Carbon Utilization and Storage Partnership of the Western United States

Final Scientific/Technical Report

Reporting Period: October 1, 2019 – September 30, 2025

DE-FE0031837

Submitting Organization:
New Mexico Institute of Mining and Technology
801 Leroy Place
Socorro, New Mexico 87801

Principal Investigator
Robert Balch

Co-Principal Investigators
George El-kaseeh, Jennifer Raney, and Brian McPherson

Prepared by Brian McPherson, George El-kaseeh, and Traci Pearson

Acknowledgment and Disclaimer

Acknowledgment: This material is based upon work supported by the Department of Energy under Award Number DE-FE0031837.

Disclaimer: This report was prepared as an account of work sponsored by an agency of the United States Government. Neither the United States Government nor any agency thereof, nor any of their employees, makes any warranty, express or implied, or assumes any legal liability or responsibility for the accuracy, completeness, or usefulness of any information, apparatus, product, or process disclosed, or represents that its use would not infringe privately owned rights. Reference herein to any specific commercial product, process, or service by trade name, trademark, manufacturer, or otherwise does not necessarily constitute or imply its endorsement, recommendation, or favoring by the United States Government or any agency thereof. The views and opinions of authors expressed herein do not necessarily state or reflect those of the United States Government or any agency thereof.

Table of Contents

Acknowledgment and Disclaimer 2
Part I – *SOPO Tasks* 23
Task 1 – Project Management and Planning 23
Subtask 1.1 – Communication and Coordination with Other Partnerships 23
Task 2 – Addressing Key Technical Challenges 23
Subtask 2.1 – Expand Characterization of Stacked and Unconventional Storage 23
Subtask 2.2 – Develop Collaborations to Integrate and Validate Key Technologies to Optimize Storage and Reduce Uncertainty in Storage Permanence and Integrity 24
Subtask 2.3 – Collaborate with Industrial Partners to Identify and Assist with Monitoring, Verification, and Accounting (MVA) Strategies as Applicable 25
Subtask 2.3.1 – Evaluation and implementation of Storage in the Permian Basin 25
Subtask 2.3.2 – CCUS Hub 2.0 Concept for ONEOK 25
Subtask 2.3.3 – Design of an Integrated CCUS Operation in a Complex Geological Structure in Osage County, Oklahoma 26
Subtask 2.3.4 – Laying the Cornerstones of a Regional Storage Hub in California 26
Subtask 2.3.5 27
Subtask 2.3.6 – CCS at the Iron Mountain Iron Mine and Direct Reduced Iron Processing Plant, Southern Utah 27
Subtask 2.4 – Development and Validation of Risk Assessment, Management, and Mitigation Strategies for Commercial-Scale Sites 27
Task 3 – Facilitating Data Collection, Sharing, and Analysis 28
Subtask 3.1 – Engaging with National Laboratories 28
Subtask 3.1.1 – Identify Data Requirements and Needs 29
Subtask 3.1.2 – Update Geologic Data for CCUS Assessment 33
Subtask 3.1.3 – Update USDW Data from All Public Sources 34
Subtask 3.1.4 – Gather and Catalogue CO_2 Emissions (Point) Source Database 34
Subtask 3.2 – Apply NRAP Tools to Assess Geologic Risks 36
Subtask 3.3 – Provide Synthesized Data to DOE's Machine Learning Initiative 36
Subtask 3.3.1 – SMART-CS Initiative Support 37
Task 4 – Evaluating Regional Infrastructure 37
References 38
Subtask 4.1 – Catalog, Map, and Evaluate Extant and Near-Term CO_2 Distribution Network 38
Subtask 4.2 – Identify and Add Rights of Way for New Pipelines (Main Lines and Otherwise) 39
Subtask 4.3 – Regulatory/Policy Impact Assessment 41
Subtask 4.4 – Economic Assessment 42

References 43
Subtask 4.5 – Focused Scenario Analysis 43
Subtask 4.5.1 – Characterization of CO_2 Storage Potential in Harquahala Basin 44
Subtask 4.5.2 – Regional-Scale Assessment of CO_2 Geological Storage in Sedimentary Basin Geothermal Reservoirs of Nevada 44
Subtask 4.5.3 – Site Characterization for CO_2 Storage to Support Escalante Hydrogen Power Plant and Logos Resources Projects 44
Subtask 4.5.4 – Feasibility Study on a Potential CCUS Project in Colorado: CO_2 Capture from a Gas Power Plant and Sequestration in the DJ Basin 44
Subtask 4.5.5 – Derisking CO_2 Mineralization Storage in Basalt Reservoirs 44
Subtask 4.6 – Develop Regional Readiness Indices 44
Methodology 46
Readiness Metrics and Scenario Generation 46
Infrastructure Modeling 48
Scenario Input Data 49
Model Decision Variables 50
Objective Function 50
Constraints 50
Infrastructure Aggregation 52
Readiness Scoring 53
Data Collection 54
Source Data 54
Storage Data 55
Induced Seismicity Data 56
Transport Data 57
References 66
Task 5 – Promoting Regional Technology Transfer 66
Subtask 5.1 – Development of Regional Readiness Indices Maps 66
Subtask 5.2 – Technology Transfer Forums 66
Data-Centric Approach to Technology Transfer 66
Data Infrastructure and Digital Tools 67
Atlas and Shared Databases 67
Analytics, Optimization, and Machine Learning 67
Enabling Class VI, MRV, and 45Q Readiness 68
Focused Projects as Technology Transfer Pilots 68
CCUS Feasibility Studies Examples 68
Harquahala Basin (Arizona) 68
Colorado Front Range Project 68
EPA Class VI - MRV - 45Q Projects 69
CCUS in Geothermal Reservoirs and Blue Hydrogen 69
CCUS in Basalts and CO_2 Plume Detection 69
Annual Meetings as Engines of Technology Transfer 69
Building a Shared Knowledge Base 70
Deepening the Data and Regulatory Toolset (2023 Annual Meeting) 70
Poster Sessions and Methodological Transfer 71
From Data to Deployment: Project Support and Commercialization 71
Lessons for Technology Transfert and Future Directions 71

References 72
Subtask 5.3 – Targeted Network Development 72
Subtask 5.4 – DOE Support 72
Subtask 5.5 – Environmental Justice Assessment 72
Part II – Focused Projects 73
Planning amongst Uncertainty: Designing CCS Infrastructure Resilient to Capture, Transport, and Storage Uncertainty 73
Objectives and Outcomes 73
Scope of Work 74
CUSP Project Team 74
CCS Modeling Background 75
Scenario Input Data 76
Model Decision Variables 77
Objective Function 77
Constraints 78
Robust Infrastructure Design 78
Heatmap Generation 80
Heatmap Filtering 80
Core Infrastructure 81
Repairable Infrastructure Design 87
Algorithm 89
MILP 1 92
MILP 2 93
Case Study 94
Scalable Infrastructure Design 97
Non-Integer Linear Program 97
Genetic Algorithm 98
Fitness Function 99
Selection Function 99
Crossover Function 100
Mutation Function 100
Genetic Algorithm 100
CPLEX Polishing 100
Optimal Search Viability 100
Case Study 103
Project Findings and Conclusions 106
Designing to Resist Failure 107
Designing to Be Repairable 107
Scaling to Large Problems 108
Overall Conclusions 108
References 108

Laboratory Feasibility Study for Eventual Field Deployment of a Downhole Source Tomographic Design for CO_2 Plume Detection 109
Final Report 110
References 114
Site Characterization for CO_2 Storage to Support Escalante Hydrogen Power Plant Project 115
Geologic Model 116
Reservoir Model 123
Evaluation of the Potential Benefit of Enhanced Coal Bed Methane (ECBM) 129
Experimental Study of Permeability Reduction in Fruitland Coal Due to CO_2 Adsorption and its Effect on Strength and Stiffness 129
Methods 130
Sample Preparation: Flow-Through and UCS 130
2.2 Laboratory Flow-Through Experiments 131
UCS Tests 132
Results and Discussion 133
Flow-Through Experiments 133
UCS and Estimated Youngs Modulus 137
References 140
BET Gas Adsorption Measurements on Powdered Coal Samples 142
Experimental Methods 143
Materials 143
Sample Preparation and Degassing 143
Nitrogen (N_2) Adsorption Measurements 143
Carbon Dioxide (CO_2) Adsorption Measurements 143
Results 143
N_2 Adsorption Measurements at -196°C 143
CO_2 Adsorption Measurements at 0°C 146
Comparison of N_2 and CO_2 Adsorption 147
Model Construction 148
History Matching 151
Performance Forecasts 154
Case #1: No CO_2 Injection 155
Case #2: Continuous CO_2 Injection 156
Case #3: Continuous N_2–CO_2 Injection 158
Case #4: Continuous CO_2 with Intermittent N_2 Injection 160
Underground Injection Control Consideration for Escalante Power Plant 163
Geologic CO_2 Storage Permits Template in New Mexico (EPA Region VI) 163
Introduction 163
Well Drilling Permit 164
UIC Class VI Well Permit 165
References 168
Regional-Scale Assessment of CO_2 Geological Storage in Sedimentary Basin Geothermal Reservoirs of Nevada 169
Objectives and Outcomes 170

CUSP Focused Project Team and Scope of Work 171
Methods 171
Geologic and Geothermal Characterization 171
Basin Configuration 171
Temperature Gradient 172
Fault Activity 173
Sedimentary Basin Geothermal Reservoir Assessment 173
CO_2 Plume Geothermal Power Plant Assessment 174
Project Findings 175
Regional-Scale Sedimentary Basin Geothermal Reservoirs of Northern Nevada 175
Basin-Scale Sedimentary Basin Geothermal Reservoirs of Northern Nevada 176
Deep Well Log Information 176
Black Rock Sedimentary Basin Analysis 177
Assessment of Low-Cost CO_2 Plume Geothermal Power Generation 179
Summary and Conclusions 180
References 181
Characterization of CO_2 Storage Potential in Harquahala Basin, Western Central Arizona 183
Project Description and Scope 184
Study Areas 184
Methods 186
Geologic Map Compilation 186
Borehole Lithology Logs 187
Vintage Seismic 2D Reflection Data and Analysis 187
Seismic Reprocessing 190
Depth Conversion 190
Gravity Data 191
Depth-to-Bedrock Contours 191
Basin Fill Storage Volume Calculations 192
Isopach Maps 192
Geologic Cross-Sections 192
Lithofacies Maps 193
Well Borehole Temperatures 194
Groundwater Total Dissolved Solids (TDS) 195
Geologic Characterization 196
Conceptual Model for Basin Formation 196
Basin Geometry and Structure 198
Stratigraphy 199
Lower Reflective Package (LRP) 199
Lower Basin Fill (LBF) 200
Upper Basin Fill (UBF) 202
Geothermal Gradient 203
Groundwater Salinity 204
Analysis and Discussion 205

Storage Reservoirs 205
Stacked Saline Formations 205
Bedded Evaporite Deposits 206
Basalt Flows 206
Volume Estimates of Basin Fill and CO_2 Storage 207
Basin Fill Sediment Volumes 207
Other Physical Parameters 207
CO_2 Storage Volume Estimate 208
Known Natural Gas Subsurface Storage Risks 210
Sealing Conditions 210
Seismic Hazard 211
Conclusions 212
Recommendations 213
New 2D Seismic 213
Gravity and Aeromagnetic Surveys 214
Stratigraphic Characterization Well 214
References 216
Derisking CO_2 Mineralization Storage in Basalt Reservoirs 218
Objectives and Outcomes 219
Scope of Work 220
Overview of Methods Used 222
CUSP Derisking CO_2 Mineralization Storage in Basalt Reservoirs Team 223
Project Publications 223
Site Investigation Planning and Preoperational Design 225
Geologic Site Characterization 226
Reservoir–Seal Framework 226
Reservoir Properties of Key Members 227
Discovery of Hyaloclastite Reservoirs 228
Hydrogeologic and Geochemical Isolation 229
Core Evidence of Mineralization 229
Structural Setting and Site Down-Selection 232
Conclusions 234
Modeling and Simulation 234
Benchmarking with Wallula Pilot Injection 234
Sensitivity Analyses and Controlling Processes 234
Reactive Transport Calibration 236
Simulation of Injection Scenarios 237
Key Findings 237
Risk Assessment 237
Technical Risks and Mitigation 237
Reservoir Heterogeneity 237
Injectivity and Capacity Uncertainty 238
Mineralization Rate Uncertainty 238

Containment and Leakage 238
Nontechnical Risks and Mitigation 238
Regulatory Familiarity and Permitting 238
Stakeholder and Public Acceptance 238
Economic Risk 239
Long-Term Liability 239
Conclusions 239
Technical/Infrastructure Issues 239
Source–Sink Matching 239
Injection Scenarios and Compression Needs 240
Transport and Pipeline Considerations 240
Coupling with Existing Infrastructure 240
In Situ Critical Mineral Recovery 240
Site Access and Permitting Logistics 241
Conclusions 241
Nontechnical Issues / Scenario Analysis 241
Land and Pore Space Ownership 241
Transport and Rights of Way 241
Water Rights 242
Liability and Long-Term Stewardship 242
Economic Assessment 242
Outreach and Engagement 242
Nontechnical Risks 243
Conclusions 244
Permitting and Regulatory Planning and Progress 244
UIC Class VI Permit Planning 244
Monitoring, Reporting, and Verification (MRV) 244
45Q Incentive Readiness 245
Stakeholder and Public Engagement 245
Other Regulatory Activities 245
Project Findings and Conclusions 245
References 246
CCS at the Iron Mountain Iron Mine and Direct Reduced Iron Processing Plant, Southern Utah 248
Outcomes and Objectives 248
Scope of Work 249
CUSP Iron Mountain Team 250
Geologic Site Characterization 251
Geologic Carbon Storage Potential in the Neck of the Escalante Desert, Iron County, Utah 251
Evaluate Well Logs and Cuttings from Nearby Wells and Determine High-Level Reservoir and Seal Properties 252
Evaluate Seal Properties of Nearby Outcrop (e.g., Lithology, Porosity, Permeability, Etc.), Including the Jurassic and Cretaceous Seal Rocks, and Igneous Intrusive Bodies 252
Evaluate Storage Potential/Reservoir Properties in Nearby Outcrops and Core – Navajo Sandstone and Kaibab Limestone 253

Gather Legacy Gravity Data and Collect New Gravity Data to Define Subsurface Characteristics and Tie to Seismic and Well Data 253
Characterization of Faults and Fractures Relevant to Seal Integrity and Lateral Compartmentalization 254
Modeling and Simulation 255
Seismic Well Tie with the Arco Three Peaks #1 Well, Velocity Model Construction, and Seismic Evaluation and Interpretation 255
Seismic Well Tie by UGS for Static Model Construction 255
2D Seismic Line Evaluation and Horizon Interpretation 256
Velocity Modeling and Fault Evaluation by LANL 257
Introduction 257
Legacy 2D Seismic Data Acquisition and Processing 260
Velocity Model Building 262
Results of Reverse-Time Migration and Fault Detection 267
Discussions 269
Conclusions 273
Geological Modeling 273
CO_2 Quality and Quantity 276
Storage Resource Assessment 277
Dynamic Numerical Simulation 280
Simulation Model Development and Setup 280
Injection Scenarios Evaluated 282
Pressure response and injectivity performance 282
CO_2 Phase Partitioning and Trapping Behavior 283
Numerical Modeling Results Conclusion 285
Plume Analysis and Area of Review Delineation 285
Plume Area Analysis 285
Area of Review Analysis 286
AoR Approach and Hydrostatic Allowable Pressure Increase 286
Allowable Pressure Increase (ΔPu) Field 288
Modeled Pressure Increase from Injection (ΔP) 289
AoR Delineation and Comparison to CO_2 Plume Footprint 294
Conclusions 299
Risk Assessment 300
Constraining Induced Seismicity Hazard on the Neck of the Desert Fault for the Proposed Iron Mountain, Utah, Carbon Sequestration Project 301
Introduction 301
Past Seismicity 302
Input Parameters 302
Fault Location, Size, and Orientation 302
Pore Pressure 304
Coefficient of Friction 305
Maximum Horizontal Stress Direction 305
Principal Stresses 305
Methodology 306
Results 307
Discussion 308
Conclusions 310
Nontechnical Issues / Scenario Analysis 310

Transport and Rights of Way 311
Economic Assessment 314
Outreach 316
Site Characterization for Geologic Carbon Storage of CO_2 from a Direct Reduced Iron Plant 317
Poster Abstract 318
Basin Analysis and Reservoir Characterization for Subsurface Geologic Carbon (CO_2) Sequestration Associated with a Direct Reduced Iron Plant, Iron County, Utah 321
Preliminary Assessment of Possible Stratigraphic Well and 3D Seismic Survey 322
Assemble Engineering Design Plans and Budget for Seismic Survey(s) 322
Assemble Engineering Design Plans and Budget for Stratigraphic Well 324
Wellbore Architecture and Drilling Approach 324
Rig Selection and Execution Readiness 325
Coring and Sample Acquisition Program 325
Mud Logging, HSE Spacing, and Operational Controls 326
Wireline Logging and Formation Evaluation 326
Cementing and Zonal Isolation Design 329
Budget Assembly (AFE Structure and Cost Reconciliation) 329
Comprehensive Plan to Prepare and Submit UIC Class VI Application 332
Comprehensive Plan to Prepare and Submit 45Q Tax Credit Application 332
Integrated Outcomes and Site Readiness 332
References 334
CCS Hub 2.0 Concept for ONEOK: Infrastructure Development for Handling of New Gaseous Products for Natural Gas Liquids Fractionation and Gas Processing Plants in Kansas and Oklahoma 337
Introduction 338
Objectives 339
CCS-Specific Objectives 340
Scope of Work 340
Project Task List 340
Task 1 – Project Management 342
Subtask 1.1 – Managing and Allocating Resources, Communications, Outreach, and Technology Transfer 342
Project Leadership and Timeline 343
Partner Contributions and Personnel 344
Subtask 1.2 – Site Visits to Confirm Findings of Technical Review 344
Subtask 1.3 – Reporting 345
Task 2 – High-Level Technical Review 345
Subtask 2.1 – Determine Quantity, Type, and Quality of Available Data Relevant to Geologic, Engineering, Infrastructure, Risk Assessment, and Economic Modeling 345
Bushton, Kansas Site 346
Medford, Oklahoma Site 349
Data Aggregation 352
Subtask 2.2 – Delineate Underground Sources of Drinking Water 352
Subtask 2.3 – Review Environmental/Social Justice Considerations 353
Subtask 2.4–Determine Area-of-Review 354

Task 3 – Subsurface Studies 356
Subtask 3.1 – Subsurface Data Aggregation and Database Build 358
Bushton Site Data 359
Medford Site Data 359
Subtask 3.2 – Static Geological Modeling 360
Bushton (KS) Geologic Models 365
Lansing/Kansas City (LKC) Static Model 365
Arbuckle Deep Static Model Details 370
Upper Arbuckle Geologic Model 378
Medford (OK) Geologic Model 378
Wilcox-Bromide Static Model Details 380
Salt Horizons CO_2 Storage Evaluation 384
Subtask 3.3 – Assess CO_2 Storage Resources 386
Subtask 3.4 – Geomechanical Assessment 391
Core Analysis 392
Acoustical Analysis 393
Petrophysical Analysis 394
1D MEM 395
Seal and Risk Assessment 401
Structural Model 404
Results and Discussion 404
Subtask 3.5 – Install and Monitor Seismometer Network for Seismic Risk Analysis 405
3.5.1 – Development and Deployment of a Low-Cost Seismic Network 405
3.5.2 – Earthquake Data Collection and Analysis 407
3.5.3 – RS-3D Earthquake Data Quality Assessment 407
Central Kansas Background Seismicity and RS-3D Monitoring 409
3.5.5 – RS-3D Earthquake Catalogue of Central Kansas Seismic Activity 411
3.5.6 – Conclusions 413
Task 4 – Dynamic Simulation 414
Subtask 4.1 – Evaluate Existing Oil Field Injection Pressures and Rates to Determine Suitability for Saline Storage Operations 415
Bushton, Kansas Site, Lansing Kansas City Reservoir 415
Saturation Function 416
Aqueous Relative Permeability Function 417
Gas Relative Permeability Function 418
Wells 418
Initial Conditions 419
Boundary Conditions 419
Simulation Results 419
Bushton, Kansas Site, Upper Arbuckle Reservoir 421
Saturation Function 423
Aqueous Relative Permeability Function 424
Gas Relative Permeability Function 425
Wells 426
Initial Conditions 426
Boundary Conditions 427
Simulation Results 427
Bushton, Kansas Site, Arbuckle Deep Reservoir 430
Saturation Function 431

Aqueous Relative Permeability Function 431
Gas Relative Permeability Function 432
Wells 433
Initial Conditions 433
Boundary Conditions 434
Simulation Results 434
Medford, Oklahoma Site, Wilcox-Bromide Reservoir 438
Saturation Function 438
Aqueous Relative Permeability Function 439
Gas Relative Permeability Function 440
Wells 440
Initial Conditions 441
Boundary Conditions 441
Simulation Results 441
Subtask 4.2 – Dynamic Simulations of CO_2 Injection Scenarios into Saline Storage Reservoirs 446
Task 5 – Risk Assessment 448
Subtask 5.1 – Risk Assessment Data Aggregation and Database Build 448
NRAP-OPEN-IAM (V 2.7.2) Model Inputs/Assumptions 450
Subtask 5.2 – Assess Well Integrity and Seal Penetrations 451
LKC Injection Scenario 451
Arbuckle Injection Scenario 457
Summary 462
Subtask 5.3 – Prepare a Ranked Matrix of Key Risk Factors for Each Seal and Reservoir Horizon AoR Addressing Key Surface and Subsurface Issues that Might Affect Injection Viability 464
Induced Seismicity 466
Potential Leakage Risk Analysis Using NRAP Tools 466
Traffic Light System to Mitigate Induced Seismicity Hazard and Risk 467
Subtask 5.5 – Economic Risk/Feasibility Assessment 468
Results and Cost-Benefit Analysis 470
Economic Risk Assessment 471
Regulatory and Policy Risk 471
Market and Price Risk 472
Financing and Interest Rate Risk 472
Community and Social Licensing Risk 472
Conclusion 472
Task 6 – Infrastructure Network Assessment 472
Subtask 6.1 – Aggregate Infrastructure Data and Build Databases 473
Subtask 6.2 – Model Pipeline Corridor and Define Surface Facilities That Would Be Required to Execute Chosen Design Concepts 475
Subtask 6.3 – Assess CO_2 Capture-Transport-Storage System 475
Subtask 6.4 – Identify Potential Business Entry Opportunities Related to Nearby Sources or Users of CO_2 483
Task 7 – Regulatory Outreach and 45Q Preparations 484
Subtask 7.1 – Meet With U.S. EPA to Discuss UIC Class VI Permit Application 484
Interview with U.S. EPA Region 7 485
Subtask 7.2 – Meet With External Teams That Have Experience Applying for EPA–UIC Class VI Permits 490
Interview with Advanced Resources International 490
Subtask 7.3– Meet With State Environmental and Petroleum Regulators 491
Interview with the Kansas Department of Health and Environment (KDHE) 491

Interview with the Kansas Corporation Commission 492
Task 8 – Technology Transfer 493
Subtask 8.1 – Maintain Website for Project 493
Subtask 8.2 – Public Presentations 493
Technical Transfer Short Course 493
Subtask 8.3 – Publications 495
Subtask 8.4 – Upload Data to DOE-EDX 495
References 495
Laying the Cornerstones of a Regional Storage Hub in California 499
Distributed Emitters 502
Identification and Selection of CO_2 Emitters 502
Capture Cost for Steam Generation and CHP 504
Identification of Potential Storage Sites 506
Technoeconomic Analysis 507
Summary 514
Subsurface Model 514
Overview of CCS Sites 514
Numerical Simulation Model 517
Storage Assessment & Plume Migration 520
pyCCUS 520
Plume Definition 521
Well Design Optimization 522
Injector Design Optimization Result 524
Dynamic Plume Quantification 526
Optimal Injector Performance Under Uncertainty 529
Assessment of Spatial Monitoring using InSAR 533
Background 533
Methodology 535
Parameter Space and Response Data 535
DGSA 537
PCA 538
Autoencoders 538
Results 540
PCA Feature Extraction 540
Autoencoders Feature Extraction 540
Discussion 544
Summary 545
Field Project 546
Background 546
CO_2 Source Selection 546
Scenario Set Up 546
Results 547
Summary 549
Risk Assessment 550

Leakage Risk Assessment 550
Overview of the Storage Site and Optimized Well Design 550
Leakage Risk Assessment Method 551
Leakage Risk through Existing Wellbores 557
Leakage through Quaternary Faults 558
Summary 560
Induced Geomechanical Risk Assessment 561
Site Characterization 561
Geomechanical Model 562
Fault Slip Analysis 563
3D Visualization of Plume–Fault Interaction 564
Modeling Effects of CO_2 Injection 565
Identifying and Responding to Induced Seismicity 566
Summary 566
Forward-Looking Regional Scenarios 567
Results 567
Summary 569
Conclusion 569
1. Emitter Identification and Capture Economics 570
2. Subsurface Model Characterization 570
3. Storage Assessment and Plume Migration 570
4. Monitoring via InSAR and Data Analytics 570
5. Infrastructure and Economic Scenarios in Field Project 570
6. Risk and Seismic Assessment 571
7. Forward-Looking Regional Scenarios 571
Acknowledgement 571
References 571
Carbon Solutions' Contributions 576
Feasibility Study on a Potential CCUS Project in Colorado: CO_2 Capture from a Refinery and Sequestration in the DJ Basin 580
Introduction 581
Study Area 582
Stratigraphic Column of DJ Basin 583
Static Modeling Construction from Post-Stack Seismic 584
Property Distribution 584
Static Model Construction 586
Fluid Flow Modeling 587
Fluid Model Setup 587
CO_2 Saturation Distribution 588
CO_2 Component Inventory 589
CO_2 Pressure Distribution 590
Risk Evaluation and Discussion 591

Confining System Evaluation 591
Fault Confinement and Induced Seismicity Potential 592
Legacy Wells Leakage Risk 593
Seismic Monitoring Feasibility 593
Conclusions and Future Work 596
Acknowledgment 597
References 597
From Site to State: Design of an Integrated CCS Operation in a Complex Geological Structure in Osage County, Oklahoma 600
Targa Resources (Formerly Lucid Energy Delaware) Acid Gas Injection Project 600
Carbon Solutions' Contributions to Focused Projects 600
Subtask 4.5.2 – Regional-Scale Assessment of CO_2 Geological Storage in Sedimentary Basin Geothermal Reservoirs of Nevada 600
Subtask 4.5.2 – Cornerstones of a Regional Storage Hub in California 602
Subtask 4.5.3 – CUSP Midstream Operator Storage of CO_2 ($MOSCO_2$) 606
Subtask 4.5.4 – From Site to State: Design of an Integrated CCUS Operation in a Complex Geological Structure in Osage County, Oklahoma 611
Subtask 4.5.5 – Iron Mountain Subsurface Characterization 612
Part III – State-by-State Summaries 614
Arizona 614
Acknowledgements 616
References 616
California 617
Subtask 3.1.2 – Update Geologic Data for CCUS Assessment 617
California CO_2 Storage Estimates and Potential Storage Sites 617
Screening Methodology for CO_2 Storage Sites 617
Potential CO_2 Storage Estimates 619
Subtask 3.1.4 – Gather and Catalogue CO_2 Emissions 621
California CO_2 Emission Sources 621
CO_2 Capture Costs by Industrial Sector in California 624
Right of Way for Potential CO_2 Pipeline 624
Technoeconomic Analysis 625
References 625
Colorado 627
Kansas 627
References 627

Nevada 627
Task 2 – Addressing Key Technical Challenges 628
Task 2.1 – Expand Characterization of Stacked and Unconventional Storage 628
Task 2.2 – Develop Collaborations to Integrate and Validate Key Technologies to Optimize Storage and Reduce Uncertainty in Storage Permanence and Integrity 628
Task 3 – Facilitating Data Collection, Sharing, and Analysis 628
Task 3.1 – Engaging with National Laboratories 628
Task 3.1.1 – Identify Data Requirements & Needs 629
Task 3.1.2 – Update Geologic Data for CCUS Assessment 630
Task 3.1.3 – Update USDW Data from All Public Sources 633
Task 3.1.4 – Gather and Catalog CO_2 Emissions (Point) Source Database 634
Summary and Conclusions 635
References 635
New Mexico / West Texas 636
Goals 637
San Juan Basin 637
Tectonics 638
Structure 641
Stratigraphy 641
Geologic Model 647
Surfaces Without Faults 649
Surfaces With Faults 683
Delaware Basin 714
Structure 724
Stratigraphy 727
Cambrian to Precambrian 727
Bliss Sandstone 727
Ordovician 727
Ellenburger Group 727
Simpson Group 729
Montoya Group 729
Ordovician – Silurian 730
Fusselman Formation 730
Lower Devonian – Silurian 730
Thirtyone and Wristen Formations 730
Upper Devonian 732
Woodford Shale 732
Mississippian 732
Mississippian Limestone 732
Barnett Shale 733
Pennsylvanian 733
Morrow Formation 733
Atoka Formation 734
Strawn Group 735
Canyon Formation 736

Cisco Formation 737
Permian 738
Wolfcampian Rocks 738
Wolfcamp/Hueco Group 738
Leonardian/Cisuralian Rocks 740
Bone Spring Formation/Abo, and Yeso Group/Victorio Peak Formations 740
Guadalupian Rocks 743
Delaware Mountain Group/San Andres and Grayburg Formations 743
Ochoan Rocks 750
Castile, Salado, and Rustler Formations 750
Geologic Model 751
Surfaces Without Faults 755
Surfaces With Faults 777
Bravo Dome 789
Background Geology 790
Geologic Model 793
CO_2 Emissions Source Database for New Mexico 803
SCO_2T^{PRO} Geologic Data 805
References 810
Oklahoma 814
References 814
Oklahoma Geological Survey Carbon Capture, Utilization, and Storage Curriculum 814
Climate Change is a Problem 816
Guiding Question 816
Topic Overview 816
Activities and Resources 816
CO_2 Holds the Sun's Energy 816
Guiding Question 816
Topic Overview 816
Activities and Resources 817
CO_2 Management Solutions Exist 817
Guiding Question 817
Topic Overview 817
Activities and Resources 817
Carbon Capture, Utilization, and Storage Removes CO_2 from the Atmosphere 817
Guiding Question 817
Topic Overview 817
Activities and Resources 817
Storing CO_2 Comes with Risks 818
Guiding Question 818
Topic Overview 818
Activities and Resources 818
Oklahoma Can Store CO_2 Underground 818
Guiding Question 818
Topic Overview 818
Activities and Resources 818

Teams of People Work on CCUS 818
Guiding Question 818
Topic Overview 818
Activities and Resources 819
References 819
Texas 820
Utah 820
Washington 820
Task 1 – Project Management and Planning 820
Task 2.1 – Expand Characterization of Stacked and Unconventional Storage 821
Task 2.2 – Develop Collaborations to Integrate and Validate Key Technologies to Optimize Storage and Reduce Uncertainty in Storage Permanence and Integrity 823
Task 2.3 – Collaborate with Industrial Partners to Identify and Assist with Monitoring, Verification, and Accounting (MVA) Strategies as Applicable 824
Task 2.4 – Development and Validation of Risk Assessment, Management, and Mitigation Strategies for Commercial-Scale Sites 826
Task 3.1 – Engaging with National Laboratories 826
Task 3.1.1 – Identify Data Requirements & Needs 827
Task 3.1.2 – Update Geologic Data for CCUS Assessment 828
Task 3.1.3 – Update USDW Data from All Public Sources 828
Task 3.1.4 – Gather and Catalog CO_2 Emissions (Point) Source Database 829
Task 3.2 – Apply NRAP Tools to Assess Geologic Risks 829
Task 4.1 – Catalog, Map, and Evaluate Extant and Near-Term CO_2 Distribution Network 829
Task 4.2 – Identify and Add Rights-of-Way for New Pipelines 829
Task 4.3 – Regulatory / Policy Impact Assessment 829
Task 4.5 – Focused Scenario Analysis 832
Task 5 – Promoting Regional Technology Transfer 832
Task 5.2 – Technology Transfer Forums 833
References 833
Wyoming 834
Part IV – National Laboratories 835
Los Alamos National Laboratory (LANL) 835
Task 1 – Apply NRAP Tools to Assess Geologic Risks 836
Subtask 1.1 – Kansas Case Study 837
LKC Injection 840
Arbuckle Injection 846
Conclusions 849
Subtask 1.2 – California Case Study 849
Case 1: Vertical Injection Scenario 850
Case 2: Deviated Injection Scenario 853
Conclusions 855
Subtask 1.3 – Colorado Case Study 856
Conclusions 859
Subtask 1.4 – Oklahoma Case Study 859

Conclusions 862
Task 2 – Evaluating Regional Infrastructure: Four Corners Case Study 863
SimCCS Introduction 863
Four Corners Case Study 864
Conclusions 865
Task 3 – Develop Regional Readiness Indices 866
Impact of Induced Seismicity Risk on Pipeline Routing 866
Impact of Leakage Risk on Pipeline Routing 868
Conclusions 870
Task 4 – Characterizing Subsurface Structures for GCS at Iron Mountain in Utah 870
Introduction 871
Legacy 2D Seismic Data Acquisition and Processing 873
Velocity Model Building 875
Results of Reverse-Time Migration and Fault Detection 881
Discussions 884
Conclusions 889
References 890
Sandia National Laboratories (SNL) 891
Task 1 – Project Management and Planning 891
Task 3 – Facilitating Data Collection, Sharing, and Analysis 892
Task 4 – Evaluating Regional Infrastructure 892
Subtask 4.4 – Economic Assessment 892
Technoeconomic Analysis 892
Cost–Benefit Analysis and Evaluation of Implication of 45Q Tax Credits 893
Subtask 4.5 – Focused Scenario Analysis 893
Regional Permian Basin Analysis 894
Report and Products 894
Future Work and Connections to Other Energy Applications – Support for Geothermal, Hydrogen, and Critical Metals and Rare Earths 895
Acknowledgments 895
References 895
Pacific Northwest National Laboratory (PNNL) 895
Part V – Working Groups 896
Economics Working Group 896
Targa Resources (Formerly Lucid Energy Delaware) Acid Gas Injection Project 896
Economic Risk–Related Objectives and Desired Outcomes 896
Economic Assessment 896
CCS Hub 2.0 Concept for ONEOK: Infrastructure Development for Handling of New Gaseous Products for Natural Gas Liquids Fractionation and Gas Processing Plants in Kansas and Oklahoma 897

Economic Risk–Related Objectives and Outcomes 897
Risk Assessment 897
Economic Assessment 897
References 898
Data Working Group 898
Analytics Working Group 899
Report Organization 900
Phase 1 – Foundational Data and Scenario Guidance 900
Defining Data Requirements 900
Partner Engagement and Education 900
Scenario Typology and Planning Guidance 901
Phase 2 – Scenario Development and Evaluation 901
California: San Joaquin Basin CCS Opportunities 902
Source Types and CO_2 Emitters 903
Case Studies and Technoeconomic Scenarios 903
Seismic Fault Avoidance and Geologic Considerations 903
Conclusions and Recommendations 904
Nevada: Resilience for CCS Networks in the Face of Uncertainty 904
CO_2 Sources and Storage Sites in Nevada 905
Modeling Reservoir Failures in CCS Networks 905
Key Findings: Balancing Infrastructure and Failure Costs 906
Conclusions and Infrastructure Recommendations 906
Kansas: Statewide CCS Deployment Potential. 907
Four Corners Region: CO_2 Transport and Environmental Justice Concerns 907
Conclusion 908
Phase 3 – Model Development 909
Phased Deployment 909
Model Formulation 910
Model Discussion 913
Heuristic Solvers 915
Problem Formulation 916
Computational Complexity 917
Algorithms 919
Greedy Add 919
Iterative LP 923
LP-Greedy Hybrid 926
Genetic Algorithm 928
Non-Integer Linear Program 929
Genetic Algorithm 930
Fitness Function 931
Selection Function 931
Crossover Function 931
Mutation Function 932
Genetic Algorithm 932
CPLEX Polishing 932

Optimal Search Viability 932
Case Study 935
Phase 4 – Readiness Indices and Mapping 939
Conclusions 939
References 939
Outreach Working Group 940
Appendices 941
Bibliography 942

Part I – *SOPO Tasks*

Task 1 – Project Management and Planning

The CUSP management team addressed Task 1 by providing overall project management, coordination, and governance for the CUSP partnership throughout the performance period. Task 1 activities ensured alignment among academic, national laboratory, industry, and state partners and supported effective execution of technical, data, infrastructure, and outreach efforts across Tasks 2 through 5. Key accomplishments included establishment and maintenance of regular coordination mechanisms among project participants; oversight of task integration and sequencing; preparation and submission of required quarterly reports; and sustained engagement with DOE to address guidance, reporting requirements, and evolving program priorities. Task 1 also supported revisions to the Statement of Project Objectives and Project Management Plan, coordinated budget modifications, and facilitated the integration of focused projects and new partners as the project evolved. Collectively, these activities provided the organizational framework and continuity necessary for successful completion of CUSP technical and programmatic objectives.

An important point to note is that Carbon Solutions provided general support for Task 1 through virtual meetings, in-person meetings, quarterly reporting, and other logistical tasks since formally being brought onto the project in September 2021.

Subtask 1.1 – Communication and Coordination with Other Partnerships

Task 1.1 efforts focused on administrative coordination and formal reporting required to support project execution and DOE oversight. Activities under this subtask included preparation and submission of quarterly Research Performance Progress Reports, coordination of inputs from project partners, and documentation of progress, milestones, and scope adjustments over the course of the project. Task 1.1 also supported administrative communication with DOE related to schedule, budget, and deliverable alignment, ensuring that changes in project scope or emphasis were appropriately documented and incorporated into project planning. These efforts maintained transparency, accountability, and compliance with DOE reporting requirements throughout the CUSP performance period.

Task 2 – Addressing Key Technical Challenges

Subtask 2.1 – Expand Characterization of Stacked and Unconventional Storage

All efforts for Subtask 2.1 focused on expanding regional understanding of stacked and unconventional CO_2 storage opportunities across the CUSP region. Activities under this subtask included compilation, synthesis, and screening of geologic data relevant to saline formations,

depleted reservoirs, and other unconventional storage settings within participating states. Project partners aggregated and evaluated publicly available and partner-provided subsurface datasets—including stratigraphy, reservoir properties, well control, and regulatory constraints—to identify storage intervals with potential for commercial deployment.

These efforts resulted in a catalog of significant stacked and unconventional storage options by state, providing a consistent regional framework for comparing storage capacity, data quality, and development readiness. The products of Subtask 2.1 informed selection and prioritization of focused projects, supported subsequent reservoir modeling and risk assessment activities, and contributed foundational data to the CUSP regional database. Detailed site-specific analyses and modeling results associated with selected focus areas are described in later sections of this report.

Subtask 2.2 – Develop Collaborations to Integrate and Validate Key Technologies to Optimize Storage and Reduce Uncertainty in Storage Permanence and Integrity

The CUSP team's efforts associated with Subtask 2.2 focused on establishing and sustaining collaborations to integrate and apply existing analytical, modeling, and risk-assessment technologies in support of geologic CO_2 storage evaluation. These efforts emphasized coordination among CUSP partners, DOE national laboratories, industry collaborators, and state and academic institutions to promote consistent and practical application of available tools, rather than development of new standalone technologies.

The CUSP team collaborated with Sandia National Laboratories, Los Alamos National Laboratory, and Pacific Northwest National Laboratory to support application of established modeling and risk-assessment frameworks—such as NRAP tools—for screening, uncertainty evaluation, and monitoring and verification planning at candidate storage sites. These laboratory collaborations provided technical input on risk pathways, uncertainty characterization, and data integration and supported alignment of project activities with DOE guidance and initiatives.

The team also worked with industry partners, most notably Lucid Energy / Targa Resources, to apply integrated workflows combining geologic characterization, reservoir modeling, and risk assessment in support of active storage projects in the Permian Basin. These efforts informed MRV planning and regulatory permitting and served as practical demonstrations of tool integration in commercial project contexts.

In parallel, the CUSP team leveraged its multi-state network of universities and state geological surveys to harmonize characterization approaches and datasets across the region, enabling comparison of stacked and unconventional storage options using shared analytical frameworks. Collaborative mechanisms—including biweekly coordination calls, topical working groups, focused-project meetings, and annual in-person meetings—supported ongoing integration of technical approaches across Tasks 2 through 4. Outcomes from Subtask 2.2 informed site screening, MRV development, and subsequent technical analyses described in later sections of this report.

Subtask 2.3 – Collaborate with Industrial Partners to Identify and Assist with Monitoring, Verification, and Accounting (MVA) Strategies as Applicable

The CUSP team's efforts associated with Subtask 2.3 focused on collaboration with industry partners to identify and support monitoring, verification, and accounting (MVA/MRV) strategies appropriate for candidate geologic CO_2 storage projects. These efforts emphasized practical application of characterization, modeling, and risk-assessment tools to inform monitoring design and regulatory requirements, rather than development of new monitoring technologies.

Through engagement with industrial partners, the CUSP team applied integrated workflows combining geologic characterization, reservoir modeling, and risk assessment to support evaluation of monitoring needs and uncertainty reduction at prospective storage sites. These activities included interpretation of subsurface data, assessment of potential leakage pathways, and application of established risk-assessment frameworks to inform MRV planning.

Subtask 2.3 activities also supported coordination between industry partners and technical teams across CUSP, ensuring that monitoring strategies were aligned with site-specific geologic conditions, regulatory expectations, and best practices emerging from DOE-supported tools and methodologies. Outcomes from this subtask informed focused project activities, MRV plan development, and permitting efforts described in later sections of this report.

Subtask 2.3.1 – Evaluation and implementation of Storage in the Permian Basin

The CUSP team's efforts associated with Subtask 2.3.1 focused on supporting evaluation and implementation of geologic CO_2 storage in collaboration with Lucid Energy and Targa Resources in the Permian Basin. Activities under this focused project emphasized application of integrated characterization, modeling, and risk-assessment workflows to active industrial projects, with the goal of informing monitoring, reporting, and verification (MRV) planning and regulatory permitting.

The CUSP team supported acquisition and interpretation of subsurface data, including core and well log information, and applied reservoir modeling and risk-assessment tools to evaluate storage performance and potential leakage pathways. These analyses informed development of MRV plans tailored to site-specific geologic conditions and regulatory requirements.

As part of this effort, the CUSP team contributed technical analyses and documentation supporting Class VI–relevant permitting activities, including preparation of MRV plans that were reviewed and approved by regulatory agencies for multiple AGI wells in New Mexico and Texas. This work provided a practical demonstration of how integrated characterization, modeling, and risk-assessment approaches can be applied to commercial-scale storage projects and informed broader CUSP guidance on MRV strategy development. Detailed technical results and site-specific analyses are described in later sections of this report.

Subtask 2.3.2 – CCUS Hub 2.0 Concept for ONEOK

The CUSP team's efforts associated with Subtask 2.3.2 supported development of the BaseCCS Hub 2.0 concept in collaboration with ONEOK, focusing on evaluation of hub-scale CO_2

capture, transport, and storage opportunities in Kansas and Oklahoma. This work addressed early- to mid-stage project planning needs, including identification of suitable subsurface storage intervals near ONEOK facilities, assessment of infrastructure and integration considerations, and evaluation of monitoring, regulatory, and economic constraints relevant to large-scale deployment.

Under this subtask, the CUSP team applied integrated geologic characterization, reservoir modeling, techno-economic analysis, and risk-assessment approaches to inform storage feasibility and project viability at a conceptual level. These efforts supported assessment of potential storage capacity, cost drivers, regulatory pathways, and economic risks associated with hub-scale CCUS development. Detailed technical analyses, modeling results, and economic assessments associated with the ONEOK BaseCCS Hub 2.0 effort are presented in later sections of this report.

Subtask 2.3.3 – Design of an Integrated CCUS Operation in a Complex Geological Structure in Osage County, Oklahoma

The CUSP team's efforts associated with Subtask 2.3.3 supported integrated evaluation of a potential CCS project in Osage County, Oklahoma, focusing on site-scale planning under geologic and infrastructure uncertainty. Activities under this subtask emphasized application of geologic characterization, reservoir modeling, and risk-assessment approaches to assess storage feasibility and inform monitoring and regulatory considerations in a structurally and stratigraphically complex setting.

The CUSP team applied integrated workflows to evaluate subsurface storage options, characterize uncertainty related to reservoir properties and structural complexity, and assess implications for monitoring strategy development and project design. This work provided a site-specific demonstration of how integrated characterization and risk-based approaches can support CCS planning in challenging geologic environments. Detailed technical analyses, modeling results, and scenario evaluations associated with the Osage County effort are presented in later sections of this report.

Subtask 2.3.4 – Laying the Cornerstones of a Regional Storage Hub in California

The CUSP team's efforts associated with Subtask 2.3.4 supported evaluation and planning of a regional CO_2 storage hub concept in California, with emphasis on integration of geologic, infrastructure, regulatory, and policy considerations. Activities under this subtask focused on assessing storage opportunities within complex geologic and regulatory environments and evaluating how subsurface suitability, transport infrastructure, and permitting frameworks interact to influence project feasibility.

The CUSP team applied integrated characterization, modeling, economic, and risk-assessment approaches to screen potential storage options, assess uncertainty and constraints, and inform hub-scale planning considerations. This work contributed to development of a conceptual framework for regional CCUS deployment in California and provided insights into challenges and opportunities unique to that setting. Detailed technical analyses, modeling results, and scenario evaluations associated with the California regional hub effort are presented in later sections of this report.

Subtask 2.3.5

This subtask corresponded to a mineralization project to be led by Alain Bonneville of PNNL. Dr. Bonneville left PNNL in 2021, and therefore CUSP management in consultation with NETL canceled this subtask and no accomplishments are associated with this subtask.

Subtask 2.3.6 – CCS at the Iron Mountain Iron Mine and Direct Reduced Iron Processing Plant, Southern Utah

The CUSP team's efforts associated with Subtask 2.3.6 supported preliminary evaluation of the feasibility of carbon capture and storage (CCS) for the Iron Mountain iron mine and associated direct reduced iron (DRI) processing facility in southern Utah. Activities under this subtask focused on early-stage assessment of CCS integration challenges and opportunities specific to mining and industrial processing operations, rather than detailed site characterization or project implementation.

The CUSP team conducted screening-level analyses to examine potential pathways for integrating CO_2 capture, transport, and storage within the regional geologic and infrastructure context. These efforts emphasized identification of key technical, economic, and regulatory uncertainties that would influence project viability and inform future decision-making. Consistent with the exploratory nature of this subtask, the work did not advance to detailed reservoir modeling, MRV planning, or permitting. Instead, the Iron Mountain assessment provided a conceptual evaluation of CCS applicability in an industrial mining setting and contributed to broader CUSP understanding of nontraditional CCS deployment contexts.

Subtask 2.4 – Development and Validation of Risk Assessment, Management, and Mitigation Strategies for Commercial-Scale Sites

The CUSP team's efforts associated with Subtask 2.4 focused on application and evaluation of risk assessment, management, and mitigation approaches to support planning and decision-making for commercial-scale CO_2 storage projects. Activities under this subtask emphasized use of established DOE-supported tools and frameworks to identify key risk drivers, assess potential leakage pathways, and evaluate uncertainty related to storage performance and integrity, rather than development of new risk methodologies.

The CUSP team applied risk-assessment approaches—including NRAP-based tools—in support of candidate storage sites and focused projects across the region. These analyses integrated geologic characterization, reservoir modeling, and site-specific data to assess potential risks associated with injectivity, containment, and monitoring, and to inform development of monitoring, reporting, and verification (MRV) strategies. Risk considerations were incorporated into site screening, scenario evaluation, and MRV planning activities conducted under Tasks 2 and 3.

Subtask 2.4 efforts also supported evaluation of risk management and mitigation options at a planning level by identifying dominant sources of uncertainty and potential strategies for monitoring design, operational controls, and regulatory compliance. These efforts provided a consistent framework for incorporating risk considerations into CCS project planning and contributed to demonstration of how integrated risk-based approaches can support commercial-

scale storage decision-making. Detailed applications and results are presented in later sections of this report.

Task 3 – Facilitating Data Collection, Sharing, and Analysis

The CUSP team's efforts under Task 3 focused on developing and sustaining the data infrastructure required to support regional CO_2 storage assessment, modeling, and risk evaluation across the CUSP region. Activities under this task emphasized identification, compilation, synthesis, and organization of geologic, infrastructure, regulatory, and emissions data needed to inform storage screening, monitoring and verification (MRV) planning, and uncertainty assessment. Rather than generating new proprietary datasets, Task 3 prioritized integration of existing public, partner-provided, and DOE-supported data to facilitate consistent analysis and reuse.

Through coordination with national laboratories, state geological surveys, academic partners, and industry collaborators, the CUSP team established a persistent regional data framework for focused project analyses, hub-scale planning efforts, and risk assessments described throughout this report. Task 3 outcomes—including curated datasets, analytical workflows, and an accessible regional database—supported application of NRAP tools, contributed to DOE machine learning initiatives, and provided a durable foundation for CCUS planning beyond the life of the project.

Subtask 3.1 – Engaging with National Laboratories

The CUSP team engaged DOE national laboratories to support identification, integration, and application of data needed for geologic CO_2 storage assessment and risk evaluation. Through this subtask, the CUSP team coordinated with national laboratory partners to align data needs, analytical workflows, and modeling approaches with project objectives and DOE program priorities.

Subtask 3.1 emphasized collaboration with Sandia National Laboratories, Los Alamos National Laboratory, and Pacific Northwest National Laboratory to support consistent use of geologic, monitoring, and risk-related datasets across the CUSP region. Our collaborative effort facilitated integration of regional and site-specific data for modeling and risk-assessment frameworks, supported application of NRAP tools, and informed monitoring and verification (MRV) planning efforts described under Tasks 2 and 3.

Activities under Subtask 3.1 included regular technical coordination, data exchange, and review of analytical approaches to ensure compatibility between CUSP-developed datasets and DOE-supported tools and initiatives. While early project periods emphasized identification of data requirements and establishment of data-sharing workflows, later phases of the project reflected steady-state application of these collaborations as data infrastructure matured. Outcomes from Subtask 3.1 are reflected throughout this report in integrated modeling analyses, risk evaluations, and data products that support focused projects, hub-scale planning efforts, and DOE machine learning initiatives.

Subtask 3.1.1 – Identify Data Requirements and Needs

CCUS includes a variety of topics that can range from chemical to geological to geographical to political to economic. As such, it represents an unusual challenge of storing and retrieving data that is very diverse in nature. To meet that challenge, the concept of a heterogeneous database/visualization system is described, along with its implementation in the form of the EGI Carbon Portal. However, since energy and resource challenges exist beyond CCUS, it is proposed that these ideas and technologies be expanded to create the EGI Resource Portal to solve similar challenges across even more fields.

Most databases tend to be specialist databases that focus on a single topic and explore it in great depth. For a warehouse database, hundreds of database tables will describe the inventory, employees and rent of a warehouse. For a geochemical database, a database can have hundreds of measurements like porosity, permeability and TOC (total organic carbon). For a census database, the population, ages and employment status of people in an area can be accurately described. Let us call each of these conventional databases homogenous databases.

Such tools are excellent but they can be over-specialized. What if the stakeholder wishes to quickly know if there is there is oil producing potential near a warehouse he owns, and if repurposing the warehouse for oil production will have a net positive or negative effect on local employment. In that case, information about the warehouse, geochemistry under the earth and local employment census data needs to be accessed in a simple but overlapping way. Let us call this concept of a multi-topic database a heterogeneous database.

CCUS is a strong candidate for a heterogeneous database. For example, when looking for a potential carbon sink, not only is it necessary to understand the carbon storing potential of formations underneath the earth, but it is also necessary to find a carbon dioxide producing facility, as well as existing pipelines for transport, and finding what public and private lands would be involved in the construction of new pipelines. Additionally, finding areas where there might already be oil wells and where the local population would benefit the most from economic growth is needed. However, the number of concepts to be considered and finding the data can be quite intimidating.

To assist in such a query, a heterogeneous database and website (called the EGI Carbon Portal) was created.

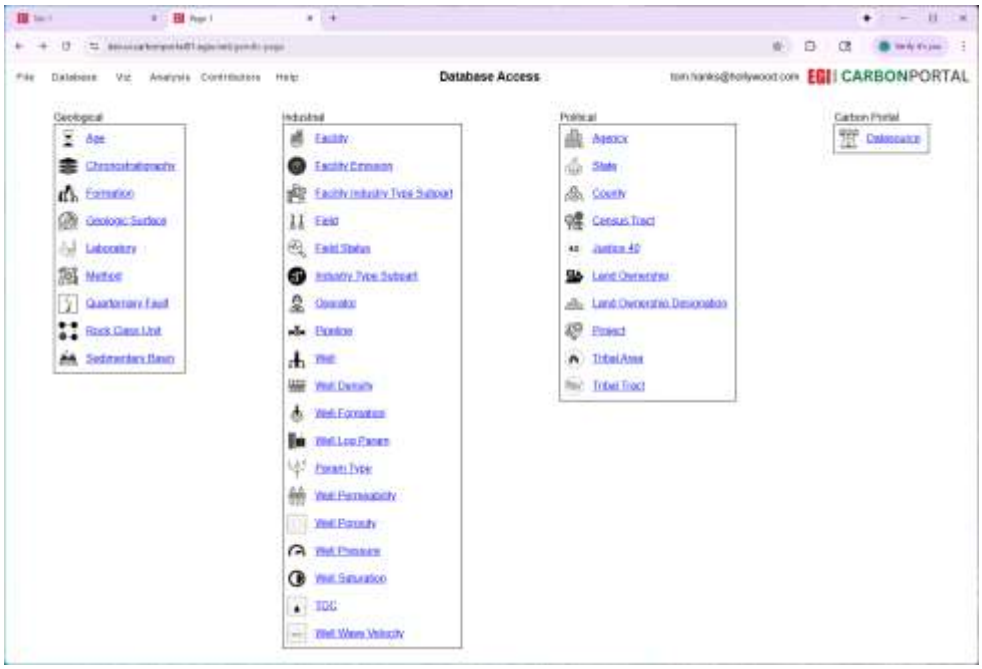


Figure 3.1.1 A heterogeneous database can include seemingly unrelated fields which have no obvious overlap but exist side by side. This seemingly unrelated data can be combined in visualizers.

While making the EGI Carbon Portal, major categories like Geological, Industrial and Political were recognized, each of which could have as many tables and fields as needed. In the computer code, there was an emphasis to be able to quickly add/remove/edit fields and tables as stakeholders' needs changed. So, the emphasis was not on the creation of a database, but on a database that could evolve.

For example, the user can search for Facilities near Lancaster, CA that produce carbon dioxide near a pipeline to be transported to wells near Cedar City, UT.



Figure 3.1.2 Carbon dioxide Emitters near Lancaster, CA; pipelines from CA to UT; wells in UT are all queried in the same website.

These three queries can be sent to a free ArcGIS page in the same website in a matter of seconds.



Figure 3.1.3 The queries from Figure 3.1.3 are combined on a map to see enhanced oil recovery opportunities.

Exploring the data, the stakeholder finds in 2011, an aeronautics company was the largest CO2 producer near Lancaster, CA. There is a pipeline that covers over 90% of the distance to Cedar City and there is a well called “Table Butte U 1” that may be a good candidate. Thus, we have

found a possible CO2 source, a well that is perhaps available for enhanced oil recovery, and an existing pipeline.

Visualizations are not limited to maps, but in fact an unlimited number of visualizations are possible. Data can be sent from database to visualizer, or from one visualizer to another in a few seconds, without leaving the website.

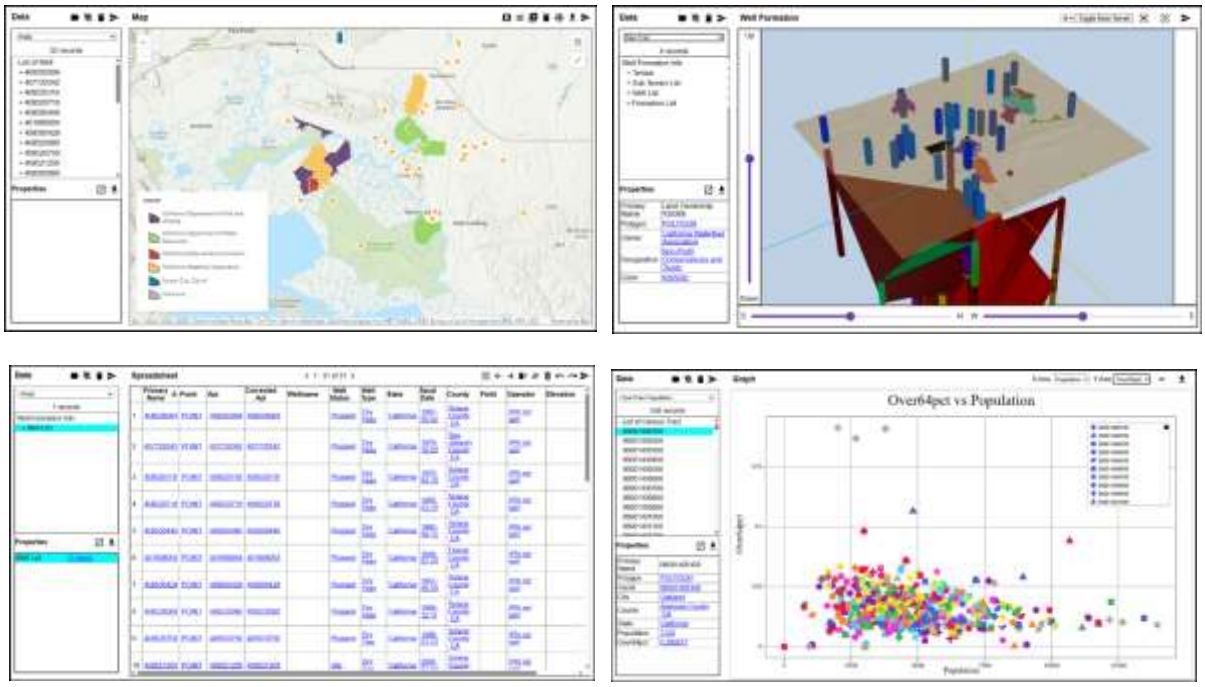


Figure 3.1.4 Wells, Land Ownership, Subsurface Geology and Population information from the San Francisco area are expressed in maps, 3D viewers, spreadsheets and graphs.

Most importantly, the data citation and its original file (or reference to the original) are stored for each piece of data. The original file can be downloaded by the stakeholder in just a few clicks.



Figure 3.1.5 On the left is a formation in the database. Notice the Metadata button conveniently placed above the image. After clicking 'Metadata', the full information about the source of the data appears on the right, along with a download button to retrieve the original data.

In short, the challenges of CCUS require the creation of a database tool that can span numerous topics, is powerful, is simple, is flexible, can continuously change, and can allow exploration of the data in an intuitive way. This tool, called EGI Carbon Portal has been partially created and shows great promise for further expansion.

The expansion envisioned is a tool called EGI Resource Portal which will expand into even more topics such as critical minerals, geothermal energy and enhanced oil recovery to allow stakeholders to explore the commercial viability of their business ideas.



Fig 3.1.6 The EGI Carbon Portal can be reimagined as the EGI Resource Portal. This heterogenous database can allow non-specialist and non-technical stakeholders to explore commercial viability of the projects they envision.

Subtask 3.1.2 – Update Geologic Data for CCUS Assessment

In the EGI Carbon Portal, one of the major categories is geology, specifically concepts deemed important for CCUS.

So far, the following concepts have been included.

Table 3.1.1 Geologic records at a Glance

Concept	Quantity	Concept	Quantity
Formations (2D Projections)	123 records	Well Porosity	14,888 records
Geologic Surfaces	313,732 records	Well Pressure	105,793 records
Quaternary Faults	112,376 records	Well Saturation	55 records
Sedimentary Basins	144 records	Well TOC	42 records
Well Permeability	1690 records	Well Wave Velocity	1368 records
Geologic data gathered so far in EGI Carbon Portal			

Geologic Surfaces, Quaternary Faults and Sedimentary Basins provide surface information. Subsurface information can be derived from well drilling records (permeability, porosity, TOC, etc.). An example where well information is utilized is the 3D viewer in Figure 3.1.4.



Fig 3.1.7 Left to right: The Arbuckle formation, the Almond Trondhjemite geologic surface, and the Albert Rim fault.

However, this is only the initial geologic data. For the EGI Resource Portal, the following geologic topics can be added.

- Formations in 3D
- Isotherms in 3D
- Hydrology
- Critical Minerals
- Nuclear Resources
- Etc.

An example would be searching for enhanced geothermal sites. A location that is above a large geological formation of the correct material, within the correct temperature range at a drillable depth, with favorable parameters for drilling, perhaps along a fault line, with a water source nearby and neither too near or too far from a populated area is desirable. Querying the EGI Resource Portal for the topics Formations in 3D, Isotherms in 3D, Quaternary Faults, Hydrology, and Census data can help find such a location.

Subtask 3.1.3 – Update USDW Data from All Public Sources

Although it has not yet been included, underground sources of drinking water (USDW) can be added alongside other topics. Similar to facility emissions (Subtask 3.1.4), these records can express changes over time. Additionally, by utilizing API calls to recent water measurement, the current values of water sources can be obtained.

Subtask 3.1.4 – Gather and Catalogue CO_2 Emissions (Point) Source Database

One of the topics inside of the EGI Carbon Portal heterogeneous database is Facility Emissions.

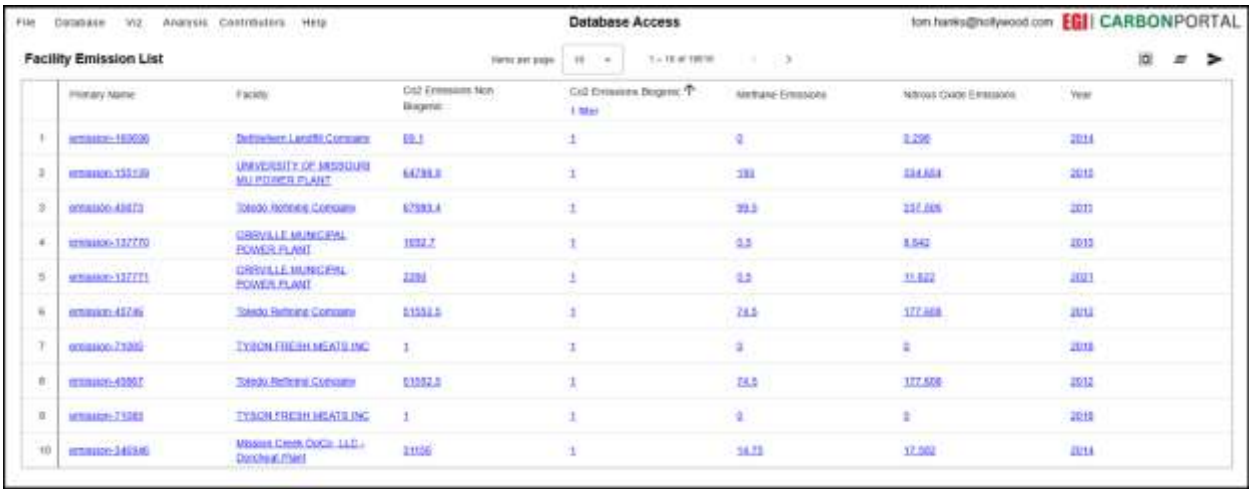


Figure 3.1.8 This database interface provides access to records for hundreds of thousands of Facility Emissions between 2010 and 2021.

In a few seconds, we can do a complex query such as "facilities emitting non-biogenic carbon dioxide in the Los Angeles area in 2021". Once again, this can then be easily mapped, and colored by emission quantity, without leaving the website.

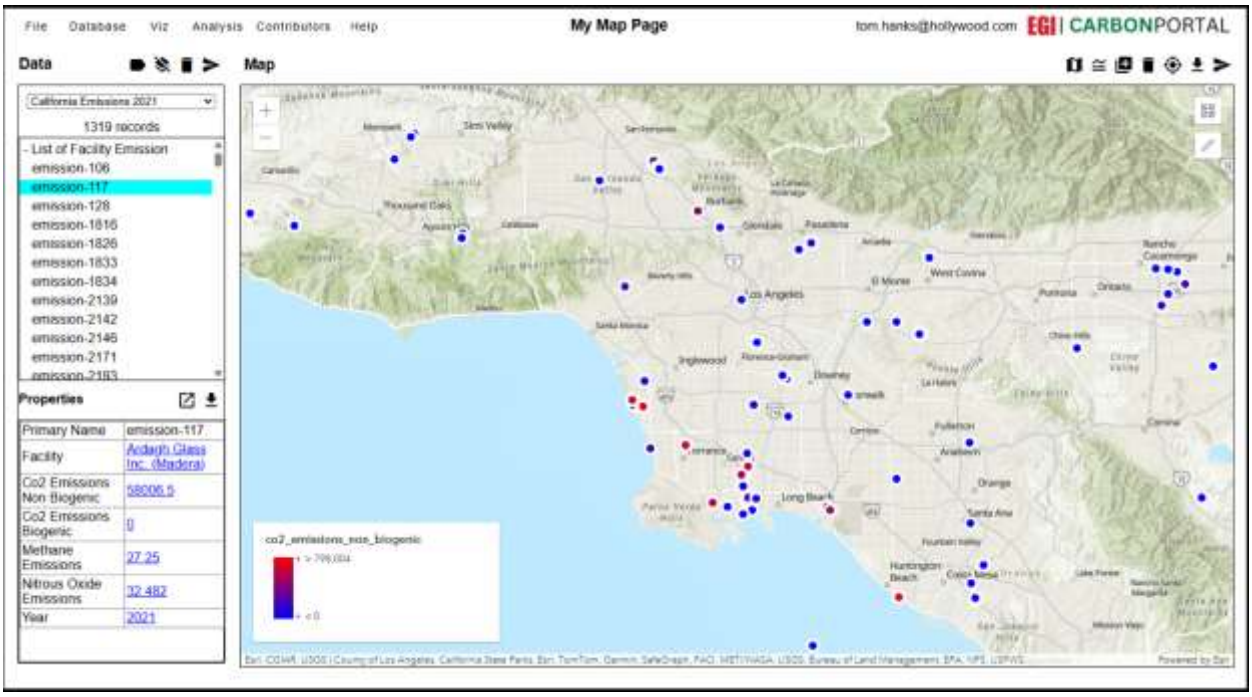


Figure 3.1.9 Facilities emitting non-biogenic carbon dioxide in the Los Angeles area in 2021

Table 3.1.2 Facility Emissions records at a Glance			
Concept	**Quantity**	**Concept**	**Quantity**

Emission Records	363,595	Non-Biogenic CO2 Emissions	363,595 records
Facilities	17,889	Biogenic CO2 Emissions	353,163 records
States	50	Methane Emissions	363,595 records
Years	2010-2021	Nitrous Oxide Emissions	363,595 records
Summary of data contained in the EGI Carbon Portal 'Facility' and 'Facility Emissions' topics.			

It is possible that API calls could obtain the latest emissions as well.

Subtask 3.2 – Apply NRAP Tools to Assess Geologic Risks

The CUSP team applied National Risk Assessment Partnership (NRAP) tools to assess geologic risks associated with CO_2 storage across the CUSP region. Building on the integrated datasets developed under Subtask 3.1, we employed NRAP-supported risk-assessment frameworks to evaluate potential leakage pathways, characterize key sources of uncertainty, and inform monitoring and verification (MRV) planning for candidate storage sites. The NRAP tool suite includes integrated assessment, induced seismicity, and monitoring-design tools intended to support quantitative risk assessment and uncertainty evaluation; the quarterly reports document application of NRAP tools broadly without attribution to specific sub-components.

NRAP tools were applied in support of both regional screening efforts and site-specific analyses conducted under Tasks 2 and 4, including multiple Focus Projects. These applications integrated geologic characterization, reservoir simulation results, USDW information, legacy well data, and site-specific operational assumptions to assess risks related to containment, injectivity, induced seismicity, and monitoring design. Across the project, NRAP-based analyses were used to identify dominant uncertainty drivers, evaluate relative importance of potential leakage pathways, and prioritize data collection and monitoring strategies appropriate to site conditions and project maturity.

Outcomes of the Subtask 3.2 effort supported risk-informed planning and decision-making for Focus Projects and hub-scale CCUS concepts described throughout this report. Detailed outcomes of specific NRAP analyses—including assessments of leakage risk, induced seismicity, well integrity, and monitoring performance—are documented in the Focus Project summaries (Part II), Task 5 Risk Assessment sections, National Laboratory contributions, and Regional Readiness Indices analyses presented elsewhere in this final report. Collectively, these sections reflect extensive application of NRAP tools over the life of the project and demonstrate how NRAP-informed risk assessment was integrated into storage screening, MRV planning, regulatory considerations, and regional CCS decision-support workflows.

Subtask 3.3 – Provide Synthesized Data to DOE's Machine Learning Initiative

The CUSP team synthesized and delivered curated datasets and analytical outputs to support DOE machine learning (ML) initiatives focused on geologic CO_2 storage assessment. Building on the regional data infrastructure developed under Subtask 3.1 and the risk-assessment

applications conducted under Subtask 3.2, we organized geologic, reservoir, risk, and Focus Project–specific data in formats suitable for use in ML workflows and decision-support tools.

In coordination with DOE national laboratories and NETL-led ML efforts (SMART and otherwise), the CUSP team provided synthesized datasets, model inputs, and metadata describing storage properties, uncertainty drivers, and risk-related attributes across multiple basins and storage settings. These contributions emphasized reuse of existing analyses and outputs—rather than development of new models—to ensure consistency with DOE-supported analytical frameworks and to facilitate integration with broader ML research activities.

Outcomes of the Subtask 3.3 effort supported DOE efforts to apply machine learning to CCUS planning and risk evaluation. CUSP-provided datasets and analytical products informed ML-based investigations of storage suitability, uncertainty characterization, and regional screening and contributed to development of scalable approaches for integrating geologic, engineering, and risk information in support of future CCS deployment.

Subtask 3.3.1 – SMART-CS Initiative Support

The CUSP team supported DOE's SMART-CS initiative through coordination and data contributions that aligned regional CCUS analyses with broader machine learning–based research efforts. Much of the technical work supporting SMART-CS was carried out by the University of Utah research team under a separate, dedicated project; however, these activities were conducted collaboratively with CUSP and leveraged data products, analytical workflows, and Focus Project outcomes developed under Task 3.

Through this collaboration, the CUSP team facilitated transfer of synthesized geologic, reservoir, risk, and infrastructure data to support SMART-CS objectives related to machine learning–enabled assessment of CO_2 storage suitability and uncertainty. These efforts emphasized consistency between CUSP-developed datasets and DOE-supported ML frameworks and ensured that regional storage assessments and risk insights generated through CUSP could be incorporated into broader, scalable analytical tools developed under SMART-CS.

Outcomes of Subtask 3.3.1 strengthened alignment between CUSP data products and DOE machine learning initiatives, enabling reuse of regional datasets and analytical insights beyond the scope of the CUSP project. This collaboration supported DOE objectives to advance data-driven approaches for CCS planning while maintaining clear delineation between CUSP deliverables and the independently funded SMART-CS research activities.

Task 4 – Evaluating Regional Infrastructure

Carbon Solutions provided support on Task 4 – Evaluating Regional Infrastructure in several states across the CUSP region by applying its SimCCS^{PRO} toolset (Carbon Solutions 2025d; including CostMAP^{PRO} [Carbon Solutions 2025b], SCO$_2$T^{PRO} [Carbon Solutions 2025c], and CO$_2$NCORD [Carbon Solutions 2025a]) to case studies for each Focused Project. Specifically, Carbon Solutions supported the following Focused Projects:

- California
- Kansas
- Montana
- Nevada

- Oklahoma
- Utah

More details about the work and support provided by Carbon Solutions can be found in targeted Focused Project final report documents. In addition to supporting these Focused Projects, Carbon Solutions also supported efforts in all four working groups: Outreach, Data Organization, Data Analytics, and Economic Analysis. Support was provided by co-leading the outreach, data analytics, and economic analysis working groups, as well as coordinating with other members and providing data.

References

Carbon Solutions LLC. 2025a. CO_2NCORD [software]. Saint Paul (MN); Carbon Solutions LLC. [accessed 2026 Jan 14]. https://www.carbonsolutionsllc.com/software/co2ncord/

Carbon Solutions LLC. 2025b. CostMAP^{PRO} [software]. Saint Paul (MN); Carbon Solutions LLC. [accessed 2025 Dec 30]. https://www.carbonsolutionsllc.com/software/costmappro/

Carbon Solutions LLC. 2025c. SCO$_2$T^{PRO} [software]. Saint Paul (MN); Carbon Solutions LLC. [accessed 2025 Dec 30]. https://www.carbonsolutionsllc.com/software/sco2tpro/

Carbon Solutions LLC. 2025d. SimCCS^{PRO} [software]. Saint Paul (MN); Carbon Solutions LLC. [accessed 2025 Dec 30]. https://www.carbonsolutionsllc.com/software/simccspro/

Subtask 4.1 – Catalog, Map, and Evaluate Extant and Near-Term CO_2 Distribution Network

Carbon Solutions worked to expand and update its existing data on CO_2 transport systems using MAPSearch pipeline data (https://www.mapsearch.com/, accessed January 14, 2026). Integrating this data into CostMAP^{PRO} allowed Carbon Solutions to better incorporate existing real-world pipelines as rights-of-way (ROWs) that might act as corridors, encouraging CCS projects in the future (Figure 1). These data were added as a new input layer when generating routing and cost surfaces used in SimCCS^{PRO} scenario runs.

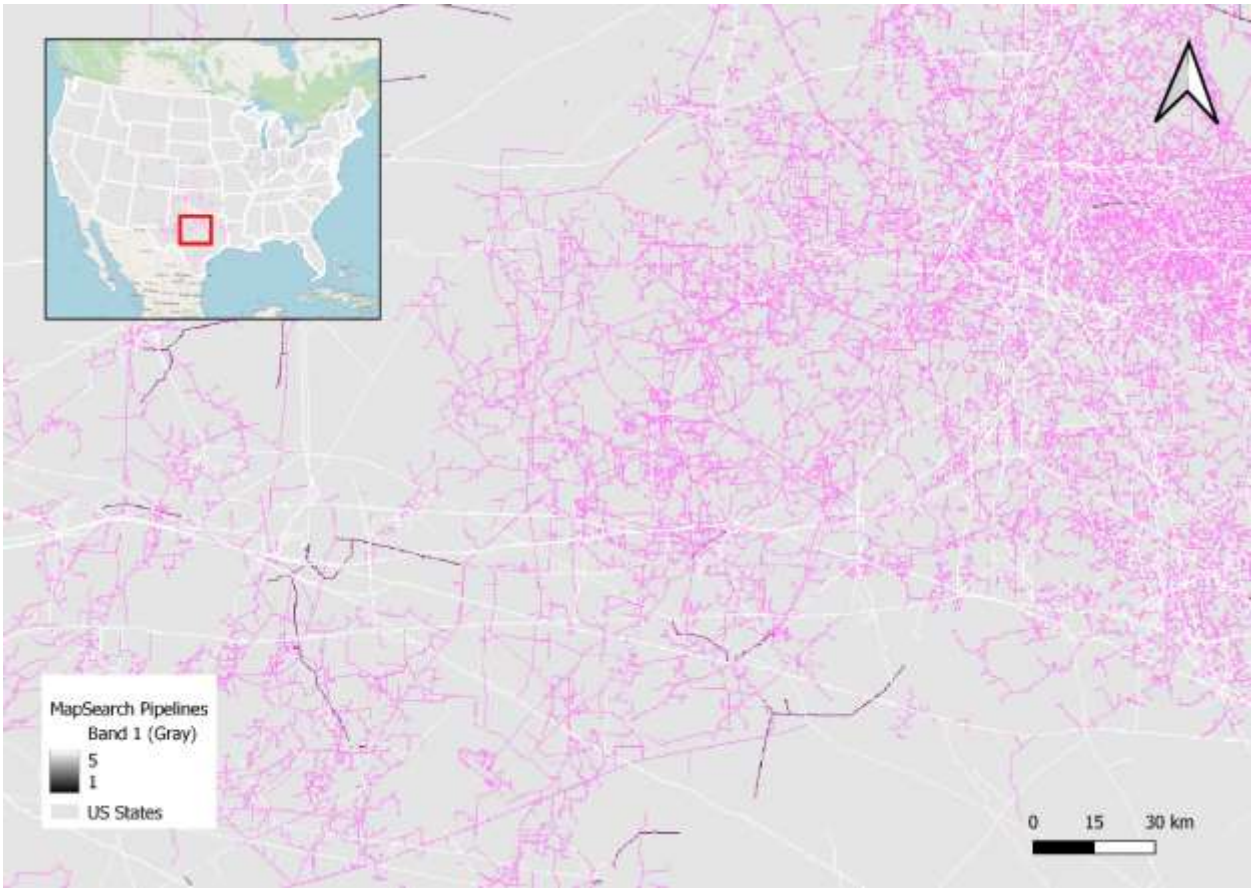


Figure 1 Pipeline data

Carbon Solutions is not affiliated with SimCCS Gateway. The Indiana University team supporting SimCCS Gateway has disbanded since project inception. The website is still live (https://SimCCS.org, accessed January 10, 2026) but is not actively supported by Indiana University.

Subtask 4.2 – Identify and Add Rights of Way for New Pipelines (Main Lines and Otherwise)

CostMAP^{PRO} integrates several geospatial data layers to create both cost and routing surfaces, or in other words, geospatial data weighted to determine the cost of moving over space (e.g., building on sloped land is more expensive than flat), and geospatial data weighted to capture the ease of siting pipelines over space (e.g., it is better to avoid building a new pipeline in densely populated areas.) This data is collected from a variety of both public and private data. Creating separate routing and cost surfaces is important to ensure both realistic pipeline costs and routes. While costs for construction is a primary concern for developers, sensitive areas such as critical habitat require additional routing concerns separated from the cost of pipeline development. Differences in the outcomes of weighting for routing versus construction costs can be seen in Figure 2.

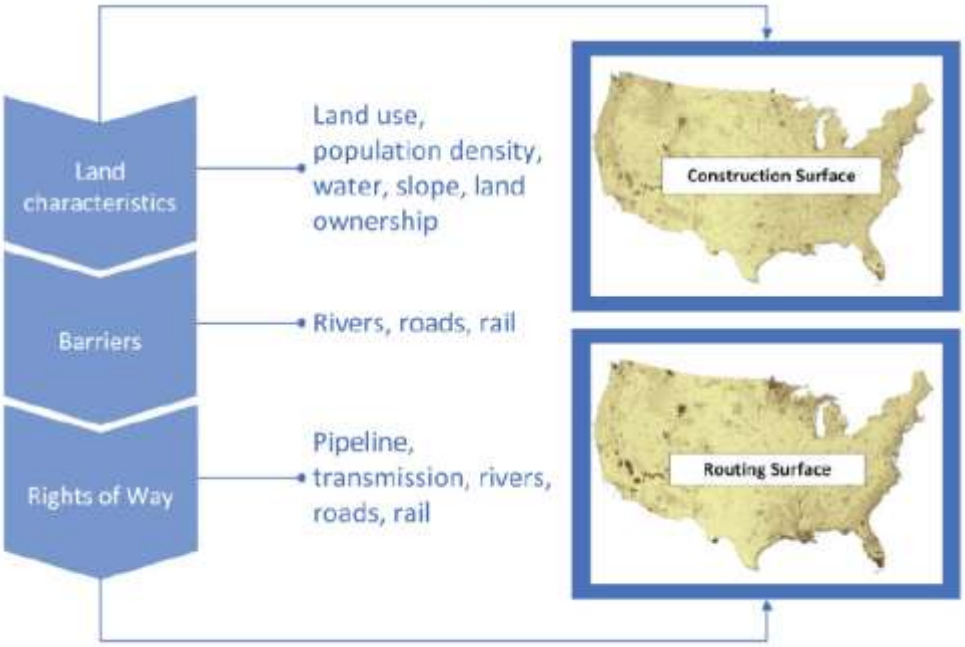


Figure 2 Example of data used to construct routing and construction cost surfaces

Within these datasets, there are features that serve as rights-of-way, potentially supporting and encouraging pipeline deployment. For example, existing pipelines or transmission lines could encourage pipeline deployment since rights-of-ways have already been secured, potentially reducing the cost of routing a pipeline that follows them. More specifically, CostMAP^{PRO} incorporates the following geospatial data that relate more directly to rights-of-way (see Table 1).

Table 1 Specific CostMAP^{PRO} data layers that impact rights-of-way decision making

Geospatial layer	Explanation and data source
Pipelines	Pipeline ROW data from state and federal sources*
Transmission lines	Data from Homeland Infrastructure Foundation-Level Data Working Group**
Railroads	Railway data from the U.S. Department of Transportation Rail Network data***
Roads	All roads from the U.S. Census Bureau TIGER/Line shapefiles**** and from the National Transportation Atlas Database for large scales*****

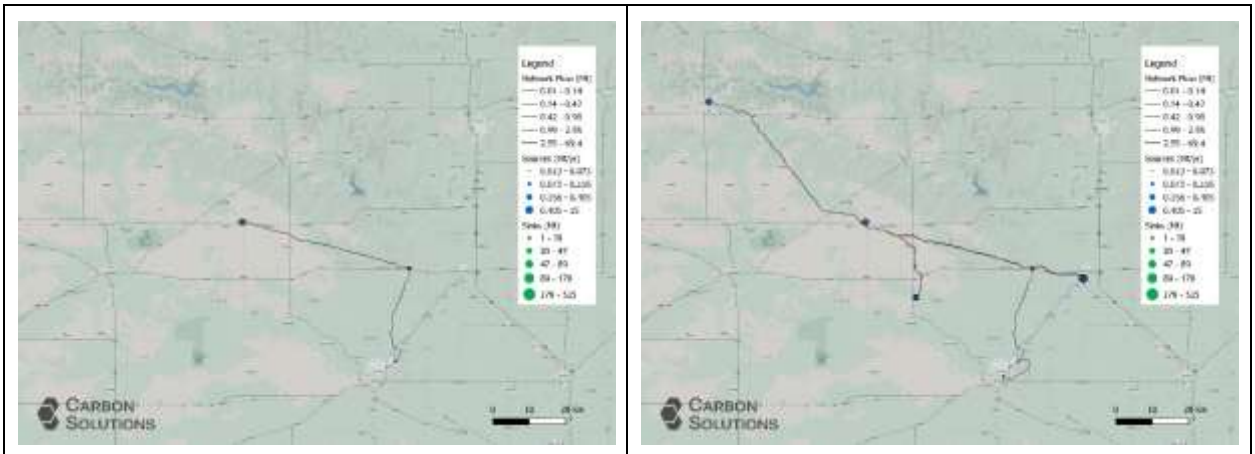
***https://www.mapsearch.com/, accessed January 14, 2026**
****At the time of data collection, these data were publicly available at https://www.dhs.gov/gmo/hifld; the site has since been removed.**
*****https://railroads.dot.gov/rail-network-development/maps-and-data/maps-geographic-information-system/maps-geographic, accessed January 14, 2026**
******https://www.census.gov/geographies/mapping-files/time-series/geo/tiger-line-file.html, accessed January 14, 2026**
*******https://geodata.bts.gov/, accessed January 14, 2026**

During the CUSP project, Carbon Solutions worked on improving and updating this data to be as accurate as possible. For example, Carbon Solutions utilized the most current deployed pipeline routes from MAPSearch (https://www.mapsearch.com/, accessed January 14, 2026). These data

layers were incorporated into each routing and cost surface across all SimCCS^{PRO} scenarios in each individual Focused Project case study.

Subtask 4.3 – Regulatory/Policy Impact Assessment

Carbon Solutions worked with Focused Project teams to determine the most useful scenarios to understand and assess different pipeline scenarios. After coordinating with Focused Project teams, SimCCS^{PRO} scenarios primarily focus on intrastate transport routes to meet CCUS targets, avoiding any potential regulatory or legal challenges to developing an interstate pipeline network. These varying Focused Project scenarios also assess potential future project partners that could join in CCUS efforts. For example, in the Kansas Focused Project, a total of 12 different scenarios were run, exploring what intrastate CCUS networks would look like if only using project partner sources or engaging with surrounding emitters of CO_2 engaged in CCUS efforts. This was done to provide information and support to the Focused Project partner ONEOK as they considered the potential for future Class VI well and CarbonSAFE applications. Two SimCCS^{PRO} result networks can be viewed in Figure 3.



A **B**

Figure 3 Two scenarios run in the Kansas Focused Project in collaboration with project partners ONEOK. Map A features a CCUS network only using current ONEOK facilities, and Map B shows the CCUS network if surrounding sources of CO_2 were to participate.

Carbon Solutions did not incorporate any federal or state tax credits into any Focused Project scenario but did provide total CCUS network unit costs. For example, in the California Focused Project the SimCCS^{PRO} the cost of CCUS networks at the proposed field site range from \$74 to \$80/tCO_2, falling below the current 45Q tax credit of \$85/tCO_2. On the other hand, the total CCUS network costs for the Kansas Focused Project range from \$86/tCO_2 to \$110/tCO_2, indicating that the current 45Q tax credit threshold might not be high enough to incentivize CCUS in Kansas. It could also be implied that some states, like Kansas, might need additional incentives on the local level before emitters of CO_2 would engage in CCUS efforts. Alternatively, in the Oklahoma Focused Project, total CCUS network costs range from \$37/tCO_2 to \$96/tCO_2. Approximately 75% of the Oklahoma Focused Project scenarios have total unit costs that fall below the current 45Q tax credit of \$85/tCO_2 suggesting that the current 45Q tax credit is sufficient to incentivize early CCUS efforts in Oklahoma.

Subtask 4.4 – Economic Assessment

Carbon Solutions provided support on Subtask 4.4 across all Focused Projects with targeted scenarios on the following projects:

- California Focused Project – Statewide CCUS scenarios comparing hub vs distributed storage.
- Kansas Focused Project – Inclusion of other nearby facilities in support of potential CarbonSAFE applications.
- Oklahoma Focused Project – Evaluation of stacked storage in support of developing a CCUS roadmap.

For example, in the California Focused Project, Carbon Solutions ran four "future" scenarios looking at statewide CCUS network deployment using either hub storage locations or the 50 km SCO_2T^{PRO} storage locations. The three hub storage locations were:

1. Northern California "Tehama County" Hub was selected because of its higher probability of being a viable geologic CO_2 storage reservoir than other options in the surrounding area.
2. Central California "San Joaquin County" Hub is located just west of San Fransico.
3. Southern California "Kern County" Hub that aggregates all 10-by-10-km cells in Kern County into one point location near the center of Kern County based on the work and analysis conducted in Kim et al. (2023).

These scenarios provided insight into how amounts of deployed pipeline (km), pipeline routes, and total CCUS network costs change when considering either hub or distributed storage. Carbon Solutions observed that distributed storage scenarios deployed fewer pipelines for the same capture target and generally had lower total CCUS network costs when compared with hub storage options (Table 2). For example, when capturing all available CO_2 emissions in California, distributed storage deployed approximately 3,359 km of pipeline with a total CCUS network cost of \$102/tCO_2. The corresponding hub scenario saw the deployment of 5,133 km of pipeline with a total CCUS network cost of \$109/tCO_2. It should be noted that these values reflect only the cost of building the deployed CCUS networks (capture, transport, and storage) and do not reflect any cost sharing or tax incentives that individual facilities may be eligible for when engaging in hub storage. Further, 80 unique storage locations are deployed in the distributed storage scenario when capturing all available CO_2 emissions in California from 246 unique facilities. This indicates that captured CO_2 emissions from multiple sources are transported to the same storage option, forming more local hubs than the three proposed by Carbon Solutions.

Table 2 Summary table of the results for all forward-looking California runs conducted using $SimCCS^{PRO}$. DS-AS refers to distributed storage and all sources, DS-SG refers to distributed storage and steam generators, HS-AS refers to hub storage and all sources, HS-SG refers to hub storage and steam generators.

Run	Annual capture target, $MtCO_2/yr$	Number of sources	Number of sinks	Network length, km	Capture cost, \$/tCO_2	Transport cost, \$/tCO_2	Storage cost, \$/tCO_2	Total cost, \$/tCO_2
DS-AS	51.55	246	80	3,358.49	68.29	26.81	6.91	102.01
DS-SG	8.64	63	13	218.10	64.38	3.87	6.88	75.13

HS-AS	51.55	246	3	5,143.38	68.29	33.79	6.63	108.71
HS-SG	8.64	63	1	616.78	64.38	10.75	6.85	81.98

The Oklahoma Focused Project featured an analysis that evaluated stacked storage as part of a roadmap for CCUS in Oklahoma. This Focused Project has 32 distinct intrastate scenarios broken into two discrete sets. In the first set of scenarios, captured CO_2 could be deployed in any county that had geologic CO_2 storage, including but not limited to counties with existing CO_2-EOR operations. The second set of scenarios limited storage options to only those counties with geologic CO_2 storage and counties with existing CO_2-EOR operations, simulating the conditions needed for stacked storage. One major finding from this analysis suggested that the cost of capture as the main driver in CCUS network deployment in Oklahoma, with the lowest cost sources of CO_2 typically deploying first. Additionally, Carbon Solutions examined how often a county was deployed across SimCCS^{PRO} scenarios, indicating those counties that would be suitable targets for future analysis and exploration (Figure 4). Several counties with existing CO_2-EOR operations and geologic CO_2 storage were deployed across the scenarios, highlighting how stacked storage could play an important role in Oklahoma CCUS development. In particular, Pontotoc County deployed as a storage option across all 32 scenarios, suggesting that regardless of future appetite for stacked storage in Oklahoma, it could serve as an important starting point for CCUS in Oklahoma.

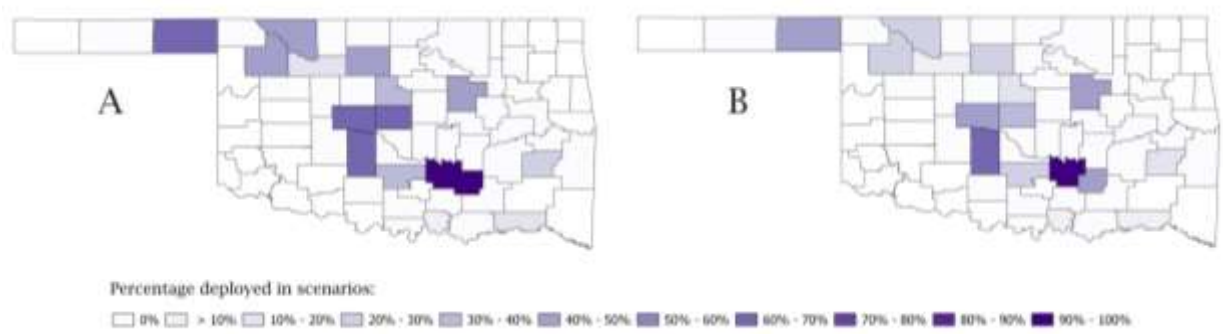


Figure 4 Percentage deployment of each county across A) scenarios where geologic CO_2 storage occurs in any county with saline storage resources (only 16 scenarios) and B) any scenario that we conducted in this analysis (32 scenarios). Source: Miranda et al. (2023).

References

Kim TW, Yaw S, Kovscek AR. 2023. Scoring, ranking, and technoeconomics of carbon capture and storage opportunities in the Central Valley of California. Int J Greenh Gas Control. 128:103968. doi:10.1016/j.ijggc.2023.103968

Miranda MW, Ogland-Hand JD, Bielicki JM, Moghanloo RG, DaneshFar J, Middleton RS. 2023. Developing a roadmap for carbon capture and storage in Oklahoma by assessing the viability of stacked storage. Greenh Gas Sci Technol. First published 09 Nov 2023. doi:10.1002/ghg.2244

Subtask 4.5 – Focused Scenario Analysis

Subtask 4.5.1 – Characterization of CO_2 Storage Potential in Harquahala Basin

See Both state- and basin-scale assessments of the geothermal favorability in Nevada have previously been made (e.g., Coolbaugh et al. 2005; Penfield et al. 2010; Iovenitti et al. 2016; **Figure 67**). These assessments, however, were performed for the exploration and development of geothermal power plants that use water or other chemicals as the primary working fluid at relatively shallow depths. There are currently no published regional-scale assessments of CO_2 geological storage in sedimentary basin geothermal reservoirs of Nevada; and previous preliminary assessments of the potential for CO_2 geological storage in the state did not consider using geologically stored CO_2 as a subsurface heat extraction fluid for geothermal electricity generation (e.g., Price et al. 2005).

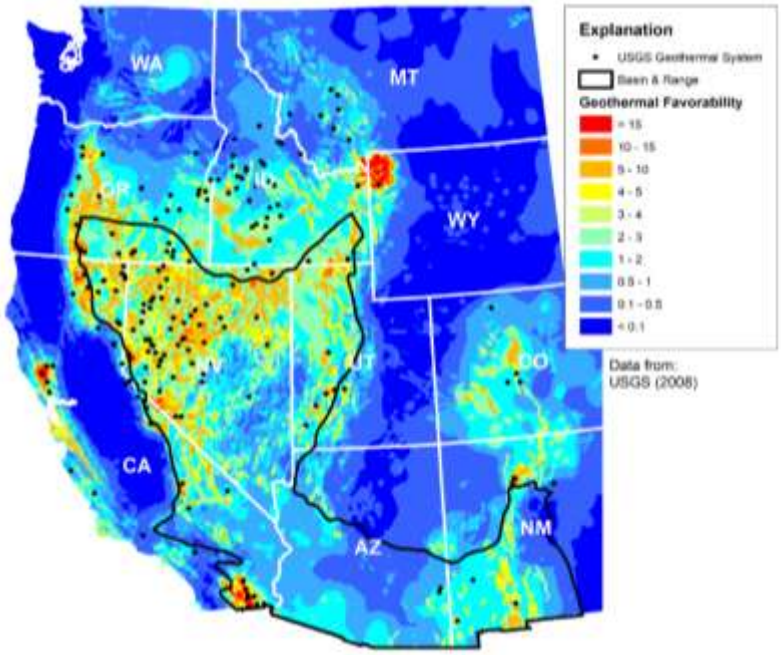


Figure 67 Map of geothermal favorability of the western United States. Much of the region with geothermal favorability of >5 is in northwestern Nevada. The extent of the Basin and Range physiographic province (black outline) and distribution of USGS geothermal systems are also shown.

Recent assessments of the favorability of using Enhanced Geothermal Systems (EGS) at basin-scales in Nevada have previously been made by developing methodologies to explore optimum subsurface conditions (Iovenitti et al. 2016). Assessments of EGS are currently being performed in Nevada, but similar assessments of sedimentary basin geothermal resources are comparatively understudied, in part because sedimentary basins have generally colder temperatures than EGS resources. But using geologically stored CO_2 as the heat-extraction fluid can more than halve the cost of sedimentary basin geothermal power generation compared to using in-situ water because CO_2 is a more efficient heat extraction fluid (e.g., Adams et al. 2021; Zhang et al. 2014). As a result, geologically stored CO_2 may "unlock" using sedimentary basin geothermal resources for electricity generation by using CO_2 plume geothermal power plants (Ogland-Hand et al. 2022). Nevada is a good test bed to assess the feasibility of using CO_2 plume geothermal power plants in the United States due to the state's high geothermal potential from its location in the

tectonically active Basin and Range physiographic province (**Figure 67**) and having existing geothermal energy infrastructure (**Figure 68**).

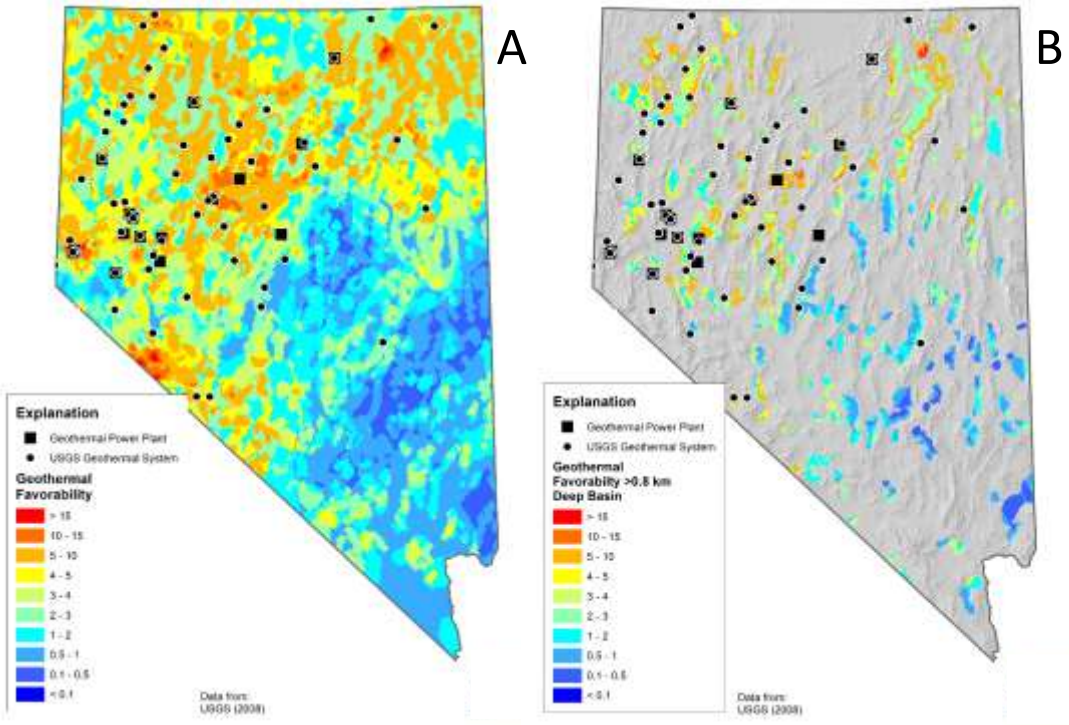


Figure 68 Maps of Nevada showing: (A) geothermal favorability of entire state, and (B) geothermal favorability in sedimentary basins with depths greater than 800 m. The location of geothermal power plants and USGS geothermal systems distributed in northwestern Nevada are also shown.

Objectives and Outcomes

The general objectives of the focused project are to (1) perform a regional-scale assessment to fill a data gap of critical information related to carbon capture, utilization, and storage (CCUS) technologies to mitigate CO_2 emissions in Nevada and (2) to develop an approach to regionally assess the potential that using CO_2 geological storage in sedimentary basin geothermal reservoirs may have for increasing the states capability for CCUS.

Sedimentary basin geothermal power plants that use plumes of geologically stored CO_2 as a subsurface heat extraction fluid can store between approximately 2 and 7 $MtCO_2$ per MW of electric power capacity and as such, they are one of the only CO_2-utilization processes that may demand megatonne, if not gigatonne, volumes of CO_2 geological storage (Adams et al. 2021). Nevada may be an especially favorable state for low-cost CO_2 plume geothermal power plants, given that: a) the cost of geothermal power decreases with increasing geothermal temperature gradient, and b) there are commercial geothermal power plants currently operating in Nevada, based on the state having high geothermal temperature gradients (e.g., Coolbaugh et al. 2005; USGS 2008; **Figure 68**).

The CUSP West-specific objectives are to (1) provide an approach that could be used to regionally assess the favorability of CO_2 geological storage in other CUSP states with

sedimentary basin geothermal resources and (2) provide a better understanding of potential areas in Nevada that could be targeted for more detailed analyses either in individual basins or at geothermal power plants with future research. The overall efforts of the focused project will demonstrate to the Department of Energy that the CUSP West is also researching alternative approaches to CCUS by taking advantage of each state specific geologic setting and capabilities, in this case, the geothermal resources of Nevada.

CUSP Focused Project Team and Scope of Work

The CUSP focused project team included collaboration between Steven Bacon (PI) and Rishi Parashar of the Desert Research Institute (DRI), Reno, Nevada and Jonathan Ogland-Hand (Co-PI), Jeff Bennett, and Richard Middleton of Carbon Solutions, LLC. The overall scope of work included the DRI team creating a 2-km grid resolution geospatial dataset of pertinent geologic and geothermal information to identify areas that are favorable for CO_2 geological storage in sedimentary basin geothermal systems in northern Nevada. The extent of areas with favorable sedimentary basin geothermal potential along with available reservoir property data from deep well logs previously analyzed for the Nevada CUSP project were integrated for a basin-scale assessment. These data were then used as model input parameters for the Carbon Solutions team to apply their computational tools to characterize the storage capacity and cost of CO_2 storage, as well as the power capacity and cost of CO_2 plume geothermal power plants across Nevada (e.g., Ogland-Hand et al. 2022).

Methods

The focused project was separated into two main tasks with each team performing specific subtasks to reach the overall objectives. The two main tasks included (1) regional- and basin-scale geologic and geothermal characterization and identification of potential sedimentary basin geothermal reservoirs and (2) estimating the storage capacity and cost of CO_2 storage at basin-scales using site-specific well log information. The geospatial datasets, approaches, and tools used in the overall assessment include:

Geologic and Geothermal Characterization

A regional-scale assessment of CO_2 geological storage in sedimentary basin geothermal reservoirs was performed using a range of geologic, geophysical, and geothermal information appropriate for making a regional-scale assessment. The geothermal potential assessment of Coolbaugh et al. (2005) shows northern Nevada has the highest geothermal potential across the state. As a result, the project scope concentrated on performing the assessment in northern Nevada because of its high geothermal temperature gradient and availability of existing deep well log information. The following gridded data layers were used in the geospatial analysis component of the assessment:

Basin Configuration

Deep sedimentary basins greater than 800 m depth were identified based on geophysical datasets including gravity inversion mapping of the depth to pre-Cenozoic basement in northern Nevada (Ponce 2004; **Figure 69**A). This dataset was double-checked with more recently published data from the USGS - National Crustal Model (NCM). The NCM dataset includes crustal properties

for the western United States on a 1-km grid scale including depth to basement and thickness of unconsolidated sediments (Shah and Boyd 2018). The data of Ponce (2004) was also used in the development of NCM dataset. The geologic map of Nevada at a scale of 1:500,000 was also used in conjunction with the geophysical datasets to refine the delineation between sedimentary basins (i.e., valley fill) and mountain highlands composed of pre-Cenozoic rocks (Stewart and Carlson 1978; **Figure 69**B).

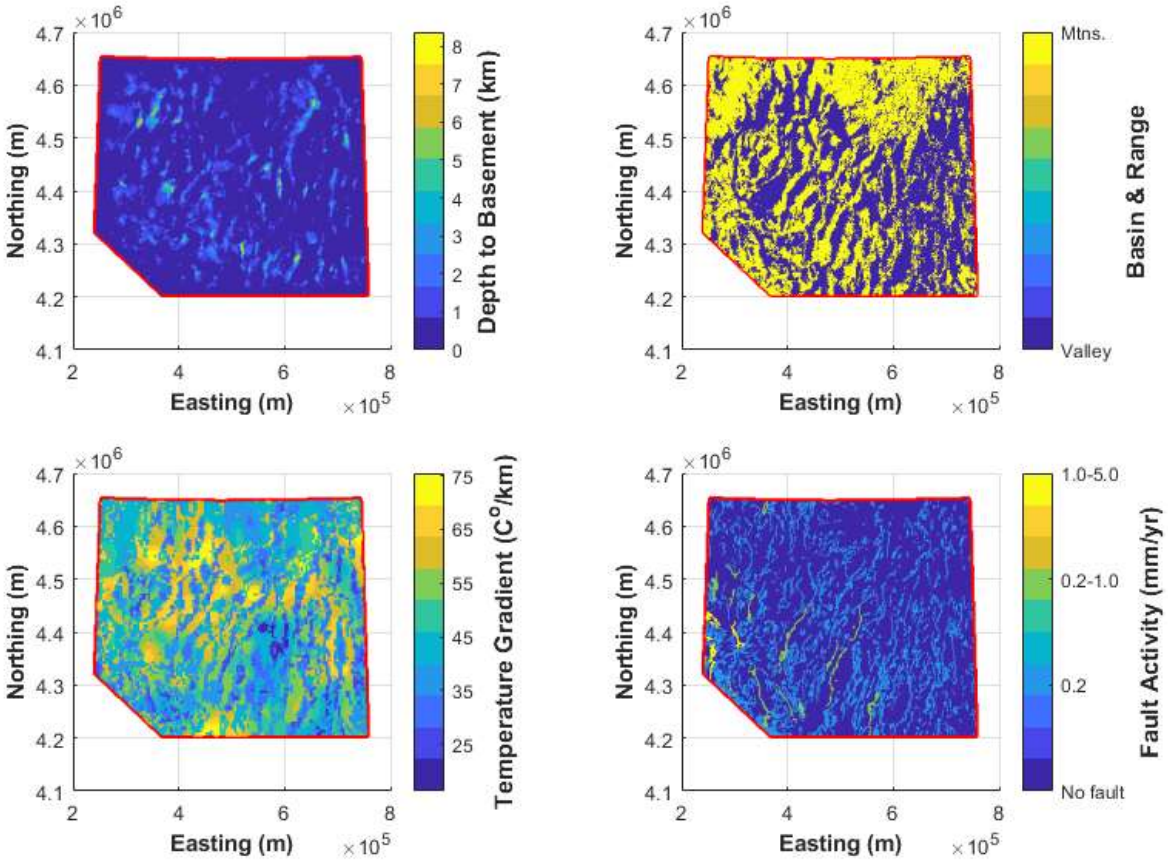


Figure 69 Maps of northern Nevada used in the regional-scale assessment of CO_2 geological storage in geothermal reservoirs: (A) depth to pre-Cenozoic basement, (B) geologic mapping to distinguish between sedimentary valley fill and mountains, (C) geothermal temperature gradient, and D) fault activity.

Temperature Gradient

Previous regional assessments of geothermal favorability and detailed information on site-specific geothermal resources were leveraged (Coolbaugh et al. 2005; USGS 2008; Penfield et al. 2010). Of the existing geothermal data available, the gridded map of geothermal temperature gradient at less than 2 km depth (Coolbaugh et al. 2005) provided the information required for the SCO_2T and genGEO computational tools (**Figure 69**C).

Fault Activity

The fault activity map of Nevada was used to identify potential areas with geothermal favorability (dePolo et al. 2009; USGS/NBMG 2016). Fault activity is directly linked to geothermal potential because fault zones can act as conduits for heat and fluids to rise to the surface (e.g., Faulds et al. 2012). The relative activity of faults in terms of slip rate (mm/yr) is used in the focused project as a proxy for the relative potential of geothermal favorability, given that fault zones with faster slip rates will likely have higher geothermal favorability compared to fault zones with slower slip rates that may have lower geothermal favorability. A 2-km buffer bounding mapped fault traces was applied to best represent the extent of high density fracturing along discrete shear zones.

Sedimentary Basin Geothermal Reservoir Assessment

The approach used to identify sedimentary basin geothermal reservoirs is principally based on an evaluation-parameter rating scheme. The rating scheme approach is commonly used in geologic hazard assessments and developed by considering intrinsic trigger parameters that are typically responsible for a given geologic hazard or geologic process (e.g., Price 2009). The approach used here for identifying sedimentary geothermal potential is partially based on applicable elements from the study of Coolbaugh et al. (2005) that produced a geothermal potential map of the Great Basin region, including both bedrock and sedimentary basin areas.

The intrinsic parameters (i.e., geological attributes) used in the assessment of sedimentary geothermal potential include (1) sedimentary valley fill at depths between 0.8 and 9 km, (2) geothermal temperature gradients ranging from 25°C/km to 75°C/km, and (3) location of faults and associated slip rate information (i.e., fault activity; **Figure 69**). A non-weighted, numerical rating class system was assigned to each intrinsic parameter based on their contribution towards influencing sedimentary geothermal potential according to logical judgments acquired from experience and literature (e.g., Pachauri and Pant 1992). A 10-fold rating class (0–9) was used for sedimentary valley fill greater than 800 m depth (i.e., depth to bedrock) and geothermal temperature gradient data layers, whereas a 4-fold rating class (0–3) was applied for the fault activity (i.e., slip rate) data layer (Table 11). Geospatial analyses were initially performed in ArcGIS to resample original datasets to have 2-km grid resolution followed by classifying the resampled data in MATLAB® programming language using the factor ratings for each data layer.

Table 11 Parameter ratings assigned to data layers in the sedimentary geothermal potential assessment.

Intrinsic Parameter	Variable	Factor Rating
Depth to basement	(km)	
Very Deep	8 - 9	9
	7 - 8	8
Deep	6 - 7	7
	5 - 6	6
Moderately Deep	4 - 5	5
	3 - 4	4
Shallow	2 - 3	3

	1 - 2	2
Very Shallow	0.8 - 1	1
Not applicable	<0.8	0
Geothermal temperature gradient	(°C/km)	
Very High	>75	9
	70 - 75	8
High	65 - 70	7
	60 - 65	6
Moderate	55 - 60	5
	50 - 55	4
Low	45 - 50	3
	40 - 45	2
Very Low	35 - 40	1
Not applicable	<35°	0
Fault activity (slip rate)	(mm/yr)	
High	1.0 - 5.0	3
Intermediate	0.2 - 1.0	2
Low	<0.2	1
Not appliable	No fault	0

CO_2 Plume Geothermal Power Plant Assessment

Sedimentary basin geothermal reservoirs with mostly High to Very High potential ratings and corresponding deep well log information for saline reservoirs were assessed for CO_2 plume geothermal power plant generation. The amount of CO_2 that will be stored in the sedimentary geothermal basins was estimated under several power plant financing assumptions (e.g., Ogland-Hand et al. 2022). The power plant financing assumptions used in the analysis include: power plant capacity factor of 95%; annual operation and management costs of 5.5% of specific capitol cost; and capitol recovery factor of 5.2%.

As the deployment of sedimentary basin CO_2 plume geothermal power plants will ultimately be driven by a currently undetermined CO_2 policy (e.g., Section 45Q of the U.S. Tax Code [Credit for Carbon…2021], CO_2 prices), the modeling performed for the focused project is principally based on the lowest cost of CO_2 plume geothermal levelized cost of electricity. The rapid tool for carbon storage science, engineering, and economics (SCO_2T: Middleton et al. 2020a, 2020b) and the generalizable GEOthermal techno-economic simulator (genGEO; Ezekiel et al. 2024) with recent tool enhancements (Ogland-Hand et al. 2022) were used to calculate: a) the cost and storage capacity of CO_2 geological storage; and b) the cost, power generation capacity, and CO_2 requirements of CO_2 plume geothermal power plants.

Project Findings

Regional-Scale Sedimentary Basin Geothermal Reservoirs of Northern Nevada

A sixteen-fold rating classification ranging from None to Very High was generated from the three intrinsic parameter data layers to estimate the regional-scale sedimentary geothermal

potential in northern Nevada. This rating class system represents the sum of the three parameter ratings for each grid cell. The sixteen-fold rating classification can be generalized into four rating classes. The four-fold rating classes provides a simplification to assess the relative sedimentary basin geothermal potential including: None (<7); Moderate (7–10); High (10–13); and Very High (13–16; **Figure 70**).

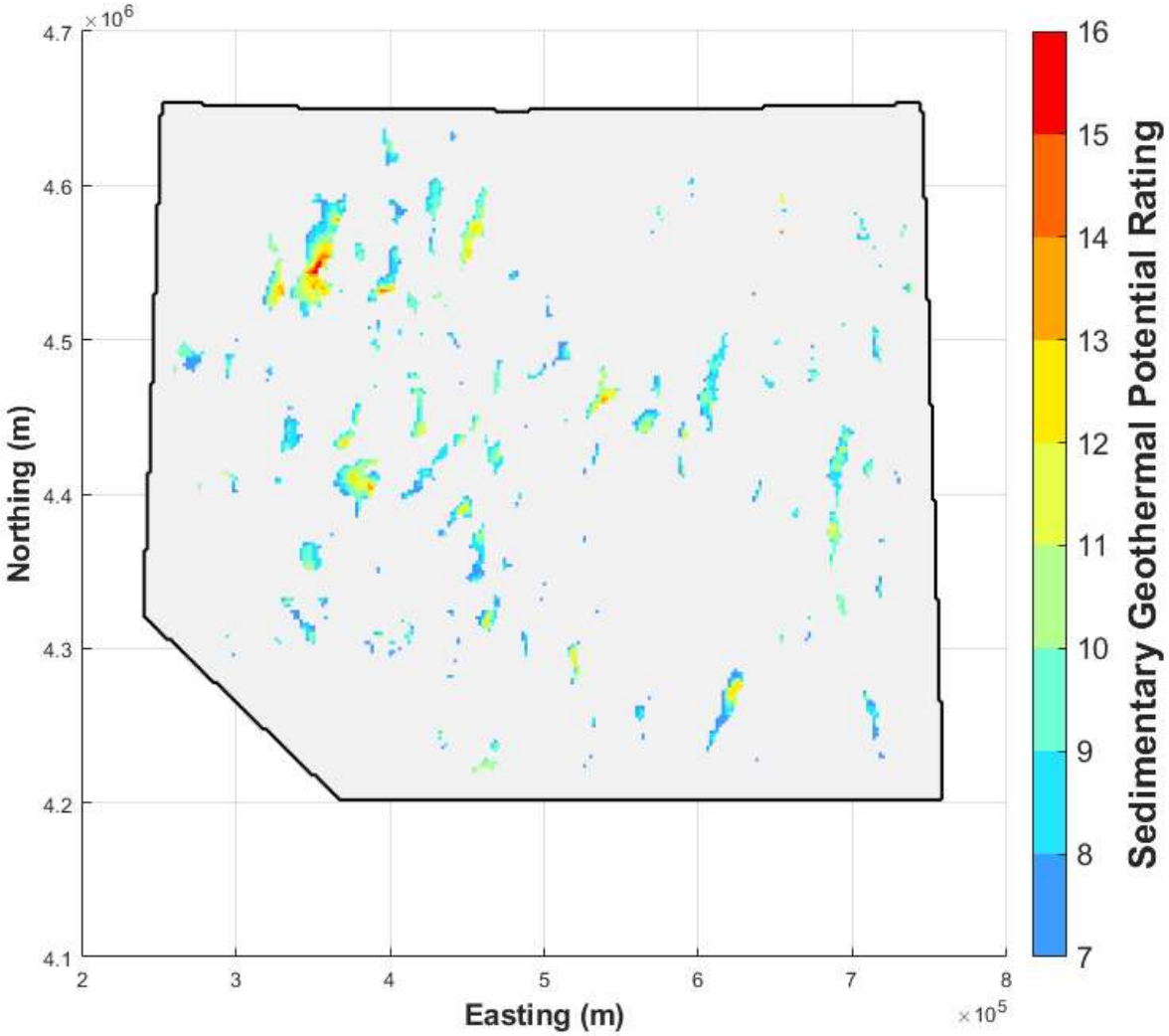


Figure 70 Map of sedimentary geothermal potential of northern Nevada. Rating classes are: None (<7); Moderate (7–10); High (10–13); and Very High (13–16). Five sedimentary basins with existing deep well log information are also shown.

Basin-Scale Sedimentary Basin Geothermal Reservoirs of Northern Nevada

Five sedimentary basins in northern Nevada with a range of sedimentary geothermal potential ratings were identified from the regional-scale assessment based on the basins having existing deep well log information (**Figure 71**). A basin-scale assessment of these areas was performed to (1) validate the regional-scale approach and (2) provide a site-specific feasibility assessment of using CO_2 plume geothermal geological storage and power generation in sedimentary basins.

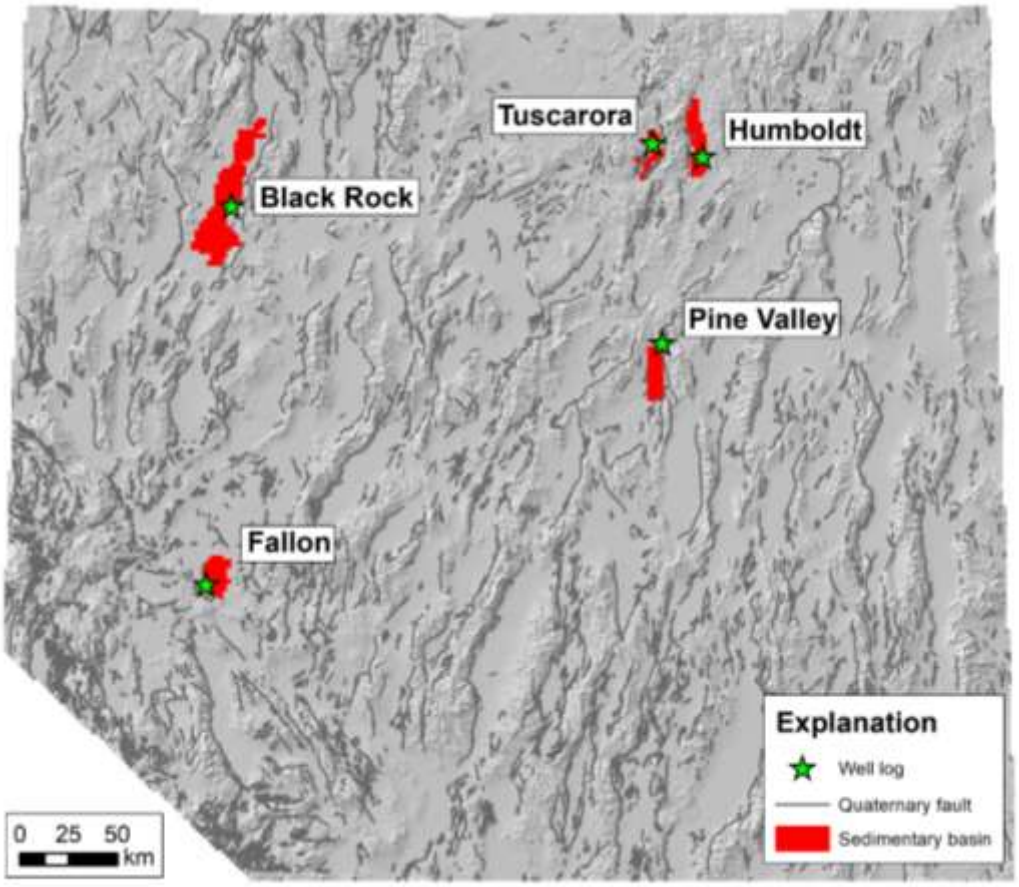


Figure 71 Map showing five sedimentary basins in northern Nevada that have a range of sedimentary geothermal potential ratings and existing deep well log information (see **Figure 70**). Quaternary faults are also shown.

Deep Well Log Information

Compared to other CUSP West states, Nevada has limited deep well log information appropriate for identifying and characterizing saline reservoirs below depths of 800 m. Of the limited number of deep wells, even fewer of these wells are in sedimentary basins having Moderate to Very High sedimentary geothermal potential. The five sedimentary basins that meet the criteria of having deep well log information and variable degrees of Moderate to Very High sedimentary geothermal potential include from west to east: Black Rock, Fallon, Tuscarora, Humboldt, and Pine Valley (**Figure 71**). Each basin consists of a single and complete geophysical well log that extends deeper than 800 m. Geophysical well logs were digitized, and resistivity, neutron porosity, and permeability were used to characterize aquifer properties and identify saline formations with salinities of 3,000 to >10,000 mg/L (see 50-km SCO_2T geologic input database). The five sedimentary basins have a wide range of sedimentary fill thickness, aquifer rock types, fault density, and geothermal gradients, which provide sufficient information to evaluate the accuracy of the regional-scale assessment, as well as assess the feasibility of using deep sedimentary basin CO_2 plume geothermal geological storage in northern Nevada.

Black Rock Sedimentary Basin Analysis

Of the five sedimentary basins identified in the regional-scale assessment, the Black Rock basin within the Black Rock Desert of northwestern Nevada was selected to be an example of a basin-scale assessment using site-specific reservoir property data. The basin was selected because of its relatively large size, has the highest sedimentary geothermal potential of the five basins evaluated (**Figure 72**), and has the highest temperature gradients in the region, ranging mostly from 60°C/km to 75°C/km (**Figure 73**).

Figure 72 Map of sedimentary geothermal potential within the Black Rock basin based on the regional-scale assessment. The extent of the 2-km grid coincides with depths greater than 1,950 m in the valley, which is the top of the first saline reservoir identified in the King Lear Federal No. 1-17 well log.

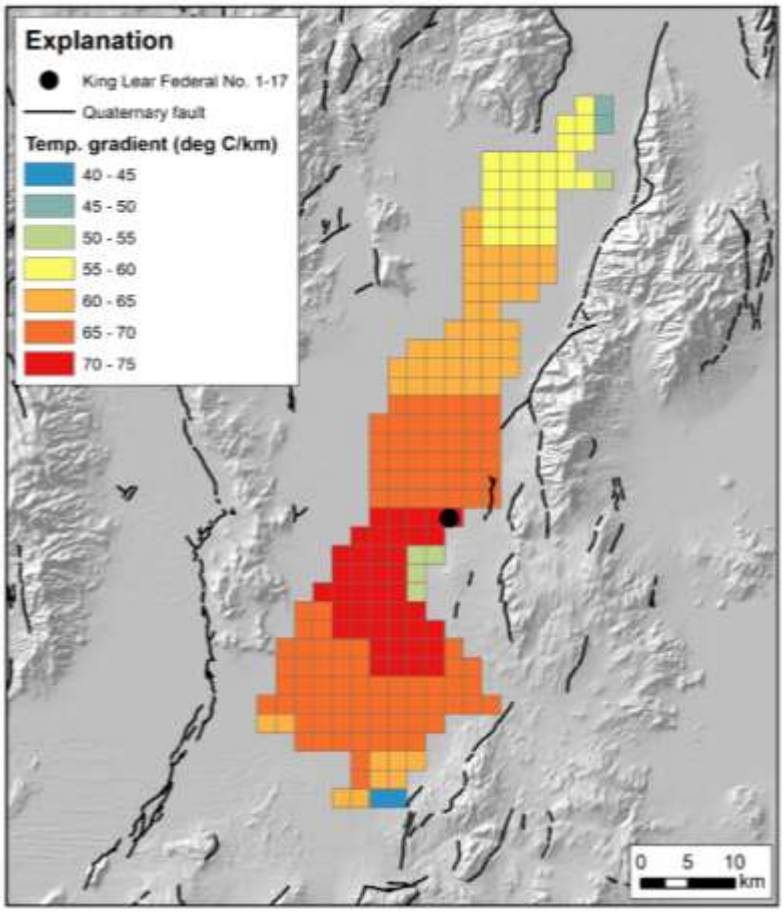


Figure 73 Map of geothermal temperature gradient within the Black Rock basin (Coolbaugh et al. 2005). The extent of the 2-km grid coincides with depths deeper than 1,950 m in the valley, which is the top of the first saline reservoir identified in the King Lear Federal No. 1-17 well log.

The Black Rock sedimentary basin is within a half graben formed between the west-dipping Jackson Mountains and Black Rock fault zones (**Figure 71** and **Figure 72**). The Black Rock sedimentary basin is the largest of the five basins evaluated. The basin has an area of 912 km^2 that was determined from the spatial extent of sedimentary fill thickness between the depths of

1,950 and 2,130 m. These depths coincide with an upper approximately 60-m thick saline formation (reservoir 1) composed of Miocene interbedded lacustrine siltstone and claystone and a lower approximately 120-m thick saline formation (reservoir 2) consisting of Miocene lacustrine siltstone with lesser interbeds of limestone and tuffaceous siltstone that were identified in a geophysical well log from the east-central sector of the basin (King Lear Federal No. 1-17 [API# 27-013-05002]; Table 12; **Figure 73**).

Table 12 Reservoir property data from analysis of geophysical log of the King Lear Federal No. 1-17 well (API# 27-013-0

Reservoir no.	Depth top (m)	Depth bottom (m)	Net thickness (m)	Mean porosity (fraction)	Minimum porosity (fraction)	Maximum porosity (fraction)	Mean permeability (mD)	Minimum permeability (mD)	Maximum permeability (mD)	Me sali (mg
1	1,951	1,981	30	0.288	0.265	0.299	1,630.1	1,043.3	1,969.5	9,0
1	1,981	2,012	30	0.288	0.263	0.300	1,622.1	1,003.1	2,004.9	11,(
2	2,012	2,042	30	0.276	0.242	0.299	1,308.0	653.9	1,969.5	11,2
2	2,042	2,073	30	0.260	0.241	0.294	953.8	640.2	1,800.3	11,1
2	2,073	2,103	30	0.257	0.223	0.300	934.3	432.1	2,004.9	10,2
2	2,103	2,133	30	0.272	0.242	0.300	1,235.1	653.9	2,004.9	11,(

Given the tectonic setting of the Black Rock basin, it is likely that the Miocene rocks are fractured having increased fracture density proximal to fault zones. Future work could also incorporate a discrete fracture network analysis that would account for a grid cell's distance from nearby fault zones. The discrete fracture network analysis could provide additional reservoir property information in terms of spatial variations in fracture density of the rock mass, which in turn can be used to provide insights on potential changes in hydraulic conductivity and permeability relative to fault distance (e.g., Jiang et al. 2025). Furthermore, a major assumption in the basin-scale analysis is the saline formations and associated aquifer properties identified in the well log are laterally and vertically continuous throughout the entire basin. As a result, long-term basin evolution and spatial variations in reservoir properties driven by tectonic ground deformation was not explicitly accounted for in the analysis.

Assessment of Low-Cost CO_2 Plume Geothermal Power Generation

Analysis of greenfield levelized cost of electricity of CO_2 plume geothermal development was performed to assess the feasibility of using deep sedimentary basin geothermal for power generation in the Black Rock sedimentary basin. Reservoir properties for two stacked saline formations of interbedded claystone and siltstone (depth: 1,950–2,012 m) and siltstone and limestone with tuffaceous siltstone (depth: 2,010–2,130), along with geothermal temperature gradient (**Figure 73**) were used with the SCO_2T and genGEO computational tools (Ogland-Hand et al. 2022) to identify sectors of the Black Rock basin with the lowest-cost power generation.

The range of levelized cost of electricity in the basin was estimated for the stacked saline formations. Analysis was performed at depths between 1,950 and 1,980 m for reservoir 1 and at depths between 2,010 and 2,100 m for reservoir 2 (**Figure 74**). The range of depths analyzed is

reflective of each reservoir's different aquifer properties and geothermal temperature gradients (Table 12 and **Figure 73**). In general, a deep and thick saline formation with high permeability and a high temperature gradient result in low-cost CO_2 plume geothermal power and in turn, low-cost geologic CO_2 storage. The results of the assessment are promising and show that most of the basin has the potential for low-cost CO_2 plume geothermal power generation ranging from \$70/MWh to \$80/MWh to less than \$70/MWh (**Figure 74**).

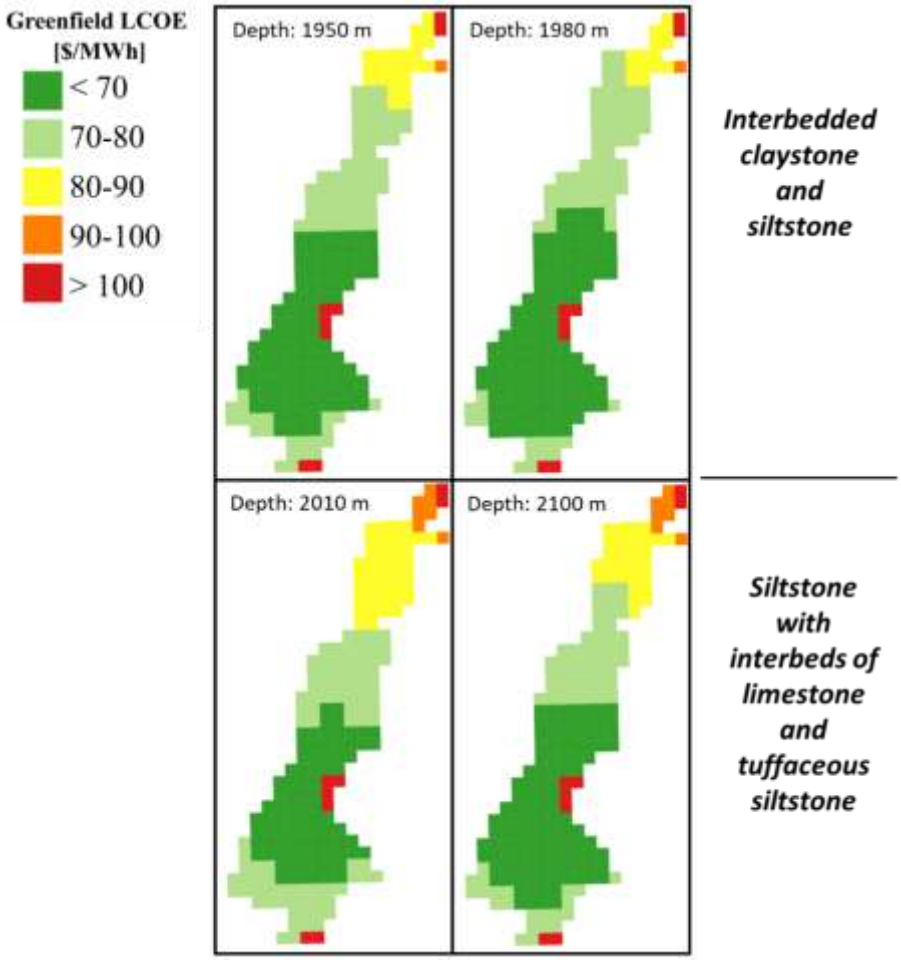


Figure 74 Maps showing greenfield levelized cost of electricity of CO_2 plume geothermal power generation for two stacked saline formations of the Black Rock sedimentary basin. The saline formations consist of an upper reservoir composed of Miocene interbedded claystone and siltstone at depths between 1,950 and 1,980 m; and a lower reservoir of Miocene siltstone with interbeds of limestone and tuffaceous siltstone at depths between 2,010 and 2,100 m.

Summary and Conclusions

The scope of the CUSP focused project is to perform a regional assessment of the CO_2-geological storage in sedimentary basin geothermal reservoirs of northern Nevada. Both regional- and basin-scale assessments of the geothermal favorability in the state have previously been made. However, there are currently no published regional-scale assessments of CO_2 geological storage in sedimentary basin geothermal reservoirs of Nevada; and previous preliminary assessments of the potential for CO_2 geological storage in the state did not consider

using geologically stored CO_2 as a subsurface heat extraction fluid for geothermal electricity generation.

The goal of the CUSP focused project is to provide an initial "first cut" regional-scale assessment of the potential for CO_2 geological storage in sedimentary basin geothermal reservoirs to fill a data gap of critical information related to CCUS technologies to mitigate CO_2 emissions in Nevada. The regional assessment was based on the integration of 2-km grid resolution geospatial datasets of geologic and geothermal information to identify areas that are favorable for deep sedimentary basin CO_2 plume geothermal geological storage. From the regional assessment, five sedimentary basins were identified for basin-scale assessments based on the presence of deep well log geophysical data that were previously analyzed for the Nevada CUSP project to characterize reservoir properties. The reservoir property data was then used as model input parameters for the SCO_2T and genGEO computational tools to characterize (1) the cost and storage capacity of CO_2 geologic storage and (2) the power capacity and cost of greenfield CO_2 plume geothermal power generation.

Analysis of the Black Rock basin was performed as a proof-of-concept of a basin-scale assessment. The analysis shows that sedimentary basins with Moderate to Very High sedimentary geothermal potential, geothermal gradients of less than 55°C/km, and interbedded claystone and siltstone saline formations with salinities ranging from approximately 6,000 to 25,600 mg/L have the lowest cost of CO_2 plume geothermal levelized cost of electricity, ranging from $80/MWh to $70/MWh to less than $70/MWh.

The regional-scale assessment of sedimentary geothermal potential provided a useful dataset to identify areas for more detailed basin-scale assessments of low-cost CO_2 plume geothermal power generation where deep well log information is available. The results of the focused project provide an alternative CCUS capability for Nevada, as well as a methodology that could be used to assess the favorability of CO_2 geological storage at both regional- and basin-scales in other CUSP states with sedimentary basin geothermal resources.

References

Coolbaugh M, Zehner R, Kreemer C, Blackwell D, Oppliger G, Sawatzky D, Blewitt G, Pancha A, Richards M, Helm-Clark C, et al. 2005. Geothermal potential map of the Great Basin, western United States. Reno (NV); Nevada Bureau of Mines and Geology. Map 151a. Scale 1:1,000,000. With geospatial data. [accessed 2025 Dec 23]. https://pubs.nbmg.unr.edu/Geoth-potential-map-Great-Basin-p/m151.htm

Credit for Carbon Oxide Sequestration, U.S.C.-2023 26 C.F.R. §1.45Q-1 (2021).

dePolo CM, Johnson GL, Price JG, Mauldin JM. 2009. Quaternary faults in Nevada—online interactive map. Reno (NV); Nevada Bureau of Mines and Geology. Open-File Report 2009-09. [accessed 2025 Dec 23]. https://maps.nbmg.unr.edu/QuaternaryFaults/

Ezekiel J, Vahrenkamp V, Hoteit HA, Finkbeiner T, Mai PM. 2024. Techno-economic assessment of large-scale sedimentary basin stored-CO_2 geothermal power generation. Appl Energy. 376(Pt B):124270. doi:10.1016/j.apenergy.2024.124270

Faulds JE, Hinz N, Kreemer C, Coolbaugh M. 2012. Regional patterns of geothermal activity in the Great Basin region, western USA: correlation with strain rates. Geotherm Resour Counc Trans. 36:897–902.

Iovenitti J, Ibser FH, Clyne M, Sainsbury J, Callahan O. 2016. The Basin and Range Dixie Valley geothermal wellfield, Nevada, USA—a test bed for developing an enhanced geothermal system exploration favorability methodology. Geothermics. 63:195–209. doi:10.1016/j.geothermics.2016.01.001

Jiang X, Wang Z, Na J, Sun Z, Hu T. 2025. Application of coupled discrete fracture–equivalent porous medium model for groundwater flow simulations in fault zones. Eng Geol. 357:108335. doi:10.1016/j.enggeo.2025.108335

Middleton RS, Chen B, Harp DR, Kammer RM, Ogland-Hand JD, Bielicki JM, Clarens AF, Currier RP, Ellett KM, Hoover BA, et al. 2020a. Great SCO_2T! rapid tool for carbon sequestration science, engineering, and economics. Appl Comput Geosci. 7:100035. doi:10.1016/j.acags.2020.100035

Middleton RS, Ogland-Hand JD, Chen B, Bielicki JM, Ellett KM, Harp DR, Kammer RM. 2020b. Identifying geologic characteristics and operational decisions to meet global carbon sequestration goals. Energy Environ Sci. 13(12):5000–5016. doi:10.1039/D0EE02488K

Ogland-Hand JD, Adams BM, Bennett JA, Middleton RS. 2022. A geospatial cost comparison of CO_2 plume geothermal (CPG) power and geologic CO_2 storage. Front Energy Res. 10:855120. doi:10.3389/fenrg.2022.855120

Pachauri AK, Pant M. 1992. Landslide hazard mapping based on geological attributes. Eng Geol. 32:81–100. doi:10.1016/0013-7952(92)90020-Y

Penfield R, Shevenell L, Garside L, Zehner R. 2010. Nevada geothermal resources. Reno (NV); Nevada Bureau of Mines and Geology. Map 161. Scale 1:750,000. With geospatial data. [accessed 2025 Dec 23]. https://pubs.nbmg.unr.edu/Nevada-geothermal-resources-p/m161.htm

Ponce DA. 2004. Geophysical methods and applications. In: Wallace AR, editor. Assessment of metallic mineral resources in the Humboldt River basin, northern Nevada. Reston (VA); U.S. Geological Survey. Bulletin 2218. Chapter 6. Digital data. [accessed 2025 Dec 23]. https://pubs.usgs.gov/bul/2218/

Price DG. 2009. Engineering geology principles and practice. Berlin (Germany); Springer-Verlag. 450 p.

Price JG, Hess RH, Fitch S, Faulds JE, Garside LG, Shevenell L, Warren S. 2005. Preliminary assessment of the potential for carbon dioxide disposal. Reno (NV); Nevada Bureau of Mines and Geology. Report 51z. With geospatial data. [accessed 2025 Dec 23]. https://pubs.nbmg.unr.edu/CO2-disposal-assessment-p/r051z.htm

Shah AK, Boyd OS. 2018. Depth to basement and thickness of unconsolidated sediments for the western United States—initial estimates for layers of the U.S. Geological Survey National Crustal Model. Reston (VA); U.S. Geological Survey. Open-File Report 2018-1115. 13 p. doi:10.3133/ofr20181115

Stewart JH, Carlson JE. 1978. Geologic map of Nevada. Reston (VA); U.S. Geological Survey. State Geologic Map Series. Scale 1:500,000. Prepared in cooperation with Nevada Bureau of Mines and Geology. [accessed 2025 Dec 23]. https://pubs.usgs.gov/map/i-1136/

[USGS] U.S. Geological Survey. 2008. Assessment of moderate- and high-temperature geothermal resources of the United States. Reston (VA); U.S. Geological Survey. Fact Sheet 2008-3082. With digital data. [accessed 2025 Dec 23]. https://pubs.usgs.gov/fs/2008/3082/

[USGS/NBMG] U.S. Geological Survey and Nevada Bureau of Mines and Geology. 2016. Quaternary fault and fold database for the United States. Reston (VA)/Reno (NV); U.S. Geological Survey & Nevada Bureau of Mines and Geology. [accessed 2026 Jan 5]. https://earthquake.usgs.gov/hazards/qfaults

Zhang L, Li D, Ren B, Cui G, Zhuang Y, Ren S. 2014. Potential assessment of CO_2 geological storage in geothermal reservoirs associated with heat mining: case studies from China. Energy Procedia. 63:7651–7662. doi:10.1016/j.egypro.2014.11.799

Characterization of CO_2 Storage Potential in Harquahala Basin, Western Central Arizona *on page 169.*

Subtask 4.5.2 – Regional-Scale Assessment of CO_2 Geological Storage in Sedimentary Basin Geothermal Reservoirs of Nevada

See Within Rio Arriba County, New Mexico, the Entrada Sandstone is both an oil reservoir, a salt water disposal target, and a potential CO_2 injection target. Since the oil reservoirs have been mostly played out, new life for the reservoir is a target for CO_2 sequestration. A potential source of the CO_2 is from the potential retrofitting "Blue Hydrogen" Escalante Power Plant (**Figure 33**). The plant will create hydrogen from natural gas while sequestering 97% of its CO_2 emissions.

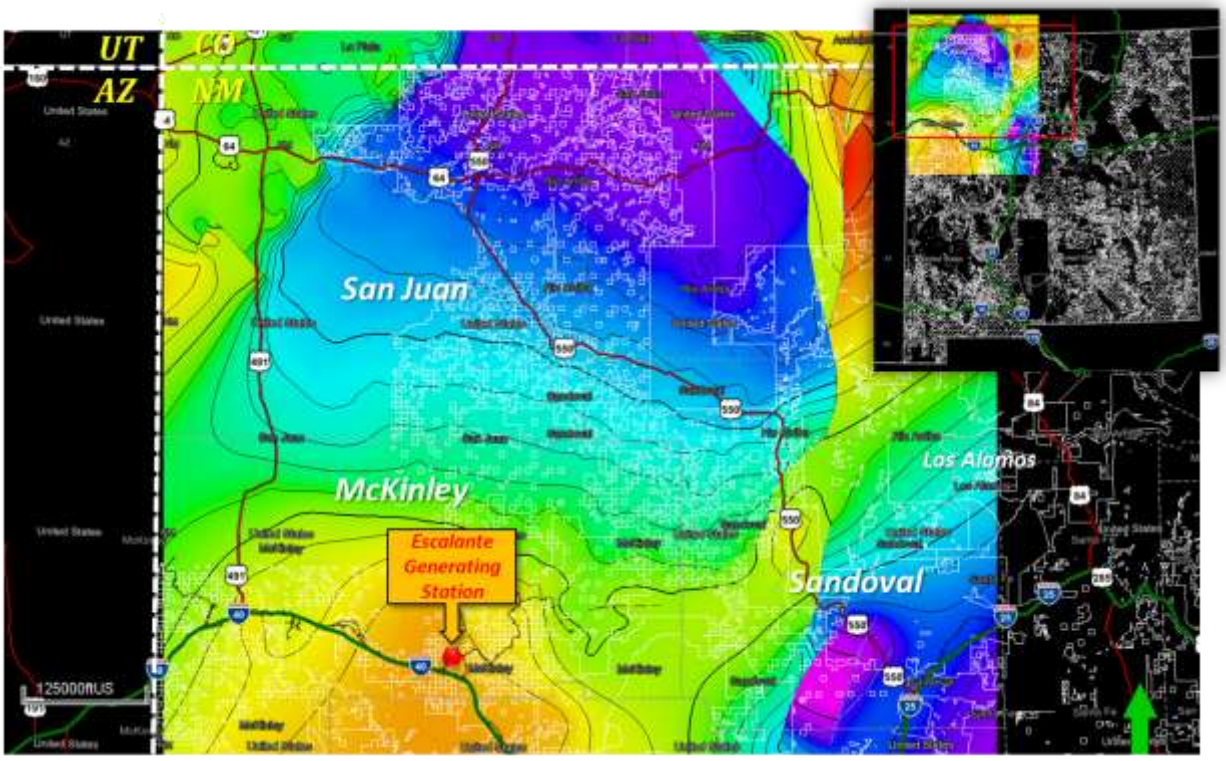


Figure 33. Subsea structure map on the Entrada Sandstone for the San Juan Basin showing the location of the Escalante Power Station.

Geologic Model

The primary reservoir identified in the area is the Jurassic Entrada Sandstone (**Figure 34**). The Entrada Sandstone is a large eolian sand erg that covers the northwestern part of New Mexico. It consists of very fine- to medium-grained sandstones that are composed of quartz and subordinate feldspars and lithic rock fragments. Potential secondary reservoirs include the Jurassic Bluff Sandstone, another eolian deposit, and the Salt Wash Member of the Morrison Formation. Bluff deposits are like the Entrada Sandstone, but they may have undergone more extensive cementation. The Salt Wash deposits consist of alluvial fan and plain sediments associated with widespread, braided stream complexes.

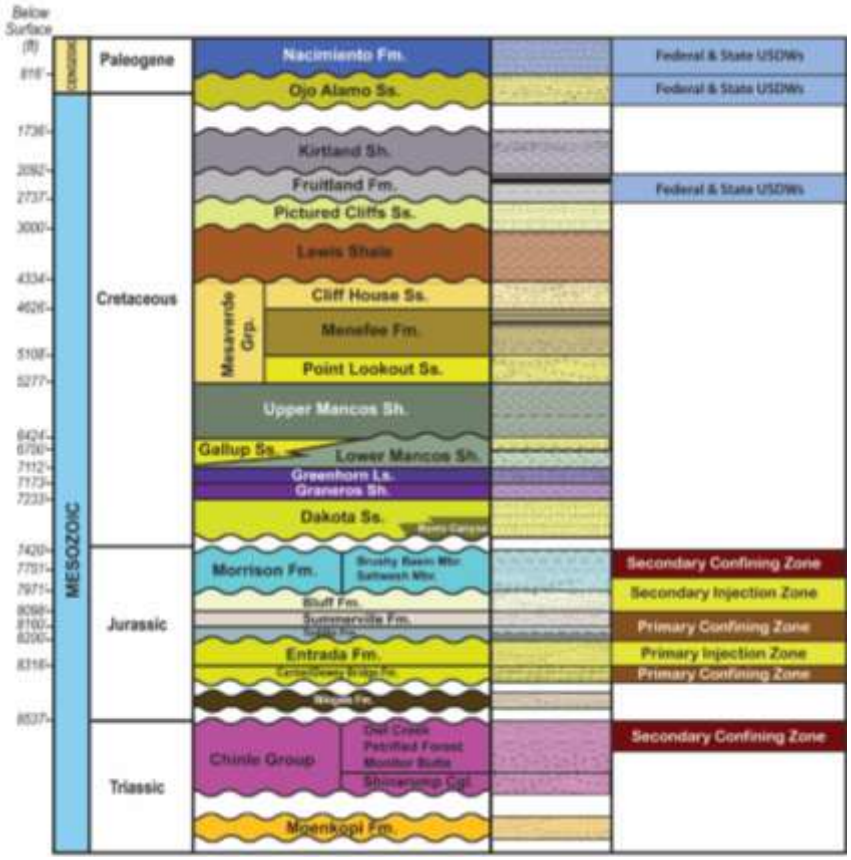


Figure 34. Stratigraphic column for the Mesozoic to Cenozoic section in the San Juan Basin.

The primary seals for the Entrada Sandstone are the overlying Todilto and Summerville Formations and the underlying Carmel Formation. The Todilto Formation fills the relief on top of the Entrada dune fields and was deposited as part of a complex coastal salina where marine and freshwater interacted. Todilto deposits consists of algally-laminated limestones with anhydrite nodules, high-energy coastal carbonates to massive anhydrite deposits. The Summerville deposits represent a change from the tidal flats to fluvial and lacustrine depositional environments. Sediments include very fine-grained sandstones, siltstones, mudstones and limestones. The Carmel Formation represents widespread sabkha deposits in the San Juan Basin and are composed of siltstones and mudstones. The secondary seal, for the Bluff and Salt Wash units, is the Brushy Basin Member of the Morrisson Formation. The Brushy Basin deposits represent a change to fluvial and lacustrine sedimentation. They have isolated fluvial sandstone channels encased by mudstones and siltstones, making it a good potential seal.

A geologic model was constructed in IHS Kingdom© based on well logs tops that were all hand-picked (**Figure 35**). For each of the units, subsea structure and isopach maps were constructed. Since the primary injection target is the Entrada Sandstone, included in the report are the maps for the Entrada to Summerville units (**Figure 36** to **Figure 38**). These surfaces, and the others created in the geologic model, were then utilized for the simulation model.

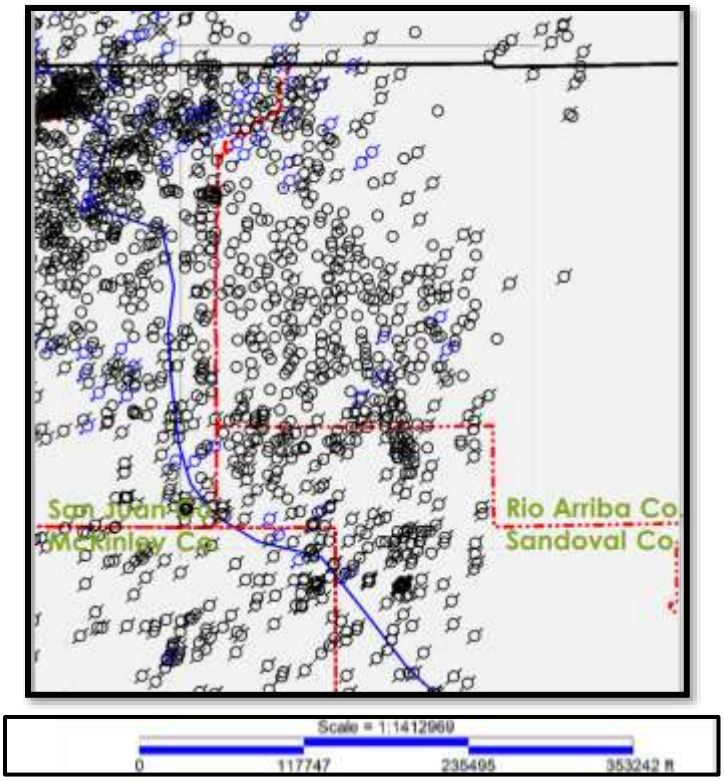


Figure 35. Base map showing the distribution of wells used for this study. The blue line is Cortez CO_2 pipeline.

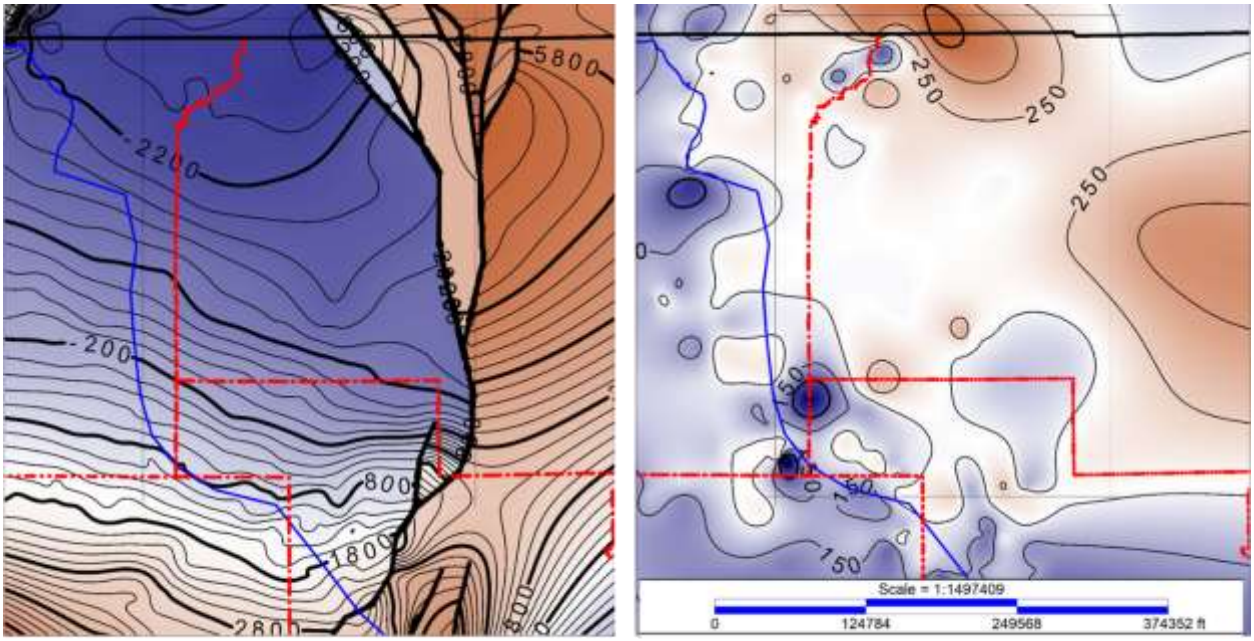


Figure 36. Entrada Sandstone subsea structure and isopach maps. The contour interval (CI) = 200 feet for the structure map and CI = 50 feet for the isopach map. The blue line is the Cortez Pipeline on this and subsequent figures. The subsea maps show the numerous faults that bound the eastern margin of the San Juan Basin and make up the Nacimiento uplift and Archuleta Anticlinorium.

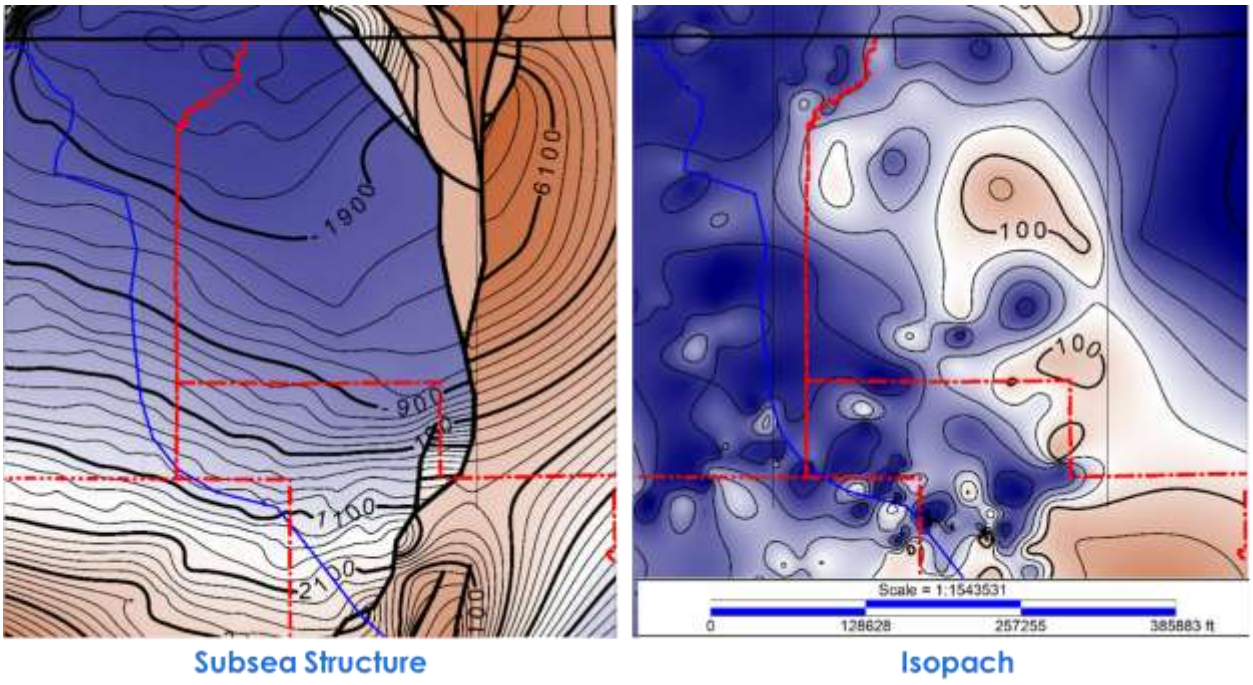


Figure 37. Todilto Formation subsea structure and isopach maps. The CI = 200 feet for the structure map and CI = 20 feet for the isopach map.

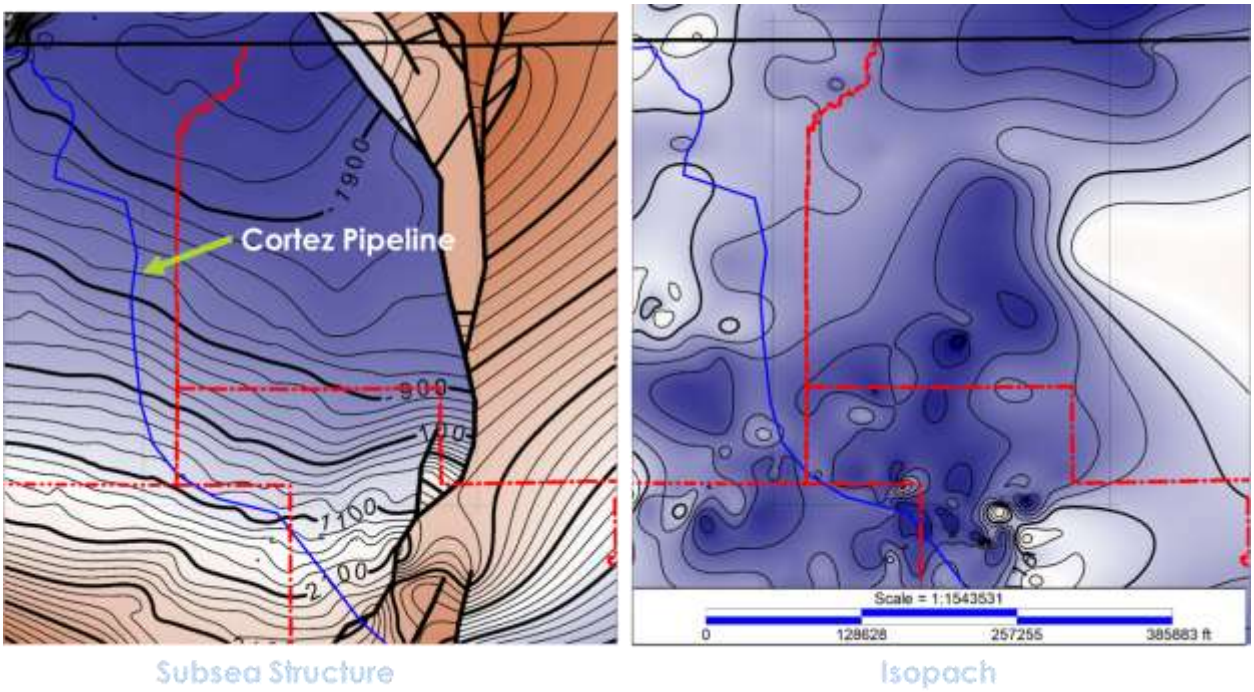


Figure 38. Summerville Formation subsea structure and isopach maps. The CI = 200 feet for the structure map and CI = 15 feet for the isopach map.

Due to several small oil fields occurring with the study area, core is available (**Figure 39**). Therefore, the Entrada Sandstone is relatively well characterized in the area with both thin section and porosity and permeability data available. The porosity and permeability data will be discussed in the model section, but it should be noted that internally, porosity and permeability vary in the Entrada Sandstone (**Figure *40***). Some logs indicate a thin zone of tight Entrada just below the contact with the Todilto Formation. This is followed by a zone of high porosity (thickness varies by well), and in the lower part of the unit, the porosity and permeability decrease with depth. This is easily seen in thin sections from the San Luis Federal #001 core (**Figure 41** and **Figure 42**).

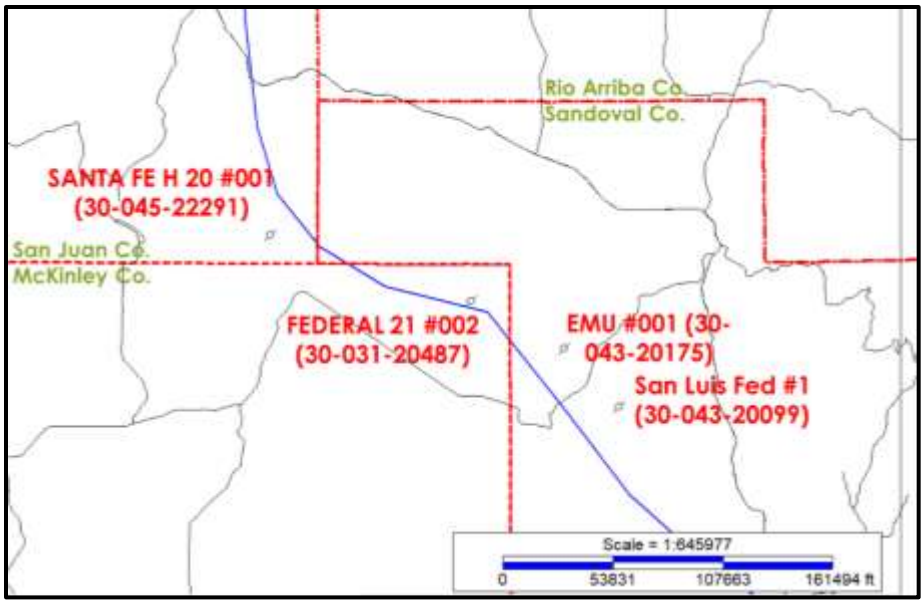


Figure 39. Map showing available cores in the area. The blue star is the approximate location of the recommended injection well.

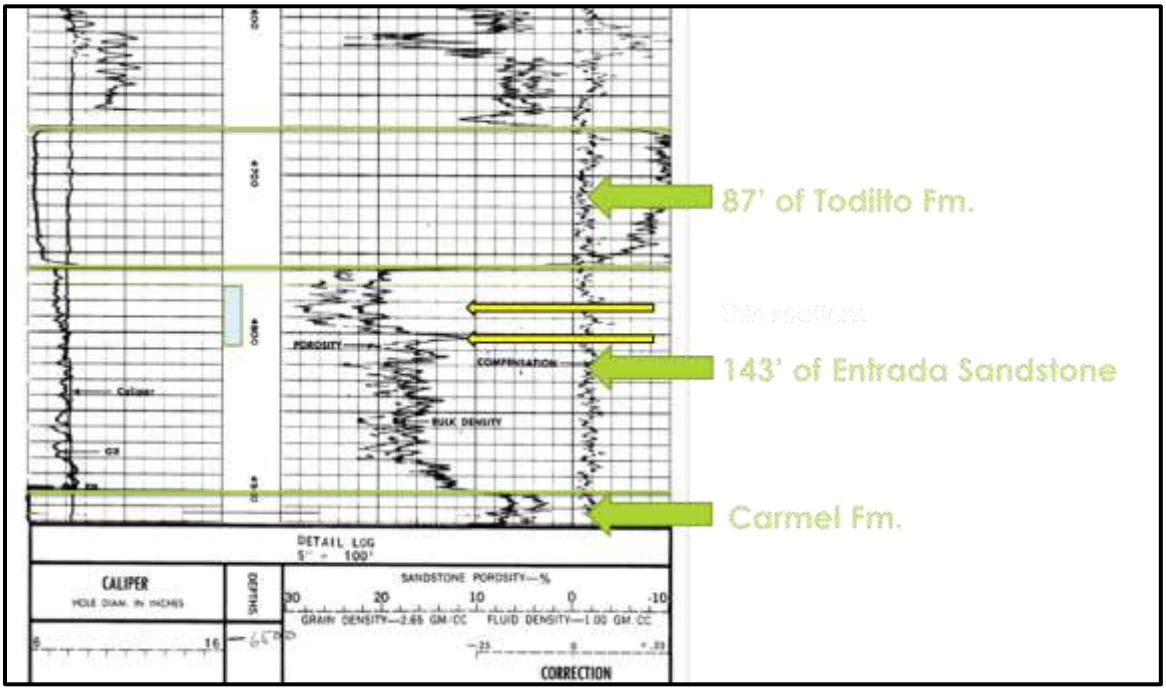


Figure 40. Log from the San Luis Federal #001 (30-043-20099) showing the 87 feet of tight Todilto Formation, followed by a zone of variable porosity in Entrada Sandstone.

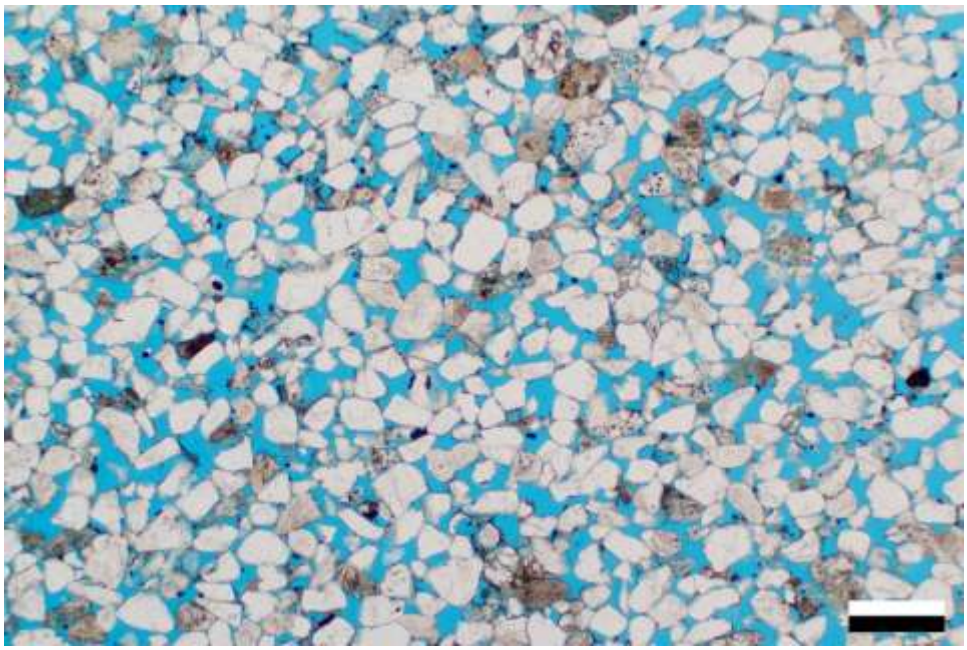


Figure 41. A plane-light photomicrograph of the Entrada Sandstone from a core in the southeastern part of the San Juan Basin in Sandoval Co., NM (San Luis Federal #1, 4,778 feet). This view contains quartz grains (white grains), feldspars (gray grains) and rock fragments (dark grains). This sample is from a dune structure in the core. Quartz overgrowths are present on a few grains, but otherwise there is little or no cement. This sample has an average porosity of 22.2%; most of the porosity is likely primary porosity, but there are numerous pores with very rounded outlines that may be a result of grains being dissolved producing secondary porosity. Scale bar = 0.51 mm.

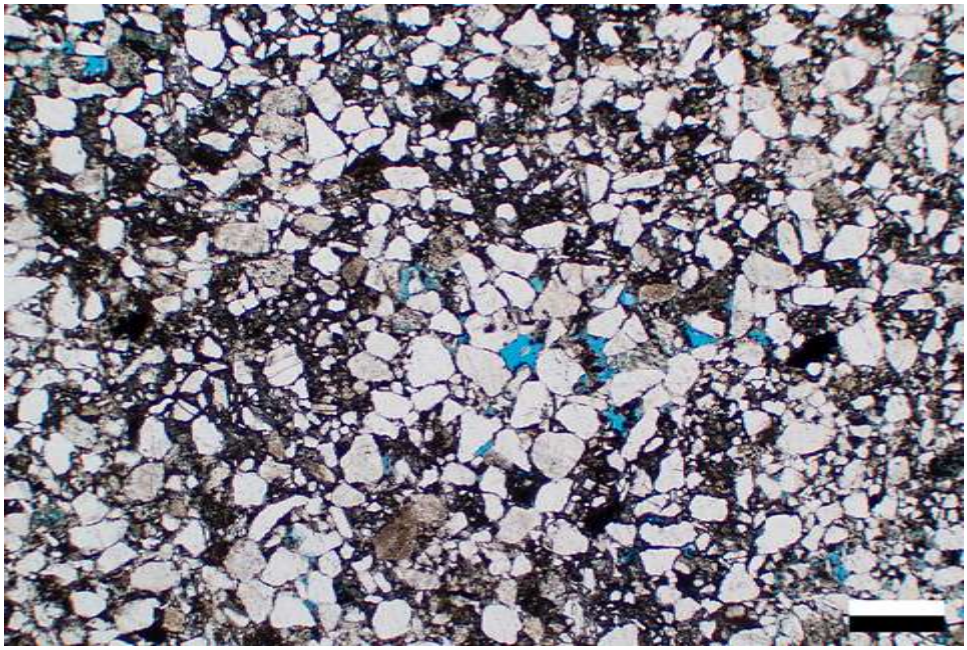


Figure 42. A plane-light photomicrograph of a sample from a tight zone of the Entrada Sandstone (San Luis Federal #1, 4,793 feet) containing quartz and feldspar grains, and rock fragments. This sample has an average porosity of 3.5%. This sample was likely deposited in an interdunal setting. Note the abundance of finer-grained material in this slide. Compaction has destroyed most of the porosity that was present in the sample. Scale bar = 0.51 mm.

In addition, analyses of produced waters indicate that the reservoir is a saline aquifer. and would not be an injection issue for going forward with detailed simulation models (**Figure 43**).

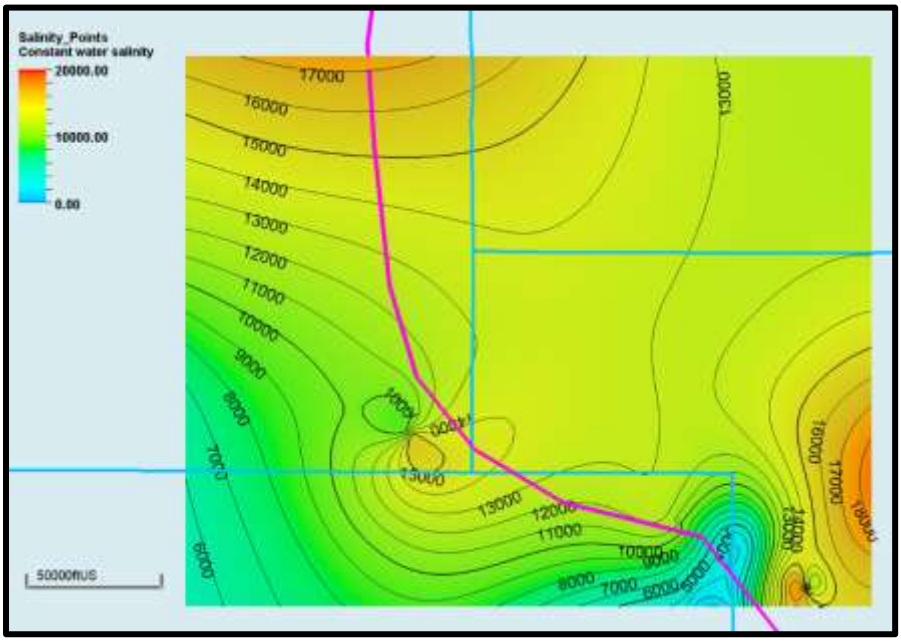


Figure 43. A contour map of total dissolved solids in produced waters within the study area.

Overall, the geologic analyses indicates that the Entrada Sandstone would be an excellent injection zone. The Bluff Sandstone and Salt Wash Member also have potential as sequestration targets, though their injection zones and associated seal's geology is less understood due to the lack of coring and porosity and permeability analyses.

Reservoir Model

Compositional reservoir simulator CMG-GEM was used to simulate the storage scenarios, and CMG-RESULTS and REPORT were used to quantitively evaluate the simulation results. The trapping mechanisms considered are geo-structural trapping, hysteresis trapping, and solubility trapping. Reservoir rock types, and fluid properties from San Juan Basin Entrada reservoir was used. As a result, the simulation group was able to analyze a simulation scenario that stores 45 Mt CO_2 over 30 yr working with the industrial partners. The proposed final development strategies will inject into Entrada Sandstone only.

The domain of the current model remains to be 60.9 miles by 57.1 miles square (**Figure 44 and Figure 45**). The grids distribute in I, J, K directions are 311 X 330 X 15 with 1,539,450 cells in total, 1,000 square feet grid size in average. It consists of seven (5) geological zones, where 'Salt Wash', 'Bluff', and 'Entrada' are the potential storage zones. The reservoir initial conditions and trapping mechanisms stay the same as the last version of the model. Carter-Tracy limited reservoir was assigned to the boundary of the simulation domain to mimic infinite reservoir response. Mid-depth (-1,850 ft – MSL, 7,760 ft - KB) reservoir pressure 3,314 psi was calculated with the pore pressure gradient of 0.427 psi/ft. The reservoir temperature was calculated to be 85.83 Celsius degree. The P-T condition was used to compute the fluid model by Peng-Robinson Equation of State in the CMG-WinProp module. Irreducible water saturation of 0.55 is used to

generate the relative permeability curves for the gas-water system (**Figure 46**). The reservoir is assumed to be initially saturated with 100% brine and exhibit hydrostatic equilibrium.



Figure 44. Aerial view of the simulation model boundary over the state map.

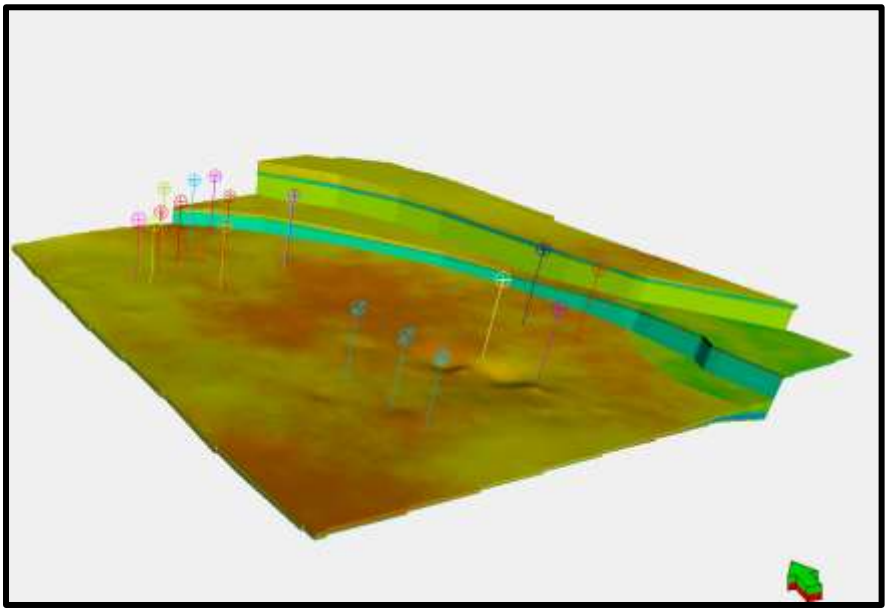


Figure 45. 3D view of the simulation model with SWDs and fault models considered.

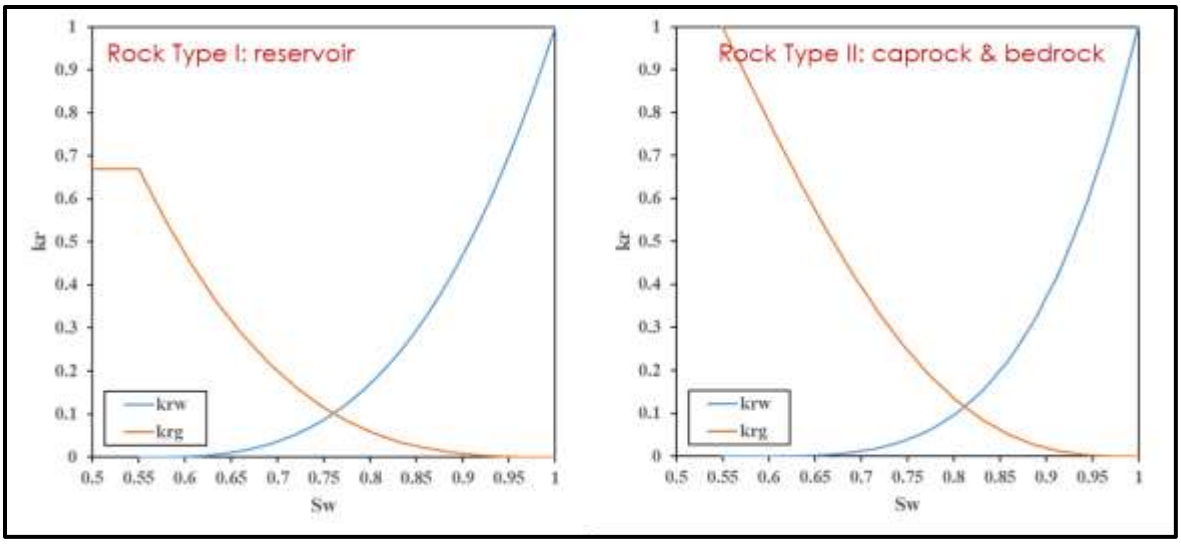


Figure 46. Relative permeability used in the reservoir simulation.

Based on the estimated maximum allowable gas injection rate per well, it is set as the primary control. Each injector is set to 1.5 Mt/yr or 79,210,173 standard cubic feet per well per day. The target is to inject CO_2 over 30 yr period. The schedule of each simulation run can be categorized into three phases: (1) history matching (1990 to 2023), (2) CO_2 injection (2023 to 2053), and (3) post-injection site care (2053 to 2073). The formations of injection are selected to be Entrada without because it is noted that Salt Wash and Bluff are beneficial to serve as a buffer zone. During the injection, Salt Wash formation prevents the CO_2 from being pushed into the caprock layer due to the high bottom hole pressure. During the PISC period, the buffer zone of Salt Wash enables the CO_2 to migrate upward while interacting with the formation solution and matrix that more CO_2 can be securely trapped by solubilization and capillary hysteresis effect. The secondary control is the maximum bottom hole pressure. It is set to equal to 5,000 psi which is estimated by the fracture gradient of 0.6 psi/ft, calculated at the shallowest perforation depth to ensure safe injection operations.

According to the well database from the State of New Mexico Oil Conservation Division, 13 Saltwater Disposal (SWD) wells that penetrate Entrada and with historical water injection data are imported into the model domain (**Table 7**). The simulation model set the injection rate as the primary constrain for SWDs. The wellhead injection pressure limit and historical wellhead pressure are converted to bottom hole pressure through an in-house program for SWDs. The purpose of this step is to justify the permeability and porosity realizations populated through statistic calculation with available core plug samples and correlations (**Table 8** and **Figure 47**).

Table 7. Petrophysical properties used for zones of the simulation model.

	Porosity, dec	Permeability, md	Average Thickness, ft
Salt Wash	0.17 to 0.23	1.9 to 21.7	287
Bluff	0.16	1.026	91
Summerville	0.04	0.006	75

Todilto	0.01	0.002	48
Entrada	0.01 to 0.25	0.01 to 507.13	100

Table 8. Active saltwater disposal wells considered in the model validation.

API	Well Name	Latitude	Longitude	TVD (ft)	Well Type	Status
3003930148	CARRACAS SWD #002	36.997990	-107.250952	9334	SWD	
3003924278	CARRACAS UNIT 27 A #082	36.953957	-107.343425	10060	SWD	Active
3003926868	CARSON SWD #001	36.787414	-107.230275	9590	SWD	
3003926214	EUL CANYON SWD #1	36.961603	-107.414712	9235	SWD	
3003925465	JILLSON FEDERAL SWD #001	36.325713	-107.180083	8800	SWD	Active
3003924236	NORTHEAST BLANCO UNIT SIMS MESA	36.830393	-107.564145	8956	SWD	Active
3003927055	ROSA UNIT SWD #001	36.884527	-107.426675	9176	SWD	
3003930812	ROSA UNIT SWD #002	36.870988	-107.314770	9334	SWD	
3003923231	RUCKER LAKE #002	36.380128	-107.004781	8975	SWD	Active
3003924807	SAN JUAN 29 6 UNIT SWD #301	36.748372	-107.423891	9112	SWD	Active
3003924518	SAN JUAN 30 6 UNIT #002	36.804575	-107.546728	8930	SWD	Active
3003924549	SAN JUAN 31 6 UNIT #301	36.846163	-107.502143	9040	SWD	Active
3003922756	SIMMS FEDERAL #001	36.809108	-107.202985	9731	SWD	Active

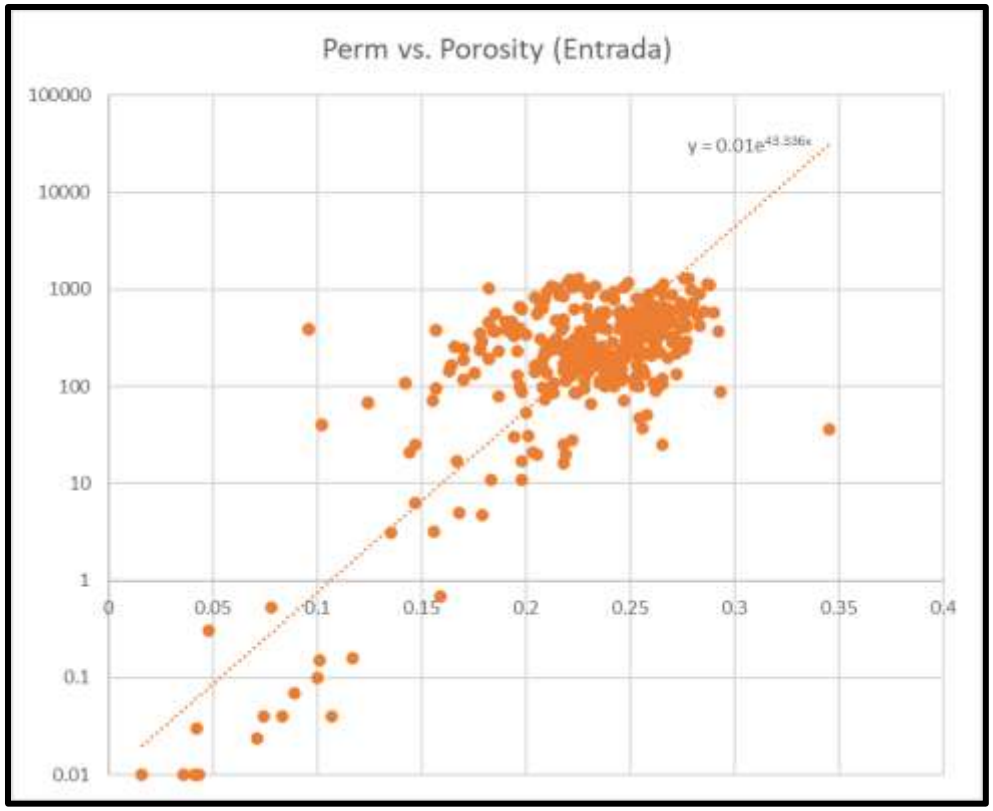


Figure 47. Petrophysical properties correlation from core plug samples.

Some representative results of the history matching are shown in **Figure 48** to **Figure 49**. The history results can be categorized into good matched. There following observations are from the history matching phase: 1) some literature indicates that the area of Entrada formation in the San Juan Basin maybe naturally fractures, which may result in parts of the region recorded better injectivity than others. As this project goes further, the geology characterization of the San Juan Basin will be better addressed, which is part of the significance of this ongoing project; 2) some wells may experience near-wellbore skin effects from formation damage and perforations. If this is true, the injectivity can be adjusted by assigning positive skin factors to certain wells; and 3) as the earliest historical data were from three decades ago, some of the records may need quality checks and adjustment.

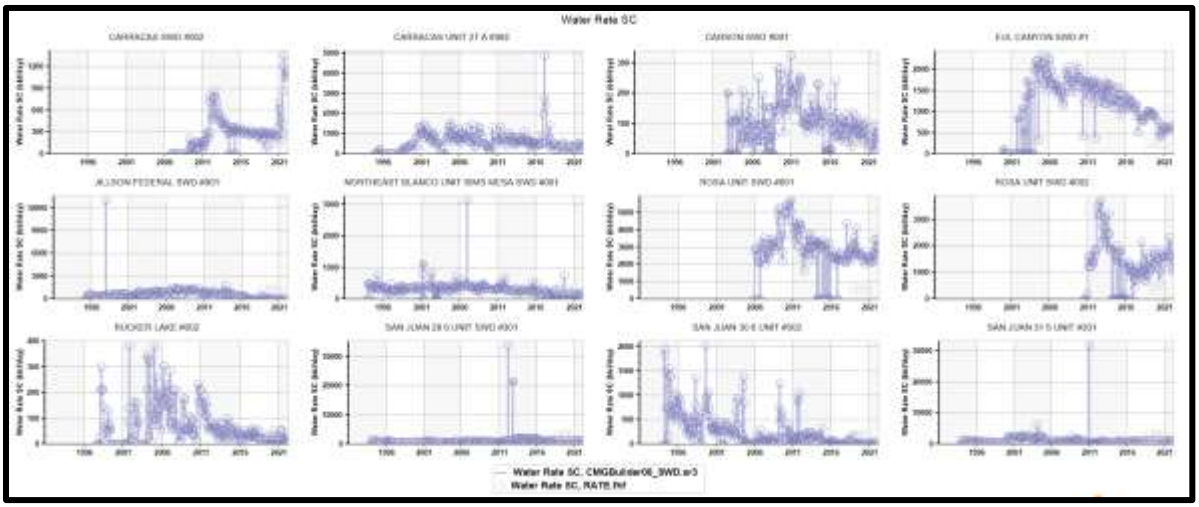


Figure 48. The injection historical injection rates of saltwater disposal wells.

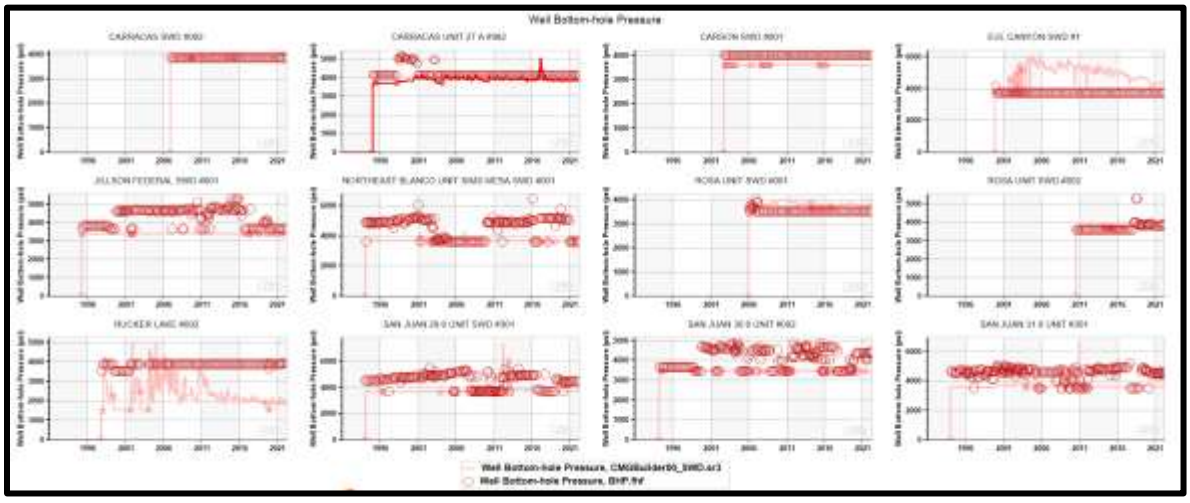


Figure 49. The injection historical bottom hole pressures of saltwater disposal wells.

The total injected CO_2 achieved 45 Mt CO_2 over 30 yr, and 1.5 million tons of injection rate maintained the entire injection period (**Figure 50**). The CO_2 plume barely migrated during the post monitoring period and the size is about 10 miles in diameter (**Figure 51**). The CO_2 is predominantly stored as supercritical phase and trapped through capillary pressure hysteresis

effect. 25% of which CO_2 was dissolved in formation brine under the reservoir temperature and pressure conditions (**Figure 52**).

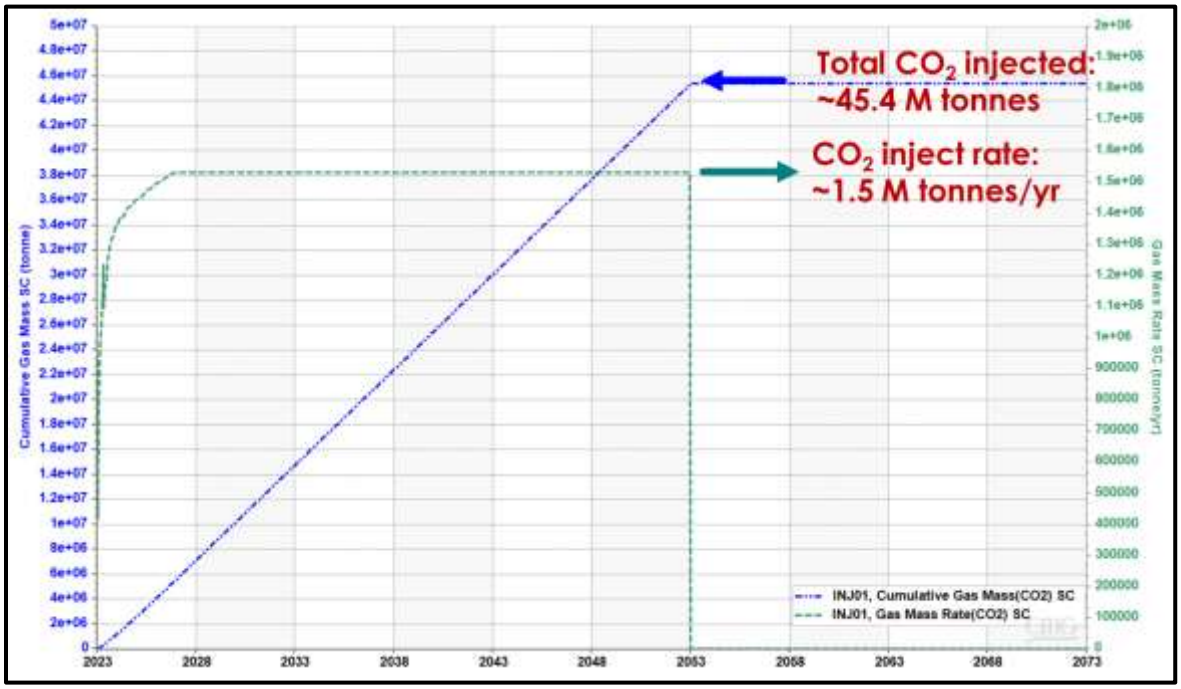


Figure 50. The total CO_2 injected over 30 yr and the yearly rates.

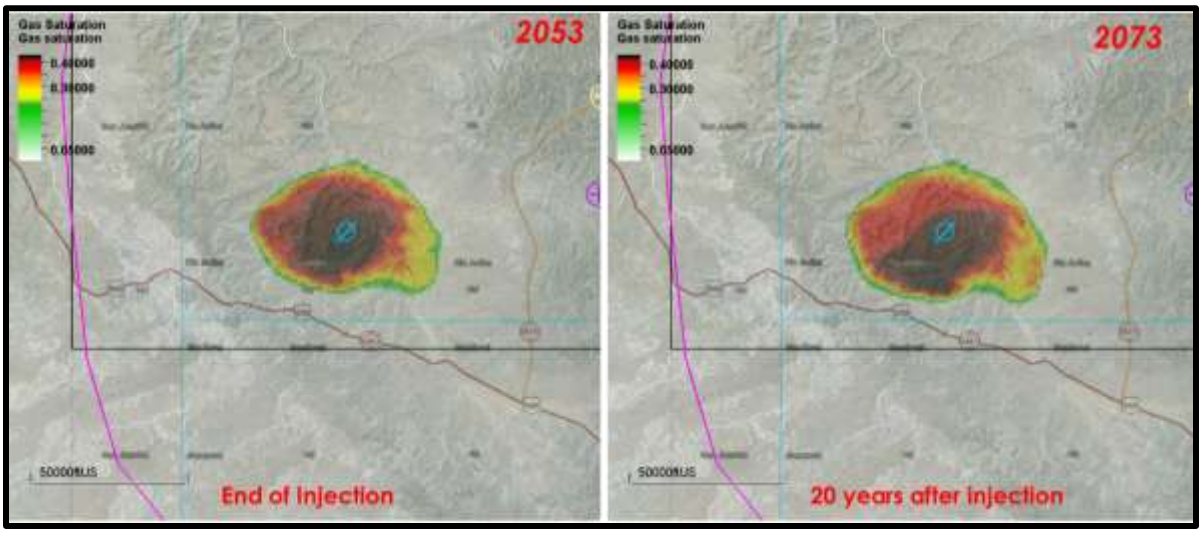


Figure 51. The injected CO_2 plume at the end of 30-yr injection and 20-yr post-injection.

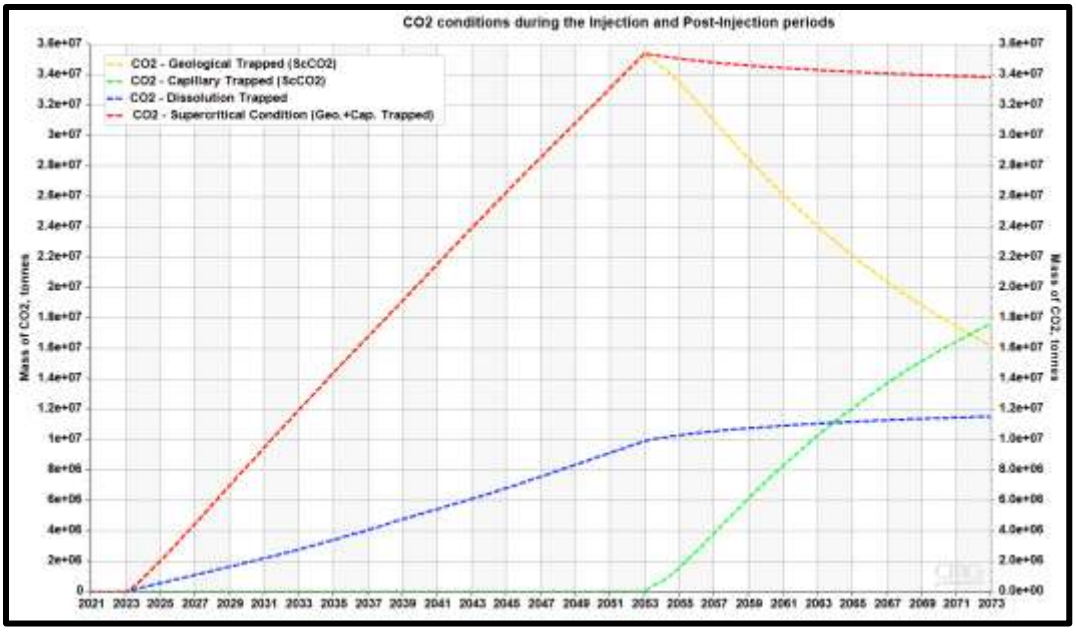


Figure 52. The injected CO_2 stored by separate mechanisms over years of sequestration.

Evaluation of the Potential Benefit of Enhanced Coal Bed Methane (ECBM)

Experimental Study of Permeability Reduction in Fruitland Coal Due to CO_2 Adsorption and its Effect on Strength and Stiffness

By Jason Simmons

The main objective of this CUSP Focused Project is to perform a feasibility assessment of site characterization to identify a suitable storage complex in New Mexico that can safely store a minimum of 1.5 million metric tons of CO_2 over a 30-year injection period. As part of this assessment the project aims to provide data which may increase the technical understanding of using coalbeds in New Mexico as part of the storage complex. One of the main challenges for the long-term storage of CO_2 in coalbeds is injectivity decline near the wellbore which has been linked to swelling induced permeability reduction as CO_2 adsorbs to the coal matrix (Siriwardane et al., 2009; Pan et al., 2010; Perera et al., 2011;Vishal and Singh, 2015; Vishal, 2017; Wang et al., 2019). To define this phenomenon and to assess the potential for storage of CO_2 in New Mexico coalbeds, we performed laboratory flow-through experiments in Fruitland coal samples under reservoir conditions to measure the permeability reduction over time. Permeability experiments were combined with unconfined compressive strength tests (UCS) on two pristine samples and flow-through samples interacted with CO_2 to determine if adsorption of CO_2 had any adverse effects on strength and stiffness within the Fruitland Coal which may affect operations. Finally, adsorption isotherms for CO_2 and N_2 in the experimental samples were developed using Brunauer-Emmett-Teller (BET) analysis.

Methods

Sample Preparation: Flow-Through and UCS

Sample selection in the Fruitland Coal was based on visual inspection and existing logs which contained proximate analysis for nearby depths. We chose interval 3739.75 – 3759 ft. from well Chicosa 35, API 3003924622 (FCC35; Figure 1; Tables 1 and 2). 3 cylindrical samples were cut parallel to general dimensions of 1.5" diameter by 2.25 - 2.5" length for the experiments using a standard press (Table 2). Due to friability, a heat shrink was molded to the samples before they were end trimmed using a Kemet Automatic Cutter 402 saw. All sample preparation was completed dry, without cooling fluids to retain sample integrity.

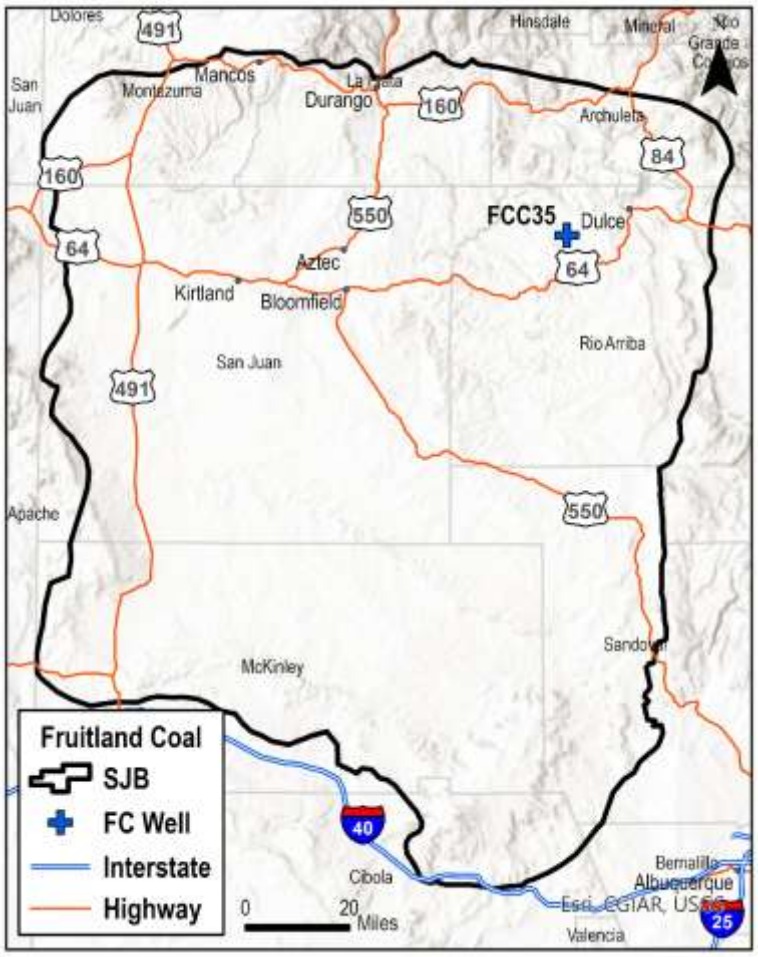


Figure 1. Well location for Fruitland Coal samples.

Table 1.Well information for sample locations within the SJB Fruitland Coal

API	Well Name	Well ID	Lat_NAD83	Lon_NAD83	MVD	Elev	Status
3003926422	Chicosa 35	FCC35	36.8615456	-107.217598	3862	7005	CBM

Table 2. Core parameters of Fruitland Coall

Sample ID	Test Type	Interval ft	Interval m	Length cm	Diameter cm
FCC35-1	CO_2/UCS	3759	1145.74	5.9479	3.8682
FCC35-2	CO_2/UCS	3758.33	1145.54	6.2009	3.8684
FCC35-3	CO_2/UCS	3758	1145.44	6.1006	3.8814
FCC35-4	Pristine UCS	3739.75	1139.88	5.7523	3.8710
FCC35-5	Pristine UCS	3740	1139.95	6.0117	3.8669

2.2 Laboratory Flow-Through Experiments

Flow-through experiments with supercritical CO_2 were conducted on 2 samples (FCC35-1 and FCC35-2) of Fruitland Coal from well Chicosa 35 at the reservoir temperature 56°C, and reservoir effective stress of 12 MPa to measure any permeability reduction through time due to adsorption. A 3rd experiment was performed using liquid CO_2 by lowering temperature to 28°C to determine if changes in CO_2 phase would affect adsorption (Table 3).

Prior to the experiment, we jacketed samples in a Buna-N sleeve wrapped in stainless steel foil inside a Core Labs hydrostatic cell. A PTFE sleeve was inserted around the jacketed sample to minimize the mass of CO_2 that will diffuse into the silicon oil confining fluid. Three Watlow ceramic heating bands controlled by a Watlow control and a Type K thermocouple inside of the vessel heated the system. Three Teledyne ISCO syringe pumps were used throughout the experiment to control pore fluid (pump A and pump B, Figure 2; 260HP and 500HP) and confining pressures (pump C, Figure. 2; 100D). During the test, two high precision (0.0129 MPa) Heise HWQ-64864 pressure transducers measured upstream and downstream pressures. Permeability was measured using a pore pressure transmission method which involved a constant gas injection pressure at the sample inlet with a downstream compartment which was isolated from any pump controls. Initially, a CO_2 cylinder was connected to pumps A and B and used to gently increase pore pressure to 6 MPa. The pumps were then filled with CO_2 and used to further pressurize the system to 7.5 MPa. Pumps A and B were set to constant pressure and pore pressure was allowed to equilibrate until no volume changes were observed in the pumps. Confining pressure was simultaneously increased to 19.5 MPa. Finally, the core sample was momentarily isolated from the upstream pressure, which was increased to 8.5 MPa, while the confining pressure was increased to 20.5 MPa to meet the in situ effective stress requirement. The downstream compartment was closed off thereby isolating the sample from the downstream pump B and the most upstream valve at the sample inlet was opened allowing a 1 MPa pressure gradient across the sample. Pressure was allowed to move freely through the sample into the downstream compartment while the change in pressure there was recorded at 5 second intervals and used to calculate flowrate according to

$$Q = \frac{dP}{dt}\beta V$$

where $\frac{dP}{dt}$ is the change in downstream pressure through time, β is the adiabatic compressibility of CO_2, and V is the volume of the downstream compartment (Siriwardane et al., 2009a and

2009b; Perera et al., 2011;Vishal and Singh, 2015; Vishal, 2017). β was calculated using the derived formula

$$\beta = \frac{Z}{P\gamma}$$

where Z is the Z-factor which accounts for the deviation of CO_2 from ideal to real gas behavior at our experimental conditions, P is the average pore pressure, and γ is the ratio of specific heat capacity ratio for CO_2 (Bear, 1972; Pipeng, 2025). Finally, permeability (k) was calculated using the standard formula

$$k = \frac{2QP_o\mu L}{A(P_i^2 - P_o^2)}$$

where Q is the downstream flowrate, μ is viscosity of the CO_2, P_i and P_o are the upstream and downstream pressures respectively, and A and L are the cross sectional area and the average length of the coal sample respectively (Perera et al., 2011;Shukla; et al., 2012; Nasvi, et al., 2013; Vishal and Singh, 2015; Vishal, 2017). Once the initial permeability was determined, CO_2 was passed through the sample for ≈ 30-36 hours, before the experiment was repeated at the exact same conditions to determine if a change permeability had occurred.

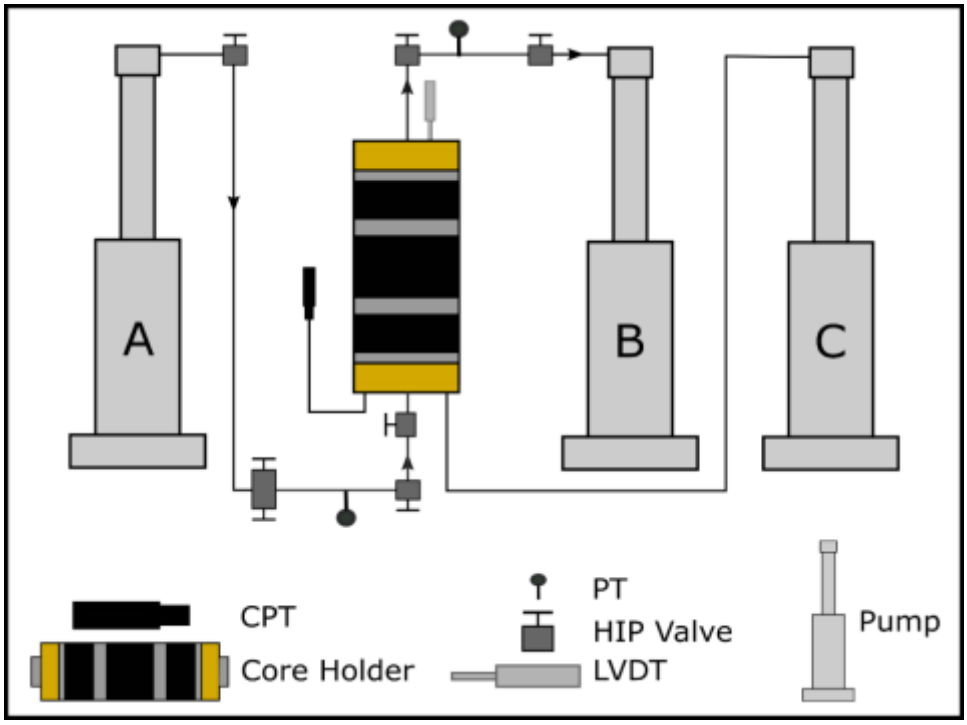


Figure 2. Permeability apparatus. Black lines represent flow lines with directional arrows.

UCS Tests

Unconfined compressive strength (UCS) tests were performed on the three experimental flow-through samples interacted with supercritical or liquid CO_2 and two pristine samples of Fruitland Coal using a MTS 793 testing system with maximum load of 600 kN (Figure 3). Sample preparation and testing protocols generally adhered to ASTM D7012. However, due to friability, cores were not ground flat but rather ends were capped with card stock according to methods

outlined in Pells (1993). Samples were placed between steel platens and capped with card stock before being loaded at a constant strain rate of 3.9 - 5.0 x 10^{-4} strain/s and displacement rate of 0.0009 - 0.0115 mm/s. UCS (σ) was calculated from the standard formula

$$\sigma = \frac{P}{A} \quad (1)$$

where P is the maximum load (kN) sustained during testing and A is the sample's cross-sectional area (mm^2; SCDOT, 2009; Gudmundson, 2011). The displacement of the card stock and platens was calibrated by applying the same loads and deformation rates to an ≈ 1.5" x 3.0 in. 316 stainless steel cylinder. Calibrated displacements were to be subtracted off from the displacements that developed during each test.



Figure 3. MTS testing machine used in UCS testing of Fruitland Coal specimens.

Results and Discussion

Flow-Through Experiments

Three experiments were conducted on Fruitland Coal samples to assess permeability reduction during injection of supercritical CO_2 and to determine if changing the CO_2 phase would affect adsorptive properties. For the two samples which were interacted with supercritical CO_2 we found that the rate of change in the downstream pressure was slow during the initial exposure, lasting ≈ 4-5 hours for a generally steady state between the upstream and downstream compartments (Figures 4a and 5a). Based on the flowrate from this pressure change, we found

that initial permeability was low at 78.1 nanodarcies (nD) and 80.4 nD for FCC35-1 and FCC35-2 respectively (Figure 6). After prolonged exposure to supercritical CO_2, the rate of change in the downstream compartment had decreased in both samples leading to reduction in permeability of 60.6 nD (22.4%) and 24.5 nD (55.9%) for FCC35-1 and FCC35-2 respectively (Table 3; Figures 4b ,5b, and 6). Opposing results occurred in the 3rd experiment performed with liquid CO_2. Where CO_2 had taken hours to move through the previous 2 samples, equilibration of the downstream pressure in sample FCC35-3 occurred in ≈ 3-4 minutes rather than hours (Figure 7a).We found that initial permeability here was 200 times greater than in the 1st two experiments at 0.0157 millidarcies (mD) or 15,683 nD (Figure 8). After the sample had been exposed to CO_2 for 30+ hours, the rate of pressure change in the downstream compartment had had sufficiently increased informing the permeability increase to .0237 mD (23,742 nD; Figure 7b and 8).

Samples flooded with supercritical CO_2 experienced 22.4% to 69.5% reduction in permeability after approximately 34-38 hours of total time (Figure 6). Because effective stress and temperature remained constant for both experiments, the reduction in permeability occurred due to adsorption of CO_2 to the coal matrix during the initial experiment and during the samples prolonged exposure to the CO_2 phase. This experimental result indicates that without a change to the cleat/fracture network, injectivity problems are likely to occur through time in this section of interval 3758.33 to 3759 ft of the Fruitland Coal. However, the permeability increase in sample FCC35-3 tells a different story. The high initial permeability in this sample is not typical of traditional tight coalbeds. Upon examination of the coal sample, we learned that an extensive network of pre-existing fractures exists throughout the full sample geometry. Fractures are a dominant channel of gas flow in coal as evidenced by the large difference in permeability from samples FCC35-1 and FCC35-2 which show no evidence of a fracture network. We also find that because the sample is so well-fractured, that adsorption of CO_2 to the matrix was insignificant through time as compared to the connectivity of the flow pathways. Because gas moved through the sample so quickly, the experiment was repeated multiple times, allowing at least 10 hours of exposure between measurements to finally equal the same total exposure time to CO_2 as occurred in the first two samples. From this we found that the permeability increased at each subsequent measurement except from the second to third where no change occurred. We believe that the 1MPa pressure gradient across the sample contributed to widening or increasing the fracture network through time which resulted in increasing the permeability (Figure 8). The increasing permeability in the previously fractured sample indicates that where there is an extensive fracture network, the Fruitland Coal is likely to have good injectivity which may increase with time as connectivity changes with increasing injection pressure. Overall, determination of the Fruitland Coal as a good storage reservoir to meet the requirement of 1.5 million metric tons of CO_2 over a 30-year injection period will be highly dependent on the cleat and fracture network which exists on the reservoir scale especially in proximity to the injection well.

Finally, because our 3rd sample had a connected fracture network, we could not determine how changing the CO_2 phase would affect adsorption in Fruitland Coal. It should be noted however that supercritical CO_2 would generally be the preferred phase during injection activities based on in situ conditions in the Fruitland Coal in most of New Mexico.

Table 3. Permeability of coal samples. Red indicates a decrease

Sample ID	CO_2 Phase	Initial (nD)	Post (nD)	Change (nD)	Change (%)
FCC35-1	SC	78.1	60.6	17.5	22.4
FCC35-2	SC	80.4	24.5	55.9	69.5
FCC35-3	Liquid	15683.4	23744.2	8060.8	51.4

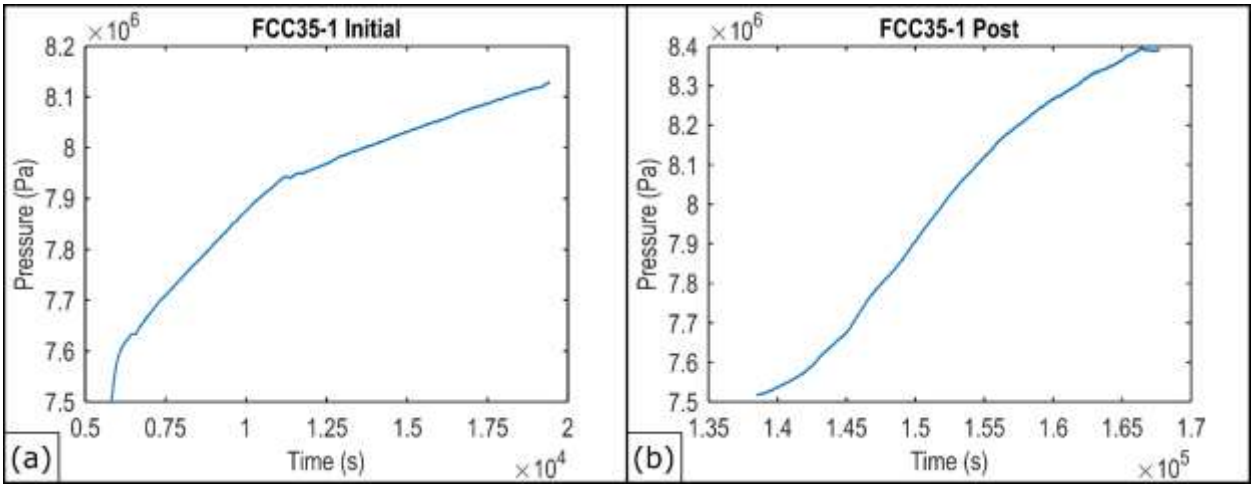


Figure 4. Downstream pressure evolution through time in experiment 1 during initial flooding of the coal sample (a) and after 30-36 hours of prolonged exposure (b).

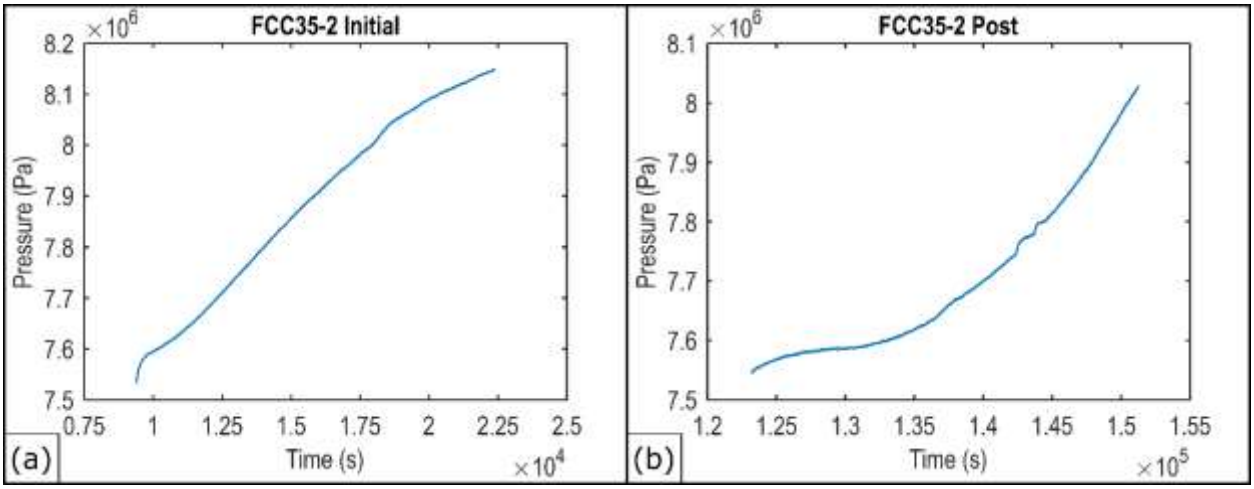


Figure 5. Downstream pressure evolution through time in experiment 2 during initial flooding of the coal sample (a) and after 30-36 hours of prolonged exposure (b).

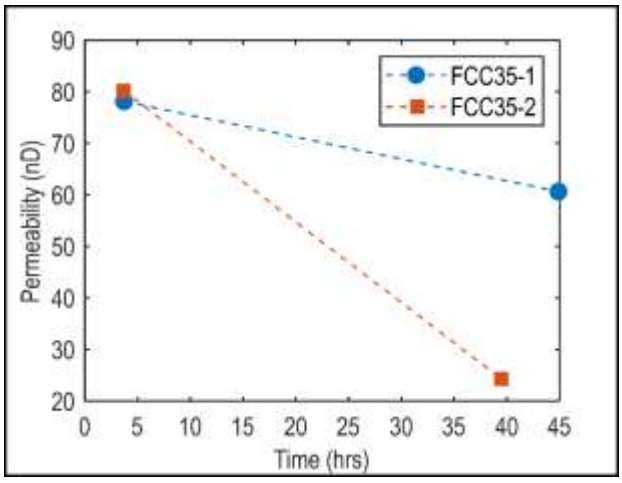


Figure 6. Permeability before and after prolonged exposure to CO_2 in samples FCC351 and FCC35-2. Decreases ranged from 22.4% to 69.5% in the two samples.

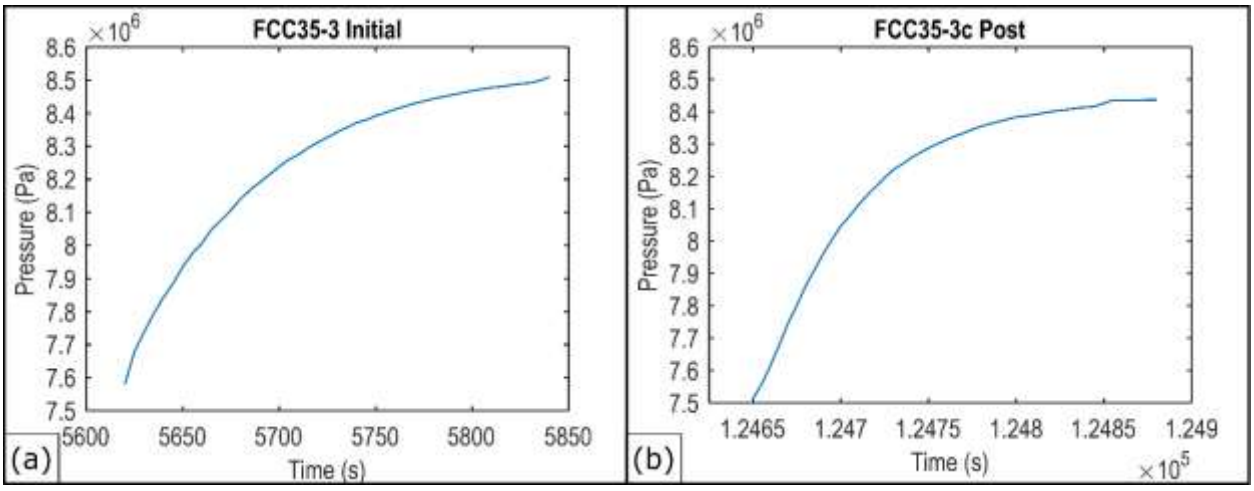


Figure 7. Downstream pressure evolution through time in experiment 3 using liquid CO_2 during initial flooding of the coal sample (a) and after 30-36 hours of prolonged exposure (b).

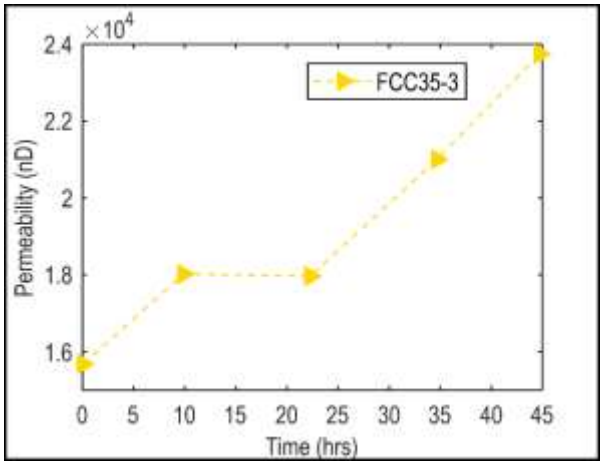


Figure 8. Permeability before and after prolonged exposure to CO_2 in sample FCC353 interacted with liquid CO_2. Because CO_2 flowed through the sample in minutes, the experiment was repeated several times to match total time

of exposure as in FCC35-1 and FCC35-2. This coal sample was extensively fractured and permeability increased by 51%.

UCS and Estimated Youngs Modulus

Unconfined compressive strength testing was performed on 5 samples of Fruitland Coal that were either interacted with CO_2 or pristine (Figure 9 and 10). Samples of the Fruitland Coal generally exhibited brittle post-peak failure behavior with several samples showing double peaks (Figure 11a and 11b). Notably, pristine sample FCC35-4 exhibited ductile failure before an abrupt brittle post-peak failure (Figure 11b). Peak load and unconfined compressive strength were determined for each experiment. For pristine samples not interacted with CO_2, peak load was 27.6 kN and 32.3 kN, and UCS was 23.4 MPa and 27.5 MPa (average 25.5 MPa) for samples FCC35-4 and FCC35-5 respectively (Table 4). For experimental samples, peak load was 38.1 kN, 32.9 kN, 26.2 kN, and UCS was 32.4 MPa, 28.0 MPa, and 22.1 MPa (average 27.5 MPa) for samples FCC35-1, FCC35-2, and FCC35-3 respectively (Table 4).

Typically, Young's modulus would easily be calculated from the slope of the linear portion of the stress strain curve during UCS testing (Gudmundsson, 2011). However, the calibration of the card stock displacement from the total displacement during testing proved to be unattainable. Therefore, the strains that developed during each test were overestimated, resulting in the underestimation of Young's modulus while leaving the UCS unaffected. However, there is significant data which positively correlates UCS with Young's modulus in geomaterials, where stronger materials typically have a higher Young's modulus (Dincer et al., 2004; Chang et al., 2006; Basu et al., 2009; Pan et al., 2013; Malkowski et al., 2018). Of these studies, Pan et al (2013) developed a direct correlation between UCS and Young's modulus for three independent coal types:

$$UCS = 3.3844e^{0.4744E} \quad (2)$$

where the unconfined compressive strength (*UCS*) is in MPa and *E* is the Young's modulus in GPa. Applying this correlation to our study, we estimated the Young's modulus which was 4.1 GPa and 4.4 GPa (average 4.2 GPa) for pristine samples FCC35-4 and FCC35-5 respectively, and 4.8 GPa, 4.5, GPa, and 4.0 GPa (average 4.4 GPa) for experimental samples FCC35-1, FCC35-2, and FCC35-3 respectively.

Based on results, the values of peak load, UCS, and estimated Young's modulus were reasonably consistent between the pristine and CO_2 interacted samples, and were within normal range for strong coal specimens found in the literature (Pan et al., 2013; Perera, 2013; Perera, 2016; Schreiber et al., 2017). The lowest values of UCS (22.1 MPa) and Young's modulus (4.0 GPa) occurred in CO_2 interacted sample FCC35-3 which contained the most connected and extensive cleat and fracture network based on fluid flow during permeability testing and physical observations of the core plug. This result is not unexpected as fractured coal generally exhibits lower strengths and elastic properties when compared to the more solid coals with a lesser cleat/fracture network (Abrar, et al, 2025). Even then, when comparing results between the experimental and pristine sample groups, we found the lowest value of UCS in the experimental group was only 1.3 MPa (6%) lower than in the pristine samples. There was also only a 2.0 MPa (8%) difference and 0.2 GPa (5%) difference between the average UCS and average Young's modulus respectively, for the pristine and experimental sample groups (Table 4). When looking for real variations which might indicate change in strength or stiffness for the coal samples post experiment, we believe a reasonable difference should be > 20% which did not occur in this

study. It is also worth noting that the largest UCS (32.4 MPa) and estimated Young's modulus (4.8 GPa) occurred in a CO_2 interacted sample (FCC35-1). This sample also underwent a permeability reduction of 22.4% during the flow-through experiments. Based on the relative similarity of results for all of the samples, relatively low % differences between sample points of the two groups, and low differences in average values for the combined samples of each group, there was no effect on the UCS or Young's modulus of the coal specimens due to adsorption of CO_2 to the coal matrix. Beyond the lowest value of UCS in experimental sample FCC35-3 due to its internal structure, the slight differences in strength are acceptable and from heterogeneities within the coal specimens themselves.

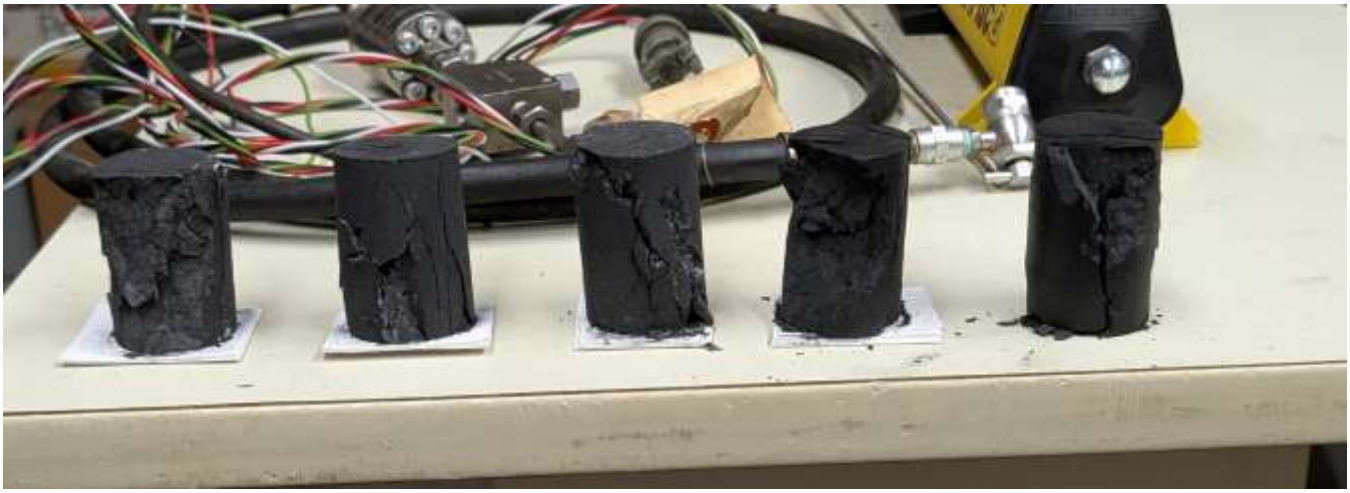


Figure 9. Coal specimens generally experienced brittle failure during UCS testing.



Figure 10. Sample FCC35-4 which exhibited ductile failure during UCS testing.

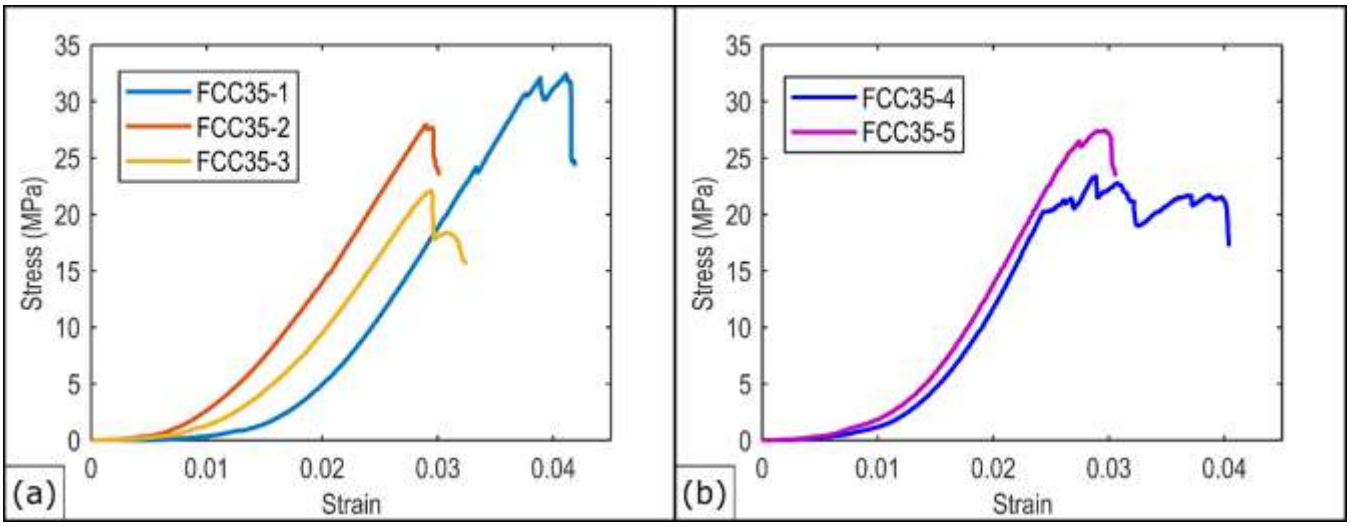


Figure 11. Failure curves for experimental samples (a) and pristine samples (b). Strain includes sample strain, and card stock (end cap) strain due to post-test calibration issues. Because of this, strain is overestimated for these tests and could not be used to determine Young's modulus while the UCS is fully represented in these figures. Sample

FCC35-4 exhibited ductile failure, and several samples show double peaks where stress increased after an initial decrease before failure.

Table 4. Results of UCS tests for Fruitland Coal. Young's modulus (E) was estimated from a correlation in Pan et al (2013)

Sample ID	Test Type	Peak Load (kN)	UCS (MPa)	E (Gpa)
FCC35-1	CO_2/UCS	38.1	32.4	4.8
FCC35-2	CO_2/UCS	32.9	28.0	4.5
FCC35-3	CO_2/UCS	26.2	22.1	4.0
FCC35-4	Pristine UCS	27.6	23.4	4.1
FCC35-5	Pristine UCS	32.3	27.5	4.4

References

Abrar SW, Mendhe VA, Kamble AD, Shukla P, Sharma P, Buragohain J, Kumari S, Kumari S, Anurag, Das AK, et al. 2025. Cleat and fracture systems in coal with implications for strength, hydrofracking, and gas–water flow mechanisms: a critical review. ACS Omega. 10:29909–29928. doi:10.1021/acsomega.5c00520

[ASTM]ASTM International. 2023. ASTM D7012-23: standard test methods for compressive strength and elastic moduli of intact rock core specimens under varying states of stress and temperatures. West Conshohocken (PA): ASTM International. 8 p.

Basu A, Celestino T, Bortolucci A. 2009. Evaluation of rock mechanical behaviors under uniaxial compression with reference to assessed weathering grades. Rock Mech Rock Eng. 42:73–93. doi:10.1007/s00603-008-0170-2

Bear J. 1972. Dynamics of fluids in porous media. New York (NY): American Elsevier Publishing Company. 764 p.

Dinçer I, Acar A, Çobanoğlu I, Uras Y. 2004. Correlation between Schmidt hardness, uniaxial compressive strength and Young's modulus for andesites, basalts and tuffs. Bull Eng Geol Environ. 63:141–148. doi:10.1007/s10064-004-0230-0

Gudmundsson A. 2011. Rock fractures in geological processes. Cambridge (UK): Cambridge University Press.

Hangx SJT, Spiers CJ, Peach CJ. 2010. Creep of simulated reservoir sands and coupled chemical-mechanical effects of CO_2 injection. J Geophys Res Solid Earth. 115:B09205. doi:10.1029/2009JB006939

Małkowski P, Ostrowski Ł, Brodny J. 2018. Analysis of Young's modulus for Carboniferous sedimentary rocks and its relationship with uniaxial compressive strength using different methods of modulus determination. J Sustain Min. 17:145–157. doi:10.1016/j.jsm.2018.07.002

Nasvi MCM, Ranjith PG, Sanjayan J, Haque A. 2013. Sub- and super-critical carbon dioxide permeability of wellbore materials under geological sequestration conditions: an experimental study. Energy. 54:231–239. doi:10.1016/j.energy.2013.01.049

Pells PJN. 1993. Uniaxial strength testing. In: Hudson JA, editor. Rock testing and site characterization: principles, practice, and projects. Oxford (UK): Pergamon Press. p. 67–85. doi:10.1016/B978-0-08-042066-0.50010-0

Pan Z, Connell LD, Camilleri M. 2010. Laboratory characterisation of coal reservoir permeability for primary and enhanced coalbed methane recovery. Int J Coal Geol. 82:252–261. doi:10.1016/j.coal.2009.10.019

Pan J, Meng Z, Hou Q, Ju Y, Cao Y. 2013. Coal strength and Young's modulus related to coal rank, compressional velocity and maceral composition. J Struct Geol. 54:129–135. doi:10.1016/j.jsg.2013.07.008

Perera MSA, Ranjith PG, Choi SK, Airey D. 2011. The effects of sub-critical and super-critical carbon dioxide adsorption-induced coal matrix swelling on the permeability of naturally fractured black coal. Energy. 36:6442–6450. doi:10.1016/j.energy.2011.09.023

Perera MSA, Ranjith PG, Viete DR. 2013. Effects of gaseous and super-critical carbon dioxide saturation on the mechanical properties of bituminous coal from the Southern Sydney Basin. Appl Energy. 110:73–81. doi:10.1016/j.apenergy.2013.03.069

Perera M, Ranathunga A, Ranjith P. 2016. Effect of coal rank on various fluid saturations creating mechanical property alterations using Australian coals. Energies. 9:440. doi:10.3390/en9060440

Pipeng. 2025. Carbon dioxide compressibility factor, density, and vapour pressure (Yaws) calculator [Internet]. [accessed 2025 Jun–Aug]. https://pipeng.com/index.php/gsts/itdmotflup004a/itdtoflup004012/.

Schreiber J, Konicek P, Stonis M. 2017. Seismological activity during room and pillar hard coal extraction at great depth. Procedia Eng. 191:67–73. doi:10.1016/j.proeng.2017.05.155

Shukla R, Ranjith PG, Choi SK, Haque A. 2012. A novel testing apparatus for hydromechanical investigation of rocks: geo-sequestration of carbon dioxide. Rock Mech Rock Eng. 45:1073–1085. doi:10.1007/s00603-012-0241-2

Siriwardane H, Haljasmaa I, McLendon R, Irdi G, Soong Y, Bromhal G. 2009a. Influence of carbon dioxide on coal permeability determined by pressure transient methods. Int J Coal Geol. 77:109–118. doi:10.1016/j.coal.2008.08.006

Siriwardane HJ, Gondle RK, Smith DH. 2009b. Shrinkage and swelling of coal induced by desorption and sorption of fluids: theoretical model and interpretation of a field project. Int J Coal Geol. 77:188–202. doi:10.1016/j.coal.2008.08.005

South Carolina Department of Transportation. 2009. SC-T-39: standard method of test for determining the unconfined compressive strength of intact rock core specimens. Columbia (SC): South Carolina Department of Transportation.

Vishal V, Singh TN. 2015. A laboratory investigation of permeability of coal to supercritical CO_2. Geotech Geol Eng. 33:1009–1016. doi:10.1007/s10706-015-9882-8

Vishal V. 2017. In-situ disposal of CO_2: liquid and supercritical CO_2 permeability in coal at multiple down-hole stress conditions. J CO2 Util. 17:235–242. doi:10.1016/j.jcou.2016.12.011

Wang L, Chen Z, Wang C, Elsworth D, Liu W. 2019. Reassessment of coal permeability evolution using steady-state flow methods: the role of flow regime transition. Int J Coal Geol. 211:103210. doi:10.1016/j.coal.2019.103210

BET Gas Adsorption Measurements on Powdered Coal Samples

by Jessie Wu and Ernest Owusu

Gas adsorption measurements based on the Brunauer–Emmett–Teller (BET) approach are commonly applied to characterize gas–solid interactions in coal and other porous materials. Adsorption isotherms are obtained by measuring the amount of gas adsorbed as a function of pressure at a controlled temperature, providing quantitative information on adsorption behavior under defined experimental conditions.

Nitrogen (N_2) adsorption experiments conducted at cryogenic temperature (−196 °C) are widely used to characterize pore structure, including pore size distribution and pore volume, over a broad pore size range. Carbon dioxide (CO_2) adsorption experiments, typically performed at higher temperatures, are often used to evaluate adsorption behavior under conditions that are more relevant to laboratory-scale and subsurface applications.

Gas adsorption measurements in this study were performed using a Micromeritics ASAP 2020 Plus surface area and porosity analyzer (Figure 1). The ASAP 2020 Plus is a fully automated volumetric gas adsorption instrument designed for high-resolution adsorption and desorption measurements under controlled temperature and pressure conditions. The system supports a wide range of adsorptive gases and is commonly used for adsorption isotherm measurements on powders and porous solids.

The instrument is equipped with precise pressure transducers and automated dosing control, enabling accurate measurement of gas uptake as a function of pressure. Integrated degassing capabilities allow samples to be evacuated and thermally treated prior to analysis to remove moisture and residual gases. During adsorption measurements, free space determination, pressure equilibration, and data acquisition are performed automatically through instrument control software, ensuring consistent and repeatable experimental procedures.



Figure 1. Micromeritics ASAP 2020 Plus instrument.

Experimental Methods

Materials

Gas adsorption experiments were conducted on three powdered coal samples: **FCC35-1, FCC35-2,** and **FCC35-3.** All samples were prepared as fine powders prior to analysis to ensure uniform packing and consistent gas–solid contact during adsorption measurements.

Sample Preparation and Degassing

Prior to adsorption measurements, each coal sample was loaded into a standard sample tube and degassed automatically on the instrument to remove moisture and residual gases. Degassing was performed under vacuum using a two-stage procedure. During the evacuation phase, samples were evacuated from approximately 5.0 mmHg to about 1.0×10^{-2} mmHg while being heated to 150°C at a ramp rate of 10°C/min. The evacuation was maintained for 60 minutes. This was followed by a heating phase in which the sample temperature was held at 150°C for an additional 120 minutes. After degassing, samples were allowed to cool and were backfilled prior to adsorption analysis.

Carbon dioxide (CO_2) experiments were conducted on powdered coal samples using a Micromeritics ASAP 2020 Plus instrument (Figure 1). All measurements were performed at 0°C with CO_2 as the adsorptive gas to obtain adsorption and desorption isotherms under controlled temperature conditions.

Nitrogen (N_2) Adsorption Measurements

Nitrogen adsorption and desorption experiments were conducted for each coal sample using N_2 as the adsorptive gas at a measurement temperature of −196°C. Adsorption isotherms were collected over a wide range of relative pressures using absolute pressure dosing. The N_2 adsorption data were used to obtain adsorption isotherms, pore size distribution, and pore volume for each sample. Ambient and analysis free space volumes were measured automatically prior to data acquisition, and pressure equilibration was applied at each dosing step to ensure stable measurements.

Carbon Dioxide (CO_2) Adsorption Measurements

Following the N_2 adsorption experiments, CO_2 adsorption and desorption measurements were conducted on the same coal samples using CO_2 as the adsorptive gas. CO_2 adsorption isotherms were collected at a measurement temperature of **0°C** using absolute pressure dosing over a pressure range from near vacuum to approximately 925 mmHg. An equilibration interval of 10 seconds was applied at each pressure step. Adsorbed gas quantities were recorded as a function of pressure and reported in units of cm^3/g at standard temperature and pressure (STP).

Results

N_2 Adsorption Measurements at -196°C

Nitrogen adsorption and desorption isotherms for **FCC35-1** measured at −196°C are shown in Figure 2. The isotherm exhibits a continuous increase in N_2 uptake with increasing relative pressure over the full measured range. A distinct separation between the adsorption and

desorption branches is observed, indicating pressure-dependent adsorption and desorption behavior.

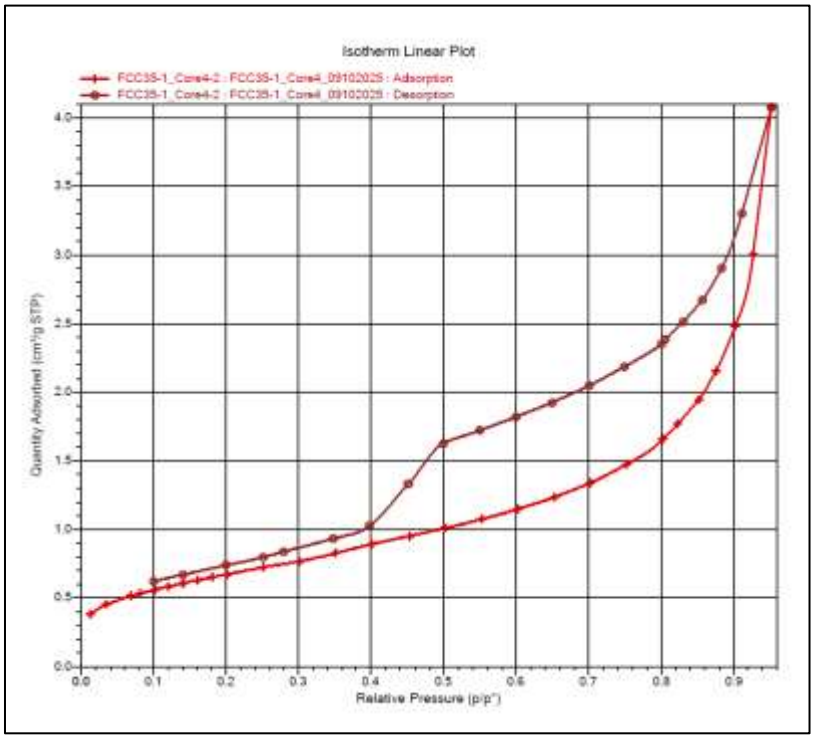


Figure 2. Nitrogen adsorption and desorption isotherms of FCC35-1 measured at −196°C

BET analysis of the N_2 adsorption data yields a BET surface area of **2.46 m²/g**. The total pore volume derived from adsorption data and **0.0064 cm³/g** from desorption data over the analyzed pore size range. The average pore diameter estimated from the BET method is approximately **10.2 nm.**

Nitrogen adsorption and desorption isotherms for FCC35-2 measured at −196°C are shown in Figure 3. The isotherm exhibits a continuous increase in N_2 uptake with increasing relative pressure over the full measured range. A distinct separation between the adsorption and desorption branches is observed, indicating pressure-dependent adsorption and desorption behavior.

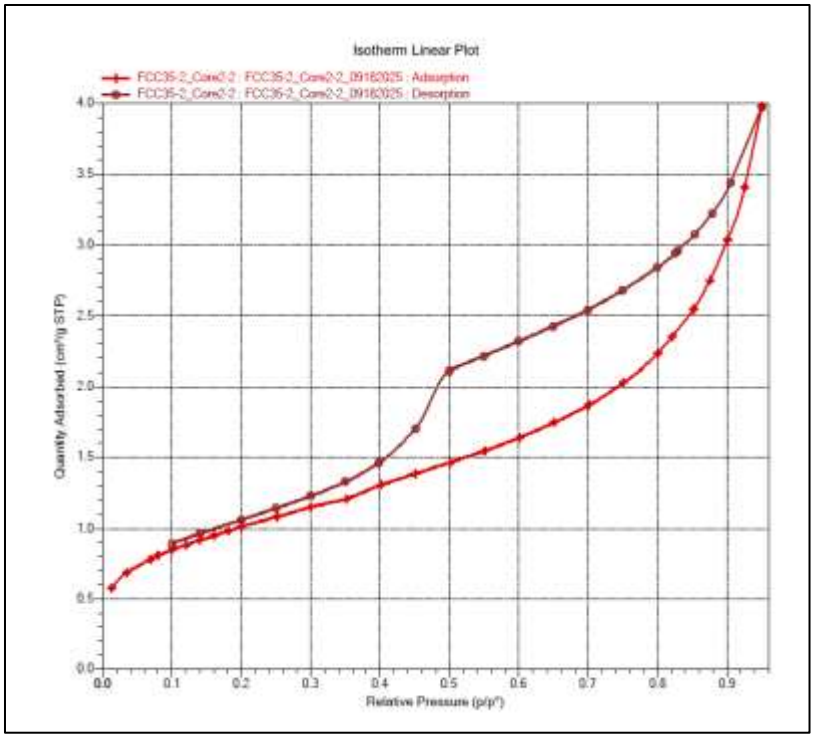


Figure 3. Nitrogen adsorption and desorption isotherms of FCC35-2 Core 2-2 measured at −196°C.

BET analysis of the N_2 adsorption data yields a BET surface area of 3.66 m^2/g. The total pore volume derived from adsorption data is 0.0064 cm^3/g, and 0.0063 cm^3/g from desorption data over the analyzed pore size range. The average pore diameter estimated from the BET method is approximately 6.72 nm.

Nitrogen adsorption and desorption isotherms for FCC35-3 measured at −196°C are shown in Figure 4. The isotherm exhibits a continuous increase in N_2 uptake with increasing relative pressure over the full measured range. A distinct separation between the adsorption and desorption branches is observed, indicating pressure-dependent adsorption and desorption behavior.

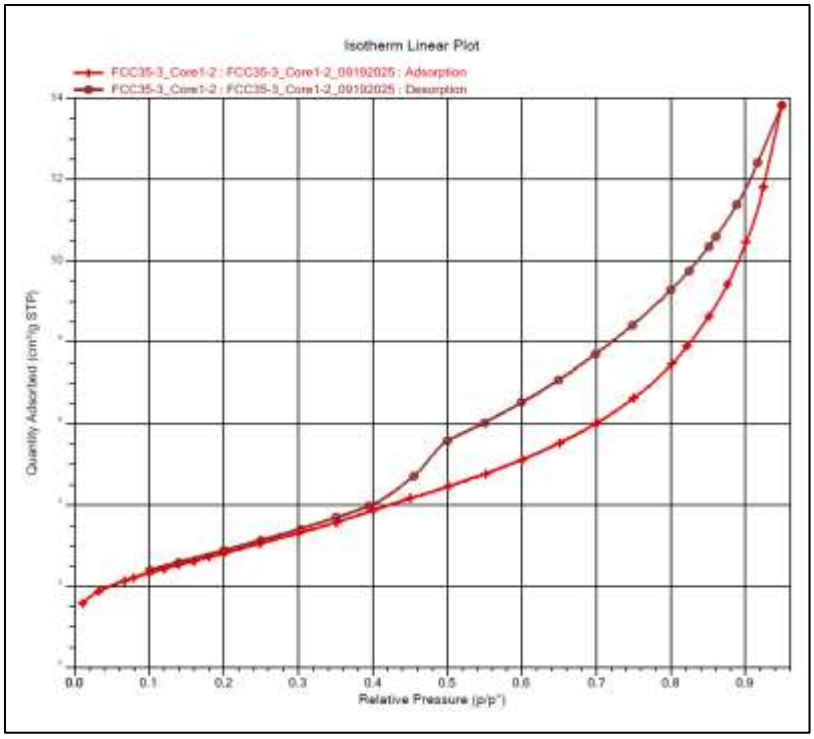


Figure 4. Nitrogen adsorption and desorption isotherms of FCC35-3 measured at −196°C. BET analysis of the N_2 adsorption data yields a BET surface area of 10.41 m²/g. The total pore volume derived from adsorption data is 0.0219 cm³/g, and 0.0217 cm³/g from desorption data over the analyzed pore size range. The average pore diameter estimated from the BET method is approximately 8.22 nm.

Comparison of the nitrogen adsorption and desorption isotherms for the three coal samples shows clear differences in adsorption capacity and overall gas uptake behavior. All three samples exhibit similar isotherm shapes, with a continuous increase in N_2 uptake as relative pressure increases and a distinct separation between adsorption and desorption branches, indicating pressure-dependent adsorption and desorption behavior.

Among the three samples, FCC35-3 shows the highest N_2 uptake across the full relative pressure range, consistent with its higher BET surface area and larger total pore volume. FCC35-2 exhibits intermediate N_2 uptake, while FCC35-1 shows the lowest overall adsorption capacity. These differences are reflected in both the magnitude of adsorption at high relative pressure and the total pore volumes derived from the N_2 data.

Despite differences in total uptake, the overall trends in adsorption and desorption behavior are similar for all three samples. The N_2 adsorption results therefore indicate systematic variability in pore-related characteristics among the coal samples while maintaining comparable adsorption behavior across the measured pressure range. These results provide a consistent basis for subsequent comparison with CO_2 adsorption measurements performed on the same samples.

CO_2 Adsorption Measurements at 0°C

Carbon dioxide adsorption and desorption isotherms for **FCC35-1** measured at **0°C** are shown in Figure 5. The isotherm exhibits a continuous increase in CO_2 uptake with increasing relative pressure over the full measured range (p/p° up to approximately 0.035). A distinct separation

between the adsorption and desorption branches is observed, indicating pressure-dependent adsorption and desorption behavior.

The CO_2 adsorption data show gradual uptake at lower relative pressures, followed by a more pronounced increase in adsorption as relative pressure approaches the upper end of the measured range. The observed hysteresis between adsorption and desorption branches indicates differences in CO_2 uptake and release behavior under the same relative pressure conditions.

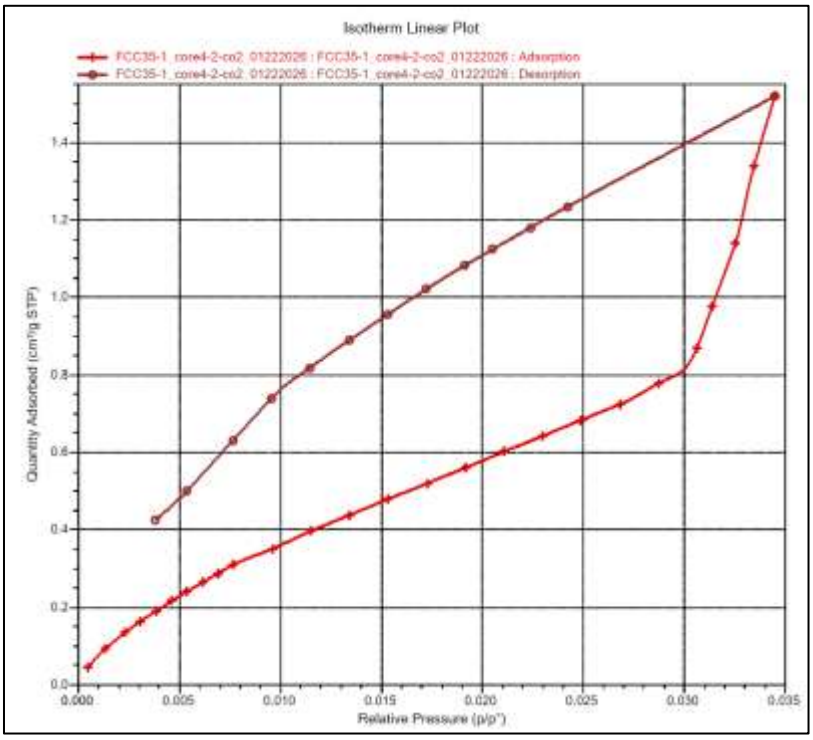


Figure 5. Nitrogen adsorption and desorption isotherms of FCC35-1 measured at 0°C.

Comparison of N_2 and CO_2 Adsorption

Nitrogen and carbon dioxide adsorption and desorption isotherms for FCC35-1 show clear differences in adsorption behavior under the respective measurement conditions. The N_2 isotherm measured at −196°C spans a broad relative pressure range and exhibits a gradual increase in gas uptake with increasing relative pressure. In contrast, the CO_2 isotherm measured at 0°C covers a narrower relative pressure range and shows a continuous increase in CO_2 uptake with increasing relative pressure.

Both isotherms exhibit hysteresis between adsorption and desorption branches, indicating pressure-dependent adsorption and desorption behavior. Differences in the shape and magnitude of the isotherms reflect variations in adsorption behavior between N_2 and CO_2 under the tested conditions. Together, the N_2 and CO_2 results provide complementary datasets for characterizing gas adsorption behavior on the same coal sample.

Model Construction

The primary goal is to develop a hydrodynamic model to calibrate the measured gas production rate at the Fruitland coal site in New Mexico. The initial field model, created using Petrel 2024,

was upscaled to Computer Modelling Group's (CMG) General Equation of State Model (GEM) 2025 to simulate fully implicit compositional fluid flow. A six-layer field double porosity model, consisting of three coal-bearing zones (upper, middle, and lower) identified from log interpretations (Weber et al. 2012), was built for the simulation study. Each coal-bearing zone includes two layers separated by non-reservoir sections, with total thicknesses ranging from 4.6 to 25 ft for the upper zone, 3.5 to 12 ft for the middle zone, and 8 to 33 ft for the lower zone. The matrix porosity of the production zones was set at 1% (assumed), while the cleat permeability was set at 78 nD based on core testing. The model grid comprised 235 × 196 × 11 blocks, totaling approximately 506,660 grid blocks, of which 276,360 are active. Each grid block measures 100 ft × 100 ft. The cleat porosity was estimated using the production index (Siriwardane et al. 2012) for each well (Error! Reference source not found.) and used as input for a Gaussian geostatistical simulation to fill the rest of the grids (**Figure 1**). A cubic power-law relationship (Siriwardane et al. 2012) between cleat permeability and porosity (Error! Reference source not found.) was used to model permeability distribution (**Figure 54**). The Langmuir volume and pressure isotherms were obtained from the Tiffany Unit N2-ECBM Pilot report (Reeves and Oudinot 2004). Wells completed in the three coal zones, with operating parameters based on gas and water surface production histories, served as model inputs. The wells were constrained to respect reservoir volume during history matching, with skin factors set to zero. Other relevant reservoir parameters are listed in **Table 9.** Reservoir parameters used in the model. The model boundaries were set as no-flow barriers to represent wells adjacent to the study area (Reeves and Oudinot 2004).

$$\emptyset_i = \frac{\emptyset_{max} - \emptyset_{min}}{R_{max} - R_{min}} \times (R_i - R_{min}) + \emptyset_{min} \quad \text{Eq. 1}$$

$$\emptyset = a\left(k_f\right)^n \quad \text{Eq. 2}$$

Where:

R_i = The relative production of each well *i* compared to maximum production ($\frac{Q_i}{Q_{max}}$)

R_{min} = Minimum relative production ratio among all producers

$\emptyset_{max}$ = Specified maximum porosity

$\emptyset_{min}$ = Specified minimum porosity

Q_i = Production rate of well *i*

Q_{max} = Maximum production rate of well *i*

$\emptyset$ = Porosity

k_f = Intrinsic permeability in the face cleat, mD

a = Variable porosity factor

n = 0.33 for coal

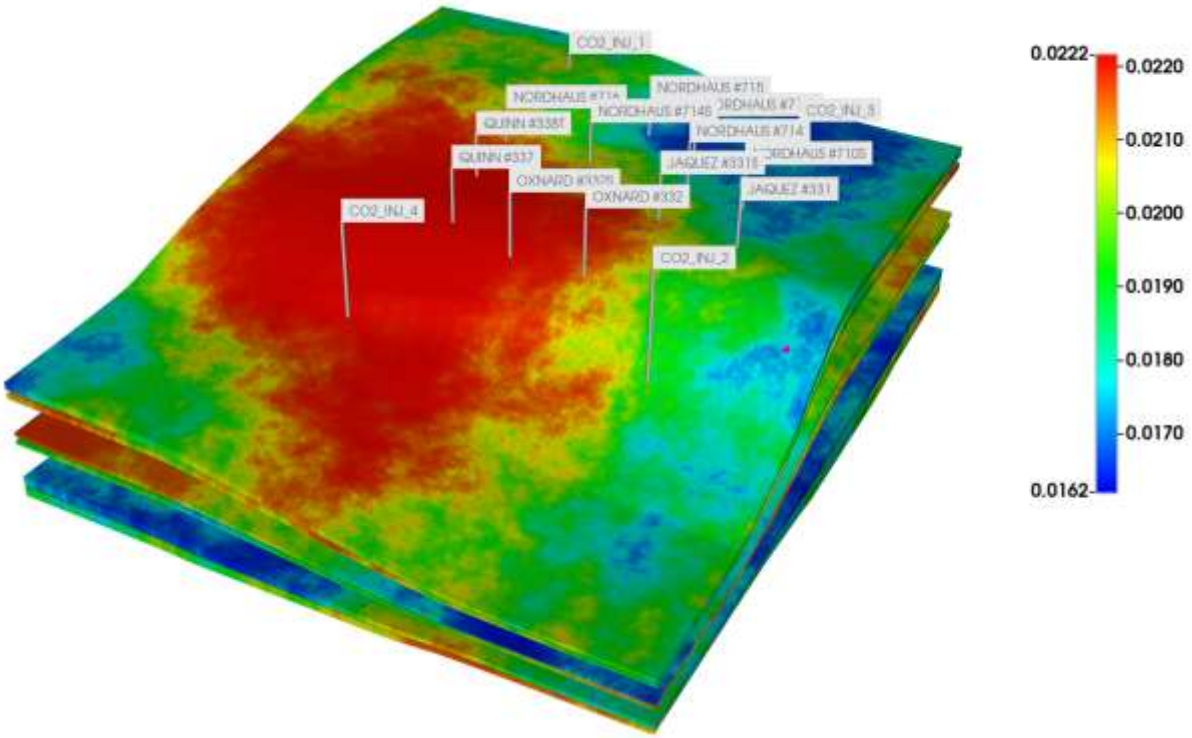


Figure 53. Face cleat porosity distribution

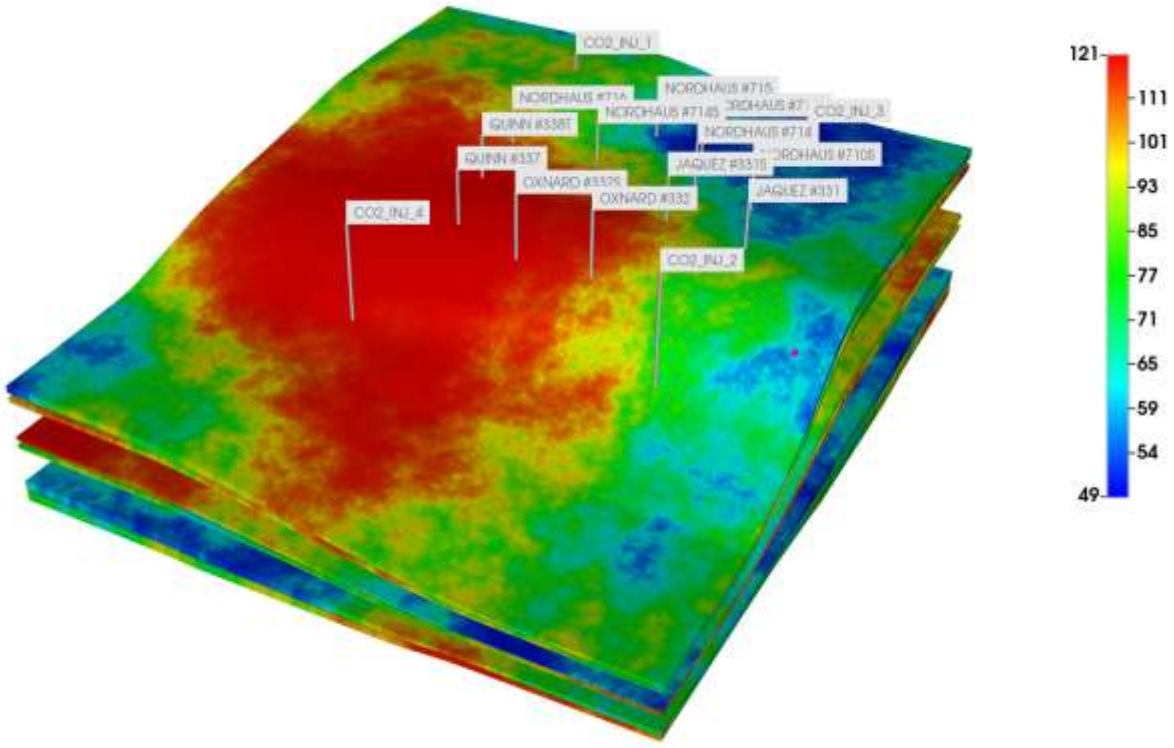


Figure 54. Face cleat permeability distribution

Table 9. Reservoir parameters used in the model

Parameter	Value	Source
Initial Pressure	1,600 psi	Well test report
Reservoir Temperature	120 deg F	(Reeves et al. 2003)
Initial Water Saturation		Assumed
Initial Gas Content	Per Isotherm	(Reeves et al. 2003)
Sorption time	10 days	(Reeves et al. 2003)
Fracture Spacing	0.25 inch	(Reeves and Oudinot 2004)
Gas Composition	95.5% CH_4 4.5% CO_2	(Reeves et al. 2003)

Relative Permeability	History Match	
Permeability Function Parameters	n = 0.33 a = 0.0024	(Siriwardane et al. 2012)

History Matching

The goal of this subtask is to calibrate the coal seam reservoir model to match field history before Enhanced Coalbed Methane (ECBM) production. The parameters chosen for adjustment are those affecting field performance and can be technically justified. The independent parameter in the reservoir model was the reservoir production rate to maintain material balance, while the dependent (history-matching) parameters were the gas and water production rates. A parametric study was performed on the permeability anisotropy ratio between the cleat and butt directions to identify the ratio at which gas production cannot be sustained while matching the field-measured rates. This step prevents selecting permeability values that could lead to overestimation during field operations. A second step involved history matching, adjusting two parameters of the relative permeability model (Chen et al. 2013) as in Error! Reference source not found. to Error! Reference source not found., where l is the cleat size distribution, h is the tortuosity, k_{rw}^{*} is the end-point relative permeability of the wetting phase, k_{rnw}^{*} is the end-point relative permeability of the nonwetting phase, S_w is the wetting phase saturation, S_{wr} is the residual wetting phase saturation and S_{nwr} is the residual nonwetting phase saturation to align gas production with the relative permeability. **Figure 55** is the resulting relative permeability curve after model calibration and used in the ECBM study.

$$k_{rw} = k_{rw}^{*}(S_w^{*})^{\eta+1+2/\lambda} \quad \text{Eq. 3}$$

$$k_{rnw} = k_{rnw}^{*}(1 - S_w^{*})^{\eta}\left[1 - (S_w^{*})^{1+2/\lambda}\right] \quad \text{Eq. 4}$$

$$S_w^{*} = \frac{S_w - S_{wr}}{1 - S_{wr} - S_{nwr}} \quad \text{Eq. 5}$$

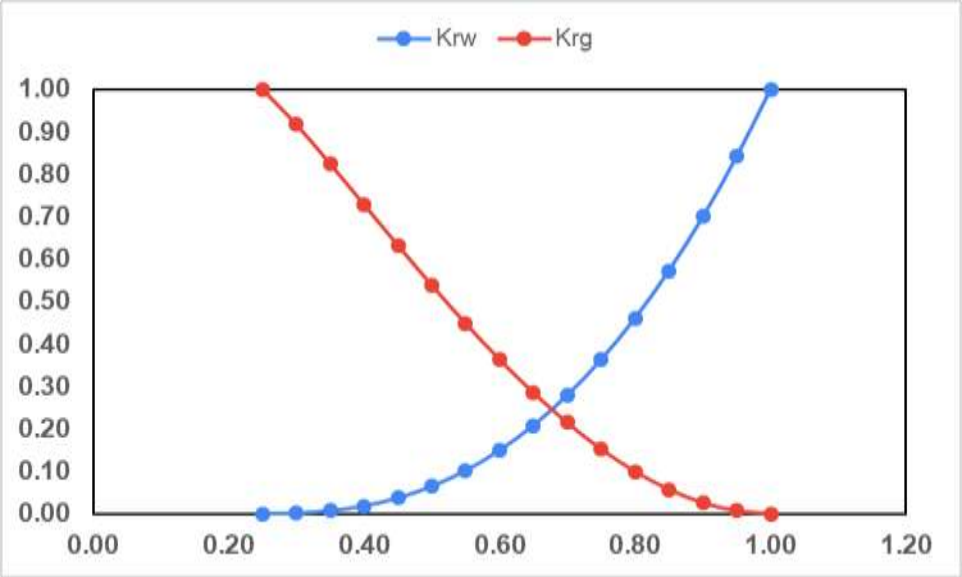
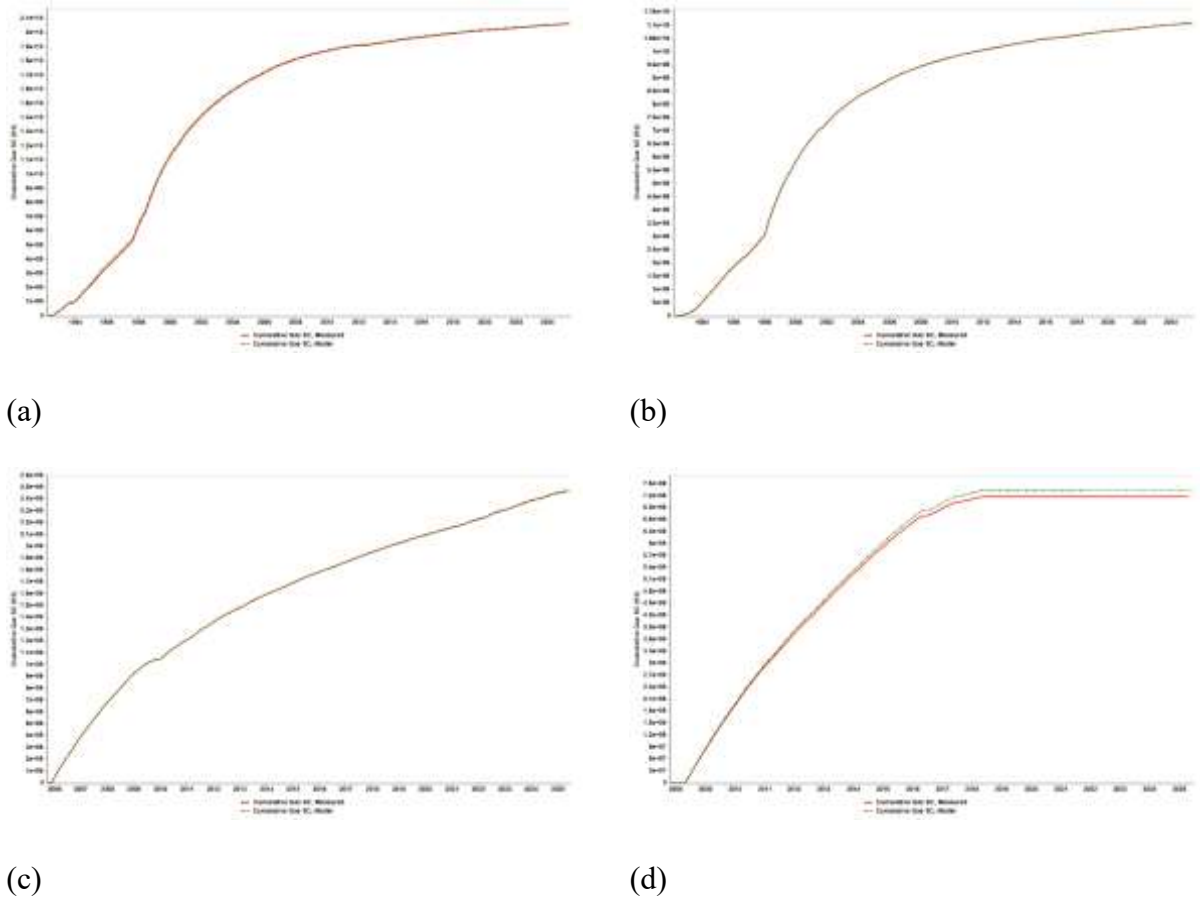


Figure 55: Calibrated relative permeability curve

A comparison of measured versus model-predicted well gas production is shown in **Figure 56** for selected wells. The only conclusion that can be drawn from this result, since the reservoir volume rate drove the model, is that the model can produce the observed gas volumes.

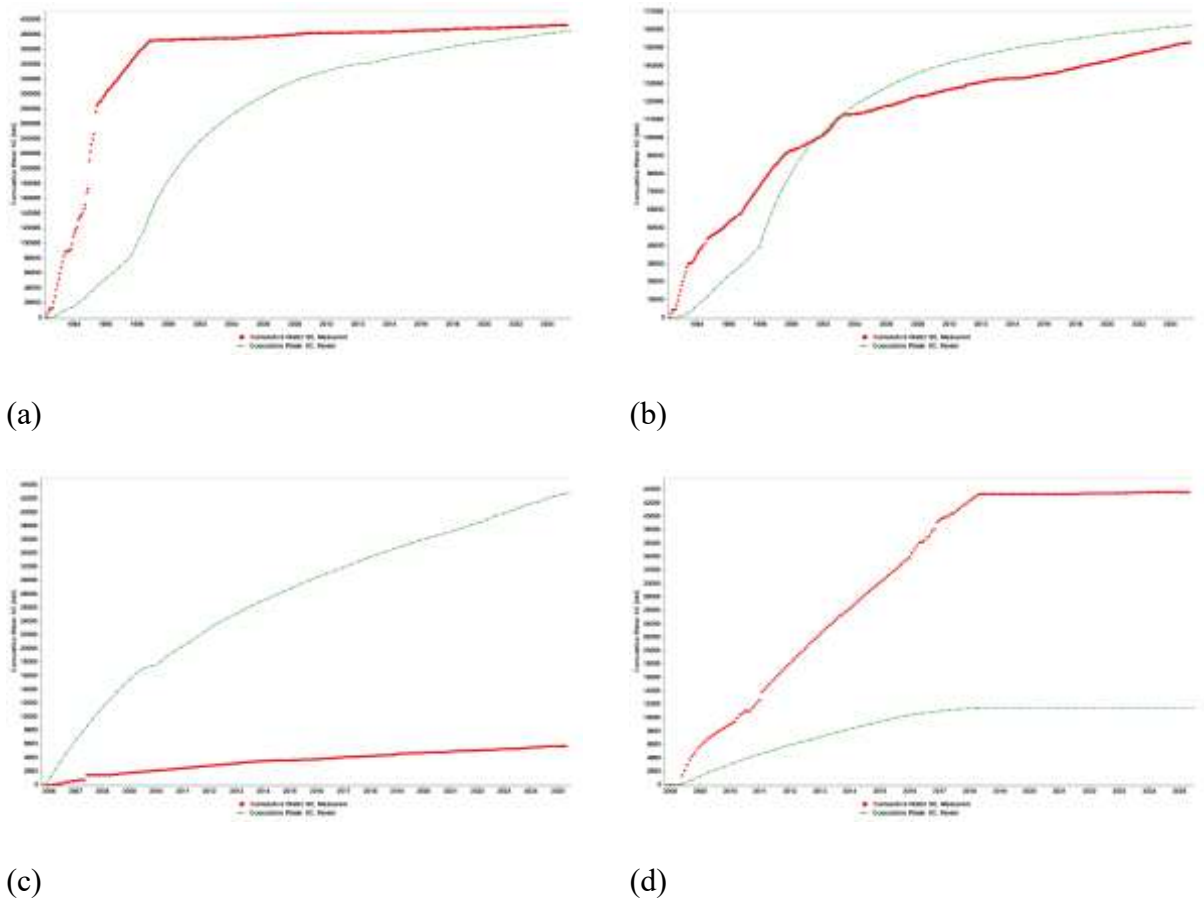


(a) (b)

(c) (d)

Figure 56: Comparison between measured and model-predicted gas production performance (a) NORDHAUS #714 (b) NORDHAUS #715 (c) JAQUEZ #331S (d) QUINN #338T

Figure 57 shows the well water production performance for selected wells. The quality of the water rate predictions varied, with some being too high (Figure 57c) and some too low (Figure 57d). However, on balance, the projections are considered reasonable, and the measured water rate appears too erratic to be accurate. It cannot be easily explained by regional variations in porosity and/or water relative permeability. Therefore, matching water rates was not a priority. Even though water production from individual wells was not prioritized, the total water produced from all wells was honored at the end of calibration (**Figure 58**). Preferably, well bottom-hole pressure, if available, should be used to validate the calibration, which was not available for this study. The use of the water rate, which is historically known not to be measured accurately, may lead to erroneous calibration pressures, which in turn affect forecast performance.



(a) (b)

(c) (d)

Figure 57. Comparison between measured and model-predicted water production performance (a) NORDHAUS #714 (b) NORDHAUS #715 (c) JAQUEZ #331S (d) QUINN #338T

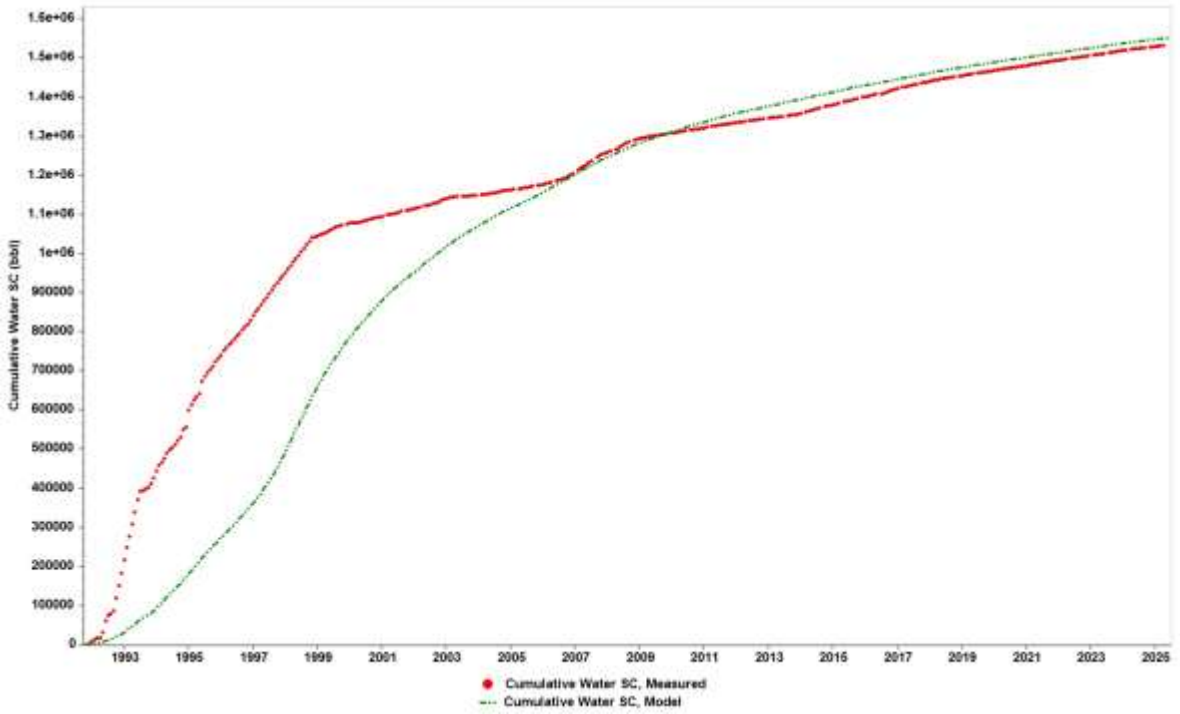


Figure 58. Field cumulative water production performance between measured and model predictions.

Performance Forecasts

To evaluate the long-term performance of the ECBM pilot under status quo conditions (i.e., no further CO_2 injection) and other "what if" future injection scenarios, performance prediction cases were simulated using the calibrated model. The specific cases evaluated included:

1) No CO_2 injection (i.e., primary production only).
2) Continuous CO_2 injection.
3) Continuous N_2–CO_2 co-injection.
4) Continuous CO_2 with intermittent N_2 injection.

For each forecast scenario, the model assumed flowing bottomhole pressures of 200 psi. The gas production rate is 1E6 ft³/day for the ECBM cases and gradually increased every 2 yr until 2034, when the maximum rate target of 3E6 ft³/day is maintained. For the No CO_2 injection case, the last known well-specific rates from history were used for forecasting. Additionally, an economic limit of 50% CO_2 content per well was imposed; exceeding this threshold prompted the layer in question to be shut in. An injection target of 100 tons per day per injection well was set, gradually increased by 50 tons every 2 yr until 2034, when the maximum injection target of 300 tons per day is reached. The maximum injection bottom-hole pressure was set to 0.7 of the initial reservoir pressure, translating to 1,120 psi. A peripheral injection scheme was implemented, coupled with staggered rate control between the injection and production wells to delay CO_2 breakthrough and prevent rapid pressure changes that could negatively impact displacement efficiency. By maintaining reservoir pressure around 0.7 of its initial value, pressure-induced injectivity loss will be minimized. **Figure 59** shows the relationship between permeability changes with pressure and concentrations (Reeves et al. 2003). The forecast aims to keep reservoir pressure within the green region. After the calibration, the average pressure within the

upper coal was 1,151 psi, while the middle and lower coal zones were around 980 psi. The upper coal was within the pressure-dependence region, while the middle and lower coals were within the matrix-shrinkage region.

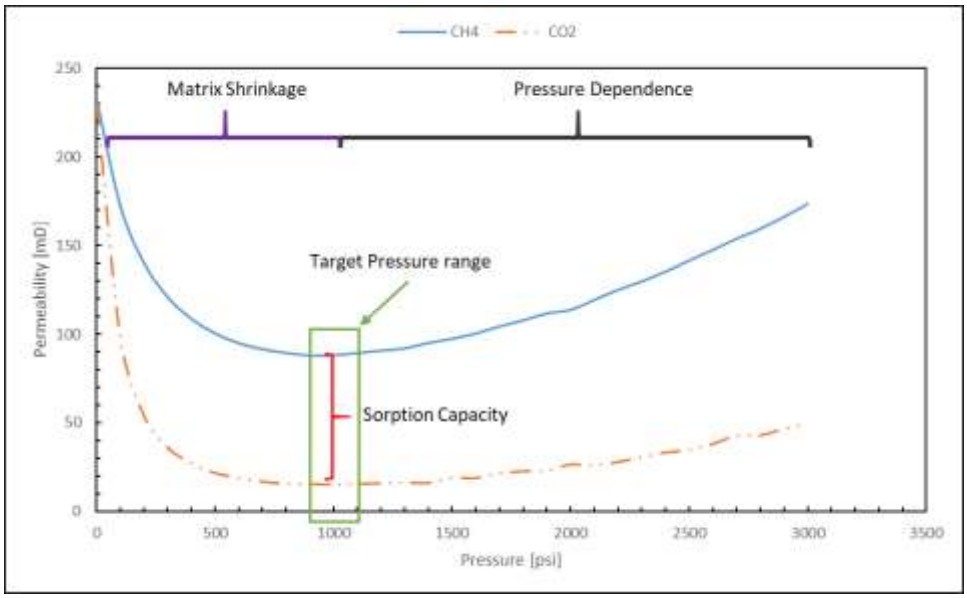


Figure 59. Permeability changes with pressure and concentration (Reeves et al. 2003)

Case #1: No CO_2 Injection

The baseline scenario assumes that no CO_2 injection occurred and that the field was produced exclusively by primary pressure depletion over 30 yr. In this case, total incremental methane recovery was 336 Mt within the active model area, yielding a recovery factor of 3.0%. The final average reservoir pressure was 971 psi (**Figure 60**).

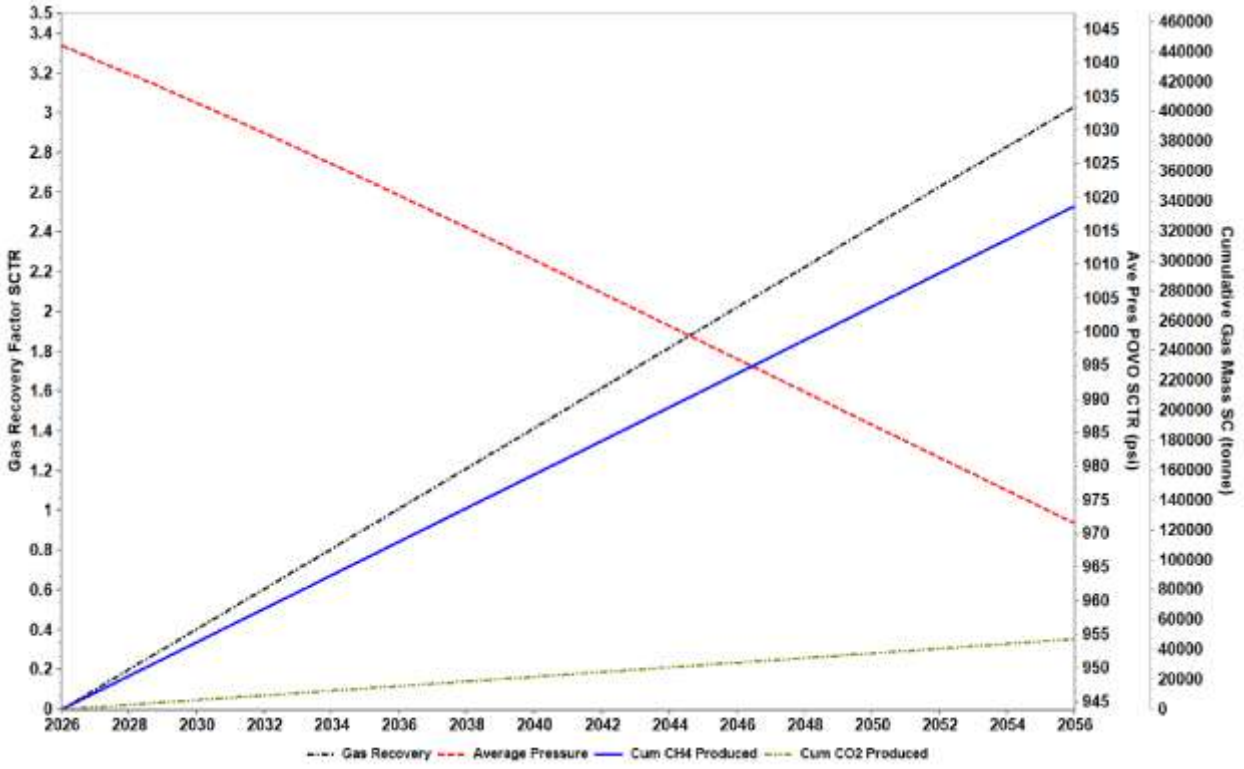


Figure 60. Average reservoir pressure and incremental gas production and recovery Case 1

Case #2: Continuous CO_2 Injection

This case assumes CO_2 injection over 30 yr, with a gradual increase in the injection rate. The incremental gas rate for Case 2 is shown in **Figure 61.** Notably, several wells were shut in due to exceeding the maximum allowable CO_2 content of 50% in the produced gas. The total methane recovery for Case 2 was approximately 3.53 Mt, approximately 3.19 Mt more than in Case 1. The total volume of CO_2 injected was approximately 21.6 Mt, resulting in a CO_2 to CH_4 ratio of 6:1. The average final pressure within the active model was 1,130 psi. The estimated incremental sequestration volume for this case is approximately 18.7 Mt of CO_2.

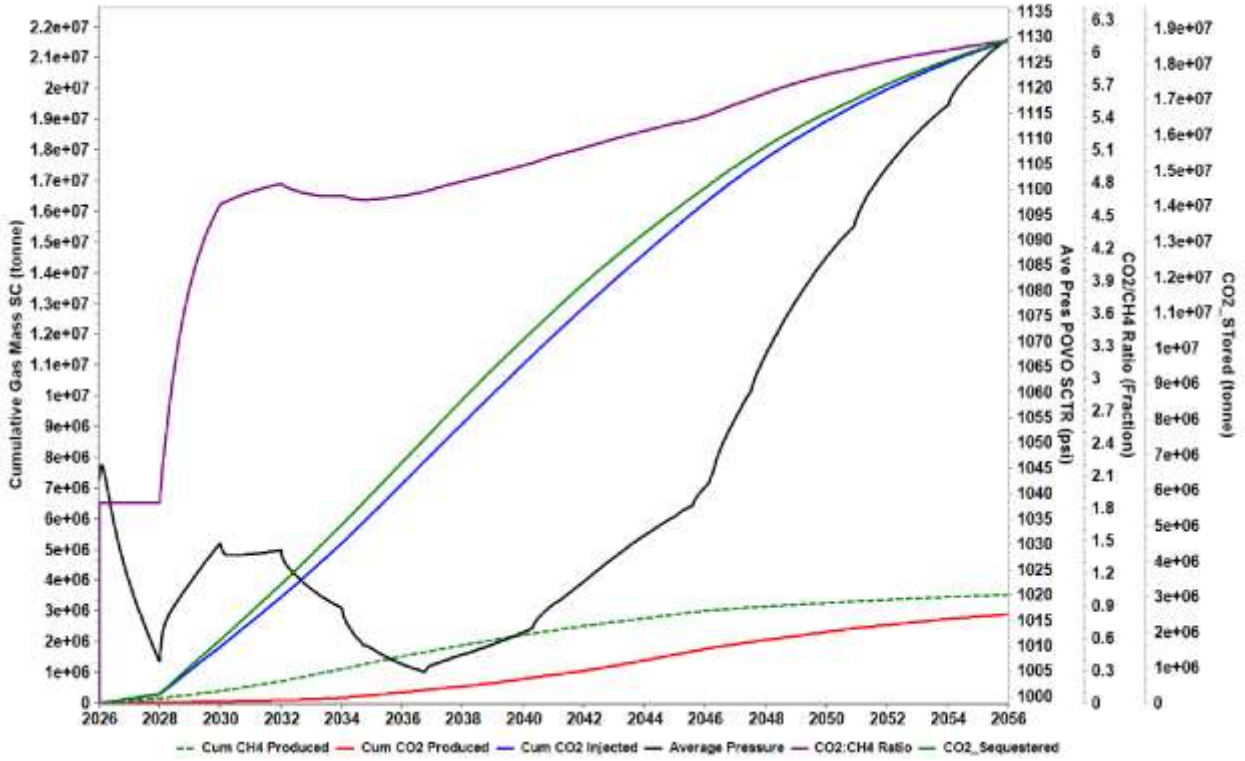
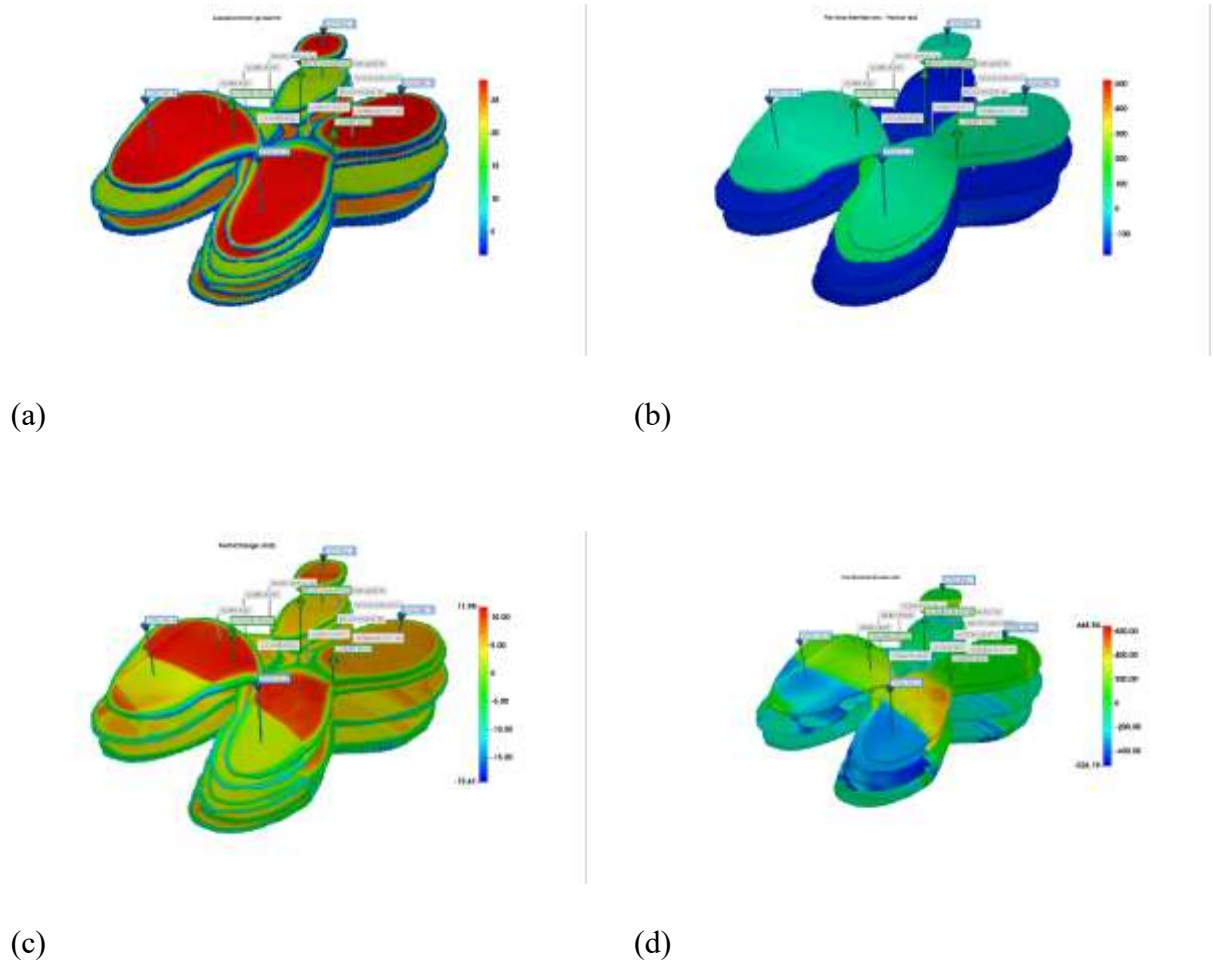


Figure 61. Continuous CO_2 injection incremental recovery performance

Figure 62a shows the CO_2 plume within the coal matrix at the end of injection, delineated as any regions with CO_2 adsorption greater than 3 gmole/ft^3. The minimum value was chosen based on the maximum final adsorption after calibration. Any adsorption value above the maximum is treated as the injected CO_2 plume region. The forecasting was designed to decrease the fracture pressure in the upper coal region and increase it in the middle and lower regions. In Figure 62b, which shows the cumulative pressure drop within the CO_2 plume, it can be observed that there is a decrease (positive fracture pressure drop) in the upper coal and an increase (negative fracture pressure drop) in the middle and lower regions. An average pressure gain of 100 psi was observed in the middle and lower regions, and an average pressure depletion of 100 psi in the upper coal region. With that pressure target, permeability increased in the upper coal region without significant loss in the middle and lower regions, as shown in the cumulative permeability change plot (Figure 62c). The permeability changes in the fractures between the injector and producers (Figure 62c) did not lead to injectivity because the matrix pressures around the producers created a significant pressure drop (Figure 62d), thereby shrinking the matrix and increasing permeability in the fractures. At the end of the injection, the pressure within all regions was within the target range, which is around the average pressure at the end of calibration.



(a) (b)

(c) (d)

Figure 62. Case 2 CO_2 adsorption: (a) CO_2 plume, (b) cumulative pressure change, (c) fracture cumulative permeability change, and (d) matrix cumulative permeability change at the end of injection

Case #3: Continuous N_2–CO_2 Injection

This case assumes CO_2–N_2 injection at a 0.95:0.05 ratio over 30 yr, with a gradual increase in injection rate. The incremental gas rate for Case 3 is shown in **Figure 63**. The total methane recovery for Case 3 was approximately 3.59 Mt, approximately 3.26 Mt more than in Case 1 but about 66 kt more than in Case 2. The total volume of CO_2 injected was approximately 20 Mt. The average final pressure within the active model was 1,117 psi which is not different from Case 2. The estimated incremental sequestration volume for this case is approximately 17.4 Mt of CO_2, about 1 Mt less than Case 2.

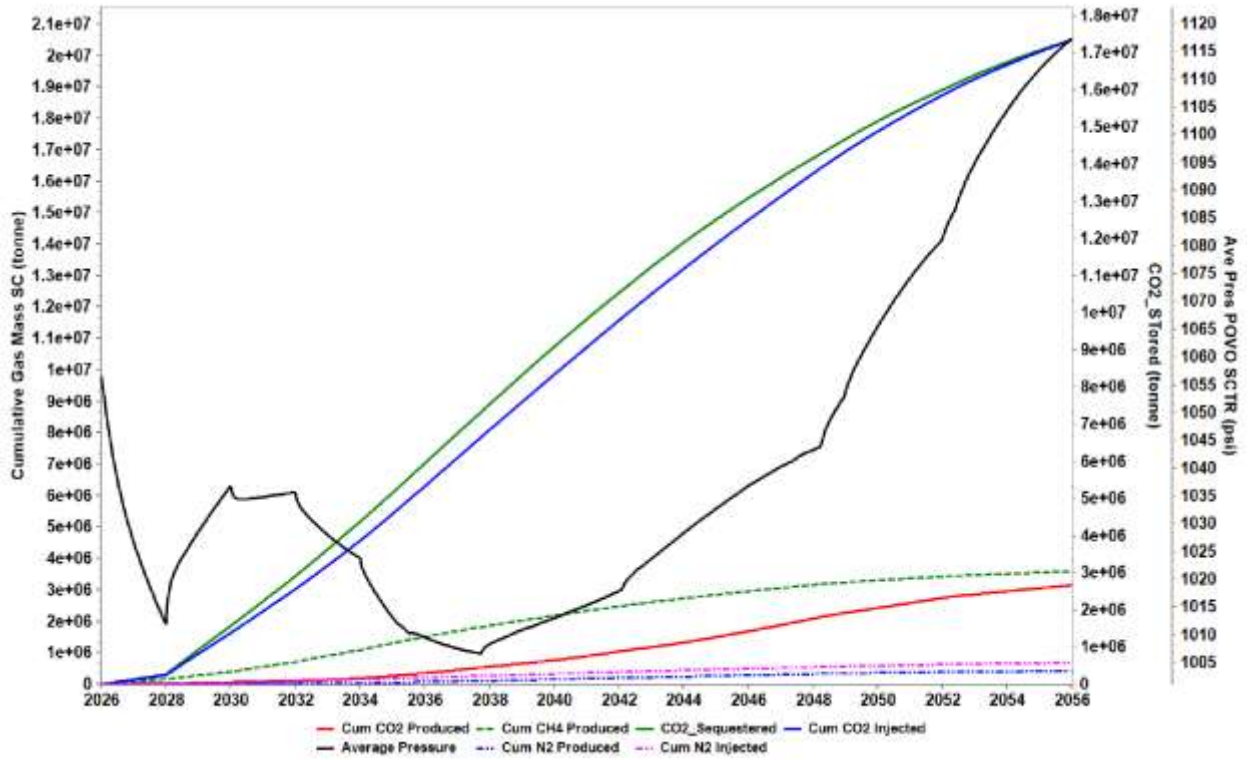
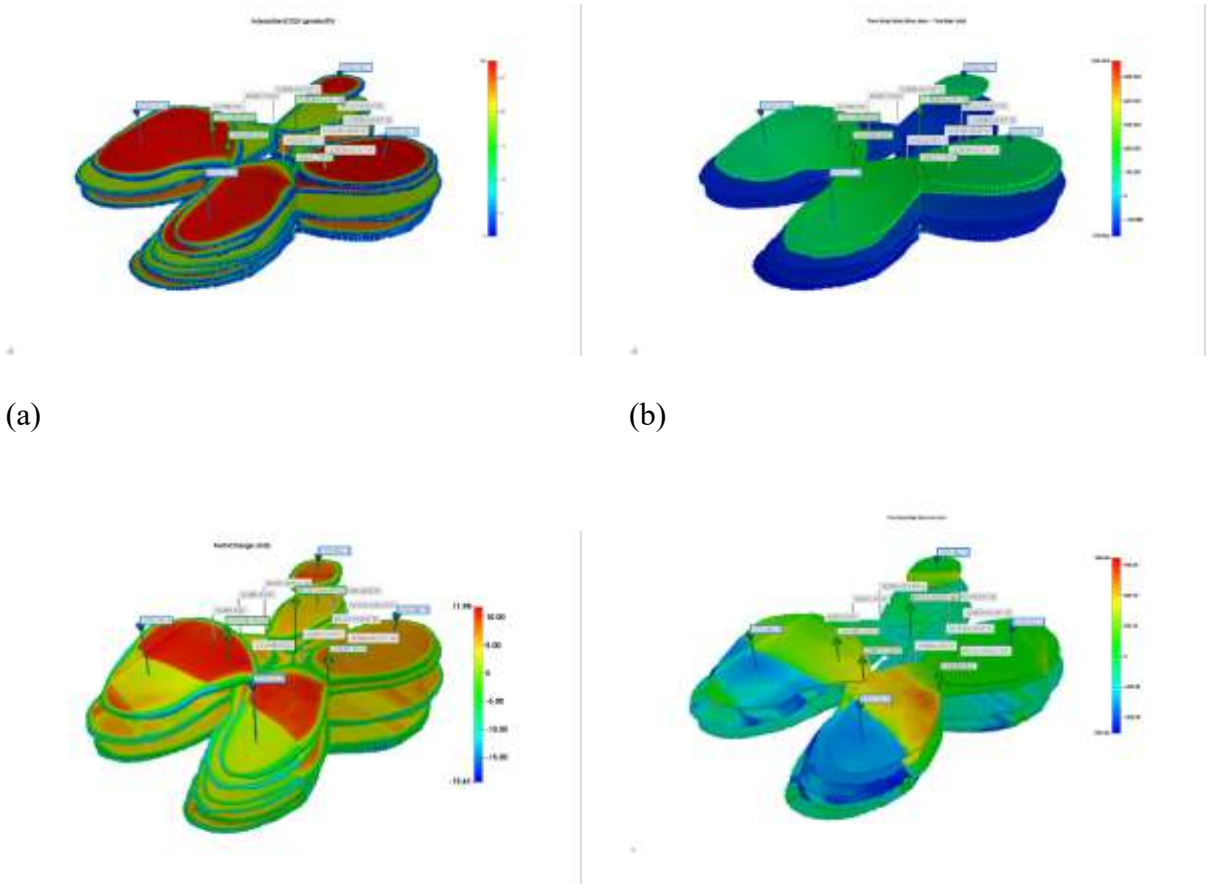


Figure 63. Continuous CO_2–N_2 injection incremental recovery performance

Figure 64a shows the CO_2 plume within the coal matrix at the end of injection, delineated as any regions with CO_2 adsorption greater than 3 gmole/ft^3. The forecasting was designed similarly to Case 2, but N_2 kept the fractures open to decrease the pressure in the upper coal region and increase it in the middle and lower regions. In Figure 64b, which shows the cumulative pressure drop within the CO_2 plume, it can be observed that there is a decrease in the upper coal and an increase in the middle and lower regions. An average pressure gain of 100 psi was observed in the middle and lower regions, and an average pressure depletion of 100 psi in the upper coal region. With that pressure target, permeability increased in the upper coal region without significant loss in the middle and lower regions, as shown in the cumulative permeability change plot (Figure 64c). At the end of the injection, the pressure within the production zone within the matrix (Figure 64d) decreased, creating a flow path between the injector and producers. Due to the distance between the injectors 1 and 3 and the producers, there was net pressure decrease which lead to permeability increase (Figure 64c).



(a) (b)

(c) (d)

Figure 64. Case 3 CO_2 adsorption: (a) CO_2 plume, (b) cumulative pressure change, (c) fracture cumulative permeability change, and (d) matrix cumulative permeability change at the end of injection

Case #4: Continuous CO_2 with Intermittent N_2 Injection

This case assumes CO_2 injection for 11 months and N_2 injection for 1 month over 30 yr, with a gradual increase in the CO_2 injection rate while the N_2 injection rate is maintained at 50 t for each of the four injection wells. The incremental performance for Case 4 is shown in **Figure 65**. The total methane recovery for Case 4 was approximately 3.65 Mt, approximately 3.32 Mt more than in Case 1, but about 126 thousand and 59 kt more than in Cases 2 and 3, respectively. The total volume of CO_2 injected was approximately 20.7 Mt. The average final pressure within the active model was 1,097 psi, which is not different from Cases 2 and 3. The estimated incremental sequestration volume for this case is approximately 17.3 Mt of CO_2, about 1 Mt less than Case 2.

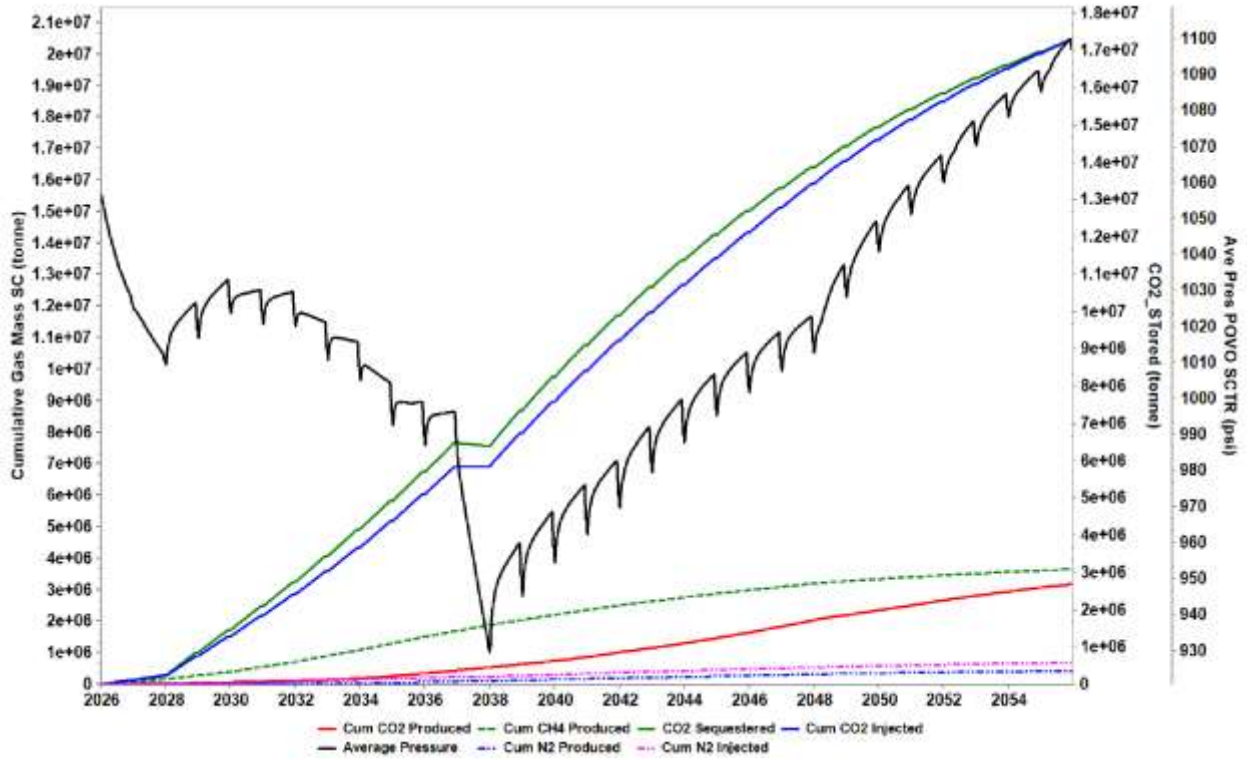
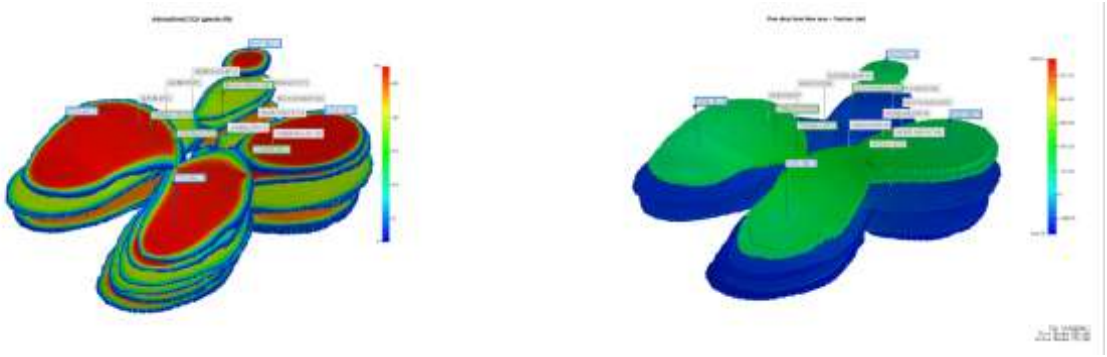
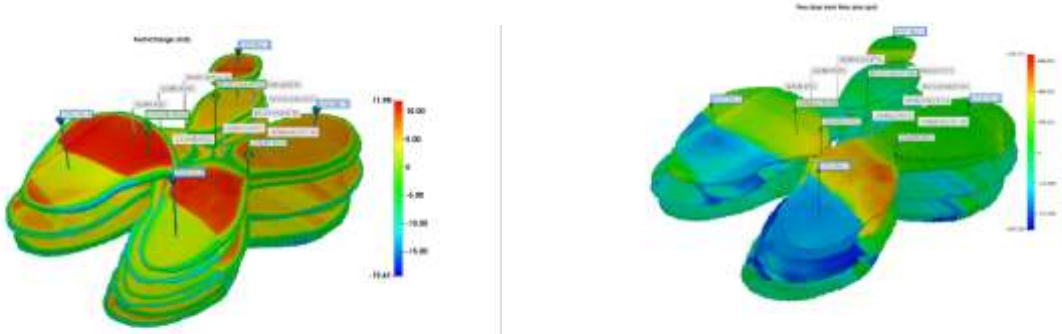


Figure 65. Intermittent CO_2–N_2 injection incremental recovery performance

Figure 66a shows the CO_2 plume within the coal matrix at the end of injection. In Figure 66b, which shows the cumulative pressure drop within the CO_2 plume, it can be observed that there is a decrease in the upper coal and an increase in the middle and lower regions. An average pressure gain of 100 psi was observed in the middle and lower regions, and an average pressure depletion of 100 psi in the upper coal region similar to Case 2 and 3. The permeability increase within the upper coal region without significant permeability loss within the middle and lower regions as shown in the cumulative permeability change plot (Figure 66c).



(a) (b)



(c) (d)

Figure 66: Case 4 CO_2 adsorption: (a) CO_2 plume, (b) cumulative pressure change, (c) fracture cumulative permeability change, and (d) matrix cumulative permeability change at the end of injection

A comparison of the forecast cases' performance relative to the no-injection case is delineated in **Table 10**. The results indicate an approximately 1% increase in recovery when N_2 was injected, despite a reduction in CO_2 storage attributable to increased CO_2 production. Because we could not attribute what amount of CO_2 or N_2 was contributed to CH_4 recovery, the CO_2:CH_4 ratio was not computed. The peripheral injection strategy and the spacing between injector and producer facilitated improved recovery, thereby permitting a larger injection volume and enhanced injectivity.

Table 10: Summary of case comparisons

	NO_CO_2_Injection	**CO_2-ECBM**	**CO_2-N_2-ECBM**	**CO_2-N_2-ECBM-Cycling**
Total CH_4 produced, t	3.37E+05	3.53E+06	3.59E+06	3.65E+06
Incremental CH_4 produced, t	0	3.19E+06	3.26E+06	3.32E+06
Total CO_2 injected, t	0	2.16E+07	2.05E+07	2.05E+07
Total CO_2 produced, t	4.70E+04	2.90E+06	3.15E+06	3.18E+06
Total N_2 injected, t	0	0	6.87E+05	6.85E+05
Total N_2 produced, t	0	0	4.25E+05	4.25E+05

CO_2:CH_4	0	6	-	-
Incremental CH_4 recovery, %OGIP	2.45	25.67	26.15	26.59
CO_2 stored, t	0	1.87E+07	1.74E+07	1.73E+07
Average pressure, psi	972	1,130	1,117	1,097

Underground Injection Control Consideration for Escalante Power Plant

Geologic CO_2 Storage Permits Template in New Mexico (EPA Region VI)

Well drilling and CO_2 storage facility permits issued by New Mexico Oil and Gas Commission and the U.S. Environmental Protection Agency (EPA) Regional VI individually are required to implement geologic CO_2 storage in New Mexico. The Petroleum Recovery Research Center at New Mexico Tech has developed one permit template to assist the operator in preparing 1) an application for permit to drill (APD) a stratigraphic test well and 2) a storage facility permit (SFP) application that are consistent with EPA Underground Injection Control (UIC) Class VI statutes and regulations. The APD template includes options for the design and permitting of a stratigraphic test well that can be transitioned for use as a UIC Class VI-compliant injection or monitoring well.

No storage facility permits have yet been issued in New Mexico. The permit application templates presented incorporate learnings and clarifications that have been garnered as the first projects advancing carbon capture and storage (CCS) in New Mexico. Each section provides a description of the intent of the section, and a description of evidence or exhibits to be included within the section. The templates incorporate formatting that is both structured to present the information required in the permit application in a functional, logical, and consistent fashion and aligned with the permit review and public hearing process.

With the assistance of the project team, Four Corners Carbon Capture LLC (Tallgrass) had successfully submitted an UIC Class VI permit to EPA Region 6. Currently the submission is pending for the final permitting determination.

Introduction

Well drilling and CO_2 storage facility permits (SFP) are required to construct and operate a geologic CO_2 storage project in New Mexico. An application of permit to drill (APD) is required to drill a stratigraphic test well, which is used to acquire the necessary downhole data to complete a CO_2 SFP in New Mexico. The New Mexico Oil and Gas Commission (NMOCD) has authority to regulate stratigraphic well drilling permit align with the Class II well permit as an acid gas injection well. As such, the stratigraphic test well is part of a critical path to achieving

UIC Class VI compliance. Several recommended practices and clarifications related to well design, geologic characterization, well testing, and the UIC Class VI requirements resulted from these permit discussions, the more significant of which are captured in call-out boxes throughout these templates.

This document provides application templates for the two permits that are required to move forward with the commercial geologic storage of CO_2 in New Mexico: the APD for Class II well and the SFP.

Well Drilling Permit

For the purposes of this template, the APD has been developed as a stratigraphic test well which classified as a Class II acid gas injection well. A complete storage facility permit requires data and information obtained from core, geologic formation testing and sampling, and wireline logging within the facility area of a geologic storage project. While there may be instances where existing data (i.e., core and log data) can be used for the SFP in lieu of drilling a stratigraphic test well, in many cases the operator will need to drill a well prior to applying for a SFP to collect the necessary data.

An option for accelerating deployment of CCS is to permit and drill a stratigraphic test well designed and constructed in a manner that provides a pathway to convert the Class II well to a UIC Class VI compliant injection well (e.g., strategic use of CO_2 resistant materials). The stratigraphic test well transition pathway is addressed in the SFP application process, which includes a request to convert the well to a CO_2 injection well and an application to inject CO_2.

The APD includes 1) an accurate well location plat certified by a registered surveyor showing the location of the proposed well with reference to the nearest lines of a governmental section and referenced to true north; 2) an accurate pad layout which indicates a cut and fill diagram and additional construction required, i.e., water bars, culverts, etc.; 3) a facility layout, i.e., location of surface facilities on well pad; and 4) road access to the well location. If drill cuttings will be buried on location (i.e., a dry-cuttings pit), the location of the dry cuttings pit needs to be on the facility layout plat.

This attachment, a geological prognosis, presents such information as the estimated depth to the top of objective horizons (measured depths [MD]); the estimated depth to the top and thickness of important geologic markers such as members or zones potentially containing usable water, USDWs, oil, gas, or other valuable deposits; and the identification of the formation at total depth, including the identification of all potential confining layers above and below the zone of interest. The drilling program and prognosis provides the technical detail of the plans for drilling and completing the injection well. Examples of the information and content of this attachment are as follows:

- Proposed total depth (including MD and true vertical depth) to which the well will be drilled
- Estimated depth to the top of important geologic markers
- Estimated depth to the top of objective horizons
- Proposed drilling mud program for surface hole and vertical hole
- Proposed openhole and cased hole logging program
- Proposed well testing, coring, and geologic characterization program
- Proposed casing program including size and weight

- Proposed depth and formation at which each casing string is to be set
- Proposed amount of cement and placement procedure to be used
- Estimated top of cement
- General completion procedure
- Other pertinent information

The storage operator should provide information regarding the proposed mud program for both the surface and production holes in this attachment. Also, the operator should include a description of the casing program, which includes the casing properties. The storage operator is required to provide a schematic of the wellbore. An evaluation program for the coring, testing, and logging of the stratigraphic test well is provided in this attachment. Additional information of importance includes the descriptions of the pressure control equipment, the drilling procedure, and the post completion plan. Examples of the content that is required for each of these topics is provided in the remainder of this section.

Well control during all phases of the drilling, logging, casing runs, cementing, testing, etc., is mandated by NMOCD and by industry best management practices. Well control equipment is typically referred to as blowout prevention equipment (BOPE). The BOPE includes a description, accompanied by exhibits, of the type of equipment that will be used, e.g., blowout preventers, choke manifolds, and accumulators, including the operational procedures and frequency for testing and documentation of this equipment.

The drilling procedure are required for each drilling interval from ground level to the total depth of the well, include the following:

- Hole size
- Type of drilling mud
- Bit and casing specifications
- Detailed drilling procedure
- Detailed coring, testing, and logging procedures
- Specific cementing procedures
- Cementing and casing evaluation procedures

Within thirty days after the conclusion of well drilling and completion activities, the storage operator is required to provide project specific reports, exhibits, documentation, and descriptions of the drilling, logging, coring, cementing, and well integrity evaluations of the stratigraphic test well.

UIC Class VI Well Permit

The UIC Class VI well permit application(s), one for each proposed Class VI well, will meet all requirements of 40 CFR 146.82 and those parts referenced therein. Required permit application materials will be entered into the ten modules of the Geologic Sequestration Data Tool (GSDT) and, after meeting data validation, will be submitted to EPA Region 6. Table 5 indicates the documents the project had been developed.

Table 5 Class VI Underground Injection Control (UIC) permit application project narrative, modified [1].

Section of Project Narrative	**Requirements**	**UIC Regulatory**

Site Characterization, including:		40 CFR 146.82(a)(2), (3), (5), and (6)
Regional Geology, Hydrogeology, and Local Structural Geology	Submittal of geologic & topographic maps & cross sections illustrating regional geology, hydrogeology, geologic structure of local area surrounding the project area	40 CFR 146.82(a)(3)(vi)
Maps and Cross Sections of the AoR	Topographic maps; geologic maps w/ cross sections & stratigraphic columns summarizing lithology, sequence of geologic units (including injection & confining zones and USDWs), approximate formation thicknesses, lateral extent of units, and correlation of units in vicinity of project and across region	40 CFR 146.82(a)(2); 40 CFR 146.82(a)(3)(i)
Faults and Fractures	Submittal of information on location, orientation, and properties of known or suspected faults & fractures that may transect the confining zone(s) in the AoR and a determination that they would not interfere with containment.	40 CFR 146.82(a)(3)(ii)
Injection and Confining Zone Details	Submittal of information on the depth, areal extent & thickness of the injection formation & confining zone(s); submittal of data on mineralogy of injection & confining zone(s); submittal of data on porosity, permeability & capillary pressure of injection & confining zones	40 CFR 146.82(a)(3)(iii)
Geomechanical and Petrophysical Information	Geomechanical information be submitted on fractures, stress, ductility, rock strength, and in situ fluid pressures within the confining zone; the use of geophysical methods for obtaining subsurface information in lieu of direct physical sampling.	40 CFR 146.82(a)(3)(iv)
Seismic History	A report on the seismic history of the project site, including the presence and depth of all seismic sources	40 CFR 146.82(a)(3)(v)
Hydrologic and Hydrogeologic Information	Submission of maps and stratigraphic cross sections indicating the general vertical and lateral limits of all USDWs, water wells, and springs within the AoR, their positions relative to the injection zone(s) and confining zone(s), and the direction of water movement	40 CFR 146.82(a)(3)(vi); 40 CFR 146.82(a)(5)
Geochemistry	Baseline geochemical information on subsurface formations including all USDWs in the AoR including both fluid and solid phase chemical analysis.	40 CFR 146.82(a)(6)

Site Suitability	Provide comprehensive data and descriptions for many properties of the proposed project site and demonstrate whether it is a good candidate for GS and meets the requirements at 40 CFR 146.83	40 CFR 146.83
Injection Well Construction Plan, including:	Ensure that all Class VI wells are constructed and completed to: (1) Prevent the movement of fluids into or between USDWs or into any unauthorized zones; (2) Permit the use of appropriate testing devices and workover tools; and (3) Permit continuous monitoring of the annulus space between the injection tubing and long string casing.	40 CFR 146.82(a)(9), (11), and (12)
Proposed Stimulation Program		40 CFR 146.82(a)(9)
Construction Procedures		40 CFR 146.82(a)(12)
Well Operation Plan, including:	Maintaining the integrity of the well and ensuring the safe sequestration of CO_2	40 CFR 146.82(a)(7) and (10)
Operational Procedures		40 CFR 146.82(a)(10)
Proposed CO_2 Stream		40 CFR 146.82(a)(7)(iii) and (iv)
Injection Depth Waiver and Aquifer Exemption Expansion	Seeking a waiver of the requirement to inject below the lowermost USDW	40 CFR 146.82(d); 40 CFR 146.95(a); 40 CFR 146.4(d); 40 CFR 144.7(d)
Other Information		40 CFR 146.82(a)(21)
Executive Summaries of:		
Financial Responsibility	The types of financial instruments that owners or operators of Underground Injection Control (UIC) Class VI Geologic Sequestration (GS) wells can choose to demonstrate compliance with the financial responsibility requirements of the Rule	40 CFR 146.82(a)(14); 40 CFR 146.85
AoR and Corrective Action Plan	Prepare, maintain, and comply with an AoR and Corrective Action Plan that includes all of the required elements of the plan; Delineate the AoR using computational modeling and identify all wells that require corrective action; Perform all required corrective action on wells in the AoR;	40 CFR 146.82(a)(4); 40 CFR 146.82(a)(13); 40 CFR 146.84(b); 40 CFR 146.84©

	Re-evaluate the AoR throughout the life of the project; Ensure that the Emergency and Remedial Response Plan and financial responsibility demonstration account for the most recently approved AoR; Retain modeling inputs and data used to support AoR re-evaluations for 10 yr.	
Pre-Operational Logging and Testing Plan	Describes how they will test the well and analyze the chemical and physical characteristics of the injection and confining zones	40 CFR 146.82(a)(8); 40 CFR 146.87
Emergency and Remedial Response Plan	Describes actions to be taken to address events that could potentially cause endangerment to a USDW during the construction, operation, and PISC phases of a project	40 CFR 146.82(a)(19); 40 CFR 146.94(a)
Testing and Monitoring Plan	Describes testing and monitoring activities that are primarily required during the injection phase	40 CFR 146.82(a)(15); 40 CFR 146.90
Injection Well Plugging Plan	Ensure that the proposed materials and procedures for injection well plugging are appropriate to the well's approved construction and the site's geology and geochemistry	40 CFR 146.82(a)(16); 40 CFR 146.92(b)
Post-Injection Site Care (PISC) and Site Closure Plan	Outlines the proposed post-injection monitoring strategies and how non-endangerment of USDWs will be ensured throughout the PISC phase	40 CFR 146.82(a)(17); 40 CFR 146.93(a)

Required permit application materials will be entered into the ten modules of the GSDT and, after meeting data validation, the package will be submitted to EPA regional offices by the site operator.

References

Chen D, Pan Z, Liu J, Connell LD. 2013. An improved relative permeability model for coal reservoirs. Int J Coal Geol. 109–110:45–57. doi:10.1016/j.coal.2013.02.002

Reeves NS, Oudinot NA. 2004. The Tiffany Unit N2–ECBM pilot: a reservoir modeling study. Morgantown (WV); U.S. Department of Energy, Office of Scientific and Technical Information. doi:10.2172/923257

Reeves S, Taillefert A, Pekot L, Clarkson C. 2003. The Allison Unit CO_2–ECBM pilot: a reservoir modeling study. Morgantown (WV); U.S. Department of Energy, Office of Scientific and Technical Information. doi:10.2172/825083

Siriwardane HJ, Bowes BD, Bromhal GS, Gondle RK, Wells AW, Strazisar BR. 2012. Modeling of CBM production, CO_2 injection, and tracer movement at a field CO_2 sequestration site. Int J Coal Geol. 96–97:120–136. doi:10.1016/j.coal.2012.02.009

Weber M, Wilson TH, Akwari B, Wells AW, Koperna G. 2012. Impact of geological complexity of the Fruitland Formation on combined CO_2 enhanced recovery/sequestration at San Juan Basin pilot site. Int J Coal Geol. 104:46–58. doi:10.1016/j.coal.2012.09.011

Regional-Scale Assessment of CO_2 Geological Storage in Sedimentary Basin Geothermal Reservoirs of Nevada *on page* 115.

Subtask 4.5.3 – Site Characterization for CO_2 Storage to Support Escalante Hydrogen Power Plant and Logos Resources Projects

See We proposed a new technology for CO2 plume detection wherein a seismic emitter will be placed beneath the plume and tomography will be performed with stations at the surface (Figure 28). This design has six hypothesized advantages over the present state-of-the-art of CO_2 plume tomographic detection, which typically only images the plume in a 2D sense at either a single time or infrequently (Ajo-Franklin et al. 2013; Gunning et al. 2020; Hu et al. 2017) and only augments the numerical modeling of the plume (Pruess et al. 2001; Pham et al. 2011). The first advantage of this technology is the inherent time-lapse nature wherein the operator would be able to image the plume at essentially any time they choose. The second significant advantage is the 3D nature of the design. So long as the surface stations are placed with sufficient coverage above the expected extent of the plume (and they can be moved in the middle of monitoring), then the plume can be imaged with accuracy throughout its full volumetric extent. The third advantage is that the tomography will be performed with direct waves rather than reflected waves, which increases the amplitude and reduces the uncertainty. Fourth, by placing the emitter in the borehole rather than using a surface source, the frequency content of the emitted wavelet can be significantly higher, which will allow for greater tomographic resolution. Such resolution could potentially offer the ability to detect leakage of supercritical carbon dioxide through the caprock should that be the case. Fifth, the source is frequency swept, which allows for correlation-based processing that offers a much higher dynamic range for imaging the system. Finally, the tomographic image can be improved by moving the source to different locations within the monitoring wellbore to gather from different source points.

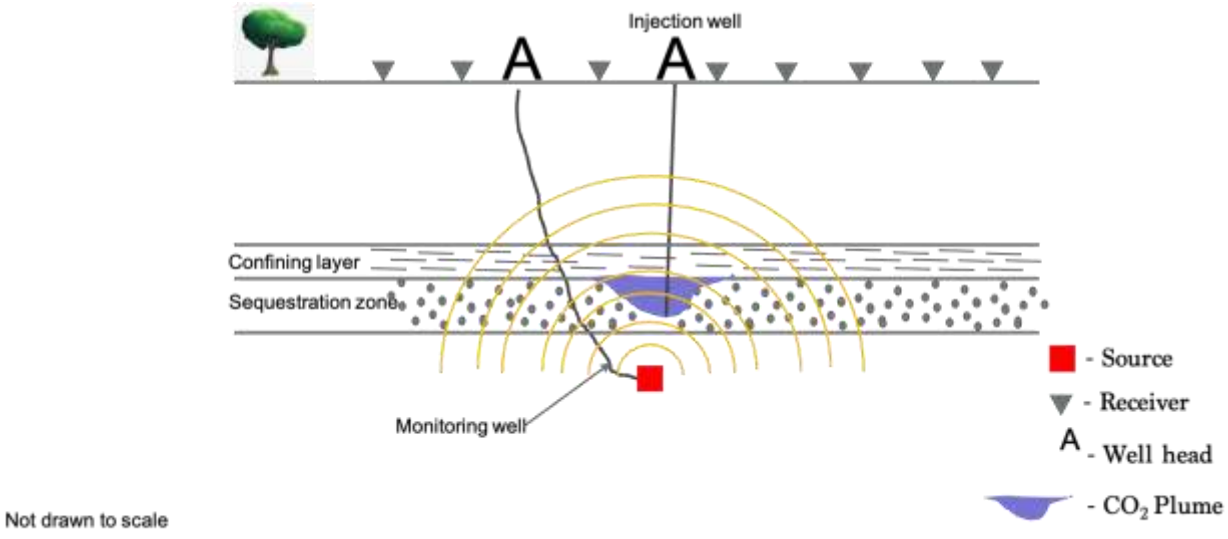


Figure 28 Proposed design of the downhole source tomographic technology to enhance the CO_2 plume migration detection

Final Report

The project team designed a laboratory-scale experiment to simulate the potential implementation of the Downhole Source Tomography technology. The proposed experiment will be conducted in a 1m x 1m x 1m cube of sandstone (Figure 29). There will be two sandstone blocks separated by a thin, impermeable epoxy seal. The bottom block will host the plume of supercritical carbon dioxide and simulate the reservoir in a deep saline sequestration project. The epoxy seal will simulate the caprock, and the upper block of sandstone will simulate the formations above the sequestration target. A single perforation will be placed into the epoxy seal at a distance of 20 cm away from the center of the cube (Figure 30). Supercritical carbon dioxide injection will take place in a "wellbore" in the center of the block completed such that carbon dioxide only goes into the bottom, reservoir block. Injection will take place for four hours at 0.01 kg/s. The rate is chosen to allow for the carbon dioxide fully to percolate through the system, including the leak, in a reasonable timeframe without risking hydraulically fracturing the sample.



Figure 29 A schematic of the sandstone cube that will host the experiment. The gray circles represent the sensors that will be placed on the sample.

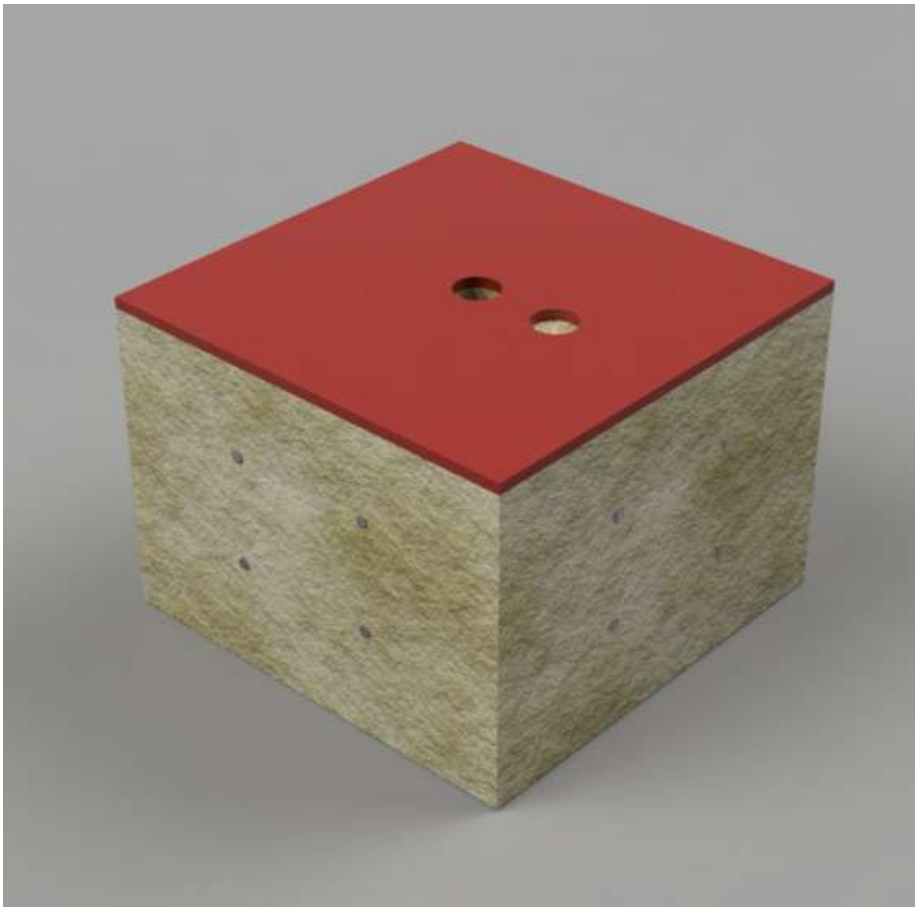


Figure 30 The perforated epoxy seal that simulates a leaky wellbore

Quotes to perform these experiments were obtained from Sandia National Laboratory and Schlumberger's Geomechanics Laboratory in Houston, TX. Sandia quoted roughly $500,000 and Schlumberger quoted about $180,000, but $45,000 of that is for sample preparation, which we have assessed will cost roughly $8,000 for the project team to perform, reducing the price to $143,000. We estimate that the Schlumberger experiment will be sufficient for the project needs. In addition to the cost of the geomechanics laboratory, the project team will also have to rent specialized sensors that can detect with a sampling frequency of at least 200 kHz. These custom sensors have been estimated to cost about $70,000. Another option at a similar price is the use of a distributed fiber optic cable that will allow for a greater spatial resolution of the experiment, but this both moves the design further from an analog of the field scale experiment, and it would be challenging to wind the cable around the sample without interfering with the true triaxial load frame. Thus, the project team has elected to use the custom transducers and Schlumberger load frame.

Two versions of numerical simulations were performed. First, we used TOUGH2 code to simulate fluid flow in the experimental apparatus. This encapsulates the flow through the bottom, reservoir rock as well as flow through the perforated epoxy seal (Figure 31). These results show that the plume of supercritical carbon dioxide occupies the reservoir rock with relatively high concentrations of carbon dioxide, and a lower concentration plume escapes into the upper, country rock. The second numerical simulation is the tomography based on the placement of the sensors (Figure 32) and the output of the fluid flow simulations. These results demonstrate a

large difference in the *P*-wave velocity as a function of the injection of the carbon dioxide. Furthermore, the smaller plume through the perforation is detectable through the tomography, which lends credence to both the ability to detect a plume and a leak with this technology. It should be noted, however, that the synthetic data in these simulations do not contain noise.

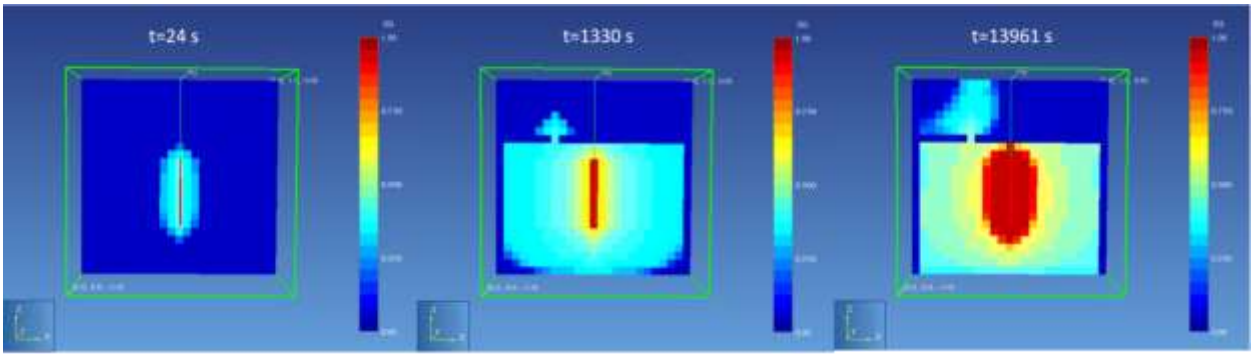


Figure 31 Numerical results of the first experiment, which show the plume hitting the seal and the one location of leakage through the perforation. The colors represent gas saturation.

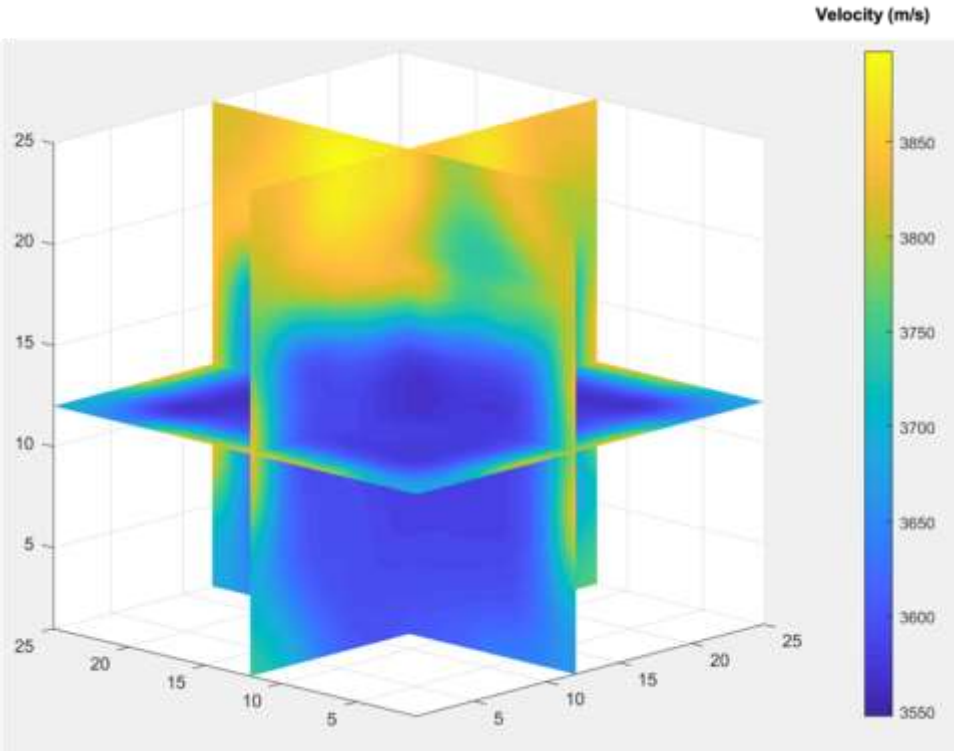


Figure 32 Tomography results after 4 hours of injection. The color bar represents *P*-wave velocity.

There will be two experiments. One with brine in the pore space of the lower block, and one with oil in the pore space of the lower block. In the first experiment, we can easily release the carbon dioxide by bringing the sample to atmospheric conditions. This will allow the carbon dioxide to leak out of the pore space, and then the experiment can be conducted again. We anticipate that each experiment will take roughly one day, and so we will repeat the experiments from Monday to Thursday. On Friday, we will switch to the second experiment, which given our inability to

withdraw the oil, cannot be repeated. By occupying one week with these experiments, we hope to optimize productivity and minimize costs.

One important consideration for the project is scale effects. A laboratory experiment objective is to replicate a plume that spans several kilometers in a real-world scenario, but it's important to account for any differences that may arise from downsizing. Although there may be variations in the length of migration and the complexity of the structure between the two scales, the response of the medium to tomography is similar. As a result, the path taken by the plume during migration may not be a representation of the field scale, but measurements of seismic body wave velocities through the medium apply to both scales, with two possible exceptions. Firstly, frequencies of seismic waves in the lab are much higher, which may cause dispersion effects. Secondly, detectors may be positioned at regular, specific intervals around the plume in the lab, but in the field, surface stations and geophones in legacy boreholes are locations of opportunity, and therefore almost always irregularly spaced. Such disparities mean the lab experiments are not directly comparable to the full design. However, we may still use the lab results to interpret whether the field-based technology may be feasible.

In summary, we successfully designed experiments that will achieve four separate results. First, we want to detect the extent of the plume throughout the duration of the experiment. Second, we want to detect the carbon dioxide leaking through the perforation in the epoxy. Third, we want to passively detect the plume with acoustic emissions, which is something that has been seen in triaxial experiments as the pore pressure changes. It would be novel if we could demonstrate and differentiate acoustic emissions associated both with the pore pressure front and with the sCO_2 plume. And fourth, we want to demonstrate the ability of our tomographic technique to distinguish between brine, sCO_2, and oil in the EOR experiment. These laboratory experiments will allow for the assessment of the downhole source tomography technology as a viable means of monitoring CO_2 plumes in the subsurface.

A funding application has been written and submitted to the Unsolicited Proposal program at the National Energy Technology Laboratory. They declined to provide additional funds.

For more perspective on our designs, please see our American Rock Mechanics Association paper (McCormack et al. 2023).

References

Ajo-Franklin JB, Peterson J, Doetsch J, Daley TM. 2013. High-resolution characterization of a CO_2 plume using crosswell seismic tomography: Cranfield, Mississippi, USA. Int J Greenh Gas Control. 18:497–509. doi:10.1016/j.ijggc.2012.12.018

Gunning J, Jackson S, Pevzner R, Barraclough P, Jenkins C. 2023. Tracking CO_2 plumes via time-lapse pressure tomography. In: Proceedings of the 84th EAGE Annual Conference & Exhibition; 2023 Jun; Vienna (Austria). p. 1–5.

Hu L, Doetsch J, Brauchler R, Bayer P. 2017. Characterizing CO_2 plumes in deep saline formations: comparison and joint evaluation of time-lapse pressure and seismic tomography. Geophysics. 82(4):ID1–ID18. doi:10.1190/geo2016-0365.1

McCormack KL, Edelman E, Moodie N, McPherson BJ, Paulsson B, He R. 2023. The design of a downhole source tomography experiment for the detection of CO_2 plumes in the subsurface.

Paper presented at: U.S. Rock Mechanics/Geomechanics Symposium (ARMA); 2023 Jun; Atlanta (GA).

Pruess K, Tsang CF, Law DHS, Oldenburg CM. 2001. An intercomparison study of simulation models for geologic sequestration of CO_2. In: Proceedings of the First National Conference on Carbon Sequestration; 2001 May; Washington (DC). Berkeley (CA); Lawrence Berkeley National Laboratory.

Pham THV, Maast TE, Hellevang H, Aagaard P. 2011. Numerical modeling including hysteresis properties for CO_2 storage in Tubåen Formation, Snøhvit Field, Barents Sea. Energy Procedia. 4:3746–3753.

Site Characterization for CO_2 Storage to Support Escalante Hydrogen Power Plant Project *on page* 109.

Subtask 4.5.4 – Feasibility Study on a Potential CCUS Project in Colorado: CO_2 Capture from a Gas Power Plant and Sequestration in the DJ Basin

See Feasibility Study on a Potential CCUS Project in Colorado: CO2 Capture from a Refinery and Sequestration in the DJ Basin *on page* 580.

Subtask 4.5.5 – Derisking CO_2 Mineralization Storage in Basalt Reservoirs

See Arizona Geological Survey, University of Arizona – Tucson, AZ

The majority of this report has been adapted from the AZGS-UA open-file report 24-01 (Wilson et al. 2024).

The Arizona Geological Survey (AZGS) conducted a Phase I pre-feasibility study of the Harquahala basin, western Maricopa County, Arizona, for subsurface geologic storage of CO_2. The purpose of this project was to evaluate subsurface geology and structure and provide site characterization for future long-term CO_2 sequestration. This work was done as part of the larger Carbon Utilization and Storage Partnership (CUSP) regional initiative with the goal of expediting the deployment of onshore carbon capture, utilization, and storage (CCUS) technologies in the western region of the United States. This project advances this goal through subsurface characterization to geologically de-risk this carbon storage prospect to help attract industry for further development. Additionally, learnings from this site can be applied to numerous geologically similar basins throughout the state.

The Phase I evaluation compiled and integrated publicly available geologic maps, wellbore lithology logs, wellbore temperature data, well water chemistry information, and published gravity surveys with proprietary datasets including legacy 2D seismic lines and detailed gravity and resistivity surveys. These data were used to produce depth-to-bedrock (DTB) contour maps, structure maps of the lower basin fill surface, and isopach maps of the total basin fill, upper basin fill, lower basin fill, and potential evaporite deposits in the basin. Our analyses yielded new information about the basin size, geometry, and structure, which improved calculations of the area and volume of the potential reservoir study area.

Harquahala basin may have the geologic conditions necessary to store natural gas permanently and safely in the subsurface, but additional geophysical and well data are needed to characterize the physical properties of storage reservoir rocks. Harquahala has thick accumulations of basin fill sediments with sufficient volumes for storage of supercritical CO_2: an estimated 1,997 Mt of CO_2 (P50). Basin fill likely contains three different potential storage reservoir types: CO_2 in stacked saline clastic sedimentary deposits, bedded evaporite deposits for compressed H_2 gas storage, and basalt lava flows for CO_2 mineralized sequestration. Hot, dry crystalline rock underlying basin fill is favorable for geothermal energy and has an unknown volume of saline groundwater. The seismicity risk is low based on the absence of Quaternary faults and historic seismicity. The basin is located close to five major (greater than 100,000 tons/yr) CO_2 point sources, existing pipeline infrastructure and Interstate 10, a transportation corridor between Arizona and southern California.

At the completion of our data analyses, three critical unknowns remain: the existence/absence of sealing strata such as bedded evaporites and fine-grained deposits, the physical properties of stacked saline reservoir rock, and the stratigraphic architecture of basin fill sediments. Harquahala basin lacks deep well borehole data to adequately characterize rock lithology, porosity, and permeability. New 2D seismic interpretations reported within suggest bedded evaporite deposits and basalt lava flows are likely components of the lower basin fill unit; however, these interpretations cannot be calibrated with physical evidence. To reduce the uncertainties about storage reservoir integrity, we recommend the acquisition of new data to include 2D active-source seismic, high-resolution gravity infilling, high resolution aeromagnetic survey, and a stratigraphic characterization well with wireline geophysical logs and a core, cutting, and fluid sampling program. These datasets, combined with data reported within, will refine our understanding of the basin fill rock properties, identify the presence/absence of sealing strata, and clarify stratigraphic architecture and basin structure.

Project Description and Scope

The AZGS conducted a phase I pre-feasibility evaluation for subsurface storage of CO_2 in Harquahala basin, western Maricopa County, Arizona. This study was funded by the U.S. Department of Energy (DOE), as a Focused Project within the regional CUSP Regional Initiative. The purpose of this work was to evaluate the basin geometry, structure, and stratigraphic architecture of Harquahala basin and provide site characterization for future potential subsurface CO_2 storage.

The scope of work required data collection, data analysis, coordination, and technical evaluation in three tasks. In Task 1, AZGS researchers synthesized geologic maps, well lithology logs, public and private gravity datasets, newly reprocessed 2D seismic data, DTB contours, and groundwater temperature and chemistry data for Harquahala basin. Task 2 involved stakeholder engagement and outreach through periodic meetings and the creation of a publicly available StoryMap. In Task 3 sites for a future characterization well and geophysical surveys were identified. Deliverables include this report, supporting maps, cross sections, model data and parameters, and future data collection recommendations.

Study Areas

The Harquahala basin is located on the border of Maricopa and La Paz counties in west-central Arizona (Figure 75 and Figure 76). The Harquahala basin underlies a rural, agricultural valley located approximately 60 miles west of Phoenix. The approximately 511 mi^2 basin area is defined by several rugged mountain ranges composed of crystalline rocks: Harquahala Mountains to the north, Big Horn Mountains to the northeast, Saddle Mountain to the southeast, and the Eagletail Mountains to the southwest. Existing infrastructure crossing Harquahala Valley includes I-10, Central Arizona Project (CAP) canal, and natural gas pipelines. Land ownership consists of 62% federal land (managed by the U.S. Bureau of Land Management), 25% private land, and 13% State Trust lands (Towne 2014).

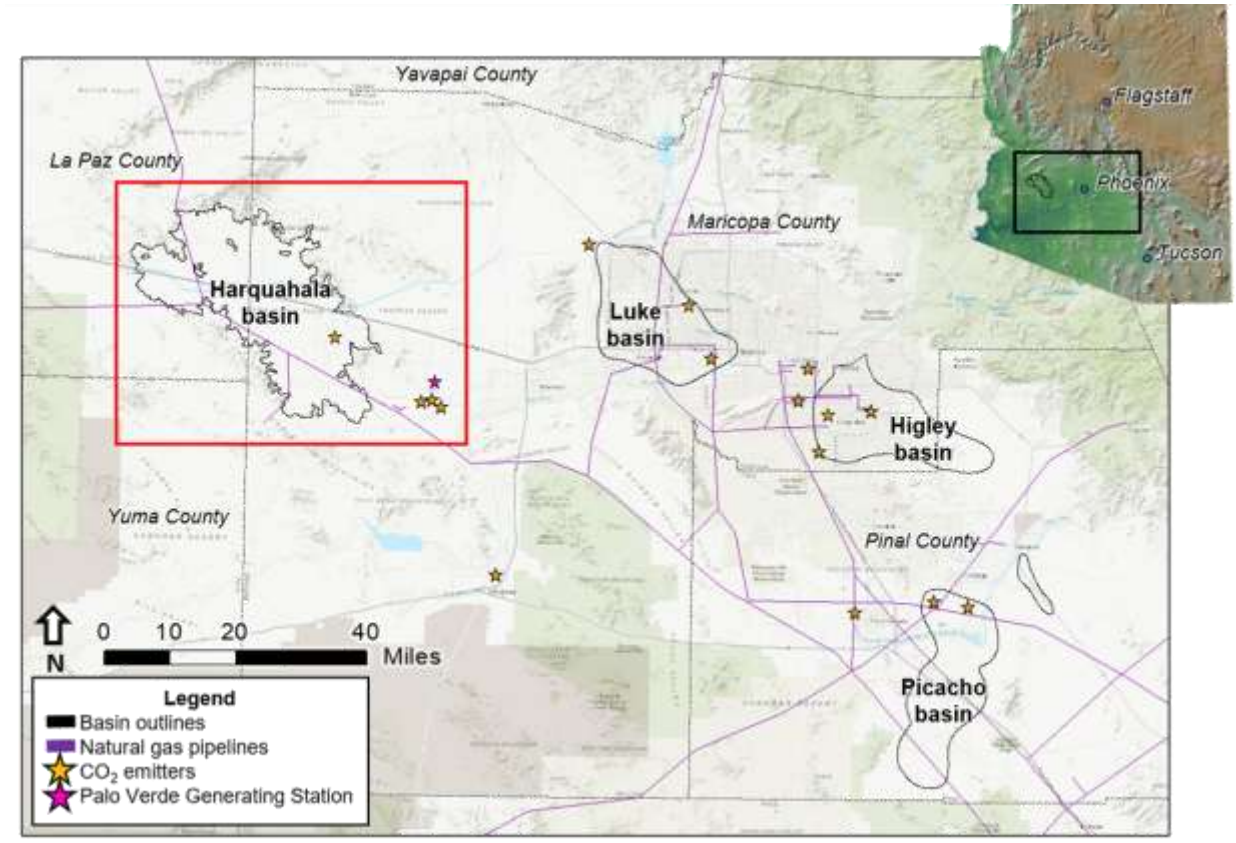


Figure 75 Map of study area in south-central Arizona (black box in state inset) showing the location of natural gas pipelines, CO_2 emission point sources (greater than 100,000 t per year), and major sedimentary basins in this region. The study area includes Harquahala basin (red box and location of Figure 76).

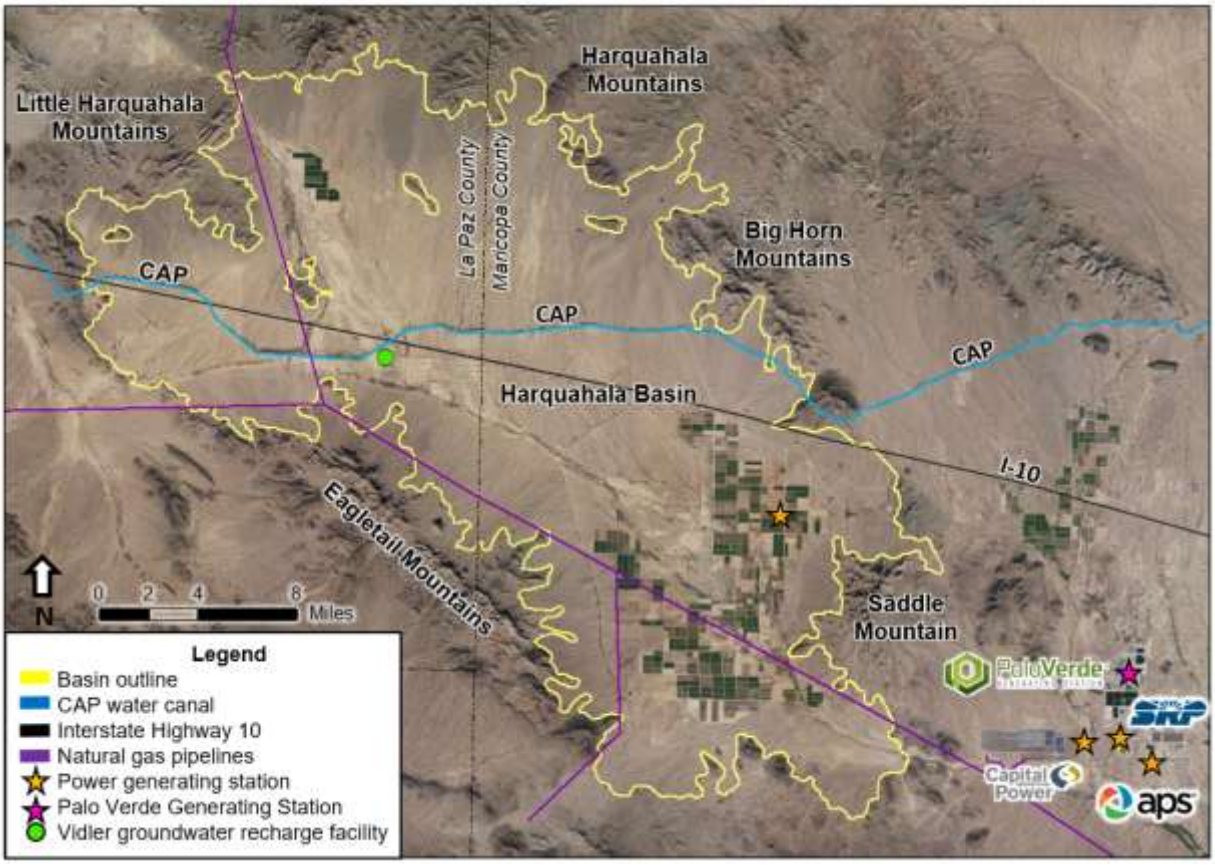


Figure 76 Location map of Harquahala basin (yellow outline), the surrounding infrastructure, and nearby energy facilities.

Four natural gas–powered energy facilities—Harquahala Generating Station, Mesquite Generating Station, Redhawk Generating Facility, and Arlington Valley Energy Facility—are located within 15 miles of the basin, three of which operate year-round. In 2021, three of the four natural gas power plants emitted over 6.32 Mt CO_2 waste to the atmosphere (U.S. EPA 2023). Palo Verde Nuclear Generating Station, the nation's largest nuclear power plant, is located 11 miles east of Harquahala basin.

Methods

All publicly available data were compiled, quality checked, and organized into an Esri ArcMap geodatabase. Data includes geologic map compilations, borehole lithology logs, 2D legacy seismic lines, public and proprietary gravity datasets, DTB contours, groundwater temperatures, and well chemistry information.

Geologic Map Compilation

Surficial geology was compiled and simplified from four 1:100,000 AZGS geologic maps (Reynolds 1997; Reynolds and Grubensky 2007; Richard et al. 2022; Spencer et al. 2022). Geologic units were simplified into 11 time-transgressive lithologic categories to highlight important compositional provenance for basin fill sediments (see Plate 2, Wilson et al. 2024). For example, crystalline bedrock units were lumped by age, while younger volcanic rocks were lumped by age and chemistry (this approach identified source areas for mafic volcanic rocks that

can be used to sequester CO_2). All surficial alluvium younger than approximately 5 Myr was omitted from the map compilation for simplicity.

Borehole Lithology Logs

Over 740 Arizona Department of Water Resources (ADWR) and Arizona Oil and Gas Conservation Commission (AZOGCC) wells were reviewed for subsurface geologic data within Harquahala basin (Appendices A and B). Within the basin center, only wells deeper than 122 m (400 ft) with lithologic borehole data were plotted. Along the basin margins, all wells regardless of depth were logged and plotted to refine depth to bedrock contours.

The review criteria resulted in 205 wells with subsurface lithologic data that have an average depth of 250 m (820 ft), with the deepest well reaching 611 m (2,005 ft; AZOGCC 2023). Wells were sorted by lithology, clast size, and/or composition at reported intervals, and plotted by lithology in cross-sections. Lithology codes were assigned to a color and resulting logs are displayed on each of the cross-sections traversing the basin.

Vintage Seismic 2D Reflection Data and Analysis

The application of 1980's vintage seismic reflection data was a major contributor to improving the understanding of the structure and stratigraphy of Harquahala basin. In this section we present the quality of legacy data, processing methods including depth conversion and limitations of these data. These seismic data are proprietary and confidential under contract between the UA Seismology Group and Conoco Phillips. Results and interpretations presented in this report may be reproduced, although original raw digital data remain confidential.

Seismic reflection profiles were acquired by petroleum exploration companies in the early 1980's to assess petroleum potential in Tertiary and older sedimentary rocks in central Arizona. The focus of the original data acquisition was to image stratigraphy and structure from a few hundred meters to several thousand meters in depth. However, the limited number of wells and lack of any deep wells to calibrate seismic velocity in both basins introduce uncertainty in velocity and depth estimates across the basin and in gaps between lines.

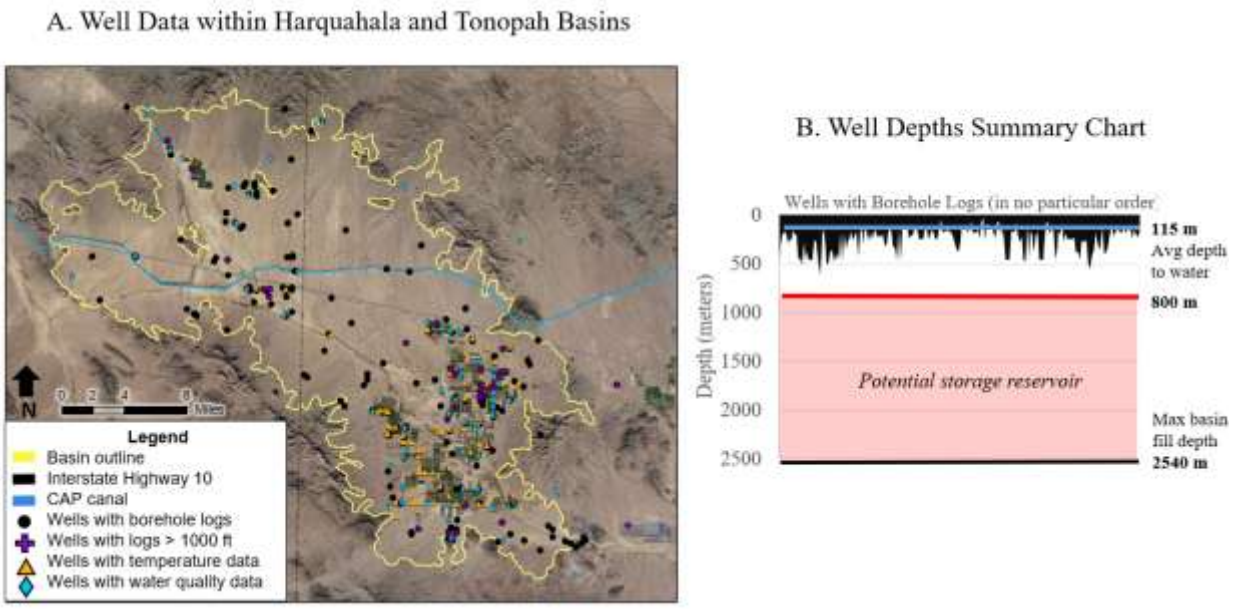


Figure 77 (A) Map of well data types within the Harquahala basin. (B) Summary chart showing wells plotted against depth. The average depth to the water table is shown as a blue line, depth to bedrock is a black line, and the potential reservoir (basin fill below 800 m and above bedrock) is shaded red. This chart highlights the lack of well data at the reservoir depths.

Reprocessing of five of these 2D seismic reflection lines was carried out by Jourdan Anoka with Anoka Geophysical LLC, Aurora, CO, in collaboration with Roy Johnson and Kurt Constenius at University of Arizona (Figure 78, Table 1). Analysis of the final stacks were made by Kurt Constenius with input from AZGS research geologists. Data quality for the five lines was variable, ranked from moderate quality to poor quality: PW24, PW23, PW22, TR12, TR10b, and TR9.

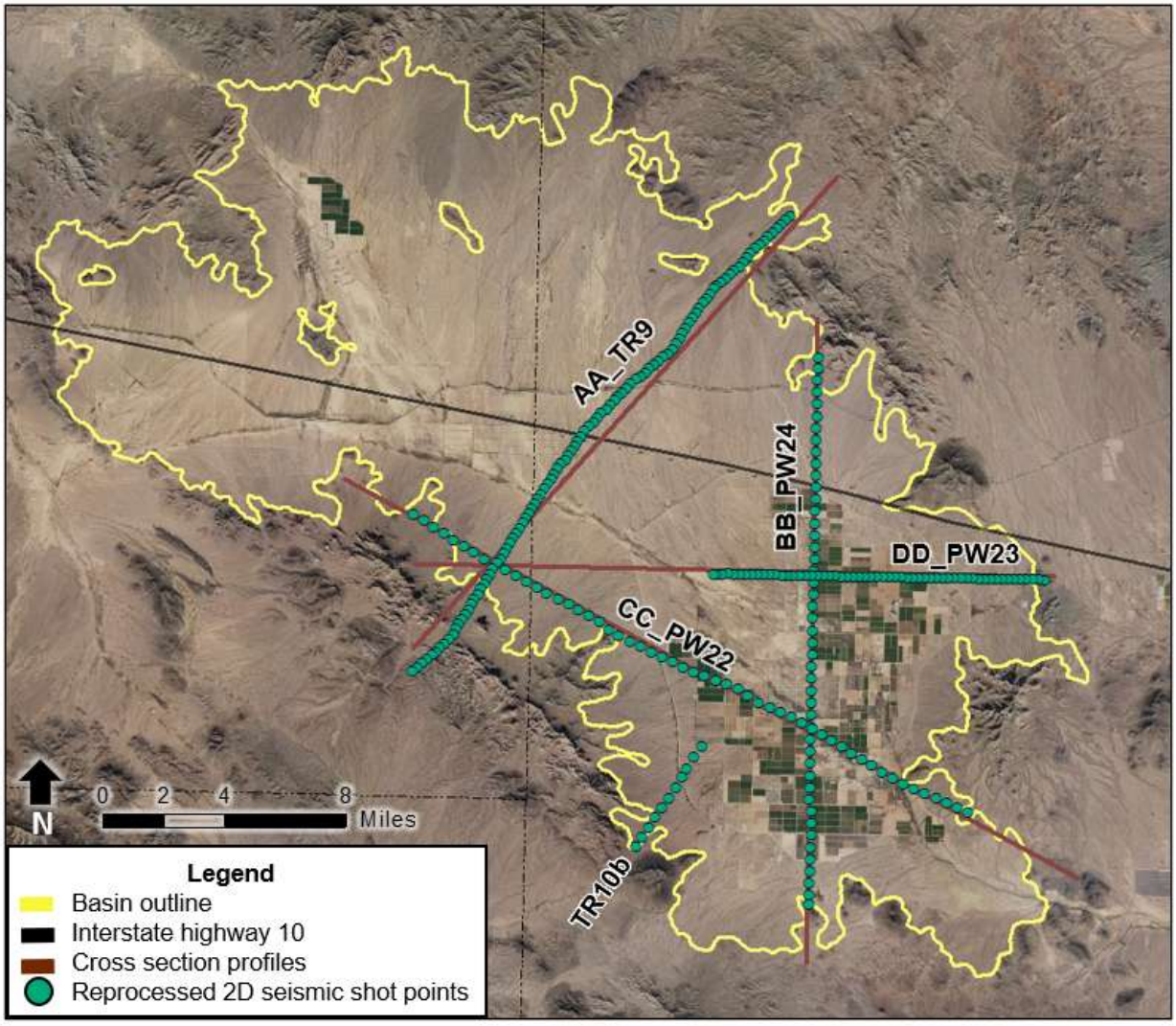


Figure 78 Map of the 2D seismic lines and cross sections profiles that traverse the Harquahala basin. 2D vintage seismic line shot points are black dots.

Table 1. List of vintage seismic lines stations used in Harquahala basin. Beginning of line (BOL) and end of line (EOL). Refer to Figure 78 for location of seismic lines and stations.

Seismic line	Reprocessed line length (km)	BOL stations	EOL stations	SP spacing (ft)	Datum elev. (m)
PW23	18.3	780	1,050	1,100	600
PW22	35.5	670	1,200	2,000	600
PW24	30.7	201	658	2,000	600
TR9	34.5	1,200	2,200	1,200	600
TR10b	6.7	0	200	2,000	600

Seismic Reprocessing

A standard processing sequence that included iterations of velocity analysis and static corrections was used for the PW and TR profiles (Table 2). Differences in processing between lines included application of normal moveout-correction velocities determined separately for each line and application of automatic static corrections, which were based on individual reflection events in each profile.

Table 2. Acquisition parameters for seismic lines used in Harquahala basin.

Acquisition Parameters	TR lines	PW lines
Acquired by	Texoma Production Co.	Anschutz Corp.
Date	1980	1980
Source	Dynamite	Vibroseis
Source size or sweep	110 lb	14-56 Hz; 18 s
Source interval	134 m	67 m
Group interval	33.5 m	67 m
Channel array	96 channels; off end	48 channels; off-end
Near offset - Far offset	805 m - 3,990 m	268 m - 3,420 m
Normal maximum fold	1,200%	2,400%
Sampling interval	2 ms	4 ms
Recording time	8 s	24 s

Depth Conversion

Depth-below-surface was determined for two interpreted event horizons using two-way travel time to the horizon and assigned interval velocities. Velocity control for the upper basin fill was provided by a sonic log from the Humble Oil and Refining State #1 well (Section 2 T8S-R8E) in the Picacho Basin. The average velocity of the upper basin fill in that well is approximately 2,133 m/s (7,000 ft/s). The lower basin fill was depth converted using velocity data from the same Humble well and sonic log data from the Suncor Development, Sunset Point #1-19 well (Section 19 T2N-R1W) in Luke basin. The lower basin fill in the Humble well is predominantly evaporites and is entirely halite in the Suncor 1-19 well with a velocity of 4,419 m/s (14,500 ft/s). Depth conversion of lower basin fill used the velocity of halite because we interpret the lower basin fill to be predominantly evaporites (see section 4).

Gravity Data

Multiple gravity datasets were used in Harquahala basin (Figure 79). Historical and statewide public gravity data were provided by the Arizona Department of Water Resources (ADWR;

2022) who maintains the regional dataset compilation derived from the Pan-American Center for Earth and Environmental Studies dataset (PACES 2016). A basin-wide gravity survey of Harquahala was conducted in 2008 but was unpublished (HGI 2009). The Complete Bougier Anomaly (CBA) gravity values from all datasets in conjunction with well, modeled DTB, and seismic data were used to identify geologic structures, anomalies, and data gaps.

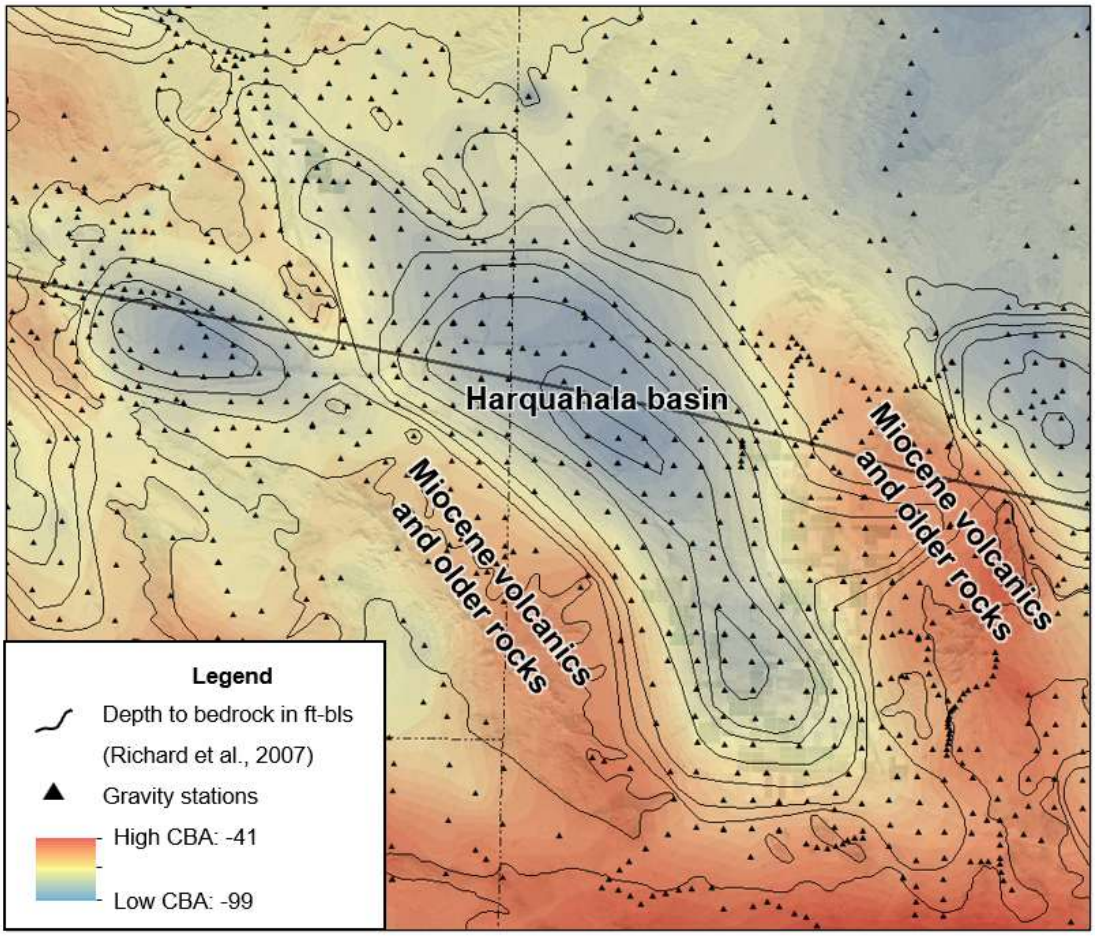


Figure 79 Map of gravity, depth-to-bedrock contours (Richard et al. 2007), and modeled CBA gravity data used in this study. Gravity point data are compiled from three separate sources (ADWR 2004, 2022; HGI 2009). Colored basemap is interpolated from Complete Bouguer Anomaly (CBA) low (blue) to high (red) values.

Depth-to-Bedrock Contours

Depth-to-bedrock data used at the start of this study were derived from a statewide DTB contour map modeled from gravity data and a limited number of borehole control points (Richard et al. 2007; Figure 79). In that report, bedrock is defined as crystalline basement overlain by clastic and volcaniclastic rocks, the same definition we use in this report. Of note, the HGI gravity study (HGI 2009) was not included in the (Richard et al. 2007) compilation.

The 2007 DTB contours were modified stepwise using detailed geologic maps, recent borehole lithology logs, and results from reprocessed vintage seismic data. Modification of DTB lines in this study were based on the hierarchy of data sources, from most confident to least confident, is as follows: (1) geologic mapping, (2) borehole lithology logs, (3) reprocessed 2D seismic lines,

and (4) gravity. Data sources for DTB contour modification are listed for each contour line in the geodatabase.

ADWR wellbore logs are of generally poor quality (specific rock types may not be mentioned or may be too generally categorized; Appendix B), which prompted an in-depth quality review of adjacent wellbore logs and their relationship to geologic mapping and known geophysical data. Wellbore logs that did not correspond with two or more other datasets were not used. Basin margin contour shapes below 122 m (400 ft) were most affected by the well log review, while basin center contours were largely unaffected (due to the lack of deep borehole data). Well terminations in granite or crystalline volcanic rock overlying granite were considered bedrock penetrations. Green dots indicate reprocessed shot points included in this analysis.

Basin Fill Storage Volume Calculations

Basin fill volume between the 2D areal extent of the 800 m depth contour and the depth to bedrock was calculated using Esri ArcMap geoprocessing tools. Volume estimations rely on gravity and seismic data and interpretations of those data. Thus, they are first order estimates of potential basin fill storage volumes below 800 meters depth and above crystalline bedrock. In these estimates, basin fill is not distinguished by lithology (i.e., clastic sedimentary, chemical sedimentary, and volcanic rocks are lumped together); however, we do assume that the basin centers consist of fine-grained clastic sediment and some percent evaporite bedding, and possible interbedded volcanic rocks, and a range of physical parameters, such porosity and permeability, commonly associated with those lithologies. Carbon dioxide injection volumes are based on these physical dimensions and used in three separate methods to calculate gross and net injection volume capacity and volumes over a 5-year period. These methods are described along with results in section 6b.

Isopach Maps

Reprocessed seismic data revealed acoustic differences within the basin fill, which gave rise to an interpretation of distinct stratigraphic units and seismic zones delineated by seismic fabric. Stratigraphic picks for top and bottom of basin fill units, and an acoustically transparent zone within the lower basin fill, were determined at each seismic shot point along TR9, PW23, PW24, and PW22 in Harquahala basin. Depths were converted to elevation and used to create contour maps of the surfaces. Contour maps were converted into raster data and later used to create isopach maps (maps of thickness) for the upper and lower basin fill units, and acoustically transparent zone in Harquahala basin.

Geologic Cross-Sections

Five geologic cross-sections were created along or adjacent to the 2D seismic lines (Figure 79). Profiles were created along each line by combining a surface digital elevation model (DEM) and DTB contours. Well lithology logs from wells located within 3,000 m of the profile were projected vertically onto each cross-section line. In areas where wells were clustered, rendering them unreadable on the profile, the well(s) located further away were removed for clarity. Basin fill unit boundaries, extent of each seismic line, extent of probable salt, and the location of faults as interpreted from seismic data were also projected onto the cross sections. The interpreted seismic lines are displayed next to their corresponding profile (see Plate 3, Wilson et al. 2024).

Lithofacies Maps

Geologic mapping of bedrock units exposed at the surface surrounding the Harquahala basin was used to predict what lithology or lithofacies would be encountered through drilling the upper few thousand feet of basin fill. The geometry of the modern watershed that supplied sediment to Harquahala basin during upper basin fill time is assumed to be consistent over the last approximately 5 Myr due to the absence of tectonism and/or major drainage reorganization. Smaller watersheds within the basin watershed, or subsheds, are also assumed to be relatively consistent.

The basin's asymmetrical geometry and location of paleodepositional centers identified in down-dip seismic reflectors were used to create paleodepositional boundaries or subsheds in the subsurface. Watershed maps were derived from the USGS Watershed Boundary Dataset (WBD). The simplified geologic map compilation (described in section 3a) was used to calculate the area of geologic map units in the basin. Geologic map units were clipped to subsheds. Areas of each map unit within each subshed were exported into Excel. Map units were lumped into broad lithologic categories (e.g., plutonic, metamorphic, volcanic, etc.) and relative percent of each lithologic category plotted for each subshed.

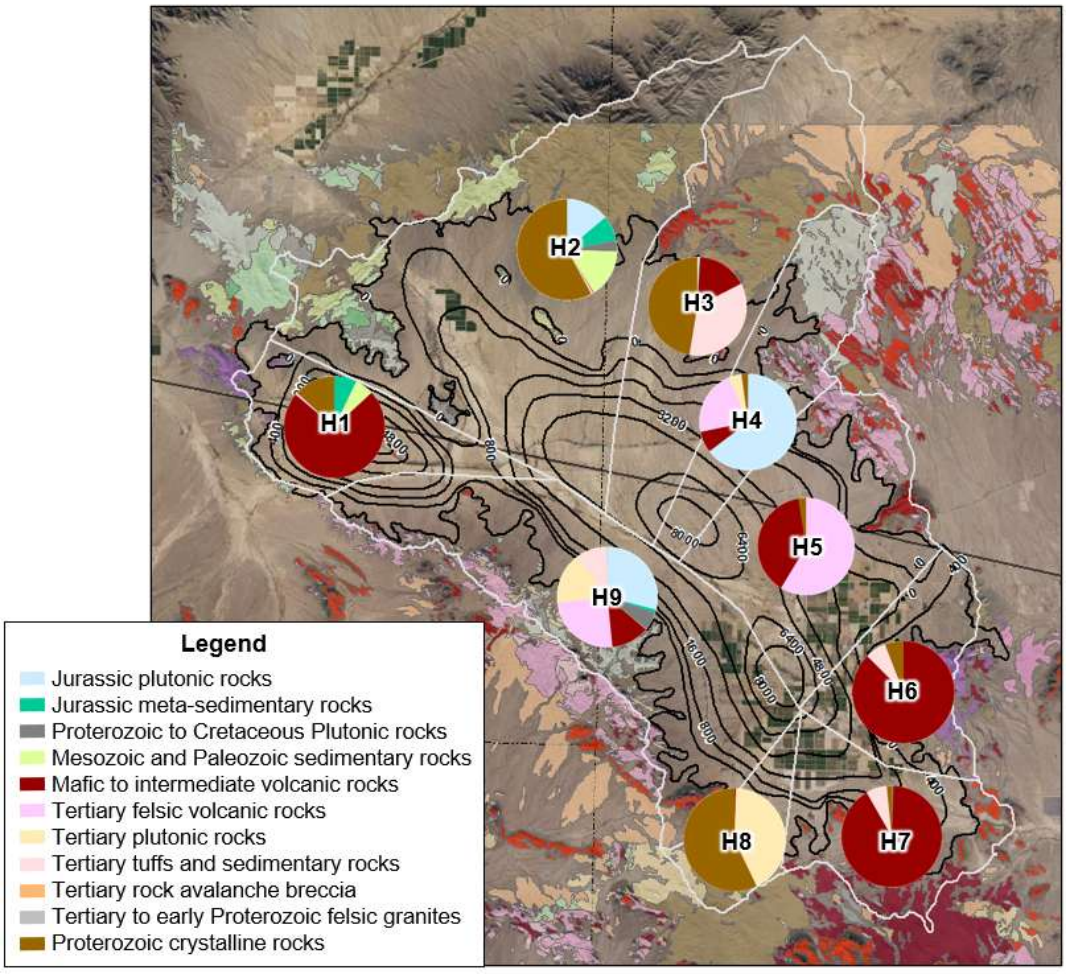


Figure 80 Lithofacies prediction map showing the percentage of rock types expected in upper basin fill based on watershed and subshed boundaries within Harquahala basin

Well Borehole Temperatures

Publicly available borehole temperature data in Harquahala basin was compiled, reviewed, and analyzed. Reported temperatures and well depths for 157 wells in Harquahala basin (Witcher 1995) are plotted in Figure 81. Overall, the quality of the data is highly variable, and data collection methods were not standardized. The borehole temperature sample depth and time collected, as well as the screened intervals sampled, are unknown. Borehole temperature data was plotted and symbolized by a color gradient representing temperature and constrained by discrete depth ranges to look for any spatial trends.

Geothermal gradients were calculated from wellbore temperatures by subtracting the bottom-hole temperature from the mean annual surface ground temperature at the well site and dividing by well depth. The mean annual surface ground temperature used for both basins was 21.1°C (70°F). This calculation yielded values between 6°C/km and 438°C/km, with many values outside of the expected range of geothermal gradients. This may be due to reporting errors of the wellbore temperature values. The worldwide average geothermal gradients are from 24°C/km to 41°C/km (1.3°F/100 ft to 2.2°F/100 ft; Peters et al. 2012). Data outside of this range was omitted in the analysis, which brought the well count from 201 to 101 wells with reasonable calculated geothermal gradient values (Appendix C).

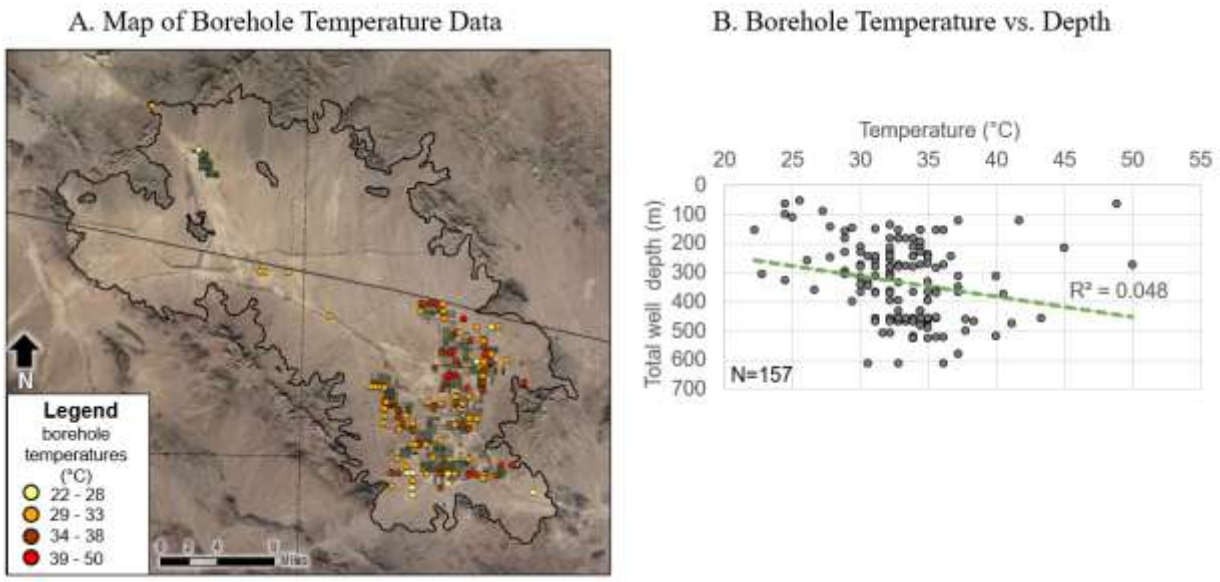


Figure 81 Borehole temperature data (A) Map displaying borehole temperatures colored by specific temperature ranges. (B) Scatter plot of temperature vs. depth for Harquahala basin. Trend lines shown in green with R2 values. Wells with depth listed as 0 were removed.

Groundwater Total Dissolved Solids (TDS)

We compiled a total of 453 wells with publicly available groundwater salinity and conductivity data in Harquahala basin (Appendix D). Of these, 51 shallow wells included direct measurements of total dissolved solids (TDS; Towne 2014). The remainder of well data lacked direct TDS values, though they did have conductivity measurements which we used as a proxy for TDS. The reported TDS value was retained where water quality records reported both TDS and conductivity values.

Conductivity values were converted to equivalent TDS values using the equation

TDS (mg/L) = k * EC (µS/cm),

where "k" is the conversion factor and EC is electrical conductivity. Wells that had both TDS and conductivity measurements (n=51) were used to determine an average conversion factor of 0.64 (range = 0.59 to 0.69). For comparison, previous work reporting statewide salinity used a conversion factor of 0.642 (Gootee et al. 2012). Figure 82 is a scatterplot of groundwater salinity vs. well depth for Harquahala basin.

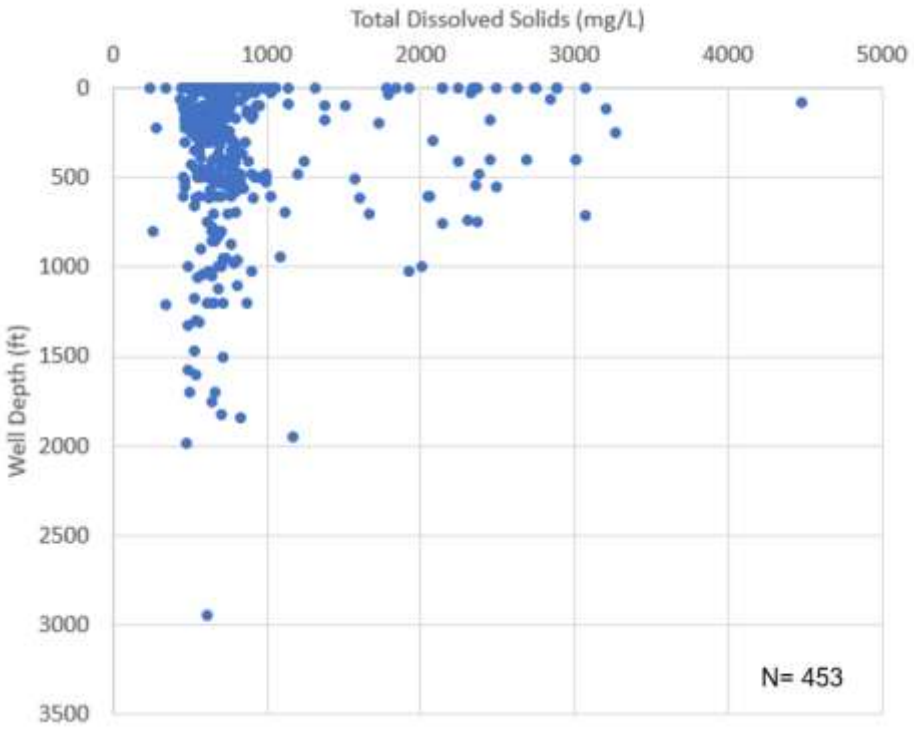


Figure 82 Groundwater salinity from wells. Scatter plot of groundwater salinity as total dissolved solids (TDS) vs. borehole depth for water wells in Harquahala basin. No trend between TDS and depth is observed.

Geologic Characterization

Conceptual Model for Basin Formation

The geology of Harquahala basin can be broadly described with a conceptual model that integrates commonalities in geologic structure and stratigraphic architecture across the Arizona Basin and Range Province (Eberly and Stanley 1978; Menges and Pearthree 1989; Spencer and Reynolds 1989).

About 30 Ma, tectonic extension in southeastern, southern, and western Arizona began to fracture, fault, and pull apart older rocks that composed Earth's crust. Through distributed low-angle normal faulting, the crust thinned, and large, linear fault blocks were uplifted to form subparallel mountain ranges. The space between those ranges gradually increased and deepened with each additional earthquake. Mountain ranges were separated by largely asymmetrical, deep

sedimentary basins into which water and sediment from the surrounding mountain ranges collected over millions of years (Figure 83).

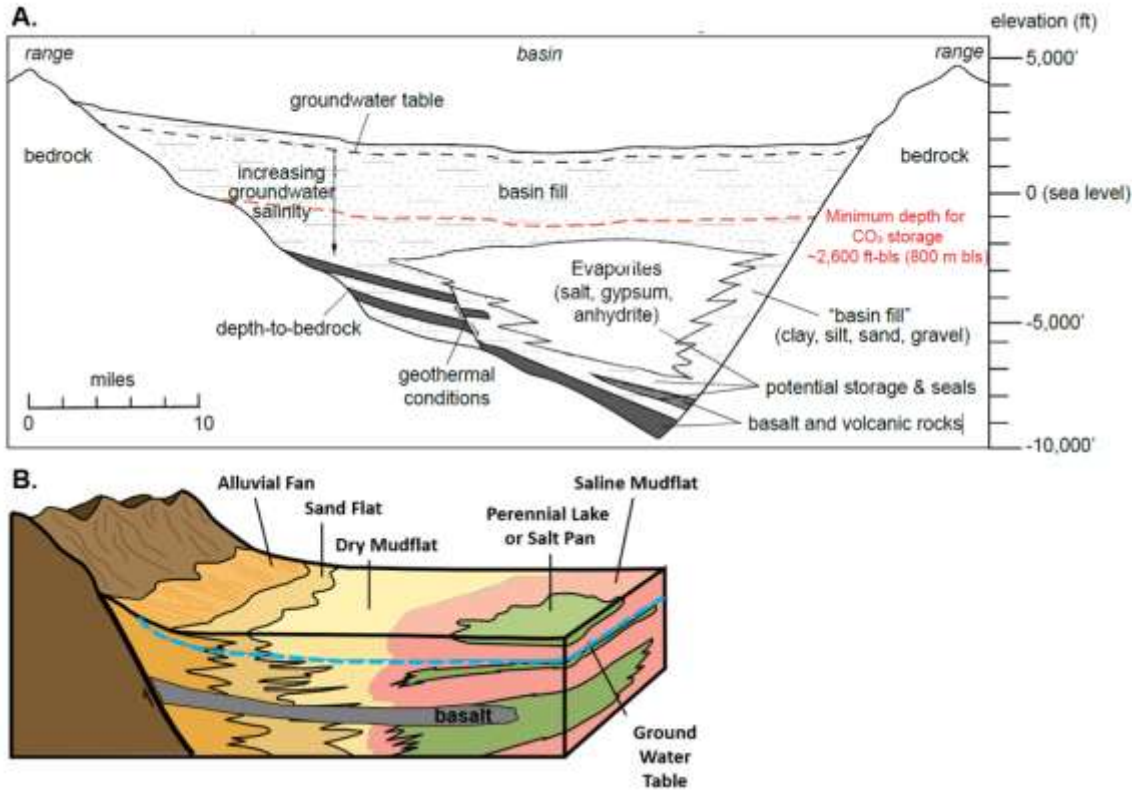


Figure 83 (A) General geologic cross section of Harquahala basin showing distribution of basin fill features and lithology. (B) Block model of depositional environments of basin fill. Modified after Faulds et al. (2016).

Early in the basin extension process between about 25 to 15 Ma, coarse sediments were concentrated near steep basin margins close to their mountain provenance and fine sediments were concentrated near sub-horizontal depositional centers where water likely ponded. The climate was semi-arid and favorable to both periods of water accumulation (forming shallow playa lakes) and extended periods of drought (water evaporation) which, in the case of closed basins, resulted in the formation of bedded evaporite deposits fed primarily by shallow groundwater high in dissolved solids within the basin center or subbasin centers (Figure 83). Deposition of these basin-fill facies were punctuated by continued crustal extension and widespread volcanic eruptions that deposited lava flows, ash, and pumice directly on crystalline bedrock-cored mountain ranges and interlayered with basin fill sediments. Continued extension during this phase accumulated thousands of feet of basin fill deposits before tectonism waned. As a result, older basin fill and interbedded volcanic deposits are progressively tilted, faulted, and compacted with depth.

Beginning about 6 to 5 Ma, extension and faulting waned while passive erosion and deposition dominated within the closed basins. These deposits are generally horizontal, less compacted and nondeformed compared to older basin fill sequences. Basin-filling continued in depocenters in a closed basin, generally fining grain sizes up section, as piedmonts backfilled bedrock topography near the base of mountain fronts. As a result, there are basin sedimentary packages with different structural histories: a lower, older sedimentary package that is tilted and faulted (during active

extension) and an upper, younger sedimentary package that is generally undeformed (as extension waned; Figure 84).

Harquahala basin is mantled by a thin veneer of Pleistocene and Holocene (about 2.6 Ma to the present) alluvium that forms low-gradient piedmonts graded to the modern valley axial washes (Centennial Wash). Both axial wash systems are integrated with the Gila River about 2 miles downstream of the Hassayampa River's confluence with the Gila River. Integration timing is not known, but it likely occurred during the Pleistocene or latest Pliocene (5 to 2.6 Ma). This basin model is generally well understood in shallow basin fill and surficial exposures, although less understood in buried basin fill deposits below about 2,500-ft depth. Harquahala basin exhibits a similar extensional history, style of faulting, and depositional environments to other neighboring basins in southern Arizona.

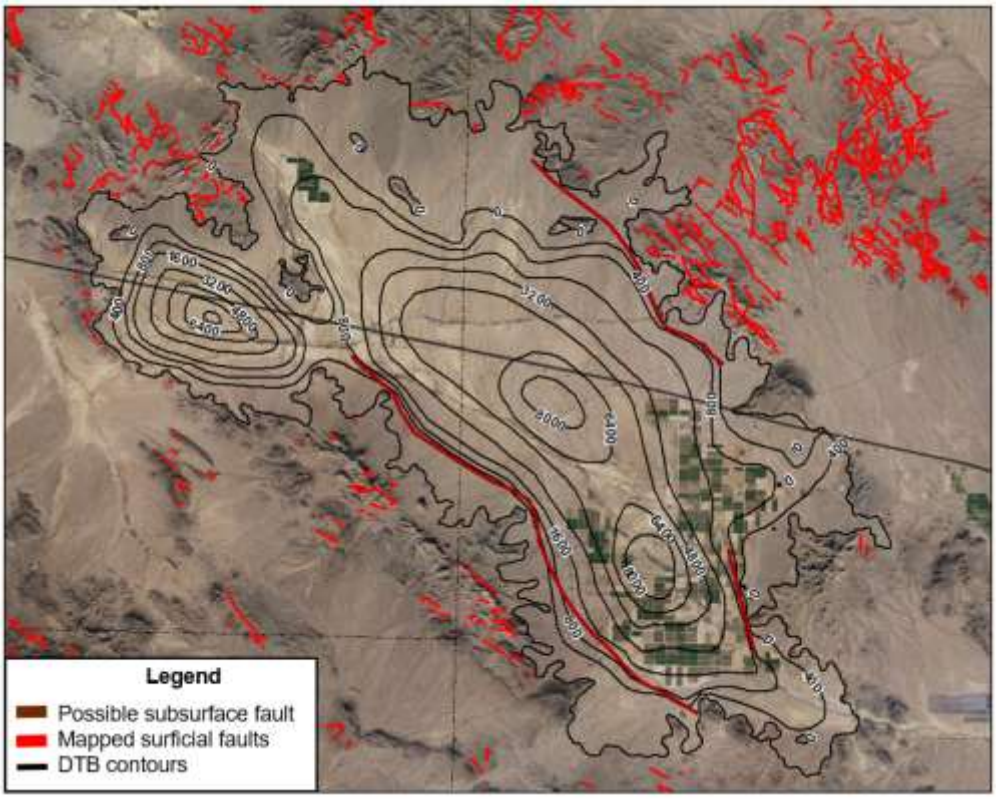


Figure 84 Map of fault traces exposed at the surface (bright red) and subsurface faults interpreted from seismic lines (brown).

Basin Geometry and Structure

Harquahala valley is surrounded by mountains composed of a diverse suite of Proterozoic crystalline igneous and metamorphic rocks, sparse outcrops of Paleozoic and Mesozoic sedimentary rocks, and Jurassic igneous and metasedimentary rocks, unconformably overlain by effusive and explosive products from Miocene volcanic eruptions (see Plate 2 , Wilson et al. 2024).

Harquahala basin is divided into three subbasins each separated by a subsurface structural high, as shown on the DTB contour map (see Plate 2, Wilson et al. 2024). The central subbasin is the

deepest with a maximum depth of 2,538 m (8,326 ft) and the southern subbasin's maximum depth is 2,530 m (8,300 ft). The northwestern subbasin is isolated and smaller than the other two with a maximum depth of 2,438 m (8,000 ft). Reprocessed 2D seismic data show the basin-bounding detachment fault is close to the southwest basin margin at the base of the NW–SE striking Eagletail Mountains (see Plate 3, Wilson et al. 2024; seismic line TR10b). As such, the deepest portion of the basin is adjacent and subparallel to that mountain range (Figure 85).

Stratigraphy

The stratigraphic architecture of basin fill in Harquahala basin is not well delineated due to lack of age constraints, few high-quality well records, and no deep well penetrations. However, basin fill could be divided into three units based on the character of the seismic reflection data and the conceptual model described in section 4a. Listed from oldest to youngest the stratigraphic packages are: lower reflective package (LRP), lower basin fill (LBF), and upper basin fill (UBF; Figure 85). Harquahala basin is not dissected, therefore all basin fill deposits are covered by Pleistocene and Holocene alluvium. Due to the lack of exposure and deep well penetrations, the porosity and permeability of each unit are unknown.

Lower Reflective Package (LRP)

The LRP, the oldest unit, is a strong reflective package and is likely comprised of interbedded lava flows and sedimentary rocks deposited directly on the crystalline basin floor (Figure 85; see Plate 3, Wilson et al. 2024, seismic lines TR9, PW22, PW23, PW24). This unit is distinguished solely through interpretations of strong, parallel, shallow-dipping seismic reflectors. The LRP is approximately 1,066 m (3,500 ft) thick near the basin center, although without velocity control the true thickness is not known and could be $\pm$ 20-30%. The apparent thickness increases to the southeast and decreases to the northwest. Extensive outcrops of early Miocene age volcanic rocks in the mountain ranges bordering Harquahala basin are evidence for widespread bimodal volcanism during early basin formation. Therefore, we suggest that the LRP is equivalent to those rocks in part by age, although contains a mix of clastic sediments interbedded with volcanic flows near now buried depocenters. The LRP may also include explosive centers or cauldrons as part of an upper-plate geometry within the Harquahala half-graben.

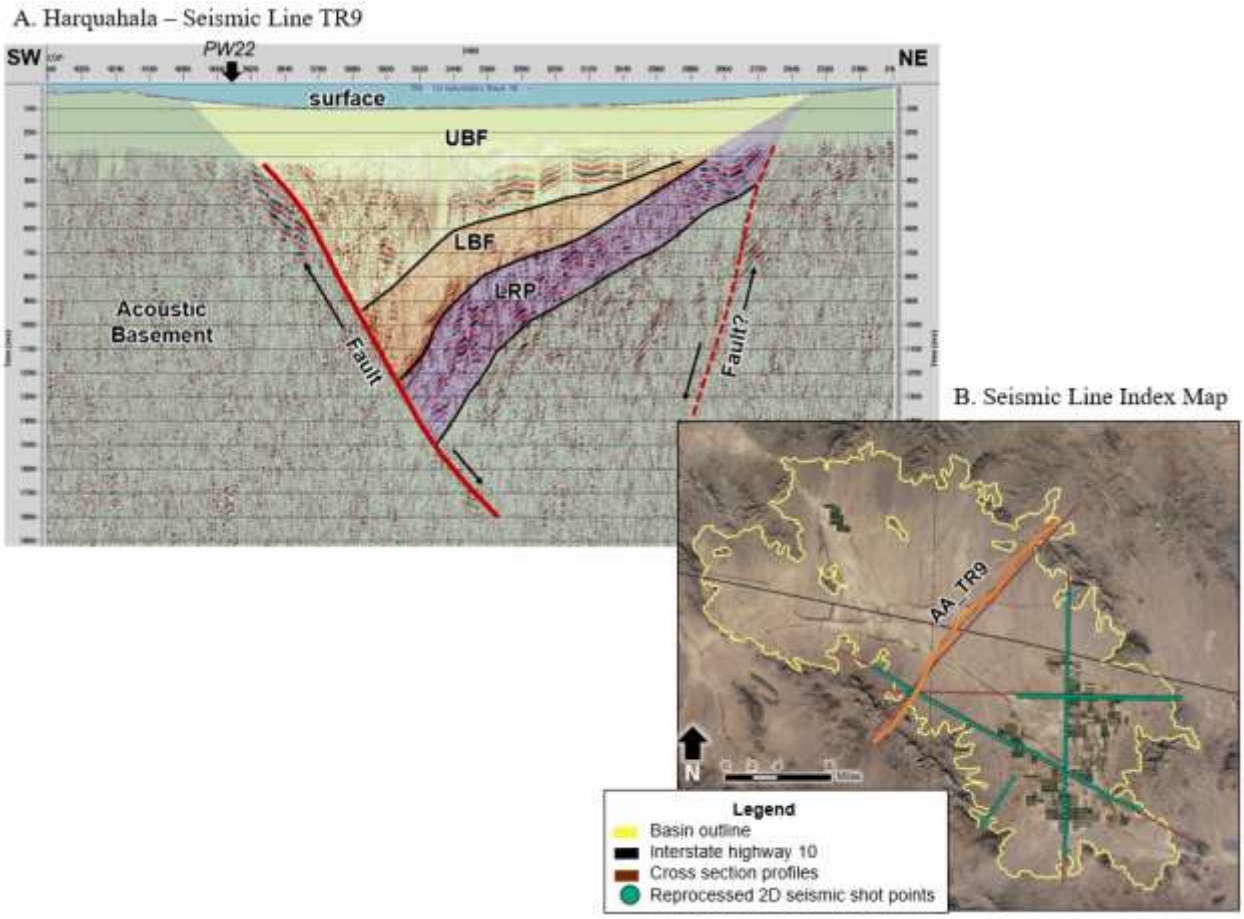


Figure 85 Examples of the basin fill units interpreted from the 2D seismic. (A) Seismic line TR9 is perpendicular to the basin axis in Harquahala basin and shows the seismic character of the lower reflective package (LRP), lower basin fill (LBF), and upper basin fill (UBF) units. (B) Index map of seismic lines.

Lower Basin Fill (LBF)

The LBF is a middle-aged sedimentary package defined by tilted and truncated seismic reflectors seen on all seismic lines (Figure 85; see Plate 3, Wilson et al. 2024). There are no direct measurements, such as borehole lithology logs, to characterize lower basin fill lithologies for Harquahala basin. Broadly, LBF is likely comprised of a wide range of clastic sediment sizes from clay to boulders sourced from nearby mountain ranges, and the package may contain interbedded mafic to intermediate lava flows and felsic explosive material. The areal extent and lateral continuity of deposits and grain size distribution is unknown; however, based on our conceptual model, coarse clastic deposits on the basin margin grade laterally down-gradient into finer sediments near basin centers. Potential capping rocks such as extensive clay deposits or evaporite deposits, if present, should be located near basin centers.

In Harquahala basin, the LBF is a maximum of 975 m (3,200 ft) thick and overlies the LRP. Seismic reflectors suggest individual LBF blocks are cut and tilted by several high-angle normal faults. The LBF isopach map in Harquahala basin (Figure 86) represents the gross thickness of rock between the LRP and UBF units and highlights three subbasins: the northwest subbasin with a maximum thickness of 785 m (2,575 ft), southern subbasin with a maximum thickness of 722 m (2,368 ft), and the central subbasin where LBF is thickest at 975 m (3,200 ft).

The LBF includes an acoustically transparent zone (ATZ) which is defined as an area of dim amplitude reflectors. The ATZ is interpreted to consist of bedded evaporite deposits based on similar, tested, ATZ's in proxy basins (Eberly and Stanley 1978) and predictions from the conceptual basin formation model (section 4a). Although the type of evaporite minerals present in Harquahala basin is not directly known, poorly reflective and chaotic-to-weak amplitudes, are indicators of halite-rich bodies (Teixeira et al. 2020). The composition of evaporite deposits in proxy basins also include significant halite – the evaporites in Luke basin are halite and Picacho basin is composed of anhydrite with lesser bedded halite (Neal and Rauzi 1996).

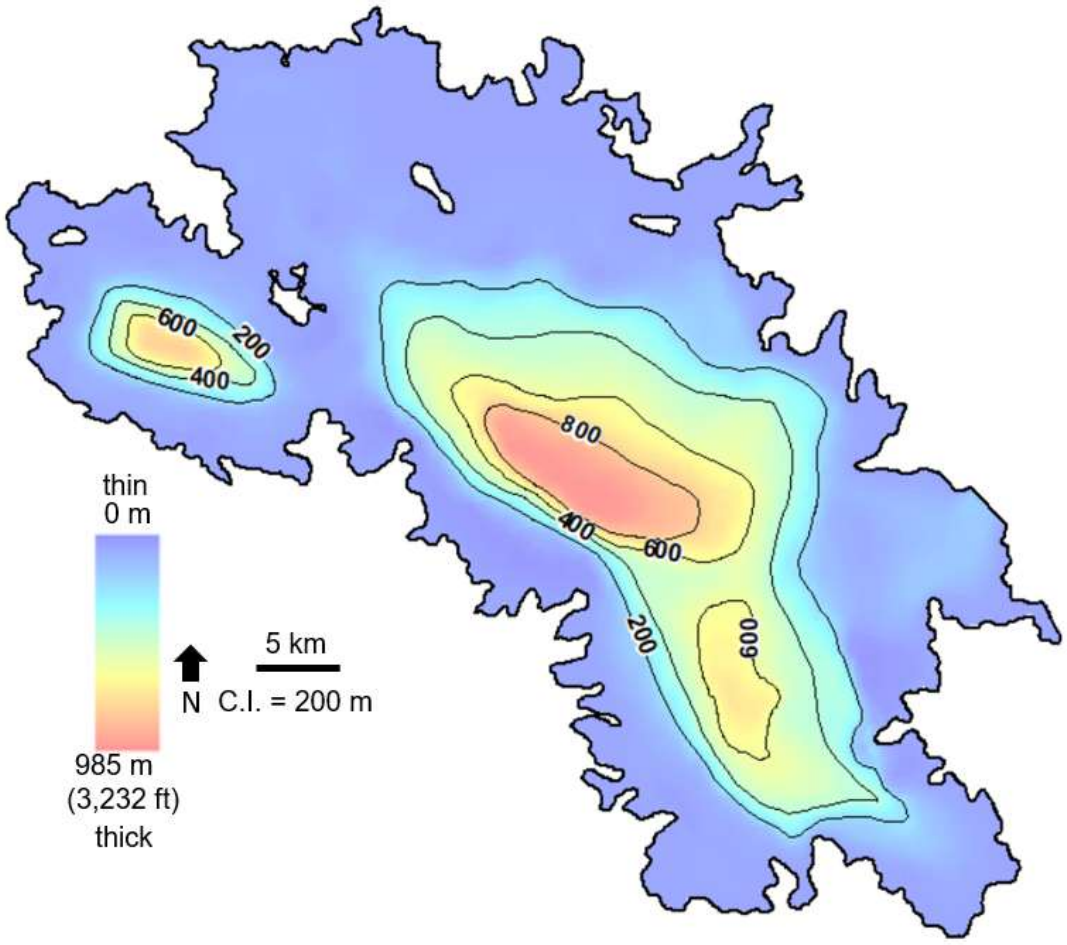


Figure 86 Isopach map of lower basin fill in Harquahala basin created by subtracting the base upper basin fill (UBF) elevation (m) grid by the base lower basin fill (LBF) elevation (m) grid

The acoustically transparent zone is observed on lines TR9 and PW23 in Harquahala basin. An approximate thickness across the zone was calculated using the difference of the travel time (ms) between the top and bottom of the seismic facies (converted to seconds) and multiplied by14,500 ft/s (the proxy evaporite velocity from sonic logs in Picacho and Luke basins). The areal extent and maximum thickness of the ATZ in Harquahala basin is 180 km^2 (112 mi^2) and 610 m (2,000 ft). Isopach maps of the ATZ show their extents are generally located adjacent to basin depocenters (Figure 87), which may represent the extensive, and shallow salt pan environment as seen on the depositional environment block model (Figure 84). Additionally, subbasins likely

migrated slightly over time which may explain why the ATZ polygon does not match the deepest parts of the subbasins. Higher resolution data is needed to better delineate ATZ extents.

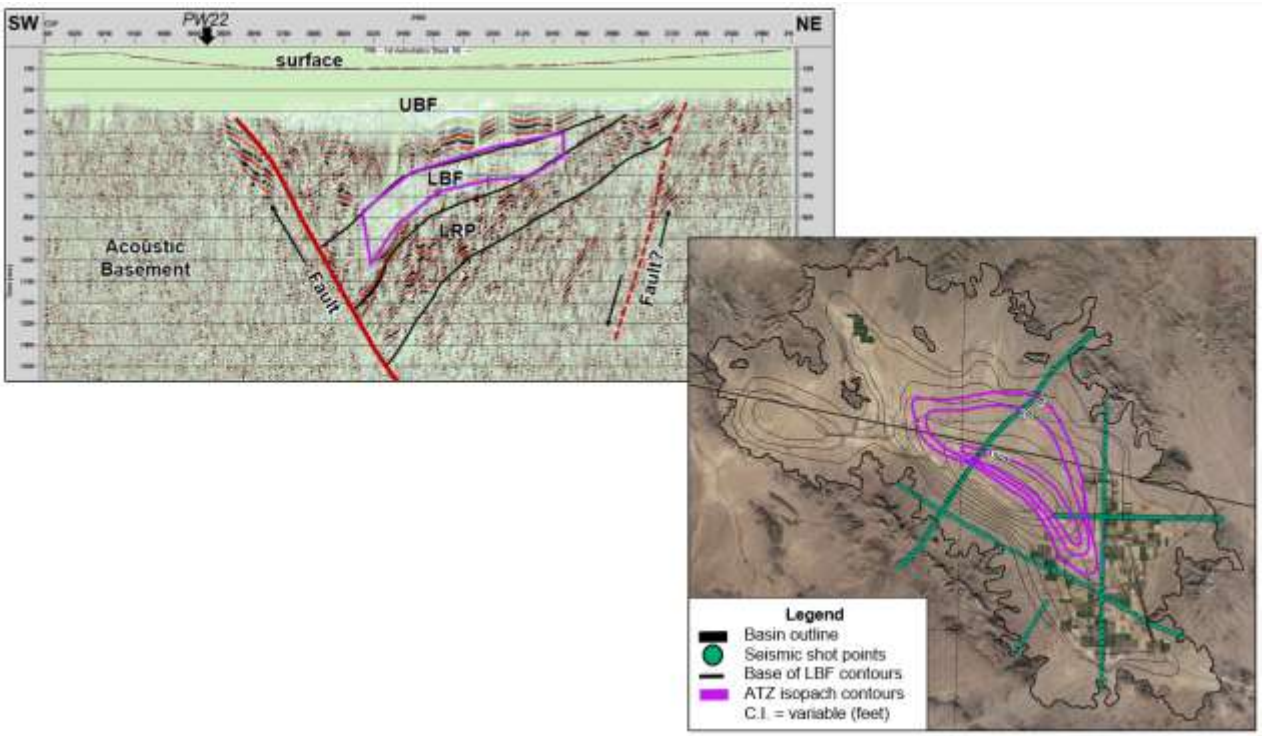


Figure 87 Seismic line TR9 with the mapped ATZ outlined in purple. Isopach map of the acoustic transparent zone (ATZ) in Harquahala basin.

Upper Basin Fill (UBF)

The youngest unit defined in this study is the upper basin fill (UBF). It is characterized by combining the conceptual basin model, proxy studies from nearby basins, well lithology logs, and lateral predictions from bedrock and surficial geologic mapping. In both basins, the UBF is relatively nondeformed (not faulted, folded, or tilted), extends to basin margins, and unconformably overlies the LBF (Figure 85). Like the LBF, the UBF is composed of clastic sediments ranging in size from clay to boulders and grain size is dependent on distance from the basin-bounding mountain ranges. At the time UBF was deposited, Basin and Range extension and volcanism was waning, therefore the UBF likely has little or no primary volcanic deposits.

The isopach map of UBF in Harquahala basin shows two distinct subbasins, the northwestern subbasin with a maximum thickness of 530 m (1,740 ft) and the central subbasin with a maximum thickness of 820 m (2,690 ft; Figure 13A).

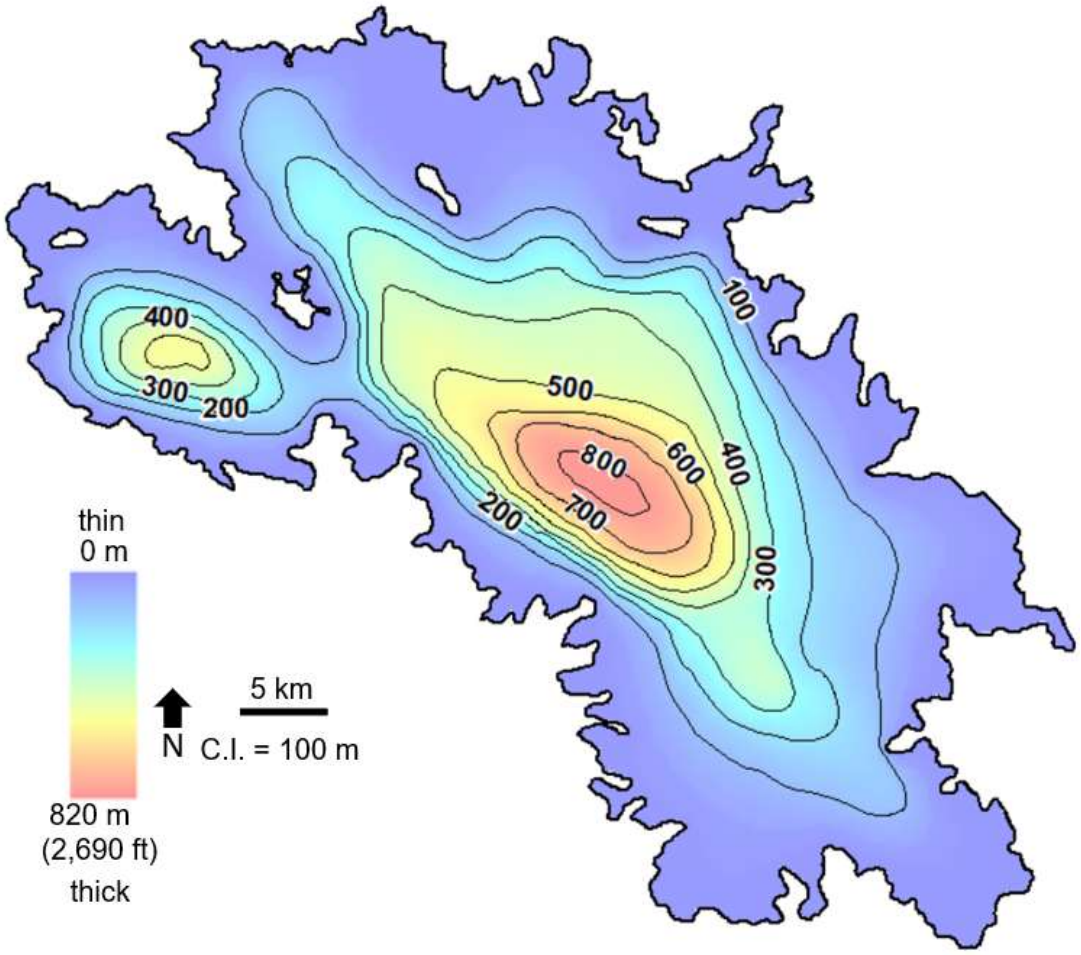


Figure 88 Isopach map of upper basin fill unit in Harquahala basin by subtracting the surface digital elevation model (DEM) grid by the base upper basin fill (UBF) elevation (m) grid

Geothermal Gradient

Hot dry crystalline rock is close to the surface in the Basin and Range Province due to millions of years of extension/faulting resulting in high heat flow (Figure 89A). Small-scale national geothermal studies of heat flow (Mullane et al. 2017; Witcher 1995) show the state of Arizona has moderate geothermal potential (Sass et al. 1994; Figure 89B).

Borehole temperature data in Harquahala basin are sparse and they show no distinct spatial trends. Measured temperatures in 84 wells that penetrate upper basin fill to the shallow depth of 611 m (2,005 ft) average 91°F (33°C). The calculated mean geothermal gradients to shallow well terminations are 87°F/mi (30.6°C/km) for Harquahala basin. These gradients are comparable to the published mean geothermal gradient for the southern Basin and Range Province of 30°C/km (Nathenson and Guffanti 1988).

Geothermal gradients for the entire basin depth cannot be directly calculated because there are no deep borehole logs. Estimates can be made, however, using two nearby proxy basins: Luke basin at 78.8°F/mi (26°C/km) with a maximum well depth of 550 m (1,804 ft) and Higley basin at 104°F/mi (40°C/km) with a maximum well depth of 2,780 m (9,118 ft). In general, geothermal gradient is dependent on crustal thickness. Thick basin fill that overlies thinner crust (at basin

centers) is expected to have a higher geothermal gradient because there is less mantle-derived heat loss within that crust. Conversely, thin basin fill that overlies thick crust (at basin margins) is expected to have a lower geothermal gradient because mantle-derived heat is widely dissipated within that crust. Additional data acquisition is required to better characterize basin heat flow and borehole temperature heterogeneity.

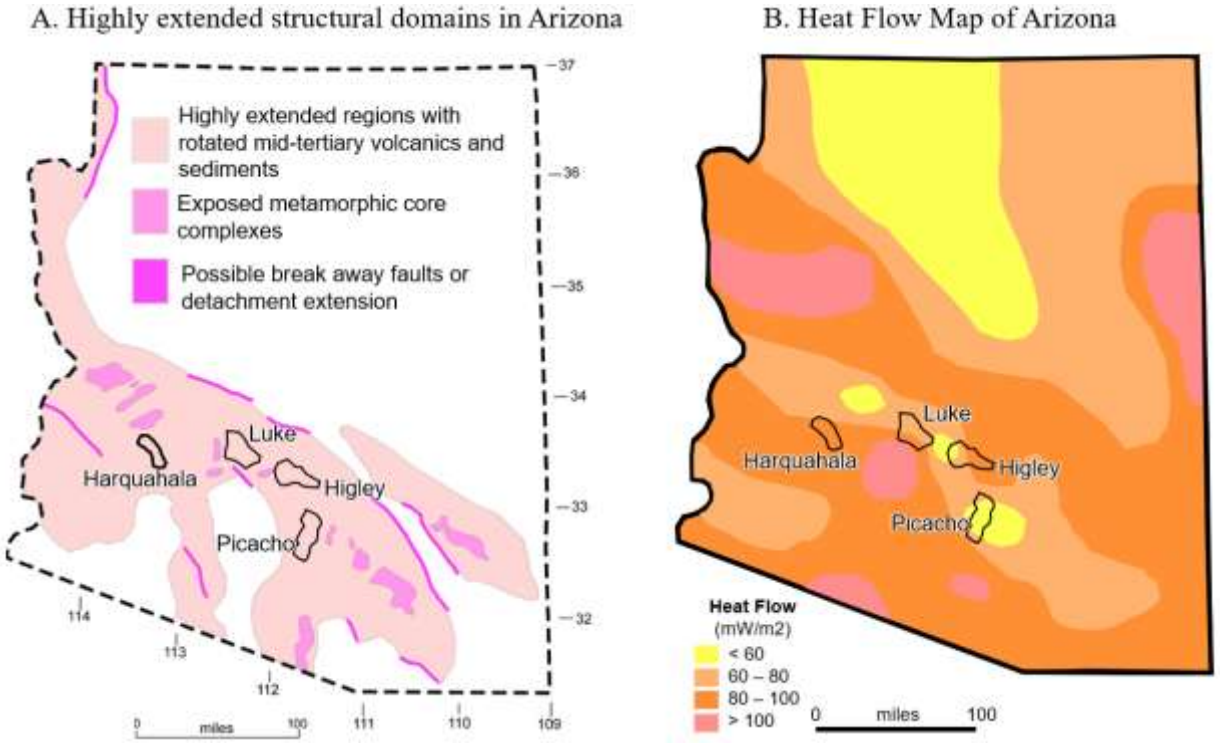


Figure 89 Map of extended crust and heat flow in Arizona (A) Map of highly extended structural domains throughout Arizona. Modified after a 2018 presentation by Witcher, originally from Spencer and Reynolds (1989). (B) Map of heat flow throughout Arizona modified after a 2018 presentation by Witcher, originally from Sass et al. (1994).

Groundwater Salinity

The U.S. Environmental Protection Agency (EPA) defines a non-potable water resource as greater than 10,000 milligrams per liter (mg/L) of total dissolved solids (TDS). Several basins in south-central Arizona have brackish, saline and hypersaline groundwater at depths generally greater than 2,500 ft (Gootee et al. 2012). Due to the lack of salinity data below 2,000 ft in Harquahala basin, we refer to proxy basins for comparison.

Figure 90 shows TDS values exceed approximately 90,000 mg/L for three proxy basins with deep well data: Luke basin, Higley basin, and Picacho basin. Measured TDS values for Harquahala basin are below the 10,000-ppm limit, but those data are limited to wells shallower than approximately 1,000 ft. Deep TDS values cannot be extracted from shallower data because the data do not trend linearly due to factors such as groundwater mixing from mountain-front recharge, mixing with deeper groundwater and recharge from agricultural uses. The basin is structurally and hydrologically isolated with deep (>5,000 ft) basin centers, and likely bedded evaporite deposits. Given this, the potential for elevated TDS concentrations at depths greater

than approximately 2,500 ft is anticipated. Additional water sampling and temperature measurements at depth are required to give a more accurate and complete assessment.

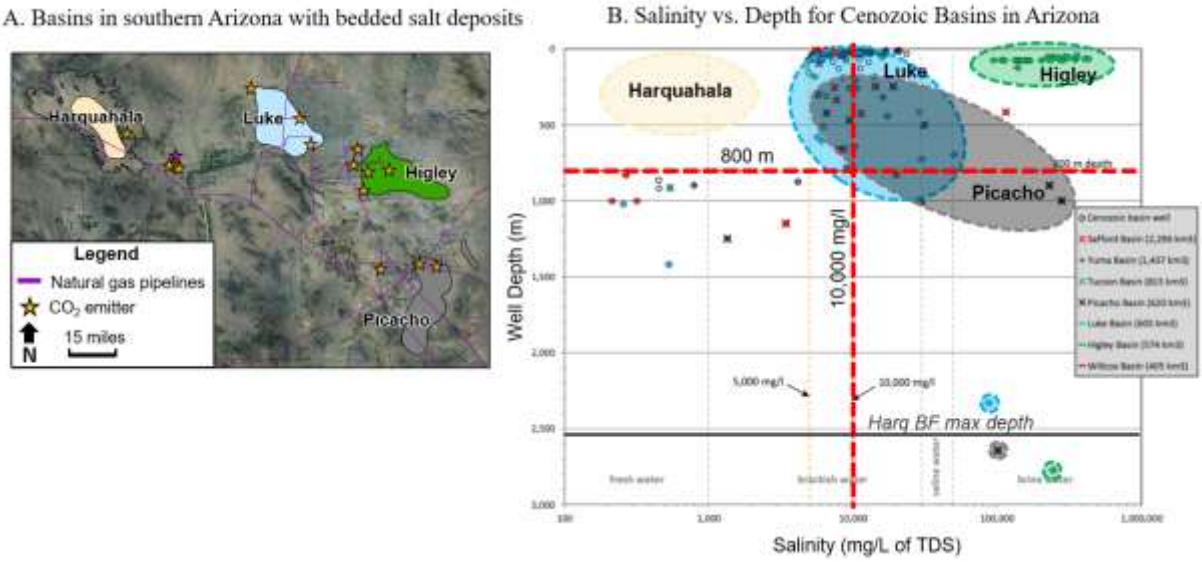


Figure 90 Bedded salt and groundwater salinity in southern Arizona (A) Location map of salt-bearing basins of interest in south-central Arizona colored to match fields shown in 16B. (B) Scatter plot of salinity vs. well depth for salt-bearing basins of interest, modified after Gootee et al. (2012). Each basin has a colored data cloud for comparison. Red dashed lines represent the salinity and depth cut offs. Black lines represent maximum basin fill depths for each basin.

Analysis and Discussion

Storage Reservoirs

Parameters necessary for a suitable carbon capture and storage (CCS) reservoir include sufficient lithostatic pressure of around 800 m depth (about 20 MPa pressure), groundwater salinity at or greater than 10,000 ppm TDS limit set by EPA, below viable underground sources of drinking water (USDW), reservoir pore space volume and permeability, and a seal or caprock above the reservoir. The types of CCS reservoirs applicable in this region would be stacked saline, mafic rocks, and geothermal. Potential seals would include claystones and bedded evaporites. A stacked saline reservoir with fine-grained clastic and bedded evaporite capping layer(s) are highly probable in Harquahala. Bedded evaporite deposits and basalt lava flows are likely but not directly measured. Storage reservoir types stated herein are each 800 m (2,624 ft) below the land surface, where lithostatic pressure is sufficient to retain CO_2 in a supercritical state, assuming regional pressure and temperature conditions.

Stacked Saline Formations

Stacked saline reservoirs are comprised of permeable clastic and chemical sedimentary rocks with saline pore water and represent the most likely and abundant type of storage by volume. The stacked saline reservoir in Harquahala basin includes both the lower reflective package (LRP) and the lower basin fill (LBF), which can also include stacked volcaniclastic and mixed volcanic and sedimentary rocks. Together these stratigraphic units occupy a total gross volume of 396 km^3 (95 mi^3): LRP = 304 km^3 (73 mi^3) and LBF = 92 km^3 (22 mi^3). Reported volumes

include rock volume and pore space. Capping or sealing stratigraphic units cannot be identified with available data. However, evaporite deposits, fine-grained siliciclastics such as clay beds, and some weathered basalt lava flows, can provide sealing conditions and are likely present in Harquahala basin based on predictions from the basin's geologic history and regional geologic map units.

Bedded Evaporite Deposits

The presence of bedded evaporites is likely based on nearby proxy basins with similar tectonic histories and tested evaporite deposits. Bedded evaporites in Harquahala basin are strongly supported by proprietary isostatic residual gravity anomaly maps and seismic patterns/fabrics observed and interpreted from 2D seismic lines in this study.

The nearby Picacho and Luke sedimentary basins, which have the same geologic history as our basin of interest, have proven salt deposits. Picacho basin, approximately 90 mi SE of Harquahala basin, has evaporite facies at depth confirmed by wireline electric logs and whole rock core. The Luke basin contains a large salt body that has been developed and used to safely store liquid natural gas since the early 1970s. The Luke basin salt deposit is characterized by gravity anomaly maps (Richard et al. 2007) and seismic data (Eberly and Stanley 1978) which have also highlighted the potential salt presence in Harquahala basin.

The acoustically transparent zone (ATZ) imaged from seismic facies likely represents a bedded evaporite deposit or interval and is present in Harquahala basin. The ATZ is defined by areas of dim amplitude reflectors. The areal extent and thickness are shown on Figure 86. The location and extent of this facies is limited by the quality of the 2D seismic lines, and it may be present elsewhere, where resolution is poor, or data is absent.

Basalt Flows

Liquified CO_2 can be reacted with buried magnesium- and iron-rich mafic rocks in situ to form a solid precipitate, permanently storing it (Raza et al. 2022). This chemical reaction takes place on short timescales ranging from hours to a few years, and the reaction is accelerated with greater exposed surface area (i.e., vesicular basalt, volcaniclastic particles, and joint surfaces). During crustal extension and formation of Harquahala basin, mafic (basaltic) volcanism was widespread and long-lived. Basalt lava flows cap bedrock in basin-bounding mountain ranges, and (at least) one large volcanic vent (Saddle Mountain) divides Harquahala and Tonopah basin to the east (see Plate 2, Wilson et al. 2024). Mafic volcanic rocks are logged in shallow wells along the basin margins (see Plate 3, Wilson et al. 2024) and lithofacies mapping predicts mafic volcanic rocks are the dominant source terrain for basin fill in the southern Harquahala basin (Figure 80). Inselbergs of basaltic flows exposed on basin margins are surrounded by young basin fill, suggesting some likelihood that these flows are interbedded with a part of basin fill. The LRP in Harquahala basin is likely comprised of volcanic flows interbedded with sedimentary rock, which may present additional basaltic storage reservoirs combined with interbeds capable of trapping CO_2 long enough to mineralize into solid carbonate minerals.

Volume Estimates of Basin Fill and CO_2 Storage

Basin Fill Sediment Volumes

Storage volume estimates are theoretical and not based on direct measurements in the Harquahala basin. Isopach maps were created to calculate the total rock volume of the stratigraphic units present. Without deep borehole lithologic and rock property logs, we assigned mean matrix porosity values derived from our interpretations of basin stratigraphy and regional proxy data from other deep sedimentary basins (Gootee 2013a, 2013b, 2015). Fracture porosity, spacing, and density was not considered in our study. Storage volumes for CO_2 mineralization in basalts were not estimated. This technique is relatively new and there are too many unknowns at this stage to achieve a reasonable estimate.

To estimate net pore space for CO_2 storage, the area of each basin fill unit and maximum thickness were calculated from isopach maps presented in section 4. The average thickness of basin fill below 800 m depth was used to calculate first-order gross volume. The UBF lies above the 800 m depth requirement for CO_2 storage, so it is not considered in the storage volume calculations. Table 3 summarizes the area, max thickness, and gross sediment volume for each basin-fill unit in Harquahala basin.

Table 3. Physical dimensions of area, thickness, and volume for basin fill units in Harquahala basin. Italicized physical parameters below 800 m depth were used in CO_2 volume analysis.

	Basin-fill units	Area (km2)	Max thickness (m)	Average thickness (m)	Gross volume (km3)
Harquahala basin	UBF	1,380	820	--	248
	LBF	1,380	975	--	92
	ATZ	185	610	--	unknown
	LRP	unknown	1,490	--	304
	below 800 m	*327*	*1,740*	*848*	*269*
	total basin fill	1,380	2,540	--	644

Other Physical Parameters

Basin fill units in Harquahala are suitable reservoirs for supercritical CO_2 storage because they likely contain permeable and porous strata under confined to semi-confined conditions in saline to hypersaline aquifers below 800 m depth. The LBF is likely composed of evaporite minerals, mixed with some fine gravel, sand, silt and possibly extensive clay, characteristic of basin fill in the region at these depths (Gootee 2015). The LRP, which underlies the LBF, is likely composed of volcanic and sedimentary rocks. A gross volume of porous rock was estimated based on these lithologies and their porosity contributions. For example, sandstone, fine gravel and volcanic lithofacies would contribute to porous and permeable strata, whereas clay and evaporites would serve as sealing strata. The percentage of the porous lithofacies was estimated based upon the conceptional basin model presented in Figure 80. In both basins, we estimate between 30% and 70% of basin fill have porous and permeable sediment suitable for CO_2 storage, thus we used the 50% median or net-to-gross ratio of 0.5. The porosity of sandstone and gravel range from 40% to

15%; we used an average porosity of 25%, excluding porosity-reduced compaction with increased depth. An effective available porosity (specific yield) between 10% and 30% was considered, based on data from general physical character of sand and fine gravel (Walton 1970), although these estimates do not take cementation into consideration. A conservative effective porosity of 15% was used, derived primarily from numerical groundwater models of older basin fill strata in nearby McMullen basin (Gootee and Noel 2015) and Phoenix basins (ADWR 2006).

The density of supercritical CO_2 at an approximate depth, temperature and pressure for supercritical CO_2 storage is based on modeled datasets (Pan et al. 2017). The temperature of the reservoir was based on scant oil and gas well data in this region, and from the geothermal gradient discussed in section 4. A summary of physical parameters and their standard deviations used to calculate volumes are listed in Table 4. All volume data, other factors, coefficients, and calculations are listed in Appendix G.

Table 4. Physical parameters of basin fill used to calculate CO_2 injection volumes.

Parameter	Units	Harquahala	Standard deviation
Area, A	km2	327	0.1
Gross thickness	m	848	0.2
Porosity, Φ	frac.	0.15	0.05
Net-To-Gross Ratio, NGR	frac.	0.5	0.25
Efficiency Factor	frac.	0.2	0.1
Density of CO_2	kg/m3	650	--
Reservoir temperature	C	75	10
Reservoir pressure	MPa	20	3

CO_2 Storage Volume Estimate

The volume of pore space available for supercritical CO_2 injection into a stacked saline reservoir was estimated by employing three different approaches using the physical input parameters listed in Table 4 – a simple linear approach, a probabilistic approach independent of time (Sarkodie-Kyeremeh et al. 2022), and a similar probabilistic simulation for 5 yr of CO_2 injection at 200,000 mt/yr using a DOE National Energy Technology Laboratory (NETL) CO_2-Screen tool v.4.1 (Sanguinito et al. 2022).

In the simplistic linear approach, the assumed net rock volume is multiplied by the estimated effective porosity to derive the estimated pore volume. To estimate the amount of CO_2 that would be stored in this calculated pore volume we used the average volume of CO_2 at a supercritical state, 0.650 g/cm^3 (650 kg/m^3) to find that 100,000 t of CO_2 would occupy approximately 0.000154 km^3 of space. This resulted in 13,550 Mt of CO_2 storage in Harquahala basin.

For the probabilistic methods the results are plotted as a percentage of uncertainty, represented by a probability distribution (Figure 91). Estimates are defined as the probability of exceedance

such that a proved (P90), the lowest value, 90% of the calculated estimates will be equal or exceed the P90 estimate. P50 is the median estimate. The P10 is the possible estimate, the highest value, or 10% of the calculated estimates will be equal or exceed the P10 estimate. Because the mean and median (P50) values are not the same, this suggests the results are slightly skewed, thus we consider the P50 values to be more representative than the mean. The P50 results yield 1,997 Mt (1.9 Gt) in Harquahala basin for total CO_2 storage. The time dependent approach resulted in a P50 of 463 Mt in Harquahala basin of CO_2 storage for 5 yr of injection.

The simplistic linear approach yields much larger values than the probabilistic approach and is likely an overestimate. The probabilistic approach takes more parameters into account and is likely more representative of the subsurface conditions, therefore we expect the total CO_2 storage volumes to be closer to the probabilistic method values. The method by Sarkodie-Kyeremeh et al. (2022) estimates a degree of uncertainty or sensitivity of most parameters listed in Table 4. The area, gross thickness, and CO_2 density presented the least degree of uncertainty, whereas the porosity, net-to-gross ratio, and efficiency factor presented the most, which will help to identify which parameters need to be refined as part of new data collection. The relative amount of uncertainty for this method is presented in more detail in Appendix G.

Table 5. Summary of CO_2 storage calculations in million metric tons (Mt) for each method.

	Total CO_2 storage, Mt		**CO_2 storage for 5 yr, Mt**
Basin	**Simple linear**	**Probabilistic (P50)**	**Probabilistic (P50) NETL CO_2-Screen**
Harquahala	13,550	1,997	463

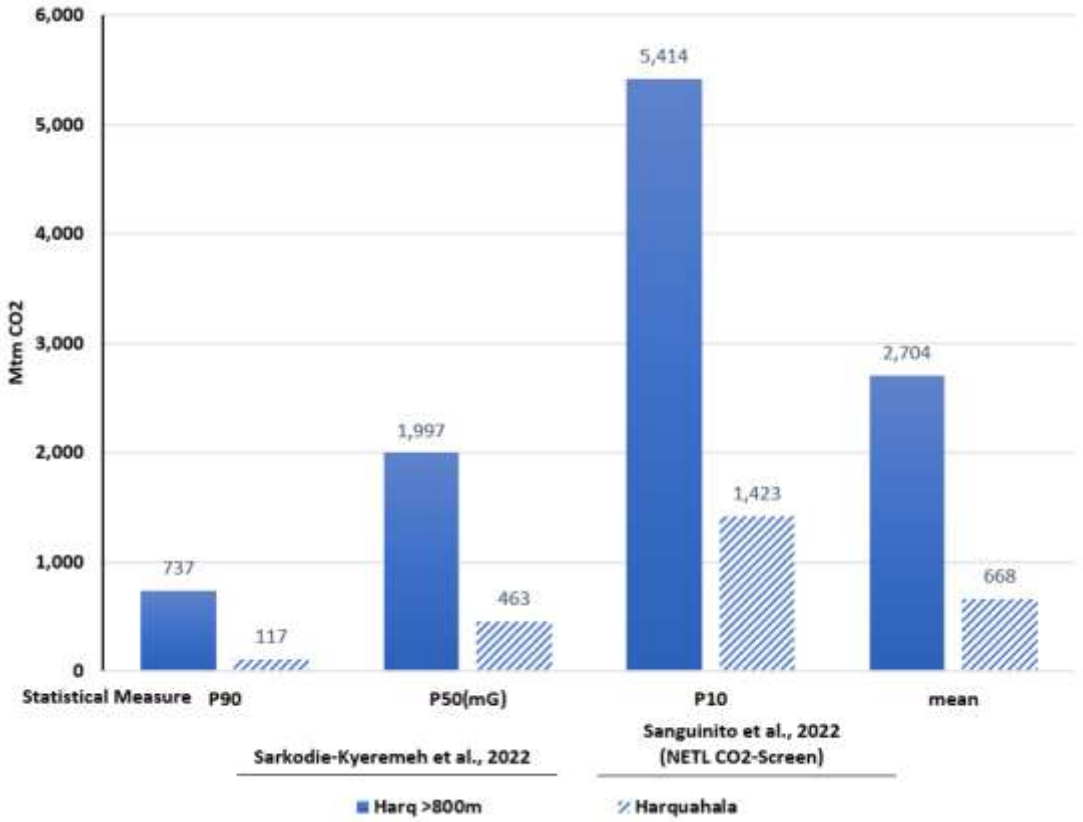


Figure 91 Calculated statistical volumes of CO_2 storage in non-differentiated basin fill units below 800 m depth in Harquahala basin for total CO_2 injection capacity in solid blue (Sarkodie-Kyeremeh et al. 2022) and CO_2 capacity after 5 yr injection in hashed blue (Sanguinito et al. 2022).

Known Natural Gas Subsurface Storage Risks

Sealing Conditions

The lack of known impermeable sealing strata is a geologic risk to subsurface natural gas storage. In Harquahala basin, potential bedded evaporite and clay deposits could be adequate seal rocks for stacked saline reservoirs. We predict these deposits are present in the lower basin fill, but we have made no direct observations of them.

Evaporite deposits are impermeable and can serve as a robust seal to trap fluid and gases underground. The lateral extent of this potential seal is shown by the zero contour on the acoustically transparent zone isopach map (equivalent to the top of this seismic facies; Figure 86). The chemistry, geomechanical properties, and lateral continuity of the evaporite deposits have not been directly measured. Fine-grained clastic sediment such as clay, silt and fine sand usually borders evaporite deposits, and the types of salts and mixed percent of lithofacies is important to map out in the subsurface to adequately de-risk storage of CO_2.

The low porosity, fine-grained facies such as clay can be a lithologic barrier to fluid migration. Lithology logs from shallow water wells suggest the presence of a laterally continuous clay layer in Harquahala basin (Towne 2014). The extent, thickness, and continuity of this clay is limited by the location of well penetrations, which are generally clustered within the agricultural area of the basin. Based on the conceptual basin model (section 4a), clay would likely be present near or

along the margin of subbasin centers. Thin interbedded clays layers could create baffles to subsurface flow and compartmentalization within the reservoir. Direct measurements such as electric wireline logs and core are needed to further de-risk the sealing integrity and conditions in these basins.

Seismic Hazard

Historical and induced seismicity can present a risk to any subsurface CO_2 storage. There are several faults surrounding Harquahala basin, and major faults interpreted in vintage seismic reflections (Figure 84); however, there are no known active or Quaternary faults (last 2.5 Myr). The nearest known Quaternary fault is the "Sand Tank" fault about 50 miles southeast of Harquahala basin near the town of Gila Bend, although no paleoseismic investigative work has been done on this fault. Based on the lack of surface ruptures, lack of springs and aseismic activity in Harquahala basin, the seismic risk is considered relatively low (Figure 92; USGS 2018).

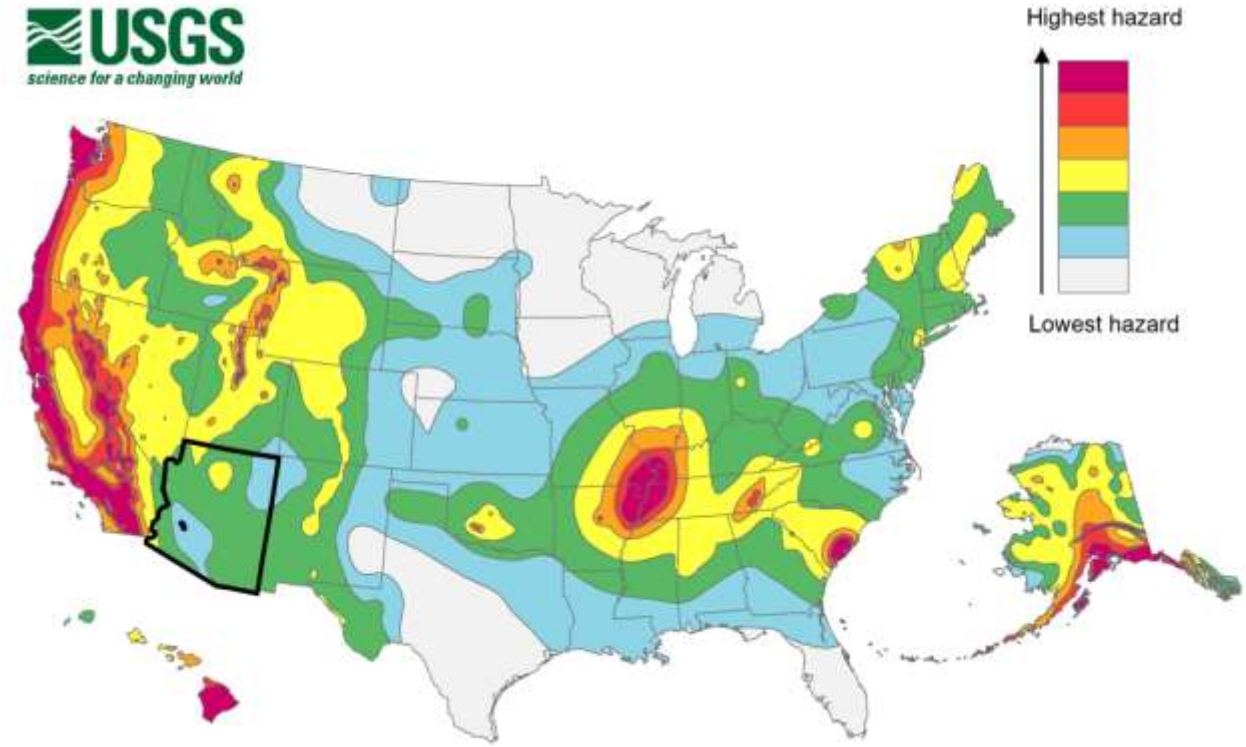


Figure 92 Earthquake hazard map showing peak ground accelerations having a 2 percent probability of being exceeded in 50 yr, for a firm rock site. Harquahala basin is shown as a solid black polygon within Arizona outline. The map is based on the most recent USGS models for the conterminous United States (2018), Hawaii (1998), and Alaska (2007; all from USGS [2018]). Models are based on seismicity, fault-slip rates and consider the frequency of earthquakes of various magnitudes. Locally, the hazard may be greater than shown because site geology may amplify ground motions.

The known seismicity rates for the Harquahala basin and surrounding area are low. Within the last several decades, no events larger than M 3.0 have occurred. Events smaller than M 3.0 may occur; however, the area has not had adequate seismic monitoring spatially or historically. In 2009, AZGS began operating a statewide seismic network, but that network only has 16 stations in the entire state. The two stations closest to Harquahala basin are located approximately 43 km

to the north near Wickenburg and about 110 km to the southwest near Mohawk Valley. Higher density seismic monitoring would improve the detection threshold for the study area if lower magnitudes were necessary.

Conclusions

This study integrated geologic maps, borehole lithology logs, newly reprocessed vintage 2D seismic lines, public and proprietary gravity datasets, and borehole temperature & TDS data to characterize Harquahala basin for geologic storage of CO_2. Permanent subsurface CO_2 storage is possible in two different geologic environments: (1) storage as a supercritical fluid within stacked saline formations below 800 m depth or (2) permanent mineralization through chemical reactions with basalt lava flows. Short term H_2 storage may be possible within the evaporite deposits likely present in the basin, though much of this study was focused on CO_2 storage potential. CO_2 storage in fractured bedrock and geothermal energy potential could be utilized in this basin, though not expanded in this study due to limited data. Harquahala basin is one of 57 extensional basins in the Arizona Basin and Range that is sufficiently deep to store CO_2. This basin formed during the same time under similar tectonic and climatic conditions. Therefore, data from nearby basins such as deep well lithology logs, TDS measurements, and geothermal temperatures can be used a proxy for missing data in Harquahala basin. A conceptual geologic model based on numerous basin studies in the Arizona Basin and Range is used to generalize lithofacies distribution, stratigraphic framework, structural history, and basin geometry.

Harquahala basin is a deep, asymmetric, extensional basin filled with a thick accumulation of clastic and (potentially) chemical sediments, lava flows, and explosive volcanic material from nearby volcanic vents. Seismic reflectors, well lithology logs, proxy data from nearby basins, and our conceptual geologic model delineate three stratigraphic packages. From oldest to youngest these are: lower reflective package (LRP), lower basin fill (LBF), and upper basin fill (UBF). The LRP is deposited on older and more extensively deformed plutonic, metamorphic, and sedimentary rocks and likely composed of a sequence of stacked lava flows interbedded with felsic tuffs and coarse clastic sediments. Deposition of the LRP began with the onset of basin extension and has only been identified from seismic imaging in Harquahala basin. The LBF is likely composed of a wide range of lithofacies and grain size, dependent on distance from the source terrains. Laterally discontinuous seismic reflectors suggest the LBF is locally tilted, folded, and/or faulted, consistent with imaging in other parts of the basin and range province at similar depths. Seismic interpretations of an acoustically transparent zone on seismic lines TR9 and PW23 suggest there may be a thick accumulation of bedded evaporite deposits within the LBF. The UBF is a relatively undeformed, laterally continuous package of clastic and (potentially) chemical sedimentary rocks that unconformably overlies the LBF. The UBF sedimentary package is entirely above 800 m depth and is therefore ineligible for stacked saline storage.

Harquahala basin has sufficient volumes of pore space in presumably saline groundwater below 800 m depth, however, we cannot identify a sealing or capping rock for those reservoirs with certainty because of the lack of deep well lithology logs. Isopach maps highlight the thicker areas in the basin that could be targeted for future exploration. The LBF and LRP are both present below 800 m (2,625 ft) and are good candidates for stacked saline storage and, potentially, mineralization in basalt lava flows. Based primarily on analysis and interpretation of seismic data, and on physical parameters from proxy basins, there is a P50 probability that about 1,997

Mt of supercritical CO_2 can be stored in Harquahala basin. To reduce uncertainty and sensitivity in these calculations, the porosity, net-to-gross storage volumes, and storage efficiency require new data collection from drilling and detailed geophysics.

From this study we have refined the basin geometry and provided new insights into basin structure and gross stratigraphy. Three critical unknowns remain: the existence/absence of a sealing strata such as bedded evaporites, the physical properties of stacked saline reservoir rock, and the stratigraphic architecture of basin fill sediments. Harquahala basin lacks the deep well borehole data needed to adequately characterize rock lithology, porosity, and permeability. We cannot diagnostically identify, for example, the presence/absence of bedded evaporite deposits, basalt lava flows, or extensive clay beds that can be used as sealing strata. The stratigraphic architecture of the basin, such as lateral extent of sealing strata, minor fault blocks, or presence/absence of anticlinal traps also remains unknown. Therefore, we recommend the acquisition of three new datasets in both basins: 2D active-source seismic (possibly passive-source too), magnetotellurics, and deep well borehole wireline geophysical logs and sampling. These datasets, combined with data reported within, will refine our understanding of the lower basin fill unit rock properties (the potential stacked saline aquifer), identify the presence/absence of sealing strata, and clarify stratigraphic architecture and basin structure.

Recommendations

CO_2 geologic storage in Harquahala basin is favorable, but more data collection is necessary to better characterize the reservoir and decrease geologic risk. For a phase II technical evaluation, our team recommends acquiring 8 new 2D seismic lines, additional in-fill gravity data, high resolution aeromagnetic survey, and drilling one stratigraphic characterization well.

The location of each method is presented in Figure 93 and discussed below. Magnetotellurics and a 3D seismic survey were considered as part of new data collection, although we recommend these methods be considered after Phase-II data are analyzed and funded as part of a Phase-III program.

New 2D Seismic

The reprocessed legacy 2D seismic data that was interpreted for this project is of moderate to poor quality and was not acquired with modern techniques. Acquiring new 2D seismic lines is advantageous because the acquisition parameters can be tailored specifically for the purpose of exploring the deep subsurface using what we now know about the stratigraphic units at depth. Line locations would target deep subbasins identified in this study. New 2D seismic would help refine basin geometry, identify faults, provide greater image resolution and seismic facies, map the extent of bedded salt deposits, and reduce uncertainty related to reservoir boundaries and potential seals.

We recommend acquiring 2D seismic reflection data along 8 different lines in Harquahala basin, totaling 105 miles. Three of these lines are longer (16–21 miles) and strike northwest-southeast and north-south. The remaining five lines are shorter (8–11 miles), cover the two main depocenters, and generally run perpendicular to the basin axis (Figure 93). The proposed 2D seismic lines were chosen based on existing roads and access points, minimizing impact to agricultural plots, utilizing land ownership maps, intersecting legacy seismic surveys, and maximizing the characterization potential of the reservoir based on our findings in this study.

The locations of these conceptual lines will likely change as part of a phase-II approach involving permitting, surveys related to permitting, ownership, and access.

Gravity and Aeromagnetic Surveys

Gravity and magnetic surveys are cost effective geophysical methods for exploring the subsurface over a large area. Gravity measurements provide information about rock density and can be used to understand the spatial distribution of those rock types in the subsurface. An aeromagnetic survey measures the intensity of the Earth's magnetic field and can yield the spatial distribution of the relative abundance of magnetic minerals. Often these types of data are used in conjunction with one another. The resulting data can help refine the boundaries of the sedimentary basin at depth and can elucidate the internal structural highs and lows (Selley and Sonnenberg 2023). Faults can also be identified using these methods which can help characterize the effectiveness of the sealing strata and potential seismicity risk, especially when combined with 2D seismic and well control. These data will be processed using the Werner Deconvolution method to also map salt extent (top and bottom), thickness, and the depth to crystalline basement.

We recommend acquiring additional gravity data and a high-resolution aeromagnetic survey over a targeted area (approximately 900 km^2) of the Harquahala Valley (Figure 93). The spatial distribution of existing gravity stations within the basin is not sufficient, as there are areas (specifically in the east) that lack control points. The goal is to develop a gravity acquisition plan that fills in the existing gravity dataset at regularly spaced intervals (1 mile apart) for the entirety of our Area of Interest (AOI). Additionally, more gravity stations along the southwest margin of the basin along seismic lines will be needed to capture the steepness of that fault margin. An aeromagnetic dataset also exists over this area but again is not sufficient for this study. This survey was collected in 2001 by the U.S. Geological Survey as part of a large statewide effort and lacks the resolution needed. We plan to collect a high-resolution aeromagnetic survey with 200 m line spacing and 2,000 m tie lines.

Stratigraphic Characterization Well

A deep characterization well is required to examine rock lithology, stratigraphy, reservoir type and depth, sealing potential, geothermal potential, and water chemistry/salinity. This will be achieved by drilling a deep borehole, running wireline logging tools, collecting cuttings, retrieving core samples, and collecting downhole water samples and pressure information. A comprehensive suite of wireline logs should include, but not be limited to triple combo (caliper, spontaneous potential, gamma ray, resistivity, density), 4-point Rx sonic, formation imager (FMI), nuclear magnetic resonance, cement bond log (CBL) and temperature log. These logs will greatly reduce uncertainty and be used to calibrate and adjust input parameters in legacy and new geophysical datasets. Continuous wireline core through the bedded salt section would provide the greatest preservation of data and likely be the most cost-effective method. Conventional whole-rock core and sidewall cores are recommended for pertinent sections and lithologies below the bedded salt portion. A detailed core analysis would include, but not be limited to: porosity, permeability, grain density, core gamma for correlating core depth with logs, core photographs, CT scan, and fluids analysis. Additional CO_2 mineralization experiments will be run on mafic rocks encountered.

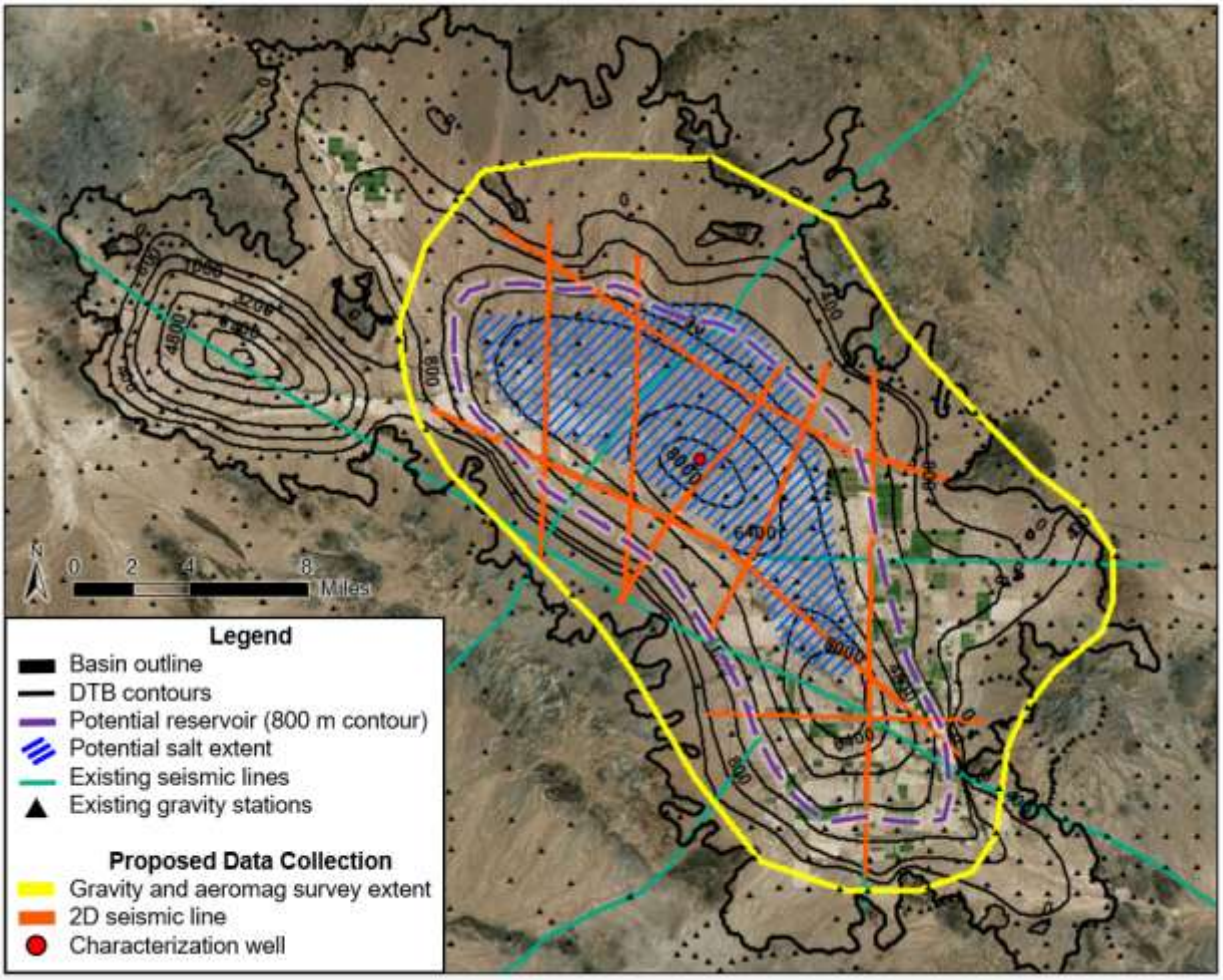


Figure 93 Map of selected existing data and proposed new data acquisition.

We recommend drilling a 10,000 ft stratigraphic characterization well in the central subbasin (Figure 93). This depth was chosen to ensure the hole penetrates the crystalline basement rock which, if fractured, will be evaluated as a potential reservoir and to determine the temperature for assessing the geothermal potential. This location will capture the deepest portion of the basin and will confirm the presence or absence of bedded evaporite deposits and interbedded basalt flows here (including their state of alteration or weathering). The proposed well location is on federal land (Bureau of Land Management) which should streamline the permitting process for CCS projects under BLM Internal Memorandum # 2022-041 (June, 2022). It is also conveniently positioned near interstate 10 and Salome Road, which provides a transportation route to support drilling operations.

References

[ADWR] Arizona Department of Water Resources. 2004. Unpublished gravity data from the Hassayampa region, south-central Arizona. Phoenix (AZ); Arizona Department of Water Resources. [Unpublished data].

[ADWR] Arizona Department of Water Resources. 2006. Salt River model geology update. Phoenix (AZ); Arizona Department of Water Resources. Modeling Report No. 16.

[ADWR] Arizona Department of Water Resources. 2022. Statewide historic and compiled gravity datasets originally from PACES (2016), maintained by ADWR. Phoenix (AZ); Arizona Department of Water Resources. [Unpublished data].

[AZOGCC] Arizona Oil and Gas Conservation Commission. 2023. Well files and production reports. Phoenix (AZ); Arizona Oil and Gas Conservation Commission. [Internet]. Accessed 2023 Jan. https://azogcc.az.gov/records

Eberly LD, Stanley TB. 1978. Cenozoic stratigraphy and geologic history of southwestern Arizona. Geol Soc Am Bull. 89:921–940. doi:10.1130/0016-7606(1978)89%3C921:CSAGHO%3E2.0.CO;2

Faulds JE, Schreiber BC, Langenheim VE, Hinz NH, Shaw TH, Heizler MT, Perkins ME, El Tabakh M, Kunk MJ. 2016. Paleogeographic implications of late Miocene lacustrine and nonmarine evaporite deposits in the Lake Mead region: immediate precursors to the Colorado River. Geosphere. 12:721–767. doi:10.1130/GES01143.1

Gootee BF. 2013a. An evaluation of carbon dioxide sequestration potential in the Luke Basin, south-central Arizona. Tucson (AZ); Arizona Geological Survey. Open-File Report 13-05.

Gootee BF. 2013b. An evaluation of carbon dioxide sequestration potential in the Higley Basin, south-central Arizona. Tucson (AZ); Arizona Geological Survey. Open-File Report 13-10.

Gootee BF. 2015. An evaluation of carbon dioxide sequestration potential in the Picacho Basin, southeastern Arizona. Tucson (AZ); Arizona Geological Survey. Open-File Report 15-09.

Gootee BF, Love DS, Mahan MK. 2012. A summary of salinities in Arizona's deep groundwater. Tucson (AZ); Arizona Geological Survey. Open-File Report 12-26.

Gootee BF, Noel SD. 2015. McMullen Valley groundwater model (supporting Arizona State Land Department application for analysis of water adequacy). Phoenix (AZ); Arizona State Land Department. [Unpublished report].

[HGI] HydroGeophysics Inc. 2009. Geophysical results for Harquahala Basin. Tucson (AZ); HydroGeophysics Inc. [Confidential report].

Menges CM, Pearthree PA. 1989. Late Cenozoic tectonism in Arizona and its impact on regional landscape evolution. In: Jenny JP, Reynolds SJ, editors. Geologic evolution of Arizona. Tucson (AZ); Arizona Geological Society. p 649–680.

Mullane, M., Gleason, M., Reber, T., McCabe, K., Mooney, M., Young, K.R., 2017. An estimate of shallow, low-temperature geothermal resources of the United States (No. NREL/CP-6A20-68523). Davis, CA: Geothermal Resources Council.

Nathenson M, Guffanti M. 1988. Geothermal gradients in the conterminous United States. J Geophys Res Solid Earth. 93(B6):6437–6450. doi:10.1029/JB093iB06p06437

Neal JT, Rauzi SL. 1996. Storage opportunities in Arizona bedded evaporites. Albuquerque (NM); Sandia National Laboratories. Report No. SAND96-1679C.

[PACES] PACES Project. 2016. Regional public gravity datasets. [Place unknown]; PACES Project. [Data set].

Pan B, Lei J, Zhang L, Guo Y. 2017. Research on the physical properties of supercritical CO_2 and the log evaluation of CO_2-bearing volcanic reservoirs. J Geophys Eng. 14:1052–1060. doi:10.1088/1742-2140/aa6f22

Peters, K.E., Curry, D.J., Kacewicz, M., 2012. An overview of basin and petroleum system modeling: definitions and concepts 1–16. doi:10.1306/13311426H4139

Raza A, Glatz G, Gholami R, Mahmoud M, Alafnan S. 2022. Carbon mineralization and geological storage of CO_2 in basalt: mechanisms and technical challenges. Earth-Sci Rev. 229:104036. doi:10.1016/j.earscirev.2022.104036

Reynolds SJ. 1997. Geologic data for the Phoenix South 30′ × 60′ quadrangle. Tucson (AZ); Arizona Geological Survey. DGI-05 v2.0.

Reynolds SJ, Grubensky MJ. 2007. Geologic data for the Phoenix North 30′ × 60′ quadrangle. Tucson (AZ); Arizona Geological Survey. DGI-04 v2.0.

Richard SM, Shipman TC, Greene L, Harris RC. 2007. Estimated depth to bedrock in Arizona. Tucson (AZ); Arizona Geological Survey. Digital Geologic Map DGM-52.

Richard SM, Spencer JE, Reynolds SJ, Pearthree PA, Demsey KA, Thompson LA, Snellen HL, Theim JP. 2022. Geologic map of the Salome 30′ × 60′ quadrangle, west-central Arizona. Tucson (AZ); Arizona Geological Survey. Digital Geologic Map DGM-157.

Sanguinito S, Hanson A, Haeri F, Myshakin E, Moore J, Crandall D. 2022. CO_2 storage prospective resource estimation Excel analysis (CO_2-SCREEN) user's manual: Python v4.1. Albany (OR); National Energy Technology Laboratory. Report No. DOE/NETL-2022/3729. doi:10.2172/1862020

Sarkodie-Kyeremeh J, Ampomah W, Tu J, Czarnota R. 2022. Advances in CO_2 geological storage: estimation of CO_2 storage efficiency factors for the San Juan Basin formations. In: Proceedings of the 16th Greenhouse Gas Control Technologies Conference (GHGT-16); 2022 Oct 23–27; Lyon (France). doi:10.2139/ssrn.4286058

Sass JH, Lachenbruch AH, Galanis SP Jr, Morgan P, Priest SS, Moses TH Jr, Munroe RJ. 1994. Thermal regime of the southern Basin and Range Province: 1. Heat flow data from Arizona and the Mojave Desert of California and Nevada. J Geophys Res Solid Earth. 99(B11):22093–22119. doi:10.1029/94JB01891

Selley RC, Sonnenberg SA. 2023. Methods of exploration. In: Selley RC, Sonnenberg SA, editors. Elements of petroleum geology. 4th ed. London (UK); Academic Press. p 43–166. doi:10.1016/B978-0-12-822316-1.00003-3

Spencer JE, Pearthree PA, Demsey KA, Thompson LA, Snellen HL, Korroch KM, Theim JP, Richard SM. 2022. Geologic map of the Little Horn Mountains 30′ × 60′ quadrangle, west-central Arizona. Tucson (AZ); Arizona Geological Survey. Digital Geologic Map DGM-153.

Spencer, J.E., Reynolds, S.J., 1989. Middle Tertiary tectonics of Arizona and adjacent areas. Geol. Evol. Ariz. Ariz. Geol. Soc. Dig. 17, 539–574.

Teixeira L, Lupinacci WM, Maul A. 2020. Quantitative seismic-stratigraphic interpretation of the evaporite sequence in the Santos Basin. Mar Pet Geol. 122:104690. doi:10.1016/j.marpetgeo.2020.104690

Towne D. 2014. Ambient groundwater quality of the Harquahala Basin: a 2009–2014 baseline study. Phoenix (AZ); Arizona Department of Environmental Quality. Open-File Report 14-04.

[U.S. EPA] U.S. Environmental Protection Agency. 2023. Greenhouse Gas Reporting Program (GHGRP): reporting year 2021 data, parts C and D (FLIGHT). Washington (DC); U.S. Environmental Protection Agency. [Internet]. https://www.epa.gov/ghgreporting/ghgrp-2021-reported-data

[USGS] U.S. Geological Survey. 2018. 2018 long-term national seismic hazard map. Reston (VA); U.S. Geological Survey. [Internet]. https://www.usgs.gov/programs/earthquake-hazards/science/2018-united-states-lower-48-seismic-hazard-long-term-model

Walton WC. 1970. Groundwater resource evaluation. New York (NY); McGraw-Hill.

Wilson TC, Thompson LA, Gootee BF. 2024. Phase I pre-feasibility study to evaluate carbon dioxide and hydrogen geologic storage potential in Harquahala Basin. Tucson (AZ); Arizona Geological Survey. Open-File Report 24-01. https://library.azgs.arizona.edu/item/AOFR-1712775909999-126

Witcher JC. 1995. Geothermal resource data base: Arizona. Idaho Falls (ID); U.S. Department of Energy. Report No. DOE/ID/13223-T9. doi:10.2172/204692

Derisking CO_2 Mineralization Storage in Basalt Reservoirs *on page* 183.

Subtask 4.6 – Develop Regional Readiness Indices

Carbon Solutions worked in tandem with Montana State University for Subtask 4.6.

This report details the methodology and resulting regional readiness indices maps for carbon capture and storage (CCS) deployment within the Carbon Utilization and Storage Partnership (CUSP) region. The goal of this report is twofold: (1) to present the workflow and methodology used for generating readiness indices and (2) to present the resulting readiness index maps that depict CCS deployment potential across the CUSP region. This report provides a structured framework for evaluating the spatial distribution of CCS opportunities and challenges in the CUSP region that was developed by integrating multiple independent metrics—including source and storage suitability, economic incentives, pipeline routing, regulatory factors, and risk considerations.

Regional readiness for CCS deployment refers to the extent to which a geographic area is prepared to support CCS infrastructure and project development. This readiness depends on a combination of technical, economic, policy, and logistical factors that influence the feasibility and efficiency of CCS projects. It helps identify locations where CCS can be implemented most effectively in the short, medium, and long term and also highlights regions that may require additional investments, regulatory adjustments, or infrastructure development.

Readiness indices quantify regional readiness by integrating multiple factors into a composite score. These indices provide a quantifiable way to compare different subregions based on their CCS deployment potential. The purposes of readiness indices are to

1) identify promising CCS deployment areas by highlighting regions best suited for CCS projects in the short, medium, and long term;

2) pinpoint avenues for improvement by identifying specific technical, economic, or regulatory barriers to CCS deployment;
3) facilitate strategic planning and investment by helping stakeholders efficiently allocate resources by prioritizing high-readiness regions; and
4) support scenario analysis and decision-making by allowing evaluation of different policy, economic, and technical conditions to assess their impact on CCS readiness.

The methodology presented in this report to generate readiness indices for the CUSP region incorporates a variety of technical and nontechnical metrics, including the following:

- Source availability – proximity, concentration, and cost of CO_2 emissions sources
- Storage suitability – geological characteristics, capacity, and injectivity of potential storage sites
- Infrastructure availability – existing and potential transport networks, including pipeline feasibility
- Economic considerations – impact of tax incentives (e.g., tax credits under Section 45Q of the U.S. Tax Code [Credit for Carbon…2021]), capture and storage costs, and financial viability
- Regulatory and policy landscape – permitting ease, legal frameworks, and government incentives
- Risk factors – environmental and operational risks, such as induced seismicity and community acceptance

The first part of this report details the workflow and methodology used to develop these readiness indices. The approach involves scenario-based modeling to simulate a portfolio of different assumptions. Using data from CUSP partners, scenarios were developed that consider CCS deployment potential (e.g., source and sink availability and performance) and variations in storage capacity estimates, tax policies, and seismic risk tolerance. The SimCCS modeling tool (Carbon Solutions 2025b) was used to identify cost-minimal configurations for CCS infrastructure under each scenario. The results were spatially aggregated into a 50 km by 50 km raster grid, in which each cell is assigned a readiness index score based on its CCS deployment potential relative to all the other cells in the region.

The second part of this report presents the actual readiness index maps generated using this methodology. These maps provide a visual representation of CCS potential across the region under different assumptions for each scenario, identifying areas with higher or lower readiness scores based on the selected metrics.

By outlining a structured methodology and presenting readiness index maps, this report establishes a framework for evaluating CCS readiness across the CUSP region.

Methodology

This section provides an overview of the workflow used to generate regional readiness indices for CCS deployment in the CUSP region. The methodology consists of several key steps: (1) Readiness metric identification and scenario generation, (2) infrastructure modeling, (3) infrastructure aggregation, and (4) readiness scoring. This workflow is presented in Figure 5 and each step is described below.

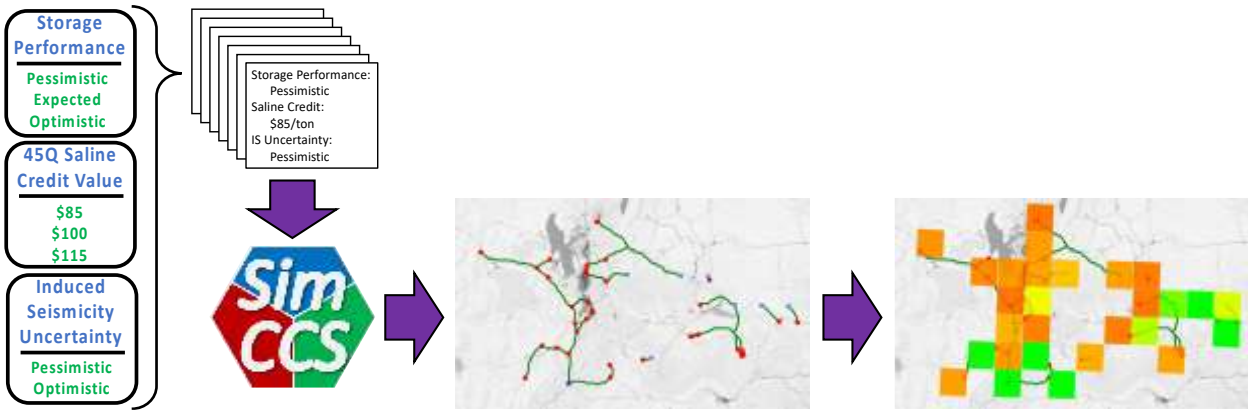


Figure 5 Readiness index generation workflow consisting of readiness metric identification, scenario generation, use of SimCCS to generate infrastructure solutions for each scenario, and aggregation of deployed infrastructure components into raster for relative readiness index scoring. IS = induced seismicity

Readiness Metrics and Scenario Generation

The first step in readiness index generation is the selection of key metrics that influence CCS deployment potential and the development of scenarios based on different parameter assumptions for each metric. The selected metrics account for critical factors that impact the feasibility and cost-effectiveness of CCS infrastructure deployment. During the CUSP project, multiple metrics were considered and explored. The readiness index software developed during the CUSP project was designed to accommodate a wider range of metrics than are discussed here, enabling future extensions and refinements beyond the scope of this report. For this report, the following metrics were selected:

- Storage performance estimates site-specific saline storage capacities and injection costs under three different performance assumptions:
  - Pessimistic – The reservoir underperforms, resulting in lower storage capacity and higher injection costs.
  - Expected – The reservoir performs as expected, with standard capacity and cost assumptions.
  - Optimistic – The reservoir exceeds expected performance, leading to higher storage capacity and lower injection costs.
- 45Q saline credit values reflect the economic incentive for CO_2 storage, modeled under three different credit values per metric ton of stored CO_2:
  - $85/t – baseline credit value reflecting current incentives
  - $100/t – increased credit scenario to assess potential policy improvements
  - $115/t – aggressive incentive scenario representing a more favorable policy environment
- Induced seismicity data uncertainty represents uncertainty in available fault data and their influence on site selection:
  - Pessimistic – assumes that critical fault lines are missing from the dataset, leading to a higher probability of seismic risks
  - Optimistic – assumes the available fault data are complete and accurate, reducing uncertainty in risk assessment

To systematically explore the impacts of these metrics on CCS deployment, multiple scenarios are generated by varying the parameter settings for each metric. By systematically combining different parameter values, we create a diverse set of scenarios that capture variations in geological performance, economic incentives, and seismic risks, ensuring a comprehensive evaluation of potential CCS deployment under a wide range of conditions. For example, one scenario assumes optimistic storage performance, $100/t 45Q saline credit, and pessimistic induced seismicity uncertainty. Given the number of parameter settings for each metric, this results in a total of 18 distinct scenarios as presented in Figure 6.

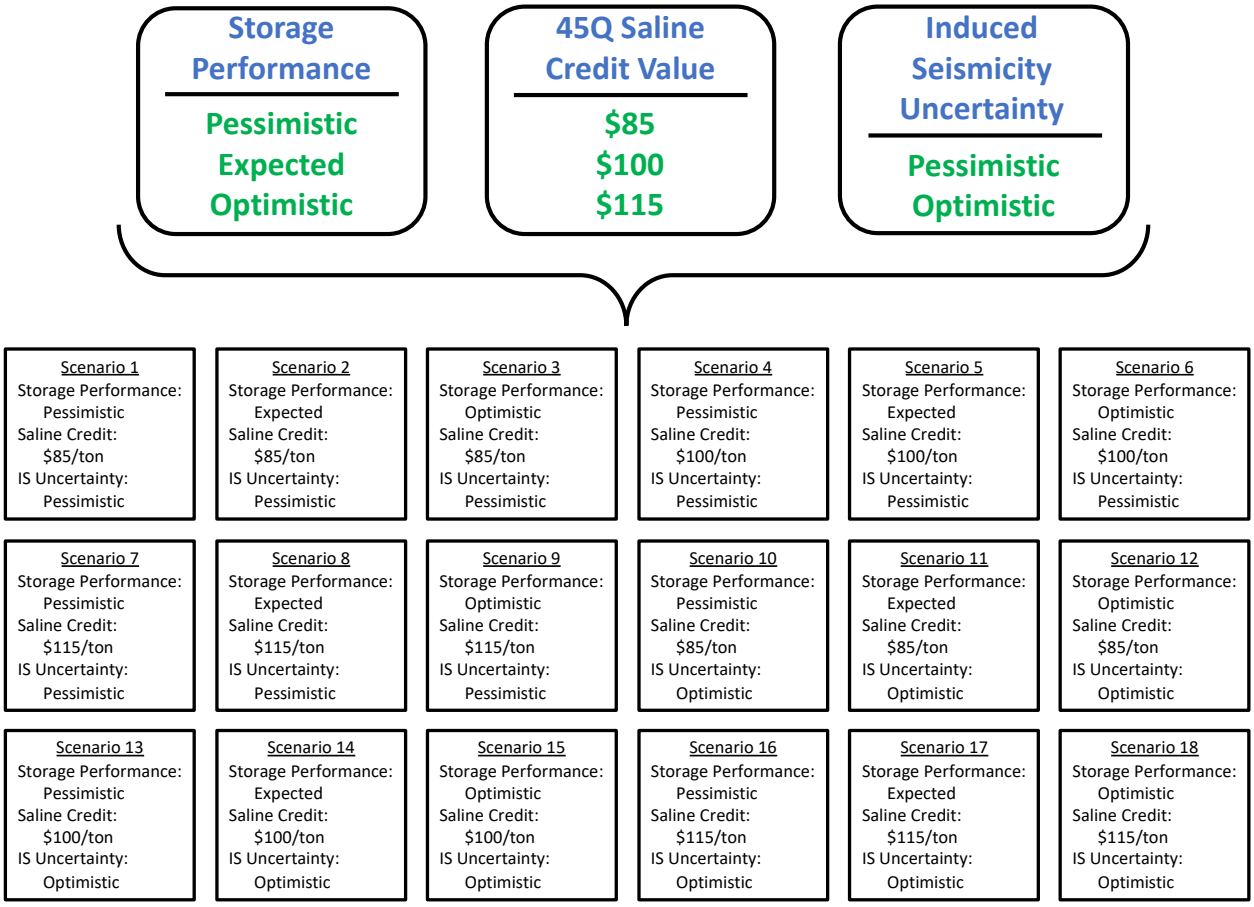


Figure 6 The 18 unique scenarios that result from generating all combinations of metric parameter values. IS = induced seismicity

For each unique scenarios, the relevant data values are adjusted according to that scenario's selected parameter values. The impacts of these parameters on scenario-specific data values are as follows:

1) Storage Performance Parameter

- Each reservoir location's storage capacity and injection cost are adjusted based on whether the scenario assumes pessimistic, expected, or optimistic performance.
- In pessimistic cases, injection costs increase and storage capacity decreases due to poorer reservoir performance.

- In optimistic cases, injection costs decrease and storage capacity increases, making storage sites more viable.

2) 45Q Credit Value Parameter
   - The selected credit value is incorporated into the effective storage cost at each reservoir location.
   - Higher credit values reduce net storage costs, making storage more financially attractive in those scenarios.

3) Induced Seismicity Parameter
   - This parameter influences which reservoir locations are available for CCS deployment in a given scenario.
   - Storage locations classified as having an elevated risk of fault activation are removed from consideration in all scenarios. However, under the pessimistic assumption—in which critical faults are assumed to be missing from the dataset—more locations are classified as high risk compared with the optimistic assumption.

By systematically varying these parameters across the 18 scenarios, a robust set of readiness conditions that reflect different economic, geological, and risk factors is generated. The infrastructure modeling process, described in the next section, then determines optimal CCS infrastructure deployments for each scenario, identifying infrastructure that would be deployed under a specific set of assumptions. The output of this step is a set of scenario-specific datasets that serve as inputs for subsequent modeling and infrastructure optimization. This structured approach ensures that key uncertainties and policy variations are systematically incorporated into the subsequent infrastructure modeling and readiness index computation.

Infrastructure Modeling

After each scenario is formalized, optimal infrastructure is calculated for each using the SimCCS infrastructure optimization software. SimCCS determines optimal CCS infrastructure by formulating the problem as a mixed-integer linear programming (MILP) problem. MILP is a mathematical optimization approach widely used for planning and decision-making in complex systems. The goal of MILP models is to minimize or maximize an objective function, which is the algebraic representation of some parameter of interest (e.g., cost, productivity, or throughput) in the system being modeled. The objective function is encoded with data from the problem and decision variables, which are unknown elements of the problem that one wishes to determine (e.g. the amount of product to produce or the location to which a resource is to be deployed). MILP models combine continuous decision variables, which represent quantities such as flow rates, with 0- or 1-valued decision variables, which indicate on/off decisions for components such as the construction (or not) of pipelines. An MILP solver (e.g. IBM's CPLEX software [IBM 2025]) manipulates the decision variables in order to optimize the objective function. Linear inequality functions called constraints are used to enforce problem properties (e.g., capacity restrictions). A solution to an MILP model is represented by specific values for the decision variables and the value of the solution is the value of the objective function.

The goal of the optimal CCS infrastructure MILP model is to determine the minimum-cost infrastructure deployment of sufficient capacity. Because the goal is to minimize CCS infrastructure cost, the scenario data that are fed into the MILP model are composed of the key cost drivers of a CCS project, including the following: source information (location, capture

costs, and emission rate), storage information (location, injection costs, and storage capacity), and transport information (pipeline routes and pipeline cost–capacity curves). Information on the scenario input data is presented below.

Scenario Input Data

S	Set of CO_2 sources
Q_i^{src}	Annual CO_2 production rate at source i ($MtCO_2$/yr)
F_i^{src}	Fixed cost of opening source i ($)
V_i^{src}	Variable cost of capturing CO_2 from source i ($/$MtCO_2$)
R	Set of storage sites
Q_j^{res}	Annual CO_2 capacity of storage site j ($MtCO_2$/yr)
F_j^{res}	Fixed cost of opening storage site j ($)
V_j^{res}	Variable cost of injecting CO_2 into storage site j ($/$MtCO_2$)
P	Set of candidate pipelines
C	Set of possible capacities for each pipeline
Q_{kc}^{min}	Minimum capacity of pipeline k with capacity c ($MtCO_2$/yr)
Q_{kc}^{max}	Maximum capacity of pipeline k with capacity c ($MtCO_2$/yr)
F_{kc}^{pipe}	Fixed cost of opening pipeline k with capacity c ($)
V_{kc}^{pipe}	Variable cost of transporting CO_2 via pipeline k with capacity c ($/$MtCO_2$)
J	Set of candidate pipeline junctions

The decision variables of the infrastructure design MILP model indicate which sources to open and how much CO_2 to capture from each, which storage locations to open and how much CO_2 to inject into each, and where to deploy pipelines and what capacity they need to be able to transport. Details on the decision variables are presented below.

Model Decision Variables

$s_i \in \{0,1\}$	Indicates if source i is opened
$a_i \in \mathbb{R}^{\geq 0}$	Annual amount of CO_2 captured from source i ($MtCO_2$/yr)
$r_j \in \{0,1\}$	Indicates if reservoir j is opened
$b_j \in \mathbb{R}^{\geq 0}$	Annual amount of CO_2 injected into reservoir j ($MtCO_2$/yr)
$p_{kc} \in \{0,1\}$	Indicates if pipeline k with capacity c is opened
$d_{kc} \in \mathbb{R}^{\geq 0}$	Annual amount of CO_2 put in pipeline k with capacity c ($MtCO_2$/yr)

The goal of the MILP model is to minimize the cost of the project. The objective function that realizes this goal quantifies the cost of the project as the sum of the cost to capture the CO_2, the cost to transport the CO_2, and the cost to store the CO_2. The cost to capture CO_2 is the cost to open each opened facility (F_i^{src}) plus the cost to capture each metric ton of CO_2 from it ($V_i^{src} a_i$). Similarly, the cost to store CO_2 is the cost to open each opened storage location (F_j^{res}) plus the cost to inject each metric ton of CO_2 into it ($V_j^{res} b_j$). The cost to transport CO_2 is the cost to build each opened pipeline (F_{kc}^{pipe}) plus the cost to use the opened pipeline ($V_{kc}^{pipe} d_{kc}$). Because the goal is minimum-cost infrastructure, this objective function is minimized. The objective function is presented below.

Objective Function

$$\min \overbrace{\sum_{i \in S} (F_i^{src} s_i + V_i^{src} a_i)}^{capture\ cost} + \overbrace{\sum_{k \in P} \sum_{c \in C} (F_{kc}^{pipe} p_{kc} + V_{kc}^{pipe} d_{kc})}^{transport\ cost} + \overbrace{\sum_{j \in R} \left(F_j^{res} r_j + V_j^{res} b_j\right)}^{storage\ cost}$$

Constraints are used to enforce realistic operational restrictions including capacity restrictions and standard network construction requirements. The constraints are presented below.

Constraints

$Q_{kc}^{\min} p_{kc} \leq d_{kc} \leq Q_{kc}^{\max} p_{kc}, \forall k \in P, \forall c \in C$	(A)
$\sum_{\substack{k \in P: \\ src(k)=n}} \sum_{c \in C} d_{kc} - \sum_{\substack{k \in P: \\ dest(k)=n}} \sum_{c \in C} d_{kc} = \begin{cases} a_n & \text{if } n \in S \\ -b_n & \text{if } n \in R, \forall n \\ 0 & \text{if } n \in J \end{cases}$ $\in S \cup R \cup J$	(B)

$a_i \leq Q_i^{src} s_i, \forall i \in S$	(C)
$b_j \leq Q_j^{res} r_j, \forall j \in R$	(D)

where constraint (A) enforces minimum and maximum pipeline capacities by ensuring that the amount of CO_2 transported by a pipeline (d_{kc}) is greater than the minimum capacity ($Q_{kc}^{\min}$) and less than the maximum capacity ($Q_{kc}^{\max}$) of that pipeline. Constraint (B) enforces conservation of flow at each node in the network to ensure that CO_2 is added to the network only when captured from sources and leaves the network only when injected into sinks. In other words, constraint (B) ensures that all CO_2 in the network comes from a source and goes to a storage site. Constraint (C) enforces limitations on source production rates by forcing the amount of CO_2 captured at each source (a_i) to be less than the available amount of CO_2 at that source (Q_i^{src}). Constraint (D) enforces limitations on reservoir storage capacities by forcing the amount of CO_2 injected into each storage site (b_j) to be less than the capacity of that site (Q_j^{res}). Because there are no constraints requiring a minimum amount of CO_2 processing, the model will only deploy simulated infrastructure that is profitable (i.e., cost negative). This is possible given the availability of tax incentives such as 45Q.

The output from this step is optimal cost-effectives CCS infrastructure for each scenario under consideration. An example of infrastructure found by SimCCS using this optimization process is presented in Figure 7. This information will be used in subsequent steps to identify specific regions that exhibit greater and lower activity in the individual solutions.

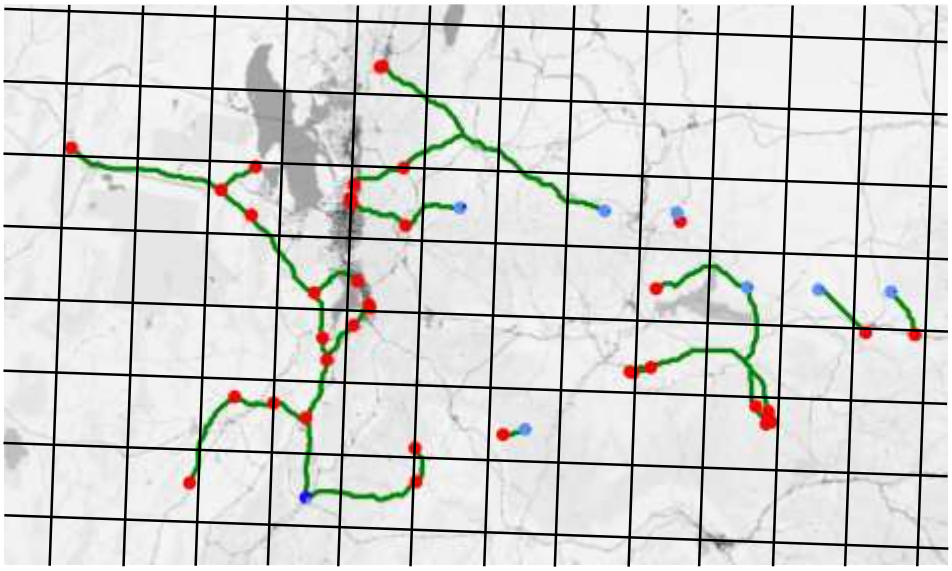


Figure 7 50 km by 50 km raster grid on deployed infrastructure calculated by SimCCS for a single scenario in a subregion of CUSP. The red circles represent deployed sources, the blue circles represent deployed storage locations, and the green lines represent deployed pipelines.

Infrastructure Aggregation

Once SimCCS has determined the optimal CCS infrastructure deployments for each scenario, the next step is to aggregate these results into a standardized spatial format. To achieve this, we rasterized the study region into 50 km by 50 km cells, a grid resolution agreed upon by CUSP's

participating organizations. Figure 7 provides an example of how this rasterization is applied to modeled CCS infrastructure within a subregion of CUSP.

This rasterization scheme is particularly important because it aligns with the methodology used for assessing storage potential across the region, ensuring direct comparability of infrastructure deployment and storage feasibility. Further details on this are provided later in this report. For each scenario, we assign every deployed source and storage site identified by SimCCS to the corresponding 50 km by 50 km cell in which it is located. This allows us to track the spatial distribution of infrastructure activity across different scenarios. Specifically, we record two key quantities for each grid cell:

1) Amount of CO_2 processed – This includes the total volume of CO_2 captured at sources within the cell and the total volume injected into storage reservoirs located in the cell.
2) Cost of processing CO_2 – This includes both capture costs and storage costs for all CO_2 processed in that cell.

Although CO_2 transport volumes through each cell were not explicitly tracked, future iterations of this methodology could incorporate pipeline flow tracking to provide a more complete picture of infrastructure use A potential challenge in cost tracking arises in cases in which it is unclear which storage site a specific source sends CO_2 to, because flow networks typically optimize flows without explicitly defining individual transport paths. However, in the case of the CUSP data, this scenario did not occur, allowing us to accurately track CO_2 processing costs per cell without ambiguity.

This aggregation process transforms the detailed, high-resolution infrastructure optimization outputs into a standardized, lower-resolution dataset that facilitiates regional comparison and supports decision making. This aggregated dataset provides a simplified yet informative representation of CCS infrastructure deployment, serving as the foundation for readiness scoring in the next step.

Readiness Scoring

At this stage of the readiness index generation process, each 50 km by 50 km raster cell contains two key values: (1) the total amount of CO_2 processed in that cell and (2) the total cost of processing CO_2 in that cell. These values are then converted into two distinct readiness indices, each highlighting different aspects of CCS deployment potential.

1) Volume-Based Readiness Index
    - This index measures the relative amount of CO_2 processed across all cells.
    - To compute this, cell values are normalized by dividing each cell's CO_2 volume by the highest volume found in any cell. This results in values ranging between 0 and 1, where 1 represents the cell with the highest CO_2 processing volume.
2) Cost-Based Readiness Index
    - This index reflects the cost-effectiveness of CCS deployment within each cell.
    - First, the per-metric-ton processing cost is calculated by dividing each cell's total processing cost by the total amount of CO_2 processed in that cell.
    - These per-metric-ton costs are then normalized using the same approach as above, in which each value is divided by the highest per-metric-ton cost observed in the dataset, resulting in a value between 0 and 1.

The volume-based index highlights regions with the greatest CO_2 processing activity, whereas the cost-based index identifies areas with the highest economic feasibility. If the primary objective is maximizing CO_2 capture and storage, the volume-based index would be most relevant. Even though all deployed infrastructure found during the infrastructure modeling phase is profitable, the cost-based index focuses on the most cost-effective regions. This is particularly important for securing industry buy-in and ensuring profitable deployment of CCS projects.

To support visual interpretation as a map, the readiness indices are translated into an orange–yellow–green color scale in which green represents high readiness and yellow–orange represents moderate readiness. Cells with no CCS activity (readiness = 0) are left blank to avoid unnecessary visual clutter. The lowest nonzero readiness values are colored orange instead of red to avoid suggesting that any CCS deployment is inherently negative; all infrastructure deployed in these scenarios is cost-effective. This color-coding approach ensures that high-priority regions for CCS deployment stand out and also maintains a clear distinction between impactful and less-impactful areas. Figure 8 presents an example of the readiness indices map.

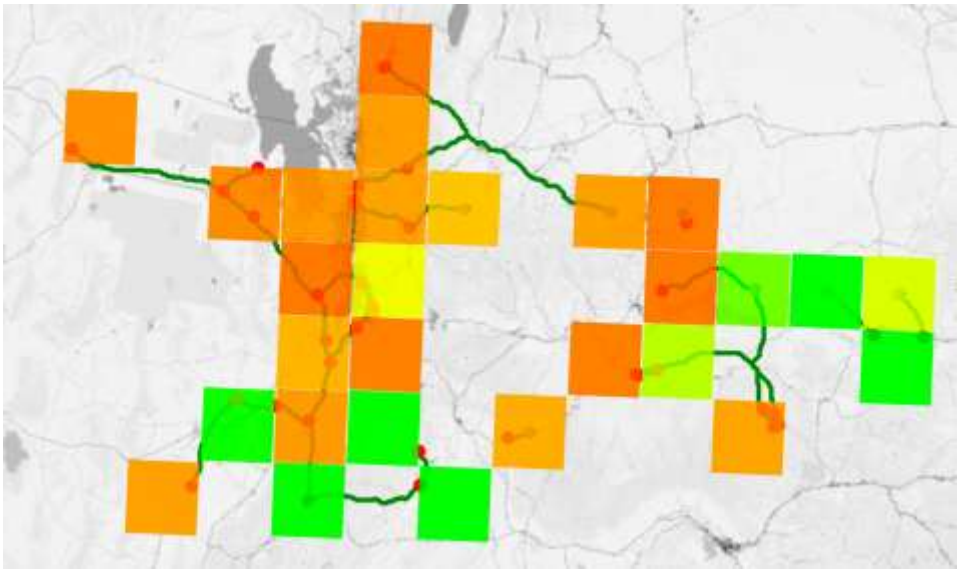


Figure 8 Readiness indices map overlayed on the corresponding infrastructure in a CUSP subregion. Color ranges from a high readiness of green (large volume of CO_2 processing or low cost per metric ton of CO_2 processing) to a low readiness of dark orange to red.

Data Collection

The readiness index generation process relies on multiple datasets that describe key components of CCS deployment potential. These datasets include information on CO_2 capture sources, storage capacity, transport infrastructure, and induced seismicity risks. Each dataset was collected, processed, and integrated into the readiness framework to ensure consistency and comparability across the CUSP region.

This section describes the four primary data categories used in this study:

1) Source data – information on CO_2 point sources, including emission rates, capture costs, and expected operational lifespan
2) Storage data – estimated saline storage capacities, injection costs, and performance assumptions derived from the SCO_2T tool (Middleton et al. 2020)

3) Transport data – potential pipeline routes, existing infrastructure, and transport cost estimates
4) Induced seismicity data – fault data and seismic risk assessments that influence storage site selection

Each of these datasets was collected from CUSP member organizations, publicly available databases, and industry reports, ensuring the most comprehensive and up-to-date data available for CCS deployment planning.

Source Data

CO_2 source data were compiled by CUSP member organizations as part of Subtask 3.1.4, which focused on assessing, verifying, and augmenting existing CO_2 point source data. This effort involved

- verifying emission volumes using facility-reported and government-sourced data;
- determining the expected lifespan of each source, both with and without CO_2 capture;
- identifying feasible CO_2 capture methods based on industry-specific characteristics;
- estimating capture costs and operational efficiencies using standardized methodologies; and
- incorporating future CO_2 capture sources where relevant.

Data were collected by CUSP partners from multiple sources including the EPA Greenhouse Gas (GHG) Emissions database and local data sources covering both CO_2 emitters across the CUSP region and smaller point sources strategically positioned near transport and storage infrastructure, because these may still play a role in CCS deployment. To ensure consistent classification and cost estimation across the CUSP region, data collection teams used a Leopold Matrix approach to categorize CO_2 emitters by industry type, emission rate, and capture cost. Capture costs were either estimated on a source-specific basis or set to industry-specific values derived from published tables.

The final dataset includes 257 unique CO_2 point sources with a combined annual emission capacity of 255.9 $MtCO_2$. These emitters represent a diverse set of industries and geographies, providing a broad foundation for evaluating CCS deployment potential across the region. Information on the capture data used in this effort is included in Table 3.

Table 3 Emission source information for the CUSP region

Industry	Number of facilities	Emission rate, Mt/yr	Share of total emissions	Average cost, $/t	Cost range, $/t
Gas power	105	105.0	41.1%	$75	$25–$131
Coal power	24	89.3	34.9%	$55	$35–$60
Petroleum refinery	17	15.6	6.1%	$61	$56–$73
Cement	22	15.2	5.9%	$59	$48–$75
Hydrogen	15	9.3	3.6%	$72	$58–$101
Gas processing	12	7.6	3.0%	$14	$14
Ammonia	4	3.7	1.4%	$20	$16–$30
Pulp and paper	8	3.4	1.3%	$56	$56–$56
Ethanol	14	1.2	0.5%	$15	$10–$23
Other	36	5.6	2.2%	$58	$30–$75
Total	**257**	**255.9**	**100%**		

Storage Data

Storage site identification and characterization was conducted using the same 50 km by 50 km raster grid as described in the Methodology section. This raster ensured consistency with the spatial framework used in the readiness indices generation process. Each raster cell centroid was designated a potential CO_2 injection site, which allowed for a standardized assessment of regional storage potential. To estimate storage capacities and injection costs, CUSP state partners collected geologic data necessary to run the SCO_2T model, a geologic sequestration tool developed to estimate saline storage potential and associated costs. SCO_2T is a machine learning–based tool trained on high-fidelity, full-physics reservoir simulations, enabling it to rapidly generate reliable estimates of CO_2 storage feasibility across large regions. CUSP state partners compiled key geologic parameters for each raster centroid, including formation depth, thickness, pressure, porosity, permeability, temperature, and geothermal gradient. Each of these parameters was estimated under three different performance assumptions:

1) Pessimistic – conservative estimates assuming lower storage performance and higher injection costs
2) Expected – standard estimates based on best-available geological data
3) Optimistic – favorable estimates assuming enhanced storage performance and lower injection costs

Once compiled, the geologic parameter dataset was provided to Carbon Solutions (https://www.carbonsolutionsllc.com/, accessed 2025 November 20), a CUSP industry partner, which ran the SCO_2T model to estimate the total CO_2 storage capacity for each centroid and the per-metric-ton injection cost under each pessimistic, expected, and optimistic assumption. These estimates formed the foundation for subsequent scenario generation and infrastructure modeling, ensuring that each simulated deployment scenario accounted for a range of geologic and economic conditions. By leveraging SCO_2T, the CUSP project was able to provide a consistent and scalable approach to assessing regional CO_2 storage potential. Details on the storage potential used in readiness indices generation is provided in Table 4.

Table 4 Storage site information for the CUSP region

Assumption	Number of sites	Total capacity, Mt	Average capacity, Mt	Average cost, $/t
Pessimistic	104	176,767.2	1,699.7	$23
Expected	194	395,724.6	2,039.8	$7
Optimistic	238	458,623.4	1,927.0	$8

Induced Seismicity Data

The assessment of induced seismicity risk for the CUSP region was conducted by PNNL and served as a filtering mechanism to determine the feasibility of potential CO_2 storage sites. The primary objective was to evaluate the likelihood of fault activation due to CO_2 injection and remove high-risk storage locations from consideration in scenario modeling. This assessment leveraged the State of Stress Analysis Tool (SOSAT; PNNL 2025), a Bayesian framework designed for geomechanical uncertainty quantification and risk assessment.

For each storage location, the risk of fault activation was evaluated under two seismicity data quality assumptions: a pessimistic scenario, in which the available fault data were assumed to be incomplete (i.e., critical blind faults may exist but are unaccounted for), and an optimistic

scenario, in which the National Seismic Hazard Model (NSHM) database of known faults was assumed to be complete (USGS 2023). Under the pessimistic assumption, the methodology presumed that a critically oriented blind fault could exist at the site and computed the risk of activation based on the increase in pore pressure after injection. Under the optimistic assumption, known faults from the NSHM database were used and the risk of activation was calculated for each fault within 50 km of the storage site. For each site, the fault with the highest activation risk within 50 km was used to classify its seismic risk. If no known fault existed within 50 km, the site was classified as "low: no fault found."

This process resulted in two independent seismic risk rankings for each storage site: one assuming incomplete fault data (pessimistic) and the other assuming complete fault data (optimistic). Each ranking was assigned a likelihood category of "low," "medium," or "elevated" based on the estimated probability of fault activation.

To integrate seismic risk into storage feasibility, sites categorized as "elevated" risk under a given seismicity data assumption were removed from consideration for that scenario. This means that the availability of a storage site depended on both storage performance assumptions (pessimistic, expected, or optimistic) and the assumed quality of seismic data (pessimistic or optimistic). For example, a storage site's fault activation risk might be classified as "low" when assuming expected storage performance and optimistic fault data quality, making it available for infrastructure modeling. However, if that same site was classified as "elevated" risk under pessimistic fault data quality, it would be excluded from the set of available storage sites in that scenario.

Ultimately, for each scenario combination of storage performance, 45Q tax credit, and seismic data quality assumption, only storage sites ranked "low" or "medium" risk were made available for use in SimCCS infrastructure modeling. This filtering ensured that only geologically viable storage locations were considered for CCS infrastructure deployment, reducing the risk of induced seismicity and maintaining flexibility across multiple scenario assumptions.

Transport Data

Pipeline routing and cost estimation are critical components of CCS infrastructure planning. SimCCS, the infrastructure optimization tool used in this study, relies on a cost surface to discretize a geospatial region and estimate the cost of deploying a pipeline along different routes. The cost surface incorporates multiple factors that influence pipeline construction and operation costs, including land ownership, land cover, population density, terrain considerations, and other geographic and environmental factors.

To establish baseline pipeline costs, we used the FECM/NETL CO_2 Transport Cost Model, (DOE 2023), which provides expected pipeline costs under idealized conditions. These costs were then adjusted using scaling factors derived from the cost surface, allowing for a more realistic representation of regional variability in pipeline deployment expenses. For cost surface generation, we used the CostMAP tool (Carbon Solutions 2025a), which produces standardized cost surfaces based on predefined input parameters. In some regions, custom cost surfaces were generated to accommodate unique geographic or regulatory constraints. For example, in California, we implemented a customized cost surface to avoid fault lines, reflecting specific regional challenges in pipeline siting.

Once the cost surface was established, SimCCS applied custom routing algorithms to determine the least-cost paths for CO_2 transport infrastructure. These routing algorithms balance cost considerations with the need to efficiently connect CO_2 sources to storage sites, ensuring that infrastructure deployment remains both economical and feasible. Figure 9 presents a map of the CUSP region showing sources (red circles), storage sites (blue circles), and candidate pipeline routes (purple edges). SimCCS uses the data to select which sources, storage sites, and pipelines to deploy in a simulated scenario to achieve a least-cost solution.

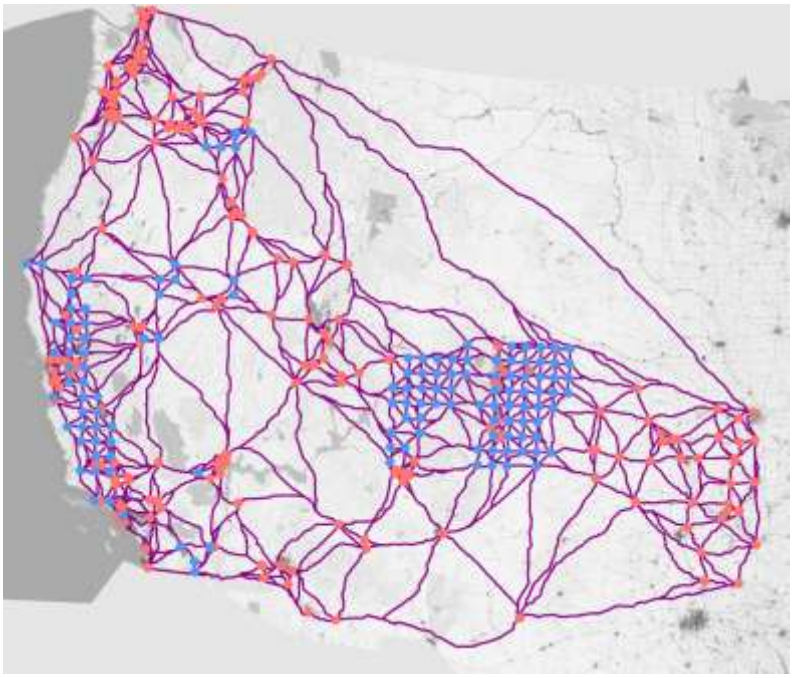


Figure 9 Map of the CUSP region with locations of sources (red circles), sinks (blue circles), and candidate pipeline paths (purple edges) highlighted.

Regional Readiness Indices Maps

This section presents the regional readiness indices maps generated using the methodology described in the previous sections. The workflow was integrated into SimCCS to provide a comprehensive readiness indices generation and visualization platform. These maps visualize the spatial distribution of CCS deployment potential across the CUSP region, providing insights into the relative feasibility of infrastructure development in different geographic areas. The readiness indices are derived from two key factors: the total amount of CO_2 processed in each grid cell and the cost-effectiveness of CO_2 processing in each cell. These values were normalized to create two distinct indices:

1) Volume-Based Readiness Index – highlights regions with the highest total volume of CO_2 processed, emphasizing large-scale capture and storage activity
2) Cost-Based Readiness Index – identifies areas where CCS deployment is most cost-effective, providing insight into regions that may attract industry investment due to favorable economic conditions

Each map represents a unique combination of storage performance assumptions, 45Q tax credit values, and seismic data quality assumptions. They are labeled according to the scheme in Figure

10. These variations allow for a more comprehensive understanding of how different factors influence CCS infrastructure deployment potential. To enhance readability, the maps use a red–yellow–green color scale to represent relative readiness, with high-readiness areas appearing in green and lower-readiness areas appearing in orange. Cells with no CCS deployment activity are left blank to maintain focus on areas with active infrastructure development. The following pages contain the regional readiness indices maps, organized by scenario type. These maps serve as a visual decision-support tool, helping stakeholders identify high-potential CCS deployment regions and evaluate how various assumptions impact infrastructure feasibility.

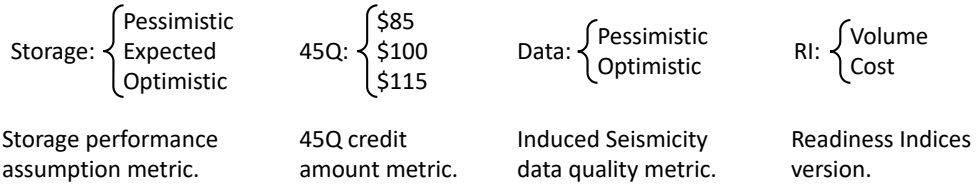
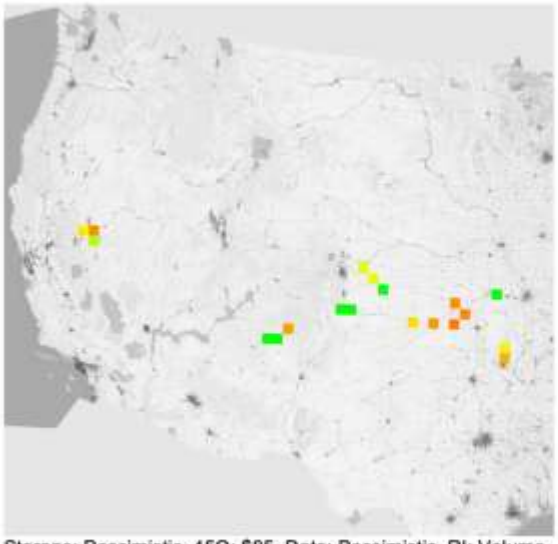
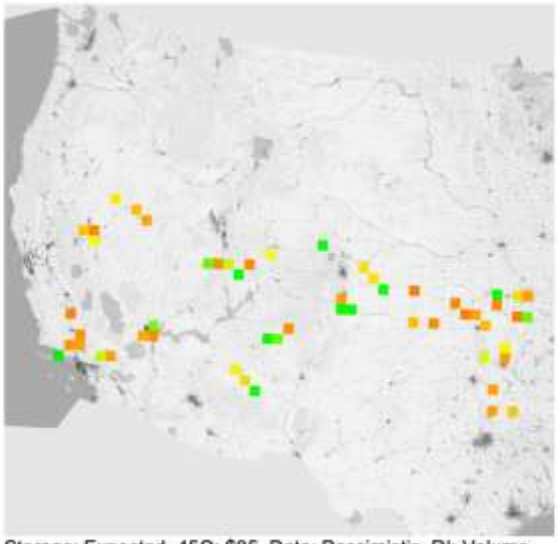


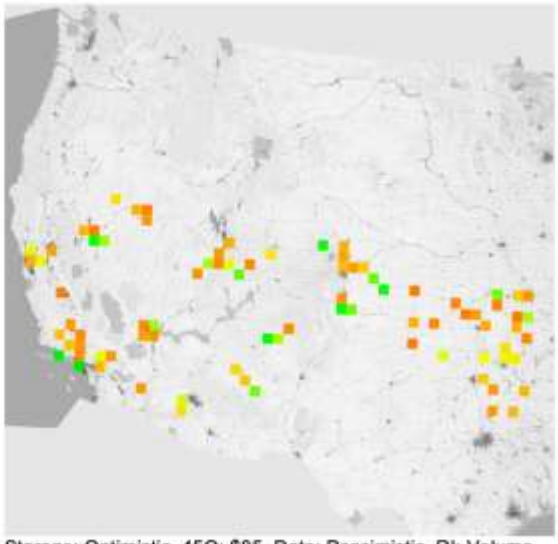
Figure 10 Regional Readiness Indices labeling scheme.



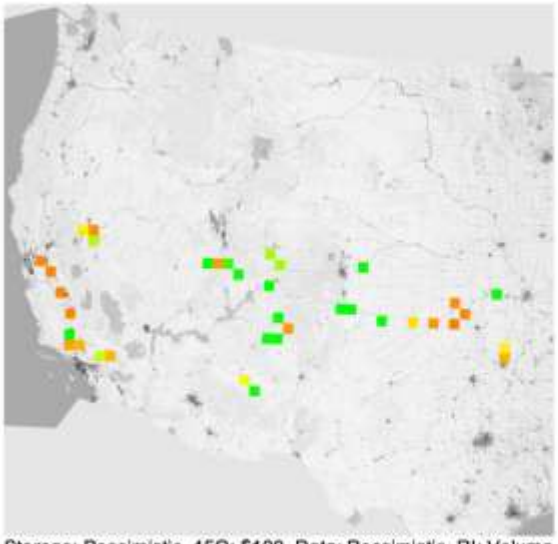
Storage: Pessimistic, 45Q: $85, Data: Pessimistic, RI: Volume



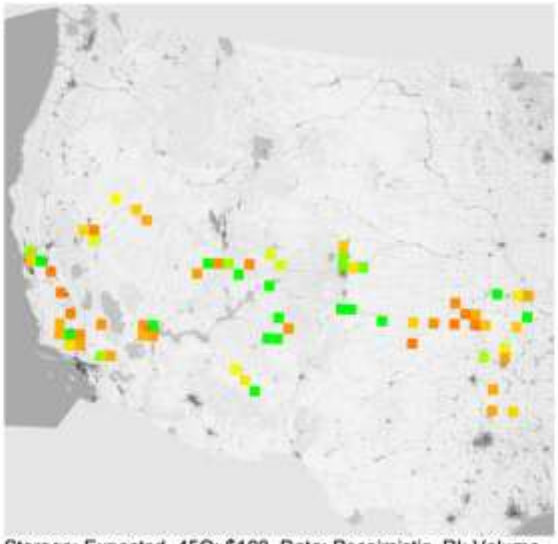
Storage: Expected, 45Q: $85, Data: Pessimistic, RI: Volume



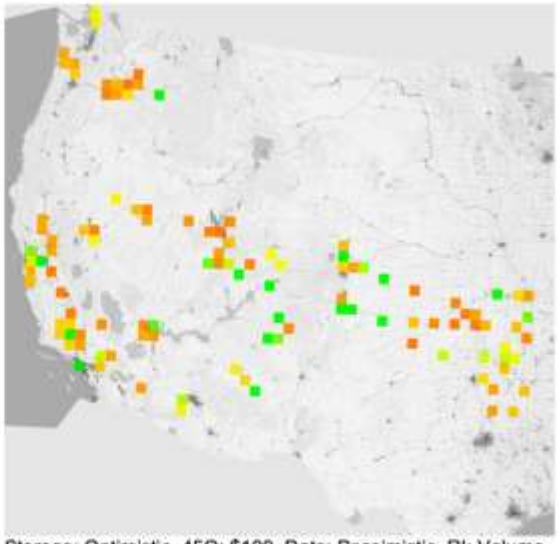
Storage: Optimistic, 45Q: $85, Data: Pessimistic, RI: Volume



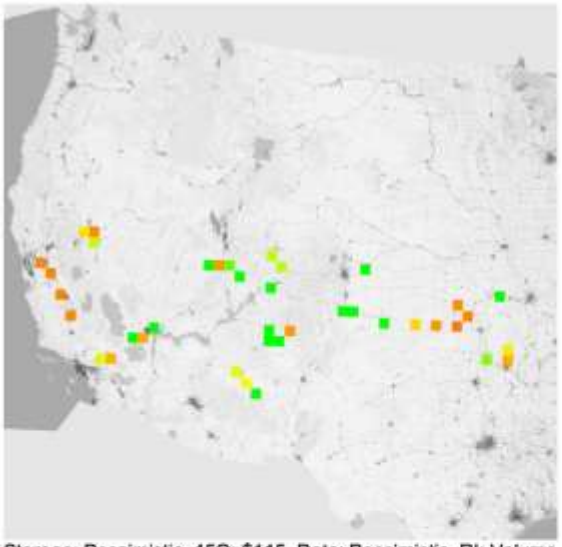
Storage: Pessimistic, 45Q: $100, Data: Pessimistic, RI: Volume



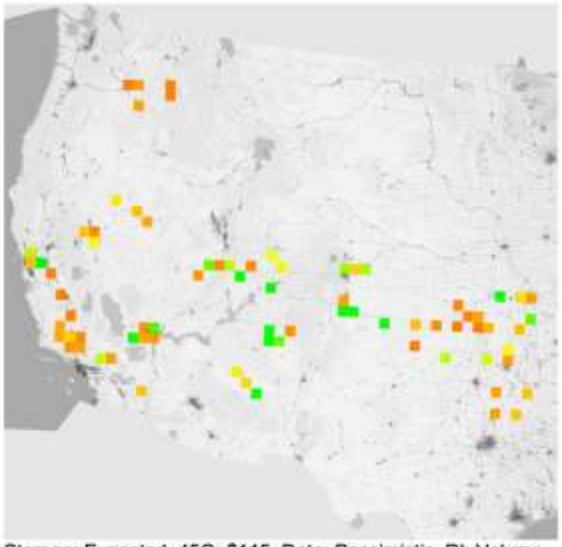
Storage: Expected, 45Q: $100, Data: Pessimistic, RI: Volume



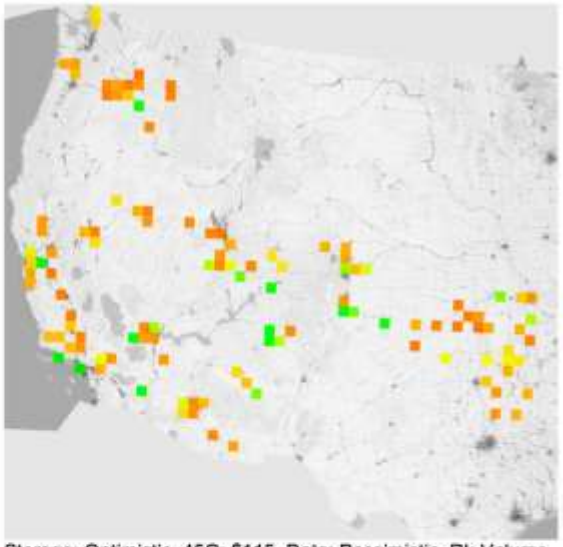
Storage: Optimistic, 45Q: $100, Data: Pessimistic, RI: Volume



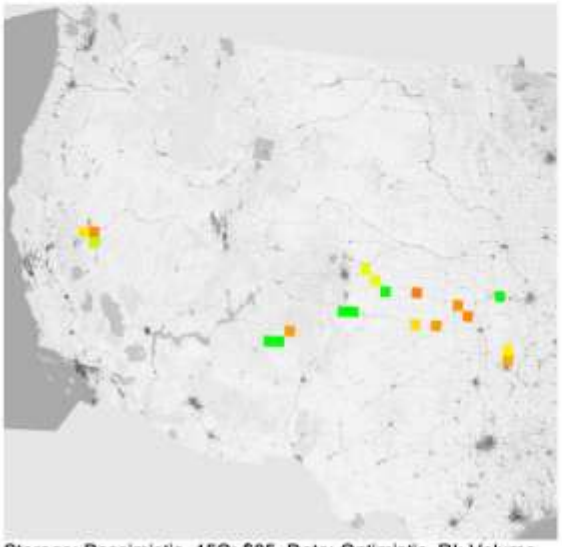
Storage: Pessimistic, 45Q: $115, Data: Pessimistic, RI: Volume



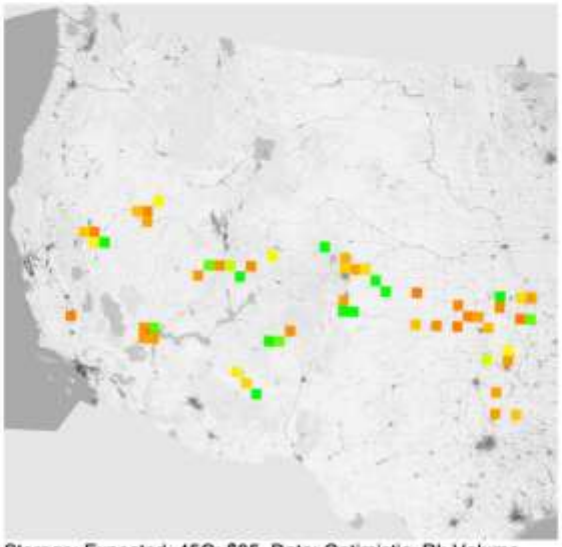
Storage: Expected, 45Q: $115, Data: Pessimistic, RI: Volume



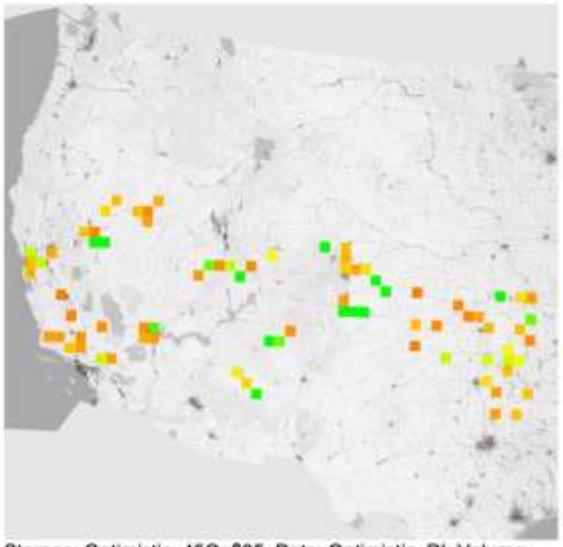
Storage: Optimistic, 45Q: $115, Data: Pessimistic, RI: Volume



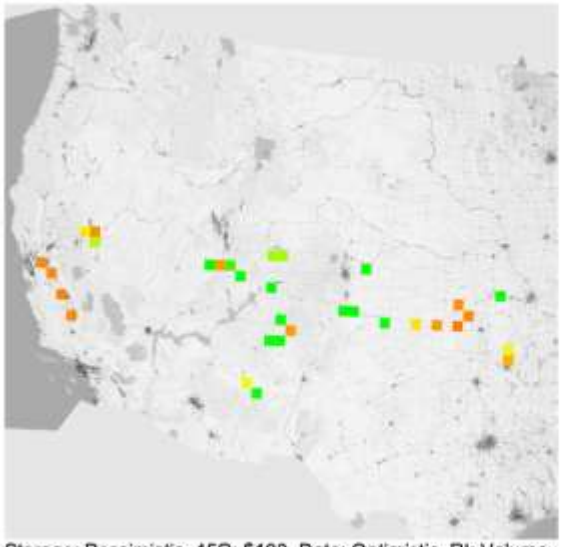
Storage: Pessimistic, 45Q: $85, Data: Optimistic, RI: Volume



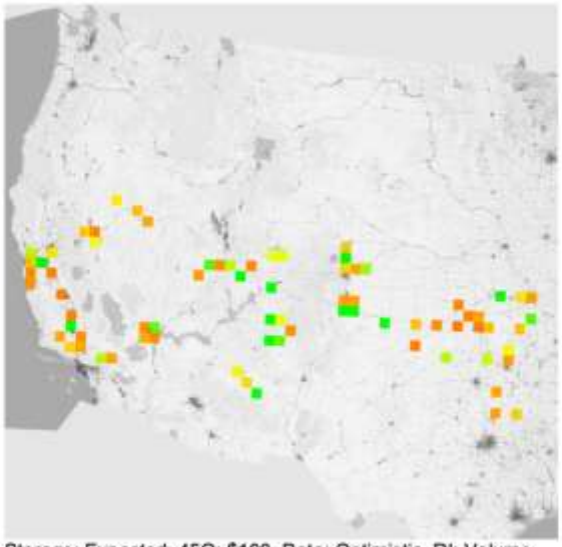
Storage: Expected, 45Q: $85, Data: Optimistic, RI: Volume



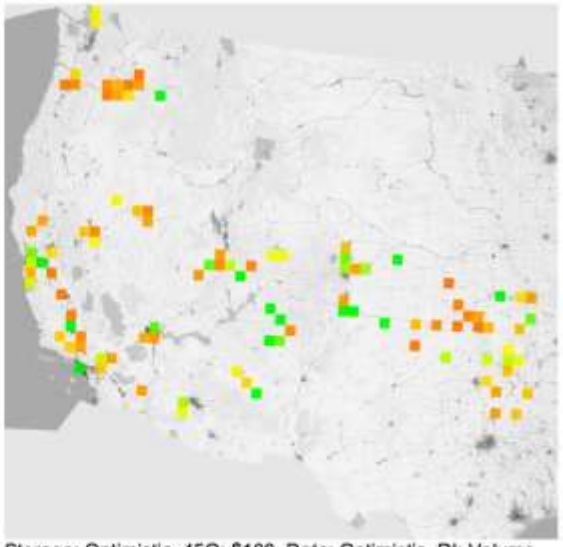
Storage: Optimistic, 45Q: $85, Data: Optimistic, RI: Volume



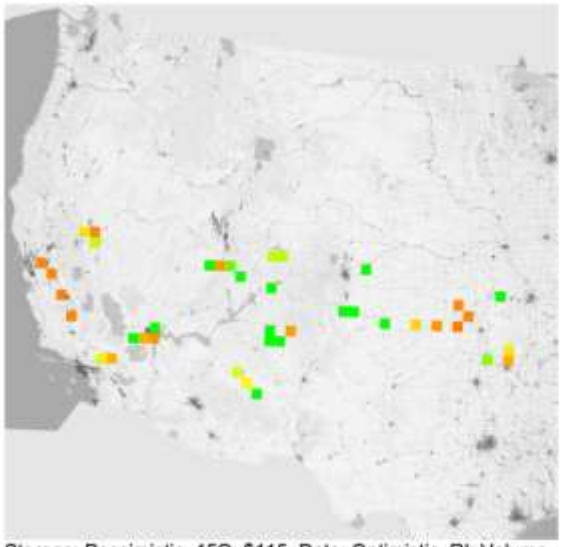
Storage: Pessimistic, 45Q: $100, Data: Optimistic, RI: Volume



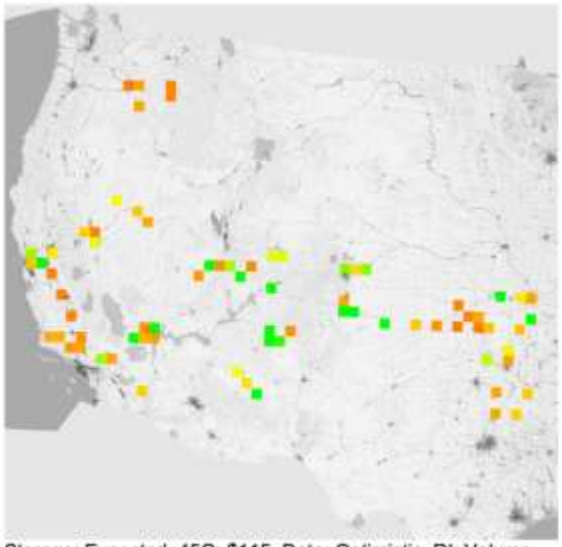
Storage: Expected, 45Q: $100, Data: Optimistic, RI: Volume



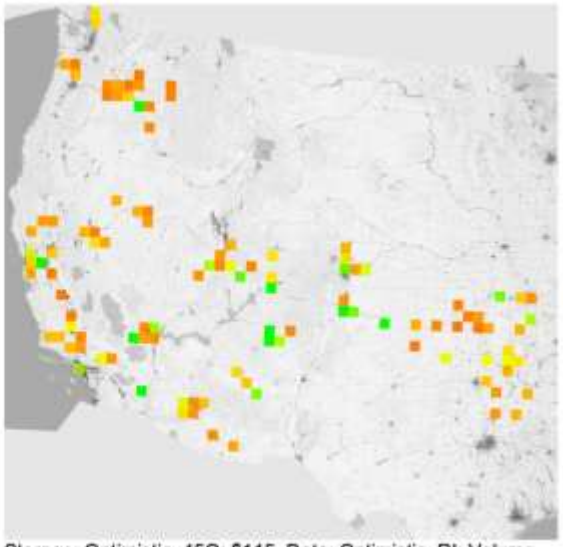
Storage: Optimistic, 45Q: $100, Data: Optimistic, RI: Volume



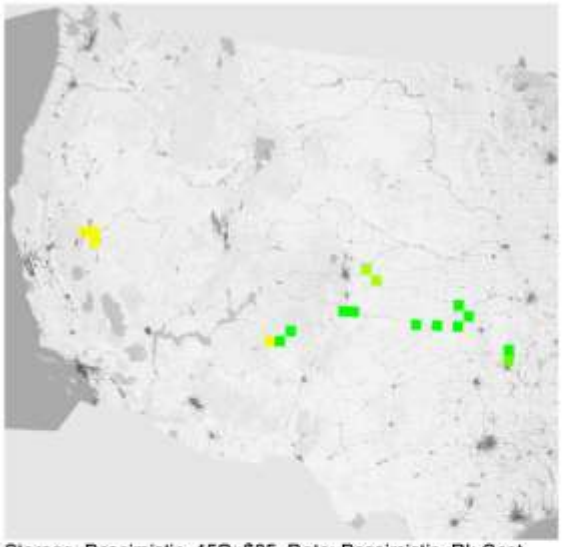
Storage: Pessimistic, 45Q: $115, Data: Optimistic, RI: Volume



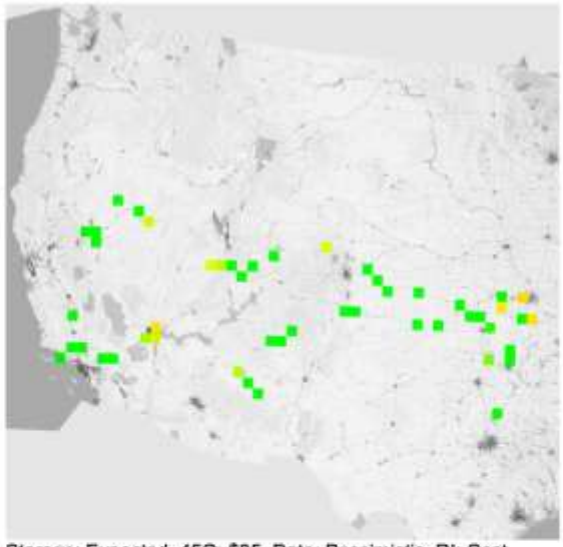
Storage: Expected, 45Q: $115, Data: Optimistic, RI: Volume



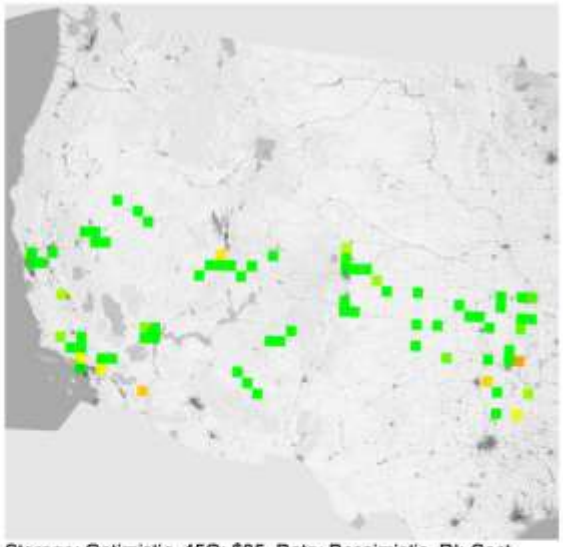
Storage: Optimistic, 45Q: $115, Data: Optimistic, RI: Volume



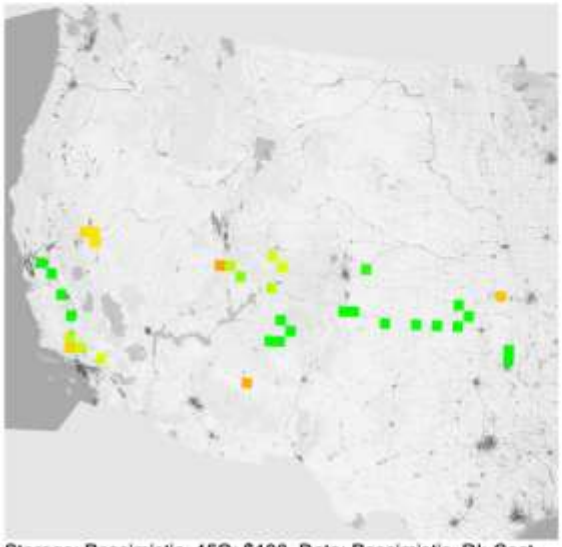
Storage: Pessimistic, 45Q: $85, Data: Pessimistic, RI: Cost



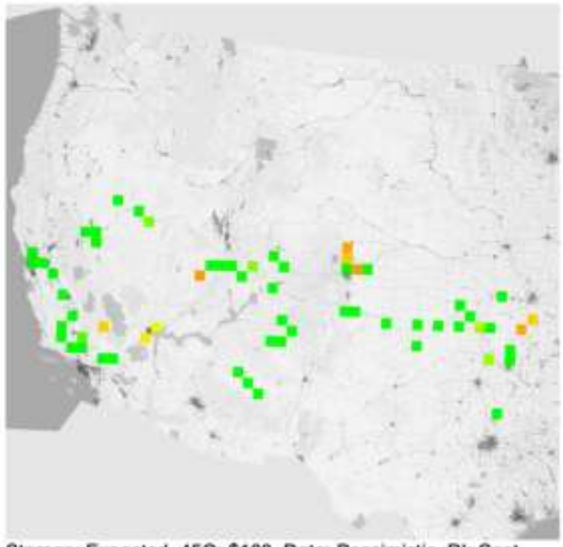
Storage: Expected, 45Q: $85, Data: Pessimistic, RI: Cost



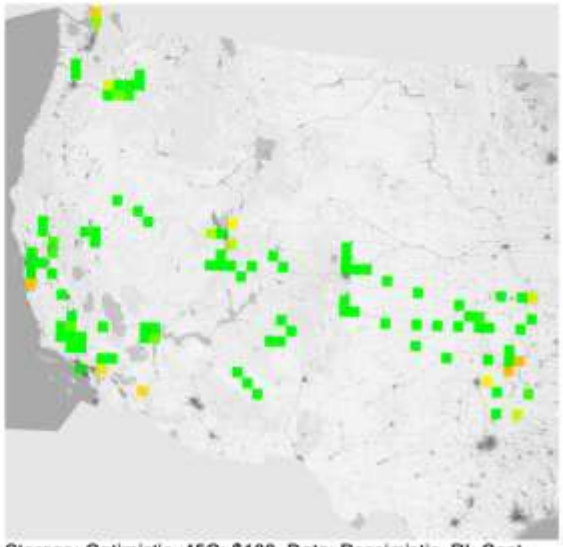
Storage: Optimistic, 45Q: $85, Data: Pessimistic, RI: Cost



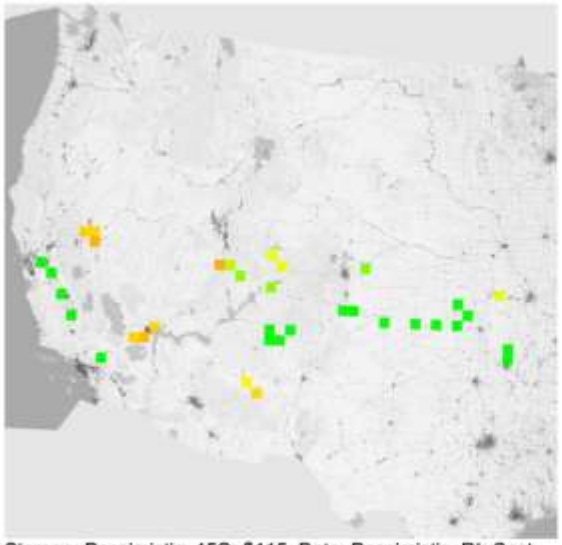
Storage: Pessimistic, 45Q: $100, Data: Pessimistic, RI: Cost



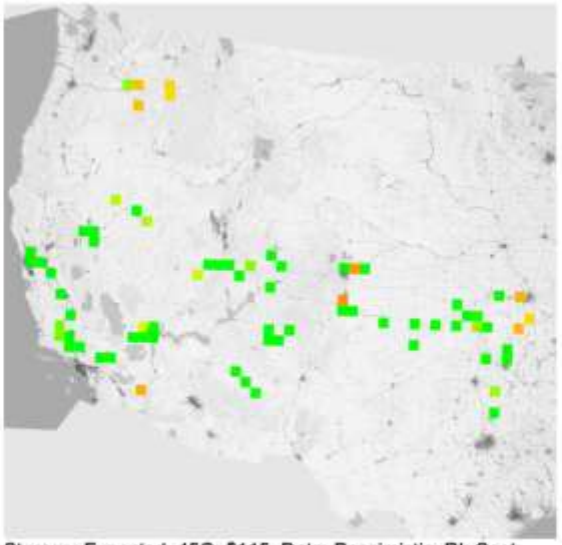
Storage: Expected, 45Q: $100, Data: Pessimistic, RI: Cost



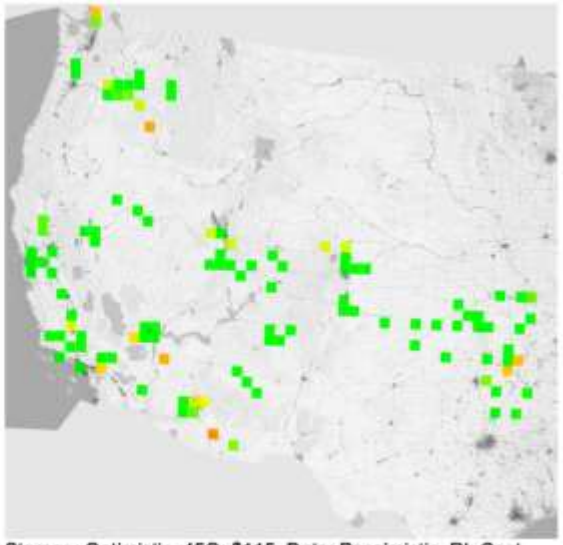
Storage: Optimistic, 45Q: $100, Data: Pessimistic, RI: Cost



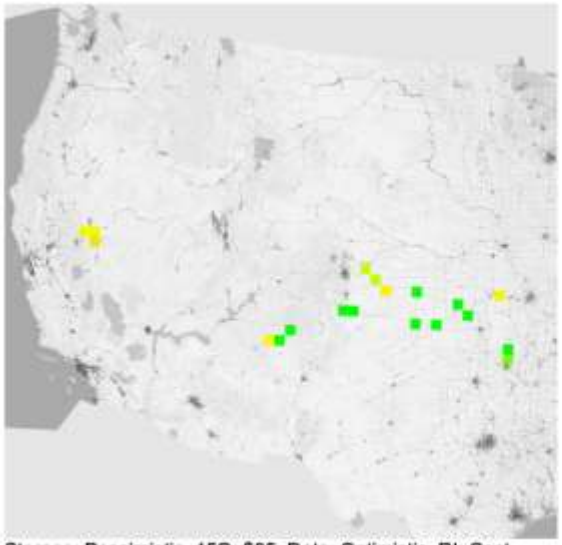
Storage: Pessimistic, 45Q: $115, Data: Pessimistic, RI: Cost



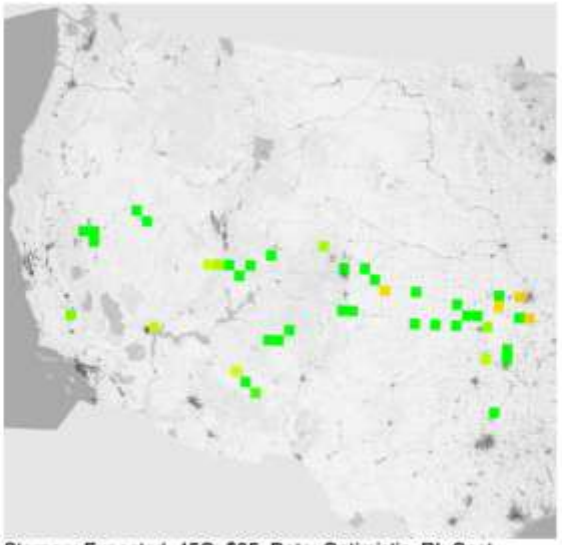
Storage: Expected, 45Q: $115, Data: Pessimistic, RI: Cost



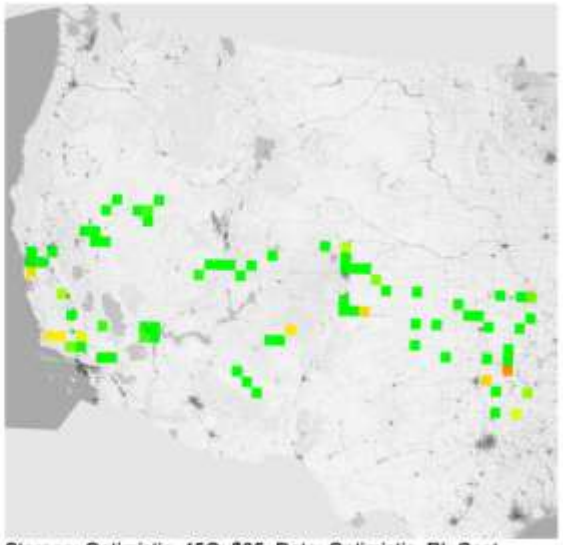
Storage: Optimistic, 45Q: $115, Data: Pessimistic, RI: Cost



Storage: Pessimistic, 45Q: $85, Data: Optimistic, RI: Cost



Storage: Expected, 45Q: $85, Data: Optimistic, RI: Cost



Storage: Optimistic, 45Q: $85, Data: Optimistic, RI: Cost

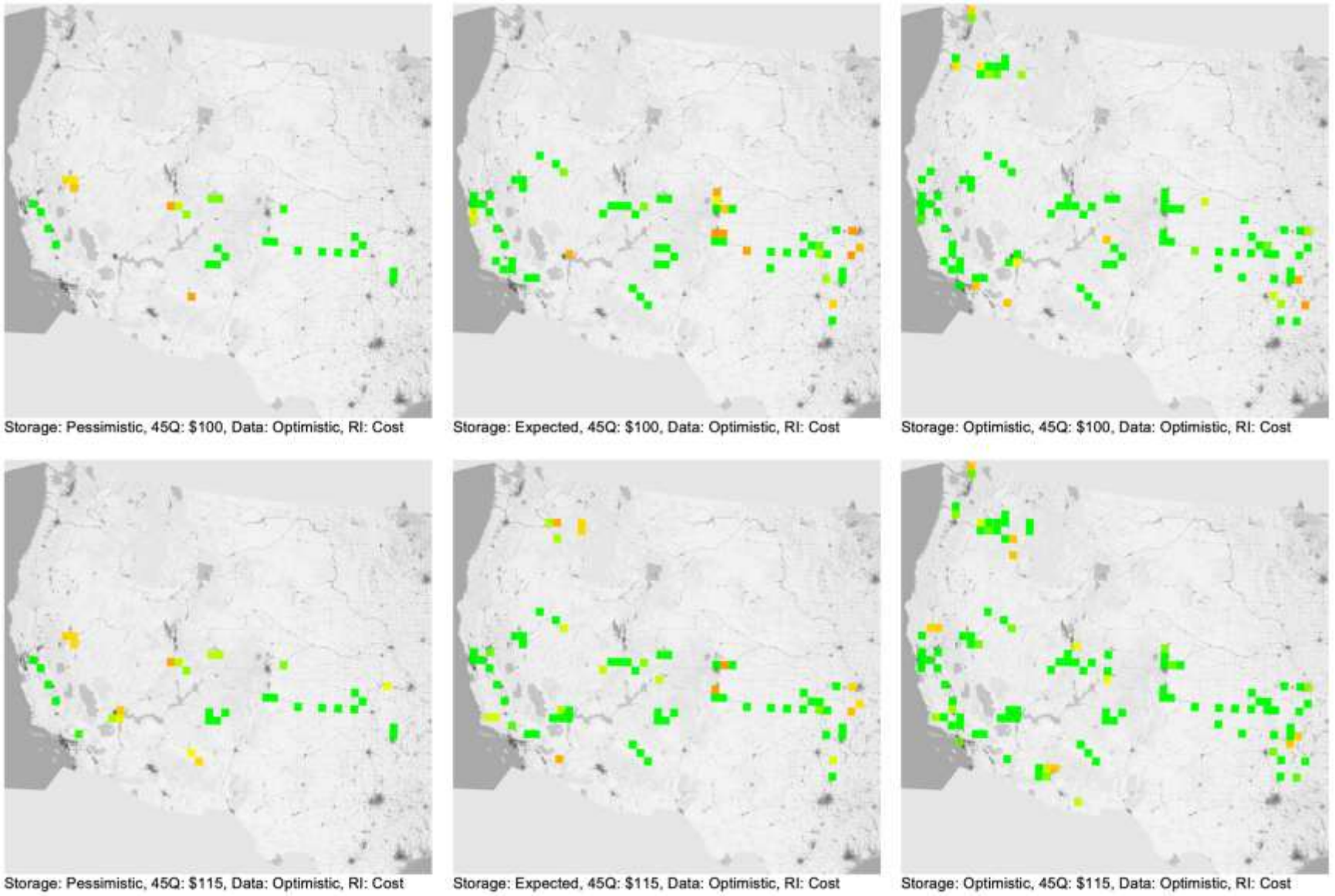


Figure 7 Readiness maps

References

Carbon Solutions LLC. 2025a. CostMAP^{PRO} [software]. Saint Paul (MN); Carbon Solutions LLC. [accessed 2025 Nov 20]. https://www.carbonsolutionsllc.com/software/costmappro/.

Carbon Solutions LLC. 2025b. SimCCS^{PRO} [software]. Saint Paul (MN); Carbon Solutions LLC. [accessed 2025 Nov 20]. https://www.carbonsolutionsllc.com/software/simccspro/.

Credit for Carbon Oxide Sequestration, U.S.C.-2023 26 C.F.R. §1.45Q-1 (2021).

IBM. 2025. IBM ILOG CPLEX Optimization Studio [software] [Internet]. Armonk (NY): IBM. [accessed 2025 Nov 20]. https://www.ibm.com/products/ilog-cplex-optimization-studio.

Middleton RS, Chen B, Harp DR, Kammer R, Ogland-Hand JD. 2020. Great SCO_2T! Rapid tool for carbon sequestration science, engineering, and economics. Appl Comput Geosci. 7:100035. doi:10.1016/j.acags.2020.100035

[PNNL] Pacific Northwest National Laboratory. 2025. State of stress analysis tool (SOSAT) [software] [Internet]. Richland (WA): Pacific Northwest National Laboratory. [accessed 2025 Nov 20]. https://www.pnnl.gov/projects/state-stress-analysis-tool.

[DOE] U.S. Department of Energy. 2023. FECM/NETL CO_2 transport cost model (2023): description and user's manual [Internet]. Pittsburgh (PA): U.S. Department of Energy, National Energy Technology Laboratory; Fossil Energy and Carbon Management. doi:10.2172/1992905 [accessed 2025 Nov 20]. https://www.osti.gov/servlets/purl/1992905.

[USGS] U.S. Geological Survey. 2023. Data release for the 2023 U.S. 50-state National Seismic Hazard Model—overview [Internet]. Reston (VA): U.S. Geological Survey. doi:10.5066/P9GNPCOD [accessed 2026 Jan 15]. https://www.sciencebase.gov/catalog/item/644af897d34e45f6ddcd13b3.

Task 5 – Promoting Regional Technology Transfer

Subtask 5.1 – Development of Regional Readiness Indices Maps

Carbon Solutions supported Montana State University and providing the key deliverable for this subtask.

Subtask 5.2 – Technology Transfer Forums

Data-Centric Approach to Technology Transfer

CUSP's technology transfer model is built mainly around data. Rather than focusing only on individual demonstration projects, the partnership invested heavily in:

- Building shared regional data sets on geology, emission sources, infrastructure, and economics
- Developing analytical and optimization tools to turn these data into actionable project designs
- Using focused projects and annual meetings to move that knowledge into industry practice and regulatory processes

In data workflow description, the partnership emphasizes three pillars: collecting, synthesizing, and using existing data sets, integrating them into analytical and optimization models to evaluate carbon management opportunities across the western United States.

This data-first orientation underpins almost every aspect of technology transfer: from pre-feasibility screening, to Class VI and MRV readiness, to infrastructure planning and long-term storage monitoring.

Data Infrastructure and Digital Tools

Atlas and Shared Databases

The core of CUSP's data work is an evolving regional "Carbon Portal." The 2023 overview describes how the partnership has assembled databases "of useful information necessary to create robust geologic models, flow models, and economic studies."

Key elements include the following:

- Geological data for saline aquifers, residual oil zones, basalts, and geothermal reservoirs
- Source inventories of power plants, gas processing facilities, refineries, hydrogen projects, and other industrial emitters
- Infrastructure layers, such as existing and potential pipeline corridors, processing plants, and transmission infrastructure
- Socio-economic and policy context needed for readiness and risk assessment

These datasets are standardized and made interoperable so they can be used across states, institutions, and tools.

Analytics, Optimization, and Machine Learning

CUSP explicitly positions itself as a provider of "intelligent computer applications" and access to national lab tools to optimize connections between sources and sinks and to support long-range development and economic analyses. This includes the following:

- Source-sink matching and cluster formation tools (e.g., SIMCCS and related workflows) used to design economically optimal CO_2 transport and storage networks under uncertainty
- Risk- and cost-based optimization, where infrastructure layouts are evaluated not only on cost but also on resilience, capacity, and risk tolerance
- NRAP-based tools for storage and leakage risk assessment, including passive seismic monitoring applications showcased in annual meeting presentations

Several research articles using datasets from the partnership illustrate this approach. Such analyses are directly transferable to real projects and are part of the technology transfer process.

Enabling Class VI, MRV, and 45Q Readiness

The partnership has built a dedicated team for Class VI permitting and MRV planning across the region, supported by its databases and modeling capabilities.

Data-enabled tech transfer here includes the following:

- Templates and workflows for Class VI permit applications based on regional experience
- MRV templates and workflows for design drawing on plume modeling, risk assessment, and monitoring technology evaluations
- Guidance for industries seeking to access 45Q tax credits (Credit for Carbon…2021), including case studies and technical support.

In practice, this means that workflows from acid gas injection and enhanced oil recovery fields projects is repurposed to support a new CCUS projects.

Focused Projects as Technology Transfer Pilots

CUSP organized its technical work into Focused Projects, which act as pilots for methods, tools, and datasets that can then be replicated elsewhere. The main themes are: CCUS feasibility studies, Class VI/MRV/45Q readiness, CCUS in geothermal systems, CCUS to support blue hydrogen, storage in basalts, and CO_2 plume detection. (See website)

CCUS Feasibility Studies Examples

Harquahala Basin (Arizona)

The "Characterization of CO_2 storage potential in Harquahala Basin, western central Arizona" project combines basin-scale mapping, stratigraphic analysis, and volumetric estimates to evaluate long-term storage potential. A follow-on pre-feasibility study and related posters show how the project uses:

- Basin-wide ranking of sedimentary basins by storage potential below 800 m
- Integration of well, seismic, and geophysical data to refine storage estimates
- Screening of risks such as sealing potential and sparse well control.

These methods are transferrable to other sedimentary basins in the region and are explicitly presented through CUSP materials and annual meeting sessions.

Colorado Front Range Project

The Colorado School of Mines feasibility study evaluates capturing CO_2 from the Front Range natural gas power plant and injecting it into nearby saline aquifers, working with Colorado Springs Utilities and Oxy Low Carbon Ventures.

The project demonstrates the following:

- Practical source-sink matching using spatial datasets and industrial input
- Joint use of geologic, engineering, and economic models to evaluate feasibility
- A repeatable workflow that can be applied to other power plants and basins

EPA Class VI - MRV - 45Q Projects

Several focused projects specifically target regulatory readiness and monitoring design, leveraging CUSP data and tools.

Relevant elements include the following:

- Regional and project-level MRV strategies, informed by CUSP's databases and NRAP tools
- Design of monitoring frameworks (e.g., NRAP tool applications presented at the 2023 annual meeting)
- Case studies like Lucid/Targa Red Hills acid gas injection in New Mexico, first introduced at the 2019 annual meeting and updated as the Targa Red Hills AGI Project, showcasing how project data feeds into regional learning and vice versa.

These activities are closely tied to 45Q readiness: the 2022 and 2023 meetings feature dedicated presentations on 45Q tax credits, explaining how data-driven MRV and reservoir modeling underpin eligibility for storage-related tax incentives.

CCUS in Geothermal Reservoirs and Blue Hydrogen

Focused projects on geothermal reservoirs in Nevada explore the dual role of geothermal formations for both energy production and CO_2 storage. Data and technology transfer aspects include:

- Combining heat-flow, permeability, and structural datasets with storage capacity modeling
- Evaluating the potential for CO_2 as a working fluid in geothermal systems at bench scale, including thermophysical properties and circulation behavior.

Similarly, projects supporting blue hydrogen evaluate integrated capture and storage options, using the same shared data infrastructure and analytics to design hydrogen-plus-storage hubs.

CCUS in Basalts and CO_2 Plume Detection

The "Derisking CO_2 mineralization storage in basalt reservoirs" project and related presentations (e.g., "Basalt for Carbon Sequestration Update to WGS") focus on basalts as long-term mineralization hosts.

Parallel work on CO_2 plume detection includes a focused project on downhole source tomography, and a New Mexico Tech focused project on 3D models and plume simulations.

These projects transfer

- laboratory and modeling methods for predicting mineralization rates and trapping mechanisms in basalts and
- monitoring technologies and plume imaging workflows, feeding directly into MRV design for Class VI projects.

Annual Meetings as Engines of Technology Transfer

The partnership's annual meetings were a central mechanism for transferring technologies, data methods, and regulatory know-how to practitioners, industries, and decision makers.

Building a Shared Knowledge Base

The annual meeting presentations always provided a state-by-state CCUS briefings and foundational capacity building:

- State CCUS overviews for Arizona, California, Colorado, Kansas, Nevada, New Mexico, Oklahoma, Texas, Utah, and Washington synthesize local data on geology, sources, and early-stage projects.
- "Introduction to 45Q Tax Credit" (Balch) and "Introduction to EPA Class VI" (Candace Cady) translate complex federal incentives and regulatory frameworks into practical guidance.
- The "CUSP Analytics Working Group" presentation (Sean Yaw) highlights the use of advanced analytics and optimization to design infrastructure under uncertainty, emphasizing the importance of shared datasets and tools.
- Project-specific talks such as "Lucid Energy Red Hills AGI Project" and "Biomass and CCS in Washington" embed local project data within a regional technology transfer context.

This structure effectively turns the meeting into a short course on CCUS project development, built on shared regional data.

Deepening the Data and Regulatory Toolset (2023 Annual Meeting)

The 2023 Annual Meeting expanded this with a more comprehensive program that directly supports technology transfer:

- Core regulatory and monitoring sessions:
  - "UIC Class VI Program" (Meissner)
  - "Monitoring, Reporting, and Verification (MRV)" (Cady)
  - "Navigating NEPA for Carbon Capture Project Developments" (Wolf & Ross)
- Sessions on financial and infrastructure enablers:
  - "45Q Tax Credit" (Balch)
  - "The Impact of IRA on CO_2 Transportation Infrastructure" (Bulbul)
- Data and modeling focused talks:
  - "Application for NRAP Passive Seismic Monitoring Tool" (Huang)
  - "Wellbore Design for Risk Management and Financial Viability" (Fisher)
  - "Core Analysis for CCS" (Walls)
- Storage and utilization frontiers:
  - "Applied CO_2 Mineralization Opportunities and Challenges" (Schaef, Cao, White)
  - "Basalt for Carbon Sequestration Update to WGS" (Gallin)
  - "CO_2 Storage Opportunities in Northern Platform of the Permian Basin" (Webster)

State update presentations for Utah, Oklahoma, New Mexico, Colorado, Kansas, Nevada, California, and Arizona further standardize data narratives across the region, showing how each jurisdiction is using CUSP data and tools.

Combined, these sessions transform CUSP's internal data and methods into shared, replicable practices for regulators, operators, and consultants.

Poster Sessions and Methodological Transfer

The 2023 poster session reinforced data-focused tech transfer. Examples include:

- "Pre-feasibility study for CO_2 sequestration in Harquahala Basin, southwestern Arizona", demonstrating basin-scale mapping and screening
- "Planning Amongst Uncertainty: Designing CCS Infrastructure Resilient to Capture, Transport, and Storage Uncertainty", illustrating how infrastructure design tools handle uncertain capture rates, storage behavior, and policy scenarios

By presenting methodologies and workflows rather than only results, these posters directly support uptake by other states and projects.

From Data to Deployment: Project Support and Commercialization

Beyond research, the partnership uses its data and tools to support commercial projects in the region. The 2023 overview notes that it has funded 15 CCUS commercialization projects and has 10 additional projects funded entirely by industry, while offering targeted support services for new initiatives.

Examples include

- Farnsworth Unit in Texas, where enhanced oil recovery operations are being repositioned toward longer-term storage, supported by modeling and MRV planning
- San Juan CarbonSAFE project in New Mexico, where CUSP assists with storage complex development to complement hydrogen conversion at the Escalante power station and supports preparation of Class VI applications
- Red Hills and Metropolis separation facilities in the Permian Basin, where acid gas injection experience and data are used to inform storage practices and 45Q strategies

Lessons for Technology Transfert and Future Directions

From a technology transfer perspective, several key lessons emerge from the partnership's work:

- **Data standardization is foundational**
  A shared atlas and interoperable databases make it possible to apply common tools and workflows across very different geological and regulatory environments. This underlies everything from source–sink matching to Class VI applications.
- **Analytics and optimization close the gap between data and decisions**
  Tools for risk-aware infrastructure design, NRAP-based risk assessment, and machine-learning–assisted screening help translate complex datasets into practical project choices that investors, regulators, and operators can act on. (ResearchGate)
- **Focused projects act as laboratories for transferable methods**
  Harquahala, the Colorado Front Range project, ONEOK Hub 2.0, Nevada geothermal reservoirs, basalt storage, and plume detection projects are all developing methods that can be reused elsewhere with minimal adaptation. (CUSP West - CUSP West)

- **Annual meetings are structured as technology transfer platforms**
  The combination of foundational talks (45Q, Class VI, MRV, NEPA), analytics sessions, project case studies, and state updates creates a continuous training and knowledge-sharing loop for stakeholders across the western states. (CUSP West - CUSP West)
- **Regulatory and financial enablers depend on strong data**
  Access to Class VI permits, 45Q, and IRA-driven infrastructure investments is fundamentally tied to robust datasets, credible models, and well-designed MRV plans. The partnership's investment in data and modeling is therefore central to its technology transfer mission, not ancillary.

References

Credit for Carbon Oxide Sequestration, U.S.C.-2023 26 C.F.R. §1.45Q-1 (2021).

Subtask 5.3 – Targeted Network Development

Subtask 5.4 – DOE Support

Subtask 5.5 – Environmental Justice Assessment

Part II – Focused Projects

Planning amongst Uncertainty: Designing CCS Infrastructure Resilient to Capture, Transport, and Storage Uncertainty

This focused project was led by Montana State University (MSU). The project's goal was to develop modeling and optimization techniques that help design carbon capture and storage (CCS) infrastructure that performs reliably under uncertainty. Large-scale CCS deployment faces inherent risks: capture costs can fluctuate, pipeline corridors can be disrupted, and storage capacities are often not fully known until injection begins. Without accounting for these uncertainties, infrastructure investments risk becoming stranded or requiring costly redesigns.

This project directly supports the broader goals of the Carbon Utilization and Storage Partnership (CUSP) project by equipping stakeholders with decision-support tools that quantify risk and highlight trade-offs among cost, capacity, and resilience. By embedding uncertainty directly into the infrastructure design process, this work helps de-risk CCS investment, supports phased development strategies, and ultimately increases confidence in achieving DOE's objectives for regional and national CO_2 mitigation.

The work was carried out at MSU with collaboration from Carbon Solutions (https://www.carbonsolutionsllc.com/, accessed 2026 Jan 14), which provided advisory input and data support. Graduate and undergraduate researchers at MSU implemented algorithms, conducted case studies, and integrated results into the open-source SimCCS platform (Middleton et al 2020b; LANL 2026), ensuring that the methods developed here are accessible to the broader CCS research and practitioner community.

Objectives and Outcomes

The primary objective of this focused project was to create a rigorous, scalable process for designing CCS infrastructure that remains effective under uncertain capture, transport, and storage conditions. Rather than relying on deterministic assumptions about source emissions or storage capacity, the project sought to develop algorithms and tools that explicitly incorporate uncertainty into infrastructure planning.

The result is a provably adaptable design process that generates deployment recommendations resilient to a wide range of possible futures. This process quantifies both the direct cost of uncertainty and the trade-offs among cost, throughput, and risk tolerance. By embedding this capability into the open-source SimCCS platform, the methods developed here can be readily applied across the CUSP region and beyond.

Scope of Work

The work carried out in this focused project centered on developing, implementing, and demonstrating a suite of algorithms for uncertainty-aware CCS infrastructure design. The scope of this focused project included 3 major components:

1) Robust design under uncertainty
    - Developed a Monte Carlo scenario generation plus mixed-integer linear programming (MILP) optimization workflow to design infrastructure that remains effective across many realizations of storage capacity and cost parameters
    - Introduced a risk index parameter that allows decision-makers to tune the level of robustness required, yielding a family of "core network" designs that balance capacity, cost, and risk
    - Applied the method to a California CUSP dataset, demonstrating how risk tolerance affects CO_2 throughput, profit, and infrastructure selection
2) Repair-aware design
    - Formulated a multi-objective optimization model that jointly determines an initial CCS network design and a repaired design if a designated pipeline segment or other component fails
    - Implemented an algorithm that enumerates the Pareto frontier of solutions, providing decision-makers with trade-offs between lower upfront costs and cheaper future repairs
    - Evaluated the approach using a Nevada CUSP dataset, illustrating how targeted overbuilding of the initial system can significantly reduce the cost of network repair if failure occurs
3) Scalable solution techniques
    - Developed a genetic algorithm (GA) with a novel solution encoding that ensures every candidate represents a valid infrastructure design, avoiding costly repair functions
    - Demonstrated that this approach produces near-optimal solutions for state-scale datasets and outperforms exact MILP solvers on national-scale datasets under fixed runtime budgets
    - Showed that this scalability is critical for running large ensembles of uncertainty scenarios, enabling tractable national-level planning studies

Each component was implemented within or alongside the SimCCS platform, ensuring that the results are accessible to researchers and practitioners throughout the CUSP network.

CUSP Project Team

This focused project was led by Montana State University under the direction of Sean Yaw, who oversaw project design, modeling methodology, and SimCCS integration.

- Graduate researchers Daniel Olson, Caleb Eardley, and Dalton Gomez were primary contributors to algorithm development, implementation, and case study analysis.
- Undergraduate researchers Ryan Dupuis and Michael Papadopoulos supported data preparation, scenario generation, and results validation.

- Collaborating organization: Carbon Solutions provided advice, cost data, and modeling context. Primary contact: Richard Middleton.

This combination of academic leadership, industry collaboration, and student involvement ensured both technical rigor and practical relevance while advancing workforce development in CCS modeling and optimization.

CCS Modeling Background

Wide-scale adoption of CCS is needed to limit the increase of global temperatures. Projects that grow from local-scale projects up to national-scale collaborations must be initiated. At all scales, CCS projects will require massive infrastructure investment. The consequences of poor infrastructure investments include failed projects and lack of wide-scale CCS adoption. A large driver of the success of a CCS project is the management of uncertainties related to capture, transport, and storage decisions. In particular, large uncertainty may surround the capacity and injectivity of potential storage locations. Even with thorough site characterization, the true performance of a storage location is not well known until injection operations commence. Infrastructure that was deployed under an assumption of incorrect storage parameters can be very expensive to provision with more injection locations or even reroute to a better storage formation. Alternatively, initially designing infrastructure that routed pipelines to provide opportunities to easily redirect CO_2 to a different storage location if the primary location underperforms would provide resiliency to storage performance uncertainty. Determining an initial infrastructure design that is adaptable to uncertainty in storage parameters could greatly reduce costs if true storage performance differs from estimated performance. The overarching aim of this project was to develop a CCS infrastructure design model that would endogenously account for uncertainty throughout the CCS supply chain, with a particular focus on storage uncertainty.

CCS modeling necessitates optimizing infrastructure deployments for hundreds of sources and reservoirs and thousands of kilometers of pipeline networks. Deploying CCS infrastructure on a massive scale requires careful and comprehensive planning to ensure investments are made in a cost-effective manner. At its core, designing CCS infrastructure is an optimization problem that aims to determine the most cost-effective locations and quantities of CO_2 to capture, route via pipeline, and inject for storage. Designing CCS infrastructure can naturally be formulated as a MILP that aims to minimize total cost while capturing and injecting a target amount of CO_2.

MILP modeling is a mathematical optimization approach widely used for planning and decision-making in complex systems. The goal of MILP models is to minimize or maximize an objective function, which is the algebraic representation of some parameter of interest (e.g., cost, productivity, or throughput) in the system being modeled. The objective function is encoded with data from the problem and decision variables, which are unknown elements of the problem that one wishes to determine (e.g., the amount of product to produce or the location to which a resource is to be deployed). MILPs combine continuous decision variables, which represent quantities such as flow rates, with binary decision variables, which indicate binary decisions for components such as the construction (or not) of pipelines. A MILP solver (e.g., IBM's CPLEX software [IBM 2025]) manipulates the decision variables in order to optimize the objective function. Linear inequality functions called constraints are used to enforce problem properties

(e.g., capacity restrictions). A solution to a MILP model is represented by specific values for the decision variables and the value of the solution is the value of the objective function.

The goal of the optimal CCS infrastructure MILP model is to determine the minimum-cost infrastructure deployment of sufficient capacity. Because the goal is to minimize CCS infrastructure cost, the scenario data that are fed into the MILP model are composed of the key cost drivers of a CCS project, including the following: source information (location, capture costs, and emission rate), storage information (location, injection costs, and storage capacity), and transport information (pipeline routes and pipeline cost–capacity curves). Information on the scenario input data is presented below.

Scenario Input Data

S	Set of CO_2 sources
Q_i^{src}	Annual CO_2 production rate at source i ($MtCO_2$/yr)
F_i^{src}	Fixed cost of opening source i ($)
V_i^{src}	Variable cost of capturing CO_2 from source i ($/$MtCO_2$)
R	Set of storage sites
Q_j^{res}	Annual CO_2 capacity of storage site j ($MtCO_2$/yr)
F_j^{res}	Fixed cost of opening storage site j ($)
V_j^{res}	Variable cost of injecting CO_2 into storage site j ($/$MtCO_2$)
P	Set of candidate pipelines
C	Set of possible capacities for each pipeline
Q_{kc}^{min}	Minimum capacity of pipeline k with capacity c ($MtCO_2$/yr)
Q_{kc}^{max}	Maximum capacity of pipeline k with capacity c ($MtCO_2$/yr)
F_{kc}^{pipe}	Fixed cost of opening pipeline k with capacity c ($)
V_{kc}^{pipe}	Variable cost of transporting CO_2 via pipeline k with capacity c ($/$MtCO_2$)

J	Set of candidate pipeline junctions

The decision variables of the infrastructure design MILP model indicate which sources to open and how much CO_2 to capture from each, which storage locations to open and how much CO_2 to inject into each, and where to deploy pipelines and what capacity they need to be able to transport. Details on the decision variables are presented below.

Model Decision Variables

$s_i \in \{0,1\}$	Indicates if source i is opened
$a_i \in \mathbb{R}^{\geq 0}$	Annual amount of CO_2 captured from source i ($MtCO_2$/yr)
$r_j \in \{0,1\}$	Indicates if reservoir j is opened
$b_j \in \mathbb{R}^{\geq 0}$	Annual amount of CO_2 injected into reservoir j ($MtCO_2$/yr)
$p_{kc} \in \{0,1\}$	Indicates if pipeline k with capacity c is opened
$d_{kc} \in \mathbb{R}^{\geq 0}$	Annual amount of CO_2 put in pipeline k with capacity c ($MtCO_2$/yr)

The goal of the MILP model is to minimize the cost of the project. The objective function that realizes this goal quantifies the cost of the project as the sum of the cost to capture the CO_2, the cost to transport the CO_2, and the cost to store the CO_2. The cost to capture CO_2 is the cost to open each opened facility (F_i^{src}) plus the cost to capture each metric ton of CO_2 from it ($V_i^{src} a_i$). Similarly, the cost to store CO_2 is the cost to open each opened storage location (F_j^{res}) plus the cost to inject each metric ton of CO_2 into it ($V_j^{res} b_j$). The cost to transport CO_2 is the cost to build each opened pipeline (F_{kc}^{pipe}) plus the cost to use the opened pipeline ($V_{kc}^{pipe} d_{kc}$). Because the goal is minimum-cost infrastructure, this objective function is minimized. The objective function is presented below.

Objective Function

$$\min \overbrace{\sum_{i \in S} (F_i^{src} s_i + V_i^{src} a_i)}^{capture\ cost} + \overbrace{\sum_{k \in P} \sum_{c \in C} (F_{kc}^{pipe} p_{kc} + V_{kc}^{pipe} d_{kc})}^{transport\ cost} + \overbrace{\sum_{j \in R} \left(F_j^{res} r_j + V_j^{res} b_j\right)}^{storage\ cost}$$

Constraints are used to enforce realistic operational restrictions including capacity restrictions and standard network construction requirements. The constraints are presented below.

Constraints

$Q_{kc}^{\min} p_{kc} \leq d_{kc} \leq Q_{kc}^{\max} p_{kc}, \forall k \in P, \forall c \in C$	(A)
$\sum_{\substack{k \in P: \\ src(k)=n}} \sum_{c \in C} d_{kc} - \sum_{\substack{k \in P: \\ dest(k)=n}} \sum_{c \in C} d_{kc} = \begin{cases} a_n & \text{if } n \in S \\ -b_n & \text{if } n \in R, \forall n \in S \cup R \cup J \\ 0 & \text{if } n \in J \end{cases}$	(B)
$a_i \leq Q_i^{src} s_i, \forall i \in S$	(C)
$b_j \leq Q_j^{res} r_j, \forall j \in R$	(D)

where constraint (A) enforces minimum and maximum pipeline capacities by ensuring that the amount of CO_2 transported by a pipeline (d_{kc}) is greater than the minimum capacity ($Q_{kc}^{\min}$) and less than the maximum capacity ($Q_{kc}^{\max}$) of that pipeline. Constraint (B) enforces conservation of flow at each node in the network to ensure that CO_2 is added to the network only when captured from sources and leaves the network only when injected into sinks. In other words, constraint (B) ensures that all CO_2 in the network comes from a source and goes to a storage site. Constraint (C) enforces limitations on source production rates by forcing the amount of CO_2 captured at each source (a_i) to be less than the available amount of CO_2 at that source (Q_i^{src}). Constraint (D) enforces limitations on reservoir storage capacities by forcing the amount of CO_2 injected into each storage site (b_j) to be less than the capacity of that site (Q_j^{res}). Because there are no constraints requiring a minimum amount of CO_2 processing, the model will deploy only infrastructure that is profitable (i.e., cost negative). This is possible given the availability of tax incentives such as those under Section 45Q of the U.S. Tax Code (Credit for Carbon…2021).

The work carried out in this focused project is organized around 3 major contributions:

1) We developed methods for designing infrastructure that resists failure, ensuring that networks remain robust even when storage performance underperforms.
2) We developed techniques for designing infrastructure that can be efficiently repaired in the event of disruption, allowing planners to weigh trade-offs between upfront cost and future adaptability.
3) We created new scalable optimization approaches that make it possible to apply uncertainty analysis at regional and national scales, where problem sizes quickly overwhelm conventional methods.

These 3 components collectively form the foundation of our approach to planning CCS infrastructure amidst uncertainty.

Robust Infrastructure Design

In this section, we introduce a heatmap-based method for identifying core CCS infrastructure that is resistant to storage capacity uncertainty (Olson et al. 2025). If all of the input parameters for a CCS infrastructure design instance were exactly known, optimal infrastructure solutions could be determined by solving the MILP model detailed in the CCS Modeling Background section on page 75. However, we assume that the actual annual capacity of each storage site,

Q_j^{res}, is uncertain and can be represented by a site-specific probability distribution. Each probability distribution is based on geologically informed estimates, reflecting the uncertainty in reservoir performance. Because the capacity of each site is not exactly known, this uncertainty prevents optimal infrastructure solutions from being determined by solving the MILP model. Instead, we propose a stochastic process for designing infrastructure that functions even with uncertain annual storage capacities. At a high level, the proposed infrastructure design process is a Monte Carlo optimization framework that first generates discrete scenarios by randomly sampling each storage site's probability distribution. Each scenario is then solved using the MILP model detailed in the CCS Modeling Background section on page 75 to determine the optimal infrastructure needed to support that scenario. The optimal infrastructure solutions for each scenario can then be aggregated into a heatmap to identify infrastructure components common to multiple solutions. Next, the heatmap is filtered to include only infrastructure that is common to a specified minimum number of solutions. Finally, a core infrastructure design is identified by finding the minimum-cost, maximum-flow solution in the filtered heatmap. An illustration of the proposed infrastructure design process is presented in Figure 11 and detailed below.

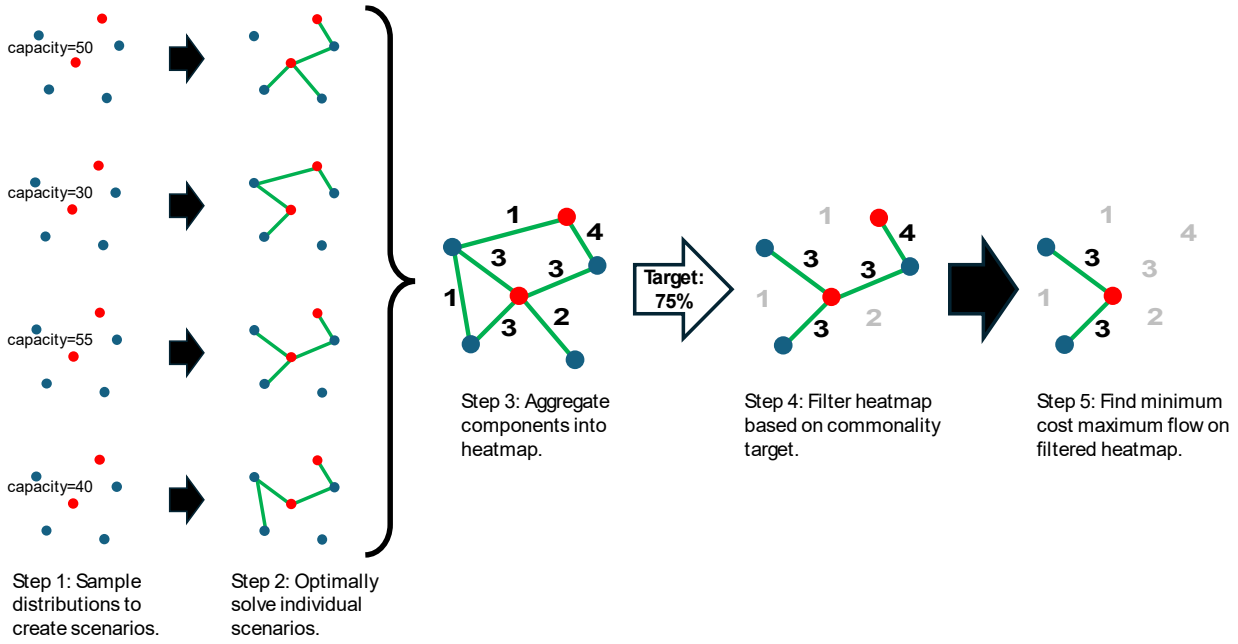


Figure 11 *Proposed process for identifying core infrastructure that is resistant to storage capacity uncertainty. Red circles are CO_2 sources and blue circles are storage sites. In Step 1, multiple scenarios are generated to reflect a range of possible values for uncertain storage capacities. In Step 2, each scenario is optimally individually solved using the MILP model. A heatmap is constructed in Step 3 by calculating the number of times each infrastructure component is used. In Step 4, the heatmap is filtered to include only a subset of all used infrastructure. Finally, the largest feasible infrastructure is calculated in Step 5.*

Scenario Generation

The MILP model detailed in the CCS Modeling Background section on page 75 requires concrete values for all input parameters, including the site-specific annual storage capacities Q_j^{res}. To construct a concrete scenario from uncertain storage capacities that can be solved using the MILP model, each storage site's capacity is selected as a random value sampled from that

site's probability distribution. This process is repeated to generate a set of scenarios, where each scenario represents a unique realization of the annual storage capacities for all storage sites. This set of scenarios captures a range of potential outcomes, ensuring that, with a sufficiently large set, the infrastructure design process will likely be exposed to storage conditions similar to what will be encountered in deployment.

Scenario Optimization

Each scenario is independently optimized using the MILP model detailed in the CCS Modeling Background section on page 75. Solving the MILP model for each scenario determines the infrastructure components needed to support that scenario, including the following:

- The set of sources to open and their associated capture rates
- The set of storage sites to open and their associated injection rates
- The network of pipelines to deploy and their capacities

Solving the MILP model for each scenario yields an optimal infrastructure solution for that specific realization of storage capacities.

Heatmap Generation

The individual solutions from all scenarios are aggregated to generate a heatmap that represents the frequency with which each infrastructure component (e.g., pipeline, source, or storage site) appears across the set of scenario solutions. A commonality score is calculated for each component as the number of scenario solutions in which that component appears. The commonality score is represented as the numerical edge weights in the graph in Step 3 of Figure 11. The result is higher commonality scores for infrastructure components with higher usage frequencies, which indicate greater importance and resilience across a range of uncertainty realizations. Each commonality score can be translated into a value in the range [0,1], representing the percentage of scenario solutions in which the component appeared, by dividing it by the number of scenarios.

Heatmap Filtering

An abstract concept of risk mitigation is incorporated into the design process in the form of a *risk index*, which assumes a value of $0\% \leq X \leq 100\%$. This index represents 2 things in the workflow that manage the risk that the core CCS infrastructure found will require repair due to storage underperformance during operation with the real storage capacities. First, for a given risk index X, a network component (e.g., pipeline, source, or storage site) must have a minimum commonality score of $(100 - X)$ to be included in the filtered heatmap. As the risk index decreases, the filtered heatmap retains only infrastructure that appears in a larger number of scenario solutions, effectively reducing the available infrastructure to the most common components. This results in a more conservative, lower-risk assessment of infrastructure availability. For example, at $X = 0\%$, only network components that appear in the optimal solutions of all scenarios (those with a commonality score of 100) are included, offering high confidence that any of those components would remain functional during actual injection operations. At $X = 15\%$, components used in at least 85% of scenarios are included in the filtered heatmap, allowing more infrastructure possibilities at an increased risk of deploying

infrastructure that will underperform with the actual storage capacities and require repair. All network components that appear in fewer than X% of the scenario solutions are excluded from the final infrastructure design.

Core Infrastructure

Although the filtered heatmap identifies infrastructure that is common to X% of all scenarios, there is no guarantee that this infrastructure forms a valid flow solution. For example, the filtered heatmap could contain pipeline components that are not connected to any other infrastructure with the same risk index. In this case, the filtered heatmap infrastructure would not serve as a stand-alone solution. To determine the largest valid solution contained within the filtered heatmap, the minimum-cost maximum flow over that network is computed. Maximum flows represent solutions in the filtered heatmap that can host the largest amount of CO_2. The minimum-cost solution among the set of maximum flow solutions represents the most cost-effective maximum flow. Minimum-cost maximum flows in the filtered heatmap infrastructure can be found by iteratively solving versions of the MILP model from the CCS Modeling Background section on page 75.

First, the maximum flow is determined by performing a binary search on values of the annual CO_2 processing target T, looking for the largest threshold value that results in a feasible MILP instance. Once the maximum flow is found, the minimum-cost maximum flow is found by solving the MILP model one more time with the processing target T set to equal the maximum flow value. However, before the MILP model from the CCS Modeling Background section on page 75 can be formulated, concrete storage capacities need to be identified from the site-specific probability distributions. This is done by again leveraging the risk index value. Given a risk index of X, the storage capacity of each site is set to the Xth percentile of the site's probability distribution.

For example, if a decision-maker with a low appetite for risk wanted to explore possible infrastructure deployments, they might choose a risk index of X = 10%. In that case, only infrastructure that was deployed in at least 90% of the scenario solutions would be considered. The storage capacity for all those storage sites would be set at the very conservative 10th percentile of their probability distributions. The resulting core infrastructure found when calculating the minimum-cost maximum flow would reflect a very conservative set of assumptions, and it is very likely that this core infrastructure would perform well with whatever storage capacities are encountered during operation. On the other hand, if the decision-maker had a large appetite for risk, they might choose a risk index of X = 75%. In this case, the amount of available infrastructure would increase greatly, and the storage capacity for all those sites would be set at the 75th percentile of their probability distributions. This would reflect a far more optimistic view and would result in core infrastructure that is larger and capable of processing significantly more CO_2 but is also at a greater risk of requiring repair due to storage site underperformance. In this way, the risk index serves as a parameter of the model that represents the appetite for risk during the infrastructure generation process. This process can also be modified to have a different storage capacity selection method (e.g., always select the expected value) should a specific case study warrant it.

Workflow Discussion

Although this proposed workflow for designing CCS infrastructure provides a framework for addressing storage capacity uncertainty, there are numerous practical details that should be considered. The underlying infrastructure design optimization problem is a known NP-hard problem. This means that although solving the MILP model will produce globally optimal solutions, the computational running time will exponentially increase as the size of the dataset increases (e.g., by increasing the number of sources, storage sites, or candidate pipelines). This can pose significant scalability challenges when applying the proposed process to very large datasets, such as those representing multi-region or nationwide CCS studies. In such cases, additional computational resources or heuristic approximations, such as those presented in the Scalable Infrastructure Design section of this report on page 97, may be required to maintain tractability.

Implementation of the proposed workflow is a straightforward process because existing CCS infrastructure modeling tools such as SimCCS and CostMAP (Carbon Solutions 2025a) can be heavily leveraged. These tools handle data organization and visualization and use off-the-shelf MILP solvers such as CPLEX or Gurobi (Gurobi Optimization 2026) to solve the core MILP model. Modifications to existing software (e.g. SimCCS) need to be made to support the stochastic component of the workflow and to aggregate solutions into heatmaps for display.

Finally, as is true of all models, the accuracy and validity of the output from the proposed process heavily depend on the quality of the input data. Important data, such as storage capacity estimates, injectivity rates, capture costs, and pipeline routing costs, must be reliable and accurate to generate meaningful results. In particular, probability distributions for storage capacity uncertainty are central to the operation of the workflow. Determining these distributions relies on geologic characterization data that may be sparse, incomplete, or uncertain. Although the stochastic nature of the process allows some mitigation of these data deficiencies by running many simulations, highly inaccurate or biased input data could still lead to suboptimal or misleading recommendations.

Case Study

To validate the efficacy of the robust infrastructure design workflow, scenarios were run on a CCS dataset collected for the state of California as part of the CUSP project. The dataset includes 62 sources with a total annual capture potential of 38.01 $MtCO_2$/yr coming from a variety of industries, as detailed in Table 5. Capture capacities and costs were generated as part of the CUSP project and include California's Low Carbon Fuel Standard (LCFS) credits when applicable for the specific source.

Table 5 Capture profiles by industry

Industry	Number of sources	Emission amount, $MtCO_2$/yr
Natural gas power	13	14.46
Combined heat and power	15	7.17
Hydrogen production	7	5.23
Cement production	5	4.76
Steam generation	16	3.38
Petroleum refineries	4	2.15

Ethanol production	2	0.87

The dataset includes 57 independent storage sites with a combined annual storage capacity expected value of 452.75 $MtCO_2$/yr. Of the 57 sites, 45 are saline storage sites (419.04 $MtCO_2$/yr expected) and 12 are enhanced oil recovery sites (33.71 $MtCO_2$/yr expected). Storage capacities and costs were generated as part of the CUSP project and include 45Q federal tax credits when applicable for the specific storage sites. A normal distribution for each storage site was generated by estimating site-specific storage capacity expected values and standard deviations across a range of parameter possibilities using the SCO_2T geologic sequestration tool (Middleton et al. 2020a).

The set of possible pipeline routes was generated using SimCCS's candidate pipeline generation tool. SimCCS generates candidate pipeline routes from a rasterized cost surface, where each grid cell represents localized routing costs and pipeline routes are calculated as piecewise linear paths through the spatial grid. The pixelated appearance of the following map-based figures is due to the underlying map being the rasterized cost surface as well as the piecewise linear pipeline routes.

The California dataset is presented in Figure 12.

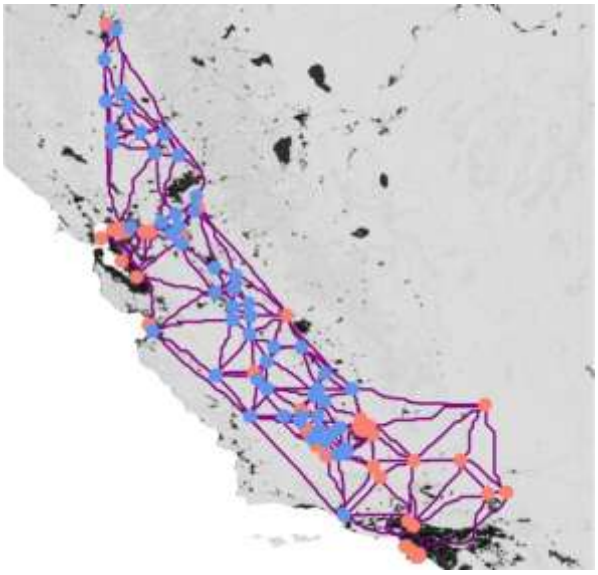


Figure 12 CCS infrastructure dataset from the state of California. The study area is bounded by (40.960, −123.659) in the top left corner and (33.636, −116.042) in the bottom right. Red circles are CO_2 sources, blue circles are storage sites, and purple edges are candidate pipeline locations.

A total of 57 scenarios were generated by sampling each of the storage sites' storage capacity probability function to obtain a random annual storage capacity value for each scenario. Each scenario is parameterized to process 17 $MtCO_2$/yr for 30 years. Optimal solutions for each scenario were found by solving the MILP from the CCS Modeling Background section on page 75 using SimCCS and IBM's CPLEX optimization software version 12.9. The heatmap was generated by aggregating the deployed infrastructure from the solutions of the 57 scenarios and calculating the commonality score for each infrastructure component. The commonality score was translated into a value in the range [0,1], representing the percentage of scenario solutions in which the component appears, by dividing by 57. The resulting heatmap is presented graphically

by mapping the commonality score into a color on the red–yellow–green color gradient, as seen in Figure 13.

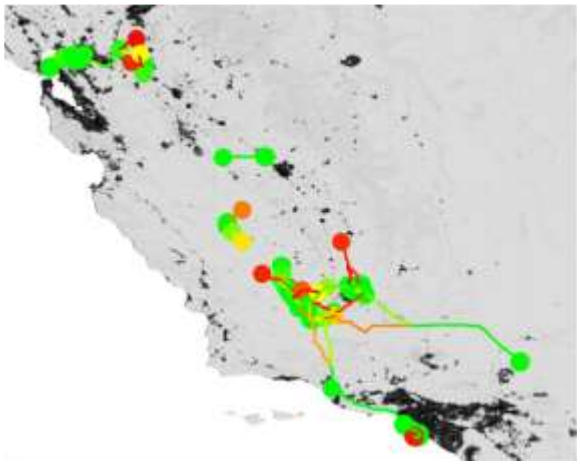
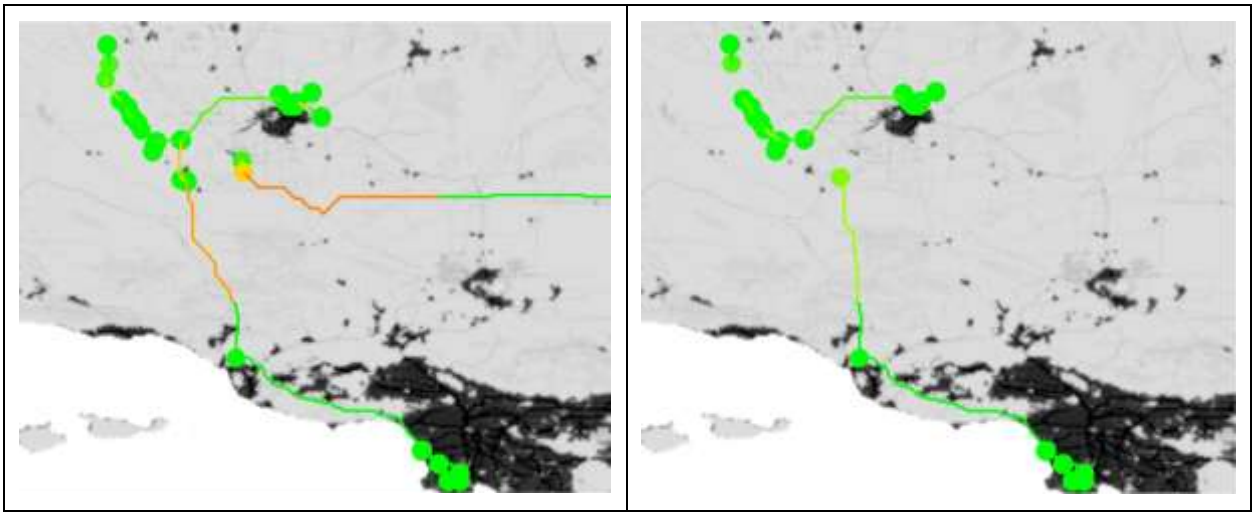


Figure 13 Aggregated heatmap of solutions from 57 scenarios with different storage capacities. Infrastructure is colored on a red–yellow–green color gradient, in which red corresponds to less commonly used infrastructure and green corresponds to more commonly used infrastructure.

The core infrastructure is constructed by first identifying the desired risk index in the range of 0% to 100%. As described in the core infrastructure subsection this threshold relates to the minimum percentage of scenarios in which each network component must appear to be available in the core infrastructure solution. The selection of a risk index filters out infrastructure from the full heatmap that is below the threshold to exclude it from possibly being in the core solution. After the infrastructure available to the core solution is identified, the capacity for each sink is set as described in the methodology to be the *X*th percentile of the corresponding probability distribution. Finally, the minimum-cost maximum flow is calculated using the standard process of first finding the maximum flow using the Ford-Fulkerson algorithm and then finding the minimum-cost flow with that value using integer linear programming. Core infrastructure found using this process for a subregion of the dataset using risk index values of 100%, 43%, 30%, and 15% is presented in Figure 14.



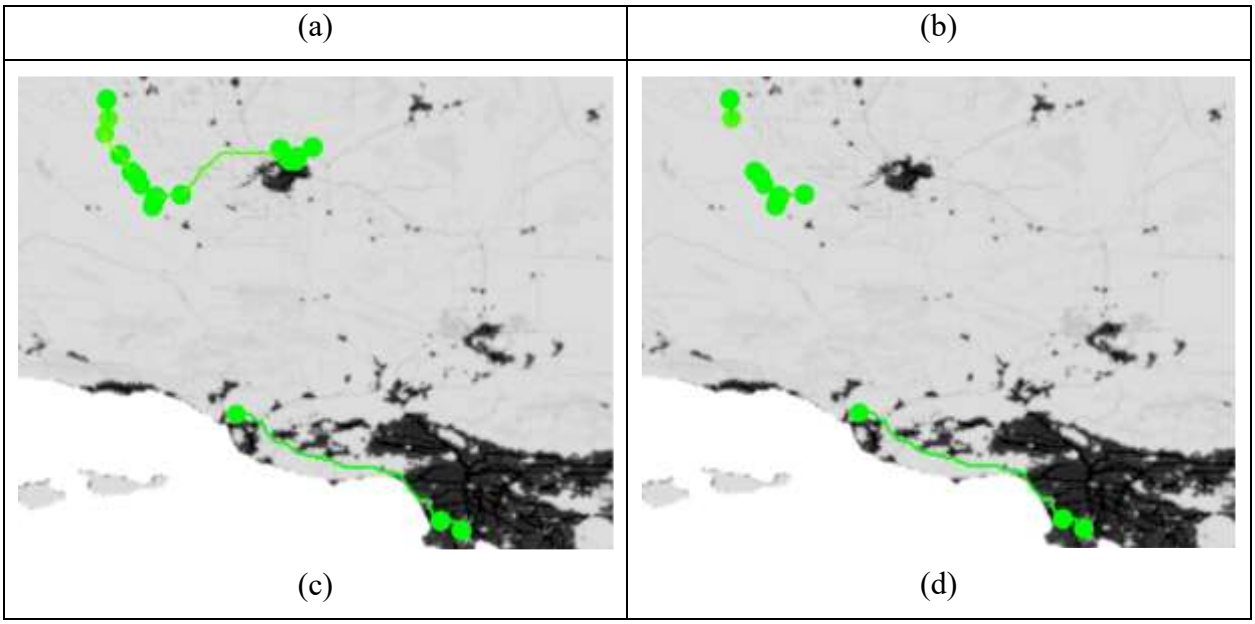


Figure 14 Core CCS infrastructure found using the proposed method for a subregion of the dataset using various risk indices. Infrastructure is colored on a red–yellow–green color gradient, in which red corresponds to less commonly used infrastructure and green corresponds to more commonly used infrastructure. (a) Risk index = 100%. (b) Risk index = 43%. (c) Risk index = 30%. (d) Risk index = 15%.

Increasing the risk index corresponds to generating more-conservative infrastructure, as the amount of available infrastructure is restricted and the storage capacity is reduced. The trade-off between the risk index and performance is important for decision-makers to consider, because this can provide insight into the potential range of performance as well as the natural risk index breakpoints that should be considered. The performance measures that are of most interest are the amount of CO_2 that the identified core infrastructure can process and the cost of the infrastructure. To quantify this trade-off, the proposed core infrastructure generation process was run for risk index values from 0% to 100% in 2.5% increments.

Figure 15 presents the trade-off curve between the selected risk index and the amount of CO_2 that can be processed by the identified infrastructure. Reducing the risk index from 15% to 0% reduced the amount of CO_2 processed by 83.7%. Likewise, reducing the risk index from 30% to 15% reduced the amount of CO_2 processed by 31.3%. This demonstrates the trade-off between infrastructure effectiveness and assumption of risk.

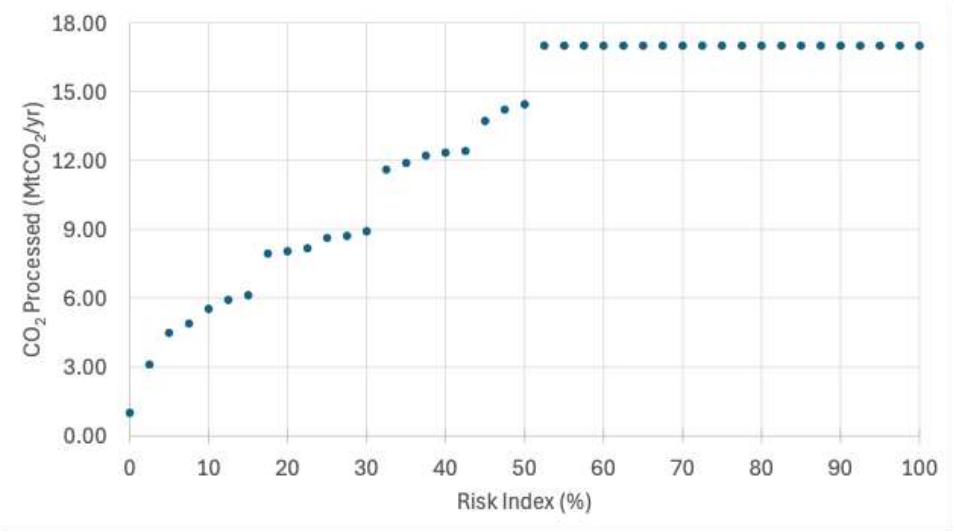


Figure 15 Annual amount of CO_2 processed versus risk index for a range of risk index values

Of particular interest are the obvious breakpoints that may help decision-makers settle on a specific risk index or small set of risk indices. For example, the difference in the amount of CO_2 processed when the risk index is decreased from 17.5% to 15% (1.81 $MtCO_2$/yr) is notably more than the difference between 20% and 17.5% (0.09 $MtCO_2$/yr) or 15% and 12.5% (0.21 $MtCO_2$/yr). These breakpoints occur when infrastructure components are added to the available infrastructure that are important enough to notably increase the amount of CO_2 that can be processed by the solution. They serve as logical spots that demonstrate the most impactful trade-offs between performance and risk index. The annual amount of CO_2 processed is constant for risk index values below 50% because, for this specific dataset, that commonality score encompasses all deployed infrastructure in all scenarios. This means that for low-risk index values, the same infrastructure is available, as opposed to higher risk index values, when the required commonality score reduces the amount of available infrastructure. The nonincreasing trend from a large amount of CO_2 processed for low-risk index values to a small amount of CO_2 processed for high-risk index values would be seen for all datasets, because the amount of available infrastructure is reduced. The constant regions, breakpoint locations, and CO_2 processed values are dataset specific; accordingly, other datasets would likely show differences in this behavior.

Figure 16 presents the trade-off curve between the selected risk index and the cost of the identified infrastructure. Note that the inclusion of LCFS and 45Q tax credits allows for the cost of processing CO_2 to be outweighed by the credits, which enables the infrastructure to have a negative cost (i.e. to be profitable). Reducing the risk index from 15% to 0% decreased the profit of the project by 77.1%. Likewise, reducing the risk index from 30% to 15% decreased the profit of the project by 28.5%. This demonstrates the trade-off between infrastructure cost and assumption of risk. The same breakpoints (for the same risk index values) are seen in the cost trade-off curve as in the trade-off curve for the amount of CO_2 processed.

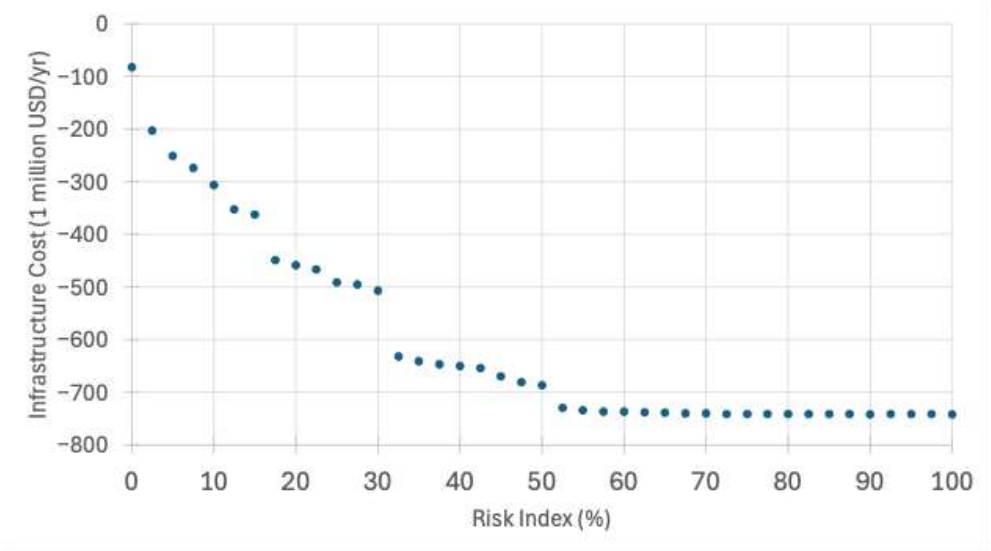


Figure 16 Annual infrastructure cost versus risk index for a range of risk index values. Note that the infrastructure cost is negative due to Low Carbon Fuel Standard and 45Q tax credits.

Repairable Infrastructure Design

In this section, we examine how CCS infrastructure should be designed when there is a possibility that a specific component (e.g., pipeline segment) may fail after deployment. If a network is initially built and one of its pipelines becomes unavailable, additional infrastructure may need to be constructed or reactivated to ensure that the planned volume of CO_2 can still be transported and stored. Because it is not known in advance whether the vulnerable pipeline will actually fail, 2 designs must be considered simultaneously: (1) the initial infrastructure design, which assumes the pipeline remains available, and (2) the repaired design, which represents the modifications required if that pipeline fails. The costs of these 2 designs are interdependent, because the fixed costs of constructing the potentially failing pipeline—and any other infrastructure abandoned when transitioning to the repaired design—contribute to the overall repaired cost. This interdependence makes the problem a multi-objective optimization with competing goals: minimizing the cost of the initial deployment while also minimizing the potential cost of repair. The set of Pareto-optimal solutions defines the trade-off frontier between these objectives, and it is along this frontier that decision-makers should select a design, guided by both the perceived likelihood of failure and their tolerance for risk.

Although the MILP described in the CCS Modeling Background section on page 75 identifies an optimal infrastructure configuration when all pipelines and storage sites perform as expected, the problem becomes more complex if a designated component fails after construction. In this project, we consider scenarios in which a specific pipeline segment may become unusable after the network has been built and its fixed construction costs have been incurred. If such a pipeline fails, the CCS network must be repaired by rerouting CO_2 through alternate infrastructure to maintain the planned capture and storage volumes. The cost of this repaired system includes not only the ongoing variable costs but also the fixed costs of any abandoned infrastructure, because those investments have already been made. This interdependence makes it difficult to determine the best initial design: even if a pipeline fails, its construction cost is sunk, and any additional abandoned pipelines also add to the effective repair cost. The problem is therefore formulated as

a multi-objective optimization, seeking to minimize both the cost of the initial design and the potential cost of repair. Because these objectives are in conflict, there is not a single optimal solution but instead a spectrum of trade-offs between inexpensive initial designs and inexpensive repairs.

To illustrate, consider the simplified CCS network in Figure 17 (top), in which edge weights represent pipeline construction costs, capacities are uniform, and the target throughput is 1 unit of CO_2. In this example, the vulnerable pipeline is the segment (b,t). The minimum-cost design (Figure 17(a), top) routes CO_2 along the direct path (s,b,t) at a cost of 9. If that pipeline does not fail, this is the uncontested best solution. However, if the pipeline does fail after construction, repairing the system requires rerouting along a longer path, yielding a total cost of 20 (Figure 17(a), bottom). The 3 additional solutions (panels b through d) require higher initial construction costs but offer lower repair costs if the vulnerable pipeline fails. Depending on the perceived likelihood of failure, the best choice lies among these alternatives.

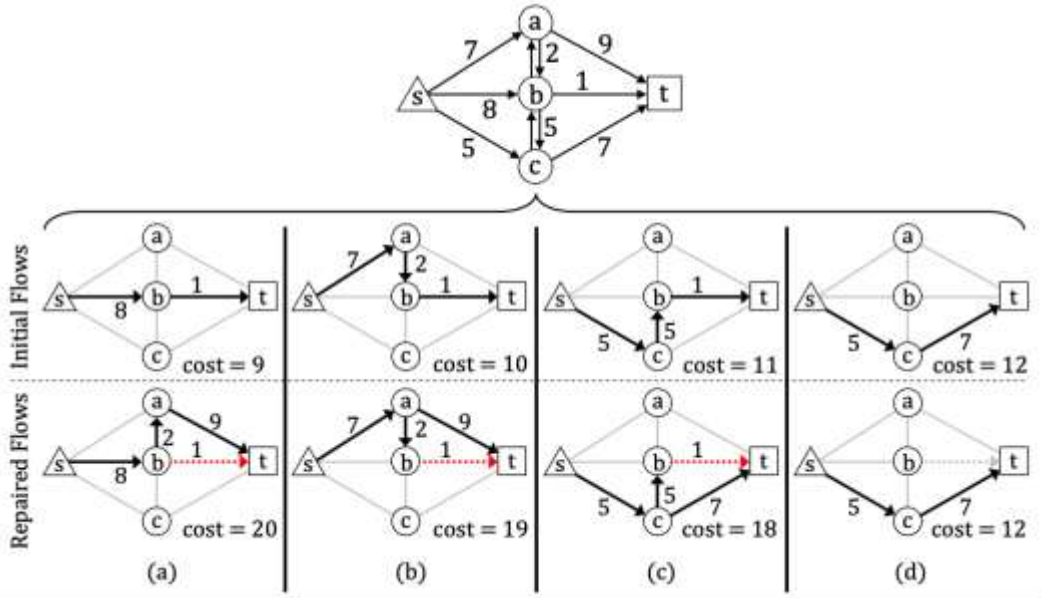


Figure 17 Sample simplified CCS network (top) with source s, storage site t, displayed fixed costs, no variable costs, unit edge capacities, and a target flow amount of 1. Panels (a) through(d) show a sequence of initial flow solutions (top) and optimal repaired flow solutions (bottom) when edge (b,t) fails.

The relevant set of designs for decision-makers is defined by the Pareto frontier between initial cost and repaired cost. At one extreme, the frontier begins with the minimum-cost design that assumes no failure (Figure 17(a), top). At the other extreme, it ends with the minimum-cost design that excludes the vulnerable pipeline entirely (Figure 17(d)), which is optimal if failure is certain. The intermediate points correspond to overbuilding the initial system: spending more up front to reduce the cost of repairing the network if the vulnerable pipeline fails. If failure is unlikely, a lower-cost initial design is appropriate, even though it carries a more expensive repair. If failure is likely, the opposite holds: investing in a more robust initial design reduces the overall cost of recovery. The contribution of this work is an algorithmic process for generating the Pareto front, thereby giving planners a structured set of trade-off solutions for resilient CCS network design.

Algorithm

In this section, we present the algorithm that finds the Pareto front between the initial flow cost and the repaired flow cost. This sequence of solutions has progressively decreasing repaired flow costs, starting with the minimum-cost flow and proceeding to the minimum-cost flow on the network with the designated edge excluded. The scenario input data input we consider is identical to the input to the MILP described in CCS Modeling Background section on page 75, with the addition of the designated edge that may or may not fail and a capture target:

w	Pipeline segment from P subject to failure
T	Target CO_2 capture amount for project (tCO_2/yr)

The algorithm presented here works by solving a series of 2 MILPs that identify the sequence of solutions that form the Pareto front. The first solution in the sequence is the minimum-cost flow and the minimum-cost repair of that flow when the designated edge fails. This solution corresponds to the initial and repaired flows shown in Figure 17(a). The 2 MILPs are run sequentially and each concurrently finds an initial flow with the designated edge not failing and a repaired flow with the designated edge failing using the following decision variables:

$s_i^{in} \in \{0,1\}$	Indicates if source i is opened in initial solution
$a_i^{in} \in \mathbb{R}^{\geq 0}$	Annual amount of CO_2 captured from source i ($MtCO_2$/yr) in initial solution
$s_i^{rep} \in \{0,1\}$	Indicates if source i is opened in repaired solution
$a_i^{rep} \in \mathbb{R}^{\geq 0}$	Annual amount of CO_2 captured from source i ($MtCO_2$/yr) in repaired solution
$r_j^{in} \in \{0,1\}$	Indicates if reservoir j is opened in initial solution
$b_j^{in} \in \mathbb{R}^{\geq 0}$	Annual amount of CO_2 injected into reservoir j ($MtCO_2$/yr) in initial solution
$r_j^{rep} \in \{0,1\}$	Indicates if reservoir j is opened in repaired solution
$b_j^{rep} \in \mathbb{R}^{\geq 0}$	Annual amount of CO_2 injected into reservoir j ($MtCO_2$/yr) in repaired solution
$p_{kc}^{in} \in \{0,1\}$	Indicates if pipeline k with capacity c is opened in initial solution

$d_{kc}^{in} \in \mathbb{R}^{\geq 0}$	Annual amount of CO_2 put in pipeline k with capacity c ($MtCO_2$/yr) in initial solution
$p_{kc}^{rep} \in \{0, 1\}$	Indicates if pipeline k with capacity c is opened in repaired solution
$d_{kc}^{rep} \in \mathbb{R}^{\geq 0}$	Annual amount of CO_2 put in pipeline k with capacity c ($MtCO_2$/yr) in repaired solution

There is significant commonality in the constraints between the 2 MILPs. These common constraints enforce the validity of the initial and repaired flows, and encode the failure of the designated edge for the repaired flow:

Initial solution	
$Q_{kc}^{\min} p_{kc}^{in} \leq d_{kc}^{in} \leq Q_{kc}^{\max} p_{kc}^{in}, \forall k \in P, \forall c \in C$	(E)
$\sum_{\substack{k \in P: \\ src(k)=n}} \sum_{c \in C} d_{kc}^{in} - \sum_{\substack{k \in P: \\ dest(k)=n}} \sum_{c \in C} d_{kc}^{in} = \begin{cases} a_n^{in}, \text{if } n \in S \\ -b_n^{in}, \text{if } n \in R \\ 0 \quad, \text{if } n \in J \end{cases}, \forall n \in S \cup R \cup J$	(F)
$a_i^{in} \leq Q_i^{src} s_i^{in}, \forall i \in S$	(G)
$b_j^{in} \leq Q_j^{res} r_j^{in}, \forall j \in R$	(H)
$\sum_{i \in S} a_i^{in} \geq T$	(I)
Repaired solution	
$Q_{kc}^{\min} p_{kc}^{rep} \leq d_{kc}^{in} \leq Q_{kc}^{\max} p_{kc}^{rep}, \forall k \in P, \forall c \in C$	(J)
$\sum_{\substack{k \in P: \\ src(k)=n}} \sum_{c \in C} d_{kc}^{rep} - \sum_{\substack{k \in P: \\ dest(k)=n}} \sum_{c \in C} d_{kc}^{rep} = \begin{cases} a_i^{rep}, \text{if } n \in S \\ -b_n^{rep}, \text{if } n \in R \\ 0 \quad, \text{if } n \in J \end{cases}, \forall n \in S \cup R \cup J$	(K)
$a_i^{rep} \leq Q_i^{src} s_i^{rep}, \forall i \in S$	(L)
$b_j^{rep} \leq Q_j^{res} r_j^{rep}, \forall j \in R$	(M)
$\sum_{i \in S} a_i^{rep} \geq T$	(N)

Edge failure	
$d_{wc}^{rep} = 0, \forall c \in C$	(O)
$p_{kc}^{rep} \geq p_{kc}^{in}, \forall k \in P, \forall c \in C$	(P)

where constraints (E) and (J) enforces minimum and maximum pipeline capacities. Constraint (F) and (K) enforce conservation of flow at each node in the network. Constraints (G) and (L) enforce limitations on source capture rates. Constraints (H) and (M) enforce limitations on reservoir injection rates. Constraints (I) and (N) require a minimum amount of CO_2 processing. Constraint (O) ensures that no CO_2 will be transported on the failed pipeline segment in the repaired solution. Constraint (P) ensures that if a pipeline segment is used in the initial solution, its fixed opening costs must still be paid in the repaired solution. This constraint is used to force the repaired solution to pay the fixed costs of any pipeline components purchased for the initial solution, even if they are not used by the repaired solution, including the failed pipeline component.

The algorithm functions in an iterative fashion, at each iteration finding an initial and repaired solution in which the cost of the repaired solution is smaller than the cost of the repaired solution from the previous iteration. It is important to actively decrease the cost of the repaired solution instead of actively increasing the cost of the initial solution. Finding an initial solution with the same cost as the preceding iteration but with a lower cost repaired solution is a useful solution for the decision-maker to consider. Conversely, an initial solution with an increased cost compared with that of the preceding iteration and the same repaired solution cost is of little utility. At each iteration of the algorithm, 2 MILPs are used to identify the next initial and repaired solutions in the sequence. An overview of the algorithm is presented in Figure 18, and the 2 MILPS are detailed is the following subsections.

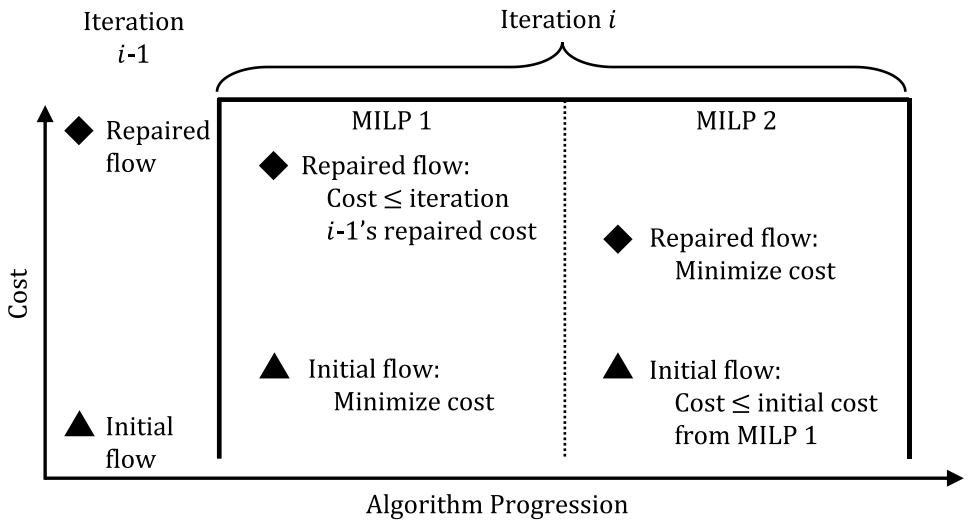


Figure 18 Overview of the objectives that the 2 MILPs optimize for when finding an initial and repaired solution during a single iteration of the algorithm. The initial and repaired solutions found by MILP 2 form the next solution on the Pareto front.

MILP 1

First, the cheapest initial solution is found such that the cost of its accompanying repaired solution is less than the cost of the previous iteration's repaired solution. These solutions can be found by formulating a MILP with the input parameters and decision variables defined above, and the following objective function that minimizes the cost of the initial solution:

$$\min \overbrace{\sum_{i \in S} \left(F_i^{src} s_i^{in} + V_i^{src} a_i^{in}\right)}^{capture\ cost} + \overbrace{\sum_{k \in P} \sum_{c \in C} \left(F_{kc}^{pipe} p_{kc}^{in} + V_{kc}^{pipe} d_{kc}^{in}\right)}^{transport\ cost} + \overbrace{\sum_{j \in R} \left(F_j^{res} r_j^{in} + V_j^{res} b_j^{in}\right)}^{storage\ cost}$$

The constraints for the MILP are Constraints (E) through (P) with the addition of a constraint that requires the cost of the repaired solution to be less than the cost of the repaired solution from the last iteration. Let R^{last} be the cost of the repaired solution from the last iteration and ϵ be some small value that represents the minimum step size for each sequential solution. This constraint limiting the cost of the repaired solution is then

$$\sum_{i \in S} \left(F_i^{src} s_i^{rep} + V_i^{src} a_i^{rep}\right) + \sum_{k \in P} \sum_{c \in C} \left(F_{kc}^{pipe} p_{kc}^{rep} + V_{kc}^{pipe} d_{kc}^{rep}\right) + \sum_{j \in R} \left(F_j^{res} r_j^{rep} + V_j^{res} b_j^{rep}\right) \leq R^{last} - \epsilon$$

Note that to find each Pareto-optimal point on the Pareto front, the value of ϵ must be small enough so that the repaired solution cost of the next Pareto-optimal point does not exceed $R^{last} - \epsilon$. If ϵ is too large, the algorithm will skip the Pareto-optimal points whose repaired solution costs are between $R^{last} - \epsilon$ and R^{last}. Because the cost differences between consecutive Pareto-optimal points are not known in advance, it is difficult to determine an appropriate minimum ϵ as a property of the graph instance. In practice, we address this by defining ϵ in as a small fraction (e.g., 0.1%) of the previous iteration's repaired solution cost. This approach

ensures meaningful cost differences between Pareto-optimal points and enables effective exploration of the Pareto front.

The result of this step is the cheapest initial solution whose corresponding repaired solution is cheaper than the previous iteration's repaired solution.

MILP 2

Second, an initial and repaired solution are found so that the cost of the repaired solution is minimized and the cost of the initial solution is, at most, the cost of the initial solution found by MILP 1. These solutions are found by a MILP with the input parameters and decision variables defined above and the following objective function that minimizes the cost of the repaired solution:

$$\min \overbrace{\sum_{i \in S} \left(F_i^{src} s_i^{rep} + V_i^{src} a_i^{rep}\right)}^{capture\ cost} + \overbrace{\sum_{k \in P} \sum_{c \in C} (F_{kc}^{pipe} p_{kc}^{rep} + V_{kc}^{pipe} d_{kc}^{rep})}^{transport\ cost} + \overbrace{\sum_{j \in R} \left(F_j^{res} r_j^{rep} + V_j^{res} b_j^{rep}\right)}^{storage\ cost}$$

The constraints for the MILP are Constraints (E) through (P) along with an additional constraint that is needed to force the cost of the initial solution to be, at most, the cost of the initial solution found by MILP 1 (I^{MILP-1}). Because the initial solution found by MILP 1 is the cheapest such solution, this constraint ensures that the initial solution will also have this minimum cost:

$$\sum_{i \in S} \left(F_i^{src} s_i^{in} + V_i^{src} a_i^{in}\right) + \sum_{k \in P} \sum_{c \in C} (F_{kc}^{pipe} p_{kc}^{in} + V_{kc}^{pipe} d_{kc}^{in}) + \sum_{j \in R} \left(F_j^{res} r_j^{in} + V_j^{res} b_j^{in}\right) \leq I^{MILP-1}$$

The result of this step is the next initial and repaired solution in the solution sequence.

This algorithm generates a sequence of initial and repaired solutions. The algorithm is initialized so that the initial solution for iteration 1 is the minimum-cost flow and the repaired solution is the minimum-cost repair of the initial solution when the designated edge fails. It is initialized to this because it is the cheapest initial solution, in which no restrictions are put on the cost of the repaired solution. The final iteration of the algorithm finds a solution in which the initial solution and repaired solution are both the minimum-cost flow on the flow network with the designated edge excluded. It finds this solution because it is the cheapest possible repaired solution. The intermediate solutions all represent trade-offs between initial solution cost and repaired solution cost. It can now be argued that the sequence of solutions found by the algorithm lie on the Pareto front between initial solution cost and repaired solution cost.

Theorem: Each initial–repaired pair solution found by the algorithm is Pareto-optimal.

Proof: Suppose that (I^{ALG}, R^{ALG}) is the cost of an initial–repaired solution pair found by the algorithm. This pair is Pareto-optimal if there does not exist any other solution pair with cost (I, R) such that

$$(I < I^{ALG} \text{and } R \leq R^{ALG}) \text{ or } (I \leq I^{ALG} \text{and } R < R^{ALG})$$

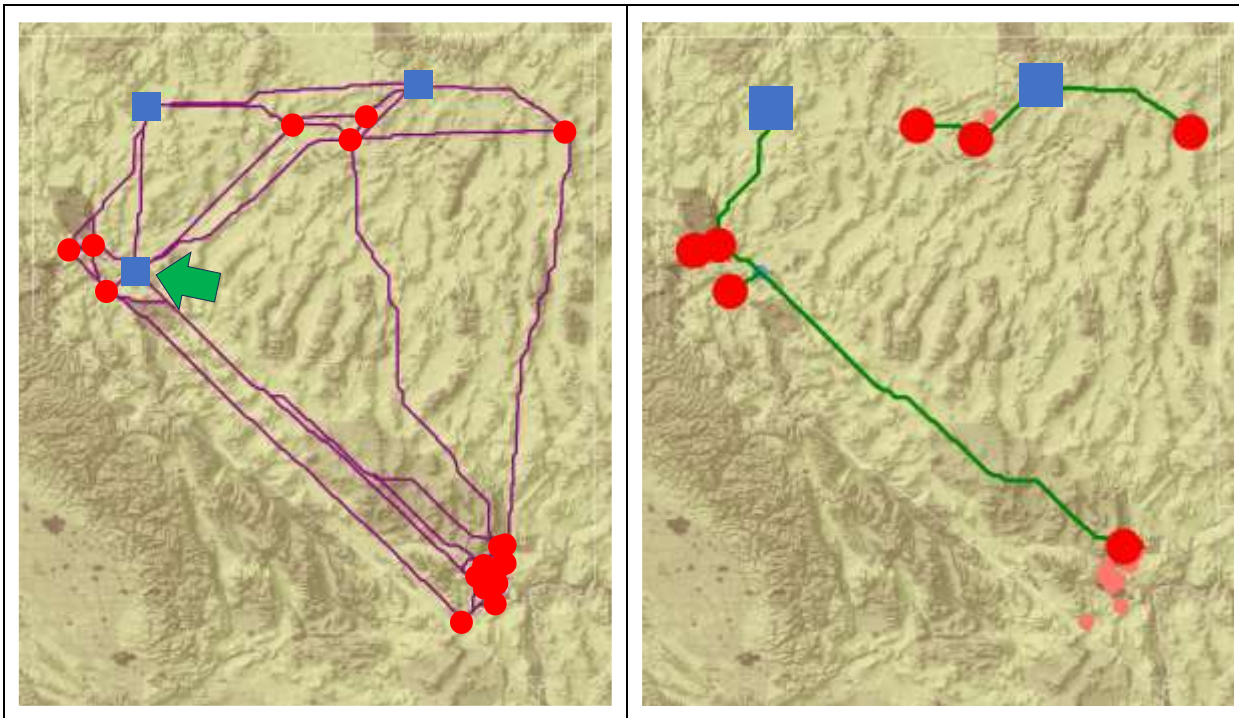
Consider any other valid solution pair with cost (I, R). Suppose that $R \leq R^{ALG}$. MILP 1 identified I^{ALG} as the cheapest initial solution compatible with any repaired solution whose cost is, at most, $R^{last} - \epsilon$. Because $R < R^{ALG} \leq R^{last} - \epsilon$, $I \geq I^{ALG}$. Suppose that $I < I^{ALG}$. MILP 2 identified R^{ALG} as the cheapest repaired solution compatible with any initial solution whose cost

is, at most, I^{ALG}. Because $I < I^{ALG}$, $R \geq R^{ALG}$. Therefore, neither condition of the Pareto-optimality condition holds and (I^{ALG}, R^{ALG}) is Pareto-optimal.

This theorem establishes that every solution produced by the algorithm is Pareto-optimal. However, it does not guarantee that every Pareto-optimal solution is found. Generating the full set of Pareto-optimal solutions depends on choosing a sufficiently small ϵ value to avoid skipping Pareto-optimal solutions, because an overly large ϵ value will cause the algorithm to bypass intermediate Pareto-optimal solutions.

Case Study

In this section, we present results from running the repairable infrastructure design algorithm on CCS infrastructure data collected by the CUSP project in the state of Nevada. The dataset consisted of 21 sources, 3 sinks, and 5,230 km of possible pipeline routes. The total annual emission amount in this dataset is 15.92 $MtCO_2$/yr. The total storage capacity in this dataset is 392.3 $MtCO_2$. Figure 19(a) shows the location of the sources (red vertices), sinks (blue vertices), and possible pipeline routes (purple edges). In this study, we selected the southernmost sink (indicated with the arrow) to be the sink that may fail. The repairable infrastructure design algorithm was implemented into the CCS infrastructure modeling tool SimCCS, which uses a MILP to concurrently determine cost-minimal capture, transport, and storage infrastructure. SimCCS also provides a standardized way to load, manipulate, and visualize CCS data. We replaced the SimCCS MILP core with the repairable infrastructure design algorithm but retained the data loading, manipulation, and visualization capabilities. An example of a solved CCS Infrastructure Design instance as viewed in SimCCS is shown in Figure 19(b).



(a) (b)

Figure 19 CCS data consisting of sources (circles), sinks (squares), and possible pipeline routes (edges). The arrow indicates the sink that fails in the evaluated scenario.

A scenario was run consisting of capturing 8 $MtCO_2$/yr for 20 years and identified sink number 2 (arrow in Figure 19) as the sink that may fail. This scenario was run on a machine with an 8-core Intel Core i9 processor running at 3.6 GHz, and 64 GB of RAM. SimCCS on this machine used IBM's CPLEX optimization tool, version 22.1.1.0. In an effort to quantify the practical computational efficiency of the proposed algorithm, 5 identical runs of the scenario were conducted and the running times were recorded for each iteration. The minimum, maximum, and average running times for each iteration is presented in Figure 20. Note that iteration 1 of the algorithm has a substantially lower running time because it is much less computationally expensive to solve the MILP from the CCS Modeling Background section on page 75 to find a single solution than it is to solve the MILPs from this section that each find 2 codependent solutions.

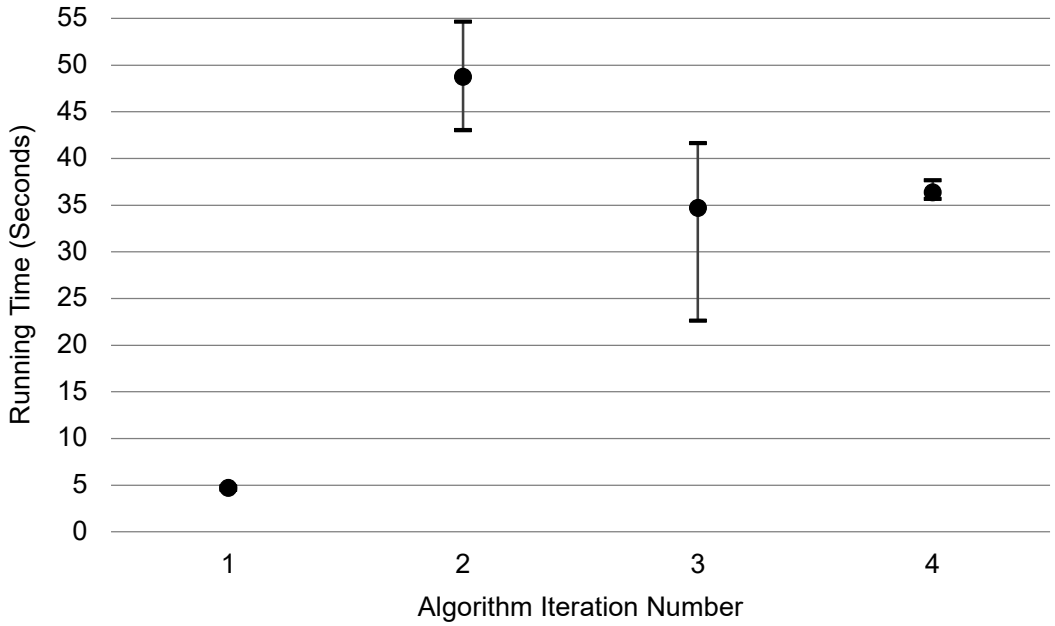


Figure 20 Minimum, maximum, and average running times for each iteration of the algorithm over 5 identical runs of the scenario

Figure 21 presents the transport cost of the initial and repaired solutions over the course of 4 iterations of the algorithm. Only the transport cost is shown because the capture cost is the same between initial and repaired solutions (due to the additional constraint) and the storage cost is the same because the dataset has identical storage costs for all storage locations. As designed, the initial solution for the first iteration is the minimum-cost flow on the network and its repaired solution is the repaired minimum-cost flow. The initial and repaired solutions of the final iteration are both the minimum-cost flow on the flow network with sink number 2 excluded. The initial and repaired solutions found in the intermediate iterations demonstrate a trade-off between increasing initial solution cost and decreasing repaired solution cost.

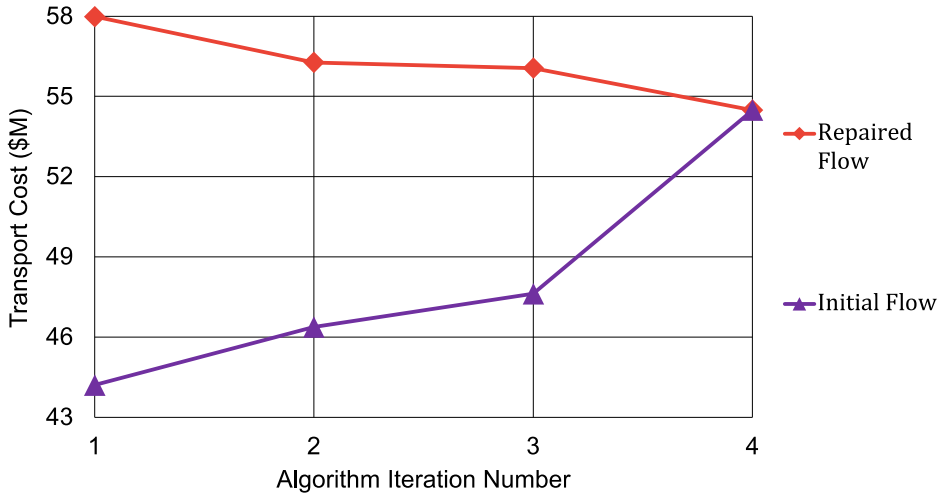


Figure 21 Progression of the initial and repaired solutions, over the course of the execution of the algorithm, from the minimum-cost flow (and its associated repaired solution) to minimum-cost flow on the network with sink number 2 excluded

Figure 22 presents the sequence of Pareto-optimal points, forming the Pareto front, between the initial solution transport cost and the repaired solution transport cost found by the algorithm for the scenario capturing 8 $MtCO_2/yr$ for 20 years. These solutions represent the options for optimal trade-offs between initial solution cost and repaired solution cost. These are the solutions that a decision-maker would take into account when determining the likelihood of the designated edge failing, the cost of such a failure, and their willingness to accept risk. This evaluation demonstrates the ability of our algorithm to identify the Pareto front in a relevant application with real-world data.

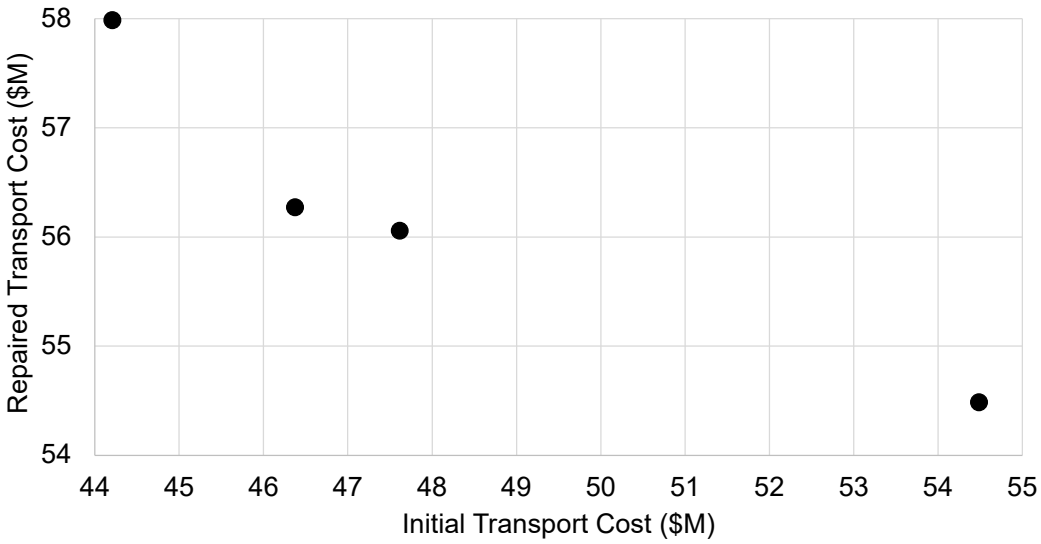


Figure 22 Pareto front between initial transport cost and repaired transport cost

Scalable Infrastructure Design

Solving CCS infrastructure design problems is fundamentally a computationally intractable problem. (Formally, it is an NP-hard optimization problem). CCS infrastructure design optimization is actually even NP-hard to approximate within the natural logarithm of the number of vertices in the graph. As such, finding optimal solutions to large instances is often computationally infeasible. The MILPs presented throughout this report are solvable with specialized software but do not scale to national-level CCS case studies. In this section, we introduce a novel GA to solve CCS infrastructure design problems (Eardley et al. 2025). The novel contribution of our GA is the representation of a flow solution by an array of parameters that scale the fixed costs for each edge in the network. This representation ensures that each array corresponds to a valid flow, thereby eliminating the need for computationally expensive repair functions that are required by other GAs for similar fixed-charge flow network problems. By avoiding costly repair functions, the proposed algorithm is able to efficiently find high-quality solutions to very large CCS infrastructure design problem instances. The proposed GA is inspired by slope scaling techniques previously used for the flow network problems. It is a *matheuristic*, in that it uses mathematical programming to calculate a flow solution from a linear program parameterized with the fixed-cost scaling arrays.

Non-Integer Linear Program

In this section, we introduce a linear program (LP) that is a modification of the MILP presented in the CCS Modeling Background section on page 75. Because it is an LP, this new formulation can be optimally solved in polynomial time. This LP forms the foundation of the GA discussed in later in this report. Two components of the integer linear program (ILP) are changed to turn it into an appropriate LP:

1) The binary decision variables s_i, r_j, and p_{kc} are removed, thereby turning the model into an LP. Because the binary variables are removed, the fixed costs are then scaled and combined with the variable costs.
2) New scaling parameters s_i^s, r_j^s, and p_{kc}^s are introduced for component that will scale the fixed cost of each entity. These parameters form the representation of a flow solution in the GA.

Let α_i, β_j, and δ_{kc} be the decision variable representing the amount of CO_2 processed by sources, sinks, and pipeline components, respectively, analogous to the a_i, b_j, and d_{kc} continuous decision variable in the MILP.

Then, the objective function of the LP is

$$\min \overbrace{\sum_{i\in S}\left(\frac{F_i^{src}}{s_i^s}+V_i^{src}\right)\alpha_i}^{capture\ cost}+\overbrace{\sum_{k\in P}\sum_{c\in C}\left(\frac{F_{kc}^{pipe}}{p_{kc}^s}+V_{kc}^{pipe}\right)\delta_{kc}}^{transport\ cost}+\overbrace{\sum_{j\in R}\left(\frac{F_j^{res}}{r_j^s}+V_j^{res}\right)\beta_j}^{storage\ cost}$$

The constraints in the LP mirror the constraints in the MILP:

$\delta_{kc} \le Q_{kc}^{\max}, \forall k \in P, \forall c \in C$	(Q)

$\sum_{\substack{k\in P:\\ src(k)=n}} \sum_{c\in C} \delta_{kc} - \sum_{\substack{k\in P:\\ dest(k)=n}} \sum_{c\in C} \delta_{kc} = \begin{cases} \alpha_n & \text{if } n \in S \\ -\beta_n & \text{if } n \in R, \forall n \in S \cup R \cup J \\ 0 & \text{if } n \in J \end{cases}$	(R)
$\alpha_i \leq Q_i^{src}, \forall i \in S$	(S)
$\beta_j \leq Q_j^{res}, \forall j \in R$	(T)
$\sum_{i\in S} \alpha_i \geq T$	(U)

The output of this LP is a value for each α_i, β_j, and δ_{kc}. Of course, the optimal flow found by the LP is likely not an optimal solution for the MILP. The true cost of the LP's solution can be determined by calculating its value when input into the MILP's objective function. This is first done by defining resource-use indicator functions s_i^z, r_j^z, and p_{kc}^z and assigning them values as follows:

$$s_i^z = \begin{cases} 1, if\ \alpha_i > 0 \\ 0, if\ \alpha_i = 0 \end{cases} \quad r_j^z = \begin{cases} 1, if\ \beta_j > 0 \\ 0, if\ \beta_j = 0 \end{cases} \quad p_{kc}^z = \begin{cases} 1, if\ \delta_{kc} > 0 \\ 0, if\ \delta_{kc} = 0 \end{cases}$$

This makes the true cost of the LP's solution equal to

$$\sum_{i\in S} (F_i^{src} s_i^z + V_i^{src} \alpha_i) + \sum_{k\in P} \sum_{c\in C} (F_{kc}^{pipe} p_{kc}^z + V_{kc}^{pipe} \delta_{kc}) + \sum_{j\in R} \left(F_j^{res} r_j^z + V_j^{res} \beta_j\right)$$

The GA described below works by varying the s_i^s, r_j^s, and p_{kc}^s scaling parameters and scoring the resulting optimal α_i, β_j, and δ_{kc} values found by this true cost equation.

Genetic Algorithm

GAs are a common evolutionary heuristic method used for searching and optimization. GAs manage a population of *organisms* that each correspond to a solution to the problem. The population evolves over iterations of the algorithm using evolutionary processes observed in nature including selection, crossover, and mutation operations. Selection is the process of deciding which organisms of the population continue into the next iteration (i.e., next generation). This is the mechanism that allows the algorithm to prioritize organisms that correspond to better solutions to the problem and control the size of the population. Crossover is the generation of a new organism from 2 existing organisms, analogous to biological reproduction. Similarly, mutation is the slight modification of an organism into a new one corresponding to a different solution. Crossover and mutation operations are the mechanisms that allow the algorithm to search for new, and possibly better, solutions.

A number of GAs have been developed to solve various versions of the fixed-charge flow network problem. In these algorithms, organisms are broadly represented as either individual edges or predefined routes through the network. Representing organisms as individual edges typically involves a binary variable for each edge indicating its availability for use. Alternatively, representing organisms as predefined routes involves a binary variable for each route in a set of

predefined routes through the network. In the case of the individual edge representation, generating the initial population, crossover operations, and mutation operations often requires repairing the organism, because random sets of edges are unlikely to result in valid flows. Using predefined routes simplifies repairing operations but may still require repair in the event of capacity constraint violations and is likely to result in suboptimal solutions due to the limited set of routing options. The GAs that use these representations address the issue by using computationally expensive repair functions to make organisms correspond to valid flows. Instead of representing an organism in this fashion, we represent it as an array of the fixed-cost scaling parameters s_i^s, r_j^s, and p_{kc}^s. Then, the solution corresponding to this organism is the set of solution values α_i, β_j, and δ_{kc} found by the LP described earlier. The result of this representation is that we can guarantee the solution corresponding to any organism is a valid flow, because the LP enforces that. This avoids costly repair functions and is the key to the efficiency of our approach.

The motivation for using the fixed-cost scaling parameters as the organism representation is that it allows control over the amount of fixed costs incurred and also removes the integer variables from the optimal MILP. As the scaling parameter decreases to 0, the scaled fixed cost increases to infinity, thereby dissuading selection of that edge by the LP. Conversely, as the scaling parameter increases to infinity, the scaled fixed cost approaches 0, thereby encouraging selection of that edge by the LP. The GA is tasked with searching for an organism of scaling parameters whose corresponding flow solution is as close to optimal for the MILP as possible. Given that the GA uses the fixed-cost scaling parameters as a proxy for a solution instead of directly using a solution, an important question is whether or not there exists a set of scaling parameters that yields an optimal flow solution. A proof that such a set of scaling parameters is guaranteed to exist is presented later in this report. The key components and workflow of the GA are described below.

Fitness Function

GAs use fitness functions to rank and compare the population of organisms to aid the selection process. Our fitness function first determines the solution for a given organism by solving the LP to get the α_i, β_j, and δ_{kc} solution values. After the α_i, β_j, and δ_{kc} values are determined, the solution's true cost in the context of the optimal ILP is calculated using the LP's true cost solution equation. This value is used as the fitness of the organism, where lower values correspond to higher fitness.

Selection Function

To keep the size of the population computationally manageable, a selection function is used to prune the population at each iteration. A selection function is also used to identify the organisms for crossover operations. Our GA implements a binary tournament selection function in an effort to prioritize high-fitness organisms while not ignoring all low-fitness organisms. In binary tournament selection, 2 random organisms are selected and the one with the higher fitness is kept while the other is discarded. This ensures that high-fitness organisms are likely to remain in the population while maintaining the possibility for low-fitness ones to survive as well. Binary tournament selection is repeated until the number of organisms in the population is at the desired size.

Crossover Function

A crossover function is used to generate a new child organism from 2 parent organisms already in the population. Our crossover function first randomly selects 2 parent organisms from the existing population. A child organism is constructed by taking a random interval of the scaling parameter array from the first parent, combined with the remaining values from the second parent.

Mutation Function

In order to mimic evolution and introduce another element of randomness into the search, a mutation function is used to further alter child organisms. After a child organism is generated with the crossover function, it may be randomly selected for mutation. During a mutation operation, a number of scaling parameter values in the organism are selected and, with equal probability, incremented either up or down a random amount between 0 and 1. Mutated scaling parameter values are not allowed to go below a lower bound to avoid negative values and divide-by-zero issues.

Genetic Algorithm

Using the functions described above, our algorithm operates as follows: First, an initial population of organisms is randomly generated. Each organism in the initial population is initialized as a scaling parameter array filled with a random value between $\epsilon > 0$ and the average value of the fixed costs in the input instance. After the initial population of organisms are created, the algorithm proceeds in an iterative fashion: At each iteration, the fitness of each organism is first calculated as described above. While the population size is less than some threshold, the crossover function is executed to generate child organisms. The child organisms are also subject to randomized mutations from the mutation function. Once the population has increased in size to the designated threshold, the selection function is run to reduce its size while statistically discarding the lower-fitness organisms. The algorithm keeps executing iterations until the running time reaches a designated time limit.

CPLEX Polishing

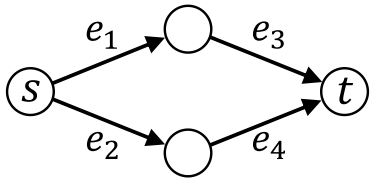
Once the time limit has been reached, the most fit organism's α_i, β_j, and δ_{kc} solution values are used as a warm start for IBM's CPLEX optimization software. CPLEX polishing is run for one-fifth of the total time limit, resulting in the final flow values returned by the algorithm.

Optimal Search Viability

The purpose of this section is to show that the GA is capable of finding the optimal solution of the ILP. This claim is not trivial, because the search space of the GA is the set of possible scaling parameter arrays, which are merely a proxy for solution values, the property we are actually optimizing for. The original motivation for formulating the LP and representing the organisms in the GA as scaling parameter arrays follows from the following false claim.

Claim: If each scaling parameter equals the optimal MILP solution value for that resource, then the optimal flow found by the resulting LP is also an optimal flow for the ILP.

The rationale for this claim is that if each scaling parameter and α_i, β_j, and δ_{kc} solution value both equal the optimal MILP flow values, then the cost of the LP's objective function will equal the optimal cost of the ILP's objective function. This claim is shown to be false with a simplified example in Figure 23 with only pipeline costs and capacities as fixed costs (a_e), variable costs (b_e), and capacities (c_e) and a capture target of 3. In this instance, the optimal ILP solution is to set the amount of flow on e_1 and e_3 to 2 and the amount of flow on e_2 and e_4 to 1 for a total cost of 20. Setting flow values for e_1 and e_3 to 2 and e_2 and e_4 to 1 yields the LP objective of minimizing $7\delta_{e_1} + 6\delta_{e_2}$. The optimal solution to this is to set the amount of flow on e_1 and e_3 to 1 and the amount of flow on e_2 and e_4 to 2 for a total cost of 21, thereby contradicting the claim.



	a_e	b_e	c_e
e_1	10	2	2
e_2	3	3	2
e_3	0	0	2
e_4	0	0	2

Figure 23 Counterexample to claim with only transportation costs and capacities having the displayed fixed costs (a_e), variable costs (b_e), and capacities (c_e) and a capture target of 3. In this instance, the optimal integer linear program solution is 20 with a flow of 2 units on e_1 and e_3 and 1 unit on e_2 and e_4. The corresponding optimal linear program solution is 21 with a flow of 1 unit on e_1 and e_3 and 2 units on e_2 and e_4.

Because the motivation claim is false, along with the fact that the scaling parameter arrays are only proxies for the flow value solutions we seek, it remains to be shown that there actually exists a set of scaling parameter values that will result in the GA finding optimal flow values for the ILP.

$s_i \in \{0, 1\}$	Indicates if source i is opened
$a_i \in \mathbb{R}^{\geq 0}$	Annual amount of CO_2 captured from source i ($MtCO_2$/yr)
$r_j \in \{0, 1\}$	Indicates if reservoir j is opened
$b_j \in \mathbb{R}^{\geq 0}$	Annual amount of CO_2 injected into reservoir j ($MtCO_2$/yr)
$p_{kc} \in \{0, 1\}$	Indicates if pipeline k with capacity c is opened
$d_{kc} \in \mathbb{R}^{\geq 0}$	Annual amount of CO_2 put in pipeline k with capacity c ($MtCO_2$/yr)

Theorem: For every problem instance, there exists a set of scaling parameter values such that the optimal flow found by the resulting LP is also an optimal flow for the ILP.

Proof: Without loss of generality, consider only a flow network with edge costs and capacities. This does not influence the conclusion in general since any CCS infrastructure modeling instance

can be represented as a network with only edge costs and capacities. Let d_{kc}^{opt} be the optimal flow values found by the MILP and define the set of p_{kc}^{s} scaling parameter values as follows:

$$p_{kc}^{s} = \begin{cases} \epsilon > 0, if\ d_{kc}^{opt} = 0 \\ \infty, \quad if\ d_{kc}^{opt} > 0 \end{cases}$$

When p_{kc}^{s} is set to an ϵ -value near 0, the scaled fixed cost F_{kc}^{pipe}/p_{kc}^{s} makes those edges prohibitively expensive to include in LP solutions, so long as valid solutions exist that do not use those edges (such as the valid solution d_{kc}^{opt}). Likewise, if p_{kc}^{s} is set to a very large value, the scaled fixed cost is near 0. These p_{kc}^{s} values effectively restrict the LP to selecting only the edges and capacities with nonzero δ_{kc}^{opt} values.

Suppose that $H \subseteq P \times C$ is the set of edge-capacity pairs where p_{kc}^{opt} equals 1. Then, given the p_{kc}^{s} values resulting from above, the objective for the LP becomes

$$\sum_{k\in P}\sum_{c\in C}\left(\frac{F_{kc}^{pipe}}{p_{kc}^{s}} + V_{kc}^{pipe}\right)\delta_{kc} = \sum_{kc\in H} V_{kc}^{pipe}\delta_{kc}$$

Let δ_{kc}^{opt} be optimal flow values to the LP. We aim to show that δ_{kc}^{opt} is also an optimal flow for the MILP. First, δ_{kc}^{opt} is a valid solution to the MILP, because δ_{kc}^{opt} is a valid flow of the MILP's target value on an identical graph with the same capacities. Showing that δ_{kc}^{opt} is optimal for the ILP can be accomplished by using δ_{kc}^{opt} to feed the definitions for p_{kc}^{z} and showing that

$$\sum_{k\in P}\sum_{c\in C}\left(F_{kc}^{pipe}p_{kc}^{z-opt} + V_{kc}^{pipe}\delta_{kc}^{opt}\right) = \sum_{k\in P}\sum_{c\in C}\left(F_{kc}^{pipe}p_{kc}^{opt} + V_{kc}^{pipe}d_{kc}^{opt}\right)$$

p_{kc}^{z-opt} must equal 1 for all edges in H. If p_{kc}^{z-opt} equals 0 for some edge in H, then the fixed costs incurred by δ_{kc}^{opt} are lower than the fixed costs incurred by d_{kc}^{opt}. Also, because δ_{kc}^{opt} is optimal for the LP,

$$\sum_{kc\in H} V_{kc}^{pipe}\delta_{kc}^{opt} \leq \sum_{kc\in H} V_{kc}^{pipe}d_{kc}^{opt}$$

Therefore, if p_{kc}^{z-opt} equals 0 for some edge in H, δ_{kc}^{opt} is a lower cost flow for the ILP than the optimal d_{kc}^{opt}, which is a contradiction. Therefore, d_{kc}^{opt} and δ_{kc}^{opt} must incur identical fixed costs and p_{kc}^{z-opt} must equal 1 for all edges in H.

Suppose that,

$$\sum_{kc\in H} V_{kc}^{pipe}\delta_{kc}^{opt} < \sum_{kc\in H} V_{kc}^{pipe}d_{kc}^{opt}$$

This implies that,

$$\sum_{kc\in H} F_{kc}^{pipe} + \sum_{kc\in H} V_{kc}^{pipe}\delta_{kc}^{opt} < \sum_{kc\in H} F_{kc}^{pipe} + \sum_{kc\in H} V_{kc}^{pipe}d_{kc}^{opt}$$

$$\Rightarrow \sum_{kc \in H} \left(F_{kc}^{pipe} + V_{kc}^{pipe} \delta_{kc}^{opt}\right) < \sum_{kc \in H} \left(F_{kc}^{pipe} + V_{kc}^{pipe} d_{kc}^{opt}\right)$$

$$\Rightarrow \sum_{k \in K} \sum_{c \in C} \left(F_{kc}^{pipe} p_{kc}^{z-opt} + V_{kc}^{pipe} \delta_{kc}^{opt}\right) < \sum_{k \in K} \sum_{c \in C} \left(F_{kc}^{pipe} p_{kc}^{opt} + V_{kc}^{pipe} d_{kc}^{opt}\right)$$

which is a contradiction, because d_{kc}^{opt} is an optimal flow value for the ILP and therefore cannot be more expensive than the valid flow δ_{kc}^{opt}. Therefore,

$$\sum_{kc \in H} V_{kc}^{pipe} \delta_{kc}^{opt} = \sum_{kc \in H} V_{kc}^{pipe} d_{kc}^{opt}$$

which implies that,

$$\sum_{k \in K} \sum_{c \in C} \left(F_{kc}^{pipe} p_{kc}^{z-opt} + V_{kc}^{pipe} \delta_{kc}^{opt}\right) = \sum_{k \in K} \sum_{c \in C} \left(F_{kc}^{pipe} p_{kc}^{opt} + V_{kc}^{pipe} d_{kc}^{opt}\right)$$

Therefore, defining the p_{kc}^{s} values as above yields an LP whose optimal flow values correspond to optimal flow values of the ILP.

Case Study

To demonstrate the efficiency and effectiveness of the GA, an evaluation was conducted using CCS data collected as part of the CUSP effort. The GA was implemented and integrated into SimCCS. Initial performance simulations guided the parameterization of the GA to have a population size of 10 and mutation and crossover probability of both 50%. A mutation probability of 50% means that each organism has a 50% chance of mutation, and a crossover probability of 50% means that 50% of the population (without organism repetition) is crossed over with a random other organism in each iteration of the GA. All reported GA values are the average of 3 runs. The optimal MILP from the CCS Modeling Background section on page 75 was implemented in SimCCS using CPLEX as well. SimCCS was used as a standardized way to represent CCS data and for problem and solution visualization. Timing was coded directly into SimCCS to ensure only the algorithm of interest was being timed during simulation. Simulations were run on a machine with Ubuntu 20.04.5, an Intel Xeon W-2255 processor running at 3.7 GHz, and 64 GB of RAM. SimCCS on this machine used IBM's CPLEX optimization tool, version 22.1.1.0.

The GA was tested on 2 CCS infrastructure design datasets. The first dataset covers the state of California and consists of 190 sources with a total annual emission rate of 88.3 $MtCO_2$/yr, 102 sinks with a total lifetime storage capacity of 37.18 $GtCO_2$, and 1,188 possible pipeline components (i.e., edges in the graph) with a total length of 17,940.88 km and 11 possible capacities on each edge. A map of this dataset is presented in Figure 24.

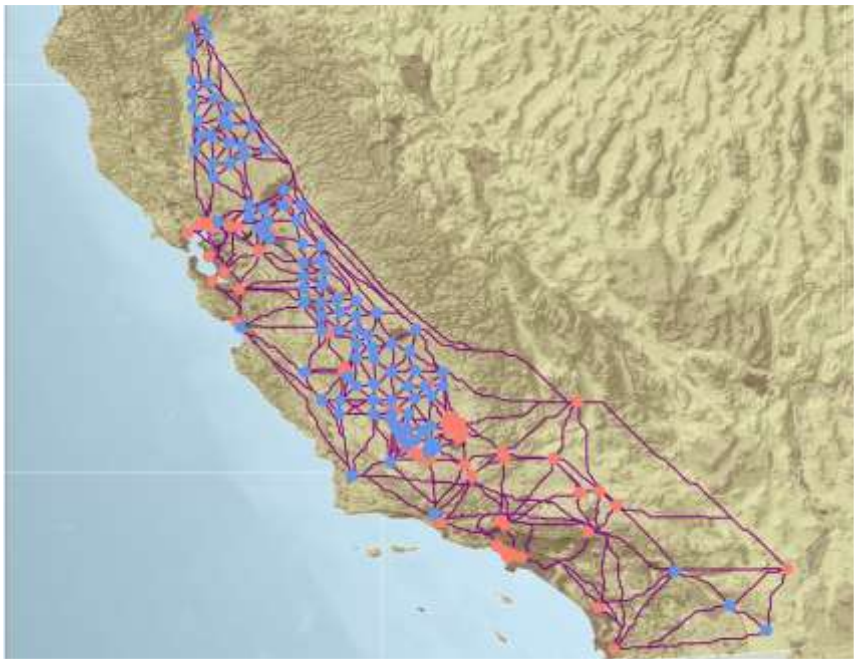


Figure 24 CCS dataset for the state of California consisting of sources (red), sinks (blue), and possible pipeline routes

The second dataset covers the contiguous United States and consists of 2,746 sources with a total annual emission rate of 532.61 $MtCO_2$/yr, 1,202 sinks with a total lifetime storage capacity of 2,691.86 $GtCO_2$, and 22,597 possible pipeline components with a total length of 424,674.41 km and 11 possible capacities on each edge. This data was collected by Carbon Solutions apart from the CUSP project as part of a study conducted by the Clean Air Task Force (Boston, MA). Storage data was generated using the SCO_2T geologic sequestration tool (Carbon Solutions 2025b). A map of this dataset is presented in Figure 25.

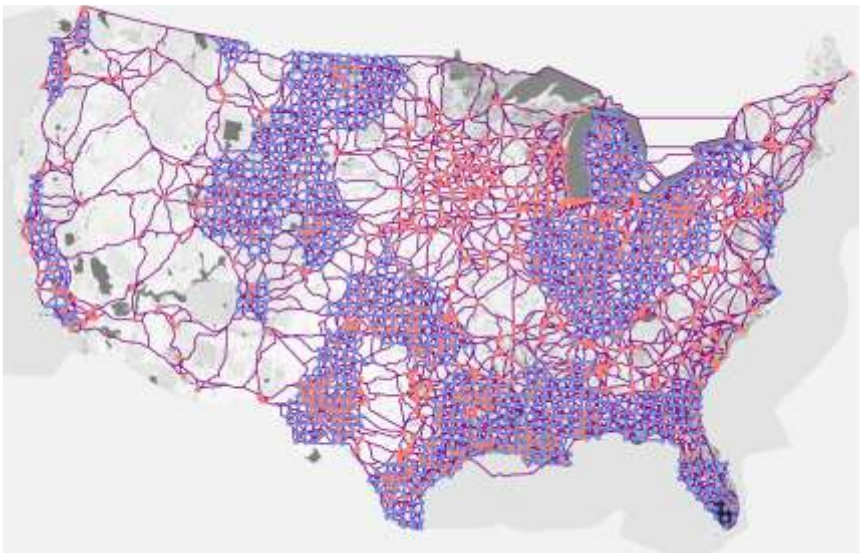


Figure 25 CCS dataset for the contiguous United States consisting of sources (red), sinks (blue), and possible pipeline routes

Candidate pipeline routes were generated in SimCCS using its candidate network generation algorithms. The National Energy Technology Laboratory's CO_2 Transport Cost Model (NETL 2023) was used by SimCCS to determine fixed construction and variable utilization costs for the 11 discrete pipeline capacity options.

To assess the efficiency of the GA, its solution cost was compared with the solution cost found by CPLEX solving the optimal ILP, with both methods being allowed to run for set running time periods. For the California dataset, those running time periods were 0.5, 1, 2, 4, and 8 hours. The target flow amount (T) was set to 80 $MtCO_2$/yr for all of the California scenarios. For the contiguous United States dataset, the running time periods were 0.5, 1, 2, 4, 8, and 16 hours. The target flow amount was set to 500 $MtCO_2$/yr for the contiguous United States scenarios. Figure 26(a) presents each algorithm's solution cost over the running time periods for the California dataset, and Figure 26(b) presents the same results for the contiguous United States dataset. The cost of the best solution found by the GA in the California dataset was within 0.5% of the ILP's solution across all running times. Conversely, the cost of the best solution found by the GA in the contiguous United States dataset was 17% lower than the ILP's solution after 1 hour, 7% lower after 4 hours, and 2% lower after 16 hours. This suggests that the GA may have utility for very large problem instances. The utility for small instances is likely limited, due to the speed of CPLEX.

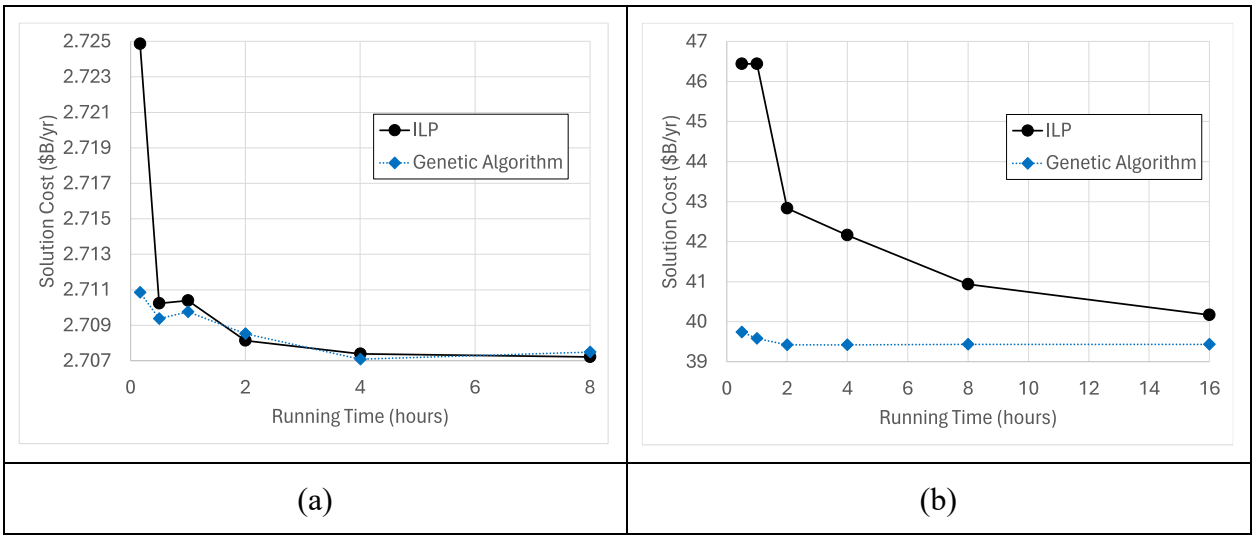


Figure 26 Solution cost versus running time for the genetic algorithm and optimal integer linear program (ILP) on (a) the California dataset and (b) the contiguous United States dataset

Problem solvability is related to not only instance size but also the amount of target flow being found. To identify the impact that target flow amount has on solution quality, scenarios were run on the contiguous United States dataset in which the target flow amount was varied from 1 to 532 $MtCO_2$/yr. The maximum annual capturable amount of CO_2 for this dataset is 532.61 $MtCO_2$/yr. Each algorithm was given 2 hours to solve each scenario. Figure 27 presents each algorithm's solution cost for the various target flow amounts. Table 6 presents the specific solution cost values and the percent improvement of the GA's solution over the ILP's solution. Other than in very low and high target flow amount scenarios, the GA was fairly consistent in its improvement over the ILP. Interestingly, in the low target flow amount scenario, the GA performed the best relative to the ILP. This suggests that the GA could have utility in a very

large problem instance, even if the target flow amount is quite small. This is likely a realistic scenario, where a relatively small target is sought amongst a very large space of options that provides a compelling argument for the utility of the GA.

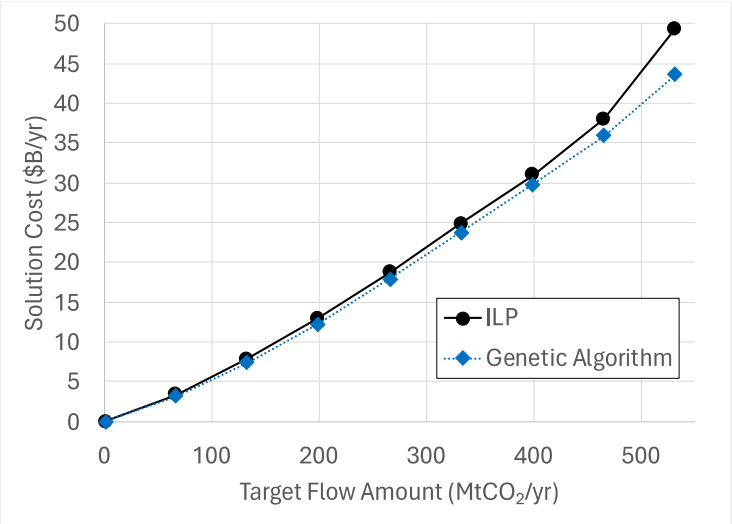


Figure 27 Solution cost versus target flow amount for the genetic algorithm and optimal integer linear program (ILP). Specific solution cost values are presented in Table 6.

Table 6 Solution values with varying flow targets

Target flow amount	MILP*	Genetic algorithm	Precent improvement
1.00	0.04	0.03	25.00
66.50	3.35	3.22	3.88
133.00	7.84	7.41	5.48
199.50	13.00	12.25	5.77
266.00	18.78	17.94	4.47
332.50	24.84	23.77	4.31
399.00	31.06	29.86	3.86
465.50	38.05	35.98	5.44
532.00	49.44	43.58	11.65

*MILP = mixed-integer linear program

Project Findings and Conclusions

This focused project demonstrated that accounting for uncertainty in CCS infrastructure planning fundamentally changes both the design process and the resulting networks. Rather than producing a single deterministic solution, our methods generate a family of risk-informed solutions that allow decision-makers to weigh cost, throughput, and resilience in a transparent, quantitative way.

Designing to Resist Failure

The first major outcome of this project was a scenario-based design framework that identifies core CCS infrastructure that remains valuable under a wide range of storage performance assumptions. By generating hundreds of Monte Carlo scenarios of storage capacities and solving a MILP for each, we were able to construct a heatmap that shows how frequently each pipeline, source, and storage site appears across all optimal designs. This allows stakeholders to focus on building the "backbone" network components that are robust to uncertainty and to phase in less certain laterals as confidence grows.

The introduction of the risk index parameter proved to be especially valuable. It allows planners to tune their desired level of robustness—for example, selecting only components present in 100% of scenario solutions for a zero-risk design or relaxing to 85% commonality to unlock more throughput at the expense of some risk. In the California case study, tightening risk tolerance from 15% to 0% resulted in an 83.7% reduction in total processing capacity and a 77.1% drop in profit, revealing sharp breakpoints where small changes in risk tolerance had large impacts on system behavior. These inflection points are natural candidates for decision-making, because they balance the cost of robustness with the benefits of increased CO_2 processing.

This result advances CUSP's mission by showing that robust infrastructure planning can prevent costly overbuilding and minimize the risk of stranded assets. It also provides DOE stakeholders with a reproducible process to quantify the cost of uncertainty itself, something that has been difficult to capture in traditional deterministic planning models.

Designing to Be Repairable

The second major contribution reframed uncertainty planning as explicitly preparing for component failure. Rather than assuming that a single network design is sufficient, we developed an approach that pairs an initial design (assuming a critical component survives) with a repaired design (if it fails after construction). The result is a Pareto frontier of trade-offs between minimizing upfront construction costs and minimizing the cost of network repair in the failure scenario.

Our results on the Nevada dataset show that a purely least-cost initial design often leaves the system highly exposed to failure, with expensive repairs required to maintain throughput. Moving along the Pareto frontier reveals designs that slightly increase initial cost—for example, by prebuilding redundant pipeline capacity—but dramatically reduce the cost of repair. This gives decision-makers a clear, quantitative way to "buy insurance" against failure by overbuilding where it is economically justified.

This approach has 2 key benefits for the CUSP region:

- It empowers stakeholders to make risk-informed investment decisions, explicitly balancing capital efficiency against resilience.
- It enables planners to price resilience at the time of initial investment, rather than discovering repair costs only after a failure has occurred.

Scaling to Large Problems

The third component addressed a practical barrier to widespread adoption of these methods: computational scale. Scenario-based planning multiplies the number of optimization problems that must be solved, and deterministic MILP solvers quickly become intractable at the regional or national scale. To address this, we developed a GA for the CCS infrastructure design problem that guarantees each candidate solution is a valid network configuration. This avoids expensive repair functions and allows for much faster exploration of the design space.

In tests on the California and United States datasets, the GA produced solutions within 0.5% of MILP optimality for state-scale problems and actually outperformed MILP under time-limited conditions on the national-scale network (by up to 17%). This demonstrates that national-scale uncertainty studies are computationally feasible, paving the way for planning studies that support DOE's long-term vision for a national CO_2 transport network.

Overall Conclusions

Together, these 3 contributions form a complete toolkit for planning CCS infrastructure amidst uncertainty:

- a process to design CCS infrastructure that resists failure by building backbone infrastructure that is robust across many plausible futures.
- a process to plan for repair of CCS infrastructure by explicitly modeling potential failures and quantifying the cost of mitigation.
- a process to solve massive CCS infrastructure design scenarios to make regional and national uncertainty analysis tractable.

These findings directly support CUSP's goal of accelerating commercial CCS deployment by providing stakeholders with tools that

- quantify risk and make it an explicit part of the design process,
- support phased investment strategies that match capital outlay to increasing certainty over time,
- improve bankability by giving financiers and project developers confidence that designs remain viable even under adverse conditions, and
- advance technology transfer through integration with the open-source SimCCS platform.

In sum, this project delivered not only new theory and algorithms but also practical, field-ready tools that will improve the resiliency, efficiency, and scalability of CCS infrastructure planning across the CUSP region and beyond.

References

Carbon Solutions LLC. 2025a. CostMAP^{PRO} [software]. Saint Paul (MN); Carbon Solutions LLC. [accessed 2025 Nov 20]. https://www.carbonsolutionsllc.com/software/costmappro/.

Carbon Solutions LLC. 2025b. SCO_2T^{PRO} [software]. Saint Paul (MN); Carbon Solutions LLC. [accessed 2025 Dec 30]. https://www.carbonsolutionsllc.com/software/sco2tpro/.

Credit for Carbon Oxide Sequestration, U.S.C.-2023 26 C.F.R. §1.45Q-1 (2021).

Eardley C, Gomez D, Dupuis R, Papadopoulos M, Yaw S. 2025. A genetic algorithm for multi-capacity fixed-charge flow network design. In: Sauer J, Schmidt M, editors. 25th Symposium on Algorithmic Approaches for Transportation Modelling, Optimization, and Systems (ATMOS 2025). Open Access Ser Inform. 137:10:1–10:14. Dagstuhl (Germany): Schloss Dagstuhl–Leibniz-Zentrum für Informatik. doi:10.4230/OASIcs.ATMOS.2025.10

Gurobi Optimization LLC. 2026. Gurobi Optimizer [software] [Internet]. Beaverton (OR): Gurobi Optimization LLC. [accessed 2026 Jan 14]. https://www.gurobi.com/.

IBM. 2025. IBM ILOG CPLEX Optimization Studio [software] [Internet]. Armonk (NY): IBM. [accessed 2025 Nov 20]. https://www.ibm.com/products/ilog-cplex-optimization-studio.

[LANL] Los Alamos National Laboratory. 2026. SimCCS platform [software] [Internet]. Los Alamos (NM): Los Alamos National Laboratory. [accessed 2026 Jan 14]. https://github.com/simccs/SimCCS.

Middleton RS, Chen B, Harp DR, Kammer RM, Ogland-Hand JD, Bielicki JM, Clarens AF, Currier RP, Ellett KM, Hoover BA, et al. 2020. Great SCO2T! Rapid tool for carbon sequestration science, engineering, and economics. Appl Comput Geosci. 7:100035. doi:10.1016/j.acags.2020.100035

Middleton RS, Yaw SP, Hoover BA, Ellett KM. 2020b. SimCCS: An open-source tool for optimizing CO_2 capture, transport, and storage infrastructure. Environ Model Softw. 124:104560. doi:10.1016/j.envsoft.2019.104560

[NETL] National Energy Technology Laboratory. 2023. NETL releases updated version of CO2_T_COM transport cost model [Internet]. [accessed 2026 Jan 14]. https://netl.doe.gov/node/12859

Olson D, Yaw S. 2025. Planning amidst uncertainty: identifying core CCS infrastructure robust to storage uncertainty. Energies. 18(4):926. doi:10.3390/en18040926

Laboratory Feasibility Study for Eventual Field Deployment of a Downhole Source Tomographic Design for CO_2 Plume Detection

We proposed a new technology for CO_2 plume detection wherein a seismic emitter will be placed beneath the plume and tomography will be performed with stations at the surface (Figure 28). This design has six hypothesized advantages over the present state-of-the-art of CO_2 plume tomographic detection, which typically only images the plume in a 2D sense at either a single time or infrequently (Ajo-Franklin et al. 2013; Gunning et al. 2020; Hu et al. 2017) and only augments the numerical modeling of the plume (Pruess et al. 2001; Pham et al. 2011). The first advantage of this technology is the inherent time-lapse nature wherein the operator would be able to image the plume at essentially any time they choose. The second significant advantage is the 3D nature of the design. So long as the surface stations are placed with sufficient coverage above the expected extent of the plume (and they can be moved in the middle of monitoring), then the plume can be imaged with accuracy throughout its full volumetric extent. The third advantage is that the tomography will be performed with direct waves rather than reflected waves, which increases the amplitude and reduces the uncertainty. Fourth, by placing the emitter in the

borehole rather than using a surface source, the frequency content of the emitted wavelet can be significantly higher, which will allow for greater tomographic resolution. Such resolution could potentially offer the ability to detect leakage of supercritical carbon dioxide through the caprock should that be the case. Fifth, the source is frequency swept, which allows for correlation-based processing that offers a much higher dynamic range for imaging the system. Finally, the tomographic image can be improved by moving the source to different locations within the monitoring wellbore to gather from different source points.

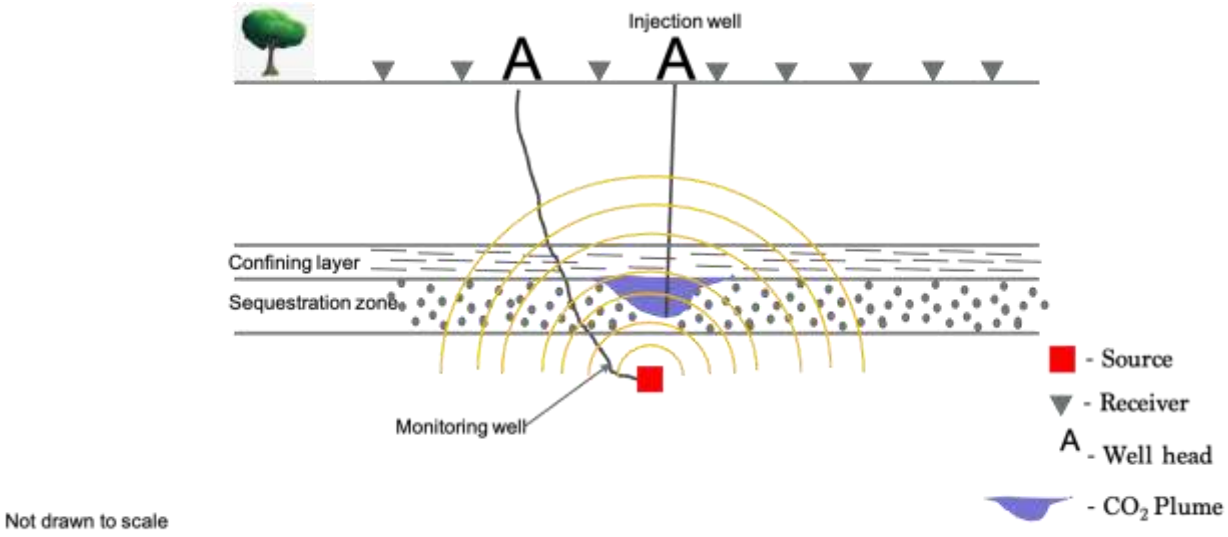


Figure 28 Proposed design of the downhole source tomographic technology to enhance the CO_2 plume migration detection

Final Report

The project team designed a laboratory-scale experiment to simulate the potential implementation of the Downhole Source Tomography technology. The proposed experiment will be conducted in a 1m x 1m x 1m cube of sandstone (Figure 29). There will be two sandstone blocks separated by a thin, impermeable epoxy seal. The bottom block will host the plume of supercritical carbon dioxide and simulate the reservoir in a deep saline sequestration project. The epoxy seal will simulate the caprock, and the upper block of sandstone will simulate the formations above the sequestration target. A single perforation will be placed into the epoxy seal at a distance of 20 cm away from the center of the cube (Figure 30). Supercritical carbon dioxide injection will take place in a “wellbore” in the center of the block completed such that carbon dioxide only goes into the bottom, reservoir block. Injection will take place for four hours at 0.01 kg/s. The rate is chosen to allow for the carbon dioxide fully to percolate through the system, including the leak, in a reasonable timeframe without risking hydraulically fracturing the sample.



Figure 29 A schematic of the sandstone cube that will host the experiment. The gray circles represent the sensors that will be placed on the sample.

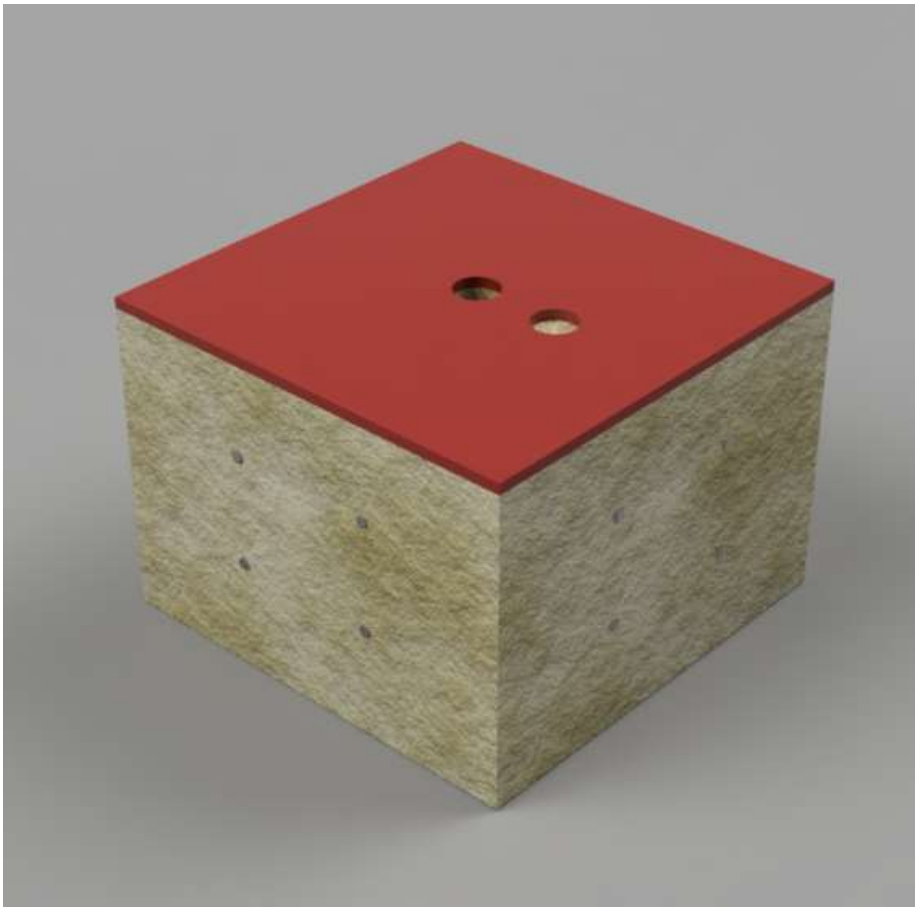


Figure 30 The perforated epoxy seal that simulates a leaky wellbore

Quotes to perform these experiments were obtained from Sandia National Laboratory and Schlumberger's Geomechanics Laboratory in Houston, TX. Sandia quoted roughly $500,000 and Schlumberger quoted about $180,000, but $45,000 of that is for sample preparation, which we have assessed will cost roughly $8,000 for the project team to perform, reducing the price to $143,000. We estimate that the Schlumberger experiment will be sufficient for the project needs. In addition to the cost of the geomechanics laboratory, the project team will also have to rent specialized sensors that can detect with a sampling frequency of at least 200 kHz. These custom sensors have been estimated to cost about $70,000. Another option at a similar price is the use of a distributed fiber optic cable that will allow for a greater spatial resolution of the experiment, but this both moves the design further from an analog of the field scale experiment, and it would be challenging to wind the cable around the sample without interfering with the true triaxial load frame. Thus, the project team has elected to use the custom transducers and Schlumberger load frame.

Two versions of numerical simulations were performed. First, we used TOUGH2 code to simulate fluid flow in the experimental apparatus. This encapsulates the flow through the bottom, reservoir rock as well as flow through the perforated epoxy seal (Figure 31). These results show that the plume of supercritical carbon dioxide occupies the reservoir rock with relatively high concentrations of carbon dioxide, and a lower concentration plume escapes into the upper, country rock. The second numerical simulation is the tomography based on the placement of the

sensors (Figure 32) and the output of the fluid flow simulations. These results demonstrate a large difference in the *P*-wave velocity as a function of the injection of the carbon dioxide. Furthermore, the smaller plume through the perforation is detectable through the tomography, which lends credence to both the ability to detect a plume and a leak with this technology. It should be noted, however, that the synthetic data in these simulations do not contain noise.

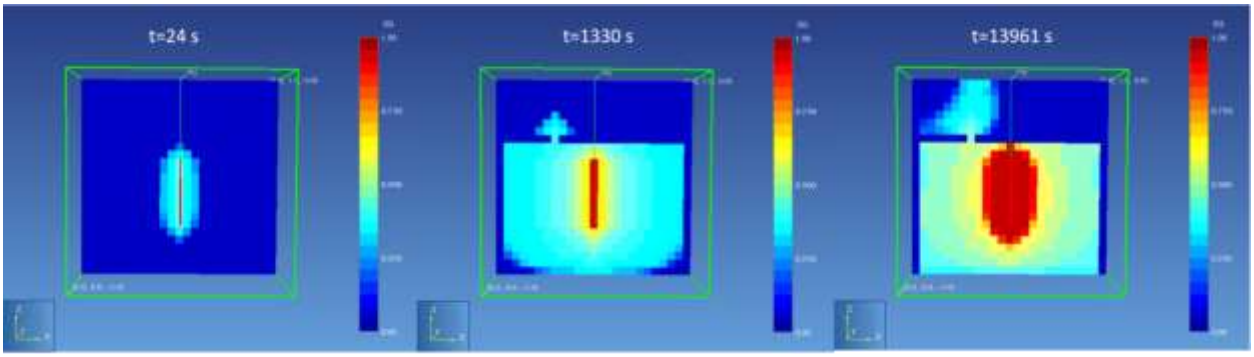


Figure 31 Numerical results of the first experiment, which show the plume hitting the seal and the one location of leakage through the perforation. The colors represent gas saturation.

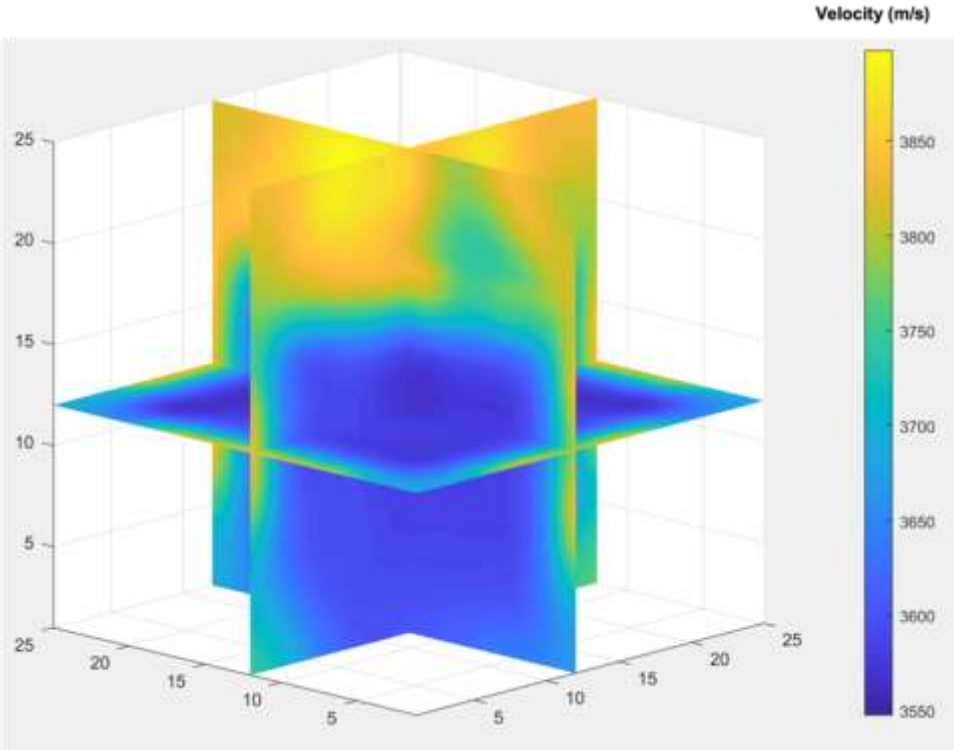


Figure 32 Tomography results after 4 hours of injection. The color bar represents *P*-wave velocity.

There will be two experiments. One with brine in the pore space of the lower block, and one with oil in the pore space of the lower block. In the first experiment, we can easily release the carbon dioxide by bringing the sample to atmospheric conditions. This will allow the carbon dioxide to leak out of the pore space, and then the experiment can be conducted again. We anticipate that each experiment will take roughly one day, and so we will repeat the experiments from Monday

to Thursday. On Friday, we will switch to the second experiment, which given our inability to withdraw the oil, cannot be repeated. By occupying one week with these experiments, we hope to optimize productivity and minimize costs.

One important consideration for the project is scale effects. A laboratory experiment objective is to replicate a plume that spans several kilometers in a real-world scenario, but it's important to account for any differences that may arise from downsizing. Although there may be variations in the length of migration and the complexity of the structure between the two scales, the response of the medium to tomography is similar. As a result, the path taken by the plume during migration may not be a representation of the field scale, but measurements of seismic body wave velocities through the medium apply to both scales, with two possible exceptions. Firstly, frequencies of seismic waves in the lab are much higher, which may cause dispersion effects. Secondly, detectors may be positioned at regular, specific intervals around the plume in the lab, but in the field, surface stations and geophones in legacy boreholes are locations of opportunity, and therefore almost always irregularly spaced. Such disparities mean the lab experiments are not directly comparable to the full design. However, we may still use the lab results to interpret whether the field-based technology may be feasible.

In summary, we successfully designed experiments that will achieve four separate results. First, we want to detect the extent of the plume throughout the duration of the experiment. Second, we want to detect the carbon dioxide leaking through the perforation in the epoxy. Third, we want to passively detect the plume with acoustic emissions, which is something that has been seen in triaxial experiments as the pore pressure changes. It would be novel if we could demonstrate and differentiate acoustic emissions associated both with the pore pressure front and with the sCO_2 plume. And fourth, we want to demonstrate the ability of our tomographic technique to distinguish between brine, sCO_2, and oil in the EOR experiment. These laboratory experiments will allow for the assessment of the downhole source tomography technology as a viable means of monitoring CO_2 plumes in the subsurface.

A funding application has been written and submitted to the Unsolicited Proposal program at the National Energy Technology Laboratory. They declined to provide additional funds.

For more perspective on our designs, please see our American Rock Mechanics Association paper (McCormack et al. 2023).

References

Ajo-Franklin JB, Peterson J, Doetsch J, Daley TM. 2013. High-resolution characterization of a CO_2 plume using crosswell seismic tomography: Cranfield, Mississippi, USA. Int J Greenh Gas Control. 18:497–509. doi:10.1016/j.ijggc.2012.12.018

Gunning J, Jackson S, Pevzner R, Barraclough P, Jenkins C. 2023. Tracking CO_2 plumes via time-lapse pressure tomography. In: Proceedings of the 84th EAGE Annual Conference & Exhibition; 2023 Jun; Vienna (Austria). p. 1–5.

Hu L, Doetsch J, Brauchler R, Bayer P. 2017. Characterizing CO_2 plumes in deep saline formations: comparison and joint evaluation of time-lapse pressure and seismic tomography. Geophysics. 82(4):ID1–ID18. doi:10.1190/geo2016-0365.1

McCormack KL, Edelman E, Moodie N, McPherson BJ, Paulsson B, He R. 2023. The design of a downhole source tomography experiment for the detection of CO_2 plumes in the subsurface. Paper presented at: U.S. Rock Mechanics/Geomechanics Symposium (ARMA); 2023 Jun; Atlanta (GA).

Pruess K, Tsang CF, Law DHS, Oldenburg CM. 2001. An intercomparison study of simulation models for geologic sequestration of CO_2. In: Proceedings of the First National Conference on Carbon Sequestration; 2001 May; Washington (DC). Berkeley (CA); Lawrence Berkeley National Laboratory.

Pham THV, Maast TE, Hellevang H, Aagaard P. 2011. Numerical modeling including hysteresis properties for CO_2 storage in Tubåen Formation, Snøhvit Field, Barents Sea. Energy Procedia. 4:3746–3753.

Site Characterization for CO_2 Storage to Support Escalante Hydrogen Power Plant Project

Within Rio Arriba County, New Mexico, the Entrada Sandstone is both an oil reservoir, a salt water disposal target, and a potential CO_2 injection target. Since the oil reservoirs have been mostly played out, new life for the reservoir is a target for CO_2 sequestration. A potential source of the CO_2 is from the potential retrofitting "Blue Hydrogen" Escalante Power Plant (**Figure 33**). The plant will create hydrogen from natural gas while sequestering 97% of its CO_2 emissions.

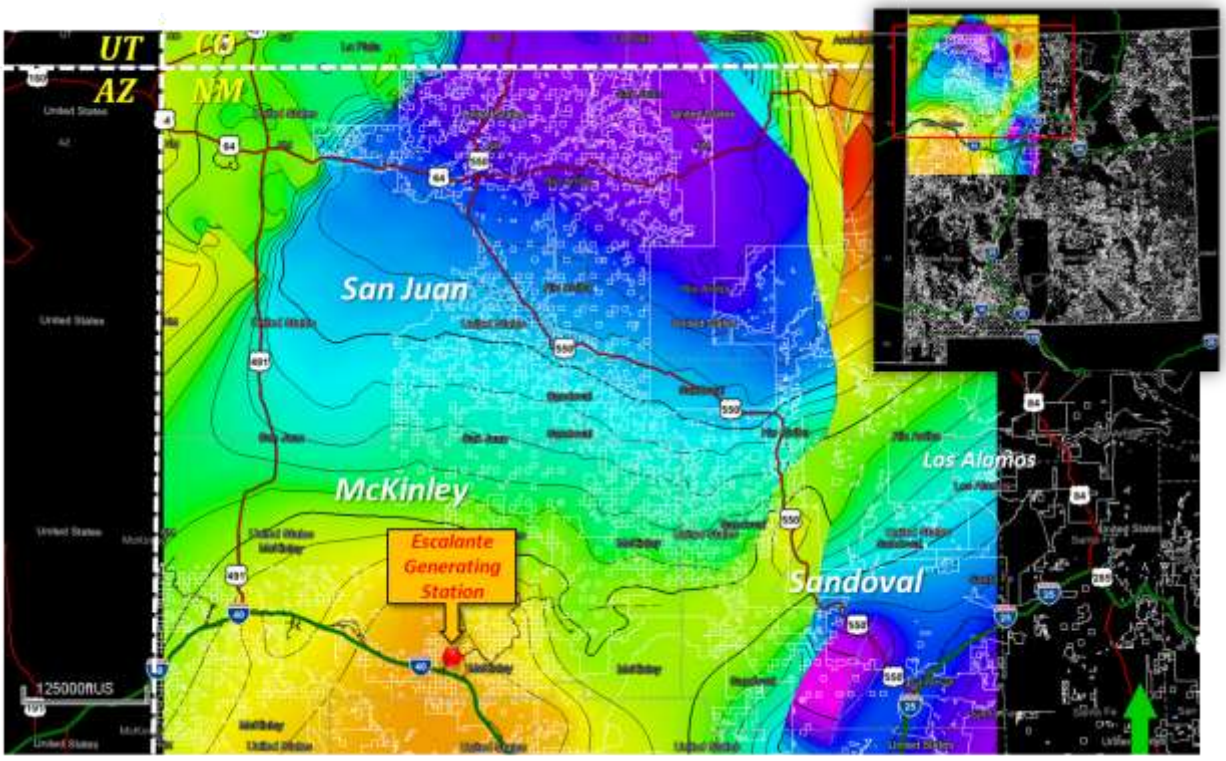


Figure 33. Subsea structure map on the Entrada Sandstone for the San Juan Basin showing the location of the Escalante Power Station.

Geologic Model

The primary reservoir identified in the area is the Jurassic Entrada Sandstone (**Figure 34**). The Entrada Sandstone is a large eolian sand erg that covers the northwestern part of New Mexico. It consists of very fine- to medium-grained sandstones that are composed of quartz and subordinate feldspars and lithic rock fragments. Potential secondary reservoirs include the Jurassic Bluff Sandstone, another eolian deposit, and the Salt Wash Member of the Morrison Formation. Bluff deposits are like the Entrada Sandstone, but they may have undergone more extensive cementation. The Salt Wash deposits consist of alluvial fan and plain sediments associated with widespread, braided stream complexes.

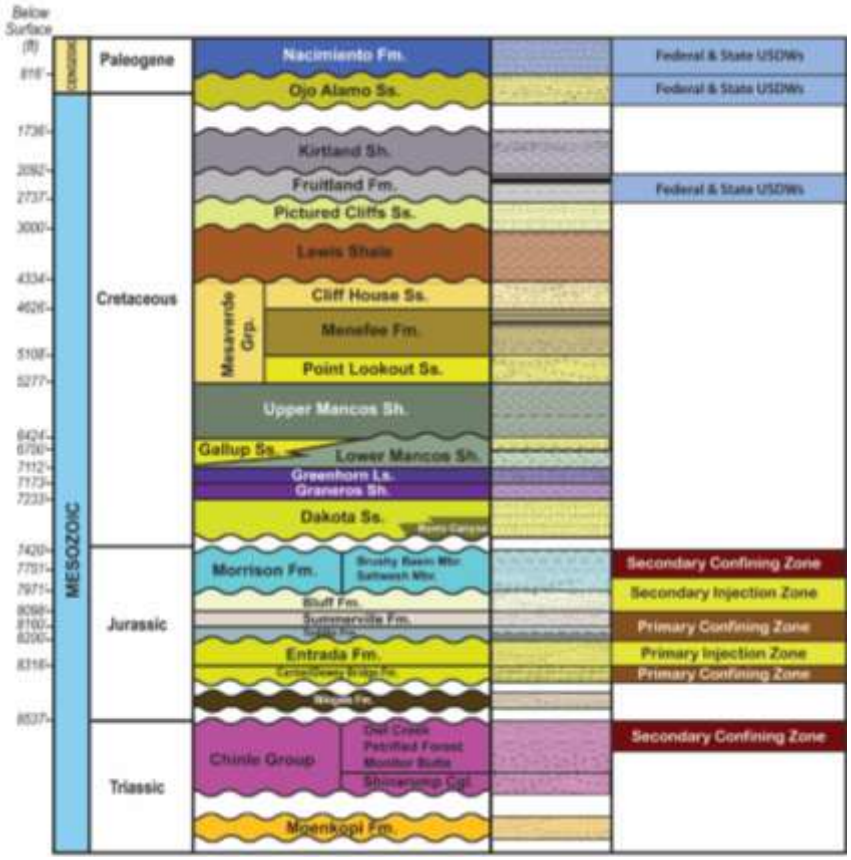


Figure 34. Stratigraphic column for the Mesozoic to Cenozoic section in the San Juan Basin.

The primary seals for the Entrada Sandstone are the overlying Todilto and Summerville Formations and the underlying Carmel Formation. The Todilto Formation fills the relief on top of the Entrada dune fields and was deposited as part of a complex coastal salina where marine and freshwater interacted. Todilto deposits consists of algally-laminated limestones with anhydrite nodules, high-energy coastal carbonates to massive anhydrite deposits. The Summerville deposits represent a change from the tidal flats to fluvial and lacustrine depositional environments. Sediments include very fine-grained sandstones, siltstones, mudstones and limestones. The Carmel Formation represents widespread sabkha deposits in the San Juan Basin and are composed of siltstones and mudstones. The secondary seal, for the Bluff and Salt Wash units, is the Brushy Basin Member of the Morrisson Formation. The Brushy Basin deposits

represent a change to fluvial and lacustrine sedimentation. They have isolated fluvial sandstone channels encased by mudstones and siltstones, making it a good potential seal.

A geologic model was constructed in IHS Kingdom© based on well logs tops that were all hand-picked (**Figure 35**). For each of the units, subsea structure and isopach maps were constructed. Since the primary injection target is the Entrada Sandstone, included in the report are the maps for the Entrada to Summerville units (**Figure 36** to **Figure 38**). These surfaces, and the others created in the geologic model, were then utilized for the simulation model.

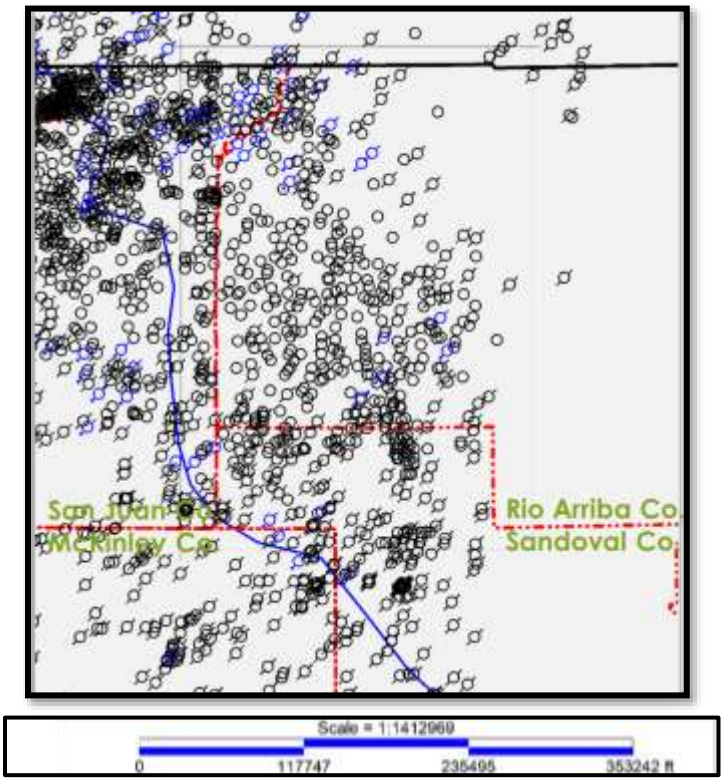


Figure 35. Base map showing the distribution of wells used for this study. The blue line is Cortez CO_2 pipeline.

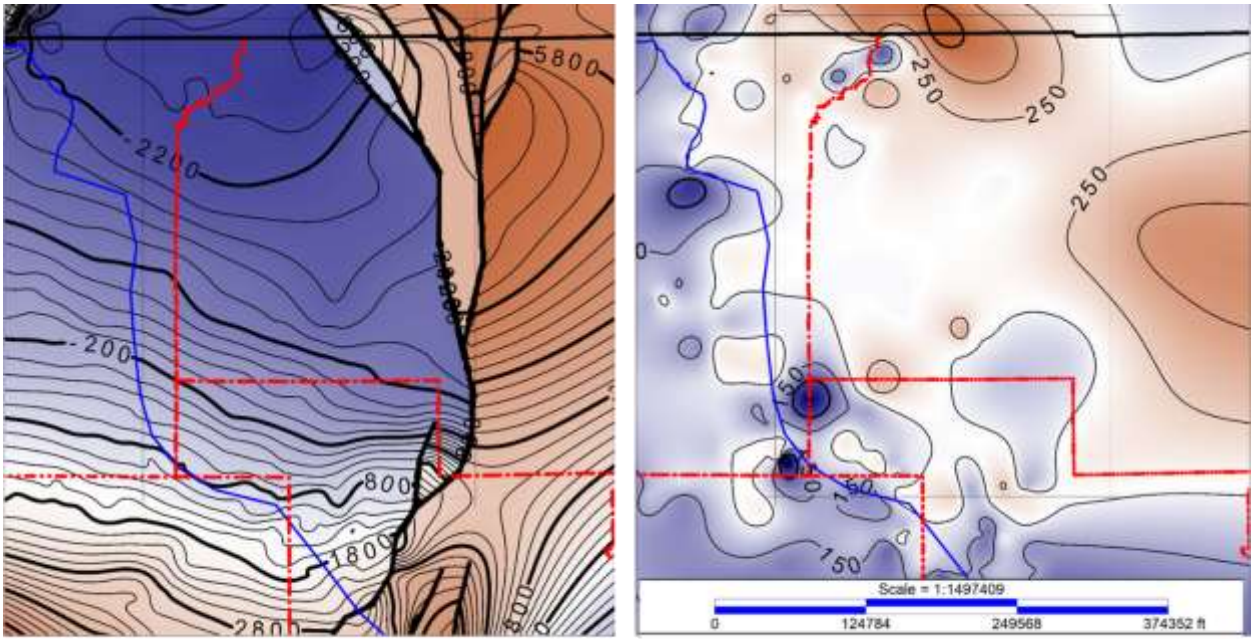


Figure 36. Entrada Sandstone subsea structure and isopach maps. The contour interval (CI) = 200 feet for the structure map and CI = 50 feet for the isopach map. The blue line is the Cortez Pipeline on this and subsequent figures. The subsea maps show the numerous faults that bound the eastern margin of the San Juan Basin and make up the Nacimiento uplift and Archuleta Anticlinorium.

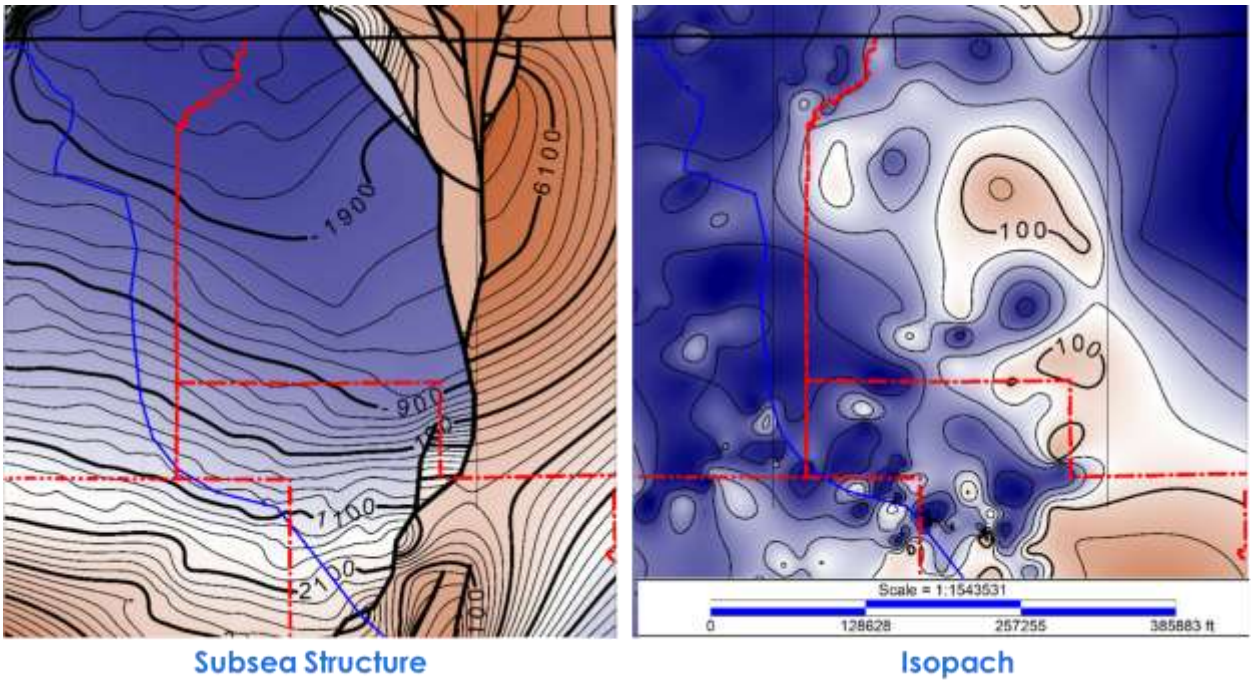


Figure 37. Todilto Formation subsea structure and isopach maps. The CI = 200 feet for the structure map and CI = 20 feet for the isopach map.

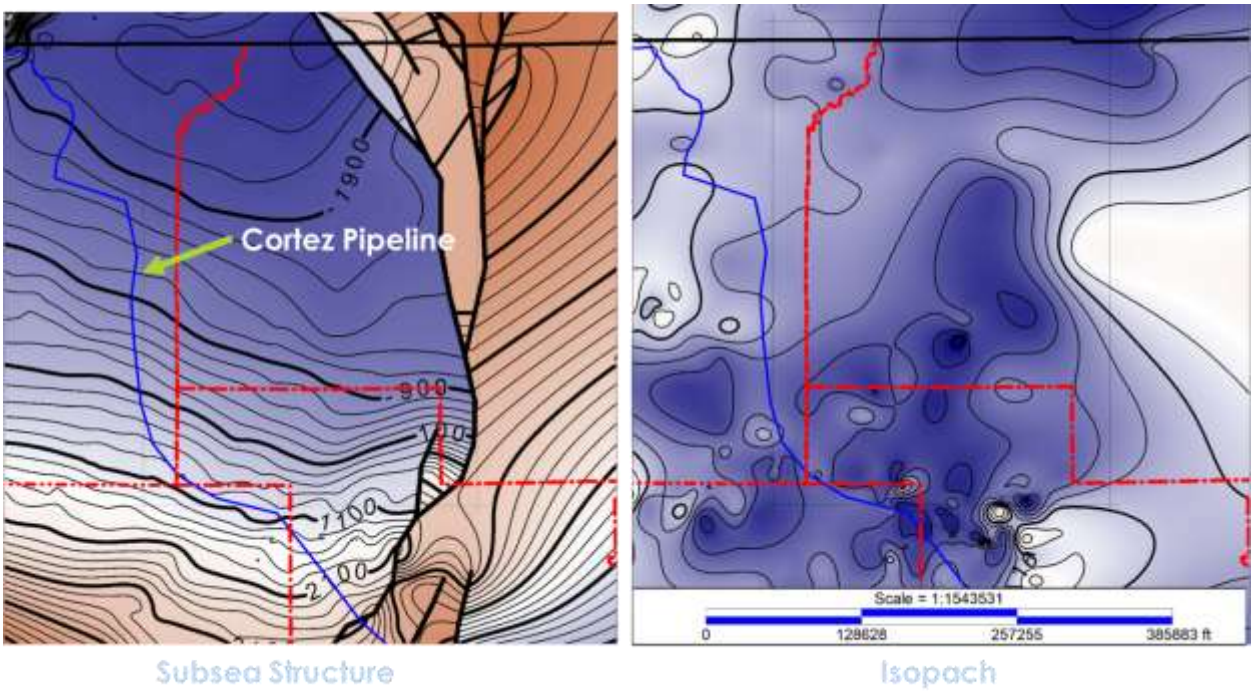


Figure 38. Summerville Formation subsea structure and isopach maps. The CI = 200 feet for the structure map and CI = 15 feet for the isopach map.

Due to several small oil fields occurring with the study area, core is available (**Figure 39**). Therefore, the Entrada Sandstone is relatively well characterized in the area with both thin section and porosity and permeability data available. The porosity and permeability data will be discussed in the model section, but it should be noted that internally, porosity and permeability vary in the Entrada Sandstone (**Figure *40***). Some logs indicate a thin zone of tight Entrada just below the contact with the Todilto Formation. This is followed by a zone of high porosity (thickness varies by well), and in the lower part of the unit, the porosity and permeability decrease with depth. This is easily seen in thin sections from the San Luis Federal #001 core (**Figure 41** and **Figure 42**).

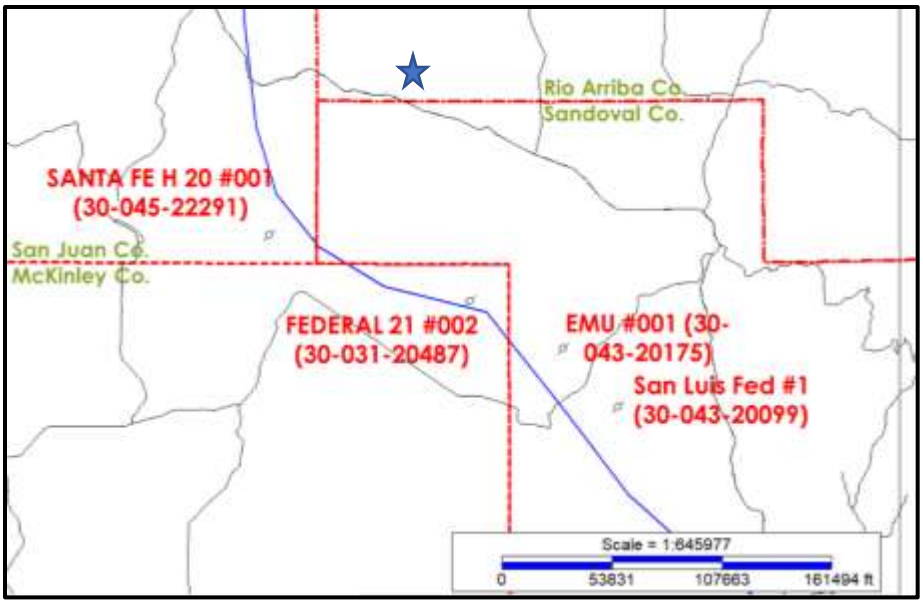


Figure 39. Map showing available cores in the area. The blue star is the approximate location of the recommended injection well.

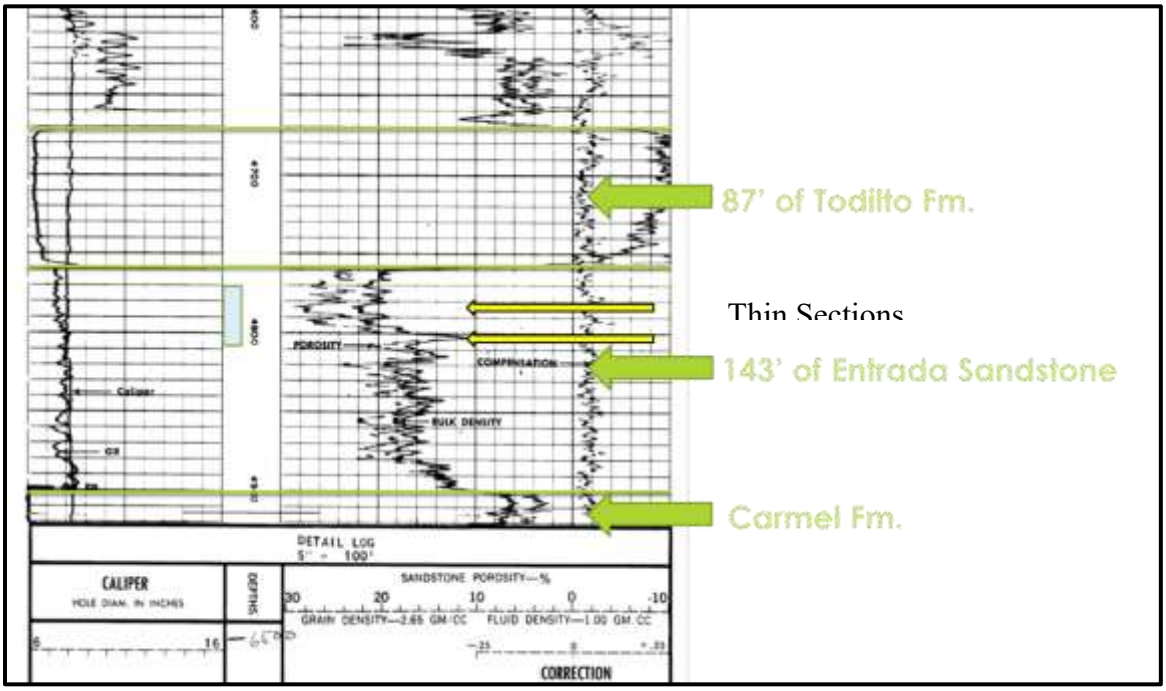


Figure 40. Log from the San Luis Federal #001 (30-043-20099) showing the 87 feet of tight Todilto Formation, followed by a zone of variable porosity in Entrada Sandstone.

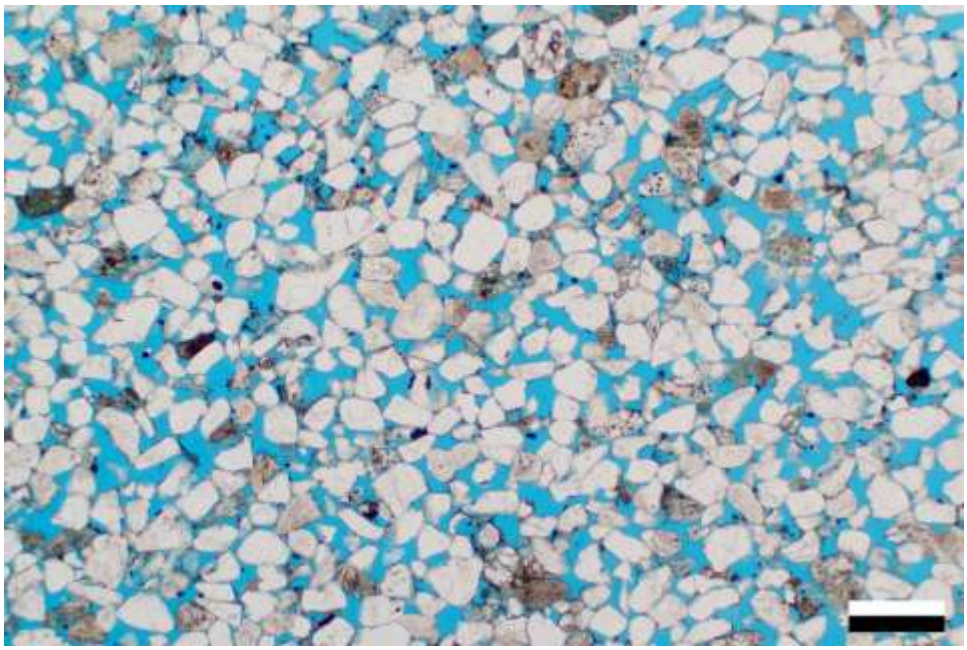


Figure 41. A plane-light photomicrograph of the Entrada Sandstone from a core in the southeastern part of the San Juan Basin in Sandoval Co., NM (San Luis Federal #1, 4,778 feet). This view contains quartz grains (white grains), feldspars (gray grains) and rock fragments (dark grains). This sample is from a dune structure in the core. Quartz overgrowths are present on a few grains, but otherwise there is little or no cement. This sample has an average porosity of 22.2%; most of the porosity is likely primary porosity, but there are numerous pores with very rounded outlines that may be a result of grains being dissolved producing secondary porosity. Scale bar = 0.51 mm.

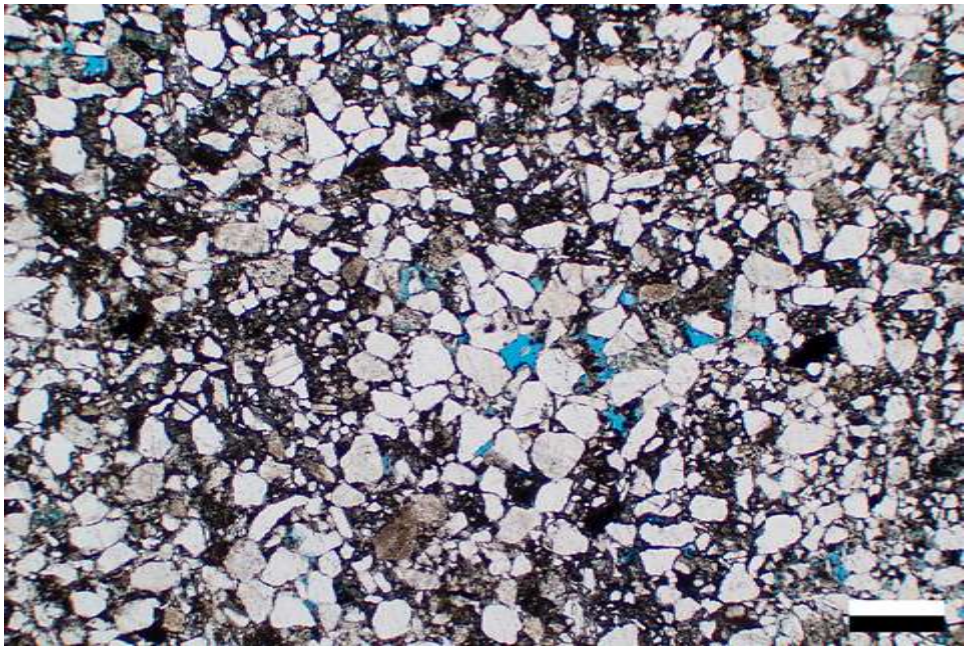


Figure 42. A plane-light photomicrograph of a sample from a tight zone of the Entrada Sandstone (San Luis Federal #1, 4,793 feet) containing quartz and feldspar grains, and rock fragments. This sample has an average porosity of 3.5%. This sample was likely deposited in an interdunal setting. Note the abundance of finer-grained material in this slide. Compaction has destroyed most of the porosity that was present in the sample. Scale bar = 0.51 mm.

In addition, analyses of produced waters indicate that the reservoir is a saline aquifer. and would not be an injection issue for going forward with detailed simulation models (**Figure 43**).

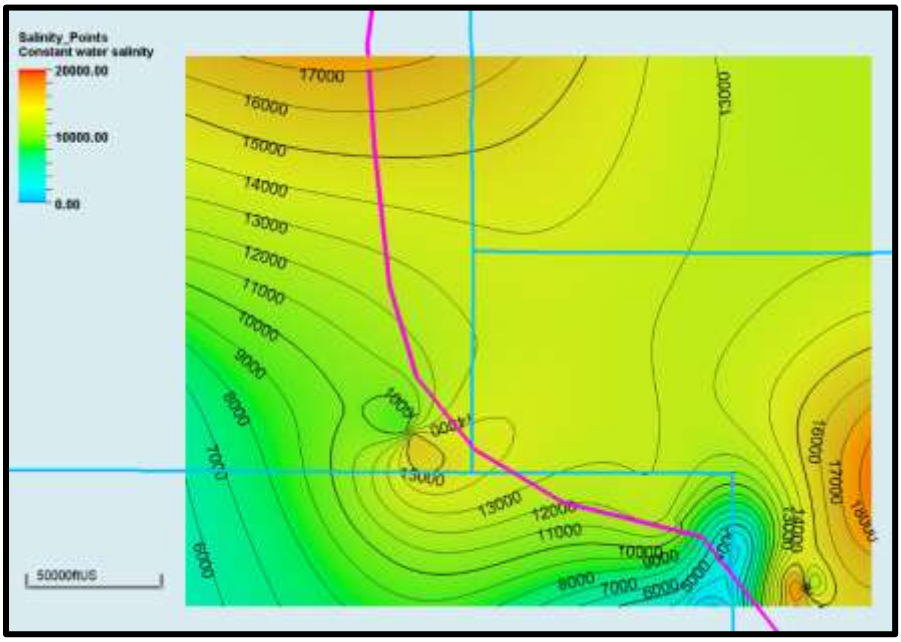


Figure 43. A contour map of total dissolved solids in produced waters within the study area.

Overall, the geologic analyses indicates that the Entrada Sandstone would be an excellent injection zone. The Bluff Sandstone and Salt Wash Member also have potential as sequestration targets, though their injection zones and associated seal's geology is less understood due to the lack of coring and porosity and permeability analyses.

Reservoir Model

Compositional reservoir simulator CMG-GEM was used to simulate the storage scenarios, and CMG-RESULTS and REPORT were used to quantitively evaluate the simulation results. The trapping mechanisms considered are geo-structural trapping, hysteresis trapping, and solubility trapping. Reservoir rock types, and fluid properties from San Juan Basin Entrada reservoir was used. As a result, the simulation group was able to analyze a simulation scenario that stores 45 Mt CO_2 over 30 yr working with the industrial partners. The proposed final development strategies will inject into Entrada Sandstone only.

The domain of the current model remains to be 60.9 miles by 57.1 miles square (**Figure 44 and Figure 45**). The grids distribute in I, J, K directions are 311 X 330 X 15 with 1,539,450 cells in total, 1,000 square feet grid size in average. It consists of seven (5) geological zones, where 'Salt Wash', 'Bluff', and 'Entrada' are the potential storage zones. The reservoir initial conditions and trapping mechanisms stay the same as the last version of the model. Carter-Tracy limited reservoir was assigned to the boundary of the simulation domain to mimic infinite reservoir response. Mid-depth (-1,850 ft – MSL, 7,760 ft - KB) reservoir pressure 3,314 psi was calculated with the pore pressure gradient of 0.427 psi/ft. The reservoir temperature was calculated to be 85.83 Celsius degree. The P-T condition was used to compute the fluid model by Peng-Robinson Equation of State in the CMG-WinProp module. Irreducible water saturation of 0.55 is used to

generate the relative permeability curves for the gas-water system (**Figure 46**). The reservoir is assumed to be initially saturated with 100% brine and exhibit hydrostatic equilibrium.



Figure 44. Aerial view of the simulation model boundary over the state map.

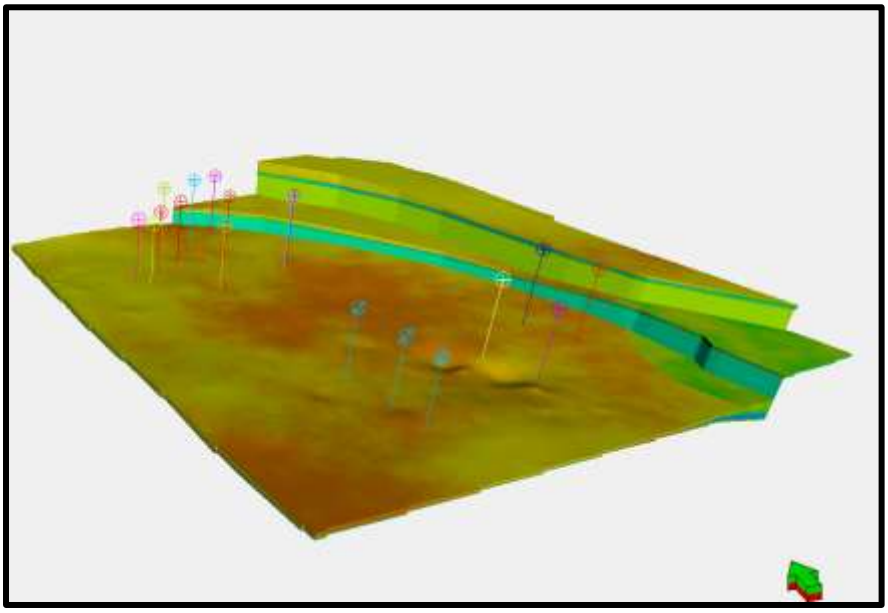


Figure 45. 3D view of the simulation model with SWDs and fault models considered.

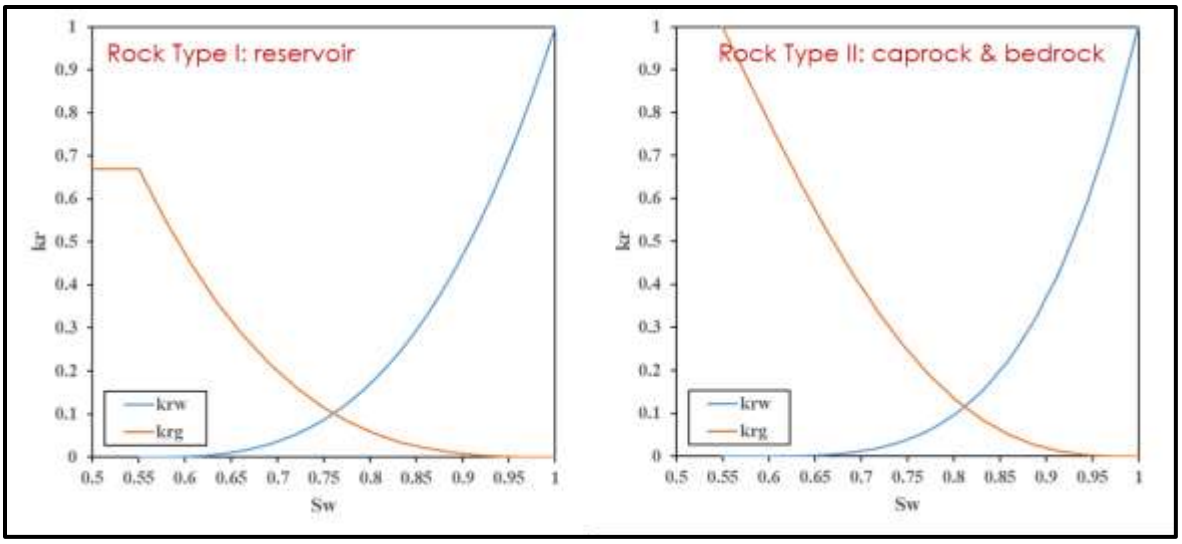


Figure 46. Relative permeability used in the reservoir simulation.

Based on the estimated maximum allowable gas injection rate per well, it is set as the primary control. Each injector is set to 1.5 Mt/yr or 79,210,173 standard cubic feet per well per day. The target is to inject CO_2 over 30 yr period. The schedule of each simulation run can be categorized into three phases: (1) history matching (1990 to 2023), (2) CO_2 injection (2023 to 2053), and (3) post-injection site care (2053 to 2073). The formations of injection are selected to be Entrada without because it is noted that Salt Wash and Bluff are beneficial to serve as a buffer zone. During the injection, Salt Wash formation prevents the CO_2 from being pushed into the caprock layer due to the high bottom hole pressure. During the PISC period, the buffer zone of Salt Wash enables the CO_2 to migrate upward while interacting with the formation solution and matrix that more CO_2 can be securely trapped by solubilization and capillary hysteresis effect. The secondary control is the maximum bottom hole pressure. It is set to equal to 5,000 psi which is estimated by the fracture gradient of 0.6 psi/ft, calculated at the shallowest perforation depth to ensure safe injection operations.

According to the well database from the State of New Mexico Oil Conservation Division, 13 Saltwater Disposal (SWD) wells that penetrate Entrada and with historical water injection data are imported into the model domain (**Table 7**). The simulation model set the injection rate as the primary constrain for SWDs. The wellhead injection pressure limit and historical wellhead pressure are converted to bottom hole pressure through an in-house program for SWDs. The purpose of this step is to justify the permeability and porosity realizations populated through statistic calculation with available core plug samples and correlations (**Table 8** and **Figure 47**).

Table 7. Petrophysical properties used for zones of the simulation model.

	Porosity, dec	Permeability, md	Average Thickness, ft
Salt Wash	0.17 to 0.23	1.9 to 21.7	287
Bluff	0.16	1.026	91
Summerville	0.04	0.006	75

Todilto	0.01	0.002	48
Entrada	0.01 to 0.25	0.01 to 507.13	100

Table 8. Active saltwater disposal wells considered in the model validation.

API	Well Name	Latitude	Longitude	TVD (ft)	Well Type	Status
3003930148	CARRACAS SWD #002	36.997990	-107.250952	9334	SWD	
3003924278	CARRACAS UNIT 27 A #082	36.953957	-107.343425	10060	SWD	Active
3003926868	CARSON SWD #001	36.787414	-107.230275	9590	SWD	
3003926214	EUL CANYON SWD #1	36.961603	-107.414712	9235	SWD	
3003925465	JILLSON FEDERAL SWD #001	36.325713	-107.180083	8800	SWD	Active
3003924236	NORTHEAST BLANCO UNIT SIMS MESA	36.830393	-107.564145	8956	SWD	Active
3003927055	ROSA UNIT SWD #001	36.884527	-107.426675	9176	SWD	
3003930812	ROSA UNIT SWD #002	36.870988	-107.314770	9334	SWD	
3003923231	RUCKER LAKE #002	36.380128	-107.004781	8975	SWD	Active
3003924807	SAN JUAN 29 6 UNIT SWD #301	36.748372	-107.423891	9112	SWD	Active
3003924518	SAN JUAN 30 6 UNIT #002	36.804575	-107.546728	8930	SWD	Active
3003924549	SAN JUAN 31 6 UNIT #301	36.846163	-107.502143	9040	SWD	Active
3003922756	SIMMS FEDERAL #001	36.809108	-107.202985	9731	SWD	Active

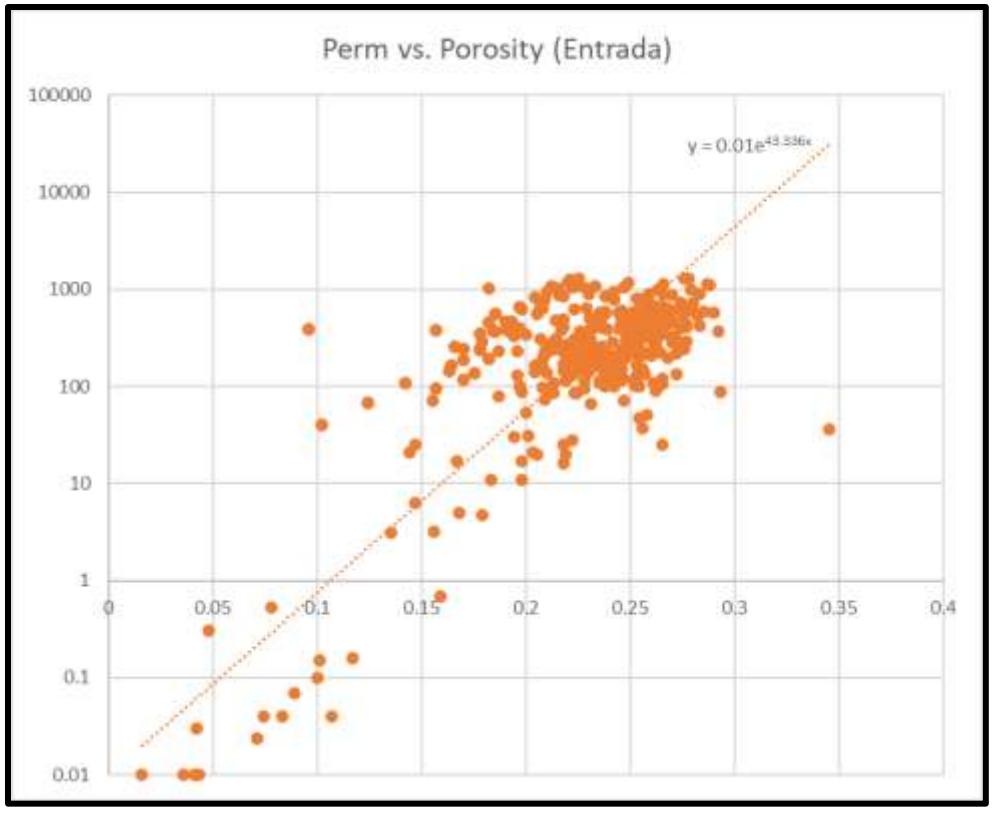


Figure 47. Petrophysical properties correlation from core plug samples.

Some representative results of the history matching are shown in **Figure 48** to **Figure 49**. The history results can be categorized into good matched. There following observations are from the history matching phase: 1) some literature indicates that the area of Entrada formation in the San Juan Basin maybe naturally fractures, which may result in parts of the region recorded better injectivity than others. As this project goes further, the geology characterization of the San Juan Basin will be better addressed, which is part of the significance of this ongoing project; 2) some wells may experience near-wellbore skin effects from formation damage and perforations. If this is true, the injectivity can be adjusted by assigning positive skin factors to certain wells; and 3) as the earliest historical data were from three decades ago, some of the records may need quality checks and adjustment.

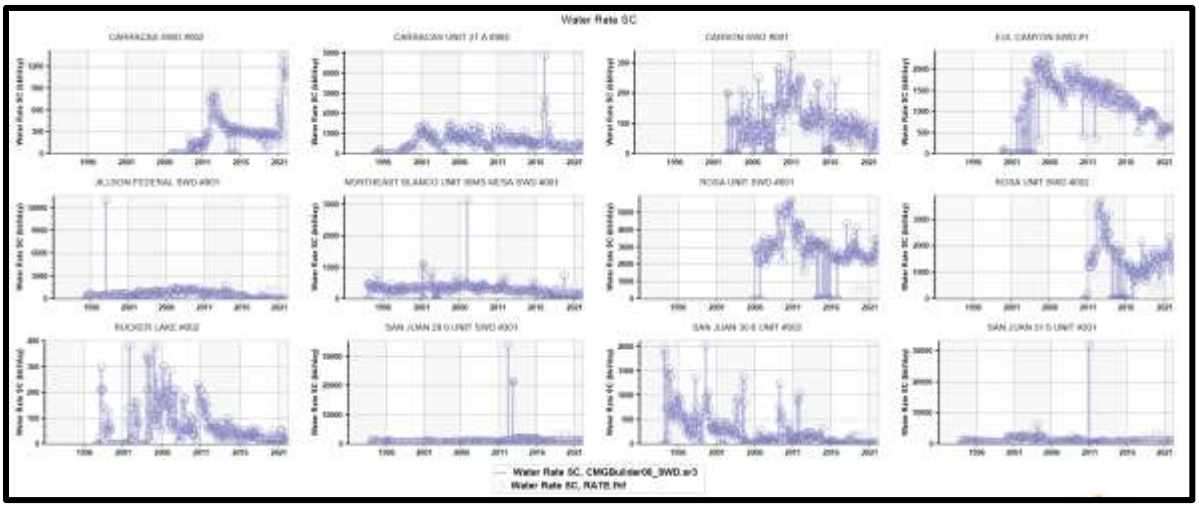


Figure 48. The injection historical injection rates of saltwater disposal wells.

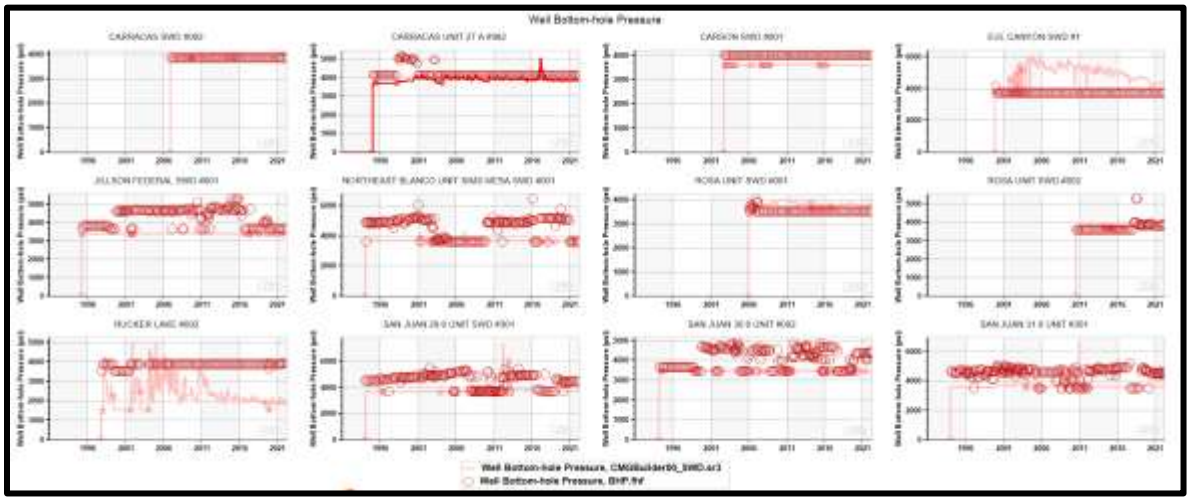


Figure 49. The injection historical bottom hole pressures of saltwater disposal wells.

The total injected CO_2 achieved 45 Mt CO_2 over 30 yr, and 1.5 million tons of injection rate maintained the entire injection period (**Figure 50**). The CO_2 plume barely migrated during the post monitoring period and the size is about 10 miles in diameter (**Figure 51**). The CO_2 is predominantly stored as supercritical phase and trapped through capillary pressure hysteresis

effect. 25% of which CO_2 was dissolved in formation brine under the reservoir temperature and pressure conditions (**Figure 52**).

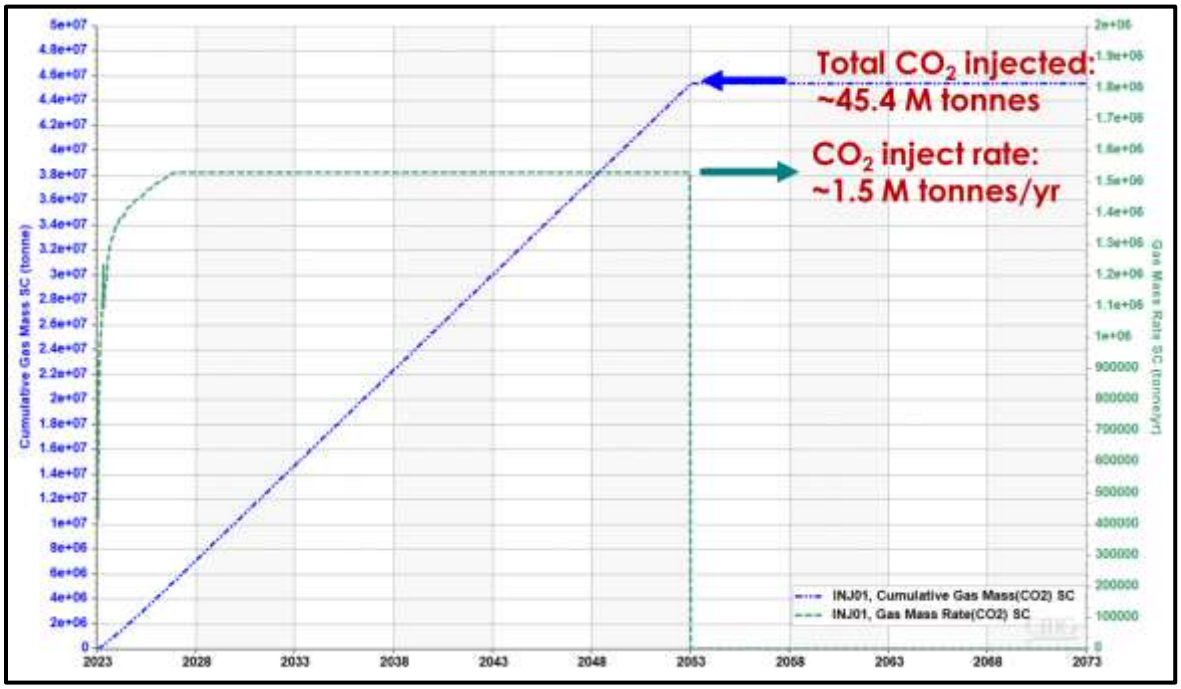


Figure 50. The total CO_2 injected over 30 yr and the yearly rates.

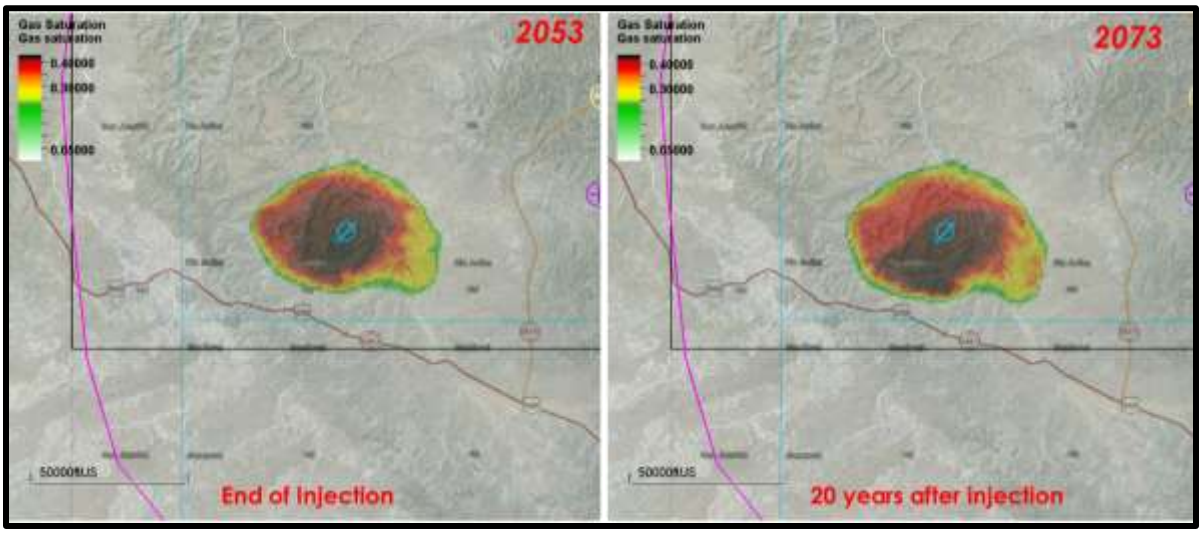


Figure 51. The injected CO_2 plume at the end of 30-yr injection and 20-yr post-injection.

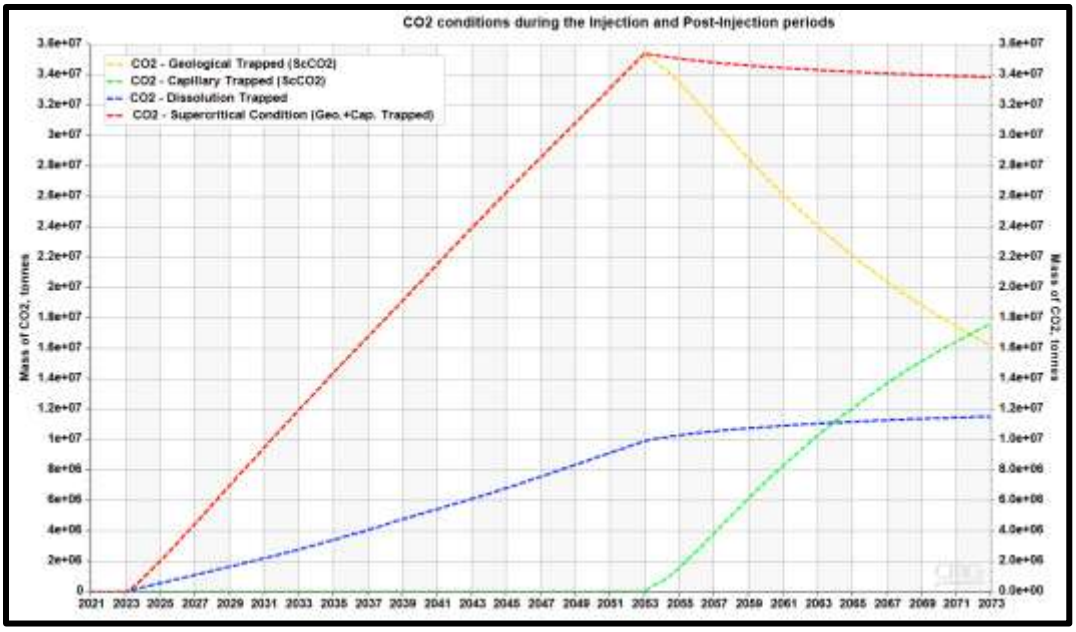


Figure 52. The injected CO_2 stored by separate mechanisms over years of sequestration.

Evaluation of the Potential Benefit of Enhanced Coal Bed Methane (ECBM)

Experimental Study of Permeability Reduction in Fruitland Coal Due to CO_2 Adsorption and its Effect on Strength and Stiffness

By Jason Simmons

The main objective of this CUSP Focused Project is to perform a feasibility assessment of site characterization to identify a suitable storage complex in New Mexico that can safely store a minimum of 1.5 million metric tons of CO_2 over a 30-year injection period. As part of this assessment the project aims to provide data which may increase the technical understanding of using coalbeds in New Mexico as part of the storage complex. One of the main challenges for the long-term storage of CO_2 in coalbeds is injectivity decline near the wellbore which has been linked to swelling induced permeability reduction as CO_2 adsorbs to the coal matrix (Siriwardane et al., 2009; Pan et al., 2010; Perera et al., 2011;Vishal and Singh, 2015; Vishal, 2017; Wang et al., 2019). To define this phenomenon and to assess the potential for storage of CO_2 in New Mexico coalbeds, we performed laboratory flow-through experiments in Fruitland coal samples under reservoir conditions to measure the permeability reduction over time. Permeability experiments were combined with unconfined compressive strength tests (UCS) on two pristine samples and flow-through samples interacted with CO_2 to determine if adsorption of CO_2 had any adverse effects on strength and stiffness within the Fruitland Coal which may affect operations. Finally, adsorption isotherms for CO_2 and N_2 in the experimental samples were developed using Brunauer-Emmett-Teller (BET) analysis.

Methods

Sample Preparation: Flow-Through and UCS

Sample selection in the Fruitland Coal was based on visual inspection and existing logs which contained proximate analysis for nearby depths. We chose interval 3739.75 – 3759 ft. from well Chicosa 35, API 3003924622 (FCC35; Figure 1; Tables 1 and 2). 3 cylindrical samples were cut parallel to general dimensions of 1.5" diameter by 2.25 - 2.5" length for the experiments using a standard press (Table 2). Due to friability, a heat shrink was molded to the samples before they were end trimmed using a Kemet Automatic Cutter 402 saw. All sample preparation was completed dry, without cooling fluids to retain sample integrity.

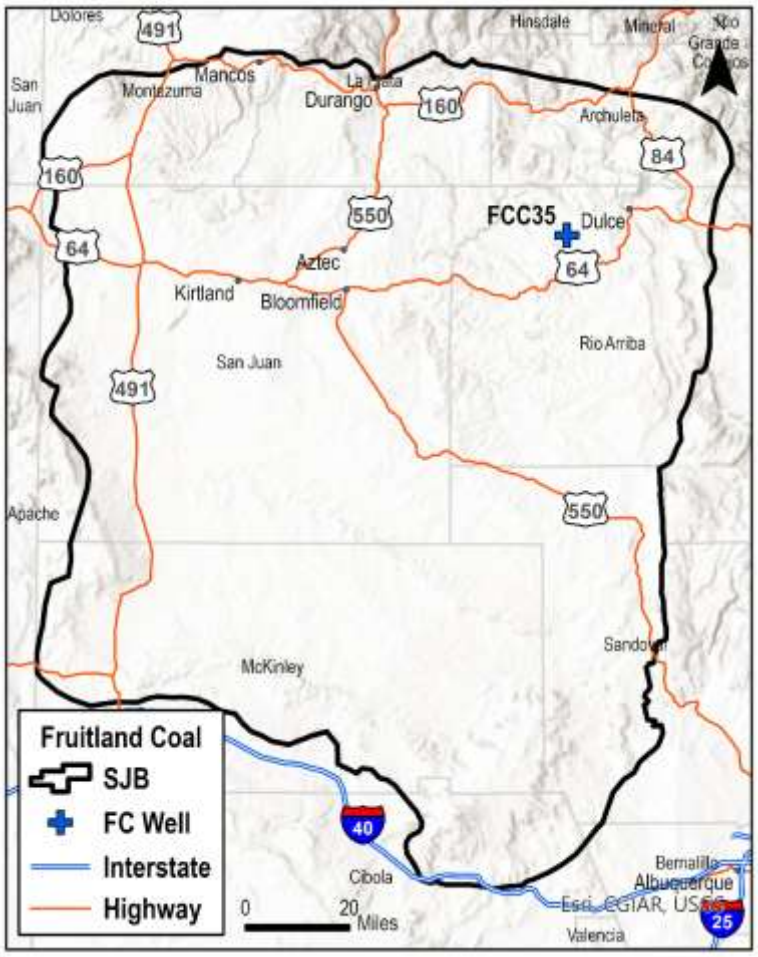


Figure 1. Well location for Fruitland Coal samples.

Table 1.Well information for sample locations within the SJB Fruitland Coal

API	Well Name	Well ID	Lat_NAD83	Lon_NAD83	MVD	Elev	Status
3003926422	Chicosa 35	FCC35	36.8615456	-107.217598	3862	7005	CBM

Table 2. Core parameters of Fruitland Coall

Sample ID	Test Type	Interval ft	Interval m	Length cm	Diameter cm
FCC35-1	CO_2/UCS	3759	1145.74	5.9479	3.8682
FCC35-2	CO_2/UCS	3758.33	1145.54	6.2009	3.8684
FCC35-3	CO_2/UCS	3758	1145.44	6.1006	3.8814
FCC35-4	Pristine UCS	3739.75	1139.88	5.7523	3.8710
FCC35-5	Pristine UCS	3740	1139.95	6.0117	3.8669

2.2 Laboratory Flow-Through Experiments

Flow-through experiments with supercritical CO_2 were conducted on 2 samples (FCC35-1 and FCC35-2) of Fruitland Coal from well Chicosa 35 at the reservoir temperature 56°C, and reservoir effective stress of 12 MPa to measure any permeability reduction through time due to adsorption. A 3rd experiment was performed using liquid CO_2 by lowering temperature to 28°C to determine if changes in CO_2 phase would affect adsorption (Table 3).

Prior to the experiment, we jacketed samples in a Buna-N sleeve wrapped in stainless steel foil inside a Core Labs hydrostatic cell. A PTFE sleeve was inserted around the jacketed sample to minimize the mass of CO_2 that will diffuse into the silicon oil confining fluid. Three Watlow ceramic heating bands controlled by a Watlow control and a Type K thermocouple inside of the vessel heated the system. Three Teledyne ISCO syringe pumps were used throughout the experiment to control pore fluid (pump A and pump B, Figure 2; 260HP and 500HP) and confining pressures (pump C, Figure. 2; 100D). During the test, two high precision (0.0129 MPa) Heise HWQ-64864 pressure transducers measured upstream and downstream pressures. Permeability was measured using a pore pressure transmission method which involved a constant gas injection pressure at the sample inlet with a downstream compartment which was isolated from any pump controls. Initially, a CO_2 cylinder was connected to pumps A and B and used to gently increase pore pressure to 6 MPa. The pumps were then filled with CO_2 and used to further pressurize the system to 7.5 MPa. Pumps A and B were set to constant pressure and pore pressure was allowed to equilibrate until no volume changes were observed in the pumps. Confining pressure was simultaneously increased to 19.5 MPa. Finally, the core sample was momentarily isolated from the upstream pressure, which was increased to 8.5 MPa, while the confining pressure was increased to 20.5 MPa to meet the in situ effective stress requirement. The downstream compartment was closed off thereby isolating the sample from the downstream pump B and the most upstream valve at the sample inlet was opened allowing a 1 MPa pressure gradient across the sample. Pressure was allowed to move freely through the sample into the downstream compartment while the change in pressure there was recorded at 5 second intervals and used to calculate flowrate according to

$$Q = \frac{dP}{dt}\beta V$$

where $\frac{dP}{dt}$ is the change in downstream pressure through time, β is the adiabatic compressibility of CO_2, and V is the volume of the downstream compartment (Siriwardane et al., 2009a and

2009b; Perera et al., 2011;Vishal and Singh, 2015; Vishal, 2017). β was calculated using the derived formula

$$\beta = \frac{Z}{P\gamma}$$

where Z is the Z-factor which accounts for the deviation of CO_2 from ideal to real gas behavior at our experimental conditions, P is the average pore pressure, and γ is the ratio of specific heat capacity ratio for CO_2 (Bear, 1972; Pipeng, 2025). Finally, permeability (k) was calculated using the standard formula

$$k = \frac{2QP_o\mu L}{A({P_i}^2 - {P_o}^2)}$$

where Q is the downstream flowrate, μ is viscosity of the CO_2, P_i and P_o are the upstream and downstream pressures respectively, and A and L are the cross sectional area and the average length of the coal sample respectively (Perera et al., 2011;Shukla; et al., 2012; Nasvi, et al., 2013; Vishal and Singh, 2015; Vishal, 2017). Once the initial permeability was determined, CO_2 was passed through the sample for ≈ 30-36 hours, before the experiment was repeated at the exact same conditions to determine if a change permeability had occurred.

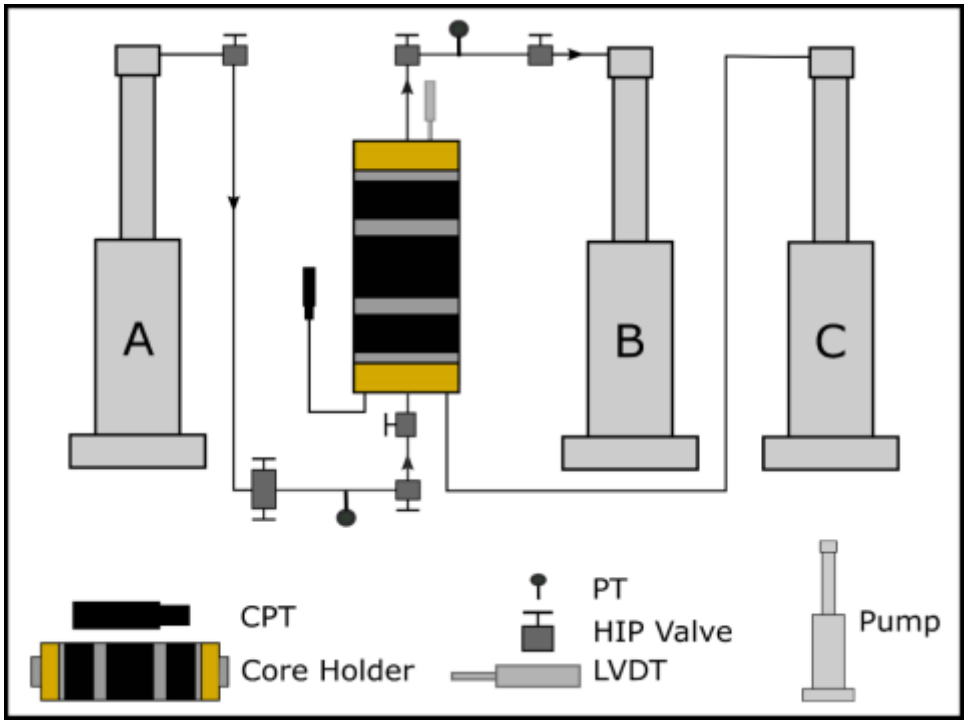


Figure 2. Permeability apparatus. Black lines represent flow lines with directional arrows.

UCS Tests

Unconfined compressive strength (UCS) tests were performed on the three experimental flow-through samples interacted with supercritical or liquid CO_2 and two pristine samples of Fruitland Coal using a MTS 793 testing system with maximum load of 600 kN (Figure 3). Sample preparation and testing protocols generally adhered to ASTM D7012. However, due to friability,

cores were not ground flat but rather ends were capped with card stock according to methods outlined in Pells (1993). Samples were placed between steel platens and capped with card stock before being loaded at a constant strain rate of 3.9 - 5.0 x 10^{-4} strain/s and displacement rate of 0.0009 - 0.0115 mm/s. UCS (σ) was calculated from the standard formula

$$\sigma = \frac{P}{A} \quad (1)$$

where P is the maximum load (kN) sustained during testing and A is the sample's cross-sectional area (mm^2; SCDOT, 2009; Gudmundson, 2011). The displacement of the card stock and platens was calibrated by applying the same loads and deformation rates to an ≈ 1.5" x 3.0 in. 316 stainless steel cylinder. Calibrated displacements were to be subtracted off from the displacements that developed during each test.



Figure 3. MTS testing machine used in UCS testing of Fruitland Coal specimens.

Results and Discussion

Flow-Through Experiments

Three experiments were conducted on Fruitland Coal samples to assess permeability reduction during injection of supercritical CO_2 and to determine if changing the CO_2 phase would affect adsorptive properties. For the two samples which were interacted with supercritical CO_2 we found that the rate of change in the downstream pressure was slow during the initial exposure,

lasting ≈ 4-5 hours for a generally steady state between the upstream and downstream compartments (Figures 4a and 5a). Based on the flowrate from this pressure change, we found that initial permeability was low at 78.1 nanodarcies (nD) and 80.4 nD for FCC35-1 and FCC35-2 respectively (Figure 6). After prolonged exposure to supercritical CO_2, the rate of change in the downstream compartment had decreased in both samples leading to reduction in permeability of 60.6 nD (22.4%) and 24.5 nD (55.9%) for FCC35-1 and FCC35-2 respectively (Table 3; Figures 4b ,5b, and 6). Opposing results occurred in the 3rd experiment performed with liquid CO_2. Where CO_2 had taken hours to move through the previous 2 samples, equilibration of the downstream pressure in sample FCC35-3 occurred in ≈ 3-4 minutes rather than hours (Figure 7a).We found that initial permeability here was 200 times greater than in the 1st two experiments at 0.0157 millidarcies (mD) or 15,683 nD (Figure 8). After the sample had been exposed to CO_2 for 30+ hours, the rate of pressure change in the downstream compartment had had sufficiently increased informing the permeability increase to .0237 mD (23,742 nD; Figure 7b and 8).

Samples flooded with supercritical CO_2 experienced 22.4% to 69.5% reduction in permeability after approximately 34-38 hours of total time (Figure 6). Because effective stress and temperature remained constant for both experiments, the reduction in permeability occurred due to adsorption of CO_2 to the coal matrix during the initial experiment and during the samples prolonged exposure to the CO_2 phase. This experimental result indicates that without a change to the cleat/fracture network, injectivity problems are likely to occur through time in this section of interval 3758.33 to 3759 ft of the Fruitland Coal. However, the permeability increase in sample FCC35-3 tells a different story. The high initial permeability in this sample is not typical of traditional tight coalbeds. Upon examination of the coal sample, we learned that an extensive network of pre-existing fractures exists throughout the full sample geometry. Fractures are a dominant channel of gas flow in coal as evidenced by the large difference in permeability from samples FCC35-1 and FCC35-2 which show no evidence of a fracture network. We also find that because the sample is so well-fractured, that adsorption of CO_2 to the matrix was insignificant through time as compared to the connectivity of the flow pathways. Because gas moved through the sample so quickly, the experiment was repeated multiple times, allowing at least 10 hours of exposure between measurements to finally equal the same total exposure time to CO_2 as occurred in the first two samples. From this we found that the permeability increased at each subsequent measurement except from the second to third where no change occurred. We believe that the 1MPa pressure gradient across the sample contributed to widening or increasing the fracture network through time which resulted in increasing the permeability (Figure 8). The increasing permeability in the previously fractured sample indicates that where there is an extensive fracture network, the Fruitland Coal is likely to have good injectivity which may increase with time as connectivity changes with increasing injection pressure. Overall, determination of the Fruitland Coal as a good storage reservoir to meet the requirement of 1.5 million metric tons of CO_2 over a 30-year injection period will be highly dependent on the cleat and fracture network which exists on the reservoir scale especially in proximity to the injection well.

Finally, because our 3rd sample had a connected fracture network, we could not determine how changing the CO_2 phase would affect adsorption in Fruitland Coal. It should be noted however that supercritical CO_2 would generally be the preferred phase during injection activities based on in situ conditions in the Fruitland Coal in most of New Mexico.

Table 3. Permeability of coal samples. Red indicates a decrease

Sample ID	CO_2 Phase	Initial (nD)	Post (nD)	Change (nD)	Change (%)
FCC35-1	SC	78.1	60.6	17.5	22.4
FCC35-2	SC	80.4	24.5	55.9	69.5
FCC35-3	Liquid	15683.4	23744.2	8060.8	51.4

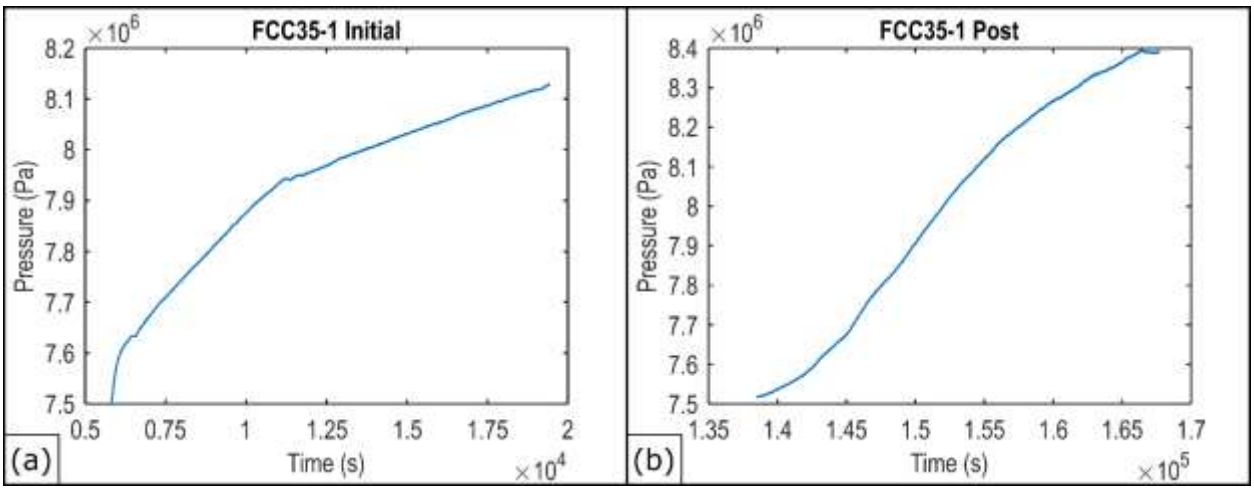


Figure 4. Downstream pressure evolution through time in experiment 1 during initial flooding of the coal sample (a) and after 30-36 hours of prolonged exposure (b).

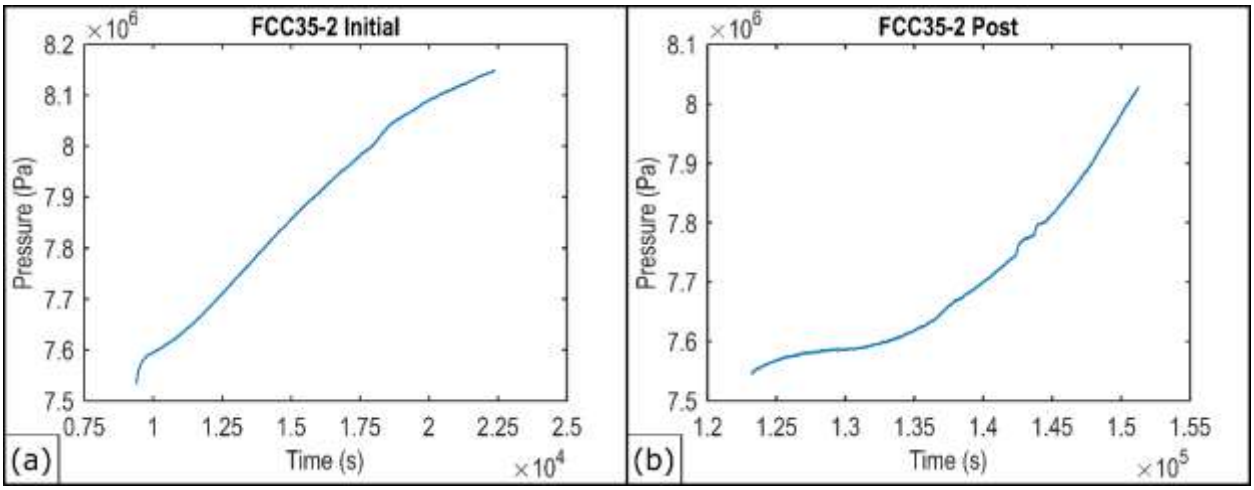


Figure 5. Downstream pressure evolution through time in experiment 2 during initial flooding of the coal sample (a) and after 30-36 hours of prolonged exposure (b).

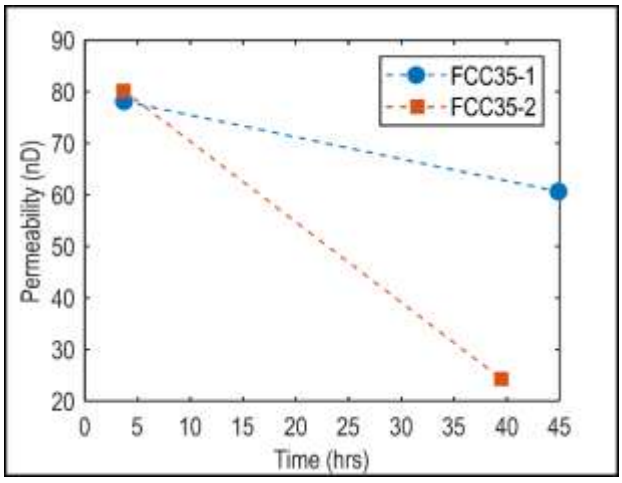


Figure 6. Permeability before and after prolonged exposure to CO_2 in samples FCC351 and FCC35-2. Decreases ranged from 22.4% to 69.5% in the two samples.

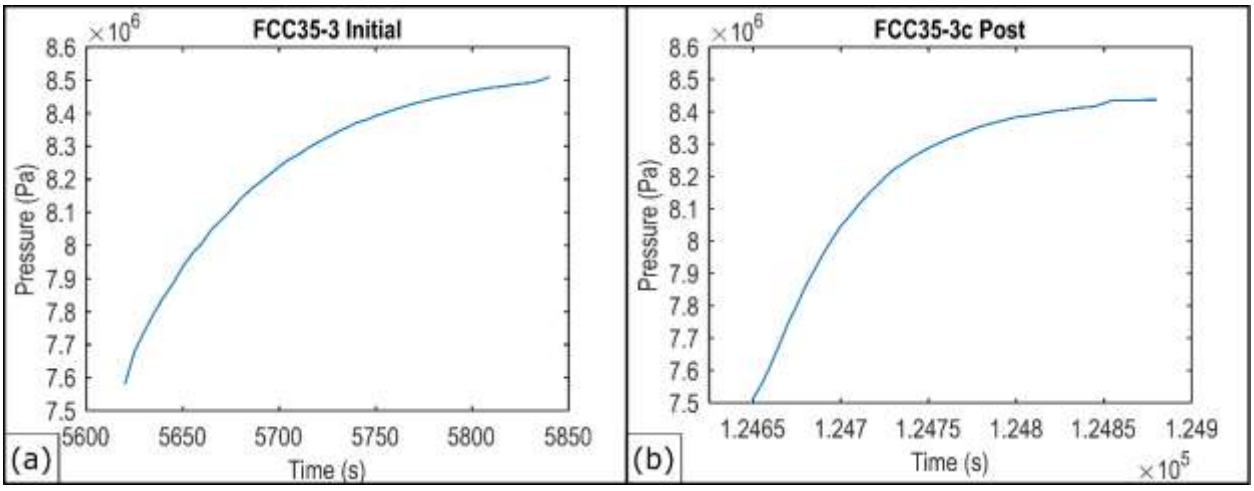


Figure 7. Downstream pressure evolution through time in experiment 3 using liquid CO_2 during initial flooding of the coal sample (a) and after 30-36 hours of prolonged exposure (b).

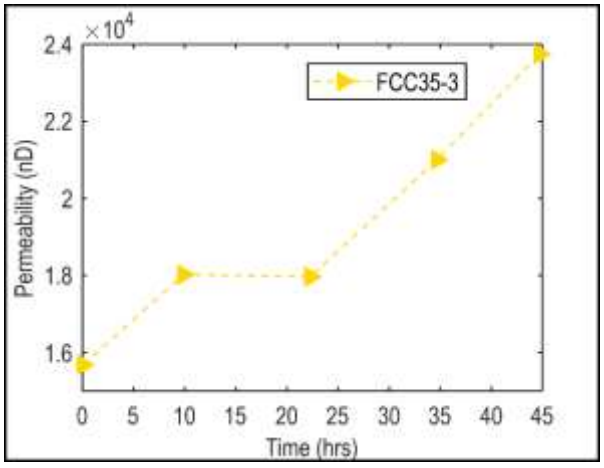


Figure 8. Permeability before and after prolonged exposure to CO_2 in sample FCC353 interacted with liquid CO_2. Because CO_2 flowed through the sample in minutes, the experiment was repeated several times to match total time of exposure as in FCC35-1 and FCC35-2. This coal sample was extensively fractured and permeability increased by 51%.

UCS and Estimated Youngs Modulus

Unconfined compressive strength testing was performed on 5 samples of Fruitland Coal that were either interacted with CO_2 or pristine (Figure 9 and 10). Samples of the Fruitland Coal generally exhibited brittle post-peak failure behavior with several samples showing double peaks (Figure 11a and 11b). Notably, pristine sample FCC35-4 exhibited ductile failure before an abrupt brittle post-peak failure (Figure 11b). Peak load and unconfined compressive strength were determined for each experiment. For pristine samples not interacted with CO_2, peak load was 27.6 kN and 32.3 kN, and UCS was 23.4 MPa and 27.5 MPa (average 25.5 MPa) for samples FCC35-4 and FCC35-5 respectively (Table 4). For experimental samples, peak load was 38.1 kN, 32.9 kN, 26.2 kN, and UCS was 32.4 MPa, 28.0 MPa, and 22.1 MPa (average 27.5 MPa) for samples FCC35-1, FCC35-2, and FCC35-3 respectively (Table 4).

Typically, Young's modulus would easily be calculated from the slope of the linear portion of the stress strain curve during UCS testing (Gudmundsson, 2011). However, the calibration of the card stock displacement from the total displacement during testing proved to be unattainable. Therefore, the strains that developed during each test were overestimated, resulting in the underestimation of Young's modulus while leaving the UCS unaffected. However, there is significant data which positively correlates UCS with Young's modulus in geomaterials, where stronger materials typically have a higher Young's modulus (Dincer et al., 2004; Chang et al., 2006; Basu et al., 2009; Pan et al., 2013; Malkowski et al., 2018). Of these studies, Pan et al (2013) developed a direct correlation between UCS and Young's modulus for three independent coal types:

$$UCS = 3.3844e^{0.4744E} \quad (2)$$

where the unconfined compressive strength (*UCS*) is in MPa and *E* is the Young's modulus in GPa. Applying this correlation to our study, we estimated the Young's modulus which was 4.1 GPa and 4.4 GPa (average 4.2 GPa) for pristine samples FCC35-4 and FCC35-5 respectively, and 4.8 GPa, 4.5, GPa, and 4.0 GPa (average 4.4 GPa) for experimental samples FCC35-1, FCC35-2, and FCC35-3 respectively.

Based on results, the values of peak load, UCS, and estimated Young's modulus were reasonably consistent between the pristine and CO_2 interacted samples, and were within normal range for strong coal specimens found in the literature (Pan et al., 2013; Perera, 2013; Perera, 2016; Schreiber et al., 2017). The lowest values of UCS (22.1 MPa) and Young's modulus (4.0 GPa) occurred in CO_2 interacted sample FCC35-3 which contained the most connected and extensive cleat and fracture network based on fluid flow during permeability testing and physical observations of the core plug. This result is not unexpected as fractured coal generally exhibits lower strengths and elastic properties when compared to the more solid coals with a lesser cleat/fracture network (Abrar, et al, 2025). Even then, when comparing results between the experimental and pristine sample groups, we found the lowest value of UCS in the experimental group was only 1.3 MPa (6%) lower than in the pristine samples. There was also only a 2.0 MPa (8%) difference and 0.2 GPa (5%) difference between the average UCS and average Young's modulus respectively, for the pristine and experimental sample groups (Table 4). When looking for real variations which might indicate change in strength or stiffness for the coal samples post experiment, we believe a reasonable difference should be > 20% which did not occur in this study. It is also worth noting that the largest UCS (32.4 MPa) and estimated Young's modulus (4.8 GPa) occurred in a CO_2 interacted sample (FCC35-1). This sample also underwent a permeability reduction of 22.4% during the flow-through experiments. Based on the relative similarity of results for all of the samples, relatively low % differences between sample points of the two groups, and low differences in average values for the combined samples of each group, there was no effect on the UCS or Young's modulus of the coal specimens due to adsorption of CO_2 to the coal matrix. Beyond the lowest value of UCS in experimental sample FCC35-3 due to its internal structure, the slight differences in strength are acceptable and from heterogeneities within the coal specimens themselves.

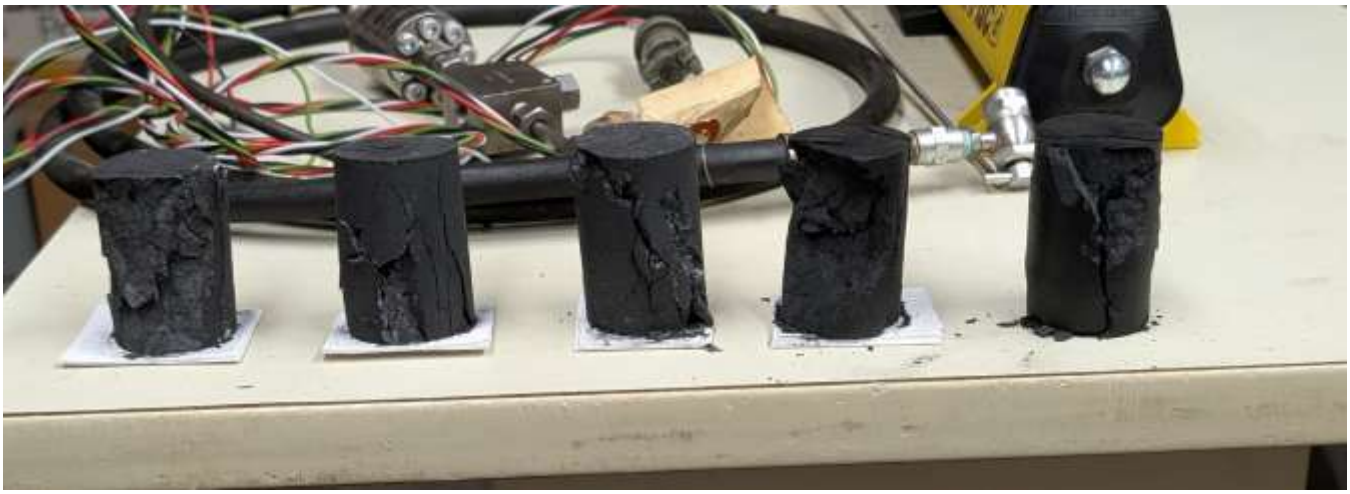


Figure 9. Coal specimens generally experienced brittle failure during UCS testing.



Figure 10. Sample FCC35-4 which exhibited ductile failure during UCS testing.

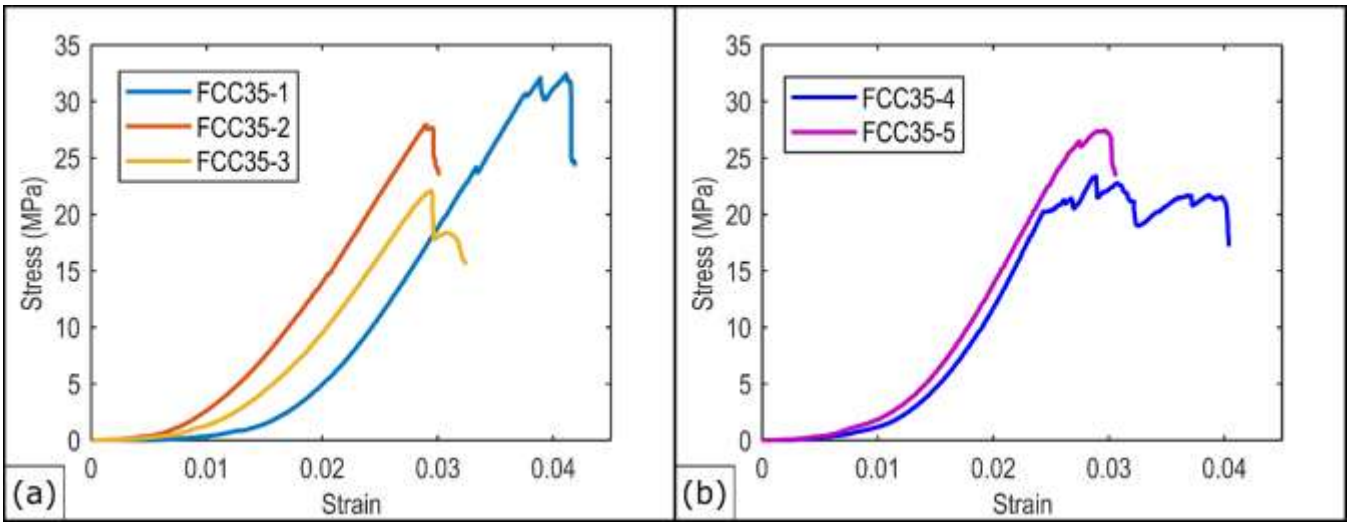


Figure 11. Failure curves for experimental samples (a) and pristine samples (b). Strain includes sample strain, and card stock (end cap) strain due to post-test calibration issues. Because of this, strain is overestimated for these tests and could not be used to determine Young's modulus while the UCS is fully represented in these figures. Sample

FCC35-4 exhibited ductile failure, and several samples show double peaks where stress increased after an initial decrease before failure.

Table 4. Results of UCS tests for Fruitland Coal. Young's modulus (E) was estimated from a correlation in Pan et al (2013)

Sample ID	Test Type	Peak Load (kN)	UCS (MPa)	E (Gpa)
FCC35-1	CO_2/UCS	38.1	32.4	4.8
FCC35-2	CO_2/UCS	32.9	28.0	4.5
FCC35-3	CO_2/UCS	26.2	22.1	4.0
FCC35-4	Pristine UCS	27.6	23.4	4.1
FCC35-5	Pristine UCS	32.3	27.5	4.4

References

Abrar SW, Mendhe VA, Kamble AD, Shukla P, Sharma P, Buragohain J, Kumari S, Kumari S, Anurag, Das AK, et al. 2025. Cleat and fracture systems in coal with implications for strength, hydrofracking, and gas–water flow mechanisms: a critical review. ACS Omega. 10:29909–29928. doi:10.1021/acsomega.5c00520

[ASTM]ASTM International. 2023. ASTM D7012-23: standard test methods for compressive strength and elastic moduli of intact rock core specimens under varying states of stress and temperatures. West Conshohocken (PA): ASTM International. 8 p.

Basu A, Celestino T, Bortolucci A. 2009. Evaluation of rock mechanical behaviors under uniaxial compression with reference to assessed weathering grades. Rock Mech Rock Eng. 42:73–93. doi:10.1007/s00603-008-0170-2

Bear J. 1972. Dynamics of fluids in porous media. New York (NY): American Elsevier Publishing Company. 764 p.

Dinçer I, Acar A, Çobanoğlu I, Uras Y. 2004. Correlation between Schmidt hardness, uniaxial compressive strength and Young's modulus for andesites, basalts and tuffs. Bull Eng Geol Environ. 63:141–148. doi:10.1007/s10064-004-0230-0

Gudmundsson A. 2011. Rock fractures in geological processes. Cambridge (UK): Cambridge University Press.

Hangx SJT, Spiers CJ, Peach CJ. 2010. Creep of simulated reservoir sands and coupled chemical-mechanical effects of CO_2 injection. J Geophys Res Solid Earth. 115:B09205. doi:10.1029/2009JB006939

Małkowski P, Ostrowski Ł, Brodny J. 2018. Analysis of Young's modulus for Carboniferous sedimentary rocks and its relationship with uniaxial compressive strength using different methods of modulus determination. J Sustain Min. 17:145–157. doi:10.1016/j.jsm.2018.07.002

Nasvi MCM, Ranjith PG, Sanjayan J, Haque A. 2013. Sub- and super-critical carbon dioxide permeability of wellbore materials under geological sequestration conditions: an experimental study. Energy. 54:231–239. doi:10.1016/j.energy.2013.01.049

Pells PJN. 1993. Uniaxial strength testing. In: Hudson JA, editor. Rock testing and site characterization: principles, practice, and projects. Oxford (UK): Pergamon Press. p. 67–85. doi:10.1016/B978-0-08-042066-0.50010-0

Pan Z, Connell LD, Camilleri M. 2010. Laboratory characterisation of coal reservoir permeability for primary and enhanced coalbed methane recovery. Int J Coal Geol. 82:252–261. doi:10.1016/j.coal.2009.10.019

Pan J, Meng Z, Hou Q, Ju Y, Cao Y. 2013. Coal strength and Young's modulus related to coal rank, compressional velocity and maceral composition. J Struct Geol. 54:129–135. doi:10.1016/j.jsg.2013.07.008

Perera MSA, Ranjith PG, Choi SK, Airey D. 2011. The effects of sub-critical and super-critical carbon dioxide adsorption-induced coal matrix swelling on the permeability of naturally fractured black coal. Energy. 36:6442–6450. doi:10.1016/j.energy.2011.09.023

Perera MSA, Ranjith PG, Viete DR. 2013. Effects of gaseous and super-critical carbon dioxide saturation on the mechanical properties of bituminous coal from the Southern Sydney Basin. Appl Energy. 110:73–81. doi:10.1016/j.apenergy.2013.03.069

Perera M, Ranathunga A, Ranjith P. 2016. Effect of coal rank on various fluid saturations creating mechanical property alterations using Australian coals. Energies. 9:440. doi:10.3390/en9060440

Pipeng. 2025. Carbon dioxide compressibility factor, density, and vapour pressure (Yaws) calculator [Internet]. [accessed 2025 Jun–Aug]. https://pipeng.com/index.php/gsts/itdmotflup004a/itdtoflup004012/.

Schreiber J, Konicek P, Stonis M. 2017. Seismological activity during room and pillar hard coal extraction at great depth. Procedia Eng. 191:67–73. doi:10.1016/j.proeng.2017.05.155

Shukla R, Ranjith PG, Choi SK, Haque A. 2012. A novel testing apparatus for hydromechanical investigation of rocks: geo-sequestration of carbon dioxide. Rock Mech Rock Eng. 45:1073–1085. doi:10.1007/s00603-012-0241-2

Siriwardane H, Haljasmaa I, McLendon R, Irdi G, Soong Y, Bromhal G. 2009a. Influence of carbon dioxide on coal permeability determined by pressure transient methods. Int J Coal Geol. 77:109–118. doi:10.1016/j.coal.2008.08.006

Siriwardane HJ, Gondle RK, Smith DH. 2009b. Shrinkage and swelling of coal induced by desorption and sorption of fluids: theoretical model and interpretation of a field project. Int J Coal Geol. 77:188–202. doi:10.1016/j.coal.2008.08.005

South Carolina Department of Transportation. 2009. SC-T-39: standard method of test for determining the unconfined compressive strength of intact rock core specimens. Columbia (SC): South Carolina Department of Transportation.

Vishal V, Singh TN. 2015. A laboratory investigation of permeability of coal to supercritical CO_2. Geotech Geol Eng. 33:1009–1016. doi:10.1007/s10706-015-9882-8

Vishal V. 2017. In-situ disposal of CO_2: liquid and supercritical CO_2 permeability in coal at multiple down-hole stress conditions. J CO2 Util. 17:235–242. doi:10.1016/j.jcou.2016.12.011

Wang L, Chen Z, Wang C, Elsworth D, Liu W. 2019. Reassessment of coal permeability evolution using steady-state flow methods: the role of flow regime transition. Int J Coal Geol. 211:103210. doi:10.1016/j.coal.2019.103210

BET Gas Adsorption Measurements on Powdered Coal Samples

by Jessie Wu and Ernest Owusu

Gas adsorption measurements based on the Brunauer–Emmett–Teller (BET) approach are commonly applied to characterize gas–solid interactions in coal and other porous materials. Adsorption isotherms are obtained by measuring the amount of gas adsorbed as a function of pressure at a controlled temperature, providing quantitative information on adsorption behavior under defined experimental conditions.

Nitrogen (N_2) adsorption experiments conducted at cryogenic temperature (−196 °C) are widely used to characterize pore structure, including pore size distribution and pore volume, over a broad pore size range. Carbon dioxide (CO_2) adsorption experiments, typically performed at higher temperatures, are often used to evaluate adsorption behavior under conditions that are more relevant to laboratory-scale and subsurface applications.

Gas adsorption measurements in this study were performed using a Micromeritics ASAP 2020 Plus surface area and porosity analyzer (Figure 1). The ASAP 2020 Plus is a fully automated volumetric gas adsorption instrument designed for high-resolution adsorption and desorption measurements under controlled temperature and pressure conditions. The system supports a wide range of adsorptive gases and is commonly used for adsorption isotherm measurements on powders and porous solids.

The instrument is equipped with precise pressure transducers and automated dosing control, enabling accurate measurement of gas uptake as a function of pressure. Integrated degassing capabilities allow samples to be evacuated and thermally treated prior to analysis to remove moisture and residual gases. During adsorption measurements, free space determination, pressure equilibration, and data acquisition are performed automatically through instrument control software, ensuring consistent and repeatable experimental procedures.



Figure 1. Micromeritics ASAP 2020 Plus instrument.

Experimental Methods

Materials

Gas adsorption experiments were conducted on three powdered coal samples: **FCC35-1, FCC35-2,** and **FCC35-3.** All samples were prepared as fine powders prior to analysis to ensure uniform packing and consistent gas–solid contact during adsorption measurements.

Sample Preparation and Degassing

Prior to adsorption measurements, each coal sample was loaded into a standard sample tube and degassed automatically on the instrument to remove moisture and residual gases. Degassing was performed under vacuum using a two-stage procedure. During the evacuation phase, samples were evacuated from approximately 5.0 mmHg to about 1.0×10^{-2} mmHg while being heated to 150°C at a ramp rate of 10°C/min. The evacuation was maintained for 60 minutes. This was followed by a heating phase in which the sample temperature was held at 150°C for an additional 120 minutes. After degassing, samples were allowed to cool and were backfilled prior to adsorption analysis.

Carbon dioxide (CO_2) experiments were conducted on powdered coal samples using a Micromeritics ASAP 2020 Plus instrument (Figure 1). All measurements were performed at 0°C with CO_2 as the adsorptive gas to obtain adsorption and desorption isotherms under controlled temperature conditions.

Nitrogen (N_2) Adsorption Measurements

Nitrogen adsorption and desorption experiments were conducted for each coal sample using N_2 as the adsorptive gas at a measurement temperature of −196°C. Adsorption isotherms were collected over a wide range of relative pressures using absolute pressure dosing. The N_2 adsorption data were used to obtain adsorption isotherms, pore size distribution, and pore volume for each sample. Ambient and analysis free space volumes were measured automatically prior to data acquisition, and pressure equilibration was applied at each dosing step to ensure stable measurements.

Carbon Dioxide (CO_2) Adsorption Measurements

Following the N_2 adsorption experiments, CO_2 adsorption and desorption measurements were conducted on the same coal samples using CO_2 as the adsorptive gas. CO_2 adsorption isotherms were collected at a measurement temperature of **0°C** using absolute pressure dosing over a pressure range from near vacuum to approximately 925 mmHg. An equilibration interval of 10 seconds was applied at each pressure step. Adsorbed gas quantities were recorded as a function of pressure and reported in units of cm^3/g at standard temperature and pressure (STP).

Results

N_2 Adsorption Measurements at -196°C

Nitrogen adsorption and desorption isotherms for **FCC35-1** measured at −196°C are shown in Figure 2. The isotherm exhibits a continuous increase in N_2 uptake with increasing relative pressure over the full measured range. A distinct separation between the adsorption and

desorption branches is observed, indicating pressure-dependent adsorption and desorption behavior.

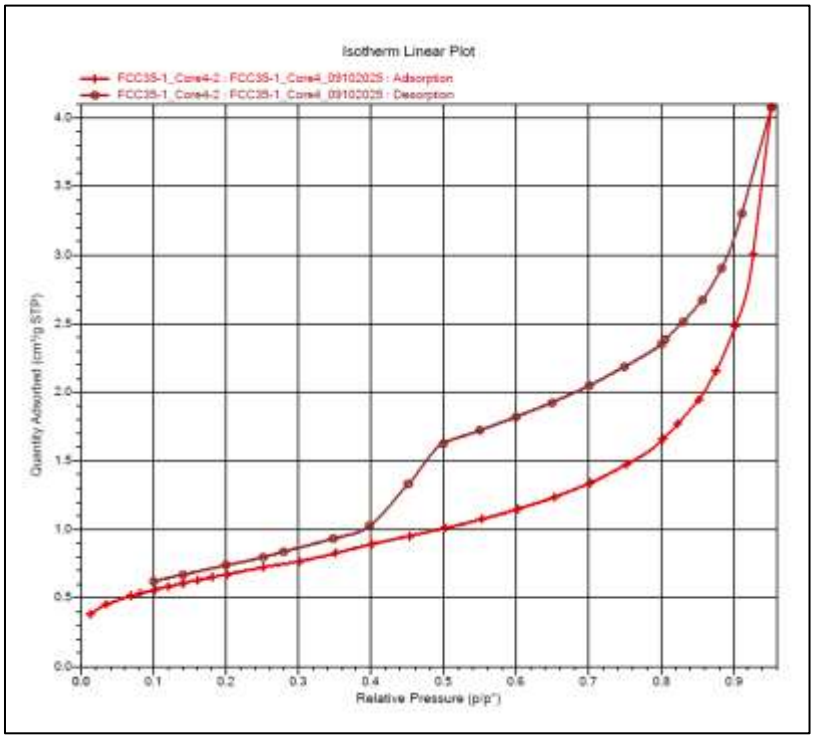


Figure 2. Nitrogen adsorption and desorption isotherms of FCC35-1 measured at −196°C

BET analysis of the N_2 adsorption data yields a BET surface area of **2.46 m²/g**. The total pore volume derived from adsorption data and **0.0064 cm³/g** from desorption data over the analyzed pore size range. The average pore diameter estimated from the BET method is approximately **10.2 nm.**

Nitrogen adsorption and desorption isotherms for FCC35-2 measured at −196°C are shown in Figure 3. The isotherm exhibits a continuous increase in N_2 uptake with increasing relative pressure over the full measured range. A distinct separation between the adsorption and desorption branches is observed, indicating pressure-dependent adsorption and desorption behavior.

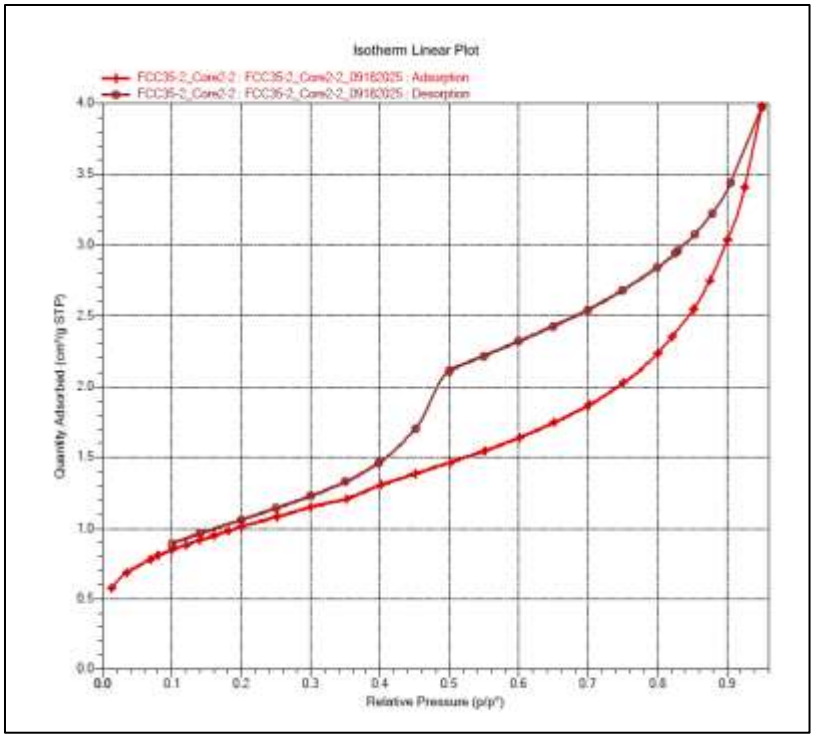


Figure 3. Nitrogen adsorption and desorption isotherms of FCC35-2 Core 2-2 measured at −196°C.

BET analysis of the N_2 adsorption data yields a BET surface area of 3.66 m^2/g. The total pore volume derived from adsorption data is 0.0064 cm^3/g, and 0.0063 cm^3/g from desorption data over the analyzed pore size range. The average pore diameter estimated from the BET method is approximately 6.72 nm.

Nitrogen adsorption and desorption isotherms for FCC35-3 measured at −196°C are shown in Figure 4. The isotherm exhibits a continuous increase in N_2 uptake with increasing relative pressure over the full measured range. A distinct separation between the adsorption and desorption branches is observed, indicating pressure-dependent adsorption and desorption behavior.

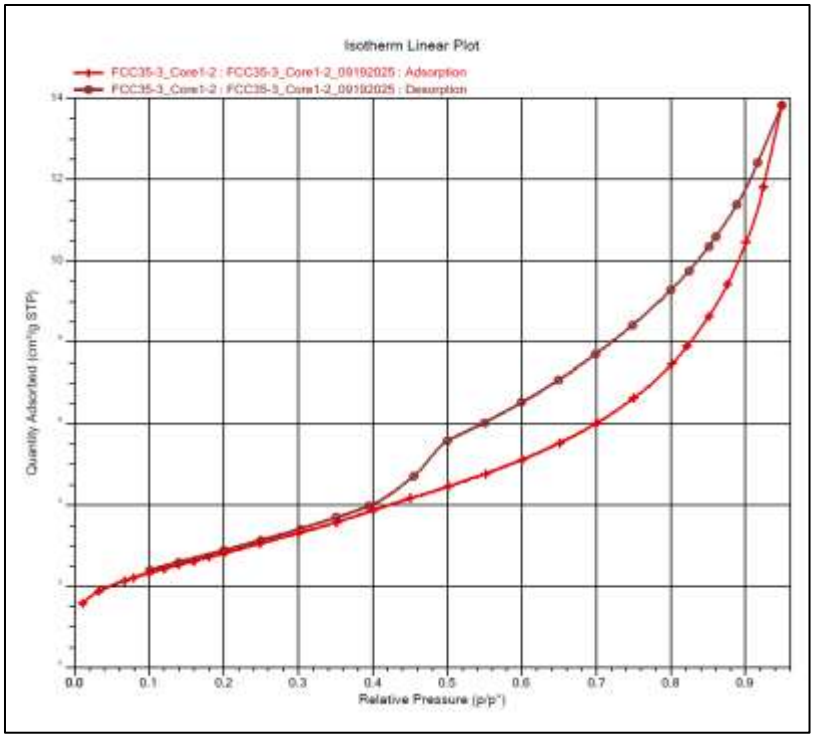


Figure 4. Nitrogen adsorption and desorption isotherms of FCC35-3 measured at −196°C. BET analysis of the N_2 adsorption data yields a BET surface area of 10.41 m²/g. The total pore volume derived from adsorption data is 0.0219 cm³/g, and 0.0217 cm³/g from desorption data over the analyzed pore size range. The average pore diameter estimated from the BET method is approximately 8.22 nm.

Comparison of the nitrogen adsorption and desorption isotherms for the three coal samples shows clear differences in adsorption capacity and overall gas uptake behavior. All three samples exhibit similar isotherm shapes, with a continuous increase in N_2 uptake as relative pressure increases and a distinct separation between adsorption and desorption branches, indicating pressure-dependent adsorption and desorption behavior.

Among the three samples, FCC35-3 shows the highest N_2 uptake across the full relative pressure range, consistent with its higher BET surface area and larger total pore volume. FCC35-2 exhibits intermediate N_2 uptake, while FCC35-1 shows the lowest overall adsorption capacity. These differences are reflected in both the magnitude of adsorption at high relative pressure and the total pore volumes derived from the N_2 data.

Despite differences in total uptake, the overall trends in adsorption and desorption behavior are similar for all three samples. The N_2 adsorption results therefore indicate systematic variability in pore-related characteristics among the coal samples while maintaining comparable adsorption behavior across the measured pressure range. These results provide a consistent basis for subsequent comparison with CO_2 adsorption measurements performed on the same samples.

CO_2 Adsorption Measurements at 0°C

Carbon dioxide adsorption and desorption isotherms for **FCC35-1** measured at **0°C** are shown in Figure 5. The isotherm exhibits a continuous increase in CO_2 uptake with increasing relative pressure over the full measured range (p/p° up to approximately 0.035). A distinct separation

between the adsorption and desorption branches is observed, indicating pressure-dependent adsorption and desorption behavior.

The CO_2 adsorption data show gradual uptake at lower relative pressures, followed by a more pronounced increase in adsorption as relative pressure approaches the upper end of the measured range. The observed hysteresis between adsorption and desorption branches indicates differences in CO_2 uptake and release behavior under the same relative pressure conditions.

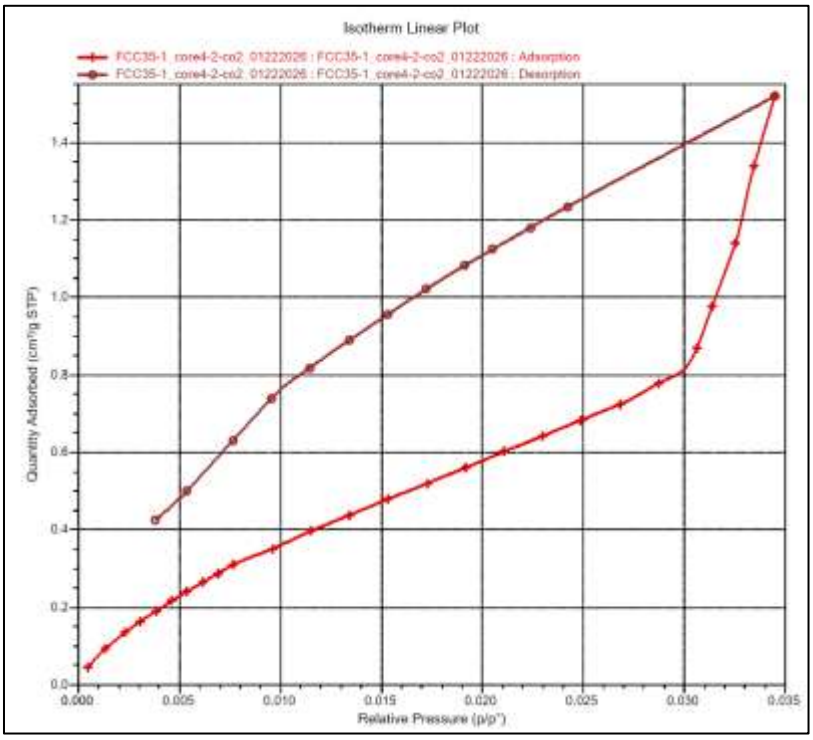


Figure 5. Nitrogen adsorption and desorption isotherms of FCC35-1 measured at 0°C.

Comparison of N_2 and CO_2 Adsorption

Nitrogen and carbon dioxide adsorption and desorption isotherms for FCC35-1 show clear differences in adsorption behavior under the respective measurement conditions. The N_2 isotherm measured at −196°C spans a broad relative pressure range and exhibits a gradual increase in gas uptake with increasing relative pressure. In contrast, the CO_2 isotherm measured at 0°C covers a narrower relative pressure range and shows a continuous increase in CO_2 uptake with increasing relative pressure.

Both isotherms exhibit hysteresis between adsorption and desorption branches, indicating pressure-dependent adsorption and desorption behavior. Differences in the shape and magnitude of the isotherms reflect variations in adsorption behavior between N_2 and CO_2 under the tested conditions. Together, the N_2 and CO_2 results provide complementary datasets for characterizing gas adsorption behavior on the same coal sample.

Model Construction

The primary goal is to develop a hydrodynamic model to calibrate the measured gas production rate at the Fruitland coal site in New Mexico. The initial field model, created using Petrel 2024, was upscaled to Computer Modelling Group's (CMG) General Equation of State Model (GEM) 2025 to simulate fully implicit compositional fluid flow. A six-layer field double porosity model, consisting of three coal-bearing zones (upper, middle, and lower) identified from log interpretations (Weber et al. 2012), was built for the simulation study. Each coal-bearing zone includes two layers separated by non-reservoir sections, with total thicknesses ranging from 4.6 to 25 ft for the upper zone, 3.5 to 12 ft for the middle zone, and 8 to 33 ft for the lower zone. The matrix porosity of the production zones was set at 1% (assumed), while the cleat permeability was set at 78 nD based on core testing. The model grid comprised 235 × 196 × 11 blocks, totaling approximately 506,660 grid blocks, of which 276,360 are active. Each grid block measures 100 ft × 100 ft. The cleat porosity was estimated using the production index (Siriwardane et al. 2012) for each well (Error! Reference source not found.) and used as input for a Gaussian geostatistical simulation to fill the rest of the grids (**Figure 1**). A cubic power-law relationship (Siriwardane et al. 2012) between cleat permeability and porosity (Error! Reference source not found.) was used to model permeability distribution (**Figure 54**). The Langmuir volume and pressure isotherms were obtained from the Tiffany Unit N2-ECBM Pilot report (Reeves and Oudinot 2004). Wells completed in the three coal zones, with operating parameters based on gas and water surface production histories, served as model inputs. The wells were constrained to respect reservoir volume during history matching, with skin factors set to zero. Other relevant reservoir parameters are listed in **Table 9.** Reservoir parameters used in the model. The model boundaries were set as no-flow barriers to represent wells adjacent to the study area (Reeves and Oudinot 2004).

$$\emptyset_i = \frac{\emptyset_{max} - \emptyset_{min}}{R_{max} - R_{min}} \times (R_i - R_{min}) + \emptyset_{min} \quad \text{Eq. 1}$$

$$\emptyset = a\left(k_f\right)^n \quad \text{Eq. 2}$$

Where:

R_i = The relative production of each well *i* compared to maximum production ($\frac{Q_i}{Q_{max}}$)

R_{min} = Minimum relative production ratio among all producers

$\emptyset_{max}$ = Specified maximum porosity

$\emptyset_{min}$ = Specified minimum porosity

Q_i = Production rate of well *i*

Q_{max} = Maximum production rate of well *i*

$\emptyset$ = Porosity

k_f = Intrinsic permeability in the face cleat, mD

a = Variable porosity factor

n = 0.33 for coal

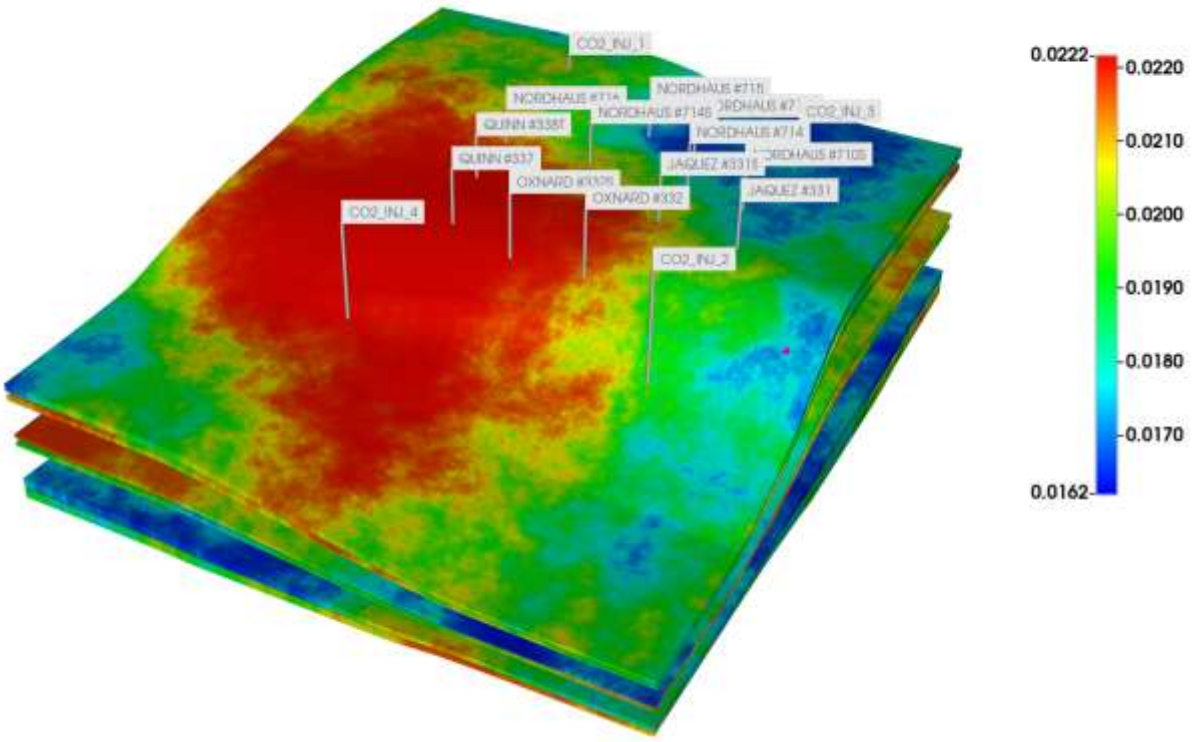


Figure 53. Face cleat porosity distribution

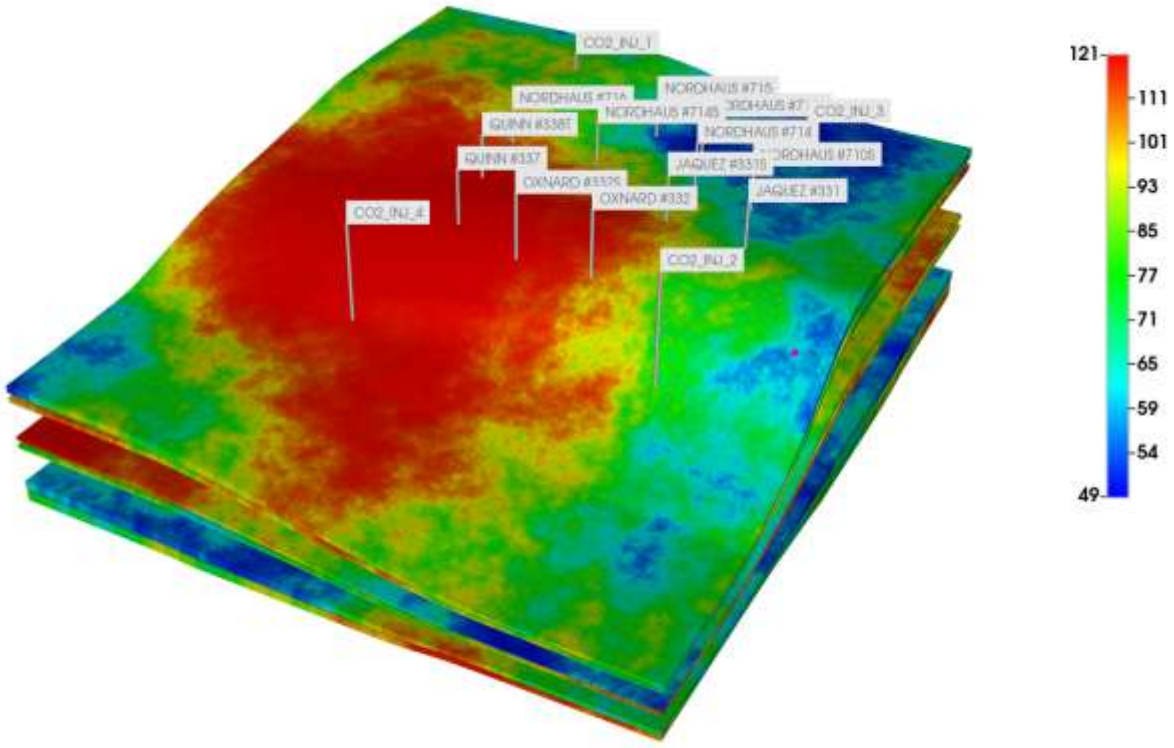


Figure 54. Face cleat permeability distribution

Table 9. Reservoir parameters used in the model

Parameter	Value	Source
Initial Pressure	1,600 psi	Well test report
Reservoir Temperature	120 deg F	(Reeves et al. 2003)
Initial Water Saturation		Assumed
Initial Gas Content	Per Isotherm	(Reeves et al. 2003)
Sorption time	10 days	(Reeves et al. 2003)
Fracture Spacing	0.25 inch	(Reeves and Oudinot 2004)

Gas Composition	95.5% CH_4 4.5% CO_2	(Reeves et al. 2003)
Relative Permeability	History Match	
Permeability Function Parameters	n = 0.33 a = 0.0024	(Siriwardane et al. 2012)

History Matching

The goal of this subtask is to calibrate the coal seam reservoir model to match field history before Enhanced Coalbed Methane (ECBM) production. The parameters chosen for adjustment are those affecting field performance and can be technically justified. The independent parameter in the reservoir model was the reservoir production rate to maintain material balance, while the dependent (history-matching) parameters were the gas and water production rates. A parametric study was performed on the permeability anisotropy ratio between the cleat and butt directions to identify the ratio at which gas production cannot be sustained while matching the field-measured rates. This step prevents selecting permeability values that could lead to overestimation during field operations. A second step involved history matching, adjusting two parameters of the relative permeability model (Chen et al. 2013) as in Error! Reference source not found. to Error! Reference source not found., where l is the cleat size distribution, h is the tortuosity, k_{rw}^{*} is the end-point relative permeability of the wetting phase, k_{rnw}^{*} is the end-point relative permeability of the nonwetting phase, S_w is the wetting phase saturation, S_{wr} is the residual wetting phase saturation and S_{nwr} is the residual nonwetting phase saturation to align gas production with the relative permeability. **Figure 55** is the resulting relative permeability curve after model calibration and used in the ECBM study.

$$k_{rw} = k_{rw}^{*}(S_w^{*})^{\eta+1+2/\lambda} \quad \text{Eq. 3}$$

$$k_{rnw} = k_{rnw}^{*}(1 - S_w^{*})^{\eta}\left[1 - (S_w^{*})^{1+2/\lambda}\right] \quad \text{Eq. 4}$$

$$S_w^{*} = \frac{S_w - S_{wr}}{1 - S_{wr} - S_{nwr}} \quad \text{Eq. 5}$$

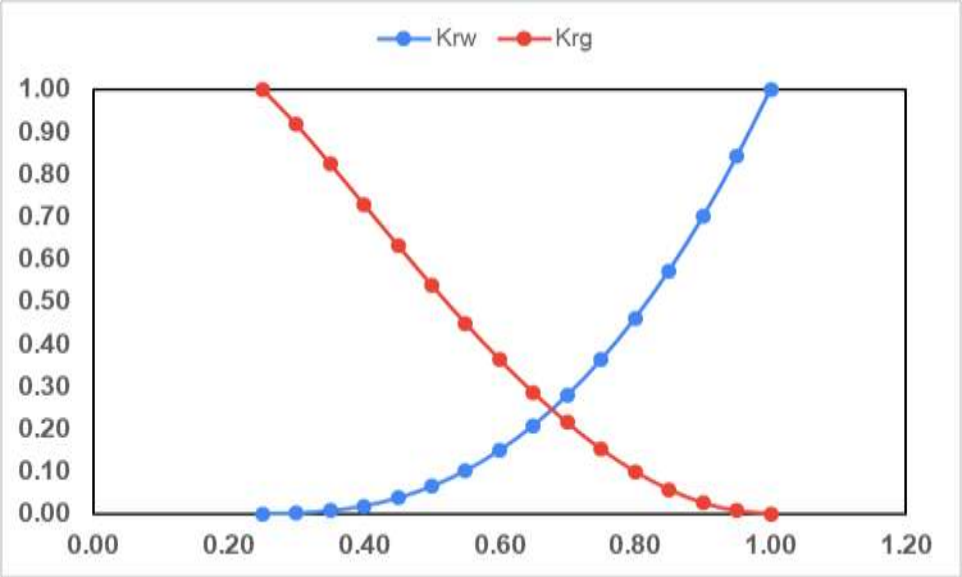
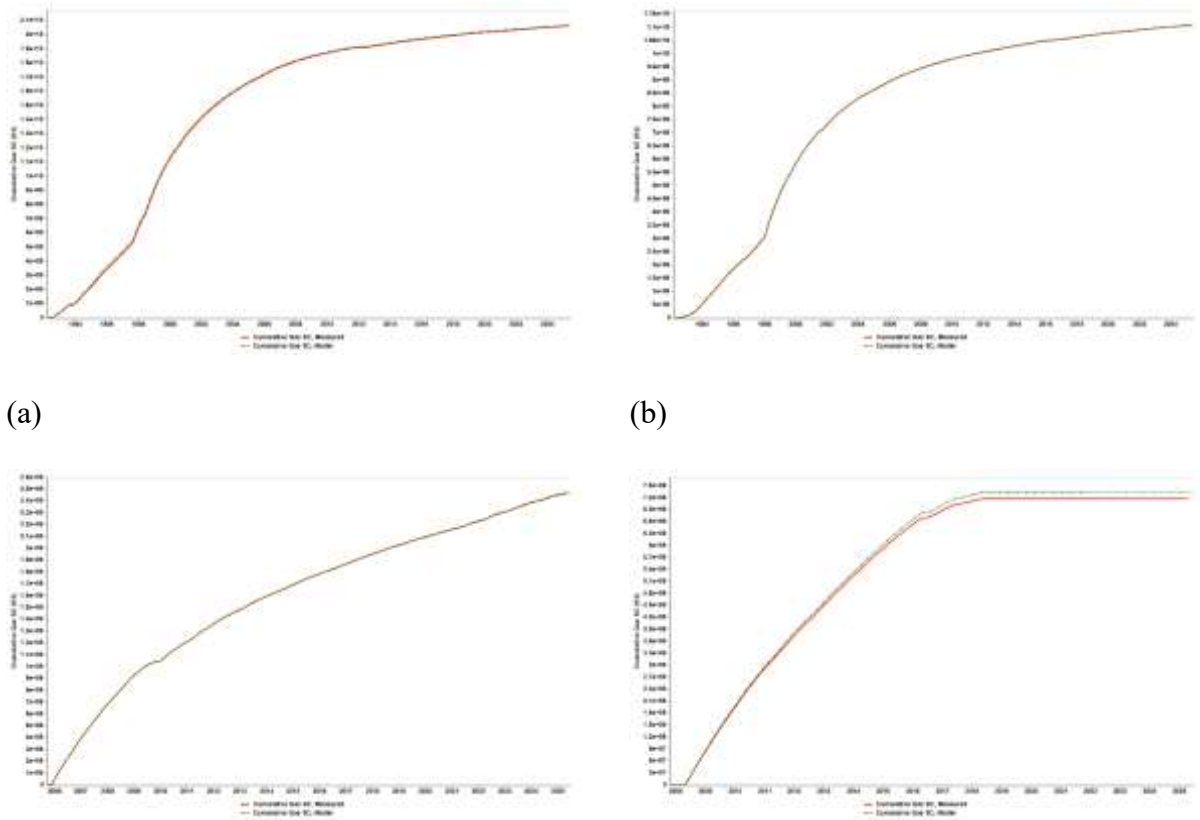


Figure 55: Calibrated relative permeability curve

A comparison of measured versus model-predicted well gas production is shown in **Figure 56** for selected wells. The only conclusion that can be drawn from this result, since the reservoir volume rate drove the model, is that the model can produce the observed gas volumes.

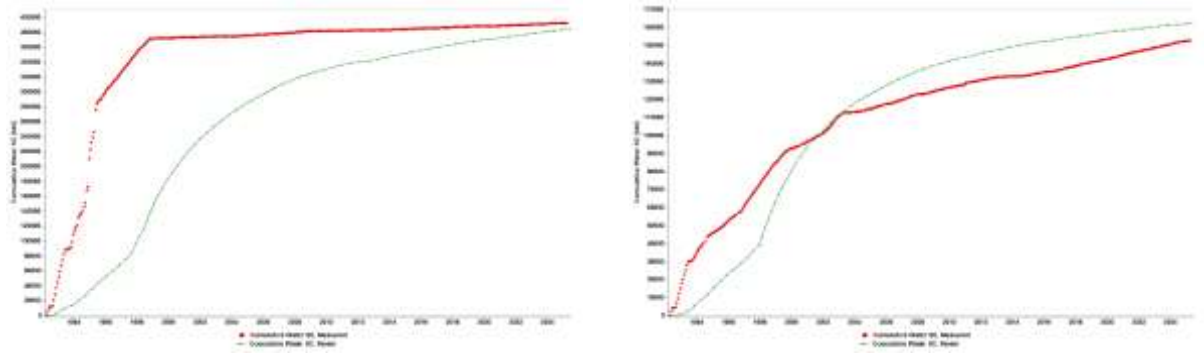


(a) (b)

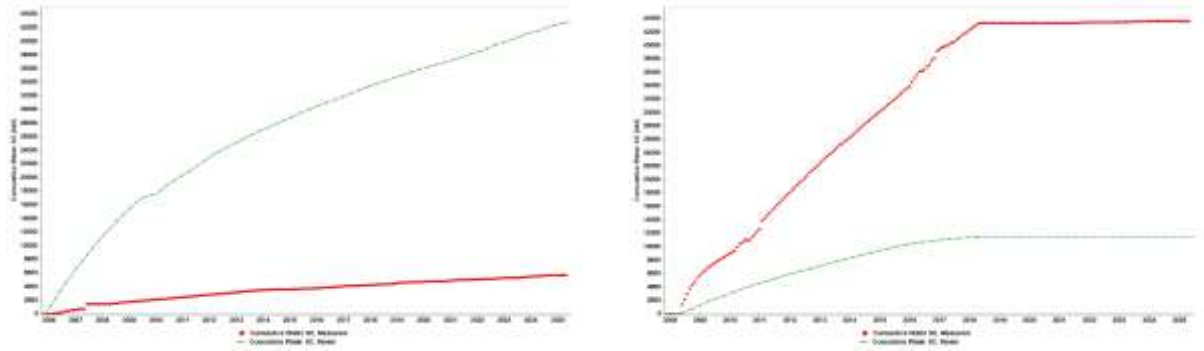
(c) (d)

Figure 56: Comparison between measured and model-predicted gas production performance (a) NORDHAUS #714 (b) NORDHAUS #715 (c) JAQUEZ #331S (d) QUINN #338T

Figure 57 shows the well water production performance for selected wells. The quality of the water rate predictions varied, with some being too high (Figure 57c) and some too low (Figure 57d). However, on balance, the projections are considered reasonable, and the measured water rate appears too erratic to be accurate. It cannot be easily explained by regional variations in porosity and/or water relative permeability. Therefore, matching water rates was not a priority. Even though water production from individual wells was not prioritized, the total water produced from all wells was honored at the end of calibration (**Figure 58**). Preferably, well bottom-hole pressure, if available, should be used to validate the calibration, which was not available for this study. The use of the water rate, which is historically known not to be measured accurately, may lead to erroneous calibration pressures, which in turn affect forecast performance.



(a) (b)



(c) (d)

Figure 57. Comparison between measured and model-predicted water production performance (a) NORDHAUS #714 (b) NORDHAUS #715 (c) JAQUEZ #331S (d) QUINN #338T

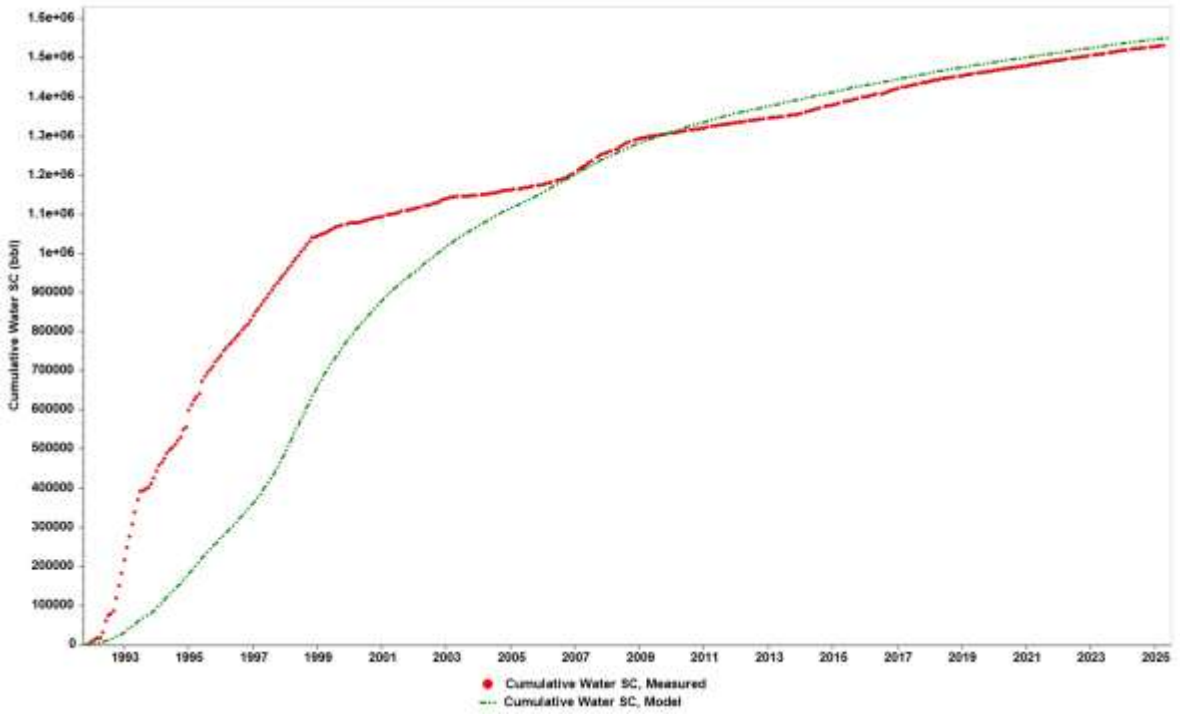


Figure 58. Field cumulative water production performance between measured and model predictions.

Performance Forecasts

To evaluate the long-term performance of the ECBM pilot under status quo conditions (i.e., no further CO_2 injection) and other "what if" future injection scenarios, performance prediction cases were simulated using the calibrated model. The specific cases evaluated included:

1) No CO_2 injection (i.e., primary production only).
2) Continuous CO_2 injection.
3) Continuous N_2–CO_2 co-injection.
4) Continuous CO_2 with intermittent N_2 injection.

For each forecast scenario, the model assumed flowing bottomhole pressures of 200 psi. The gas production rate is 1E6 ft³/day for the ECBM cases and gradually increased every 2 yr until 2034, when the maximum rate target of 3E6 ft³/day is maintained. For the No CO_2 injection case, the last known well-specific rates from history were used for forecasting. Additionally, an economic limit of 50% CO_2 content per well was imposed; exceeding this threshold prompted the layer in question to be shut in. An injection target of 100 tons per day per injection well was set, gradually increased by 50 tons every 2 yr until 2034, when the maximum injection target of 300 tons per day is reached. The maximum injection bottom-hole pressure was set to 0.7 of the initial reservoir pressure, translating to 1,120 psi. A peripheral injection scheme was implemented, coupled with staggered rate control between the injection and production wells to delay CO_2 breakthrough and prevent rapid pressure changes that could negatively impact displacement efficiency. By maintaining reservoir pressure around 0.7 of its initial value, pressure-induced injectivity loss will be minimized. **Figure 59** shows the relationship between permeability changes with pressure and concentrations (Reeves et al. 2003). The forecast aims to keep reservoir pressure within the green region. After the calibration, the average pressure within the

upper coal was 1,151 psi, while the middle and lower coal zones were around 980 psi. The upper coal was within the pressure-dependence region, while the middle and lower coals were within the matrix-shrinkage region.

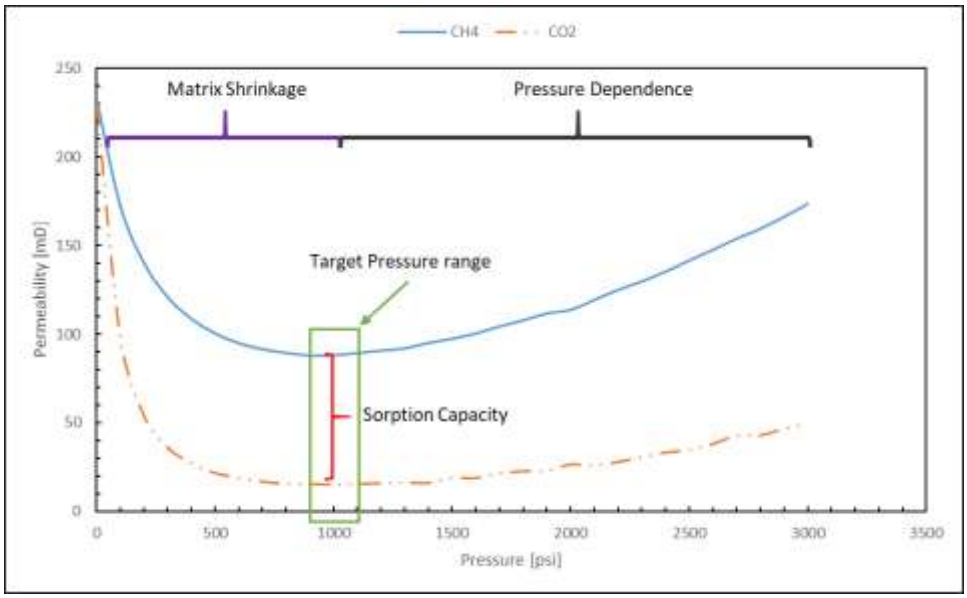


Figure 59. Permeability changes with pressure and concentration (Reeves et al. 2003)

Case #1: No CO_2 Injection

The baseline scenario assumes that no CO_2 injection occurred and that the field was produced exclusively by primary pressure depletion over 30 yr. In this case, total incremental methane recovery was 336 Mt within the active model area, yielding a recovery factor of 3.0%. The final average reservoir pressure was 971 psi (**Figure 60**).

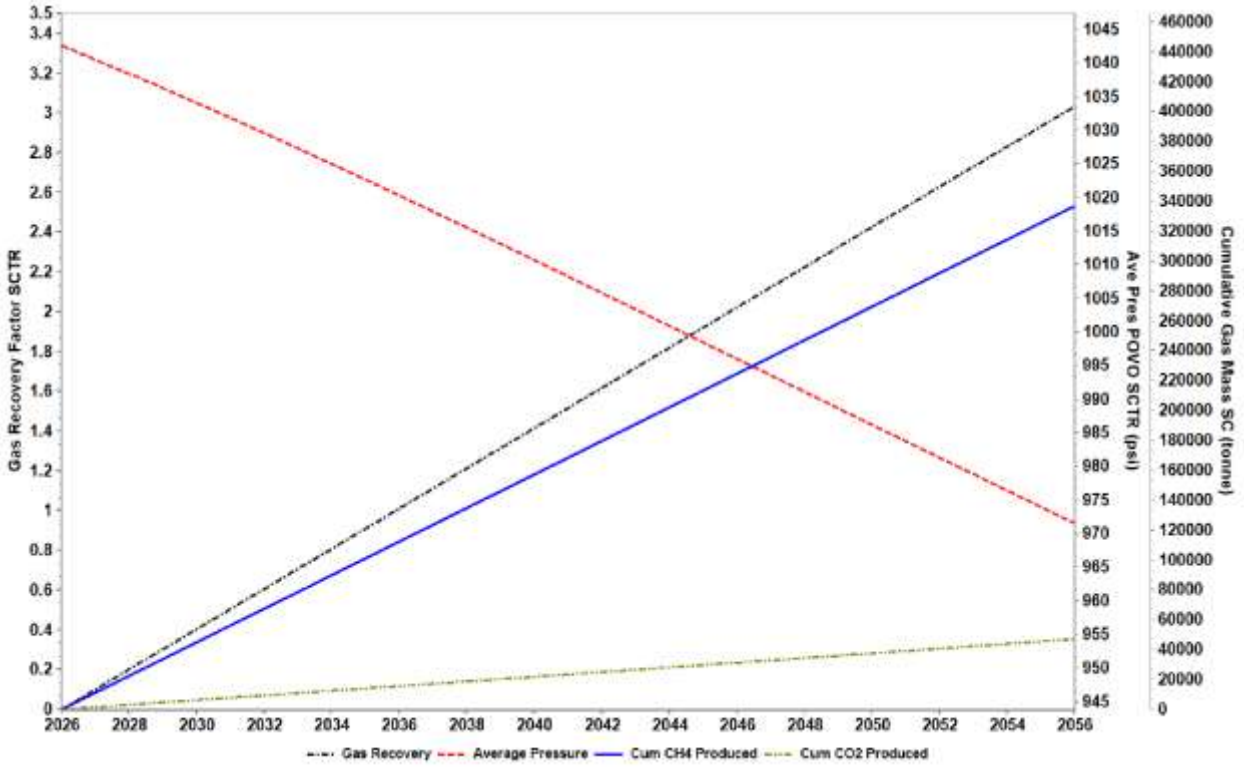


Figure 60. Average reservoir pressure and incremental gas production and recovery Case 1

Case #2: Continuous CO_2 Injection

This case assumes CO_2 injection over 30 yr, with a gradual increase in the injection rate. The incremental gas rate for Case 2 is shown in **Figure 61.** Notably, several wells were shut in due to exceeding the maximum allowable CO_2 content of 50% in the produced gas. The total methane recovery for Case 2 was approximately 3.53 Mt, approximately 3.19 Mt more than in Case 1. The total volume of CO_2 injected was approximately 21.6 Mt, resulting in a CO_2 to CH_4 ratio of 6:1. The average final pressure within the active model was 1,130 psi. The estimated incremental sequestration volume for this case is approximately 18.7 Mt of CO_2.

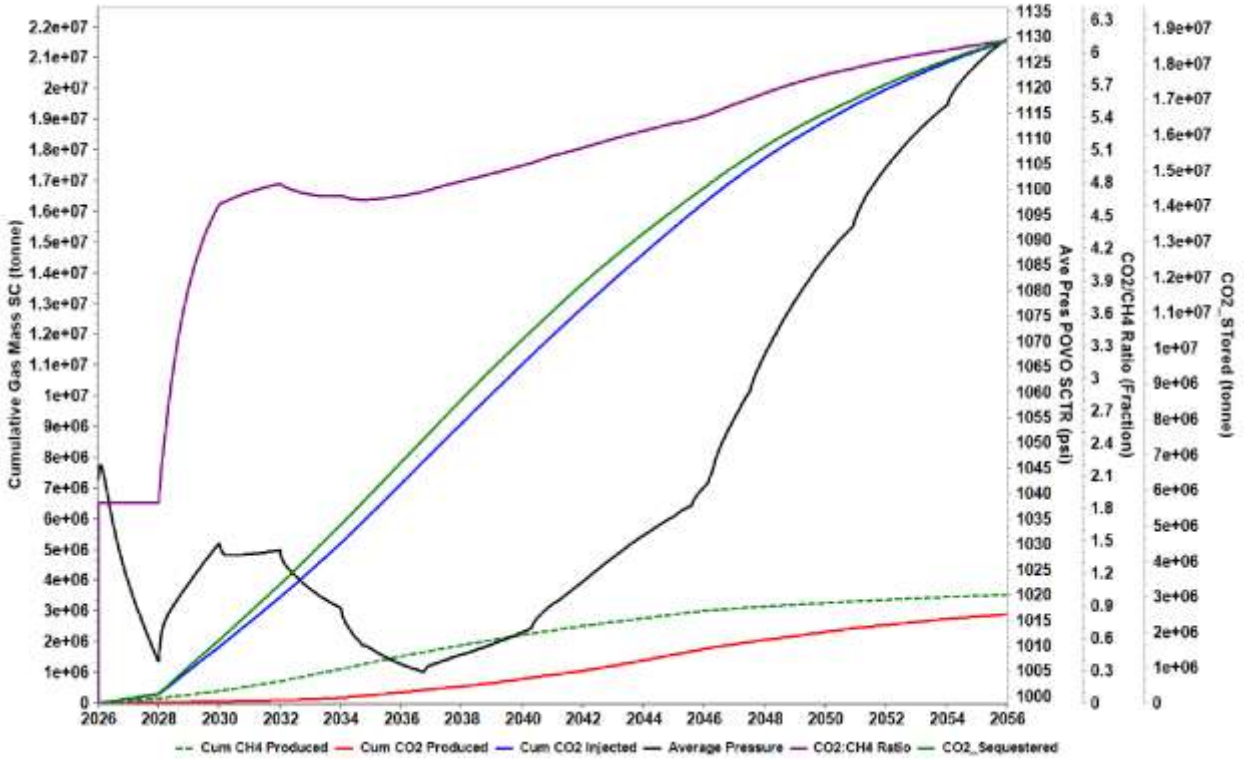
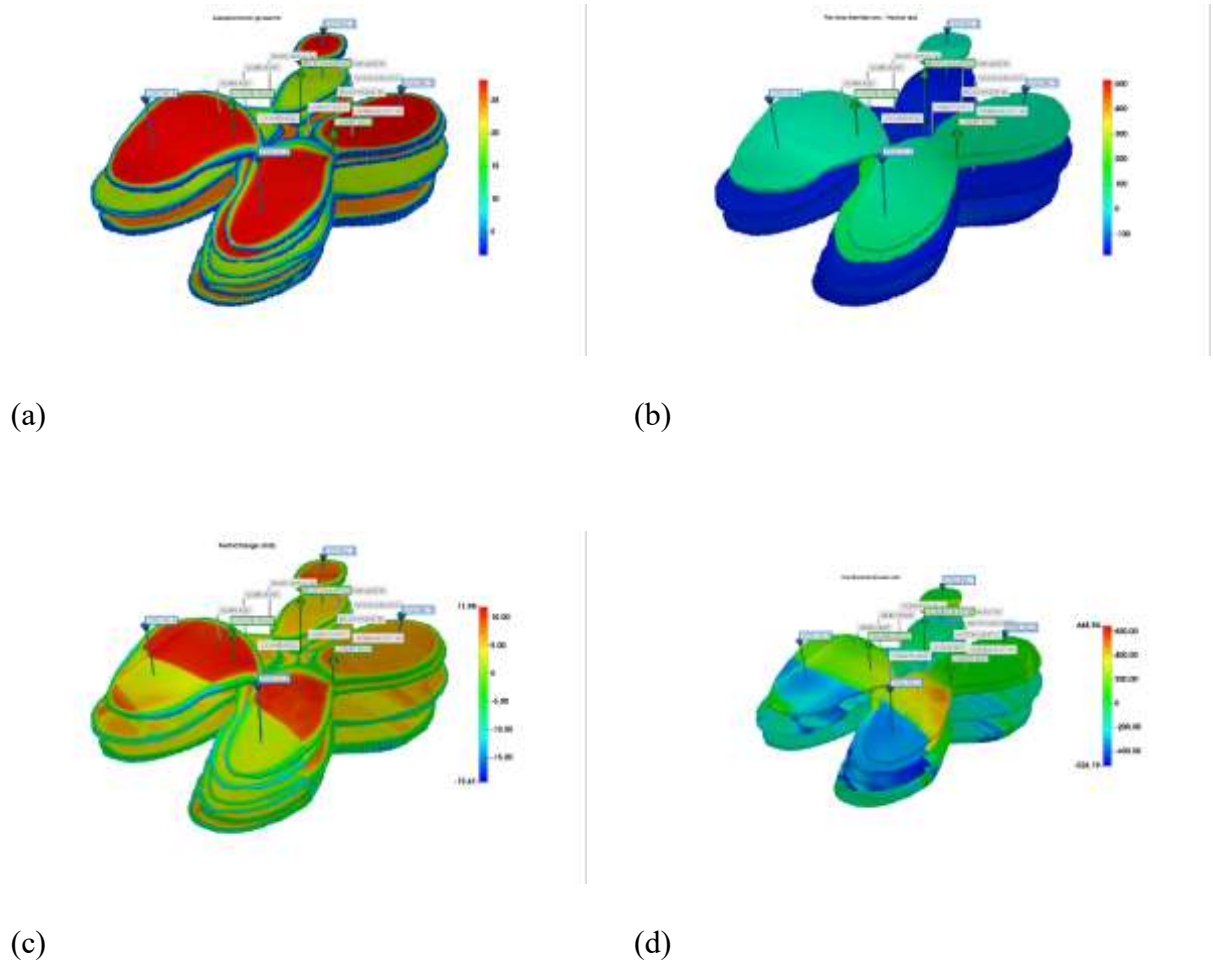


Figure 61. Continuous CO_2 injection incremental recovery performance

Figure 62a shows the CO_2 plume within the coal matrix at the end of injection, delineated as any regions with CO_2 adsorption greater than 3 gmole/ft^3. The minimum value was chosen based on the maximum final adsorption after calibration. Any adsorption value above the maximum is treated as the injected CO_2 plume region. The forecasting was designed to decrease the fracture pressure in the upper coal region and increase it in the middle and lower regions. In Figure 62b, which shows the cumulative pressure drop within the CO_2 plume, it can be observed that there is a decrease (positive fracture pressure drop) in the upper coal and an increase (negative fracture pressure drop) in the middle and lower regions. An average pressure gain of 100 psi was observed in the middle and lower regions, and an average pressure depletion of 100 psi in the upper coal region. With that pressure target, permeability increased in the upper coal region without significant loss in the middle and lower regions, as shown in the cumulative permeability change plot (Figure 62c). The permeability changes in the fractures between the injector and producers (Figure 62c) did not lead to injectivity because the matrix pressures around the producers created a significant pressure drop (Figure 62d), thereby shrinking the matrix and increasing permeability in the fractures. At the end of the injection, the pressure within all regions was within the target range, which is around the average pressure at the end of calibration.



(a) (b)

(c) (d)

Figure 62. Case 2 CO_2 adsorption: (a) CO_2 plume, (b) cumulative pressure change, (c) fracture cumulative permeability change, and (d) matrix cumulative permeability change at the end of injection

Case #3: Continuous N_2–CO_2 Injection

This case assumes CO_2–N_2 injection at a 0.95:0.05 ratio over 30 yr, with a gradual increase in injection rate. The incremental gas rate for Case 3 is shown in **Figure 63**. The total methane recovery for Case 3 was approximately 3.59 Mt, approximately 3.26 Mt more than in Case 1 but about 66 kt more than in Case 2. The total volume of CO_2 injected was approximately 20 Mt. The average final pressure within the active model was 1,117 psi which is not different from Case 2. The estimated incremental sequestration volume for this case is approximately 17.4 Mt of CO_2, about 1 Mt less than Case 2.

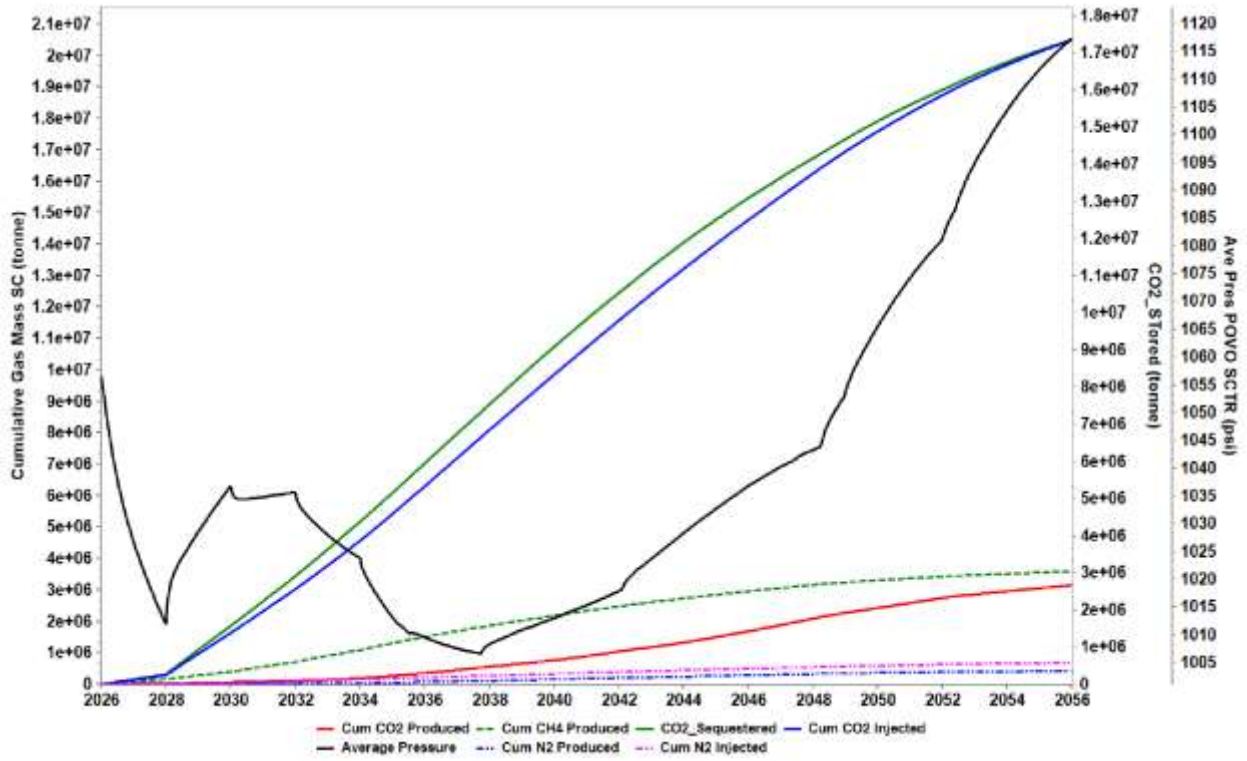
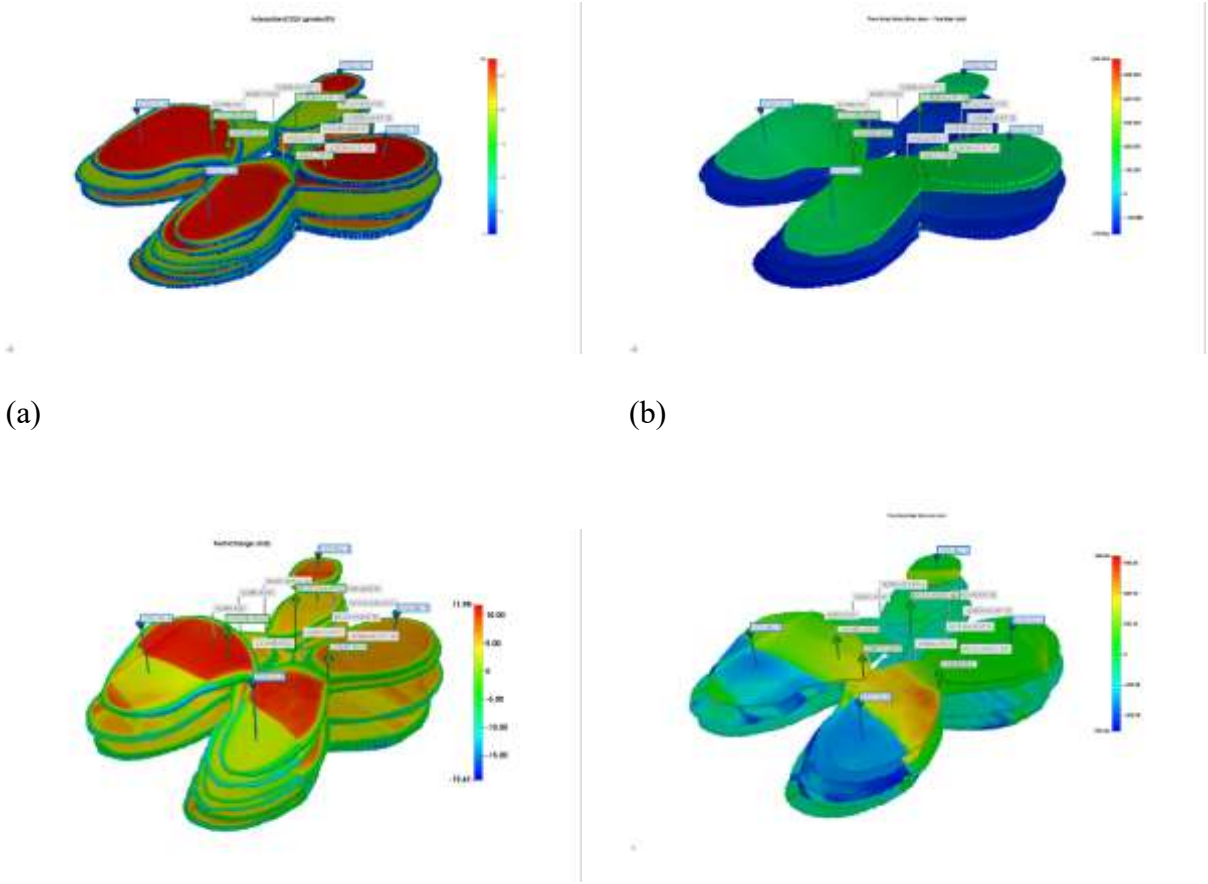


Figure 63. Continuous CO_2–N_2 injection incremental recovery performance

Figure 64a shows the CO_2 plume within the coal matrix at the end of injection, delineated as any regions with CO_2 adsorption greater than 3 gmole/ft^3. The forecasting was designed similarly to Case 2, but N_2 kept the fractures open to decrease the pressure in the upper coal region and increase it in the middle and lower regions. In Figure 64b, which shows the cumulative pressure drop within the CO_2 plume, it can be observed that there is a decrease in the upper coal and an increase in the middle and lower regions. An average pressure gain of 100 psi was observed in the middle and lower regions, and an average pressure depletion of 100 psi in the upper coal region. With that pressure target, permeability increased in the upper coal region without significant loss in the middle and lower regions, as shown in the cumulative permeability change plot (Figure 64c). At the end of the injection, the pressure within the production zone within the matrix (Figure 64d) decreased, creating a flow path between the injector and producers. Due to the distance between the injectors 1 and 3 and the producers, there was net pressure decrease which lead to permeability increase (Figure 64c).



(a) (b)

(c) (d)

Figure 64. Case 3 CO_2 adsorption: (a) CO_2 plume, (b) cumulative pressure change, (c) fracture cumulative permeability change, and (d) matrix cumulative permeability change at the end of injection

Case #4: Continuous CO_2 with Intermittent N_2 Injection

This case assumes CO_2 injection for 11 months and N_2 injection for 1 month over 30 yr, with a gradual increase in the CO_2 injection rate while the N_2 injection rate is maintained at 50 t for each of the four injection wells. The incremental performance for Case 4 is shown in **Figure 65**. The total methane recovery for Case 4 was approximately 3.65 Mt, approximately 3.32 Mt more than in Case 1, but about 126 thousand and 59 kt more than in Cases 2 and 3, respectively. The total volume of CO_2 injected was approximately 20.7 Mt. The average final pressure within the active model was 1,097 psi, which is not different from Cases 2 and 3. The estimated incremental sequestration volume for this case is approximately 17.3 Mt of CO_2, about 1 Mt less than Case 2.

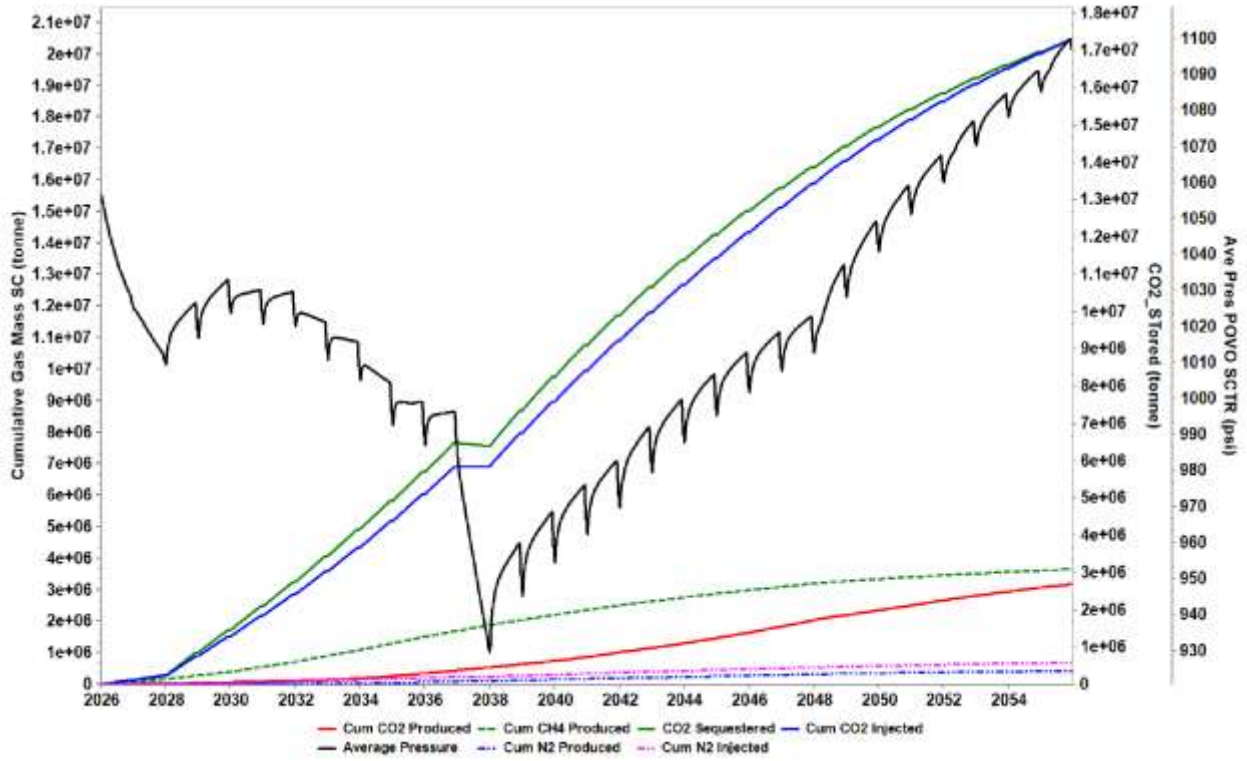
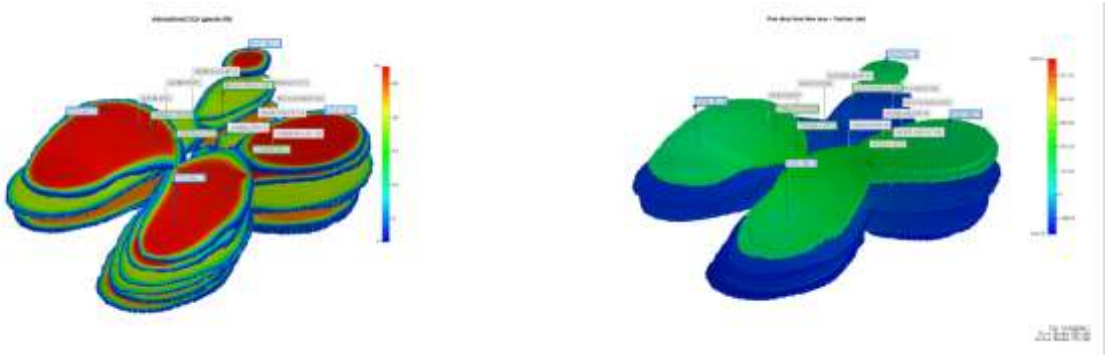
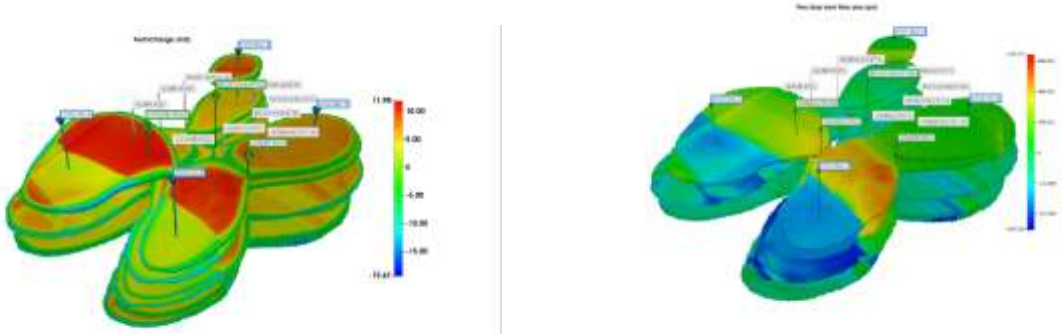


Figure 65. Intermittent CO_2–N_2 injection incremental recovery performance

Figure 66a shows the CO_2 plume within the coal matrix at the end of injection. In Figure 66b, which shows the cumulative pressure drop within the CO_2 plume, it can be observed that there is a decrease in the upper coal and an increase in the middle and lower regions. An average pressure gain of 100 psi was observed in the middle and lower regions, and an average pressure depletion of 100 psi in the upper coal region similar to Case 2 and 3. The permeability increase within the upper coal region without significant permeability loss within the middle and lower regions as shown in the cumulative permeability change plot (Figure 66c).



(a) (b)



(c) (d)

Figure 66: Case 4 CO_2 adsorption: (a) CO_2 plume, (b) cumulative pressure change, (c) fracture cumulative permeability change, and (d) matrix cumulative permeability change at the end of injection

A comparison of the forecast cases' performance relative to the no-injection case is delineated in **Table 10**. The results indicate an approximately 1% increase in recovery when N_2 was injected, despite a reduction in CO_2 storage attributable to increased CO_2 production. Because we could not attribute what amount of CO_2 or N_2 was contributed to CH_4 recovery, the CO_2:CH_4 ratio was not computed. The peripheral injection strategy and the spacing between injector and producer facilitated improved recovery, thereby permitting a larger injection volume and enhanced injectivity.

Table 10: Summary of case comparisons

	NO_CO_2_Injection	**CO_2-ECBM**	**CO_2-N_2-ECBM**	**CO_2-N_2-ECBM-Cycling**
Total CH_4 produced, t	3.37E+05	3.53E+06	3.59E+06	3.65E+06
Incremental CH_4 produced, t	0	3.19E+06	3.26E+06	3.32E+06
Total CO_2 injected, t	0	2.16E+07	2.05E+07	2.05E+07
Total CO_2 produced, t	4.70E+04	2.90E+06	3.15E+06	3.18E+06
Total N_2 injected, t	0	0	6.87E+05	6.85E+05
Total N_2 produced, t	0	0	4.25E+05	4.25E+05

CO_2:CH_4	0	6	-	-
Incremental CH_4 recovery, %OGIP	2.45	25.67	26.15	26.59
CO_2 stored, t	0	1.87E+07	1.74E+07	1.73E+07
Average pressure, psi	972	1,130	1,117	1,097

Underground Injection Control Consideration for Escalante Power Plant

Geologic CO_2 Storage Permits Template in New Mexico (EPA Region VI)

Well drilling and CO_2 storage facility permits issued by New Mexico Oil and Gas Commission and the U.S. Environmental Protection Agency (EPA) Regional VI individually are required to implement geologic CO_2 storage in New Mexico. The Petroleum Recovery Research Center at New Mexico Tech has developed one permit template to assist the operator in preparing 1) an application for permit to drill (APD) a stratigraphic test well and 2) a storage facility permit (SFP) application that are consistent with EPA Underground Injection Control (UIC) Class VI statutes and regulations. The APD template includes options for the design and permitting of a stratigraphic test well that can be transitioned for use as a UIC Class VI-compliant injection or monitoring well.

No storage facility permits have yet been issued in New Mexico. The permit application templates presented incorporate learnings and clarifications that have been garnered as the first projects advancing carbon capture and storage (CCS) in New Mexico. Each section provides a description of the intent of the section, and a description of evidence or exhibits to be included within the section. The templates incorporate formatting that is both structured to present the information required in the permit application in a functional, logical, and consistent fashion and aligned with the permit review and public hearing process.

With the assistance of the project team, Four Corners Carbon Capture LLC (Tallgrass) had successfully submitted an UIC Class VI permit to EPA Region 6. Currently the submission is pending for the final permitting determination.

Introduction

Well drilling and CO_2 storage facility permits (SFP) are required to construct and operate a geologic CO_2 storage project in New Mexico. An application of permit to drill (APD) is required to drill a stratigraphic test well, which is used to acquire the necessary downhole data to complete a CO_2 SFP in New Mexico. The New Mexico Oil and Gas Commission (NMOCD) has authority to regulate stratigraphic well drilling permit align with the Class II well permit as an acid gas injection well. As such, the stratigraphic test well is part of a critical path to achieving

UIC Class VI compliance. Several recommended practices and clarifications related to well design, geologic characterization, well testing, and the UIC Class VI requirements resulted from these permit discussions, the more significant of which are captured in call-out boxes throughout these templates.

This document provides application templates for the two permits that are required to move forward with the commercial geologic storage of CO_2 in New Mexico: the APD for Class II well and the SFP.

Well Drilling Permit

For the purposes of this template, the APD has been developed as a stratigraphic test well which classified as a Class II acid gas injection well. A complete storage facility permit requires data and information obtained from core, geologic formation testing and sampling, and wireline logging within the facility area of a geologic storage project. While there may be instances where existing data (i.e., core and log data) can be used for the SFP in lieu of drilling a stratigraphic test well, in many cases the operator will need to drill a well prior to applying for a SFP to collect the necessary data.

An option for accelerating deployment of CCS is to permit and drill a stratigraphic test well designed and constructed in a manner that provides a pathway to convert the Class II well to a UIC Class VI compliant injection well (e.g., strategic use of CO_2 resistant materials). The stratigraphic test well transition pathway is addressed in the SFP application process, which includes a request to convert the well to a CO_2 injection well and an application to inject CO_2.

The APD includes 1) an accurate well location plat certified by a registered surveyor showing the location of the proposed well with reference to the nearest lines of a governmental section and referenced to true north; 2) an accurate pad layout which indicates a cut and fill diagram and additional construction required, i.e., water bars, culverts, etc.; 3) a facility layout, i.e., location of surface facilities on well pad; and 4) road access to the well location. If drill cuttings will be buried on location (i.e., a dry-cuttings pit), the location of the dry cuttings pit needs to be on the facility layout plat.

This attachment, a geological prognosis, presents such information as the estimated depth to the top of objective horizons (measured depths [MD]); the estimated depth to the top and thickness of important geologic markers such as members or zones potentially containing usable water, USDWs, oil, gas, or other valuable deposits; and the identification of the formation at total depth, including the identification of all potential confining layers above and below the zone of interest. The drilling program and prognosis provides the technical detail of the plans for drilling and completing the injection well. Examples of the information and content of this attachment are as follows:

- Proposed total depth (including MD and true vertical depth) to which the well will be drilled
- Estimated depth to the top of important geologic markers
- Estimated depth to the top of objective horizons
- Proposed drilling mud program for surface hole and vertical hole
- Proposed openhole and cased hole logging program
- Proposed well testing, coring, and geologic characterization program
- Proposed casing program including size and weight

- Proposed depth and formation at which each casing string is to be set
- Proposed amount of cement and placement procedure to be used
- Estimated top of cement
- General completion procedure
- Other pertinent information

The storage operator should provide information regarding the proposed mud program for both the surface and production holes in this attachment. Also, the operator should include a description of the casing program, which includes the casing properties. The storage operator is required to provide a schematic of the wellbore. An evaluation program for the coring, testing, and logging of the stratigraphic test well is provided in this attachment. Additional information of importance includes the descriptions of the pressure control equipment, the drilling procedure, and the post completion plan. Examples of the content that is required for each of these topics is provided in the remainder of this section.

Well control during all phases of the drilling, logging, casing runs, cementing, testing, etc., is mandated by NMOCD and by industry best management practices. Well control equipment is typically referred to as blowout prevention equipment (BOPE). The BOPE includes a description, accompanied by exhibits, of the type of equipment that will be used, e.g., blowout preventers, choke manifolds, and accumulators, including the operational procedures and frequency for testing and documentation of this equipment.

The drilling procedure are required for each drilling interval from ground level to the total depth of the well, include the following:

- Hole size
- Type of drilling mud
- Bit and casing specifications
- Detailed drilling procedure
- Detailed coring, testing, and logging procedures
- Specific cementing procedures
- Cementing and casing evaluation procedures

Within thirty days after the conclusion of well drilling and completion activities, the storage operator is required to provide project specific reports, exhibits, documentation, and descriptions of the drilling, logging, coring, cementing, and well integrity evaluations of the stratigraphic test well.

UIC Class VI Well Permit

The UIC Class VI well permit application(s), one for each proposed Class VI well, will meet all requirements of 40 CFR 146.82 and those parts referenced therein. Required permit application materials will be entered into the ten modules of the Geologic Sequestration Data Tool (GSDT) and, after meeting data validation, will be submitted to EPA Region 6. Table 5 indicates the documents the project had been developed.

Table 5 Class VI Underground Injection Control (UIC) permit application project narrative, modified [1].

Section of Project Narrative	**Requirements**	**UIC Regulatory**

Site Characterization, including:		40 CFR 146.82(a)(2), (3), (5), and (6)
Regional Geology, Hydrogeology, and Local Structural Geology	Submittal of geologic & topographic maps & cross sections illustrating regional geology, hydrogeology, geologic structure of local area surrounding the project area	40 CFR 146.82(a)(3)(vi)
Maps and Cross Sections of the AoR	Topographic maps; geologic maps w/ cross sections & stratigraphic columns summarizing lithology, sequence of geologic units (including injection & confining zones and USDWs), approximate formation thicknesses, lateral extent of units, and correlation of units in vicinity of project and across region	40 CFR 146.82(a)(2); 40 CFR 146.82(a)(3)(i)
Faults and Fractures	Submittal of information on location, orientation, and properties of known or suspected faults & fractures that may transect the confining zone(s) in the AoR and a determination that they would not interfere with containment.	40 CFR 146.82(a)(3)(ii)
Injection and Confining Zone Details	Submittal of information on the depth, areal extent & thickness of the injection formation & confining zone(s); submittal of data on mineralogy of injection & confining zone(s); submittal of data on porosity, permeability & capillary pressure of injection & confining zones	40 CFR 146.82(a)(3)(iii)
Geomechanical and Petrophysical Information	Geomechanical information be submitted on fractures, stress, ductility, rock strength, and in situ fluid pressures within the confining zone; the use of geophysical methods for obtaining subsurface information in lieu of direct physical sampling.	40 CFR 146.82(a)(3)(iv)
Seismic History	A report on the seismic history of the project site, including the presence and depth of all seismic sources	40 CFR 146.82(a)(3)(v)
Hydrologic and Hydrogeologic Information	Submission of maps and stratigraphic cross sections indicating the general vertical and lateral limits of all USDWs, water wells, and springs within the AoR, their positions relative to the injection zone(s) and confining zone(s), and the direction of water movement	40 CFR 146.82(a)(3)(vi); 40 CFR 146.82(a)(5)
Geochemistry	Baseline geochemical information on subsurface formations including all USDWs in the AoR including both fluid and solid phase chemical analysis.	40 CFR 146.82(a)(6)

Site Suitability	Provide comprehensive data and descriptions for many properties of the proposed project site and demonstrate whether it is a good candidate for GS and meets the requirements at 40 CFR 146.83	40 CFR 146.83
Injection Well Construction Plan, including:	Ensure that all Class VI wells are constructed and completed to: (1) Prevent the movement of fluids into or between USDWs or into any unauthorized zones; (2) Permit the use of appropriate testing devices and workover tools; and (3) Permit continuous monitoring of the annulus space between the injection tubing and long string casing.	40 CFR 146.82(a)(9), (11), and (12)
Proposed Stimulation Program		40 CFR 146.82(a)(9)
Construction Procedures		40 CFR 146.82(a)(12)
Well Operation Plan, including:	Maintaining the integrity of the well and ensuring the safe sequestration of CO_2	40 CFR 146.82(a)(7) and (10)
Operational Procedures		40 CFR 146.82(a)(10)
Proposed CO_2 Stream		40 CFR 146.82(a)(7)(iii) and (iv)
Injection Depth Waiver and Aquifer Exemption Expansion	Seeking a waiver of the requirement to inject below the lowermost USDW	40 CFR 146.82(d); 40 CFR 146.95(a); 40 CFR 146.4(d); 40 CFR 144.7(d)
Other Information		40 CFR 146.82(a)(21)
Executive Summaries of:		
Financial Responsibility	The types of financial instruments that owners or operators of Underground Injection Control (UIC) Class VI Geologic Sequestration (GS) wells can choose to demonstrate compliance with the financial responsibility requirements of the Rule	40 CFR 146.82(a)(14); 40 CFR 146.85
AoR and Corrective Action Plan	Prepare, maintain, and comply with an AoR and Corrective Action Plan that includes all of the required elements of the plan; Delineate the AoR using computational modeling and identify all wells that require corrective action; Perform all required corrective action on wells in the AoR;	40 CFR 146.82(a)(4); 40 CFR 146.82(a)(13); 40 CFR 146.84(b); 40 CFR 146.84©

	Re-evaluate the AoR throughout the life of the project; Ensure that the Emergency and Remedial Response Plan and financial responsibility demonstration account for the most recently approved AoR; Retain modeling inputs and data used to support AoR re-evaluations for 10 yr.	
Pre-Operational Logging and Testing Plan	Describes how they will test the well and analyze the chemical and physical characteristics of the injection and confining zones	40 CFR 146.82(a)(8); 40 CFR 146.87
Emergency and Remedial Response Plan	Describes actions to be taken to address events that could potentially cause endangerment to a USDW during the construction, operation, and PISC phases of a project	40 CFR 146.82(a)(19); 40 CFR 146.94(a)
Testing and Monitoring Plan	Describes testing and monitoring activities that are primarily required during the injection phase	40 CFR 146.82(a)(15); 40 CFR 146.90
Injection Well Plugging Plan	Ensure that the proposed materials and procedures for injection well plugging are appropriate to the well's approved construction and the site's geology and geochemistry	40 CFR 146.82(a)(16); 40 CFR 146.92(b)
Post-Injection Site Care (PISC) and Site Closure Plan	Outlines the proposed post-injection monitoring strategies and how non-endangerment of USDWs will be ensured throughout the PISC phase	40 CFR 146.82(a)(17); 40 CFR 146.93(a)

Required permit application materials will be entered into the ten modules of the GSDT and, after meeting data validation, the package will be submitted to EPA regional offices by the site operator.

References

Chen D, Pan Z, Liu J, Connell LD. 2013. An improved relative permeability model for coal reservoirs. Int J Coal Geol. 109–110:45–57. doi:10.1016/j.coal.2013.02.002

Reeves NS, Oudinot NA. 2004. The Tiffany Unit N2–ECBM pilot: a reservoir modeling study. Morgantown (WV); U.S. Department of Energy, Office of Scientific and Technical Information. doi:10.2172/923257

Reeves S, Taillefert A, Pekot L, Clarkson C. 2003. The Allison Unit CO_2–ECBM pilot: a reservoir modeling study. Morgantown (WV); U.S. Department of Energy, Office of Scientific and Technical Information. doi:10.2172/825083

Siriwardane HJ, Bowes BD, Bromhal GS, Gondle RK, Wells AW, Strazisar BR. 2012. Modeling of CBM production, CO_2 injection, and tracer movement at a field CO_2 sequestration site. Int J Coal Geol. 96–97:120–136. doi:10.1016/j.coal.2012.02.009

Weber M, Wilson TH, Akwari B, Wells AW, Koperna G. 2012. Impact of geological complexity of the Fruitland Formation on combined CO_2 enhanced recovery/sequestration at San Juan Basin pilot site. Int J Coal Geol. 104:46–58. doi:10.1016/j.coal.2012.09.011

Regional-Scale Assessment of CO_2 Geological Storage in Sedimentary Basin Geothermal Reservoirs of Nevada

Both state- and basin-scale assessments of the geothermal favorability in Nevada have previously been made (e.g., Coolbaugh et al. 2005; Penfield et al. 2010; Iovenitti et al. 2016; **Figure 67**). These assessments, however, were performed for the exploration and development of geothermal power plants that use water or other chemicals as the primary working fluid at relatively shallow depths. There are currently no published regional-scale assessments of CO_2 geological storage in sedimentary basin geothermal reservoirs of Nevada; and previous preliminary assessments of the potential for CO_2 geological storage in the state did not consider using geologically stored CO_2 as a subsurface heat extraction fluid for geothermal electricity generation (e.g., Price et al. 2005).

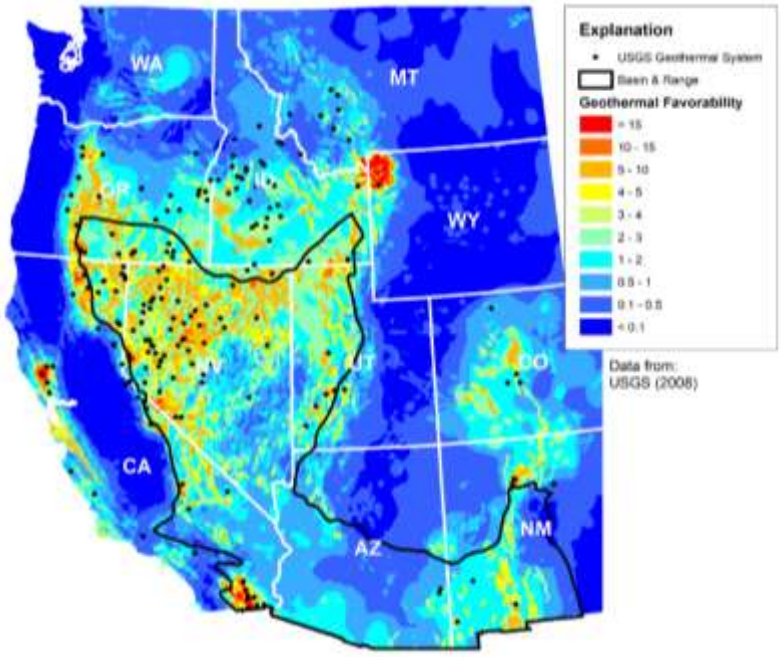


Figure 67 Map of geothermal favorability of the western United States. Much of the region with geothermal favorability of >5 is in northwestern Nevada. The extent of the Basin and Range physiographic province (black outline) and distribution of USGS geothermal systems are also shown.

Recent assessments of the favorability of using Enhanced Geothermal Systems (EGS) at basin-scales in Nevada have previously been made by developing methodologies to explore optimum subsurface conditions (Iovenitti et al. 2016). Assessments of EGS are currently being performed in Nevada, but similar assessments of sedimentary basin geothermal resources are comparatively understudied, in part because sedimentary basins have generally colder temperatures than EGS resources. But using geologically stored CO_2 as the heat-extraction fluid can more than halve the cost of sedimentary basin geothermal power generation compared to using in-situ water because CO_2 is a more efficient heat extraction fluid (e.g., Adams et al. 2021; Zhang et al. 2014). As a result, geologically stored CO_2 may "unlock" using sedimentary basin geothermal resources for electricity generation by using CO_2 plume geothermal power plants (Ogland-Hand et al. 2022).

Nevada is a good test bed to assess the feasibility of using CO_2 plume geothermal power plants in the United States due to the state's high geothermal potential from its location in the tectonically active Basin and Range physiographic province (**Figure 67**) and having existing geothermal energy infrastructure (**Figure 68**).

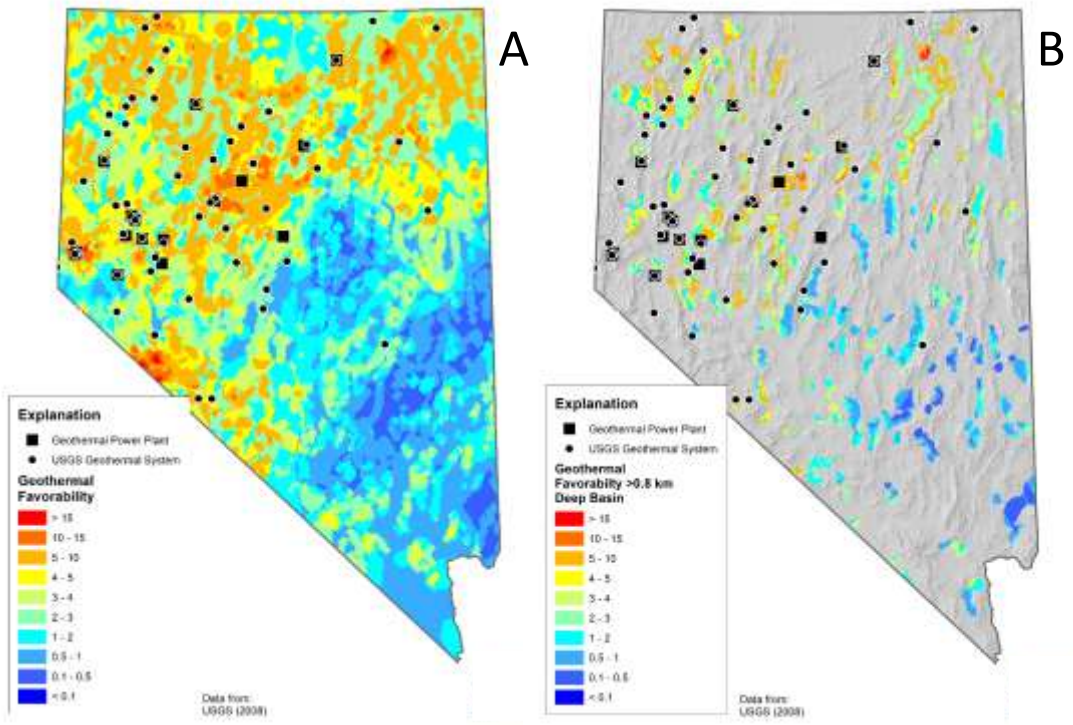


Figure 68 Maps of Nevada showing: (A) geothermal favorability of entire state, and (B) geothermal favorability in sedimentary basins with depths greater than 800 m. The location of geothermal power plants and USGS geothermal systems distributed in northwestern Nevada are also shown.

Objectives and Outcomes

The general objectives of the focused project are to (1) perform a regional-scale assessment to fill a data gap of critical information related to carbon capture, utilization, and storage (CCUS) technologies to mitigate CO_2 emissions in Nevada and (2) to develop an approach to regionally assess the potential that using CO_2 geological storage in sedimentary basin geothermal reservoirs may have for increasing the states capability for CCUS.

Sedimentary basin geothermal power plants that use plumes of geologically stored CO_2 as a subsurface heat extraction fluid can store between approximately 2 and 7 $MtCO_2$ per MW of electric power capacity and as such, they are one of the only CO_2-utilization processes that may demand megatonne, if not gigatonne, volumes of CO_2 geological storage (Adams et al. 2021). Nevada may be an especially favorable state for low-cost CO_2 plume geothermal power plants, given that: a) the cost of geothermal power decreases with increasing geothermal temperature gradient, and b) there are commercial geothermal power plants currently operating in Nevada, based on the state having high geothermal temperature gradients (e.g., Coolbaugh et al. 2005; USGS 2008; **Figure 68**).

The CUSP West-specific objectives are to (1) provide an approach that could be used to regionally assess the favorability of CO_2 geological storage in other CUSP states with sedimentary basin geothermal resources and (2) provide a better understanding of potential areas in Nevada that could be targeted for more detailed analyses either in individual basins or at geothermal power plants with future research. The overall efforts of the focused project will demonstrate to the Department of Energy that the CUSP West is also researching alternative approaches to CCUS by taking advantage of each state specific geologic setting and capabilities, in this case, the geothermal resources of Nevada.

CUSP Focused Project Team and Scope of Work

The CUSP focused project team included collaboration between Steven Bacon (PI) and Rishi Parashar of the Desert Research Institute (DRI), Reno, Nevada and Jonathan Ogland-Hand (Co-PI), Jeff Bennett, and Richard Middleton of Carbon Solutions, LLC. The overall scope of work included the DRI team creating a 2-km grid resolution geospatial dataset of pertinent geologic and geothermal information to identify areas that are favorable for CO_2 geological storage in sedimentary basin geothermal systems in northern Nevada. The extent of areas with favorable sedimentary basin geothermal potential along with available reservoir property data from deep well logs previously analyzed for the Nevada CUSP project were integrated for a basin-scale assessment. These data were then used as model input parameters for the Carbon Solutions team to apply their computational tools to characterize the storage capacity and cost of CO_2 storage, as well as the power capacity and cost of CO_2 plume geothermal power plants across Nevada (e.g., Ogland-Hand et al. 2022).

Methods

The focused project was separated into two main tasks with each team performing specific subtasks to reach the overall objectives. The two main tasks included (1) regional- and basin-scale geologic and geothermal characterization and identification of potential sedimentary basin geothermal reservoirs and (2) estimating the storage capacity and cost of CO_2 storage at basin-scales using site-specific well log information. The geospatial datasets, approaches, and tools used in the overall assessment include:

Geologic and Geothermal Characterization

A regional-scale assessment of CO_2 geological storage in sedimentary basin geothermal reservoirs was performed using a range of geologic, geophysical, and geothermal information appropriate for making a regional-scale assessment. The geothermal potential assessment of Coolbaugh et al. (2005) shows northern Nevada has the highest geothermal potential across the state. As a result, the project scope concentrated on performing the assessment in northern Nevada because of its high geothermal temperature gradient and availability of existing deep well log information. The following gridded data layers were used in the geospatial analysis component of the assessment:

Basin Configuration

Deep sedimentary basins greater than 800 m depth were identified based on geophysical datasets including gravity inversion mapping of the depth to pre-Cenozoic basement in northern Nevada

(Ponce 2004; **Figure 69**A). This dataset was double-checked with more recently published data from the USGS - National Crustal Model (NCM). The NCM dataset includes crustal properties for the western United States on a 1-km grid scale including depth to basement and thickness of unconsolidated sediments (Shah and Boyd 2018). The data of Ponce (2004) was also used in the development of NCM dataset. The geologic map of Nevada at a scale of 1:500,000 was also used in conjunction with the geophysical datasets to refine the delineation between sedimentary basins (i.e., valley fill) and mountain highlands composed of pre-Cenozoic rocks (Stewart and Carlson 1978; **Figure 69**B).

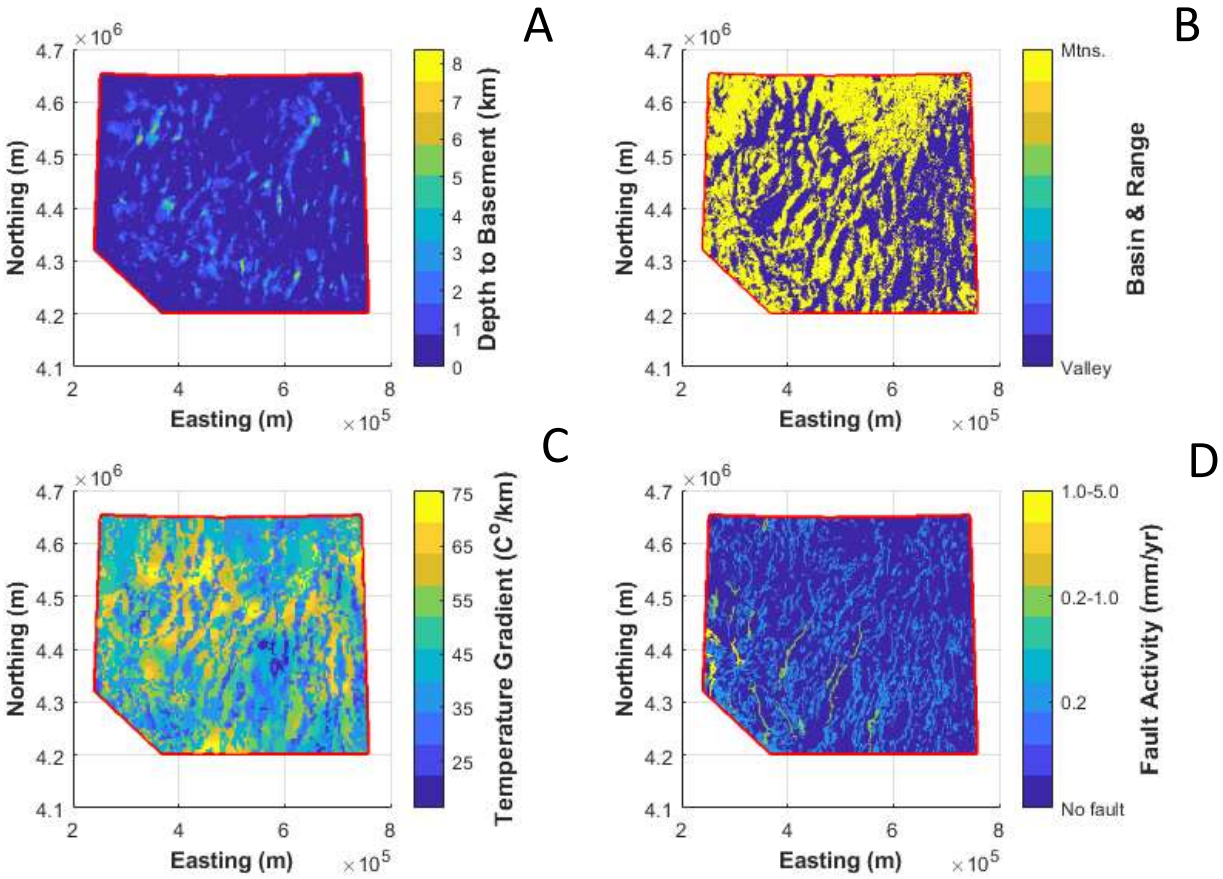


Figure 69 Maps of northern Nevada used in the regional-scale assessment of CO_2 geological storage in geothermal reservoirs: (A) depth to pre-Cenozoic basement, (B) geologic mapping to distinguish between sedimentary valley fill and mountains, (C) geothermal temperature gradient, and D) fault activity.

Temperature Gradient

Previous regional assessments of geothermal favorability and detailed information on site-specific geothermal resources were leveraged (Coolbaugh et al. 2005; USGS 2008; Penfield et al. 2010). Of the existing geothermal data available, the gridded map of geothermal temperature gradient at less than 2 km depth (Coolbaugh et al. 2005) provided the information required for the SCO_2T and genGEO computational tools (**Figure 69**C).

Fault Activity

The fault activity map of Nevada was used to identify potential areas with geothermal favorability (dePolo et al. 2009; USGS/NBMG 2016). Fault activity is directly linked to geothermal potential because fault zones can act as conduits for heat and fluids to rise to the surface (e.g., Faulds et al. 2012). The relative activity of faults in terms of slip rate (mm/yr) is used in the focused project as a proxy for the relative potential of geothermal favorability, given that fault zones with faster slip rates will likely have higher geothermal favorability compared to fault zones with slower slip rates that may have lower geothermal favorability. A 2-km buffer bounding mapped fault traces was applied to best represent the extent of high density fracturing along discrete shear zones.

Sedimentary Basin Geothermal Reservoir Assessment

The approach used to identify sedimentary basin geothermal reservoirs is principally based on an evaluation-parameter rating scheme. The rating scheme approach is commonly used in geologic hazard assessments and developed by considering intrinsic trigger parameters that are typically responsible for a given geologic hazard or geologic process (e.g., Price 2009). The approach used here for identifying sedimentary geothermal potential is partially based on applicable elements from the study of Coolbaugh et al. (2005) that produced a geothermal potential map of the Great Basin region, including both bedrock and sedimentary basin areas.

The intrinsic parameters (i.e., geological attributes) used in the assessment of sedimentary geothermal potential include (1) sedimentary valley fill at depths between 0.8 and 9 km, (2) geothermal temperature gradients ranging from 25°C/km to 75°C/km, and (3) location of faults and associated slip rate information (i.e., fault activity; **Figure 69**). A non-weighted, numerical rating class system was assigned to each intrinsic parameter based on their contribution towards influencing sedimentary geothermal potential according to logical judgments acquired from experience and literature (e.g., Pachauri and Pant 1992). A 10-fold rating class (0–9) was used for sedimentary valley fill greater than 800 m depth (i.e., depth to bedrock) and geothermal temperature gradient data layers, whereas a 4-fold rating class (0–3) was applied for the fault activity (i.e., slip rate) data layer (Table 11). Geospatial analyses were initially performed in ArcGIS to resample original datasets to have 2-km grid resolution followed by classifying the resampled data in MATLAB® programming language using the factor ratings for each data layer.

Table 11 Parameter ratings assigned to data layers in the sedimentary geothermal potential assessment.

Intrinsic Parameter	Variable	Factor Rating
Depth to basement	(km)	
Very Deep	8 - 9	9
	7 - 8	8
Deep	6 - 7	7
	5 - 6	6
Moderately Deep	4 - 5	5
	3 - 4	4

Shallow	2 - 3	3
	1 - 2	2
Very Shallow	0.8 - 1	1
Not applicable	<0.8	0
Geothermal temperature gradient	(°C/km)	
Very High	>75	9
	70 - 75	8
High	65 - 70	7
	60 - 65	6
Moderate	55 - 60	5
	50 - 55	4
Low	45 - 50	3
	40 - 45	2
Very Low	35 - 40	1
Not applicable	<35°	0
Fault activity (slip rate)	(mm/yr)	
High	1.0 - 5.0	3
Intermediate	0.2 - 1.0	2
Low	<0.2	1
Not appliable	No fault	0

CO_2 Plume Geothermal Power Plant Assessment

Sedimentary basin geothermal reservoirs with mostly High to Very High potential ratings and corresponding deep well log information for saline reservoirs were assessed for CO_2 plume geothermal power plant generation. The amount of CO_2 that will be stored in the sedimentary geothermal basins was estimated under several power plant financing assumptions (e.g., Ogland-Hand et al. 2022). The power plant financing assumptions used in the analysis include: power plant capacity factor of 95%; annual operation and management costs of 5.5% of specific capitol cost; and capitol recovery factor of 5.2%.

As the deployment of sedimentary basin CO_2 plume geothermal power plants will ultimately be driven by a currently undetermined CO_2 policy (e.g., Section 45Q of the U.S. Tax Code [Credit for Carbon…2021], CO_2 prices), the modeling performed for the focused project is principally based on the lowest cost of CO_2 plume geothermal levelized cost of electricity. The rapid tool for carbon storage science, engineering, and economics (SCO_2T: Middleton et al. 2020a, 2020b) and the generalizable GEOthermal techno-economic simulator (genGEO; Ezekiel et al. 2024) with recent tool enhancements (Ogland-Hand et al. 2022) were used to calculate: a) the cost and storage capacity of CO_2 geological storage; and b) the cost, power generation capacity, and CO_2 requirements of CO_2 plume geothermal power plants.

Project Findings

Regional-Scale Sedimentary Basin Geothermal Reservoirs of Northern Nevada

A sixteen-fold rating classification ranging from None to Very High was generated from the three intrinsic parameter data layers to estimate the regional-scale sedimentary geothermal potential in northern Nevada. This rating class system represents the sum of the three parameter ratings for each grid cell. The sixteen-fold rating classification can be generalized into four rating classes. The four-fold rating classes provides a simplification to assess the relative sedimentary basin geothermal potential including: None (<7); Moderate (7–10); High (10–13); and Very High (13–16; **Figure 70**).

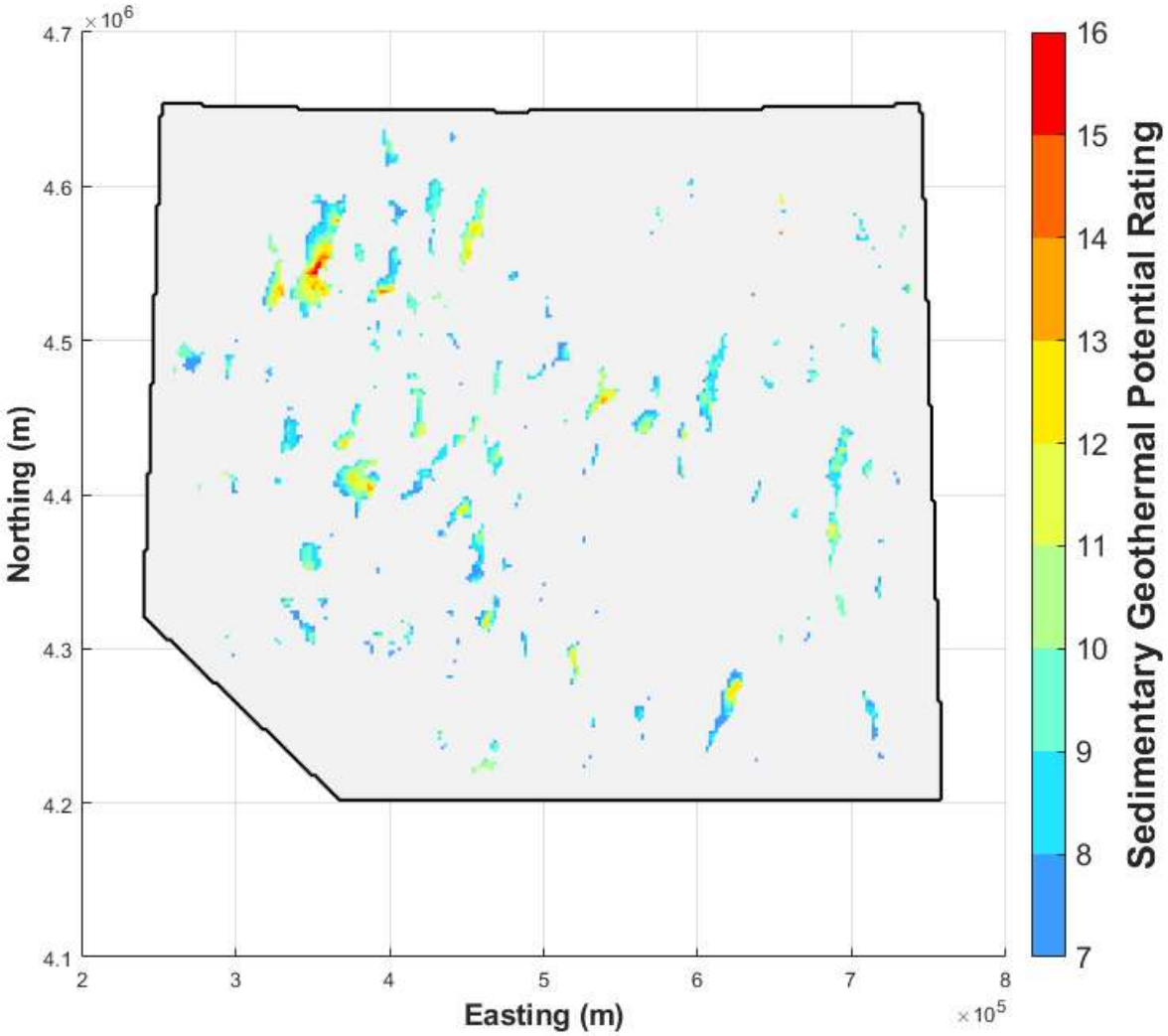


Figure 70 Map of sedimentary geothermal potential of northern Nevada. Rating classes are: None (<7); Moderate (7–10); High (10–13); and Very High (13–16). Five sedimentary basins with existing deep well log information are also shown.

Basin-Scale Sedimentary Basin Geothermal Reservoirs of Northern Nevada

Five sedimentary basins in northern Nevada with a range of sedimentary geothermal potential ratings were identified from the regional-scale assessment based on the basins having existing deep well log information (**Figure 71**). A basin-scale assessment of these areas was performed to (1) validate the regional-scale approach and (2) provide a site-specific feasibility assessment of using CO_2 plume geothermal geological storage and power generation in sedimentary basins.

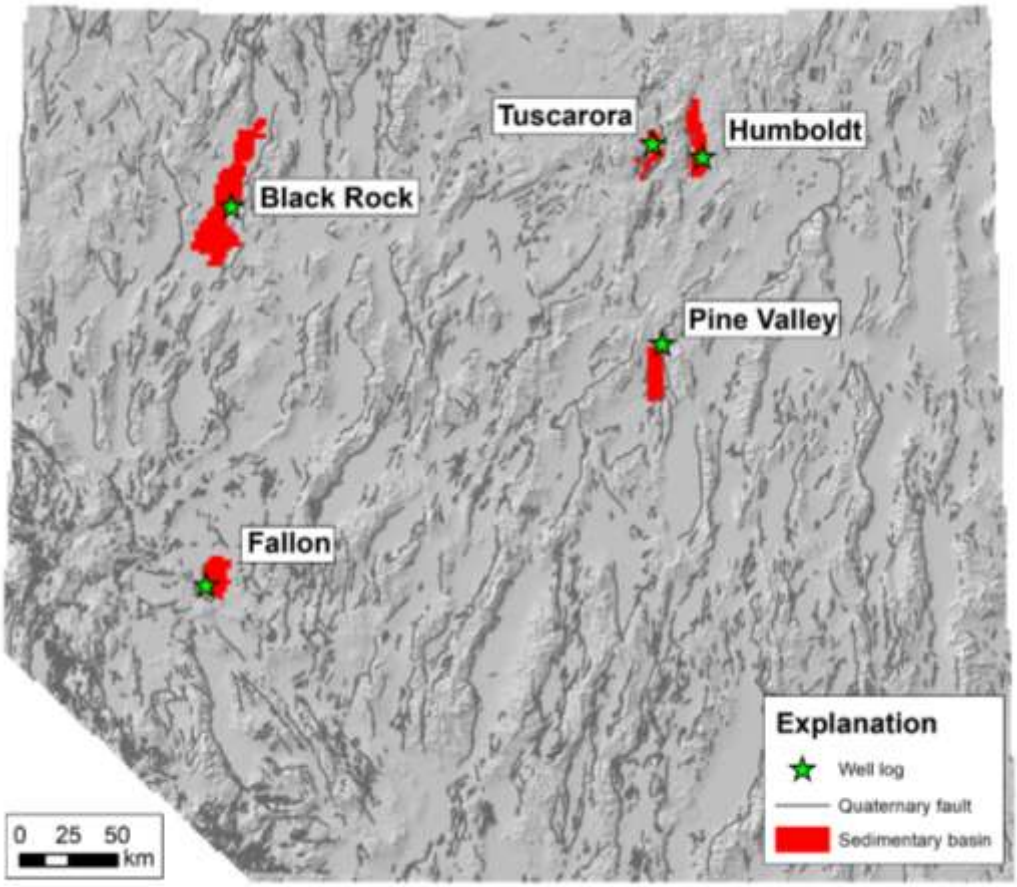


Figure 71 Map showing five sedimentary basins in northern Nevada that have a range of sedimentary geothermal potential ratings and existing deep well log information (see **Figure 70**). Quaternary faults are also shown.

Deep Well Log Information

Compared to other CUSP West states, Nevada has limited deep well log information appropriate for identifying and characterizing saline reservoirs below depths of 800 m. Of the limited number of deep wells, even fewer of these wells are in sedimentary basins having Moderate to Very High sedimentary geothermal potential. The five sedimentary basins that meet the criteria of having deep well log information and variable degrees of Moderate to Very High sedimentary geothermal potential include from west to east: Black Rock, Fallon, Tuscarora, Humboldt, and Pine Valley (**Figure 71**). Each basin consists of a single and complete geophysical well log that

extends deeper than 800 m. Geophysical well logs were digitized, and resistivity, neutron porosity, and permeability were used to characterize aquifer properties and identify saline formations with salinities of 3,000 to >10,000 mg/L (see 50-km SCO_2T geologic input database). The five sedimentary basins have a wide range of sedimentary fill thickness, aquifer rock types, fault density, and geothermal gradients, which provide sufficient information to evaluate the accuracy of the regional-scale assessment, as well as assess the feasibility of using deep sedimentary basin CO_2 plume geothermal geological storage in northern Nevada.

Black Rock Sedimentary Basin Analysis

Of the five sedimentary basins identified in the regional-scale assessment, the Black Rock basin within the Black Rock Desert of northwestern Nevada was selected to be an example of a basin-scale assessment using site-specific reservoir property data. The basin was selected because of its relatively large size, has the highest sedimentary geothermal potential of the five basins evaluated (**Figure 72**), and has the highest temperature gradients in the region, ranging mostly from 60°C/km to 75°C/km (**Figure 73**).

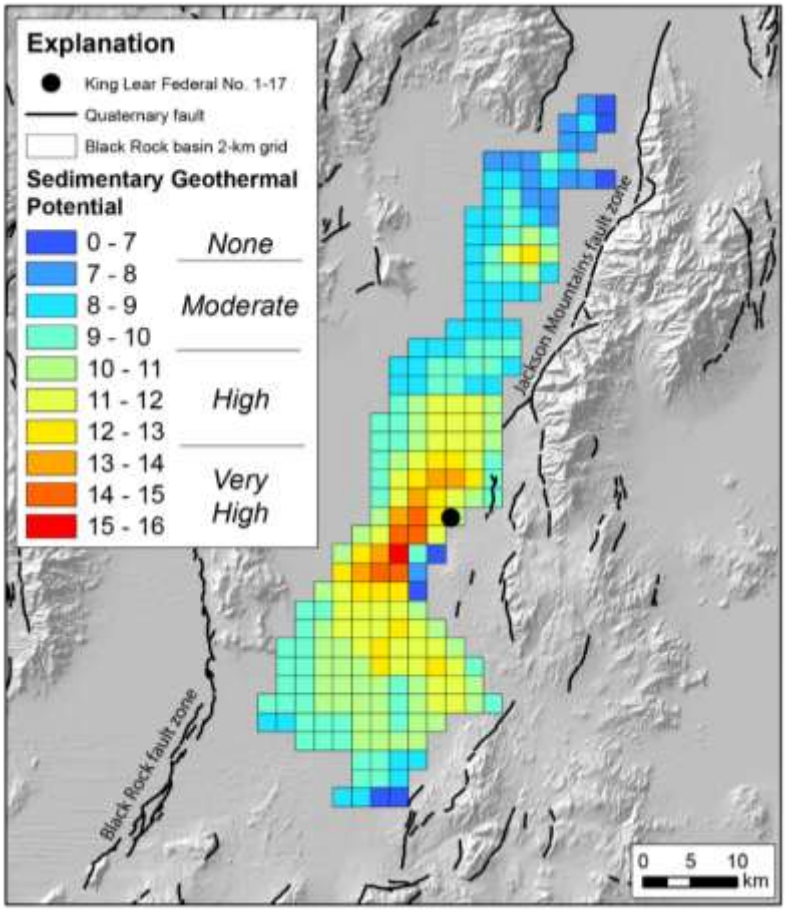


Figure 72 Map of sedimentary geothermal potential within the Black Rock basin based on the regional-scale assessment. The extent of the 2-km grid coincides with depths greater than 1,950 m in the valley, which is the top of the first saline reservoir identified in the King Lear Federal No. 1-17 well log.

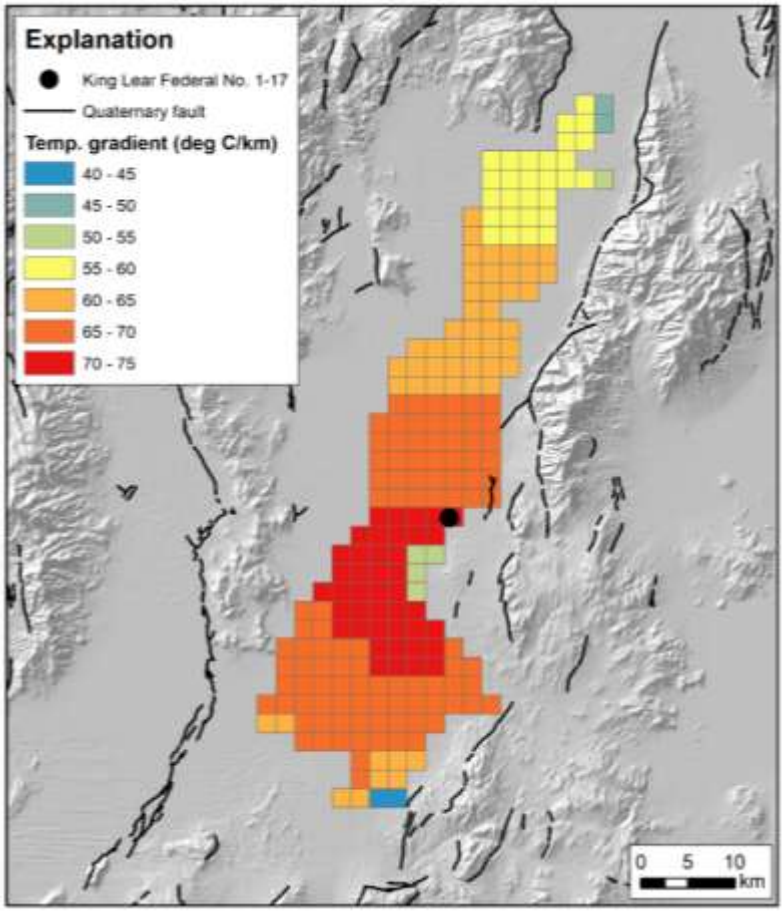


Figure 73 Map of geothermal temperature gradient within the Black Rock basin (Coolbaugh et al. 2005). The extent of the 2-km grid coincides with depths deeper than 1,950 m in the valley, which is the top of the first saline reservoir identified in the King Lear Federal No. 1-17 well log.

The Black Rock sedimentary basin is within a half graben formed between the west-dipping Jackson Mountains and Black Rock fault zones (**Figure 71** and **Figure 72**). The Black Rock sedimentary basin is the largest of the five basins evaluated. The basin has an area of 912 km^2 that was determined from the spatial extent of sedimentary fill thickness between the depths of 1,950 and 2,130 m. These depths coincide with an upper approximately 60-m thick saline formation (reservoir 1) composed of Miocene interbedded lacustrine siltstone and claystone and a lower approximately 120-m thick saline formation (reservoir 2) consisting of Miocene lacustrine siltstone with lesser interbeds of limestone and tuffaceous siltstone that were identified in a geophysical well log from the east-central sector of the basin (King Lear Federal No. 1-17 [API# 27-013-05002]; Table 12; **Figure 73**).

Table 12 Reservoir property data from analysis of geophysical log of the King Lear Federal No. 1-17 well (API# 27-013-0

Reservoir no.	Depth top (m)	Depth bottom (m)	Net thickness (m)	Mean porosity (fraction)	Minimum porosity (fraction)	Maximum porosity (fraction)	Mean permeability (mD)	Minimum permeability (mD)	Maximum permeability (mD)	Me sali (mg
1	1,951	1,981	30	0.288	0.265	0.299	1,630.1	1,043.3	1,969.5	9,04

1	1,981	2,012	30	0.288	0.263	0.300	1,622.1	1,003.1	2,004.9	11,(
2	2,012	2,042	30	0.276	0.242	0.299	1,308.0	653.9	1,969.5	11,2
2	2,042	2,073	30	0.260	0.241	0.294	953.8	640.2	1,800.3	11,1
2	2,073	2,103	30	0.257	0.223	0.300	934.3	432.1	2,004.9	10,2
2	2,103	2,133	30	0.272	0.242	0.300	1,235.1	653.9	2,004.9	11,(

Given the tectonic setting of the Black Rock basin, it is likely that the Miocene rocks are fractured having increased fracture density proximal to fault zones. Future work could also incorporate a discrete fracture network analysis that would account for a grid cell's distance from nearby fault zones. The discrete fracture network analysis could provide additional reservoir property information in terms of spatial variations in fracture density of the rock mass, which in turn can be used to provide insights on potential changes in hydraulic conductivity and permeability relative to fault distance (e.g., Jiang et al. 2025). Furthermore, a major assumption in the basin-scale analysis is the saline formations and associated aquifer properties identified in the well log are laterally and vertically continuous throughout the entire basin. As a result, long-term basin evolution and spatial variations in reservoir properties driven by tectonic ground deformation was not explicitly accounted for in the analysis.

Assessment of Low-Cost CO_2 Plume Geothermal Power Generation

Analysis of greenfield levelized cost of electricity of CO_2 plume geothermal development was performed to assess the feasibility of using deep sedimentary basin geothermal for power generation in the Black Rock sedimentary basin. Reservoir properties for two stacked saline formations of interbedded claystone and siltstone (depth: 1,950–2,012 m) and siltstone and limestone with tuffaceous siltstone (depth: 2,010–2,130), along with geothermal temperature gradient (**Figure 73**) were used with the SCO_2T and genGEO computational tools (Ogland-Hand et al. 2022) to identify sectors of the Black Rock basin with the lowest-cost power generation.

The range of levelized cost of electricity in the basin was estimated for the stacked saline formations. Analysis was performed at depths between 1,950 and 1,980 m for reservoir 1 and at depths between 2,010 and 2,100 m for reservoir 2 (**Figure 74**). The range of depths analyzed is reflective of each reservoir's different aquifer properties and geothermal temperature gradients (Table 12 and **Figure 73**). In general, a deep and thick saline formation with high permeability and a high temperature gradient result in low-cost CO_2 plume geothermal power and in turn, low-cost geologic CO_2 storage. The results of the assessment are promising and show that most of the basin has the potential for low-cost CO_2 plume geothermal power generation ranging from \$70/MWh to \$80/MWh to less than \$70/MWh (**Figure 74**).

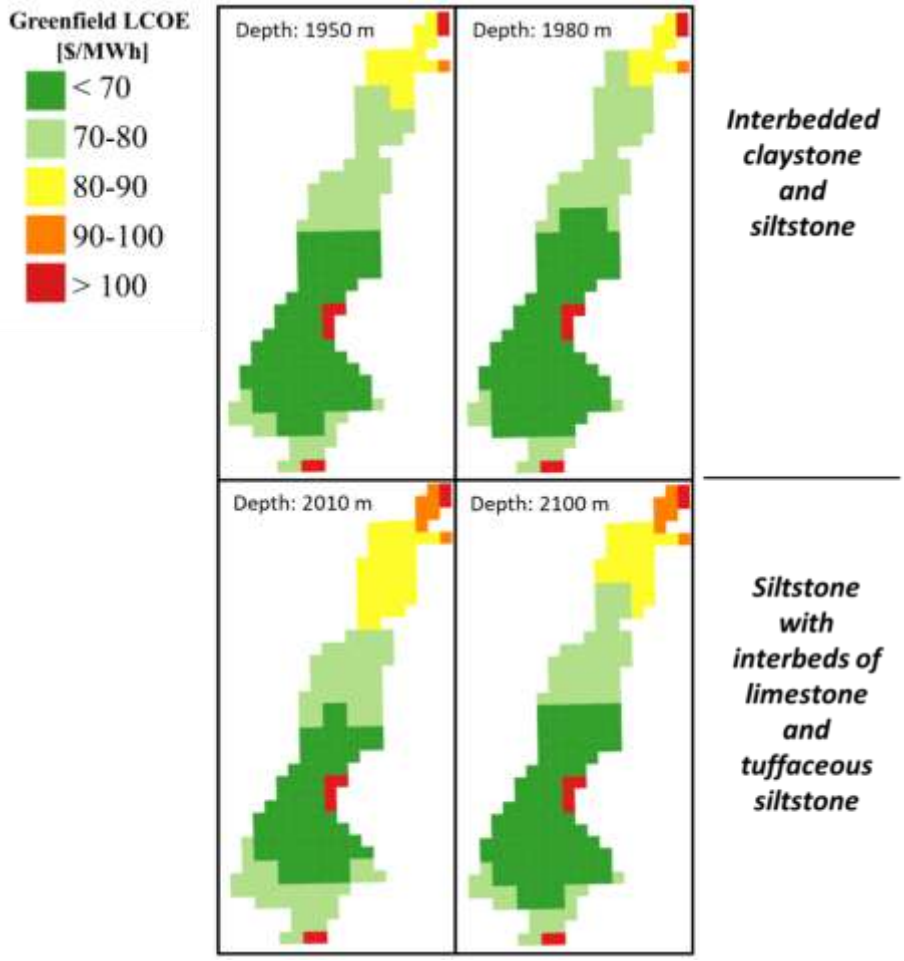


Figure 74 Maps showing greenfield levelized cost of electricity of CO_2 plume geothermal power generation for two stacked saline formations of the Black Rock sedimentary basin. The saline formations consist of an upper reservoir composed of Miocene interbedded claystone and siltstone at depths between 1,950 and 1,980 m; and a lower reservoir of Miocene siltstone with interbeds of limestone and tuffaceous siltstone at depths between 2,010 and 2,100 m.

Summary and Conclusions

The scope of the CUSP focused project is to perform a regional assessment of the CO_2-geological storage in sedimentary basin geothermal reservoirs of northern Nevada. Both regional- and basin-scale assessments of the geothermal favorability in the state have previously been made. However, there are currently no published regional-scale assessments of CO_2 geological storage in sedimentary basin geothermal reservoirs of Nevada; and previous preliminary assessments of the potential for CO_2 geological storage in the state did not consider using geologically stored CO_2 as a subsurface heat extraction fluid for geothermal electricity generation.

The goal of the CUSP focused project is to provide an initial “first cut” regional-scale assessment of the potential for CO_2 geological storage in sedimentary basin geothermal reservoirs to fill a data gap of critical information related to CCUS technologies to mitigate CO_2 emissions in Nevada. The regional assessment was based on the integration of 2-km grid

resolution geospatial datasets of geologic and geothermal information to identify areas that are favorable for deep sedimentary basin CO_2 plume geothermal geological storage. From the regional assessment, five sedimentary basins were identified for basin-scale assessments based on the presence of deep well log geophysical data that were previously analyzed for the Nevada CUSP project to characterize reservoir properties. The reservoir property data was then used as model input parameters for the SCO_2T and genGEO computational tools to characterize (1) the cost and storage capacity of CO_2 geologic storage and (2) the power capacity and cost of greenfield CO_2 plume geothermal power generation.

Analysis of the Black Rock basin was performed as a proof-of-concept of a basin-scale assessment. The analysis shows that sedimentary basins with Moderate to Very High sedimentary geothermal potential, geothermal gradients of less than 55°C/km, and interbedded claystone and siltstone saline formations with salinities ranging from approximately 6,000 to 25,600 mg/L have the lowest cost of CO_2 plume geothermal levelized cost of electricity, ranging from $80/MWh to $70/MWh to less than $70/MWh.

The regional-scale assessment of sedimentary geothermal potential provided a useful dataset to identify areas for more detailed basin-scale assessments of low-cost CO_2 plume geothermal power generation where deep well log information is available. The results of the focused project provide an alternative CCUS capability for Nevada, as well as a methodology that could be used to assess the favorability of CO_2 geological storage at both regional- and basin-scales in other CUSP states with sedimentary basin geothermal resources.

References

Coolbaugh M, Zehner R, Kreemer C, Blackwell D, Oppliger G, Sawatzky D, Blewitt G, Pancha A, Richards M, Helm-Clark C, et al. 2005. Geothermal potential map of the Great Basin, western United States. Reno (NV); Nevada Bureau of Mines and Geology. Map 151a. Scale 1:1,000,000. With geospatial data. [accessed 2025 Dec 23]. https://pubs.nbmg.unr.edu/Geoth-potential-map-Great-Basin-p/m151.htm

Credit for Carbon Oxide Sequestration, U.S.C.-2023 26 C.F.R. §1.45Q-1 (2021).

dePolo CM, Johnson GL, Price JG, Mauldin JM. 2009. Quaternary faults in Nevada—online interactive map. Reno (NV); Nevada Bureau of Mines and Geology. Open-File Report 2009-09. [accessed 2025 Dec 23]. https://maps.nbmg.unr.edu/QuaternaryFaults/

Ezekiel J, Vahrenkamp V, Hoteit HA, Finkbeiner T, Mai PM. 2024. Techno-economic assessment of large-scale sedimentary basin stored-CO_2 geothermal power generation. Appl Energy. 376(Pt B):124270. doi:10.1016/j.apenergy.2024.124270

Faulds JE, Hinz N, Kreemer C, Coolbaugh M. 2012. Regional patterns of geothermal activity in the Great Basin region, western USA: correlation with strain rates. Geotherm Resour Counc Trans. 36:897–902.

Iovenitti J, Ibser FH, Clyne M, Sainsbury J, Callahan O. 2016. The Basin and Range Dixie Valley geothermal wellfield, Nevada, USA—a test bed for developing an enhanced geothermal system exploration favorability methodology. Geothermics. 63:195–209. doi:10.1016/j.geothermics.2016.01.001

Jiang X, Wang Z, Na J, Sun Z, Hu T. 2025. Application of coupled discrete fracture–equivalent porous medium model for groundwater flow simulations in fault zones. Eng Geol. 357:108335. doi:10.1016/j.enggeo.2025.108335

Middleton RS, Chen B, Harp DR, Kammer RM, Ogland-Hand JD, Bielicki JM, Clarens AF, Currier RP, Ellett KM, Hoover BA, et al. 2020a. Great SCO_2T! rapid tool for carbon sequestration science, engineering, and economics. Appl Comput Geosci. 7:100035. doi:10.1016/j.acags.2020.100035

Middleton RS, Ogland-Hand JD, Chen B, Bielicki JM, Ellett KM, Harp DR, Kammer RM. 2020b. Identifying geologic characteristics and operational decisions to meet global carbon sequestration goals. Energy Environ Sci. 13(12):5000–5016. doi:10.1039/D0EE02488K

Ogland-Hand JD, Adams BM, Bennett JA, Middleton RS. 2022. A geospatial cost comparison of CO_2 plume geothermal (CPG) power and geologic CO_2 storage. Front Energy Res. 10:855120. doi:10.3389/fenrg.2022.855120

Pachauri AK, Pant M. 1992. Landslide hazard mapping based on geological attributes. Eng Geol. 32:81–100. doi:10.1016/0013-7952(92)90020-Y

Penfield R, Shevenell L, Garside L, Zehner R. 2010. Nevada geothermal resources. Reno (NV); Nevada Bureau of Mines and Geology. Map 161. Scale 1:750,000. With geospatial data. [accessed 2025 Dec 23]. https://pubs.nbmg.unr.edu/Nevada-geothermal-resources-p/m161.htm

Ponce DA. 2004. Geophysical methods and applications. In: Wallace AR, editor. Assessment of metallic mineral resources in the Humboldt River basin, northern Nevada. Reston (VA); U.S. Geological Survey. Bulletin 2218. Chapter 6. Digital data. [accessed 2025 Dec 23]. https://pubs.usgs.gov/bul/2218/

Price DG. 2009. Engineering geology principles and practice. Berlin (Germany); Springer-Verlag. 450 p.

Price JG, Hess RH, Fitch S, Faulds JE, Garside LG, Shevenell L, Warren S. 2005. Preliminary assessment of the potential for carbon dioxide disposal. Reno (NV); Nevada Bureau of Mines and Geology. Report 51z. With geospatial data. [accessed 2025 Dec 23]. https://pubs.nbmg.unr.edu/CO2-disposal-assessment-p/r051z.htm

Shah AK, Boyd OS. 2018. Depth to basement and thickness of unconsolidated sediments for the western United States—initial estimates for layers of the U.S. Geological Survey National Crustal Model. Reston (VA); U.S. Geological Survey. Open-File Report 2018-1115. 13 p. doi:10.3133/ofr20181115

Stewart JH, Carlson JE. 1978. Geologic map of Nevada. Reston (VA); U.S. Geological Survey. State Geologic Map Series. Scale 1:500,000. Prepared in cooperation with Nevada Bureau of Mines and Geology. [accessed 2025 Dec 23]. https://pubs.usgs.gov/map/i-1136/

[USGS] U.S. Geological Survey. 2008. Assessment of moderate- and high-temperature geothermal resources of the United States. Reston (VA); U.S. Geological Survey. Fact Sheet 2008-3082. With digital data. [accessed 2025 Dec 23]. https://pubs.usgs.gov/fs/2008/3082/

[USGS/NBMG] U.S. Geological Survey and Nevada Bureau of Mines and Geology. 2016. Quaternary fault and fold database for the United States. Reston (VA)/Reno (NV); U.S.

Geological Survey & Nevada Bureau of Mines and Geology. [accessed 2026 Jan 5]. https://earthquake.usgs.gov/hazards/qfaults

Zhang L, Li D, Ren B, Cui G, Zhuang Y, Ren S. 2014. Potential assessment of CO_2 geological storage in geothermal reservoirs associated with heat mining: case studies from China. Energy Procedia. 63:7651–7662. doi:10.1016/j.egypro.2014.11.799

Characterization of CO_2 Storage Potential in Harquahala Basin, Western Central Arizona

Arizona Geological Survey, University of Arizona – Tucson, AZ

The majority of this report has been adapted from the AZGS-UA open-file report 24-01 (Wilson et al. 2024).

The Arizona Geological Survey (AZGS) conducted a Phase I pre-feasibility study of the Harquahala basin, western Maricopa County, Arizona, for subsurface geologic storage of CO_2. The purpose of this project was to evaluate subsurface geology and structure and provide site characterization for future long-term CO_2 sequestration. This work was done as part of the larger Carbon Utilization and Storage Partnership (CUSP) regional initiative with the goal of expediting the deployment of onshore carbon capture, utilization, and storage (CCUS) technologies in the western region of the United States. This project advances this goal through subsurface characterization to geologically de-risk this carbon storage prospect to help attract industry for further development. Additionally, learnings from this site can be applied to numerous geologically similar basins throughout the state.

The Phase I evaluation compiled and integrated publicly available geologic maps, wellbore lithology logs, wellbore temperature data, well water chemistry information, and published gravity surveys with proprietary datasets including legacy 2D seismic lines and detailed gravity and resistivity surveys. These data were used to produce depth-to-bedrock (DTB) contour maps, structure maps of the lower basin fill surface, and isopach maps of the total basin fill, upper basin fill, lower basin fill, and potential evaporite deposits in the basin. Our analyses yielded new information about the basin size, geometry, and structure, which improved calculations of the area and volume of the potential reservoir study area.

Harquahala basin may have the geologic conditions necessary to store natural gas permanently and safely in the subsurface, but additional geophysical and well data are needed to characterize the physical properties of storage reservoir rocks. Harquahala has thick accumulations of basin fill sediments with sufficient volumes for storage of supercritical CO_2: an estimated 1,997 Mt of CO_2 (P50). Basin fill likely contains three different potential storage reservoir types: CO_2 in stacked saline clastic sedimentary deposits, bedded evaporite deposits for compressed H_2 gas storage, and basalt lava flows for CO_2 mineralized sequestration. Hot, dry crystalline rock underlying basin fill is favorable for geothermal energy and has an unknown volume of saline groundwater. The seismicity risk is low based on the absence of Quaternary faults and historic seismicity. The basin is located close to five major (greater than 100,000 tons/yr) CO_2 point sources, existing pipeline infrastructure and Interstate 10, a transportation corridor between Arizona and southern California.

At the completion of our data analyses, three critical unknowns remain: the existence/absence of

sealing strata such as bedded evaporites and fine-grained deposits, the physical properties of stacked saline reservoir rock, and the stratigraphic architecture of basin fill sediments. Harquahala basin lacks deep well borehole data to adequately characterize rock lithology, porosity, and permeability. New 2D seismic interpretations reported within suggest bedded evaporite deposits and basalt lava flows are likely components of the lower basin fill unit; however, these interpretations cannot be calibrated with physical evidence. To reduce the uncertainties about storage reservoir integrity, we recommend the acquisition of new data to include 2D active-source seismic, high-resolution gravity infilling, high resolution aeromagnetic survey, and a stratigraphic characterization well with wireline geophysical logs and a core, cutting, and fluid sampling program. These datasets, combined with data reported within, will refine our understanding of the basin fill rock properties, identify the presence/absence of sealing strata, and clarify stratigraphic architecture and basin structure.

Project Description and Scope

The AZGS conducted a phase I pre-feasibility evaluation for subsurface storage of CO_2 in Harquahala basin, western Maricopa County, Arizona. This study was funded by the U.S. Department of Energy (DOE), as a Focused Project within the regional CUSP Regional Initiative. The purpose of this work was to evaluate the basin geometry, structure, and stratigraphic architecture of Harquahala basin and provide site characterization for future potential subsurface CO_2 storage.

The scope of work required data collection, data analysis, coordination, and technical evaluation in three tasks. In Task 1, AZGS researchers synthesized geologic maps, well lithology logs, public and private gravity datasets, newly reprocessed 2D seismic data, DTB contours, and groundwater temperature and chemistry data for Harquahala basin. Task 2 involved stakeholder engagement and outreach through periodic meetings and the creation of a publicly available StoryMap. In Task 3 sites for a future characterization well and geophysical surveys were identified. Deliverables include this report, supporting maps, cross sections, model data and parameters, and future data collection recommendations.

Study Areas

The Harquahala basin is located on the border of Maricopa and La Paz counties in west-central Arizona (Figure 75 and Figure 76). The Harquahala basin underlies a rural, agricultural valley located approximately 60 miles west of Phoenix. The approximately 511 mi^2 basin area is defined by several rugged mountain ranges composed of crystalline rocks: Harquahala Mountains to the north, Big Horn Mountains to the northeast, Saddle Mountain to the southeast, and the Eagletail Mountains to the southwest. Existing infrastructure crossing Harquahala Valley includes I-10, Central Arizona Project (CAP) canal, and natural gas pipelines. Land ownership consists of 62% federal land (managed by the U.S. Bureau of Land Management), 25% private land, and 13% State Trust lands (Towne 2014).

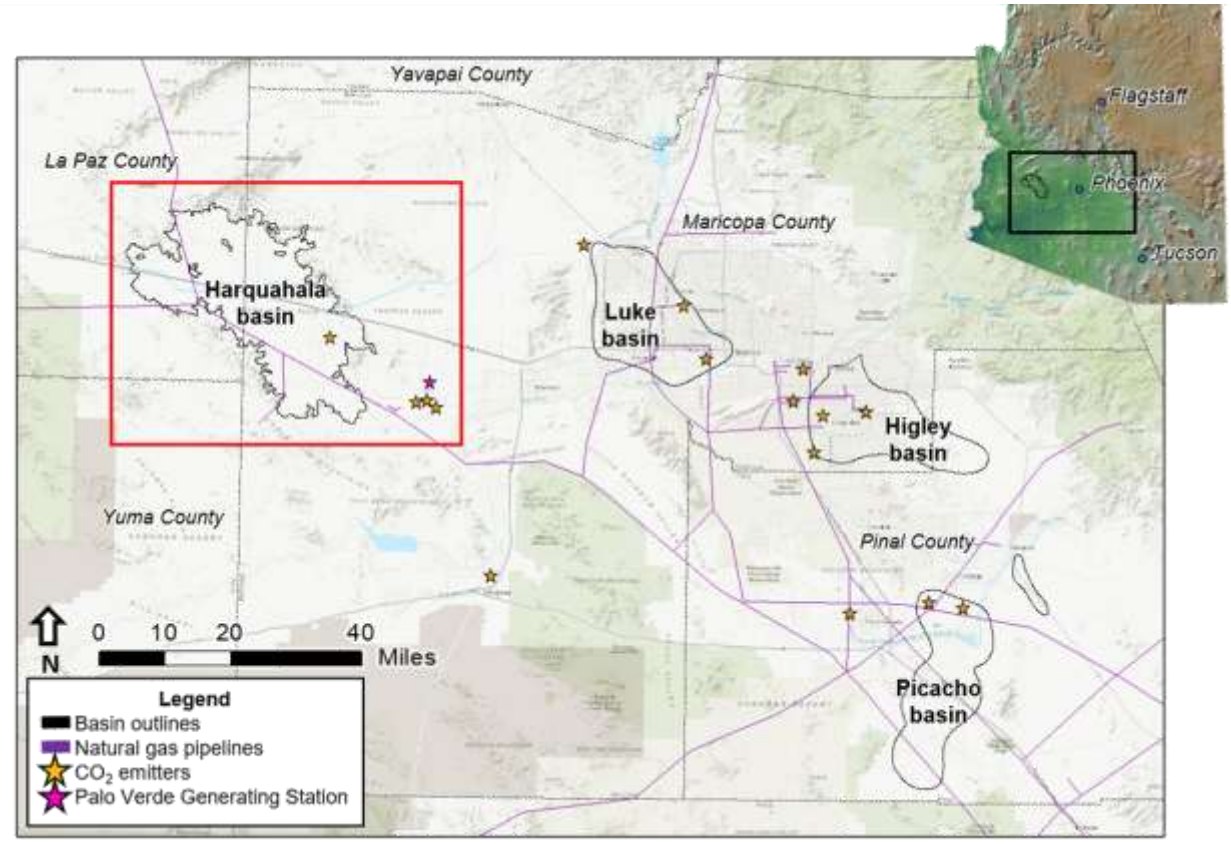


Figure 75 Map of study area in south-central Arizona (black box in state inset) showing the location of natural gas pipelines, CO_2 emission point sources (greater than 100,000 t per year), and major sedimentary basins in this region. The study area includes Harquahala basin (red box and location of Figure 76).

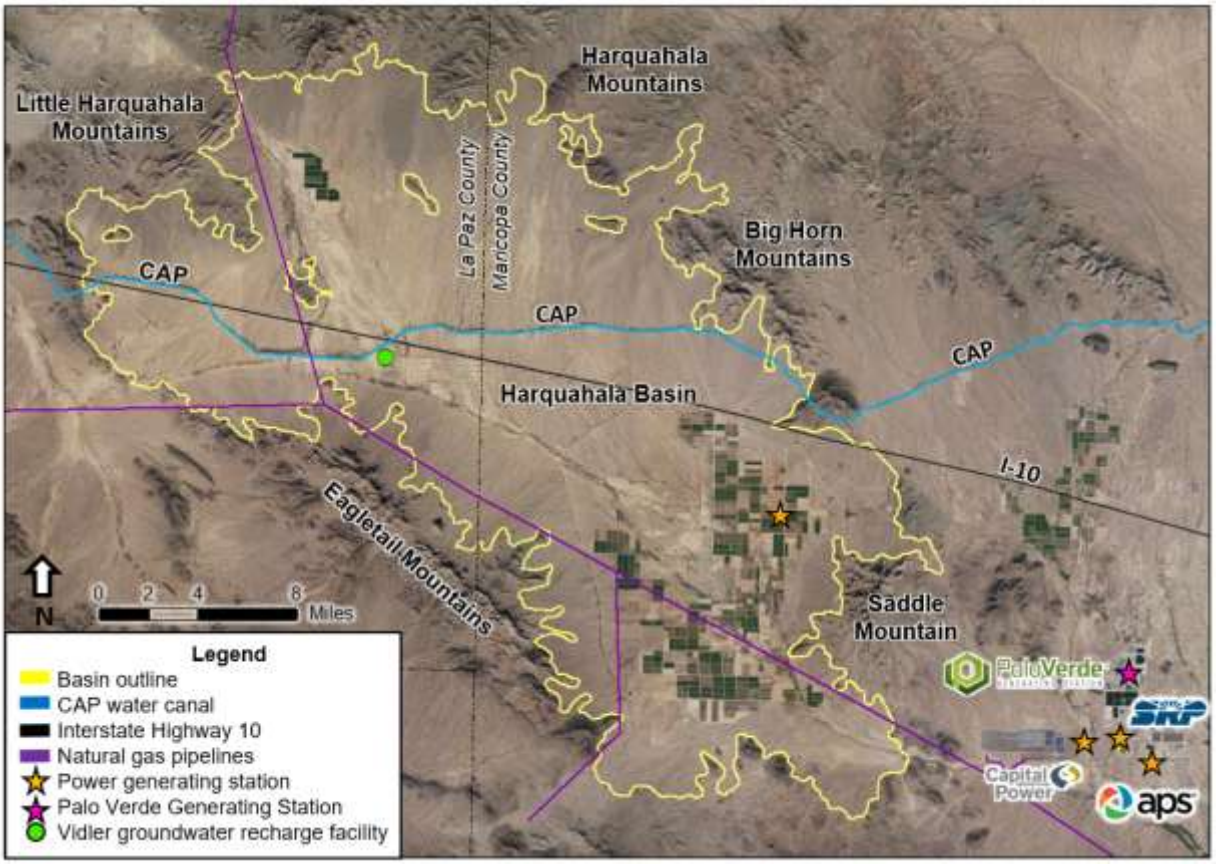


Figure 76 Location map of Harquahala basin (yellow outline), the surrounding infrastructure, and nearby energy facilities.

Four natural gas–powered energy facilities—Harquahala Generating Station, Mesquite Generating Station, Redhawk Generating Facility, and Arlington Valley Energy Facility—are located within 15 miles of the basin, three of which operate year-round. In 2021, three of the four natural gas power plants emitted over 6.32 Mt CO_2 waste to the atmosphere (U.S. EPA 2023). Palo Verde Nuclear Generating Station, the nation's largest nuclear power plant, is located 11 miles east of Harquahala basin.

Methods

All publicly available data were compiled, quality checked, and organized into an Esri ArcMap geodatabase. Data includes geologic map compilations, borehole lithology logs, 2D legacy seismic lines, public and proprietary gravity datasets, DTB contours, groundwater temperatures, and well chemistry information.

Geologic Map Compilation

Surficial geology was compiled and simplified from four 1:100,000 AZGS geologic maps (Reynolds 1997; Reynolds and Grubensky 2007; Richard et al. 2022; Spencer et al. 2022). Geologic units were simplified into 11 time-transgressive lithologic categories to highlight important compositional provenance for basin fill sediments (see Plate 2, Wilson et al. 2024). For example, crystalline bedrock units were lumped by age, while younger volcanic rocks were

lumped by age and chemistry (this approach identified source areas for mafic volcanic rocks that can be used to sequester CO_2). All surficial alluvium younger than approximately 5 Myr was omitted from the map compilation for simplicity.

Borehole Lithology Logs

Over 740 Arizona Department of Water Resources (ADWR) and Arizona Oil and Gas Conservation Commission (AZOGCC) wells were reviewed for subsurface geologic data within Harquahala basin (Appendices A and B). Within the basin center, only wells deeper than 122 m (400 ft) with lithologic borehole data were plotted. Along the basin margins, all wells regardless of depth were logged and plotted to refine depth to bedrock contours.

The review criteria resulted in 205 wells with subsurface lithologic data that have an average depth of 250 m (820 ft), with the deepest well reaching 611 m (2,005 ft; AZOGCC 2023). Wells were sorted by lithology, clast size, and/or composition at reported intervals, and plotted by lithology in cross-sections. Lithology codes were assigned to a color and resulting logs are displayed on each of the cross-sections traversing the basin.

Vintage Seismic 2D Reflection Data and Analysis

The application of 1980's vintage seismic reflection data was a major contributor to improving the understanding of the structure and stratigraphy of Harquahala basin. In this section we present the quality of legacy data, processing methods including depth conversion and limitations of these data. These seismic data are proprietary and confidential under contract between the UA Seismology Group and Conoco Phillips. Results and interpretations presented in this report may be reproduced, although original raw digital data remain confidential.

Seismic reflection profiles were acquired by petroleum exploration companies in the early 1980's to assess petroleum potential in Tertiary and older sedimentary rocks in central Arizona. The focus of the original data acquisition was to image stratigraphy and structure from a few hundred meters to several thousand meters in depth. However, the limited number of wells and lack of any deep wells to calibrate seismic velocity in both basins introduce uncertainty in velocity and depth estimates across the basin and in gaps between lines.

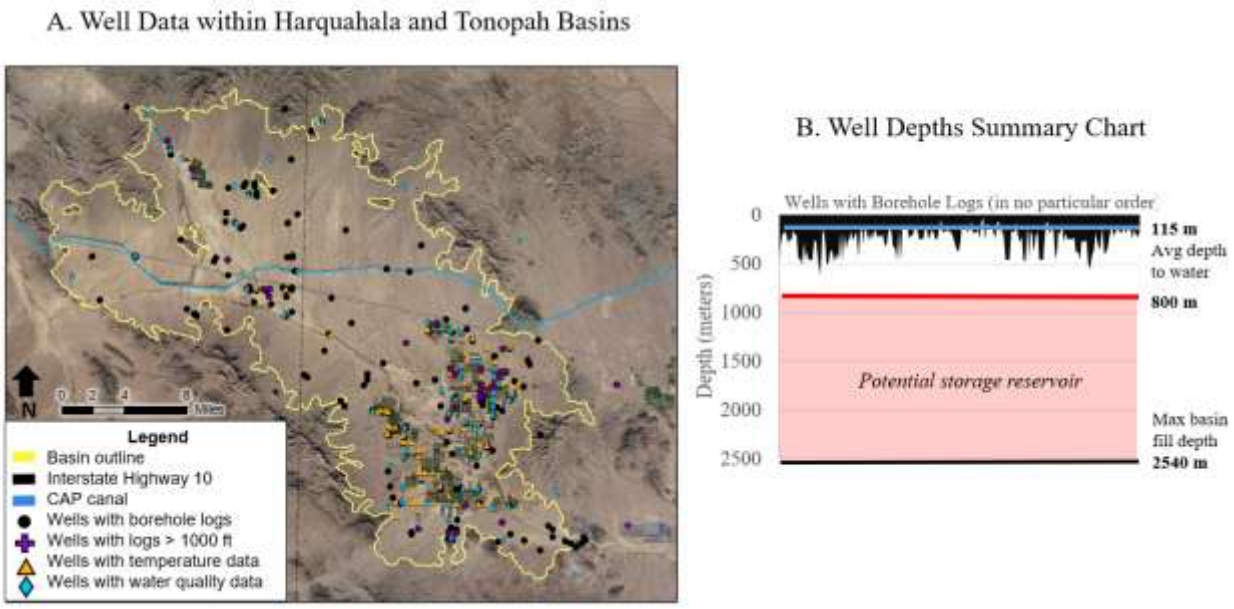


Figure 77 (A) Map of well data types within the Harquahala basin. (B) Summary chart showing wells plotted against depth. The average depth to the water table is shown as a blue line, depth to bedrock is a black line, and the potential reservoir (basin fill below 800 m and above bedrock) is shaded red. This chart highlights the lack of well data at the reservoir depths.

Reprocessing of five of these 2D seismic reflection lines was carried out by Jourdan Anoka with Anoka Geophysical LLC, Aurora, CO, in collaboration with Roy Johnson and Kurt Constenius at University of Arizona (Figure 78, Table 1). Analysis of the final stacks were made by Kurt Constenius with input from AZGS research geologists. Data quality for the five lines was variable, ranked from moderate quality to poor quality: PW24, PW23, PW22, TR12, TR10b, and TR9.

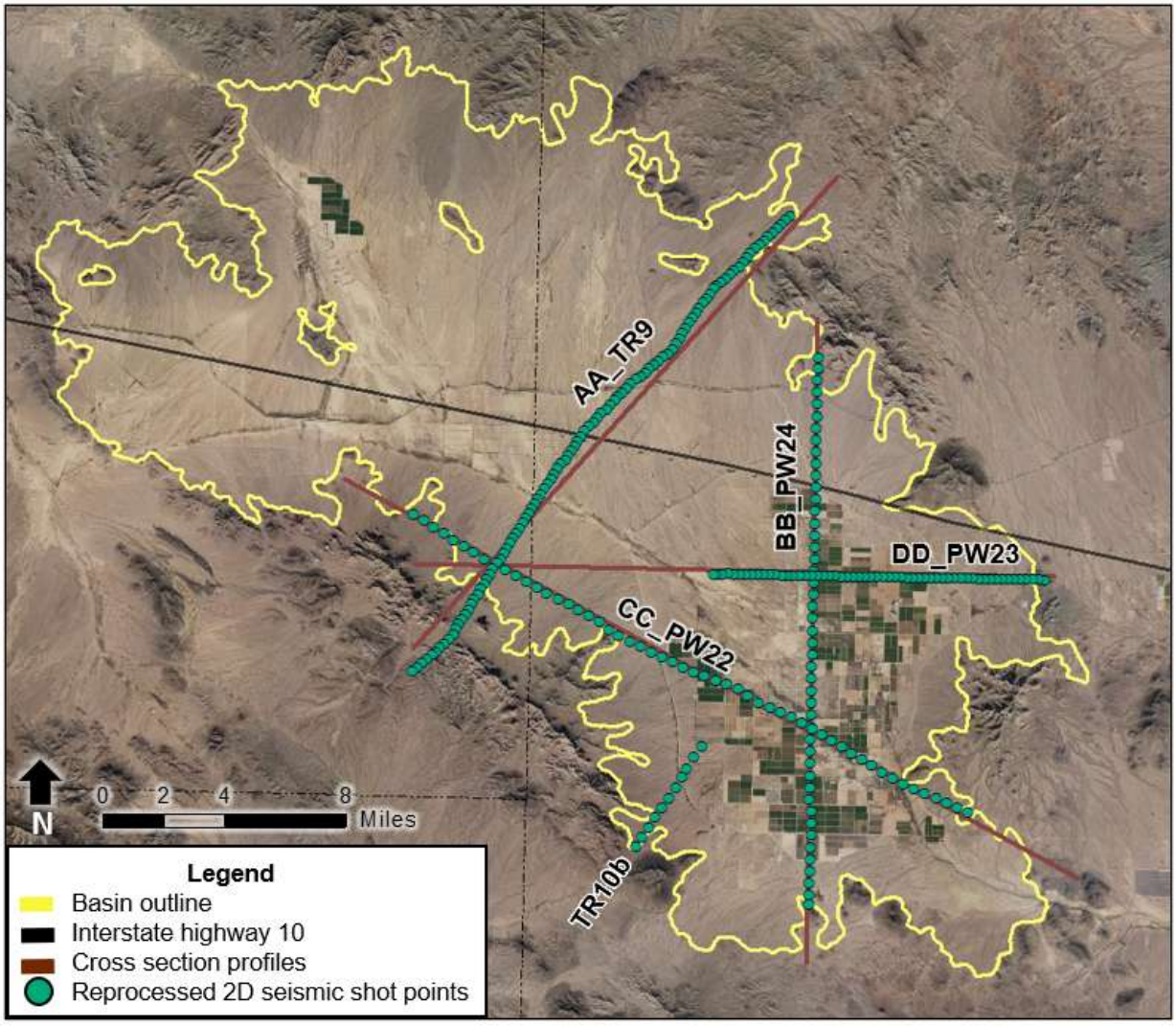


Figure 78 Map of the 2D seismic lines and cross sections profiles that traverse the Harquahala basin. 2D vintage seismic line shot points are black dots.

Table 1. List of vintage seismic lines stations used in Harquahala basin. Beginning of line (BOL) and end of line (EOL). Refer to Figure 78 for location of seismic lines and stations.

Seismic line	Reprocessed line length (km)	BOL stations	EOL stations	SP spacing (ft)	Datum elev. (m)
PW23	18.3	780	1,050	1,100	600
PW22	35.5	670	1,200	2,000	600
PW24	30.7	201	658	2,000	600
TR9	34.5	1,200	2,200	1,200	600
TR10b	6.7	0	200	2,000	600

Seismic Reprocessing

A standard processing sequence that included iterations of velocity analysis and static corrections was used for the PW and TR profiles (Table 2). Differences in processing between lines included application of normal moveout-correction velocities determined separately for each line and application of automatic static corrections, which were based on individual reflection events in each profile.

Table 2. Acquisition parameters for seismic lines used in Harquahala basin.

Acquisition Parameters	TR lines	PW lines
Acquired by	Texoma Production Co.	Anschutz Corp.
Date	1980	1980
Source	Dynamite	Vibroseis
Source size or sweep	110 lb	14-56 Hz; 18 s
Source interval	134 m	67 m
Group interval	33.5 m	67 m
Channel array	96 channels; off end	48 channels; off-end
Near offset - Far offset	805 m - 3,990 m	268 m - 3,420 m
Normal maximum fold	1,200%	2,400%
Sampling interval	2 ms	4 ms
Recording time	8 s	24 s

Depth Conversion

Depth-below-surface was determined for two interpreted event horizons using two-way travel time to the horizon and assigned interval velocities. Velocity control for the upper basin fill was provided by a sonic log from the Humble Oil and Refining State #1 well (Section 2 T8S-R8E) in the Picacho Basin. The average velocity of the upper basin fill in that well is approximately 2,133 m/s (7,000 ft/s). The lower basin fill was depth converted using velocity data from the same Humble well and sonic log data from the Suncor Development, Sunset Point #1-19 well (Section 19 T2N-R1W) in Luke basin. The lower basin fill in the Humble well is predominantly evaporites and is entirely halite in the Suncor 1-19 well with a velocity of 4,419 m/s (14,500 ft/s). Depth conversion of lower basin fill used the velocity of halite because we interpret the lower basin fill to be predominantly evaporites (see section 4).

Gravity Data

Multiple gravity datasets were used in Harquahala basin (Figure 79). Historical and statewide public gravity data were provided by the Arizona Department of Water Resources (ADWR; 2022) who maintains the regional dataset compilation derived from the Pan-American Center for Earth and Environmental Studies dataset (PACES 2016). A basin-wide gravity survey of Harquahala was conducted in 2008 but was unpublished (HGI 2009). The Complete Bougier Anomaly (CBA) gravity values from all datasets in conjunction with well, modeled DTB, and seismic data were used to identify geologic structures, anomalies, and data gaps.

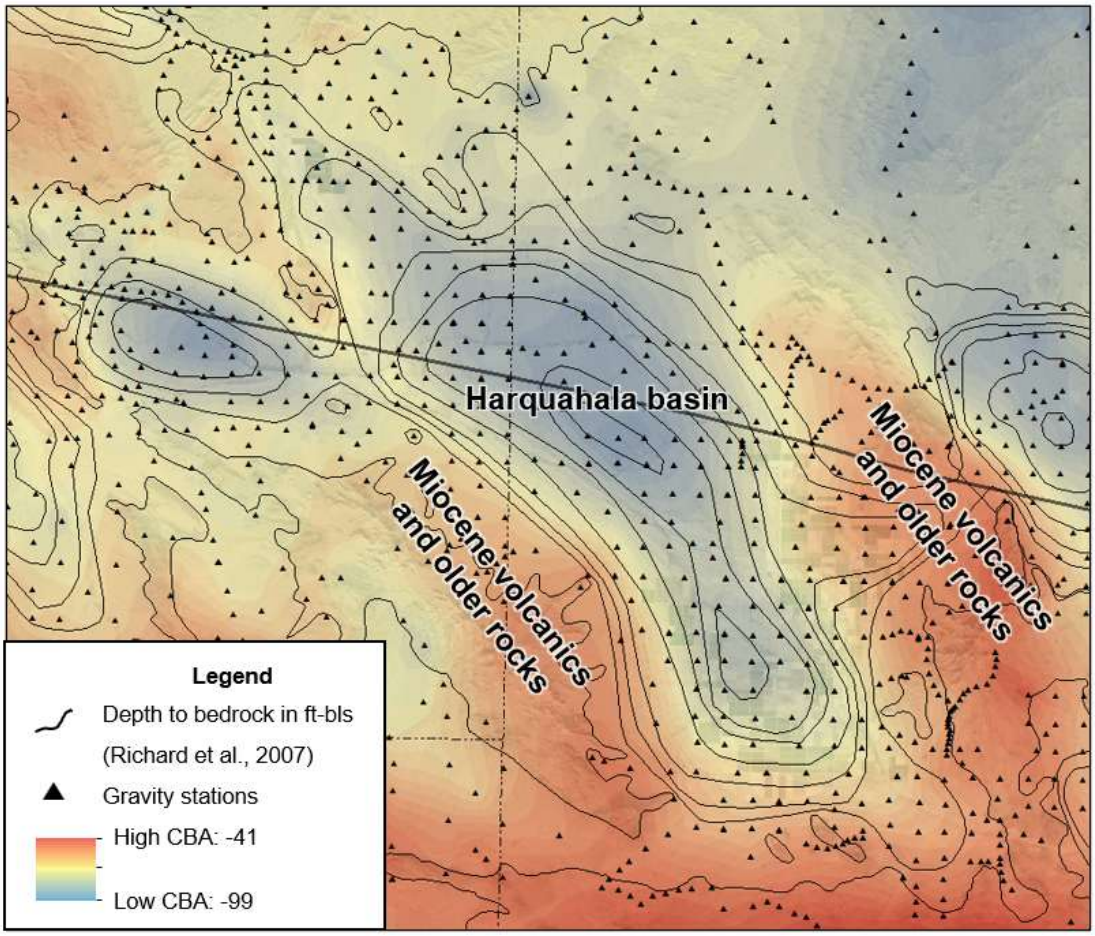


Figure 79 Map of gravity, depth-to-bedrock contours (Richard et al. 2007), and modeled CBA gravity data used in this study. Gravity point data are compiled from three separate sources (ADWR 2004, 2022; HGI 2009). Colored basemap is interpolated from Complete Bouguer Anomaly (CBA) low (blue) to high (red) values.

Depth-to-Bedrock Contours

Depth-to-bedrock data used at the start of this study were derived from a statewide DTB contour map modeled from gravity data and a limited number of borehole control points (Richard et al. 2007; Figure 79). In that report, bedrock is defined as crystalline basement overlain by clastic and volcaniclastic rocks, the same definition we use in this report. Of note, the HGI gravity study (HGI 2009) was not included in the (Richard et al. 2007) compilation.

The 2007 DTB contours were modified stepwise using detailed geologic maps, recent borehole lithology logs, and results from reprocessed vintage seismic data. Modification of DTB lines in this study were based on the hierarchy of data sources, from most confident to least confident, is as follows: (1) geologic mapping, (2) borehole lithology logs, (3) reprocessed 2D seismic lines, and (4) gravity. Data sources for DTB contour modification are listed for each contour line in the geodatabase.

ADWR wellbore logs are of generally poor quality (specific rock types may not be mentioned or may be too generally categorized; Appendix B), which prompted an in-depth quality review of adjacent wellbore logs and their relationship to geologic mapping and known geophysical data. Wellbore logs that did not correspond with two or more other datasets were not used. Basin margin contour shapes below 122 m (400 ft) were most affected by the well log review, while basin center contours were largely unaffected (due to the lack of deep borehole data). Well terminations in granite or crystalline volcanic rock overlying granite were considered bedrock penetrations. Green dots indicate reprocessed shot points included in this analysis.

Basin Fill Storage Volume Calculations

Basin fill volume between the 2D areal extent of the 800 m depth contour and the depth to bedrock was calculated using Esri ArcMap geoprocessing tools. Volume estimations rely on gravity and seismic data and interpretations of those data. Thus, they are first order estimates of potential basin fill storage volumes below 800 meters depth and above crystalline bedrock. In these estimates, basin fill is not distinguished by lithology (i.e., clastic sedimentary, chemical sedimentary, and volcanic rocks are lumped together); however, we do assume that the basin centers consist of fine-grained clastic sediment and some percent evaporite bedding, and possible interbedded volcanic rocks, and a range of physical parameters, such porosity and permeability, commonly associated with those lithologies. Carbon dioxide injection volumes are based on these physical dimensions and used in three separate methods to calculate gross and net injection volume capacity and volumes over a 5-year period. These methods are described along with results in section 6b.

Isopach Maps

Reprocessed seismic data revealed acoustic differences within the basin fill, which gave rise to an interpretation of distinct stratigraphic units and seismic zones delineated by seismic fabric. Stratigraphic picks for top and bottom of basin fill units, and an acoustically transparent zone within the lower basin fill, were determined at each seismic shot point along TR9, PW23, PW24, and PW22 in Harquahala basin. Depths were converted to elevation and used to create contour maps of the surfaces. Contour maps were converted into raster data and later used to create isopach maps (maps of thickness) for the upper and lower basin fill units, and acoustically transparent zone in Harquahala basin.

Geologic Cross-Sections

Five geologic cross-sections were created along or adjacent to the 2D seismic lines (Figure 79). Profiles were created along each line by combining a surface digital elevation model (DEM) and DTB contours. Well lithology logs from wells located within 3,000 m of the profile were projected vertically onto each cross-section line. In areas where wells were clustered, rendering

them unreadable on the profile, the well(s) located further away were removed for clarity. Basin fill unit boundaries, extent of each seismic line, extent of probable salt, and the location of faults as interpreted from seismic data were also projected onto the cross sections. The interpreted seismic lines are displayed next to their corresponding profile (see Plate 3, Wilson et al. 2024).

Lithofacies Maps

Geologic mapping of bedrock units exposed at the surface surrounding the Harquahala basin was used to predict what lithology or lithofacies would be encountered through drilling the upper few thousand feet of basin fill. The geometry of the modern watershed that supplied sediment to Harquahala basin during upper basin fill time is assumed to be consistent over the last approximately 5 Myr due to the absence of tectonism and/or major drainage reorganization. Smaller watersheds within the basin watershed, or subsheds, are also assumed to be relatively consistent.

The basin's asymmetrical geometry and location of paleodepositional centers identified in down-dip seismic reflectors were used to create paleodepositional boundaries or subsheds in the subsurface. Watershed maps were derived from the USGS Watershed Boundary Dataset (WBD). The simplified geologic map compilation (described in section 3a) was used to calculate the area of geologic map units in the basin. Geologic map units were clipped to subsheds. Areas of each map unit within each subshed were exported into Excel. Map units were lumped into broad lithologic categories (e.g., plutonic, metamorphic, volcanic, etc.) and relative percent of each lithologic category plotted for each subshed.

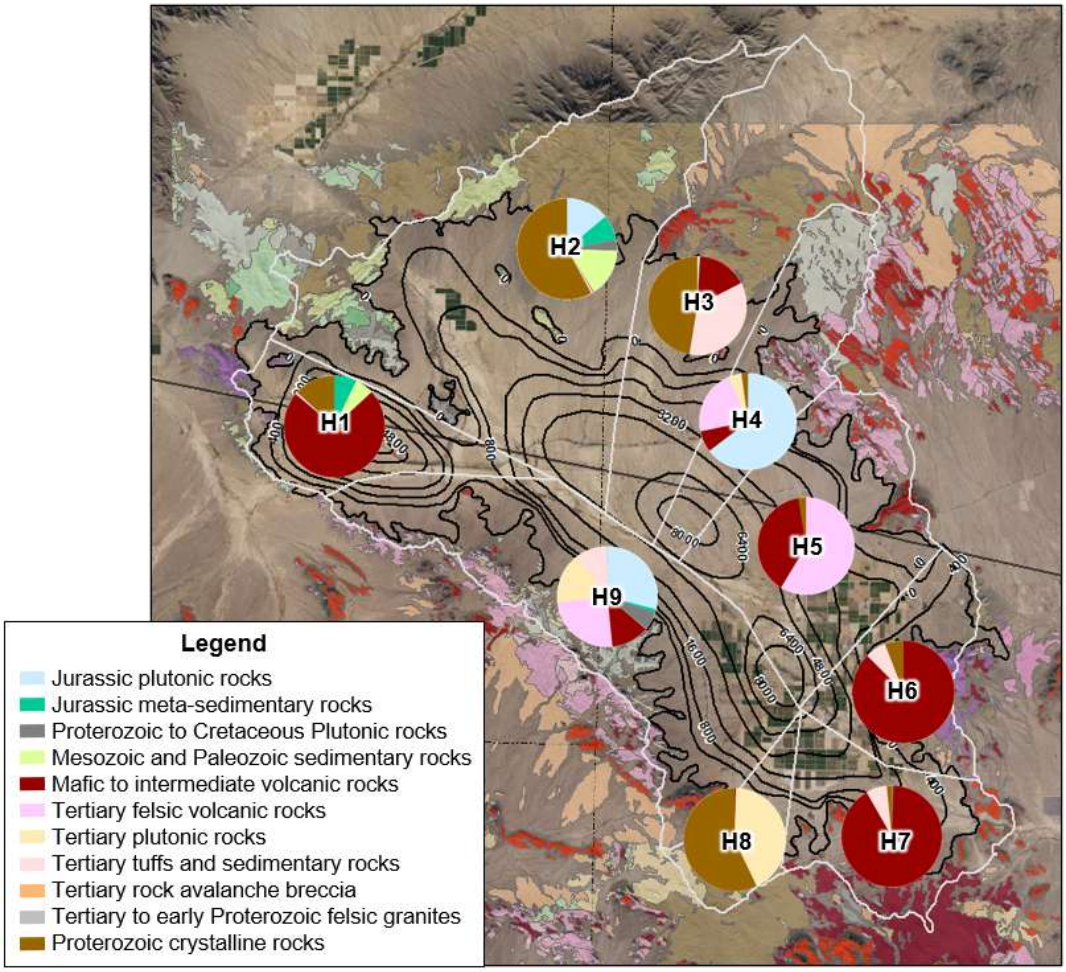


Figure 80 Lithofacies prediction map showing the percentage of rock types expected in upper basin fill based on watershed and subshed boundaries within Harquahala basin

Well Borehole Temperatures

Publicly available borehole temperature data in Harquahala basin was compiled, reviewed, and analyzed. Reported temperatures and well depths for 157 wells in Harquahala basin (Witcher 1995) are plotted in Figure 81. Overall, the quality of the data is highly variable, and data collection methods were not standardized. The borehole temperature sample depth and time collected, as well as the screened intervals sampled, are unknown. Borehole temperature data was plotted and symbolized by a color gradient representing temperature and constrained by discrete depth ranges to look for any spatial trends.

Geothermal gradients were calculated from wellbore temperatures by subtracting the bottom-hole temperature from the mean annual surface ground temperature at the well site and dividing by well depth. The mean annual surface ground temperature used for both basins was 21.1°C (70°F). This calculation yielded values between 6°C/km and 438°C/km, with many values outside of the expected range of geothermal gradients. This may be due to reporting errors of the wellbore temperature values. The worldwide average geothermal gradients are from 24°C/km to 41°C/km (1.3°F/100 ft to 2.2°F/100 ft; Peters et al. 2012). Data outside of this range was omitted

in the analysis, which brought the well count from 201 to 101 wells with reasonable calculated geothermal gradient values (Appendix C).

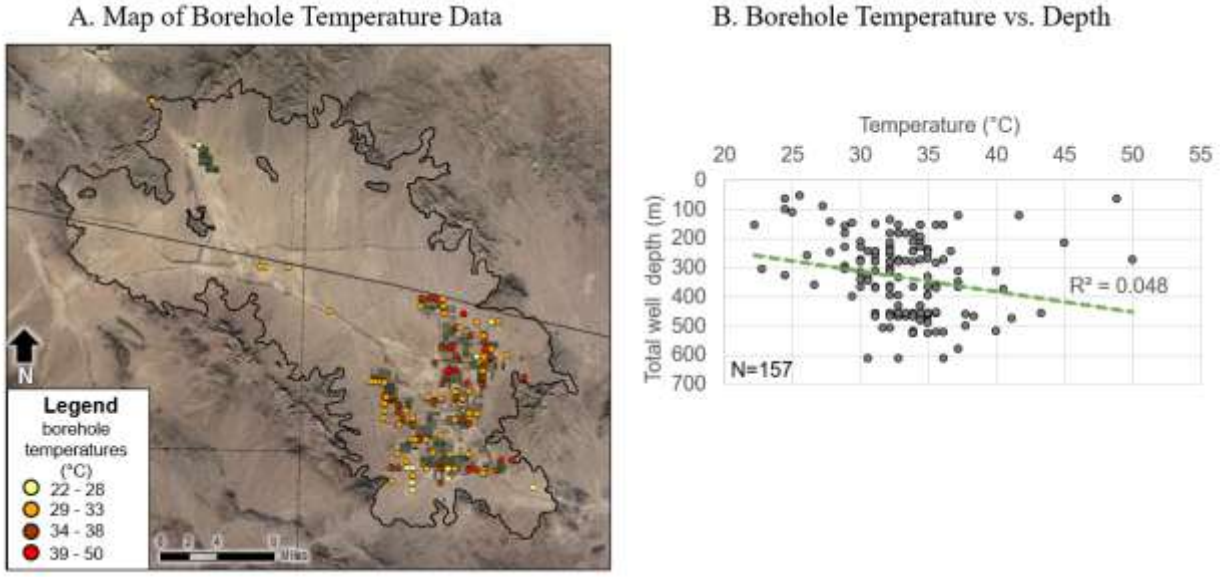


Figure 81 Borehole temperature data (A) Map displaying borehole temperatures colored by specific temperature ranges. (B) Scatter plot of temperature vs. depth for Harquahala basin. Trend lines shown in green with R2 values. Wells with depth listed as 0 were removed.

Groundwater Total Dissolved Solids (TDS)

We compiled a total of 453 wells with publicly available groundwater salinity and conductivity data in Harquahala basin (Appendix D). Of these, 51 shallow wells included direct measurements of total dissolved solids (TDS; Towne 2014). The remainder of well data lacked direct TDS values, though they did have conductivity measurements which we used as a proxy for TDS. The reported TDS value was retained where water quality records reported both TDS and conductivity values.

Conductivity values were converted to equivalent TDS values using the equation

TDS (mg/L) = k * EC (µS/cm),

where "k" is the conversion factor and EC is electrical conductivity. Wells that had both TDS and conductivity measurements (n=51) were used to determine an average conversion factor of 0.64 (range = 0.59 to 0.69). For comparison, previous work reporting statewide salinity used a conversion factor of 0.642 (Gootee et al. 2012). Figure 82 is a scatterplot of groundwater salinity vs. well depth for Harquahala basin.

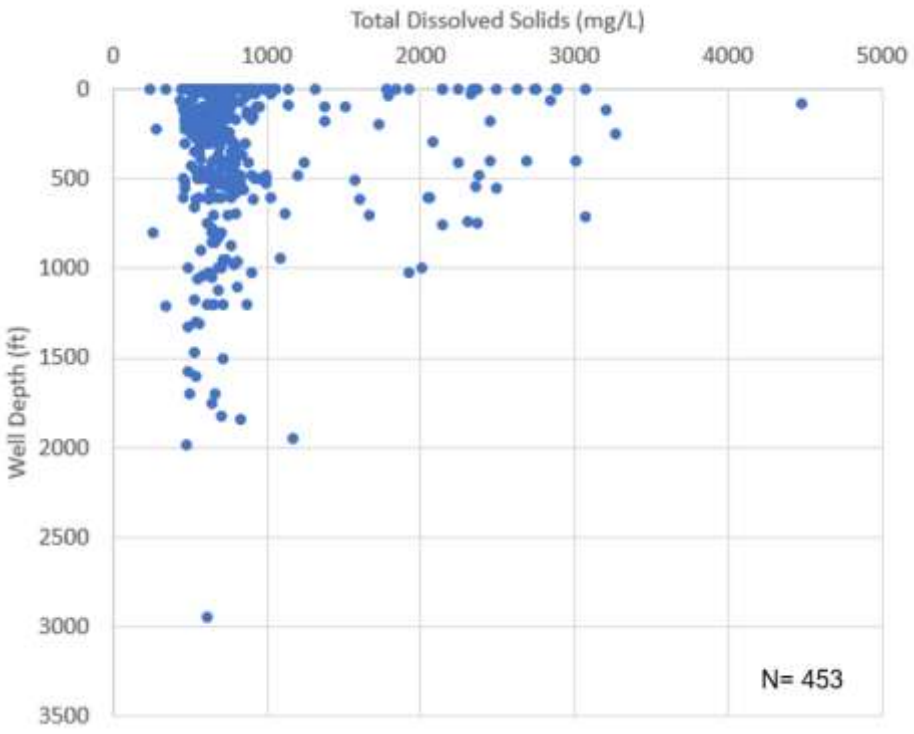


Figure 82 Groundwater salinity from wells. Scatter plot of groundwater salinity as total dissolved solids (TDS) vs. borehole depth for water wells in Harquahala basin. No trend between TDS and depth is observed.

Geologic Characterization

Conceptual Model for Basin Formation

The geology of Harquahala basin can be broadly described with a conceptual model that integrates commonalities in geologic structure and stratigraphic architecture across the Arizona Basin and Range Province (Eberly and Stanley 1978; Menges and Pearthree 1989; Spencer and Reynolds 1989).

About 30 Ma, tectonic extension in southeastern, southern, and western Arizona began to fracture, fault, and pull apart older rocks that composed Earth's crust. Through distributed low-angle normal faulting, the crust thinned, and large, linear fault blocks were uplifted to form subparallel mountain ranges. The space between those ranges gradually increased and deepened with each additional earthquake. Mountain ranges were separated by largely asymmetrical, deep sedimentary basins into which water and sediment from the surrounding mountain ranges collected over millions of years (Figure 83).

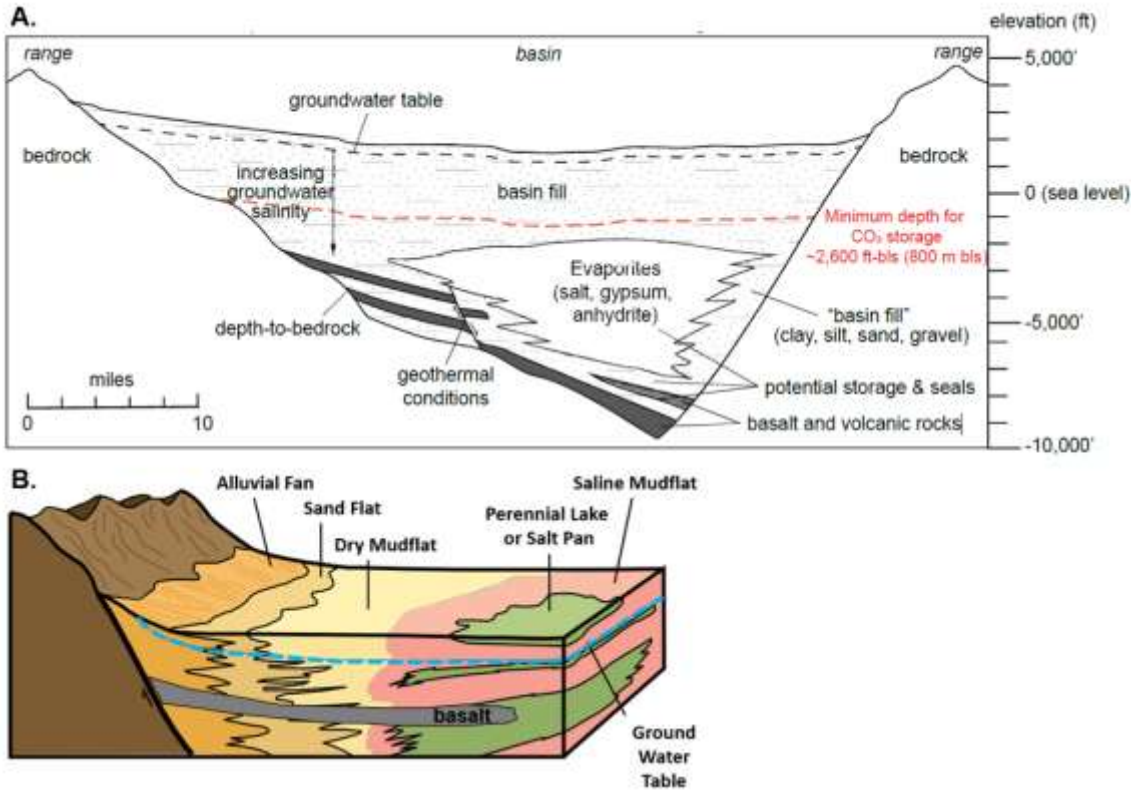


Figure 83 (A) General geologic cross section of Harquahala basin showing distribution of basin fill features and lithology. (B) Block model of depositional environments of basin fill. Modified after Faulds et al. (2016).

Early in the basin extension process between about 25 to 15 Ma, coarse sediments were concentrated near steep basin margins close to their mountain provenance and fine sediments were concentrated near sub-horizontal depositional centers where water likely ponded. The climate was semi-arid and favorable to both periods of water accumulation (forming shallow playa lakes) and extended periods of drought (water evaporation) which, in the case of closed basins, resulted in the formation of bedded evaporite deposits fed primarily by shallow groundwater high in dissolved solids within the basin center or subbasin centers (Figure 83). Deposition of these basin-fill facies were punctuated by continued crustal extension and widespread volcanic eruptions that deposited lava flows, ash, and pumice directly on crystalline bedrock-cored mountain ranges and interlayered with basin fill sediments. Continued extension during this phase accumulated thousands of feet of basin fill deposits before tectonism waned. As a result, older basin fill and interbedded volcanic deposits are progressively tilted, faulted, and compacted with depth.

Beginning about 6 to 5 Ma, extension and faulting waned while passive erosion and deposition dominated within the closed basins. These deposits are generally horizontal, less compacted and nondeformed compared to older basin fill sequences. Basin-filling continued in depocenters in a closed basin, generally fining grain sizes up section, as piedmonts backfilled bedrock topography near the base of mountain fronts. As a result, there are basin sedimentary packages with different structural histories: a lower, older sedimentary package that is tilted and faulted (during active extension) and an upper, younger sedimentary package that is generally undeformed (as extension waned; Figure 84).

Harquahala basin is mantled by a thin veneer of Pleistocene and Holocene (about 2.6 Ma to the present) alluvium that forms low-gradient piedmonts graded to the modern valley axial washes (Centennial Wash). Both axial wash systems are integrated with the Gila River about 2 miles downstream of the Hassayampa River's confluence with the Gila River. Integration timing is not known, but it likely occurred during the Pleistocene or latest Pliocene (5 to 2.6 Ma). This basin model is generally well understood in shallow basin fill and surficial exposures, although less understood in buried basin fill deposits below about 2,500-ft depth. Harquahala basin exhibits a similar extensional history, style of faulting, and depositional environments to other neighboring basins in southern Arizona.

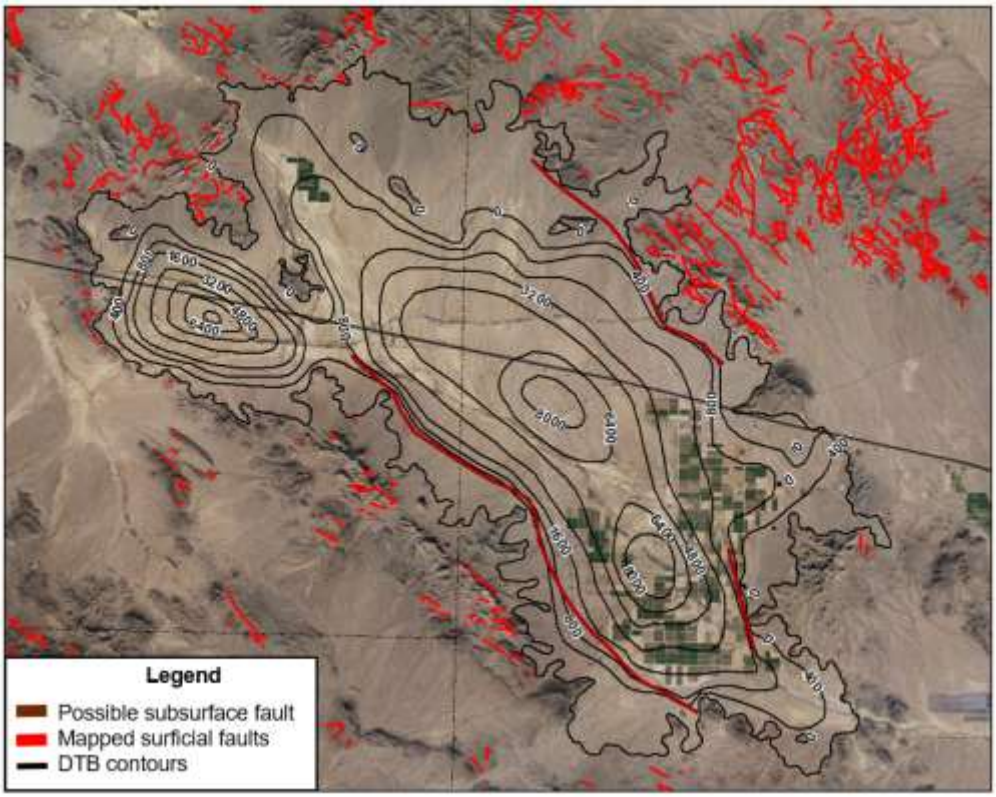


Figure 84 Map of fault traces exposed at the surface (bright red) and subsurface faults interpreted from seismic lines (brown).

Basin Geometry and Structure

Harquahala valley is surrounded by mountains composed of a diverse suite of Proterozoic crystalline igneous and metamorphic rocks, sparse outcrops of Paleozoic and Mesozoic sedimentary rocks, and Jurassic igneous and metasedimentary rocks, unconformably overlain by effusive and explosive products from Miocene volcanic eruptions (see Plate 2 , Wilson et al. 2024).

Harquahala basin is divided into three subbasins each separated by a subsurface structural high, as shown on the DTB contour map (see Plate 2, Wilson et al. 2024). The central subbasin is the deepest with a maximum depth of 2,538 m (8,326 ft) and the southern subbasin's maximum depth is 2,530 m (8,300 ft). The northwestern subbasin is isolated and smaller than the other two

with a maximum depth of 2,438 m (8,000 ft). Reprocessed 2D seismic data show the basin-bounding detachment fault is close to the southwest basin margin at the base of the NW–SE striking Eagletail Mountains (see Plate 3, Wilson et al. 2024; seismic line TR10b). As such, the deepest portion of the basin is adjacent and subparallel to that mountain range (Figure 85).

Stratigraphy

The stratigraphic architecture of basin fill in Harquahala basin is not well delineated due to lack of age constraints, few high-quality well records, and no deep well penetrations. However, basin fill could be divided into three units based on the character of the seismic reflection data and the conceptual model described in section 4a. Listed from oldest to youngest the stratigraphic packages are: lower reflective package (LRP), lower basin fill (LBF), and upper basin fill (UBF; Figure 85). Harquahala basin is not dissected, therefore all basin fill deposits are covered by Pleistocene and Holocene alluvium. Due to the lack of exposure and deep well penetrations, the porosity and permeability of each unit are unknown.

Lower Reflective Package (LRP)

The LRP, the oldest unit, is a strong reflective package and is likely comprised of interbedded lava flows and sedimentary rocks deposited directly on the crystalline basin floor (Figure 85; see Plate 3, Wilson et al. 2024, seismic lines TR9, PW22, PW23, PW24). This unit is distinguished solely through interpretations of strong, parallel, shallow-dipping seismic reflectors. The LRP is approximately 1,066 m (3,500 ft) thick near the basin center, although without velocity control the true thickness is not known and could be $\pm$ 20-30%. The apparent thickness increases to the southeast and decreases to the northwest. Extensive outcrops of early Miocene age volcanic rocks in the mountain ranges bordering Harquahala basin are evidence for widespread bimodal volcanism during early basin formation. Therefore, we suggest that the LRP is equivalent to those rocks in part by age, although contains a mix of clastic sediments interbedded with volcanic flows near now buried depocenters. The LRP may also include explosive centers or cauldrons as part of an upper-plate geometry within the Harquahala half-graben.

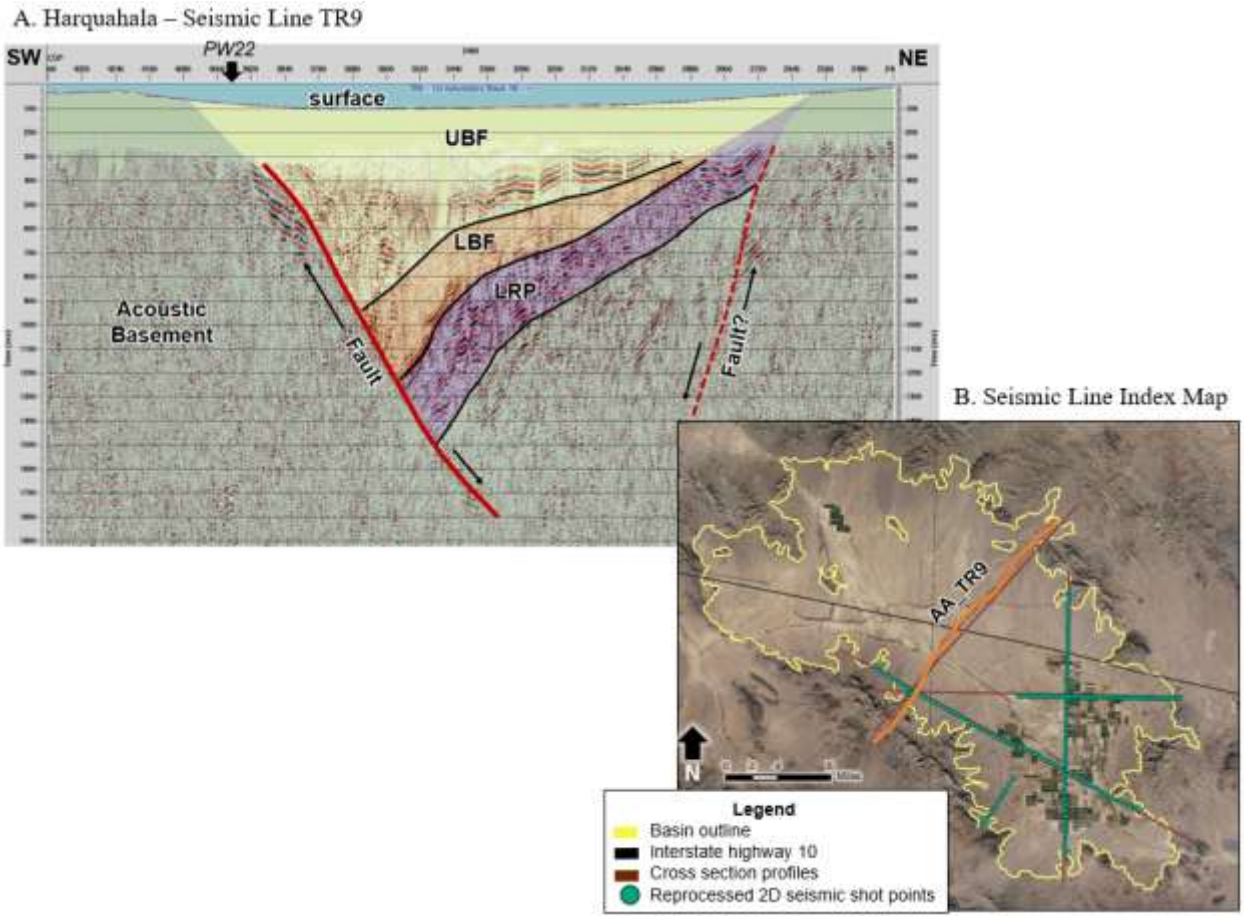


Figure 85 Examples of the basin fill units interpreted from the 2D seismic. (A) Seismic line TR9 is perpendicular to the basin axis in Harquahala basin and shows the seismic character of the lower reflective package (LRP), lower basin fill (LBF), and upper basin fill (UBF) units. (B) Index map of seismic lines.

Lower Basin Fill (LBF)

The LBF is a middle-aged sedimentary package defined by tilted and truncated seismic reflectors seen on all seismic lines (Figure 85; see Plate 3, Wilson et al. 2024). There are no direct measurements, such as borehole lithology logs, to characterize lower basin fill lithologies for Harquahala basin. Broadly, LBF is likely comprised of a wide range of clastic sediment sizes from clay to boulders sourced from nearby mountain ranges, and the package may contain interbedded mafic to intermediate lava flows and felsic explosive material. The areal extent and lateral continuity of deposits and grain size distribution is unknown; however, based on our conceptual model, coarse clastic deposits on the basin margin grade laterally down-gradient into finer sediments near basin centers. Potential capping rocks such as extensive clay deposits or evaporite deposits, if present, should be located near basin centers.

In Harquahala basin, the LBF is a maximum of 975 m (3,200 ft) thick and overlies the LRP. Seismic reflectors suggest individual LBF blocks are cut and tilted by several high-angle normal faults. The LBF isopach map in Harquahala basin (Figure 86) represents the gross thickness of rock between the LRP and UBF units and highlights three subbasins: the northwest subbasin

with a maximum thickness of 785 m (2,575 ft), southern subbasin with a maximum thickness of 722 m (2,368 ft), and the central subbasin where LBF is thickest at 975 m (3,200 ft).

The LBF includes an acoustically transparent zone (ATZ) which is defined as an area of dim amplitude reflectors. The ATZ is interpreted to consist of bedded evaporite deposits based on similar, tested, ATZ's in proxy basins (Eberly and Stanley 1978) and predictions from the conceptual basin formation model (section 4a). Although the type of evaporite minerals present in Harquahala basin is not directly known, poorly reflective and chaotic-to-weak amplitudes, are indicators of halite-rich bodies (Teixeira et al. 2020). The composition of evaporite deposits in proxy basins also include significant halite – the evaporites in Luke basin are halite and Picacho basin is composed of anhydrite with lesser bedded halite (Neal and Rauzi 1996).

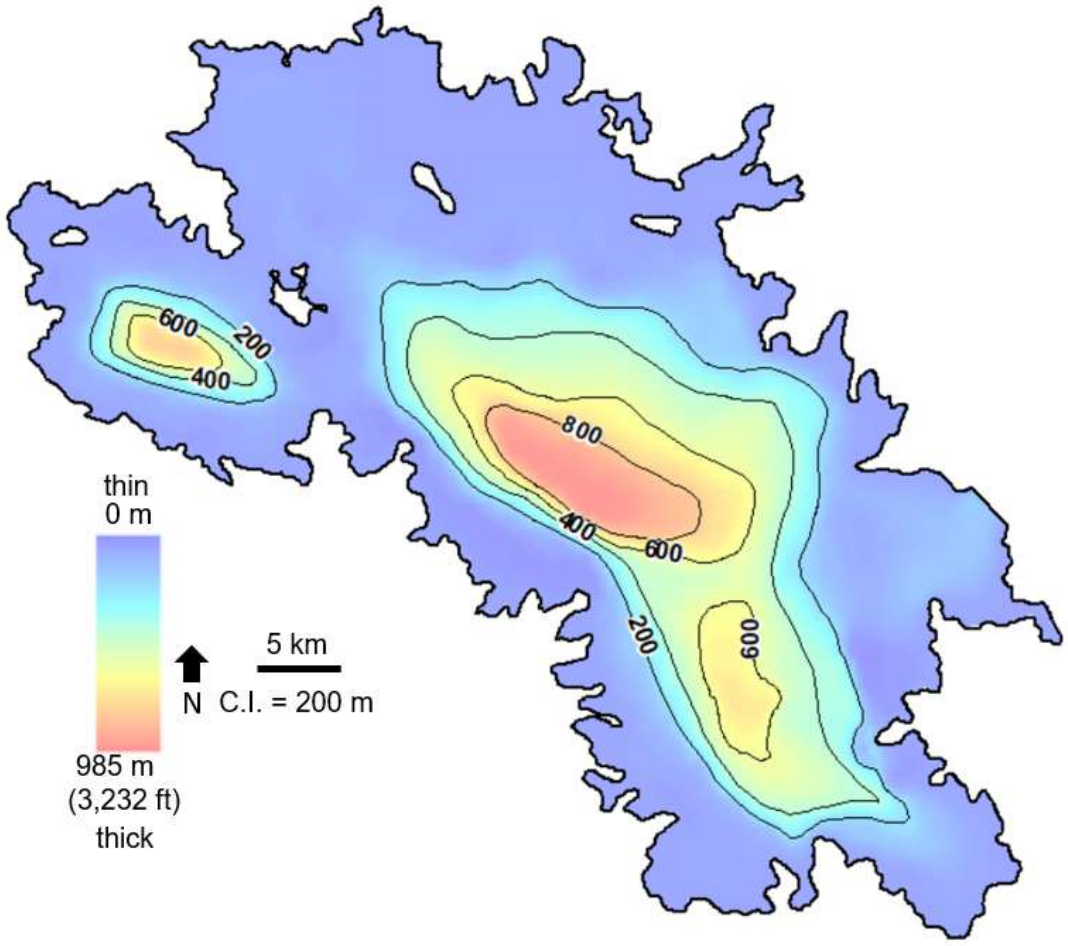


Figure 86 Isopach map of lower basin fill in Harquahala basin created by subtracting the base upper basin fill (UBF) elevation (m) grid by the base lower basin fill (LBF) elevation (m) grid

The acoustically transparent zone is observed on lines TR9 and PW23 in Harquahala basin. An approximate thickness across the zone was calculated using the difference of the travel time (ms) between the top and bottom of the seismic facies (converted to seconds) and multiplied by14,500 ft/s (the proxy evaporite velocity from sonic logs in Picacho and Luke basins). The areal extent and maximum thickness of the ATZ in Harquahala basin is 180 km^2 (112 mi^2) and 610 m (2,000 ft). Isopach maps of the ATZ show their extents are generally located adjacent to basin

depocenters (Figure 87), which may represent the extensive, and shallow salt pan environment as seen on the depositional environment block model (Figure 84). Additionally, subbasins likely migrated slightly over time which may explain why the ATZ polygon does not match the deepest parts of the subbasins. Higher resolution data is needed to better delineate ATZ extents.

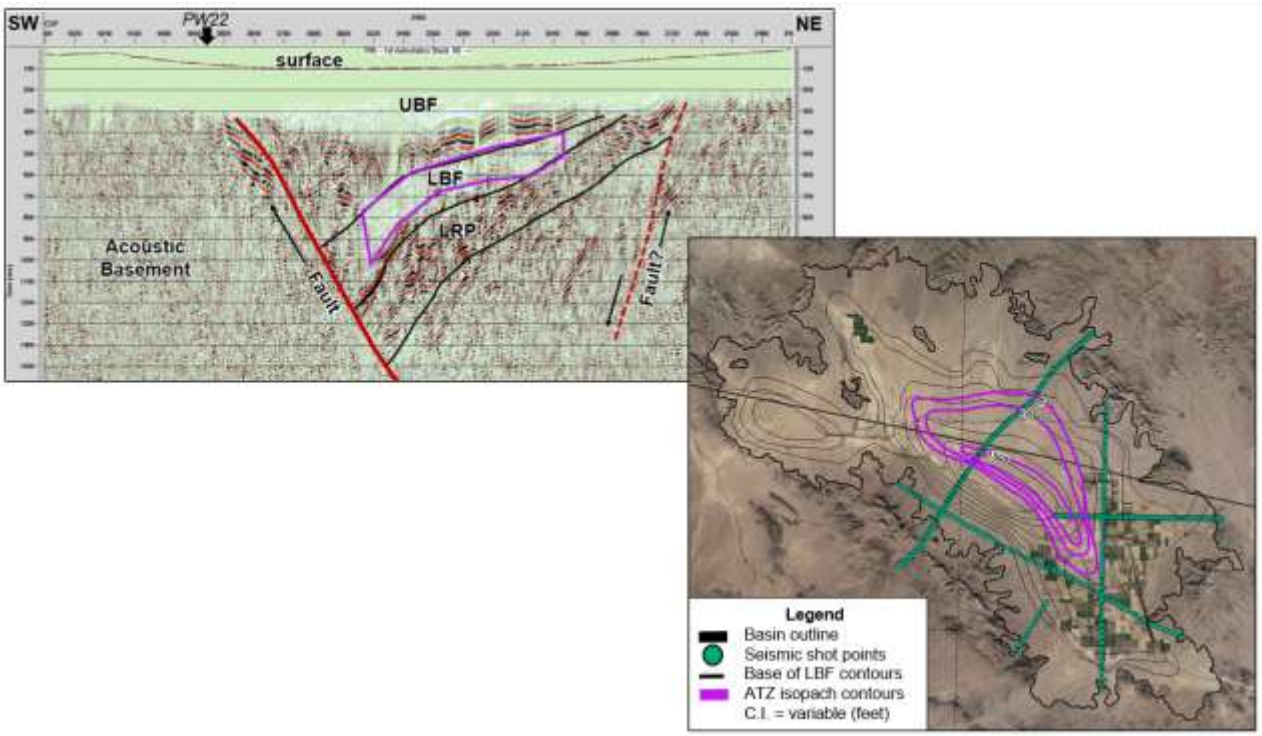


Figure 87 Seismic line TR9 with the mapped ATZ outlined in purple. Isopach map of the acoustic transparent zone (ATZ) in Harquahala basin.

Upper Basin Fill (UBF)

The youngest unit defined in this study is the upper basin fill (UBF). It is characterized by combining the conceptual basin model, proxy studies from nearby basins, well lithology logs, and lateral predictions from bedrock and surficial geologic mapping. In both basins, the UBF is relatively nondeformed (not faulted, folded, or tilted), extends to basin margins, and unconformably overlies the LBF (Figure 85). Like the LBF, the UBF is composed of clastic sediments ranging in size from clay to boulders and grain size is dependent on distance from the basin-bounding mountain ranges. At the time UBF was deposited, Basin and Range extension and volcanism was waning, therefore the UBF likely has little or no primary volcanic deposits.

The isopach map of UBF in Harquahala basin shows two distinct subbasins, the northwestern subbasin with a maximum thickness of 530 m (1,740 ft) and the central subbasin with a maximum thickness of 820 m (2,690 ft; Figure 13A).

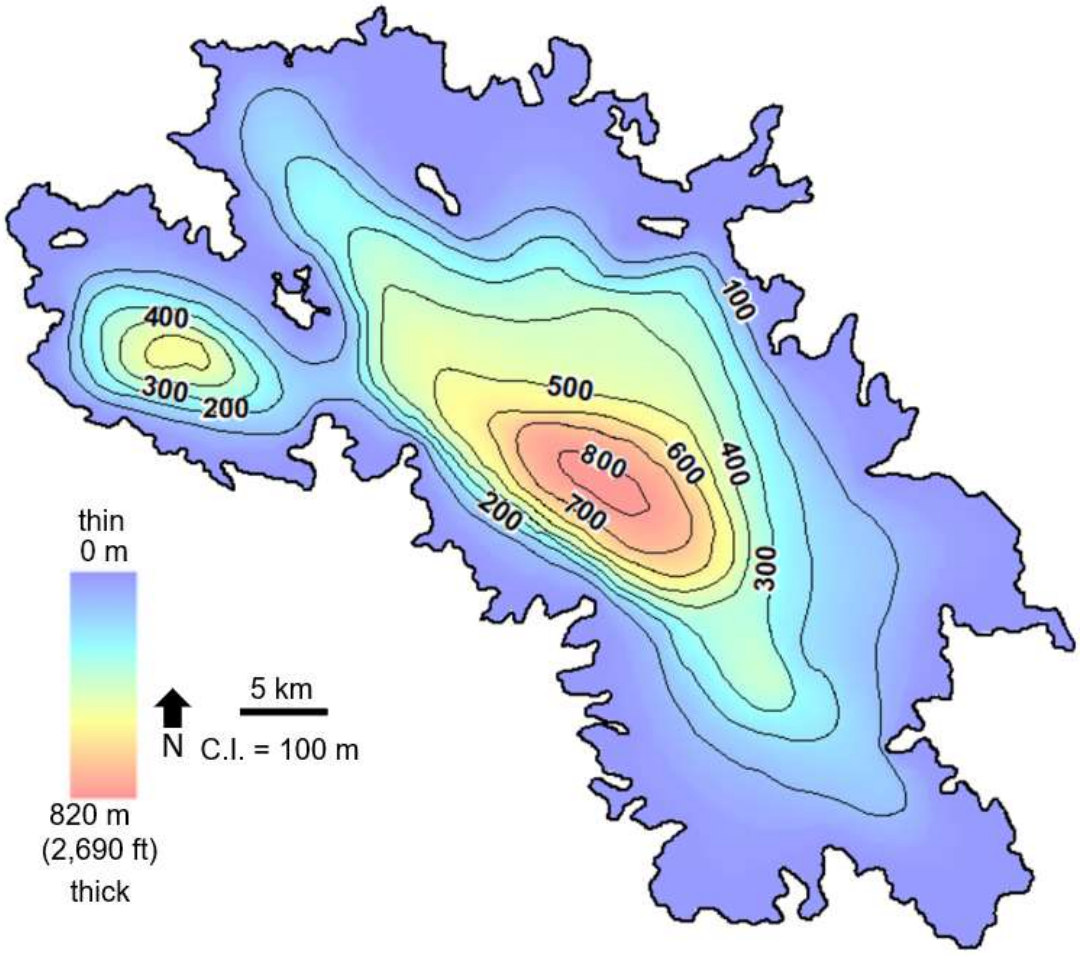


Figure 88 Isopach map of upper basin fill unit in Harquahala basin by subtracting the surface digital elevation model (DEM) grid by the base upper basin fill (UBF) elevation (m) grid

Geothermal Gradient

Hot dry crystalline rock is close to the surface in the Basin and Range Province due to millions of years of extension/faulting resulting in high heat flow (Figure 89A). Small-scale national geothermal studies of heat flow (Mullane et al. 2017; Witcher 1995) show the state of Arizona has moderate geothermal potential (Sass et al. 1994; Figure 89B).

Borehole temperature data in Harquahala basin are sparse and they show no distinct spatial trends. Measured temperatures in 84 wells that penetrate upper basin fill to the shallow depth of 611 m (2,005 ft) average 91°F (33°C). The calculated mean geothermal gradients to shallow well terminations are 87°F/mi (30.6°C/km) for Harquahala basin. These gradients are comparable to the published mean geothermal gradient for the southern Basin and Range Province of 30°C/km (Nathenson and Guffanti 1988).

Geothermal gradients for the entire basin depth cannot be directly calculated because there are no deep borehole logs. Estimates can be made, however, using two nearby proxy basins: Luke basin at 78.8°F/mi (26°C/km) with a maximum well depth of 550 m (1,804 ft) and Higley basin at 104°F/mi (40°C/km) with a maximum well depth of 2,780 m (9,118 ft). In general, geothermal

gradient is dependent on crustal thickness. Thick basin fill that overlies thinner crust (at basin centers) is expected to have a higher geothermal gradient because there is less mantle-derived heat loss within that crust. Conversely, thin basin fill that overlies thick crust (at basin margins) is expected to have a lower geothermal gradient because mantle-derived heat is widely dissipated within that crust. Additional data acquisition is required to better characterize basin heat flow and borehole temperature heterogeneity.

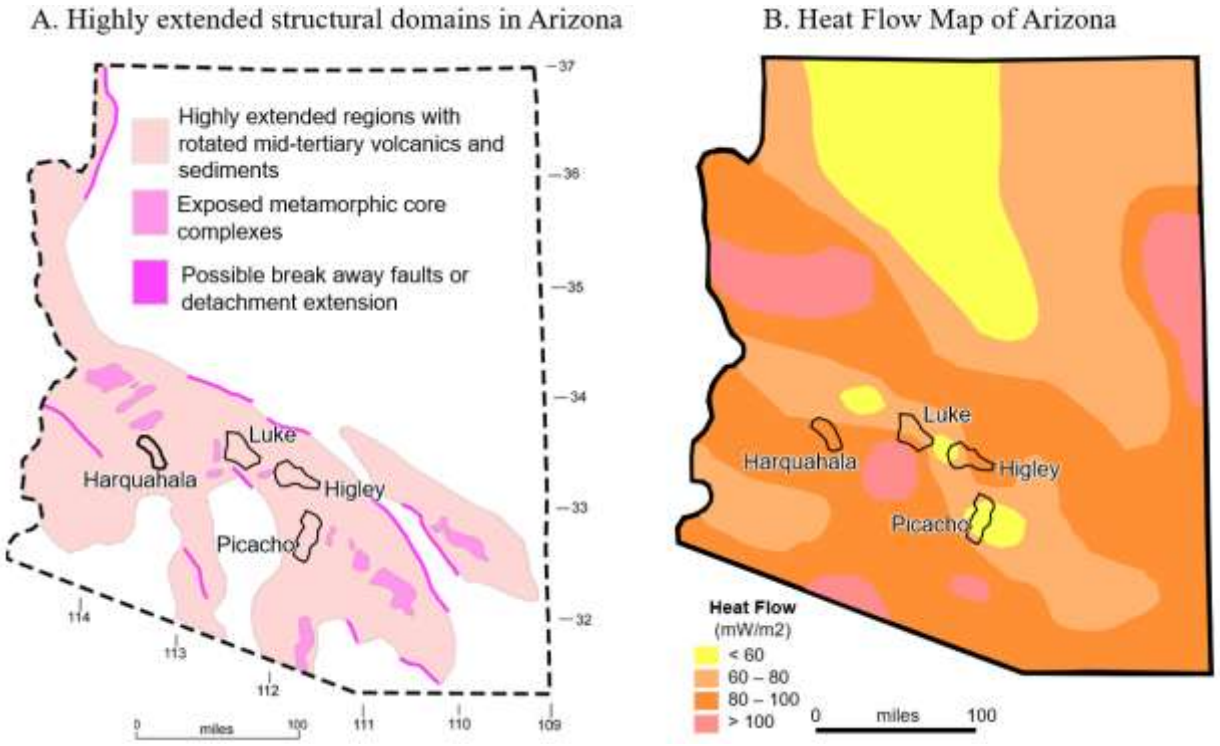


Figure 89 Map of extended crust and heat flow in Arizona (A) Map of highly extended structural domains throughout Arizona. Modified after a 2018 presentation by Witcher, originally from Spencer and Reynolds (1989). (B) Map of heat flow throughout Arizona modified after a 2018 presentation by Witcher, originally from Sass et al. (1994).

Groundwater Salinity

The U.S. Environmental Protection Agency (EPA) defines a non-potable water resource as greater than 10,000 milligrams per liter (mg/L) of total dissolved solids (TDS). Several basins in south-central Arizona have brackish, saline and hypersaline groundwater at depths generally greater than 2,500 ft (Gootee et al. 2012). Due to the lack of salinity data below 2,000 ft in Harquahala basin, we refer to proxy basins for comparison.

Figure 90 shows TDS values exceed approximately 90,000 mg/L for three proxy basins with deep well data: Luke basin, Higley basin, and Picacho basin. Measured TDS values for Harquahala basin are below the 10,000-ppm limit, but those data are limited to wells shallower than approximately 1,000 ft. Deep TDS values cannot be extracted from shallower data because the data do not trend linearly due to factors such as groundwater mixing from mountain-front recharge, mixing with deeper groundwater and recharge from agricultural uses. The basin is structurally and hydrologically isolated with deep (>5,000 ft) basin centers, and likely bedded

evaporite deposits. Given this, the potential for elevated TDS concentrations at depths greater than approximately 2,500 ft is anticipated. Additional water sampling and temperature measurements at depth are required to give a more accurate and complete assessment.

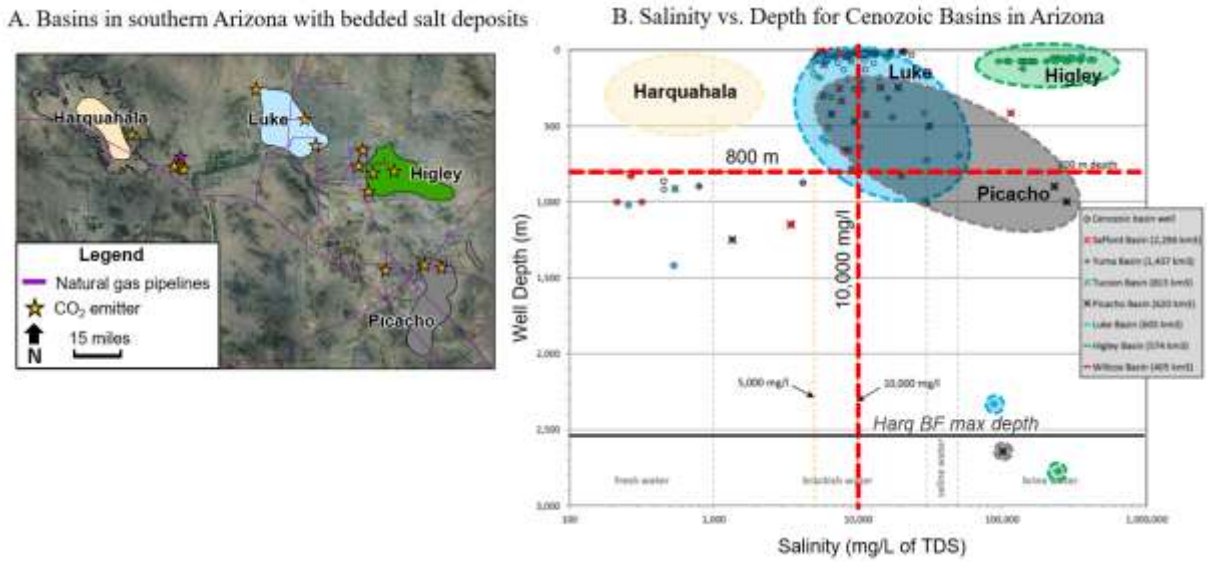


Figure 90 Bedded salt and groundwater salinity in southern Arizona (A) Location map of salt-bearing basins of interest in south-central Arizona colored to match fields shown in 16B. (B) Scatter plot of salinity vs. well depth for salt-bearing basins of interest, modified after Gootee et al. (2012). Each basin has a colored data cloud for comparison. Red dashed lines represent the salinity and depth cut offs. Black lines represent maximum basin fill depths for each basin.

Analysis and Discussion

Storage Reservoirs

Parameters necessary for a suitable carbon capture and storage (CCS) reservoir include sufficient lithostatic pressure of around 800 m depth (about 20 MPa pressure), groundwater salinity at or greater than 10,000 ppm TDS limit set by EPA, below viable underground sources of drinking water (USDW), reservoir pore space volume and permeability, and a seal or caprock above the reservoir. The types of CCS reservoirs applicable in this region would be stacked saline, mafic rocks, and geothermal. Potential seals would include claystones and bedded evaporites. A stacked saline reservoir with fine-grained clastic and bedded evaporite capping layer(s) are highly probable in Harquahala. Bedded evaporite deposits and basalt lava flows are likely but not directly measured. Storage reservoir types stated herein are each 800 m (2,624 ft) below the land surface, where lithostatic pressure is sufficient to retain CO_2 in a supercritical state, assuming regional pressure and temperature conditions.

Stacked Saline Formations

Stacked saline reservoirs are comprised of permeable clastic and chemical sedimentary rocks with saline pore water and represent the most likely and abundant type of storage by volume. The stacked saline reservoir in Harquahala basin includes both the lower reflective package (LRP) and the lower basin fill (LBF), which can also include stacked volcaniclastic and mixed

volcanic and sedimentary rocks. Together these stratigraphic units occupy a total gross volume of 396 km^3 (95 mi^3): LRP = 304 km^3 (73 mi^3) and LBF = 92 km^3 (22 mi^3). Reported volumes include rock volume and pore space. Capping or sealing stratigraphic units cannot be identified with available data. However, evaporite deposits, fine-grained siliciclastics such as clay beds, and some weathered basalt lava flows, can provide sealing conditions and are likely present in Harquahala basin based on predictions from the basin's geologic history and regional geologic map units.

Bedded Evaporite Deposits

The presence of bedded evaporites is likely based on nearby proxy basins with similar tectonic histories and tested evaporite deposits. Bedded evaporites in Harquahala basin are strongly supported by proprietary isostatic residual gravity anomaly maps and seismic patterns/fabrics observed and interpreted from 2D seismic lines in this study.

The nearby Picacho and Luke sedimentary basins, which have the same geologic history as our basin of interest, have proven salt deposits. Picacho basin, approximately 90 mi SE of Harquahala basin, has evaporite facies at depth confirmed by wireline electric logs and whole rock core. The Luke basin contains a large salt body that has been developed and used to safely store liquid natural gas since the early 1970s. The Luke basin salt deposit is characterized by gravity anomaly maps (Richard et al. 2007) and seismic data (Eberly and Stanley 1978) which have also highlighted the potential salt presence in Harquahala basin.

The acoustically transparent zone (ATZ) imaged from seismic facies likely represents a bedded evaporite deposit or interval and is present in Harquahala basin. The ATZ is defined by areas of dim amplitude reflectors. The areal extent and thickness are shown on Figure 86. The location and extent of this facies is limited by the quality of the 2D seismic lines, and it may be present elsewhere, where resolution is poor, or data is absent.

Basalt Flows

Liquified CO_2 can be reacted with buried magnesium- and iron-rich mafic rocks in situ to form a solid precipitate, permanently storing it (Raza et al. 2022). This chemical reaction takes place on short timescales ranging from hours to a few years, and the reaction is accelerated with greater exposed surface area (i.e., vesicular basalt, volcaniclastic particles, and joint surfaces). During crustal extension and formation of Harquahala basin, mafic (basaltic) volcanism was widespread and long-lived. Basalt lava flows cap bedrock in basin-bounding mountain ranges, and (at least) one large volcanic vent (Saddle Mountain) divides Harquahala and Tonopah basin to the east (see Plate 2, Wilson et al. 2024). Mafic volcanic rocks are logged in shallow wells along the basin margins (see Plate 3, Wilson et al. 2024) and lithofacies mapping predicts mafic volcanic rocks are the dominant source terrain for basin fill in the southern Harquahala basin (Figure 80). Inselbergs of basaltic flows exposed on basin margins are surrounded by young basin fill, suggesting some likelihood that these flows are interbedded with a part of basin fill. The LRP in Harquahala basin is likely comprised of volcanic flows interbedded with sedimentary rock, which may present additional basaltic storage reservoirs combined with interbeds capable of trapping CO_2 long enough to mineralize into solid carbonate minerals.

Volume Estimates of Basin Fill and CO_2 Storage

Basin Fill Sediment Volumes

Storage volume estimates are theoretical and not based on direct measurements in the Harquahala basin. Isopach maps were created to calculate the total rock volume of the stratigraphic units present. Without deep borehole lithologic and rock property logs, we assigned mean matrix porosity values derived from our interpretations of basin stratigraphy and regional proxy data from other deep sedimentary basins (Gootee 2013a, 2013b, 2015). Fracture porosity, spacing, and density was not considered in our study. Storage volumes for CO_2 mineralization in basalts were not estimated. This technique is relatively new and there are too many unknowns at this stage to achieve a reasonable estimate.

To estimate net pore space for CO_2 storage, the area of each basin fill unit and maximum thickness were calculated from isopach maps presented in section 4. The average thickness of basin fill below 800 m depth was used to calculate first-order gross volume. The UBF lies above the 800 m depth requirement for CO_2 storage, so it is not considered in the storage volume calculations. Table 3 summarizes the area, max thickness, and gross sediment volume for each basin-fill unit in Harquahala basin.

Table 3. Physical dimensions of area, thickness, and volume for basin fill units in Harquahala basin. Italicized physical parameters below 800 m depth were used in CO_2 volume analysis.

	Basin-fill units	Area (km2)	Max thickness (m)	Average thickness (m)	Gross volume (km3)
Harquahala basin	UBF	1,380	820	--	248
	LBF	1,380	975	--	92
	ATZ	185	610	--	unknown
	LRP	unknown	1,490	--	304
	below 800 m	*327*	*1,740*	*848*	*269*
	total basin fill	1,380	2,540	--	644

Other Physical Parameters

Basin fill units in Harquahala are suitable reservoirs for supercritical CO_2 storage because they likely contain permeable and porous strata under confined to semi-confined conditions in saline to hypersaline aquifers below 800 m depth. The LBF is likely composed of evaporite minerals, mixed with some fine gravel, sand, silt and possibly extensive clay, characteristic of basin fill in the region at these depths (Gootee 2015). The LRP, which underlies the LBF, is likely composed of volcanic and sedimentary rocks. A gross volume of porous rock was estimated based on these lithologies and their porosity contributions. For example, sandstone, fine gravel and volcanic lithofacies would contribute to porous and permeable strata, whereas clay and evaporites would serve as sealing strata. The percentage of the porous lithofacies was estimated based upon the conceptional basin model presented in Figure 80. In both basins, we estimate between 30% and 70% of basin fill have porous and permeable sediment suitable for CO_2 storage, thus we used the

50% median or net-to-gross ratio of 0.5. The porosity of sandstone and gravel range from 40% to 15%; we used an average porosity of 25%, excluding porosity-reduced compaction with increased depth. An effective available porosity (specific yield) between 10% and 30% was considered, based on data from general physical character of sand and fine gravel (Walton 1970), although these estimates do not take cementation into consideration. A conservative effective porosity of 15% was used, derived primarily from numerical groundwater models of older basin fill strata in nearby McMullen basin (Gootee and Noel 2015) and Phoenix basins (ADWR 2006).

The density of supercritical CO_2 at an approximate depth, temperature and pressure for supercritical CO_2 storage is based on modeled datasets (Pan et al. 2017). The temperature of the reservoir was based on scant oil and gas well data in this region, and from the geothermal gradient discussed in section 4. A summary of physical parameters and their standard deviations used to calculate volumes are listed in Table 4. All volume data, other factors, coefficients, and calculations are listed in Appendix G.

Table 4. Physical parameters of basin fill used to calculate CO_2 injection volumes.

Parameter	Units	Harquahala	Standard deviation
Area, A	km2	327	0.1
Gross thickness	m	848	0.2
Porosity, Φ	frac.	0.15	0.05
Net-To-Gross Ratio, NGR	frac.	0.5	0.25
Efficiency Factor	frac.	0.2	0.1
Density of CO_2	kg/m3	650	--
Reservoir temperature	C	75	10
Reservoir pressure	MPa	20	3

CO_2 Storage Volume Estimate

The volume of pore space available for supercritical CO_2 injection into a stacked saline reservoir was estimated by employing three different approaches using the physical input parameters listed in Table 4 – a simple linear approach, a probabilistic approach independent of time (Sarkodie-Kyeremeh et al. 2022), and a similar probabilistic simulation for 5 yr of CO_2 injection at 200,000 mt/yr using a DOE National Energy Technology Laboratory (NETL) CO_2-Screen tool v.4.1 (Sanguinito et al. 2022).

In the simplistic linear approach, the assumed net rock volume is multiplied by the estimated effective porosity to derive the estimated pore volume. To estimate the amount of CO_2 that would be stored in this calculated pore volume we used the average volume of CO_2 at a supercritical state, 0.650 g/cm^3 (650 kg/m^3) to find that 100,000 t of CO_2 would occupy approximately 0.000154 km^3 of space. This resulted in 13,550 Mt of CO_2 storage in Harquahala basin.

For the probabilistic methods the results are plotted as a percentage of uncertainty, represented by a probability distribution (Figure 91). Estimates are defined as the probability of exceedance such that a proved (P90), the lowest value, 90% of the calculated estimates will be equal or exceed the P90 estimate. P50 is the median estimate. The P10 is the possible estimate, the highest value, or 10% of the calculated estimates will be equal or exceed the P10 estimate. Because the mean and median (P50) values are not the same, this suggests the results are slightly skewed, thus we consider the P50 values to be more representative than the mean. The P50 results yield 1,997 Mt (1.9 Gt) in Harquahala basin for total CO_2 storage. The time dependent approach resulted in a P50 of 463 Mt in Harquahala basin of CO_2 storage for 5 yr of injection.

The simplistic linear approach yields much larger values than the probabilistic approach and is likely an overestimate. The probabilistic approach takes more parameters into account and is likely more representative of the subsurface conditions, therefore we expect the total CO_2 storage volumes to be closer to the probabilistic method values. The method by Sarkodie-Kyeremeh et al. (2022) estimates a degree of uncertainty or sensitivity of most parameters listed in Table 4. The area, gross thickness, and CO_2 density presented the least degree of uncertainty, whereas the porosity, net-to-gross ratio, and efficiency factor presented the most, which will help to identify which parameters need to be refined as part of new data collection. The relative amount of uncertainty for this method is presented in more detail in Appendix G.

Table 5. Summary of CO_2 storage calculations in million metric tons (Mt) for each method.

	Total CO_2 storage, Mt		**CO_2 storage for 5 yr, Mt**
Basin	**Simple linear**	**Probabilistic (P50)**	**Probabilistic (P50) NETL CO_2-Screen**
Harquahala	13,550	1,997	463

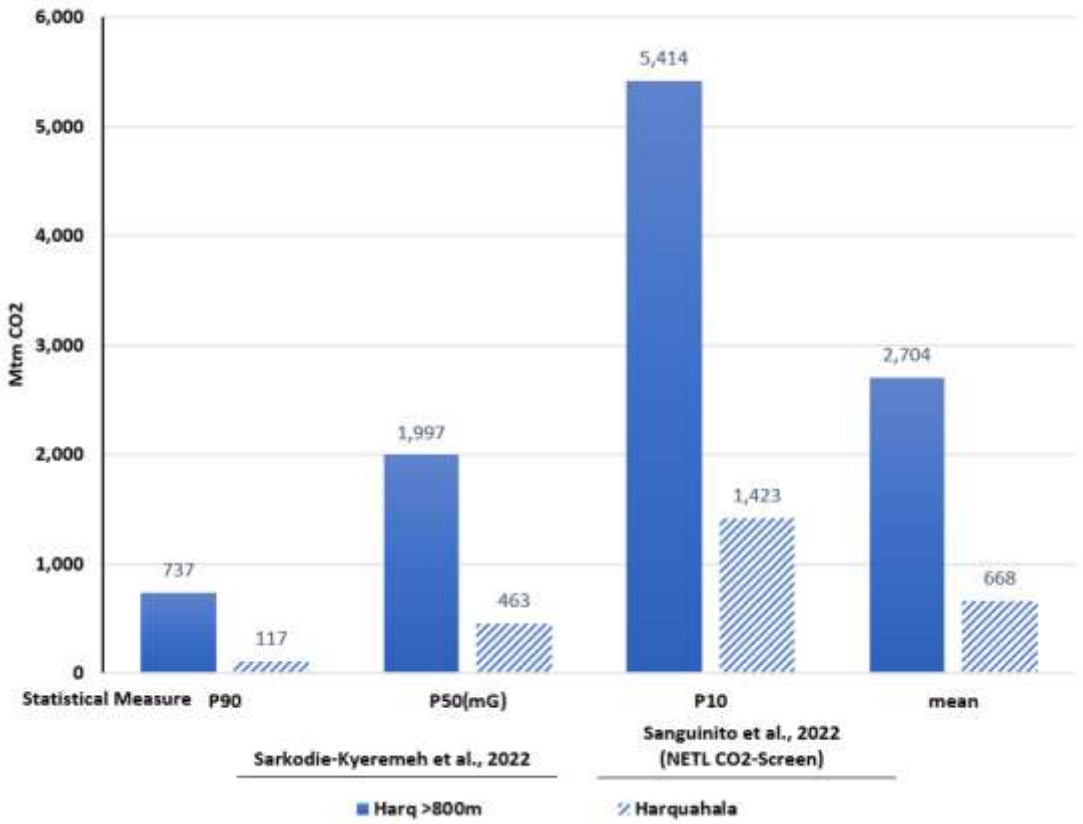


Figure 91 Calculated statistical volumes of CO_2 storage in non-differentiated basin fill units below 800 m depth in Harquahala basin for total CO_2 injection capacity in solid blue (Sarkodie-Kyeremeh et al. 2022) and CO_2 capacity after 5 yr injection in hashed blue (Sanguinito et al. 2022).

Known Natural Gas Subsurface Storage Risks

Sealing Conditions

The lack of known impermeable sealing strata is a geologic risk to subsurface natural gas storage. In Harquahala basin, potential bedded evaporite and clay deposits could be adequate seal rocks for stacked saline reservoirs. We predict these deposits are present in the lower basin fill, but we have made no direct observations of them.

Evaporite deposits are impermeable and can serve as a robust seal to trap fluid and gases underground. The lateral extent of this potential seal is shown by the zero contour on the acoustically transparent zone isopach map (equivalent to the top of this seismic facies; Figure 86). The chemistry, geomechanical properties, and lateral continuity of the evaporite deposits have not been directly measured. Fine-grained clastic sediment such as clay, silt and fine sand usually borders evaporite deposits, and the types of salts and mixed percent of lithofacies is important to map out in the subsurface to adequately de-risk storage of CO_2.

The low porosity, fine-grained facies such as clay can be a lithologic barrier to fluid migration. Lithology logs from shallow water wells suggest the presence of a laterally continuous clay layer in Harquahala basin (Towne 2014). The extent, thickness, and continuity of this clay is limited by the location of well penetrations, which are generally clustered within the agricultural area of

the basin. Based on the conceptual basin model (section 4a), clay would likely be present near or along the margin of subbasin centers. Thin interbedded clays layers could create baffles to subsurface flow and compartmentalization within the reservoir. Direct measurements such as electric wireline logs and core are needed to further de-risk the sealing integrity and conditions in these basins.

Seismic Hazard

Historical and induced seismicity can present a risk to any subsurface CO_2 storage. There are several faults surrounding Harquahala basin, and major faults interpreted in vintage seismic reflections (Figure 84); however, there are no known active or Quaternary faults (last 2.5 Myr). The nearest known Quaternary fault is the "Sand Tank" fault about 50 miles southeast of Harquahala basin near the town of Gila Bend, although no paleoseismic investigative work has been done on this fault. Based on the lack of surface ruptures, lack of springs and aseismic activity in Harquahala basin, the seismic risk is considered relatively low (Figure 92; USGS 2018).

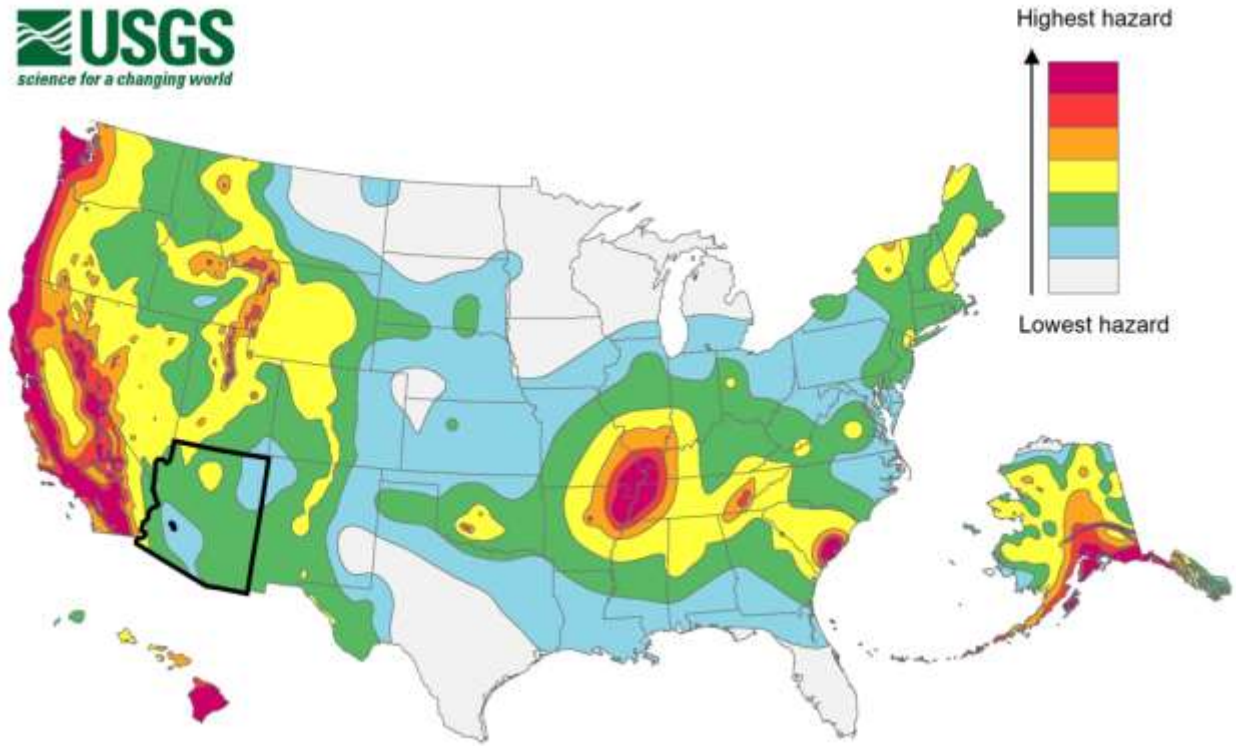


Figure 92 Earthquake hazard map showing peak ground accelerations having a 2 percent probability of being exceeded in 50 yr, for a firm rock site. Harquahala basin is shown as a solid black polygon within Arizona outline. The map is based on the most recent USGS models for the conterminous United States (2018), Hawaii (1998), and Alaska (2007; all from USGS [2018]). Models are based on seismicity, fault-slip rates and consider the frequency of earthquakes of various magnitudes. Locally, the hazard may be greater than shown because site geology may amplify ground motions.

The known seismicity rates for the Harquahala basin and surrounding area are low. Within the last several decades, no events larger than M 3.0 have occurred. Events smaller than M 3.0 may occur; however, the area has not had adequate seismic monitoring spatially or historically. In

2009, AZGS began operating a statewide seismic network, but that network only has 16 stations in the entire state. The two stations closest to Harquahala basin are located approximately 43 km to the north near Wickenburg and about 110 km to the southwest near Mohawk Valley. Higher density seismic monitoring would improve the detection threshold for the study area if lower magnitudes were necessary.

Conclusions

This study integrated geologic maps, borehole lithology logs, newly reprocessed vintage 2D seismic lines, public and proprietary gravity datasets, and borehole temperature & TDS data to characterize Harquahala basin for geologic storage of CO_2. Permanent subsurface CO_2 storage is possible in two different geologic environments: (1) storage as a supercritical fluid within stacked saline formations below 800 m depth or (2) permanent mineralization through chemical reactions with basalt lava flows. Short term H_2 storage may be possible within the evaporite deposits likely present in the basin, though much of this study was focused on CO_2 storage potential. CO_2 storage in fractured bedrock and geothermal energy potential could be utilized in this basin, though not expanded in this study due to limited data. Harquahala basin is one of 57 extensional basins in the Arizona Basin and Range that is sufficiently deep to store CO_2. This basin formed during the same time under similar tectonic and climatic conditions. Therefore, data from nearby basins such as deep well lithology logs, TDS measurements, and geothermal temperatures can be used a proxy for missing data in Harquahala basin. A conceptual geologic model based on numerous basin studies in the Arizona Basin and Range is used to generalize lithofacies distribution, stratigraphic framework, structural history, and basin geometry.

Harquahala basin is a deep, asymmetric, extensional basin filled with a thick accumulation of clastic and (potentially) chemical sediments, lava flows, and explosive volcanic material from nearby volcanic vents. Seismic reflectors, well lithology logs, proxy data from nearby basins, and our conceptual geologic model delineate three stratigraphic packages. From oldest to youngest these are: lower reflective package (LRP), lower basin fill (LBF), and upper basin fill (UBF). The LRP is deposited on older and more extensively deformed plutonic, metamorphic, and sedimentary rocks and likely composed of a sequence of stacked lava flows interbedded with felsic tuffs and coarse clastic sediments. Deposition of the LRP began with the onset of basin extension and has only been identified from seismic imaging in Harquahala basin. The LBF is likely composed of a wide range of lithofacies and grain size, dependent on distance from the source terrains. Laterally discontinuous seismic reflectors suggest the LBF is locally tilted, folded, and/or faulted, consistent with imaging in other parts of the basin and range province at similar depths. Seismic interpretations of an acoustically transparent zone on seismic lines TR9 and PW23 suggest there may be a thick accumulation of bedded evaporite deposits within the LBF. The UBF is a relatively undeformed, laterally continuous package of clastic and (potentially) chemical sedimentary rocks that unconformably overlies the LBF. The UBF sedimentary package is entirely above 800 m depth and is therefore ineligible for stacked saline storage.

Harquahala basin has sufficient volumes of pore space in presumably saline groundwater below 800 m depth, however, we cannot identify a sealing or capping rock for those reservoirs with certainty because of the lack of deep well lithology logs. Isopach maps highlight the thicker areas in the basin that could be targeted for future exploration. The LBF and LRP are both present

below 800 m (2,625 ft) and are good candidates for stacked saline storage and, potentially, mineralization in basalt lava flows. Based primarily on analysis and interpretation of seismic data, and on physical parameters from proxy basins, there is a P50 probability that about 1,997 Mt of supercritical CO_2 can be stored in Harquahala basin. To reduce uncertainty and sensitivity in these calculations, the porosity, net-to-gross storage volumes, and storage efficiency require new data collection from drilling and detailed geophysics.

From this study we have refined the basin geometry and provided new insights into basin structure and gross stratigraphy. Three critical unknowns remain: the existence/absence of a sealing strata such as bedded evaporites, the physical properties of stacked saline reservoir rock, and the stratigraphic architecture of basin fill sediments. Harquahala basin lacks the deep well borehole data needed to adequately characterize rock lithology, porosity, and permeability. We cannot diagnostically identify, for example, the presence/absence of bedded evaporite deposits, basalt lava flows, or extensive clay beds that can be used as sealing strata. The stratigraphic architecture of the basin, such as lateral extent of sealing strata, minor fault blocks, or presence/absence of anticlinal traps also remains unknown. Therefore, we recommend the acquisition of three new datasets in both basins: 2D active-source seismic (possibly passive-source too), magnetotellurics, and deep well borehole wireline geophysical logs and sampling. These datasets, combined with data reported within, will refine our understanding of the lower basin fill unit rock properties (the potential stacked saline aquifer), identify the presence/absence of sealing strata, and clarify stratigraphic architecture and basin structure.

Recommendations

CO_2 geologic storage in Harquahala basin is favorable, but more data collection is necessary to better characterize the reservoir and decrease geologic risk. For a phase II technical evaluation, our team recommends acquiring 8 new 2D seismic lines, additional in-fill gravity data, high resolution aeromagnetic survey, and drilling one stratigraphic characterization well.

The location of each method is presented in Figure 93 and discussed below. Magnetotellurics and a 3D seismic survey were considered as part of new data collection, although we recommend these methods be considered after Phase-II data are analyzed and funded as part of a Phase-III program.

New 2D Seismic

The reprocessed legacy 2D seismic data that was interpreted for this project is of moderate to poor quality and was not acquired with modern techniques. Acquiring new 2D seismic lines is advantageous because the acquisition parameters can be tailored specifically for the purpose of exploring the deep subsurface using what we now know about the stratigraphic units at depth. Line locations would target deep subbasins identified in this study. New 2D seismic would help refine basin geometry, identify faults, provide greater image resolution and seismic facies, map the extent of bedded salt deposits, and reduce uncertainty related to reservoir boundaries and potential seals.

We recommend acquiring 2D seismic reflection data along 8 different lines in Harquahala basin, totaling 105 miles. Three of these lines are longer (16–21 miles) and strike northwest-southeast and north-south. The remaining five lines are shorter (8–11 miles), cover the two main

depocenters, and generally run perpendicular to the basin axis (Figure 93). The proposed 2D seismic lines were chosen based on existing roads and access points, minimizing impact to agricultural plots, utilizing land ownership maps, intersecting legacy seismic surveys, and maximizing the characterization potential of the reservoir based on our findings in this study. The locations of these conceptual lines will likely change as part of a phase-II approach involving permitting, surveys related to permitting, ownership, and access.

Gravity and Aeromagnetic Surveys

Gravity and magnetic surveys are cost effective geophysical methods for exploring the subsurface over a large area. Gravity measurements provide information about rock density and can be used to understand the spatial distribution of those rock types in the subsurface. An aeromagnetic survey measures the intensity of the Earth's magnetic field and can yield the spatial distribution of the relative abundance of magnetic minerals. Often these types of data are used in conjunction with one another. The resulting data can help refine the boundaries of the sedimentary basin at depth and can elucidate the internal structural highs and lows (Selley and Sonnenberg 2023). Faults can also be identified using these methods which can help characterize the effectiveness of the sealing strata and potential seismicity risk, especially when combined with 2D seismic and well control. These data will be processed using the Werner Deconvolution method to also map salt extent (top and bottom), thickness, and the depth to crystalline basement.

We recommend acquiring additional gravity data and a high-resolution aeromagnetic survey over a targeted area (approximately 900 km^2) of the Harquahala Valley (Figure 93). The spatial distribution of existing gravity stations within the basin is not sufficient, as there are areas (specifically in the east) that lack control points. The goal is to develop a gravity acquisition plan that fills in the existing gravity dataset at regularly spaced intervals (1 mile apart) for the entirety of our Area of Interest (AOI). Additionally, more gravity stations along the southwest margin of the basin along seismic lines will be needed to capture the steepness of that fault margin. An aeromagnetic dataset also exists over this area but again is not sufficient for this study. This survey was collected in 2001 by the U.S. Geological Survey as part of a large statewide effort and lacks the resolution needed. We plan to collect a high-resolution aeromagnetic survey with 200 m line spacing and 2,000 m tie lines.

Stratigraphic Characterization Well

A deep characterization well is required to examine rock lithology, stratigraphy, reservoir type and depth, sealing potential, geothermal potential, and water chemistry/salinity. This will be achieved by drilling a deep borehole, running wireline logging tools, collecting cuttings, retrieving core samples, and collecting downhole water samples and pressure information. A comprehensive suite of wireline logs should include, but not be limited to triple combo (caliper, spontaneous potential, gamma ray, resistivity, density), 4-point Rx sonic, formation imager (FMI), nuclear magnetic resonance, cement bond log (CBL) and temperature log. These logs will greatly reduce uncertainty and be used to calibrate and adjust input parameters in legacy and new geophysical datasets. Continuous wireline core through the bedded salt section would provide the greatest preservation of data and likely be the most cost-effective method. Conventional whole-rock core and sidewall cores are recommended for pertinent sections and lithologies below the bedded salt portion. A detailed core analysis would include, but not be limited to:

porosity, permeability, grain density, core gamma for correlating core depth with logs, core photographs, CT scan, and fluids analysis. Additional CO_2 mineralization experiments will be run on mafic rocks encountered.

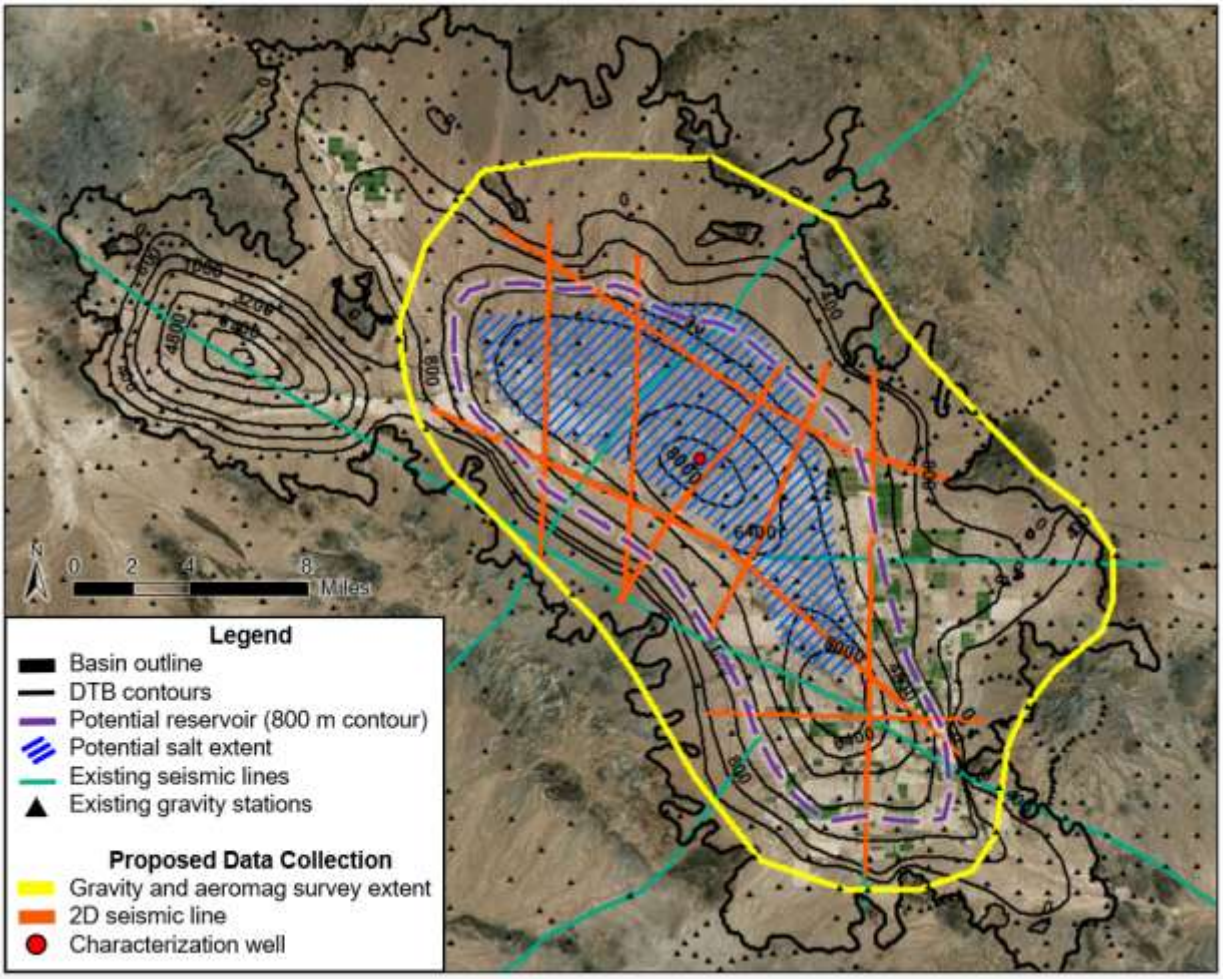


Figure 93 Map of selected existing data and proposed new data acquisition.

We recommend drilling a 10,000 ft stratigraphic characterization well in the central subbasin (Figure 93). This depth was chosen to ensure the hole penetrates the crystalline basement rock which, if fractured, will be evaluated as a potential reservoir and to determine the temperature for assessing the geothermal potential. This location will capture the deepest portion of the basin and will confirm the presence or absence of bedded evaporite deposits and interbedded basalt flows here (including their state of alteration or weathering). The proposed well location is on federal land (Bureau of Land Management) which should streamline the permitting process for CCS projects under BLM Internal Memorandum # 2022-041 (June, 2022). It is also conveniently positioned near interstate 10 and Salome Road, which provides a transportation route to support drilling operations.

References

[ADWR] Arizona Department of Water Resources. 2004. Unpublished gravity data from the Hassayampa region, south-central Arizona. Phoenix (AZ); Arizona Department of Water Resources. [Unpublished data].

[ADWR] Arizona Department of Water Resources. 2006. Salt River model geology update. Phoenix (AZ); Arizona Department of Water Resources. Modeling Report No. 16.

[ADWR] Arizona Department of Water Resources. 2022. Statewide historic and compiled gravity datasets originally from PACES (2016), maintained by ADWR. Phoenix (AZ); Arizona Department of Water Resources. [Unpublished data].

[AZOGCC] Arizona Oil and Gas Conservation Commission. 2023. Well files and production reports. Phoenix (AZ); Arizona Oil and Gas Conservation Commission. [Internet]. Accessed 2023 Jan. https://azogcc.az.gov/records

Eberly LD, Stanley TB. 1978. Cenozoic stratigraphy and geologic history of southwestern Arizona. Geol Soc Am Bull. 89:921–940. doi:10.1130/0016-7606(1978)89%3C921:CSAGHO%3E2.0.CO;2

Faulds JE, Schreiber BC, Langenheim VE, Hinz NH, Shaw TH, Heizler MT, Perkins ME, El Tabakh M, Kunk MJ. 2016. Paleogeographic implications of late Miocene lacustrine and nonmarine evaporite deposits in the Lake Mead region: immediate precursors to the Colorado River. Geosphere. 12:721–767. doi:10.1130/GES01143.1

Gootee BF. 2013a. An evaluation of carbon dioxide sequestration potential in the Luke Basin, south-central Arizona. Tucson (AZ); Arizona Geological Survey. Open-File Report 13-05.

Gootee BF. 2013b. An evaluation of carbon dioxide sequestration potential in the Higley Basin, south-central Arizona. Tucson (AZ); Arizona Geological Survey. Open-File Report 13-10.

Gootee BF. 2015. An evaluation of carbon dioxide sequestration potential in the Picacho Basin, southeastern Arizona. Tucson (AZ); Arizona Geological Survey. Open-File Report 15-09.

Gootee BF, Love DS, Mahan MK. 2012. A summary of salinities in Arizona's deep groundwater. Tucson (AZ); Arizona Geological Survey. Open-File Report 12-26.

Gootee BF, Noel SD. 2015. McMullen Valley groundwater model (supporting Arizona State Land Department application for analysis of water adequacy). Phoenix (AZ); Arizona State Land Department. [Unpublished report].

[HGI] HydroGeophysics Inc. 2009. Geophysical results for Harquahala Basin. Tucson (AZ); HydroGeophysics Inc. [Confidential report].

Menges CM, Pearthree PA. 1989. Late Cenozoic tectonism in Arizona and its impact on regional landscape evolution. In: Jenny JP, Reynolds SJ, editors. Geologic evolution of Arizona. Tucson (AZ); Arizona Geological Society. p 649–680.

Mullane, M., Gleason, M., Reber, T., McCabe, K., Mooney, M., Young, K.R., 2017. An estimate of shallow, low-temperature geothermal resources of the United States (No. NREL/CP-6A20-68523). Davis, CA: Geothermal Resources Council.

Nathenson M, Guffanti M. 1988. Geothermal gradients in the conterminous United States. J Geophys Res Solid Earth. 93(B6):6437–6450. doi:10.1029/JB093iB06p06437

Neal JT, Rauzi SL. 1996. Storage opportunities in Arizona bedded evaporites. Albuquerque (NM); Sandia National Laboratories. Report No. SAND96-1679C.

[PACES] PACES Project. 2016. Regional public gravity datasets. [Place unknown]; PACES Project. [Data set].

Pan B, Lei J, Zhang L, Guo Y. 2017. Research on the physical properties of supercritical CO_2 and the log evaluation of CO_2-bearing volcanic reservoirs. J Geophys Eng. 14:1052–1060. doi:10.1088/1742-2140/aa6f22

Peters, K.E., Curry, D.J., Kacewicz, M., 2012. An overview of basin and petroleum system modeling: definitions and concepts 1–16. doi:10.1306/13311426H4139

Raza A, Glatz G, Gholami R, Mahmoud M, Alafnan S. 2022. Carbon mineralization and geological storage of CO_2 in basalt: mechanisms and technical challenges. Earth-Sci Rev. 229:104036. doi:10.1016/j.earscirev.2022.104036

Reynolds SJ. 1997. Geologic data for the Phoenix South 30′ × 60′ quadrangle. Tucson (AZ); Arizona Geological Survey. DGI-05 v2.0.

Reynolds SJ, Grubensky MJ. 2007. Geologic data for the Phoenix North 30′ × 60′ quadrangle. Tucson (AZ); Arizona Geological Survey. DGI-04 v2.0.

Richard SM, Shipman TC, Greene L, Harris RC. 2007. Estimated depth to bedrock in Arizona. Tucson (AZ); Arizona Geological Survey. Digital Geologic Map DGM-52.

Richard SM, Spencer JE, Reynolds SJ, Pearthree PA, Demsey KA, Thompson LA, Snellen HL, Theim JP. 2022. Geologic map of the Salome 30′ × 60′ quadrangle, west-central Arizona. Tucson (AZ); Arizona Geological Survey. Digital Geologic Map DGM-157.

Sanguinito S, Hanson A, Haeri F, Myshakin E, Moore J, Crandall D. 2022. CO_2 storage prospective resource estimation Excel analysis (CO_2-SCREEN) user's manual: Python v4.1. Albany (OR); National Energy Technology Laboratory. Report No. DOE/NETL-2022/3729. doi:10.2172/1862020

Sarkodie-Kyeremeh J, Ampomah W, Tu J, Czarnota R. 2022. Advances in CO_2 geological storage: estimation of CO_2 storage efficiency factors for the San Juan Basin formations. In: Proceedings of the 16th Greenhouse Gas Control Technologies Conference (GHGT-16); 2022 Oct 23–27; Lyon (France). doi:10.2139/ssrn.4286058

Sass JH, Lachenbruch AH, Galanis SP Jr, Morgan P, Priest SS, Moses TH Jr, Munroe RJ. 1994. Thermal regime of the southern Basin and Range Province: 1. Heat flow data from Arizona and the Mojave Desert of California and Nevada. J Geophys Res Solid Earth. 99(B11):22093–22119. doi:10.1029/94JB01891

Selley RC, Sonnenberg SA. 2023. Methods of exploration. In: Selley RC, Sonnenberg SA, editors. Elements of petroleum geology. 4th ed. London (UK); Academic Press. p 43–166. doi:10.1016/B978-0-12-822316-1.00003-3

Spencer JE, Pearthree PA, Demsey KA, Thompson LA, Snellen HL, Korroch KM, Theim JP, Richard SM. 2022. Geologic map of the Little Horn Mountains 30′ × 60′ quadrangle, west-central Arizona. Tucson (AZ); Arizona Geological Survey. Digital Geologic Map DGM-153.

Spencer, J.E., Reynolds, S.J., 1989. Middle Tertiary tectonics of Arizona and adjacent areas. Geol. Evol. Ariz. Ariz. Geol. Soc. Dig. 17, 539–574.

Teixeira L, Lupinacci WM, Maul A. 2020. Quantitative seismic-stratigraphic interpretation of the evaporite sequence in the Santos Basin. Mar Pet Geol. 122:104690. doi:10.1016/j.marpetgeo.2020.104690

Towne D. 2014. Ambient groundwater quality of the Harquahala Basin: a 2009–2014 baseline study. Phoenix (AZ); Arizona Department of Environmental Quality. Open-File Report 14-04.

[U.S. EPA] U.S. Environmental Protection Agency. 2023. Greenhouse Gas Reporting Program (GHGRP): reporting year 2021 data, parts C and D (FLIGHT). Washington (DC); U.S. Environmental Protection Agency. [Internet]. https://www.epa.gov/ghgreporting/ghgrp-2021-reported-data

[USGS] U.S. Geological Survey. 2018. 2018 long-term national seismic hazard map. Reston (VA); U.S. Geological Survey. [Internet]. https://www.usgs.gov/programs/earthquake-hazards/science/2018-united-states-lower-48-seismic-hazard-long-term-model

Walton WC. 1970. Groundwater resource evaluation. New York (NY); McGraw-Hill.

Wilson TC, Thompson LA, Gootee BF. 2024. Phase I pre-feasibility study to evaluate carbon dioxide and hydrogen geologic storage potential in Harquahala Basin. Tucson (AZ); Arizona Geological Survey. Open-File Report 24-01. https://library.azgs.arizona.edu/item/AOFR-1712775909999-126

Witcher JC. 1995. Geothermal resource data base: Arizona. Idaho Falls (ID); U.S. Department of Energy. Report No. DOE/ID/13223-T9. doi:10.2172/204692

Derisking CO_2 Mineralization Storage in Basalt Reservoirs

Lead Institution: Pacific Northwest National Laboratory (PNNL), Richland, WA
Primary Investigator: H. Todd Schaef

The Derisking CO_2 Mineralization Storage in Basalt Reservoirs project was designed to show that basalts, specifically the Columbia River Basalt Group (CRBG), can provide both a permanent and a gigaton-scale carbon storage option for the Pacific Northwest. Unlike conventional sedimentary reservoirs, basalts react with injected CO_2 and formation fluids to form solid carbonate minerals. This process ensures rapid and irreversible trapping of carbon, reducing both long-term risks and the need for extended postinjection monitoring.

Within the broader goals of the Carbon Utilization and Storage Partnership (CUSP), the project expands the range of viable storage reservoirs, develops technical and economic frameworks for basalt deployment, and builds the public relationships needed for eventual commercial operations in the Pacific Northwest. By integrating laboratory experiments, field observations from the Wallula pilot project, and advanced Subsurface Transport Over Multiple Phases for

CO_2 (STOMP-CO_2) reactive transport modeling, the project addressed uncertainties in injectivity, mineralization rates, and long-term storage capacity.

Ultimately, this effort strengthens CUSP's mission by showing that basalt storage can be cost competitive with sedimentary basins while offering the added benefit of permanent mineral trapping. It also provides regional stakeholders, regulators, and industry with the technical, economic, and social foundations needed to advance Class VI permitting and demonstration-scale projects in mafic–ultramafic reservoirs.

The project was led by Pacific Northwest National Laboratory (PNNL), with Todd Schaef serving as Principal Investigator and a multidisciplinary team of researchers contributing expertise in geologic modeling, reactive transport simulation, mineralogy, and stakeholder engagement. PNNL worked in close collaboration with the U.S. Department of Energy's Office of Fossil Energy and Carbon Management (DOE-FECM), which provided funding and strategic guidance. Supporting organizations included the University of Idaho and the University of Texas at Austin, which partnered on student engagement, outreach, and modeling activities, as well as the Confederated Tribes of the Umatilla Indian Reservation (CTUIR) and other regional groups, which played a key role in stakeholder engagement and workforce development discussions. Industry and utility partners, along with the CarbonSAFE network, provided additional support by contributing insights into infrastructure, permitting pathways, and commercial deployment readiness. Together, these organizations created a collaborative framework that advanced the technical, social, and economic dimensions of in situ mineralization CO_2 storage.

Objectives and Outcomes

This project seeks to address research gaps crucial to derisking and demonstrating commercial scale basalt storage (Figure 94) and to provide critical information to key stakeholders and developers seeking CO_2 storage opportunities in our region, and beyond. We plan to screen, evaluate, and select site(s) for further characterization and permitting of CO_2 injection in the CRBG, with the goal of reducing technical and nontechnical risks currently facing R&D implementation. To accomplish this, we will focus on 2 key areas: (1) regional-scale site screening and sensitivity analyses on key parameters governing reservoir viability for sustainable injection over decadal project lifetimes (Phase 1) and (2) validation of simulation, characterization, and monitoring approaches necessary to support successful Class VI application and demonstration for this reservoir class (Phase 2).

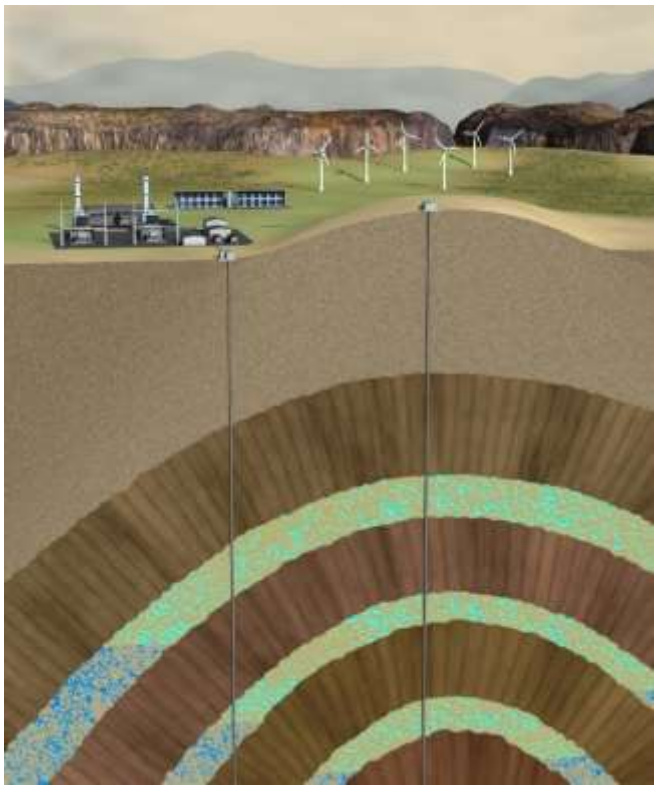


Figure 94 Conceptual model of commercial-scale CO_2 capture and storage hub with geologic carbon dioxide removal (CDR) via injection into stacked Columbia River Basalt Group reservoirs with regional anticlinal structures

Scope of Work

This scope is focused exclusively on R&D needed to accelerate the adoption of CCS in basalt reservoirs. This prioritizes efforts to address key uncertainties impacting project cost and risk, including injectivity, mineralization rates, and realizable storage capacity. This Phase 1 scope will lay the groundwork to characterize and permit a basalt injection, and to help develop the industrial, regulatory and public partnerships needed to successfully demonstrate the technology at commercial scale in Phase 2. Based on over 20 yr of screening, siting, characterizing, permitting, and developing geologic CO_2 storage projects, including the first Class VI permit for FutureGen (Gilmore et al. 2014, 2016; Vermuel et al. 2016; White et al. 2016) and the world's first and only supercritical CO_2 ($scCO_2$) basalt project at Wallula, this proposal prioritizes these tasks and outcomes:

- **Task 1** – Develop regional geologic models using existing geological and hydrogeochemical data
- **Task 2** – Perform numerical simulation of large-scale $scCO_2$ injection to provide uncertainty-bounded estimates of storage capacity and injection rates for key target intervals
- **Task 3** – Identify priority areas and options for acquisition of new datasets to resolve key uncertainties
- **Task 4** – Define a development plan focused on characterization, permitting and certification of basalt-based storage critical to CCS deployment in the Pacific Northwest

- **Task 5** – Engage with regional stakeholders, including regulatory, policy, industry, environmental and other groups to understand regional deployment dynamics and help develop support

The project advanced through five main tasks, with milestones and core activities spanning fiscal year (FY) 22 through FY24.

Task 1 (Regional Geologic Model) centered on feasibility analysis of the Columbia River Basalt Group (CRBG) for CO_2 storage. Beginning in FY22 fiscal quarter 3 (Q3), geological and hydrochemical data were assembled into stratigraphic and GIS frameworks, supported by correlations of deep boreholes (Wallula Pilot, 100 Circles, and K2H). By FY23, feasibility studies expanded to include basal hyaloclastite facies reservoirs, which exhibited porosities as high as 86%. In FY23 Q4, these reservoirs were added as a new high-injectivity class, and by FY24 Q2, 2 priority sites, the Yakima Fold Belt and Palouse Slope, were down selected for future stratigraphic wells. These activities laid the groundwork for characterizing stacked saline aquifers and anticlinal traps suitable for commercial-scale injection.

Task 2 (Numerical Simulation) advanced in parallel, focused on modeling and validation. Early efforts in FY22 benchmarked STOMP-CO_2 simulations against outcomes from the Wallula pilot project, which showed approximately 60% mineralization of injected CO_2 within 2 yr. A major milestone, Milestone 2.2, was met in FY23 Q3 with a publication on reactive transport modeling, integrating laboratory-derived kinetics into reservoir-scale simulations. Sensitivity analyses demonstrated mineralization extents of approximately 20% in baseline cases and up to 90% under accelerated clinopyroxene dissolution, underscoring the importance of mineral dissolution rates. By FY24 Q2, the modeling workflow was enhanced through PEST parameter estimation, enabling multiparameter calibration with field groundwater chemistry data. This progression represented a key leap in predictive capability, a requirement for permitting and risk assessment.

Task 3 (Preliminary Site Screening) integrated field data acquisition and geologic modeling to identify favorable injection zones. Initial down selection in FY22 Q4 estimated storage capacity up to 351 Gt CO_2 in northeastern Oregon, a transformative finding for regional feasibility. Subsequent screening emphasized hyaloclastite facies as promising reservoirs due to their high porosity, permeability, and reactivity. In FY23 Q4 and FY24 Q2, field and laboratory analyses, including X-ray microtomography and geochemical studies, provided additional support for the Yakima Fold Belt and Palouse Slope sites. These activities refined the focus toward data-rich regions with structurally stable formations and robust sealing capacity.

Task 4 (Characterization, Permitting, and Development Planning) built on Tasks 1 to 3 to evaluate infrastructure requirements and economic feasibility. In FY24 Q1, Milestone 4.1 was achieved with a preliminary cost analysis comparing supercritical CO_2 and aqueous-dissolved injection methods. This analysis showed clear advantages for supercritical CO_2, with levelized storage costs of approximately $11.9/t compared with approximately $23.5/t for aqueous injection, largely due to lower water demand, reduced footprint, and fewer monitoring wells. By FY24 Q4, Milestone 4.2 was completed with a comprehensive cost and permitting report, estimating total levelized storage costs between $13/t and $25/t. These figures demonstrated basalt storage to be competitive with sedimentary basins while offering permanent mineral trapping as an additional advantage.

Task 5 (Stakeholder Engagement) was continuous across the project and integrated into all other activities. Early outreach in FY22 included the Carbon Interactive Workshop in Richland, WA, followed by milestone 5.1 in FY23 Q1 through a series of workshops and university engagements. Field and laboratory demonstrations, such as lab tours for DOE officials, collaborations with Heritage University, and hands-on outreach at Nueva Esperanza Leadership Academy, ensured that public perspectives informed technical progress. In FY24 Q3, Milestone 3.2 was met with the release of a regional stakeholder workshop report, synthesizing input from more than 120 participants across five events. This work ensured that regulatory, social, and workforce development considerations were integrated alongside technical and economic readiness. Although the stakeholder engagement task is the least technical, our experience at Wallula suggests it is every bit as critical to success as reservoir models, seismic surveys and permits. The characterization and simulation will come into play only if we work from the beginning to establish strong relationships and ongoing dialog with developers, financers, regulators, landowners, and communities whose partnership will be essential to this effort. Ultimately, our technical work exists to help inform the decisions of the stakeholder groups that will capitalize, finance, host and operate these projects.

Together, these tasks and their associated core activities moved the project from regional feasibility analysis and laboratory-scale experiments to calibrated reservoir modeling, costed infrastructure design, and broad stakeholder engagement. The consolidation of technical and nontechnical milestones provides a comprehensive foundation for advancing basalt mineralization storage to Class VI permitting and commercial demonstration.

Overview of Methods Used

The project applied a multi-scale, multidisciplinary set of methods to evaluate and derisk CO_2 mineralization in basalt reservoirs:

- **Geologic characterization** – Regional stratigraphic and structural models of the CRBG were constructed using borehole logs, well correlations, and geophysical datasets (seismic surveys, gravity, and magnetic anomaly maps). Existing U.S. Geological Survey (USGS) aquifer models were integrated to identify permeable flow tops, stacked saline aquifers, and basal hyaloclastite facies with high porosity and permeability.
- **Laboratory experiments** – Controlled carbonation experiments were performed on basalt glass, crystalline enstatite ($MgSiO_3$), and amorphous Mg–silicate analogues under water-saturated supercritical CO_2 conditions. These experiments quantified reaction pathways and mineralization kinetics. Postinjection sidewall cores from the Wallula pilot project were analyzed using X-ray diffraction (XRD), scanning electron microscopy (SEM), transmission electron microscopy (TEM), and X-ray microtomography (micro-CT) to characterize carbonate phases and pore structures across nano- to macroscale resolutions.
- **Numerical modeling and simulation** – The Subsurface Transport Over Multiple Phases simulator for CO_2 (STOMP-CO_2), developed at PNNL, was coupled with the Equilibrium-Conservation-Kinetic Equation Chemistry (ECKEChem) reactive transport module to simulate multiphase flow, geochemical reactions, and mineral trapping. Simulations were benchmarked against Wallula pilot injection data. Sensitivity analyses tested mineral dissolution kinetics, diffusion, and reservoir heterogeneity. The Parameter ESTimation

(PEST) software package was integrated to optimize model calibration and align simulated groundwater chemistry with field observations.

- **Economic and infrastructure assessment** – Cost models compared 2 injection scenarios: pure $scCO_2$ injection and dissolved CO_2 in water. Analyses included capital expenditures (CAPEX), operations and maintenance (O&M), water use, and monitoring requirements. Areas of Review (AORs) for Class VI permitting were determined based on simulated pressure fronts from 30-year injection scenarios.
- **Stakeholder engagement** – Public input was gathered through interactive workshops, university outreach, and laboratory tours. Engagement methods emphasized 2-way dialogue, workforce development considerations, and the consolidation of public priorities into planning for Class VI permitting and deployment.

CUSP Derisking CO_2 Mineralization Storage in Basalt Reservoirs Team

The project was led by Todd Schaef at Pacific Northwest National Laboratory (PNNL), who served as Principal Investigator and provided overall direction across geologic characterization, laboratory studies, and stakeholder engagement. Quin Miller played a central role in modeling and pore-scale analyses, linking laboratory experiments with reservoir-scale simulations conducted by Katie Muller. Ruoshi Cao led regional geologic modeling and economic assessments, including the comparison of injection scenarios and cost analyses for Class VI permitting. Nabajit Lahiri directed nanoscale and atomic-scale characterization of carbonate nodules, identifying novel mineral phases critical to understanding long-term storage security. Emily Nienhuis contributed expertise in mineral reactivity and basalt glass carbonation experiments, while Anil Battu advanced pore network modeling and 3D quantification of basalt flow structures. Casie Davidson coordinated stakeholder engagement and regional outreach, ensuring that public perspectives were integrated into technical planning. Together, this collaborative structure, anchored by PNNL with support from university partners, public organizations, and DOE program managers, ensured that the project balanced technical rigor with regional relevance and readiness for deployment, along with a long list of publications, shown below with cover highlights in Figure 95.

Project Publications

Year	Citation
2025	Lahiri, N., L.A. Kovarik, S.D. Taylor, J.V. Crum, C.T. Depp, Q.R.S. Miller, H.T. Schaef. Complex carbonate phases drive geologic CO_2 mineralization. Communications Earth & Environment. 2025, 6 (1), 344. doi:10.1038/s43247-025-02273-6
2024	Cao, R., Q.R.S. Miller, C.L. Davidson, W. Gallin, S.P. Reidel, Z. Jiao, J.F. McLaughlin, H.T. Schaef. Gigaton Commercial-Scale Carbon Storage and Mineralization Potential in Stacked Columbia River Basalt Reservoirs. International Journal of Greenhouse Gas Control. 2024. doi:10.1016/j.ijggc.2024.104206
2024	Stanfield, C.H., Q.R.S. Miller, A.K. Battu, N. Lahiri, A.B. Nagurney, R. Cao, E.T. Nienhuis, D.J. DePaolo, D.E. Latta, H.T. Schaef. Carbon Mineralization and Critical Mineral Resource

	Evaluation Pathways for Mafic-Ultramafic Assets. ACS Earth and Space Chemistry, 2024, 8 (6), 1204–1213. doi:10.1021/acsearthspacechem.4c00005 (cover highlight)
2024	Battu, A.K., Q.R.S. Miller, R. Cao, A.T. Owen, H.T. Schaef. 3D Quantification of Pore Networks and Anthropogenic Carbon Mineralization in Stacked Basalt Reservoirs. Environmental Science and Technology, 2024, 58 (8), 3747–3754. doi:10.1021/acs.est.3c06163 (cover highlight)
2024	Li, X., E.T. Nienhuis, A.B. Nagurney, Q.R.S. Miller, X. Zhang, H. Todd Schaef. Resolving nanoscale processes during carbon mineralization using identical location transmission electron microscopy. Environmental Science and Technology Letters, 2024, 11 (2), 79–88. doi:10.1021/acs.estlett.3c00699 (cover highlight)
2023	Lahiri, N., Q.R.S. Miller, R. Cao, C.T. Depp, H.T. Schaef. Facile Metal Release from Pore-Lining Phases Enables Unique Carbonate Zonation in a Basalt Carbon Mineralization Demonstration. Environmental Science and Technology, 2023, 57 (32), 11843–11851. doi:10.1021/acs.est.3c02075
2023	Aguila, B., L. Hardee, H.T. Schaef, S. Zare, M.J.A. Qomi, J.V. Crum, J.E. Holliman, E.T. Rodriguez, L.M. Anovitz, K.M. Rosso, Q.R.S. Miller. Kinetics of Diopside Reactivity for Carbon Mineralization in Mafic-Ultramafic Rocks. Environmental Science: Nano, 2023, 10, 2672. doi:10.1039/D3EN00087G (cover highlight)
2022	Holliman, J.E., H.T. Schaef, B.P. McGrail, Q.R.S. Miller. Review of foundational and emerging directions in metamaterial research: Design, phenomena, and applications. Materials Advances, 2022, 3, 8390–8406. doi:10.1039/D2MA00497F (cover highlight)
2022	Depp, C.T., Q.R.S. Miller, J.V. Crum, J.A. Horner, H. Todd Schaef. Pore-scale Microenvironments Control Anthropogenic Carbon Mineralization Outcomes in Basalt. ACS Earth and Space Chemistry, 2022, 6 (12), 2836–2847. doi:10.1021/acsearthspacechem.2c00165 (cover highlight)
2022	Polites, E.G., H.T. Schaef, J.A. Horner, A.T. Owen, J.E. Holliman, B.P. McGrail, Q.R.S Miller. Exotic Carbonate Mineralization Recovered from a Deep Basalt Carbon Storage Demonstration. Environmental Science and Technology, 2022, 56 (20), 14713–14722. doi:10.1021/acs.est.2c03269
2022	Qomi, M.J., Q.R.S. Miller, S. Zare, H.T. Schaef, J.P. Kaszuba, K.M. Rosso. Molecular-Scale Mechanisms of CO_2 Mineralization in Nanoscale Interfacial Water Films. Nature Reviews Chemistry, 2022, 6, 598–613. doi:10.1038/s41570-022-00418-1 (cover highlight)
2022	Miller, Q.R.S., H.T. Schaef. Activation Energy of Magnesite ($MgCO_3$) Precipitation: Recent Insights from Olivine Carbonation Studies. Environmental Science: Advances, 2022, 1, 426–429. doi:10.1039/D2VA00066K (cover highlight)

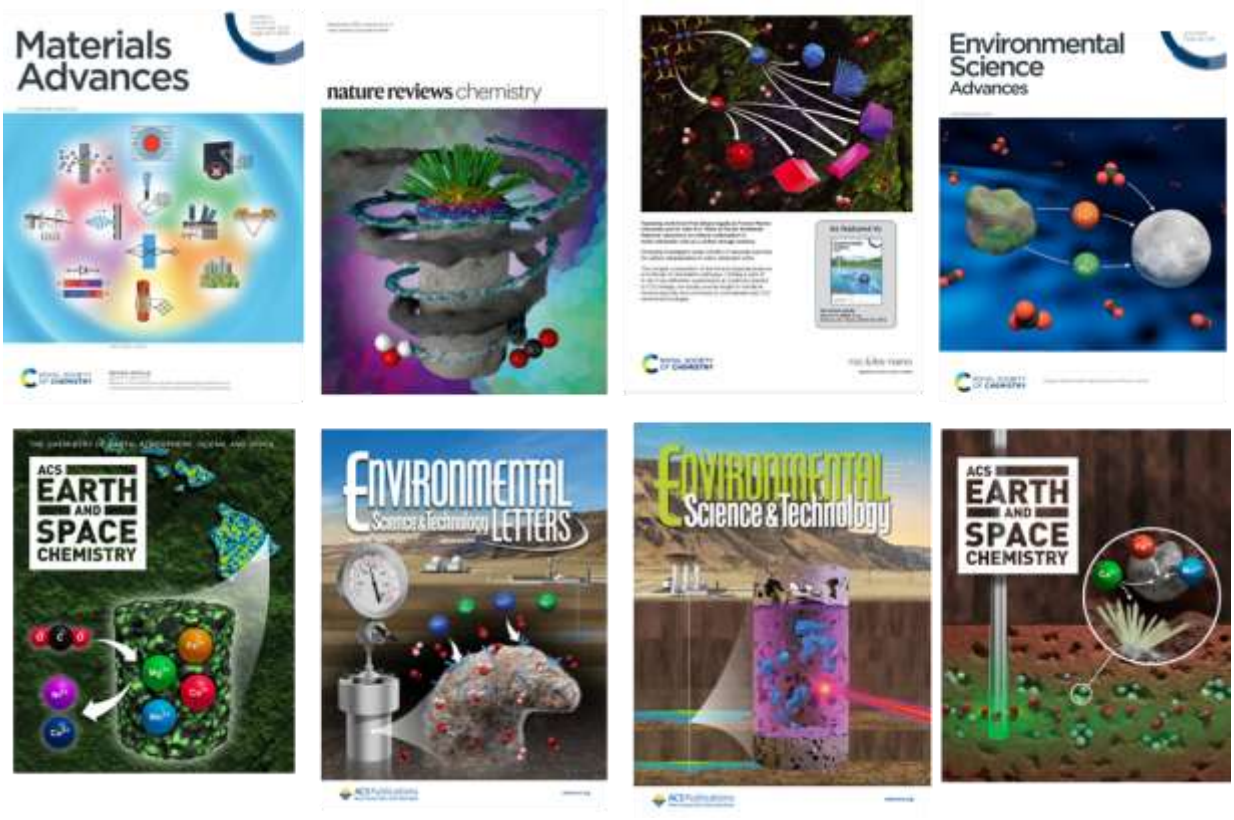


Figure 95 Published paper cover highlights under the project

Site Investigation Planning and Preoperational Design

Preoperational planning for basalt CO_2 storage focused on identifying, evaluating, and prioritizing sites within the Columbia River Basalt Group (CRBG) that offered both technical feasibility and long-term security. Early assessments leveraged decades of data from the Wallula Basalt Pilot Project and the Hanford Basalt Waste Isolation Project, along with new well log correlations and geophysical surveys. These datasets were synthesized into a regional stratigraphic framework, which provided the foundation for down selection of 2 priority areas. Both sites were chosen based on their favorable geology, depth (greater than 800 meters to ensure supercritical CO_2 conditions), and absence of significant surface hazards such as landslides or flooding risks.

Engineering planning considered the requirements for stratigraphic test wells and seismic surveys to refine subsurface understanding. Preliminary designs outlined drilling strategies for targeting basal hyaloclastite facies in the Grande Ronde and Wanapum Basalts, where porosities of 40% to 86% had been documented in prior well cuttings. These reservoirs are highly permeable and reactive and are therefore prime candidates for injection testing, because they can store large quantities of CO_2 and then react to permanently store it as carbonate minerals. Plans also included the combination of advanced logging tools and core recovery to capture high-resolution data on reservoir properties as well as establishing baseline groundwater chemistry for regulatory compliance.

Even in the absence of active fieldwork, strategic preparation ensured that future operations could proceed efficiently once funding and permitting pathways were secured. This preparatory work included identifying seismic survey corridors to map structural closures, estimating well depths and casing designs for stratigraphic drilling, and aligning proposed activities with regulatory expectations under the U.S. Environmental Protection Agency's Class VI Underground Injection Control (UIC) program. Importantly, preoperational design also factored in public feedback gathered through workshops, ensuring that site planning would be responsive to environmental concerns, local land use, and long-term benefits.

Together, these preliminary assessments and engineering plans established a clear roadmap for transitioning from regional feasibility studies to field-based site characterization. By addressing technical, regulatory, and social considerations early in the planning process, the project positioned the Columbia Basin to host one of the first commercial-scale demonstrations of basalt mineralization storage in the United States.

Geologic Site Characterization

The geologic site characterization work evaluated the suitability of the CRBG as a large-scale CO_2 storage complex. This effort brought together decades of subsurface information with new interpretations and laboratory analyses to assess reservoir quality, containment integrity, and reactivity. Characterization was central to derisking basalt storage: it established a detailed stratigraphic framework, defined reservoir–seal pairings, identified new classes of high-injectivity reservoirs, and provided direct evidence of rapid mineralization from cores collected after injection.

Reservoir–Seal Framework

The CRBG is composed of hundreds of individual lava flows emplaced during the Miocene. Each flow typically consists of a vesicular, fractured top and bottom and a dense, massive interior. The flow tops and bottoms act as porous and permeable horizons where CO_2 can be injected and distributed, whereas the dense interiors provide effective vertical seals. Together, these create a layer-cake reservoir–seal architecture that repeats over thousands of meters of stratigraphy. In the Grande Ronde Formation alone, up to one-third of the section is composed of reservoir-quality flow tops, amounting to more than 150 m of net porous rock in some wells (Figure 96). This stacked arrangement provides both significant capacity and built-in redundancy: If one horizon underperforms, neighboring horizons remain available for injection.

Borehole dip azimuth and angle data show that these flows are subhorizontal with gentle dips of 5° to 25°, indicating excellent lateral continuity and structural stability across the Columbia Basin. Such stability reduces risks of fault-controlled leakage and makes the geology predictable for long-term storage operations.

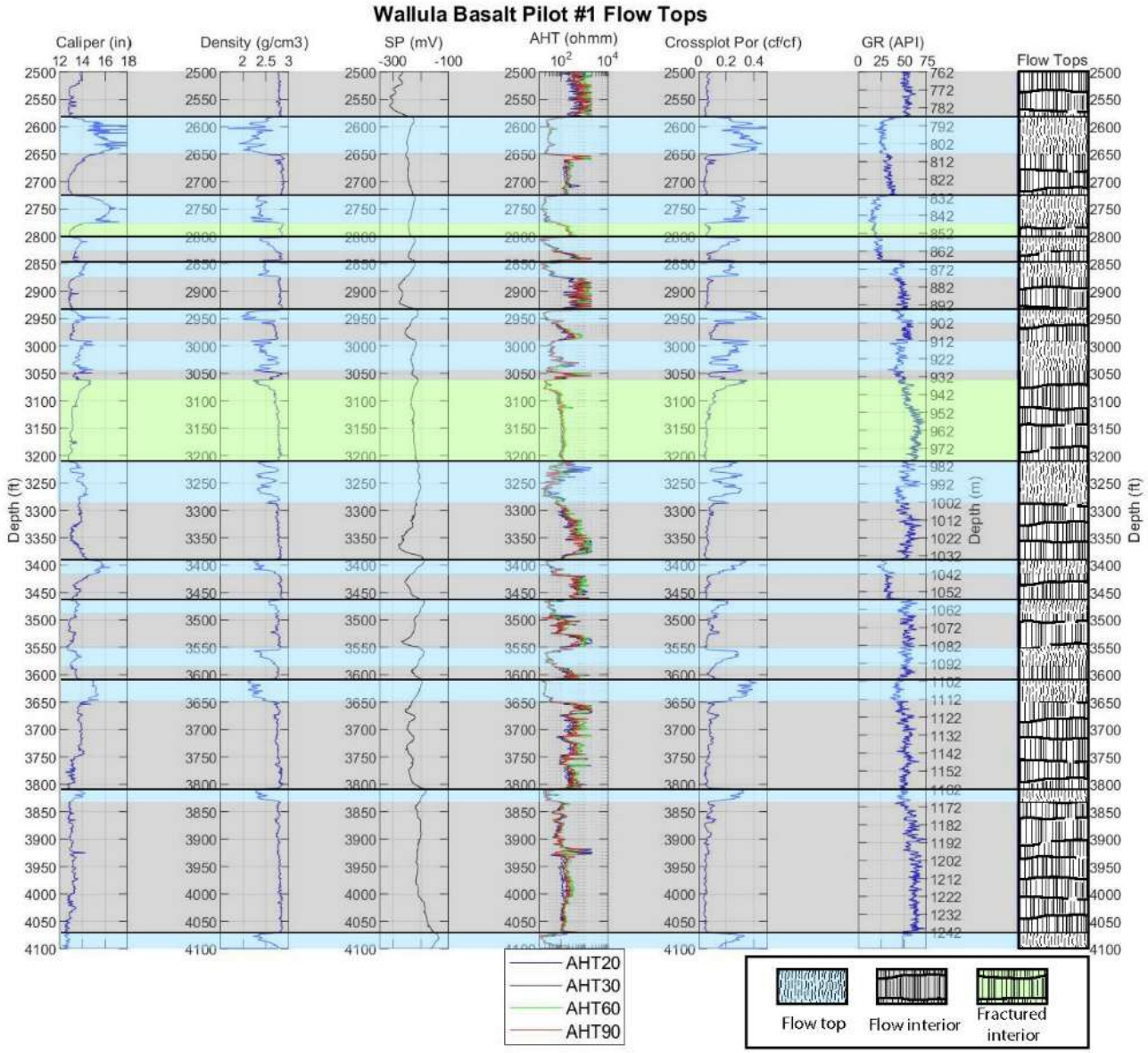


Figure 96 Interpreted flow tops and flow interiors from the supercritical CO_2 region of the Wallula Basalt Pilot No. 1 well. Log acronyms: SP = spontaneous potential; AHT = array induction two foot resistivity; Crossplot Por = computed porosity from density porosity and neutron porosity; GR = gamma ray.

Reservoir Properties of Key Members

Three stratigraphic intervals within the Grande Ronde Formation stand out as especially promising for injection:

- Winter Water Member – Located between approximately 700 and 850 m depth, this unit contains porous flow tops with 20% to 30% porosity and approximately 20 m of net thickness. Its lateral continuity makes it a reliable candidate horizon.

- Indian Ridge Member – Around 780 to 820 m depth, this member demonstrates porosities up to nearly 40%. Hydraulic testing reported transmissivity values equivalent to permeabilities as high as 2,500 mD, confirming the ability to sustain high injection rates.
- Ortley Member – Found between approximately 860 and 1,050 m depth, this interval contains at least nine flow tops with a combined net thickness of approximately 58 m. Porosities average 15% to 32%, and transmissivity tests indicate moderate injectivity. Its multiple stacked horizons make it particularly valuable for operational flexibility.

Collectively, these members confirm that the Grande Ronde Formation hosts laterally continuous, thick sequences of reservoir rock with favorable storage properties, directly overlaid and underlain by dense basalt interiors acting as seals.

Discovery of Hyaloclastite Reservoirs

A major new finding during the project was the identification of basal hyaloclastite deposits, fragmented basalt formed when lava erupted into water, as a new reservoir class. These facies were encountered in several wells and showed porosities of 60% to 86% and permeabilities reaching multiple darcies (Figure 97). Their high glass content indicates high chemically reactive, offering even faster mineralization than typical flow tops. Mapping of paleochannels demonstrated that hyaloclastites occur at the base of the Grande Ronde and Wanapum Basalts, particularly in the Yakima Valley and northern Columbia Basin.

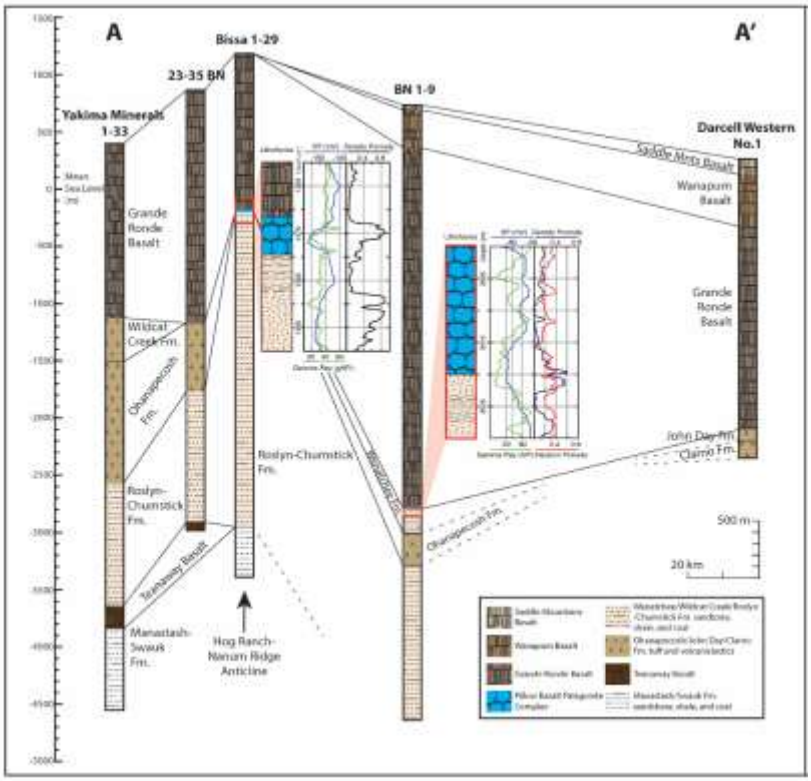


Figure 97 Well sections showing the hyaloclastite occurrences and petrophysical properties

The recognition of hyaloclastite as a reservoir type greatly expands the range of viable injection zones in the CRBG. Instead of relying solely on traditional flow tops, developers can now

consider these highly permeable, glass-rich deposits that combine excellent injectivity with rapid reactivity.

Hydrogeologic and Geochemical Isolation

Hydrologic testing showed that injection zones below 800 m depth are hydraulically isolated from overlying potable aquifers. Formation waters at these depths are non-potable, with chloride concentrations of 300 to 400 mg/L, fluorine exceeding 20 mg/L (far above the 4 mg/L drinking water limit), and iron concentrations up to 6,300 µg/L. The reducing, anoxic environment supports carbonate precipitation once CO_2 is dissolved. Together, the hydrogeologic and chemical data confirm compliance with EPA Class VI requirements: Injection occurs below underground sources of drinking water (USDWs) in brines that are chemically distinct and naturally confined (FY22 Q4, representative water-chemistry figure).

Core Evidence of Mineralization

The Wallula pilot project provided direct, physical confirmation that basalts not only react with injected CO_2 but do so on timescales relevant to project lifetimes. Sidewall cores collected 2 yr after the injection revealed abundant carbonate nodules embedded within the fractured flow tops of the Grande Ronde Basalt (Depp et al. 2022; Lahiri et al. 2023, 2025; Polites et al. 2022) . These nodules displayed distinct compositional zoning, with manganese- and calcium-rich interiors transitioning to iron-rich rims. Such zoning is consistent with sequential precipitation under evolving geochemical conditions: early stages dominated by Ca- and Mn-bearing phases, followed by Fe incorporation as groundwater chemistry shifted during continued reaction with the host rock.

High-resolution imaging and spectroscopy provided unprecedented insight into these mineralization processes. Scanning electron microscopy (SEM) and energy dispersive spectroscopy (EDS) confirmed the chemical zonation at the micron scale (Figure 98), whereas transmission electron microscopy (TEM) enabled direct visualization of the carbonate lattice at the atomic scale (Figure 99). These analyses identified novel carbonate phases, including cation-ordered ankerite (which the PNNL team has called “wallulite”) and calcian siderite, whose crystallographic ordering had not been observed in natural or synthetic systems before (Lahiri et al. 2025). The discovery of these previously unreported mineral phases highlights the unique reactive environment that arises when supercritical CO_2 interacts with basalt under subsurface conditions.

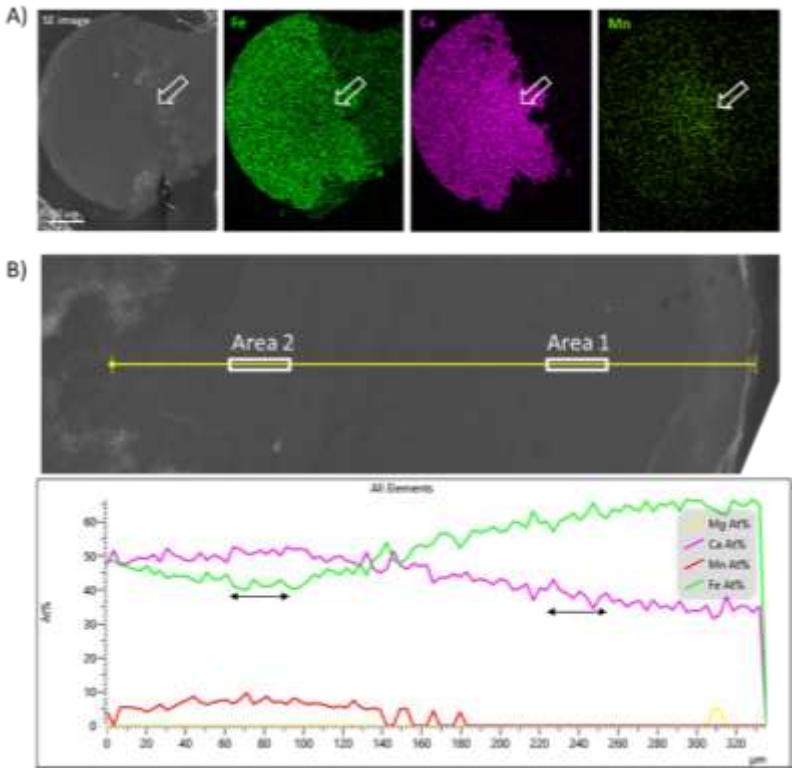
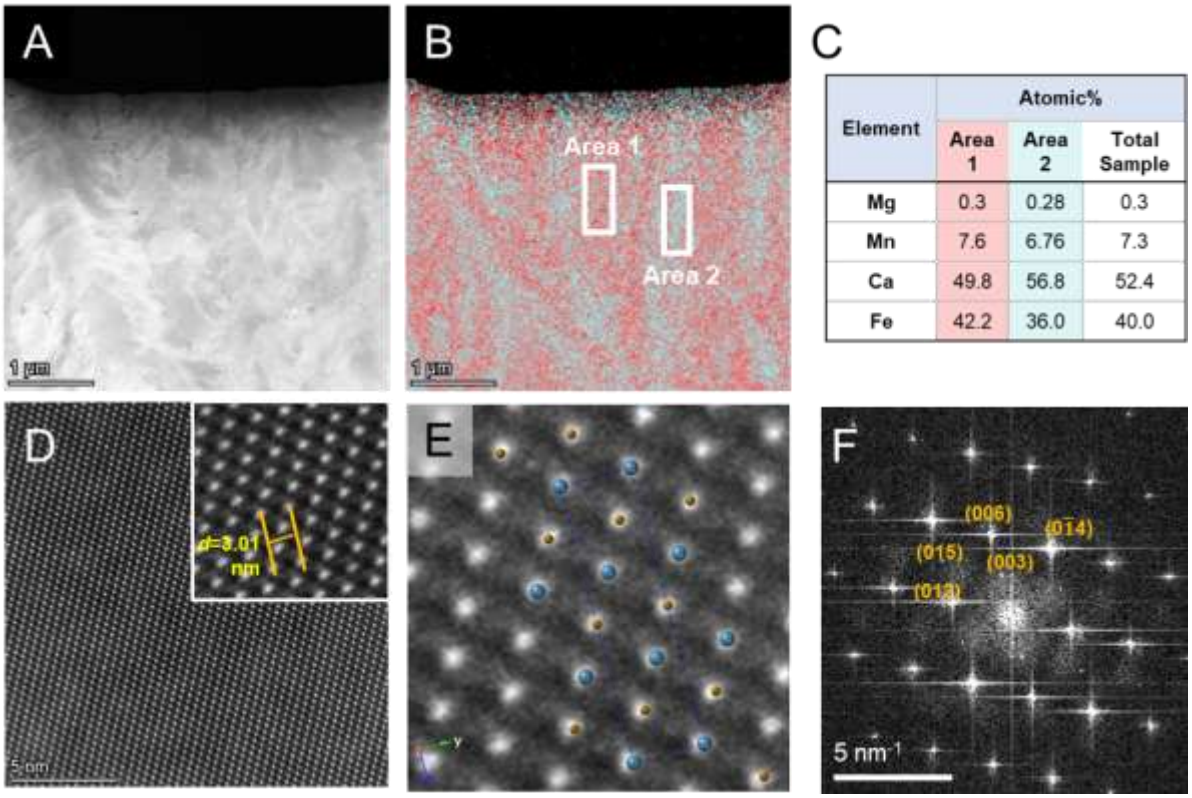


Figure 98 SEM-EDS analysis of carbonate nodule extracted from a depth of 857.1 m (2812 ft) bgs, (Zone No. 2). A) SEM-EDS chemical maps highlighting elemental zonation. B) EDS line scan, measuring the composition along the radius of the nodule at the micrometer scale. The highlighted rectangular areas represent the regions analyzed by TEM.



Element	Atomic%		
	Area 1	Area 2	Total Sample
Mg	0.3	0.28	0.3
Mn	7.6	6.76	7.3
Ca	49.8	56.8	52.4
Fe	42.2	36.0	40.0

Figure 99 TEM analysis of FIB lift-out from Mn-rich outer rim of carbonate nodule. A) STEM image showing the microstructure of the core region. B) STEM-EDS chemical mapping of the region. C) Table representing compositions corresponding to the two mineral phases. D) Atomic resolution imaging of the major phase identified in the core region. E) Ankerite structural model (using CrystalMaker) overlaid on magnified STEM HAADF image showing only the metal lattice structure. Blue = Ca; brown = Fe/Mn. F) FFT of the STEM-HAADF image showing the diffraction pattern revealing ordering reflections.

The physical occurrence of these carbonates also aligned with model predictions. Numerical simulations had indicated that mobile supercritical CO_2 would transition into dissolved CO_2, which in turn would react with basalt to liberate divalent cations such as Ca^{2+}, Mg^{2+}, Fe^{2+}, and Mn^{2+}. The precipitation of multi-cation carbonate nodules, observed directly in Wallula cores, confirmed that these pathways operate in situ. Moreover, the textures of the nodules, including sharp compositional gradients and concentric growth rims, suggest that mineralization was both rapid and ongoing at the time of sampling.

These findings carry significant implications for risk reduction. By showing that injected $scCO_2$ becomes immobilized in solid carbonate minerals within years, the Wallula results reduce uncertainty about long-term containment and diminish concerns over leakage or the need for extended postinjection monitoring. The immobility of carbonate minerals provides a permanence that far exceeds solubility or structural trapping mechanisms in sedimentary reservoirs.

Equally important, the identification of exotic carbonate phases highlights the potential for unanticipated but stable mineral products in basalt storage settings. This not only enriches scientific understanding of CO_2–rock interactions but also reinforces confidence in the durability of storage, because the minerals formed are crystalline, stable, and unlikely to rerelease CO_2 under geologic conditions. Together, these core observations form one of the strongest lines of

evidence that basalt reservoirs can deliver on the promise of permanent, gigaton-scale CO_2 storage through rapid mineralization.

Structural Setting and Site Down-Selection

Regional analysis identified two structurally distinct but complementary storage settings and evaluated specific CRBG flow members (Table 13). In the Yakima Fold Belt, doubly plunging anticlines provide additional structural closure to contain injected CO_2 (Figure 100). In the Palouse Slope province, thick, undeformed sections of the Grande Ronde Basalt provide broad, laterally continuous reservoirs free of major faulting. Together, these settings offer both localized trap security and regional scalability. After integrating structural, reservoir, and geochemical criteria, 2 priority sites were down selected: site A in the Yakima Fold Belt and site B on the Palouse Slope (Figure 100).

Table 13. Summary of potential injection formation members with key petrophysical data and attributes.

Reservoir Unit	Approx. Depth (m)	Net Thickness (m)	Porosity (%)	Permeability/ Injectivity	Key Attributes
Winter Water Member	700–850	Approx. 20	20–30	Moderate	Laterally continuous, favorable flow tops
Indian Ridge Member	780–820	Approx. 30	20–39	High (up to approx. 2,500 mD)	Strong injectivity, well tested
Ortley Member	860–1050	Approx. 58 (9 flow tops)	15–32	Moderate (approx. 20 mD average)	Multiple stacked injection horizons
Grande Ronde Formation (general flow tops)	800–1250	Approx. 150 (stacked)	25 average up to 39	Variable: flow interiors act as seals	Layered reservoir-seal geometry
Basal Hyaloclastite (Grande Ronde)	1,300–3,500+	10–50+	60–86	Very high (multi-darcy)	Exceptional porosity and reactivity
Basal Hyaloclastite (Wanapum)	270–670	10–30	60–84	High; up to 6,000 mD	Glass-rich, highly reactive facies

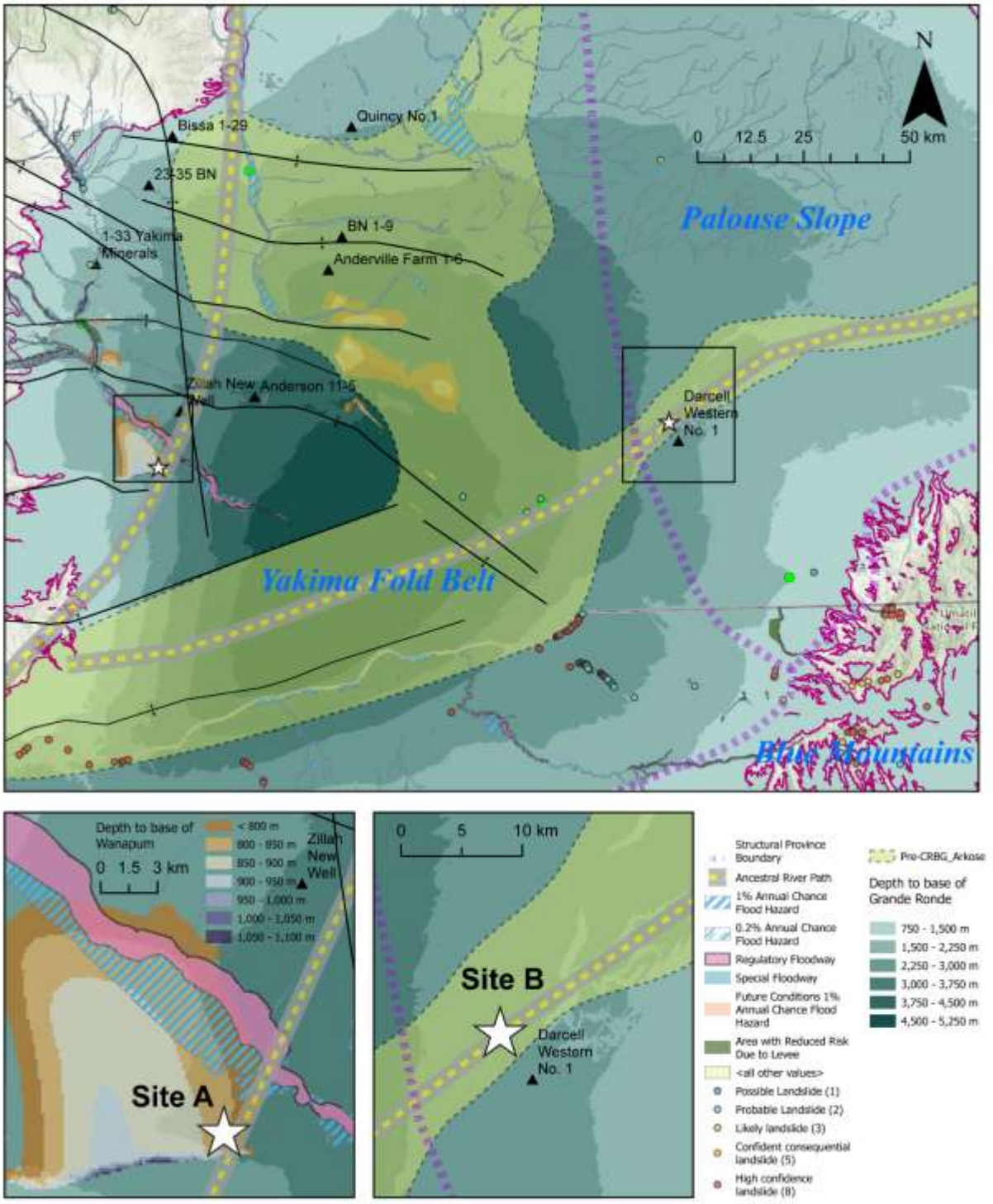


Figure 100. The selected 2 priority sites in the Columbia Basin are shown on the maps as white stars. The site selection is based on the interpreted ancestral Columbia River channels with sufficient storage depth. A stratigraphic well drilled at Site A is targeting both the basal Wanapum Basalt and the basal Grande Ronde Basalt hyaloclastite reservoirs at approximately 850 m and approximately 2,250 m below ground, respectively. Site B is targeting the basal Grande Ronde Basalt hyaloclastite reservoir at approximately 2,000 m. Site A is located in the Yakima Fold Belt structural province, about 15 km away from the Zilla New Well and away from surface sensitivities such as

land slide or flooding hazard. Site B is located in the structurally stable Palouse Slope province, about 5 km away from the Darcell Western No. 1 well.

Conclusions

Geologic site characterization confirmed that the Columbia River Basalt Group offers a unique combination of attributes for CO_2 storage: thick stacks of reservoir-quality flow tops, laterally continuous aquitards, newly recognized hyaloclastite reservoirs with exceptional porosity and reactivity, non-potable and isolated formation waters, and robust structural settings that minimize leakage risk. Core analyses provided direct evidence of rapid and permanent mineralization. These findings demonstrate that the Columbia Basin is among the most promising geologic settings globally for large-scale carbon mineralization storage, and provide the technical foundation for advancing to stratigraphic test wells and future Class VI demonstration projects.

Modeling and Simulation

Numerical modeling and simulation were critical for understanding how injected CO_2 would behave in basalt reservoirs over time. Using the Subsurface Transport Over Multiple Phases for CO_2 (STOMP-CO_2) simulator, PNNL researchers integrated geologic data, mineral kinetics, and hydrogeologic parameters to reproduce field-scale injection at Wallula and extend predictions to commercial scenarios. The modeling program advanced stepwise: benchmarking against known results, sensitivity testing to identify controlling processes, calibrating with laboratory and field data, and scenario analysis to assess storage security and mineralization potential.

Benchmarking with Wallula Pilot Injection

Initial simulations replicated the 2013 Wallula pilot, which injected approximately 1,000 t of supercritical CO_2 into a Grande Ronde Basalt reservoir (McGrail et al. 2009, 2011, 2014, 2017). Previous monitoring had shown that approximately 60% of the CO_2 mineralized within 2 yr (White et al. 2020), with nearly all expected to mineralize within a decade. STOMP-CO_2 simulations successfully reproduced these outcomes, providing confidence that the model captured key flow and geochemical processes. Benchmark runs confirmed the multiphase distribution of injected CO_2: a mobile supercritical phase near the wellbore, a dissolved fraction spreading into formation waters, and carbonate precipitation concentrated in reactive flow tops.

Sensitivity Analyses and Controlling Processes

Once benchmarked, the model was used to explore how reservoir properties and reaction kinetics influence storage outcomes. Two key findings emerged:

1) **Diffusion controls dissolution rates.** Simulations showed that CO_2 begins dissolving into formation waters immediately upon contact, but the overall rate of dissolution is governed by molecular diffusion. Even when other factors such as brine salinity or aqueous species concentrations were varied, diffusion remained the dominant control (Figure 101 and Figure 102).

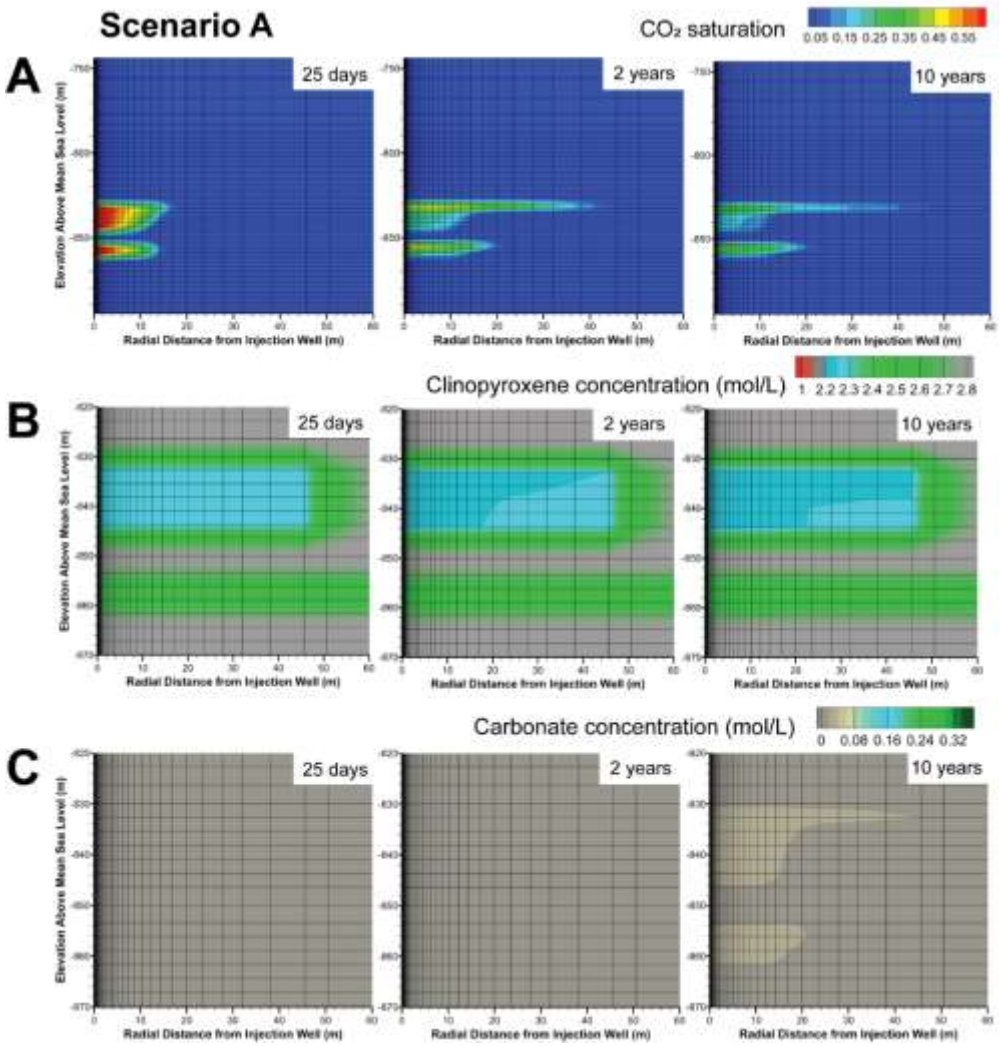


Figure 101 (A) CO_2 saturation, (B) clinopyroxene concentration, and (C) carbonate concentration in Scenario A at 25 days (the end of injection), 2 yr, and 10 yr after injection started.

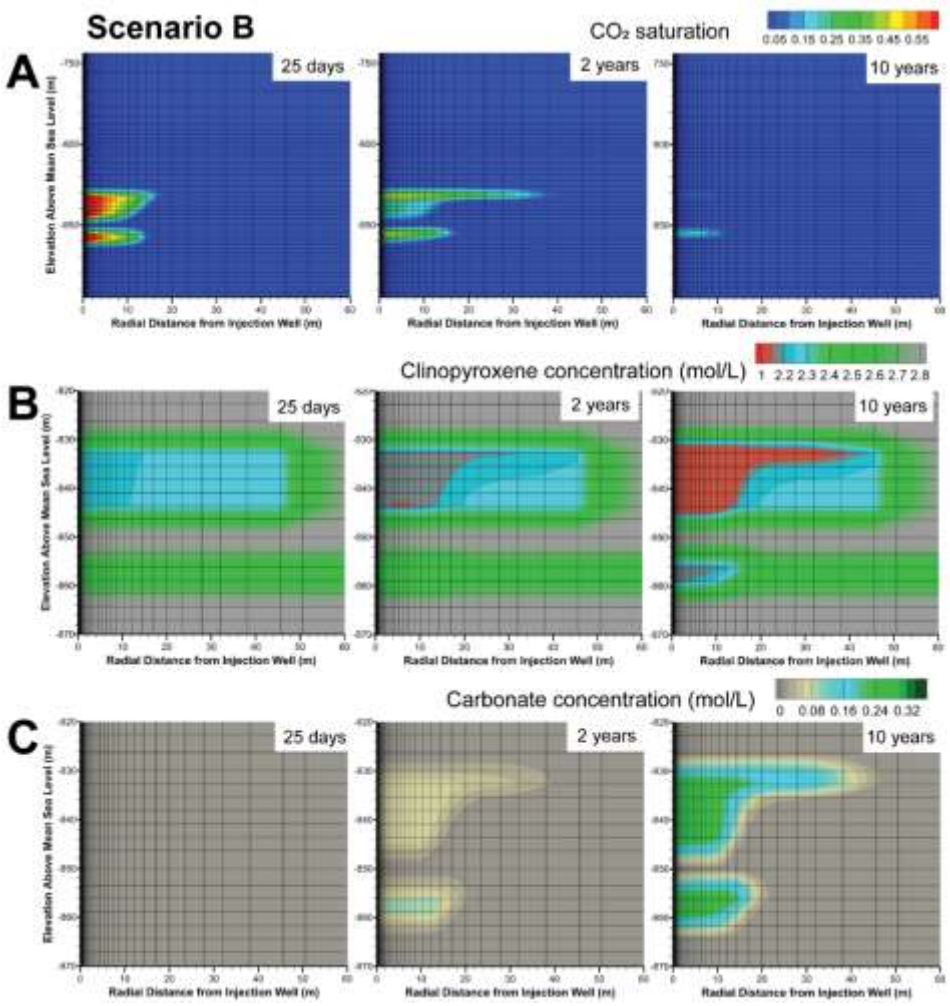


Figure 102 (A) CO_2 saturation, (B) clinopyroxene concentration, and (C) carbonate concentration in Scenario B at 25 days (the end of injection), 2 yr, and 10 yr after injection started.

2) **Mineral dissolution kinetics drive long-term mineralization.** In baseline cases, approximately 20% of injected CO_2 mineralized over 10 yr (Figure 101). When the dissolution rate of clinopyroxene, a primary basalt mineral, was increased by one order of magnitude, the extent of mineralization rose dramatically to approximately 90% over the same period (Figure 102). This demonstrated that uncertainties in primary mineral reactivity translate directly into uncertainty in long-term storage security.

Reactive Transport Calibration

To reduce uncertainty, a calibration workflow was developed that coupled STOMP-CO_2 outputs with PEST software. This approach allowed multiparameter fitting of model results to field data, including temporal groundwater chemistry ($_{e.g.}$ Ca, Mg, Fe, Mn concentrations, and pH) and postinjection pressure responses. The calibrated models achieved reaction networks consistent with 62% mineralization within 2 yr, aligning with Wallula pilot observations. The remaining refinements focused on adjusting precipitation rates of secondary minerals such as ankerite and aragonite to match core observations from postinjection samples.

Simulation of Injection Scenarios

Beyond reproducing pilot outcomes, simulations explored injection at commercial scale (approximately 1 $MtCO_2$/yr). These runs tested different reservoir architectures, injection rates, and geochemical settings. Results showed

- Plume behavior – Injected CO_2 remained confined within target flow tops, spreading laterally less than 50 m from the wellbore in 10-year simulations. Dense flow interiors effectively limit vertical migration.
- Mineral trapping timeline – All scenarios converged on rapid dissolution followed by precipitation. Even conservative cases predicted most injected CO_2 would transition into mineral phases within decades.
- Impact of glassy/amorphous vs. crystalline basalt – Simulations parameterized with amorphous glass data (from lab carbonation tests) yielded faster mineralization than crystalline enstatite cases, underscoring the importance of reservoir mineralogy.

Key Findings

- Rapid permanence – Both modeling and field calibration confirm that CO_2 injected into basalt reservoirs transitions to stable carbonate minerals within years to decades, ensuring permanent storage.
- Critical uncertainties – The rate of primary mineral dissolution (especially clinopyroxene and basalt glass) is the main uncertainty influencing predicted mineralization rates.
- Reservoir confinement – Flow interiors act as strong seals, and modeled plumes remained tightly confined, reducing risk of leakage.
- Scalability – Simulations demonstrate that mineralization can occur at scales relevant to commercial projects, not just pilots, making basalt storage competitive with sedimentary basins.

Risk Assessment

Risk assessment for CO_2 storage in basalt reservoirs required addressing both technical risks (injectivity, mineralization rates, reservoir heterogeneity, and containment) and nontechnical risks (regulatory pathways, stakeholder acceptance, infrastructure, and long-term liability). The project advanced risk management through laboratory validation, numerical simulations, hydrogeologic and geochemical testing, and stakeholder workshops. Together these efforts established a framework for anticipating, quantifying, and mitigating risks to enable Class VI permitting and commercial deployment.

Technical Risks and Mitigation

Reservoir Heterogeneity

Basalt formations are inherently heterogeneous, with properties varying among porous flow tops, massive flow interiors, and hyaloclastite facies. This variability poses uncertainty in predicting injectivity and storage capacity. To mitigate, the project integrated multiple borehole datasets (Wallula, 100 Circles, K2H, Zillah New Well) into a regional geologic model, providing a more complete picture of lateral continuity. Stacked reservoir–seal sequences demonstrated that even

if one flow top underperforms, neighboring horizons can sustain injection, reducing reliance on any single interval.

Injectivity and Capacity Uncertainty

Initial risk centered on whether basalt flow tops could support high injection rates at commercial scale. Hydraulic tests in the Indian Ridge Member demonstrated transmissivity values greater than 2,000 mD, confirming robust injectivity. The discovery of hyaloclastite reservoirs with porosities up to 86% and multi-darcy permeability further reduced injectivity risk, offering high-capacity injection zones that exceed those typical of sedimentary saline formations.

Mineralization Rate Uncertainty

The pace of mineralization is critical to long-term containment. Simulations of the Wallula pilot reproduced approximately 60% mineralization within 2 yr, consistent with core analyses. Sensitivity tests showed mineralization could range from approximately 20% (conservative scenario) to approximately 90% (accelerated clinopyroxene dissolution) over 10 yr. These results identified mineral dissolution kinetics as the key uncertainty. Laboratory experiments on basalt glass and enstatite helped narrow parameter ranges, and model calibration with groundwater chemistry (Ca, Mg, Fe, Mn, pH) further improved confidence.

Containment and Leakage

Risk of upward migration was assessed through structural and hydrogeologic analysis. Anticlinal structures in the Yakima Fold Belt and thick, undeformed basalt in the Palouse Slope provide natural confinement (Figure 100). Massive flow interiors serve as aquitards, with hydraulic head and water-chemistry data confirming minimal vertical connectivity between injection zones and overlying potable aquifers. Modeled plumes spread less than 50 m from the wellbore over 10 yr, indicating strong lateral confinement (Figure 101 and Figure 102).

Nontechnical Risks and Mitigation

Regulatory Familiarity and Permitting

Basalt reservoirs are novel for U.S. regulators accustomed to sedimentary saline formations. This introduces risk in Class VI permitting pathways. To mitigate, the project developed a permitting and cost framework specific to basalt, including definition of Areas of Review (AORs) for 30-year injections (approximately 14 km radius for 50 $MtCO_2$). Cost of permitting and characterization was estimated at approximately \$1.4/tCO_2, demonstrating feasibility within DOE expectations.

Stakeholder and Public Acceptance

Public unfamiliarity with CCS and concern about subsurface risks represent significant roadblocks. Engagement through five workshops (Richland, Ellensburg, Toppenish, Washington, D.C., and Richland Integrated Mineralization Workshop) brought together more than 120 participants, including Tribal Nations, local governments, NGOs, and public groups. Concerns about groundwater safety, pipeline infrastructure, and long-term liability were openly discussed. Input was incorporated into planning, particularly on-site access and workforce development.

Economic Risk

Cost competitiveness was another risk. Analyses compared supercritical CO_2 injection (approximately \$11.9/tCO_2) with aqueous dissolved injection (approximately \$23.5/tCO_2). Although both were within the ranges reported for sedimentary saline formations (typically approximately \$8/tCO_2 to \$20/tCO_2 depending on depth, reservoir quality, and monitoring requirements), supercritical injection offered clear cost advantages, reducing the risk of economic nonviability. For estimations specific to the Columbia Basin, costs ranged from \$13.3/tCO_2 for supercritical CO_2 to \$24.9/tCO_2 for aqueous CO_2 injection, placing basalt storage at the upper end of sedimentary basin costs but with the added advantage of rapid mineralization and permanent immobilization of injected carbon.

Long-Term Liability

The permanence of storage is essential for reducing monitoring costs and liability exposure. Mineralization in basalts provides unique assurance: Once CO_2 is converted to solid carbonate, it cannot migrate. This outcome directly addresses one of the largest risks in sedimentary CCS projects—postinjection care—by reducing the required monitoring timeframe.

Conclusions

Risk assessment demonstrated that although basalts pose unique uncertainties, especially regarding heterogeneity and reaction kinetics, these risks are mitigated by their equally unique advantages: stacked aquifer–seal architecture, rapid mineralization, and natural geochemical isolation. Technical analyses reduced uncertainty in injectivity and mineralization rates, whereas nontechnical engagement reduced regulatory and public risks. The combined findings show risks are manageable and, in some cases, lower than for conventional saline reservoirs, making basalt storage not only viable but highly attractive for long-term CO_2 management.

Technical/Infrastructure Issues

Although the scientific focus of this project was on geologic suitability and mineralization kinetics, technical and infrastructure considerations were also evaluated to understand feasibility of scaling basalt storage from pilot to commercial levels. These considerations included identifying potential CO_2 sources, matching with prospective sinks in the Columbia Basin, assessing transport and compression needs, and comparing engineering designs for different injection approaches. This work informed economic assessments and provided a realistic picture of how a commercial basalt storage project might be deployed in the Pacific Northwest.

Source–Sink Matching

The Columbia Basin is home to multiple potential point sources of CO_2, including natural gas combined-cycle (NGCC) power plants, industrial facilities, and pulp and paper operations. The Hermiston Power Project, a 546-MW natural gas–fired facility, was specifically evaluated as a capture candidate. Its location near the down selected storage sites in the Yakima Fold Belt and Palouse Slope minimizes transport distance and costs (Figure 100). Analyses assumed post-combustion capture at the power plant, with injection either directly onsite or via short pipeline routing.

Injection Scenarios and Compression Needs

Two injection strategies were compared:

- $scCO_2$ injection – requires compression of captured CO_2 to pressures greater than 7.4 MPa and delivery to depths greater than 800 m. Modeling and cost assessments showed this option has lower water requirements, a smaller surface and subsurface footprint, and fewer monitoring wells.
- Aqueous dissolved CO_2 injection (CO_2 (aq)) – requires dissolving CO_2 into large volumes of water before injection. For a 50-Mt injection scenario, approximately 1.25 Gt of water would be required, leading to higher capital costs (more wells, pumps) and higher O&M costs.

Transport and Pipeline Considerations

Pipeline construction and routing were recognized as key infrastructure elements. Although long-distance transport was not required for the modeled Hermiston case, regional deployment would involve building new CO_2 pipelines or repurposing existing rights-of-way. Workshops and stakeholder input highlighted concerns about pipeline safety, permitting, and land use, consistent with broader CCS infrastructure challenges. Although detailed routing analyses ($_{e.g.}$ using SimCCS optimization) were not conducted in this project, preliminary cost estimates assumed short-distance pipelines linking capture facilities to nearby basalt sinks.

Coupling with Existing Infrastructure

The Columbia Basin has several advantages for infrastructure combination:

- Energy infrastructure is already established in Hermiston and Tri-Cities, with power generation, transmission lines, and rail networks.
- Industrial partners (e.g. Boise Cascade pulp mill at Wallula) have prior engagement in CO_2 projects, creating opportunities for early adoption.
- Regional geology aligns with infrastructure corridors, meaning many candidate sinks are close to existing industrial centers, reducing transport challenges.

In Situ Critical Mineral Recovery

Recent analyses also suggest that basalt reservoirs hold potential for co-benefits through critical mineral recovery, particularly titanium (Ti), vanadium (V), and rare earth elements present in glassy mesostasis phases. During carbonation reactions, dissolution of basalt glass liberates not only divalent cations (Ca, Mg, Fe, and Mn) that drive carbonate formation but also trace elements of economic value. Experimental and nanoscale studies have shown that Ti-bearing oxides and silicates undergo partial alteration in CO_2-bearing fluids, releasing Ti and other critical minerals into solution where it may be recoverable under controlled conditions (Jacobs et al. 2025; Miller et al. 2025; Murchland et al. 2025; Stanfield et al, 2024). Although the primary goal of injection is permanent carbon storage, the potential for dual outcomes—CO_2 mineralization and critical mineral mobilization through CO_2 enhanced mineral recovery (CO_2-EMR)—adds value to basalt reservoirs and aligns with U.S. priorities for securing domestic supplies of strategic materials.

Site Access and Permitting Logistics

From a logistical standpoint, site access and permitting were considered in preoperational planning. Candidate sites were chosen in areas with minimal surface hazards (e.g. away from floodplains or landslide-prone zones) and close to existing roads and utilities. Early engagement with landowners and Tribal Nations informed site location discussions, whereas regulatory planning anticipated the requirements of EPA Class VI permitting, including definition of Areas of Review (AORs), well design standards, and monitoring networks.

Conclusions

Technical and infrastructure assessments confirmed that basalt storage in the Columbia Basin can be integrated with nearby power and industrial facilities using existing infrastructure corridors, supplemented by new injection and short pipeline systems. Comparative analysis showed that supercritical CO_2 injection is the most practical and cost-effective option, with significantly lower water demand and fewer wells than aqueous dissolved injection. These findings reduce infrastructure uncertainty and demonstrate that basalt storage can be deployed at commercial scale with realistic engineering and logistical requirements.

Nontechnical Issues / Scenario Analysis

Beyond technical feasibility, the success of commercial-scale CO_2 mineralization projects depends on addressing nontechnical factors such as property rights, regulatory pathways, public acceptance, and long-term liability. These issues often determine whether technically sound projects can be permitted, financed, and sustained. For basalt storage in the Columbia River Basalt Group (CRBG), the project team evaluated land and pore space ownership, transport and rights of way, water availability, liability frameworks, economics, and outreach activities. Collectively, these assessments revealed both challenges and opportunities and shaped strategies for building social license and regulatory readiness.

Land and Pore Space Ownership

The CRBG spans multiple states, counties, and private landholdings, introducing complexity around pore space rights. In many U.S. jurisdictions, subsurface pore space is considered part of the surface estate, although interpretations vary. This uncertainty poses risk for permitting Class VI injection wells, where landowner agreements are required. To mitigate, the project identified target areas (Yakima Fold Belt and Palouse Slope) with relatively simple ownership structures, avoiding urbanized or highly fragmented parcels (Figure 100). Early engagement with landowners and Tribal Nations emphasized transparent communication about the use of pore space for long-term carbon storage.

Transport and Rights of Way

Transporting captured CO_2 to injection sites requires access to pipeline corridors or the development of new rights of way. Although the Hermiston and Tri-Cities areas already host extensive energy infrastructure, new CO_2 pipelines may face siting challenges, including opposition from landowners or environmental groups. Stakeholders expressed concerns about pipeline safety, permitting delays, and public disruption. Although detailed routing optimization

(e.g. with SimCCS) was not performed under this project, economic analyses assumed short-haul transport from local NGCC power plants to basalt sinks. Future work will need to integrate routing studies, permitting strategies, and right-of-way negotiations into early project planning.

Water Rights

Injection strategies requiring water, such as dissolved CO_2 injection (CO_2 (aq)), introduce significant water rights challenges. For a 50-MtCO_2 injection, approximately 1.25 Gt of water would be needed, placing enormous strain on already contested water resources in the Columbia Basin. By contrast, supercritical CO_2 injection has minimal water demand, making it more feasible in regions where agricultural and municipal water use dominates. Water scarcity in the Yakima Valley and Eastern Oregon was flagged by stakeholders as a critical nontechnical issue, strongly influencing the project team's preference for supercritical injection pathways.

Liability and Long-Term Stewardship

A persistent roadblock to CO_2 storage projects is uncertainty about long-term liability. In sedimentary projects, liability often extends for decades postinjection, with operators responsible for monitoring and potential leakage remediation. Basalt mineralization reduces this burden: Once CO_2 is converted into stable carbonates, leakage pathways are effectively eliminated. This geochemical permanence could shorten the period of required postinjection site care, reducing both financial and regulatory liabilities. Nevertheless, clarity is still needed on how liability would be transferred to state or federal entities once monitoring is complete.

Economic Assessment

Economic feasibility is central to commercial deployment. Analyses compared supercritical CO_2 injection (approximately \$11.9/tCO_2) with aqueous injection (approximately \$23.5/tCO_2). Supercritical injection offered lower capital and operating costs due to reduced water demand, smaller well fields, and fewer monitoring requirements. Permitting and site characterization costs added approximately \$1.4/tCO_2, bringing total levelized storage costs into the range of \$13/tCO_2 to \$25/tCO_2. These figures are competitive with sedimentary basin projects, providing confidence that basalt mineralization can attract investment if regulatory and policy frameworks support tax credits under Section 45Q of the U.S. Tax Code (Credit for Carbon…2021) and other incentives.

Outreach and Engagement

Outreach activities were central to addressing nontechnical risks. Over five workshops were held in FY22–FY24, engaging more than 120 participants, including Tribal Nations, local communities, NGOs, industry, and regulators. The Carbon Interactive Workshop (Richland, WA), the "Big Questions" workshop (Ellensburg, WA), and outreach to Heritage University (Toppenish, WA) each provided forums for stakeholders to voice priorities and concerns (Figure 103). Issues raised included groundwater protection, pipeline safety, and land use. The project team emphasized early information sharing and opportunities for student internships and workforce development to build trust and regional readiness.



Figure 103 PNNL mineralization team presenting posters, showcase basalt reservoir core samples with microscopes, and discussing among working groups at the "Big Questions" workshop

Nontechnical Risks

Key nontechnical risks identified include

- public unfamiliarity with CCS leads to misconceptions about safety,
- opposition to CO_2 pipelines due to safety or land use concerns,
- water rights conflicts in regions where dissolved injection would compete with agriculture,

- regulatory uncertainty about permitting basalt reservoirs under Class VI, and
- long-term liability frameworks for mineralization-based storage that are not yet tested.

Mitigation strategies included prioritizing supercritical CO_2 injection, selecting sites in structurally stable and less densely populated areas, and conducting extensive outreach. Early adoption of public feedback was identified as essential to avoiding delays during permitting and operation.

Conclusions

Nontechnical assessments underscored that public trust, regulatory clarity, and water resource management are as critical as technical feasibility. By proactively addressing pore space ownership, rights of way, liability, and economic competitiveness, and by engaging stakeholders in open dialogue, the project reduced roadblocks to future demonstration projects. These efforts position basalt mineralization storage not only as a technically sound option but also as a socially and economically viable pathway for large-scale carbon management in the Pacific Northwest.

Permitting and Regulatory Planning and Progress

UIC Class VI Permit Planning

The EPA's Class VI well program governs the injection of CO_2 for the purpose of long-term storage. Although prior Class VI permits have been issued for saline formations, none have yet been granted for basalts, introducing regulatory uncertainty. To reduce risk, the project team applied lessons from the Wallula pilot (globally, the only prior basalt injection) and from sedimentary projects such as FutureGen. Class VI–relevant activities included

- Area of Review (AOR) analysis that used modeled pressure fronts, with a 30-year injection of 50 $MtCO_2$ generating a critical pressure radius of approximately 14 km used to delineate the AOR (FY23–FY24 modeling outputs);
- Well construction planning that anticipated casing, cementing, and monitoring requirements tailored to fractured flow tops and hyaloclastite facies; and
- Reservoir and seal characterization that demonstrated lateral continuity, low vertical connectivity, and non-potable groundwater at target depths, prerequisites for Class VI approval.

These activities provide the technical foundation for an eventual permit application once a demonstration site is selected.

Monitoring, Reporting, and Verification (MRV)

A Class VI permit requires a robust monitoring, reporting, and verification (MRV) plan to ensure injected CO_2 remains contained. The project prepared for this by integrating

- Reactive transport simulations that were calibrated to field chemistry, which enabled predictions of plume extent, mineralization rates, and long-term fate;
- Baseline groundwater chemistry datasets that included iron, manganese, and fluorine concentrations, which exceeded potable standards and support non-USDW classification; and

- Proposed monitoring strategies that included pressure observation wells, seismic surveys, and geochemical sampling, which aligned with Wallula pilot experience.

Together, these elements provide the basis for MRV plans that regulators and stakeholders can trust.

45Q Incentive Readiness

Economic viability of basalt storage depends in part on the federal 45Q tax credit, which rewards secure CO_2 storage. The project team evaluated how basalt mineralization fits within 45Q frameworks. Although current rules were developed for saline and depleted hydrocarbon reservoirs, the permanence of mineralization offers an even stronger assurance of storage. Cost assessments ($13/t$CO_2$ to $25/t$CO_2$ for basalt storage in the Columbia Basin) align with 45Q thresholds, and stakeholder discussions emphasized that early basalt projects should be prioritized for credit eligibility. Positioning basalt mineralization within 45Q enhances its competitiveness with sedimentary basin projects.

Stakeholder and Public Engagement

Because regulatory unfamiliarity with basalt reservoirs represents a risk, stakeholder engagement was incorporated into regulatory planning. Five workshops between FY22 and FY24—Richland, WA; Ellensburg, WA; Toppenish, WA; Washington, D.C.; and Richland Integrated Mineralization Workshop—brought together more than 120 participants, including Tribal Nations, regulators, DOE officials, and public representatives. These events provided opportunities to

- explain the permitting process and Class VI requirements;
- address public concerns about groundwater protection, pipeline safety, and site access; and
- build support for early basalt demonstration projects through transparent dialogue.

This engagement not only advanced social license but also gave regulators confidence that public acceptance was being addressed proactively.

Other Regulatory Activities

In addition to Class VI planning, the project addressed related regulatory considerations:

- State-level water rights and land use policies, which strongly influence site selection.
- Cross comparison with sedimentary Class VI permits, such as FutureGen and Illinois Basin projects, to identify transferable best practices.
- Synergy with DOE's CarbonSAFE program, which provides a pathway for large-scale demonstration and future commercialization.

Project Findings and Conclusions

The project demonstrated that the Columbia River Basalt Group (CRBG) possesses the geologic, geochemical, and structural characteristics necessary to support secure, commercial-scale CO_2 storage. Site characterization confirmed that flow tops within the Grande Ronde Formation provide laterally extensive, permeable reservoirs, whereas massive flow interiors act as effective aquitards. The discovery of basal hyaloclastite deposits as a new reservoir class expanded

injection opportunities by revealing zones with extremely high porosity, permeability, and glass content, which are ideal for both injectivity and rapid mineralization. Hydrogeologic and geochemical testing further showed that target formations occur well below potable groundwater and are chemically isolated, strengthening the case for long-term containment.

Modeling and simulation results validated that mineralization occurs on decadal or shorter timescales, with up to 60% of injected CO_2 mineralized within 2 yr at the Wallula pilot site. Sensitivity analyses highlighted diffusion and mineral dissolution kinetics as the main controls on long-term outcomes, whereas calibration with groundwater chemistry aligned predictions with field data. Core analyses provided direct, physical evidence of permanent storage through the formation of novel carbonate phases, including cation-ordered ankerite and calcian siderite. These findings demonstrated that basalt storage not only matches but, in some ways, exceeds the permanence guarantees of sedimentary reservoirs.

Collectively, the project derisked CO_2 mineralization in basalts by addressing geologic uncertainty, validating reactive transport models, and establishing permitting and economic frameworks. Cost estimates for Columbia Basin storage ($13–25/t$CO_2$) are comparable with those reported for sedimentary saline formations, but with the added benefit of permanent mineralization that reduces the need for long-term postinjection monitoring and liability. Nontechnical risks, such as pore space ownership, pipeline rights of way, and stakeholder acceptance, were proactively managed through workshops, engagement with Tribal Nations and communities, and development of permitting readiness pathways.

The overall conclusion of the project is that basalts in the Pacific Northwest represent a gigaton-scale, permanent, and economically competitive storage resource. With both technical feasibility and stakeholder frameworks now in place, the region is ready to advance to Class VI permitting and demonstration-scale injection projects. This work positions basalt mineralization as a cornerstone of carbon management in the western United States and as a globally relevant option for durable, geologic-scale carbon dioxide removal with potential for coupling with other subsurface technologies, such as in situ critical mineral recovery.

References

Battu AK, Miller QRS, Cao R, Owen AT, Schaef HT. 2024. 3D quantification of pore networks and anthropogenic carbon mineralization in stacked basalt reservoirs. Environ Sci Technol. 58(8):3747–3754. doi:10.1021/acs.est.3c06163

Credit for Carbon Oxide Sequestration, U.S.C.-2023 26 C.F.R. §1.45Q-1 (2021).

Depp CT, Miller QRS, Crum J, Horner JA, Schaef HT. 2022. Pore-scale microenvironments control anthropogenic carbon mineralization outcomes in basalt. ACS Earth Space Chem. 6(12):2836–2847. doi:10.1021/acsearthspacechem.2c00165

Gilmore T, Bonneville A, Sullivan C, Kelley M, Appriou D, Vermeul V, White, S, Zhang F, Bjornstad B, Cornet F, et al. 2016. Characterization and design of the FutureGen 2.0 carbon storage site. Int J Greenh Gas Control. 53:1–10. doi:10.1016/j.ijggc.2016.07.022

Gilmore TJ, Bonneville A, Vermeul V, Spane F, Kelley ME, Sullivan C, Hoffmann J. 2014. Overview of the CO_2 geological storage site for the FutureGen project in Morgan County Illinois, USA. Energy Procedia. 63:6361–6367. doi:10.1016/j.egypro.2014.11.671

Jacobs JE, Stanfield CH, Miller QRS, Villante MA, Marcial J, Nienhuis ET, Silverstein JA, Polites EG, Bartels MF, Gooch BT, et al. 2025. Technoeconomic potential for carbon mineralization with enhanced recovery of critical minerals in the Pacific Northwest. ACS Sustainable Resour Manage. 2(5):775–785. doi:10.1021/acssusresmgt.4c00541

Lahiri N, Kovarik L, Taylor SD, Crum JV, Ilton ES, Depp CT, Miller QRS, Schaef HT. 2025. Complex carbonate phases drive geologic CO_2 mineralization. Commun Earth Environ. 6(1):344. doi:10.1038/s43247-025-02273-6

Lahiri N, Miller QRS, Cao R, Depp CT, Schaef HT. 2023. Facile metal release from pore-lining phases enables unique carbonate zonation in a basalt carbon mineralization demonstration. Environ Sci Technol. 57(32):11843–11851. doi:10.1021/acs.est.3c02075

McGrail BP, Schaef HT, Spane FA, Horner JA, Owen AT, Cliff JB, Qafoku O, Thompson CJ, Sullivan EC. 2017. Wallula basalt pilot demonstration project: post-injection results and conclusions. Energy Procedia. 114:5783–5790. doi:10.1016/j.egypro.2017.03.1716

McGrail BP, Spane FA, Amonette JE, Thompson CR, Brown CF. 2014. Injection and monitoring at the Wallula basalt pilot project. Energy Procedia. 63:2939–2948. doi:10.1016/j.egypro.2014.11.316

McGrail BP, Spane FA, Sullivan EC, Bacon DH, Hund G. 2011. The Wallula basalt sequestration pilot project. Energy Procedia. 4:5653–5660. doi:10.1016/j.egypro.2011.02.557

McGrail BP, Sullivan EC, Spane FA, Bacon DH, Hund G, Thorne PD, Thompson CJ, Reidel SP, Colwell FS. 2009. Preliminary hydrogeologic characterization results from the Wallula basalt pilot study. PNWD-4129. Richland (WA): Battelle Pacific Northwest Division. p. i–5.4.

Miller QR, Nagurney A, Blondes M, Thakurta J, Liu J, Gadikota G, Lahiri N, Schaef HT. 2025. Carbon-negative nickel mining to meet global mineral resource demands [preprint]. EarthArXiv [Internet]. [accessed 2026 Jan 16]. https://eartharxiv.org/repository/view/9174/. doi:10.31223/X5S15S

Murchland MA, Miller QRS, Nagurney AB, Stanfield CH, Lahiri N, Silverstein JA, Teng Y, Nienhuis ET, Engelhard MH, Mulcahy C, et al. 2025. CO_2-based leaching of sulfidic peridotite drives critical mineral mobilization and carbonate precipitation. Environ. Sci. Technol Lett. 12(9):1252–1263. doi:10.1021/acs.estlett.5c00603

Polites EG, Schaef HT, Horner JA, Owen AT, Holliman JE Jr, McGrail BP, Miller QRS. 2022. Exotic carbonate mineralization recovered from a deep basalt carbon storage demonstration. Environ Sci Technol. 56(20):14713–14722. doi:10.1021/acs.est.2c03269

Stanfield CH, Miller QRS, Battu AK, Lahiri N, Nagurney AB, Cao R, Nienhuis ET, DePaolo DJ, Latta DE, Schaef HT. 2024. Carbon mineralization and critical mineral resource evaluation pathways for mafic–ultramafic assets. ACS Earth Space Chem. 8(6):1204–1213. doi:10.1021/acsearthspacechem.4c00005

Vermeul VR, Amonette JE, Strickland CE, Williams MD, Bonneville A. 2016. An overview of the monitoring program design for the FutureGen 2.0 CO_2 storage site. Int J Greenh Gas Control. 51:193–206. doi:10.1016/j.ijggc.2016.05.023

White SK, Spane FA, Schaef HT, Miller QRS, White MD, Horner JA, McGrail BP. 2020. Quantification of CO_2 mineralization at the Wallula basalt pilot project. Environ Sci Technol. 54(22):14609–14616. doi:10.1021/acs.est.0c05142

White SK, Zhang ZF, Oostrom M. 2016. Simulation of carbon dioxide injection at the FutureGen2.0 site: Class VI permit model and local sensitivity analysis. Int J Greenh Gas Control. 55:177–194. doi:10.1016/j.ijggc.2016.10.009

CCS at the Iron Mountain Iron Mine and Direct Reduced Iron Processing Plant, Southern Utah

The CUSP Iron Mountain Subsurface Characterization Focused Project evaluated the technical feasibility of geologic CO_2 storage to support a planned direct-reduced iron (DRI) facility in the Iron Springs District near Cedar City, Utah. The project focused on establishing the feasibility for a storage complex concept in a data-limited setting, with the Jurassic Navajo Sandstone as the primary storage reservoir and associated Jurassic–Triassic units and intrusive rock bodies evaluated as sealing units. Work was structured to (1) assemble and quality-control the critical subsurface datasets needed for storage assessment, (2) develop a geological model and simulation study, (3) evaluate storage performance and key containment risks, and (4) define the engineering scope required to close remaining uncertainties through a dedicated stratigraphic characterization well.

Across the project, partners integrated legacy and newly generated geoscience and engineering inputs, including well logs and sample-based observations, outcrop and laboratory measurements, and regional geophysical constraints. Legacy 2D seismic data were reprocessed using updated velocity modeling to improve structural interpretation, supported by automated fault detection products where appropriate. New terrestrial gravity data were acquired and merged with regional datasets to better constrain basin geometry and structural context. These inputs were incorporated into an iterative geological modeling workflow, progressing from updated surfaces and interpretations (v2/v3) to a complete stratigraphic sequence model from surface (DEM) through the Moenkopi (v4), with corresponding updates to petrophysical property representations.

Using the resulting models, the team performed site-scale performance assessment to evaluate injectivity, pressure evolution, CO_2 plume behavior and stabilization trends, and Area of Review (AoR) sensitivities under multiple operating scenarios. The project also produced a preliminary engineering basis for next-phase field work, including a defined scope and budget framework for a stratigraphic characterization well with coring, logging, and sampling intended to reduce key uncertainties for future Class VI and 45Q documentation. Collectively, these outcomes establish a technically grounded foundation for advancing Iron Mountain toward a field characterization phase and subsequent EPA Class VI storage complex design.

Outcomes and Objectives

The CUSP Iron Mountain Subsurface Characterization Focused Project evaluated the feasibility of geologic CO_2 storage associated with a planned direct-reduced iron (DRI) facility in the Iron Springs District near Cedar City, Utah. The work concentrated on the Navajo Sandstone and

associated formations as a potential storage complex, with the Carmel and Temple Cap formations and the Three Peaks quartz monzonite laccolith acting as the confining units. The overarching goals were to assemble sufficient geologic, petrophysical, and geomechanical information to support a geological model suitable for dynamic simulation, to characterize key geologic risks such as induced seismicity and seal integrity, and to prepare the technical and non-technical foundation for eventual Class VI and 45Q work.

The primary objectives of this proposed project include (1) detailed site characterization and analysis of storage capacity, risks and economic options for CCUS at Iron Mountain, and (2) developing a plan for drilling a stratigraphic well and/or acquiring a 3D seismic survey of the area of interest, and (3) comprehensive plans for assembling UIC Class VI and 45Q tax credit applications. The nature and success of these objectives depend explicitly on the target storage formation and its specific geologic setting.

The target formation for this project is the Navajo Sandstone, with a possible secondary target of the Kaibab Limestone. The Jurassic-aged Navajo Ss. is a prolific aquifer south of the Pine Valley Mountains and oil reservoir in other areas throughout SW Utah. At depths suitable for CO_2 storage (> 800 m, to maintain supercritical state), two key reservoir/seal pairs include (1) the Jurassic Navajo Sandstone (and possibly the overlying Temple Cap Formation) that is stratigraphically sealed by the heterolithic, mudstone and gypsum-rich Carmel Formation and, in certain areas, is intruded with several thousand feet of the Three Peaks quartz monzonite laccolith and (2) the Permian Kaibab Limestone with (potentially) self-sealing intraformational gypsum layers and overlain by the mudstone-rich Triassic Chinle and Moenkopi Formations.

Scope of Work

Preliminary analysis suggests that the Navajo SS and/or the Kaibab are both capable of storing at least 50 million tons of CO_2 in the area of Iron Mountain, also known as the Iron Spring District. Geologic carbon sequestration in these formations in this area is favorable for several reasons, including the presence of several reservoir/seal pairs at different depth intervals as mentioned above, which provides potential for multiple targets. Additionally, lack of hydrocarbons may lower the risk of unavailable pore space or associated overpressures. And, given that these units are deep (7,000+ ft) but not excessively so translates to relatively low drilling and injection costs. Ultimately, the project objectives included assessment of commercial-scale storage potential with nominal risks, with 21 and 50 million tons over 30 years evaluated. Additionally, the demonstration of CCUS with an iron-processing plant specifically has never been attempted to date, and this project would provide a meaningful example for other iron and steel industry projects coming on line in the next decade.

Key outcomes achieved during the project include:

1. Integration and QA/QC of legacy and newly generated datasets, including the ARCO Three Peaks #1 well logs and cuttings, analogue well information, outcrop observations and sampling, petrographic products, laboratory petrophysical and geomechanical measurements, and regional geophysical datasets.
2. Reprocessing and depth imaging of legacy 2D seismic data using updated velocity models and reverse-time migration, followed by automated fault detection to improve structural interpretation in areas affected by complex geology.

3. Acquisition and interpretation of new terrestrial gravity data, merged with regional datasets, to constrain basin geometry and the extent of the Three Peaks intrusion and to provide independent structural constraints for model building.
4. Progressive development of a 3D geological model suitable for simulation, including iterative updates to formation surfaces and property models as new interpretations and measurements became available.
5. Site-scale performance assessment using numerical simulation and supporting analyses to evaluate pressure evolution, injectivity, CO_2 plume behavior and stabilization, and Area of Review sensitivities under multiple operating scenarios.
6. Development of preliminary engineering planning products (scope, basis of estimate, and cost framework) for a stratigraphic characterization well and associated coring, logging, and sampling program to close key data gaps identified by the subsurface characterization and modeling work."

CUSP Iron Mountain Team

Project management focused on coordinating a geographically distributed team, managing budgets and cost-share, and enabling data access critical for geophysical reprocessing and modeling.

The project was executed by a multi-institutional team that included the University of Utah (UU/EGI), Utah Geological Survey (UGS), Oklahoma Geological Survey and the IC3 laboratory (OGS/IC3), Los Alamos National Laboratory (LANL), Carbon Solutions/MSU, and state policy partners. Work began in mid 2022, included a pause related to funding and a subsequent no-cost extension, and continued through mid 2024.

From project initiation, the management team organized a technical kickoff meeting and field visit in Cedar City that combined presentations with a tour of the mine and key outcrops of the Navajo Sandstone and overlying formations. This visit helped align the team on both the industrial context and the subsurface geology. Routine bi-weekly all-hands meetings were maintained through most of the project, with alternating geology-focused meetings hosted by UGS. These meetings were used to track progress across site characterization, laboratory testing, modeling, and risk assessment, and to avoid duplication of efforts.

A substantial management effort went into enabling LANL to reprocess legacy 2D seismic data using the Echos processing system at the University of Houston. This required negotiating and executing a multi-party non-disclosure and data-sharing arrangement among the University of Utah, LANL, Seismax, and the University of Houston so that existing processing flows and velocity models could be transferred and interrogated. In parallel, the UU team worked with UGS to plan around budget constraints and a no-cost extension, pausing some work streams (particularly at UGS) when BP2 funds were exhausted and restarting them once additional support became available.

Management also developed and maintained standardized quarterly reporting templates, a Gantt chart, and a Final Report outline keyed to the Statement of Project Objectives. Toward the end of the project, effort shifted toward synthesizing results into the final report, preparing slides for the DOE annual review, and ensuring that all partner contributions, particularly UGS's Open File

Report and LANL's fault imaging results, could be integrated into a coherent end-of-project narrative.

Geologic Site Characterization

The UGS lead the geologic site characterization effort and are in the process of writing a manuscript that details their work. The following title and abstract are from this in-process manuscript. Additional information from the project reporting is documented in the following subsections.

Geologic Carbon Storage Potential in the Neck of the Escalante Desert, Iron County, Utah

Eugene Szymanski[1], Christian L. Hardwick[1], Michael D. Vanden Berg[1], Elliot A. Jagniecki[1], Kayla Smith[1], Gabriela A.E. St. Pierre[1], Nathan Moodie[2], Eric Edelman[2], and Julia S. Mulhern[1,3]

1. Utah Geological Survey, 1594 W. North Temple, Suite 3110, Salt Lake City, UT 84116

2. The University of Utah Energy & Geoscience Institute, 423 Wakara Way, Suite 300, Salt Lake City, UT 84108

3. National Energy Technology Laboratory, 1011 Highway 6 S., Suite 309, Houston, TX 77077

The Iron Springs District in southwest Utah lies at the eastern boundary of the Basin and Range Province as it transitions into the Colorado Plateau and it is one of the largest iron ore producing regions in the western United States. In 2022, a local mining company proposed building a direct reduced iron (DRI) plant to optimize their operations and increase the domestic steel supply. A DRI plant would also generate approximately 500,000 t of carbon dioxide (CO_2) annually, and to reduce the amount of carbon-rich byproducts released into the atmosphere, a rigorous subsurface characterization project was conducted under the purview of the Carbon Utilization and Storage Partnership (CUSP; U.S. Department of Energy Award DE-FE0031837) to assess the potential for industrial-scale geologic carbon sequestration in a nearby basin. The approximately 180-km² study area within the Neck of the Escalante Desert comprises north-northeast-trending basement-cored horst and graben structures that juxtapose thick sequences of Paleozoic and Mesozoic sedimentary strata and extensive Eocene and younger volcanics, all of which have been heavily faulted and sometimes cross-cut and intruded by Miocene-age plutonism. This structural complexity, combined with a lack of data from few local well penetrations, meant significant uncertainty for geological risk elements like reservoir and seal quality and a subsurface characterization study was framed to determine the favorability of local subsurface conditions for geological carbon storage and create reliable data for quantitative reservoir modeling. Our multidisciplinary workflow integrated new and existing geological and geophysical control points including reprocessed 2D seismic lines, newly acquired terrestrial gravity surveys with refined inter-station spacing, petrographic data from local and regional outcrop exposures representing a range of depositional realms and diagenetic conditions, and geophysical logs, core and cuttings from three nearby petroleum exploration wells, particularly the 1984 ARCO Three Peaks #1 (ATP-1) well. The primary reservoir targeted for CO2 injection is the approximately 1,500-foot-thick Jurassic Navajo Sandstone that lies entirely in the subsurface locally at a mean depth of 7,000 feet below ground. In the ATP-1 well, the Navajo Sandstone is overlain by multiple sealing units including anhydrite-carbonate beds in the Manganese Wash Member of the

Jurassic Temple Cap Formation and gypsiferous shale and limestone of the Co-Op Creek Member of the Carmel Formation. These sealing units were intruded during the Oligocene-Miocene (ca. 22 Ma) by the Three Peaks quartz monzonite laccolith, creating a complex volcano-stratigraphic caprock. Metasomatic fluids generated during laccolith development likely precipitated pore-occluding CaCO3 and CaSO4 in the uppermost Navajo Sandstone after filtering through anhydrite-carbonate beds in the Manganese Wash Member and overpressure created during laccolith development created several crosscutting, healed calcite-filled fracture sets in the Carmel Formation. Yet despite a range of complex conditions where diagenetic events impacted highly favorable native rock properties, numerical reservoir models indicate that available pore space in the Navajo Sandstone may sufficiently accommodate the volumes of CO2 byproducts expected from the planned DRI plant. This study demonstrates how practical reservoir characterization can improve geologic carbon storage models that require a detailed understanding of the extent, architecture, and inherent rock properties of subsurface strata, even in data-poor environments.

Evaluate Well Logs and Cuttings from Nearby Wells and Determine High-Level Reservoir and Seal Properties

The ARCO Three Peaks #1 well provided the primary subsurface control for the Iron Mountain project. UGS compiled and interpreted digital logs, organized cuttings from the full depth range, and integrated existing core from key intervals in the Carmel and Kaibab formations. Stratigraphic interpretation from this well was carried into Petrel and served as the backbone for the geological model.

To complement the ARCO well, UGS identified an additional analogue well (Delta Federal 23-44) in the Parowan Gap region, whose cuttings and logs provide constraints on the lateral variability of the stratigraphy and rock properties near the project area. Cuttings and core materials from the ARCO well—particularly from the Carmel Formation and the target depth range for storage and seal units—were distributed to UU and OGS/IC3 for petrophysical and geomechanical testing.

By early 2024 the project reported Subtask 2.1 as complete: the evaluation of well logs and cuttings had defined high-level reservoir and seal properties, identified key reservoir and seal intervals, and provided calibrated 1D property profiles for use in the geological model.

Evaluate Seal Properties of Nearby Outcrop (e.g., Lithology, Porosity, Permeability, Etc.), Including the Jurassic and Cretaceous Seal Rocks, and Igneous Intrusive Bodies

Outcrop analogs around Cedar City and Parowan Gap were used to characterize both reservoir and seal units and to provide physical samples for laboratory testing.

UGS conducted multiple field campaigns to collect oriented core plugs and hand samples from the Navajo Sandstone, Carmel Formation, Temple Cap Formation, and the Three Peaks quartz monzonite. Navajo samples included both typical high-quality eolian sandstone and a “siltier” facies (NAV-6) to represent lower-permeability reservoir or baffle units. Temple Cap samples were chosen from evaporite-rich layers that may act as caprock or intra-formational seals. The Three Peaks quartz monzonite samples were collected at and away from its contact with Carmel,

targeting both the intrusive body and contact aureole. These samples were prepared as both 1-inch oriented core plugs and thin sections to support integrated petrographic, petrophysical, and mechanical analyses.

Thin section production was contracted to a commercial lab for both outcrop samples and ARCO cuttings from the formations of interest. The resulting sections were split between UGS and OGS/IC3 for petrographic analysis, which identified lithofacies, diagenetic features, and mineral assemblages controlling porosity, permeability, and sealing potential. UGS used these petrographic results combined with outcrop observations to refine facies interpretations that feed into the facies and property modeling components of the geological model.

At OGS/IC3, seal and reservoir samples were subjected to a systematic laboratory program that included Fourier-transform infrared (FTIR) mineralogical assessment, helium-expansion porosity, NMR porosity and pore-size distributions, and mercury intrusion capillary pressure or analogous pore-throat characterization to estimate capillary entry pressures, tortuosity, and diffusivity. Nanoindentation experiments provided localized Young's modulus and hardness for seal units, while scanning electron microscopy documented microstructural controls on sealing behavior. A subset of seal samples was exposed to supercritical CO_2 for periods of several weeks to evaluate potential chemo-mechanical degradation, with pre- and post-exposure properties compared.

In parallel, UU's rock mechanics laboratory conducted triaxial tests on Carmel and Navajo samples under different fluid conditions (dry, nitrogen-saturated, and planned brine and CO_2-saturated states) to determine strength and failure envelopes and to evaluate the effect of pore fluid composition on mechanical behavior. Mechanical problems with the triaxial apparatus delayed some planned tests, but the sample suite and experimental design for both reservoir and seal units were in place by the end of the project period.

Taken together, these efforts produced a rich dataset of reservoir and seal properties—porosity, permeability proxies, capillary behavior, elastic moduli, and microstructure—for use in the geological model, dynamic simulations, and risk assessment.

Evaluate Storage Potential/Reservoir Properties in Nearby Outcrops and Core – Navajo Sandstone and Kaibab Limestone

The work under this sub-task is reported in the previous section above, Sub-Task 2.2.

Gather Legacy Gravity Data and Collect New Gravity Data to Define Subsurface Characteristics and Tie to Seismic and Well Data

To better constrain the geometry of the Three Peaks laccolith and the broader basin structure, UGS acquired and processed new ground gravity data in the Iron Mountain region. Fieldwork added 25 new stations in late 2022, bringing the total dataset to more than 200 gravity measurements. These were merged with existing regional data and aeromagnetic information to generate complete Bouguer anomaly maps, horizontal gradient maps, and inversion models of the laccolith body (**Figure 104**).

By mid 2024, UGS had compiled these products into an ArcPro layer package for the project, including station locations, regional and detailed grids, and contour maps. These products inform

the structural framework of the geological model by constraining the depth and extent of the intrusive body, as well as highlighting density contrasts that may be associated with major fault zones and basin geometry.

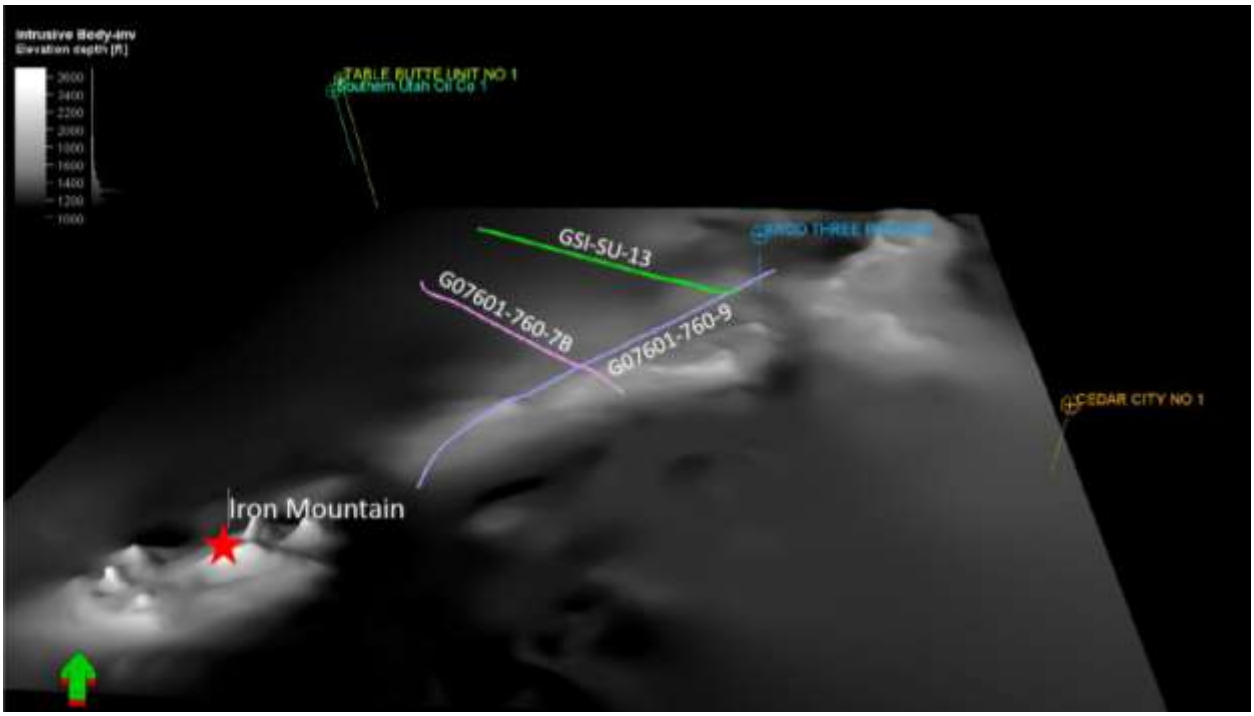


Figure 104 Volcanic intrusive body

Characterization of Faults and Fractures Relevant to Seal Integrity and Lateral Compartmentalization

Legacy 2D seismic lines in the Iron Mountain area were reinterpreted and reprocessed to support the structural component of the geological model and to inform fault-related risk assessments.

OGS interpreted three 2D time-domain seismic sections tied to the ARCO Three Peaks #1 well. Key reflectors corresponding to the Carmel, Navajo, and Kaibab formations were identified, and a time–depth relationship was developed using the well log–based velocity information. This work produced preliminary formation tops and highlighted areas of structural complexity, especially northwest of the main area of interest.

LANL, after gaining access to the Echos processing system under the negotiated NDA, investigated and adapted the original seismic processing flow and developed new velocity models suitable for prestack depth migration. Reverse-time migration (RTM) was applied to selected lines, significantly improving imaging quality in areas with complex structure.

On these RTM images LANL deployed a nested residual U-Net deep learning workflow for automatic fault detection. The method successfully mapped faults on key lines and was subsequently extended with a new architecture capable of detecting high-angle as well as low- and variable-angle faults. This allowed a more comprehensive mapping of the local fault

network, including elements associated with the Neck of the Desert and Antelope Range fault systems.

Fault and fracture characterization at the surface, led by UGS, included analysis of LiDAR-derived fault traces and field observations that documented Quaternary normal faults trending across the region. These data were integrated with seismic interpretations to identify structures that might intersect the intended storage interval. By early 2024, Subtask 2.5 Characterization of faults and fractures relevant to seal integrity and lateral compartmentalization, was reported as complete.

As site characterization transitioned from data acquisition to synthesis, UGS began assembling a comprehensive Open File Report that integrates well, outcrop, gravity, aeromagnetic, and seismic interpretation into a coherent description of the Iron Mountain storage complex. Drafting of this report, and coordination of contributions from UU, OGS, and LANL, was a major focus of UGS activities in the final year.

Modeling and Simulation

The modeling and simulation work was carried out by UU, UGS, LANL, and OGS. UGS performed the seismic well tie work (Task 3.1) and OGS interpreted the three 2-D seismic lines (Task 3.2). Then using data provided by UGS and OGS, UU and OGS developed the geologic model (Task 3.2). Utah Iron provided the CO_2 quality and quantity (Task 3.3). The UU then performed the CO_2 storage assessment (Task 3.4), developed the numerical simulation model and performed the dynamic simulations (Task 3.5), and AoR modeling (Task 3.6).

Seismic Well Tie with the Arco Three Peaks #1 Well, Velocity Model Construction, and Seismic Evaluation and Interpretation

Seismic Well Tie by UGS for Static Model Construction

A time–depth conversion was assembled using available sonic-log data and seismic velocities from the ARCO Three Peaks #1 well. Three 2D seismic lines (G07601-760-7B, G07601-760-9, and GSI-SU-13) were purchased from SEI Seismic Exchange, Inc. that provided raw, processed, and enhanced post stack migration dataset formats per 2D line. Enhanced stack migration format contained best visual quality for comparing picked formation tops interpreted from Van Kooten (1988) along the SW-NE trending seismic line G07601-760-9 adjacent to the nearby ARCO Three Peaks #1 well. Geophysical logs (density, sonic, and gamma), as well as formation tops at depth, from the ARCO Three Peaks #1 well and TWT amplitude horizons provided by Van Kooten (1988), allowed for creation of a synthetic checkshot associated with the well. The primary formation tops used for generating a reliable interval velocity alignment at depth and time were the top of the Three-Peaks monzonite laccolith, Carmel, Navajo Sandstone, Kaibab, and Redwall Limestone formations. Proceeding wavelet calibration from density and sonic logs and formation tops, a coherent velocity model was created for time-depth conversion for further interpretations and sequential forward reservoir modeling.

This depth migrated data was then given to the OGS for seismic horizon interpretation (subtask 3.1.2) and LANL for fault identification (subtask 3.1.3). Figure 105 shows the three seismic lines in time.

2D Seismic Line Evaluation and Horizon Interpretation

OGS used the time-migrated 2D seismic sections from subtask 3.1.1 and the ARCO Three Peaks #1 well to interpret the following formation horizons; the Three Peaks monzonite laccolith, Carmel, Navajo Sandstone, Kayenta, Moenave, Chinle, Moenkopi, Kaibab limestone, and Redwall Limestone formations. Seismic lines G07601-760-9 and G07601-7B showed good reflectors across the lines for each of these formations. Seismic line GSI-SU-13 showed poor resolution across most of the western portion of the line, with only the area intersecting Go7601-760-9 having easily picked horizons. This could be due to a combination of factors, including poor acquisition parameters and/or structural complexity possibly related to the laccolith intrusion. Seismic horizons away from the intersection with G07601-760-9 were interpreted with lower confidence with some horizons, such as the Carmel, not being able to be discerned. **Figure 105** shows the three seismic lines in time and interpreted seismic horizons.

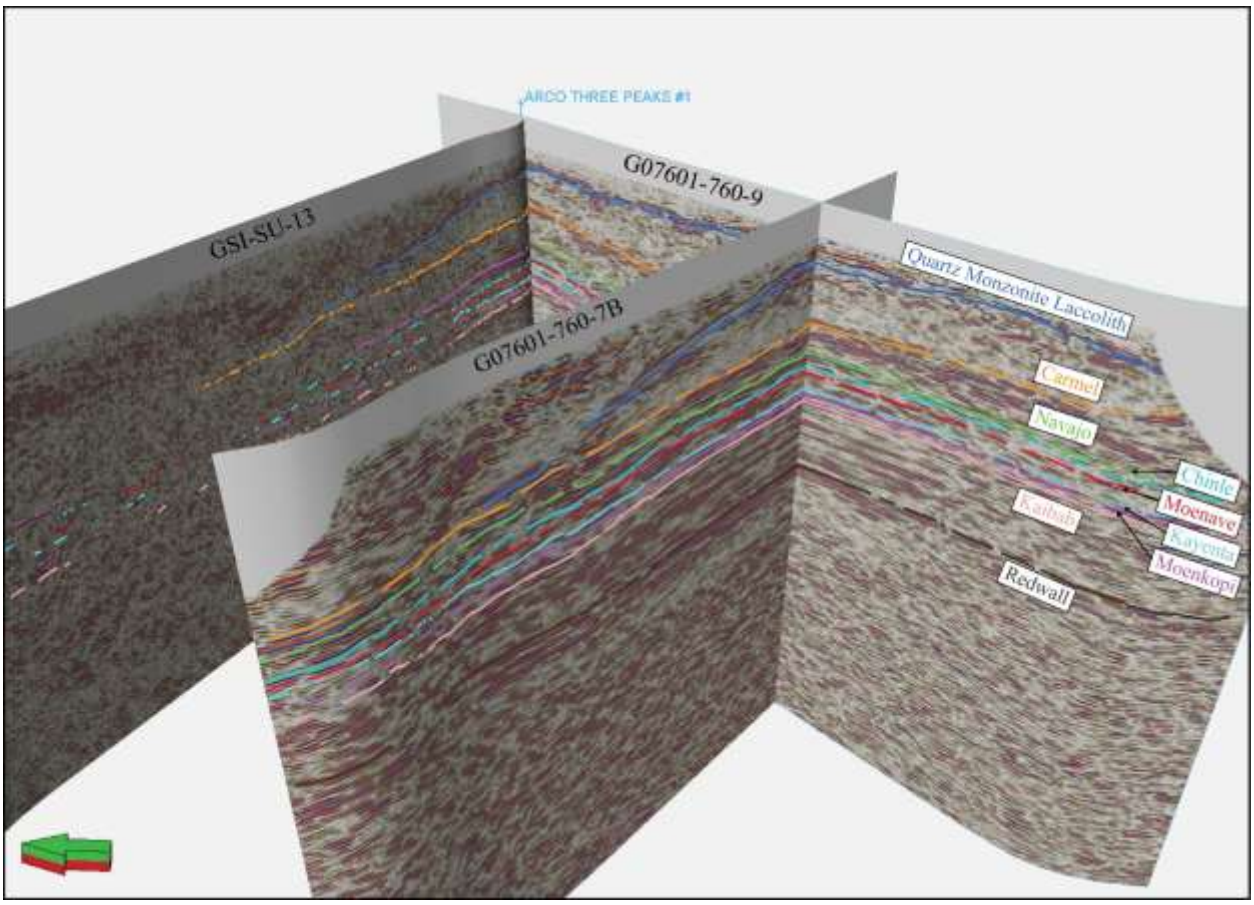


Figure 105 Three seismic lines in time at 5x vertical exaggeration showing the interpreted surfaces

Formation surfaces were then generated for each interpreted 2D seismic horizon shown in Figure 105 and converted from time to depth using the velocity model. Seismic resolution was not sufficient to confidently identify and map faults. No obvious faults were observed on lines G07601-760-9 and G07601-760-7B, and the overall data quality of line GSI-SU-13 was too poor to support reliable fault interpretation. In addition, because LANL did not complete their fault evaluation prior to the project end date, a fault framework was not developed, and faults were not

incorporated into the 3D geologic model. See Figure 106 for the formation surfaces in depth used to construct the geological model.

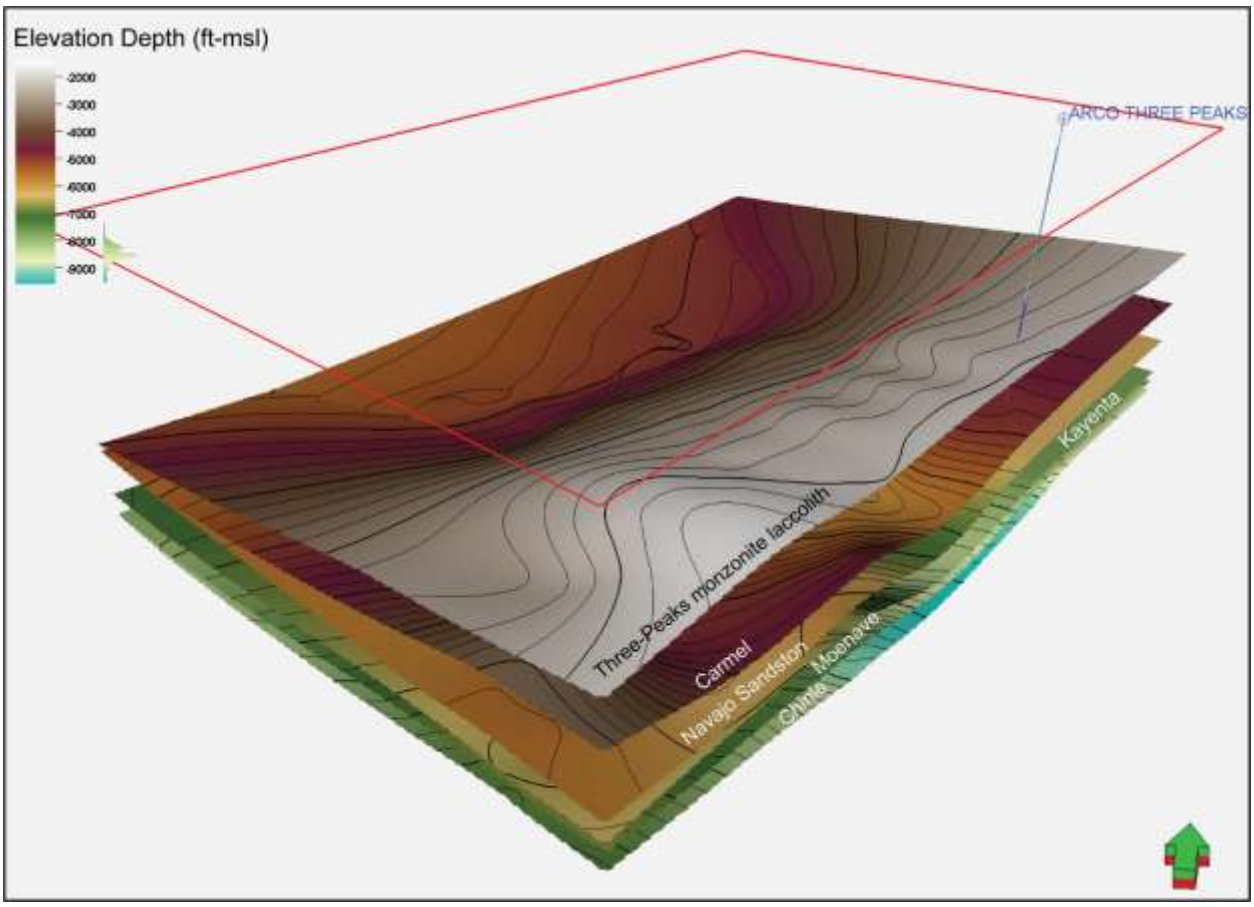


Figure 106 Formations used to construct the 3D geological model in depth

Velocity Modeling and Fault Evaluation by LANL

Subsurface structure imaging and fault detection are essential for site characterization and risk assessment in geologic carbon storage. In this study, we use 2D surface seismic data acquired at Iron Mountain, Utah, USA, to characterize subsurface structures. The data were collected with vibroseis sources along three 2D walkaway lines, with a source spacing of approximately 91 m, receiver spacing of about 45 m, and line lengths ranging from 9 to 15 km. We analyze two of these lines, Line 7B and Line 9, to construct 2D velocity models using first-arrival travel time tomography and pre-stack depth migration velocity analysis (MVA). Reverse-time migration with the MVA-updated velocity models produces high-resolution images of the subsurface, and a machine learning algorithm is subsequently applied to delineate faults in the migration results. These analyses provide critical insights into the subsurface structures and support the assessment of geologic carbon storage feasibility at Iron Mountain.

Introduction

To mitigate anthropogenic CO_2 emissions, researchers are focusing on decarbonizing heavy industries such as iron production. In conventional processes, iron is refined by reacting iron ore,

which contains iron oxides (Fe_2O_3), with carbon monoxide (CO) to yield pure iron and carbon dioxide (CO_2). Traditionally, CO is generated by burning coal in a low-oxygen environment or within a blast furnace. However, this method releases significant amounts of greenhouse gases and other pollutants into the atmosphere.

In contrast, the direct reduced iron (DRI) process refines iron by reacting iron ore in a reactor vessel with synthesis gas (syngas), a mixture of CO and hydrogen (H_2), produced through the catalytic reforming of methane (CH_4) rather than the combustion of coal. In DRI, iron ore reacts with CO and H_2 to produce pure iron, CO_2, and water (Battelle et al. 2024). The resulting CO_2 stream is relatively pure and can be dried and either utilized for industrial applications or permanently stored through geological carbon sequestration.

To evaluate a potential site for carbon capture and storage (CCS) associated with direct reduced iron (DRI) production, we characterized the subsurface of a proposed DRI plant in southern Utah using legacy seismic data acquired in the 1980s. The prospective DRI-CCS field is located in the Iron Springs District in the southwestern part of Utah. A geologic map of the area, modified from Blank and Mackin (1967), is presented in Figure 107.

The target formation for CO_2 sequestration is the Navajo Sandstone, a Jurassic-aged, porous sandstone situated at a depth of approximately 1,890 m (6,200 ft) below the surface. Preliminary studies suggest that this formation has the capacity to store at least 15 million tons of CO_2 (Moodie et al. 2022). The Navajo Sandstone is overlain by several potential caprock formations, including the Jurassic Temple Formation, composed primarily of evaporites, and the Jurassic Carmel Formation, which consists of mudstones and limestones.

In certain areas of the site, outlined by the red dashed line in Figure 107, the Jurassic Carmel Formation is intruded by several hundred meters of quartz monzonite laccolith (Rowley and Barker 1978; van Kooten 1988). A geologic cross-section illustrating these formations is shown in **Figure 108**.

To assess the feasibility of carbon capture and storage (CCS) for direct reduced iron (DRI) production in this region, we analyzed 2D legacy active seismic land data acquired along two walkaway lines (shown as red and blue lines in **Figure 107**) to characterize subsurface structures. An initial layered velocity model was constructed by applying a median filter to the sonic slowness log obtained from the Arco Three Peaks #1 well, located at the northernmost green circle in **Figure 107**.

First-arrival traveltime tomography (Leung and Qian 2006; Taillander et al. 2009; Fomel et al. 2009; Tong 2021) was then applied using the first arrival times of P-waves to refine the shallow portions (less than 1 km) of the P-wave velocity (Vp) model. Migration velocity analysis (MVA; Liu and Bleistein 1995) was subsequently used to update the deeper sections of the model.

After obtaining the MVA-updated Vp models, reverse-time migration (RTM; McMechan 1983; Fei et al 2015) was employed to produce pre-stack depth migration images of the subsurface. Finally, a machine learning algorithm (Gao 2024) was applied to reduce noise, enhance image resolution, and automatically detect faults within the migration images.

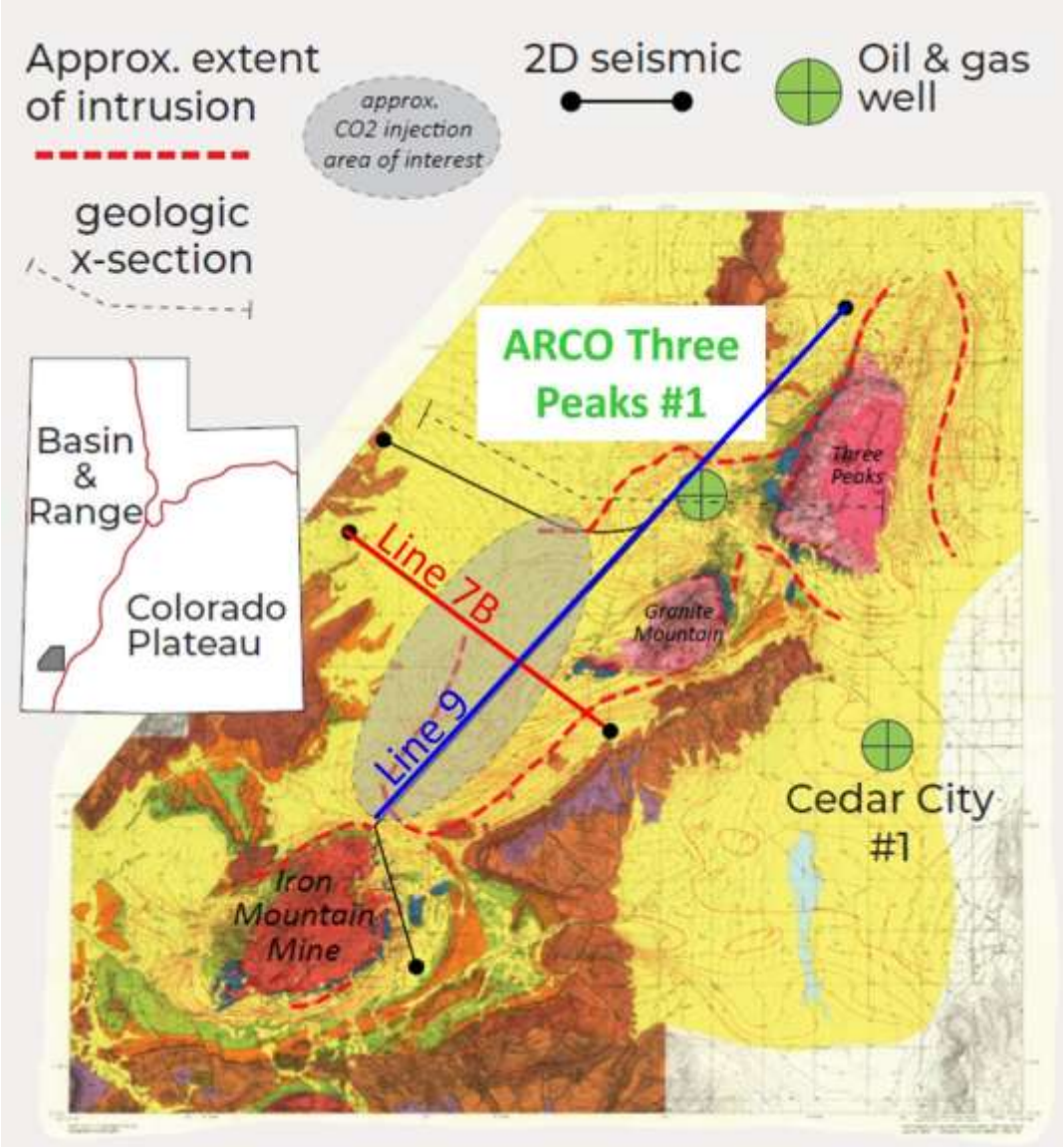


Figure 107 Geologic map of Iron Mountain, Utah, showing Seismic Line 7B (red) and Line 9 (blue). Green dots indicate wells drilled in the region, and the gray ellipse marks the CO_2 injection area of interest. Modified from Blank and Mackin (1967).

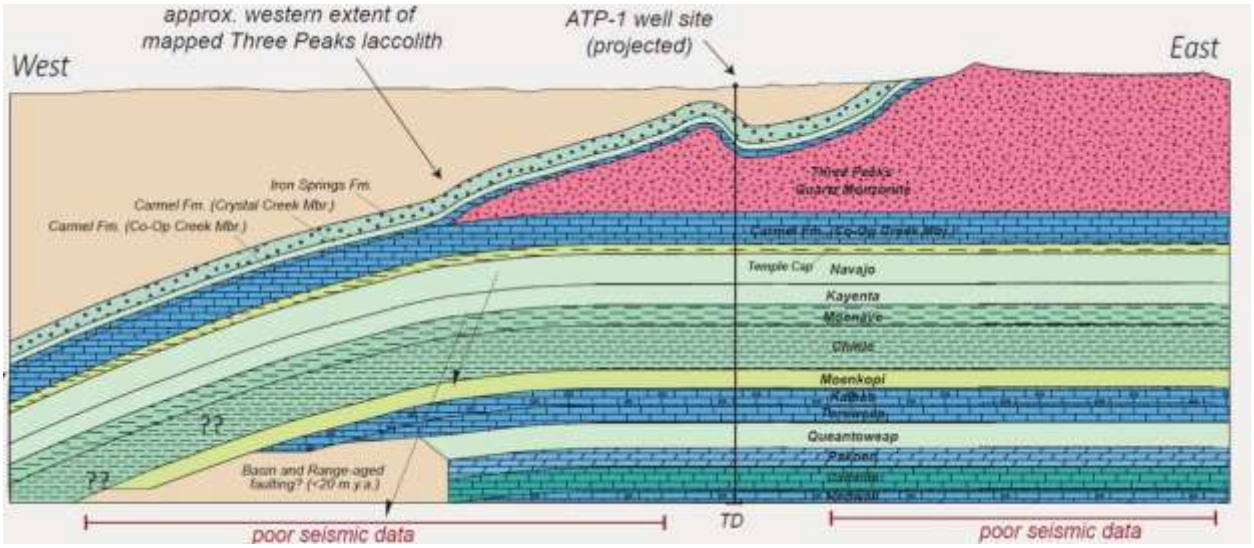


Figure 108 Geologic cross-section from west to east across the Iron Mountain area showing the Jurassic Navajo Sandstone reservoir layer, the Temple Formation caprock, the Carmel Formation, and the quartz monzonite intrusion. Modified from Moodie et al. 2022.

Legacy 2D Seismic Data Acquisition and Processing

The 2D legacy seismic data were acquired at Iron Mountain, Utah, along three walkaway lines: 7B, 9, and 13. For this study, only Lines 7B and 9 were analyzed because the data quality for Line 13 was extremely poor, preventing the extraction of any meaningful information. The limitations of Line 13 will be discussed further in the discussion section. The geometries of Lines 7B and 9 are shown in **Figure 109**.

The linear portion of Line 7B (red line) trends northwest–southeast and includes 118 common-shot gathers, while Line 9 (blue line) trends southwest–northeast and includes approximately 183 shots. For each common-shot gather, up to 96 receiver channels were used for data acquisition. The shot spacing was approximately 91 m, and the receiver spacing was about 45 m. The data were sampled at a 2 ms interval, with a total recording time of 3 s.

Following standard preprocessing procedures (Yilmaz 2001), automatic gain control was applied to attenuate ground roll noise, and a band-pass filter of 3–8–20–25 Hz was used to suppress high-frequency noise. Two processed mid-spread common-shot gathers from Lines 7B and 9 are shown in **Figure 110**. After pre-processing, P-wave velocity (Vp) models were constructed for pre-stack depth migration.

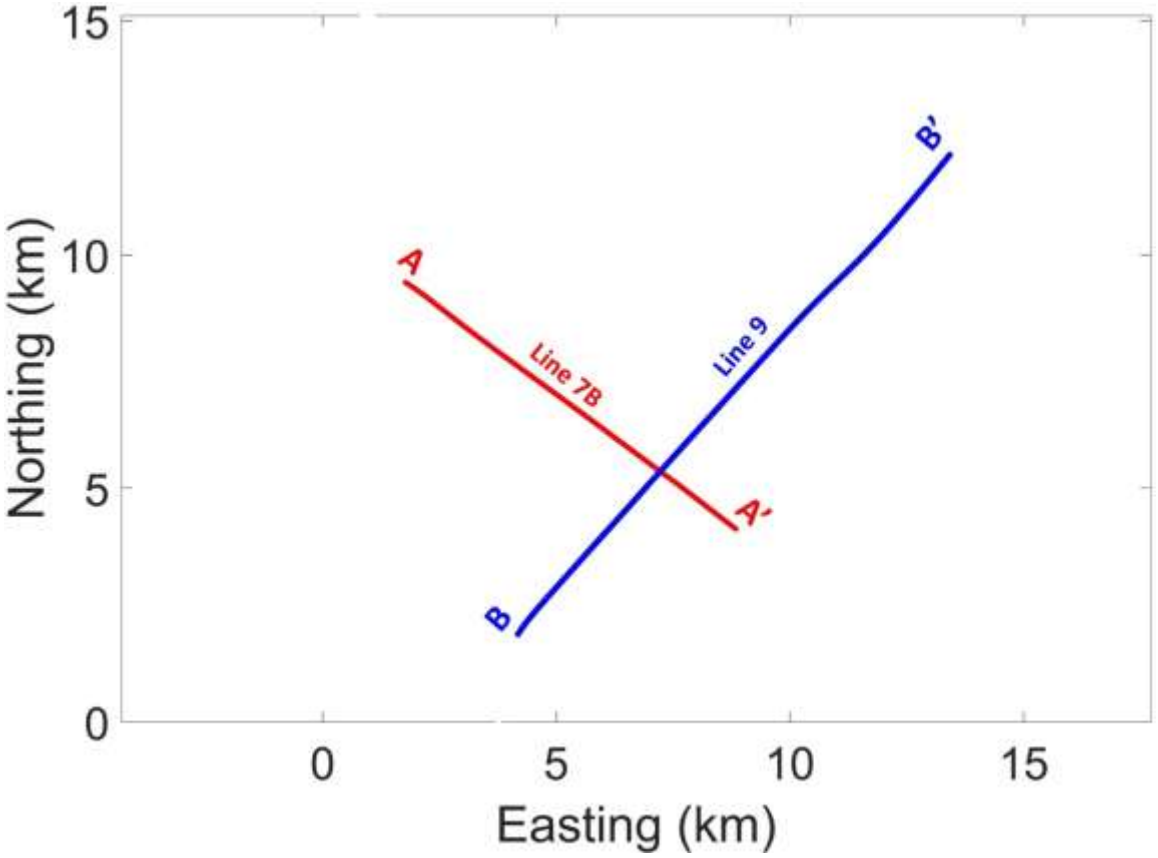


Figure 109 Map showing the location of Line 7B (red) extending from A to A′ and Line 9 (blue) extending from B to B′

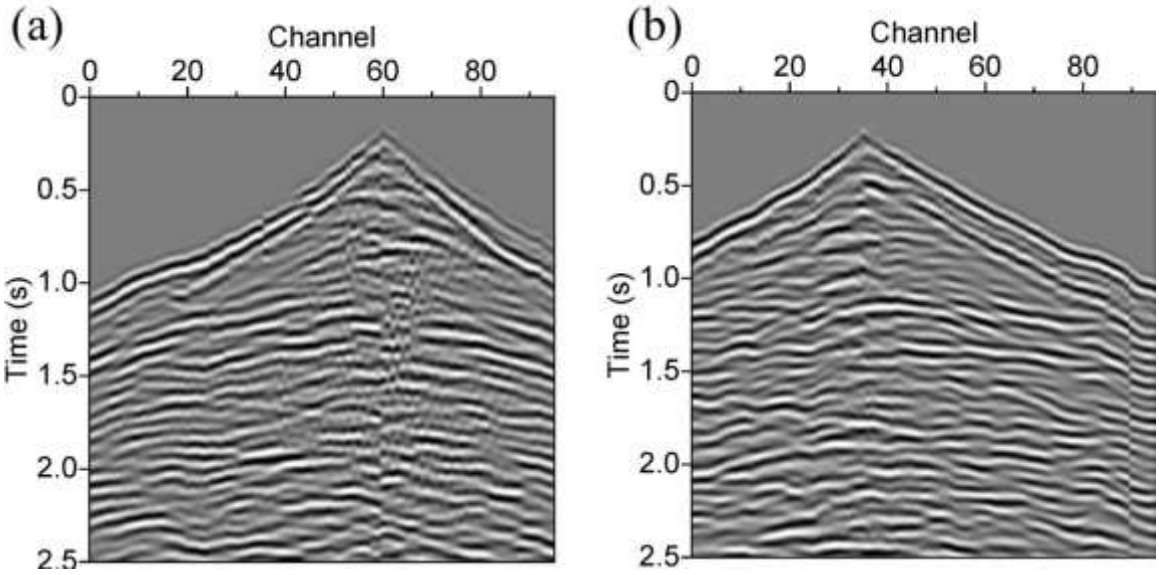


Figure 110 Two mid-spread common-shot gathers for (a) Line 7B and (b) Line 9 after applying automatic gain control and band-pass filtering from 3–8–20–25 Hz

Velocity Model Building

To construct the P-wave velocity (Vp) models for migration imaging using the legacy 2D surface seismic data at Iron Mountain, we first developed an initial layered velocity model based on sonic well log data from the Arco Three Peaks #1 well and interpreted formation boundaries. The shallow portions of the Vp model along each 2D walkaway line were then refined using first-arrival traveltime tomography (FATT). Following the FATT update, we performed pre-stack Kirchhoff depth migration and subsequently refined the deeper parts of the model through migration velocity analysis (MVA).

To build the initial layered velocity models, we began with well log data and interpreted formation boundaries from the Arco Three Peaks #1 well. The well logging data were acquired by Schlumberger in January 1985, covering measured depths from 16.46 m (54 ft) to 3,761.2 m (12,340 ft) at 0.1524 m (0.5 ft) intervals. A datum of 1,785 m was used for the velocity models and migration images, and the depths of the logging data were adjusted to account for elevation differences between the well and the seismic data reference. Median values were selected within layer intervals on the compression slowness log to derive the layered Vp velocity profiles. Constant velocity values were assigned to regions beyond the logged interval, and the resulting 1D velocity profile was used to build the layered initial models down to a depth of 4.5 km. The median velocity layers and corresponding sonic log velocities are shown in **Figure 111**, and the initial Vp models for each walkaway line are presented in **Figure 114**.

Traveltime tomography was then applied using the first arrivals of P-waves to refine the shallow portions of the velocity models. After 40 iterations, the traveltime misfit was reduced by more than 95% for both Lines 7B and 9. The convergence curves for relative misfit, along with histograms of traveltime misfits before and after tomography, are shown in **Figure 112** and **Figure 113**, respectively. The updated Vp models after FATT for Lines 7B and 9 are displayed in **Figure 115**, showing significant improvements in the shallow regions of the models (approximately the upper 1 km). These FATT models were then used for MVA.

Following the FATT updates, pre-stack Kirchhoff depth migration was performed along both walkaway lines using the FATT velocity models to produce pre-stack depth migration images. Horizons were interpreted from these images, and the velocities between horizons were adjusted by flattening reflection events on common-image gathers. The final Vp models after MVA are shown in **Figure 116**. These MVA-updated velocity models were subsequently used in reverse-time migration to generate high-resolution subsurface images of the structural features.

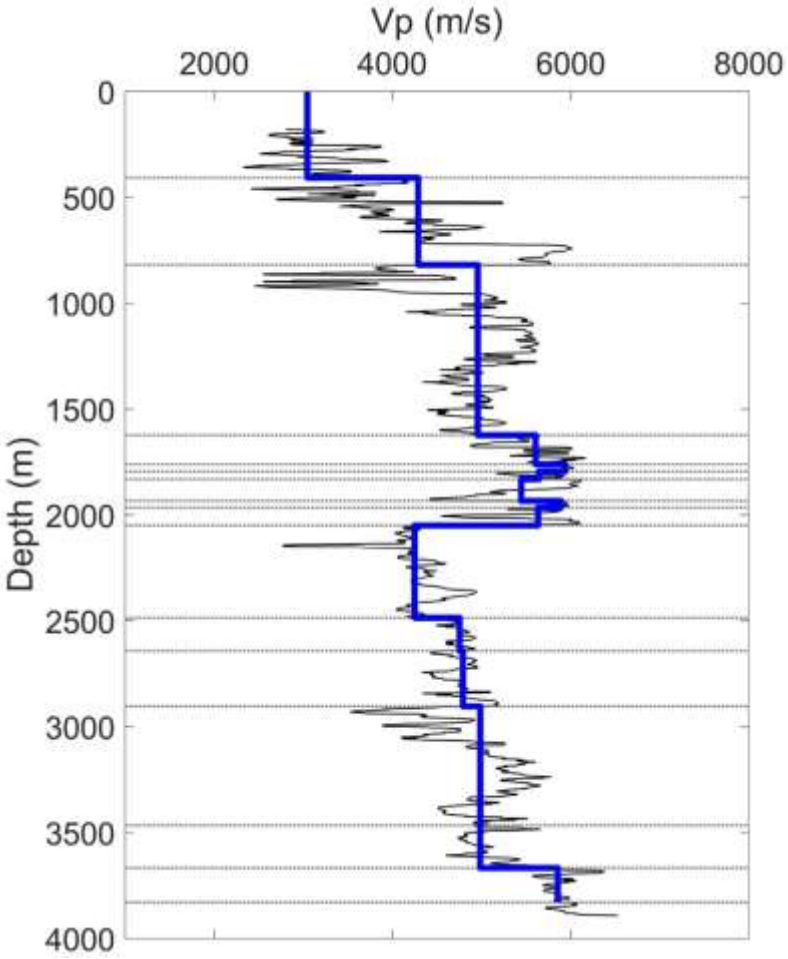


Figure 111 Velocity profile from sonic logging data (black) alongside median-filtered velocities between interpreted formation boundaries (blue). The median-filtered velocity is used to construct the initial velocity models for Line 7B and Line 9.

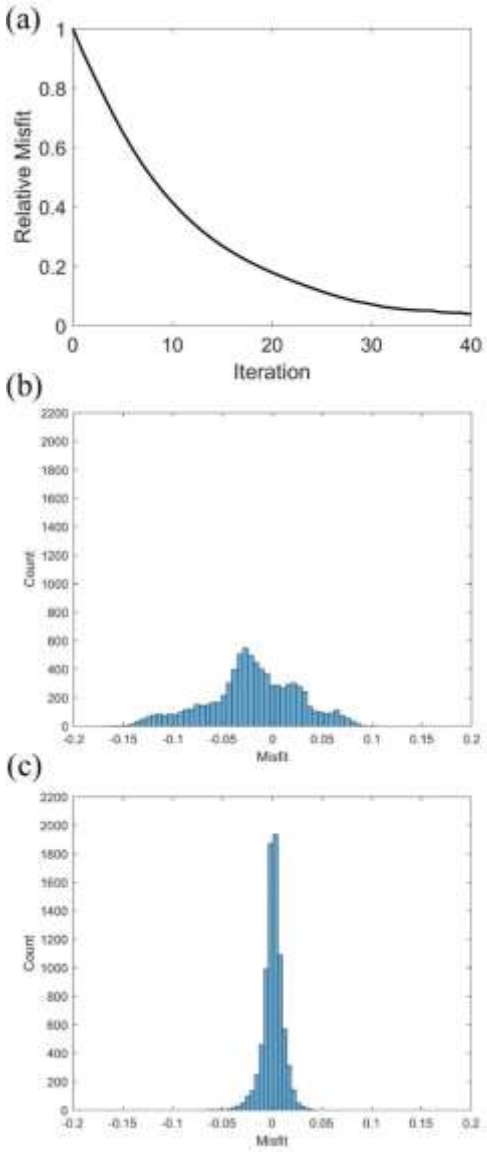


Figure 112 (a) Relative traveltime misfit convergence curve, (b) histogram of traveltime misfits before tomography, and (c) histogram of traveltime misfits after 40 iterations for Line 7B

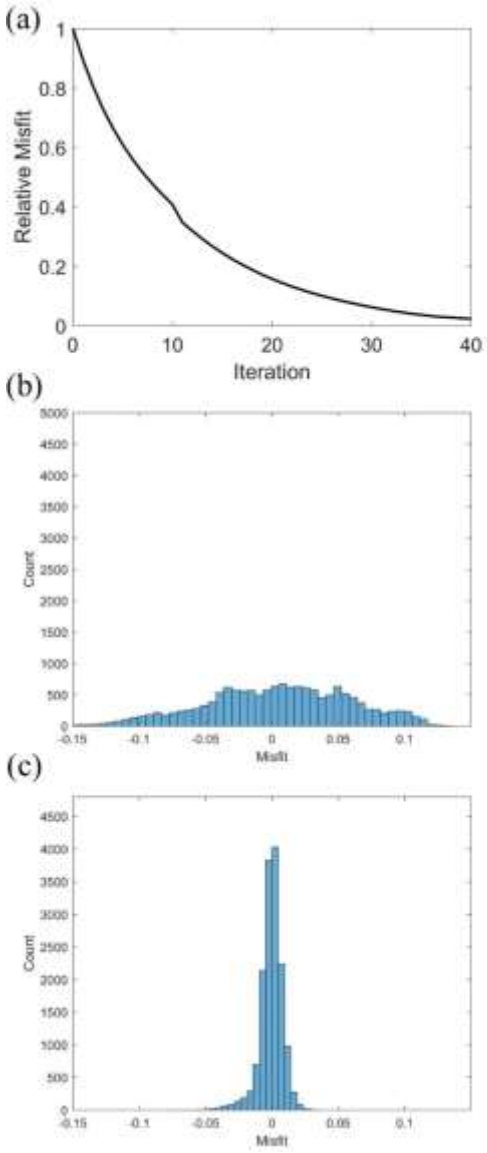


Figure 113 (a) Relative traveltime misfit convergence curve, (b) histogram of traveltime misfits before tomography, and (c) histogram of traveltime misfits after 40 iterations for Line 9

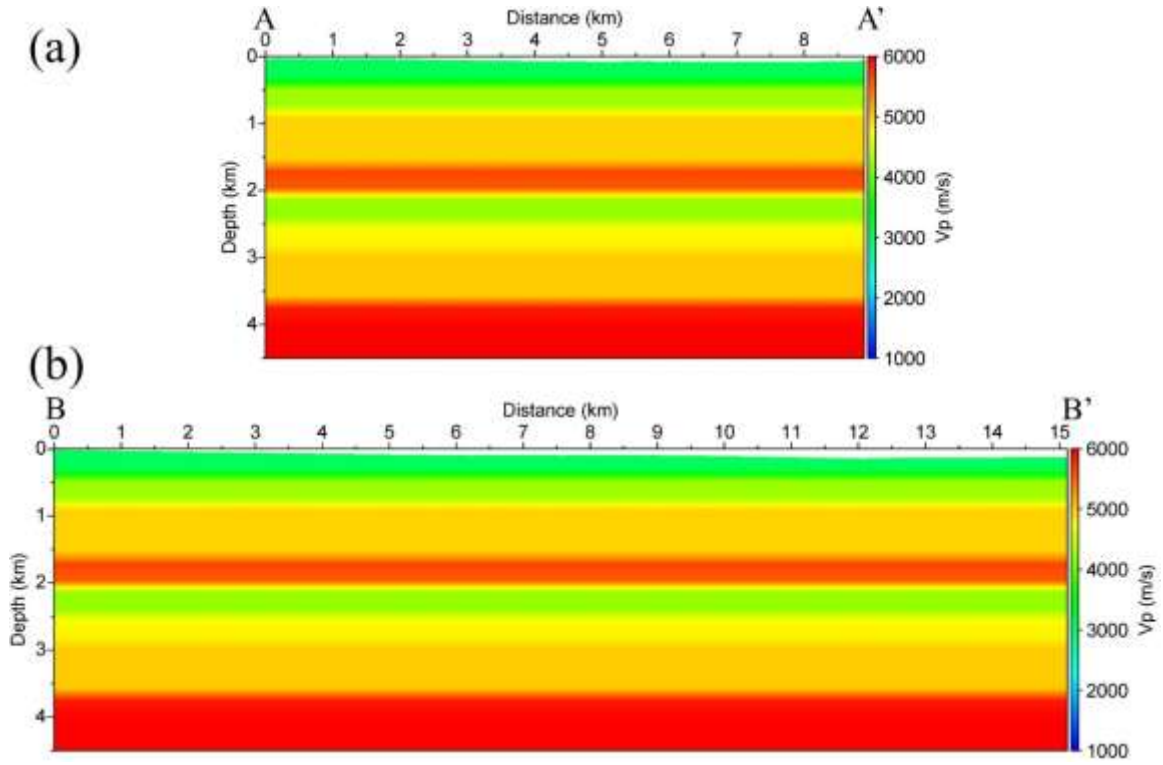


Figure 114 Initial layered P-wave velocity (Vp) model for (a) Line 7B extending from A to A′ and (b) Line 9 extending from B to B′

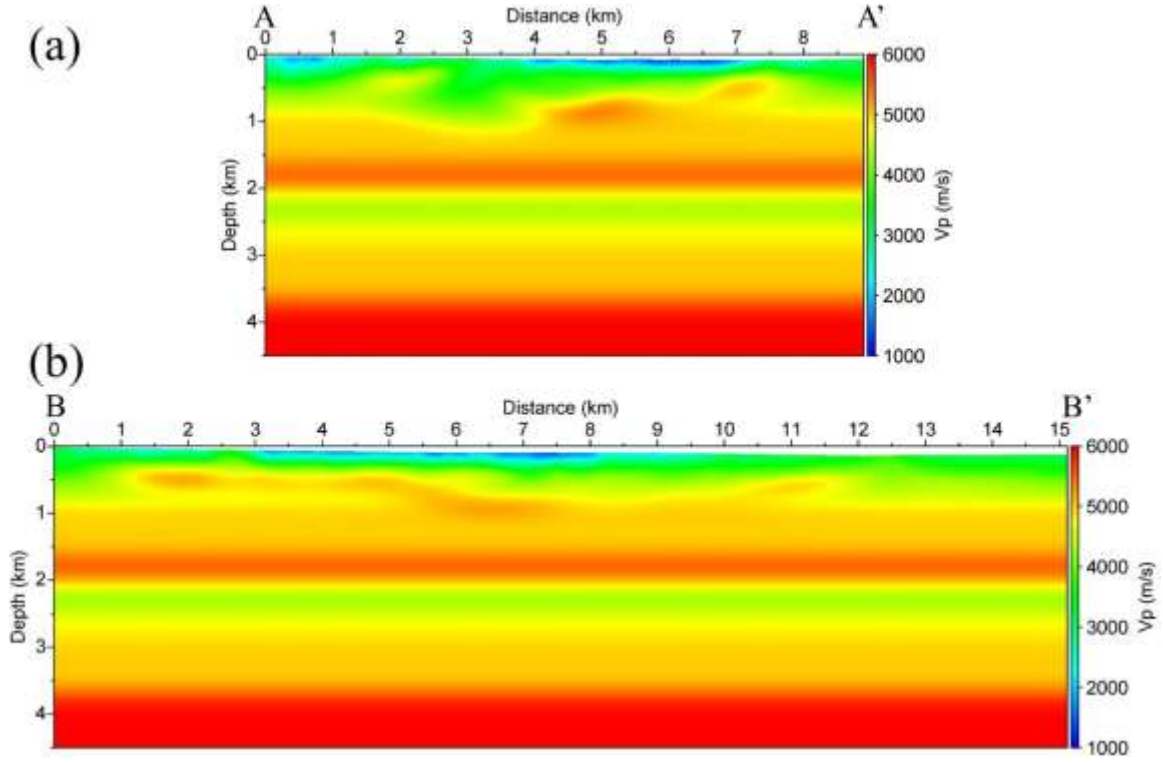


Figure 115 P-wave velocity (Vp) models after first-arrival traveltime tomography (FATT) for (a) Line 7B extending from A to A′ and (b) Line 9 extending from B to B′

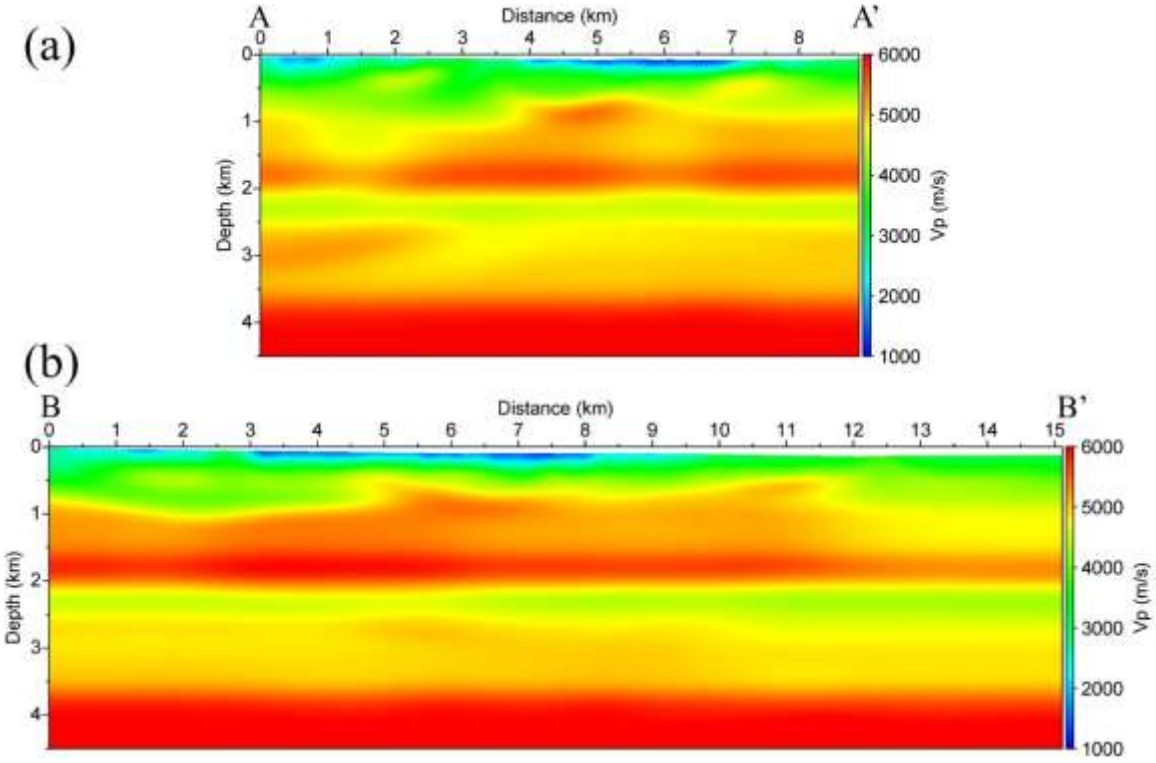


Figure 116 P-wave velocity (Vp) models after first-arrival traveltime tomography (FATT) and migration velocity analysis (MVA) for (a) Line 7B extending from A to A′ and (b) Line 9 extending from B to B′

Results of Reverse-Time Migration and Fault Detection

After constructing the velocity models using sonic logging data, first-arrival traveltime tomography (FATT), and migration velocity analysis (MVA), and processing the PP reflections, we applied reverse-time migration (RTM) to obtain high-resolution PP images of the subsurface structures beneath Iron Mountain. Each common-shot gather was migrated individually, and a spatial taper mask was applied to suppress migration artifacts resulting from limited source and receiver coverage. The raw PP RTM migration images for each line, generated using the MVA velocity models, are shown in **Figure 117**.

To further enhance the imaging results, we employed a multitask machine learning (ML) approach to denoise the RTM images, improve spatial resolution, and automatically detect faults. The ML-denoised RTM images for Lines 7B and 9 are shown in **Figure 118**. Compared to the raw RTM images, the denoised results reveal greater structural detail, with reflectors appearing more continuous and better defined, particularly along the edges of the profiles where the raw images exhibited smiling artifacts.

The ML-denoised RTM images with automatically detected faults are presented in **Figure 119**. These results indicate the presence of numerous high-angle faults distributed throughout the entire profiles of Lines 7B and 9, highlighting the complex structural framework of the subsurface in the Iron Mountain region.

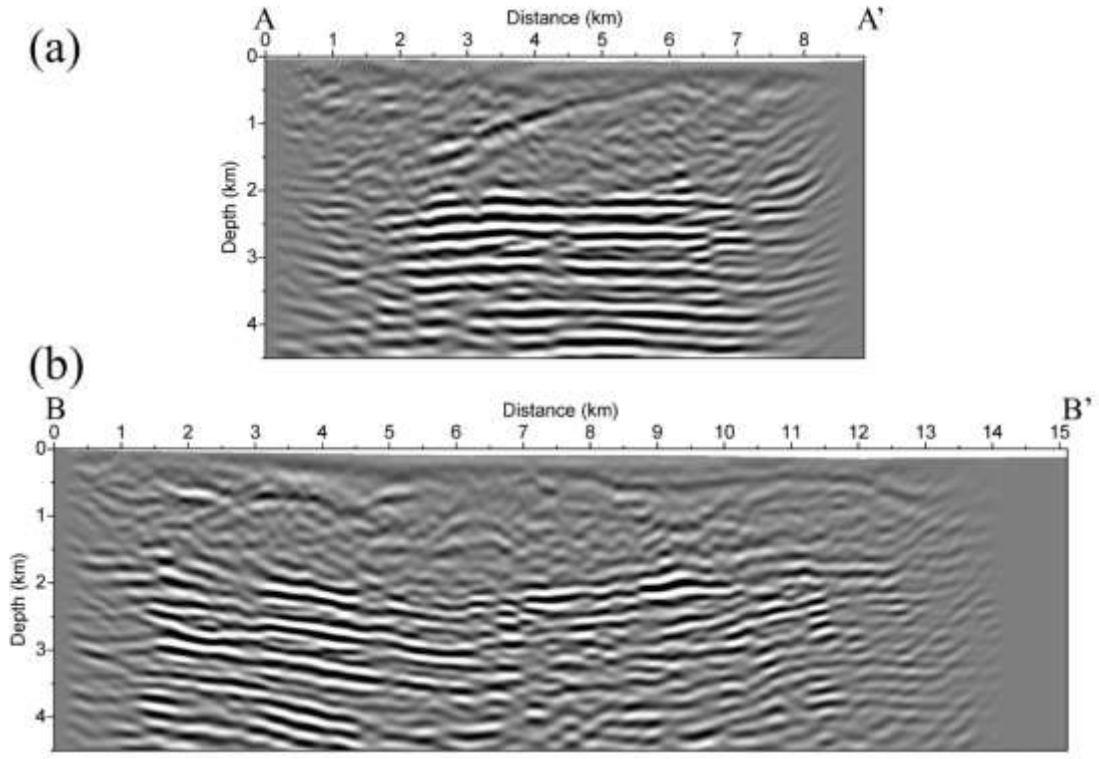


Figure 117 Raw reverse-time migration (RTM) images obtained using the migration velocity analysis (MVA) updated P-wave velocity (Vp) models for (a) Line 7B extending from A to A′ and (b) Line 9 extending from B to B′

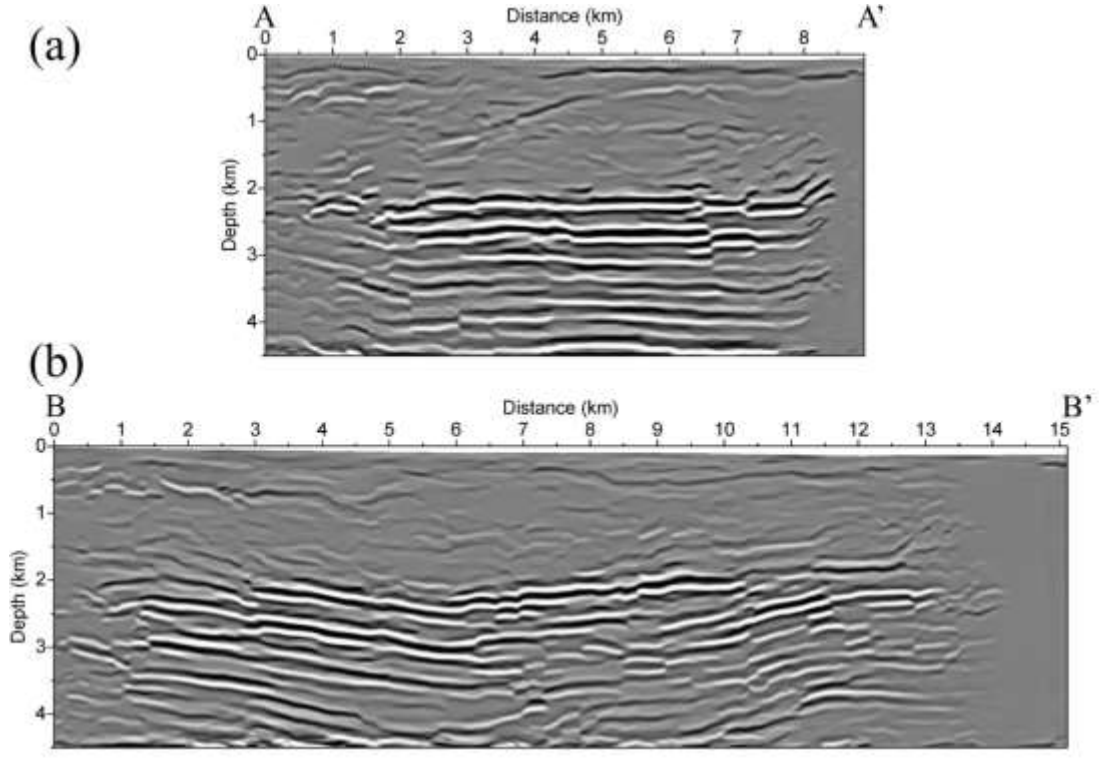


Figure 118 Reverse-time migration (RTM) images after machine learning (ML) denoising for (a) Line 7B extending from A to A′ and (b) Line 9 extending from B to B′

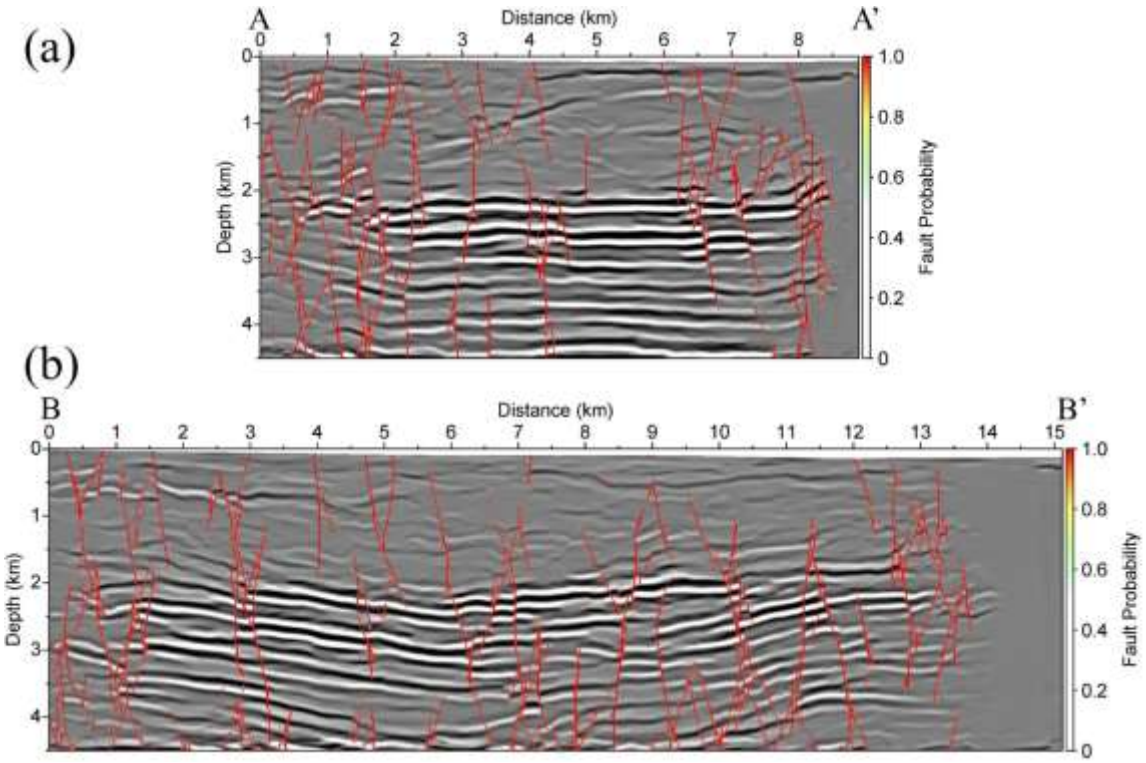


Figure 119 Machine learning (ML) denoised reverse-time migration (RTM) images with automatically detected faults shown in red for (a) Line 7B extending from A to A′ and (b) Line 9 extending from B to B′

Discussions

We overlaid the velocity models on the machine learning (ML) noise-removed migration images, as shown in **Figure 120**. From the figure, there is a strong correspondence between the velocity contrasts and the seismic reflectors. In **Figure 120**a, the edge of the high-velocity zone aligns closely with the dipping reflector observed at approximately 1.5 to 0.5 km depth and 2 to 7 km horizontal distance. This structure corresponds well with the quartz monzonite intrusion identified in the conceptual geologic cross-section (**Figure 108**). Furthermore, **Figure 120**a indicates that our migration velocity analysis successfully resolved the lower-velocity lithologies surrounding the quartz monzonite intrusion. The low-velocity region between 0 and 3 km horizontal distance and 1 and 2 km depth is clearly visible in the MVA-derived Vp model (**Figure 120**a), whereas it was not evident in either the initial layered Vp model (**Figure 114**a) or the FATT-updated model (**Figure 115**a).

The ML-denoised migration images for Lines 7B and 9 were plotted in 3D at different azimuthal viewpoints, as shown in **Figure 121**. From this figure, we observe good continuity and alignment of reflectors between Lines 7B and 9. Minor variations in reflector positions are likely due to slight differences in the velocity fields of the two lines, as each line was processed independently in 2D. For a more complete and accurate characterization of the subsurface structures and fault systems, a dedicated 3D seismic survey of the region is recommended.

As mentioned in previous sections, Line 13 was excluded from the main analysis due to poor data quality. A common-shot gather from Line 13 is shown in **Figure 122**. In contrast to the gathers from Lines 7B (**Figure 122**a) and 9 (**Figure 122**b), where distinct parabolic reflection

patterns are visible, no clear reflections are observed in the Line 13 data. Instead, the data are dominated by strong ringing noise. We attempted to remove this noise using Wiener deconvolution; however, this approach did not yield any usable signal.

First-arrival traveltime tomography (FATT) was performed using the first-arrival picks from Line 13 and the initial layered Vp model. Unlike the successful convergence observed for Lines 7B and 9, the FATT results for Line 13 did not converge satisfactorily. The relative convergence curve, along with traveltime misfit histograms before and after tomography, are shown in **Figure 123**. After FATT, the traveltime misfits for Lines 7B and 9 are centered near zero, while those for Line 13 exhibit a systematic bias toward negative misfit values, indicating poor model fitting.

Reverse-time migration (RTM) was applied to the processed Line 13 data using the FATT velocity model, and the resulting image is shown in **Figure 124**. Unlike the raw RTM images of Lines 7B and 9 (**Figure 117**), the RTM result for Line 13 shows no coherent reflectors corresponding to the major formations. As a result, we were unable to identify and pick any horizons to perform MVA for this line. Due to these limitations in data quality and processing, Line 13 was excluded from further analysis.

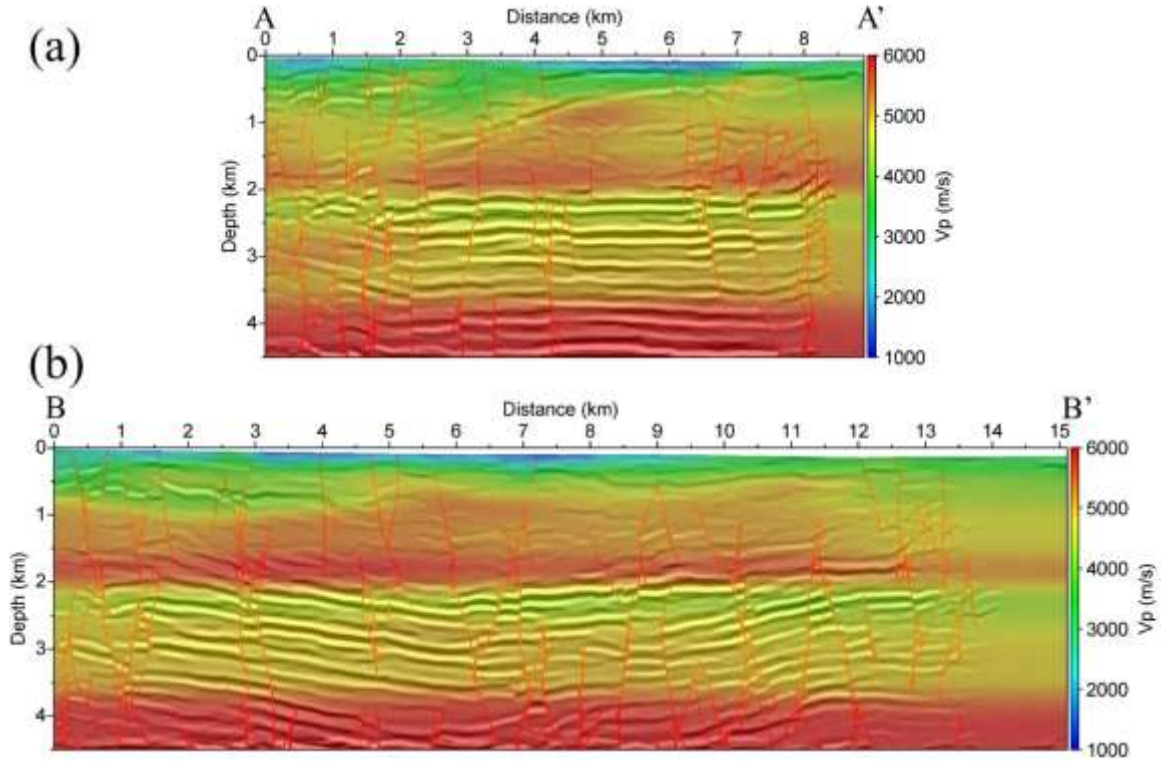


Figure 120 Machine learning (ML) denoised reverse-time migration (RTM) images with automatically detected faults (red) plotted alongside P-wave velocity (Vp) models for (a) Line 7B extending from A to A′ and (b) Line 9 extending from B to B′

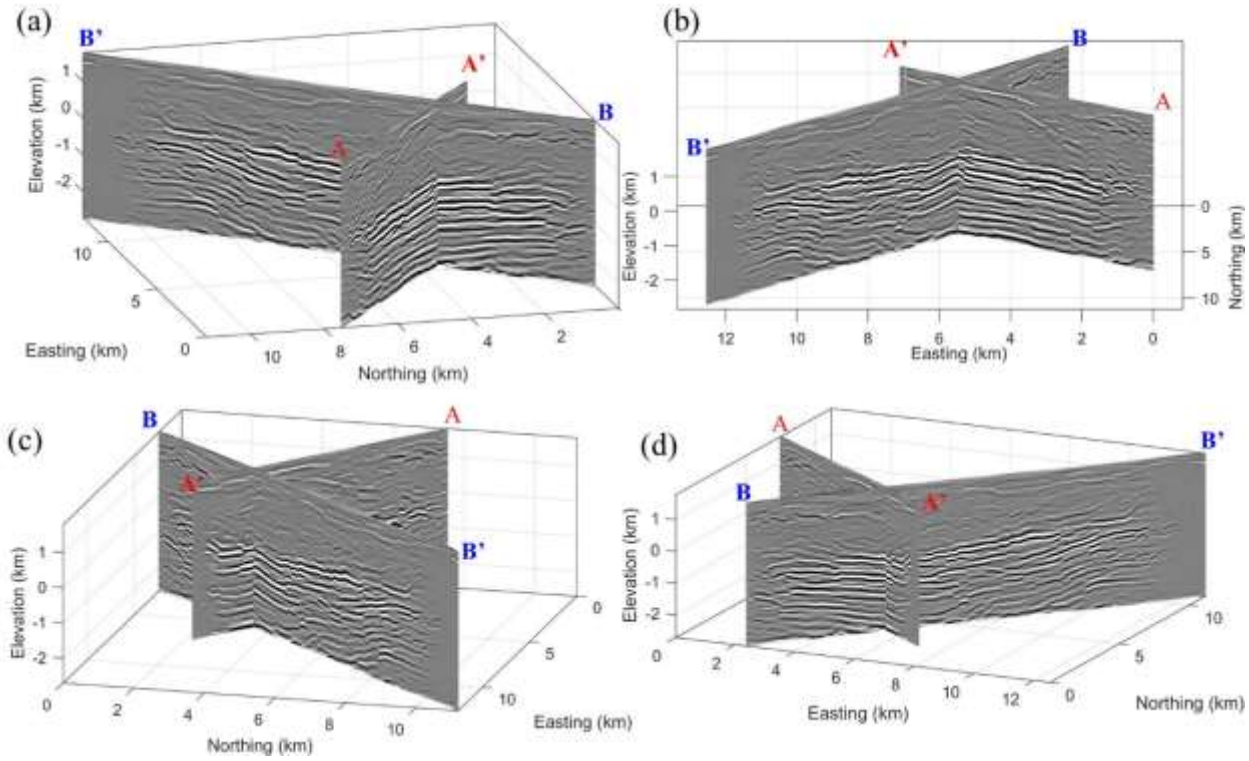


Figure 121 3D plot of migration images for Line 7B extending from A to A′ and Line 9 extending from B to B′, viewed from multiple azimuth angles

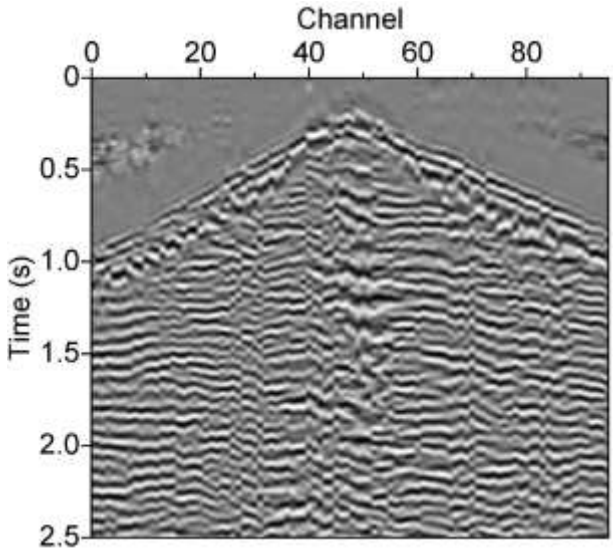


Figure 122 Common-shot gather from Line 13. In comparison with data from Lines 7B and 9, no clear reflections are observed. The dataset is also heavily contaminated by strong ringing noise, which obscures coherent seismic signals.

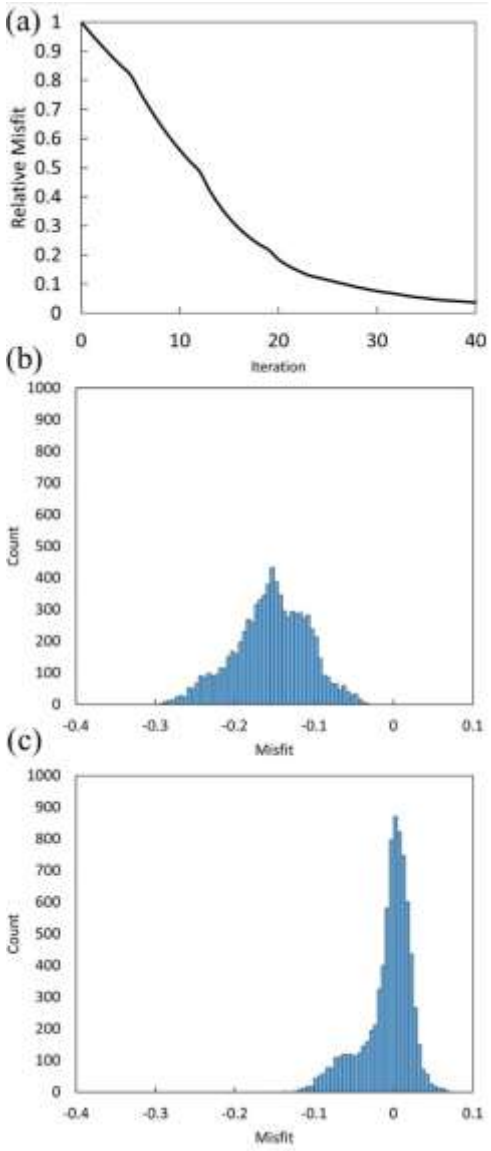


Figure 123 (a) Relative traveltime misfit convergence curve, (b) histogram of traveltime misfits before tomography, and (c) histogram of traveltime misfits after 40 iterations for Line 13

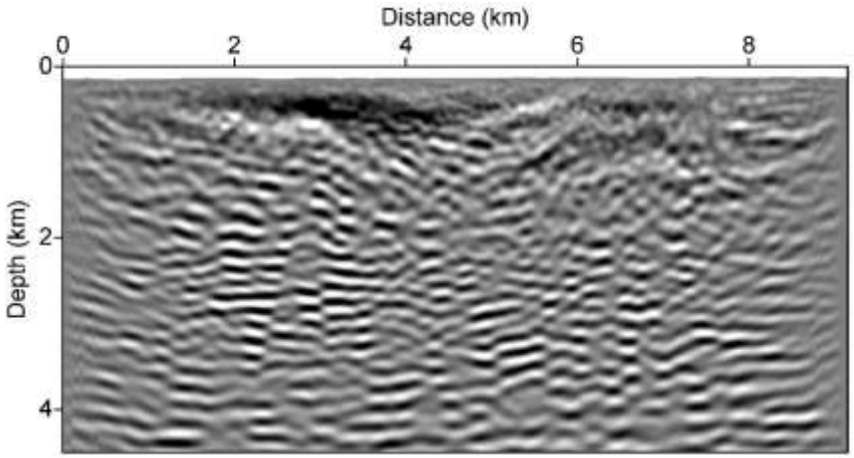


Figure 124 (a) Relative traveltime misfit convergence curve, (b) histogram of traveltime misfits before tomography, and (c) histogram of traveltime misfits after 40 iterations for Line 13

Conclusions

We analyzed two 2D legacy walkaway seismic datasets acquired in the Iron Mountain area of Utah. Initial P-wave velocity (Vp) models were constructed using sonic log data and subsequently refined through first-arrival traveltime tomography (FATT) and migration velocity analysis (MVA). Reverse-time migration (RTM) was then applied to generate pre-stack depth migration images of the subsurface. Following RTM, a machine learning (ML) algorithm was used to denoise the migration images and automatically detect faults.

By overlaying the Vp models on the denoised images, we demonstrated that the boundary of the quartz monzonite laccolith was successfully resolved along Line 7B. The denoised migration images from Lines 7B and 9 were also visualized together in 3D, revealing good correspondence in layer continuity and structural alignment. Minor discrepancies between the two profiles are attributed to slight variations in the Vp models at corresponding locations.

Overall, the results indicate that the processed 2D seismic data effectively delineate key subsurface features in the study area. However, to achieve a more detailed and reliable characterization of the subsurface structures and fault systems, acquisition and analysis of a 3D seismic survey are recommended.

Geological Modeling

The geological model with an area of 122.4 square miles was constructed in Petrel® using three legacy 2D seismic lines, well control from the ARCO Three Peaks #1 well (API: 4302130006) and supporting analyses of outcrop samples. Petrophysical properties were derived primarily from cuttings from the ARCO Three Peaks #1 well and limited core from the sealing interval (Carmel Formation). Additional porosity and permeability measurements were incorporated from Navajo Sandstone core acquired at the Covenant oil field, approximately 45 miles northeast of the project area, collected under the Rock Mountain Carbon Capture and Sequestration (RMCCS) project (DE-FE0001812). Table 14 summarizes the porosity and permeability datasets used for each modeled formation.

The structural framework was developed from the depth-migrated formation surfaces interpreted in Subtask 3.1. These surfaces include the Three Peaks quartz monzonite laccolith, Carmel Formation, Navajo Sandstone, Kayenta Formation, Moenave Formation, and Chinle Formation. These horizons were used to generate a 3D gridded framework, within which the stratigraphy was discretized into model layers as follows: the laccolith (4 layers), Carmel Formation (5 layers), Navajo Sandstone injection interval (10 layers), Kayenta Formation (4 layers), and Moenave Formation (2 layers). The resulting grid contains 123 × 128 × 25 cells, for a total of 393,600 active cells, with an average lateral cell dimension of approximately 220 ft × 200 ft.

Porosity was upscaled to the model grid from neutron and density porosity logs in the ARCO Three Peaks #1 well, using the arithmetic mean of density porosity and neutron porosity (porosity = (DPHI + NPHI)/2). **Figure 125** shows the porosity distribution in the Navajo Sandstone and the wells logs in the ARCO Three Peaks well. Permeability was calculated in the ARCO Three Peaks well from porosity using an industry-standard porosity–permeability correlation and then upscaled to the model grid. Permeability was populated throughout the model volume using sequential Gaussian simulation (SGS) with co-kriging to the porosity volume, applying a spherical variogram with correlation lengths of 12,300 ft × 12,300 ft. **Figure 126** shows the permeability distribution in the Navajo Sandstone.

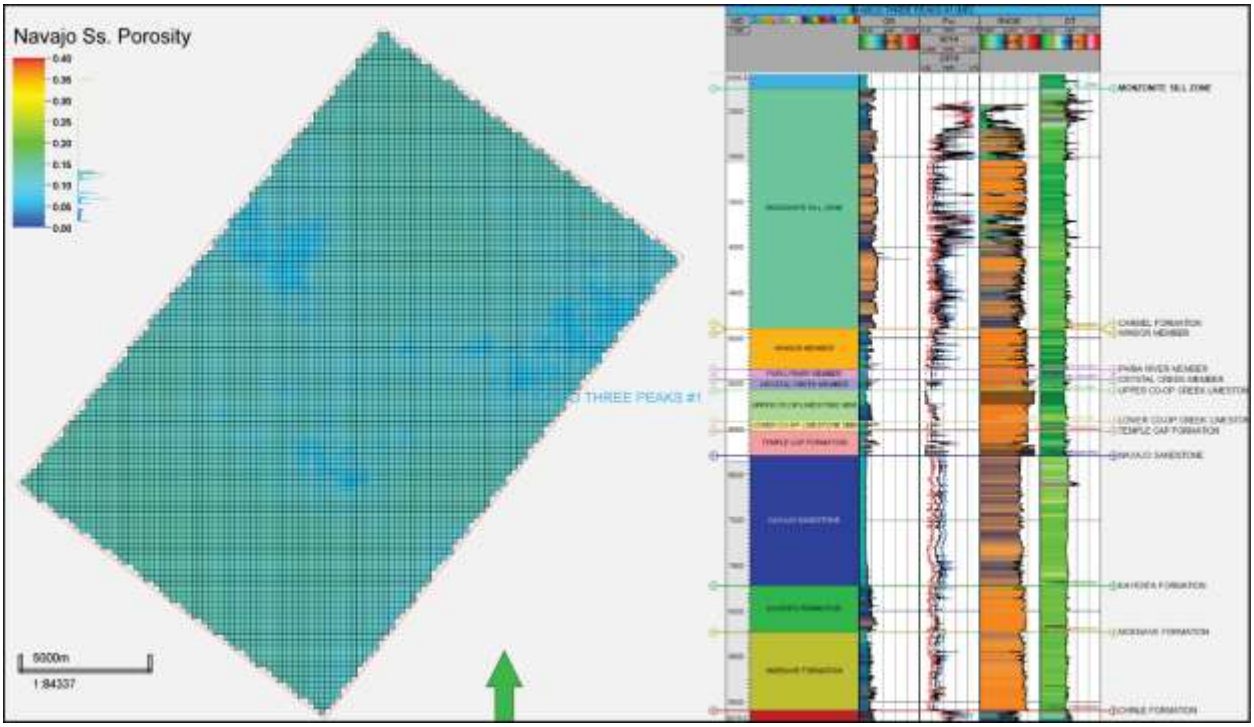


Figure 125 Porosity distribution in the 3D model and the Arco Three Peaks well log

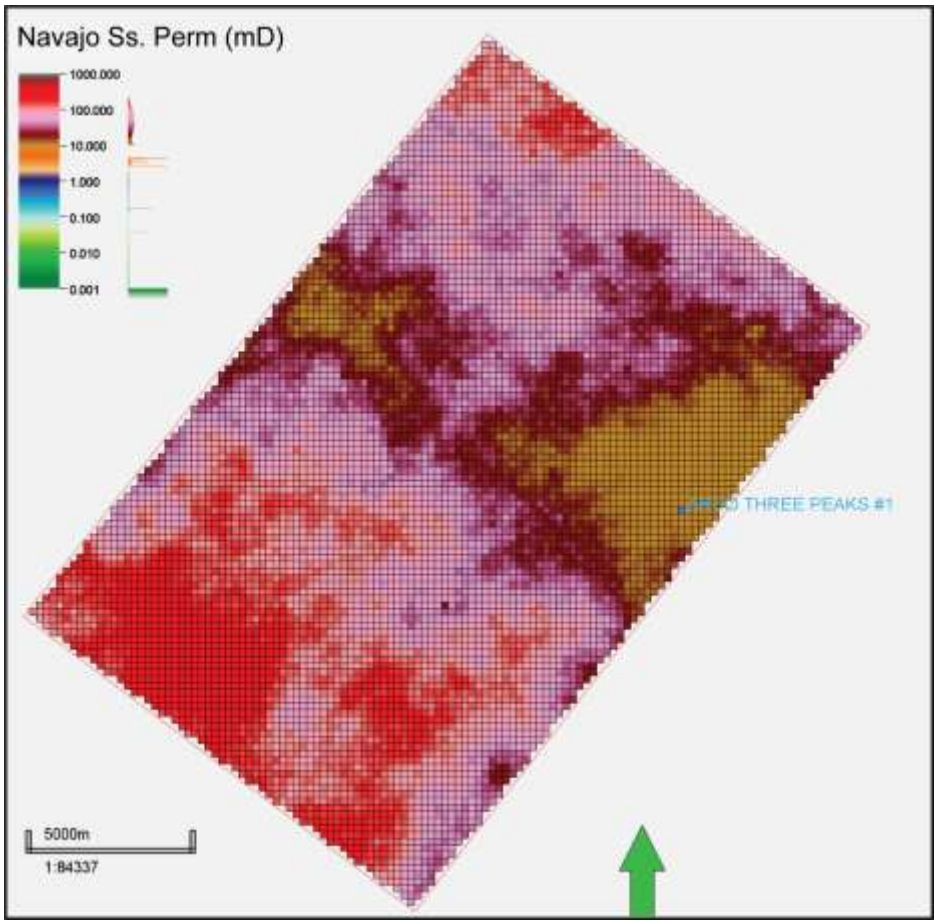


Figure 126 Permeability in the Navajo Ss.

Initial pressure conditions were set using a hydrostatic pressure gradient. The model was initialized as fully water-saturated (no free-phase CO_2 present), with brine salinity set to 20,000 ppm total dissolved solids (TDS). A reference temperature of 160°F was applied, along with a Navajo Sandstone reference pressure of 2,462 psi. The compositional fluid description for subsequent simulation consists of CO_2 and water only; however, the initial state of the full model includes water only (0% CO_2).

Table 14 Petrophysical data for the geological model.

Grid cells (nI x nJ x nK)	123 x 128 x 25					
Total number of grid cells:	393,600					
Formation	Monzonite		Carmel		Navajo	
Total number of defined cells	23,484		37,340		76,710	
Type of data:	Permeability (mD)	Porosity	Permeability (mD)	Porosity	Permeability (mD)	Porosity
Min:	0.0009	0.1254	0	0.0144	0.4831	0.0684

Max:	0.1741	0.3509	0.0008	0.1129	213	0.1328
Delta:	0.1732	0.2255	0.0008	0.0985	212.5169	0.0644
Mean:	0.0824	0.24	0.0002	0.0395	54.8234	0.1192
Std. dev.	0.0718	0.0887	0.0003	0.025	42.3164	0.0144

Formation	Kayenta		Moenave	
Total number of defined cells	30,684		15,342	
Type of data:	Permeability (mD)	Porosity	Permeability (mD)	Porosity
Min:	2.521	0.0555	0.0394	0.0808
Max:	4.2089	0.0723	3.1724	0.0837
Delta:	1.6879	0.0168	3.133	0.0029
Mean:	3.4597	0.0655	1.5762	0.082
Std. dev.	0.717	0.0055	1.3398	0.0011

CO_2 Quality and Quantity

Utah Iron's proposed direct reduced iron (DRI) facility will produce a concentrated CO_2 stream as an inherent byproduct of reducing iron oxide (magnetite) to metallic iron using a reducing gas composed primarily of CO and H_2. In the shaft furnace, CO and H_2 react with oxygen in the ore to form CO_2 and H_2O (steam), and the resulting "top gas" also contains variable amounts of unreacted reducing gas (CO and H_2) and other minor constituents depending on plant configuration and feed gas composition (Midrex Technologies 2018).

The furnace effluent is conditioned upstream of CO_2 capture to enable efficient recycle of the reducing gas. Gas conditioning typically includes cooling (often with direct contact cooling or heat exchange) and knock-out/separation steps that remove bulk water condensed from the high-moisture furnace effluent, along with entrained solids. While this front-end conditioning removes a substantial fraction of water, the gas entering the CO_2 capture unit remains humid, and moisture management is a primary design consideration because the reduction reactions generate water and because cooling/condensation behavior varies with operating conditions (Midrex Technologies 2018).

CO_2 is then separated using an amine-based capture system. In this configuration, CO_2 is selectively absorbed from the conditioned top gas into an aqueous amine solvent, and the CO_2-lean gas (enriched in CO and H_2) is recycled back to the shaft furnace as part of the closed-loop reducing gas circuit. Amine-based capture is a mature post-combustion/industrial separation approach and is capable of producing a high-purity CO_2 product suitable for compression and geologic storage when paired with standard downstream conditioning (Hack et al. 2022).

A key implication of amine capture is that the CO_2 product leaving the regenerator/stripper is typically saturated with water vapor (and may contain trace solvent carryover), because the

separation process is water-based and the CO_2 is liberated at elevated temperature in contact with aqueous solvent. Accordingly, dehydration is required to produce a CO_2 stream that is compatible with compression, dense-phase transport (if applicable), and injection operations. In practice, dehydration is commonly implemented in combination with compression: interstage cooling during multi-stage CO_2 compression condenses and removes additional water, followed by a dedicated dehydration unit to meet the final moisture specification. Dehydration technologies used in CCUS service commonly include triethylene glycol (TEG) contactors and/or molecular sieve systems, sometimes in series, with upstream protection (e.g., coalescers or guard beds) to limit solvent/impurity impacts on the dehydration media (Kemper et al. 2014).

For CO_2 transport and injection system integrity, the target water content is typically very low to minimize corrosion risk and to avoid hydrate-related operability issues under compression and pipeline/injection conditions. A commonly cited design target for "dry" CO_2 in CCUS transport service is on the order of less than 50 ppmv water, with the final specification set by the chosen operating pressure–temperature envelope and materials strategy (Cao et al. 2024).

After CO_2 capture and dehydration, the conditioned product stream is expected to be a high-purity, dry CO_2 stream ready for compression and sequestration at depth in the Navajo Sandstone (eolian strata). This study indicates that the Navajo Sandstone in the Iron Springs Mining District is capable of storing at least 50 million tons of CO_2. In terms of supply, based on Utah Iron's estimates of unmined ore and planned operations, the project anticipates capturing approximately 750,000 t of CO_2 per year, with a source lifetime exceeding 30 years.

Storage Resource Assessment

A storage resource assessment was completed for the Neck of the Desert area adjacent to the Iron Springs mining district using the NETL CO2SCREEN tool. The assessment area covers 104.4 km^2 (**Figure 127**) and was selected to represent the portion of the Navajo Sandstone storage complex relevant to Utah Iron's planned CO_2 sequestration project. The CO2SCREEN workflow was implemented as a probabilistic (distribution-based) volumetric assessment, with key geologic inputs populated from the project geological model. Specifically, the model provided the reservoir thickness and porosity statistics for the Navajo Sandstone, as well as representative pressure and temperature conditions used to characterize in situ CO_2 behavior.

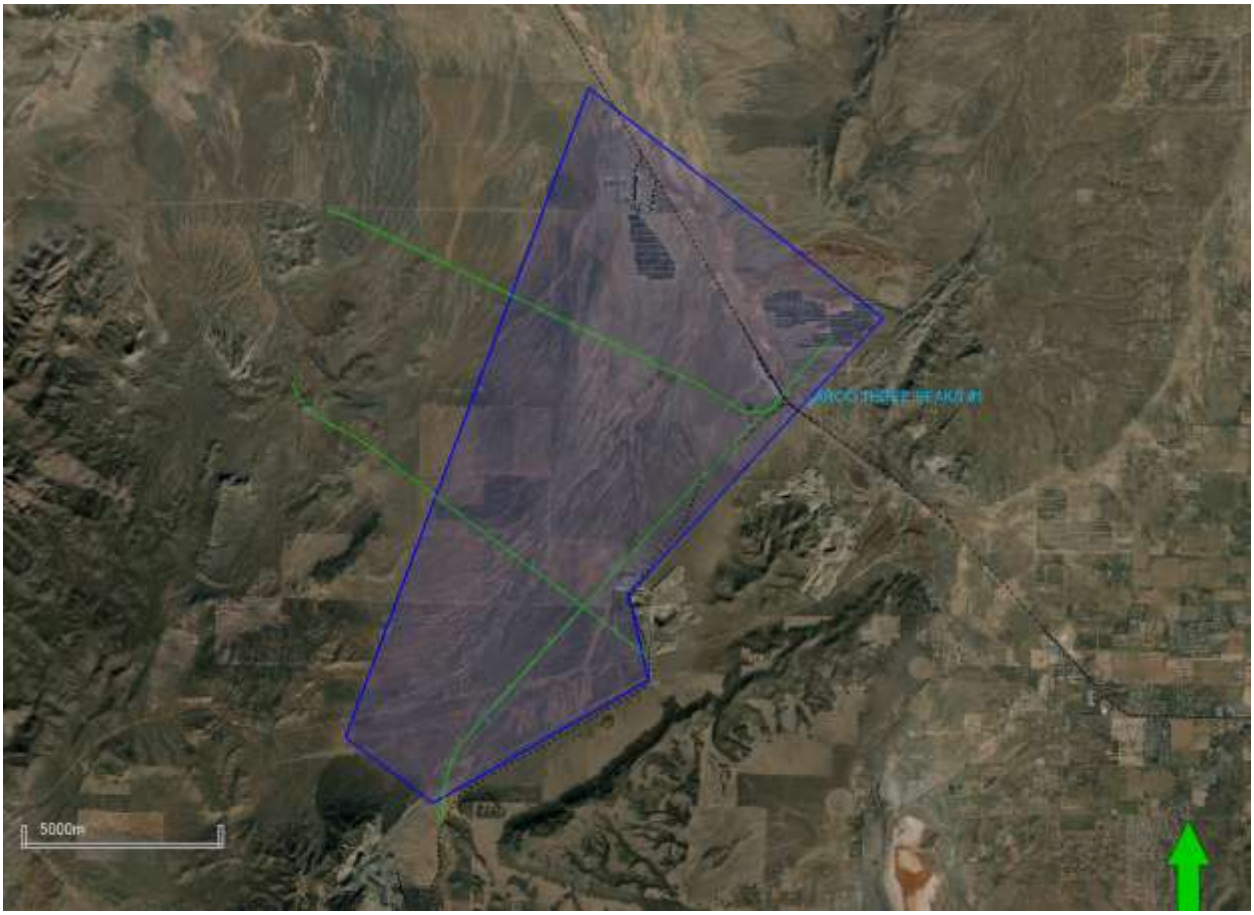


Figure 127 Neck of the Desert CO_2 resource assessment area

Table 15 summarizes the primary CO2SCREEN inputs for the Navajo Sandstone. The Navajo Sandstone average thickness across the assessment area is 372.5 m with a standard deviation of 83.8 m, reflecting lateral and vertical variability captured in the structural framework and gridded geologic model. Average porosity was set to 0.12 with a standard deviation of 0.10 based on available petrophysical interpretation and well log properties. Reservoir pressure was represented by an average of 18.4 MPa with a standard deviation of 1 MPa, corresponding to the hydrostatic pressure estimate used in the model at the Navajo Sandstone reference depth. Reservoir temperature was set to 71.1°C, consistent with the project temperature model and intended to represent the injection interval conditions used in the screening calculations.

Table 15 CO2SCREEN input parameters for the Navajo Sandstone.

	Average	Std Dev	
Neck of the Desert Area	104.4	n/a	km2
Navajo Average Thickness	372.5	83.8	m
Navajo Porosity	0.12	0.1	

Navajo Pressure	18.4	1	Mpa
Navajo Temperature	71.1	n/a	°C

CO2SCREEN applies a storage efficiency framework to translate gross pore volume into an effective storage resource estimate. For this assessment, eolian sandstone efficiency factors were used because the Navajo Sandstone is an eolian reservoir characterized by high lateral continuity, dune-scale heterogeneity, and strong stratigraphic controls on flow and plume migration. Table 16 lists the efficiency factors applied for the Iron Mountain site. The net-to-total area, net-to-gross thickness, and effective-to-total porosity factors were taken from the IEA (2009) database values implemented within CO2SCREEN. The volumetric displacement and microscopic displacement factors were sourced from the CO2BRA (2022) database, with one site-specific modification: the P90 volumetric displacement factor was adjusted to reflect project-specific expectations for displacement behavior within the assessed closure and migration setting. This modification was applied to better align the high-case displacement assumption with the local geological understanding derived from the site characterization rather than relying solely on generalized database values.

*Table 16 Efficiency factors used for the Iron Mountain site. *The P90 volumetric displacement has been modified to be site specific.*

Efficiency Factors – From IEA and Cobra Databases

	P10	P90	database
net-to-total area	0.2	0.8	IEA 2009
net-to-gross thickness	0.21	0.76	IEA 2009
effective-to-total porosity	0.64	0.77	IEA 2009
volumetric displacement	0.114	0.8	CO2BRA 2022*
microscopic displacement	0.432	0.502	CO2BRA 2022

The CO2SCREEN results are presented in Table 17 as probabilistic percentiles (P10, P50, and P90) for storage resource (MMt) and the corresponding implied storage efficiency (%). For the Neck of the Desert assessment area, the estimated CO_2 storage resource ranges from 8.78 MMt (P10) to 206.73 MMt (P90), with a P50 (median) estimate of 54.92 MMt. The associated storage efficiencies are 0.33% (P10), 2.0% (P50), and 7.3% (P90). In this context, the storage efficiency represents the fraction of the gross pore volume (defined by the assessed area, average thickness, and porosity) that is effectively available for CO_2 storage after accounting for geologic and displacement constraints embedded in the efficiency factor framework.

Table 17 CO2SCREEN resource assessment results.

CO2 Storage Statistics	P_{10}	P_{50}	P_{90}

Storage Resource (MMt)	8.78	54.92	206.73
Storage Efficiency (%)	0.33	2	7.3

When considered alongside Utah Iron's projected captured CO_2 supply (approximately 0.75 MMt/yr), the CO2SCREEN results indicate that the assessed portion of the Navajo Sandstone can accommodate multi-decade injection in the median and higher cases, with the low-case outcome representing a more conservative capacity bound. This relationship between forecasted CO_2 supply and screened storage resource is used in subsequent sections to inform injection scenario design and to guide additional data needs that would reduce uncertainty in the thickness, porosity, and efficiency assumptions used in the screening-level assessment.

Dynamic Numerical Simulation

Simulation Model Development and Setup

A dynamic numerical simulation model was constructed from the geological model and executed in Eclipse®. The simulation domain covers approximately 22.0 km × 14.4 km and uses the same grid architecture as the geological model (123 × 128 × 25 cells; 393,600 active cells). The intent of matching the geological and simulation grids was to minimize grid translation effects and avoid introducing additional uncertainty from a second upscaling step. Accordingly, porosity and permeability properties from the geological model were applied directly to the simulation grid.

Relative permeability for the Navajo Sandstone was assigned using core-derived data measured on Navajo Sandstone samples from the Covenant field by the Rocky Mountain CarbonSAFE Phase I project (DE-FE0029280; **Figure 128**).

Boundary conditions were specified as open along all lateral model boundaries and closed at the top and bottom. This configuration approximates laterally extensive flow within the Navajo Sandstone while restricting vertical mass exchange outside the modeled stratigraphic interval. The model was initialized under hydrostatic conditions with brine salinity set to 200,000 ppm. **Figure 129** shows the initial pressure distribution at the top of the Navajo Sandstone.

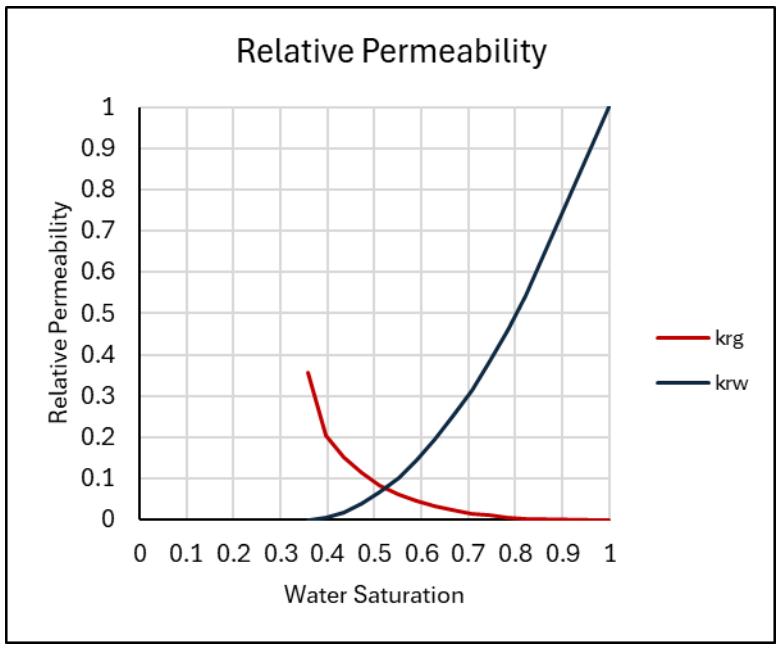


Figure 128 Relative permeability measured on Navajo Sandstone core from the Covenant oil field

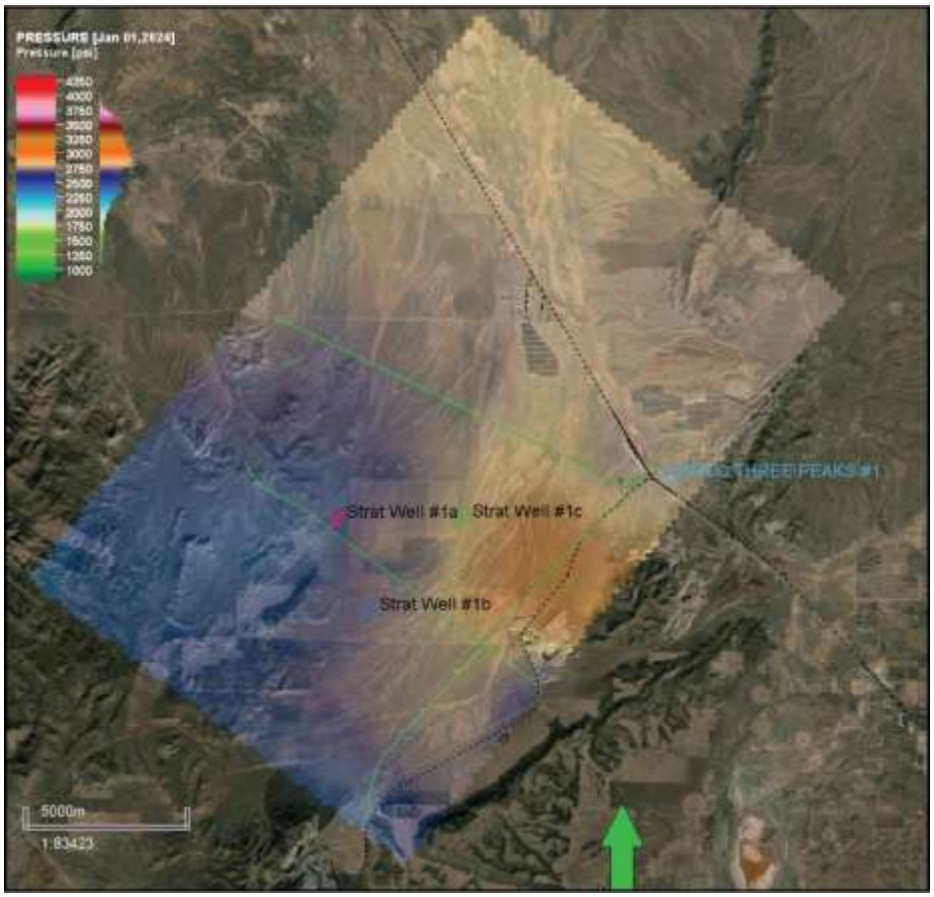


Figure 129 Initial pressure at the top of the Navajo Ss

Injection Scenarios Evaluated

Three candidate injection locations were evaluated (Well #1a, Well #1b, and Well #1c; **Figure 129**). These sites were selected within the portion of the 2D seismic coverage exhibiting the most coherent and laterally continuous reflectors, interpreted to indicate well-defined stratigraphy and favorable storage conditions. Among the three sites, the Well #1a location is associated with the most continuous and interpretable stratigraphic character.

Four injection scenarios were simulated. All scenarios include 30 years of active CO_2 injection followed by a 50-year post-injection site care (PISC) period, for a total simulation duration of 80 years (2024–2104). Two injection rates were evaluated at Well #1a, while only the higher rate was evaluated at Well #1b and Well #1c. The four cases are as follows:

1. Well #1a, 36,649 MSCF/d (0.704 Mt CO_2/yr), 30-year injection (21.1 MMT case)
2. Well #1a, 81,442.3 MSCF/d (1.56 Mt CO_2/yr), 30-year injection (50 MMT case)
3. Well #1b, 81,442.3 MSCF/d (1.56 Mt CO_2/yr), 30-year injection (50 MMT case)
4. Well #1c, 81,442.3 MSCF/d (1.56 Mt CO_2/yr), 30-year injection (50 MMT case)

Pressure response and injectivity performance

Figure 130 shows cumulative injected CO_2 and average field pressure over time for all scenarios. Under the assumptions represented in this model (grid extent, open lateral boundaries, hydrostatic initialization, and assigned rock/fluid properties), the Navajo Sandstone accommodates both the lower-rate (0.704 MMT/year) and higher-rate (1.56 MMT/year) injection scenarios without reaching the bottomhole pressure limit and without injection-rate throttling.

For the 21.1 MMT scenario (Well #1a), average reservoir pressure declines from 2,369.1 psi initially to 2,318.8 psi at the end of the simulation (a net decrease of 50.3 psi). At the end of the 30-year injection period, average pressure is 2,343.3 psi (25.8 psi below the initial condition).

For the 50 MMT scenarios, the average pressure response is characterized by a small initial decline during the first few years followed by a gradual increase during continued injection. At the end of injection, average reservoir pressure ranges from 2,366.7 to 2,367.3 psi across the injection locations, representing only about 2 psi below the initial pressure. During the 50-year PISC period, pressure decreases and converges toward about 2,319 psi, consistent with the long-term equilibration trend observed in the lower-rate scenario.

There is no meaningful difference in cumulative injected volume or pressure evolution among the three candidate well sites for the 50 MMT scenarios, indicating that, at the scale represented by this model and under the applied boundary conditions, site selection within the tested area does not materially change the pressure-limited injectivity outcome. Average pressure statistics for each scenario are summarized in Table 18.

Table 18 Average reservoir pressure.

Pressure Data (psi)	Initial	Final	Delta	End Inj	Delta Inj Period
21.1 MMT 1a	2369.1	2318.8	50.3	2343.3	25.8
50 MMT 1a	2369.1	2319.6	49.4	2367.3	1.8

50 MMT 1b	2369.1	2319.8	49.3	2366.7	2.4
50 MMT 1c	2369.1	2319.7	49.4	2367.1	2.0

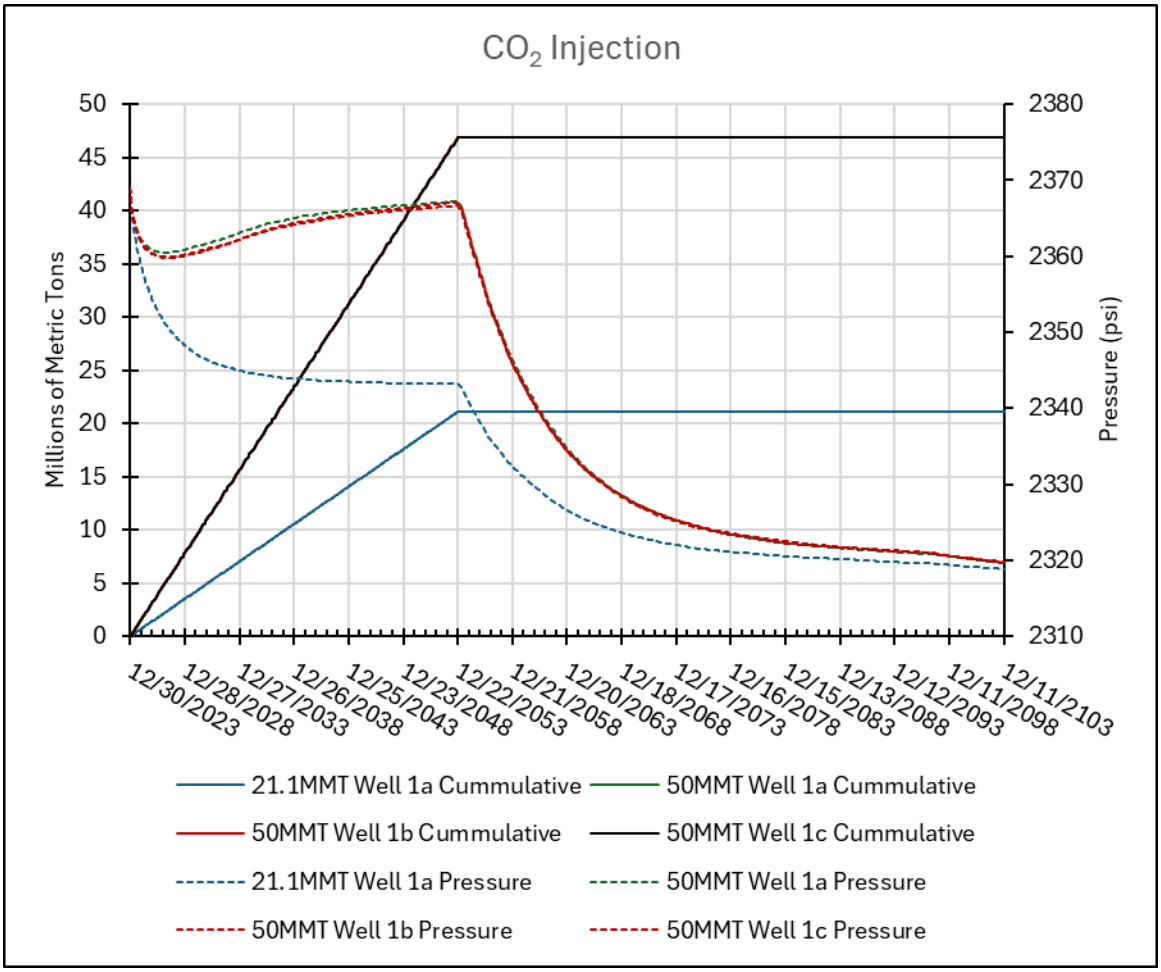


Figure 130 CO_2 injection masses and field pressure for each injection scenario

CO_2 Phase Partitioning and Trapping Behavior

CO_2 phase behavior in the reservoir is consistent with expectations for deep saline aquifer storage, with injected CO_2 partitioning between a mobile/supercritical phase and a dissolved phase in brine over time. The dissolved CO_2 mass increases throughout both the injection and post-injection periods (dashed lines in **Figure 131**), while the mass of supercritical CO_2 increases during injection and then decreases post-injection as dissolution progresses (solid lines in **Figure 131**).

For the 21.1 MMT scenario (Well #1a), 3.99 MMT of CO_2 is dissolved by the end of the simulation, corresponding to 18.9% of the total injected mass. For the 50 MMT scenarios, dissolved CO_2 at the end of the simulation ranges from 7.54 to 8.35 MMT, corresponding to approximately 16.1% to 17.8% of the total injected mass. The remaining CO_2 is present as a supercritical phase at the end of the simulation, ranging from 17.14 MMT in the 21.1 MMT

scenario to approximately 38.6 to 39.4 MMT in the 50 MMT scenario. CO_2 phase totals for each scenario are summarized in Table 19.

Table 19 CO_2 Phase composition for each injection scenario.

	Dissolved Phase				Supercritical Phase				Total
CO_2 Data (MMT)	**End Inj**	**End Sim**	**Max**	**% Total**	**End Inj**	**End Sim**	**Max**	**% Total**	
21.1 MMT 1a	2.58	3.99	3.99	18.9%	18.54	17.14	18.54	81.2%	21.11
50 MMT 1a	5.09	7.54	7.54	16.1%	41.85	39.41	41.85	84.0%	46.92
50 MMT 1b	5.06	8.35	8.35	17.8%	41.88	38.59	41.88	82.3%	46.92
50 MMT 1c	5.01	8.28	8.28	17.6%	41.93	38.66	41.93	82.4%	46.92

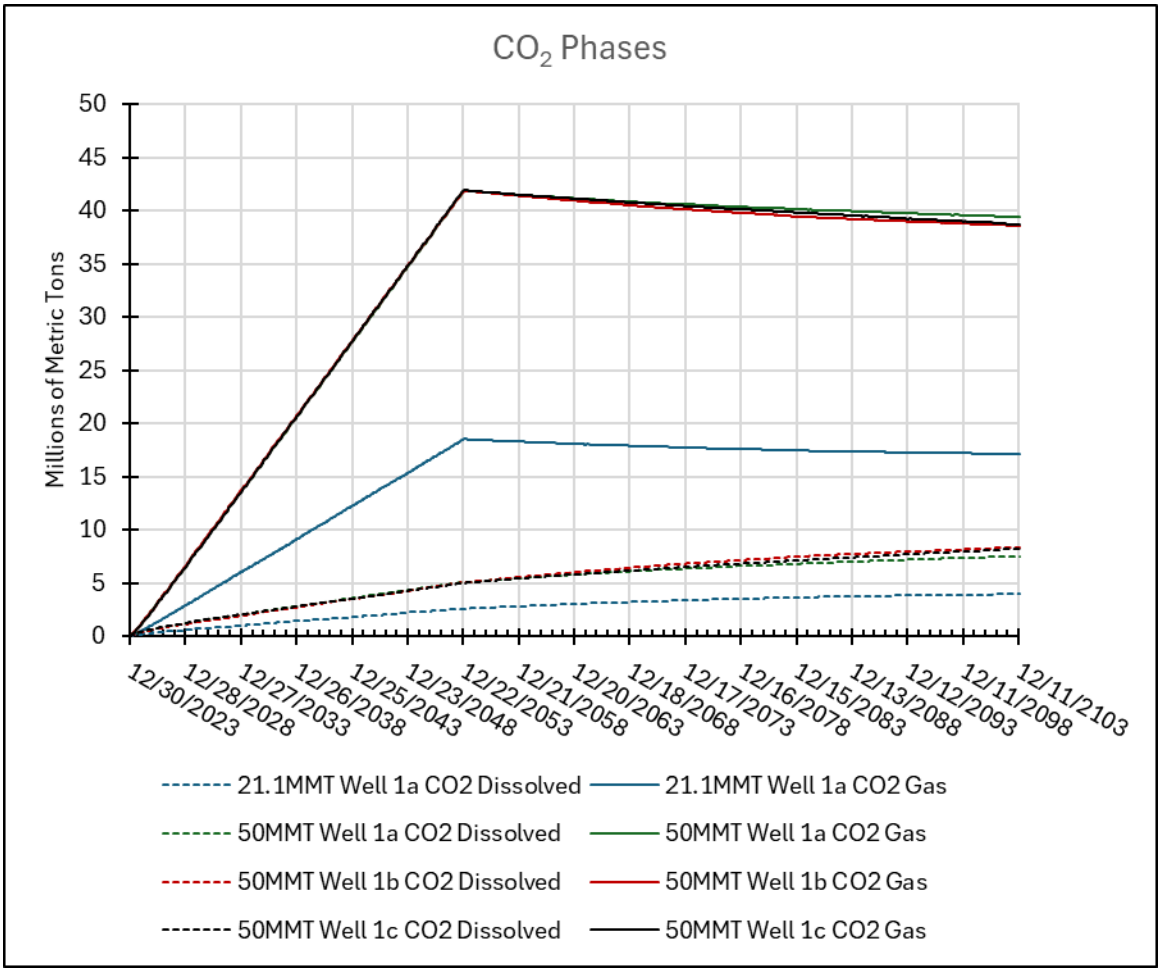


Figure 131 Mass of CO_2 phases present in the reservoir for each injection scenario

Numerical Modeling Results Conclusion

Across all four scenarios, the modeled Navajo Sandstone injection interval demonstrates sustained injectivity over 30 years of injection without pressure-limited rate reduction, and the pressure response remains modest under both the 21.1 MMT and 50 MMT scenarios. Differences among the three candidate well locations are negligible at the modeled scale, suggesting that injectivity performance is primarily controlled by the regional reservoir framework and boundary condition assumptions rather than by local variations among the tested sites. CO_2 partitioning indicates progressive dissolution over time, with approximately 19% of injected CO_2 dissolved in the lower-rate scenario and approximately 16% to 18% dissolved in the higher-rate scenarios by the end of the 80-year simulation, consistent with expected trapping evolution in a deep saline aquifer setting.

Plume Analysis and Area of Review Delineation

CO_2 plume footprint, plume growth rate, and the EPA Class VI Area of Review (AoR) were evaluated to provide an initial indication of permitting-relevant performance for the modeled injection scenarios. Plume metrics were derived from the dynamic simulation results (Section 3.5), and AoR delineations were developed using a hydrostatic USDW protection basis consistent with EPA Class VI AoR and corrective action guidance.

Plume Area Analysis

For all four scenarios, the CO_2 plume area expands during the active injection period in an approximately linear manner (**Figure 132**). After injection ceases, the plume footprint continues to grow, but the rate of areal expansion decreases steadily as the plume approaches stabilization. Consistent with this behavior, the post-injection rate of change falls to less than approximately 2% per year as plume growth tapers and the footprint asymptotically approaches a stable maximum extent (**Figure 132**).

Unlike the injectivity and pressure behavior described in Section 3.5, where differences among the three candidate sites were minor, the plume footprint is strongly site dependent. The lower-rate, 21.1 MMT scenario produces the smallest plume area, as expected. For the higher-rate (50 MMT) scenarios, the final plume extent varies materially among Well #1a, Well #1b, and Well #1c, indicating that local stratigraphic/structural differences and heterogeneity expressed in the model have an impact on plume migration and areal containment. This finding reinforces the importance of site selection and local subsurface characterization for plume management and monitoring design.

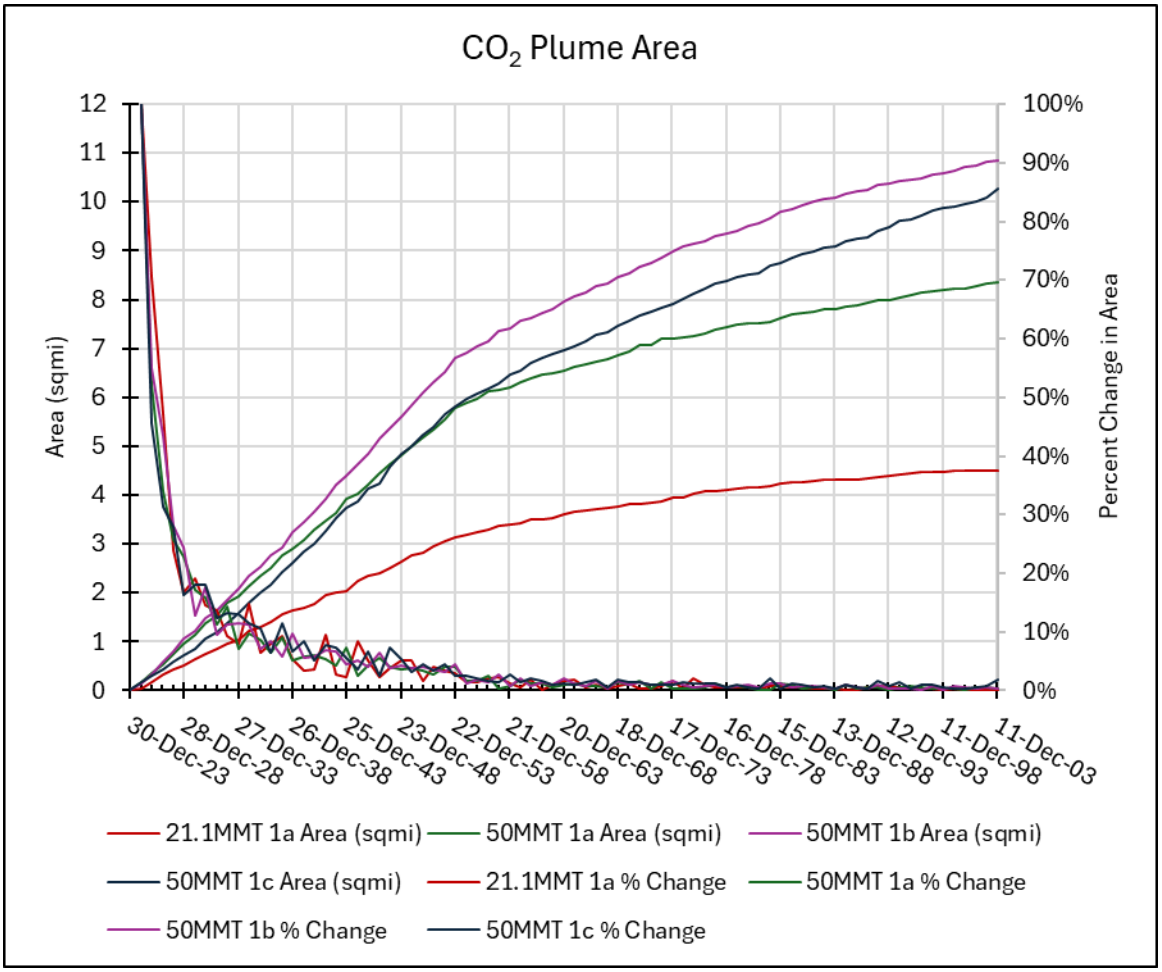


Figure 132 *CO_2 plume area and change in area through time*

Area of Review Analysis

AoR Approach and Hydrostatic Allowable Pressure Increase

An AoR analysis was performed to evaluate the extent of the pressure front relative to an allowable reservoir pressure increase intended to protect Underground Sources of Drinking Water (USDWs). Because the reservoir was initialized under hydrostatic conditions, the hydrostatic AoR formulation from EPA AoR and Corrective Action guidance was applied (Equations 1 and 2; adapted to the imperial unit system used in the numerical model; EPA 2013).

Equation 1 $\Delta Pc = 0.5 * \frac{g}{gc} * \xi * (z_u - z_i)^2$

Equation 2 $\xi = \frac{(\rho_i - \rho_u)}{(z_u - z_i)}$

Where gc is the gravitation conversion constant from lbm to lbf, ρ_u is the density of the USDW, ρ_i is the density of the injection reservoir, z_u is the elevation (depth) of the USDW relative to mean sea level (msl), and z_i is the elevation (depth) of the injection reservoir relative to msl. Table 7 lists the constants and the source of each variable used in the calculation.

Table 20 Inputs to the EPA Class VI hydrostatic AoR formula to calculate delta Pu.

Constants		
32.174	g	ft/s^2
32.174	gc	$lbm*ft/lbf*s^2$
1	g/gc	
62.37	ρ_u	lbm/ft^3
Model output	ρ_i	lbm/ft^3
Model output	z_u	ft
Model output	z_i	ft

To estimate z_u (base of USDW), the base of the USDW was assumed to be 200 ft below ground surface. Practically, this surface was constructed by subtracting 200 ft from a digital elevation model (DEM) of the ground surface and smoothing the result to approximate the expected behavior of a shallow groundwater system that broadly follows topography (**Figure 133**). The depth to the injection interval (z_i) was computed by subtracting the DEM from the mapped top Navajo Sandstone surface. The reservoir brine density (ρ_i) was extracted from the simulation initialization state (time step 0) for consistency with the model's fluid and salinity assumptions. The USDW density (ρ_u) was taken as the average density of freshwater (62.37 lbm/ft^3).

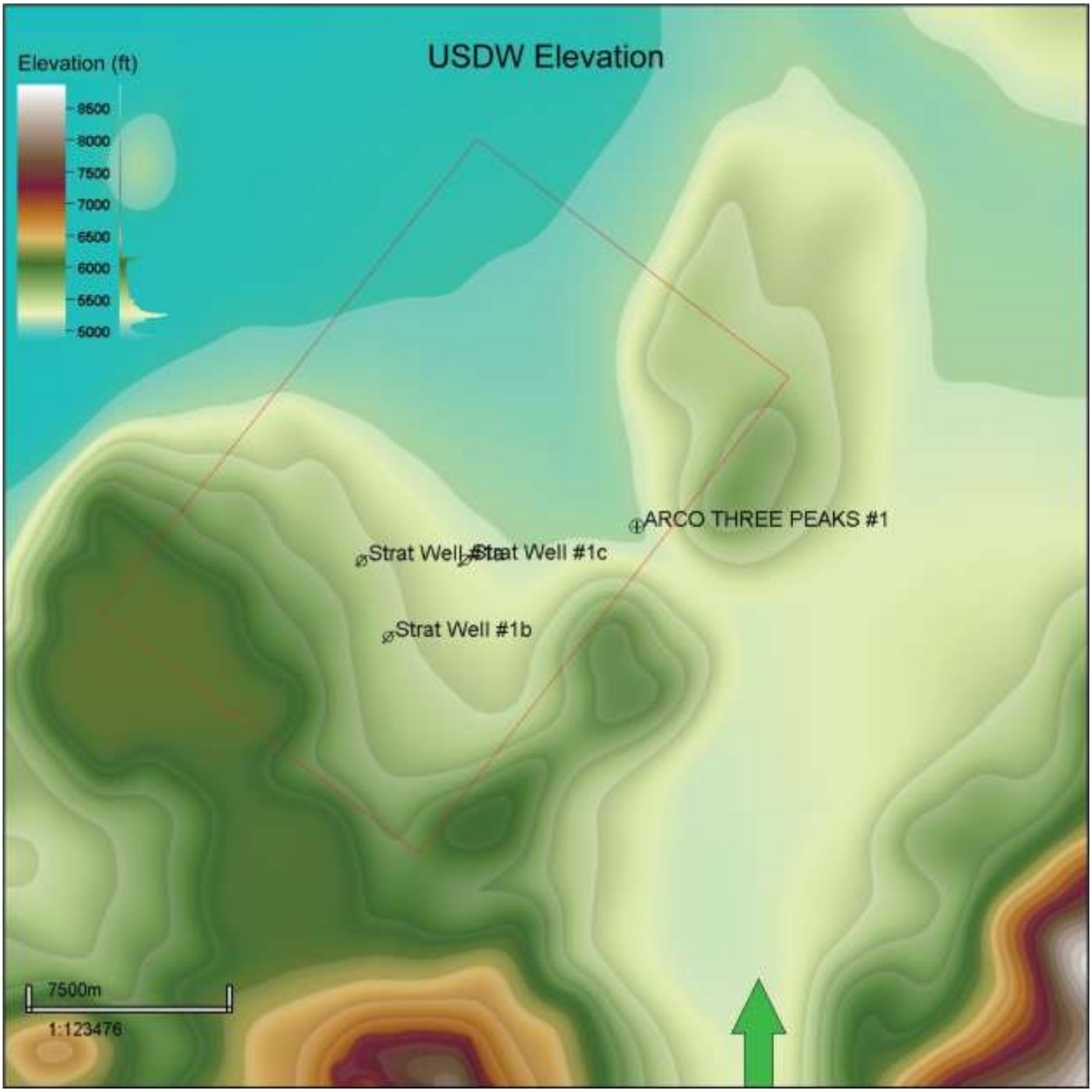


Figure 133 Estimated elevation of the USDW. The red polygon is the model boundary

Allowable Pressure Increase (ΔPu) Field

Using these inputs, an allowable pressure increase field (ΔPu) was calculated and mapped to the Navajo Sandstone surface (**Figure 134**). The allowable pressure increase grows toward the head of the valley nearer to Iron Mountain, reflecting increasing surface elevation while the Navajo Sandstone remains comparatively flat over the modeled area. From a siting perspective, this trend is favorable: locating injection closer to Iron Mountain increases the allowable pressure increase before a USDW-protection threshold is exceeded.

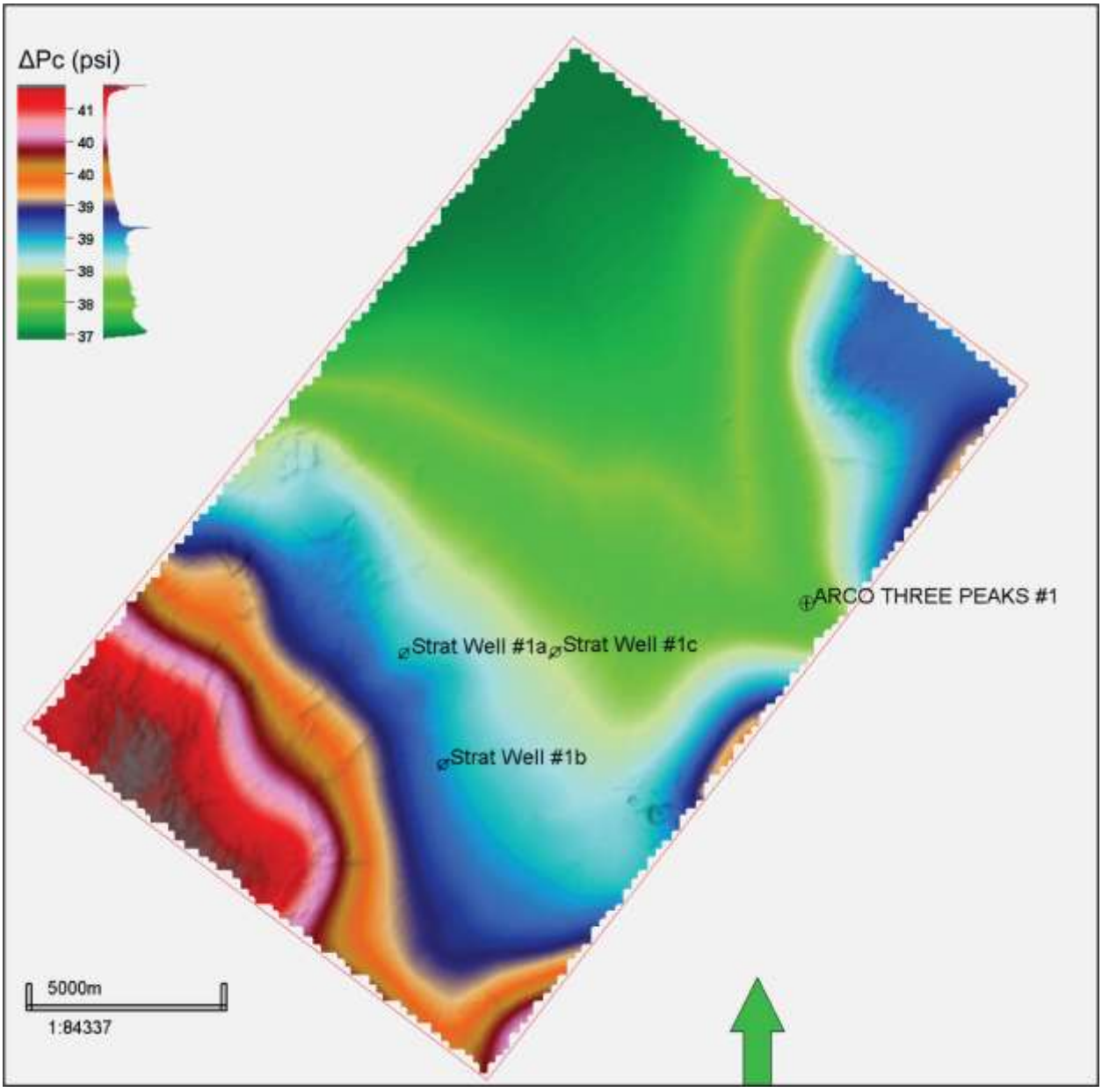


Figure 134 Pressure map showing the allowable increase in pressure under hydrostatic conditions (ΔPc) based on EPA Class VI Guidance for AoR delineation

Modeled Pressure Increase from Injection (ΔP)

For each scenario, the modeled pressure increase due to injection was computed by subtracting initial reservoir pressure from the pressure at the end of injection. The resulting ΔP field at the top of the Navajo Sandstone was then mapped to the Navajo surface for each scenario (Figures 31–34). As expected, the 21.1 MMT scenario yields the smallest pressure perturbation, with an increase of approximately 31 psi at the Well #1a location (**Figure 135**). The 50 MMT scenarios produce larger pressure increases, with well-site pressure increases ranging from approximately 96 to 130 psi and a broader area of elevated pressure persisting across the southern half of the

model at the end of injection (Figures 33–34). Table 21 summarizes the modeled pressure increase at each well site.

Table 21 Pressure increase at each of the well site for each scenario.

	Pressure Increase (psi)
21.1 MMT Well #1a	31
50 MMT Well #1a	102
50 MMT Well #1b	96
50 MMT Well #1c	130

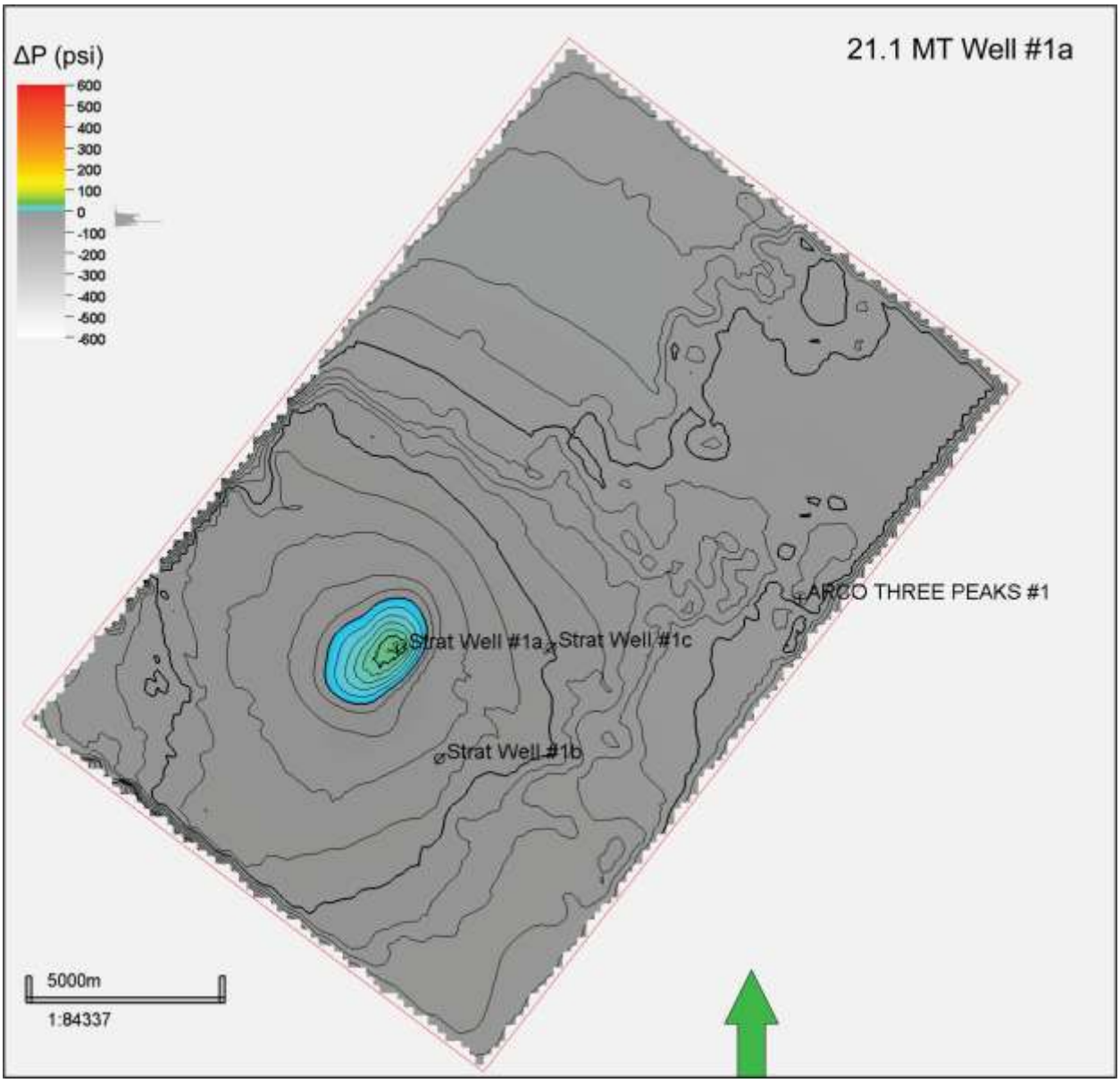


Figure 135 Pressure delta at Well #1a between the initial pressure and the pressure at the end of injection (2054) for 21.1 Mt of injected CO_2

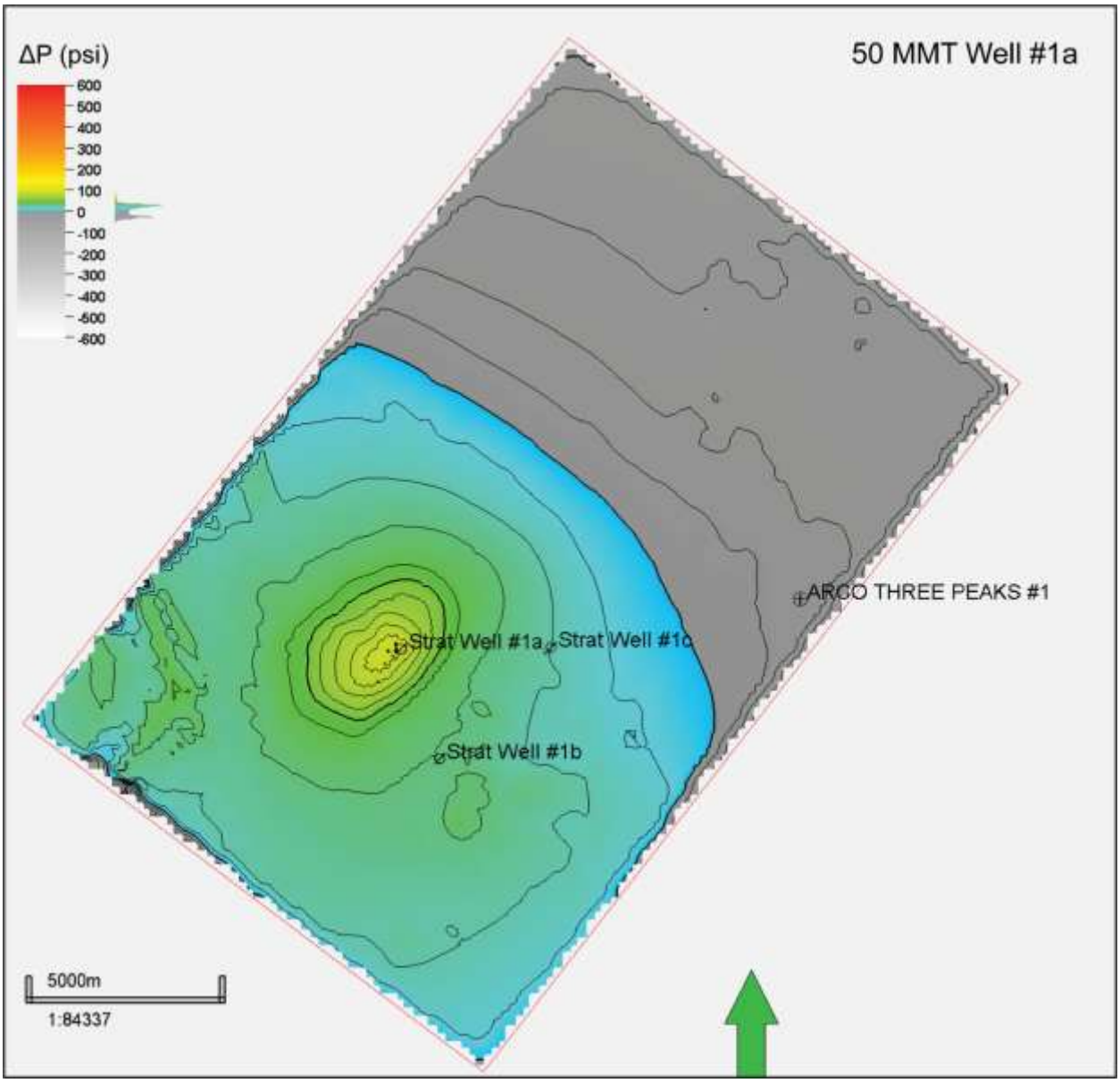


Figure 136 Pressure delta at Well #1a between the initial pressure and the pressure at the end of injection (2054) for 50 Mt of injected CO_2

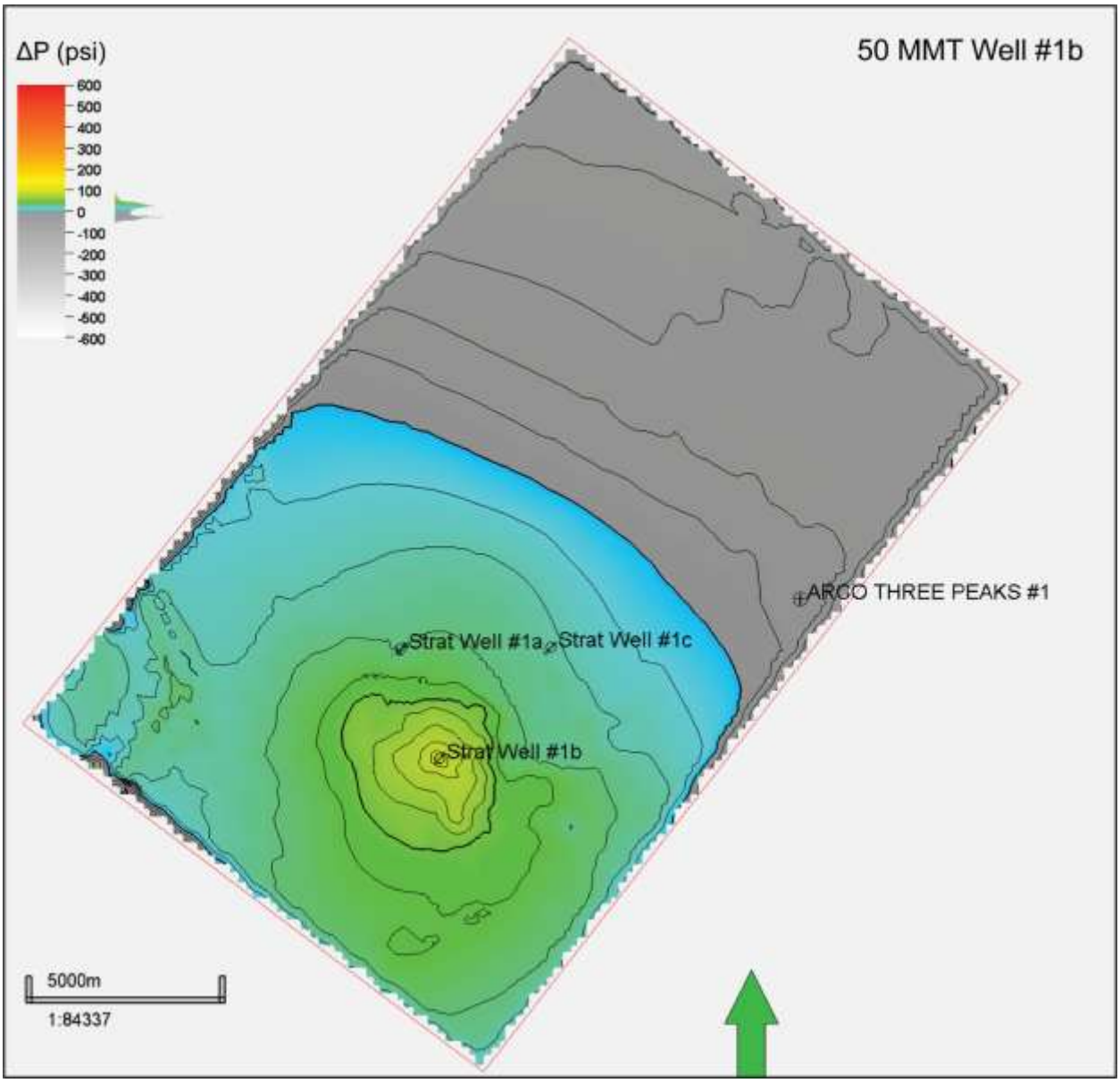


Figure 137 Pressure delta at Well #1b between the initial pressure and the pressure at the end of injection (2054) for 50 Mt of injected CO_2

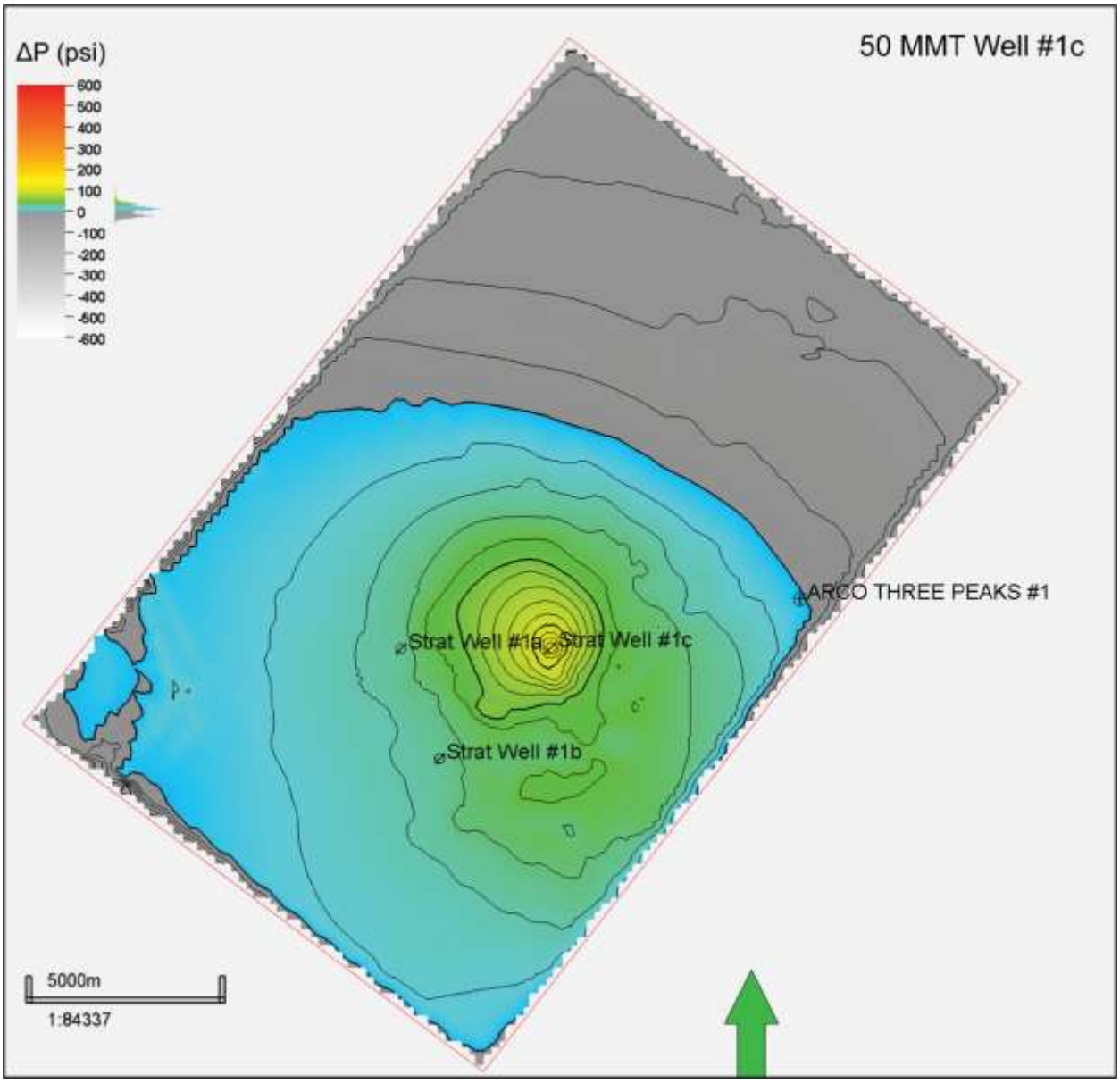


Figure 138 Pressure delta at Well #1c between the initial pressure and the pressure at the end of injection (2054) for 50 Mt of injected CO_2

AoR Delineation and Comparison to CO_2 Plume Footprint

The AoR was delineated by comparing the modeled pressure increase (ΔP) to the allowable pressure increase (ΔPu). Practically, this was implemented by subtracting ΔPu from ΔP; locations where the resulting value is positive define the AoR footprint for that scenario (i.e., where modeled pressure increase exceeds the allowable increase). The resulting AoR polygons are shown with the CO_2 plume footprints in Figures 35 through 38.

A critical outcome is that the 21.1 MMT scenario produces no AoR, because the modeled pressure increase remains below the allowable pressure increase across the model domain. This result is favorable for the anticipated operational case at the Iron Springs mine, given that

planned CO_2 capture volumes from DRI operations are expected to be a maximum of 0.75 Mt per year. Figure 35 shows the CO_2 plume footprint without an associated AoR polygon.

For the 50 MMT scenarios, AoR footprints are present and range from 5.30 to 10.58 square miles. Even in these higher-rate cases, the AoR remains comparable in magnitude to the plume footprint, rather than substantially exceeding it. Specifically, in the 50 MMT Well #1a scenario, the AoR polygon is 5.30 square miles compared to a plume area of 5.79 square miles (**Figure 140**). In the 50 MMT Well #1b scenario, the AoR increases to 10.58 square miles relative to a plume area of 6.82 square miles (**Figure 141**). In the 50 MMT Well #1c scenario, the AoR is 8.63 square miles relative to a plume area of 5.81 square miles (**Figure 142**). Table 22 summarizes AoR and plume areas used for these comparisons.

Table 22 Area of the AoR

	AoR area (sqmi)	Plume Area (sqmi)
21.1 MMT 1a	0	3.13
50 MMT 1a	5.30	5.79
50 MMT 1b	10.58	6.82
50 MMT 1c	8.63	5.81

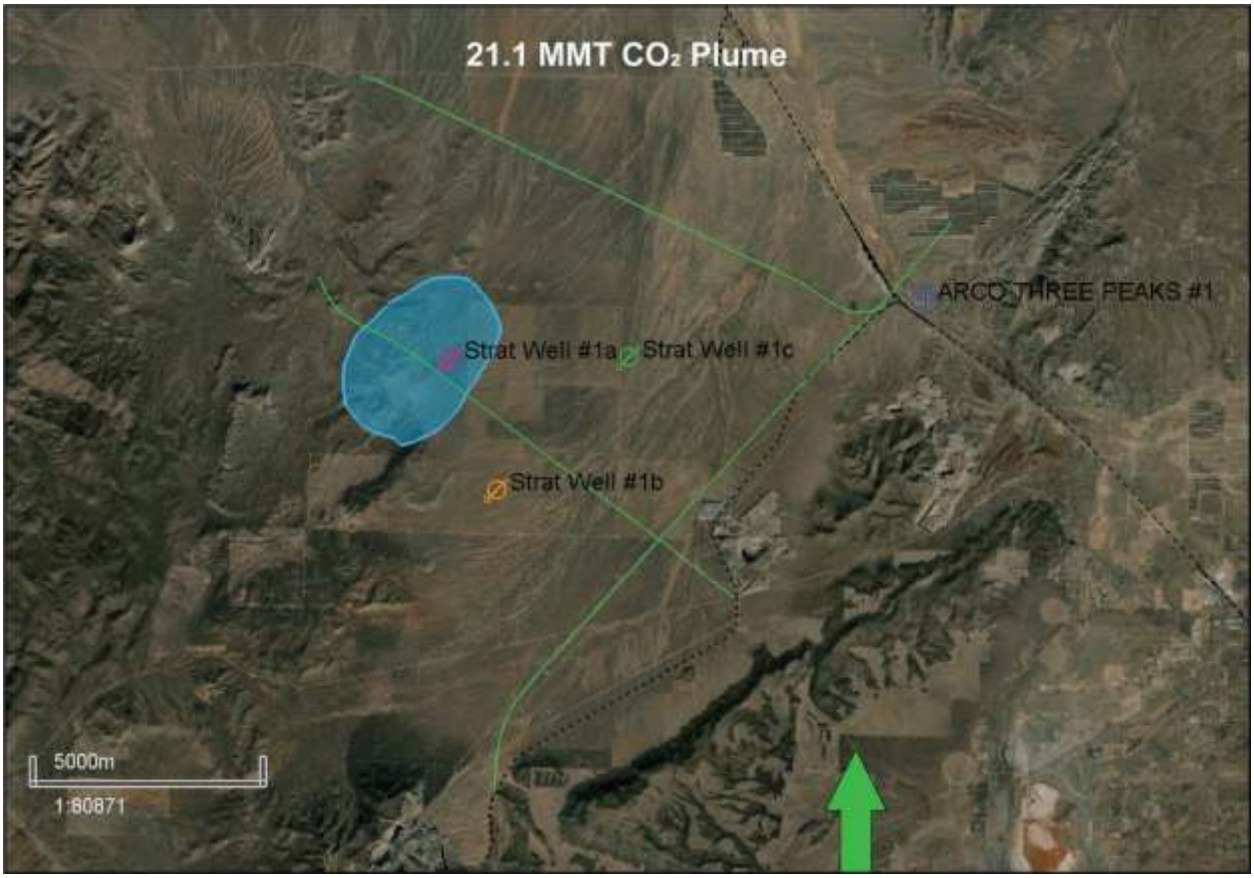


Figure 139 CO_2 plume size at the end of injection (2054) for the 21.1-million-ton injection volume at well 1a. The pressure delta at the top of the Navajo Ss. is below the ΔPc, so there is no AoR.

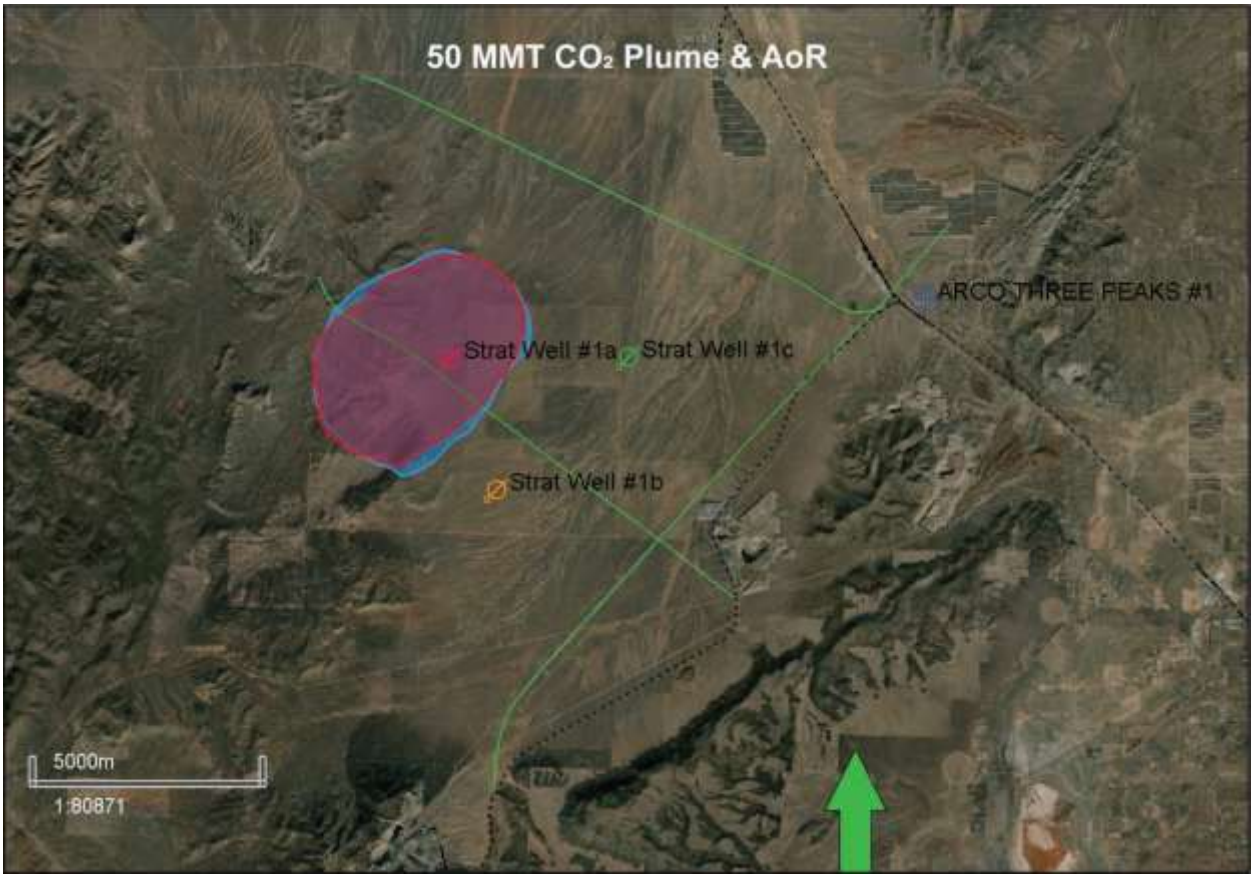


Figure 140 CO_2 plume size (blue polygon) and AoR (red polygon) at the end of injection (2054) for the 50-million-ton injection volume at well 1a

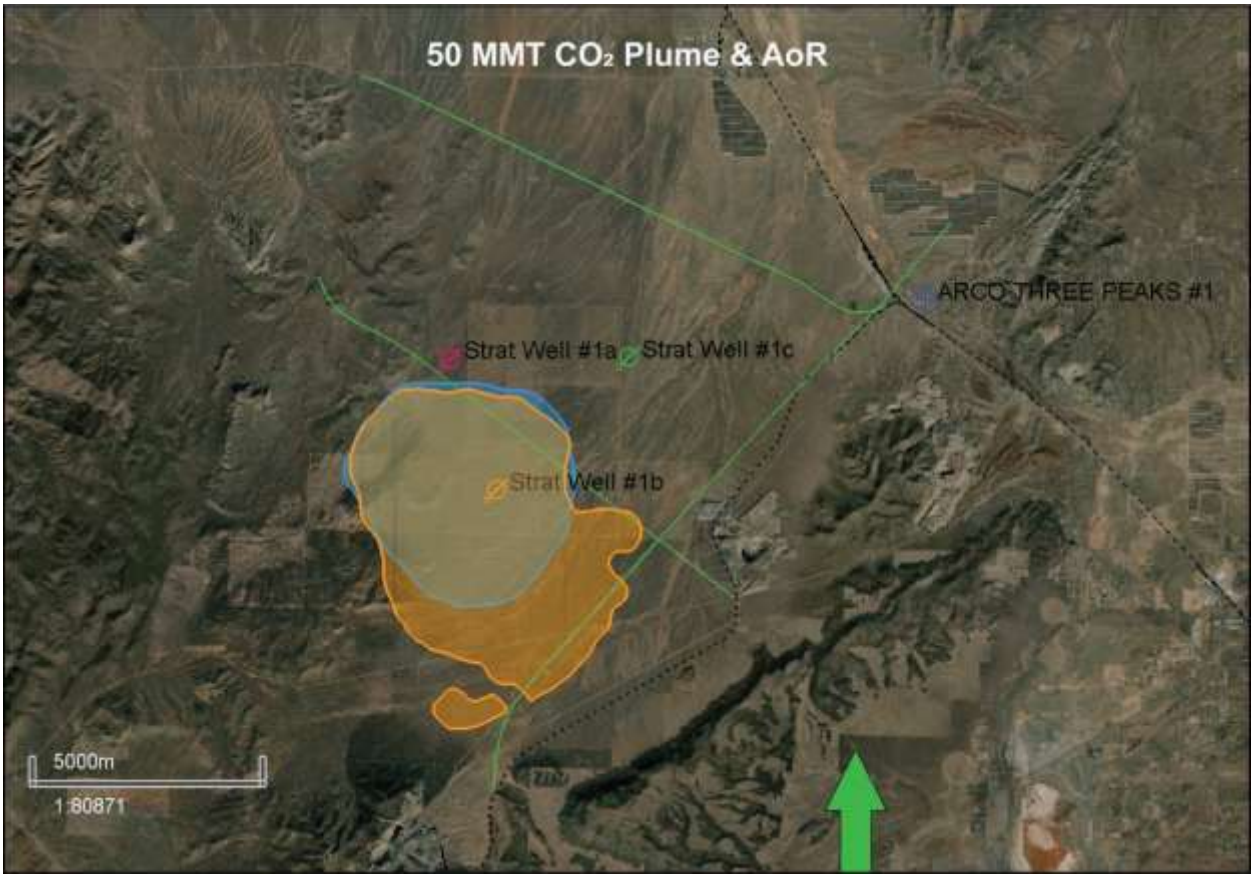


Figure 141 CO_2 plume size (blue polygon) and AoR (orange polygon) at the end of injection (2054) for the 50-million-ton injection volume at well 1b

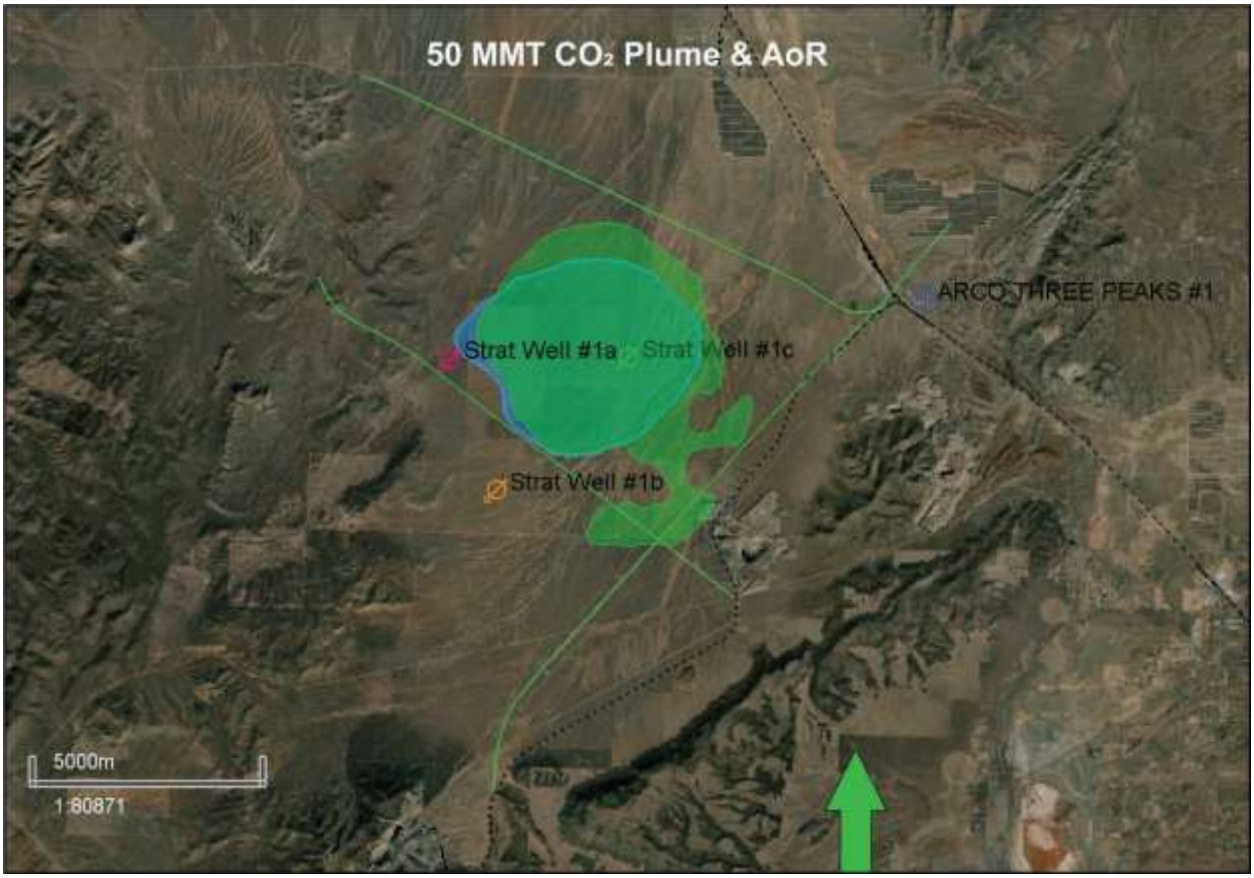


Figure 142 CO_2 plume size (blue polygon) and AoR (green polygon) at the end of injection (2054) for the 50-million-ton injection volume at well 1c

Conclusions

Task 3 integrated legacy 2D seismic interpretation, well control from the ARCO Three Peaks #1 well, petrophysical data from cuttings/core and outcrop analyses, and screening- to simulation-level modeling to evaluate CO_2 storage feasibility in the Navajo Sandstone beneath the Iron Mountain project area. Collectively, this workflow establishes a technical basis for injection scenario design and Class VI relevant performance metrics (injectivity, pressure response, plume footprint, and AoR extent), while also identifying the subsurface uncertainties that most strongly control storage performance.

Seismic processing and interpretation demonstrate that the legacy 2D datasets can resolve key structural and stratigraphic features, including imaging of the quartz monzonite laccolith boundary along the better-quality lines. LANL's RTM reprocessing and ML-assisted fault detection further indicate that faults can be mapped on the improved images, supporting ongoing refinement of the structural understanding; however, the limited 2D geometry and variable data quality (particularly on Line GSI-SU-13) remain a fundamental constraint on confidently defining a complete fault framework without additional 3D seismic coverage.

The Petrel® geological model (built from the interpreted horizons and available petrophysical constraints) provided the structural and property framework for screening and dynamic simulation. CO_2SCREEN results for the 104.4 km² Neck of the Desert assessment area indicate a

probabilistic storage resource ranging from 8.78 to 206.73 MMt, with a median (P50) estimate of 54.92 MMt, supporting multi-decade storage of Utah Iron's anticipated captured CO_2 volumes under most plausible parameter combinations.

Dynamic simulations executed in Eclipse (30 years injection plus 50 years PISC) show sustained injectivity without pressure-limited rate reduction under the modeled assumptions, for both the anticipated operational-rate case (0.704 MMt/yr; 21.1 MMt total) and higher-rate stress-test cases (1.56 MMt/yr; approximately 50 MMt total). The modeled pressure response remains modest across all scenarios, with the maximum well-site pressure increase reaching about 130 psi in the evaluated cases. CO_2 trapping evolution is consistent with expectations for deep saline injection: dissolution progresses throughout the simulation period, reaching about 19% dissolved in the lower-rate scenario and between 16% to 18% dissolved in the higher-rate scenarios by the end of the 80-year modeled period.

CO_2 Plume behavior is characterized by approximately linear areal growth during injection and a decreasing post-injection growth rate as the plume stabilizes (with postinjection areal growth declining to less than approximately 2% per year). Unlike the pressure response, which shows minimal differences among the candidate sites at the modeled scale, final plume footprint is distinctly site dependent, indicating that well placement and local stratigraphic/structural variability can influence plume migration and therefore monitoring design.

Under the hydrostatic AoR framework applied here, the operational-rate case (21.1 MMt total injected) produces no AoR because modeled pressure increases remain below the allowable pressure increase across the modeled domain, an outcome that is favorable for the planned DRI capture scale (0.75 MMt/yr). For the higher-rate cases, AoR footprints are present but remain broadly comparable in magnitude to plume footprints, ranging from 5.30 to 10.58 square miles, with the maximum AoR extent occurring at the Well #1b location.

Overall, all three sites are excellent candidates for CO_2 sequestration of effluent from the planned DRI plant, a positive picture for CCUS at the Iron Springs mine.

Risk Assessment

The primary technical focus under Task 4 was induced seismicity risk, particularly related to the Antelope Range Fault and other Basin-and-Range style normal faults in the vicinity of the proposed storage complex.

Dr. McCormack compiled historical seismicity data and focal mechanisms from regional catalogs, confirming a normal-fault dominated stress regime consistent with extension in southwestern Utah. The state of stress at depth was estimated using stress gradients and coefficients from published relationships, assuming that the least principal stress is near frictional failure and that pore pressures are initially hydrostatic.

Using these stress models, the team developed probabilistic geomechanical analyses for the Antelope Range Fault, treating fault dip and depth extent as key uncertain parameters. A Monte Carlo approach, with multiple realizations over plausible dip scenarios, yielded Coulomb failure function distributions that show the fault system is within roughly one hundred psi of frictional failure under baseline conditions. This result implies that modest perturbations in pore pressure or stress associated with CO_2 injection could, in principle, bring portions of the fault to failure if they hydraulically communicate with the storage interval.

The work concluded that induced seismicity risk at Iron Mountain is not prohibitive but is highly sensitive to the precise geometry and connectivity of major faults, as well as to the true in-situ stress state. These findings emphasize the importance of improved imaging and characterization of the Antelope Range Fault and related structures, as well as careful operational planning for injection rates and pressure management. Subtask 4.1 was reported as complete by early 2024, with results prepared for publication and for inclusion in the project's Final Report.

Constraining Induced Seismicity Hazard on the Neck of the Desert Fault for the Proposed Iron Mountain, Utah, Carbon Sequestration Project

As significantly more focus is placed on carbon sequestration as a means to help mitigate the progression of climate change, the need to adequately characterize an injection target for its induced seismicity potential becomes more apparent. In the Iron Mountain project in Southern Utah, a single fault is identified in the Neck of the Desert near Iron Mountain. The dip of the fault is unknown, and the geomechanical stability of the fault (i.e., distribution of Coulomb failure functions (CFFs)) is highly dependent upon the dip. For some dips, such as 15 degrees, the hazard from injection is low. For other dips, such as 75 degrees, the hazard is high. Another key consideration is the depth of penetration of the fault. Should the fault not penetrate the stress and pressure perturbed region from injection, it will not be induced to fail. Thus, understanding the dip and the depth of penetration of the fault will greatly improve our understanding of the likelihood of inducing an earthquake.

Introduction

The process of reducing iron typically requires heating the ore to high temperatures (>1,000°F), but the technique of direct reduced iron utilizes a syngas to catalyze the reduction process at lower temperatures (Anameric and Kawatra 2007). A byproduct of this reaction is carbon dioxide. The Iron Mountain iron mine in Southern Utah will upgrade its reduction facilities to use this process and is actively seeking an environmentally sound means to dispose of the carbon dioxide waste. Geologic carbon sequestration has been proposed in the Navajo Sandstone at a depth of roughly 6300 feet in the Neck of the Desert near the mine. Federally funded characterization efforts for the subsurface in the region of interest are being undertaken by a consortium of universities, private industry, and national labs.

One element of the characterization is the assessment of induced seismicity potential. While carbon sequestration has yet to induce a damaging earthquake, the largest was possibly a magnitude 4.4 in the Cogdell oilfield in Texas (Gan and Frohlich 2013; White and Foxall 2016), the potential exists for more potent events, especially as more projects become funded. To ensure that the social license to operate subsurface injection projects remains intact, it is essential to do an initial assessment of the potential for seismicity (Vilarrasa et al. 2019; Templeton et al. 2023). This paper illustrates the methodology applied to the LiDAR-identified Neck of the Desert fault, using probabilistic Mohr-Coulomb theory, and demonstrates that the hazard of the fault is highly dependent on the dip, which is a difficult parameter to constrain.

Past Seismicity

Prior to initiating injection projects, it is important to examine the seismic activity in the region. **Figure 143** shows the recorded seismic events on instruments from the United States Geological Survey between October 1998 and October 2023 (25 years). In total, there are 831 events in the region, and they concentrate in the Cedar Valley. To the west, in the Neck of the Desert, there are fewer events recorded, but seismicity is still present. The inset of **Figure 143** shows that the maximum magnitude event was 4.1 with a magnitude of completion of the catalog of roughly 1.5. The majority of the events have magnitudes below 2.0 although larger events are also present. Of note as well is the geologically mapped Antelope Range Fault in the western portion of the study area, which does not appear to have been seismically active in the last 25 years. The degree of seismicity present in the Neck of the Desert and the surrounding area, especially the Cedar Valley, should be considered carefully by the project team as they develop their injection plan.

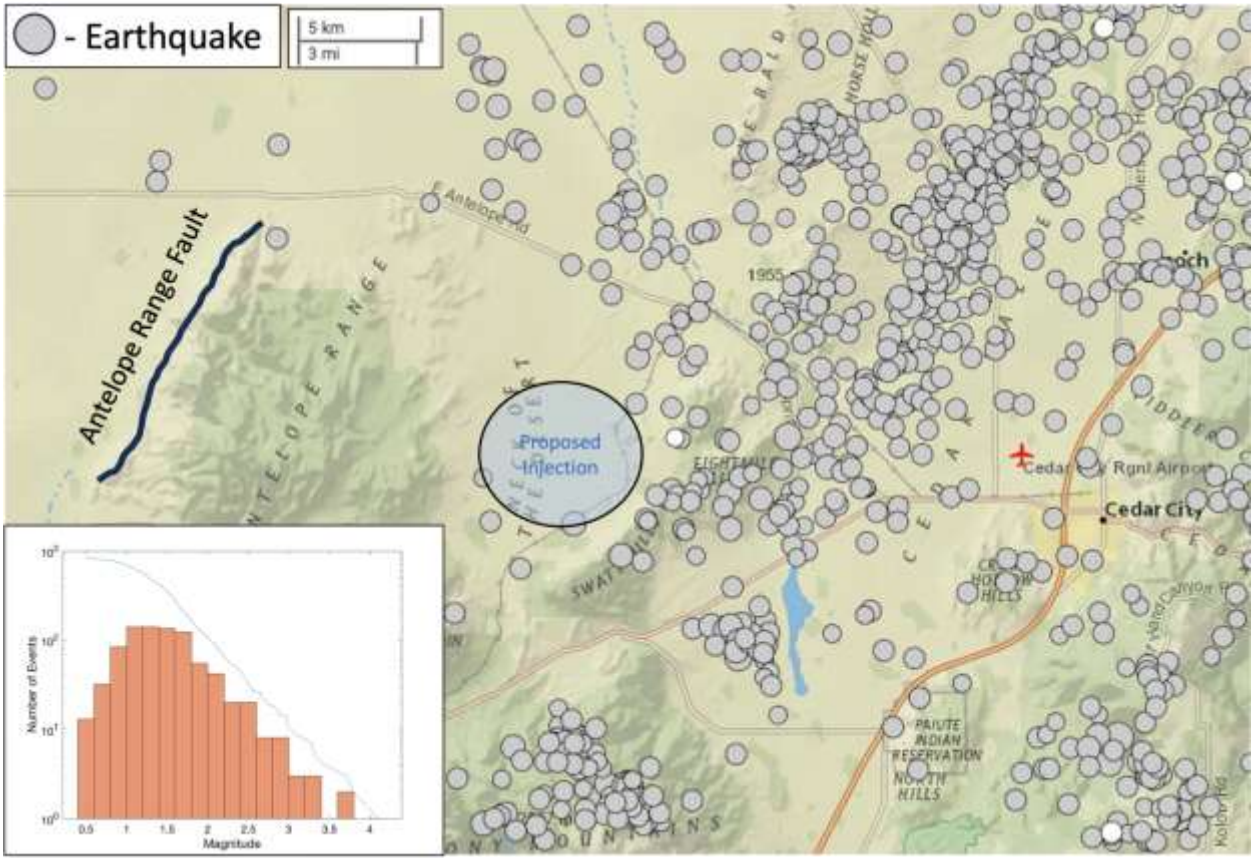


Figure 143 A map of the past seismicity in the Neck of the Desert and surrounding regions. The inset shows a Gutenberg–Richter plot of the 831 events depicted on the map.

Input Parameters

Fault Location, Size, and Orientation

The first input parameter of the characterization is the fault geometry. This has been inferred from LiDAR data collected by the Utah Geological Survey. While it is open to interpretation, the

data indicate that a fault striking at roughly 10 degrees cuts through the target location for the injection (**Figure 144**). We term this fault the Neck of the Desert fault. Other faults may exist in the region but are not expressed at the surface. Some researchers have demonstrated that often faults that host large, induced events, such as the Pawnee Mw 5.8 event, are not capable of being detected beforehand (Brocher et al. 2015; Kolawale et al. 2019). The hazard associated with such faults cannot be fully mitigated (Templeton et al. 2023), but in the event that there is a large, known fault oriented close to failure relative to the stress field, the project team needs to be made aware of the hazard. Should the project proceed, extra efforts must be made to avoid pressurizing the problematic fault. Therefore, although not every fault can be detected prior to injection, those faults that can must be scrutinized for their ability to host large earthquakes. Also, the Neck of the Desert fault appears to transect the proposed injection site, which could be problematic for storage regardless of seismic potential.

The surface trace of the Neck of the Desert fault is several miles long, yet the subsurface structure is unknown. For the purposes of being conservative, this paper assumes that the fault reaches to the depth of the Navajo Sandstone (the injection reservoir), the top of which is roughly 6290 feet deep. This assumption, however, is critical. Should the depth of penetration of the fault not reach the region around the injection, it will unlikely host an induced event. Soliva et al. (2008) indicated that in most normal faults, the surface extent typically is larger when the depth of penetration is larger. Therefore, the large surface extent of the fault implies a deeper depth of penetration, but more data is needed before we can ascertain if it reaches the Navajo Sandstone.

The strike of the fault is roughly ten degrees, but the dip is unconstrained. Given its location at the edge of the Basin and Range, it is reasonable to assume that this is a low-angle normal fault (Wernicke 1981), but we do not limit our investigation by this possibility. Instead, we analyze the fault for a suite of possible dips ranging from 0 degrees to 90 degrees.

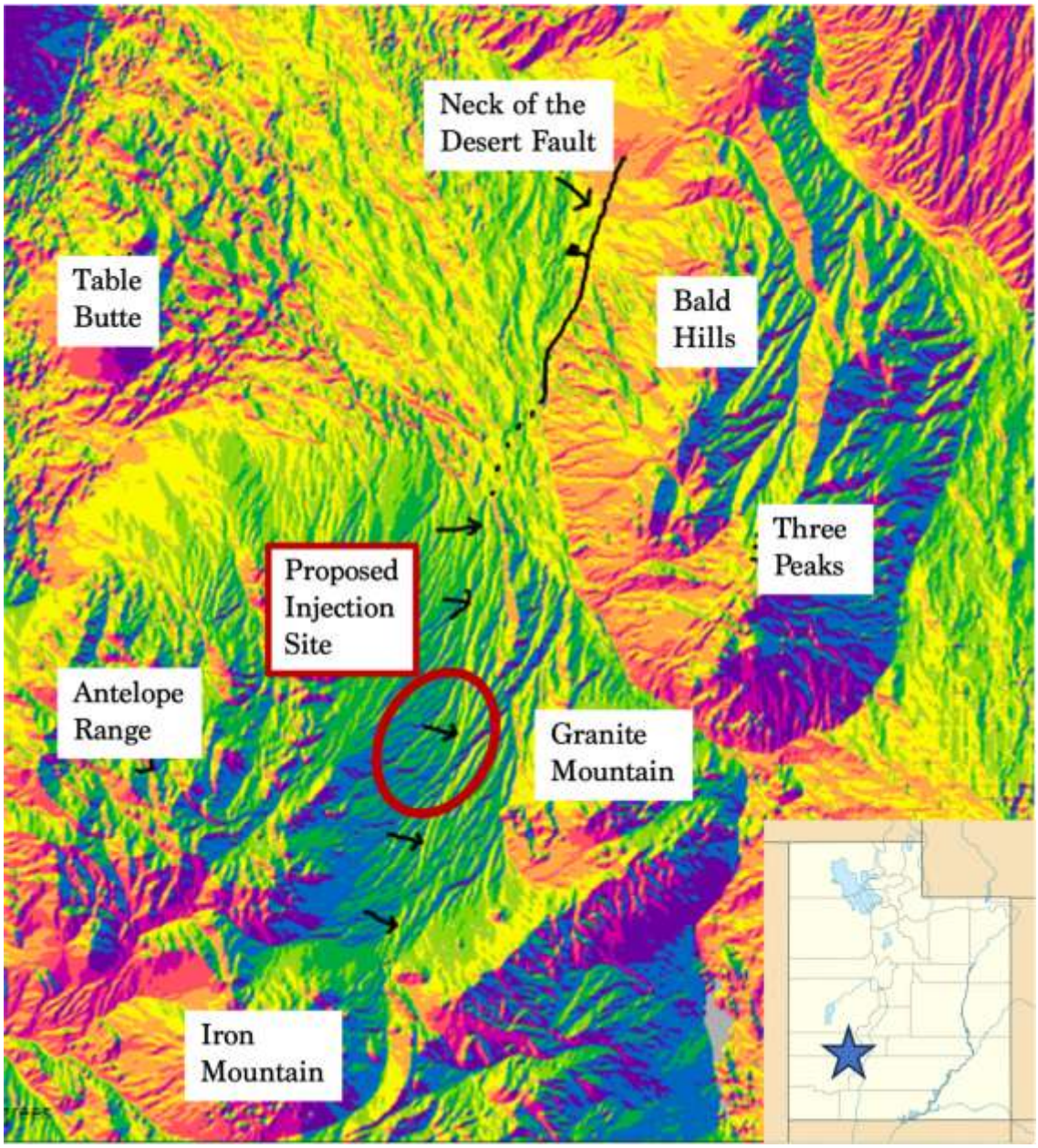


Figure 144 LiDAR data in the region of interest. The black arrows point to the inferred fault studied in this paper.

Pore Pressure

There is not sufficient information to determine the pore pressure at depth in the Neck of the Desert region. Therefore, we make the assumption that the pore pressure is nearly hydrostatically pressured, which is not always a valid assumption in deep sedimentary formations, but when the sedimentation rate is slow, hydrostatic conditions are common (Zhang 2011). As a result, we assume that there is error in our assumption of hydrostatic pore pressure, but not to the degree that it obfuscates the analysis.

Coefficient of Friction

Geologic materials have been seen to have coefficients of friction between 0.6 and 0.8 (Dieterich 1972). Other authors have shown coefficients as high as 1.0 (Dieterich and Conrad 1984). Byerlee (1978) showed that a value of 0.6 describes most materials, so we elect to use this value as the mean of our distribution for the coefficient of friction.

Maximum Horizontal Stress Direction

The maximum horizontal principal stress direction is often considered to be a function of tectonics and physiographic provinces (Zoback and Zoack 1980). In our case, we obtain this parameter from regional maps (Lund Snee and Zoback 2022). The closest indicators are within roughly 100 miles and agree on a measurement of roughly 40 degrees of azimuth.

Principal Stresses

The vertical stress is assumed to have a gradient of 1.07 psi/ft. This value is observed in the Paradox Basin about a hundred miles to the east of the Neck of the Desert (McCormack et al. 2023). The vertical stress is typically measured with density logs, which are not present for this region. Thus, we need to use the nearby proxy of the Paradox Basin.

The least horizontal principal stress is calculated using frictional faulting equilibrium (Zoback 2007). This calculation assumes the same coefficient of friction of 0.6. The assumption here is that the stress in the earth cannot fall below the threshold because well-oriented faults will slip, relaxing the stress. Furthermore, the assumption that the earth is close to critically stressed in most regions (Townend and Zoback 2000) indicates that the least horizontal stress will not greatly exceed this threshold.

The maximum horizontal principal stress is calculated using Simpson's coefficient method (McCormack et al. 2023). This method takes the Simpson's coefficient from regional maps (Lund Snee and Zoback 2022) to approximate a lower bound for the maximum horizontal principal stress by using the pore pressure and the equation of frictional faulting equilibrium for a normal faulting environment. Normal faulting is essential for this method to work, and in the Neck of the Desert, the vertical stress appears to be the maximum stress as determined from regional maps. The model of the stress state that we use is show in **Figure 145**.

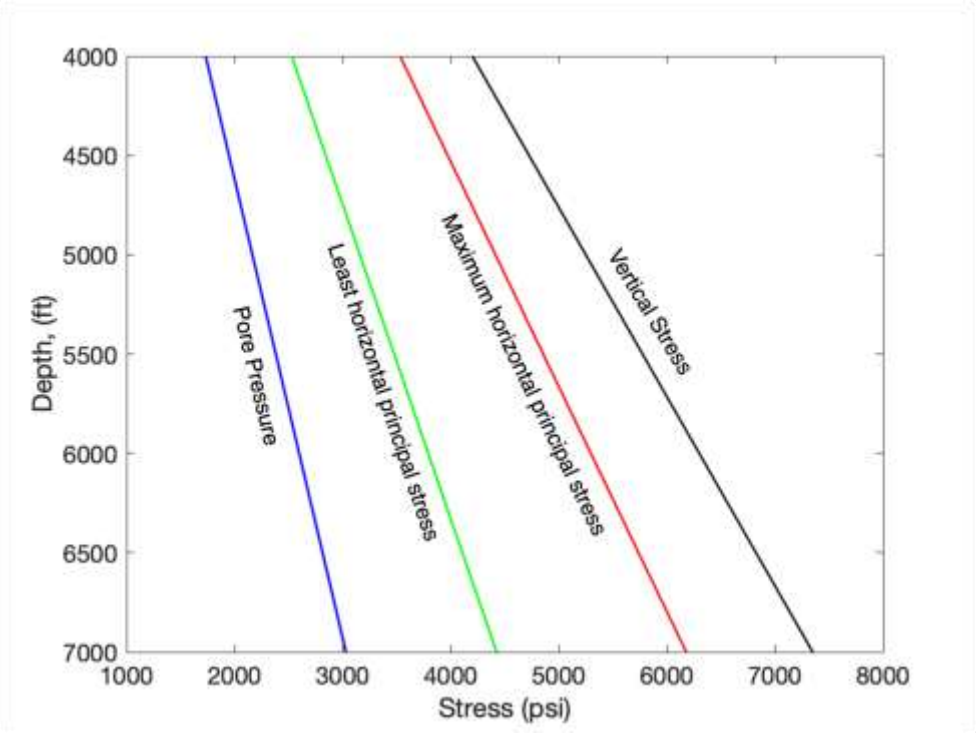


Figure 145 The stress state obtained from the Simpson's coefficient method.

The stress state is a model that suffers from the lack of available data. We use hydrostatic pore pressure, and a Simpson's coefficient value of 0.6 to obtain this model. If additional data were available, such as core data, diagnostic fracture injection test data, or image logs, the state of stress could be more reliably constrained. Nonetheless, this simple model represents the best of our knowledge, and can be used in the subsequent analyses of the hazard of induced seismicity.

Methodology

After choosing distributions for the input parameters, the next step in the probabilistic geomechanics workflow is to sample from each distribution in a Monte Carlo fashion and propagate the realizations through a geomechanical model (Walsh and Zoback 2016; McCormack et al. 2022). **Figure 146** shows the Mohr circles of this forward propagation on twenty realizations out of twenty thousand for six scenarios of the dip: Uniform, 15 degrees, 30 degrees, 45 degrees, 60 degrees, and 75 degrees. These values are chosen to elucidate the difference in the final distribution of Coulomb failure functions that results in different input distributions for the dip. The direction of dip, that is, east or west, was also tested but was found to have a minimal impact. The minimal impact is due to the similarity between the strike and the direction of maximum horizontal principal stress.

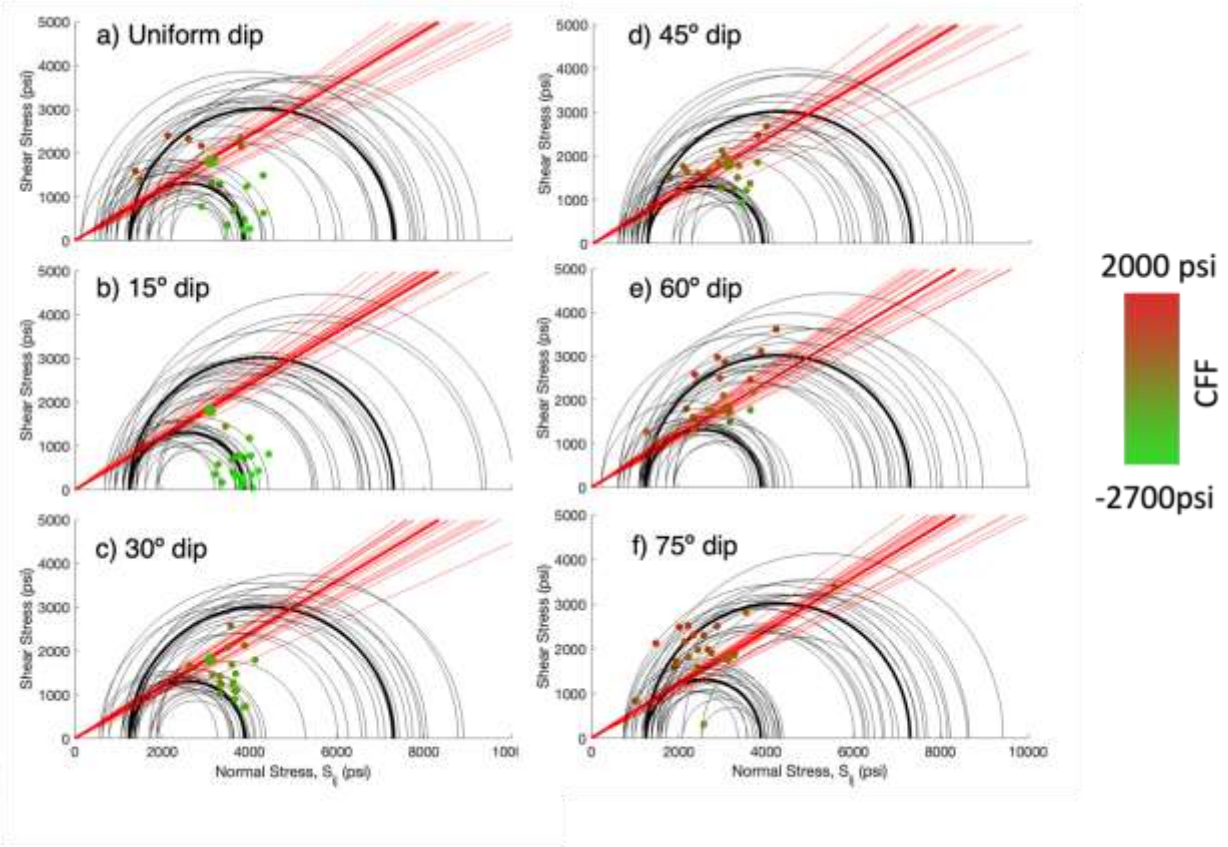


Figure 146 Probabilistic Mohr circles for the six scenarios of dip. a) Uniform dip, b) 15° dip, c) 30° dip, d) 45° dip, e) 60° dip, and f) 75° dip. The bold lines represent the mean values for the stresses and the coefficienct of friction.

Results

The distributions of the Coulomb failure functions for each of the six scenarios of dip are shown in **Figure 147**. There is a clear dependence of the distributions of the Coulomb failure functions on the dip. In the case of the uniform dip ranging from 0 degrees to 90 degrees, the distribution has the highest standard deviation as more possible orientations are sampled. As the sampling becomes narrower in the subsequent dip distributions, the resulting distributions of the Coulomb failure function also become narrower. The lower the mean dip, the lower the CFF due to the relation between the fault orientation and the stress state, and conversely, when the mean dip is higher, the hazard is also higher. The mean of the CFF distribution for the uniform dip input and the 45-degree dip input is similar because the mean of the uniform distribution is also 45 degrees. The difference is sampling a narrower normal distribution in the 45-degree case versus a wider uniform distribution. We do not analyze a dip of 90 degrees because as a normal fault, it is unrealistic for the dip to be that high.

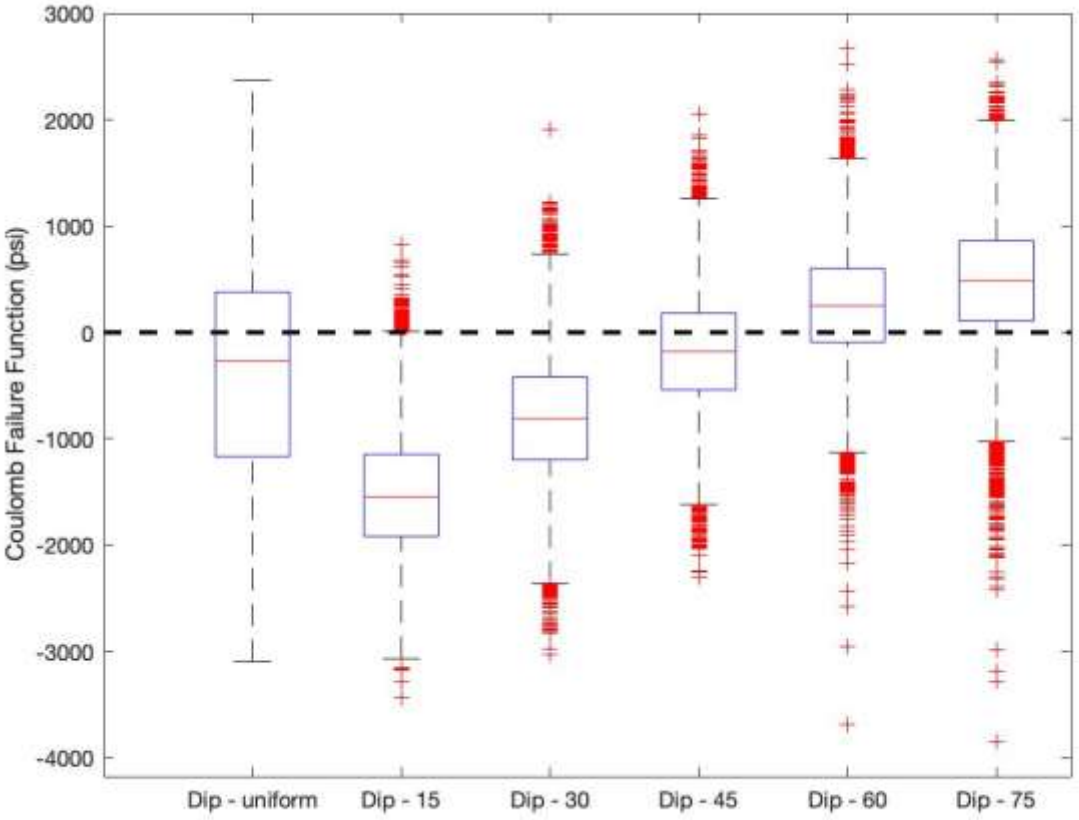


Figure 147 Six distributions of CFFs using six different inputs of the dip of the Neck of the Desert fault

Discussion

The difference between the CFF distributions for the different mean dips underscores the importance of constraining this parameter. Seismic surveys, especially 3D surveys, have the potential to vastly improve our understanding of the orientation of the Neck of the Desert fault (Gibson et al. 2005; Bahorich and Farmer 1995). Currently, there is substantial work in the literature to use machine learning to automatically detect faults in 3D seismic volumes, which may elucidate additional features that should be analyzed in the same manner as the Neck of the Desert fault (Li et al. 2022; Bi et al. 202; Wang et al. 2018).

In addition to seismic surveys, geologic inference can also constrain the orientation of the faults. Cross sections such as that in Rowley and Barker (1978) can inform which dips are more likely to be present in the larger faults, such as the Neck of the Desert fault. While geologic inference is not as reliable as seismic surveys, it is a reasonable first approach to narrow the breadth of the investigation.

The relative sensitivities of the different input parameters in the model are shown for the uniform dip distribution in **Figure 148**. These sensitivities clearly show the importance of the dip, but other parameters such as the coefficient of friction or the principal stresses also have an impact. Additional data will further improve the uncertainty in the input parameters. Specifically,

laboratory tests of friction, in situ measurements of least principal stress, direct borehole measurements of pore pressure, borehole failures related to the direction of the maximum horizontal principal stress, as well as a more detailed, site-specific understanding of the Simpson's coefficient will all benefit the analysis.

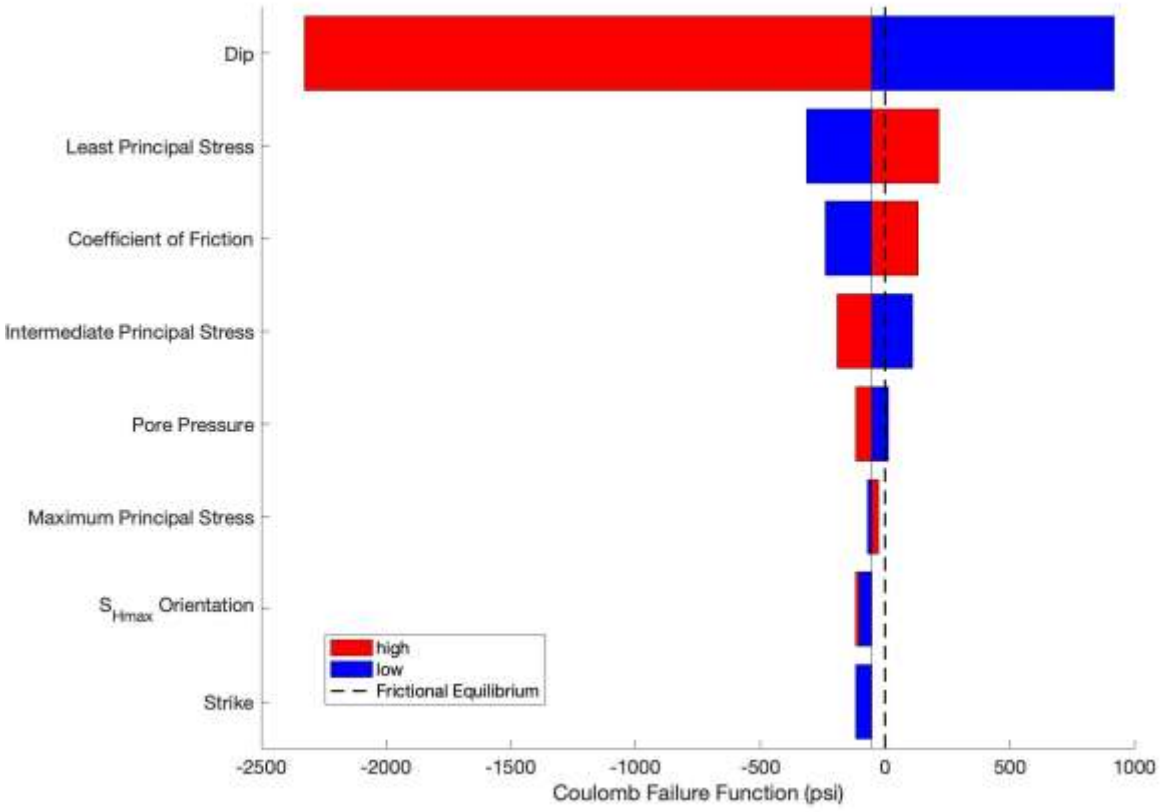


Figure 148 The sensitivity of the CFF to each of the input parameters in the uniform distribution of dip. The dip is the most sensitive.

The hazard associated with the Neck of the Desert fault is dependent on whether or not it reaches depths of the injection. Around the injection there is a 3D region, which possesses elevated pore pressures, and around that region, there is another volume, which possesses altered stresses due to poroelasticity (Detournay and Cheng 1993). If the fault does not interact with these regions, the hazard is significantly lessened. Also, the fault can only provide a conduit for the escape of carbon dioxide or migration of brine if it intersects the Navajo Sandstone. Therefore, it is important to assess the depth of penetration of this major fault.

The major faults are not the only faults that may be induced to fail in the event of the injection of the carbon dioxide. Smaller faults, even so small that they cannot be detected, can also host microseismic events. In an EOR field in Texas, Qin et al. (2023) showed that the preponderance of earthquakes were relatively small magnitude and concentrated in certain layers of higher density of fractures. Thus, it is important that the subsurface is fully characterized to avoid

fractures that may host microseismicity near the caprock because that could denigrate the integrity of the seal.

Conclusions

Using the available data at the Neck of the Desert proposed carbon sequestration site, we have detailed the hazard along an identified fault that cuts the proposed injection site. Even in the event that the fault is not close to failure, it may have implications for the ability to store the carbon because it may provide a pathway for leakage. A key consideration both in terms of seismicity and leakage is the depth to which the fault penetrates. Both the depth of penetration and the dip of the fault are, at present, highly uncertain. The hazard of the fault failing is higher for higher dips and conversely, lower for lower dips. Further characterization is required to understand how problematic the Neck of the Desert fault might be for the proposed injection.

Nontechnical Issues / Scenario Analysis

Task 5 activities addressed pipeline routing, non-technical risks, and the broader policy and outreach context for Iron Mountain.

Carbon Solutions and MSU used the CostMAP and SimCCS toolchain to explore pipeline routing between the Utah Iron plant and candidate injection sites. Cost surfaces incorporated land cover, slope, population density, roads, railways, rivers, transmission lines, and the plant boundary, and distinguished barriers from potential corridors. An early analysis considered multiple candidate source–sink combinations and produced optimal pipeline alignments in a multi-source/multi-sink framework. Subsequent work explicitly incorporated Utah Iron rights-of-way, testing how strongly weighting these corridors in the cost surface alters the optimal route. This demonstrated that preferential use of existing rights-of-way can significantly re-route pipelines in the near-plant vicinity while leaving distal route segments largely unchanged.

The same workflow was then applied to “Plan B” injection sites located north of the primary Iron Mountain site, including candidate locations in the Escalante Desert and west of Parowan. New cost surfaces and pipeline routes were generated, and digital well logs were acquired for at least two of the alternate storage sites to begin evaluating their subsurface suitability. This pipeline-routing and scenario-analysis framework is designed to be reused and refined in future phases as additional storage sites or capacity expansion options are considered.

On the policy and regulatory side, the project benefitted from significant progress within the State of Utah. Earlier legislation established a carbon sequestration liability fund and a pathway for eventual transfer of long-term liability to the state. During the project period, Utah passed additional carbon capture and storage legislation (e.g., a Carbon Capture Amendments bill) that clarified aspects of long-term liability and financial assurance for Class VI projects. In parallel, the Utah Division of Oil, Gas and Mining advanced work on a state Class VI rule and preparations for seeking Class VI primacy from EPA. Project personnel were engaged in these discussions, ensuring that the technical work at Iron Mountain is aligned with the emerging regulatory framework that will ultimately govern a Class VI application and 45Q claims.

Outreach and non-technical risk activities included field trips for the UGS Advisory Board to Iron Mountain, presentations at scientific conferences (GSA, AAPG Rocky Mountain Section, AGU, SSA), and invited talks on Utah's emerging CCS portfolio. These efforts raised awareness of the Iron Mountain project among scientists, regulators, and the public, and helped position the site within the broader context of Utah's decarbonization strategy.

Formal economic assessments and detailed analyses of water rights, land and pore-space ownership, and long-term liability were largely deferred to future phases, but the groundwork laid through policy engagement and scenario analysis will facilitate those efforts.

Transport and Rights of Way

The goal of Subtask 5.1 is to build a cost surface for the vicinity of the Iron Mountain site to support identifying feasible pipeline transport corridors. Geospatial data was used to assess the economic viability of pipeline routing. Existing rights of way owned by Utah Iron were incorporated into the cost surface to reduce the logistical and economic burdens of pipeline routing. In particular, the team focused on pipeline routes that will transport captured CO_2 from the Iron Mountain capture site to nearby possible sequestration sites. This subtask is a key component of ensuring the economic and logistical feasibility of the Iron Mountain CCS effort.

To aid the construction of a cost surface to be used in the subsequent economic analysis, the team performed a preliminary transport and rights of way analysis using CostMAP^{PRO}. An area of interest was first identified that includes possible CO_2 storage sites along with the planned CO_2 source, Utah Iron (**Figure 149**).

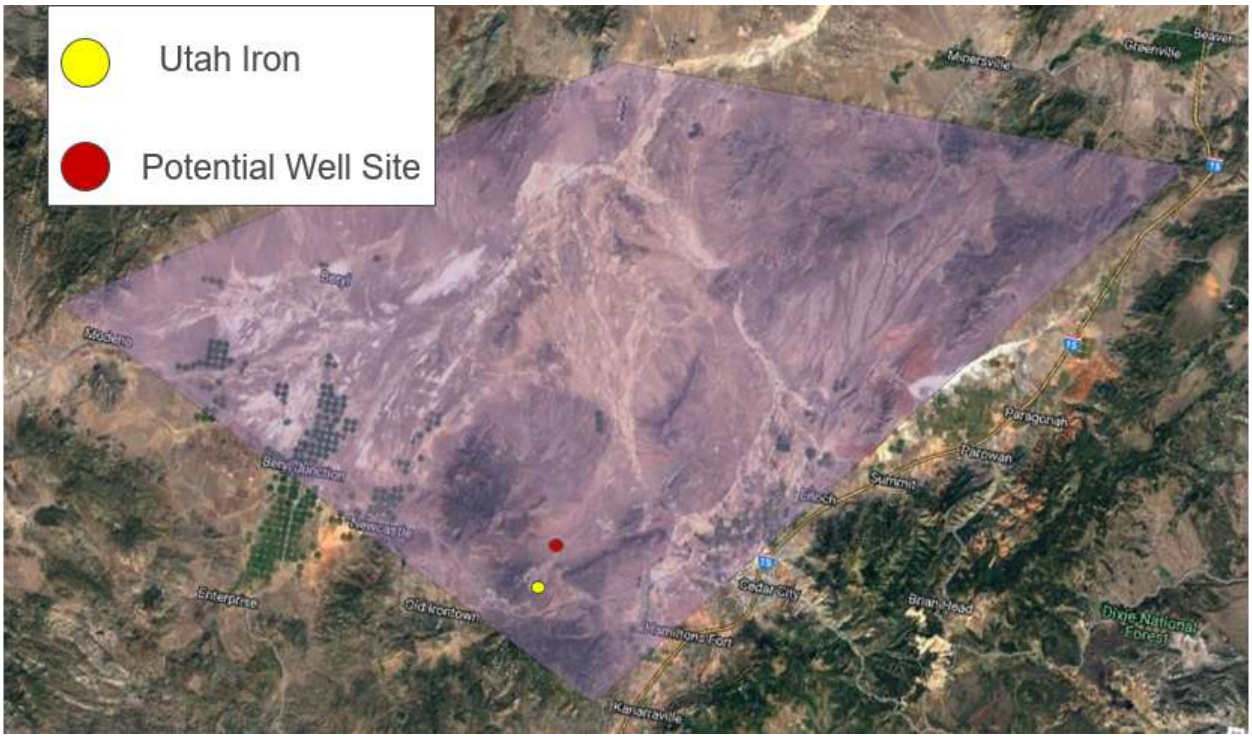


Figure 149 Delineated Area of Interest

Using this area of interest, relevant GIS data for the region was aggregated to help understand what geospatial locations were best suited to routing. This included data such as landcover, population, federal lands, and slope (**Figure 150**).

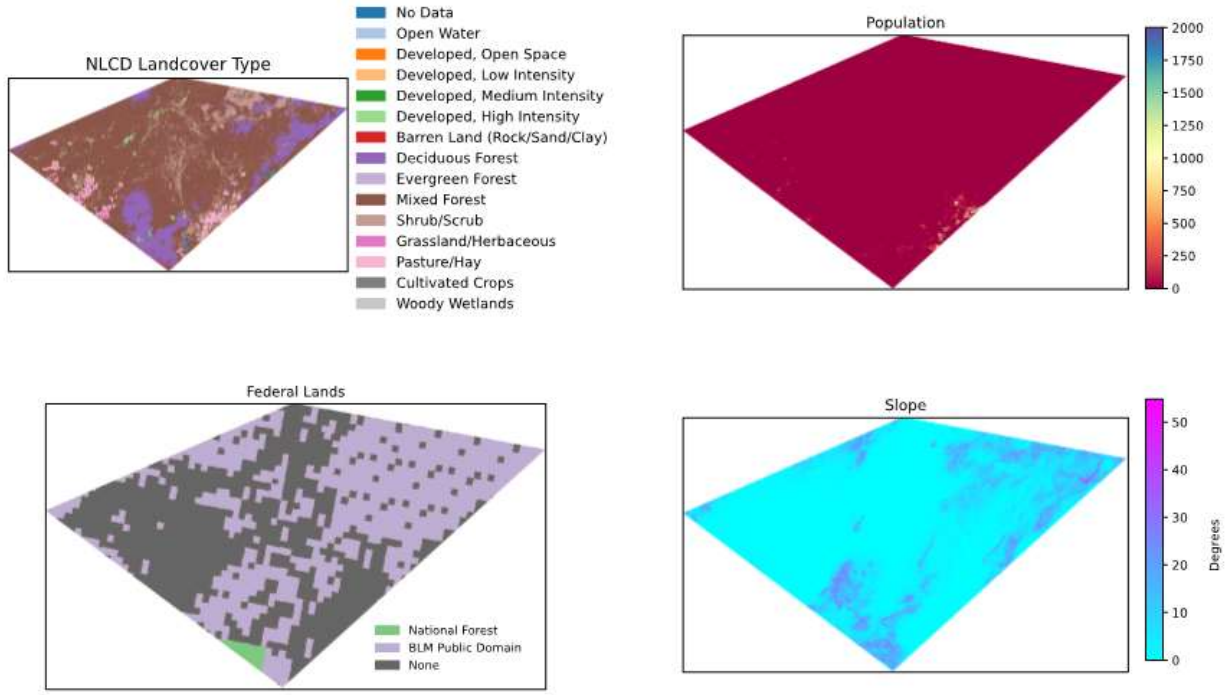


Figure 150 GIS data used by CostMAP^{PRO}

The CostMAP^{PRO} tool was used to identify barriers (**Figure 151**) and corridors (**Figure 152**) for pipeline routing in the area of interest. Barriers represent zones that ideally would not have a pipeline crossing, such as a road or railway. Conversely, corridors represent paths that are preferential to routing a pipeline, such as routing alongside a transmission line.



Figure 151 Barriers identified by CostMAP^{PRO}

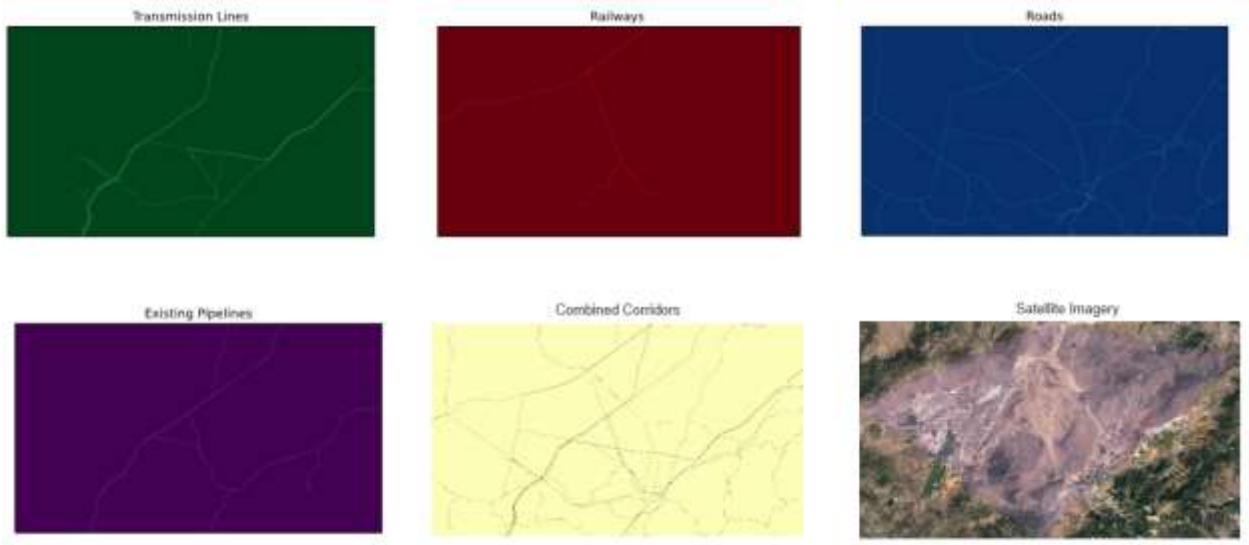


Figure 152 Corridors as identified by CostMAP[PRO]

The team was provided GIS data on existing rights of way owned by Utah Iron to be integrated into the pipeline modeling framework. **Figure 153** shows the rights of way supplied by Utah Iron for the project. These rights of way include electrical lines, gas pipelines, railroads, roadways, as well as the plant boundary.

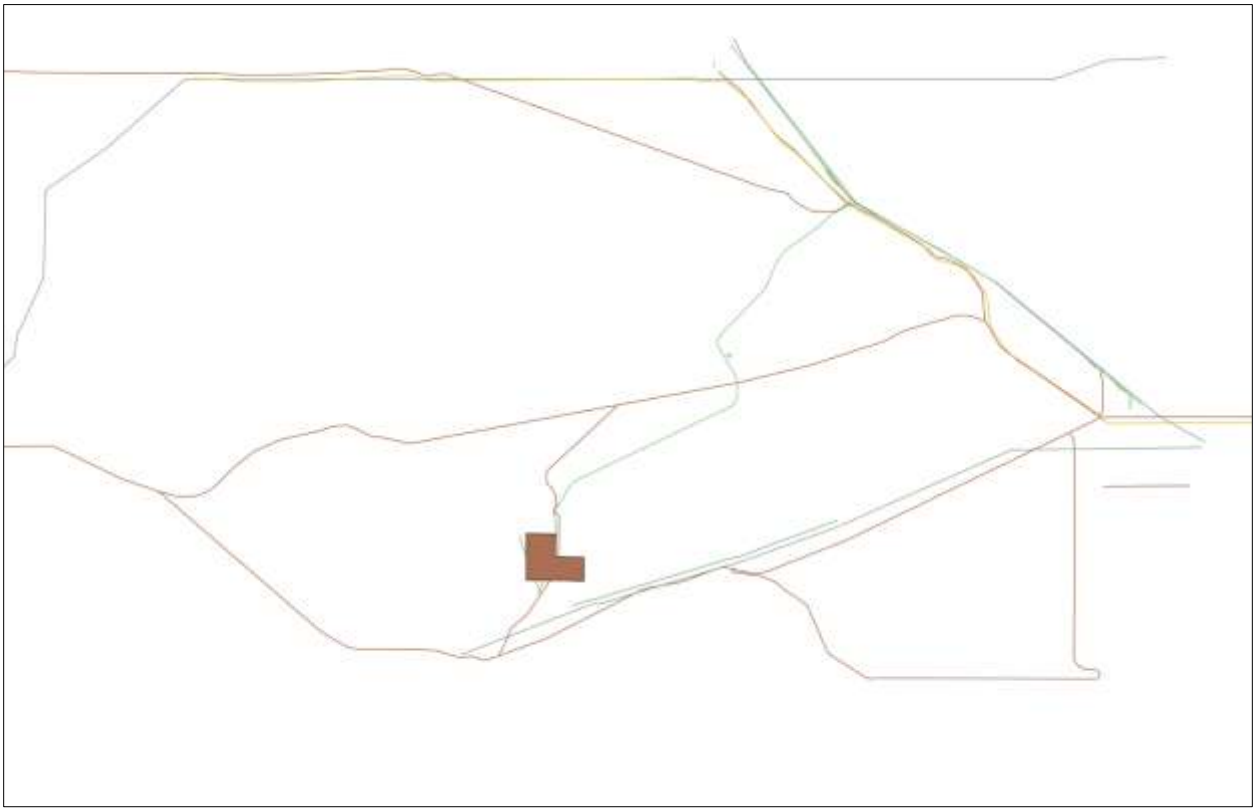


Figure 153 Utah Iron rights of way with plant boundary shape in center

All of the preceding GIS layers, barriers and corridors, and existing Utah Iron rights of way were combined in CostMAP^{PRO} to create a cost surface representing the cost of installing a pipeline (**Figure 154**).

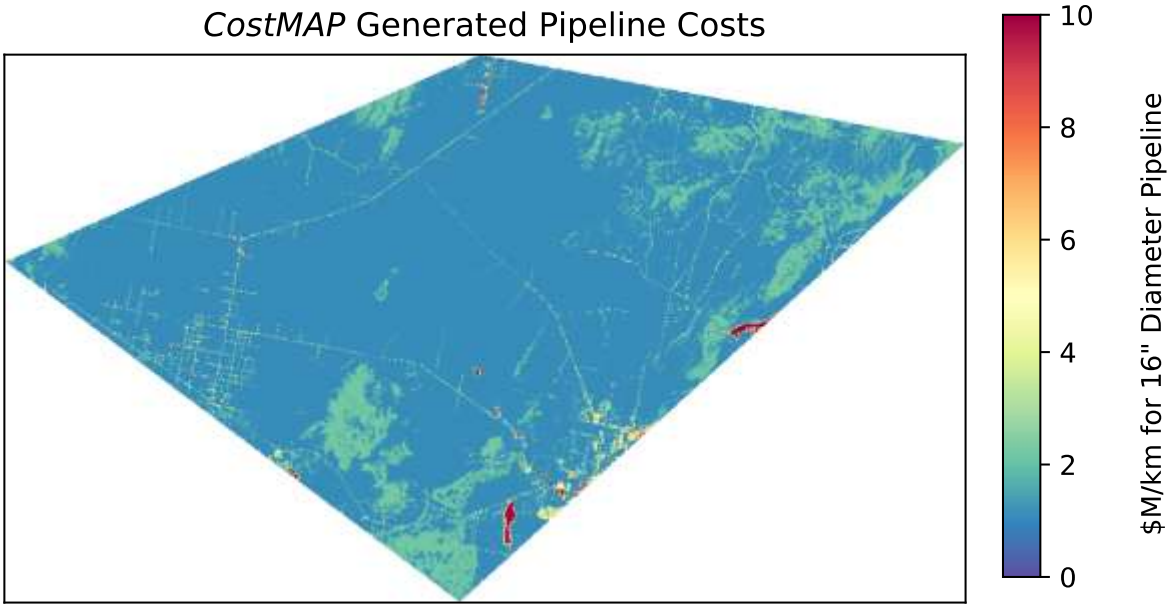


Figure 154 Pipeline cost calculated by CostMAP^{PRO}

The output of this Subtask was this cost surface that reflects the cost of routing pipelines in the vicinity of Iron Mountain. This cost surface is used by SimCCS^{PRO} to perform the Economic Assessment of Subtask 5.2.

Economic Assessment

The goal of Subtask 5.2 is to assess the economic implications of the proposed CCUS project. During the project, the team focused on exploring the most economically viable routing of CO_2 pipelines subject to various assumptions. Economic information related to pipeline routing was embedded in the cost surface constructed during Subtask 5.1. Cheapest pipeline routes were identified using SimCCS^{PRO} which implements a shortest path network construction scheme. The assumptions considered in this analysis included both the weighting of right of way priorities and contingency storage location planning.

The team explored two different ways of incorporating existing Utah Iron rights of way into the pipeline routing. The first was to merely add new rights of way to the existing cost surface while maintaining the weights normally allocated for right of ways. The second was to heavily bias the cost surface weights to prioritize using right of ways whenever possible. Cost surfaces for both of these options were generated. To test the effect of the two options on pipeline routing, cheapest pipeline routes were calculated by SimCCS^{PRO} in the cost surfaces between the anticipated capture location and the primary targeted storage location. The two paths generated are seen in **Figure 155**.

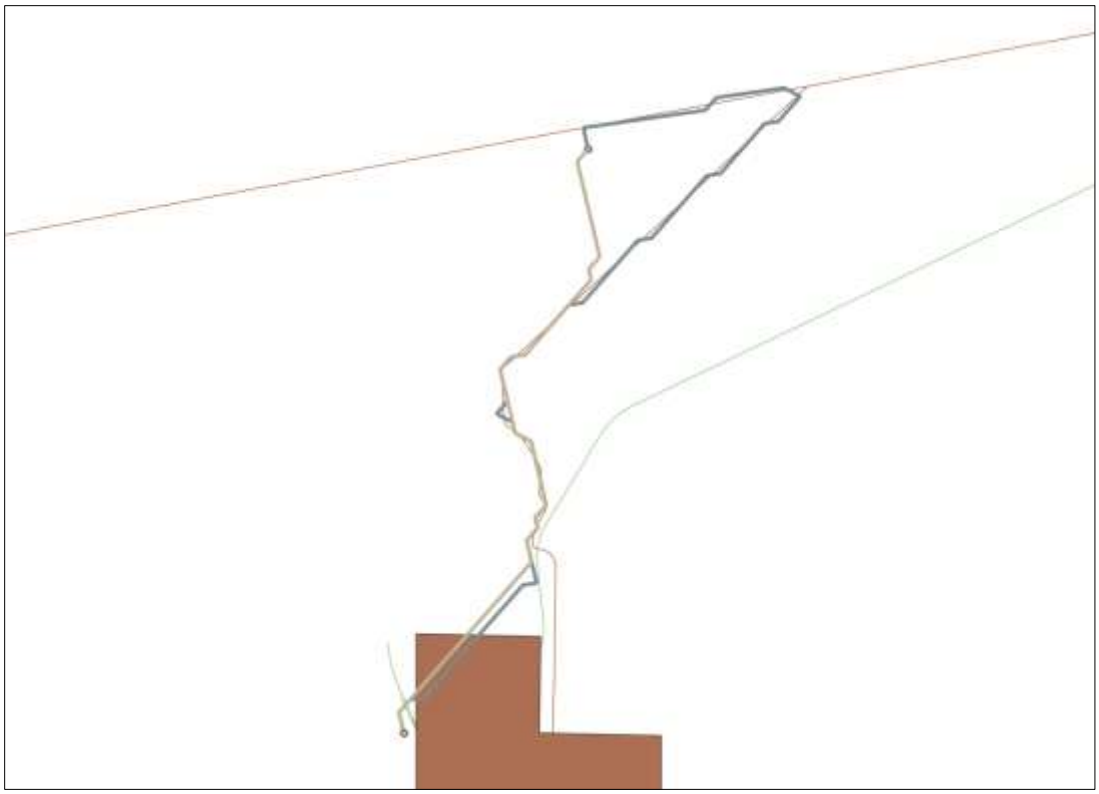


Figure 155 Optimal pipeline routs through cost surfaces with differing rights of way prioritization

The source location is the circle near the plant boundary shape and the storage location is the circle to the north. The tan source-to-storage path is the cheapest pipeline route generated through the cost surface where rights of way carry the default weight. The grey source-to-storage path is the cheapest pipeline route generated through the cost surface where rights of way are heavily prioritized. It can be seen that the grey path minimizes the distance travelled off of right of ways. Note that the jagged nature of the paths is due to the raster nature of the cost surface. The result of this exercise is to show that the Utah Iron designated right of ways have the potential to influence pipeline routing.

The team explored pipeline routes to alternate injection sites (Parowan site and Beaver Valley site) that was identified to the north of the primary injection site. Two new surfaces with a revised extent, beyond the initial area of interest, to include the new alternate injection sites were constructed to support this analysis. The first cost surface employed standard weighting techniques for rights of way prioritization. The second cost surface heavily biased routing to prioritize the existing rights of way owned by Utah Iron.

These new cost surfaces were used to calculate minimum cost pipeline routes between the capture location at Utah Iron and the alternate injection sites. **Figure 156** shows the pipeline routes generated by SimCCS^{PRO}, where the purple route is the route that uses standard weighting of rights of way and the green route is the route that heavily biases routing towards existing rights of way. The routes differ in the vicinity of Utah Iron, where the existing rights of way are highly prioritized. Outside of the Utah Iron vicinity, the routes coincide.

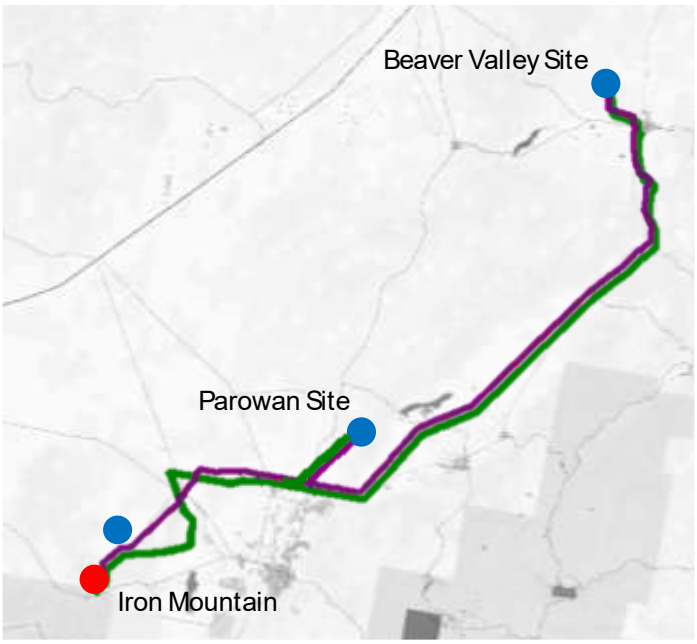


Figure 156 Pipeline routes from capture location to alternate storage sites. The green route heavily prioritizes existing Utah Iron rights of way and the purple route does not.

The analysis conducted as part of Subtask 5.2 demonstrated that leveraging existing rights of way could be a critical factor in determining CO_2 pipeline transport networks for the project. The ability to prioritize these corridors could reduce potential delays and logistical challenges associated with securing new land for pipeline routing. Additionally, the exploration of alternative storage locations provides a flexible, cost-effective contingency plan, ensuring the project can remain economically viable even in the face of unforeseen challenges. This is particularly true given the colocation of pipelines to the two alternate storage locations.

Outreach

Multiple outreach efforts were made throughout the focused project.

- CUSP annual meeting in 2022 a presentation was given showing the initial progress on the project
    1. Team was highlighted
    2. We highlighted that we were one of 12 focused projected selected and funded by CSUP.
    3. Presented the project concept and work plan and goals, including:
        - Site characterization, storage capacity assessment, and risks
        - Highlighted the goal to develop a “plan for a 3D seismic survey, and data collection to support a future MRV and/or UIC Class VI application”
    4. Highlighted the direct reduced iron process and why CCS was easily implementable into this process
    5. Showed the focus project location and existing seismic and well data
    6. Highlighted the plan to collect additional data and analysis
- AGU 2022 conference a poster was presented
    1. Show poster

Site Characterization for Geologic Carbon Storage of CO_2 from a Direct Reduced Iron Plant

Authors: Nathan Moodie(1), Eugene Szymanski(2), Michael D. Vanden Berg(2), Brian McPherson(3)

1. University of Utah, Energy & Geoscience Institute, Salt Lake City, UT
2. Utah Geological Survey, 1594 W. North Temple, Suite 3110, Salt Lake City, UT 84116
3. University of Utah, Department of Civil & Environmental Engineering, Salt Lake City, UT

Decarbonizing the industrial sector of our economy to meet climate goals and slow climate change is a challenging prospect. To meet these goals, industrial plants that process ethanol, fertilizer, cement, and iron and steel will need to either decarbonize or capture and sequester their CO_2 emissions. The primary objective of this study is decarbonization of iron processing through direct reduced iron (DRI) with CCS, in place of a traditional blast furnace. Iron ore is reduced to elemental iron by exposing the ore to a high-temperature (800–1,200°C) syngas (H_2 and CO) in a reactor vessel. The reaction releases CO_2, water, and unreacted syngas. The CO_2 and water are separated and unreacted syngas is recycled back into the reactor. This separation results in a source of low pressure, wet, nearly pure CO_2 that may be dried, compressed, transported and injected for permanent geologic sequestration or used for other industrial needs.

This analysis is a case study ("focus project") under the auspices of the Carbon Utilization and Storage Partnership (CUSP; U.S. Department of Energy Award DE-FE0031837). We are assessing the carbon storage potential of local subsurface geology near a proposed DRI plant in southern Utah. The primary objectives of this focused project include: (1) rigorous site characterization and analysis of storage capacity, risks and economic options for CCS, (2) a detailed plan for drilling a stratigraphic well and performing a 3D seismic survey, and (3) comprehensive plans for assembling UIC Class VI and 45Q tax credit applications. The targeted reservoir formation is the Jurassic Navajo Sandstone (SS) at about a 6,200 ft depth, which is stratigraphically overlain by potential sealing units of evaporite-rich Jurassic Temple Cap and limestone/mudstone-dominated Carmel Formations which, in certain areas, were intruded approximately 22 Ma by several thousand feet of quartz monzonite laccolith. Preliminary analysis indicate that the Navajo SS in this area is capable of storing at least 15 million tons of CO_2.

A goal of this study is to facilitate decision making needed to implement commercial-scale geologic carbon storage at a DRI facility. Demonstration of CCS with an iron-processing plant has not been attempted to date, and a goal is to provide a meaningful example for other iron and steel plants.

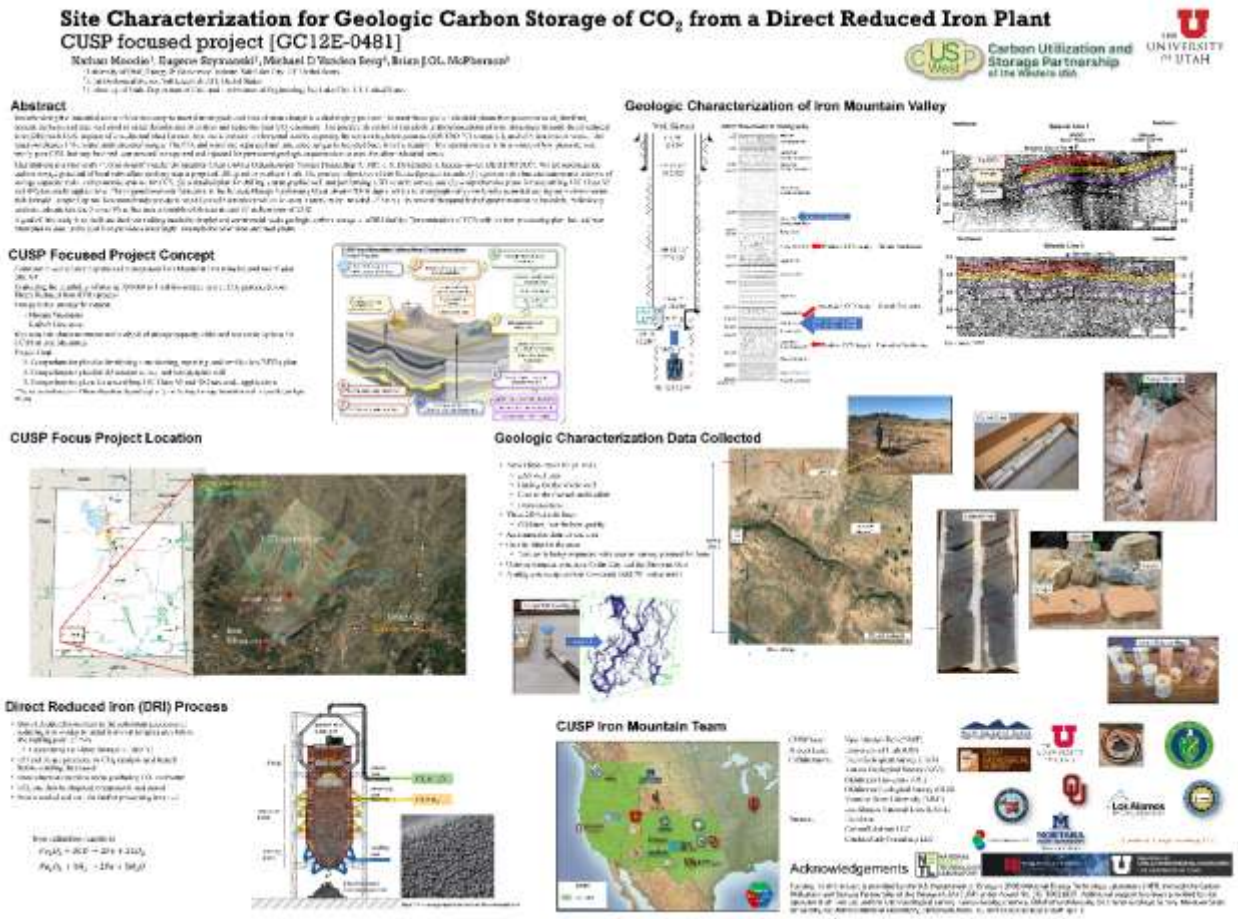


Figure 157 AGU 2022 poster

- Project progress was presented at the CUSP Annual Meeting in 2023 in the form of a poster highlighting the work done.

Poster Abstract

Decarbonizing the industrial sector of our economy to meet climate goals and slow climate change is a challenging prospect. To meet these goals, industrial plants that process ethanol, fertilizer, cement, and iron and steel will need to either decarbonize or capture and sequester their CO_2 emissions. The primary objective of this study is decarbonization of iron processing through direct reduced iron (DRI) with CCS, in place of a traditional blast furnace. Iron ore is reduced to elemental iron by exposing the ore to a high-temperature (800–1,200°C) syngas (H_2 and CO) in a reactor vessel. The reaction releases CO_2, water, and unreacted syngas. The CO_2 and water are separated and unreacted syngas is recycled back into the reactor. This separation results in a source of low pressure, wet, nearly pure CO_2 that may be dried, compressed, transported and injected for permanent geologic sequestration or used for other industrial needs.

This analysis is a case study ("focus project") under the auspices of the Carbon Utilization and Storage Partnership (CUSP). We are assessing the carbon storage potential of local subsurface geology near a proposed DRI plant in southern Utah. The primary objectives of this focused project include: (1) rigorous site characterization and analysis of storage capacity, risks and

economic options for CCS, (2) a detailed plan for drilling a stratigraphic well and performing a 3D seismic survey, and (3) comprehensive plans for assembling UIC Class VI and 45Q tax credit applications. The targeted reservoir formation is the Jurassic Navajo Sandstone (SS) at about 6200 ft depth, which is stratigraphically overlain by potential sealing units of evaporite-rich Jurassic Temple Cap and limestone/mudstone-dominated Carmel Formations which, in certain areas, were intruded approximately 22 Ma by several thousand feet of quartz monzonite laccolith. Preliminary analysis indicate that the Navajo SS in this area is capable of storing at least 15 million tons of CO_2.

A goal of this study is to facilitate decision making needed to implement commercial-scale geologic carbon storage at a DRI facility. Demonstration of CCS with an iron-processing plant has not been attempted to date, and a goal is to provide a meaningful example for other iron and steel plants.

Site Characterization for Geologic Carbon Storage of CO_2 from a Direct Reduced Iron Plant

Nathan Moodie, Eugene Szymanski, Son Dang, Chadra S. Rai, Emilio Torres, Michael D. Vanden Berg, Nicholas Hayman, Brian McPherson

Schlumberger Carbon Services

Abstract

Decarbonizing the industrial sector of our economy to meet climate goals and slow climate change is a challenging prospect. To meet these goals, industrial plants that process ethanol, fertilizer, cement, and iron and steel will need to either decarbonize or capture and sequester their CO_2 emissions. The primary objective of this study is decarbonization of iron processing through direct reduced iron (DRI) with CCS, in place of a traditional blast furnace. Iron ore is reduced to elemental iron by exposing the ore to a high-temperature (800-1200 °C) syngas (H_2 and CO) in a reactor vessel. The reaction releases CO_2, water, and unreacted syngas. The CO_2 and water are separated and unreacted syngas is recycled back into the reactor. This separation results in a source of low pressure, wet, nearly pure CO_2 that may be dried, compressed, transported and injected for permanent geologic sequestration or used for other industrial needs.

This analysis is a case study ("focus project") under the auspices of the Carbon Utilization and Storage Partnership (CUSP). We are assessing the carbon storage potential of local subsurface geology near a proposed DRI plant in southern Utah. The primary objectives of this focused project include: (1) rigorous site characterization and analysis of storage capacity, risks and economic options for CCS; (2) a detailed plan for drilling a stratigraphic well and performing a 3D seismic survey, and (3) comprehensive plans for assembling EIC Class VI and 45Q tax credit applications. The targeted reservoir formation is the Jurassic Navajo Sandstone (SS) at about 6200 ft depth, which is stratigraphically overlain by potential sealing units of evaporite-rich Jurassic Temple Cap and limestone/mudstone-dominated Carmel Formations which, in certain areas, were intruded ~22 m.y.a. by several thousand feet of quartz monzonite laccolith. Preliminary analysis indicate that the Navajo SS in this area is capable of storing at least 15 million tons of CO_2.

A goal of this study is to facilitate decision making needed to implement commercial-scale geologic carbon storage at a DRI facility. Demonstration of CCS with an iron-processing plant has not been attempted to date, and a goal is to provide a meaningful example for other iron and steel plants.

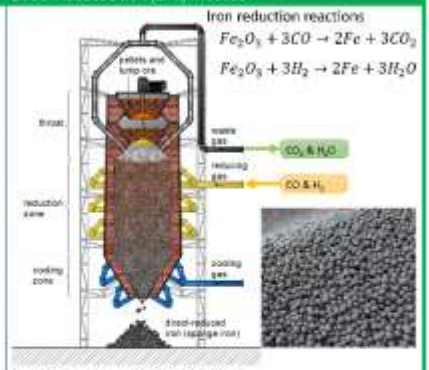
CUSP Focused Project Concept





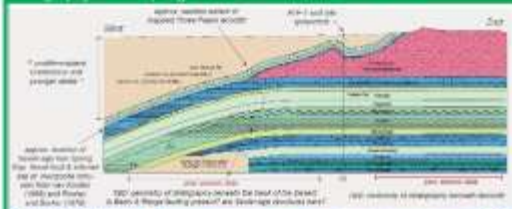
Generalized geologic maps of the greater Iron Springs District, Utah, showing the location of wells and schematic outline of laccolith (modified from Blank and Mackin, 1967)

Direct Reduced Iron (DRI) Process



Direct Reduced Iron refers to the solid-state process of reducing iron oxides to metallic iron at temperatures below the melting point of iron, <1,000 °C. CO and H_2 are produced by CH_4 catalysis and heated before entering the reactor. Iron reduction reactions occur producing CO_2 and water. CO_2 can then be stripped, compressed, and piped to a permanent storage site.

Stratigraphy of Iron Springs District / Neck of the Desert Area





The igneous intrusion has historically been interpreted as a continuous, sheet-like intrusion which migrated by way of an old fault plane. Questions remain about the orientation and extent of the laccolith due to the limitations of the legacy seismic data. The extent of faulting and complexities from regional tectonism are also unknown at depth and could impact seal integrity.

Thin Section - Navajo Well Cuttings



Cross-polarized light (XPL) images show a range of grain sizes and shapes as well as open pore space in the central rock fragment. Visual porosity estimate range: ~10-15%† (6,587-6,596' MD)

Field Work, Outcrop, & Core

Navajo Ss displays a range of depositional facies from outcrop analogues located east of Cedar City; zones of relatively greater permeability in cross-bedded strata often contain cements that create positive relief during weathering

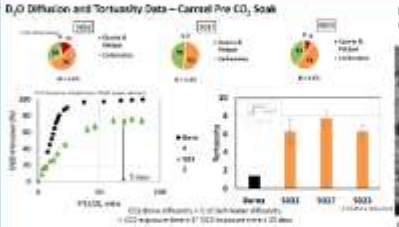


Rock core from the Co-Op Creek Mbr. of the Carmel Formation (just below the Three Peaks quartz monzonite intrusive body) shows at least two calcite-filled fracture sets cross-cutting and obstructing primary bedding structures, remobilized, high-Ca fluid from the Carmel Fm. may be responsible for relatively high Ca values in upper Navajo SS, precipitating $CaCO_3$ in the pores

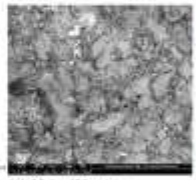


Sample Characterization Effort

D_2O Diffusion and Tortuosity Data – Carmel Pre CO_2 Soak



Navajo Ss. before and after two weeks extended contact with CO_2



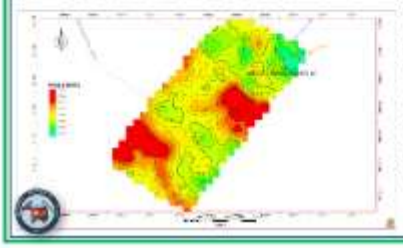
NAV-2 Before CO_2 exposure

CO_2 in Brine Contact Angle of the Navajo Ss.



CO_2 (2.5%KCl Contact angle of 40.8° at 3000 psi and 60 °C (NAV-1 Sample)

Porosity of the Navajo Ss in the 3D geocellular model





NAV-1 after two weeks of CO_2 exposure



CO_2 (2.5%KCl Contact angle of 55.4° at 3000 psi and 60 °C (NAV-1 Sample)

Acknowledgements:

Funding for this project is provided by the U.S. Department of Energy's (DOE) National Energy Technology Laboratory (NETL) through the Carbon Utilization and Storage Partnership of the Western USA (CUSP) under Award No. DE-FE0031837. Additional support has been provided by site operator Utah Iron LLC and the Utah Geological Survey, Kansas Geologic Survey, Oklahoma University, Oklahoma Geologic Survey, Montana State University, Los Alamos National Laboratory, CarbonSolutions LLC, and CandaceDaileyConsulting LLC.

Figure 158 CUSP Annual Meeting 2023 poster

- AAPG 2023 conference presentation by UGS

Basin Analysis and Reservoir Characterization for Subsurface Geologic Carbon (CO_2) Sequestration Associated with a Direct Reduced Iron Plant, Iron County, Utah

Eugene Szymanski[1], Michael D. Vanden Berg[1], Julia Mulhern[1], Elliot A. Jagniecki[1], Austin Jensen[1], Kayla Smith[1], Nathan Moodie[2], Eric Edelman[2], Carl W. Symcox[3], and Emilio J. Torres Parada[3]

[1]Utah Geological Survey

[2]The University of Utah Energy & Geoscience Institute

[3]Oklahoma Geological Survey

The Iron Springs district in southwest Utah is one of the largest iron producing regions in the western United States. A local mine recently proposed building a direct reduced iron plant to optimize their operations and increase the domestic supply of steel. Funded by the U.S. Department of Energy (Award DE-FE0031837), we are conducting rigorous site characterization to assesses the CO_2 sequestration potential of subsurface geologic strata near the proposed plant to accommodate carbon-rich byproducts on a commercial scale. The region possesses world-class reservoir/seal packages at depths suitable for CO_2 storage and lacks evidence of an active petroleum system which lowers the risk of occluded pore space and overpressure, but considerable geologic uncertainty remains due to complex and poorly constrained subsurface conditions. Our characterization leverages geological and geophysical data to assess CO_2 reservoir and seal quality and drilling hazards. Primary injection targets lie within eolian sequences of the Jurassic Navajo Sandstone (porosity 15%; permeability 156 mD), overlain by stacked confining units that include anhydrite-carbonate beds in the Temple Cap Fm. (Manganese Wash Mbr.) and gypsiferous shale and limestone of the Carmel Fm. (Co-Op Creek Mbr.), which itself was intruded by the Three Peaks quartz monzonite. Locally, the Navajo Sandstone lies entirely in the subsurface and preliminary thin section petrography work on cuttings samples from the ARCO Three Peaks #1 well reveals a range of lithofacies and fabrics that appear promising for CO_2 storage. Reservoir analog data from nearby outcrop exhibit a range of structural and depositional realms rock mechanics and petrographic data from these locations provide potential end-member values for reservoir quality. Attribute analysis of reprocessed 2D seismic data indicates laterally continuous subsurface reflectors and viable structural, stratigraphic, and volcano-stratigraphic trap styles, suggesting favorable reservoir / seal presence and continuity. A new gravity survey reveals an intrusive sealing unit with greater volume and more complex geometry than previously identified. Each of these data inputs will be combined into a geomodel to simulate flow and CO2 storage potential. This study highlights how integrated basin analysis and reservoir characterization can provide key inputs for site selection and facility design, a first step on the path toward onsite CO_2 sequestration for industrial projects.

- CUSP Annual meeting 2024 presented the final project results in a presentation.

Slides are available on the CUSP website.

Preliminary Assessment of Possible Stratigraphic Well and 3D Seismic Survey

Although no stratigraphic test well or 3D seismic survey was drilled or acquired under this focused project, substantial planning and costing work was completed.

For the 3D seismic survey, the team obtained a detailed proposal from Explor Seismic for a high-density survey of approximately 15 to 16 square miles north of the mine, using micro-vibrator source technology and dense receiver and source spacing. The proposed design, with trace density corresponding to roughly 33-foot bin sizes and more than four million traces, would provide finely resolved images of the upper crustal structure, including the geometry of the laccolith and major faults, and would be well-suited to both structural interpretation and advanced fault detection workflows.

In parallel, preliminary engineering and cost estimates were assembled for a stratigraphic test well located just north of the mine. This work, led by project staff working with multiple vendors, outlined requirements for rig mobilization, drilling, coring, logging, and laboratory testing. While no contracts were executed, this bid package provides a ready-to-implement plan that could be activated in a future CarbonSAFE phase once funding is available.

Assemble Engineering Design Plans and Budget for Seismic Survey(s)

A 3D seismic survey was designed by Explor. The “Iron Mountain 3D Seismic Acquisition Proposal” is a turnkey acquisition plan for collecting a high-density 3D seismic survey to support geologic evaluation of CO_2 storage potential near the Iron Mountain mining facility (Neck of the Desert / Iron Springs area), see **Figure 159**. The proposal scope is a 15.5 mi^2 3D survey designed to address complex near-surface conditions while also attempting to image as deep as practicable, including requested maximum offsets of approximately 9,000 ft.

The project setting is characterized as a Basin and Range physiographic/ecological context (EPA Level III Central Basin and Range, near boundaries with adjacent ecoregions; Level IV “Woodland and Shrub-Covered Low Mountains”). It notes the southern portion of the survey area lies on a flat valley plain with ephemeral drainage and good access and is therefore well suited to efficient high-density vibroseis acquisition.



Figure 159 Proposed 3D seismic survey acquisition area

The recommended acquisition design is an “all-live” high-density 3D geometry (every receiver records every source point) intended to maximize offset and azimuth distribution and improve imaging and seismic attribute reliability. Key proposed parameters include receiver line interval 330 ft and receiver station interval 66 ft with source line interval 330 ft and source point interval 66 ft. This would give approximately 20,000 receiver nodes deployed “all live” and approximately 20,000 vibroseis source points on about a 33 ft × 33 ft bin size fully populated across azimuths and offsets. The nearest far-offset near-offset on any source point would be 233 ft with an estimated total traces on the order of about 400 million (reported as approximately 10 million traces/km² at all offsets). The proposal indicates single-vibe, single-sweep operations with independent simultaneous sweeping using nodes, and 24-hour source operations to improve efficiency.

Operationally, Explor proposes using its IntelliSeis system (a GIS-enabled dashboard and project hub) to support survey design, stakeless deployment, near-real-time tracking, QC, and KPI analytics accessible to the client and stakeholders during execution (**Figure 160**). The proposal emphasizes flexibility to adapt to changing field conditions through stakeless methods and integrated positioning/timing workflows.

Explor provides an all-inclusive turnkey acquisition price of $674,250 (stated as approximately $43.5k/sq mi), excluding permitting and processing, with a proposed field acquisition window in Q3 2023 and a recommended start prior to the end of September to avoid winter impacts.

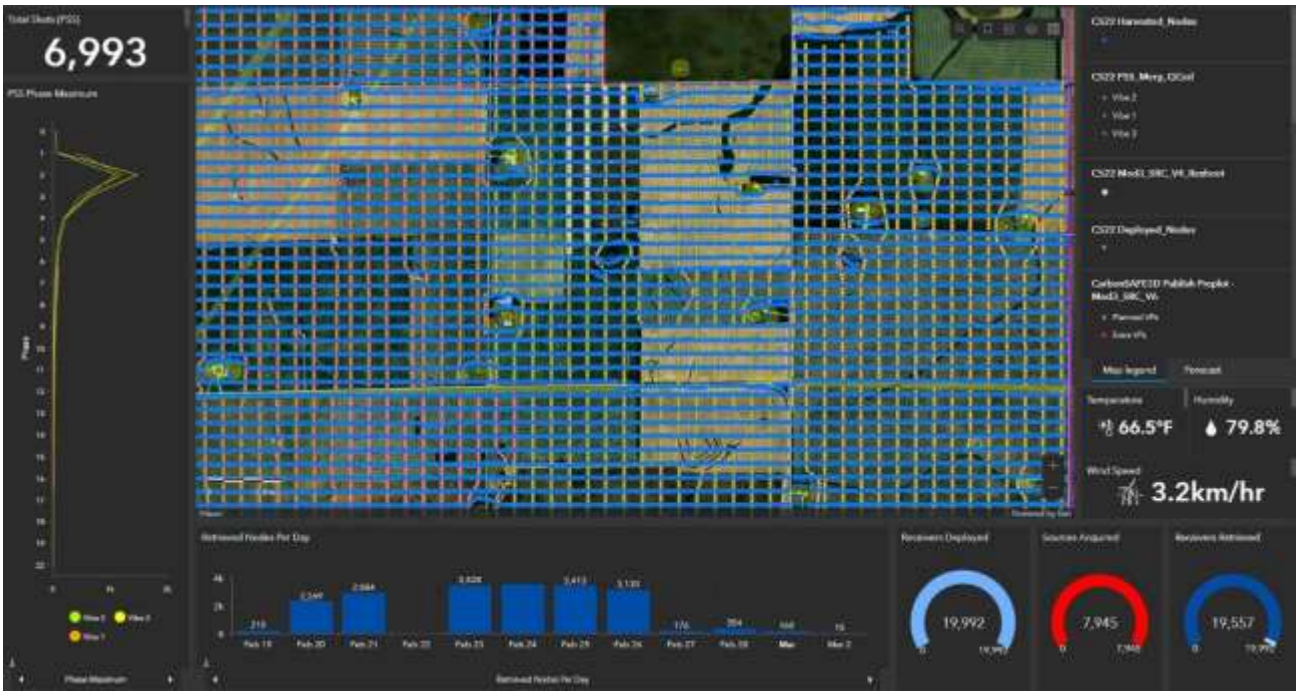


Figure 160 Screenshot showing the Explor IntelliSeis Dashboard for a recent Explor 3D project

Assemble Engineering Design Plans and Budget for Stratigraphic Well

The engineering design basis for the stratigraphic well was established to obtain the subsurface datasets required to evaluate storage feasibility and to support future characterization and Class VI permitting. The design integrated drilling, coring, mud logging, and wireline logging requirements into a single operational program, and then translated that program into a budget with vendor-backed costs for the major services.

According to project engineering and service-provider quote packages prepared in June–July 2023 (rig, mobilization, drilling bits/fluids, mud logging, coring, and wireline logging), the stratigraphic well engineering design and budget were assembled to support a deep characterization well near Iron Mountain with (1) continuous core across target storage and seal intervals, (2) comprehensive open hole logging and formation testing for reservoir and caprock evaluation, and (3) cemented casing strings designed to enable safe drilling through the USDW interval and reliable isolation of deeper sections

Wellbore Architecture and Drilling Approach

The planned well configuration utilized a staged hole-and-casing architecture to (1) set shallow conductor casing for near-surface stability, (2) isolate the USDW interval behind cemented surface casing, and (3) drill deeper intermediate/production-size intervals suitable for coring and open hole logging. A representative staged design (used for drilling bit estimation and consistent

with the planned deep characterization objective) included: 20-in hole to approximately 120 ft (roller cone), 12-1/4 in hole to approximately 1,500 ft, 8-1/2 in hole to approximately 8,500 ft, and 6-1/8-in hole to approximately 12,500 ft (multiple PDC bits planned for the deeper intervals). The staged concept was selected specifically to support large-diameter casing through shallow zones and then maintain a stable borehole at depth that could be easily logged and cored.

Rig Selection and Execution Readiness

A trailer-mounted drilling package with deep capacity and a modern top drive system was selected for budgeting and execution planning. The IronHand Rig 118 package was quoted with a 25,000-ft depth rating, 750,000-lb hook load, a TDS-11SA top drive, dual F-1600 mud pumps, and supporting solids-control and tubular-handling equipment. Commercial terms included a daywork drilling rate and defined standby/mobilization-related conditions, which were rolled into the drilling cost model used for the budget.

Coring and Sample Acquisition Program

Continuous core was treated as a primary project deliverable and therefore a primary cost driver. The coring program was budgeted using a dedicated coring provider, with pricing structured around (1) core acquisition, (2) core handling, and (3) core processing and ancillary services. The ProCoring estimate provided a total coring-services budget on the order of approximately $0.63MM, comprising a core acquisition estimate of approximately $0.47MM and core processing of approximately $0.16MM (with the understanding that final cost scales with final core footage, tool selection, and downhole conditions). This coring scope was intentionally paired with a mud logging and sample management plan to ensure continuous lithologic description, gas monitoring, and chain-of-custody documentation for core and cuttings. See **Figure 161** for a coring diagram highlighting the intervals being targeted.

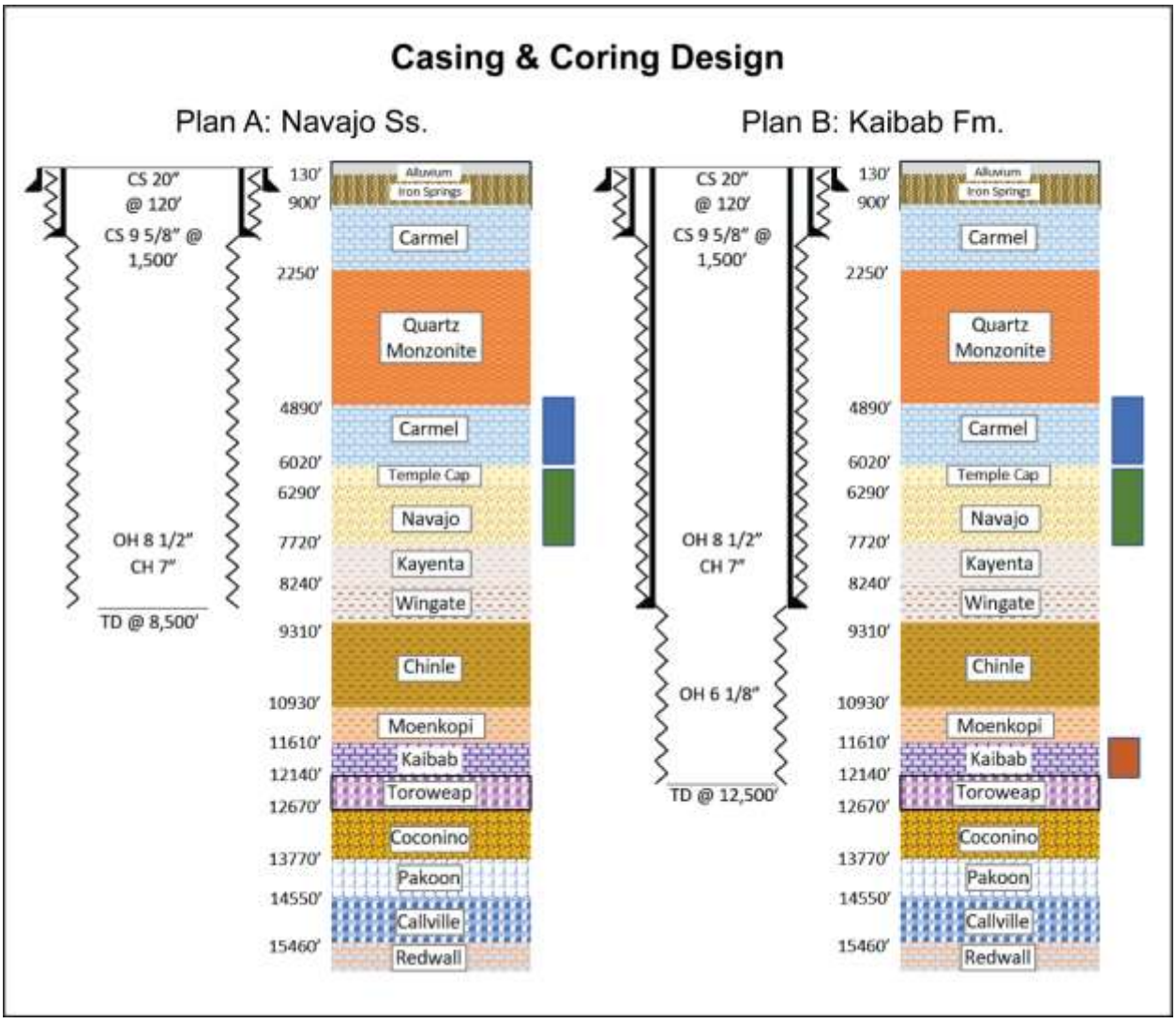


Figure 161 Casing and coring design

Mud Logging, HSE Spacing, and Operational Controls

Mud logging was included as a continuous safety and characterization function during drilling and coring operations. The mud logging quote (Suttles' Logging) was structured as a two-person computerized unit with a daily rate and standard adders (synthetic mud system charge, communications, lodging, and one-time rig up/down trailer charges), and included explicit safety placement requirements (e.g., logging unit located at least 100 ft from the wellbore, flare line, and generators/diesel engines) to support safe operations on location.

Wireline Logging and Formation Evaluation

Wireline logging was scoped to support reservoir quality, caprock integrity, geomechanics, and fluid characterization objectives. Because logging suite selection strongly controls total cost, multiple vendor quotes were obtained. The SLB RFP package provided section-by-section grand totals (12-1/4 in, 8-1/2 in, and 6-1/8 in intervals) and optional adders (e.g., certain specialty services). Halliburton and Baker Hughes quotes provided alternative toolstring configurations

and pricing, including options that bundle more advanced formation testing and specialty measurements. The budget consolidated these alternatives into a single “logging / fluid sampling / mini-fracs” line item sized to capture a comprehensive formation evaluation program rather than a minimal triple-combo log suite. See Table 23 and Table 24 for the logging plan for the Navajo and Kaibab intervals respectively.

Table 23 Logging program plan for the Navajo drilling plan A.

Logging Program Plan: Navajo		**Stage**		
		1	**2**	**3**
		Hole Size		
		24"	**12 1/4"**	**8 1/2"**
		Depth [ft]		
Logs	**Requirement**	**120**	**1500**	**8500**
Gamma Ray	Triple Combo (Res/Dens/Poro)	1	1	1
Resistivity		1	1	1
Neutron-Density			1	1
Dipolar Sonic + Anysotrophy	Sonic Scanner			2
Imaging	FMI			2
Elemental Spectroscopy	Litho Scanner			2
CMR	CMR			2
Formation Tester - Pretests	MDT/XPT (10 pretest)			2
Formation Tester - Sampling	MDT (4 samples)			2
Formation Tester- MiniFrac	MDT Minifrac (1 measurement)			3
Sidewall Cores	20 cores			3
CBL-VDL				1

	Priority	
	1	Needed
	2	Recommended
	3	Budget dependent

Table 24 Logging program plan for the Kaibab drilling plan B.

Logging Program Plan: Kaibab		**Stage**		
		1	**2**	**3**
		Hole Size		
		24"	**12 1/4"**	**8 1/2"**
		Depth [ft]		
Logs	**Requirement**	**120**	**1500**	**12500**
Gamma Ray	Triple Combo (Res/Dens/Poro)	1	1	1
Resistivity		1	1	1
Neutron-Density			1	1
Dipolar Sonic + Anysotrophy	Sonic Scanner			2
Imaging	FMI			2
Elemental Spectroscopy	Litho Scanner			2
CMR	CMR			2
Formation Tester - Pretests	MDT/XPT (10 pretest)			2
Formation Tester - Sampling	MDT (4 samples)			2

Formation Tester- MiniFrac	MDT Minifrac (1 measurement)			3
Sidewall Cores	20 cores			3
CBL-VDL				1

	Priority	
	1	Needed
	2	Recommended
	3	Budget dependent

Cementing and Zonal Isolation Design

Cementing costs were included explicitly in the budget to cover surface and intermediate casing strings and associated additives/contingencies. The Halliburton cement correspondence documented candidate additive systems (e.g., ThermaLock / latex options and loss-circulation/coal-related considerations), and the budget carried cement allowances at a level consistent with deep intermediate casing requirements and the associated pumping, blending, and contingency needs typical for the anticipated drilling environment.

Budget Assembly (AFE Structure and Cost Reconciliation)

The University of Utah Iron Mountain Drilling budget workbook was used to get a rough estimate of expected costs with a cored and logged stratigraphic well. It captured two planning cases (a shallower case and a deeper case) to bound schedule and cost uncertainty. For each case, the budget included (1) pre-spud civil/site costs (survey, roads/pits, damages/ROW), (2) drilling contractor daywork costs (rate × days), (3) major service lines (coring, mud, cement, logging), (4) rentals/trucking/fishing/safety, (5) supervision and professional support, and (6) a project administration fee. The total “intangibles” were $6.30MM (shallower case) and $7.08MM (deeper case). See Table 25 for a detailed breakdown of the drilling costs for the two drilling plans.

Estimate cases used in the budget:

- Case A: 8,500 ft TD; 45 days; approximately 3,000 ft core (AFE column “Iron Mountain (NAVAJO)”)
- Case B: 12,000 ft TD; 60 days; approximately 600 ft core (AFE column “Iron Mountain (KAIBAB)”)

Table 25 Iron Mountain drilling estimates for a stratigraphic well and core.

	Iron Mountain (NAVAJO)	Iron Mountain (KAIBAB)
Days:	**45**	**60**
TD:	**8500 ft**	**12000 ft**
Cores:	**3000 ft**	**600 ft**
Title/Curative/Permit/Insurance	$30,000	$30,000
Damages/Right of Way	$120,000	$120,000
Survey/Stake Location	$200,000	$200,000
Location/Pits/Road Expense	$200,000	$200,000
Drilling/Completion Overhead	$0	$0
Daywork Contract ($22,000/day)	$990,000	$1,320,000
Mobilization and Demobilization	$75,000	$75,000
Directional Drilling Services	$250,000	$250,000
Fuel, Power, and Water	$400,000	$400,000
Bits	$40,000	$50,000
Drilling Monitoring (vibration, high-res. Drill data)	$26,000	$26,000
Mud & Chemicals	$100,000	$100,000
Coring	$550,000	$600,000
Core Handling	$100,000	$185,000
Core Analysis	$300,000	$350,000
Cement (Surface)	$150,000	$150,000
Cement (1st Intermediate)	$350,000	$350,000
Cement (Production)	$0	$0
Float Equipment, Centralizers	$30,000	$30,000
Casing/Tubing Crews & Equipment	$35,000	$35,000
Geologic/Eng./Reg./Drilling & Comp. Supervision	$260,000	$260,000
Contract Supervision - Engineering Spt.	$50,000	$50,000
Company Supervision including Company Man	$170,000	$170,000
Contract Labor	$10,000	$10,000

Health & Safety Supervision	$40,000	$40,000
Testing Casing/Tubing	$30,000	$30,000
Mud Logging Unit	$10,000	$10,000
Logging /Fluid sampling/Mini fracs	$700,000	$850,000
Perforating	$0	$0
Perforation Cleanup	$0	$0
Rentals - Surface and Subsurface	$160,000	$210,000
Trucking/Forklift/Welding Services	$80,000	$100,000
Step Rate & Injectivity Testing	$0	$0
Wellhead Services	$50,000	$50,000
Solid and Liquid Disposal	$56,000	$75,000
Lighting, Utilities, Internet, Trash, etc.	$20,000	$26,000
Trailer Rentals (3 drilling)	$20,000	$26,000
Repair, Maintenance, & Miscellaneous	$35,000	$45,000
Closed Loop & Environmental	$150,000	$150,000
Geolex Administrative Fee (10%)	$509,900	$509,900
TOTAL INTANGIBLES	**$6,296,900**	**$7,082,900**
TANGIBLE COSTS		
Conductor Casing	$15,000	$15,000
Surface Casing	$14,000	$14,000
1st Intermediate	$373,175	$373,175
Production Csg.)	$261,250	$261,250
CRA Prod. Csg.		
Tubing		
Wellhead Equipment (Tree, hanger, etc.)	$50,000	$50,000
Diesel for Tubing Annulus	$0	$0
Retrievable SSSV & Surface Panel		
Bottom Hole P/T Gauge & Surf. Panel	$0	$0
Packer	$5,000	$5,000
Miscellaneous	$3,500	$3,500

Geolex Administrative Fee (10%)	$0	$0
TOTAL TANGIBLES	**$721,925**	**$721,925**
TOTAL (TANGIBLE & INTANGIBLE COSTS)	**$7,018,825**	**$7,804,825**

Comprehensive Plan to Prepare and Submit UIC Class VI Application

Detailed work on the Class VI application plan (Task 7) was scheduled for later in the broader CUSP program and did not proceed beyond preliminary planning within this focused project. However, the technical outputs produced here, geological model, reservoir and seal property datasets, induced seismicity risk assessment, and pipeline-routing scenarios, were developed with an eye toward their eventual inclusion in a Class VI permit application.

The concurrent progress in Utah's regulatory framework and efforts toward Class VI primacy means that the Iron Mountain site, once fully characterized and modeled, will be well positioned to move into formal permitting and tax-credit qualification.

Comprehensive Plan to Prepare and Submit 45Q Tax Credit Application

Detailed work on the 45Q Tax Credit application plan (Task 8) was scheduled for later in the broader CUSP program and did not proceed beyond preliminary planning within this focused project. However, the technical outputs produced here, geological model, reservoir and seal property datasets, induced seismicity risk assessment, and pipeline-routing scenarios, were developed with an eye toward their eventual inclusion in 45Q documentation.

The concurrent progress in Utah's regulatory framework and efforts toward Class VI primacy means that the Iron Mountain site, once fully characterized and modeled, will be well positioned to move into formal permitting and tax-credit qualification.

Integrated Outcomes and Site Readiness

Across its duration, the CUSP Iron Mountain Subsurface Characterization Focused Project achieved its central objective: to move the Iron Mountain CO_2 storage concept from a reconnaissance-level idea to a technically grounded, partially modeled site with a clear path toward a future CarbonSAFE Phase II/III.

The project produced a geological model that integrates well, outcrop, gravity, aeromagnetic, and reprocessed seismic data into a coherent structural framework with facies and property modeling appropriate for reservoir simulation. It generated a substantial rock-property database for both reservoir and seal units, including porosity, permeability, capillary pressure, geomechanical properties, and CO_2 reactivity, derived from coordinated UGS, UU, and OGS/IC3 laboratory

programs. Preliminary dynamic simulations demonstrated that plausible injection scenarios of 0.5 to 1.0 Mt per year over 20 years yield compact CO_2 plumes under the assumed reservoir conditions.

The induced seismicity work showed that major normal faults in the region, particularly the Antelope Range Fault, may be close to frictional failure, underscoring the need for improved structural imaging and careful pressure management, but did not reveal any fundamental barriers to storage. Pipeline-routing and scenario analysis established how CO_2 could be transported from the plant to primary and alternate storage sites while leveraging existing rights-of-way. Policy and outreach efforts kept the project aligned with an evolving state regulatory environment that is increasingly supportive of CCUS.

Some key elements, most notably acquisition of a stratigraphic test well and 3D seismic survey, fully coupled dynamic simulations with pressure and leakage risk analysis, and detailed Class VI and 45Q plans, remain future work. Nevertheless, the integrated technical, modeling, and non-technical outputs of this project provided a strong foundation from which a subsequent CarbonSAFE Phase II project proposal was submitted and accepted by the Department of Energy, and is currently under review. This project provided the key data and technical knowledge to make that successful proposal a reality and will facilitate permitting and deployment of CO_2 storage to support low-carbon iron production at Iron Mountain.

Acknowledgment

Funding for this project is provided by the U.S. Department of Energy's (DOE) National Energy Technology Laboratory (NETL through the Carbon Utilization and Storage Partnership of the Western USA (CUSP) under Award No. DE-FE0031837.

References

Anameric B, Kawatra SK. 2007. Properties and features of direct reduced iron. Miner Process Extr Metall Rev. 28(1):59–116. doi:10.1080/08827500600943473

Bahorich M, Farmer S. 1995. 3-D seismic discontinuity for faults and stratigraphic features: the coherence cube. Lead Edge. 14(10):1053–1058. doi:10.1190/1.1437077

Battelle T, Srivastava U, Kopfle J, Hunter R, McClelland J. 2024. The direct reduction of iron. In: Treatise on process metallurgy. Amsterdam (Netherlands): Elsevier. p. 89–149. doi:10.1016/B978-0-323-85373-6.00011-9

Bi Z, Wu X, Geng Z, Li H. 2021. Deep relative geologic time: a deep learning method for simultaneously interpreting 3-D seismic horizons and faults. J Geophys Res Solid Earth. 126(9):e2021JB021882. doi:10.1029/2021JB021882

Blank HR, Mackin JH. 1967. Geologic interpretation of an aeromagnetic survey of the Iron Springs district, Utah. U.S. Geol Surv Prof Pap 516. Washington (DC): U.S. Government Printing Office.

Brocher TM, Baltay AS, Hardebeck JL, Pollitz FF, Murray JR, Llenos AL, Scharer KM, Dawson TE, Boatwright J, Dreger DS, et al. 2015. The Mw 6.0 24 August 2014 South Napa earthquake. Seismol Res Lett. 86(2A):309–326. doi:10.1785/0220140242

Byerlee J. 1978. Friction of rocks. In: Rock friction and earthquake prediction. Basel (Switzerland): Birkhäuser. p. 615–626. doi:10.1007/978-3-0348-7182-2_4

Cao H, Greene M, Kuppler J, Ali M. 2024. CO_2 transport specification, purification, and dehydration solutions. In: Abu Dhabi International Petroleum Exhibition and Conference. SPE paper D031S094R002.

Detournay E, Cheng AHD. 1993. Fundamentals of poroelasticity. In: Analysis and design methods. Oxford (UK): Pergamon Press. p. 113–171.

Dieterich JH. 1972. Time-dependent friction in rocks. J Geophys Res. 77(20):3690–3697. doi:10.1029/JB077i020p03690

Dieterich JH, Conrad G. 1984. Effect of humidity on time- and velocity-dependent friction in rocks. J Geophys Res Solid Earth. 89(B6):4196–4202. doi:10.1029/JB089iB06p04196

Fei TW, Luo Y, Yang J, Liu H, Qin F. 2015. Removing false images in reverse time migration: the concept of de-primary. Geophysics. 80(6):S237–S244. doi:10.1190/geo2014-0605.1

Fomel S, Luo S, Zhao H. 2009. Fast sweeping method for the factored eikonal equation. J Comput Phys. 228(17):6440–6455. doi:10.1016/j.jcp.2009.05.008

Gan W, Frohlich C. 2013. Gas injection may have triggered earthquakes in the Cogdell oil field, Texas. Proc Natl Acad Sci U S A. 110(47):18786–18791. doi:10.1073/pnas.1311316110

Gao K. 2024. Iterative multitask learning and inference from seismic images. Geophys J Int. 236(1):565–592. doi:10.1093/gji/ggad418

Gibson D, Spann M, Turner J, Wright T. 2005. Fault surface detection in 3-D seismic data. IEEE Trans Geosci Remote Sens. 43(9):2094–2102. doi:10.1109/TGRS.2005.853185

Hack J, Maeda N, Meier DM. 2022. Review on CO_2 capture using amine-functionalized materials. ACS Omega. 7(44):39520–39530. doi:10.1021/acsomega.2c05020

Kemper J, Sutherland L, Watt J, Santos S. 2014. Evaluation and analysis of the performance of dehydration units for CO_2 capture. Energy Procedia. 63:7568–7584. doi:10.1016/j.egypro.2014.11.793

Kolawole F, Johnston CS, Morgan CB, Chang JC, Marfurt KJ, Lockner DA, Carpenter BM, Brown JR, Chen X, Hennings PH, et al. 2019. The susceptibility of Oklahoma's basement to seismic reactivation. Nat Geosci. 12(10):839–844. doi:10.1038/s41561-019-0424-8

Leung S, Qian J. 2006. An adjoint state method for three-dimensional transmission traveltime tomography using first arrivals. Geophys J Int. 165(2):497–512. doi:10.1111/j.1365-246X.2006.02907.x

Li S, Liu N, Li F, Gao J, Ding J. 2022. Automatic fault delineation in 3-D seismic images with deep learning: data augmentation or ensemble learning? IEEE Trans Geosci Remote Sens. 60:1–14. doi:10.1109/TGRS.2021.3128057

Liu Z, Bleistein N. 1995. Migration velocity analysis: theory and an iterative algorithm. Geophysics. 60(1):142–153. doi:10.1190/1.1443741

McCormack KL, Bratton TR, Chen T, McPherson BJ. 2022. Induced seismicity potential based on probabilistic geomechanics for the San Juan Basin CarbonSAFE project. Geophysics. 87(6):EN69–EN79. doi:10.1190/geo2021-0667.1

McCormack KL, McLennan JD, Jagniecki EA, McPherson BJ. 2023. Discrete measurements of the least horizontal principal stress from core data: an application of viscoelastic stress relaxation. SPE Res Eval Eng. 26(3):827–841. doi:10.2118/220255-PA

McMechan GA. 1983. Migration by extrapolation of time-dependent boundary values. Geophys Prospect. 31(3):413–420. doi:10.1111/j.1365-2478.1983.tb01060.x

Midrex Technologies Inc. 2018. MidrexNG: optimizing DRI production using natural gas. Charlotte (NC): Midrex Technologies Inc.

Moodie N, Szymanski E, Vanden Berg MD, McPherson BJ. 2022. Site characterization for geologic carbon storage from a direct reduced iron plant. In: AGU Fall Meeting Abstracts. Chicago (IL). Abstract GC12E-0481.

Qin Y, Li J, Huang L, Gao K, Li D, Chen T, McPherson B, Pawar R, Zhang Y, White M, et al. 2023. Microseismic monitoring at the Farnsworth CO_2-EOR field. Energies. 16(10):4177. doi:10.3390/en16104177

Rowley PD, Barker DS. 1978. Geology of the Iron Springs mining district, Utah. Utah Geol Mineral Surv Bull. 110. Salt Lake City (UT): Utah Geological and Mineral Survey.

Snee JEL, Zoback MD. 2022. State of stress in areas of active unconventional oil and gas development in North America. AAPG Bull. 106(2):355–385. doi:10.1306/08122120053

Soliva R, Benedicto A, Schultz RA, Maerten L, Micarelli L. 2008. Displacement and interaction of normal fault segments branched at depth: implications for fault growth and potential earthquake rupture size. J Struct Geol. 30(10):1288–1299. doi:10.1016/j.jsg.2008.07.004

Taillandier C, Noble M, Chauris H, Calandra H. 2009. First-arrival traveltime tomography based on the adjoint-state method. Geophysics. 74(6):WCB1–WCB10. doi:10.1190/1.3250266

Templeton DC, Schoenball M, Layland-Bachmann CE, Foxall W, Guglielmi Y, Kroll KA, White JA, McClure MW, Walsh FR, Zoback MD, et al. 2023. A project lifetime approach to the management of induced seismicity risk at geologic carbon storage sites. Seismol Res Lett. 94(1):113–122. doi:10.1785/0220220206

Tong P. 2021. Adjoint-state traveltime tomography: eikonal equation-based methods and application to the Anza area in southern California. J Geophys Res Solid Earth. 126(5):e2021JB021818. doi:10.1029/2021JB021818

Townend J, Zoback MD. 2000. How faulting keeps the crust strong. Geology. 28(5):399–402. doi:10.1130/0091-7613(2000)28<399:HFKTCS>2.0.CO;2

[EPA] U.S. Environmental Protection Agency. 2013. Underground injection control (UIC) program Class VI well area of review evaluation and corrective action guidance. Washington (DC): U.S. Environmental Protection Agency.

Van Kooten GK. 1988. Structure and hydrocarbon potential beneath the Iron Springs laccolith, southwestern Utah. Geol Soc Am Bull. 100(10):1533–1540. doi:10.1130/0016-7606(1988)100<1533:SAHPBI>2.3.CO;2

Vilarrasa V, Carrera J, Olivella S, Rutqvist J, Laloui L. 2019. Induced seismicity in geologic carbon storage. Solid Earth. 10(3):871–892. doi:10.5194/se-10-871-2019

Walsh FR, Zoback MD. 2016. Probabilistic assessment of potential fault slip related to injection-induced earthquakes: application to north-central Oklahoma, USA. Geology. 44(12):991–994. doi:10.1130/G38275.1

Wang Z, Di H, Shafiq MA, Alaudah Y, AlRegib G. 2018. Successful leveraging of image processing and machine learning in seismic structural interpretation: a review. Lead Edge. 37(6):451–461. doi:10.1190/tle37060451.1

Wernicke B. 1981. Low-angle normal faults in the Basin and Range Province: nappe tectonics in an extending orogen. Nature. 291(5817):645–648. doi:10.1038/291645a0

White JA, Foxall W. 2016. Assessing induced seismicity risk at CO_2 storage projects: recent progress and remaining challenges. Int J Greenh Gas Control. 49:413–424. doi:10.1016/j.ijggc.2016.03.007

Yilmaz Ö. 2001. Seismic data analysis: processing, inversion, and interpretation of seismic data. Tulsa (OK): Society of Exploration Geophysicists.

Zhang J. 2011. Pore pressure prediction from well logs: methods, modifications, and new approaches. Earth Sci Rev. 108(1–2):50–63. doi:10.1016/j.earscirev.2011.06.001

Zoback MD. 2007. Reservoir geomechanics. Cambridge (UK): Cambridge University Press.

Zoback ML, Zoback MD. 1980. State of stress in the conterminous United States. J Geophys Res Solid Earth. 85(B11):6113–6156. doi:10.1029/JB085iB11p06113

CCS Hub 2.0 Concept for ONEOK: Infrastructure Development for Handling of New Gaseous Products for Natural Gas Liquids Fractionation and Gas Processing Plants in Kansas and Oklahoma

The project team evaluated the feasibility of carbon capture and storage (CCS) at ONEOK's natural gas liquids (NGL) fractionation facilities in Bushton, Kansas, and Medford, Oklahoma. In 2020 and 2021, the two sites combined emitted over 500,000 t of CO_2 annually. Capturing and geologically storing this CO_2 presents an opportunity to reduce environmental impact, improve facility economics, and establish eligibility for federal incentives under Section 45Q of the U.S. Tax Code (Credit for Carbon…2021).

To support this goal, the team conducted geologic screening to identify subsurface formations near the Bushton and Medford facilities that may be suitable for long-term CO_2 storage. Initial site assessments were followed by the development of static geocellular models, dynamic simulations, and infrastructure planning, including conceptual routing for a CO_2 transportation network that considers land use, easements, and proximity to population centers.

Due to changes in site access and infrastructure planning at the Medford facility during the project period, detailed field activities and site-specific permitting work were concentrated at the Bushton location. However, preliminary modeling was still conducted for a Medford-area reservoir based on available data.

Study conclusions:

- ONEOK's Bushton NGL facility is a promising candidate for CCS development and regulatory planning.
- Two potential storage targets were identified at Bushton: the Lansing–Kansas City and Arbuckle formations.
- Geocellular models were constructed for both Bushton targets, with simulations showing that while the Lansing–Kansas City may offer secondary injection potential, the Arbuckle formation is more favorable as a primary target. Further coordination with nearby oil, gas, and water operators will be needed to mitigate potential subsurface interactions.
- A single geocellular model was also developed for the Wilcox-Bromide formation near Medford using publicly available and digitized data.

This work provides a technical foundation for future development of a CO_2 transportation and sequestration facility in Kansas, with a focus on economic feasibility, integration with existing midstream infrastructure, and alignment with regulatory pathways in Kansas.

Project accomplishments:

- Designed, deployed, and monitored a cost-effective seismic network in central Kansas, including the area surrounding the ONEOK Bushton facility.
- Constructed three subsurface geocellular property models: two at Bushton (Lansing–Kansas City and Arbuckle) and one at Medford (Wilcox–Bromide).

- Conducted multiple simulation cases to assess CO_2 injection behavior across modeled scenarios.
- Completed a comprehensive subsurface data audit, digitization effort, and integration of historical geologic and well data to support model development and risk analysis.

Introduction

The CUSP Midstream Operator Storage of CO_2 ($MOSCO_2$) project aimed to address the annual CO_2 production from ONEOK's natural gas liquids (NGL) fractionation plants in Bushton, Kansas, and Medford, Oklahoma. The primary objective was to identify and evaluate suitable subsurface reservoirs for the long-term geologic storage of captured CO_2. This work supports ONEOK's ability to leverage U.S. IRS 45Q tax credits, improve operational economics, and reduce its environmental footprint.

This technical report summarizes progress toward the primary objective, including reservoir characterization, geomechanical and seismic risk analyses, dynamic simulation of injection scenarios, and infrastructure network modeling. The report also includes preliminary work on temporary on-site CO_2 storage and integrated options to support the conceptual design of a CO_2 transportation and sequestration facility, with potential future linkage to hydrogen production emissions.

In 2021, the United States Congress introduced the Storing CO_2 and Lowering Emissions (SCALE) Act, a bipartisan initiative designed to expand the deployment of carbon capture technologies and reduce greenhouse gas emissions (Beck and Ross 2021). The act enhanced the existing Section 45Q tax credit by broadening eligibility criteria and improving financial incentives for CCS projects. Under the revised provisions, the credit increased to $120 per metric ton for CO_2 removed via direct air capture and to $75 per ton for CO_2 used in enhanced oil recovery applications (Ochu 2021). The legislation also introduced a direct-pay option, allowing developers to receive the tax credit through annual returns without needing taxable income (Ochu 2021).

These expanded incentives have generated strong interest from industrial operators in pursuing Class VI injection wells. To secure a Class VI permit, applicants must meet detailed site characterization, well design, and monitoring requirements defined by the U.S. Environmental Protection Agency (EPA 2013). Permitted injection operations are contingent on maintaining seismic activity below thresholds established through analysis of regional tectonic setting, historical earthquake records, and baseline monitoring data (Templeton et al. 2022). The report includes results from initial analyses of these factors.

This report is organized according to the Project Task List developed collaboratively by New Mexico Tech (NMT) and the University of Kansas (KU) as part of a U.S. Department of Energy (DOE) sponsored focused study under the Western Region of the Carbon Utilization and Storage Partnership (CUSP) collaborative initiative. Technical work and coordination were provided by the Kansas Geological Survey (KGS) as a research institution of KU. Project selection, administration, and review were provided by the Petroleum Recovery Research Center (PRRC), a research center of NMT.

The original project scope included feasibility assessments for CO_2 storage at both the Bushton and Medford ONEOK facilities. Planned activities encompassed site characterization, subsurface

modeling, infrastructure analysis, and evaluation of regulatory readiness. However, following changes in site access and corporate infrastructure planning beginning in July 2022 following a fire incident at the Medford facility (McDonnell 2022), field activities in Oklahoma were deferred or scaled back.

In early 2023, ONEOK announced new development plans to expand processing capacity in Texas, and in August 2024, it released plans to construct a new fractionator facility at Medford, Oklahoma (Sellers 2023; ONEOK 2023). These updates resulted in a shift in project focus, with the Bushton, Kansas site emerging as the primary location for detailed CO_2 storage assessment. Accordingly, Oklahoma-specific work was adjusted in consultation with ONEOK.

The Oklahoma Geological Survey (OGS), originally designated for a broader technical role, continued to contribute by providing publicly available geologic data and participating in CUSP-West coordination. Field resources were redirected to other regional initiatives. Final project deliverables emphasize Kansas-based analysis while incorporating lessons learned from the broader multi-state collaboration. The following subtasks were affected by the change in site access and scope:

- **Subtask 1.2 – Site Visits:** Site visits to the ONEOK field sites in Bushton, KS, and Medford, OK, were originally planned to validate findings from technical reviews (e.g. well status) and facilitate in-person discussions with facility personnel. The Bushton visit was completed. The Medford visit was not conducted due to site inaccessibility.
- **Subtask 3.3 – Storage Resource Assessment:** Planned assessments for potential CO_2 storage reservoirs near Medford were not conducted.
- **Subtask 7.1 - UIC Class VI Regulatory Engagement:** A planned meeting with U.S. EPA Region 6 to discuss permit data requirements for the Medford location was cancelled.
- **Subtask 7.2 - External Team Engagement:** Coordination with other teams experienced in UIC Class VI permitting was not pursued for Oklahoma-specific benchmarking.
- **Subtask 7.3 - State Regulatory Discussions:** Scheduled meetings with Oklahoma environmental and petroleum regulators were suspended.

The work summarized herein represents the collaborative effort of multiple institutions with complementary expertise in geology, engineering, simulation, infrastructure, and risk analysis, brought together under the leadership of KGS and with support from DOE through PRRC.

Objectives

This project aimed to evaluate the viability of long-term geologic storage of CO_2 emissions from ONEOK's NGL fractionation plants at Bushton, Kansas and Medford, Oklahoma by identifying suitable subsurface reservoirs near the emitting sites. A key driver was to support ONEOK's eligibility for U.S. IRS 45Q tax credits, while simultaneously enhancing operational economics and reducing environmental impact. In addition to evaluating permanent storage options, the project explored the feasibility of temporary on-site CO_2 storage prior to pipeline transport or injection.

CCS-Specific Objectives

With the project's CCS assessment ultimately focusing on the Bushton, KS facility, the technical and planning goals included:

1) **Evaluate Potential CO_2 Storage Reservoirs:** Conduct preliminary characterization of subsurface formations near the Bushton NGL fractionator to assess their suitability for long-term CO_2 storage. This included geological screening, early modeling, and petrophysical analysis to support future Class VI permitting.
2) **Support UIC Class VI Permit Planning:** Compile data and develop technical guidance to inform a future U.S. EPA UIC Class VI application, including site-specific inputs for reservoir integrity, injectivity, and Area-of-Review (AoR) delineation.
3) **Assess 45Q Tax Credit Eligibility:** Estimate potential CO_2 volumes for capture and storage to determine whether anticipated emissions meet the threshold for federal tax credit qualification under IRS 45Q guidelines.
4) **Support Planning for a CO_2 Transportation and Sequestration Facility:** Develop a conceptual design for a CO_2 capture and delivery system that integrates emissions from multiple sources and supports long-term transport and storage.
5) **Analyze Pipeline and Infrastructure Needs:** Use SimCCS^{PRO} (Carbon Solutions 2025) modeling software to evaluate optimal routing scenarios for new CO_2 pipelines, considering existing infrastructure, surface constraints, and economic feasibility.
6) **Explore Integration with Hydrogen Production:** Consider synergies with future hydrogen generation facilities in the region, particularly the potential to co-manage CO_2 emissions streams from multiple industrial sources.

Scope of Work

This study evaluated the potential for long-term geologic storage of CO_2 near ONEOK's NGL fractionation plants in Bushton, KS, and Medford, OK. The original project scope included identification of suitable saline reservoirs, assessment of permitting pathways, and development of monitoring strategies for CCS implementation.

To support project viability and tax credit eligibility under IRS 45Q, the study also investigated opportunities to increase CO_2 capture volumes, including the potential development of an integrated capture and delivery system that leverages existing infrastructure, particularly the NGL pipeline network. Essentially, the study provides a technical basis for establishing a CO_2 transportation and sequestration facility.

Project Task List

The following task structure guided project implementation and deliverable tracking throughout the performance period.

Task 1 – Project Management

Subtask 1.1–Managing and allocating resources, communications, outreach, and technology transfer.

Subtask 1.2–Site visits to confirm findings of technical review.

Subtask 1.3–Reporting.

Task 2 – High-Level Technical Review

Subtask 2.1–Inventory relevant geological, engineering, infrastructure, risk, and economic data.

Subtask 2.2–Delineate underground sources of drinking water (USDWs).

Subtask 2.3–Review environmental/social justice considerations.

Subtask 2.4–Determine Area-of-Review.

Task 3 – Subsurface Studies

Subtask 3.1–Subsurface data aggregation and database build.

Subtask 3.2–Static geological modeling.

Subtask 3.3–Assess CO_2 storage resources.

Subtask 3.4–Geomechanical assessment.

Subtask 3.5–Install and monitor seismometer network for seismic risk analysis.

Task 4 – Dynamic Simulation

Subtask 4.1–Evaluate existing oil field injection pressures and rates to determine suitability for saline storage operations.

Subtask 4.2–Dynamic simulations of CO_2 injection scenarios into saline storage reservoirs.

Task 5 – Risk Assessment

Subtask 5.1–Risk assessment data aggregation and database build (e.g. NRAP Tools).

Subtask 5.2–Assess well integrity and seal penetrations.

Subtask 5.3–Prepare a ranked matrix of key risk factors for each seal and reservoir horizon and AoR addressing key surface and subsurface issues that might affect injection viability.

Subtask 5.4–Perform induced seismicity and potential leakage risk analysis using NRAP tools and develop strategies for risk mitigation.

Subtask 5.5–Economic risk/feasibility assessment.

Task 6 – Infrastructure Network Assessment

Subtask 6.1–Aggregate infrastructure data and build databases.

Subtask 6.2–Model pipeline corridor; Define surface facilities that would be required to execute chosen design concepts.

Subtask 6.3–Assess CO_2 capture-transport-storage system.

Subtask 6.4–Identify potential business entry opportunities related to nearby sources or users of CO_2.

Task 7 – Regulatory Outreach and 45Q Preparations

Subtask 7.1–Meet with U.S. EPA (Regions 6-OK, 7-KS) to discuss UIC Class VI permit application.

Subtask 7.2–Meet with external teams that have experience applying for EPA-UIC Class VI permits.

Subtask 7.3–Meet with state environmental and petroleum regulators.

Subtask 7.4–Identify necessary U.S. IRS 45Q compliance documentation.

Task 8 – Technology Transfer

Subtask 8.1–Maintain website for project.

Subtask 8.2–Public presentations.

Subtask 8.3–Publications.

Subtask 8.4–Upload data to DOE-EDX.

Task 1 – Project Management

Task 1 focused on managing and coordinating the $MOSCO_2$ project across a diverse set of partners, technical domains, and deliverables. KGS led this effort, guiding the project from early mobilization through final reporting while ensuring deliverables met DOE expectations for schedule, budget, and scope.

This task emphasized centralized oversight to align the work of national laboratories, academic institutions, and private sector contributors. Institutional differences in workflow and pacing highlighted the need for strong project integration and scheduling discipline. As detailed in the Introduction, the July 2022 incident at ONEOK's Medford facility required a rapid shift in scope, concentrating field activities and technical focus at the Bushton site in Kansas.

Despite evolving field access and budgetary conditions, Task 1 ensured that technical outputs remained both robust and aligned with ONEOK's commercial objectives and DOE regulatory frameworks.

Subtask 1.1 – Managing and Allocating Resources, Communications, Outreach, and Technology Transfer

KGS led Subtask 1.1, coordinating resource management, internal communications, partner integration, and all external reporting and outreach activities. This included milestone tracking, quarterly reporting, DOE correspondence, and logistical coordination supporting subsurface evaluation, modeling, risk assessment, and infrastructure planning across five primary institutional partners. Early coordination meetings with ONEOK, Carbon Solutions, and national lab teams established data-sharing protocols and clarified simulation input requirements.

Project Leadership and Timeline

Project leadership transitioned across four principal investigators (PIs) during the performance period. Intentional knowledge handoffs and continuity planning were implemented to maintain alignment, particularly as project scope narrowed. Table 26 summarizes PI responsibilities and associated milestones. Table **27** provides a Gantt-style timeline of task execution, with blue vertical lines indicating PI transitions. KGS maintained consistent oversight throughout, leveraging internal expertise and administrative support to ensure continuity of communication and deliverable pacing.

Table 26 Project PI timeline and key deliverables

Period	Project PI	Key deliverables and milestones
Pre-Award	E. Holubnyak	Proposal developed and submitted
Apr 2022 – Oct 2022	F. Hasiuk	Kickoff held, team formed, Medford planning initiated
Oct 2022 – Jul 2023	C. Ridley	Bushton site visit, modeling integrated, seismometer deployed
Jul 2023 – Nov 2023	F. Hasiuk	Progress synthesized, budget aligned
Nov 2023 – Jul 2025	B. Bream	Partner deliverables integrated, report finalized

Table 27 Project timeline and task assignments. Blue vertical lines indicate PI transitions.

Task	Task Name	Task Assignments	Calendar Year (CY) 2022 Q2	Q3	Q4	CY 2023 Q1	Q2	Q3	Q4	CY 2024 Q1
1	Project Management	**KGS**, OGS, ONEOK								
2	High Level Technical Review	**KGS**, CS, ONEOK, OGS, PNNL, LANL, Sandia								
3	Subsurface Studies	**KGS**, OGS, CS, ONEOK, KGO								
4	Dynamic Simulations	**PNNL**, KGS, LANL								
5	Risk Assessment	**LANL**, CS, KGS, PNNL, Sandia								
6	Infrastructure Needs Assessment	**CS**, ONEOK, KGS, Sandia								
7	Regulatory outreach and 45Q Preparations	**KGS**, ONEOK, OGS								
8	Technology Transfer	**KGS**, All								

Partner Contributions and Personnel

KGS coordinated a multidisciplinary team drawn from academic, governmental, and private sector institutions with roles aligned to major technical tasks. Letters from partners detailing contributions are attached in the Appendix.

At **KGS**, the Energy Research Section led technical work, including key personnel Brendan Bream (PI), Jason Eleson, Jason Gumble, and Hannah Horinek. Subsurface engineering support was provided as needed. The KU Department of Geology led seismic risk monitoring, with contributions from George Tsoflias and graduate research assistant Hannah Proffitt, who also supported field instrumentation.

The **Oklahoma Geological Survey (OGS)** provided public geologic data and well records for Medford. Following the revised project scope, OGS redirected technical support to other CUSP-West priorities but continued sharing Petrel resources and engaging regional stakeholders. Key staff included Nick Hayman and Cesalea Ray.

ONEOK, Inc. contributed cost-share personnel time and facilitated access to regional facility data, infrastructure records, and analytics. Key contacts included Chad Schneeberger and Gregg Eichorn.

Pacific Northwest National Laboratory (PNNL) participated in early modeling discussions and later led dynamic reservoir simulation tasks (Tasks 3 and 4) using STOMP-CO_2 and STOMPX-CO_2. Mark White also coordinated NRAP tool integration with KGS.

Carbon Solutions LLC (CS) led Task 6 on infrastructure network modeling, collecting pipeline and facility data in collaboration with ONEOK and supporting facility planning and CO_2 transport analysis using SimCCS^{PRO} software. Key personnel included Richard Middleton, Erin Middleton, Marcos Miranda.

Los Alamos National Laboratory (LANL) provided early-stage guidance on risk assessment and reservoir modeling and NRAP tool use. Staff included Rajesh Pawar, Shoaping Chu, and Bailian Chen.

Sandia National Laboratories conducted economic modeling to assess commercial viability and IRS 45Q credit eligibility. Team members included Shruti Mishra and Jason Heath.

Subtask 1.2 – Site Visits to Confirm Findings of Technical Review

Site visits were conducted to validate infrastructure conditions and technical review findings, particularly around injection feasibility and field logistics.

As noted in the Introduction, the planned kickoff meeting at Medford in September 2022 was held virtually. The site visit was canceled, and a reduced-scope review continued using public data provided by OGS and references from ONEOK.

The Bushton site visit took place on November 2, 2022, with participation from F. Hasiuk, C. Ridley, J. Raney, and the KU seismic team (G. Tsoflias, H. Proffitt). ONEOK staff hosted the walkthrough, which covered injection wellheads, storage units, compressors, and pipeline points. This visit confirmed infrastructure feasibility and informed modeling and monitoring strategies. Additional field visits by H. Proffitt supported seismometer installation and maintenance.

Subtask 1.3 – Reporting

KGS led all reporting activities, including quarterly technical reports and final deliverables. These products facilitated proactive identification of risks and scope adjustments, especially as site-specific conditions evolved. Reports were produced in collaboration with project partners and reviewed by PRRC. Quarterly technical reports are available at https://www.kgs.ku.edu/Publications/OFR/2025/OFR2025-51.pdf.

Task 2 – High-Level Technical Review

Task 2 provides the foundational technical screening necessary to evaluate the feasibility of CO_2 storage at ONEOK's midstream facilities, focusing on geological integrity, regulatory compliance, and site-specific data readiness. Led by the KGS, this task integrated geologic, engineering, risk, and infrastructure expertise across institutional partners, establishing the basis for simulation, permitting, and risk analysis in subsequent tasks.

Effective CCS site screening requires consideration of both geologic suitability and interaction with existing subsurface infrastructure (DOE NETL 2017). These factors include:

- Presence of permeable and laterally continuous reservoirs;
- Effective top seals or intraformational barriers to prevent vertical CO_2 migration;
- Temperature and pressure conditions exceeding 88°F and 1,070 psi (supercritical threshold);
- Absence of faults, fractures, or legacy wellbores that could serve as leakage pathways;
- Appropriate formation pressures and stress regimes to minimize induced seismicity;
- Isolation from Underground Sources of Drinking Water (USDWs);
- Compatibility with existing injection operations;
- Suitability for robust monitoring, reporting, and verification (MRV) systems.

Key deliverables included:

- Compilation and QA/QC of subsurface geologic and petrophysical datasets;
- Delineation of USDWs and evaluation of salinity gradients;
- Environmental justice (EJ) screening;
- Preliminary Area-of-Review (AoR) delineation to support Class VI permitting.

These outputs directly supported reservoir modeling (Task 3), simulation (Task 4), risk assessment (Task 5), and permitting strategy (Task 6).

Subtask 2.1 – Determine Quantity, Type, and Quality of Available Data Relevant to Geologic, Engineering, Infrastructure, Risk Assessment, and Economic Modeling

KGS coordinated a multi-institutional review of data relevant to CO_2 storage feasibility, with participation from KGS, OGS, PNNL, LANL, Sandia, Carbon Solutions, and ONEOK. Activities included:

- Reviewing UIC permit materials for ONEOK's Bushton facility;
- Conducting alignment meetings to define modeling inputs and deliverables;
- Aggregating well logs, core data, and legacy records for both study areas.

Bushton, Kansas Site

The Bushton study area (Figure 162) is located on the southeastern flank of the Central Kansas Uplift (CKU), where Paleozoic carbonate reservoirs, especially the Arbuckle Formation, are common (Figure 163). This area benefits from dense well control, existing infrastructure, and robust production histories. Challenges include legacy wellbores, incomplete records, and complex subsurface structure.



Figure 162 Bushton study area map

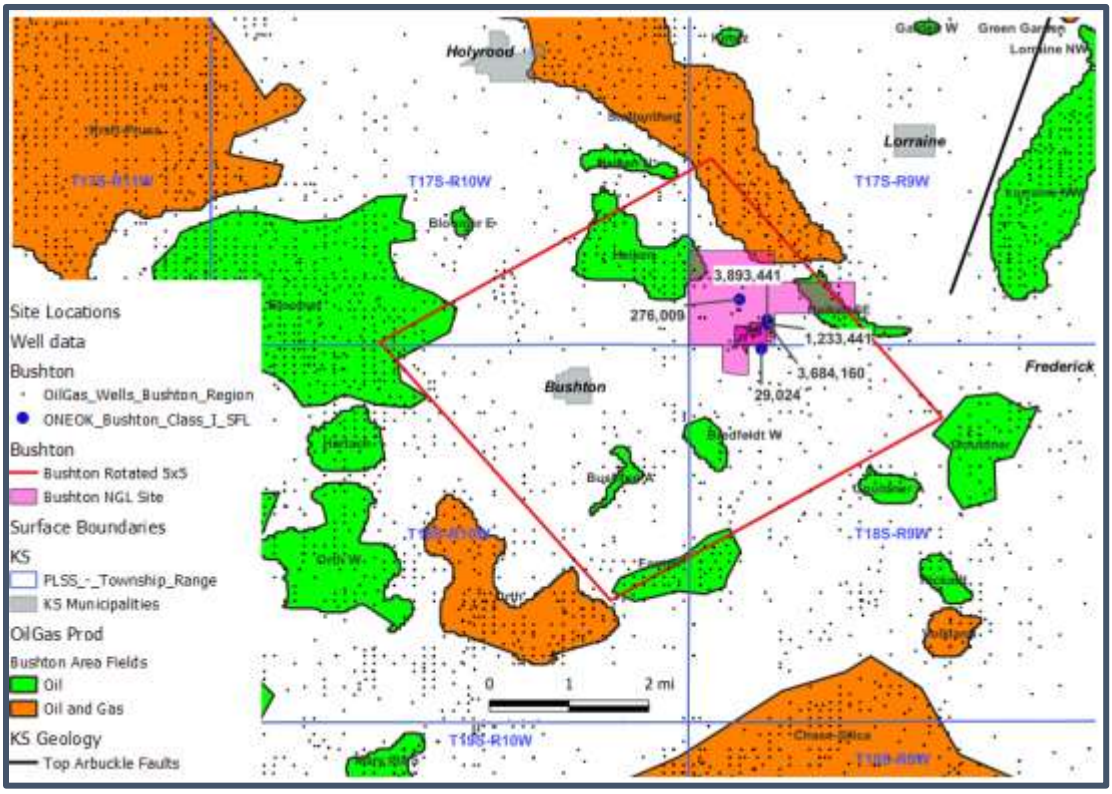


Figure 163 Initial screening map of the Bushton site, showing the distribution of oil and gas fields and the spatial extent of Class I and Class II wastewater disposal activity. Significant volumes of water have historically been injected into the Arbuckle reservoir, informing injectivity and pressure conditions for CCS evaluation.

An initial 3-by-3-mile model was expanded and rotated approximately 35° to define a 5-by-5-mile area better aligned with regional fracture orientations and less affected by legacy production. This area captures higher quality logs, maintains proximity to infrastructure, and avoids interference from high-producing fields and nearby wastewater injection (e.g. by Northern Natural Gas). Two target reservoirs were selected; their reservoir properties are summarized in Figure 164:

1. **Lansing–Kansas City (LKC) Group**: fractured oomoldic grainstones and packstones, moderate production rates, known shoal geometries;
2. **Arbuckle Formation**: fractured, karst dolostone with matrix and non-matrix porosity systems; permeabilities often exceed 1,000 mD.

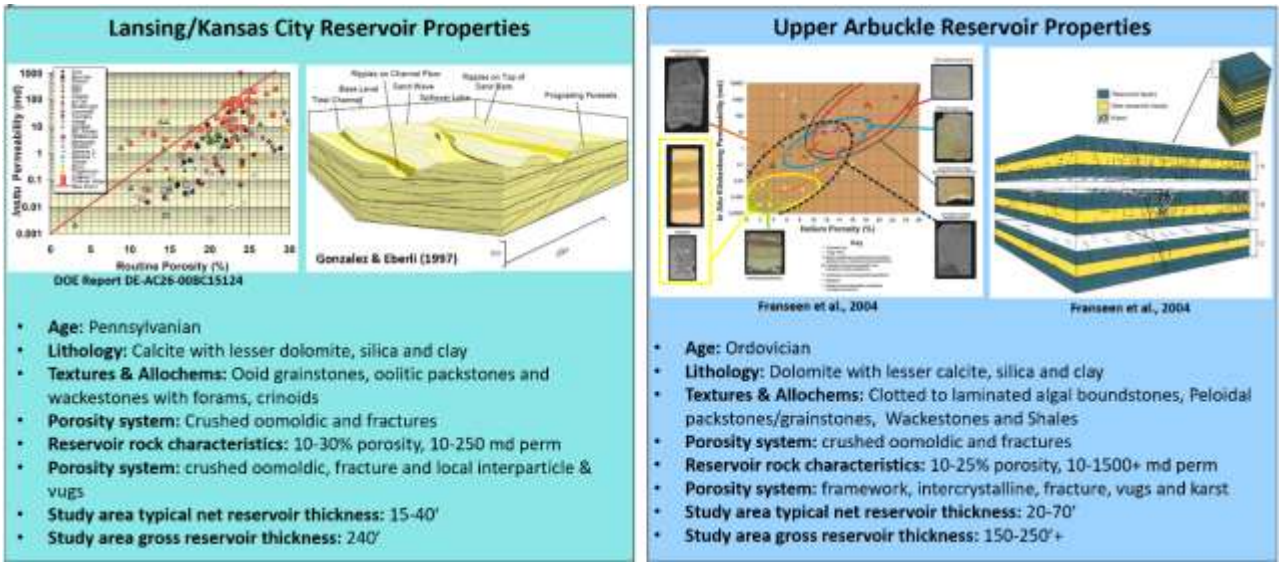


Figure 164 Reservoir properties for the two target reservoirs at the Bushton site

Small basement uplifts and irregular Arbuckle weathering contribute to warping of overlying units and likely influence fracture trends (predominantly NW/SE, consistent with CKU orientation), affecting both target formations. Regional seals include the Simpson and Douglas Shales; the Simpson may include interbedded sands that reduce seal quality in structural lows (Figure 165). The thick, high-quality seals are not expected to be compromised by fractures due to their ductility and overall thickness.

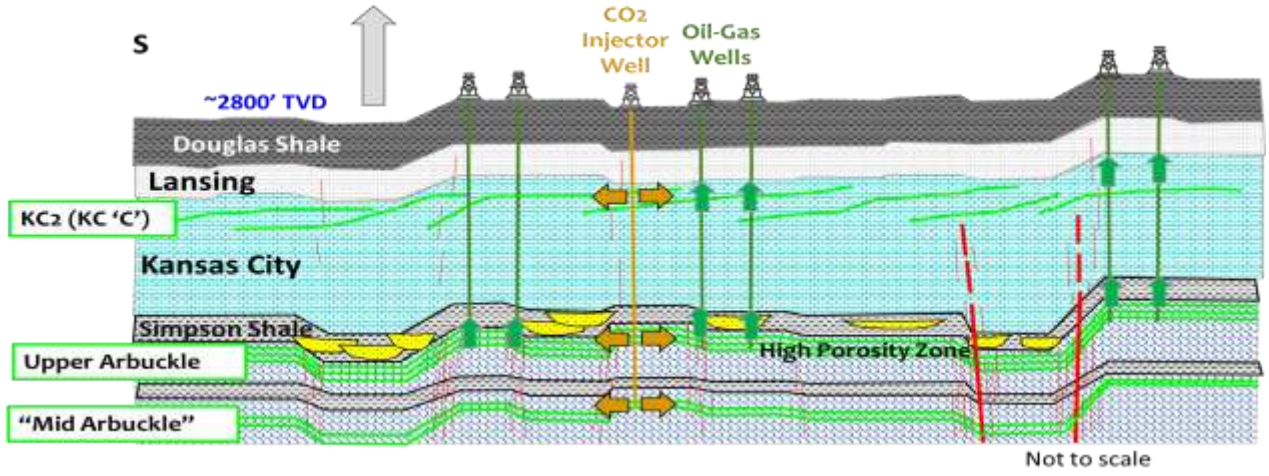


Figure 165 Bushton area conceptual model

The Bushton site hosts numerous oil and gas wells, most of which terminate in the Upper Arbuckle (UA). Injector wells and a subset of deeper producers penetrate the "Mid Arbuckle," a zone with especially high permeability (Figure 165). This distribution complicates AoR and injectivity due to potential legacy wellbore impacts.

Medford, Oklahoma Site

The Medford area is located at the southern margin of the Sedgwick Basin in central Grant County (Figure 166), adjacent to legacy production from the Mississippian Chat, Wilcox, and Arbuckle formations. Prior activity has included horizontal drilling and injection, though induced seismicity concerns have curtailed some operations.

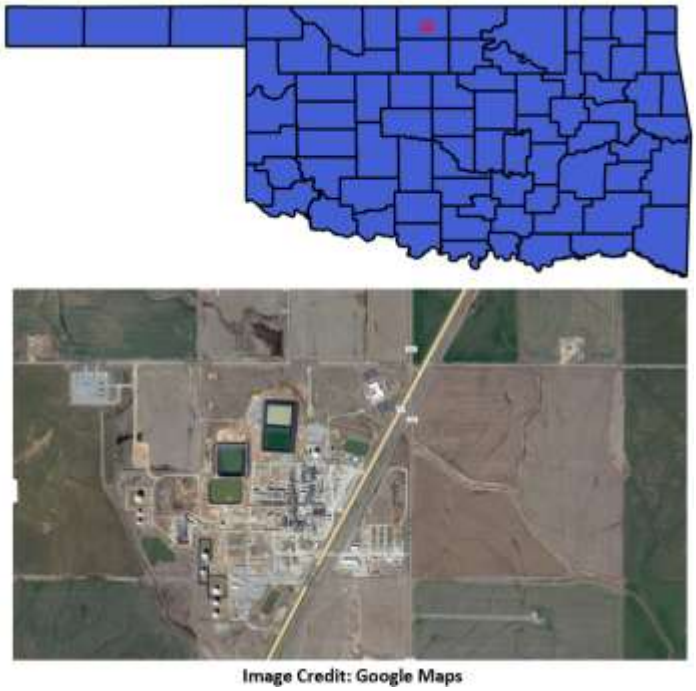


Figure 166 Location and satellite image of ONEOK facility at Medford, Oklahoma

OGS provided 128 raster logs and header metadata over a 6x6-mile area. KGS digitized ten wells for Petrel integration, four of which included modern porosity–permeability data.

The Wilcox–Bromide interval was prioritized over the Mississippian Chat based on:

- Stratigraphic thickening toward the Texas Arch, influenced by Ouachita-related subsidence (Figure 167);
- Deposition within a distributive system sourced from Canadian Shield clastics with high net-to-gross ratios;
- Consistent thickness and quality in distal shoreface sandstones (Figure 168);
- Sufficient well control for preliminary modeling;
- Reduced reservoir pressure from prior production, potentially improving injectivity and reducing seismic risk.

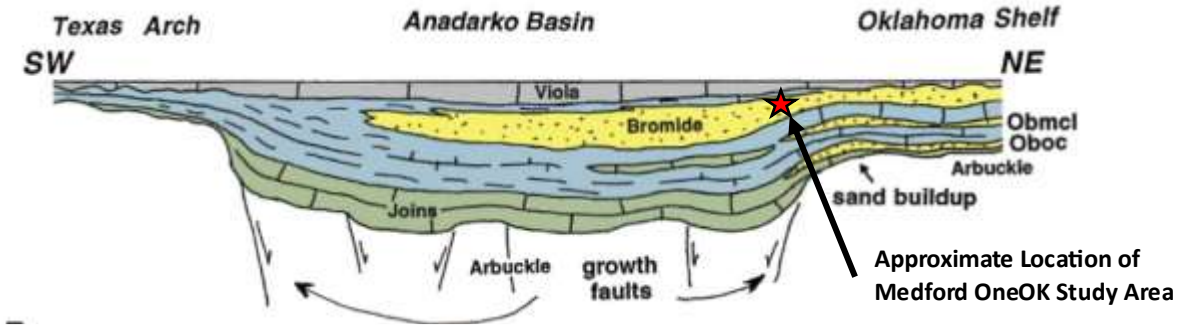


Figure 167 Conceptual stratigraphic section through the Medford area. From Suhm (2016).

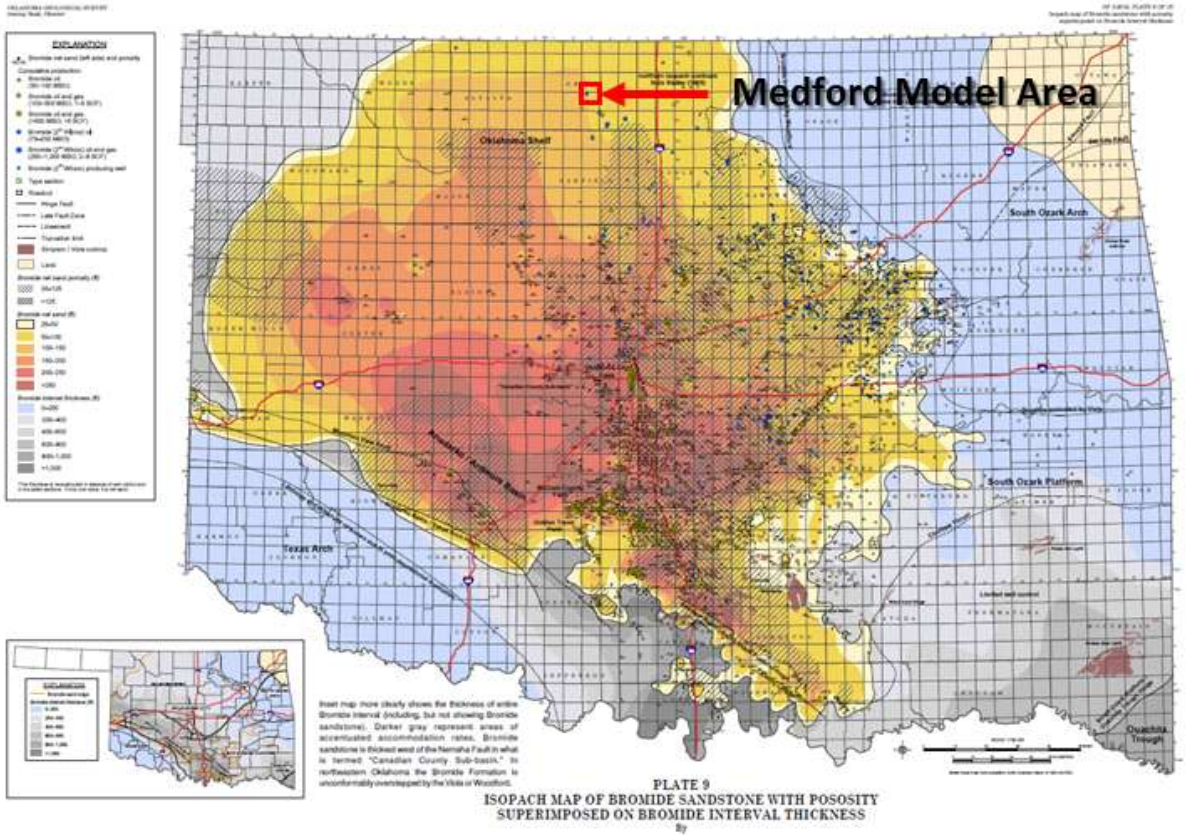


Figure 168 Isopach of Bromide-Wilcox Sandstone. From Suhm (2016).

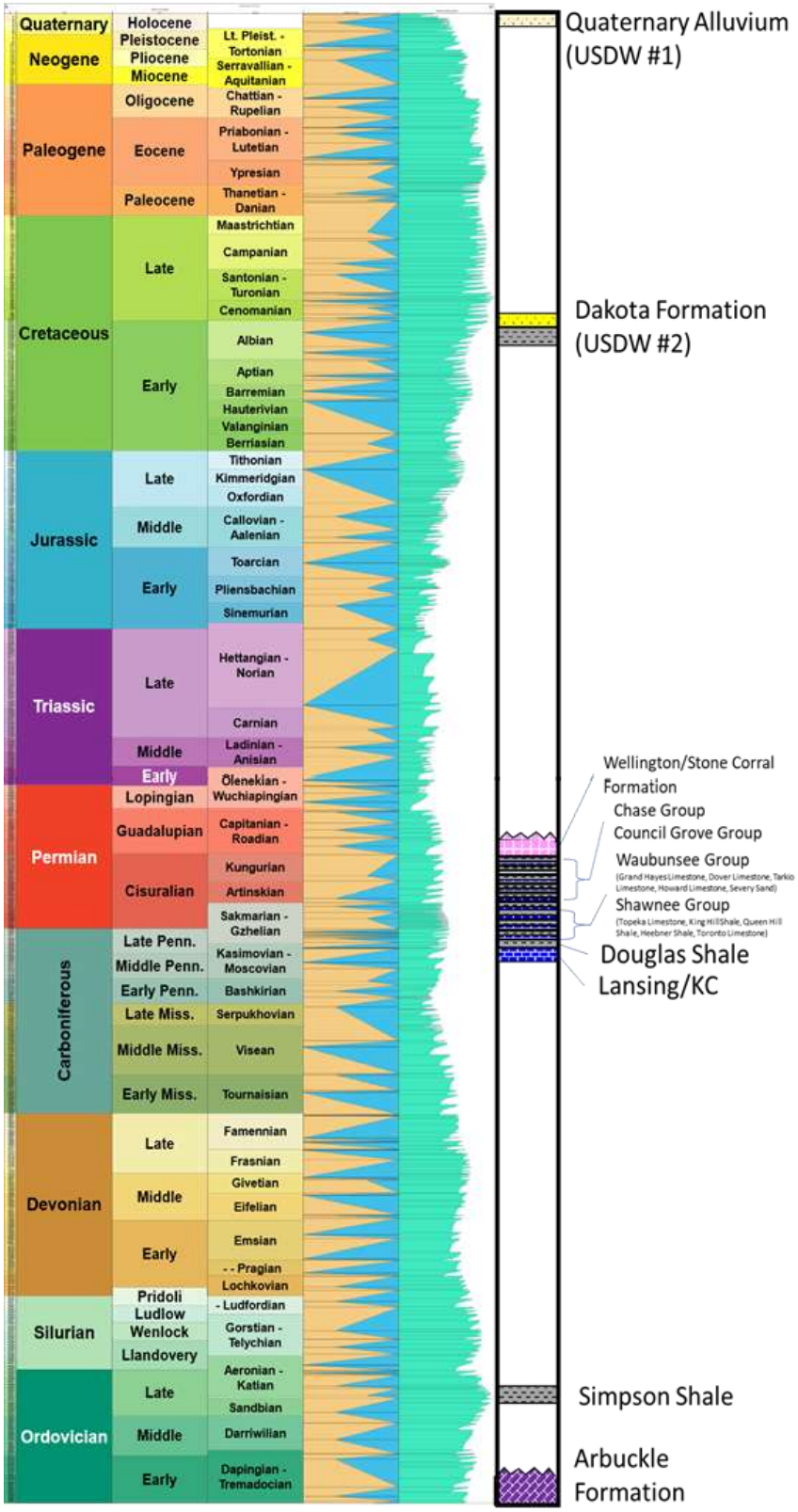


Figure 169 Stratigraphy and USDWs in Rice County, Kansas

The Bromide Formation, part of the Simpson Group, accumulated rapidly in response to subsidence within a sediment-loaded tectonic basin west of the Nemaha Fault, sometimes exceeding 250 feet in thickness (Figure 168). It is among the region's most productive and high-quality sandstone reservoirs.

The Mississippian Chat showed locally favorable porosity development in the northern part of the study area. However, that zone had been extensively drilled and included active production, making it less favorable due to the risk of CO_2 intrusion into hydrocarbon streams and higher abundance of legacy wellbores that could increase leakage risk. In contrast, areas farther south lacked adequate porosity, likely due to reduced karst development.

The Arbuckle Formation, while technically attractive, was excluded from detailed modeling due to a limited number of well penetrations in the Medford area and heightened concerns regarding induced seismicity. This formation lies closer to the Precambrian basement and is intersected by faults known to be critically stressed. Prior wastewater disposal in the region has been linked to seismic events, and informal consultation with OGS staff indicated that injection into the Arbuckle would face significant regulatory obstacles.

Data Aggregation

KGS conducted data integration and QA/QC, producing:

- 265 digitized log curves from 36 wells, loaded and stretched in Petrel;
- Porosity-permeability data from routine core analyses (RCA);
- Drill stem test (DST) and falloff test data;
- Type logs and regional well top correlation in both project areas;
- Petrel-ready datasets for use in static modeling (Subtask 3.2), simulation (Task 4), and AoR analysis (Subtask 2.4).

Subtask 2.2 – Delineate Underground Sources of Drinking Water

KGS delineated USDWs at both sites using stratigraphic interpretations and water quality datasets from KGS and OGS, supplemented by regional brine chemistry and salinity cross-sections developed for this study.

At the Bushton site, the base of the USDW was placed near the top of the Hutchinson Salt Member of the Wellington Formation at approximately 950 feet below ground surface (bgs), based on halite occurrence and salinity increase (Figure 169). Shallower sediments include Holocene alluvium and eolian deposits, while the Cretaceous Dakota Sandstone forms the base of the USDW.

At the Medford site, USDWs are associated with Quaternary alluvium and Permian Garber-Wellington and Chase Groups. Below the Simpson Group, TDS exceeds 10,000 mg/L. The Wilcox-Bromide target lies well below and is isolated from these zones.

These delineations supported reservoir selection and AoR boundaries, ensuring vertical and lateral isolation from potable aquifers.

Subtask 2.3 – Review Environmental/Social Justice Considerations

An EJ screening was conducted to assess whether either of the candidate sites are located within or near disadvantaged communities (DACs) that could be disproportionately affected by carbon storage activities (Figure 170A). The analysis followed guidance from the U.S. Department of Energy's Office of Fossil Energy and Carbon Management (FECM), using the Climate and Economic Justice Screening Tool (CEJST) and archived EPA EJScreen data (https://edgi-govdata-archiving.github.io/j40-cejst-2/en/#3/33.47/-97.5).

Bushton, Kansas: Rural Rice County showed no DAC indicators within 5 miles (Figure 170B). Air quality and hazard exposure were low, and no Tribal lands were nearby.

Medford, Oklahoma: While not classified as disadvantaged, poverty and energy burden indicators approach threshold levels. No elevated risk indicators were identified within 5 miles (Figure 170C), but future stakeholder engagement is recommended.



Figure 170 Disadvantaged communities (A) at regional scale, (B) near Bushton, KS, and (C) near Medford, OK.

Nearby DACs and Tribal Context: Nearby DACs (within 100 miles) were noted for future consideration. These include Hoisington (approximately 20 mi), Great Bend (approximately 25 mi), and Reno County (approximately 60 mi), Kansas, and Enid (approximately 30 mi), Woods County (approximately 60 mi), and nearby Tribal communities such as the Tonkawa (approximately 30 mi), Ponca (approximately 50 mi), and Osage (approximately 90 mi) Nations were noted in Oklahoma. While no direct EJ concerns were identified, early outreach is recommended for future Class VI development.

Subtask 2.4–Determine Area-of-Review

The work completed for this study is not adequate to rigorously delineate an Area-of-Review (AoR) per current EPA Class VI Well Area of Review Evaluation and Corrective Action Guidance. This work is useful as a preliminary benchmark for injection into a single deterministic subsurface property model; additional data collection (e.g. seismic, core, post-production formation pressures, etc.) are highly recommended. While these models are not intended to serve as an EPA-ready AoR, they demonstrate a viable workflow for future permit application development. All necessary simulation data for a formal Class VI AoR evaluation are contained within LANL's model output files but were not post-processed for regulatory compliance in this study as the underlying static property is under-constrained and numerous critical assumptions were required (e.g. reservoir connectivity within and adjacent to the model; current formation pressure). Additional technical work is recommended to refine these AoRs, including acquisition of 3D seismic, advanced logging data, formation pressure measurements, and conventional core from both storage and seal units. The spatial geometry of modeled plume and pressure behavior aligns with regional injectivity trends and provides a strong technical foundation for advancing future site characterization and risk-informed project design. Below is summary of the most relevant outputs generated from the technical work completed at Los Alamos National Laboratory.

The AoR for a geologic sequestration project is a delineation on a surface map of the region over which USDWs may be endangered by the injection activity (EPA 2013). This area encompasses two regions, both of which are determined from computational modeling that accounts for the characterization of the subsurface site and the thermodynamic, chemical and transport properties of the fluid phases in the reservoir pore space (40 CFR 146.84(a) and 40 CFR 146.84(c)(1)). The first region is the areal extent of the CO_2 over time, from the commencement of injection until the CO_2 plume (free and dissolved components) movement ceases. One methodology for determining this region is selecting a cutoff value for the vertically integrated mass per area (VIMPA; Zhang et al. 2015). The second method uses areal extent of the pressure within injection reservoir that could result in the upward migration of reservoir fluid into an overlying USDW as delineated by dynamic simulation model outputs. As with the CO_2 plume region, this region is delineated from the commencement of injection until pressure differentials sufficient to cause the movement of injected fluids or formation fluids into a USDW cease to exist (40 CFR 146.84(c)(1)).

KGS conducted preliminary AoR analysis for the Bushton site using static and dynamic reservoir simulation tools. These conceptual models delineate the expected spatial extent of pressure propagation and CO_2 plume migration for two potential injection intervals: the LKC Group and the Arbuckle Formation. Simulations were conducted with STOMP-CO_2 and STOMPX-CO_2, incorporating formation-specific parameters such as porosity, permeability, and pressure. For the LKC reservoir, simulation results indicated limited CO_2 plume expansion, primarily due to poor injectivity and low reservoir pressure. Fracture gradient scenarios of 0.6, 0.7, and 0.8 psi/ft yielded top-hole pressure limits of approximately 1,740 to 2,750 psi, limiting injection rates below viable thresholds. As a result, the LKC was assessed to be a marginal candidate for sustained CO_2 injection unless active fracture management strategies are employed or legacy fracture systems allow for diffusion of CO_2 plumes and associated pressure fronts. In contrast, the Arbuckle Formation demonstrated greater injectivity and a broader CO_2 plume footprint.

Calibration of permeability inputs was based on historical data from five nearby disposal wells. Additional modeling scenarios evaluated three hypothetical injection wells placed in deeper sections of the Arbuckle not commonly penetrated by existing wells. To support this, KGS integrated logs from four deep penetrations located approximately 7 miles south of Bushton. These inputs allowed for conceptual modeling of deep Arbuckle behavior at depths comparable to legacy Class I injection operations. Although these models are exploratory and cannot yet be fully validated with site-specific data, they provide valuable insight into the storage potential of deeper Arbuckle intervals.

Pressure-based AoRs were developed for both intervals, incorporating simulation outputs (see Task 4) and risk considerations (see Task 5). For the LKC, the AoR reflects the fracture and karst geometries embedded in the property model (**Figure 171**). For the Arbuckle Deep scenario, the pressure-based footprint was smaller due to favorable reservoir properties, including thickness, fracture-enhanced porosity, connectivity, and permeability. The maximum projected extent of both CO_2 plume migration and pressure increase was used to define the preliminary AoRs.

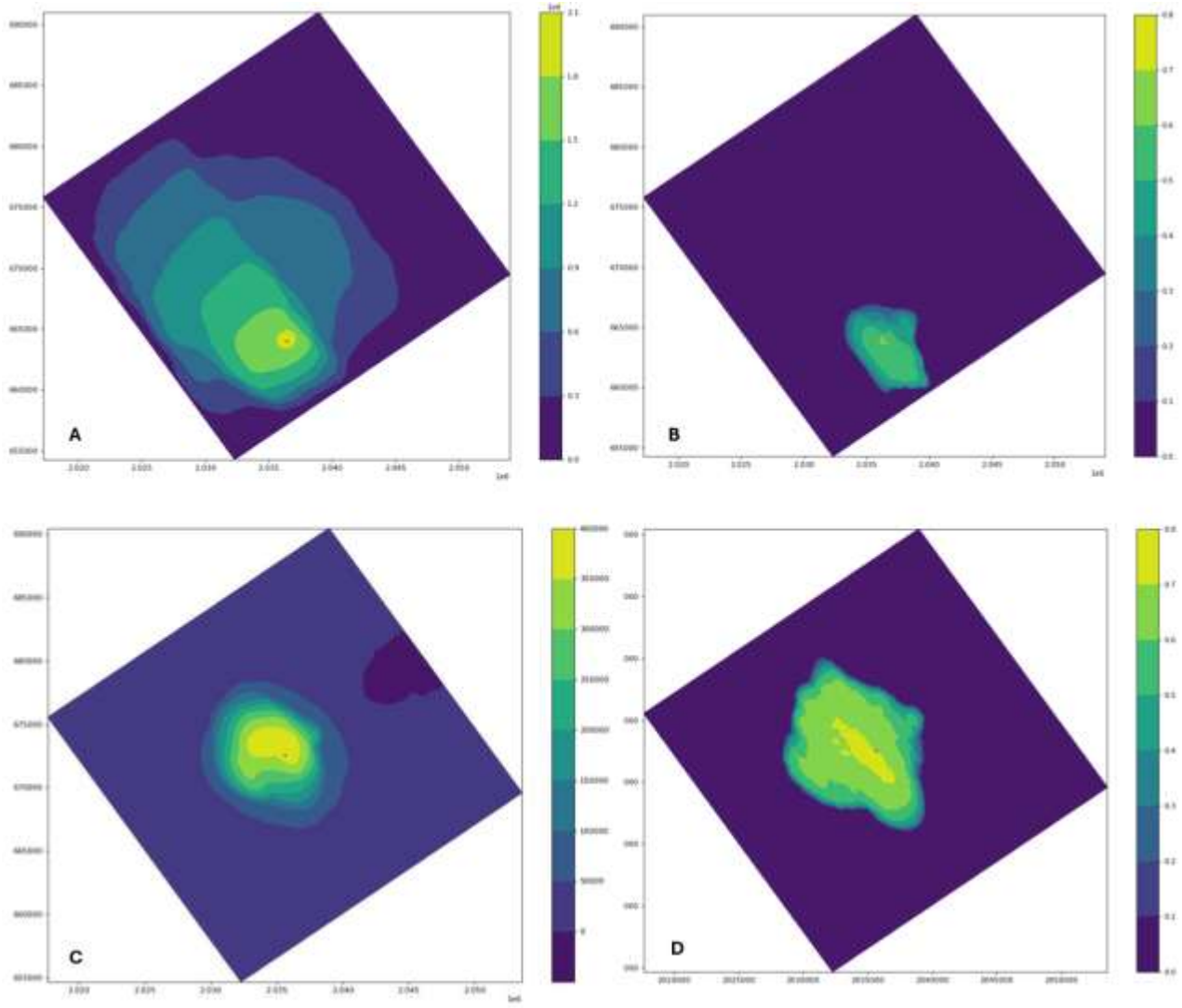


Figure 171 Pressure and CO_2 plume extents for the Lansing-Kansas City and Arbuckle Deep simulations. A) Pressure increase from injection for the LKC; B) CO_2 plume after 51 yr of injection for the LKC; C) Pressure increase from injection for the Arbuckle Deep; D) CO_2 plume after 50 yr of injection for the Arbuckle Deep.

Task 3 – Subsurface Studies

Subsurface screening and evaluation for ONEOK facilities in Medford, OK and Bushton, KS were conducted under this CUSP-West focused study. This work represents a preliminary technical foundation for future site-specific Class VI application development. Establishing a viable regional CCS hub in the midcontinent will require substantial additional geologic and engineering assessment. The results frame future work by identifying existing data assets, technical gaps, and key elements required to reduce subsurface uncertainty.

This relied on publicly available geologic resources, including regional syntheses for Kansas and Oklahoma (e.g. Bream et al. 2025; Buchanan and Carr 2008; OGS 2021), detailed reservoir-scale assessments (e.g. Benmadi et al. 2024; Holubnyak and Dubois 2018), and ongoing DOE FOA 2711 work in Kansas. Long-term CO_2 storage potential in Kansas aligns, in descending viability:

(1) Arbuckle Formation (deep saline aquifer); (2) younger porous carbonate reservoirs (Mississippian, LKC); and (3) mineralization in Precambrian mafic rocks of the Midcontinent Rift System.

Existing reservoir distribution and property studies supported model construction and parameter selection, for example, Watney (2009) for the LKC, Franseen et al. (2004) for the Arbuckle, and Suhm (2016) for the Wilcox-Bromide. Figure 172 maps regional play adequacy relevant to Bushton (Bream et al. 2025). Probabilistic play evaluation remains recommended to frame Value-Of-Information (VOI) decisions for new data (seismic, core, wireline) and develop high/low/best-case scenarios reflecting uncertainty.

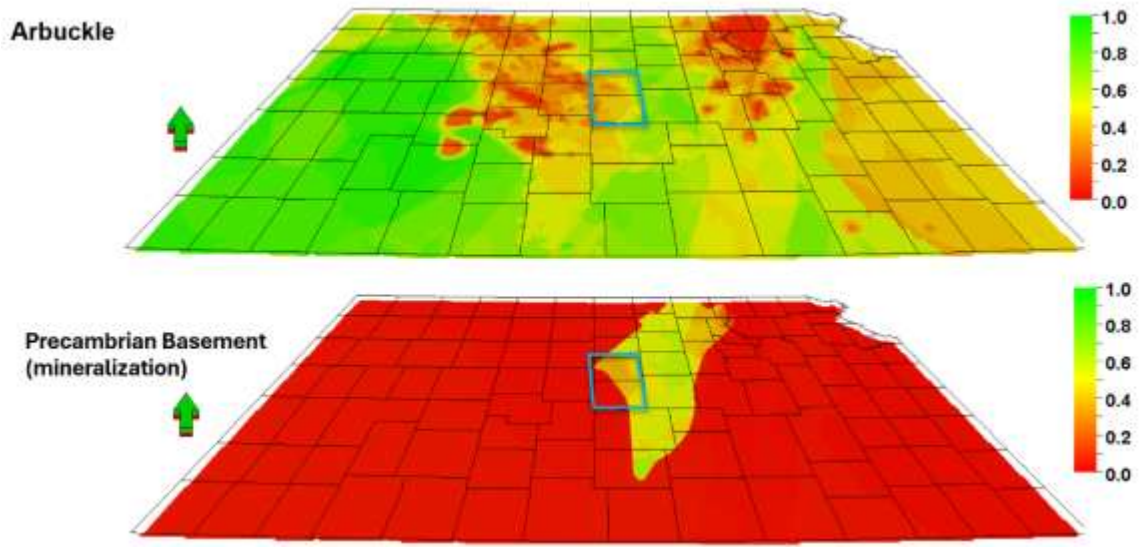


Figure 172 Example of two aggregated regional play assessment adequacy maps for Kansas (Bream et al. 2025). The color bar represents the aggregated chance of adequacy of CCS potential for four different play elements (reservoir presence, reservoir quality, CO_2 phase, and seal). The highlighted counties are Ellsworth (North) and Rice (South); the ONEOK Bushton facility is about 6.5 miles from the western edge of this county boundary.

Geocellular models, integrated with dynamic simulation, are essential screening tools. However, deterministic realizations are non-unique and must be interpreted considering data quality, facies interpretation, and geologic uncertainty. These models provide representative—not comprehensive—subsurface scenarios, useful for guiding screening, economic evaluation, and regulatory planning.

A generalized subsurface workflow, reflective of Class VI application needs, is recommended:

1) Identify, assemble, and assess local subsurface data (see Subtask 3.1).
2) Evaluate regional reservoir/seal properties, including trends in thickness, porosity, permeability, salinity, etc.
3) Assess regional existing seismicity (see Subtask 3.5).
4) Evaluate regional and subregional structural influences, including previously recognized faults, fault trends, and fracture or geomechanical data obtainable from offset wells, for example, published maps, core descriptions, dipole sonic and microresistivity imaging logs (see Subtask 3.4).

5) Assess subregional dynamic factors (e.g. nearby field production, wastewater injection, impact of legacy wellbores for leakage risk).
6) Collect baseline geochemical data to understand impact of CO_2 brines on seals, reservoir injectivity, and legacy boreholes.
7) Define reasonable property distributions based on available data or analogues.
8) Perform probabilistic assessment of key subsurface field inputs with dependencies (e.g. porosity and permeability).
9) Qualify subsurface parameters by quality and confidence (e.g. Callas et al. 2024).
10) Construct simplified scenario-based subsurface representations that capture at least high-side, low-side, and best-estimate cases.
11) Build one or more static geologic models that integrate the available data into viable subsurface solutions (see Subtask 3.3).
12) Add static models tied to probabilistic assessment inputs (e.g. P10 porosity), probabilistic outputs (e.g. P50 capillary seal capacity), or revised interpretations (e.g. from new wells or seismic).

Bushton and Medford illustrate typical midcontinent CCS challenges: well density and reservoir knowledge coexist with legacy data formats, limited coverage, and proprietary restrictions. This study generated viable geologic models that support simulation (Task 4) and risk assessment (Task 5), while defining future refinement paths. The outlook for long-term CO_2 storage in central Kansas remains favorable, though technically complex.

Subtask 3.1 – Subsurface Data Aggregation and Database Build

KGS, with support from OGS and Carbon Solutions, compiled subsurface data for Petrel modeling near Bushton and Medford. The integrated project includes well locations, raster and digital well logs, stratigraphic correlation picks, core-derived porosity–permeability data, and type well control. Figure 173 shows the Petrel interface for the Bushton model.

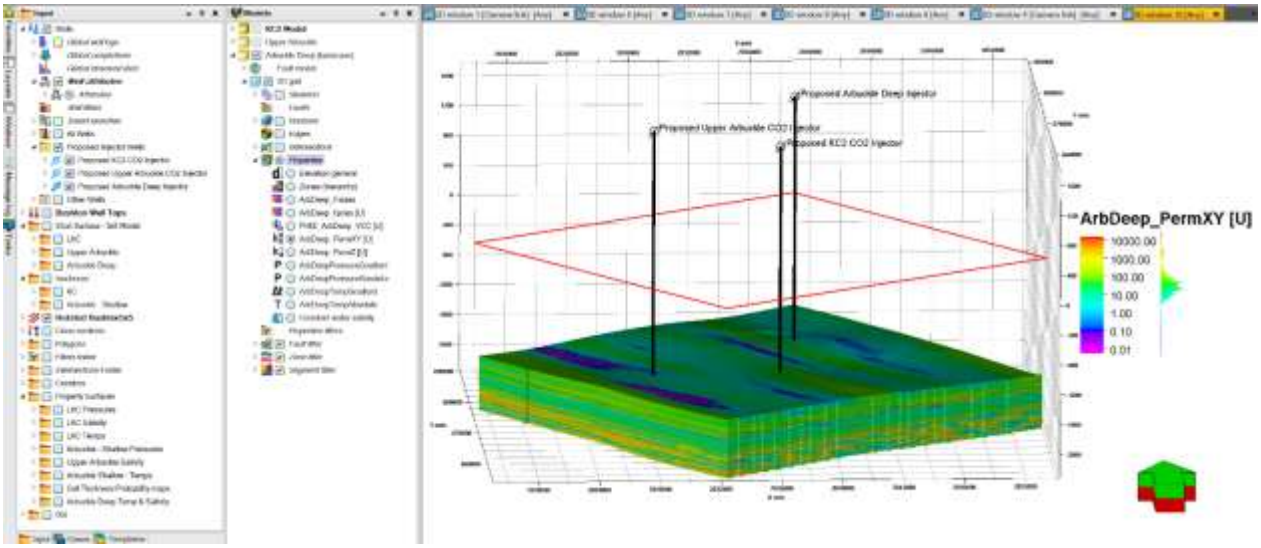


Figure 173 SLB Petrel Input, Model and 3D Window highlighting data that was identified and loaded for the Bushton subsurface evaluation with the resulting 3D geocellular model. The model property displayed is horizontal permeability in millidarcies for the Arbuckle Deep static model. NOTE: model is displayed at 5X vertical exaggeration.

Bushton Site Data

Two primary target reservoirs were selected: LKC Group and Arbuckle Formation, chosen for supercritical CO_2 conditions and data availability. A 5×5-mile modeling area includes 40 wells with raster logs, composed of a mix of legacy suites (e.g. spontaneous potential [SP], gamma ray [GR], and deep resistivity [RESD]) and more modern log suites (e.g. GR, resistivity, neutron porosity [NPHI], density [RHOB], and photoelectric factor [Pe]). Digitization efforts focused on modern logs, resulting in 26 wells with digital logs, and 11 with complete triple-combo logs (Figure 174). Injector data include cased-hole logs, falloff tests, and free-water levels. Regional salinity is constrained via the KGS Brine Database and the USGS Produced Water database. No new seismic data was acquired. Analog data for geologic modeling were drawn from the Hall-Gurney Field, a DOE-supported CO_2-EOR project in the LKC Group, and the Wellington and North Hugoton CCS projects, which are Arbuckle Group characterization studies.

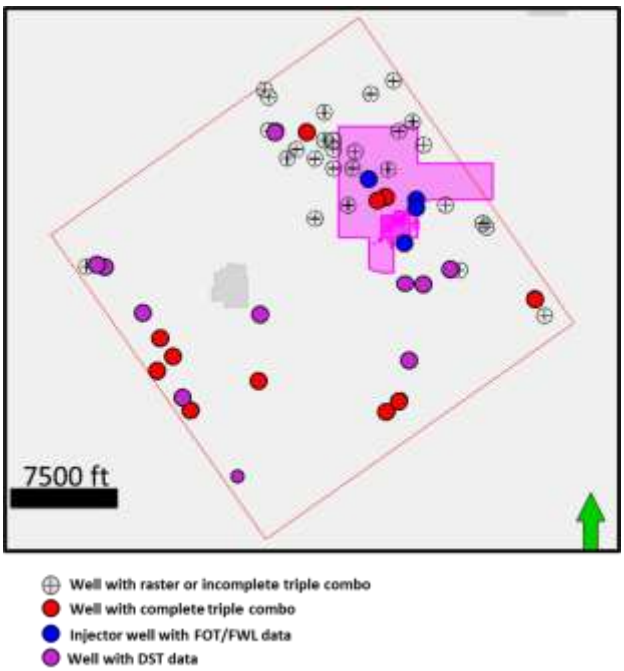


Figure 174 Available data for the 5-by-5-mile Bushton study area

Medford Site Data

Two primary target reservoirs were selected: Mississippian Chat and Wilcox–Bromide system. Over 125 raster logs were provided by OGS; ten wells were digitized by KGS for model development, including two injector wells. Only four wells contained complete modern log suites sufficient for porosity and permeability estimation. Most wells were drilled to total depth above the target Wilcox-Bromide intervals, and no core data from these reservoirs were available. KGS supported the effort by providing core-derived porosity, permeability, and grain density data from the Simpson sandstone, which is time-equivalent to the Wilcox-Bromide. Additionally, one well with DST records was identified through GeoIntegra's *Enverus* subscription.

To enhance modeling relevance, the AOI was shifted approximately 2 miles north for data quality and to avoid active production. A 6×6-mile grid was defined around the facility (Figure 175).

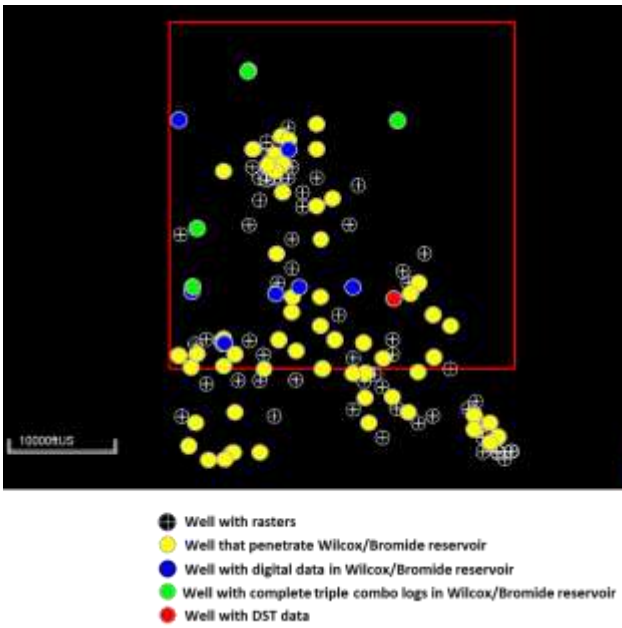


Figure 175 Available data for the 6-by-6-mile Medford study area

Subtask 3.2 – Static Geological Modeling

Geocellular models were developed to support static and dynamic analysis for CCS screening near ONEOK facilities. These Petrel-based models integrate well log, core, and structural data, and are archived with NMT/CUSP-West and uploaded to DOE EDX. Modeling outputs informed simulation efforts (Task 4), AoR development (Task 2.4), and risk assessment (Task 5). **Figure 176** illustrates the modeling workflow used to build 3D static models for each site. Table 28 summarizes the utility of each static model across key technical assessments.

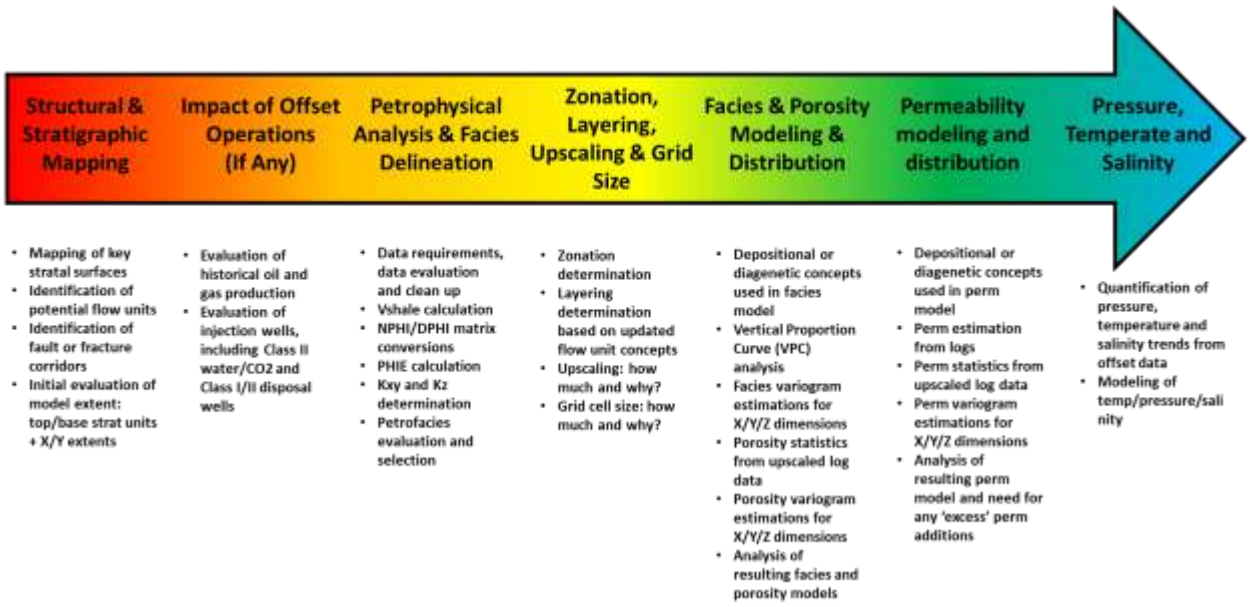


Figure 176 Overall geologic static modeling workflow

Table 28 Subsurface static models highlighting which models were utilized in key technical assessments and outputs for this research project.

Project name	Task 4: Dynamic Simulation	Subtask 5.2: Well Integrity and Seal Penetration Assessment	Subtask 5.5: Economic Risk/Feasibility Assessment	Task 6: Infrastructure Network Assessment
Lansing-KC (Bushton)	✓	✓	✓	
Arbuckle Deep (Bushton)	✓	✓	✓	✓
Upper Arbuckle (Bushton)	✓		✓	
Wilcox-Bromide (Medford)	✓		✓	

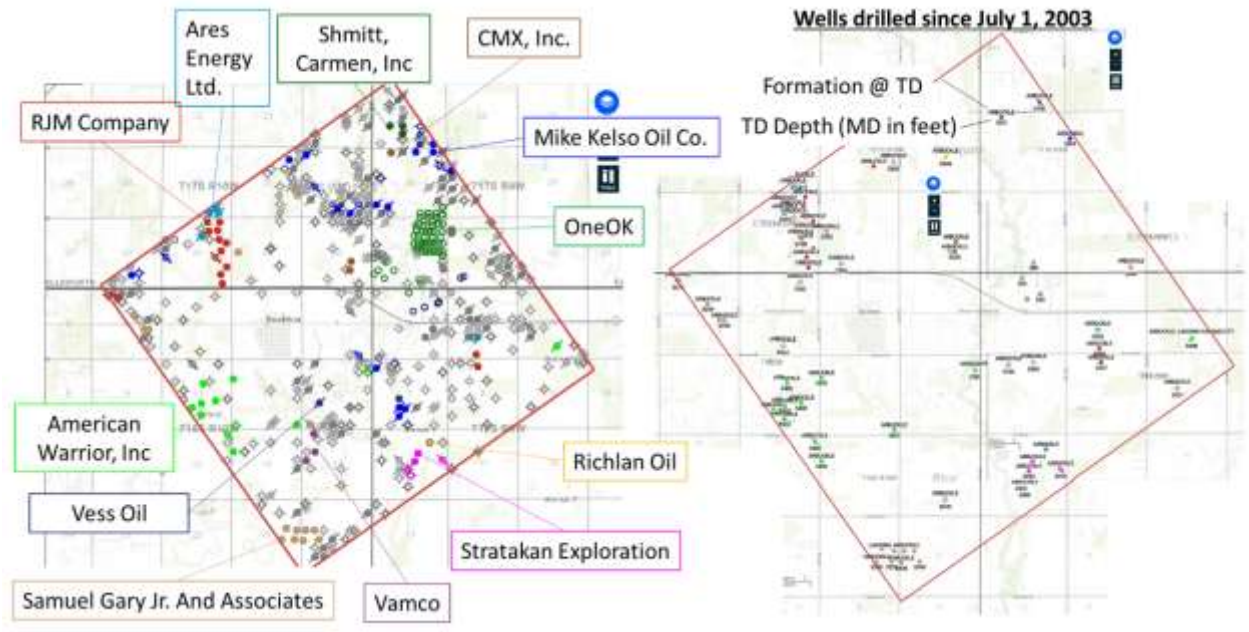


Figure 177 Active operators in the area surrounding the ONEOK Bushton facility (left). Wells drilled since 2003 with total depth (TD) and reservoir at TD (right).

Stratigraphic and structural interpretations were used to define zone and layering schemes (**Figure 178**), with petrophysical data guiding porosity and permeability distribution. Reservoirs were evaluated using analogues and adjusted for injection performance scenarios.

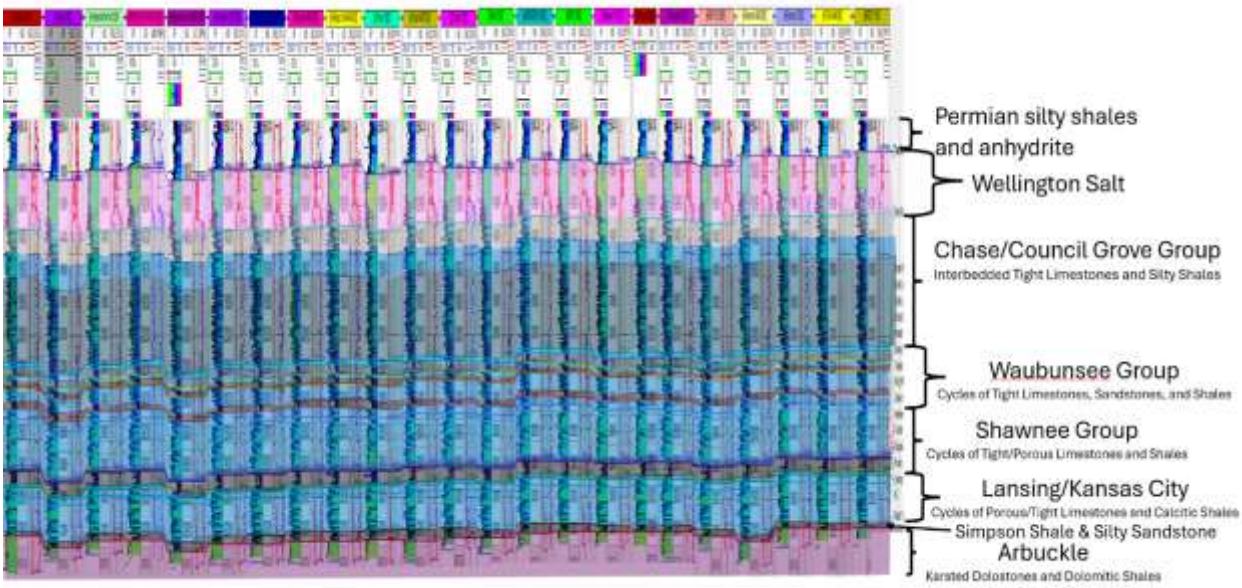


Figure 178 Composite well section (roughly west to east) at Bushton, showing stratigraphy and total depth of wells. Note the Arbuckle Deep model utilizes log data from outside of the model due to insufficient penetration of the Arbuckle Group.

Initial subsurface screening must consider salt thickness and salt depth below the surface to determine the feasibility of a facility near the ONEOK Bushton site or within the broader CO_2 producer pipeline network (**Figure 177**). Additional evaluation is needed to characterize the salt's geomechanical properties to ensure supercritical CO_2 conditions can be maintained. The Hutchinson Salt near the Bushton site is relatively shallow (500–1,000 feet below surface; approximately 950 feet at the facility) and thins near the evaporitic basin's depositional edge (**Figure 179**).

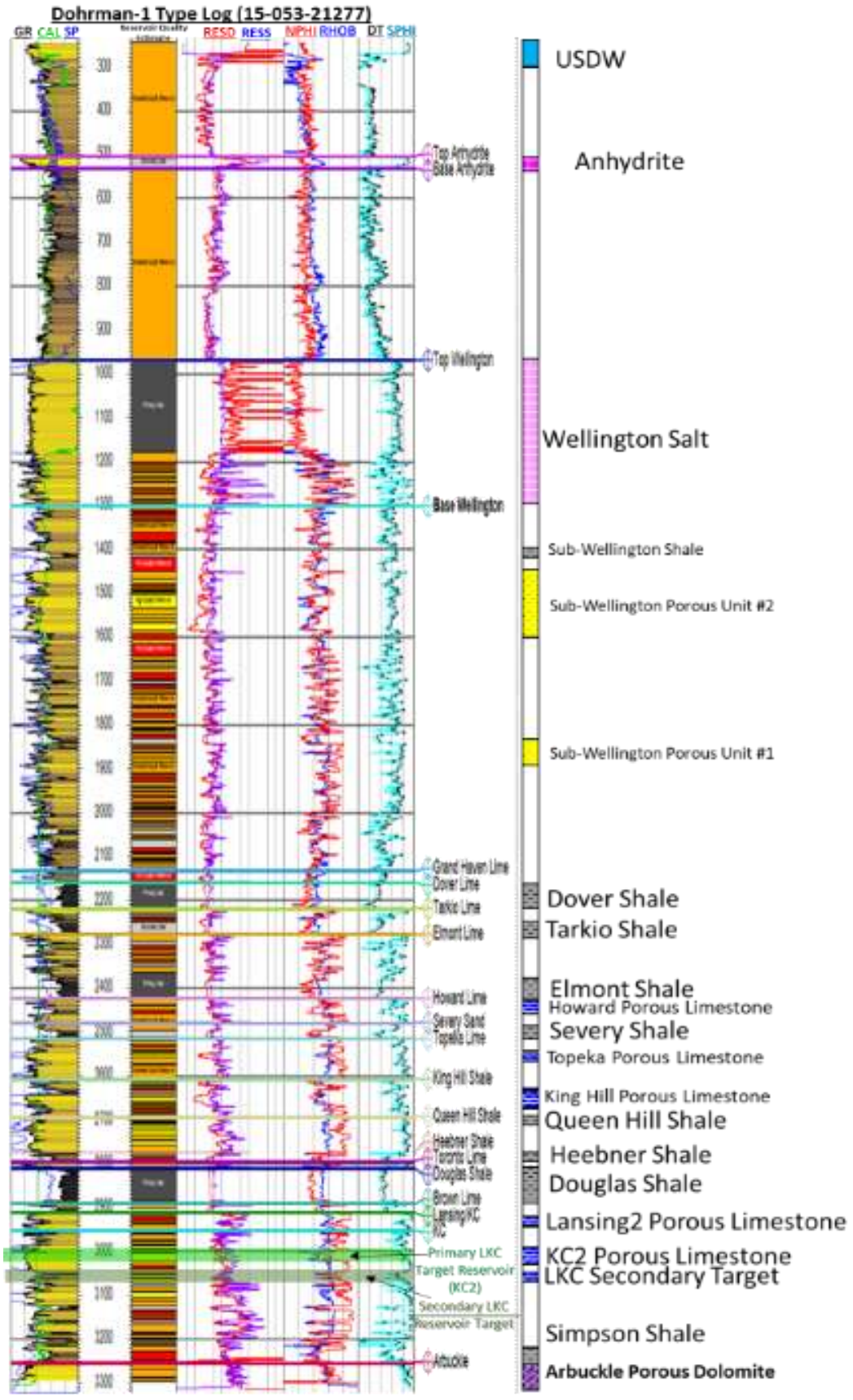

Dohrman-1 Type Log (15-053-21277)
GR CAL SP
RESD RESS NPHI RHOB DT SPHI
Top Anhydrite
Base Anhydrite
Top Wellington
Base Wellington
Grand Haven Lime
Dover Lime
Tarkio Lime
Elmont Lime
Howard Lime
Severy Sand
Topeka Lime
King Hill Shale
Queen Hill Shale
Heebner Shale
Toronto Lime
Douglas Shale
Brown Lime
Lansing/KC
Primary LKC Target Reservoir (KC2)
Secondary LKC Reservoir Target
Arbuckle
USDW
Anhydrite
Wellington Salt
Sub-Wellington Shale
Sub-Wellington Porous Unit #2
Sub-Wellington Porous Unit #1
Dover Shale
Tarkio Shale
Elmont Shale
Howard Porous Limestone
Severy Shale
Topeka Porous Limestone
King Hill Porous Limestone
Queen Hill Shale
Heebner Shale
Douglas Shale
Lansing2 Porous Limestone
KC2 Porous Limestone
LKC Secondary Target
Simpson Shale
Arbuckle Porous Dolomite

Figure 179 Dohrman-1 well log used to illustrate key porous and sealing intervals in central Kansas at the edge of the Central Kansas Uplift

Bushton (KS) Geologic Models

Three Bushton models were created: Lansing–Kansas City (KC2), Upper Arbuckle, and Arbuckle Deep (AD). The Upper Arbuckle model was discontinued due to poor regional correlation and pressure alignment. The KC2 and AD models were selected for simulation (Subtask 4.2).

Lansing/Kansas City (LKC) Static Model

The LKC Group model is shown in **Figure 180**.

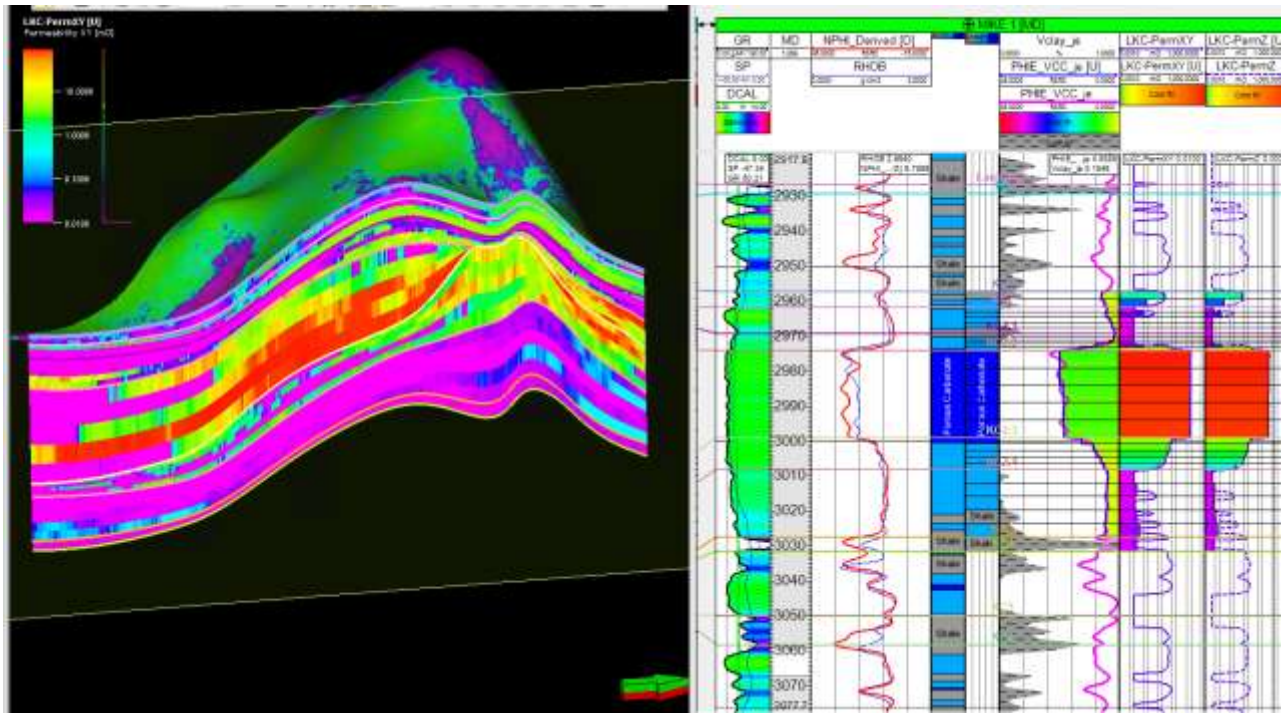


Figure 180 Permeability and petrophysical model for the Lansing-Kansas City Group

Reservoir analogue: Hall-Gurney Field (approximately 25 miles NW), with DOE-supported data (Watney et al. 2009). The best reservoir quality was observed in the upper Kansas City interval. Progradational shoals displayed high permeability (hundreds of millidarcies) and were "shingled" over time in depositional patterns comparable to modern Bahamas analogues (Gonzalez and Eberli 1997). These high-permeability zones are bordered by deeper water carbonates with lower permeability (tens of millidarcies). Results from the Hall-Gurney CO_2 WAG program showed permeability anisotropy aligned NW/SE, interpreted as controlled by basement-involved fractures and paleotopographic highs.

Well log correlation: Within the study area, stretched raster and digital well logs were used to create the geologic model zones that honor the Hall-Gurney analogue with compensational and shingling of shoal systems within the Lansing/Kansas City reservoir at Bushton. Over time, the locus of deposition shifts from the NW corner, to the central area, to the south/southwest portion

of the study area as lateral migration of carbonate shoals fill in the available accommodation space (**Figure 181**). Similar to the Hall-Gurney reservoir analogue, the porous units (shown as green bars) are more commonly found in the thicker deposits near the top of coarsening upward sequences. An interpreted fracture trend was also created for the Bushton study site.

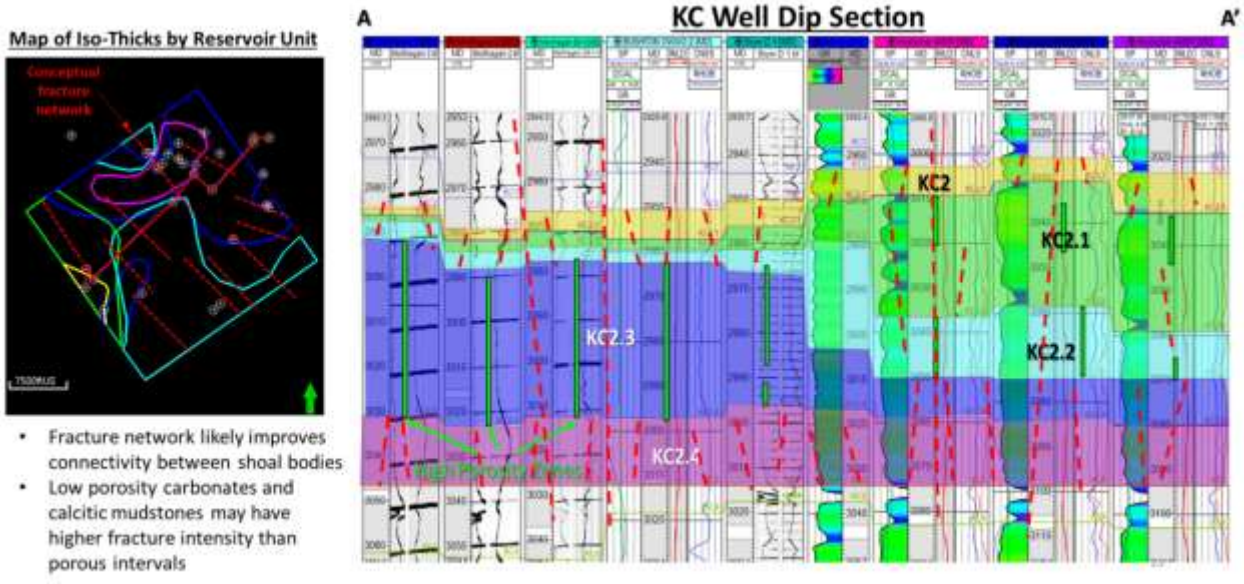


Figure 181 Stacking trends within the Lansing-Kansas City reservoir system. Note that there are significant thickness variations as interpreted across the study site that could impact connectivity and plume evolution.

Zone model/layering: Lansing/Kansas City reservoir zonation and layering was a function of (1) the stratal framework built for the region and (2) the desire to adequately represent high and lower permeability intervals that were mappable across some or all of the study area. The result is a 28-layer model covering approximately 75 feet of section in the upper portion of the Kansas City Formation (**Figure 182**). The layers were mapped as conformable and proportional, thus allowing for pinching and swelling that is expected in the depositional systems. The shingling nature of sediments in the Bushton LKC study area is comparable to what is observed at Hall-Gurney field. Each zone contains between 1 and 5 layers, averaging 4.8 to 17.6-feet thick. Proportional layering was applied and deemed appropriate for the expected stratal geometries.

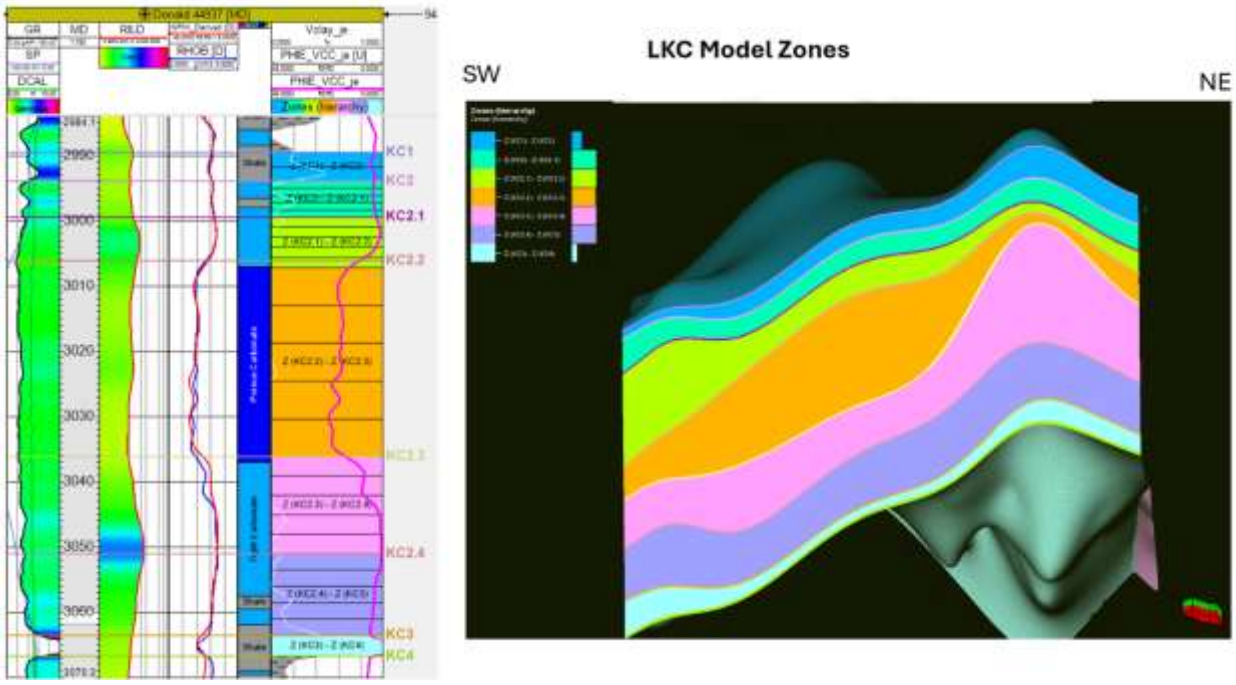


Figure 182 LKC modeled zones highlighting thickness variation and proportional layering applied.

Facies modeling: Using matrix-corrected NPHI porosity and GR as a proxy for clay, three facies were identified (porous carbonate, tight carbonate, and shale). Vertical Proportion Curves were built using the vertical variations observed in the 4 pseudo-wells used in this project (**Figure 183**). Different stratigraphic units contained different facies percentages. Furthermore, lateral thickness variations commonly resulted in different facies percentages for the same stratigraphic interval. Vertical proportion curves and layer thickness (i.e. thicker intervals had more high porosity carbonates) were used to distribute the facies within the model.

Vertical Proportion Curves used to propagate distribution of each facies type within each zone

1. **Porous carbonate**
   - More common in thicker units high N:G units like the KC2.2 and KC2.1 (shoal crest)
2. **Tight carbonate**
   - Common in all units, particularly in thinner strata (inter-shoal)
3. **Shales**
   - Most common in thinner zones or within zones that likely represent high order flood events

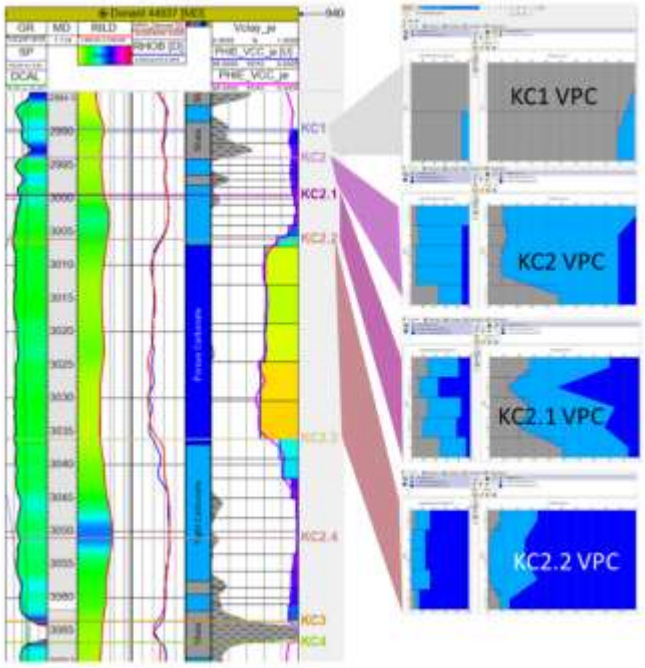


Figure 183 LKC facies modeling in the Donald 44397 well

Effective porosity: Porosity was upscaled at the wells using an arithmetic mean of the calculated PHIE well log. Resulting upscaled porosity values match the PHIE curve reasonably well as seen in the histogram of well logs vs. upscaled cells (**Figure 184**).

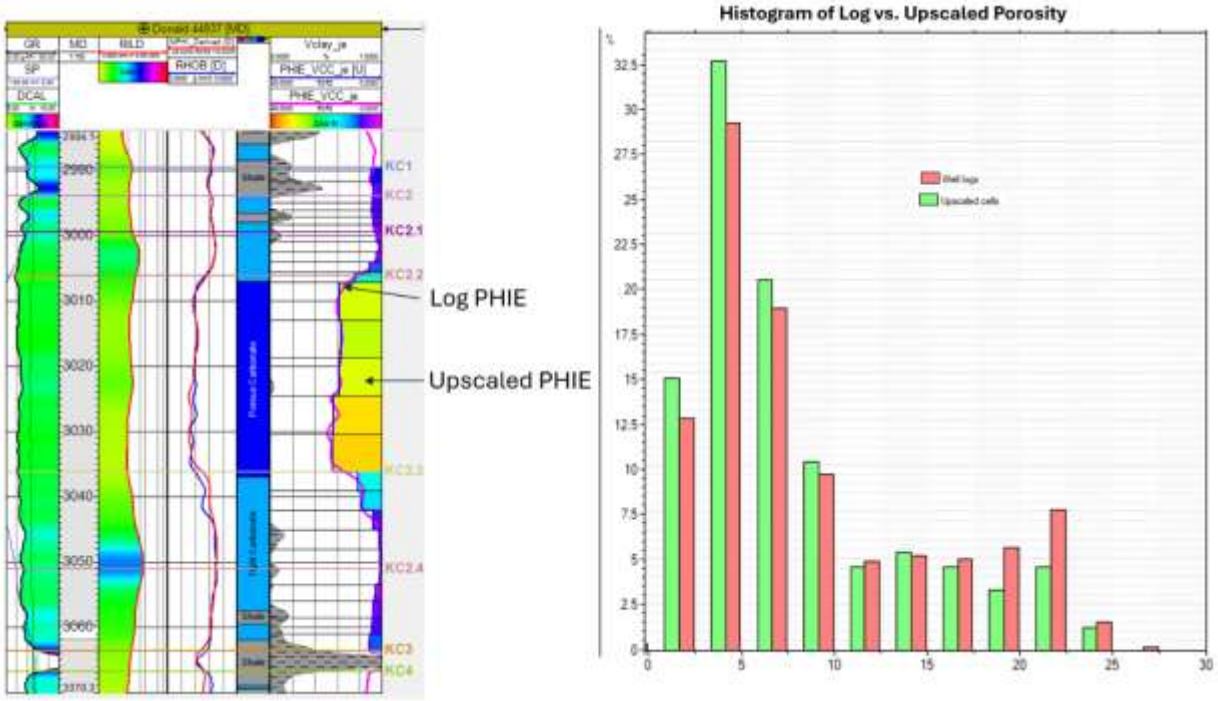


Figure 184 Effective porosity log and upscaling example from the Donald 44937 well

Variograms were also used to guide facies distribution in the model (**Figure 185**). Shales are interpreted to represent flooding events and have an equal aspect ratio in major and minor directions. The tight carbonate facies have a moderate major/minor aspect ratio to represent the more laterally continuous off-shoal facies. Porous carbonate facies have the highest major/minor aspect ratio compared to other facies due to the linear nature of shoal crests. Default values for vertical variogram length (100') were used because the fractured nature of this reservoir likely results in high vertical permeability and/or continuity of permeability systems. The vertical variogram from shale was derived from the vertical variogram plots and is lower than the other facies because the high clay content within renders it less likely to fracture.

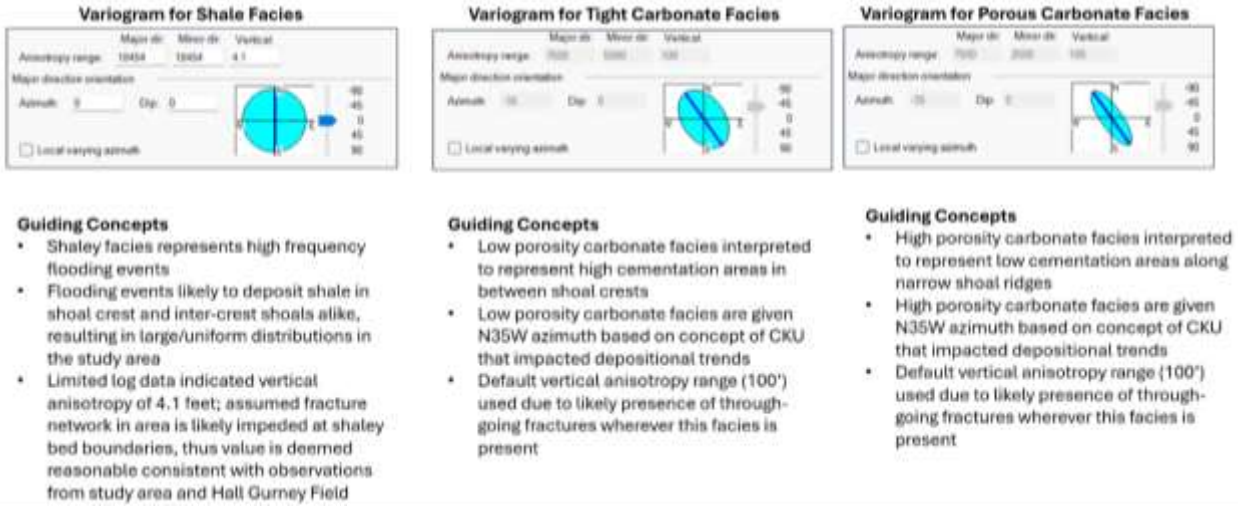


Figure 185 LKC variograms applied for the three modeled facies

Final PHIE property model trends show similar patterns as those observed in the Hall-Gurney Field (**Figure 186**). Shoal bodies within individual zones mostly show higher porosity distributions; this is most notable in the younger, thicker carbonate shoal bodies.

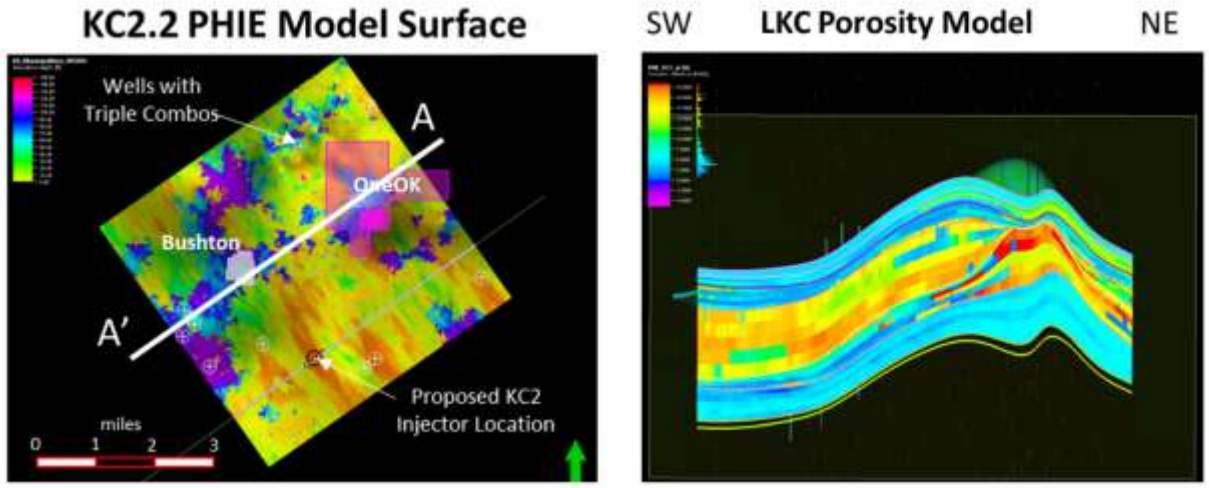


Figure 186 LKC porosity model

Permeability values were derived from the core-based porosity-permeability transform at Hall-Gurney field. The model's horizontal permeability (Kh) was enhanced to account for non-matrix pore systems, including fractures and connected vugs, based on production data from Hall-Gurney field. Vertical permeability (Kv) was set at 30% of Kh, following recommendations from Battelle's Midcontinent Storage report (Battelle Memorial Institute 2018). This ratio aligns with values observed in carbonate reservoirs analyzed by KGS in the Patterson and Wellington CCS reports.

Production data from Hall-Gurney revealed elevated permeability and reservoir connectivity along a northwest-southeast axis, suggesting that lineaments identified in seismic data may represent fracture corridors. Analysis indicates that permeability systems in these reservoirs are controlled by both depositional geometries and fracture networks. These findings guided permeability modeling in the Bushton LKC model (**Figure 187**).

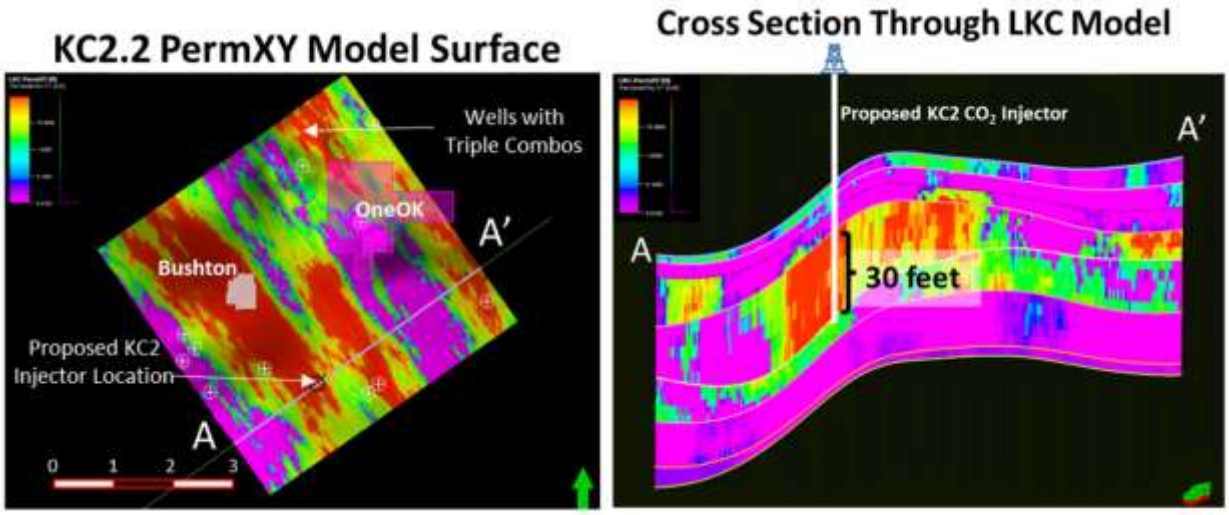


Figure 187 LKC horizontal permeability model

The modeling approach incorporated porosity-permeability transforms from Hall-Gurney and vertical-to-horizontal permeability ratios from the Battelle Midcontinent Storage study. Similar to the porosity model, higher permeability streaks were oriented northwest-southeast but with tighter distribution to simulate the impact of fracture corridors on prograding shoal bodies extending south-southwest. The resulting permeability model displays northwest-southeast oriented permeability systems reflecting both depositional geometries and fracture systems.

Note: Future phases of CCS screening will require development of a dual porosity/dual permeability model for the LKC to account for distinct behaviors of matrix and fracture porosity systems. This advanced modeling approach requires additional data including 3D seismic, Formation MicroImager (FMI) data, and conventional core descriptions that were not available during this study phase.

Arbuckle Deep Static Model Details

After the initial Arbuckle model had been constructed (see section 3.2.4), ONEOK provided additional well data from wastewater disposal wells in the area. Injection top and base for those

wells were deeper than any of the wells used for the initial Arbuckle reservoir modeling (**Figure 188**). The shallow Arbuckle wells likely penetrate most of the Cotter Dolomite and some of the Jefferson City Dolomite, but none of the Roubidoux and Gasconade formations. These formations have been shown to have the best porosity and permeability development in the Arbuckle Group. As such, it was necessary to pull in wells from offsite that penetrated these intervals for use as pseudo-wells for the Arbuckle Deep static model. The stratigraphy from the shallow wells was used as a guide in the pseudo-wells, but the stratigraphic tops used were at a lower resolution to ensure that the entire reservoir section could be modeled efficiently. This highlights the importance of a stratigraphic well to fully characterize the reservoir and delineate zones for injection.

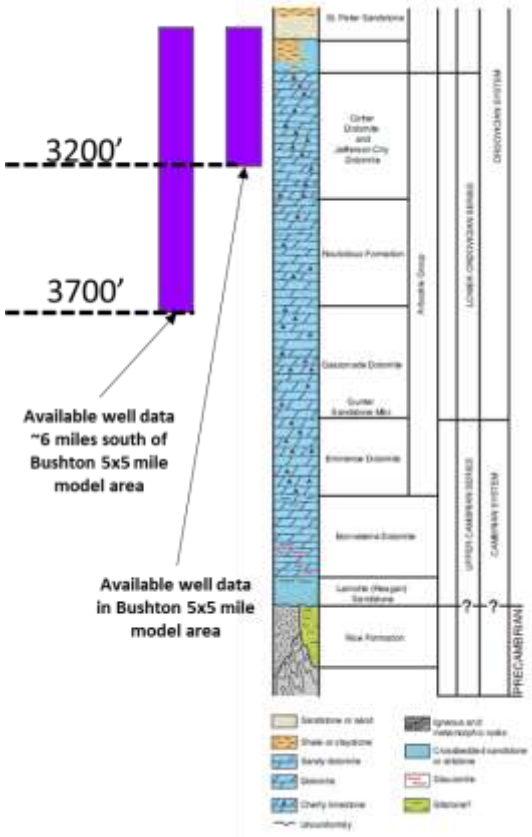


Figure 188 Arbuckle Group stratigraphy highlighting the well control within the modeled area and the additional information from wells outside of the area versus the total Arbuckle interval thickness

Reservoir analogue: Prior KGS research indicates that stratiform layering is common in the Arbuckle formation, particularly at reservoir scales used for CCS. The figures above demonstrate that the Arbuckle has relatively continuous reservoir and non-reservoir facies, but this is heavily impacted by fracturing and karst, as described by Franseen et al. (2004). The KGS researchers built a simulation model for the Wellington site with stratiform layering, as shown in the figure above. This concept agrees with similar stratigraphic architecture observed at the Bushton site.

Well log correlation: The final stratigraphic correlation used in Arbuckle Deep is shown in **Figure 189**. Conformable stratigraphy seen from pseudo-wells matches regional trends within the model area. Higher resolution picks were carried out in middle/lower portion of Arbuckle

(ArbDeep4-ArbDeep7) to add additional zone (and potentially flow) detail as well as to increase reservoir heterogeneity. The beds are largely conformable, though they display thickening and thinning trends. Higher resolution mapping was carried out in the deeper intervals (i.e. ArbDeep4-ArbDeep7) based on the prominent, mappable porosity variations observed in the logs.

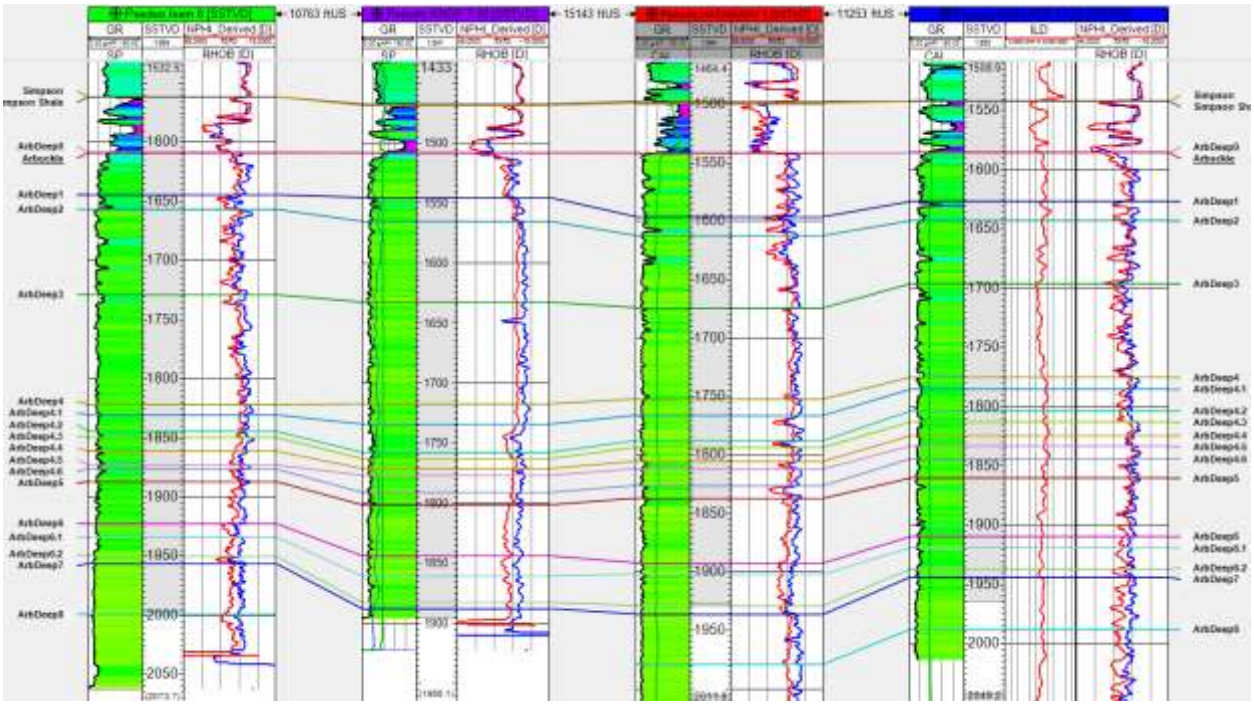


Figure 189 Well log correlation of the Arbuckle Group in the Bushton model area

Zone model and layering: The Arbuckle Deep zone model was derived from stratigraphic correlation and associated structure maps (**Figure 190**). Model layering was proportional. An additional 150' of strata were added to the lowermost zone to mimic the deeper portions of the Arbuckle that are likely present in the Bushton area that will likely impact the behavior of the CO_2 plume and associated pressure front during and after a CO_2 injection program. Zones were

broken out based on stratigraphy picked from well logs. Layers were kept conformable to match the stratigraphic models seen in literature and verified by mapping in this project.

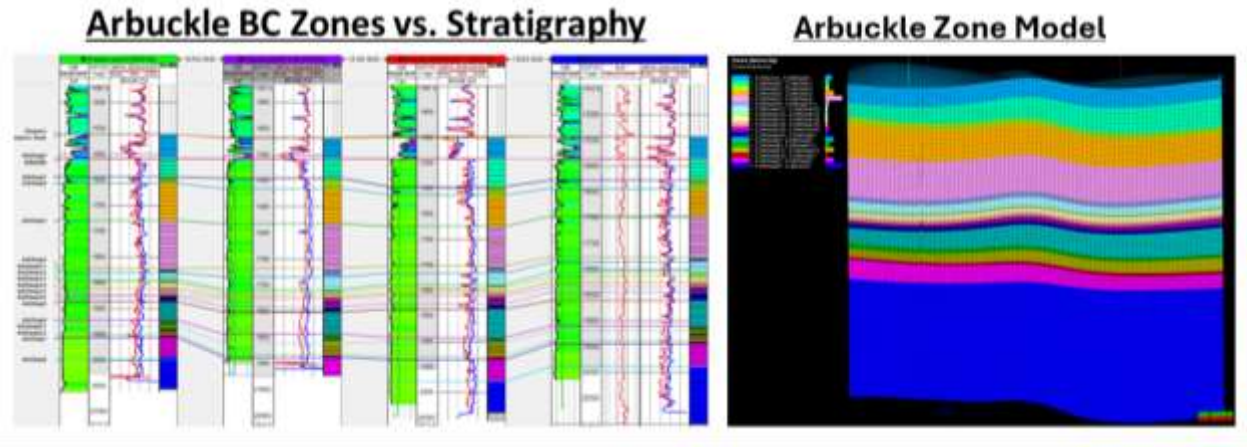


Figure 190 Arbuckle Deep zone model. Well correlation section (left) and 3D perspective (right).

Facies model: Log-based facies for the Arbuckle reservoir were split into the following facies based on interpreted permeability and clay abundance:

- **High perm dolomites** – 75 mD+ that likely represent karst intervals, mimetic dolomites in prior high energy grainstone or framework deposits
- **Moderate perm dolomites** - 75 mD>PermXY>5 that likely represent more heavily cemented grainstones/packstones or muddy and recrystallized sediments
- **Low Perm Dolomite** – PermXY<5 mD that likely represents lower energy depositional environments (mudstones, wackestones) or very heavily cemented shallow water deposits
- **Shales** – Vclay >50% that likely represents depositional lows along the Ordovician-Silurian carbonate ramp and/or local high level flooding events

Vertical proportion curves were derived from the available log data to guide the relative abundance of the log facies in each zone (**Figure 191**). There was significant vertical and lateral variability in the interpreted facies, though the upper units were generally lower reservoir quality and the lower units were generally higher reservoir quality. Shales were relatively rare, which is expected on a high-energy shallow water carbonate ramp with low accommodation space.

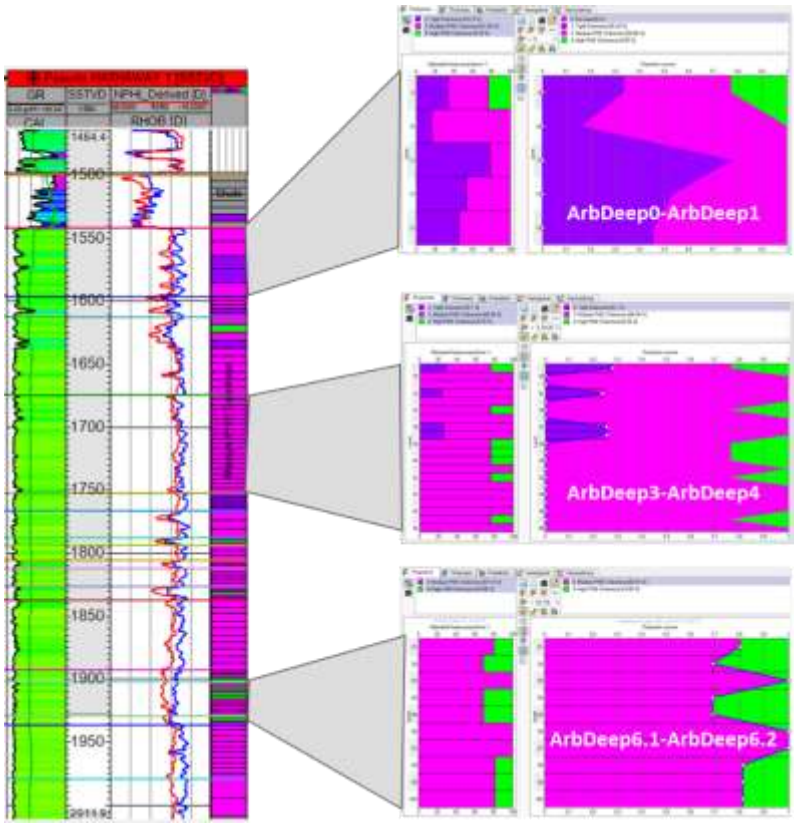


Figure 191 Arbuckle Deep facies model with examples showing the vertical distribution of dolomite facies within the Arbuckle Group

Vertical Proportion Curves used to propagate distribution of each facies type within each zone:

- **High Perm Dolomite -** More common in lower portion of middle Arbuckle; likely represents recrystallized grainstones or boundstones with preserved framework porosity
- **Moderate Dolomite –** Ubiquitous throughout all Arbuckle intervals, represents moderately cemented dolomites without leaching or karsting
- **Tight Dolomite** – Scattered throughout, but more common in shallow Arbuckle and middle portion of model; likely the result of pervasive early cementation in these intervals
- **Shale –** Ubiquitous in Simpson top seal interval; present but in lower abundance in local marls scattered throughout the vertical Arbuckle section seen in logs

Variograms were defined for each of the four facies based on previous modeling efforts of the Arbuckle in Kansas and to accentuate the narrowness of the high perm dolomite facies (**Figure 192**). General depositional characteristics are based on carbonate reservoir analogs where shales = flooding events with similar properties in X/Y direction; high perm dolostones represent narrow shallow water carbonate facies; moderate perm dolostones are shallow subtidal carbonate facies; and tight dolostones are deep subtidal carbonate facies.



Figure 192 Arbuckle Deep variograms used for the four modeled facies

The conceptual model was used to guide the facies model (**Figure 193**). The top seal (Simpson shale) shows variability, but is a competent seal, and is known to seal reasonably tall hydrocarbon columns. The upper 500' of the modeled facies are similar to the conceptual model, and the lower 150 feet of the model used stochastic distributions of the facies from all other logged Arbuckle intervals from the pseudo-wells to distribute facies.

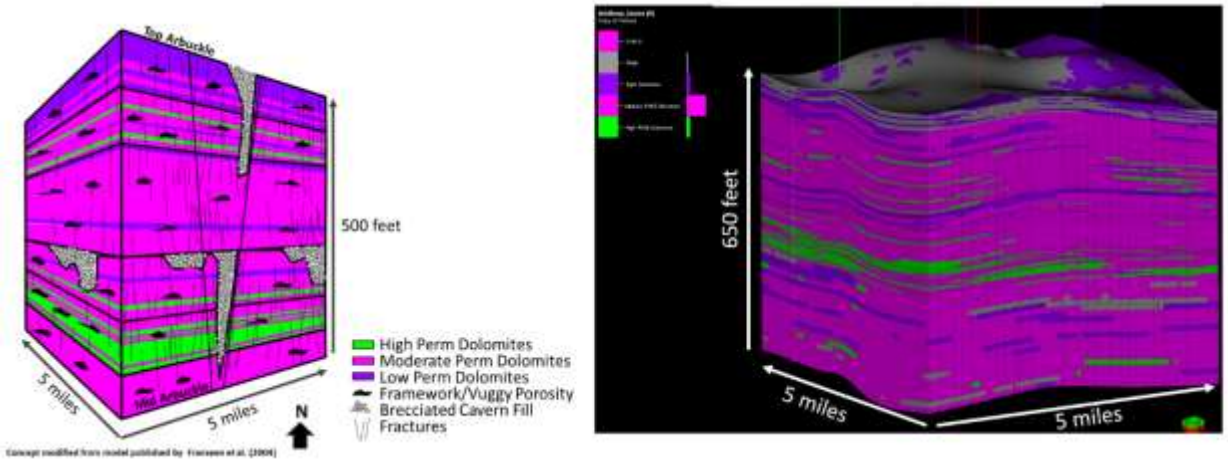


Figure 193 Arbuckle Deep conceptual model

Effective porosity: Evaluation of available well data covered down to approximately 3,200 ft, whereas ONEOK Class I wells inject waste brines at depths of 3,310 to 3,745 ft. Deeper wells with TDs greater than 3,600 ft were identified approximately 7 miles south of study area and were used as pseudo-wells within study area. Final porosity-permeability distributions were based on the data from these wells. The stratigraphy from the shallow wells was used as a guide in the pseudo-wells, but the stratigraphic tops used were at a lower resolution to ensure that the entire reservoir section could be modeled efficiently. Upscaled porosity (blocked color fill in log on the right) displays general conformance to calculated porosity (**Figure 194**; magenta line in log on the right). Some high porosity streaks, as seen in interval between 1,550 and 1,600 ft, average out to a lower porosity, and may reflect decreased flow or storage behavior.

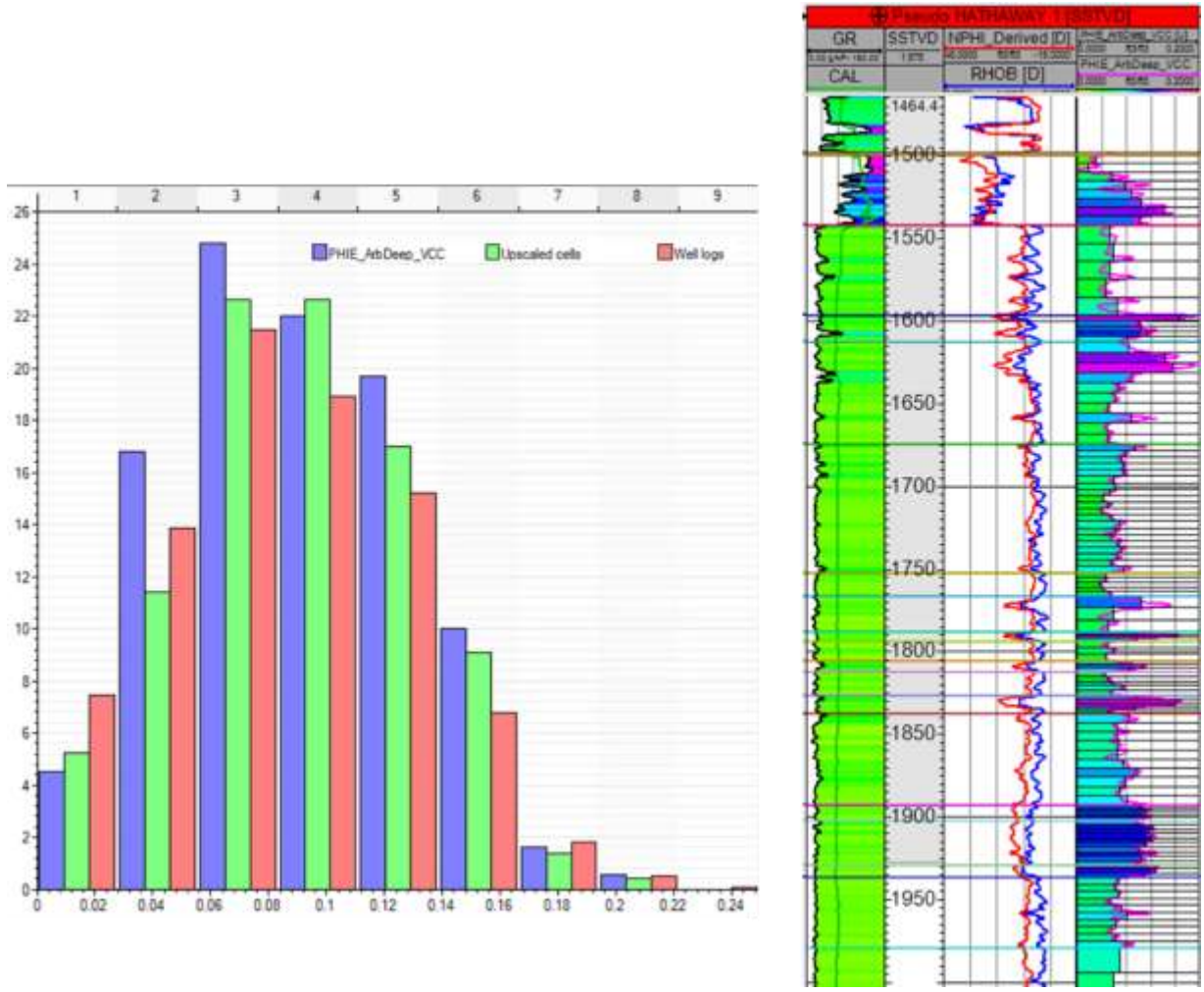


Figure 194 Effective porosity model for the Arbuckle Deep geologic model

The final effective porosity model shows general conformance between well logs, upscaled values at the well, and the conceptual geologic model (**Figure 195**). The porosity model inherits the variogram dimensions from facies modeling. Karst and fractures were not explicitly built into the porosity model but are not likely to significantly impact overall storage volumes. They will likely impact permeability and are addressed in the permeability model. The Gaussian Random Function Simulation was used to distribute porosities in the model based on associated values found in log calculations for each zone. Porosity in karst or heavily fractured zones was not included in model, as no known karst/fracture zones were encountered in logs evaluated for the model.

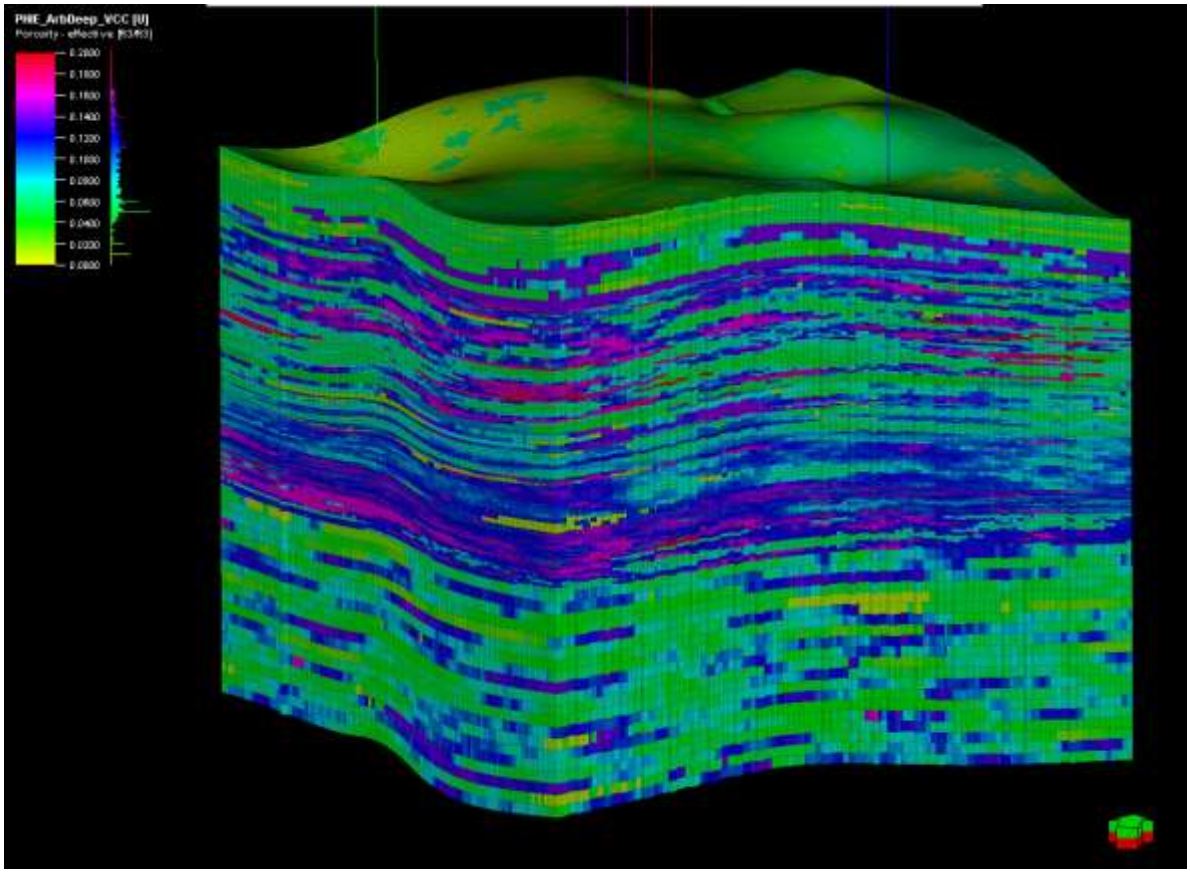


Figure 195 3D view of the Arbuckle Deep effective porosity model

Permeability: The permeability trends in the model are like those from the porosity model, with a N35W orientation, but overall magnitude of permeability is higher in the upper 1/3 and lower half of the model (**Figure 196**). Water injection rates from Class I water injectors were used to history match the Arbuckle Deep model. Simulation of the early Arbuckle Deep static model experienced rapid pressure rise and required a substantial drop in injection rates to prevent frac gradient from being exceeded. The permeability was iteratively increased until the model could handle the known water disposal rates and a 5X permeability multiplier was applied to the static model permeability properties. Lack of conformance between original perm model and history-matched permeabilities is attributed to the lack of dual porosity and dual permeability in the model. Future models should include DFN (discrete fracture network) and attempt to quantify porosity and permeability in fractures and brecciated cavern fill in Arbuckle Group. No core available in study area, so leveraged prior KGS research to derive reasonable Arbuckle perm estimate ICKan quarterly report by Bidgoli and Dubois (07/07/2018) which contains a core-corrected poro-perm transform derived from NMR log measurements. Intervals with Kh>75 mD received a 5X boost to match perms seen in ONEOK #4 injector wells. The upscaling process resulted in a muted impact on permeability boost in some intervals. Core data from Hadley-1 well in Bemis Shutts field was used to estimate Kv/Kh ratio of 0.202.

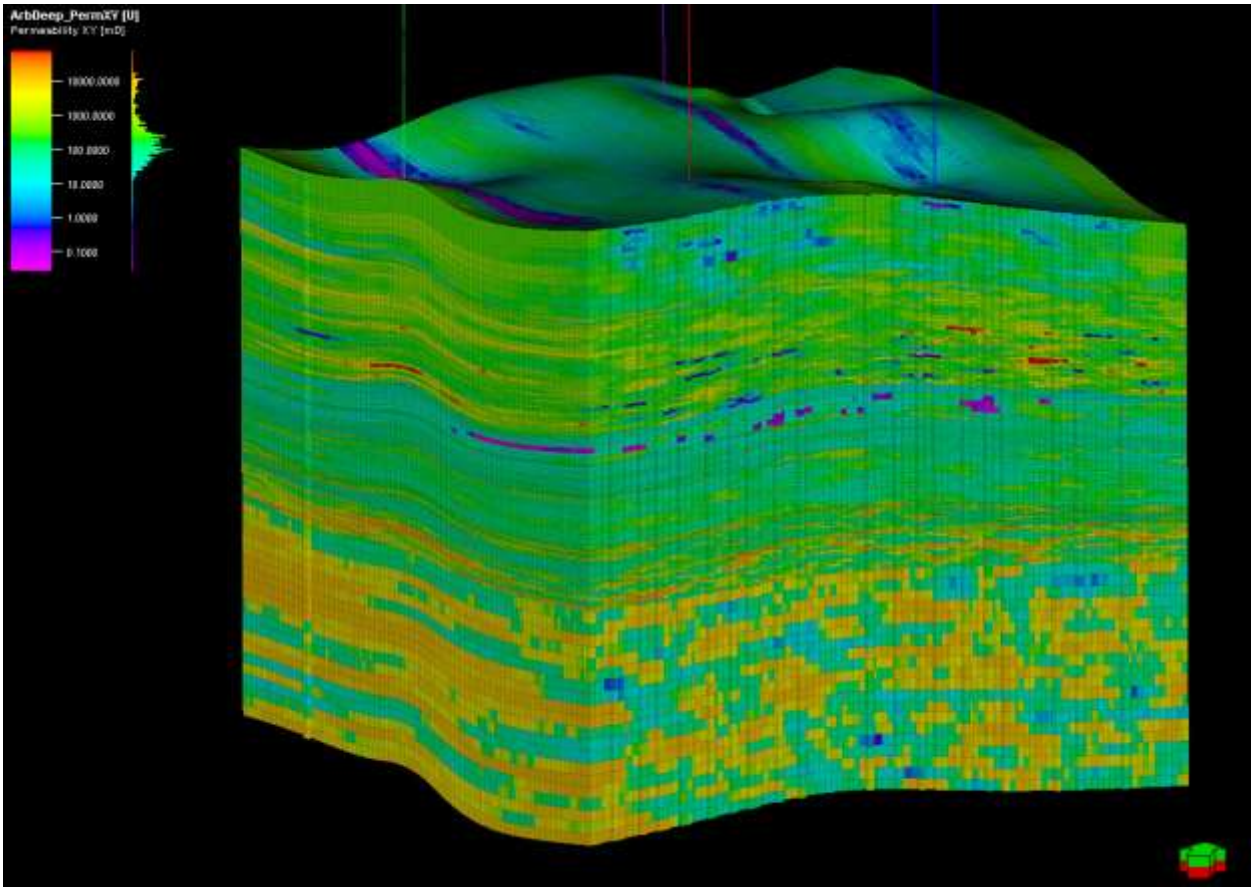


Figure 196 Arbuckle Deep model horizontal permeability

Upper Arbuckle Geologic Model

The Upper Arbuckle Geologic Model represents the first Arbuckle model built for the Bushton site. It was limited to just the shallower portion of the Arbuckle Group as the wells within the modeled area did not penetrate the deeper Roubidoux and Gasconade formations which have some of the best developed porosity and permeability. The modeling methodology outlined for the Deep Arbuckle geologic model (Section 3.2.3) utilized the methodology established for the Upper Arbuckle model therefore it is not redocumented here.

Medford (OK) Geologic Model

A model of the Wilcox-Bromide sandstones was constructed in an area of central Grant County that includes the ONEOK facility. The model boundary was positioned to take advantage of existing well data without being too close to extant Wilcox production in the northern and southern areas. This would allow for reasonable modeling that included areas with undrilled potential that would not interfere with ongoing oil and gas operations (**Figure 197**).

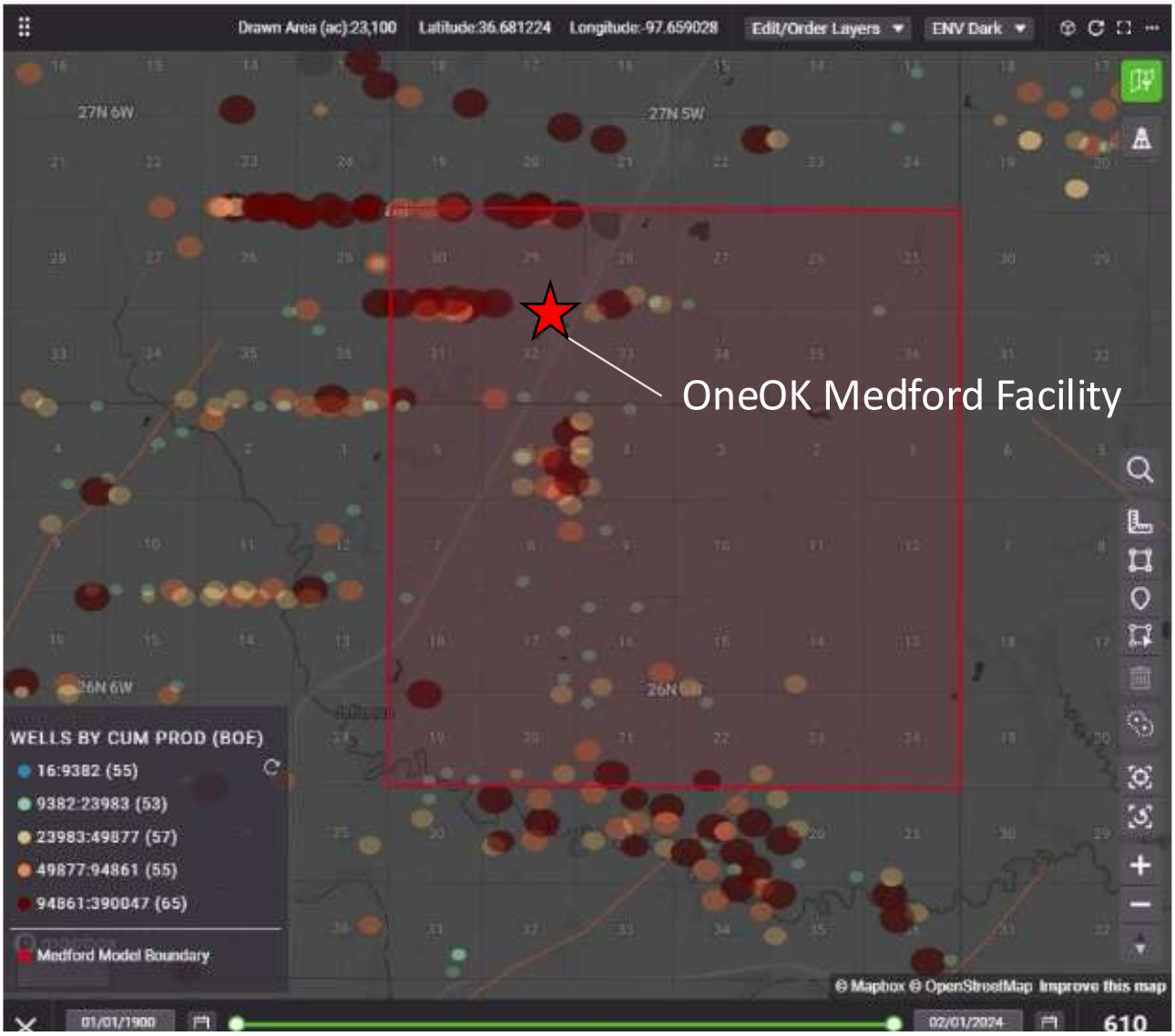


Figure 197 Map showing the area of the Medford subsurface model (red outline) with production wells displayed with cumulative production in units of barrel of oil equivalent

Model location resulted from prioritization of several goals:

- Proximity to ONEOK Medford facility
- Avoiding faulted areas or intervals with high oil and gas production that could lead to lower formation pressures, relative permeability issues, etc.
- "Goldilocks" zone for data needs vs. undrilled potential, resulting in:
    - Sufficient data coverage that permits reservoir seal characterization
    - Undrilled areas that would have comparable reservoir/seal properties but with lower leakage potential from legacy boreholes

A marine slope clastic depositional model was utilized to develop a local conceptual stratigraphic framework for the reservoir.

After initial well log correlation and evaluation of reservoir and seal intervals in the area, the Wilcox-Bromide sands were selected for subsurface modeling (**Figure 198**). The Bromide-Wilcox sandstones produce large volumes of oil and gas within Oklahoma and have some of the best reservoir quality of all oil and gas reservoirs in the region.

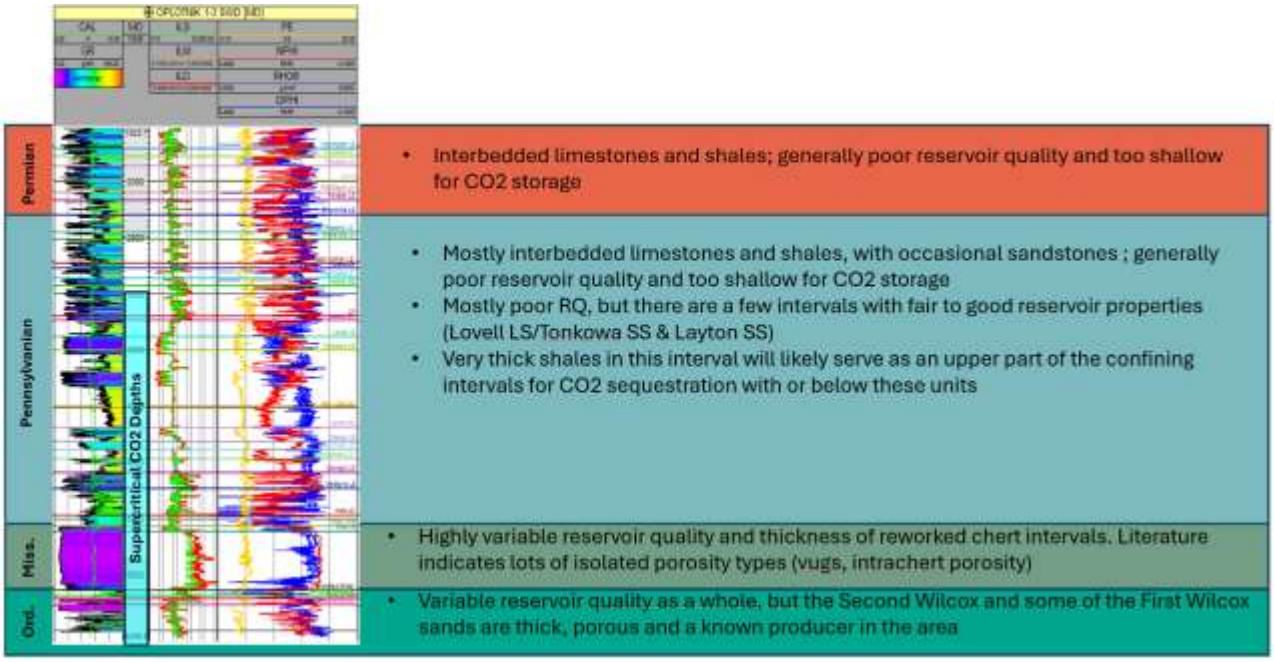


Figure 198 *Type well summary of the key intervals in the Medford area*

Wilcox-Bromide Static Model Details

Reservoir analogue: The Wilcox-Bromide sandstones are part of a larger marine clastic distributive system that sourced sediments from the Canadian Shield. The Wilcox-Bromide sandstones produce large volumes of oil and gas within Oklahoma and have some of the best reservoir quality of all oil and gas reservoirs in the region. For these reasons, we decided to focus on the Wilcox-Bromide sandstones over the Mississippian Chat reservoirs. These sediments were funneled into the study area via shelfal clastic systems that existed between structural highs. Upon entering Oklahoma, these clastic sediments moved beyond the shelf/slope break, resulting in increased accommodation space and a change in overall depositional style to lobate turbidite systems. These sediments thicken to the south, where they abruptly terminate against the Texas Arch that was created by the pre-collision phase of the Ouachita orogeny.

Well log correlation: Raster logs were depth registered to perform the initial stratigraphic correlation. Available log data indicates a lateral compensational stacking pattern within the Wilcox-Bromide sandstone. This pattern likely represents high frequency (parasequence scale), autochthonous sedimentation distributive systems within the broader clastic depositional system. There is likely minor scouring occurring, but no major erosive events, leading to mostly conformable sedimentation in the area.

Zone model and layering: Six sand zones with an upper shale-prone zone were correlated and modeled (**Figure 199**). There are more wells that penetrate the upper portion of the Wilcox sands (Wilcox_6 to Wilcox_3) and thus more confidence in the thickness trends in those intervals.

Nevertheless, all intervals show apparent compensational stacking patterns as sediment filled in local lows created by turbidite distribute systems nearby. Well clustering and data quality issues in the raster logs create uncertainty in the reservoir dimensions. As a result, analogues from Doveton et al. (1990) in Kansas were used as a reference in the geologic model.

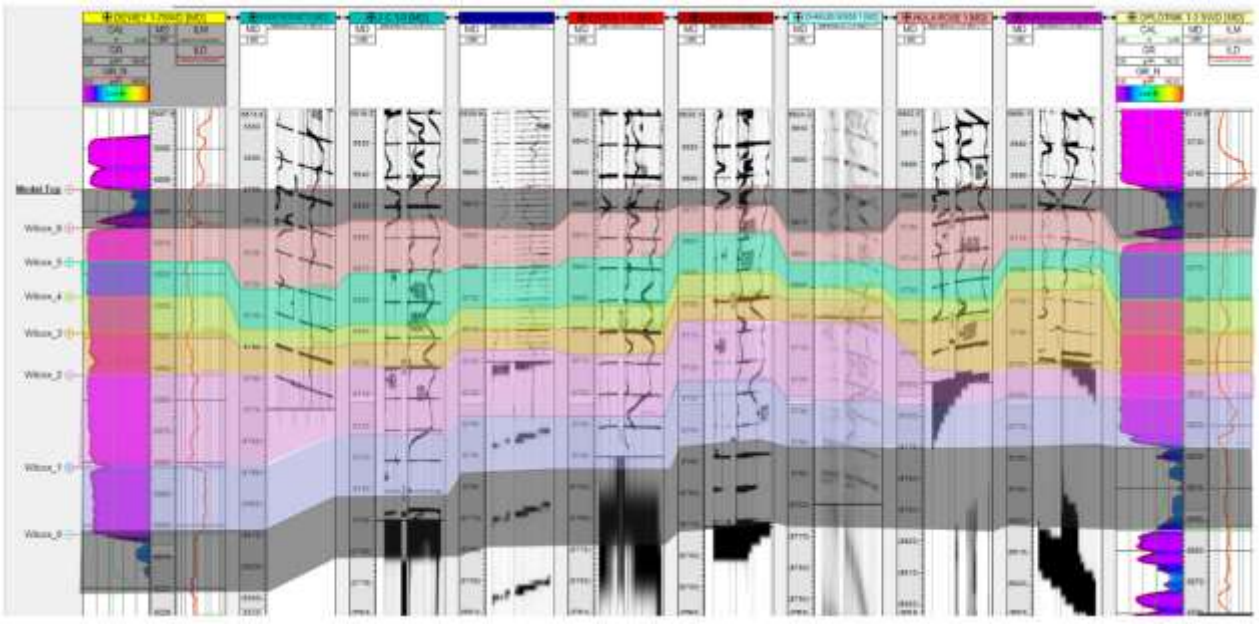


Figure 199 Zone model showing 10 wells from NW (left) to the SE (right) within the modeled area

Facies model: The Wilcox-Bromide sandstone likely represents multiple turbidite depositional sequences, with higher quality sands representing Ta and Tb beds. The lower equality sands likely represent Tc and Td beds, with shales representing Te beds or pelagic sedimentation. No clear trend of the high- or low-quality sands was discerned from the available wells, so vertical proportion curves relied on the average facies abundance across all four wells in the study area (**Figure 200**).

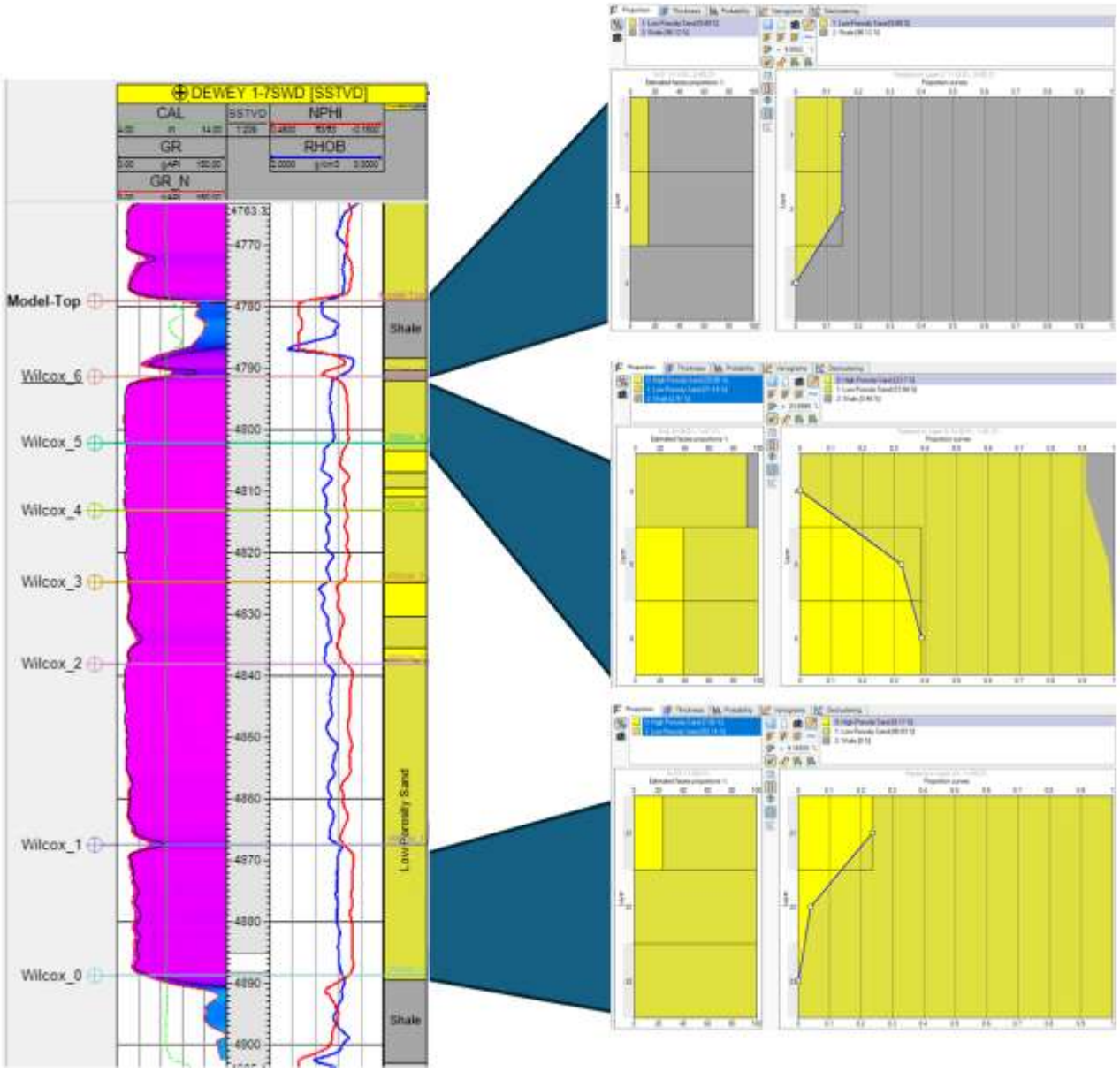


Figure 200 Vertical proportion curves used to distribute each of the 3 facies (high porosity sandstone, low porosity sandstone, shale) within the Wilcox zone

Effective porosity: Modeled porosity trends compare favorably with those taken from the well logs or upscaled values (PHIE) (**Figure 201**). Low porosities are less abundant in the model than in well logs due to upscaling and facies and porosity distributions in the model. The lack of lower porosities is not expected to have a material impact on the model during simulation.

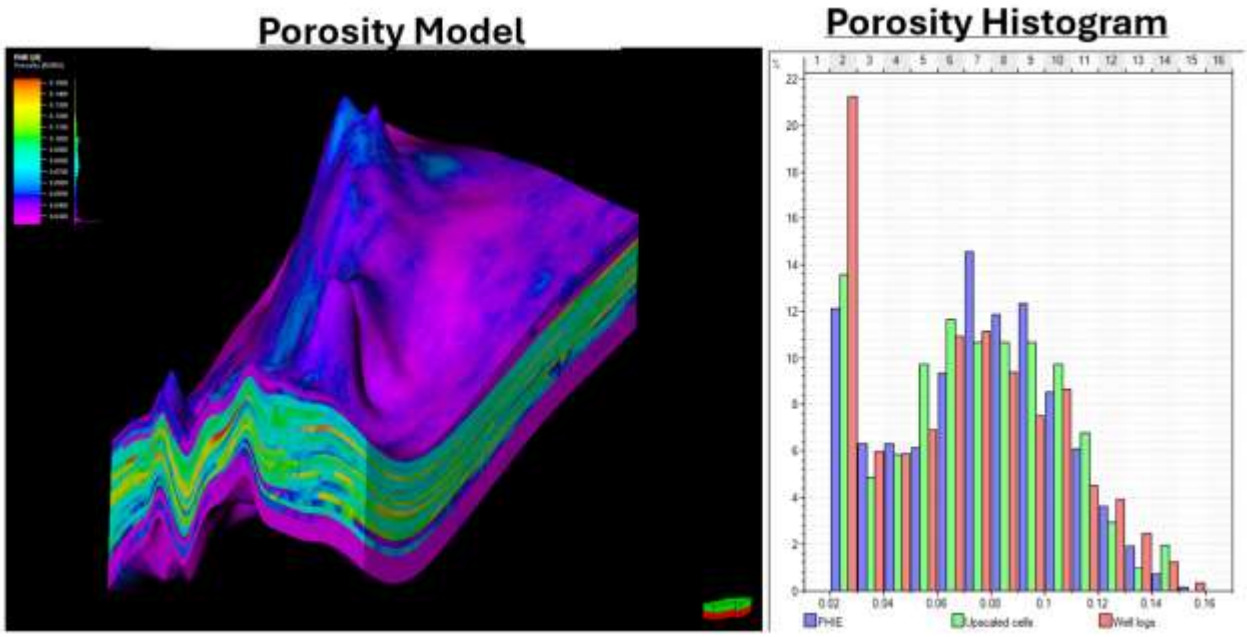


Figure 201 Porosity property model (left) and histogram (right) of the Wilcox reservoir. The histogram shows the distribution of the PHIE property in the model; upscaled well logs; and the well logs.

Permeability: Permeability trends are based on the poro-perm transform created using KGS Simpson core data and highlight the key elements of the conceptual geologic model (**Figure 202**). It is important to note that the wells used in the model area did not contain porosities as high as observed in the KGS Simpson core data, thus overall permeability is lower than predicted from the Kansas analogues. The lower porosity at the Medford site vs. the KGS core data is likely a function of porosity loss via compaction due to deeper burial in Oklahoma; KGS core depths are approximately 3,200 to 3,400 ft below the surface whereas the Wilcox-Bromide sands in the Medford area are approximately 4,600 to 4,900 ft below the surface (**Figure 202**).

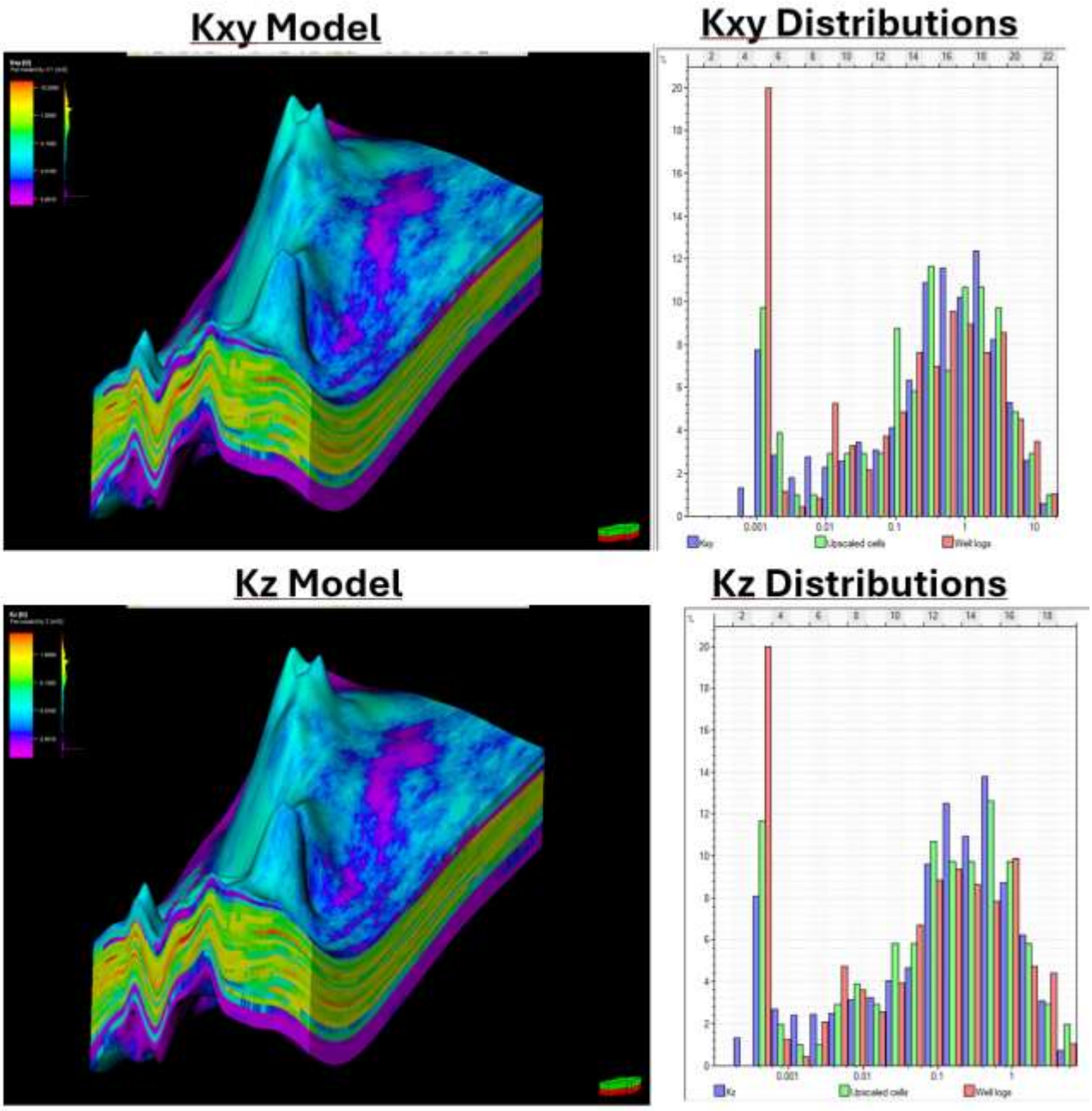


Figure 202 Permeability property models (left) and histograms (right) of the Wilcox reservoir. The histograms show the distribution of the PHIE property in the model; upscaled well logs; and the well logs.

Salt Horizons CO_2 Storage Evaluation

CO_2 sequestration in salt caverns was initially considered as part of this study's scope but was ultimately determined to be non-feasible for the Bushton site. This determination was based on several critical technical and economic constraints identified during preliminary evaluation.

Technical Challenges: The primary technical obstacles include the shallow depth of the Hutchinson Salt Member near the ONEOK Bushton facility. The salt formation is approximately

200 feet thick with the top of salt located around 950 feet below the surface (**Figure 203**). This shallow depth presents significant challenges for maintaining CO_2 at supercritical conditions, which typically require greater depths and pressures for effective storage. The Hutchinson Salt thickness nearest the ONEOK Bushton site is relatively thin and located near the depositional edge of the evaporitic basin (**Figure 204**, **Figure 203**).

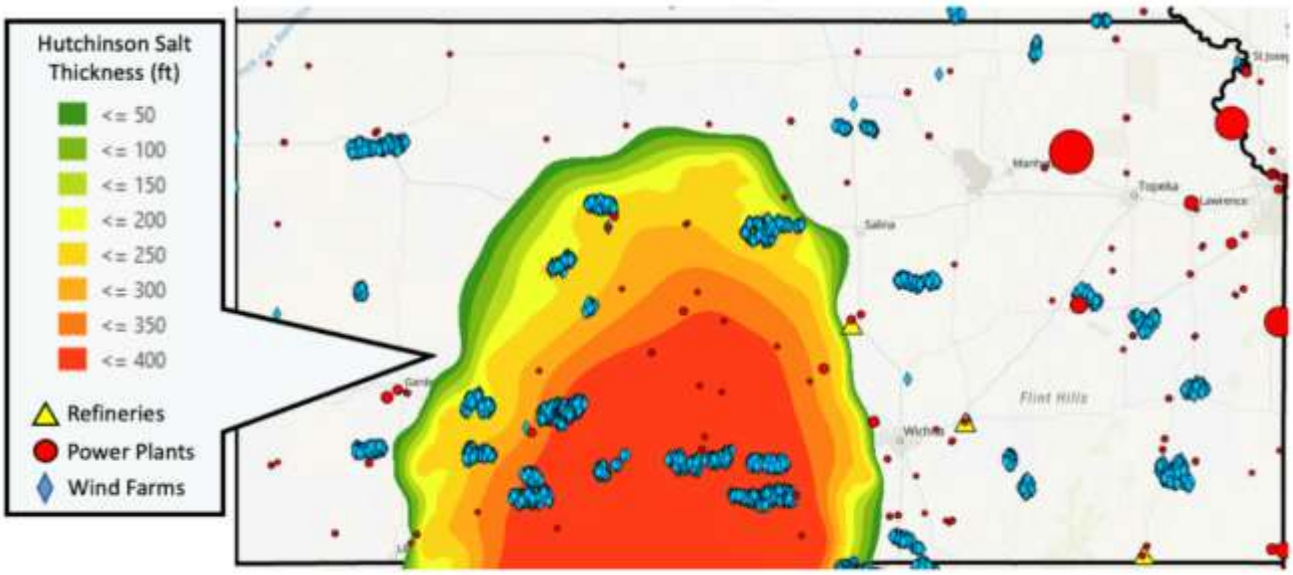


Figure 203 Hutchison salt thickness map for Kansas. From a KU News press release (Jan 14, 2022). https://news.ku.edu/news/article/2022/01/14/kansas-geological-survey-study-hydrogen-storage-underground-salt-beds.

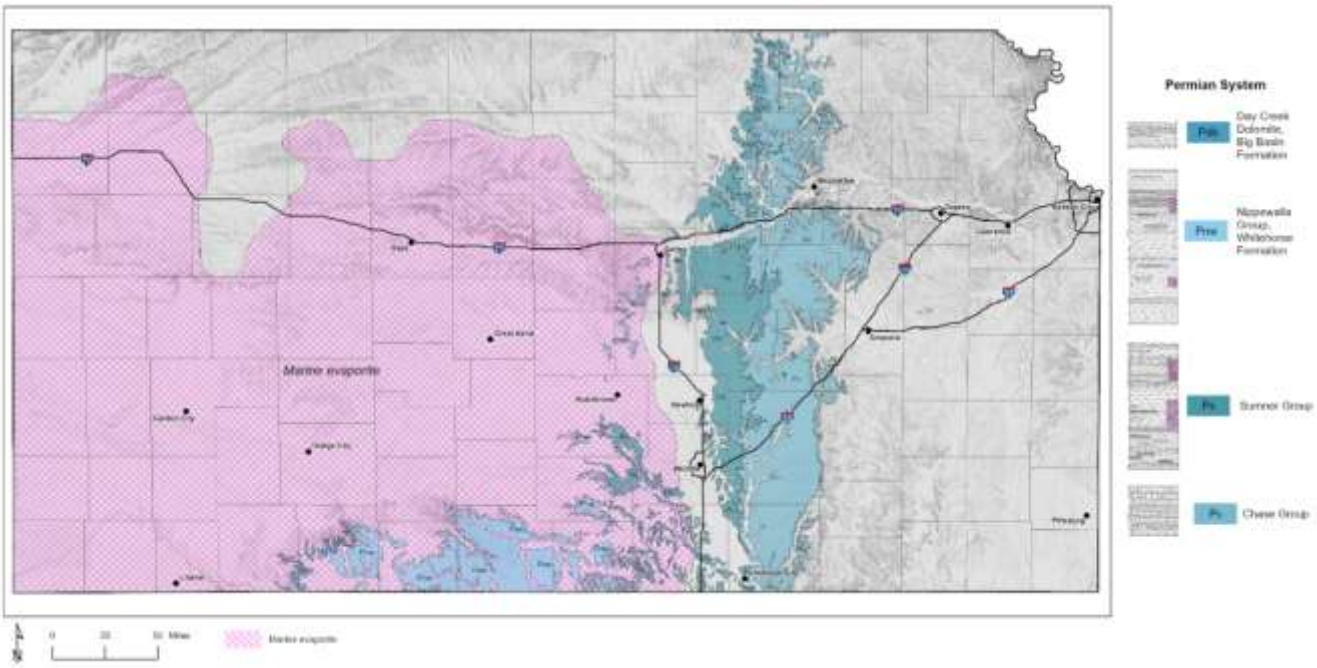


Figure 204 Maximum extent of Lower Permian evaporite deposits associated with the Blaine Formation, Flower-pot Shale, Ninnescah Shale unit, and Wellington Formation (Hutchinson Salt Member)

Additional technical concerns include:

- Risk of salt dissolution and surface subsidence, as evidenced by numerous sinkholes that have developed along shallow salt margins from both natural dissolution and wastewater disposal activities (Knapp et al. 1989)
- Geomechanical uncertainties regarding the salt's ability to maintain structural integrity under supercritical CO_2 conditions
- Potential for induced seismicity and long-term monitoring challenges common to CO_2 sequestration methods (Zhang et al. 2022; Mwakipunda et al. 2024)

Economic and Logistical Considerations: While deeper salt formations in the region could theoretically overcome some technical limitations, accessing these would require extensive pipeline infrastructure extending well beyond the existing ONEOK facility network. The associated capital investment and operational complexity would likely exceed the economic viability compared to conventional saline aquifer sequestration approaches. Given the combination of shallow salt depths, geomechanical uncertainties, dissolution risks, and prohibitive infrastructure requirements, salt cavern CO_2 storage was determined to be non-feasible for this project. The study therefore focused on more technically and economically viable sequestration options, including saline aquifer storage in deeper formations.

Subtask 3.3 – Assess CO_2 Storage Resources

Accurate evaluation of long-term subsurface CO_2 storage potential requires dynamic assessment of the reservoir to better understand reservoir behavior within the reservoir while injecting at rates that satisfy project economics. While dynamic modeling results are presented in Task 4, this subtask focuses on volumetric analysis of the Arbuckle Group to estimate potential CO_2 storage resources across central Kansas.

The Arbuckle Group underlies much of the state and has been extensively studied due to its historical significance as a hydrocarbon reservoir. It is well characterized in most areas and exhibits significant pore space potential through both primary and secondary porosity (e.g. Merriam 1963; Franseen et al. 2004). Although not funded through this CUSP-West study, the KGS has recently produced a regional model of Arbuckle storage potential (Figure 205), from which maximum CO_2 storage values were derived for each county in the state (e.g. Bream et al. 2025). These volumetric estimates were calculated using mapped formation thicknesses, bulk rock volume, and average net porosity derived from well log analysis.

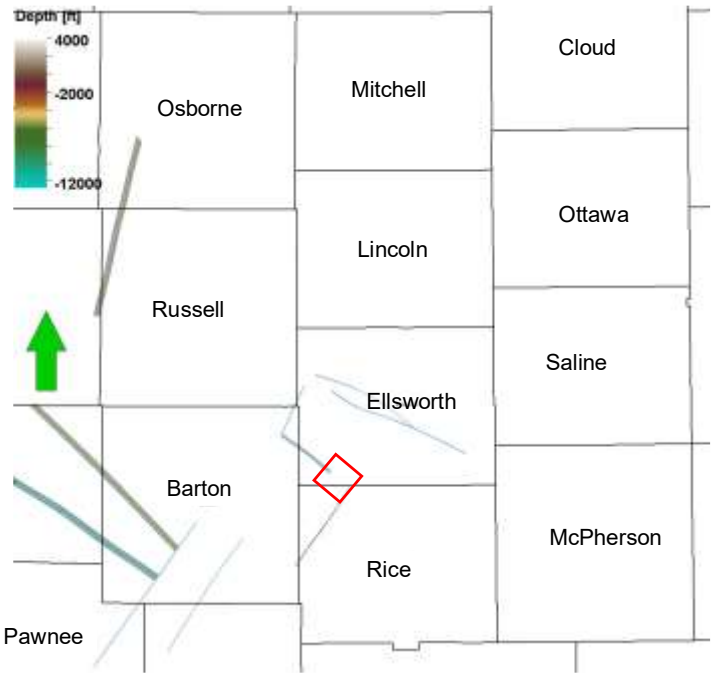


Figure 205 Approximate location of the model area (red outline) in central Kansas; labels are counties. Regional faults identified from well tops in the KGS database. Note that the fault offset is minimal for these faults in the modeled area.

Figure 206 shows depth structure maps (relative to Mean Sea Level) of the top of the Arbuckle formation (A) and the top of the Precambrian basement (B).

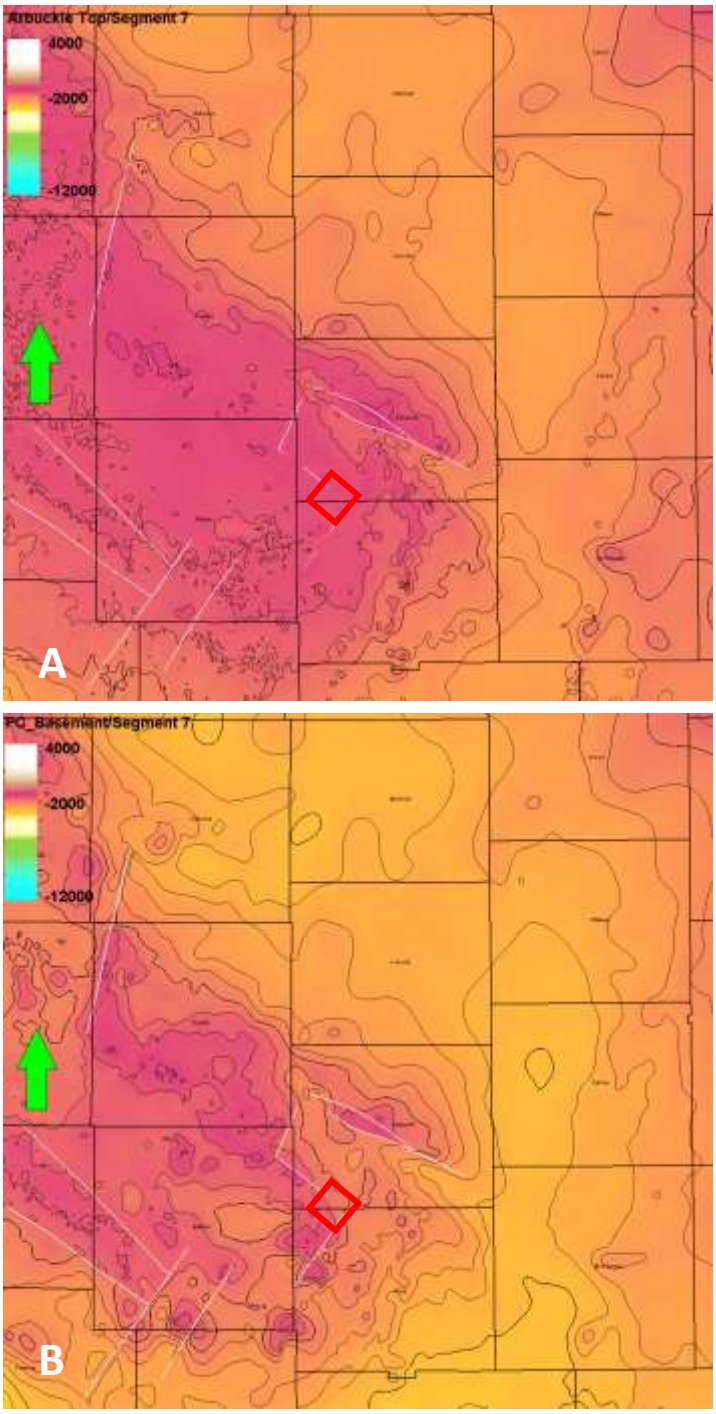


Figure 206 (A) Approximate location of the model area (red outline) against the top of the Arbuckle formation. (B) Approximate location of the model area (red outline) against the top of the Precambrian basement.

Note: This work is ongoing and was not supported as part of this focused study.

The average net neutron porosity of the Arbuckle formation in the area around the Bushton site is above average for the state (**Figure 207**). The net pore volume for these counties highlights the storage potential in area around the ONEOK Bushton facility on a county-wide basis compared to counties west of the Nemaha Uplift (Table 29 ;**Figure 208**). When converted to billion cubic

feet (BCF) and normalized by square mile, the counties have the following potential (Barton 0.93 BCF/mi^2; Ellsworth 1.39 BCF/mi^2; Lincoln 0.72 BCF/mi^2; McPherson 2.12 BCF/mi^2; Ottawa 0.45 BCF/mi^2; Rice 2.24 BCF/mi^2; Russell 0.70 BCF/mi^2; Saline 1.24 BCF/mi^2).

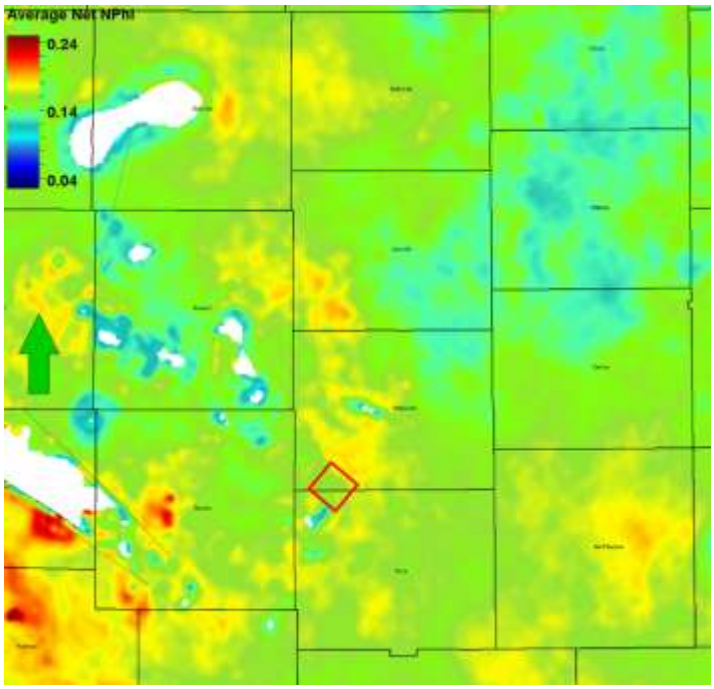


Figure 207 Average net porosity map of the Bushton, Kansas site (and surrounding counties) showing the distribution of Arbuckle Group porosity across the region. NOTE: Overall storage potential depends on numerous factors but at a minimum must consider both pore space (fraction) and reservoir bulk volume (ft^3); porosity as estimated from neutron wireline logs.

Table 29 Results of CO_2 storage resources by county

County Name	Area (sq.m.)	Area (sq.mi.)	Net Por Vol (cu.ft.)	Net Por Vol (cu.m.)	NPV/Area (cu.ft./sq.mi.)	NPV/Area (cu.m./sq.mi.)
Mcpherson	2,332,422,320.55	900.553293	1,906,837,000,000	53,995,521,962	2,117,406,061	59,958,163.9
Saline	1,868,384,581.82	721.38732	891,773,800,000	25,252,180,340	1,236,192,785	35,005,023.8
Ottawa	1,868,858,451.42	721.570282	328,227,500,000	9,294,352,472	454,879,460	12,880,730.7
Rice	1,885,288,716.68	727.914043	1,628,748,000,000	46,120,931,366	2,237,555,403	63,360,408.8
Ellsworth	1,873,412,586.65	723.328644	1,002,550,000,000	28,389,007,840	1,386,022,811	39,247,730.7
Lincoln	1,866,465,337.57	720.646296	516,833,200,000	14,635,062,358	717,180,124	20,308,246.1
Russel	2,329,948,196.34	899.598028	632,532,300,000	17,911,290,633	703,127,708	19,910,326.7

Barton	2,332,568,035.87	900.609554	836,094,900,000	23,675,532,064	928,365,568	26,288,342.1

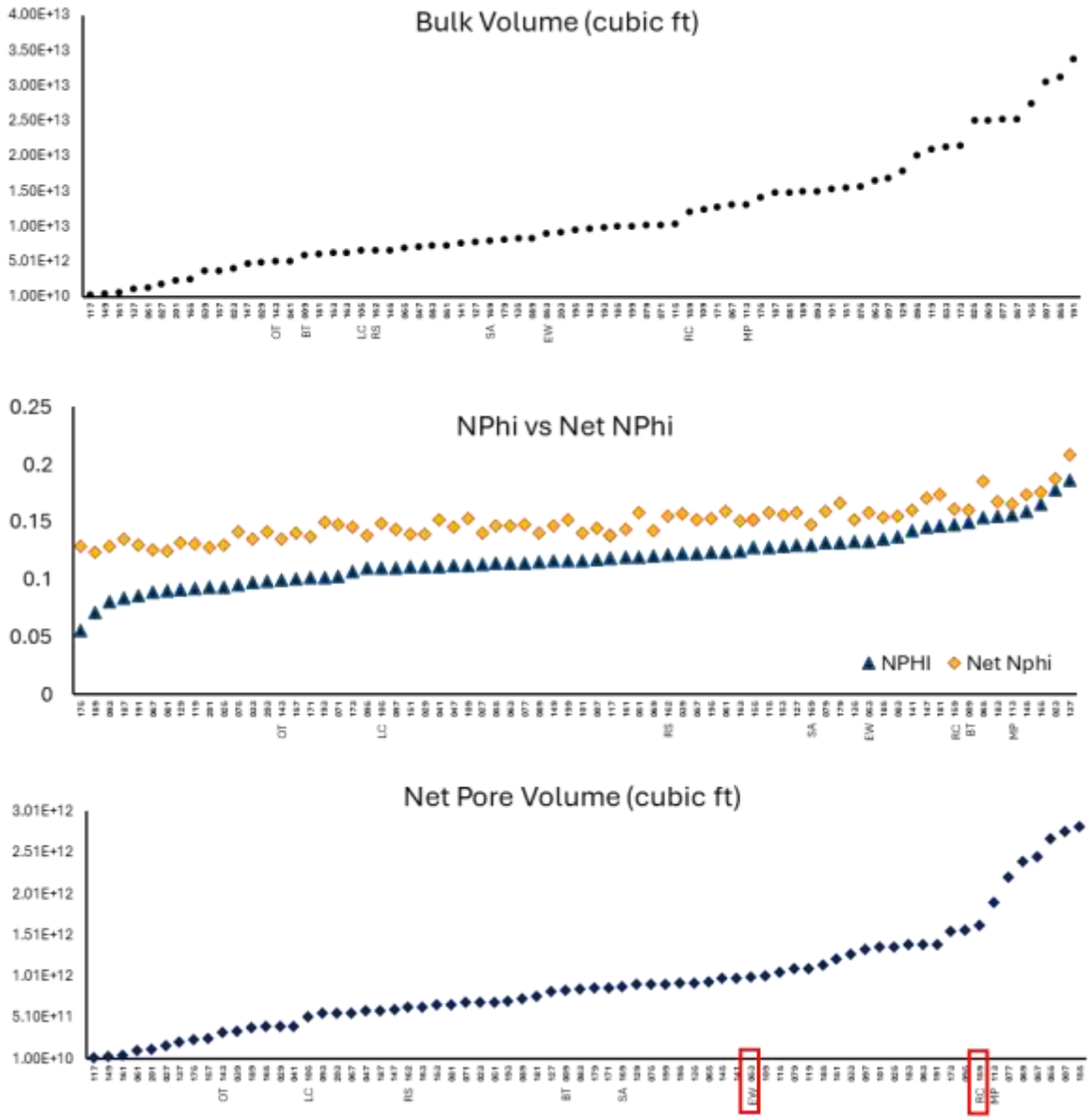


Figure 208 Values by county for Bulk Volume (ft3), neutron porosity and net neutron porosity (fraction); and net pore volume (ft3) for the Arbuckle reservoir. The counties surrounding the ONEOK Bushton facility are labeled. Data and plots courtesy of S. Bhattacharjee (KGS) and are as presented in Bream et al. (2025). NOTE: Net porosity used a 0.1 (fraction) cut-off such that modeled cells below that value were not included in the net pore volume values.

These estimated maximum storage potential values serve as a meaningful regional screening tool; however, they do not address numerous factors that would decrease the local storage potential of a project within one of these counties (e.g. relative permeability, gas buoyancy, local permeability heterogeneity, reactivity of carbonate reservoirs to CO_2 injection, irreducible water

saturation, impact from decades of hydrocarbon production). Storage estimates alone, whether at the scale of a county or a smaller geologic model, do not capture other critical subsurface elements necessary for a successful CCS project (e.g. seal presence and quality, quality of cement in existing wells, nearby wastewater disposal, etc.).

Subtask 3.4 – Geomechanical Assessment

A 1D Mechanical Earth Model (MEM) for the proposed ONEOK, Bushton, Medford CCS site was constructed. Some petrophysical modeling was incorporated as well to augment previous petrophysical models generated by the well logging service company. The well data utilized is located at a site known as the Wellington CCS site, in Ellis County, due to the absence of the required well log, core, and other data required at the Bushton site. The analog well is located in the Bemis Shutts oil field, approximately sixty miles from the Bushton site.



Figure 209 Location of the analog study well in relation to the proposed ONEOK Bushton injection site

This work centers on the utilization of well logging data focusing on, but not limited to, the analysis of the dipole sonic log (Halliburton's WaveSonic tool) and the density log. These data were taken from the McCord 20H pilot well, a science well that was drilled prior to a horizontal injection well used in a pilot carbon sequestration study as the injection well.

This work would ultimately provide the basis for microseismic and time-lapse seismic monitoring, as well as integrate into advanced reservoir simulation models. However, for this analysis to relate directly to the Bushton site, additional data would have to be acquired in a project pilot well. This data should include advanced acoustic logs, formation micro-imaging logs, and core data to undergo triaxial testing, in order to calibrate the 1D model for the Bushton site and to ensure the most accurate starting point for 3D geomechanical and reservoir flow simulation modeling.

Although some data is unavailable, the well-bore geomechanics is presented in six sections, giving a high-level review of areas that would need to be addressed in the event this project moved forward. The six sections are: 1) core analysis, 2) acoustic analysis, 3) petrophysics analysis, 4) construction of the 1D MEM, 5) integration of geomechanical data with reservoir flow modeling via coupled geomechanical flow modeling, and 6) structural model.

Core Analysis

As previously mentioned, no core data exists at the Bushton site. The closest core data available is in an offset well to the 1D MEM, the KGS 1-32H; these data are discussed in more detail in section 3.4.5, as they are part of a previous study at the Wellington site. To fully constrain the MEM, various tests should be performed on core data recovered from a pilot well in the Arbuckle and additional sealing formations located at Bushton. Tests should include geochemistry, petrophysical rock properties, and geomechanical rock properties. Stress-strain curves for both the intended storage formation and seal formations can be derived from triaxial testing, which would provide insight into the mechanical properties of these formations.

Figure 210 shows a typical stress-strain curve resulting from laboratory testing of core data. The stress-strain curve has been divided into four regions of geomechanical behavior, chronicling the increased axial stress during the lab experiment. Region one is defined as concave upward and results from the closing of microcracks typically introduced during retrieval. Region two demonstrates the linear stress-strain curve that is typically assumed during the bulk of geomechanical modeling and flow modeling. The end of the linear portion is the yield strength of the sample. Region three is concave down, due to the development of new cracks as the result of the experiment. The maximum load is dictated by the peak of this curve, known as peak strength, the point at which the sample has failed. Region four occurs post-failure, demonstrating the residual strength of the sample post-failure. This shows the importance of laboratory testing, as understanding the end points of these regions and the associated yield strength, peak strength, and residual strength would allow for calibration of well log data. There are other pertinent measurements to be derived from these tests as well, such as failure ratio, which not only facilitate calibration but also allow for the analyst to determine at which state of stress the formation exists in nature, whether it is in failure (as most unconventional reservoirs), elastoplastic, or elastic (Bratton et al. 2025). Most workflows assume the formation is linear elastic, as we will treat the Arbuckle in the upcoming well log analysis.

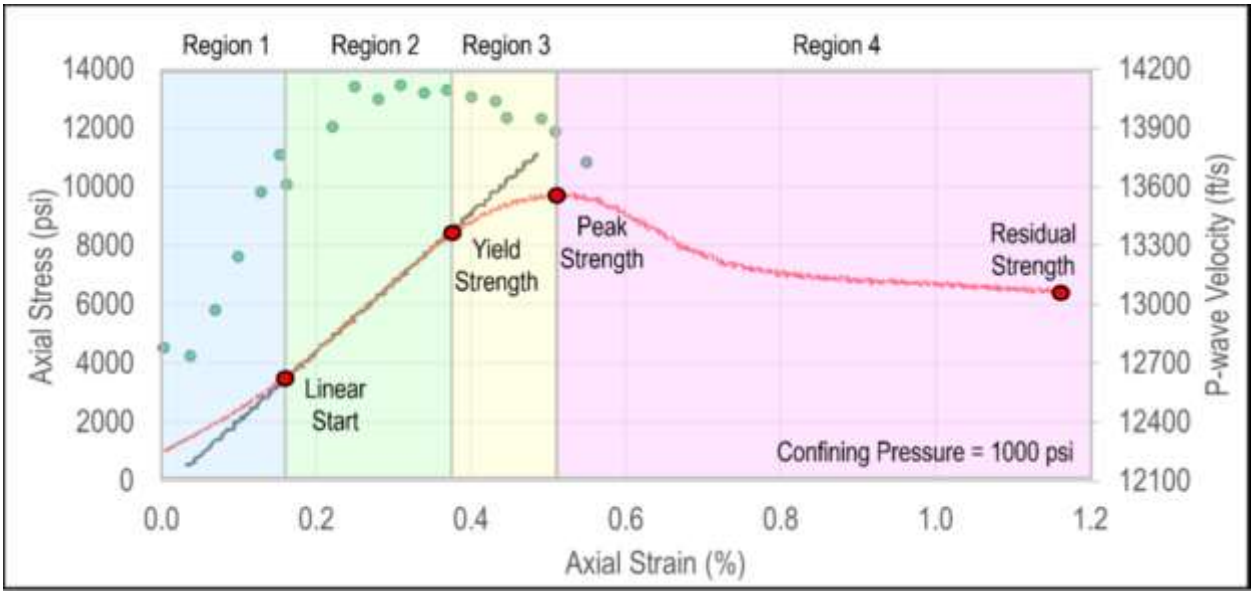


Figure 210 Typical stress test on the core for a brittle formation. The strain curve is shown in red as a function of the applied axial stress. Ultrasonic velocities are shown as green dots. (From Bratton, Geophysics and the Energy Transition.)

In addition to physical, destructive mechanical testing of the formation samples, sonic measurements will be made of the core. This will allow the petrophysical analyst to relate the sonic velocity measurements made at different scales, as the core measurements are much higher resolution than the log scale, though the log scale is typically more indicative of the in situ mechanical properties, depending on how the formation is classified. Note the behavior of the ultrasonic velocities (shown in green) in **Figure 210**. In this case, the ultrasonic measurements mimic the stress-strain curve. As a result, this formation *may* be classified as continuous, homogeneous, isotropic, linear, elastic. This is an indication that borehole measurements of sonic velocities will be sensitive to stress. If the sonic velocities did not vary with stress, this indicates that the sonic velocities will *not* be sensitive to the state of stress of the formation. If the formation is stress sensitive, then the sonic velocities will vary with stress loading. Equation 1 shows how compressional (P) and shear (S) waves will change with stress.

$$\Delta Vp,s=(Vp,s\partial\sigma)(\Delta\sigma) \quad (1)$$

The first term is the stress sensitivity variable, and the second term is the differential stress variable. Each term must be greater than zero for us to observe a change in velocity (Bratton et al. 2025).

Acoustical Analysis

Full waveform sonic log processing is an advanced and complex field, requiring highly specialized tools and expertise. Modern logs are capable of classifying and differentiating complex relationships between stress-induced, and intrinsic velocity anisotropy. Understanding the relationship between the speed of different waves in different directions within the formation enables the petrophysical analyst to characterize the state of stress in the formation much more effectively, particularly when understanding the relationship between maximum horizontal and minimum horizontal stress (Shmax and Shmin).

One of tools at the analyst's disposal is shown in **Figure 210**40. Modern dipole sonic tools measure not only the P and S -waves (compressional and shear, respectively), but also the Stonely wave. All waves are recorded over a wide range of frequencies, as formation and stress anisotropy are dispersive, or frequency dependent, but formation and stress dispersion will vary independently, allowing for differentiation between the two (Bratton et al. 2025).

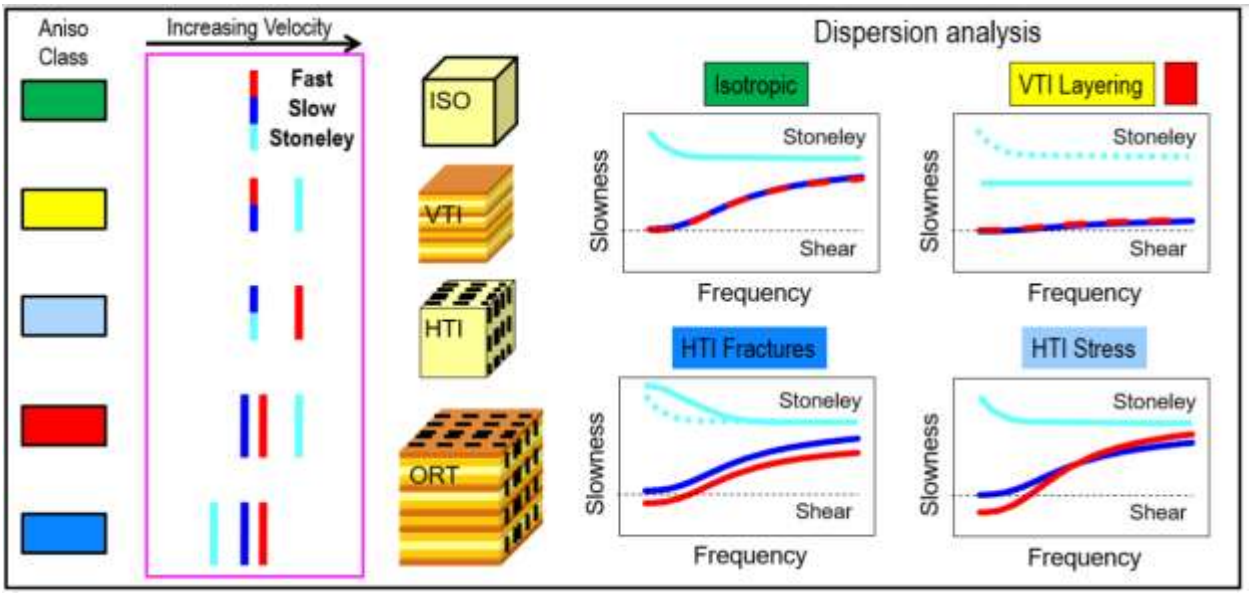


Figure 211 Anisotropy classification based on dispersion. (From Bratton, Geophysics and the Energy Transition.)

The WaveSonic tool deployed in the McCord 20H, was an early attempt to record all the above waveforms. Today the WaveSonic tool is a best-in-class sonic evaluation tool, but at the time of data acquisition of the McCord 20H (2011), the WaveSonic was hampered by hardware limitations, preventing full characterization of all waveforms. Also, although the data were recorded, the specialized processing required to separate the wave fields to fully understand the anisotropy was not performed. These factors limit the use of these data to a strictly isotropic, linear elastic mechanical earth model.

Petrophysical Analysis

Petrophysical analysis was carried out in part by the service company (Halliburton) and augmented in part in house by the KGS where needed for the development of the MEM. It should be noted that these analyses can also be calibrated to core data where available as they center on the estimation of rock properties such as porosity, permeability, and total organic content (TOC). Logs run in the McCord A-20H Pilot hole are shown in Table 30, additional logging runs were made in the horizontal well but are not the subject of this study.

Table 30 Logging runs on the McCord A-20H Pilot well. GR – Gamma Ray, SP – Spontaneous Potential, GTET – Gamma Ray, ACRT – Array Combination Resistivity Tool, Holefinder – caliper tool, IDT – LOGIQ directional tool, WSTT – LOGIQ WaveSonic tool.

Logging Run	Depths (feet)	Logging Tools

Run 1	12.5'-3,748'	GR
	1,279'-3,748	SP, GTET, ACRT, Holefinder
Run 2	1,260'-3,747	Sp, GTET, IDT, WSTT

Rock physics-based models, and therefore the resultant geomechanical models can benefit from further calibration of petrophysical properties to core data when available. For example, well established relationships between elastic moduli and porosity can be calibrated utilizing the methods of Lev Vernik (Vernik 1998) and Krief (Krief 1990).

1D MEM

A MEM is intended to provide the required input data to run a geomechanical simulation. Tom Bratton (Bratton et al. 2025) summarized the components of the MEM as follows:

"1) a framework model to characterize the structure of the formation including formation horizons and major faults, 2) a petrophysical model to quantify the lithology, porosity, water saturation, matrix permeability, and dynamic elastic moduli, 3) a mechanical stratigraphy model to characterize the stratigraphic column, load bearing facies, and natural and drilling induced fracture attributes, 4) a rock property model to characterize the static moduli, deformation, yield, and failure properties of the formation, 5) an overburden model to characterize the vertical loading, 6) a pore pressure model to quantify the pore pressure, 7) a stress orientation model to characterize the dip and azimuth of the far-field stresses, and finally 8) a stress magnitude model to quantify the horizontal loading on the formations."

A mechanical stratigraphy model was constructed utilizing Schlumberger's Techlog™ software. The approach is based on the cross-plot methods (Herron et al. 1992).

Rock properties were modeled utilizing standard geomechanical correlations (**Figure 212** and **Figure 213**). Static Young's modulus was derived both from the Morales correlation (Morales 1993) and the Canaday correlation (Canaday 2011) and exhibit a strong match, the Morales method was utilized for further calculations. The friction angle is derived utilizing the Plumb correlation (Plumb 1994) while the unconfined compressive strength (UCS) is derived from the Coates-Denoo correlation (Coates 1981).

Figure 212 shows the static moduli, rock strength, and corresponding dipole sonic measurements for the entirety of the McCord A-20H pilot well. The red curve labeled "AppAni" represents an apparent anisotropy derived from the shear wave measurements aligned in the X and Y directions respectively. As previously mentioned, further processing is required to align the shear waves to the formation fast and slow directions to fully characterize formation and stress anisotropy. This will further inform the magnitude of minimum and maximum horizontal stress, as well as characterize the presence of fractures. **Figure 213** shows the same data over the depth interval comprising the proposed injection formation (Arbuckle) and the overlying formations. There exist some areas of relatively high apparent anisotropy, which will most likely indicate some formation fracturing in both the Stark and Kansas City formations.

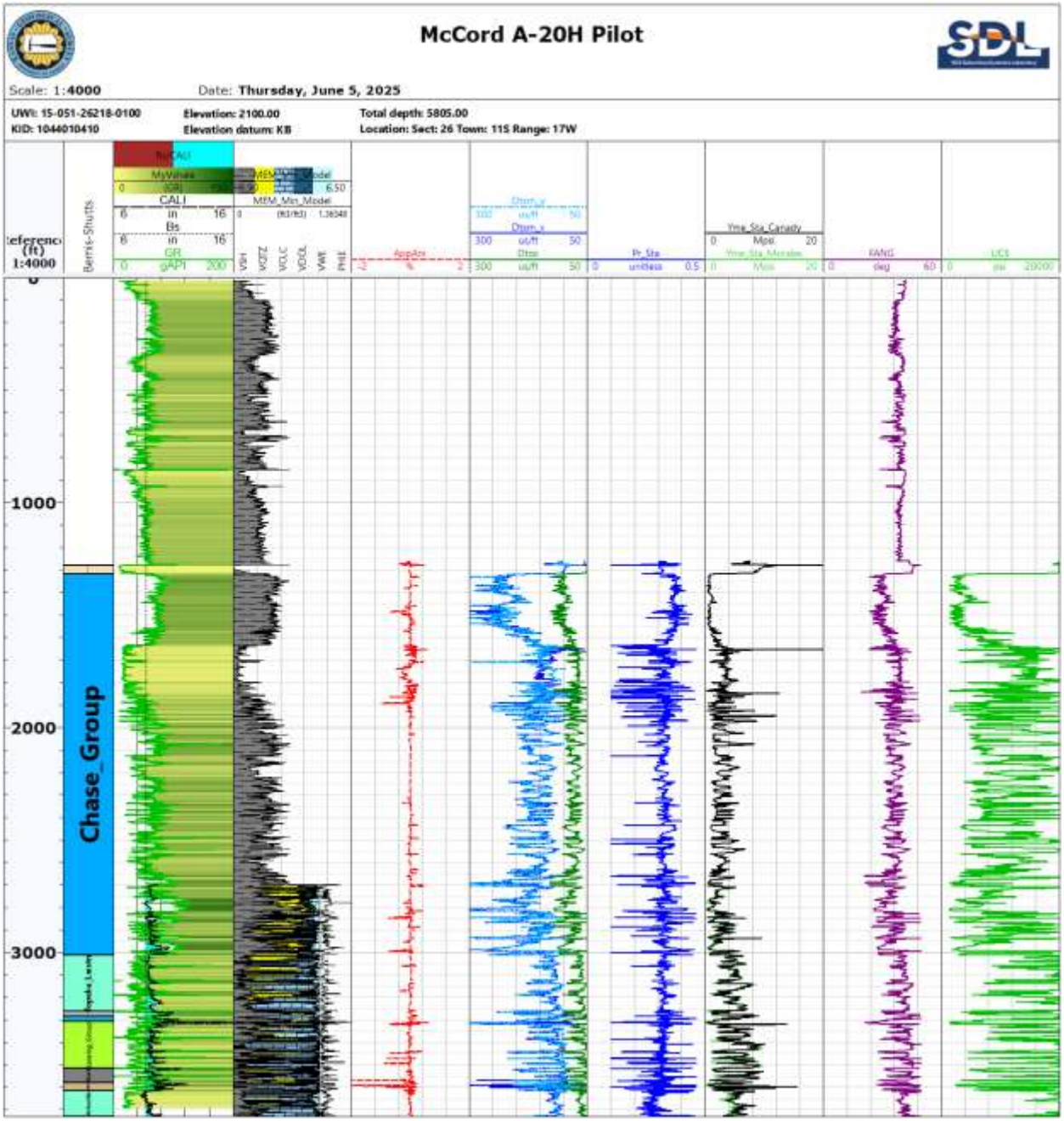


Figure 212 Static moduli, rock strength parameters and diploe sonic measurements shown for the McCord A-20H Pilot well. Track 1 is the depth track, track 2 shows the stratigraphic column, track 3 shows the correlation curves, track 4 shows the fractional volumes, track 5 shows and apparent anisotropy, track 6 shows the vertical sonic velocities, track 7 shows the static Poisson's ratio, track 8 shows both of the calculated static Young's moduli, track 9 the friction angle and track 10 the unconfined compressive strength (UCS).

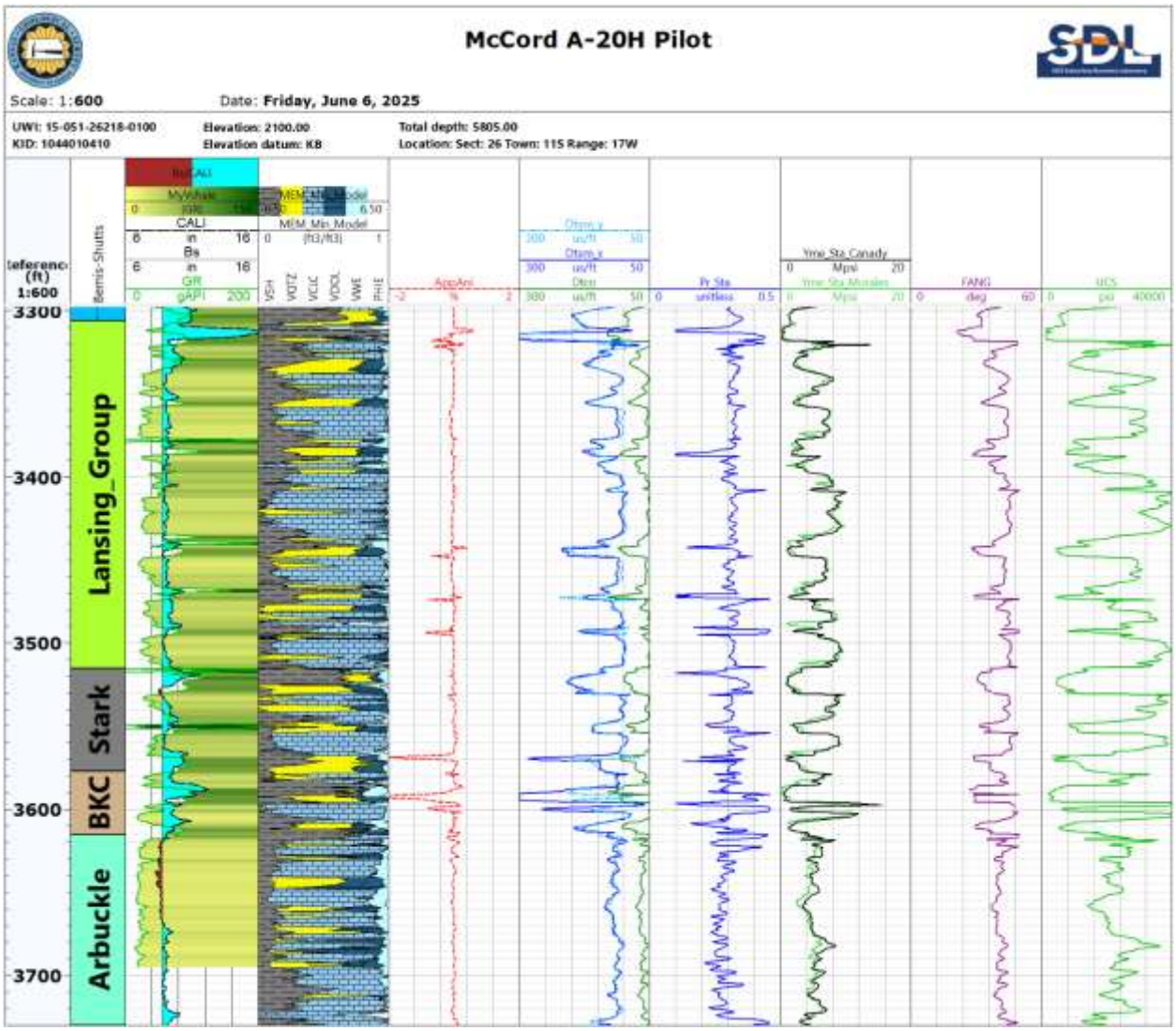


Figure 213 Static moduli, rock strength parameters and diploe sonic measurements shown for the McCord A-20H Pilot well highlighting the section from the top of the Lansing Group to the Arbuckle. Track 1 is the depth track, track 2 shows the stratigraphic column, track 3 shows the correlation curves, track 4 shows the fractional volumes, track 5 shows and apparent anisotropy, track 6 shows the vertical sonic velocities, track 7 shows the static Poisson's ratio, track 8 shows both of the calculated static Young's moduli, track 9 the friction angle and track 10 the unconfined compressive strength (UCS).

An overburden model is required to calculate both vertical stress, pore pressure and subsequent geomechanical parameters. Wireline bulk density is integrated over depth from the surface to within the Arbuckle formation. Where there exists no direct density measurement an exponential model is used to continue the density and overburden gradient to the surface. Pore pressure was compared to borehole derived formation hydrostatic pressure measurements (labeled FHP 31 and FHP 33 in **Figure 214** and **Figure 215**) and found to be in direct agreement with no need for further calibration.

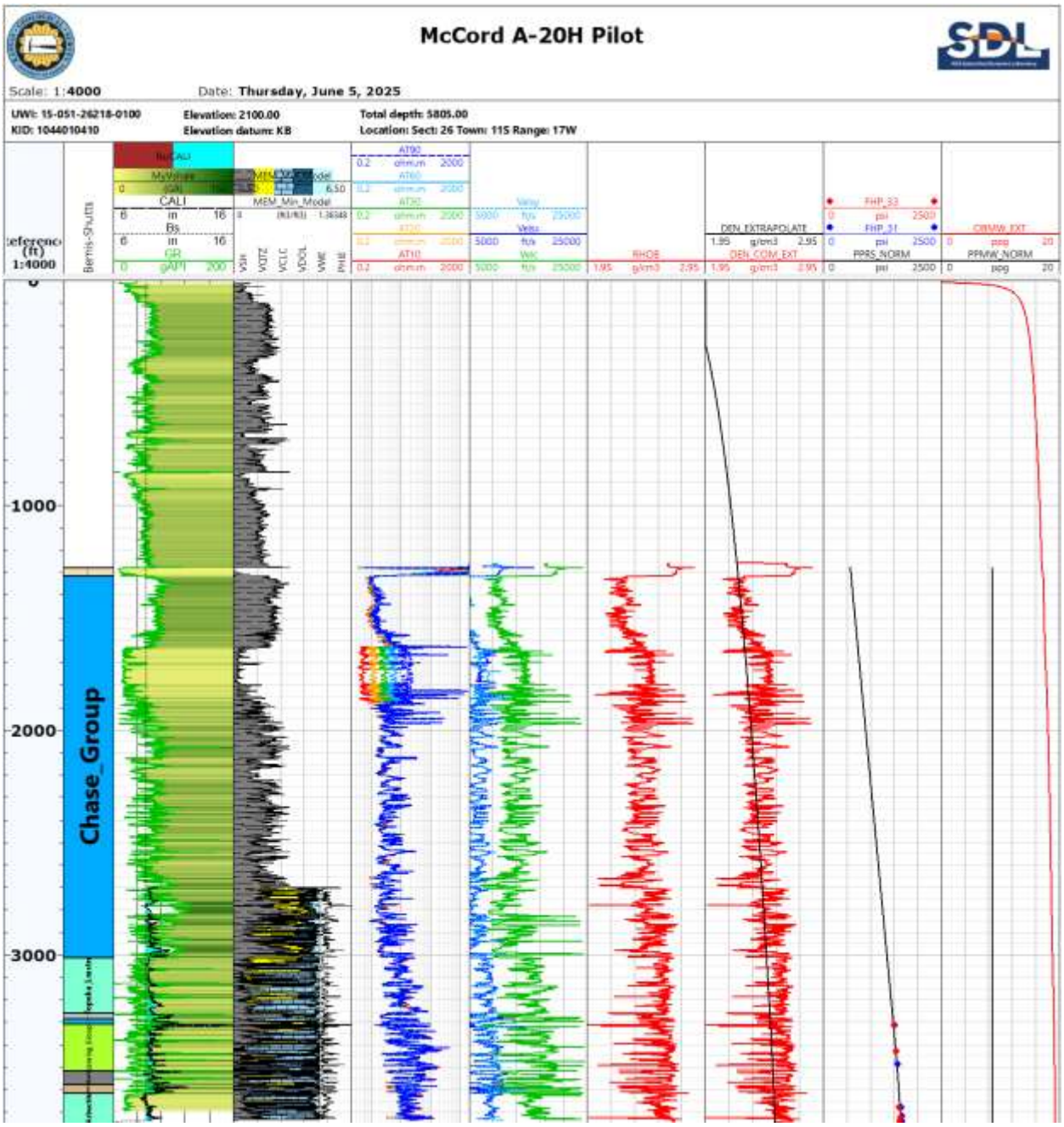


Figure 214 The overburden and pore pressure model. Track 1 is the depth track, track 2 shows the stratigraphic column, track 3 shows the correlation curves, track 4 shows the fractional volumes, track 5, shows the resistivity curves, track 6 shows the vertical sonic velocities, track 7 shows the measured density in red, track 8 shows the measured density in red and an exponential model in black, track 8 shows the resulting pore pressure and measured formation hydrostatic pressures from borehole measurements (dots) and track 10 shows the overburden stresses in ppg as well as pressure gradient.

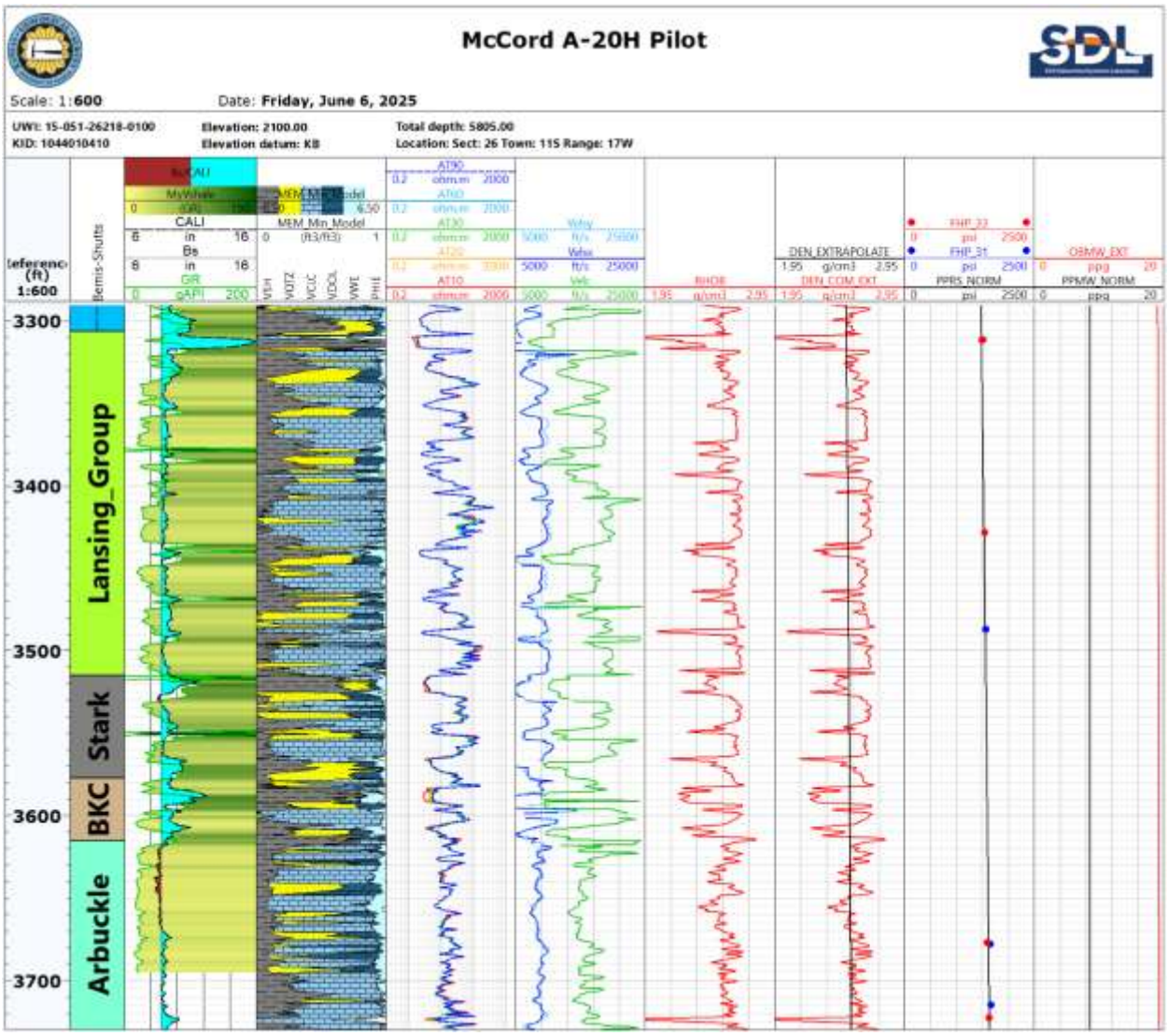


Figure 215 The overburden and pore pressure model shown from the top of the Lansing Group to the Arbuckle. Track 1 is the depth track, track 2 shows the stratigraphic column, track 3 shows the correlation curves, track 4 shows the fractional volumes, track 5, shows the resistivity curves, track 6 shows the vertical sonic velocities, track 7 shows the measured density in red, track 8 shows the measured density in red and an exponential model in black, track 8 shows the resulting pore pressure and measured formation hydrostatic pressures from borehole measurements (dots) and track 10 shows the overburden stresses in ppg as well as pressure gradient.

Assuming that all layers in the 1D MEM will be within the elastic domain, the standard poroelastic horizontal strain equations were used to estimate horizontal stress. The minimum horizontal stress equation is shown in Equation 2 and the maximum horizontal stress is shown in Equation 3.

$$\sigma_h = \left(\frac{\nu}{1-\nu}\right)(\sigma_V - \alpha P_p) + \left(\frac{E}{1-\nu^2}\right)\varepsilon_h + \left(\frac{E\nu}{1-\nu^2}\right)\varepsilon_H + \alpha P_p \quad (2)$$

$$\sigma_H = \left(\frac{\nu}{1-\nu}\right)(\sigma_V - \alpha P_p) + \left(\frac{E\nu}{1-\nu^2}\right)\varepsilon_h + \left(\frac{E}{1-\nu^2}\right)\varepsilon_H + \alpha P_p \quad (3)$$

Static elastic moduli were used and a Biot's alpha coefficient of one. The strain values used were 0.00 for the minimum horizontal strain and 0.15 for the maximum horizontal strain. Resulting in an estimated lower bound SHmin and a best estimate Shmax (**Figure 216** and **Figure 217**).

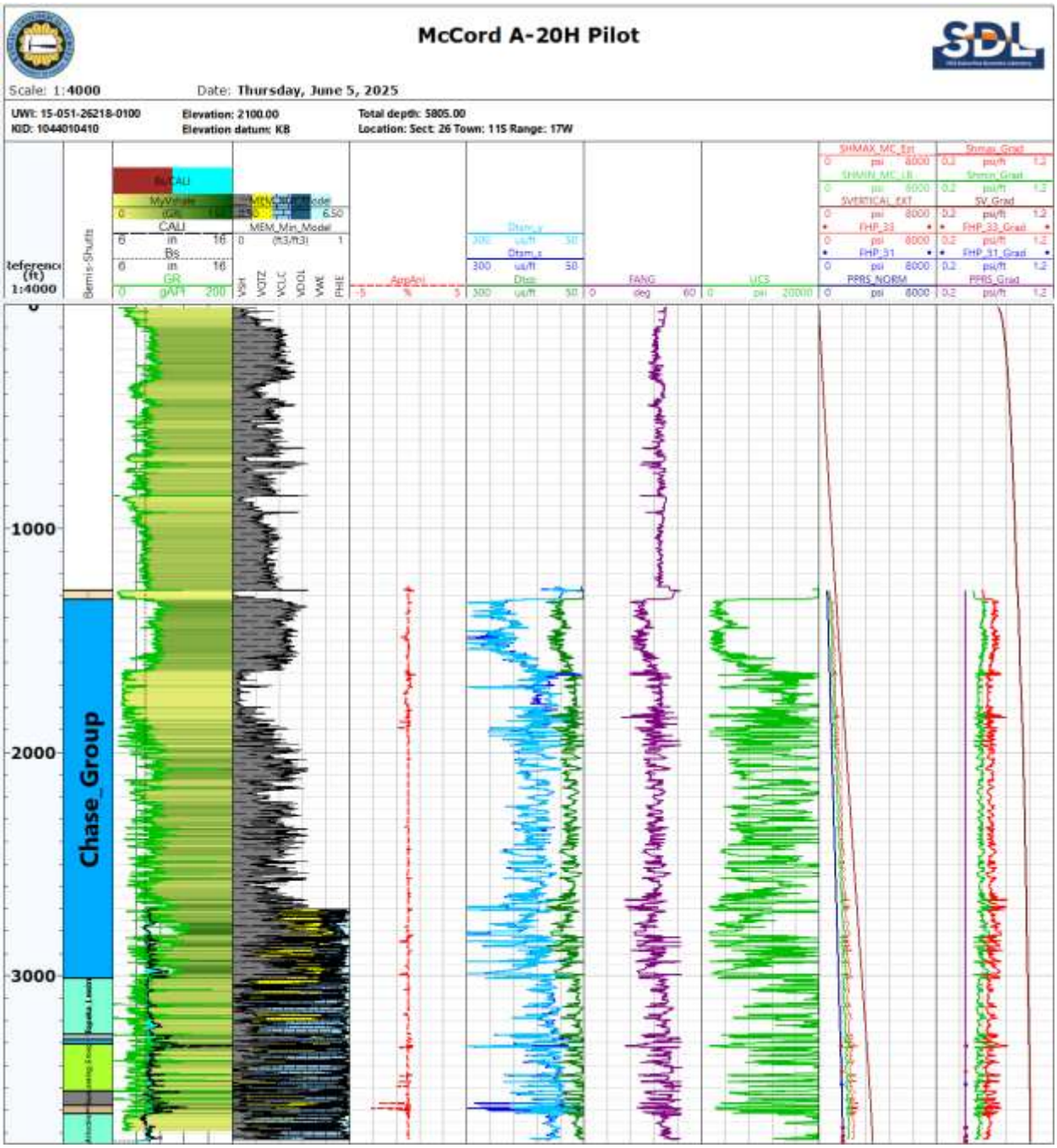


Figure 216 Horizontal stress magnitude analysis. Track 1 shows the measured depth, track 2 shows the formation names, track 3 shows the standard correlation curves, track 4 shows the mineralogical fractional volumes, track 5 shows an apparent anisotropy, track 6 shows the dipole sonic slownesses, track 7 shows the friction angle, track 8 shows the UCS, track 9 shows the pore pressure, stress curves, and formation hydrostatic pressure measurements (dots) and track 10 shows the pore pressure and stress gradients, along with the formation hydrostatic pressure measurements (dots).

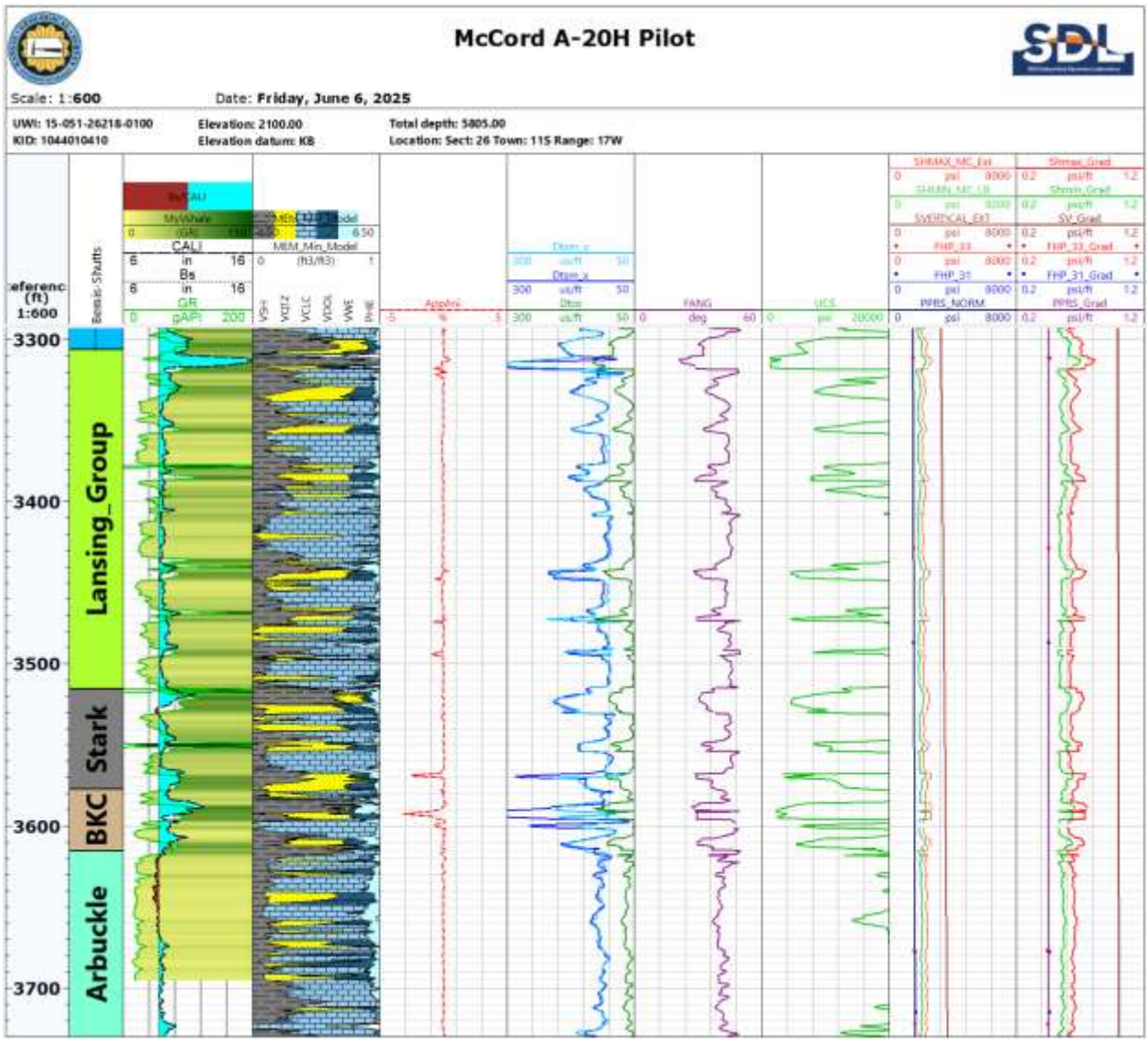


Figure 217 Horizontal stress magnitude analysis shown from the top of the Lansing Group to the Arbuckle. Track 1 shows the measured depth, track 2 shows the formation names, track 3 shows the standard correlation curves, track 4 shows the mineralogical fractional volumes, track 5 shows an apparent anisotropy, track 6 shows the dipole sonic slownesses, track 7 shows the friction angle, track 8 shows the UCS, track 9 shows the pore pressure, stress curves, and formation hydrostatic pressure measurements (dots) and track 10 shows the pore pressure and stress gradients, along with the formation hydrostatic pressure measurements (dots).

Seal and Risk Assessment

The potential for injection-induced fault reactivation in the Arbuckle Group reservoir at the Wellington site was addressed in a previous study incorporating subsurface structural mapping and stress field conditions related to increased seismicity in the region (Schwab et al. 2017). This work will be used in addition to the McCord 20H Pilot well-log data as an analog for the ONEOK Bushton site.

To analyze geomechanical caprock integrity concerning CO_2 injection and its effects on subsurface stability at the Wellington site, triaxial tests were conducted in the KGS 1-32 well, an

offset to the McCord A20H Pilot. CO_2 injection increases pore pressure, potentially reactivating fractures or faults. Geomechanical studies are essential to examine fault reactivation potential and ensure CO_2 remains confined. In these studies, three failure modes would be investigated: new fractures, slippage along faults, and opening of existing fractures.

Subsurface stress fields involve lithostatic and horizontal compressive stresses. Mohr's Circle can be used to represent stress states and failure envelopes for fault stability (Mavko et al. 2009). Effective stress is influenced by pore pressure, which can facilitate fault movement. Future work would include calibrating the 1D mechanical model in the McCord A20H Pilot to the triaxial measurements made on core extracted from the KGS 1-32 (Table 31).

Table 31 Triaxial tests conducted on core samples from depths of 3,630 to 5,151 ft.

Depth (ft)	Confining Pressure (psi)	Compressive Strength (psi)	Static Young's Modulus (x10^6 psi)	Static Poisson's Ratio
3,630.46	1,350	22,754	2.4	0.15
3,696.17	1,700	13,988	2.62	0.25
3,724.05	1,700	34,131	4.53	0.34
3,932.76	1,500	41,979	5.71	0.39
4,005.7	1,500	39,389	4.75	0.31
4,053.85	1,500	20,350	3.07	0.37
4,084.94	1,600	24,233	5.19	0.33
4,109.31	1,600	17,487	2.97	0.12
4,132.61	1,600	17,089	1.96	0.22
4,197.65	1,750	23,418	6.62	0.25
4,323.02	1,750	29,337	7.46	0.3
4,476.05	1,750	42,375	10.73	0.3
4,646.4	1,750	43,343	10.53	0.32
4,945.15	1,750	32,543	10.23	0.29
5,151.84	1,900	47,455	9.72	0.29

The weakest sample at 4,132.61' can be interpreted to suggest that no new fractures would be expected due to injection, however, calibration of the 1D model, and incorporation into the 3D simulation through coupled geomechanics simulation would need to be performed to verify this interpretation.

The increase in seismic activity in Kansas correlates with brine disposal operations, indicating that pore fluid pressure is reactivating preexisting faults. This study evaluates the potential for injection-induced earthquakes in Wellington Field, focusing on subsurface fault mapping and stress analysis. Kansas has seen a rise in seismicity linked to brine disposal since 2009 with over 100 M3.0+ earthquakes that occurred from 2013 to 2017, with significant events in western Sumner County. The majority of seismic events are located within the crystalline basement, suggesting a hydraulic connection with basement faults. A detailed characterization of subsurface faults utilizing 3D seismic imaging was made at the Wellington site to determine orientations and stresses for assessing induced seismic hazards. A similar study would be necessary at the proposed Bushton site. These studies will determine which faults are stable. As an analog, it was determined that at the Wellington site, that faults striking <020° are stable, while those striking 020°–049° may be prone to reactivation with increased pore fluid pressure. At Wellington, the proposed injection volume of 40,000 t was determined unlikely to reactivate faults at reservoir depths, but higher rates of injection could exceed critical thresholds in the basement.

The orientation and magnitudes of principal stresses were estimated at Wellington through analysis of drilling-induced fractures and moment tensor solutions from recent earthquakes. The study found consistent stress orientations across the region, with significant implications for fault reactivation potential.

- SHmax estimated at approximately 075°, with no local trends in nodal plane orientation.
- Stress magnitudes at 1,484 m: Sv = 36.6 MPa, Shmin = 18.4 MPa, SHmax = 31.3–45.9 MPa.
- Stress gradients: Sv = 24 MPa/km, Shmin = 12.4 MPa/km, SHmax = 21–31 MPa/km.
- Pore fluid pressure at 1,484 m is 14.5 MPa.

Slip and dilation tendency analysis assessed the likelihood of fault reactivation by calculating slip and dilation tendencies based on observed fault geometries and estimated stress states. Results indicated varying potential for fault slip under different stress conditions.

- Slip tendency values for SS (strike-slip; lateral movement expected) stress state ranged from 0.46 to 0.01.
- For NS (normal stress; extensional movement expected) stress state, slip tendency values were less than 0.34.
- Critical pore fluid pressure changes required for failure ranged from 1.1 MPa to 9.8 MPa, depending on the stress state and fault orientation.
- Dilation tendency values were generally low, indicating a higher likelihood of slip over dilation.

The study evaluated the potential for fault reactivation in both the Mississippian and Arbuckle reservoirs, revealing that many faults are moderately oriented for failure under current stress conditions. The analysis highlighted the influence of pore fluid pressure on fault stability. The author's analysis indicated a low likelihood of reactivating faults in the Mississippian and Arbuckle, but highlighted concerns regarding basement faults. These faults may provide pathways for pressure changes that could induce seismicity (Schwab et al. 2017). If the injection reservoirs in the Bushton areas have additional permeability from non-matrix porosity systems like fractures or karst, this would further decrease the chances of fault or fracture reactivation.

Structural Model

The structural model, incorporating the static 3D model is documented in section 3.2. A 1D MEM serves as a calibration point for further coupled geomechanical flow simulation, where iterative updates are made to the 3D MEM as pore pressure and other stresses evolve during injection. This represents the final and most comprehensive integration of all data types and models reviewed thus far.

Results and Discussion

We have introduced all the necessary steps to generate a comprehensive, integrated 3D mechanical earth model. This includes core, petrophysical, and well log based geomechanical models as input into a coupled 3D reservoir/geomechanical flow model. A 1D MEM was created in the nearest offset well, and a thorough review of previous work incorporating core analysis and fault slip potential within the intended storage formation (Arbuckle) and overlying sealing rock. Necessary components are provided here:

- a framework model to characterize the structure of the formation including formation horizons and major faults;
- a petrophysical model to quantify the lithology, porosity, water saturation, matrix permeability, and dynamic elastic moduli;
- a mechanical stratigraphy model to characterize the stratigraphic column, load bearing facies, and natural and drilling induced fracture attributes;
- a rock property model to characterize the static moduli, deformation, yield, and failure properties of the formation;
- an overburden model to characterize the vertical loading;
- a pore pressure model to quantify the pore pressure;
- a stress orientation model to characterize the dip and azimuth of the far-field stresses;
- a stress magnitude model to quantify the horizontal loading on the formations.

Recommended further work at the Wellington site includes additional integration of the available triaxial test in the KGS 1-32H and complete (re)-processing of the sonic data in the McCord A20H. The integration of the core data will provide calibration to the well-based 1D MEM as well as set upper and lower bounds for principal horizontal stresses. Reprocessed sonic data will enable the determination of the stress orientation, and differentiation between stress and fracture induced anisotropy. These results can further be incorporated into a fully realized, reservoir coupled, 3D mechanical earth model. Risk assessment at the Wellington site was also facilitated through seismic imaging interpretation of horizons and faults within the formations of interest.

At the Bushton site, core data and modern sonic logs are required to develop a local MEM, which would be significantly enhanced through integration of a FMI, which provides further insight into formation stress magnitude and orientation, as well as enabling quantification of pre-existing faults and fractures. As with the Wellington site, 3D seismic imaging is highly recommended to realize a full risk assessment of injection induced fault slippage and induced seismicity.

In summary, the results demonstrate that building a detailed Mechanical Earth Model (MEM)—integrating core, log, and stress data—is essential for reliably assessing induced seismicity and leakage risk at injection sites. For Bushton, this means that to ensure safe CO_2 or brine injection,

similar site-specific data (core analyses, modern well logs, and especially 3D seismic imaging) are needed to characterize faults, rock properties, and stress conditions. Applying this approach will allow for targeted risk assessment of fault reactivation and leakage at Bushton, helping identify safe injection pressures and minimizing the potential for induced earthquakes or loss of containment. In short, thorough geomechanical characterization—like what was done at Wellington—is critical before proceeding with injection operations at Bushton.

Subtask 3.5 – Install and Monitor Seismometer Network for Seismic Risk Analysis

Induced seismicity in Kansas and Oklahoma has been studied extensively by researchers and regulatory agencies in both states for more than a decade. Well site monitoring guidelines (EPA 2013; EPA 2018) require that CO_2 injection at Class VI wells may proceed only if baseline seismicity levels are not exceeded. Prior to injection, local monitoring networks must be installed to establish baseline seismicity levels using historical data and regional tectonic assessments (Templeton et al. 2022). These networks should be capable of detecting local earthquake magnitudes of at least M1 and recording all ground motions associated with such events. Once sequestration begins, projects must adhere to the EPA's 7-Step protocol and associated traffic light system for managing induced seismicity risks (Templeton et al. 2022; 40 CFR 146.94(a)).

Subtask 3.5 accomplishments:

- Developed and field-tested a low-cost seismic network using the Raspberry Shake 3D (RS-3D) seismometers, offering a viable alternative to conventional broadband stations. Each station, including peripheral components, cost approximately $3,500, substantially lower than commonly used broadband seismometers that cost more than $35,000 per station. RS-3D station recordings were validated against broadband seismic recordings from regional USGS and KGS networks in Kansas (Proffitt 2024).
- Conducted 11 months of continuous seismic monitoring near the ONEOK Bushton facility and established local background seismicity for future seismic risk analysis. The RS-3D network detected 440 earthquakes in the state of Kansas and 140 local earthquakes within a 45-mile (72.4 km) radius of the study site. The RS-3D network revealed local, low-level seismicity not reported by the distant USGS and KGS networks (Templeton et al. 2022).

3.5.1 – Development and Deployment of a Low-Cost Seismic Network

The RS-3D is an all-in-one, plug-and-play seismograph consisting of three electronically extended 4.5 Hz short period geophone sensors capable of capturing signals down to a 2 second period (Raspberry Shake 2023). The incorporated computer is the Raspberry Pi 3 – Model B, which comes with pre-installed Raspberry Shake software, making it ready for immediate use. This seismometer provides real-time miniSEED data compatible with various seismological software such as SeisComP, Earthworm, ObsPy, and Seisan (Raspberry Shake 2023).

Five RS-3D seismic stations were constructed and installed at three locations: three co-located at the ONEOK facility in Bushton, one in Holyrood Cemetery (approximately 6.1 km NW), and one at the Kansas Wetlands Education Center (approximately 25.3 km SW). Each unit was installed approximately 2 ft underground in a waterproof enclosure, with an above-ground system powered by solar panel, 12 V deep cycle battery, and equipped with GPS and wireless

telemetry components (Figure 218). For detailed description of station fabrication, refer to Proffitt (2024, Appendix A).

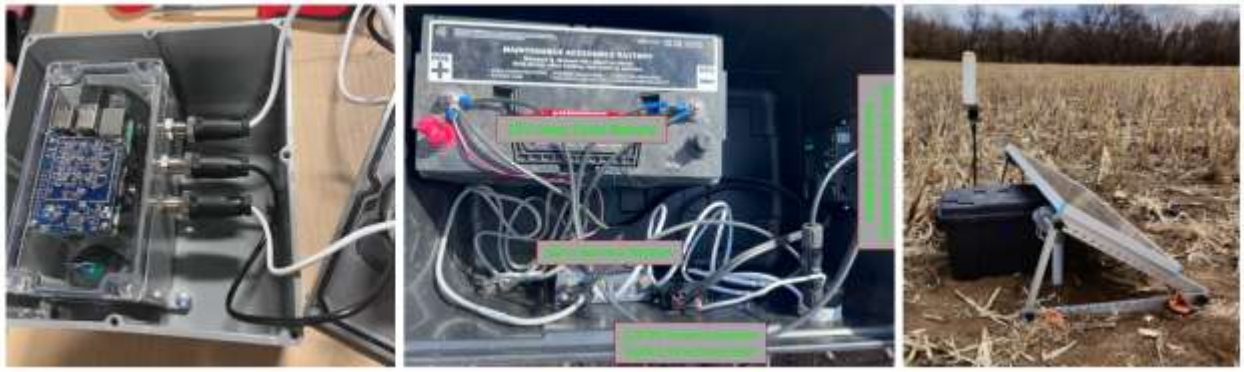


Figure 218 (left) RS-3D seismometer shown in the waterproof case. (middle) Above ground case housing station components. (right) A completed seismic station installation at the ONEOK Bushton site. Surface components housed inside the black tote, antennas for cellular and GPS signals, and a solar panel to power the components. The PVC piping extending above the ground allows cables connected to the seismometer below ground to reach the tote.

Before field deployment each seismometer was manually configured for continuous data recording and streaming, and for minimizing network disconnections. Stations were remotely accessible using the free VPN service ZeroTier (https://www.zerotier.com/) safeguarding network data and privacy. Additionally, an in-house developed script enabled each seismometer to reconnect online in the event of a system reboot. Remote station access reduced significantly the need for maintenance visits to the network stations. For a detailed description of the station setup, see Proffitt (2024, Appendix A).

The five RS-3D stations were installed at three locations forming the RS-3D network (**Figure 219**). The first installation was located at ONEOK facility in Bushton, and consisted of 3 stations spaced approximately 100 m apart in a N-S orientation. Multiple station deployments at the ONEOK facility allowed for multiplicity of observations providing nearly uninterrupted monitoring and confidence in low magnitude recordings at an industrial, noisy site. A second location was set up in Holyrood cemetery, 6.1 km northwest from the ONEOK facility, and a third location southwest at the Kansas Wetlands Education Center, 25.3 km away from the ONEOK facility. Site selection was challenging due to the limited availability of public land and the few contact points for requesting permission to use private land. The Holyrood location, a cemetery on the southeast edge of the city limits, proved ideal due to its consistently quiet environment and regular monitoring lasted 11-months with the exception of a two-week period in November due to power outage caused by a winter freeze. While the stations at the ONEOK facility recorded significant operational noise, having multiple stations at this location improved the signal quality for earthquake detection.

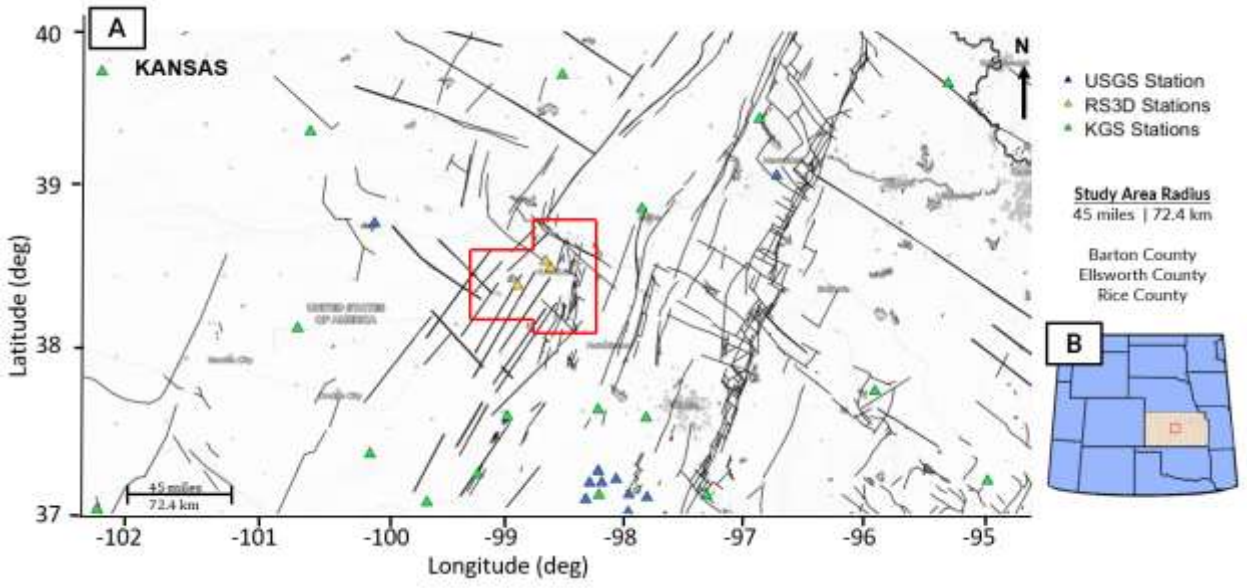


Figure 219 Map (A) showing the geographic locations of seismic monitoring stations from the USGS (blue triangles), KGS (green triangles), and RS-3D (yellow triangles). The immediate study area is outlined in red. Inset (B) shows the location of the study area within the state of Kansas. Basemap modified from Dicken et al. (2001).

3.5.2 – Earthquake Data Collection and Analysis

Throughout the project, the use of open-source software for documentation, forums, and accessibility was maintained. Remote monitoring of the Bushton area began at the University of Kansas campus, where data was collected using a telemetry-based connection for processing and interpretation. As data was retrieved directly from the stations, it was automatically downloaded in miniSEED format. The Standard for the Exchange of Earthquake Data (SEED), developed by the USGS and the Albuquerque Seismic Laboratory, has become the standard for delivering unprocessed earthquake data to various laboratories (Bormann 2012). The free SeisAn software package (Havskov and Ottemoller 1999) was used for earthquake detection, location, and magnitude calculations. A subsurface seismic velocity model used in this study was calculated using two well logs (Kinzel well and Schepmann Trust Well) near the ONEOK facility (Proffit 2024, Appendix C).

For visualization and data compilation, Python and its extension, ObsPy (Beyreuther et al. 2010) were used. Python was utilized to develop an SFTP (Secure File Transfer Protocol) script that automated the data collection process. The Python script accessed each station and channel, transferring the data to a specified folder. ObsPy, a Python toolbox for seismology, was employed for waveform analysis and signal detection. The analysis utilized a recursive STA/LTA (Short-Term Average/Long-Term Average) network trigger, which applies two moving windows (short-term and long-term) to a continuous data stream to calculate the average signal power, or signal-to-noise ratio (SNR). For detailed description of data collection and analysis methods refer to Proffitt (2024, Appendix A).

3.5.3 – RS-3D Earthquake Data Quality Assessment

Critical information for accurate earthquake detection—such as arrival time, location, and magnitude—was collected and compared across all three seismic networks (RS-3D, USGS, and

KGS; **Figure 219**). However, the overlap where all three networks recorded the same events was limited due to differences in coverage area and time constraints.

Continuous monitoring was conducted by the RS-3D network over a period of 11 months (from May 17, 2023, to April 30, 2024), but the network experienced 15 days in total data loss in November due to harsh winter conditions causing power outages and animal damage to surface wiring. Additionally, the USGS network's spatial coverage in Kansas is limited due to the sparse distribution of stations within the state.

For the earthquake data comparison, six events that were recorded by all three networks were analyzed (Table 32 and **Figure 220**). The earthquakes occurred at least 80 km from the RS-3D network, classifying them as regional events. Each arrival time from the USGS, RS-3D, and KGS stations agreed while the magnitudes and epicenters calculated showed some variability across all three networks (Table 32). Varying magnitudes and earthquake epicenters may be expected depending on the network location relative to the earthquake, calibration of the user's velocity model, response file, and spectral frequency fit. While small differences in magnitude and epicenter location are observed between the RS-3D and USGS/KGS stations, these differences are attributed to variations in network geometry and station placement. We note that the RS-3D station locations are not optimal as they were limited by site availability The uncertainty in earthquake magnitude and location increased with the distance from the RS-3D stations. Conversely, seismic events closer to the RS-3D stations were determined with higher confidence in both location and magnitude.

Table 32 Comparison table for six earthquakes detected by the USGS, KGS, and RS-3D networks. The table includes arrival times from both the USGS and RS-3D seismometers, demonstrating an exact match. However, all three networks recorded matching arrival times. The magnitudes reported by each network are shown along with the standard deviation for each earthquake. The epicenter locations calculated by each network were compared by measuring the distance between their reported epicenters to assess location variation.

Date	Arrival Time USGS	Arrival Time RS3D	Magnitude USGS	Magnitude RS3D	Magnitude KGS	St Dev	Epicenter Distance USGS-RS3D	Epicenter Distance USGS-KGS	Epicenter Distance RS3D-KGS
4-Jun	13:55:24	13:55:24	3.2	3.4	3.3	0.08	2 km	5 km	7 km
6-Jun	2:19:14	2:19:14	2.3	2.3	2.4	0.05	2 km	2 km	2 km
8-Jun	4:56:56	4:56:56	2.5	2.8	2.7	0.12	9 km	2 km	10 km
23-Aug	7:13:17	7:13:17	2.5	3	2.8	0.21	6 km	2 km	4 km
25-Oct	21:43:42	21:43:42	2.3	2.5	2.5	0.09	10km	3 km	7 km
25-Nov	7:05:50	7:05:50	3.4	3.6	3.6	0.09	3 km	2 km	4 km

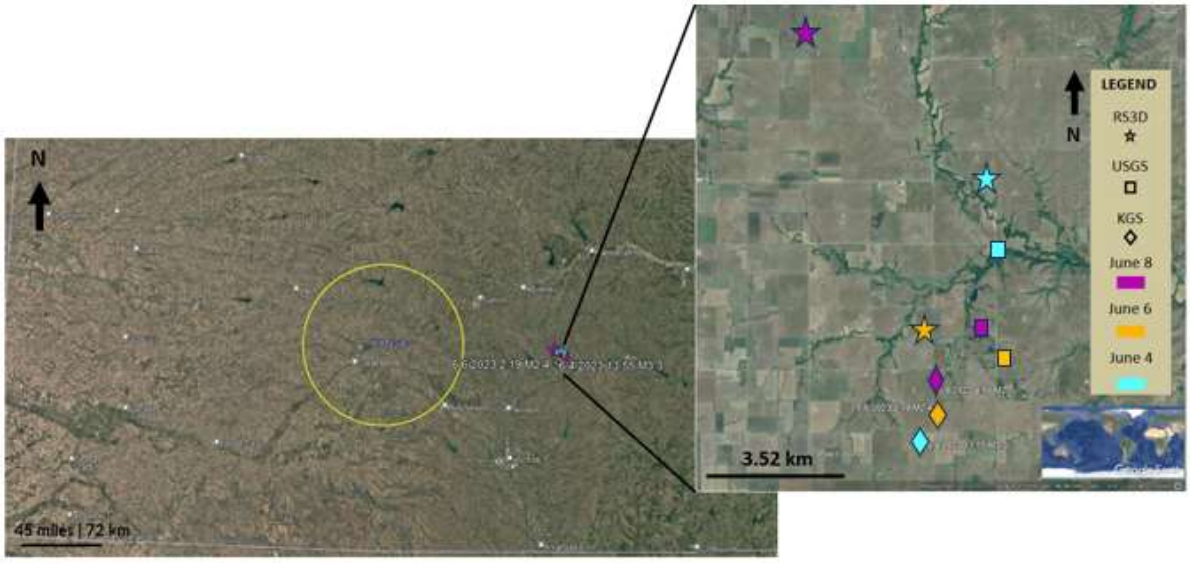


Figure 220 Map of three earthquakes recorded in June 2023 (see Table 32). The stars are the epicenters reported from the RS-3D network, the squares are reported from the USGS, and the diamonds are reported from the KGS. These epicenters are located near the town of Marion, Kansas.

Central Kansas Background Seismicity and RS-3D Monitoring

Historically, Kansas experienced relatively low seismicity. Figure 221 summarizes statewide seismic activity from 1867 to 2018. From 1867 to 1977, only approximately 30 felt earthquakes were reported. Between 1977 and 2012, a total of 197 earthquakes were recorded by the statewide network, with fifteen of those having a magnitude of M3 or larger (KGS Data 2024). The onset of widespread wastewater disposal activities in the south central and north central part of the state led to a significant increase in earthquakes from 2013 to 2023 (Figure 221). Very few earthquakes are reported in the central part of the state near Bushton, as shown in the region near the RS-3D stations (Figure 222), despite established wastewater disposal operations in the region. The lack of reported seismicity may be due to the lack of local monitoring networks. Figure 222 shows the location of seismic stations of the KGS and USGS networks that are 100's of Km from each other in central Kansas limiting a network's ability to report with confidence on small magnitude events. Using the RS-3D network this study compiled an earthquake catalog from May 17, 2023, through April 30, 2024, documenting 440 earthquakes across the state of Kansas (**Figure 223**). Each event was analyzed to determine its epicenter location and magnitude, with recorded magnitudes ranging from M_w0.7 to M_w4.2. During the same period, the KGS reported 228 earthquakes with magnitudes between M_w2.0 and M_w4.3. Meanwhile, the USGS reported 26 events, with magnitudes ranging from M_w1.4 to M_w4.0. **Error! Reference source not found.** shows the epicenters of each earthquake recorded and its reporting institution. There was a period of 19 days out of the total 333 days that all RS-3D network seismometers were down due to a winter storm. The freezing temperatures caused the power convertors from the deep cycle batteries to the seismometers to stop delivering power to the seismometers. The number of days without data equals 5.7% of the total monitoring period.

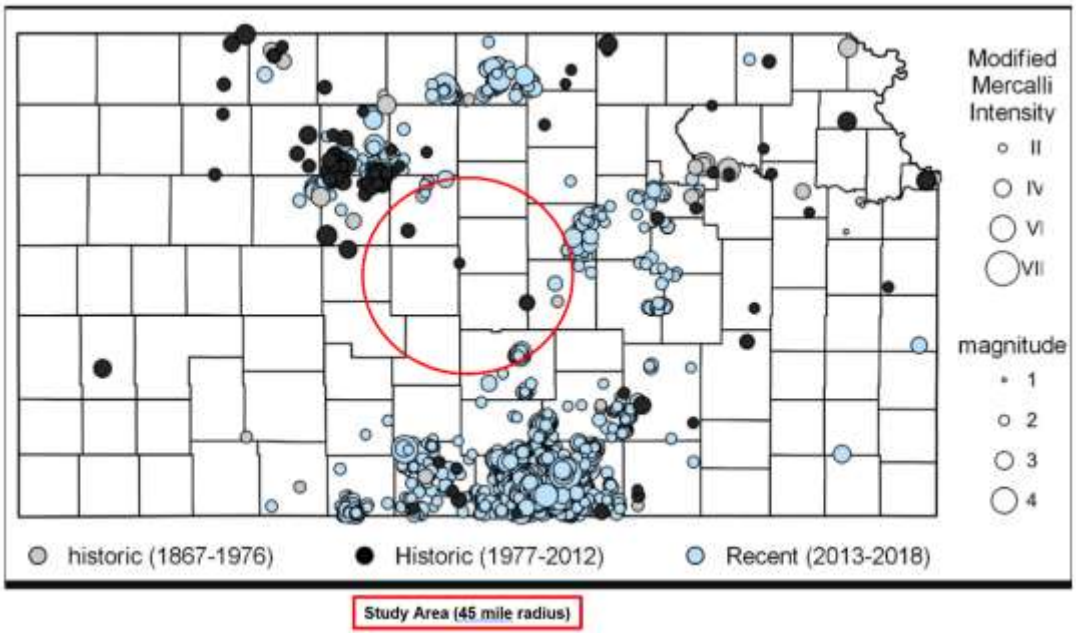


Figure 221 Summary figure of seismicity in Kansas between 1867 and 2018 (Kansas Geological Survey 2023). The red circle identifies the area of interest in central Kansas.

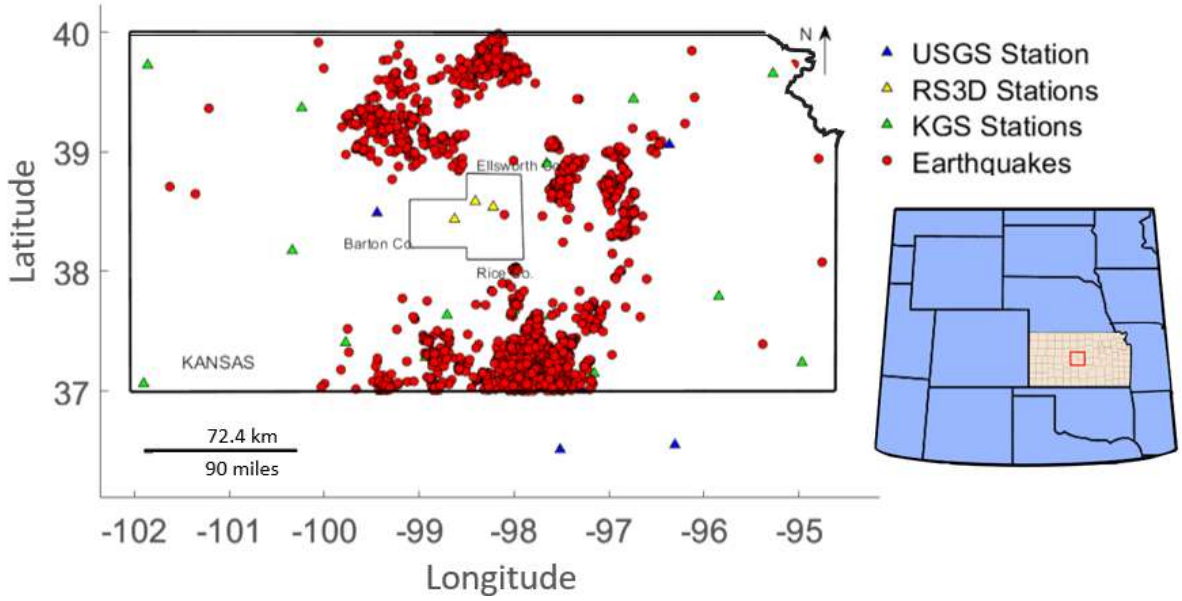


Figure 222 Seismicity map of Kansas showing the recorded earthquake locations (red circles) starting in 2013 through 2023 (Accessed from the Kansas Geological Survey Interactive Earthquake Map; https://maps.kgs.ku.edu/earthquakes/) and seismic station locations (triangles). The earthquakes typically occur in clusters located in south-central Kansas, and north-central Kansas. Occasionally, an earthquake will be recorded in central Kansas; however, the area is deemed as "seismically quiet." Central Kansas has had 3 earthquakes reported over the past 12 yr and 3 earthquakes reported prior to 2013.

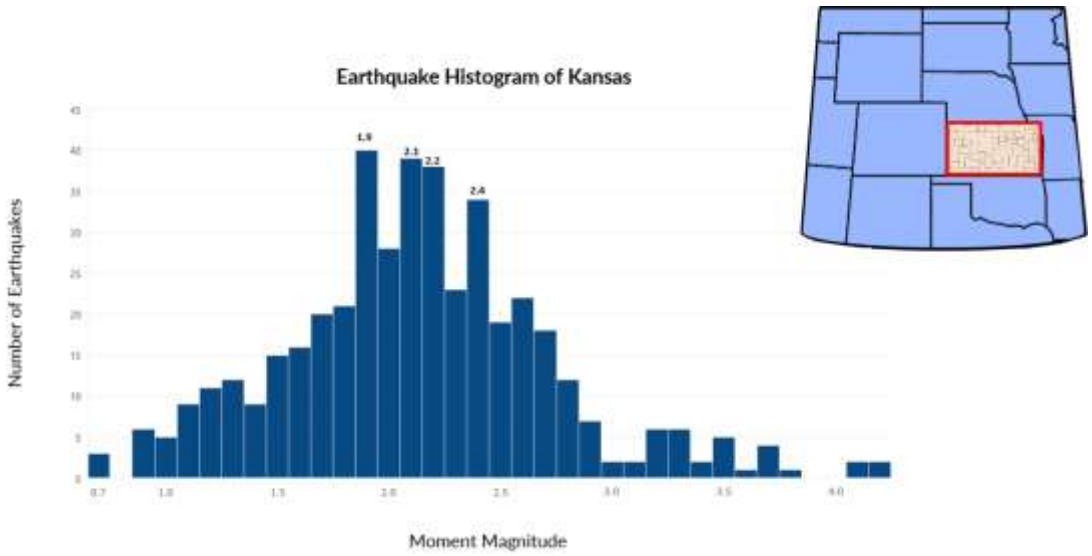


Figure 223 Histogram showing the number of earthquakes recorded by the RS-3D seismometers within the entire state of Kansas. The majority of earthquakes had magnitudes of M_w1.9 to M_w2.4 with the range of earthquakes detected occurring between M_w0.7 and M_w4.2.

3.5.5 – RS-3D Earthquake Catalogue of Central Kansas Seismic Activity

Earthquake monitoring in Kansas has historically shown that the central Kansas region is seismically quiet. However, central Kansas is located on the edge of the Central Kansas Uplift and the area has numerous faults (e.g. **Figure 219**). Knowing these conditions, the lack of earthquakes in the area may be due to a lack of local monitoring networks. In **Figure 224**, all earthquakes reported by the USGS and KGS are plotted in conjunction with the earthquakes detected from the RS-3D network. The locations of the RS-3D earthquake epicenters agree with the regional events reported by the USGS and the KGS while also filling in the central Kansas area that was once thought to be seismically quiet. Additionally, the epicenter locations within the study area have a higher confidence in time arrivals, magnitude calculations, and earthquake epicenter locations.

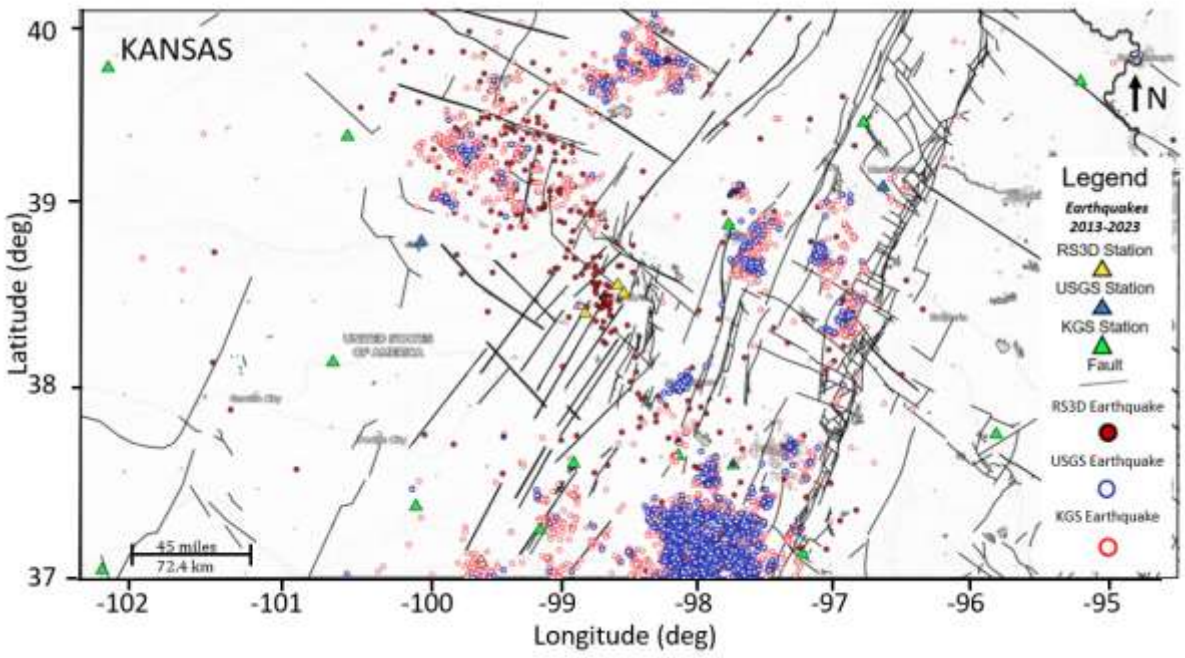


Figure 224 Map of all earthquakes reported by the USGS and KGS from 2013 to 2023, overlaid with RS-3D seismic events recorded during the study period. Central Kansas, previously interpreted as seismically quiet, shows significant low-magnitude activity based on RS-3.

Within the study area the RS-3D network recorded 140 earthquakes with magnitudes ranging from M_w0.7 to M_w3.4 (Figure 225 and Figure 226). In contrast, the KGS reported only 10 earthquakes within the study area, while the USGS did not report any seismic activity in the region during the study period. The RS-3D earthquake catalogue is available in Proffitt (2024, Appendix B).

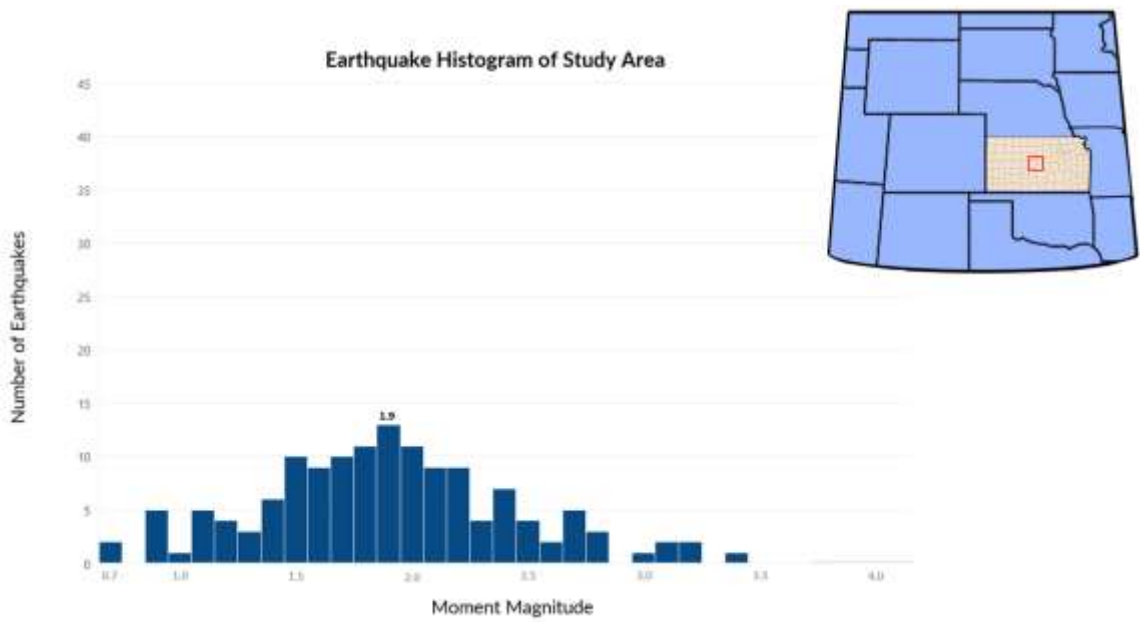


Figure 225 A histogram showing the earthquake magnitude distribution recorded by the RS-3D stations within the study area. The range of magnitudes recorded are M_w0.7 to M_w3.4 with most earthquake magnitudes occurring from M_w1.5 to M_w2.2.

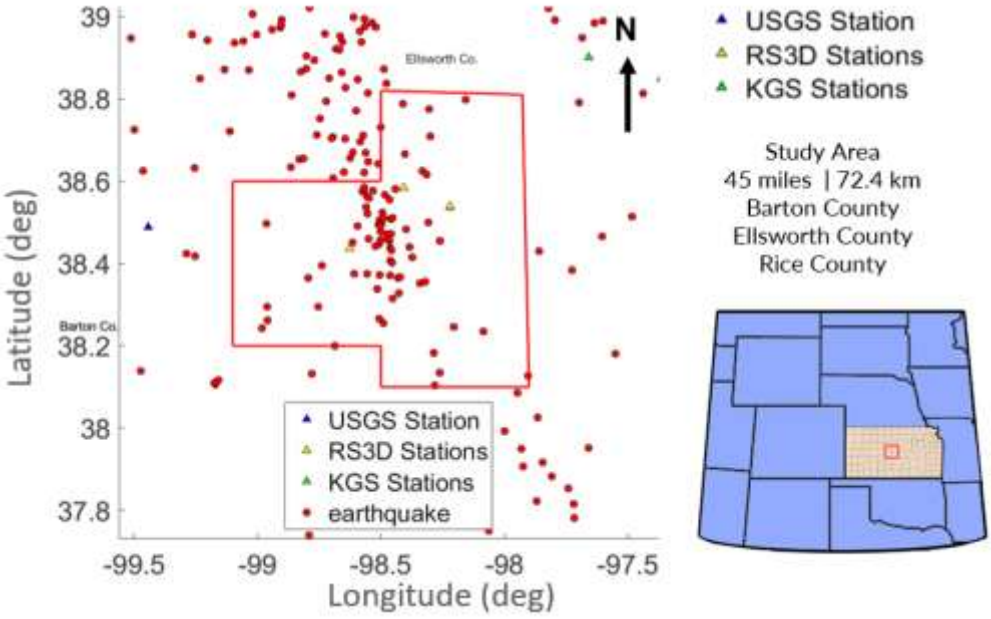


Figure 226 A map zoomed into the study area for the project and showing the 140 earthquakes located within the red study area boundaries

3.5.6 – Conclusions

This study demonstrated the viability of using low-cost RS-3D seismometers for local seismic monitoring, particularly in industrial settings requiring continuous monitoring, such as CO_2 sequestration and wastewater injection. Given the growing interest in CCS as a strategy to

mitigate climate change, efficient and affordable earthquake detection systems are essential to meet EPA guidelines for managing induced seismicity risks.

The research focused on two primary objectives, a) Developing low-cost seismic stations using RS-3D seismometers and readily available components (solar panels, wireless modems and antennas, GPS units, and 12V batteries) and evaluating their performance; and b) Assessing background seismicity in central Kansas, specifically around the ONEOK facility in Bushton, KS. This region has historically experienced low seismicity, making it an ideal case study for CO_2 sequestration projects.

Over 333 days of continuous data collection, 19 days of data were lost due to a winter storm on October 27th, which caused all stations to go offline simultaneously. Field investigations revealed that the $5.00 power converters had frozen during the storm. Use of more robust components will alleviate the issue. Despite this setback, the RS-3D stations reliably collected seismic data, detecting small-magnitude earthquakes while maintaining GPS timing and operating on solar power.

The RS-3D stations proved to be a cost-effective alternative to traditional broadband seismometers, which are significantly more expensive. At approximately $1,500 per unit, RS-3D seismometers offer substantial savings while delivering accurate real-time seismic data. The total cost of each seismic station was approximately $3,500. By integrating GPS timing and utilizing weather-resistant enclosures and solar panels, the stations achieved continuous operation with minimal maintenance. The research team processed and analyzed the collected earthquake data efficiently using open-source software such as SeisAn and ObsPy, validating the RS-3D's performance against data from USGS and KGS stations.

While minor discrepancies in magnitude and epicenter location were observed between the RS-3D and USGS/KGS stations, these differences were attributed to variations in network geometry and station placement. The uncertainty in earthquake magnitude and location increased with the distance from the RS-3D stations. Conversely, seismic events closer to the RS-3D stations were determined with higher confidence in both location and magnitude. This study demonstrated that RS-3D seismometers could detect seismic events with magnitudes as low as $M_w0.7$, meeting EPA requirements for CO_2 sequestration operations.

During the monitoring period the RS-3D network identified 140 local earthquakes with magnitudes ranging from $M_w1.5$ to $M_w2.2$. While these earthquakes are too small to be felt by humans and to be detected reliably by the distant KGS and USGS networks, the RS-3D local network confirmed the occurrence of low-level seismicity in central Kansas.

Task 4 – Dynamic Simulation

The PNNL participated in the CCUS Hub 2.0 Concept for ONEOK project, led by the KGS for the CUSP-West study, as a consultant and dynamic reservoir simulation provider. PNNL's scope on this project was to collaboratively work with the KGS to model the fate of CO_2 injected into selected target project reservoirs. These results were then passed to LANL for risk analyses with the NRAP tools. Reservoir modeling was completed with the PNNL developed STOMP-CO_2 and STOMPX-CO_2 reservoir simulators (White et al. 2012). KGS provided a series of static geologic models to PNNL, which included three storage reservoirs at two sites, near Bushton, Kansas and Medford, Oklahoma. Two storage reservoirs were considered at the Bushton site: 1)

Lansing Kansas City and 2) Arbuckle and one storage reservoir was considered at the Medford site: 1) Wilcox-Bromide. Whereas the STOMP-CO_2 and STOMPX-CO_2 simulators have modeling capabilities that include geochemistry and geomechanics, neither of these was exercised during this phase of the project. The static geologic models comprised a structured hexahedral computational mesh and data concerning the intrinsic permeability, porosity, initial pressure, initial salinity, and initial pressure at the centroids of each grid cell, in Petrel format.

Unique static geologic models were provided for each storage reservoir, and in the case of the Bushton, Arbuckle reservoir, two static geologic models were investigated: 1) Upper Arbuckle and Arbuckle Deep. These static geologic models, provided as ASCII formatted GRDECL files, were converted to STOMP input format and then combined with other required STOMP input, such as saturation functions, relative permeability functions, well models, initial conditions, boundary conditions, and output options to create a simulation model. These models were then executed with STOMPX-CO_2 (i.e. the MPI parallel implementation of STOMP-CO_2) on PNNL's supercomputer "constance," which has 520 compute nodes, each with 24 cores. Constance is being phased out, but when installed in November 2014, it was ranked 297th on the Top 500 supercomputer list. As the computational domains were modest in size computations were restricted to single nodes, using either 20 or 24 cores. This technical memo is designed to document the series of simulations executed to model the fate of CO_2 injected into the three reservoirs, located at two sites.

Subtask 4.1 – Evaluate Existing Oil Field Injection Pressures and Rates to Determine Suitability for Saline Storage Operations

Bushton, Kansas Site, Lansing Kansas City Reservoir

The static geologic model for the Bushton LKC Reservoir was provided to PNNL as a series of four data files, as shown in Table 33. Three scenarios were considered for this site/reservoir, that differed with respect to the fracture gradient (i.e. the allowable injection pressure), as shown in Table 33. Simulation times varied with the complexity of the simulation, with shorter times being associated with the scenarios where the injection well was pressure controlled, yielding injection rates less than specified, as shown in Table 33. The density range for pure CO_2 over the initial temperature and pressure range of the simulations is shown in Figure 227, as Lansing Kansas City.

Table 33 LKC completed simulations

Computational Domain	Depth Range	Areal Extent	Time Range
267 x 265 x 28 (5.9 million unknowns)	2,909 to 3,088 ft bgs	37,010 ft x 36,965 ft	0 to 51 yr
Static Geologic Model Data Files			
KC2_Model_ASCII_072523_UpdatedPressures_3_ACTNUM.GRDECL			
KC2_Model_ASCII_072523_UpdatedPressures_3_COORD.GRDECL			

KC2_Model_ASCII_072523_UpdatedPressures_3.GRDECL			
KC2_Model_ASCII_072523_UpdatedPressures_3_ZCORN.GRDECL			
Scenario	**Fracture Gradient**	**Top of Well Pressure Limit**	**Number of Time Steps (Simulation Time, hr:min)**
LKC-S1	0.6 psi/ft	1,740 psi	377 (7:44)*
LKC-S2	0.7 psi/ft	2,030 psi	344 (8:13)*
LKC-S2	0.95 psi/ft	2,750 psi	674 (13:18)*

* default PETSc PC and KSP.

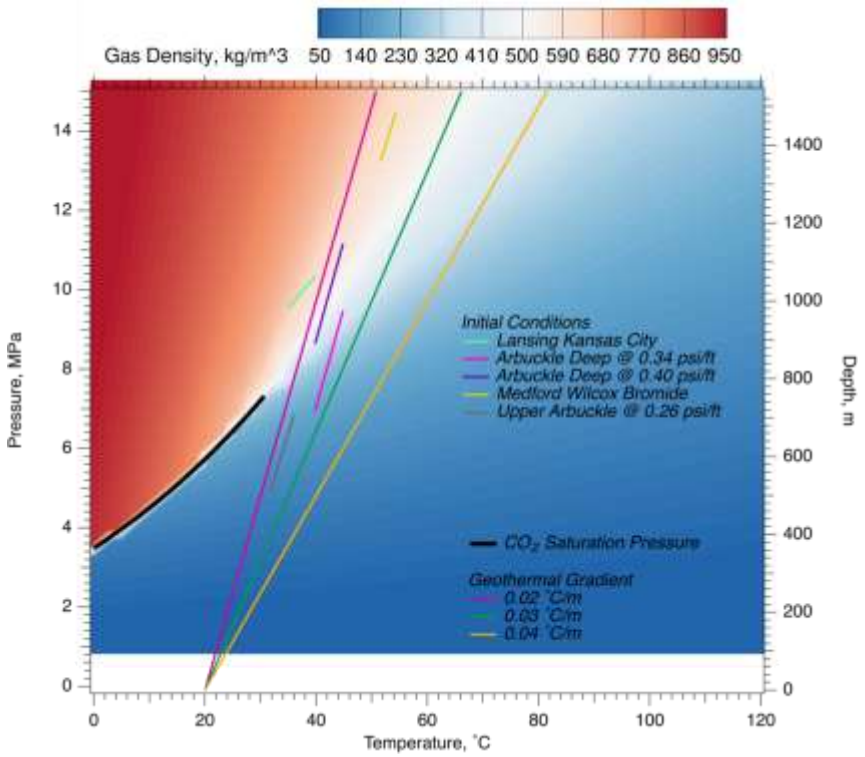


Figure 227 Pure CO_2 density over the initial temperature and pressure range of the simulations

Saturation Function

Saturation functions relate capillary pressure (i.e. the difference between gas and aqueous pressure) to aqueous saturation. As parameters for this function were not included in the data package a representative saturation function was used, based on the Brooks and Corey (1964) function with the Webb (2000) extension and hysteretic nonwetting fluid entrapment (**Figure 228**).

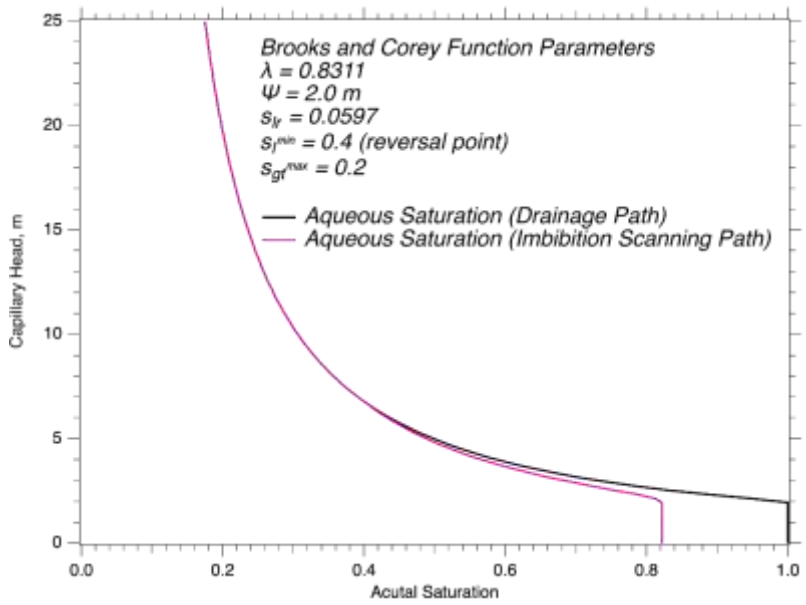


Figure 228 Saturation function, based on the Brooks and Corey Model with Webb extension and hysteretic gas entrapment, showing drainage and imbibition scanning paths for a reversal saturation of 0.4

Aqueous Relative Permeability Function

Aqueous relative permeability functions relate the relative permeability of the aqueous phase to aqueous saturation. As parameters for this function were not included in the data package a representative saturation function was used, based on Burdine (1953) function (Figure 229).

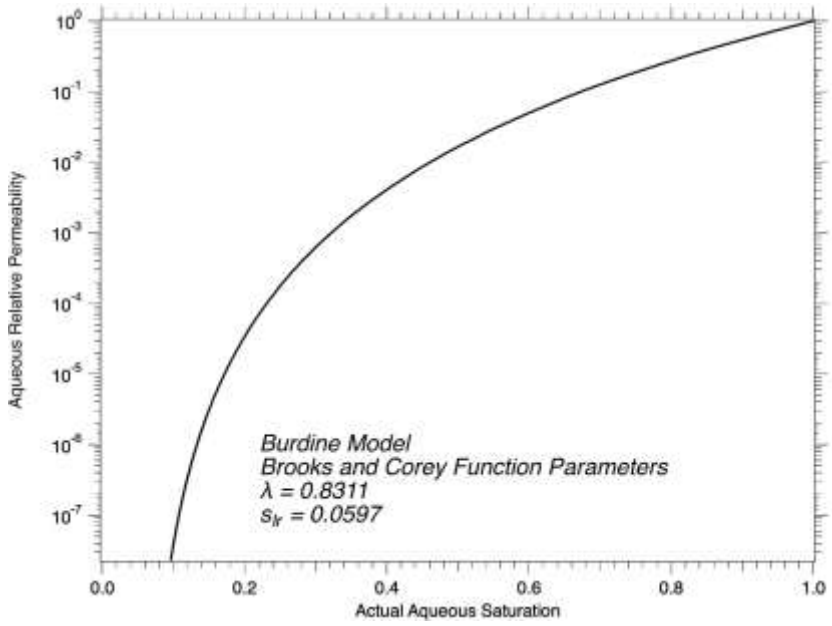


Figure 229 Aqueous relative permeability function based on the coupled Burdine and Brooks and Corey models

Gas Relative Permeability Function

Gas relative permeability functions relate the relative permeability of the gas phase to aqueous saturation. As parameters for this function were not included in the data package a representative saturation function was used, based on Burdine (1953) function, as shown in Figure 230.

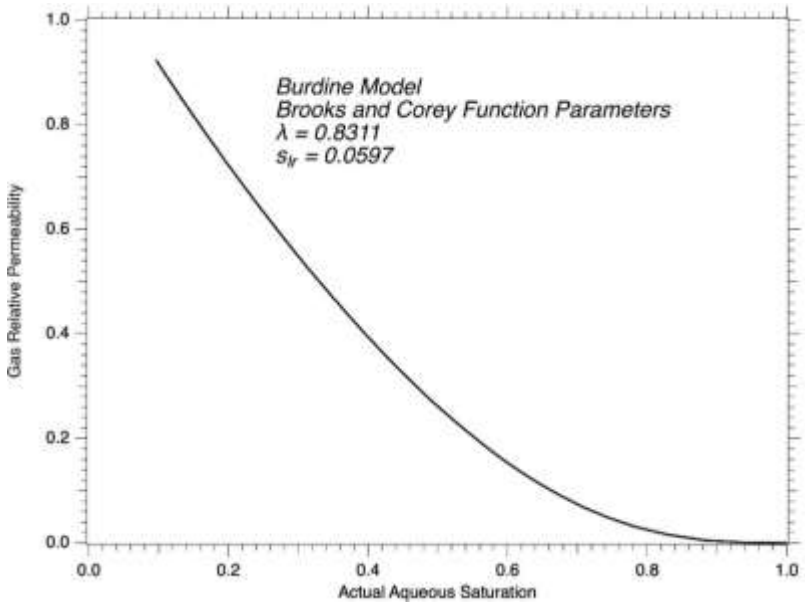


Figure 230 Gas relative permeability function based on the coupled Burdine and Brooks and Corey models

Wells

A single CO_2 injection well was modeled with the parameters shown in Table 34. Injected CO_2 was specified as dry (i.e. no water). Note the well was placed in the southeastern corner of the model in order to 1) decrease the likelihood of interference with oil and gas producing wells located in other regions of the model area, and 2) utilize a high porosity/permeability reservoir trend in the static model.

Table 34 LKC well parameters

Scenario	Well Type	Top Coordinates	Bottom Coordinates	Time Range	Injection Rate	Pressure Limit (top)	Skin Factor	Borehole Radius
LKC-S1	Class VI	2,036,408 ft 664,012 ft 2,910 ft	2,036,408 ft 664,012 ft 3,088 ft	1 to 31 yr	0.35 MMT/yr	1,740 psi	0.0	10.16 cm
LKC-S2	Class VI	2,036,408 ft 664,012 ft 2,910 ft	2,036,408 ft 664,012 ft 3,088 ft	1 to 31 yr	0.35 MMT/yr	2,030 psi	0.0	10.16 cm
LKC-S3	Class VI	2,036,408 ft 664,012 ft 2,910 ft	2,036,408 ft 664,012 ft 3,088 ft	1 to 31 yr	0.35 MMT/yr	2,750 psi	0.0	10.16 cm

Initial Conditions

The initial pressure and temperature were specified to vary laterally across the domain per the data in the static geologic model data files (Table 33). These specifications were imposed at a depth of 3,088.06 ft. From that point the computational domain was initialized as being saturated with water under hydrostatic conditions with a temperature gradient of 0.0392°F/m. Zero salinity was specified.

Boundary Conditions

Boundary conditions were specified for the six boundary surfaces of the computational domain, as shown in Table 35.

Table 35 LKC boundary condition specifications

Bottom	Top	West	East	South	North
Zero Flux	Zero Flux	Equilibrium with Initial State	Equilibrium with Initial State	Equilibrium with Initial State	Equilibrium with Initial State

Simulation Results

Simulation results were recorded in a series of binary formatted files. The output.bin file contains a record user specified reference variables (Table 36) at each time step, and the plot_xxxxxxx.bin files contain a record of user specified plot variables (Table 36) at specified points in time (Table 36). Binary formatted files were converted to ASCII formatted files. The output.bin file was converted to output, and the plot_xxxxxxx.bin files were converted to contours_xxxyr.dat files. The implications of these simulation results will be discussed in Section 4.2.

Table 36 LKC output variables

Reference Variables		Plot Variables	
Temperature, ˚F	Gas Density, kg/m^3	Temperature, ˚F	CO_2 Aqueous Concentration, gm/cm^3
Gas Saturation	Aqueous Density, kg/m^3	Rock/Soil Type	Salt Aqueous Mass Fraction
Trapped Gas Saturation	Gas Pressure, psia	Diffusive Porosity	CO_2 Aqueous Mass Fraction
Integrated CO_2 Mass, kg	Aqueous Pressure, psia	X-Intrinsic Permeability, mD	Gas Pressure, psia
Integrated CO_2 Aqueous Mass, kg	Diffusive Porosity	Z-Intrinsic Permeability, mD	Aqueous Pressure, psia
Integrated CO_2 Gas Mass, kg	Coupled-Well Press, 1, psia	Gas Saturation	Gas Density, kg/m^3
Integrated CO_2 Trapped-Gas Mass, kg	Coupled-Well CO_2 Mass Rate, 1, kg/s	Trapped Gas Saturation	Aqueous Density, kg/m^3
Salt Aqueous Mass Fraction	Coupled-Well CO_2 Mass Integral, 1, kg	Plot Times	
CO_2 Aqueous Mass Fraction		0.0 yr, 5 at 0.1 yr, 50 at 1.0 yr	

The output file was used to generate plots of integrated CO_2 mass, well pressure, and well injection rate versus time (Figure 231 and Figure 232). The contours_xxxyr.dat files were used to create color contours of gas saturation at the specified plot times (Figure 233 and **Figure 234**). Slices of the contours_xxxyr.dat files were created across the top tier of the domain at the specified plot times and stored in a series of zslice_x.xx.dat files and transferred to LANL for use with the NRAP tools.

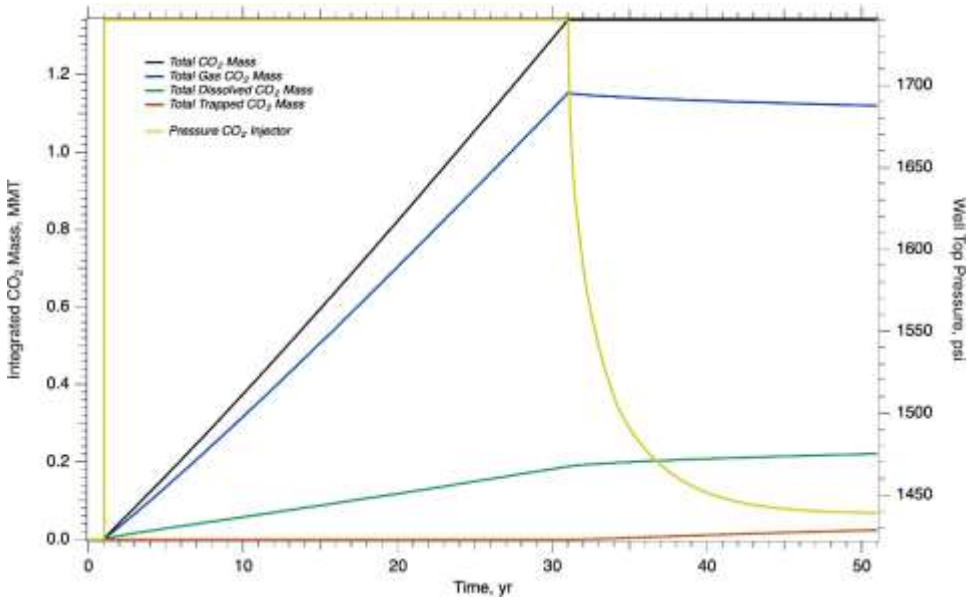


Figure 231 LKC-S1 integrated CO_2 mass and well pressure history

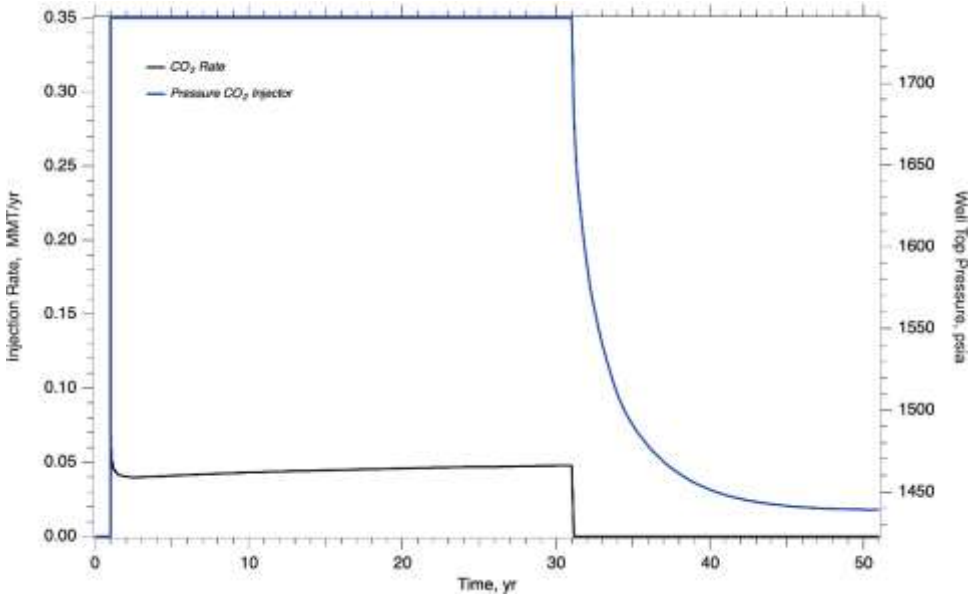


Figure 232 LKC-S1 injection rate and well pressure history

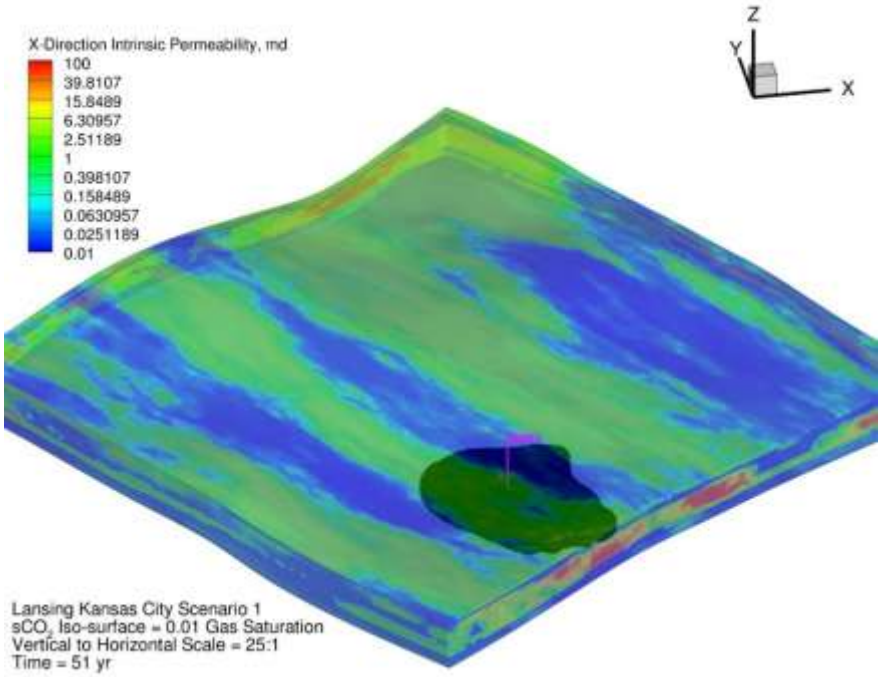


Figure 233 LKC-S1 iso-surface of gas saturation within color-scaled permeability field at 51 yr, oblique view

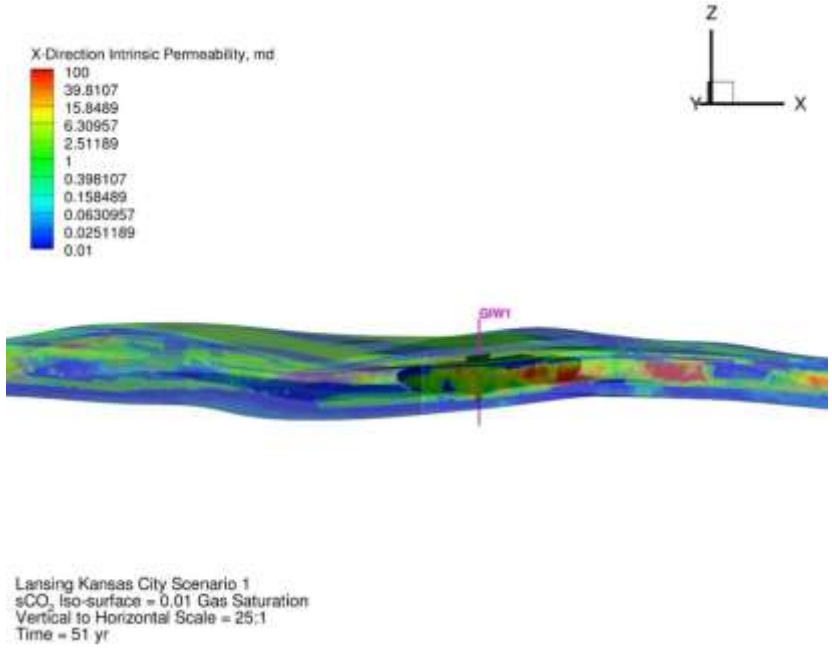


Figure 234 LKC-S1 iso-surface of gas saturation within color-scaled permeability field at 51 yr, section view

Bushton, Kansas Site, Upper Arbuckle Reservoir

The static geologic model for the Bushton, Kansas Site, Upper Arbuckle Reservoir (UA) was provided to PNNL as a series of four data files, as shown in Table 37. Seven preliminary scenarios were modeled that were directed at establishing the permeability of the reservoir, using the five Class 1 injector wells as a benchmark. These wells were injecting at a known rate under

hydrostatic conditions from the ground surface. The scenarios labeled cropped used trajectories for these wells that were restricted in depth to remain above the lower permeability layer in the static geology model, and those labeled actuals used the actual trajectories, which extended below the low permeability layer for some wells. These simulations, which were executed for 10 yr, established that a permeability scaling factor of 5.0 was required to achieve the injection rates for the five Class 1 injectors under hydrostatic pressure conditions. This permeability field was then used in a final simulation scenario with the five Class 1 injectors and a single Class VI (CO_2 injector) injector well. Simulation times varied with the complexity of the simulation, with shorter times being associated with the scenarios where the injection well was pressure controlled, yielding injection rates less than specified, as shown in Table 37. The density range for pure CO_2 over the initial temperature and pressure range of the simulations is shown in Figure 227, as Upper Arbuckle @ 0.26 psi/ft.

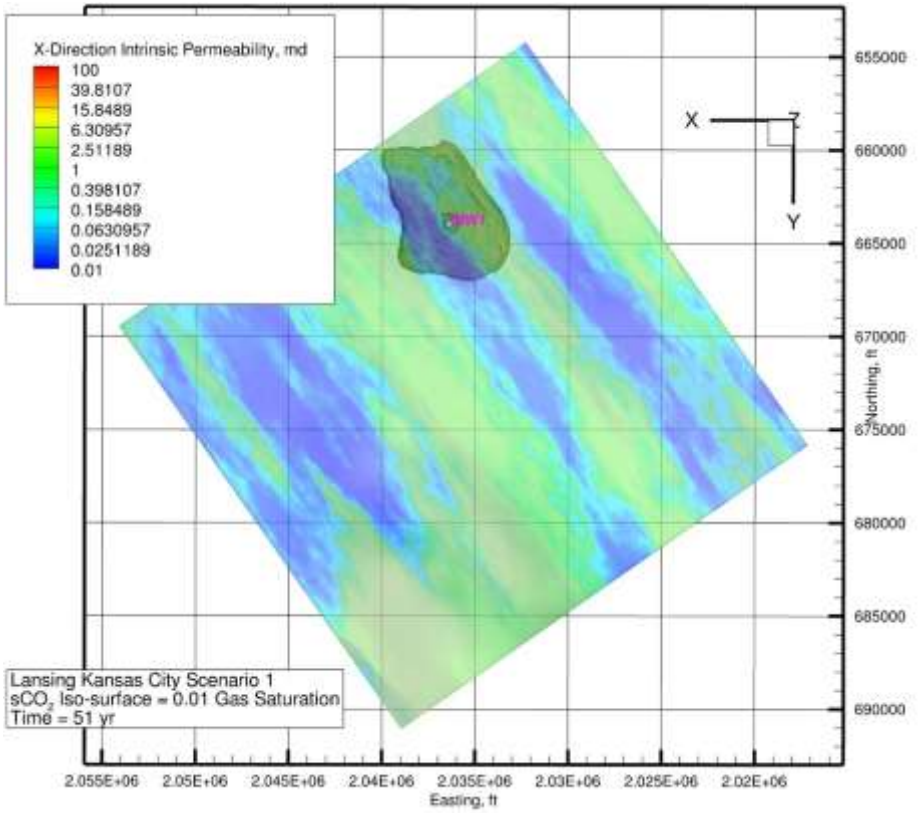


Figure 235 LKC-S1 iso-surface of gas saturation within color-scaled permeability field at 51 yr, areal view

Table 37 UA completed simulations

Computational Domain	Depth Range	Areal Extent	Time Range
267 x 265 x 47 (10.0 million unknowns)	3,069 to 3,841 ft bgs	37,010 ft x 36,965 ft	0 to 10 yr 0 to 50 yr
Static Geologic Model Data Files			

Upper_Arbuckle_Model_GlobalCoordinates_ACTNUM.GRDECL			
Upper_Arbuckle_Model_GlobalCoordinates_COORD.GRDECL			
Upper_Arbuckle_Model_GlobalCoordinates.GRDECL			
Upper_Arbuckle_Model_GlobalCoordinates_ZCORN.GRDECL			
Scenario	**Wells**	**Characteristics**	**Number of Time Steps (Simulation Time, hr:min)**
UA-S1	Class 1 (cropped)	Hetero. Temperature 1.0 x Permeability	112 (3:17)*
UA-S2	Class 1 (actuals)	Hetero. Temperature 1.0 x Permeability	112 (3:20)*
UA-S3	Class 1 (cropped)	Uniform Temperature 1.0 x Perm	112 (3:15)*
UA-S4	Class 1 (actuals)	Uniform Temperature 1.0 x Perm	112 (3:13)*
UA-S5	Class 1 (cropped)	Uniform Temperature 1.5 x Perm	112 (4:37)*
UA-S6	Class 1 (actuals)	Uniform Temperature 1.5 x Perm	112 (4:03)*
UA-S7	Class 1 (cropped)	Uniform Temperature 5.0 x Perm	112 (5:04)*
UA-S8	Class 1 (actuals)	Uniform Temperature 5.0 x Perm	112 (4:44)*
UA-S10	Class 1 and Class 6 (cropped)	Uniform Temperature 5.0 x Perm	4,124 (162:42)*

* default PETSc PC and KSP.

Saturation Function

Saturation functions relate capillary pressure (i.e. the difference between gas and aqueous pressure) to aqueous saturation. As parameters for this function were not included in the data package a representative saturation function was used, based on the Brooks and Corey (1964) function with the Webb (2000) extension and hysteretic nonwetting fluid entrapment, as shown in Figure 236.

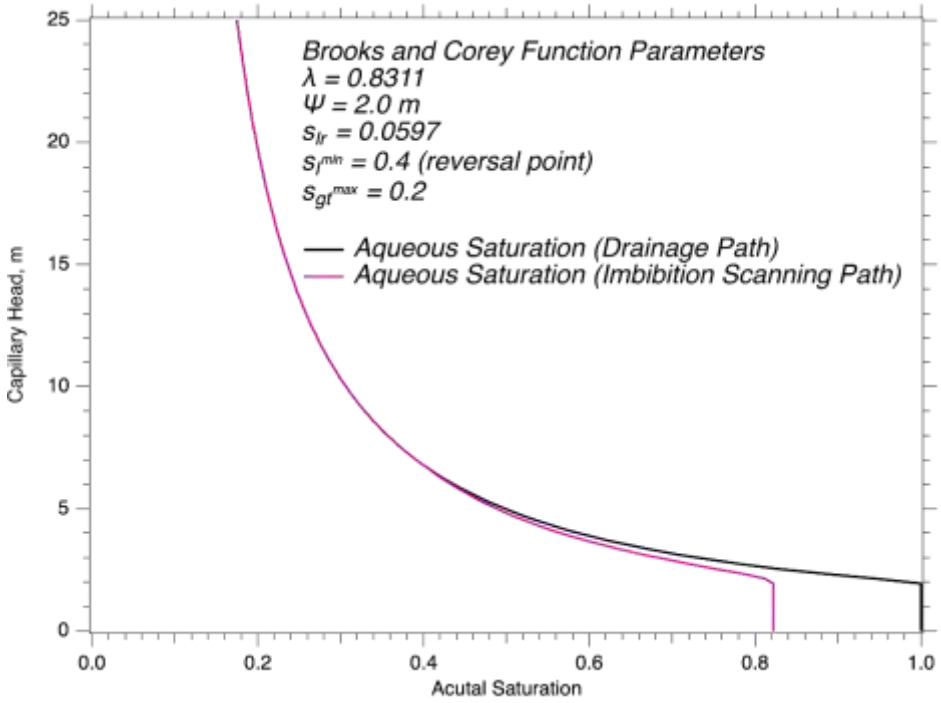


Figure 236 Saturation function, based on the Brooks and Corey Model with Webb extension and hysteretic gas entrapment, showing drainage and imbibition scanning paths for a reversal saturation of 0.4

Aqueous Relative Permeability Function

Aqueous relative permeability functions relate the relative permeability of the aqueous phase to aqueous saturation. As parameters for this function were not included in the data package a representative saturation function was used, based on Burdine (1953) function, as shown in Figure 237.

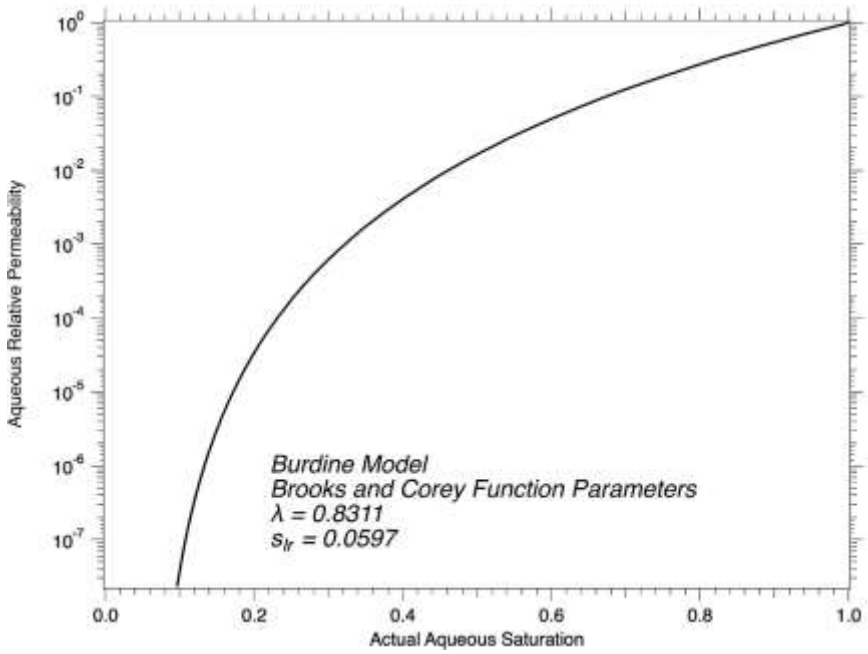


Figure 237 Aqueous relative permeability function based on the coupled Burdine and Brooks and Corey models

Gas Relative Permeability Function

Gas relative permeability functions relate the relative permeability of the gas phase to aqueous saturation. As parameters for this function were not included in the data package a representative saturation function was used, based on Burdine (1953) function, as shown in Figure 238.

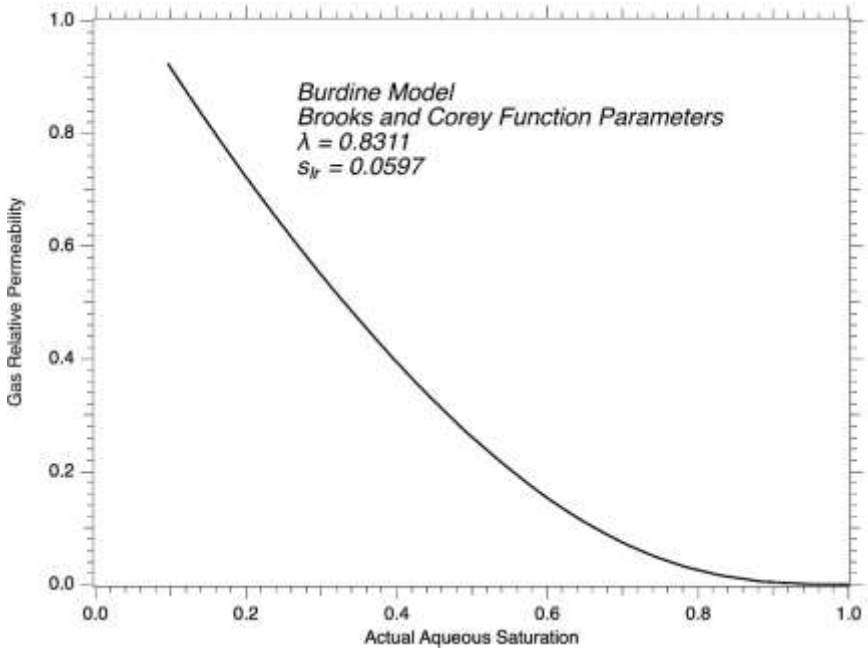


Figure 238 Gas relative permeability function based on the coupled Burdine and Brooks and Corey models

Wells

There is a total of five Class 1 wastewater injector wells at the UA reservoir, but since the well trajectories for the ONEOK #003 and #006 were sufficiently close to one another, they were modeled as a single well with a combined injection rate. CO_2 was injected as dry-CO_2 via a single injector and the water was injected as pure water without dissolved solids. Specifications for the Class 1 and 6 wells are shown in Table 38, where (c) refers to cropped and (a) refers to actual.

Table 38 UA well parameters

Well Name	Well Type	Top Coordinates	Bottom Coordinates	Time Range	Injection Rate	Pressure Limit (top)	Skin Factor	Borehole Radius
ONEOK_#003_#006	Class I	2,042,591 ft 677,309 ft 3,200 ft (c) 3,326 ft (a)	2,042,591 ft 677,309 ft 3,450 ft (c) 3,670 ft (a)	0 to 50 yr	11.587 kg/s	1,388 psi	0.0	10.16 cm
NNGC_#0001_RC	Class I	2,042,137 ft 675,226 ft 3,200 ft (c) 3,310 ft (a)	2,042,137 ft 675,226 ft 3,450 ft (c) 3,400 ft (a)	0 to 50 yr	0.1619 kg/s	1,388 psi	0.0	10.16 cm
ONEOK_#004	Class I	2,042,518 ft 679,386 ft 3,200 ft (c) 3,316 ft (a)	2,042,518 ft 679,386 ft 3,450 ft (c) 3,745 ft (a)	0 to 50 yr	1.772 kg/s	1,388 psi	0.0	10.16 cm
ONEOK_#005	Class I	2,042,519 ft 677,681 ft 3,200 ft (c) 3,327 ft (a)	2,042,519 ft 677,681 ft 3,450 ft (c) 3,630 ft (a)	0 to 50 yr	9.2229 kg/s	1,388 psi	0.0	10.16 cm
CO2_#001	Class VI	2,034,868 ft 665,251 ft 3,200 ft	2,034,868 ft 665,251 ft 3,450 ft	10 to 40 yr	0.35 MMT/yr	2,080 psi	0.0	10.16 cm

Initial Conditions

The initial pressure and temperature, derived from Bushton fall-off test data provided by ONEOK, were specified to vary vertically with a temperature of 97˚F (36.1˚C) and pressure of 1,000 psi (6.89 MPa) imposed at a depth of 3,782.97 ft (1,153 m) bgs. From that point the computational domain was initialized as being saturated with water under hydrostatic conditions with a temperature gradient of 0.0392°F/m. Zero salinity was specified.

Boundary Conditions

Boundary conditions were specified for the six boundary surfaces of the computational domain, as shown in Table 39.

Table 39 UA boundary condition specifications

Bottom	Top	West	East	South	North
Zero Flux	Zero Flux	Equilibrium with Initial State	Equilibrium with Initial State	Equilibrium with Initial State	Equilibrium with Initial State

Simulation Results

The simulation was executed to the 15-yr point and then halted due to the large size of the free gas plume. Simulation results were recorded in a series of binary formatted files. The output.bin file contains a record user specified reference variables (Table 40) at each time step, and the plot_xxxxxxx.bin files contain a record of user specified plot variables (Table 40) at specified points in time (Table 40). Binary formatted files were converted to ASCII formatted files. The output.bin file was converted to output, and the plot_xxxxxxx.bin files were converted to contours_xxxyr.dat files. The output file was used to generate plots of well injection rate and well pressure (top of screened interval) versus time (**Figure 239** and **Figure 240**). The contours_xxxyr.dat files were used to create color contours of water and free gas plumes and free gas density at the specified plot times. Plots at 15 yr are shown in **Figure 241** and **Figure 242**. The implications of these simulation results will be discussed in Section 4.2.

Table 40 UA output variables

Reference Variables		Plot Variables	
Temperature, ˚F	NNGC_1, Water Mass Integral, kg	XNC Aqueous Volumetric Flux, m/s,	X-Intrinsic Permeability, mD
Aqueous Density, kg/m^3	ONEOK-4 Pressure, psia	YNC Aqueous Volumetric Flux, m/s	Z-Intrinsic Permeability, mD
Gas Pressure, psia	ONEOK-4, Water Mass Rate, kg/s	ZNC Aqueous Volumetric Flux, m/s	CO_2 Aqueous Mass Fraction
Aqueous Pressure, psia	ONEOK-4, Water Mass Integral, kg	Temperature, ˚F	Aqueous Pressure, psia
Diffusive Porosity	ONEOK-5 Pressure, psia	Diffusive Porosity	Aqueous Density, kg/m^3
ONEOK-3/6 Pressure, psia	ONEOK-5, Water Mass Rate, kg/s	Plot Times	
ONEOK-3/6, Water Mass Rate, kg/s	ONEOK-5, Water Mass Integral, kg	0.0 yr, 20 at 0.5 yr	
ONEOK-3/6, Water Mass Integral, kg	CO_2 Injector, Pressure, psia		
NNGC-1, Pressure, psia	CO_2 Injector, CO_2 Mass Rate, kg/s		

NNGC-1, Water Mass Rate, kg/s	CO_2 Injector, CO_2 Mass Integral, kg

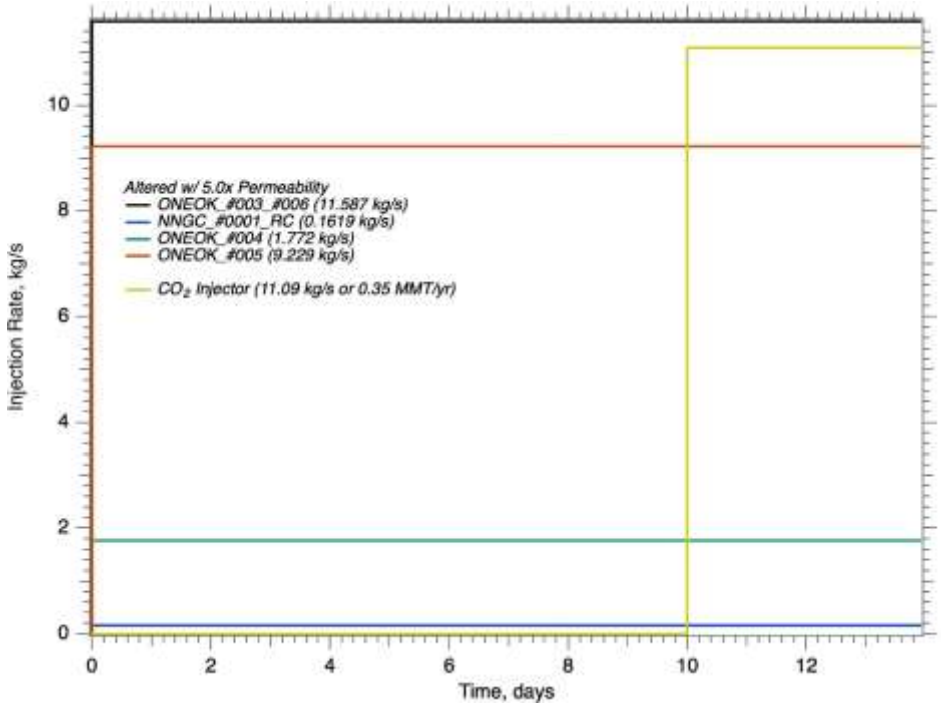


Figure 239 UA well mass injection rate history

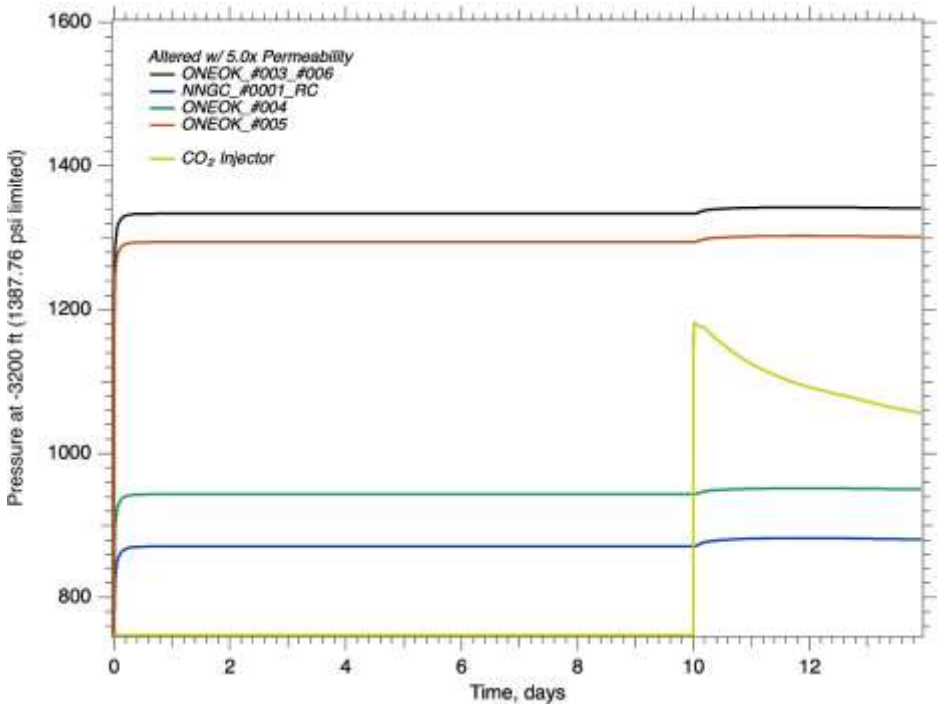


Figure 240 UA well pressure history

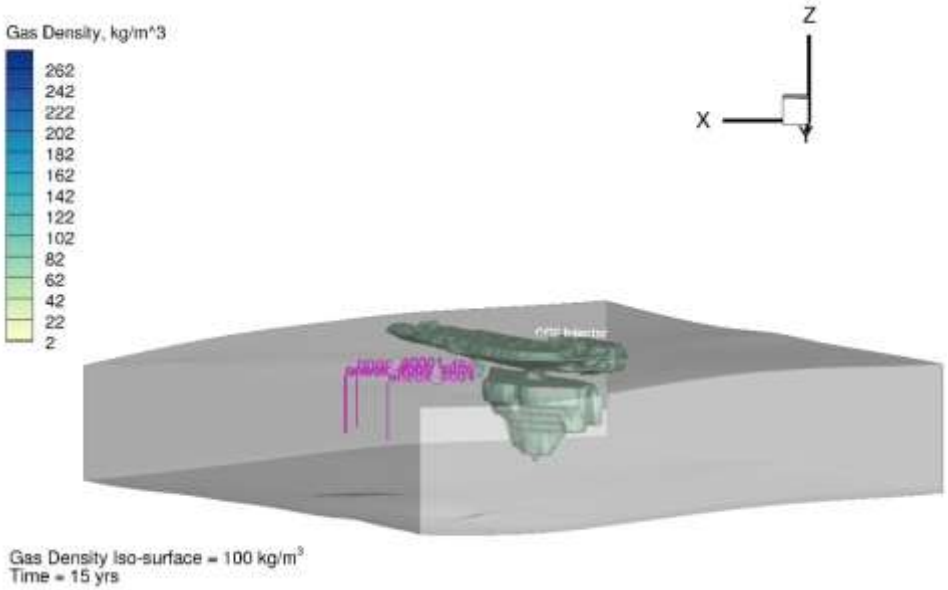


Figure 241 UA-S10 water and free gas plumes at 15 yr (iso-surfaces of CO_2 mass fraction)

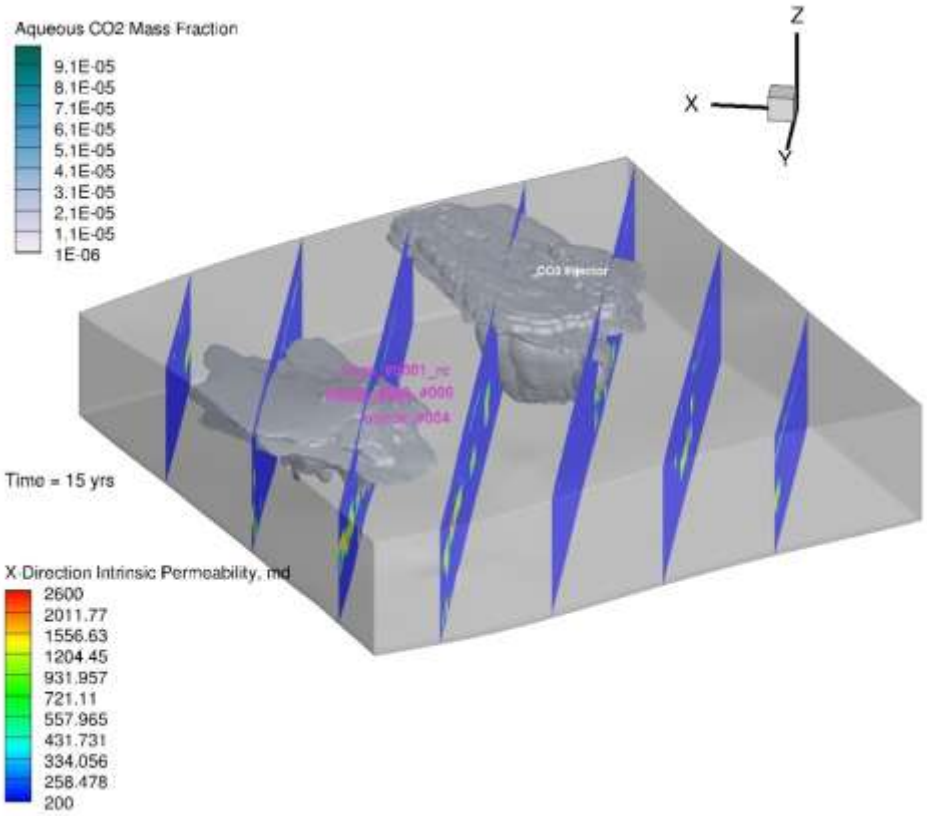


Figure 242 UA-S10 free gas density at 15 yr (iso-surface at 100 kg/m3)

Bushton, Kansas Site, Arbuckle Deep Reservoir

The static geologic model for the Bushton, Kansas Site, Arbuckle Deep (AD) was provided to PNNL as a series of four data files, as shown in Table 41. Ten scenarios were considered for this site/reservoir, that differed with respect the initial fluid pressure gradient, total dissolved solids (TDS) concentrations, well location, and simulation period, as shown in Table 41. Simulation times varied with the complexity of the simulation, with longer simulation times being associated with increased plume interference and lower free gas density, as shown in Table 41, where the number in the scenario name refers to the well location (i.e. 1, 2, or 3). The density range for pure CO_2 over the initial temperature and pressure range of the simulations is shown in Figure 227, as either Arbuckle Deep @ 0.34 psi/ft or Arbuckle Deep @ 0.40 psi/ft.

Table 41 AD completed simulations

Computational Domain	Depth Range	Areal Extent	Time Range
107 x 105 x 133 (4.5 million unknowns)	3,152 to 4,136 ft bgs	37,720 ft x 36,703 ft	0 to 50 yr or 0 to 100 yr
Static Geologic Model Data Files			
Arbuckle_Deep_V3_ACTNUM.GRDECL			
Arbuckle_Deep_V3_COORD.GRDECL			
Arbuckle_Deep_V3.GRDECL			
Arbuckle_Deep_V3_ZCORN.GRDECL			

Scenario	TDS	Fluid Pressure Gradient	Simulation Period	Number of Time Steps (Simulation Time, hr:min)
AD-S1A	0 ppm	0.34 psi/ft	50 yr	1,167 (73:44)*
AD-S1B	500 ppm	0.40 psi/ft	50 yr	1,960 (28:16)
AD-S1C	220,000 ppm	0.40 psi/ft	50 yr	7,824 (93:46)
AD-S1E	220,000 ppm	0.40 psi/ft	100 yr	15,242 (177:38)
AD-S2A	0 ppm	0.34 psi/ft	50 yr	1,617 (86:59)*
AD-S2B	500 ppm	0.40 psi/ft	50 yr	2,070 (30:13)
AD-S2B	220,000 ppm	0.40 psi/ft	50 yr	6,175 (81:19)
AD-S3A	0 ppm	0.34 psi/ft	50 yr	1,515 (72:01)*
AD-S3B	500 ppm	0.40 psi/ft	50 yr	2,997 (40:22)
AD-S3C	220,000 ppm	0.40 psi/ft	50 yr	10,802 (137:16)

* default PETSc PC and KSP.

Saturation Function

Saturation functions relate capillary pressure (i.e. the difference between gas and aqueous pressure) to aqueous saturation. As parameters for this function were not included in the data package a representative saturation function was used, based on the Brooks and Corey (1964) function with the Webb (2000) extension and hysteretic nonwetting fluid entrapment, as shown in **Figure 228**.

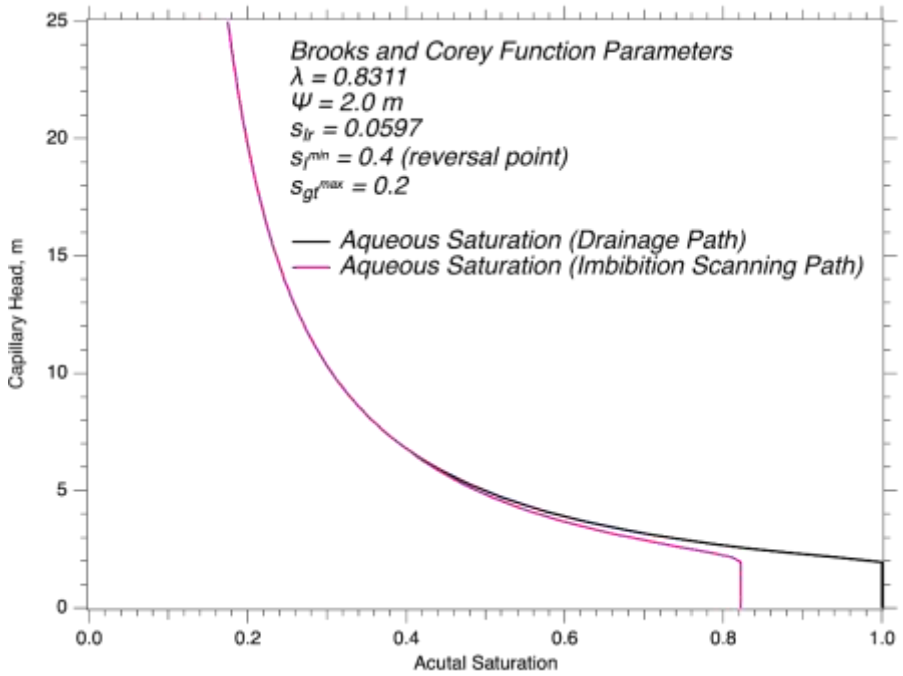


Figure 243 Saturation function, based on the Brooks and Corey Model with Webb extension and hysteretic gas entrapment, showing drainage and imbibition scanning paths for a reversal saturation of 0.4

Aqueous Relative Permeability Function

Aqueous relative permeability functions relate the relative permeability of the aqueous phase to aqueous saturation. As parameters for this function were not included in the data package a representative saturation function was used, based on Burdine (1953) function, as shown in **Figure 229**.

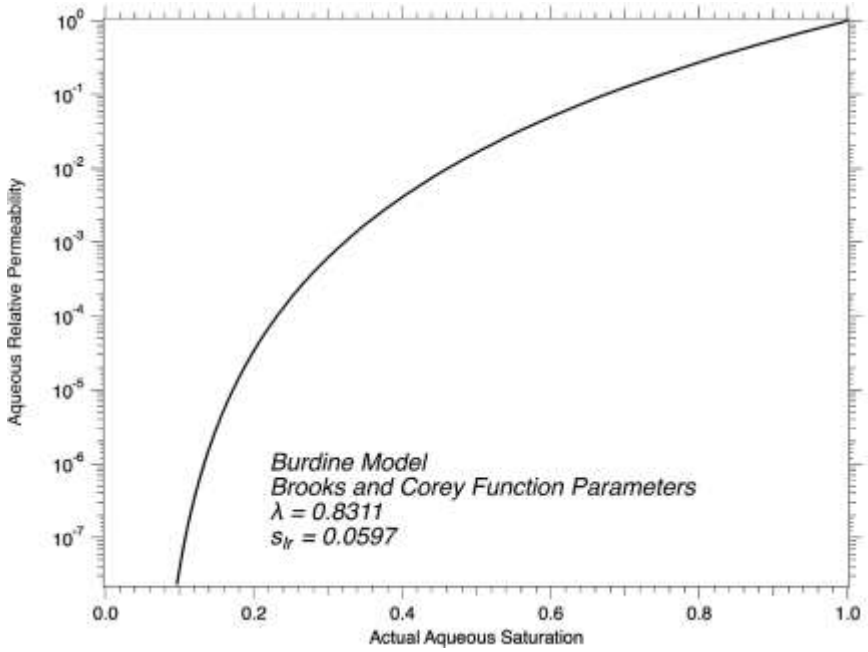


Figure 244 Aqueous relative permeability function based on the coupled Burdine and Brooks and Corey models

Gas Relative Permeability Function

Gas relative permeability functions relate the relative permeability of the gas phase to aqueous saturation. As parameters for this function were not included in the data package a representative saturation function was used, based on Burdine (1953) function, as shown in **Figure 245**.

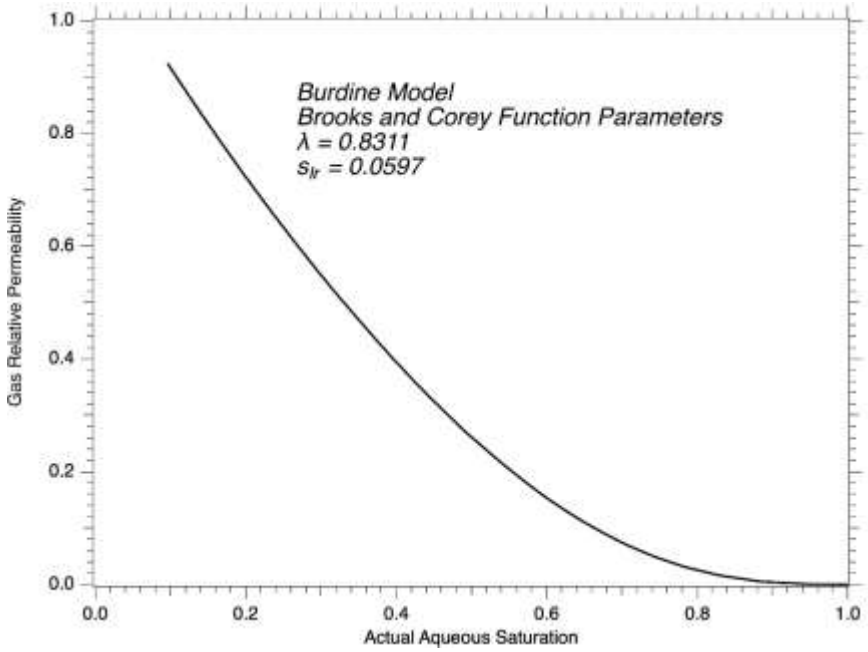


Figure 245 Gas relative permeability function based on the coupled Burdine and Brooks and Corey models

Wells

There is a total of five Class 1 wastewater injector wells at the UA reservoir, but since the well trajectories for the ONEOK #003 and #006 were sufficiently close to one another, they were modeled as a single well with a combined injection rate. CO_2 was injected as dry-CO_2 via a single injector and the water was injected as pure water without dissolved solids. Specifications for the Class 1 and 6 wells are shown in Table 38, where (c) refers to cropped and (a) refers to actual.

Table 42 AD well parameters

Well Name	Well Type	Top Coordinates	Bottom Coordinates	Time Range	Injection Rate	Pressure Limit (top)	Skin Factor	Borehole Radius
ONEOK_#003_#006	Class I	2,042,591 ft 677,309 ft 3,326 ft	2,042,591 ft 677,309 ft 3,670 ft	0 to 50 100 yr	11.587 kg/s	1,388 psi	0.0	10.16 cm
NNGC_#0001_RC	Class I	2,042,137 ft 675,226 ft 3,310 ft	2,042,137 ft 675,226 ft 3,400 ft	0 to 50 100 yr	0.1619 kg/s	1,388 psi	0.0	10.16 cm
ONEOK_#004	Class I	2,042,518 ft 679,386 ft 3,316 ft	2,042,518 ft 679,386 ft 3,745 ft	0 to 50 100 yr	1.772 kg/s	1,388 psi	0.0	10.16 cm
ONEOK_#005	Class I	2,042,519 ft 677,681 ft 3,327 ft	2,042,519 ft 677,681 ft 3,630 ft	0 to 50 100 yr	9.2229 kg/s	1,388 psi	0.0	10.16 cm
CO_2 Injector Location 1	Class VI	2,035,610 ft 672,567 ft 3,800 ft	2,035,610 ft 672,567 ft 4,000 ft	10 to 40 yr	0.35 MMT/yr	2,080 psi	0.0	10.16 cm
CO_2 Injector Location 2	Class VI	2,039,543 ft 681,797 ft 3,800 ft	2,039,543 ft 681,797 ft 4,000 ft	10 to 40 yr	0.35 MMT/yr	2,080 psi	0.0	10.16 cm
CO_2 Injector Location 3	Class VI	2,041,982 ft 677,401 ft 3,800 ft	2,041,982 ft 677,401 ft 4,000 ft	10 to 40 yr	0.35 MMT/yr	2,080 psi	0.0	10.16 cm

Initial Conditions

The initial pressure and temperature were specified to vary vertically with a temperature of 112.8˚F (44.9˚C) and pressure of 1,646 psi (11.3 MPa) for the 0.40 psi/ft scenarios or 1,399 psi (9.65 MPa) for the 0.34 psi/ft scenarios, imposed at a depth of 4,115 ft (1,254 m) bgs. From that

point the computational domain was initialized as being saturated with water under hydrostatic conditions with a temperature gradient of 0.01 ˚F/m. Zero salinity was specified.

Boundary Conditions

Boundary conditions were specified for the six boundary surfaces of the computational domain, as shown in Table 43.

Table 43 AD boundary condition specifications.

Bottom	Top	West	East	South	North
Zero Flux	Zero Flux	Equilibrium with Initial State	Equilibrium with Initial State	Equilibrium with Initial State	Equilibrium with Initial State

Simulation Results

Simulations were executed to either 50 or 100 yr. During the first 10 yr, only wastewater injection was active, in order to mimic the legacy brine disposal into the Arbuckle aquifer in the region. Then during the next 30 yr both wastewater and CO_2 injection was active. Finally, during the closing 10 or 60 yr, only wastewater injection was active. Simulation results were recorded in a series of binary formatted files. The output.bin file contains a record user specified reference variables (Table 44) at each time step, and the plot_xxxxxxx.bin files contain a record of user specified plot variables (Table 44) at specified points in time (Table 44). Binary formatted files were converted to ASCII formatted files. The output.bin file was converted to output, and the plot_xxxxxxx.bin files were converted to contours_xxxyr.dat files. The output file was used to generate plots of forms of integrated CO_2 mass, well pressure (top of screened interval), and well mass injection rate versus time (**Figure 246** and **Figure 247**). The contours_xxxyr.dat files were used to create color contours of brine and free gas plumes at the specified plot times (**Figure 248** through **Figure 250**). The implications of these simulation results will be discussed in Section 4.2.

Table 44 AD output variables

Reference Variables		Plot Variables	
Temperature, ˚F	NNGC-1, Pressure, psia	XNC Aqueous Volumetric Flux, m/s,	Trapped Gas Saturation
Integrated CO_2 Mass, kg	NNGC-1, Water Mass Rate, kg/s	YNC Aqueous Volumetric Flux, m/s	CO_2 Aqueous Concentration, gm/cm^3
Integrated CO_2 Aqueous Mass, kg	NNGC_1, Water Mass Integral, kg	ZNC Aqueous Volumetric Flux, m/s	Salt Aqueous Mass Fraction
Integrated CO_2 Gas Mass, kg	ONEOK-4 Pressure, psia	Temperature, ˚F	CO_2 Aqueous Mass Fraction
Integrated CO_2 Trapped-Gas Mass, kg	ONEOK-4, Water Mass Rate, kg/s	Diffusive Porosity	Gas Pressure, psia
Salt Aqueous Mass Fraction	ONEOK-4, Water Mass Integral, kg	X-Intrinsic Permeability, mD	Aqueous Pressure, psia

Aqueous Density, kg/m^3	ONEOK-5 Pressure, psia	Z-Intrinsic Permeability, mD	Gas Density, kg/m^3
Gas Pressure, psia	ONEOK-5, Water Mass Rate, kg/s	Gas Saturation	Aqueous Density, kg/m^3
Aqueous Pressure, psia	ONEOK-5, Water Mass Integral, kg	**Plot Times**	
Diffusive Porosity	CO_2 Injector, Pressure, psia	0.0 yr, 20 at 0.5 yr	
ONEOK-3/6 Pressure, psia	CO_2 Injector, CO_2 Mass Rate, kg/s		
ONEOK-3/6, Water Mass Rate, kg/s	CO_2 Injector, CO_2 Mass Integral, kg		
ONEOK-3/6, Water Mass Integral, kg			

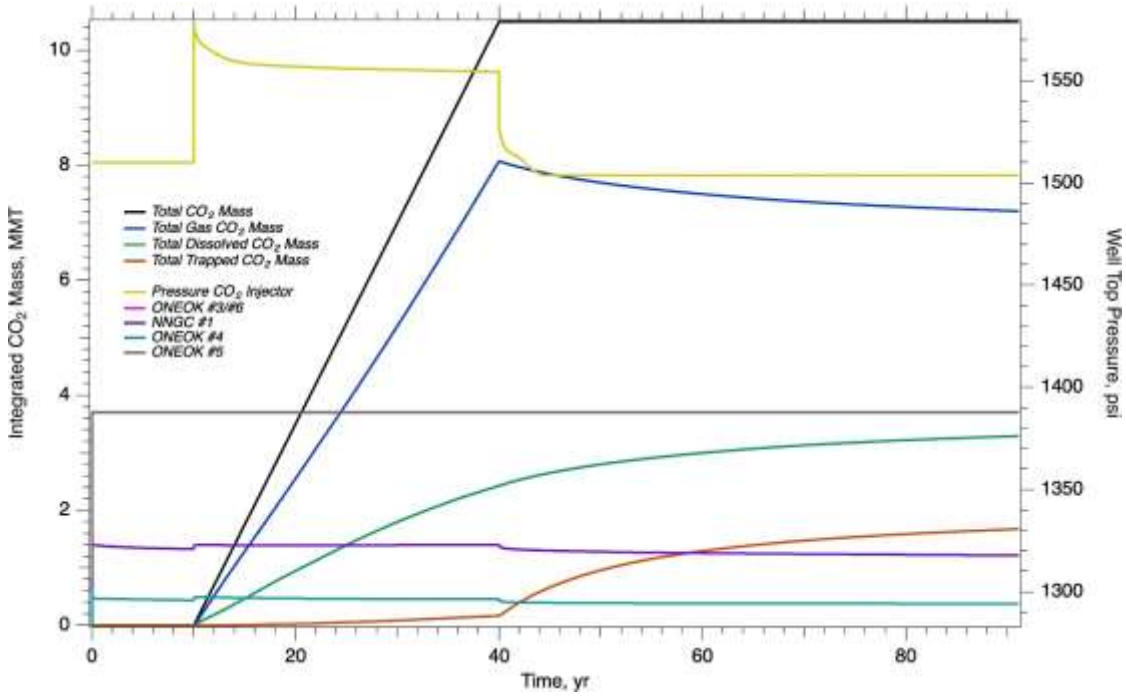


Figure 246 AD-S1E forms of integrated CO_2 mass and injection well pressures (top of screened interval)

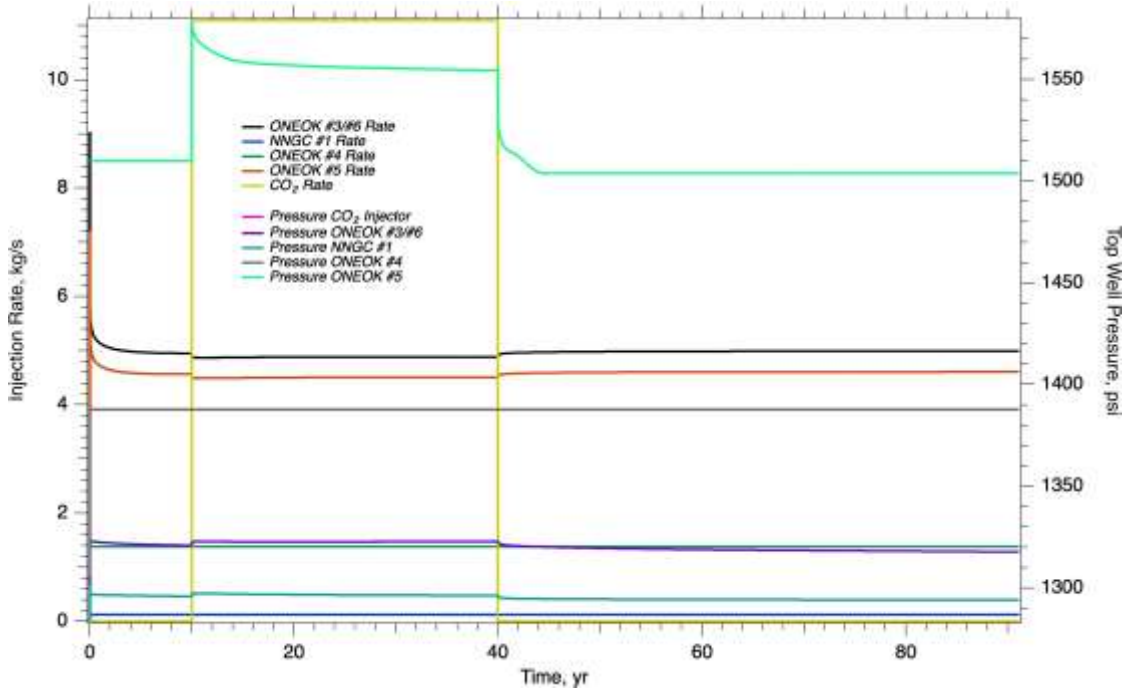


Figure 247 AD-S1E well mass injection rate and well pressure (top of screened interval)

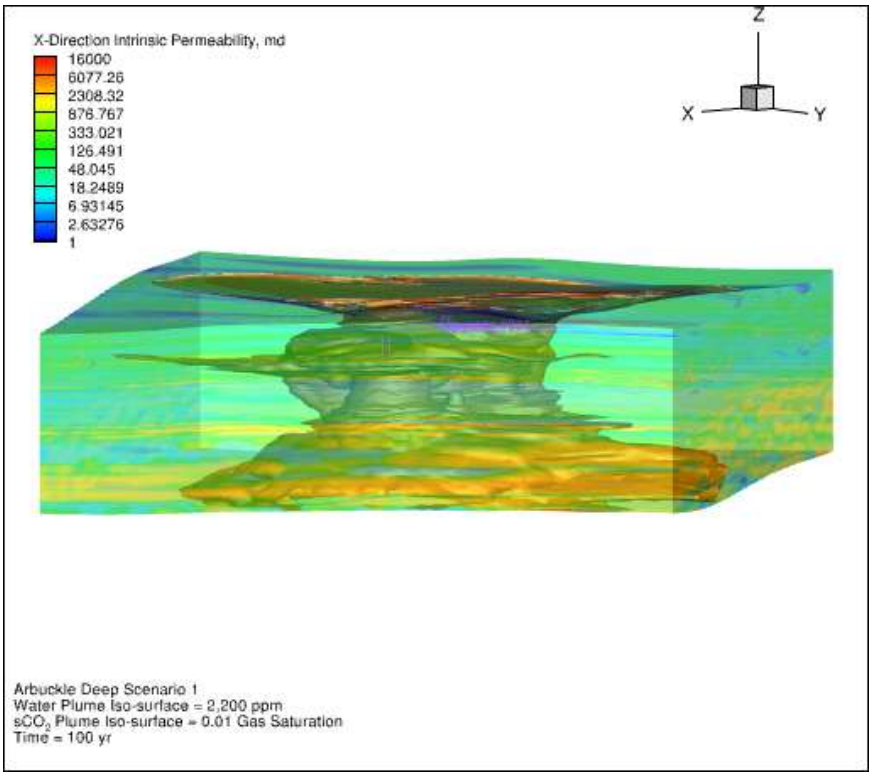


Figure 248 AD-S1E brine and free gas plumes at 100 yr over horizontal intrinsic permeability (section view)

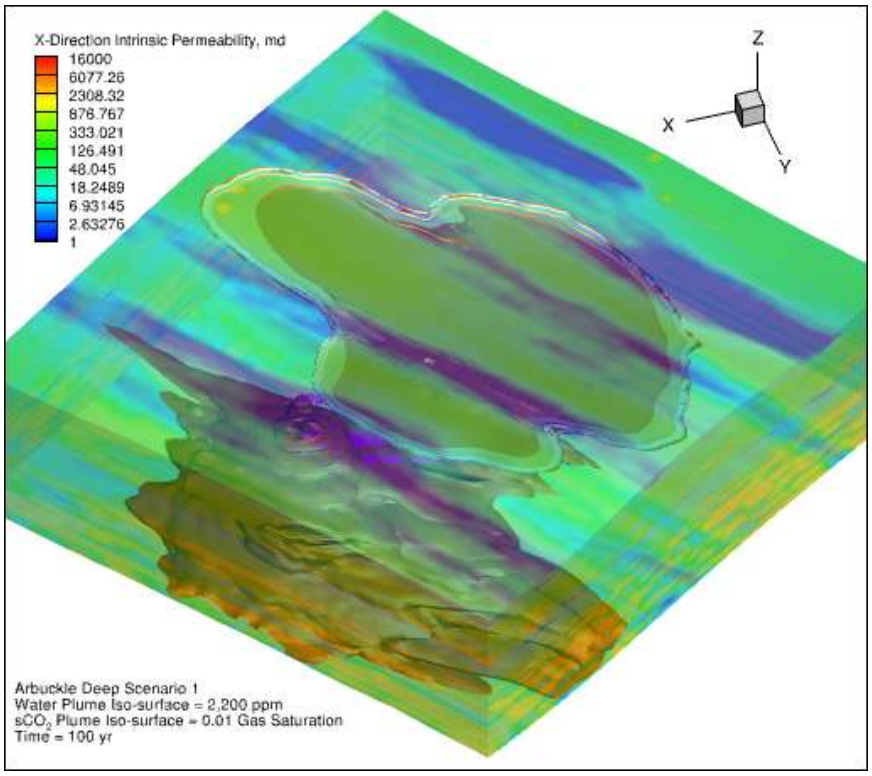


Figure 239 AD-S1E brine and free gas plumes at 100 yr over horizontal intrinsic permeability (oblique view)

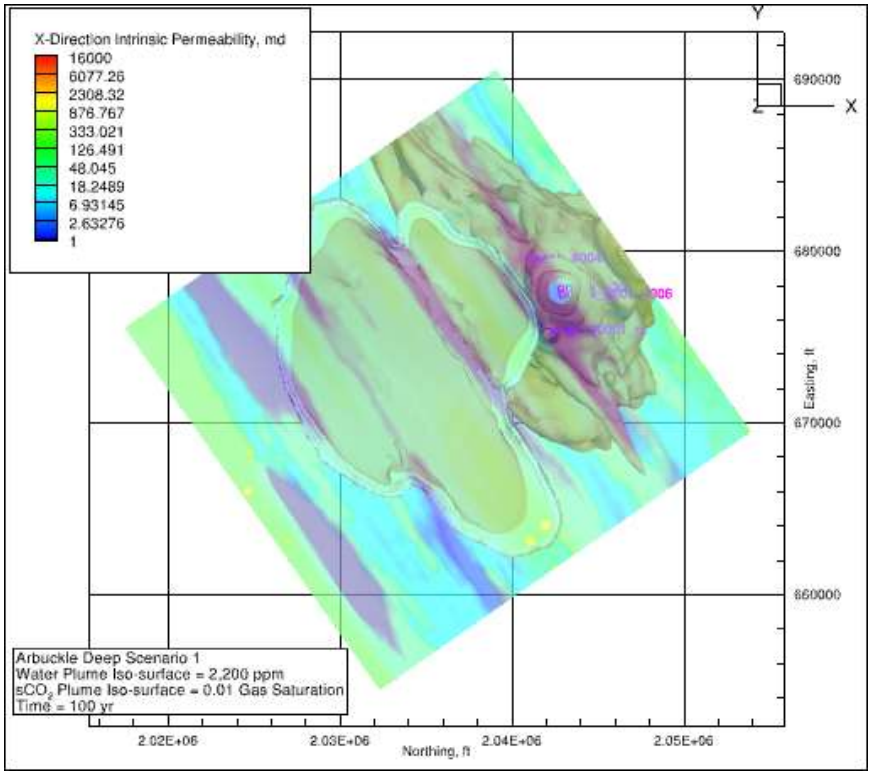


Figure 250 AD-S1E brine and free gas plumes at 100 yr over horizontal intrinsic permeability (areal view)

Medford, Oklahoma Site, Wilcox-Bromide Reservoir

The static geologic model for the Medford, Oklahoma, Wilcox-Bromide (MWB) site was provided to PNNL as one data file, as shown in Table 45. Four scenarios were considered for this site/reservoir, that differed with respect the well location and grid type, as shown in Table 45. Simulation times were generally comparable across the scenarios, as the wells were pressure limited, as shown in Table 45. The density range for pure CO_2 over the initial temperature and pressure range of the simulations is shown in Table 45.

Table 45 MWB completed simulations

Computational Domain	Depth Range	Areal Extent	Time Range
158 x 158 x 26 (1.9 million unknowns)	4,563 to 4,993 ft bgs	31,600 ft x 31,600 ft	0 to 50 yr
Static Geologic Model Data Files			
Medford-Wilcox-Bromide.GRDECL			

Scenario	Well Location	Grid Type	Simulation Period	Number of Time Steps (Simulation Time, hr:min)
MWB-S1	southwest quadrant	Petrel	50 yr	269 (00:41)
MWB-S2	center	Petrel	50 yr	269 (00:45)
MWB-S3	northeast quadrant	Petrel	50 yr	269 (00:41)
MWB-S4	center	Cartesian	50 yr	269 (00:46)

Saturation Function

Saturation functions relate capillary pressure (i.e. the difference between gas and aqueous pressure) to aqueous saturation. As parameters for this function were not included in the data package a representative saturation function was used, based on the Brooks and Corey (1964) function with the Webb (2000) extension and hysteretic nonwetting fluid entrapment, as shown in **Figure 236**.

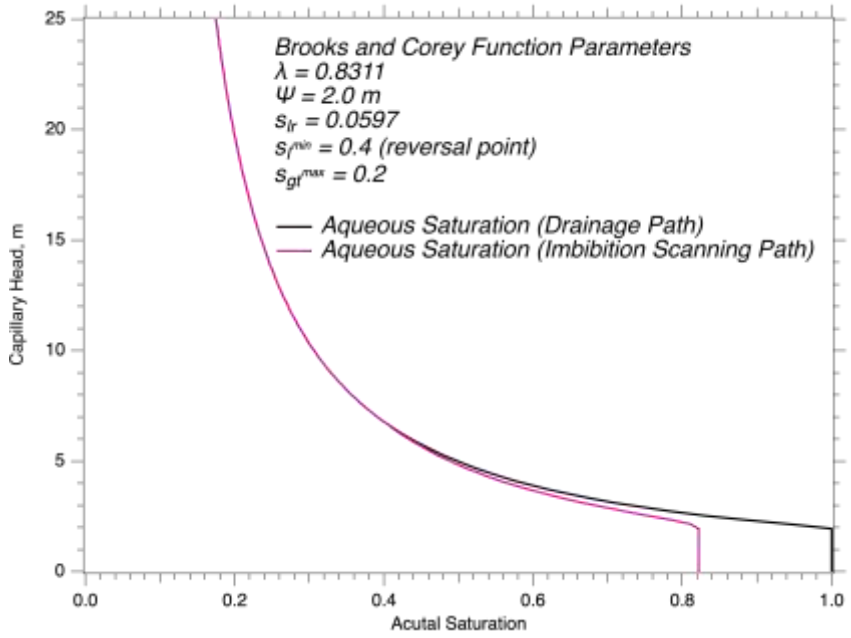


Figure 241 Saturation function, based on the Brooks and Corey Model with Webb extension and hysteretic gas entrapment, showing drainage and imbibition scanning paths for a reversal saturation of 0.4

Aqueous Relative Permeability Function

Aqueous relative permeability functions relate the relative permeability of the aqueous phase to aqueous saturation. As parameters for this function were not included in the data package a representative saturation function was used, based on Burdine (1953) function, as shown in **Figure 242**.

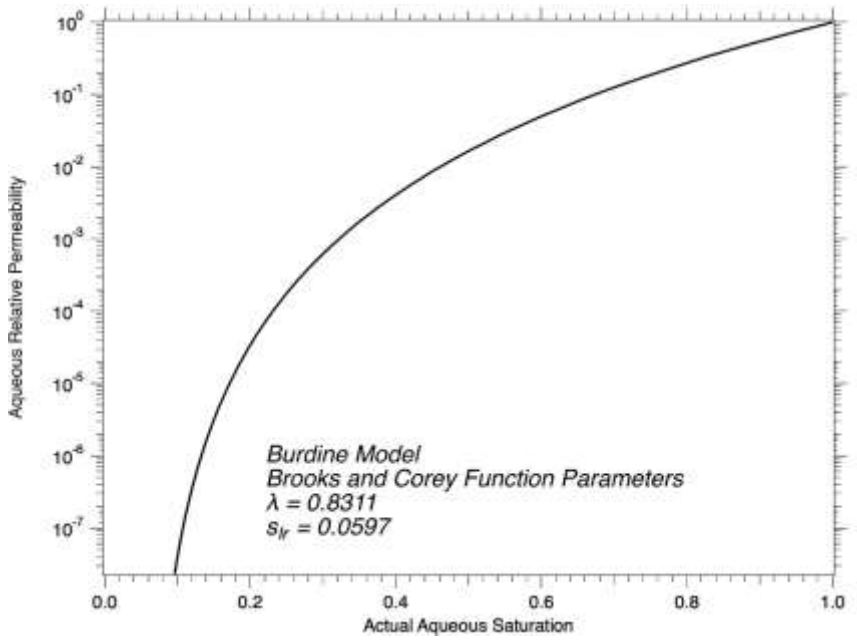


Figure 242 Aqueous relative permeability function based on the coupled Burdine and Brooks and Corey models

Gas Relative Permeability Function

Gas relative permeability functions relate the relative permeability of the gas phase to aqueous saturation. As parameters for this function were not included in the data package a representative saturation function was used, based on Burdine (1953) function, as shown in **Figure 243**.

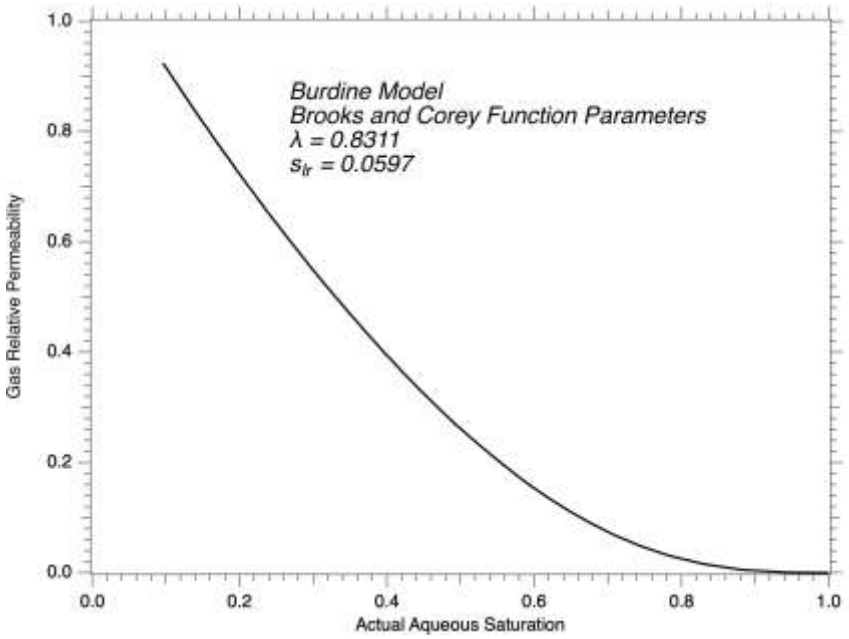


Figure 243 Gas relative permeability function based on the coupled Burdine and Brooks and Corey models

Wells

A single CO_2 injection well was modeled with the parameters shown in Table 34. Injected CO_2 was specified as dry (i.e. no water).

Table 46 MWB well parameters

Scenario	Well Type	Top Coordinates	Bottom Coordinates	Time Range	Injection Rate	Pressure Limit (top)	Skin Factor	Borehole Radius
MWB-S1	Class VI	2,068,821 ft 646,954 ft 4,660 ft	2,068,821 ft 646,954 ft 4,760 ft	0 to 30 yr	0.35 MMT/yr	2,796 psi	0.0	10.16 cm
MWB-S2	Class VI	2,079,184 ft 636,729 ft 4,655 ft	2,079,184 ft 636,729 ft 4,755 ft	0 to 30 yr	0.35 MMT/yr	2,799 psi	0.0	10.16 cm
MWB-S3	Class VI	2,090,016 ft 625,381 ft 4,828 ft	2,090,016 ft 625,381 ft 4,928 ft	0 to 30 yr	0.35 MMT/yr	2,897 psi	0.0	10.16 cm

MWB-S4	Class VI	2,079,184 ft 636,729 ft 4,803 ft	2,079,184 ft 636,729 ft 4,918 ft	0 to 30 yr	0.35 MMT/yr	2,882 psi	0.0	10.16 cm

Initial Conditions

The initial pressure and temperature were specified to vary vertically with a temperature of 125.4˚F (51.9˚C) and pressure of 1,940.0 psi (13.4 MPa), imposed at a depth of 4,618 ft (1,407 m) bgs. From that point the computational domain was initialized as being saturated with water under hydrostatic conditions with a temperature gradient of 0.01 ˚F/m. Zero salinity was specified.

Boundary Conditions

Boundary conditions were specified for the six boundary surfaces of the computational domain, as shown in Table 47.

Table 47 MWB boundary condition specifications

Bottom	Top	West	East	South	North
Zero Flux	Zero Flux	Equilibrium with Initial State	Equilibrium with Initial State	Equilibrium with Initial State	Equilibrium with Initial State

Simulation Results

Table 48 MWB output variables

Reference Variables		Plot Variables	
Temperature, ˚F	Gas Density, kg/m^3	XNC Aqueous Volumetric Flux, m/s,	Trapped Gas Saturation
Gas Saturation	Aqueous Density, kg/m^3	YNC Aqueous Volumetric Flux, m/s	CO_2 Aqueous Concentration, gm/cm^3
Trapped Gas Saturation	Gas Pressure, psia	ZNC Aqueous Volumetric Flux, m/s	Salt Aqueous Mass Fraction
Integrated CO_2 Mass, kg	Aqueous Pressure, psia	Temperature, °F	CO_2 Aqueous Mass Fraction
Integrated CO_2 Aqueous Mass, kg	Diffusive Porosity	Diffusive Porosity	Gas Pressure, psia
Integrated CO_2 Gas Mass, kg	CO_2 Injector, Pressure, psia	X-Intrinsic Permeability, mD	Aqueous Pressure, psia
Integrated CO_2 Trapped-Gas Mass, kg	CO_2 Injector, CO_2 Mass Rate, kg/s	Z-Intrinsic Permeability, mD	Gas Density, kg/m^3
Salt Aqueous Mass Fraction	CO_2 Injector, CO_2 Mass Integral, kg	Gas Saturation	Aqueous Density, kg/m^3
CO_2 Aqueous Mass Fraction		**Plot Times**	
		0.0 yr, 50 at 1.0 yr	

Simulations were executed to 50 yr. During the first 30 yr, CO_2 injection was active and then during the final 20 yr the CO_2 migrated under buoyancy forces. Simulation results were recorded in a series of binary formatted files. The output.bin file contains a record user specified reference variables (Table 48) at each time step, and the plot_xxxxxxx.bin files contain a record of user specified plot variables (Table 48Table 48 MWB output variables) at specified points in time. Binary formatted files were converted to ASCII formatted files. The output.bin file was converted to output, and the plot_xxxxxxx.bin files were converted to contours_xxxyr.dat files. The output file was used to generate plots of forms of integrated CO_2 mass, well pressure (top of screened interval), and well mass injection rate versus time (**Figure 244** and **Figure 245**). The contours_xxxyr.dat files were used to create color contours of brine and free gas plumes at the specified plot times (**Figure 246** through **Figure 248**). The implications of these simulation results will be discussed in Section 4.2.

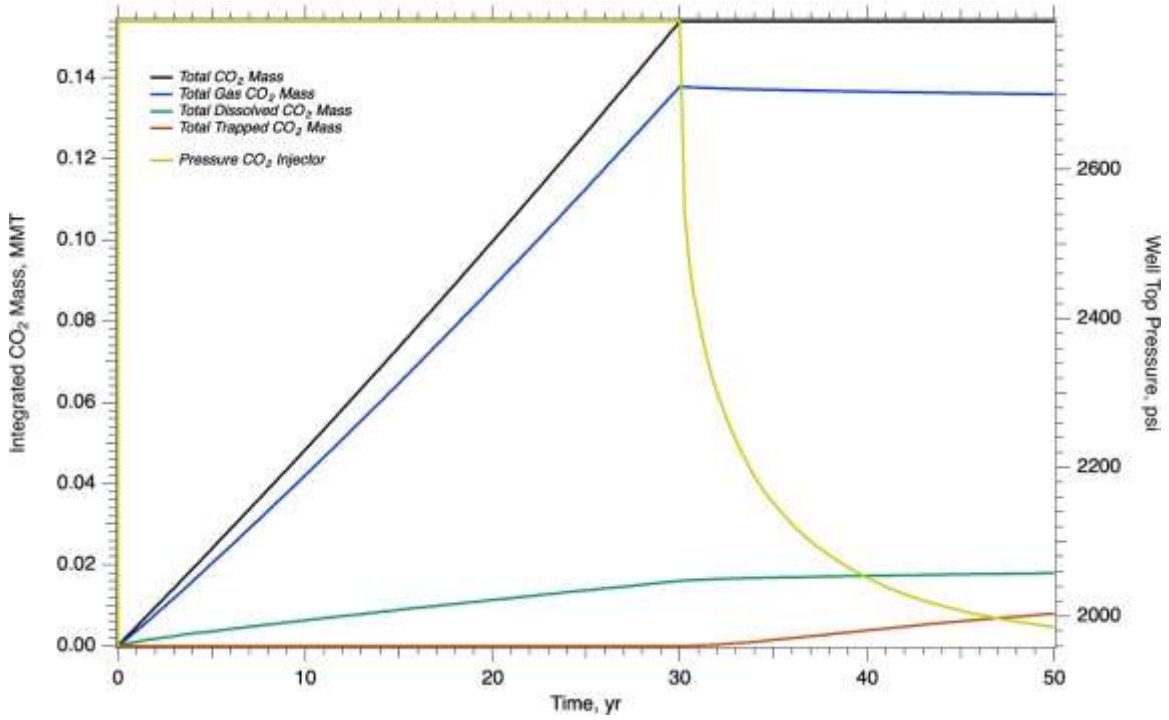


Figure 244 MWB-S2 forms of integrated CO_2 mass and injection well pressures (top of screened interval)

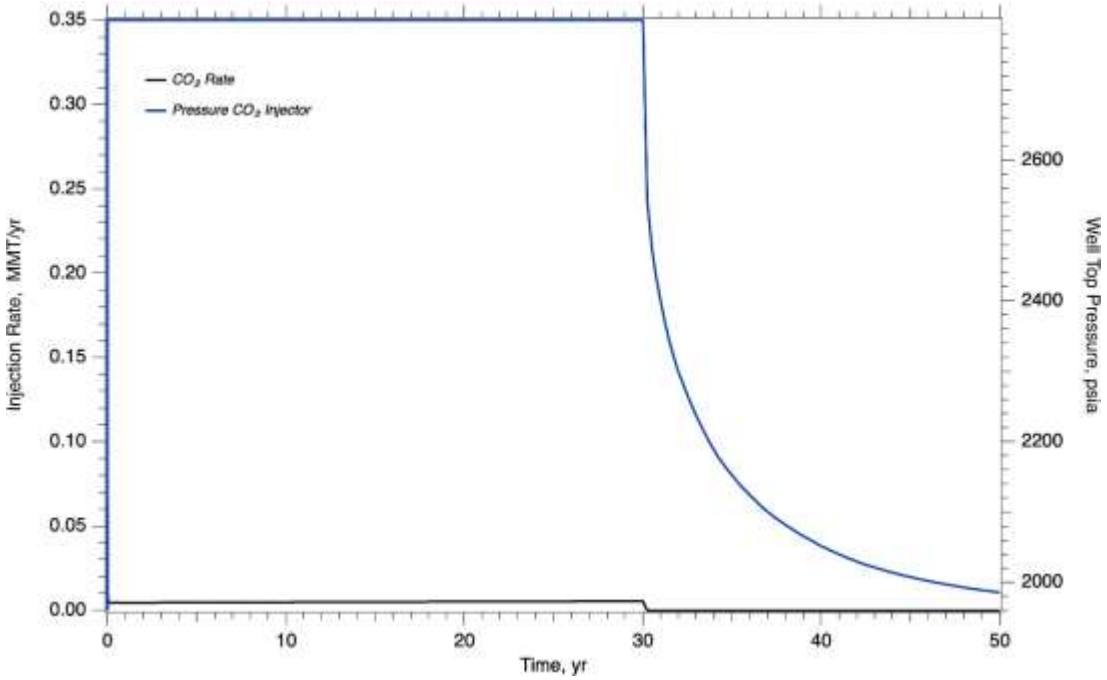


Figure 245 MWB-S2 free gas plume at 50 yr over horizontal intrinsic permeability (oblique view)

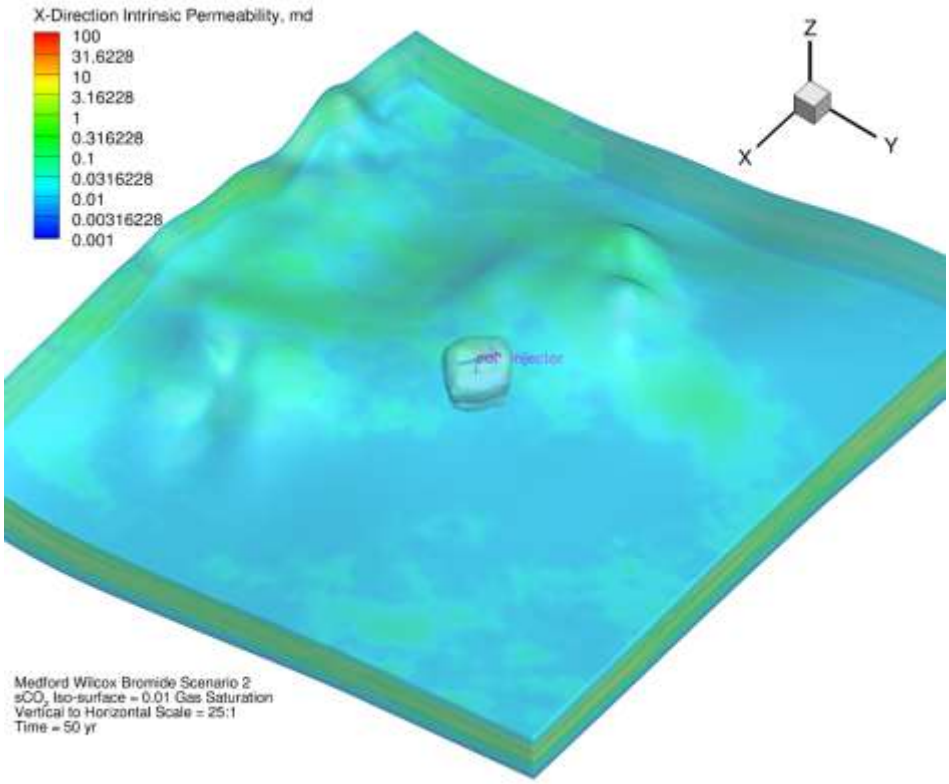


Figure 246 MWB-S2 free gas plume at 50 yr over horizontal intrinsic permeability (oblique view)

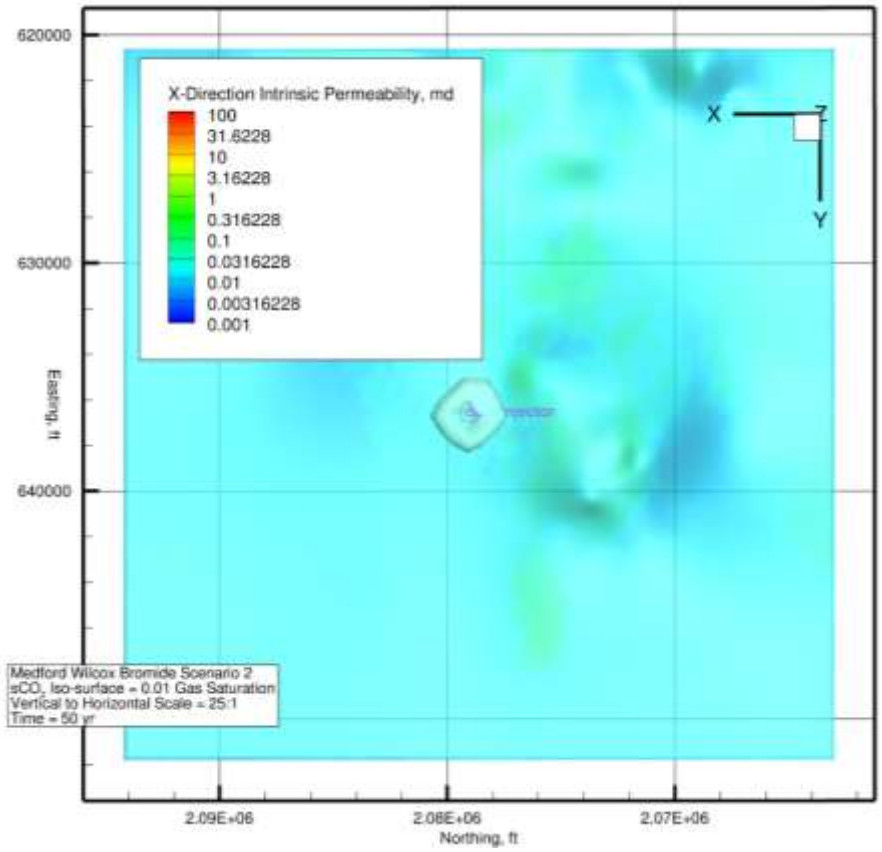


Figure 247 MWB-S2 free gas plume at 50 yr over horizontal intrinsic permeability (areal view)

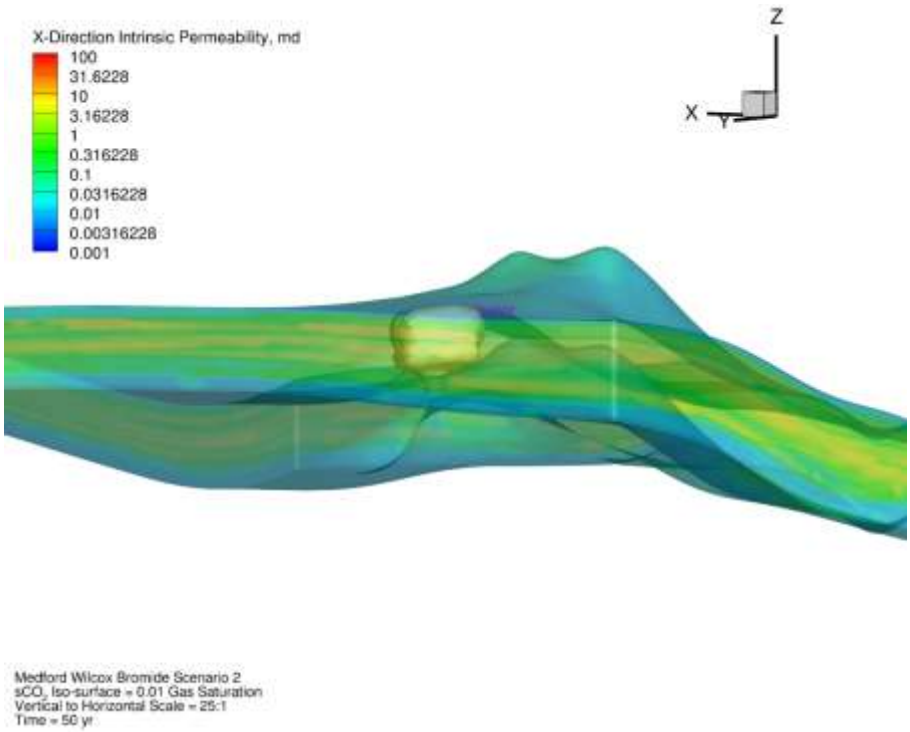


Figure 248 MWB-S2 free gas plume at 50 yr over horizontal intrinsic permeability (section view)

Subtask 4.2 – Dynamic Simulations of CO_2 Injection Scenarios into Saline Storage Reservoirs

A series of numerical simulations were executed with STOMPX-CO_2, PNNL developed parallel reservoir simulator for modeling the fate of CO_2 injected into deep saline reservoirs. These simulations were executed on PNNL's "constance," a supercomputer based on the Intel Haswell CPU architecture and is the generalized system for parallel applications requiring dozens to thousands of compute cores. The STOMPX-CO_2 reservoir simulator is a Message Passing Interface (MPI) based implementation of STOMP-CO_2, which has been benchmarked against problems from two international code comparison studies: 1) GeoSeq (Pruess et al. 2002) comprising 8 test problems and 2) Stuttgart Benchmark Study (Class et al. 2009), comprising 3 test problems. This series of simulations were designed to provide a preliminary assessment of two sites and four reservoirs to meet the carbon storage needs of a carbon capture and storage (CCS) hub for ONEOK at 0.35 MMT/yr for 30 yr. The sites were located near Bushton, Kansas and Medford, Oklahoma. At the Bushton, Kansas site, three reservoirs were considered: 1) Lansing Kansas City, 2) Upper Arbuckle, and 3) Deep Arbuckle. At the Medford, Oklahoma site, a single reservoir was considered: 1) Wilcox Bromide. As with most subsurface modeling projects, several simulations were executed for each reservoir beyond those reported in this document. Included in these simulations were those used to conduct auxiliary investigations (e.g. closed versus open boundaries, neglecting interference from neighboring injectors) and those that had input errors.

This technical memo was specifically written to document this series of preliminary numerical simulations, providing a readable log of the data contained in the input and output files for the reportable simulations completed. This series of simulations are considered preliminary, as they

are based on a single realization of the geology and associated petrophysical and transport properties for each reservoir. Moreover, for most of the simulations completed, the boundary conditions influenced the simulation results (i.e. pressure field, plume migration behavior), thus a larger areal computational domain extent is required to avoid this influence. Another context for which these simulations should be considered preliminary is that of geochemistry. CO_2 dissolution in water is dependent on the pressure of the gaseous CO_2 and the pH of aqueous solutions of CO_2 is inversely proportional to dissolved CO_2 concentration (i.e. higher concentrations yield lower pH solutions). This yields the potential for dissolution of reservoir minerals and precipitation of carbonate minerals, potential altering porosity, intrinsic permeability and other petrophysical properties, including the geomechanical strength of the rock. Though modeling capabilities for these processes is a capability of the STOMPX-CO_2, simulator geochemical processes were not considered during this study.

As modeled the temperature range of the LKC reservoir is influenced by historical petroleum industry activities, making it lower than the levels expected for the regional geothermal gradient. As shown in Figure 227, this creates moderate gas densities (i.e. approximately 600 kg/m^3) under the initial temperature and pressure conditions. The LKC simulations generally showed injectivity much lower than the specified 0.35 MMT/yr, with the actual injection being dependent on the injection pressure limit, based on fracturing pressure. A characterization well would provide opportunities to confirm the reservoir porosity and permeability, including non-matrix porosity systems like fractures or karst, plus minimum horizontal stress or fracture initiation pressures.

The static geologic model for the UA reservoir included a low permeability horizon, designed to separate the Arbuckle formation into two layers. Historical records of injectivity of five wastewater injectors provided an excellent benchmark for defining the in-situ permeability of the formation (i.e. combined matrix and fracture permeability). For these simulations, an initial and boundary condition state of the initial pressure and temperature varying vertically with a temperature of 97˚F (36.1˚C) and pressure of 1,000 psi (6.89 MPa) imposed at a depth of 3,782.97 ft (1,153 m) bgs. As shown in Figure 227, this yields subcritical-gas CO_2 conditions for the gas with associated low gas densities. The series of UA simulations with the wastewater injectors established that permeabilities 5 times that of the matrix permeabilities would be sufficient to show agreement with the historical inject records. During the simulation with combined injections of wastewater and CO_2, however, the low initial pressure yielded large gas-plume volumes, which was consistent with the density of CO_2 for those temperature and pressure states. These simulations were halted after 15 yr.

Following the investigations with the UA geologic model, the DA static geologic model was developed, which comprised the entirety of the Arbuckle formation, but did not include a low-permeability layer. The initial pressure used in the UA models was revised to agree with recent field measurements. The principal objective for the DA series of simulations was to quantify the interference in pressure and plume extents between wastewater and CO_2 injectors, with the wastewater plume being a density brine and the CO_2 plume being a less dense gas. These simulations considered three well locations for the CO_2 injectors: 1) orthogonal from the trends of permeability to the wastewater injectors, 2) in line with the trends of permeability to the wastewater injectors, and 3) amid the wastewater injectors. For all three locations, the CO_2 injector was screened at greater depths than those for the wastewater injectors. The third location

was selected to determine if the wastewater injections could increase the amount of trapped gas. Preliminary findings from these simulations indicate that pressure interference between the wastewater and CO_2 injectors is minor due, in part to the density contrasts between the brine (more dense) and the CO_2 (less dense) fluid phase. However, more accurate data concerning the current state of formation pressure in the Arbuckle is required. Multiple realizations of the static geologic model well also be required to quantify the uncertainty of the fate of the injected CO_2 and AoR over the course of the project.

The MWB reservoir offers advantages of being more remote from other subsurface activities (i.e. wastewater injections and petroleum production) and is located at the deepest horizon of the investigated reservoirs. The greater depth means higher temperatures but also higher fluid pressures, yielding gas densities in the 600 kg/m^3 range. The downside to the MWB reservoir is the lower permeability. Further characterization could indicate a different permeability and pre-injection stimulations could improve injectivity. Simulations of the MWB considered three different well locations, but all three simulations showed the CO_2 injection well as being pressure limited with injection rates being well below the target value of 0.35 MMT/yr.

Task 5 – Risk Assessment

This task summarizes a quantitative risk assessment of CO_2 and brine leakage and the potential impacts on the USDW at the Bushton, Kansas ONEOK site. The team developed a workflow to import pressure and CO_2 saturation results obtained by physics-based reservoir simulator (STOMP) into NRAP Open-source Integrated Assessment Model (NRAP-Open-IAM). The integrated modeling enabled quantitative assessment of CO_2/brine leakage and aquifer exposure risks. Preliminary 30-yr injection risk modeling in both the Bushton-LKC and Arbuckle formations suggests low leakage potential within the AoR. However, modeling limitations—and uncertainties in legacy well sealing and subsurface faulting—highlight the need for further site characterization.

Subtask 5.1 – Risk Assessment Data Aggregation and Database Build

The modeled domain spans approximately 37,000 × 37,000 feet and includes wells that penetrate both targeted storage formations (LKC and Arbuckle). Injection well locations and all existing wells intersecting the Arbuckle and LKC formations were catalogued. Legacy wells located nearest to the proposed injectors were selected for detailed leakage risk evaluation (Table 49). Within the AoR, 69 wells intersect the LKC, while 124 wells reach the Arbuckle interval and therefore also penetrate the LKC formation. **Figure 249** maps the injection and existing wells that intersect each CO_2 storage target formation (LKC and Arbuckle). Red markers indicate proposed injectors; blue markers represent all other penetrations; orange markers denote legacy wells selected for risk analysis.

Table 49 Injection well and existing well locations and well permeability for each injection scenario

Well API	Well number	X(ft)	Y(ft)	Distance to injection well (ft)	Well permeability (mD)

	Injection to LKC	2,036,408.18	664,011.95		
15159064950000	1	2,035,809.96	665,274.30	1,396.93	1
15159003220000	2	2,037,790.46	664,610.56	1,506.33	0.01
15159063970000	3	2,038,203.06	662,612.42	2,276.02	1
15159004820000	4	2,035,151.19	661,965.14	2,401.97	1
15159033100000	5	2,034,490.18	663,950.47	1,918.98	1
	Injection to Arbuckle	2,035,610.00	672,566.50		
15-159-03010-00	1	2,035,777.97	670,543.25	2,030.21	1
15-159-30207-00	2	2,035,772.78	673,843.40	1,287.23	0.01
15-159-21540-00	3	2,036,436.02	675,162.73	2,724.47	1
15-159-00269-00	4	2,039,493.28	672,529.89	3,883.46	1
15-159-06496-00	5	2,034,111.21	668,259.54	4,560.29	1
15-159-00046-00	6	2,031,718.05	675,263.21	4,734.92	0.01

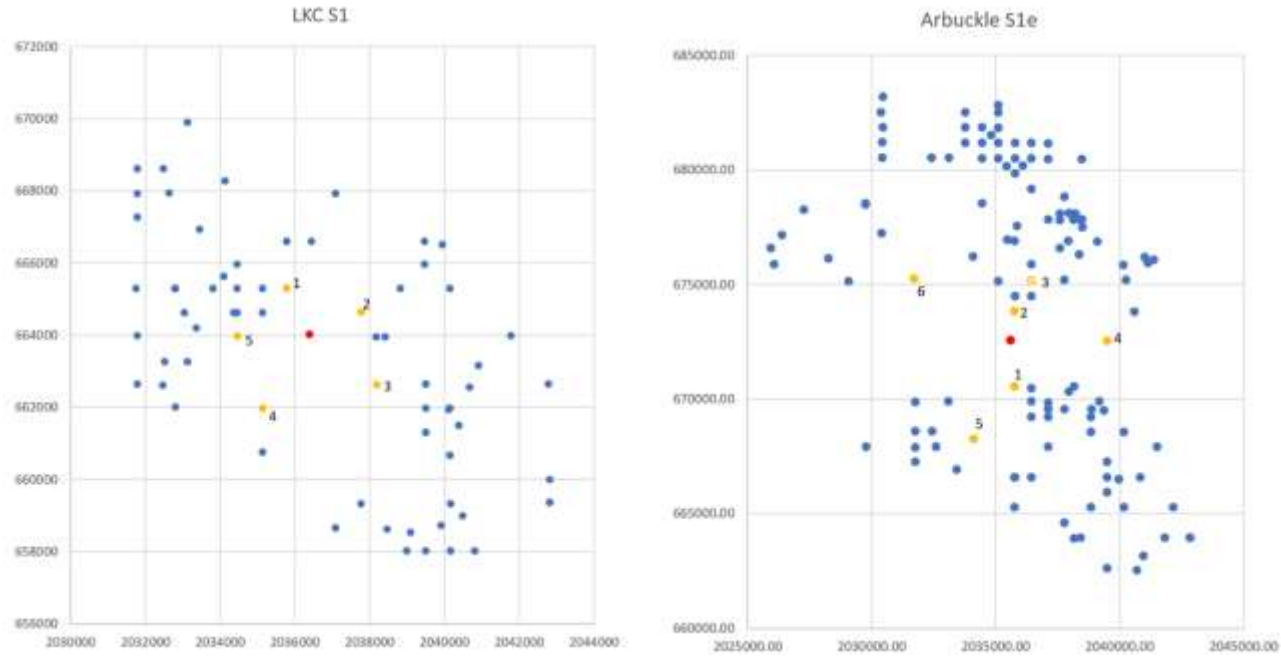


Figure 249 LKC and Arbuckle injection well and existing well locations. Red dots denote injection wells, blue dots denote existing wells, and orange dotes denote chosen wells for leakage risk analysis for this study.

NRAP-OPEN-IAM (V 2.7.2) Model Inputs/Assumptions

Input parameters are provided from the collected site data.

Simulation setting:

Time

LKC: 30-yr injection (year 0.5 to 30.5) and 20-yr post injection monitoring period (total duration 51 yr), time step 1 yr

Arbuckle: 30-yr injection (year 10 to 40) and 60-yr post injection monitoring period (total duration 100 yr), time step 1 yr

Storage reservoir:

One final set of reservoir simulation pressure and CO_2 saturation results from STOMP are selected to covert to Lookup Table input for CO_2 injection to each formation.

Stratigraphy:

Because few wells had complete stratigraphic data, the stratigraphy listed in Table 50 was used for all selected wells in this study.

Table 50 Stratigraphic data for potential leaky wells, with reservoir as the deepest layer and USDW (Dakota formation) as the shallow aquifer

Stratigraphy data (ft)	LKC	Arbuckle
USDW thickness	148	148
Depth of potential leakage	200	200
Reservoir thickness	39.5	80
Depth to top of storage reservoir	3,000	3,250

Wellbore:

Input parameters were selected from site data, with most values representing conservative estimates. Table 51 lists input parameters for the wellbore component model.

Table 51 Input parameters for wellbore model. (Note: NRAP default values are used for missing data.)

Wellbore parameter	Reservoir ranges
Wellbore effective permeability (mD)	0.001 to 1 (details see Table 5.1)
Aquifer permeability (mD)	10 to 100, USDW (Dakota 3mD)
Caprock permeability (mD)	0.001 to 0.01
Well diameter (inch)	5.5 to 7 (To ensure a conservative estimate, a diameter of 7 inches was used for all selected wells.)
Brine density (kg/m3)	977
CO_2 density (kg/m3)	648
Brine viscosity (Pa s)	0.002535 (NRAP default)

CO_2 viscosity (Pa s)	3.95 × 10-5 (NRAP default)
Compressibility (Pa-1)	5.1 × 10-11 (NRAP default)
Brine saturation	0.1 (NRAP default)

Subtask 5.2 – Assess Well Integrity and Seal Penetrations

For this study, potential CO_2 and brine leakage risks from selected representative wells in the domain were analyzed separately for injections to LKC and Arbuckle storage formations. A conservative approach was taken, selecting legacy wells closest to the injection wells to evaluate the highest potential for leakage.

LKC Injection Scenario

The LKC simulation included a 30-yr injection period (year 0.5 to 30.5) and a 20-yr post-injection monitoring period. A few representative wells close to the injection well are chosen for analysis, the distance of these existing wells to the injection well ranging from 1,400 ft to 2,400 ft surrounding the injector. Well locations are listed in Table 49 and **Figure 249** show the predicted reservoir pressure increase (ΔP) due to injection and the CO_2 saturation plume at the end of the simulation period (year 51), respectively. Results indicate a maximum ΔP of 2.1 MPa at the injector. The CO_2 saturation plume peaks at 0.8 in year 51 and exhibits an oval shape.

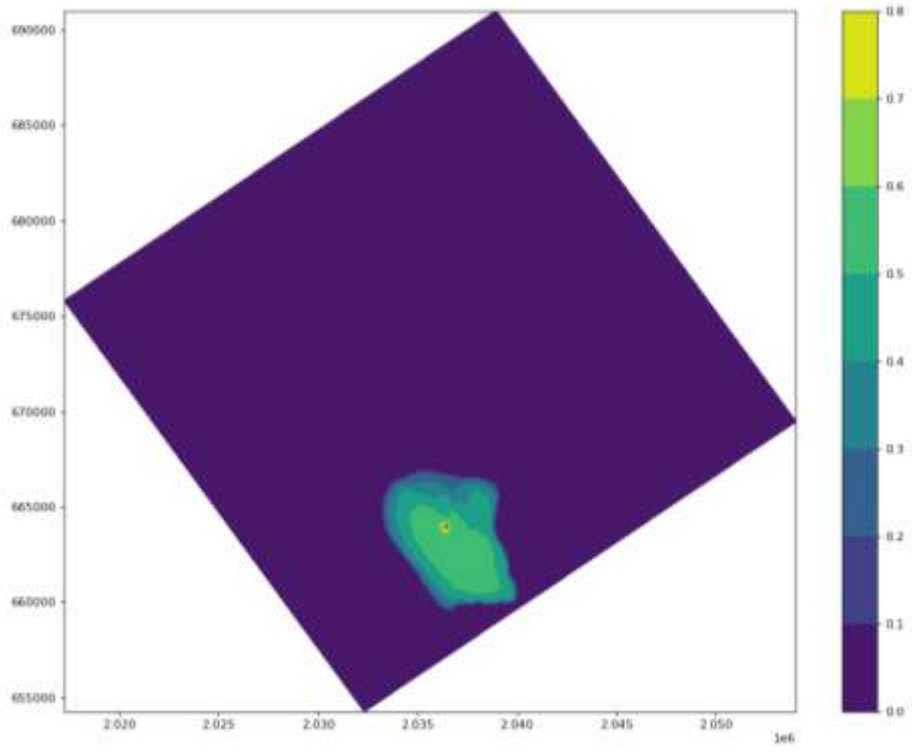


Figure 250 LKC CO_2 plume at year 51

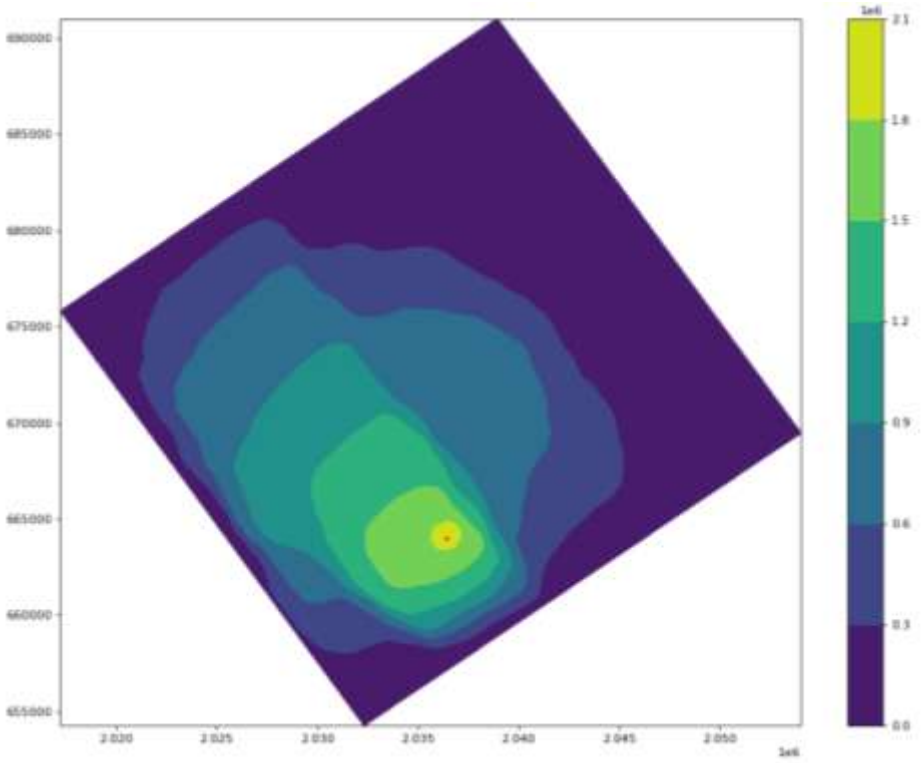


Figure 251 LKC reservoir pressure increase due to injection

Figure 252 and **Figure 253** present the predicted reservoir pressure and maximum CO_2 saturation for the representative wells, respectively.

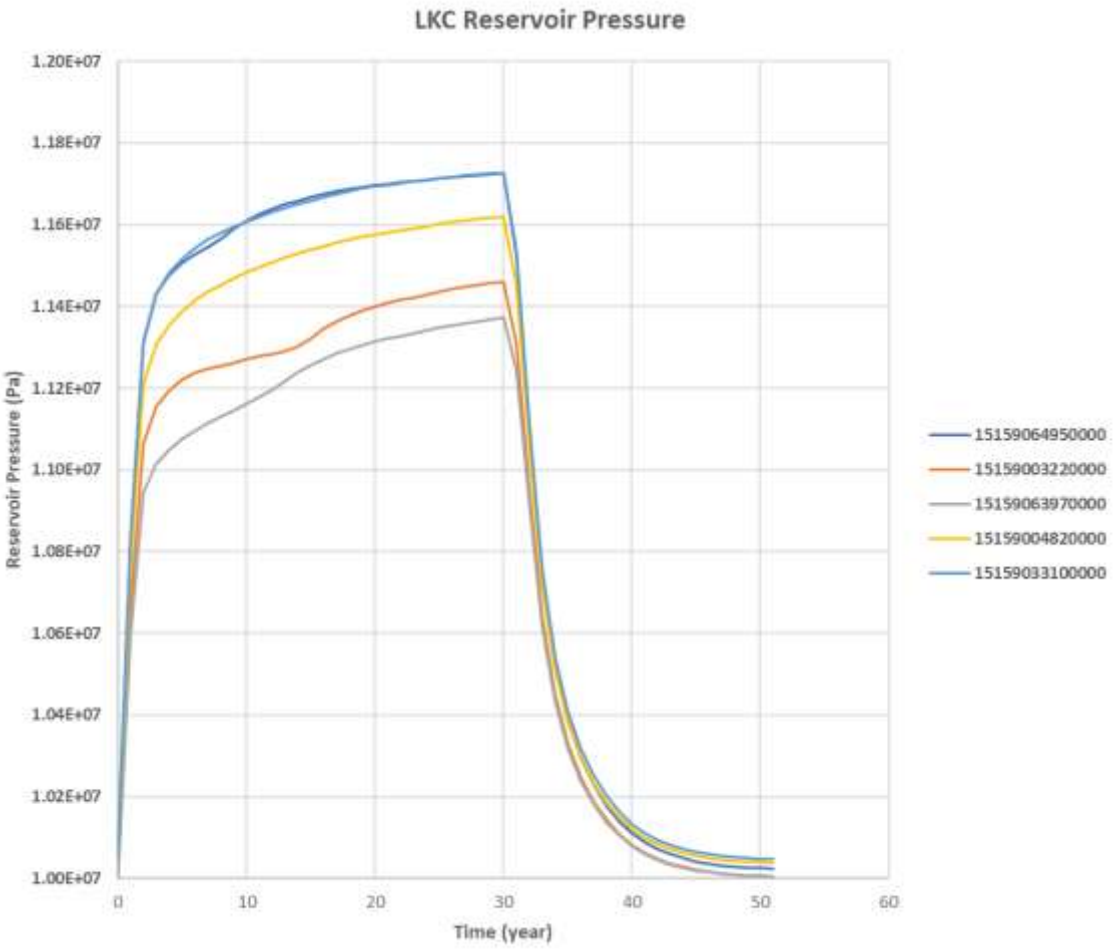


Figure 252 Reservoir pressure at the top of LKC storage formation for representative wells

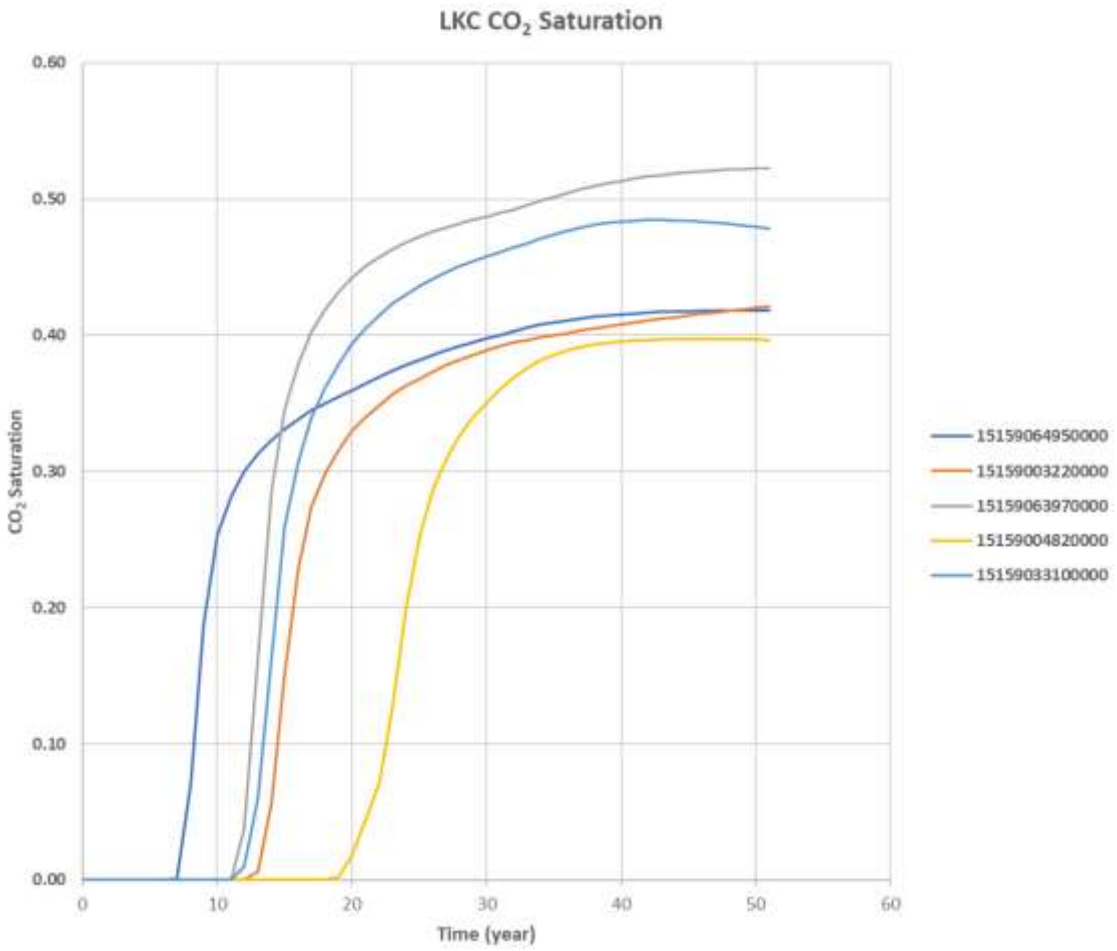


Figure 253 Maximum CO_2 saturation at LKC formation for representative wells

The highest reservoir pressure and earliest CO_2 plume breakthrough occurred at well1 (API 15159064950000), while the lowest reservoir pressure and highest CO_2 saturation occurred at well3 (API 15159063970000). Pressures at all five well locations increased during injection, reached a maximum before injection ceased, and then declined during the post-injection period. The maximum ΔP due to injection was approximately 1.7 MPa.

CO_2 saturation in wells closest to the injection well begins to break through early in the injection period, demonstrating earlier plume arrival; farther wells are generally reached later (e.g. well4), and saturation at some wells begins to decline shortly after injection ceases (e.g. well5).

Figure 254 shows minimal CO_2 leakage from representative wells to the USDW, with a maximum leakage rate of 2 kg/yr at well3 during year 51. Cumulative leakage calculations indicate that well1 had the highest total CO_2 leaked to the USDW among the five representative wells: 41.5 kg over 51 yr. Relative to the total amount of CO_2 injected (0.35 MMT/yr over 30 yr), the percentage leaked from well1 over 51 yr was approximately 4×10^{-7}%.

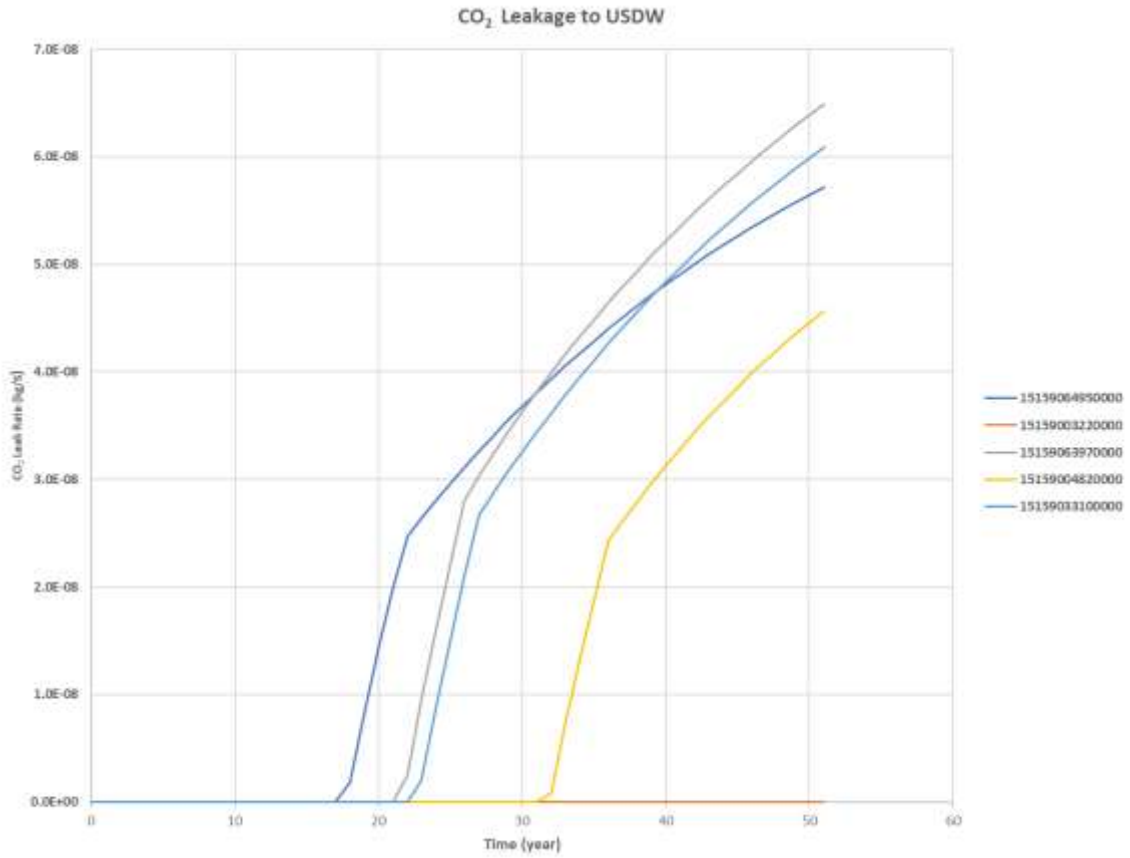


Figure 254 LKC leakage rate of CO_2 to USDW for representative wells

Using well1 as an example, **Figure 255** and **Figure 256** illustrate minimal brine leakage and associated impact on the USDW. **Figure 255** shows that the cumulative brine leakage to the USDW over 51 yr was approximately 0.3 kg. **Figure 256** depicts the pH change in the USDW due to leakage. The volume of the pH plume with an absolute change greater than 0.2 is less than 7.5 m^3.

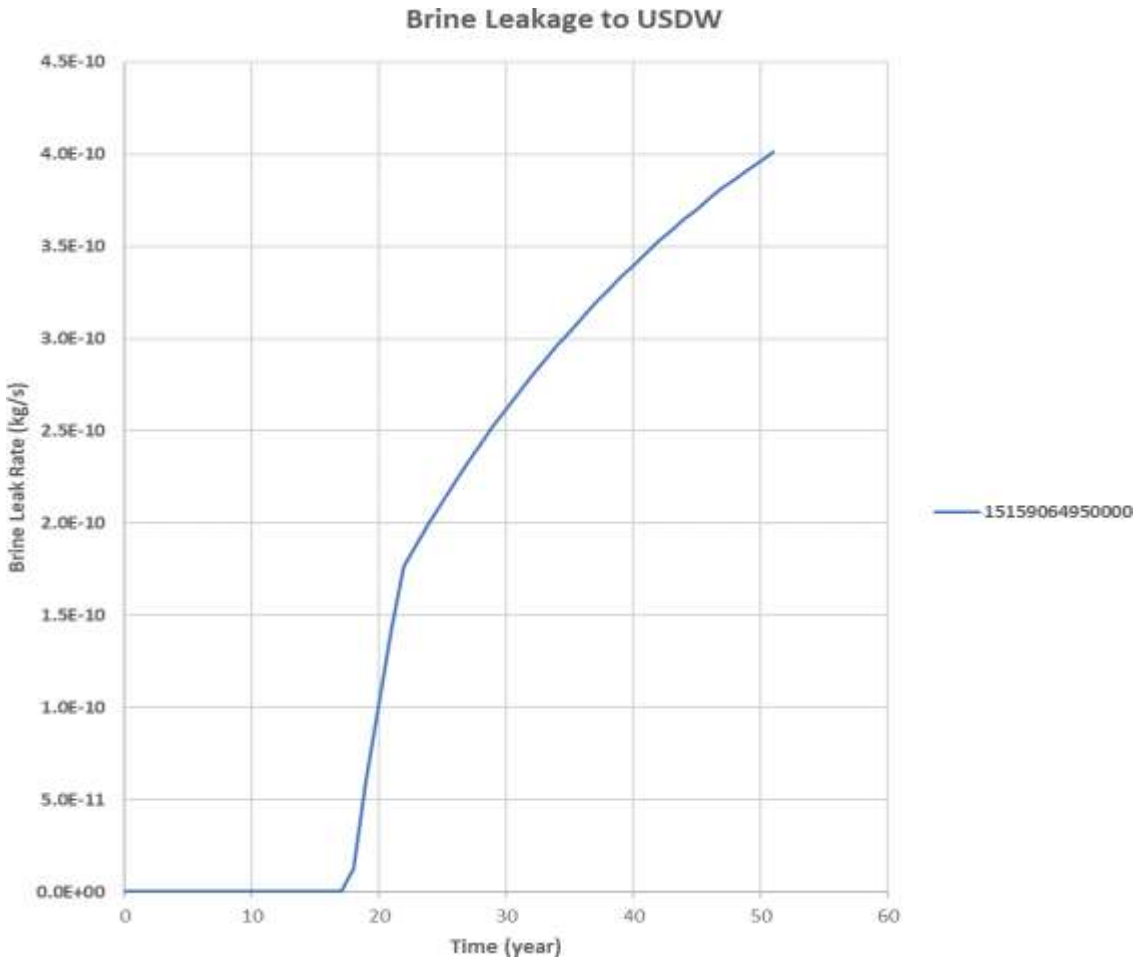


Figure 255 LKC leakage rate of brine to USDW for well 1 (API 15159064950000)

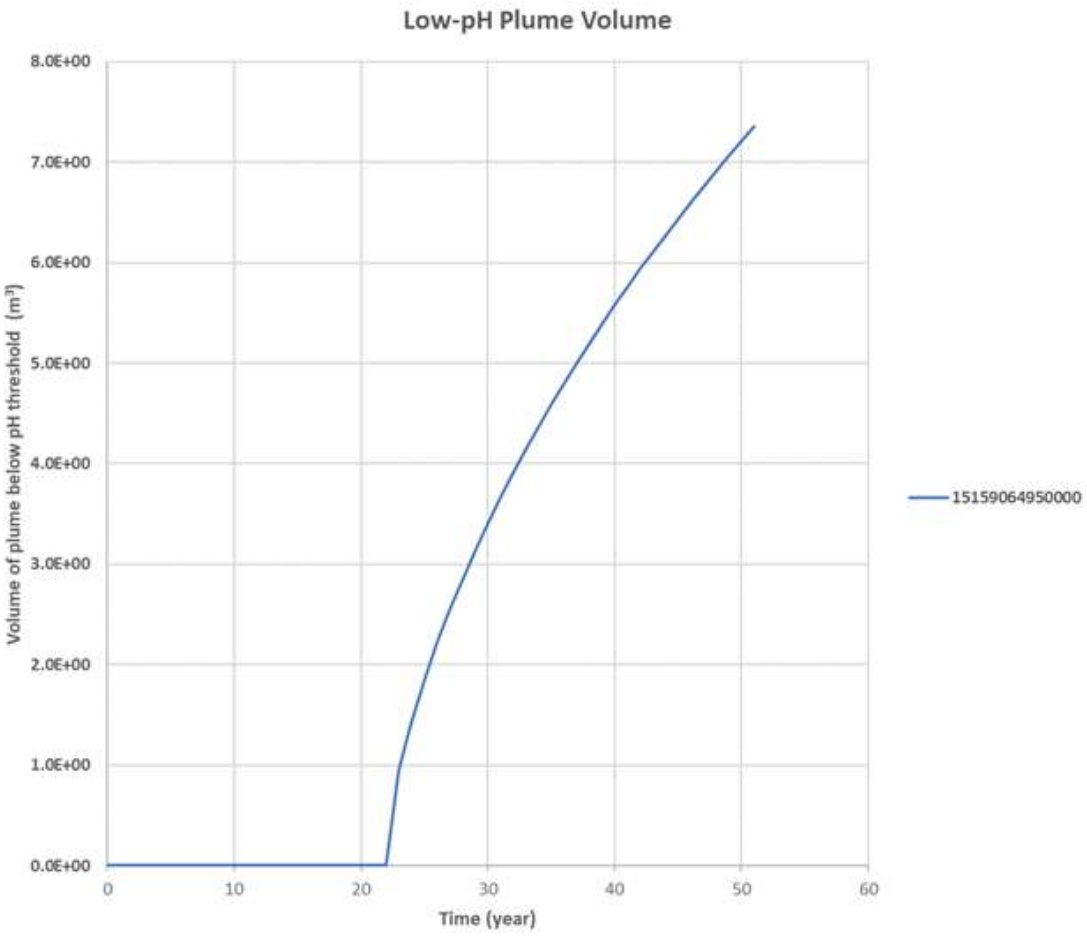


Figure 256 LKC Low-pH plume volume in USDW for well 1 (API 15159064950000)

Arbuckle Injection Scenario

The simulation for Arbuckle: 30-yr injection (year 10 to year 40) plus 60-yr post injection monitoring period. A few representative wells close to injection well are chosen for analysis, the distance of these existing wells to the injection well ranging from 1,300 ft to 4,700 ft surrounding the injector. The locations for these wells are listed in Table 49. Figure 257 shows the predicted reservoir pressure increase (delta P) due to injection. **Figure 258** and **Figure 259** show the CO_2 saturation plume at year 50 and at the end of simulation duration (year 100), respectively. The results show that delta P maximum at injector reaches 0.4 MPa which is much lower (1/5) compared to the delta P max for LKC injection scenario. Note the negative delta P shown on Figure 257 is due to water injection in that area. CO_2 saturation plume (Figure 257 and **Figure 258**) show peak at approximately 0.8, the plume size increase during injection, and migrate/change in size during the postinjection monitoring period.

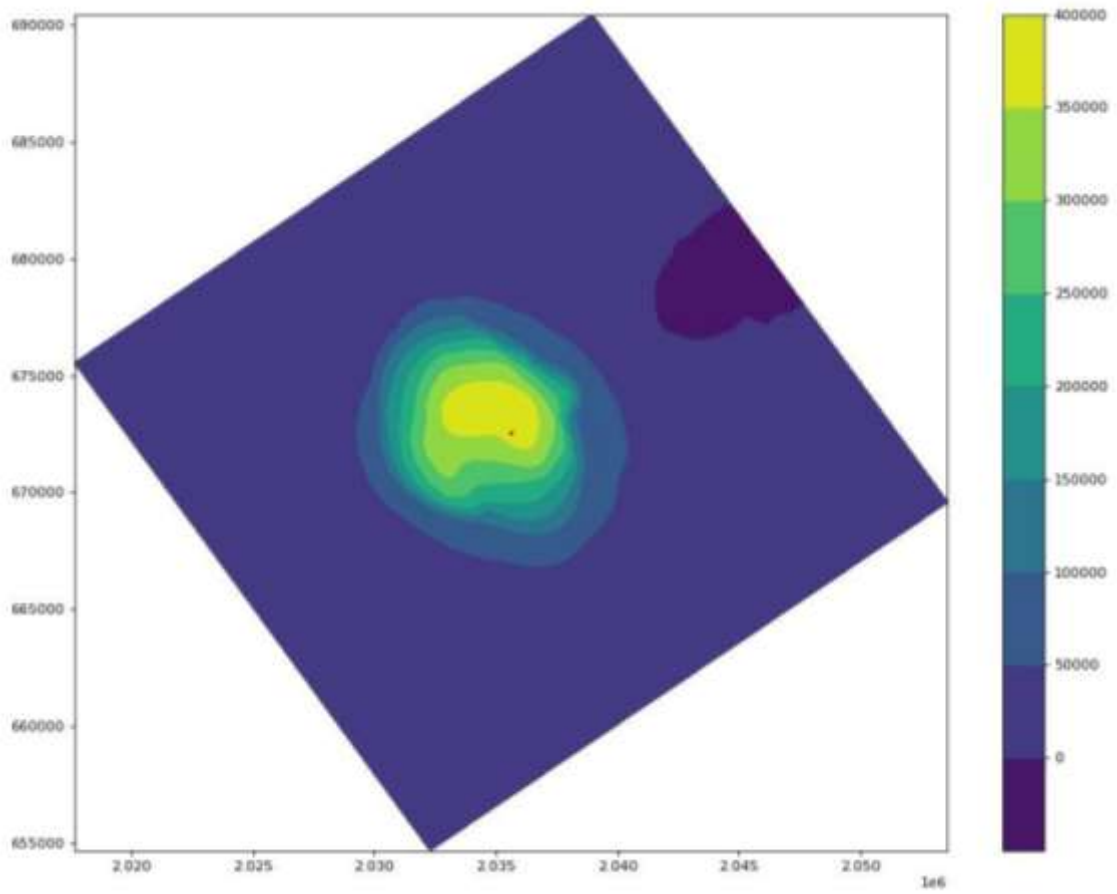


Figure 257 Arbuckle reservoir pressure increases due to injection

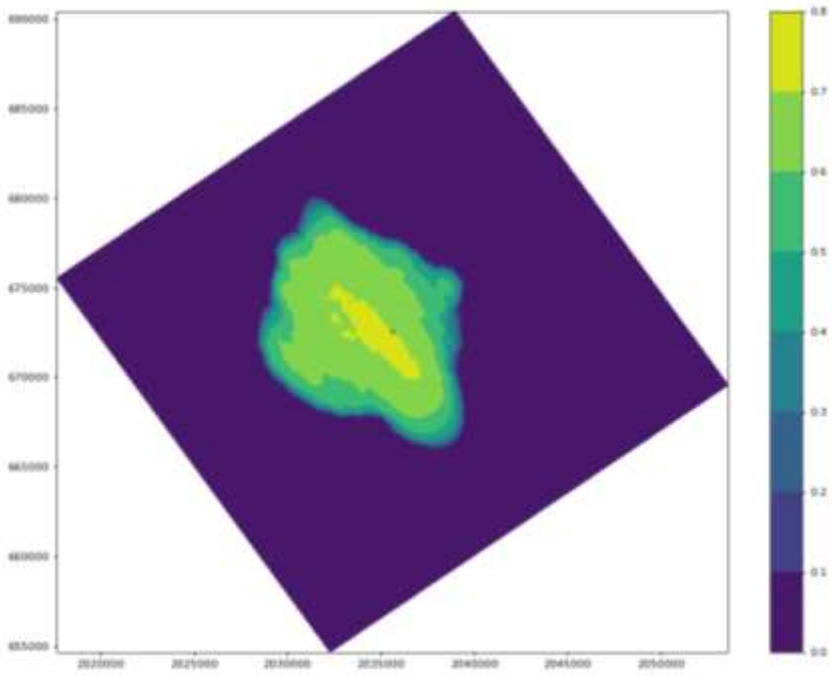


Figure 258 Arbuckle CO_2 plume at year 50

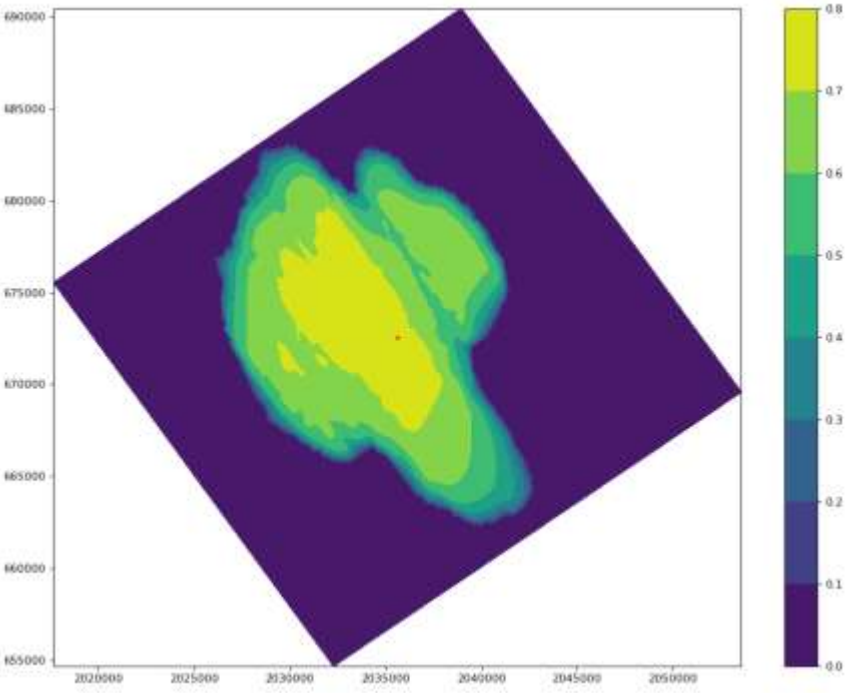


Figure 259 Arbuckle CO_2 plume at year 100

Figure 260 and **Figure 261** show the predicted reservoir pressure and maximum CO_2 saturation for the Arbuckle representative wells, respectively.

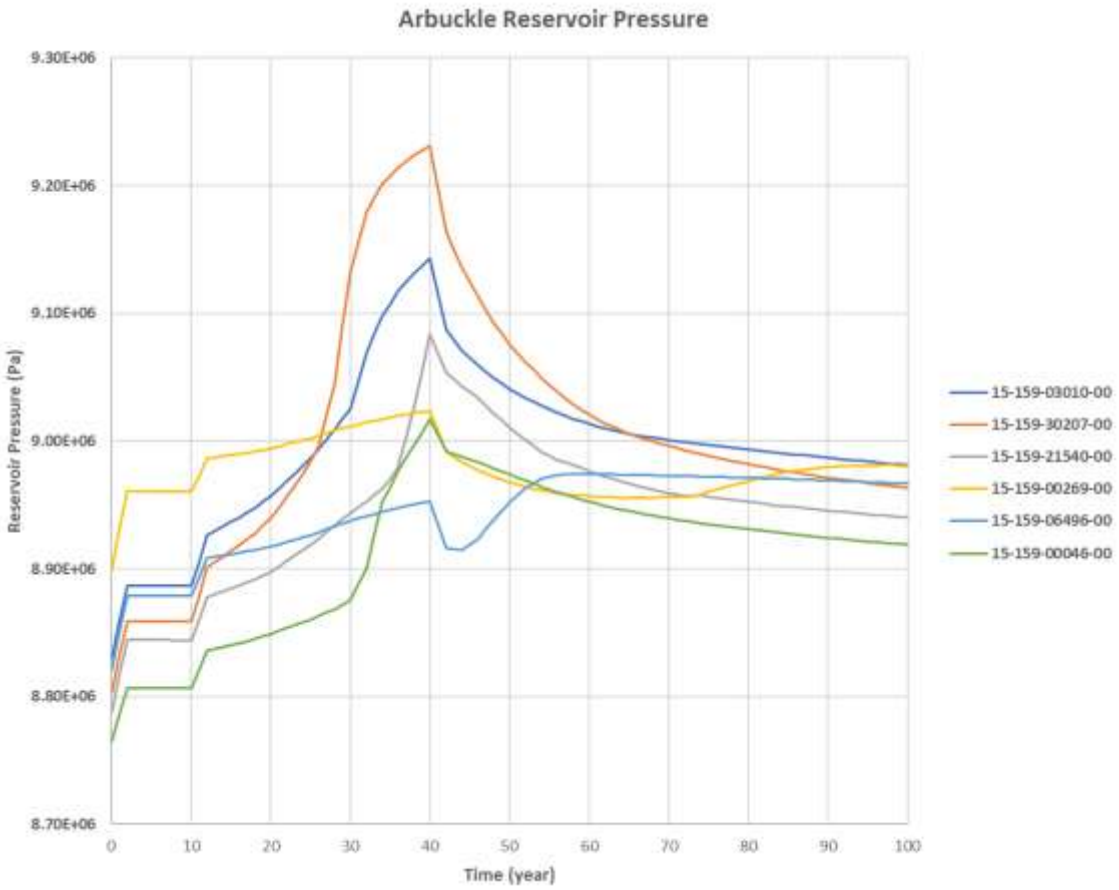


Figure 260 Reservoir pressure at the top of Arbuckle storage formation for representative wells

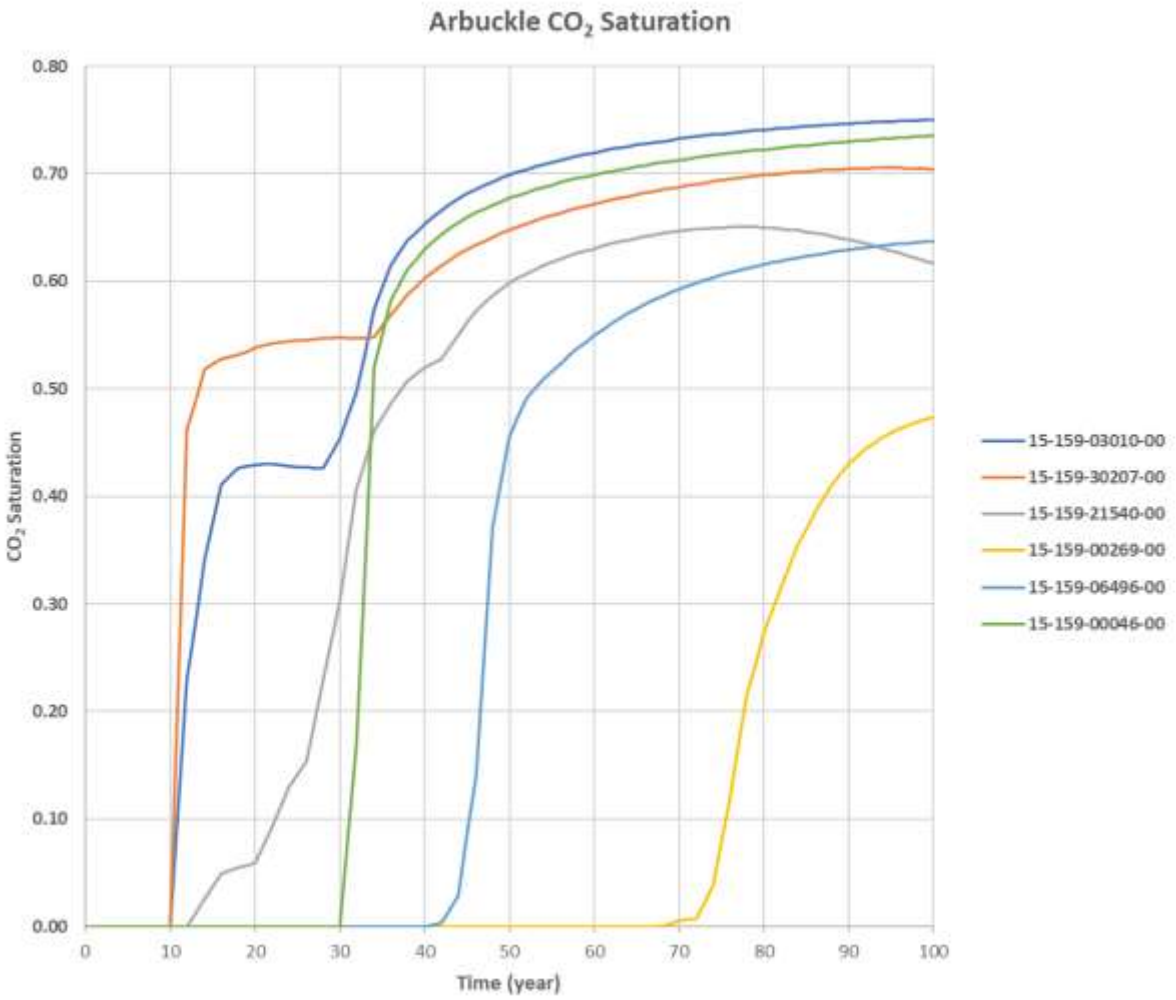


Figure 261 Maximum CO_2 saturation at Arbuckle formation for representative wells

The highest reservoir pressure and earliest CO_2 plume reaching well is well 2 (API 15-159-30207-00), the last CO_2 plume reaching well is well 4 (API 15-159-00269-00). Pressures at 6 well locations all increase during injection and reach maximum value until injection is stopped. They then start to decline in the post-injection period. Maximum delta P due to injection is approximately 0.4 MPa.

CO_2 saturation in wells that are closest to injection well start breakthrough early on during injection (depends on CO_2 plume shape and size), demonstrate that CO_2 plume reaching them earlier while other farther away wells are reached later (e.g. well 4), and some wells with saturation decreasing earlier once injection is stopped (e.g. well 3).

Leakage calculations for Arbuckle injection show that there are no CO_2 and brine leakage for all representative wells, and no impact to USDW on pH and TDS beyond natural background variability.

Summary

Among legacy wells that have been drilled in the study domain, wells penetrating to the two targeted storage formations have been identified. Leakage risk analyses for chosen representative wells show that the pressure build up and wellbore permeability strongly influence the CO_2 and brine leakage from the reservoir to the USDW.

For LKC formation injection, analysis of chosen representative wells in the reservoir domain shows there are very small CO_2 and brine leakage, and small USDW impact for wells 1, 3, 4, and 5. The percent of CO_2 leaked in comparison to the total amount injected is less than 4×10^{-7} % for the highest potential leaky well. There is no CO_2 and brine leakage, and no impact to USDW on pH and TDS beyond natural background variability for well 2 (API 15159003220000).

For Arbuckle formation injections, analysis of chosen existing wells on the reservoir domain shows that there is no CO_2 and brine leakage and no impact to USDW on pH and TDS beyond natural background variability for any well.

For this study we take a conservative approach for leakage risk assessment, choosing the legacy wells that are closest surrounding the injection well to evaluate the highest CO_2 and brine leakage potentials for existing legacy wells. For Class VI well permit application at the ONEOK site, AoR delineation will confine the leakage risk concerned area. Individual well leakage situations are different based on each well's degradation status, more complete wellbore and site characterization data will help facilitate the site-specific leakage risk assessment accurately.

5.2 Subtask 5.2 – Assess well integrity and seal penetrations. To determine risk for leakage from storage vessels, seal assessment is necessary in the Area of Review

Well integrity broadly includes all elements of well construction that are in place to prevent uncontrolled release of fluids into other formations or the environment. Casing, cement, wellhead components, and other downhole elements (e.g. sliding sleeves) represent physical barriers between a producing reservoir and its produced fluids and gases with other permeable formations penetrated by the wellbore and the surface environment. Carbon sequestration-specific well integrity considerations and suggestions for additional research needs are summarized in Iyer et al. (2022); research recommendations of these authors included the following:

- Improve the availability of existing well construction and inspection data through digitization of historical regulatory records.
- Establish quantitative relationships between well information in regulatory databases and indicators of leakage risks for use in prioritizing well inspection and remediation efforts.
- Develop and test methods to quantify leakage risk and uncertainty when well attribute data are missing.
- Evaluate different mitigation and risk management approaches when leakage risk of legacy wells is unacceptable.
- Incorporate improved characterizations of well barrier integrity, leak detectability, and mitigation into quantitative risk assessment and management frameworks for improved decision support.

As discussed in Subtask 5.1, this study applied a relatively conservative leakage risk assessment that focused on legacy wells nearest the proposed injection well at the Bushton site and did not

include a rigorous well-by-well evaluation for each of the 100+ wells within the AoR. An audit and evaluation of well integrity at the Medford site was not completed. The approach applied at the Bushton site was necessary and reviewed with the team during the study for the following reasons:

- Location of the injection well in the simulation is conceptual
- The static geologic model is under-constrained and lacks a "stratigraphic well" that would redefine trends within the model to more properly delineate an AoR.
- Existing drilling, completion, plugging, and status for wells in the model area is variable. A thorough evaluation of all wells (including those operated by ONEOK) will be necessary for any future carbon sequestration considerations in the area.
- Most wells were drilled prior to 2010 with some approaching 100 yr since their spud date (**Figure 262** and **Figure 263**). Newer wells are likely to have better casing and cement; however, recent production could decrease formation pressure below pre-production conditions which were not assessed during this study.

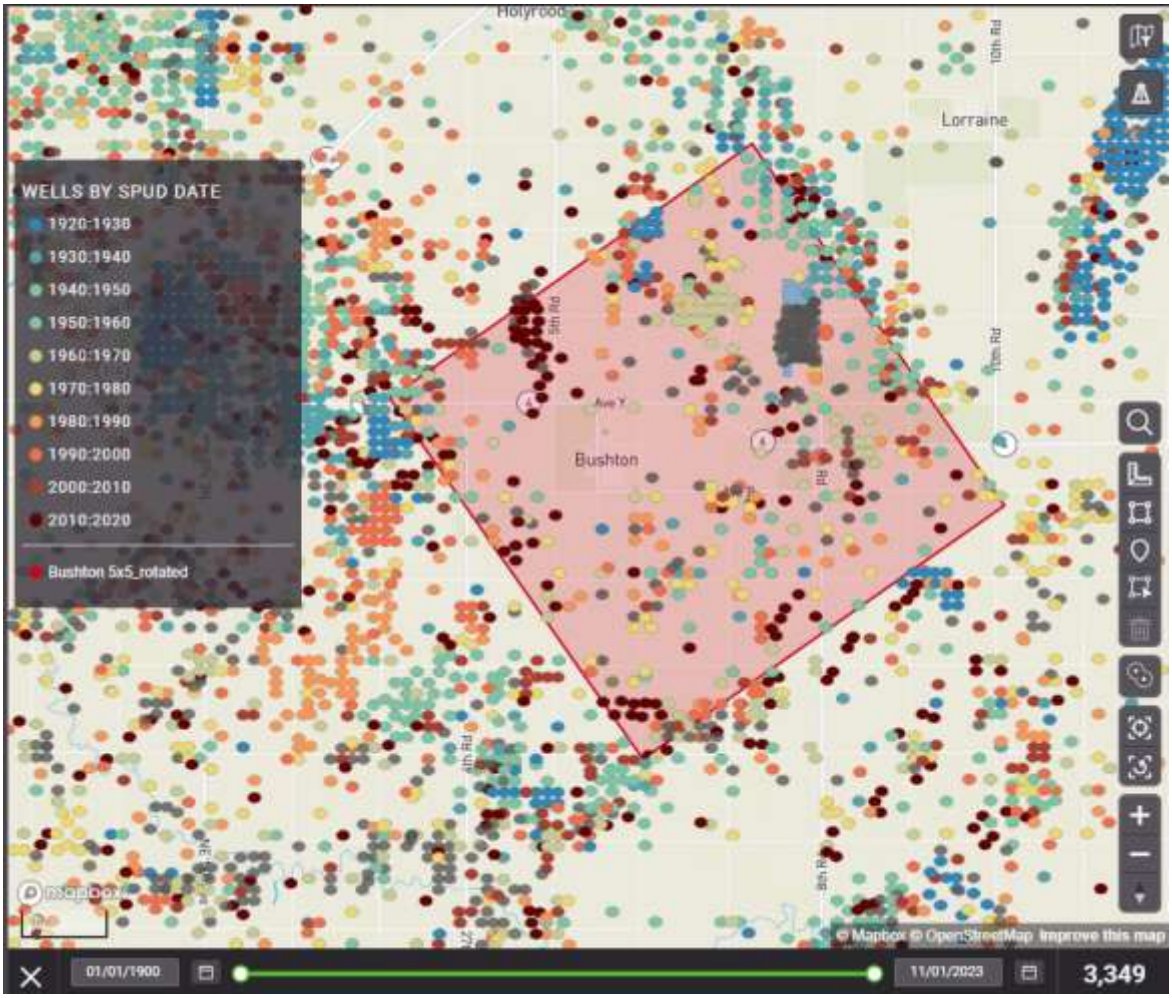


Figure 262 Map showing spud date by decade for wells in the Bushton area. NOTE: Most wells drilled to the Arbuckle Group. Data as compiled by Enverus 2023.

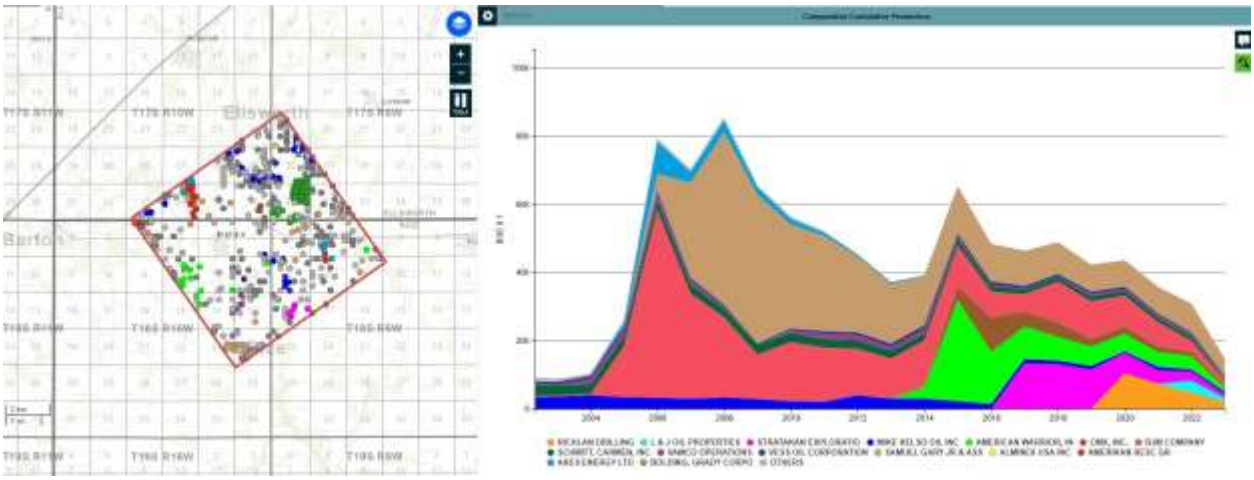


Figure 263 Map showing wells in the modeled area with current operator (left). Cumulative production by operator since 2010 (right). Data as compiled by Enverus.

At the Bushton site an evaluation of well and seal integrity will require analysis of original well documentation; additionally, a review with the Kansas Corporation Commission regarding historical activity in the area and current operators is recommended. If third party data aggregation services are utilized (e.g. Enverus), the underlying data must be validated with documented and publicly available information. As recommended by Iyer et al. (2022), a method to apply leakage risk and uncertainty where documentation and attributes are unknown will need to be established as well as strategies for mitigation and risk management where wellbores with known integrity issues are identified. A detailed vessel and pipeline to the well injection site (with appropriate leakage/seal evaluation and monitoring) will need to be developed by the operator of the injection well. As discussed in Subtask 3.2.6, it is not recommended without additional technical evaluation that salt cavern storage of CO_2 be considered at the Bushton site.

Subtask 5.3 – Prepare a Ranked Matrix of Key Risk Factors for Each Seal and Reservoir Horizon AoR Addressing Key Surface and Subsurface Issues that Might Affect Injection Viability

This subtask synthesizes the data audit, modeling, and simulation results into a comparative framework, addressing qualitative subsurface risk profiles relevant to viability, and permitting. Additionally, it illustrates where additional effort might be invested to reduce subsurface uncertainty and define the value of information related to collecting new data (e.g. seismic, cased-hole wireline, new drillwell, etc.). It is inherently a qualitative exercise based on relative quality of the selected elements. Importantly, it highlights the tradeoff between areas that have reasonable subsurface datasets (e.g. Bushton Arbuckle) vs. those without (e.g. Medford Wilcox Bromide). At the Bushton site there are numerous wells with valuable information (top depths, thickness, reservoir properties, etc.) and offset information (injection and production rates) whereas at the Medford site there are fewer wells and an under-constrained reservoir system. The Medford site, however, carries significantly lower seal containment and offset operation risk.

Figure 264 is the summary ranked matrix of the key risk factors that were considered in the evaluation of the reservoirs, sealing formations, and the USDWs (KS only). It is important to note that in both Kansas and Oklahoma multiple sealing facies exist above the Arbuckle,

Wilcox-Bromide sandstone, and the Lansing-Kansas City systems. The Arbuckle has the advantage in both states of being deeper, having well characterized reservoir characteristics, and high injectivity. This evaluation highlights the importance of considering multiple reservoir targets to identify the best candidate(s) and to consider redundant/backup injection options within injection wells should initial injection performance prove to be inadequate. It also highlights the importance of understanding the current formation pressure; specifically for the Bushton site, it is critical to understand the current regional pressure sources (injection) and sinks (production) that might cause local perturbations in the system and create unexpected injection plume formation.

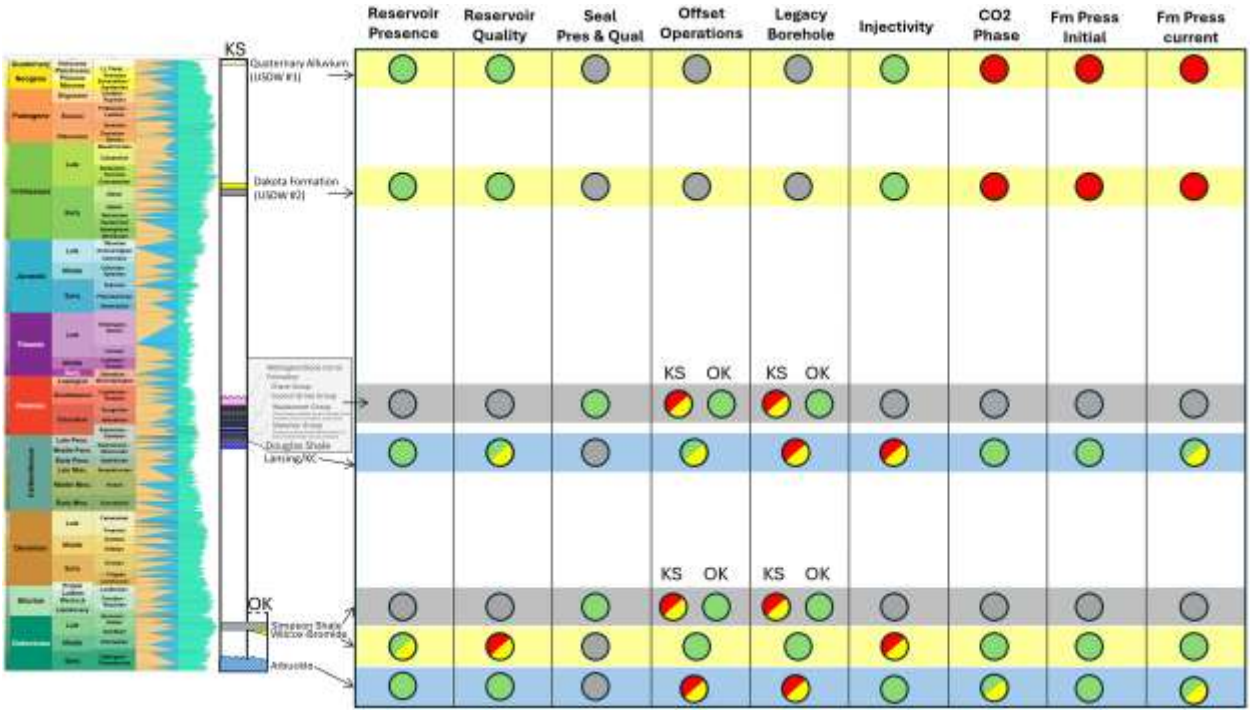


Figure 264 Stoplight style risk matrix for each seal and reservoir horizon and AoR addressing key surface and subsurface issues that might affect injection viability. The KS USDWs are also included for context.

The AoRs defined in this study are preliminary (see Subtask 2.4 of this report) but highlight the information density, quality, and availability near the ONEOK operational facilities at Bushton, Kansas and Medford, Oklahoma. Future evaluation at either site should benefit from this preliminary work which has assembled many of the fundamental elements necessary for a successful CCS project. In particular, it should be noted that the reservoir property modeling (e.g. porosity and permeability) represent non-unique solutions to the dataset and additional static scenarios could possibly generate plumes and pressure response quite different than those presented in this report. The risk from induced seismicity was not included in the risk matrix because neither site currently has evidence of seismicity above background levels or mapped faults (see Subtask 3.5 of this report). Both Bushton reservoir formations had favorable outcomes in the LANL relative leakage risk rankings by well and formation with the LKC showing minimal leakage and the Arbuckle showing none (see Subtask 5.1 of this report).

Induced Seismicity

As outlined in Subtask 3.5, induced seismicity in Kansas and Oklahoma has been studied extensively by researchers and regulators for over a decade. Kansas historically experienced low seismicity, with only approximately 30 felt earthquakes between 1867 and 1977. However, increased saltwater disposal activities since 2000 have been linked to a sharp rise in earthquake frequency. From 1977 to 2012, more than 200 seismic events were recorded in association with Arbuckle Group injection. summarizes statewide seismic activity from 1867 to 2018.

Seismic events from 2014 to 2022 are shown in **Figure 265**, overlaid with mapped fault traces and newly deployed seismic monitoring stations, including the RS-3D network described in Subtask 3.5. These observations demonstrate that central Kansas, previously considered seismically quiet, does exhibit low-magnitude seismic activity detectable with a localized network.

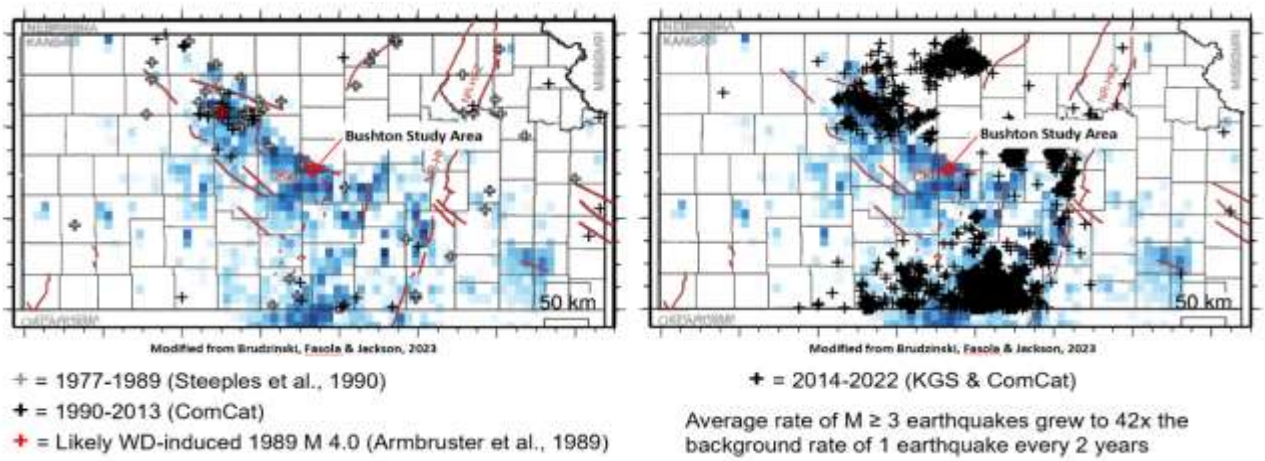


Figure 265 Induced seismicity in study area is low risk, despite high wastewater injection volumes. (From Fasola et al. in prep.)

The relationship between elevated pore pressure and induced seismicity is well established (Langenbruch and Zoback 2016; Rubinstein 2018; Dempsey et al. 2019; Chang and Segall 2016; Zhai et al. 2019; **Figure 221**). Given these risks, injection into the Arbuckle is discouraged by the Oklahoma Geological Survey and regional stakeholders. As a result, the Arbuckle was excluded from dynamic modeling at the Medford site, even though some static characterization was completed. Simulations instead focused on more geologically favorable intervals, such as the Wilcox–Bromide system.

While explicit seismicity modeling was not conducted, PNNL's dynamic simulations evaluated spatial and temporal pressure changes, including plume overlap and pressure interference between CO_2 and wastewater injectors in the Arbuckle. These are important precursors for assessing fault reactivation potential. PNNL concluded that further seismic risk evaluation would require detailed fault mapping and geomechanical modeling, which was beyond the current project scope.

Potential Leakage Risk Analysis Using NRAP Tools

To evaluate the potential for CO_2 and brine leakage from legacy wells within the AoR, the NRAP open-source Integrated Assessment Model (IAM) was employed. This toolset

incorporates reduced-order models (ROMs) for key subsurface components, including the reservoir, wellbore, and overlying aquifer systems.

A preliminary AoR containing 69 legacy wells was assessed using pressure and saturation outputs from STOMP-based reservoir simulations (Task 4). Wellbore integrity was evaluated using the cemented wellbore ROM, which accounts for well construction, material degradation, and pressure gradients. Reservoir simulation results Reservoir simulation results for Well1, located 380 feet west of the CO_2 injector, indicated a peak reservoir pressure of approximately 8.5 MPa after 5 yr of injection and a CO_2 saturation peak of approximately 32% at year 35 (**Figure 266**). These values served as inputs to the wellbore ROM. The analysis confirmed that, under modeled conditions, no significant leakage of CO_2 or brine into the USDW occurred, and no adverse aquifer impacts were observed.

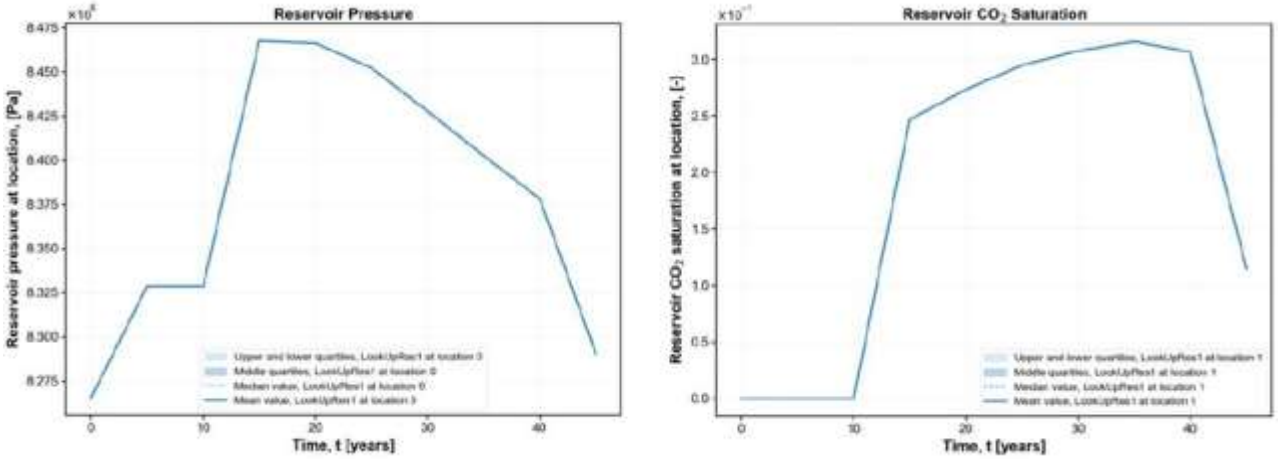


Figure 266 Reservoir pressure (left) and CO_2 saturation (right)

Traffic Light System to Mitigate Induced Seismicity Hazard and Risk

A structured approach for managing induced seismicity in geologic carbon storage (GCS) has been recommended by Templeton et al. (2022) and adopted by the U.S. EPA as part of Class VI well permitting requirements (**Figure 267**). The federal regulations relevant to this process are codified in 40 CFR 146.94(a), as part of the Emergency and Remedial Response Plan, and elaborated in EPA's Class VI guidance documents.

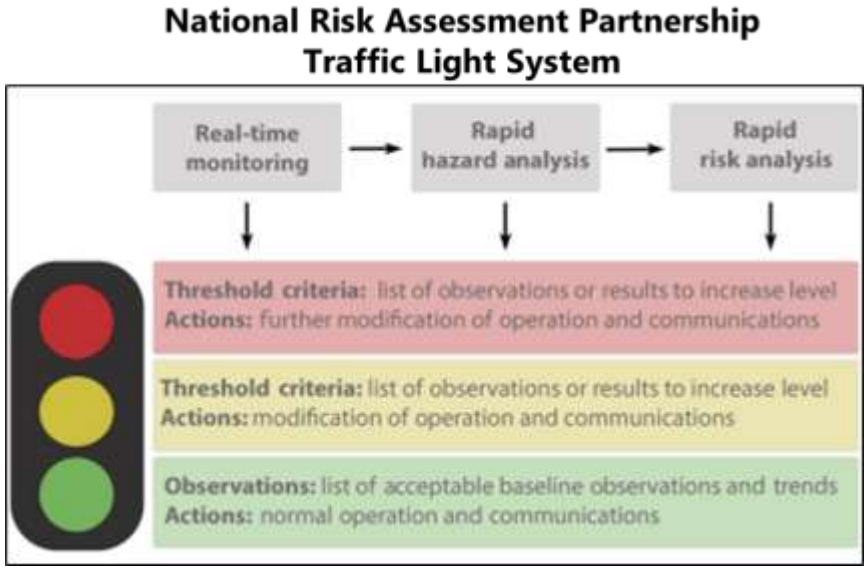


Figure 267 The recommended 7-step approach and the adaptive traffic light from the National Risk Association Partnership in collaboration with Templeton et al. (2022)

Effective risk management requires real-time monitoring of seismic, hydraulic, and operational parameters. These inputs can trigger pre-defined response levels or inform rapid hazard and risk assessments that warrant operational changes. Establishing a baseline of local seismicity is a prerequisite for implementing a site-specific risk management protocol.

As described in Subtask 3.5, a local seismic monitoring network was installed near the Bushton facility and operated for 11 months. This network provided a new earthquake catalog for establishing background seismicity and evaluating risk thresholds. It also demonstrated the utility of low-cost RS-3D instruments for continuous local monitoring in industrial settings.

Although PNNL did not explicitly model induced seismicity, their reservoir simulations did capture spatial and temporal pressure trends relevant to seismic risk. These included evaluations of pressure buildup and plume interference with legacy wastewater injection into the Arbuckle. Such conditions are recognized precursors for fault reactivation.

As concluded by PNNL, a detailed seismic risk assessment would require fault mapping and mechanical modeling, which exceeded the current project scope. However, their findings helped define preliminary AoR boundaries and highlighted the sensitivity of model outcomes to initial pressure distributions, permeability assumptions, and legacy well characteristics (e.g. plugging methods and construction age).

Subtask 5.5 – Economic Risk/Feasibility Assessment

Sandia National Laboratories conducted a detailed economic analysis to evaluate the feasibility of CO_2 storage at four proposed injection scenarios near ONEOK's facilities in Bushton, Kansas, and Medford, Oklahoma. The study integrated three key methods: (1) techno-economic analysis (TEA) to estimate capital (CAPEX) and operational (OPEX) expenses and levelized CO_2 storage costs (LCOS); (2) cost-benefit analysis (CBA) using Section 45Q tax incentives to compute net present value (NPV); and (3) evaluation of financial and regulatory risks affecting project viability.

The TEA was conducted following methods from Mishra et al. (2025), using both site-specific data from ONEOK and generalized cost models. The CBA included baseline and sensitivity scenarios and incorporated key project parameters such as well depth, injection rate, and lifetime. Economic risk was evaluated by categorizing regulatory, market, financing, and social risks.

The analysis evaluated four proposed CCS sites: Bushton-LKC, Bushton-UArb, Bushton-DArb, and Medford-WilBro. Table 52 summarizes key reservoir and injection parameters used for cost modeling, including injection rate, total CO_2 volume, and well depth.

Table 52 ONEOK Carbon sequestration site characteristics

	Bushton-LKC	Bushton-UArb	Buston-DArb	Medford- WilBro
Injection rate (MMSCFD)	17	17	52	17
Injection rate, t/day	998.86	998.86	2,996.58	998.86
Injection rate, t/Yr	350,000	350,000	1,050,000	350,000
Total CO_2 sequestered, t	10,500,000	10,500,000	31,500,000	10,500,000
Depth	3,088	3,841	4,136	4,993
Number of injection wells	1	1	3	1

Capital and operating costs were estimated using the techno-economic framework developed by Mishra et al. (2025). CAPEX included geologic site characterization, AoR studies, well construction, compressors, monitoring stations, and administrative costs. These were calculated using depth, number of wells, and injection volumes. The techno-economic results indicate that CO_2 injection at all four sites is capital intensive but operationally efficient. Total capital costs range from approximately $8.2 million to $18.7 million, with higher CAPEX at deeper sites like Bushton-DArb. Operating expenses are dominated by compression energy requirements, with COMC consistent across sites due to similar injection volumes.

Calculated LCOS range from $10.86 to $11.13 per metric ton, with overlapping confidence intervals (Table 5.6), indicating economic comparability across sites despite differing depths and injection configurations.

Cost-benefit analysis using Section 45Q tax credits yielded benefit-cost ratios >1 and NPVs exceeding $100 million for all sites under all scenarios. Table 5.7 summarizes NPV and B/C ratios across three economic scenarios.

These results suggest all four CCS projects are economically feasible under current tax credit structures and operating assumptions. The analysis highlights high CAPEX but favorable long-term financial performance.

An additional 20% of total capital cost was added as fixed general administrative cost.

OPEX included COMC and WOMC, calculated using energy requirements and site-specific well parameters.

Table 53 Median capital expenditure for storage site development (in million USD)

	Bushton-LKC	Bushton-UArb	Buston-DArb	Medford- WilBro

Storage site	8.21	8.47	17.82	8.68
Geologic Site Characterization	0.69	0.69	0.69	0.58
Permit	0.24	0.25	0.52	0.26
Injection well construction	1.97	2.22	5.75	2.53
AoR Study & corrective action	0.27	0.27	0.72	0.27
Compressors	5.00	5.00	10.00	5.00
Well operating equipment	0.05	0.05	0.14	0.05
Total	16.42	16.93	35.64	17.36

The LCOS was computed from total CAPEX and OPEX using the following equation:

$$LCCO_2 = LTCC + OM_{COM} + OM_W \text{ Eq. } 1$$

where LTCC (levelized total capital cost) is calculated as:

$$LTCC = \frac{TCC * CRF}{CF} \text{ Eq. } 2$$

with CRF (capital recovery factor) computed as:

$$CRF = \frac{r * (1+r)^t}{(1+r)^t - 1} \text{ Eq. } 3$$

A discount rate of 10% and project lifetime of 30 yr were used, yielding a CRF of 0.11. Levelized costs per ton of CO_2 are presented in Table 54.

Results and Cost-Benefit Analysis

The techno-economic results indicate that CO_2 injection at all four sites is capital intensive but operationally efficient. Total capital costs range from approximately $8.2 million to $18.7 million, with higher CAPEX at deeper sites like Bushton-DArb. Operating expenses are dominated by compression energy requirements, with COMC consistent across sites due to similar injection volumes.

Calculated LCOS range from $10.86 to $11.13 per metric ton, with overlapping confidence intervals (Table 54), indicating economic comparability across sites despite differing depths and injection configurations.

Cost-benefit analysis using Section 45Q tax credits yielded benefit-cost ratios >1 and NPVs exceeding $100 million for all sites under all scenarios. Table 55 summarizes NPV and B/C ratios across three economic scenarios.

These results suggest all four CCS projects are economically feasible under current tax credit structures and operating assumptions. The analysis highlights high CAPEX but favorable long-term financial performance.

Table 54 Levelized cost of CO_2 storage

	Bushton-LKC	Bushton-UArb	Buston-DArb	Medford- WilBro
LTCC	0.08 (0.07-0.12)	0.09 (0.07-0.12)	0.06 (0.05-0.07)	0.09 (0.07-0.13)
WOMC	0.65 (0.47-0.75)	0.73 (0.54-0.85)	0.60 (0.44-0.7)	0.85 (0.62-0.98)
COMC	10.19 (8.35 – 12.03)	10.19 (8.35 – 12.03)	10.19 (8.35 – 12.03)	10.19 (8.35 – 12.03)
LCOS	10.92 (9.08-12.76)	11.01 (9.17-12.85)	10.86 (9.02-12.69)	11.13 (9.29-12.96)

The techno-economic analysis conducted for the ONEOK site demonstrates that the total capital and operational costs associated with CO_2 injection are highly dependent on well depth, equipment selection, and site-specific geological conditions. The estimated levelized cost of CO_2 storage provides a useful benchmark for evaluating the economic feasibility of the proposed ONEOK carbon sequestration projects. However, the results of any site-specific analysis are not generalizable for the whole region.

Table 55 The benefit cost ratios and net present value of the ONEOK sites

		Bushton-LKC	Bushton-UArb	Buston-DArb	Medford-WilBro
Scenario 1	**Benefit:Cost Ratio**	5.6	5.6	6.3	5.6
	Net Present Value (million USD)	182.3	182.03	522.4	181.7
Scenario 2	**Benefit:Cost Ratio**	2.8	2.7	2.9	2.7
	Net Present Value (million USD)	167.5	167.1	508.8	166.7
Scenario 3	**Benefit:Cost Ratio**	1.2	1.2	1.3	1.1
	Net Present Value (million USD)	138.1	137.39	421.7	136.6

Economic Risk Assessment

Sandia's analysis also identified key financial risks that could affect project feasibility. These are categorized as follows:

Regulatory and Policy Risk

The CCS policy landscape remains dynamic. Uncertainty in Section 45Q tax credit duration, value, and eligibility introduce risk, as many CCS projects rely on full realization of these incentives for viability. Compliance with monitoring and verification requirements, long-term liability, and evolving Class VI permitting standards can also increase costs and delay implementation (EPA 2008).

Market and Price Risk

Volatile input prices, particularly for compressors, drilling, and electricity, directly affect CAPEX and OPEX. Between 2021 and 2025, equipment costs rose significantly. As CCS is energy-intensive, fluctuations in power prices can notably alter LCOS, potentially undermining economic viability.

Financing and Interest Rate Risk

All four sites require substantial upfront investment ($8.2M–$35.6M; see techno-economic results). Large capital requirements combined with uncertain returns reduce investor confidence. Interest rate variability further influences project viability; even small increases in borrowing costs significantly affect NPV in high CAPEX projects with long lifespans.

Community and Social Licensing Risk

Local community acceptance is critical. Concerns around groundwater protection, induced seismicity, and long-term site stewardship may delay or block development. Transparent risk communication, stakeholder engagement, and environmental monitoring are essential to mitigate opposition and secure social license.

Conclusion

Based on available site data and the methodology of Mishra et al. (2025), all four proposed ONEOK wells appear economically feasible. The analysis used conservative assumptions and focused exclusively on injection-site costs, excluding capture and transportation expenses. Net Present Values exceeding $100 million for each site suggest sufficient economic headroom to accommodate additional upstream costs.

The results should be interpreted as preliminary indicators, not definitive project valuations. TEA and NPV outputs are sensitive to input assumptions, particularly cost, operational efficiency, and policy parameters. Improved accuracy in site-specific data will refine future assessments.

Additionally, while the techno-economic analysis identified economically viable scenarios, it did not include all financial risks. Sections above outline key uncertainties—regulatory, market, financing, and community-related—that may influence future project implementation. The accompanying risk framework provides a tool for CCS developers to evaluate these uncertainties and enhance financial planning.

This analysis demonstrates that all four ONEOK CCS project sites are technically and economically promising candidates for development, contingent on further data acquisition, regulatory alignment, and proactive risk management.

Task 6 – Infrastructure Network Assessment

Carbon Solutions utilized SimCCS^{PRO} and other supporting tools to assess the infrastructure network required to transport CO_2 from emitting facilities to sites for permanent geological storage. SimCCS^{PRO} is an economic-engineering, mixed-integer linear programming model that determines where and how much CO_2 to capture, where and how much CO_2 to store, and the pipeline network that connects these point locations. SimCCS^{PRO} utilizes a series of inputs

generated by the other proven software of CO_2NCORD (Carbon Solutions 2025d), SCO_2T^{PRO} (Carbon Solutions 2025b), and CostMAP. Together, these software provide estimates for capturable CO_2 emissions and capture costs, estimates for underground CO_2 injection capacities and storage costs, and a weighted cost surface, respectively.

Subtask 6.1 – Aggregate Infrastructure Data and Build Databases

Carbon Solutions assessed existing infrastructure within the defined region by aggregating potential sources of CO_2 and using the geology characterization provided by the team's leading Task 3 and Task 4 to assess storage options. Carbon Solutions used its proprietary software, CO_2NCORD, to determine all the potential CO_2 emitters within the Area of Interest (AOI) before working with industry partner ONEOK to identify which emitters would be included in the analysis. Ultimately, eight unique facilities across six industries with a total of 12 capturable streams of CO_2 were selected (**Figure 268**). These facilities have a cumulative amount of 2.1 Mt of capturable CO_2 emissions with capture costs that range from \$36.89/tCO_2 to \$71.13/tCO_2. Capture costs were generated in CO2NCORD using the best available public data, which includes literature, expert elicitation, and recent reports from NETL (Bennett et al. 2024). These emitters represent partnership opportunities for ONEOK in developing and deploying a CCS network in Kansas and represent the entire extent of emitters in the AOI regardless of their inclusion in final scenarios (**Figure 269**).

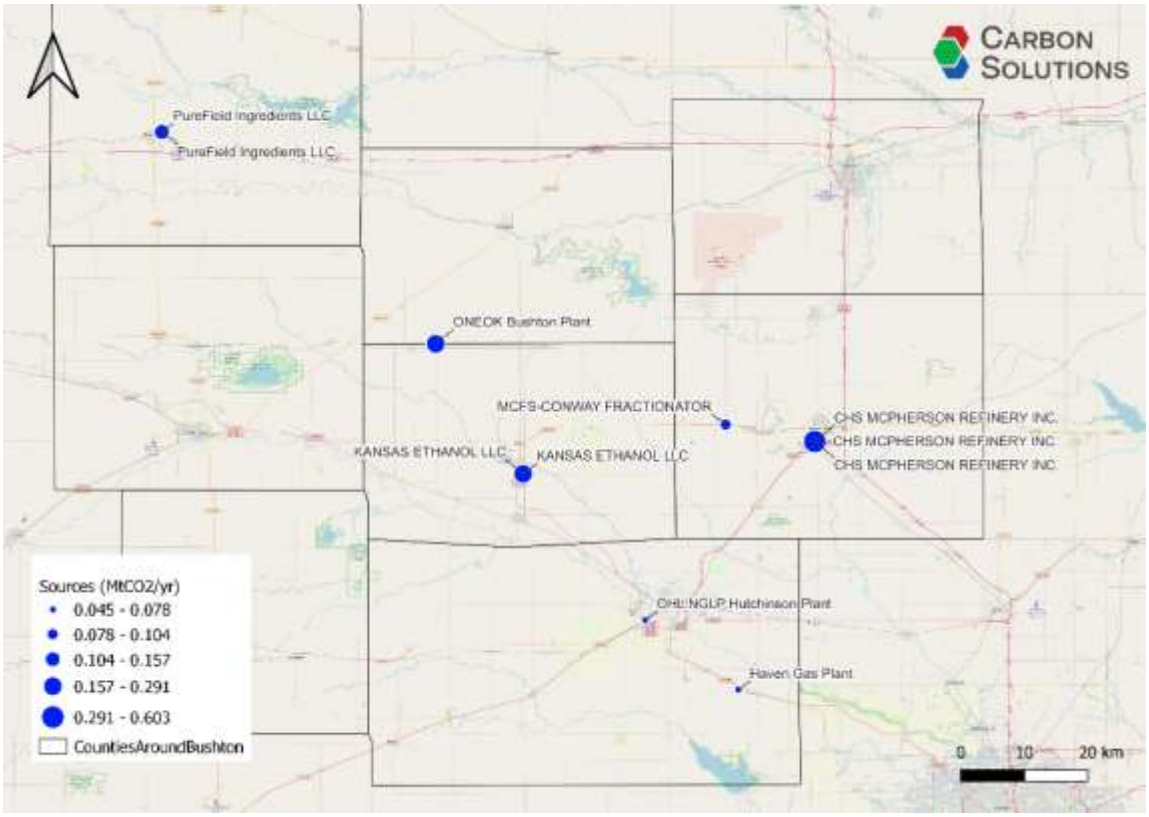


Figure 268 Map of all potential emitters within the AOI

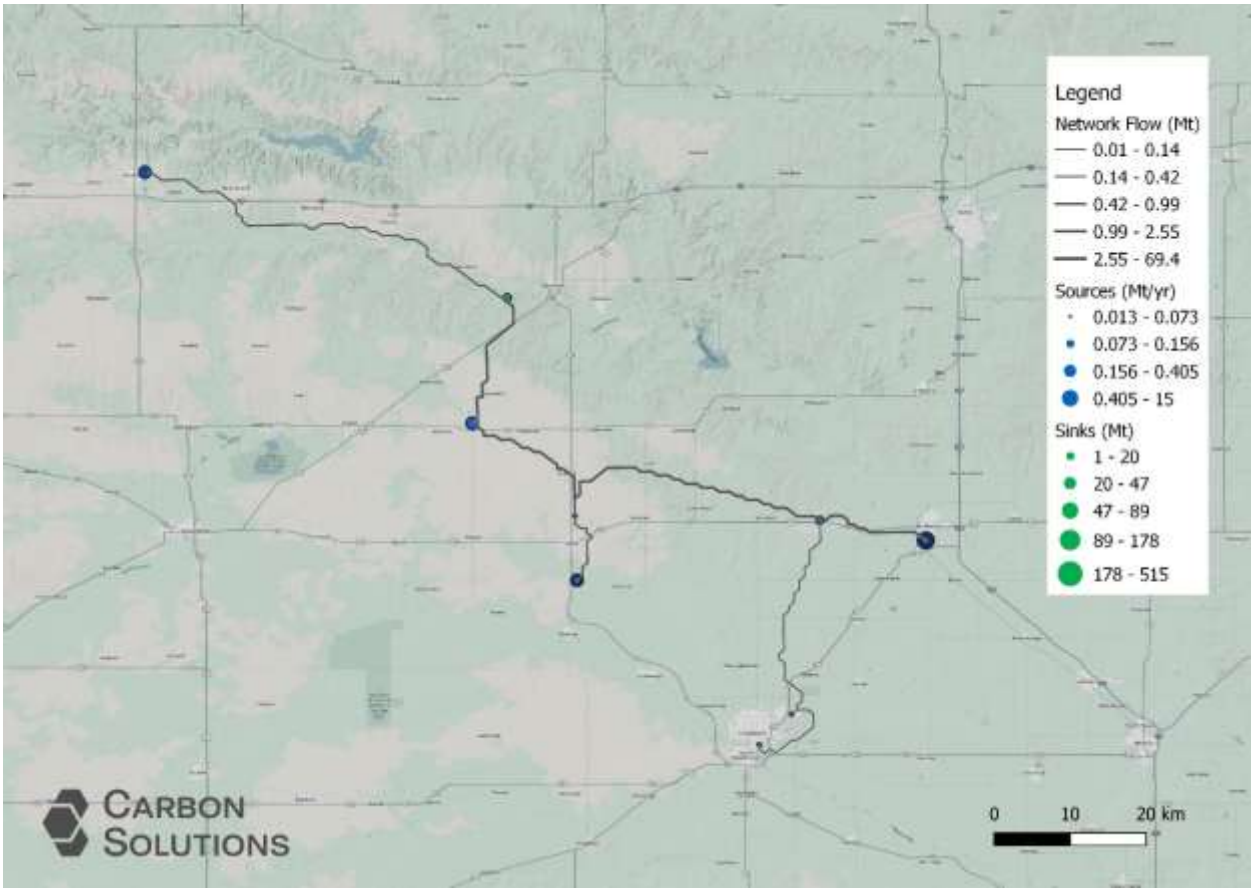


Figure 269 Map of source distributions and capacities

The teams leading Task 3 and Task 4 provided detailed geological characterizations of potential storage formations within the defined region including anticipated injection rates ($MtCO_2$/yr) into each formation. Carbon Solutions utilized the geologic data as input into its proprietary model SCO_2T^{PRO} which estimates storage costs ($/t$CO_2$) and formation storage capacities ($MtCO_2$) for given geological data. This was done for the three different storage locations (Bushton, Alternate Site 1, and Alternate Site 2) and three different formations (Lansing-KC, Arbuckle, and Wilcox-Bromide). This was also modeled for two different injection rates: 0.3 $MtCO_2$/yr and 1 $MtCO_2$/yr. Estimates for storage capacities and storage costs from SCO_2T^{PRO} can be found in Table 56 for each of the different formations, locations, and geological characteristics.

Table 56 Outline of different scenario sets and runs for each scenario set that were completed using SimCCS^{PRO} by Carbon Solutions

Scenario Location	Geology Context	Run 1	Run 2	Run 3	Run 4
Bushton	Arbuckle Formation: 30 Mt Storage Capacity	Hutchinson, Conway Fractionator, Bushton	Run 1 + Cargill Salt, KS Ethanol, NA Salt	Run 2 + McPherson Facilities	Run 4 + Purefield

Alternate Site 1	Arbuckle Formation: 30 Mt Storage Capacity	Hutchinson, Conway Fractionator, Bushton	Run 1 + Cargill Salt, KS Ethanol, NA Salt	Run 2 + McPherson Facilities	Run 4 + Purefield
Alternate Site 2	Arbuckle Formation: 30 Mt Storage Capacity	Hutchinson, Conway Fractionator, Bushton	Run 1 + Cargill Salt, KS Ethanol, NA Salt	Run 2 + McPherson Facilities	Run 4 + Purefield
Total Annual Emissions ($MtCO_2$/yr)		0.442	0.842	1.916	2.118
10-yr Emissions ($MtCO_2$)		4.42	8.42	19.16	21.18

Subtask 6.2 – Model Pipeline Corridor and Define Surface Facilities That Would Be Required to Execute Chosen Design Concepts

CostMAP is used to determine the potential transportation network that connects sources to storage sites by creating a cost surface that includes a variety of data, such as rights-of-way, land use changes, population densities, elevation changes, and more. Each layer that is put into CostMAP is assigned its own routing and cost weights separately. The cost weights are intended to account for the actual costs of constructing pipelines in each area. Routing weights are intended to capture non-economic factors such as environmental considerations or important areas to local communities. The result is both a routing network, that shows where pipelines can go, and a cost network that provides cost estimates for these potential routes. Keeping routing and cost separate is important because while one route might have a lower cost, it could pass through areas that are important to local community or protected lands. Therefore, having separate routing and cost networks helps to choose the least cost option that includes environmental, economic, and social factors. These routing and cost weights help to identify potential barriers, features that prohibit or restrict pipeline deployment like rights-of-ways and roads.

After routing and cost weights have been chosen, a stepwise process computes the cost of moving from cell to cell, calculated as the average cost of the corresponding nodes normalized by the distance needed to travel between nodes (rook vs bishop movement). More details on the function of CostMAP^{PRO} can be found in Hoover et al. (2019). The result is more realistic pipeline routing. More details on potential pipeline corridors and surface facilities that would be involved in capture-transport-storage systems can be found in Subtask 6.3.

Subtask 6.3 – Assess CO_2 Capture-Transport-Storage System

Working with ONEOK, Carbon Solutions identified scenarios that contained different emitters as desirable candidates that should be included in modeling the capture-transport-storage system. Table 56 shows the scenarios that were agreed upon and modeled in Subtask 6.3. Table 6.2

shows summary results for each run. These scenarios show potential pathways by which ONEOK and surrounding industries can work together to deploy CCS networks.

Table 2 Summary results for all Bushton scenario runs

Run	Annual Capture Amount ($MtCO_2/yr$)	# Sources	# Sinks	Network Length (km)	Source Cost ($/tCO_2$)	Transport Cost ($/tCO_2$)	Sink Cost, $/tCO_2$	Total Cost ($/tCO_2$)
Run One	0.44	3	1	89.09	69.39	22.68	11.34	103.41
Run Two	0.84	7	1	127.09	60.71	20.05	11.34	92.10
Run Three	1.92	10	1	145.51	65.53	11.15	11.34	88.01
Run Four	2.12	12	1	215.88	63.50	13.74	11.34	88.58

CO_2NCORD uses an amine-based capture technology for estimating capture costs from all sources of CO_2 and pipeline routing in CostMAP^{PRO} is based on NETL's CO_2 Transport Cost Model. Using the weighted cost surface generated by CostMAP, some of the non-technical challenges are addressed by accounting for factors like pre-existing rights-of-way that can encourage new pipeline deployment.

To maintain consistency across the software and modeling efforts used in Task 6, the following assumptions are maintained:

- A 10-yr financing period.
- An interest rate of 10%.
- A capital recovery factor of 0.163.

This means that after 10 yr, all capital cost expenditures have been paid and the only remaining costs are operation and maintenance costs associated with the capture-transport-storage system. Therefore, the costs beyond the 10-yr financing period are expected to be lower than those presented in fulfillment of this report since the presented costs include both capital and operating costs associated with the designed systems.

All inputs and financing assumptions were entered into SimCCS^{PRO}. For the Bushton scenario, total network unit costs went from \$103/tCO_2 in the first run to \$88/tCO_2 in the last final run using all sources. It is observed that unlike scenarios 1 (Figure 6.3) and 3 (Figure 6.5), the CCS network in scenario 2 (Figure 6.4) moves more northwest first instead of moving directly north to connect with the sources. Despite the increase in the amount of transport pipeline deployed (89 km to 216 km), there was a reduction in transportation costs (\$23/tCO_2 to \$14/tCO_2). This is

explained by economies of scale, despite more pipelines being needed these larger pipelines can handle a larger flow of captured CO_2 emissions.

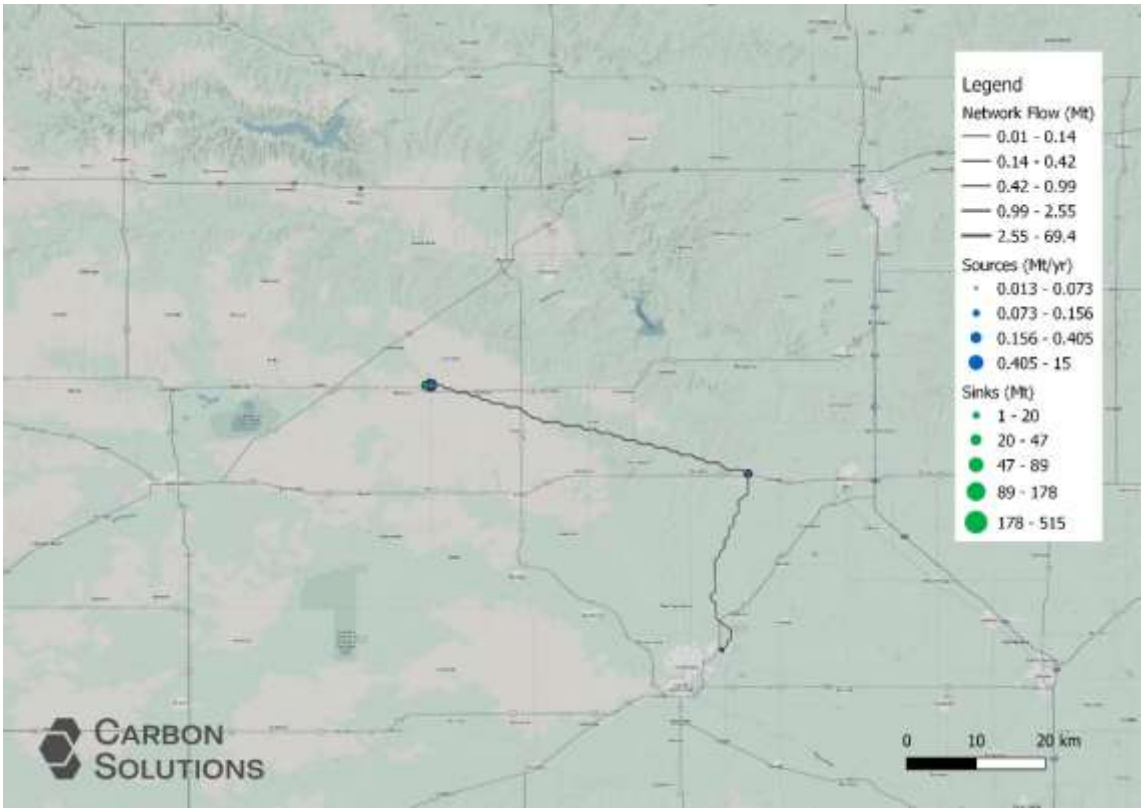


Figure 270 Deployed CCS network for Bushton scenario run 1. It should be noted that the top left set of points represents both a source of CO_2 and the co-located Bushton storage location.

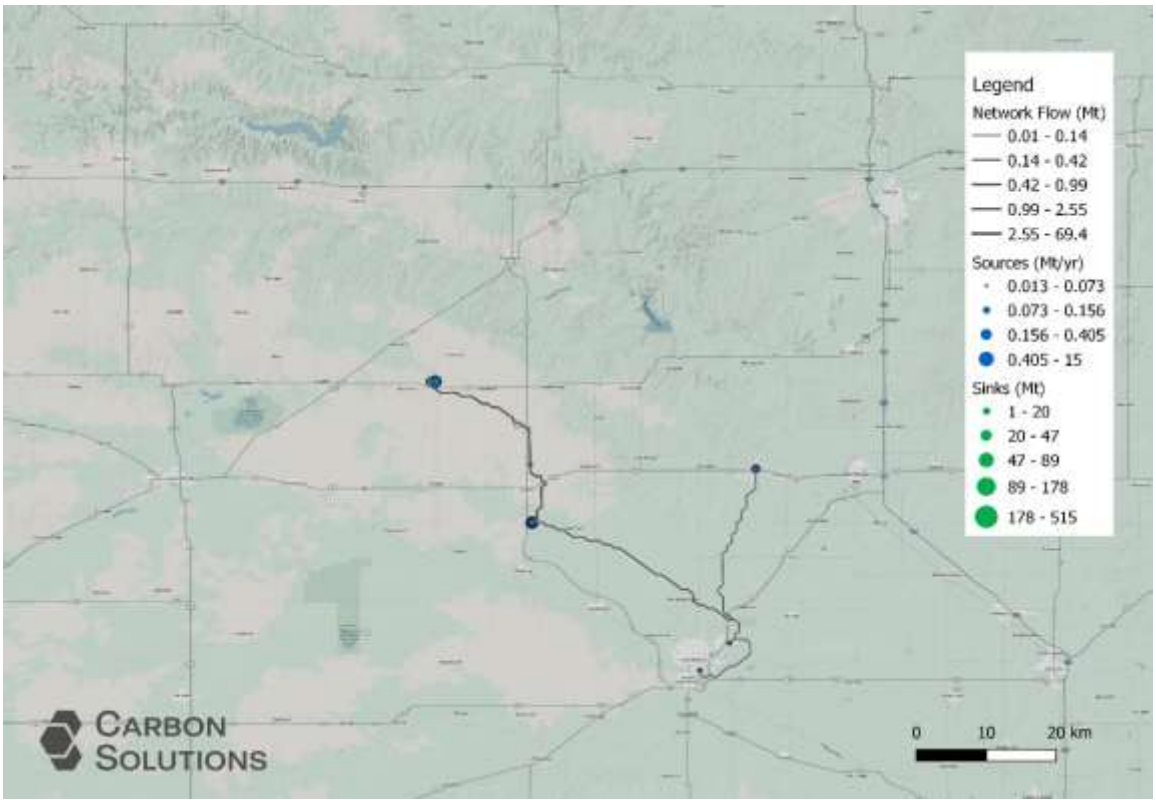


Figure 271 Deployed CCS network for Bushton scenario run 2, including all sources from run 1

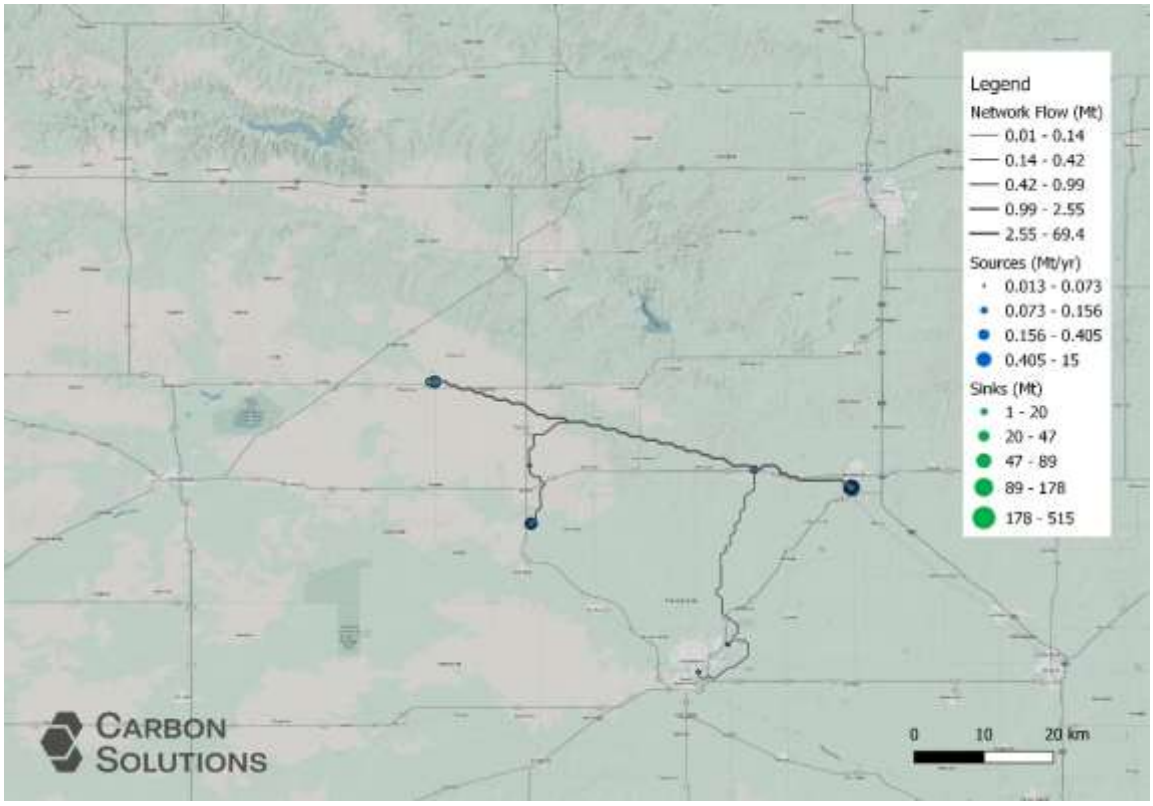


Figure 272 Deployed CCS network for Bushton scenario run 3, including all sources from runs 1 and 2

For the runs in the Alternate Site 1 Scenario, total CCS network cost goes from \$106/tCO_2 in the first run to \$86/tCO_2 in the final run using all the candidate capturable CO_2 emissions identified while working with the commercial partner. When using Alternate Site 1 instead of Bushton as the geologic CO_2 storage option, the total network lengths for each run increase, ranging from 113 km to 226 km (Figure 6.6 and Figure 6.7). Transportation cost decreases from Run 1 to Run 4, starting at \$29/tCO_2 for Run 1 (Figure 6.6) to \$15/tCO_2 for Run 4 (Figure 6.7). The run with the lowest transportation cost is Run 3, \$13/tCO_2, which includes capturing from all potential sources of CO_2 except Purefield.

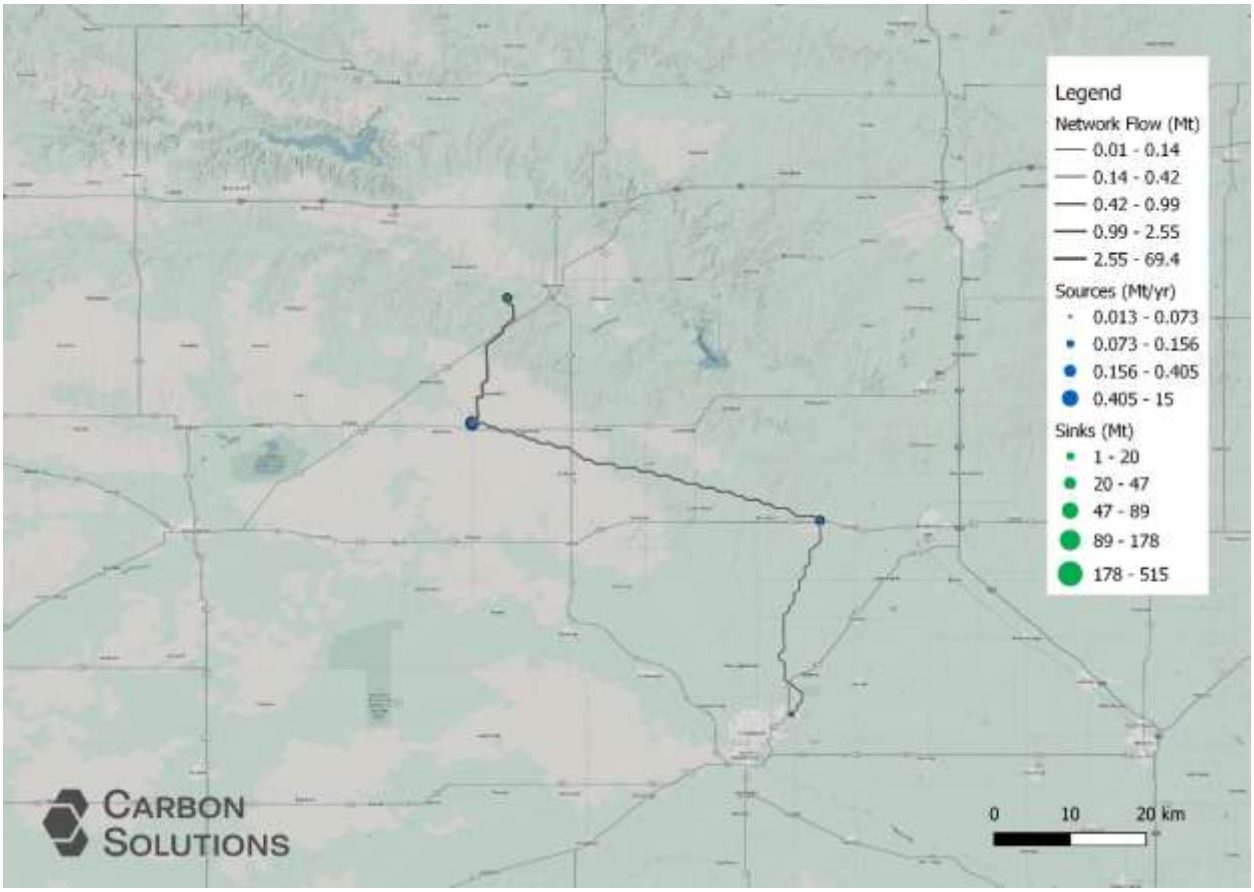


Figure 273 Deployed CCS network for alternate Site 1 – Run 1

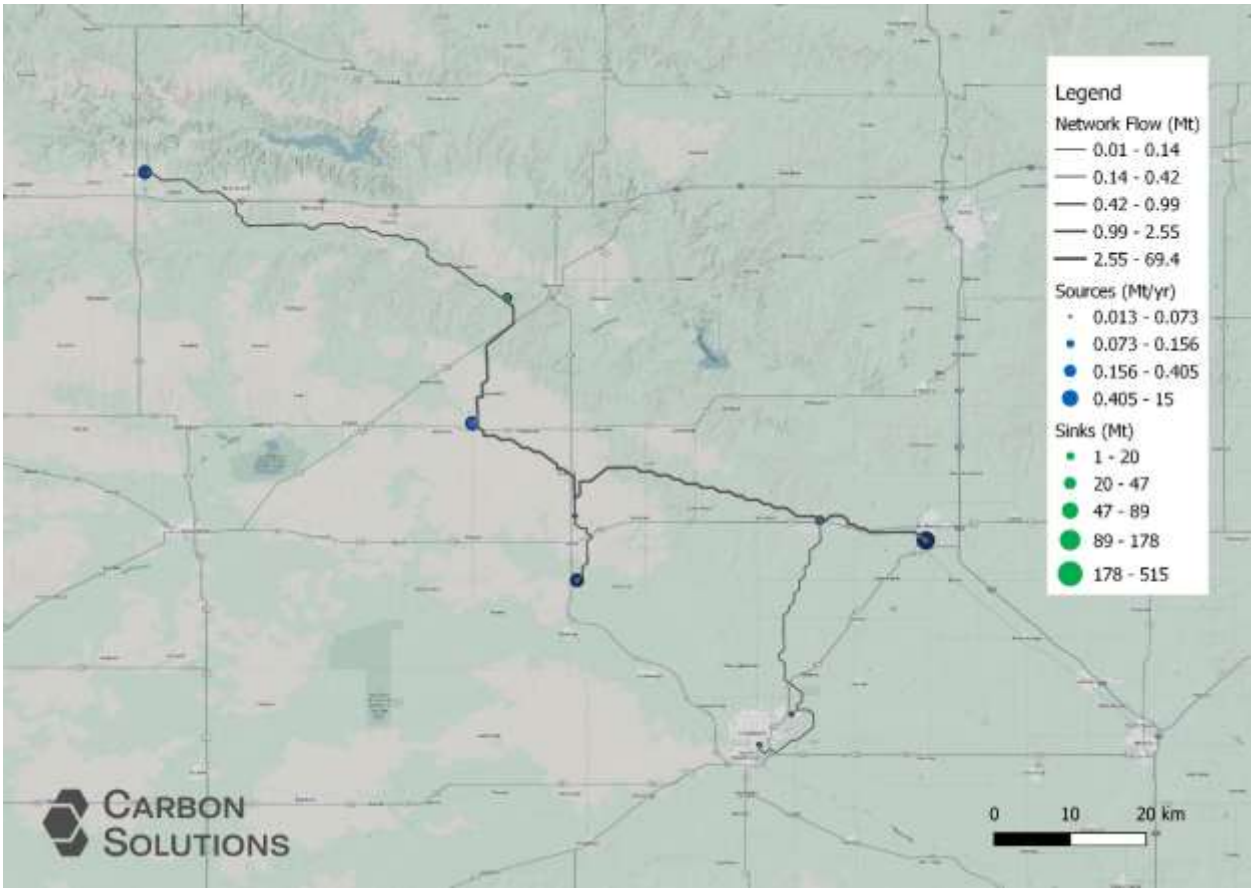


Figure 274 Deployed CCS network for alternate Site 1 – Run 4

For the runs in the Alternate Site 1 Scenario, total CCS network cost goes from \$106/tCO_2 in the first run to \$86/tCO_2 in the final run using all the candidate capturable CO_2 emissions identified while working with the commercial partner. When using Alternate Site 1 instead of Bushton as the geologic CO_2 storage option, the total network lengths for each run increase, ranging from 113 km to 226 km (Figure 6.6 and Figure 6.7). Transportation cost decreases from Run 1 to Run 4, starting at \$29/tCO_2 for Run 1 (Figure 6.6) to \$15/tCO_2 for Run 4 (Figure 6.7). The run with the lowest transportation cost is Run 3, \$13/tCO_2, which includes capturing from all potential sources of CO_2 except Purefield.

For the runs in the Alternate Site 2 Scenario, the total CCS network cost starts at \$110/tCO_2 for Run 1 (Figure 6.8) to \$88/tCO_2 for Run 4 (Figure 6.9). Source cost for each run matches the corresponding runs in the other two scenario sets, since the same set of sources are being used in each run. Storage costs remain constant across runs because only Alternate Site 2 is considered as a storage option. Due to the location of Alternate Site 2 in relation to sources of CO_2, more transport pipelines are deployed with CCS networks ranging from 128 km to 253 km. As a result, transport costs for each run in the Alternate Site 2 Scenario are higher than the two previous scenario sets, going from \$33/tCO_2 in Run 1 to the lowest cost of \$14/tCO_2 in Run 3. Nevertheless, there is an overlap between deployed CCS pipeline routes regardless of which storage site was considered, indicating that some CCS pipeline deployment could be robust regardless of final storage consideration.

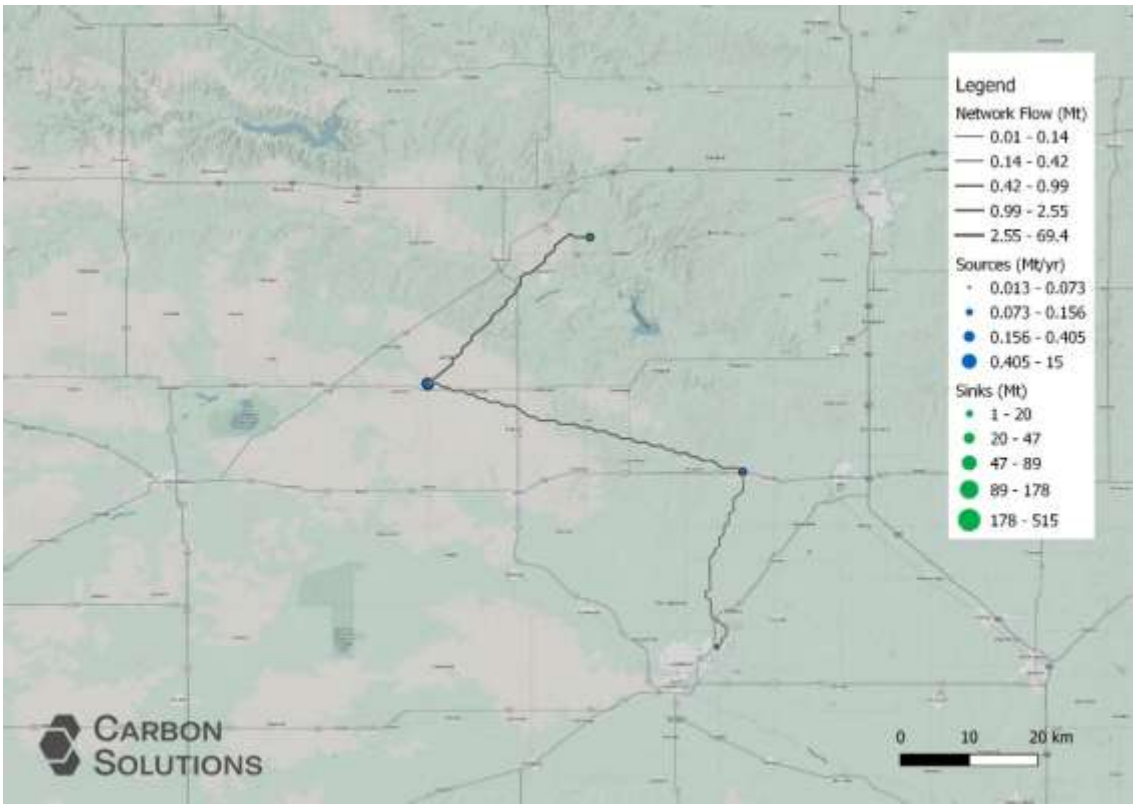


Figure 275 Deployed CCS network for Alternate Site 2 – Run 1

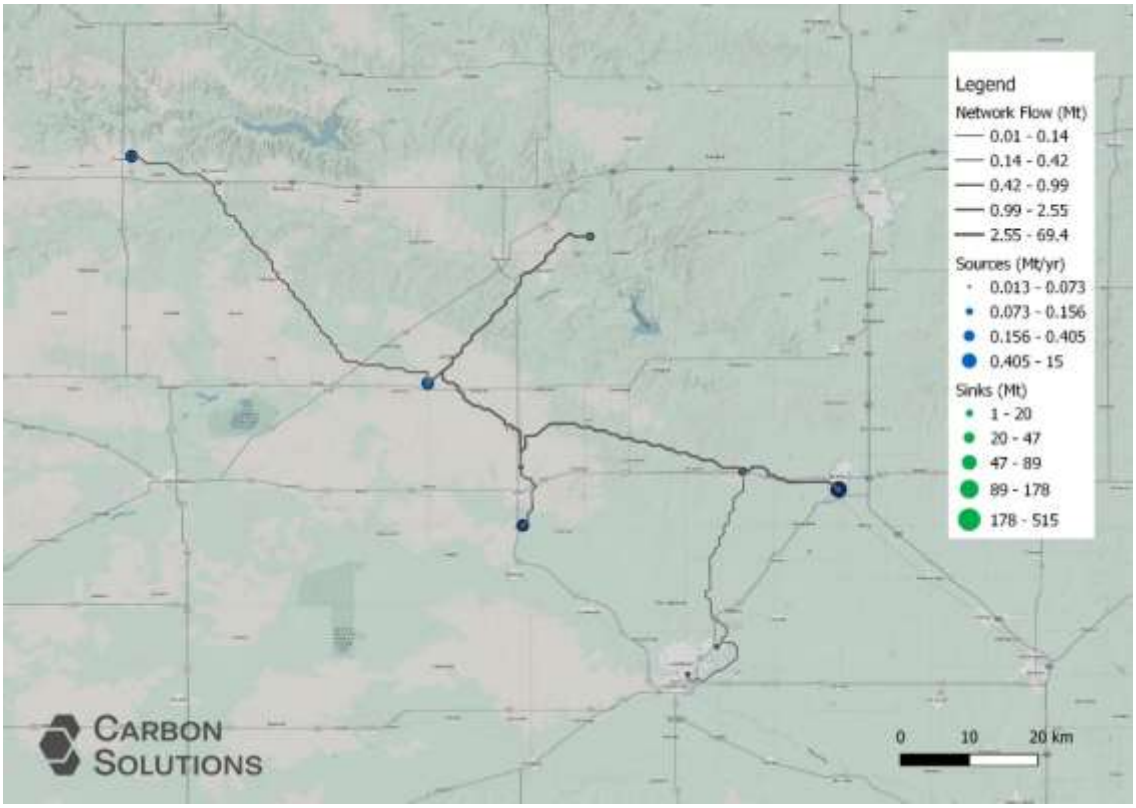


Figure 276 Deployed CCS network for Alternate Site 2 – Run 4

Going from run 3 to run 4, across all scenarios, the only difference is the addition of the Purefield ethanol plant to the list of potential sources. Looking at each scenario set, going from run 3 to run 4 typically results in less than a \$1/tCO_2 difference in total network costs. This is to say that despite needing more pipelines to transport captured CO_2 from Purefield, the CO_2 at Purefield is a relatively large and pure stream, reducing the average total capture cost of the system.

Subtask 6.4 – Identify Potential Business Entry Opportunities Related to Nearby Sources or Users of CO_2

Through this analysis, several different facilities were consistently deployed across scenarios. These sites are potential viable candidates for engaging in future business development for CCS. These facilities include industries such as the oil and gas, ethanol, chemicals manufacturing, refineries, and food and agriculture. Some industries, like ethanol manufacturing, produce high purity CO_2 streams at a relatively low capture cost. These ethanol facilities, specifically Kansas Ethanol LLC and PureField Ingredients LLC, could be ideal candidates to be "first-movers" or support early CCS efforts, highlighting their potential importance to CCS efforts in Kansas. Additionally, the CHS McPherson Refinery has some of the largest streams of capturable CO_2 emissions in the AOI, making it a potentially important partner for CCS engagement and business development.

There is growing demand for captured CO_2 for utilization in applications such as CO_2 enhanced oil recovery (EOR) operations, chemical manufacturing, and construction efforts. Each of these

end uses have the opportunity to be profitable. For example, captured CO_2 emissions not only potentially qualify for the 45Q tax credit for utilization but then has the opportunity to sell these captured emissions to any of these utilization industries, allowing them to be potentially profitable.

Total CCS costs are between \$87.52/tCO_2 to \$110.22/tCO_2, across all scenarios Carbon Solutions analyzed. It should be noted that this is higher than some CCS policy support such as 45Q which provides \$85/tCO_2 for CO_2 that is captured and permanently sequestered in underground geologic storage. Nevertheless, the total CCS network cost decreases with an increasing number of potential sources and the higher the capture target goes. For example, when considering storage at the Bushton location CCS network costs go from \$103.41/tCO_2 when only considering three sources to \$88.58/tCO_2 when considering eight sources. This trend is reflected when storage is placed at either of the alternate sites. This reflects the potential for economies of scale that CCS networks can benefit from when bringing in new sources.

One of the biggest challenges in this region is the rate at which CO_2 can be injected. In the future, there may be opportunities for other industries to join or engage with CCS by utilizing the existing infrastructure, given that the storage formations can sustain higher injection rates. It is important to note that additional infrastructure may be needed to connect these nearby sources (i.e. additional pipeline deployment). The development of a proposed CCS network will reduce uncertainty and risk that can be associated with CCS, thereby encouraging future nearby sources to engage with CCS.

In 2022, the U.S. Congress passed the Inflation Reduction Act (IRA) which, amongst other things, included updates to the 45Q tax credit to encourage widespread deployment and development of CCS activities in the United States. This change increased the tax credit from \$50/tCO_2 to \$85/tCO_2 for captured CO_2 that is geologically sequestered. Further, this update also extended the commence construction window for projects to 2033 and allowed for the credit to be realized after 12 yr after CCS equipment is in place and active (citation). All facilities chosen in this analysis meet the eligibility criteria for qualified facilities under 45Q, emitting at least 12,500 t of CO_2, even if they did not feature in the final proposed networks.

These tax credits are transferable, meaning that eligible facilities can elect to sell their credits to willing buyers. This transferability means there are opportunities for other industries in the region to participate in CCS especially if they are not initially part of proposed CCS networks. This also should help with cost sharing between different participants in the proposed CCS networks.

Task 7 – Regulatory Outreach and 45Q Preparations

Subtask 7.1 – Meet With U.S. EPA to Discuss UIC Class VI Permit Application

The Kansas Geological Survey (KGS) met with U.S. EPA Region 7 representatives to discuss the UIC Class VI permit application process and to identify the data and analyses required for the application. Note that due to the fire at the Medford site early in the project, Oklahoma's involvement in the project was limited, therefore interviews with the EPA were conducted solely for Region 7 (Kansas). This section documents salient information obtained during interviews

and provides a framework for a permit application in Region 7, following guidelines set forth by the U.S. EPA (EPA 2013).

Interview with U.S. EPA Region 7

On March 31, 2025, representatives of KGS met with Ben Meissner and Marina Mailer of EPA Region 7's Water Division to discuss the Class VI well permitting application process. The process occurs in four stages, followed by a fifth phase once injection operations are complete:

i. Phase 1: Pre-construction to determine site suitability
ii. Phase 2: Permit to construct
iii. Phase 3: Pre-operations
    a. Verify information provided in the pre-construction phase
    b. Move into an authorization to inject
iv. Phase 4: Injection Operations
v. Phase 5: Post-injection site care.

Permit applications are evaluated on the following content:

i. Site characterization, including a narrative description of the geologic structures, hydrogeologic properties, injection and confining zones, and fluid and solid geochemistry to meet the requirements of 40 CFR 146.82(a)(3,5,6) and 146.83. Items and data required for the geologic narrative are described in Table 57.
ii. Pre-op testing, well construction
    a. In regions with sufficient well control data, data may be accessed and used
    b. In regions lacking sufficient well control, a stratigraphic test well may be drilled to ensure the AoR is adequate for sequestration
iii. Area-of-Review and Corrective Action (Table 58).
iv. Testing and Monitoring Plan (Table 59)
v. Plugging Plan. The Well Plugging Plan may be a narrative (sometimes step-by-step) description of plugging procedures for the injection well. It may be accompanied by schematics and tables. The plan must include the following information:
    a. Tests or measures for determining bottomhole reservoir pressure.
    b. External mechanical integrity testing methods
    c. The type and number of plugs to be used.
    d. The placement of each plug, including the elevation of the top and bottom of each plug.
    e. The type, grade, and quantity of material to be used in plugging.
    f. The method of placement of the plugs.
vi. Emergency and remedial response plan. The Emergency and Remedial Response Plan will be a narrative description of local resources and infrastructure, potential emergency events and response actions, personnel, and equipment to address USDW endangerment. It may be accompanied by maps, illustrations, and tables.
vii. Construction Details.
    a. Description of the casing and cement. Well schematics (either planned or as-built) that show the surface casing and at least one long string casing. The schematics may be accompanied by a narrative step-by-step process for installing casing strings, description of centralizers, cementing procedures, cement and cement

additives. The application may also include a narrative description of how the casing and cement will be compatible with fluids with which they may come into contact and meet or exceed API/ASTM standards. See Table 60 for description of required information

b. Description of the Tubing and Packer. The tubing and packer may be depicted on the well schematics described above, and the information below may be summarized in tables. The application may also include a narrative description of how the tubing and packer materials will be compatible with fluids with which they may come into contact and meet or exceed API/ASTM standards. See Table 60 for description of required information.
c. Continuous Recording Devices and Automatic Shutoff Devices. The well schematics should show continuous recording devices and automatic shutoff devices to monitor: injection pressure; the rate, volume and/or mass, and temperature of the CO_2 stream; and the pressure on the annulus between the tubing and the long string casing and annulus fluid volume.

viii. Pre-operational Testing. A narrative plan that describes the testing that the applicant has performed or plans to perform to characterize the well and all relevant geologic formations. The plan may include step-by-step procedures and be accompanied by tables or graphics. At a minimum, the logs and tests must address the information and testing required at 146.87 (a) through (e), including: logs, surveys and tests to determine or verify information about relevant geologic formations; tests to verify internal and external mechanical integrity; reports/analysis of injection zone and confining zone cores and formation fluid samples; and characterization of the injection zone(s).

ix. Stimulation Plan. The stimulation plan should include a narrative description of stimulation fluids to be used and a determination that stimulation will not interfere with containment.

x. Post Injection Site Care and Site Closure Plan

xi. Regulatory processes

Table 57 Regional geologic structure and hydrogeologic properties required for a permit application. The description of the geologic structure and hydrogeologic properties of the proposed storage site and overlying formations must include these items and data/analyses.

Required Item	Description	Data or Analyses
Maps and Cross Sections of the AoR	The maps and cross sections may be accompanied by a brief narrative description interpreting the figures and providing an overview of key features important to the project.	Maps and cross sections
Information on Faults and Fractures	A narrative description of the location, orientation, and properties of known or suspected faults and fractures and a discussion supporting a determination that they would not interfere with containment.	Maps, cross sections, core sample analyses, geophysical survey results, pore pressure data

Data on the Injection Zone(s)	A narrative description of plans to collect, or the results of, geologic cores, outcrop data, seismic surveys, well logs, lithologic descriptions, and other field data used to characterize the injection zone(s), including geology/facies changes.	Depth, areal extent, thickness, mineralogy, porosity, permeability, capillary pressure
Data on the Confining Zone(s)	A narrative description of plans to collect, or the results of, geologic cores, outcrop data, seismic surveys, well logs, lithologic descriptions, and other field data used to characterize the confining zone(s), including geology/facies changes.	Depth, areal extent, thickness, mineralogy, porosity, permeability, capillary pressure
Geomechanical and Petrophysical Information about the Confining Zone(s)	A narrative description of the confining zone(s) may describe the testing performed (or planned) and available results in a tabular and/or graphical form.	Fractures, stress, ductility, rock strength, in situ fluid pressures, maps, seismic or other geophysical data, core data, well logs
Information on Seismic History	A narrative description of the presence and depth of seismic sources and a determination that seismicity would not interfere with containment.	Tables and/or maps of seismic events, sources, and depths
Geologic and Topographic Maps and Cross Sections	Maps and cross sections of regional geology, hydrogeology, and local geologic structure may be accompanied by a narrative description or interpretations of logs or core data.	Maps and cross sections
Hydrologic Information/Maps and Cross Sections of USDWs	The maps and stratigraphic cross sections of the vertical and lateral limits of all USDWs may be accompanied by a narrative interpretation of the figures.	Maps of water wells and springs within the AoR, their position relative to the injection zone, the direction of water movement, where known
Baseline Geochemical Data	The narrative description of available geochemical data on fluid- and solid-phase geochemistry of all subsurface formations (including USDWs) in the AoR; it may be accompanied by tabular or graphical data, statistics, and maps.	Results or planned sampling/testing, the parameters analyzed, and any geochemical modeling that was performed, along with data sources, data quality or gaps, and sampling/testing methods
Demonstration of Site Suitability	This narrative demonstration must describe the suitability of the injection zone and the suitability of the confining zone. It may also describe additional confining zone(s); note a description of additional confining zones is not required of all projects.	Maps, cross sections, tables of relevant geological data, or descriptions of model inputs/results

Table 58 Area of review (AoR) and corrective action plan requirements

Required Item	Description
The Method for Delineating the AoR	A narrative description of the AoR delineation model used, which may include assumptions made, any available outputs/results, and the inputs on which the model is based. It may be accompanied by tables, figures and graphics, or raw data in a tabular format.
AoR Reevaluation Schedule and Criteria	A description of the minimum fixed frequency, not to exceed 5 yr, for AoR reevaluations. The monitoring and operational conditions that would warrant a reevaluation of the AoR prior to the next scheduled reevaluation. How monitoring and operational data will be used to inform an AoR reevaluation.
Corrective Action Information	A narrative discussion of how corrective action was/will be conducted. If phased corrective action is planned, the application must describe: 1. How the phasing will be determined, 2. How corrective action will be adjusted if there are changes in the AoR, and 3. How site access for future correction action will be guaranteed.
Tabulation of Wells in the AoR	The AoR and Corrective Action Plan must include a table listing wells within the AoR that penetrate the injection or confining zones or a statement there are no wells that penetrate the confining zone within the AoR. Other penetrations of the confining zone(s), such as underground mines, also must be identified. If a table is submitted, it must include the following information: well type, description of the well's construction, date drilled, location, depth, record of plugging and/or completion.

Table 59 Testing and monitoring plan requirements. The testing and monitoring plan will be a narrative description of planned injection-phase testing activities that is accompanied by maps, tables, illustrations, or step-by-step procedures that describe the following.

Required Item	Description
CO_2 Stream Analysis	Narrative description that may describe analytical parameters, sampling methods, sampling locations, and frequencies.
Continuous Recording of Operational Parameters	Narrative description of devices to continuously monitor and record injection pressure, rate, and volume; tubing-casing annulus pressure; and annulus fluid volume added. May be depicted on well schematics.
Corrosion Monitoring	Narrative description of corrosion monitoring methods that may describe sampling methods/locations or testing frequency.
Above Confining Zone Monitoring	Narrative description of planned water quality monitoring that may describe well locations; analytical methods and parameters; sampling locations and methods, formations/depths, and frequencies. The description may be accompanied by maps, monitoring well schematics, or tables of analytical parameters and methods.
External Mechanical Integrity Testing	Narrative (sometimes step-by-step) description of mechanical integrity tests (MITs) and their planned frequency.
Pressure Fall-Off Testing	Narrative (sometimes step-by-step) description of pressure fall-off tests and their planned frequency.

Direct CO_2 Plume and Pressure Front Tracking	Narrative description of planned direct methods to track the CO_2 plume and pressure front that may include well locations; analytical methods and parameters; sampling locations and formations/depths; and frequencies. The description may be accompanied by maps, monitoring well schematics, or tables of analytical parameters and methods.
Indirect CO_2 Plume and Pressure Front Tracking	Narrative description of planned indirect methods to track the CO_2 plume and pressure front; it may describe: well locations; monitoring equipment; or geophysical survey extent/resolution. The description may be accompanied by maps, monitoring well or equipment schematics, or tables.
Surface Air Monitoring and/or Soil Gas Monitoring	This type of monitoring is not required for all projects; if it is included, it would be a narrative description of planned methods detecting CO_2 in the soil or atmosphere (including monitoring locations, equipment, and frequencies) that may be accompanied by maps or illustrations.
Other Monitoring	Additional monitoring is not required for all projects; if it is included, it would be a narrative description of the types of monitoring (e.g. seismic), including: methods, equipment, locations, and frequencies that may be accompanied by maps, illustrations, or tables.
Quality Assurance and Surveillance Plan	Narrative description of planned quality assurance procedures for all testing and monitoring activities.

Table 60 Information required for the injection well construction plan

Casing and Cement Information	**Tubing and Packer Information**
Depth to injection zone(s)	Depth of setting
Injection pressure, external pressure, internal pressure, and axial loading	Characteristics of the CO_2 stream and formation fluids
Hole size.	Maximum proposed injection pressure
Size and grade of all casing strings	Maximum proposed annular pressure
Corrosiveness of the CO_2 stream and formation fluids	Proposed injection rate and volume and/or mass of the CO_2 stream
Down-hole temperatures	Size of tubing and casing
Lithology of the injection and confining zone(s)	Tubing tensile, burst, and collapse strengths
Type or grade of cement and cement additives	
Quantity, chemical composition, and temperature of the CO_2 stream	

To date, Region 7 has received four Class VI permit applications: two in Kansas, others are in Nebraska. Primacy will be determined by the States' goals for the program and whether there is an industry push to justify entering the primacy process. Applications for primacy will typically fall to a state's regulatory agency. It would be advantageous for states pursuing primacy to partner with the State Geological Survey, given the vast amounts of regional data that surveys have.

Recommendations for entities interested in applying for a Class VI permit include reviewing all requirements of the permitting process before beginning the process. EPA's website contains all information and lists of required data. It was also recommended that the suitability of well construction materials be considered, as well as supply chain delays. Applicants should assume 6-8 months lead time in securing certain materials. Overall, CCUS is being taken more seriously and there is interest in moving CCS projects forward with investment by industry.

Subtask 7.2 – Meet With External Teams That Have Experience Applying for EPA–UIC Class VI Permits

KGS met with an external team who has experience applying for EPA-UIC Class VI permits to discuss the application process. This section documents information obtained during the interview.

Interview with Advanced Resources International

On March 25, 2025, representatives of KGS met with Dave Riestenberg and Manoj Valluri of Advanced Resources International (ARI). ARI specializes in global unconventional gas resources, enhanced recovery, and CO_2 storage, with research on these topics dating back to 1980 for the U.S. Department of Energy. Over the past two decades, the company has conducted extensive R&D on shale oil, gas shales, coalbed methane, and tight sands, focusing on geology, engineering, economics, and environmental impacts worldwide. ARI has also explored CO_2 storage opportunities for over 50 power plants and industrial facilities, assessing regional and site-specific geological feasibility, storage capacity, and project development plans. Since 2022, ARI has led the application for multiple Class VI injection wells in Kansas, California, Alabama, Florida, Illinois, Louisiana, Missouri, Texas, and Ohio. The company has also been a consortia participant on applications for Colorado and Alaska.

ARI has partnered with only one state with primacy over Class VI systems at the time of application (Louisiana; Texas was close to obtaining primacy at the time of their application). There is a greater synergy between the EPA and states with primacy during the Class VI application process, leading to more actionable feedback from the EPA that results in the application process happening faster. Main differences ARI noted between working with the EPA versus working with states on Class VI applications include:

- States that have received primacy (i.e. Louisiana, North Dakota, West Virginia, Wyoming) are taking a more careful approach and add local-scale nuances with respect to environmental regulation.
- Regulatory bodies are variable due to their experience, established protocols (or lack thereof), efficiency, etc. For example, Region 7 (Kansas) has a streamlined system that is

very efficient, likely related to workload and regulatory environment, and as a result response times are very quick.

Efficiency and expediency of the application process is also dependent upon the characteristics of the geological unit and stratigraphy that proposed injection wells to be penetrated. Application complexity and time-to-approval can be a function of regionally specific sub-surface traits (e.g. seismic activity in the Midwest vs. brine/brackish water in coastal plain states).

ARI noted that, in some regions, there is tension between CCUS and Oil and Gas industries, though there are advantages to the two industries working together. This tension could be attributed to a perceived competition for land/subsurface access and use rights, materials and services. Research consortia such as CUSP-West, in partnership with State Geological Surveys and private industry could enhance the evaluation of regional sub-surface challenges like overpressure and seismic activity. By sharing data and coordinating outreach initiatives, they can collaboratively address risk mitigation, particularly regarding basin-scale concerns and opportunities. Although private partnerships have seen some success with advancing through tax credits for carbon storage, most of the work on advancing the industry has benefited from public partnerships. Pairing public dollars to nudge commercialization would grow the industry.

Near- and mid-term challenges ARI noted for CCUS projects in the U.S. include:

- Uncertainty around DOE funding availability and timeline
- Stability of incentives and tax credits such as 45Q
- Inflation, potential impact of tariffs on materials and services
- Evolving/developing regulatory environment
- Investor confidence in the global economy
- Supply chain issues
- A lack of certainty in CCS well design requirements

Despite these challenges, CCS maintains bipartisan political support, provides jobs, and offers an industry-friendly solution to carbon reduction. States are continuing to pursue primacy and receiving approval, signaling expansion of the industry. The relatively small size of the CCS industry has allowed for agility when compared to the oil and gas industry, providing opportunities for growth across a range of sectors, including finance, manufacturing, transportation, science, and more.

Subtask 7.3– Meet With State Environmental and Petroleum Regulators

KGS met with state environmental and petroleum regulators to discuss the current regulatory framework for CO_2 injection scenarios. This section summarizes information obtained during the interview.

Interview with the Kansas Department of Health and Environment (KDHE)

On April 30, 2025, representatives of KGS met with Sue Funk, Wakil Balumi, and Riley Biel of the Kansas Department of Health and Environment (KDHE). KDHE's Division of Environment protects public health and the environment through environmental regulatory programs and other programs that remediate contamination, lessen nonpoint pollution, and evaluate environmental

conditions across the state. Included in the responsibilities of KDHE are regulation of the Underground Injection Control Program. KDHE would work with the Kansas Corporation Commission (KCC; see section 7.3.2) to establish the process of Kansas pursuing primacy.

The main change needed to facilitate injection scenarios in Kansas is a greater demand for it by industry. As of the date of the interview, only 2 ethanol plants in Kansas are interested in primacy. Overall, companies would prefer to deal with the state governments, rather than the Federal Government, because state governments are familiar with local scale activities and are more accessible.

If the demand for primacy were to grow in Kansas, the state would model their efforts after other states that have successfully secured primacy (Wyoming, Texas, Louisiana). These states have shared with other states their experience with obtaining primacy, which seems to be positive. The main limitations in Kansas are demand and resources; if the demand was high, the Kansas state agencies working on obtaining primacy will collaborate to submit the primacy application. If Kansas were to pursue primacy, KGS, KCC and KDHE have the expertise to write and review technical submissions for Class VI applications.

Interview with the Kansas Corporation Commission

On April 29, 2025, representatives from KGS met with Ryan Hoffman, the director of the Kansas Corporation Commission (KCC). The (KCC) regulates five cornerstone industries in the Kansas economy. The Commission has the responsibility of ensuring that natural gas, electricity, telephone and transportation vendors provide safe, adequate and reliable services at reasonable rates. The Commission also has the mandate of assuring that oil and gas producers protect correlative rights and environmental resources.

At the time of this report, Kansas has not initiated the process to establish state primacy and there are two UIC Class VI permit applications in Region 7 under review by the EPA.

The EPA approves and oversees Class VI wells in Kansas. Once an application to drill a Class VI well is submitted, the EPA will partner with the KCC through the application's completion. The current process for drilling new stratigraphic wells involves initial permitting by KCC. New wells may be drilled as disposal wells and are not initially authorized for injection. Such wells can be used to determine a site's suitability for CO_2 injection through data collection and stratigraphic tests to assess, for example, subsurface geological and hydrogeologic characteristics. Once testing is completed, entities have 90 days to apply for a permit to inject. During the testing period, it is under the jurisdiction of KCC. Once it is approved for injection, EPA has oversight of all injection activities.

State primacy generally results in a more efficient and rapid turnaround on applications than currently occurs when applications are submitted to EPA. Demand for primacy in Kansas is currently low, but subject to change should industry show more interest. Primacy interests in Kansas will likely remain stagnant until a utility or major refiner takes the lead and provides the resources needed to support the application process. The uncertain future of the 45Q tax credit for carbon capture projects also plays a role in low industry demand. In the meantime, Kansas' CCS industry is "closely watching and learning" from nearby states such as Nebraska as they move through the primacy process.

Should the demand for primacy in Kansas increase, KCC sees the KGS as an integral part of the application team owing to its extensive subsurface modeling and stratigraphic studies of the Arbuckle Group, a prospective environment for CO_2 sequestration. If Kansas were to obtain primacy, KGS has the in-house expertise to, for example, conduct original site-specific evaluations and perform technical review in support of applications to the state.

The greatest risks of CO_2 injection in Kansas, as with many states, is potential seismic activity arising from brine injection, and determination of the triggering mechanism of injection-induced seismicity.

Task 8 – Technology Transfer

KGS, with contributions from partner organizations, led the technology transfer activities for the ONEOK-focused CUSP-West study. These efforts aimed to enhance public engagement, promote technical knowledge-sharing, and disseminate research findings to both scientific and stakeholder audiences.

Subtask 8.1 – Maintain Website for Project

A dedicated website for the project is maintained by KGS at https://kgs.ku.edu/kgs-cusp-west. This online platform serves as a central repository for selected outputs and supporting materials from the study. It was developed to facilitate transparent access to key technical resources and to support broader outreach objectives by increasing visibility into the project's scope, progress, and outcomes.

Subtask 8.2 – Public Presentations

Throughout the project, team members presented findings and engaged with professional communities at a range of scientific meetings. In June 2023, two posters highlighting different aspects of the study were presented at the Annual CUSP meeting. One provided a general project overview, while the other described the development and implementation of the seismic monitoring network. The latter was recognized with third place in the student poster category.

Additional dissemination activities included a technical presentation by KGS staff at the AAPG International Meeting for Applied Geoscience and Energy (IMAGE) in Houston in August 2023. In September 2024, Brendan Bream delivered an update on the study during the Annual CUSP-West meeting in Santa Fe, which served to introduce the KGS team preparing the final technical report. This engagement continued at the 2025 Annual CUSP-West meeting in Salt Lake City, where Bream presented a comprehensive summary of the completed study to the broader research community.

Technical Transfer Short Course

As part of its professional development and technical outreach efforts, KGS organized and hosted a four-day advanced modeling short course titled *STOMPing at the KGS: Subsurface Simulator* from March 17 to 20, 2025 (Fig. 8.1). This course was conducted as part of the project's broader objectives to enhance technical capacity related to subsurface energy systems and carbon storage.

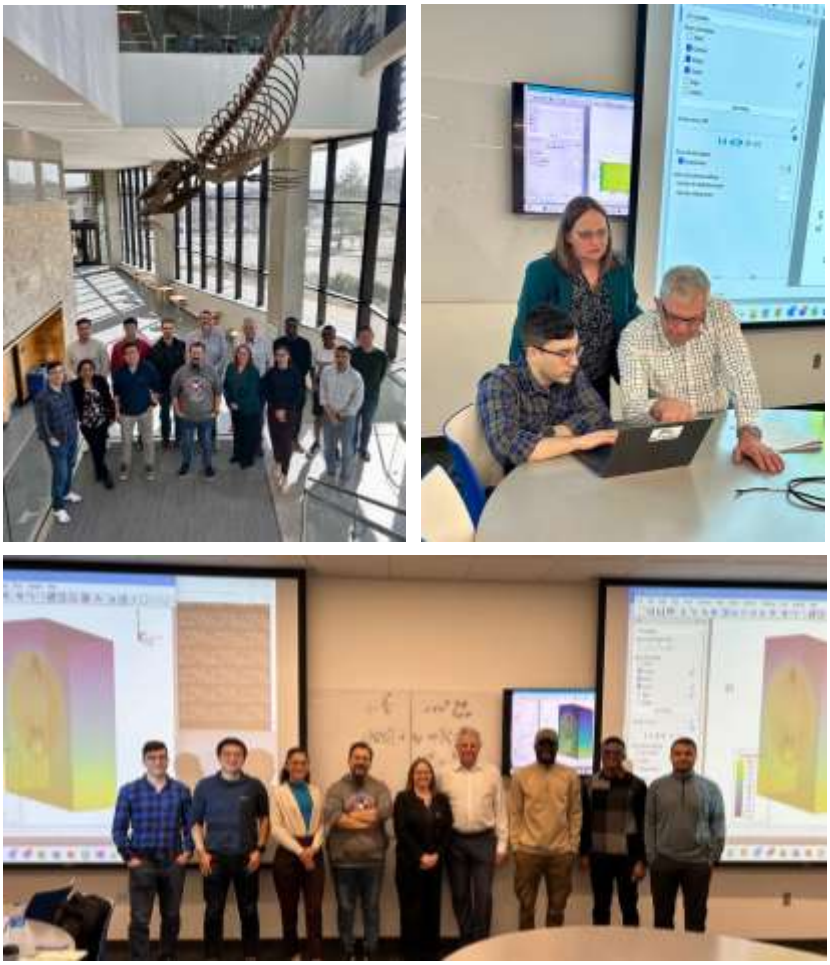


Figure 277 Photos from KGS technology transfer short course

The short course engaged 15 participants from the U.S. and the UK, including professionals from Burns & McDonnell and INTERA, KGS researchers, and graduate students from the University of Kansas. Participants brought expertise from disciplines spanning engineering, geology, geophysics, and geochemistry. The course was led by Mark White (PNNL) and Signe White (INTERA), recognized experts in the STOMP simulation platform.

Course content focused on applied scenario modeling across a diverse range of geologic processes relevant to carbon management and energy transition, including:

- Geologic carbon sequestration
- Natural gas hydrate production
- Geologic hydrogen systems
- Enhanced oil recovery
- Reactive transport
- Coupled geomechanics
- Hydrothermal systems
- Closed-loop and enhanced geothermal technologies
- Nuclear waste repository performance
- Microbial and biological processes in the subsurface

The course functioned as a pilot for a continuing education series hosted by KGS, designed to strengthen applied modeling skills in support of CCUS deployment. All participants completed scenario-based modeling exercises, with content tailored to simulate the kinds of geologic systems encountered in regional carbon hub development.

KGS coordinated course planning, logistics, and CEU certification internally, with operational support from Brendan Bream and Souvik Bhattacharjee and coordination by Hannah Horinek. Instruction was delivered through a combination of structured modules and hands-on sessions, contributing directly to the project's goal of expanding simulation expertise among collaborators and external stakeholders.

Subtask 8.3 – Publications

In addition to presentations and outreach activities, the project generated several technical publications. Most notably, Hannah Proffitt produced a detailed manual documenting the seismic network design and associated data workflows developed for the project. This work also formed the basis of her master's thesis at the University of Kansas and was presented at the Geological Society of America national meeting in 2023.

The thesis, titled *Development of Efficient Seismic Networks to Detect Local Earthquakes* (Proffitt 2024), provides a transferable framework for monitoring seismicity in CCS projects and has informed the broader discussion on best practices for subsurface monitoring. The combination of technical documentation, academic scholarship, and field implementation represents a successful integration of research, education, and applied geotechnical development.

Subtask 8.4 – Upload Data to DOE-EDX

All relevant project data associated with this report is being made available via the DOE Energy Data eXchange (EDX) system and can be accessed using the report title for reference.

References

Battelle Memorial Institute. 2018. Integrated mid-continent stacked carbon storage hub phase I final report. Columbus (OH); Battelle Memorial Institute. Prepared for U.S. Department of Energy.

Beck L, Ross S. 2021. Introduction of a bipartisan SCALE Act—landmark CO_2 capture, transport and storage infrastructure bill. Boston (MA); Clean Air Task Force. https://www.catf.us/2021/03/introduction-of-a-bipartisan-scale-act-landmark-co2-capture-transport-and-storage-infrastructure-bill/

Benmadi M, Moghanloo RG, Hayman NW. 2024. Assessing CO_2 geological storage in the Arbuckle Group in northeast Oklahoma. Fuel. 356:129323. doi:10.1016/j.fuel.2023.129323

Bennett et al., 2024 [added by Carbon Solutions]

Bormann P, editor. 2012. Seismic networks. In: New manual of seismological observatory practice 2 (NMSOP-2). Potsdam (Germany); German Research Centre for Geosciences.

Bratton T. 2025. The geomechanics of carbon storage. In: Wilson M, Davis T, Landrø M, editors. Geophysics and the energy transition. Amsterdam (Netherlands); Elsevier. p 275–303. doi:10.1016/B978-0-323-95941-4.00010-0

Bream BR, Bhattacharjee S, White M, Gumble J. 2025. Preliminary screening approach to support carbon sequestration efforts in Kansas. Paper presented at: Carbon Capture, Utilization, and Storage Conference (CCUS); 2025 Mar 3–5; Houston (TX).

Brooks RH, Corey AT. 1964. Hydraulic properties of porous media. Fort Collins (CO); Colorado State University. Hydraulic Paper No. 3.

Buchanan R, Carr TR. 2008. Geologic sequestration of carbon dioxide in Kansas. Revised 2011. Lawrence (KS); Kansas Geological Survey. Public Information Circular No. 27. https://www.kgs.ku.edu/Publications/PIC/PIC27_2011.pdf

Burdine NT. 1953. Relative permeability calculation from size distribution data. Trans AIME. 198:71–78.

Callas C, Davis JS, Saltzer SD, Hashemi SS, Wen G, Gold PO, Zoback MD, Benson SM, Kovscek AR. 2024. Criteria and workflow for selecting saline formations for carbon storage. Int J Greenh Gas Control. 135:104138. doi:10.1016/j.ijggc.2024.104138

Canady W. 2011. A method for full-range Young's modulus correction. Paper presented at: North American Unconventional Gas Conference and Exhibition; 2011 Jun; The Woodlands (TX).

Carbon Solutions LLC. 2025a. CostMAP^{PRO} [software]. Saint Paul (MN); Carbon Solutions LLC. [accessed 2025 Dec 30]. https://www.carbonsolutionsllc.com/software/costmappro/

Carbon Solutions LLC. 2025b. SCO_2T^{PRO} [software]. Saint Paul (MN); Carbon Solutions LLC. [accessed 2025 Dec 30]. https://www.carbonsolutionsllc.com/software/sco2tpro/

Carbon Solutions LLC. 2025c. SimCCS^{PRO} [software]. Saint Paul (MN); Carbon Solutions LLC. [accessed 2025 Dec 30]. https://www.carbonsolutionsllc.com/software/simccspro/

Carbon Solutions LLC. 2025d. CO_2NCORD [software]. Saint Paul (MN); Carbon Solutions LLC. [accessed 2026 Jan 14]. https://www.carbonsolutionsllc.com/software/co2ncord/

Chang KW, Segall P. 2016. Injection-induced seismicity on basement faults including poroelastic stressing. J Geophys Res Solid Earth. 121(4):2708–2726. doi:10.1002/2015JB012561

Class H, Ebigbo A, Helmig R, Dahle HK, Nordbotten JM, Celia MA, Bandilla KW, Darcis M, Flemisch B, Gasda SE, et al. 2009. A benchmark study on problems related to CO_2 storage in geologic formations. Comput Geosci. 13(4):409–434. doi:10.1007/s10596-009-9146-x

Coates G, Denoo S. 1981. Mechanical properties program using borehole analysis and Mohr's circle. Paper presented at: SPWLA 22nd annual logging symposium; 1981 Jun 23–26; Mexico City (Mexico). Paper DD.

Credit for Carbon Oxide Sequestration, U.S.C.-2023 26 C.F.R. §1.45Q-1 (2021).

Dempsey D, Riffault J. 2019. Response of induced seismicity to injection rate reduction: models of delay, decay, quiescence, recovery, and Oklahoma. Water Resour Res. 55(1):656–681. doi:10.1029/2018WR023587

Dicken CL, Pimley SG, Cannon WF. 2001. Precambrian basement map of the northern midcontinent, USA: a digital representation of the 1990 P.K. Sims map. Reston (VA); U.S. Geological Survey. Open-File Report 01-021. https://pubs.usgs.gov/of/2001/of01-021/

Doveton JH, Charpentier RR, Metzger EP. 1990. Lithofacies analysis of the Simpson Group in south-central Kansas. Lawrence (KS); Kansas Geological Survey. Petrophysical Series No. 5. https://www.kgs.ku.edu/Publications/Bulletins/PS5/

Franseen EK, Byrnes AP, Cansler JR, Steinhauff DM, Carr TR. 2004. The geology of Kansas—Arbuckle Group. Curr Res Earth Sci. 250:1–43.

Herron M, Herron S, Plumb R. 1992. Identification of clay-supported and framework-supported domains from geochemical and geophysical well log data. Richardson (TX); Society of Petroleum Engineers. SPE Paper 24726.

Holubnyak Y, Dubois M. 2018. Integrated CCS for Kansas (ICKan) final technical report. Pittsburgh (PA); U.S. Department of Energy. Report No. DE-FE0029474.

Hoover et al. 2019 (from Task 6 – Carbon Solutions; cited in text but no reference provided)

Iyer J, Lackey G, Edvardsen L, Bean A, Carroll SA, Huerta N, Smith MM, Torsæter M, Dilmore RM, Cerasi P. 2022. A review of well integrity based on field experience at carbon utilization and storage sites. Int J Greenh Gas Control. 113:103533. doi:10.1016/j.ijggc.2021.103533

Knapp RW, Steeples DW, Miller RD, McElwee CD. 1989. Seismic-reflection surveys at sinkholes in central Kansas. In: Steeples DW, editor. Geophysics in Kansas. Lawrence (KS); Kansas Geological Survey. p 95–116.

Krief M, Garat J, Stellingwerff J, Ventre J. 1990. A petrophysical interpretation using the velocities of P and S waves (full-waveform sonic). Log Analyst. 31(6):355–369.

Langenbruch C, Zoback MD. 2016. How will induced seismicity in Oklahoma respond to decreased saltwater injection rates? Sci Adv. 2(11):e1601542. doi:10.1126/sciadv.1601542

Mavko G, Mukerji T, Dvorkin J. 2009. Elasticity and Hooke's law. In: The rock physics handbook: tools for seismic analysis of porous media. 2nd ed. Cambridge (UK); Cambridge University Press. p 21–80.

McDonnell A. 2022 Jul 11. Medford ONEOK natural gas plant fire displaces residents. News9 [Internet]. Oklahoma City (OK). https://www.news9.com/story/62cca1cc92065407260f79a4/medford-oneok-natural-gas-plant-fire-displaces-residents

Merriam DF. 1963. The geologic history of Kansas. Lawrence (KS); Kansas Geological Survey. Bulletin 162.

Mishra SK, Henderson MA, Tu DJ, Erwin A, Trentham RC, Earnhart DH, Heath JE. 2025. Can Section 45Q tax credit foster decarbonization? A case study of geologic carbon storage at acid gas injection wells in the Permian Basin. Int J Greenh Gas Control. 140:104284. doi:10.1016/j.ijggc.2024.104284

Mwakipunda GC, Mgimba MM, Ngata MR, Yu L. 2024. Recent advances on carbon dioxide sequestration potentiality in salt caverns: a review. Int J Greenh Gas Control. 133:104109. doi:10.1016/j.ijggc.2024.104109

NRAP Open-IAM. 2024. NRAP open-source integrated assessment model. Pittsburgh (PA); U.S. Department of Energy National Energy Technology Laboratory. https://edx.netl.doe.gov/dataset/phase-iii-nrap-open-iam

Ochu E. 2021 Jun 24. Proposed 45Q tax credit reform could give a big boost to carbon capture projects. Columbia Climate School [Internet]. New York (NY). https://news.climate.columbia.edu/2021/06/24/proposed-45q-tax-credit-reform-carbon-capture/

[OGS] Oklahoma Geological Survey. 2021. Geological carbon management in Oklahoma. Norman (OK); Oklahoma Geological Survey. Fact Sheet No. 1. https://www.ou.edu/content/dam/ogs/documents/fact-sheets/OGS_FactSheet_No1.pdf

ONEOK Inc. 2023 Jan 9. ONEOK reaches agreement on Medford NGL facility insurance claim for $930 million [Press release]. Tulsa (OK); ONEOK Inc. https://ir.ONEOK.com/news-and-events/press-releases/2023/01-09-2023-211553651

Plumb R. 1994. Influence of composition and texture on the failure properties of clastic rocks. In: Eurock ‘94. Rotterdam (Netherlands); Balkema.

Proffitt HR. 2024. Development of efficient seismic networks to detect local earthquakes. Lawrence (KS); University of Kansas. Master’s thesis.

Proffitt H, Tsoflias G. 2023. Monitoring induced seismicity using low-cost seismometers: a case study in central Kansas. Geol Soc Am Abstr Programs. 55:394501.

Pruess K, Garcia J, Kovscek T, Oldenburg C, Rutqvist J, Steefel C, Xu T. 2002. Intercomparison of numerical simulation codes for geologic disposal of CO_2. Berkeley (CA); Lawrence Berkeley National Laboratory. Report No. LBNL-51813.

Raspberry Shake. n.d. Technical specifications. San Jose (CA); Raspberry Shake. https://manual.raspberryshake.org/specifications.html#techspecs

Rubinstein JL, Ellsworth WL, Dougherty SL. 2018. The 2013–2016 induced earthquakes in Harper and Sumner Counties, southern Kansas. Bull Seismol Soc Am. 108(2):674–689. doi:10.1785/0120170209

Sellers C. 2023 Jan 9. ONEOK reaches agreement on Medford NGL insurance claim after gas explosion. KFOR Oklahoma News [Internet]. Oklahoma City (OK).

Schwab DR, Bidgoli TS, Taylor MH. 2017. Characterizing the potential for injection-induced fault reactivation through subsurface structural mapping and stress field analysis, Wellington Field, Sumner County, Kansas. J Geophys Res Solid Earth. 122:10132–10154. doi:10.1002/2017JB014071

Templeton DC, Schoenball M, Layland-Bachmann CE, Foxall W, Guglielmi Y, Kroll KA, Burghardt JA, Dilmore R, White JA. 2022. A project lifetime approach to the management of induced seismicity risk at geologic carbon storage sites. Seismol Res Lett. 94(1):113–122. doi:10.1785/0220210284

[DOE NETL] U.S. Department of Energy National Energy Technology Laboratory. 2017. Best practices: site screening, site selection, and site characterization for geologic storage projects. Pittsburgh (PA); U.S. Department of Energy. Report No. DOE/NETL-2017/1844. https://www.netl.doe.gov/sites/default/files/2018-10/BPM-SiteScreening.pdf

[EPA] U.S. Environmental Protection Agency Office of Water. 2013. Geologic sequestration of carbon dioxide: underground injection control (UIC) program Class VI well area of review evaluation and corrective action guidance. Washington (DC); U.S. Environmental Protection Agency. Report No. EPA 816-R-13-005.

[EPA] U.S. Environmental Protection Agency. 2013. Class VI—geologic sequestration permit application and permitting tools. Washington (DC); U.S. Environmental Protection Agency. https://www.epa.gov/uic/class-vi-geologic-sequestration-permit-application-and-permitting-tools

[EPA] U.S. Environmental Protection Agency. 2014. Emergency and remedial response plan: 40 CFR §146.94(a). Washington (DC); U.S. Environmental Protection Agency.

Vasylkivska V, Dilmore R, Lackey G, Zhang Y, King S, Bacon D, Chen B, Mansoor K, Harp D. 2021. NRAP-open-IAM: a flexible open-source integrated-assessment model for geologic carbon storage risk assessment and management. Environ Model Softw. 143:105114. doi:10.1016/j.envsoft.2021.105114

Vernik L. 1998. Acoustic velocity and porosity systematics in siliciclastics. Log Analyst. 39(4):27–35.

Webb SW. 2000. A simple extension of two-phase characteristic curves to include the dry region. Water Resour Res. 36(6):1425–1430. doi:10.1029/2000WR900066

White MD, Bacon DH, McGrail BP, Watson DJ, White SK, Zhang ZF. 2012. STOMP: subsurface transport over multiple phases—STOMP-CO_2 and -CO_2e guide. Richland (WA); Pacific Northwest National Laboratory. Report No. PNNL-21268.

Zhai G, Shirzaei M, Manga M, Chen X. 2016. Pore-pressure diffusion, enhanced by poroelastic stresses, controls induced seismicity in Oklahoma. Proc Natl Acad Sci USA. 113(33):16228–16233. doi:10.1073/pnas.1819225116

Zhang ZF, White SK, White MD. 2015. Delineating the horizontal plume extent and CO_2 distribution at geologic sequestration sites. Int J Greenh Gas Control. 43:141–148.

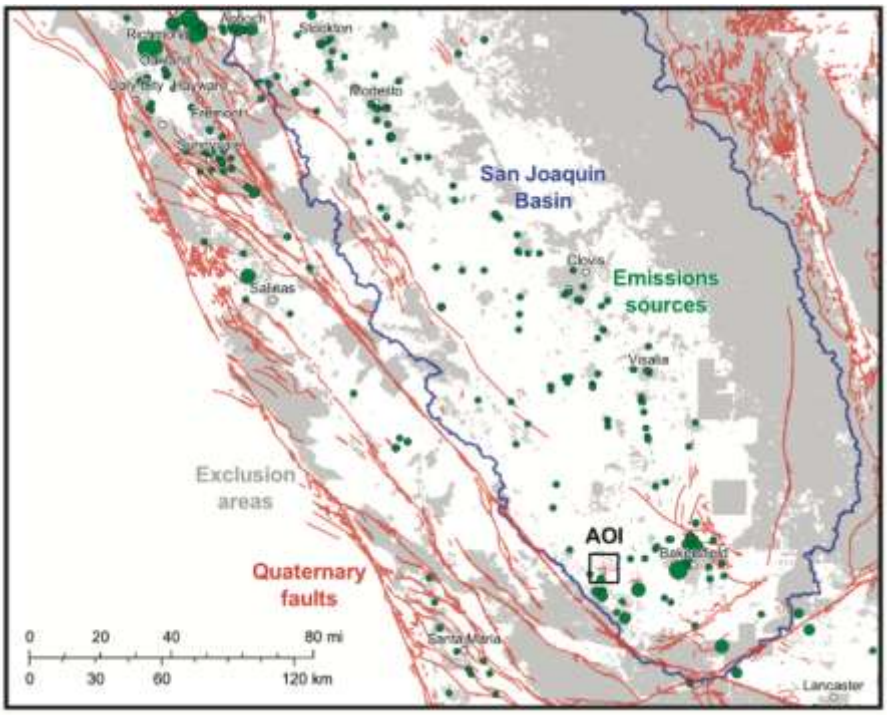
Zhang X, Liu W, Chen J, Jiang D, Fan J, Daemen JJK, Qiao W. 2022. Large-scale CO_2 disposal/storage in bedded rock salt caverns of China: an evaluation of safety and suitability. Energy. 249:123727. doi:10.1016/j.energy.2022.123727

Laying the Cornerstones of a Regional Storage Hub in California

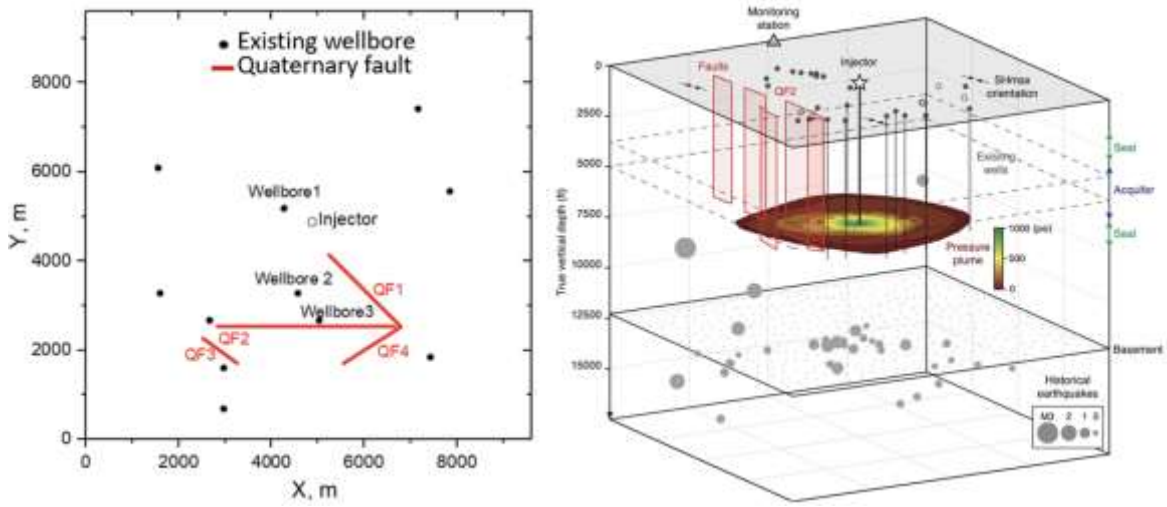
The overarching goal of the California Cornerstone project was to provide foundational engineering analysis across immediate, near-term, and medium-term time frames to accelerate the implementation of a shovel-ready project that has the potential to scale and address the 12.3 $MtCO_2$/yr emitted from upstream oil and gas operations in the San Joaquin Valley (SJV), see **Error! Reference source not found.**(a). This represents a first-mover carbon capture and storage (CCS) project on the Pacific Coast and the involvement of the Carbon Utilization and Storage Partnership (CUSP) to help establish a pathway for additional projects in California, including a regional storage hub. The project's physical location is one of the closest prospective

storage sites to the Los Angeles (LA) Basin. Within the LA Basin any subsurface storage is unlikely due to population density and seismic activity making the SJV especially interesting.

The area of interest (AOI) for CO_2 storage is located in Kern County, CA, in the southern San Joaquin Basin. Previously, Kim et al. (2023a) found that the southern San Joaquin Basin is a good location for geological carbon storage (GCS) projects based on geological properties and technoeconomic aspects. The potential storage site is 50 km west of Bakersfield, CA, as shown in **Error! Reference source not found.**(a). Also, the simplified maps of the AOI in 2D and 3D are shown in **Error! Reference source not found.**(b) and **Error! Reference source not found.**(c), respectively. The potential CO_2 injector is located in the middle of the AOI, and the existing wellbores and Quaternary faults (QF) are shown in **Error! Reference source not found.**(b). In addition, the historic seismicity near AOI is shown in **Error! Reference source not found.**(c).



(a)



(b) (c)

Figure 278 (a) Map of CO_2 storage opportunities in the San Joaquin Basin and the area of interest (AOI) of this study. (b) 2D map for AOI. (c) 3D map for AOI with existing wellbores and Quaternary faults. Source of **Error! Reference source not found.**b and **Error! Reference source not found.**c: Kim et al. (2025), licensed under CC BY-NC.

The objective was to provide technical and economic analysis to support a first-of-its-kind capture and storage project aimed at reducing emissions from upstream oil production operations. Project goals were to (1) leverage low-carbon fuel standard (LCFS) credits and CUSP technical expertise to move a CCS project in California from concept to permitting to implementation, (2) add certainty to storage volumes and dynamic storage capacity of relatively poorly characterized saline formations in the SJV, (3) forge a pathway for others to follow with similar projects, and (4) lay the foundations of a regional storage hub.

Our previous analysis of capacity in California for CUSP found a storage capacity of 864 $MtCO_2$ in the oil fields of the SJV (Kim et al. 2022). This is a substantial volume but not a large enough volume to construct a carbon storage hub and to have sufficient storage volume to scale. Our study also suggested significant potential of saline formations in the SJV that far exceeds the capacity of oil fields. These saline formations are not well characterized and understood from a storage engineering perspective. Hence, we have a specific objective to conduct further evaluation to obtain more certain estimates of saline formation storage capacity and storage rates.

We achieved our goals using 7 tasks with collaboration among team members. The outline of each task was as follows.

1) Distributed emitters – Identify the spatial locations of SGs in Kern County for integration into ArcGIS (Esri 2025), enabling analysis of potential surface infrastructure and association of emissions with individual generators to prioritize sources. Conduct a techno-economic analysis to assess the value generated from capturing these emissions.
2) Subsurface model – Develop a reservoir model of a typical saline formation in the SJV, including key features such as geology, aquifers, permeability, porosity, and capillary pressure. The model aligned with Sentinel Peak Resources' recent geological assessment of saline formations and was used to demonstrate the site's capacity to confine effectively CO_2.

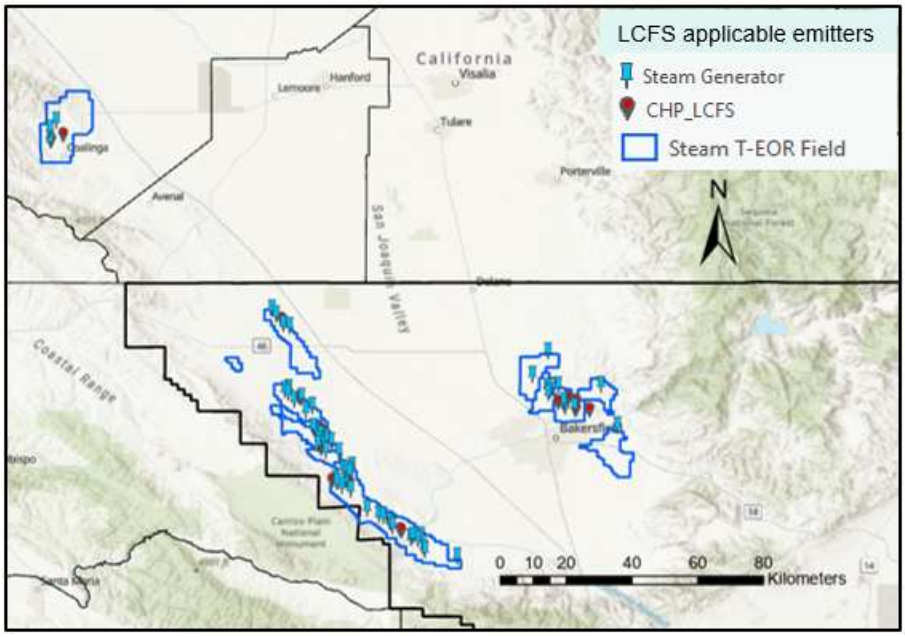
3) Storage assessment – Evaluate the dynamic CO_2 storage capacity over time using reservoir simulation to guide injection well operations. Use uncertainty analysis to explore the range of possible outcomes.
4) Plume migration – Using the subsurface model, conduct simulation studies incorporating uncertainty to predict the transport and fate of the CO_2 injected and simulate plume dynamics and pressure buildup incorporating uncertainty quantification. Additionally, we evaluate and assess an InSAR (Interferometric Synthetic Aperture Radar)-based surveillance approach for GCS to demonstrate the potential use of satellite images to monitor a CCS project in Kern County, CA.
5) Field project – Support the planning, infrastructure development, and monitoring of a field project. Use the SimCCS^{PRO} (Carbon Solutions 2025c) toolset to visualize the Sentinel Peak Resources project with pipeline routing (using CostMAP^{PRO} [Carbon Solutions 2025a]) and evaluate potential well placements and configurations using SCO_2T^{PRO} (Carbon Solutions 2025b) and related tools.
6) Risk assessment – Incorporate reservoir mechanics if needed and simulate deformation of the storage formation and conduct a geomechanical risk assessment to establish that proposed storage sites(s) are low risk. Also, evaluate the risk of CO_2 leakage from existing wellbores.
7) Forward-looking regional scenarios – Consider 2 expansion scenarios: first, capturing and storing 90% of emissions from thermal enhanced oil recovery (EOR) SGs in California, and second, developing a regional CO_2 storage hub. Use the SimCCS^{PRO} toolset to model both scenarios. The regional hub would serve as a CCS complex, helping to launch the CCS industry in the SJV and beyond.

Distributed Emitters

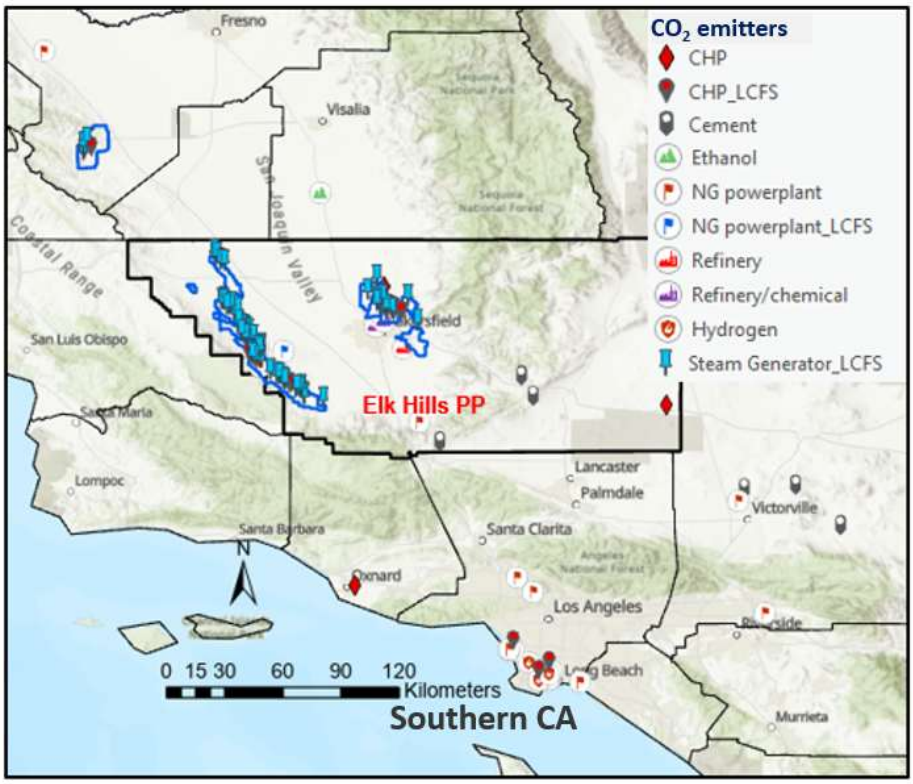
We conducted a comprehensive assessment of CCS opportunities within California's southern San Joaquin Basin, in particular Kern County laying the groundwork for a regional storage hub. The analysis involved a detailed methodology to identify and characterize CO_2 emitters and a thorough techno-economic evaluation to prioritize CCS projects under current and potential financial incentives. The detailed results in this section are provided in Kim et al. (2023a); see the Appendix.

Identification and Selection of CO_2 Emitters

We identified the emission sources and spatial locations for oil and gas thermal EOR production facilities, specifically steam generators (SGs) and combined heat and power (CHP) plants, in Kern County. The thermal enhanced oil production facilities (SGs and CHP) are shown in Figure 279(a). Also, additional CO_2 emitting regions, throughout Southern California are shown in Figure 279(b). There are 125 large CO_2-emitting facilities (EPA 2021a) in Southern California, with a significant concentration of oil and gas production operations in Kern County. These facilities include SGs and CHP systems that support thermal EOR.



(a)



(b)

Figure 279 The distribution of (a) thermal enhanced oil recovery production facilities (steam generation and combined heat and power [CHP]) and (b) large CO_2 emitters throughout Southern California. CHP_LCFS represents the low- carbon fuel standard (LCFS)-applicable CHP sites. Source: Kim et al. (2023a), licensed under CC BY-NC.

A systematic selection process was used to identify candidate sites for carbon capture:

- **SGs –** We used the California Air Resource Board (CARB 2021a) and California Department of Conservation (CA DOC 2021) databases, along with Google Earth, to locate thermal EOR sites. A key criterion for selection was an annual emission rate of 0.025 $MtCO_2$ or greater. This process resulted in the identification of 63 SG sites, which contain approximately 380 individual units.
- **CHP Plants –** Starting with 1,695 sites from the EPA's eGRID database (EPA 2021b), we filtered for industrial and independent CHP facilities that produce both power and steam for oil and gas production, making them applicable for the LCFS credit. After applying an emissions threshold of at least 0.025 $MtCO_2$/yr, our procedure identified 20 CHP sites as suitable candidates.

Capture Cost for Steam Generation and CHP

Previous studies were consulted for GHG capture cost estimates for California (EFI and Stanford 2020) and the United States as a whole (Abramson et al. 2020; Pilorgé et al. 2020). The capture cost for industrial facilities in California ranged from \$58/tCO_2 to \$131/tCO_2 (EFI and Stanford 2020), whereas the capture cost for the United States was reported as \$36/tCO_2 to \$75/tCO_2 (Abramson et al. 2020). It is assumed that the carbon capture facility is an amine-based solvent unit. In particular, the capture cost for a natural gas powerplant, which is an application similar to CHP, ranged from \$53/tCO_2 to \$63/tCO_2 at the national level (Abramson et al. 2020). The difference in capture cost for CO_2 emitters in California was considered related to specific conditions of operation and maintenance.

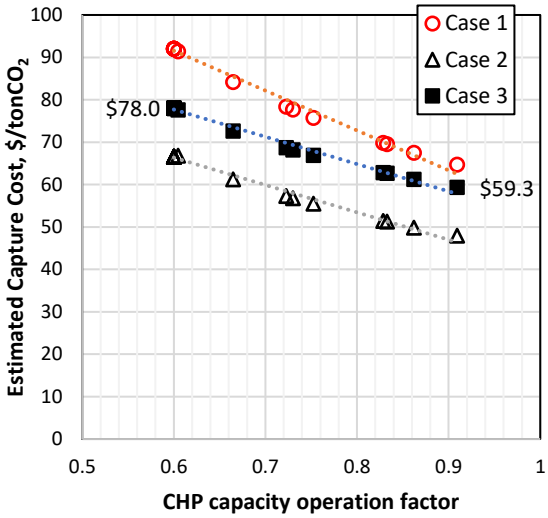
Unit capture cost is expressed in Eq. (1). The total capture cost ($Capture_{total\ cost}$) consists of capital expenditures (CAPEX) and operating expenditures (OPEX). The OPEX is composed of operating costs (C_{op}) and energy costs (C_E). A 20-year time period was assumed for economics, but actual plant lifetime may be longer. The detailed parameters to calculate capture cost are shown in the Appendix.

$$Capture_{unit}\left(\$/_{tCO_2}\right) = \frac{Capture_{\ total\ cost}}{\sum_i^n Capture\ amount} = \frac{\sum_{i=1}^n CAPEX_i + OPEX_i}{\sum_i^n Capture\ amount} = \frac{\sum_{i=1}^n CAPEX_i + C_{op,i} + C_{E,i}}{\sum_i^n Capture\ amount} \quad (1)$$

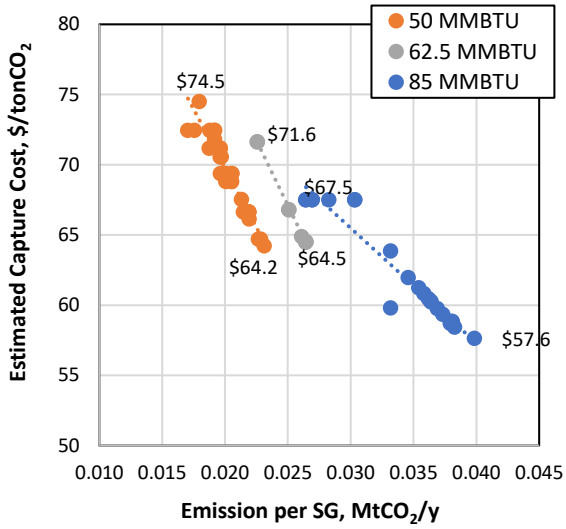
The CAPEX included the capture unit and engineering fee. CAPEX were spread over the first 2 years. The operating costs were calculated at 5% of CAPEX for both CHP plants and steam generators The OPEX includes labor, tax, materials, and insurance (EFI and Stanford 2020). The energy cost (C_E) considers both electricity and natural gas expenses. The electricity cost and natural gas costs are \$50/MWh and \$3.5/MMBTU, respectively (NPC 2019). Regarding the capture cost of CHP, there were 3 cases depending on CAPEX and energy costs. The base case was estimated using the average CAPEX from a previous study (EFI and Stanford 2020). The capture cost for steam generation assumed parameters identical to CHP except CAPEX and gas consumption. Based on the capacity of the SG, 50, 62.5, and 85 MMBTU, the retrofit CAPEX costs were determined to be \$7 million, \$8.1 million, and \$10 million, respectively. The detailed parameters for each case are in the Supplementary Material.

The estimated capture cost for oil production facilities (CHP and steam generation) is shown in Figure 280. In particular, the capture cost for CHP has 3 different cases based on the capacity operation factor. We assumed that the capacity operation factor ranged from 0.6 to 0.9. As the operation factor increased, the capture cost decreased. The capture cost in Case3 for CHP ranged from \$59.3/tCO_2 to \$78.0/tCO_2. The capture cost of steam generation was estimated based on

emissions per steam generation unit with the capacity operation factor from 0.7 to 0.9. The capture cost decreases with the increase of capacity operation factor and steam generation capacity type. The capture cost of steam generation in our model ranges from \$57.6/tCO_2 to \$74.5/tCO_2 depending on the estimated operating conditions of each site. The mean capture cost for 50, 62.5, and 85 MMBTU steam generation units are \$69.0/tCO_2, \$66.6/tCO_2, and \$62.2/tCO_2, respectively.



(a)



(b)

Figure 280 Estimated capture cost for (a) combined heat and power (CHP) and (b) steam generation for common steam generator (SG) heat rates. Source: Kim et al. (2023a), licensed under CC BY-NC.

Identification of Potential Storage Sites

We evaluated and ranked potential CO_2 storage sites, considering both saline formations and hydrocarbon fields in the southern San Joaquin Basin. We used a 3-stage procedure below. Detailed explanations are found in the Appendix.

- **Stage 1 – Geological Screening:** Candidate sites were first evaluated against qualifying geological thresholds for properties such as depth (>800 m), reservoir thickness (>10 m), and permeability (>10 mD) to ensure their suitability for secure, long-term storage.
- **Stage 2 – Exclusion Zones:** We then defined and applied exclusion zones to minimize risk and potential land-use conflicts. These zones removed areas based on seismic risk (e.g., a 4-km buffer around Quaternary faults), high population density, sensitive habitats, and restricted lands.
- **Stage 3 – Qualification and Ranking:** After removing exclusion zones, the remaining areas were evaluated and their storage resource estimates revised. Despite this conservative method, the region still showed an estimated storage capacity of 0.45 to 1.15 $GtCO_2$ in qualified hydrocarbon fields and 16.6 to 52.0 $GtCO_2$ in saline formations. A scoring system using 12 criteria—such as storage capacity, permeability, and seal integrity—was applied to identify the most promising sites.

This comprehensive screening and scoring process resulted in the selection of 41 high-priority storage sites for the techno-economic analysis. These 41 sites, which include 7 hydrocarbon fields and 34 saline or stacked formations, represent a total storage resource of 5.8 $GtCO_2$. Finally, Figure 281 shows the 41 target CO_2 storage sites in the available saline formations in the southern San Joaquin Basin.

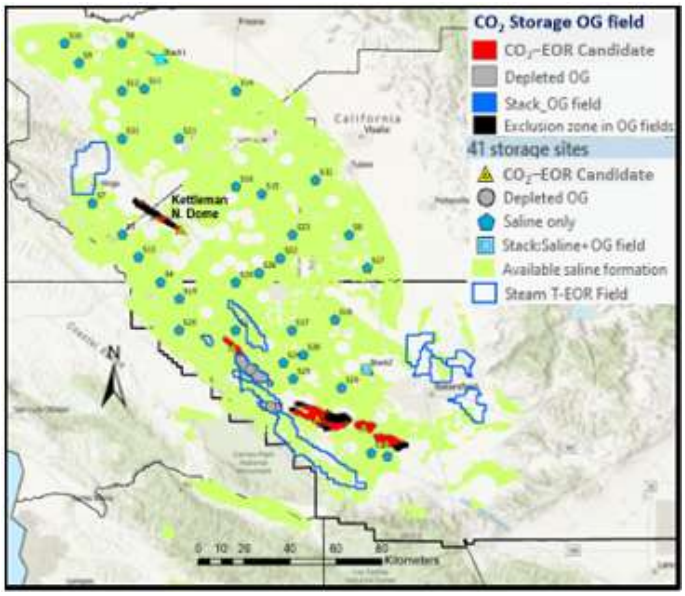


Figure 281 Prospective CO_2 storage sites among available saline formations and hydrocarbon fields. Source: Kim et al. (2023a), licensed under CC BY-NC.

Technoeconomic Analysis

The version of SimCCS used in this study is the temporal model and is different from the previous version (Middleton 2020). An overview of the SimCCS model is given in the Supplementary Material. Tax credits are modeled in SimCCS as modifications to capture or storage costs. If the state-level credit varies based on the source (e.g., LCFS credits), then the credit is applied to the capture cost as

$$\text{Total Capture Cost} = \text{Raw Capture Cost} - \text{Tax Credit} \quad (2)$$

The LCFS credit was conservatively considered to be \$100/tCO_2 with a 100% LCFS assumption. The maximum LCFS credit (2021) price was posted as \$221.67 (CARB 2021b). LCFS credits are only applied for refineries, SGs, CHP plants, and ethanol refineries based on LCFS pathways. Steam generators, refinery, and hydrogen facilities received 80% of \$100/tCO_2 LCFS credit. The ethanol facility receives 100% of the \$100/tCO_2 LCFS credit. The LCFS percentage of CHP facilities varied from 50 to 60% based on the contribution of steam generation for oil production (Supplementary Material, Table S2 in Appendix A-1). The cement and powerplant facility cannot receive the LCFS credit except Elk Hills powerplant (40% LCFS) that provides electricity to oil production. In the scenario case study, the LCFS credits used were \$70/tCO_2, \$100/tCO_2 and \$150/tCO_2.

The 45Q tax credit (Section 45Q of the U.S. Tax Code; Credit for Carbon…2021) was applied to the cost of storage for the maximum credit period of 12 years. The updated (Inflation Reduction Act of 2022) 45Q credit for saline and CO_2-EOR fields was \$85/tCO_2 and \$60/tCO_2, respectively. The injection cost of CO_2 in saline formations and depleted hydrocarbon fields was simply assumed to be \$10/tCO_2, which is consistent with previous studies (DOE 2014; Rubin et al. 2015). We note that actual injection cost of CO_2 is variable based on formation depth and injectivity. So, the storage cost per metric ton of CO_2 in saline formations was −\$75/tCO_2 with the net benefit computed as

$$\text{Total storage cost} = \$10\ (CO_2 \text{ injection cost}) - \$85\ (45Q \text{ credit}) \quad (3)$$

Regarding the cost of storage for CO_2-EOR, we conservatively considered the revenue from the additional hydrocarbon production as an additional credit. In particular, the cost of CO_2 purchase and recycling price ranges from 25% to 50% of the cost per barrel oil produced at \$70/bbl (NETL 2010). Based on the condition of operation, the revenue generated by CO_2 injection and operation (\$/tCO_2) was varied. We conservatively assumed revenue of \$17.5/tCO_2, whereas another study assumed the revenue from CO_2-EOR projects was \$15/tCO_2 (EFI and Stanford 2020). The storage cost for CO_2-EOR fields was estimated as −\$67.5/tCO_2 with the net benefit computed as

$$\text{Total storage cost} = \$10\ (\text{Injection Cost}) - \$17.5\ (\text{Revenue from } CO_2\text{-EOR}) - \$60\ (45Q \text{ credit}) \quad (4)$$

The storage cost in CO_2-EOR fields needs to be further investigated. In this study, the injection rate limit for saline formations and hydrocarbon fields was constrained to 2 and 1 $MtCO_2$/yr, respectively. Also, the pipeline network rights-of-way (ROWs) used existing natural gas and crude oil pipeline ROWs.

Generally, the SimCCS optimization model operates in 3 modes: (1) CAP, (2) PRICE, and (3) TIME. SimCCS formulates these optimization models as mixed integer linear programming

(MILPs). In all modes, SimCCS aims to minimize infrastructure cost subject to various constraints. Equation (7) represents infrastructure cost as shown below.

$$\min \overbrace{\sum_{i \in S} V_i^s a_i}^{capture\ cost} + \overbrace{\sum_{k \in K} \sum_{c \in C} \alpha_{kc} p_{kc}}^{pipeline\ use\ cost} + \overbrace{\sum_{k \in K} \sum_{c \in C} \beta_{kc} y_{kc}}^{pipeline\ build\ cost} + \overbrace{\sum_{j \in R} V_j^w b_j}^{storage\ cost} \quad (5)$$

The objective function contains the capture (V_i^s) and storage (V_j^w) cost data provided to SimCCS as well as transportation costs calculated from the cost surface (α_{kc} and β_{kc}). The other variables in the objective function are *decision variables* that represent the amount of CO_2 captured at a location (a_i), the amount of CO_2 stored at a location (b_j), the amount of CO_2 transported in a pipeline component (p_{kc}), and an indicator for whether or not a pipeline component is constructed (y_{kc}). Further explanation is provided in the Supplementary Material.

The different modes of SimCCS reflect variations in the model as follows.

CAP Mode. This mode is the model presented, but with an additional constraint that forces the resulting infrastructure to capture a certain amount of CO_2. This mode is used for scenarios that target capture amounts. In this study, CAP mode was used to collect and store all capturable emissions.

PRICE Mode. This mode has no constraint requiring the capture of a specific amount of CO_2. This is possible only with negative costs (or profit) in the system. Therefore, infrastructure is deployed only if the cost of the objective function is less than zero. Generally, this mode depends on 45Q credit, LCFS credit, or EOR sales profit at a storage site. This mode is used to find the profitable scenarios under deployment. We conducted several scenarios depending on the variation of credits including the 45Q tax credit, LCFS credit, and the capture threshold for the 45Q tax credit.

TIME Mode. This mode is more complicated than the CAP and PRICE models. The project period is broken up into phases and each phase has its own set of cost and capacity parameters. Infrastructure for each phase is designed to minimize total project cost, so infrastructure that can be shared across phases is prioritized over infrastructure that needs to be rebuilt in subsequent phases (Jones et al. 2023). This mode is used for scenarios in which evolution is expected (e.g., tax credit values, capture costs, source and reservoir availability, and capture targets change). A simple phasing study was applied to gauge the effect of the 45Q credit period using 12-, 16-, and 20-year durations of 45Q.

Table 61 presents the deployment scenarios with different parameters. The current threshold of capture amount for the 45Q tax credit is 0.0125 $MtCO_2$/yr (industrial emitter) and 0.0185 $MtCO_2$/yr (powerplant). All scenarios operate for 20 years. The base-case scenarios with current 45Q capture thresholds and credit value were used in CAP and PRICE modes. Sensitivity studies were conducted based upon 45Q credit duration (12, 16, 20 years) and LCFS credit value ($70/t, $100/t, $150/t). Case studies with the 45Q tax criteria before 2022 are reported in the Supplementary Material. The all-storage option refers to considering all kinds of storage sites including CO_2-EOR candidate sites.

Table 61 Parameters for the SimCCS case studies. Shaded columns represent the parameters varied for each case study. Modified from Kim et al. (2023a).

	Operation year	Credit year	Mode	Capture threshold	Storage sites	Credit 45Q, $/tCO$_2$	LCFS* credit, $/tCO$_2$	No. of scenarios
Base study	20	12	CAP/PRICE	Current capture criteria ***	All storage	$60 (EOR**)/ $85 (saline)	$100	2
Case study 1 (45Q credit year)	20	12 16 20	CAP/PRICE		All storage	$60/$85	$100	6
Case study 2 (variation of LCFS credit)	20	12	PRICE		All storage	$60/$85	$70 $100 $150	3
Other case studies in the Supplementary Material	12 20	12 16 20	CAP/PRICE	Previous capture criteria ****	All storage/ no-EOR site	$35/$50 $60/$85 $70/$100	$100 $150 $200	25

*LCFS = low-carbon fuel standard
**EOR = enhanced oil recovery
***Current threshold (industrial emitter: 0.0125 MtCO$_2$/yr and powerplant: 0.01875 MtCO$_2$/yr)
****Previous threshold (industrial emitter: 0.1 MtCO$_2$/yr and powerplant: 0.5 MtCO$_2$/yr)

The 41 storage sites and 125 CO_2 emitters in the target region and Southern California were considered using SimCCS. Based on proposed scenarios (Table 61), the results of SimCCS are presented using CAP and PRICE mode. Also, a simple phasing study (Time mode) was applied to understand the effect of 45Q credit periods of 12, 16, and 20 years. The effect of the LCFS credit value was investigated with the current 45Q credit and capture threshold. In the Supplementary Material, there are several additional case studies of the effect of 45Q credit duration, the value of the 45Q credit, and the value of the LCFS credit with the 45Q capture threshold before 2022.

Figure 282 shows the results of the base study with the current capture threshold condition under the current 45Q tax credit period of 12 years and 20 years. Each case uses CAP and PRICE modes. A negative cost represents a profitable CO_2 storage project. The net cost is shown with a red bar and represents the sum of storage costs in gray, capture costs in yellow, and transport costs in blue. Also, the annual amount captured and stored is marked with a black square and the number of storage sites marked with green triangles are shown in Figure 288. The number of CO_2-EOR candidate sites is shown with a red triangle. These legends and marks are similar in the rest of the figures.

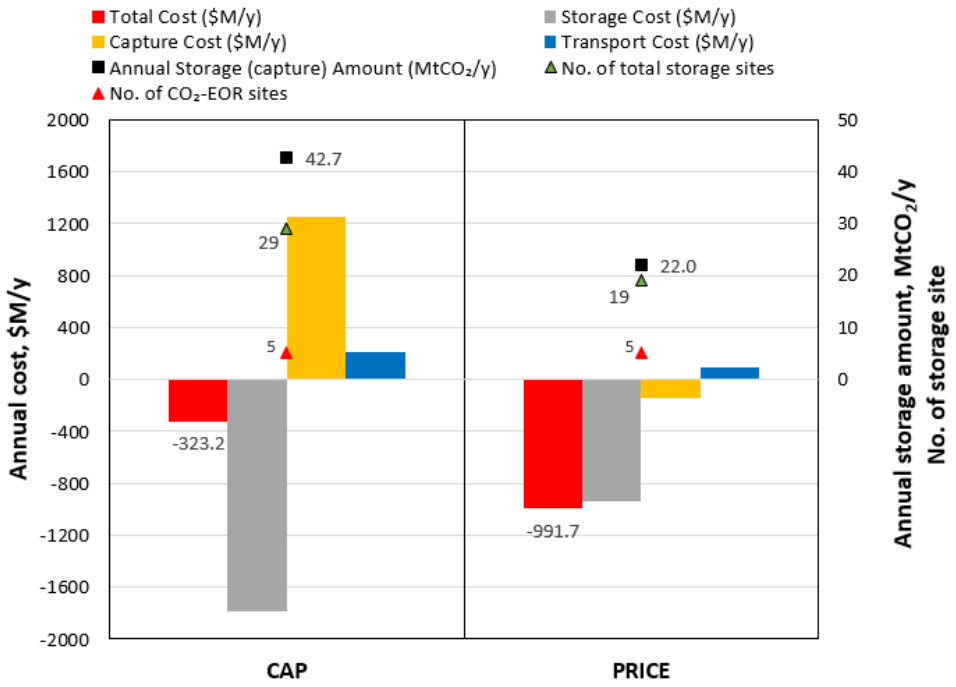


Figure 282 The results of CAP and PRICE scenarios assuming 20 project life, 12 years of 45Q credits, and \$100/tCO$_2$ low-carbon fuel standard credit in the base study. Source: Kim et al. (2023a), licensed under CC BY-NC.

As discussed above, the CAP mode operates to collect and store all capturable emissions where PRICE mode finds the profitable individual CCS project under deployment. As a result, the capturable amount in the PRICE mode shows 22 MtCO$_2$/yr amounting to around 50% of the total capturable amount (42.7 MtCO$_2$/yr) in the CAP mode. Therefore, the number of storage sites is less in the PRICE mode. We notice that the total project cost in the CAP mode was profitable with the 2022 45Q tax credit value.

Figure 293 shows the distribution of capture amount and number of emitters within each industrial field. In the CAP mode, all capturable emissions (42.7 MtCO$_2$) and emitters (125) were engaged. In the PRICE mode, the majority of emissions from cement manufacture and natural gas power plants can not be captured with an economic benefit under the current 45Q tax credit value except the emissions from Elk Hills natural gas power plant because they are not LCFS eligible. About 50% of emissions from CHP can be economically captured and stored. The emissions from ethanol, steam generation, refinery and hydrogen production can be mostly captured with economic benefit. Note that more than 90% of steam generation emissions and refinery hydrogen production can be captured and stored with economic benefit because they receive both the LCFS credit and the 45Q credit.

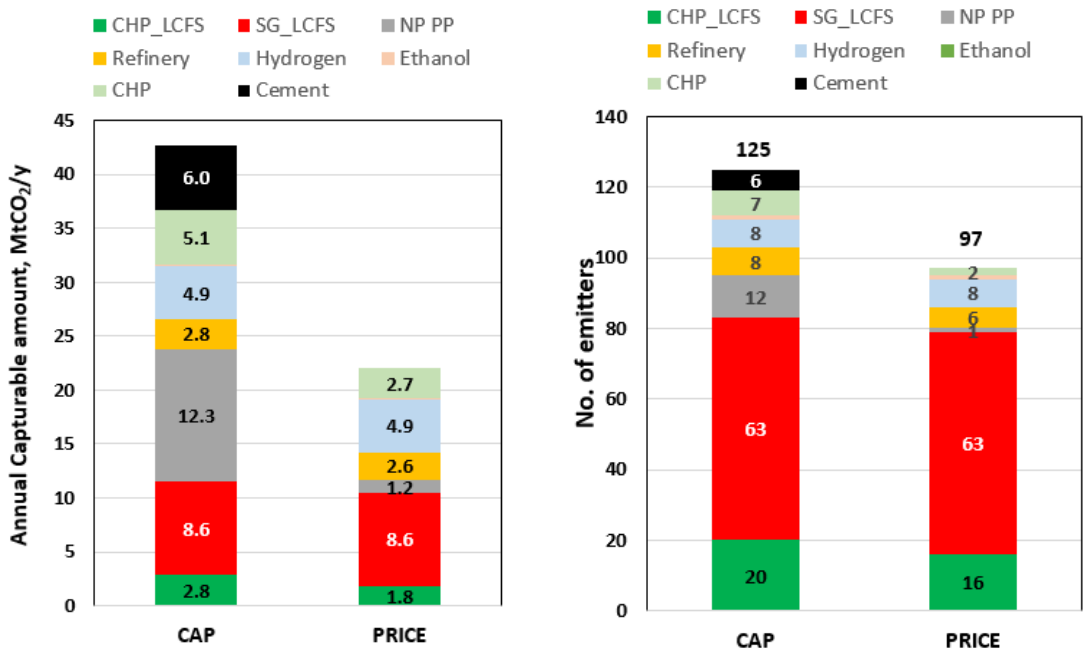
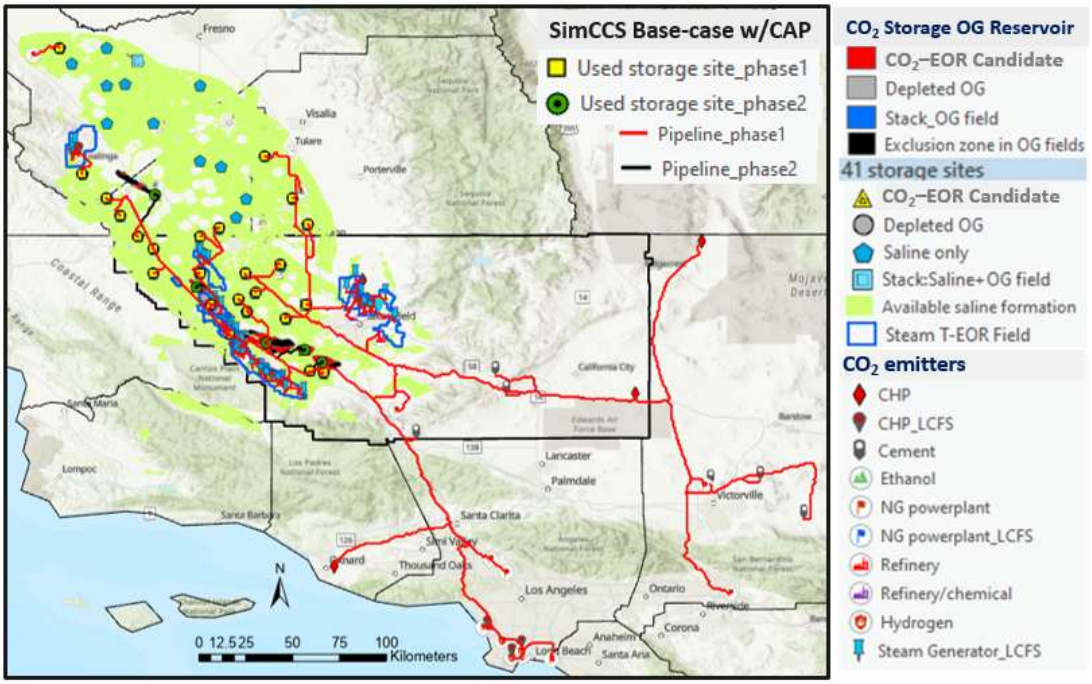


Figure 293 SimCCS results for (a) CO_2 capturable amount ($MtCO_2$/yr) and (b) number of engaged emitters in the base study. Source: Kim et al. (2023a), licensed under CC BY-NC.

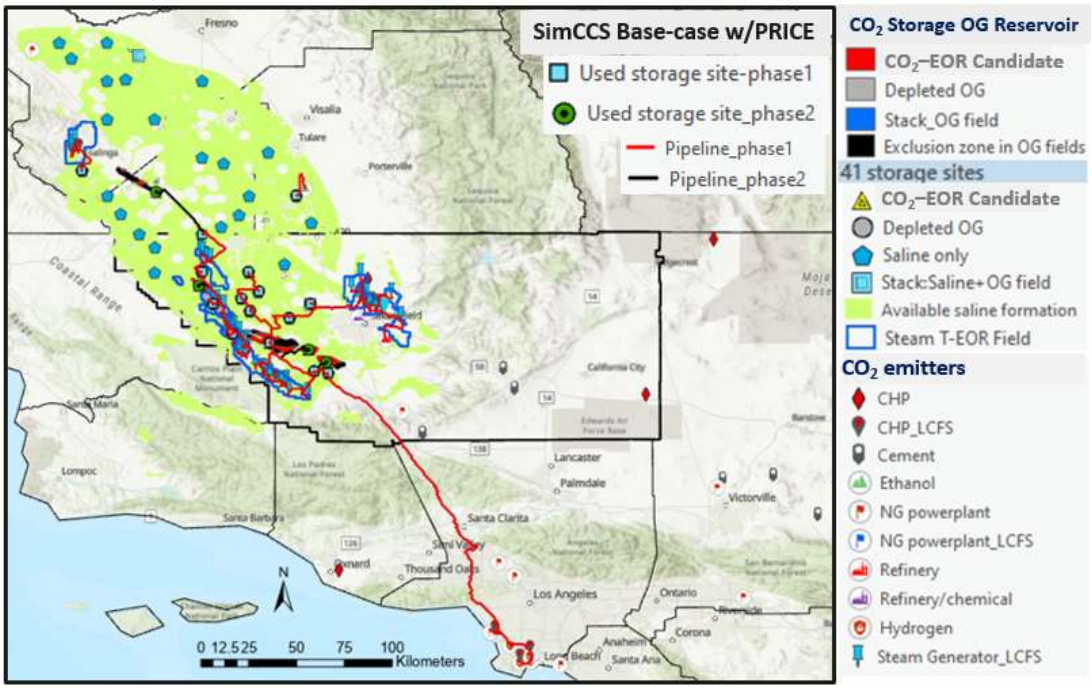
Figure 294 shows base-case results for CAP and PRICE mode with all storage option. We assume there are 2 phases for the pipeline construction due to the different 45Q credit coverage. The period of 1st and 2nd phases is 12 years (45 Q credit period) and 8 years (no-45Q credit period), respectively. The pipeline network is shown with solid red and black lines for phases 1 and 2. The CO_2 storage sites chosen are marked with yellow squares and a double circle green mark (filled radio button).-The network of CO_2 emitters and storage sites in CAP mode is shown in Figure 300(a). All emitters were connected with CO_2 storage sites because the CAP mode is designed to store all capturable emissions. As noted above, 29 sites shown with yellow squares among 41 storage sites were connected.

In PRICE mode, 97 CO_2 emitters were connected with 19 storage sites, Figure 294(b). The CO_2 storage sites chosen are marked with light blue squares and a double circle green mark. In the 2nd phase, 4 storage locations (CO_2-EOR candidate sites except Elk Hill site) are engaged with a new pipeline (black color).

Again, the emissions from natural gas power plant and cement industries cannot be connected economically because these emitters are not eligible for LCFS credits. Also the capture cost and transportation cost of these facilites exceeds the current 45Q credit benefit. In the PRICE mode, there was only 1 pipeline network to construct between CO_2 emtters and CO_2 storage sites.



(a)



(b)

Figure 294 SimCCS base-case scenario using (a) CAP mode and (b) PRICE mode with the "All" storage option. The low- carbon fuel standard (LCFS) credit is \$100/tCO_2 and project lifetime is 20 years with 12 years of 45Q credit. Source: Kim et al. (2023a), licensed under CC BY-NC.

The sensitivity of 45Q tax credit value assuming a 20-year project lifetime was investigated to explore expansion of capture. We assume \$100/tCO_2 LCFS credit and the "all storage" option.

The current 45Q credit is \$60/\$85/tCO_2 for EOR/no-EOR sites. The effect of CO_2 capturable amount on different industries is shown in Figure 295. The current 45Q tax credit with the assumption of 12 year and 20 year credit life can capture 22 and 31.7 $MtCO_2$/yr, respectively, in PRICE mode. This results suggests that the current 45Q tax credit lifetime of 12 years is too short to improve the economic viability of many CCS actions. Unfortunately, the emissions from cement and powerplant sectors are not captured and stored due to the lack of economic benefit with a 12 year credit life. Increasing the 45Q credit life increases the capturable amount to 31.7 $MtCO_2$/yr. In this scenario, all emissions from the cement industry can be captured and stored economically. The greater 45Q credit value (\$70/\$100/tCO_2) with a 12-year credit life leads to storage amounts (22.9 $MtCO_2$/yr) similar to the current 45Q credit value. The scenario with 20-year 45Q credit life mostly captures and stores all emissions. This results in 41.3 $MtCO_2$/yr, which is almost 97% of the total capturable amount (42.7 $MtCO_2$/yr) in the target region. The carbon capture cost has a critical role within the technoeconomic analysis. The capture cost should decrease over time with technology innovation to fulfill a carbon neutral economy. The results from SimCCS showed that carbon capture from some large emitters in natural gas power plant and cement industries did not have an economic benefit with the current 45Q tax credit lifetime and the retrofit costs for carbon capture. The target capture cost for these industrial fields should be less than \$40/tCO_2 to \$50/tCO_2 with current tax credit and storage cost. Detailed analysis of target capture costs and pipeline network construction will be conducted in the future. An aggressive 45Q tax credit strategy, cost-effective capture units, and optimal pipeline networks will speed deployment of carbon storage.

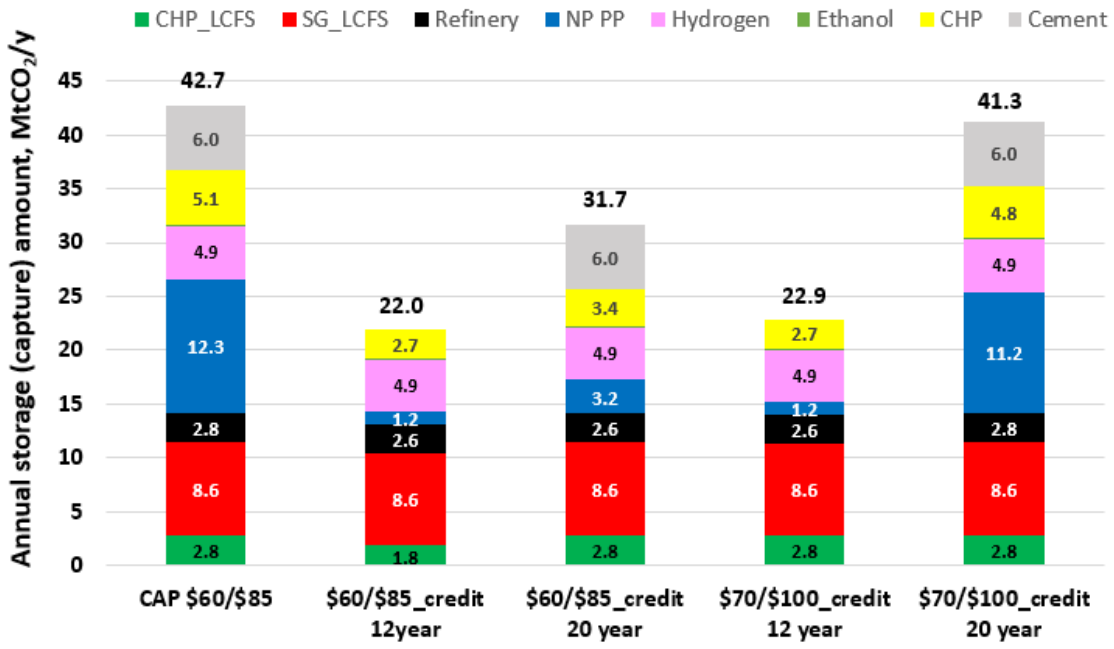


Figure 295 Sensitivity of capture and storage amount in each industry as a function of 45Q credit value with PRICE mode. Credit durations are 12 and 20 years (as noted) with a 20-year project lifetime. Source: Kim et al. (2023a), licensed under CC BY-NC.

Summary

Steam generation and combined heat and power operations within oil and gas production facilities were identified and located using public data in and around Kern County. These facilities were selected as eligible for the LCFS credit if their emissions were equal to or greater than 0.025 $MtCO_2$/yr. The capturable cumulative GHG emissions from 63 SGs and 20 CHP plants with LCFS applicable facilities were 8.6 and 2.8 $MtCO_2$/yr, respectively. Additionally, another 42 selected large emitters in the Kern County vicinity and Southern California were estimated as having capturable emissions of 42.7 $MtCO_2$/yr. The capture cost for CHP ranged from \$59/tCO_2 to \$78/tCO_2 depending on the operating conditions whereas the capture cost for emissions from steam generation ranged from \$58/tCO_2 to \$74.5/tCO_2 depending on the estimates for each site.

CO_2 storage resources were reevaluated and investigated using a 3-stage screening procedure. Conservative risk exclusion zones were used to increase the security of potential CO_2 storage in geological formations. The exclusion zones consist of risk category (Quaternary fault and seismic activity), population density, restricted lands, and sensitive ecological habitats. Even with a significantly conservative approach, the resulting estimated storage resources for hydrocarbon fields and saline formations were 0.45 to 1.15 $GtCO_2$ and 16.6 to 52.0 (mean 34.3) $GtCO_2$, respectively. These resources were then scored and storage sites with high and medium priority scores and greater than 20 $MtCO_2$ storage resource were defined as the target sites for technoeconomic analysis. All fields passing through screening with exclusion zones have desirable qualities for storage. In this way, 7 hydrocarbon fields were selected. Among them, 5 fields were CO_2-EOR candidates and 2 fields were depleted oil fields only for storage. Also, a total of 34 saline formations including 2 stacked formations were selected. The 41 storage sites chosen totaled 5.8 $GtCO_2$ of storage resource.

Subsequently, in our study, the 125 emitters in Kern County and Southern California were connected with 41 prospective storage sites and a regional technoeconomic analysis conducted. The capture costs for the additional 42 large emitters were adopted from a previous study (EFI and Stanford 2020). The proposed regional scenarios were conducted to find the optimal CCS project with proper credit assumptions. Oil and gas production facilities are predicted to break even or profit under current 45Q tax and LCFS credit conditions. Almost all oil and gas facilities can receive both credits. The base-case results using CAP and PRICE mode in the SimCCS tool illustrated that cement manufacture and natural gas power plants do not receive enough credit to break even. Therefore, there are limitations to deploying CCS projects under the current 45Q and LCFS credits.

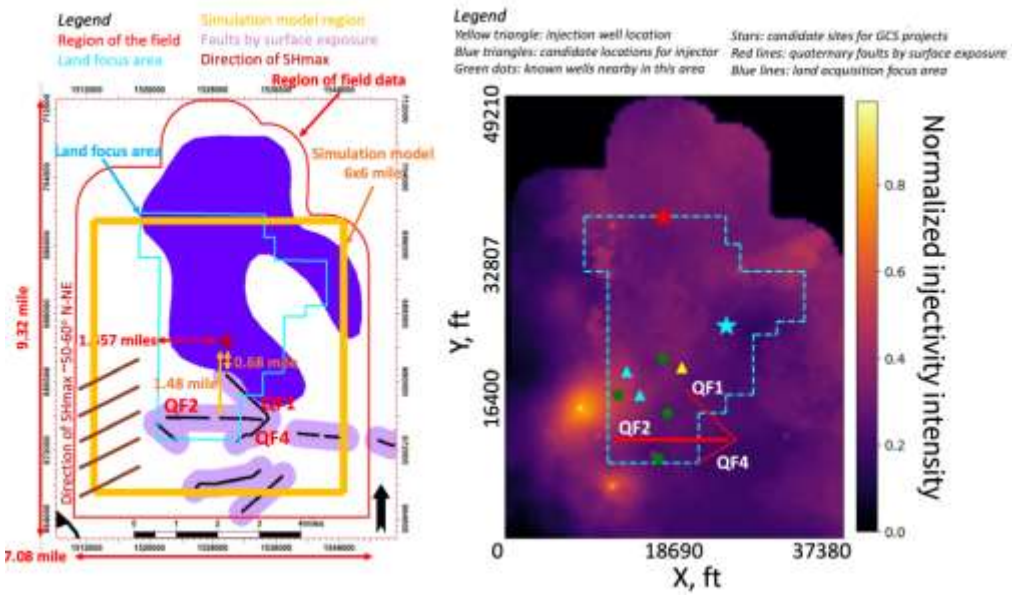
Subsurface Model

We modeled the pilot-scale CCS site incorporating geomechanics to quantify the rock deformation at land surface and subsurface. The detailed results in this section are provided in Li et al. (2024); see the Appendix.

Overview of CCS Sites

The potential GCS site is located in Kern County in the southern SJV in California. Significant CO_2 emissions exist throughout the region (Kim et al. 2023a). Figure 296(a) shows an overview

of the study area, which is 66.0 square miles (7.08 miles in width and 9.32 miles in height) at the land surface. The target storage formation is a saline aquifer, and it is around 3,861 ft (1,177 m) in depth dipping to the west and south. Within this site, a 6-by-6-mile (10-by-10-km) area, shown as the orange square, is selected to build the subsurface model for numerical simulation. The blue polygon in Figure 296(a) is the potential land focus area at the early stage of this project, and we aim to constrain the majority of the injected CO_2 within a small area to preserve the site for future activities. The injection well location is selected according to the injectivity map (Figure 296(b)). The injectivity is defined as the product of permeability and effective pay thickness. Figure 296(b) shows that the large injectivity regions are unfortunately out of the land acquisition area. The injection well is placed at the location of the yellow triangle by considering the distances to the boundaries of the land focus area and the injectivity potential. The blue triangles are other candidate injection locations, and they are not selected because they are very close to the west boundaries of the land focus area. The dashed line in Figure 296(b) shows the exact land focus area, as shown in Figure 296(a). The green dots in Figure 296(b) are the known wells in this area, and the star icons represent the other candidate injection sites that were studied and found to not be as advantageous as the selected site. The identified injection well is 1.56 miles away from the west boundary of the land focus area. There are surface exposures of faults in this area, and the injection well location is 0.68 miles to the QF1 fault and 1.48 miles to the QF2 fault.



(a) (b)

Figure 296 Map view of the geological carbon storage pilot site. (a) Boundaries and potential fault observations through surface exposure (represented by the lavender-shaded area around the faults) with the direction of SHmax indicated as 50° to 60° north-northeast. (b) Normalized injectivity (kh) map in this region. The triangles and stars represent candidate injector locations, and the yellow triangle is selected for injection. The green circles show the known existing wells. The blue dashed line describes the so-called land focus area or main project area. The red solid lines show the location of Quaternary faults (QF1, QF2, and QF4) according to surface exposures. Note that QF1 is nearly normal to the direction of SHmax. Source: Li et al. (2024), licensed under CC BY-NC.

The subsurface geological stratigraphy demonstrates subsurface layers in Figure 297. The subsurface geological stratigraphy is summarized in Figure 297 and is based on well logs. This

given well is about 1.5 km away from the potential injection well. In this work, we mainly focus on the Etchegoin Formation as our CO_2 storage reservoir. In general, the Etchegoin Formation is around 3,862 ft (1,177 m) in depth and has an average thickness of 2,258 ft (688.2 m). The Etchegoin Formation also dips to the west with an approximate angle of 9°. This imposes further challenges for CO_2 storage due to the fact that a dipping formation drives CO_2 plume migration. The Etchegoin Formation is modeled with overburden shale layers (SJ shale 1 and SJ shale 2) of 1,912 ft (582.3 m) thickness in total. It also has bottom seal at the depth of 6,120 ft (1,865.4 m). The Etchegoin Formation has significant potential for CO_2 storage. The underground source of drinking water (USDW) starts in the middle of the San Joaquin Formation (above 1,320 ft [402.3 m] depth).

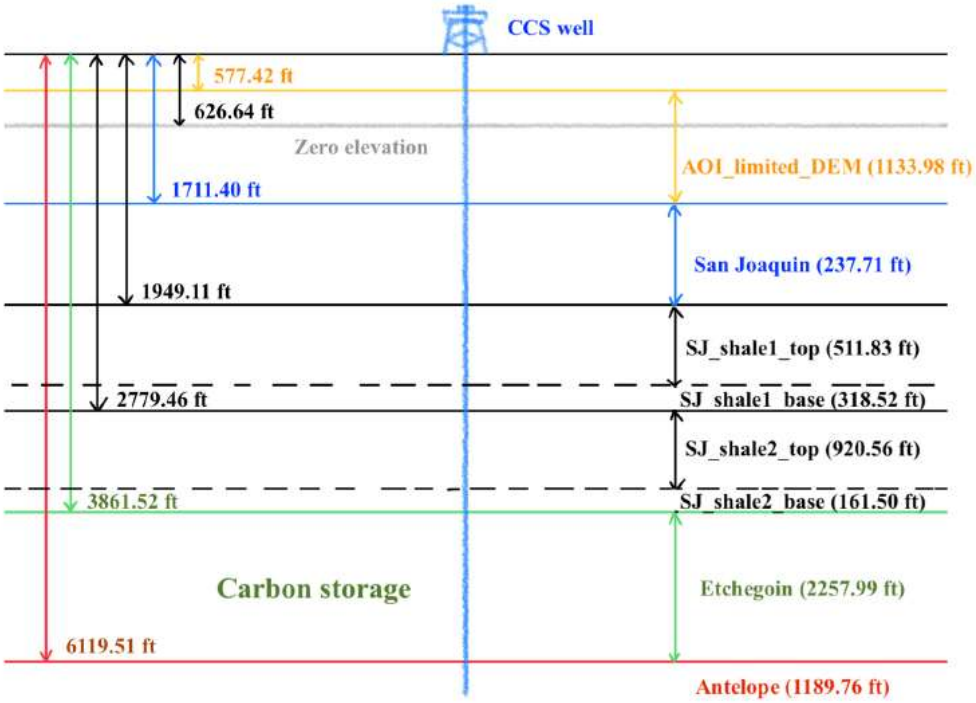
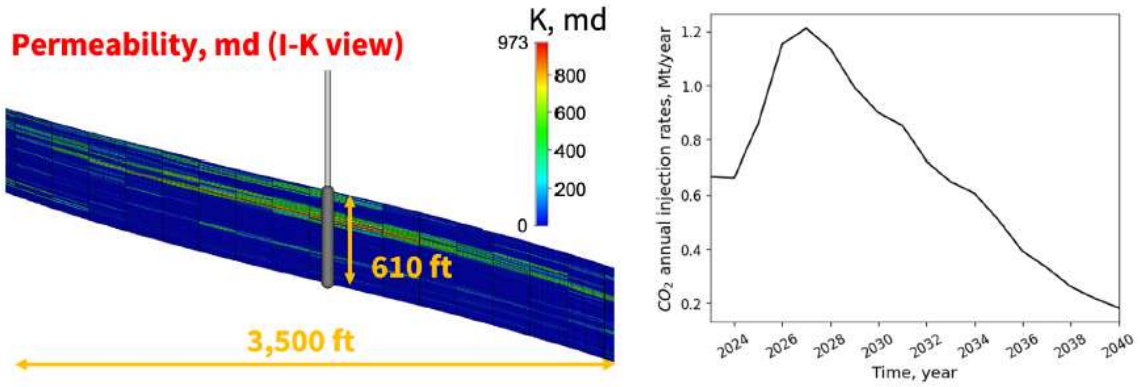


Figure 297 Schematic vertical section of geological strata adjacent to the injection well. The middle of the storage formation is over a mile (1.6 km) deep. Source: Kim et al. (2023b), licensed under CC BY-NC.

One of the site-specific challenges in this work is the heterogeneous storage formation with low-permeability layers as shown in Figure 288(a). We need to limit CO_2 migration while maximizing the storage amount in this dipping saline formation. In addition, the predefine injection scheme is shown in Figure 288(b). Annual injection rates peak in 2027 at 1.2 $MtCO_2$/yr as defined by a potential project. The variable injection rate poses significant challenges for this GCS case study because the pressure response needs to be managed carefully to avoid fracturing the storage formation seal and to reduce the risk of leakage. It is necessary to address the changing injection rate challenge because the imbalance of CO_2 supply and demand in the region may happen (Davis et al. 2011; Naims 2016). This project plans to inject a total amount of 12.3 $MtCO_2$ within 18 years followed by a monitoring period of 100 years after shut-in of the well to ensure that the CO_2 plume becomes stationary.



(a) (b)

Figure 288 Site-specific design for the geological carbon storage problem. (a) I–K cross-sectional view (610 ft [185.9 m] tall by 3,500 ft [1,066.8 m] wide) of the horizontal permeability to demonstrate the heterogeneous storage formation and (b) Injection schedule for 18 years of injection following the predefined annual rates. Injection in the lower portions of the storage formation where permeability is lower is judged optimal so that plume migration updip is limited. Source: Li et al. (2024), licensed under CC BY-NC.

It is important to avoid injection into large permeability channels because the CO_2 will be very mobile and a large areal CO_2 plume extent will result. The buoyancy-driven CO_2 migration updip during the postinjection period (after shut-in of the injector) further enlarges the final plume size. The low-permeability zones, however, are not fully capable of storing large amounts of CO_2 given the pressure buildup constraint. We measure this trade-off quantitatively throughout the dynamic GCS simulation. The surface exposures of the Quaternary faults in this site are another challenge we need to tackle. According to the geomechanical analysis and the state of stress at the project site, we need to be extremely careful about slip on the QF2 fault. The orientation of the QF2 fault within the stress field, as shown in Figure 278(a), presents an angle that is not normal or parallel to the regional stress in this area. This suggests that QF2 is of great interest during the design of the injector and the accompanying response to injection. We control the pressure increase at the location of the QF2 fault with a large safety margin to avoid fault activation.

Numerical Simulation Model

The geological structure of the storage formation is analyzed using well logs in order to interpret the permeability and porosity distribution. There is a dipping tidal channel in the southwest. The mud in the northeast region leads to low permeability zones. To model the saline storage formation, the initial water saturation is set to be 1 and the salinity of the brine is equal to 15,300 ppm. The hydrostatic pressure gradient is set to be 0.47 psi/ft (10.63 kPa/m) and the 2.5 °F (1.39 °C) geothermal gradient is per 100 ft (30.48 m). The grid block design for the Etchegoin storage formation is 33 by 33 by 75, as is shown in Figure 299 with red layers. There are 40 extra layers on top of the storage formation (shown in Figure 299 using blue) serving as the cap rock to represent the sealing formation. The grid blocks are refined in the area close to the injector to describe the CO_2 plume and migration with greater geospatial resolution. The grid blocks far away from the injector are very large in order to cover the entire 6 by 6 miles (9.66 by 9.66 km) area of the model.

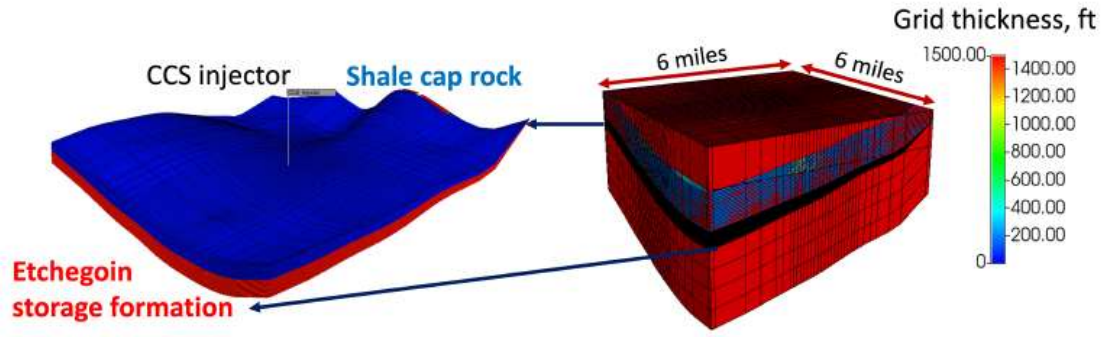


Figure 299 Numerical simulation model set-up in the 6-by-6-mile (9.66-by-9.66 km) study area. Fluid flow occurs in the storage formation overlain by a caprock (left) and the storage zone is 2-way coupled geomechanically to the land surface and below the storage formation (right). Source: Li et al. (2024), licensed under CC BY-NC.

The geomechanical model is used to understand rock deformation, stress, and strain change due to injection. The fluid flow model is 2-way coupled with the geomechanical model to simulate the case with 18 years of injection following the injection scheme in Figure 288(b). We simulated a 100-year postinjection period after shut-in. We extended the geomechanical grids upward with 25 extra layers to fill in the gap between the top surface of the sealing formation and the land surface. Therefore, we are capable to compute the land surface movement due to CO_2 injection. Figure 299 demonstrates the fluid flow model on the left and the 2-way coupled geomechanical model on the right.

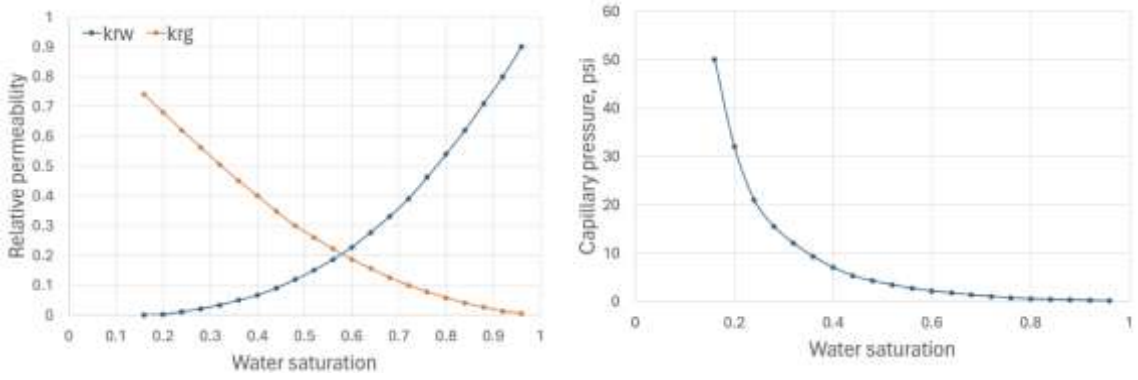
The storage formation is thin compared with the entire subsurface system in this model. This 2-way coupled model follows a structure of sandstone–shale–sandstone–shale from top to bottom. The top sandstone represents the rock from land surface to the sealing formation. The next shale structure represents the ultra-low permeability cap formation to seal the CO_2 storage and prevent upward motion by buoyancy. The next sandstone rock represents the storage formation, and the shale rock next to it represents the bottom sealing formation. This structure defines different rock mechanics characteristics in order to compute the solid deformation. The geomechanical model assumes that the rock follows elastic deformation because we limit pressure increase due to injection to avoid plastic deformation or potential rock fractures. The Mohr-Coulomb model is implemented for rock failure due to the normal and shear stresses in the subsurface system.

The pressure–volume–temperature (PVT) model is summarized in Table 62. The main fluids in this subsurface system include CO_2 and brine. The solubility is modelled according to Henry's Law, and the Henry's Law constant is a function of temperature and pressure. Rock fluid models include relative permeability and capillary pressure and are shown in Figure 300(a) and Figure 300(b), respectively. Gas relative permeability hysteresis is considered to determine the imbibition curve as a function of a given drainage curve according to the maximum residual gas saturation, which is defined to be 0.4. We do not consider any geochemical reactions in this work.

Table 62 Component properties in the baseline numerical simulation model (modified from Li et al. [2024])

Component	CO_2	Water
Molecular weight, g/mol	44	18

Critical pressure, psi (kPa)	1,073 (7,398.1)	3,200 (22,063.2)
Critical temperature, °C	31	374
Acentric factor	0.225	0.343



(a) (b)

Figure 300 (a) Relative permeability curves and (b) draining capillary pressure for the baseline simulation model. Source: Li et al. (2024), licensed under CC BY-NC.

The geomechanical model is detailed in Table 63 and includes storage and sealing formations as rock types. The storage formation is represented as sandstone for CO_2 sequestration. Sandstone also describes the rock mechanical properties for the layers from the land surface to the top of the cap rock seal. The sealing formation represents the cap rock on top of the storage formation, and it also serves as the bottom seal below the storage formation. The values of Young's modulus and Poisson's ratio come from literature to represent SJV rock conditions (Holstein and Lake 2007; Sone and Zoback 2013; Molina et al. 2017). The unconfined compressive strength and friction angle are computed based on the empirical relations from the literature (Horsrud 2001; Chang et al. 2006). The Biot coefficients are close to unity because this model tends to represent a close-to-perfect coupling effect between pore pressure and the rock frame (Zimmerman 1990). We model a fully saturated saline aquifer in the subsurface where the majority of the pore pressure increment is expected to contribute to the effective stress change. In addition, the pore pressure management is essential for GCS projects, and a large Biot coefficient allows conservative consideration of pore pressure change effects due to the CO_2 injectivity.

Table 63 Geomechanical model details model (modified from Li et al. [2024])

Quantity	Storage formation	Sealing formation	Unit
Young's modulus	1.47×10^6 (1.0147×10^7)	2.18×10^6 (1.50×10^7)	psi (kPa)
Poisson's ratio	0.20	0.25	
Unconfined compressive strength	8.38×10^4 (5.78×10^5)	9.57×10^4 (6.60×10^5)	psi (kPa)
Friction angle	28.4	22.6	degrees
Biot coefficient	0.98	0.95	

A sensitivity analysis of grid block size confirms that there are minimal boundary effects related to pressure, and hence geomechanics, within the 2-way coupled flow and mechanical simulation. The unit grid block size ranges from 92.7 by 92.7 by 150 ft (28.3 by 28.3 by 45.7 m) to 183.5 by 183.5 by 150 ft (55.9 by 55.9 by 45.7 m) and further to 374.4 by 374.4 by 150 ft (114.1 by 114.1

by 45.7 m) to represent a wide range of dimensions for 3 distinct scenarios. The thickness of the grid blocks is uniformly 150 ft (45.7 m) in the *z*-direction because initial results showed consistent observations for different layer thicknesses of 38, 75, and 150 ft (11.6, 22.9, and 45.7 m). We examine the simulated pressure behavior at the boundary of the site (north of the injector), and the results show constant pressure with an average CO_2 injectivity of around 0.68 Mt/yr. This aligns with assumptions of GCS projects that have a large extent of volume for subsurface storage. The model size is sufficient for minimal boundary effects related to pressure. Although we observe marginal differences in results when zoomed into the curves, the accuracy is well maintained so that we balance the grid block sizes with the simulation runtime. For the same overall dimension of the model, using a much larger amount of small grid blocks significantly increases the simulation complexity and expected runtime.

Storage Assessment & Plume Migration

We evaluate the dynamic storage performance of the Kern County pilot site using the optimized subsurface model. This engineering assessment simulates realistic CO_2 injection and monitoring periods to measure total storage volume, plume behavior, pressure propagation, and mechanical integrity under operational constraints.

The in-house toolbox pyCCUS (Li et al. 2024) leverages the base-case numerical model and facilitates computations efficiently. The capacity of high-performance computing resources enables parallel computations to accelerate the workflow. The post-processing components evaluate the dynamic simulation quantitatively and combine all the necessary information together for analysis, visualization, and validation. The definitions of CO_2 plume and pressure footprint are stated. The well design optimization setup demonstrates one of the applications using the in-house toolbox to find the best injection well trajectory for this GCS case study. The detailed results in this section are provided in Li et al. (2024, 2025); see the Appendix.

pyCCUS

We have developed an in-house toolbox to automate the large number of simulations needed to analyze GCS outcomes during optimization. This toolbox interacts with the commercial software CMG so that the numerical model is parsed by CMG for computations. Our toolbox extracts the results from CMG for post-processing and analysis. Figure 301 shows an overview of the workflow with essential components noted. At the beginning, we need to build the base simulation model. We may also need the inputs from users as an optional choice if the goal is to drive pyCCUS to create many reservoir simulation models. For example, users could provide a list of parameters with ranges or distributions, and the design-of-experiment algorithms in pyCCUS would take over the task of generating the design-of-experiment setup. Therefore, our toolbox writes a number of simulation model input files accordingly. This function is applicable for uncertainty quantification or global sensitivity analysis. In this paper, we implemented a novel module to generate deviated injector trajectories for optimization. When the numerical simulation models are created according to user needs, the next step is to run all simulations. The toolbox is capable of deploying the work in different environments, including the Windows operating system, Linux operating system, and multiple high-performance computing resources. The toolbox submits all jobs prioritizing parallel over sequential computations depending on the computational resources allocated.

The numerical simulation results are extracted from CMG to Python for post-processing and analysis. The "sanity check" component ensures the success of the simulation and filters out cases that do not satisfy our settings. For example, the actual injection profile may not be the same as the predefined injection scheme due to the well bottomhole pressure constraint. For GCS-specific tasks, we highlighted the 2D and 3D CO_2 delineation, CO_2 migration distances with uncertainties, case design optimization, and potential artificial intelligence applications. The CO_2 migration distance and pressure plume are essential information for induced seismicity analysis and management (Kohli et al. 2023). Additionally, the land surface uplift due to injectivity could be a significant method to monitor the significant extent of the pressure plume and is discussed later.

In terms of optimization, pyCCUS is capable of both forward and looped optimization. The looped optimization is favored when performing a history match using a relatively simple model because the optimizer needs to learn from previous iterations to propose a better set of values. Example cases include chemical kinetics history matching with experimental measurements (Li et al. 2023). In this study, we use forward optimization because it reduces the computational cost. We are capable of requesting enough computational resources to simulate all cases in parallel so that the amount of time needed for all cases is the same as the time needed for 1 simulation. If the looped optimization is applied, however, there are at least a few iterations required for optimization and the total computational cost is expected to be many times larger than the forward optimization.

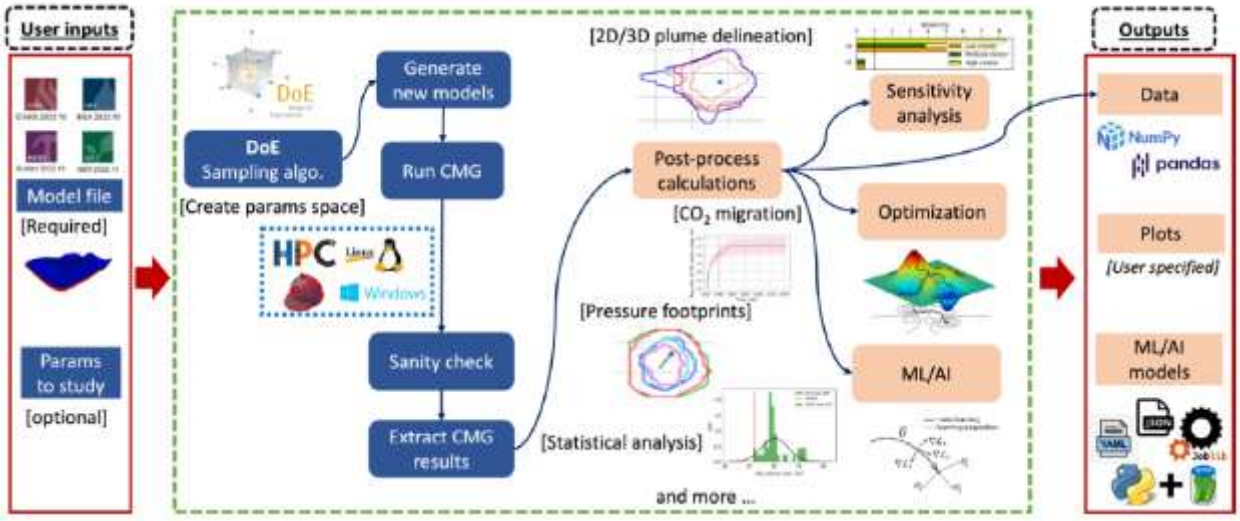


Figure 301 End-to-end workflow in pyCCUS including the major components from simulation to user-specified outputs. The model demonstrated in the user inputs section (required input) represents a 6-by-6-mile (9.66-by-9.66 km) field model. Source: Li et al. (2024), licensed under CC BY-NC.

Plume Definition

Plume definition is part of the post-processing of pyCCUS so that we are capable of quantifying the progress of GCS projects. We delineated the 2D and 3D CO_2 plumes according to the CO_2 gas saturation of the storage formation. The threshold value is defined to be the irreducible gas

saturation (5% in this work) because we aim to quantify the mobile CO_2 in the subsurface. To delineate the areal extent of the CO_2 plume, we first classify the grid blocks as with or without CO_2 and then draw the boundary lines. The CO_2 plume size is computed by integrating the area within the boundary of the 2D plume at the land surface. Eq. (6) describes the criterion to classify the grids to be inside of the CO_2 plume or not as

$$\text{CO}_2\ \text{plume}_{i,j,t} \in \{0,1\}\ \ \text{s.t.} \begin{cases} 1 & \text{if } \max_k \text{SG}_{i,j,k,t} \geq \text{SG}_{\text{threshold}} \\ 0 & \text{otherwise,} \end{cases} \tag{6}$$

where SG represents gas saturation of the target property; t represents the time; i, j, and k represent the grid coordinates; and k shows the vertical direction. Similarly, the pressure footprints are characterized following an approach similar to that in Eq. (7) and we compare the pressure increase with a threshold value that the user defines. The pressure buildup quantifies the pressure increment compared with the initial value. The pressure response at the fault is defined to be the maximum pressure buildup within the vertical plane at the QF2 fault location among all timesteps. The geological description of the QF2 fault is not available yet and we observe it only from surface exposures. Therefore, we minimize the fault leakage risk by restricting the pressure increment at the location of the QF2 fault as

$$\text{PRES footprint}_{i,j,t} \in \{0,1\}\ \ \text{s.t.} \begin{cases} 1 & \text{if } \max_k \Delta P_{i,j,k,t} \geq \Delta P_{\text{threshold}} \\ 0 & \text{otherwise,} \end{cases} \tag{7}$$

where $\Delta P_{i,j,k,t}$ represents the pressure buildup in each gridblock at each timestep.

Well Design Optimization

The injector optimization looks for the best trajectory of the deviated well or vertical well following the objective function in Eq. (8). The optimization process has 3 goals: (1) minimize the CO_2 plume size at the land surface, (2) minimize the pressure buildup in the storage formation, and (3) minimize the pressure change at the QF2 fault. The constraints include that the well location is fixed and the injection schedule is fixed, as shown in Figure 288(a). The loss function in Eq. (8) computes all 3 goals quantitatively for all cases. The well trajectory is the only independent variable in this work. To combine all optimization goals in 1 loss function, we normalize the properties and make the terms dimensionless. The terms are normalized by the minimum values of the population to quantify how far it is from the best achievable case regarding each optimization goal as

$$\begin{gathered} \text{Loss} = w_1 * \frac{\text{plumesize}_{CO_2}(\text{injector})}{\min \text{plumesize}_{CO_2}(\text{injector})} + w_2 * \frac{\Delta P(\text{injector})}{\min \Delta P(\text{injector})} + w_3 * \frac{\Delta P_{\text{fault}}(\text{injector})}{\min \Delta P_{\text{fault}}(\text{injector})} \\ \text{s.t.}\ \ w_1 + w_2 + w_3 = 1 \\ \underset{\text{injector}}{\text{argmin}}\ \ \text{Loss}(\text{injector}) \end{gathered} \tag{8}$$

where "injector" represents the independent variable in well design optimization, w1, w2, and w3 are weighting factors for 3 different aspects, and the default values are all equal to 1/3 to assign equal weights. The minimum values are known given all simulations finished from the forward optimization process.

We use 4 parameters to describe the injector trajectory in Figure 302. They include depth, deviation, direction, and perforation length. The depth describes the distance from the land surface to the center of the injector. The deviation is the angle between the deviated portion of the well and the direction of gravity. The direction is the angle between the projection of the well on the land surface and the base direction, which is defined to be positive in the east direction. The length of perforations controls the total length of the well and perforation length is the contact area of the injector with the storage formation. The combinations of different values of these 4 parameters generate many potential injector trajectories. Each trajectory is defined by a unique set of 4 parameters, and each combination of those parameters describes a unique injector.

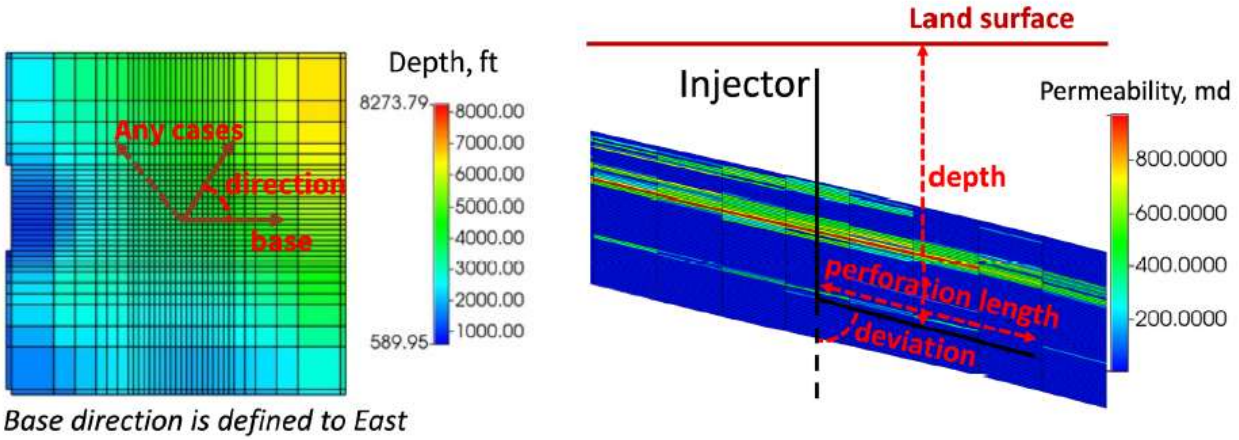
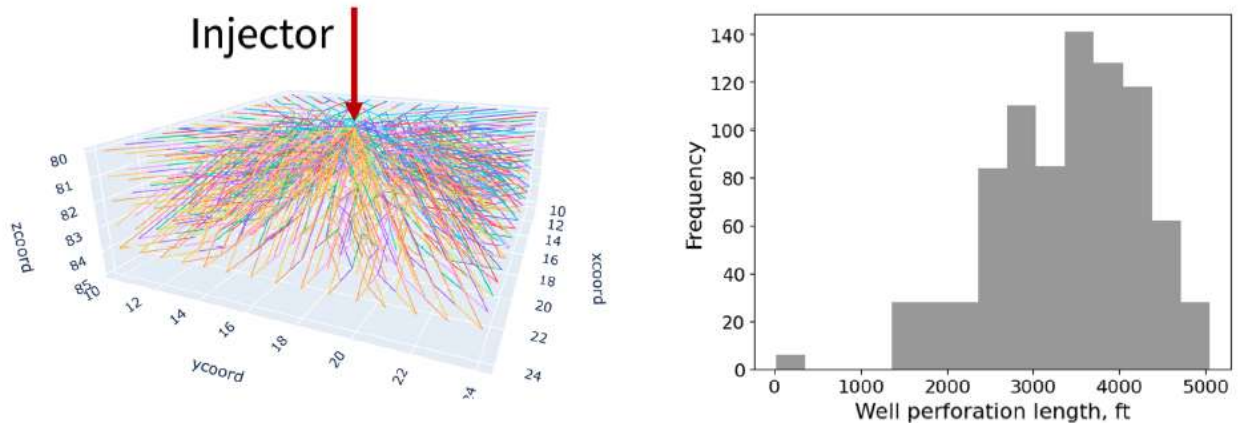


Figure 302 Parameter definition for injector design optimization. (left) Areal view (6 by 6 miles) illustrating depth. (right) 610 ft (185.9 m) tall by 3,500 ft (1,066.8 m) wide cross section of storage formation with permeability indicated. Source: Li et al. (2024), licensed under CC BY-NC.

The well depth ranges from 4,100 to 4,900 ft (1,249.7 to 1,493.5 m) due to the subsurface geometry. Essential test cases show that the CO_2 plume migrates beyond the study region if injected into the large permeability layers. Therefore, we need deeper wells injecting into lower permeability layers to control the plume size. The deviation angle ranges from 78° to 98° for a wide spread of the subsurface space. The direction ranges from 0° to 360° to consider all possible angles for tilt. The perforation length ranges from 80 to 5,000 ft (24.4 to 1,524 m), as shown in Figure 303(b), including scenarios of both vertical wells that are partially perforated at the deep layers of the storage formation and deviated horizontal wells. There are more than 800 cases generated for all potential trajectories of the injectors, as shown in Figure 303(a). The injector location is fixed and the trajectory varies to fulfill the entire potential space of the storage formation.



(a) (b)

Figure 303 Injector optimization experiment design. (a) All injector trajectories for optimization. (b) Histogram of the injector perforation length in the storage formation. Source: Li et al. (2024), licensed under CC BY-NC.

Injector Design Optimization Result

The optimization result for the injector trajectories in Figure 293(a) is shown in Figure 294. This figure evaluates the performance of injector design regarding CO_2 plume size at the end of the 100-year postinjection period, pressure buildup in the subsurface, the pressure response at the QF2 fault, and the loss function value. Each bubble in Figure 304 represents a unique injector trajectory. The size of the bubble demonstrates the pressure response at the QF2 fault, and the color bar shows the loss function value following Eq. (8). The horizontal axis represents the maximum pressure buildup in the subsurface. We evaluate GCS cases by looking for the maximum value across the entire project horizon for all grid blocks. The vertical axis demonstrates the CO_2 plume size at the end of the project, which is the year 2142, after 100 years of postinjection monitoring. We select Case130 as the optimal injector due to the smallest value of the objective function computed using Eq. (3). We reserve the capability for users to assign different weights in Eq. (3) to multiple aspects of GCS projects. The result shows that it is possible to further reduce the CO_2 plume size, but the pressure buildup tends to be larger. This is a trade-off for project designers to weigh.

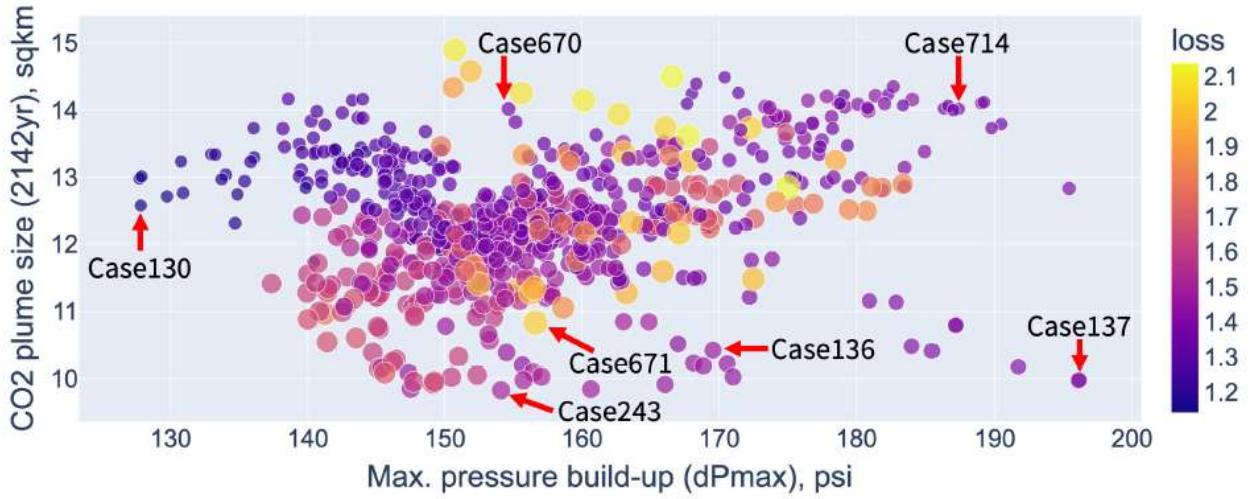


Figure 304 Injector design optimization results. Plume size 100 years after injection vs. the maximum pressure increase at the top of the storage formation. The size of the bubble represents the maximum pressure buildup at the QF2 fault plane through all timesteps. The color bar shows the loss value defined by the objective function in Eq. (8). Representative well trajectories are noted for further analysis. Source: Li et al. (2024), licensed under CC BY-NC.

As the bubbles in Figure 304 move downward for smaller CO_2 plume size, they tend to be larger (greater pressure buildup at the fault) and shift to the right. This pattern explains the trade-off between pressure response and the CO_2 plume size. We demonstrate the results favoring a risk-averse strategy; therefore, we define Case130 as the optimal case. Managing subsurface risks is difficult, and it is easier to restrict the pressure response to avoid leakage or fault activation risks. There is a list of trajectories selected in Table 64 because they are the extreme cases among the entire population of cases. The optimal injector shows the minimum pressure buildup either in the subsurface or at the QF2 fault compared with all other cases. Although the CO_2 plume size is 12.6 km^2 at the end of the monitoring period, this scenario reduces the pressure buildup by 35% (68 psi [468.8 kPa]) in the storage formation while the plume area required increases by 22% compared with Case243. The optimal injector trajectory demonstrates significant strength to avoid fault risk by reducing 175 psi (1,206.6 kPa) of the pressure increase at the QF2 fault (73%) for an extra 1.75 km^2 of land area compared with Case671.

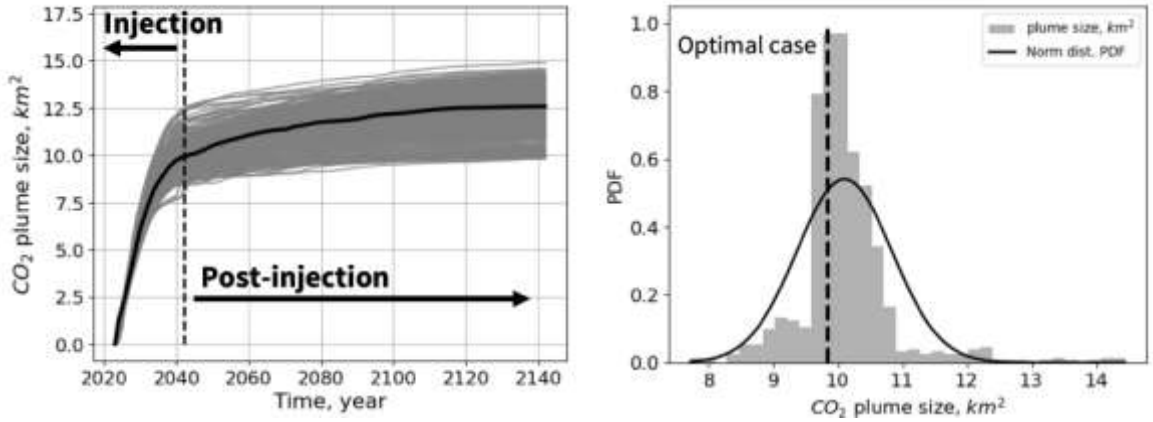
Table 64 Deviated injection well performance in terms of the optimization objectives model (modified from Li et al. [2024])

		Well trajectory ID							
		115	**130**	**136**	**137**	**243**	**670**	**671**	**714**
Well trajectory parameters	Depth, ft (m)	4,532.7 (1,381.6)	4,299.3 (1,310.4)	4,201 (1,280.5)	4,234.5 (1,290.7)	4,149.2 (1,264.7)	4,666 (1,422.2)	4,236.4 (1,291.3)	4,856.2 (1,480.2)
	Deviation, °	85.7	92.5	96.8	96.3	96.2	81.4	94.9	78.8
	Length, ft (m)	3,509.9 (1,069.8)	4,614.2 (1,406.4)	3,377.8 (1,029.6)	3,018.4 (920.0)	4,637.2 (1,413.4)	3,540 (1,079.0)	3,822.1 (1,165.0)	4,698.9 (1,432.2)
	Direction, °	90	310.6	243.6	270	229.7	8.6	156.3	41.9

Results	CO_2 plume size, km^2	13.7	12.6	10.4	10.0	9.8	14.0	10.8	14.0
	ΔP_{max}, psi (kPa)	174.9 (1,205.9)	127.8 (881.1)	169.5 (1,168.7)	196.1 (1,352.1)	154.1 (1,062.5)	154.6 (1,065.9)	156.6 (1,079.7)	187.4 (1,292.1)
	$\Delta P_{max,QF2}$, psi (kPa)	134.7 (928.7)	66.5 (458.5)	124.8 (860.5)	105.1 (724.6)	143.6 (990.1)	83.6 (576.4)	241.1 (1,662.3)	68.1 (469.5)
	Loss value	1.65	1.14	1.47	1.42	1.50	1.35	2.04	1.36

Dynamic Plume Quantification

The CO_2 plume size is quantified in a dynamic manner, and we show the growth vs. time for all cases in Figure 305(a). The highlighted thick black curve represents the optimal case we identified based on the objective function. Figure 305 shows that the plume size grows very fast during the first 5 years of the injection due to the large annual injection rates shown in Figure 288(a). The growth rate tends to drop afterward, but the plume size still increases during the injection period. After the shut-in, there is no CO_2 added to the storage formation, but CO_2 migration happens due to the increase of formation pressure and the buoyancy force. The plume size only increases slightly after injection stops.



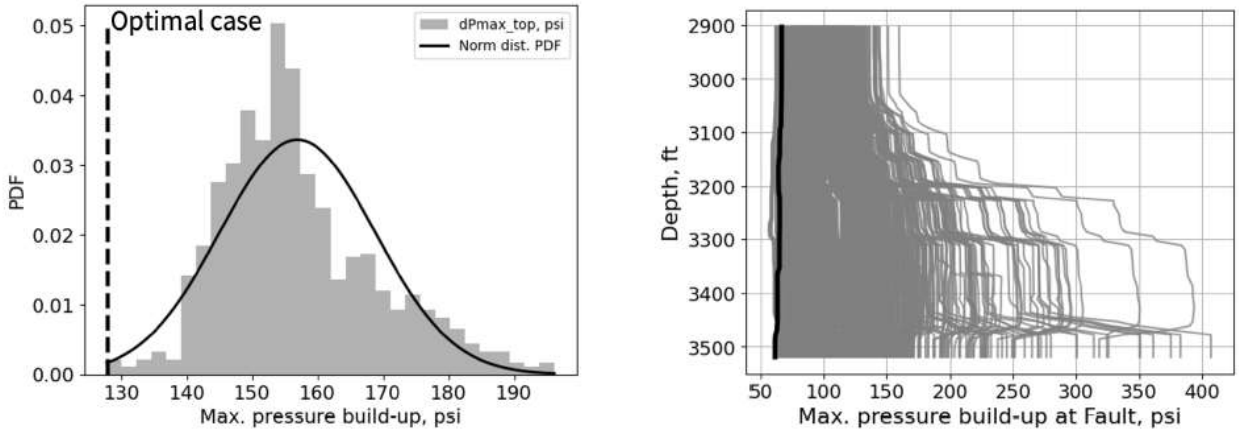
(a) (b)

Figure 305 CO_2 plume size for all injector trajectories. (a) Plume size vs. time (the solid line represents the optimal case). (b) Histogram distribution of the CO_2 plume size after shut-in for all injector design cases. Source: Li et al. (2024), licensed under CC BY-NC.

Throughout the postinjection period, the plume size tends to be stable and the growth rate gradually drops to zero. The gray thin curves represent all other cases in this work and we observe cases following different growth patterns regarding the plume size. This happens because the heterogeneous rock allows mass transfer at different rates. The histogram in Figure 305(b) shows the optimal case stands at a good position among the entire population of cases. Although there are cases on the left of the optimal case, they may show a large pressure response in the subsurface. In addition, some cases show small plume sizes because they do not follow the injection scheme defined in Figure 288(a). In the numerical simulation, the injection well is

constrained from injection rate or bottomhole pressure. If the injector reaches the bottomhole pressure limit, the numerical model reduces the injection rate, and therefore we see cases with smaller plume sizes. We filtered out cases not following the injection scheme from further analysis.

Pressure responses are very important to GCS project development, so we show the distribution of all cases in Figure 306(a). The optimal case shows that the pressure buildup is less than the majority of the design cases, and the maximum pressure buildup is 196 psi (1,351.4 kPa). The average of the cases shows 156-psi (1,075.6 kPa) pressure buildup, with a standard deviation of 11.8 psi (81.4 kPa). The pressure increase is a very important evaluation factor to make sure that injection does not fracture the rock. In addition, we also care about the pressure response at the QF2 fault for this specific site. The maximum pressure change along the vertical plane of the QF2 fault is shown in Figure 296(b). We show the maximum pressure change at each depth to capture the extreme conditions for safety concerns. The thick black curve represents the optimal design, and all other cases are represented by gray curves. Figure 306 shows that some cases have significant pressure change from 3,330 to 3,500 ft (1,005.8 to 1,066.8 m) because the deviated well tilts to a certain direction in the storage formation that stimulates the pressure change. It is critical to manage the pressure change along the fault to be uniform to avoid the possibility of fault slip or leakage risks.



(a) (b)

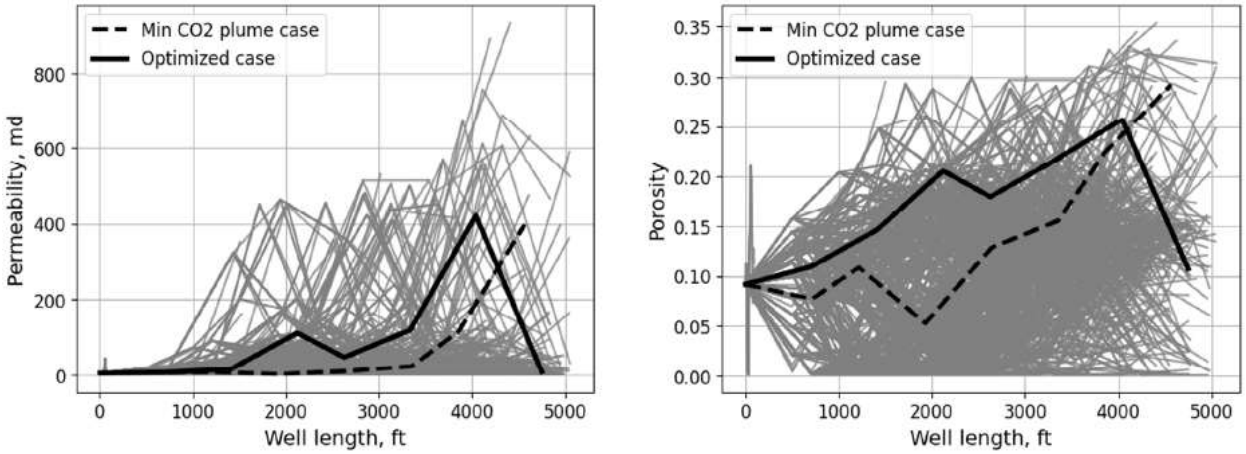
Figure 306 Pressure responses in the storage formation due to CO_2 injection (a) Distribution of the maximum pressure buildup within the top layer of the formation through both injection and postinjection periods. (b) Population of maximum pressure buildup within the plane of the QF2 fault during both injection and postinjection periods. The black solid line in (b) represents the response from the optimal injector in this work. Source: Li et al. (2024), licensed under CC BY-NC.

Figure 307 further explains the trade-off between the CO_2 plume size and the pressure change in the storage formation. The permeability and porosity are important to understand the trade-off. The large permeability zone allows mass transfer at a larger rate or a smaller pressure change consistent with single-phase Darcy's law in Eq. (9) as

$$q = -\frac{k}{\mu}\nabla p \tag{9}$$

where q is the flow rate, k is the permeability of the rock, μ is the viscosity of the fluid, and ∇p is the pressure gradient. To understand the optimization process, we demonstrate the permeability

and porosity along the trajectory of injectors for all cases in Figure 307. The plot shows that the optimal case seeks fairly good permeability and porosity because managing the pressure response favors better rock. The well does not deviate to the more permeable rock region because minimizing the CO_2 plume size is included in the objective function. The comparison case is the injector having the minimum CO_2 plume size, and it clearly shows this design particularly seeks a storage region with low permeability and porosity. The low permeability leads to a small rate of CO_2 movement and the plume size is well controlled to be small. The well length is also important because it determines the contact area within the storage formation. The optimal case has a slightly longer well compared with the case having a minimal CO_2 plume size. A deviated well with a long perforation length is favored, but it does not necessarily mean that the longest well is the best.



(a) (b)

Figure 307 Storage formation rock properties visualized along the trajectory of injectors for all cases. (a) Permeability and (b) porosity vs. injector perforation length. The bold black line shows the rock properties along the optimal well in this work. The black dashed line shows the well trajectory for the case with the smallest plume size. Source: Li et al. (2024), licensed under CC BY-NC.

The rock deformation is evaluated based on the optimal injector, and the result indicates a promising monitoring approach. In Figure 308, we show the land surface uplift computed from the 2-way coupled geomechanical model at the location of the injector. The uplift increases up to 2.14 cm in 2027, having the largest annual injection rate during the injection period. The simulation also shows the pressure change at the injector in the storage formation, and it demonstrates a strong correlation between the pressure change and the land surface uplift. They both increase at the beginning due to the increasing annual injection rates. In short, the chosen gridding balances numerical accuracy and simulation runtime. Substantially finer grids change the computed pressure response negligibly. After 2027, both pressure and land uplift decrease due to the decreasing injection rates after the peak. Some uplift and elevated pressure exist throughout the injection period. After the shut-in of the well, the pressure and land uplift decline due to the relatively infinite subsurface storage formation (relative to the total injection). This allows pressure dissipation. The redistribution of the CO_2 away from the injector after shut-in leads to a slight continued evolution of the pressure plume and uplift. The pressure and uplift dynamics still show a strong correlation, and the marginal change in uplift computed after shut-in does not impact the optimization objectives. The imposed pressure gradient, capillary

pressure, and buoyancy forces drive CO_2 migration after injector shut-in. The land surface uplift images are captured at 2 representative timesteps: 2024 and 2027, respectively. The uplift region is not at the center of the site due to the injector trajectory.

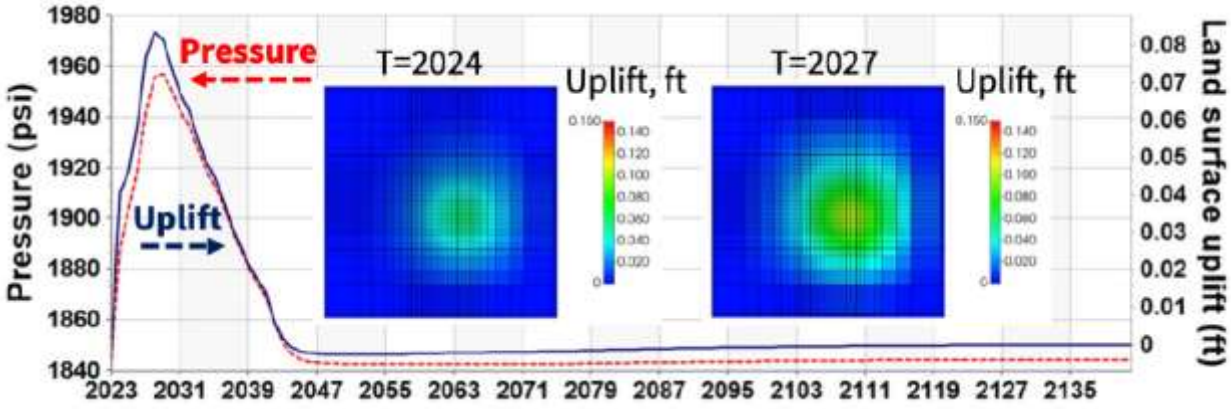
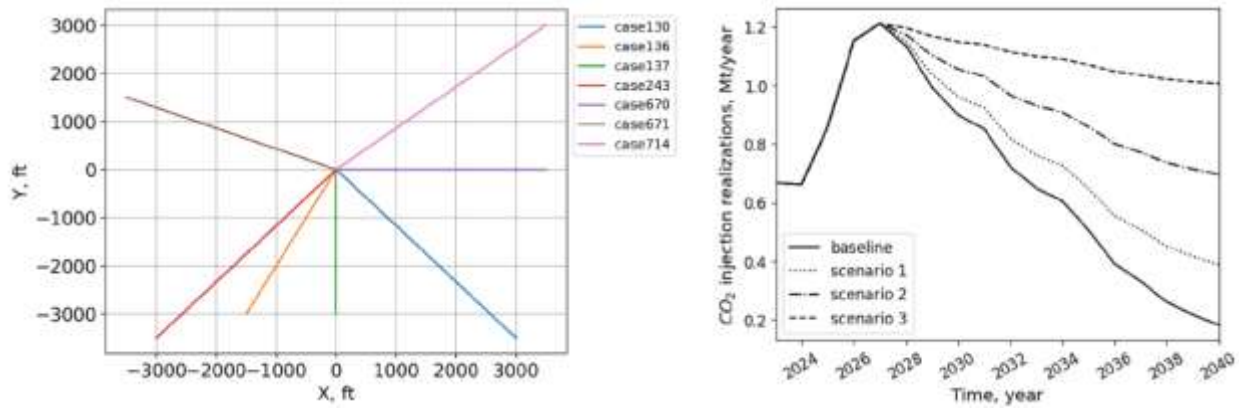


Figure 308 Correlation of pressure and land surface uplift throughout the CCS project in the 6-by-6-mile (9.66 by 9.66 km) study area according to the optimal injector design. Warmer colors indicate greater uplift. The land surface displacement figures are captured after 1 year (T = 2024) and 4 years (T = 2027) of injection, respectively. Source: Li et al. (2024), licensed under CC BY-NC.

Optimal Injector Performance Under Uncertainty

To validate the robust performance of the optimal design, we selected 6 representative cases among the entire population to quantify uncertainties from injection schemes and geological realizations. The details of the selected wells are in Table 64. The selected cases represent the entire population because they are extreme cases regarding CO_2 plume size and pressure responses. In addition, we ensure that the selected wells have diverse directions to span the majority of the parameter space. In Figure 309(a), we visualize the projection of the injectors to the land surface, and the wells deviate throughout all directions. Figure 304 highlights all selected wells to provide an additional perspective for visualization. We design 3 additional injection schemes to explore the capability of the optimal injector for larger amounts of CO_2 injection. The baseline comes from the field in Figure 309(b), and scenarios 1, 2, and 3 are designed to increase the total amount of injection. Scenario 1 has a total injection amount of 13.9 Mt, showing a 13% increment compared with the baseline. The average injection rate is around 0.77 Mt/yr for 18 years of injection. For Scenario 2, we further increase the average annual injection rate to 0.91 Mt/yr. It has a total of 16.3 Mt CO_2 injection, showing a 32.5% increment compared with the baseline. Scenario 3 is designed to be challenging because the average injection rate is greater than 1 Mt/yr (injection rate is 1.04 Mt/yr). Scenario 3 injects a total of 18.7 Mt with a 52.0% increase compared with the baseline. We keep the annual injection rates before 2027 to be the same because the peak injection rate is already large. It appears to be better to ramp up and then maintain a relatively large annual injection rate as a matter of controlling risks while increasing the total storage amount.



(a) (b)

Figure 309 (a) Map view of selected wells for uncertainty quantification in terms of injection schemes and permeability and porosity realizations. The origin is the injector location so that negative values in *x* or *y* coordinates represent a point that is left or below the injector. (b) Demonstration of the injection scheme scenarios for selected wells. Source: Li et al. (2024), licensed under CC BY-NC.

The uncertainties of the injection schemes do not impact the performance of the optimal case, as shown in Figure 310. The size of the bubbles represents the pressure buildup at the QF2 fault, and the color represents different injection schemes. All injectors keep their relative positions compared with Figure 304. For each case, the larger injection rates increase the CO_2 plume size and the pressure buildup in the storage formation. The pressure response at the QF2 fault is more related to the injector trajectory as compared with the injection schemes. The CO_2 plume size and the pressure buildup in the storage formation are impacted by the injection schemes in different manners, depending on the well trajectory. For example, Case714 does not represent any extreme factors, but it has a large pressure buildup in the storage formation but small pressure responses at the fault. More importantly, it deviates in a direction that is different from all other wells. It shows that the pressure buildup in the storage formation is not as impactful as CO_2 plume size when increasing the injection rates. For Case137, however, it shows the pressure buildup in the storage formation is influenced more by the large injection rates. In general, most cases are capable of supporting larger injection rates with greater total CO_2 injection and these results confirm the strong potential of this GCS site for further development.

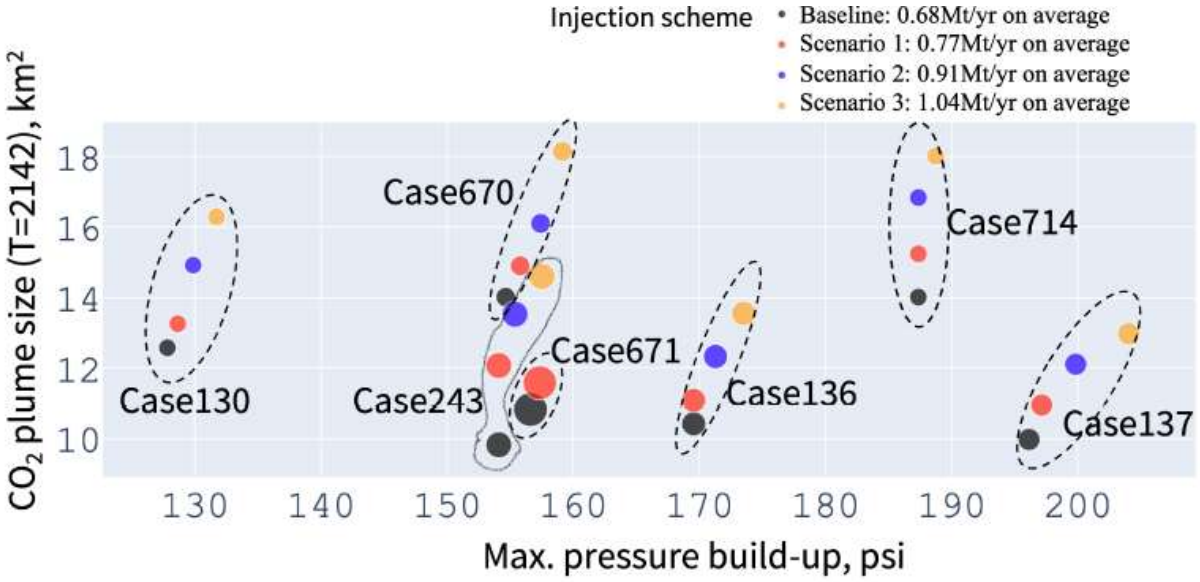
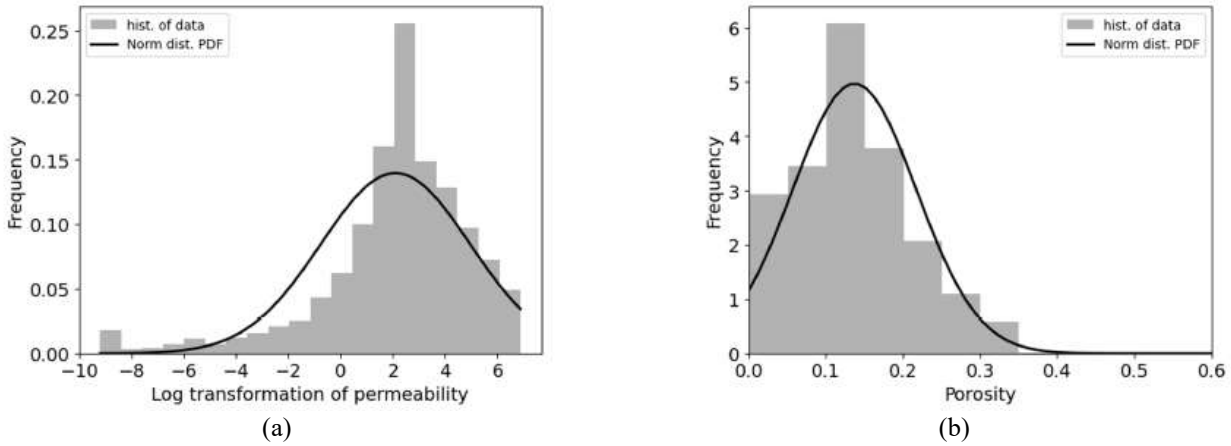


Figure 310 Comparison of selected wells under different injection scheme realizations. This plot describes plume size 100 years after injection vs. the maximum pressure increase at the top of the storage formation. The injection rates in the legend represent the average annual injection rate over the geological carbon storage project life. The color represents cases under different injection schemes as shown in the legend. The size of the bubble represents the maximum pressure responses at the QF2 fault plane across all timesteps. Source: Li et al. (2024), licensed under CC BY-NC.

Uncertainties from the geological property characterization need to be quantified for risk management. According to the field information, we already have the 3D baseline model in terms of permeability and porosity. To generate different geological realizations with variances, we resample the distribution of the properties following the same prior. Based on the existing geological properties, as shown in Figure 311, the permeability has the best fit with a lognormal distribution, whereas the porosity could be characterized by a normal distribution. Therefore, we present the log transformation of the permeability in Figure 311(a) and the normal distribution of porosity in Figure 311(b). With the explicit distribution function, we resample the data and generate 10 new and different realizations of the 3D geological maps for reservoir simulation. The results from the selected wells are presented in Figure 302.



(a) (b)

Figure 311 Distributions of (a) permeability and (b) porosity in the target storage formation. The permeability follows a lognormal distribution and the porosity follows a normal distribution. The geological realizations are

generated based on these priors but resampled for the 3D model for exploration of geological uncertainty. Source: Li et al. (2024), licensed under CC BY-NC.

To analyze and quantify the differences in results engendered by the geological model realizations, we present the results using box plots in Figure 312. Mean and variance are compared for all selected cases. The orange line in the box is the median of the results from 10 realizations. The box shows the interquartile range (IQR) with boundaries representing Q_1 (25th percentile) and Q_3 (75th percentile), respectively. The outliers (shown as circles) may appear if they are less than the threshold of $Q_1 - 1.5 \times IQR$ or greater than the threshold of $Q_3 + 1.5 \times IQR$. Our optimal well design demonstrates robust performance and outperforms all selected wells with excellent balance regarding the 3 optimization goals. The optimal design has the best overall performance and manages the risks at a decent level. Although some cases show smaller CO_2 plume size or pressure responses, they could not handle other aspects of the goals well. Therefore, we believe that our optimal design maximizes the subsurface CO_2 storage security and manages the risks presented by uncertain data.

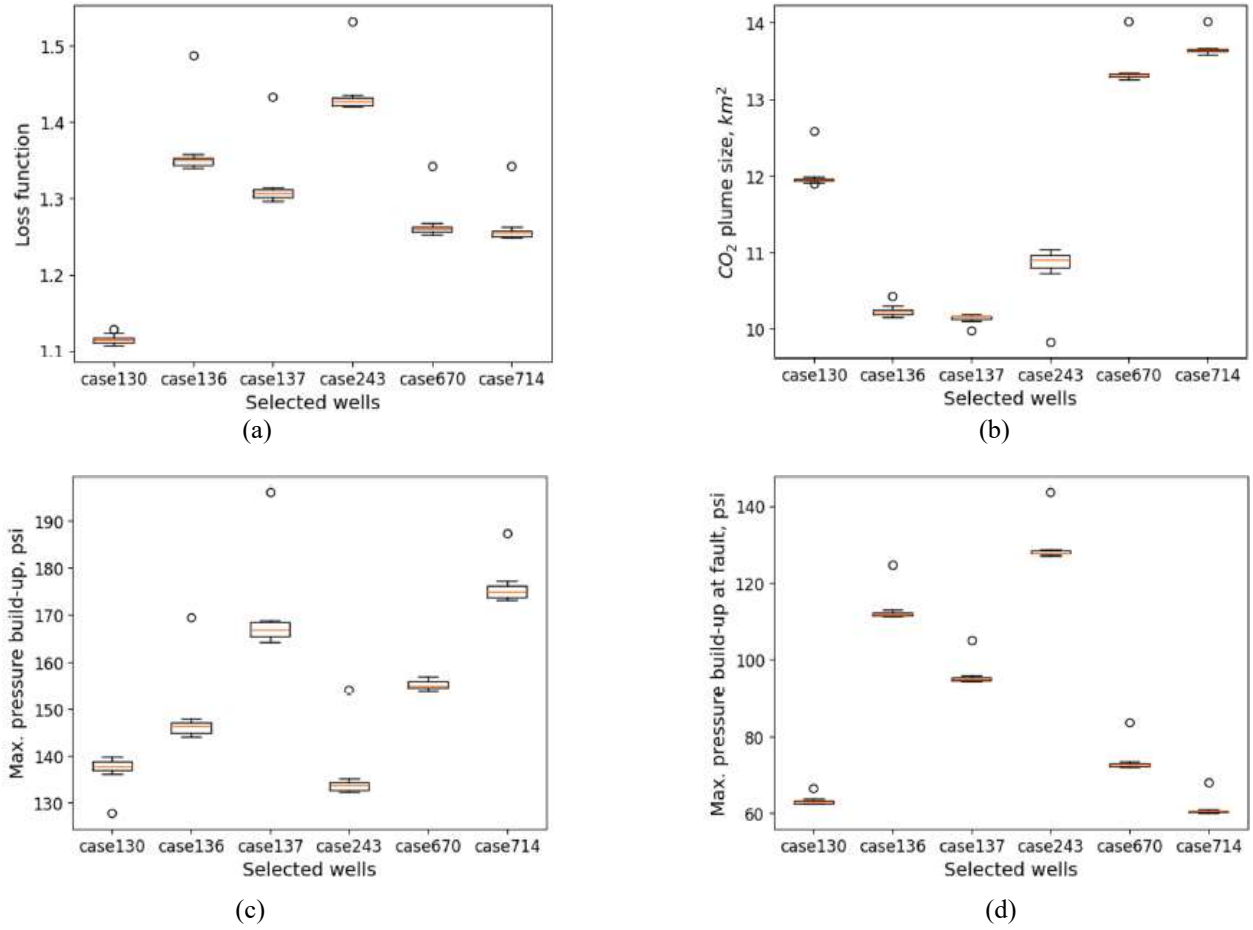


Figure 312 Quantification of geological uncertainty for selected cases of well trajectory. The orange line is the median outcome from 10 realizations. The bars indicate outcomes in the 25th and 75th percentiles. Outliers are shown as circles. The evaluation matrices include (a) loss function in optimization, (b) CO_2 plume size, (c) maximum pressure buildup within the storage formation, and (d) maximum pressure responses at the QF2 fault. Source: Li et al. (2024), licensed under CC BY-NC.

Assessment of Spatial Monitoring using InSAR

We evaluate and assess an InSAR-based surveillance approach for GCS to demonstrate the potential use of satellite images to monitor the potential CCS project site in Kern County, CA. The scope of work includes identifying appropriate subsurface and surface conditions for project success and presenting the data recoverable through InSAR. The detailed methods and results in this section are provided in the published paper in the Appendix.

Background

InSAR may be cost effective for onshore GCS projects either as a stand-alone solution or in combination with other techniques. Remote sensing has advantages in observing an extensive area in real time, and it has been successfully applied for various GCS assets (Zhang et al. 2021). Under the umbrella of remote sensing, ground-based observation has high resolution and precision but covers a small area (Zhang et al. 2021). Satellite platforms such as Sentinel-2 provide sufficient resolution (10–60 m) for GCS monitoring (Chen et al. 2019). InSAR measures surface deformation by tracking phase differences in radar waves, enabling quantification of both the extent and the magnitude of land displacement. Compared with GPS, it is significantly less expensive for monitoring large regions (Dzurisin and Lu 2007) and has been successfully applied to geomorphology, hydrology, natural hazards, and subsurface processes, including steam stimulation (Maharramov and Zoback 2018) and EOR (Bazargan et al. 2020).

For GCS, the primary challenge is that pressure-induced rock deformation is subtle, because storage security requires limited pressure buildup. Demonstrating measurable surface uplift and its correlation with reservoir pressure is therefore critical. As we discussed above, our study focuses on a 6-by-6-mile (9.66 by 9.66 km) area underlain by a 3,861-ft (1,176.8-m)-deep saline sandstone aquifer sealed by approximately 1,000 ft (304.8 m) of shale (Kohli et al. 2023; Li et al. 2024). Planned injection will occur below 4,000 ft (1,219.2 m) via a long, deviated well. Historical InSAR data (2015–2023) from a commercial provider confirm detectable surface signals (Guilhot et al. 2021). As shown in Figure 313, the project site (outlined in blue) remained stable before injection, with green-coded regions indicating no surface movement. In contrast, adjacent red-coded zones represent subsidence from oil production but do not overlap the project boundary. Five stable reference polygons within the site were selected for quality control. The flat and stable baseline demonstrated in Figure 313 highlights the site's suitability for InSAR-based surveillance during and after CO_2 injection.

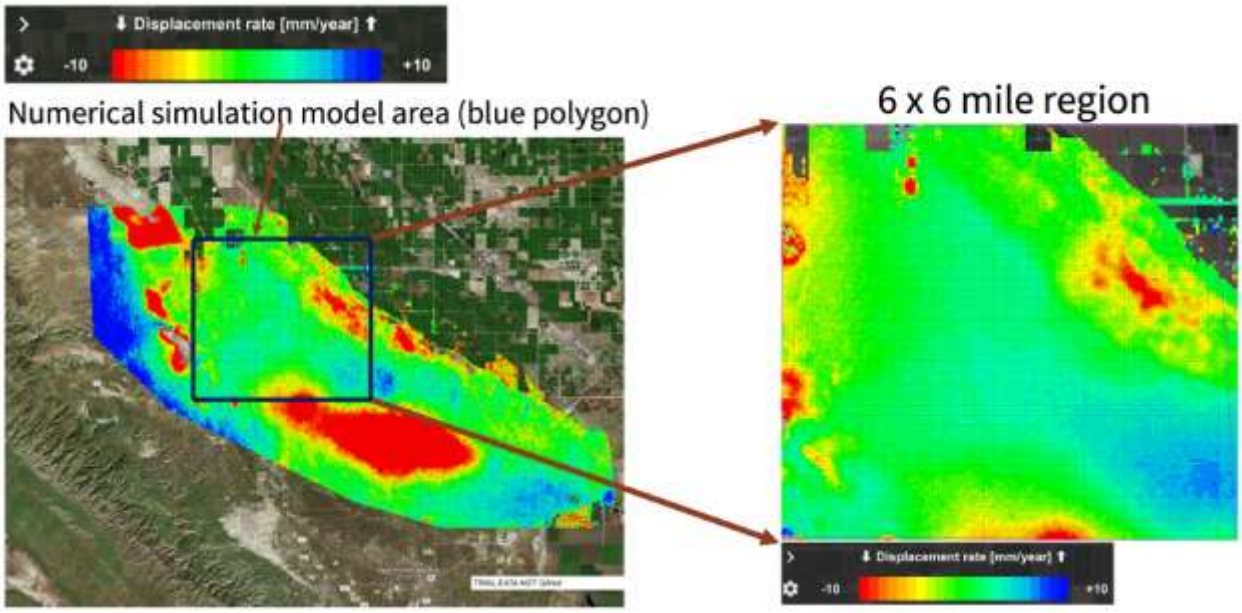
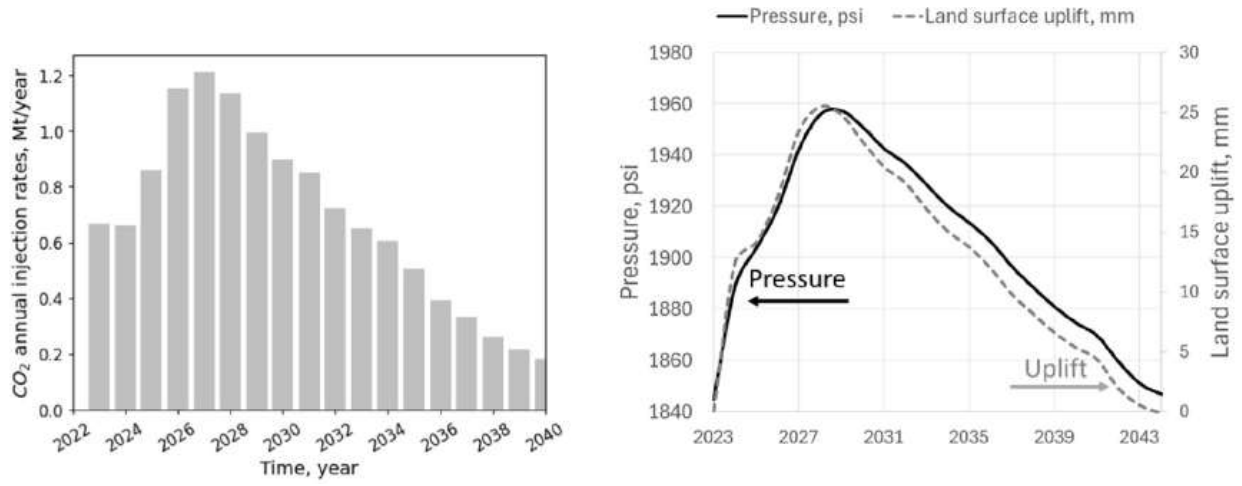


Figure 313 InSAR observations in the vicinity of the geological carbon storage site (left). The inset (right) provides more detail on the project site. The color represents the displacement rate in mm/yr according to the color bar. A positive value shows land uplift in blue and a negative value shows land subsidence in red. The color green signifies areas with stable surface measurements and close to zero land-surface displacement. Source: Li et al. (2025), licensed under CC BY-NC.

Figure 314(a) provides the planned CO_2 injection schedule for the project. Our simulation can predict land uplift of approximately 25 mm (Figure 314(b)), which shows a strong correlation with pressure buildup during injection. Notably, the greatest uplift occurs when the annual CO_2 injection rate reaches its peak. This finding demonstrates that surface deformation can serve as an indirect indicator of subsurface processes and may provide valuable information for monitoring CO_2 storage projects.



(a) (b)

Figure 314 Baseline geological carbon storage site details with (a) injection scheme determined by business need and (b) correlation between the pressure change and land surface uplift from geomechanical computations. Source: Li et al. (2025), licensed under CC BY-NC.

To quantify uncertainty, a global sensitivity analysis of the coupled transport–geomechanical model was performed using distance-based generalized sensitivity analysis (DGSA). DGSA was selected because it is computationally efficient, accounts for 2-way parameter interactions, and treats all data points equally. This provides a systematic framework to evaluate how uncertain parameters collectively affect system response over time. Because land uplift data are complex and high dimensional, feature extraction methods were applied to identify dominant patterns. Autoencoders, a neural network approach, were particularly effective in reducing dimensionality and capturing nonlinear features from uplift images. The encoder compresses input data into a latent representation, whereas the decoder reconstructs the images, ensuring the essential features are preserved. Synthetic InSAR observations generated from the model demonstrate how simulation and remote sensing can be integrated for monitoring. These results establish a foundation for advanced surveillance strategies, including history-matched model calibration, inversion-based property estimation, and AI-driven mapping of subsurface processes.

This section proceeds with a description of the numerical simulation methodology followed by the computation of synthetic InSAR observations from model results. These efforts provide a foundation for advancing InSAR surveillance in future work, such as calibration of history-matched models to reduce uncertainty, inversion methods, and AI-based mapping tools that predict subsurface behavior using InSAR data.

Methodology

We use the pyCCUS toolbox for massive numerical simulation to compute essential data needed to understand sensitivity. We sample 500 cases from the parameter space identified, and 2 different types of response data are used for global sensitivity analysis.

DGSA demonstrates strong capability for complex subsurface modelling systems, and we extend the applicability of DGSA on complex datasets by incorporating principal component analysis (PCA) and autoencoders. Both PCA and the autoencoders contribute to extract essential features and reduce dimensionality of the complex response data for clustering.

Parameter Space and Response Data

To initialize the global sensitivity study, we do Monte Carlo sampling on selected parameters for numerical simulation to generate the dataset. There are 3 main aspects of the parameters that play essential roles throughout GCS projects, including rock mechanics, petrophysics, and operational control. Table 61 indicates the range of parameter values that are from field operators and literature (Lin et al. 2010; Li et al. 2024). To provide valuable information for this particular site, we set up the field model as the baseline for sensitivity analysis. The rock mechanics parameters include the Young's modulus and Poisson's ratio as defined in Eq. (10), for both the sealing formation (shale layers) and the storage formation (sandstone layers).

$$E = \frac{\sigma}{\varepsilon} \tag{10a}$$

$$\nu = \frac{d\epsilon_{trans}}{d\epsilon_{axial}} \tag{10b}$$

where E is Young's modulus, σ is uniaxial stress, ε is strain, ν is Poisson's ratio, ϵ_{trans} is transverse strain, and ϵ_{axial} is axial strain.

The shale layers have low permeability and porosity, and they serve as the sealing formation for GCS. They are fine grained mudstone under significant compaction at this specific site. In comparison, the sandstone layers in the saline aquifer show much larger porosity. The Young's modulus for shale in Table 61 is assumed to be greater than sandstone for this GCS site (Lin et al. 2010; Li et al. 2024).

The petrophysical parameters define the porous medium for multiphase flow. We include the vertical-to-horizontal permeability ratio (kv:kh) to capture differences in vertical and lateral mass transfer. Permeability and porosity models are derived from well logs across the project area (Li et al. 2024), and multiple realizations are sampled from prior distributions to remain geologically-consistent. Relative permeability and capillary pressure functions are held constant across all cases.

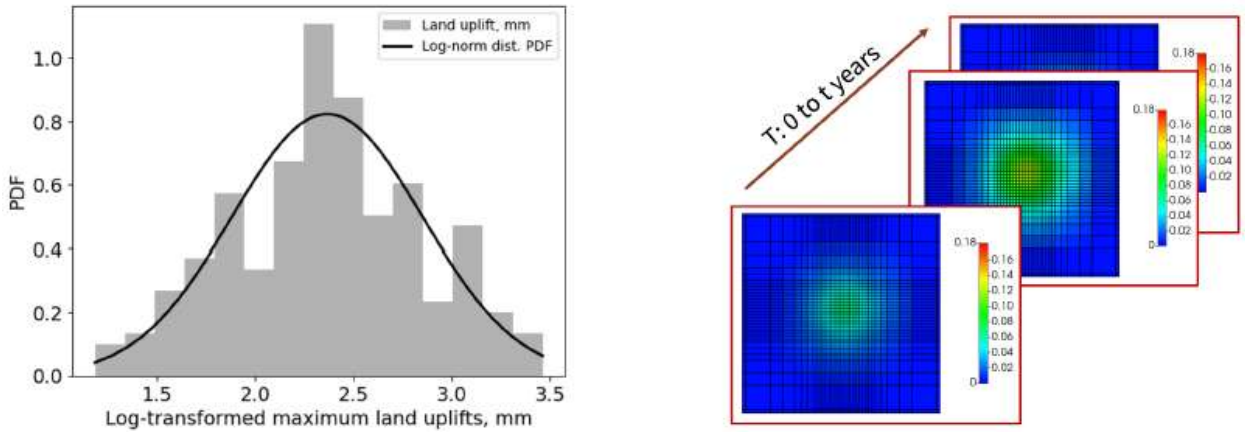
For GCS projects, we mainly care about the injection rate and years of injection. The combination informs the total amount of CO_2 storage in the subsurface. Operational parameters include injection rate and duration in Table 65, which together define the total CO_2 stored. We sampled 500 cases using uniform distributions and a Latin hypercube algorithm to ensure broad coverage of parameter space. Simulations were run with the pyCCUS toolbox (Li 2024a) using a 2-way coupled flow–geomechanics model to predict land surface displacement.

Table 65 Parameter space for global sensitivity analysis and clarification of nomenclature (modified from Li et al. [2025])

Parameter*	Unit	Lower bound	Upper bound	Note
E_{shale}	psi (kPa)	4.74×10^6 (3.27×10^7)	1.17×10^7 (8.07×10^7)	Young's modulus, shale layers
$E_{\text{sandstone}}$	psi (kPa)	2.76×10^6 (1.90×10^7)	8.31×10^6 (5.73×10^7)	Young's modulus, sandstone layers
ν_{shale}		0.255	0.287	Poisson's ratio of shale layers
$\nu_{\text{sandstone}}$		0.137	0.272	Poisson's ratio of sandstone layers
$k_u \cdot k_h$		0.1	2	Ratio of vertical permeability to horizontal permeability
Inj. rate	Mt/yr	0.7	2	CO_2 constant annual injection rate
Inj. hrzn	Y	10	30	Number of years during the injection
k/ϕID		1	10	Integer category of k/ϕ realizations

*Inj. = injection ; hrzn = horizon.

For the global sensitivity analysis, we examined parameter impacts on 2 response datasets. Response 1 is the maximum land uplift over the project lifetime (Figure 315(a)). Values follow a log-normal distribution, with uplift rates of 3.52 to 24.10 mm/yr (see Appendix A-4), equivalent to 3.0 to 31.8 mm net uplift (Figure 315(a)). The first derivative of displacement was also calculated to evaluate deformation rates. This dataset is relatively simple for clustering and directly reflects the magnitude of surface uplift.



(a) (b)

Figure 315 Response data for global sensitivity analysis with different levels of complexity. Panel (a) shows the log-normal distribution of the maximum land uplift for all samples and panel (b) demonstrates the complex synthetic InSAR dataset including annual land uplift images at various time steps during the injection period. The color bar in (b) represents the land uplift in feet. Source: Li et al. (2025), licensed under CC BY-NC.

Response 2 captures the spatiotemporal evolution of land displacement as a time series of uplift images (Figure 315(b)). Its analysis is more complex due to high dimensionality and varying time horizons (10–30 years). Sensitivity quantification for Response 2 helps determine what information InSAR observations can reliably recover.

Because injection has not yet started at the site, validation relies on literature comparisons. For example, the Bredasdorp Basin in South Africa showed pressure buildup of 120 to 140 psi (827.4 to 965.3 kPa) at approximately 0.5 Mt/yr injection (Afolayan et al. 2023), which aligns with our simulated outcomes (Figure 314).

DGSA

DGSA is a computationally efficient sensitivity analysis approach to handle complex response datasets. The DGSA method classifies the entire experimental sample space into different clusters, according to the response data or their distance matrix. Next, it computes the distances of cumulative distribution functions (CDFs) in each cluster to its prior to quantify the variance of an independent variable to the response. The sensitivity index is described in Eq. (11) as

$$d_{i,k} = d\big(CDF(X_i), CDF(X_i|k)\big) \tag{11a}$$

$$Sensitivity(X_i) = \frac{1}{K}\sum_{k=1}^{K}\frac{d_{i,k}}{d_{i,k}^{q}} \tag{11b}$$

where X_i is the independent variable, K is the total number of clusters, and $d_{i,k}^{q}$ is the bootstrapped CDF distance for quantile q.

DGSA is a way to figure out which factors (such as rock strength or injection rate) matter most for how the system behaves. It works by grouping all simulation results into clusters that look similar and then checking how much each parameter changes those groups. If a parameter makes a big difference, it is considered “sensitive.” This method is efficient for handling very complex datasets because it avoids focusing on just a small part of the data. It also looks at interactions among parameters, which is important in subsurface systems where multiple factors act together.

PCA

PCA is a typical method to reduce the dimensionality of a large and complex dataset. In particular, if the large dataset contains the interrelated variables, which is common for time series data, PCA is powerful to transform linearly the large dataset to a new set of variables that are orthogonal to each other (Wold et al. 1987). The new set of variables are the principal components (PCs) selected to represent the entire raw dataset. Similarly, the raw dataset could be reconstructed according to the PCs. One of the main steps is to compute the eigen vectors and eigenvalues of the matrix, because the eigenvalues represent variance. In order to select the top K PCs, we define the criterion to collect cumulative variance greater than 96%.

To tackle the variable time length challenge, we pad the dataset with zeroes, because land uplift is expected to drop back to its initial condition as pressure buildup decreases to zero. The injectivity induced pressure change will dissipate in the storage formation after shut-in of the injection well. For GCS projects, we assume rock elastic deformation because the rock mechanical response is carefully monitored to avoid breaking or fracturing the subsurface storage and sealing formation. The PCA process is shown in Eq. (12).

$$K = \arg min_k \sum_{i=1}^{k} \lambda_i \geq 96\% \tag{12a}$$

$$PC_{i=1,\ldots..k} = PCA\left(M_{n,-1}\right) \tag{12b}$$

$$M_{n,-1} \in R^{n\times(-1)} \tag{12c}$$

where n is the number of samples, λ_i is the ith eigenvalue of the dataset, $M_{n,-1}$ is a 2D matrix including all samples with land uplift images at all is a 2D matrix including all samples with land uplift images at all time query steps from the first year until the shut-in. The K PCs for all samples come from the first K columns of the matrix transformed from PCA. Therefore, the number of PCs selected is the same for all samples, although they show different time dimensions due to the injection horizon ranges from 10 to 30 years.

Autoencoders

Autoencoders are powerful to extract complex nonlinear features from a large dimensional dataset. Autoencoders are a type of artificial neural network to learn efficient representations of unlabeled data. They are typically used for dimensionality reduction and feature. Autoencoders are composed of 2 main components, that are encoder and decoder as shown in Figure 316. They work by compressing data into a smaller “latent space” (the bottleneck) and then reconstructing it. If the reconstruction looks very similar to the original, it means the autoencoder has learned the important features. Unlike PCA, which captures only linear patterns, autoencoders can detect complex nonlinear relationships. In this study, autoencoders helped identify subtle spatial and temporal patterns in land uplift images, providing a more powerful tool for feature extraction compared with PCA.

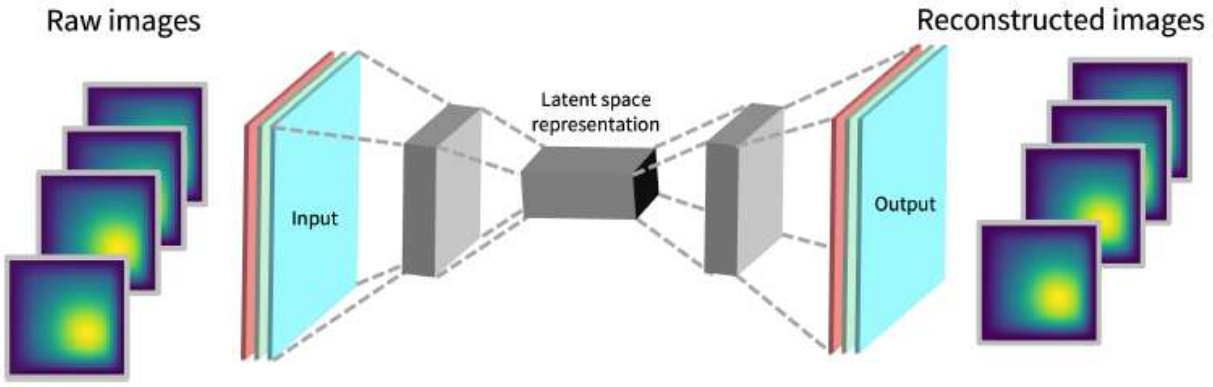


Figure 316 Autoencoder structure from raw images to reconstructed images. The latent vector space represents the feature extracted from raw images with the reduced dimension. Source: Li (2024b), licensed under CC BY-NC.

The loss function of the autoencoder is the mean absolute error (MAE) of outputs ($\hat{x_i}$) from the autoencoder and inputs (x_i) for all samples, as is shown in Eq. (13)

$$Loss = \frac{1}{n}\sum_{i=1}^{n}|x_i - \hat{x_i}| \tag{13}$$

The MAE is less sensitive to outliers compared with mean square error (MSE), and it maintains the balance among all errors to avoid extra emphasis on large errors (Chai et al. 2014; Chicco et al. 2021). The autoencoder contains 14 layers in both the encoder and the decoder. The encoder starts with a linear layer to adjust the dimensionality of the data, and a Leaky ReLU is used ~~followed~~ to add nonlinearity. Compared with PCA, which is an orthogonal linear transformation of the dataset to a new coordinate, the autoencoder approach incorporates nonlinear relationships in its structure for complex datasets. Eq. (14) is an option for the activation function to describe a nonlinear mapping from inputs to outputs, but the gradient vanishing problem exists particularly in multilayer structures due to its saturation nature (Tan and Lim 2019).

$$Sigmoid(x) = \frac{1}{1+e^{-x}} \tag{14}$$

The rectified linear unit (ReLU) function mitigates this concern by providing a linear function for positive input values. The ReLU dying problem, however, is an issue (Lu et al. 2020) because the neurons from ReLU output are 0 when input x is less than 0, as is shown in Eq. (15).

$$ReLU\ (x) = max(0, x) \tag{15}$$

A Leaky ReLU (shown in Eq. (16), where a = 0.01) is selected as our activation function because it improves the ReLU and avoids problems with dying. The Leaky ReLU allows a small positive gradient when the unit is not active, and it solves the problem that the missing values exist in reconstructed images due to ReLU dying (Xu et al. 2020).

$$Leaky\ ReLU\ (x) = \max(ax, x) \tag{16}$$

The network has about 93.9 million parameters. Training uses 500 simulation samples, each a 33 × 33 image of land uplift per year. About 8,130 images (85%) are used for training and 1,433 (15%) for validation. We apply the Adam optimizer (Kingma and Ba 2015) with weight decay 10^{-8} for stability and learning rate 10^{-6}. Training runs for 512 epochs until convergence. The bottleneck (latent space) is 8 dimensions, chosen to capture essential features while keeping model size small.

Results

We presented and compared PCA feature extraction and Autoencoder features extraction.

PCA Feature Extraction

The PCA result relies on the cumulative variance of the data to select a few top PCs for further analysis. In order to maintain the majority of information from the raw dataset in this paper, we define the criterion to be 96%, meaning that the selected PCs account for at least 96% of the total variance of the entire dataset. We need at least 8 PCs to maintain over 96% of the cumulative variance. It also shows that the cumulative variance achieves 100% with at least 18 PCs, which means that the raw data contains intercorrelations within the matrix. It is essential to validate the performance of PCs by comparing the reconstructed images with raw images. We compare a selected reconstructed image with its raw image in order to validate the performance of PCA. That is, the PCs are capable of collecting all essential information of an image. In Figure 317, the reconstructed image preserves the shape and magnitude of the land surface uplift, with the absolute difference in Figure 317(c) below 0.2 mm.

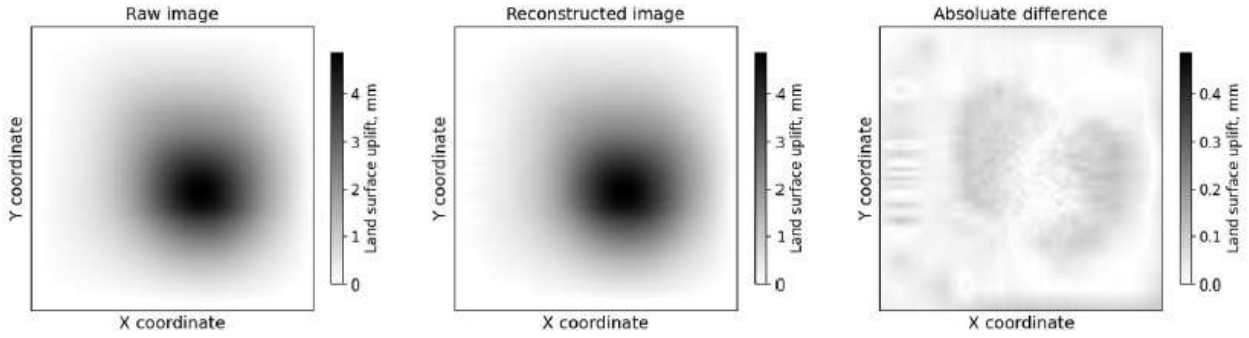


Figure 317 Comparison of the (b) reconstructed image with its (a) raw image with the (c) image of absolute error. The example is based on the principal component analysis feature extraction method. Source: Li et al. (2025), licensed under CC BY-NC.

Autoencoders Feature Extraction

Training an autoencoder is an alternative option to tackle the com plex dataset challenge for classification. The loss function quantifies differences between input images and output data from the encoder–decoder structure. We aim to train the autoencoder as an identical function to enforce the outputs to be the same as inputs. We train the autoencoder model with 512 epochs and batch size of 32 until the loss function gradually stabilizes. The architecture of the autoencoders is configured to produce a latent vector space with a dimensionality of 8. We plot all dimensions to examine their relationships. Overall, we observe no strong correlations among the illustrated dimensions, indicating that each extracted dimension captures unique patterns from the complex dataset.

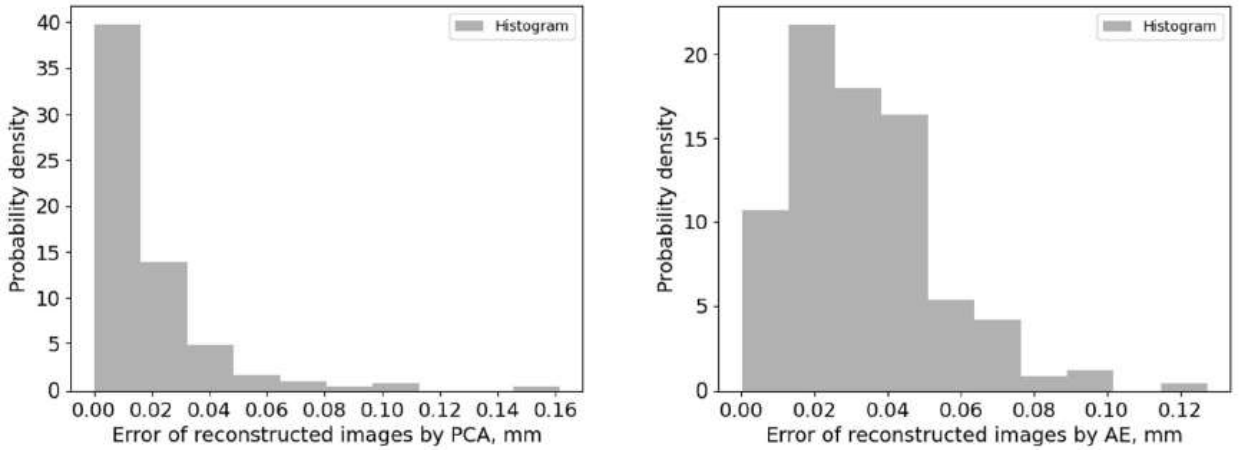
We validate the strength of autoencoders in a similar way, that is to compare reconstructed images with raw images. We use the same example case (Case10) after 5 years of injection to demonstrate the details of autoencoder performance. The autoencoder learns features of input images as the latent vectors after the bottleneck layer. A few layers in the encoder part gradually

reduces the dimensionality of raw images to bottleneck layer dimension. The decoder part parses the latent vectors and reconstructs images as outputs, that are expected to be the same as inputs. This validates the latent vectors to represent the entire raw dataset with essential features and key information. The classification step therefore relies on the reduced dimensionality of latent vectors to group all samples into multiple clusters. In addition, we compute the error of the reconstructed data compared with its raw images for all samples according to Eq. (17)

$$\epsilon_i = \frac{1}{MNT}\sum_{t=1}^{T}\sum_{m=1}^{M}\sum_{n=1}^{N}\left|\hat{y}_{i,t,m,n} - y_{i,t,m,n}\right| \quad (17)$$

This allows the error evaluation from a holistic view of the entire population of samples, that complements to the image-to-image comparison for a selected sample in Figure 317.

We confirm the performance of both PCA and autoencoders according to their histogram distributions in Figure 318(a) and Figure 318(b), respectively. Although errors are observed, the maximum errors are both below 0.16 mm, which is accepted for dimensionality reduction. The autoencoder demonstrates a smaller potential error, compared with PCA; however, the majority of samples by PCA present good performance. A few cases do have larger errors than cases that use autoencoders.



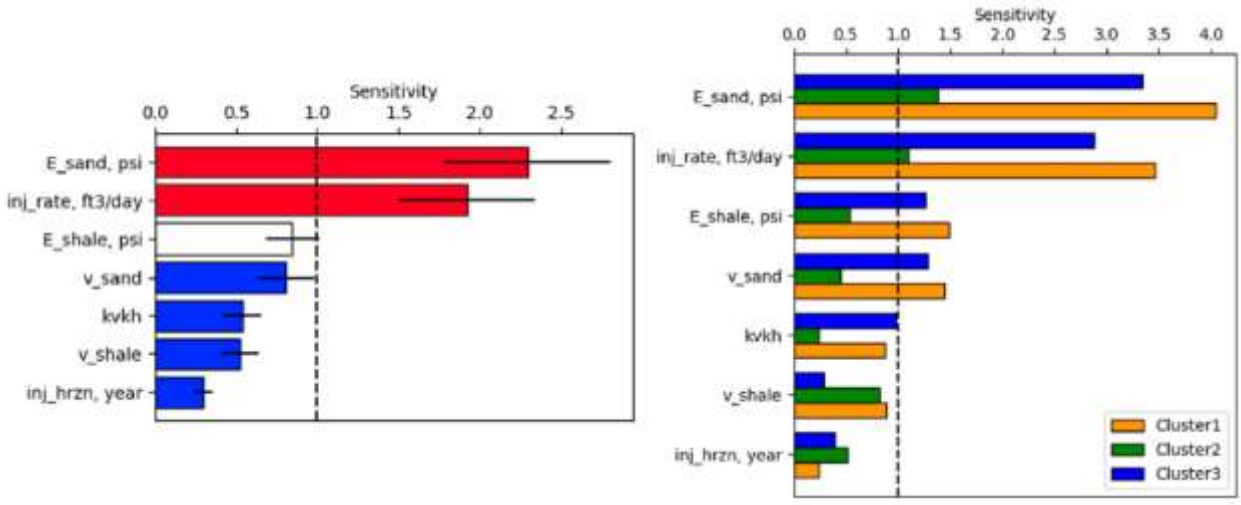
(a) (b)

Figure 318 The histogram distribution of the error between reconstructed images and raw images for all samples. Panel (a) displays the error from principal component analysis, and panel (b) shows the error by using autoencoders as the feature extraction method. Source: Li et al. (2025), licensed under CC BY-NC.

The global sensitivity analysis shows both rock mechanics and field operation parameters are essential to the magnitude of land uplift in Figure 319. The Young's modulus of the sandstone storage formation is one of the most important factors because it describes rock deformation according to the enforced stress in Eq. (10a). Carbon dioxide is injected into the sandstone layers defined in the numerical simulation model. The injectivity induced pressure buildup leads to uplift within the storage formation, and uplift therefore propagates toward the land surface. The injection rate is another significant factor because it leads to pressure buildup directly, assuming all other conditions are the same. The injection horizon is the parameter nonsensitive to response 1 data, because the number of years of injection does not contribute to maximum land uplift during the injection period. The response 1 data is the magnitude of the land uplift throughout the lifespan of GCS projects, which is independent of injection horizon. All samples are set to have constant injection schemes but with different rates. The permeability and porosity models

are very important to the land displacement. These effects, however, are not well reflected in Figure 319 because our realizations are constrained to follow the prior distributions and patterns from the field.

The details in Figure 319(b) show sensitivity index by each cluster. Results clearly show that a cluster may demonstrate statistical significance (a sensitivity of 1) or may not, depending on the clusters. The overall results are evaluated as the average of sensitivity index for all clusters to be robust. Cluster 1 in orange shows a very different pattern in terms of the first 2 dimensions. The CDFs for all parameters within all clusters are shown in Figure 320. The visualization allows comparison in a qualitative way. For example, the distances of CDFs for sandstone Young's modulus and injection rate are significantly larger than other parameters. In comparison, the CDFs of the injection horizon are very close to each other and they are the least sensitive factor to the response 1 dataset.



(a) (b)

Figure 319 Global sensitivity results based on response 1 data (maximum land uplift throughout geological carbon storage lifespan). The dashed line represents the threshold value of the statistical significance validation. The red color in (a) means sensitive parameters and blue means unsensitive parameters. Items without a color mean the sensitivity is at the edge of statistical significance tests. Panel (b) shows details of sensitivity index of the parameters for each cluster, and the average of all clusters is the overall sensitivity. E_sand represents the Young's modulus for sand layers, inj_rate represents the injection rate for CO_2, E_shale represents the Young's modulus of shale layers, inj_hrzn represents the number of years for CO_2 injection, v_sand represents the Poisson's ratio for sand layers, v_shale represents the Poisson's ratio for shale layers, kvkh represents the ratio of vertical permeability to horizontal permeability. Source: Li et al. (2025), licensed under CC BY-NC.

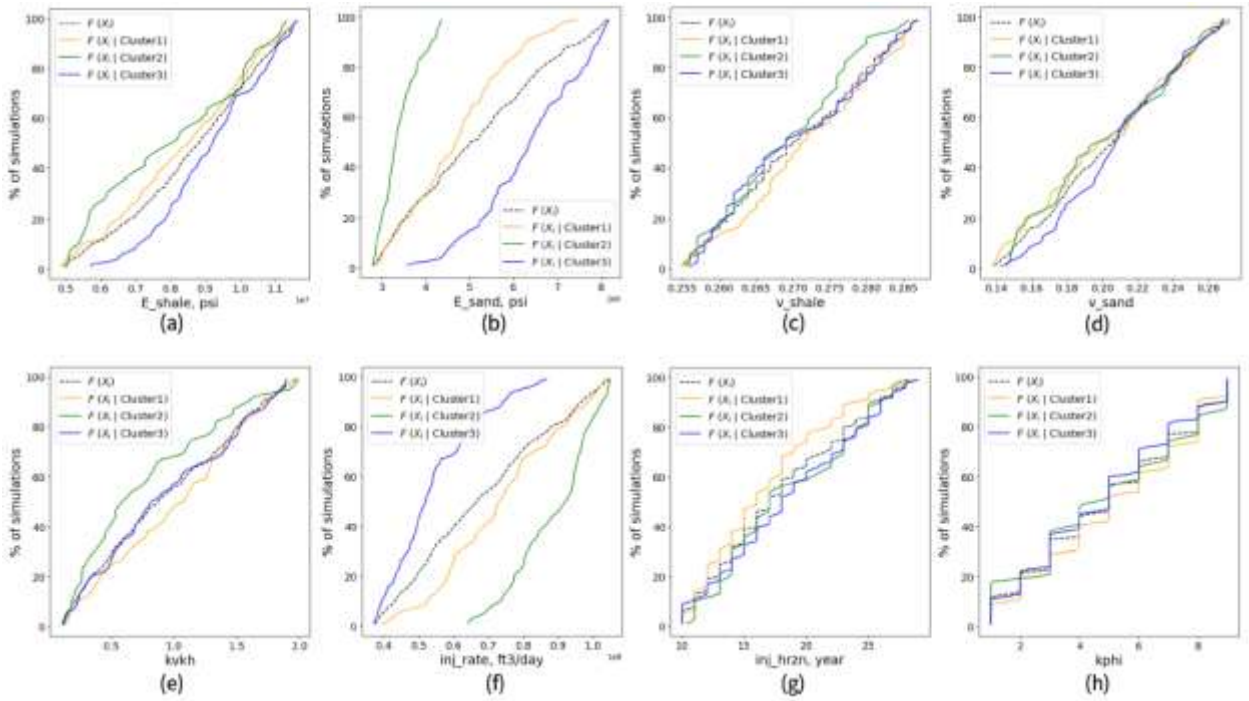


Figure 320 The cumulative distribution function (CDF) of each parameter in terms of response 1 dataset (maximum land uplift throughout geological carbon storage lifespan). The distribution plots display CDFs for samples within all clusters in terms of (a) Young's modulus of shale, (b) Young's modulus of sandstone, (c) Poisson's ratio of shale, (d) Poisson's ratio of sandstone, (e) kv:kh, (f) injection rate, (g) injection horizon (number of years for injection), and (h) kphi realizations. Source: Li et al. (2025), licensed under CC BY-NC.

The operational parameters are factors under control for GCS projects, including the injection rate and injection horizon. The geological parameters describe the subsurface system, that are intrinsic by nature. They include permeability and porosity fields, reservoir formation models, and so on. They play essential roles to impact the pressure change by operational parameters, and the response caused by pressure increase. The response in this work refers to the land deformation at the surface. We are motivated to quantify the sensitivity index of selected parameters to pressure change and also the pressure change to our response. Detailed results are shown in the Appendix.

The global sensitivity analysis successfully displays the factors that influence land movement most sensitively. It confirms the potential to recover subsurface information according to land surface displacement. The InSAR satellite is capable of observing land movement with a resolution of 1 mm/yr thereby validating the possibility of InSAR surveillance for this specific GCS site. We show the computed synthetic InSAR data in Figure 321, according to a 2-way coupled reservoir simulation model reported in the methodology of our prior work (Li et al. 2024). The simulation starts in 2023 and continues for 18 years of injection following a specific injection scheme in Figure 314(a). The annual land displacement rate changes with the injection of CO_2 and it is predicted to peak in 2027 due to the largest annual injection rate. Before 2027, the land uplifts faster in the southeast area due to the deviated injection well and the increasing annual injection rates. After 2027, the land uplift rate gradually drops until it shows land displaces downward due to the declining formation pore pressure. With a lesser injection rate, the pressure change decreases and therefore the land uplift drops compared with previous years.

Thereafter, the land displacement rates become negative. The land uplift drops to its initial condition, and the land displacement rate becomes zero until the end of the injection period. The simulation results indicate land surface deformation due to the CO_2 injection with induced pressure increment (Li 2024a; Li et al. 2024), whereas the synthetic InSAR images provide a view in time series to understand the land movements according to injectivity.

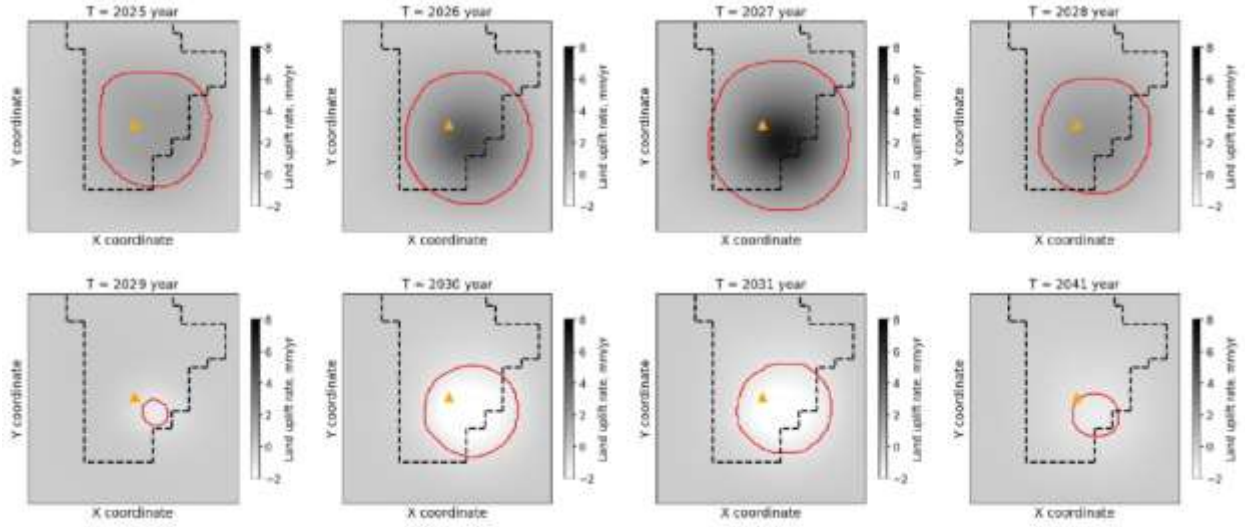


Figure 321 Synthetic InSAR observations for the geological carbon storage site from reservoir simulation of flow 2-way coupled with a geomechanical model to compute land surface displacement rates in mm/yr. Land uplift and subsidence is within the sensitivity of current InSAR measurements. The dashed black region shows the land acquisition focus area, and red solid lines represent detectability of InSAR in this region, and the orange triangle represents the location of the deviated injection well at land surface. Source: Li et al. (2025), licensed under CC BY-NC.

Discussion

This work evaluates the potential use of InSAR time series images as a monitoring tool for a GCS project. This study evaluates InSAR time series imaging as a monitoring tool for GCS in Kern County, CA. Numerical simulations reveal a strong correlation between CO_2-induced pressure changes and net surface displacement, confirming that InSAR signals reflect subsurface processes. A global sensitivity analysis (DGSA) was performed for 2 responses. Response 1 (net displacement) shows that sandstone Young's modulus and injection rate are the most sensitive parameters controlling land uplift. Response 2 (time series InSAR observations) recovers additional information, with sensitivity extending to sandstone Young's modulus, injection rate, and injection horizon. Parameters such as Poisson's ratio of shale or sandstone and vertical-to-horizontal permeability ratios are found to be relatively insensitive.

By modeling elastic rock behavior in a saline aquifer, the study avoids scenarios of fracturing and leakage, although future work should extend to fractured reservoirs. Synthetic InSAR data successfully recover land deformation signals above background noise, demonstrating detectability in the project area where surface vegetation and topographic noise are minimal. The results suggest that InSAR can complement numerical models by providing real-time geospatial monitoring, reducing uncertainty through history matching, and improving risk management. Future directions include broader uncertainty quantification and extension to multiple GCS sites

to assess global sensitivities. Overall, InSAR shows strong potential as a cost effective, reliable component of monitoring, measurement, and verification (MMV) strategies for carbon storage projects.

Summary

The main challenges of the prospective site include heterogeneous rock properties, a dipping storage formation, a large peak annual rate of the injection scheme, and the potential existence of faults in the storage formation. We developed an in-house toolbox, pyCCUS, to automate the GCS injector-design workflow and address the challenges. The proposed deviated well keeps the pressure increase in the storage formation as small as possible while meeting the specified injection rates. It is essential to quantify the trade-off between CO_2 plume size and pressure responses systematically. This workflow standardizes the process from building the 2-way coupled numerical model for parallel computations to the postprocessing targeting GCS-specific needs. The workflow therefore optimizes the well trajectory in the subsurface to maximize CO_2 storage security and minimize risk.

We demonstrate the work following a risk-averse strategy that reduces risks caused by the pressure responses in the storage formation and at the fault. The geomechanical model boundary is confirmed to comply with assumptions, that we have a stable land surface due to the constant pressure at the edge. We examine the pressure change at the boundary of this model to ensure the constant pressure condition is valid for all timesteps. The optimal injector demonstrates the capability to reduce the pressure buildup by 54% while increasing CO_2 plume size by only 21%. The optimal injector is validated by its performance under uncertainties of the injection schemes and geological realizations compared with selected representative cases. Sensitivity analysis indicates that the optimal injector is capable of injecting more CO_2 while maintaining storage integrity. The uncertainty analysis from multiple geological realizations offers additional validation to confirm the robust performance of our optimal injector design. A long, deviated, injection well benefits this GCS project with maximal storage security and minimal geomechanical risk.

We successfully detect the historical net surface displacement signals to establish background signal as the noise level of InSAR. The spatial information together with vertical resolution satisfy requirements for using InSAR to monitor the plume for this project because the uplift signal is distinguishable from the background noise. The analysis confirms that the features learned from these complex response data are sufficient and representative. The global sensitivity study of the coupled CO_2 transport and geomechanical model shows that InSAR observations are most sensitive to injection rate and storage formation mechanical parameters, Youngs modulus. The study also suggests that some model parameters could be recovered reliably from InSAR images.

It is also challenging to monitor GCS projects throughout their lifespan. We identify the clear correlation between the land surface uplift and the pressure change in the storage formation for this site. This response indicates the strong potential to monitor subsurface events according to the signals from land movements. The 2-way coupled flow and mechanical simulation predicts that the maximum land uplift will be 2.1 cm in 2027, according to the initial model predictions based on the SJV conditions. Interestingly, this amount of deformation is measurable using

satellite observations. The satellite images could provide cost-effective information to monitor the site spatially in near real time.

Field Project

Field Project – Assist with preliminary planning, implementation of infrastructure, and monitoring of a field project. Provide input on well construction that can withstand CO_2 contact over the project lifetime. Apply the SimCCS^{PRO} toolset and scenario analysis to understand how the SPR project might look with pipelines and how well locations might look.

Background

Carbon Solutions collaborated with Sentinel Peak Resources (https://sentinelpeakresources.com/) to identify sources of CO_2 and to assess the storage potential and cost of the proposed field project location. Carbon Solutions ran 2 different sets of scenarios at the field project location. The first set of runs used a "constrained" storage potential, reflecting the subsurface storage simulations from the SCO$_2$T^{PRO} model. The second set of runs used an "unconstrained" storage potential, allowing the capture of all available CO_2 emissions. Capture targets depend on available capturable CO_2 emissions and storage capacity. Every run uses a project duration of 30 years and a capital recovery factor (CRF) of 0.1627, which corresponds to a 10-year financing period and 10% discount rate.

CO_2 Source Selection

Carbon Solutions identified sources of CO_2, including SGs based on previous work (Kim et al. 2022), that exist around the proposed storage location within buffer ranges of 10, 20, 30, 40, 50, and 65 km. For each buffer zone, Carbon Solutions examined the count of facilities and cumulative capturable CO_2 emissions across different industries. For example, in the 20-km buffer there are 18 different facilities across 5 industrial sectors with total capturable emissions of 4.89 MtCO$_2$/yr. Additionally, going from a buffer range of 50 to 65 km brings in an additional 15 facilities and 1.26 MtCO$_2$/yr of capturable CO_2 emissions.

Scenario Set Up

Carbon Solutions ran a total of 12 SimCCS^{PRO} runs broken into 2 different sets, 1 group featuring a "constrained storage capacity," that is, using the storage capacity produced from Carbon Solutions' SCO$_2$T^{PRO} model, and the other group featuring an "unconstrained storage capacity" where there is sufficient storage to capture all emissions within the 65 km buffer radius. The proposed field project location identified in earlier tasks was the only storage location considered. The first run of each scenario set features only distributed SGs as sources of CO_2 emissions. Each subsequent run features the SGs and the differing buffer ranges starting at 20 km going to 65 km. A complete breakdown of the runs can be found in Table 66.

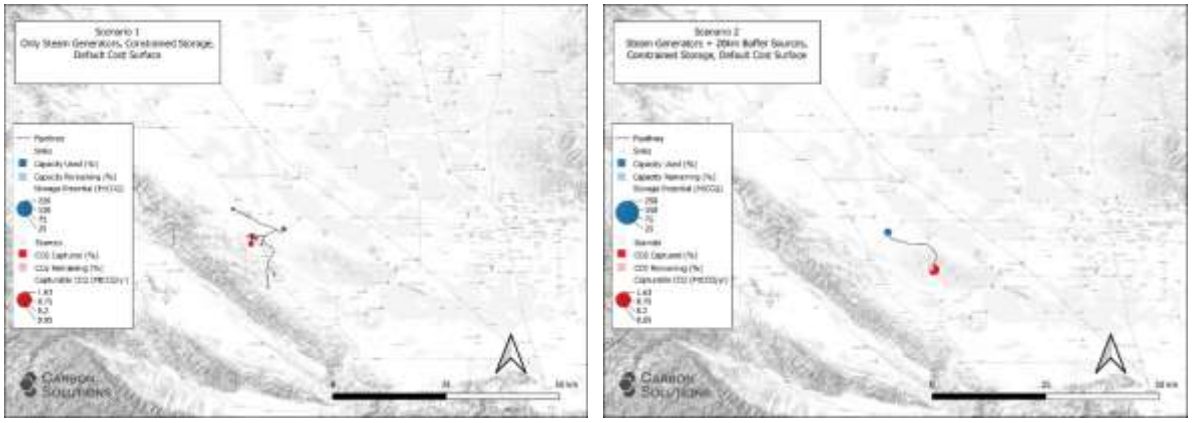
Table 66 Breakdown of all runs for the proposed field project site

Scenario – Run	Sources	Sinks	Capture target
Constrained capacity – 1	Steam generators (SGs) only	Field project location	0.78
Constrained capacity – 2	SGs + 20 km buffer	Field project location	0.79

Constrained capacity – 3	SGs + 30 km buffer	Field project location	0.79
Constrained capacity – 4	SGs + 40 km buffer	Field project location	0.79
Constrained capacity – 5	SGs + 50 km buffer	Field project location	0.79
Constrained capacity – 6	SGs + 65 km buffer	Field project location	0.79
Unconstrained capacity – 1	SGs only	Field project location	0.78
Unconstrained capacity – 2	SGs + 20 km buffer	Field project location	5.67
Unconstrained capacity – 3	SGs + 30 km buffer	Field project location	7.35
Unconstrained capacity – 4	SGs + 40 km buffer	Field project location	7.39
Unconstrained capacity – 5	SGs + 50 km buffer	Field project location	7.42
Unconstrained capacity – 6	SGs + 65 km buffer	Field project location	8.83

Results

Under the constrained capacity runs, the total storage potential of the proposed field project is just under 24 $MtCO_2$/yr, resulting in a maximum annual capture target of 0.79 $MtCO_2$/yr for a 30-year project duration. The cumulative capturable emissions for all SGs are 0.78 $MtCO_2$/yr; therefore, the deployed CCS networks using only SGs look like the network show on Figure 322(a), regardless of whether storage is constrained or unconstrained.



(a) (b)

Figure 322 Deployed CCS networks for the constrained storage scenarios featuring only steam generators (left) and steam generators with sources in the 20-km buffer (right). For constrained scenarios all remaining networks look exactly like the right image.

Because the maximum annual capture target under constrained capacity runs is 0.79 $MtCO_2$/yr, all runs in the constrained capacity scenarios capture only from the Elk Hills Power project, a 550 MW natural gas combined-cycle cogeneration power plant located in Kern County in Figure 323 (CEC 2024). Although the Elk Hills Power Project does not have the lowest capture cost, its proximity to the proposed storage location and sufficient capturable CO_2 emissions most likely offset increased costs from transportation that would pull from farther-away, lower cost sources.

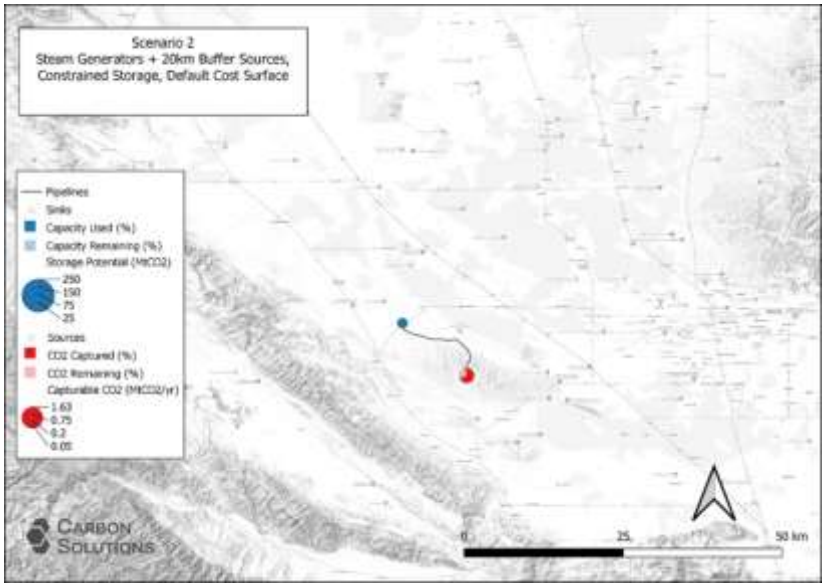


Figure 323 Deployed CCS network for all constrained storage scenarios when more than steam generators are considered a source of CO_2.

Figure 324 shows the deployed CCS networks for the 65 km buffer, which adds 209 km of pipeline deployment from the scenario using sources in the 50 km buffer. This additional pipeline deployment results in the unit transport cost going from \$6.62/tCO_2 to \$9.52/tCO_2. Despite a small reduction in the unit capture cost, the increase in transportation cost increases the total unit CCS network cost from \$77.97/tCO_2 to \$80.78/tCO_2 when extending the buffer. Increasing the buffer from 50 km to 65 km, on the assumption there is sufficient storage potential at or near the proposed field project site, would enable the capture and storage of up to an additional 1.26 MtCO_2/yr.

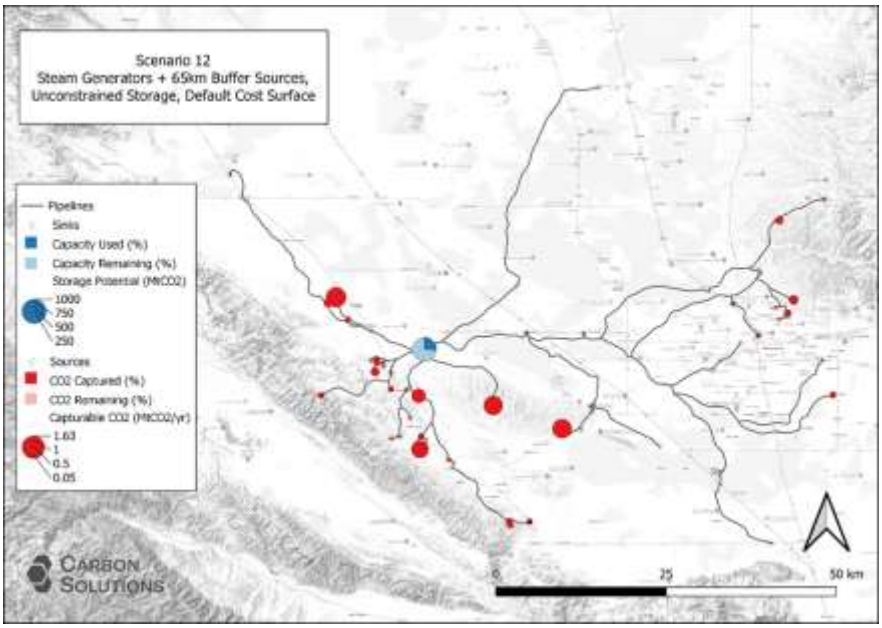


Figure 324 Deployed CCS network for the unconstrained storage scenario, steam generators and sources within a 65 km buffer run at the field project site.

Table 67 shows the summary results for all project runs carried out by Carbon Solutions. Network lengths range from approximately 18 km (when considering a constrained storage capacity at the proposed field project location) to approximately 500 km (when using sources in a 65 km buffer). The per unit capture and storage costs remain relatively constant while transport costs range from between \$3/tCO_2 and \$10/tCO_2. Regardless of whether geologic CO_2 storage capacity is constrained or unconstrained, total CCS network costs range from \$74/tCO_2 and \$81/tCO_2, falling below some current CO_2 tax credit thresholds (Jones and Marples 2023). In the unconstrained storage capacity runs, the count of sources ranges from 11 to 67, with the latter representing the maximum number of sources within the 65-km buffer. When considering 30 years of storage, under constrained storage conditions, the maximum annual capture target is 0.79 $MtCO_2$/yr, whereas when storage capacity is unconstrained, the capture target goes from 0.78 to 8.83 $MtCO_2$/yr.

Table 67 Summary table of the results for all proposed field project site runs conducted using SimCCS^{PRO}

Run no.	Annual capture target, $MtCO_2$/yr	Number of sources	Number of sinks	Network length, km	Capture cost, \$/tCO_2	Transport cost, \$/tCO_2	Storage cost, \$/tCO_2	Total cost, \$/tCO_2
1	0.78	11	1	44.36	64.95	7.23	5.30	77.48
2	0.79	1	1	17.69	64.45	4.58	5.30	74.34
3	0.79	1	1	17.69	64.45	4.58	5.30	74.34
4	0.79	1	1	17.69	64.45	4.58	5.30	74.34
5	0.79	1	1	17.69	64.45	4.58	5.30	74.34
6	0.79	1	1	17.69	64.45	4.58	5.30	74.34
7	0.78	11	1	82.09	64.96	4.18	5.30	74.45
8	5.67	28	1	132.49	66.27	3.67	5.30	75.25
9	7.35	39	1	190.82	66.05	4.26	5.30	75.62
10	7.39	42	1	251.45	66.06	5.40	5.30	76.78
11	7.42	46	1	300.66	66.04	6.62	5.30	77.97
12	8.83	67	1	509.11	65.96	9.52	5.30	80.78

Summary

Carbon Solutions was tasked with "assisting with preliminary planning, implementation of infrastructure, and monitoring of a field project" by applying the SimCCS^{PRO} toolset in a scenario analysis. Carbon Solutions ran a total of 12 scenarios at the proposed field project location. One set of scenarios (6 total) used the storage potential generated by SCO_2T^{PRO} whereas the other set of scenarios (6 total) used an unconstrained storage potential that was able to store the maximum amount of capturable CO_2 emissions. Industry types and counts of sources were adjusted across scenarios using buffer ranges from 10 to 65 km. Results indicate that when using the SCO_2T^{PRO} storage potential, only 1 facility deploys for 5 of the scenarios resulting in the same network route being deployed. This network has a total cost of approximately \$74/tCO_2 and a network length of almost 18 km. When using unconstrained storage, total network costs range from \$74/tCO_2 to \$81/tCO_2 with network lengths going from 82 km to approximately 509 km while capturing between 0.79 and 8.83 $MtCO_2$ annually.

Risk Assessment

We conducted the leakage risk assessment through the existing wellbores and Quaternary faults with different trajectory scenarios using the NRAP-OPEN-IAM (NRAP 2023a) tool. Also, we calculated the probability of induced slip on faults under a range of injection scenarios.

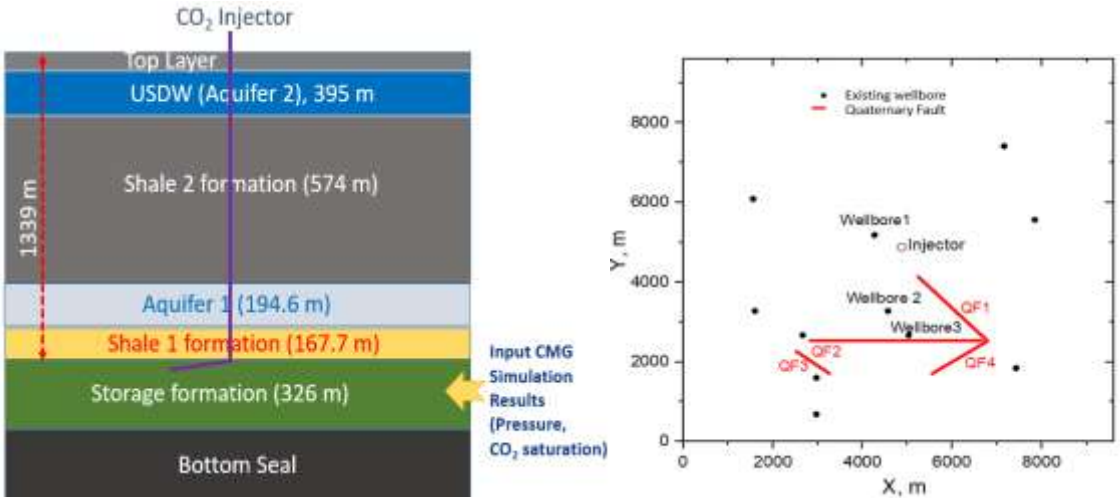
Leakage Risk Assessment

To ensure the security of a prospective regional storage hub in California's southern San Joaquin Basin, we conducted a detailed leakage risk assessment for a potential storage site. This assessment established a protocol for evaluating potential CO_2 leakage through 2 primary pathways: preexisting, plugged-and-abandoned wellbores and Quaternary faults. The analysis demonstrates that with an optimized injection strategy, the risk of leakage is negligible, providing confidence in the long-term security of the site. The detailed results in this section are provided in Kim et al. (2025); see the Appendix.

Overview of the Storage Site and Optimized Well Design

The AOI for CO_2 storage is located in Kern County, CA, in the southern San Joaquin Basin. Previously, Kim et al. (2023a) found that the southern San Joaquin Basin is a good location for GCS projects based on geological properties and technoeconomic aspects. The potential storage site is 50 km west of Bakersfield, CA, as previously shown in Figure 278(a). The target storage formation is the Etchegoin sandstone at a depth of about 1,400 m. Detailed information about the potential storage site and the available capturable CO_2 is provided in a previous study (Kim et al. 2023b).

The simplified stratigraphy of the storage formation is shown in Figure 325(a) and used to assess leakage. The average top of the storage formation is at 1,339 m. There is a shale layer (Shale 1) that acts as a primary seal in case of upward CO_2 movement. The USDW layer is 395 m thick and starts at a depth of 402.3 m. The potential pathways for leakage including Quaternary faults (red solid lines) and existing wellbores (black circles) are shown in map view in Figure 325(b). The domain is 9.7 km by 9.7 km (6 by 6 miles). Wellbores 1, 2, and 3 penetrate the storage formation. We assume that all faults are vertical and also penetrate the storage formation. The injector (open circle) is located in the middle of the domain. The operational conditions are 18 years of injection at an average of 0.683 $MtCO_2$/yr, reaching a total stored amount of 12.3 $MtCO_2$. The postinjection monitoring time is taken as 100 years. We assume that the first and last years of injection are 2023 and 2041, respectively.



(a) (b)

Figure 325 (a) Map of CO_2 storage opportunities in the San Joaquin Basin and the area of interest (AOI) of this study. (b) Simplified stratigraphic diagram used for leakage calculations in the NRAP-OPEN-IAM tool. (c) AOI map of wells and Quaternary faults (QF1 to QF4) near the prospective CO_2 injector. Source: Kim et al. (2025), licensed under CC BY-NC.

Leakage Risk Assessment Method

The NRAP-OPEN-IAM tool was used to assess the risk of leakage to the USDW (Lackey et al. 2019; Vasylkivska et al. 2021; NRAP 2023b). Four reduced-order models (ROMs) were used: Lookup Table Reservoir component, Multisegmented Wellbore component, Fault Flow component, and Deep Alluvium Aquifer component. The reservoir pressure and CO_2 saturation profiles, were obtained from a 3D reservoir model reported elsewhere (Li et al. 2024) and used in the Lookup Table Reservoir component model. The optimized deviated well trajectory was chosen to minimize the overall CO_2 plume size, pressure increase on QF2, and pressure buildup within the storage formation. The detailed explanation of the well design process is found in Li et al. (2024). QF2 is predicted to be more likely to slip due to the orientation of the maximum horizontal stress (Kohli et al. 2023), even though it is farther from the injector than QF1. The optimized case reduces the pressure change by 67% at QF2 compared with a vertical well and the plume footprint is 12.6 km^2 on the land surface 100 years after injection. The footprint on the land surface decreased by 3% compared with vertical well cases.

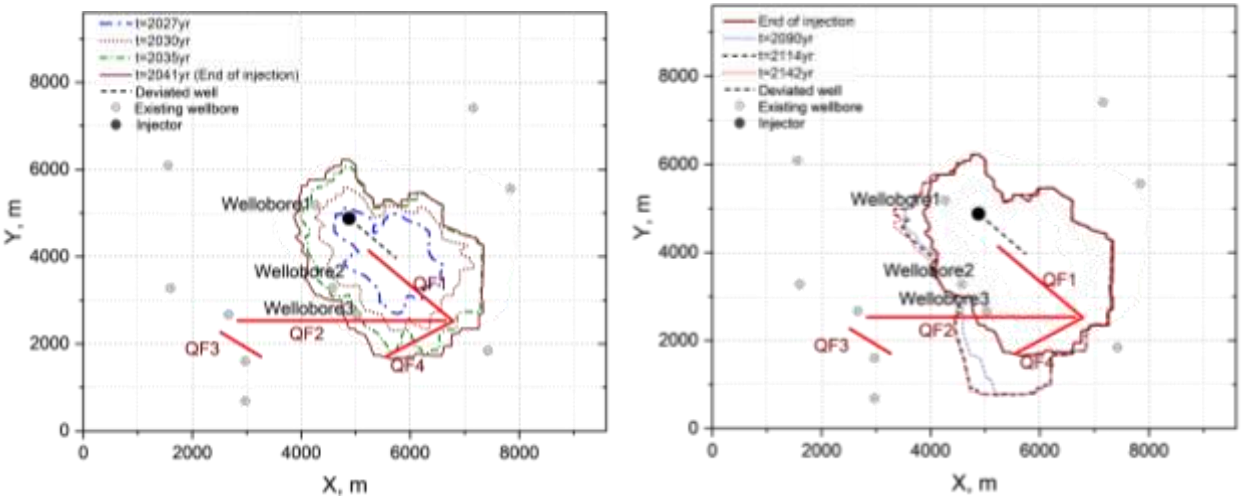
Figure 326 shows CO_2 plume migration and pressure footprint with pressure buildup for injection and postinjection periods. The threshold of CO_2 saturation was 0.05 as a residual saturation. Two pressure thresholds were used for the pressure footprint: 1 and 0.2 MPa**.** The value of 1 MPa was decided from the threshold pressure (ΔP_{thr}) for the critical pressure region with an estimated brine density of 1,105 kg/m^3 computed using Eq. (18) (EPA 2013),

$$\Delta P_{thr} = g \times \Delta z \times \Delta \rho \quad (18)$$

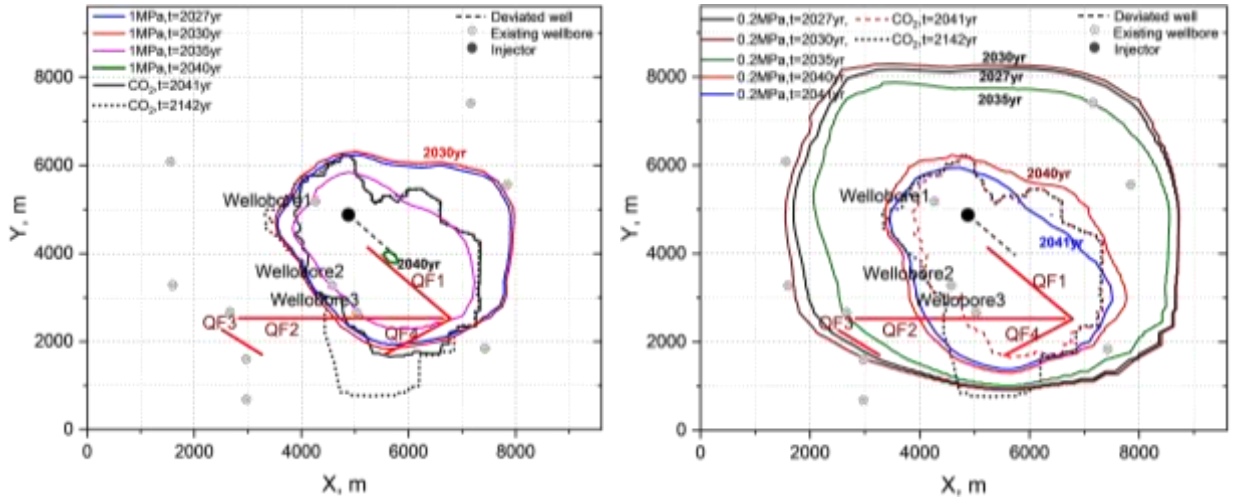
where g is the gravity constant of 9.81 m/s^2, Δz (m) is the depth from the bottom of the USDW layer (403 m) to the top depth of the injection formation (1,339 m), and $\Delta \rho$ presents the difference in density for the USDW water and formation brine. The density of USDW water was taken as 1,000 kg/m³. The alternate 0.2-MPa threshold was used to account for potential uncertainty in brine density. This value was calculated assuming a brine density of 1,022 kg/m³

from Fig. A-1 of Li et al. (2024). These thresholds ensure a robust evaluation of pressure impacts, their potential effects on the USDW, and the Area of Review (AoR).

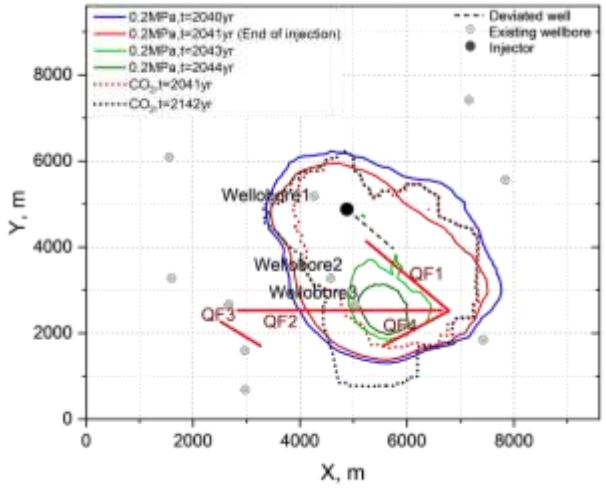
The CO_2 plumes are characterized in the years 2027, 2030, 2035, and 2041 during the injection period (Figure 326(a)) and further to 2090, 2114, and 2142 during the postinjection period as shown in Figure 326(b). The later periods are needed to understand the migration and plume growth driven by buoyancy after injector shut-in. In the region of CO_2 plume migration, there were 3 wellbores and 3 QFs (QF1, QF2, and QF4) to be impacted. The pressure plumes are evaluated during the injection period in the years 2024, 2027, 2030, 2035, 2040, and 2041 for better visualization. The pressure footprint rapidly increased until 2030 and then decreased continuously until the end of injection. Figure 326(c) and Figure 326(d) show results with 1- and 0.2-MPa thresholds. Due to the dissipation of pressure during the postinjection period, the pressure threshold of 1 MPa existed until 2040. For the case of a 0.2-MPa threshold, pressure dissipated by 2044, Figure 326(e). After injector shut-in, pressure relaxes relatively rapidly in the subsurface system and the pressure plume tends to dissipate. The delineation of the AoR, based on a pressure footprint threshold of 0.2 MPa and CO_2 plume migration with a residual saturation of 0.05, is provided in the Supplementary Information of Kim et al. (2025).



(a) (b)



(c) (d)



(e)

Figure 326 Dynamic evaluation of (a) CO_2 plumes during injection, (b) CO_2 plumes for the postinjection period, (c) pressure footprints during injection with 1 MPa threshold, (d) pressure footprints during injection with 0.2-MPa threshold, and (e) pressure footprints with 0.2-MPa threshold for the postinjection period for the optimal well trajectory (Case130). The faults are represented by the red lines, and the existing wellbores 1, 2, and 3 are illustrated by orange dots. The injector location is illustrated by the black dot, and the projection of the long deviated well to land surface is shown by the black dashed line. Gray dots represent other existing wellbores. Source: Kim et al. (2025), licensed under CC BY-NC.

Table 68 shows the average geological properties from well log data (Kim et al. 2023b). Data on both existing wellbores and Quaternary faults are obtained from the California Department of Conservation (CA DOC 2024a, 2024b) and the U.S. Geological Survey (USGS 2024). The effective wellbore permeability was assumed to be 1 to 10 mD based on previous studies (Lackey et al. 2019; Kim et al. 2023b). We note that the permeability of an intact cemented wellbore is generally much less than 1 μD and damaged wellbore permeability was reported between 10 μD and 10 mD (Tao and Bryant 2014). In this AoR, the existing wellbores are all plugged wellbores with cement according to public data. Therefore, the wellbore permeability is assumed as a worst case. For the leakage assessment through existing wellbores, we used the

Multisegmented Wellbore Component ROM in the NRAP-OPEN-IAM tool. The model calculates CO_2 and brine leakage along existing cemented wellbores. It allows for segmenting of the legacy wells passing through the overlying stratigraphy into several intervals to simulate a site's specific stratigraphic and hydrogeologic properties (Vasylkivska et al. 2021; Baek et al. 2021). The depth of the injection was 1,420 m. The Deep Alluvium Aquifer Component ROM was used to predict the changes in underground water if CO_2 and brine were to leak out of the storage zone.

Table 68 Geological properties for risk assessment. See Figure 278(b) for geological stratigraphy (modified from Kim et al. [2025])

Property	Formation type	Top depth, m	Thickness, m	Porosity (ϕ), %	Perm (k), mD
Stratigraphic layer	Top layer (caprock)	0	8	–	0.01
	Aquifer 2 (USDW*)	8	395	20	10
	Shale 2	403	574	15	0.01
	Aquifer 1	977	194.6	35	150
	Shale 1	1,171.6	167.7	28	0.02
	Storage formation (Etchegoin Formation)	1,339.3	326	32	30
	Bottom seal	1,665.3	363	2.5	0.001
Existing wellbores	**Leakage pathway type**	**Well radius (r_w), m**	**Effective wellbore perm.** range, mD**	**Distance from injector, m**	
	Existing wellbore 1	0.135	1–10	657	
	Existing wellbore 2	0.125		1,547	
	Existing wellbore 3	0.125		2,221	
Quaternary faults	**Leakage pathway type**	**Strike (direction of fault)***	**Length, m**	**Starting point**** (x, y), m	
	QF1	133°	2,276	(5,238.2, 4,135.9)	
	QF2	91°	3,730.6	(2,836.4, 2,529.7)	
	QF3	128°	1,005.3	(2,522.3, 2,261.8)	
	QF4	60°	1,480.3	(5,551.5, 1,702.7)	

*USDW = underground source of drinking water
**perm. = permeability
***Direction of fault strike taken clockwise from north
****Coordinate of the fault start point taken as the left point of fault trace

Table 69 shows the fault parameters in the leakage risk assessment. In general, fault zones may serve either as potential CO_2 leakage pathways or barriers depending on geological properties including fracture aperture size, connectivity, lithology, stress state, and so on (Xiao et al. 2024). There are many studies that show small leakage risk along fault zones (Rinaldi et al. 2014; Miocic et al. 2019; Guglielmi et al. 2021).

In this study, we use the surface trace of the Quaternary faults and vary both the permeability and the depth to assess CO_2 leakage along faults. Fault permeability is controlled by the effective

fault aperture, which is assumed to vary from 2×10^{-6} to 2.5×10^{-2} m (0.0002 to 2.5 cm) and 2×10^{-6} to 1×10^{-1} m (0.0002 to 10 cm). In similar CO_2 leakage studies, the effective fault aperture varied from 0.1 to 2 mm. Shear displacement was also varied from 0 to 40 mm to predict the fault's permeability (Pasala et al. 2013; Huang et al. 2019). We consider various scenarios for fault depth (403, 1,200, 1,400, and 1,419 m). We assume that the faults are continuous from the surface to the specific depth. The depth of the injector is set at 1,420 m. Each fault is divided into 4 segments to capture slight changes in orientation. The maximum permeability ratios (CO_2 to brine) of each fault are chosen as 0.6 and 1.5. We use the Fault Flow Component ROM in the NRAP-OPEN-IAM tool to calculate leakage rates.

Table 69 Fault parameters in the leakage risk assessment (modified from Kim et al. [2025])

Parameter	Value	Explanation
Fault segments	4	Number of separate fault divisions of the fault
Fault aperture, m	2×10^{-6} to 2.5×10^{-2} 2×10^{-6} to 1×10^{-1}	Fault effective aperture
Fault depth, m	403, 800, 1,200, 1,400, and 1,419	Fault depth from the surface
Maximum permeability ratio	0.6, 1.5	Ratio of maximum nonwetting permeability to the maximum wetting permeability

The process to minimize pressure buildup is explained in detail by Li et al. (2024). Figure 327 demonstrates the multi-objective optimization results considering the minimization of CO_2 plume size, pressure buildup, and pressure responses at the QF2 fault region. From a geomechanical point of view, QF2 is more likely to slip due to the orientation of the maximum horizontal stress (Kohli et al. 2023), even though it is farther from the injector than QF1. The color of the bubble represents the pressure increase along the QF2 fault. The *y*-axis represents CO_2 plume size at the year 2142 and the *x*-axis represents the maximum pressure buildup in the subsurface over the 118-year project life. Among these cases, Case130 is capable of minimizing the pressure responses due to CO_2 injection while restricting the mass flow in the subsurface for acceptable CO_2 plume size. Figure 327 presents 8 cases selected for comparison with the optimal Case130, based on their well trajectory directions. This comparative analysis is discussed in a later section.

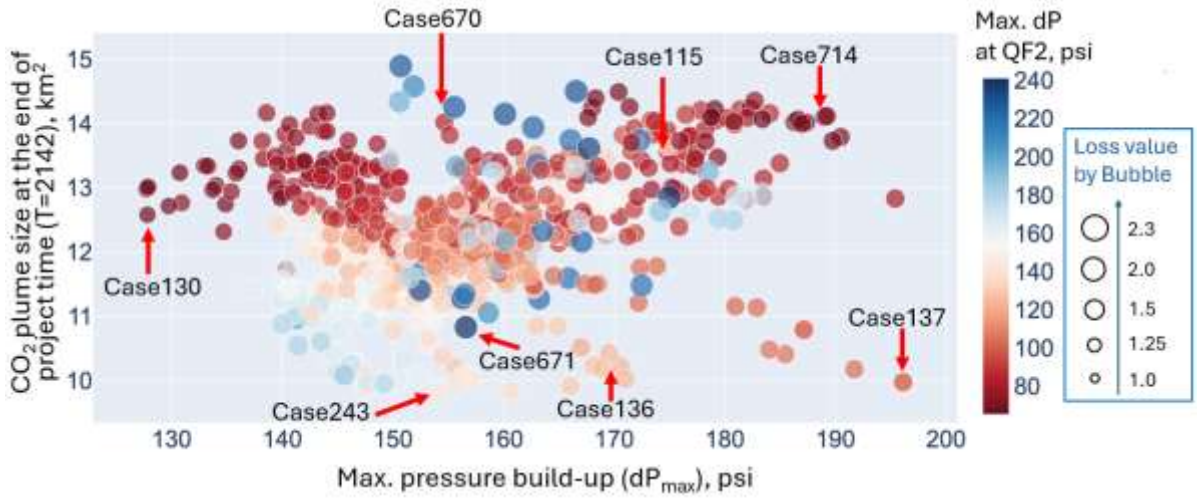


Figure 327 Injector design optimization results. The size of the bubble represents the maximum pressure buildup at the fault plane through all time steps. The color bar also shows the maximum pressure change at the QF2 fault for better visualization. Source: Kim et al. (2025), licensed under CC BY-NC. Representative well trajectories are noted for further analysis (Li et al. 2024).

Table 70 shows well trajectory parameters and results for 8 representative cases including the optimal case (Case130). As discussed in the optimal case (Case130), the optimal injector shows minimum pressure buildup in the subsurface and at the QF2 fault compared with all other cases. Although the CO_2 plume size is 12.6 km^2 at the end of the monitoring period, this scenario reduces the pressure buildup by 35% (68.3 psi [470.9 kPa]) in the storage formation while the plume area required increases by 26% compared with Case137. The optimal injector trajectory demonstrates significant robustness to avoid fault risk by reducing 174.6 psi (1,203.8 kPa) of the pressure increase at the QF2 fault (72.4%) while increasing the plume size by 1.8 km^2 compared with Case671. Among the results of simulations, the well trajectory to the north (Case115) made pressure buildup at the top of the storage formation and QF2 greater than those of Case130. Also, the CO_2 plume size of Case115 was greater than that of Case130.

Table 70 Deviated injection well performance in terms of the optimization objectives (modified from Kim et al. [2025])

		Well trajectory ID							
		115	**130**	**136**	**137**	**243**	**670**	**671**	**714**
Well trajectory parameters	Depth, ft (m)	4,532.7 (1,381.6)	4,299.3 (1,310.4)	4,201 (1,280.5)	4,234.5 (1,290.7)	4,149.2 (1,264.7)	4,666 (1,422.2)	4,236.4 (1,291.3)	4,856.2 (1,480.2)
	Deviation, °	85.7	92.5	96.8	96.3	96.2	81.4	94.9	78.8
	Length, ft (m)	3,509.9 (1,069.8)	4,614.2 (1,406.4)	3,377.8 (1,029.6)	3,018.4 (920.0)	4,637.2 (1,413.4)	3,540 (1,079.0)	3,822.1 (1,165.0)	4,698.9 (1,432.2)
	Direction, °	90	310.6	243.6	270	229.7	8.6	156.3	41.9
Results	CO_2 plume size, km^2	13.7	12.6	10.4	10.0	9.8	14.0	10.8	14.0

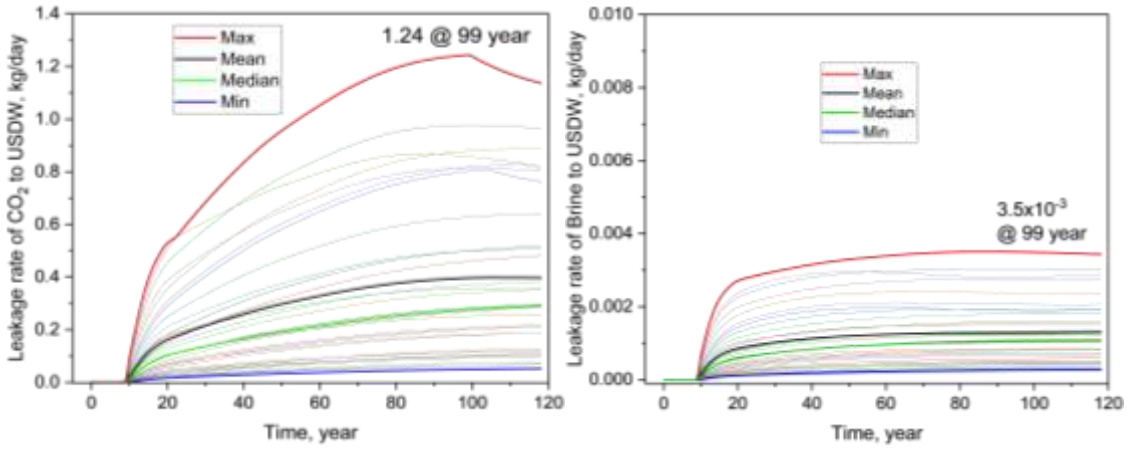
ΔP_{max}, psi (kPa)	174.9 (1,205.9)	127.8 (881.1)	169.5 (1,168.7)	196.1 (1,352.1)	154.1 (1,062.5)	154.6 (1,065.9)	156.6 (1,079.7)	187.4 (1,292.1)
$\Delta P_{max,QF2}$, psi (kPa)	134.7 (928.7)	66.5 (458.5)	124.8 (860.5)	105.1 (724.6)	143.6 (990.1)	83.6 (576.4)	241.1 (1,662.3)	68.1 (469.5)
Loss value	1.65	1.14	1.47	1.42	1.50	1.35	2.04	1.36

Leakage Risk through Existing Wellbores

Based on the worst-case scenario of large wellbore permeability, we found that there was leakage of CO_2 and brine from wellbore 1 and wellbore 2, as shown in Figure 328. To conduct stochastic simulations, we used Latin hypercube sampling (LHS), a random parameter sampling method. The primary variables included wellbore permeability, fault effective aperture, and brine density. The maximum leakage rates of CO_2 and brine are 1.24 kg/d and 3.5×10^{-3} kg/d, respectively, at year 99 from the existing wellbore 1, Figure 328(a). Also, the maximum leakage rates of CO_2 and brine are 7.6×10^{-2} kg/d and 4.8×10^{-4} kg/s, respectively, at year 15 from the existing wellbore 2, as shown in Figure 328(b). Year 15 corresponds approximately to the maximum pressure increase. There was no leakage of CO_2 and brine from wellbore 3. The cumulative leakage ratio by mass into the USDW per total CO_2 injection (CLR) is defined as

$$CLR = \frac{Cumulative\ leakage\ of\ CO_{2,mass}\ into\ USDW}{Total\ injected\ CO_{2,mass}\ in\ storage\ formation} \quad (19)$$

During the project lifespan of 118 years, the ratio of the cumulative leaked CO_2 to the total mass injected (i.e., cumulative leakage fraction) in the worst-case scenario at wellbore 1 was 2.8×10^{-6} to 1.23×10^{-5}, Figure 328(c). The maximum cumulative CO_2 leakage fractions at wellbore 2 were an order of magnitude less than those at wellbore 1. The combined cumulative leakage fraction of the 2 existing wellbores reaches 1.44×10^{-5} in the worst-case scenario. Therefore, the leakage ratio was estimated to range from 0.0003% to 0.001% among the total CO_2 injection amounts by mass where cumulative injection is 12.3 $MtCO_2$.



(a) (b)

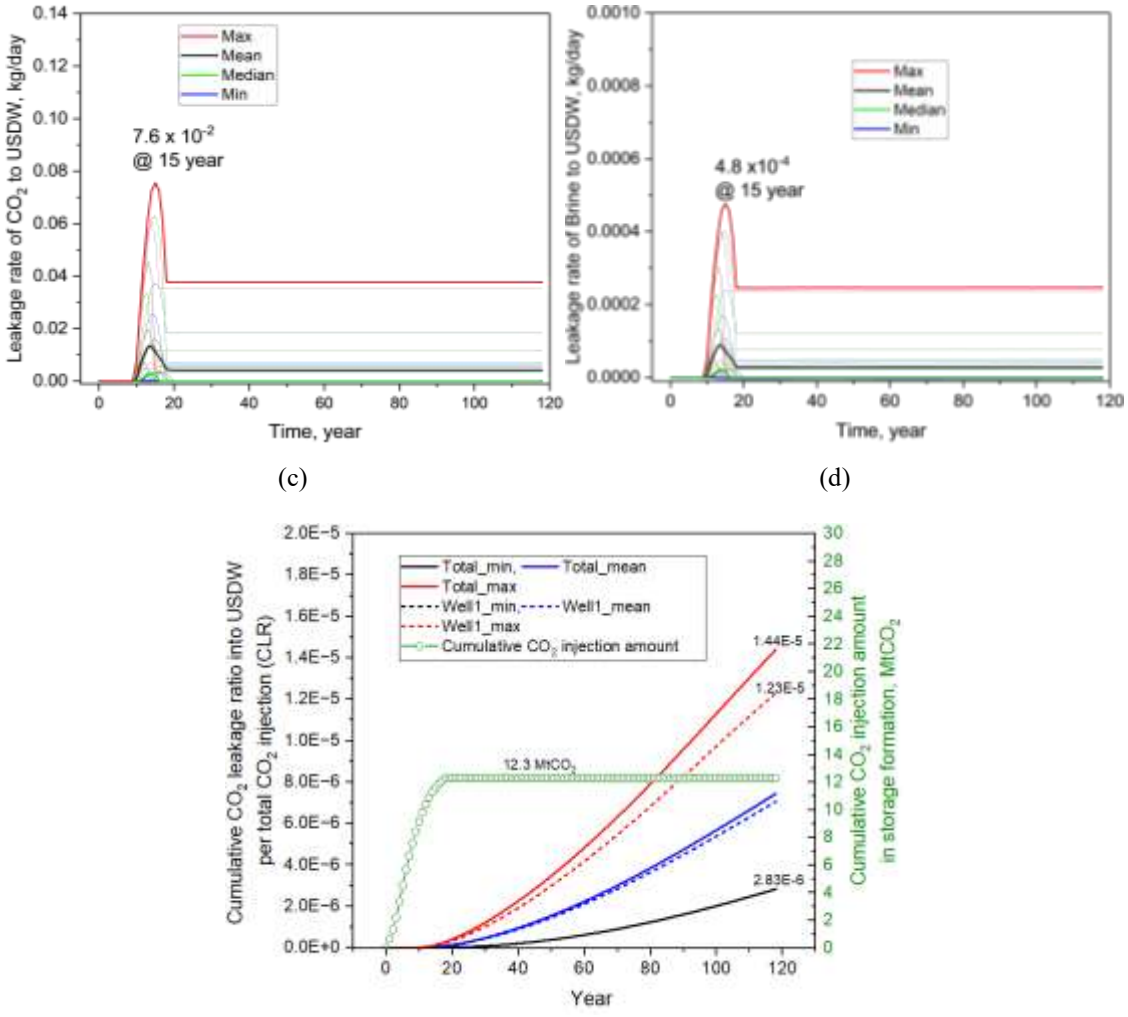
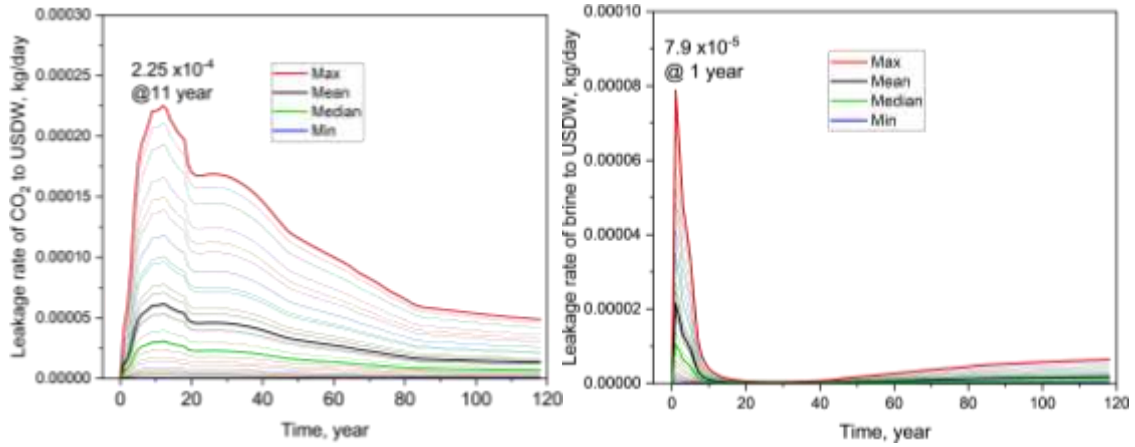


Figure 328 CO_2 and brine leakage rates at (a) wellbore 1, (b) wellbore 2, and (c) cumulative CO_2 leakage fraction compared with total injected CO_2. The amount of CO_2 that leaks is estimated to be 0.0003% to 0.001% of the cumulative injected amount at 118 years after the start of injection. Source: Kim et al. (2025), licensed under CC BY-NC.

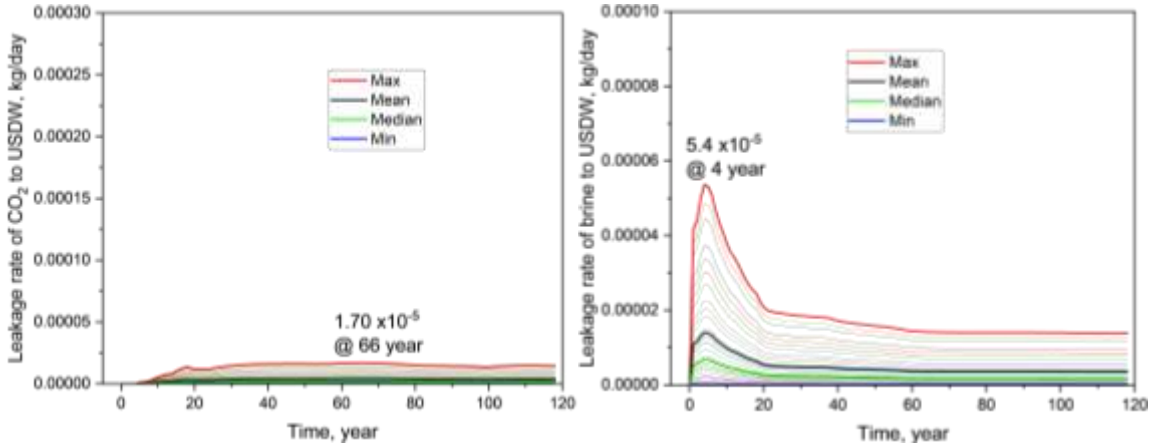
Leakage through Quaternary Faults

Quaternary faults may also serve as leakage pathways. Figure 329 shows the CO_2 and brine leakage rate on faults with a maximum permeability ratio of 0.6, aperture of 2×10^{-6} to 2.5×10^{-2} m, and 1,400 m fault depth. In this model, fault aperture serves as the primary input parameter for controlling fault permeability. Based on the stress conditions within the storage formation, the fault aperture was recalculated. The fault permeability was subsequently determined using the updated aperture and calculated according to the 'Cubic Law' method (Durham and Bonner 1994; Renshaw et al. 2000). Based on these fault conditions, we found that QF1 has the greatest risk of leakage among all faults. The range of the *y*-axis for each fluid is identical. At QF1, the maximum leakage rates for CO_2 and brine are 2.25×10^{-4} kg/d in year 11 and 7.9×10^{-5} kg/d in year 1, respectively. The rate of brine leakage at QF1 gradually increased from year 40 because brine was expelled as the CO_2 plume migrated. The CO_2 leakage rate on

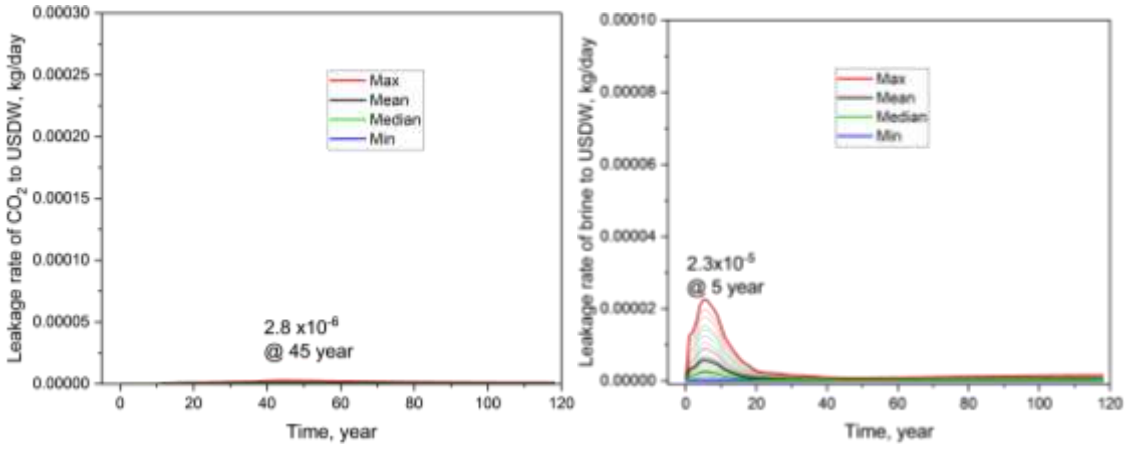
QF2 and QF4 are both 1 to 2 orders of magnitude less than those of QF1. At both QF2 and QF4, the brine leakage rate is greater than the CO_2 leakage rate. Nevertheless, the leakage of CO_2 and brine through these faults is found to be negligible compared with the leakage from the existing wellbores, see Figure 329(d).



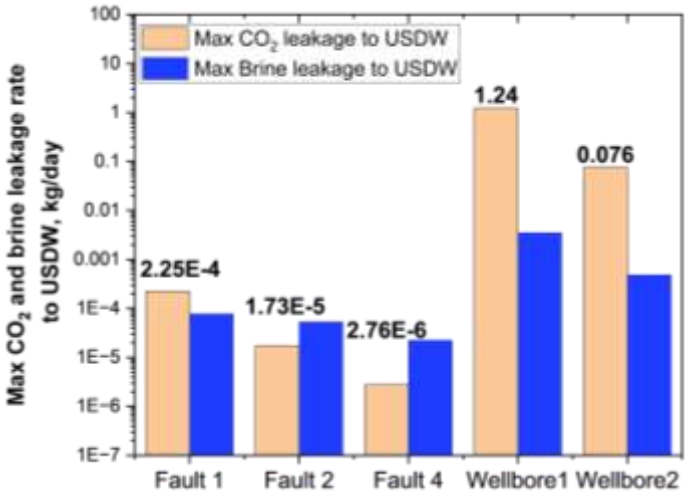
(a)



(b)



(c)



(d)

Figure 329 CO_2 and brine leakage rates along (a) QF1, (b) QF2, and (c) QF4 and (d) maximum leakage rates for CO_2 and brine on each fault and wellbore. The range of the *y*-axis on each fluid is identical. The maximum leak rate (kg/d) is listed on each subfigure. Source: Kim et al. (2025), licensed under CC BY-NC.

Summary

We assessed the potential for CO_2 leakage along preexisting wellbores and Quaternary faults near a possible CO_2 storage site using the NRAP-OPEN-IAM Tool. Both pressure and CO_2 saturation profiles are input to NRAP-OPEN-IAM and were obtained using a 3D reservoir model. The optimized design of the CO_2 injection scenarios from a companion study was selected to minimize pressure buildup at faults along with a relatively small-sized CO_2 plume. This is a key initial step in minimizing the risk of leakage.

Starting from an optimized injection scenario and making conservative assumptions to obtain a worst case for leakage, we found that 2 existing wellbores and 2 Quaternary faults (QF1 and QF2) were the main leakage pathways in the AoR. The maximum leakage rates of CO_2 and brine at wellbore 1, which is closest to the injector, were 1.24 kg/d and 3.5×10^{-3} kg/d, respectively, at year 99 from the start of injection. Estimated leakage rates from wellbore 2 were 1 order of

magnitude less than wellbore 1. The cumulative CO_2 leakage, as a percentage of the total injected mass is estimated to range from 0.0003% to 0.001% for the 118-year project lifetime through existing wellbores. Therefore, leakage rates for CO_2 and brine to the USDW did not show any change in total dissolved solids (TDS) and pH above background.

Also, leakage along Quaternary faults was obtained with estimated fault parameters. We found that the maximum CO_2 leakage rate of 2.25×10^{-4} kg/d from QF1 is the greatest amount among all faults because QF1 is the fault closest to the injector. Results showed that CO_2 leakage along Quaternary faults is much less compared with leakage from the existing wellbores. We found that the leakage through faults was strongly dependent on fault depth, aperture, and relative permeability, so further characterization of fault properties is needed to predict leakage rates more accurately.

In addition, we investigated the leakage from wellbores and Quaternary faults based on different injection well trajectories. The other injection scenarios show different leakage rates due to the relative position of the injector and existing wellbores. Overall, the ratio of leaked to injected CO_2 remains small and wellbores are the primary means of leakage. We did not find any significant change in the pH and TDS of the USDW in any scenario.

Induced Geomechanical Risk Assessment

Our objective was to build a geomechanical model for the prospective storage site and conduct a seismic hazard assessment to quantify the risk of induced slip on preexisting faults during the propose to CO_2 injection. The detailed results in this section are provided in Kohli et al. (2023); see the Appendix.

In this study, we take a 3-part approach to evaluating seismic hazard at a candidate site in the southern San Joaquin Basin of California. First, we build a geomechanical model and evaluate the stress state on mapped faults near the injection site. We then examine the probability of induced fault slip due to CO_2 injection using random populations of faults and a distribution of geomechanical parameters. From these analyses, we delineate the pressure conditions minimize the increase in seismic hazard on preexisting faults, given the spatial extent and magnitude of the predicted pressure plume. Finally, we characterize the natural patterns of seismicity at the site and establish criteria for differentiating induced events during the injection storage periods and for responding to events at different thresholds using a traffic light system.

Site Characterization

Figure 330 shows stress, seismicity, and fault map for the candidate CO_2 injection site.

- Stress state – The region is in a strike-slip faulting environment. The maximum horizontal stress (SHmax) is the greatest principal stress, with a consistent northeast–southwest orientation across the southern San Joaquin Basin.
- Faults – Eight major preexisting faults from the USGS Quaternary Faults database (USGS 2024) were identified within a 10-km radius of the proposed injection site. These represent risk factors for reactivation during CO_2 injection.
- Background seismicity – The prospective site is in an area of relatively low seismic activity compared with other parts of the basin. Analysis of a 20-year seismic record established a natural background seismicity rate of 0.2 to 0.3 events/$mo^{-1}km^{-2}$. Analysis of the regional

earthquake catalog revealed a Gutenberg–Richter *b*-value of approximately 0.7, which is typical for California's Central Valley. The magnitude of catalog completeness is approximately M1.7, indicating that the current seismic network does not detect all smaller events.

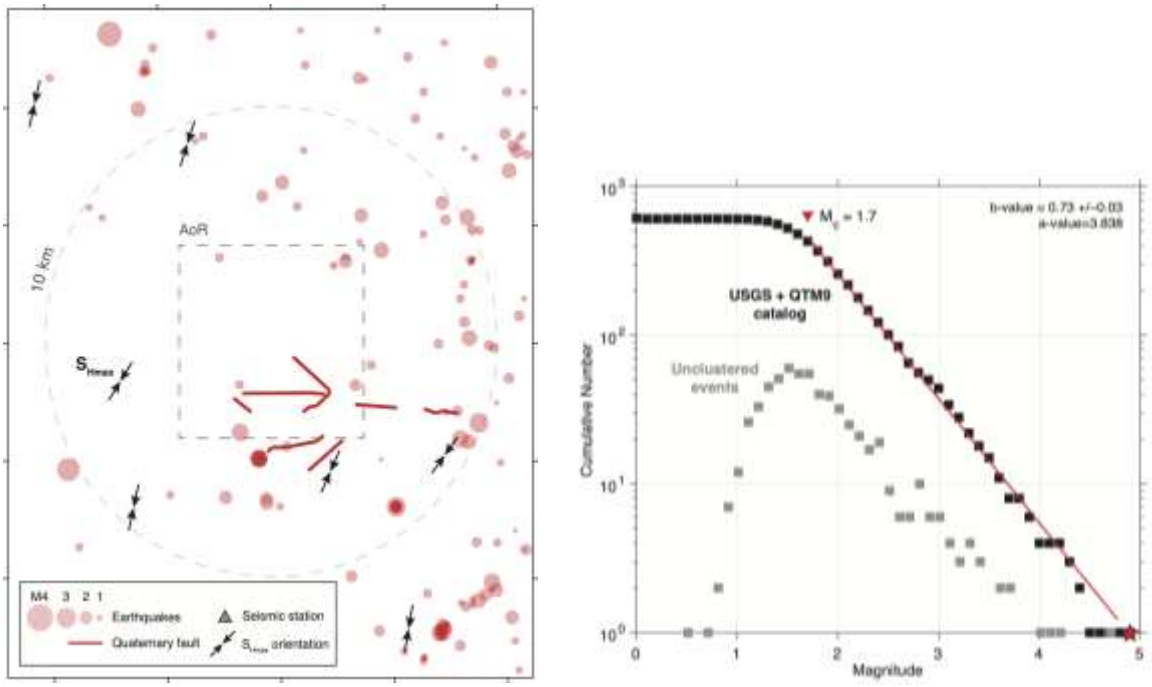


Figure 330 (left) Stress, seismicity, and fault map for the candidate CO_2 injection site. Black lines represent the orientation of the maximum horizontal stress. Red lines represent faults from the USGS Quaternary Faults database. Red circles represent historical seismic events and are sized by magnitude. (right) Gutenberg–Richter plot of historical seismicity at the prospective storage site. Source: Kohli et al. (2023), licensed under CC BY-NC.

Geomechanical Model

A geomechanical model was built to understand the preexisting stress conditions of the reservoir and seal units in Figure 331.

- Rock properties – Porosity and permeability data from logs from a nearby vertical well were used to estimate the Young's modulus of the storage reservoir and seal sequence. The porosity and permeability of the storage formation are 0.28 to 32 and 1 to 10 mD. Based on core data for similar lithologies, these porosity–permeability values correspond to Young's modulus values approximately 20 to 30 GPa.
- Viscous relaxation model – Young's modulus and lithologic data were used to estimate the variations of the fracture gradient or the minimum horizontal stress, Shmin, with depth due to viscous relaxation over geologic time.
- Model results – The storage reservoir is between 4,000 and 6,000 ft (1,219.2 and 1,828.8 m) deep and is overlain by a series of shale seal units. The model predicts a slightly lower Shmin gradient than frictional equilibrium and shows little to no significant variations in Shmin within the storage or seal formations.

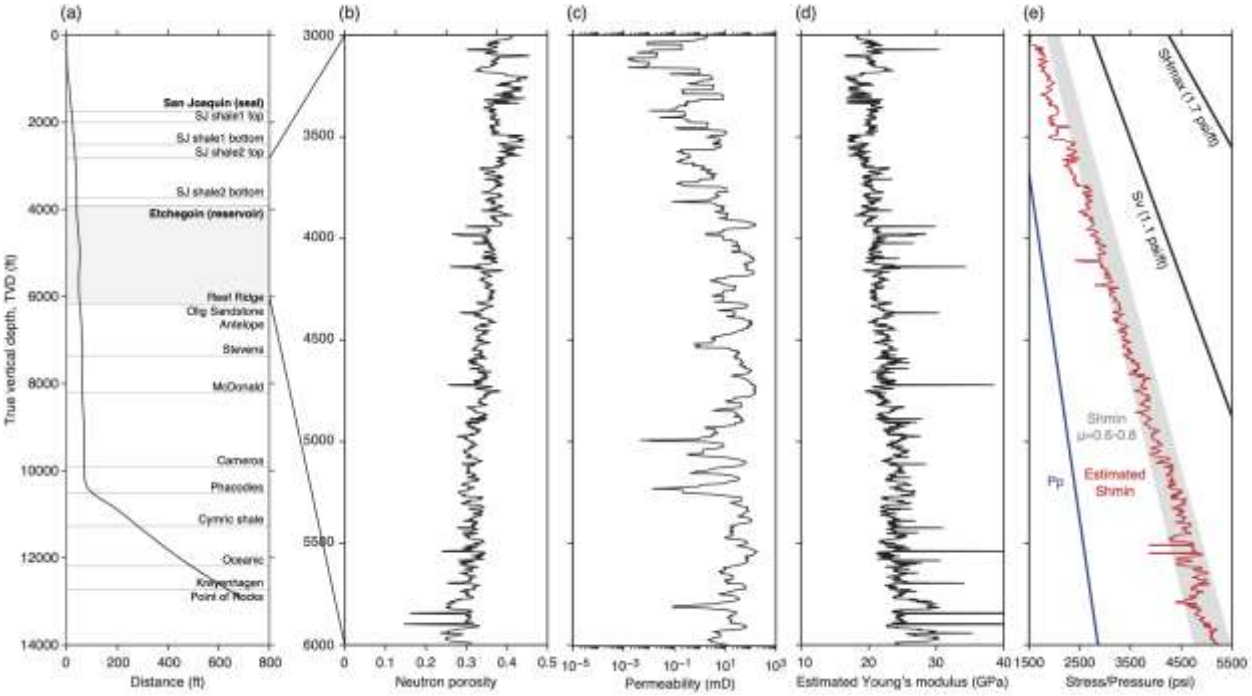


Figure 331 Pilot well logs and reservoir stress profile. (a) Pilot well trajectory and detailed stratigraphy. (b) Neutron porosity log. (c) Permeability estimated from porosity log. (d) Young's modulus estimated from porosity–permeability relationship. (e) Stress and pore pressure gradients. (grey) Minimum horizontal stress, Shmin estimated assuming faults in frictional equilibrium (red) Shmin estimated from relating Young's modulus to viscous stress relaxation over geologic time Source: Kohli et al. (2023), licensed under CC BY-NC.

Fault Slip Analysis

The geomechanical model was used to evaluate the potential for induced slip on the Quaternary faults in Figure 332.

- Mohr-Coulomb analysis – Using the geomechanical model, the conditions for slip on each fault was calculated. Faults 2, 7, and 8 were well oriented for slip in the current stress field. The analysis indicates that the pressure change due to CO_2 injection should be limited to less 500 psi (3,447.4 kPa) within 2 km of the injector.
- Probabilistic fault slip analysis – To account for geomechanical parameter uncertainty, a probabilistic analysis was conducted using Monte Carlo simulations. The probability of slip was calculated for each fault as a function of the change in pore pressure. The analysis showed that the initial probability of slip for the most hazardous faults is between 0.1 and 0.3 and increases to over 0.5 if the pore pressure change exceeds 500 psi (3,447.4 kPa).

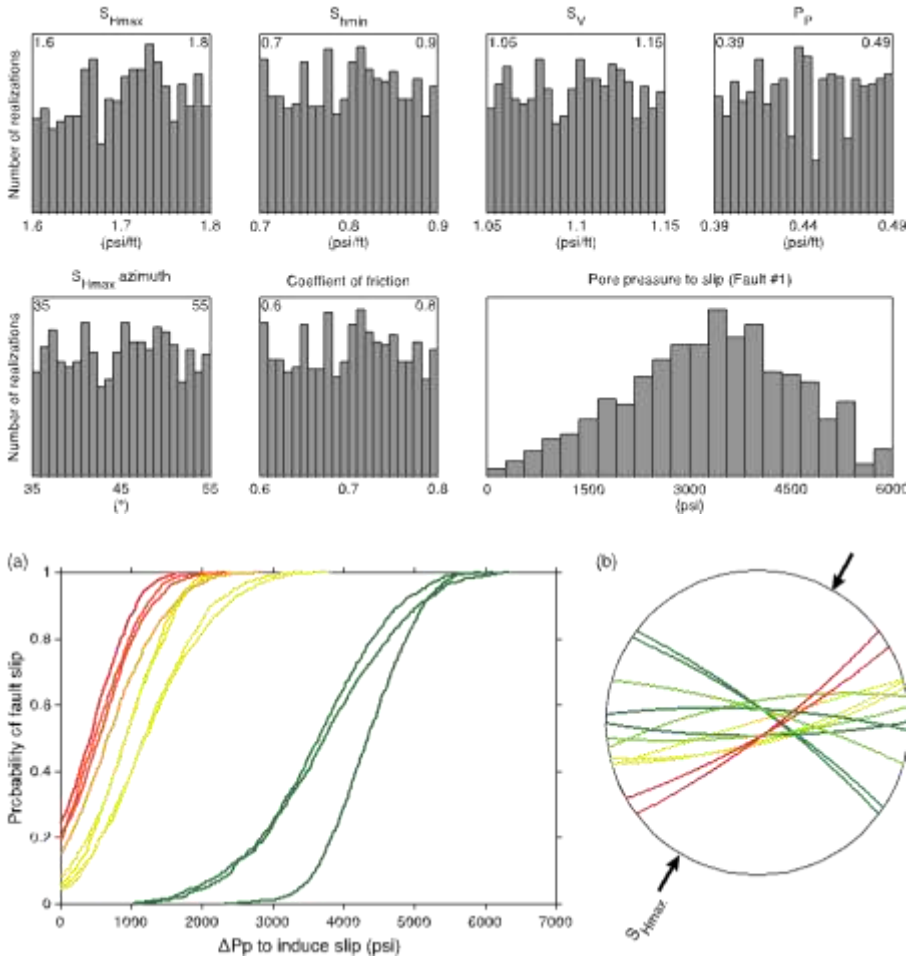


Figure 332 (top) Histograms showing the distributions of geomechanical parameters used to in the Monte Carlo simulations. (bottom) Probability of fault slip for Quaternary faults as a function of the change in pore pressure. Stereonet of fault orientations with respect to SHmax. Faults are colored by probability of slip. Source: Kohli et al. (2023), licensed under CC BY-NC.

3D Visualization of Plume–Fault Interaction

A 3D model was developed to visualize the dynamic interaction among the simulated CO_2 plume, the Quaternary faults, and historical seismicity in Figure 333. Only QF1 through QF4 are impacted by the simulated pressure plume. QF2 is of particular interest because it is the largest fault segment, it is near the injector, and it is well oriented for slip in strike-slip motion. There is no geophysical data to constrain the fault structure at depth, so for this analysis it is assumed that the faults intersect the full thickness storage zone and are vertically dipping. Visualizing the historical seismicity in 3D shows that the majority of earthquakes in this area occur far below the storage reservoir in the crystalline basement. There are several events M1-M2 that were located within the upper and lower seal units, but no events were detected on any of the Quaternary faults at the depth of the storage reservoir.

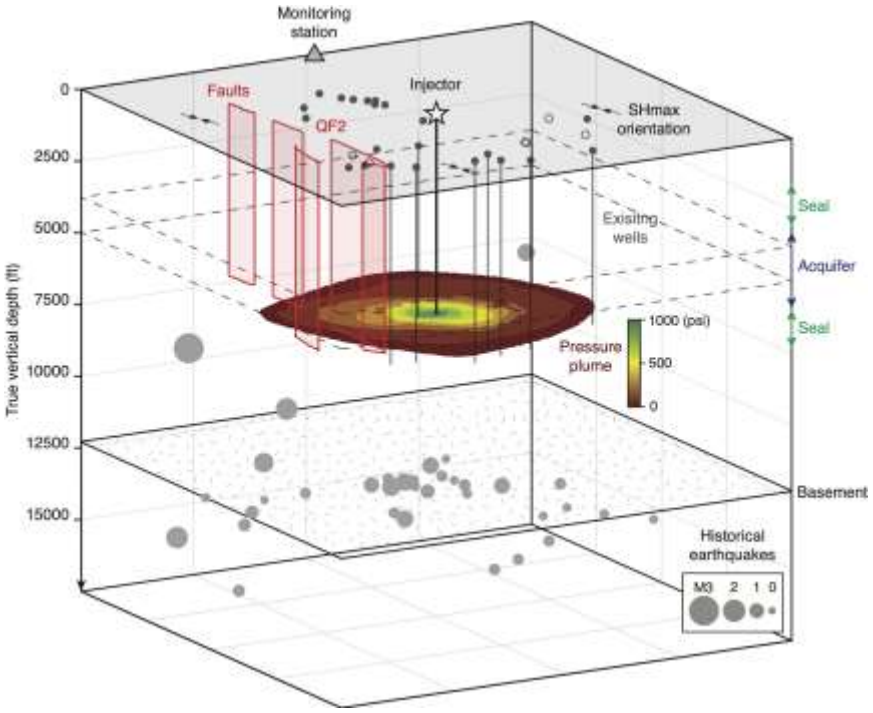


Figure 333 3D map of the proposed storage site illustrating injector (star), existing wells penetrating the storage formation (closed circles) and the seal (open circles), faults (red polygons), the orientation of the maximum horizontal stress (arrows), historical seismicity (grey circles sized by magnitude), the location of the nearest seismic monitoring station (triangle), and the simulated CO_2 pressure plume. Source: Kim et al. (2025), licensed under CC BY-NC.

Modeling Effects of CO_2 Injection

The results of the 3D hydrological model were used to calculate the impact of CO_2 injection on the probability of fault slip in Figure 334.

- The 3D hydrological model shows how the pressure changes in space and time due to CO_2 injection. At the peak of injection in 2028, pressure was predicted to increase by up to 1,200 psi (8,273.7 kPa) in the immediate vicinity of the injector. However, increase in pressure on the Quaternary faults was significantly lower, reaching a maximum of approximately 400 psi (2,757.9 kPa) on QF1 and less than 200 psi (1,379.0 kPa) on other faults.
- The probabilistic fault slip model shows the likelihood of induced seismicity for different injection scenarios. Based a distribution of reservoir simulations with different injection schemes, the range of probabilities for slip on QF2 is between 0.2 and 0.3. The probability of slip changes over time as the pressure plume builds up and then dissipates. This model can be used to iteratively improve injection designs to reduce the risk of induced seismicity.

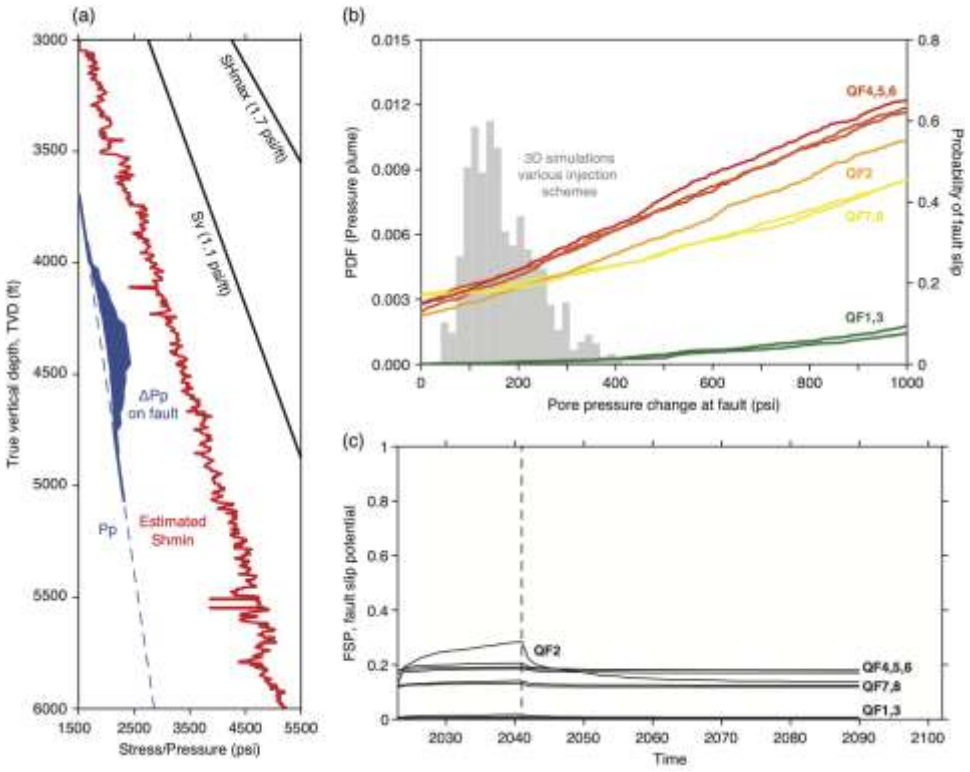


Figure 334 Impact of pressure plume on state of stress and faults at depth (a) Change in pore pressure with depth due to CO_2 injection. The blue range represents optimal and worst-case injection scenarios. (b) Probability of fault slip as a function of pore pressure change for Quaternary faults. Probability distribution function of change in pressure at QF2 for various injection schemes. (c) Change in fault slip potential over time for 8 Quaternary faults. The dotted line represents the end of injection and the start of monitoring.

Identifying and Responding to Induced Seismicity

Finally, a framework was developed to monitor, identify, and respond to any induced seismicity due to CO_2 injection.

- Identification criteria: Three categories for flagging an event for further review.

  1) Area of interest: Event occurs in a region mechanically influenced by injection.

  2) Seismic characteristics: Event is part of a sequence with anomalous characteristics (e.g., changes in seismicity rate, *b*-value, or average event depth).

  3) Ground shaking: The event causes felt reports or ground motion exceeding predefined thresholds at seismic stations.

- Response protocol: A CO_2 storage specific traffic light protocol was developed for the site and defines thresholds for action and specific operational responses.

Summary

Our study highlights the need for detailed, site-specific assessments of induced seismicity risk for CO_2 injection projects in California. In the AOI of the prospective site, mapped faults are not associated with any located earthquakes suggesting that these faults are not active in the current

tectonic regime. However, increasing pore pressure through CO_2 injection drives faults closer to failure and may induce slip if the magnitude and the footprint of the pressure plume are not controlled. Our geomechanical analysis suggests that the risk of reactivating mapped faults in the area is low if pressures are kept below 500 psi (3,447.4 kPa) within 1 to 2 km of the injector. The probabilistic fault slip analysis indicates fault slip may change by up to 20% under the proposed injection conditions. The greatest risk is presented by well oriented faults within 2 km of the injector, where pressure changes are greatest and occur relatively rapidly. Sensitivity analysis indicates that stress magnitudes and orientations are the greatest sources of variability in fault slip probability, which demonstrates the need for borehole stress measurements at the site.

The risk for induced seismicity under the proposed condition appears to low, but more data are needed to resolve naturally occurring seismicity in the estimated AOI. Based on our analysis, we recommend the following strategies to further characterize and mitigate the risk of induced seismicity at the prospective site:

- Fortify the earthquake catalog by deploying more surface seismic stations around the injector and borehole seismic stations in nearby a monitoring well
- Conduct image logs and stress measurements in both the injector and the monitoring well to characterize depth variations in stress and locate zones with active faults
- Acquire seismic imaging to identify hidden faults in the subsurface
- Design the permanent monitoring array around the predicted plume footprint
- Take corrective action if the pressure plume extent and magnitude of pressure increase deviates from simulation results and adhere to corrective actions proposed in the traffic light system

Forward-Looking Regional Scenarios

Carbon Solutions ran all forward-looking scenarios for the entire state of California to better understand what potential buildouts of CCS infrastructure within the state could look like depending on distributed or hub geologic storage locations. Here distributed storage refers to using a 50 km by 50 km grid to generate individual storage points. 3 hub storage locations were selected: the Northern California Tehama County Hub, the Central California San Joaquin County Hub, and the Southern California Kern County Hub (Kim et al. 2022).

A total of 4 scenarios were run, 2 using hub storage and 2 using distributed storage in Table 71.

Table 71 Summary of runs conducted for California forward-looking runs using SimCCS^{PRO}

Scenario	Runs	Sources	Sinks	Capture target
Distributed storage	1	All sources	50 x 50 km grid	51.55
Distributed storage	2	Steam generators	50 x 50 km grid	8.64
Hub storage	3	All sources	3 target locations	51.55
Hub storage	4	Steam generators	3 target locations	8.64

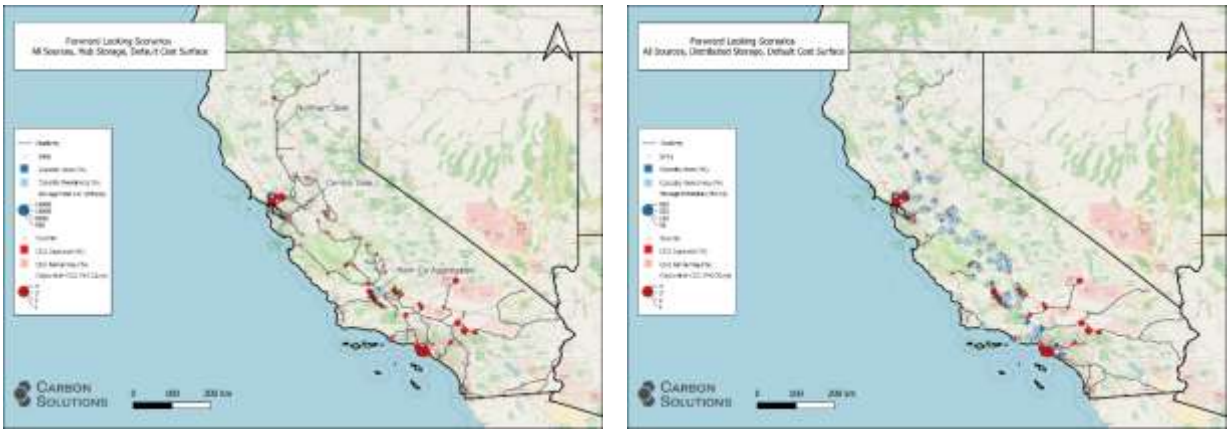
Results

Figure 335 shows what a CCS network, using all sources of CO_2 in California, would look like when using hub (A) and distributed (B) storage options. The most used hub storage option in the

hub scenario was the Southern California "Kern County" Hub. Furthermore, the overall CCS network deployment in this scenario splits into 2 main networks, one going from northern to central California and another that goes from central to southeastern California. The latter network hub features the Southern California "Kern County" Hub.

The CCS network in Figure 335(a) deploys approximately 5,143 km of pipeline to capture almost 52 $MtCO_2/yr$ for a network total cost of $\$109/tCO_2$. The additional pipeline results from needing to connect farther-away sources with the targeted hub storage locations. This can be observed when realizing that using hub storage involves an additional 1,785 km of pipeline when compared with the equivalent distributed storage scenario (Figure 335(b)). This increase in pipeline deployment results in approximately $\$7/tCO_2$ difference in the total CCS network cost between the 2 scenarios.

Figure 335(b) shows the distributed storage CCS network for California when capturing all available CO_2 emissions (52 $MtCO_2/yr$). This distributed storage network involves the deployment of 3,359 km of pipeline with a total unit network cost of $\$102/tCO_2$. Approximately 80 different individual geologic storage locations are deployed in this run, highlighting how the least cost option often involves transporting captured CO_2 emissions to nearby low cost and high storage potential options. For example, the unit storage cost for distributed and hub storage is $\$6.91/tCO_2$ and $\$6.63/tCO_2$, respectively. Yet the higher total unit cost for hub storage can be explained by the fact that the difference in unit transportation costs is approximately $\$7/tCO_2$, or in other words the difference in total CCS network cost.



(a) (b)

Figure 335 Deployed CCS networks in California using either hub (a) or distributed (b) storage.

Table 72 shows the summary results for all 4 forward-looking runs. There are large fluctuations in network length, ranging from 218 to 5,143 km, primarily driven by the geospatial location and number of SGs compared with all facilities within California. For example, in this analysis there are 246 facilities in California with 63 of them being SGs predominately located in Kern County. Network lengths are longer for each scenario that uses all sources in California.

Capture and storage costs stay relatively similar across all scenarios while unit transport costs fluctuate, driven by the changing network lengths. Overall network costs range from $\$75/tCO_2$ to $\$109/tCO_2$, with networks that use all sources having a higher overall network cost. Nevertheless, total costs are lower when comparing total costs for networks that use distributed storage as opposed to hub storage, regardless of which sources are used. Once again this is

largely driven by differences in transportation costs with it being slightly more expensive to route all sources to hub storage locations.

Table 72 Summary table of the results for all forward-looking California runs conducted using SimCCS^{PRO}. DS-AS refers to distributed storage and all sources, DS-SG refers to distributed storage and steam generators, HS-AS refers to hub storage and all sources, and HS-SG refers to hub storage and steam generators.

Run	Annual capture target, $MtCO_2/yr$	Number of sources	Number of sinks	Network length, km	Capture cost, $/$tCO_2$	Transport cost, $/$tCO_2$	Storage cost, $/$tCO_2$	Total cost, $/$tCO_2$
DS-AS	51.55	246	80	3,358.49	68.29	26.81	6.91	102.01
DS-SG	8.64	63	13	218.10	64.38	3.87	6.88	75.13
HS-AS	51.55	246	3	5,143.38	68.29	33.79	6.63	108.71
HS-SG	8.64	63	1	616.78	64.38	10.75	6.85	81.98

Summary

Carbon Solutions was tasked with applying the SimCCS^{PRO} toolset to "develop a conceptual model of how to stimulate regional CCS for more than 50 MtCO2/yr." To achieve this objective Carbon Solutions ran 4 scenarios using either hub or distributed storage options. In hub storage scenarios, Carbon Solutions designated 3 hubs for the state of California while distributed storage scenarios use the 50-km SCO_2T^{PRO} grid of storage locations. Scenarios also featured either of 2 options for sources: SGs only (8.64 $MtCO_2/yr$) and all sources of CO_2 in California (51.55 $MtCO_2/yr$). Carbon Solutions results indicate that total network costs are lower when using distributed storage when compared with hub storage. For example, when using all sources in California the total network costs for hub storage is approximately $\$109/tCO_2$ while distributed storage has a total network cost of $\$102/tCO_2$. This is further supported by looking at network lengths, where distributed storage has a network length of 3,358 km and hub storage has a network length of 5,143 km.

Conclusion

The goal of this work is to provide foundational engineering analysis across immediate, near-term, and medium-term time frames to accelerate the implementation of a shovel-ready project that has the potential to scale and address the 12.3 $MtCO_2$/year emitted from upstream oil and gas operations in the SJV. The project's physical location is one of the closest prospective storage sites to the Los Angeles (LA) Basin. Within the LA Basin any subsurface storage is unlikely due to population density and seismic activity making the SJV especially interesting. The area of interest (AOI) for CO_2 storage site is located near 50 km west of Bakersfield, California in the southern San Joaquin Basin. Previously, Kim et al. (2023a) found that the southern San Joaquin Basin is a good location for GCS projects based on geological properties and technoeconomic aspects.

The objective is to provide technical and economic analysis to support a first-of-its-kind capture and storage project aimed at reducing emissions from upstream oil production operations. Project goals are (1) to leverage low carbon fuel standard (LCFS) credits and CUSP technical expertise to move a CCS project in California from concept to permitting to implementation, (2) add

certainty to storage volumes and dynamic storage capacity of relatively poorly characterized saline formations in the SJV, (3) forge a pathway for others to follow with similar projects, and (4) lay the foundations of a regional storage hub. We intend to achieve our goals using several tasks with collaboration among team members. The result of each task is as follows.

1. Emitter Identification and Capture Economics

A detailed inventory identified 63 steam generators (SR) and 20 combined heat and power (CHP) plants emitting roughly 11.4 Mt CO_2 per year. Capture cost analysis using amine-based systems revealed an average cost of $57 to $78 per metric ton CO_2, depending on plant type and load factor. Economies of scale significantly improve capture affordability. Forty-one potential storage sites were screened, yielding an estimated 5.8 Gt CO_2 capacity.

SimCCS modeling incorporating 45Q and LCFS incentives revealed economic viability for most enhanced oil recovery facilities (SR and CHP) at $70 to $80 per metric ton CO_2, while power and cement facilities become competitive only with extended credit durations.

2. Subsurface Model Characterization

The Etchegoin Formation was selected as the primary pilot target, characterized by a 2.3 km-deep saline sandstone sealed by around 600 m of shale. Coupled flow-geomechanical simulations predict that injecting 12.3 Mt CO_2 over 18 years results in pressure increases below 130 psi and surface uplift under 2 cm, safely below fracture thresholds. The optimal well geometry analysis using pyCCUS indicates a long, deviated injector minimizes pressure on nearby faults by over 70% compared with a vertical well, confirming safe operational margins and improved reservoir performance.

3. Storage Assessment and Plume Migration

CMG and pyCCUS simulations estimate a stabilized plume footprint of approximately 12 km^2 after 100 years. Sensitivity analyses show limited uncertainty impacts, confirming containment reliability. The optimized design reduces reservoir overpressure by more than half while maintaining equivalent storage efficiency.

4. Monitoring via InSAR and Data Analytics

Analysis of Sentinel-1 InSAR data (2015–2023) established a stable pre-injection baseline. Synthetic deformation modeling predicts 20 to 25 mm of uplift during injection, consistent with expected pressure buildup. Sensitivity tests identify rock stiffness and injection rate as key uplift drivers, supporting the use of InSAR-based monitoring for regulatory compliance and safety assurance.

5. Infrastructure and Economic Scenarios in Field Project

Using $SimCCS^{PRO}$, Carbon Solutions evaluated multiple field development scenarios. In a capacity-limited (“constrained”) case, network costs reached approximately $74 per metric ton CO_2 with short pipeline distances, while “unconstrained” cases expanded injection and transport networks up to 509 km with total costs near $81 per metric ton. Capture and storage remain the

dominant cost drivers. All scenarios fall below the effective 45Q credit value, supporting the economic feasibility of pilot deployment.

6. Risk and Seismic Assessment

The leakage assessment with the NRAP-Open-IAM tool demonstrated extremely low leakage risk—less than or equal to 0.001% of total injected CO_2—through both faults and wells. Probabilistic analyses show fault-slip likelihood below 0.3 when maintaining pressure increases under 500 psi. Historical seismic data confirms the absence of active faults within the injection horizon. A traffic-light protocol was developed for operational management of induced seismicity.

7. Forward-Looking Regional Scenarios

Statewide simulations comparing centralized ("hub") and distributed storage architectures found that distributed networks across Kern, Tehama, and San Joaquin Counties minimize total system costs. Capturing all industrial emissions (approximately 52 Mt CO_2/yr) would require approximately 5,000 km of pipeline infrastructure at $102 to 109 per metric ton CO_2, while restricting to oil and gas emitters lowers cost to approximately $75 per metric ton CO_2. The southern SJV thus emerges as the most strategic location for initial large-scale deployment.

Finally, we demonstrated that the San Joaquin Basin offers the geologic, economic, and infrastructural readiness for CCS hub development. The findings confirmed technical feasibility, low leakage risk, and cost competitiveness under current credit regimes. The integrated approach—combining advanced modeling, economic optimization, and InSAR monitoring—lays the foundation for a pilot project and a scalable statewide CO_2 storage network.

Acknowledgement

The authors acknowledge the support of the DOE Office of Fossil Energy through the "Carbon Utilization and Storage Partnership (CUSP) for the Western USA" (Award No. DE-FE0031837). Additional funding was provided by the Stanford Center for Carbon Storage. The authors thank our colleagues from the SUETRI-A research group and SkyGeo for valuable discussion and support. In particular, we thank Industrial partner Sentinel Peak Resources to provide well data and the 3D geologic model.

References

Abramson E, McFarlane D, Brown J. 2020. Transport infrastructure for carbon capture and storage: regional infrastructure for midcentury decarbonization [Internet]. Minneapolis (MN): Great Plains Institute. 41 p. [accessed 2026 Jan 15]. https://www.betterenergy.org/wp-content/uploads/2020/06/GPI_RegionalCO2Whitepaper.pdf.

Afolayan B, Mackay E, Opuwari M. 2023. Dynamic modeling of geological carbon storage in an oil reservoir, Bredasdorp Basin, South Africa. Sci Rep. 13(1):16573. doi:10.1038/s41598-023-43773-9

Baek S, Bacon DH, Huerta NJ. 2021. NRAP-Open-IAM multisegmented wellbore reduced-order model. PNNL-32364. Richland (WA): Pacific Northwest National Laboratory.

Bazargan M, Leezenberg PB, Kovscek AR. 2020. In-situ combustion front monitoring and tracking using InSAR. Lead Edge. 39(4):272–278. doi:10.1190/tle39040272.1

[CARB] California Air Resources Board. 2021a. CARB Pollution Mapping Tool [Internet]. [accessed 2026 Jan 15]. https://ww3.arb.ca.gov/ei/tools/pollution_map/pollution_map.htm.

[CARB] California Air Resources Board. 2021b. Monthly LCFS credit price and transaction volume [Internet]. [accessed 2026 Jan 15]. https://ww2.arb.ca.gov/resources/documents/lcfs-credit-clearance-market.

[CA DOC] California Department of Conservation. 2021. WellSTAR data dashboard [Internet]. [accessed 2026 Jan 15]. https://www.conservation.ca.gov/calgem/Online_Data/Pages/WellSTAR-Data-Dashboard.aspx.

[CA DOC] California Department of Conservation. 2024a. Well Finder (CalGEM GIS) [Internet]. [accessed 2026 Jan 15]. https://maps.conservation.ca.gov/doggr/wellfinder/#/-118.94276/37.12009/6.

[CA DOC] California Department of Conservation. 2024b. WellSTAR data dashboard [Internet]. [accessed 2026 Jan 15]. https://www.conservation.ca.gov/calgem/Online_Data/Pages/WellSTAR-Data-Dashboard.aspx.

[CEC] California Energy Commission. 2024. Elk Hills Power Project [Internet]. [accessed 2026 Jan 15]. https://www.energy.ca.gov/powerplant/combined-cycle/elk-hills-power-project.

Carbon Solutions LLC. 2025a. CostMAP^{PRO} [software]. Saint Paul (MN); Carbon Solutions LLC. [accessed 2025 Dec 30]. https://www.carbonsolutionsllc.com/software/costmappro/.

Carbon Solutions LLC. 2025b. SCO$_2$T^{PRO} [software]. Saint Paul (MN); Carbon Solutions LLC. [accessed 2025 Dec 30]. https://www.carbonsolutionsllc.com/software/sco2tpro/.

Carbon Solutions LLC. 2025c. SimCCS^{PRO} [software]. Saint Paul (MN); Carbon Solutions LLC. [accessed 2025 Dec 30]. https://www.carbonsolutionsllc.com/software/simccspro/.

Chai T, Draxler RR. 2014. Root mean square error (RMSE) or mean absolute error (MAE)? Arguments against avoiding RMSE in the literature. Geosci Model Dev. 7(3):1247–1250. doi:10.5194/gmd-7-1247-2014

Chang C, Zoback MD, Khaksar A. 2006. Empirical relations between rock strength and physical properties in sedimentary rocks. J Pet Sci Eng. 51(3–4):223–237. doi:10.1016/j.petrol.2006.01.003

Chen Y, Guerschman JP, Cheng Z, Guo L. 2019. Remote sensing for vegetation monitoring in carbon capture storage regions: a review. Appl Energy. 240:312–326. doi:10.1016/j.apenergy.2019.02.027

Chicco D, Warrens MJ, Jurman G. 2021. The coefficient of determination R-squared is more informative than SMAPE, MAE, MAPE, MSE and RMSE in regression analysis evaluation. PeerJ Comput Sci. 7:e623. doi:10.7717/peerj-cs.623

Credit for Carbon Oxide Sequestration, U.S.C.-2023 26 C.F.R. §1.45Q-1 (2021).

Davis SJ, Peters GP, Caldeira K. 2011. The supply chain of CO_2 emissions. Proc Natl Acad Sci U S A. 108(45):18554–18559. doi:10.1073/pnas.1107409108

Durham WB, Bonner BP. 1994. Self-propping and fluid flow in slightly offset joints at high effective pressures. J Geophys Res Solid Earth. 99(B5):9391–9399. doi:10.1029/94JB00242

Dzurisin D, Lu Z. 2007. Interferometric synthetic-aperture radar (InSAR). In: Dzurisin D, editor. Volcano deformation: geodetic monitoring techniques. Berlin (Germany): Springer. p. 153–194.

[EFI and Stanford] Energy Futures Initiative and Stanford University. 2020. An action plan for carbon capture and storage in California: opportunities, challenges, and solutions [Internet]. Stanford (CA): Energy Futures Initiative and Stanford Center for Carbon Storage. [accessed 2026 Jan 15]. https://crsreports.congress.gov.

[Esri] Environmental Systems Research Institute. 2025. ArcGIS Pro Desktop [software]. Redlands (CA); Environmental Systems Research Institute. [accessed 2026 Jan 8]. https://www.esri.com/en-us/arcgis/products/arcgis-pro/overview.

Guglielmi Y, Nussbaum C, Cappa F, De Barros L, Rutqvist J, Birkholzer J. 2021. Field-scale fault reactivation experiments by fluid injection highlight aseismic leakage in caprock analogs: implications for CO_2 sequestration. Int J Greenh Gas Control. 111:103471. doi:10.1016/j.ijggc.2021.103471

Guilhot D, Martínez del Hoyo T, Bartoli A, Ramakrishnan P, Leemans G, Houtepen M, Salzer J, Metzger JS, Maknavicius G. 2021. Internet-of-things-based geotechnical monitoring boosted by satellite InSAR data. Remote Sens. 13(14):2757. doi:10.3390/rs13142757

Holstein ED, Lake LW. 2007. Reservoir engineering and petrophysics. In: Lake LW, editor. Petroleum engineering handbook. Vol. 5. Richardson (TX): Society of Petroleum Engineers.

Horsrud P. 2001. Estimating mechanical properties of shale from empirical correlations. SPE Drill Compl. 16(2):68–73. doi:10.2118/56017-PA

Huang N, Liu R, Jiang Y, Cheng Y, Li B. 2019. Shear-flow coupling characteristics of a three-dimensional discrete fracture network–fault model considering stress-induced aperture variations. J Hydrol. 571:416–424. doi:10.1016/j.jhydrol.2019.01.046

Inflation Reduction Act of 2022. Pub L No 117-169, 136 Stat 1818 [Internet]. [accessed 2026 Jan 15]. https://www.govinfo.gov/content/pkg/PLAW-117publ169/pdf/PLAW-117publ169.pdf.

Jones AC, Marples DJ. 2023. The Section 45Q tax credit for carbon sequestration [Internet]. Washington (DC): Congressional Research Service. [accessed 2026 Jan 15]. https://crsreports.congress.gov.

Kim TW, Li Y, Kohli AH, Kovscek AR. 2025. Assessment of CO_2 leakage through existing wells and faults for a prospective storage site in the southern San Joaquin Basin, California. Int J Greenh Gas Control. 144:104381. doi:10.1016/j.ijggc.2025.104381

Kim TW, Kohli AH, Li Y, Kovscek AR. 2023b. Wellbore leakage and seismic risk assessments for geological carbon dioxide storage in saline formations in Kern County, California. SPE Western Regional Meeting. SPE-212989-MS.

Kim TW, Yaw S, Kovscek AR. 2022. Evaluation of geological carbon storage opportunities in California and a deep look in the vicinity of Kern County. SPE Western Regional Meeting. SPE-209340-MS. doi:10.2118/209340-MS

Kim TW, Yaw S, Kovscek AR. 2023a. Scoring, ranking, and technoeconomics of carbon capture and storage opportunities in the Central Valley of California. Int J Greenh Gas Control. 128:103968. doi:10.1016/j.ijggc.2023.103968

Kingma DP, Ba J. 2015. Adam: a method for stochastic optimization. In: Proc Int Conf Learn Representations; 2015 May 7–9; San Diego (CA). arXiv:1412.6980.

Kohli A, Li Y, Kim TW, Kovscek AR. 2023. Induced seismicity hazard assessment for a potential CO_2 storage site in the southern San Joaquin Basin, California. GeoHazards. 4(4):421–436. doi:10.3390/geohazards4040022

Lackey G, Vasylkivska VS, Huerta NJ, King S, Dilmore RM. 2019. Managing well leakage risks at a geologic carbon storage site with many wells. Int J Greenh Gas Control. 88:182–194. doi:10.1016/j.ijggc.2019.06.011

Li Y. 2024b. Dynamic modelling and monitoring of geological carbon sequestration assets. PhD dissertation. Stanford (CA): Stanford University.

Li Y. 2024a. pyCCUS-public [software] [Internet]. [accessed 2026 Jan 15]. https://github.com/AndyStudio/pyCCUS-public.

Li Y, Leezenberg PB, Kovscek AR. 2025. Assessment of spatial monitoring of geological carbon storage using InSAR. Gas Sci Eng. 138:205591. doi:10.1016/j.gaseng.2025.205591

Li Y, Manrique EJ, Kovscek AR. 2023. Progress toward pilot-scale simulation of in-situ combustion incorporating geomechanics. SPE Res Eval Eng. 26(1):152–166. doi:10.2118/212266-PA

Li Y, O'Neal R, Whitezell M, Kovscek AR. 2024. Optimizing injection well trajectory to maximize CO_2 storage security and minimize geomechanical risk. SPE J. 29(11):6547–6562. doi:10.2118/218506-PA

Lin G, Thurber CH, Zhang H, Hauksson E, Shearer PM, Waldhauser F, Brocher TM, Hardebeck J. 2010. A California statewide three-dimensional seismic velocity model from both absolute and differential times. Bull Seismol Soc Am. 100(1):225–240. doi:10.1785/0120090028

Lu L, Shin Y, Su Y, Karniadakis GE. 2020. Dying ReLU and initialization: theory and numerical examples. Commun Comput Phys. 28(5):1671–1706. doi:10.4208/cicp.OA-2020-0165

Maharramov M, Zoback MD. 2018. Monitoring of cyclic steam stimulation by inversion of surface tilt measurements. Lead Edge. 37(5):350–355. doi:10.1190/tle37050350.1

Middleton RS, Yaw SP, Hoover BA, Ellett KM. 2020. SimCCS: an open-source tool for optimizing CO_2 capture, transport, and storage infrastructure. Environ Model Softw. 124:104560. doi:10.1016/j.envsoft.2019.104560

Miocic JM, Gilfillan SM, Frank N, Schroeder-Ritzrau A, Burnside NM, Haszeldine RS. 2019. 420,000-year assessment of fault leakage rates shows geological carbon storage is secure. Sci Rep. 9(1):769. doi:10.1038/s41598-018-36975-0

Molina O, Vilarrasa V, Zeidouni M. 2017. Geologic carbon storage for shale gas recovery. Energy Procedia. 114:5748–5760. doi:10.1016/j.egypro.2017.03.1713

Naims H. 2016. Economics of carbon dioxide capture and utilization: a supply and demand perspective. Environ Sci Pollut Res Int. 23(22):22226–22241. doi:10.1007/s11356-016-6810-2

[NETL] National Energy Technology Laboratory. 2010. Carbon dioxide enhanced oil recovery: untapped domestic energy supply and long term carbon storage solution [Internet]. Pittsburgh (PA): U.S. Department of Energy, National Energy Technology Laboratory. [accessed 2026 Jan 15]. https://www.netl.doe.gov/sites/default/files/netl-file/CO2_EOR_Primer.pdf.

[NPC] National Petroleum Council. 2019. Meeting the dual challenge: a roadmap to at-scale deployment of carbon capture, use, and storage [Internet]. Washington (DC): National Petroleum Council. [accessed 2026 Jan 15]. https://dualchallenge.npc.org/files/CCUS-Chap_2-030521.pdf.

[NRAP] National Risk Assessment Partnership. 2023a. NRAP-Open-IAM version 2.7 [software] [Internet]. [accessed 2026 Jan 15]. https://edx.netl.doe.gov/sites/nrap/nrap-open-iam/.

[NRAP] National Risk Assessment Partnership. 2023b. Overview of NRAP-Open-IAM [Internet]. [accessed 2026 Jan 15]. https://gitlab.com/NRAP/OpenIAM.

Pasala SM, Forster CB, Deo M, Evans JP. 2013. Simulation of the impact of faults on CO_2 injection into sandstone reservoirs. Geofluids. 13(3):344–358. doi:10.1111/gfl.12021

Pilorgé H, McQueen N, Maynard D, Psarras P, He J, Rufael T, Wilcox J. 2020. Cost analysis of carbon capture and sequestration of process emissions from the US industrial sector. Environ Sci Technol. 54(12):7524–7532. doi:10.1021/acs.est.0c00577

Renshaw CE, Dadakis JS, Brown SR. 2000. Measuring fracture apertures: a comparison of methods. Geophys Res Lett. 27(2):289–292. doi:10.1029/1999GL008401

Rinaldi AP, Rutqvist J, Cappa F. 2014. Geomechanical effects on CO_2 leakage through fault zones during large-scale underground injection. Int J Greenh Gas Control. 20:117–131. doi:10.1016/j.ijggc.2013.11.001

Rubin ES, Davison JE, Herzog HJ. 2015. The cost of CO_2 capture and storage. Int J Greenh Gas Control. 40:378–400. doi:10.1016/j.ijggc.2015.05.018

Sone H, Zoback MD. 2013. Mechanical properties of shale-gas reservoir rocks—Part 2: ductile creep, brittle strength, and their relation to the elastic modulus. Geophysics. 78(5):D393–D402. doi:10.1190/geo2013-0051.1

Tan HH, Lim KH. 2019. Vanishing gradient mitigation with deep learning neural network optimization. In: 2019 7th International Conference on Smart Computing and Communications (ICSCC). Piscataway (NJ): IEEE. p. 1–4.

Tao Q, Bryant SL. 2014. Well permeability estimation and CO_2 leakage rates. Int J Greenh Gas Control. 22:77–87. doi:10.1016/j.ijggc.2013.12.013

[DOE] U.S. Department of Energy. 2014. FE/NETL CO_2 saline storage cost model: model description and baseline results. Report No. DOE/NETL-2014/1659. Pittsburgh (PA): U.S. Department of Energy, National Energy Technology Laboratory.

[EPA] U.S. Environmental Protection Agency. 2021b. 2019 emissions and generation resource integrated database (eGRID 2019) [Internet]. Washington (DC): U.S. Environmental Protection Agency. [accessed 2026 Jan 15]. https://www.epa.gov/egrid.

[EPA] U.S. Environmental Protection Agency. 2021a. 2019 greenhouse gas emissions for large facilities [Internet]. Washington (DC): U.S. Environmental Protection Agency, FLIGHT Program. [accessed 2026 Jan 15]. https://ghgdata.epa.gov/ghgp/main.do.

[EPA] U.S. Environmental Protection Agency. 2013. Geologic sequestration of carbon dioxide—underground injection control (UIC) program Class VI well area of review evaluation and corrective action guide [Internet]. Washington (DC): U.S. Environmental Protection Agency, Office of Water. [accessed 2026 Jan 15]. https://www.epa.gov/sites/default/files/2015-07/documents/epa816r13006.pdf.

[USGS] U.S. Geological Survey. 2024. Quaternary fault and fold database for the United States [Internet]. Reston (VA): U.S. Geological Survey. [accessed 2026 Jan 8]. https://www.usgs.gov/programs/earthquake-hazards/faults.

Vasylkivska V, Dilmore R, Lackey G, Zhang Y, King S, Bacon D, Chen B, Mansoor K, Harp D. 2021. NRAP-open-IAM: a flexible open-source integrated-assessment-model for geologic carbon storage risk assessment and management. Environ Model Softw. 143:105114. doi:10.1016/j.envsoft.2021.105114

Wold S, Esbensen K, Geladi P. 1987. Principal component analysis. Chemometr Intell Lab Syst. 2(1–3):37–52. doi:10.1016/0169-7439(87)80084-9

Xiao T, Chen T, Ma Z, Tian H, Meguerdijian S, Chen B, Pawar R, Huang L, Xu T, Cather M, et al. 2024. A review of risk and uncertainty assessment for geologic carbon storage. Renew Sustain Energy Rev. 189:113945. doi:10.1016/j.rser.2023.113945

Xu J, Li Z, Du B, Zhang M, Liu J. 2020. Reluplex made more practical: leaky ReLU. In: 2020 IEEE Symposium on Computers and Communications (ISCC). Piscataway (NJ): IEEE. p. 1–7.

Zhang T, Zhang W, Yang R, Liu Y, Jafari M. 2021. CO_2 capture and storage monitoring based on remote sensing techniques: a review. J Clean Prod. 281:124409. doi:10.1016/j.jclepro.2020.124409

Zimmerman RW. 1990. Compressibility of sandstones. Amsterdam (Netherlands): Elsevier.

Carbon Solutions' Contributions

Carbon Solutions primarily supported work on the California Focused Project by applying its SimCCS^{PRO} toolset to support the following tasks:

- Task 6 – Field Project Assessment
- Task 9 – Forward Looking Scenarios

To begin with, Carbon Solutions identified all sources of CO_2 around the proposed project field site at buffer ranges from 20 km to 50 km with one additional buffer of 65 km considered. In the 20 km buffer there are 18 unique facilities from five different industrial sectors with total annual capturable emissions of 4.89 $MtCO_2$. When going from the 50 km buffer to the 65 km buffer adds an additional 15 facilities with 1.26 $MtCO_2$/yr in capturable CO_2 emissions.

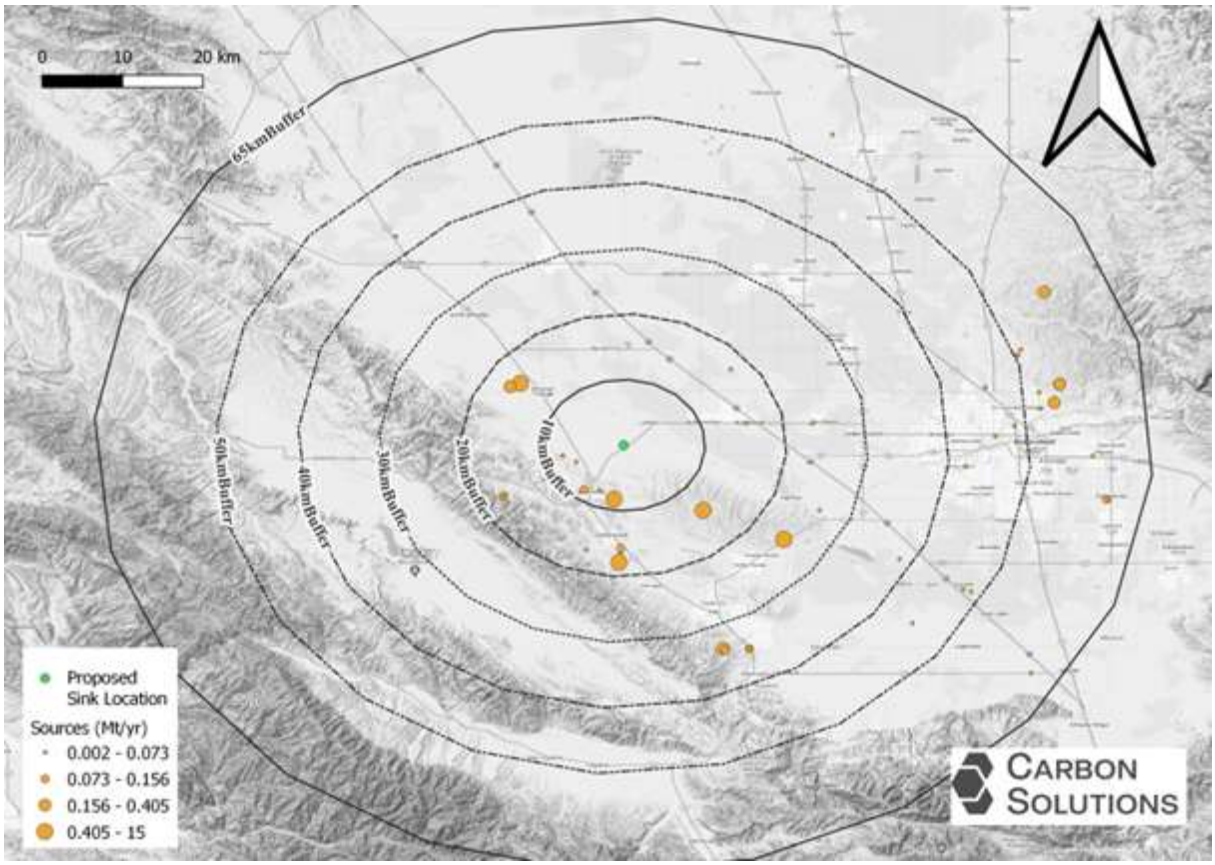


Figure 336. **Figure 337** Geospatial location and capturable emissions for sources of CO_2 within various buffer ranges around the proposed field project site

A total of 12 SimCCS^{PRO} scenarios were run around the field project site, with the first set of scenarios (6) using the "constrained" SCO_2T^{PRO} defined storage potential at the field project site and the second set of scenarios (6) using an "unconstrained" storage potential that will enable the capture of all emissions. Sets of scenarios are further divided by sources within buffer ranges to determine annual capturable CO_2 emissions.

The first scenario of each set at the field project site only captures CO_2 emissions from steam generators. There is sufficient capacity regardless of using constrained or unconstrained storage potential to capture all emissions from steam generators around the proposed field project site. The resulting CCS network features 44 km of CO_2 transport pipelines with a total unit cost of \$77.48/tCO_2 (Figure 358).

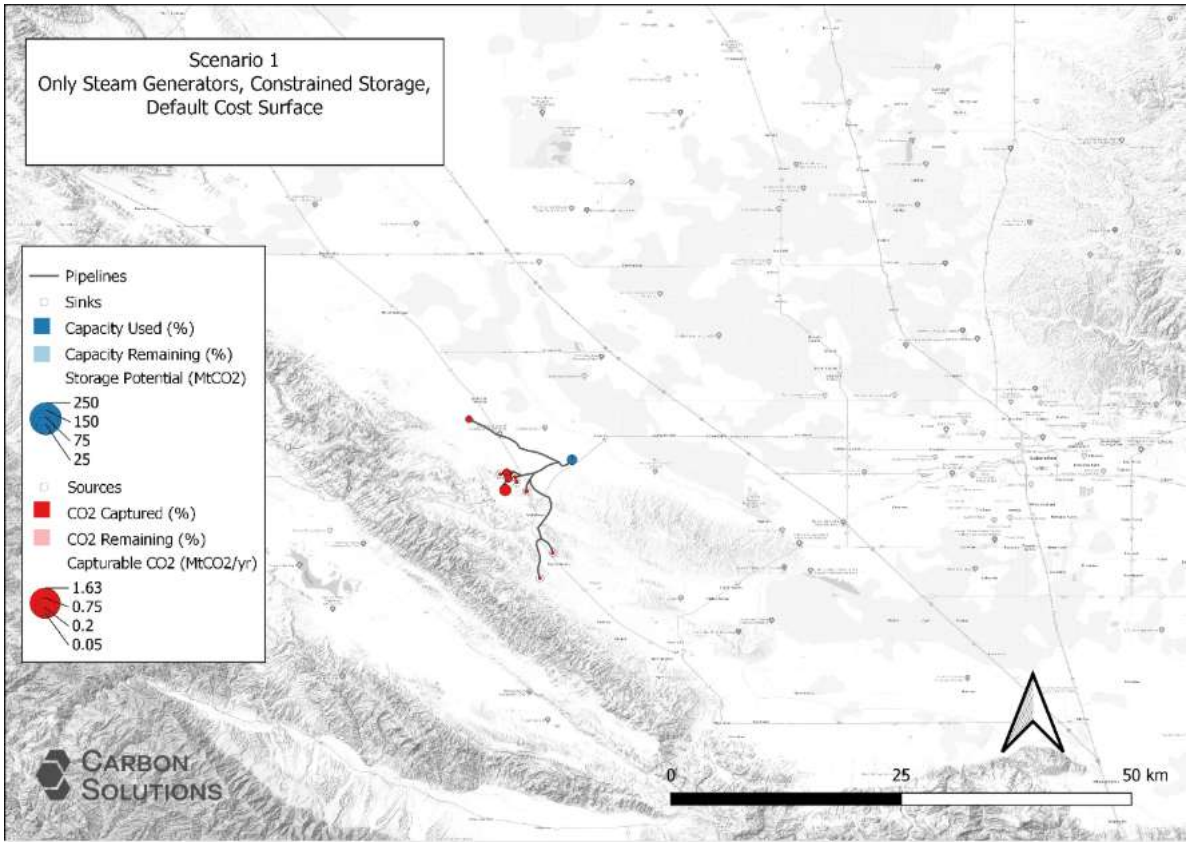


Figure 338 SimCCS^{PRO} CCS results network when using SCO$_2$T^{PRO} defined storage potential and capturing only from steam generators

When using the SCO$_2$T^{PRO} defined storage potential there is sufficient storage potential to capture approximately 0.79 MtCO$_2$/yr for 30 years. This results in CO$_2$ only being captured from the Elk Hills Power project for all constrained storage potential scenarios except for the first one which only captures from steam generators (Figure 359).

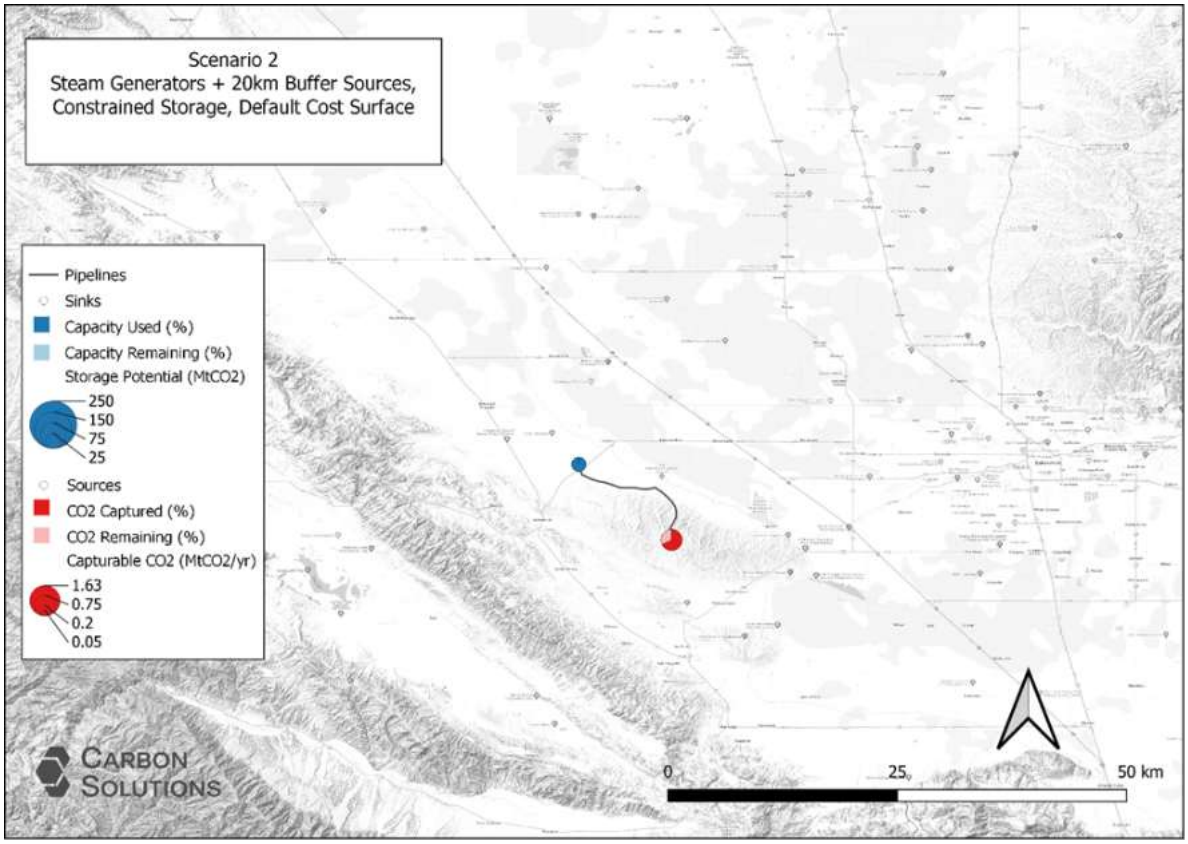


Figure 339 Deployed SimCCS^{PRO} results network when using SCO$_2$T^{PRO} defined storage potential. Due to the storage limitations all scenarios using the SCO$_2$T^{PRO} defined storage potential are the same as this one shown here

For the second set of scenarios using "unconstrained" storage potential, networks differ depending on the annual capture target. For example, Figure 360 shows what a CCS network would look like around the field project site if CO_2 is captured from all available sources within the 65 km buffer. This network features approximately 509 km of CO_2 transport pipeline with a total unit cost of almost \$81/tCO_2 and captures 8.83 MtCO_2/yr. This represents an almost \$3/tCO_2 increase in total CCS network costs when going from the 50 km buffer of sources to the 65 km buffer. Nevertheless, total CCS network unit costs range from \$74/tCO_2 - \$81/tCO_2 across all 12 scenarios Carbon Solutions modeled.

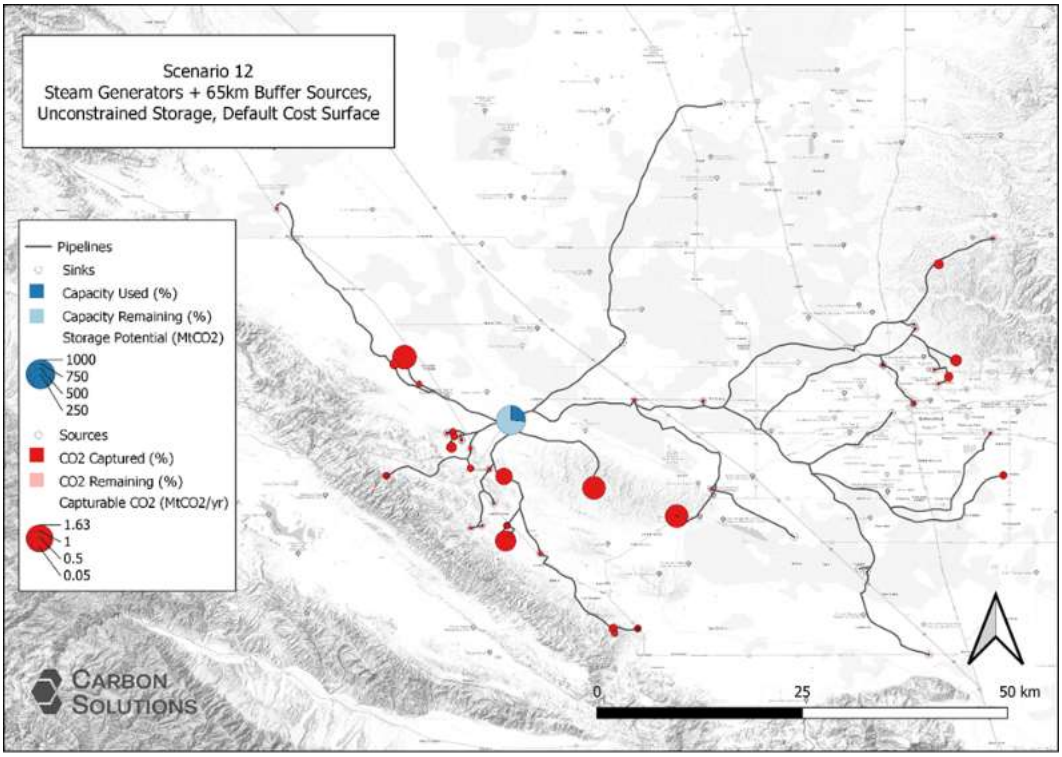


Figure 340 Deployed SimCCS^{PRO} results network when using unconstrained storage potential and capturing from all sources in the 65 km buffer

Carbon Solutions also ran four forward looking scenarios to evaluate hub or distributed storage as a foundation for future CCS networks in California. Ultimately, these scenarios indicated that regardless of what sources are being used, CCS networks that use distributed storage are always less expensive than the corresponding CCS networks that use hub storage. For example, when capturing CO_2 from all sources in California, the distributed storage CCS network has a total cost of \$102/tCO_2 while the hub storage CCS network has a total cost of \$109/tCO_2. There are notable differences in amounts of pipeline deployed with hub storage adding almost 1,800 km of additional CO_2 pipeline deployment (see Table 2 on page 42).

Feasibility Study on a Potential CCUS Project in Colorado: CO_2 Capture from a Refinery and Sequestration in the DJ Basin

This study evaluates the feasibility of storing over 50 million metric tons of CO_2 within a 30-yr period in southern Colorado. The target for injection is the 7,000 ft (2,134 m)-deep Lyons saline aquifer formation, with the overlying alternating layers of anhydrite and shale serving as seals. Geological static models were constructed using seismic, well log and core data, followed by fluid flow modeling to understand the CO_2 injection strategy, saturation distribution and plume size. The results indicate that approximately 60 million metric tons of CO_2 can be injected with 2 wells into the formation over 30 yr, with 85% of the CO_2 existing in a supercritical phase during the injection stage. After 70 yr of shut-in, about 30% of the injected CO_2 becomes immobilized due to hysteresis. Seismic data shows no faulting within the injection and seal formations, and no

legacy wells penetrate the Lyons formation within the study area, which reduces the risks of fault slippage and leakage through legacy wells. However, the small dip angle of the structure may present challenges to CO_2 plume containment, highlighting the importance of implementing strategies such as enhanced monitoring systems, detailed geomechanical modeling, and plume migration simulations to mitigate and better understand potential risks. This study offers early insights into CCUS potential in southern Colorado using seismic and limited data, and will ultimately provide valuable guidance for future implementation of CO_2 injection in the region.

Introduction

Carbon Capture, Utilization, and Storage (CCUS) has emerged as a pivotal technology in the global effort to mitigate climate change by reducing CO_2 emissions from industrial sources. As the world seeks to transition to a low-carbon economy, CCUS offers a pathway to capture CO_2 before it reaches the atmosphere, either repurposing it for industrial applications or permanently storing it underground (e.g., Metz et al. 2005; Lal 2008; Orr 2018). Geological CO_2 sequestration (GCS), a key component of CCUS, involves the long-term storage of captured CO_2 in deep subsurface formations. This method is particularly promising due to its potential to store large quantities of CO_2 securely and sustainably, thereby playing a critical role in achieving net-zero emissions targets (e.g., Page et al. 2020; McCulloch 2021).

Deep saline aquifers—also known as deep saline formations—are porous rock units saturated with non-potable brine and are considered optimal reservoirs for geological CO_2 storage due to their vast capacity and widespread availability (SPE 2017; Page et al. 2020). The sequestration process involves injecting CO_2 into these deep underground formations, where it is stored through various mechanisms (Metz et al. 2005), including structural and stratigraphic trapping by impermeable cap rocks, residual trapping in pore spaces, solubility trapping as CO_2 dissolves into saline water, and mineral trapping where CO_2 reacts with minerals to form stable carbonates. However, effective deployment of large-scale CO_2 storage also requires careful evaluation of potential risks—such as leakage through faults or legacy wells, pressure-induced fault reactivation, and long-term monitoring challenges. These factors can significantly influence storage integrity, regulatory approval (e.g., Class VI permitting), and public confidence. Therefore, in addition to evaluating storage capacity and plume behavior, this study also assesses site-specific containment risks and monitoring feasibility using geologic, geophysical, and reservoir simulation data. The focus on a southern Colorado site offers new insights into the viability of CO_2 sequestration in this underexplored region.

Globally, several commercial CCUS projects have been successfully implemented, demonstrating the viability of this technology at scale. Notable examples include the Sleipner project in Norway, which has been operated since 1996 (e.g., Chadwick et al. 2004, 2010), the Quest project in Canada, operated by Shell since 2015 (e.g., Duong et al. 2019; Brown et al. 2023), and the Gorgon project in Australia, led by Chevron since 2019 (e.g., Trupp et al. 2021; Quinn 2022). In the United States, several large-scale projects are underway, many as part of the DOE Carbon Storage Assurance Facility Enterprise (CarbonSAFE) program, further contributing to the growing momentum of CCUS deployment (Sullivan et al. 2020; DOE 2024). These projects require the storage of over 50 million metric tons of CO_2 over a 30-yr period. Examples include the storage of 3.2 million metric tons of CO_2 annually in central North Dakota (Peck et al. 2019), the sequestration of 6 to 7 million metric tons of CO_2 yearly in northwest New Mexico

over 30 yr (Ampomah et al. 2022), and the accelerated deployment of CCUS at coal-based power plants with CO_2 storage in Wyoming's Powder River Basin (McLaughlin et al. 2019). Based on the analysis of Young et al. (2007) and Ning et al. (2025), Colorado is a state with significant potential for geological CO_2 sequestration.

The goal of this study is to assess the feasibility of storing CO_2 in a deep saline aquifer of southern Colorado and to lay the groundwork for future commercial-scale CCUS projects. In alignment with the DOE's commercial-scale CCUS project requirements, the study aims to explore the potential to sequester more than 50 million metric tons of CO_2 over 30 yr. To achieve this, the geological properties of the Lyons saline aquifer and its overlying confining units are first characterized, followed by dynamic reservoir simulations to evaluate plume migration, pressure buildup, and CO_2 phase behavior. In addition to assessing storage capacity, this study also evaluates key containment risks, including legacy well integrity, fault reactivation potential, and the feasibility of seismic monitoring, based on available geological and geophysical data. These considerations are critical for site selection, permitting, and the design of long-term monitoring strategies in future CCUS applications.

Study Area

Colorado hosts numerous industrial facilities and is underlain by extensive geologic formations with significant potential for CO_2 storage (Figure 341). In 2021, Colorado emitted a total of 85.4 million metric tons of CO_2, representing 1.7% of the total U.S. emissions (EIA 2024). In response to escalating climate concerns, Colorado aims for a 50% reduction in greenhouse gas emissions by 2030 and achieving net-zero emissions by 2050 compared to its 2005 levels, positioning CCUS as a critical strategy in meeting these goals (Colorado Energy Office 2024).

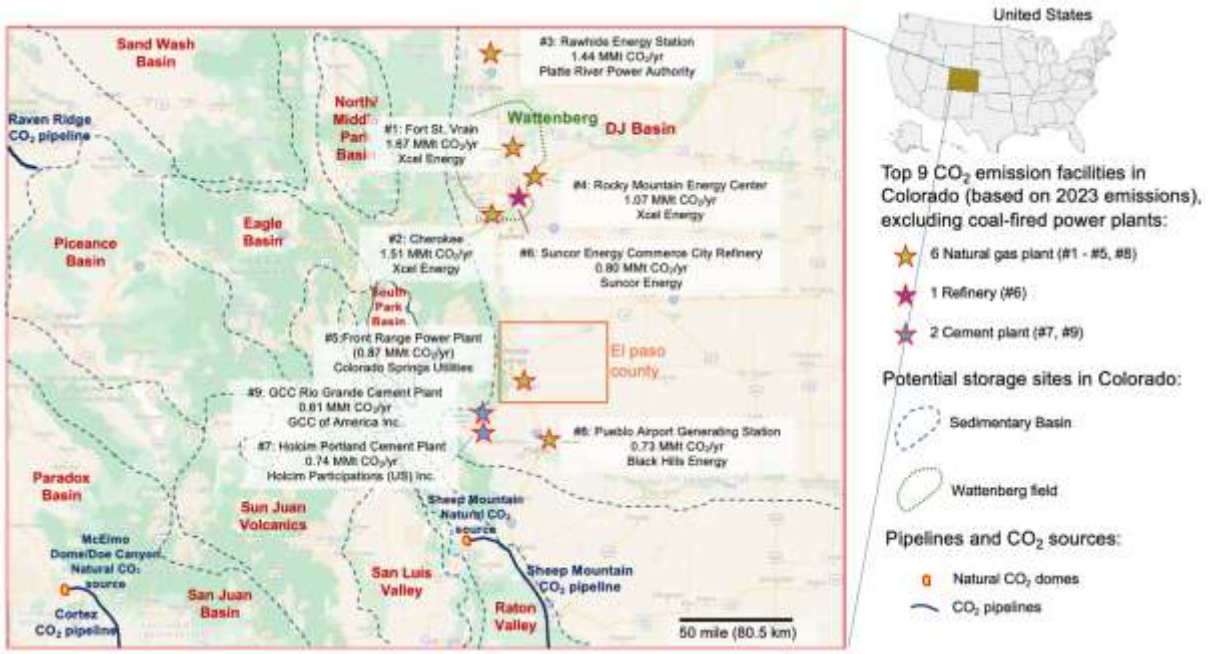


Figure 341 The leading CO_2 emission facilities, potential storage basins, and CO_2 pipelines in Colorado. Coal-fired power plants are excluded as they are scheduled for retirement by 2034.

Deep saline formations that have been identified as potential CO_2 storage units in Colorado include the Fountain, Weber, Morrison, Entrada, Lyons, and Dakota formations, which are distributed across several basins, including the DJ, Piceance, San Juan, and Sand Wash Basins, in the state (Figure 341). Assuming a storage efficiency factor of 1%, the total estimated storage resource for deep saline aquifers in Colorado is approximately 152 billion metric tons (Young et al. 2007). Notably, the Lyons formation in southern Colorado is estimated to have a storage resource of 876 million metric tons, making it a prime candidate for the target injection zone in this study. Our study area focuses on a 50-square-mile (130-square-km) area in southern Colorado, located in El Paso County (Figure 341), where several large emission facilities are situated nearby.

Stratigraphic Column of DJ Basin

The area for this study is located on the west edge of the DJ Basin, which is highly asymmetric and serves as Colorado's principal oil and gas producing region, accounting for 80% of the state's crude oil output. Bounded by the Front Range thrusts to the west and gradually shallowing towards the east, the basin's axis extends north to south parallel to the Front Range (Figure 342). Predominantly, the Cretaceous rock layers, including the Niobrara, Codell, and Dakota formations, are concentrated in the Wattenberg field just north of Denver and are key to the majority of the basin's hydrocarbon production.

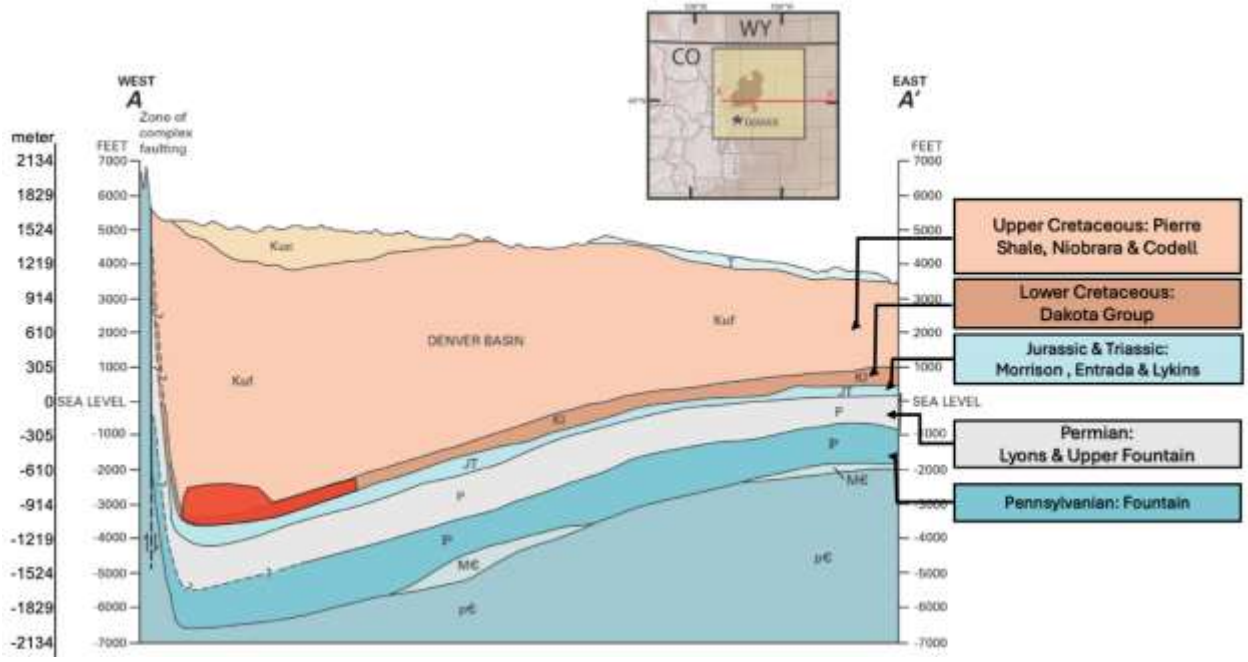


Figure 342 The stratigraphic column of the DJ Basin west (modified from Nelson and Santus [2011] and Young et al. [2007]) following the West-east cross-section A–A'. This section intersects the southwest portion of the Wattenberg gas field. The red-shaded area indicates the approximate location of gas accumulation in the Codell-Niobrara and Dakota intervals.

Several studies have explored the potential for carbon sequestration in the DJ Basin, evaluating formations like Lyons and Fountain as possible deep saline aquifers for carbon storage (e.g., Young et al. 2007; Drake et al. 2014). While the Fountain Formation has been identified as a

potential CO_2 storage unit at the state level, in the specific study area it transitions from a favorable outcrop sandstone to a tighter, less permeable limestone toward the east, suggesting limited suitability for storage at this location. Consequently, this study concentrates on assessing the Permian Lyons Sandstone's suitability for CO_2 injection, particularly within the southwestern part of the basin, or El Paso County in Colorado. Notably, the eastern sections of the Lyons formation are active oil-producing zones; however, these do not overlap with our targeted western region designated for CO_2 storage. The Lyons sandstone is primarily composed of quartz and feldspar, with depths ranging from approximately 2,000 ft (610 m) in the east to 10,000 ft (3,048 m) at the basin's axis (Garbarini and Veal 1968). The formation exhibits a porosity range of 4.4% to 26.1% and permeability between 0.1 and 88 millidarcies (mD; Levandowski et al. 1973). It is widely distributed across the DJ Basin, with thicknesses varying from less than 25 ft (8 m) to over 250 ft (76 m; Sonnenberg et al. 2024).

Static Modeling Construction from Post-Stack Seismic

Property Distribution

To model CO_2 injection accurately, the structural surfaces extracted from the seismic data must be populated with the physical properties of the deep saline aquifer, specifically porosity and permeability. These properties are crucial as porosity has a direct relationship with acoustic impedance, whereas permeability can be exponentially correlated to porosity within a formation. Figure 343 shows the seal and formation in the study area. The saline aquifer, between 7,316 ft (2,230 m) and 7,448 ft (2,270 m), is indicated by the interval with minimal separation between porosity (POR) and density log (RHOB), indicating a clean formation. The variance maps on the right side of Figure 343, derived from post-stack seismic data, indicate no faulting in either the upper or lower anhydrite layers. Seismic variance is a discontinuity attribute that highlights changes in reflection amplitude and continuity; high variance values typically indicate structural features such as faults or fractures, whereas low variance values reflect continuous, undisturbed strata.

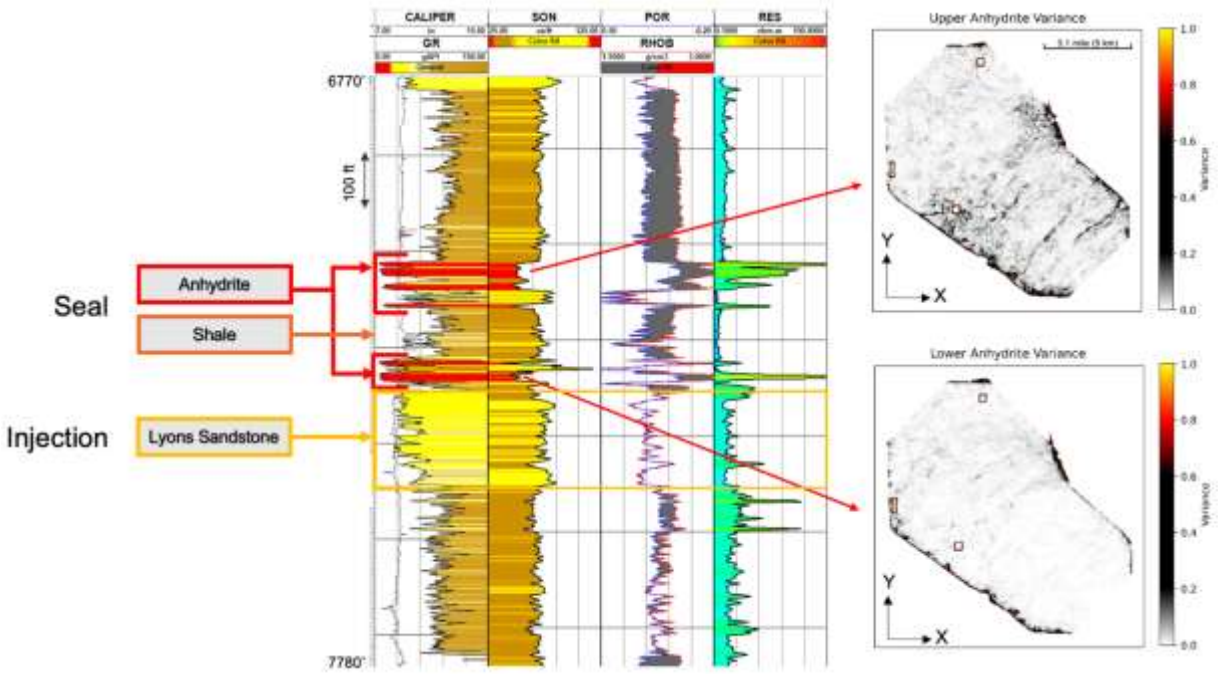


Figure 343 Gamma ray (GR), caliper (CALIPER), sonic (SON), density (RHOB), porosity (POR), and resistivity (RES) logs through the saline aquifer, over burden, and under burden formations. Depth is shown in ft. GR, CALIPER, and SON logs are color-coded by lithology as interpreted from the logs: red for anhydrite, yellow for sandstone, and brown for shales. POR (blue) and RHOB (red) are plotted together, with gray shading between them. Variance attribute for Anhydrite is derived from post-stack seismic volumes and shown on right.

The static model building process begins with the calculation of acoustic impedance for the seismic volume through a post-stack seismic inversion. This model-based inversion involves building a low-frequency initial (background) model from seismic horizons and well data, which correlates to the seismic horizons within the volume. Acoustic impedance from the well is propagated throughout the seismic volume, using multiple horizons as guides. The statistically estimated wavelet in the inversion zone and the initial model is then used to generate acoustic impedances and synthetic seismic data, which is compared to the original seismic data (Herman 2024). The inversion process iteratively updates the acoustic impedances in order to minimize the residual differences between the synthetic and field data, leading to the final acoustic impedance model.

This inverted acoustic impedance model is then correlated to porosity and lithology using well-log information. Two wells were utilized in this study: Well A, penetrating the Lyons formation but located 30 miles (48.3 km) outside the 3D seismic area, and Well B, situated within the 3D seismic but lacking the depth necessary to provide properties of the Lyons formation. The P-impedance vs porosity cross-plot from Well A for the Lyons formation shown in Figure 344. In this particular case, since there is no fluid change, no pressure change, and no facies change, the seismic impedance is mostly impacted by porosity changes. Using this linear relationship, the P-impedance obtained from the post-stack seismic inversion is transformed into porosity. The average porosity value was seen to be 13%. Subsequently, porosity was transformed into permeability using operator-derived empirical relationships and core testing, yielding an average horizontal permeability of 80 mD. Vertical permeability is lower than horizontal permeability, with a horizontal-to-vertical ratio of 17:1, as indicated by core measurements.

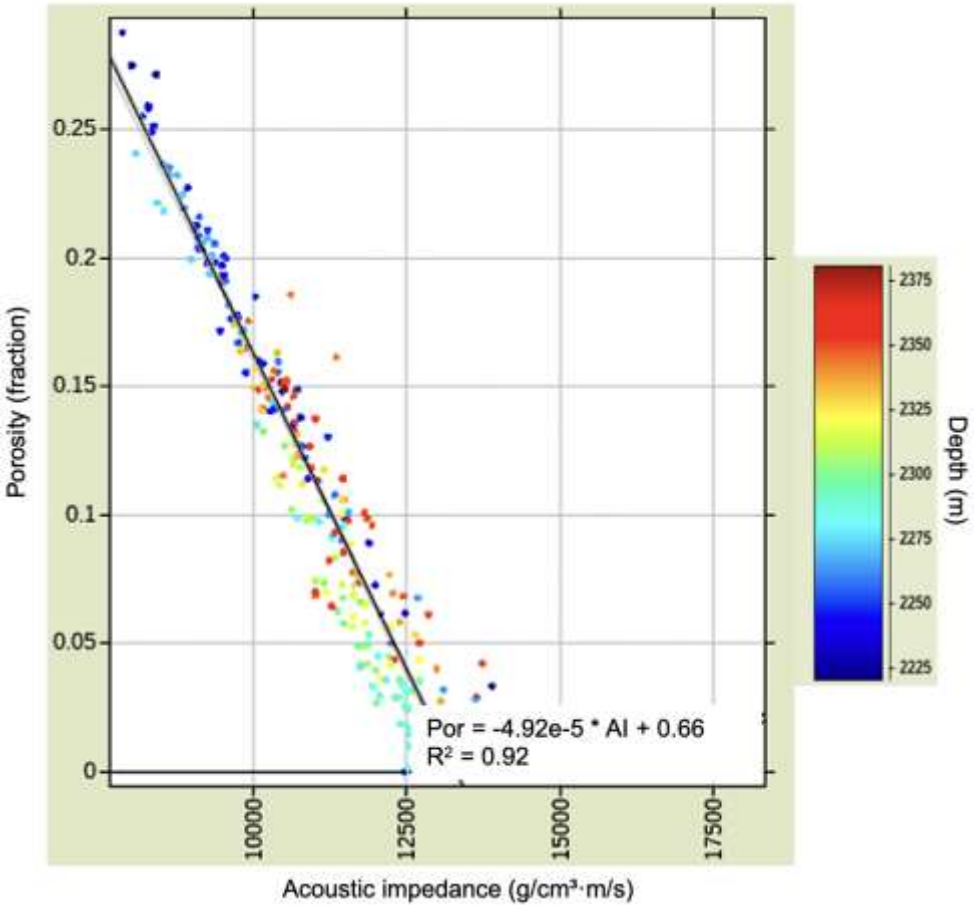


Figure 344 Cross-plot of P-impedance with porosity in Lyons formation from well log. Color Scale is depth (m). A linear trend is used to calculate porosity values from P-impedance inversion values.

Static Model Construction

The static geological model was constructed using four key seismic horizons: the top of the Lyons Formation, the top and bottom of the saline aquifer interval, and the top of the Fountain Formation. These horizons define a model framework composed of 15 layers, which were selected to adequately represent the vertical heterogeneity of the geologic units. The horizontal grid consists of 132 × 138 cells, covering the area of interest with approximately one-quarter million total grid blocks. Each grid cell has a horizontal resolution of approximately 330 ft (100 m), and vertical thicknesses ranging from 10 ft (3 m) to 25 ft (8 m), depending on the local stratigraphy.

Seismic-to-depth conversion was performed using calibrated interval velocities and time-depth relationships derived from Well A, which lies approximately 30 miles outside the 3D seismic area. These relationships were used to tie the interpreted seismic horizons to depth and to convert post-stack seismic inversion results from time to depth domain. Porosity and permeability values were estimated by correlating acoustic impedance from the inversion volume with well log data and core-derived empirical relationships. Specifically, porosity was estimated using a linear relationship with P-impedance from Well A, and permeability was derived using a porosity-permeability transform calibrated to core data.

Each grid cell was populated with porosity, horizontal permeability, and vertical permeability values, with a horizontal-to-vertical permeability ratio of 17:1 based on core analysis. The resulting static model was then exported to the dynamic simulator for fluid flow analysis.

This static model is based on a single well (Well A) located outside the seismic volume, and Well B within the seismic survey does not reach the Lyons Formation. Therefore, key petrophysical properties such as porosity and permeability rely on extrapolation from an analog location. Additionally, the model is derived from post-stack seismic inversion, which has inherent resolution and vertical smearing limitations. These factors introduce uncertainty into the property distribution, particularly in the absence of local well control and core validation. The current model should be viewed as a first-order approximation to support feasibility assessment. Future site-specific characterization, including a stratigraphic test well, will be critical for model refinement and validation.

Fluid Flow Modeling

Fluid Model Setup

CO_2 injection modeling within the saline aquifers was conducted using the reservoir simulation software CMG-GEM. The static model served as the input, with fluid-related parameters incorporated to estimate the CO_2 saturation distribution and pressure change within the reservoir. A closed boundary condition was used to represent a conservative pressure buildup scenario, given the absence of reliable data on lateral pressure communication.

The Lyons Formation, situated at a depth of approximately 7,000 ft (2,134 m), has an aquifer thickness of 150 ft (46 m), with a temperature of 161°F (71.1 °C) and a pressure of 1,800 psi (12.4 MPa). This reservoir pressure was determined from Drill Stem Test (DST) data using shut-in pressure measurements. These reservoir conditions allow the injected CO_2 to exist in a supercritical state. According to EPA guidelines, the injection pressure cannot exceed 90% of the fracture pressure of the injection zone (EPA 2008), which places the maximum allowable injection pressure in the study area at 3,400 psi (23.4 MPa). The fracture gradient was calculated using poroelastic equations based on mechanical rock properties derived from compressional and shear sonic logs, along with density log data.

Lyons formation is naturally underpressured (0.26 psi/ft pressure gradient), which offers a substantial pressure buffer that enhances injectivity and allows for large-volume storage before approaching geomechanical limits. The low formation pressure permits high CO_2 injection rates at relatively modest wellhead pressures, with reduced risk of exceeding fracture pressure or compromising caprock integrity. Moreover, the presence of long-standing underpressure often implies an effective, intact sealing unit that has prevented fluid equilibration over geologic time, enhancing storage security (Neuzil 1995). Importantly, the low baseline stress state reduces the likelihood of fault reactivation or induced seismicity during injection. Together, these characteristics make naturally underpressured saline aquifers compelling targets for CO_2 sequestration, though careful site-specific characterization is essential to quantify plume behavior and long-term containment.

The simulation was conducted in two phases: a 30-yr injection period followed by a 70-yr shut-in period. During the injection phase, two vertical wells were used, each injecting at a rate of 1.2

million metric tons of CO_2 annually. The injectors were strategically placed at the northern and southern sites of the study area to mitigate localized pressure buildup (Figure 345). As Layers 3-10 are the aquifer layers, the perforations for both injectors are set at Layer 10 to model the upward migration of the CO_2 plume.

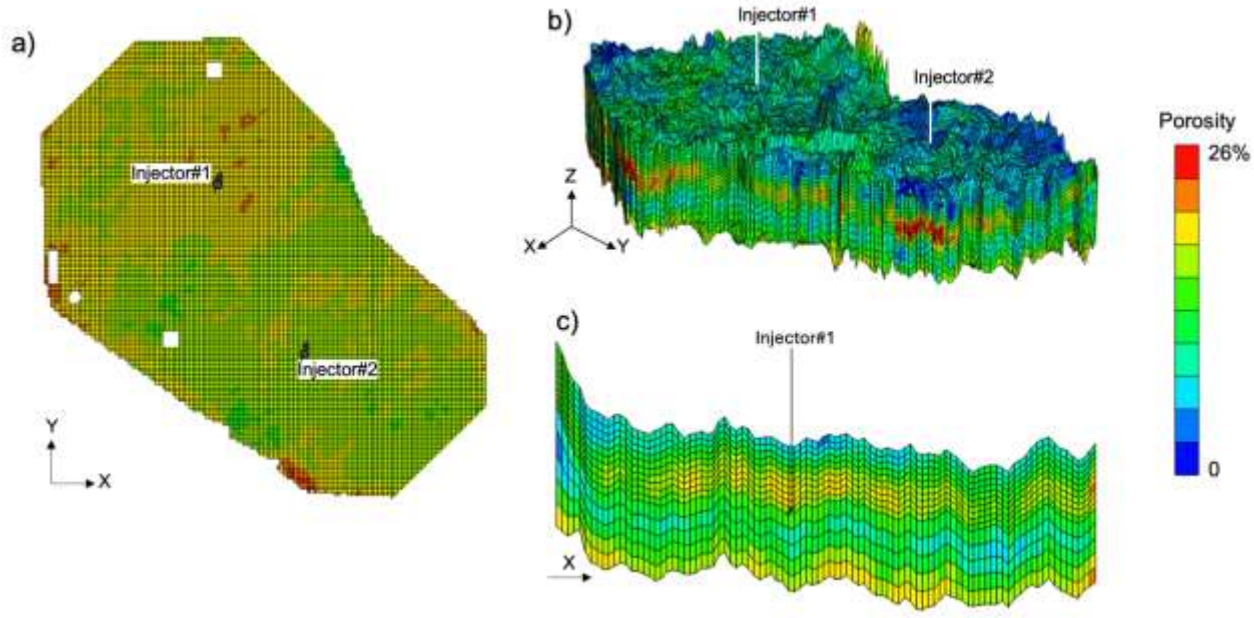


Figure 345 a) Top view of the study area, where warmer colors indicate higher porosity. The northern site exhibits relatively higher porosity compared to the southern side. Two injection wells are positioned at the northern and southern parts of the study area; b) a 3D view of the reservoir model with vertical exaggeration by a factor of 56; c) a side view of the model, showing 15 vertical layers. There is no structural trapping in this study due to the low dip angle of about 1%.

When CO_2 is injected into a deep saline aquifer formation, four primary trapping mechanisms are typically considered: structural trapping, mineral trapping, solubility trapping, and residual trapping. In this study, the first two mechanisms are neglected because there is no structural trap present in the study area (Figure 345), and the Lyons formation consists of over 95% quartz, which does not react with CO_2 under normal conditions. The latter two mechanisms, however, are considered. Solubility trapping involves the dissolution of CO_2 in water, forming aqueous ions such as HCO_3^- and CO_3^{2-}. Residual trapping occurs due to hysteresis; after CO_2 injection ceases, CO_2 at the leading edge of the plume continues to displace water through a drainage process, while water displaces CO_2 in an imbibition process at the trailing edge. This imbibition process leads to the trapping of CO_2. To account for this, the study modifies the relative permeability curves to simulate the hysteresis effect, resulting in the immobilization of a residual CO_2 trail behind the plume.

CO_2 Saturation Distribution

The CO_2 saturation distribution across various layers at Year 30 and Year 100 of CO_2 injection is illustrated in Figure 346. CO_2 is injected through Layer 10, and the lateral and upward migration of the CO_2 plume can be observed. Notably, the plume sizes in the shallower layers (e.g., Layer 1) are larger compared to deeper layers (e.g., Figure 346a vs. Figure 346c). When comparing the

two injectors, Injector#1 exhibits a larger plume size in Layer 1 (4-mile diameter for Injector#1 vs. 2.5-mile diameter for Injector#2), whereas in Layer 10, Injector#2 shows a larger plume size (1.8-mile diameter for Injector#2 vs. 1.5-mile diameter for Injector#1) (Figure 346a vs. Figure 346c). This difference is likely due to the higher porosity and permeability in the northern area compared to the south, resulting in faster CO_2 upward migration in the northern well, Injector#1. Additionally, when comparing the CO_2 plume size at Year 100 with that at Year 30, it is evident that CO_2 continues to migrate upward, resulting in a larger plume size and higher CO_2 saturation in the top layer over time (Figure 346a vs. Figure 346d). Note that the maximum simulated CO_2 saturation is approximately 0.6, reflecting moderate injectivity and upward migration in a formation with limited vertical permeability and conservative trapping assumptions, which could result in broader lateral plume distribution, slower CO_2 accumulation, and reduced localized peak saturation.

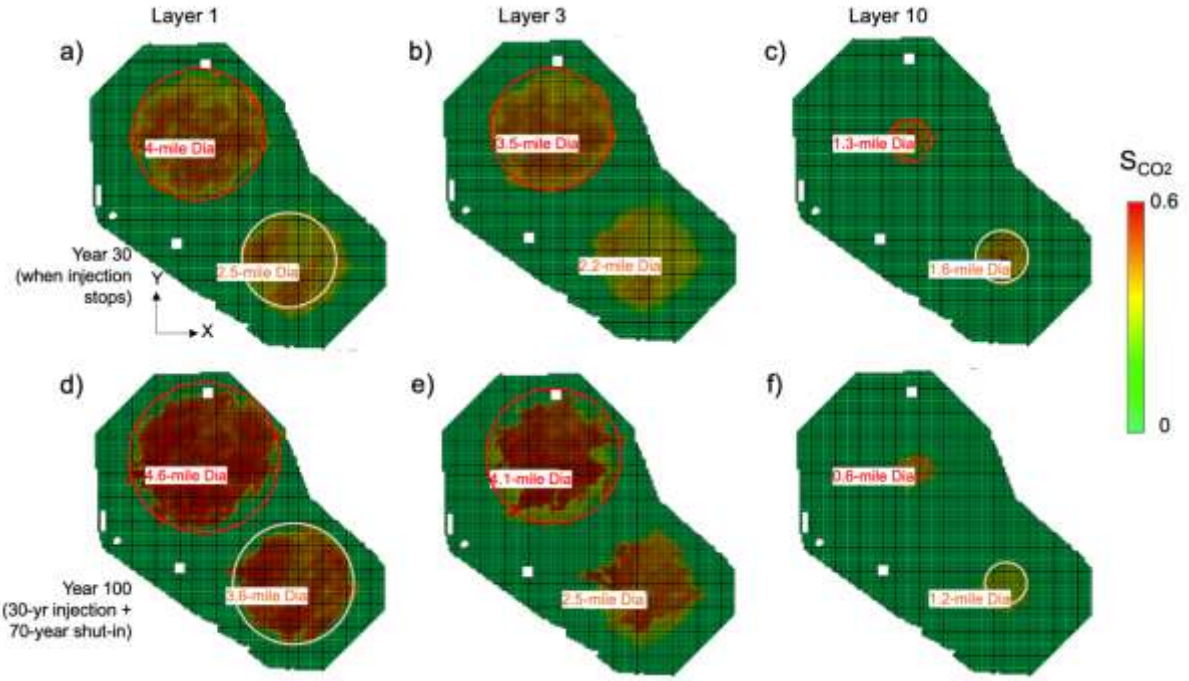


Figure 346 CO_2 saturation distribution across various layers at Year 30 and Year 100. a-c) represent the CO_2 saturation at Year 30 (end of injection), while d-f) present the saturation at Year 100 (after a 70-yr shut-in). CO_2 was injected through Layer 10, leading to significant lateral and upward migration. The color scale represents CO_2 saturation, with warm color indicating higher saturation levels. The observed plume geometry reflects the influence of the closed boundary condition, which limits lateral migration and results in more confined plume shapes.

CO_2 Component Inventory

In addition to estimating the CO_2 plume, it is crucial to evaluate the distribution of injected CO_2 among its various phases. The phase distribution of injected CO_2 was modeled using the compositional simulator CMG-GEM, which applies an equation-of-state (EOS) approach to simulate multiphase fluid behavior. The simulator distinguishes between supercritical and dissolved CO_2 based on local pressure and temperature conditions. Supercritical CO_2 is tracked as a separate phase, while solubility trapping is modeled through CO_2 dissolution into brine. Residual trapping is incorporated by applying hysteresis to the relative permeability curves,

allowing for the immobilization of CO_2 following injection. The simulator outputs mass distributions of each phase over time, enabling quantification of mobile, dissolved, and immobilized CO_2.

Figure 347a) illustrates the CO_2 inventory over the 30-yr injection period, showing that approximately 85% of the injected CO_2 exists in a supercritical phase, while the remaining portion is dissolved in water. Figure 347b) depicts the amount of immobile CO_2 that becomes trapped due to hysteresis, occurring only during the shut-in period. It reveals that 18 out of the 60 million metric tons of total injected CO_2, or 30%, becomes immobile, while the remaining CO_2 pools beneath a low-dip seal. The low dip angle in this study area (as shown in Figure 345) may reduce the effectiveness of structural trapping, making lateral plume migration more likely. While this does not imply an immediate risk of leakage, it underscores the importance of incorporating monitoring strategies and further geomechanical analysis to ensure long-term containment.

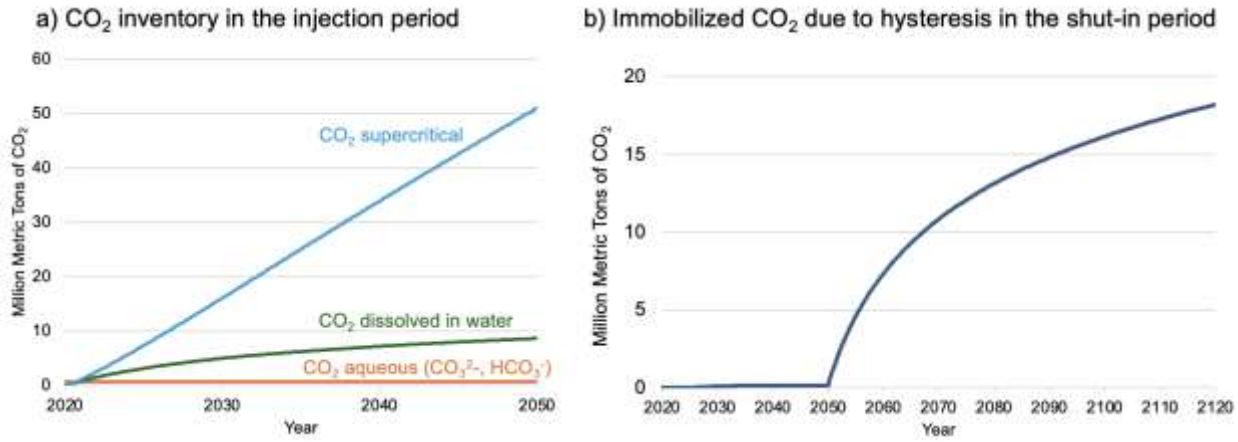


Figure 347 Distribution of injected CO_2 among different phases over time. a) shows the CO_2 inventory during the 30-yr injection period, with approximately 85% of the injected CO_2 existing in a supercritical phase and the remaining CO_2 dissolved in water; b) illustrates the immobile CO_2 trapped due to hysteresis during the shut-in period, where around 18 million metric tons of the total injected CO_2 becomes immobile. The low dip angle of the study area suggests a potential for lateral CO_2 migration, increasing the risk of plume containment.

CO_2 Pressure Distribution

Understanding pressure distribution during and after CO_2 injection is critical for evaluating reservoir integrity and containment performance. Given the closed-boundary condition used in this study, pressure buildup is expected to be conservative, with limited lateral pressure dissipation. Figure 348a) illustrates the simulated pressure distribution in Layer 3 at Year 30, immediately after injection ends, while Figure 348b) shows the pressure evolution over a 100-yr period at the grid cell corresponding to Injector #1. At the end of injection, the maximum pressure at this location reaches approximately 21 MPa (3,046 psi), remaining about 10% below the maximum allowable injection pressure of 3,400 psi. This peak pressure represents the conservative behavior imposed by the closed system model, as pressure dissipation into surrounding formations is not permitted. Following shut-in, reservoir pressure gradually declines due to equilibration within the system, stabilizing around 18.8 MPa (approximately 2,730 psi) after 100 yr. This trend suggests that, despite the lack of pressure relief boundaries, long-term

containment within the Lyons Formation remains within acceptable limits under the modeled scenario.

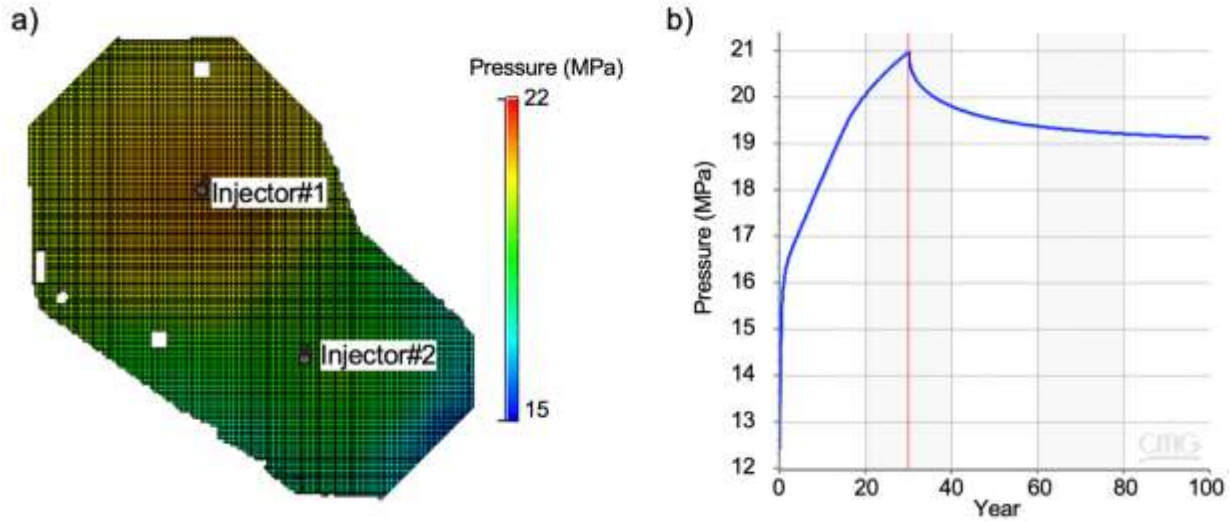


Figure 348 a) Pressure distribution in Layer 3 at Year 30, immediately after injection ends. b) Pressure changes over 100 yr near Injector #1. The maximum simulated pressure is approximately 21 MPa (3,046 psi), remaining approximately 10% below the maximum allowable injection pressure of 3,400 psi.

Risk Evaluation and Discussion

Confining System Evaluation

The Lyons Formation is overlain by the Lykins Formation, which serves as the *primary confining system* and is composed of alternating layers of anhydrite and shale (Young et al. 2007; Herman 2024). These sealing units are observed both in outcrop and in subsurface datasets across the basin and appear laterally continuous at the regional scale. In the study area, well log data (Figure 343) confirm the presence of multiple overlying seal intervals characterized by very low porosity, consistent with their role as effective vertical flow barriers.

The anhydrite beds, which dominate the seal, are associated with low gamma ray (GR), low sonic (SON), near-zero porosity (POR), high density (RHOB), and high resistivity (RES) responses—log signatures indicative of dense, non-permeable lithologies (Herman 2024). These anhydrite units are interbedded with shale layers that also exhibit low porosity, further enhancing the sealing effectiveness. The vertical thickness of the composite sealing interval is approximately 100 ft, providing a significant barrier to vertical CO_2 migration and contributing to capillary entry pressure.

In addition to petrophysical characteristics, structural integrity of the seal was assessed using variance attribute maps extracted from 3D seismic data (Figure 3, right panels). These maps reveal no evidence of faulting within the upper or lower anhydrite intervals, indicating that the confining system is structurally intact at seismic scale. Variance anomalies observed are interpreted as minor vertical heterogeneities, likely associated with depositional or diagenetic features, rather than through-going faults or fractures.

Based on the combination of well log data, stratigraphic thickness, and seismic variance analysis, the overburden above the Lyons Formation demonstrates the properties of an effective confining system. Each layer appears laterally continuous and shows no indication of transmissive features or structural discontinuities. Therefore, the risk of vertical leakage through the confining system is considered low within the study area.

Fault Confinement and Induced Seismicity Potential

Identifying faults in the study area is essential to evaluating both the potential for CO_2 migration through structural discontinuities and the risk of stress-induced fault reactivation. Seismic variance analysis across the stratigraphic column, from the Niobrara Formation to the basement, indicates that all identified seismic-scale faults are confined above the Dakota Formation (Figure 9). The Niobrara contains a well-developed system of décollement-style faults (Figure 9b), but fault frequency decreases with depth. No faults were identified that offset the Lyons Formation or its overlying confining units based on the resolution of the available seismic data.

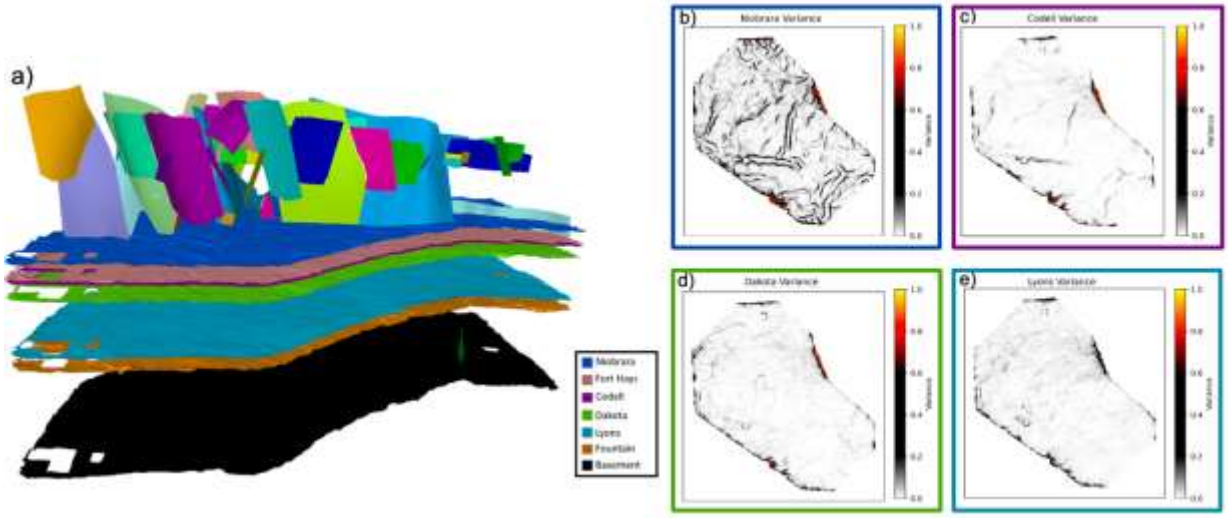


Figure 349 a) 3D view of faults in the 3D seismic survey. Horizon tops are labeled and color-coded. No faulting is observed between the top of the Dakota and the basement, except for the one fault (green-colored) in the basement shown in the bottom right; b-d) The variance map of various layers indicates that the fault system intersects with shallower formations, such as the Niobrara and Codell, while deeper formations show no evidence of faulting.

While no faults intersect the injection interval, the potential for pressure-induced fault activation must still be considered. While this indicates that fault activation or new fracturing is unlikely under the modeled conditions, it does not rule out the possibility that elevated pore pressures could reactivate undetected or basement-rooted faults under specific geological or operational scenarios. Notably, a sequence of induced seismic events associated with fluid injection into the Lyons Formation was reported in the northern DJ Basin (GWPC 2015), highlighting the need for site-specific stress evaluation. In contrast, our study area is located in the southern DJ Basin in the El Paso County, where the Precambrian basement lies at approximately 13,000 ft (4,000 m) depth. With the Lyons Formation situated at around 7,000 feet, this results in a vertical separation of about 6,000 ft from the basement—providing a substantial buffer from basement-rooted faults. Nevertheless, ongoing monitoring and further geomechanical analysis, including

data from a planned stratigraphic well, will be critical to fully assess the potential for fault activation under site-specific conditions.

Legacy Wells Leakage Risk

The primary risks associated with legacy wells arise from their potential to act as conduits for CO_2 migration out of the injection zone—either into underground sources of drinking water (USDWs), such as the Fox Hills and Arapahoe formations (approximately 600 ft or 183 m depth), or ultimately to the surface. These risks are not confined to wells within the immediate CO_2 plume, but may extend across the entire Area of Review (AoR), where elevated reservoir pressure can mobilize fluids along compromised wellbores.

The Denver-Julesburg (DJ) Basin contains thousands of legacy oil and gas wells, many of which were drilled decades ago under less stringent standards. While most of these wells do not penetrate the Lyons Formation in the immediate study area, their presence at the regional scale must be considered in long-term storage risk assessments. Within the 3D seismic survey boundary, no legacy wells are known to intersect the Lyons Formation, based on a thorough review of public well data. Consequently, leakage risk from legacy wells is considered low within the modeled domain, but may require further evaluation when defining the regulatory AoR.

Additionally, the static model was constructed with limited well control in the Lyons Formation—only one well (Well A) penetrates the formation and lies approximately 30 miles (48.3 km) outside the seismic volume. This limitation contributes to uncertainty in both structural interpretation and petrophysical calibration, and it reinforces the need for further site characterization, including a stratigraphic test well.

The primary well-related risks in this study are therefore associated with new injection and monitoring wells, which will be designed and constructed in accordance with Class VI requirements. These standards—enforced during the permitting process—mandate best practices in well siting, casing, cementing, and long-term monitoring, thereby significantly reducing the potential for CO_2 leakage through engineered wellbores.

Seismic Monitoring Feasibility

With the construction of a static and dynamic model, rock physics relationships can be used to estimate if a time-lapse seismic monitoring signal can be detected for this study. For this purpose, fluid changes on P- and S-impedance are calculated using Gassmann fluid substitution for sandstone using water and CO_2 fluid properties, temperature and pore pressure to calculate saturated bulk modulus and density. Stress changes on bulk and shear modulus are calculated using pressure sensitivity from dry core testing on Lyons sandstone. Rock physics properties of the Lyons sandstone, fluid properties at reservoir temperature and pore pressure of the water and CO_2, and stress changes with changes in pore pressure are used to calculate changes in saturated bulk modulus, shear modulus and density and used to calculate changes P- and S-impedance at each grid point of the dynamic model. Figure 10 shows these changes from pre-injection baseline (all water) to after 30 yr of CO_2 injection. The modeling shows that up to a 4% change in P-impedance can be expected. It would be important to compare this to the expected time-lapse noise level from seismic data acquisition to understand if monitoring will be successful. The change in P- or S-impedance with stress is observed to be very small or undetectable, based on

core measurements from Well A located approximately 30 miles from the study area, assuming those measurements are representative of in-situ conditions in the modeled location.

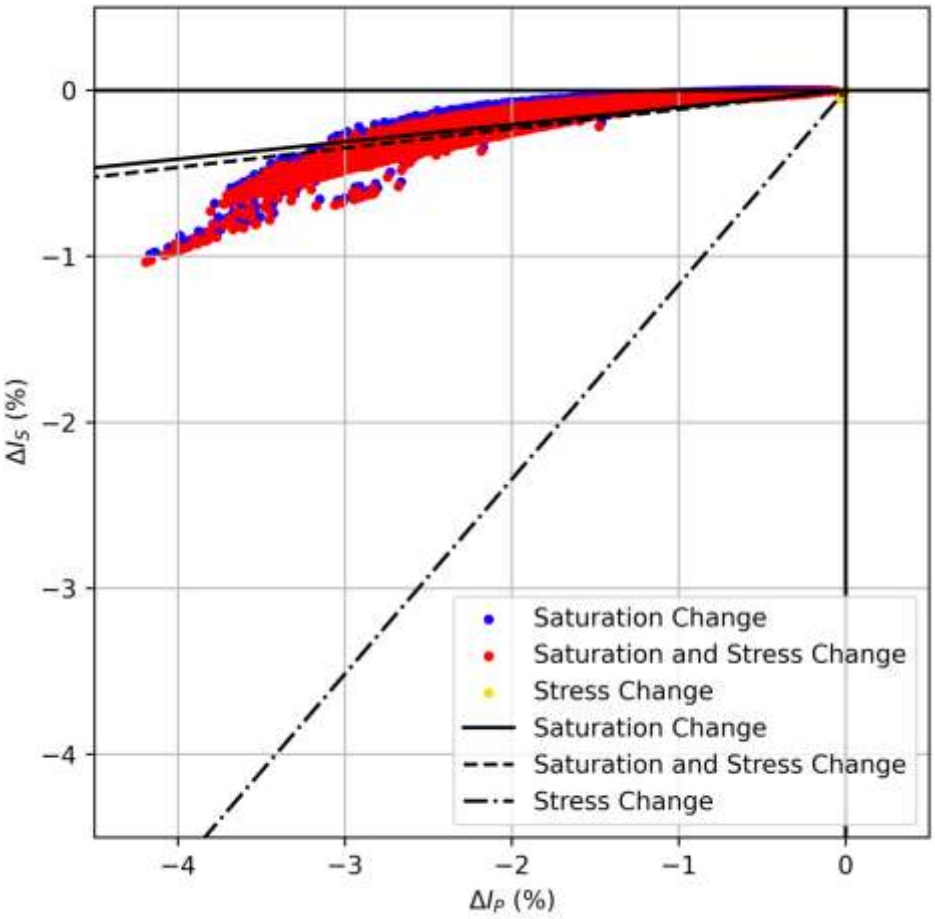


Figure 350 Precent change in P-impedance vs S-impedance from pre-injection to 30 yr of injection. A maximum of 4% change in P-impedance can be expected where CO_2 has replaced water. This reservoir is not seen to be very sensitive to stress changes provided the core measurements are representative of the field. This analysis supports feasibility for 4D seismic monitoring primarily driven by saturation effects.

The time-lapse impedance changes can be computed field wide, convolved with the wavelet estimated for the reservoir from seismic field data, and converted to industry standard seismic amplitude-versus-offset (AVO) products of intercept (I) and gradient (G). Here the time-lapse intercept and gradient AVO parameters after 30 yr of injection were calculated, as shown in Figure 11. CO_2 saturated zones are clearly seen as decreases in both intercept and gradient. The center of each plume, where there is higher CO_2 saturation and the plume is thicker, demonstrates a greater decrease in I and G. Nearing the edge of the plume, change in I and G drops until reaching zero. Outside the plume, there is a small positive difference caused by a small increase in bulk modulus and density, and subsequently P-impedance in the pore fluid from increased pore pressure. In the center of each plume there is a zone where this trend is not observed, and there is less change in I and G. Located at the injection points, these correspond to the highest saturation of CO_2 in the plume and the highest pore pressure and is more apparent in the change in G.

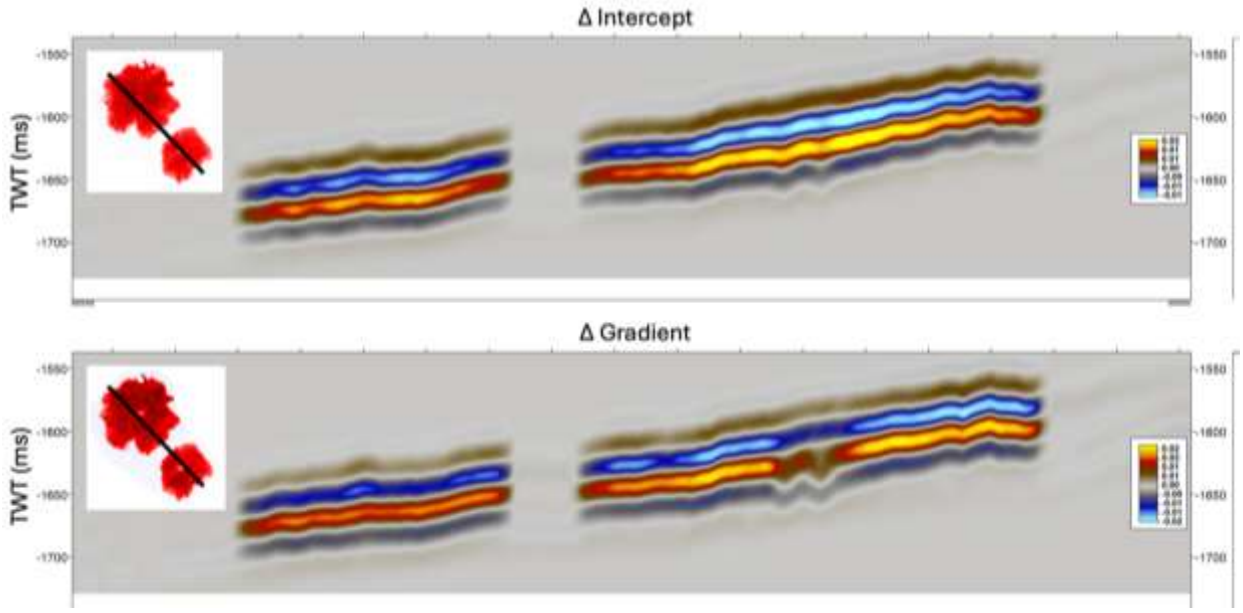


Figure 351 Cross-sectional view of time-lapse seismic attribute response after 30 yr of CO_2 injection. The top panel shows changes in intercept (ΔI), and the bottom panel shows changes in gradient (ΔG). These AVO attributes reflect changes in acoustic properties due to CO_2 saturation. The maximum decreases in ΔI and ΔG correspond to the plume tops, indicating potential detectability with properly designed 4D surface seismic monitoring. Inset map shows the seismic line orientation used for cross-section extraction.

Next, the seismic repeatability requirement was analyzed utilizing normalized root mean square (NRMS) measure between the baseline and monitor surveys to understand the time-lapse seismic signal level (Calvert 2005). NRMS is calculated for the base and 30-yr monitor and for the base and 100-yr monitor. The NRMS cross sections of these synthetic modeled plumes can be seen in Figure 12. In the reservoir region we observe an average NRMS value of 15%. Based on published NRMS data from various fields (Calvert 2005), a maximum range of 16.4 ft (5 m) to 32.8 ft (10 m) position difference between shot and receiver locations for baseline and monitor data will be required to observe the reservoir time-lapse signal. On land, the repeatability between the baseline and monitor survey may need to be even better or less than 16.4 ft (5 m).

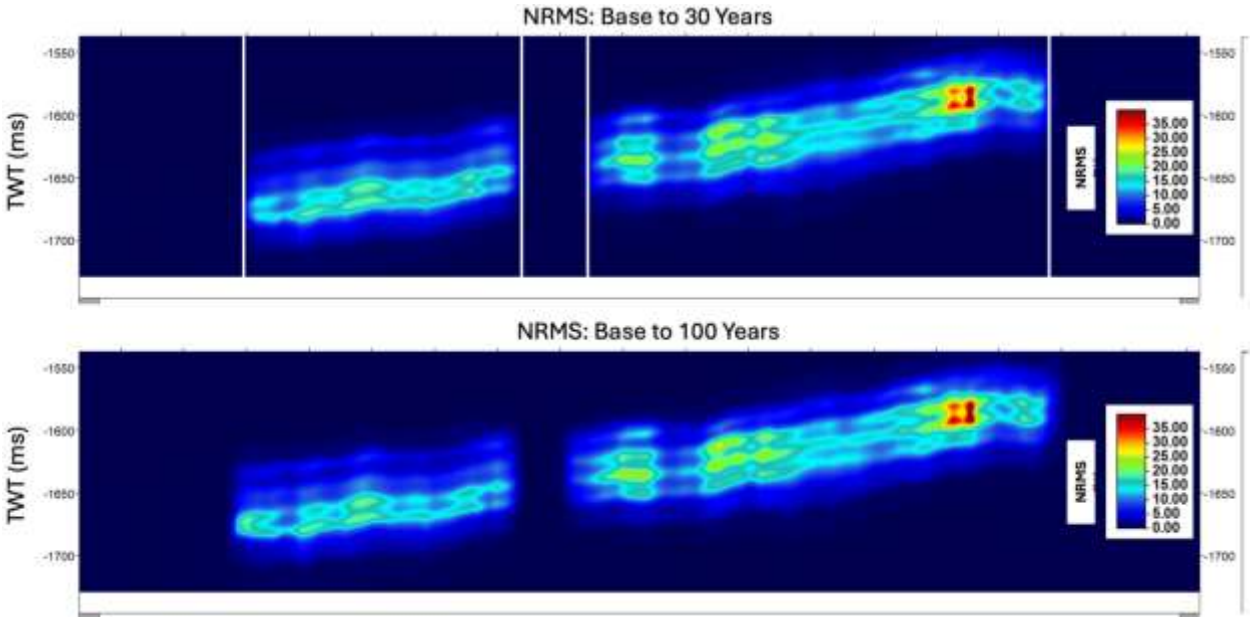


Figure 352 NRMS calculated between the base and 30-yr monitor (top). NRMS calculated between the base and 100-yr monitor (bottom). NRMS is used to quantify the repeatability of seismic surveys and the detectability of CO_2 plume signals. Values in the reservoir interval average around 15%, with localized zones exceeding 20–30%, suggesting that time-lapse signal detectability is achievable with acquisition repeatability better than 16.4 ft (5 m), as recommended in published 4D seismic monitoring studies.

Conclusions and Future Work

This study evaluates the feasibility of commercial-scale CO_2 sequestration in the Lyons saline aquifer in El Paso County, southern Colorado, using geological modeling, reservoir simulation, and containment risk assessment. Based on the current dataset, the following conclusions can be drawn:

- Storage feasibility: Simulation results indicate that approximately 60 million metric tons of CO_2 can be injected over 30 yr using two vertical wells. During injection, 85% of the CO_2 remains in a supercritical state, and after a 70-yr shut-in period, about 30% becomes immobilized via residual trapping. These findings support the technical viability of long-term storage in this formation under modeled conditions.
- Reservoir suitability: The Lyons Formation exhibits favorable reservoir depth, porosity, permeability, and multiple overlying confining units, making it a promising target for CO_2 injection in the study area.
- Containment assessment: Within the study area, containment risk is considered low, supported by the absence of seismically visible faults intersecting the injection zone and the lack of legacy wells penetrating the Lyons Formation. However, this conclusion is specific to the modeled area and should not be generalized to the broader region.
- Plume containment risk: The primary site-specific risk is the low structural dip of the formation, which limits structural trapping and may enhance lateral plume migration. For improved containment, anticlinal or low-dip regions may be more favorable.
- Monitoring feasibility: The detectability of CO_2 plume development using surface seismic methods presents a challenge, given the relatively small changes in impedance. This

monitoring risk may be mitigated through the use of high-repeatability seismic acquisition (<5 m offset) and deployment of 3D vertical seismic profiling (VSP) systems. This has direct implications for monitoring design and regulatory compliance under Class VI standards.

While the current results demonstrate the potential suitability of the Lyons Formation, they are based on limited site data. To reduce uncertainty and advance toward project deployment, the following actions are recommended:

- Site characterization: Drill a stratigraphic test well to collect well logs, core data, fluid properties, and pressure measurements to improve understanding of reservoir and caprock behavior.
- Model refinement: Use newly acquired data to refine static and dynamic models, verify assumptions related to permeability, stress distribution, and seal integrity, and improve confidence in plume evolution and pressure buildup predictions.
- Boundary condition validation: Incorporate more realistic regional boundary conditions based on pressure communication data to evaluate regional flow behavior, plume migration, AoR definition, and containment risks under more representative field conditions.
- Monitoring strategy development: Conduct detailed monitoring feasibility analysis to define appropriate acquisition geometries, frequency, and resolution requirements for surface and borehole seismic data—ensuring regulatory alignment and early detection capability.

These steps will strengthen the technical basis for a Class VI permit application, support risk-based project design, and inform best practices for safe and effective CO_2 storage in underexplored areas of southern Colorado.

Acknowledgment

The authors would like to thank the U.S. Department of Energy (#DE-FE0031837) and the Carbon Utilization and Storage Project (CUSP) for their financial support of this study.

References

Ampomah W, Wang S, El-Kaseeh G. 2022. Overview of safe subsurface storage of CO_2 in saline reservoirs: San Juan Basin CarbonSAFE Phase III. In: Proceedings of the 16th Greenhouse Gas Control Technologies Conference (GHGT-16); 2022 Oct 23–27; Lyon (France). doi:10.2139/ssrn.4285750

Brown CF, Lackey G, Mitchell N, Baek S, Schwartz B, Dean M, Dilmore R, Blanke H, O'Brien S, Rowe C. 2023. Integrating risk assessment methods for carbon storage: a case study for the Quest carbon capture and storage facility. Int J Greenh Gas Control. 129:103972. doi:10.1016/j.ijggc.2023.103972

Calvert R. 2005. Insights and methods for 4D reservoir monitoring and characterization. Tulsa (OK); Society of Exploration Geophysicists. doi:10.1190/1.9781560801696

Chadwick A, Williams G, Delepine N, Clochard V, Labat K, Sturton S, Buddensiek ML, Dillen M, Nickel M, Lima AL, et al. 2010. Quantitative analysis of time-lapse seismic monitoring data at the Sleipner CO_2 storage operation. Lead Edge. 29(2):170–177. doi:10.1190/1.3304820

Chadwick RA, Zweigel P, Gregersen U, Kirby GA, Holloway S, Johannessen PN. 2004. Geological reservoir characterization of a CO_2 storage site: the Utsira Sand, Sleipner, northern North Sea. Energy. 29(9–10):1371–1381. doi:10.1016/j.energy.2004.03.071

Colorado Energy Office. 2024. Colorado greenhouse gas pollution reduction roadmap 2.0. Denver (CO); Colorado Energy Office. [accessed 2025 Dec 23]. https://energyoffice.colorado.gov/ghg-pollution-reduction-roadmap

Drake RM, Brennan ST, Covault JA, Blondes MS, Freeman PA, Cahan SM, DeVera CA, Lohr CD. 2014. Geologic framework for the national assessment of carbon dioxide storage resources: Denver Basin, Colorado, Wyoming, and Nebraska. Reston (VA); U.S. Geological Survey.

Duong C, Bower C, Hume K, Rock L, Tessarolo S. 2019. Quest carbon capture and storage offset project: findings and learnings from first reporting period. Int J Greenh Gas Control. 89:65–75. doi:10.1016/j.ijggc.2019.08.006

Garbarini GS, Veal HK. 1968. Potential of Denver Basin for disposal of liquid wastes. Denver (CO); Colorado Geological Survey.

[GWPC] Ground Water Protection Council, Interstate Oil and Gas Compact Commission. 2015. Potential injection-induced seismicity associated with oil and gas development: a primer on technical and regulatory considerations informing risk management and mitigation. Oklahoma City (OK); GWPC. [accessed 2025 Dec 23]. https://www.gwpc.org/sites/default/files/IMAG/Primer%20Final.pdf

Herman D. 2024. Potential implementation of geologic carbon sequestration in southern Colorado. Golden (CO); Colorado School of Mines. Master's thesis.

Lal R. 2008. Carbon sequestration. Philos Trans R Soc B Biol Sci. 363(1492):815–830. doi:10.1098/rstb.2007.2185

Levandowski D, Kaley M, Smalley R. 1973. Cementation in the Lyons Sandstone and its role in oil accumulation, Denver Basin, Colorado. AAPG Bull. 57(11):2217–2244.

McCulloch S. 2021. Carbon capture in 2021: off and running or another false start? Paris (France); International Energy Agency. [accessed 2025 Dec 23]. https://www.iea.org/commentaries/carbon-capture-in-2021-off-and-running-or-another-false-start

McLaughlin F, Quillinan S, Ganshin Y, Jiao Z, Phillips E, Wang H, Moore T, Bagdonas D, Nye C, Johnson M, et al. 2019. Integrated commercial carbon capture and storage pre-feasibility study at Rock Springs Uplift, Wyoming. Laramie (WY); University of Wyoming. Report No. DOE-UW-FE0029302.

Metz B, Davidson O, De Coninck HC, Loos M, Meyer L, editors. 2005. IPCC special report on carbon dioxide capture and storage. Cambridge (UK); Cambridge University Press.

Nelson PH, Santus SL. 2011. Gas, oil, and water production from Wattenberg field in the Denver Basin, Colorado. Reston (VA); U.S. Geological Survey. Open-File Report 2011-1175. 23 p. 2 plates. [accessed 2025 Dec 23]. https://pubs.usgs.gov/of/2011/1175/

Neuzil CE. 1995. Abnormal pressures as hydrodynamic phenomena. Am J Sci. 295(6):742–786. doi:10.2475/ajs.295.6.742

Ning Y, Boak J, Tura A, Prasad M. 2025. Assessment of CO_2 sequestration potential and economics in Colorado, USA. Int J Greenh Gas Control. 141:104301. doi:10.1016/j.ijggc.2024.104301

Orr FM Jr. 2018. Carbon capture, utilization, and storage: an update. SPE J. 23(6):2444–2455. doi:10.2118/186597-PA

Page B, Turan G, Zapantis A, Burrows J, Consoli C, Erikson J, Havercroft I, Kearns D, Liu H, Rassool D, et al. 2020. The global status of CCS 2020: vital to achieve net zero. Melbourne (Australia); Global CCS Institute.

Peck WD, Ayash SC, Klapperich RJ, Gorecki CD. 2019. The North Dakota integrated carbon storage complex feasibility study. Int J Greenh Gas Control. 84:47–53. doi:10.1016/j.ijggc.2019.03.007

Quinn M. 2022. Carbon capture and storage: a review of Australian projects. APPEA J. 62(1):334–341. doi:10.1071/AJ21114

[SPE] Society of Petroleum Engineers. 2017. CO_2 storage resources management system (SRMS). Richardson (TX); Society of Petroleum Engineers. [accessed 2025 Dec 23]. https://www.spe.org/industry/docs/SRMS.pdf

Sonnenberg SA, Matson CC, Alzahrani R, Eaton M. 2024. The Permian Lyons Sandstone, central Denver Basin: an emerging CCS reservoir. In: SPE/AAPG/SEG Unconventional Resources Technology Conference; 2024 Jun 17–19; Houston (TX). Paper D031S054R003. doi:10.15530/urtec-2024-4049373

Sullivan M, Rodosta T, Mahajan K, Damiani D. 2020. An overview of the Department of Energy's CarbonSAFE initiative: moving CCUS toward commercialization. AIChE J. 66(4):e16855. doi:10.1002/aic.16855

Trupp M, Ryan S, Barranco Mendoza I, Leon D, Scoby-Smith L. 2021. Developing the world's largest CO_2 injection system—a history of the Gorgon carbon dioxide injection system. In: Proceedings of the 15th Greenhouse Gas Control Technologies Conference (GHGT-15); 2021 Mar; Abu Dhabi (United Arab Emirates). doi:10.2139/ssrn.3815492

[DOE] U.S. Department of Energy. 2024. CarbonSAFE initiative. Washington (DC); U.S. Department of Energy. [accessed 2025 Dec 23]. https://netl.doe.gov/carbon-management/carbon-storage/carbonsafe

[EIA] U.S. Energy Information Administration. 2024. Colorado state energy profile. Washington (DC); U.S. Energy Information Administration. [accessed 2025 Dec 23]. https://www.eia.gov/state/print.php?sid=CO

[EPA] U.S. Environmental Protection Agency. 2008. Federal requirements under the Underground Injection Control (UIC) Program for carbon dioxide (CO_2) geological sequestration wells; proposed rule. Fed Regist. 73:43492–43541.

Young GB, Lintz VA, Widmann BL, Bird DA, Cappa JA. 2007. CO_2 sequestration potential of Colorado. Golden (CO); Colorado Geological Survey.

From Site to State: Design of an Integrated CCS Operation in a Complex Geological Structure in Osage County, Oklahoma

Targa Resources (Formerly Lucid Energy Delaware) Acid Gas Injection Project

In 2022, the New Mexico Tech CUSP team partnered with Lucid Energy to permit an acid gas injection (AGI) well for their Red Hills site in New Mexico. The effort was partially funded by the CUSP project. The goal of the project was to identify a subsurface geological formation to inject acid gas (CO_2 and H_2S), captured during sour natural gas treatment. The acid gas is compressed and injected in the formation.

The CUSP team prepared a "Permit to Inject" application (C-108). Preparation of the permit application involved building a geological model, well log analysis, and geophysical interpretation. Members of the team attended the NMOCD hearing as expert witnesses. Lucid Energy was granted the permit. The well was drilled and completed according to the plan.

The CUSP team supported Lucid Energy's engineers and drillers in developing (1) core collection and analysis programs, (2) a well logging program, and 3) a well design.

Based on the successful completion of the focused project, Targa Resources awarded New Mexico Tech's Petroleum Recovery Center (PRRC) several permitting projects as well as several monitoring, reporting and verification projects.

Carbon Solutions' Contributions to Focused Projects

Carbon Solutions provided support across five different CUSP Focused Projects by providing detailed information on transport, capture, and storage in support of CCS infrastructure assessment. This was done by applying the SimCCS^{PRO} toolset to meet project specific needs. Carbon Solutions support the Subtask 4.5 deliverable Report: Focused Scenario Analysis results on Candidate Sites in the CUSP Region submitted in 2024.

The following section summarizes Carbon Solutions efforts for each Focused Project.

Subtask 4.5.2 – Regional-Scale Assessment of CO_2 Geological Storage in Sedimentary Basin Geothermal Reservoirs of Nevada

Carbon Solutions provided a preliminary assessment of subsurface sedimentary geothermal potential in support of the Nevada Focused Project. The 10 km SCO_2T^{PRO} geospatial dataset was integrated with geothermal data to identify areas favorable for deep sedimentary basin CO_2 plume geothermal (CPG) geologic storage for northern Nevada. A sedimentary geothermal potential was developed based on combining the following variables:

- Sedimentary valley fill thickness
- Geothermal temperature gradient
- Fault activity or no-fault activity

Through this work it was identified that the Black Rock sedimentary basin had the highest sedimentary geothermal potential of all evaluated basins. Furthermore, the Black Rock sedimentary basin is the largest of the basins evaluated with an area of 912 km^2. This work is based on the assumption that all the properties of the saline formations, identified from well logs, are vertically and laterally continuous throughout the Black Rock sedimentary basin. A detailed view of the geothermal potential for the Black Rock sedimentary basin can be seen in Figure 353.

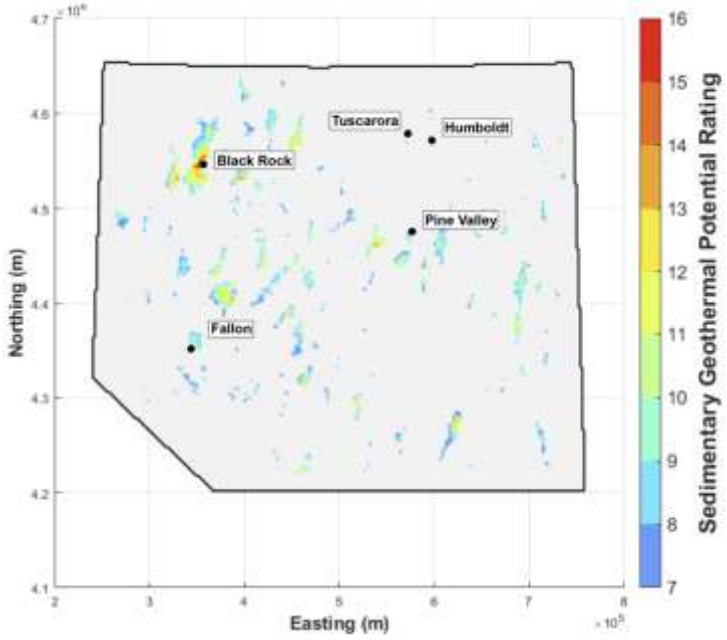


Figure 353 Regional-scale sedimentary basin geothermal reservoirs in northern Nevada

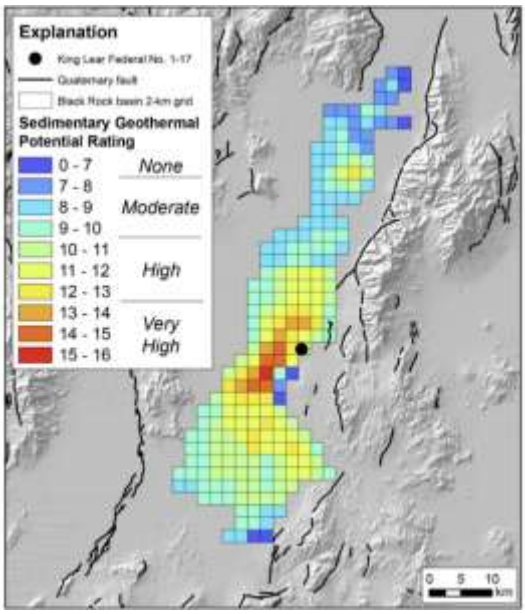


Figure 354 Figure 355 Sedimentary geothermal potential rating for the Black Rock sedimentary basin

The aggregated data, in conjunction with temperature gradient data, was then run through the SCO_2T^{PRO} tool to generate estimated greenfield levelized costs of electricity (LCOE) for CPG development. LCOE values were calculated using the following assumptions: a 95% power plant capacity factor, A capital recovery factor of 5.2%, and annual O&M costs of 5.5% of specific capital costs. The objective was to identify the lowest-cost power generation sectors of the Black Rock sedimentary basin. This analysis highlighted that large parts of the basin have the potential for low-cost CPG power generation with most of the basin having estimated LCOEs of less than $90/MWh.

Subtask 4.5.2 – Cornerstones of a Regional Storage Hub in California

Carbon Solutions primarily supported work on the California Focused Project by applying its $SimCCS^{PRO}$ toolset to support the following tasks:

- Task 6 – Field Project Assessment
- Task 9 – Forward Looking Scenarios

To begin with, Carbon Solutions identified all sources of CO_2 around the proposed project field site at buffer ranges from 20 km to 50 km with one additional buffer of 65 km considered. In the 20 km buffer there are 18 unique facilities from five different industrial sectors with total annual capturable emissions of 4.89 $MtCO_2$. When going from the 50 km buffer to the 65 km buffer adds an additional 15 facilities with 1.26 $MtCO_2$/yr in capturable CO_2 emissions.

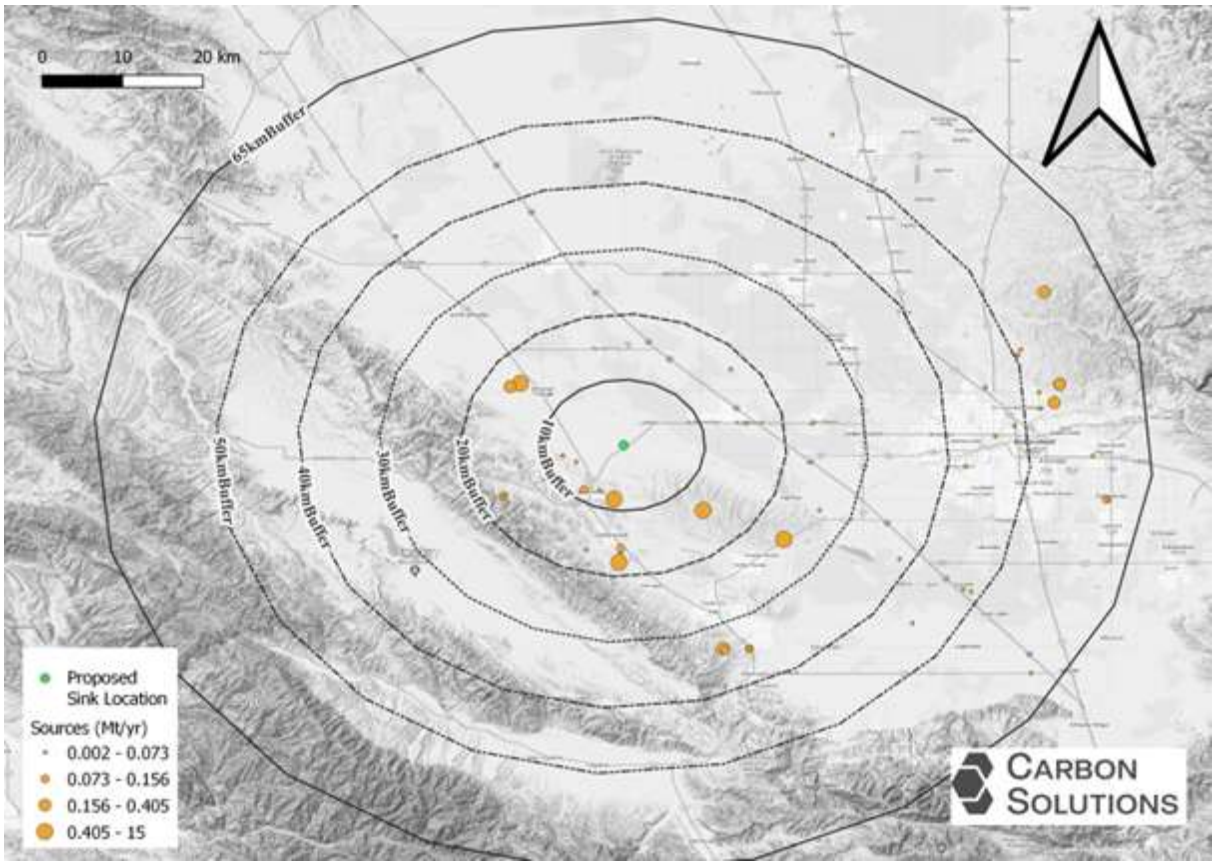


Figure 356. **Figure 357** Geospatial location and capturable emissions for sources of CO_2 within various buffer ranges around the proposed field project site

A total of 12 SimCCS^{PRO} scenarios were run around the field project site, with the first set of scenarios (6) using the "constrained" SCO_2T^{PRO} defined storage potential at the field project site and the second set of scenarios (6) using an "unconstrained" storage potential that will enable the capture of all emissions. Sets of scenarios are further divided by sources within buffer ranges to determine annual capturable CO_2 emissions.

The first scenario of each set at the field project site only captures CO_2 emissions from steam generators. There is sufficient capacity regardless of using constrained or unconstrained storage potential to capture all emissions from steam generators around the proposed field project site. The resulting CCS network features 44 km of CO_2 transport pipelines with a total unit cost of \$77.48/tCO_2 (Figure 358).

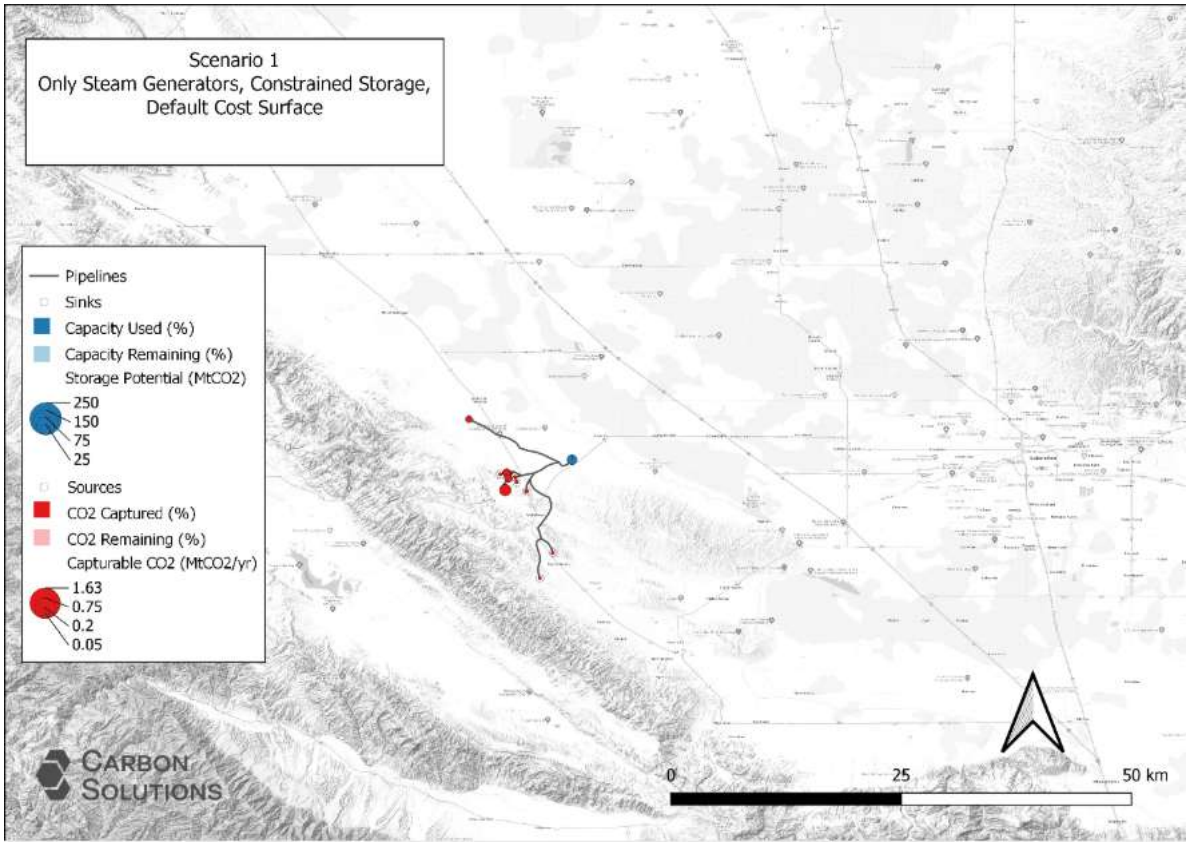


Figure 358 SimCCS^{PRO} CCS results network when using SCO$_2$T^{PRO} defined storage potential and capturing only from steam generators

When using the SCO$_2$T^{PRO} defined storage potential there is sufficient storage potential to capture approximately 0.79 MtCO$_2$/yr for 30 years. This results in CO$_2$ only being captured from the Elk Hills Power project for all constrained storage potential scenarios except for the first one which only captures from steam generators (Figure 359).

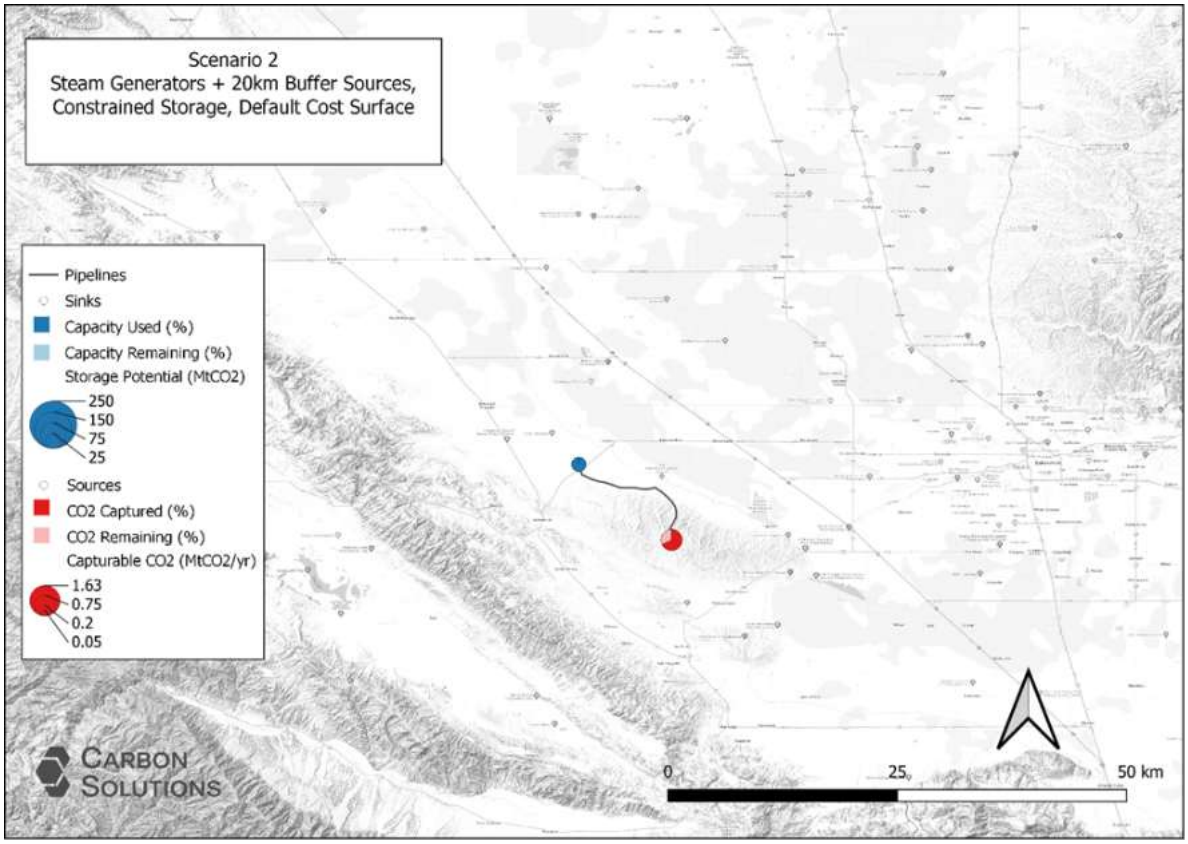


Figure 359 Deployed SimCCS^{PRO} results network when using SCO$_2$T^{PRO} defined storage potential. Due to the storage limitations all scenarios using the SCO$_2$T^{PRO} defined storage potential are the same as this one shown here

For the second set of scenarios using "unconstrained" storage potential, networks differ depending on the annual capture target. For example, Figure 360 shows what a CCS network would look like around the field project site if CO_2 is captured from all available sources within the 65 km buffer. This network features approximately 509 km of CO_2 transport pipeline with a total unit cost of almost \$81/tCO_2 and captures 8.83 MtCO_2/yr. This represents an almost \$3/tCO_2 increase in total CCS network costs when going from the 50 km buffer of sources to the 65 km buffer. Nevertheless, total CCS network unit costs range from \$74/tCO_2 - \$81/tCO_2 across all 12 scenarios Carbon Solutions modeled.

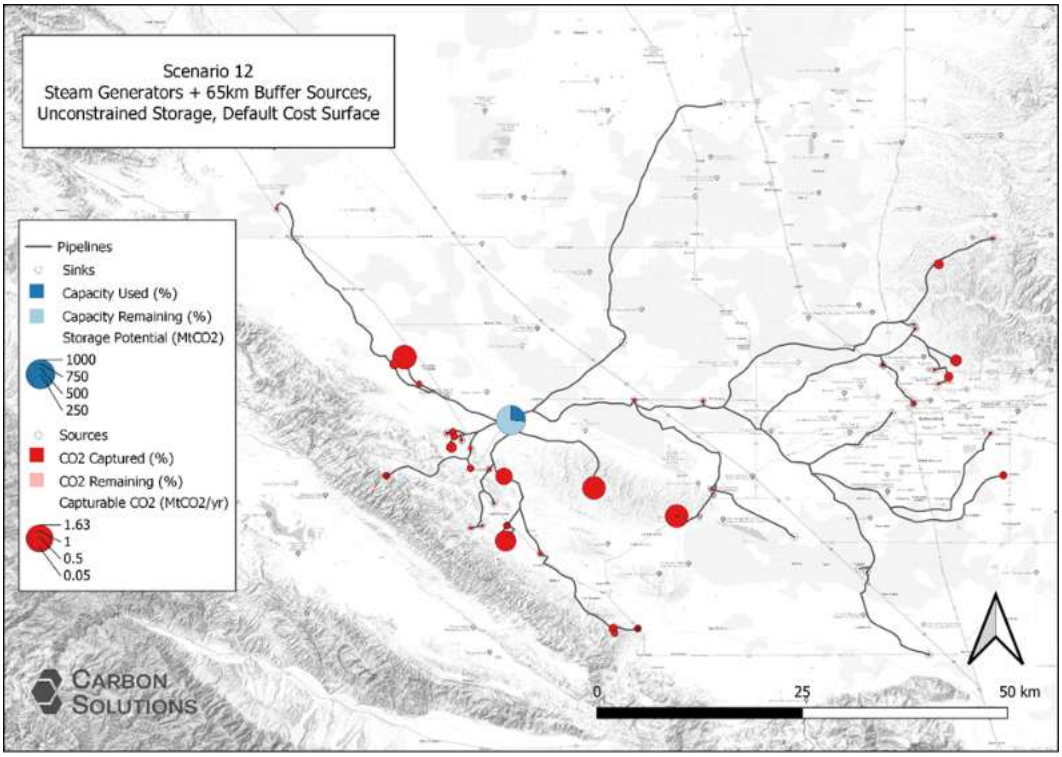


Figure 360 Deployed SimCCS^{PRO} results network when using unconstrained storage potential and capturing from all sources in the 65 km buffer

Carbon Solutions also ran four forward looking scenarios to evaluate hub or distributed storage as a foundation for future CCS networks in California. Ultimately, these scenarios indicated that regardless of what sources are being used, CCS networks that use distributed storage are always less expensive than the corresponding CCS networks that use hub storage. For example, when capturing CO_2 from all sources in California, the distributed storage CCS network has a total cost of \$102/tCO_2 while the hub storage CCS network has a total cost of \$109/tCO_2. There are notable differences in amounts of pipeline deployed with hub storage adding almost 1,800 km of additional CO_2 pipeline deployment (see Table 2 on page 42).

Subtask 4.5.3 – CUSP Midstream Operator Storage of CO_2 (MOSCO$_2$)

Carbon Solutions applied its entire SimCCS^{PRO} toolset to meet Task 6 Infrastructure Network Assessment of the Kansas Focused Project. Sources of CO_2, including capturable emissions and estimated capture costs, in Kansas were aggregated using the CO_2NCORD tool. After collaboration with project partners, Carbon Solutions focus on eight unique facilities across six different industries with total capturable emissions of 2.12 MtCO_2/yr and capture costs ranging from \$36.89/tCO_2 to \$71.13/tCO_2 (Figure 361). Geology parameters were provided by the teams leading Task 3 and Task 4 of the Focused Project and were input into SCO$_2$T^{PRO} to provide estimated storage potential and storage costs for three unique injection locations.

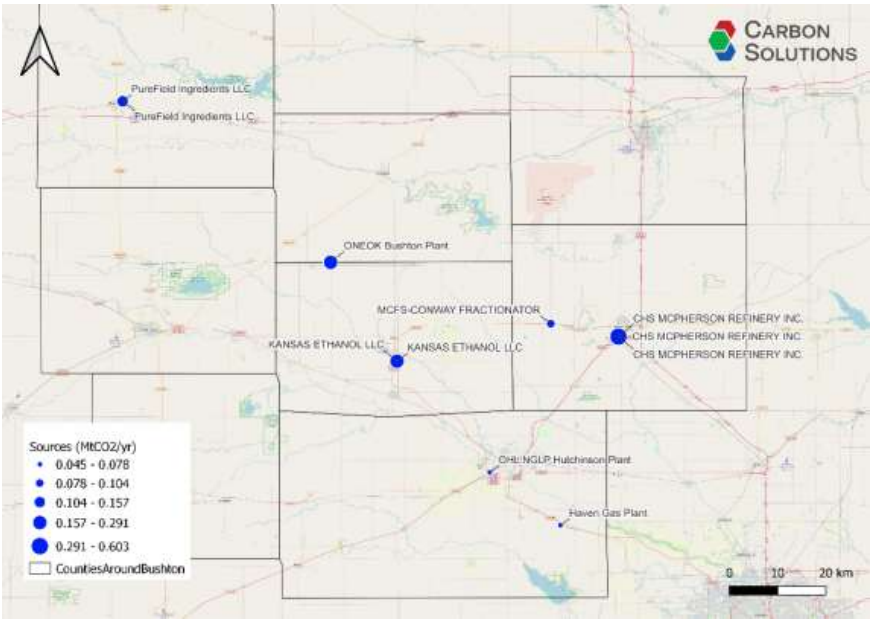


Figure 361 Map of all potential emitters considered for Task 6 SimCCS^{PRO} scenarios

Carbon Solutions took all input data and, in collaboration with project partners, developed 12 distinct scenarios to be in SimCCS^{PRO} (Table 73). These scenarios were intended to capture likely combinations of different facilities engaging with CCS in Kansas beginning with just those facilities controlled by project partners. Annual capture targets ranged from 0.442 to 2.118 $MtCO_2$/yr depending on which facilities were included in the scenario. All storage formations were assumed to have 30 Mt of storage potential.

Table 73 Summary of scenarios run in support of the Kansas Focused Project

Scenario location	**Geology Context**	**Run 1**	**Run 2**	**Run 3**	**Run 4**
Bushton	Arbuckle Formation: 30 Mt storage capacity	Hutchinson, Conway Fractionator, Bushton	Run 1 + Cargill Salt, KS Ethanol, NA Salt	Run 2 + McPherson Facilities	Run 4 + Purefield
Alternate site 1	Arbuckle Formation: 30 Mt storage capacity	Hutchinson, Conway Fractionator, Bushton	Run 1 + Cargill Salt, KS Ethanol, NA Salt	Run 2 + McPherson Facilities	Run 4 + Purefield
Alternate site 2	Arbuckle Formation: 30 Mt storage capacity	Hutchinson, Conway Fractionator, Bushton	Run 1 + Cargill Salt, KS Ethanol, NA Salt	Run 2 + McPherson Facilities	Run 4 + Purefield
Total annual emissions, $MtCO_2$/yr		0.442	0.842	1.916	2.118
10-year emissions, $MtCO_2$		4.42	8.42	19.16	21.18

All scenarios were run using a 10-year financing period and a 10% interest rate to give a capital recovery factor of 0.163. When using the storage location controlled by the project partner, total CCS network costs range from \$103/tCO_2 to \$88/tCO_2, with the networks becoming less expensive as the CO_2 capture target increases. This could be explained by economies of scale where pipelines can be made larger to handle more CO_2 thereby reducing the unit cost of transport. Additionally, the results indicate that some pipeline routes are deployed across multiple scenarios, highlighting their robustness to different scenario options (Figure 362 and Figure 363).

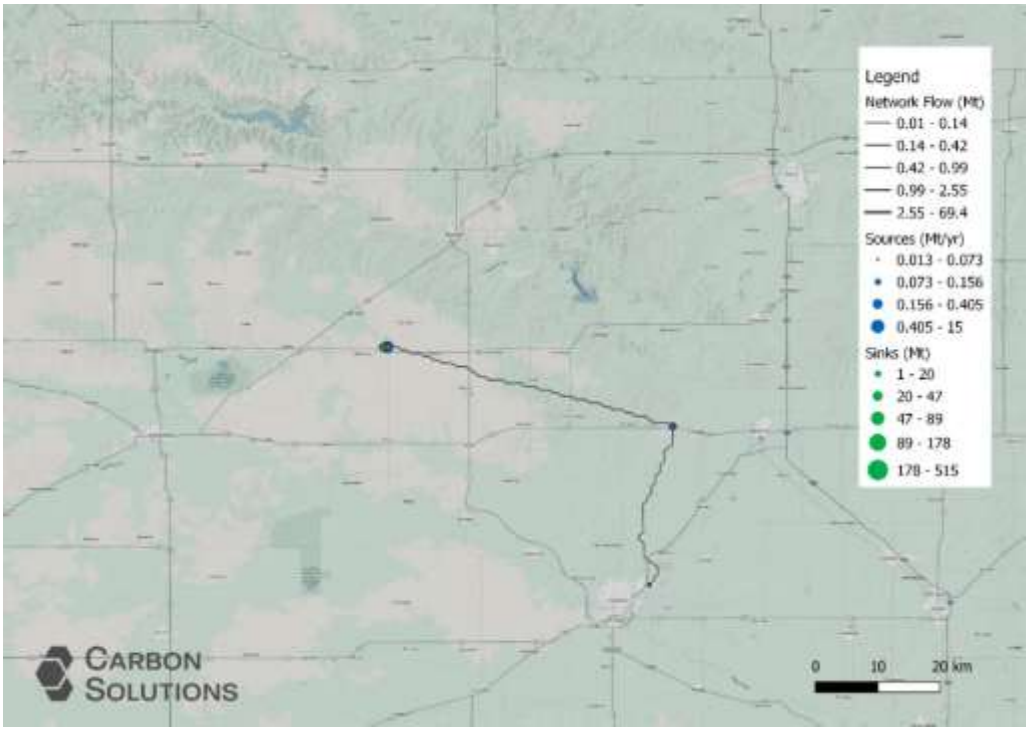


Figure 362 Deployed CCS network for Bushton scenario run 1. It should be noted that the top left set of points represents both a source of CO2 and the co-located Bushton storage location.

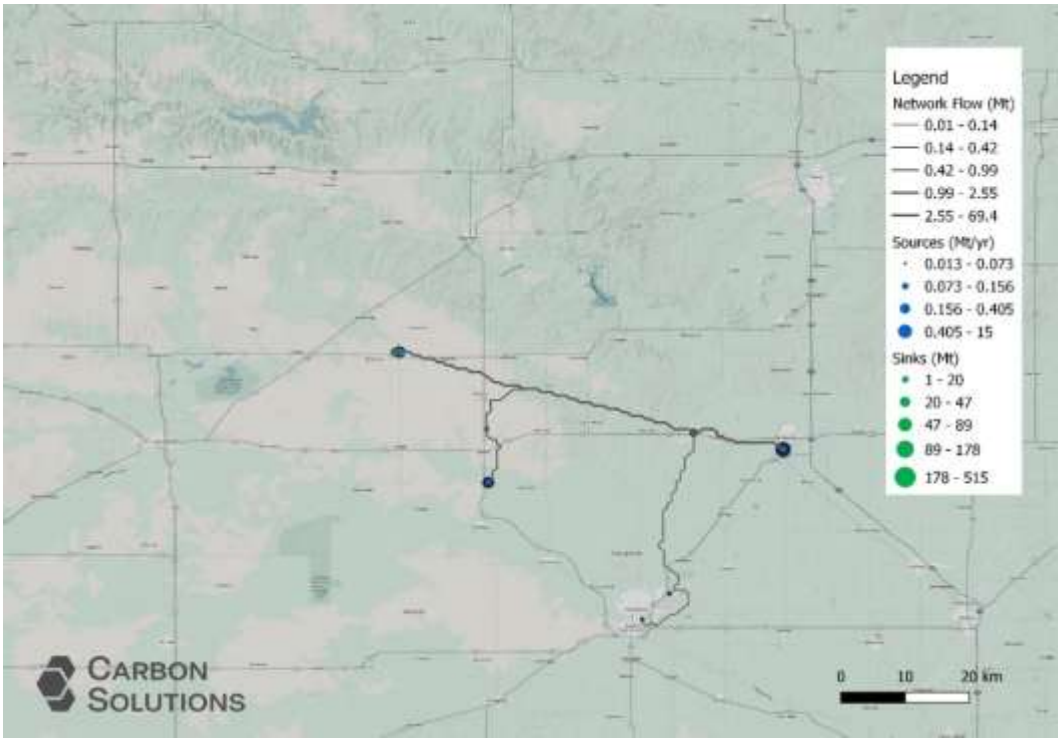


Figure 363 Deployed CCS network for Bushton scenario run 3, including all sources from runs 1 and 2

These costs largely align with total network costs when using either of the alternative storage sites. While the storage locations are different, several parts of the CO_2 transport networks align with the results presented in Figure 362 and Figure 363, once again highlighting their robust nature. When using alternative site 1, network lengths range from 113 km to 226 km, depending on which sources are included in the analysis. Similarly, when using alternative site 2 as the storage option, network lengths range from 128 km to 253 km. Figure 364 and Figure 365 show the CCS networks for alternative site 1 (Figure 364) and alternative site 2 (Figure 365) when capturing all possible CO_2 emissions.

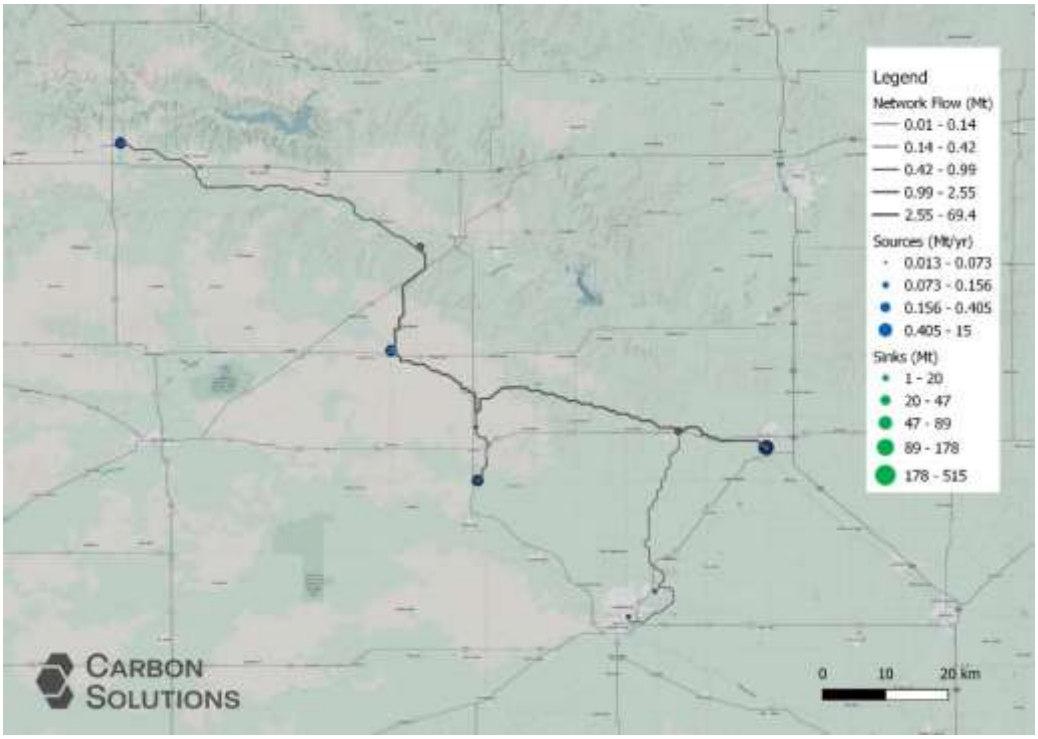


Figure 364 CCS network for alternate site 1 when capturing all available CO_2 emissions from selected sources

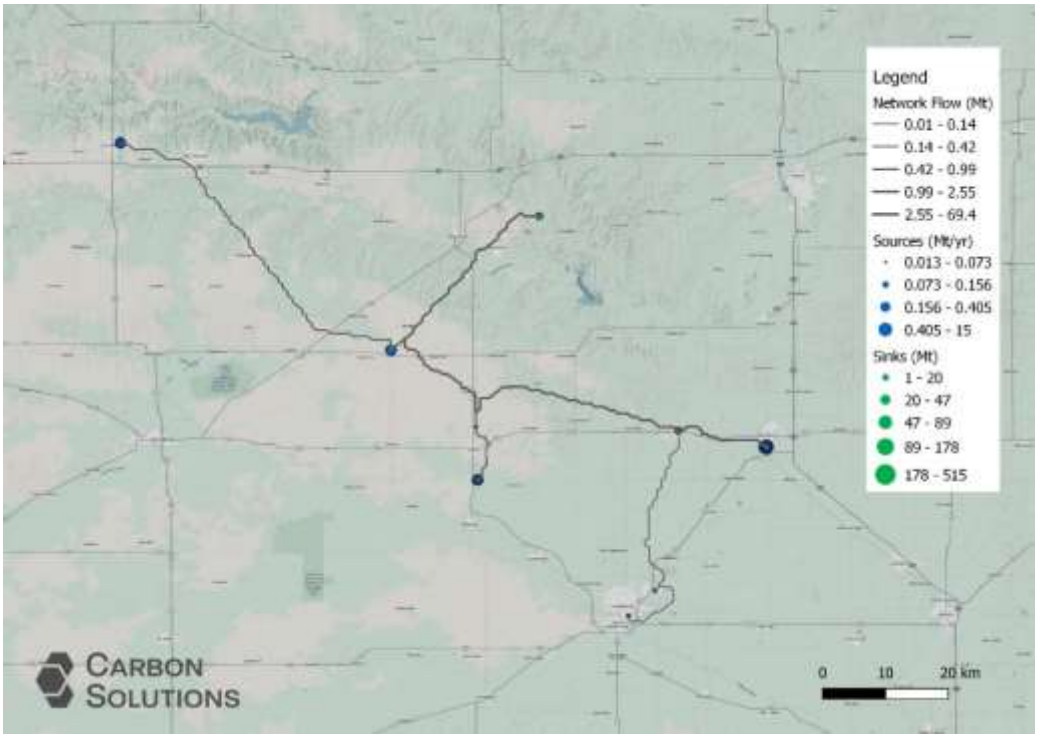


Figure 365 CCS network for alternate site 2 as a storage option when capturing all available CO_2 emissions from selected sources

Subtask 4.5.4 – From Site to State: Design of an Integrated CCUS Operation in a Complex Geological Structure in Osage County, Oklahoma

Carbon Solutions supported the Oklahoma Focused Project by applying its SimCCS^{PRO} toolset to evaluate a CCUS roadmap for Oklahoma that features stacked storage. Data on subsurface geology was provided at a county-level resolution using open-hole logs analyzed at Oklahoma University. Carbon Solutions applied its CO_2NCORD tool to determine capturable emissions and capture costs from facilities in Oklahoma.

Through collaboration with project partners, Carbon Solutions ran 32 distinct scenarios, separated into two distinct sets. The first set of scenarios (16) featured CO_2 storage in any county with geologic CO_2 storage resources, while the second set of scenarios (16) featured CO_2 storage in any county with geologic CO_2 storage resources and existing CO_2-EOR operations. The second set of scenarios simulates the conditions for stacked storage without directly modeling the unique subsurface geology. Figure 366 shows the estimated storage cost for each county and those counties with existing CO_2-EOR projects.

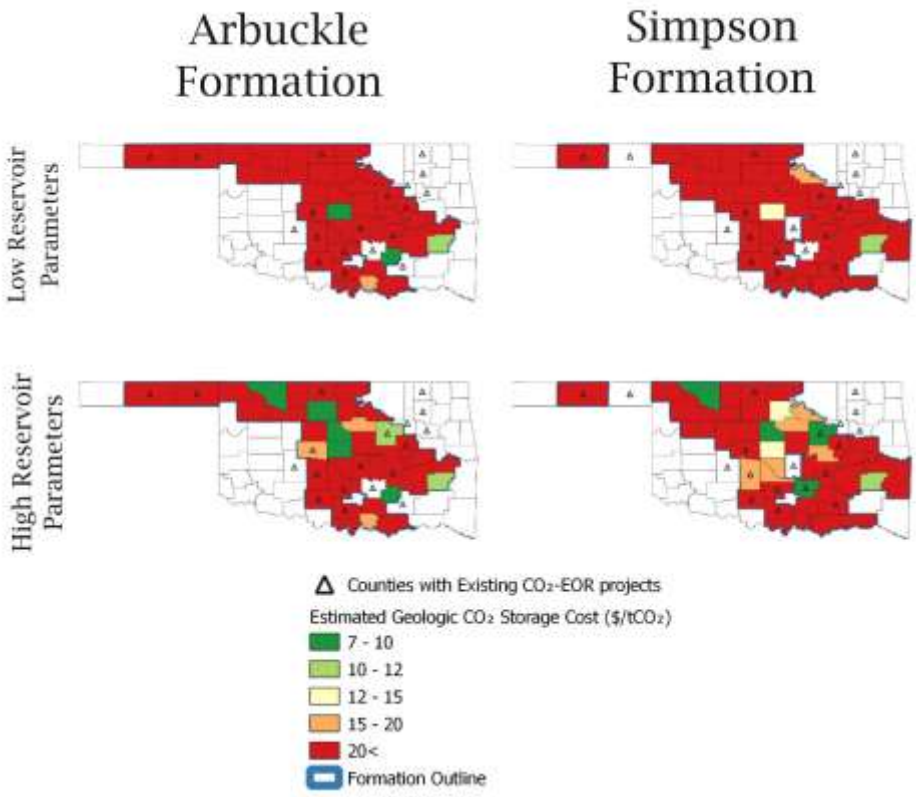


Figure 366 Estimated geologic CO_2 storage costs ($/t$CO_2$) for high and low reservoir parameters in the Arbuckle and Simpson formation. Counties with existing CO_2-EOR operations are indicated by the black triangles. Source: Miranda et al. (2023).

Once all input data had been collected all 32 scenarios were run using SimCCS^{PRO}. Results indicate that counties with existing CO_2-EOR operations do not coincide with the lowest storage cost. Further, total CCUS network costs are higher when limiting storage to only those counties with geologic CO_2 storage and existing CO_2-EOR operations. This could be explained by increase in pipeline transports costs, as more pipelines are needed to connect sources to counties that simulate the conditions for stacked storage. In meeting task objectives, Carbon Solutions identified those counties most deployed across all 32 scenarios, indicating those counties that might serve as starting points for CCUS networks in Oklahoma based on stacked storage (Figure 366). An outcome of Carbon Solutions work on the Oklahoma Focused Project is the publication Miranda et al. (2023).

Subtask 4.5.5 – Iron Mountain Subsurface Characterization

Carbon Solutions provided support for this Focused Project specifically for Subtask 5.2 Transport and Rights of Way. During the first quarter of the Focused Project, Carbon Solutions took the project AOI and applied its CostMAP^{PRO} tool to generate a cost surface for estimating costs associated with pipeline routing (Figure 367).

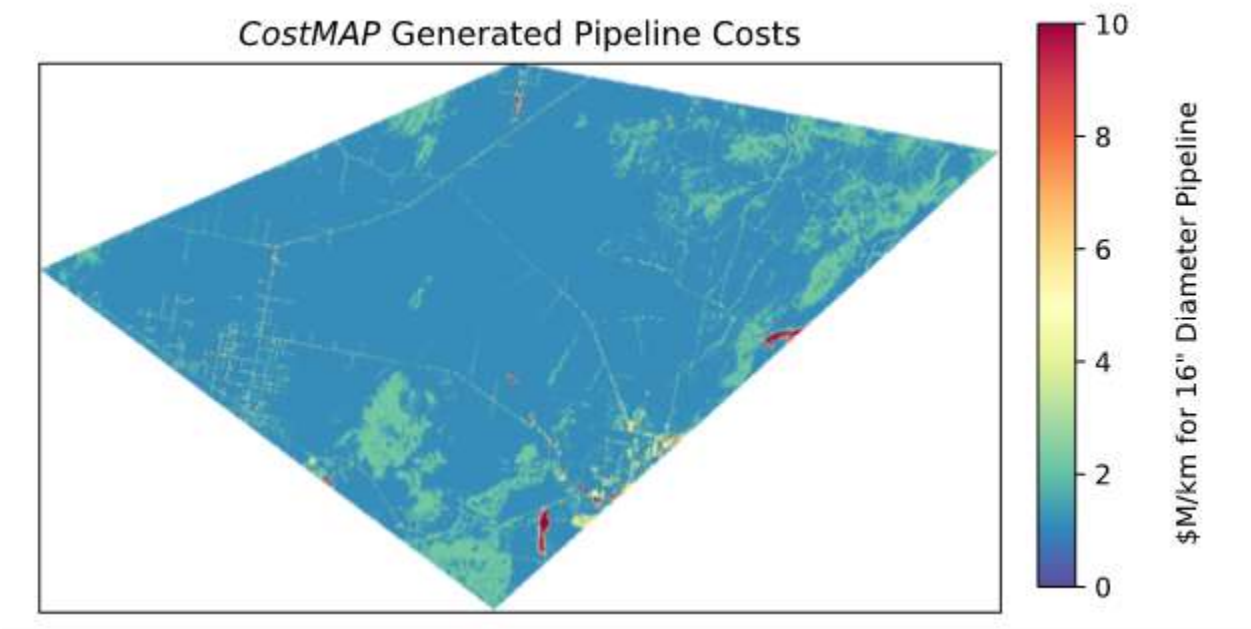


Figure 367 CO_2 pipeline cost surface generated by CostMAP^{PRO} for the project AOI

During subsequent quarters the Carbon Solutions team investigated ways to integrate known Utah Iron rights of way into the cost surface. The first method was to add the existing rights of way to the existing cost surface while maintaining default weighting values. The second method was to lower the weighting values for the existing rights of way to "bias" the cost surface into prioritizing the existing infrastructure whenever possible. Both options were made available for future CCS infrastructure assessments when using SimCCS^{PRO}.

This methodology was followed for additional cost surfaces that were generated to consider an alternate injection site. This alternate cost surface was used in SimCCS^{PRO} to generate pipeline routes (Figure 368).

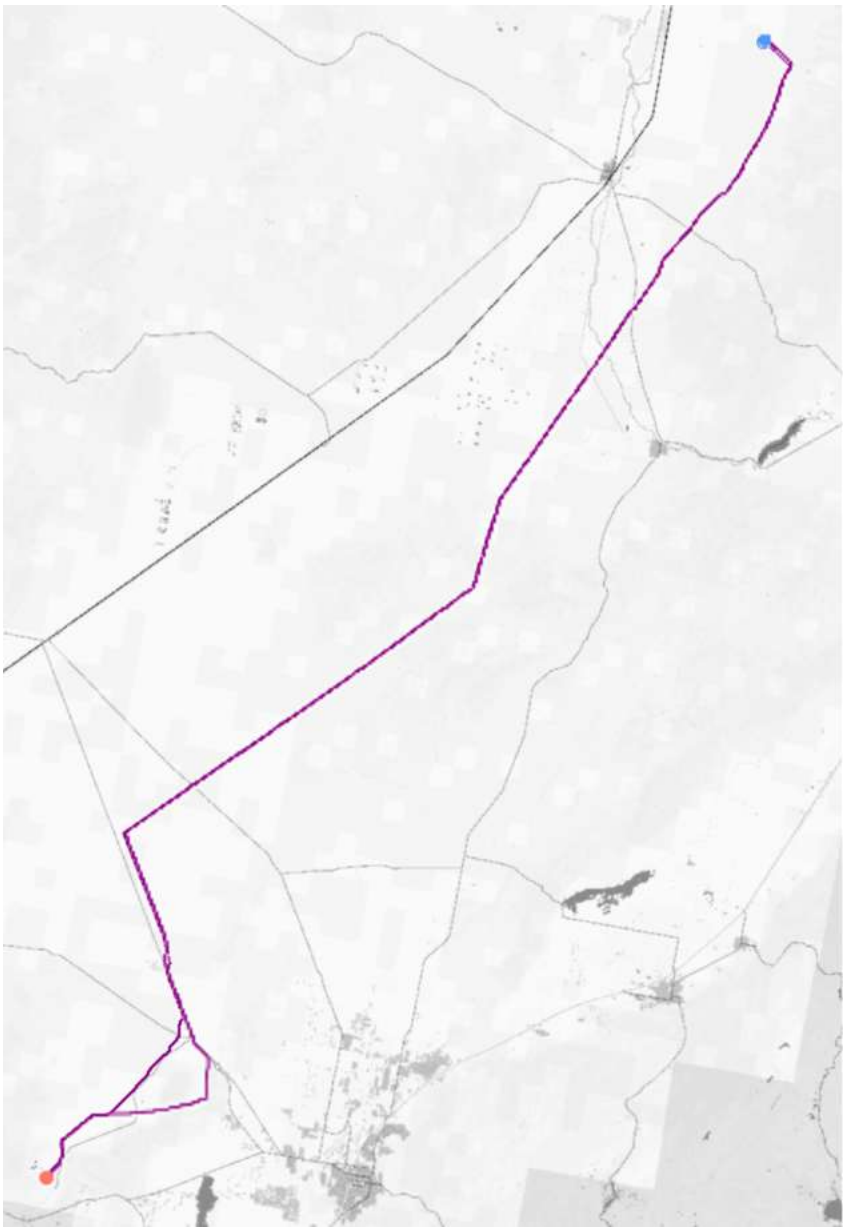


Figure 368 SimCCS^{PRO} CO_2 pipeline route from the proposed capture location to the alternate storage location

Part III – State-by-State Summaries

Arizona

Since 2008, the Arizona Geological Survey (AZGS) has participated in Carbon Capture, Utilization, and Storage (CCUS) research funded by the U.S. Department of Energy (DOE). These projects include the Southwest Regional Partnership on Carbon Sequestration (SECARB), the West Coast Regional Carbon Sequestration Partnership (WESTCARB), and the Rocky Mountain Carbon Capture and Storage (RMCCS). In 2020, AZGS was awarded funding to continue this research as part of the Carbon Utilization and Storage Partnership (CUSP) West, a 4-yr-long DOE grant led by the Petroleum Recovery Research Center at the New Mexico Institute for Mining and Technology (PRRC-NMT). CUSP West is a 13-state and 3-national-lab coalition of academic and institutional partners whose purpose is to advance existing carbon capture, utilization, and storage research and development.

As part of CUSP West, AZGS conducted a statewide sedimentary basin data review and data analyses to locate, catalogue, analyze, and rank subsurface geologic resources that can be used for long-term carbon sequestration and utilization. The scope of work required data collection, analysis, and inter-agency/state coordination in five tasks: (1) increase resolution of CCUS resource potential for all sedimentary basins (updated from Spencer [2011]), (2) catalogue CO_2 emissions point-source data, (3) map existing infrastructure pipeline right of ways (ROWs), (4) data assessment and synthesis of sedimentary basins, and (5) technology/data transfer and dissemination. Participation in multiple CUSP working groups with state partners was extremely helpful in sharing information, strategies, and much more towards meeting CUSP's objectives, milestones, and deliverables. Importantly, CUSP work fostered partnerships with industry stakeholders, including major power companies, carbon storage facility operators, and Arizona's major power and water utilities.

Four deliverables were produced: (1) a statewide map of the sedimentary basins ranked based on their potential to store CO_2 (**Figure 369**); (2) subsurface data tables shared with the CUSP group for input into SCO_2T^{PRO} (Sequestration of CO_2 Tool; Carbon Solutions 2025) and a regional CUSP database and EDX deliverable (**Figure 369**); (3) an outreach tool in the form of a web-based ArcGIS Story Map (AZGS 2022) about CCUS, highlighting basin architecture of sedimentary basins with increased storage potential; and (4) a publicly available Arizona Subsurface Viewer web map (AZGS 2025) of the subsurface storage resources in Arizona for outreach and knowledge transfer.

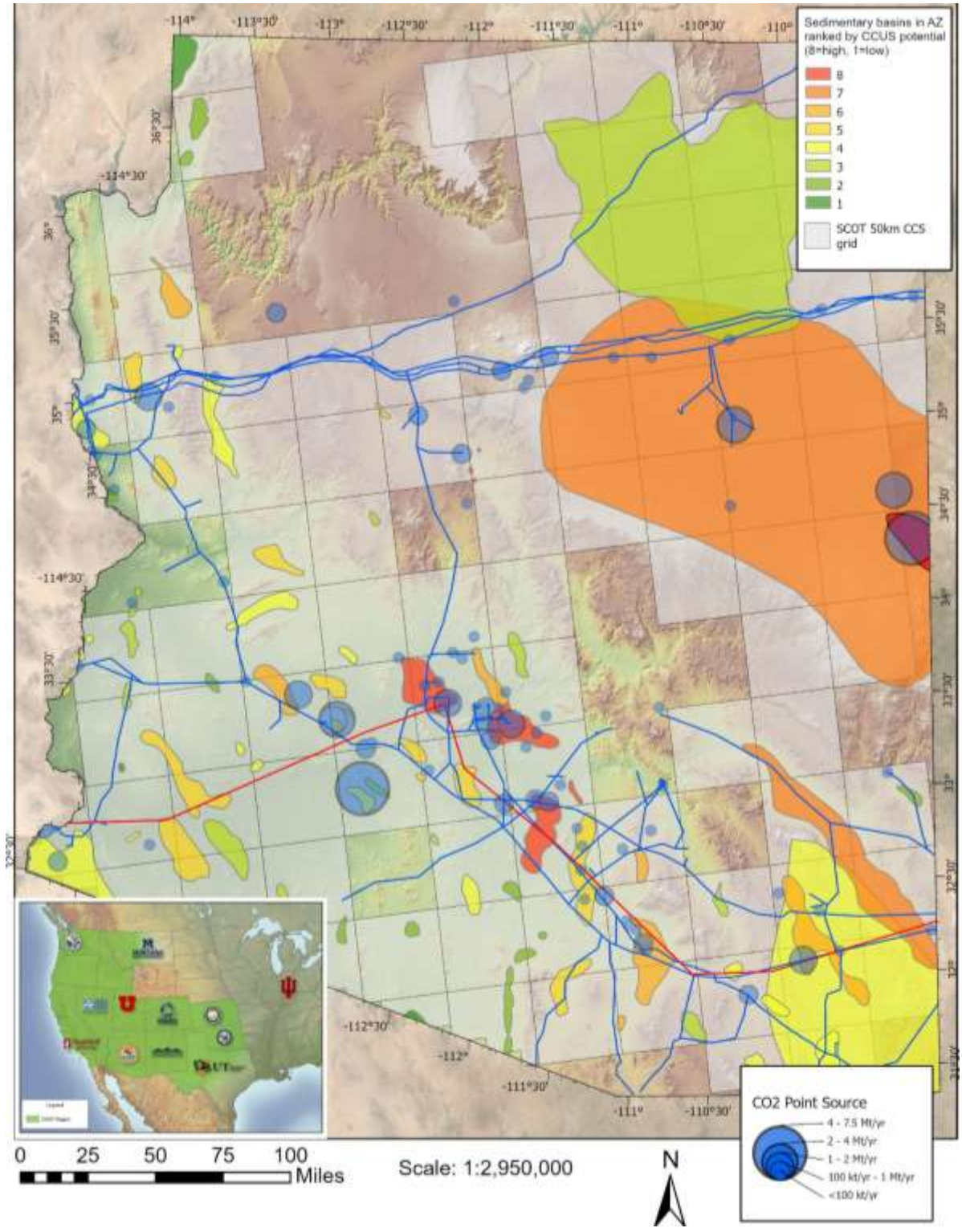


Figure 369 Location of CO_2-emission point sources and emissions (U.S. EPA 2023), pipeline ROWs of natural gas (blue) and petroleum (red), and sedimentary basins ranked by their CCUS storage potential. The SCO_2T 50-km grid represents a coarse matrix of storativity. The CUSP partnership map shown on the lower left. Basemap is a color shaded-relief DEM.

CUSP West had several positive impacts on Arizona's outlook for CCUS and related synergies. During CUSP, Arizona received UIC primacy and is pursuing regulatory pore space legislation. NMT and AZGS engaged with industry and utilities in south-central Arizona that resulted in a separately funded focused evaluation of the Harquahala Basin (Wilson et al. 2024). Results of this feasibility study led to a successful $9M DOE CarbonSAFE II award. Also, during CUSP, AZGS was awarded funding to lead a $1M DOE project to characterize mafic rock resources for CO_2 mineralization from Direct Air Capture of CO_2, in partnership with Northern Arizona University and Arizona State University. CUSP also led to two additional projects: CUSP Four Corners Regional Initiative (led by NMT), and the Southwest Regional Direct Air Capture Hub (led by Arizona State University), both of which AZGS is a subrecipient. The CUSP West Initiative put Arizona in a stronger position to leverage its subsurface resources for CCUS and synergistic energy-related efforts. Beyond CUSP, AZGS will continue to pursue collection of new data and development of new subsurface storage (CCUS and other gases) and energy-resilient opportunities such as geothermal through the state government and its stakeholders to attract industry and workforce to the state.

Acknowledgements

The success of CUSP in Arizona is due in large part to collaboration and engagement with our CUSP state partners across borders. We would like to recognize consistent support and engagement with NMT, helping to share their experiences and develop new opportunities in Arizona. We thank Arizona's power and water utilities for consistent and positive discussions and collaboration on long-term carbon management in Arizona. We also thank Arizona's Oil and Gas Conservation Commission and the Arizona Department of Environmental Quality (ADEQ) for regular engagement and discussion related to Arizona's Underground Injection Control Primacy and pore space legislation.

References

[AZGS]Arizona Geological Survey. 2022. Permanent underground CO_2 storage in southern Arizona [web-based ArcGIS StoryMap]. Tucson (AZ): Arizona Geological Survey. [accessed 2026 Jan 5]. https://storymaps.arcgis.com/stories/ecdda6f98e8541ebbfcae041aeb15970

[AZGS] Arizona Geological Survey. 2025. Arizona Subsurface Viewer [web-based interactive map]. Tucson (AZ): Arizona Geological Survey. [accessed 2026 Jan 5]. https://experience.arcgis.com/experience/235b07239c1e4435bfcd8021de4308f2

Carbon Solutions LLC. 2025. SCO_2T^{PRO} [software]. Saint Paul (MN); Carbon Solutions LLC. [accessed 2025 Dec 30]. https://www.carbonsolutionsllc.com/software/sco2tpro/

Spencer JE. 2011. Preliminary evaluation of Cenozoic basins in Arizona for carbon dioxide sequestration potential. Tucson (AZ); Arizona Geological Survey. Open-File Report 11-05. 14 p.

[U.S. EPA] U.S. Environmental Protection Agency. 2023. Greenhouse Gas Reporting Program (GHGRP), Office of Atmospheric Protection: reporting year 2021, parts C and D from FLIGHT. Washington (DC); U.S. Environmental Protection Agency. [accessed 2025 Dec 30]. https://ghgdata.epa.gov/ghgp/main.do

Wilson TC, Thompson LA, Gootee BF. 2024. Phase I pre-feasibility study to evaluate carbon dioxide and hydrogen geologic storage potential in Harquahala Basin. Tucson (AZ); Arizona Geological Survey; University of Arizona. Open-File Report 24-01. 22 p. 6 appendices. 3 plates.

California

As state's effort, we examined and investigated CO_2 storage potential, CO_2 emission sources, capture costs, potential right of way for CO_2 pipelines in California. The results demonstrate that California has sufficient geological capacity to store hundreds of years for industrial emissions at a current trend.

The statewide assessment, however, did not include comprehensive techno-economic analysis. Instead, such analyses were performed for selected Focused Project regions. Our study, titled Laying the Cornerstones of a Regional Storage Hub in California, serves as one of these Focused Projects. Detailed methodologies and case-specific results are provided in the "Distributed Emitters" section of the Focused Project report.

Additionally, we used the NRAP-OPEN-IAM tool to assess the leakage risk through the existing wellbores and Quaternary faults within the potential CO_2 storage site in our Focused Project in Kern County. The corresponding methods and case-specific results for leakage assessment are found in 'Risk assessment' section of the Focused Project report.

Subtask 3.1.2 – Update Geologic Data for CCUS Assessment

California CO_2 Storage Estimates and Potential Storage Sites

Screening Methodology for CO_2 Storage Sites

Previous studies of CO_2 storage resource in California examined oil and gas fields as well as saline formations (Downey and Clinkenbeard 2011; USGS 2013; NETL 2015a, 2015b; Long et al. 2018; Teletzke et al. 2018; Baker et al. 2020). The mean CO_2 saline formation storage estimates from USGS (2013) and NATCARB (NETL 2015a) are 90.5 $GtCO_2$ and 147.6 $GtCO_2$, respectively. In addition, a recent study that re-examined saline formations suggested the mean storage resource is at least 69.1 $GtCO_2$ in California (EFI and Stanford 2020). Baker et al. (2020) evaluated selected saline formations and hydrocarbon fields for geological carbon storage in the Sacramento and southern San Joaquin basins. The estimated CO_2 storage resources for only 4 formations in the southern San Joaquin basin ranged from 14.1 to 56.4 $GtCO_2$. Therefore, we examined both hydrocarbon reservoirs and saline formations were considered as CO_2 storage sites. We used a three-stage procedure to screen potential CO_2 storage site.

In the first stage, geological properties were applied to select qualified sites from the result of previous studies. Table 74 shows the qualifying thresholds based on geological properties. A detailed description and discussion of storage optimization parameters is given elsewhere (Kim et al. 2022). Parameters except reservoir thickness are identical to the previous study. Here, the minimum reservoir thickness, 10 m, is taken as identical to (Ramirez et al. 2010). Previously, we used a minimum reservoir thickness of 3 m. As risk minimization parameters, both salinity and top seal thickness were only applied to saline formations. The top seal thickness of hydrocarbon

formations was not found in public databases; however, a hydrocarbon accumulation indicates the presence of a seal, in most cases. The water in hydrocarbon reservoirs is typically not suitable for drinking or for agricultural purposes without significant treatment; hence, all water in oil reservoirs is assumed to be unsuitable for these purposes. Additionally, offshore sites were eliminated because they are not eligible for the LCFS credit.

Table 74 Qualifying thresholds for storage sites in this study. Modified from Callas et al. (2022) and Kim et al. (2022).

Category	Geological parameter	Qualifying threshold
Storage optimization	Storage resource (high estimate)	> 3 $MtCO_2$ (OG field)
	Depth (to top of formation)	> 800 m
	Permeability	> 10 mD (mean)
	Porosity	> 10% (mean)
	Reservoir Thickness	Target one layer, > 10 m
Risk minimization	Secondary confining	Exist secondary confining unit
	Salinity	> 10,000 ppm (TDS): Saline formation only
	Top seal thickness	> 25 m: Saline formation only
Others	Offshore location	Consider only onshore location

In the second stage, the exclusion zones were developed using four different categories as detailed in Table 75 (Kim et al. 2022). Risk categories include quaternary faults and seismically active regions. Risk categories include Quaternary faults and seismically active regions. A 2 km-wide buffer zone was applied to each side (total 4 km width) of Quaternary faults. Due to the use of publicly available data, there are, potentially, undetected faults and an incomplete seismicity catalogue. Site specific risk assessment is also needed (Kim et al. 2023). Seismicity buffer zones were assigned depending on the magnitude (M) of historical earthquakes. A 10 km diameter buffer was used for magnitude greater than 5 whereas a 5 km diameter buffer zone was used for magnitude less than 5. Active hydrocarbon fields consider exclusion zones as well. These fields are assumed to be mainly used for CO_2-EOR. Both non-active hydrocarbon fields and saline formations considered all categories including risk, population density, restricted lands, and sensitive zone/habitats as total exclusion zones.

Table 75 Exclusion zone definitions with data sources. Adopted from EFI and Stanford (2020) and Kim et al. (2022).

Category zone		Exclusion area/conditions	Data sources	Application formation	
Risk	Quaternary faulting	4 km wide "buffer zone" around all Quaternary faults	California Geologic Hazard Data and Maps (CA DOC 2010)	Active hydrocarbon field	Non-active hydrocarbon field and saline
	Seismic activity	10 km diameter for M>5 (from 1769 – present), 5 km diameter for 1.5<M<5 (from 2015 – present)	USGS Earthquake Hazards Program (USGS 2020)		
Population density		Above 75 persons/ km^2 (including city boundary)	LandScan (ORNL 2018)	-	

Restricted lands	National landmarks, conservation lands, all military installation zones, Federal lands, state lands, and Native American lands	Protected area (USGS 2019)		
Sensitive zones/habitats	Cultural sites (national park/monument, national register properties), Ecology habitats, Wildlife habitat	Wind Energy Development Exclusions and Resource Sensitivities zone (ANL 2016)		

In the third stage, the exclusion zones were subtracted from the identified hydrocarbon fields or saline formations from the first stage to obtain available storage sites. The fraction of available storage area of each original site (first stage) was multiplied by the CO_2 storage resource estimate from previous studies. In this way, new CO_2 storage resource estimates were computed. These potential CO_2 storage sites were prioritized with a scoring system.

Potential CO_2 Storage Estimates

Initially, we conducted the state-level CO_2 storage estimate for hydrocarbon field and saline formation with a 3-stage procedure. As a result, 61 potential oil & gas fields were selected with an estimated storage resource of 1.0 to 2.0 $GtCO_2$. These sites include 21 CO_2-EOR sites, mainly located in the southern San Joaquin, southern Sacramento, and Ventura Basins (Kim et al. 2022). This storage resource of 61 potential sites is sufficient for 26 to 50 yr of storage with an injection rate of 42.5 $MtCO_2$/year. This storage rate amounts to 10% of California GHG emissions averaged over 2018 and 2019.

Saline formations showed greater total storage potential than oil & gas fields as we expected. We analyzed the state-wide geological datasets for the storage site on 50 km by 50 km grid cells. The original assigned number of grid cells (50 km by 50 km) in California was 193. The number of focus grid cells in the potential CO_2 storage formations decreased to 48 grid cells. We collected data on storage formations including depth, pressure, storage thickness, permeability, porosity, temperature, temperature gradient, and storage estimated capacity (P10, P50, P90). The estimated storage capacity ranged from 52 $GtCO_2$ to 168 $GtCO_2$ before considering the exclusion criteria (in stage 1). After considering the exclusion criteria (stage 2), the final optimal estimate storage capacity in stage 3 ranged from 34 $GtCO_2$ to 104 $GtCO_2$ in California in Figure 370. In addition, we provided the potential 100 storage sites including EOR, depleted, stacked, and saline formations, total mean capacity around 37 $GtCO_2$.

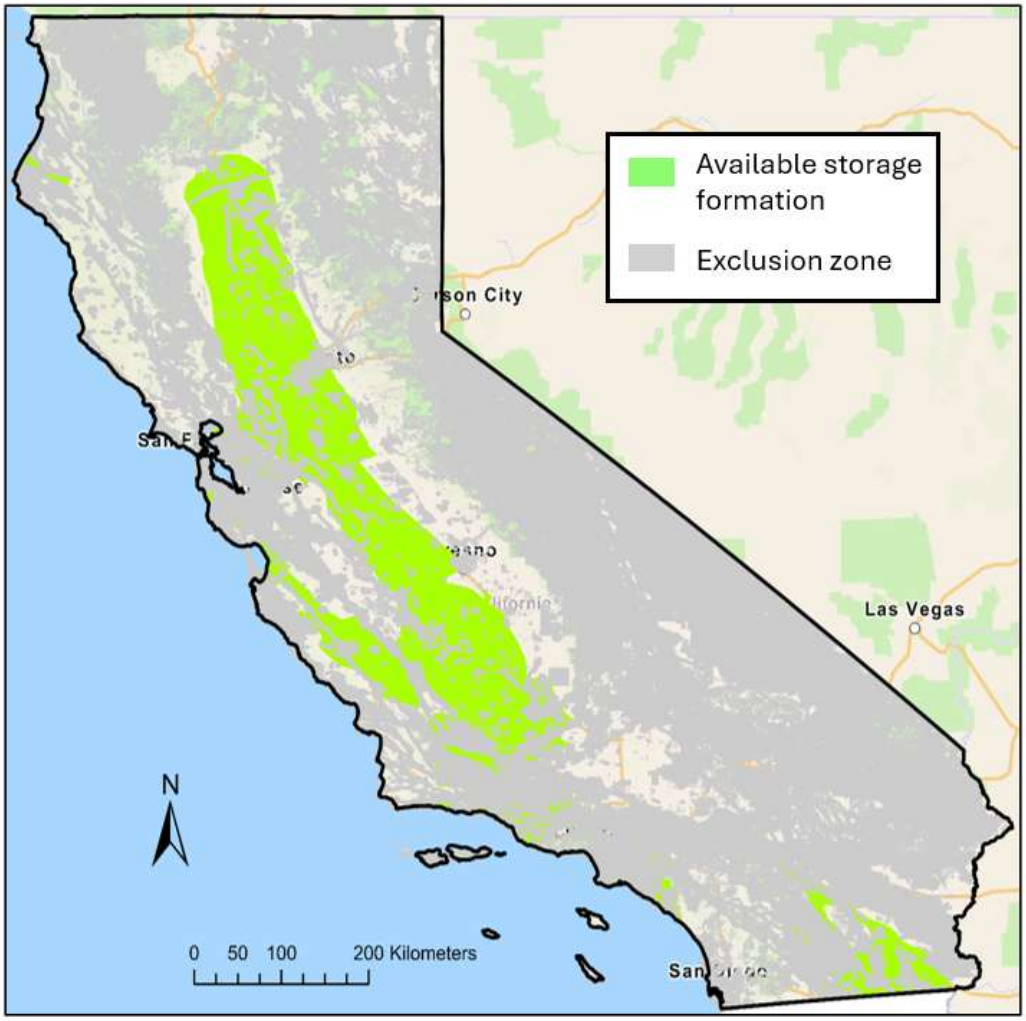


Figure 370 Available CO_2 storage formation in California using a 3-stage procedure

The southern San Joaquin Basin, which hosts the Focused Project's primary region, was examined in detail to evaluate its potential for CO_2 storage using a 3-stage procedure (Kim et al. 2023). Conservative risk exclusion zones were employed to increase the security of potential CO_2 storage in geological formations. The exclusion zones consist of risk category (Quaternary fault and seismic activity), population density, restricted lands, and sensitive ecological habitats. Even with a significantly conservative approach, the resulting estimated storage resources for hydrocarbon fields and saline formations were 0.45 - 1.15 $GtCO_2$ and 16.6 – 52.0 (mean 34.3) $GtCO_2$, respectively. These resources were then scored and storage sites with high/medium priority scores and greater than 20 $MtCO_2$ storage resource were defined as the target sites for technoeconomic analysis. All fields passing through screening with exclusion zones have desirable qualities for storage. In this way, 7 hydrocarbon fields were selected. Among them, 5 fields were CO_2-EOR candidates and 2 fields were depleted oil fields only for storage. Also, a total of 34 saline formations including 2 stacked formations were selected. The 41 storage sites chosen totaled 5.8 $GtCO_2$ of storage resource (see Figure 371).

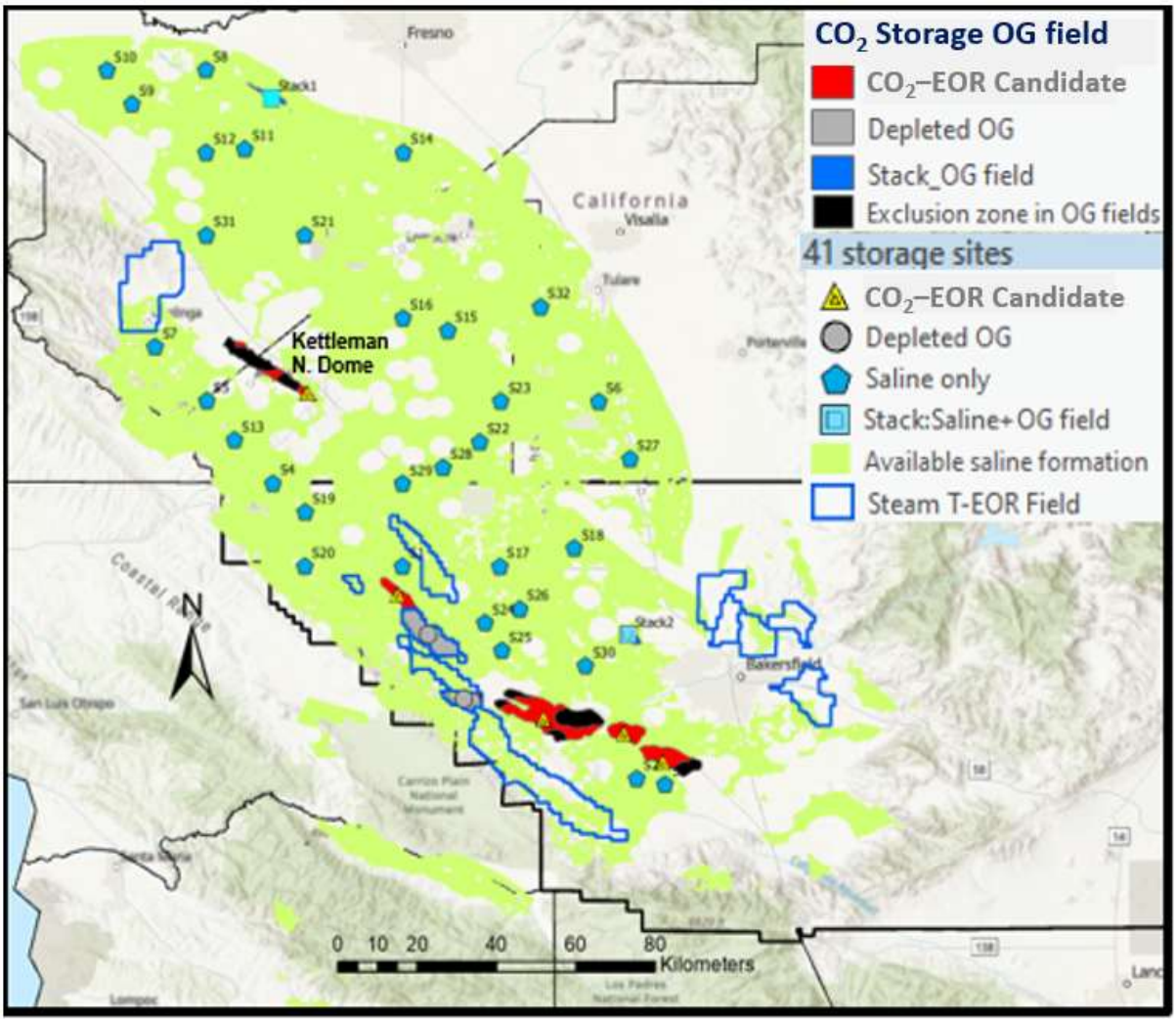


Figure 371 Prospective CO_2 storage sites among available saline formations and hydrocarbon fields in the southern San Joaquin Basin

Subtask 3.1.4 – Gather and Catalogue CO_2 Emissions

California CO_2 Emission Sources

The California Air Resources Board (CARB) reports annual emissions from greenhouse gas (GHG) generating activities statewide in 2018 of 425.3 Mt of carbon dioxide (CO_2) equivalent ($MtCO_2e$; CARB 2020). This amount is similar to 2017 levels and is 6 $MtCO_2e$ below the 2020 GHG target limit of 431 $MtCO_2e$ for California (CARB 2019, 2020). Among GHG emissions, CO_2 makes up about 81% of the total in the United States (EPA 2020a). California GHG emissions were around 6.4% of the United States total of 6,677 $MtCO_2e$ in 2018 (EPA 2020a). California contributes about 1% of global emissions. Figure 372 shows the distribution of all GHG emissions in California by economic sector-including transportation, industrial, electricity, commercial, and so on in 2018 expressed as CO_2 equivalent to account for the differing global warming potentials among GHG (CARB 2020).

Industrial and electricity sector GHG emissions tend to occur from relatively large point sources. Hence, we focus on these two sectors that account for 39% or 166 $MtCO_2e$/year of emissions. Solutions to reduce emissions or capture emissions from these sources are important to meeting California's climate goals in a timely and cost-effective manner (EFI and Stanford 2020).

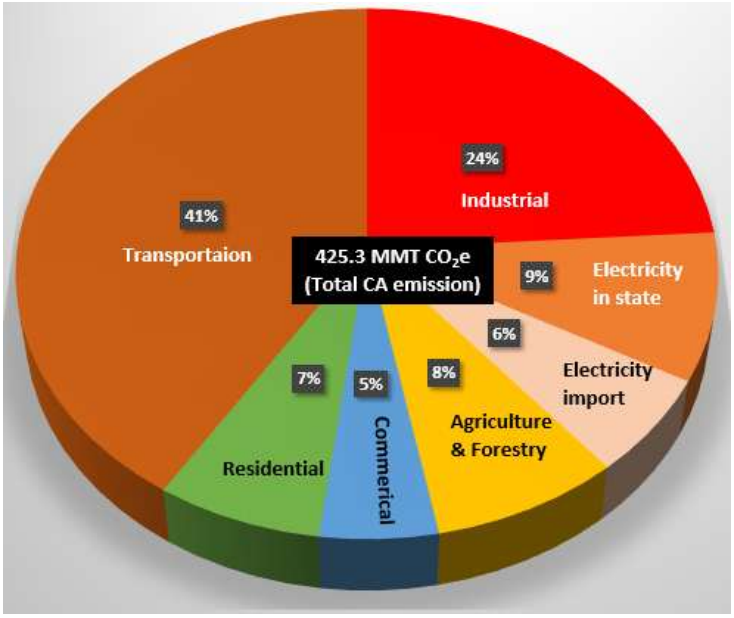


Figure 372 California greenhouse gas (GHG) emission in 2018 by economic sector expressed as CO_2 equivalent (CARB 2020)

The Environmental Protection Agency (EPA) provides facility level information on greenhouse gas tool (FLIGT) to identify the emission amount for industrial and electric sector facilities (EPA 2020b). In particular, the EPA Greenhouse Gas Reporting Program (GHGRP) is an open source to access. We found 541 industrial facilities and powerplants in California in 2018. But, GHGRP does not include combined heat and power (CHP) plants and ethanol plants as an industrial facility. Therefore, both CHP and ethanol facilities are investigated from EPA Emission & Generation Resource Integrated Database (eGRID) and GHGRP subpart D, respectively (EPA 2020c, 2021).

We eliminated any facilities in the industrial sector that are not suitable for CO_2 capture (e.g., waste) and had low emissions level, less than or equal to 100,000 t CO_2 (tCO_2e) per year. The detailed selection for each industrial subsector is shown in Table 76. The sum of emissions from these facilities estimates around 34.2 $MtCO_2e$, of which the capturable emissions totaled approximately 30.8 $MtCO_2e$ with 90% capture.

Table 76 Screen CO_2 emission from industrial and power sectors

Type	Industrial sector						Power sector (NGCC plant)	Total
	H_2 (Steam Reformer)	**CHP**	**Refinery**	**Cement**	**Ethanol**	**Total**		
Emission*, $MtCO_2e$	10.3	10.0	5.5	7.8	0.57	**34.2**	**22.8**	**57.0**

No. of facilities	15	15	8	8	4	**50**	**25**	**75**
*Average (2018 to 2019) emission data								

The GHG emission of electric sector is classified with in-state and out-of-state. Among in-state powerplants, 47% electricity is generated by natural gas in 2018. So, we have a focus on natural gas combined cycle power (NGCC) plants, because there are no coal-power plants in California and CHP plants are already included under the industrial sector. Natural gas (NG) powerplants that have a capacity of 250 MW or greater and were constructed after 2000 were selected as potential sources. The average GHG emissions from 2018 to 2019 were used identical to industrial sources. There is total 25 plants to emit total 22.8 $MtCO_2$/yr. Among them, 18 plants were greater than 500 MW and built after 2000. Finally, Figure 373 shows large emitters for both sectors in California.

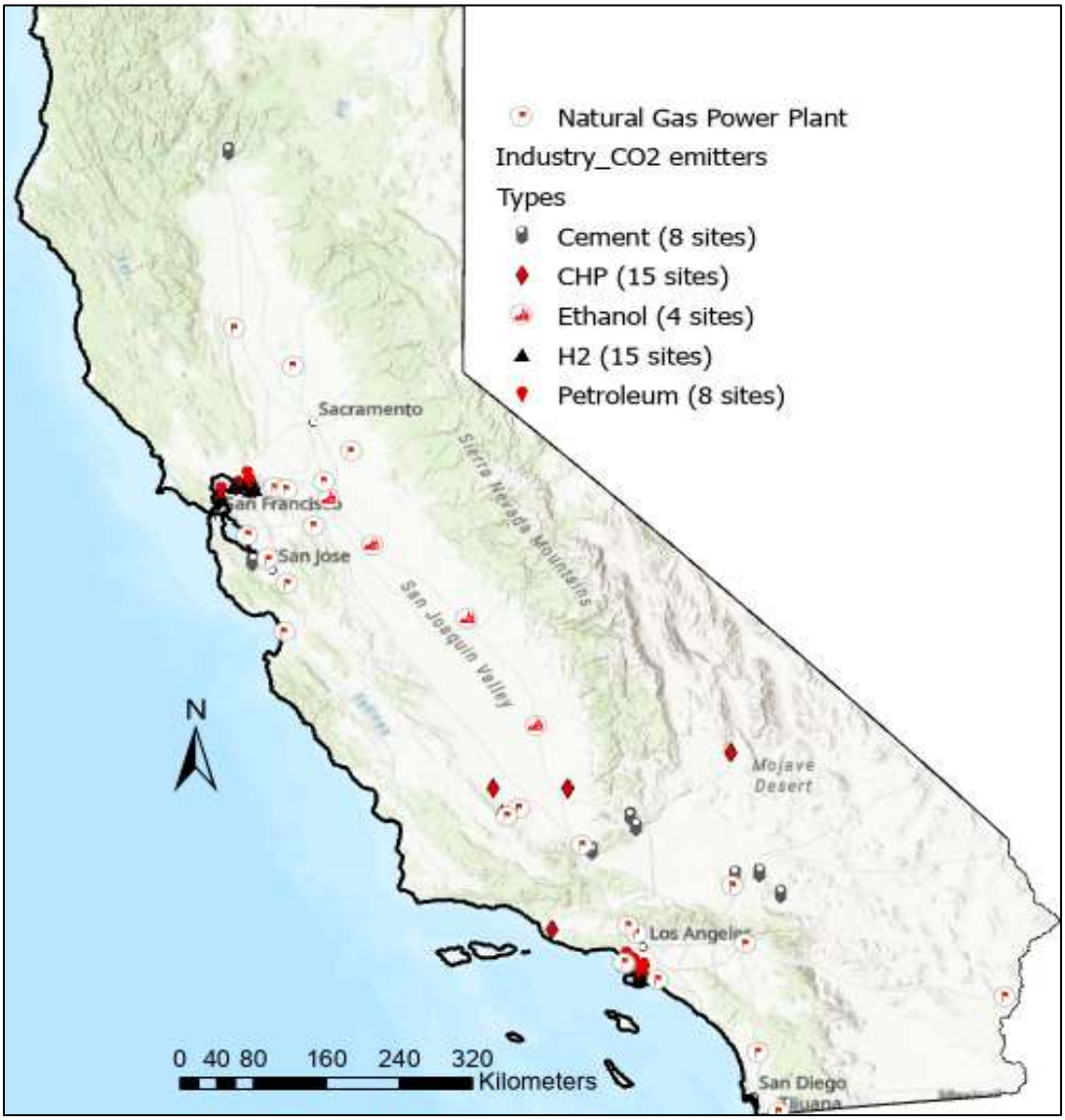


Figure 373 Large CO_2 emitters on industrial and power sectors in California

In addition, thermal enhanced oil recovery (EOR) with steam injection and CHP is responsible for nearly half of all California's crude oil production. Steam injection relies on natural gas as the fuel. It noticed that the CO_2 emissions from these facilities are considered, but specific data were difficult to obtain because the emissions levels are not reported separately. Still, CO_2 capture and storage from steam generators can claim the low carbon fuel standard (LCFS) credit in California. Therefore, we investigated and identified the CO_2 emissions from these facilities under the Focused Project. The total CO_2 emission from steam generators and CHPs had estimated 8.6 $MtCO_2$ and 2.6 $MtCO_2$/yr, respectively. The detailed approach and result were shown in the section of 'Distributed emitters' in the Focused Project report.

CO_2 Capture Costs by Industrial Sector in California

We examined and adopted CO_2 capture costs for six different industries and power sectors in Table 74 (EFI and Stanford 2020). This data can be used to assess technoeconomic analysis for CO_2 storage projects for large-scale emission sources. Table 77 shows average and range of CO_2 capture costs by different sectors (EFI and Stanford 2020). The CO_2 capture cost varies significantly depending on the purity of the emission stream, composition of the flue gas, and energy intensity of the capture process. Higher CO_2 concentrations significantly reduce capture cost. For example, ethanol fermentation streams are nearly pure CO_2 (approximately 100%), requiring minimal separation effort, while natural-gas-fired power plants (NGCC) and CHP units have dilute CO_2 streams (7–10%), which demand larger absorber columns, higher solvent circulation rates, and more regeneration energy.

Table 77 CO_2 capture costs by sectors

Type / Sector	CO_2 capture cost range, $/t$CO_2$	Average cost, $/t$CO_2$	CO_2 concentration in emission gas
H_2 (steam reformer)	58–101	71.7	12%
CHP	60–131	95.7	7–10%
Refinery	58–72.5	64.4	15%
Cement	48.2–75.2	58.5	22.5%
Ethanol	20–22.6	21.1	approximately 100%
Power (NGCC plant)	62.4–95.9	77.4	7–10%

Additionally, we conservatively estimated the capture costs for enhanced oil recovery facilities—specifically steam generation (SG) and combined heat and power (CHP) systems—based on operating parameters from previous studies (Kim and Kovscek 2017). Capture costs for CHP facilities ranged from \$59 to \$78/tCO_2, while those for SG systems ranged from \$57.6 to \$74.5/tCO_2, depending on the operating conditions at each site. Detailed methodologies and site-specific results are presented in 'Distributed emitters' section of the Focused Project report.

Right of Way for Potential CO_2 Pipeline

Pipelines are very important infrastructure to deliver CO_2 from emitters to sink sites. There is no CO_2 pipeline in California. Therefore, the new CO_2 pipeline should be constructed with secure right of way (ROW). Regarding the ROW, there are several pipelines, canals, aqueducts line, and railroad to investigate. The detailed list is in Table 78.

Table 78 Pipelines in California		
Type	**Sources**	**Organization**
Nature Gas Pipeline	https://www.eia.gov/maps/	U.S. Energy Information Administration (EIA)
Crude oil pipeline/Petrochemical pipeline		
Railroad	https://www.bts.gov/geospatial/national-transportation-atlas-database.	National Transportation Atlas Database (NTAD)
Canals and Aqueducts line	https://gis.water.ca.gov/arcgis/rest/services/InlandWaters/i12_Canals_and_Aqueducts_local/MapServer	Department of Water Resources (DWR)

Technoeconomic Analysis

Based on the characteristics of storage sites and CO_2 capture cost under the tax credit, we conducted technoeconomic analysis of the specific region in the Focused Project. Detailed methodologies and case-specific results are presented in 'Distributed emitters' section of the Focused Project report.

References

[ANL] Argonne National Laboratory. 2016. West-wide wind mapping project maps and data: wind energy development exclusions and resource sensitivities area. Lemont (IL); Argonne National Laboratory. [accessed 2025 Dec 30]. http://wwmp.anl.gov/maps-data

Baker SE, Peridas G, Stolaroff JK, Goldstein HM, Pang SH, Lucci FR, Li W, Slessarev EW, Pett-Ridge J, Ryerson FR, et al. 2020. Getting to neutral: options for negative carbon emissions in California. Livermore (CA); Lawrence Livermore National Laboratory.

[CA DOC] California Department of Conservation. 2010. Geologic hazard data and maps. Sacramento (CA); California Department of Conservation. [accessed 2025 Dec 30]. http://maps.conservation.ca.gov/geologichazards

[CARB] California Air Resources Board. 2019. GHG 1990 emissions level and 2020 limit. Sacramento (CA); California Air Resources Board. [accessed 2025 Dec 30]. https://ww2.arb.ca.gov/ghg-2020-limit

[CARB] California Air Resources Board. 2020. California greenhouse gas emissions for 2000 to 2018. Sacramento (CA); California Air Resources Board. [accessed 2025 Dec 30]. https://ww3.arb.ca.gov/cc/inventory/pubs/reports/2000_2018/ghg_inventory_trends_00-18.pdf

Callas C, Saltzer SD, Davis JS, Hashemi S, Kovscek AR, Okorofor ER, Wen G, Zoback MD, Benson SM. 2022. Criteria and workflow for selecting depleted hydrocarbon reservoirs for carbon storage. Appl Energy. 324:119668. doi:10.1016/j.apenergy.2022.119668

Downey C, Clinkenbeard JP. 2011. Studies impacting geologic carbon sequestration potential in California: offshore carbon sequestration potential, Sacramento Basin salinity investigation of select formations, Sacramento Basin hydrocarbon pool size distribution. Sacramento (CA); California Energy Commission. CEC-500-2011-044.

[EFI and Stanford] Energy Futures Initiative and Stanford University. 2020. An action plan for carbon capture and storage in California: opportunities, challenges, and solutions. Stanford (CA); Energy Futures Initiative and Stanford Center for Carbon Storage.

Kim TW, Callas C, Saltzer SD, Kovscek AR. 2022. Assessment of oil and gas fields in California as potential CO_2 storage sites. Int J Greenh Gas Control. 114:103579. doi:10.1016/j.ijggc.2022.103579

Kim TW, Kovscek AR. 2017. High-temperature imbibition for enhanced recovery from diatomite. Paper presented at: SPE Western Regional Meeting; 2017 Apr; Bakersfield (CA). SPE-185632-MS. doi:10.2118/185632-MS

Kim TW, Yaw S, Kovscek AR. 2023. Scoring, ranking, and technoeconomics of carbon capture and storage opportunities in the Central Valley of California. Int J Greenh Gas Control. 128:103968. doi:10.1016/j.ijggc.2023.103968

Long JCS, Birkholzer JT, Mace AJ, Brady SE. 2018. Long-term viability of underground natural gas storage in California. Sacramento (CA); California Council on Science and Technology.

[NETL] National Energy Technology Laboratory. 2015a. Carbon storage atlas. 5th ed. Pittsburgh (PA); U.S. Department of Energy, National Energy Technology Laboratory. [accessed 2025 Dec 30]. https://www.netl.doe.gov/sites/default/files/2018-10/ATLAS-V-2015.pdf

[NETL] National Energy Technology Laboratory. 2015b. The national carbon sequestration database (NATCARB). Pittsburgh (PA); National Energy Technology Laboratory. [accessed 2025 Dec 30]. https://edx.netl.doe.gov/dataset/natcarb-alldata-v1502

[ORNL] Oak Ridge National Laboratory. 2018. LandScan database. Oak Ridge (TN); Oak Ridge National Laboratory. [accessed 2025 Dec 30]. https://landscan.ornl.gov/landscan-datasets

Ramírez A, Hagedoorn S, Kramers L, Wildenborg T, Hendriks C. 2010. Screening CO_2 storage options in the Netherlands. Int J Greenh Gas Control. 4(2):367–380. doi:10.1016/j.ijggc.2009.11.002

Teletzke G, Palmer J, Drueppel E, Sullivan MB, Hood K, Dasari G, Shipman G. 2018. Evaluation of practicable subsurface CO_2 storage capacity and potential CO_2 transportation networks, onshore North America. In: Proceedings of the 14th Greenhouse Gas Control Technologies Conference; 2018 Oct; Melbourne (Australia). p. 21–26.

[EPA] U.S. Environmental Protection Agency. 2020a. Inventory of U.S. greenhouse gas emissions and sinks: 1990–2018. Washington (DC); U.S. Environmental Protection Agency. EPA 430-R-20-002.

[EPA] U.S. Environmental Protection Agency. 2020b. 2018 greenhouse gas emissions for large facilities. Washington (DC); U.S. Environmental Protection Agency, FLIGHT program.

[EPA] U.S. Environmental Protection Agency. 2020c. 2018 emission and generation resource integrated database (eGRID). Washington (DC); U.S. Environmental Protection Agency.

[EPA] U.S. Environmental Protection Agency. 2021. 2019 emission and generation resource integrated database (eGRID). Washington (DC); U.S. Environmental Protection Agency.

[USGS] U.S. Geological Survey. 2013. National assessment of geologic carbon dioxide storage resources: results. Reston (VA); U.S. Geological Survey. Circular 1386. [accessed 2025 Dec 30]. https://pubs.er.usgs.gov/publication/cir1386

[USGS] U.S. Geological Survey. 2019. Protected areas database of the United States. Reston (VA); U.S. Geological Survey. [accessed 2025 Dec 30]. https://www.usgs.gov/core-science-systems/science-analytics-and-synthesis/gap/science/protected-areas

[USGS] U.S. Geological Survey. 2020. Earthquake hazards program. Reston (VA); U.S. Geological Survey. [accessed 2025 Dec 30]. https://www.usgs.gov/natural-hazards/earthquake-hazards/earthquakes

Colorado

Kansas

The Kansas Geological Survey (KGS) participated in CUSP activities and led the CUSP Midstream Operator Storage of CO_2 ($MOSCO_2$) focused project under current P.I. Brendan Bream. On behalf of the State of Kansas, Brendan Bream presented at the annual CUSP meetings in 2024 and 2025; Franek Hasiuk (and Jennifer Raney?) presented at annual CUSP meetings in 2022 and 2023. The KGS facilitated several workshops with state stakeholders including regulatory and industry representatives that would be relevant and/or impacted by Kansas seeking Class VI primacy. The KGS also hosted the 2023(?) annual CUSP meeting in Lawrence, Kansas at the University of Kansas as well as the 2025 reactive transport STOMP short course. Outside of CUSP, the KGS remains engaged with CCS stakeholders and is conducting relevant research (e.g., Bhattacharjee and Bream 2025; Bream et al. 2025) that will be important to future CCS activity within Kansas and the region.

References

Bhattacharjee S, Bream BR. 2025. Top Arbuckle, Kansas—depth structure map. Lawrence (KS); Kansas Geological Survey. 3 p. Open-File Report 2025-50. [accessed 2025 Dec 30]. https://www.kgs.ku.edu/Publications/OFR/2025/OFR2025-50.pdf

Bream BR, Bhattacharjee S, White M, Gumble J. 2025. Preliminary screening approach to support carbon sequestration efforts in Kansas. In: Carbon Capture, Utilization, and Storage (CCUS) Conference; 2025 Mar 3–5; Houston (TX).

Nevada

A preliminary and regional assessment of the potential for CO_2 storage within a variety of geological settings was previously performed for the State of Nevada (Price et al. 2005). This assessment, however, was performed without oil and gas well log information. An assessment of using enhanced oil recovery (EOR) for CO_2 geological storage at existing oil fields in Nevada was also performed that used site-specific oil and well gas well logs to evaluate the favorability of EOR in the state (LaPointe et al. 2007). Saline formations were previously assessed as having

the best potential for CO_2 geological storage in Nevada compared to other capacities, such as EOR and chemical reactions with mafic and ultramafic rocks (Price et al. 2005; LaPointe et al. 2007; Sturmer et al. 2007).

The role of the Nevada CUSP West project was to leverage previous assessments of CO_2 geological storage in the state, as well as perform a more detailed assessment of CO_2 geological storage in saline formations using oil and gas well log information. The Desert Research Institute (DRI), Reno, Nevada participated in CUSP West activities and was led by Steven Bacon, Ph.D., P.G., C.E.G. The DRI team members also included Jay Arnone, Ph.D., Richard Jasoni, Ph.D., Rish Parashar, Ph.D., and Jessica Larsen. Included in this report are details of state-level accomplishments for the State of Nevada that are directly related to specific subtasks related to Tasks 2 and 3 of the CUSP West project.

Task 2 – Addressing Key Technical Challenges

Task 2.1 – Expand Characterization of Stacked and Unconventional Storage

Nevada CUSP West activities included the identification of five deep sedimentary basins with stacked saline formations in northern Nevada that have the potential to be sites for CO_2 geological storage based on the evaluation of oil and gas well log data. Additional activities included the completion of a focused project to assess the potential of using CO_2 geological storage in sedimentary basin geothermal reservoirs (see Part II Focused Project section and report in Appendix).

Task 2.2 – Develop Collaborations to Integrate and Validate Key Technologies to Optimize Storage and Reduce Uncertainty in Storage Permanence and Integrity

The DRI team developed new collaborations through the focused project. The focused project team included collaboration between Steven Bacon (PI) and Rishi Parashar of DRI and Jonathan Ogland-Hand (Co-PI), Jeff Bennett, and Richard Middleton of Carbon Solutions, LLC.

Task 3 – Facilitating Data Collection, Sharing, and Analysis

Task 3.1 – Engaging with National Laboratories

The DRI team had several email discussions at the beginning of the project with Lianjie Huang of LANL regarding potential collaborations with his group and operators at the Patua Geothermal Power Plant in Fernley, Nevada where they are evaluating the use of CO_2 as a fracking fluid to enhance heat generation and transfer. Possible joint work was internally discussed with the DRI team to include developing a near-surface CO_2 monitoring network near the injection well site to potentially measure CO_2 leakage. The overall goals of this specific research effort would be to better understand the spatiotemporal patterns of leaked CO_2 during injection and post injection, that in turn, could be used provide insight on how geothermal systems potentially store CO_2. Ultimately, this effort would be performed in anticipation for when supercritical CO_2 is used as a geothermal working fluid for geological storage in the future

(e.g., focused project). Furthermore, the research effort would also provide information to evaluate if this type of CO_2 monitoring approach is feasible in quantifying CO_2 leakage across all CCUS technologies.

Task 3.1.1 – Identify Data Requirements & Needs

Deep well-log data in Nevada are limited given the relatively low potential for oil and gas resources in the state (e.g., Price et al. 2005). Early exploration of oil and gas resources across Nevada and continued development of a few small oil fields in the eastern part of the state have resulted in up to 1,125 well logs in the Nevada Bureau of Mines and Geology oil and gas well information database. The DRI team initially screened 300 well logs from the database based on the criteria of well logs having depths greater than 800 m (**Figure 374**). A subset of 30 well logs was further screened for further evaluation based on well sites located outside the regionally extensive and deep fresh-groundwater aquifer system of eastern-southeastern Nevada that is an important resource for native habitats and water supply in the southern parts of the state (Sweetkind et al. 2011; **Figure 374**).

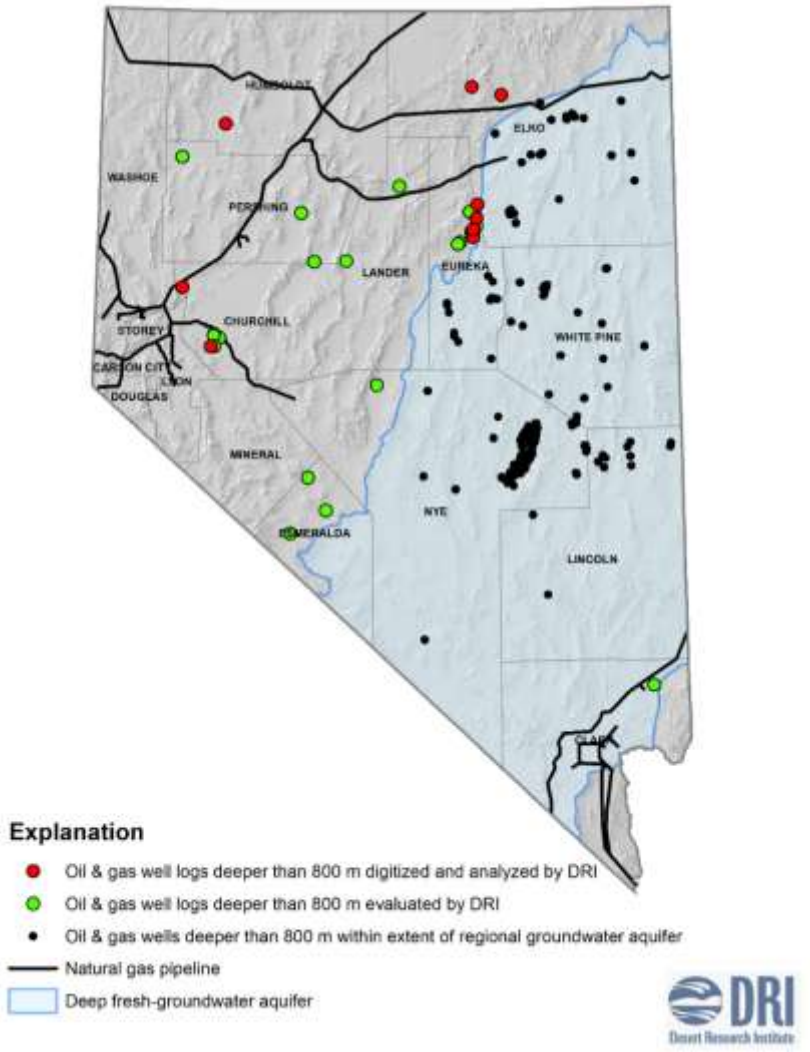


Figure 374 Map showing the location of oil and gas wells deeper than 800 m and the extent of the regional, deep fresh-groundwater aquifer in Nevada (e.g., Price et al. 2005; Sweetkind et al. 2011). The location of well logs evaluated and analyzed by DRI outside of the deep fresh-groundwater aquifer, along with the network of existing natural gas pipelines are also shown.

Lithologic and geophysical logs from the 30 well sites were evaluated to identify data deficiencies. Of the 30 well logs, only nine logs contained the minimum required data to assess the potential for stacked saline formations at each well site based on the CUSP screening parameters for the SCO_2T database. The required data in our analysis included a lithologic log, bottom-hole temperature, and geophysical wire logs of gamma ray, long-normal resistivity, and neutron porosity.

Task 3.1.2 – Update Geologic Data for CCUS Assessment

Saline formations were targeted for CO_2 geologic storage in north-northwestern Nevada. Nine well sites were evaluated based on meeting screening criteria and minimum requirements of oil and gas well logs for the SCO_2T database (**Figure 374**). Geophysical wire logs from the nine wells were digitized using Neuralog Pro software prior to analysis. Gamma ray data were used to verify general grain size in combination with lithologic logs to characterize rock type. Salinity

and intrinsic permeability of formations were estimated from resistivity and neutron porosity wire logs, along with temperature gradient based on a variety of analytical solutions and methods commonly used to estimate the quality of groundwater and permeability of aquifers (e.g., Jorgensen 1989; Hudson 1996; USBR 2019). Analytical solutions were derived and resulting analyses were performed using MATLAB programming language (see Nevada Appendix).

The analysis of the nine well logs yielded five candidate well sites that have the hydrogeologic properties favorable for CO_2 storage in stacked saline formations with salinities greater than 3,000 mg/L per the CUSP screening parameters (**Figure 375**). The stacked saline formations of the five well sites have reservoir thicknesses ranging from 61 to 122 m, mean depths ranging from 1,040 to 2,010 m, porosity ranging from 0.22 to 0.38, and salinity greater than 3,000 mg/L, averaging around 10,000 mg/L. The lithology of the saline formations consists of Tertiary sedimentary basin fill composed mostly of sandstone, siltstone/claystone, limestone with tuffaceous layers and Miocene basalt (see 50-km SCO_2T geologic input database).

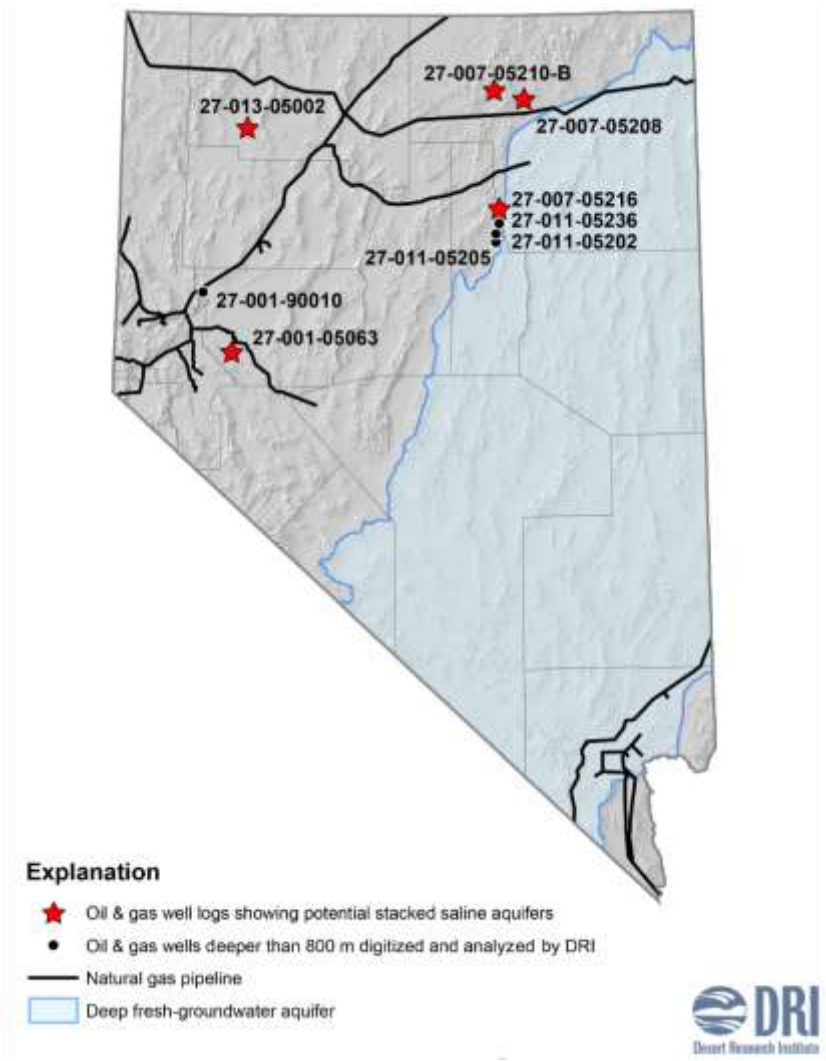


Figure 375 Map showing the location of oil and gas wells deeper than 800 m and the logs digitized and analyzed by DRI. Of the nine well sites analyzed, five sites were identified as having characteristics that could potentially

support CO_2 geologic storage in stacked saline formations (red stars). The API numbers for each well, the network of existing natural gas pipelines, and the extent of the regional fresh-groundwater aquifer are also shown.

The area of saline reservoirs was estimated at 2-km resolution using geospatial datasets that show depth to basement from gravity surveys (Ponce 2004; Price et al. 2005) and mapped Quaternary faults (USGS/NBMG 2016). Depth to pre-Cenozoic rock was used to define the base of sedimentary basins given a lack of multiple wells at the five candidate CO_2 storage sites. The basement dataset was reclassified to limit areas within sedimentary basins with depths greater than 800 m. Following the approach of Price et al. (2005), we further reduced the basement dataset by not including areas near Quaternary faults in order to limit CO_2 leakage along shear zones by including setbacks of 2 km on both sides of normal faults and 1 km on both sides of strike slip faults (**Figure 376**).

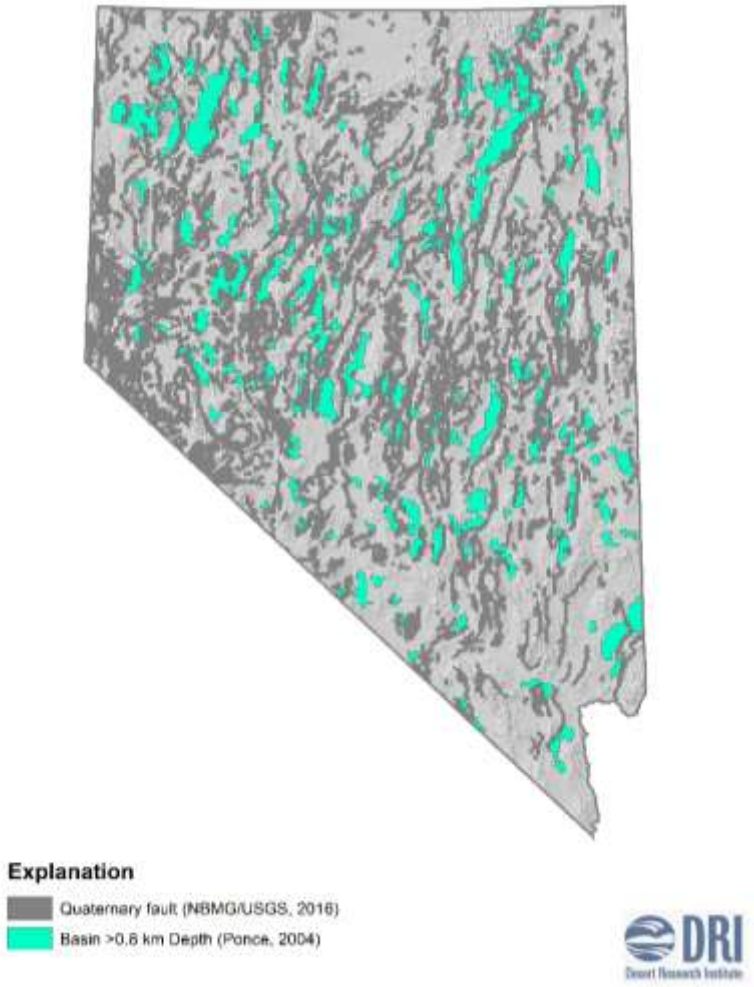


Figure 376 Map showing the location of sedimentary basins with depths greater than 800 m (0.8 km) and Quaternary faults with 2-km setbacks on normal faults and 1-km setbacks on strike slip faults.

The areal extent of identified stacked saline formations at well sites were extrapolated across the entire sedimentary basin to include areas with depths greater than 800 m and outside fault setbacks. Additional refinement of basin area was determined from the spatial extent of sedimentary fill thickness between the depths of identified stacked saline formations. The five

sedimentary basins that meet the criteria of having deep well log information and acceptable CUSP screening parameters include from west to east: Black Rock, Fallon, Tuscarora, Humboldt, and Pine Valley. The area and associated aquifer properties of each sedimentary basin were included in the 50-km SCO_2T geology input database. The five-candidate geological CO_2 storage sites are also located relatively close to the network of existing natural gas pipelines in northern Nevada (**Figure 377**).

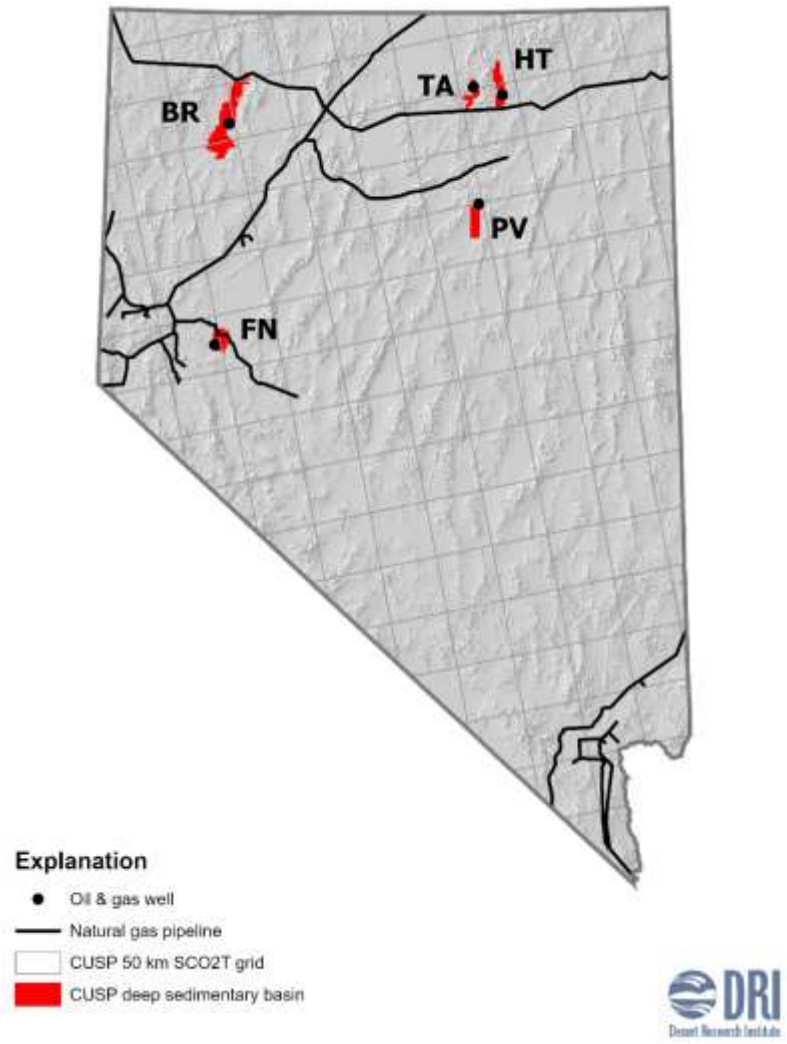


Figure 377 Map showing the location of oil and gas wells and extent of 2-km resolution deep sedimentary basins identified as potential CO_2 geological storage sites in northern Nevada. The 50-km SCO_2T grid and network of existing natural gas pipelines are also shown. Sedimentary basin names: BR – Black Rock; FN – Fallon; TA – Tuscarora; HT – Humboldt; and PV – Pine Valley.

Task 3.1.3 – Update USDW Data from All Public Sources

The extent of the regional and deep fresh-groundwater aquifer system in south-southeastern Nevada (e.g., Sweetkind et al. 2011) was used in the selection of oil and gas well sites (**Figure 374**). Wells located in the deep fresh-groundwater aquifer system were not considered in the CO_2 geological storage assessment.

Task 3.1.4 – Gather and Catalog CO_2 Emissions (Point) Source Database

Carbon dioxide point source data for Nevada were collected from the Environmental Protection Agency (EPA) Facility Level Information on Greenhouse Gasses Tool (FLIGHT; EPA FLIGHT) database (U.S. EPA 2025, the U.S. Energy Information Administration (EIA) database (EIA 2025), information about NV Energy-owned generating resources on the NV Energy website (NV Energy 2025). Carbon dioxide source data collected during the project period includes: CO_2 source site name, latitude and longitude of the site, CO_2 source type, number of CO_2 streams, total CO_2 emitted (Mt CO_2/yr, site owner name, site operator name, county, and state (all data were cataloged into the "Partner_Site_Selection_Database.xlsx" spreadsheet).

A total of 20 CO_2 point sources from power, minerals, and chemical plants were identified near Reno and Elko in the northern part of the state and Las Vegas in the southern part. Assessment of point source quantities included identifying CO_2 point sources that emitted greater than 0.100 Mt/yr. Total emissions in Nevada were greater than 100 Mt/yr in 2019, where the highest emissions were centered near Las Vegas in southern Nevada (**Figure 378**).

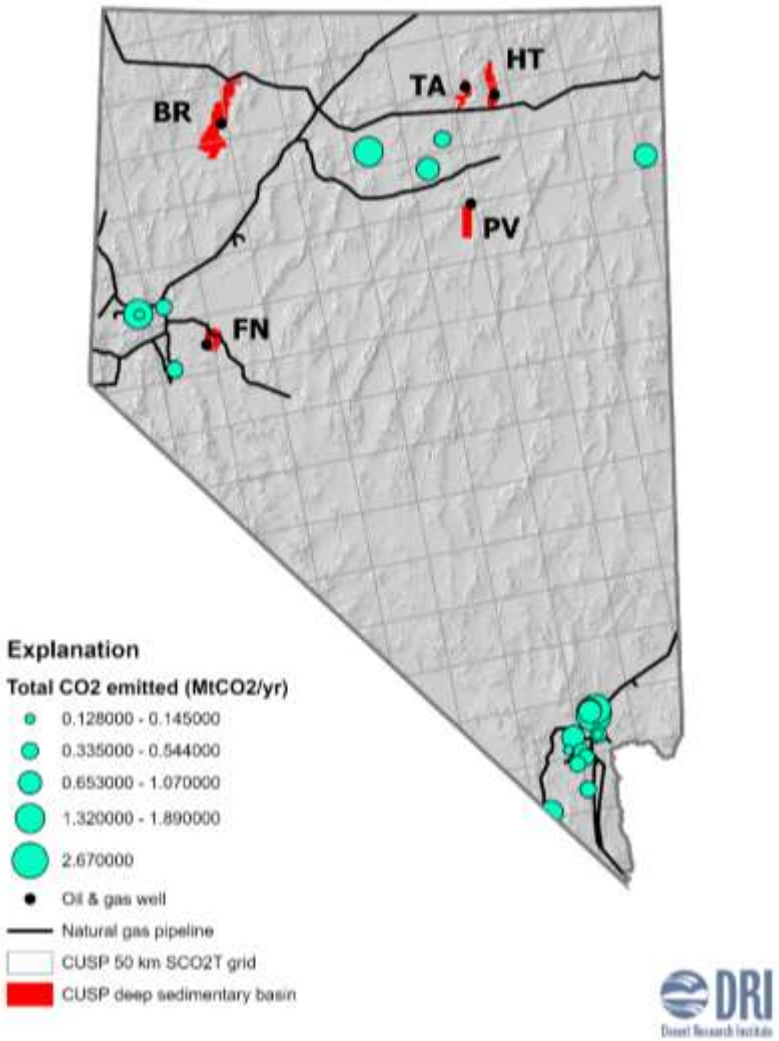


Figure 378 Map showing the distribution of point source total CO_2 emission in Nevada. The location of oil and gas wells, extent of 2-km resolution deep sedimentary basins identified as potential CO_2 geological storage sites, and

network of existing natural gas pipelines are also shown. Sedimentary basin names: BR – Black Rock; FN – Fallon; TA – Tuscarora; HT – Humboldt; and PV – Pine Valley.

The major point sources of CO_2 emissions in northern Nevada are located relatively close to the five-candidate geological CO_2 storage sites and network of existing natural gas pipelines, thereby increasing the favorability of the storage sites as being economically developed (**Figure 378**).

Summary and Conclusions

Previous assessments of Nevada's CO_2 geological storage potential identified saline formations as the most promising option, but were limited by a lack of supporting oil and gas well-log data. Under the Nevada CUSP West project, the DRI expanded upon these earlier assessments by conducting a more detailed evaluation using available oil and well log information. Led by Steven Bacon, Ph.D., P.G., C.E.G., the DRI team focused their efforts on Tasks 2 and 3 of the CUSP project, which centered on identifying and characterizing stacked saline formations for long-term CO_2 storage.

Because Nevada has limited oil and gas resources, only 1,125 well logs exist statewide, and just 300 wells exceed depths of 800 m. After screening for hydrogeologic suitability and avoidance of major freshwater aquifer systems, only 30 wells were examined in detail, and nine contained sufficient data for full analysis using SCO_2T screening parameters. Digitized geophysical logs, including gamma ray, resistivity, and neutron porosity were used to estimate lithology, porosity, salinity, and intrinsic permeability. Of these wells, five sites demonstrated favorable reservoir properties for CO_2 storage in saline formations composed of Tertiary sedimentary and volcanic rocks having thicknesses of 61 to 122 m, depths of 1,040 to 2,010 m, porosity of 0.22 to 0.38, and salinities greater than 3,000 mg/L, averaging approximately 10,000 mg/L.

The areas of the five candidate sites, located in the Black Rock, Fallon, Tuscarora, Humboldt, and Pine Valley sedimentary basins, were mapped using depth-to-basement geophysical and fault-location datasets, incorporating setbacks to minimize leakage risks. Twenty CO_2 emission point sources were identified statewide, with over 100 Mt CO_2 emitted in 2019, primarily near Reno and Elko in the northern parts, and Las Vegas in the southern part of Nevada. The candidate sites are near existing natural gas pipeline infrastructure and major CO_2 point sources, improving their potential economic viability. The proximity of point sources and existing infrastructure to the five candidate CO_2 storage sites provides a potential carbon capture utilization and storage capability for northern Nevada that was unidentified in previous CO_2 geologic storage assessments.

References

Hudson JD. 1996. Use of geophysical logs to estimate the quality of groundwater and the permeability of aquifers. Reston (VA); U.S. Geological Survey. Water-Resources Investigations Report 95-4300. 62 p. [accessed 2025 Dec 23]. https://pubs.usgs.gov/wri/1995/4300/

Jorgensen DG. 1989. Using geophysical logs to estimate porosity, water resistivity, and intrinsic permeability. Reston (VA); U.S. Geological Survey. Water-Supply Paper 2321. 24 p. [accessed 2025 Dec 23]. https://pubs.usgs.gov/wsp/2321/

LaPointe DD, Price JG, Hess RH. 2007. Assessment of the potential for carbon dioxide sequestration with enhanced oil recovery in Nevada. Reno (NV); Nevada Bureau of Mines and

Geology. Open-File Report 2007-07. 24 p. [accessed 2025 Dec 23]. https://pubs.nbmg.unr.edu/CO2-sequestration-EOR-NV-p/of2007-07.htm

NV Energy. 2025. Power supply. Reno (NV)/Las Vegas (NV); NV Energy. [accessed 2026 Jan 5]. https://www.nvenergy.com/about-nvenergy/our-company/power-supply

Ponce DA. 2004. Geophysical methods and applications. In: Wallace AR, editor. Assessment of metallic mineral resources in the Humboldt River basin, northern Nevada. Reston (VA); U.S. Geological Survey. Bulletin 2218. Chapter 6. Digital data. [accessed 2025 Dec 23]. https://pubs.usgs.gov/bul/2218/

Price JG, Hess RH, Fitch S, Faulds JE, Garside LG, Shevenell L, Warren S. 2005. Preliminary assessment of the potential for carbon dioxide disposal by sequestration in geological settings in Nevada. Reno (NV); Nevada Bureau of Mines and Geology. Report 51. 35 p. [accessed 2025 Dec 23]. https://pubs.nbmg.unr.edu/CO2-disposal-NV-p/r051.htm

Sturmer DM, LaPointe DD, Price JG, Hess RH. 2007. Assessment of the potential for carbon dioxide sequestration by reactions with rocks in Nevada. Reno (NV); Nevada Bureau of Mines and Geology. Report 52. 46 p. [accessed 2025 Dec 23]. https://pubs.nbmg.unr.edu/CO2-rock-reactions-NV-p/r052.htm

Sweetkind DS, Masbruch MD, Heilweil VM, Buto SG. 2011. Groundwater flow. In: Heilweil VM, Brooks LE, editors. Conceptual model of the Great Basin carbonate and alluvial aquifer system. Reston (VA); U.S. Geological Survey. Scientific Investigations Report 2010-5193. p 51–72. [accessed 2025 Dec 23]. https://pubs.usgs.gov/sir/2010/5193/

[USBR] U.S. Bureau of Reclamation. 2019. Refining well log interpretation techniques for determining brackish aquifer water quality. Denver (CO); U.S. Bureau of Reclamation, Research and Development Office, Science and Technology Program. Final Report ST-2018-7106-01. 111 p. Plus appendices. [accessed 2025 Dec 23]. https://www.usbr.gov/research/projects/detail.cfm?id=7106

[EIA] U.S. Energy Information Administration. 2025. EIA Open Data. Washington (DC); U.S. Energy Information Administration. [accessed 2026 Jan 5]. https://www.eia.gov/opendata/

[U.S. EPA] U.S. Environmental Protection Agency. 2025. Greenhouse Gas Reporting Program (GHGRP). Washington (DC); U.S. Environmental Protection Agency. [accessed 2026 Jan 5]. https://www.epa.gov/ghgreporting

[USGS/NBMG] U.S. Geological Survey, Nevada Bureau of Mines and Geology. 2016. Quaternary fault and fold database for the United States. Reston (VA); U.S. Geological Survey. [accessed 2016 Jun; accessed again 2025 Dec 23]. https://earthquake.usgs.gov/hazards/qfaults/

New Mexico / West Texas

The overall project objective is to implement a Regional Initiative in order to accelerate onshore CCUS technology deployment in the western region of the United States. The Carbon Utilization and Storage Partnership (CUSP), covering all or parts of 13 states, consists of organizations throughout the western United States including academia, government agencies, national laboratories, and industry.

CUSP will coordinate the capabilities and experience of the diverse organizations to accelerate CCUS deployment by performing four key activities: (1) addressing key technical challenges; (2) facilitating data collection, sharing, and analysis; (3) evaluating regional infrastructure; and (4) promoting regional technology transfer.

The project scope of work encompasses data collection and synthesis, data analysis, modeling, and scenario development to support more rapid implementation of commercial-scale CCUS. There is an emphasis on collaborative efforts, knowledge dissemination and technology transfer that will engage and inform stakeholders with the data and knowledge necessary to undertake CCUS projects throughout the region. The project's activities span the western United States with data collection efforts but will identify and focus on specific areas that exhibit higher commercial CCUS deployment readiness or that have promise but also pose specific surmountable challenges requiring more detailed examination.

Goals

- Develop a data inventory for New Mexico (Appendix A)
- Develop a sink spreadsheet for New Mexico (Appendix B)
- Develop databases for the major basins and sub-basins in New Mexico
- San Juan Basin
- Delaware Basin, NM and TX
- Bravo Dome
- Create a geologic model for Escalante Hydrogen Power Plant Project
- Create a model to evaluate the benefit of Enhanced Coal Bed Methane (ECBM)
- Create a CO_2 emissions source database for New Mexico
- Develop a SCO_2T^{PRO} geologic input database (Appendix C)

San Juan Basin

The San Juan Basin is an asymmetric structural depression covering approximately 21,600 square miles of the east-central Colorado Plateau area in northwestern New Mexico, southwestern Colorado, a small portion of northeastern Arizona, and southeastern Utah (**Figure 1**). It was formed during the Late Cretaceous to Eocene age Laramide Orogeny, which occurred approximately 75 to 35 Ma (Dickinson and Snyder 1978). Strata in the basin reaches a maximum thickness of 14,000 ft and consists primarily of sedimentary and igneous rocks ranging in age from Devonian to Lower Tertiary. Faulting is prevalent along the basin margins and in the northeastern, southeastern, and south-central portions of the San Juan Basin.

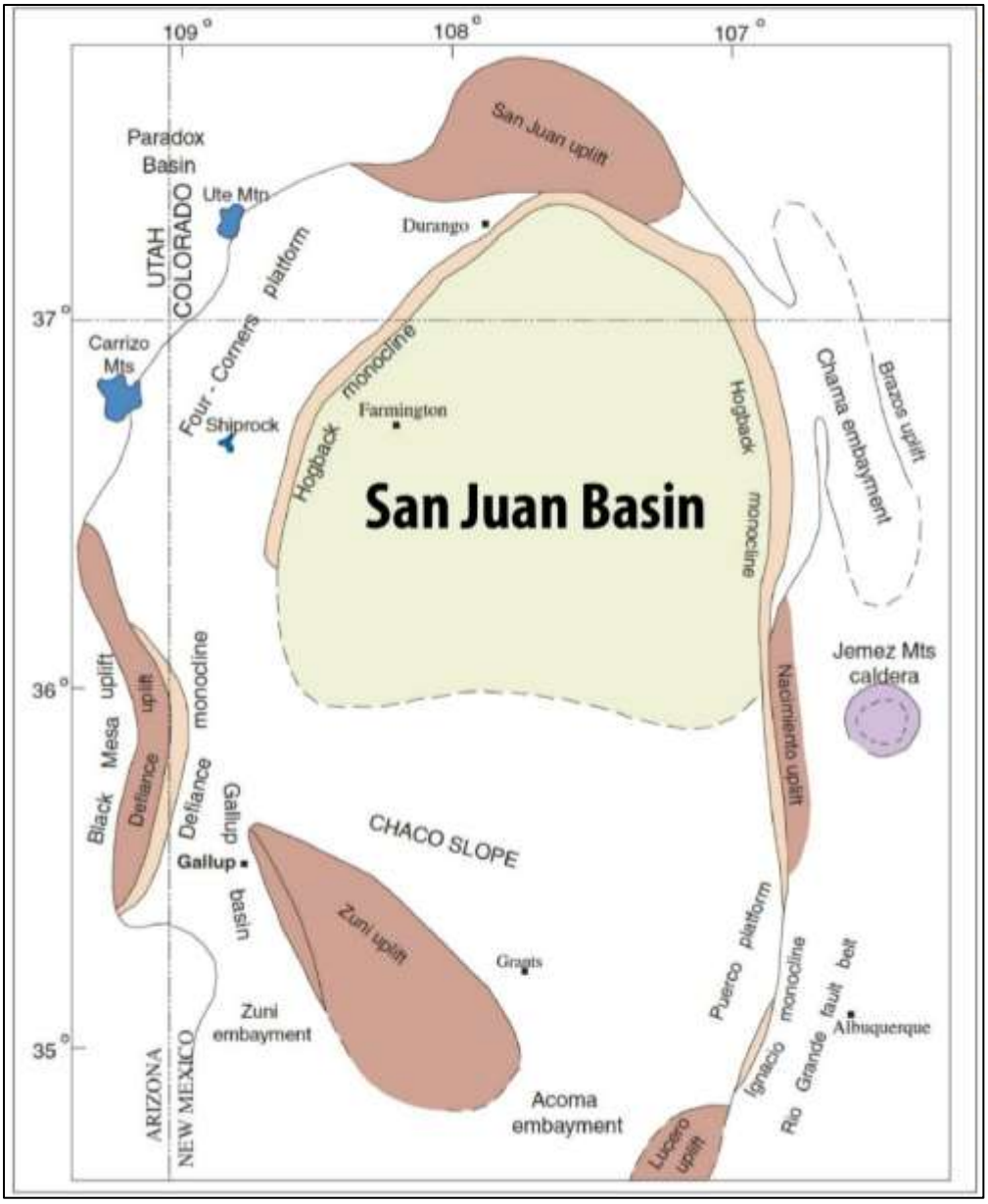


Figure 1. Structural elements within the San Juan Basin area.

Tectonics

The tectonic evolution of the San Juan Basin began by at least the late Paleozoic Period following Precambrian metamorphism, deformation, erosion, and subsequent burial. There is little evidence to suggest a structural depression existed during the Precambrian. Recurrent tectonism adjacent to the present-day San Juan Basin began during the late Paleozoic and extended through Mesozoic Periods, forming the building blocks of the future San Juan, Zuni, Defiance, and Nacimiento uplifts. Although minor deformation and uplift occurred throughout most of the Mesozoic, the San Juan Basin began to resemble its current configuration during the Laramide Period (Cooper and Lorenz 2020).

The Hogback monocline, a feature that bounds the northwestern limit of the central San Juan Basin, was initiated during the early Laramide orogeny (Figure 1 and **Figure 2**). Other bordering uplifts, including the Defiance to the southwest, the Zuni to the south, the San Juan to the north, and the Nacimiento to the east, were recurrently active during both the Paleozoic and Mesozoic periods; however, these uplifts were far more pronounced during late Cretaceous and the earliest phase of the Eocene Laramide Orogeny (Kelley 1951). Based on the distribution of post-Cretaceous sediments, uplift of the outer rim areas was localized during the earliest phase of the Laramide Orogeny and gradually spread to the inner rim of the basin during the later phase that concluded by the end of the Eocene (Kelley 1951).

Middle and late Tertiary deposits unconformably rest on much older strata, including wide regions of Precambrian rocks exposed in the cores of some of the earlier uplifts. By the Pliocene, both the San Juan Basin and Colorado Plateau were uplifted, resulting in drainages developing to both the east and west of the continental divide. These drainages incised into the basin filling sediments and removing much of the late and middle Tertiary deposits from the central portion of the basin (Kelley 1951).

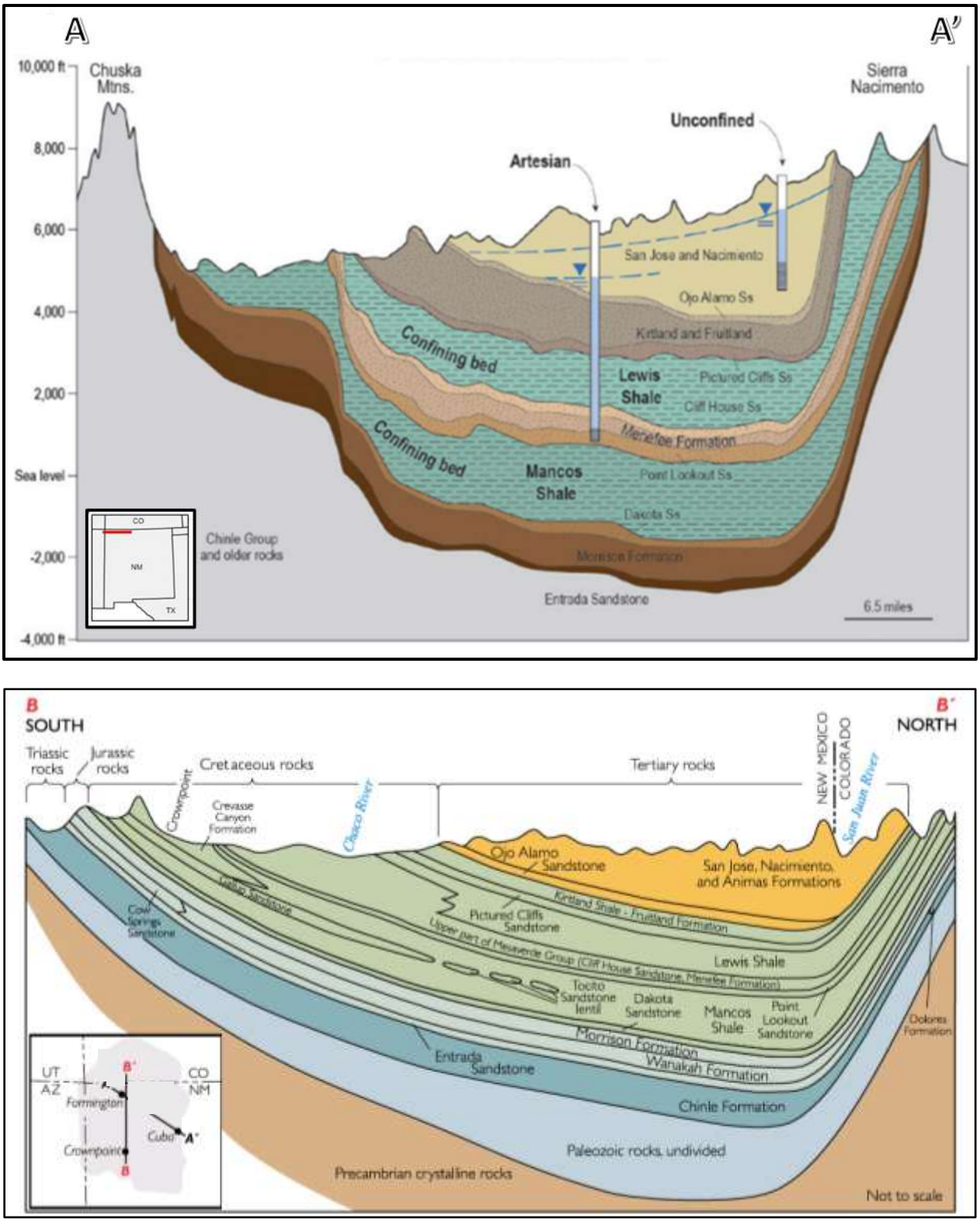


Figure 2. (A) Schematic (not to scale) west to east cross section through the San Juan Basin at the approximate latitude of the proposed injection well showing the Entrada Sandstone injection zone (after Kelley et al. [2014]). (B) Schematic (not to scale) northeast to southwest cross section (after Stone et al. [1983]).

Structure

The interior of the basin consists of strata that exhibits a gentle, regional dip with numerous tectonic features that surround the perimeter of the basin, separating it from the Colorado Plateau. These tectonic features played a predominant role in generating the present basin configuration. The major structural features adjacent to and within the San Juan Basin are categorized into three types: large uplifts, low structural arches and embayments, and monoclines (Figure 1). The Nacimiento fault, on the eastern margin of the basin, resulted in Precambrian granite being uplifted to the east. It is an example of a fault determining a basin boundary. The Defiance and Nutria monoclines are also clear basin-bounding features. Features like the Gallup and Acoma sags form less distinct boundaries where the San Juan Basin merges across structural saddles with adjacent basins or embayments (Kernodle 1995). The major structural features bounding the San Juan Basin.

Stratigraphy

The San Juan Basin contains a thick sequence of sedimentary and igneous rock ranging from the Precambrian to the Tertiary Period with the largest section deposited from Pennsylvanian Period to the Tertiary Period. The maximum thickness of the San Juan sedimentary sequence is approximately 14,400 ft within the central basin region (Figure 1). **Figure 3** from Craigg (2001) presents the stratigraphic framework and nomenclature of the San Juan Basin. **Figure 4** presents the stratigraphic framework and nomenclature for the San Juan Basin. **Figure 5** is the type log for the San Juan Basin from NMT's CarbonSAFE Strat Test Well #1. **Table 1** provides a list of the formations, rock types, depositional environments, and resources.

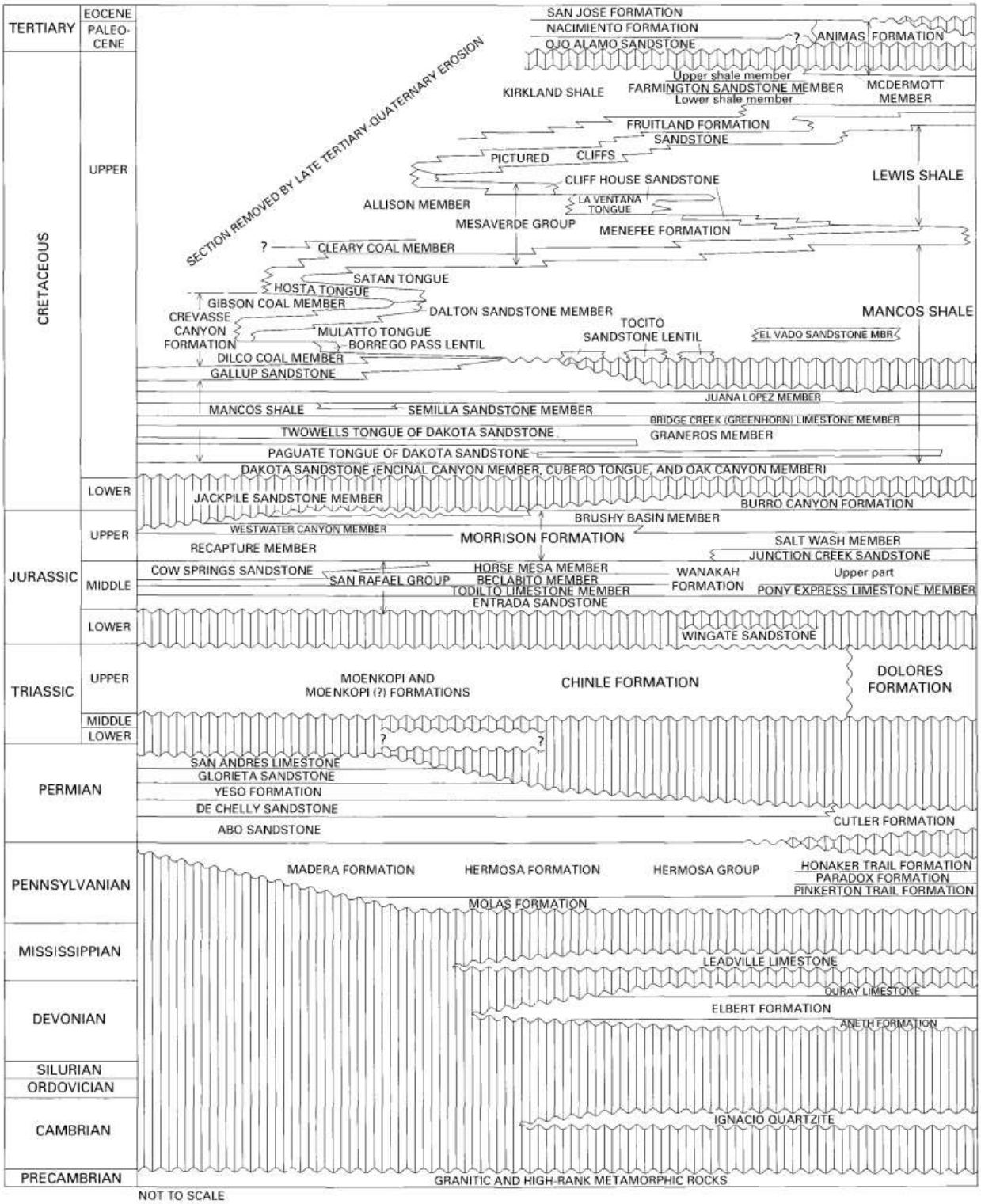


Figure 3. Stratigraphic framework and nomenclature of the San Juan Basin (Craigg 2001).

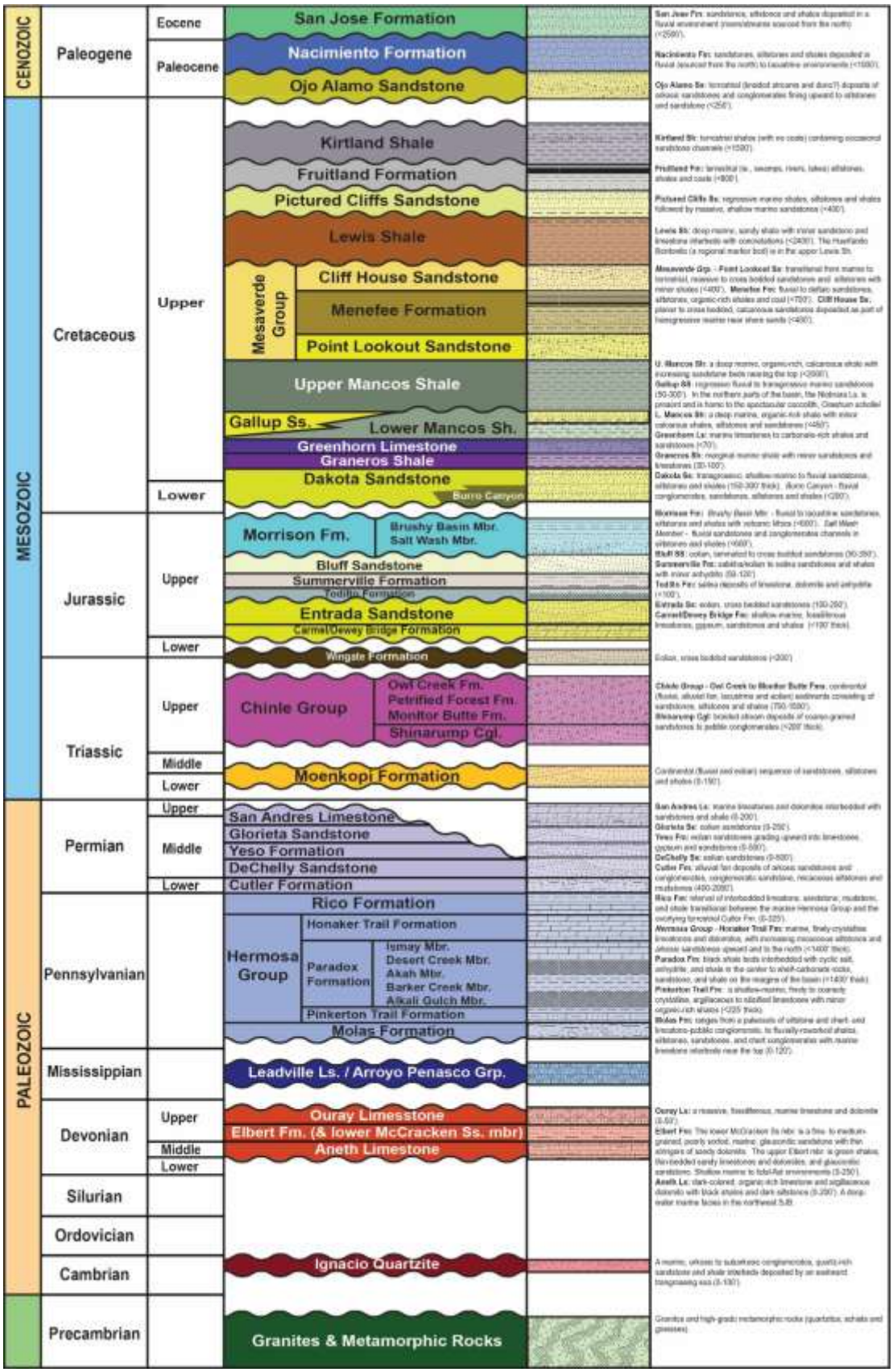

CENOZOIC
MESOZOIC
PALEOZOIC
Paleogene
Eocene
Paleocene
Cretaceous
Upper
Lower
Jurassic
Upper
Lower
Triassic
Upper
Middle
Lower
Permian
Upper
Middle
Lower
Pennsylvanian
Mississippian
Devonian
Upper
Middle
Lower
Silurian
Ordovician
Cambrian
Precambrian
San Jose Formation
Nacimiento Formation
Ojo Alamo Sandstone
Kirtland Shale
Fruitland Formation
Pictured Cliffs Sandstone
Lewis Shale
Mesaverde Group
Cliff House Sandstone
Menefee Formation
Point Lookout Sandstone
Upper Mancos Shale
Gallup Ss.
Lower Mancos Sh.
Greenhorn Limestone
Graneros Shale
Dakota Sandstone
Burro Canyon
Morrison Fm.
Brushy Basin Mbr.
Salt Wash Mbr.
Bluff Sandstone
Summerville Formation
Todilto Formation
Entrada Sandstone
Carmel/Dewey Bridge Formation
Wingate Formation
Chinle Group
Owl Creek Fm.
Petrified Forest Fm.
Monitor Butte Fm.
Shinarump Cgl.
Moenkopi Formation
San Andres Limestone
Glorieta Sandstone
Yeso Formation
DeChelly Sandstone
Cutler Formation
Rico Formation
Hermosa Group
Honaker Trail Formation
Paradox Formation
Ismay Mbr.
Desert Creek Mbr.
Akah Mbr.
Barker Creek Mbr.
Alkali Gulch Mbr.
Pinkerton Trail Formation
Molas Formation
Leadville Ls. / Arroyo Penasco Grp.
Ouray Limesstone
Elbert Fm. (& lower McCracken Ss. mbr)
Aneth Limestone
Ignacio Quartzite
Granites & Metamorphic Rocks

Figure 4. San Juan Basin specific stratigraphic column and UIC significance.

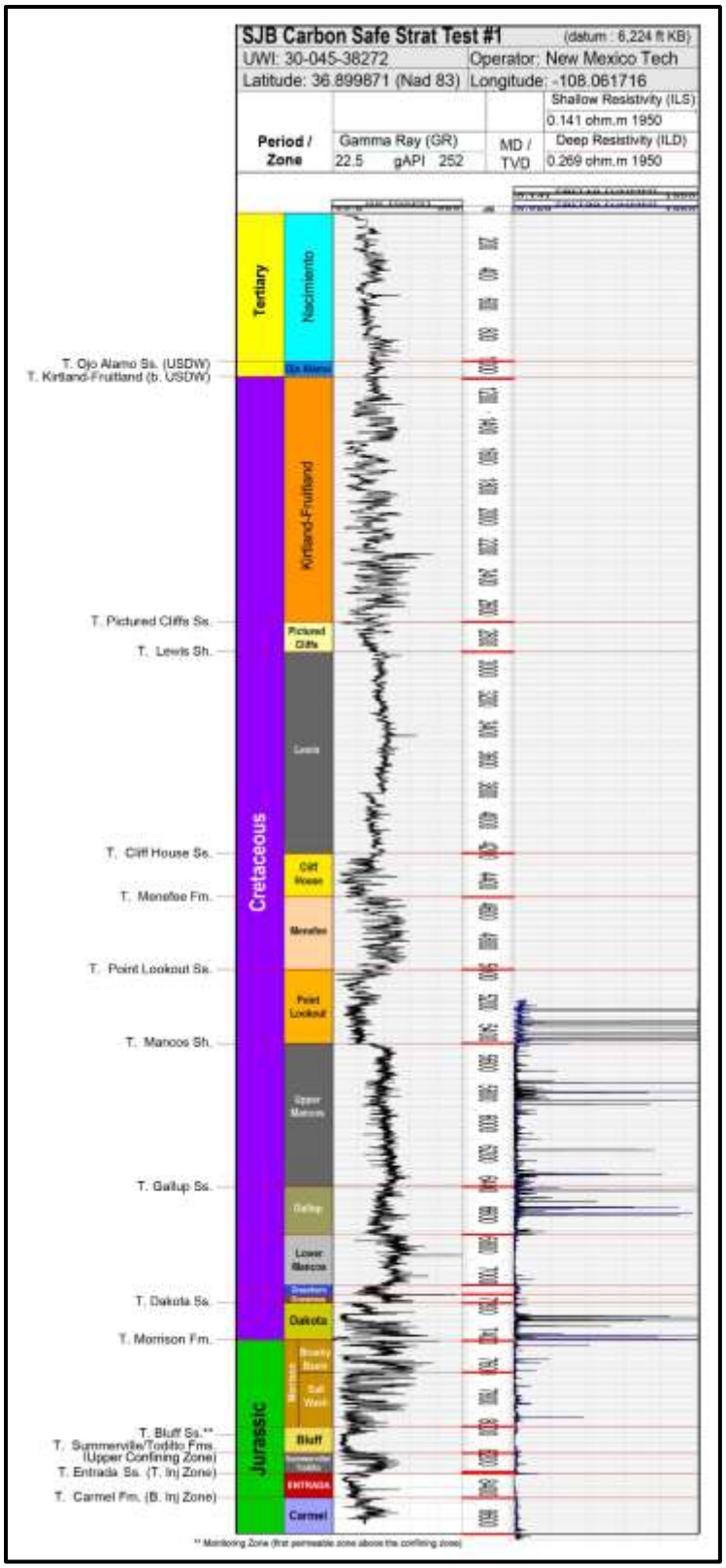

SJB Carbon Safe Strat Test #1
(datum : 6,224 ft KB)
UWI: 30-045-38272
Operator: New Mexico Tech
Latitude: 36.899871 (Nad 83)
Longitude: -108.061716
Shallow Resistivity (ILS)
0.141 ohm.m 1950
Period / Zone
Gamma Ray (GR)
22.5 gAPI 252
MD / TVD
Deep Resistivity (ILD)
0.269 ohm.m 1950
Tertiary
Nacimiento
T. Ojo Alamo Ss. (USDW)
T. Kirtland-Fruitland (b. USDW)
Kirtland-Fruitland
T. Pictured Cliffs Ss.
Pictured Cliffs
T. Lewis Sh.
Lewis
T. Cliff House Ss.
Cliff House
T. Menefee Fm.
Menefee
T. Point Lookout Ss.
Point Lookout
T. Mancos Sh.
Upper Mancos
T. Gallup Ss.
Gallup
Lower Mancos
Cretaceous
T. Dakota Ss.
Dakota
T. Morrison Fm.
Jurassic
Bluff
T. Bluff Ss.**
T. Summerville/Todilto Fms. (Upper Confining Zone)
T. Entrada Ss. (T. Inj Zone)
ENTRADA
T. Carmel Fm. (B. Inj Zone)
Carmel
** Monitoring Zone (first permeable zone above the confining zone)

Figure 5. Type well log for the project area showing all key stratigraphic markers and zones from surface down to the lower confining zone. Track 1 provides period and zone, track 2 contains gamma ray (GR), and track three contains shallow (ILS) and deep resistivity (ILD).

Table 1. Generalized description of the Cenozoic, Cretaceous, and Jurassic rock units in the San Juan Basin (after Kelley et al. 2014; Cather 2020).

	Formation	Rock Type (major rock listed first)	Depositional Environment	Resources	Geologic Symbol
Cenozoic	San Jose Fm	Sandstone and shale	Continental rivers	Water, Gas	Tsj
	Nacimiento Fm	Shale and sandstone	Continental rivers	Water, Gas	Tn
	Ojo Alamo Sandstone	Sandstone and shale	Continental rivers	Water, Gas	Toa
Cretaceous	Kirtland Shale	Interbedded shale, sandstone	Coastal to alluvial plain	Water, Oil, Gas	Kk
	Fruitland Fm	Interbedded shale, sandstone, and coal	Coastal plain	Coal, CBM[1]	Kf
	Pictured Cliffs Sandstone	Sandstone	Regressive marine, beach	Oil, Gas	Kpc
	Lewis Shale	Shale, thin limestones	Offshore marine	Gas	Kls
	Cliff House Sandstone	Sandstone	Transgressive marine, beach	Oil, Gas	Kch
	Menefee Fm	Interbedded shale, sandstone, and coal	Coastal plain	Coal, CBM[1], Gas	Kmf
	Point Lookout Sandstone	Sandstone	Regressive marine, beach	Oil, Gas, Water	Kpl
	Upper Mancos Shale	Shale, thin sandstones	Offshore marine	Oil, Gas	Kmf
	Gallup Sandstone	Sandstone, a few shales, and coals	Regressive marine to coastal deposit	Oil, Gas, Water	Kg
	Lower Mancos Shale	Shale, thin sandstones	Offshore marine	Oil, Gas	Kmf
	Dakota Sandstone	Sandstone, shale, and coals	Transgressive coastal plain to marine shoreline	Oil, Gas, Water	Kd
Jurassic	Morrison Fm	Mudstones, sandstone	Continental rivers	Uranium, Oil, Gas, Water	Jm
	Bluff Sandstone	Sandstone	Eolian sand dunes	Water	
	Summerville Fm	Sandstone, siltstone and shale	Alluvial plain		

[1] Coalbed methane

Todilto Fm	Limestone and siltstone	Salina and sabkha deposits		
Entrada Sandstone	Sandstone	Eolian sand dunes	Oil, Gas, Water	Je
Carmel Fm	Siltstone and shale	Alluvial plain		
Wingate Sandstone?	Sandstone	Eolian sand dunes		

Geologic Model

The model developed for the San Juan Basin includes over 2,750 wells (**Figure 6**). The tops for each well were handpicked for all the formations present in the logs (Figure 3). A database was built in S&P Kingdom that includes well header information, formation tops, bottom hole temperatures, and calculated geothermal gradients.

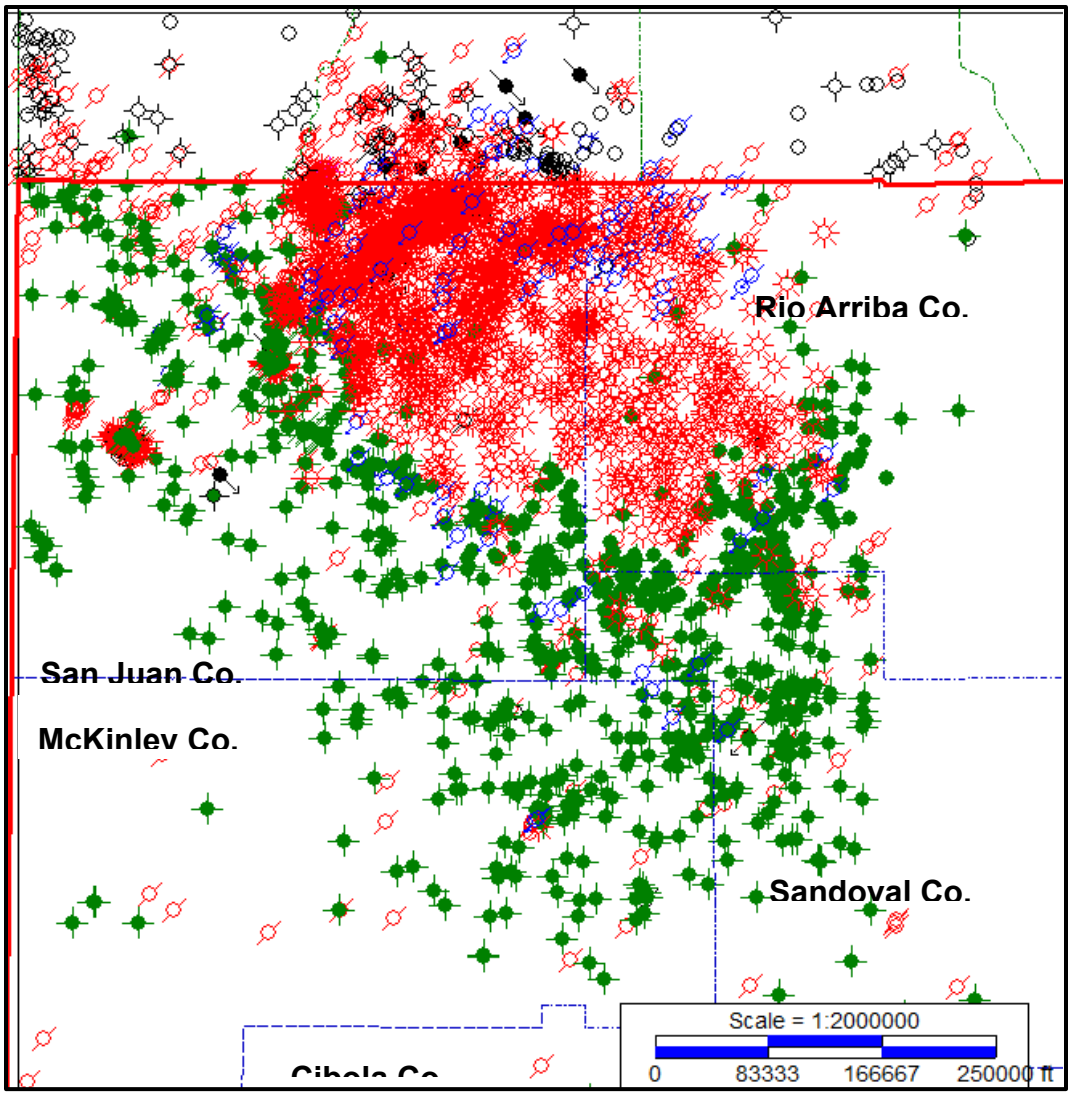


Figure 6. Base map of the San Juan Basin with the wells that have been used to develop the database. The green symbols are P&A or Active oil wells. The red symbols are P&A or active gas wells, and the Black and blue symbols are injection or SWD wells.

The following maps (**Figure 7 to Figure 40**) are subsea structure maps for all the formation tops starting at the Precambrian and to the Tertiary Ojo Alamo Sandstone for the over 2,750 wells. North is at the top of the maps. The first set of maps do not include the fault interpretations and have a contour interval of 200 ft; whereas the second set of subsea structure maps include our initial fault interpretation and have a contour interval of 250 ft (**Figure 41** to **Figure 72**).

Surfaces Without Faults

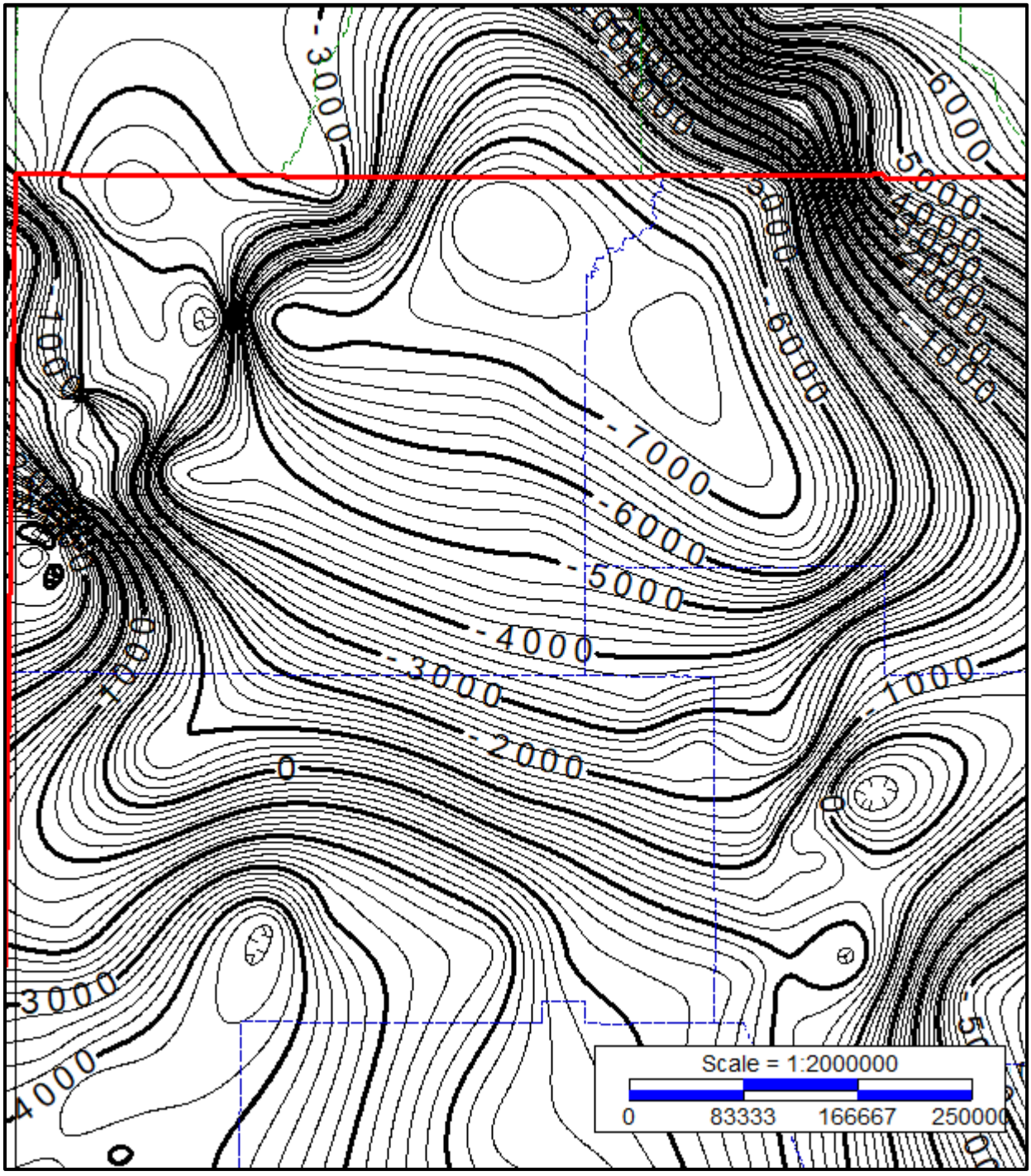


Figure 7. The subsea structural map on the Precambrian surface.

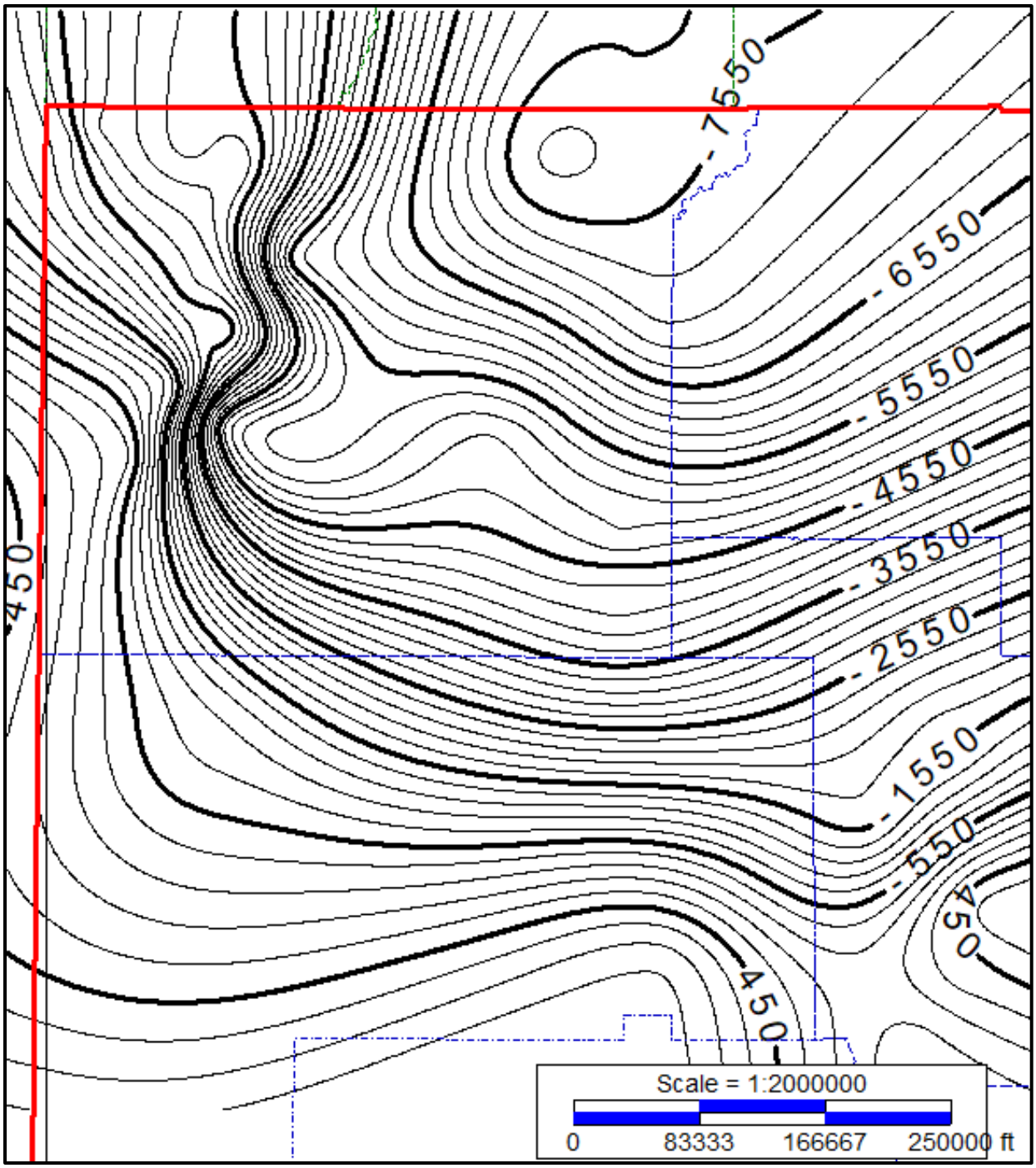


Figure 8. The subsea structural map on the Ignacio Quartzite surface.

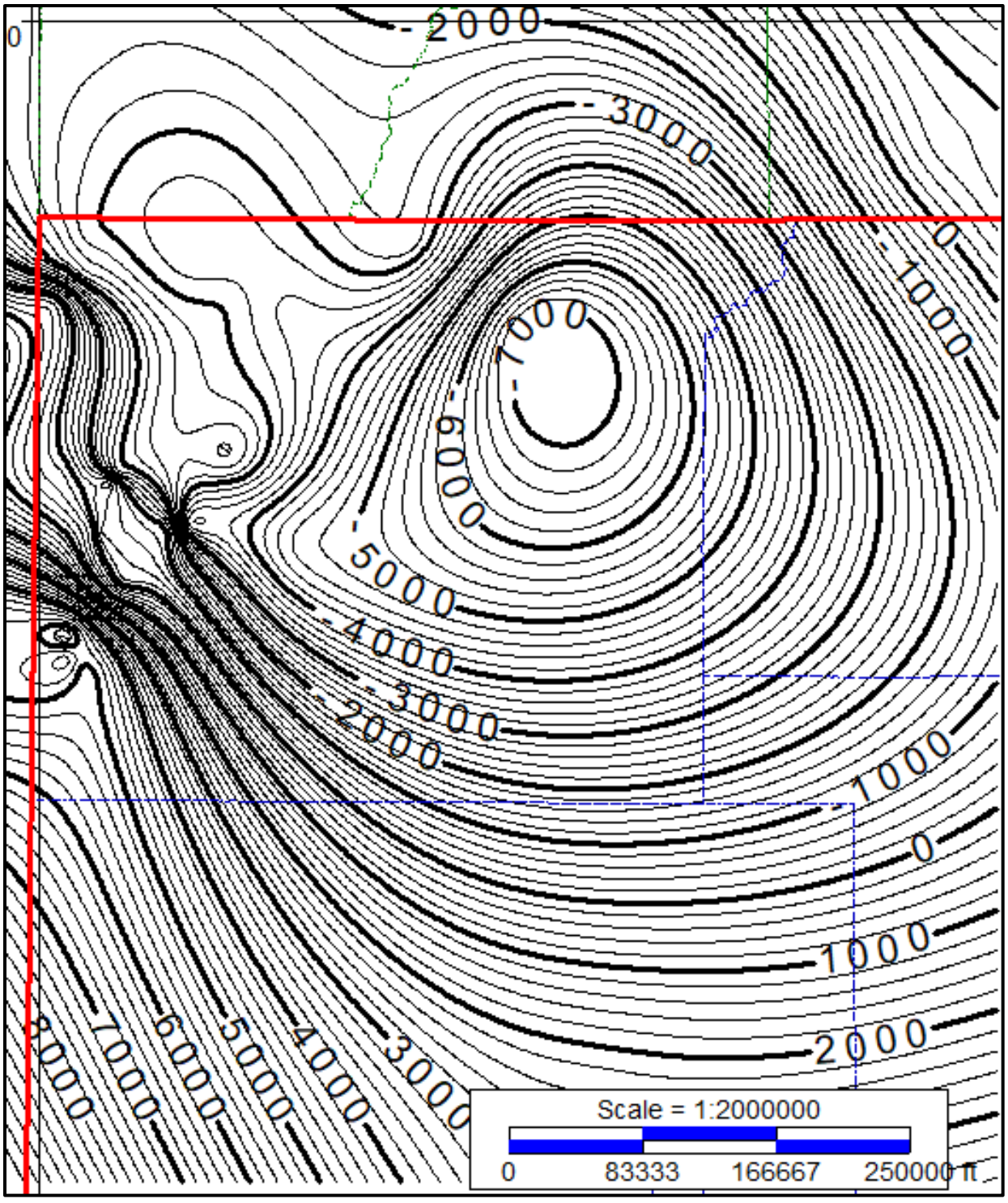


Figure 9. The subsea structural map on the Aneth Limestone surface.

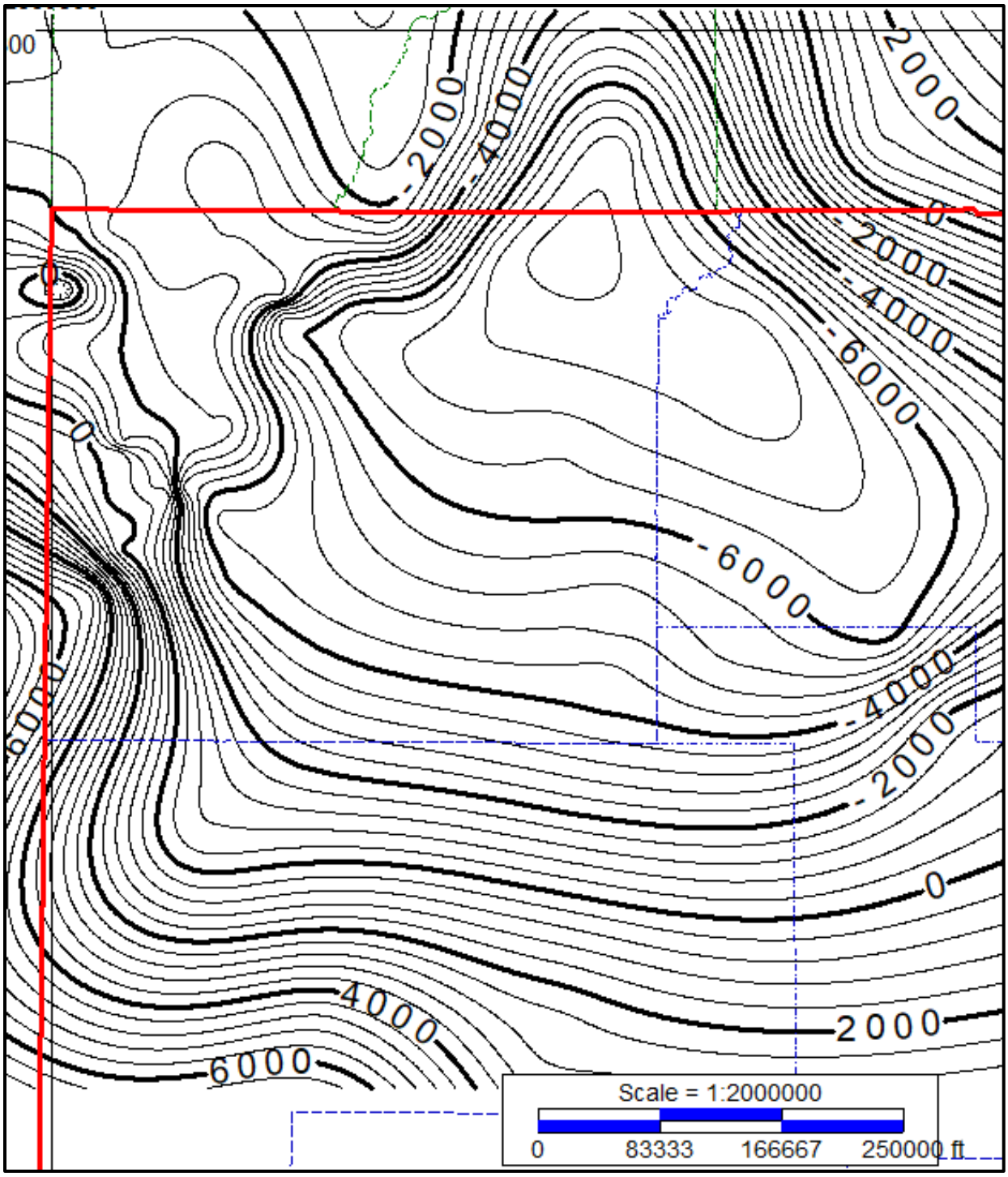


Figure 10. The subsea structural map on the Elbert Formation surface.

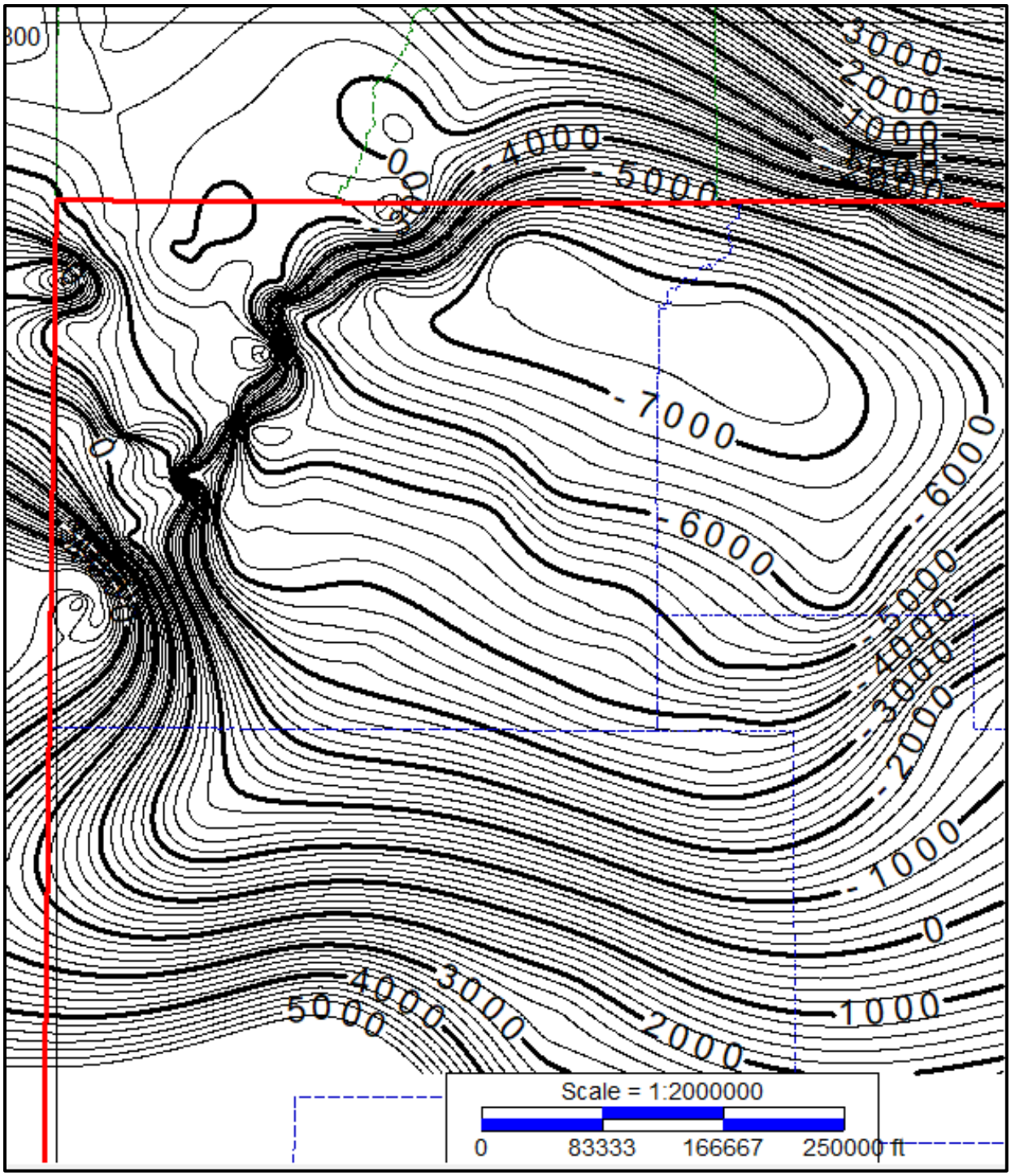


Figure 11. The subsea structural map on the Ouray Limestone surface.

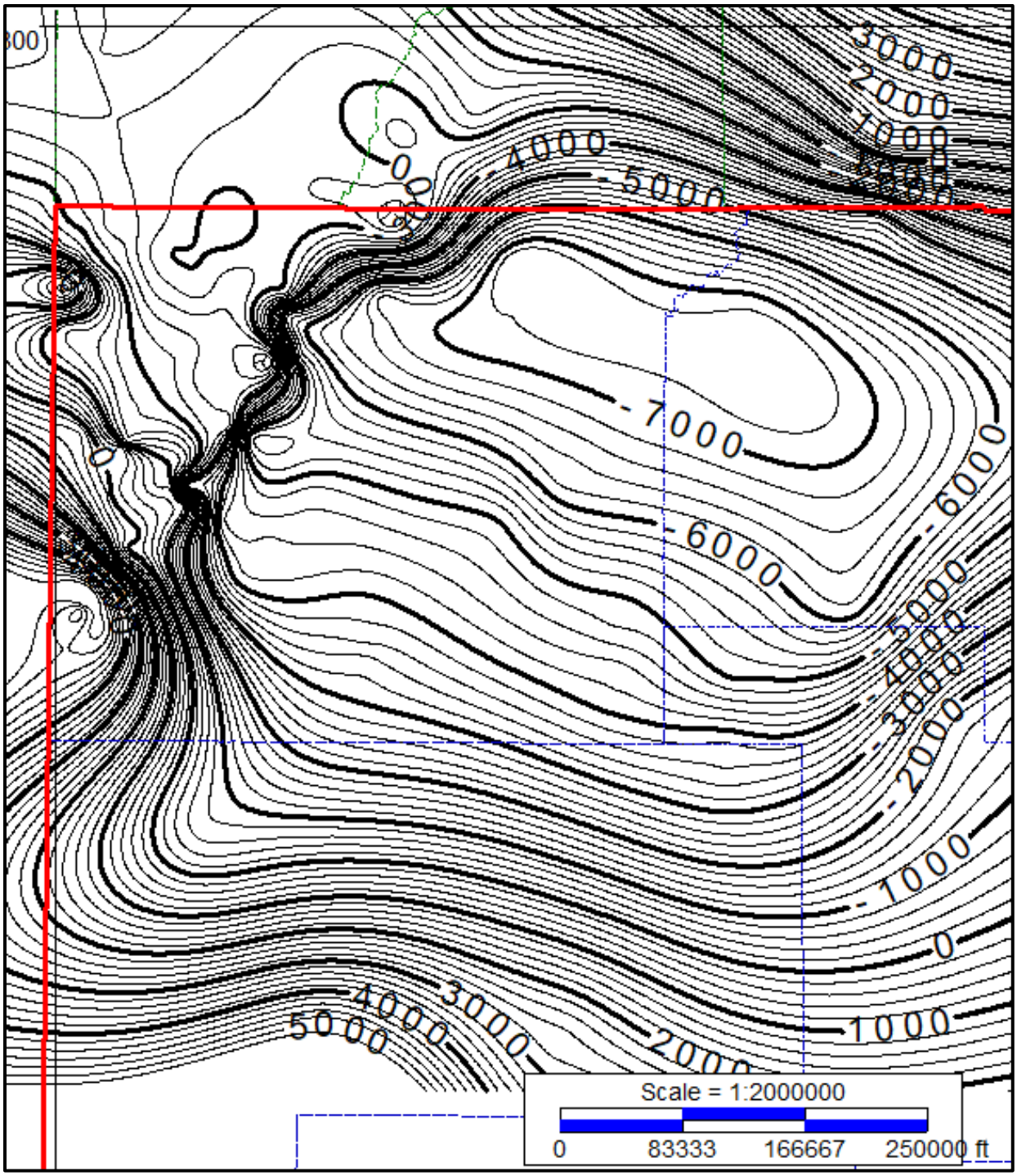


Figure 12. The subsea structural map on the Leadville Limestone surface.

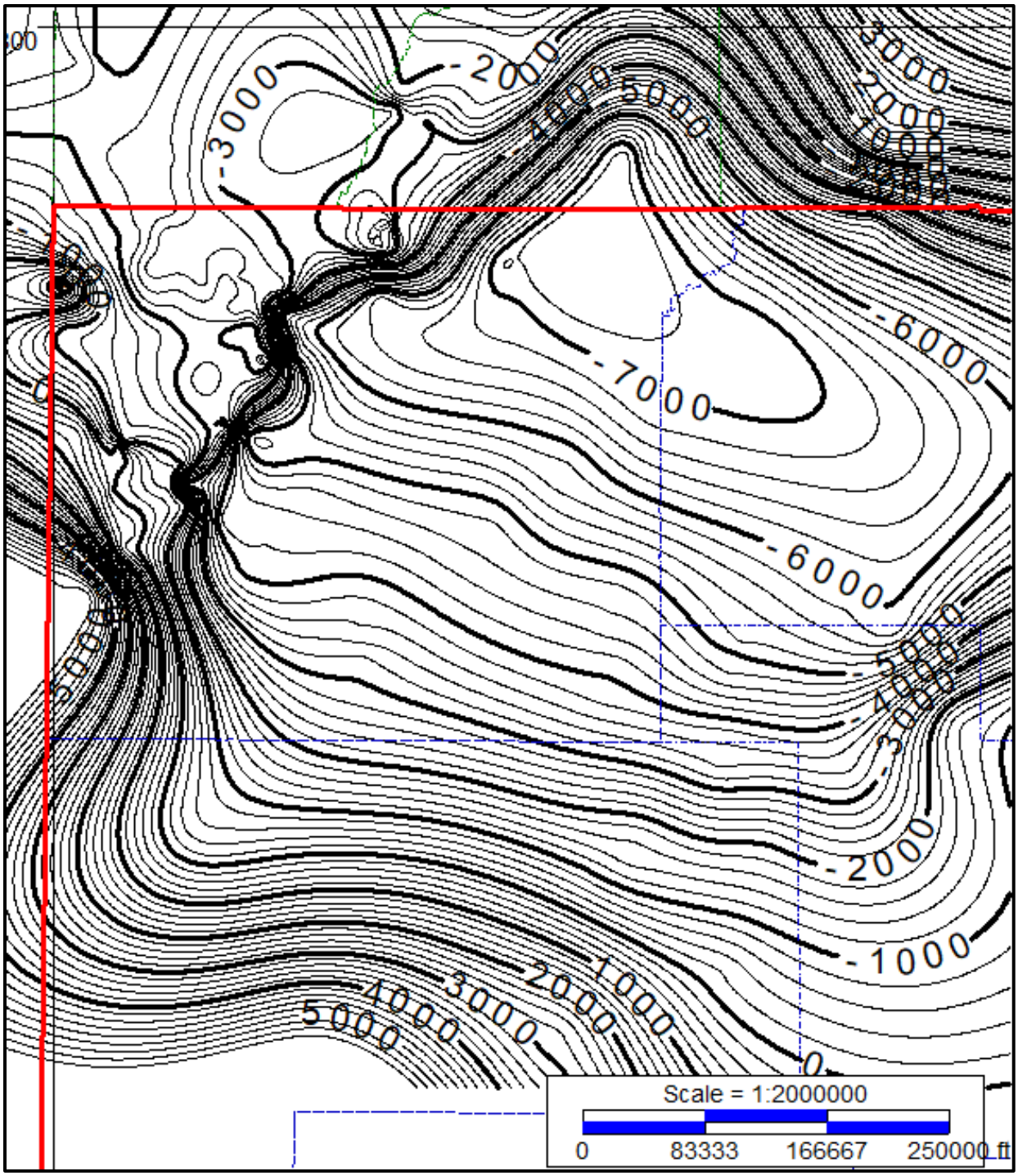


Figure 13. The subsea structural map on the Molas Formation surface.

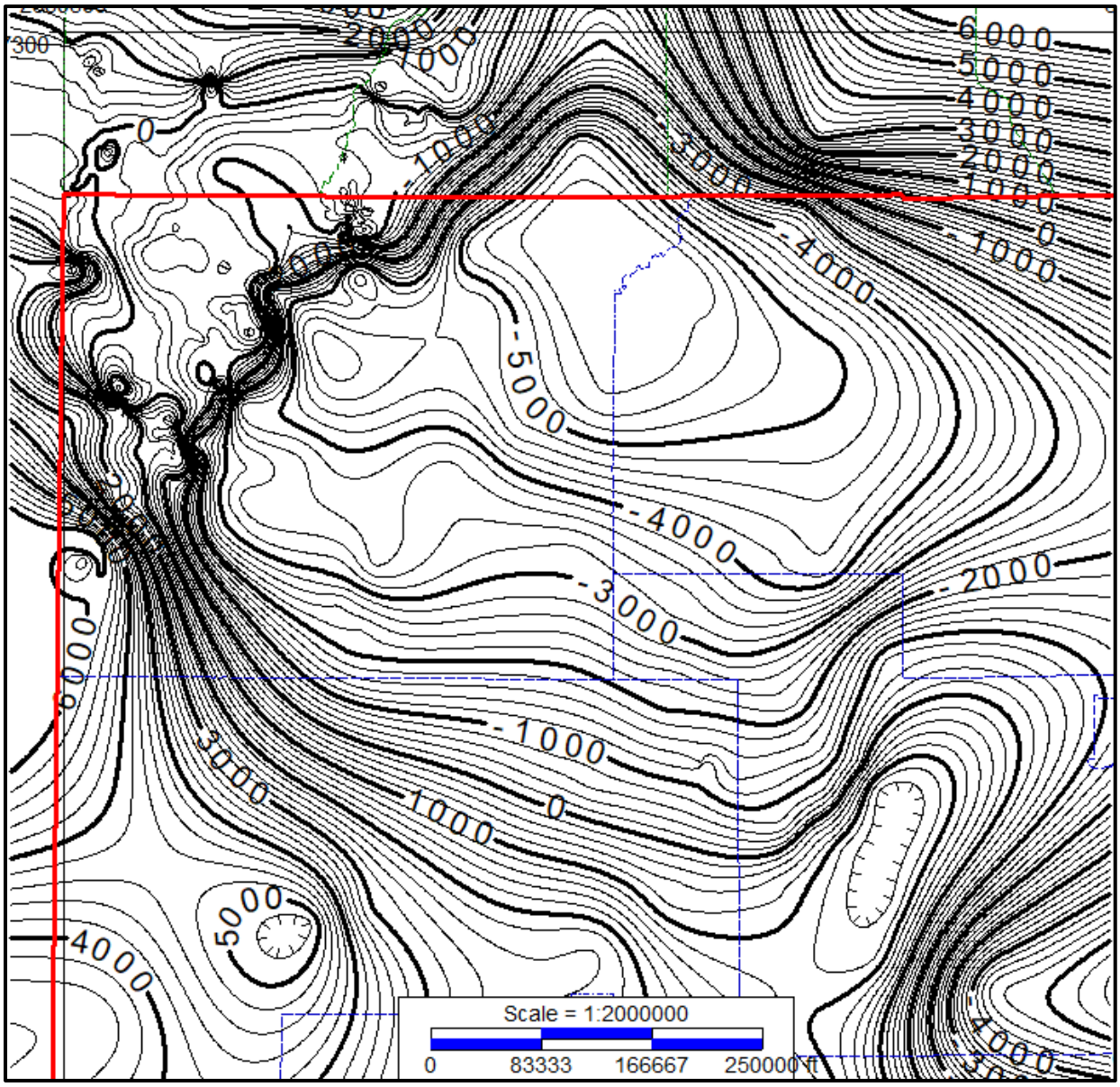


Figure 14. The subsea structural map on the Hermosa Group surface.

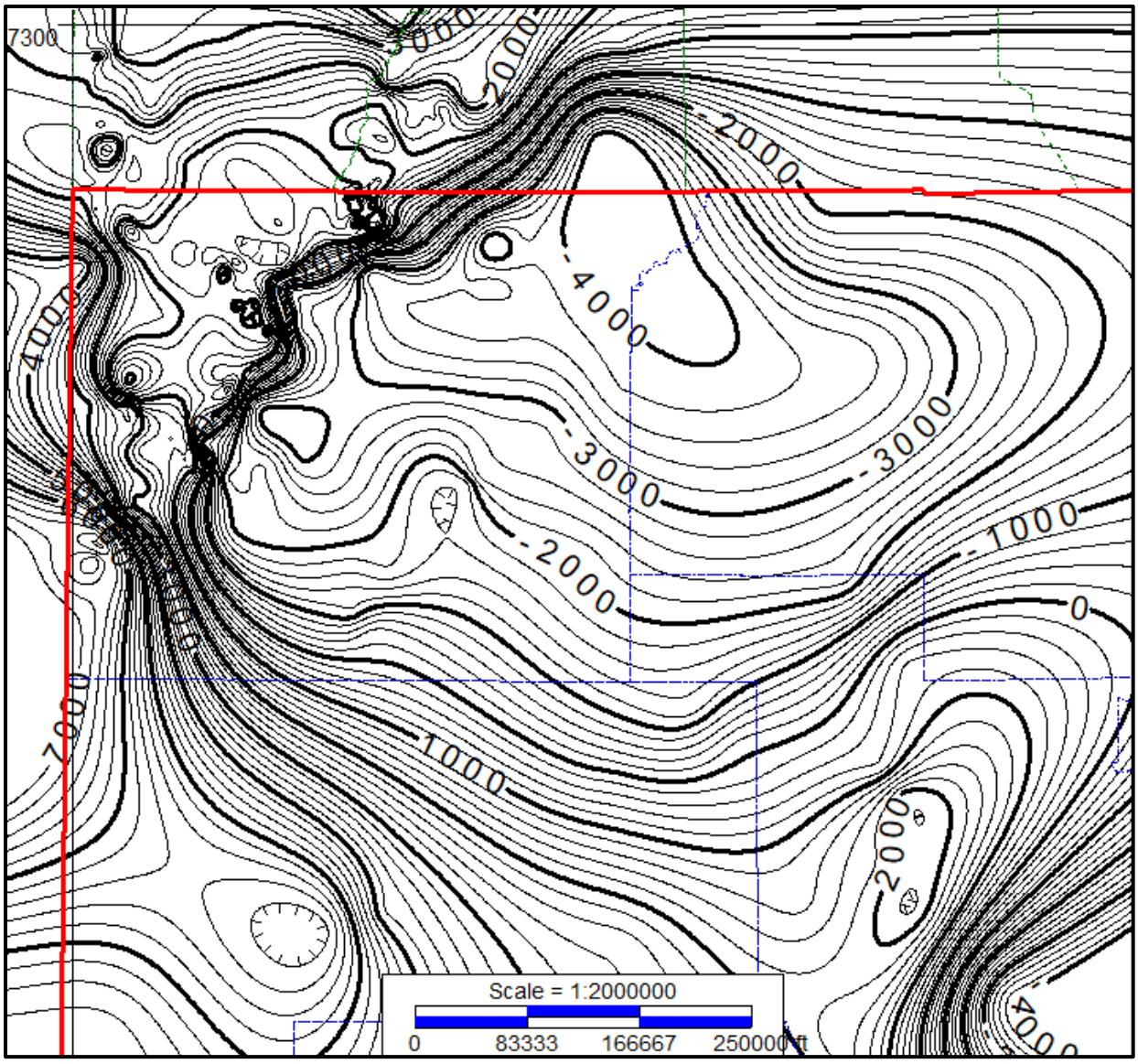


Figure 15. The subsea structural map on the Cutler Formation surface.

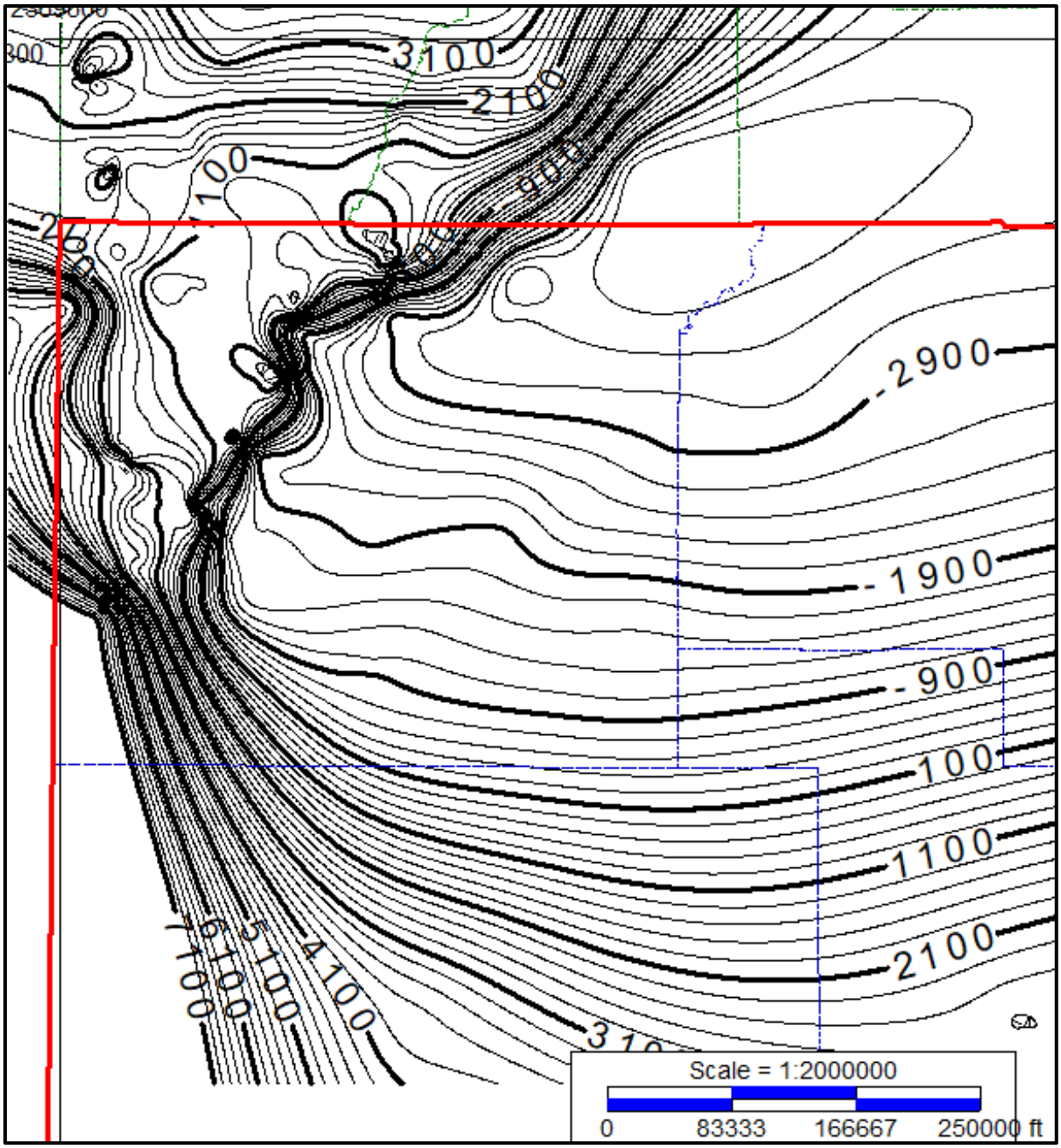


Figure 16. The subsea structural map on the DeChelly Sandstone surface.

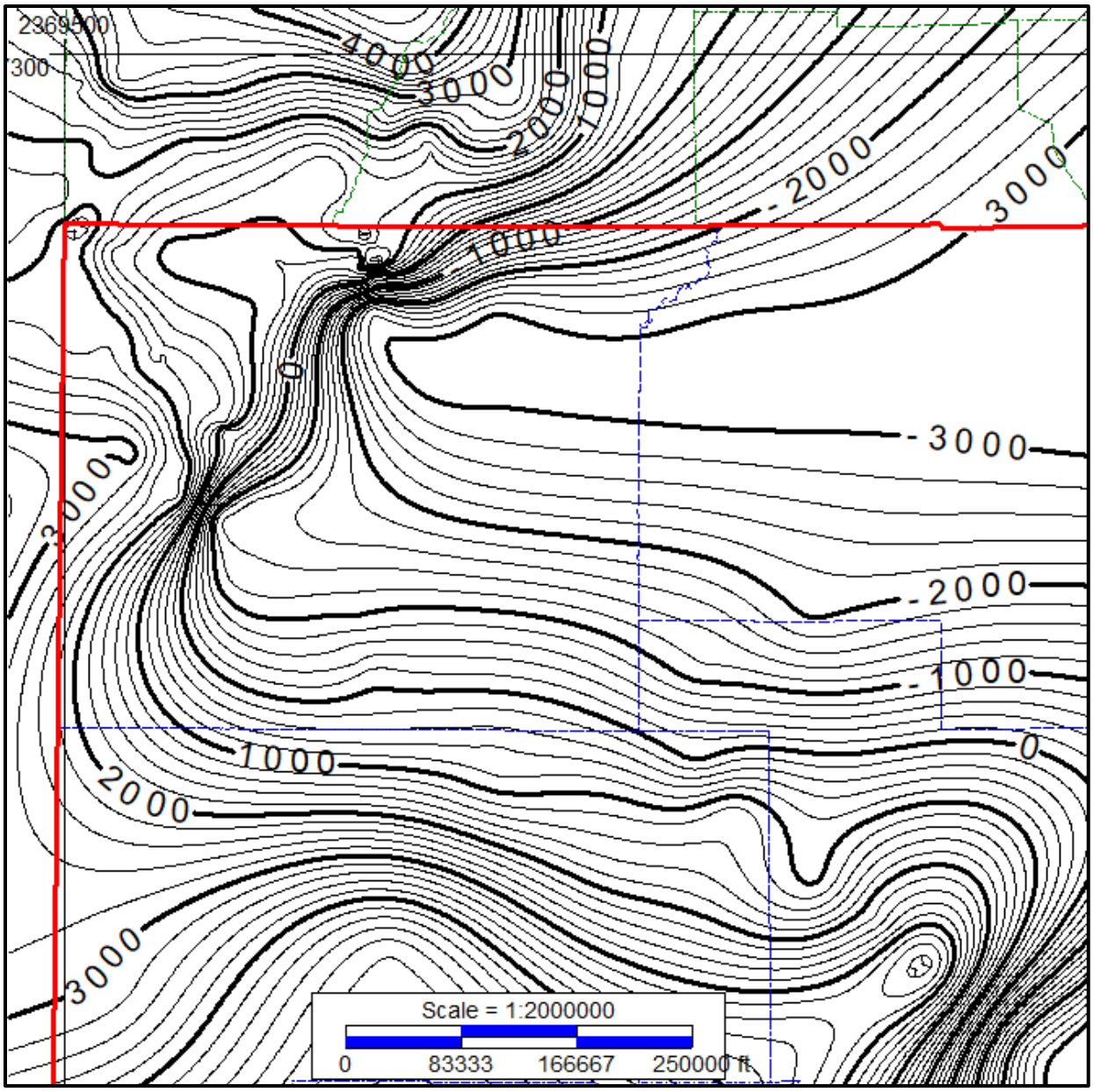


Figure 17. The subsea structural map on the Moenkopi Formation surface.

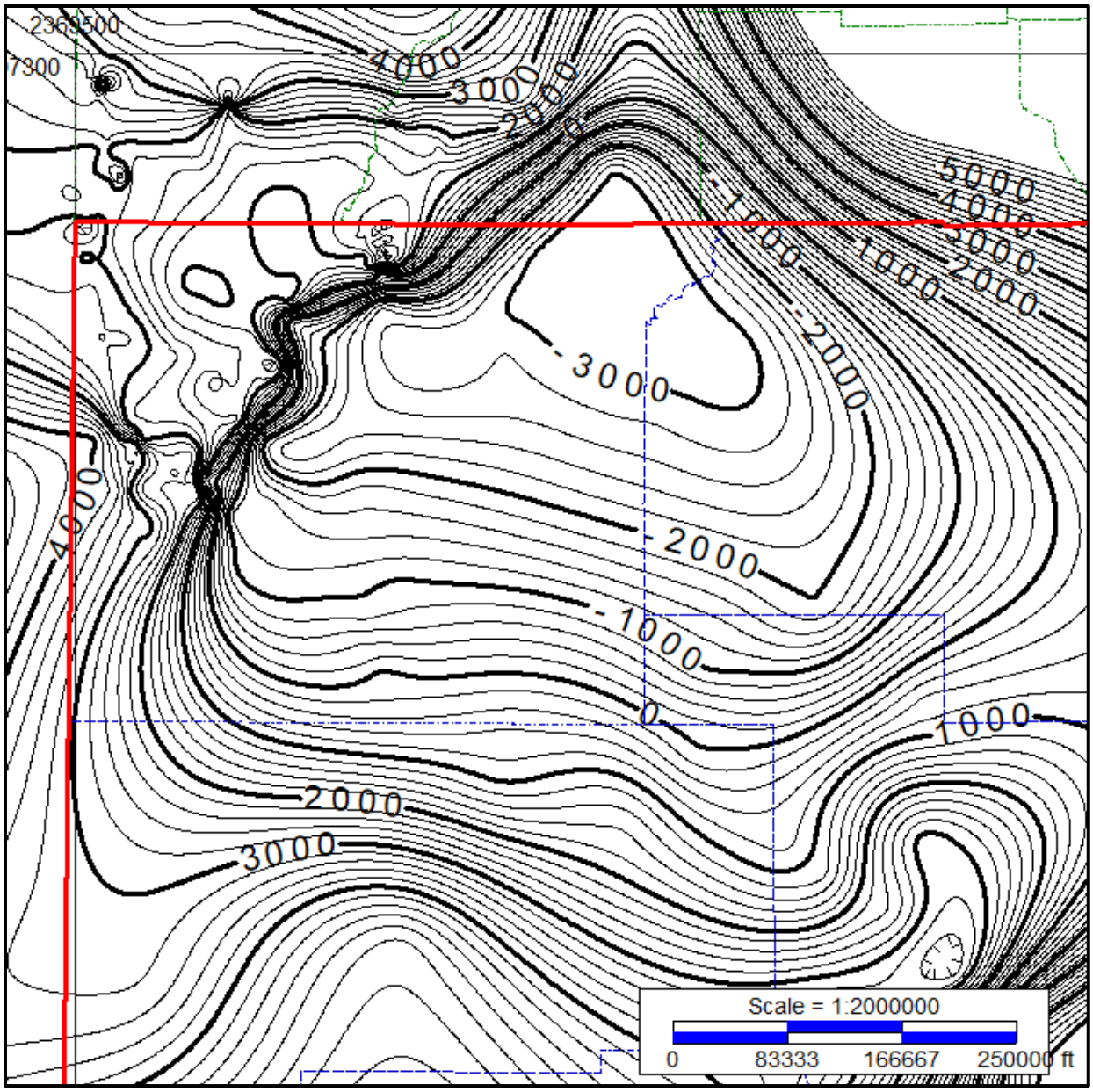


Figure 18. The subsea structural map on the Shinarump Conglomerate surface.

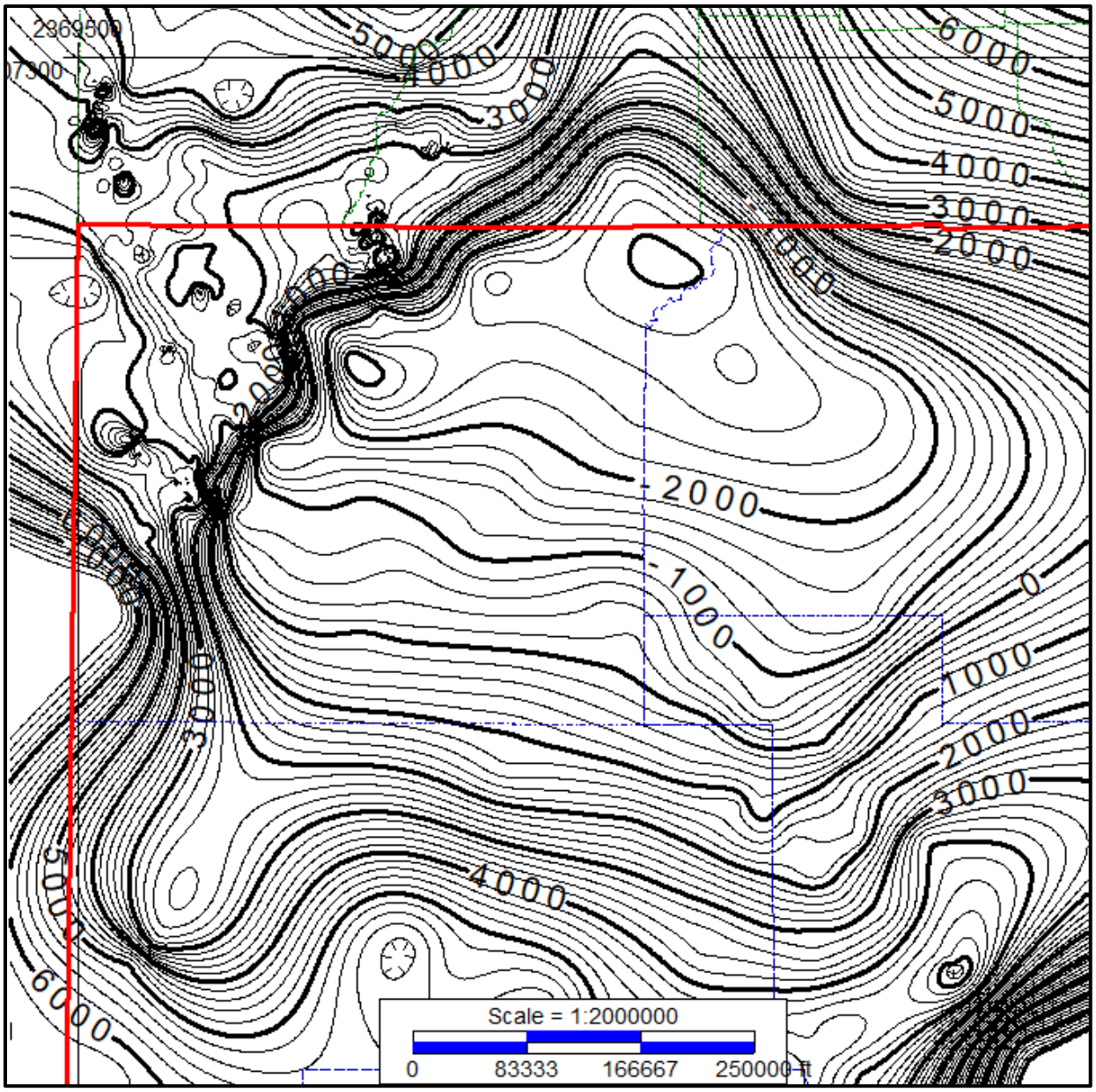


Figure 19. The subsea structural map on the Chinle Group surface.

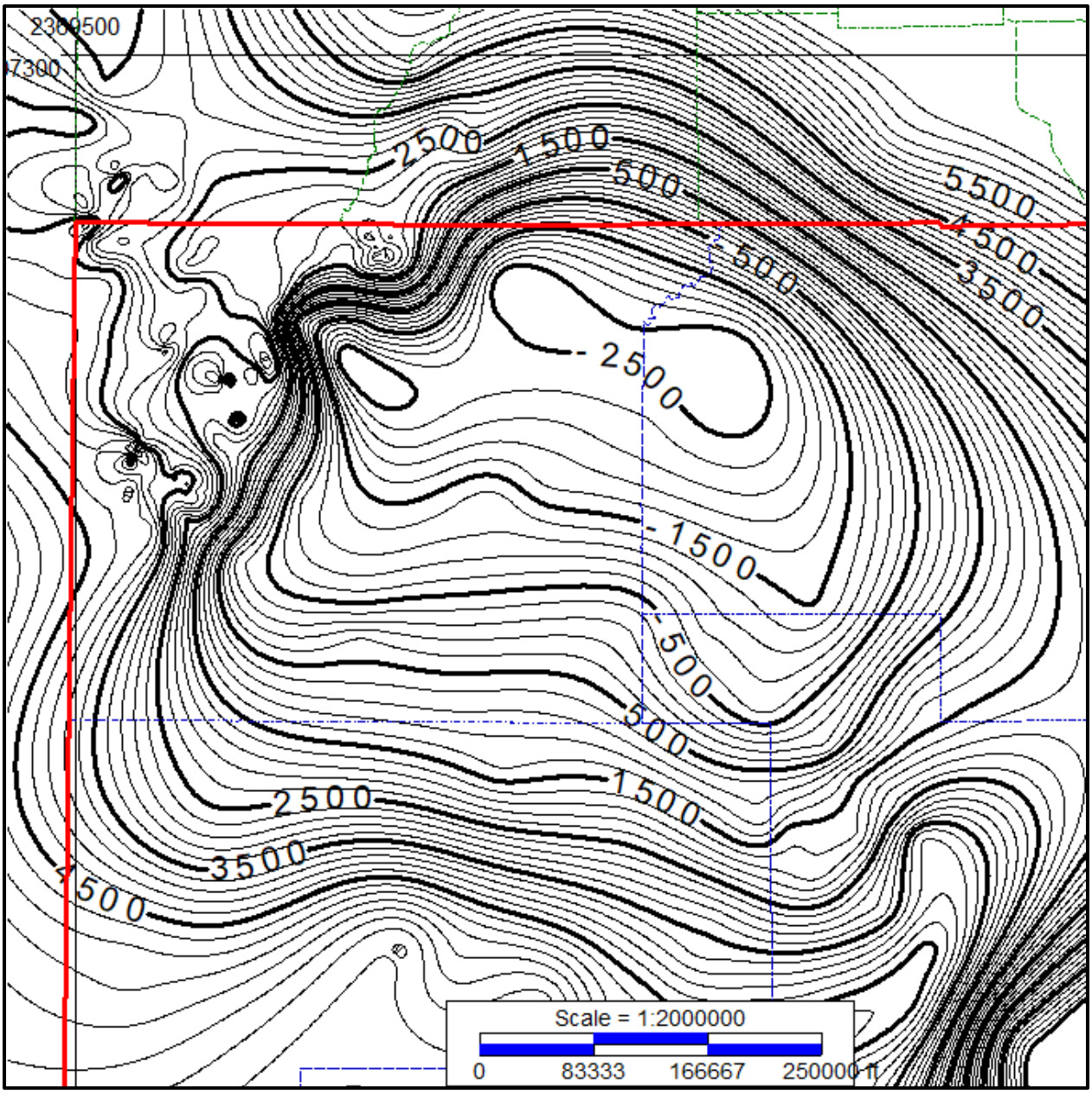


Figure 20. The subsea structural map on the Wingate Formation surface.

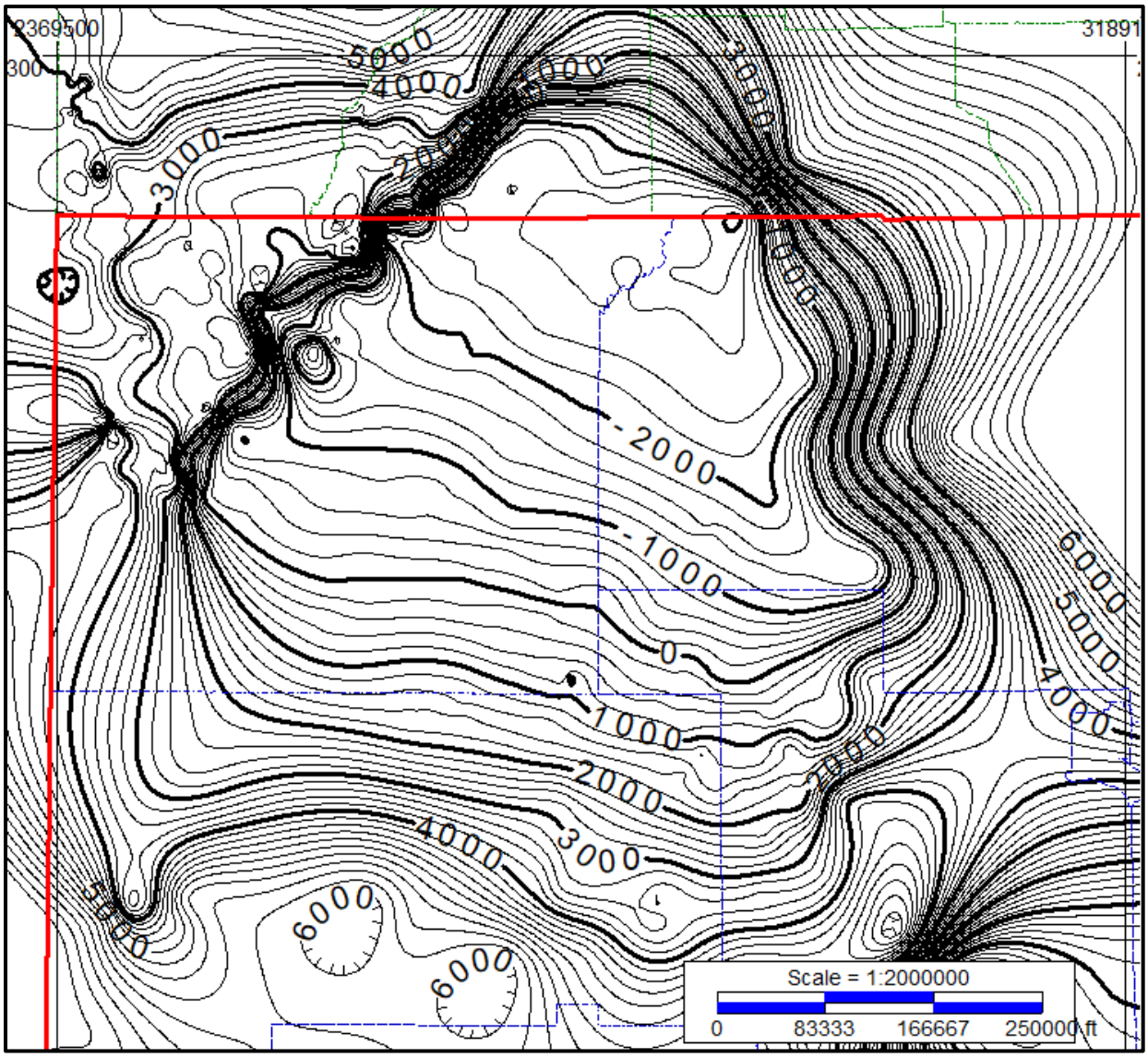


Figure 21. The subsea structural map on the Carmel Formation surface.

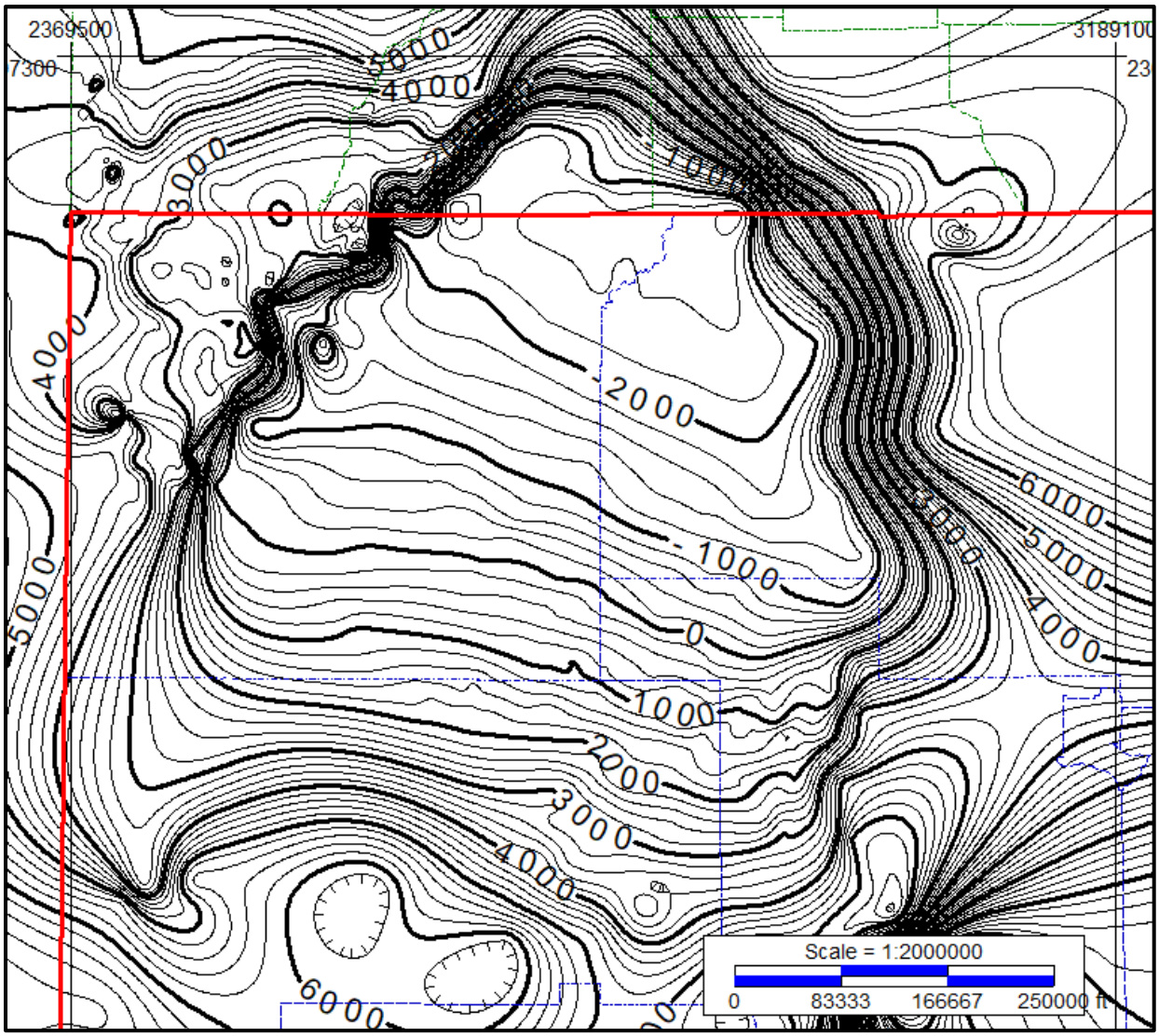


Figure 22. The subsea structural map on the Entrada Sandstone surface.

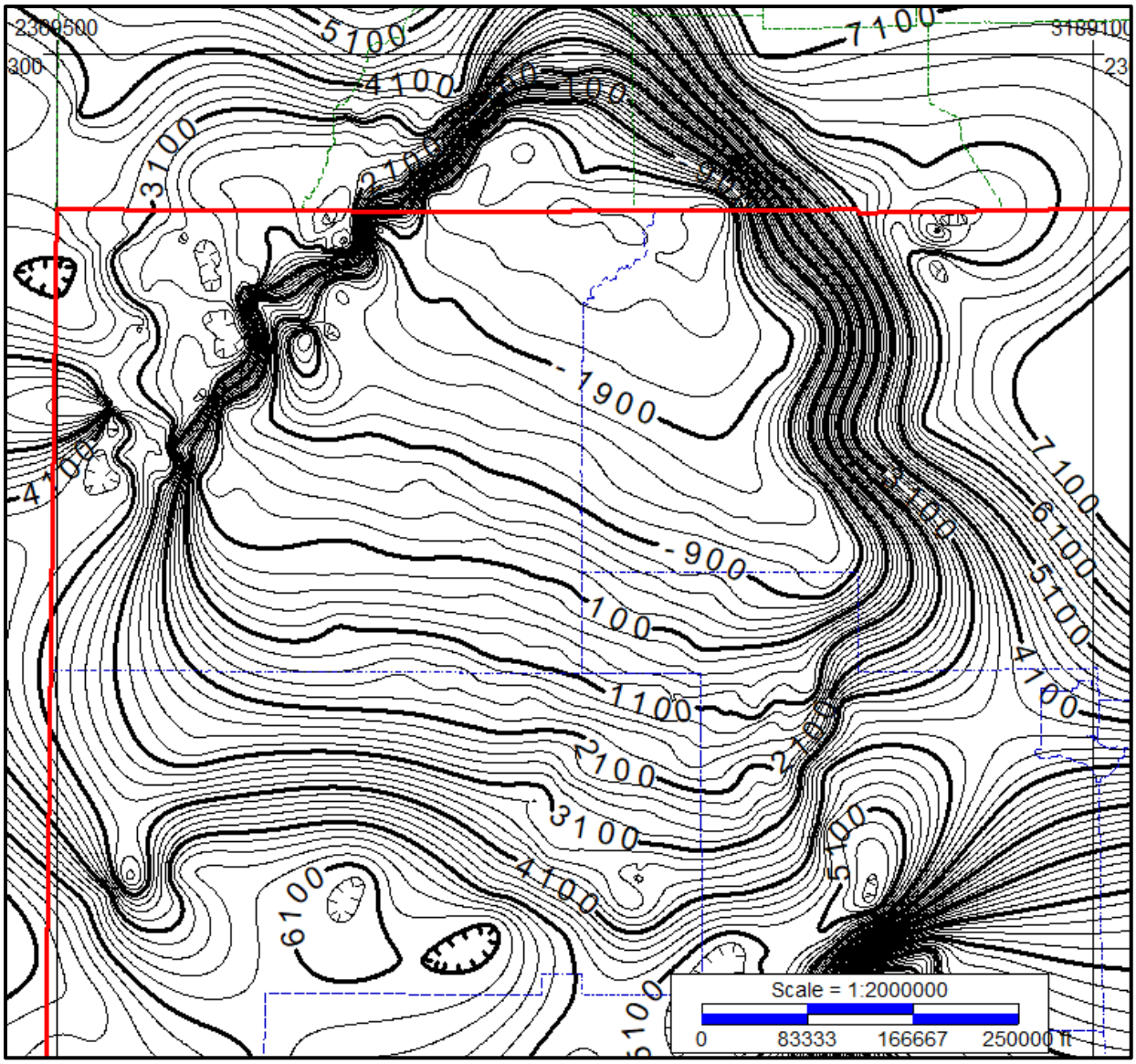


Figure 23. The subsea structural map on the Todilto Formation surface.

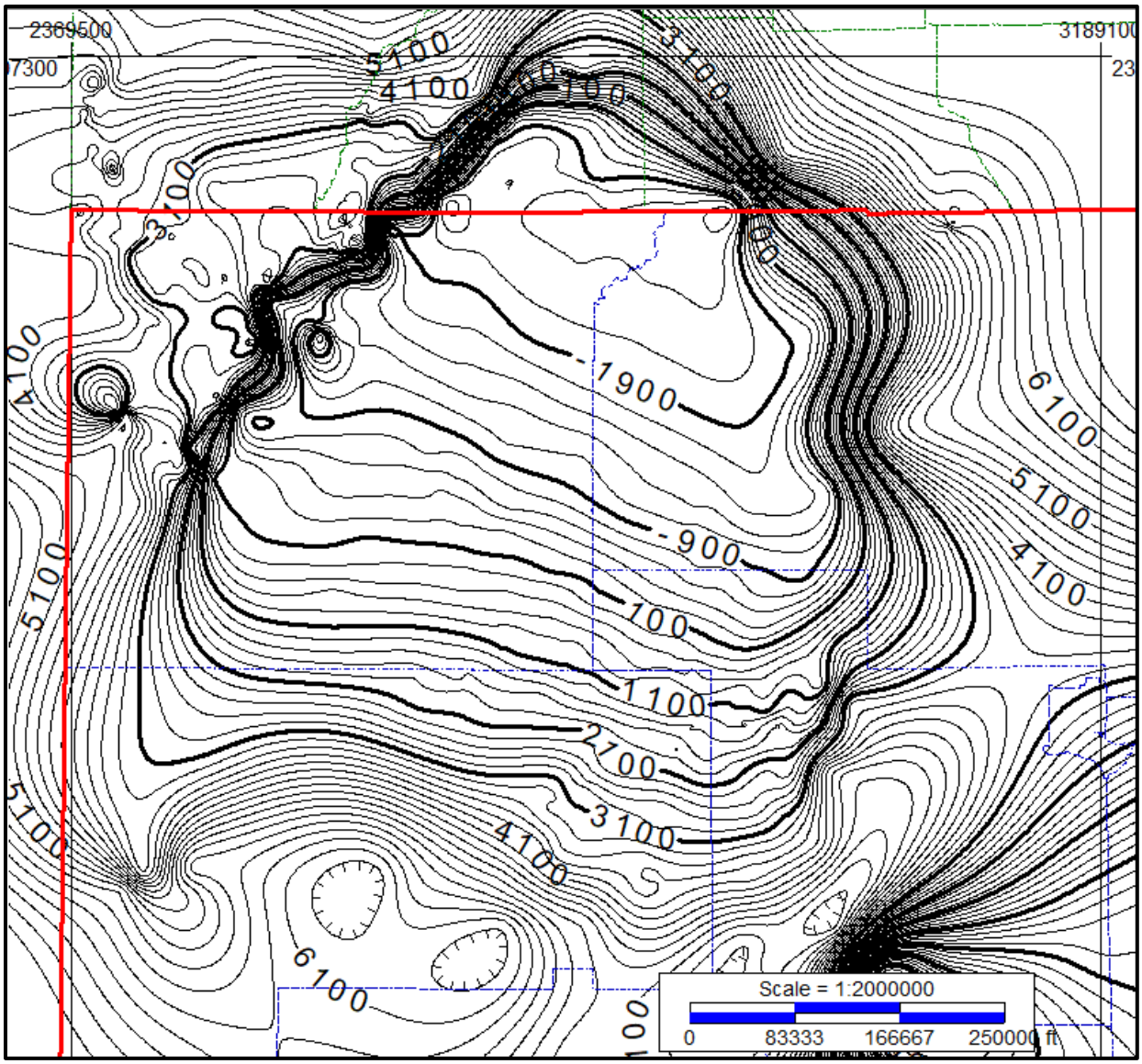


Figure 24. The subsea structural map on the Summerville Formation surface.

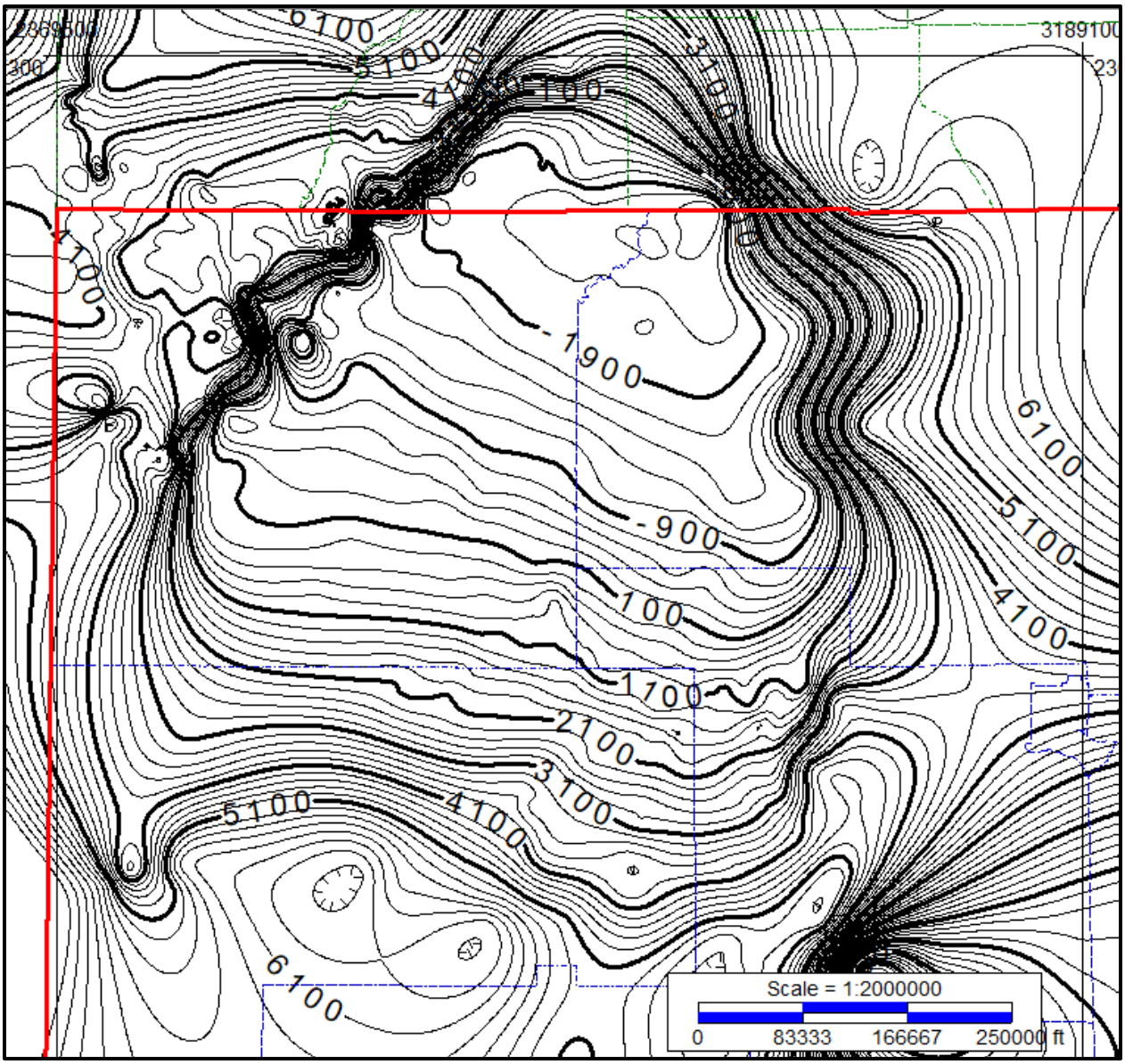


Figure 25. The subsea structural map on the Bluff Sandstone surface.

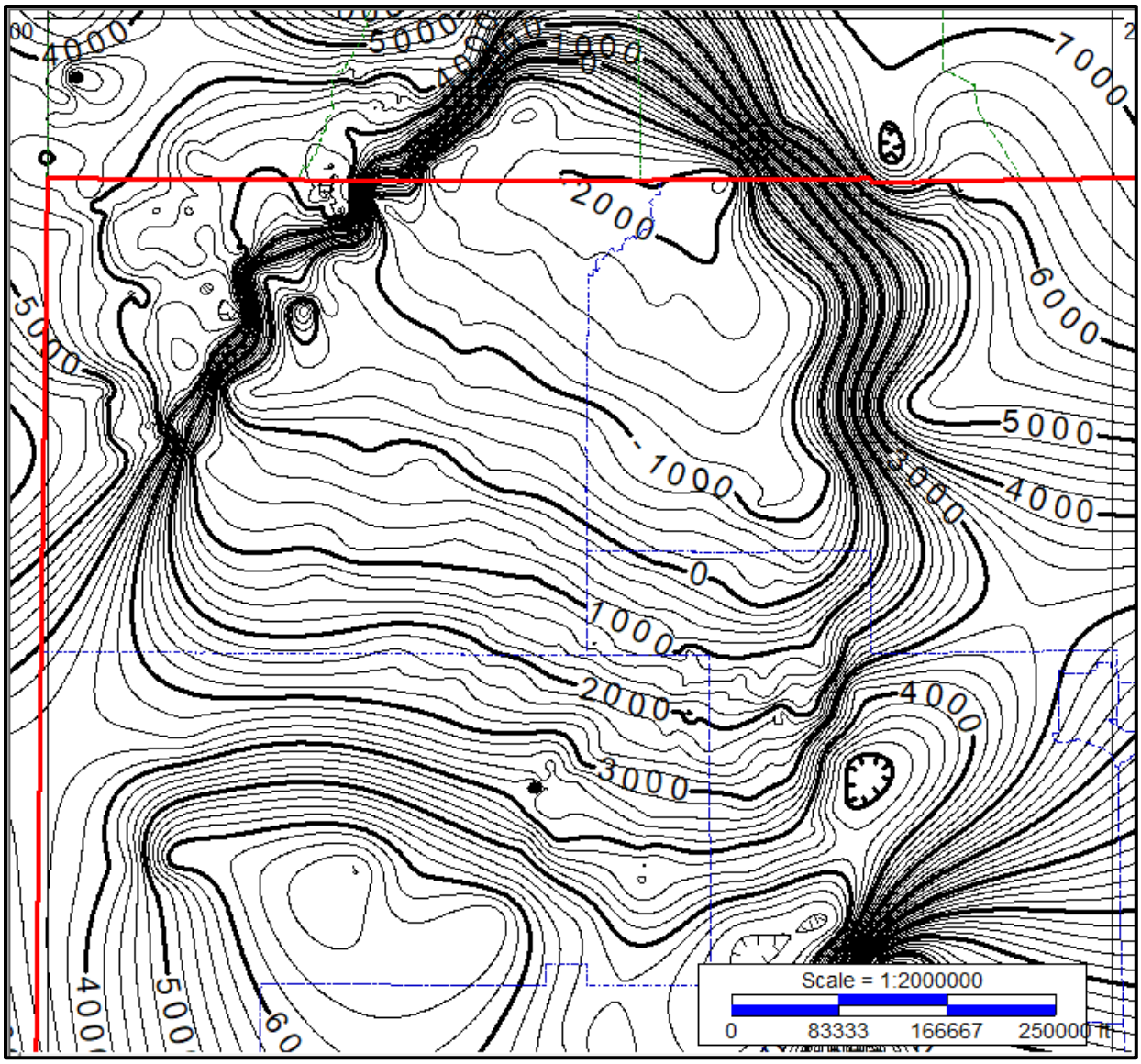


Figure 26. The subsea structural map on the Salt Wash Member of the Morrison Formation surface.

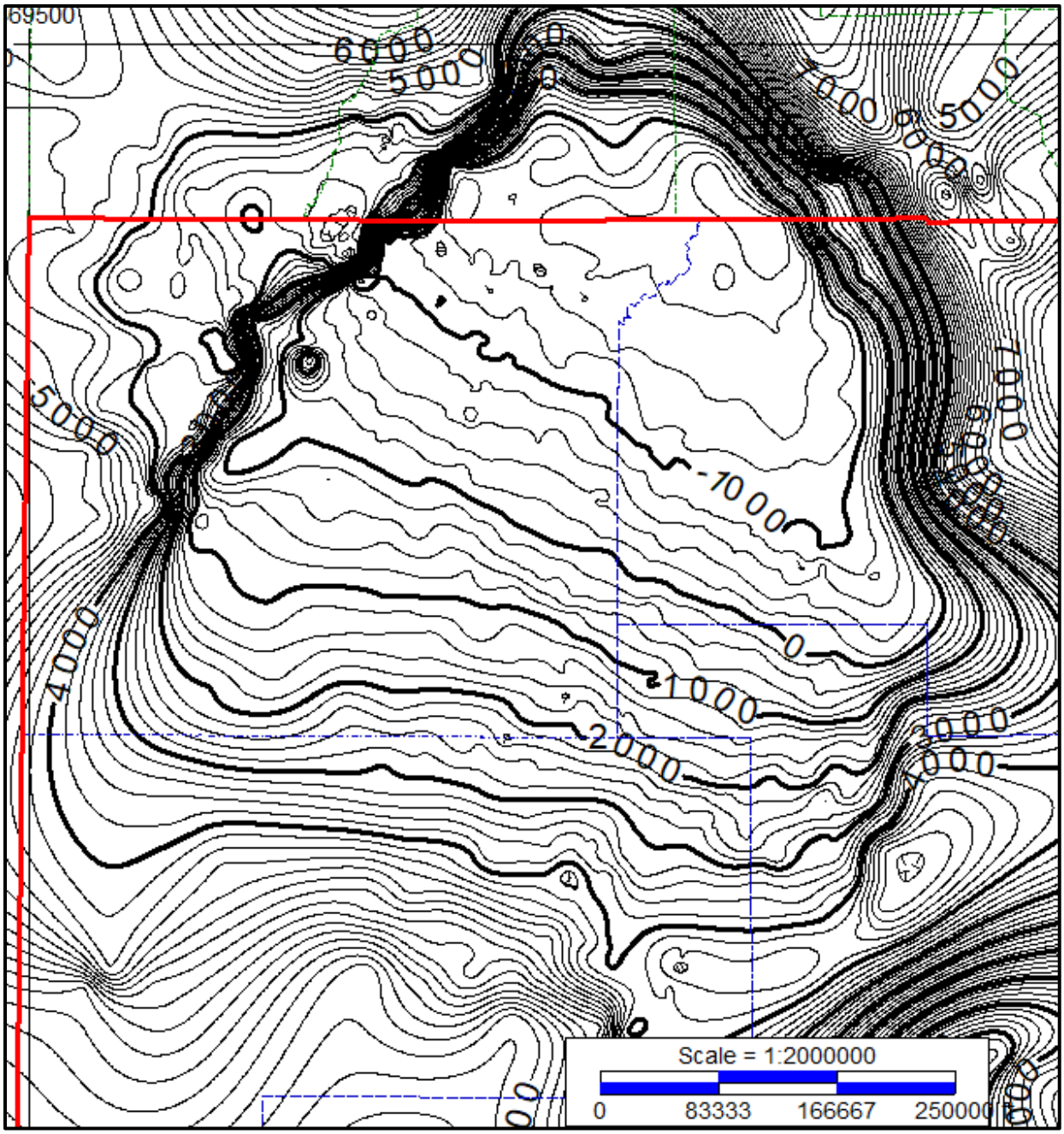


Figure 27. The subsea structural map on the Brushy Basin Member of the Morrison Formation surface.

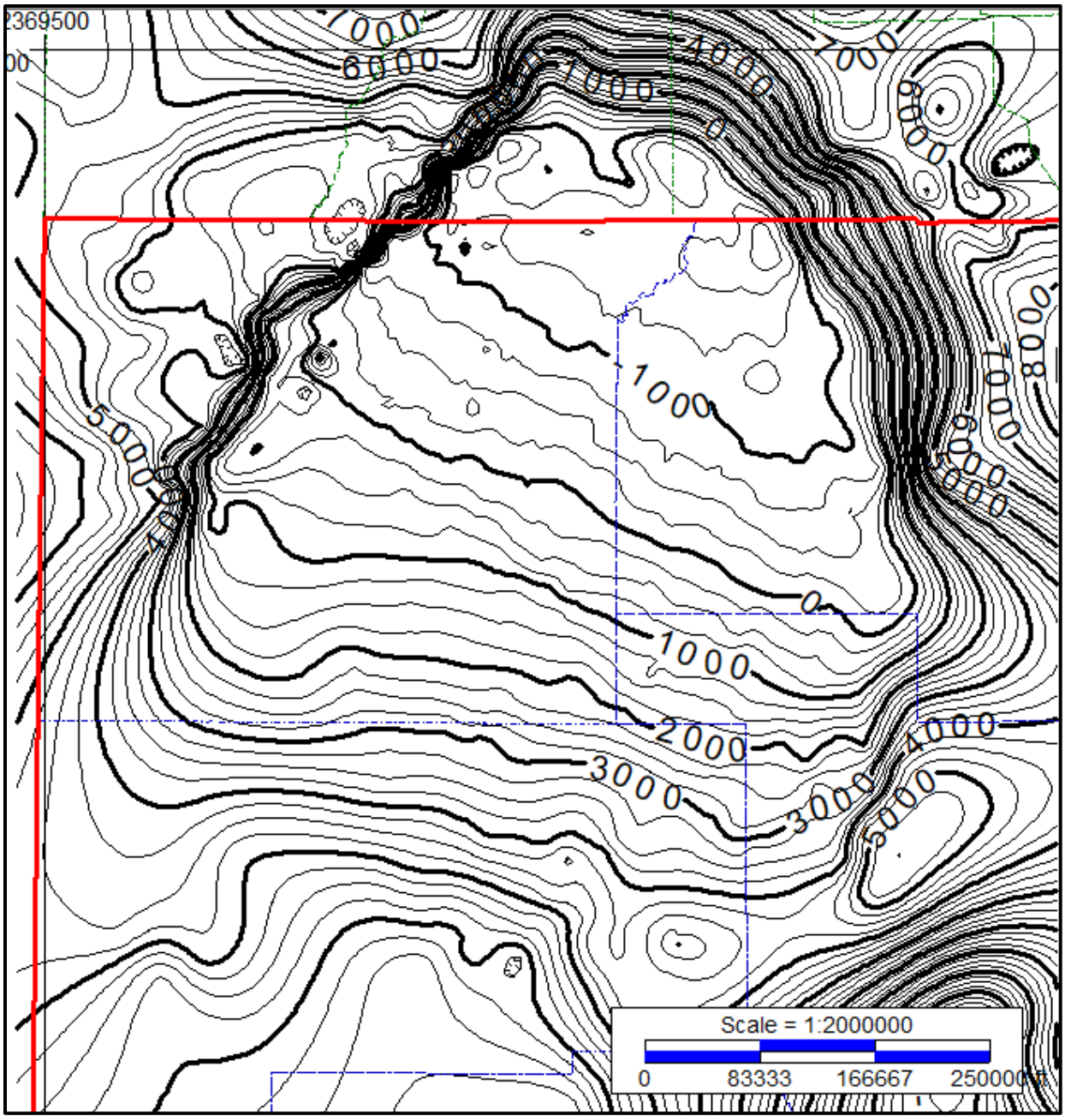


Figure 28. The subsea structural map on the Dakota Sandstone surface.

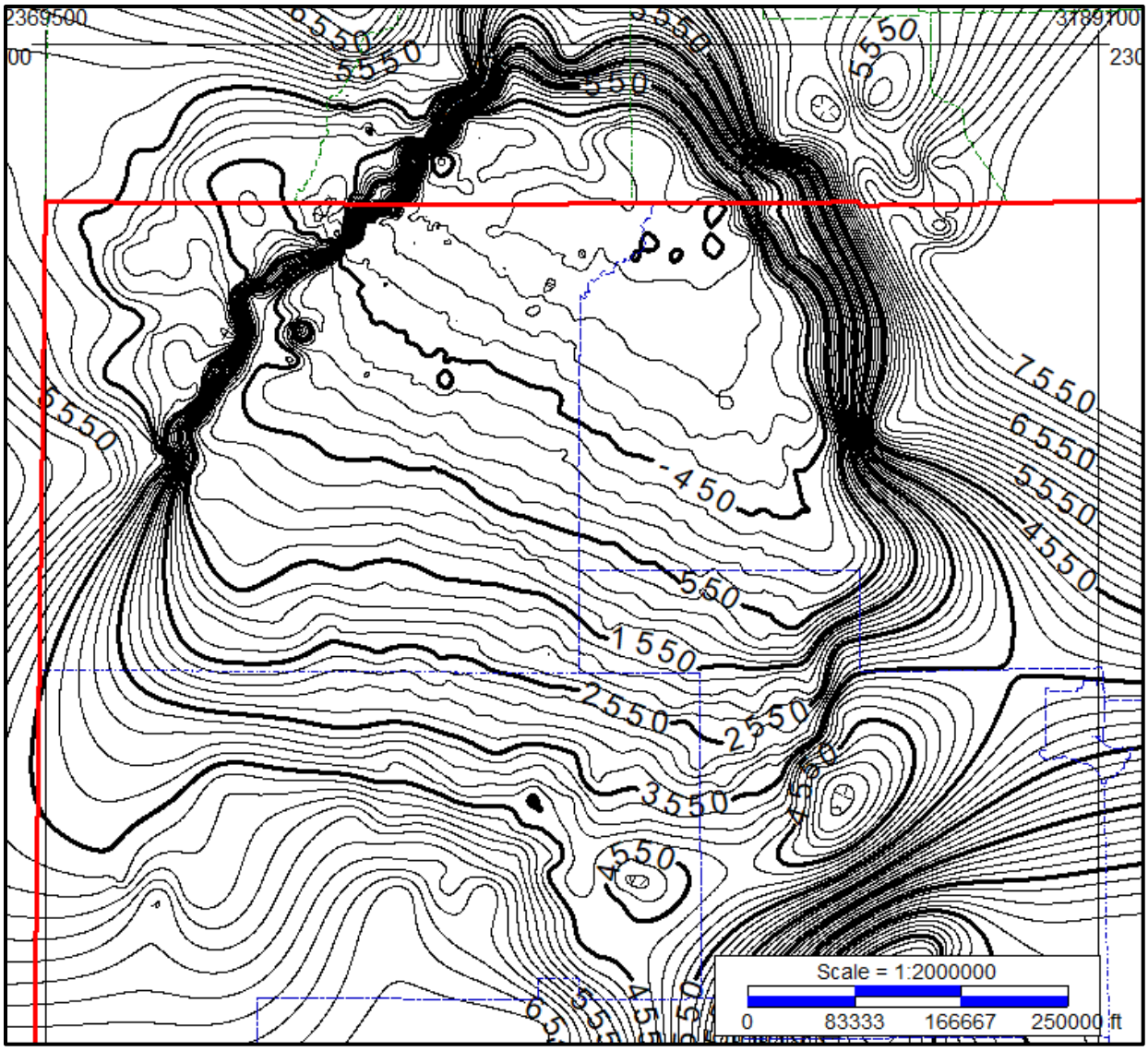


Figure 29. The subsea structural map on the Graneros Shale surface.

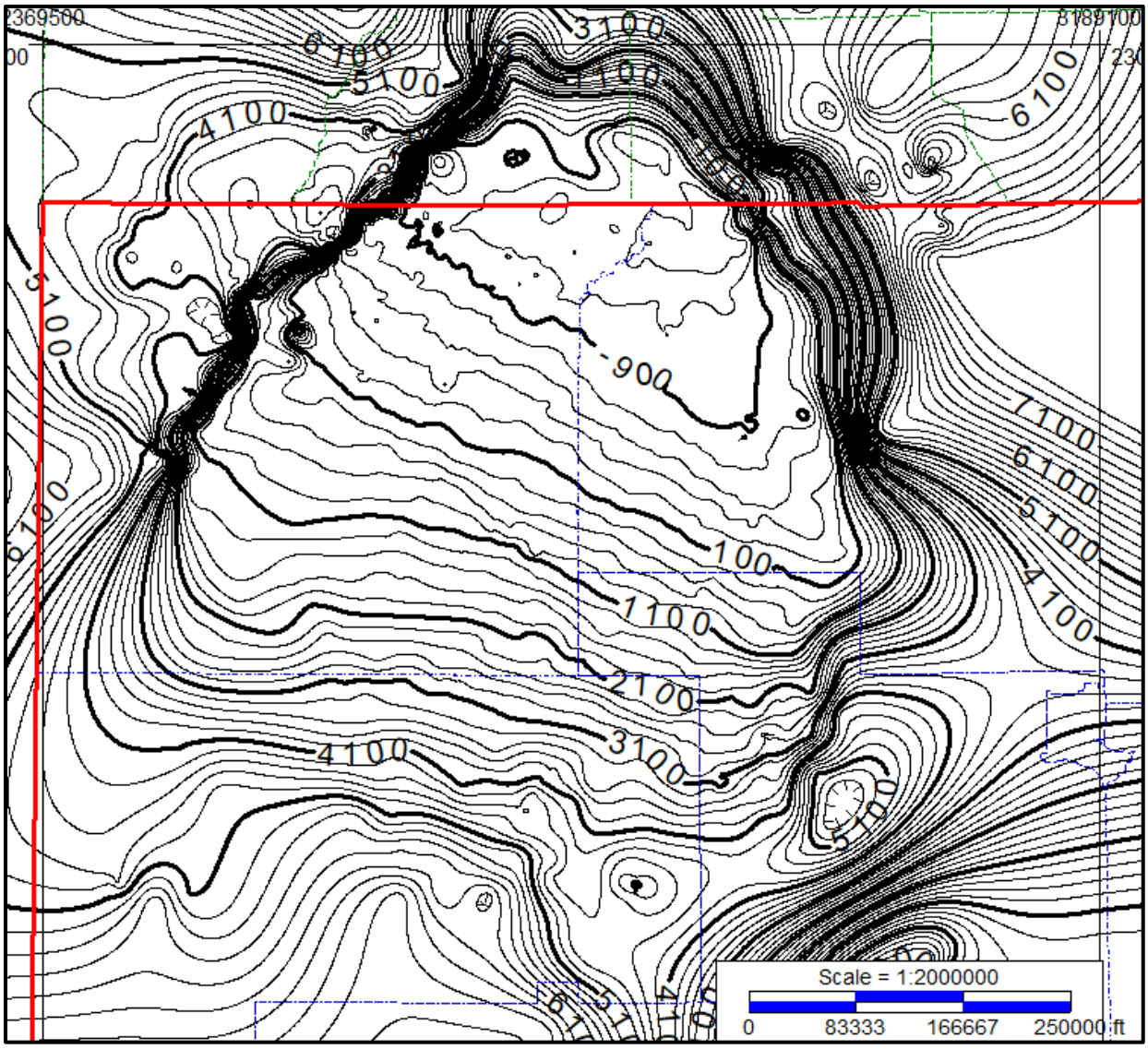


Figure 30. The subsea structural map on the Greenhorn Limestone surface.

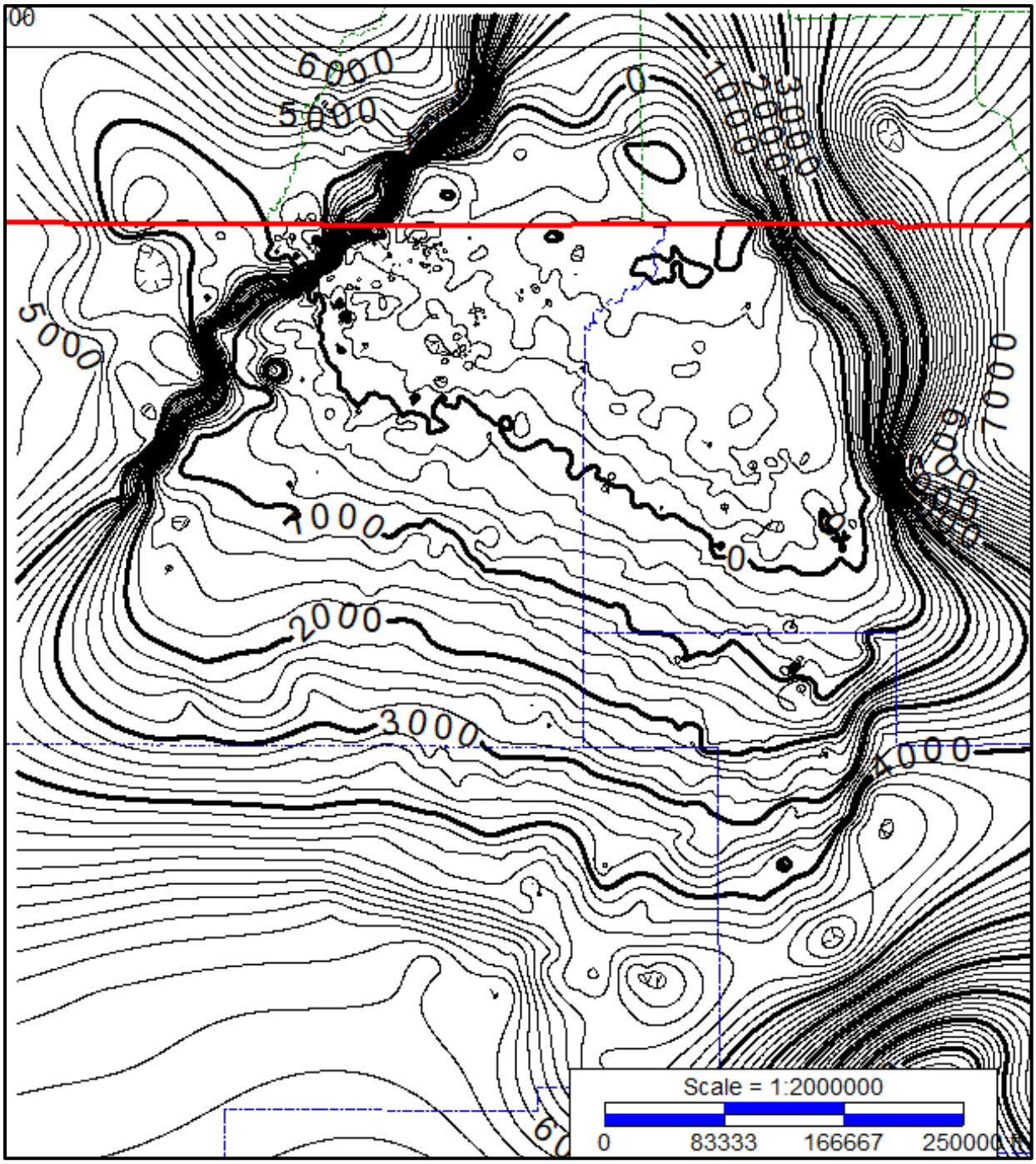


Figure 31. The subsea structural map on the lower Mancos Shale surface.

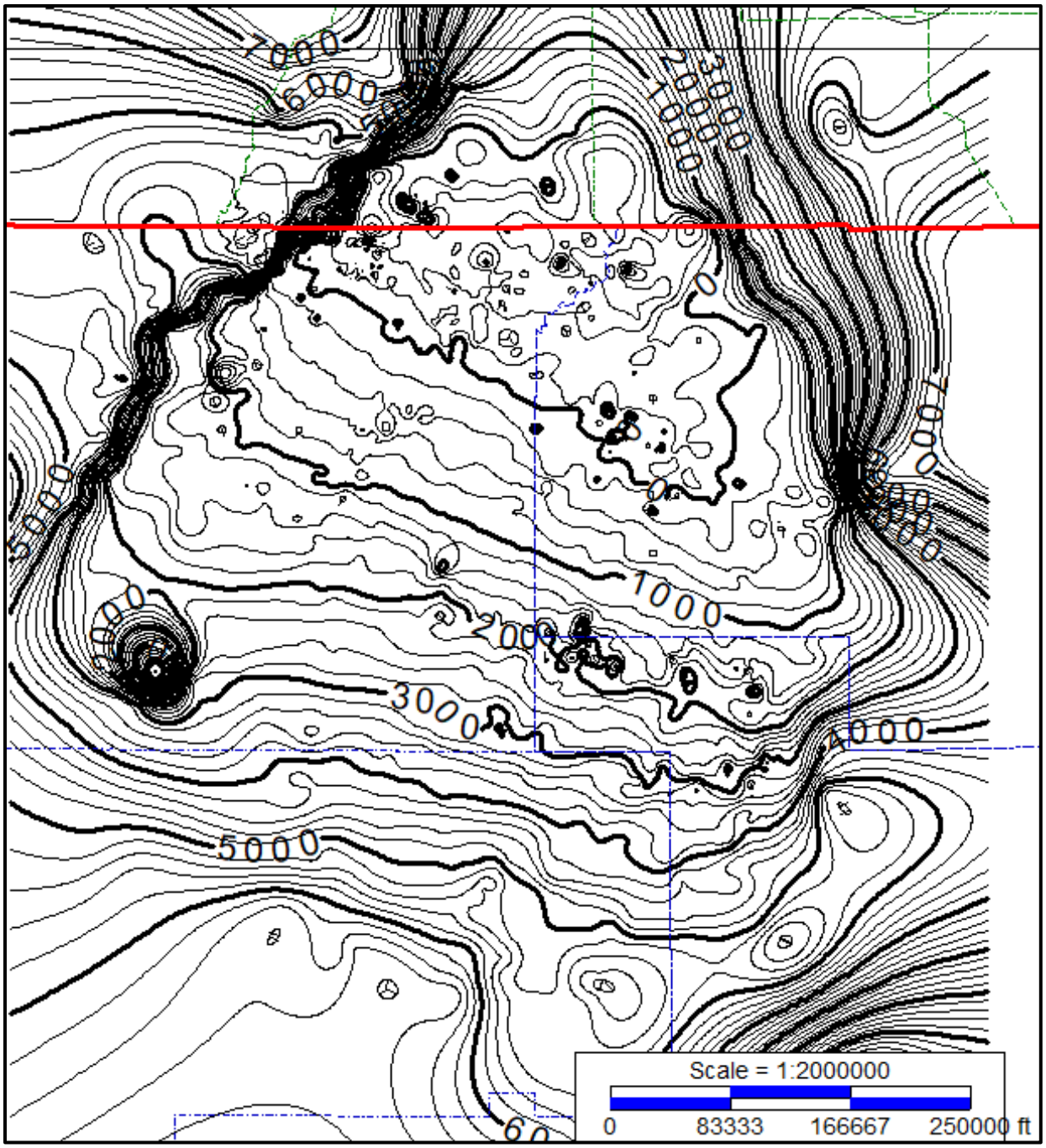


Figure 32. The subsea structural map on the Gallup Sandstone surface.

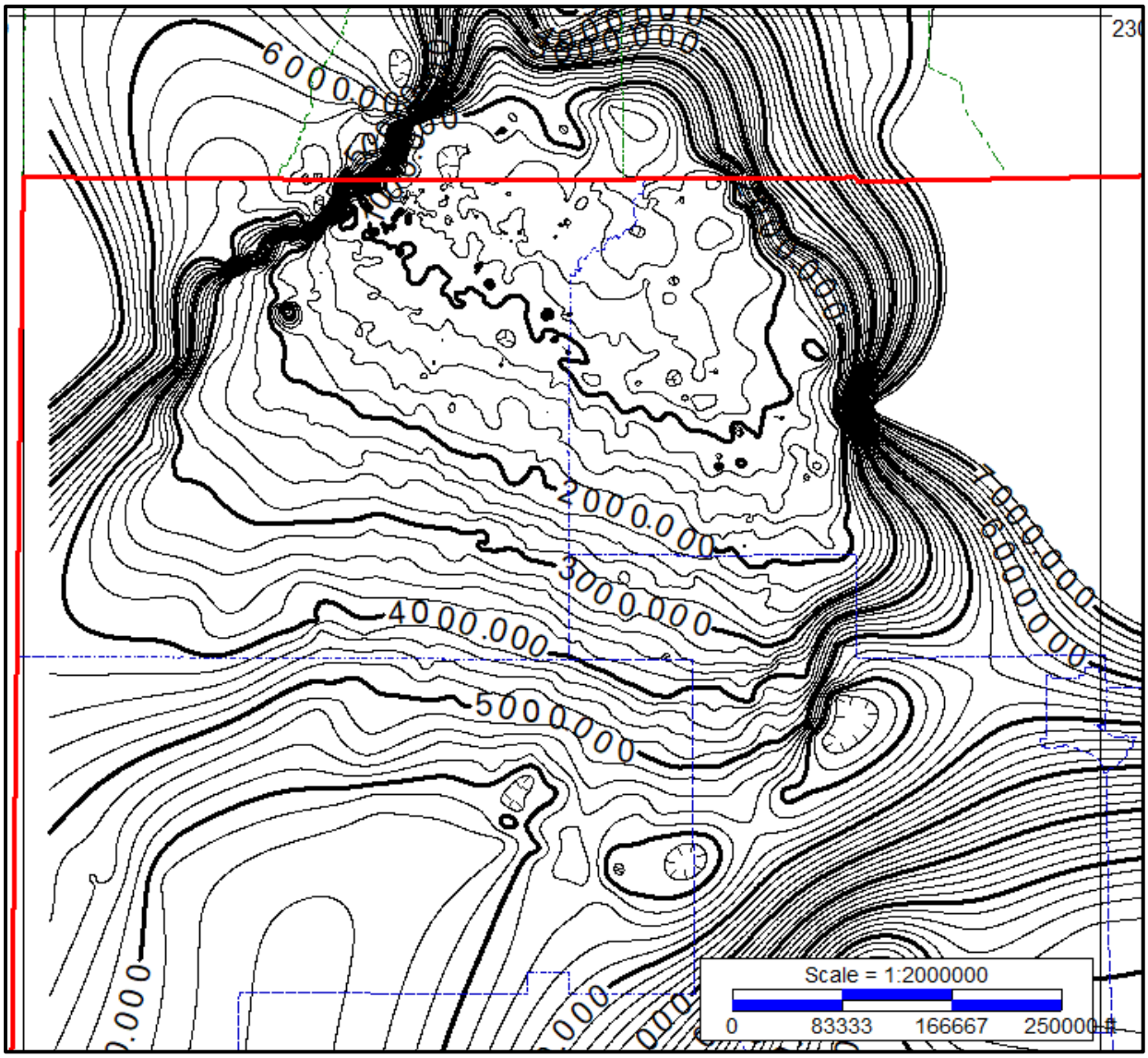


Figure 33. The subsea structural map on the upper Mancos Shale surface.

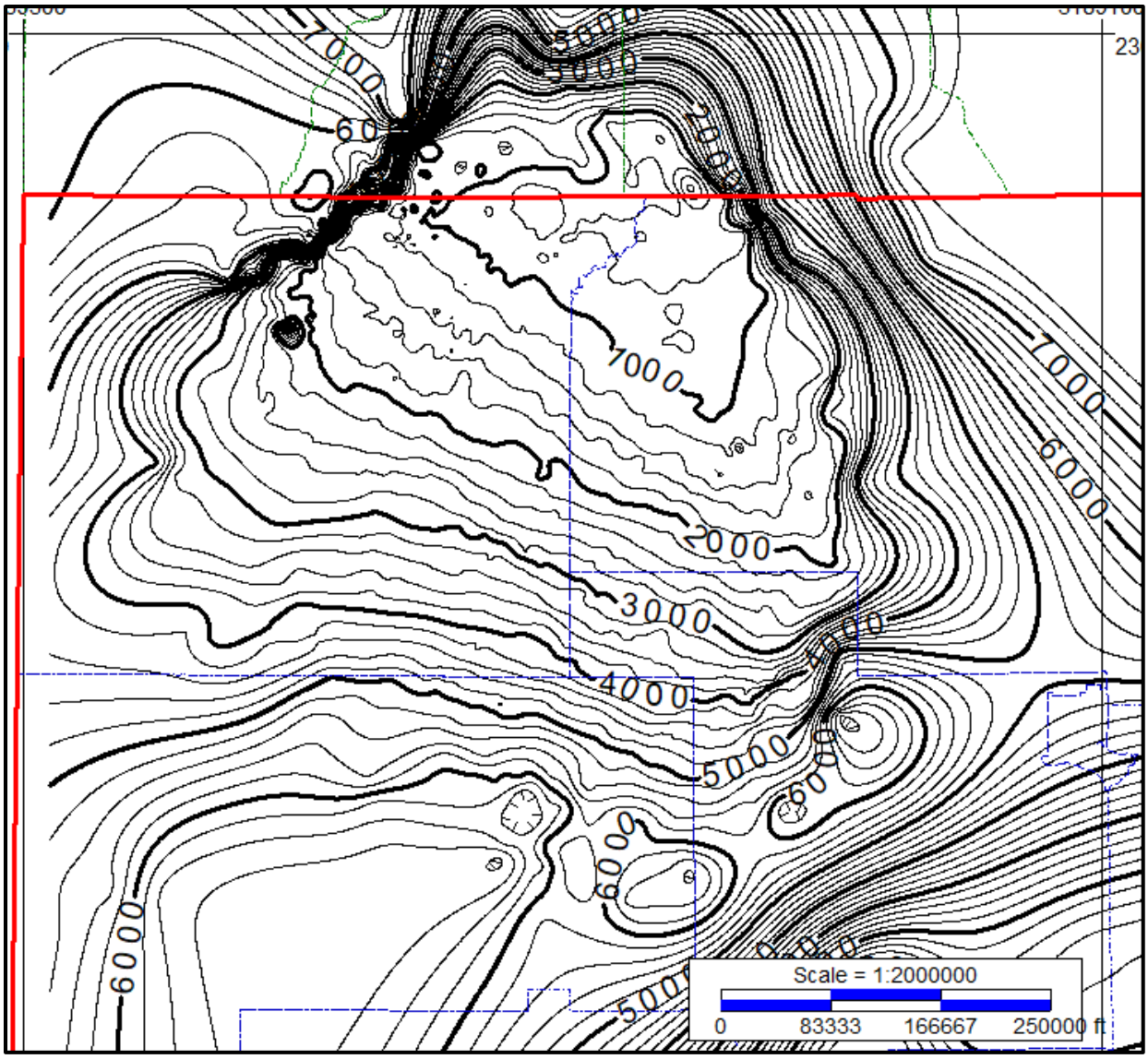


Figure 34. The subsea structural map on the Point Lookout Sandstone surface.

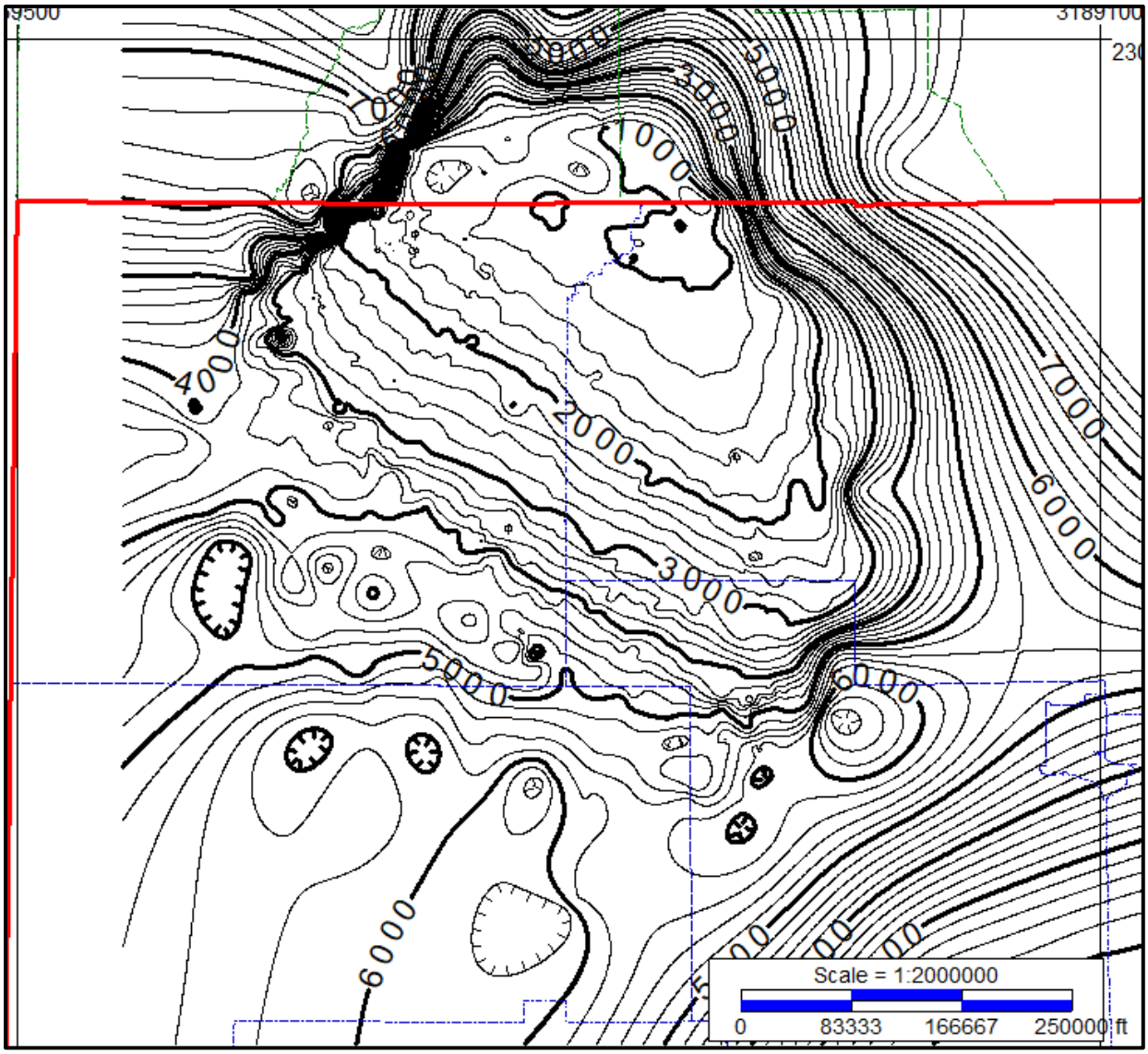


Figure 35. The subsea structural map on the Menefee Formation surface.

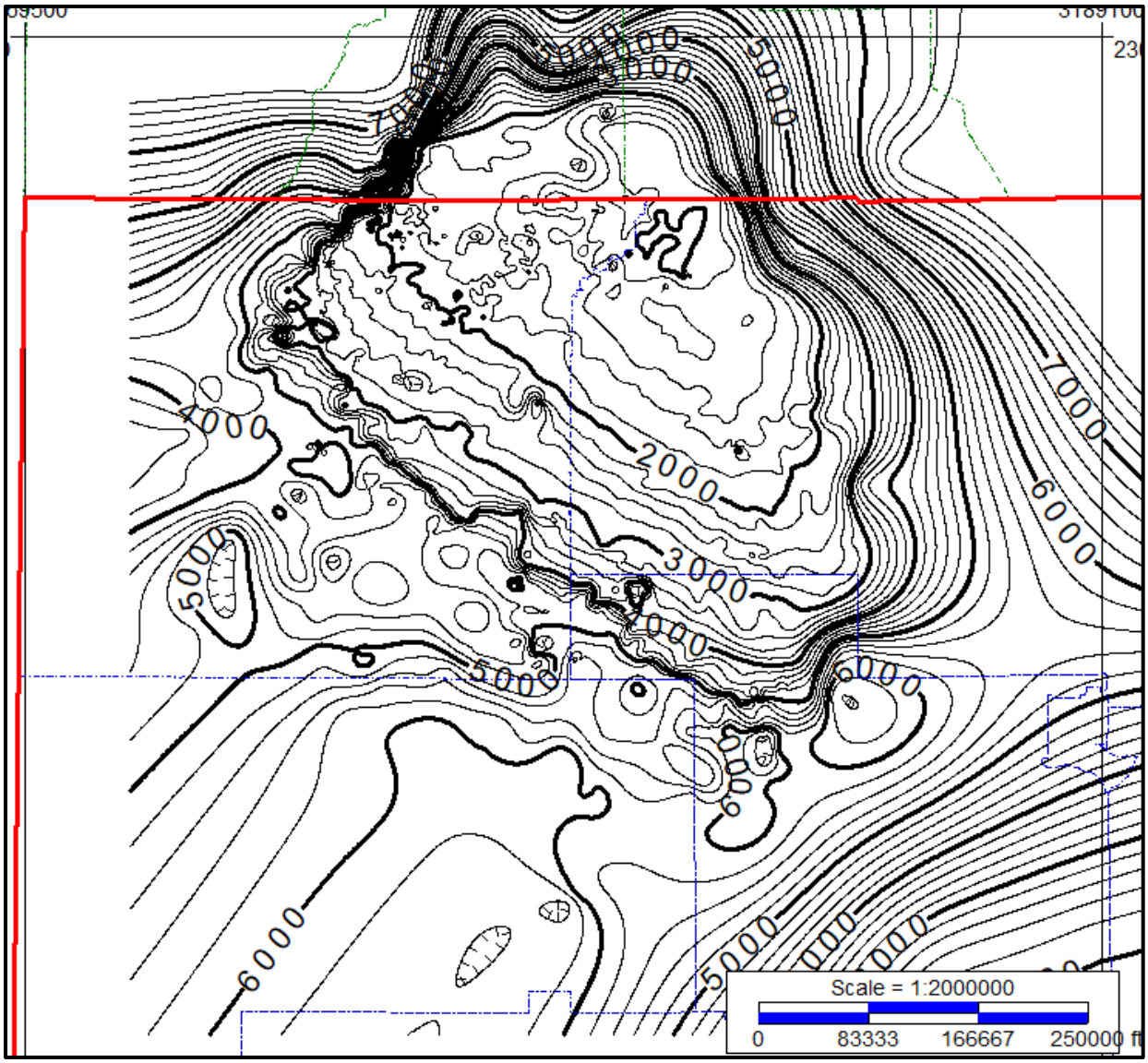


Figure 36. The subsea structural map on the Cliff House Sandstone surface.

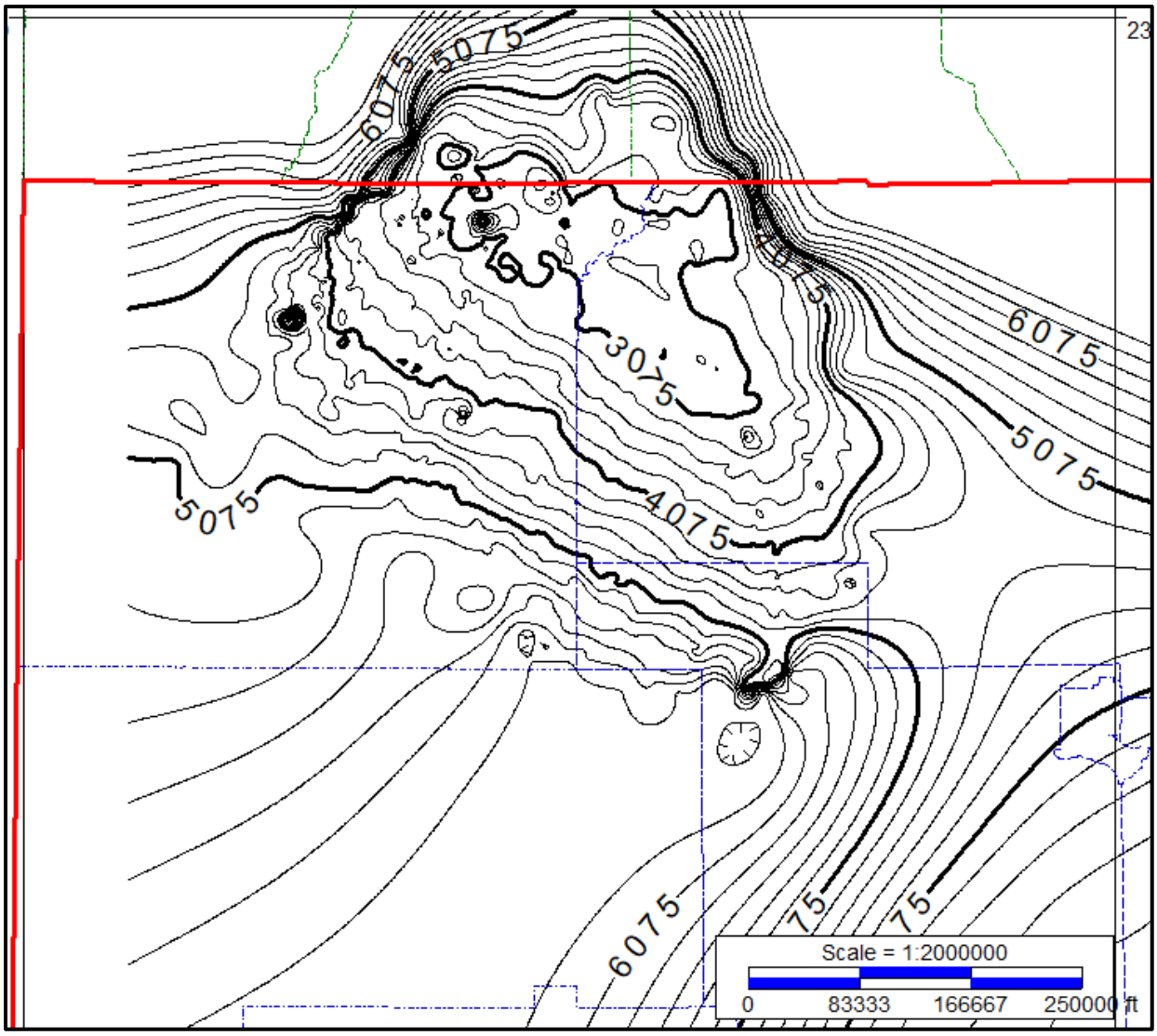


Figure 37. The subsea structural map on the Lewis Shale surface.

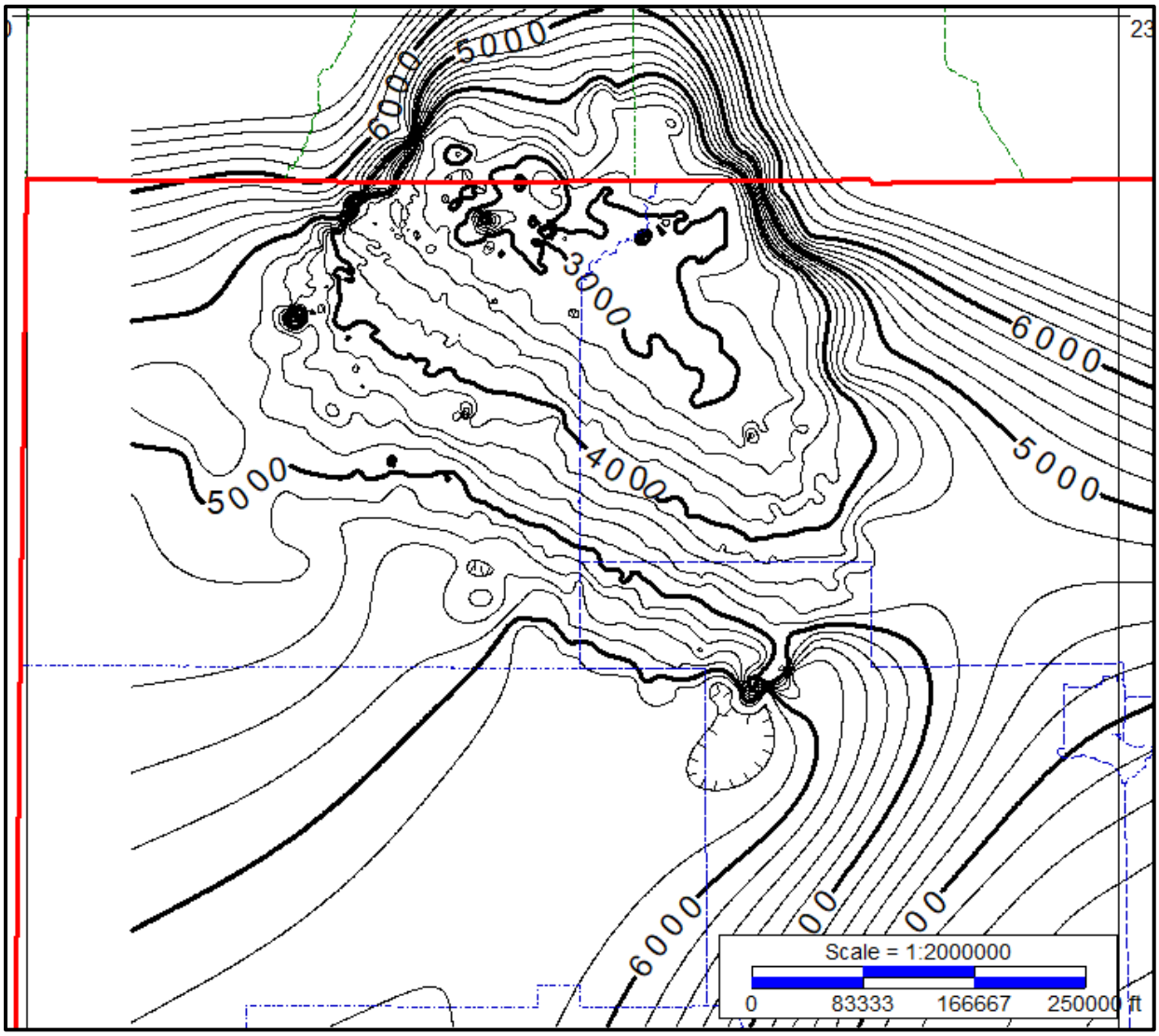


Figure 38. The subsea structural map on the Pictured Cliffs Sandstone surface.

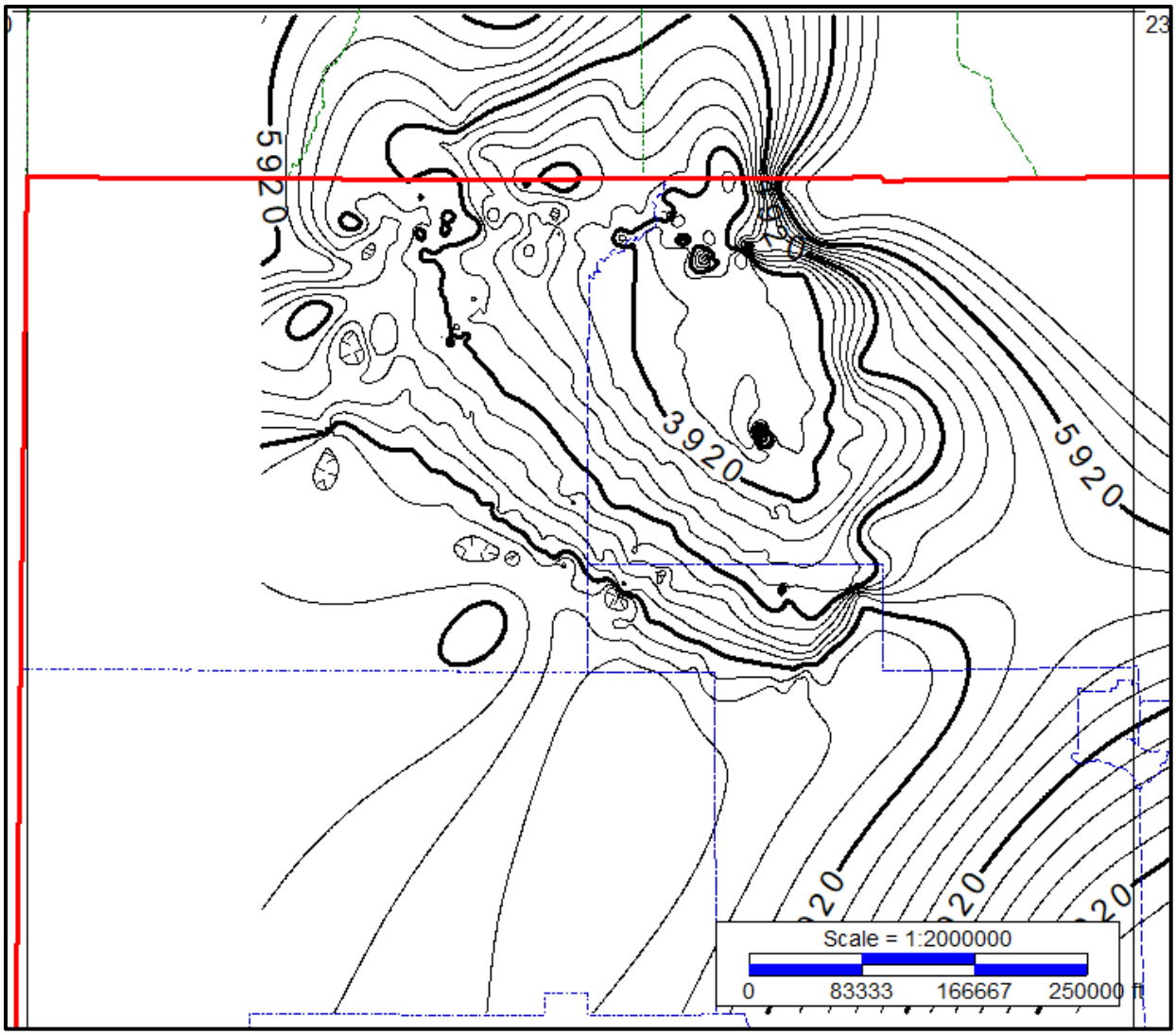


Figure 39. The subsea structural map on the Kirtland Shale surface.

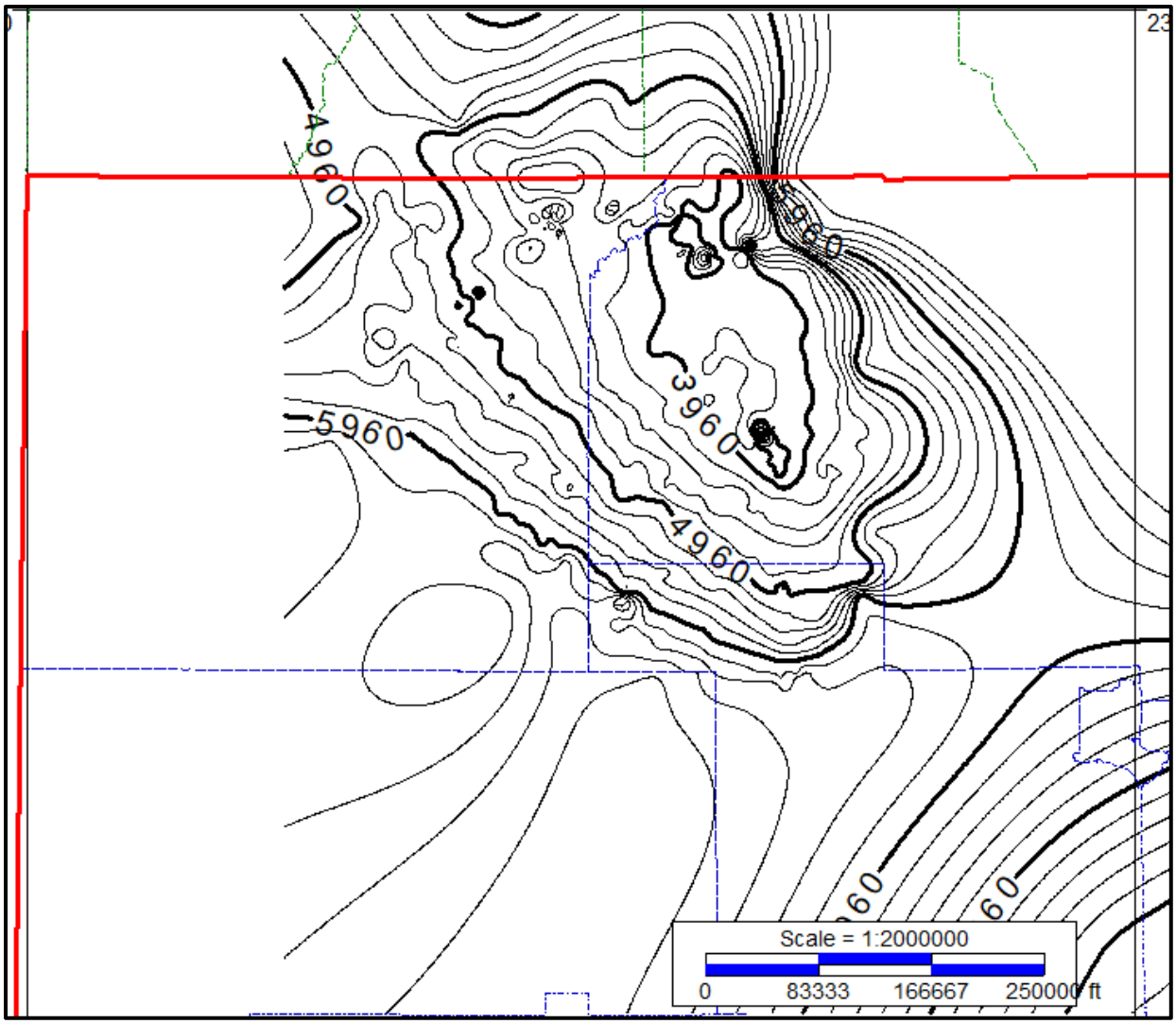


Figure 40. The subsea structural map on the Ojo Alamo Sandstone surface.

Surfaces With Faults

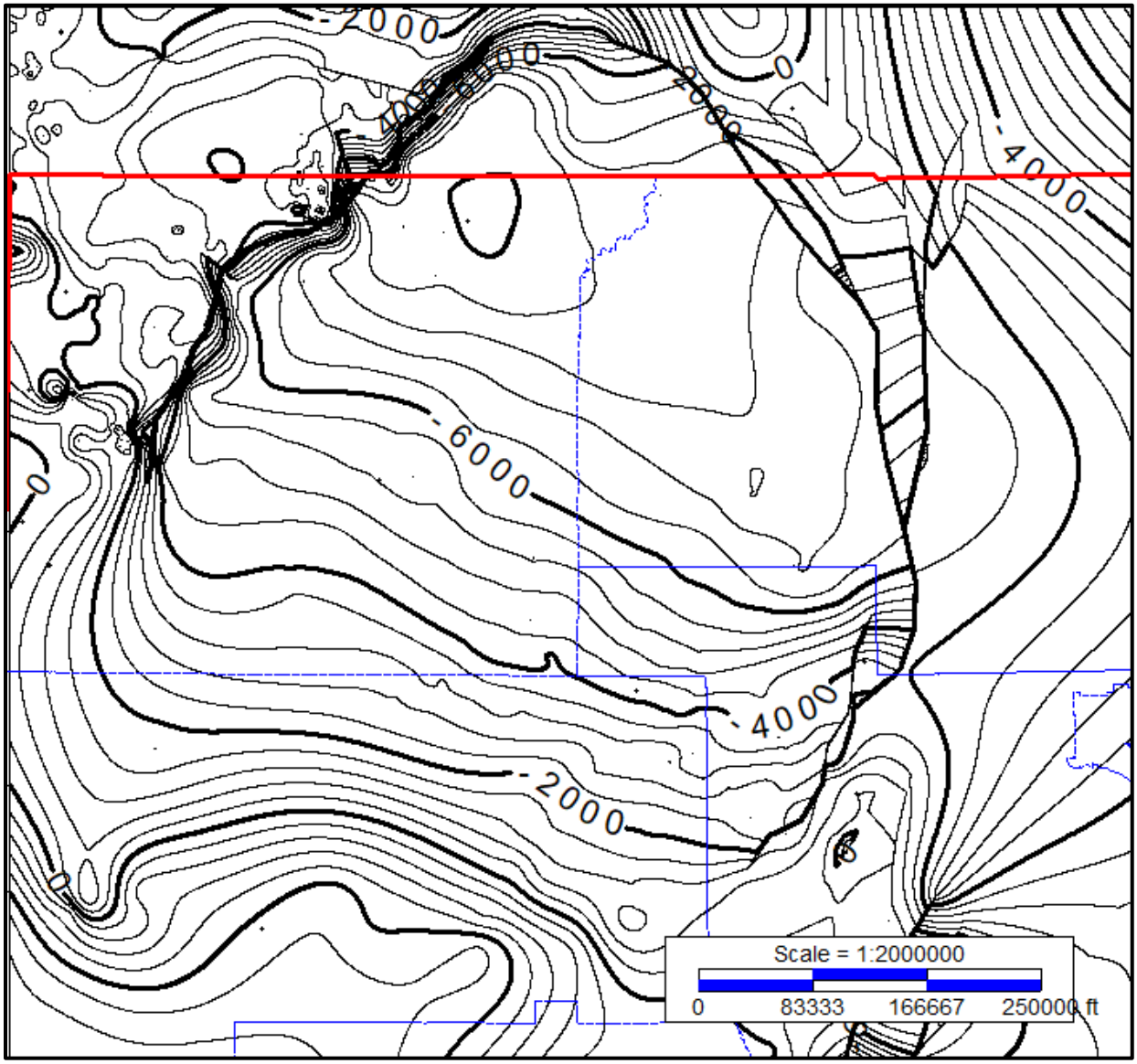


Figure 41. The subsea structural map on the Precambrian surface with potential faults.

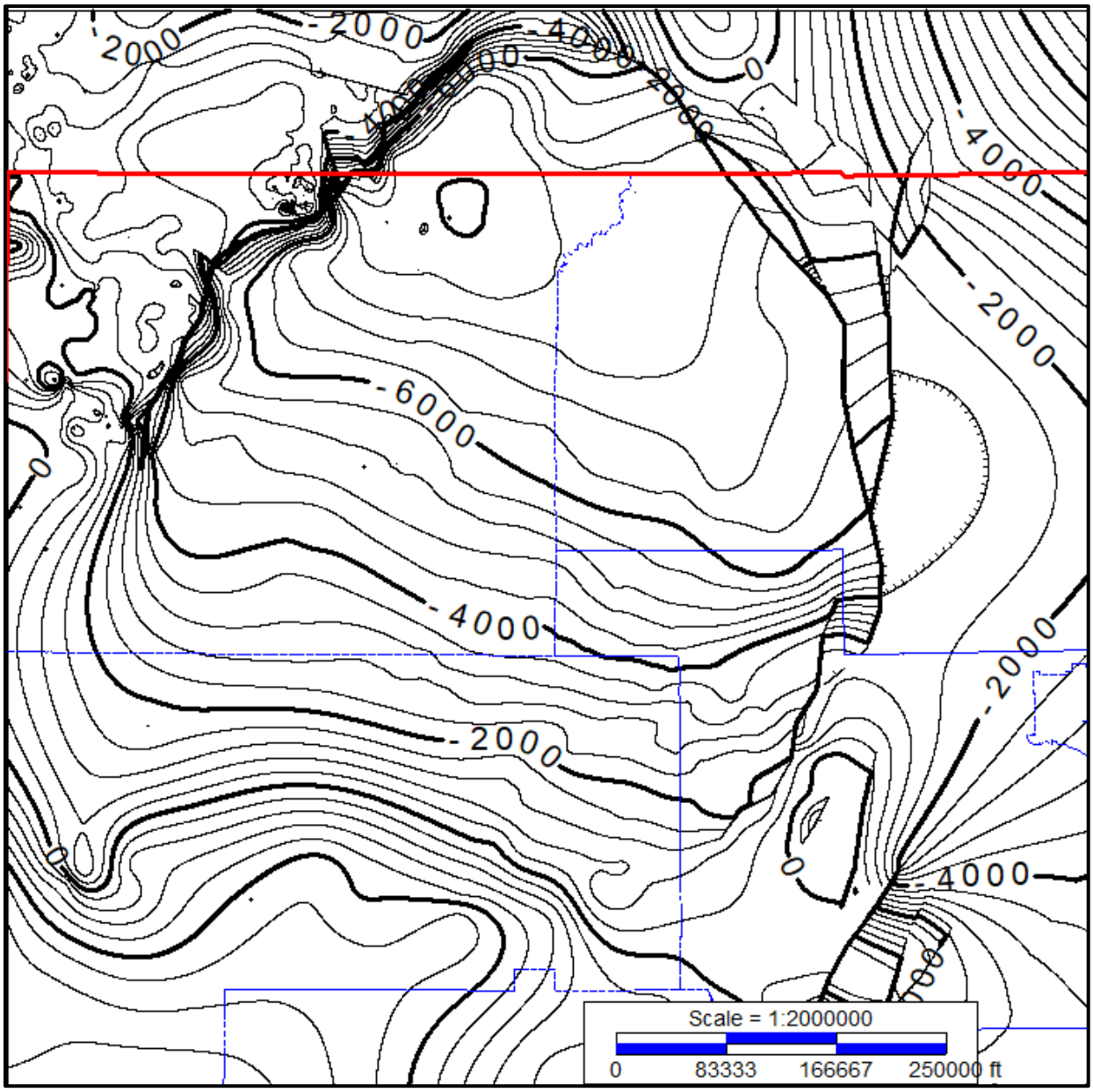


Figure 42. The subsea structural map on the Aneth Limestone surface with potential faults.

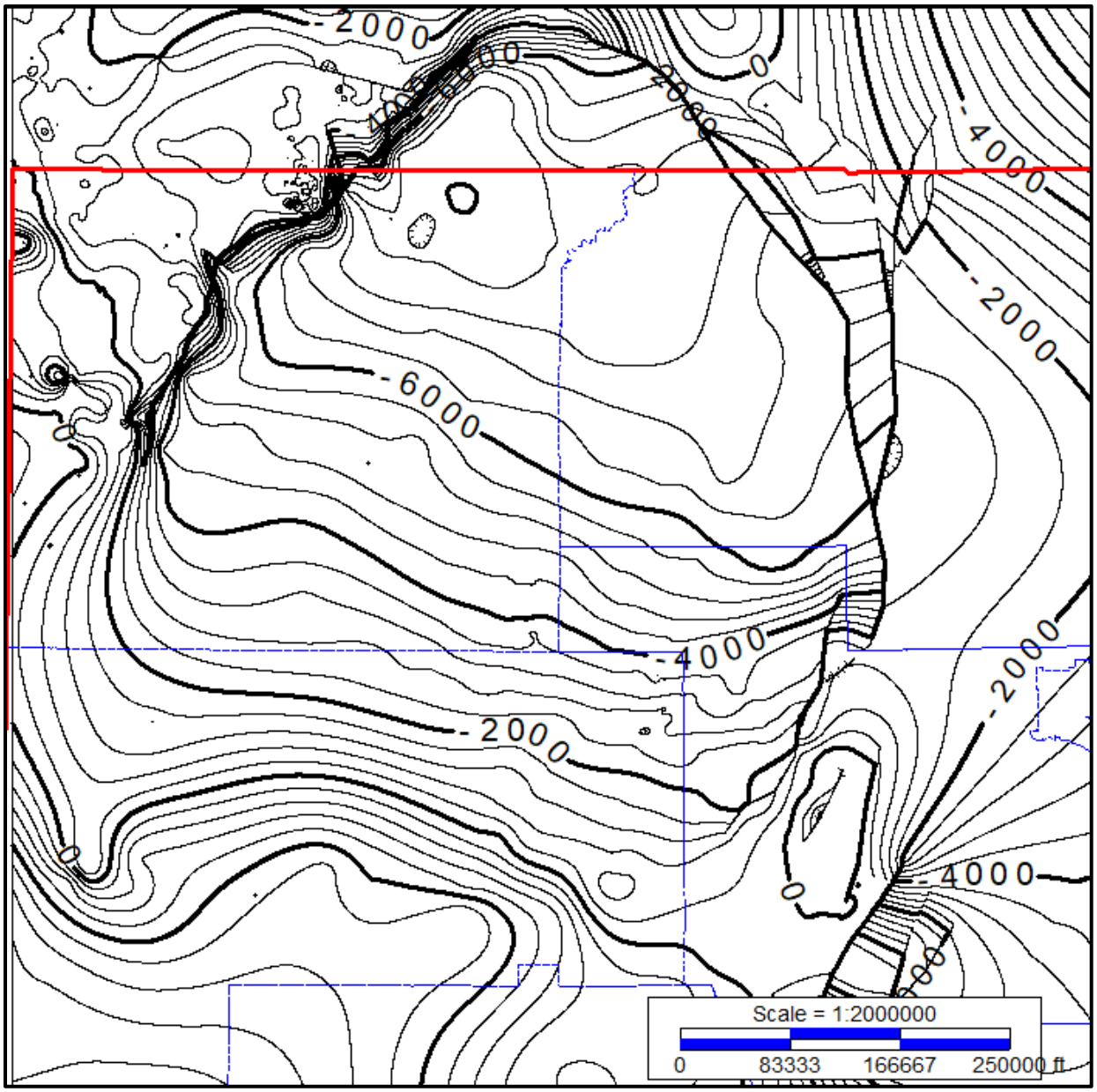


Figure 43. The subsea structural map on the Elbert Formation surface with potential faults.

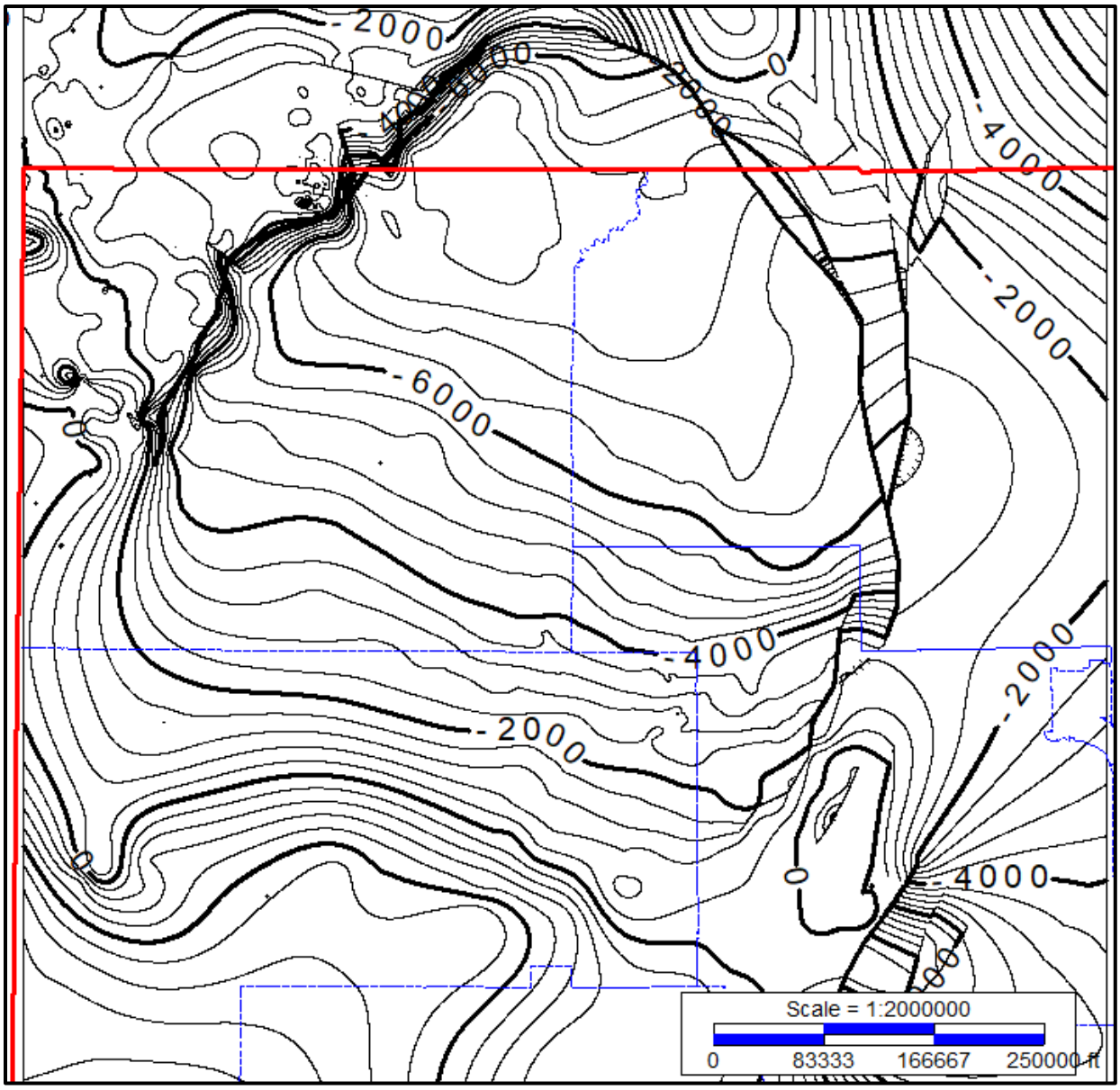


Figure 44. The subsea structural map on the Ouray Limestone surface with potential faults.

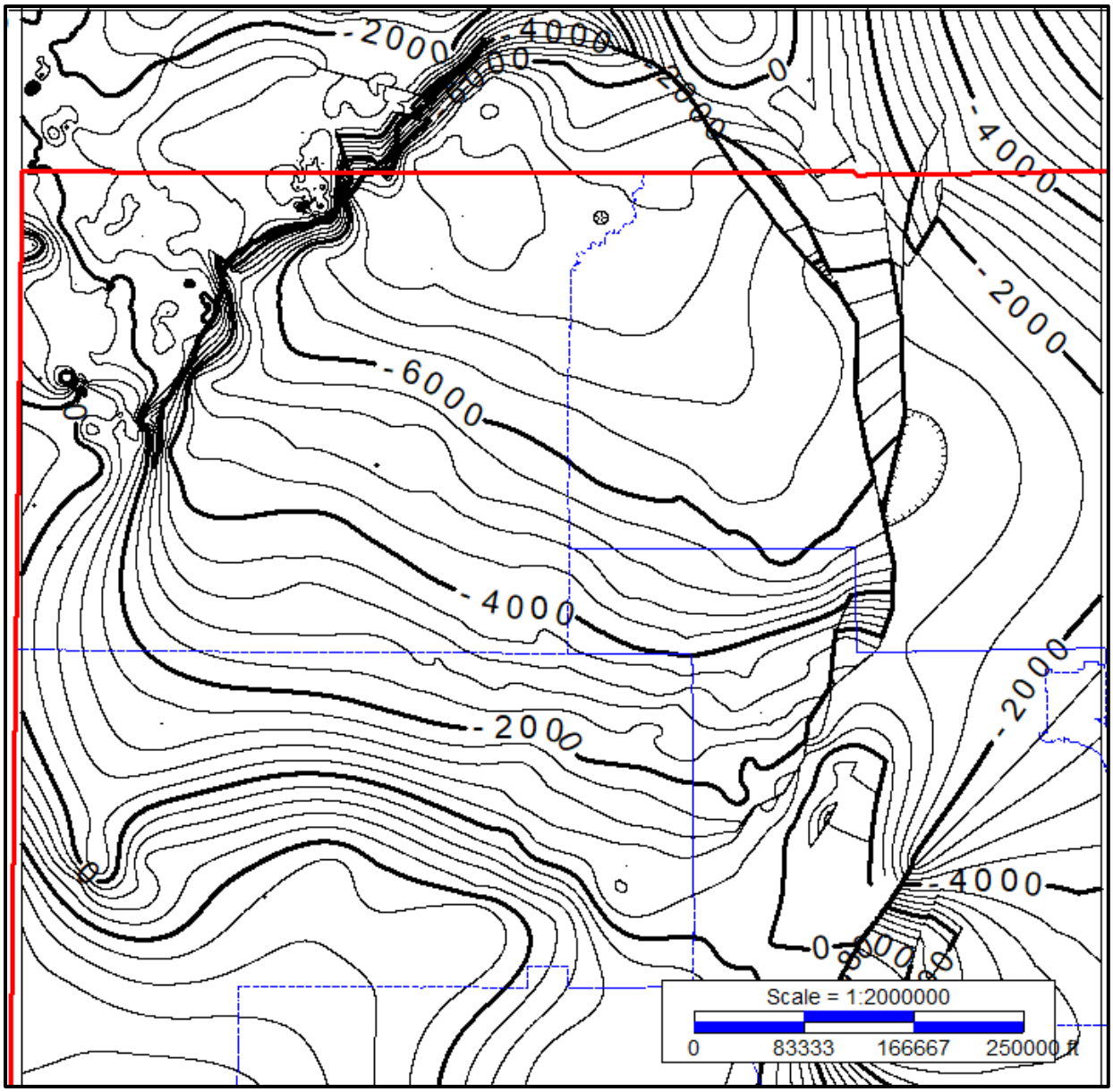


Figure 45. The subsea structural map on the Leadville Limestone surface with potential faults.

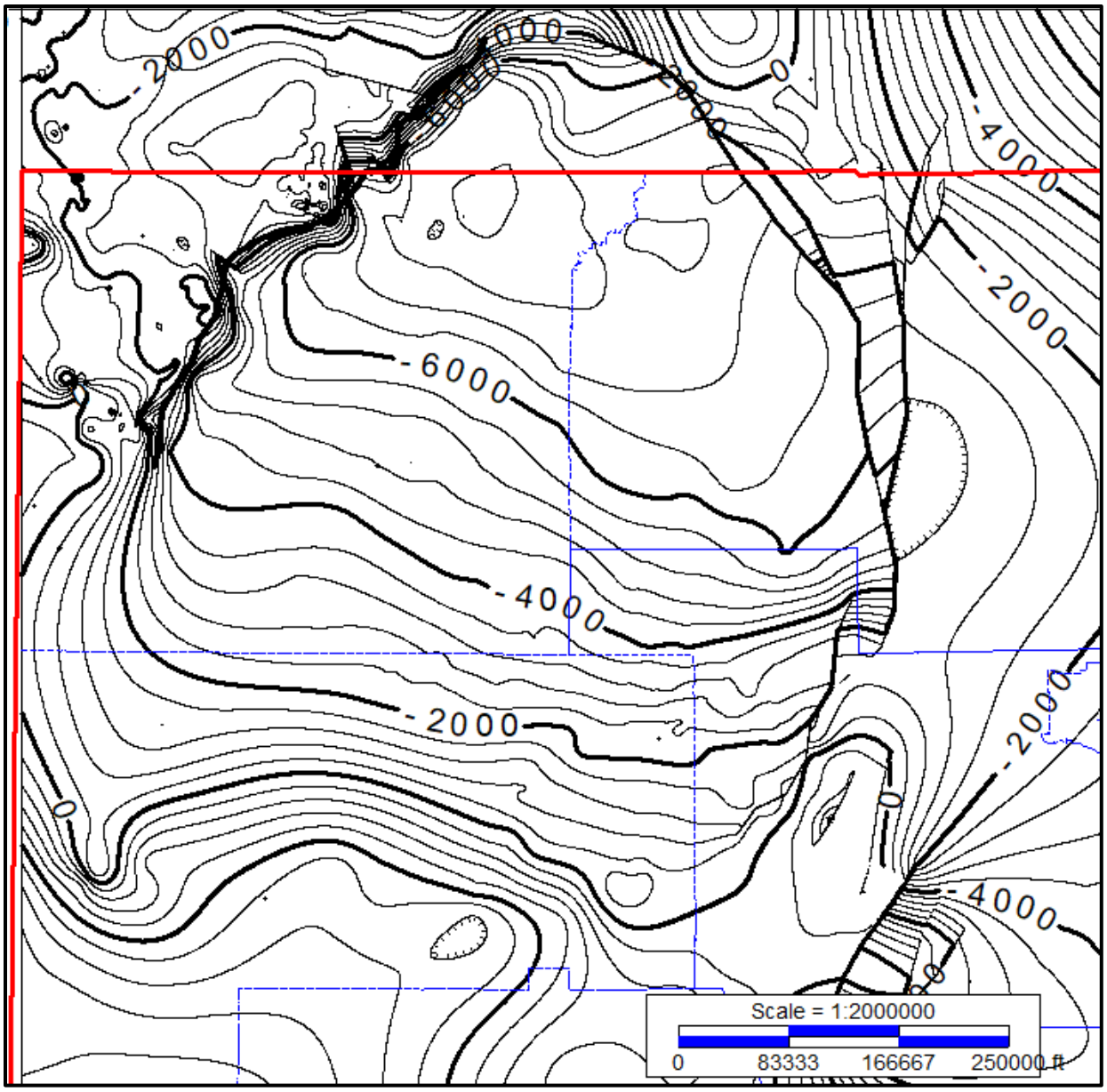


Figure 46. The subsea structural map on the Molas Formation surface with potential faults.

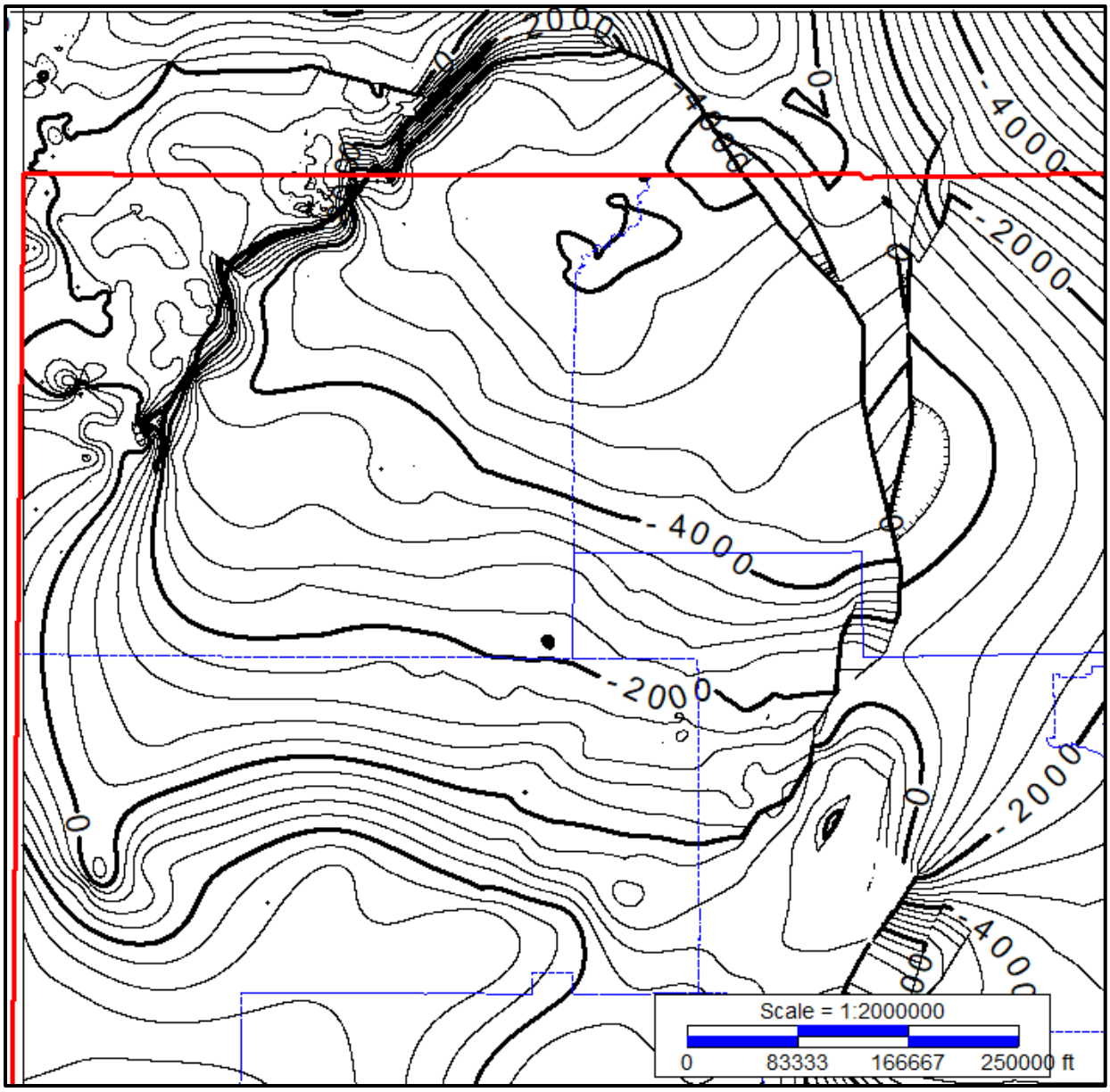


Figure 47. The subsea structural map on the Hermosa Group surface with potential faults.

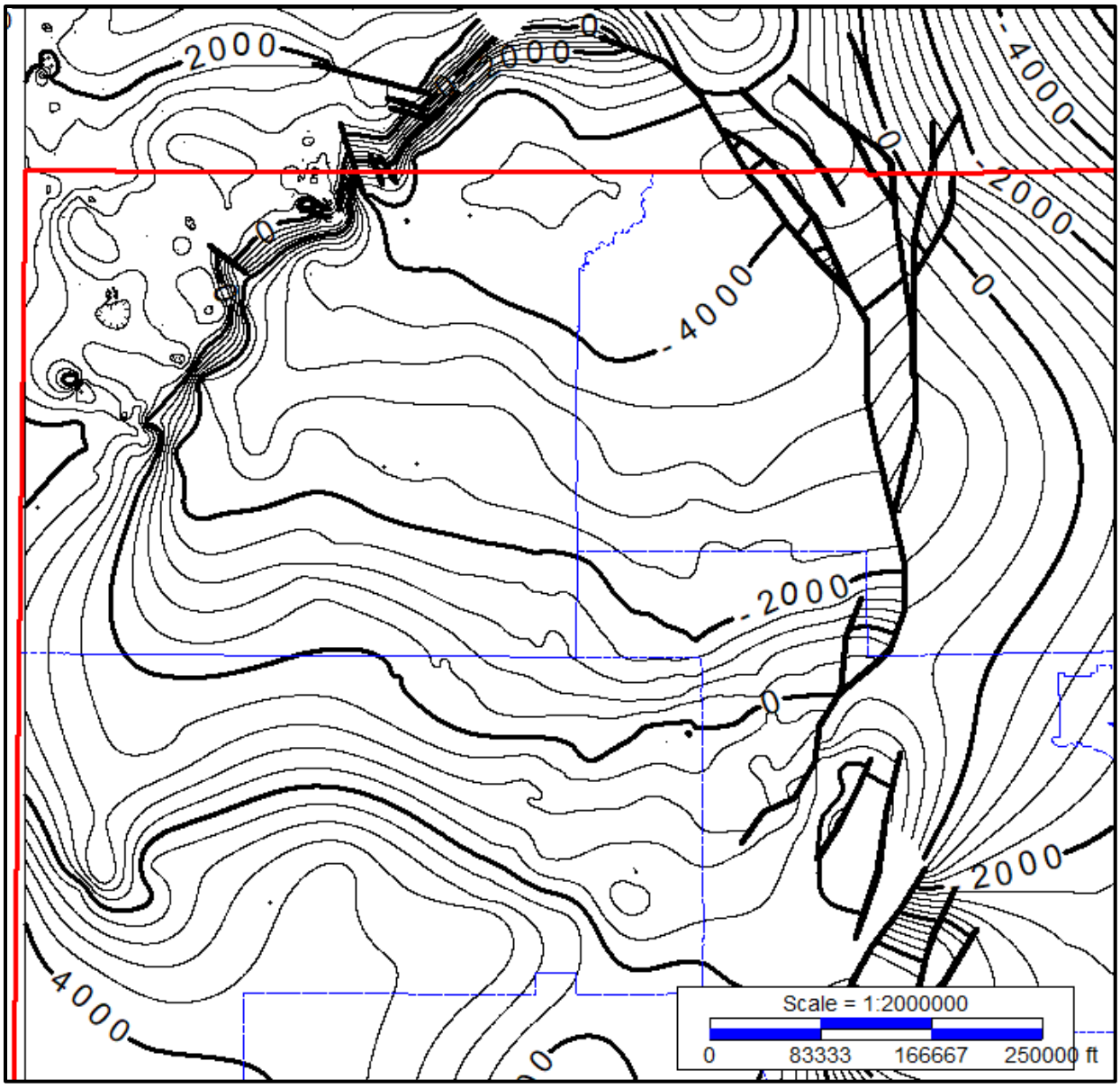


Figure 48. The subsea structural map on the Cutler Formation surface with potential faults.

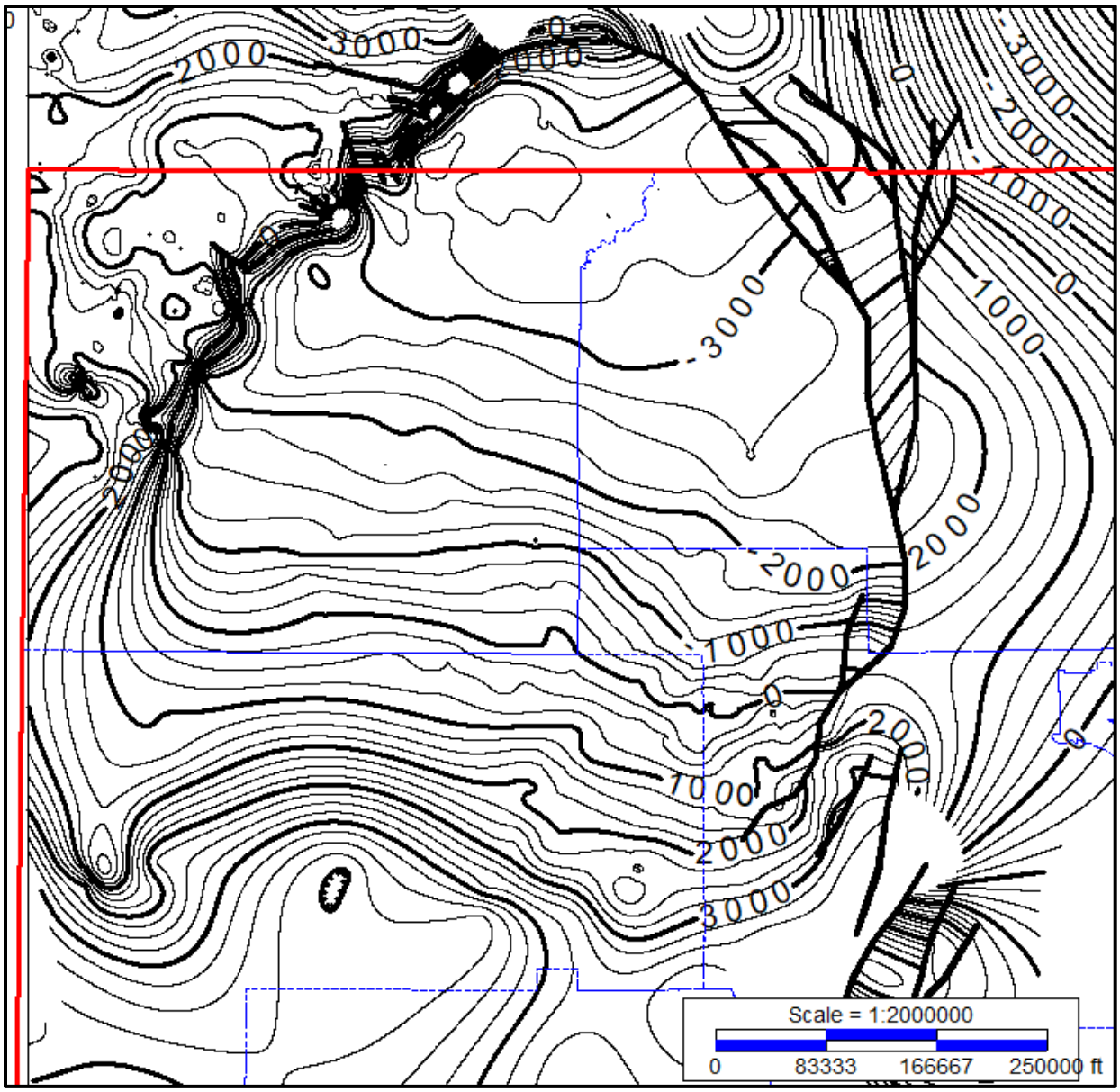


Figure 49. The subsea structural map on the Moenkopi Formation surface with potential faults.

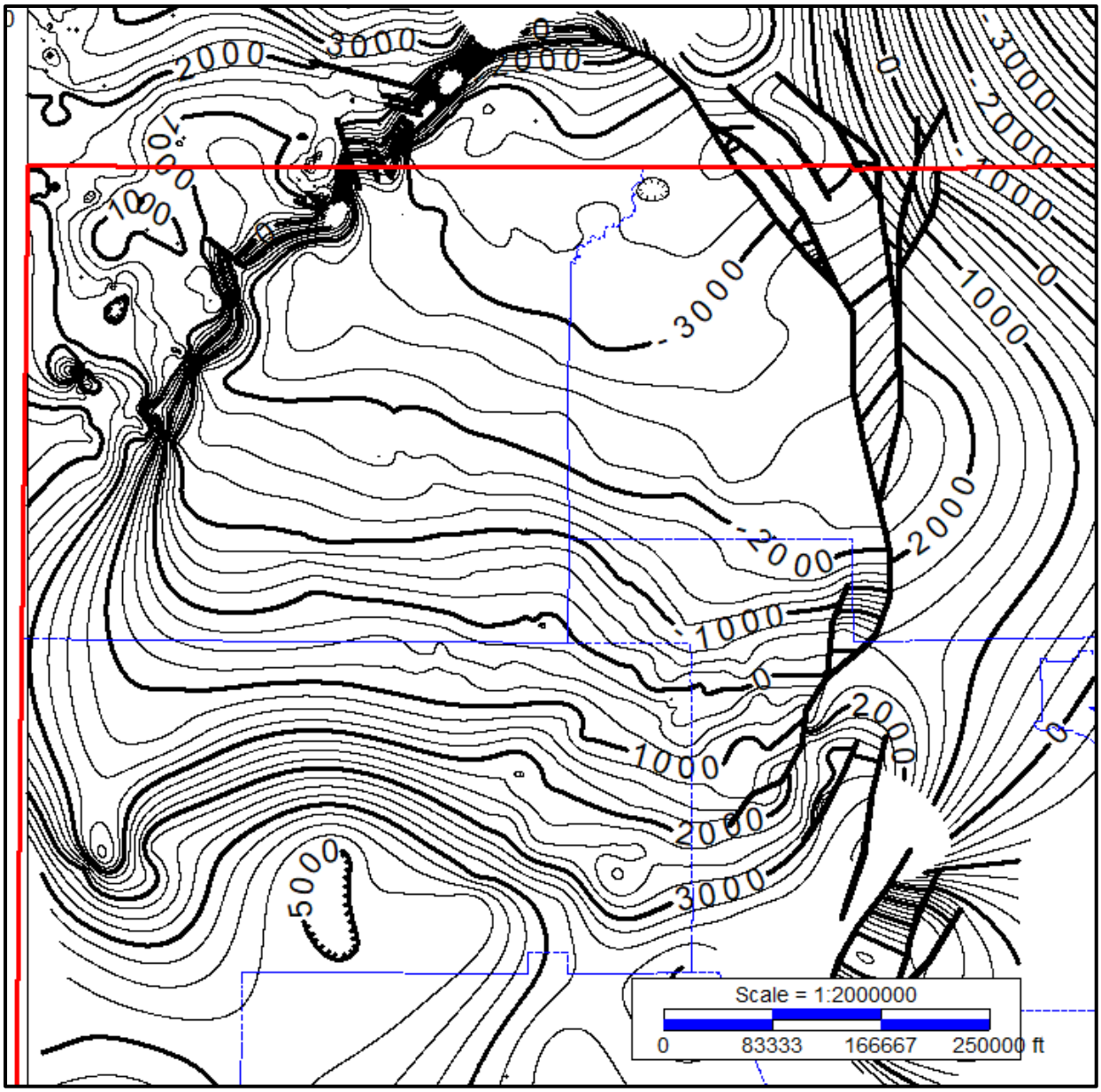


Figure 50. The subsea structural map on the Shinarump Conglomerate surface with potential faults.

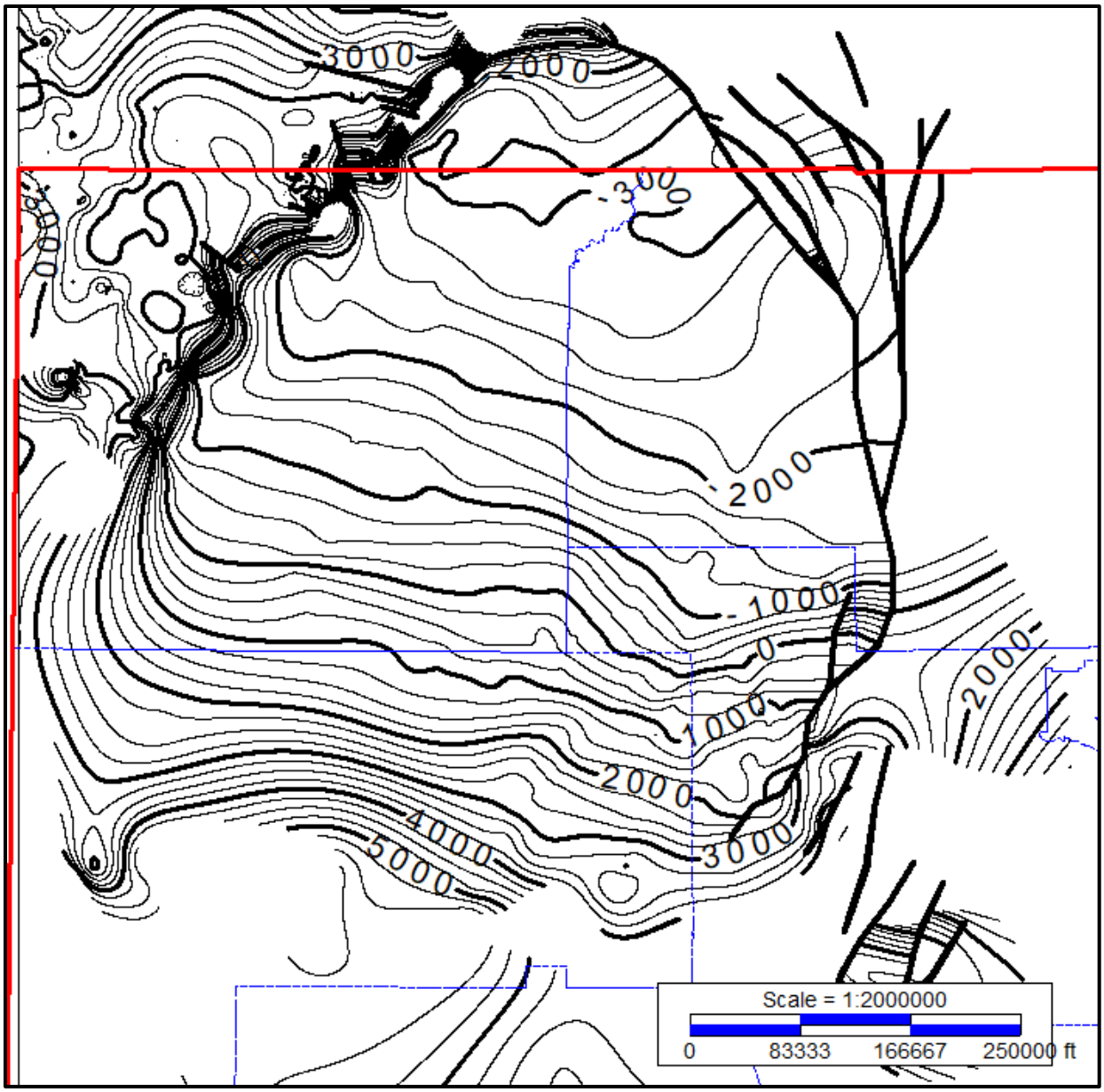


Figure 51. The subsea structural map on the Chinle Group surface with potential faults.

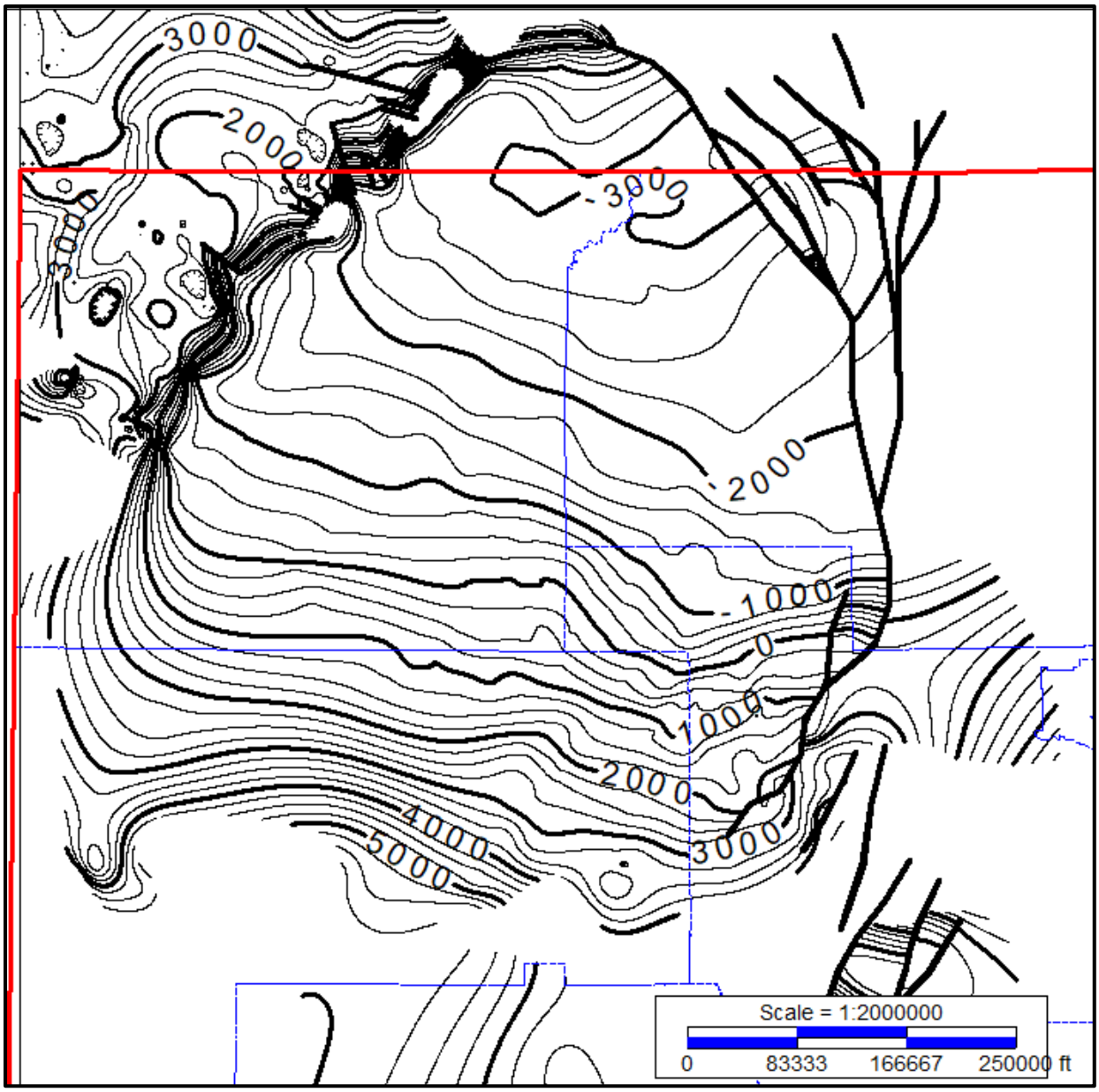


Figure 52. The subsea structural map on the Wingate Formation surface with potential faults.

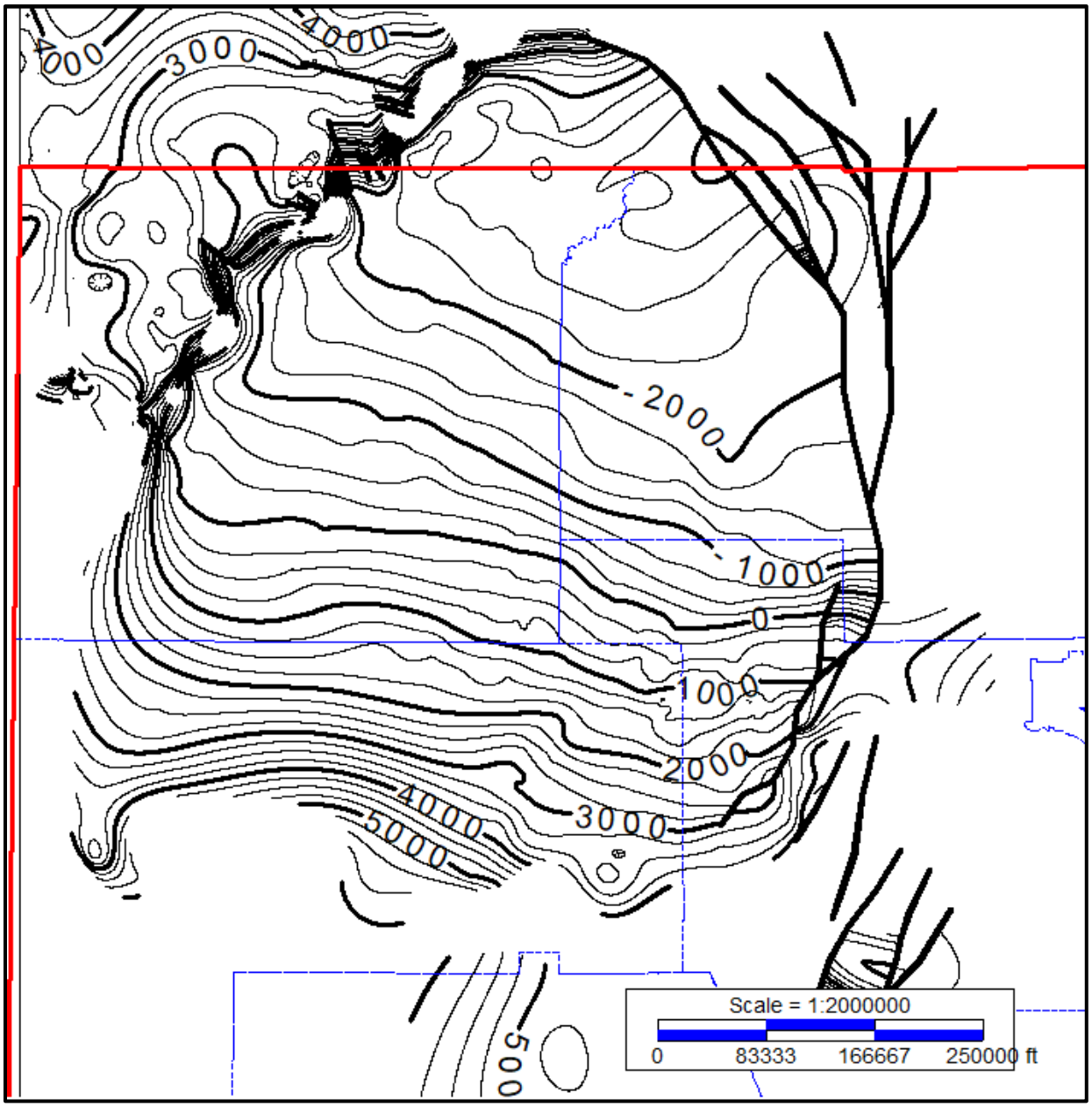


Figure 53. The subsea structural map on the Carmel Formation surface with potential faults.

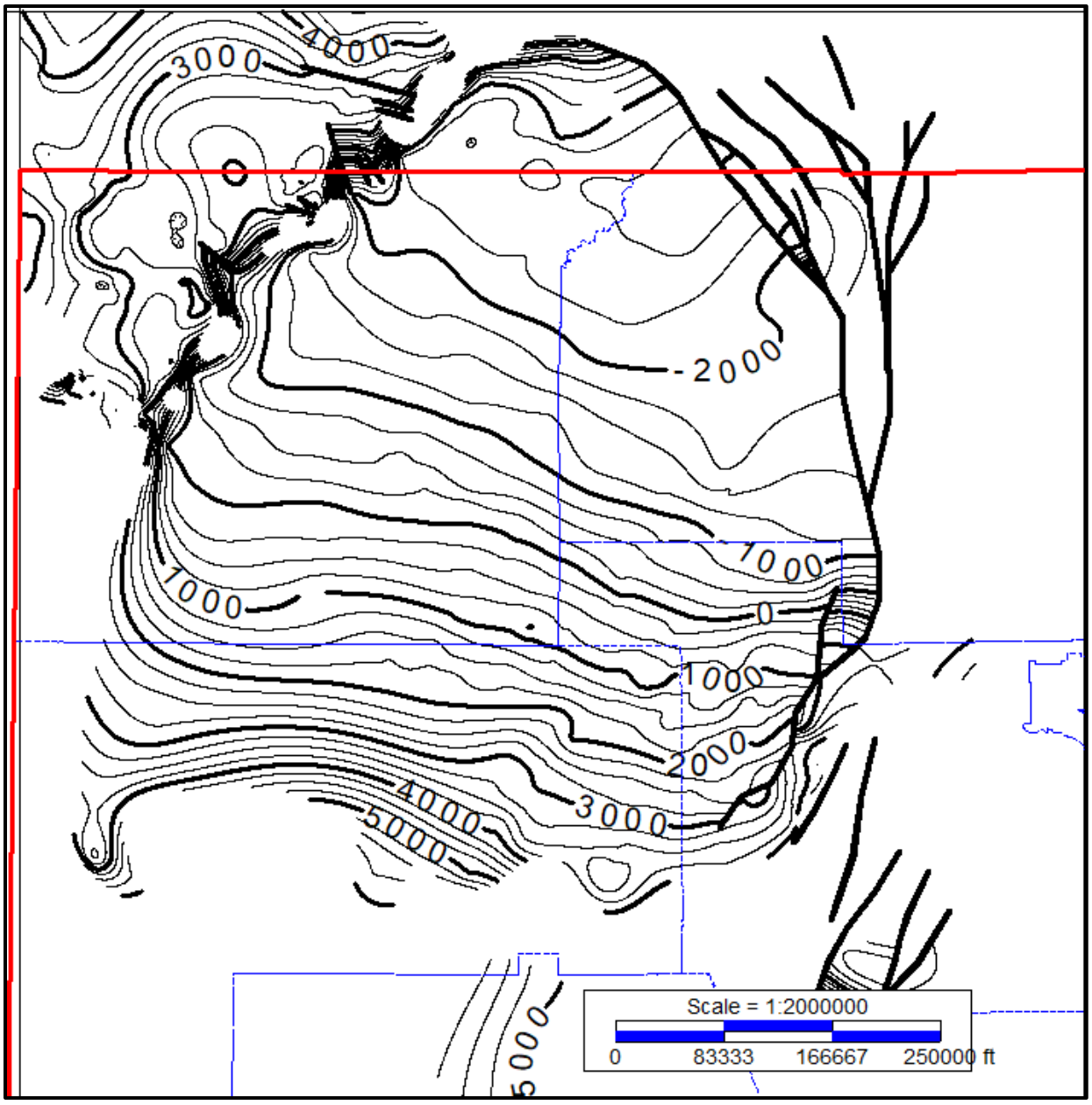


Figure 54. The subsea structural map on the Entrada Sandstone surface with potential faults.

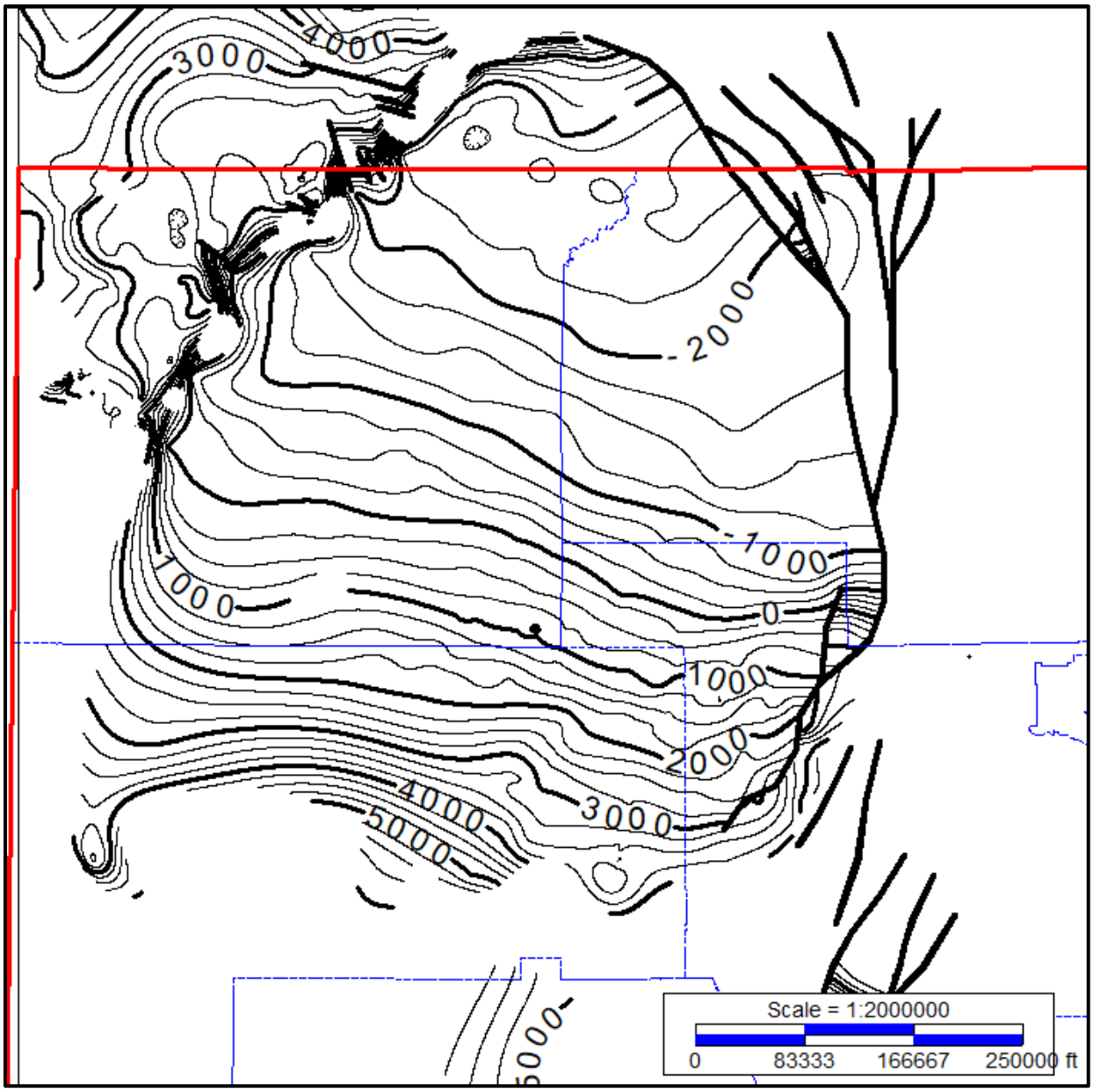


Figure 55. The subsea structural map on the Todilto Formation surface with potential faults.

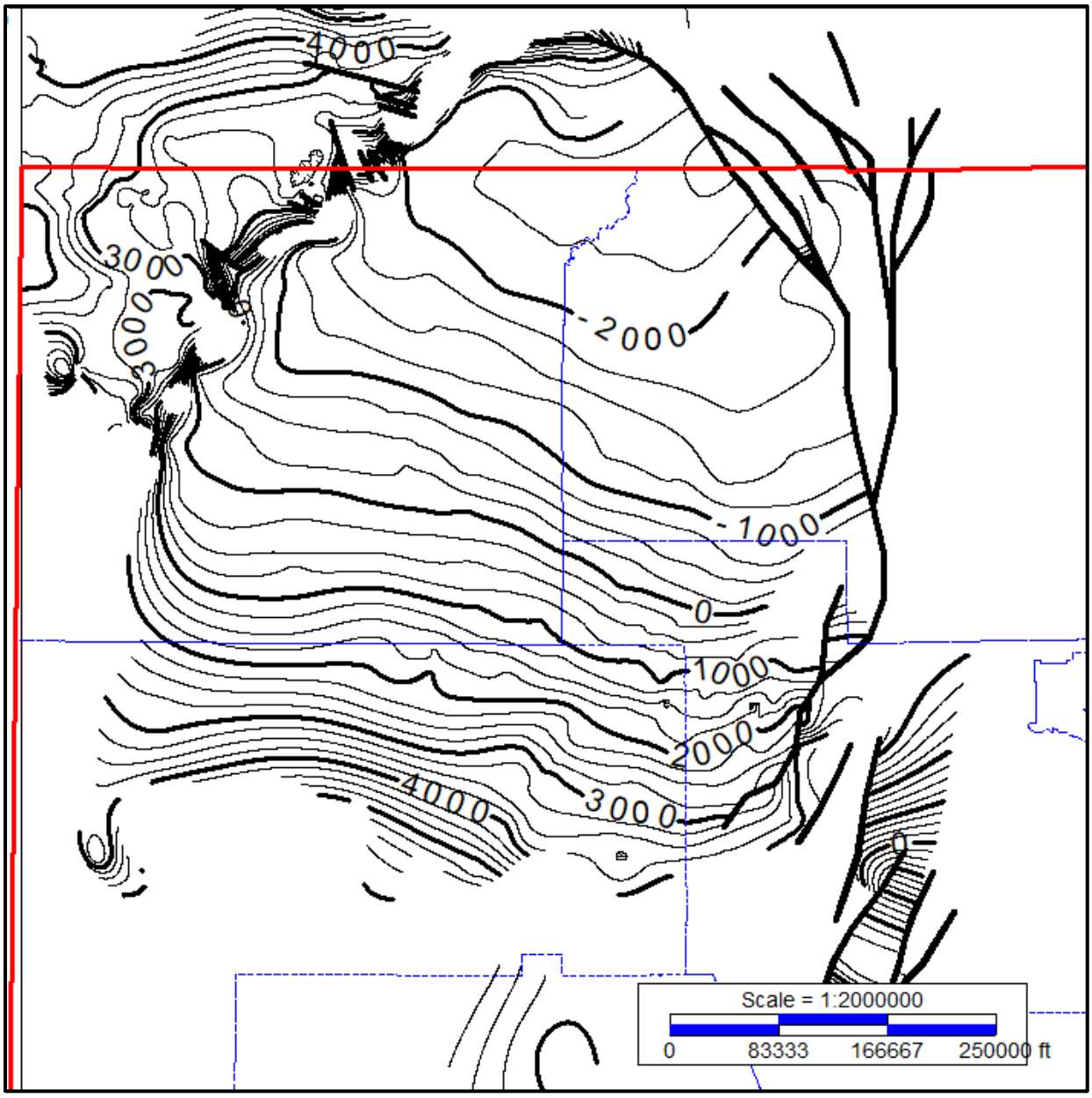


Figure 56. The subsea structural map on the Summerville Formation surface with potential faults.

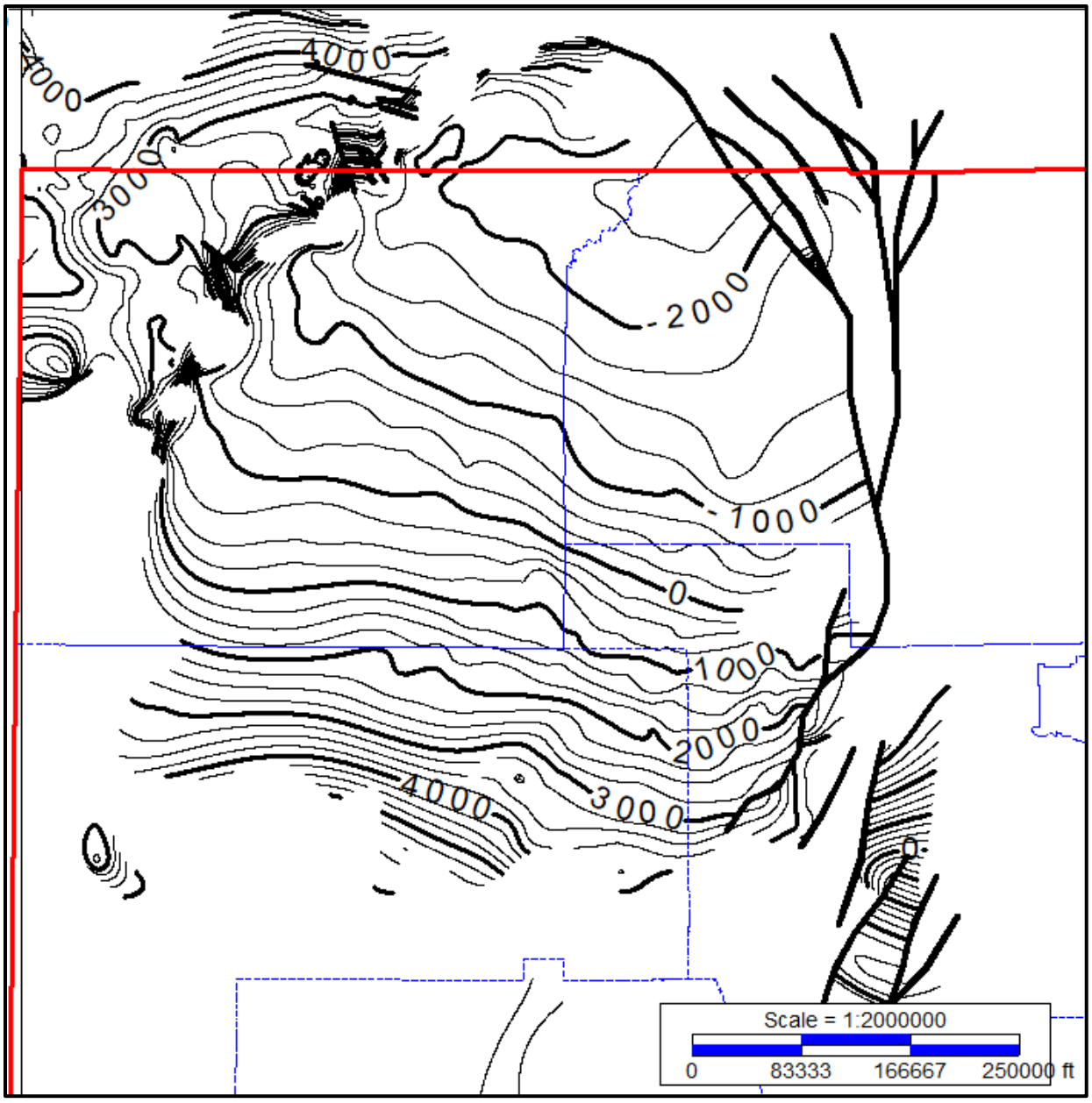


Figure 57. The subsea structural map on the Bluff Sandstone surface with potential faults.

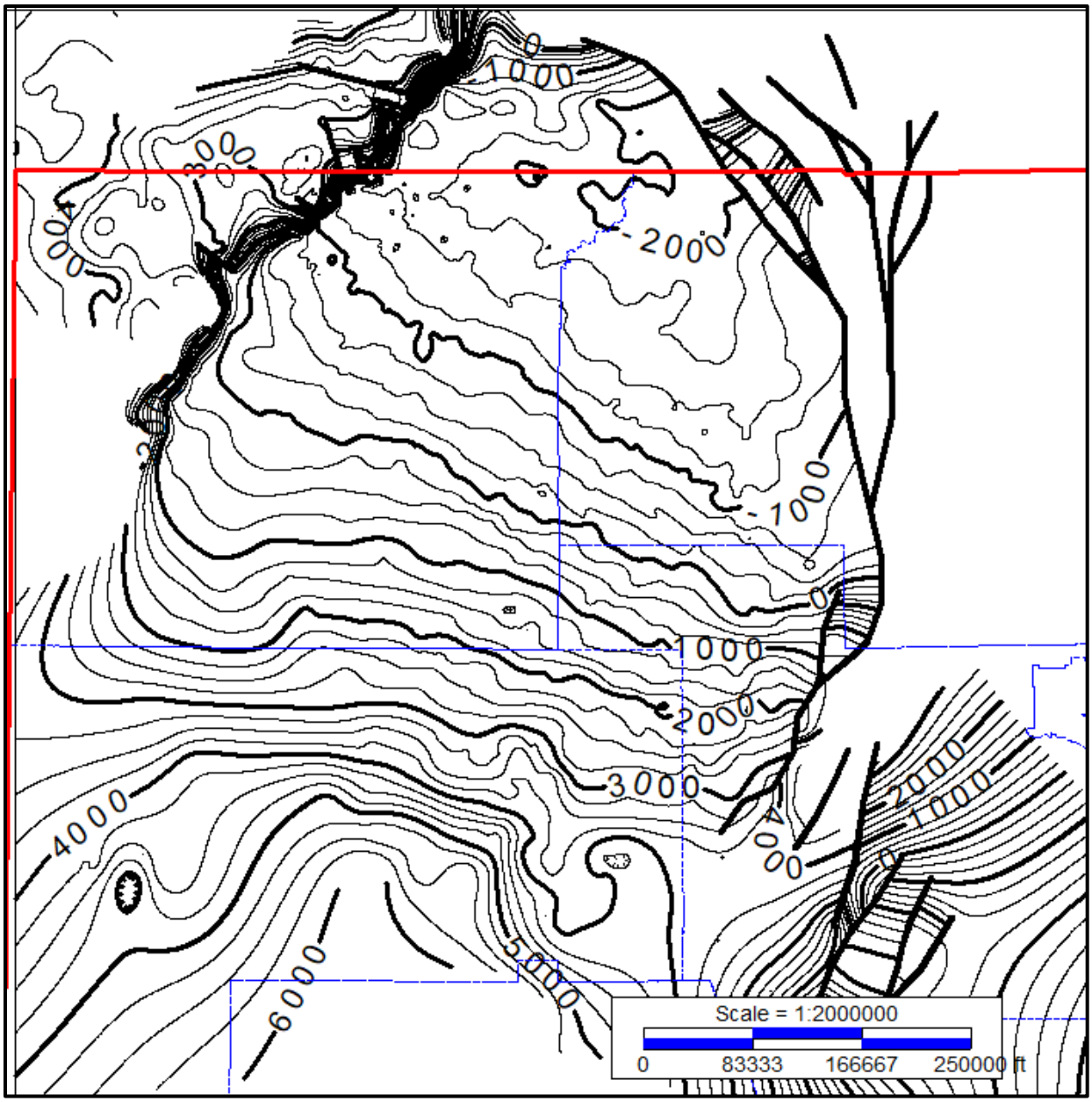


Figure 58. The subsea structural map on the Salt Wash Member of the Morrison Formation surface with potential faults.

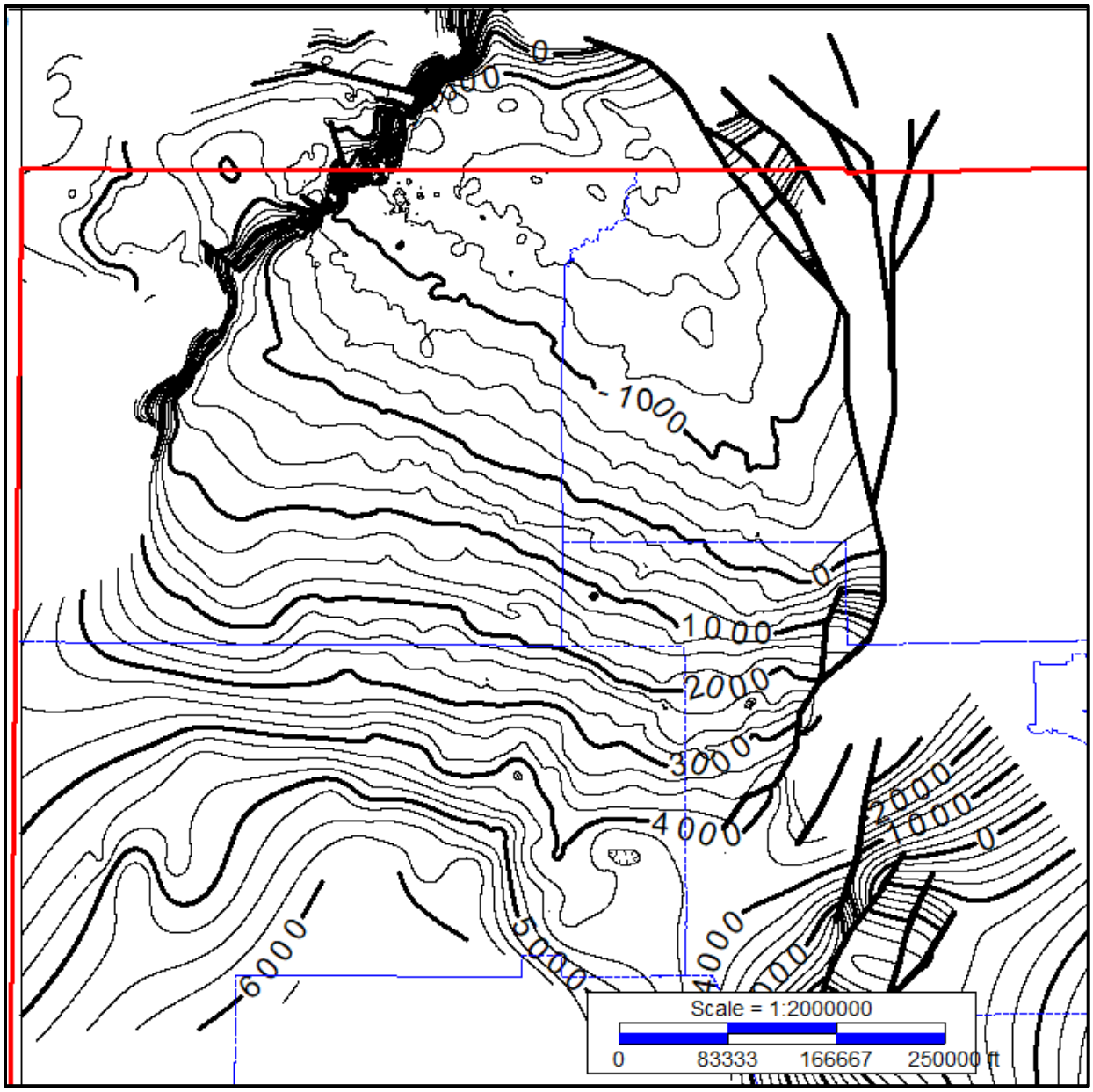


Figure 59. The subsea structural map on the Brushy Basin Member of the Morrison Formation surface with potential faults.

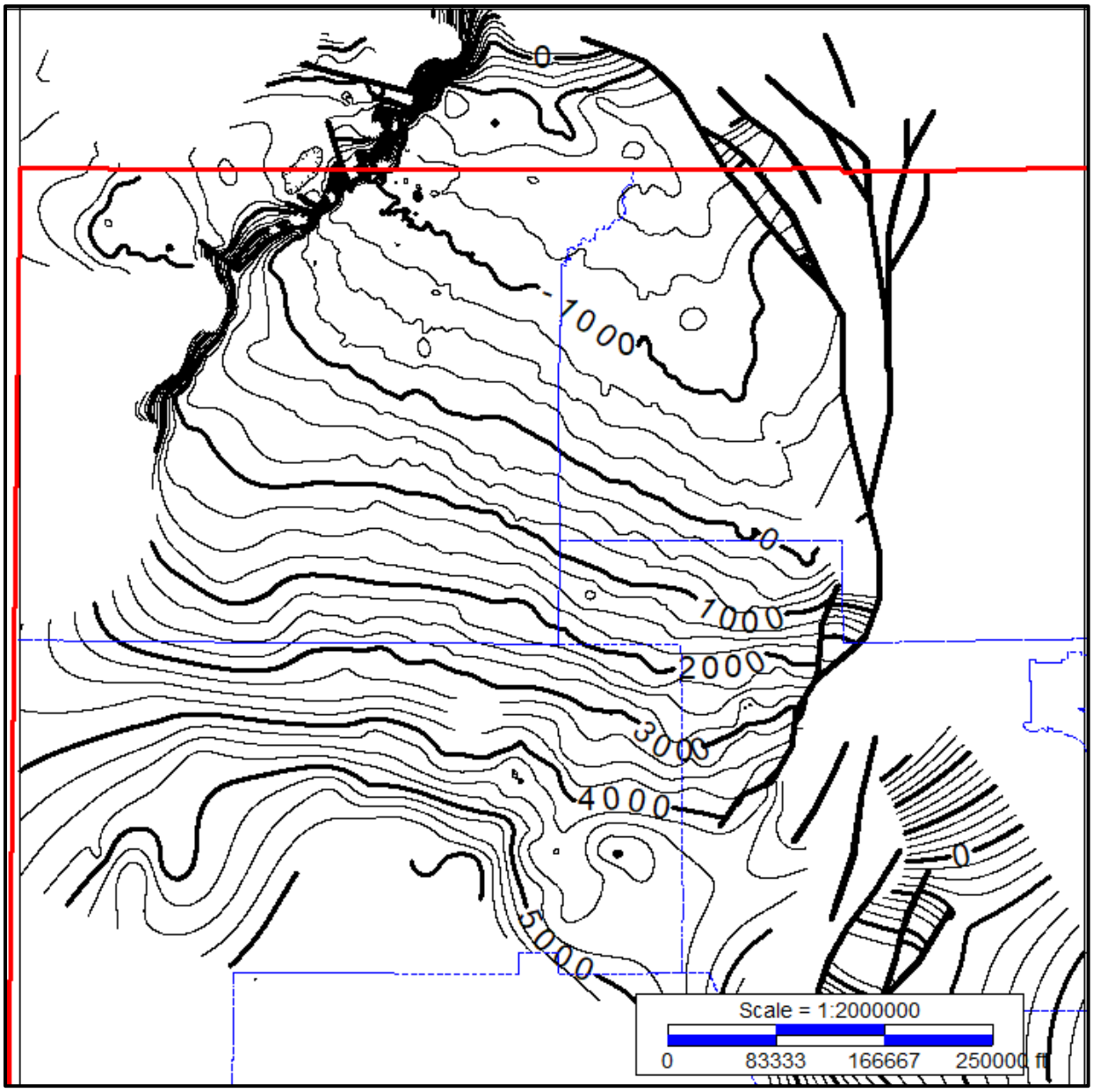


Figure 60. The subsea structural map on the Dakota Sandstone surface with potential faults.

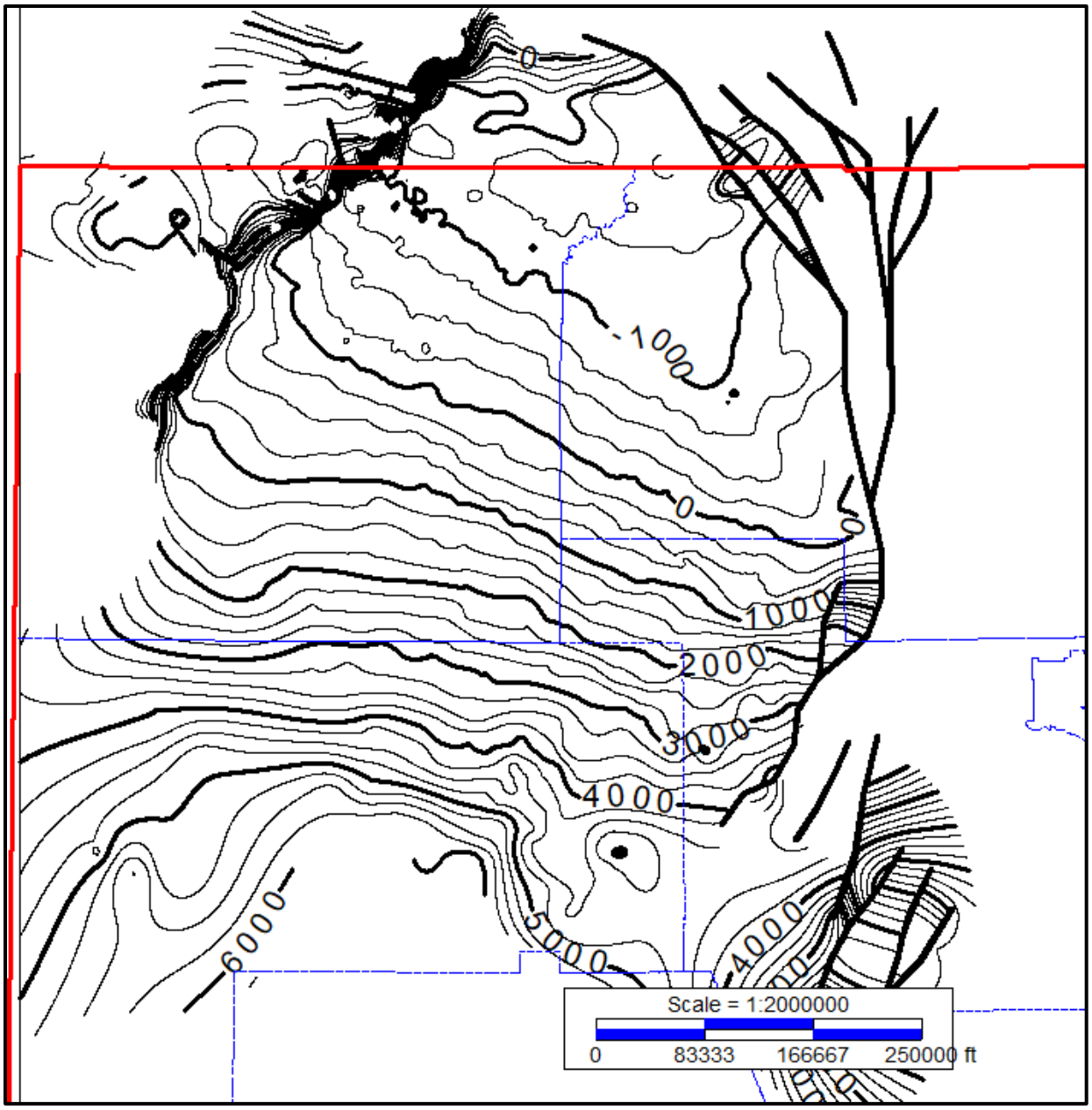


Figure 61. The subsea structural map on the Graneros Shale surface with potential faults.

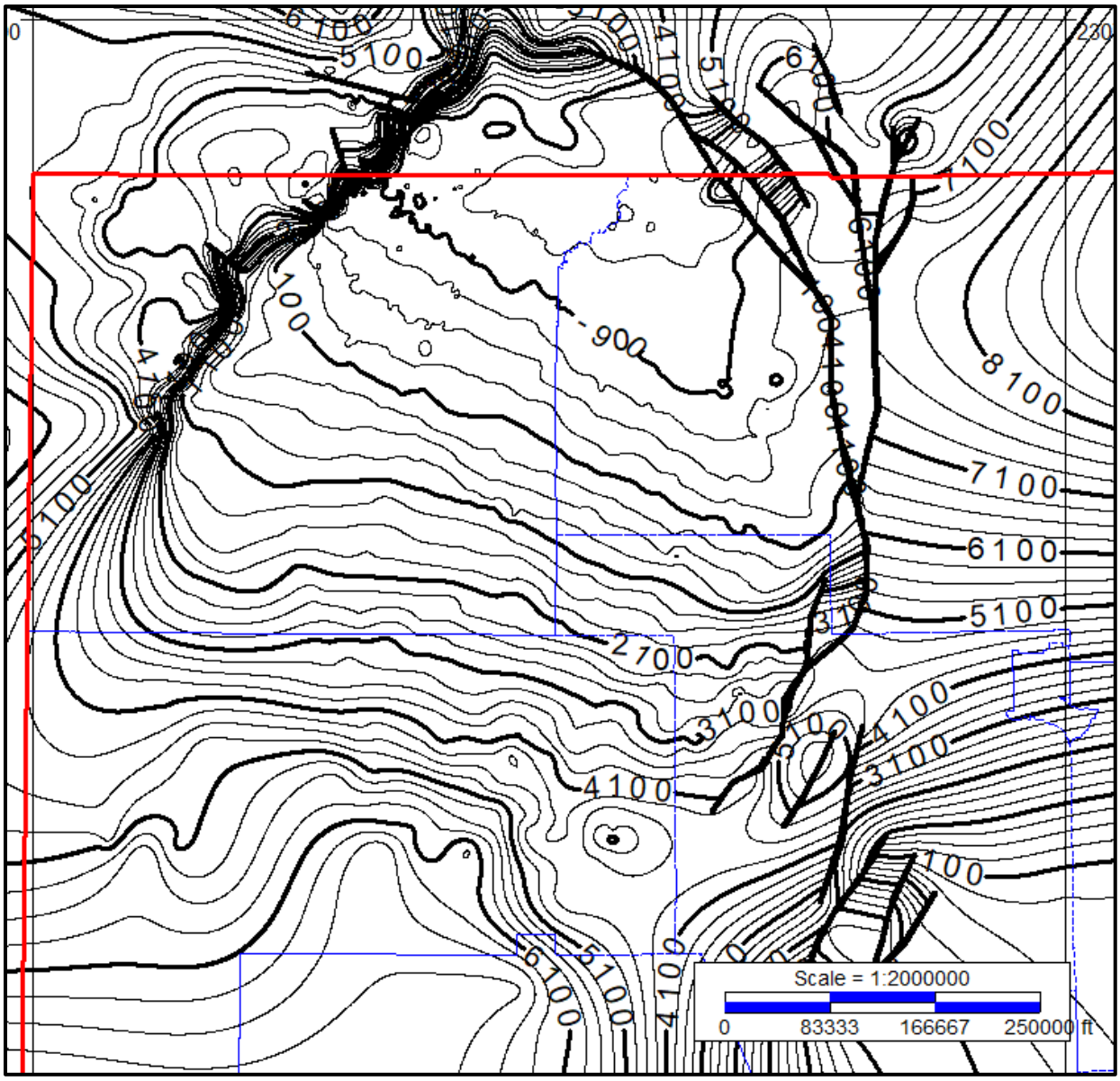


Figure 62. The subsea structural map on the Greenhorn Limestone surface with potential faults.

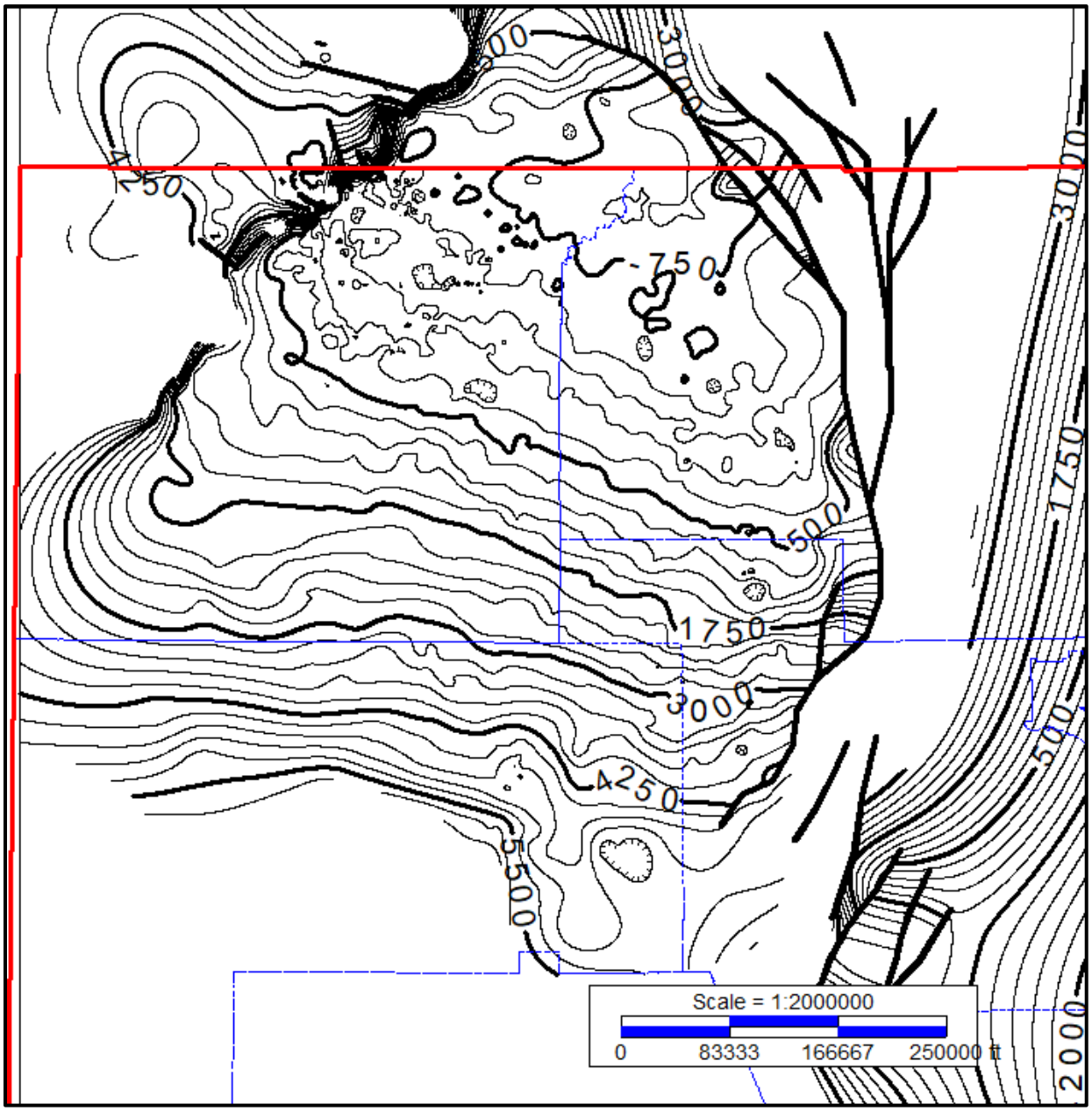


Figure 63. The subsea structural map on the lower Mancos Shale surface with potential faults.

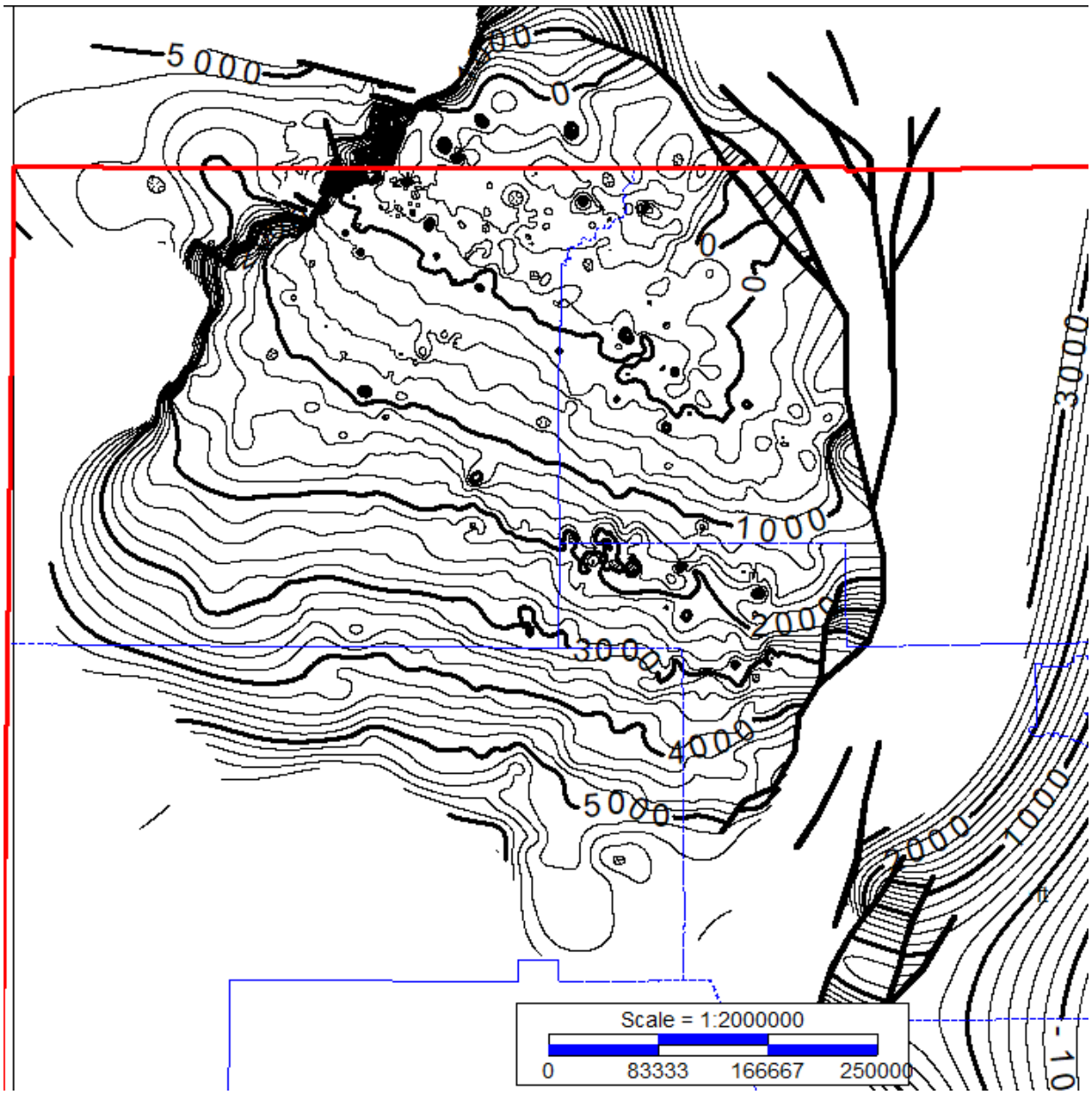


Figure 64. The subsea structural map on the Gallup Sandstone surface with potential faults.

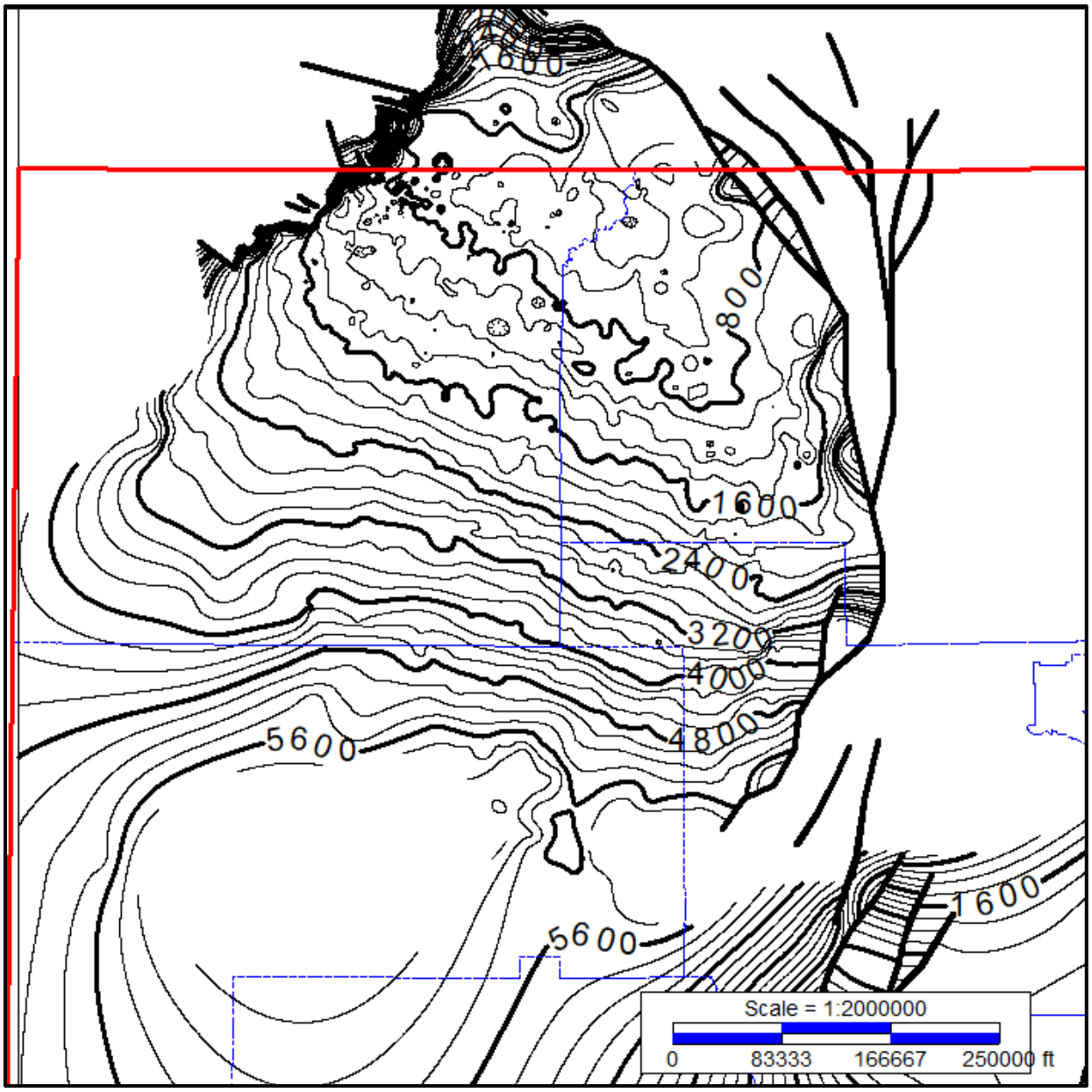


Figure 65. The subsea structural map on the upper Mancos Shale surface with potential faults.

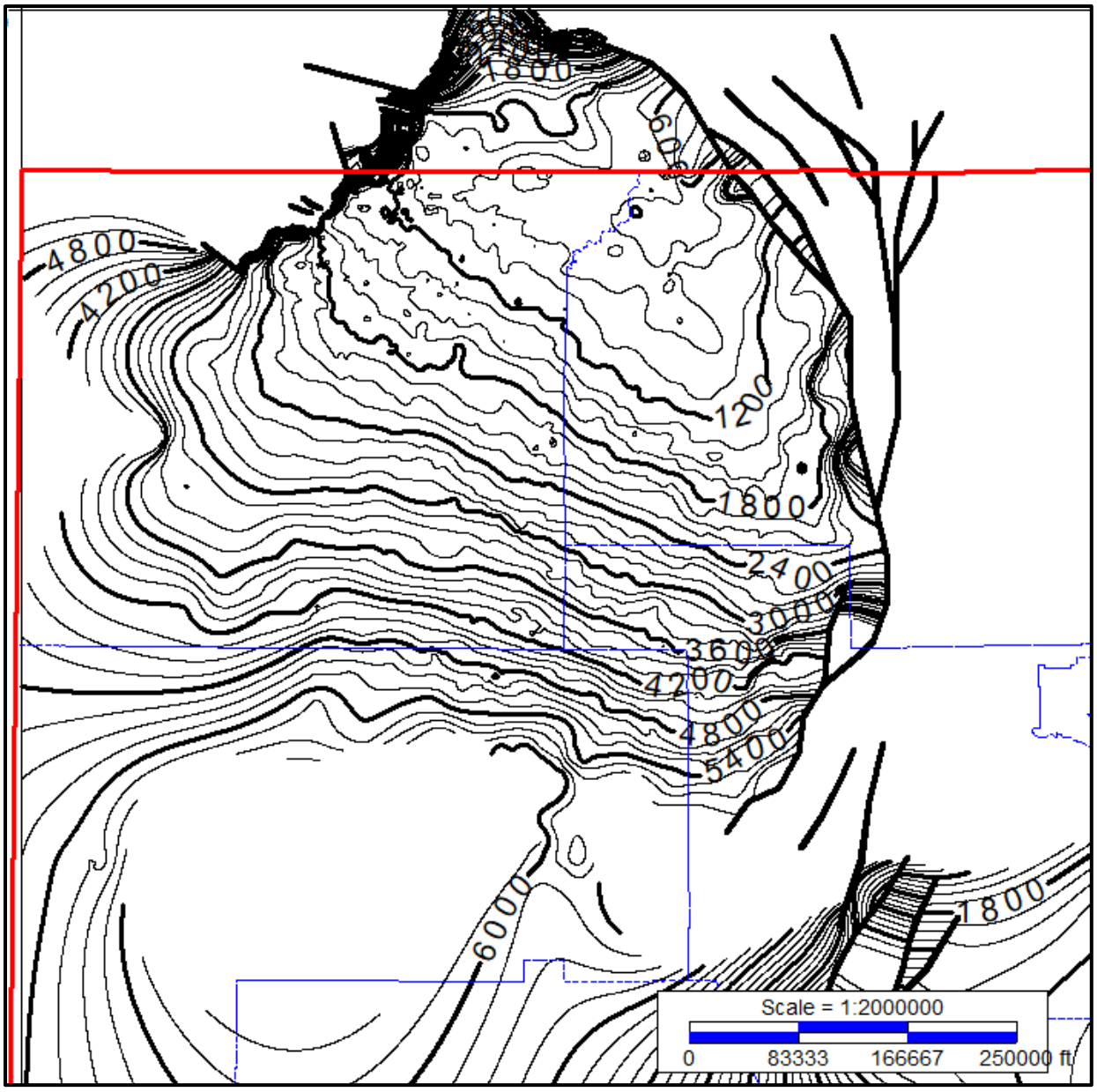


Figure 66. The subsea structural map on the Point Lookout Sandstone surface with potential faults.

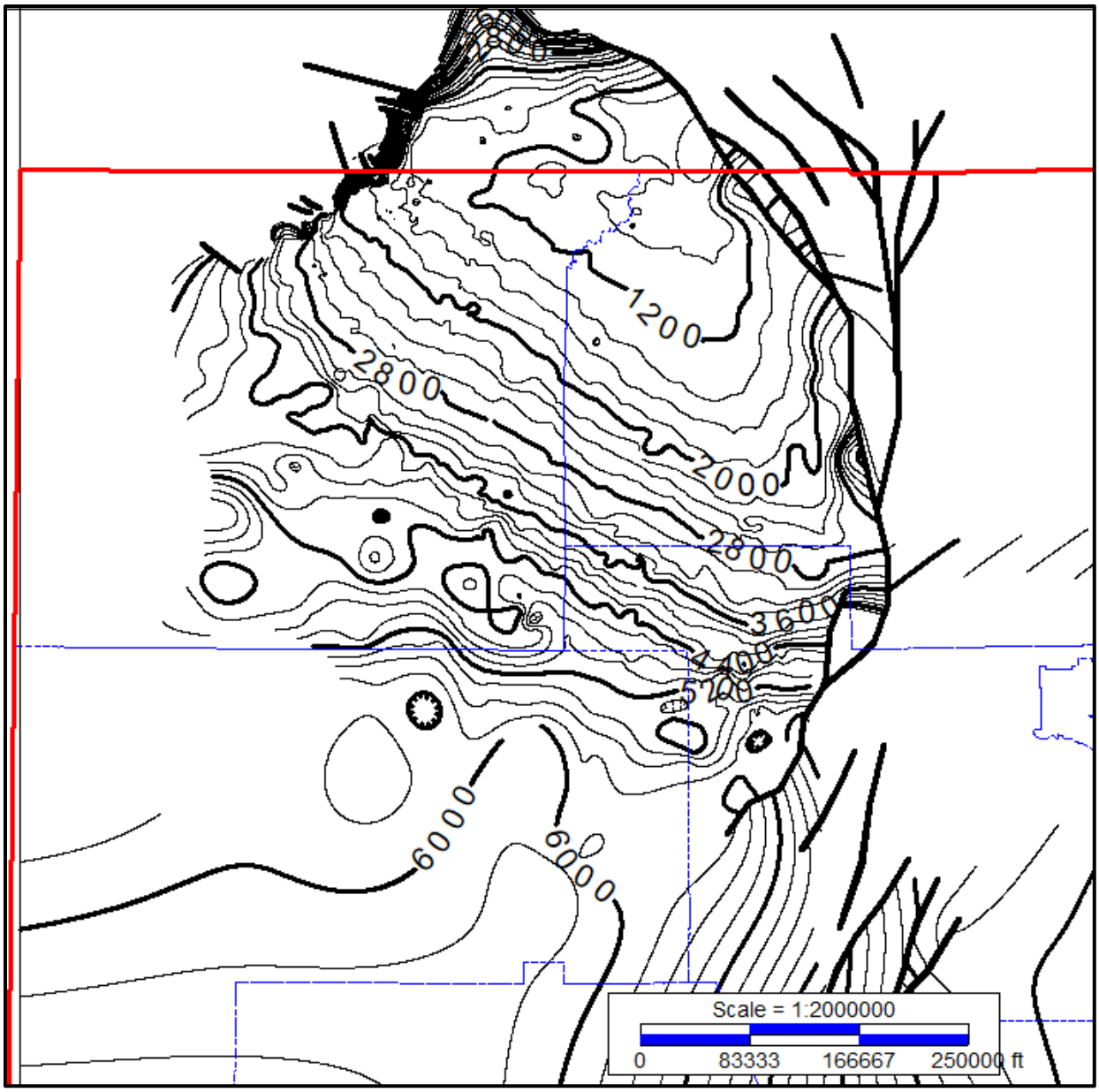


Figure 67. The subsea structural map on the Menefee Formation surface with potential faults.

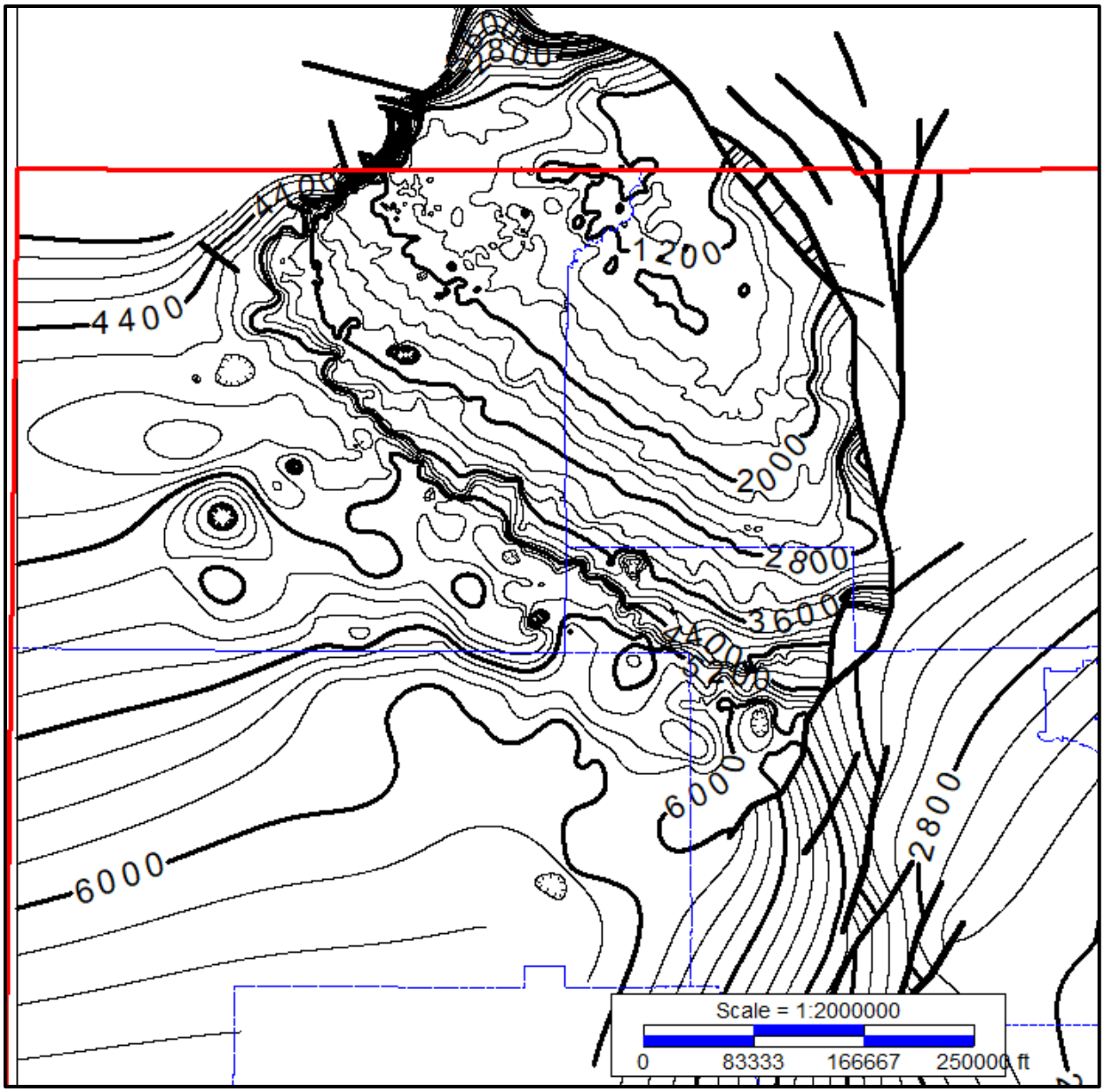


Figure 68. The subsea structural map on the Cliff House Sandstone surface with potential faults.

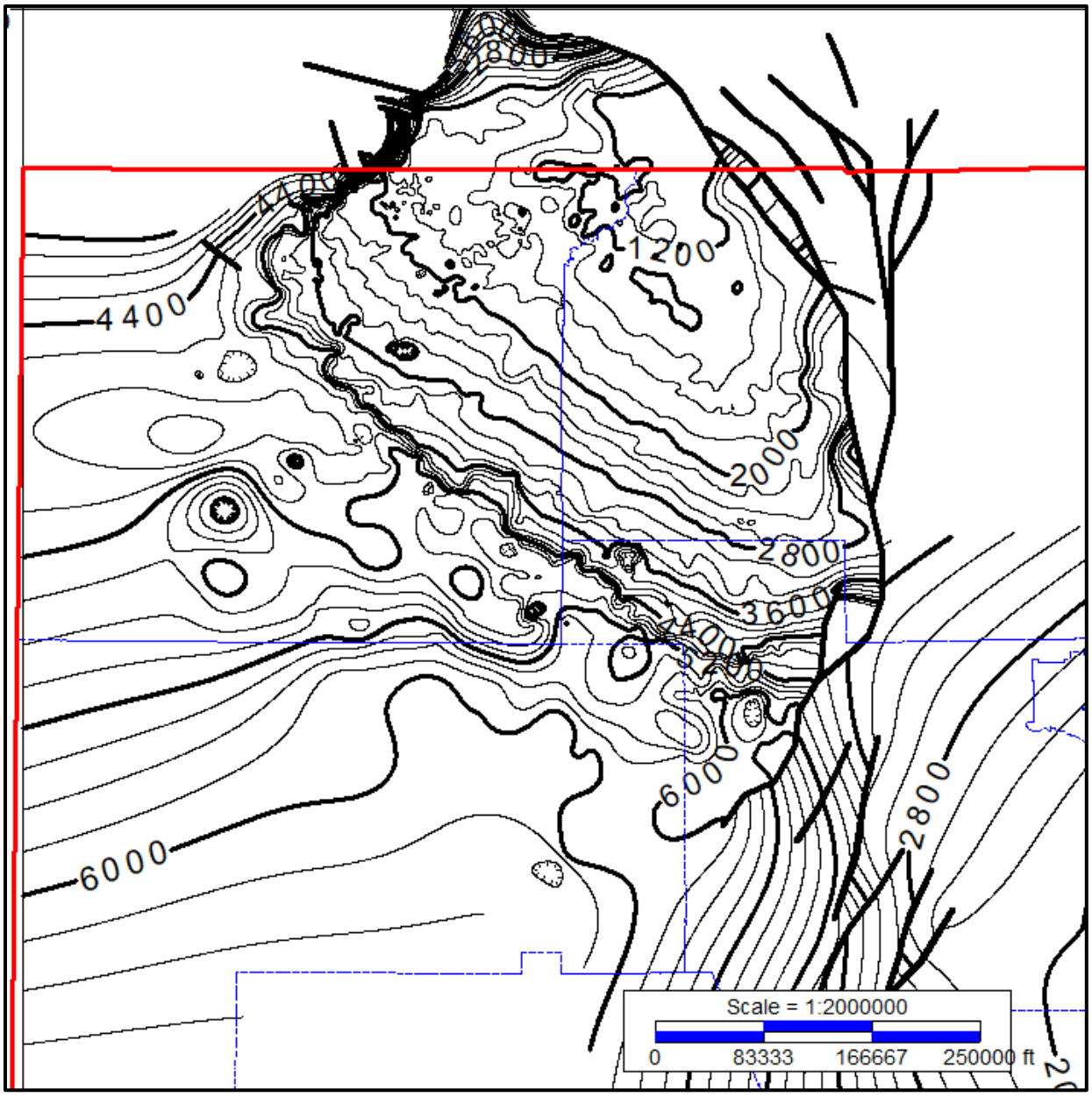


Figure 69. The subsea structural map on the Lewis Shale surface with potential faults.

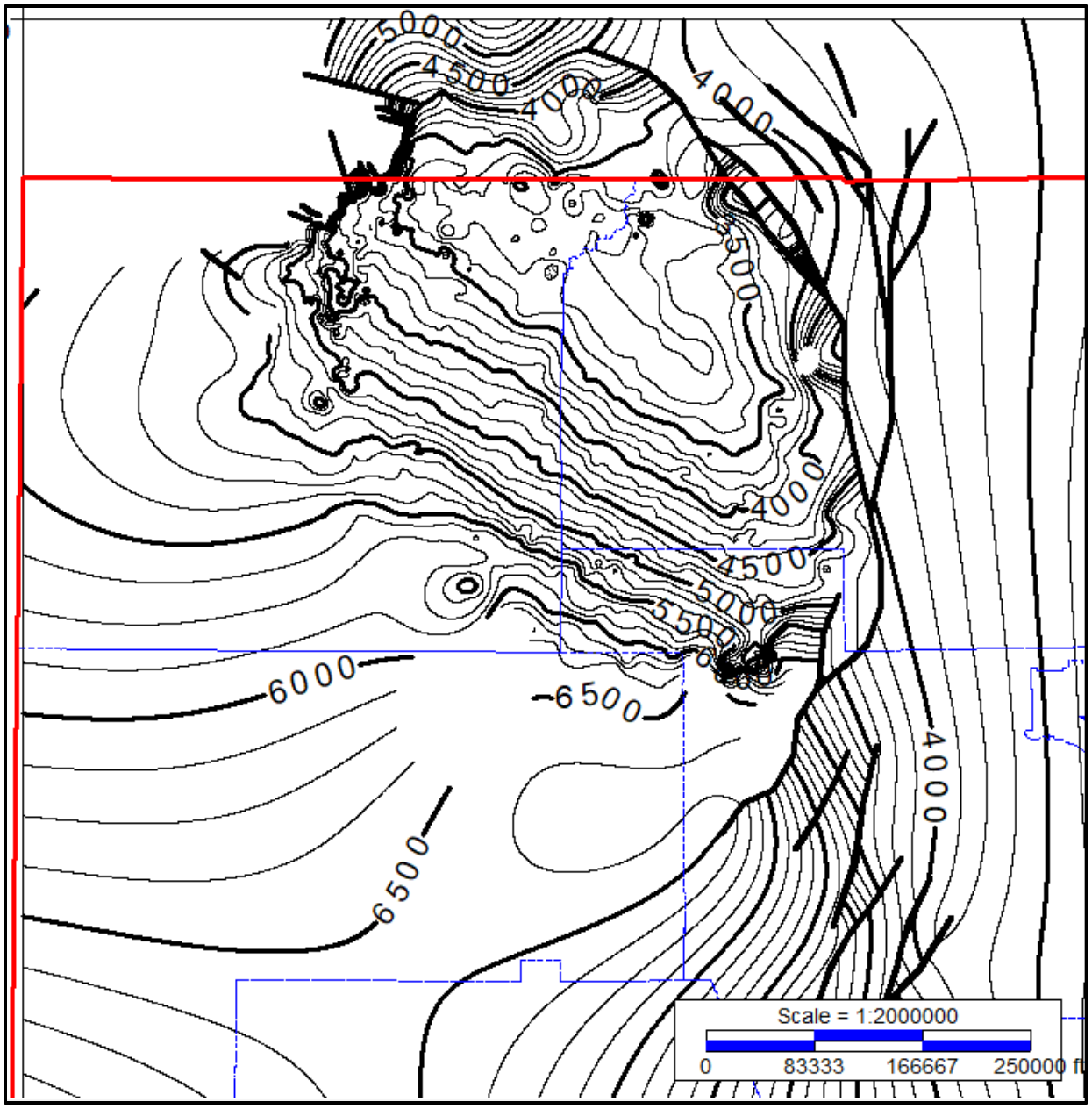


Figure 70. The subsea structural map on the Pictured Cliffs Sandstone surface with potential faults.

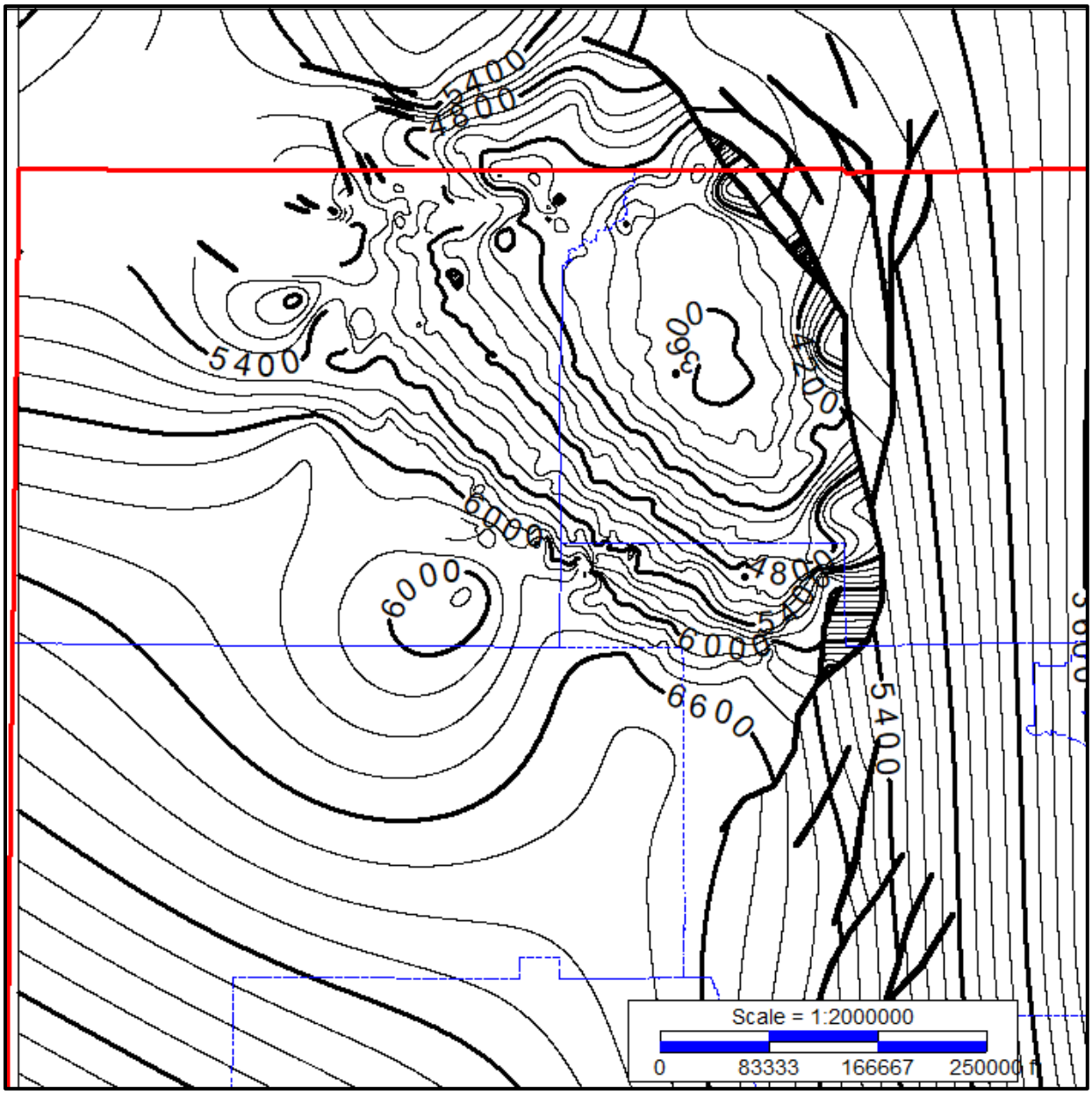


Figure 71. The subsea structural map on the Kirtland Shale surface with potential faults.

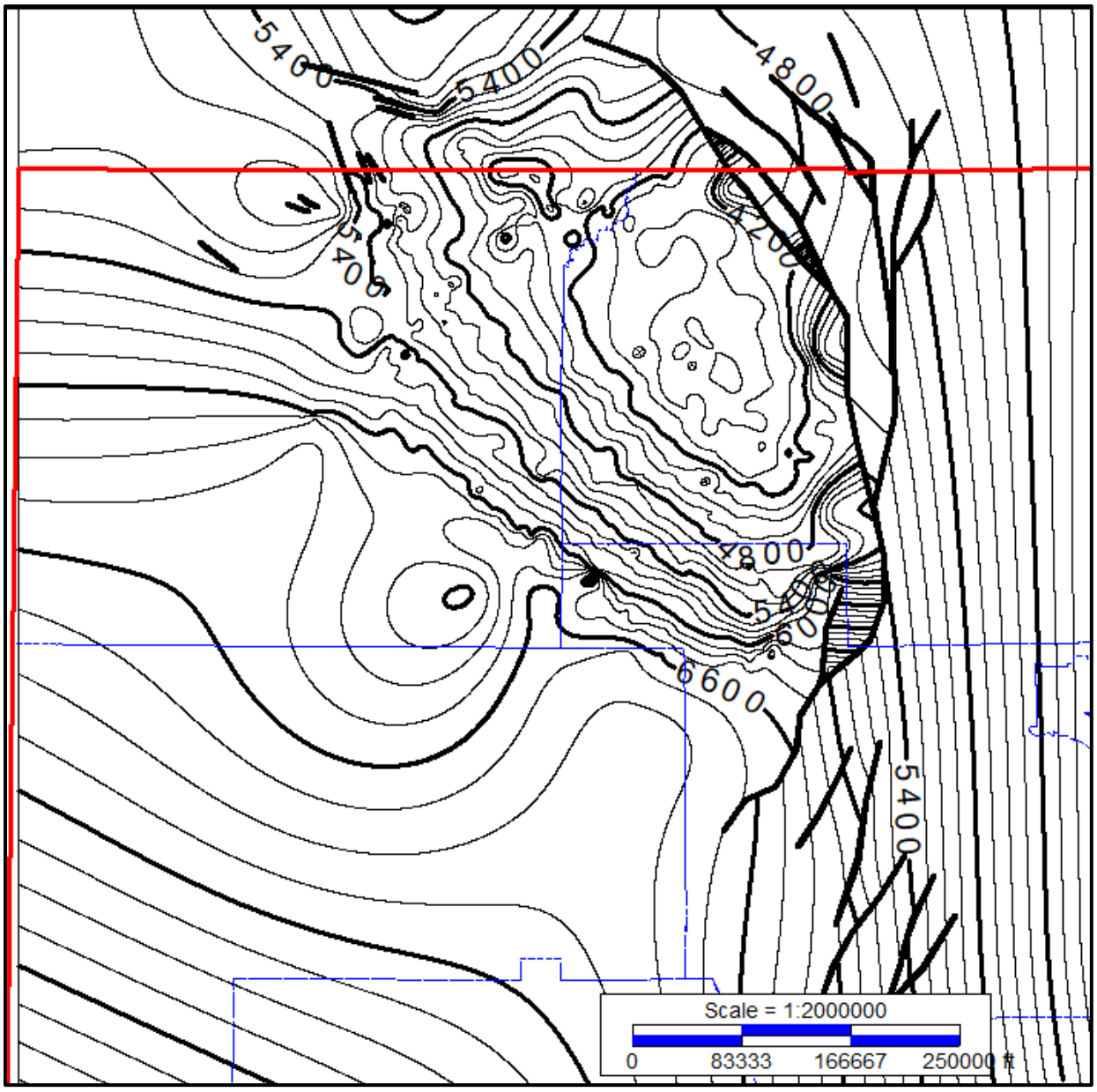


Figure 72. The subsea structural map on the Ojo Alamo Sandstone surface with potential faults.

Delaware Basin

The Permian Basin, the largest hydrocarbon producing area in the United States, contains the Delaware and Midland Basins. The Delaware Basin, the larger of the two, is found in southeastern New Mexico and western Texas (**Figure 73**). Sediments in the area date back to the Cambrian Bliss Sandstone (Broadhead 2017; **Figure 74**) and overlay Precambrian granites. These late Cambrian transgressive sandstones were the initial deposits within (**Figure 75**) a shallow marine sea that covered most of North America and Greenland. With continued down warping or sea-level rise, a broad, relatively shallow marine basin formed: the proto-Tobosa Basin. The Ellenburger Formation (0–1,000 ft) is dominated by dolostones and limestones that

were deposited on a restricted carbonate shelves (Broadhead 2017; Loucks and Kerans 2019). Tectonic activity near the end of Ellenburger deposition resulted in subaerial exposure and karstification of these carbonates which increased the unit's overall porosity and permeability.

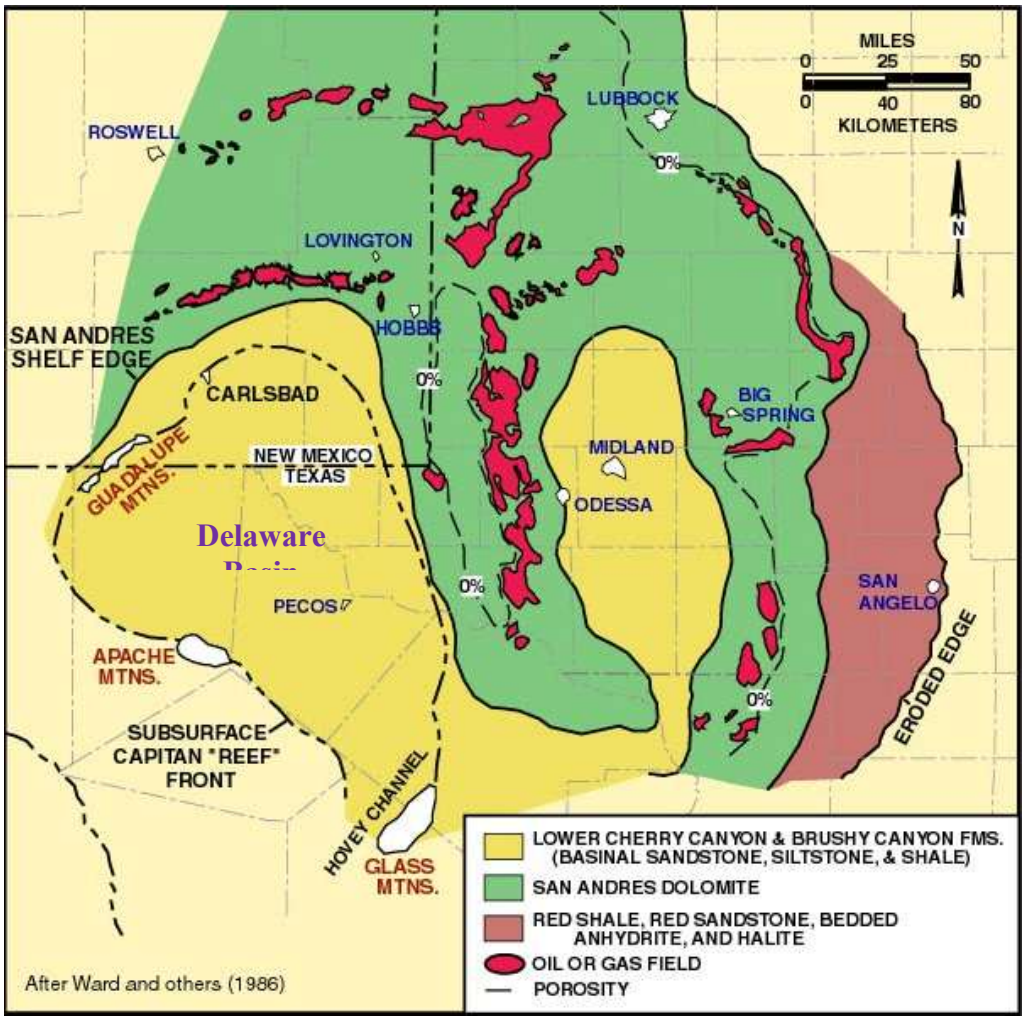


Figure 73. Location of the Delaware Basin with respect to Permian physiographic features (modified from Ward et al. 1986; Scholle et al. 2007).

AGE		CENTRAL BASIN PLATFORM-NORTHWEST SHELF	DELAWARE BASIN
Cenozoic		Alluvium	Alluvium
Triassic		Chinle Formation	Chinle Formation
		Santa Rosa Sandstone	Santa Rosa Sandstone
Permian	Lopingian (Ochoan)	Dewey Lake Formation	Dewey Lake Formation
		Rustler Formation	Rustler Formation
		Salado Formation	Salado Formation
			Castile Formation
	Guadalupian	Artesia Group: Tansill Formation	Delaware Mountain Group: Lamar Limestone
		Artesia Group: Yates Formation	Delaware Mountain Group: Bell Canyon Formation
		Artesia Group: Seven Rivers Formation	Delaware Mountain Group: Bell Canyon Formation
		Artesia Group: Queen Formation	Delaware Mountain Group: Cherry Canyon Formation
		Artesia Group: Grayburg Formation	Delaware Mountain Group: Cherry Canyon Formation
		San Andres Formation	Delaware Mountain Group: Brushy Canyon Formation
		Glorieta Formation	Delaware Mountain Group: Brushy Canyon Formation
	Cisuralian (Leonardian)	Yeso: Paddock Mbr.	Bone Spring Formation
		Yeso: Blinebry Mbr	Bone Spring Formation
		Yeso: Tubb Sandstone Mbr.	Bone Spring Formation
		Yeso: Drinkard Mbr.	Bone Spring Formation
	Wolfcampian	Abo Formation	Bone Spring Formation
		Hueco ("Wolfcamp") Fm.	Hueco ("Wolfcamp") Fm.
Pennsylvanian	Virgilian	Cisco Formation	Cisco
	Missourian	Canyon Formation	Canyon
	Des Moinesian	Strawn Formation	Strawn
	Atokan	Atoka Formation	Atoka
	Morrowan	Morrow Formation	Morrow
Mississippian	*Upper*	Barnett Shale	Barnett Shale
	Lower	"Mississippian limestone"	"Mississippian limestone"
Devonian	*Upper*	Woodford Shale	Woodford Shale
	Middle		
	Lower	Thirtyone Formation	Thirtyone Formation
Silurian	*Upper*	Wristen Group	Wristen Group
	Middle		
	Lower	Fusselman Formation	Fusselman Formation
Ordovician	*Upper*	Montoya Formation	Montoya Formation
	Middle	Simpson Group	Simpson Group
	Lower	Ellenburger Formation	Ellenburger Formation
Cambrian		Bliss Ss.	Bliss Ss.
Precambrian		Miscellaneous igneous, metamorphic, volcanic rocks	Miscellaneous igneous, metamorphic, volcanic rocks

Figure 74. General stratigraphic chart for southeastern New Mexico (modified from Broadhead [2017]).

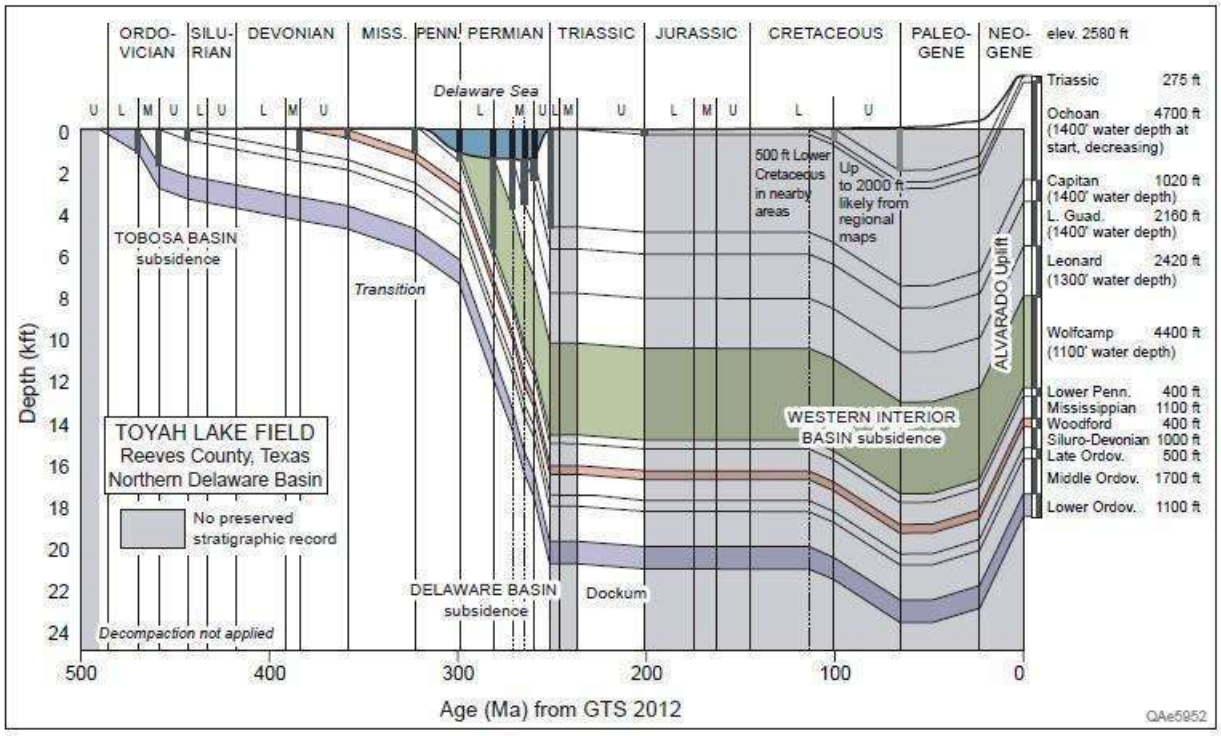
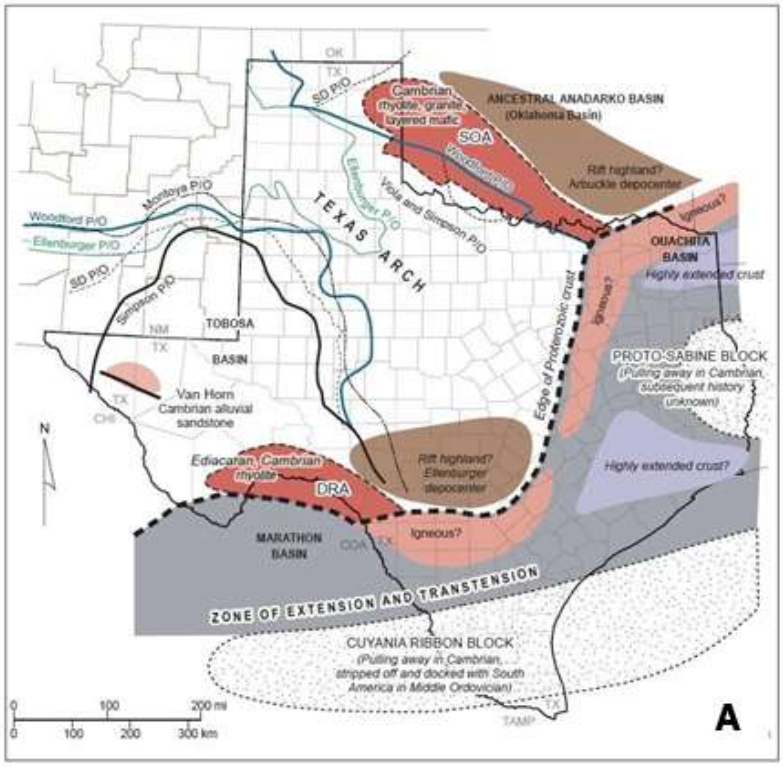


Figure 75. A subsidence chart from Reeves County, Texas showing the timing of development of the Tobosa and Delaware basins during Paleozoic deposition (from Ewing [2019]).

During Middle to Upper Ordovician time, the seas once again covered the area and deposited the carbonates, sandstones and shales of, first, the Simpson Group (0–1,000 ft) and then the Montoya Formation (0–600 ft). This is the time when the Tobosa Basin formed due to the Pedernal Uplift and development of the Texas Arch (**Figure 76**; Harrington 2019) shedding Precambrian crystalline clasts into the basin. Reservoirs in New Mexico are typically within the shoreline sandstones (Broadhead 2017). Another subaerial exposure and karstification event followed the deposition of the Simpson Group. The Montoya Formation marked a return to dominantly carbonate sedimentation with minor siliciclastic sedimentation within the Tobosa Basin (Broadhead 2017; Harrington and Ruppel 2019). Like the Ellenburger and Simpson carbonates, the subaerial exposure event at the end of Montoya deposition resulted in karstification.


Cambrian rhyolite, granite, layered mafic
SOA
ANCESTRAL ANADARKO BASIN (Oklahoma Basin)
Rift highland? Arbuckle depocenter
Igneous?
OUACHITA BASIN
Highly extended crust
TEXAS ARCH
Woodford P/O
Montoya P/O
Ellenburger P/O
Viola and Simpson P/O
SD P/O
Simpson P/O
TOBOSA BASIN
Van Horn Cambrian alluvial sandstone
Edge of Proterozoic crust
PROTO-SABINE BLOCK
(Pulling away in Cambrian, subsequent history unknown)
Highly extended crust?
Ediacaran, Cambrian rhyolite
DRA
Rift highland? Ellenburger depocenter
MARATHON BASIN
ZONE OF EXTENSION AND TRANSTENSION
CUYANIA RIBBON BLOCK
(Pulling away in Cambrian, stripped off and docked with South America in Middle Ordovician)
A

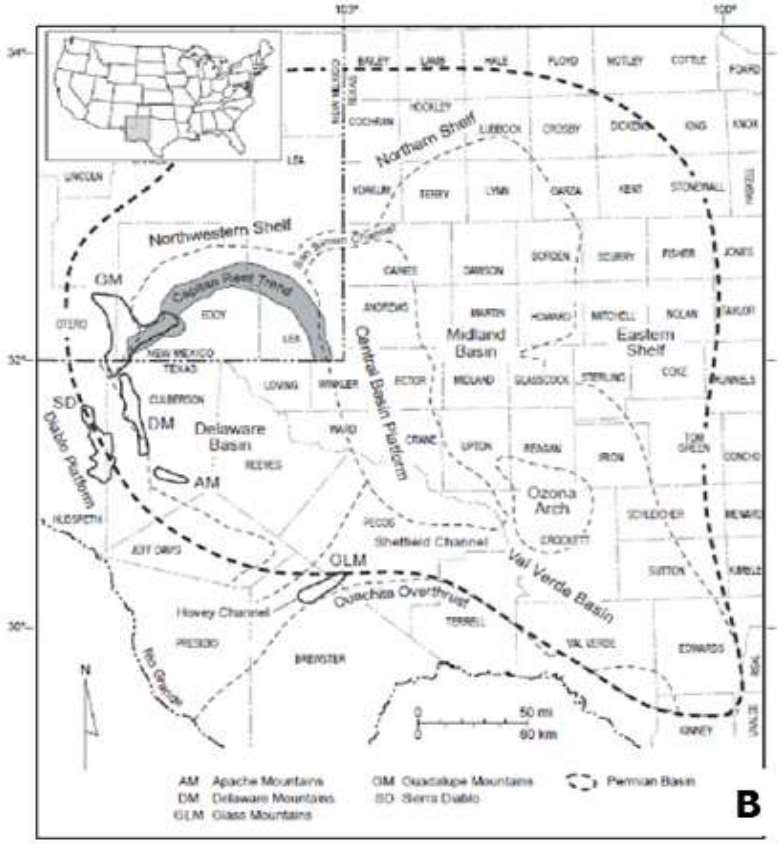

Northern Shelf
Northwestern Shelf
GM
Capitan Reef Trend
Central Basin Platform
Midland Basin
Eastern Shelf
SD
Diablo Platform
DM
Delaware Basin
AM
Ozona Arch
Sheffield Channel
GLM
Ouachita Overthrust
Val Verde Basin
Hovey Channel
Rio Grande
AM Apache Mountains
DM Delaware Mountains
GLM Glass Mountains
GM Guadalupe Mountains
SD Sierra Diablo
Permian Basin
B

Figure 76. Tectonic development of the Tobosa and Permian Basins. A) Late Mississippian (Ewing 2019). Note the lateral extent (pinchout) for the lower Paleozoic strata. B) Late Permian (Ruppel 2019a).

Silurio-Devonian formations consist of the Upper Ordovician to Lower Silurian Fusselman Formation (0–1,500 ft), the Upper Silurian to Lower Devonian Wristen Group (0–1,400 ft), and the Lower Devonian Thirtyone Formation (0–250 ft). The Fusselman Formation are shallow-marine platform deposits of dolostones and limestones (Broadhead 2017; Ruppel 2019b). Subaerial exposure and karstification associated with another unconformity at top of the Fusselman Formation as well as intraformational exposure events created brecciated fabrics, widespread dolomitization, and solution-enlarged pores and fractures (Broadhead 2017). The Wristen and Thirtyone units appear to be conformable. The Wristen Group consists of tidal to high-energy platform margin carbonate deposits of dolostones, limestones, and cherts with minor siliciclastics (Broadhead 2017; Ruppel et al. 2020a). The Thirtyone Formation is present in the southeastern corner of New Mexico and appears to be either removed by erosion or not deposited (**Figure 77**). It is shelfal carbonate with varying amounts of chert nodules and represents the last carbonate deposition in the area during Devonian time (Ruppel et al. 2020a).

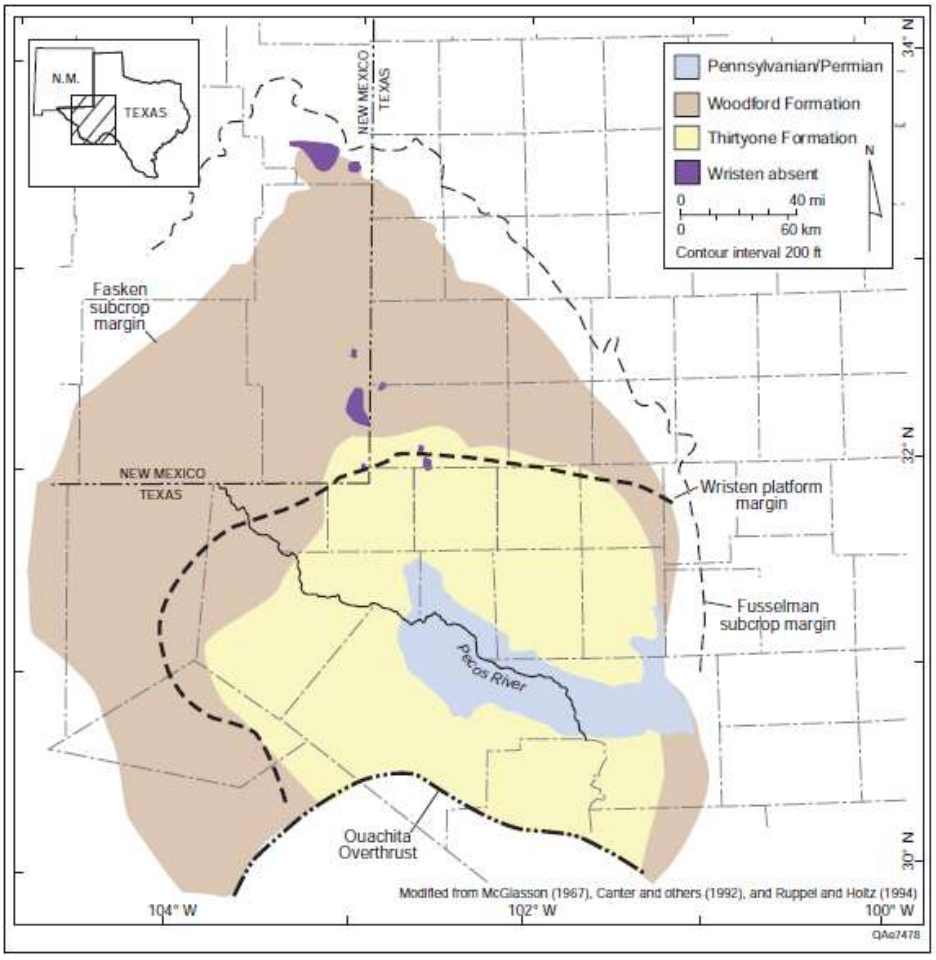


Figure 77. A subcrop map of the Thirtyone and Woodford formations. The Woodford (brown) lies unconformably on top of the Wristen Group where there is no Thirtyone sediments (yellow). Diagram is from Ruppel et al. (2020a).

The Siluro-Devonian units are saltwater injection zones within the Delaware Basin and are typically dolomitized, shallow marine limestones that have secondary porosity produced by subaerial exposure, karstification and later fracturing/faulting.

The Devonian Woodford Shale, an un-named Mississippian limestone, and the Upper Mississippian Barnett Shale are seals for the underlying Siluro-Devonian strata. While the Mississippian recrystallized limestones have minor porosity and permeability, the Woodford and Barnett shales have extremely low porosity and permeability and would be effective barriers to upward migration of acid gas out of the injection zone. The Woodford Shale (0–300 ft) ranges from an organic-rich argillaceous mudstones with abundant siliceous microfossils to organic-poor argillaceous mudstones (Ruppel et al. 2020b). The Woodford sediments represent stratified deeper marine basinal deposits with its organic content being a function of the oxygenation within the bottom waters; the more anoxic the waters, the higher the organic content.

The Mississippian strata within the northern Delaware Basin consists of an un-named carbonate member and the Barnett Shale and unconformably overlies the Woodford Shale. The lower Mississippian limestone (0–800 ft) are mostly carbonate mudstones with minor argillaceous mudstones and cherts. These units were deposited on a Mississippian ramp/shelf and have mostly been overlooked because of the reservoirs limited size. Where the units have undergone karstification, porosity may approach 4 to 9% (Broadhead 2017), otherwise it is tight. The Barnett Shale (0–400 ft) unconformably overlies the Lower Mississippian carbonates and consists of Upper Mississippian carbonates deposited on a shelf to basinal, siliciclastic deposits (the Barnett Shale). Within part of the basin, there is at least one tongue of Chesterian limestone within the Barnett Shale and numerous sandstone/siltstone interbeds within the mudstone deposits.

Pennsylvanian sedimentation in the area is influenced by glacio-eustatic sea-level cycles producing numerous shallowing upward cycles within the rock record; the intensity and number of cycles increase upward in the Pennsylvanian section. The cycles normally start with a sea-level rise that drowns the platform and deposits marine mudstones. As sea-level starts to fall, the platform becomes shallower and deposition switches to marine carbonates and coastal siliciclastic sediments. Finally, as the seas withdraw from the area, the platform is exposed causing subaerial diagenesis and the deposition terrestrial mudstones, siltstones, and sandstones in alluvial fan to fluvial deposits. This is followed by the next cycle of sea-level rise and drowning of the platform.

Lower Pennsylvanian units consist of the Morrow and Atoka formations. The Morrow Formation (0–2,000 ft) within the northern Delaware Basin was deposited as part of a deepening upward cycle with depositional environments ranging from fluvial/deltaic deposits at the base, sourced from the crystalline rocks of the Pedernal Uplift to the northwest, to high-energy, near-shore coastal sandstones and deeper and/or low-energy mudstones (Broadhead 2017; Wright 2020). The Atoka Formation (0–500 ft) was deposited during another sea-level transgression within the area. Within the area, the Atoka sediments are dominated by siliciclastic sediments, and depositional environments range from fluvial/deltas, shoreline to near-shore coastal barrier bar systems to occasional shallow-marine carbonates (Broadhead 2017; Wright 2020).

Middle Pennsylvanian units consist of the Strawn group (an informal name used by industry). Strawn sediments (250–1,000 ft) within the area consists of marine sediments that range from

ramp carbonates, containing patch reefs, and marine sandstone bars to deeper marine shales (Broadhead 2017).

Upper Pennsylvanian Canyon (0–1,200 ft) and Cisco (0–500 ft) group deposits are dominated by marine, carbonate-ramp deposits and basinal, anoxic, organic-rich shales.

Deformation, folding and high-angle faulting, associated with the Upper Pennsylvanian/Early Permian Ouachita Orogeny, created the Permian Basin and its two sub-basins, the Midland and Delaware basins (King 1948; Hills 1984), the Northwest Shelf (NW Shelf), and the Central Basin Platform (CBP; Figure 76, **Figure 78, Figure 79**). The Early Permian and older rocks have been fractured, faulted, and folded during this period of deformation and basin formation resulting in the deposition of the Wolfcamp and truncation of Wolfcampian and older units (**Figure 78**).

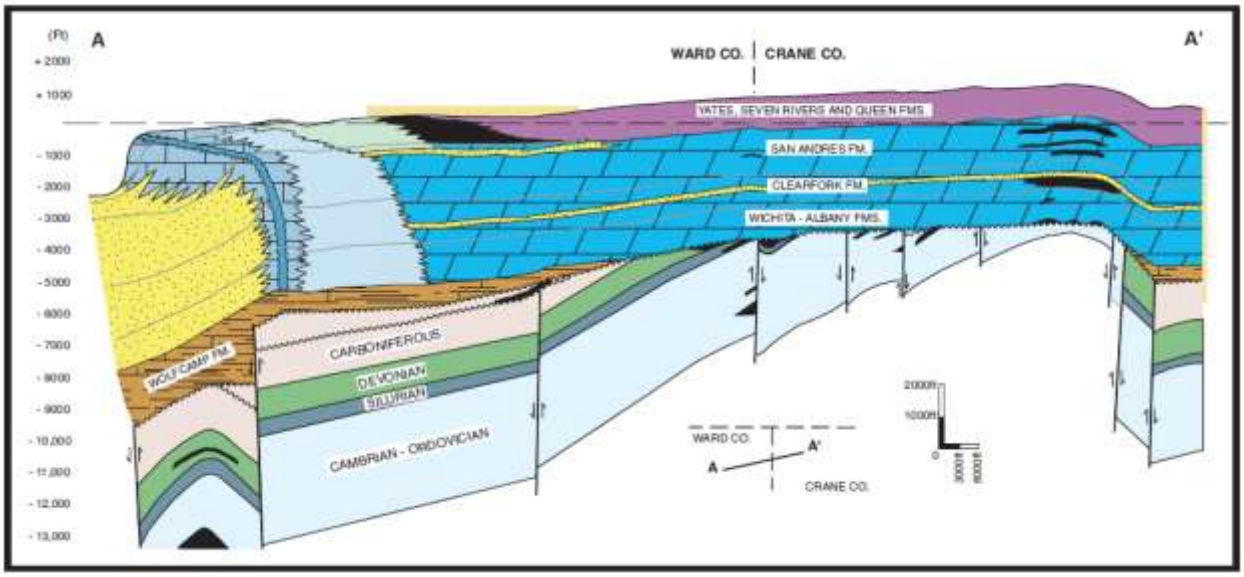


Figure 78. Cross section through the western Central Basin Platform showing the structural relationship between the Pennsylvanian and older units and Permian strata (modified from Ward et al. [1986]; from Scholle et al. [2007]).

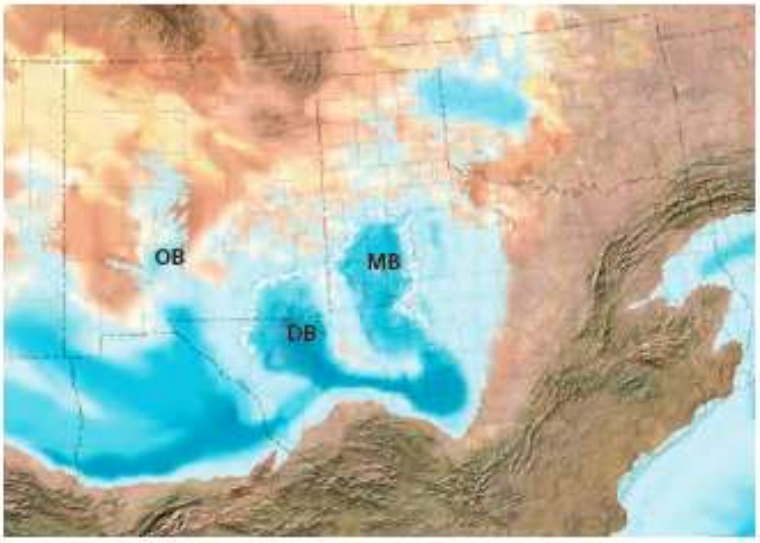


Figure 79. Reconstruction of southwestern United States about 278 Ma. The Midland Basin (MB), Delaware Basin (DB) and Orogrande Basin (OB) were the main depositional centers at that time (Scholle et al. 2020a).

The Wolfcampian Hueco Group is informally known as the Wolfcamp and this terminology will be used in this document. The Wolfcamp Group (approximately 400 ft on the NW Shelf, greater than 2,000 ft in the Delaware Basin) consists of shelf margin deposits ranging from barrier reefs and fore slope deposits, bioherms, shallow-water carbonate and sandstone shoals, and basinal carbonate mudstones (Broadhead 2017; Fu et al. 2020).

Differential sedimentation, continual subsidence, and glacial eustasy impacted Permian sedimentation after Wolfcamp deposition and produced carbonate shelves around the edges of deep sub-basins. Within the Delaware Basin, this subsidence resulted in deposition of roughly 12,000 ft of siliciclastics, carbonates, and evaporites (King 1945). Eustatic sea-level changes and differential sedimentation, played an important role in the distribution of sediments/facies within the Permian Basin. During sea-level lowstands, thousands of feet of siliciclastic sediments bypassed the shelves and were deposited in the basin. Scattered, thin sandstones and siltstones as well as fracture and pore filling sands found up on the shelves correlate to those lowstands. During sea-level highstands, thick sequences of carbonates were deposited by a “carbonate factory” on the shelf and shelf edge. Carbonate debris beds shedding off the shelf margin were transported into the basin (Wilson 1972; Scholle et al. 2007). Individual debris flows thinned substantially from the margin to the basin center (from hundreds of feet to feet).

Unconformably overlying the Hueco Group is the Abo Formation (700–1,400 ft). Abo deposits range from carbonate grainstone banks and buildups along NW Shelf margin and shallow-marine carbonates to the northwest of the margin. Further back on the margin, the backreef sediments grade into intertidal carbonates to siliciclastic-rich sabkha red beds to eolian and fluvial deposits closer to the Sierra Grande and Uncompahgre uplifts (Broadhead 2017; Ruppel 2020a). Sediments basinward of the Abo margin are equivalent to the lower Bone Spring Formation. The Yeso Formation (1,500–2,500 ft), like the Abo Formation, consists of carbonate banks and buildups along the Abo margin, which is roughly in the same area, just south of Dagger Draw. Unlike Abo sediments, the Yeso Formation contains more siliciclastic sediments associated with eolian, sabkha, and tidal flat facies (Ruppel 2020a). The Yeso shelf sandstones are commonly

subdivided into the Drinkard, Tubb, Blinebry, Paddock members (from base to top of section). The Yeso Formation is equivalent to the upper Bone Spring Formation. Overlying the Yeso, are the clean, white eolian sandstones of the Glorietta Formation. It is a key marker bed in the region, both on the surface and subsurface. Within the basin, it is equivalent to the Lower Brushy Canyon Formation of the Delaware Mountain Group.

The Guadalupian San Andres Formation (600–1,600 ft) and Artesia Group (greater than 1,800 ft) reflect the change in the shelf margin from a distally steepened ramp to a well-developed barrier reef complex at the end carbonate deposition within the Delaware Basin. The individual highstand carbonate units are separated by lowstand sandstones/siltstones that moved out over the exposed shelf. The San Andres Formation consists of supratidal to sandy subtidal carbonates and banks deposited a distally steepened ramp. Within the San Andres Formation, several periods of subaerial exposure have been identified that have resulted in karstification and pervasive dolomitization of the unit. Within the Delaware Basin, it is equivalent to the Brushy and lower Cherry Canyon Formations.

The Artesia Group (Grayburg, Queen, Seven Rivers, Yates, and Tansill formations, ascending order) is equivalent to Capitan Limestone, the Guadalupian barrier/fringing reef facies. Within the basin, the Artesia Group is equivalent to the upper Cherry and Bell Canyon formations. The Queen and Yates formations contain more sandstones than the Grayburg, Seven Rivers, and Tansill formations. The Artesia units and the shelf edge equivalent Capitan reef sediments represent the time when the carbonate factory was at its greatest productivity with the shelf margin/Capitan reef prograding nearly 6 miles into the basin (Scholle et al. 2007). The Artesia Group sediments were deposited in back-reef, shallow marine to supratidal/evaporite environments. Like the San Andres Formation, the individual formations were periodically exposed during lowstands.

The final stage of Permian deposition on the NW Shelf consists of the Ochoan/Lopingian Salado Formation (greater than 2,800 ft; Nance 2020). Within the basin, the Castile Formation, a thick sequence (total thickness approximately 1,800 ft; Scholle et al. 2007) of cyclic laminae of deep-water gypsum/anhydrite interbedded with calcite and organics, formed due to the restriction of marine waters flowing into the basin. Gypsum/anhydrite laminae precipitated during evaporative conditions, and the calcite and organic-rich horizons were a result of seasonal “freshening” of the basin waters by both marine and freshwaters. Unlike the Castile Formation, the Salado Formation is a relatively shallow water evaporite deposit. Halite, sylvite, anhydrite, gypsum, and numerous potash minerals were precipitated. The Rustler Formation (500 ft; Nance 2020) consists of gypsum/anhydrite, a few magnesitic and dolomitic limestone horizons, and red beds. These are mostly shallow marginal marine deposits and represents the last Permian marine deposits in the Delaware Basin. The Rustler Formation was followed by terrestrial sabkha red beds of the Dewey Lake Formation (approximately 350 ft; Nance 2020), ending Permian deposition in the area.

Beginning early in the Triassic, uplift and the breakup of Pangea resulted in another regional unconformity and the deposition of non-marine, alluvial Triassic sediments (Santa Rosa Sandstone and Chinle Formation). They are unconformably overlain by Cenozoic alluvium (which is present at the surface). Cenozoic Basin and Range tectonics resulted in the current configuration of the region and reactivated numerous Paleozoic faults.

Structure

The Delaware Basin is surrounded by the Central Basin Platform on the east, the San Simon Channel that separates the Central Basin Platform and the Northwest Shelf, the Diablo Platform to the southwest and west, the Hovey and Sheffield Channels to the south (**Figure 80**).

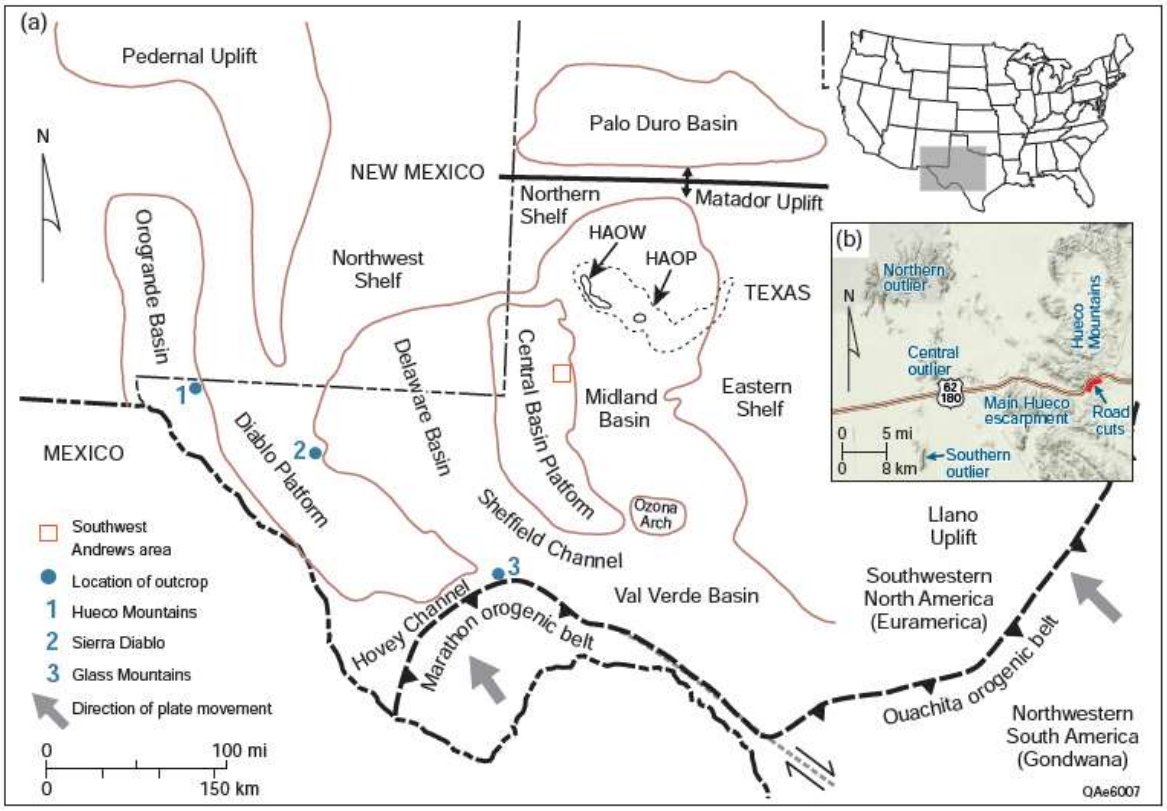


Figure 80. Map of the Delaware Basin with the major topographic features of the Permian Basin (from Fu et al. 2020).

The structural evolution of the basin was discussed in the previous section, but **Figure 81** summarizes these events as well as provide a type log for the basin (not shelf) stratigraphy.

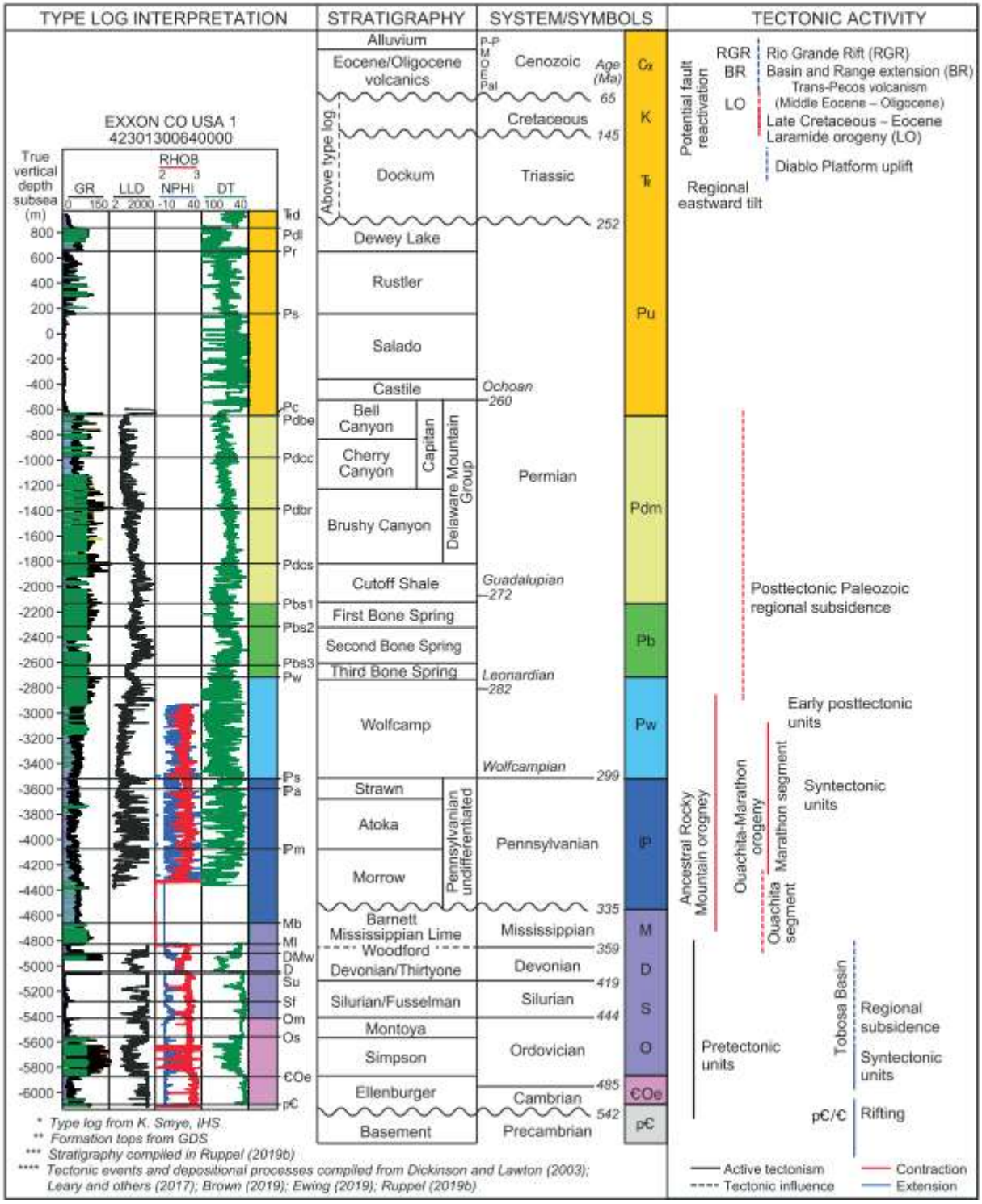


Figure 81. A type log for the Delaware Basin with the major structural events (from Horne et al. [2021]).

Horne et al. (2021), using seismic, lidar, and petrophysical well logs, has developed a regional fault map for the Delaware Basin. Their shape files were utilized in our geologic models the was developed for the New Mexico and part of the Texas Delaware Basin. Horne et al. (2022) have also produced a shallow fault map that was utilized for the shallower horizons. Most of shallow

faults occur in the Texas portion of the Delaware Basin and are with the Guadalupian Delaware Mountain and the Ochoan Castile, Salado and Rustler formations.

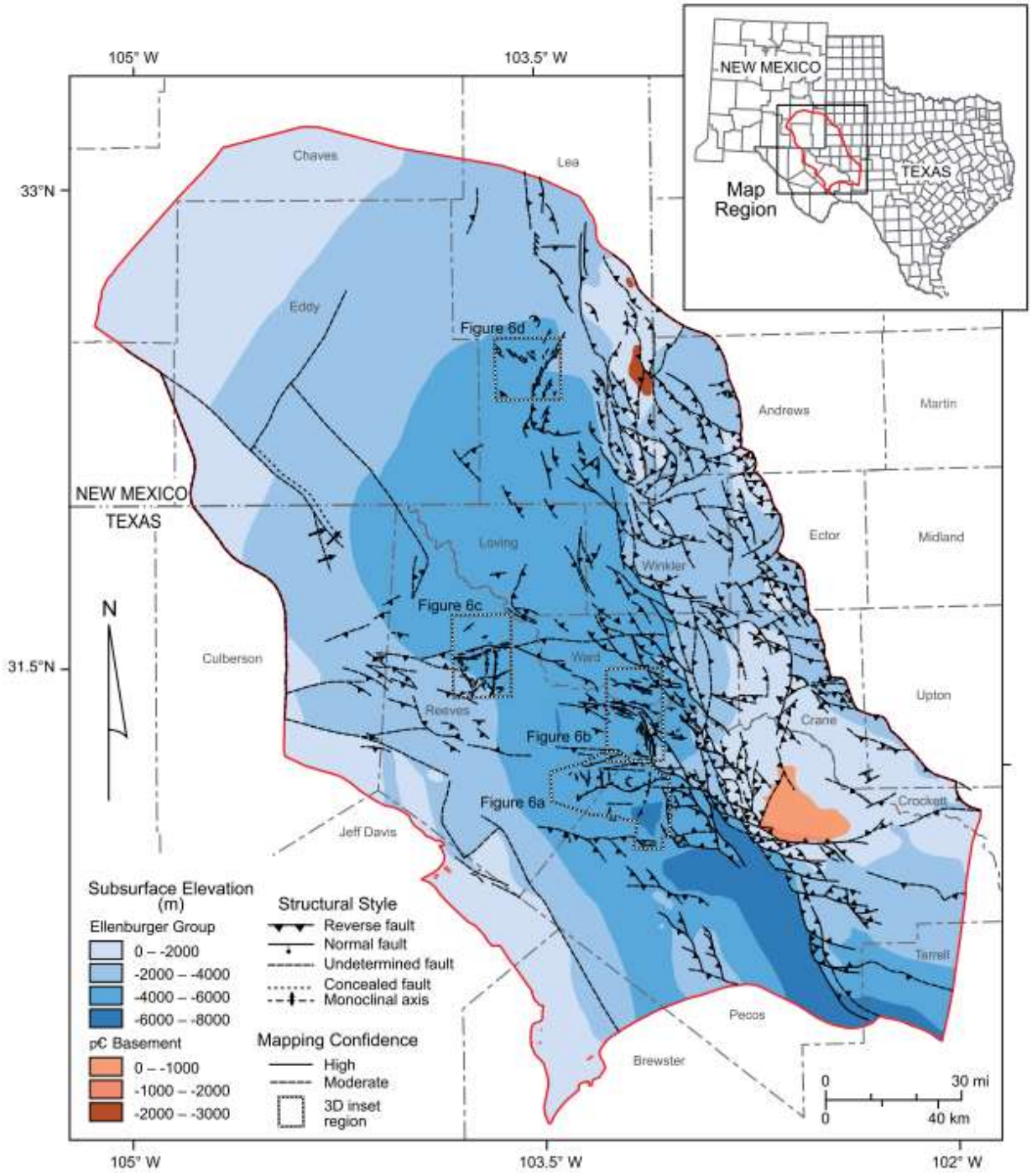


Figure 82. Regional basement fault map for the Delaware Basin from Horne et al. (2021). The map shows the subsurface elevation for the Ellenburger and Precambrian (in meters).

Stratigraphy

Cambrian to Precambrian

Bliss Sandstone

The oldest sedimentary unit in the basin is the Cambrian Bliss Sandstone (Broadhead 2017; **Figure 83**), which overlies Precambrian granites. These late Cambrian transgressive sandstones were the initial deposits from a shallow marine sea that covered most of North America and Greenland. With continued down warping and/or sea-level rise, a broad, relatively shallow marine basin formed. The Bliss Sandstone and the underlying crystalline Precambrian rocks are potential lower seals. Porosity and permeability data indicates that in shallower wells, the Bliss is an aquifer. In deeper wells, the compactional history and potential diagenetic alteration, the Bliss sandstones and associated granitic debris (from weathering of the basement rock) are probably relatively tight.

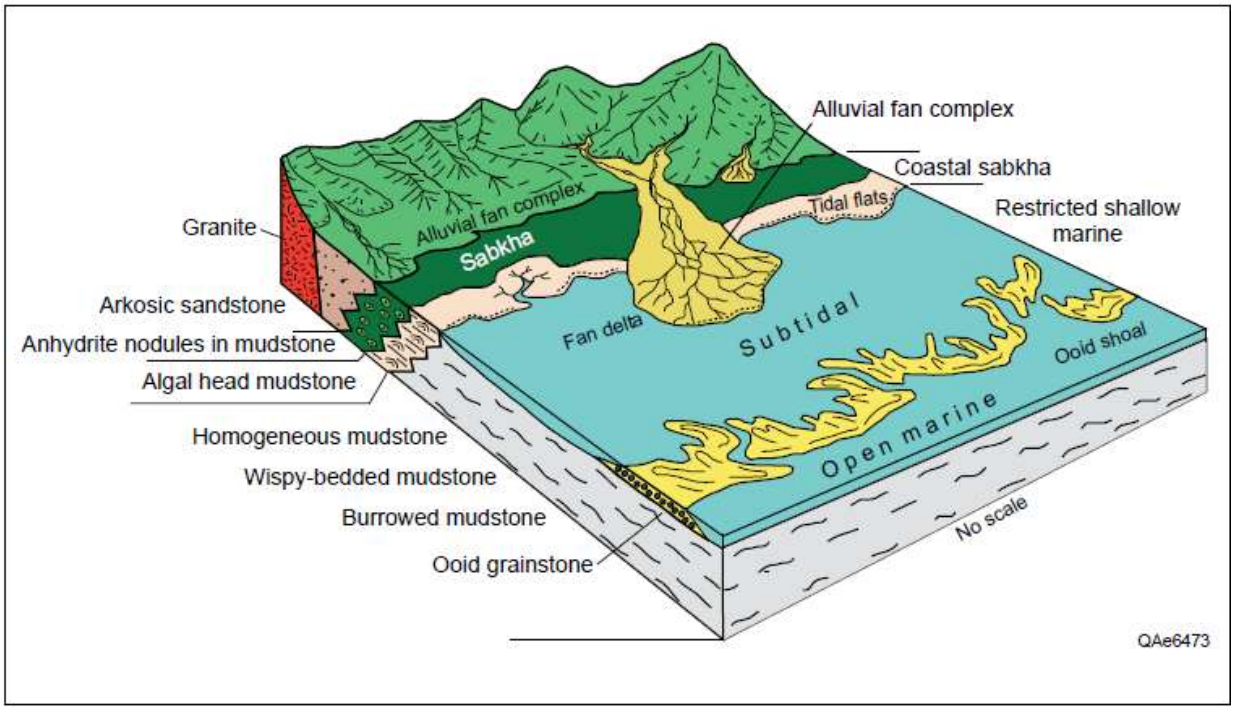


Figure 83. Depositional environments for the bliss Sandstone to early Ellenburger in the proto-Tobosa basin (from Loucks and Kerans 2019).

Ordovician

Ellenburger Group

The Ordovician Ellenburger Group is comprised of dolomites and limestones. These sediments were deposited in subtropical to tropical belt of shallow-water platform carbonates that covered most of what is now North America and Greenland. The carbonates in the Permian Basin area have been extensively altered by later diagenesis that includes several intervals of exposure and

karstification, dolomitization, and fracturing and faulting during later tectonic events (**Figure 84**).

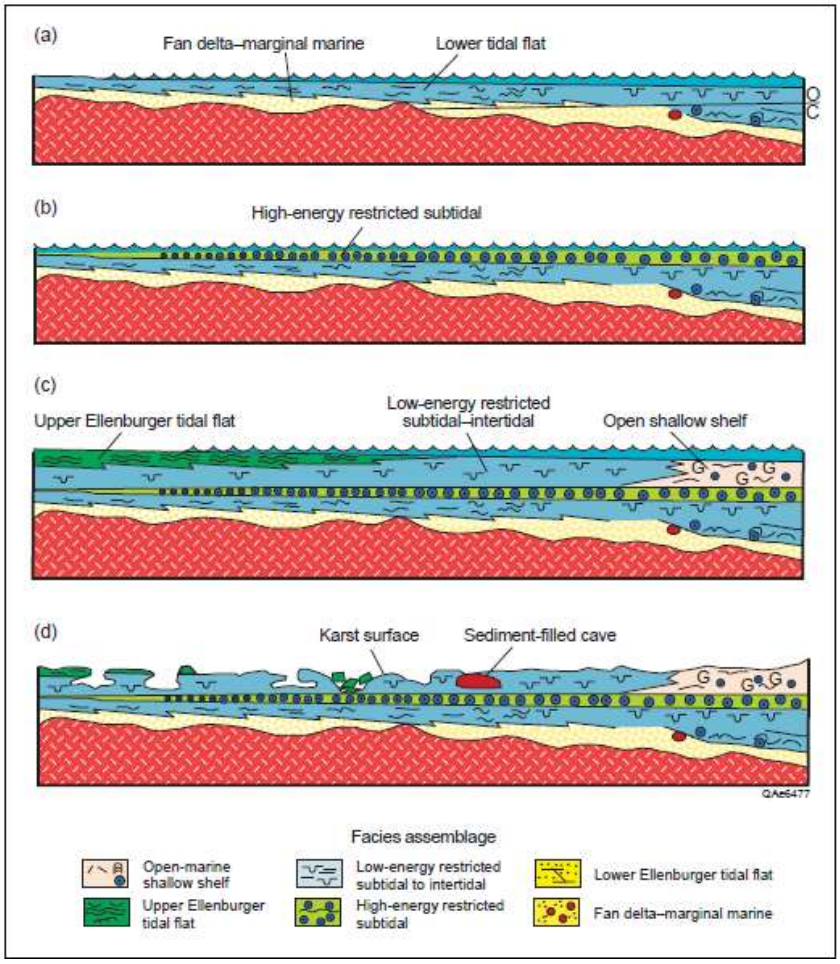


Figure 84. Depositional model for the Ellenburger Group deposits. The diagram shows a sequence of transgressive sandstones (Bliss Sandstone, yellow) to carbonates (Panels A through C followed by a regressive sequence (Panels C and D) with exposure and karstification in Panel D (from Loucks and Kerans [2019]).

Within the Ellenburger Group strata, the upper and middle section typically has the highest porosity and permeability due to karsting and cave development as well as later faulting and fracturing (**Figure 85**). Late diagenesis plays an important role in porosity destruction and resurrection. Based on work by Loucks (2016), the best karst-related porosity is to the east of the Bull Moose area, whereas the Bull Moose area is in the zone of porosity due to tectonically controlled faulting and fracturing. Porosity and permeability in the Ellenburger section can vary greatly due to the above considerations (Loucks and Kerans 2019).

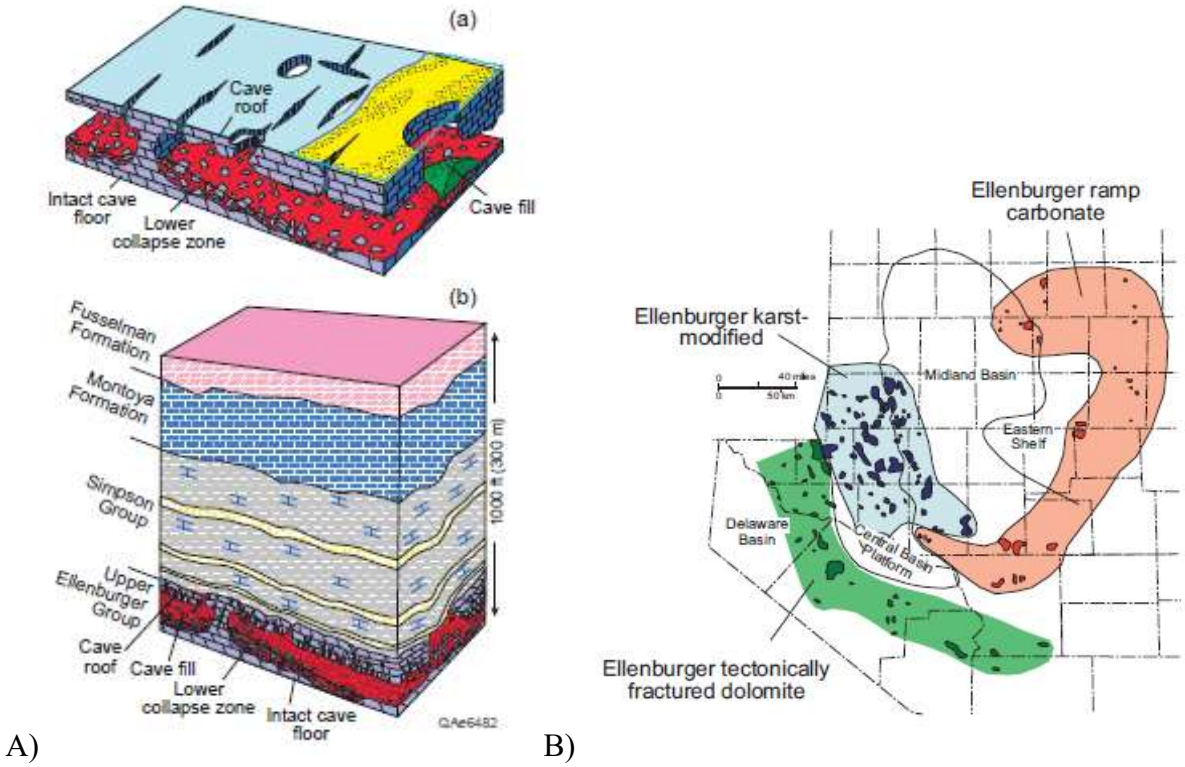


Figure 85. Karst development. A) Cave development in the upper Ellenburger rocks and their potential impact to produce porosity and permeability (from Loucks and Kerans [2019]). B) Zones of potential porosity creation: karst related (blue), fault and fracture (green) and enhanced primary porosity (orange; Loucks [2016]).

Simpson Group

The deposits of the Simpson Group represent a regional transgression after the unconformity at the end of Ellenburger deposition. This group is a thick sequence of carbonates, sandstones, and shales (approximately 1,000 ft) which has a depocenter roughly equivalent to the Delaware Basin/Tobosa Basin. There are several transgressive/regressive cycles within the section, but only the transgressive sandstone sections have significant porosity. The rest of the section typically consists of mud-rich carbonates and shales. Within the sandstones (particularly the McKee Sandstone member), well logs indicate porosity averages around 15%.

Montoya Group

The Montoya deposits are dominated by shallow-water, ramp limestones that were deposited in the Tobosa Basin (**Figure 86**). Like the Ellenburger Group, the porosity within the Montoya Group is dependent on depositional environment and diagenesis. The higher energy environments tend to have better initial porosity than the low-energy environments. Compaction destroys the porosity, and dolomitization produces secondary porosity. Based on the well logs, the average porosity is approximately 3%, with scattered zones over 5%. The probable average permeability is probably less than 1 mD, but fracturing may enhance it.

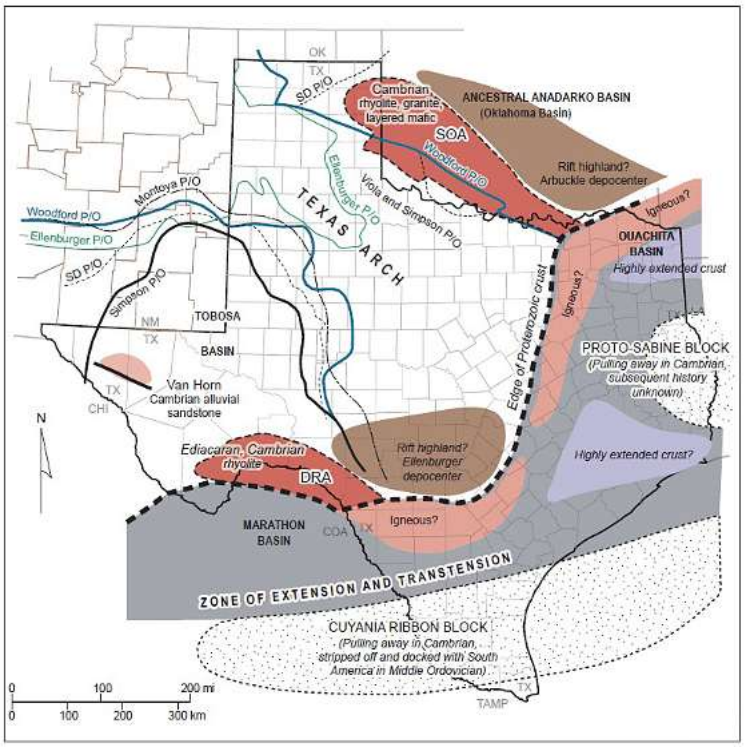


Figure 86. Tectonic features during development of the Tobosa and Permian Basins during Late Mississippian time (Ewing 2019).

Ordovician – Silurian

Fusselman Formation

The Fusselman Formation is a shallow-water carbonate system that was deposited in the Tobosa Basin. In the Delaware Basin, the Fusselman thickens to around 1,000 ft of high-energy packstones to grainstones. Like the Montoya Group, these high-energy sediments started out with the best primary porosity, but diagenesis usually has decreased both the porosity and permeability unless impacted by exposure and dissolution. Based on well logs, the porosity averages around 2%. Reported permeability for shallower sections range from 0.001 to 10 mD (Ruppel 2019b).

Lower Devonian – Silurian

Thirtyone and Wristen Formations

Underlying the Woodford Shale are the interbedded dolomites and dolomitic limestones of the Devonian Thirtyone Formation and the Silurian Wristen Group, collectively referred to as the Siluro-Devonian section. Unlike the Fusselman, Montoya and Ellenburger carbonates, these deposits represent deposition in deeper waters. These deposits range from deep ramp mudstones and wackestones, to chert- and sponge/radiolarian-rich hemipelagic mudstones (Wristen/Thirtyone) to outer ramp packstones (**Figure 87**; Ruppel et al. 2020a, 2020b). Porosity and permeability in the Wristen are limited in the main body of the unit (1-2%), but exposure events and carbonate dissolution can improve the porosity (approximately 5%). Within Thirtyone

deposits, the chert-rich hemipelagic deposits maintain the best porosity (up to 40%, up to 80 mD), while the limestones have less than 7% porosity and less than 1 mD of permeability (Ruppel et al. 2020a).

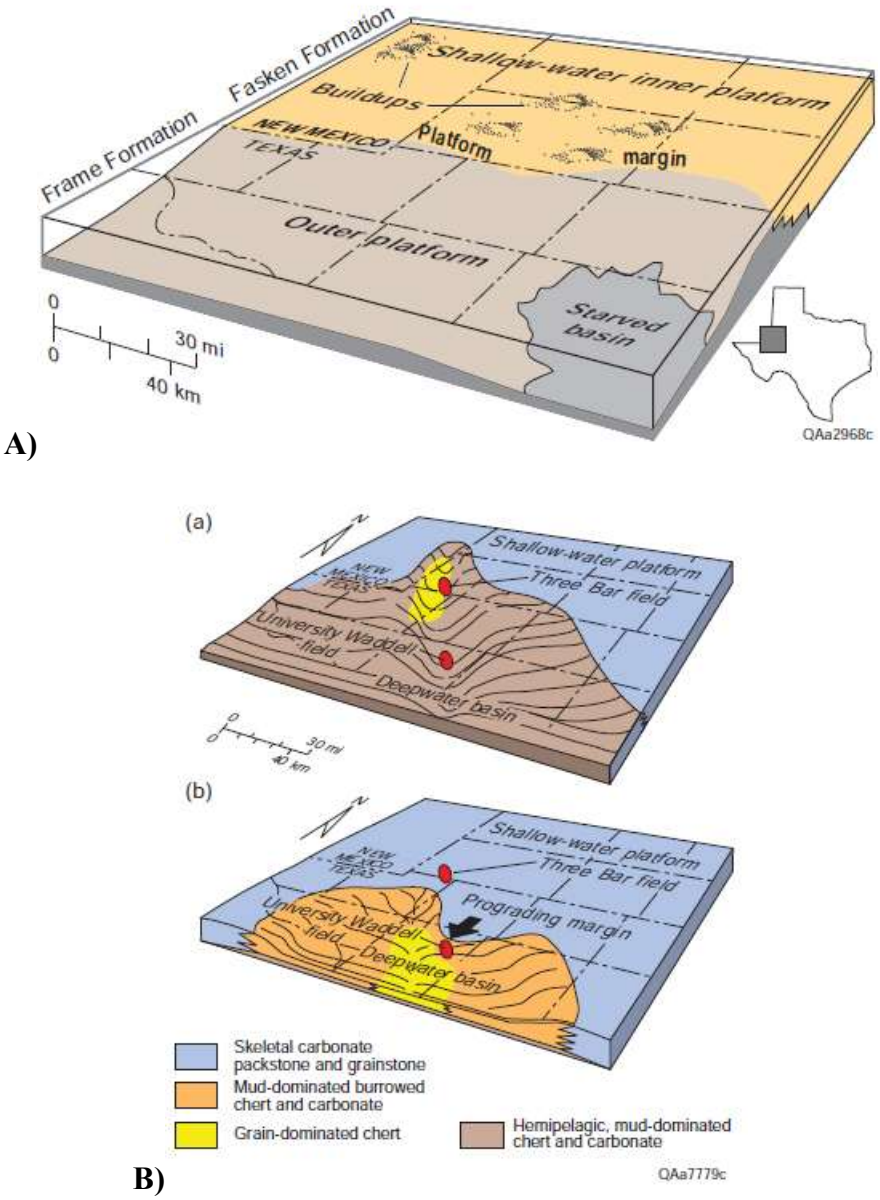


Figure 87. Generalized Paleogeography. A) Generalized paleogeography for the Wristen Group (from Ruppel [2020b]). B) Generalized paleogeography for the Thirtyone Formation. (a) represents the earliest deposition and the presence of deep-water environments. (b) represents the latter deposition (from Ruppel et al. [2020a]).

Upper Devonian

Woodford Shale

Within the Permian Basin, the Upper Devonian Woodford Shale serves as a seal to hydrocarbon migration out of Devonian and older units (Wright 1979). In combination with the Mississippian section, it makes an excellent seal for potential injection. The Woodford Shale is laterally continuous, organic- and shale-rich, siliceous (radiolarians) mudstone. The porosity that occurs in the Woodford Shale is usually micro-porosity associated with organic material and not connected (i.e., low permeability). Porosity can reach as much as 10% (Jarvie et al. 2001), but it averages around 1% with very low permeabilities.

Mississippian

Mississippian Limestone

The Lower Mississippian limestone (an informal name) is a dark colored, deep marine limestone with minor cherts and shales (**Figure 88**). In parts of the Delaware Basin, there is a second carbonate tongue informally known as the Chesterian limestone. Known production from this limestone consists of one to two well plays that normally have poor porosity (4-9%) and permeability (Broadhead 2017) in New Mexico and a few isolated fields in the shallow water, high-energy limestones in Texas.

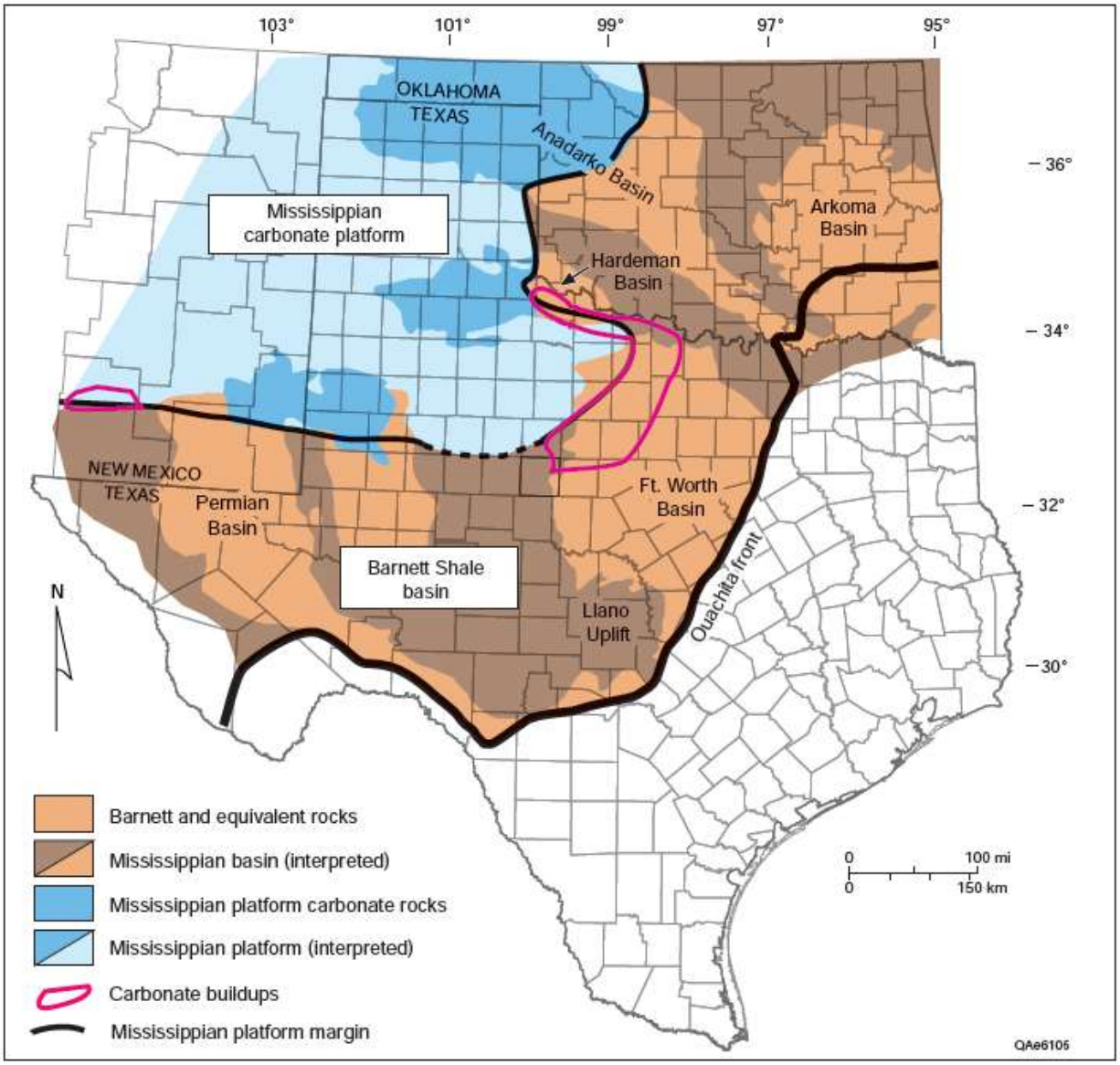


Figure 88. Map showing the distribution of platform carbonates of the Mississippian limestone and basin siliciclastic sediments of the Barnett Shale (from Ruppel et al. [2020c]).

Barnett Shale

The Barnett Shale is a widespread, dark, organic shale with very low porosity and permeability (Figure 88). Overall, the Mississippian units would be good seals in preventing upward fluid movement through the section.

Pennsylvanian

Morrow Formation

The Morrow Formation consists mainly of shale-dominated grading upward to sandstone-dominated strata as you move upward through the section. In parts of the basin, the sequence is

capped by oolitic limestones. The Morrow sediments were deposited within the basin as part of several transgressive (shales)/regressive cycles during Morrowan time. They represent deposition in deltas, shoreface, shallow to deeper water platform environments, basinal shales and submarine fans (**Figure 89**). The main reservoirs are within the sandstone lenses with porosities from 5% to 8% (Broadhead 2017).

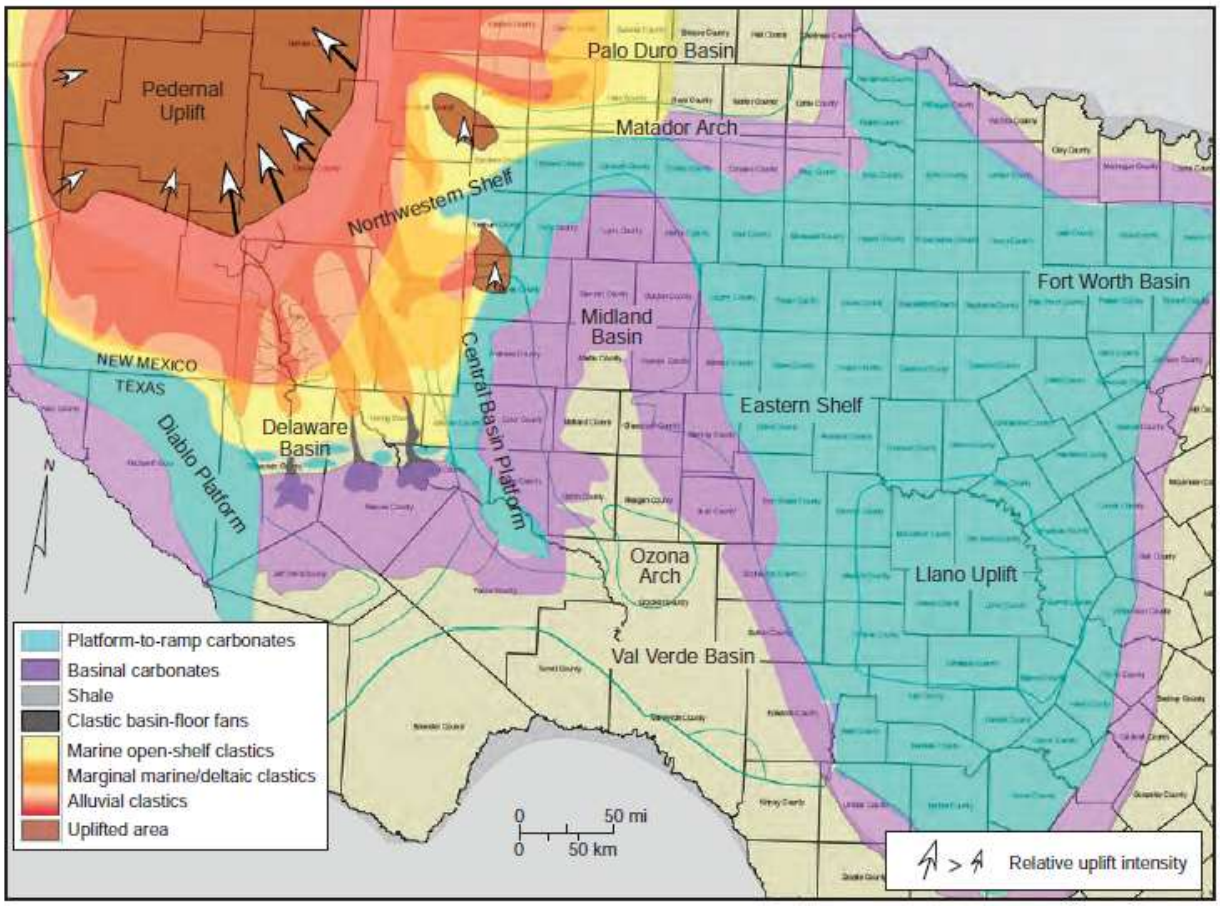


Figure 89. Paleodepositional map of Morrowan sedimentation (from Wright [2020])

Atoka Formation

Atokan units are dominated deltaic and shoreface deposits formed during a transgression, with occasional carbonate buildups (**Figure 90**; Broadhead 2017; Wright 2020). The Permian Basin starts forming during Atokan time (Wright 2020) with the deposition basin forming in the area of the Midland Basin. Gas production dominates production in the Atoka Formation with porosities ranging from 8% to 12% (Broadhead 2017).

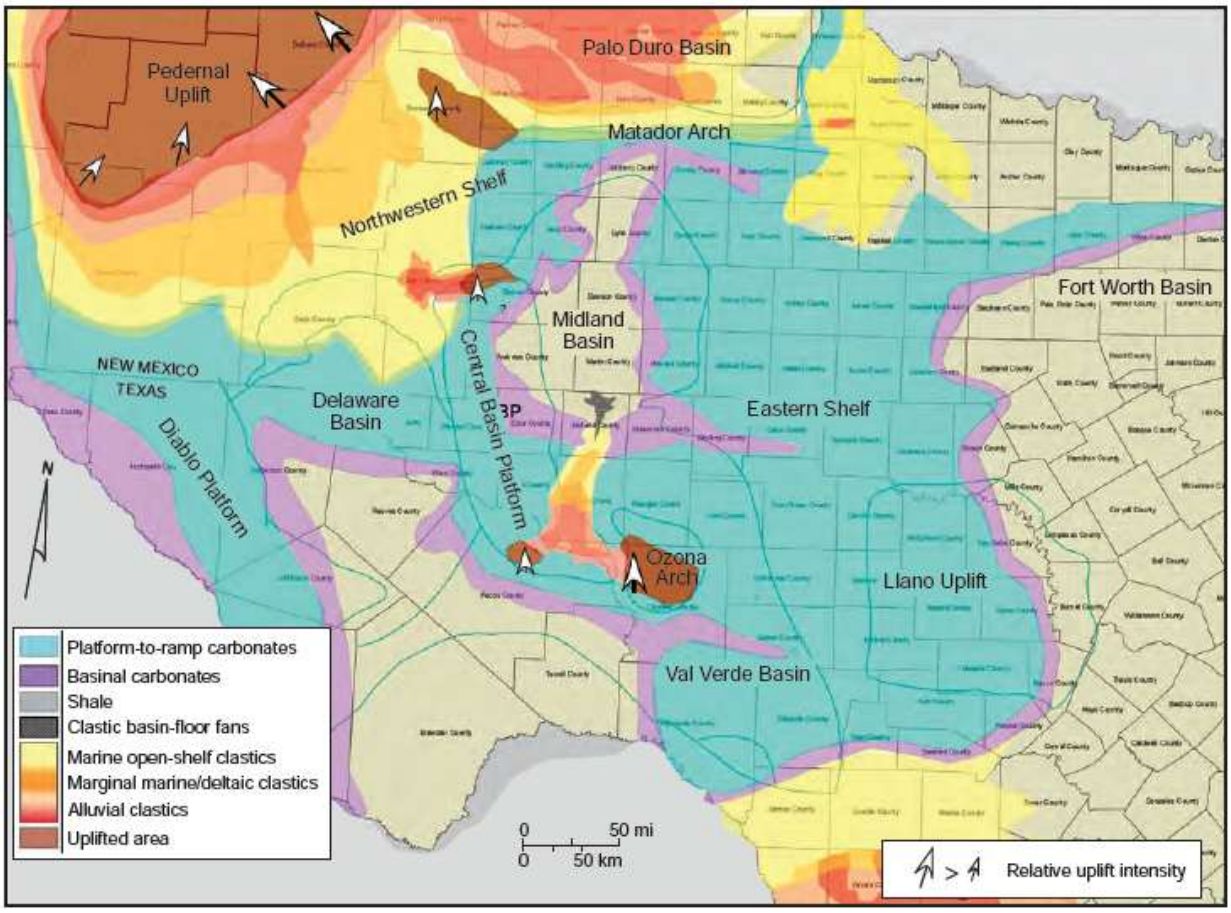


Figure 90. Paleodepositional map of Atokan sedimentation (from Wright [2020])

Strawn Group

Desmoinesian sedimentation consists of the Strawn Group. A second depositional low develops in the area of the Delaware Basin. Within the Delaware Basin, the Strawn sediments are dominated by limestones and sandstones deposited on a ramp (**Figure 91**) to basinal sediments in the Texas part of the basin. The limestones consist of patch reefs encased by shales (during a later transgression). A second depositional low develops in the area of the Delaware Basin. Reservoirs are common in the patch reefs of coralline algae and foraminiferal packstones and have porosities of approximately 10% and high permeabilities (Broadhead 2017).

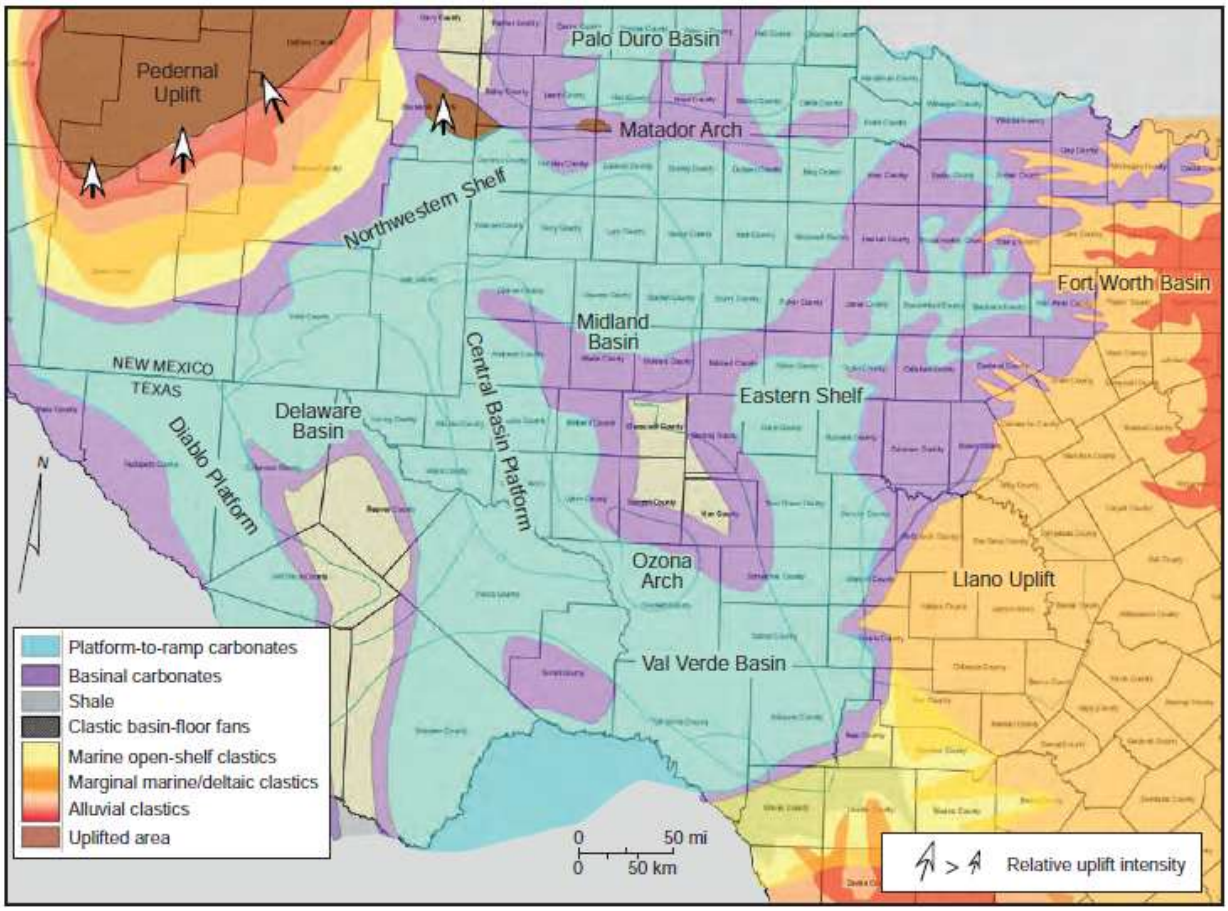


Figure 91. Paleodepositional map of Desmoinesian sedimentation (from Wright [2020])

Canyon Formation

The Canyon Formation comprise Missourian sedimentation, respectively. This is the time period of active tectonism and the completion of the Permian Basin formation (**Figure 92**). The sediments range from basinal, organic-rich shales and siltstones, basin to platform carbonates, and clastic deltaics and submarine fans (Error! Reference source not found.). Phylloid algae mounds and bioclastic packstones are the major reservoirs within these sediments. They have porosities up to 15%, mostly secondary porosity.

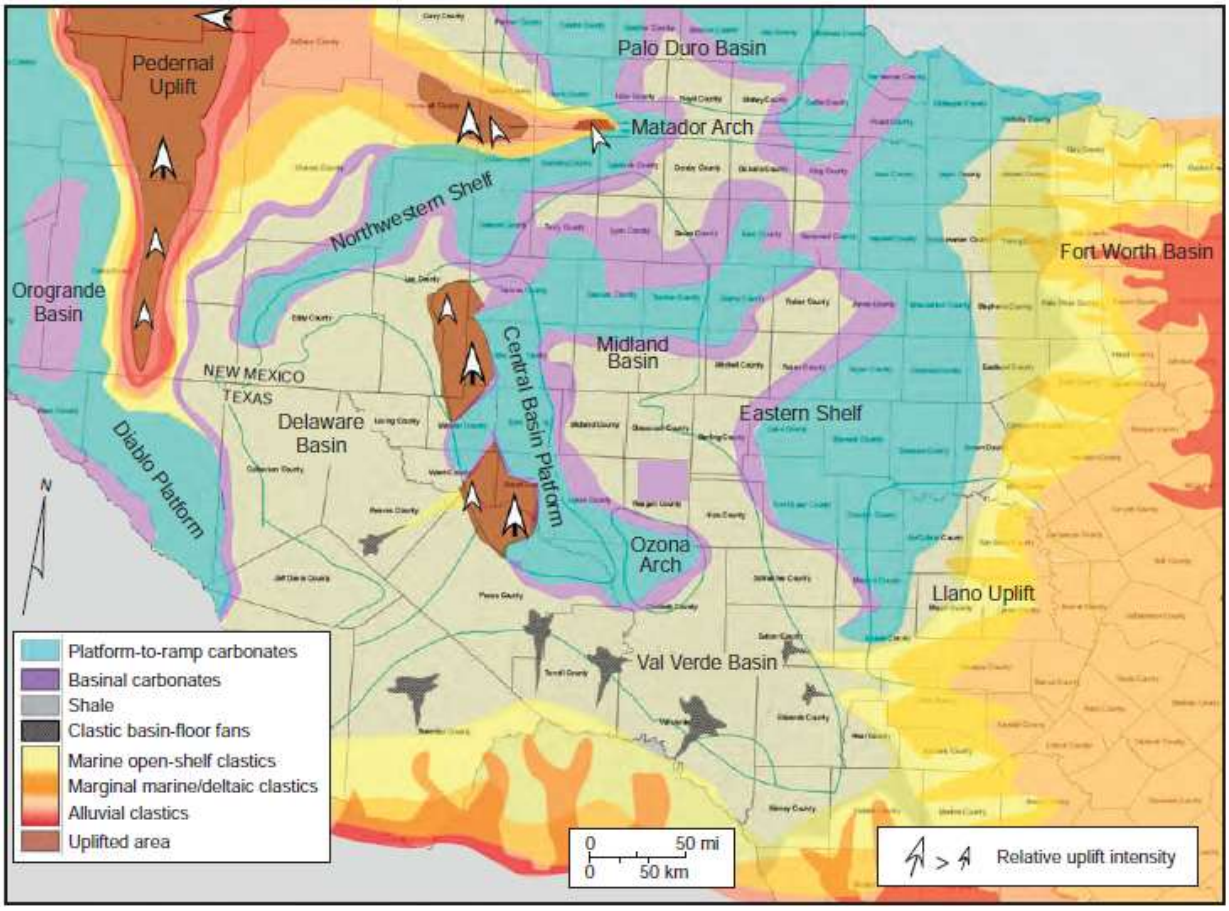


Figure 92. Paleodepositional map of Missourian sedimentation (from Wright [2020]).

Cisco Formation

The Ancestral Rocky Mountain deformation and the Ouachita Orogeny, starting in Late Pennsylvanian (Missourian) and going through Wolfcampian time, resulted in the formation of the Delaware and Midland basins. This produced changes in the shelf to basin margin throughout Pennsylvanian time. The Cisco Formation consists of interbedded carbonates, sandstones, and shales. Deeper marine sediments were dominated by organic-rich shales, the shelf edge was dominated by fusulinid-rich *Syringopora*-phylloid algal bioherms and carbonate grainstone shoals, and the platform shelf, which shallows northward, progressively changing from marine backreef and lagoonal deposits to subtidal deposits with increasing amounts of sandstone that was sourced from the Pedernal Uplift (**Figure 93**; Scholle et al. 2007; Broadhead 2017). The Cisco Formation is one of several highly productive zones in the Delaware Basin. The nearby Dagger Draw field has produced more than 70 billion barrels of oil. Oil production with Dagger Draw and Tatum field is restricted mostly to the platform-edge carbonate bioherms and, to a lesser extent, the high-energy carbonate grainstones. The bioherms have seen variable amounts of dolomitization, dissolution, and secondary porosity development. Productive zones typically have porosities that range from 7% to 12% (Broadhead 2017). The interbedded shales, interior platform carbonates and sandstones have minimal porosity.

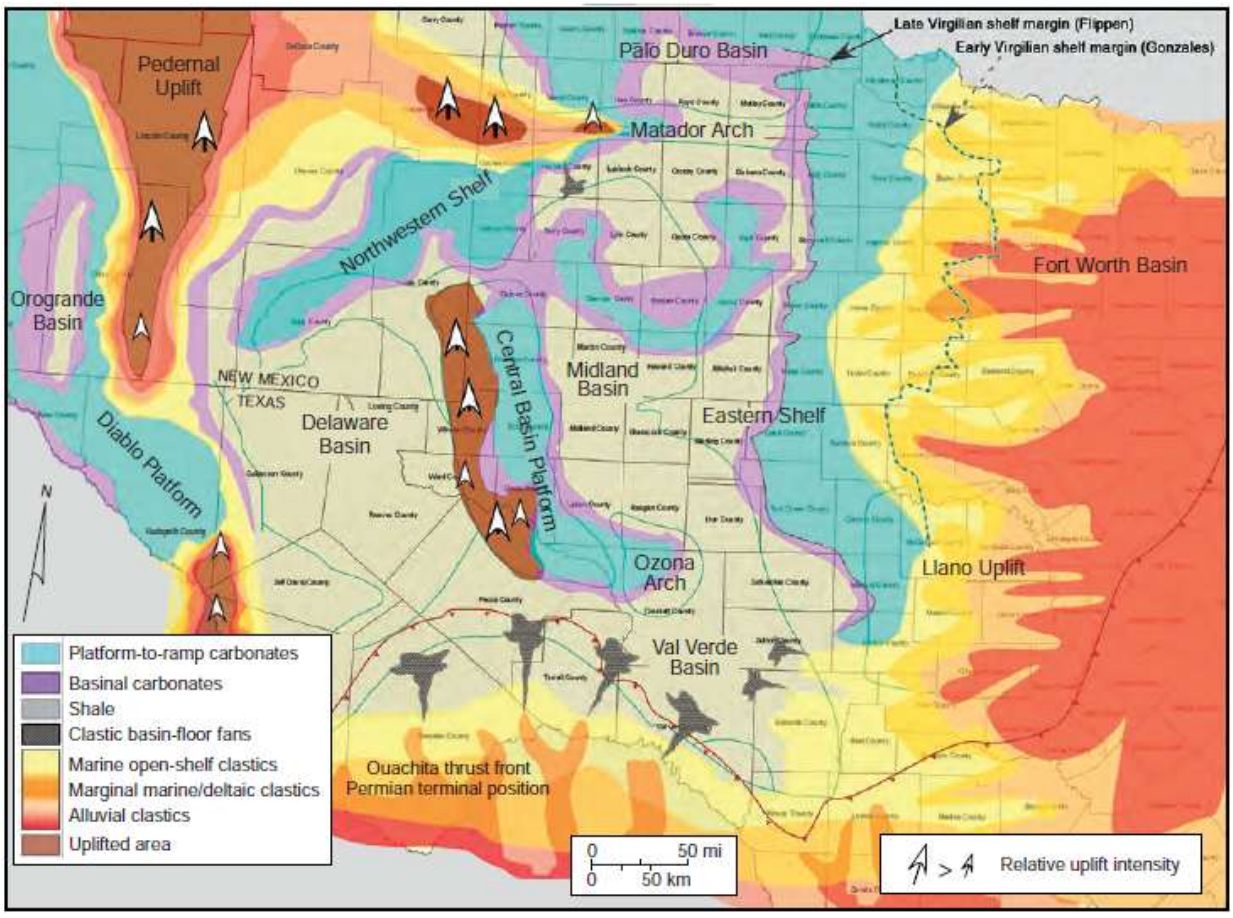


Figure 93. Paleodepositional map of Virgilian sedimentation (from Wright [2020]).

Permian

Wolfcampian Rocks

Wolfcamp/Hueco Group

Wolfcampian rocks in the Delaware Basin area have been assigned to the Hueco Group, but they are informally called the "Wolfcamp." The Wolfcamp was deposited on shelf margin during a time of high-frequency, high-amplitude sea-level fluctuations (Fu et al. 2020). The shelf deposits range from low-energy lagoonal/subtidal mudstones/wackestones to high-energy packstone/grainstone shoals (**Figure 94**). Along the shelf margin, phylloid algal bioherms (boundstones) rim the shelf margin. On many of the bioherms, oolitic grainstones occur as caps and were deposited in a very high-energy environment (Scholle et al. 2007). On the foreslope and proximal basin margin, shelf detritus makes up most of the sediments. In more distal areas within the basin, carbonate- and radiolarian-rich mudstones and shales were deposited.

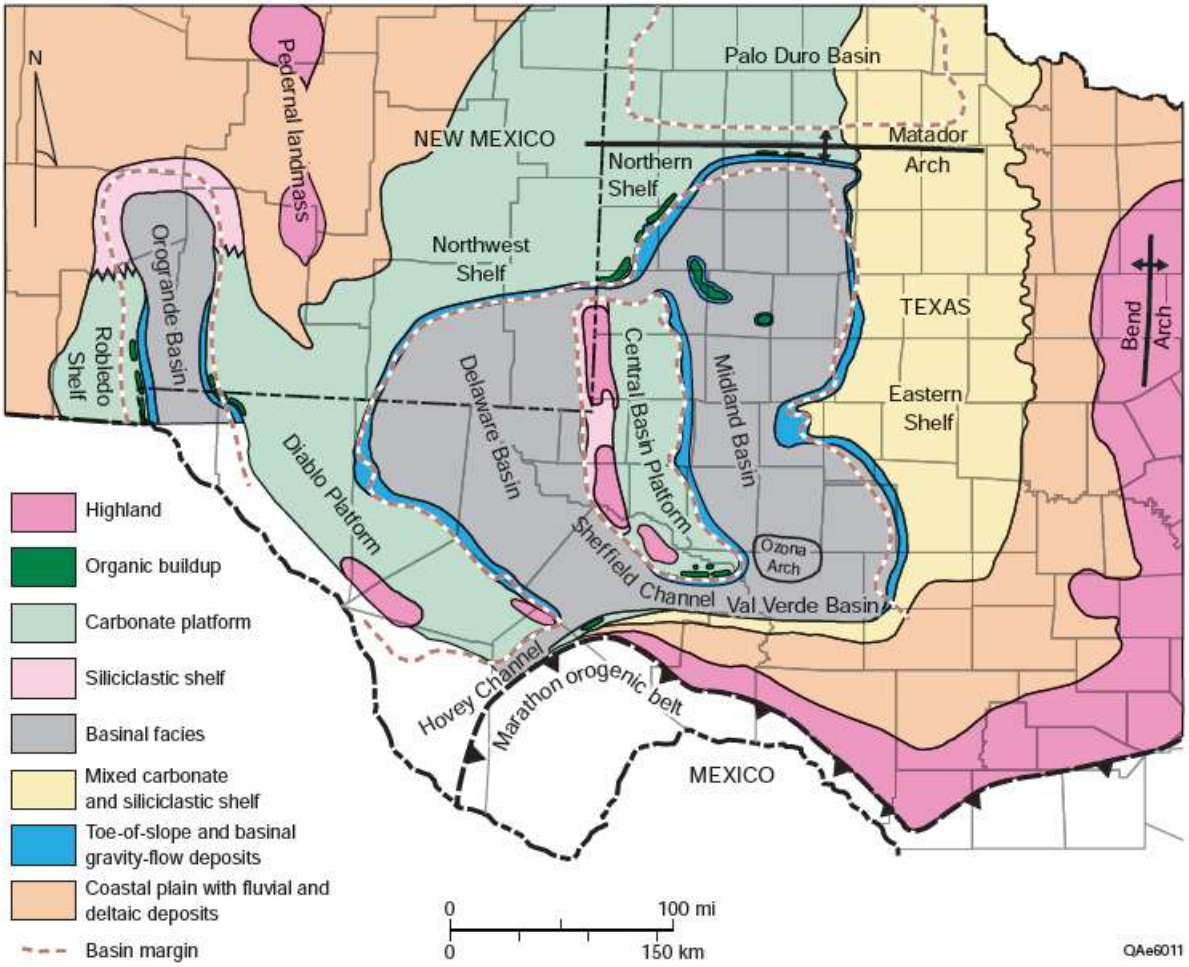


Figure 94. Paleodepositional environments within the Permian Basin area during late Wolfcampian deposition (from Fu et al. 2020).

Within the Wolfcamp strata, carbonate horizons are made up of foraminiferal-phylloid algal mounds and associated debris beds. Because of their location on the shelf edge, the location and size of the mounds are impacted by sea-level fluctuations that dominate most of Pennsylvanian and Permian deposition. Foraminiferal-algal mounds build up during sea-level highstands, and during lowstands, these mounds are reworked and redeposited in debris fans surrounding the mounds and into the basin (Figure 95**)**. The positioning and size of the mounds is controlled by the accommodation space created during sea-level highstands. During lowstands, the mounds become exposed, undergoing both physical and chemical diagenesis and forming debris beds around the mounds.

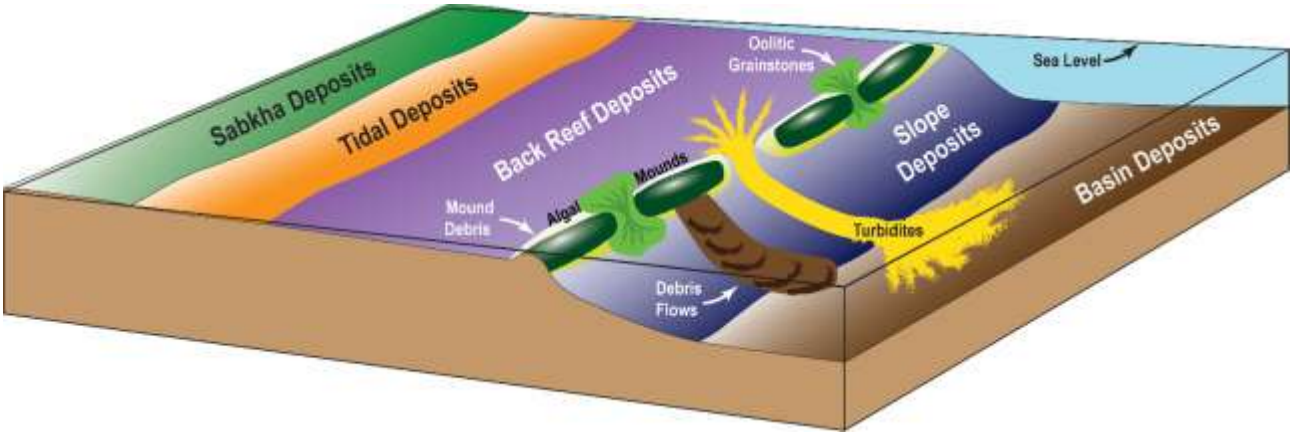


Figure 95. A depositional model for the Wolfcamp sediments in the Delaware Basin

Wolfcamp reservoirs have porosities average approximately 7 to 10% and occur mainly in the reef margin facies (Broadhead 2017). During the Ouachita Orogeny, faults and compression produced uplift in the east forming the CBP and folding resulting in the formation of the NW Shelf and the Delaware Basin. This deformation resulted in the erosion on the CBP of lower Paleozoic units (down to the Ordovician strata). Within the basin, Wolfcamp sediments were partially eroded on fault block and fold highs and redeposited in topographic lows. By the end of Wolfcamp sedimentation, most of the faulting had ceased, but down warping of the basins continued.

Leonardian/Cisuralian Rocks

Bone Spring Formation/Abo, and Yeso Group/Victorio Peak Formations

Leonardian strata consists of the Abo Formation and Yeso Group on the Central Basin Platform, the Victorio Peak Formation on the Northwest Shelf and the Bone Spring Formation within the Delaware Basin. Both the Abo, Yeso and Bone Springs formations are prolific producers with the Delaware basin area. The highstand deposits of the Abo and Yeso formations consist of dolomitized fringing barrier reef boundstones at the shelf break and dolomitized backreef deposits that grade into dolomitized and anhydrite-bearing tidal flat and supratidal deposits to red bed sabkha and fluvial/deltaic sandstone and shale deposits to the north (**Figure 96, Figure 97**). The lowstand deposits consist of eolian and fluvial deposits on the platform and turbidites going out into the basin and breaking up the Bone Spring carbonates. The main Abo reservoirs are in dolomitized reefal facies and have porosity ranging from 5 to 15% (Broadhead 2017). The fine-grained backreef deposits act as both lateral and vertical seals, produced by changing sea levels and migration of the facies across the shelf.

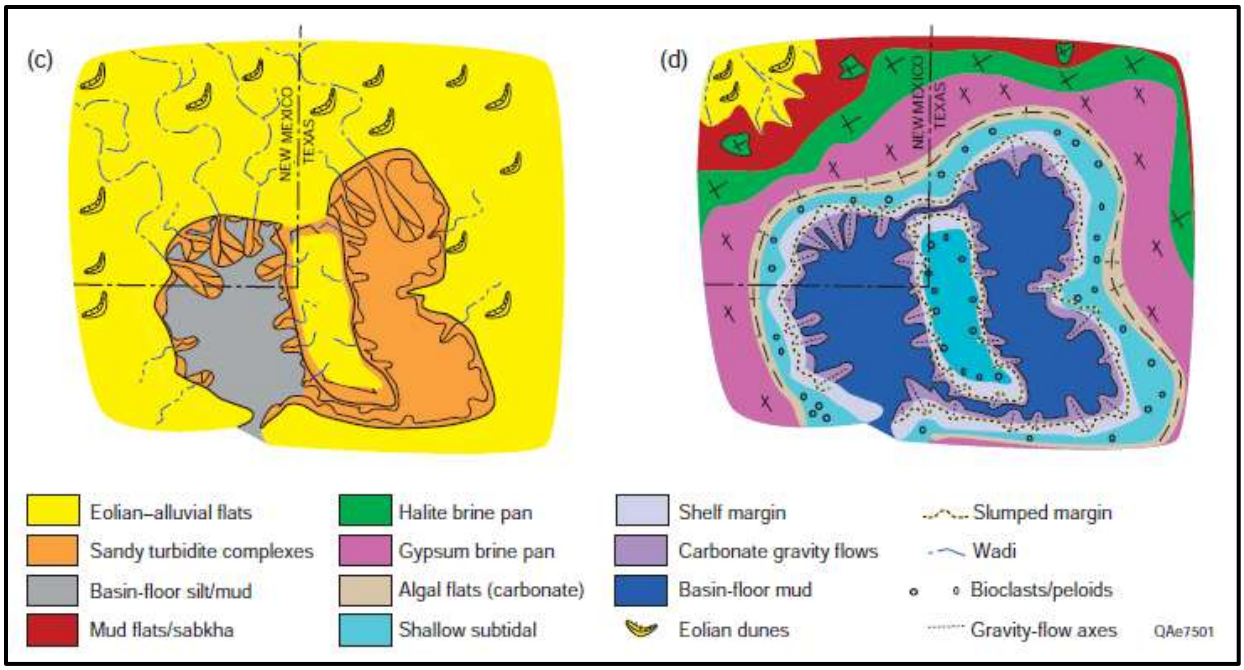


Figure 96. Detailed Leonardian paleodepositional environment for the Permian Basin during sea-level lowstands (c) and highstands (d) from Nance and Hamlin (2020).

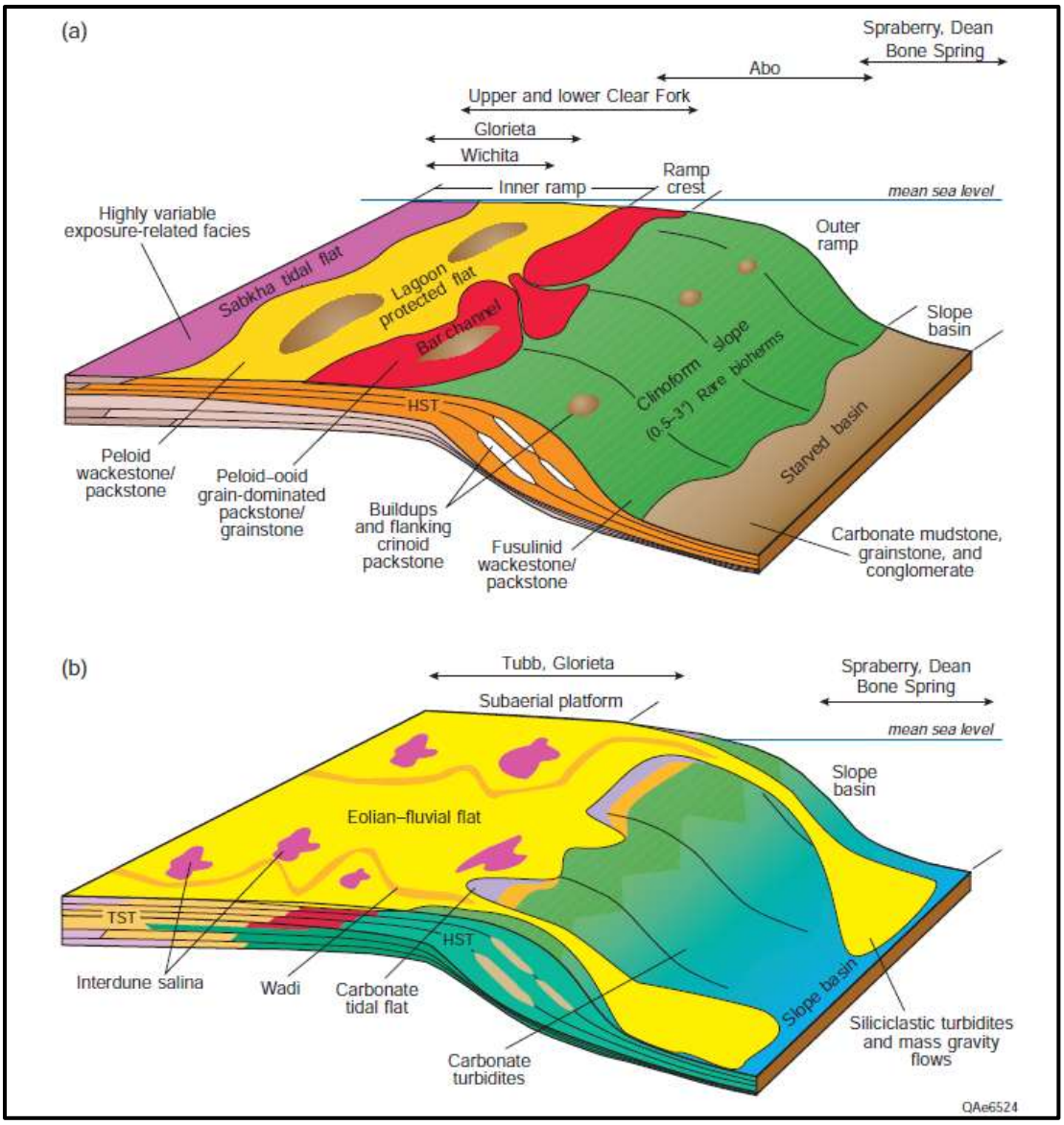


Figure 97. Depositional environments for sea-level highstand (a) and lowstand (b) times from Nance and Hamlin (2020).

The Bone Spring Formation is the basin equivalent to the Abo and overlying Yeso formations. Bone Spring sediments are characterized by >3,000 ft of basin-deposited carbonate and siliciclastic sediments. The Bone Spring Formation is more carbonate rich than the Delaware Mountain Group and consists of rockfalls, debris flows, and submarine fans deposited during sea-level highstand periods and widespread carbonate deposition. Sandstone turbidites and submarine fan complexes move sandstones out into the basin during sea-level lowstands, when the carbonate factory has been shut down up on the shelf and siliciclastic sands move across the shelf.

The Bone Spring Formation contains both conventional and unconventional fields within the Delaware Basin in both the sandstone-rich and carbonate-rich facies. Most of these plays usually occur within toe-of-slope carbonate and siliciclastic deposits or the turbidite facies in the deeper

sections of the basin (Nance and Hamlin 2020). The upper most Bone Spring is usually dense carbonate mudstone with limited porosity and low porosity. Carbonate debris derived from the shelf Bone Spring reservoirs are dominated by turbidite sandstones with porosities averaging between 7 and 20% (Broadhead 2017).

Guadalupian Rocks

Delaware Mountain Group/San Andres and Grayburg Formations

Like the Leonardian section, sea-level fluctuations and tectonics played a major role on the depositional environments on the shelf, slope and basin deposits. On the shelves, the highstand deposits range from seaward to shoreward: fringing reefs on the edge of the platform, to subtidal carbonate deposits, to barrier island facies, to lagoonal dolomites and evaporites to sabkha sand, dolomites and evaporites (**Figure 98** to **Figure 101**). During sea-level lowstand deposition, the shelves are dominated by clastic deposition: eolian, fluvial and sabkha sands and evaporites. These high frequency sea-level cycles on the shelves resulted in thick carbonate cycles during periods when the carbonate factory was active (highstands) separated by exposure surfaces with thin to very thin sandstones (lowstands).

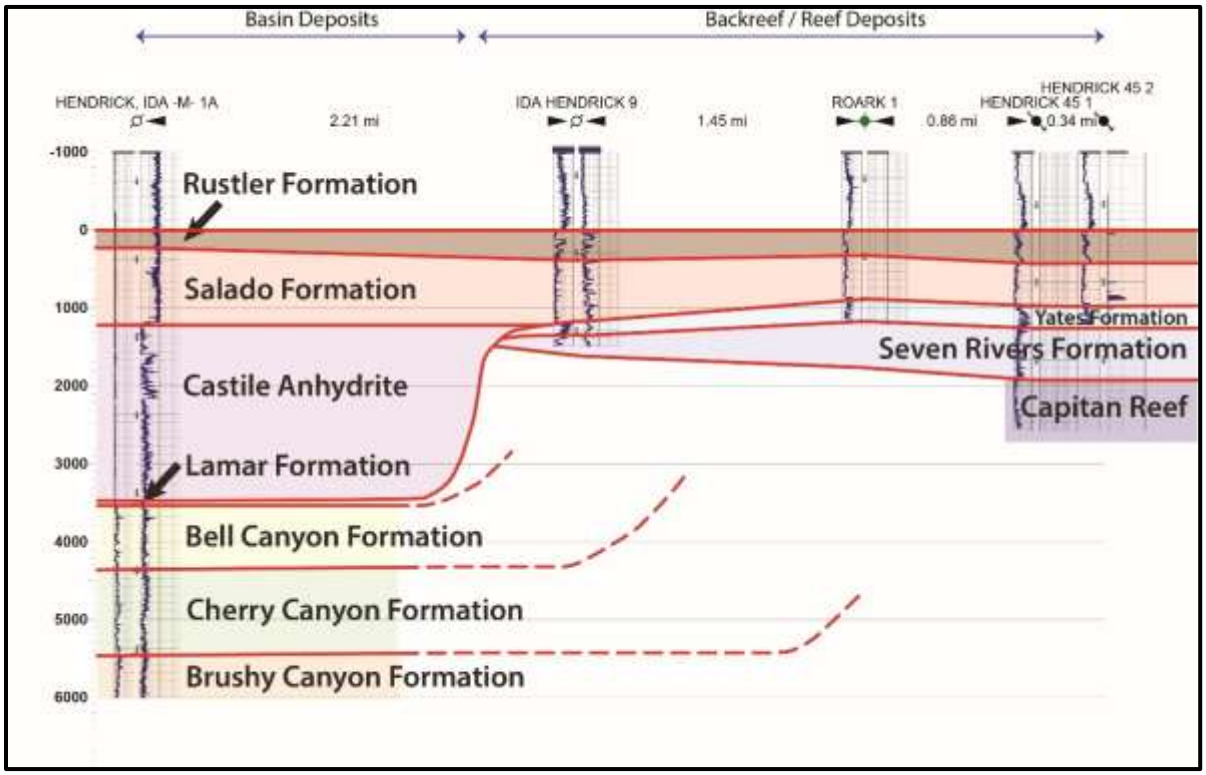


Figure 98. Relationship between the backreef, basin and later basin fill during Guadalupian deposition.

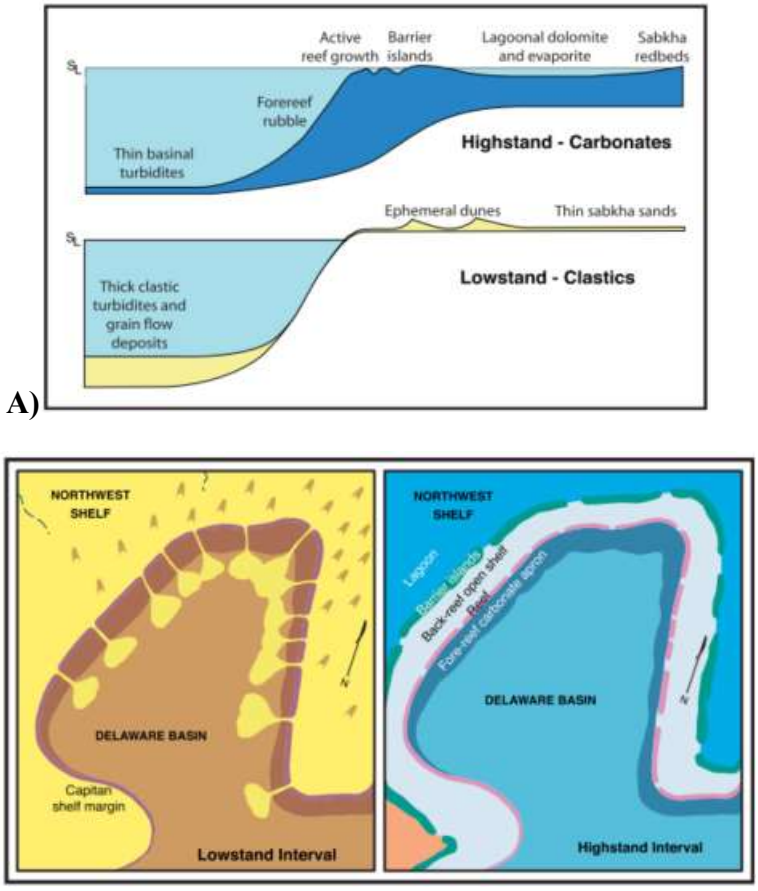


Figure 99. The impact of sea-level fluctuations (also known as reciprocal sedimentation) on the depositional systems within the Delaware Basin. A) A diagrammatic representation of sea-level variations impact on deposition. B) Model showing basin-wide depositional patterns during lowstand and highstand periods (from Scholle et al. 2007).

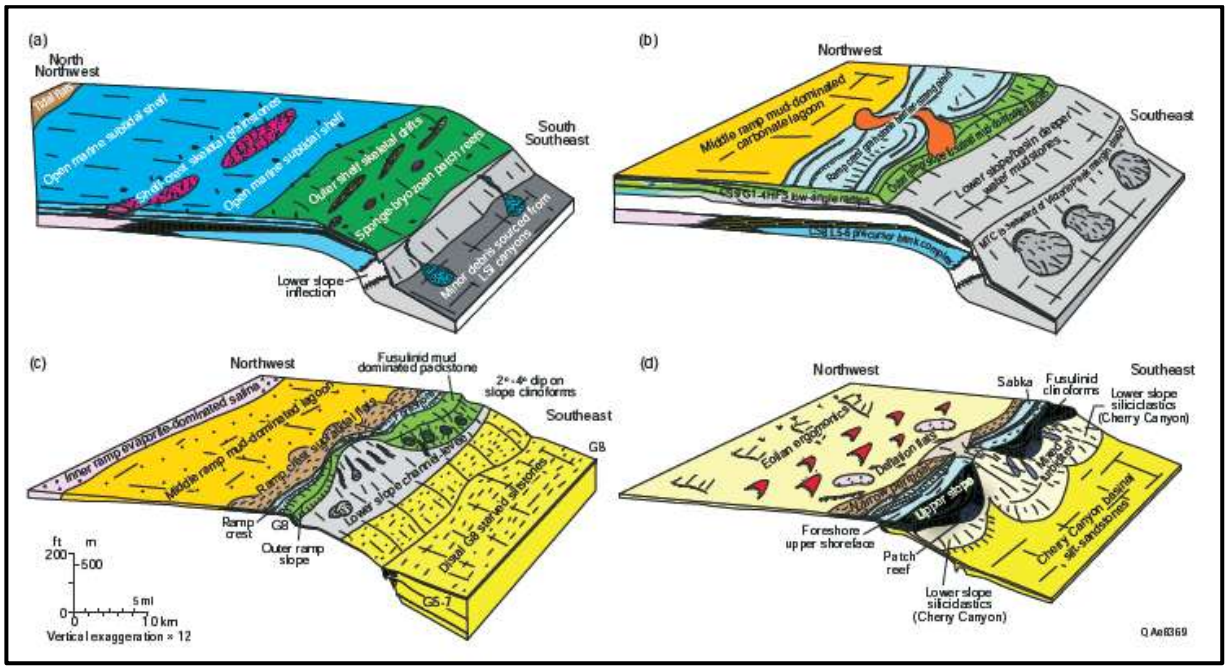


Figure 100. Depositional systems within lower Guadalupian San Andres tracts. A. sea-level highstand environments. B. Lower San Andres deposits, C. Middle San Andres deposits, and D. Upper San Andres deposits (from Kerans and Ruppel [2020]).

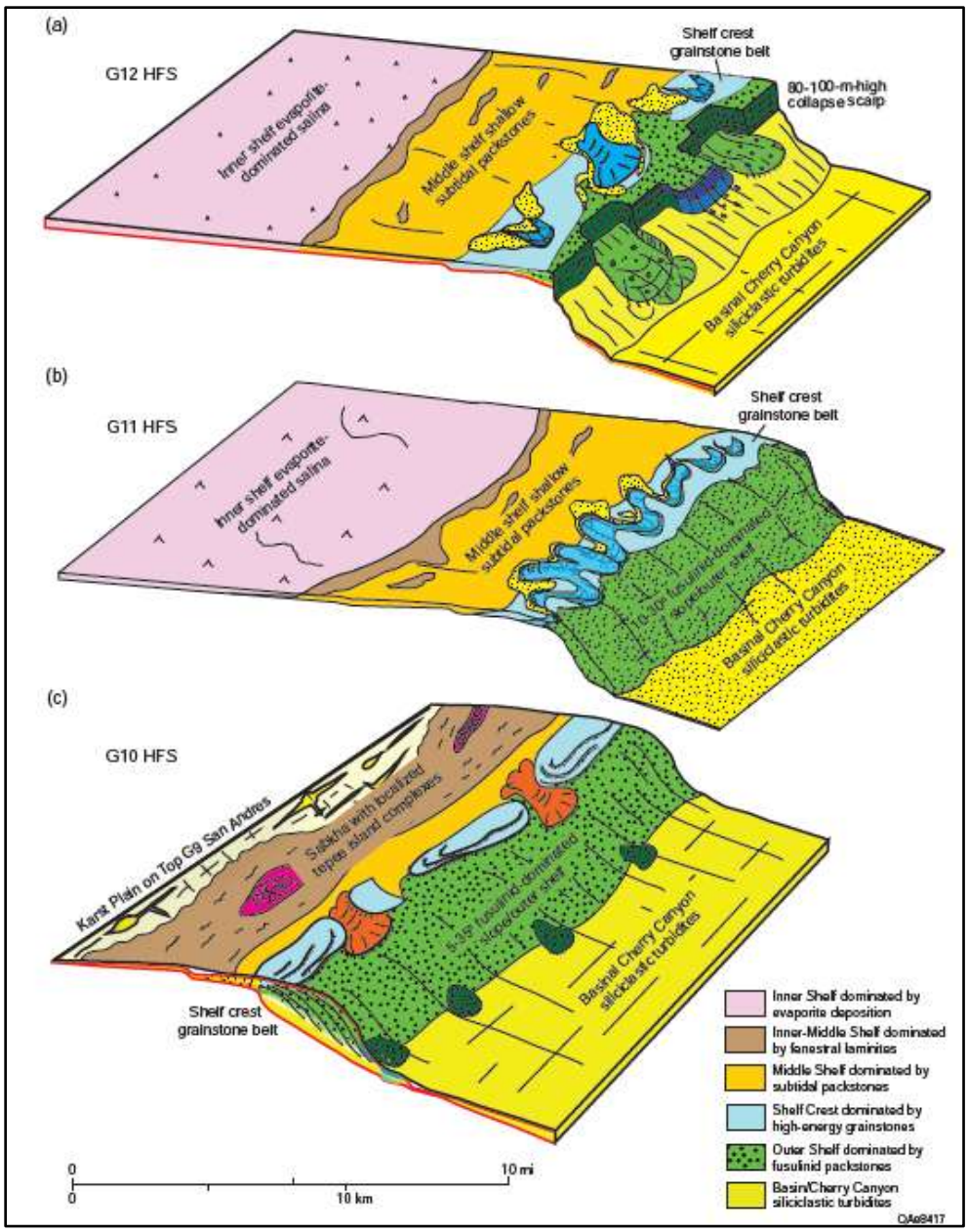


Figure 101. Upper Guadalupian Grayburg formation depositional environments. From Kerans and Ruppel (2020).

Sediments of the Delaware Mountain Group (descending, Bell Canyon, Cherry Canyon, and Brushy Canyon formations) are marine units that represent deposition within the Delaware Basin. Despite being within a basin that continuously had water in it, sea level fluctuations and tectonism had as much of an impact on these deposits as it did on the shelves. Lowstand deposits in the basin are associated with submarine canyons that incise the carbonate platform that surrounds most of the Delaware Basin. Low stand depositional environments include submarine fan complexes that encircle the Delaware Basin margin. These submarine canyons that incised the carbonate platform margin produced complexes of submarine fans consisting of turbidite channels, splays, and levee/overbank deposits (**Figure 102**).

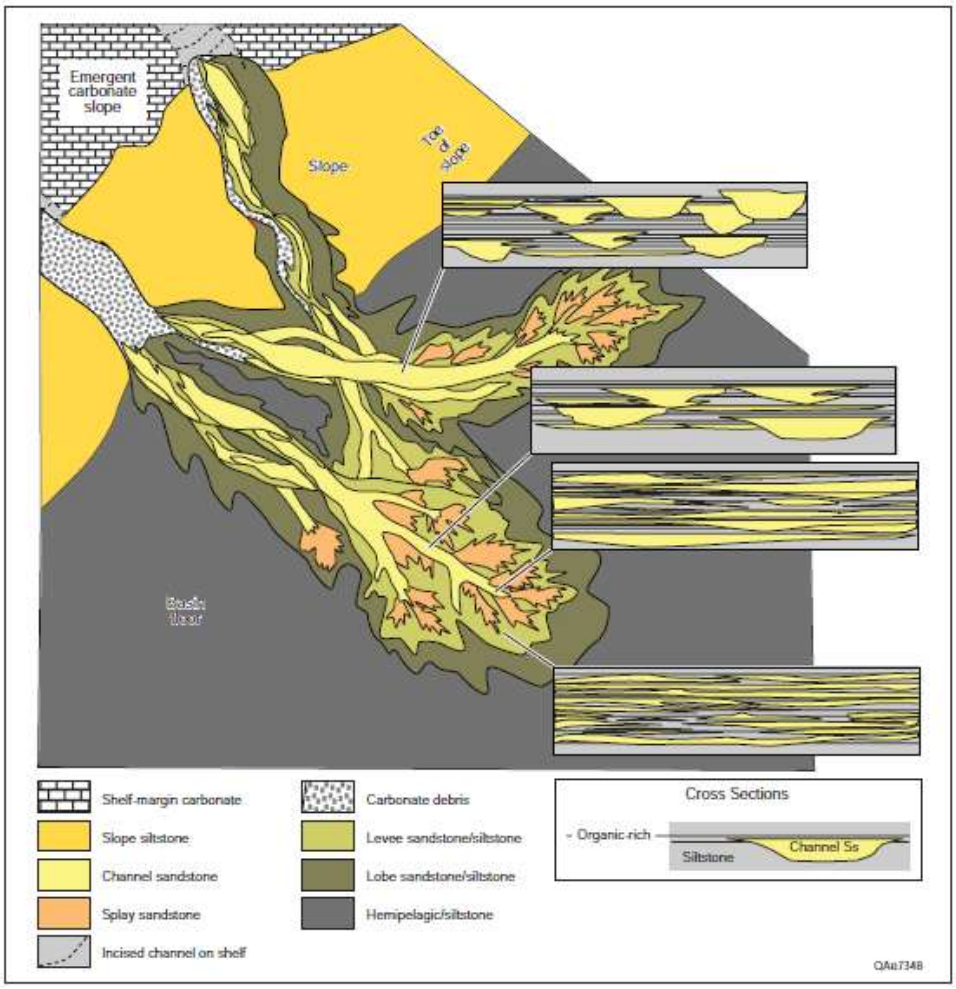


Figure 102. A diagram of typical Delaware Mountain Group basinal siliciclastic deposition patterns (from Nance [2020]). The channel and splay sandstones have the best porosity, but some of the siltstones also have potential as injection zones.

Additionally, debris flows and density currents formed units that went far out into the basin. These isolated coarse-grained to boulder-sized carbonate debris flows and grain falls within the lowstand clastic sediments likely resulted from erosion and failure of the carbonate shelf margin during sea-level lowstands or slope failure due to tectonic activity (earthquakes).

Density current deposits resulted from stratified basin waters. The basal waters were likely stratified and so dense, that turbidity flows containing sands, silts and clays were unable to displace those bottom waters and instead flowed out over the density interface (**Figure 103**). Eventually, the entrained sediments would settle out in a constant rain of sediment forming laminated deposits with little evidence of traction (bottom flowing) deposition.

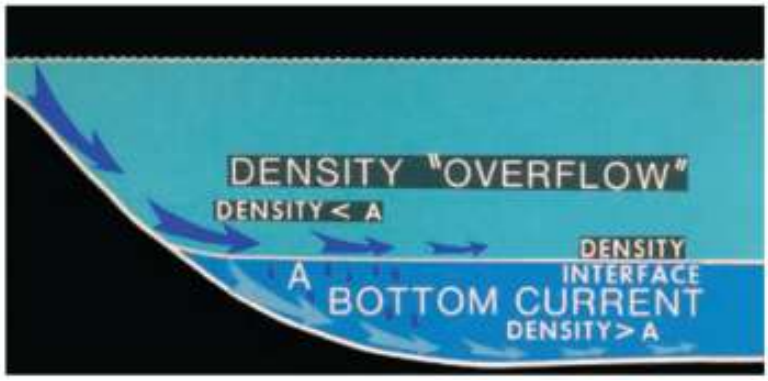


Figure 103. Harms (1974) density overflow model explains the deposition of laminated siliciclastic sediments in the Delaware Basin. Low density sand-bearing fluids flow over the top of dense, saline brines at the bottom of the basin. The sands gradually drop out as the flow loses velocity creating uniform, finely laminated deposits (from Scholle et al. [2007]).

Unlike the shelves, the basin deposits contain very thick, siliciclastic lowstand sequences that are interbedded with thin, highstand deep-water limestones and mudstones. These deposits are thickest around the edge (toe-of-slope) of the basin and thin to the basin center (Figure 99). The limestones are dark, finely crystalline, radiolarian-rich micrites to biomicrites. These highstand deposits are a combination of suspension and pelagic sediments that also thin towards the basin center. These relatively thin units are time equivalent to the massive highstand carbonate deposits on the shelf.

The top of the Guadalupian Series is the Lamar Limestone, which is the source of hydrocarbons found in underlying Delaware Sand (an upper member of the Bell Canyon Formation). The Bell Canyon Formation is roughly 1,000 ft thick in the Red Hills area and contains numerous turbidite input points around the basin margin (**Figure 104**). During Bell Canyon deposition, the relative importance of discrete sand sources varied (Giesen and Scholle 1990), creating network of channel and levee deposits that also varied in their size and position within the basin. Based on well log analyses, the Bell Canyon 2 and 3 had the thickest sand deposits.

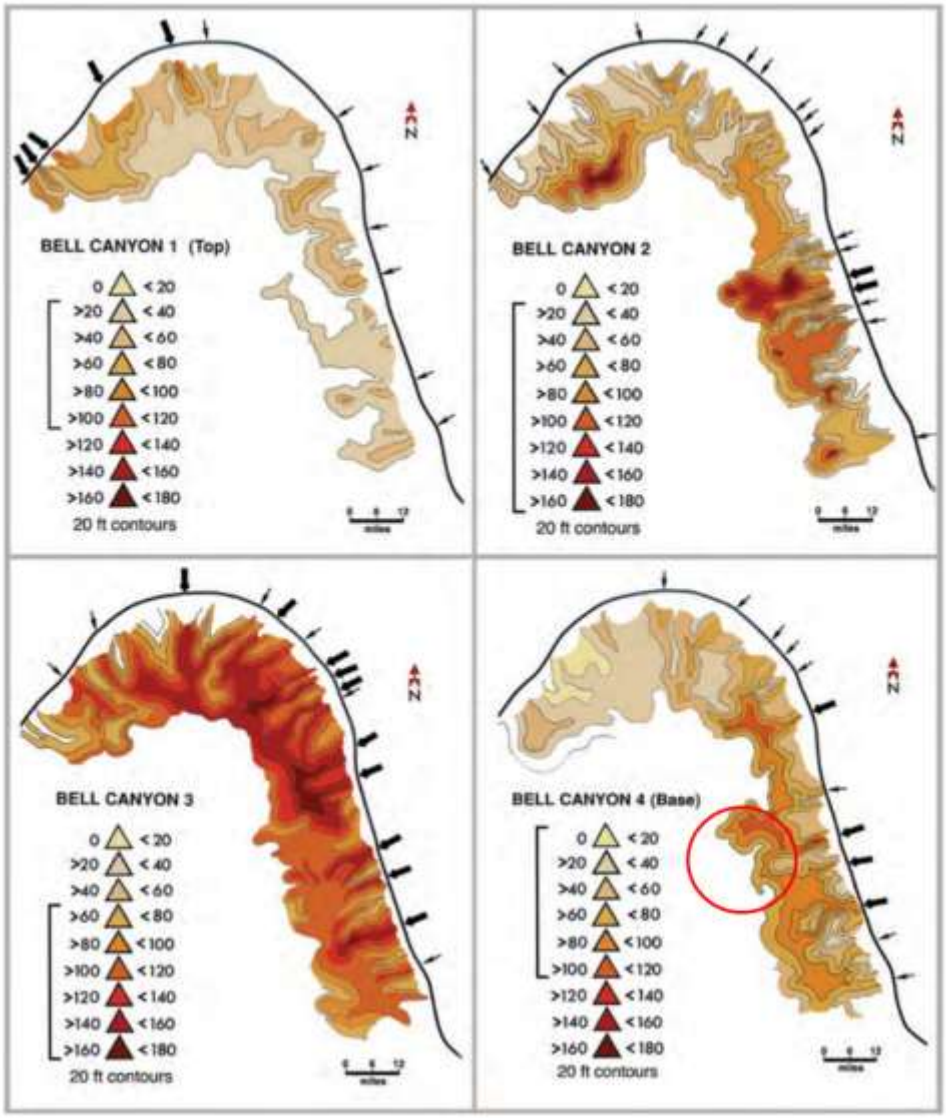


Figure 104. These maps of Bell Canyon Formation were created by measuring sandstone thicknesses on well logs in four regionally correlatable intervals (from Giesen and Scholle [1990]). The red circle on the last map surrounds the Red Hills area.

Like the Bell Canyon and Brushy Canyon formations, the Cherry Canyon Formation is approximately 1,300 ft thick and contains numerous turbidite source points. Unlike the Bell Canyon and Brushy Canyon deposits, the channel deposits are not as large (Giesen and Scholle 1990), and the source of the sands appears to be dominantly from the eastern margin (**Figure 105**). Cherry Canyon 1 and 5 have the best channel development and the thickest sands. Overall, the Cherry Canyon Formation, on outcrop, is less influenced by traction current deposition than the rest of the Delaware Mountain Group deposits and is more influenced by sedimentation by density overflow currents (Figure 103). The Brushy Canyon has notably more discrete channel deposits and coarser sands than the Cherry Canyon and Bell Canyon. The Brushy Canyon Formation is approximately 1,500 ft thick.

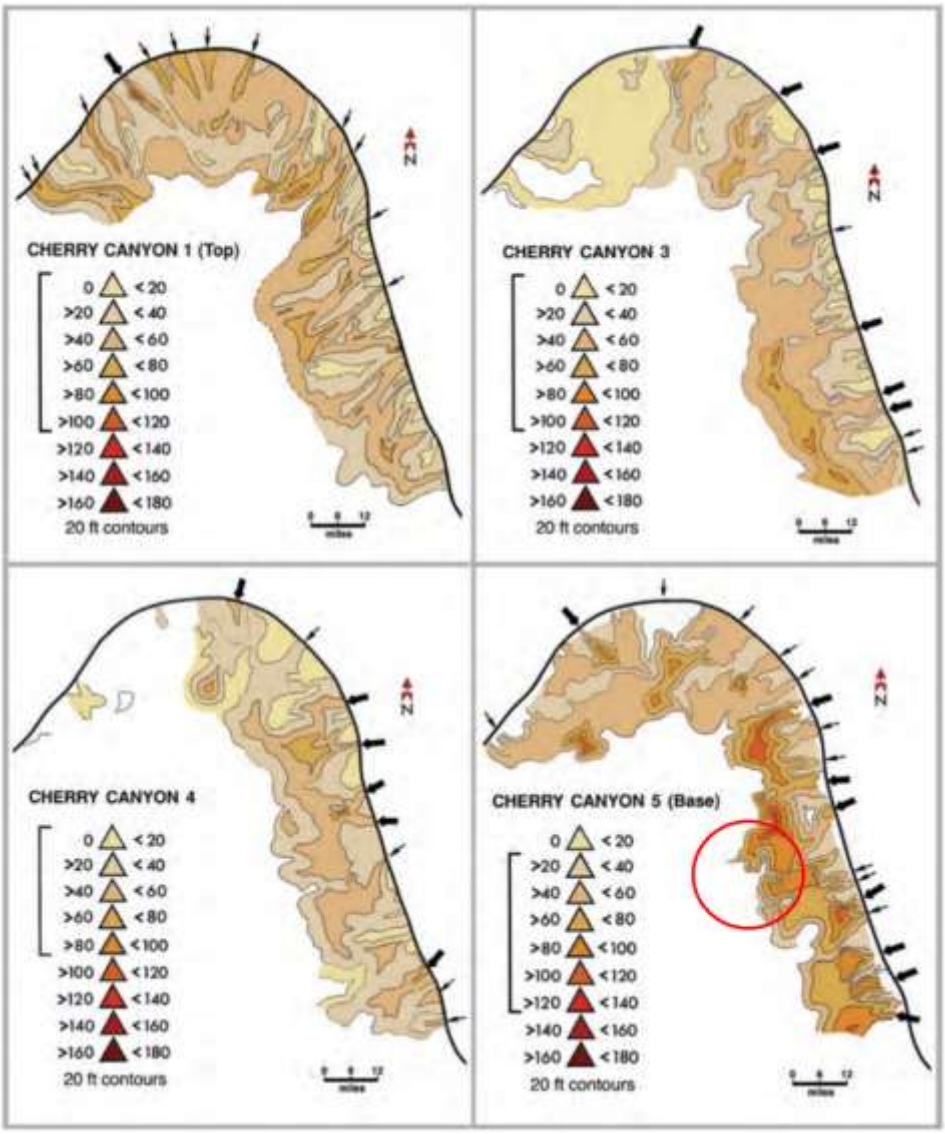


Figure 105. These maps of Cherry Canyon Formation were created by measuring sandstone thicknesses on well logs in five regionally correlatable intervals (from Giesen and Scholle [1990]). Unlike the Bell Canyon sandstones, the Cherry Canyon sands are thinner and contain fewer channels. The red circle on the last map surrounds the Red Hills area.

Within the Delaware Mountain Group, the Bell Canyon and Cherry Canyon have the best porosity (averaging 15–25% within channel/splay sandstones) and permeability (averaging 2–13 mD) than the Brushy Canyon (approximately 14% porosity, an <3 mD; Ge et al. 2022; Smye et al. 2021).

Ochoan Rocks

Castile, Salado, and Rustler Formations

The youngest of the Permian sediments, the Ochoan- or Lopingian-aged deposits, consists of evaporites, carbonates, and red beds. The Castile Formation is made of cyclic laminae of deep-water gypsum/anhydrite beds interlaminated with calcite and organics. This basin-occurring unit

can be up to 1,800 ft thick. The Castile evaporites were followed by the Salado Formation (approximately 1,500 ft thick). The Salado Formation is a shallow water evaporite deposit, when compared to the Castile Formation, and consists of halite, sylvite, anhydrite, gypsum, and numerous potash/bittern minerals. Salado deposits fill the basin and lap onto the older Permian shelf deposits. The Rustler Formation (up to 500 ft; Nance 2020) consists of gypsum/anhydrite, a few magnesitic and dolomitic limestone horizons, and red beds. These are mostly shallow marginal marine deposits and represents the last Permian marine deposits in the Delaware Basin. The Ochoan evaporitic units are superb seals (usually <1% porosity and <0.01 mD permeability) and are the reason that the Permian Basin is such a hydrocarbon-rich region despite its less than promising total organic carbon (TOC) content.

Geologic Model

The model developed for the Delaware Basin area includes over 2,280 wells (**Figure 106**). The tops for each well were handpicked for all the formations present in the logs (**Figure 107, Figure 108**). A database was built in S&P Kingdom that includes well header information, formation tops, bottom hole temperatures, and calculated geothermal gradients.

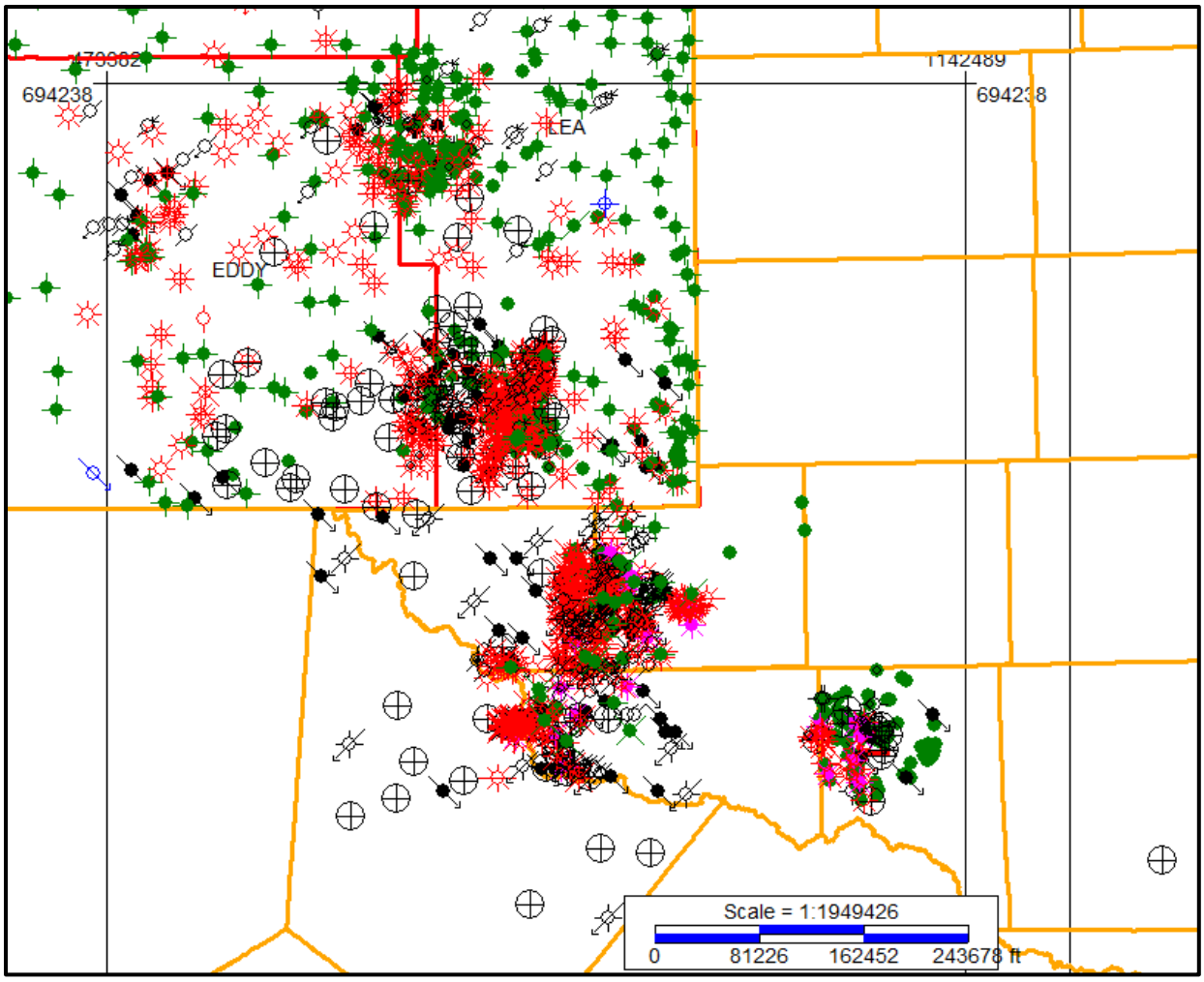


Figure 106. Base map of the Delaware Basin with the wells that have been used to develop the database. The green symbols are P&A or Active oil wells. The red symbols are P&A or active gas wells, and the Black and blue symbols are injection or SWD wells.

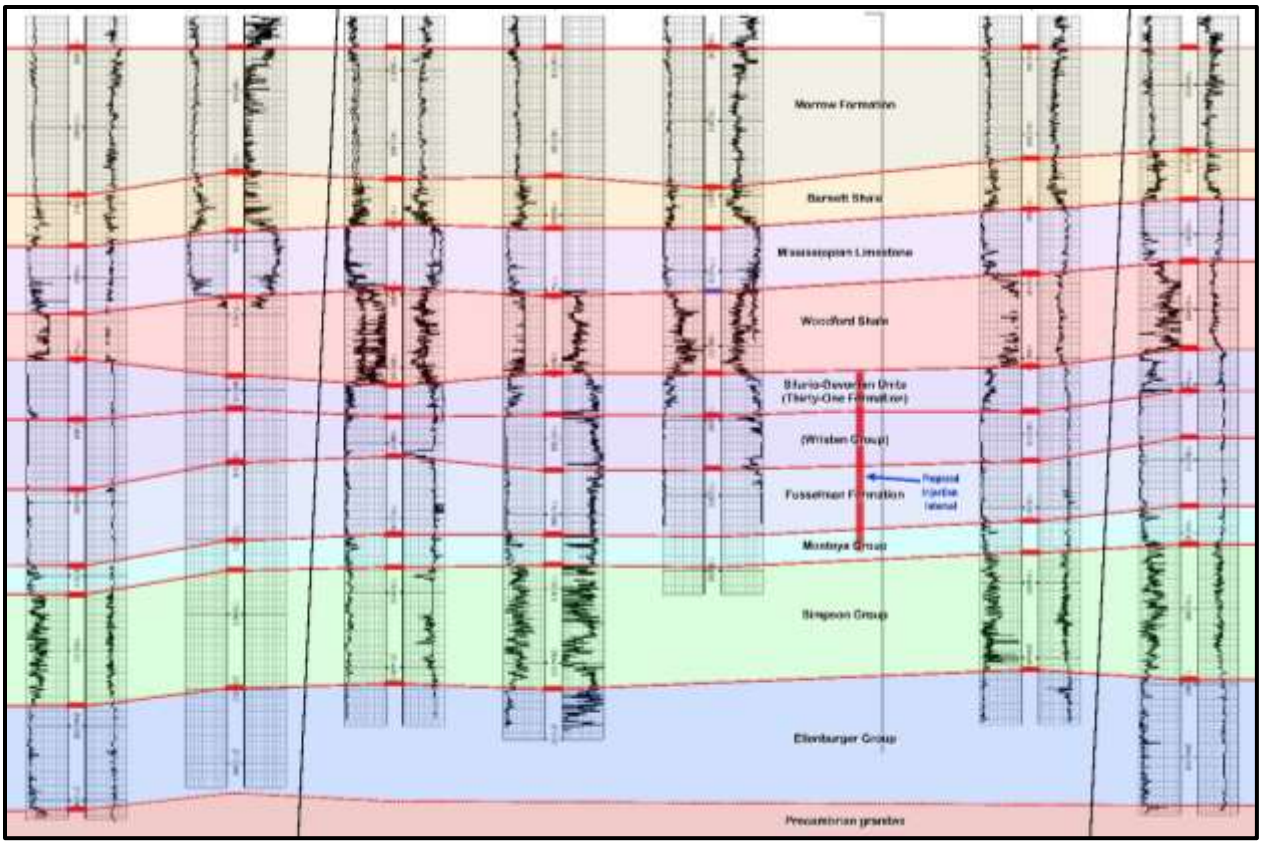


Figure 107. A typical cross section through the lower Paleozoic sediments within the basin from the Precambrian to Morrow formations.

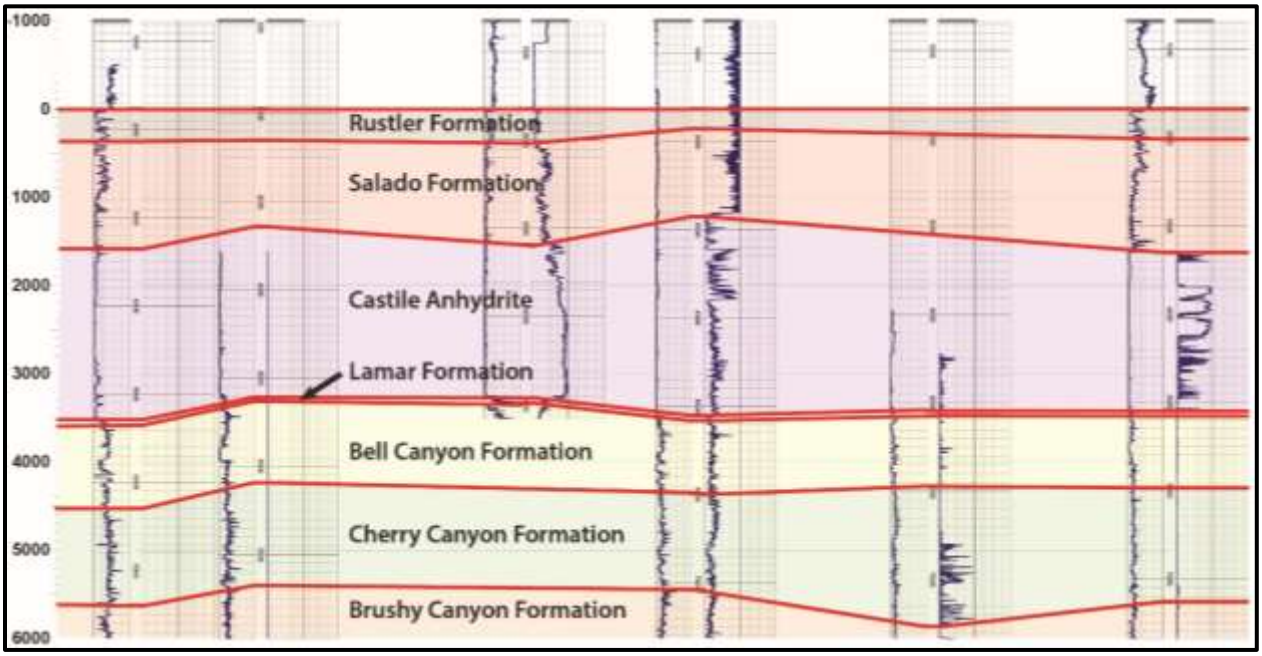


Figure 108. A typical cross section through the Guadalupian basin sediments from the Bone Spring to Rustler formations.

The following maps (**Figure 109** to **Figure 143**) are subsea structure maps for all the formation tops starting at the Precambrian and to the Permian Rustler Formation. North is at the top of the map. The first set of maps (Figure 109 to Figure 140) do not include the fault interpretations and have a contour interval of 250 ft; whereas the second set of subsea structure maps include the faults interpretated by Horne et al. (2021) and have a contour interval of 250 ft (Figure 131 to Figure 143). The fault surfaces are from Precambrian to the Strawn horizons. After that time, the majority of the basin forming faulting ended.

Surfaces Without Faults

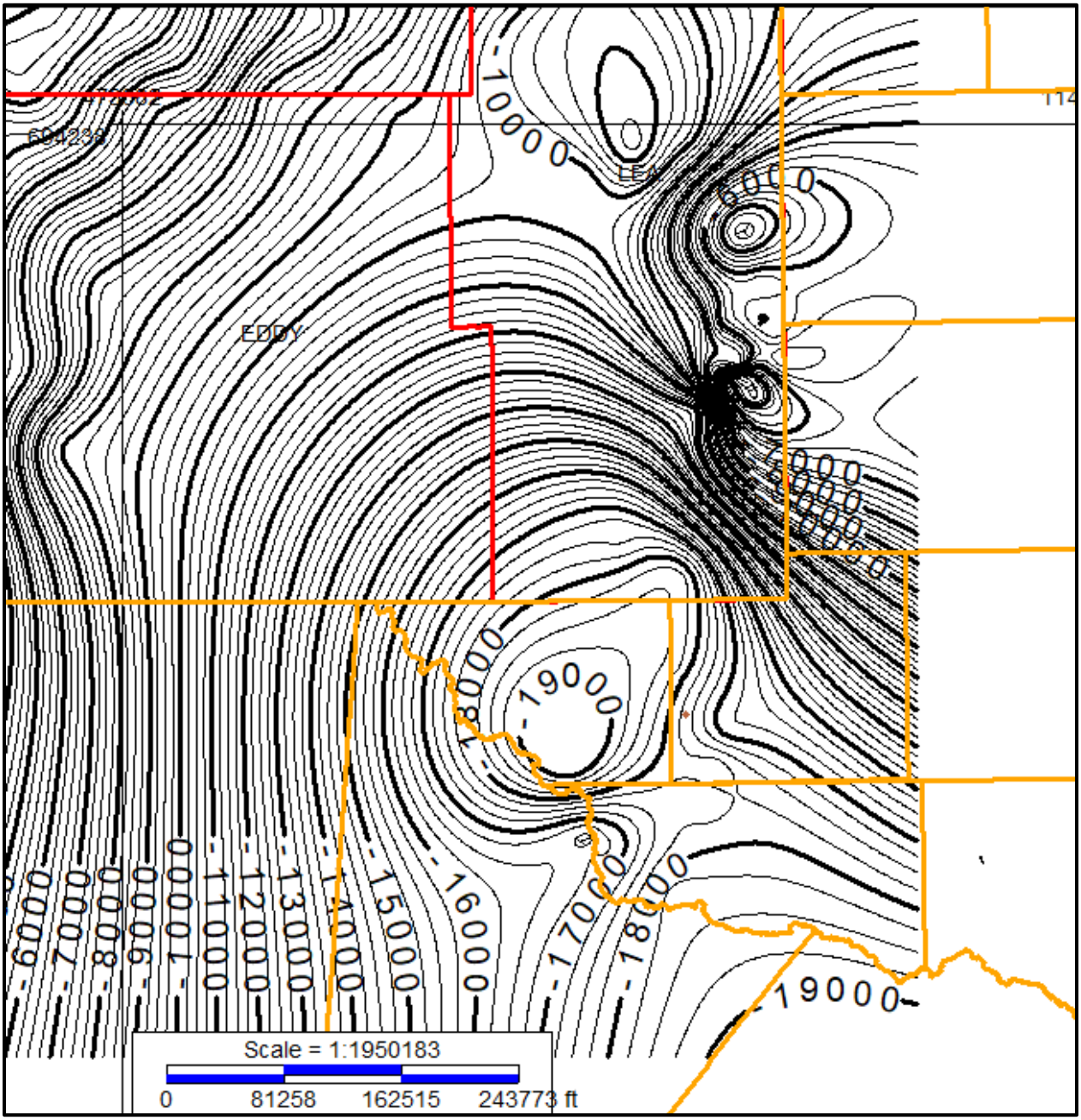


Figure 109. The Precambrian Subsea contour map within the Delaware basin in Southeastern New Mexico (red outlined counties) and west Texas (gold counties).

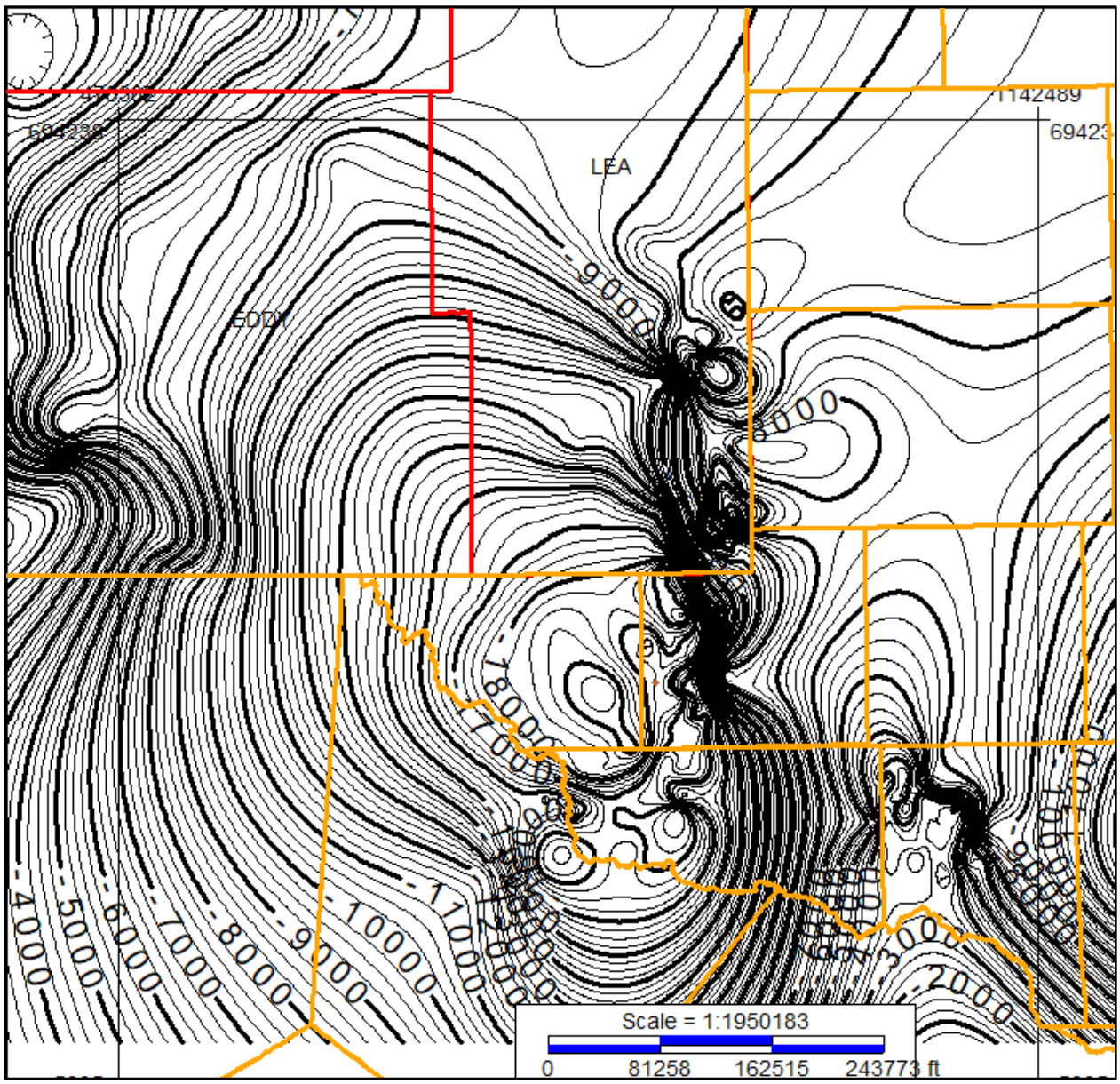


Figure 110. The Ellenburger Formation Subsea contour map within the Delaware basin in Southeastern New Mexico (red outlined counties) and west Texas (gold counties).

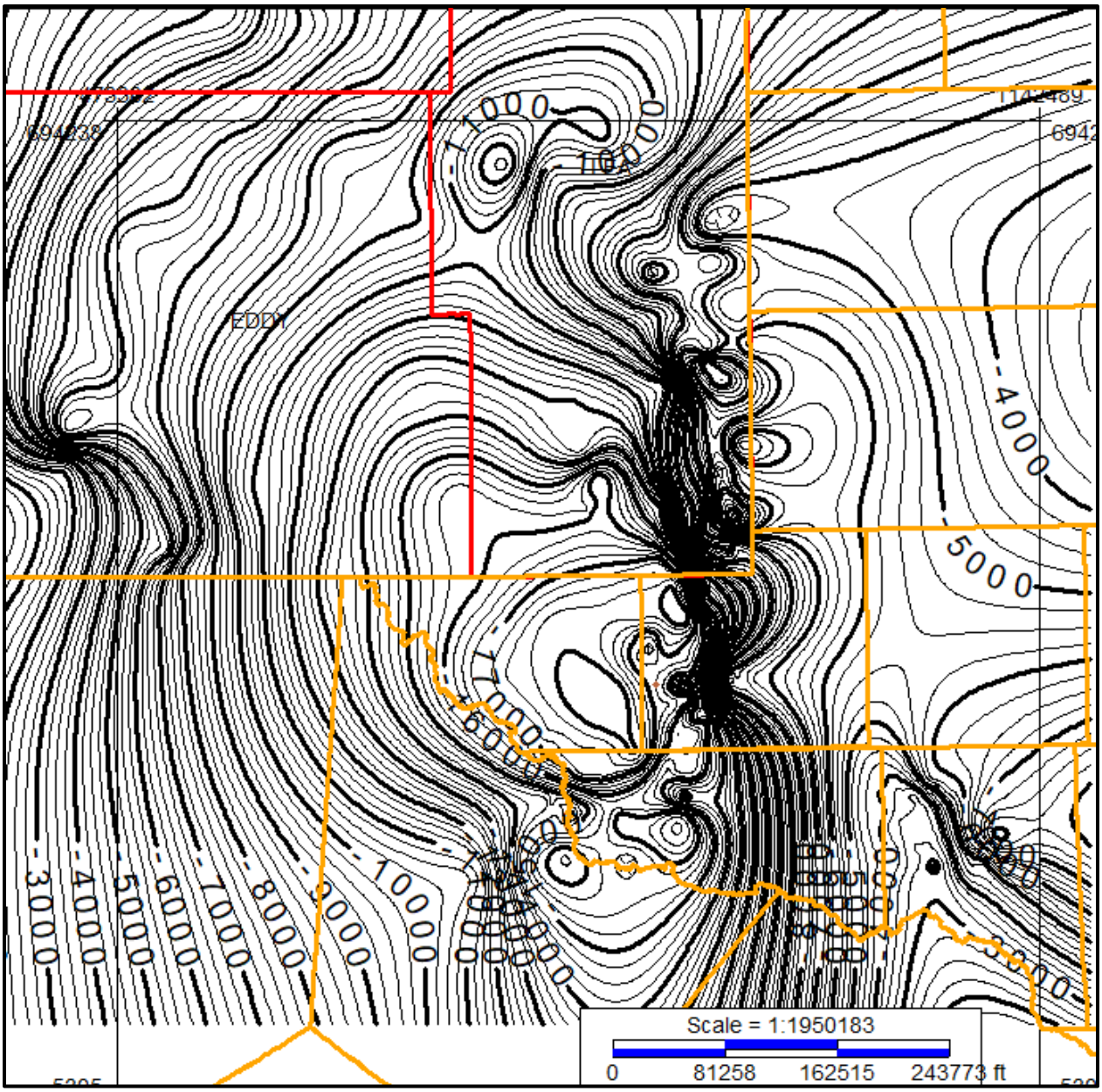


Figure 111. The Simpson Group Subsea contour map within the Delaware basin in Southeastern New Mexico (red outlined counties) and west Texas (gold counties).

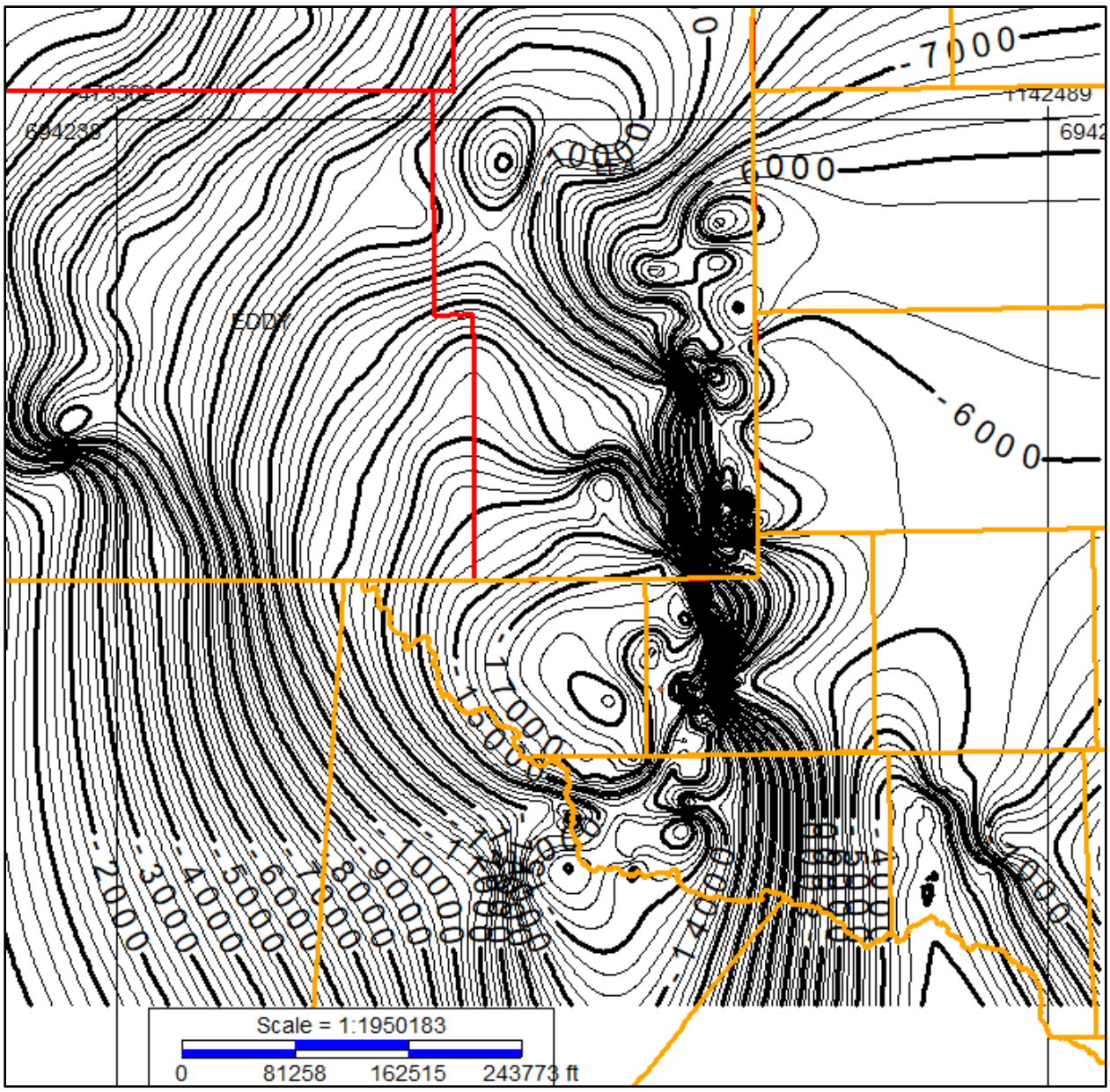


Figure 112. The Montoya Formation Subsea contour map within the Delaware basin in Southeastern New Mexico (red outlined counties) and west Texas (gold counties).

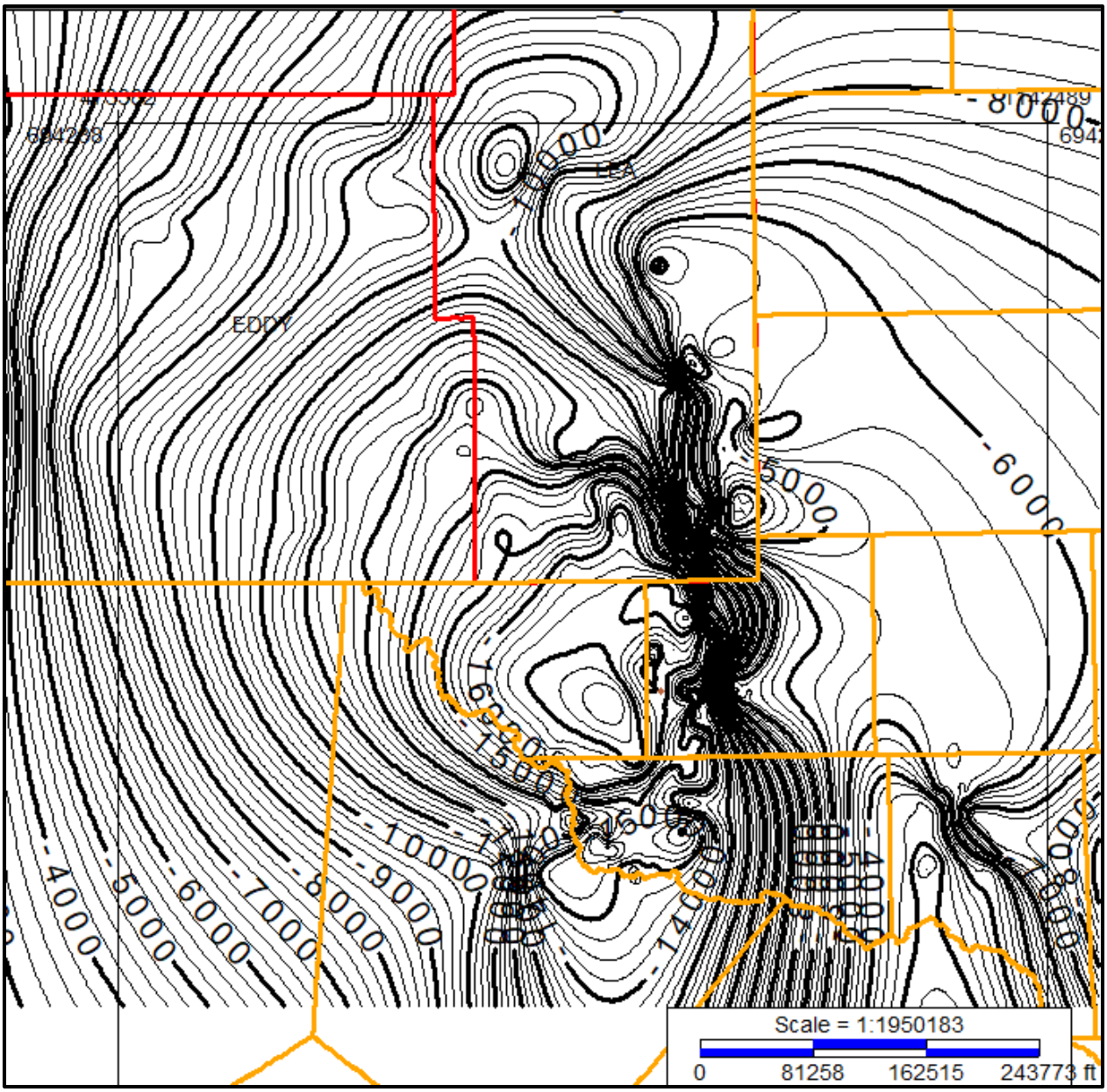


Figure 113. The Fusselman Formation Subsea contour map within the Delaware basin in Southeastern New Mexico (red outlined counties) and west Texas (gold counties).

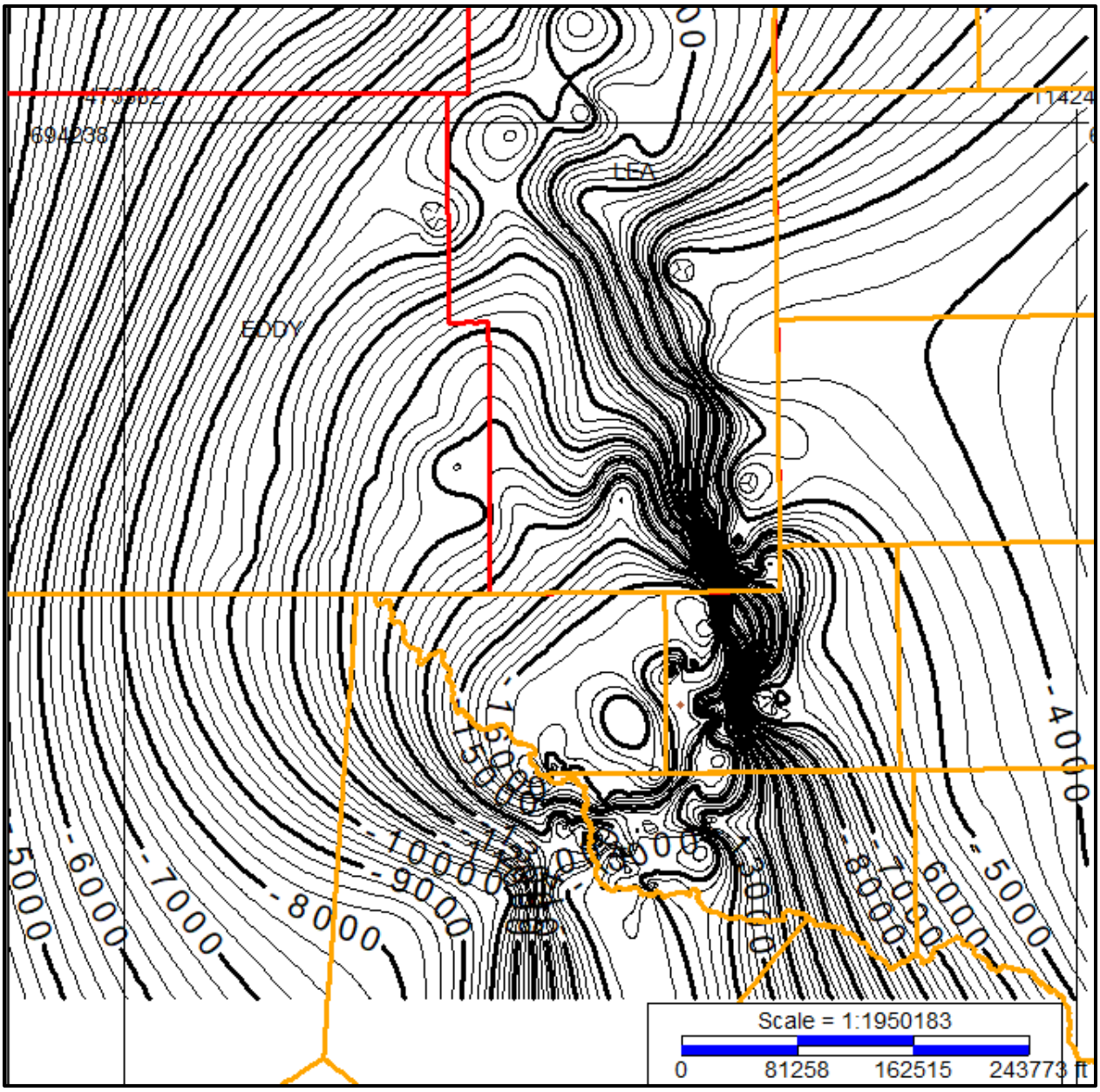


Figure 114. The Wristen Group Subsea contour map within the Delaware basin in Southeastern New Mexico (red outlined counties) and west Texas (gold counties).

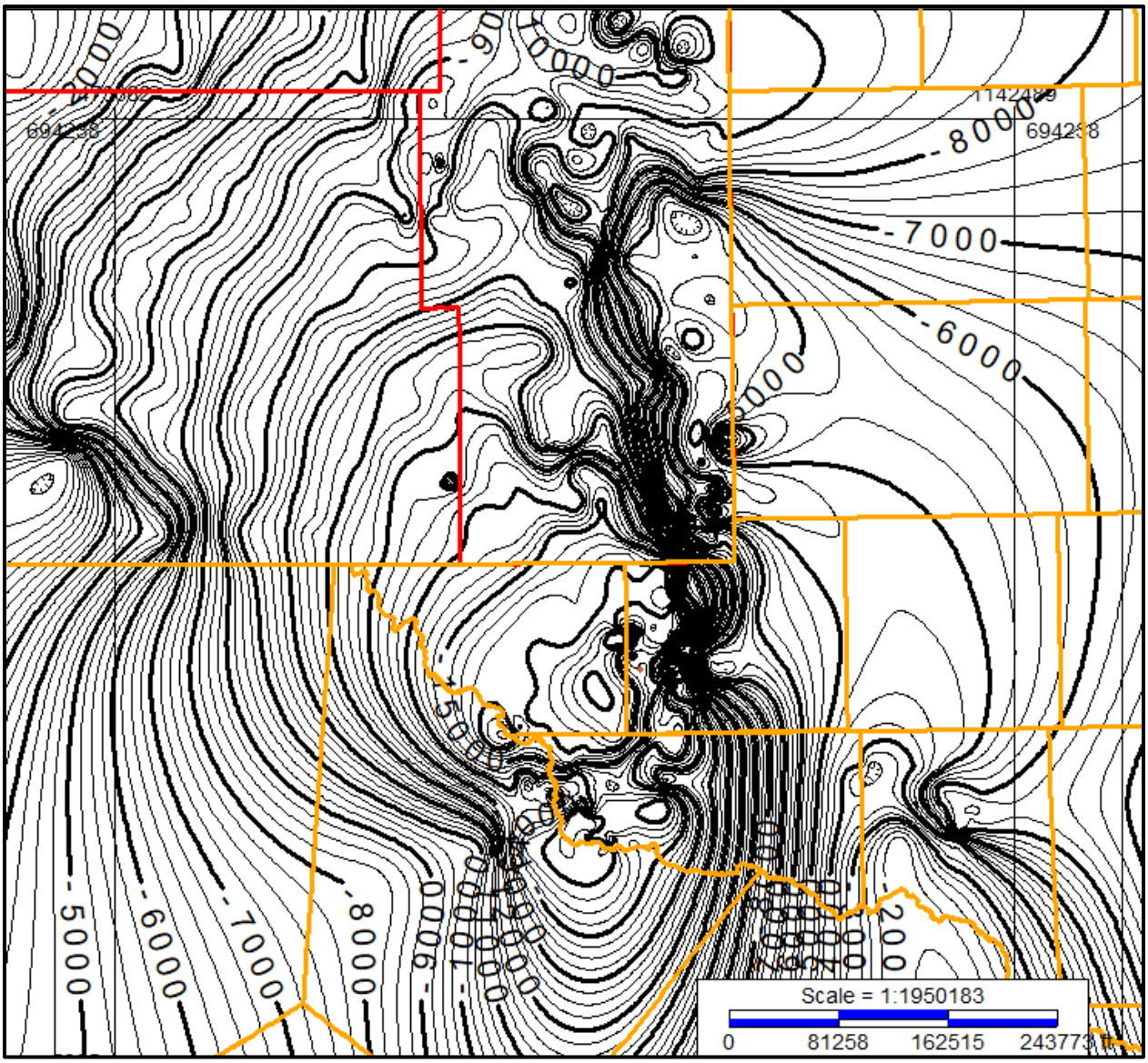


Figure 115. The top of the Siluro-Devonian strata (Thirtyone Formation) Subsea contour map within the Delaware basin in Southeastern New Mexico (red outlined counties) and west Texas (gold counties).

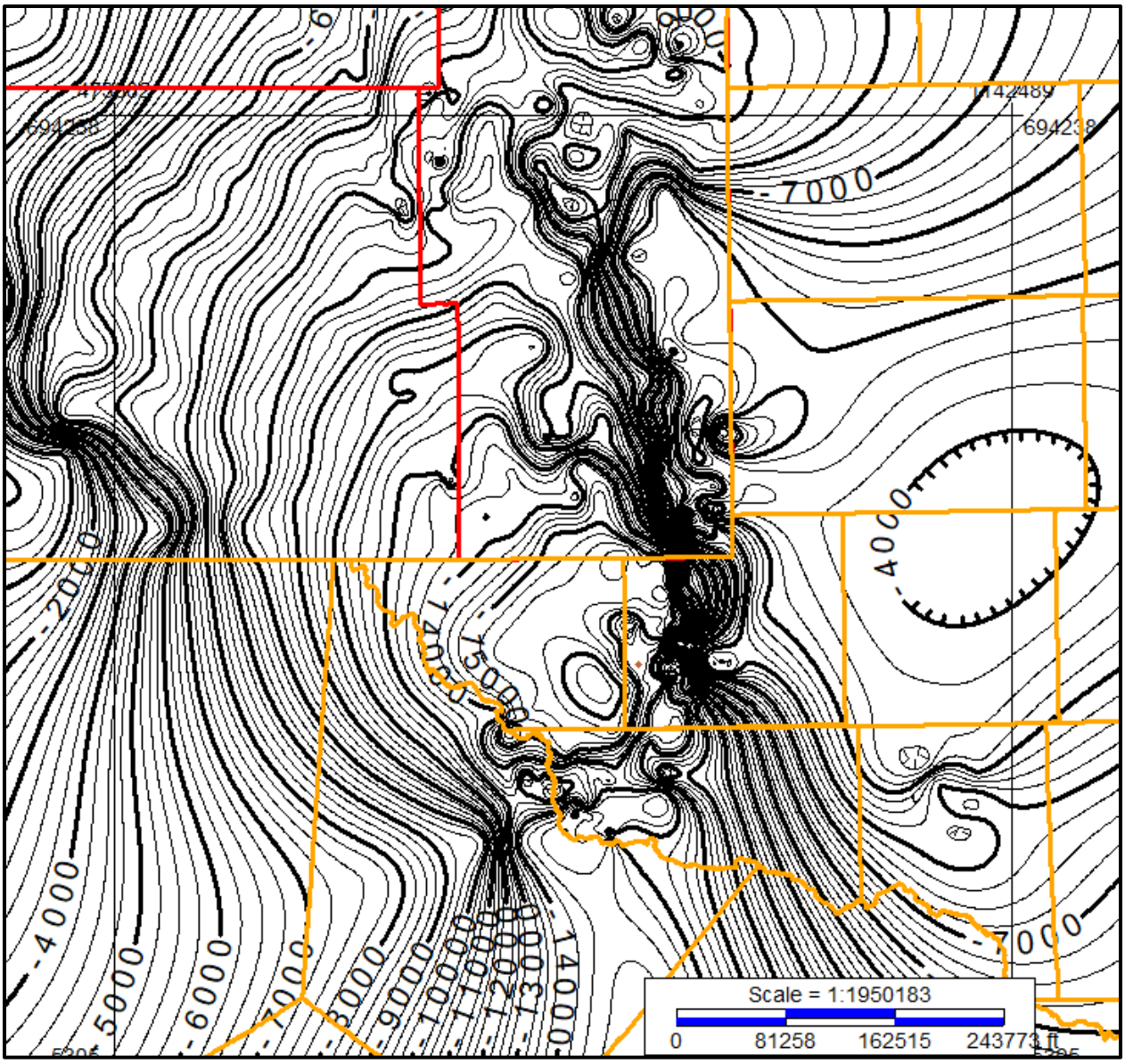


Figure 116. The top of the Woodford Shale Subsea contour map within the Delaware basin in Southeastern New Mexico (red outlined counties) and west Texas (gold counties).

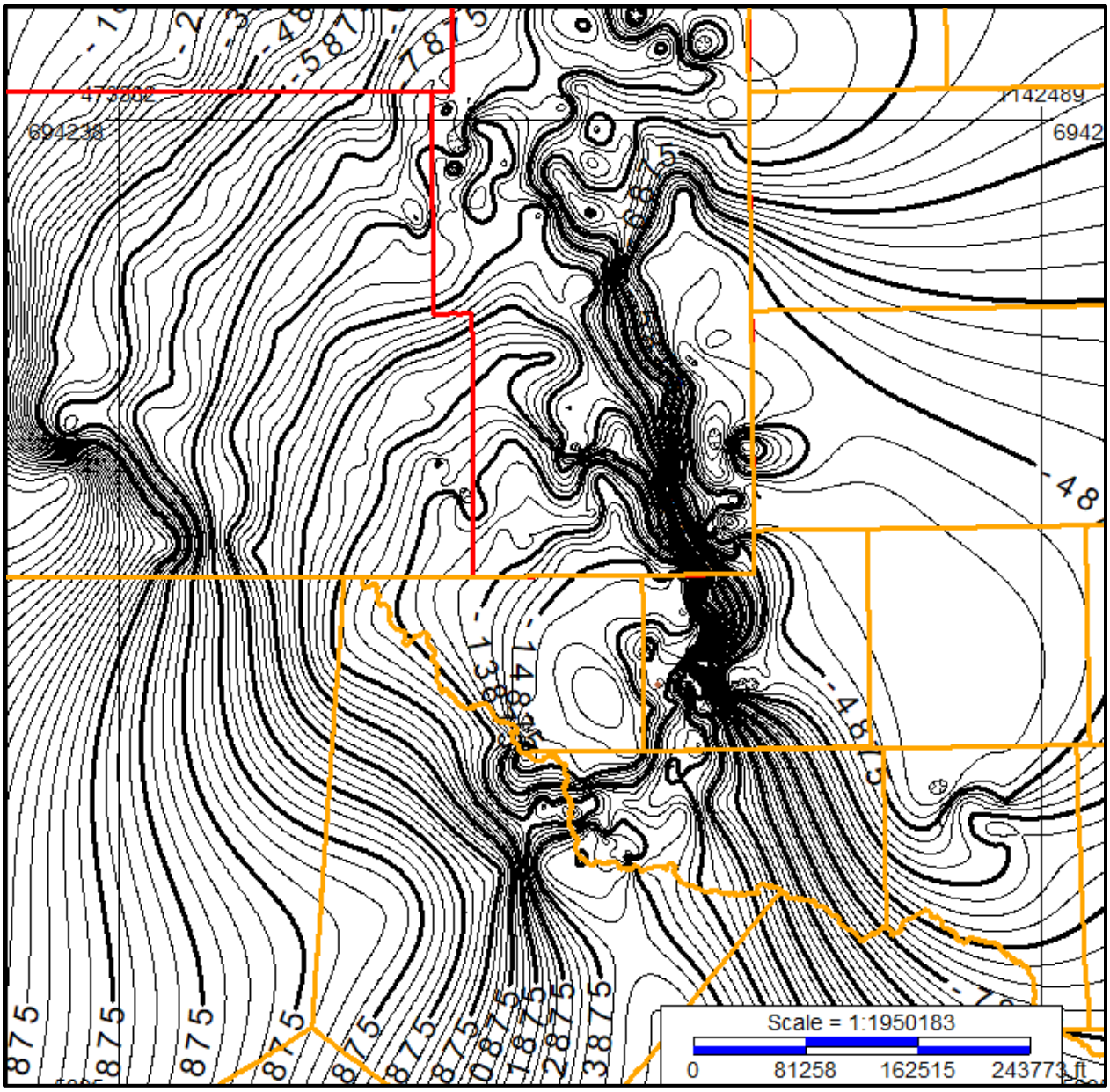


Figure 117. The top of the Mississippian limestone Subsea contour map within the Delaware basin in Southeastern New Mexico (red outlined counties) and west Texas (gold counties).

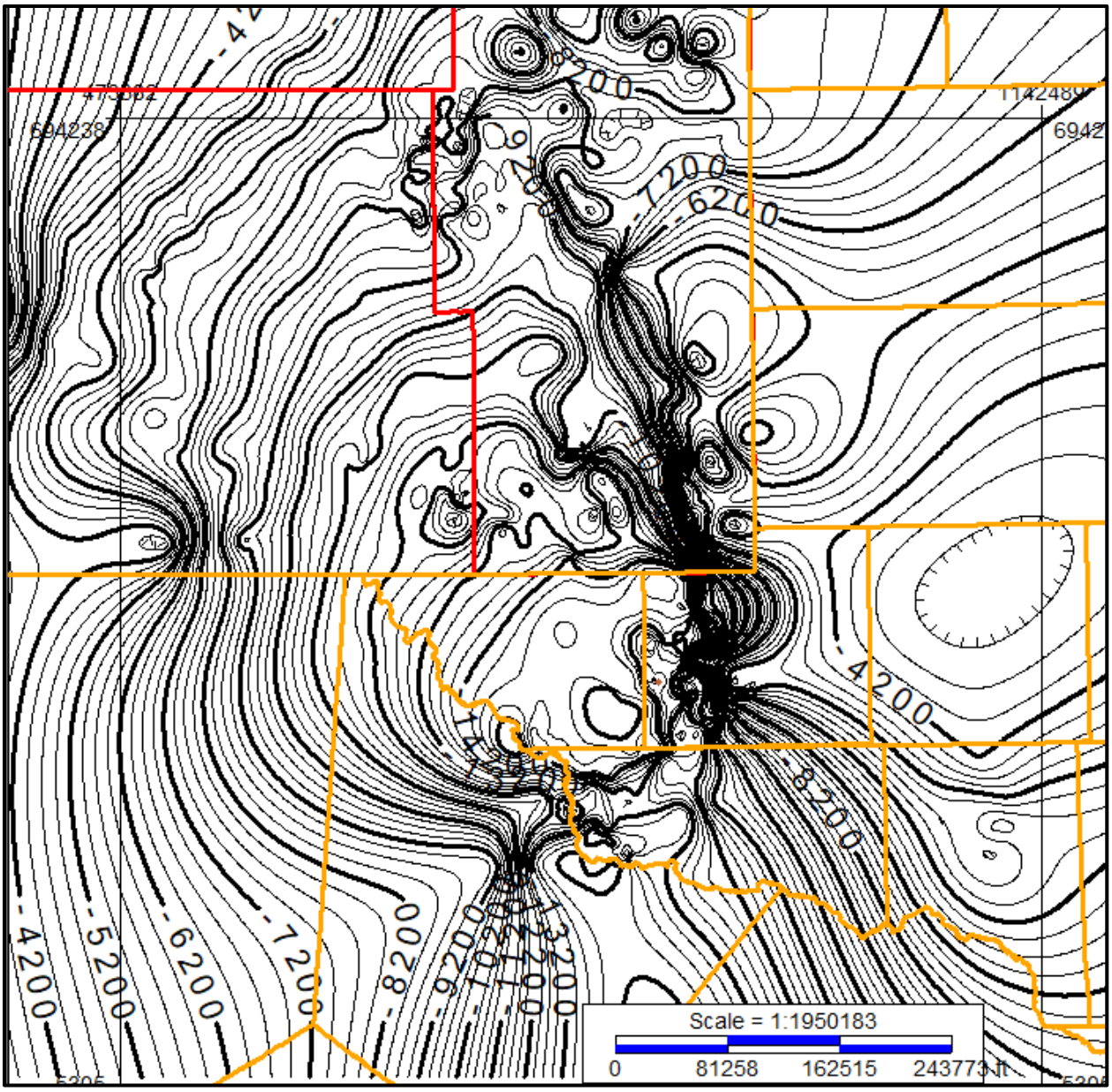


Figure 118. The top of the Barnett Shale Subsea contour map within the Delaware basin in Southeastern New Mexico (red outlined counties) and west Texas (gold counties).

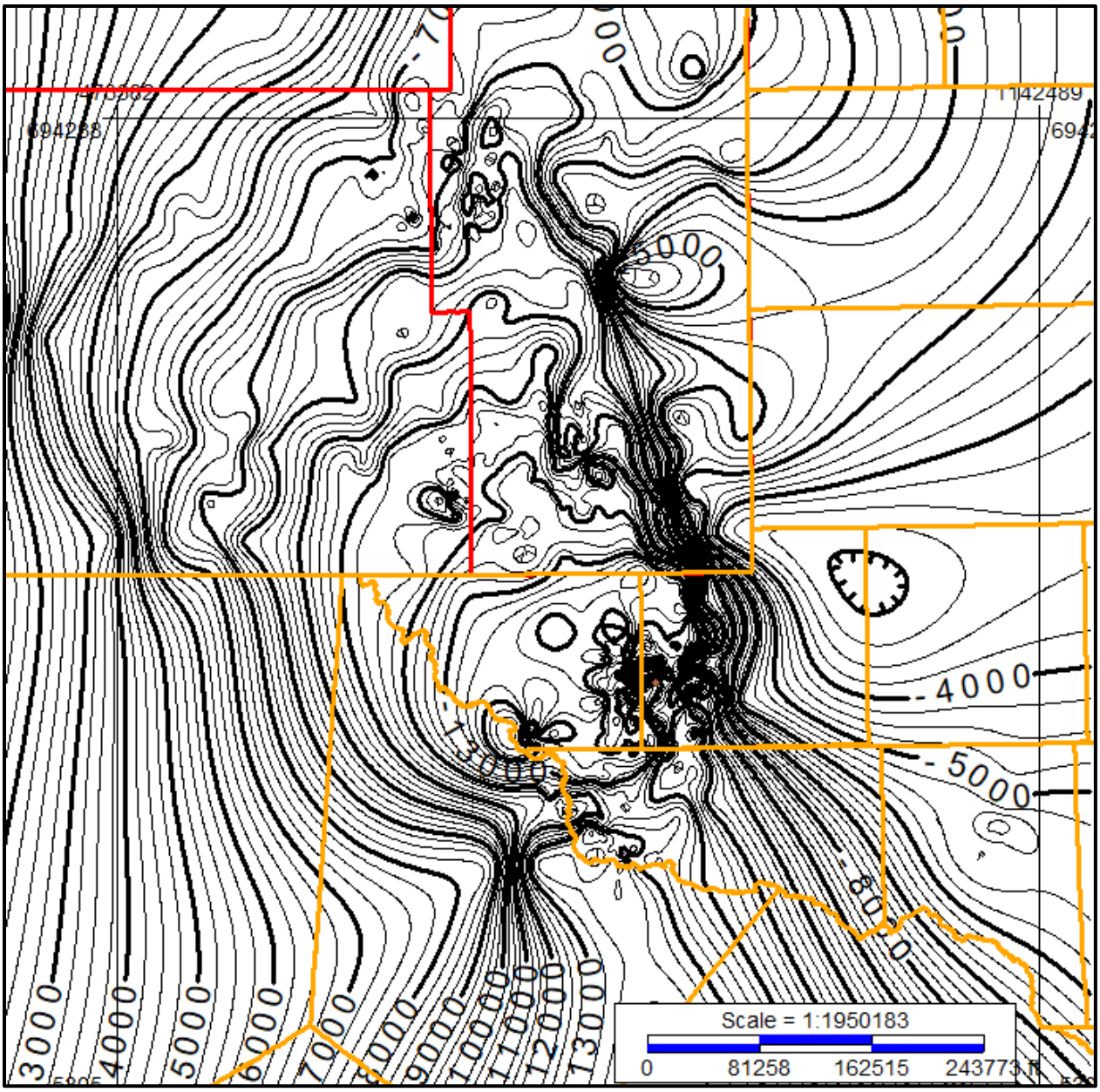


Figure 119. The top of the Morrow Formation Subsea contour map within the Delaware basin in Southeastern New Mexico (red outlined counties) and west Texas (gold counties).

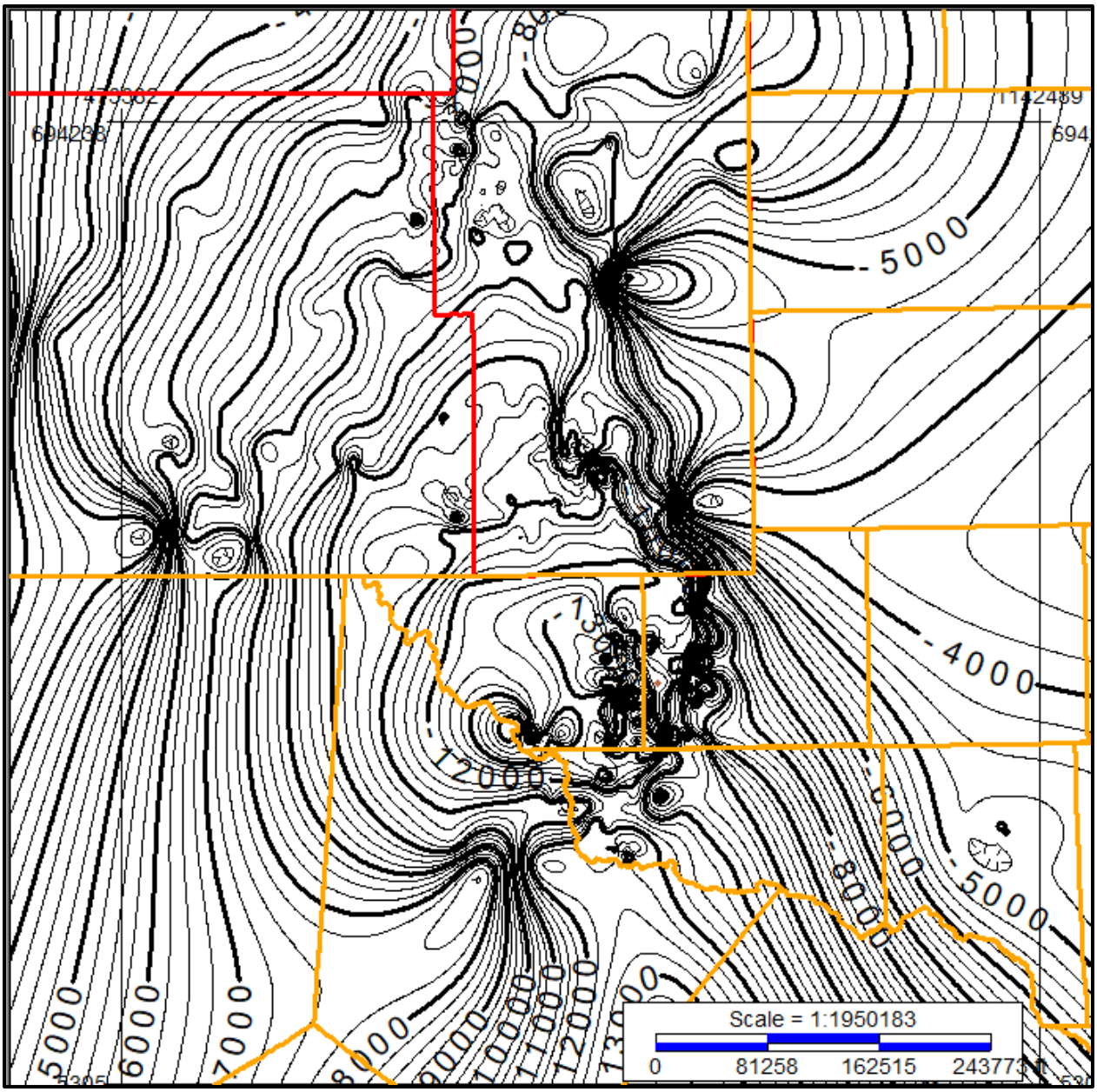


Figure 120. The top of the Atoka Formation Subsea contour map within the Delaware basin in Southeastern New Mexico (red outlined counties) and west Texas (gold counties).

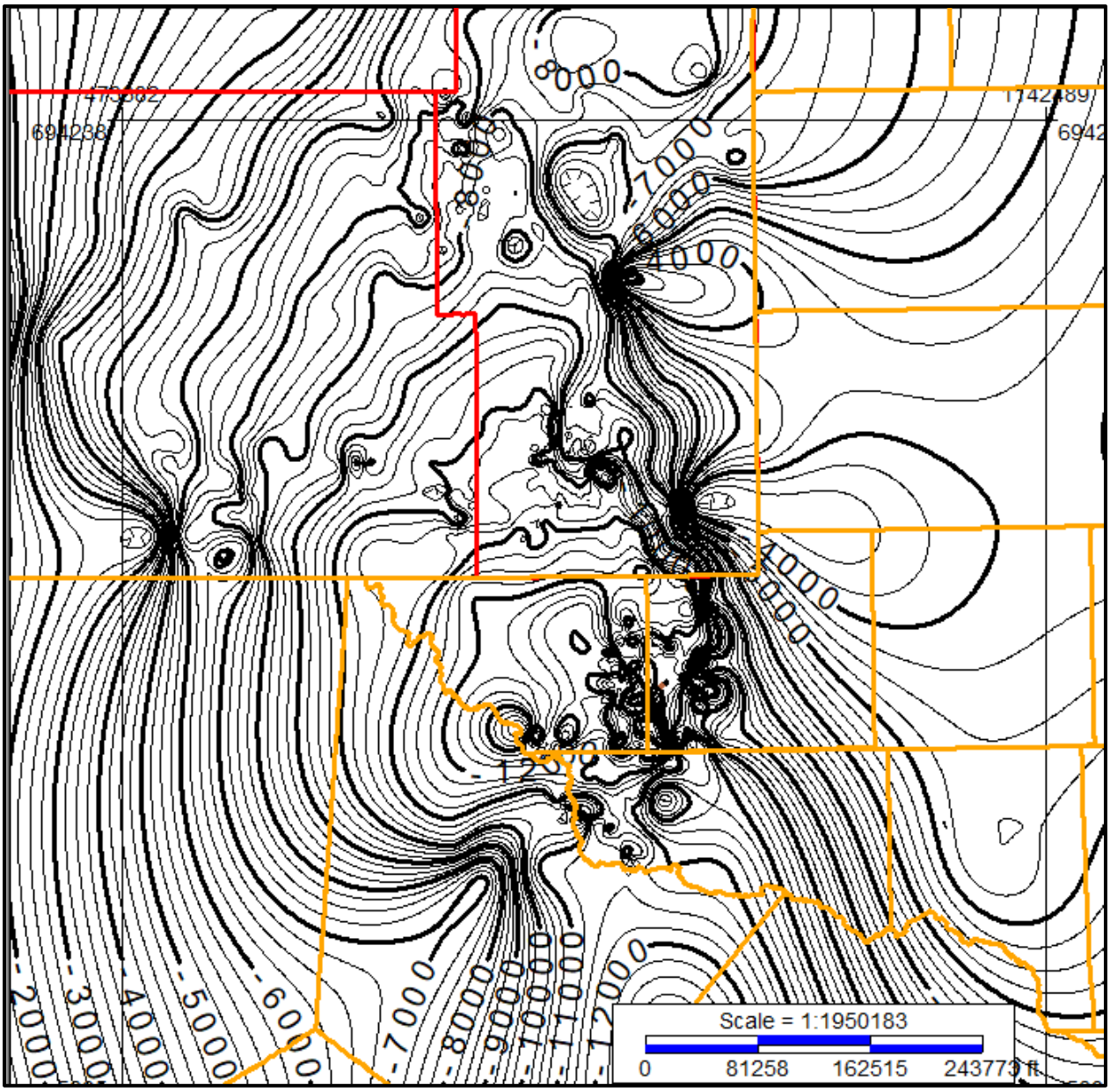


Figure 121. The top of the Atoka Formation Subsea contour map within the Delaware basin in Southeastern New Mexico (red outlined counties) and west Texas (gold counties).

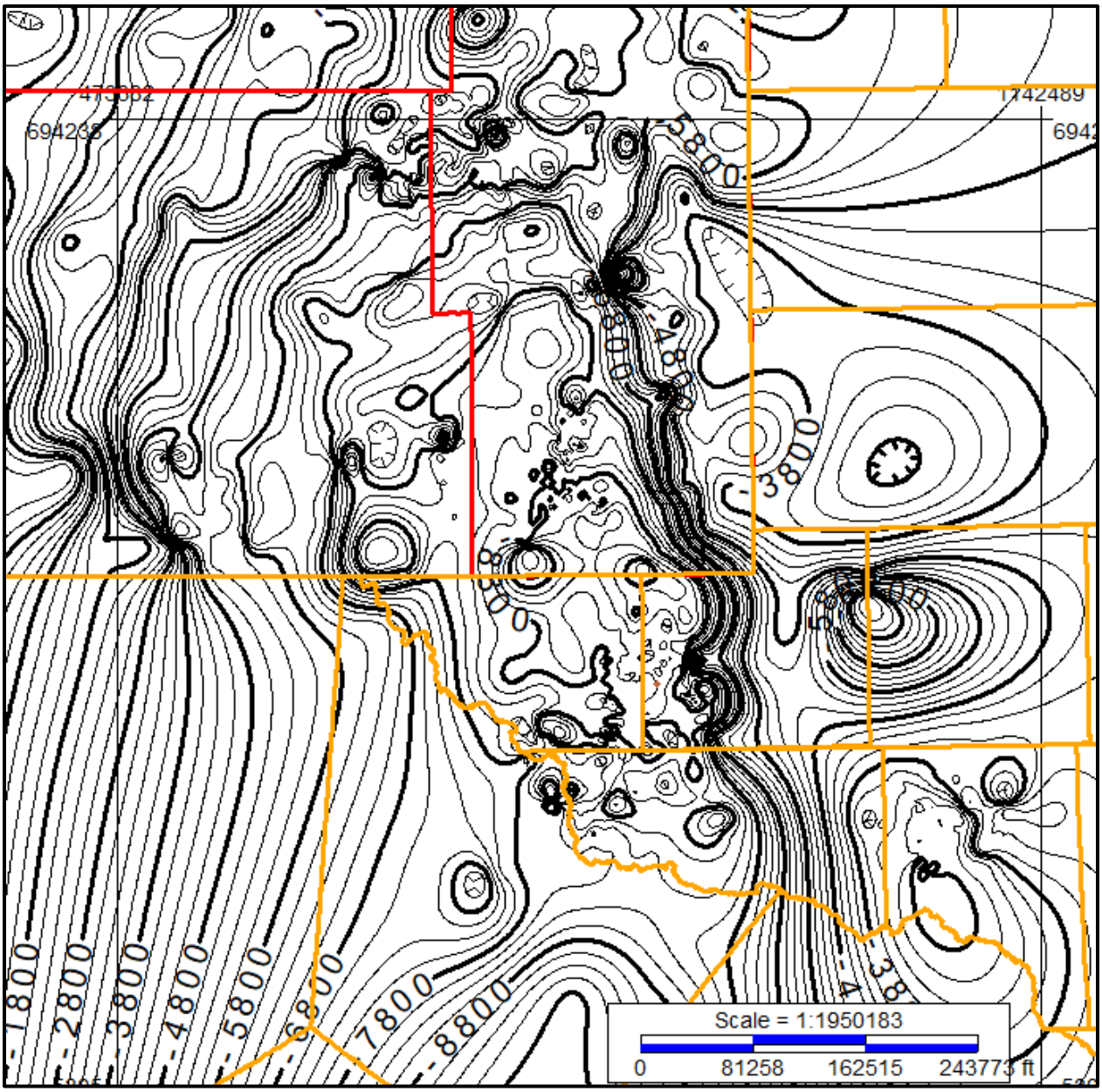


Figure 122. The top of the Wolfcamp formation (Hueco Formation) Subsea contour map within the Delaware basin in Southeastern New Mexico (red outlined counties) and west Texas (gold counties).

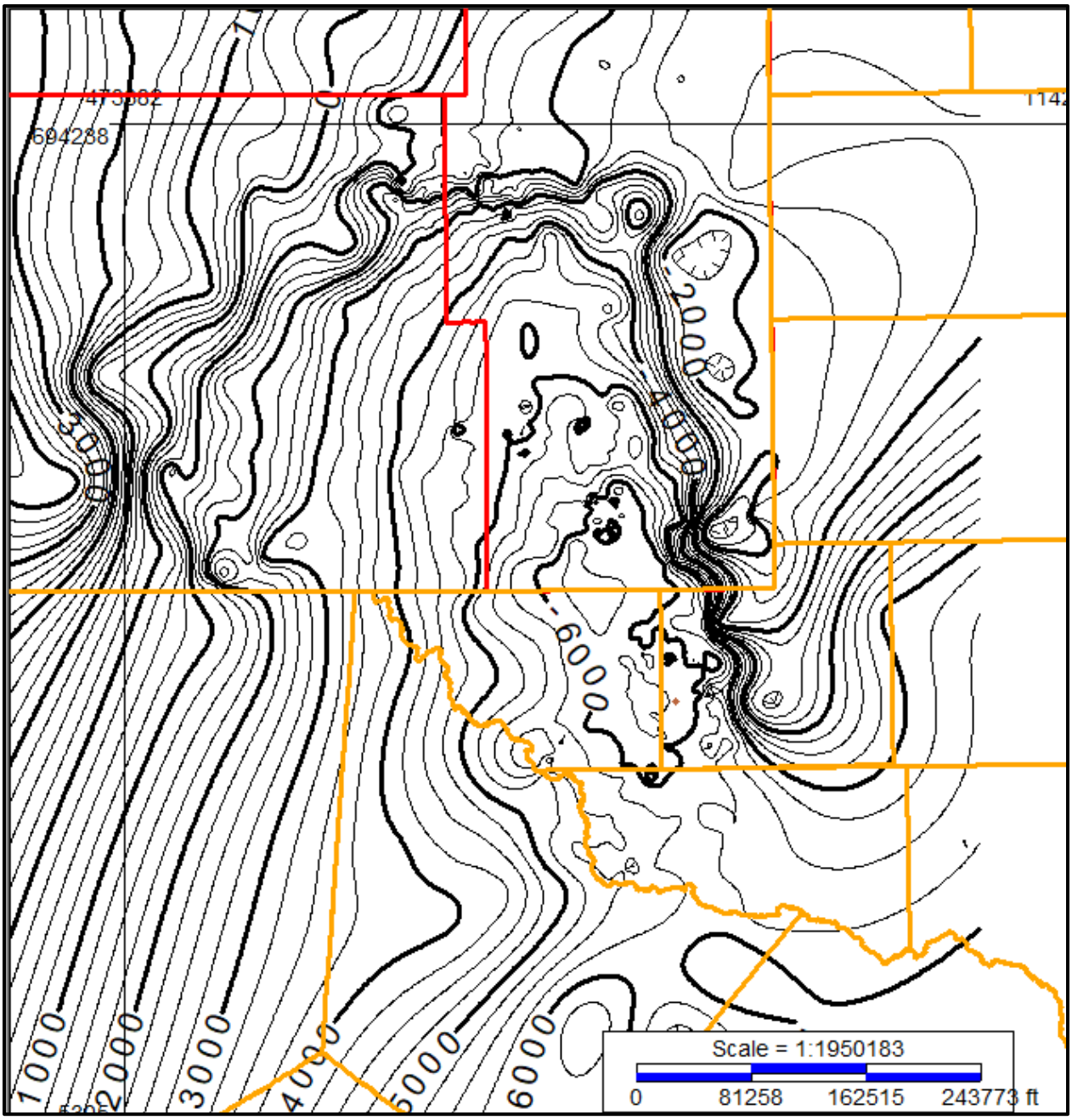


Figure 123. The top of the Bone Spring Formation Subsea contour map within the Delaware basin in Southeastern New Mexico (red outlined counties) and west Texas (gold counties).

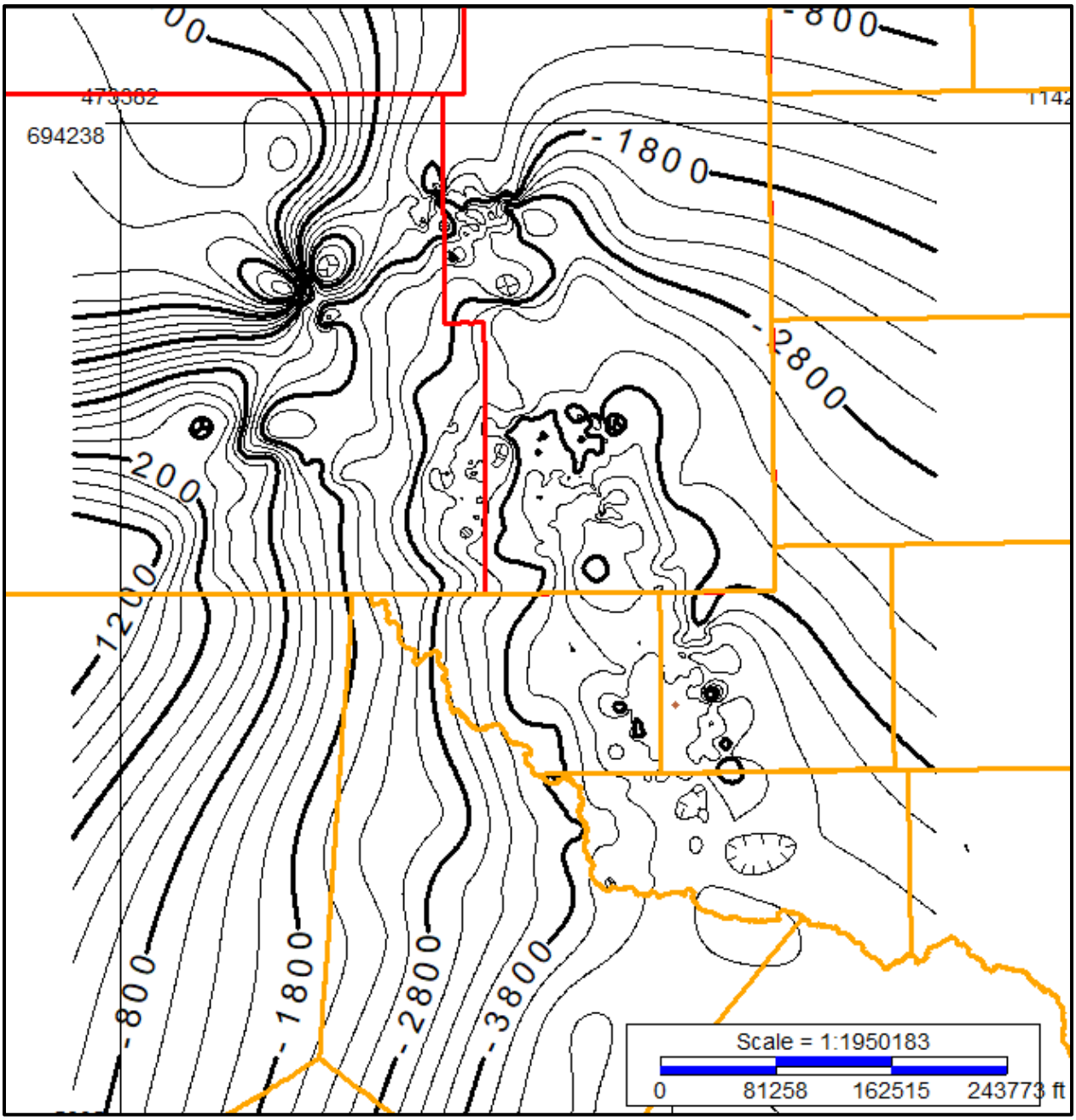


Figure 124. The top of the Brushy Canyon Formation Subsea contour map within the Delaware basin in Southeastern New Mexico (red outlined counties) and west Texas (gold counties).

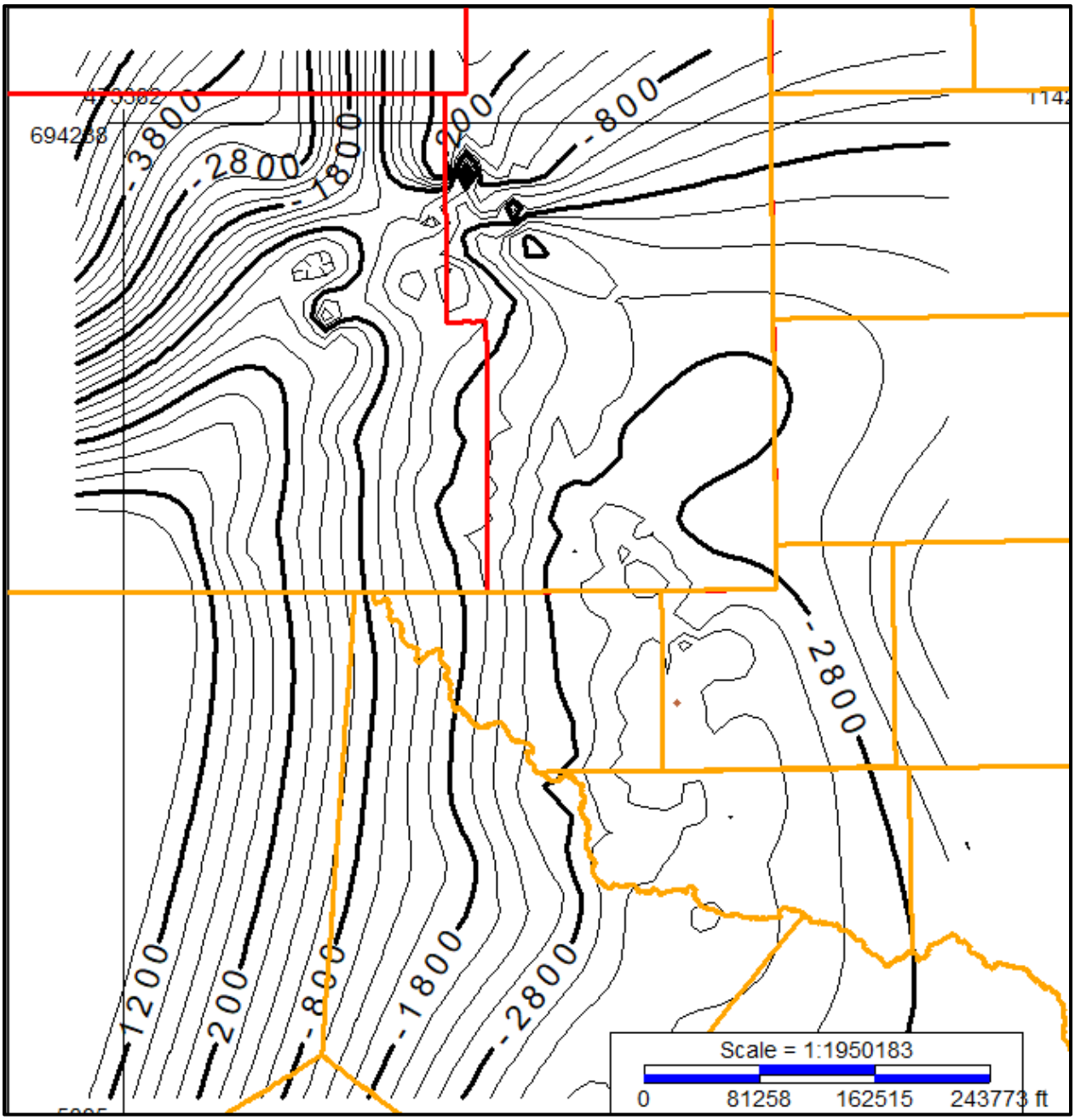


Figure 125. The top of the Cherry Canyon Formation Subsea contour map within the Delaware basin in Southeastern New Mexico (red outlined counties) and west Texas (gold counties).

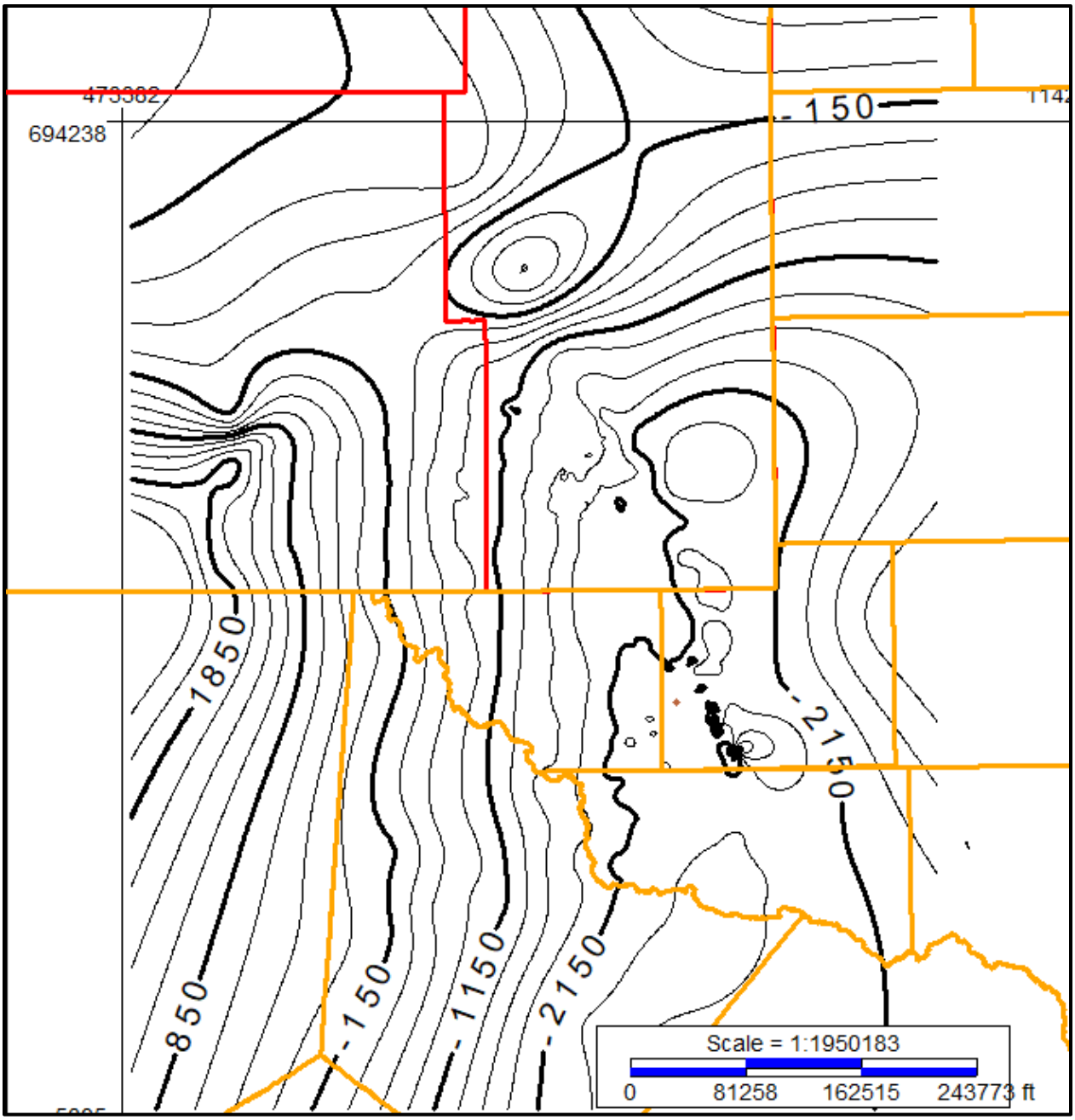


Figure 126. The top of the Bell Canyon Formation Subsea contour map within the Delaware basin in Southeastern New Mexico (red outlined counties) and west Texas (gold counties).

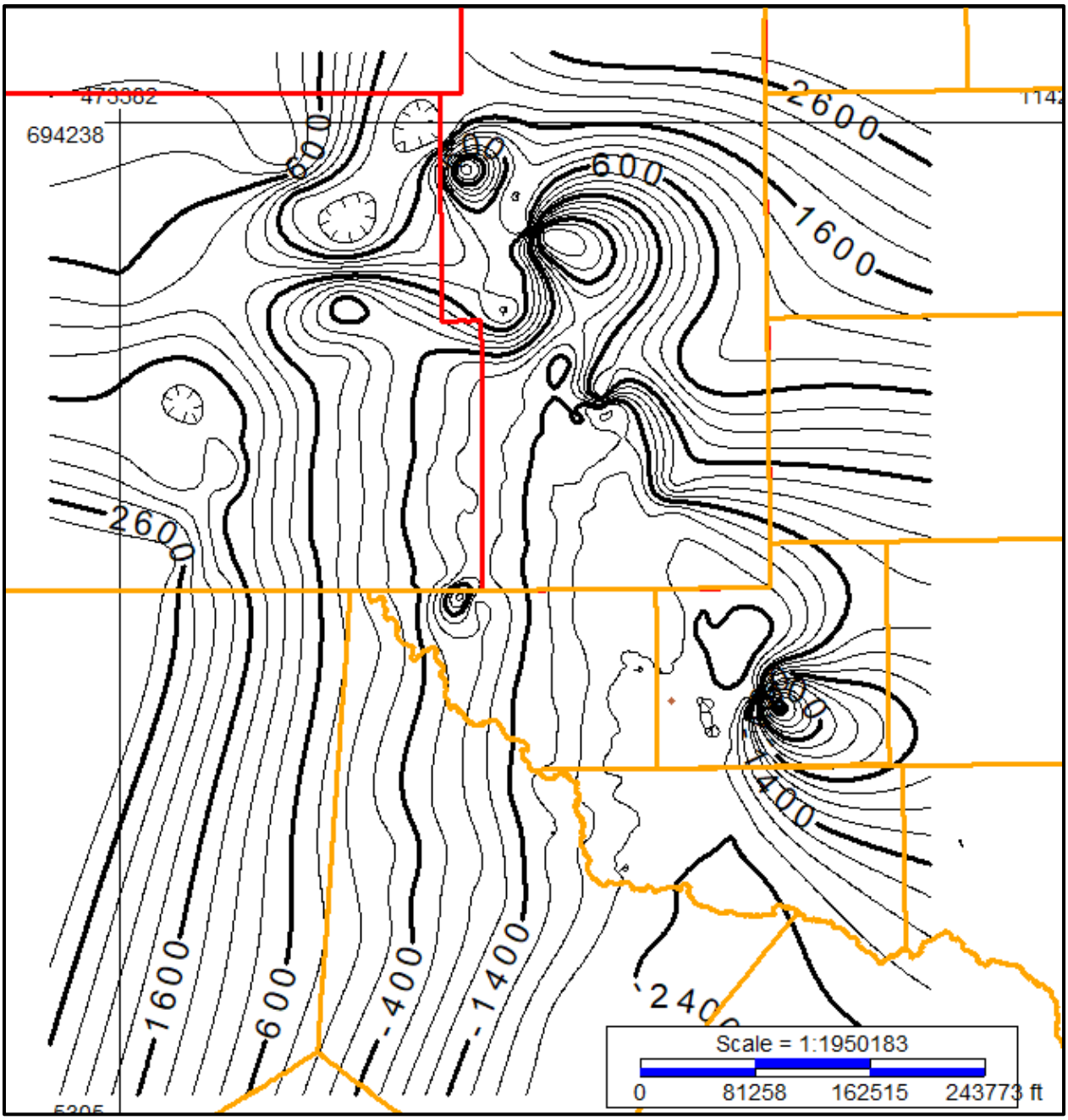


Figure 127. The top of the Lamar Limestone Subsea contour map within the Delaware basin in Southeastern New Mexico (red outlined counties) and west Texas (gold counties).

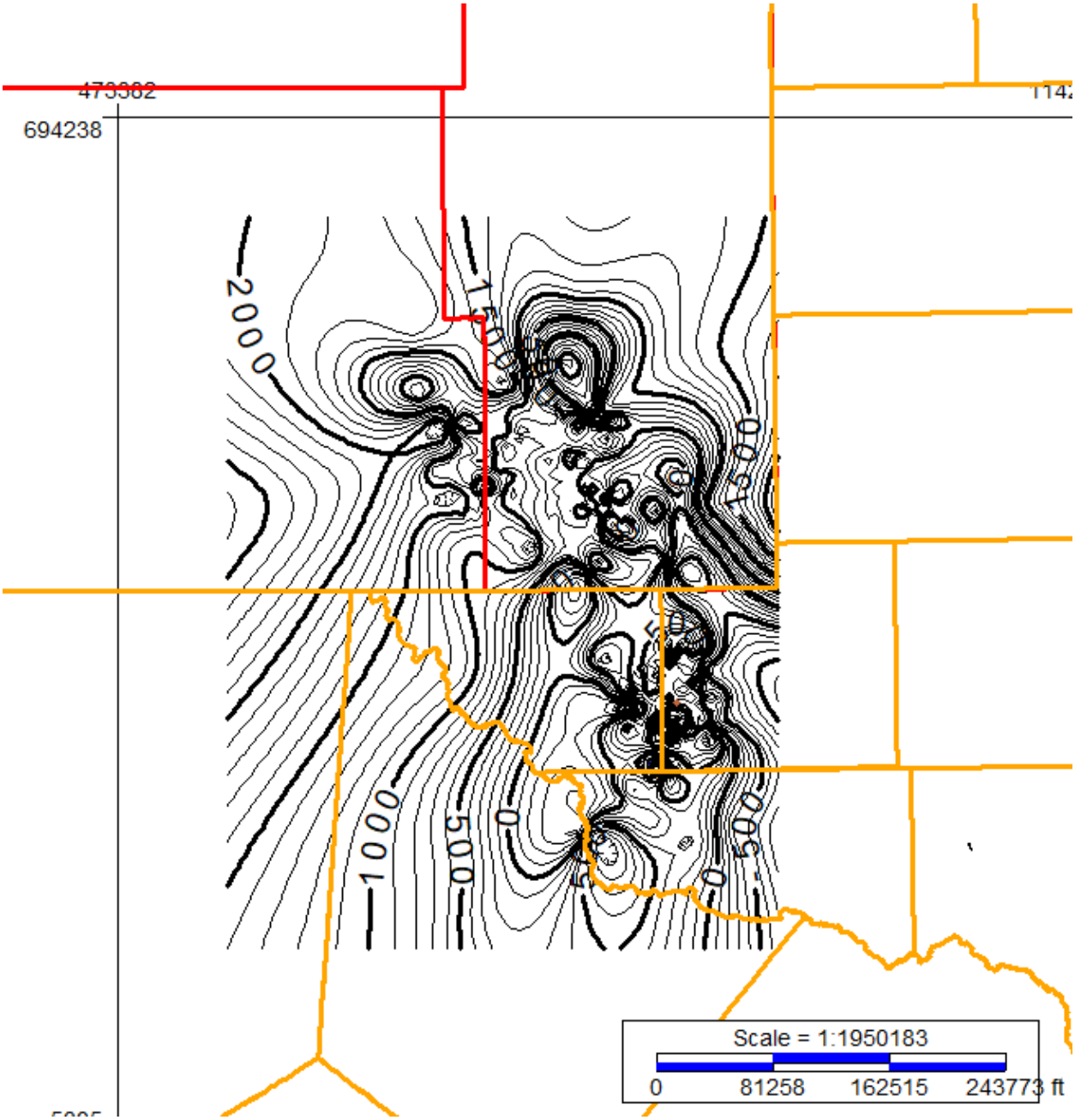


Figure 128. The top of the Castile Formation Subsea contour map within the Delaware basin in Southeastern New Mexico (red outlined counties) and west Texas (gold counties).

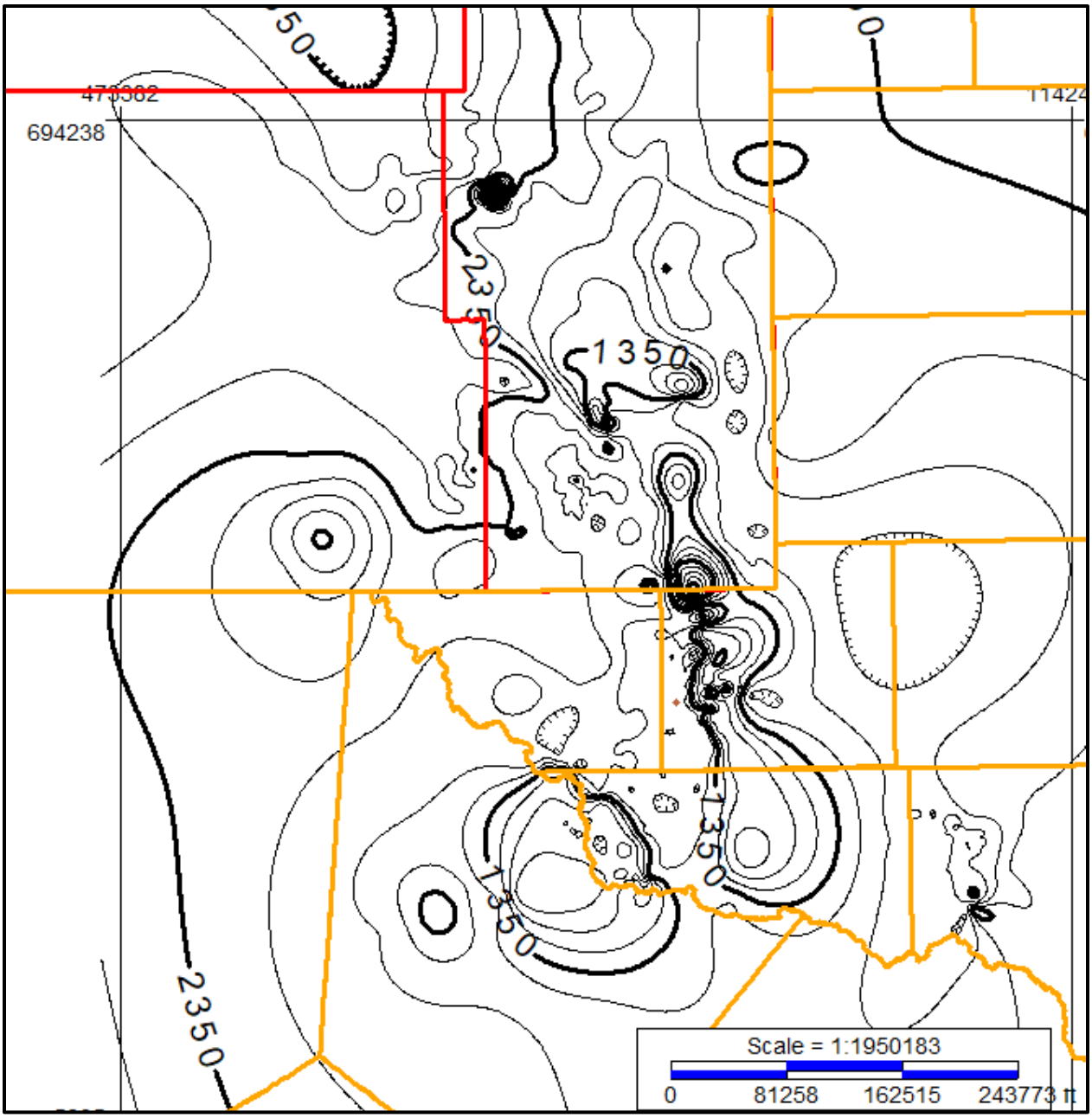


Figure 129. The top of the Salado Formation Subsea contour map within the Delaware basin in Southeastern New Mexico (red outlined counties) and west Texas (gold counties).

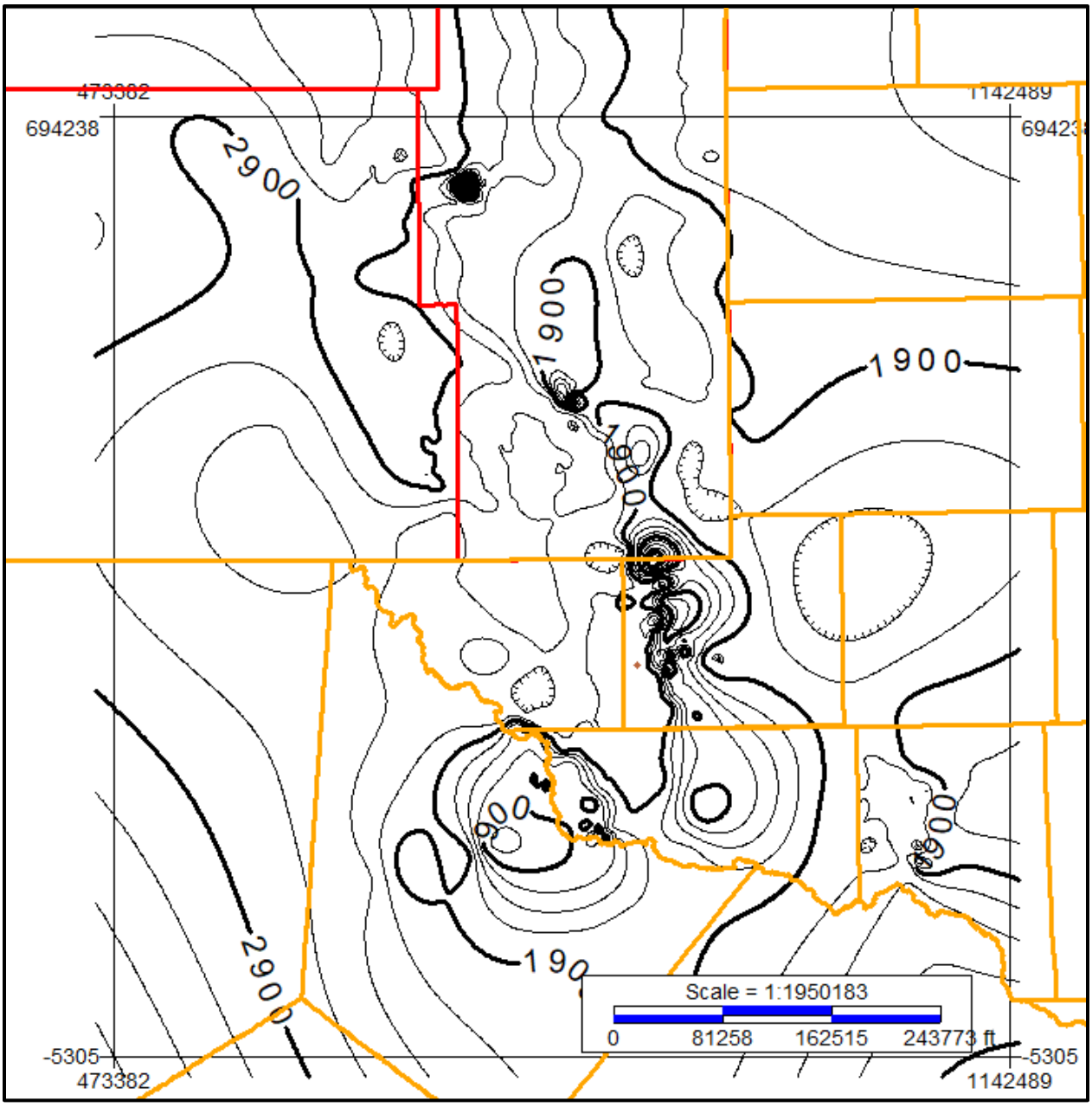


Figure 130. The top of the Rustler Formation Subsea contour map within the Delaware basin in Southeastern New Mexico (red outlined counties) and west Texas (gold counties).

Surfaces With Faults

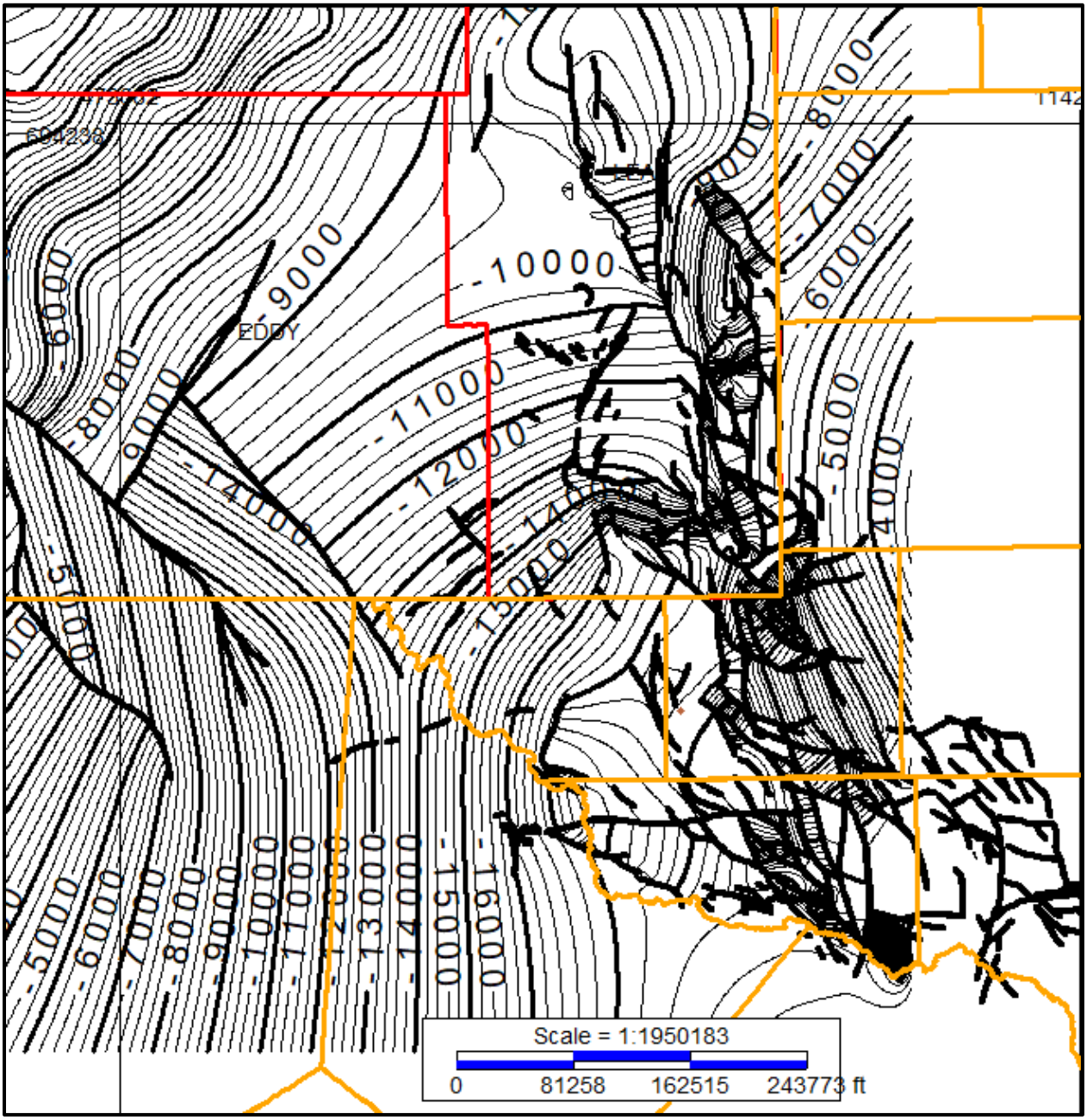


Figure 131. The Precambrian Subsea contour map using the deep-seated faults of Horne et al. (2021) within the Delaware basin in Southeastern New Mexico (red outlined counties) and west Texas (gold counties).

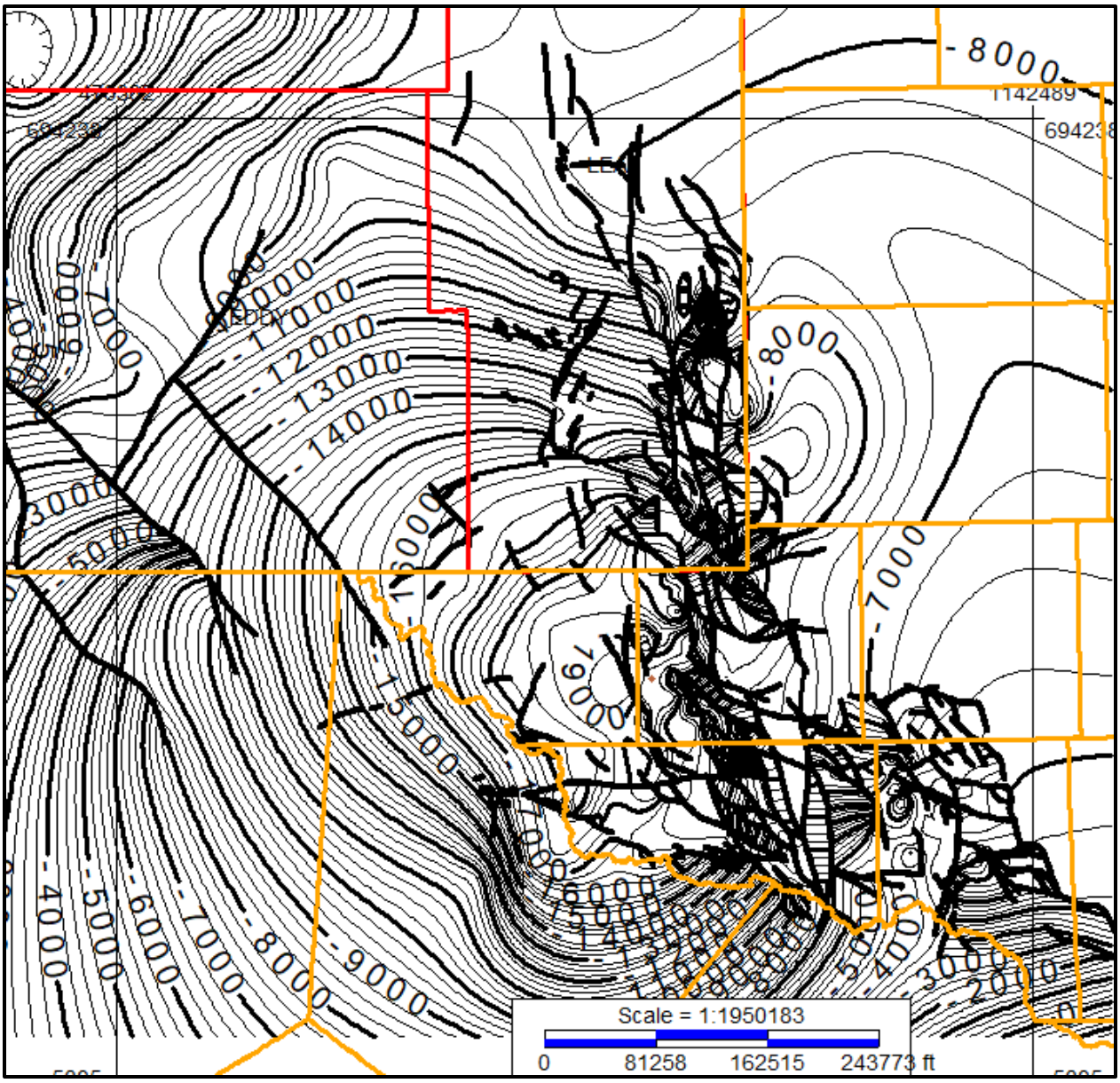


Figure 132. The Ellenburger Formation Subsea contour map using the deep-seated faults of Horne et al. (2021) within the Delaware basin in Southeastern New Mexico (red outlined counties) and west Texas (gold counties).

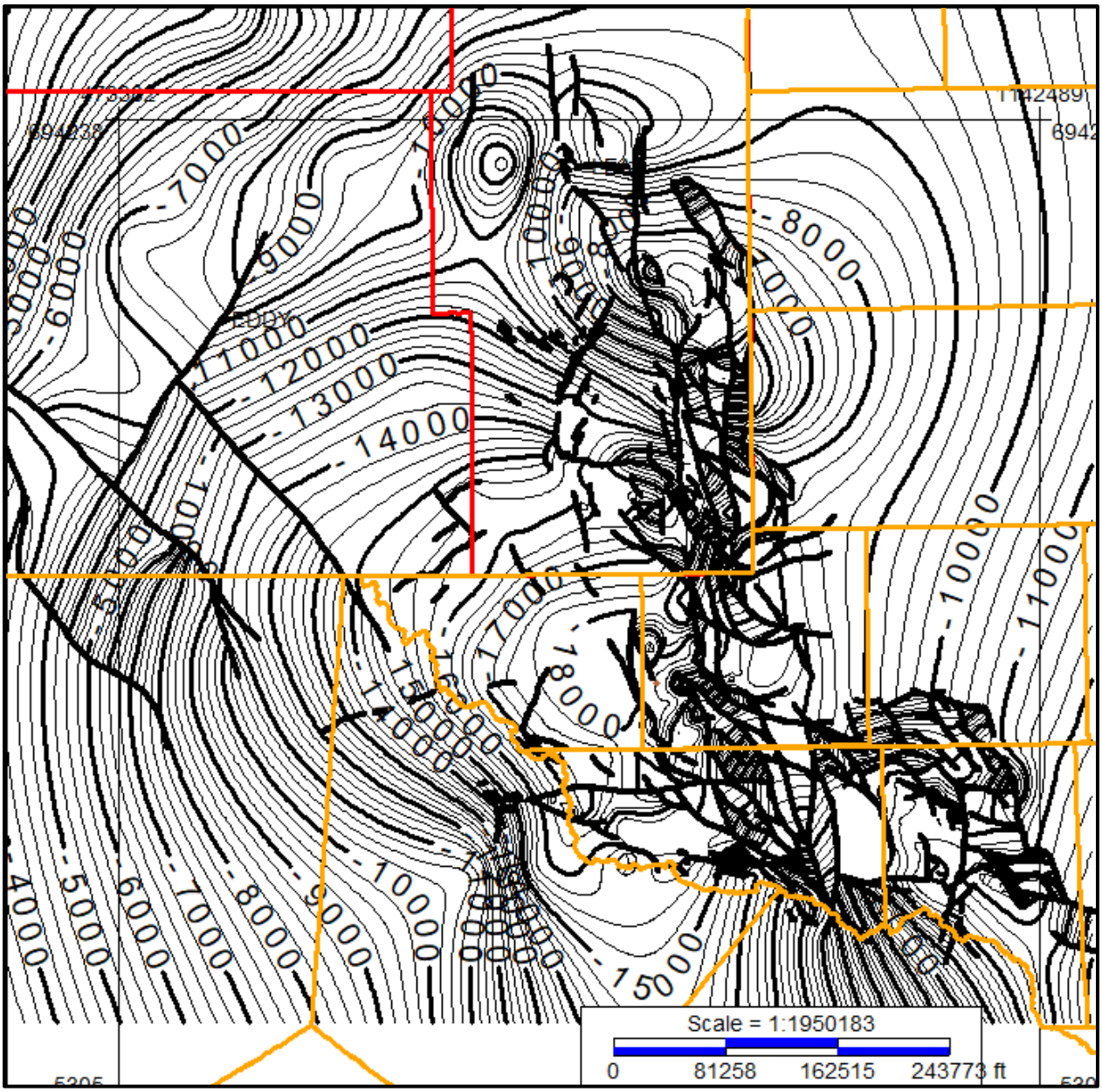


Figure 133. The Simpson Group Subsea contour map using the deep-seated faults of Horne et al. (2021) within the Delaware basin in Southeastern New Mexico (red outlined counties) and west Texas (gold counties).

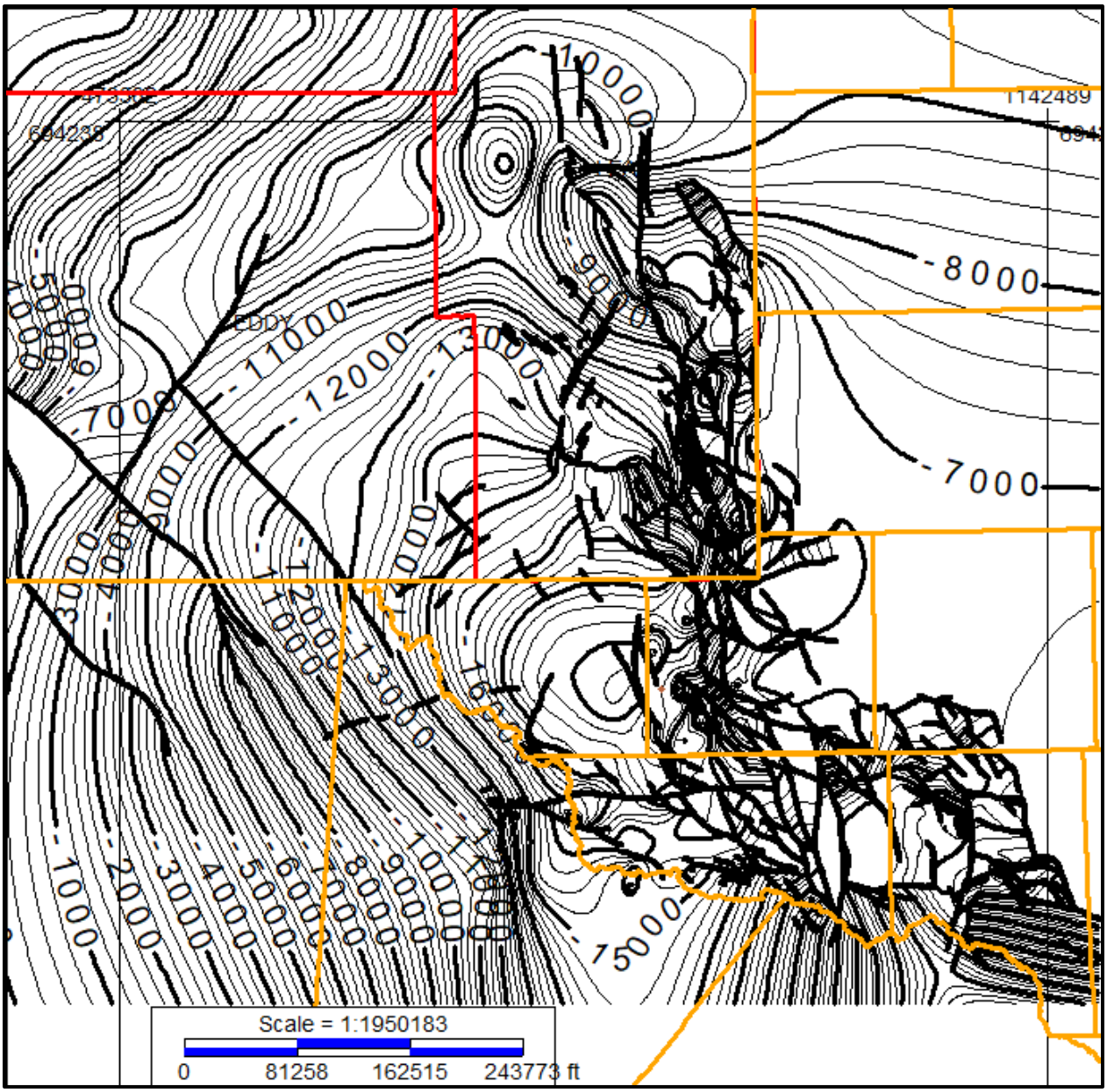


Figure 134. The Montoya Formation Subsea contour map using the deep-seated faults of Horne et al. (2021) within the Delaware basin in Southeastern New Mexico (red outlined counties) and west Texas (gold counties).

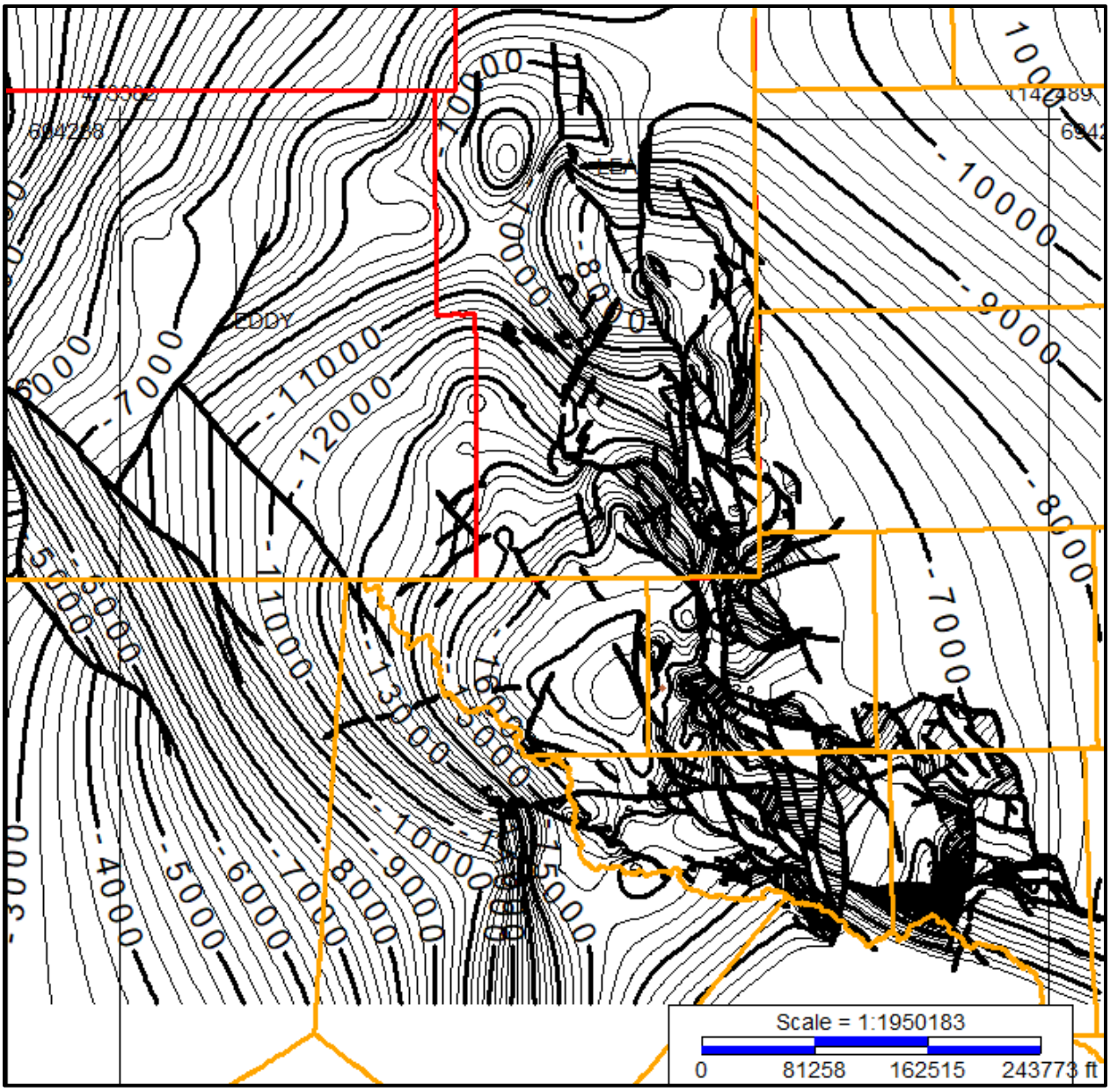


Figure 135. The Fusselman Formation Subsea contour map using the deep-seated faults of Horne et al. (2021) within the Delaware basin in Southeastern New Mexico (red outlined counties) and west Texas (gold counties).

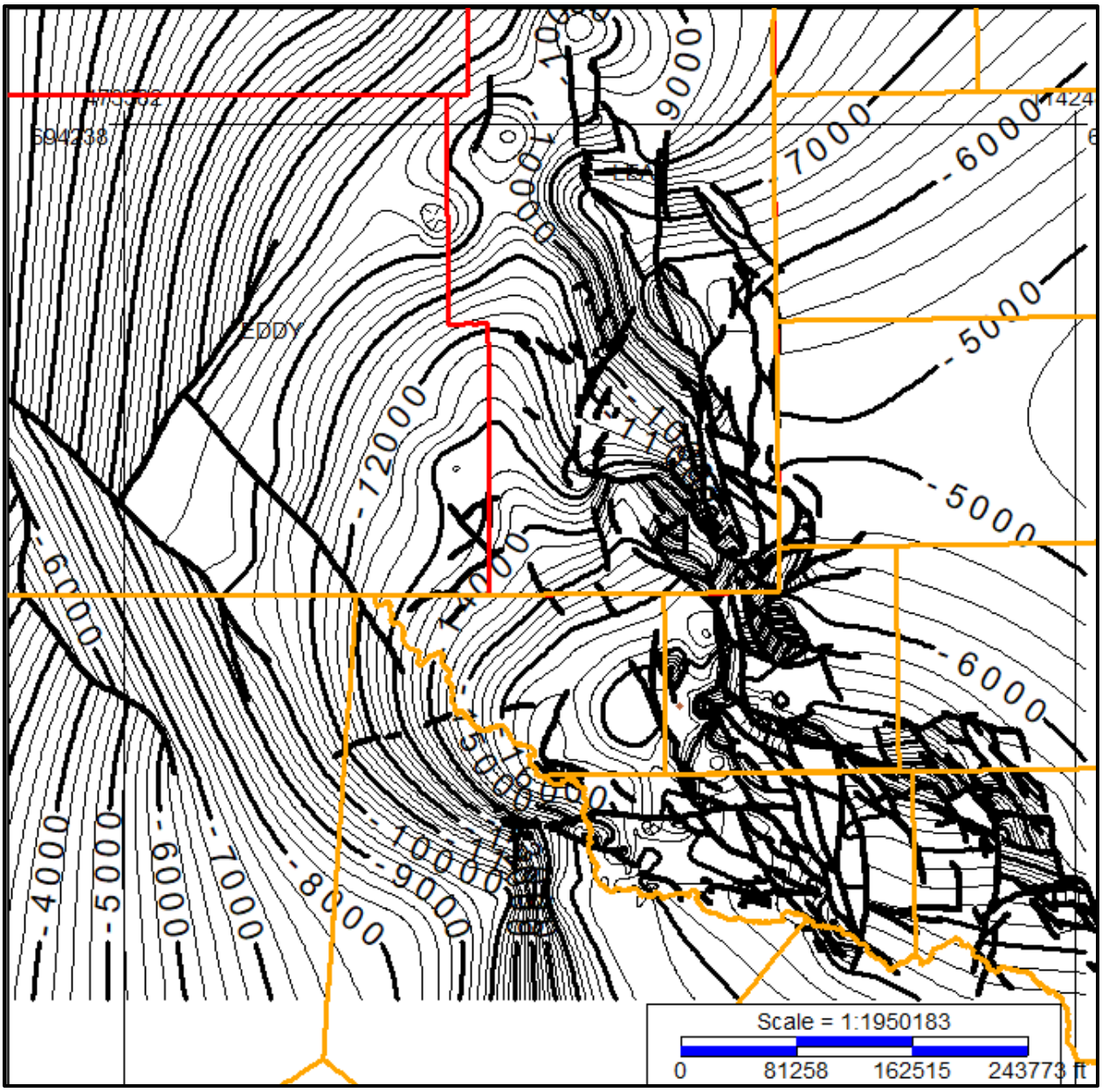


Figure 136. The Wristen Group Subsea contour map using the deep-seated faults of Horne et al. (2021) within the Delaware basin in Southeastern New Mexico (red outlined counties) and west Texas (gold counties).

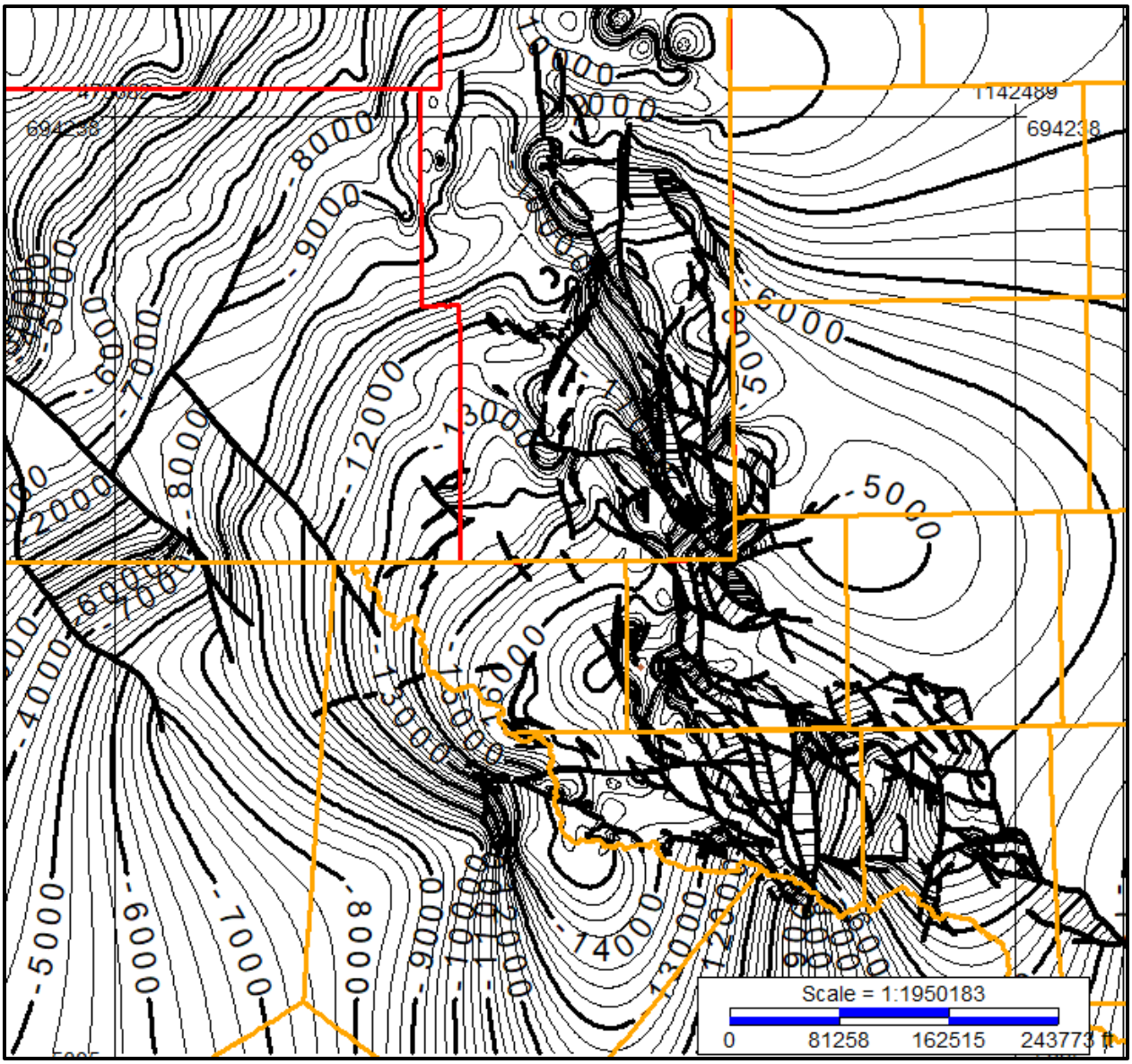


Figure 137. The top of the Siluro-Devonian strata (Thirtyone Formation) Subsea contour map using the deep-seated faults of Horne et al. (2021) within the Delaware basin in Southeastern New Mexico (red outlined counties) and west Texas (gold counties).

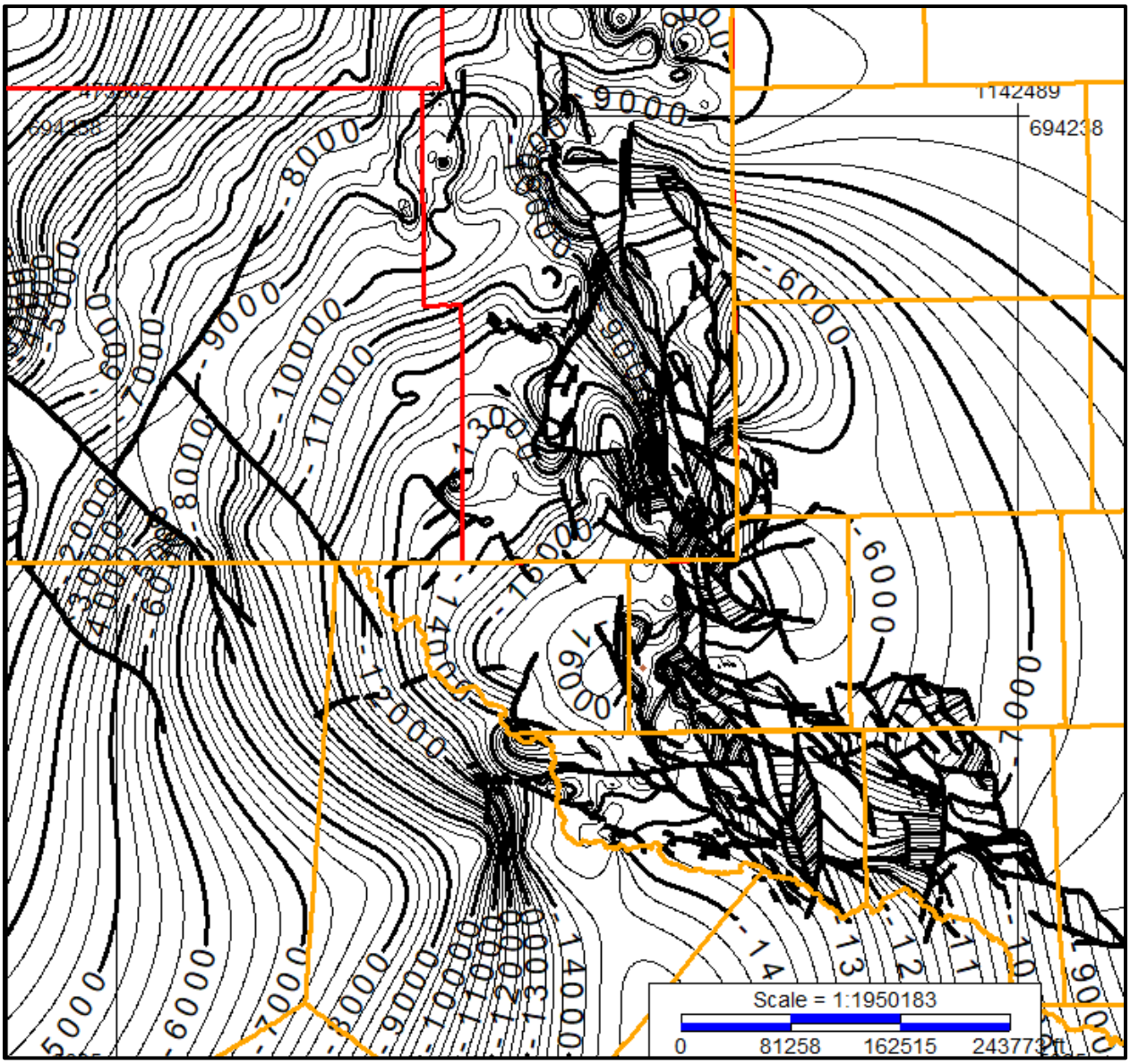


Figure 138. The top of the Woodford Shale Subsea contour map using the deep-seated faults of Horne et al. (2021) within the Delaware basin in Southeastern New Mexico (red outlined counties) and west Texas (gold counties).

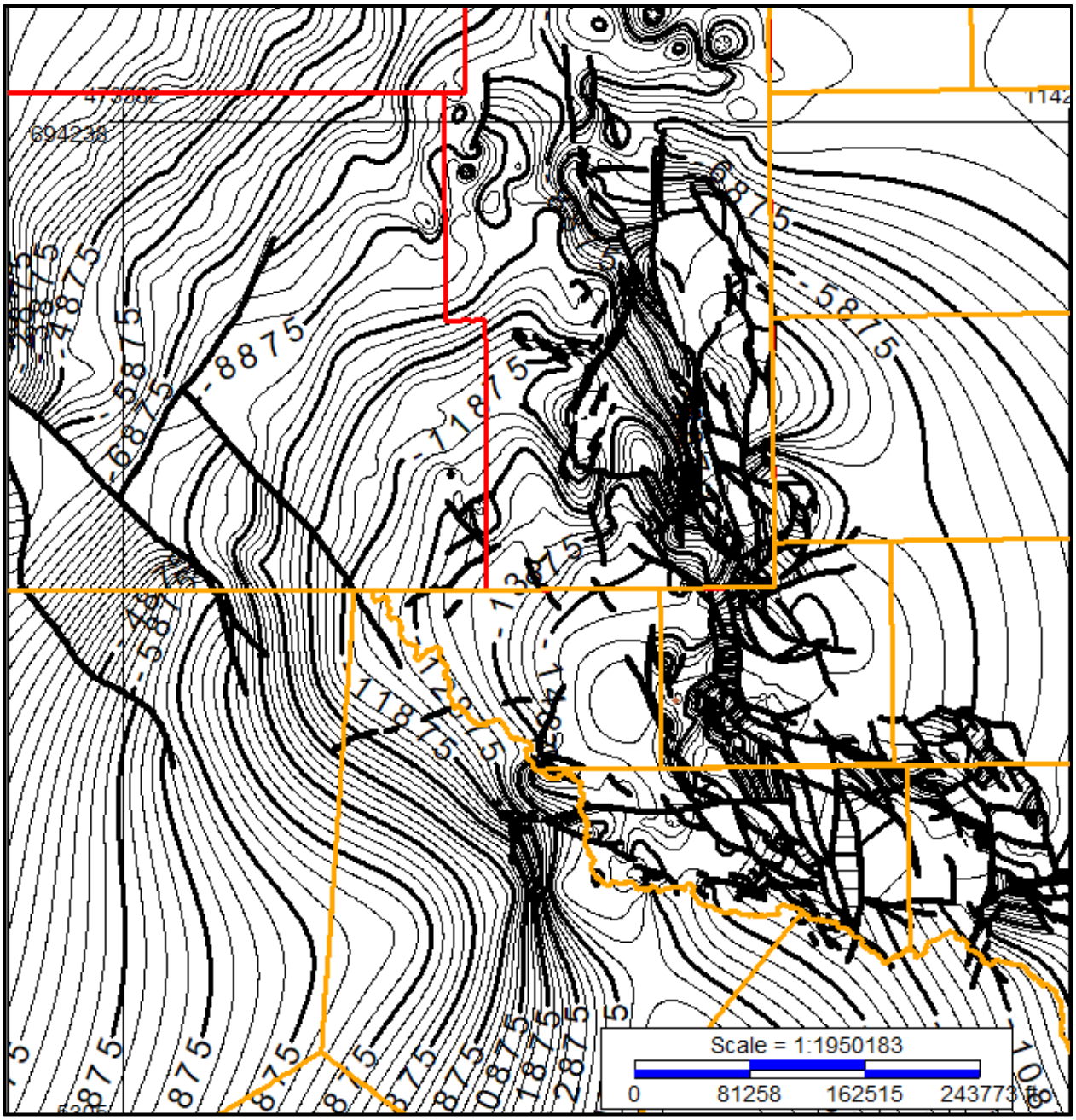


Figure 139. The top of the Mississippian limestone Subsea contour map using the deep-seated faults of Horne et al. (2021) within the Delaware basin in Southeastern New Mexico (red outlined counties) and west Texas (gold counties).

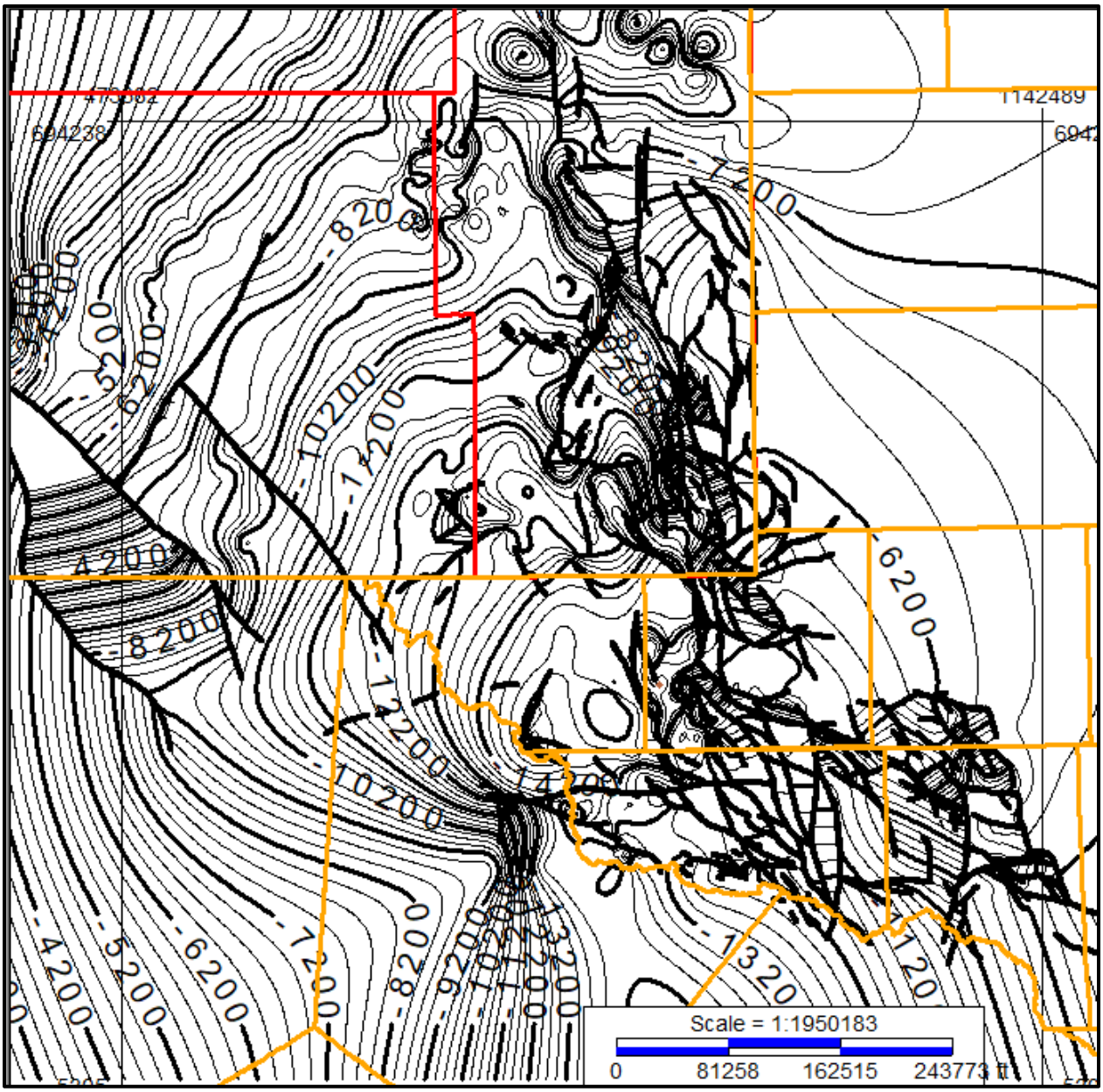


Figure 140. The top of the Barnett Shale Subsea contour map using the deep-seated faults of Horne et al. (2021) within the Delaware basin in Southeastern New Mexico (red outlined counties) and west Texas (gold counties).

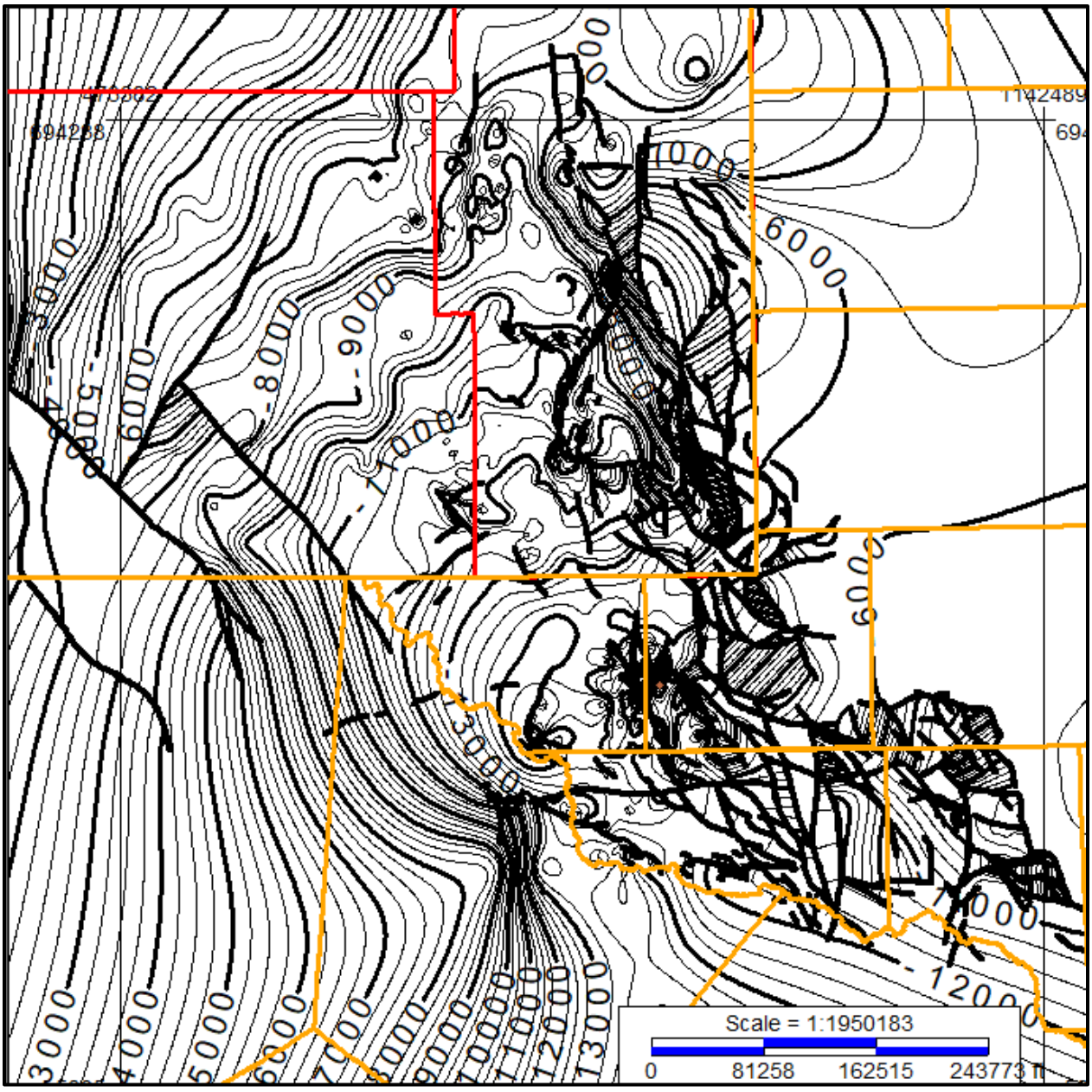


Figure 141. The top of the Morrow Formation Subsea contour map using the deep-seated faults of Horne et al. (2021) within the Delaware basin in Southeastern New Mexico (red outlined counties) and west Texas (gold counties).

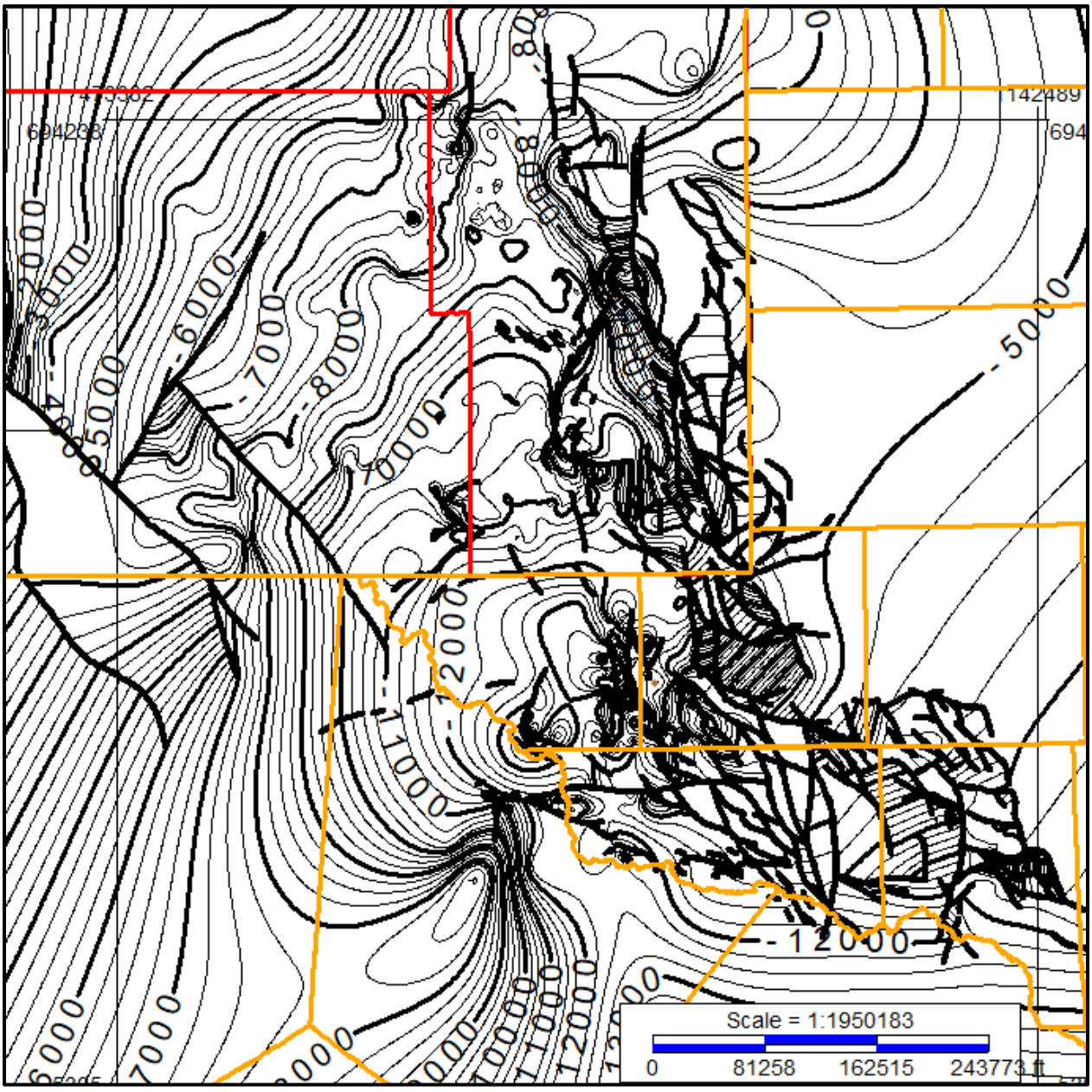


Figure 142. The top of the Atoka Formation Subsea contour map using the deep-seated faults of Horne et al. (2021) within the Delaware basin in Southeastern New Mexico (red outlined counties) and west Texas (gold counties).

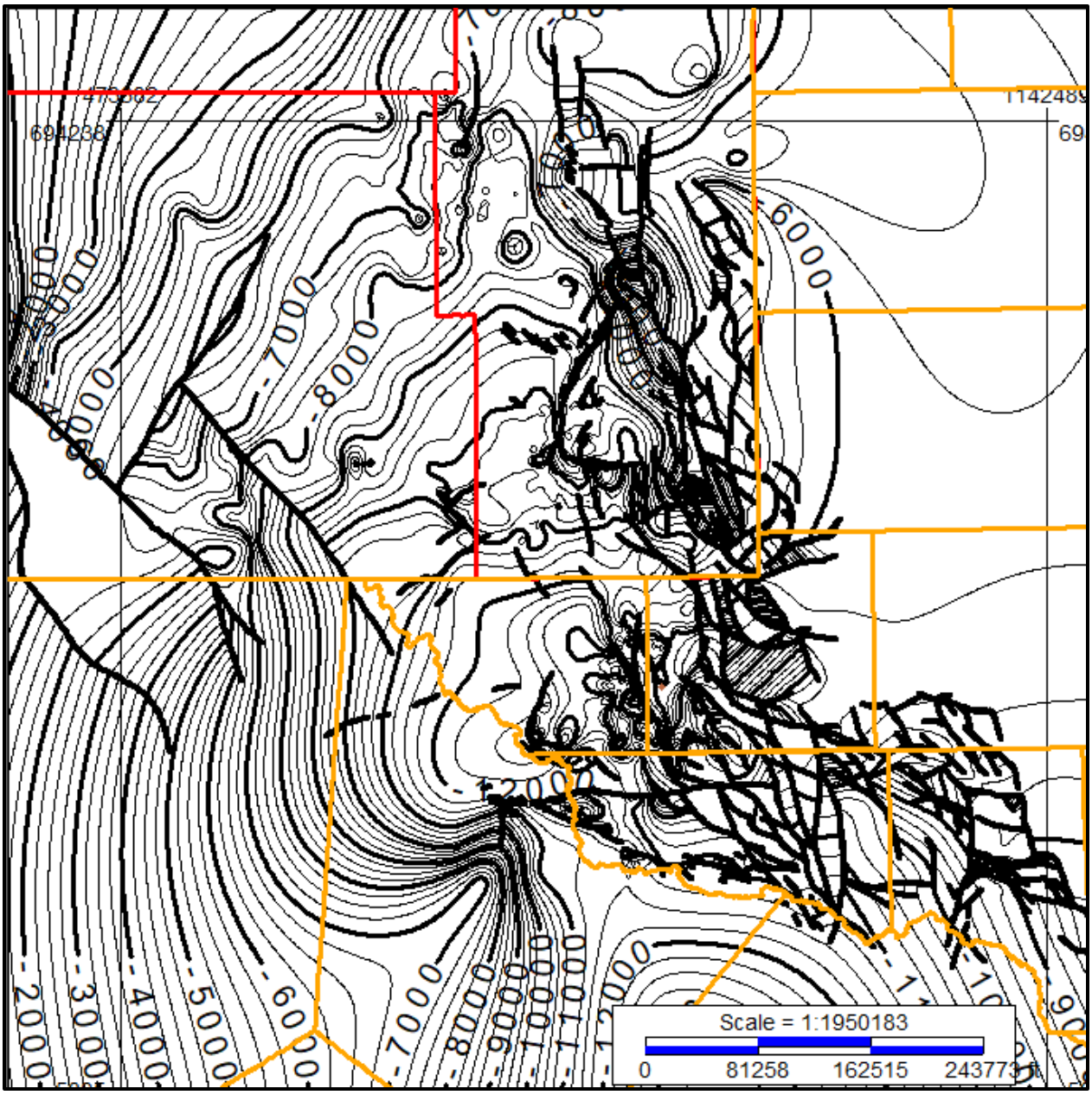


Figure 143. The top of the Atoka Formation Subsea contour map using the deep-seated faults of Horne et al. (2021) within the Delaware basin in Southeastern New Mexico (red outlined counties) and west Texas (gold counties).

Bravo Dome

The Bravo Dome area was another area selected for detailed mapping for the CUSP project. Bravo Dome is a large natural CO_2 gas field that has been utilized for many years (since the 1930s) for refrigeration and carbonation of drinks; later (1980s), this area was developed for enhanced oil recovery (EOR) CO_2 flooding projects in the Permian Basin. The wells produce 98-99% CO_2 gas from the main reservoirs (Broadhead 2017). While the exact limits of the field are yet to be determined (Broadhead 2017), mapping of the area to understand the stratigraphic and

structural trapping mechanism can provide opportunities in the future as wells become depleted, adding potential sequestration opportunities.

Background Geology

Bravo Dome Field is a large domal feature in northeastern New Mexico (**Figure 144**). It is located between the Sierra Grande uplift, Dalhart Basin and the Tucumcari Basin. Like the Permian Basin region, Bravo Dome formed during the Ouachita Orogeny and the formation of Pangea. This Pennsylvanian to Permian event eroded the structural highs to Precambrian volcanic and metamorphic rocks (like the Central Basin Platform). Younger deposits (pre-Pennsylvanian) occur off the structural highs in the basins.

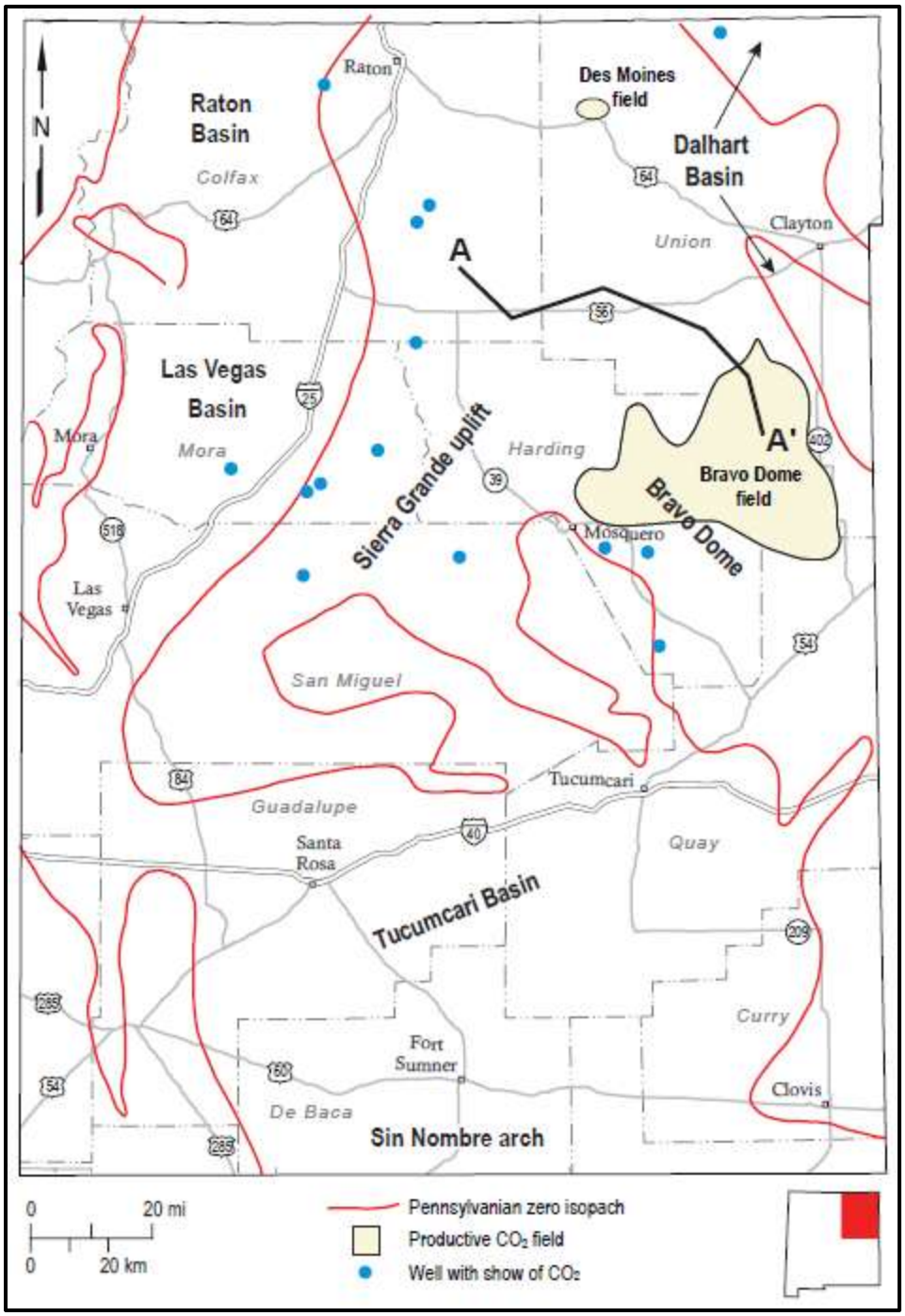


Figure 144. Location of Bravo Dome, New Mexico (from Broadhead 2017)

The Wolfcampian Abo Formation is the first unit to cover the highs, followed by the Tubb Sandstone **(Figure 145)**. The Tubb Sandstone, the main CO_2 reservoir within the field, is part of the lower Yeso Formation. It ranges from 100 to 450 ft thick throughout most of the area. Overlying the Tubb Sandstone, the Cimarron Anhydrite is a thin (approximately 15 ft) anhydrite layer that seals the Tubb Sandstone. There is upward leakage of the CO_2 where faults cut the

anhydrite (Broadhead 2017). This CO_2 has migrated up section into other permeable sandstones (Santa Rosa Sandstone).

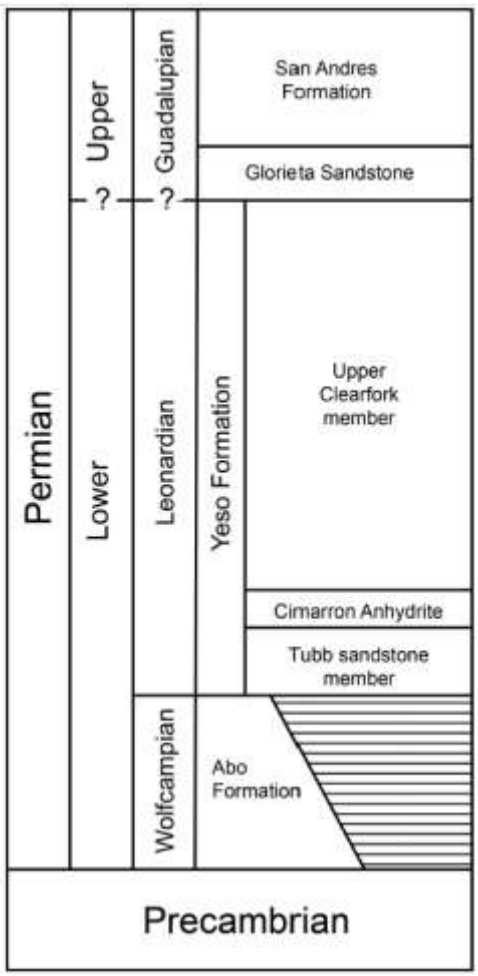


Figure 145. Stratigraphic column from Broadhead (2019). Between the Abo and Precambrian units, there are other units present in the off-structure areas.

The upper Yeso Formation consists of interbedded sandstone, siltstone, shale, carbonate, and anhydrite. Overlying the Yeso Formation, the Glorieta Sandstone, a white fine-grained, shallow marine sandstone, contains minor amounts of CO_2. The Glorieta Sandstone grades upward into the dolomite and anhydrite of the sabkha to shallow marine carbonates of the San Andres Formation. The clastics of the Bernal Formation is the final Permian deposits within the area. Like the Glorieta Sandstones, it has minor CO_2 resources.

The Triassic Santa Rosa Sandstone are alluvial and fluvial sandstones that are next major reservoir for CO_2 in the area. The shales of the overlying Chinle Formation provide an excellent seal to prevent upward gas migration.

The Jurassic Entrada Sandstone and the Cretaceous Dakota Sandstones are visible in some of the wells.

Geologic Model

The model developed for the Bravo Dome area includes over 2,500 wells (**Figure 146**). The tops for each well were handpicked for all the formations present in the logs. **Figure 147** is a cross section the goes along the crest of the structure from the northwest to the southeast. A database was built in S&P Kingdom that includes well header information, formation tops, bottom hole temperatures, and calculated geothermal gradients.

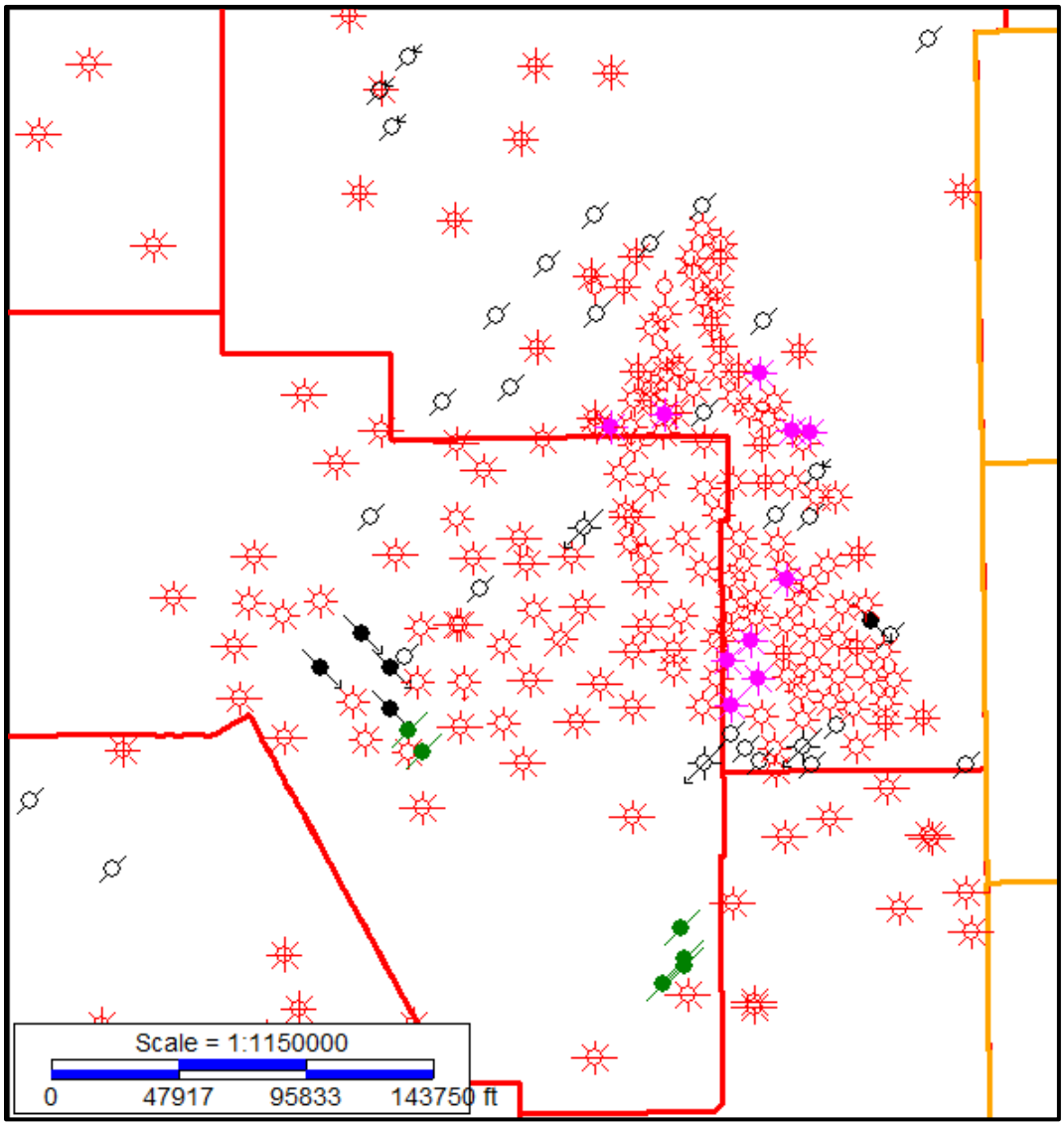


Figure 146. A base map for the Bravo Dome area and the wells that were interpretated. The Black symbols are injection wells, green symbols are plugged oil wells, and the red and purple symbols are for producing and plugged gas wells.

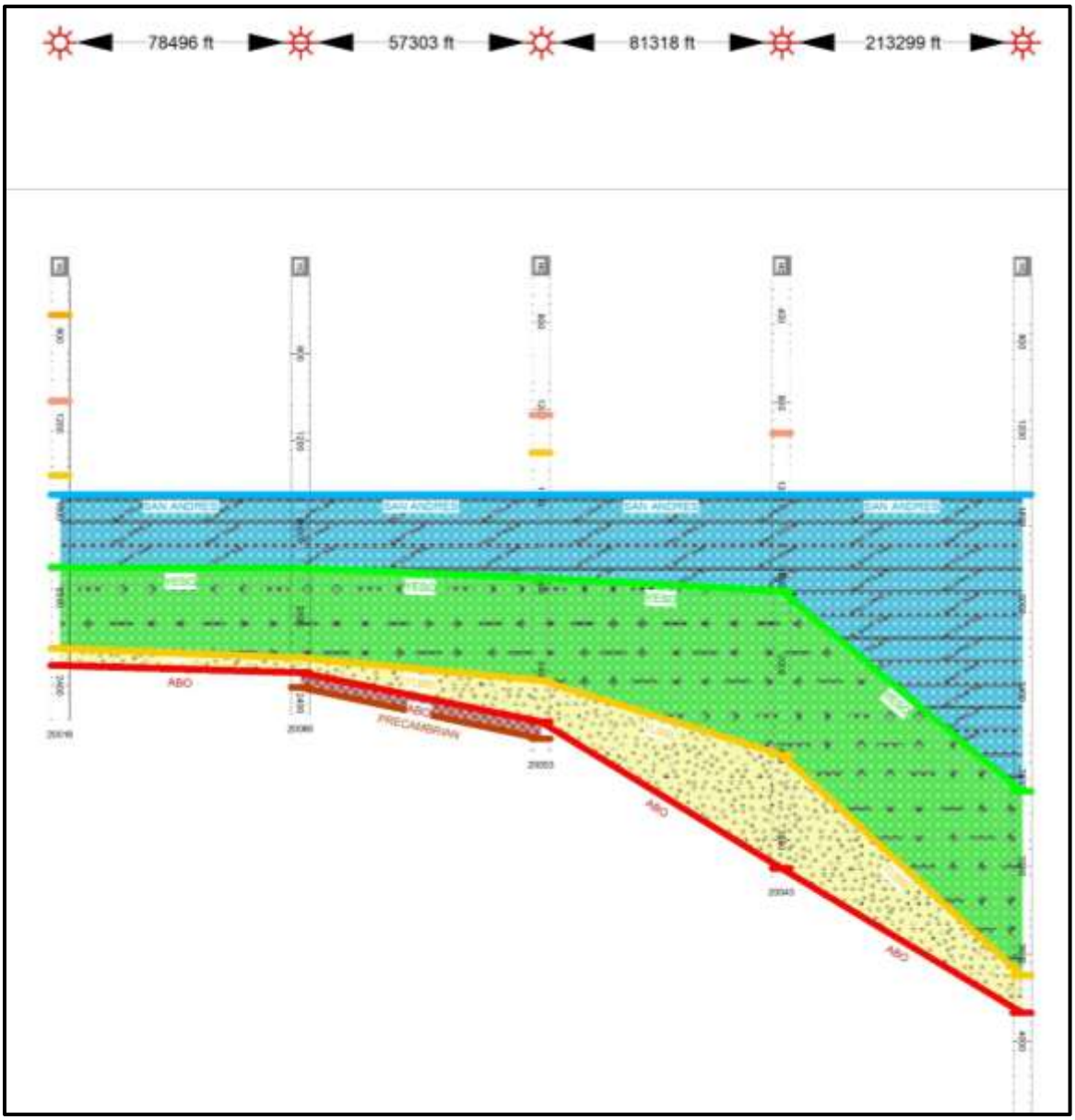


Figure 147. A cross section from the northwest (left side) to the southeast (right side) along the crest of the structure.

The following maps (**Figure 148** to **Figure 156**) are subsea structure maps for all the formation tops starting at the Precambrian to the Santa Rosa Formation. North is at the top of the map. The maps do not include the fault interpretations (on the Precambrian) and have a contour interval of 100 ft. Since the Cimarron Anhydrite is so thin, it was not picked.

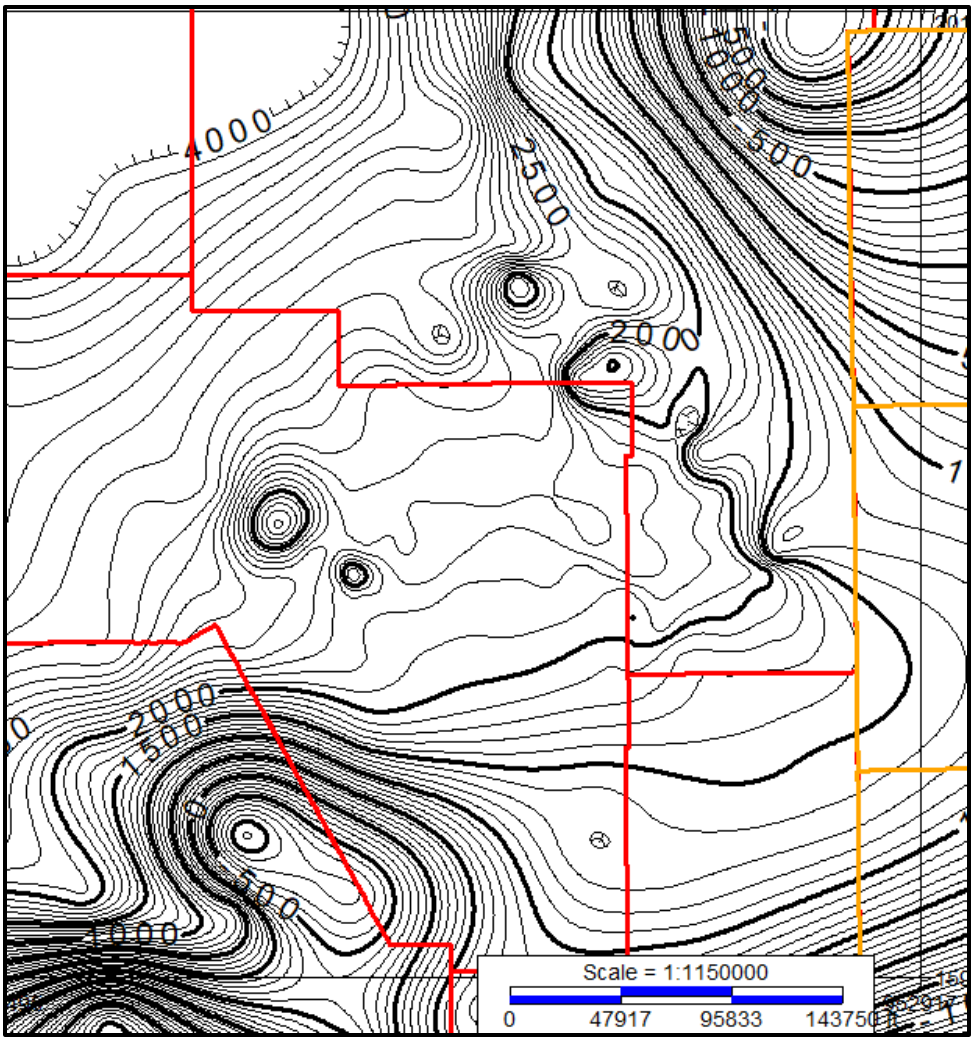


Figure 148. A structure map on the top of the Precambrian subsea surface.

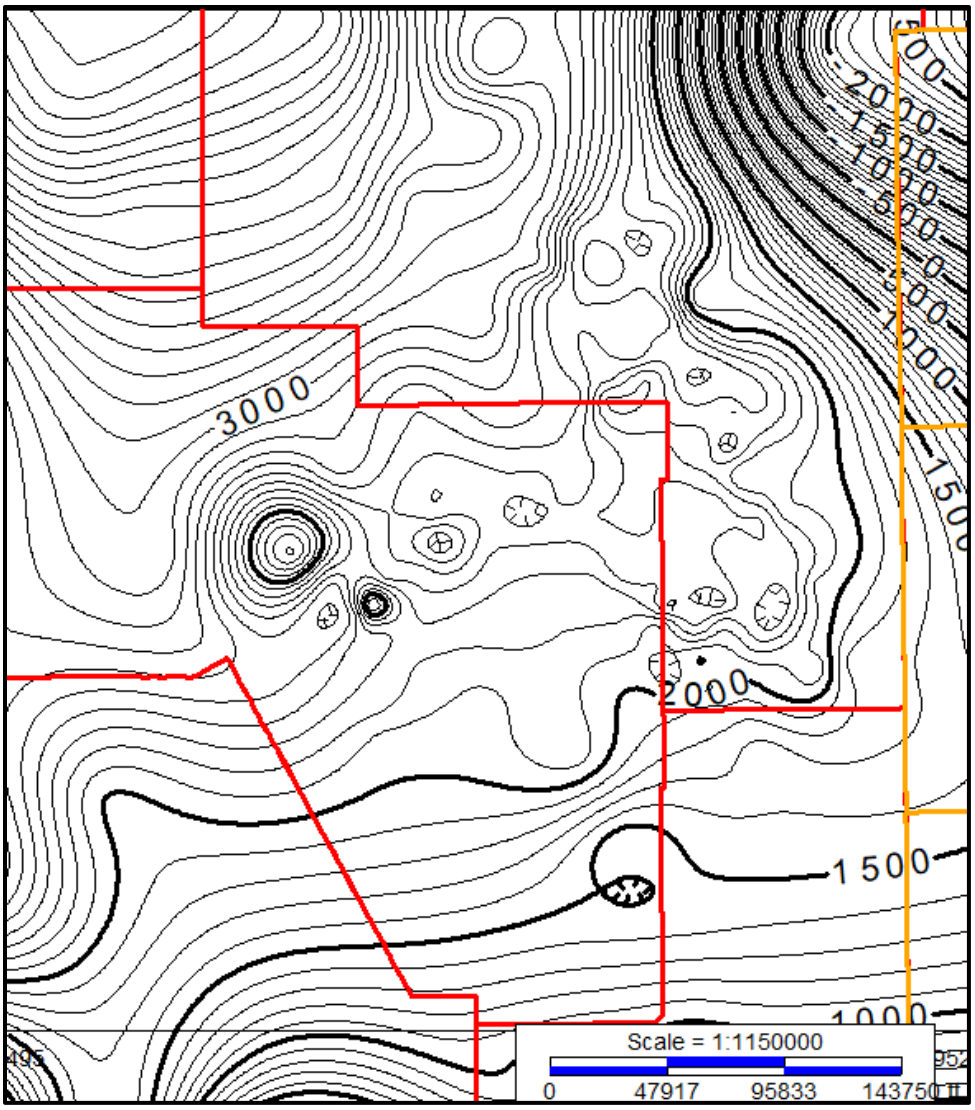


Figure 149. A structure map on the top of the Abo Formation subsea surface. Older interpretations have the Abo sediments as Granite Wash.

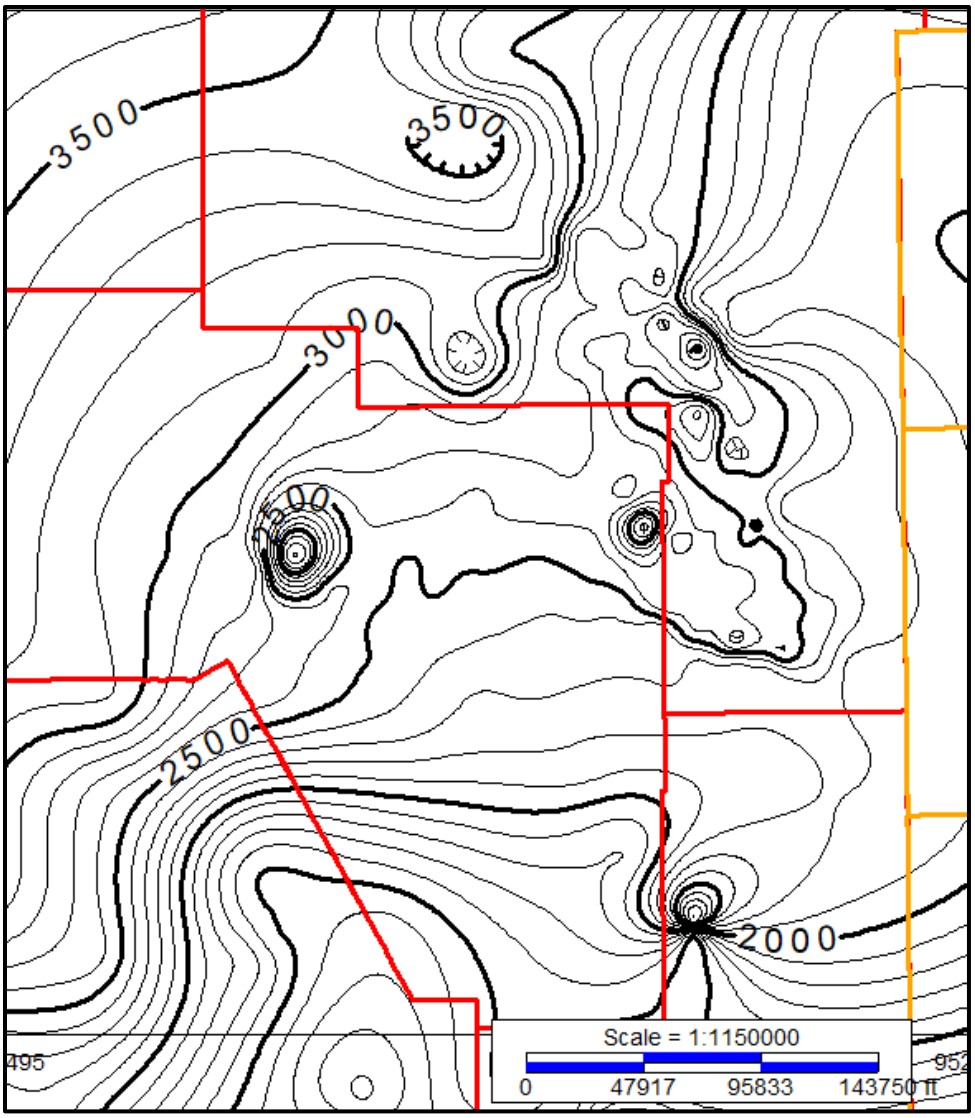


Figure 150. A structure map on the top of the Tubb Sandstone member of the Yeso Formation subsea surface. Overlying the Tubb Sandstone is the Cimarron Anhydrite. It is roughly 15 ft thick, and was not mapped.

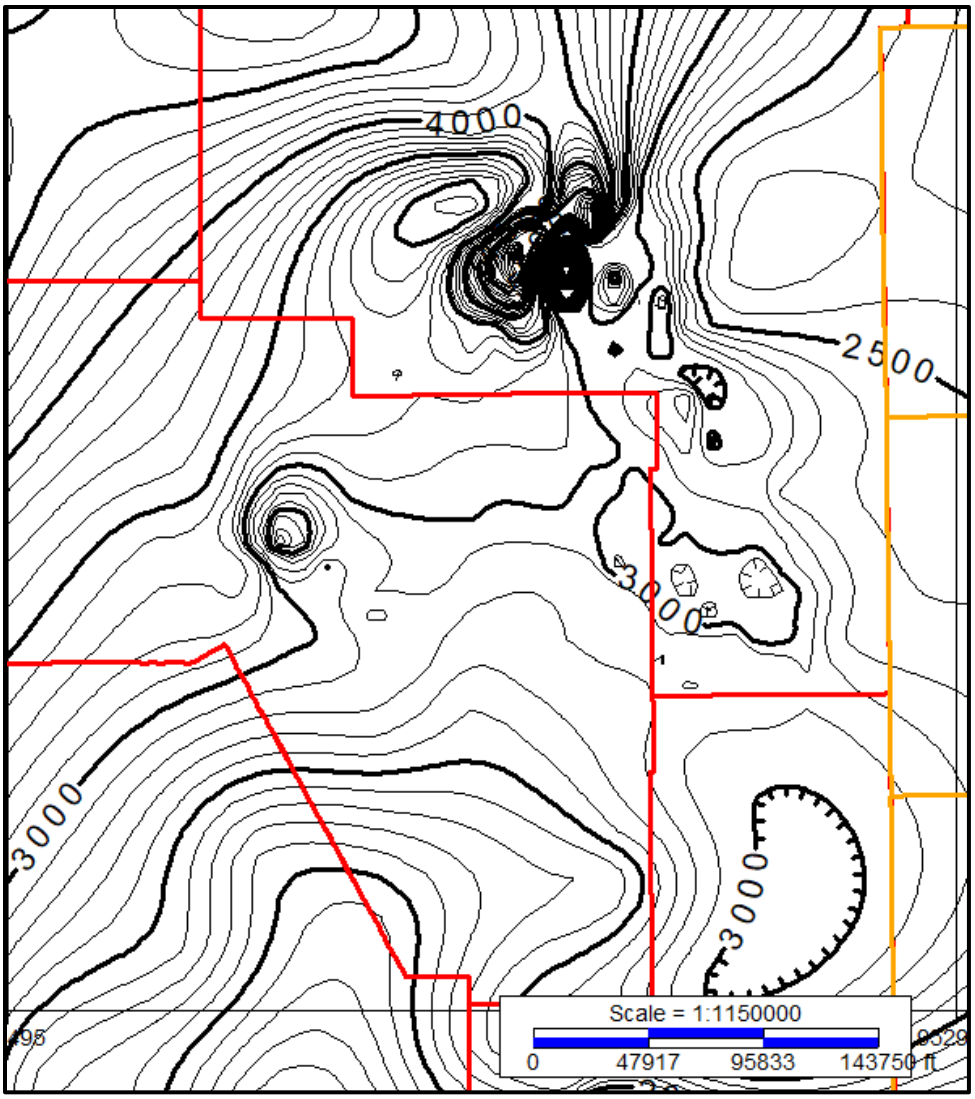


Figure 151. A structure map on the top of the Yeso Formation subsea surface.

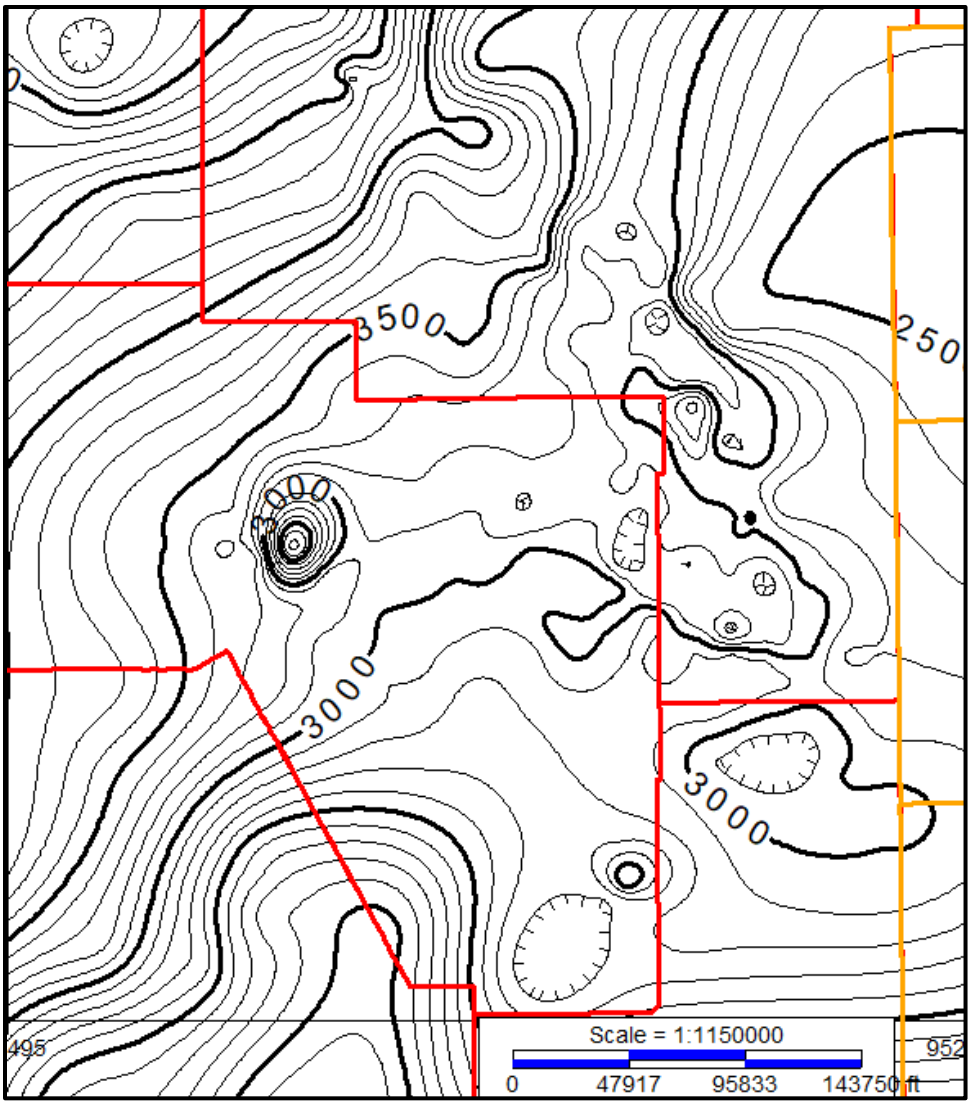


Figure 152. A structure map on the top of the Glorieta Sandstone subsea surface.

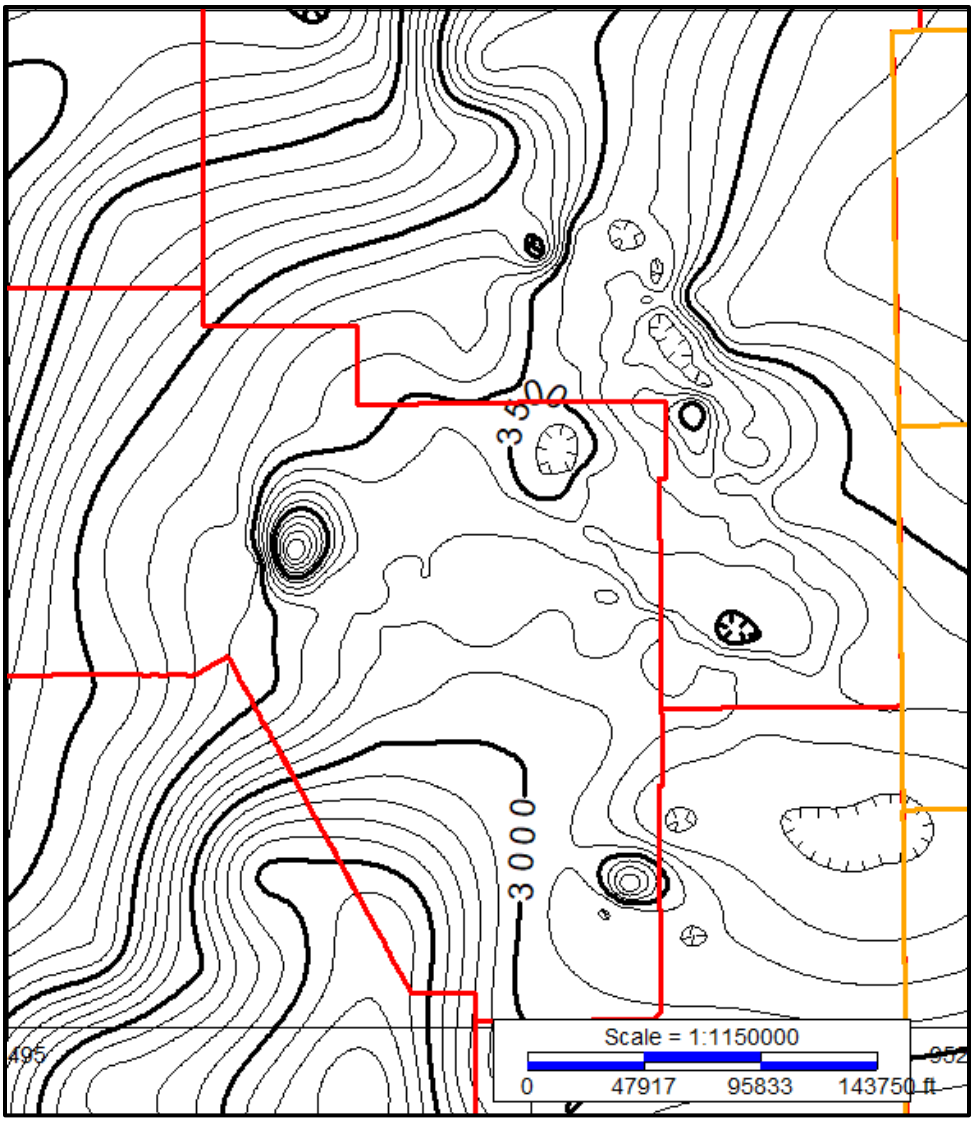


Figure 153. A structure map on the top of the San Andres Formation subsea surface.

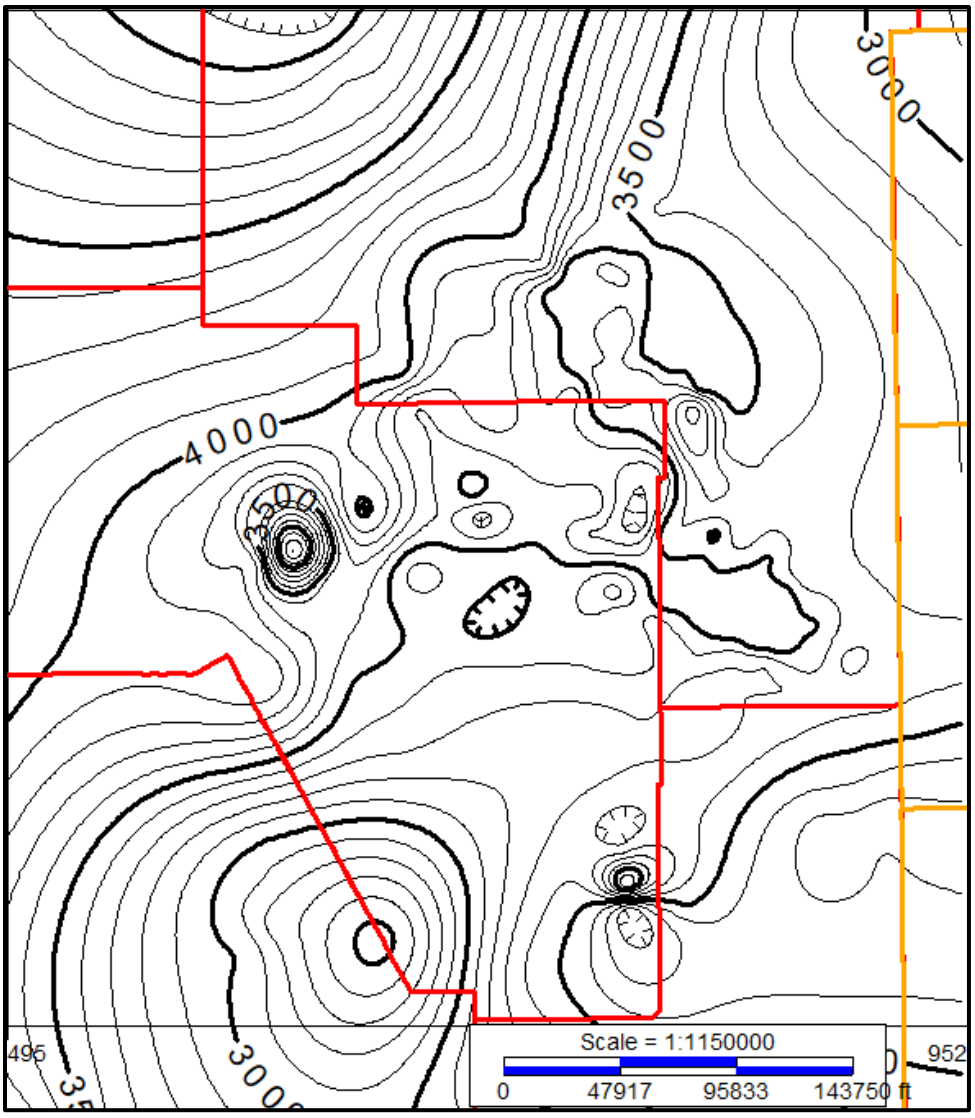


Figure 154. A structure map on the top of the Permian Bernal Formation subsea surface.

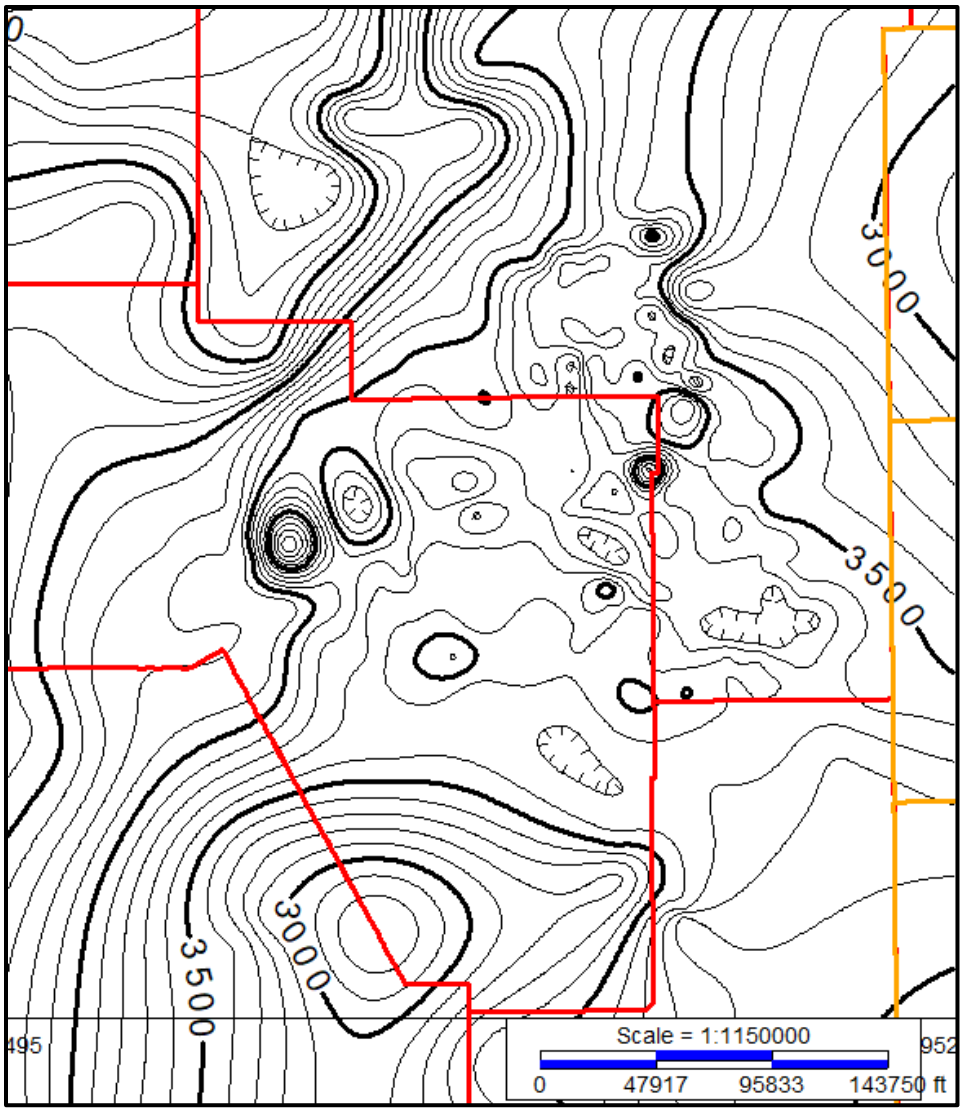


Figure 155. A structure map on the top of the Triassic Santa Rosa Sandstone subsea surface. The Santa Rosa Sandstone is a secondary CO_2 reservoir with the overlying Chinle shales sealing it.

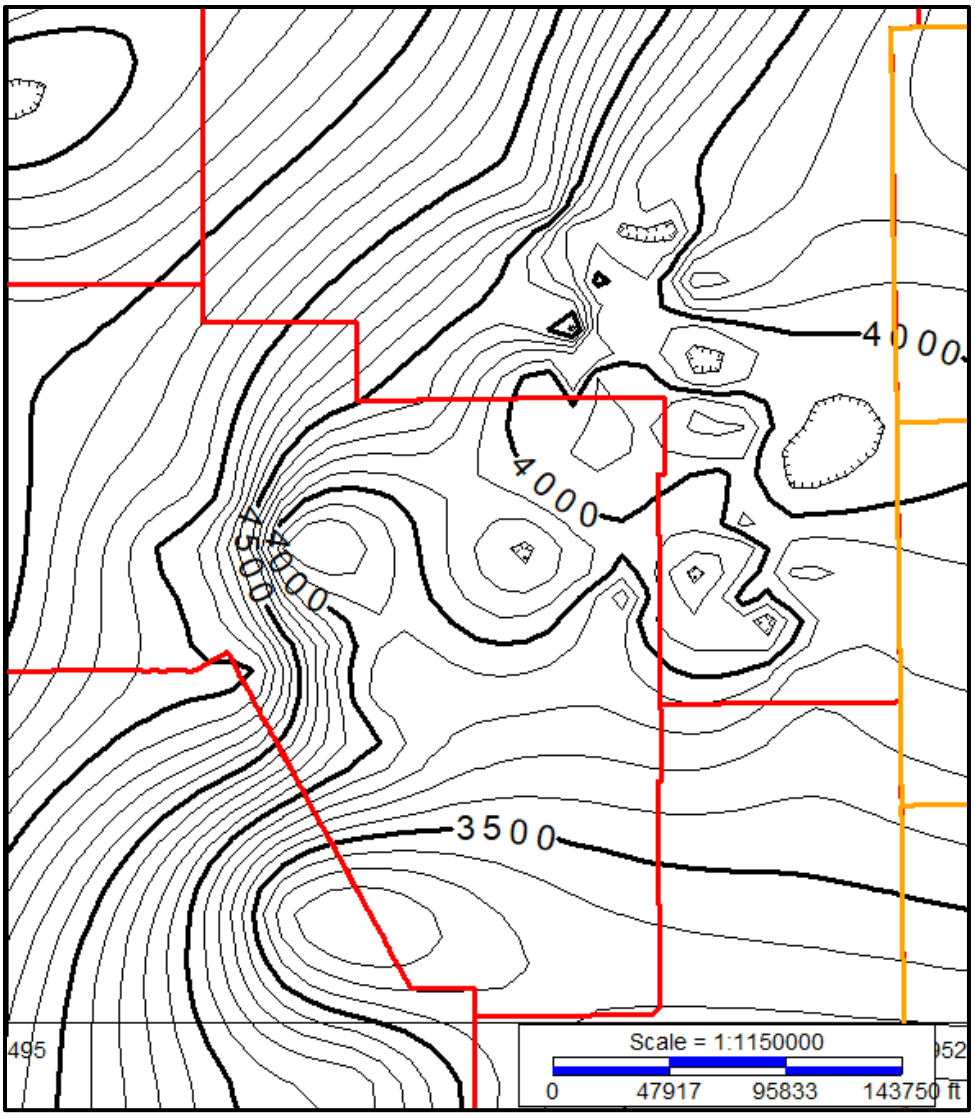


Figure 156. A structure map on the top of the Triassic Santa Rosa Sandstone subsea surface. The Santa Rosa Sandstone is a secondary CO_2 reservoir with the overlying Chinle shales sealing it.

CO_2 Emissions Source Database for New Mexico

Developed and refined second version using group feedback of Leopold framework for evaluating source viability beyond source size (Leopold Matrix) and distributed to state leads for characterization of "top 5" sources from each state.

Received and QA'd "top 5" source data from all states and first runs with all states' top 5 sources into SimCCS runs with Sean Yaw.

Using states top 5 sources, SimCCS: Price (above) and capture (below) mode results shown below:

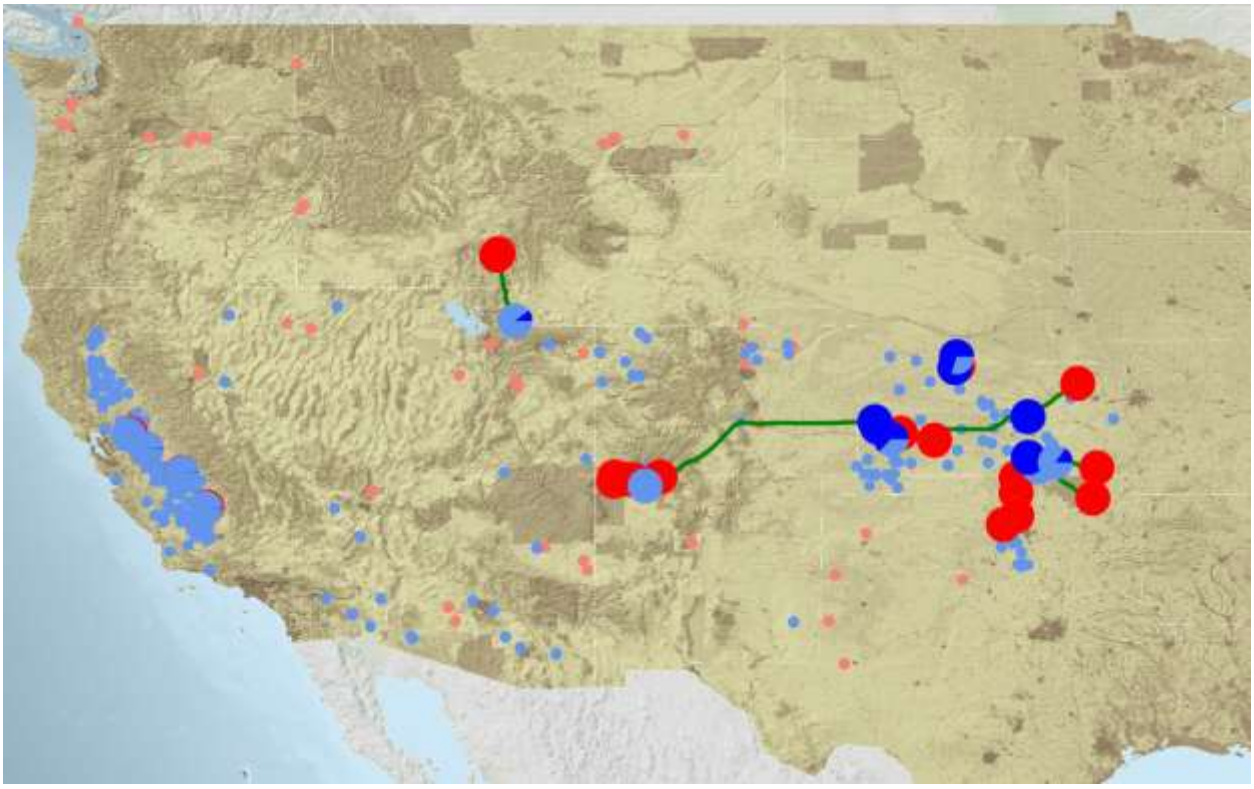


Figure 191 SimCCS price in the CUSP region is shown

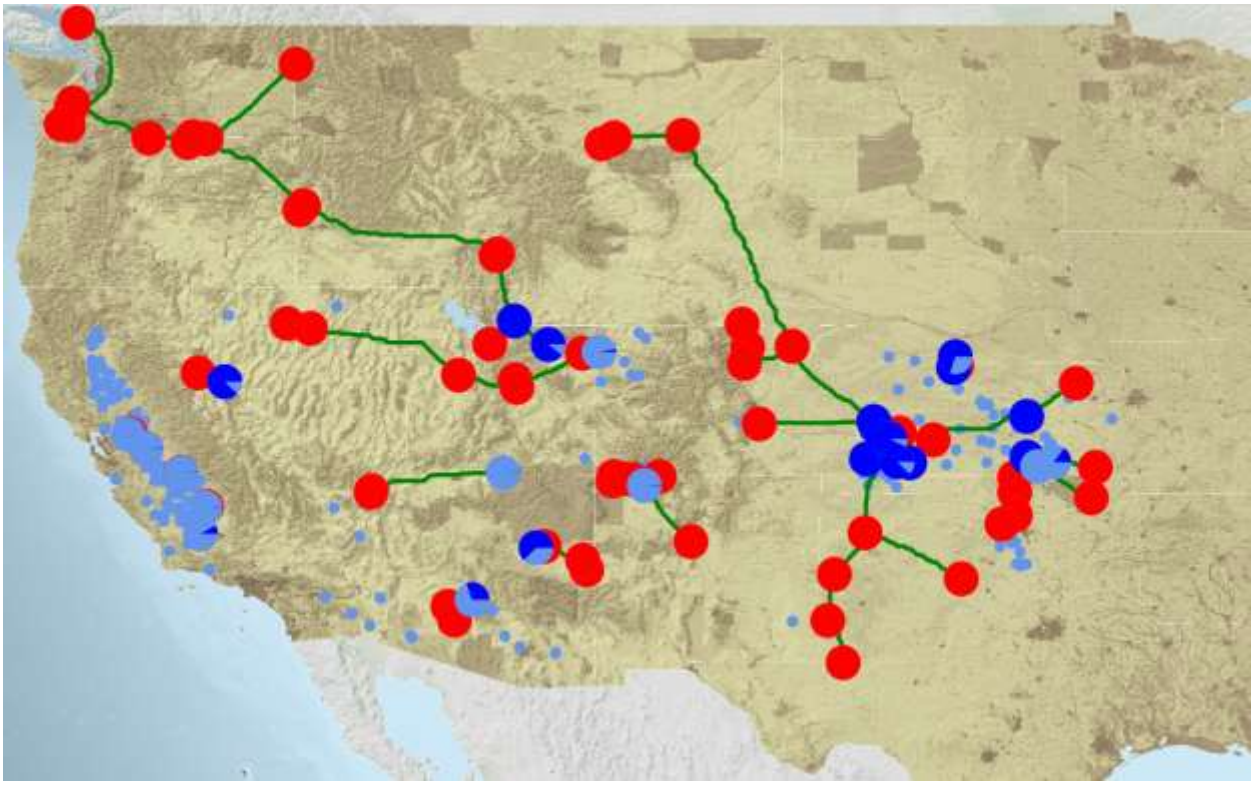


Figure 192 SimCCS cost of capture in the CUSP region is shown

- NM and other 4C states major CO_2 source data is ready in v 1.0 form
    - CO_2 source data input into SimCCS model in first CUSP wide studies shown above
- Leading 4 Corners case study group (mostly internal meetings this quarter with Dana to finalize sink data from NM as below)
- Preliminary version of V1.0 sink data for Four Corners states being readied for SimCCS runs (example formations mapped below)

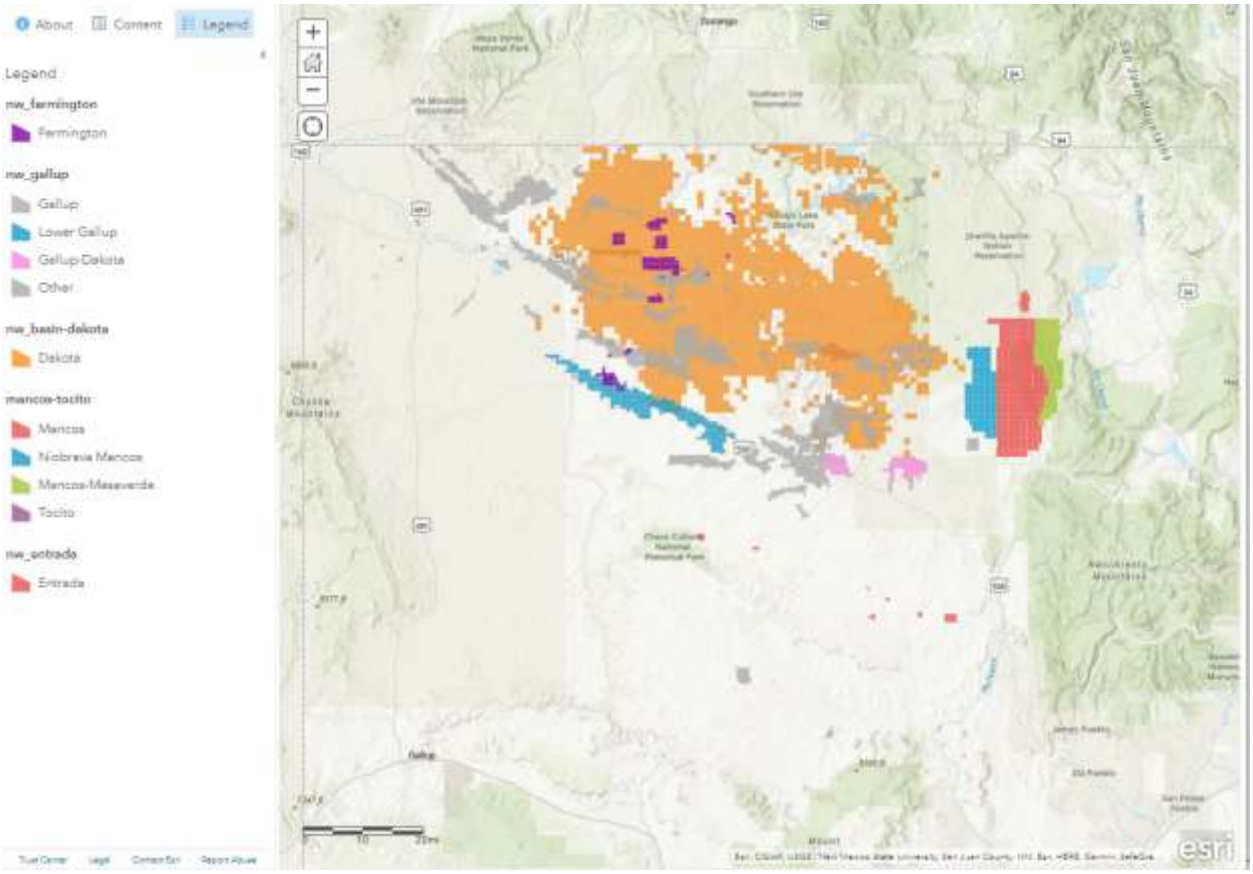


Figure 193 Potential sinks from the oil and gas reservoirs in the San Juan Basin region

SCO_2T^{PRO} Geologic Data

CUSP utilized the SCO_2T^{pro} Tool to rapidly characterize large areas of saline storage for carbon sequestration. Geologic parameters utilized by the include: depth (m), net thickness (m), porosity (fraction), permeability (mD), pressure (MPa), temperature (°C), and area (km^2). The center point of each 50 by 50 km grid was use to populate the data. For data-rich states like New Mexico, this was a simplification of the data. Future models might include a finer grid size.

Appendix C provides the geologic information utilized to develop the New Mexico maps (**Figure 191** to **Figure 195**). The outputs for the grid include injection rates, reservoir storage capacities, plume dimensions, and injection costs. Storage capacities represent how much CO_2 could be stored using multiple hypothetical wells within the grid cell.

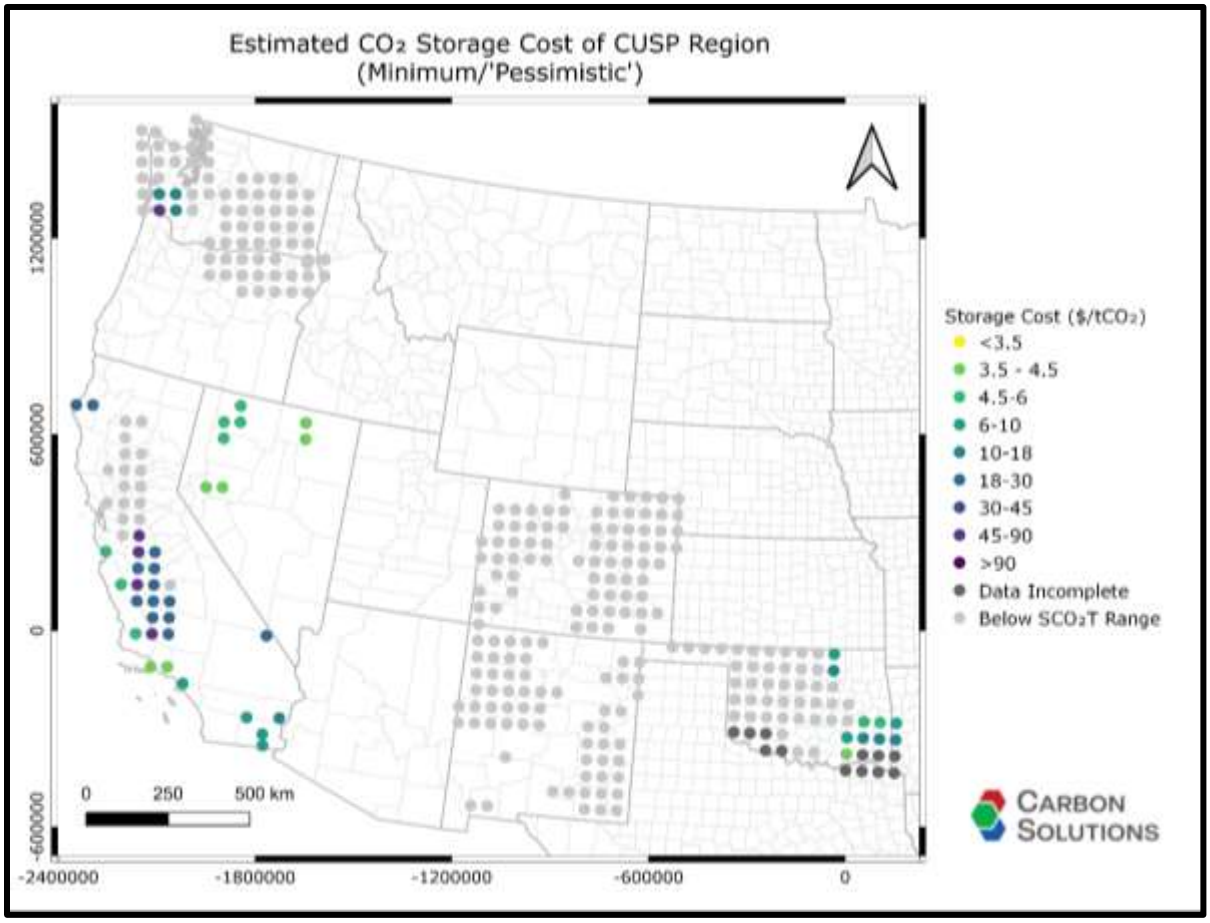


Figure 194 Minimum (pessimistic) cost of CO_2 storage in the CUSP region

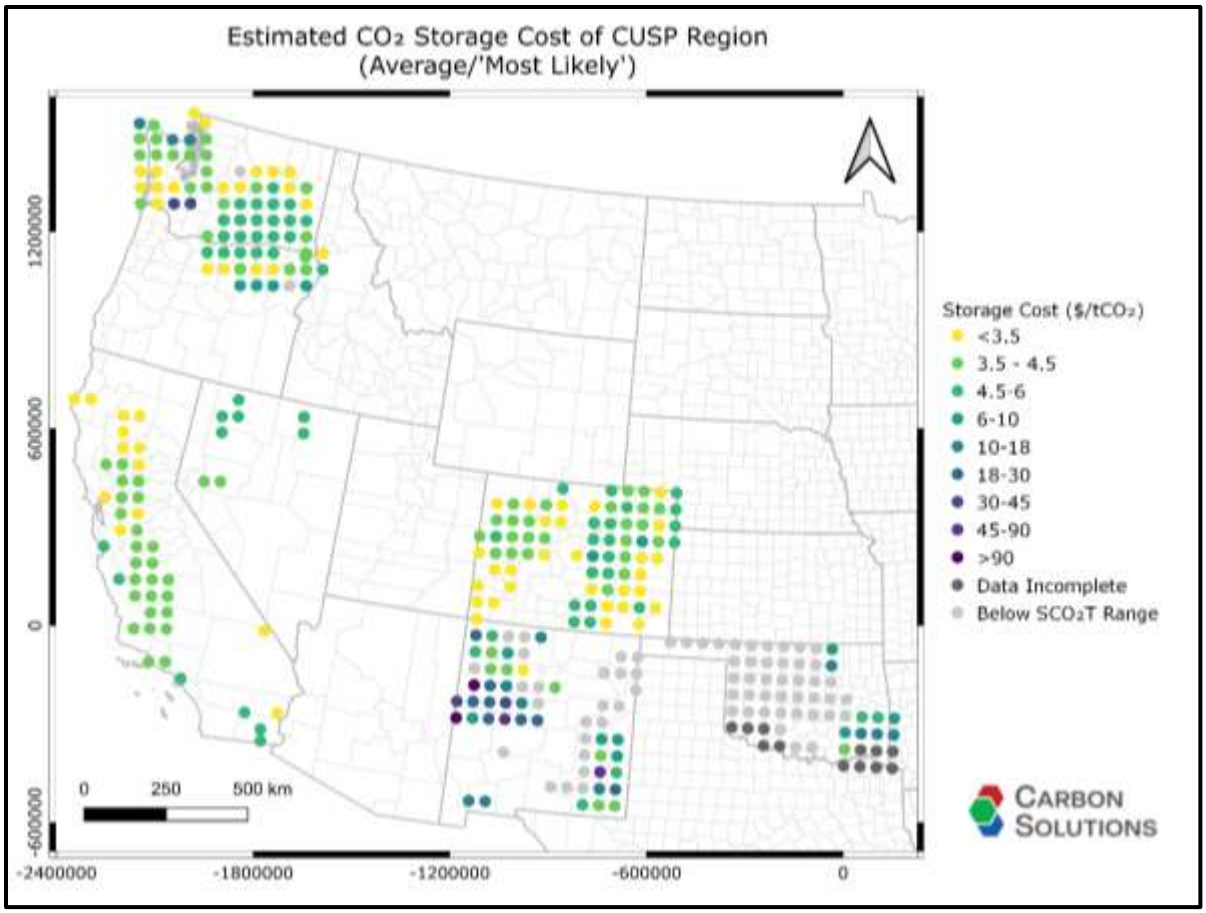


Figure 195 Average ("most likely") cost of CO_2 storage in the CUSP region

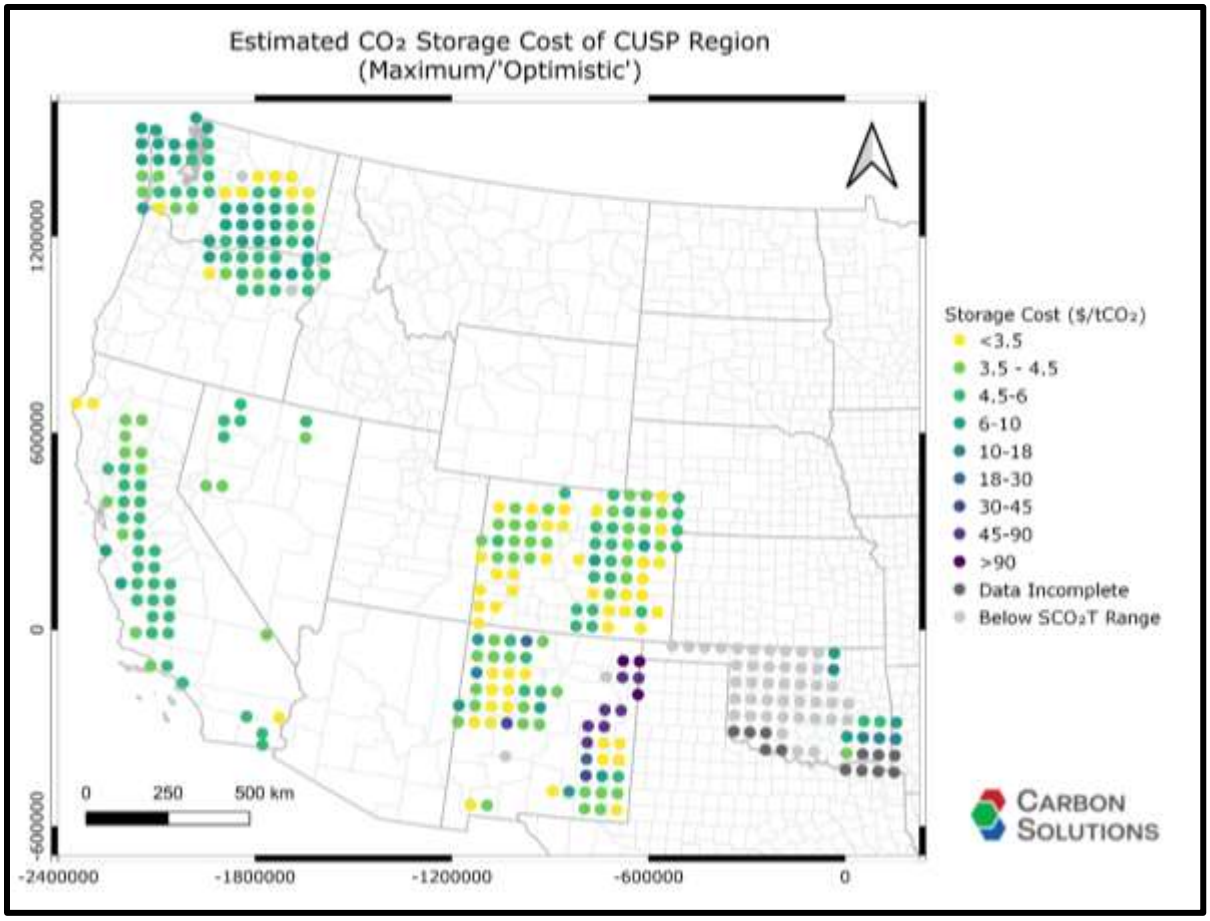


Figure 196 Maximum (optimistic) cost of CO_2 storage in the CUSP region

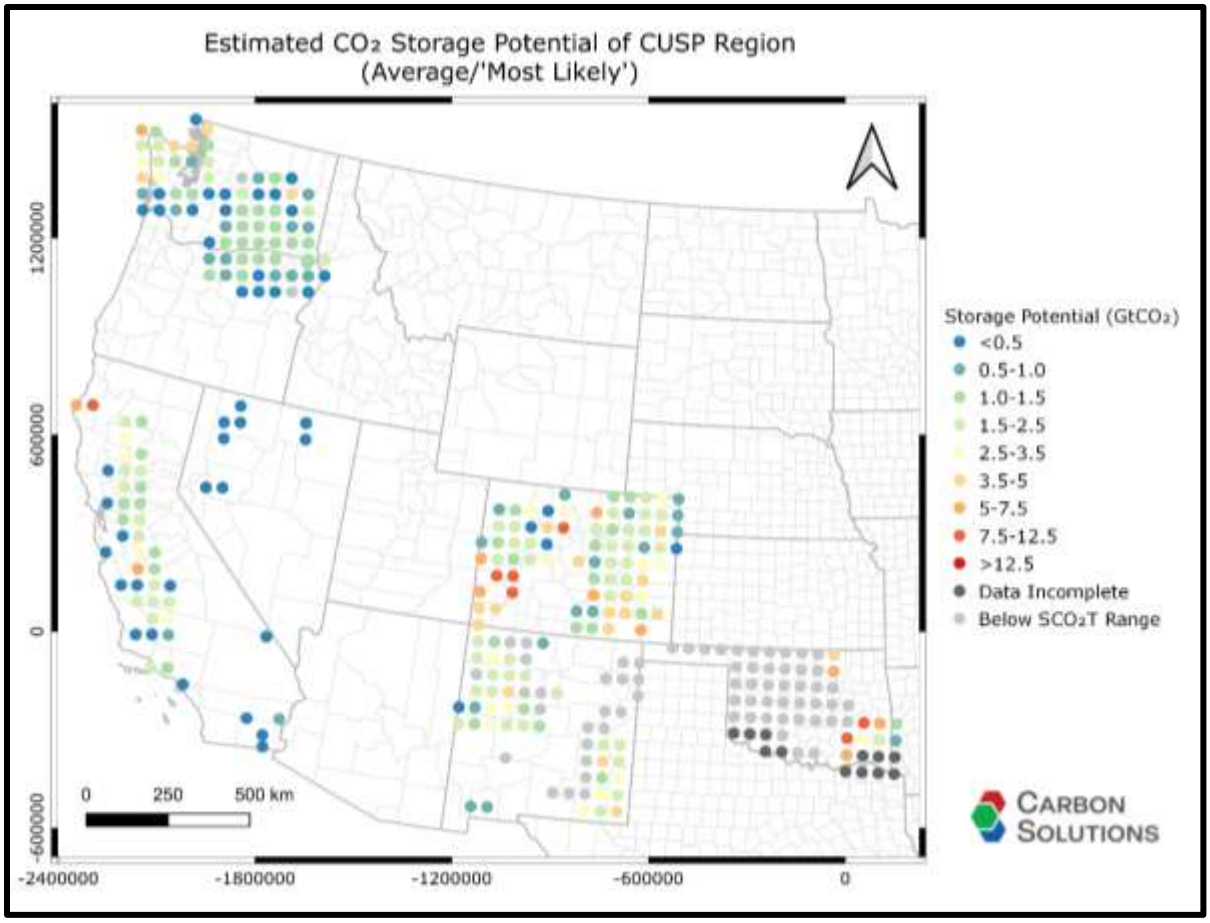


Figure 197 Average storage potential of CO_2 storage in the CUSP region

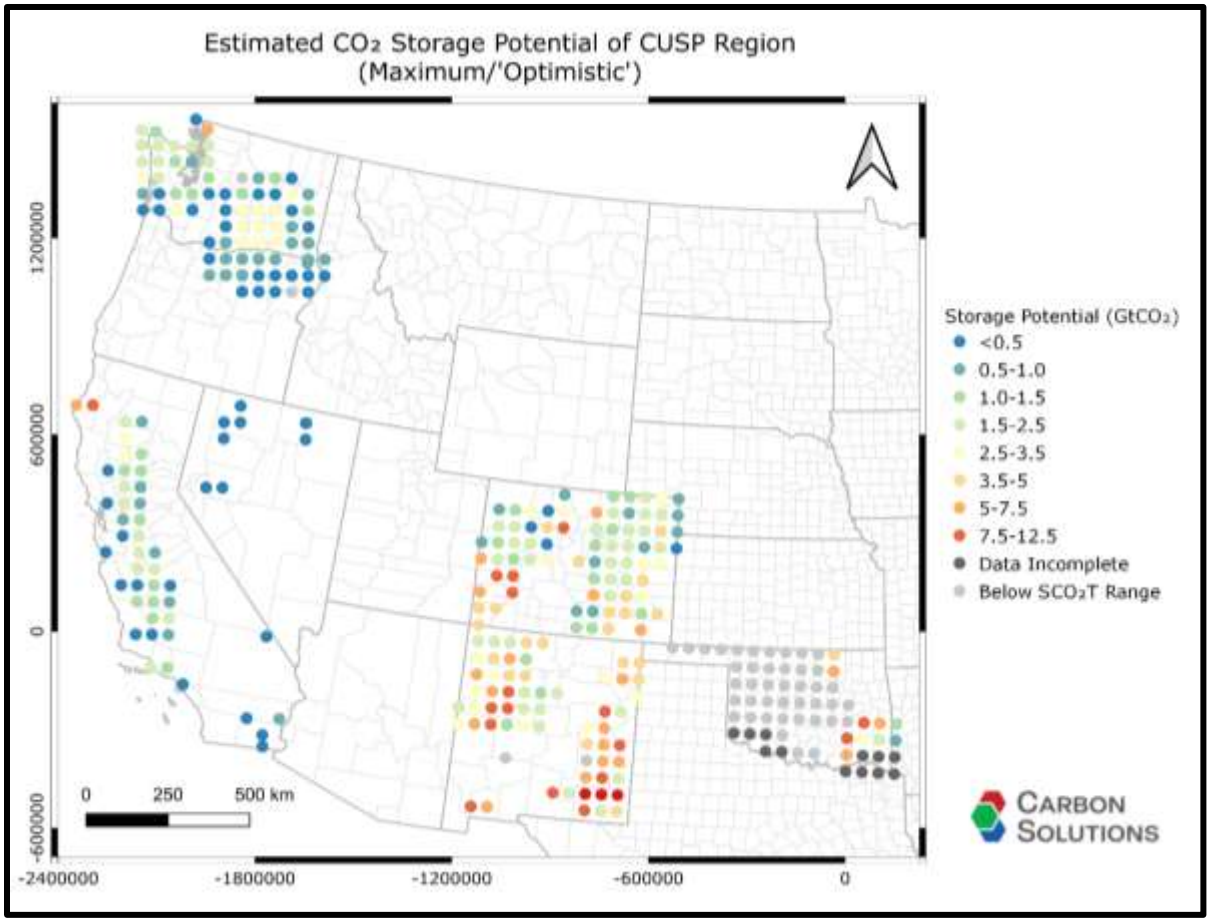


Figure 198 Maximum (optimistic) storage potential of CO_2 storage in the CUSP region

References

Broadhead RF. 2017. Energy and mineral resources of New Mexico: petroleum geology. Socorro (NM); New Mexico Bureau of Geology and Mineral Resources. Memoir 50A. 104 p.

Broadhead RF. 2019. Carbon dioxide in the subsurface of northeastern New Mexico. In: Ramos F, Zimmerer MJ, Zeigler K, Ulmer-Scholle DS, editors. Geology of the Raton–Clayton area. Socorro (NM); New Mexico Geological Society. 70th Field Conference. p. 101–108.

Cather SM. 2020. Jurassic stratigraphic nomenclature for northwestern New Mexico. In: Frey B, Kelley S, Zeigler K, McLemore V, Goff F, Ulmer-Scholle DS, editors. The geology of the Mount Taylor area. Socorro (NM); New Mexico Geological Society. Special Publication 14. p. 145–152.

Cooper SP, Lorenz JC. 2020. Fracture analysis of Wolfcamp core from the Pure Oil Red Hills Unit No. 1 well (BM 1827), Lea County, New Mexico. Houston (TX): FractureStudies LLC. 70 p. [accessed 2026 Jan 2]. https://www.fracturestudies.com/index.html

Craigg SD. 2001. Geologic framework of the San Juan structural basin of New Mexico, Colorado, Arizona, and Utah, with emphasis on Triassic through Tertiary rocks. Washington (DC); U.S. Geological Survey. Professional Paper 1420. 63 p.

Dickinson WR, Snyder WS. 1978. Plate tectonics of the Laramide orogeny. In: Matthews VE, editor. Laramide folding associated with basement block faulting in the western United States. Boulder (CO); Geological Society of America. Memoir 151. p. 355–365.

Ewing E. 2019. Tectonics of the West Texas (Permian) Basin—origins, structural geology, subsidence, and later modification. In: Ruppel S, editor. Anatomy of a Paleozoic basin: the Permian Basin, USA. Vol. 1. Austin (TX); University of Texas at Austin, Bureau of Economic Geology. Report of Investigations 285; AAPG Memoir 118. p. 63–96.

Fu Q, Baumgardner RW Jr, Hamlin HS. 2020. Early Permian (Wolfcampian) succession in the Permian Basin: icehouse platform, slope carbonates, and basinal mudrocks. In: Ruppel S, editor. Anatomy of a Paleozoic basin: the Permian Basin, USA. Vol. 2. Austin (TX); University of Texas at Austin, Bureau of Economic Geology. Report of Investigations 285; AAPG Memoir 118. p. 185–225.

Ge J, Nicot JP, Hennings PH, Smye KM, Hosseini SA, Gao RS, Breton CL. 2022. Recent water disposal and pore pressure evolution in the Delaware Mountain Group, Delaware Basin, southeast New Mexico and west Texas, USA. J Hydrol Reg Stud. 40:100987. doi:10.1016/j.ejrh.2022.101041

Giesen JH, Scholle PA. 1990. Regional basinal sandstone depositional patterns during the Guadalupian (Late Permian), Delaware Basin, west Texas–New Mexico. AAPG Bull. 74:660–661.

Harms J. 1974. Brushy Canyon Formation, Texas: a deepwater density current deposit. Geol Soc Am Bull. 85:1763–1784.

Harrington R. 2019. The Middle–Upper Ordovician Simpson Group of the Permian Basin: stratigraphy, lithofacies, and reservoir development. In: Ruppel S, editor. Anatomy of a Paleozoic basin: the Permian Basin, USA. Vol. 1. Austin (TX); University of Texas at Austin, Bureau of Economic Geology. Report of Investigations 285; AAPG Memoir 118. p. 331–352.

Harrington R, Ruppel S. 2019. Patterns of Montoya Group (Middle Ordovician) deposition, diagenesis, and reservoir development in the Permian Basin. In: Ruppel S, editor. Anatomy of a Paleozoic basin: the Permian Basin, USA. Vol. 1. Austin (TX); University of Texas at Austin, Bureau of Economic Geology. Report of Investigations 285; AAPG Memoir 118. p. 353–378.

Hills JM. 1984. Sedimentation, tectonism, and hydrocarbon generation in the Delaware Basin, west Texas and southeastern New Mexico. AAPG Bull. 68:250–267.

Horne EA, Hennings PH, Zahm CK. 2021. Basement-rooted faults of the Delaware Basin and Central Basin Platform, Permian Basin, west Texas and southeastern New Mexico. In: Callahan OA, Eichhubl P, editors. The geologic basement of Texas. Austin (TX); University of Texas at Austin, Bureau of Economic Geology. p. 1–37.

Horne EA, Hennings PH, Smye KM, Staniewicz S, Chen J, Savvaidis A. 2022. Structural characteristics of shallow faults in the Delaware Basin. Interpretation. 10:T807–T835.

Jarvie DM, Claxton BL, Henk B, Breyer JT. 2001. Oil and shale gas from the Barnett Shale, Fort Worth Basin, Texas. AAPG Bull. 85:A100.

Kelley VC. 1951. Tectonics of the San Juan Basin. In: Guidebook of the south and west sides of the San Juan Basin, New Mexico and Arizona. Durango (CO); Four Corners Geological Society. 1st Field Conference. p. 53–55.

Kelley SA, Engler T, Cather M, Pokorny C, Yang CH, Mamer E, Hoffman G, Wilch J, Johnson P, Zeigler K. 2014. Hydrologic assessment of oil and gas resource development of the Mancos Shale in the San Juan Basin, New Mexico. Socorro (NM); New Mexico Bureau of Geology and Mineral Resources. Open-File Report 566. 65 p.

Kerans C, Ruppel SC. 2020. Composite and high-frequency cyclicity in middle Permian shelf carbonates: the San Andres and Grayburg succession in the Permian Basin. In: Ruppel S, editor. Anatomy of a Paleozoic basin: the Permian Basin, USA. Vol. 2. Austin (TX); University of Texas at Austin, Bureau of Economic Geology. Report of Investigations 285; AAPG Memoir 118. p. 349–397.

Kernodle JM. 1995. Hydrogeology and steady-state simulation of ground-water flow in the San Juan Basin, New Mexico, Colorado, Arizona, and Utah. Washington (DC); U.S. Geological Survey. Water-Resources Investigations Report 95-4187. 117 p.

King RE. 1945. Stratigraphy and oil-producing zones of the pre–San Andres formations of southeastern New Mexico. Socorro (NM); State Bureau of Mines and Mineral Resources. Bulletin 23. 34 p.

King PB. 1948. Oil and shale gas from the Barnett Shale, Fort Worth Basin, Texas. Washington (DC); U.S. Geological Survey. Professional Paper 215. 183 p.

Loucks RL. 2016. Review of the Lower Ordovician Ellenburger Group of the Permian Basin, west Texas. Houston (TX): Bureau of Economic Geology, The University of Texas at Austin. 95 p. https://www.researchgate.net/publication/267850454

Loucks R, Kerans C. 2019. A geologic review of the Lower Ordovician Ellenburger Group of the Permian Basin, west Texas and southeast New Mexico. In: Ruppel S, editor. Anatomy of a Paleozoic basin: the Permian Basin, USA. Vol. 1. Austin (TX); University of Texas at Austin, Bureau of Economic Geology. Report of Investigations 285; AAPG Memoir 118. p. 295–330.

Nance HS. 2020. Guadalupian (Artesia Group) and Ochoan shelf successions of the Permian Basin: effects of deposition, diagenesis, and structure on reservoir development. In: Ruppel S, editor. Anatomy of a Paleozoic basin: the Permian Basin, USA. Vol. 2. Austin (TX); University of Texas at Austin, Bureau of Economic Geology. Report of Investigations 285; AAPG Memoir 118. p. 437–496.

Nance HS, Hamlin HS. 2020. The Bone Spring Formation (Leonardian) of the Delaware Basin: deepwater lithofacies and stratigraphy. In: Ruppel S, editor. Anatomy of a Paleozoic basin: the Permian Basin, USA. Vol. 2. Austin (TX); University of Texas at Austin, Bureau of Economic Geology. Report of Investigations 285; AAPG Memoir 118. p. 321–348.

Ruppel S. 2019a. Anatomy of a Paleozoic basin: the Permian Basin, USA—introduction, overview, and evolution. In: Ruppel S, editor. Anatomy of a Paleozoic basin: the Permian Basin, USA. Vol. 1. Austin (TX); University of Texas at Austin, Bureau of Economic Geology. Report of Investigations 285; AAPG Memoir 118. p. 1–27.

Ruppel S. 2019b. The Fusselman of the Permian Basin: depositional and diagenetic facies development on a stable platform during the Late Ordovician–Early Silurian icehouse. In: Ruppel S, editor. Anatomy of a Paleozoic basin: the Permian Basin, USA. Vol. 2. Austin (TX); University of Texas at Austin, Bureau of Economic Geology. Report of Investigations 285; AAPG Memoir 118. p. 379–399.

Ruppel S. 2020a. Lower Permian (Leonardian) platform carbonate succession: deposition and diagenesis during a waning icehouse period. In: Ruppel S, editor. Anatomy of a Paleozoic basin: the Permian Basin, USA. Vol. 2. Austin (TX); University of Texas at Austin, Bureau of Economic Geology. Report of Investigations 285; AAPG Memoir 118. p. 27–281.

Ruppel S, Hovorka S, Barnaby R. 2020a. Proximal shallow-water carbonates and distal biosiliceous cherts of the Lower Devonian Thirtyone Formation, Permian Basin. In: Ruppel S, editor. Anatomy of a Paleozoic basin: the Permian Basin, USA. Vol. 2. Austin (TX); University of Texas at Austin, Bureau of Economic Geology. Report of Investigations 285; AAPG Memoir 118. p. 37–74.

Ruppel SC, Rowe H, Reed R, Barrick JE, James EW, Loucks RG. 2020b. The Woodford Formation of the Permian Basin: regional Middle to Late Devonian transgression and accompanying global anoxia. In: Ruppel S, editor. Anatomy of a Paleozoic basin: the Permian Basin, USA. Vol. 2. Austin (TX); University of Texas at Austin, Bureau of Economic Geology. Report of Investigations 285; AAPG Memoir 118. p. 75–124.

Ruppel SC, Rowe H, Reed R, Loucks RG. 2020c. The Mississippian System in the Permian Basin: proximal platform carbonates and distal organic-rich mudrocks. In: Ruppel S, editor. Anatomy of a Paleozoic basin: the Permian Basin, USA. Vol. 2. Austin (TX); University of Texas at Austin, Bureau of Economic Geology. Report of Investigations 285; AAPG Memoir 118. p. 125–158.

Scholle P, Broadhead RF, McLemore V. 2020a. The Permian Basin. In: Scholle P, Ulmer-Scholle DS, Cather S, Kelley S, editors. The geology of southern New Mexico parks, monuments, and public lands. Socorro (NM); New Mexico Bureau of Geology and Mineral Resources. p. 285–295.

Scholle PA, Goldstein RH, Ulmer-Scholle DS. 2007. Classic Upper Paleozoic reefs and bioherms of west Texas and New Mexico: field guide to the Guadalupe and Sacramento Mountains. Socorro (NM); New Mexico Bureau of Geology and Mineral Resources. 178 p.

Smye KM, Hennings PH, Horne EA. 2021. Variations in vertical stress in the Permian Basin region. AAPG Bull. 105:1893–1907.

Stone WJ, Lyford FP, Frenzel PF, Mizell NH, Padgett ET. 1983. Hydrogeology and water resources of the San Juan Basin, New Mexico. Socorro (NM); New Mexico Bureau of Mines and Mineral Resources. 72 p.

Ward RF, Kendall CGSC, Harris PM. 1986. Upper Permian (Guadalupian) facies and their association with hydrocarbons—Permian Basin, west Texas and New Mexico. AAPG Bull. 70:239–262.

Wilson JL. 1972. Cyclic and reciprocal sedimentation in Virgilian strata of southern New Mexico. In: Elam JG, Chuber S, editors. Cyclic sedimentation in the Permian Basin. 2nd ed. Midland (TX); West Texas Geological Society. Publication 72-60. p. 82–99.

Wright WF. 1979. Petroleum geology of the Permian Basin. Midland (TX): West Texas Geological Society. 103 p.

Wright W. 2020. Pennsylvanian (upper Carboniferous) paleodepositional evolution of the greater Permian Basin, Texas and New Mexico: depositional systems and hydrocarbon reservoir analysis. In: Ruppel S, editor. Anatomy of a Paleozoic basin: the Permian Basin, USA. Vol. 2. Austin (TX); University of Texas at Austin, Bureau of Economic Geology. Report of Investigations 285; AAPG Memoir 118. p. 159–183.

Oklahoma

The Oklahoma Geological Survey (OGS) assisted University of Oklahoma (OU) PI Professor Rouzbeh Moghanloo with the CUSP activities related to Oklahoma. On behalf of the State of Oklahoma, Moghanloo presented at the annual CUSP meeting in 2022 and 2023. OGS activities included presenting state updates at the 2024 and 2025 CUSP annual meetings, working with the Oklahoma Secretary of Energy and the Environment on state legislation for carbon management (a prerequisite for Class VI primacy), and contributing to focused projects. One focused project, "From Site to State: Design of an Integrated CCS Operation in a Complex Geological Structure in Osage County, Oklahoma," was led by Moghanloo and is discussed in this report by Benmadi Milad. The other focused projects are the Utah Iron Mountain project and the Kansas–Oklahoma ONEOK project, discussed in this report by Nathan Moodie ("CCS at the Iron Mountain Iron Mine and Direct Reduced Iron Processing Plant, Southern Utah") and Brendan Bream ("Infrastructure Development for Handling of New Gaseous Products for Natural Gas Liquids Fractionation and Gas Processing Plants in Kansas and Oklahoma"), respectively. Lastly, Ming Suriamin (of the OGS) contributed OGS data to the SCO_2T database. Moghanloo coauthored the publication by Miranda et al. (2023) that described an economic model for carbon capture and storage (CCS) deployment in Oklahoma using geologic data provided by a third party (not OGS).

References

Miranda MW, Ogland-Hand JD, Bielicki JM, Moghanloo RG, DaneshFar J, Middleton RS. 2023. Developing a roadmap for carbon capture and storage in Oklahoma by assessing the viability of stacked storage. Greenh Gases Sci Technol. 13(6):763–779. doi:10.1002/ghg.2244

Oklahoma Geological Survey Carbon Capture, Utilization, and Storage Curriculum

CCUS deployment depends on local community support (NETL 2017) but over a third of American adults are unfamiliar with this technology (Bedle et al. 2024). Accelerating CCUS technology deployment in the Western Region thus requires an informed citizenry and a prepared workforce.

In 2023, the Oklahoma Geological Survey (OGS; https://www.ou.edu/ogs, accessed December 2, 2025), a CUSP partner and agency representing Oklahoma, received DOE funding from the Regional Initiative to Accelerate Carbon Capture, Utilization, and Storage CCUS) Deployment: Technical Assistance for Large-Scale Data Gathering, Analysis, Sharing, and Engagement (DOE-FOA-0002799). The 2-yr project, "Oklahoma Geological Survey coordination of mid-continent carbon management" (DE-FE0032374), began in early 2024 and included a required plan for community and stakeholder engagement (Hayman et al. 2023). The project also promised coordination and collaboration with regional initiatives like CUSP.

Throughout 2024, the OGS Education and Outreach team developed outreach activities for different stakeholder groups, including academia, state and federal agencies, industry partners, Tribal Nations, K-12 teachers, K-12 students, special interest groups, and the public. These efforts included informational materials about CCUS and cutting-edge projects in Oklahoma and creation of a professional development curriculum. These materials are freely available to the public via the OGS website and are shared with CUSP and other regional partners for dissemination.

Prior to January of 2025, the OGS Education and Outreach team collaborated with OGS research scientists on other teams, including Energy Geoscience, the Seismic Network, and the Oklahoma Petroleum Information Center (OPIC) to develop a series of hands-on activities to demonstrate the CCS processes. Unique to OGS, the CCS Challenge invited visitors to choose a geological storage site for carbon dioxide. Participants overlayed simplified subsurface data maps of a single county and applied four main criteria necessary for safe carbon storage to choose the best underground reservoir. First deployed at the Women in STEAM Conference on October 8, 2024, and again on October 26, 2024, at the Oklahoma Mineral and Gem Show, this display engaged more than 2,500 Oklahomans and began to create new connections with local industry partners.

Following these successful deployments, the OGS Education and Outreach team began to develop a curriculum guide for a planned teacher workshop in February 2025. Using the activities from the interactive CCS display as a jumping point to create "Carbon Capture, Utilization, and Storage: A Crash Course for Teachers, Students, and Communities."

In accordance with best practices, this curriculum provides information using simple, accurate, and direct language (Atkinson et al. 2024), models (Otto and Gross 2021) and multiple means of visualization to aid understanding (Greenberg and Gavreau 2014). In a commitment to maintaining transparency and public trust, the OGS Education & Outreach team prioritized clear explanations of common CCS project motivations (Szizybalski et al. 2014). Rather than prescribing research questions, the team promotes using data resources to investigate locally relevant questions (Young and Sacuta 2014). Finally, the OGS Education & Outreach team focused on activities that facilitate connection and perspective-sharing among community members to empower local decision-making (Sacuta et al. 2017; Wade and Greenberg 2009).

In December 2024, the OGS hosted a workshop, "Building Foundations for Carbon Capture and Storage in Oklahoma." This workshop gathered a group of approximately 50 industry and technical professionals to facilitate communication among industry partners, state and federal agencies, and representatives from Tribal Nations. The workshop focused specifically on creating meaningful discussion about Class VI wells and CCS in Oklahoma. A brief presentation of the interactive CCS display and future professional development curriculum was met with enthusiasm from several workshop attendees, including representatives of CUSP.

In accordance with new direction from the DOE in late January 2025, and in alignment with Executive Orders, the OGS Education & Outreach team suspended all work on, and use of community engagement efforts related to the OGS project. After additional instruction and clarification from the DOE and given interest from industry partners and regional initiatives, including CUSP, the OGS Education & Outreach team resumed completion of the CCUS curriculum to provide resources promoting an informed citizenry and workforce development for the CCUS/EOR economic sectors.

Carbon Capture, Utilization, and Storage: A Crash Course for Teachers, Students, and Communities is in its final stages of development. Currently at 86 pages, the final page count is projected to fall at or around 100 pages, divided into seven main chapters. Within each chapter are three main sections: presentation slides, a topic overview, and a resource and activity overview, followed by activity instructions and materials. Upon completion, this resource will be hosted at https://www.ou.edu/ogs/education/teacherresources (accessed December 2, 2025).

An expanded table of contents summarizes the curriculum content in more detail.

Climate Change is a Problem

Guiding Question

How is your community affected by climate change?

Topic Overview

Weather and climate are defined and predictability of each is discussed.

Activities and Resources

- Use a graph of annual yearly temperature in Oklahoma to inspire observation and questioning.
- Ask long-term residents in your community about childhood recollections of weather patterns.
- Use public data collections to investigate questions about changes in local weather patterns important or interesting to the individual.

CO_2 Holds the Sun's Energy

Guiding Question

What is the relationship between carbon dioxide and climate change?

Topic Overview

Identifies chemical properties of carbon dioxide, gases comprising Earth's atmosphere, and atmospheric absorption and reflection of solar energy. Introduces carbon dioxide as a byproduct of combustion while focusing on the societal benefits of burning fuels for energy. Ends by connecting carbon dioxide, atmospheric energy, and weather patterns.

Activities and Resources

- Make observations and ask questions about a graph of atmospheric carbon dioxide and emissions from NOAA.
- Observe properties of carbon dioxide, especially density.
- Explore relationships between temperature and gases in a contained system.

CO_2 Management Solutions Exist

Guiding Question

How can we lower the amount of carbon dioxide in the atmosphere?

Topic Overview

Discusses open and closed systems, simplifying Earth's complex systems using models, and natural carbon cycles. Defines "NetZero" and briefly introduces reduction and removal as carbon management methods. Identifies sources of carbon dioxide beyond burning fuels and the highly unlikely nature of complete decarbonization.

Activities and Resources

- Follow the pathway of a carbon molecule using a kinesthetic model of the carbon cycle.
- Analyze the message of a figure explaining the idea of NetZero.
- Explore resources to evaluate or create a local Priority Climate Action Plan.

Carbon Capture, Utilization, and Storage Removes CO_2 from the Atmosphere

Guiding Question

What is carbon capture, utilization, and storage?

Topic Overview

Clarifies terminology associated with carbon management, explains sources of carbon dioxide, scaling innovation for commercial use, and lists multiple solutions for carbon capture. Outlines the process of compressing carbon dioxide and identifies transportation methods for captured carbon dioxide, and commercial uses for carbon dioxide.

Activities and Resources

- Assemble a model CCUS facility.
- Investigate compression as a property of gases.
- Explore Oklahoma's legacy of contributions to CCUS innovation through historic news articles.

Storing CO_2 Comes with Risks

Guiding Question

How can we watch for and protect against potential problems from CCUS?

Topic Overview

Identifies potential risks associated with CCUS in four main categories: environmental, technical, economic, and social. Underscores the risks OGS has the capacity and expertise to investigate and publish data for public use. Defines monitoring and mitigation, pointing out Oklahoma's Seismic Network, extensive subsurface data repository, and methods used to create models to identify potential storage reservoirs.

Activities and Resources

- Brainstorm a list of potential risks of storing or transporting carbon dioxide within the community.
- Find and interpret data from the Oklahoma Seismic Network.
- Train AI to detect earthquakes in a dataset from the Oklahoma Seismic Network.

Oklahoma Can Store CO_2 Underground

Guiding Question

What are the characteristics of a good storage site for carbon dioxide?

Topic Overview

Reviews four main criteria of a good geologic storage reservoir for carbon dioxide: a thick layer of porous rock to hold CO_2 with a layer of caprock on top to trap CO_2, at a depth at least 800 meters (½ a mile deep) so compressed CO_2 remains a supercritical liquid, in an area with few earthquakes to prevent CO_2 leaks.

Activities and Resources

- Test the porosity and permeability of different types of rocks.
- Calculate reservoir storage capacity using data from OGS models.
- Choose a potential storage site using maps of areas underground that meet the required criteria for a good storage reservoir.

Teams of People Work on CCUS

Guiding Question

Who works on carbon capture and storage projects?

Topic Overview

Identifies major career pathways within CCUS stakeholder groups, particularly academia and research labs, associated industries, and regulatory agencies.

Activities and Resources

- Use local and regional career exploration resources to research CCUS-related career opportunities.
- Chart CCUS career pathways and navigate job announcements
- Interview a local CCUS professional.

References

Atkinson L, Dankel DJ, Romanak KD. 2024. The effect of monitoring complexity on stakeholder acceptance of CO_2 geological storage projects in the US Gulf Coast region. Front Mar Sci. 10:1154543. doi:10.3389/fmars.2023.1154543

Bedle H, Beutel AM, Garneau GRH. 2024. SPEER23 survey report: investigating climate, weather, and energy attitudes in the United States through the lens of social and psychological factors. Norman (OK); University of Oklahoma, Mewbourne College of Earth and Energy. [accessed 2024 Nov 11]. https://ou.edu/content/dam/mcee/new-mcee-website/labs/speer/documents/pdfs/SPEER%202023%20Survey%20Report.pdf

Greenberg SE, Gauvreau LM. 2014. Communicating science and technology while engaging the public at the Illinois Basin–Decatur Project. Greenh Gas Sci Technol. 4:596–603. doi:10.1002/ghg.1435

Hayman NW, Walter J, Suriamin F, Yunker M, Burkhart B, Knapp C. 2023. Oklahoma Geological Survey coordination of mid-continent carbon management. Project narrative. Pittsburgh (PA); U.S. Department of Energy, Office of Fossil Energy and Carbon Management. DOE Award No. DE-FE0032374 (FOA0002799).

[NETL] National Energy Technology Laboratory. 2017. Best practices: public outreach and education for geologic storage projects. 2017 revised ed. Houston (TX); U.S. Department of Energy, Office of Fossil Energy. [accessed 2025 Dec 23]. https://www.netl.doe.gov/sites/default/files/2018-10/BPM_PublicOutreach.pdf

Otto D, Gross M. 2021. Stuck on coal and persuasion? A critical review of carbon capture and storage communication. Energy Res Soc Sci. 82:102306. doi:10.1016/j.erss.2021.102306

Sacuta N, Daly D, Botnen B, Worth K. 2017. Communicating about the geological storage of carbon dioxide—comparing public outreach for CO_2 EOR and saline storage projects. Energy Procedia. 114:7245–7259. doi:10.1016/j.egypro.2017.03.1855

Szizybalski A, Kollersberger T, Möller F, Martens S, Liebscher A, Kühn M. 2014. Communication supporting the research on CO_2 storage at the Ketzin pilot site, Germany—a status report after ten years of public outreach. Energy Procedia. 51:274–280. doi:10.1016/j.egypro.2014.07.032

Wade S, Greenberg S. 2009. Afraid to start because the outcome is uncertain? Social site characterization as a tool for informing public engagement efforts. Energy Procedia. 1:4641–4647. doi:10.1016/j.egypro.2009.02.286

Young A, Sacuta N. 2014. Farmers, open houses, and technical knowledge: public outreach in Aquistore. Energy Procedia. 63:7043–7046. doi:10.1016/j.egypro.2014.11.737

Texas

Utah

Washington

The overall objective of the CUSP Regional Initiative was to accelerate onshore CCUS technology deployment in the Western United States. The Washington State Geological Survey (WGS) supported this objective by accomplishing the following:

- Digitization of oil and gas well logs to LAS format
- Sequestration of CO_2 Tool (SCO_2T) reservoir input data deliverable
- Salinity data collection from oil and gas wells
- Provided CCUS information to industry in WA
- Answered public inquiries on CCUS
- Gathered and shared state geologic data with National Laboratories
- Answered state agency policy and regulatory inquiries on CCUS
- Summarized point source emissions data to identify high potential sources for sequestration

The following summarizes the timeline of WGS work on CUSP that produced these accomplishments, organized by SOPO task.

Task 1 – Project Management and Planning

October through December 2019 – Attended twice-monthly teleconferences.

January through March 2020 – Attended twice-monthly teleconferences.

April through June 2020 – Attended twice-monthly teleconferences. Attended and presented background on Washington State subsurface data to CUSP kickoff meeting.

July through September 2020 – Attended twice-monthly CUSP general teleconference. Attended data collection, data analytics, and outreach work group teleconferences.

October through December 2020 – Attended twice-monthly CUSP general teleconference. Attended data collection, data analytics, and outreach work group teleconferences.

January through March 2021 – Attended twice-monthly CUSP general teleconference. Attended data collection, data analytics, and outreach work group teleconferences. Led writing of white paper on incorporating social equity and environmental health disparities in CCUS decision-making. This is in cooperation with Carbon Solutions, LLC., SNL, PNNL, and Montana State University. The white paper proposes a project for public outreach.

April through June 2021 – Attended twice-monthly CUSP general teleconference. Attended data collection, data analytics, and outreach work group teleconferences.

July through September 2021 – Attended twice-monthly CUSP general teleconference. Attended data collection, data analytics, and outreach work group teleconferences.

October through December 2021 – Attended twice-monthly CUSP general teleconference. Attended data collection, data analytics, and outreach work group teleconferences.

January through March 2022 – Attended twice-monthly CUSP general teleconference. Attended data collection, data analytics, and outreach work group teleconferences.

April through June 2022 – Attended twice-monthly CUSP general teleconference. Attended data collection, data analytics, and outreach work group teleconferences. First in-person CUSP annual meeting in Las Vegas.

July through September 2022 – Attended twice-monthly CUSP general teleconference. Attended data collection, data analytics, and outreach work group teleconferences.

October through December 2022 – Attended twice-monthly CUSP general teleconference. Attended data collection, data analytics, and outreach work group teleconferences.

April through June 2023 – Resumed twice-monthly CUSP general teleconference. Attended data collection, data analytics, and outreach work group teleconferences. CUSP annual meeting in Lawrence, Kansas.

July through September 2023 – Attended twice-monthly CUSP general teleconference. Attended data collection, data analytics, and outreach work group teleconferences.

October through December 2023 – Attended twice-monthly CUSP general teleconference. Attended data collection, data analytics, and outreach work group teleconferences.

January through March 2024 – Attended CUSP general teleconferences.

April through June 2024 – Attended CUSP general teleconferences.

July through September 2024 – Attended CUSP general teleconferences. Attended CUSP annual meeting in New Mexico.

April through June 2025 – Attended CUSP general teleconferences. Attended CUSP annual meeting in Salt Lake City.

Task 2.1 – Expand Characterization of Stacked and Unconventional Storage

January through March 2020 – Initiated data review, literature review, and well log evaluation. Researched software vendors to assist well log digitization and interpretation. Began hiring process for office assistant (OA3) to assist well log digitization.

April through June 2020 – Continued data review, literature review, and well log evaluation. Purchased NeuraLog Pro well log digitizing software license. Hired office assistant for well log digitization.

July through September 2020 – Continued data review, literature review, and well log evaluation for digitization. Onboarded office assistant (Jordanna Averett) and trained her for well log digitization.

October through December 2020 – Gathered well data (we have a primitive oil and gas well database). Of 3,271 scanned documents, identified 1,909 candidates to digitize into LAS format. Determined 430 candidates for digitization to LAS format. Prioritized 151 first and second tier

LAS candidates. OA3 digitized 57 well logs from October through December for a total of 84 well logs digitized.

January through March 2021 – OA3 digitized 81 well logs for a total of 165 well logs digitized. Evaluated 991 Puget Basin well logs. Prioritized 249 well logs to digitize in next two quarters.

April through June 2021 – OA3 digitized 15 remaining well logs of the high priority basalt logs from the Columbia Basin in April. Digitized first 84 well logs from the siliciclastic reservoirs of the Puget Basin (Chehalis sub-basin), for a total of 252 well logs digitized.

July through September 2021 – OA3 digitized 99 well logs from the Puget Basin (Chehalis and Bellingham sub-basins) for a total of 201 well logs digitized to-date from the siliciclastic reservoirs of the Puget Basin. To-date, we have digitized 163 well logs from the basaltic Columbia Basin. Mapped rough draft of possible closures and strat trap leads in the Columbia Basin. Discussed closure maps with Scott Cameron, contractor to Yale CCL partners.

October through December 2021 – OA3 digitized 25 well logs from the Columbia Basin (basalt). These were Hanford borehole data from the 1980s. Also digitized 61 well logs from the Puget Basin (45 from the Kummer Anticline play; 16 from outside play areas). To-date, we have digitized 183 basalt well logs and 262 well logs from siliciclastic reservoirs of the Puget Basin for a total of 445 well logs digitized for the CUSP project. Also gathered reservoir input data for SCO_2T.

January through March 2022 – OA3 digitized 23 well logs from the Willapa Basin. Digitized 36 well logs from Outside Play Areas. Outside Play Area logs are scattered in the Puget Sound Basin. They are significant enough to warrant digitization but do not fall within the key play areas within the Puget Basin (Chehalis Play, Bellingham Play, and Kummer Anticline Play). To-date, we have digitized 183 basalt well logs and 305 well logs from siliciclastic reservoirs of the Puget Basin for a total of 488 well logs digitized for the CUSP project. Our digitization slowed in this quarter since our digitization staff member started working part time (January through June 2022).

April through June 2022 – OA3 digitized 7 well logs from the Willapa Basin for a total of 495 well logs digitized for the CUSP project. This is the final quarter with funding for the OA3. Created stacked storage inputs and submitted them to the CUSP Google spreadsheet and formatted them for SCO_2T. Working with Carbon Solutions on creating ranges and adding Oregon and Idaho data for the PNW SimCCS model.

July through September 2022 – Added Oregon and Idaho reservoir estimates for the PNW SimCCS model. These data are good for a pilot project, but these states should refine these data in the future.

January through March 2023 – Researched old O&G well paper files for data gaps on water chemistry, rock chemistry, driller's logs, pressure and other well flow tests, temperature, mud program, and VSPs.

April through June 2023 – Completed data collection on water chemistry, rock chemistry, driller's logs, pressure and other well flow tests, temperature, mud program, and VSPs from Columbia Basin paper well documents. These data were eventually included in a much larger dataset of water wells published as Svadlenak and Florea (2025).

July through September 2023 – Completed revision of SCO_2T reservoir inputs and made corrections in collaboration with Carbon Solutions. The original draft of SCO_2T for WA, ID, and OR were rough estimates. This revision includes more thorough literature research and source documentation. This revision is only for WA state. Further refinement for OR and ID should be done by those states when they are brought on to CUSP.

Task 2.2 – Develop Collaborations to Integrate and Validate Key Technologies to Optimize Storage and Reduce Uncertainty in Storage Permanence and Integrity

April through June 2020 – Began communication with individual subject matter experts at PNNL, SNL, LANL, NMT, KGS, DRI, and EGI.

July through September 2020 – Continued communication with the groups above.

January through March 2021 – Social equity white paper (see task 1.1).

April through June 2021 – Started communication with a new group at PNNL. Previously had been communicating with the modeling group; now communicating with the basalt research group.

July through September 2021 – Continued communications with PNNL.

October through December 2021 – Continued communications with Yale CCL and PNNL.

January through March 2022 – Continued communications with Yale CCL and PNNL. Communicated with WSU group working on CCUS feasibility study for Phillips 66 refinery in Whatcom County; provided chemical engineers with geologic information.

April through June 2022 – Continued communications with Yale CCL and PNNL.

July through September 2022 – Continued communications with Yale CCL, PNNL, and Carbon Solutions LLC. Worked with Carbon Solutions to make workflow document and presentation on how to fill in SCO_2T cell data, which Carbon Solutions presented to CUSP.

October through December 2022 – Continued communications with Yale CCL, PNNL, and Carbon Solutions LLC. Began collaboration with DOGAMI (Oregon Department of Geology and Minerals) which is Oregon's state geological survey. To-date CUSP does not have participation from Oregon or Idaho agencies, although these states are within the CUSP region. DOGAMI is recovering from budgetary issues, but they have a new State Geologist with an oil & gas background who is energizing their agency and is eager to collaborate. Collaboration with DOGAMI is especially important since the primary basalt target for sequestration are in the Pasco Basin, which straddles the WA / OR border. Furthermore, while there are storage opportunities in WA, there are heavy emissions on the OR side of the border.

January through March 2023 – Held Big Questions Workshop for Columbia River Basalt Group subject matter experts (SME) as part of state-funded Earth Resources Program (ERP), including CUSP-funded participation on carbon sequestration. This workshop, led by ERP manager, Lee Florea, included SMEs from PNNL, USGS, State of Washington Department of Ecology, University of Washington, WGS STATEMAP, and others. The theme of the meeting was gaining consensus on big questions and how to answer them in the Columbia Basin, regarding carbon sequestration, geothermal energy, and water resources.

April through June 2023 – Worked NMT and SLB to determine feasibility of seismic acquisition within the Canoe Ridge area of the Columbia Basin. Identified large contiguous properties associated with structural closure and amenable land use in the Canoe Ridge area as possible candidates for exploration.

July through September 2023 – Continued work with NMT to determine feasibility of seismic acquisition within the Canoe Ridge area of the Columbia Basin.

October through December 2023 – Continued work with George El-Kaseeh (NMT) to determine feasibility of seismic acquisition within the Canoe Ridge area of the Columbia Basin. This work supported the development of a successful grant application from Breakthrough Energy for $490,000 to collect the first 3D seismic survey ever shot in WA. Although the survey will cover a small area and will not be exploration scale, it will serve to demonstrate what current seismic technology can image in the challenging geophysical environment of basalt. This will not only show what is possible in basalt CCUS exploration, but also show what can reasonably be expected for data input in a basalt UIC Class VI permit.

Task 2.3 – Collaborate with Industrial Partners to Identify and Assist with Monitoring, Verification, and Accounting (MVA) Strategies as Applicable

April through June 2020 – Participated in monthly CUSP subcommittee outreach working group (teleconference).

July through September 2020 – Examined BECCS (biomass energy carbon capture and sequestration) opportunities with cooperating lab at Yale University. Communication with a dunite mine and peridotite sequestration researcher at Columbia University. Conducted initial stage of Washington industrial partner screening based on geographic location, magnitude of emissions and state/DNR strategic priorities. Communicated with PSE (Puget Sound Energy) reservoir/drilling engineer at Jackson Prairie, WA underground natural gas storage facility, to learn about reservoir properties and injection / induced seismicity risk. Researched Mist underground natural gas storage facility in Oregon.

October through December 2020 – Continued communication with Yale Carbon Containment Lab. Answered their geology questions and discussed funding strategies for industrial partnerships. Their concept for CCUS in WA considers forest health / wildfire mitigation combined with BECCS.

January through March 2021 – Continued communication with Yale Carbon Containment Lab. Presented to the DNR GHG Reduction Team (state facilities and fleets) to learn more about their industrial partners and consultants. Made contacts with PSE and Cascadia Consulting from them. Presented to Puget Sound Energy (PSE), largest utility in the state. Discussed possibility for basalt injection from PSE Goldendale natural gas-fired power plant.

April through June 2021 – Continued communication with Yale CCL.

July through September 2021 – Continued communication with Yale CCL. A private investment coordinator associated with this work is in the preliminary stages of considering a multiple-well basalt drilling campaign. Introduced CUSP and communicated with Phillips 66, which has a refinery in Ferndale, WA. P66 provided feedback on facilities questions for our emissions

Leopold Matrix. Made first contact with Weyerhaeuser regarding CCUS. Met Weyerhaeuser land professionals at NALTA conference and connected with Weyerhaeuser Oil & Gas Director. Introduced WA work on CUSP to Carbon America.

October through December 2021 – Met with Weyerhaeuser Oil & Gas. Met with Drax, a UK power company focused on decarbonization projects.

January through March 2022 – Met with TransAlta (Canadian coal power company) regarding a BECCS concept we created. The Centralia coal plant will cease operations in 2025, and we proposed a retrofit for BECCS. Facility is connected to transmission lines and is in close proximity to a proven storage reservoir in Eocene sandstone at sufficient depth for supercritical sequestration (Jackson Prairie gas storage field operated by PSE). The facility is close to mills to provide mill waste for biomass and working forests to provide nearby slash for biomass. Transportation costs for biomass are a significant hurdle, and this facility's proximity to fuel will help decrease those costs. There is community and local government support for continued operations at the facility after coal operations cease, and this concept will help save direct and indirect jobs in the area. TransAlta was interested in the proposal. We connected them with Yale CCL and Drax who are interested in BECCS projects in the region. Held meetings between Drax Group, PLC and DNR policy advisors regarding BECCS opportunities in WA.

April through June 2022 – Introduced Yale CCL to DNR Product Sales & Leasing Division for land use license permitting for parcels of interest. Land use license are non-competitive, non-exclusive contracts with the state for exploring resource opportunities on state land. These licenses can last for 5 yr. They can be followed at any time by competitive, exclusive leases for CO_2 injection. Met with Invenergy which owns and operates the Grays Harbor Energy Center natural gas facility. Discussed opportunities in western WA. Connected them to subsurface team at PNNL and Carbon America.

July through September 2022 – Ongoing coordination with Yale CCL and DNR Product Sales & Leasing Division for land use license permitting for parcels of interest. Met with UNDO, a company that grinds basalt for terrestrial sequestration in agriculture. Met with Heirloom, a CA-based DAC company focused on CaO calcination and sequestration. They have carbon credit funding from Microsoft and are interested in basalt sequestration in Washington State. Assisted with their questions and passed their contact to PNNL, who then met with them, and to our CUSP partners in California at Stanford. Met with Emissol, a Washington-based DAC company focused on solid solution capture and sequestration. Answered their questions on sequestration opportunities in Washington.

October through December 2022 – Ongoing coordination with Yale CCL and DNR Product Sales & Leasing Division (PSLD) for land use license permitting for parcels of interest. Met with RMI (formerly Rocky Mountain Institute) which is considering leading a carbon sequestration in basalt in WA. They hope to partner with CarbFix, the Icelandic company that injects CO_2 from geothermal energy operations into basalt. Met with CarbFix (Iceland). They may consider partnering with Climeworks (Switzerland) on a DAC project. Their sequestration process in Iceland uses dissolved CO_2 instead of supercritical CO_2. This has serious implications for sequestration in the Columbia River Basalt Group of WA because of that basin's aridity and the high water use of dissolved CO_2 sequestration. However, CarbFix says they are currently testing sequestration with seawater. If this proves practicable, they may be able to use saline formation water for sequestration in arid regions. They will also have to address risk of aquifer acidification

in dissolved CO_2 sequestration. They are the primary global player in basalt sequestration, so it would be exciting for them to enter the CRBGs in WA. Met with Heirloom to discuss potential sequestration opportunities in WWA. Their DAC technology would benefit from a more humid environment than the arid CRBGs.

January through March 2023 – Meetings with RMI and Carbfix regarding DAC. Meetings with Carbon America regarding sequestration in WA.

July through September 2023 – Met in-person with Carbon America about a conventional (sandstone) sequestration project in western WA.

October through December 2023 – Resumed meetings with Yale CCL and Invenergy regarding their interest in CO_2 storage exploration on the east side (basalt) and west side (sandstone) of the state, respectively. These meetings may lead to CarbonSAFE and RITAP proposals.

Task 2.4 – Development and Validation of Risk Assessment, Management, and Mitigation Strategies for Commercial-Scale Sites

July through September 2020 – Worked with PNNL to collect case study examples of gas injection in WA and OR to test NETL Short Term Seismic Forecasting Tool (STSF). Negative results; WA and OR data are poor candidate to test STSF tool. We have seismological events but lack overpressured injection. NETL will use Kansas or Oklahoma data instead.

October through December 2022 – Preliminary work with PNNL on remote sensing mapping of previously unmapped faults, dikes, and joints in the Columbia Basin. This work helps determine recent and past stress fields in the basin, which is essential to mitigating risk from induced seismicity and hydraulic fracturing. This remote sensing technique uses red relief image maps (RRIM) derived from lidar.

January through March 2023 – Learned how to make RRIM maps. Next step is to divide Columbia Basin lidar into parcels to convert to RRIM.

Task 3.1 – Engaging with National Laboratories

January through March 2020 – Began regular communications with PNNL.

April through June 2020 – Communication with PNNL regarding Wallula Pilot Project results and basalt expertise. Participated in twice-monthly CUSP subcommittee data analysis working group (SimCCS), run by LANL.

July through September 2020 – Worked with Mark White (PNNL) on STSF tool. Communication with LANL. Contributed WA Health Disparities and Social Equity map to data analysis group for a model layer.

July through September 2021 – Twice-monthly meetings with PNNL basalt team.

October through December 2021 – Twice-monthly meetings with PNNL basalt team.

January through March 2022 – Twice-monthly meetings with PNNL basalt team.

April through June 2022 – Twice-monthly meetings with PNNL basalt team. Met INL at CUSP annual meeting. They have not joined CUSP yet, but we informally discussed reservoir data gathering for Idaho for PNW SimCCS model.

July through September 2022 – Twice-monthly meetings with PNNL basalt team. See task 2.2.

October through December 2022 – Twice-monthly meetings with PNNL basalt team. See task 2.2 and 2.4. Discussions with PNNL about collaborating on DE-FOA-0002799 for a basalt project.

January through March 2023 – Twice-monthly meetings with PNNL basalt team.

October through December 2023 – Resumed twice-monthly meetings with PNNL basalt team.

Task 3.1.1 – Identify Data Requirements & Needs

July through September 2020 – Introduction to Open Subsurface Data Universe (OSDU, led by Shell) at data organization working group.

July through September 2021 – Obtained Columbia River Basalt Group well logs that we don't already have, with assistance from PNNL. Built maps of well data distribution and discussed them with Yale CCL partners, PNNL, and a regional basalt expert.

October through December 2021 – Digitized well logs obtained from the DOE Basalt Waste Insolation Project (BWIP nuclear waste) from the 1980s.

January through March 2022 – Completed Data Catalog deliverable. Catalog identifies data gaps and strategies for mitigating these gaps.

April through June 2022 – Completed stacked storage deliverable. Submitted reservoir data to CUSP Google spreadsheet. Tracked down out of state core (WA core at TXBEG) pertinent to carbon sequestration, especially Columbia Basin (basalt).

July through September 2022 – Submitted SCO_2T cell data for Washington, Oregon, and Idaho. These data include high/mid/low stacked storage estimates for reservoir properties, updated emissions data based on the CUSP economics team's Leopold Matrix weighting system, and cells to exclude for environmental justice reasons in a SimCCS pilot project for the Pacific Northwest (PNW). This pilot project will provide a screening tool for industry to choose SimCCS scenarios with high/mid/low cases for reservoir, an economic scenario choice of 45Q/carbon credit cases (Section 45Q of the U.S. Tax Code; Credit for Carbon…2021), and a choice of excluding or including areas for environmental justice reasons. The lack of Columbia Basin data and missing reservoir properties for other WA basins in NATCARB data necessitates SCO_2T inputs.

October through December 2022 – Assisted data analysis and data organization working groups with their questions about how to input SCO_2T data.

July through September 2023 – Estimated costs for seismic acquisition in basalt of eastern WA.

October through December 2023 – Estimating costs for seismic acquisition in basalt of eastern WA. Our STATEMAP program (field mapping for 7.5 minute, 1:24k quads) held their meeting this quarter among local, state, and federal partners to determine next year's mapping quads. CUSP provided information to the Earth Resources Program manager to make the case at the STATEMAP meeting to map parts of the Columbia Basin (basalt sequestration) in southern Benton and southeastern Klickitat Counties. Such mapping would refine crucial structural information in this potential sequestration lead. Target reservoir units do not crop out in this area; however outcropping units may provide reservoir analogs.

Task 3.1.2 – Update Geologic Data for CCUS Assessment

October through December 2020 – See task 2.1. Also continued literature review of basalt reservoir characteristics.

January through March 2021 – See task 2.1. Also continued literature review of basalt reservoir characteristics.

July through September 2021 – Initiated SCO_2T pilot project for the Pacific Northwest with Carbon Solutions LLC and PNNL because the pre-existing NATCARB data is very poor to non-existent in the PNW.

October through December 2021 – See task 2.1. Continued SCO_2T reservoir data research and inputs.

April through June 2022 – See task 2.1. Continued to refine reservoir inputs as we discovered new data. Met with USGS Water Science Center (Tacoma) who supplied more accurate permeability and temperature data for the Columbia Basin.

July through September 2022 – See task 2.1.

July through September 2023 – Revised SCO_2T inputs. See task 2.1.

Task 3.1.3 – Update USDW Data from All Public Sources

July through September 2020 – Reviewed petrophysical analysis process for determining salinity from electric logs.

October through December 2020 – Explored Washington Department of Ecology water well database including extracting deep water wells (1,000–5,000 ft depth) in the Columbia Basin.

October through December 2021 – Prepared to hire new WGS hydrogeologist who will help collect USDW data.

January through March 2022 – Hired new WGS hydrogeologist with state funding (no Federal funding). This position eventually published a geochemistry report for waters in the Columbia River Basalt Group (Svadlenak and Florea 2025), which may be helpful for assessments, but we never got the specific USDW products necessary for CUSP before this position ended in 2024.

April through June 2022 – Learned about the Ginkgo Dike from regional basalt experts, which is a possible compartmentalizing barrier for fresh and saline groundwater in Columbia Basin aquifers. This is important for sequestration well depth. It is possible there are more saline waters to the NE of this NNW-SSE trending dike, but more data is needed to prove this concept.

October through December 2022 – Researched salinity data from Canoe Ridge natural gas storage exploration wells.

January through March 2023 – Continued salinity data gathering from published Hanford borehole data and O&G paper well files.

April through June 2023 – Completed salinity data gathering from published Hanford borehole data and O&G paper well files (see subtask 2.1).

October through December 2023 – Encouraged WGS hydrogeologist and Earth Resources Program manager to produce some kind of USDW map, even if deep data is scarce in the Columbia Basin.

Task 3.1.4 – Gather and Catalog CO_2 Emissions (Point) Source Database

April through June 2020 – Gathered most recent emissions data from EPA FLIGHT database.

July through September 2021 – Cataloged CO_2 emissions point source database for Washington, Oregon, and Idaho using Leopold Matrix formulated by CUSP (Kip Carrico and Maohong Fan). Cataloged Oregon and Idaho because they do not have representation in CUSP. Ranked top five emissions sites in each state according to Leopold Matrix system. Shared rankings with neighboring CUSP states to confer with their suggestions.

July through September 2022 – Updated Oregon and Idaho emissions data for SimCCS model (in addition to WA data already submitted).

Task 3.2 – Apply NRAP Tools to Assess Geologic Risks

July through September 2020 – Attended NRAP webinar on State of Stress Analysis Tool (SOSAT). Attended NRAP webinar on Short Term Seismic Forecasting Tool (STSF).

October through December 2020 – Reviewed full suite of NRAP tools as preparation for responding to public inquiries about sequestration risk mitigation.

January through March 2021 – Attended NRAP presentation on modeling CO_2 blowouts.

October through December 2021 – Attended STOMP CO_2 injection modeling training run by PNNL.

Task 4.1 – Catalog, Map, and Evaluate Extant and Near-Term CO_2 Distribution Network

April through June 2021 – Assessed draft of the Leopold Matrix made by the CUSP economics working group (defines attributes of high impact emissions sources).

July through September 2021 – See Task 3.1.4.

Task 4.2 – Identify and Add Rights-of-Way for New Pipelines

October through December 2022 – Presented CUSP to the Jackson Foundation, a policy not-for-profit based in Seattle. Discussed pipeline regulation in a separate meeting with the Foundation's board chair, a lawyer with experience working with FERC. It is unclear who will permit CO_2 pipeline siting in WA. These meetings led to a contact at the Washington Utilities and Transportation Commission (UTC). However, UTC did not respond to inquiries.

Task 4.3 – Regulatory / Policy Impact Assessment

October through December 2020 – Analyzed bill for proposed Washington State legislation of a low carbon fuel standard (called clean fuels standard in proposed legislation). Proposed legislation focuses on terrestrial sequestration (afforestation and reforestation) as credit offset projects. Recommended emphasis on geologic carbon sequestration to State Geologist.

January through March 2021 – Tracked and analyzed state legislature bills regarding carbon sequestration as a potential offset credit program for environmental policy:

- SB5126, WA Climate Commitment Act (cap and trade), passed Senate, currently in House committee.
- HB1036/SB5231 – LCFS (called Clean Transportation Fuels Standard [CTFS]), stalled in committee, replaced by HB1091/SB5231 (below).
- HB1050 – HFC restrictions, stalled in committee.
- HB1091/SB5231 – Reducing GHG Emissions by Reducing the Carbon Intensity of Transportation Fuel (LCFS), passed House and Senate, awaiting governor's signature.
- HB1513/SB5373 WA STRONG Act (carbon tax, CTFS, issuing environmental bonds), stalled in committee.
- Tracked federal legislation and informed DNR policy on proposed legislation such as the SCALE Act.

Presented CUSP in teleconference with state Rep. Alex Ramel. His district includes Anacortes, home to two of five WA refineries. Presented CUSP to new climate advisor to the Commissioner of Public lands. Attended information session on state Environmental Justice Task Force. Review by task force will soon be a requirement for projects involving state resources. This (along with similar task force in CA) is a significant impetus for the social equity and environmental health disparity focused project proposal.

April through June 2021 – Met with State Lands leasing team to discuss the future of sequestration in the state and DNR policy toward communication with potential industrial partners. Result: continue to communicate with leasing team. Ask for their advice before continuing to discuss opportunities with potential industrial partners.

July through September 2021 – Continued work with state lands leasing team. Built "traffic light" land ownership map for the Columbia Basin (basalt reservoir). This map identifies areas where drilling an injection well may be prospective, difficult, or impossible. Communicated with state land leasing team on state mineral right ownership.

October through December 2021 – Presented BECCS business model to DNR executive management in preparation for Yale Carbon Containment Lab presentation to Commissioner of Public Lands (CPL). CPL is an statewide elected official in WA, responsible for managing state land. Since there is no income tax in WA, this is a significant position with respect to state revenue. BECCS is an important model in WA because biomass energy is integrated with wildfire mitigation (forest thinning projects) and the timber business (mill waste). The BECCS model proposes a market for forest thinning projects (slash is currently control-burned which contributes to CO_2 emissions) and mill waste while also assisting the state with wildfire mitigation by improving overgrown forest health. In addition to managing revenue from state lands, DNR is also the state firefighting agency. Helped facilitate meeting of the Yale Carbon Containment lab with CPL. Met with Drax (also a BECCS model) in collaboration with DNR executive policy advisors, including Chief Resilience Officer. These meetings also collaborate with state uplands leasing and forest resources divisions of DNR.

January through March 2022 – Department of Ecology (ECY) had a vacancy for their UIC coordinator for several months at the end of 2021. Met with the Water Quality Program manager who oversees the UIC program to talk about primacy. He said ECY was interested in applying

for primacy. However, he said it would take approximately 18 months to get legislation written. Legislation would have to align with legislative sessions (long session in odd numbered years, e.g., January–April 2023; short session in even numbered years, e.g., January–February 2024). After legislation passes (written into law called the Revised Code of Washington [RCW]), it would take 12-24 months for an agency to write up the rules (Washington Administrative Code [WAC]) based on the RCW. Therefore, expect that ECY cannot obtain primacy for another 4 yr from January 2022, at the earliest. Once ECY obtains primacy there will be a period of hiring and training before the agency is equipped to permit UIC Class VI wells. As of 2025, ECY has taken no action on UIC Class VI primacy.

In the meantime, EPA will permit these wells. They have two staff members for this task in Region 10 (PNW). Neither of them have permitted a Class VI well before. No agency has permitted a Class VI well for basalt anywhere in the U.S. The only basalt CO_2 injection well (Wallula, WA, in 2009) was permitted as a Class V. It was considered an experimental well, and Class VI does not exist in the RCW. The last time the RCW was updated was before Class VI existed.

Separate from permitting, there is the issue of credit offset program rule-making, administered by a separate ECY division. In the 2021 WA legislative session, both cap and trade (called cap and invest in WA, and commonly referred to by the name of the act – Climate Commitment Act [CCA]) and low carbon fuel standard legislation (called clean fuels standard in WA [CFS]) passed, and two separate teams at ECY for CCA and CFS are working on rule-making (WAC writing) for these laws. We met with the CCA and CFS groups to ensure that geologic carbon sequestration is included where applicable in the credit offset program rule-making. This is a forest-focused state, and we don't want geological carbon sequestration to be sidelined. ECY is largely following CA state protocols which include geologic carbon sequestration.

Washington has two kinds of legislative sessions that start in January of each year: regular sessions in odd years are 105 days, and short sessions in even years are 60 days. We monitor bills related to carbon sequestration. The bills we followed this session were as follows:

- SB 5910: hydrogen incentives. This bill does not directly affect carbon sequestration. However, it excludes incentives for hydrogen produced from steam reformation, including reformation of hydrocarbons. Hydrogen is a byproduct of BECCS and could be marketed to assist a BECCS project economics. While the BECCS process produces hydrogen through steam reformation, biomass is not fossil fuel. If a BECCS project proceeds, we will have to clarify with rule-makers at the Department of Commerce to determine whether BECCS will be eligible for H2 incentives.
- SB 5961: biochar incentives. This bill does not directly affect geologic carbon sequestration but I receive a lot of inquiries about it as the state's carbon sequestration geologist.
- SB 5842: modifications to the 2021 CCA. This bill does not directly affect geologic carbon sequestration.

This quarter we met with Assistant Attorneys General (AAG) for DNR to introduce CUSP to them and explain carbon sequestration. These AAGs will be responsible in the future for dealing with CCUS leases. We explained the concept and uncertainties of pore space ownership to them.

April through June 2022 – Attended Department of Ecology rule-making meetings for Climate Commitment Act and Clean Fuel Standard. WA is referencing the CA protocols. These programs

(cap and trade, or cap and invest as they are branding it in WA; and Clean Fuels Standard, which is LCFS in CA) will go into effect in WA on January 1, 2023.

July through September 2022 – Continued to monitor of ECY rule-making for cap & invest (cap & trade) and clean fuels standard (LCFS) programs that will be effective January 1, 2023. Reviewed Inflation Reduction Act effects on CCUS in WA.

October through December 2022 – Continued monitoring of WA Dept. of Ecology rule-making for cap & invest (cap & trade) and clean fuels standard (LCFS) programs that will be effective January 1, 2023. With respect to subtask 2.3, DNR PSLD for the first time clarified that they are proceeding under the assumption that pore space belongs to the surface estate. The legal analogy for this is that RCW 78.60.040 (geothermal sui generis) is analogous to CO_2 injection. The geothermal law states that since geothermal resources are neither a mineral nor a water right, they belong to the surface estate. This position is still an assumption, and there is currently no move at the state level to codify pore space ownership in statute. There are no state agency positions held on amalgamating pooling at this time. Also monitored pre-filed bills for CCUS / emissions reduction content for upcoming state legislative session (January–April 2023). Although there is legislative language regarding amendments to recent (2021–2022) emissions legislation, the pre-filed bills have not had an impact on CCUS.

January through March 2023 – Met with Lauren Boldrick, EPA Region 10 (AK) who is tasked with accelerating Region 10 knowledge about UIC Class VI and carbon sequestration. Monitored legislative session. All the carbon sequestration legislation that arose this session concerned terrestrial (forest/wood) carbon sequestration. Legislators do not appear to be aware of geologic sequestration. Began working with new Environmental Justice (EJ) team at DNR to learn how they can help us with EJ components of carbon sequestration project planning.

July through September 2023 – Met with WA Department of Commerce manager for federal policy alignment.

Task 4.5 – Focused Scenario Analysis

July through September 2022 – Submitted data for PNW SimCCS model. Worked with Montana State University on the model.

Task 5 – Promoting Regional Technology Transfer

October through December 2020 – Presented “Geologic Carbon Sequestration in Washington State” to the Quimper Geological Society (education branch of the Jefferson County Land Trust) on December 12, 2020. Meetings are free and the audience was the general public. Eighty-two people attended.

January through March 2021 – Presented introduction to CUSP to two full-DNR videoconferences (approximately 70 people at each).

July through September 2021 – Considered LEAP grant for local community CCUS tie-in with CUSP. Discussed environmental justice focus project proposal from the spring with full CUSP team meeting and Data Organization working group. Presented Washington CCUS and land issues in CCUS to the National Association of Lease and Title Analysts (NALTA, the professional organization of Certified Professional Landmen) annual conference in Bellevue,

WA. Leaders for CUSP states assisted in the land issues presentation by offering questions from their own states. The questions focused on legal issues of pore space ownership, forced unitization for injection reservoirs, and regulatory complexities. Also communicated with Elysian Ventures, which responded with legal answers.

April through June 2022 – Began to define readiness indices with data analytics team at CUSP annual meeting and analytics working group meetings.

Task 5.2 – Technology Transfer Forums

July through September 2021 – Attended CUSP Data Symposium. Presented at NALTA in Bellevue (Gallin 2021).

October through December 2022 – Participated in DOE's first public outreach forum in Richland, WA, November 30, 2022. Representatives from environmental groups and tribes gave their feedback on CCUS. There is concern about pipelines. There is also the perspective from some of these groups that CCUS will slow down decarbonization and is therefore problematic. DOE (DC), PNNL, City of Richland, WSU, EPA, PHMSA, Yale CCL were also in attendance.

April through June 2023 – Met with DOE OCED regarding public outreach on CCUS in the Columbia Basin. Met separately with the Clean Air Task Force on the same subject.

October through December 2023 – Presented SCO_2T for PNW at GSA in Pittsburgh (Gallin et al. 2023).

January through March 2024 – Presented WA CCUS opportunities at AAPG CCUS Houston conference (Gallin and Florea 2024a).

April through June 2024 – Presented on UIC Class VI at the Washington Hydrogeology Symposium in Auburn (Gallin and Florea 2024b). Presented on basalt sequestration at GSA in Spokane (Gallin and Florea 2024c). Published volumetric analysis for mineralized sequestration in Columbia River basalt reservoirs with PNNL as first author (Cao et al. 2024).

References

Cao R, Miller QRS, Davidson CA, Gallin W, Reidel SP, Jiao Z, McLaughlin F, Nienhuis ET, Schaef HT. 2024. Gigaton commercial-scale carbon storage and mineralization potential in stacked Columbia River Basalt reservoirs. Int J Greenh Gas Control. 137:104206. doi:10.1016/j.ijggc.2024.104206

Gallin W. 2021. On the CUSP: land issues in an emerging CO_2 market—the Carbon Utilization and Storage Partnership for the Western US. Keynote address presented at: National Association of Lease and Title Analysts Annual Conference; 2021 Sep 9; Bellevue (WA).

Gallin W, Cox K, Florea L. 2023. Modeling reservoir and cost estimates for geologic carbon sequestration in Washington State using SCO_2T PRO. Geol Soc Am Abstr Programs. 55(6):395241.

Gallin W, Florea L. 2024a. Carbon sequestration risks and rewards in Washington State. Poster abstract 4015126. Presented at: AAPG/SPE/SEG Carbon Capture, Utilization, and Storage Conference; 2024; Houston (TX).

Gallin W, Florea L. 2024b. Geologic carbon sequestration: what is the status of Underground Injection Control Class VI? Presentation abstract. Presented at: 14th Washington Hydrogeology Symposium; 2024; Auburn (WA).

Gallin W, Florea L. 2024c. The current state of research and commercial geologic carbon sequestration in basalt and ultramafic rocks. Presentation abstract 399762. Presented at: Joint 120th Annual Cordilleran Section and 74th Annual Rocky Mountain Section Meeting of the Geological Society of America; 2024; Spokane (WA).

Svadlenak E, Florea L. 2025. Groundwater chemistry in the Columbia River Basalt Group, Columbia Basin, Washington. Olympia (WA); Washington Geological Survey. Report of Investigations 48. 21 p. Text and 1 Microsoft Excel file. [accessed 2025 Dec 23]. https://www.dnr.wa.gov/publications/ger_ri48_groundwater_chemistry_crbg.pdf

Wyoming

Part IV – National Laboratories

Los Alamos National Laboratory (LANL)

This report presents a suite of technical analyses conducted by LANL as part of the CUSP West project to support regional-scale planning and risk assessment for geologic carbon storage (GCS) across multiple western U.S. states. The work integrates advanced modeling tools from the National Risk Assessment Partnership (NRAP), infrastructure optimization using SimCCS, geologic risk quantification, and seismic characterization to evaluate the feasibility, safety, and readiness of emerging CO_2 storage opportunities. These efforts provide a consistent and scientifically grounded framework for assessing GCS performance under diverse geological, operational, and socio-environmental conditions.

In **Task 1**, NRAP-Open-IAM was applied to evaluate potential CO_2 and brine leakage risks for candidate storage sites in Kansas, California, Colorado, and Oklahoma. By linking reservoir simulation outputs with reduced-order models for wellbore leakage and aquifer response, the system-level analyses showed that predicted leakage rates are generally small and do not produce measurable impacts on underground sources of drinking water (USDWs). Across all case studies, only limited CO_2 or brine migration occurred through selected legacy wells, and cumulative leakage remained orders of magnitude below levels of concern, demonstrating that each site exhibits low leakage risk under the modeled conditions.

Task 2 used the SimCCS optimization platform to examine phase-based CO_2 transport network development in the Four Corners region. The analysis quantified how environmental justice (E&J) constraints, specifically, avoiding disadvantaged and tribal communities, affect pipeline routing, network length, and system-wide costs. Results show that enforcing E&J constraints increases pipeline length by 4 to 11% across development phases and raises transport and storage costs, but the overall system remains economically viable under current tax credits. These findings highlight the importance of integrating community considerations into early-stage CCS infrastructure design.

In **Task 3**, LANL developed and demonstrated methods for incorporating geologic risk factors into Regional Readiness Indices (RRIs). Two key risks were examined: induced seismicity, represented through capacity multipliers limiting allowable injection volumes, and leakage risk from legacy wells, represented through well-density-dependent storage cost adjustments. Both risk types were shown to significantly influence optimal pipeline routing and storage-site selection, underscoring the need to incorporate geologic and operational risks directly into regional CCS planning frameworks.

Finally, **Task 4** focused on subsurface characterization at Iron Mountain, Utah, using legacy 2D seismic data. Through traveltime tomography, migration velocity analysis, reverse-time migration, and machine-learning-based fault detection, high-resolution images of subsurface structures were generated to assess the suitability of deep formations for CO_2 storage associated with direct reduced iron (DRI) production. The results delineate key stratigraphic and structural features, including the geometry of the Navajo Sandstone reservoir and overlying caprocks, and

identify faults that may influence storage integrity, thereby providing essential inputs for future site evaluation.

Overall, the combined results of Tasks 1-4 demonstrate that the western U.S. region contains promising and diverse opportunities for GCS deployment, but that successful and responsible implementation requires integrating geologic risk assessment, infrastructure optimization, and detailed subsurface characterization. The tools and workflows presented in this report offer a scalable framework to support ongoing CCS planning and regulatory readiness across the region.

Task 1 – Apply NRAP Tools to Assess Geologic Risks

This work was conducted as part of the effort under "Subtask 3.2 – Apply NRAP Tools to Assess Geologic Risks" in the CUSP main project and Kansas Focused Project. This task evaluates potential geologic risks associated with CO_2 storage across multiple candidate sites in the western United States as part of the CUSP project. The primary objective is to quantify the likelihood and consequences of CO_2 and brine leakage from deep geologic storage reservoirs into overlying underground sources of drinking water (USDWs) or the atmosphere. To support this effort, LANL applies the National Risk Assessment Partnership's NRAP-Open-IAM framework—a flexible, system-level modeling tool designed to translate site characterization data and detailed reservoir simulations into probabilistic assessments of whole-system risk (Vasylkivska et al. 2022). Through this task, NRAP tools are used to analyze a variety of geological settings, wellbore conditions, and injection scenarios for Kansas, California, Colorado, and Oklahoma case studies, enabling consistent comparison of leakage behavior and potential impacts across all sites.

NRAP-Open-IAM is a modular integrated assessment model developed by the U.S. Department of Energy's National Risk Assessment Partnership to support rapid yet scientifically defensible evaluations of CO_2 storage system performance. The framework links reduced-order models (ROMs) representing key subsurface components—including reservoir pressure and plume migration, wellbore leakage pathways, and USDW aquifer response—into a computationally efficient system model capable of running thousands of simulations to explore parameter uncertainty. By coupling site-specific simulation outputs (e.g., pressure and CO_2 saturation from CMG or STOMP) with NRAP's component ROMs, NRAP-Open-IAM provides a consistent and transparent method for screening potential storage sites, identifying influential parameters, and estimating probabilistic leakage risks.

The overall NRAP workflow is illustrated in Fig. 4.1.1, which outlines the five-step approach used to predict whole-system risk performance. Step 1 divides the geologic storage system into discrete components, such as reservoir, wellbore, and aquifer units. Step 2 develops detailed component models for each subsystem, calibrated and validated against laboratory experiments and field data. Step 3 transforms these detailed physics-based models into efficient reduced-order models (ROMs) that accurately replicate component behavior while enabling rapid computation. Step 4 links the ROMs within an integrated assessment model (IAM), allowing system-level interactions and feedbacks to be simulated. Finally, Step 5 exercises the full-model framework to explore system performance and evaluate CO_2 and brine leakage risks across a wide range of operational and geologic uncertainties. This structured, hierarchical approach enables NRAP-Open-IAM to provide rigorous, site-specific risk insights while maintaining computational efficiency suitable for broad regional assessments.

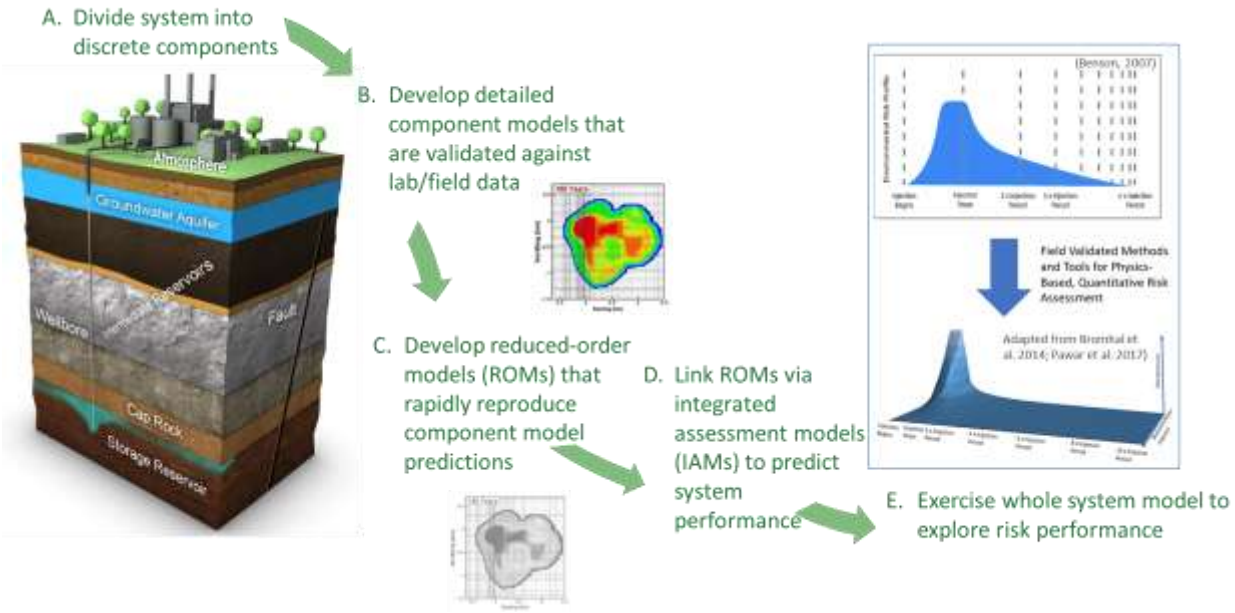


Fig. 4.1.1. NRAP's Approach for Rapid Prediction of Whole-system Risk Performance.

Subtask 1.1 – Kansas Case Study

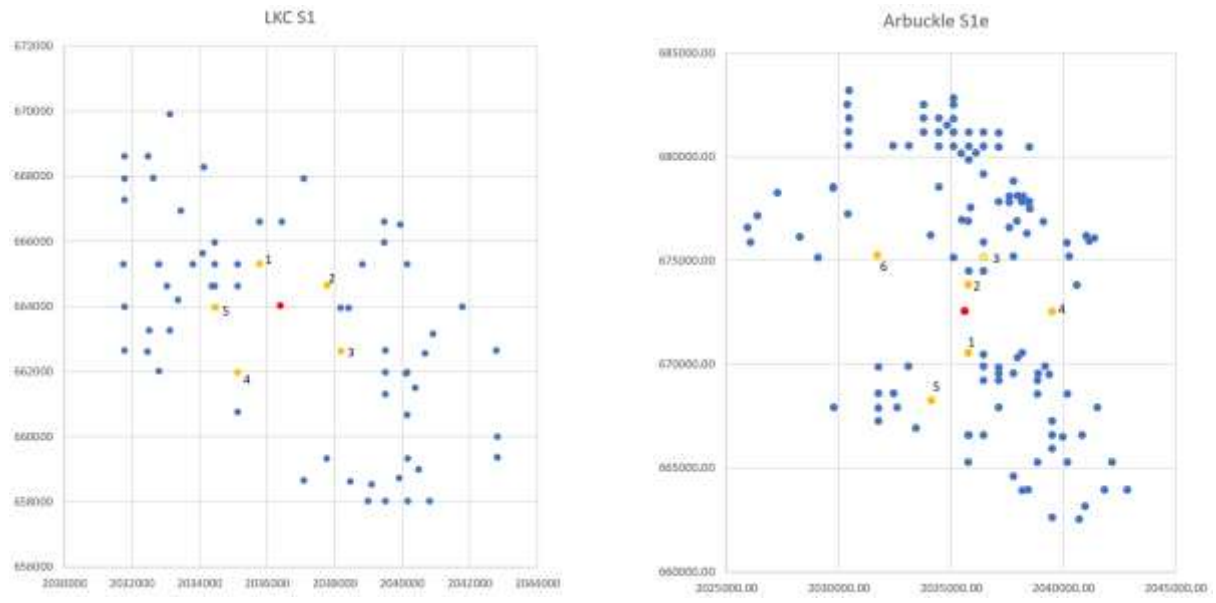
This subtask summarizes risk analysis of potential CO_2 and brine leakage and their impact on the underground source of drinking water (USDW) at the Kansas ONEOK site. This work is supported by the CUSP Western focused study project ONEOK. A workflow was developed importing pressure and CO_2 saturation results obtained by physics-based reservoir simulator (STOMP) into NRAP Integrated Assessment Model (NRAP-Open-IAM). Quantitative risk assessment of CO_2 and brine leakage, and their aquifer impact was carried out. Preliminary leakage risk analysis for 30-yr injection into two targeted storage formations (Bushton-LKC, Arbuckle) shows promising results with minimal leakages in the concerned domain area.

Following component models of the NRAP-Open-IAM system model were included for this study: Stratigraphy for the vertical structure of the system, Lookup Table Reservoir for heterogeneous CO_2 storage reservoir, Wellbore component for potential leaky wells, FutureGen2 Aquifer component for USDW. The numerical simulations for this analysis consider an approximately 37,000 by 37,000 square ft area with wells penetrating to two storage formations. Injection well locations and existing wells penetrating each targeted storage formation in the domain are identified. The legacy wells closely surrounding injection wells are chosen for leakage risk analysis for this study (Table 4.1.1). There are 69 existing wells penetrating the concerned domain area for LKC formation, and 124 existing wells for Arbuckle storage formation. Figs 4.1.2a and 4.1.2b show the locations of injection well and existing wells that penetrate the CO_2 injection formation for the two targeted storage reservoir, respectively.

Table 4.1.1. Injection well and existing well locations and well permeability for each injection scenario.

Well API	Well number	X, ft	Y, ft	Distance to injection well, ft	Well permeability, mD

	Injection to LKC	2,036,408.18	664,011.95		
15159064950000	1	2,035,809.96	665,274.30	1,396.93	1
15159003220000	2	2,037,790.46	664,610.56	1,506.33	0.01
15159063970000	3	2,038,203.06	662,612.42	2,276.02	1
15159004820000	4	2,035,151.19	661,965.14	2,401.97	1
15159033100000	5	2,034,490.18	663,950.47	1,918.98	1
	Injection to Arbuckle	2,035,610.00	672,566.50		
15-159-03010-00	1	2,035,777.97	670,543.25	2,030.21	1
15-159-30207-00	2	2,035,772.78	673,843.40	1,287.23	0.01
15-159-21540-00	3	2,036,436.02	675,162.73	2,724.47	1
15-159-00269-00	4	2,039,493.28	672,529.89	3,883.46	1
15-159-06496-00	5	2,034,111.21	668,259.54	4,560.29	1
15-159-00046-00	6	2,031,718.05	675,263.21	4,734.92	0.01



(a) (b)

Figure 4.1.2. (a) LKC, (b) Arbuckle injection well and existing well locations. Red dots denote injection wells, blue dots denote existing wells, orange dotes denote chosen wells for leakage risk analysis for this study.

NRAP-OPEN-IAM (V 2.7.2) simulations assume a 30-yr injection period for LKC (from year 0.5 to 30.5) followed by 20 yr of post-injection monitoring, giving a total duration of 51 yr with a 1-yr time step. For the Arbuckle formation, a 30-yr injection period (years 10 to 40) is followed by 60 yr of post-injection monitoring for a total of 100 yr, also using a 1-yr time step. A single final set of reservoir simulation outputs—pressure and CO_2 saturation—from STOMP is selected and converted into Lookup Table inputs for the injection scenarios in each formation. Because only a limited number of wells contain complete geological stratigraphy information, the stratigraphy described in Table 4.1.2 is applied uniformly to all selected wells in this study.

Table 4.1.2. Stratigraphy for potential leaky wells, with reservoir as the deepest layer, USDW (Dakota formation) as the shallow aquifer.

Stratigraphy data (ft)	LKC	Arbuckle
USDW thickness	148	148
Depth of potential leakage	200	200
Reservoir thickness	39.5	80
Depth to top of storage reservoir	3,000	3,250

Input parameters for wellbore are chosen from site data with most values using the conservative values for model inputs. Table 4.1.3 lists input parameters for the wellbore component model.

Table 4.1.3. Input parameters for wellbore model (Note: NRAP default values are used for missing data).

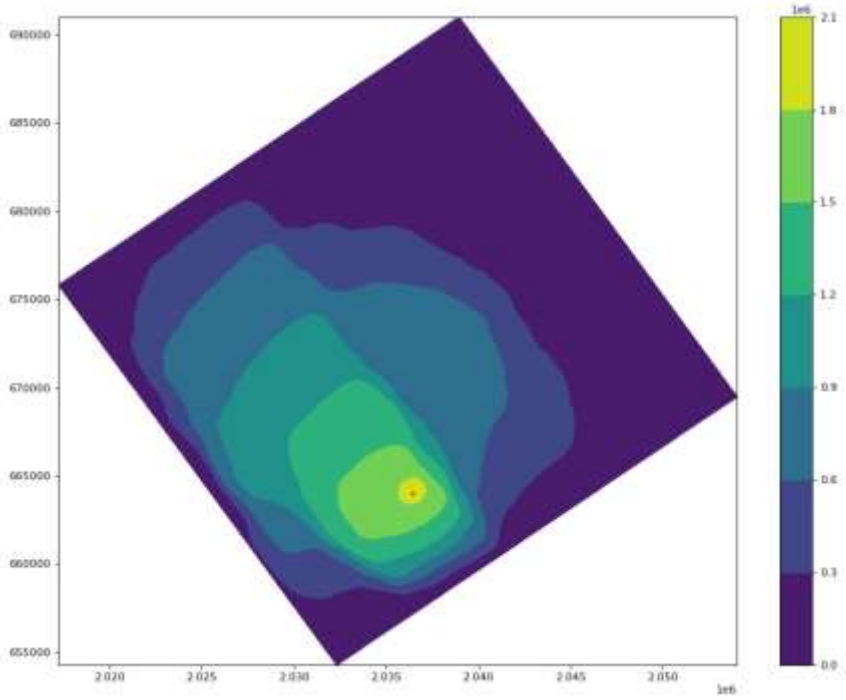
Wellbore parameter	LKC	Arbuckle

Wellbore effective permeability (mD)	0.001 to 1 (details see Table 1)
Aquifer permeability (mD)	10 to 100, USDW (Dakota 3mD)
Caprock permeability (mD)	0.001 to 0.01
Well diameter (inch)	5.5 to 7 (To be conservative, this study used 7 for all chosen wells.)
Brine density (kg/m^3)	977
CO_2 density (kg/m^3)	648
Brine viscosity (Pa s)	0.002535 (NRAP default)
CO_2 viscosity (Pa s)	3.95×10^{-5} (NRAP default)
Compressibility (Pa^{-1})	5.1×10^{-11} (NRAP default)
Brine saturation	0.1 (NRAP default)

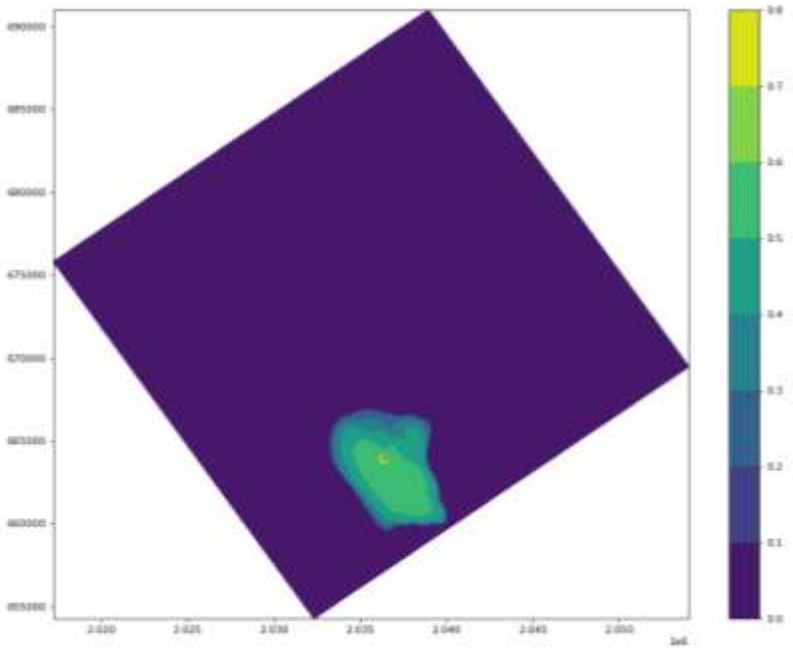
For this study, potential CO_2 and brine leakage risk from chosen representative existing wells in the domain are analyzed separately for injection to LKC and Arbuckle storage formations.

LKC Injection

The simulation for LKC: 30 yr injection (year 0.5 to year 30.5) plus 20 yr postinjection monitoring period. A few representative wells close to the injection well are chosen for analysis, the distance of these existing wells to the injection well ranging from 1,400 to 2,400 ft surrounding the injector. The locations for these wells are listed in Table 4.1.1. Figs 4.1.3a and 4.1.3b show the predicted reservoir pressure increase (delta P) due to injection, and CO_2 saturation plume at the end of simulation duration (year 51), respectively. The results show that delta P maximum at injector reaches 2.1 MPa. CO_2 saturation plume shows peak at 0.8 at year 51, with oval plume shape.



(a) LKC reservoir pressure increase due to injection.

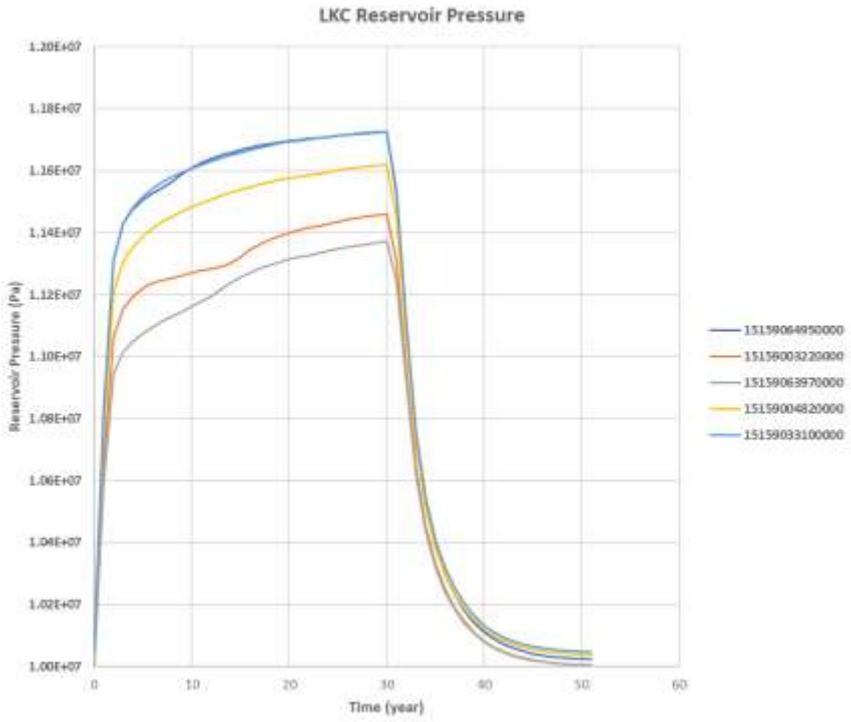


(b) LKC CO_2 plume at year 51.

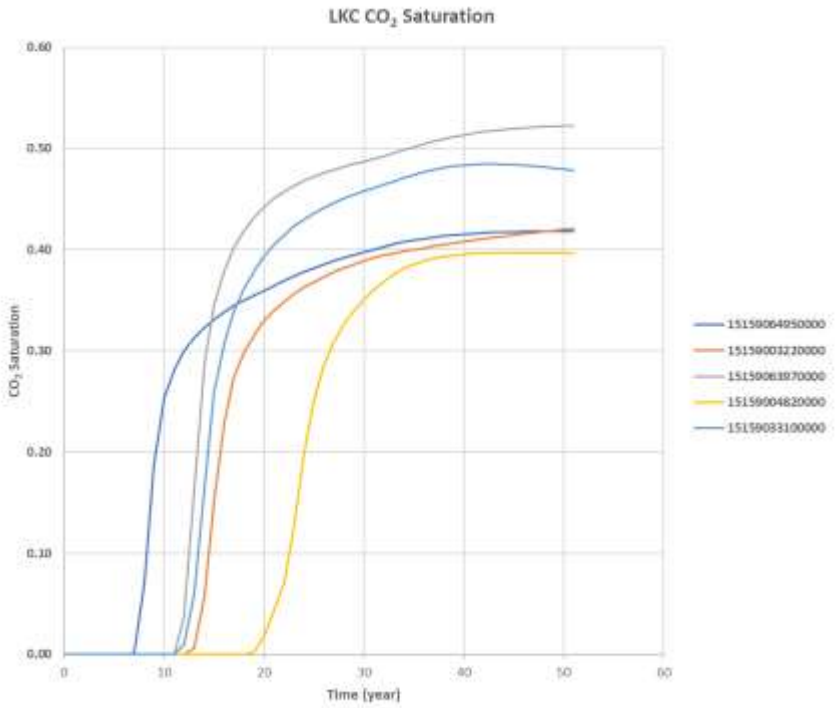
Figure 4.1.3. LKC pressure and saturation distribution at year 51.

Figs 4.1.4a and 4.1.4b show the predicted reservoir pressure and maximum CO_2 saturation for the representative wells, respectively. The highest reservoir pressure and earliest CO_2 plume reaching well is well 1 (API 15159064950000), the lowest reservoir pressure and the highest

CO_2 saturation well is well 3 (API 15159063970000). Pressures at 5 well locations all increase during injection and increasing to maximum value until injection is stopped, and then start decline in the post-injection period. Maximum delta P due to injection is approximately 1.7 MPa. CO_2 saturation in wells that are closest to injection well start breakthrough early on during injection, demonstrate that CO_2 plume reaching them earlier while other farther away wells are generally reached later (e.g., well4), and some wells with saturation decreasing earlier once injection is stopped (e.g., well5).



(a)



(b)

Figure 4.1.4. (a) Reservoir pressure at the top of LKC storage formation for representative wells; (b) maximum CO_2 saturation at LKC formation for representative wells

Figure 4.1.5 shows the very small CO_2 leakage from representative wells to USDW, with the maximum leakage rate of 2 kg/yr (well3) at year 51. Calculations of cumulative CO_2 leaked to USDW show that well 1 has the maximum of total amount CO_2 leaked to USDW among 5 representative wells, 41.5 kg over 51 yr. Comparing to the total amount of CO_2 injected (0.35 Mt/yr over 30 yr), the percentage of CO_2 leaked from well1 over 51 yr is 4×10^{-7}%.

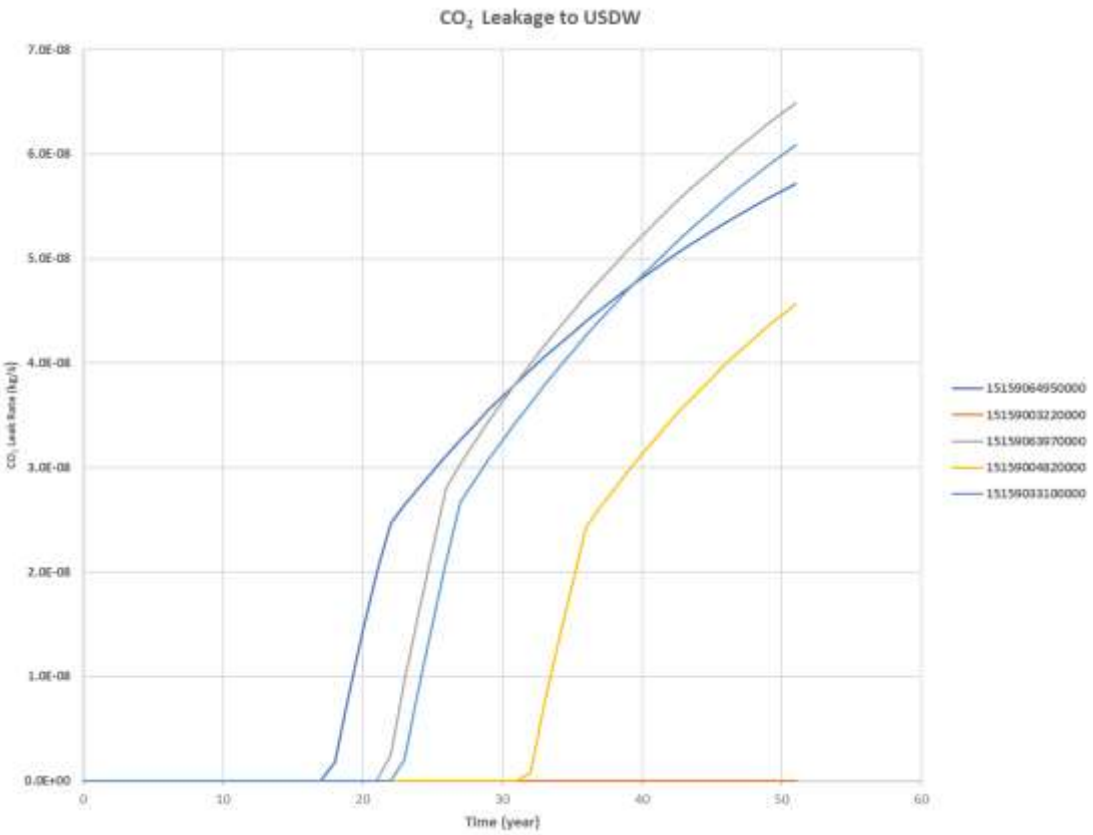


Figure 4.1.5. LKC leakage rate of CO_2 to USDW for representative wells

Take well 1 as example, Figs 4.4.6 and 4.1.7 shows the very small brine leakage and USDW impact. Fig. 4.1.6 calculation shows the cumulative brine leaked to USDW over 51 yr is approximately 0.3 kg. Fig. 4.1.7 shows the leakage impact to USDW for pH change. The pH plume volume where absolute change in pH > 0.2 is less than 7.5 m^3.

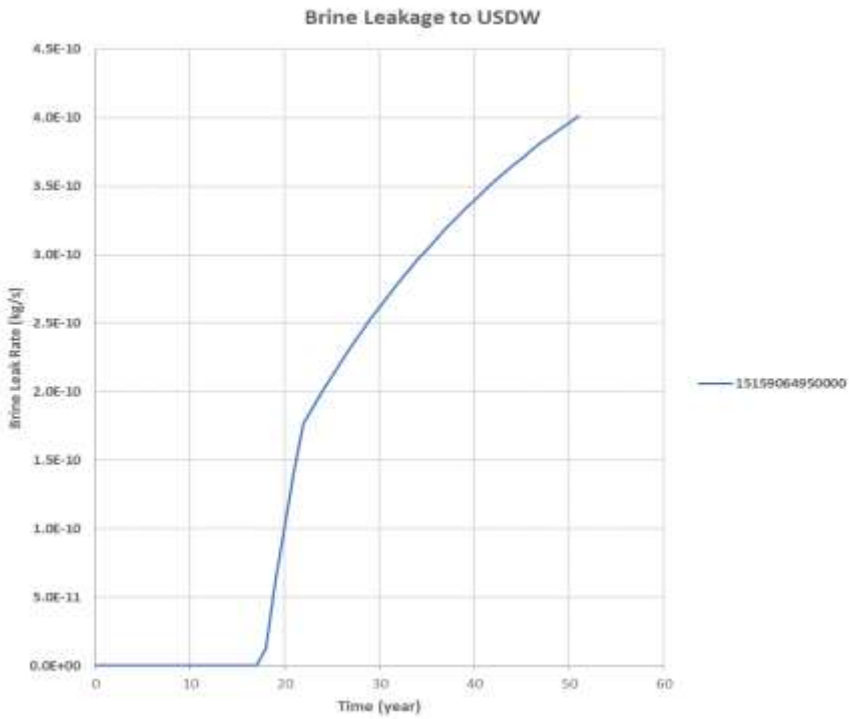


Figure 4.1.6. LKC leakage rate of brine to USDW for well 1 (API 15159064950000)

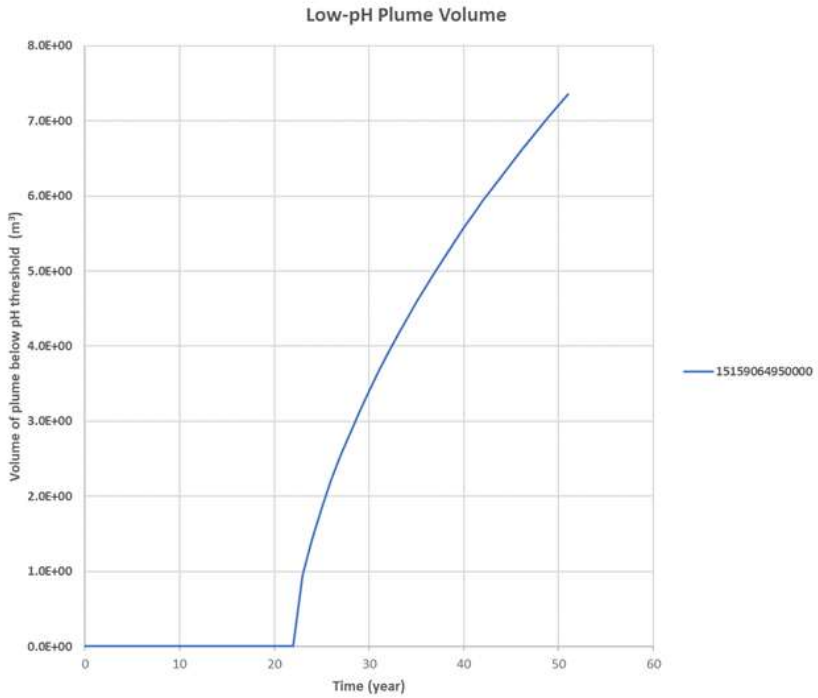


Figure 4.1.7. LKC Low-pH plume volume in USDW for well 1 (API 15159064950000)

Arbuckle Injection

The simulation for Arbuckle: 30 yr injection (year 10 to year 40) plus 60 yr postinjection monitoring period. A few representative wells close to injection well are chosen for analysis, the distance of these existing wells to the injection well ranging from 1,300 to 4,700 ft surrounding the injector. The locations for these wells are listed in Table 4.1.1. Fig. 4.1.8 shows the predicted reservoir pressure increase (delta P) due to injection. Figures 8a and 8b show the CO_2 saturation plume at year 50 and at the end of simulation duration (year 100), respectively. The results show that delta P maximum at injector reaches 0.4 MPa which is much lower (1/5) comparing to the delta P max for LKC injection scenario. Note the negative delt P shown on Fig. 4.1.8 is due to water injection in that area. CO_2 saturation plume (Figs 4.1.9a and 4.1.9b) show peak at approximately 0.8, the plume size increase during injection, and migrate/change in size during the post injection monitoring period.

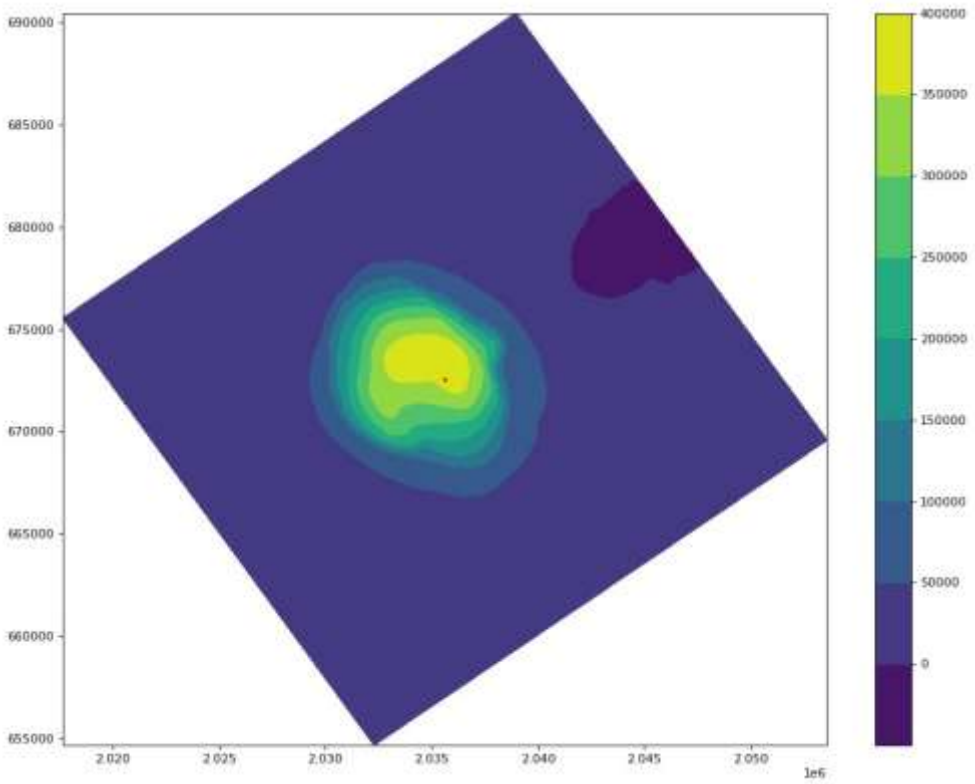
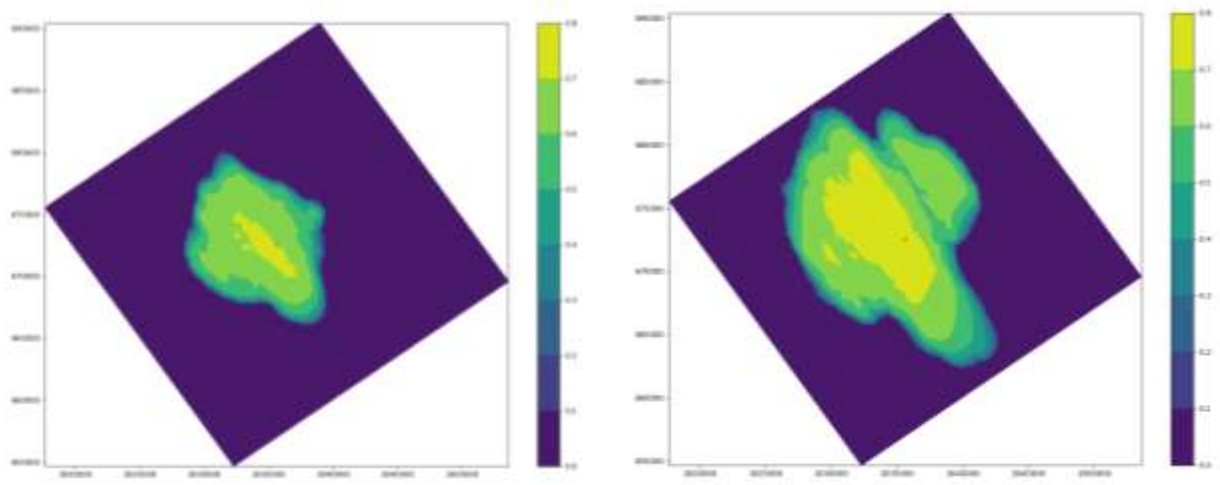


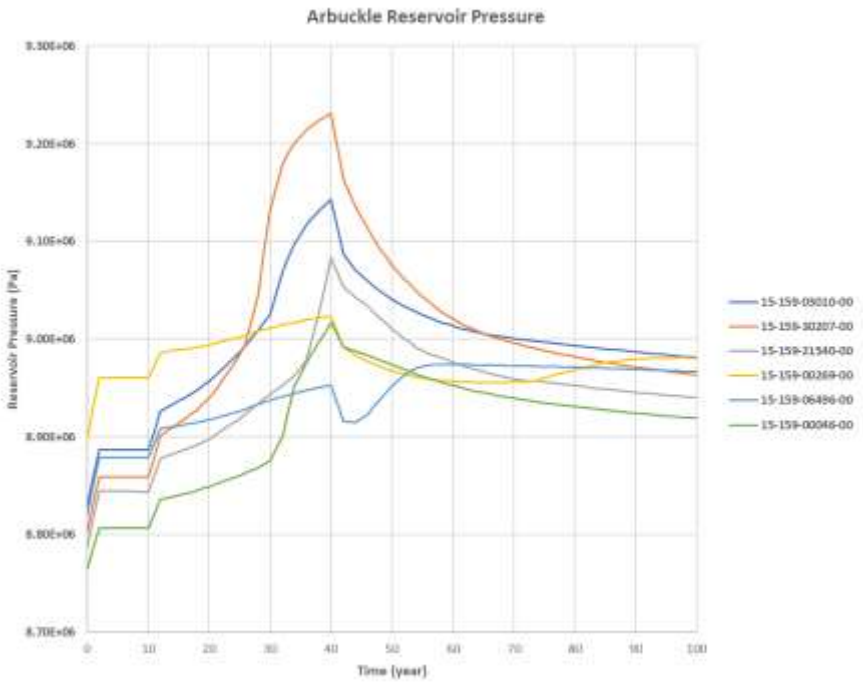
Figure 4.1.8. Arbuckle reservoir pressure increase due to injection



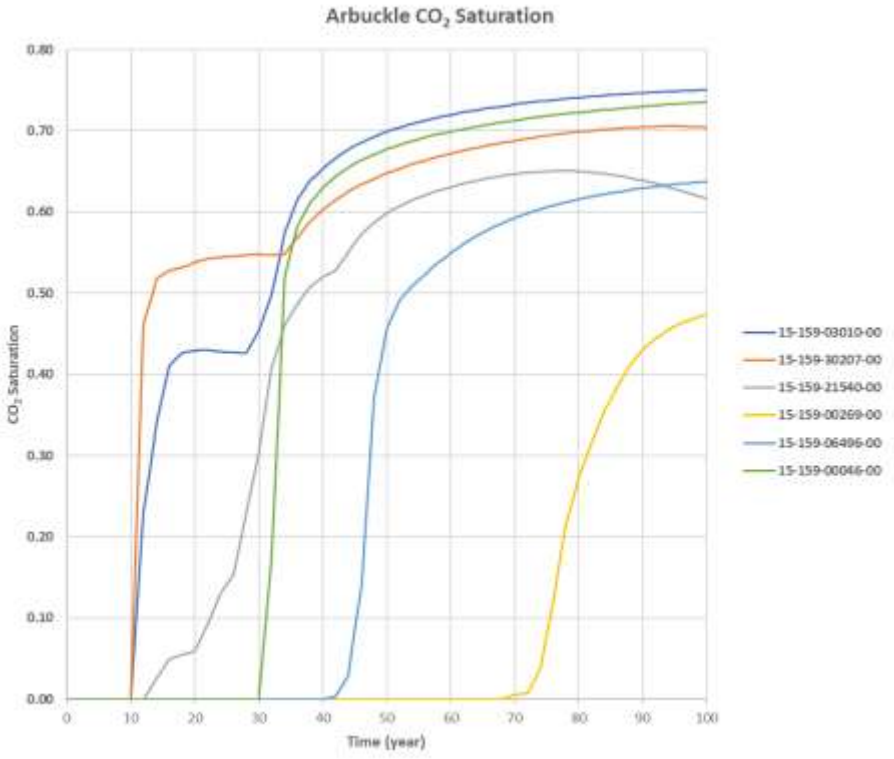
(a) (b)

Figure 4.1.9. (a) Arbuckle CO_2 plume at year 50; (b) Arbuckle CO_2 plume at year 100.

Figures 4.1.10a and 4.1.10b show the predicted reservoir pressure and maximum CO_2 saturation for the Arbuckle representative wells, respectively. The highest reservoir pressure and earliest CO_2 plume reaching well is well 2 (API 15-159-30207-00), the last CO_2 plume reaching well is well 4 (API 15-159-00269-00). Pressures at 6 well locations all increase during injection and reaching to maximum value until injection is stopped, and then start decline in the post-injection period. Maximum delta P due to injection is approximately 0.4 MPa. CO_2 saturation in wells that are closest to injection well start breakthrough early on during injection (depends on CO_2 plume shape and size), demonstrate that CO_2 plume reaching them earlier while other farther away wells are reached later (e.g., well 4), and some wells with saturation decreasing earlier once injection is stopped (e.g., well 3).



(a)



(b)

Figure 4.1.10. (a) Reservoir pressure at the top of Arbuckle storage formation for representative wells; (b) maximum CO_2 saturation at Arbuckle formation for representative wells.

Leakage calculations for Arbuckle injection show that there are no CO_2 and brine leakage for all representative wells, and no impact to USDW on pH and TDS beyond natural background variability.

Conclusions

Among legacy wells that have been drilled in the study domain, wells penetrating to the two targeted storage formations have been identified. Leakage risk analyses for chosen representative wells show that the pressure build up and wellbore permeability strongly influence the CO_2 and brine leakage from the reservoir to the USDW. For LKC formation injection, analysis of chosen representative wells in the reservoir domain shows there are very small CO_2 and brine leakage, and small USDW impact for wells 1, 3, 4, and 5. The percent of CO_2 leaked in comparison to the total amount injected is less than 4×10^{-7}% for the highest potential leaky well. There is no CO_2 and brine leakage, and no impact to USDW on pH and TDS beyond natural background variability for well 2 (API 15159003220000). For Arbuckle formation injection, analysis of chosen existing wells on the reservoir domain shows that there is no CO_2 and brine leakage and no impact to USDW on pH and TDS beyond natural background variability for any well. For this study we take a conservative approach for leakage risk assessment, choosing the legacy wells that are closest surrounding the injection well to evaluate the highest CO_2 and brine leakage potentials for existing legacy wells. For Class VI well permit application at the ONEOK site, AoR delineation will confine the leakage risk concerned area. Individual well leakage situations are different based on each well's degradation status, more complete wellbore and site characterization data will help facilitate the site-specific leakage risk assessment accurately.

Subtask 1.2 – California Case Study

This subtask evaluates the potential for CO_2 and brine leakage from two existing legacy wells in a candidate storage site in California. All data for this study were provided by Stanford University. The analysis couples reservoir-model outputs from two CMG simulation scenarios—a vertical injection well and a deviated injection well—with NRAP-Open-IAM (v2.7.2) system-model components to perform deterministic and probabilistic leakage risk assessments. A 100-yr simulation period was considered, consisting of 47 yr of CO_2 injection followed by 53 yr of post-injection monitoring. The primary receptor of concern is an overlying USDW aquifer, and the main potential leakage pathways include two dry-hole legacy wells located 615 m (Well 1) and 1,336 m (Well 2) from the injector (Fig. 4.1.11).

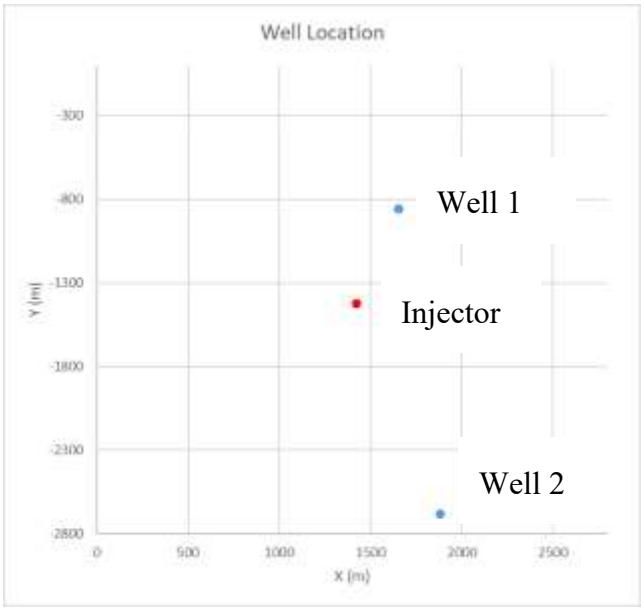


Figure 4.1.11. Storage reservoir domain and well locations

Lookup Table Reservoir components were generated directly from CMG-simulated reservoir pressure and CO_2 saturation fields, and were used to inform wellbore leakage calculations through the Cemented Wellbore reduced-order model (ROM). The Deep Alluvium Aquifer ROM was applied to evaluate potential USDW impacts. A uniform stratigraphy was adopted across all wells, and Monte Carlo simulations were performed to quantify the effects of parameter uncertainty on leakage potential.

The modeled reservoir spans approximately 3 km × 3 km, with homogeneous properties of 30 mD permeability and 0.25 porosity. The maximum injection rate was 0.6 Mt CO_2/yr. Both existing wells have low effective permeabilities (< 30 mD) and differ slightly in wellbore radius (0.135 m for Well 1; 0.125 m for Well 2). The overlying USDW has a permeability of 150 mD.

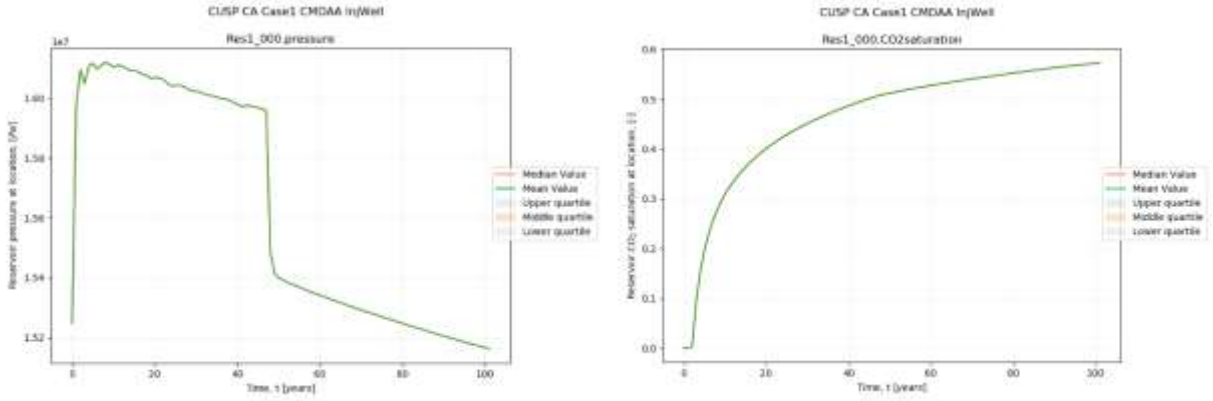
Reservoir pressure and CO_2 saturation outputs from CMG were provided for two injection configurations:

1. Case 1 — Vertical Injection Well
2. Case 2 — Deviated Injection Well

These outputs drive all NRAP-Open-IAM wellbore and aquifer ROMs used to simulate leakage rates and potential impacts on USDW pH, and TDS.

Case 1: Vertical Injection Scenario

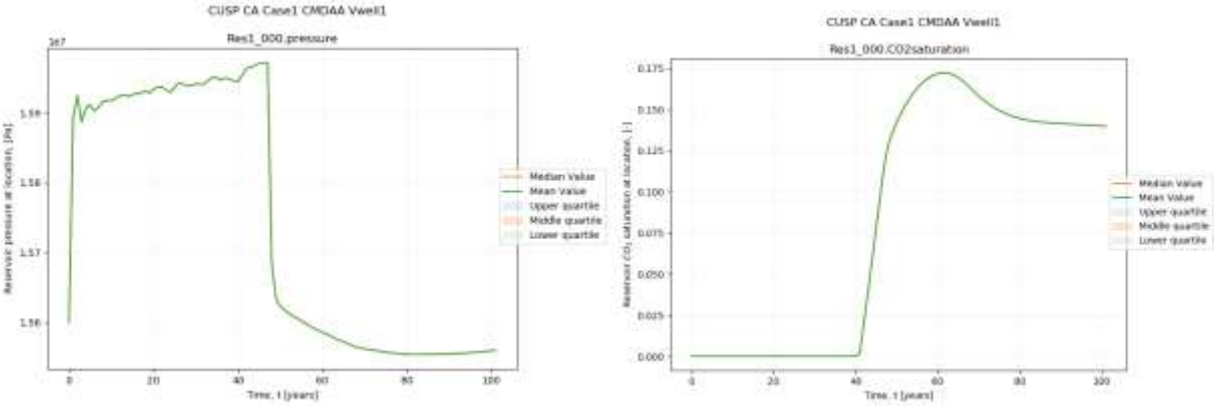
Figure 4.1.12 shows the reservoir pressure and CO_2 saturation at the injection well. Reservoir pressure peaks at approximately 16.1 MPa early in the injection period, gradually decreases as injection continues, and drops sharply following injection cessation at Year 47. CO_2 saturation increases rapidly during early injection, reaching a maximum of approximately 60% by the end of the 100-yr simulation.



(a) (b)

Figure 4.1.12. Reservoir pressure (a) and CO_2 saturation (b) at injection well, Case 1.

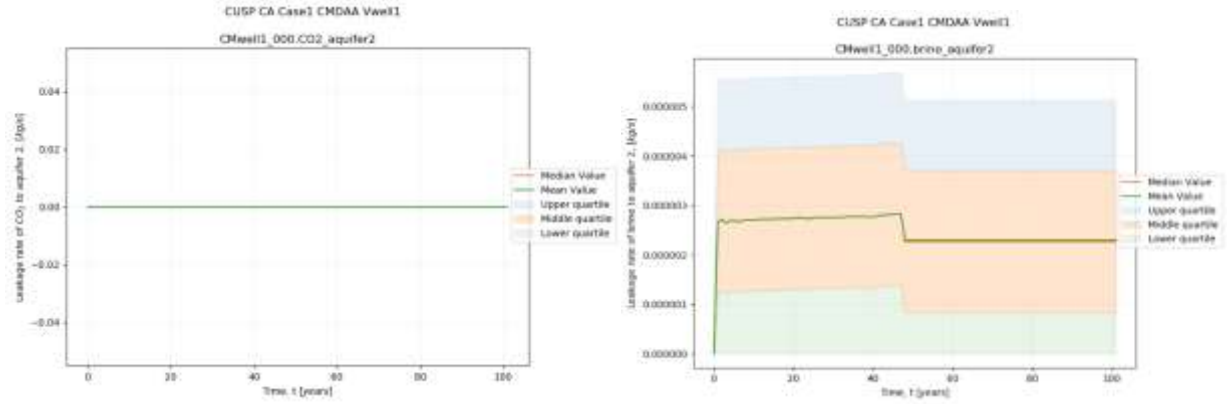
Figure 4.1.13 presents reservoir pressure and CO_2 saturation at Well 1, located 615 m from the injection well. Pressure rises throughout the injection period, reaching a maximum of approximately 15.97 MPa at Year 47 before declining sharply in the post-injection period. CO_2 saturation begins to increase late in injection (around Year 40), peaks at 17.2% near Year 60, then decreases slowly through Year 100.



(a) (b)

Figure 4.1.13. Reservoir pressure (a) and CO_2 saturation (b) at well 1, Case 1.

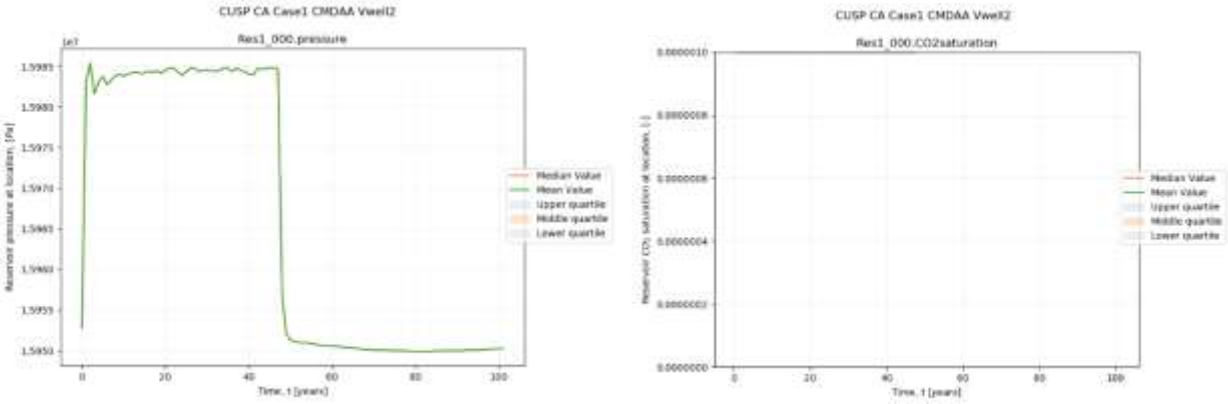
Figure 4.1.14 illustrates CO_2 and brine leakage rates from Well 1. No CO_2 leakage to the USDW is predicted. Brine leakage begins during the injection period, peaks at $<5.7\times10^{-6}$ kg s^{-1} at the end of injection, and stabilizes during the post-injection period. No measurable impacts to USDW pH, and TDS are predicted.



(a) (b)

Figure 4.1.14. CO_2 (a) and brine (b) leakage rate from well 1 to USDW, Case 1.

Pressure and saturation at Well 2 are shown in Fig. 4.1.15. Pressure increases steadily during injection, reaching approximately 15.98 MPa, and decreases sharply once injection ceases. CO_2 saturation at Well 2 remains at a negligible approximately 0.0001% throughout the 100-yr simulation, reflecting its greater distance from the injection well. As shown in Fig. 4.1.16, Well 2 exhibits no CO_2 leakage to the USDW. Small brine leakage ($<4.4\times10^{-6}$ kg s^{-1}) occurs, peaking early during injection and remaining stable throughout the monitoring period. No USDW impacts are predicted.



(a) (b)

Figure 4.1.15. Reservoir pressure (a) and CO_2 saturation (b) at well 2, Case 1

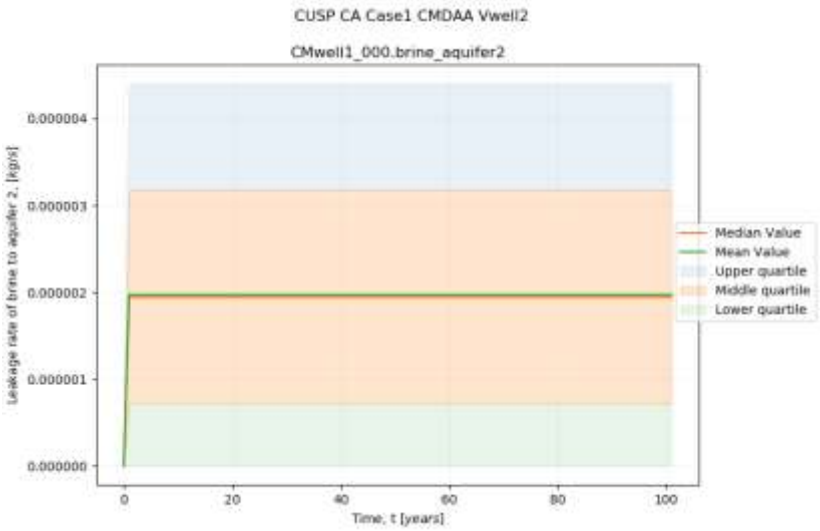
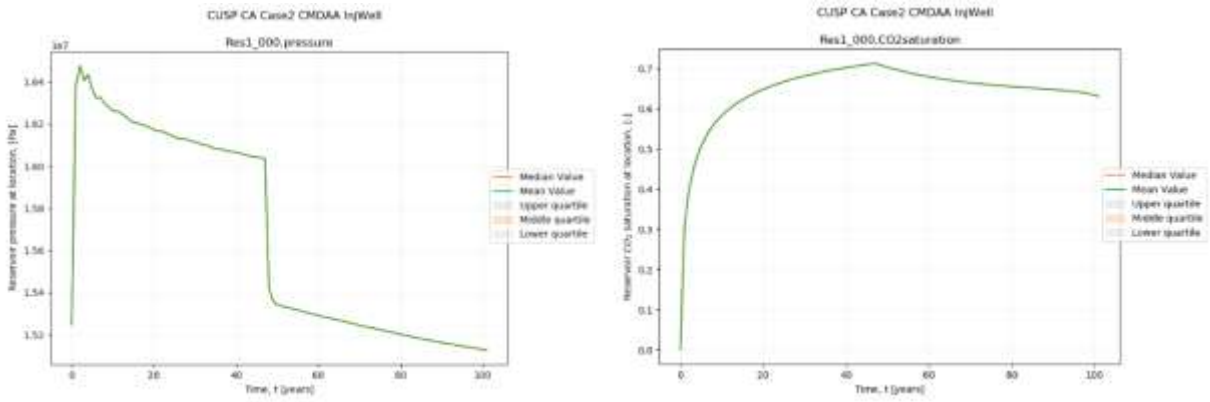


Figure 4.1.16. Brine leakage rate from well 2 to USDW, Case 1.

Case 2: Deviated Injection Scenario

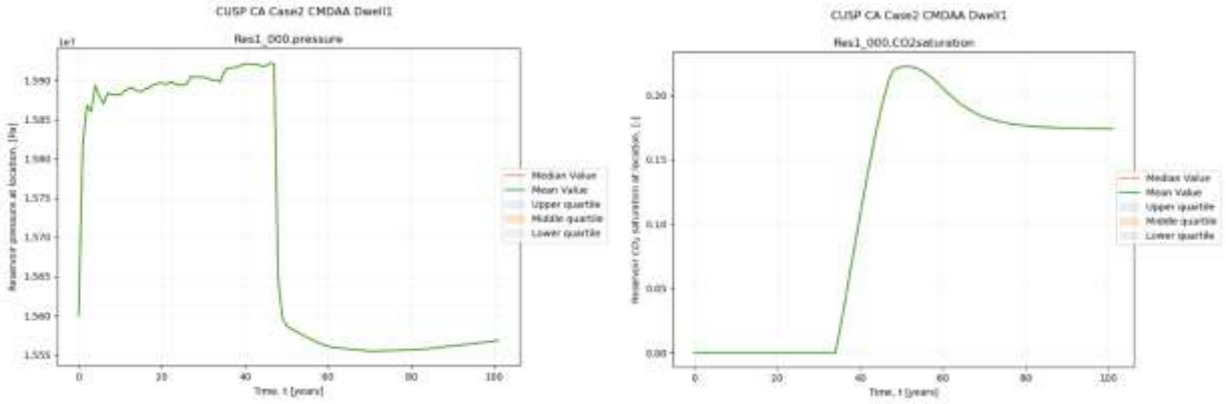
Figure 4.1.17 shows reservoir pressure and CO_2 saturation for the deviated injection scenario. Pressure peaks at approximately 16.48 MPa early in injection, then decreases similarly to Case 1. CO_2 saturations near the injector are higher than in Case 1, reaching a peak of approximately 71% at the end of the 47-yr injection period before gradually declining during post-injection.



(a) (b)

Figure 4.1.17. Reservoir pressure (a) and CO_2 saturation (b) at injection well, Case 2

At Well 1, pressure behavior mirrors Case 1, with a peak of approximately 15.92 MPa (Fig. 4.1.18). CO_2 saturation increases around Year 35, reaches a maximum of 22.2% near Year 50, and gradually declines to approximately 17% by Year 100. Figure 4.1.19 presents the predicted leakage behavior for Dwell 1. No CO_2 leakage is observed. Small brine leakage ($<5.6\times10^{-6}$ kg s^{-1}) occurs, with the highest rates near the end of injection and stable behavior during the post-injection period. No USDW impacts are detected.



(a) (b)

Figure 4.1.18. Reservoir pressure (a) and CO_2 saturation (b) at well 1, Case 2.

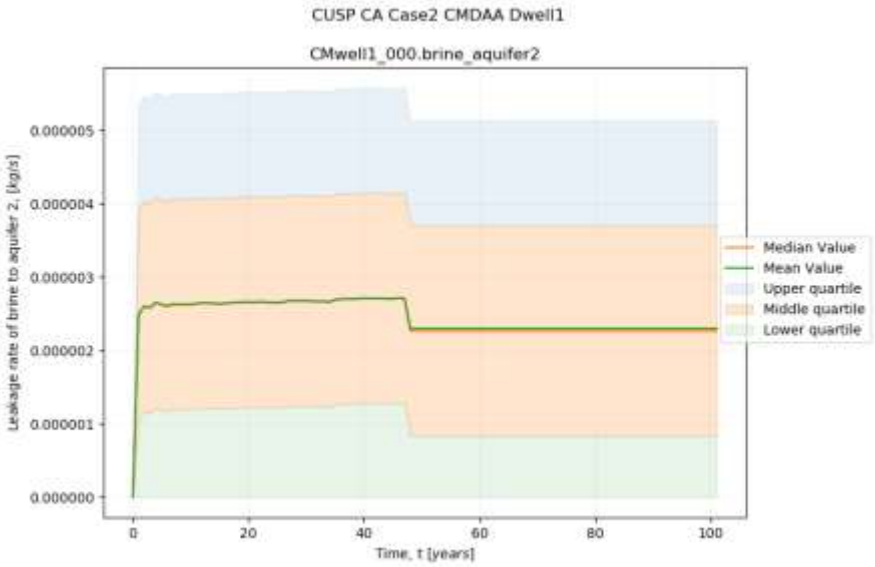
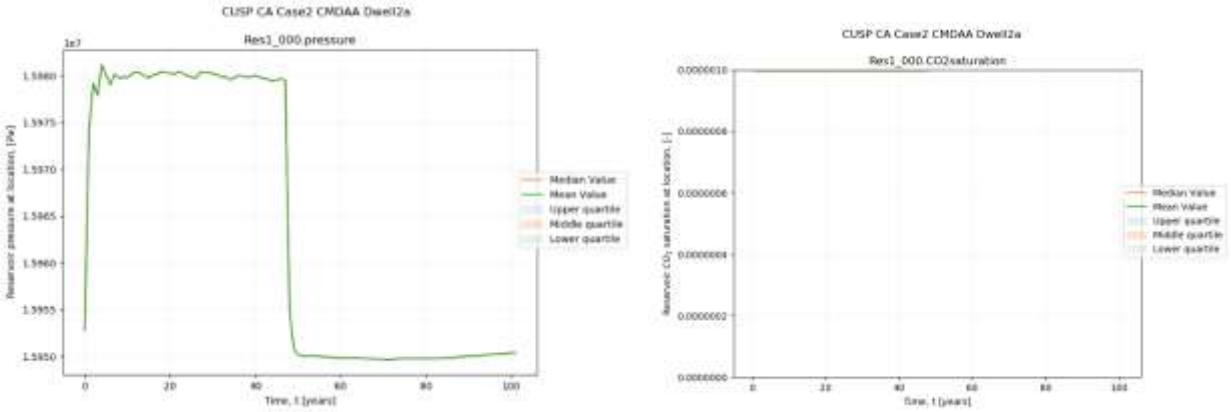


Figure 4.1.19. Brine leakage rate from well 1 to USDW, Case 2

Figure 4.1.20 shows the pressure and saturation at Well 2. Pressure increases during injection and decreases sharply after Year 47, similar to other wells. CO_2 saturation remains extremely low (approximately 0.0001%) throughout the entire period. Figure 4.1.21 shows the predicted brine leakage behavior for Well 2. No CO_2 leakage is observed. Brine leakage remains very small ($<4.4\times10^{-6}$ kg s^{-1}) and changes little throughout the simulation. No USDW impacts are predicted.



(a) (b)

Figure 4.1.20. Reservoir pressure (a) and CO_2 saturation (b) at deviated well (Dwell) 2, Case 2

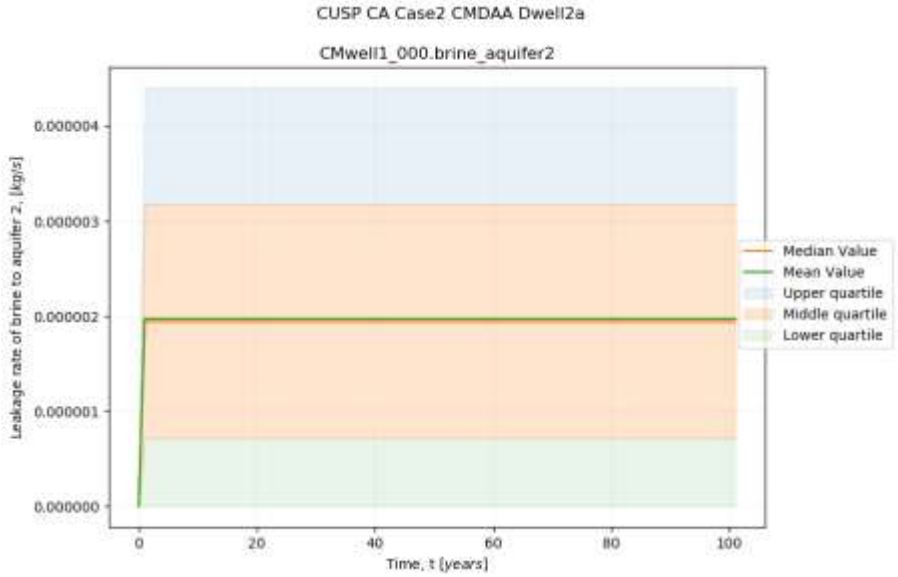


Figure 4.1.21. Brine leakage rate from well 2 to USDW, Case 2

Conclusions

Across both vertical and deviated injection scenarios, the California case study indicates a consistently low risk of leakage from the storage reservoir to the overlying USDW. No CO_2 leakage is predicted for any existing well, and only very small brine leakage rates—always less than 5.7×10^{-6} kg s^{-1}—occur, remaining stable throughout the 100-yr simulation period. These low leakage rates do not produce any measurable impacts on USDW pH, or TDS. As expected, CO_2 saturation is highest near the injection well, with the deviated-well scenario (Case 2) producing slightly greater peak saturations than the vertical-well scenario (Case 1). Wells located farther from the injector, particularly Well 2, exhibit negligible CO_2 breakthrough under all modeled conditions. Overall, the results demonstrate that the California site presents a very low potential for CO_2 or brine leakage to USDW across all tested configurations, even under conservative assumptions.

Subtask 1.3 – Colorado Case Study

This effort is part of the CUSP main project with data provided by Colorado School of Mines. This subtask presents a preliminary assessment of CO_2 and brine leakage risks for a potential geologic CO_2 storage site in Colorado. Using NRAP-Open-IAM (v2.7.2), the analysis evaluates potential leakage through a selected legacy production well located near the proposed injection location. The study integrates reservoir pressure and CO_2 saturation outputs from CMG simulations with reduced-order models (ROMs) representing the wellbore system and an overlying carbonate USDW aquifer. The primary objective is to quantify the magnitude, timing, and uncertainty associated with potential leakage to shallow groundwater and the atmosphere under a 130-yr simulation period, including 30 yr of injection followed by 100 yr of post-injection site care (PISC).

Figure 4.1.22 summarizes the stratigraphic configuration and the modeled storage domain. The target reservoir is the Pierre Sandstone, represented as a one-square-mile domain with permeability ranging from 0.1 to 8 mD. The CO_2 injection well is positioned at the center of this domain, with a constant injection rate of 1 Mt CO_2/yr during the 30-yr injection period. Among the 15 existing wells (4 vertical and 11 horizontal) that penetrate the reservoir interval, a single legacy well—Prod_v1, located approximately 348 m from the injector—was selected for detailed leakage risk evaluation due to its proximity and potential to represent a worst-case leakage pathway.

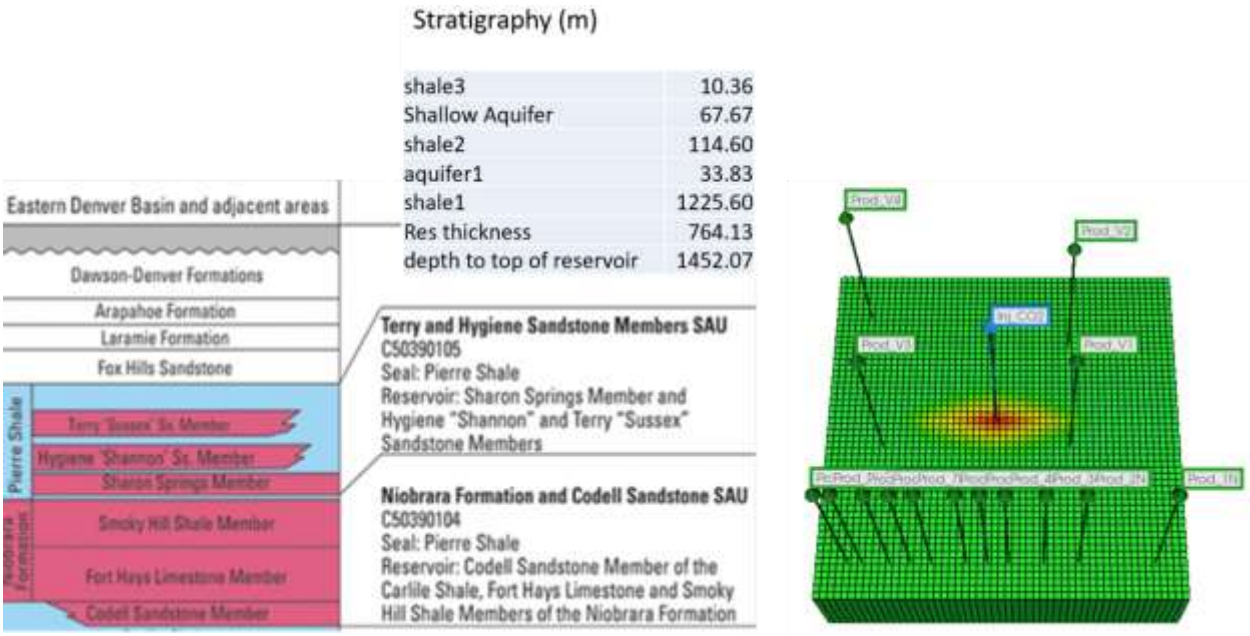


Figure 4.1.22. Stratigraphic information and reservoir model domain

NRAP-Open-IAM simulations for this subtask incorporate:

- Lookup Table Reservoir ROM, derived from CMG-simulated reservoir pressure and CO_2 saturation fields.
- Multi-Segmented Wellbore ROM, used to estimate CO_2 and brine leakage rates through Prod_v1 under variable pressure and saturation conditions.

- Carbonate Aquifer ROM, representing the overlying Arapahoe USDW, which is used to evaluate potential groundwater impacts (pH and TDS) resulting from any CO_2 or brine leakage.

Probabilistic simulations were conducted to account for uncertainty in key parameters, including wellbore permeability, aquifer properties, and reservoir conditions, enabling the computation of mean leakage rates, breakthrough timing, and upper-bound behaviors across the full simulation duration.

The Colorado case study results indicate small but nonzero CO_2 and brine leakage through the legacy well Prod_v1, beginning approximately 40 yr into the simulation. Fig. 4.1.23 shows the predicted CO_2 leakage rate to the shallow aquifer. Peak CO_2 leakage rates remain below 3.5×10^{-4} kg/s, and mean CO_2 leakage rates flatten toward the end of the 130-yr simulation, indicating stabilization under declining reservoir pressures during the PISC period.

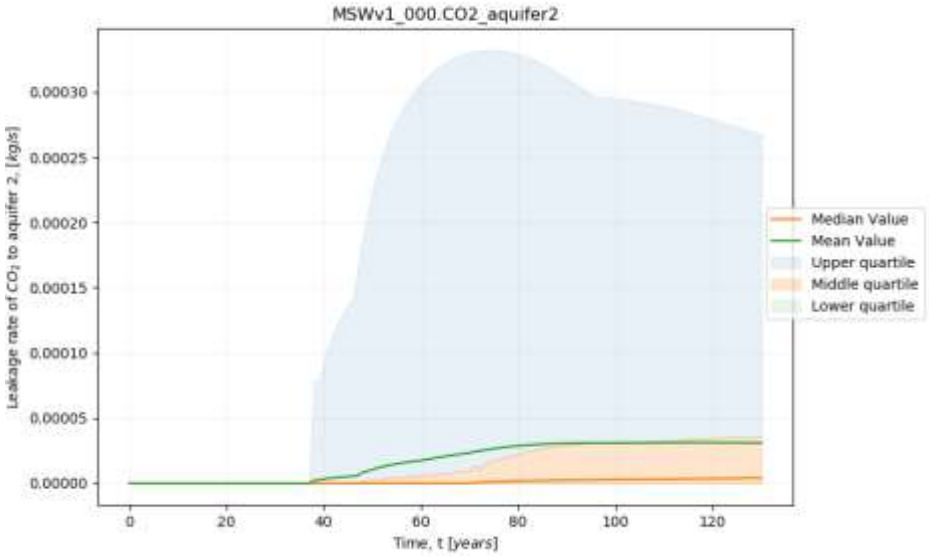


Figure 4.1.23. CO_2 leakage rate to shallow aquifer (USDW)

Fig. 4.1.24 presents the corresponding brine leakage rates, which peak at less than 7.1×10^{-7} kg/s. Brine leakage begins around the same time as CO_2 breakthrough and follows a similar stabilizing trend during the post-injection monitoring period. Despite the measurable leakage, simulated impacts to the overlying Arapahoe USDW remain below all no-impact thresholds, with pH and TDS plumes staying within natural background variability throughout the 130-yr analysis. No atmospheric leakage pathway was identified for the selected well configuration.

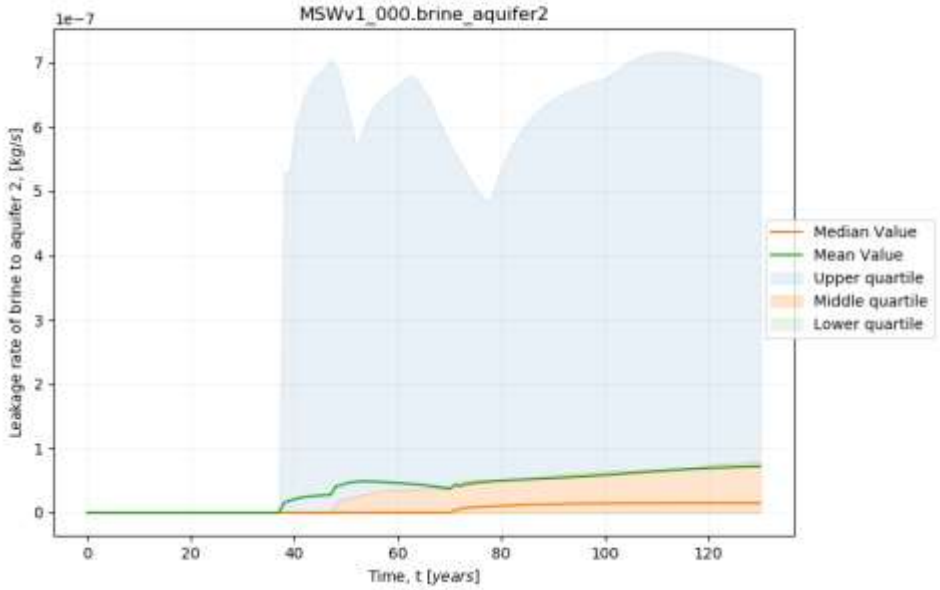


Figure 4.1.24. Brine leakage rate to shallow aquifer (USDW)

Fig. 4.1.25 displays the cumulative mass of CO_2 leaked to the USDW across the simulation period. At the end of the 100-yr PISC interval, the total CO_2 leaked is less than 1.84×10^{-5}% of the total injected mass (1 Mt/yr × 30 yr), with a mean value of approximately 7.1×10^{-6}%. These values indicate that leakage occurs at extremely small fractions relative to total injection, even under conservative assumptions regarding wellbore conditions and reservoir behavior.

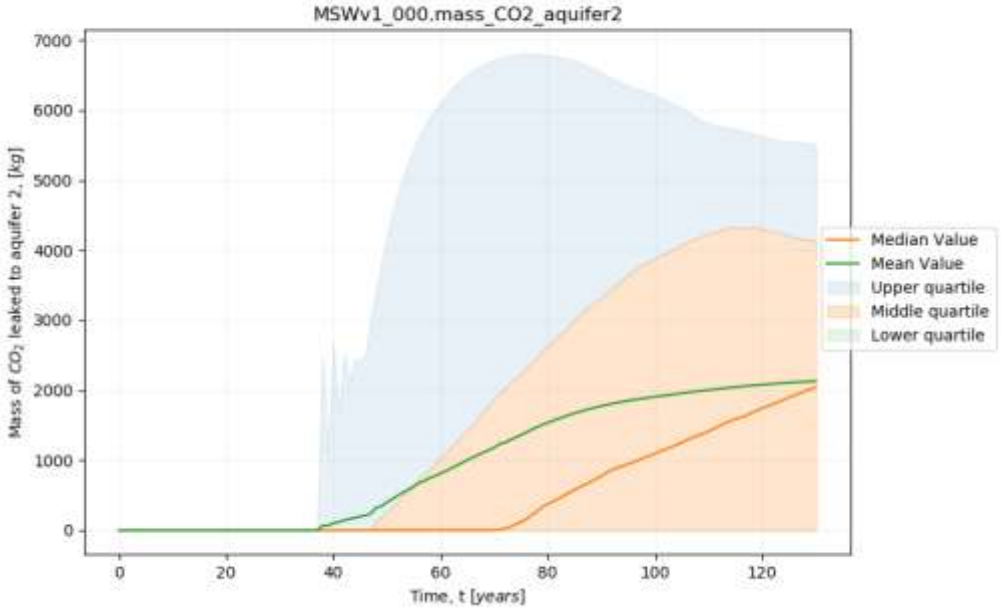


Figure 4.1.25. Mass of CO_2 leaked to shallow aquifer (USDW)

Conclusions

Preliminary leakage risk analysis for the Colorado case study shows that while limited CO_2 and brine leakage may occur through the identified legacy well, the rates remain very small, with breakthroughs occurring only after several decades of injection and monitoring. Importantly, these leakage rates do not produce any measurable impacts on shallow groundwater quality, and cumulative leakage amounts remain orders of magnitude below levels of concern relative to injected mass. Although the presence of legacy wells warrants careful consideration for future Class VI permitting and monitoring strategies, the results indicate that the Colorado site exhibits low overall leakage risk under the modeled conditions. Continued refinement of wellbore characterization, site-specific data collection, and expanded probabilistic analysis will further support robust risk assessment for potential storage development in the region.

Subtask 1.4 – Oklahoma Case Study

This effort is part of the CUSP main project with data provided by University of Oklahoma. This subtask presents an initial evaluation of CO_2 and brine leakage risks for two potential geologic carbon storage locations in Oklahoma. Working collaboratively with Oklahoma project participants, available site data were refined and integrated into NRAP-Open-IAM to conduct preliminary system-level risk assessments. Two injection areas—one located in the northern part of the study region and one in the south—were analyzed to evaluate differences in leakage behavior across varying well distributions. For each location, leakage risks were assessed for legacy wells positioned at two representative distances from the injector: near-field wells approximately 5 km away and far-field wells approximately 20 km from the injection location.

Figure 4.1.26 illustrates the simulated reservoir pressure history at legacy well locations. Pressure increases rapidly following the onset of injection and reaches a plateau after approximately 30 yr, reflecting stabilization of reservoir flow conditions as injection continues. These pressure trends influence the timing and magnitude of potential leakage from nearby wells.

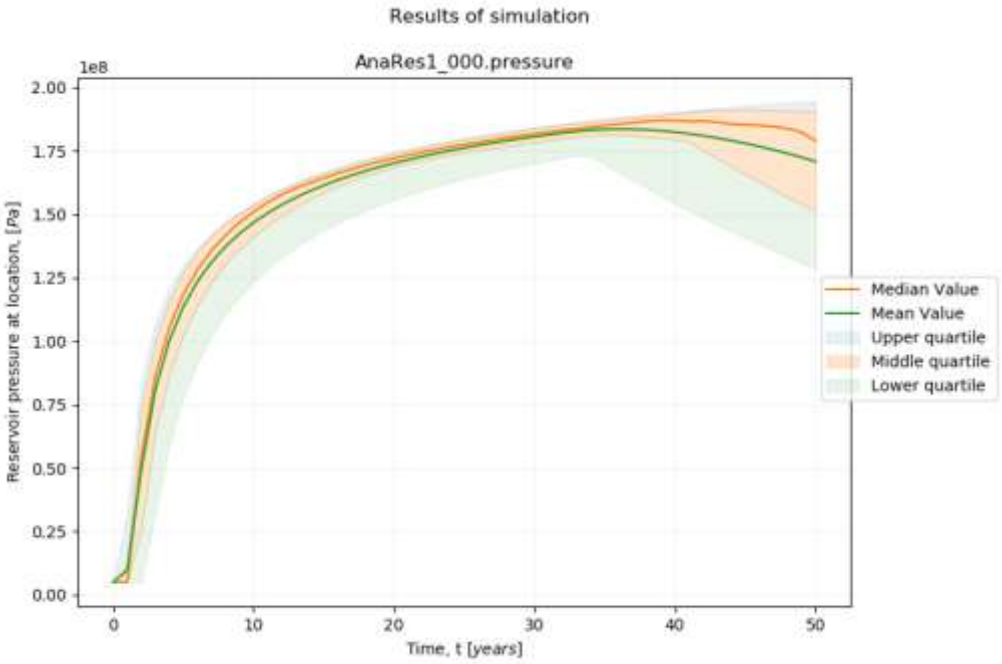


Figure 4.1.26. Reservoir pressure at legacy well location

Figures 4.1.27 and 4.1.28 show the predicted CO_2 and brine leakage rates to the shallow aquifer. The results indicate that only small quantities of both CO_2 and brine reach the shallow system, with leakage initiating during the injection period and gradually stabilizing. At the end of the 50-yr simulation window, the cumulative CO_2 leaked from the highest-risk configuration is less than 0.005% of the total mass injected, demonstrating that leakage remains extremely limited even under conservative assumptions.

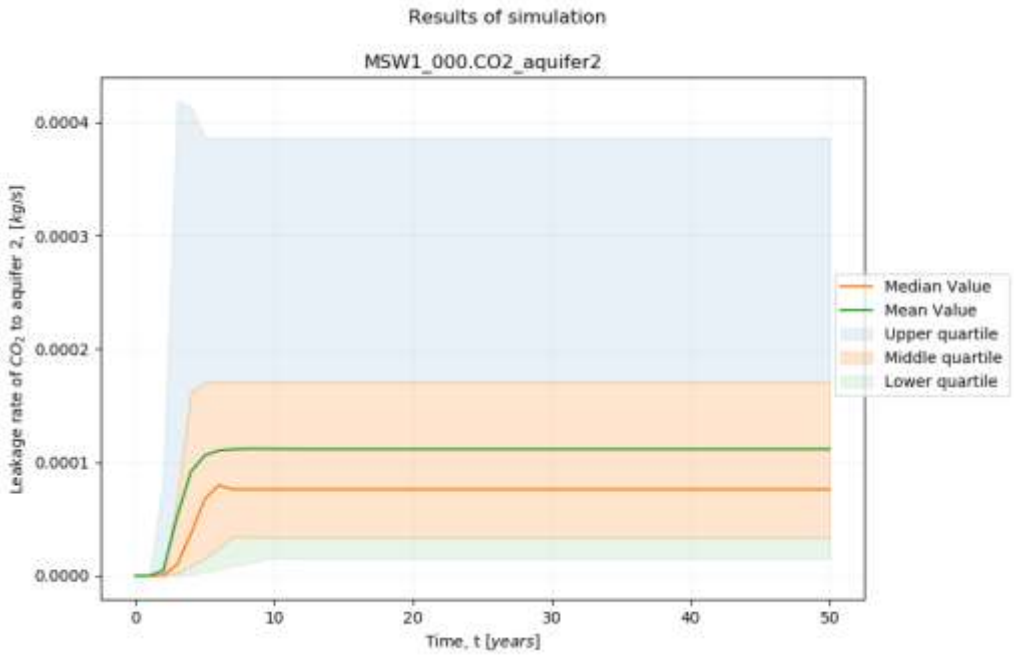


Figure 4.1.27. CO_2 leakage rate to shallow aquifer

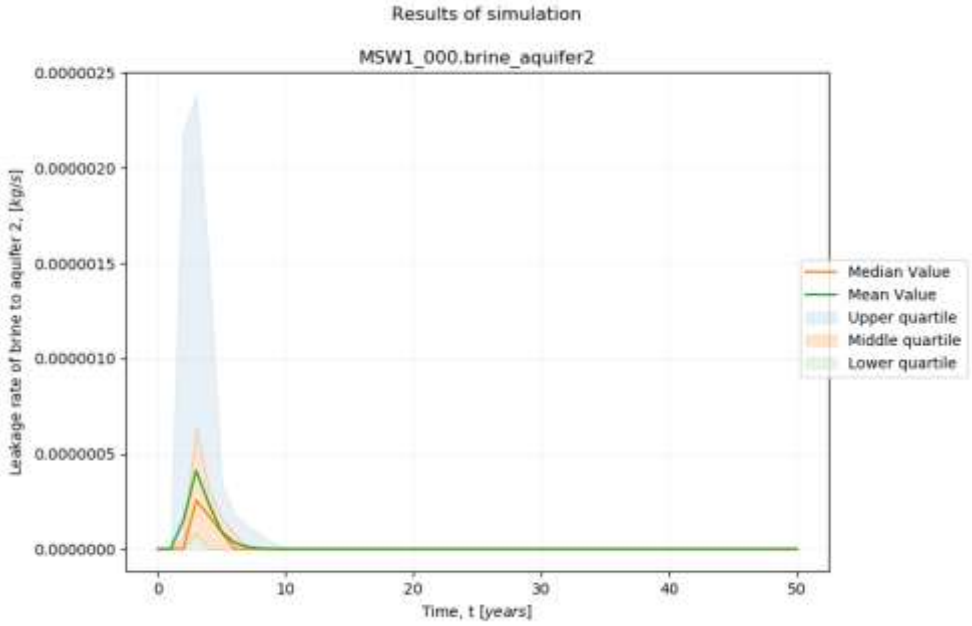


Figure 4.1.28. Brine leakage rate to shallow aquifer

Aquifer impacts were further evaluated using pH and total dissolved solids (TDS) plume metrics relative to established no-impact thresholds. Figures 4.1.29 and 4.1.30 present the simulated volumes of aquifer impacted by changes exceeding 0.2 pH units and 10% relative TDS increase, respectively. The pH plume volumes are noticeably larger than the TDS plumes, but both remain within acceptable bounds and do not exceed thresholds associated with meaningful water-quality

degradation. These results confirm that although limited leakage occurs, it does not produce significant chemical changes in the overlying USDW.

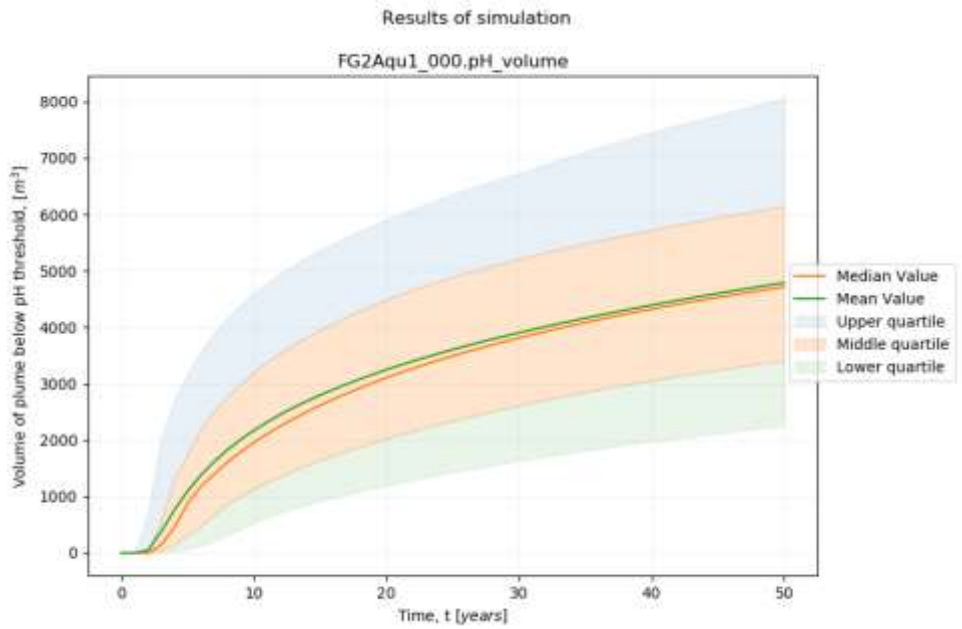


Figure 4.1.29. Volume of plume where absolute change in pH > 0.2

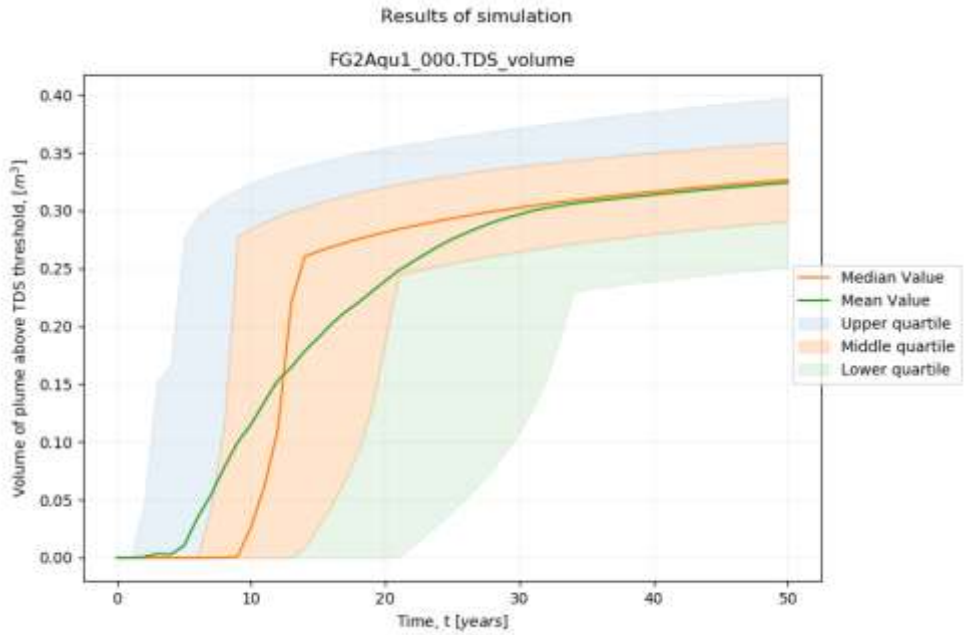


Figure 4.1.30. Volume of plume where relative change in TDS > 10%

Conclusions

Overall, this preliminary assessment suggests that the Oklahoma sites exhibit low CO_2 and brine leakage risk for both near-field and far-field legacy wells. While some leakage is predicted, the

magnitudes are small and the resulting aquifer impacts remain below regulatory concern levels. These initial findings provide a foundation for more detailed site characterization and future iterations of NRAP-based analysis as additional subsurface data and well integrity information become available.

Task 2 – Evaluating Regional Infrastructure: Four Corners Case Study

This effort is part of the "Subtask 4.1 – Catalog, Map, and Evaluate Extant and Near-Term CO_2 Distribution Network" in the CUSP main project. This task evaluates regional CO_2 transport and storage infrastructure in the Four Corners region using the SimCCS optimization framework (Chen et al. 2024). The analysis focuses on phase-based pipeline network development and quantifies how environmental justice (E&J) constraints influence pipeline routing, total network distance, and system-wide costs. By comparing scenarios with and without restrictions that prevent pipelines from crossing disadvantaged or tribal communities, the study reveals how incorporating E&J considerations affects capture, transport, energy consumption, and storage costs. Results indicate that E&J constraints consistently increase overall pipeline length and system costs, demonstrating the importance of explicit socioeconomic considerations in CO_2 infrastructure planning.

SimCCS Introduction

SimCCS (Scalable Infrastructure Model for Carbon Capture and Storage) is an optimization platform designed to identify cost-effective, large-scale CO_2 capture, transport, and storage infrastructures across a region. It integrates spatial data, engineering constraints, and economic parameters to generate optimized solutions for pipeline routing, facility siting, and storage allocation. The model simultaneously determines:

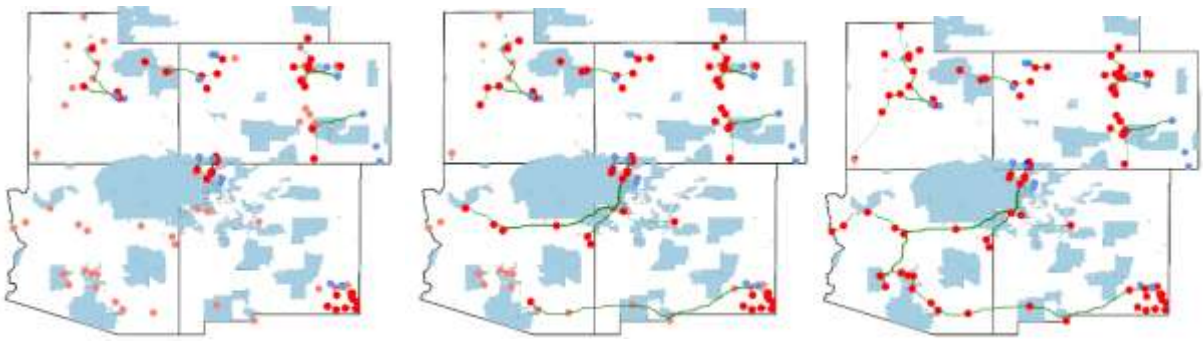
- The optimal set of point sources to implement CO_2 capture
- The pipeline network topology and phasing strategy
- CO_2 flow and capacity requirements across the network
- Storage site selection and injection allocation

SimCCS uses a mixed-integer linear programming (MILP) formulation that balances system-wide cost minimization with user-defined constraints. These constraints may include land-use restrictions, terrain, rights-of-way, community impacts, phase-wise infrastructure development, or regulatory boundaries. The tool is therefore well suited for evaluating emerging CCS regions—such as Four Corners—where infrastructure must be planned holistically to integrate multiple emitters and storage sites within a diverse social and environmental landscape.

In this task, SimCCS is applied to examine the impact of environmental justice (E&J) constraints on CO_2 pipeline development. Specifically, the model is used to compare optimized buildouts that *allow* pipelines to cross disadvantaged or tribal communities versus those that *exclude* such routes. This comparison isolates the effects of E&J considerations on routing feasibility, pipeline length, and overall system costs.

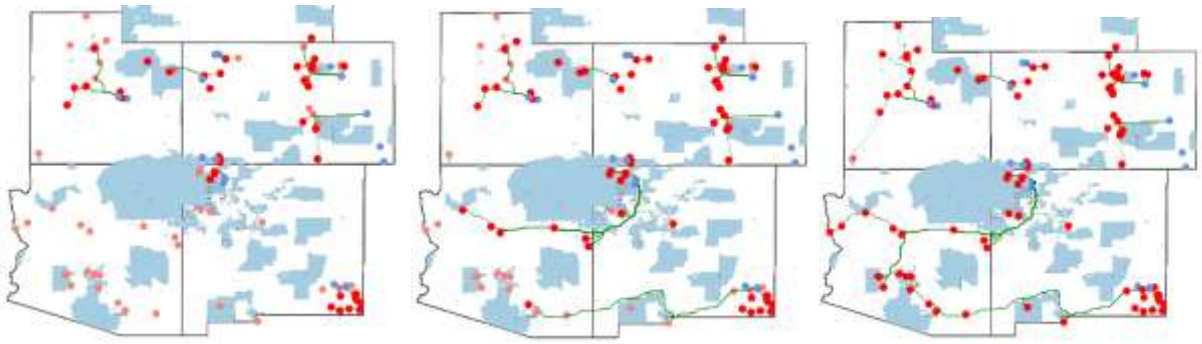
Four Corners Case Study

To evaluate how environmental justice (E&J) constraints influence CO_2 infrastructure planning, SimCCS was used to generate optimized pipeline networks for three sequential development phases that represent progressively larger volumes of CO_2 becoming capturable and transported across the region, culminating in approximately 66.4 Mt/yr CO_2 capture in Phase 3. For each phase, the model was run both with and without routing restrictions. In the constrained scenario, pipeline segments are prohibited from crossing census-defined disadvantaged communities and tribal lands, requiring the system to reroute infrastructure around these protected areas. Figs 4.2.1 and 4.2.2 summarize the resulting pipeline networks for all phases: Figure 4.2.1 shows the optimized Phase 1 through 3 routes without E&J restrictions whereas Figure 4.2.2 presents the corresponding networks when constraints are applied. A comparison between the two sets of results shows that E&J constraints systematically increase total pipeline length—by 10.8% in Phase 1, 4.5% in Phase 2, and 7.5% in Phase 3—reflecting the additional distance required to circumvent restricted zones as CO_2 capture volumes scale upward. These longer pipeline corridors directly translate into higher CO_2 transport-related construction, operation and maintenance (O&M), and energy costs, and some storage costs also increase due to shifts in CO_2 allocation among injection sites. Table 4.2.1 provides a detailed cost breakdown for Phase 3, illustrating consistent increases in construction, O&M, energy, and storage categories when E&J constraints are enforced.



(a) Phase 1 (b) Phase 2 (c) Phase 3

Figure 4.2.1. Phase-based pipeline routes without the constraint of E&J. Light blue areas correspond to the E&J communities.



(a) Phase 1 (b) Phase 2 (c) Phase 3

Figure 4.2.2. Phase-based pipeline routes with the constraint of E&J. Light blue areas correspond to the E&J communities.

The Phase 3 cost results highlight how environmental justice (E&J) routing constraints affect both CO_2 transport and storage economics in the Four Corners region. Because construction, O&M, and energy costs in Table 1 all represent transport-related costs, the increase in pipeline length from 5,198.65 km (without E&J constraints) to 5,589.99 km (with constraints) directly drives higher transport expenditures. Specifically, construction cost rises from \$0.04/tCO_2 to \$0.07/tCO_2, while transport O&M cost increases from \$0.08/tCO_2 to \$0.11/tCO_2. Energy cost shows the largest relative change among the transport components, increasing from \$0.49/tCO_2 to \$0.71/tCO_2 due to greater compression requirements and frictional losses along the longer pipeline routes. Storage costs also increase slightly, from \$4.76/tCO_2 to \$4.94/tCO_2, reflecting changes in injection allocation once routing detours are imposed. In contrast, capture costs remain unchanged at \$48.89/tCO_2 because they are independent of pipeline routing. With an updated tax credit of \$80/tCO_2, these results collectively demonstrate that while E&J constraints introduce measurable increases in transport and storage costs, the system remains economically favorable overall, and the added expense represents a manageable tradeoff for incorporating social-equity considerations into regional CCS infrastructure planning.

Table 4.2.1. Phase 3 optimized results w/o the constraint of E&J.

	Without E&J	**With E&J**
Pipeline length (km)	5,198.65	5,589.99
Pipeline construction cost ($/$tCO_2$)	0.04	0.07
Pipeline O&M ($/$tCO_2$)	0.08	0.11
Energy ($/$tCO_2$)	0.49	0.71
Storage cost ($/$tCO_2$)	4.76	4.94
Capture Cost ($/$tCO_2$)	48.89	48.89
Tax credits($/$tCO_2$)	80	80

Conclusions

SimCCS modeling for the Four Corners region shows that incorporating environmental justice (E&J) constraints has a clear and measurable impact on CO_2 transport network design and associated infrastructure costs. Requiring pipelines to avoid disadvantaged and tribal communities consistently increases total pipeline length across all development phases, which in turn raises transport-related expenses—including construction, O&M, and energy costs—

because longer and less direct routes require more materials, increased maintenance, and greater compression power. Storage costs also increase modestly as CO_2 injection patterns shift to accommodate changes in transport routing, while capture costs remain unaffected. Even with these cost increases, the system remains economically favorable under the updated \$80/tCO_2 tax credit, demonstrating that E&J considerations can be integrated without compromising the viability of regional CCS development. Overall, the results highlight the importance of SimCCS as a decision-support tool for balancing cost efficiency with social-equity objectives, enabling the design of CO_2 infrastructure networks that are both technically optimized and aligned with broader community and environmental priorities.

Task 3 – Develop Regional Readiness Indices

This task is part of "Subtask 4.6 – Develop Regional Readiness Indices" in the CUSP main project. In this task, we investigated two types of storage site risks—induced seismicity risk and leakage risk of the storage site—on regional pipeline network routing. For the first type of risk, we introduced a "capacity multiplier" for each storage site to limit the maximum cumulative CO_2 injection volume, thus, mitigating potential induced seismicity. As for the second type of risk, considering the leakage potential due to the presence of legacy wells penetrating a storage formation, it becomes necessary to implement corrective action (such as well cleaning and well plugging) and ensure the safety of CO_2 injection operations. The two risk factors evaluated in Task 3—induced seismicity and leakage risk associated with legacy wells—directly impact regional readiness for large-scale CO_2 storage. Induced seismicity risk limits the effective storage capacity that can be safely utilized, which in turn alters pipeline routing, flow allocation, and overall infrastructure design. Similarly, leakage risk increases storage cost due to required corrective actions and can change which storage sites are economically viable. These risks influence the technical, economic, and regulatory feasibility of deploying regional CO_2 transport and storage networks, making them essential components of the Regional Readiness Indices.

Impact of Induced Seismicity Risk on Pipeline Routing

The risk for induced seismicity increases with the cumulation of the amount of CO_2 injected for geologic CO_2 storage operation. To reduce this risk, it is recommended to limit the maximum volume of CO_2 injection. In this subtask, we first performed experiments using SCO_2T tool to understand the correlation between CO_2 injectivity and a predefined "safety factor", which is the ratio of actual CO_2 injection pressure and the maximum allowable injection pressure (90% of formation fracture pressure). A larger safety factor indicates a higher CO_2 injection pressure is allowed for the geologic CO_2 storage operation. We found that CO_2 injectivity is almost linearly correlated with the safety factor, that is, the higher safety factor corresponds to a higher CO_2 injectivity. Based on this observation, we incorporate a capacity multiplier (equal to or less than one) into our modeling. Specially, we first adjust the maximum CO_2 storage capacity by multiplying the capacity multiplier (equivalent to safety factor) and next use the adjusted storage capacity for pipeline design using SimCCS tool.

To test and evaluate this, we designed a simple hypothetical case study as shown in Fig. 4.3.1. This case is in the western region of Colorado and comprises 8 CO_2 sources and 4 CO_2 storage sites. The entire CCS project lasts for 20 yr, and the optimization was conducted using our newly developed temporal modeling capability in SimCCS. The maximum CO_2 capture amount is 20.8

Mt CO_2/yr from the 8 sources. For this subtask, the maximum CO_2 storage capacity for K1 to K4 is 150, 300, 200, and 200 Mt, respectively. We designed four scenarios as presented in Table 4.3.1. Specifically, we set the capacity multiplier to 1.0 for all four storage sites in Run 1. Starting from Run 2, we gradually reduced the capacity multipliers for K1 and K2 to simulate the increased risk of induced seismicity, while keeping the capacity multipliers for K3 and K4 unchanged.

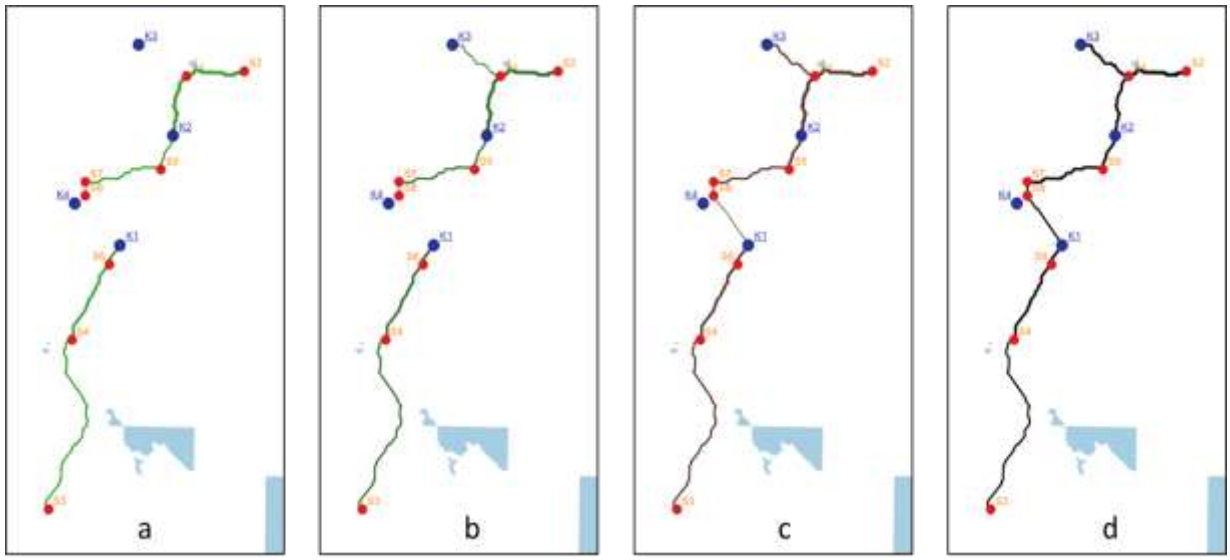


Figure 4.3.1. Optimized pipeline route at the end of 20 yr for induced seismicity risk: (a) Run 1 with capacity multiplier of 1.0, (b) Run 2 with capacity multiplier of 0.9 for storage sites K1 and K2, (c) Run 3 with capacity multiplier of 0.8 for storage sites K1 and K2, and (d) Run 4 with capacity multiplier of 0.7 for storage sites K1 and K2. In each subplot, the lines indicate the optimized pipeline routes. The red circles are CO_2 sources while the blue circles are the CO_2 storage sites.

Table 4.3.1. Capacity factors for each scenario for the case study.

Scenarios	**Capacity factor**			
	K1	**K2**	**K3**	**K4**
Run 1	1.0	1.0	1.0	1.0
Run 2	0.9	0.9	1.0	1.0
Run 3	0.8	0.8	1.0	1.0
Run 4	0.7	0.7	1.0	1.0

The optimization results are shown in Fig. 4.3.1. For Run 1, the captured CO_2 (130 Mt) from sources S3, S4, and S6 are transported to K1, which is below the CO_2 storage capacity of K1 (150 Mt). Similarly, the 286 Mt captured CO_2 from the remaining sources is transported to K2 for storage. Again, this amount is below the CO_2 storage capacity of K1 (300 Mt). For Run 2, because the capacity multipliers for K1 and K2 are reduced to 0.9, thus, the corresponding CO_2 storage capacities become 135 and 270 Mt, respectively. As shown in Figure 4.3.1(b), the

updated storage capacity of K1 still meets the storage capacity requirement, therefore, no change is necessary for the lower portion of the pipeline network. However, the updated capacity of K2 (270 Mt) due to the risk of induced seismicity is below the cumulative capture amount at S1, S2, S5, S7, and S8 (286 Mt), therefore, K3 is used as a secondary storage site to store 16 Mt CO_2. We can see that a pipeline is modeled to be constructed to connect S1 and K3. Similar observations can be found in the remaining runs. In Runs 3 and 4, the CO_2 storage capacities for K1 and K2 are further reduced to simulate a higher risk for induced seismicity. The storage site K1 no longer meets the required storage capacity, therefore the additional CO_2 from S3, S4, and S6 has to be transported to K3.

Impact of Leakage Risk on Pipeline Routing

In this subtask, we developed an approach to take into account the risk of increase in storage cost due to the presence of legacy wells and potential leakage risk. A brownfield generally has a larger number of legacy wells than a greenfield. After a detailed analysis using SimCCS' storage model SCO_2T tool, we found that the CO_2 storage cost can be impacted by the corrective action cost for legacy wells at a given storage site. Thus, we used well density (with the unit of wells/mile^2) as one parameter to describe the number of wells. A higher well density indicates more legacy well penetrating a storage site. Here, well density for a greenfield is equal to 0 wells/mile^2 because there are no existing legacy wells penetrating the site. In our previous simulations, we assumed that the well density is 0.25 wells/mile^2. According to SLB's field experience, the suggested minimum distance between two wells is 900 ft, which corresponds to a well density of 34.4 wells/mile^2, which was chosen as the largest legacy well density if we consider CO_2 storage in a brownfield.

In this subtask, we investigated the impact of legacy well density on storage cost (see Fig. 4.3.2) based on NATCARB database with 314 saline storage formations. Scenario 2 corresponding to legacy well density of 0.25 wells/mile^2, is our base scenario for comparison. Scenario 1 is assumed to be a greenfield with a well density of 0 wells/mile^2. The well density for Scenarios 3 to 6 is 1, 10, 20, and 34.4 wells/mile^2, respectively. Clearly, as well density increases, the overall CO_2 storage cost increases. Compared with the base scenario, there is a cost reduction of 1.74% for greenfield. If the well density is increased from 0.25 to 1 well/mile^2, the cost increases by 5.23% compared to the base scenario. The highest increase in cost can be found for Scenario 6 when the well density is 34.4 wells/mile^2 (maximum allowable legacy well density). This analysis indicates that well density (i.e., the number of legacy wells) has a big impact on the final storage cost due to the cost of potential corrective actions for the legacy wells.

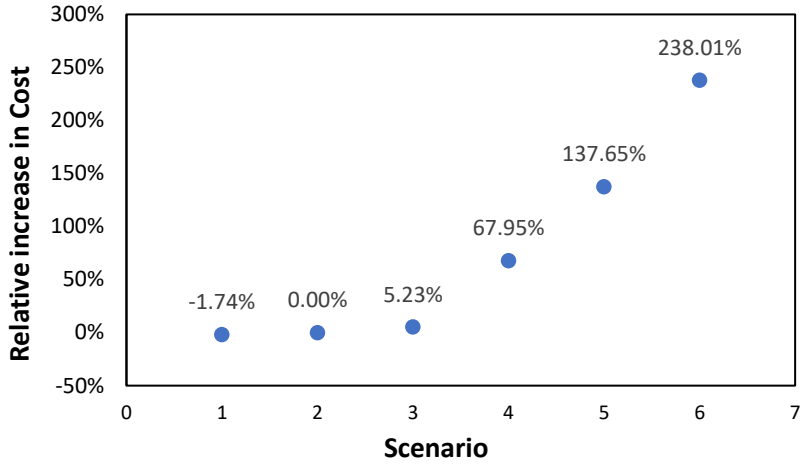


Figure 4.3.2. Relative increase in storage cost with-respective-to the base scenario (scenario 2)

To assess the impact of the well density on the final CO_2 pipeline network, we designed 5 runs in this subtask, as presented in Table 4.3.2. Again, we used the same case study as presented previously for demonstration. Specifically, we set Run 1 as the base case with a well density of 0.25 wells/mile^2 and gradually increase the legacy well density of K1 and K2 for the following runs. For Run 1, the CO_2 storage cost for K1 to K4 is 6.663, 5.61, 6.66, and 14.349 \$/tCO_2, respectively.

The final optimized pipeline routes from our SimCCS modeling are presented in Fig. 4.3.3. Clearly, for Run 1 (see in Fig. 4.3.3(a)), the captured CO_2 from sources S1, S2, S5, S7, and S8 are transported to K2 for storage. K1 is used to store the captured CO_2 from the remaining three sources. For Run 2 in Fig. 4.3.3(b), because the well density of K1 and K2 increases to 1 well/mile^2, the corresponding storage costs also increase. In particular, the storage cost of K2 becomes 7.295 instead of 6.663 \$/tCO_2. The higher storage cost makes the actual CO_2 storage operation at K1 uneconomical. Therefore, all the captured CO_2 from S3, S4, and S6 are also transported to K2 for storage. For Runs 3 to 5, the well density of K1 and K2 is larger than 10. Therefore, the corresponding storage costs also increase significantly. For example, the storage cost of K2 increases to 9.63 \$/tCO_2 for Run 3. It is not economically feasible to store CO_2 in K2 for these scenarios. Therefore, the lowest cost site, i.e., K3 (6.66 \$/tCO_2) is selected for CO_2 storage. As shown in Fig. 4.3.3(c), a new pipeline network is optimized to connect CO_2 sources to K3.

Table 4.3.2. Well density for each scenario for the case study.

Scenarios	**Well density (wells/mile^2)**			
	K1	K2	K3	K4
Run 1	0.25	0.25	0.25	0.25
Run 2	1	1	0.25	0.25
Run 3	10	10	0.25	0.25

Run 4	20	20	0.25	0.25
Run 5	34.4	34.4	0.25	0.25

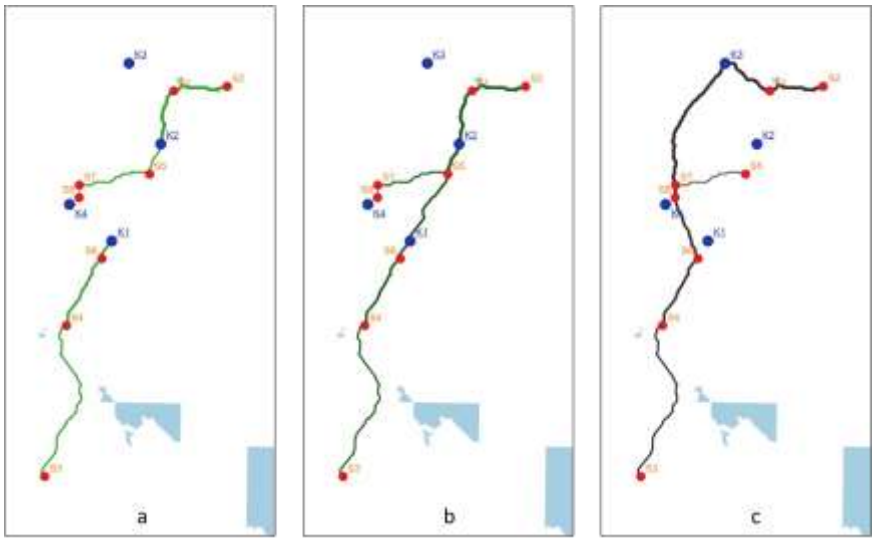


Figure 4.3.3. Final optimized pipeline infrastructures at the end of 20 yr for the case study: (a) base scenario with well density of 0.25, (b) scenario #2 with well density of 1.0 for storage sites K1 and K2, and (c) scenarios #3-5 with well density of over 10.0 for storage sites K1 and K2. In each subplot, the lines indicate the optimized pipeline routes. The red circles are CO_2 sources while the blue circles are the CO_2 storage sites.

Conclusions

The results of Task 3 show that both induced seismicity risk and leakage risk associated with legacy wells significantly influence regional readiness for CO_2 storage by altering effective storage capacity, storage cost, and optimized pipeline routing. When seismicity-related capacity multipliers reduce the usable volume at a storage site, SimCCS shifts CO_2 flows to alternative sites, resulting in new pipeline connections and higher system costs. Likewise, increased leakage risk—represented through higher legacy well densities—raises corrective-action costs and can render certain storage sites uneconomic, prompting rerouting of CO_2 to lower-risk formations even if they lie farther from major emission sources. These findings demonstrate that geologic risk factors shape the technical and economic feasibility of regional CO_2 transport and storage systems, and therefore need to be incorporated directly into Regional Readiness Indices to accurately assess a region's preparedness for large-scale CCS deployment.

Task 4 – Characterizing Subsurface Structures for GCS at Iron Mountain in Utah

This effort is part of Utah focused project "CCS at the Iron Mountain Iron Mine and Direct Reduced Iron Processing Plant, Southern Utah". Subsurface structure imaging and fault detection are essential for site characterization and risk assessment in geologic carbon storage. In this study, we use 2D surface seismic data acquired at Iron Mountain, Utah, USA, to characterize subsurface structures. The data were collected with Vibroseis sources along three 2D walkaway

lines, with a source spacing of approximately 91 m, receiver spacing of about 45 m, and line lengths ranging from 9 to 15 km. We analyze two of these lines, Line 7B and Line 9, to construct 2D velocity models using first-arrival traveltime tomography and pre-stack depth migration velocity analysis (MVA). Reverse-time migration with the MVA-updated velocity models produces high-resolution images of the subsurface, and a machine learning algorithm is subsequently applied to delineate faults in the migration results. These analyses provide critical insights into the subsurface structures and support the assessment of geologic carbon storage feasibility at Iron Mountain.

Introduction

To mitigate anthropogenic CO_2 emissions, researchers are focusing on decarbonizing heavy industries such as iron production. In conventional processes, iron is refined by reacting iron ore, which contains iron oxides ($Fe2O_3$), with carbon monoxide (CO) to yield pure iron and carbon dioxide (CO_2). Traditionally, CO is generated by burning coal in a low-oxygen environment or within a blast furnace. However, this method releases significant amounts of greenhouse gases and other pollutants into the atmosphere.

In contrast, the direct reduced iron (DRI) process refines iron by reacting iron ore in a reactor vessel with synthesis gas (syngas), a mixture of CO and hydrogen (H2), produced through the catalytic reforming of methane (CH_4) rather than the combustion of coal. In DRI, iron ore reacts with CO and H_2 to produce pure iron, CO_2, and water (Battle et al. 2024). The resulting CO_2 stream is relatively pure and can be dried and either utilized for industrial applications or permanently stored through geological carbon sequestration.

To evaluate a potential site for carbon capture and storage (CCS) associated with direct reduced iron (DRI) production, we characterized the subsurface of a proposed DRI plant in southern Utah using legacy seismic data acquired in the 1980s. The prospective DRI-CCS field is located in the Iron Springs District in the southwestern part of Utah. A geologic map of the area, modified from Blank and Mackin (1967), is presented in Fig. 4.4.1.

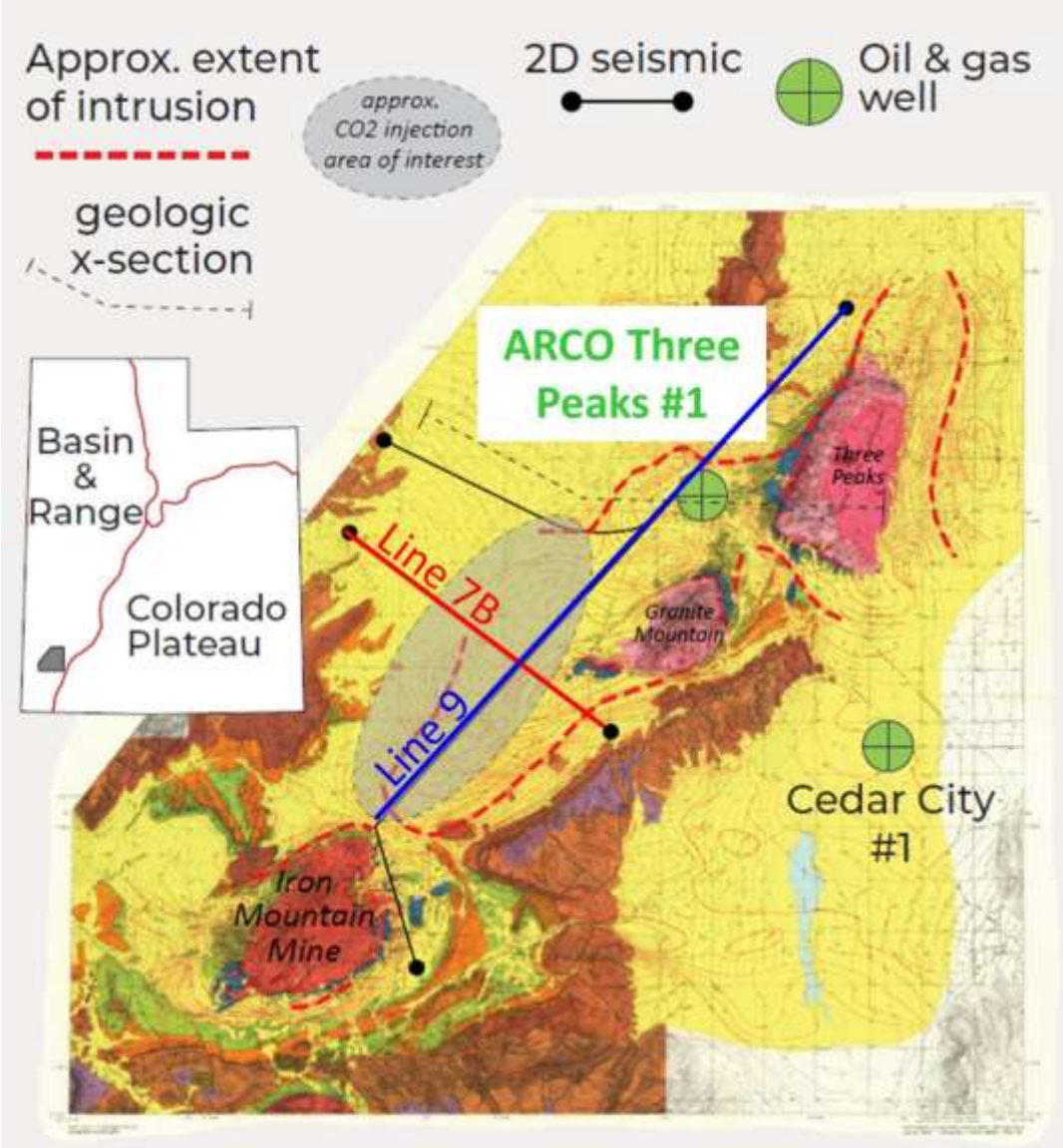


Figure 4.4.1. Geologic map of Iron Mountain, Utah, showing Seismic Line 7B (red) and Line 9 (blue). Green dots indicate wells drilled in the region, and the gray ellipse marks the CO_2 injection area of interest. Modified from Blank and Mackin (1967).

The target formation for CO_2 sequestration is the Navajo Sandstone, a Jurassic-aged, porous sandstone situated at a depth of approximately 1,890 m (6,200 ft) below the surface. Preliminary studies suggest that this formation has the capacity to store at least 15 million tons of CO_2 (Moodie et al. 2022). The Navajo Sandstone is overlain by several potential caprock formations, including the Jurassic Temple Formation, composed primarily of evaporites, and the Jurassic Carmel Formation, which consists of mudstones and limestones.

In certain areas of the site, outlined by the red dashed line in Figure 1, the Jurassic Carmel Formation is intruded by several hundred meters of quartz monzonite laccolith (Rowley and Barker 1978; van Kooten 1988). A geologic cross-section illustrating these formations is shown in Fig. 4.4.2.

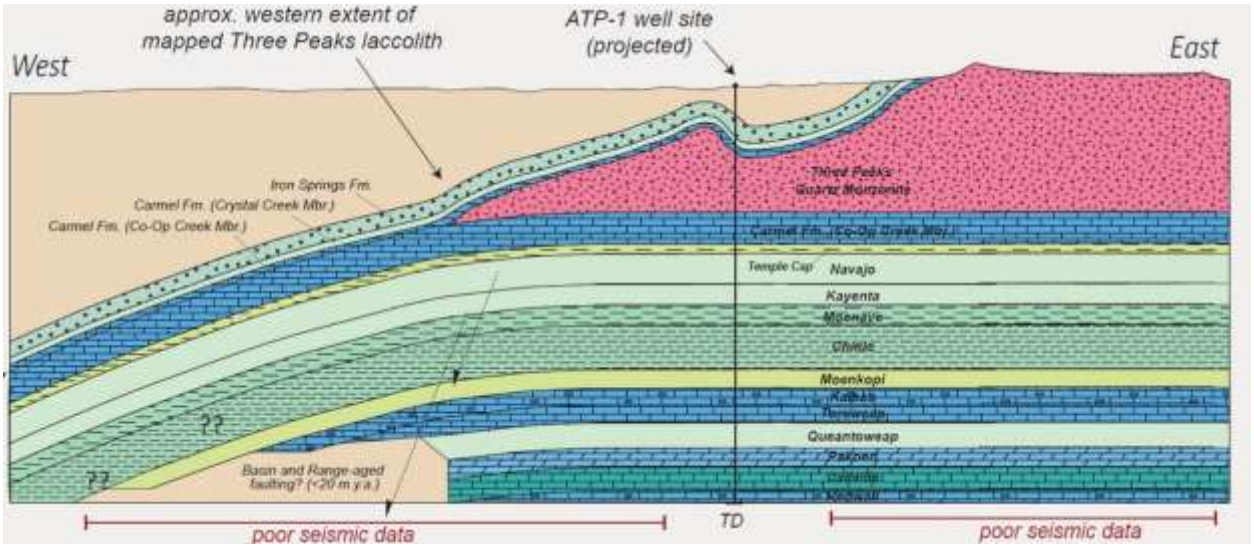


Figure 4.4.2. Geologic cross-section from west to east across the Iron Mountain area showing the Jurassic Navajo Sandstone reservoir layer, the Temple Formation caprock, the Carmel Formation, and the quartz monzonite intrusion. Modified from Moodie et al. 2022.

To assess the feasibility of carbon capture and storage (CCS) for direct reduced iron (DRI) production in this region, we analyzed two-dimensional (2D) legacy active seismic land data acquired along two walkaway lines (shown as red and blue lines in **Figur**) to characterize subsurface structures. An initial layered velocity model was constructed by applying a median filter to the sonic slowness log obtained from the Arco Three Peaks #1 well, located at the northernmost green circle in **Figur**.

First-arrival traveltime tomography (Leung and Qian 2006; Taillandier et al. 2009; Fomel et al. 2009; Tong 2021) was then applied using the first arrival times of P-waves to refine the shallow portions (less than 1 km) of the P-wave velocity (Vp) model. Migration velocity analysis (MVA) (Liu and Bleistein 1995) was subsequently used to update the deeper sections of the model.

After obtaining the MVA-updated Vp models, reverse-time migration (RTM; McMechan 1983; Fei et al. 2015) was employed to produce pre-stack depth migration images of the subsurface. Finally, a machine learning algorithm (Gao 2024) was applied to reduce noise, enhance image resolution, and automatically detect faults within the migration images.

Legacy 2D Seismic Data Acquisition and Processing

The two-dimensional (2D) legacy seismic data were acquired at Iron Mountain, Utah, along three walkaway lines: 7B, 9, and 13. For this study, only Lines 7B and 9 were analyzed because the data quality for Line 13 was extremely poor, preventing the extraction of any meaningful information. The limitations of Line 13 will be discussed further in the discussion section. The geometries of Lines 7B and 9 are shown in Fig. 4.4.3.

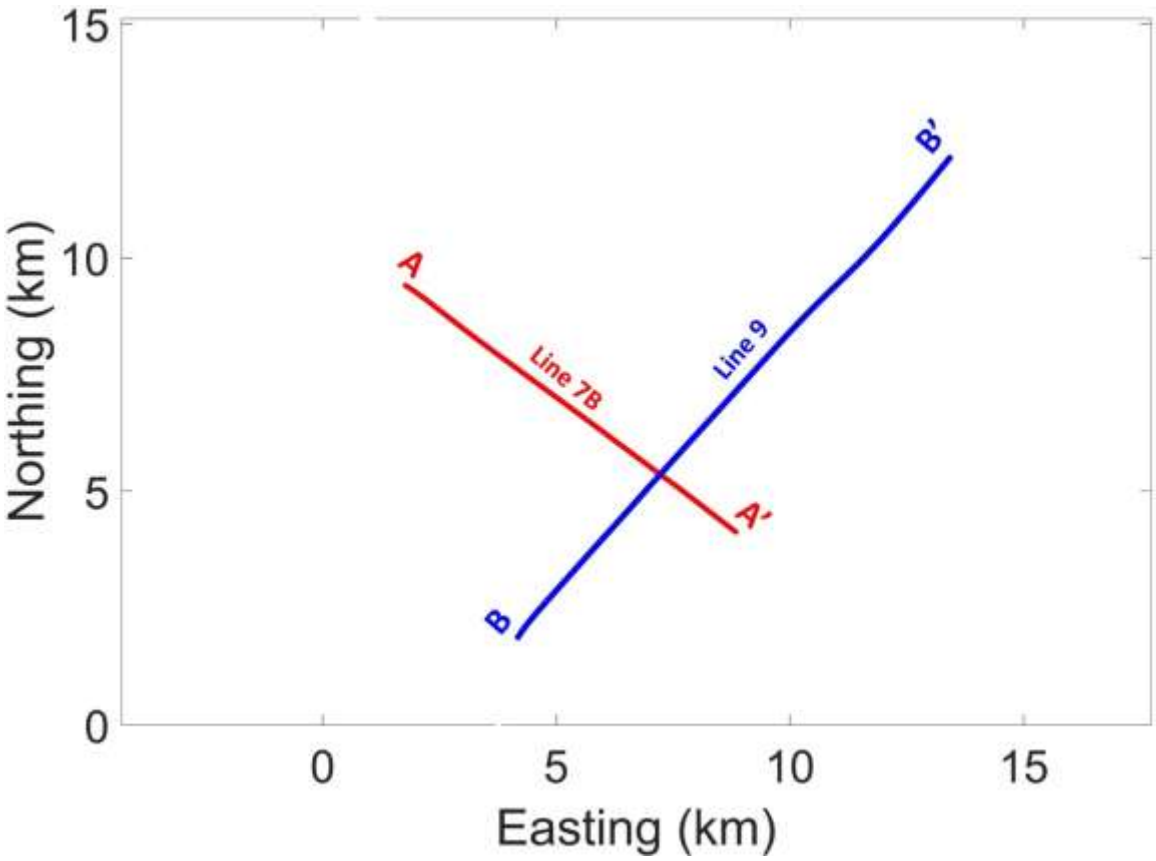


Figure 4.4.3. Map showing the location of Line 7B (red) extending from A to A' and Line 9 (blue) extending from B to B'.

The linear portion of Line 7B (red line) trends northwest–southeast and includes 118 common-shot gathers, while Line 9 (blue line) trends southwest–northeast and includes approximately 183 shots. For each common-shot gather, up to 96 receiver channels were used for data acquisition. The shot spacing was approximately 91 m, and the receiver spacing was about 45 m. The data were sampled at a 2-ms interval, with a total recording time of 3 s.

Following standard pre-processing procedures (Yilmaz 2001), automatic gain control was applied to attenuate ground roll noise, and a band-pass filter of 3–8–20–25 Hz was used to suppress high-frequency noise. Two processed mid-spread common-shot gathers from Lines 7B and 9 are shown in Fig. 4.4.4. After pre-processing, P-wave velocity (Vp) models were constructed for pre-stack depth migration.

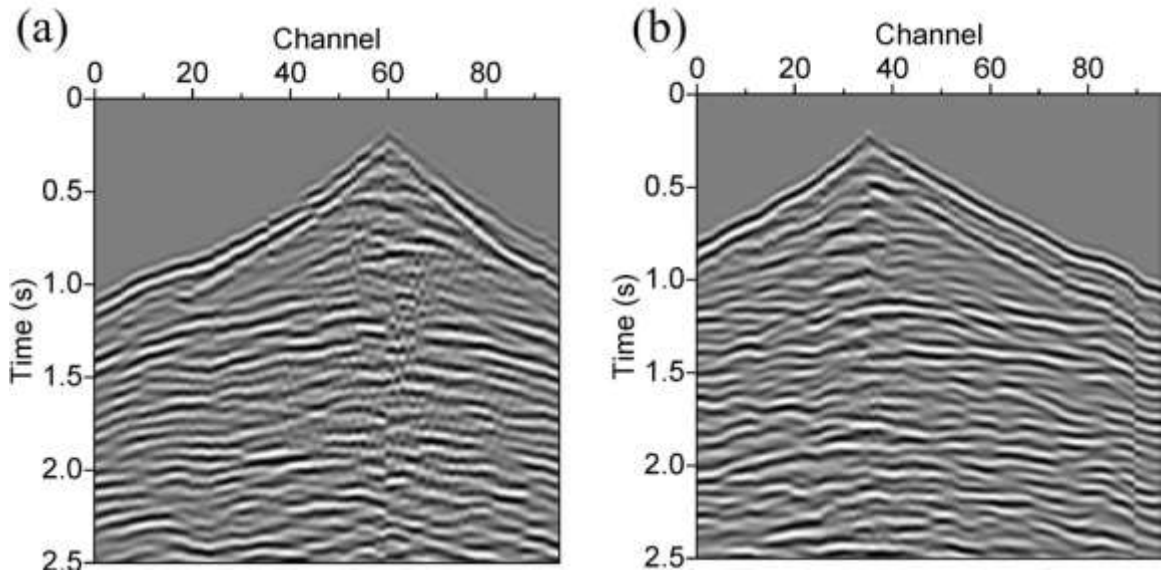


Figure 4.4.4. Two mid-spread common-shot gathers for (a) Line 7B and (b) Line 9 after applying automatic gain control and band-pass filtering from 3–8–20–25 Hz.

Velocity Model Building

To construct the P-wave velocity (Vp) models for migration imaging using the legacy two-dimensional (2D) surface seismic data at Iron Mountain, we first developed an initial layered velocity model based on sonic well log data from the Arco Three Peaks #1 well and interpreted formation boundaries. The shallow portions of the Vp model along each 2D walkaway line were then refined using first-arrival traveltime tomography (FATT). Following the FATT update, we performed pre-stack Kirchhoff depth migration and subsequently refined the deeper parts of the model through migration velocity analysis (MVA).

To build the initial layered velocity models, we began with well log data and interpreted formation boundaries from the Arco Three Peaks #1 well. The well logging data were acquired by Schlumberger in January 1985, covering measured depths from 16.46 m (54 ft) to 3,761.2 m (12,340 ft) at 0.1524 m (0.5 ft) intervals. A datum of 1,785 m was used for the velocity models and migration images, and the depths of the logging data were adjusted to account for elevation differences between the well and the seismic data reference. Median values were selected within layer intervals on the compression slowness log to derive the layered Vp velocity profiles. Constant velocity values were assigned to regions beyond the logged interval, and the resulting one-dimensional (1D) velocity profile was used to build the layered initial models down to a depth of 4.5 km. The median velocity layers and corresponding sonic log velocities are shown in Fig. 4.4.5, and the initial Vp models for each walkaway line are presented in Fig. 4.4.8.

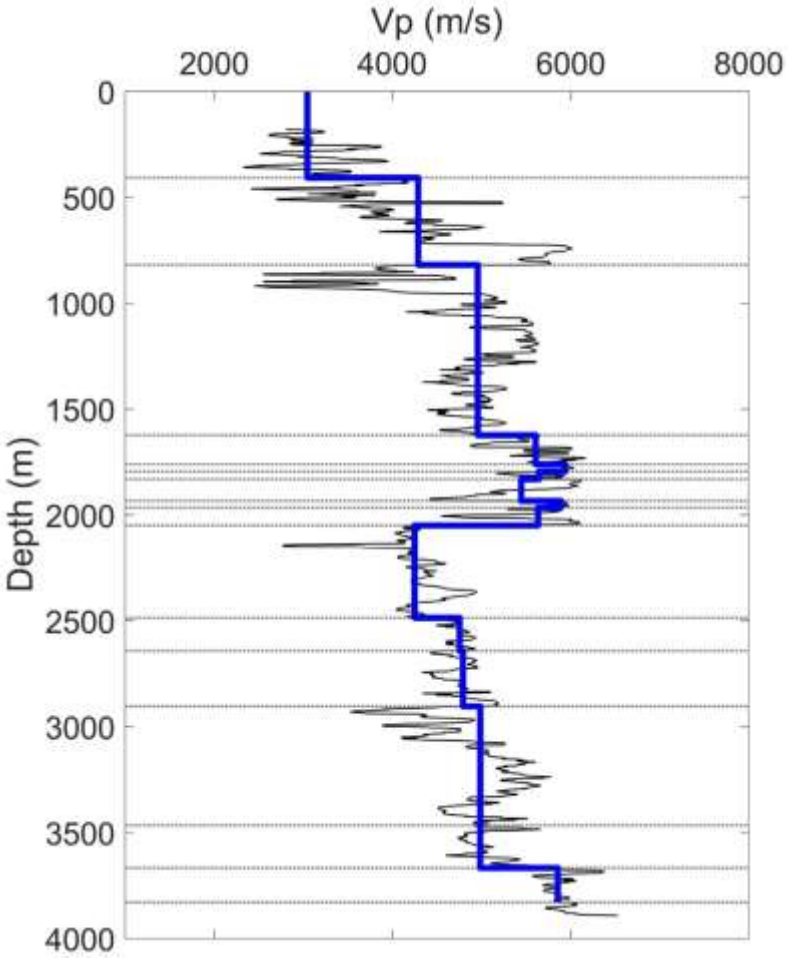


Figure 4.4.5. Velocity profile from sonic logging data (black) alongside median-filtered velocities between interpreted formation boundaries (blue). The median-filtered velocity is used to construct the initial velocity models for Line 7B and Line 9.

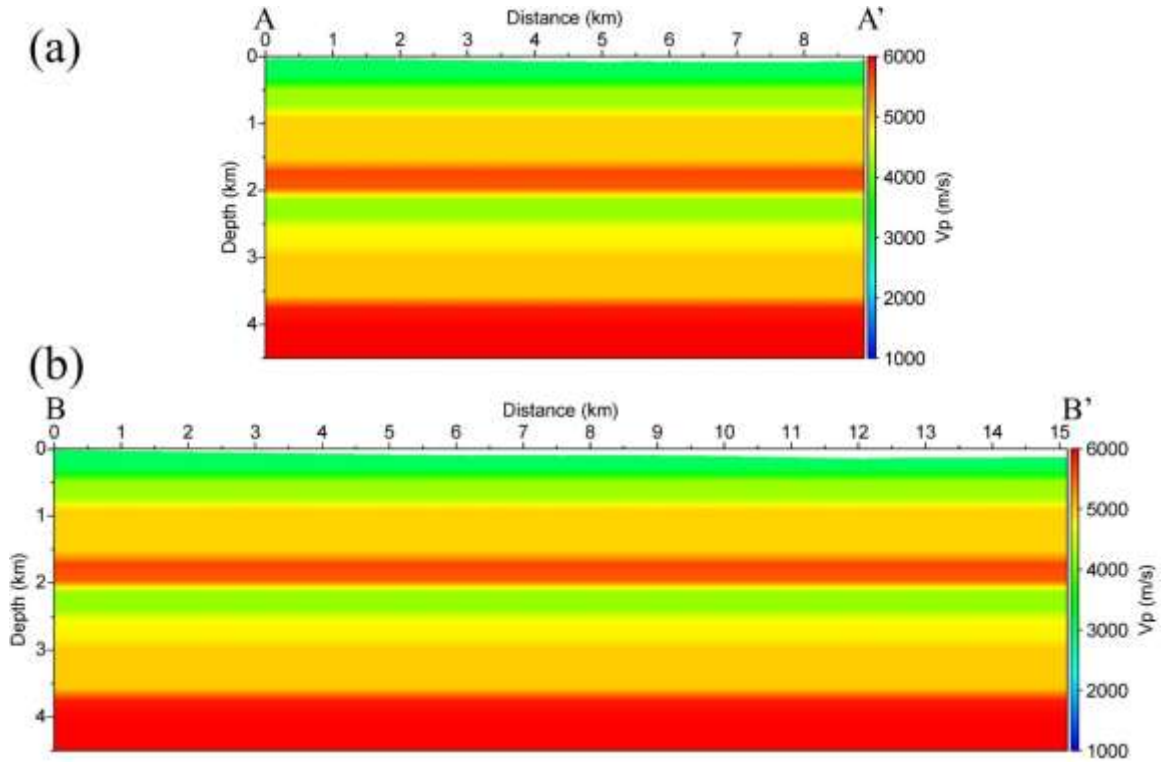


Figure 4.4.8. Initial layered P-wave velocity (Vp) model for (a) Line 7B extending from A to A' and (b) Line 9 extending from B to B'.

Traveltime tomography was then applied using the first arrivals of P-waves to refine the shallow portions of the velocity models. After 40 iterations, the traveltime misfit was reduced by more than 95% for both Lines 7B and 9. The convergence curves for relative misfit, along with histograms of traveltime misfits before and after tomography, are shown in Figs. 4.4.6 and 4.4.7, respectively. The updated Vp models after FATT for Lines 7B and 9 are displayed in Fig. 4.4.9, showing significant improvements in the shallow regions of the models (approximately the upper 1 km). These FATT models were then used for MVA.

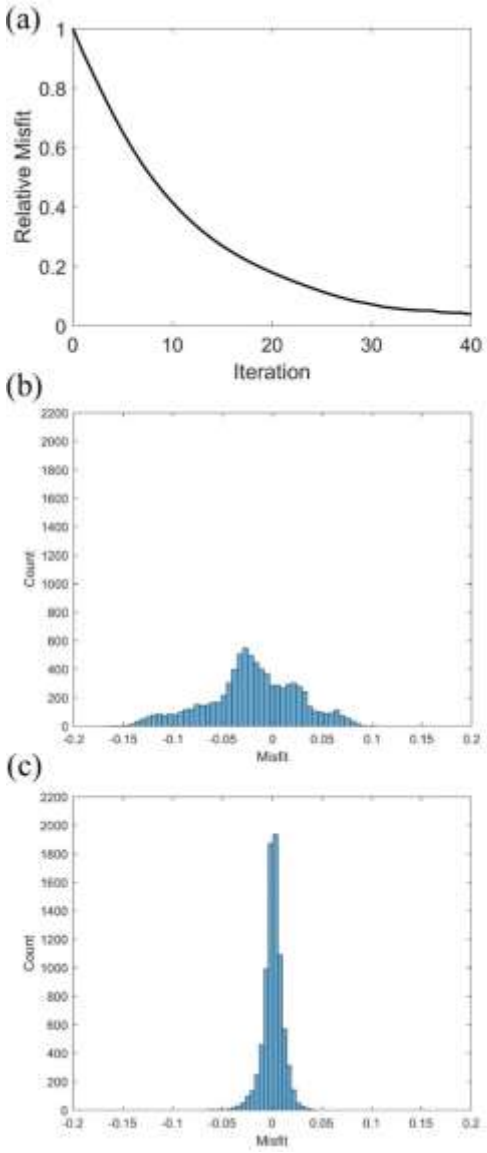


Figure 4.4.6. (a) Relative traveltime misfit convergence curve, (b) histogram of traveltime misfits before tomography, and (c) histogram of traveltime misfits after 40 iterations for Line 7B.

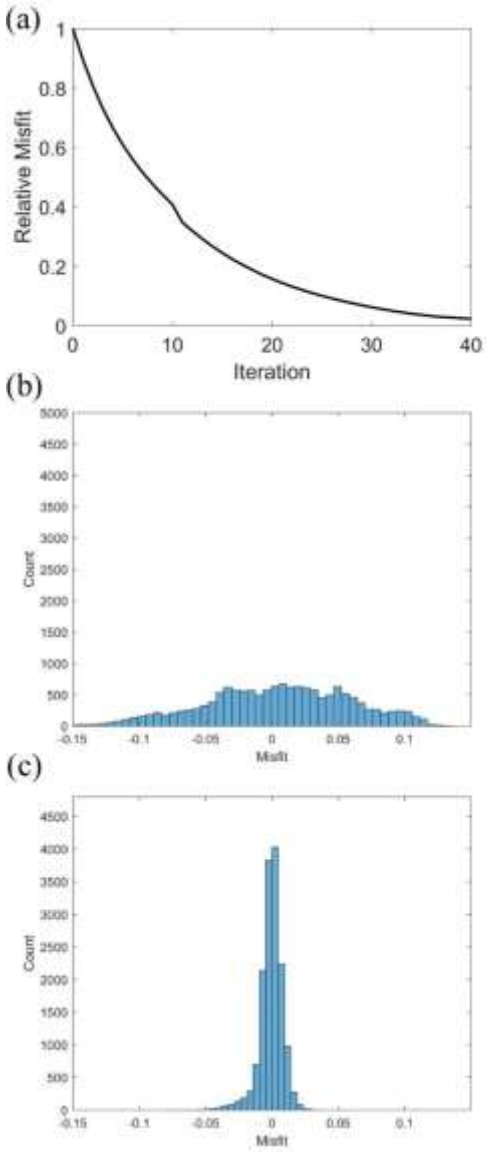


Figure 4.4.7. (a) Relative traveltime misfit convergence curve, (b) histogram of traveltime misfits before tomography, and (c) histogram of traveltime misfits after 40 iterations for Line 9.

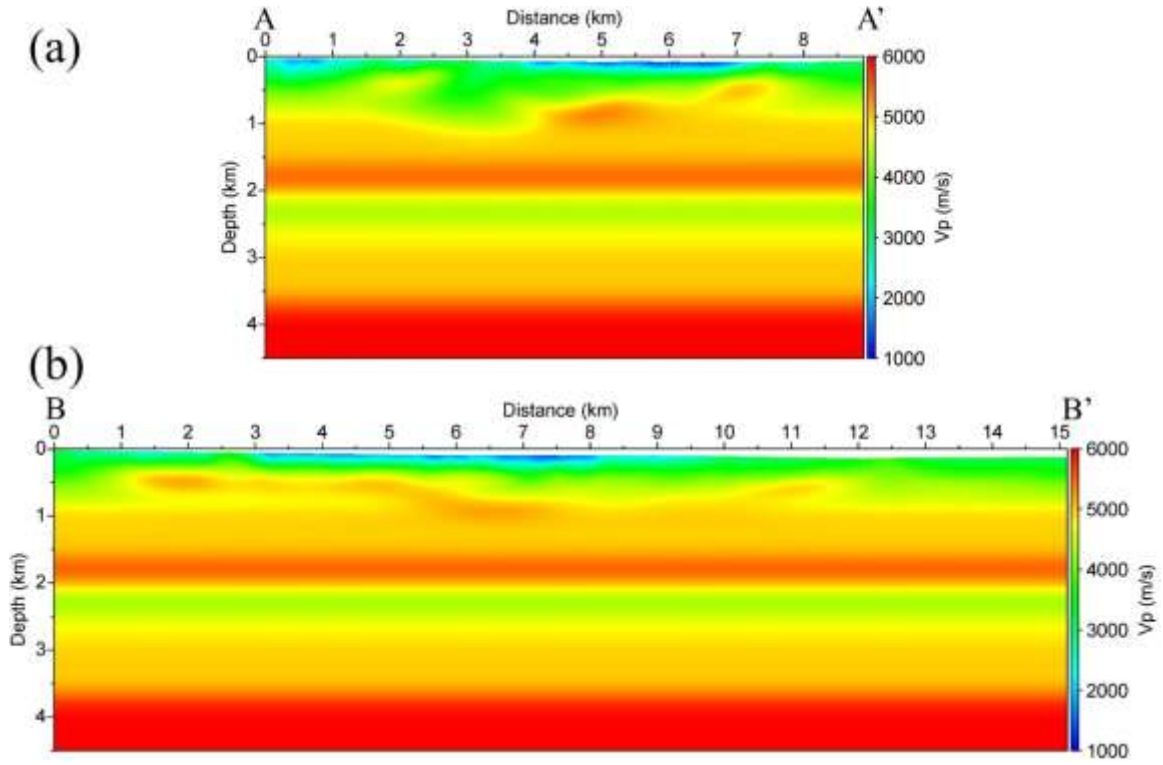


Figure 4.4.9. P-wave velocity (Vp) models after first-arrival traveltime tomography (FATT) for (a) Line 7B extending from A to A' and (b) Line 9 extending from B to B'.

Following the FATT updates, pre-stack Kirchhoff depth migration was performed along both walkaway lines using the FATT velocity models to produce pre-stack depth migration images. Horizons were interpreted from these images, and the velocities between horizons were adjusted by flattening reflection events on common-image gathers. The final Vp models after MVA are shown in Fig. 4.4.10. These MVA-updated velocity models were subsequently used in reverse-time migration to generate high-resolution subsurface images of the structural features.

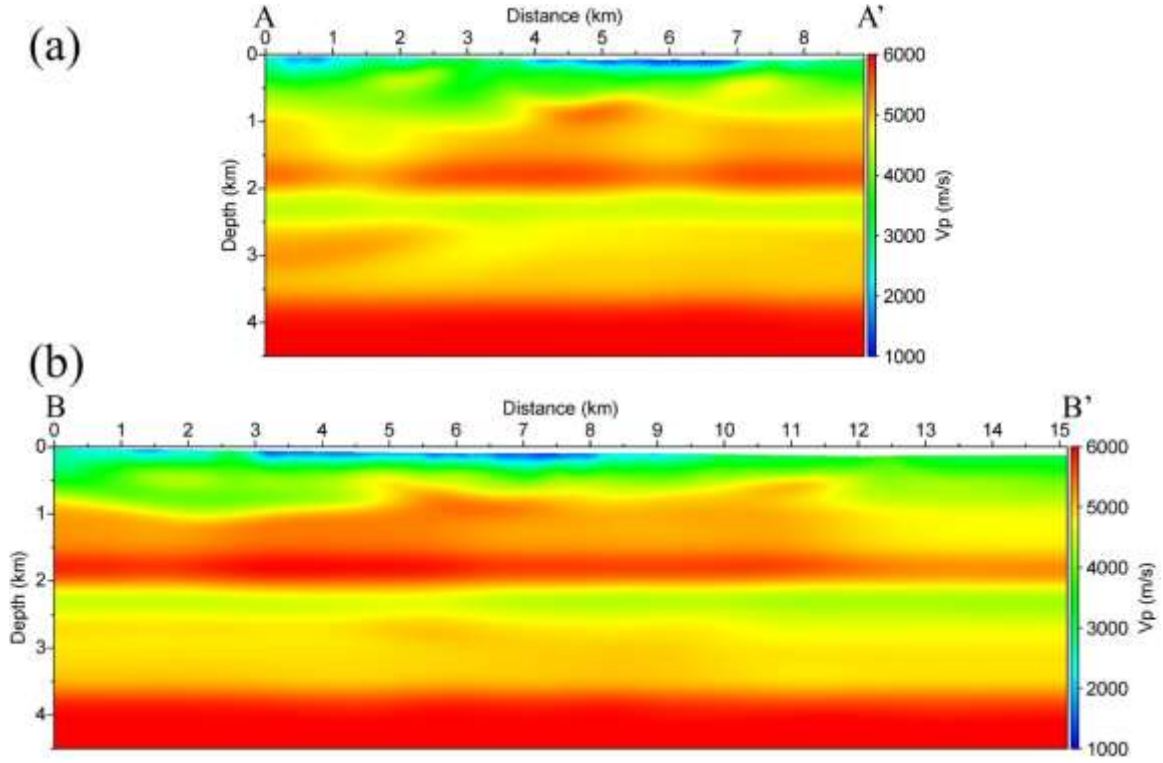


Figure 4.4.10. P-wave velocity (Vp) models after first-arrival traveltime tomography (FATT) and migration velocity analysis (MVA) for (a) Line 7B extending from A to A' and (b) Line 9 extending from B to B'.

Results of Reverse-Time Migration and Fault Detection

After constructing the velocity models using sonic logging data, first-arrival traveltime tomography (FATT), and migration velocity analysis (MVA), and processing the PP reflections, we applied reverse-time migration (RTM) to obtain high-resolution PP images of the subsurface structures beneath Iron Mountain. Each common-shot gather was migrated individually, and a spatial taper mask was applied to suppress migration artifacts resulting from limited source and receiver coverage. The raw PP RTM migration images for each line, generated using the MVA velocity models, are shown in Fig. 4.4.11.

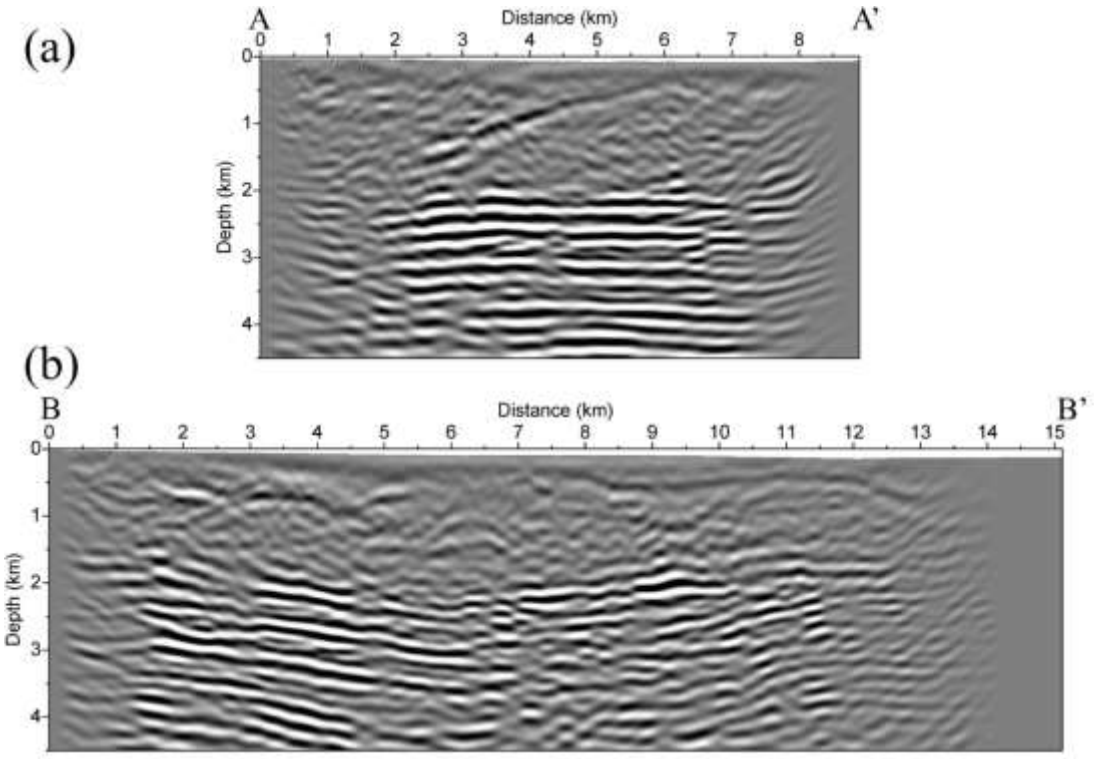


Figure 4.4.11. Raw reverse-time migration (RTM) images obtained using the migration velocity analysis (MVA) updated P-wave velocity (Vp) models for (a) Line 7B extending from A to A' and (b) Line 9 extending from B to B'.

To further enhance the imaging results, we employed a multitask machine learning (ML) approach to denoise the RTM images, improve spatial resolution, and automatically detect faults. The ML-denoised RTM images for Lines 7B and 9 are shown in Fig. 4.4.12. Compared to the raw RTM images, the denoised results reveal greater structural detail, with reflectors appearing more continuous and better defined, particularly along the edges of the profiles where the raw images exhibited smiling artifacts.

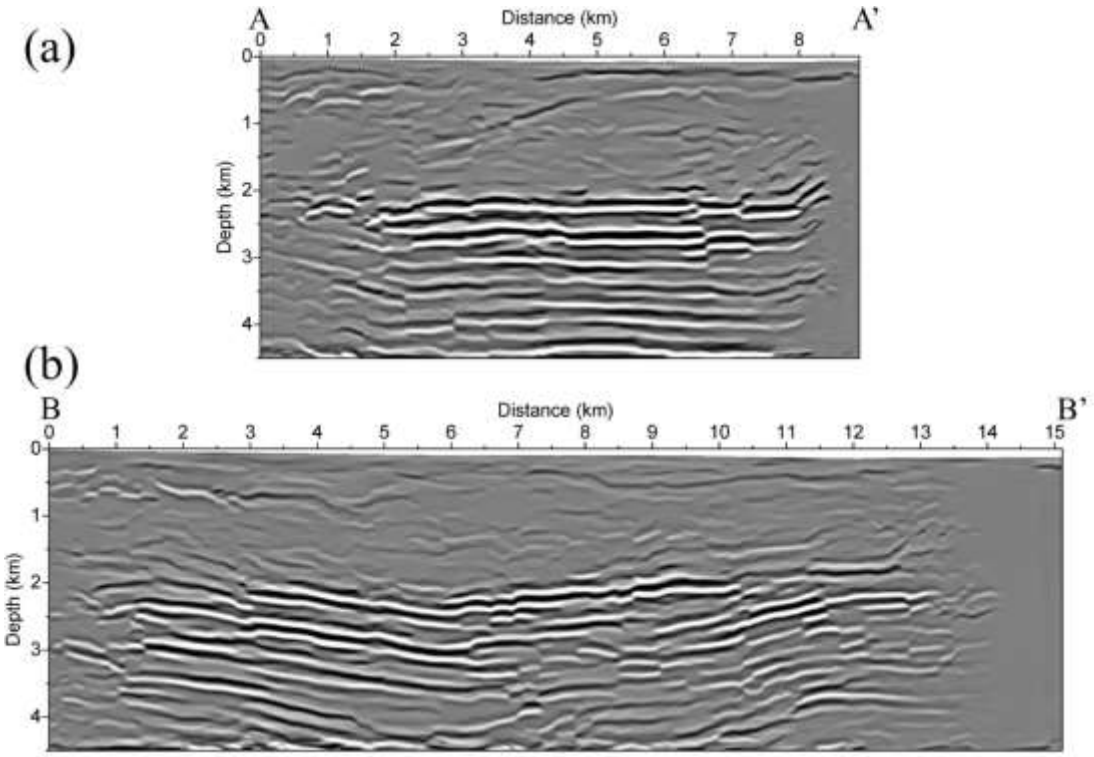


Figure 4.4.12. Reverse-time migration (RTM) images after machine learning (ML) denoising for (a) Line 7B extending from A to A' and (b) Line 9 extending from B to B'.

The ML-denoised RTM images with automatically detected faults are presented in Fig. 4.4.13. These results indicate the presence of numerous high-angle faults distributed throughout the entire profiles of Lines 7B and 9, highlighting the complex structural framework of the subsurface in the Iron Mountain region.

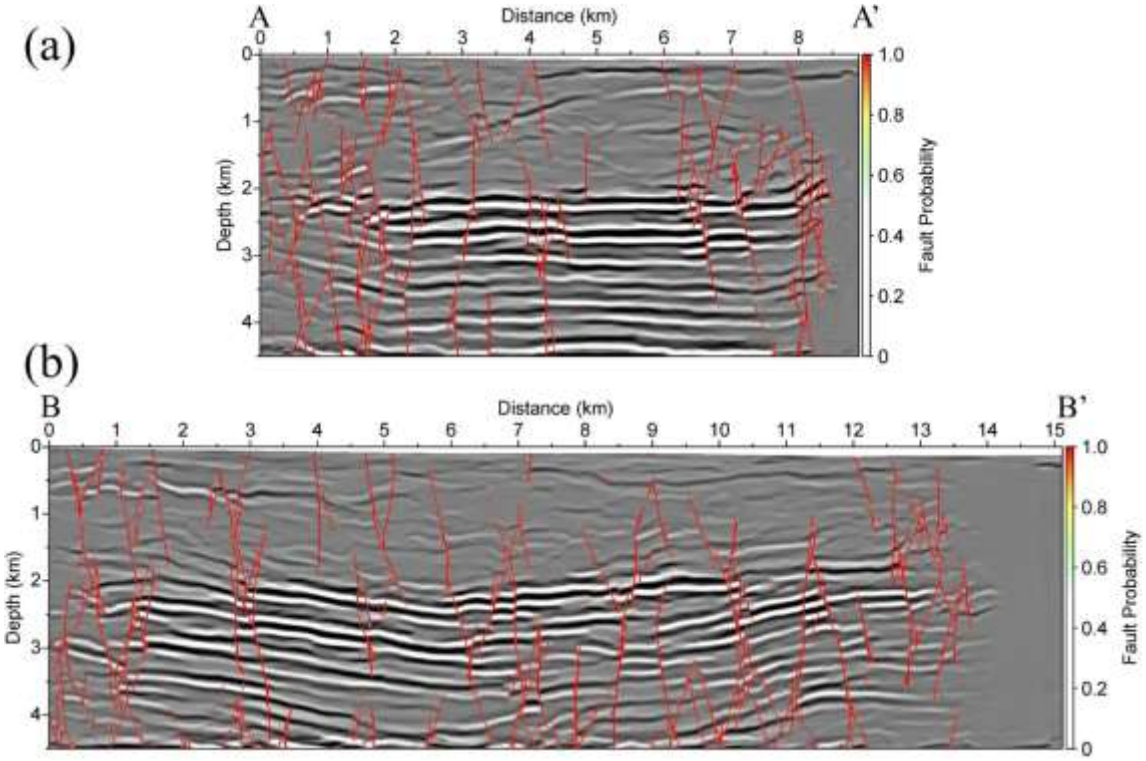


Figure 4.4.13. Machine learning (ML) denoised reverse-time migration (RTM) images with automatically detected faults shown in red for (a) Line 7B extending from A to A' and (b) Line 9 extending from B to B'.

Discussions

We overlaid the velocity models on the machine learning (ML) noise-removed migration images, as shown in Fig. 4.4.14. From the figure, there is a strong correspondence between the velocity contrasts and the seismic reflectors. In Fig. 4.4.14a, the edge of the high-velocity zone aligns closely with the dipping reflector observed at approximately 1.5 to 0.5 km depth and 2 to 7 km horizontal distance. This structure corresponds well with the quartz monzonite intrusion identified in the conceptual geologic cross-section (Fig. 4.4.2). Furthermore, **Error! Reference s ource not found.**a indicates that our migration velocity analysis successfully resolved the lower-velocity lithologies surrounding the quartz monzonite intrusion. The low-velocity region between 0 and 3 km horizontal distance and between 1 and 2 km depth is clearly visible in the MVA-derived Vp model (Fig. 4.4.14a), whereas it was not evident in either the initial layered Vp model (Fig. 4.4.8a) or the FATT-updated model (Fig. 4.4.9a).

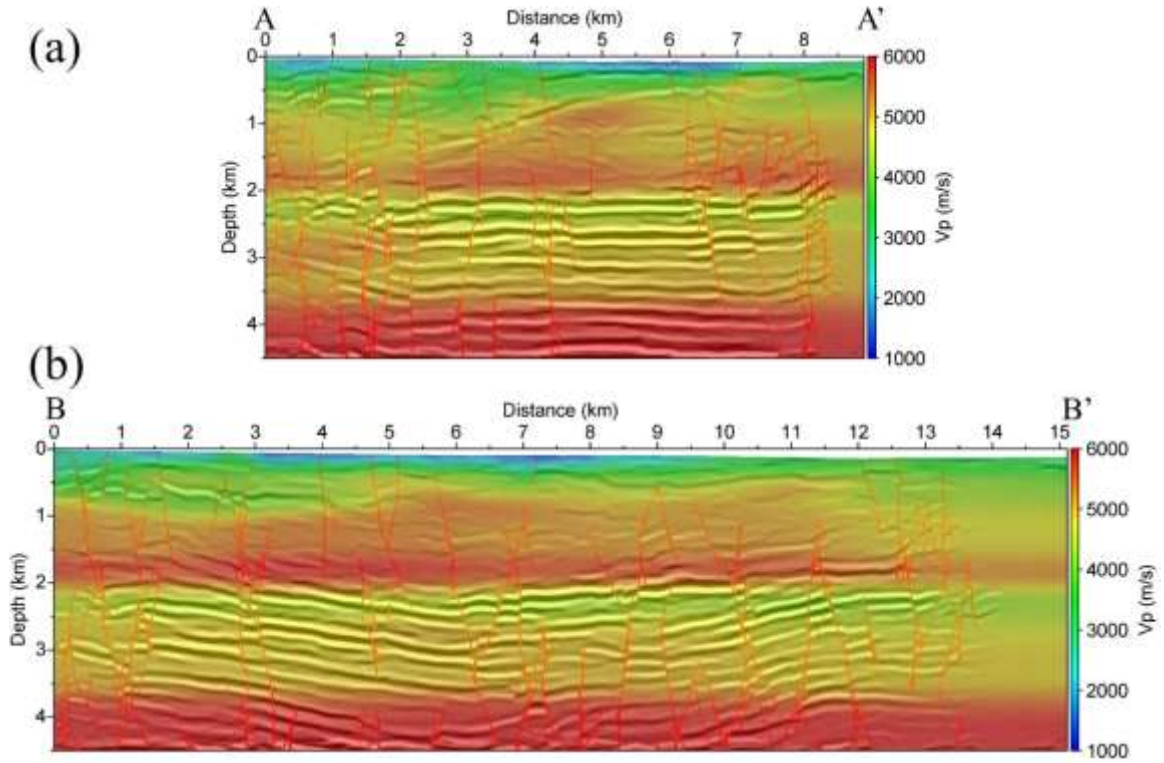


Figure 4.4.14. Machine learning (ML) denoised reverse-time migration (RTM) images with automatically detected faults (red) plotted alongside P-wave velocity (Vp) models for (a) Line 7B extending from A to A' and (b) Line 9 extending from B to B'.

The ML-denoised migration images for Lines 7B and 9 were plotted in three dimensions (3D) at different azimuthal viewpoints, as shown in Fig. 4.4.15. From this figure, we observe good continuity and alignment of reflectors between Lines 7B and 9. Minor variations in reflector positions are likely due to slight differences in the velocity fields of the two lines, as each line was processed independently in 2D. For a more complete and accurate characterization of the subsurface structures and fault systems, a dedicated 3D seismic survey of the region is recommended.

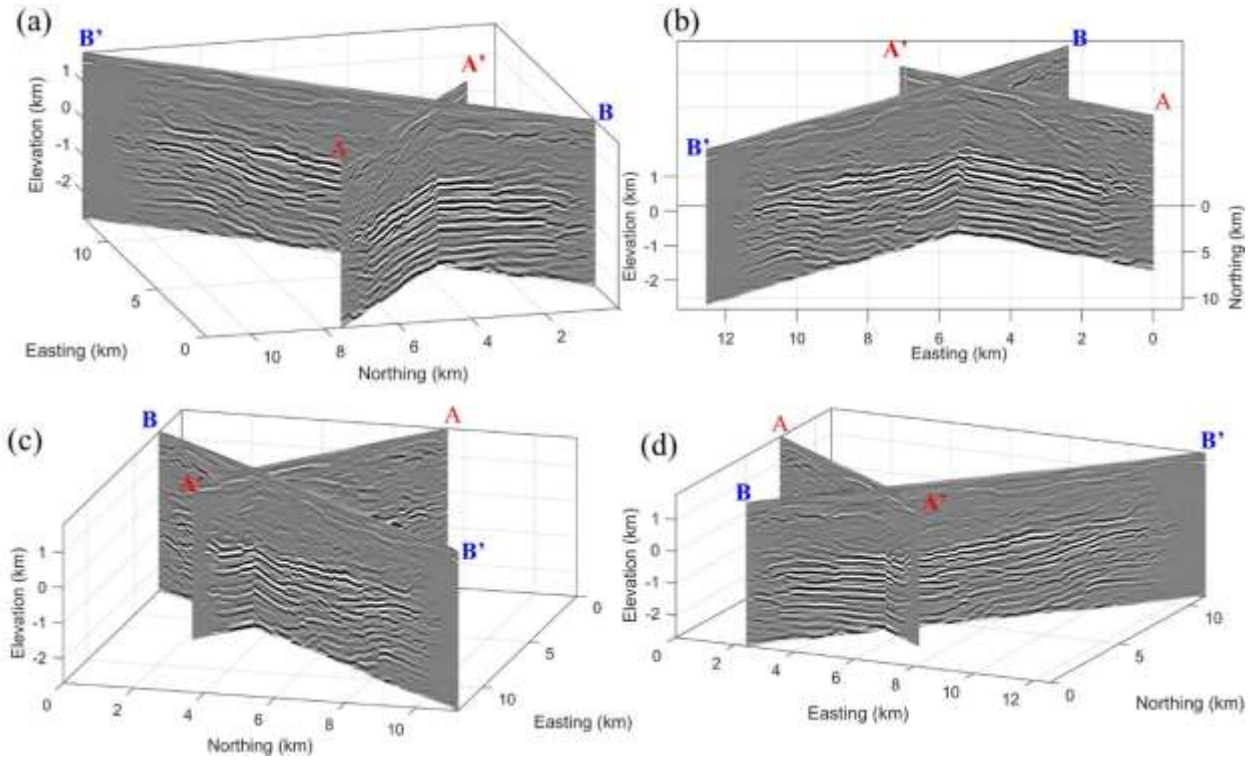


Figure 4.4.15. Three-dimensional (3D) plot of migration images for Line 7B extending from A to A' and Line 9 extending from B to B', viewed from multiple azimuth angles.

As mentioned in previous sections, Line 13 was excluded from the main analysis due to poor data quality. A common-shot gather from Line 13 is shown in Figure 16. In contrast to the gathers from Lines 7B (Fig. 4.4.16a) and 9 (Fig. 4.4.16b), where distinct parabolic reflection patterns are visible, no clear reflections are observed in the Line 13 data. Instead, the data are dominated by strong ringing noise. We attempted to remove this noise using Wiener deconvolution; however, this approach did not yield any usable signal.

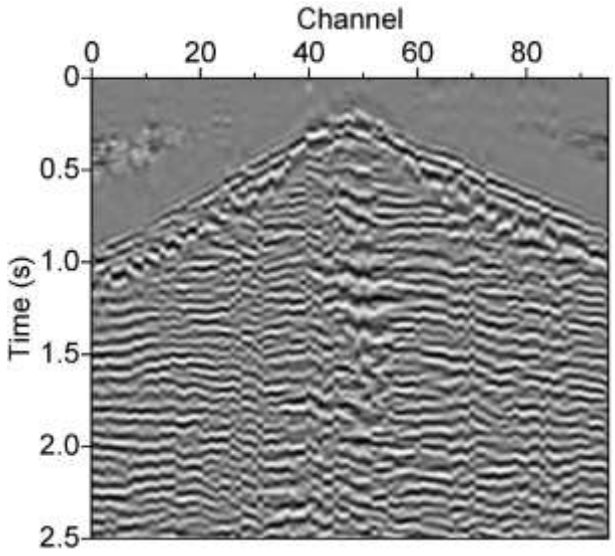


Figure 4.4.16. Common-shot gather from Line 13. In comparison with data from Lines 7B and 9, no clear reflections are observed. The dataset is also heavily contaminated by strong ringing noise, which obscures coherent seismic signals.

First-arrival traveltime tomography (FATT) was performed using the first-arrival picks from Line 13 and the initial layered Vp model. Unlike the successful convergence observed for Lines 7B and 9, the FATT results for Line 13 did not converge satisfactorily. The relative convergence curve, along with traveltime misfit histograms before and after tomography, are shown in Fig. 4.4.17. After FATT, the traveltime misfits for Lines 7B and 9 are centered near zero, while those for Line 13 exhibit a systematic bias toward negative misfit values, indicating poor model fitting.

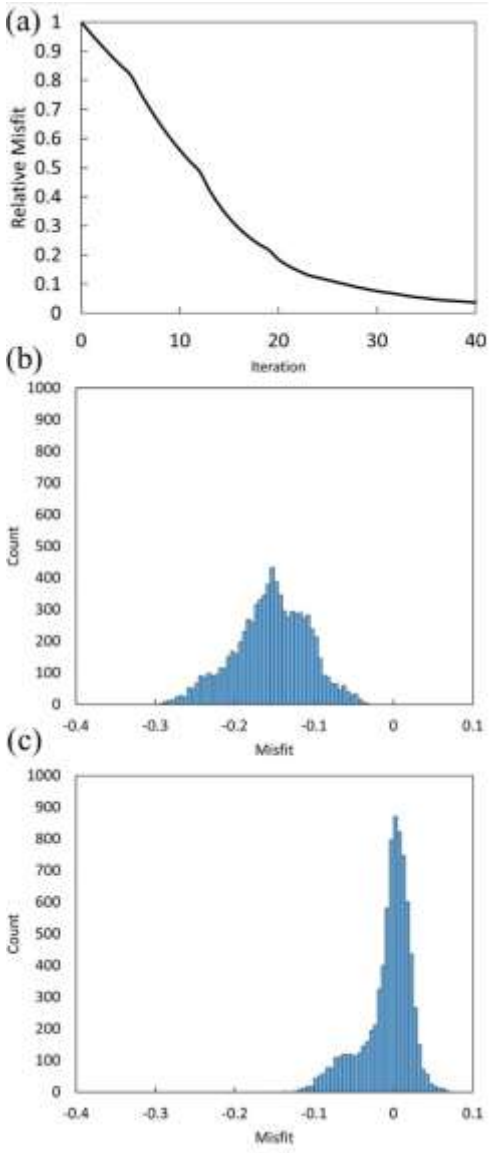


Figure 4.4.17. (a) Relative traveltime misfit convergence curve, (b) histogram of traveltime misfits before tomography, and (c) histogram of traveltime misfits after 40 iterations for Line 13.

Reverse-time migration (RTM) was applied to the processed Line 13 data using the FATT velocity model, and the resulting image is shown in Fig. 4.4.18. Unlike the raw RTM images of Lines 7B and 9 (Fig. 4.4.11), the RTM result for Line 13 shows no coherent reflectors corresponding to the major formations. As a result, we were unable to identify and pick any horizons to perform MVA for this line. Due to these limitations in data quality and processing, Line 13 was excluded from further analysis.

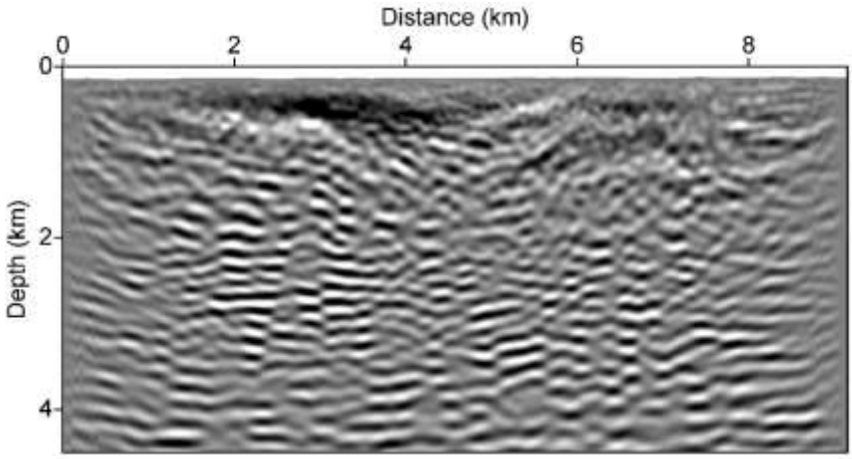


Figure 4.4.18. (a) Relative traveltime misfit convergence curve, (b) histogram of traveltime misfits before tomography, and (c) histogram of traveltime misfits after 40 iterations for Line 13.

Conclusions

We analyzed two two-dimensional (2D) legacy walkaway seismic datasets acquired in the Iron Mountain area of Utah. Initial P-wave velocity (Vp) models were constructed using sonic log data and subsequently refined through first-arrival traveltime tomography (FATT) and migration velocity analysis (MVA). Reverse-time migration (RTM) was then applied to generate pre-stack depth migration images of the subsurface. Following RTM, a machine learning (ML) algorithm was used to denoise the migration images and automatically detect faults.

By overlaying the Vp models on the denoised images, we demonstrated that the boundary of the quartz monzonite laccolith was successfully resolved along Line 7B. The denoised migration images from Lines 7B and 9 were also visualized together in three dimensions, revealing good correspondence in layer continuity and structural alignment. Minor discrepancies between the two profiles are attributed to slight variations in the Vp models at corresponding locations.

Overall, the results indicate that the processed 2D seismic data effectively delineates key subsurface features in the study area. However, to achieve a more detailed and reliable characterization of the subsurface structures and fault systems, acquisition and analysis of a three-dimensional (3D) seismic survey are recommended.

References

Battle T, Srivastava U, Kopfle J, Hunter R, McClelland J. 2024. The direct reduction of iron. In: Seetharaman S, editor. Treatise on process metallurgy. Oxford (UK); Elsevier. p 89–149. doi:10.1016/B978-0-323-90206-8.00001-3

Blank HR, Mackin JH. 1967. Geologic interpretation of an aeromagnetic survey of the Iron Springs district, Utah. Washington (DC): U.S. Government Printing Office. (US Geol Surv Prof Pap 516-B). [accessed 2025 Dec 29]. https://pubs.er.usgs.gov/publication/pp516B.

Chen B, Ma Z, Ahmmed B, Guo Q, Li W, Mehana M, Pawar R. 2024. Unified SimCCS platform for decision-making in carbon capture, transport, and storage infrastructure. In: Proceedings of the 17th International Conference on Greenhouse Gas Control Technologies (GHGT-17); 2024 Oct 20–24; Calgary (Canada). [accessed 2025 Dec 29]. https://www.osti.gov/servlets/purl/2478611

Fei TW, Luo Y, Yang J, Liu H, Qin F. 2015. Removing false images in reverse time migration: the concept of de-primary. Geophysics. 80(6):S237–S244. doi:10.1190/geo2015-0289.1

Fomel S, Luo S, Zhao H. 2009. Fast sweeping method for the factored eikonal equation. J Comput Phys. 228(17):6440–6455. doi:10.1016/j.jcp.2009.05.029

Gao K. 2024. Iterative multitask learning and inference from seismic images. Geophys J Int. 236(1):565–592. doi:10.1093/gji/ggad424

Leung S, Qian J. 2006. An adjoint state method for three-dimensional transmission traveltime tomography using first-arrivals. Commun Math Sci. 4(1):1–20. doi:10.4310/CMS.2006.v4.n1.a10

Liu Z, Bleistein N. 1995. Migration velocity analysis: theory and an iterative algorithm. Geophysics. 60(1):142–153. doi:10.1190/1.1443743McMechan GA. 1983. Migration by extrapolation of time-dependent boundary values. Geophys Prospect. 31(3):413–420. doi:10.1111/j.1365-2478.1983.tb01060.x

McMechan GA. 1983. Migration by extrapolation of time-dependent boundary values. Geophys Prospect. 31(3):413–420. doi:10.1111/j.1365-2478.1983.tb01060.x

Moodie N, Szymanski E, Vanden Berg MD, McPherson BJ. 2022. Site characterization for geologic carbon storage of CO_2 from a direct reduced iron plant. Paper presented at: AGU Fall Meeting 2022; 2022 Dec; Chicago (IL). Abstract GC12E-0481.

Rowley PD, Barker DS. 1978. Geology of the Iron Springs mining district, Utah. In: Shawe DR, Rowley PD, James LP, editors. Guidebook to mineral deposits of southwestern Utah. Salt Lake City (UT): Utah Geological Association. p. 49–60.

Taillandier C, Noble M, Chauris H, Calandra H. 2009. First-arrival traveltime tomography based on the adjoint-state method. Geophysics. 74(6):WCB1–WCB10. doi:10.1190/1.3250266

Tong P. 2021. Adjoint-state traveltime tomography: eikonal equation-based methods and application to the Anza area in southern California. J Geophys Res Solid Earth. 126(5):e2021JB021818. doi:10.1029/2021JB021818

van Kooten GK. 1988. Structure and hydrocarbon potential beneath the Iron Springs laccolith, southwestern Utah. Geol Soc Am Bull. 100(10):1533–1540.

Vasylkivska V, King S, Bacon D, Harp D, Lindner E, Baek S, Keating E, Yang Y, Zhang Y, Chen B, et al. 2022. NRAP-Open-IAM user's guide, release alpha 2.6.1-22.09.30. Pittsburgh (PA); National Energy Technology Laboratory (US). [accessed 2025 Dec 29]. https://edx.netl.doe.gov/dataset/08f396c8-bc5f-44ad-a028-6e98a6ea6d70/resource/8b27335a-343c-4836-b8a3-3ad0bdc9e669

Yilmaz Ö. 2001. Seismic data analysis: processing, inversion, and interpretation of seismic data. 2nd ed. Tulsa (OK); Society of Exploration Geophysicists. doi:10.1190/1.9781560801580

Sandia National Laboratories (SNL)

The contributions of the Sandia National Laboratories (SNL) are under the following technical tasks as well as project management and support tasks:

I. Technical Tasks

Deliverable 1. Develop a blueprint for cost benefit analysis of carbon capture, utilization and storage projects

Deliverable 2. Develop technoeconomic analysis and demonstrate the framework for a focused project with industrial partner (LUCID/TARGA) =

Deliverable 3. Regional Implications of Section 45 Q Tax Credits for the Acid Gas Injection wells in the Permian Basin =

II. Project management and support tasks.

- Task 1 – Project Management and Planning
  - Subtask 1.1 – Communication and Coordination with Other Partnerships
- Task 3 – Facilitating Data Collection, Sharing, and Analysis
  - Subtask 3.1 – Engaging with National Laboratories
    - Subtask 3.1.1 – Identify Data Requirements & Needs
    - Subtask 3.1.4 – Gather and Catalogue CO_2 Emissions (Point) Source Database
- Task 4 – Evaluating Regional Infrastructure
  - Subtask 4.4 – Economic Assessment
  - Subtask 4.5 – Focused Scenario Analysis
    - Site-specific techno-economic analysis for the TARGA (formerly LUCID) acid-gas project
    - Economic risk and feasibility assessment for the ONEOK project

Task 1 – Project Management and Planning

SNL engaged in the CUSP Data Organization and Economics working groups to define key economic inputs—capture, transport, storage, monitoring, and permitting cost drivers—and to

coordinate with other national laboratories, universities, and state geological surveys on assembling a standardized CCUS dataset. SNL also led the development of the blueprint for economic analysis of geologic carbon sequestration, laying out a common cost–benefit framework.

Task 3 – Facilitating Data Collection, Sharing, and Analysis

SNL worked with other CUSP national laboratory and academic partners to identify and prioritize the datasets needed for techno-economic and cost–benefit analyses—spanning CO_2 capture performance, cost drivers, subsurface storage parameters, monitoring requirements, and permitting inputs. As part of the CUSP Data Organization Working Group, SNL supported compiling the CO_2 emissions point-source database by integrating EPA Greenhouse Gas Reporting Program (GHGRP) records with partner inventories, harmonizing data formats, and establishing version-control and hand-off procedures to ensure all analyses draw from a single, validated dataset.

Task 4 – Evaluating Regional Infrastructure

SNL authored a unified cost-benefit economic-assessment that partners can use to compare CCUS investments at both regional and site levels. This toolkit standardizes cost–benefit workflows in Excel and underpins all subsequent techno-economic and policy-scenario studies.

Subtask 4.4 – Economic Assessment

- SNL developed the blueprint for cost-benefit analysis of carbon, capture utilization and storage projects
- SNL developed a framework for technoeconomic analysis of carbon capture, utilization and storage project
- SNL scaled up the framework and demonstrated regional cost analysis focusing on the Permian basin Region
- SNL also developed and demonstrated investigating the implications of Section 45 Q tax credits on economic feasibility of CCUS projects.

Technoeconomic Analysis

The TEA framework SNL developed allows looking into the major cost drivers of CCUS, cost minimization achieved through optimization in system component(s), as well as the levelized cost of hydrogen storage under various scenarios. The framework consists of the following:

1. Scoping (project boundaries, capture-transport-storage scenarios)
2. Metric specification (CAPEX categories—site characterization, AOR studies, well construction, compressor/pipeline infrastructure, monitoring/permit costs; OPEX categories – Compressor O&M cost, Well O& M cost, Fixed O&M costs, other costs)
3. Analysis design (levelized costs calculation using CAPEX, capital-recovery-factor, and OPEX; mapping key capex/opex drivers; and sensitivity analysis)

The demonstration of the framework is available in the report and published paper (see the Reports and Products section below).

Cost–Benefit Analysis and Evaluation of Implication of 45Q Tax Credits

For this task, SNL developed a technoeconomic analysis method, evaluated the economic feasibility of CCS at the acid gas injection (AGI) wells, and assessed the implication of tax credits under Section 45Q of the U.S. Tax Code (Credit for Carbon…2021) for CCS at the AGIs. We included the following additional components on the TEA framework discussed under Technoeconomic Analysis section.

1. Discounted-cash-flow modeling; NPV, IRR, and Benefit Cost Ratio
2. Integration of costs and benefits (45Q tax-credit revenues) into NPV, IRR, and benefit:cost outputs.

All formulas and data tables are built into Excel templates that partners can adapt to local inputs. This standardized model gives all partners a transparent, consistent way to compare CCUS projects—across technologies, geologies, and policy scenarios—reducing uncertainty and guiding strategic investment and permitting decisions.

The following is the abstract from our scientific journal article publication (Mishra et al., 2025; see Section Report and Products for the full reference):

Carbon capture, utilization, and storage (CCUS) is an important pathway for meeting climate mitigation goals. While the economic viability of CCUS is well understood, previous studies do not evaluate the economic feasibility of carbon capture and storage (CCS) in the Permian Basin specifically regarding the new Section 45Q tax credits. We developed a technoeconomic analysis method, evaluated the economic feasibility of CCS at the acid gas injection (AGI) wells, and assessed the implication of Section 45Q tax credits for CCS at the AGIs. We find that the compressors, well depth, and the permit and monitoring costs drive the facility costs. Compressors are the predominant contributors to capital and operating expenditure driving the levelized cost of CO_2 storage. Strategic cost reduction measures identified include (1) sourcing of low-cost electricity and (2) optimizing operational efficiency in well operations. In evaluating the impact of the tax credits on CCS projects, facility scale proved decisive. We found that facilities with an annual injection rate exceeding 10,000 Mt storage capacity demonstrate economic viability contingent upon the procurement of inputs at the least cost. The new construction of AGI wells was found to be economically viable at a storage capacity of 100,000 Mt. The basin is heavily focused on CCUS (tax credit – \$65/Mt CO_2), which overshadows CCS (\$85/Mt CO_2) opportunities. Balancing the dual objectives of CCS and CCUS requires planning and coordination for optimal resource and pore space utilization to attain the basin's decarbonization potential. We also found that CCS on AGI is a lower cost CCS option as compared to CCS on other industries.

Subtask 4.5 – Focused Scenario Analysis

SNL performed technoeconomic analysis for the following site-specific or regional applications:

- TARGA (formerly LUCID) Acid-Gas Project: Applied the technoeconomic analysis framework developed for geologic carbon dioxide storage site at a TARGA facility in the Permian Basin, focusing on estimating the levelized cost of carbon dioxide storage. We leveraged information provided by TARGA to validate the capital and operational costs associated with the establishment and maintenance of Acid Gas Injection wells-based CO_2 storage, including site characterization, well construction, and monitoring expenses. The

analysis highlights the significant cost drivers, such as compressor expenses and well depth, mapping key capex/opex drivers, and running sensitivity analyses.

- ONEOK CO_2 Storage Concept (Subtask 5.5 deliverable): Sandia conducted economic risk assessment to support the overarching goal of the project – to identify potential carbon dioxide (CO_2) reservoirs for long-term saline storage in the area surrounding ONEOK natural gas liquids fractionation plants near Bushton, KS, and Medford, OK, as well as several gas processing plants in Oklahoma that emit approximately 1 Mt CO_2 per annum. We employed a three-pronged approach to assess CO_2 sequestration, calculating costs at identified ONEOK sites, evaluating cost-benefit ratios, and analyzing economic risks based on the methods outlined in a Subtask 5.5 Economic risk/feasibility assessment project report. This included identifying factors affecting economic viability and quantifying risks for two factors with available project-specific data.

Regional Permian Basin Analysis

Scaled the technoeconomic analysis approach across approximately 40 acid-gas injection wells in New Mexico and in the Permian Basin. Additionally, we conducted analysis in quantifying the impacts of Section 45 Q tax credit on economic viability of carbon sequestration projects using acid gas injection wells in the Permian region.

Together, these contributions give CUSP partners transparent, repeatable economic metrics—enabling data-driven site prioritization and investment planning across the Western region.

Report and Products

Reports and a peer-reviewed journal publication produced by SNL and team members under Task 4 are the following:

- Mishra SK, Gagarin H, Potter J, Ford M, Heath J, Trentham R, Henderson M, El-Kaseeh G. 2023. Site-specific techno-economic analysis of geologic carbon storage in acid gas injection wells. Albuquerque (NM); Sandia National Laboratories. CUSP Focus Project Deliverable #11. 18 p.
- Mishra SK, Henderson MA, Heath JE, Tu DJ, Irwin A, Trentham R, Earnhart D, Fonquergne J, Gagarin H, Heath J. 2025. Can Section 45Q tax credit foster decarbonization? A case study of geologic carbon storage at acid gas injection wells in the Permian Basin. Int J Greenh Gas Control. 140:104284. doi:10.1016/j.ijggc.2024.104284
- Mishra SK, Potter J, Ford M, Heath J. 2023. A blueprint for economic analysis of geologic carbon sequestration. Albuquerque (NM); Sandia National Laboratories. CUSP Project Deliverable #9. 14 p.

SNL's economic-assessment work was showcased at several key events:

- A dedicated webinar on August 12, 2021 to the full CUSP team
- A breakout session at the CUSP Annual Meeting (May 24–25, 2022)
- A poster presentation at the DOE/NETL Carbon Management Review in Pittsburgh (August 15–19, 2022)
- Economic Analysis of Geologic Carbon Sequestration Project
- CO_2 Conference, Midland, TX (December 2022)

- A poster presented at the DOE/NETL Carbon Management Review in Pittsburgh (August 2023): Regional Economic Analysis of Geologic Carbon Sequestration in Permian Basin AGI Wells
- Oral presentation at the CUSP annual meeting September 2024, Santa Fe, New Mexico: Economic Analysis of Geologic Carbon Sequestration
- Oral presentation at the CUSP annual meeting June 2025, Salt Lake City, Utah: Economics of Carbon Capture, Utilization, & Storage

Future Work and Connections to Other Energy Applications – Support for Geothermal, Hydrogen, and Critical Metals and Rare Earths

SNL's CUSP economic-assessment—built around modular Excel workbooks for cost–benefit and DCF analyses—can be directly adapted to other subsurface resource applications. Building on this, we have refined a Technoeconomic analysis and economic feasibility analysis working with an industry partner on a separate project. We also developed and published on Technoeconomic analysis and economic feasibility analysis of underground hydrogen storage on a separate project. Furthermore, the python-based TEA algorithms we developed are easily adaptable to technoeconomic analysis of carbon, hydrogen and other sub-surface cost-analysis. By applying geothermal-specific inputs (e.g., well-drilling and stimulation costs, plant-capacity factors), hydrogen-production parameters (e.g., deep-drill and separation expenditures, storage-cavern economics), or critical-metal and rare-earth recovery metrics (e.g., mining, processing, and adsorbent-regeneration costs), and defining parallel benefit streams (e.g., power sales, hydrogen revenues, rare-earth commodity values), the user could generate levelized-cost, NPV, IRR, and sensitivity reports across any of these domains. This cross-sector reuse ensures transparent, apples-to-apples economic comparisons, streamlining investment and policy decisions in geothermal, hydrogen, and critical-mineral projects.

Acknowledgments

Sandia National Laboratories is a multi-mission laboratory managed and operated by National Technology & Engineering Solutions of Sandia, LLC, a wholly owned subsidiary of Honeywell International, Inc., for the U.S. Department of Energy's National Nuclear Security Administration under contract DE-NA0003525. SAND2026-15660O.

References

Credit for Carbon Oxide Sequestration, U.S.C.-2023 26 C.F.R. §1.45Q-1 (2021).

Mishra SK, Henderson MA, Heath JE, Tu DJ, Irwin A, Trentham R, Earnhart D, Fonquergne J, Gagarin H, Heath J. 2025. Can Section 45Q tax credit foster decarbonization? A case study of geologic carbon storage at acid gas injection wells in the Permian Basin. Int J Greenh Gas Control. 140:104284. doi:10.1016/j.ijggc.2024.104284

Pacific Northwest National Laboratory (PNNL)

For details on PNNL's work for the CUSP project, please see the Focused Project Arizona Geological Survey, University of Arizona – Tucson, AZ

The majority of this report has been adapted from the AZGS-UA open-file report 24-01 (Wilson et al. 2024).

The Arizona Geological Survey (AZGS) conducted a Phase I pre-feasibility study of the Harquahala basin, western Maricopa County, Arizona, for subsurface geologic storage of CO_2. The purpose of this project was to evaluate subsurface geology and structure and provide site characterization for future long-term CO_2 sequestration. This work was done as part of the larger Carbon Utilization and Storage Partnership (CUSP) regional initiative with the goal of expediting the deployment of onshore carbon capture, utilization, and storage (CCUS) technologies in the western region of the United States. This project advances this goal through subsurface characterization to geologically de-risk this carbon storage prospect to help attract industry for further development. Additionally, learnings from this site can be applied to numerous geologically similar basins throughout the state.

The Phase I evaluation compiled and integrated publicly available geologic maps, wellbore lithology logs, wellbore temperature data, well water chemistry information, and published gravity surveys with proprietary datasets including legacy 2D seismic lines and detailed gravity and resistivity surveys. These data were used to produce depth-to-bedrock (DTB) contour maps, structure maps of the lower basin fill surface, and isopach maps of the total basin fill, upper basin fill, lower basin fill, and potential evaporite deposits in the basin. Our analyses yielded new information about the basin size, geometry, and structure, which improved calculations of the area and volume of the potential reservoir study area.

Harquahala basin may have the geologic conditions necessary to store natural gas permanently and safely in the subsurface, but additional geophysical and well data are needed to characterize the physical properties of storage reservoir rocks. Harquahala has thick accumulations of basin fill sediments with sufficient volumes for storage of supercritical CO_2: an estimated 1,997 Mt of CO_2 (P50). Basin fill likely contains three different potential storage reservoir types: CO_2 in stacked saline clastic sedimentary deposits, bedded evaporite deposits for compressed H_2 gas storage, and basalt lava flows for CO_2 mineralized sequestration. Hot, dry crystalline rock underlying basin fill is favorable for geothermal energy and has an unknown volume of saline groundwater. The seismicity risk is low based on the absence of Quaternary faults and historic seismicity. The basin is located close to five major (greater than 100,000 tons/yr) CO_2 point sources, existing pipeline infrastructure and Interstate 10, a transportation corridor between Arizona and southern California.

At the completion of our data analyses, three critical unknowns remain: the existence/absence of sealing strata such as bedded evaporites and fine-grained deposits, the physical properties of stacked saline reservoir rock, and the stratigraphic architecture of basin fill sediments. Harquahala basin lacks deep well borehole data to adequately characterize rock lithology, porosity, and permeability. New 2D seismic interpretations reported within suggest bedded evaporite deposits and basalt lava flows are likely components of the lower basin fill unit; however, these interpretations cannot be calibrated with physical evidence. To reduce the uncertainties about storage reservoir integrity, we recommend the acquisition of new data to include 2D active-source seismic, high-resolution gravity infilling, high resolution aeromagnetic survey, and a stratigraphic characterization well with wireline geophysical logs and a core, cutting, and fluid sampling program. These datasets, combined with data reported within, will refine our understanding of the basin fill rock properties, identify the presence/absence of sealing

strata, and clarify stratigraphic architecture and basin structure.

Project Description and Scope

The AZGS conducted a phase I pre-feasibility evaluation for subsurface storage of CO_2 in Harquahala basin, western Maricopa County, Arizona. This study was funded by the U.S. Department of Energy (DOE), as a Focused Project within the regional CUSP Regional Initiative. The purpose of this work was to evaluate the basin geometry, structure, and stratigraphic architecture of Harquahala basin and provide site characterization for future potential subsurface CO_2 storage.

The scope of work required data collection, data analysis, coordination, and technical evaluation in three tasks. In Task 1, AZGS researchers synthesized geologic maps, well lithology logs, public and private gravity datasets, newly reprocessed 2D seismic data, DTB contours, and groundwater temperature and chemistry data for Harquahala basin. Task 2 involved stakeholder engagement and outreach through periodic meetings and the creation of a publicly available StoryMap. In Task 3 sites for a future characterization well and geophysical surveys were identified. Deliverables include this report, supporting maps, cross sections, model data and parameters, and future data collection recommendations.

Study Areas

The Harquahala basin is located on the border of Maricopa and La Paz counties in west-central Arizona (Figure 75 and Figure 76). The Harquahala basin underlies a rural, agricultural valley located approximately 60 miles west of Phoenix. The approximately 511 mi^2 basin area is defined by several rugged mountain ranges composed of crystalline rocks: Harquahala Mountains to the north, Big Horn Mountains to the northeast, Saddle Mountain to the southeast, and the Eagletail Mountains to the southwest. Existing infrastructure crossing Harquahala Valley includes I-10, Central Arizona Project (CAP) canal, and natural gas pipelines. Land ownership consists of 62% federal land (managed by the U.S. Bureau of Land Management), 25% private land, and 13% State Trust lands (Towne 2014).

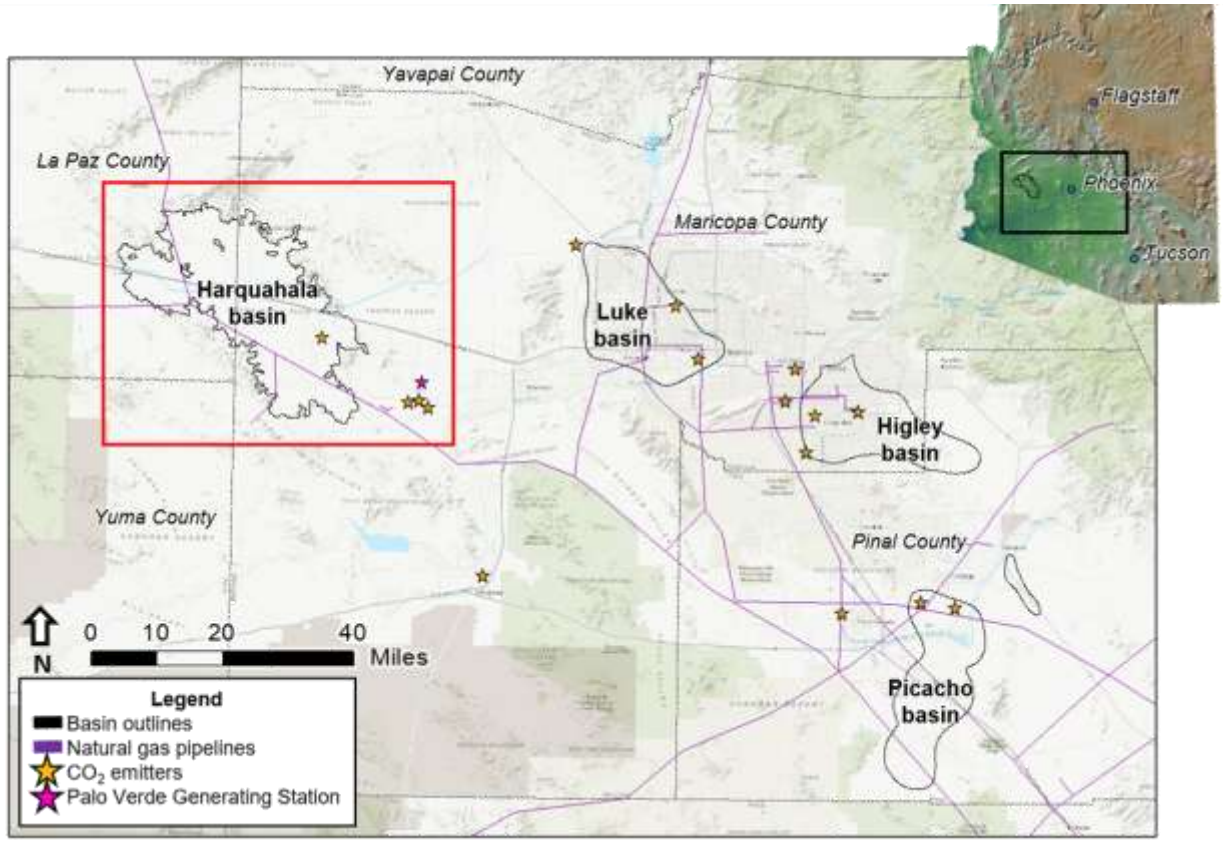


Figure 75 Map of study area in south-central Arizona (black box in state inset) showing the location of natural gas pipelines, CO_2 emission point sources (greater than 100,000 t per year), and major sedimentary basins in this region. The study area includes Harquahala basin (red box and location of Figure 76).

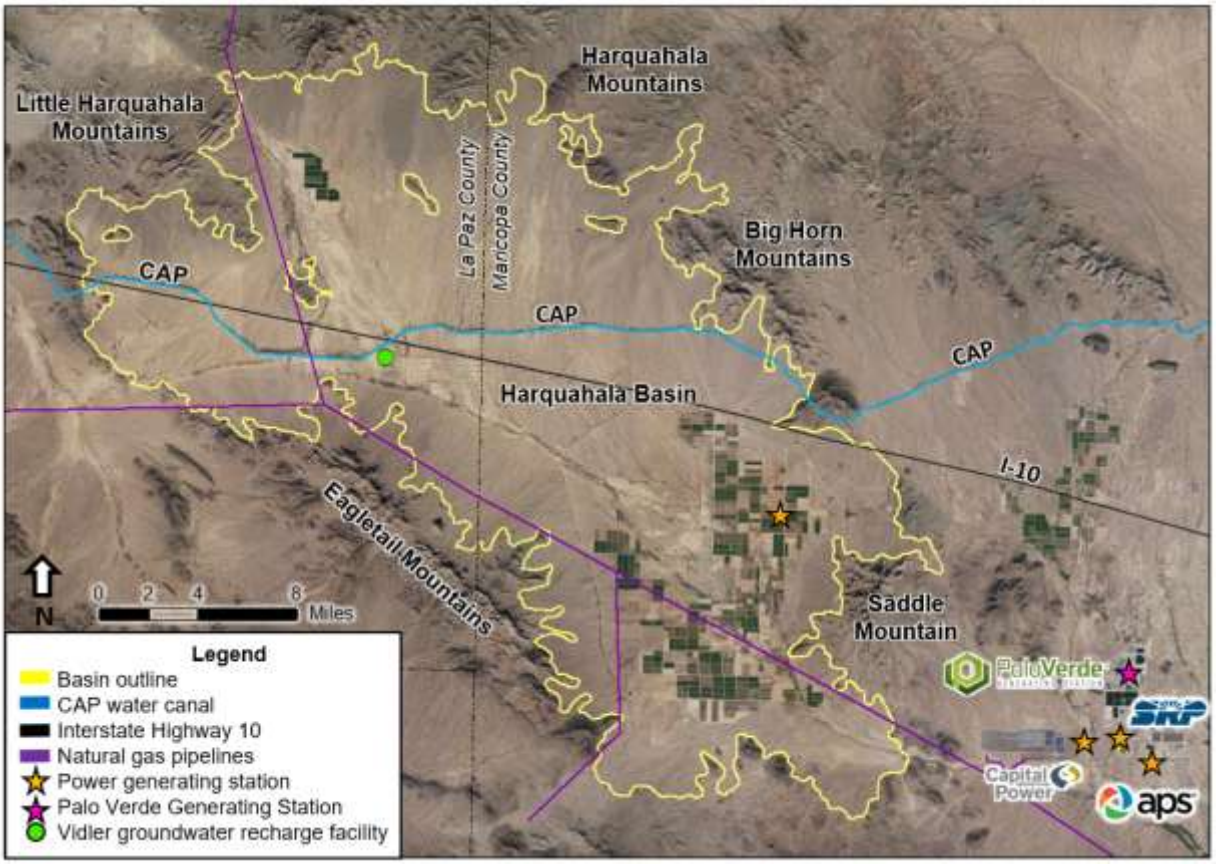


Figure 76 Location map of Harquahala basin (yellow outline), the surrounding infrastructure, and nearby energy facilities.

Four natural gas–powered energy facilities—Harquahala Generating Station, Mesquite Generating Station, Redhawk Generating Facility, and Arlington Valley Energy Facility—are located within 15 miles of the basin, three of which operate year-round. In 2021, three of the four natural gas power plants emitted over 6.32 Mt CO_2 waste to the atmosphere (U.S. EPA 2023). Palo Verde Nuclear Generating Station, the nation's largest nuclear power plant, is located 11 miles east of Harquahala basin.

Methods

All publicly available data were compiled, quality checked, and organized into an Esri ArcMap geodatabase. Data includes geologic map compilations, borehole lithology logs, 2D legacy seismic lines, public and proprietary gravity datasets, DTB contours, groundwater temperatures, and well chemistry information.

Geologic Map Compilation

Surficial geology was compiled and simplified from four 1:100,000 AZGS geologic maps (Reynolds 1997; Reynolds and Grubensky 2007; Richard et al. 2022; Spencer et al. 2022). Geologic units were simplified into 11 time-transgressive lithologic categories to highlight important compositional provenance for basin fill sediments (see Plate 2, Wilson et al. 2024). For example, crystalline bedrock units were lumped by age, while younger volcanic rocks were

lumped by age and chemistry (this approach identified source areas for mafic volcanic rocks that can be used to sequester CO_2). All surficial alluvium younger than approximately 5 Myr was omitted from the map compilation for simplicity.

Borehole Lithology Logs

Over 740 Arizona Department of Water Resources (ADWR) and Arizona Oil and Gas Conservation Commission (AZOGCC) wells were reviewed for subsurface geologic data within Harquahala basin (Appendices A and B). Within the basin center, only wells deeper than 122 m (400 ft) with lithologic borehole data were plotted. Along the basin margins, all wells regardless of depth were logged and plotted to refine depth to bedrock contours.

The review criteria resulted in 205 wells with subsurface lithologic data that have an average depth of 250 m (820 ft), with the deepest well reaching 611 m (2,005 ft; AZOGCC 2023). Wells were sorted by lithology, clast size, and/or composition at reported intervals, and plotted by lithology in cross-sections. Lithology codes were assigned to a color and resulting logs are displayed on each of the cross-sections traversing the basin.

Vintage Seismic 2D Reflection Data and Analysis

The application of 1980's vintage seismic reflection data was a major contributor to improving the understanding of the structure and stratigraphy of Harquahala basin. In this section we present the quality of legacy data, processing methods including depth conversion and limitations of these data. These seismic data are proprietary and confidential under contract between the UA Seismology Group and Conoco Phillips. Results and interpretations presented in this report may be reproduced, although original raw digital data remain confidential.

Seismic reflection profiles were acquired by petroleum exploration companies in the early 1980's to assess petroleum potential in Tertiary and older sedimentary rocks in central Arizona. The focus of the original data acquisition was to image stratigraphy and structure from a few hundred meters to several thousand meters in depth. However, the limited number of wells and lack of any deep wells to calibrate seismic velocity in both basins introduce uncertainty in velocity and depth estimates across the basin and in gaps between lines.

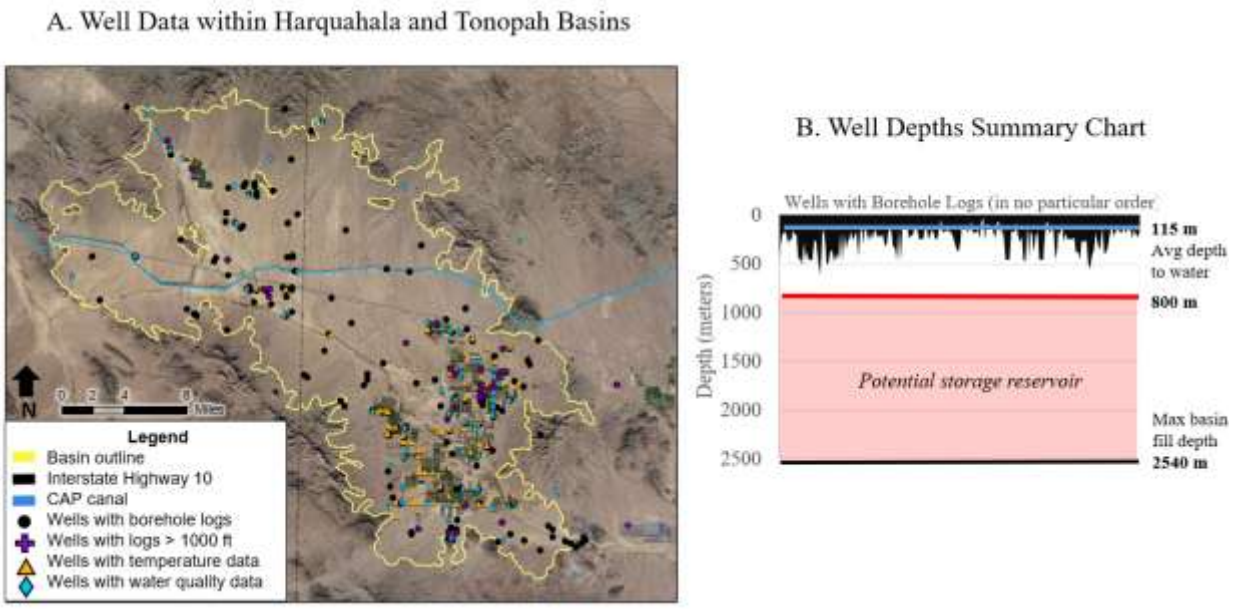


Figure 77 (A) Map of well data types within the Harquahala basin. (B) Summary chart showing wells plotted against depth. The average depth to the water table is shown as a blue line, depth to bedrock is a black line, and the potential reservoir (basin fill below 800 m and above bedrock) is shaded red. This chart highlights the lack of well data at the reservoir depths.

Reprocessing of five of these 2D seismic reflection lines was carried out by Jourdan Anoka with Anoka Geophysical LLC, Aurora, CO, in collaboration with Roy Johnson and Kurt Constenius at University of Arizona (Figure 78, Table 1). Analysis of the final stacks were made by Kurt Constenius with input from AZGS research geologists. Data quality for the five lines was variable, ranked from moderate quality to poor quality: PW24, PW23, PW22, TR12, TR10b, and TR9.

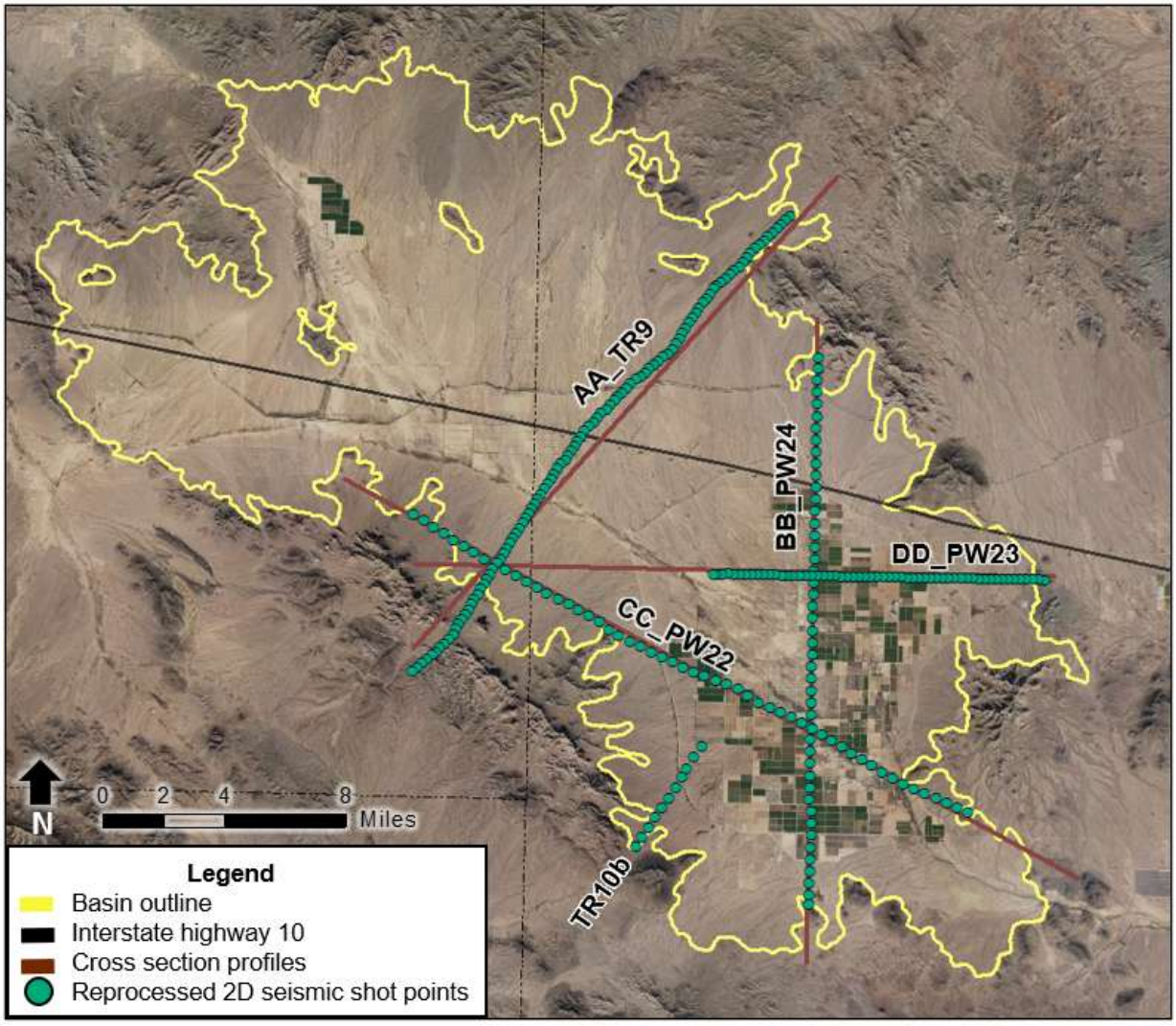


Figure 78 Map of the 2D seismic lines and cross sections profiles that traverse the Harquahala basin. 2D vintage seismic line shot points are black dots.

Table 1. List of vintage seismic lines stations used in Harquahala basin. Beginning of line (BOL) and end of line (EOL). Refer to Figure 78 for location of seismic lines and stations.

Seismic line	Reprocessed line length (km)	BOL stations	EOL stations	SP spacing (ft)	Datum elev. (m)
PW23	18.3	780	1,050	1,100	600
PW22	35.5	670	1,200	2,000	600
PW24	30.7	201	658	2,000	600
TR9	34.5	1,200	2,200	1,200	600
TR10b	6.7	0	200	2,000	600

Seismic Reprocessing

A standard processing sequence that included iterations of velocity analysis and static corrections was used for the PW and TR profiles (Table 2). Differences in processing between lines included application of normal moveout-correction velocities determined separately for each line and application of automatic static corrections, which were based on individual reflection events in each profile.

Table 2. Acquisition parameters for seismic lines used in Harquahala basin.

Acquisition Parameters	TR lines	PW lines
Acquired by	Texoma Production Co.	Anschutz Corp.
Date	1980	1980
Source	Dynamite	Vibroseis
Source size or sweep	110 lb	14-56 Hz; 18 s
Source interval	134 m	67 m
Group interval	33.5 m	67 m
Channel array	96 channels; off end	48 channels; off-end
Near offset - Far offset	805 m - 3,990 m	268 m - 3,420 m
Normal maximum fold	1,200%	2,400%
Sampling interval	2 ms	4 ms
Recording time	8 s	24 s

Depth Conversion

Depth-below-surface was determined for two interpreted event horizons using two-way travel time to the horizon and assigned interval velocities. Velocity control for the upper basin fill was provided by a sonic log from the Humble Oil and Refining State #1 well (Section 2 T8S-R8E) in the Picacho Basin. The average velocity of the upper basin fill in that well is approximately 2,133 m/s (7,000 ft/s). The lower basin fill was depth converted using velocity data from the same Humble well and sonic log data from the Suncor Development, Sunset Point #1-19 well (Section 19 T2N-R1W) in Luke basin. The lower basin fill in the Humble well is predominantly evaporites and is entirely halite in the Suncor 1-19 well with a velocity of 4,419 m/s (14,500 ft/s). Depth conversion of lower basin fill used the velocity of halite because we interpret the lower basin fill to be predominantly evaporites (see section 4).

Gravity Data

Multiple gravity datasets were used in Harquahala basin (Figure 79). Historical and statewide public gravity data were provided by the Arizona Department of Water Resources (ADWR; 2022) who maintains the regional dataset compilation derived from the Pan-American Center for Earth and Environmental Studies dataset (PACES 2016). A basin-wide gravity survey of Harquahala was conducted in 2008 but was unpublished (HGI 2009). The Complete Bougier Anomaly (CBA) gravity values from all datasets in conjunction with well, modeled DTB, and seismic data were used to identify geologic structures, anomalies, and data gaps.

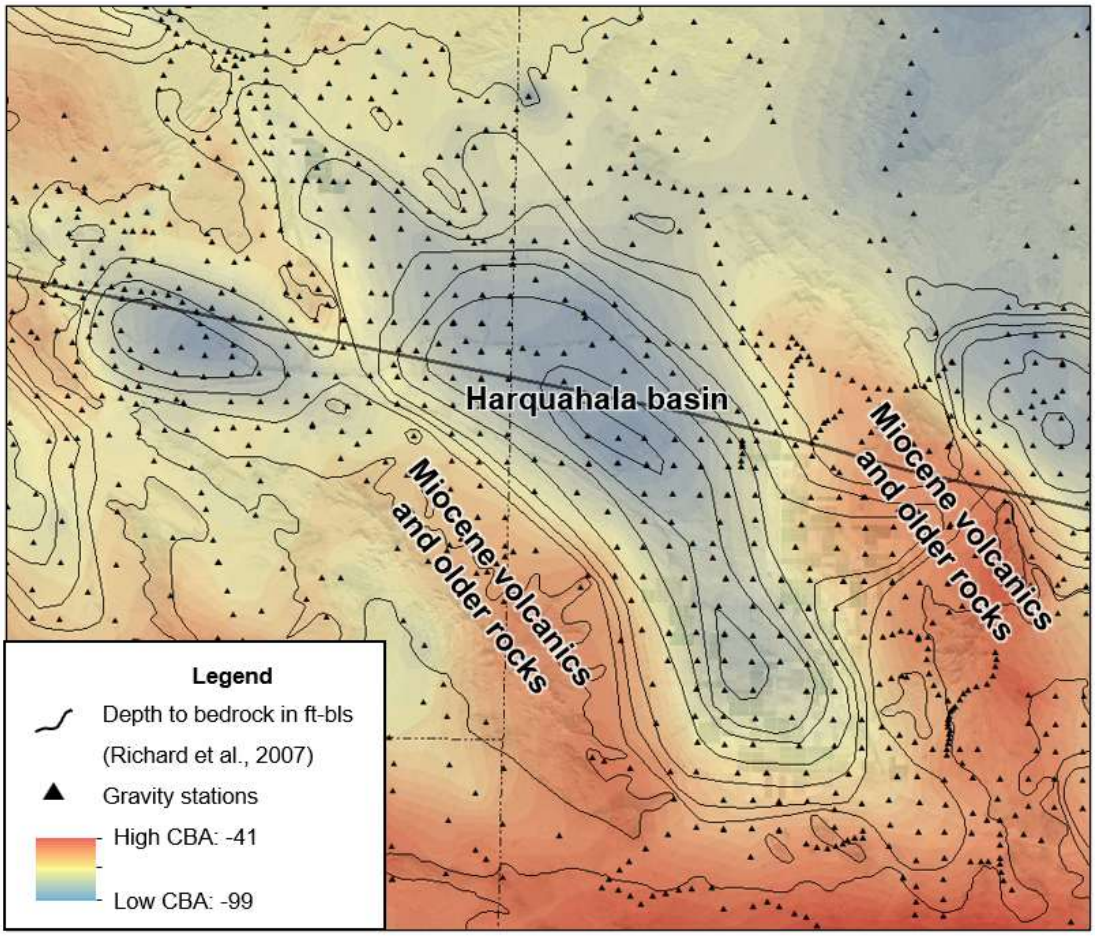


Figure 79 Map of gravity, depth-to-bedrock contours (Richard et al. 2007), and modeled CBA gravity data used in this study. Gravity point data are compiled from three separate sources (ADWR 2004, 2022; HGI 2009). Colored basemap is interpolated from Complete Bouguer Anomaly (CBA) low (blue) to high (red) values.

Depth-to-Bedrock Contours

Depth-to-bedrock data used at the start of this study were derived from a statewide DTB contour map modeled from gravity data and a limited number of borehole control points (Richard et al. 2007; Figure 79). In that report, bedrock is defined as crystalline basement overlain by clastic and volcaniclastic rocks, the same definition we use in this report. Of note, the HGI gravity study (HGI 2009) was not included in the (Richard et al. 2007) compilation.

The 2007 DTB contours were modified stepwise using detailed geologic maps, recent borehole lithology logs, and results from reprocessed vintage seismic data. Modification of DTB lines in this study were based on the hierarchy of data sources, from most confident to least confident, is as follows: (1) geologic mapping, (2) borehole lithology logs, (3) reprocessed 2D seismic lines, and (4) gravity. Data sources for DTB contour modification are listed for each contour line in the geodatabase.

ADWR wellbore logs are of generally poor quality (specific rock types may not be mentioned or may be too generally categorized; Appendix B), which prompted an in-depth quality review of adjacent wellbore logs and their relationship to geologic mapping and known geophysical data. Wellbore logs that did not correspond with two or more other datasets were not used. Basin margin contour shapes below 122 m (400 ft) were most affected by the well log review, while basin center contours were largely unaffected (due to the lack of deep borehole data). Well terminations in granite or crystalline volcanic rock overlying granite were considered bedrock penetrations. Green dots indicate reprocessed shot points included in this analysis.

Basin Fill Storage Volume Calculations

Basin fill volume between the 2D areal extent of the 800 m depth contour and the depth to bedrock was calculated using Esri ArcMap geoprocessing tools. Volume estimations rely on gravity and seismic data and interpretations of those data. Thus, they are first order estimates of potential basin fill storage volumes below 800 meters depth and above crystalline bedrock. In these estimates, basin fill is not distinguished by lithology (i.e., clastic sedimentary, chemical sedimentary, and volcanic rocks are lumped together); however, we do assume that the basin centers consist of fine-grained clastic sediment and some percent evaporite bedding, and possible interbedded volcanic rocks, and a range of physical parameters, such porosity and permeability, commonly associated with those lithologies. Carbon dioxide injection volumes are based on these physical dimensions and used in three separate methods to calculate gross and net injection volume capacity and volumes over a 5-year period. These methods are described along with results in section 6b.

Isopach Maps

Reprocessed seismic data revealed acoustic differences within the basin fill, which gave rise to an interpretation of distinct stratigraphic units and seismic zones delineated by seismic fabric. Stratigraphic picks for top and bottom of basin fill units, and an acoustically transparent zone within the lower basin fill, were determined at each seismic shot point along TR9, PW23, PW24, and PW22 in Harquahala basin. Depths were converted to elevation and used to create contour maps of the surfaces. Contour maps were converted into raster data and later used to create isopach maps (maps of thickness) for the upper and lower basin fill units, and acoustically transparent zone in Harquahala basin.

Geologic Cross-Sections

Five geologic cross-sections were created along or adjacent to the 2D seismic lines (Figure 79). Profiles were created along each line by combining a surface digital elevation model (DEM) and DTB contours. Well lithology logs from wells located within 3,000 m of the profile were projected vertically onto each cross-section line. In areas where wells were clustered, rendering

them unreadable on the profile, the well(s) located further away were removed for clarity. Basin fill unit boundaries, extent of each seismic line, extent of probable salt, and the location of faults as interpreted from seismic data were also projected onto the cross sections. The interpreted seismic lines are displayed next to their corresponding profile (see Plate 3, Wilson et al. 2024).

Lithofacies Maps

Geologic mapping of bedrock units exposed at the surface surrounding the Harquahala basin was used to predict what lithology or lithofacies would be encountered through drilling the upper few thousand feet of basin fill. The geometry of the modern watershed that supplied sediment to Harquahala basin during upper basin fill time is assumed to be consistent over the last approximately 5 Myr due to the absence of tectonism and/or major drainage reorganization. Smaller watersheds within the basin watershed, or subsheds, are also assumed to be relatively consistent.

The basin's asymmetrical geometry and location of paleodepositional centers identified in down-dip seismic reflectors were used to create paleodepositional boundaries or subsheds in the subsurface. Watershed maps were derived from the USGS Watershed Boundary Dataset (WBD). The simplified geologic map compilation (described in section 3a) was used to calculate the area of geologic map units in the basin. Geologic map units were clipped to subsheds. Areas of each map unit within each subshed were exported into Excel. Map units were lumped into broad lithologic categories (e.g., plutonic, metamorphic, volcanic, etc.) and relative percent of each lithologic category plotted for each subshed.

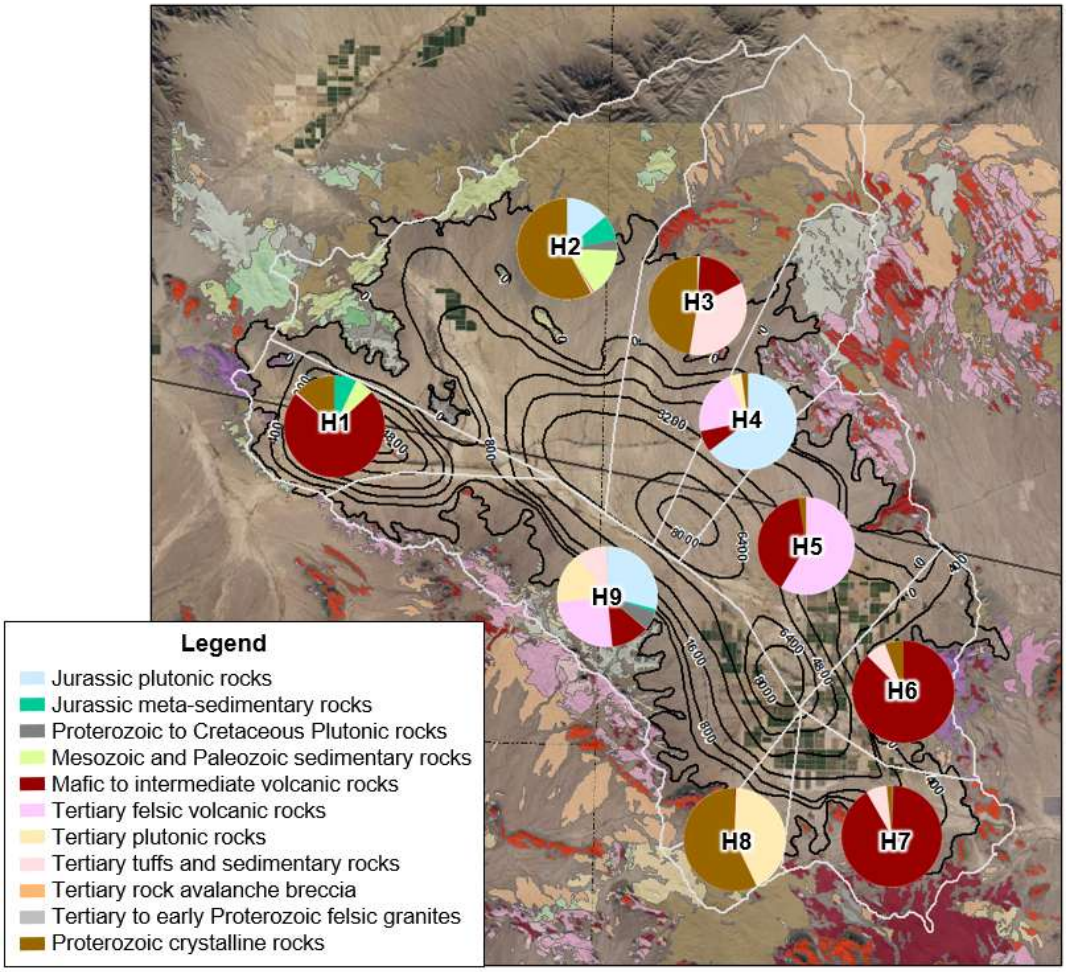


Figure 80 Lithofacies prediction map showing the percentage of rock types expected in upper basin fill based on watershed and subshed boundaries within Harquahala basin

Well Borehole Temperatures

Publicly available borehole temperature data in Harquahala basin was compiled, reviewed, and analyzed. Reported temperatures and well depths for 157 wells in Harquahala basin (Witcher 1995) are plotted in Figure 81. Overall, the quality of the data is highly variable, and data collection methods were not standardized. The borehole temperature sample depth and time collected, as well as the screened intervals sampled, are unknown. Borehole temperature data was plotted and symbolized by a color gradient representing temperature and constrained by discrete depth ranges to look for any spatial trends.

Geothermal gradients were calculated from wellbore temperatures by subtracting the bottom-hole temperature from the mean annual surface ground temperature at the well site and dividing by well depth. The mean annual surface ground temperature used for both basins was 21.1°C (70°F). This calculation yielded values between 6°C/km and 438°C/km, with many values outside of the expected range of geothermal gradients. This may be due to reporting errors of the wellbore temperature values. The worldwide average geothermal gradients are from 24°C/km to 41°C/km (1.3°F/100 ft to 2.2°F/100 ft; Peters et al. 2012). Data outside of this range was omitted

in the analysis, which brought the well count from 201 to 101 wells with reasonable calculated geothermal gradient values (Appendix C).

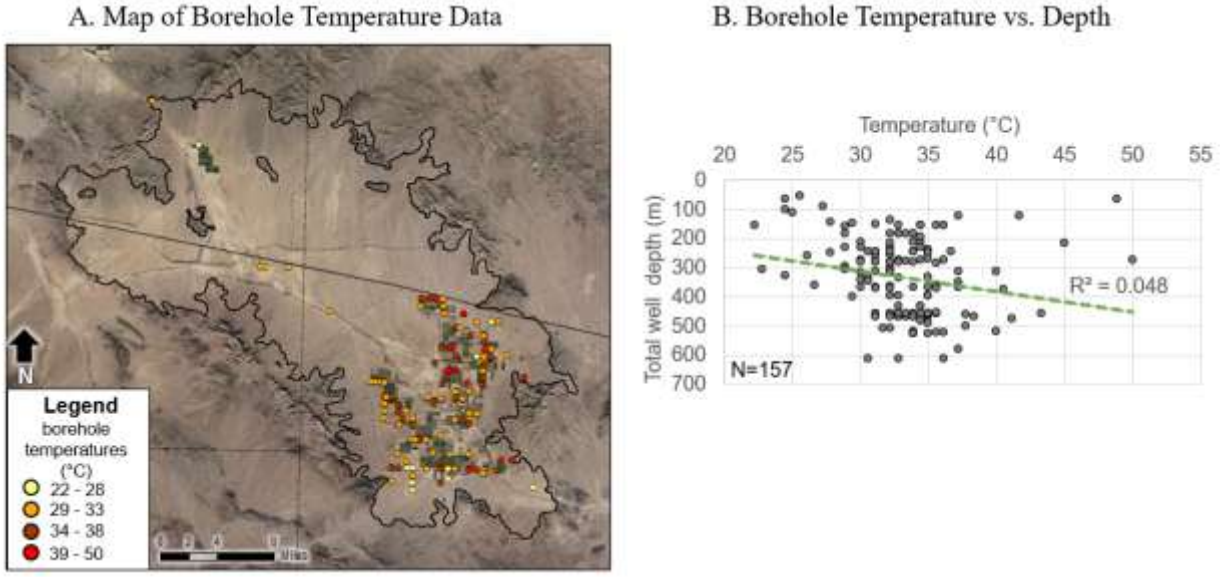


Figure 81 Borehole temperature data (A) Map displaying borehole temperatures colored by specific temperature ranges. (B) Scatter plot of temperature vs. depth for Harquahala basin. Trend lines shown in green with R2 values. Wells with depth listed as 0 were removed.

Groundwater Total Dissolved Solids (TDS)

We compiled a total of 453 wells with publicly available groundwater salinity and conductivity data in Harquahala basin (Appendix D). Of these, 51 shallow wells included direct measurements of total dissolved solids (TDS; Towne 2014). The remainder of well data lacked direct TDS values, though they did have conductivity measurements which we used as a proxy for TDS. The reported TDS value was retained where water quality records reported both TDS and conductivity values.

Conductivity values were converted to equivalent TDS values using the equation

TDS (mg/L) = k * EC (µS/cm),

where "k" is the conversion factor and EC is electrical conductivity. Wells that had both TDS and conductivity measurements (n=51) were used to determine an average conversion factor of 0.64 (range = 0.59 to 0.69). For comparison, previous work reporting statewide salinity used a conversion factor of 0.642 (Gootee et al. 2012). Figure 82 is a scatterplot of groundwater salinity vs. well depth for Harquahala basin.

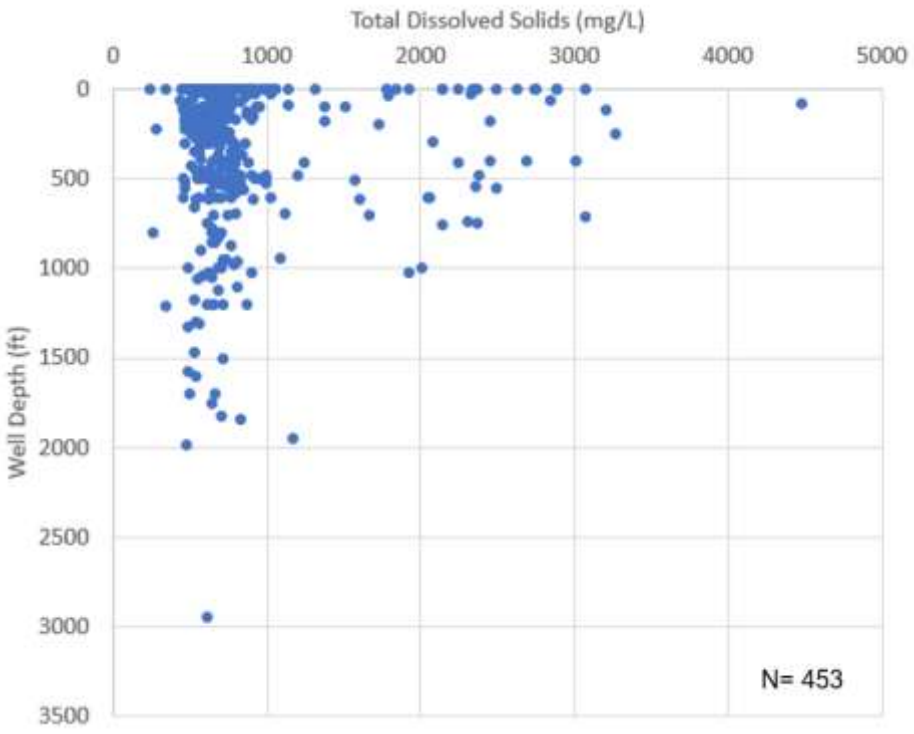


Figure 82 Groundwater salinity from wells. Scatter plot of groundwater salinity as total dissolved solids (TDS) vs. borehole depth for water wells in Harquahala basin. No trend between TDS and depth is observed.

Geologic Characterization

Conceptual Model for Basin Formation

The geology of Harquahala basin can be broadly described with a conceptual model that integrates commonalities in geologic structure and stratigraphic architecture across the Arizona Basin and Range Province (Eberly and Stanley 1978; Menges and Pearthree 1989; Spencer and Reynolds 1989).

About 30 Ma, tectonic extension in southeastern, southern, and western Arizona began to fracture, fault, and pull apart older rocks that composed Earth's crust. Through distributed low-angle normal faulting, the crust thinned, and large, linear fault blocks were uplifted to form subparallel mountain ranges. The space between those ranges gradually increased and deepened with each additional earthquake. Mountain ranges were separated by largely asymmetrical, deep sedimentary basins into which water and sediment from the surrounding mountain ranges collected over millions of years (Figure 83).

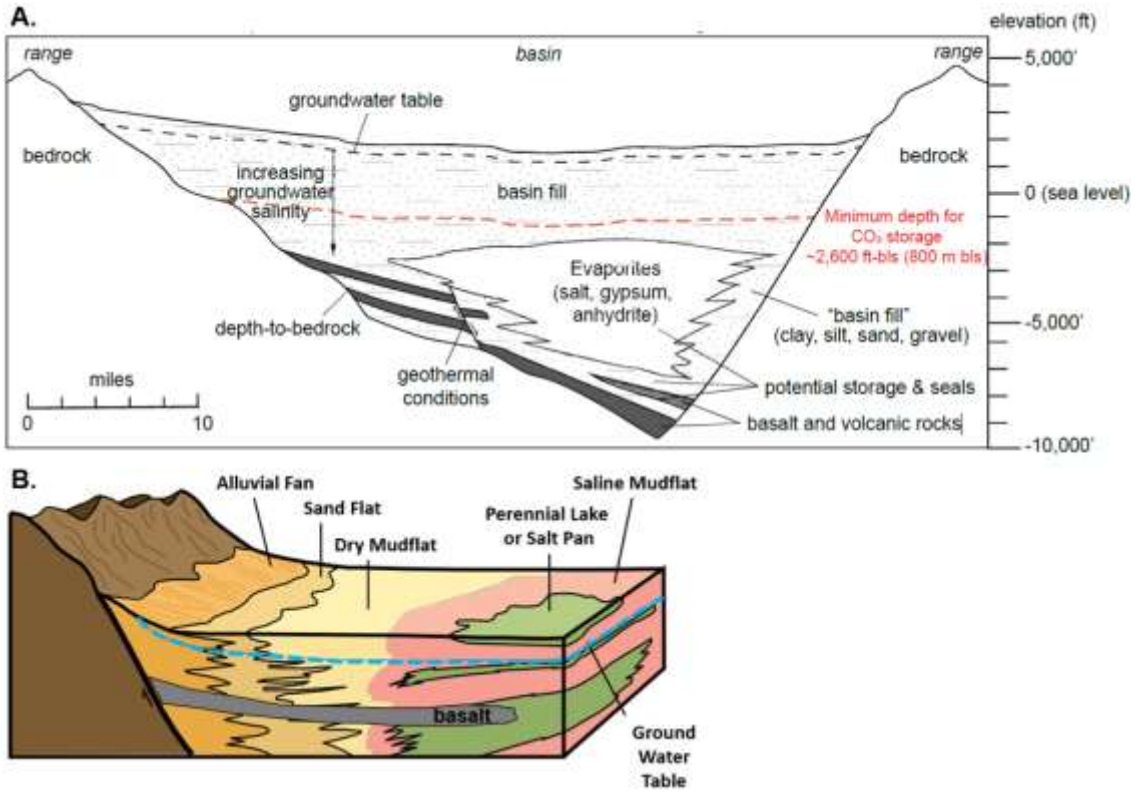


Figure 83 (A) General geologic cross section of Harquahala basin showing distribution of basin fill features and lithology. (B) Block model of depositional environments of basin fill. Modified after Faulds et al. (2016).

Early in the basin extension process between about 25 to 15 Ma, coarse sediments were concentrated near steep basin margins close to their mountain provenance and fine sediments were concentrated near sub-horizontal depositional centers where water likely ponded. The climate was semi-arid and favorable to both periods of water accumulation (forming shallow playa lakes) and extended periods of drought (water evaporation) which, in the case of closed basins, resulted in the formation of bedded evaporite deposits fed primarily by shallow groundwater high in dissolved solids within the basin center or subbasin centers (Figure 83). Deposition of these basin-fill facies were punctuated by continued crustal extension and widespread volcanic eruptions that deposited lava flows, ash, and pumice directly on crystalline bedrock-cored mountain ranges and interlayered with basin fill sediments. Continued extension during this phase accumulated thousands of feet of basin fill deposits before tectonism waned. As a result, older basin fill and interbedded volcanic deposits are progressively tilted, faulted, and compacted with depth.

Beginning about 6 to 5 Ma, extension and faulting waned while passive erosion and deposition dominated within the closed basins. These deposits are generally horizontal, less compacted and nondeformed compared to older basin fill sequences. Basin-filling continued in depocenters in a closed basin, generally fining grain sizes up section, as piedmonts backfilled bedrock topography near the base of mountain fronts. As a result, there are basin sedimentary packages with different structural histories: a lower, older sedimentary package that is tilted and faulted (during active extension) and an upper, younger sedimentary package that is generally undeformed (as extension waned; Figure 84).

Harquahala basin is mantled by a thin veneer of Pleistocene and Holocene (about 2.6 Ma to the present) alluvium that forms low-gradient piedmonts graded to the modern valley axial washes (Centennial Wash). Both axial wash systems are integrated with the Gila River about 2 miles downstream of the Hassayampa River's confluence with the Gila River. Integration timing is not known, but it likely occurred during the Pleistocene or latest Pliocene (5 to 2.6 Ma). This basin model is generally well understood in shallow basin fill and surficial exposures, although less understood in buried basin fill deposits below about 2,500-ft depth. Harquahala basin exhibits a similar extensional history, style of faulting, and depositional environments to other neighboring basins in southern Arizona.

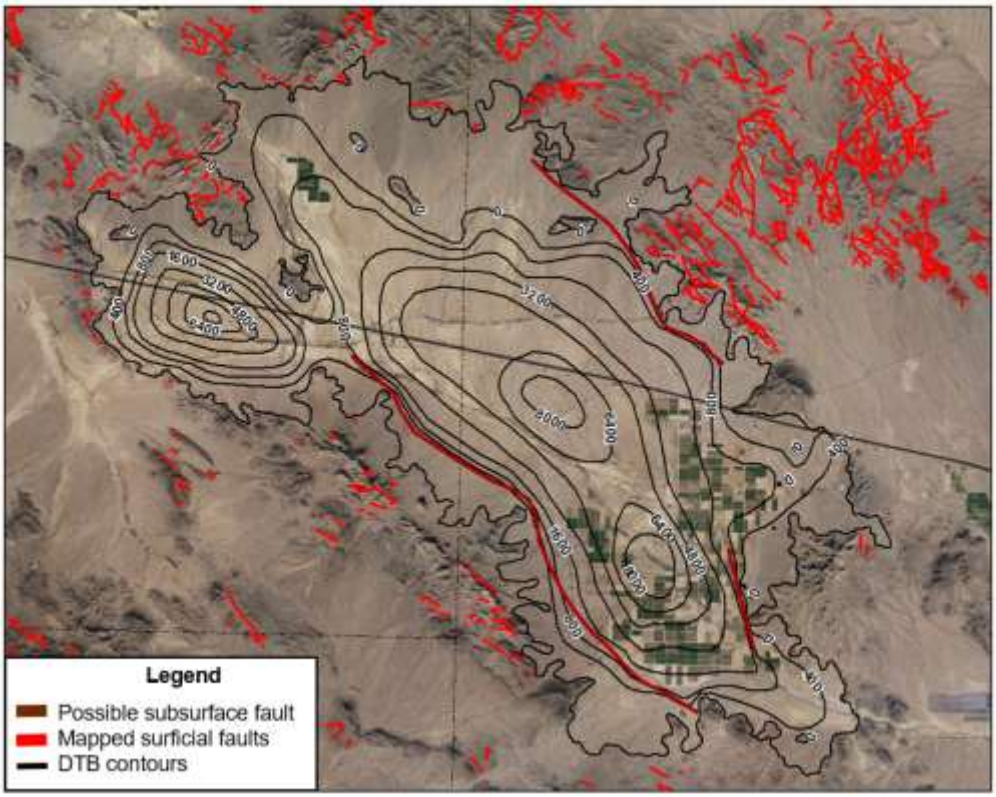


Figure 84 Map of fault traces exposed at the surface (bright red) and subsurface faults interpreted from seismic lines (brown).

Basin Geometry and Structure

Harquahala valley is surrounded by mountains composed of a diverse suite of Proterozoic crystalline igneous and metamorphic rocks, sparse outcrops of Paleozoic and Mesozoic sedimentary rocks, and Jurassic igneous and metasedimentary rocks, unconformably overlain by effusive and explosive products from Miocene volcanic eruptions (see Plate 2 , Wilson et al. 2024).

Harquahala basin is divided into three subbasins each separated by a subsurface structural high, as shown on the DTB contour map (see Plate 2, Wilson et al. 2024). The central subbasin is the deepest with a maximum depth of 2,538 m (8,326 ft) and the southern subbasin's maximum depth is 2,530 m (8,300 ft). The northwestern subbasin is isolated and smaller than the other two

with a maximum depth of 2,438 m (8,000 ft). Reprocessed 2D seismic data show the basin-bounding detachment fault is close to the southwest basin margin at the base of the NW–SE striking Eagletail Mountains (see Plate 3, Wilson et al. 2024; seismic line TR10b). As such, the deepest portion of the basin is adjacent and subparallel to that mountain range (Figure 85).

Stratigraphy

The stratigraphic architecture of basin fill in Harquahala basin is not well delineated due to lack of age constraints, few high-quality well records, and no deep well penetrations. However, basin fill could be divided into three units based on the character of the seismic reflection data and the conceptual model described in section 4a. Listed from oldest to youngest the stratigraphic packages are: lower reflective package (LRP), lower basin fill (LBF), and upper basin fill (UBF; Figure 85). Harquahala basin is not dissected, therefore all basin fill deposits are covered by Pleistocene and Holocene alluvium. Due to the lack of exposure and deep well penetrations, the porosity and permeability of each unit are unknown.

Lower Reflective Package (LRP)

The LRP, the oldest unit, is a strong reflective package and is likely comprised of interbedded lava flows and sedimentary rocks deposited directly on the crystalline basin floor (Figure 85; see Plate 3, Wilson et al. 2024, seismic lines TR9, PW22, PW23, PW24). This unit is distinguished solely through interpretations of strong, parallel, shallow-dipping seismic reflectors. The LRP is approximately 1,066 m (3,500 ft) thick near the basin center, although without velocity control the true thickness is not known and could be $\pm$ 20-30%. The apparent thickness increases to the southeast and decreases to the northwest. Extensive outcrops of early Miocene age volcanic rocks in the mountain ranges bordering Harquahala basin are evidence for widespread bimodal volcanism during early basin formation. Therefore, we suggest that the LRP is equivalent to those rocks in part by age, although contains a mix of clastic sediments interbedded with volcanic flows near now buried depocenters. The LRP may also include explosive centers or cauldrons as part of an upper-plate geometry within the Harquahala half-graben.

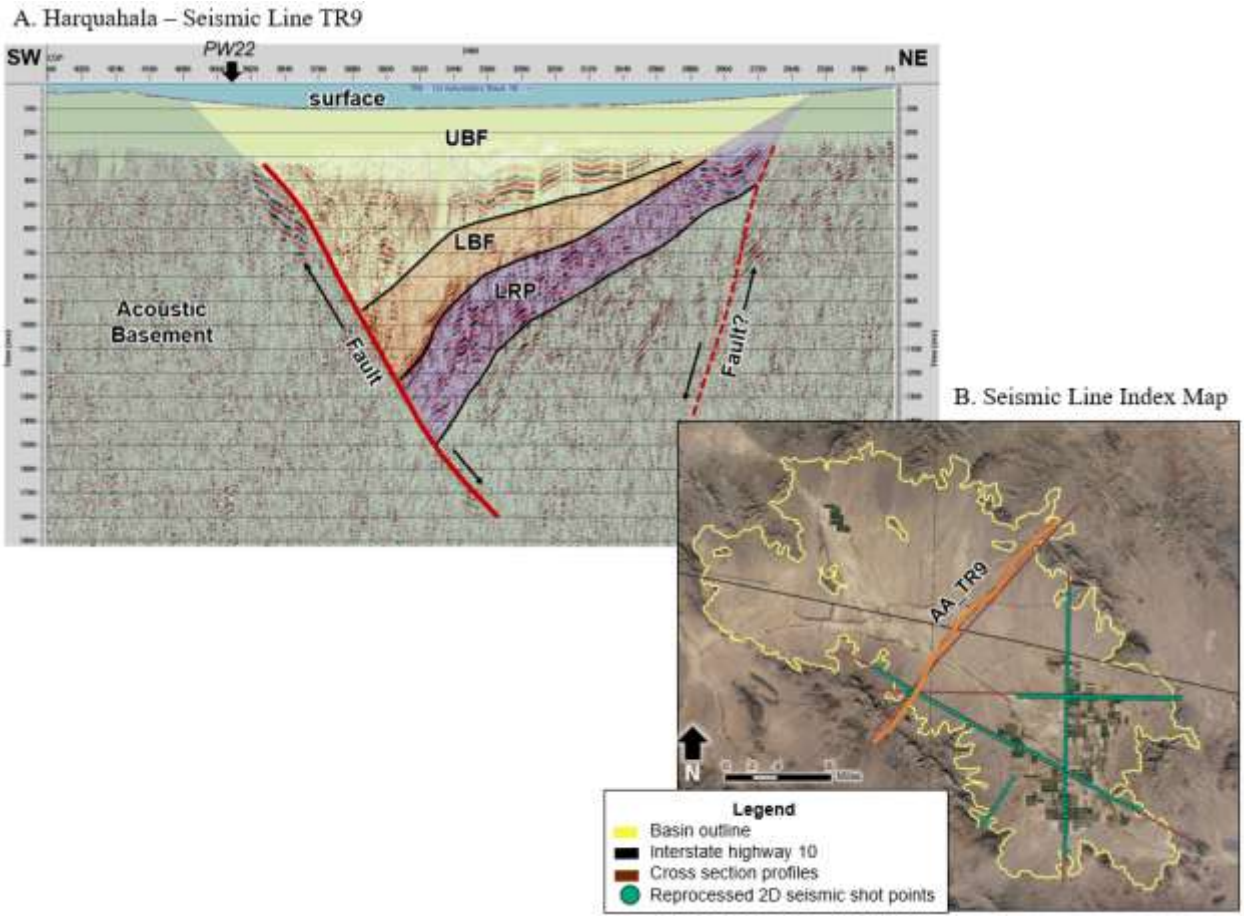


Figure 85 Examples of the basin fill units interpreted from the 2D seismic. (A) Seismic line TR9 is perpendicular to the basin axis in Harquahala basin and shows the seismic character of the lower reflective package (LRP), lower basin fill (LBF), and upper basin fill (UBF) units. (B) Index map of seismic lines.

Lower Basin Fill (LBF)

The LBF is a middle-aged sedimentary package defined by tilted and truncated seismic reflectors seen on all seismic lines (Figure 85; see Plate 3, Wilson et al. 2024). There are no direct measurements, such as borehole lithology logs, to characterize lower basin fill lithologies for Harquahala basin. Broadly, LBF is likely comprised of a wide range of clastic sediment sizes from clay to boulders sourced from nearby mountain ranges, and the package may contain interbedded mafic to intermediate lava flows and felsic explosive material. The areal extent and lateral continuity of deposits and grain size distribution is unknown; however, based on our conceptual model, coarse clastic deposits on the basin margin grade laterally down-gradient into finer sediments near basin centers. Potential capping rocks such as extensive clay deposits or evaporite deposits, if present, should be located near basin centers.

In Harquahala basin, the LBF is a maximum of 975 m (3,200 ft) thick and overlies the LRP. Seismic reflectors suggest individual LBF blocks are cut and tilted by several high-angle normal faults. The LBF isopach map in Harquahala basin (Figure 86) represents the gross thickness of rock between the LRP and UBF units and highlights three subbasins: the northwest subbasin

with a maximum thickness of 785 m (2,575 ft), southern subbasin with a maximum thickness of 722 m (2,368 ft), and the central subbasin where LBF is thickest at 975 m (3,200 ft).

The LBF includes an acoustically transparent zone (ATZ) which is defined as an area of dim amplitude reflectors. The ATZ is interpreted to consist of bedded evaporite deposits based on similar, tested, ATZ's in proxy basins (Eberly and Stanley 1978) and predictions from the conceptual basin formation model (section 4a). Although the type of evaporite minerals present in Harquahala basin is not directly known, poorly reflective and chaotic-to-weak amplitudes, are indicators of halite-rich bodies (Teixeira et al. 2020). The composition of evaporite deposits in proxy basins also include significant halite – the evaporites in Luke basin are halite and Picacho basin is composed of anhydrite with lesser bedded halite (Neal and Rauzi 1996).

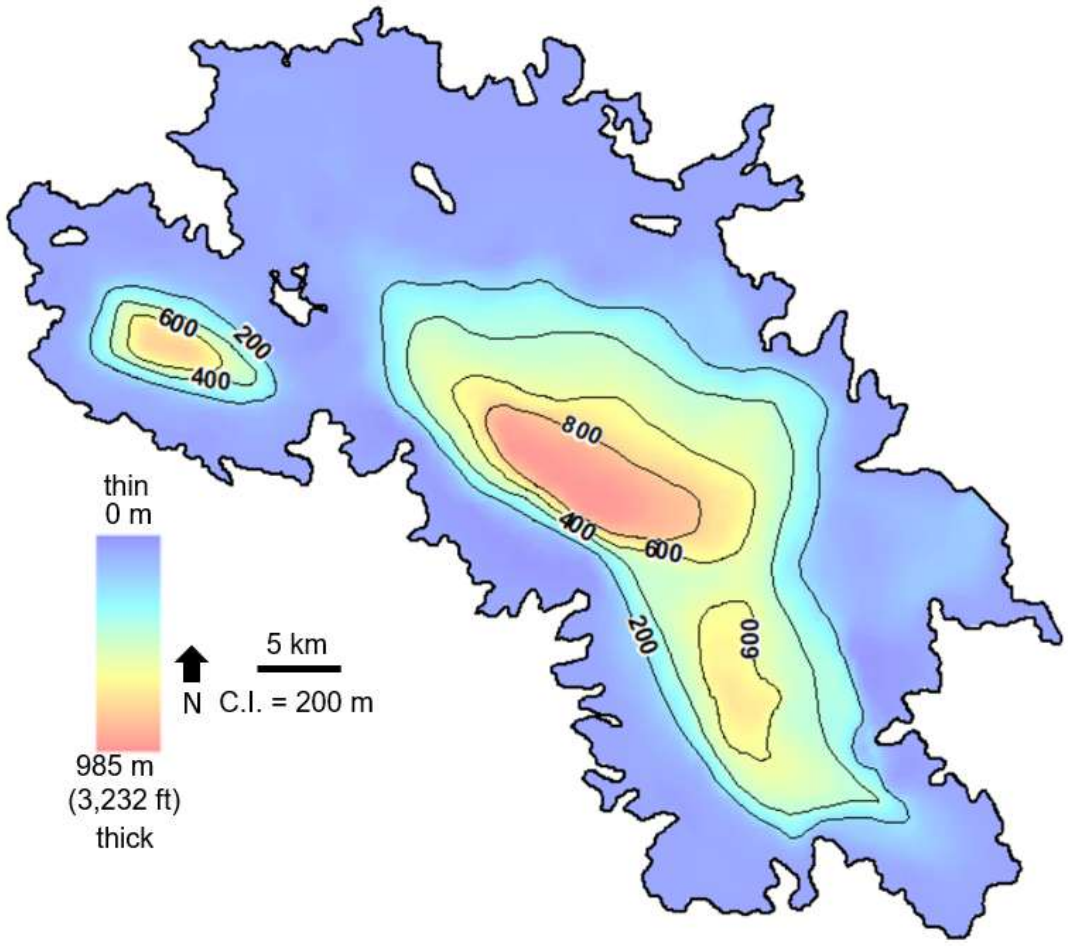


Figure 86 Isopach map of lower basin fill in Harquahala basin created by subtracting the base upper basin fill (UBF) elevation (m) grid by the base lower basin fill (LBF) elevation (m) grid

The acoustically transparent zone is observed on lines TR9 and PW23 in Harquahala basin. An approximate thickness across the zone was calculated using the difference of the travel time (ms) between the top and bottom of the seismic facies (converted to seconds) and multiplied by14,500 ft/s (the proxy evaporite velocity from sonic logs in Picacho and Luke basins). The areal extent and maximum thickness of the ATZ in Harquahala basin is 180 km^2 (112 mi^2) and 610 m (2,000 ft). Isopach maps of the ATZ show their extents are generally located adjacent to basin

depocenters (Figure 87), which may represent the extensive, and shallow salt pan environment as seen on the depositional environment block model (Figure 84). Additionally, subbasins likely migrated slightly over time which may explain why the ATZ polygon does not match the deepest parts of the subbasins. Higher resolution data is needed to better delineate ATZ extents.

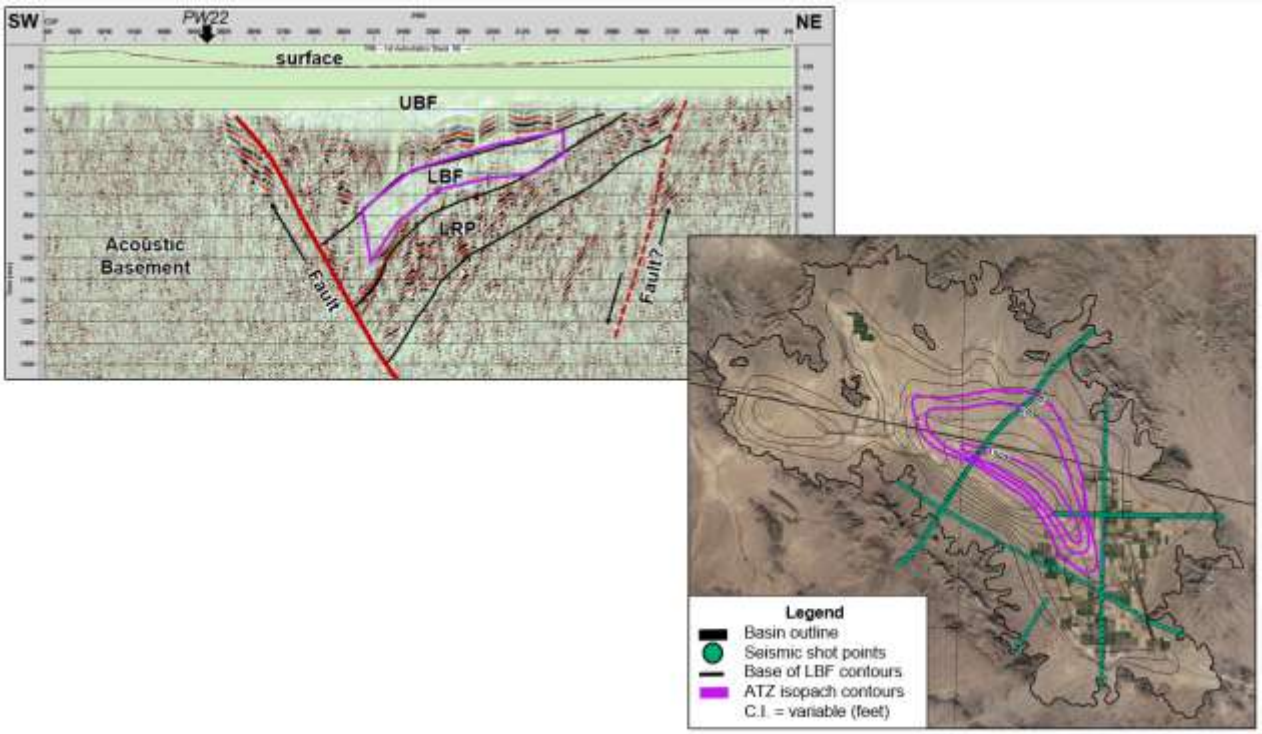


Figure 87 Seismic line TR9 with the mapped ATZ outlined in purple. Isopach map of the acoustic transparent zone (ATZ) in Harquahala basin.

Upper Basin Fill (UBF)

The youngest unit defined in this study is the upper basin fill (UBF). It is characterized by combining the conceptual basin model, proxy studies from nearby basins, well lithology logs, and lateral predictions from bedrock and surficial geologic mapping. In both basins, the UBF is relatively nondeformed (not faulted, folded, or tilted), extends to basin margins, and unconformably overlies the LBF (Figure 85). Like the LBF, the UBF is composed of clastic sediments ranging in size from clay to boulders and grain size is dependent on distance from the basin-bounding mountain ranges. At the time UBF was deposited, Basin and Range extension and volcanism was waning, therefore the UBF likely has little or no primary volcanic deposits.

The isopach map of UBF in Harquahala basin shows two distinct subbasins, the northwestern subbasin with a maximum thickness of 530 m (1,740 ft) and the central subbasin with a maximum thickness of 820 m (2,690 ft; Figure 13A).

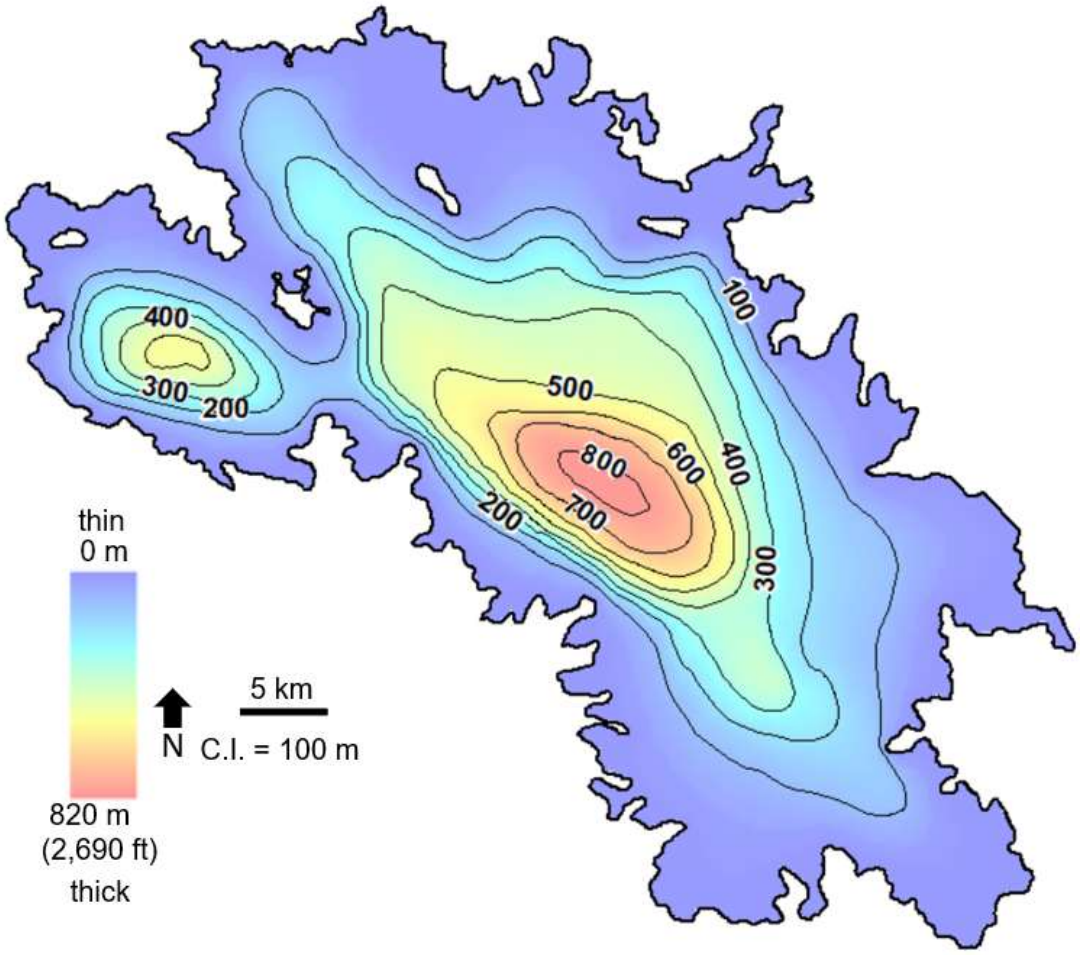


Figure 88 Isopach map of upper basin fill unit in Harquahala basin by subtracting the surface digital elevation model (DEM) grid by the base upper basin fill (UBF) elevation (m) grid

Geothermal Gradient

Hot dry crystalline rock is close to the surface in the Basin and Range Province due to millions of years of extension/faulting resulting in high heat flow (Figure 89A). Small-scale national geothermal studies of heat flow (Mullane et al. 2017; Witcher 1995) show the state of Arizona has moderate geothermal potential (Sass et al. 1994; Figure 89B).

Borehole temperature data in Harquahala basin are sparse and they show no distinct spatial trends. Measured temperatures in 84 wells that penetrate upper basin fill to the shallow depth of 611 m (2,005 ft) average 91°F (33°C). The calculated mean geothermal gradients to shallow well terminations are 87°F/mi (30.6°C/km) for Harquahala basin. These gradients are comparable to the published mean geothermal gradient for the southern Basin and Range Province of 30°C/km (Nathenson and Guffanti 1988).

Geothermal gradients for the entire basin depth cannot be directly calculated because there are no deep borehole logs. Estimates can be made, however, using two nearby proxy basins: Luke basin at 78.8°F/mi (26°C/km) with a maximum well depth of 550 m (1,804 ft) and Higley basin at 104°F/mi (40°C/km) with a maximum well depth of 2,780 m (9,118 ft). In general, geothermal

gradient is dependent on crustal thickness. Thick basin fill that overlies thinner crust (at basin centers) is expected to have a higher geothermal gradient because there is less mantle-derived heat loss within that crust. Conversely, thin basin fill that overlies thick crust (at basin margins) is expected to have a lower geothermal gradient because mantle-derived heat is widely dissipated within that crust. Additional data acquisition is required to better characterize basin heat flow and borehole temperature heterogeneity.

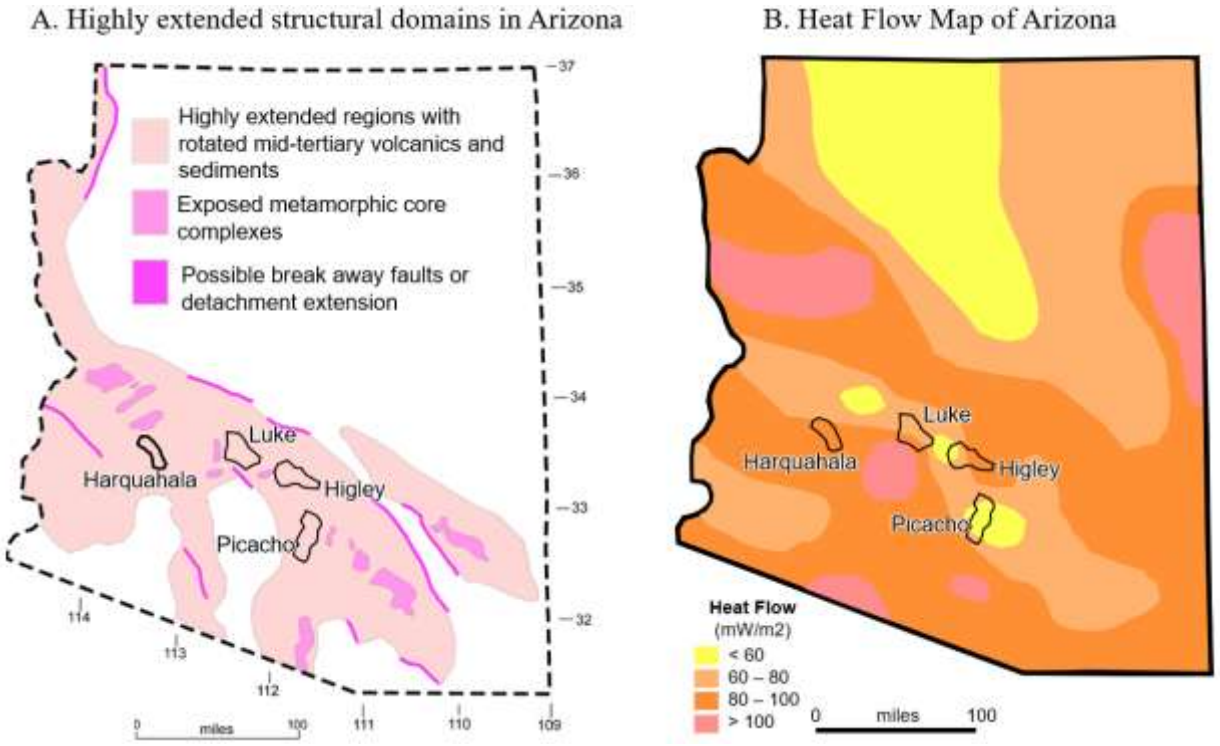


Figure 89 Map of extended crust and heat flow in Arizona (A) Map of highly extended structural domains throughout Arizona. Modified after a 2018 presentation by Witcher, originally from Spencer and Reynolds (1989). (B) Map of heat flow throughout Arizona modified after a 2018 presentation by Witcher, originally from Sass et al. (1994).

Groundwater Salinity

The U.S. Environmental Protection Agency (EPA) defines a non-potable water resource as greater than 10,000 milligrams per liter (mg/L) of total dissolved solids (TDS). Several basins in south-central Arizona have brackish, saline and hypersaline groundwater at depths generally greater than 2,500 ft (Gootee et al. 2012). Due to the lack of salinity data below 2,000 ft in Harquahala basin, we refer to proxy basins for comparison.

Figure 90 shows TDS values exceed approximately 90,000 mg/L for three proxy basins with deep well data: Luke basin, Higley basin, and Picacho basin. Measured TDS values for Harquahala basin are below the 10,000-ppm limit, but those data are limited to wells shallower than approximately 1,000 ft. Deep TDS values cannot be extracted from shallower data because the data do not trend linearly due to factors such as groundwater mixing from mountain-front recharge, mixing with deeper groundwater and recharge from agricultural uses. The basin is structurally and hydrologically isolated with deep (>5,000 ft) basin centers, and likely bedded

evaporite deposits. Given this, the potential for elevated TDS concentrations at depths greater than approximately 2,500 ft is anticipated. Additional water sampling and temperature measurements at depth are required to give a more accurate and complete assessment.

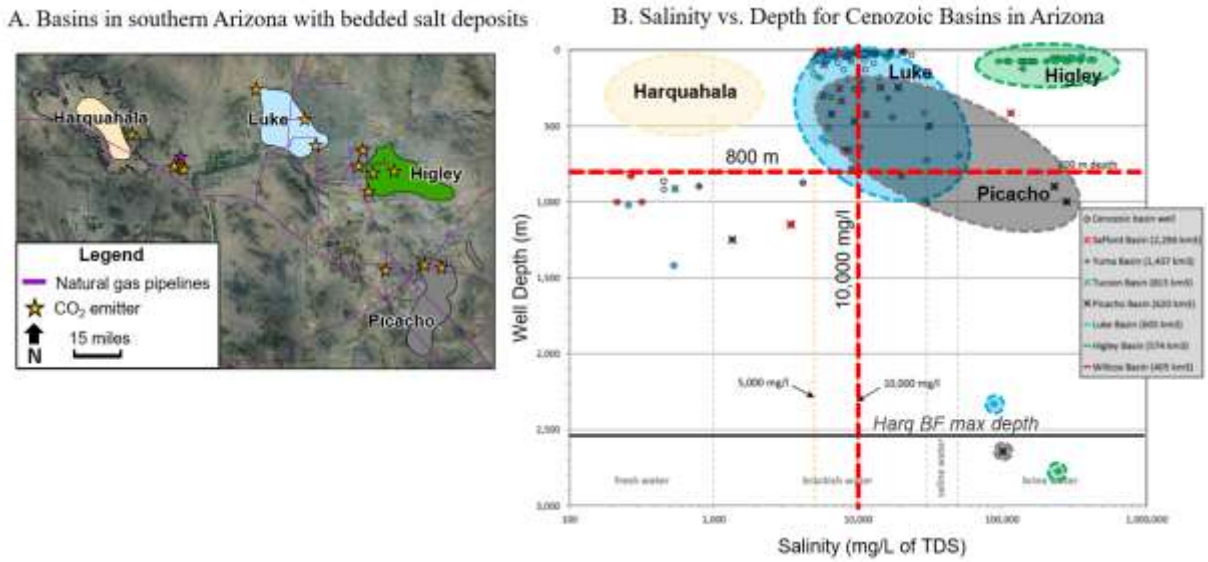


Figure 90 Bedded salt and groundwater salinity in southern Arizona (A) Location map of salt-bearing basins of interest in south-central Arizona colored to match fields shown in 16B. (B) Scatter plot of salinity vs. well depth for salt-bearing basins of interest, modified after Gootee et al. (2012). Each basin has a colored data cloud for comparison. Red dashed lines represent the salinity and depth cut offs. Black lines represent maximum basin fill depths for each basin.

Analysis and Discussion

Storage Reservoirs

Parameters necessary for a suitable carbon capture and storage (CCS) reservoir include sufficient lithostatic pressure of around 800 m depth (about 20 MPa pressure), groundwater salinity at or greater than 10,000 ppm TDS limit set by EPA, below viable underground sources of drinking water (USDW), reservoir pore space volume and permeability, and a seal or caprock above the reservoir. The types of CCS reservoirs applicable in this region would be stacked saline, mafic rocks, and geothermal. Potential seals would include claystones and bedded evaporites. A stacked saline reservoir with fine-grained clastic and bedded evaporite capping layer(s) are highly probable in Harquahala. Bedded evaporite deposits and basalt lava flows are likely but not directly measured. Storage reservoir types stated herein are each 800 m (2,624 ft) below the land surface, where lithostatic pressure is sufficient to retain CO_2 in a supercritical state, assuming regional pressure and temperature conditions.

Stacked Saline Formations

Stacked saline reservoirs are comprised of permeable clastic and chemical sedimentary rocks with saline pore water and represent the most likely and abundant type of storage by volume. The stacked saline reservoir in Harquahala basin includes both the lower reflective package (LRP) and the lower basin fill (LBF), which can also include stacked volcaniclastic and mixed

volcanic and sedimentary rocks. Together these stratigraphic units occupy a total gross volume of 396 km^3 (95 mi^3): LRP = 304 km^3 (73 mi^3) and LBF = 92 km^3 (22 mi^3). Reported volumes include rock volume and pore space. Capping or sealing stratigraphic units cannot be identified with available data. However, evaporite deposits, fine-grained siliciclastics such as clay beds, and some weathered basalt lava flows, can provide sealing conditions and are likely present in Harquahala basin based on predictions from the basin's geologic history and regional geologic map units.

Bedded Evaporite Deposits

The presence of bedded evaporites is likely based on nearby proxy basins with similar tectonic histories and tested evaporite deposits. Bedded evaporites in Harquahala basin are strongly supported by proprietary isostatic residual gravity anomaly maps and seismic patterns/fabrics observed and interpreted from 2D seismic lines in this study.

The nearby Picacho and Luke sedimentary basins, which have the same geologic history as our basin of interest, have proven salt deposits. Picacho basin, approximately 90 mi SE of Harquahala basin, has evaporite facies at depth confirmed by wireline electric logs and whole rock core. The Luke basin contains a large salt body that has been developed and used to safely store liquid natural gas since the early 1970s. The Luke basin salt deposit is characterized by gravity anomaly maps (Richard et al. 2007) and seismic data (Eberly and Stanley 1978) which have also highlighted the potential salt presence in Harquahala basin.

The acoustically transparent zone (ATZ) imaged from seismic facies likely represents a bedded evaporite deposit or interval and is present in Harquahala basin. The ATZ is defined by areas of dim amplitude reflectors. The areal extent and thickness are shown on Figure 86. The location and extent of this facies is limited by the quality of the 2D seismic lines, and it may be present elsewhere, where resolution is poor, or data is absent.

Basalt Flows

Liquified CO_2 can be reacted with buried magnesium- and iron-rich mafic rocks in situ to form a solid precipitate, permanently storing it (Raza et al. 2022). This chemical reaction takes place on short timescales ranging from hours to a few years, and the reaction is accelerated with greater exposed surface area (i.e., vesicular basalt, volcaniclastic particles, and joint surfaces). During crustal extension and formation of Harquahala basin, mafic (basaltic) volcanism was widespread and long-lived. Basalt lava flows cap bedrock in basin-bounding mountain ranges, and (at least) one large volcanic vent (Saddle Mountain) divides Harquahala and Tonopah basin to the east (see Plate 2, Wilson et al. 2024). Mafic volcanic rocks are logged in shallow wells along the basin margins (see Plate 3, Wilson et al. 2024) and lithofacies mapping predicts mafic volcanic rocks are the dominant source terrain for basin fill in the southern Harquahala basin (Figure 80). Inselbergs of basaltic flows exposed on basin margins are surrounded by young basin fill, suggesting some likelihood that these flows are interbedded with a part of basin fill. The LRP in Harquahala basin is likely comprised of volcanic flows interbedded with sedimentary rock, which may present additional basaltic storage reservoirs combined with interbeds capable of trapping CO_2 long enough to mineralize into solid carbonate minerals.

Volume Estimates of Basin Fill and CO_2 Storage

Basin Fill Sediment Volumes

Storage volume estimates are theoretical and not based on direct measurements in the Harquahala basin. Isopach maps were created to calculate the total rock volume of the stratigraphic units present. Without deep borehole lithologic and rock property logs, we assigned mean matrix porosity values derived from our interpretations of basin stratigraphy and regional proxy data from other deep sedimentary basins (Gootee 2013a, 2013b, 2015). Fracture porosity, spacing, and density was not considered in our study. Storage volumes for CO_2 mineralization in basalts were not estimated. This technique is relatively new and there are too many unknowns at this stage to achieve a reasonable estimate.

To estimate net pore space for CO_2 storage, the area of each basin fill unit and maximum thickness were calculated from isopach maps presented in section 4. The average thickness of basin fill below 800 m depth was used to calculate first-order gross volume. The UBF lies above the 800 m depth requirement for CO_2 storage, so it is not considered in the storage volume calculations. Table 3 summarizes the area, max thickness, and gross sediment volume for each basin-fill unit in Harquahala basin.

Table 3. Physical dimensions of area, thickness, and volume for basin fill units in Harquahala basin. Italicized physical parameters below 800 m depth were used in CO_2 volume analysis.

	Basin-fill units	Area (km2)	Max thickness (m)	Average thickness (m)	Gross volume (km3)
Harquahala basin	UBF	1,380	820	--	248
	LBF	1,380	975	--	92
	ATZ	185	610	--	unknown
	LRP	unknown	1,490	--	304
	below 800 m	*327*	*1,740*	*848*	*269*
	total basin fill	1,380	2,540	--	644

Other Physical Parameters

Basin fill units in Harquahala are suitable reservoirs for supercritical CO_2 storage because they likely contain permeable and porous strata under confined to semi-confined conditions in saline to hypersaline aquifers below 800 m depth. The LBF is likely composed of evaporite minerals, mixed with some fine gravel, sand, silt and possibly extensive clay, characteristic of basin fill in the region at these depths (Gootee 2015). The LRP, which underlies the LBF, is likely composed of volcanic and sedimentary rocks. A gross volume of porous rock was estimated based on these lithologies and their porosity contributions. For example, sandstone, fine gravel and volcanic lithofacies would contribute to porous and permeable strata, whereas clay and evaporites would serve as sealing strata. The percentage of the porous lithofacies was estimated based upon the conceptional basin model presented in Figure 80. In both basins, we estimate between 30% and 70% of basin fill have porous and permeable sediment suitable for CO_2 storage, thus we used the

50% median or net-to-gross ratio of 0.5. The porosity of sandstone and gravel range from 40% to 15%; we used an average porosity of 25%, excluding porosity-reduced compaction with increased depth. An effective available porosity (specific yield) between 10% and 30% was considered, based on data from general physical character of sand and fine gravel (Walton 1970), although these estimates do not take cementation into consideration. A conservative effective porosity of 15% was used, derived primarily from numerical groundwater models of older basin fill strata in nearby McMullen basin (Gootee and Noel 2015) and Phoenix basins (ADWR 2006).

The density of supercritical CO_2 at an approximate depth, temperature and pressure for supercritical CO_2 storage is based on modeled datasets (Pan et al. 2017). The temperature of the reservoir was based on scant oil and gas well data in this region, and from the geothermal gradient discussed in section 4. A summary of physical parameters and their standard deviations used to calculate volumes are listed in Table 4. All volume data, other factors, coefficients, and calculations are listed in Appendix G.

Table 4. Physical parameters of basin fill used to calculate CO_2 injection volumes.

Parameter	Units	Harquahala	Standard deviation
Area, A	km2	327	0.1
Gross thickness	m	848	0.2
Porosity, Φ	frac.	0.15	0.05
Net-To-Gross Ratio, NGR	frac.	0.5	0.25
Efficiency Factor	frac.	0.2	0.1
Density of CO_2	kg/m3	650	--
Reservoir temperature	C	75	10
Reservoir pressure	MPa	20	3

CO_2 Storage Volume Estimate

The volume of pore space available for supercritical CO_2 injection into a stacked saline reservoir was estimated by employing three different approaches using the physical input parameters listed in Table 4 – a simple linear approach, a probabilistic approach independent of time (Sarkodie-Kyeremeh et al. 2022), and a similar probabilistic simulation for 5 yr of CO_2 injection at 200,000 mt/yr using a DOE National Energy Technology Laboratory (NETL) CO_2-Screen tool v.4.1 (Sanguinito et al. 2022).

In the simplistic linear approach, the assumed net rock volume is multiplied by the estimated effective porosity to derive the estimated pore volume. To estimate the amount of CO_2 that would be stored in this calculated pore volume we used the average volume of CO_2 at a supercritical state, 0.650 g/cm^3 (650 kg/m^3) to find that 100,000 t of CO_2 would occupy approximately 0.000154 km^3 of space. This resulted in 13,550 Mt of CO_2 storage in Harquahala basin.

For the probabilistic methods the results are plotted as a percentage of uncertainty, represented by a probability distribution (Figure 91). Estimates are defined as the probability of exceedance such that a proved (P90), the lowest value, 90% of the calculated estimates will be equal or exceed the P90 estimate. P50 is the median estimate. The P10 is the possible estimate, the highest value, or 10% of the calculated estimates will be equal or exceed the P10 estimate. Because the mean and median (P50) values are not the same, this suggests the results are slightly skewed, thus we consider the P50 values to be more representative than the mean. The P50 results yield 1,997 Mt (1.9 Gt) in Harquahala basin for total CO_2 storage. The time dependent approach resulted in a P50 of 463 Mt in Harquahala basin of CO_2 storage for 5 yr of injection.

The simplistic linear approach yields much larger values than the probabilistic approach and is likely an overestimate. The probabilistic approach takes more parameters into account and is likely more representative of the subsurface conditions, therefore we expect the total CO_2 storage volumes to be closer to the probabilistic method values. The method by Sarkodie-Kyeremeh et al. (2022) estimates a degree of uncertainty or sensitivity of most parameters listed in Table 4. The area, gross thickness, and CO_2 density presented the least degree of uncertainty, whereas the porosity, net-to-gross ratio, and efficiency factor presented the most, which will help to identify which parameters need to be refined as part of new data collection. The relative amount of uncertainty for this method is presented in more detail in Appendix G.

Table 5. Summary of CO_2 storage calculations in million metric tons (Mt) for each method.

	Total CO_2 storage, Mt		**CO_2 storage for 5 yr, Mt**
Basin	**Simple linear**	**Probabilistic (P50)**	**Probabilistic (P50) NETL CO_2-Screen**
Harquahala	13,550	1,997	463

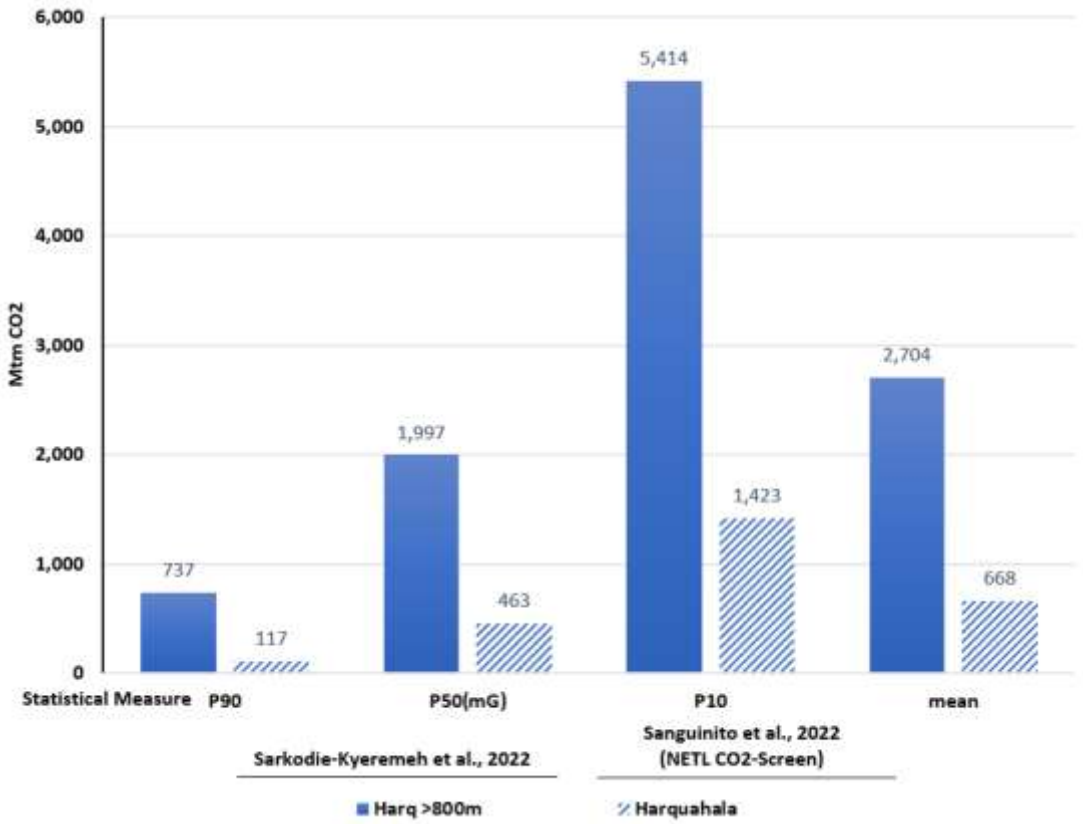


Figure 91 Calculated statistical volumes of CO_2 storage in non-differentiated basin fill units below 800 m depth in Harquahala basin for total CO_2 injection capacity in solid blue (Sarkodie-Kyeremeh et al. 2022) and CO_2 capacity after 5 yr injection in hashed blue (Sanguinito et al. 2022).

Known Natural Gas Subsurface Storage Risks

Sealing Conditions

The lack of known impermeable sealing strata is a geologic risk to subsurface natural gas storage. In Harquahala basin, potential bedded evaporite and clay deposits could be adequate seal rocks for stacked saline reservoirs. We predict these deposits are present in the lower basin fill, but we have made no direct observations of them.

Evaporite deposits are impermeable and can serve as a robust seal to trap fluid and gases underground. The lateral extent of this potential seal is shown by the zero contour on the acoustically transparent zone isopach map (equivalent to the top of this seismic facies; Figure 86). The chemistry, geomechanical properties, and lateral continuity of the evaporite deposits have not been directly measured. Fine-grained clastic sediment such as clay, silt and fine sand usually borders evaporite deposits, and the types of salts and mixed percent of lithofacies is important to map out in the subsurface to adequately de-risk storage of CO_2.

The low porosity, fine-grained facies such as clay can be a lithologic barrier to fluid migration. Lithology logs from shallow water wells suggest the presence of a laterally continuous clay layer in Harquahala basin (Towne 2014). The extent, thickness, and continuity of this clay is limited by the location of well penetrations, which are generally clustered within the agricultural area of

the basin. Based on the conceptual basin model (section 4a), clay would likely be present near or along the margin of subbasin centers. Thin interbedded clays layers could create baffles to subsurface flow and compartmentalization within the reservoir. Direct measurements such as electric wireline logs and core are needed to further de-risk the sealing integrity and conditions in these basins.

Seismic Hazard

Historical and induced seismicity can present a risk to any subsurface CO_2 storage. There are several faults surrounding Harquahala basin, and major faults interpreted in vintage seismic reflections (Figure 84); however, there are no known active or Quaternary faults (last 2.5 Myr). The nearest known Quaternary fault is the "Sand Tank" fault about 50 miles southeast of Harquahala basin near the town of Gila Bend, although no paleoseismic investigative work has been done on this fault. Based on the lack of surface ruptures, lack of springs and aseismic activity in Harquahala basin, the seismic risk is considered relatively low (Figure 92; USGS 2018).

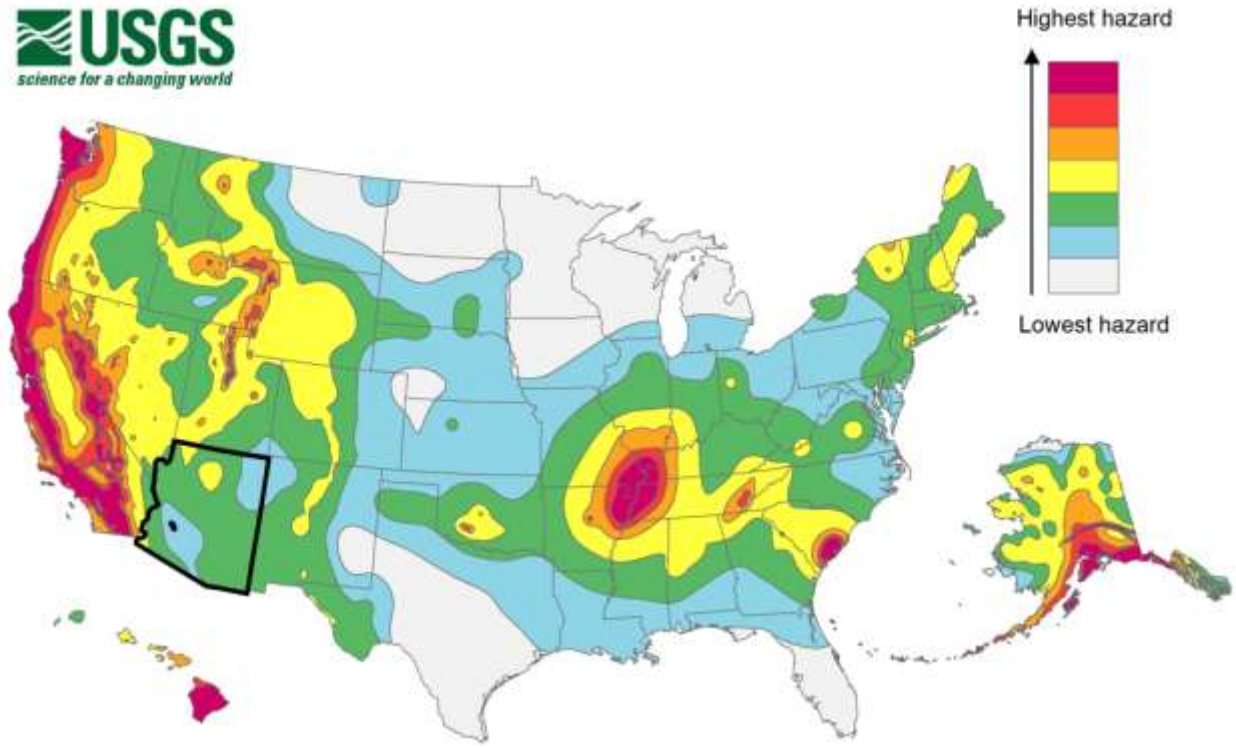


Figure 92 Earthquake hazard map showing peak ground accelerations having a 2 percent probability of being exceeded in 50 yr, for a firm rock site. Harquahala basin is shown as a solid black polygon within Arizona outline. The map is based on the most recent USGS models for the conterminous United States (2018), Hawaii (1998), and Alaska (2007; all from USGS [2018]). Models are based on seismicity, fault-slip rates and consider the frequency of earthquakes of various magnitudes. Locally, the hazard may be greater than shown because site geology may amplify ground motions.

The known seismicity rates for the Harquahala basin and surrounding area are low. Within the last several decades, no events larger than M 3.0 have occurred. Events smaller than M 3.0 may occur; however, the area has not had adequate seismic monitoring spatially or historically. In

2009, AZGS began operating a statewide seismic network, but that network only has 16 stations in the entire state. The two stations closest to Harquahala basin are located approximately 43 km to the north near Wickenburg and about 110 km to the southwest near Mohawk Valley. Higher density seismic monitoring would improve the detection threshold for the study area if lower magnitudes were necessary.

Conclusions

This study integrated geologic maps, borehole lithology logs, newly reprocessed vintage 2D seismic lines, public and proprietary gravity datasets, and borehole temperature & TDS data to characterize Harquahala basin for geologic storage of CO_2. Permanent subsurface CO_2 storage is possible in two different geologic environments: (1) storage as a supercritical fluid within stacked saline formations below 800 m depth or (2) permanent mineralization through chemical reactions with basalt lava flows. Short term H_2 storage may be possible within the evaporite deposits likely present in the basin, though much of this study was focused on CO_2 storage potential. CO_2 storage in fractured bedrock and geothermal energy potential could be utilized in this basin, though not expanded in this study due to limited data. Harquahala basin is one of 57 extensional basins in the Arizona Basin and Range that is sufficiently deep to store CO_2. This basin formed during the same time under similar tectonic and climatic conditions. Therefore, data from nearby basins such as deep well lithology logs, TDS measurements, and geothermal temperatures can be used a proxy for missing data in Harquahala basin. A conceptual geologic model based on numerous basin studies in the Arizona Basin and Range is used to generalize lithofacies distribution, stratigraphic framework, structural history, and basin geometry.

Harquahala basin is a deep, asymmetric, extensional basin filled with a thick accumulation of clastic and (potentially) chemical sediments, lava flows, and explosive volcanic material from nearby volcanic vents. Seismic reflectors, well lithology logs, proxy data from nearby basins, and our conceptual geologic model delineate three stratigraphic packages. From oldest to youngest these are: lower reflective package (LRP), lower basin fill (LBF), and upper basin fill (UBF). The LRP is deposited on older and more extensively deformed plutonic, metamorphic, and sedimentary rocks and likely composed of a sequence of stacked lava flows interbedded with felsic tuffs and coarse clastic sediments. Deposition of the LRP began with the onset of basin extension and has only been identified from seismic imaging in Harquahala basin. The LBF is likely composed of a wide range of lithofacies and grain size, dependent on distance from the source terrains. Laterally discontinuous seismic reflectors suggest the LBF is locally tilted, folded, and/or faulted, consistent with imaging in other parts of the basin and range province at similar depths. Seismic interpretations of an acoustically transparent zone on seismic lines TR9 and PW23 suggest there may be a thick accumulation of bedded evaporite deposits within the LBF. The UBF is a relatively undeformed, laterally continuous package of clastic and (potentially) chemical sedimentary rocks that unconformably overlies the LBF. The UBF sedimentary package is entirely above 800 m depth and is therefore ineligible for stacked saline storage.

Harquahala basin has sufficient volumes of pore space in presumably saline groundwater below 800 m depth, however, we cannot identify a sealing or capping rock for those reservoirs with certainty because of the lack of deep well lithology logs. Isopach maps highlight the thicker areas in the basin that could be targeted for future exploration. The LBF and LRP are both present

below 800 m (2,625 ft) and are good candidates for stacked saline storage and, potentially, mineralization in basalt lava flows. Based primarily on analysis and interpretation of seismic data, and on physical parameters from proxy basins, there is a P50 probability that about 1,997 Mt of supercritical CO_2 can be stored in Harquahala basin. To reduce uncertainty and sensitivity in these calculations, the porosity, net-to-gross storage volumes, and storage efficiency require new data collection from drilling and detailed geophysics.

From this study we have refined the basin geometry and provided new insights into basin structure and gross stratigraphy. Three critical unknowns remain: the existence/absence of a sealing strata such as bedded evaporites, the physical properties of stacked saline reservoir rock, and the stratigraphic architecture of basin fill sediments. Harquahala basin lacks the deep well borehole data needed to adequately characterize rock lithology, porosity, and permeability. We cannot diagnostically identify, for example, the presence/absence of bedded evaporite deposits, basalt lava flows, or extensive clay beds that can be used as sealing strata. The stratigraphic architecture of the basin, such as lateral extent of sealing strata, minor fault blocks, or presence/absence of anticlinal traps also remains unknown. Therefore, we recommend the acquisition of three new datasets in both basins: 2D active-source seismic (possibly passive-source too), magnetotellurics, and deep well borehole wireline geophysical logs and sampling. These datasets, combined with data reported within, will refine our understanding of the lower basin fill unit rock properties (the potential stacked saline aquifer), identify the presence/absence of sealing strata, and clarify stratigraphic architecture and basin structure.

Recommendations

CO_2 geologic storage in Harquahala basin is favorable, but more data collection is necessary to better characterize the reservoir and decrease geologic risk. For a phase II technical evaluation, our team recommends acquiring 8 new 2D seismic lines, additional in-fill gravity data, high resolution aeromagnetic survey, and drilling one stratigraphic characterization well.

The location of each method is presented in Figure 93 and discussed below. Magnetotellurics and a 3D seismic survey were considered as part of new data collection, although we recommend these methods be considered after Phase-II data are analyzed and funded as part of a Phase-III program.

New 2D Seismic

The reprocessed legacy 2D seismic data that was interpreted for this project is of moderate to poor quality and was not acquired with modern techniques. Acquiring new 2D seismic lines is advantageous because the acquisition parameters can be tailored specifically for the purpose of exploring the deep subsurface using what we now know about the stratigraphic units at depth. Line locations would target deep subbasins identified in this study. New 2D seismic would help refine basin geometry, identify faults, provide greater image resolution and seismic facies, map the extent of bedded salt deposits, and reduce uncertainty related to reservoir boundaries and potential seals.

We recommend acquiring 2D seismic reflection data along 8 different lines in Harquahala basin, totaling 105 miles. Three of these lines are longer (16–21 miles) and strike northwest-southeast and north-south. The remaining five lines are shorter (8–11 miles), cover the two main

depocenters, and generally run perpendicular to the basin axis (Figure 93). The proposed 2D seismic lines were chosen based on existing roads and access points, minimizing impact to agricultural plots, utilizing land ownership maps, intersecting legacy seismic surveys, and maximizing the characterization potential of the reservoir based on our findings in this study. The locations of these conceptual lines will likely change as part of a phase-II approach involving permitting, surveys related to permitting, ownership, and access.

Gravity and Aeromagnetic Surveys

Gravity and magnetic surveys are cost effective geophysical methods for exploring the subsurface over a large area. Gravity measurements provide information about rock density and can be used to understand the spatial distribution of those rock types in the subsurface. An aeromagnetic survey measures the intensity of the Earth's magnetic field and can yield the spatial distribution of the relative abundance of magnetic minerals. Often these types of data are used in conjunction with one another. The resulting data can help refine the boundaries of the sedimentary basin at depth and can elucidate the internal structural highs and lows (Selley and Sonnenberg 2023). Faults can also be identified using these methods which can help characterize the effectiveness of the sealing strata and potential seismicity risk, especially when combined with 2D seismic and well control. These data will be processed using the Werner Deconvolution method to also map salt extent (top and bottom), thickness, and the depth to crystalline basement.

We recommend acquiring additional gravity data and a high-resolution aeromagnetic survey over a targeted area (approximately 900 km^2) of the Harquahala Valley (Figure 93). The spatial distribution of existing gravity stations within the basin is not sufficient, as there are areas (specifically in the east) that lack control points. The goal is to develop a gravity acquisition plan that fills in the existing gravity dataset at regularly spaced intervals (1 mile apart) for the entirety of our Area of Interest (AOI). Additionally, more gravity stations along the southwest margin of the basin along seismic lines will be needed to capture the steepness of that fault margin. An aeromagnetic dataset also exists over this area but again is not sufficient for this study. This survey was collected in 2001 by the U.S. Geological Survey as part of a large statewide effort and lacks the resolution needed. We plan to collect a high-resolution aeromagnetic survey with 200 m line spacing and 2,000 m tie lines.

Stratigraphic Characterization Well

A deep characterization well is required to examine rock lithology, stratigraphy, reservoir type and depth, sealing potential, geothermal potential, and water chemistry/salinity. This will be achieved by drilling a deep borehole, running wireline logging tools, collecting cuttings, retrieving core samples, and collecting downhole water samples and pressure information. A comprehensive suite of wireline logs should include, but not be limited to triple combo (caliper, spontaneous potential, gamma ray, resistivity, density), 4-point Rx sonic, formation imager (FMI), nuclear magnetic resonance, cement bond log (CBL) and temperature log. These logs will greatly reduce uncertainty and be used to calibrate and adjust input parameters in legacy and new geophysical datasets. Continuous wireline core through the bedded salt section would provide the greatest preservation of data and likely be the most cost-effective method. Conventional whole-rock core and sidewall cores are recommended for pertinent sections and lithologies below the bedded salt portion. A detailed core analysis would include, but not be limited to:

porosity, permeability, grain density, core gamma for correlating core depth with logs, core photographs, CT scan, and fluids analysis. Additional CO_2 mineralization experiments will be run on mafic rocks encountered.

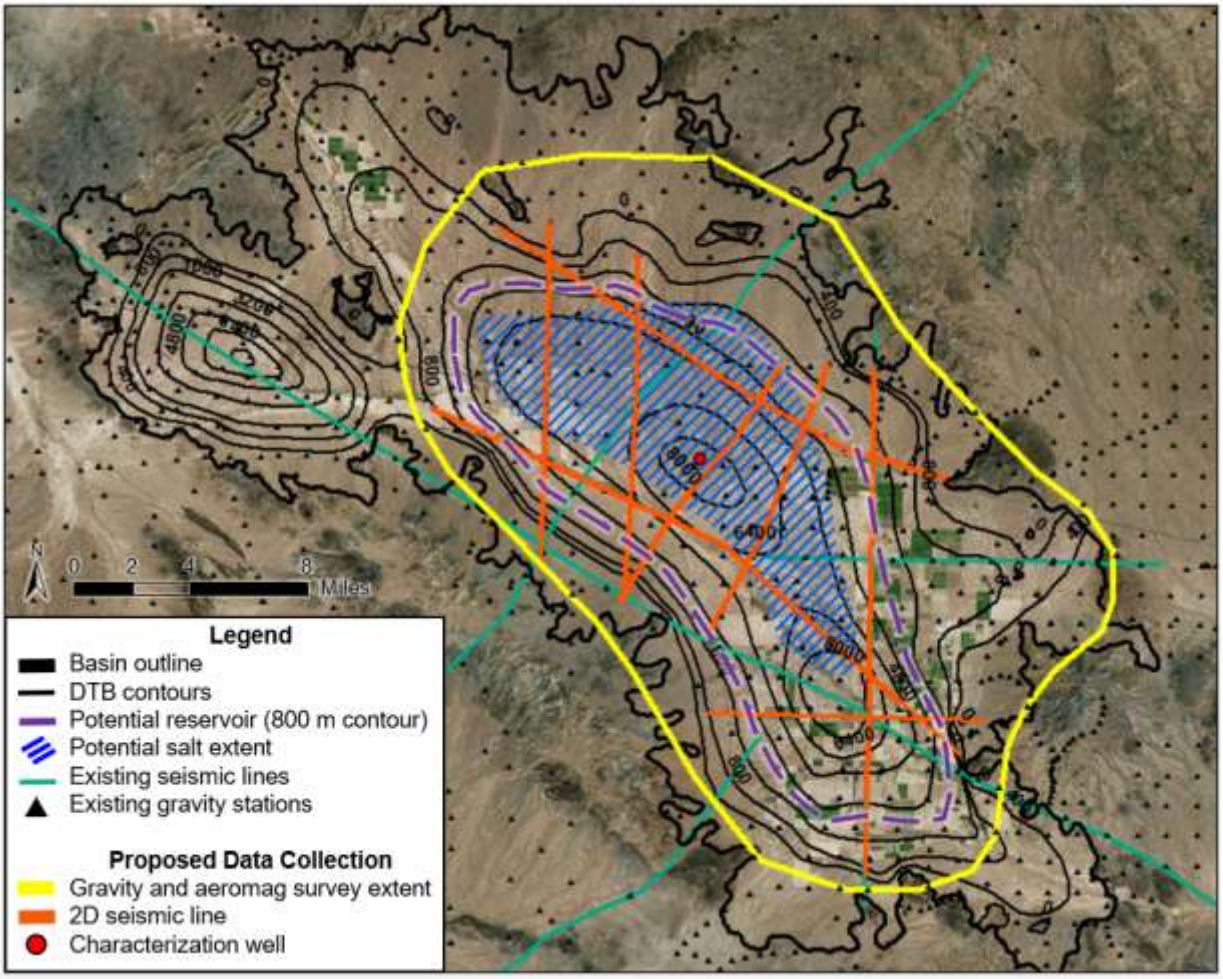


Figure 93 Map of selected existing data and proposed new data acquisition.

We recommend drilling a 10,000 ft stratigraphic characterization well in the central subbasin (Figure 93). This depth was chosen to ensure the hole penetrates the crystalline basement rock which, if fractured, will be evaluated as a potential reservoir and to determine the temperature for assessing the geothermal potential. This location will capture the deepest portion of the basin and will confirm the presence or absence of bedded evaporite deposits and interbedded basalt flows here (including their state of alteration or weathering). The proposed well location is on federal land (Bureau of Land Management) which should streamline the permitting process for CCS projects under BLM Internal Memorandum # 2022-041 (June, 2022). It is also conveniently positioned near interstate 10 and Salome Road, which provides a transportation route to support drilling operations.

References

[ADWR] Arizona Department of Water Resources. 2004. Unpublished gravity data from the Hassayampa region, south-central Arizona. Phoenix (AZ); Arizona Department of Water Resources. [Unpublished data].

[ADWR] Arizona Department of Water Resources. 2006. Salt River model geology update. Phoenix (AZ); Arizona Department of Water Resources. Modeling Report No. 16.

[ADWR] Arizona Department of Water Resources. 2022. Statewide historic and compiled gravity datasets originally from PACES (2016), maintained by ADWR. Phoenix (AZ); Arizona Department of Water Resources. [Unpublished data].

[AZOGCC] Arizona Oil and Gas Conservation Commission. 2023. Well files and production reports. Phoenix (AZ); Arizona Oil and Gas Conservation Commission. [Internet]. Accessed 2023 Jan. https://azogcc.az.gov/records

Eberly LD, Stanley TB. 1978. Cenozoic stratigraphy and geologic history of southwestern Arizona. Geol Soc Am Bull. 89:921–940. doi:10.1130/0016-7606(1978)89%3C921:CSAGHO%3E2.0.CO;2

Faulds JE, Schreiber BC, Langenheim VE, Hinz NH, Shaw TH, Heizler MT, Perkins ME, El Tabakh M, Kunk MJ. 2016. Paleogeographic implications of late Miocene lacustrine and nonmarine evaporite deposits in the Lake Mead region: immediate precursors to the Colorado River. Geosphere. 12:721–767. doi:10.1130/GES01143.1

Gootee BF. 2013a. An evaluation of carbon dioxide sequestration potential in the Luke Basin, south-central Arizona. Tucson (AZ); Arizona Geological Survey. Open-File Report 13-05.

Gootee BF. 2013b. An evaluation of carbon dioxide sequestration potential in the Higley Basin, south-central Arizona. Tucson (AZ); Arizona Geological Survey. Open-File Report 13-10.

Gootee BF. 2015. An evaluation of carbon dioxide sequestration potential in the Picacho Basin, southeastern Arizona. Tucson (AZ); Arizona Geological Survey. Open-File Report 15-09.

Gootee BF, Love DS, Mahan MK. 2012. A summary of salinities in Arizona's deep groundwater. Tucson (AZ); Arizona Geological Survey. Open-File Report 12-26.

Gootee BF, Noel SD. 2015. McMullen Valley groundwater model (supporting Arizona State Land Department application for analysis of water adequacy). Phoenix (AZ); Arizona State Land Department. [Unpublished report].

[HGI] HydroGeophysics Inc. 2009. Geophysical results for Harquahala Basin. Tucson (AZ); HydroGeophysics Inc. [Confidential report].

Menges CM, Pearthree PA. 1989. Late Cenozoic tectonism in Arizona and its impact on regional landscape evolution. In: Jenny JP, Reynolds SJ, editors. Geologic evolution of Arizona. Tucson (AZ); Arizona Geological Society. p 649–680.

Mullane, M., Gleason, M., Reber, T., McCabe, K., Mooney, M., Young, K.R., 2017. An estimate of shallow, low-temperature geothermal resources of the United States (No. NREL/CP-6A20-68523). Davis, CA: Geothermal Resources Council.

Nathenson M, Guffanti M. 1988. Geothermal gradients in the conterminous United States. J Geophys Res Solid Earth. 93(B6):6437–6450. doi:10.1029/JB093iB06p06437

Neal JT, Rauzi SL. 1996. Storage opportunities in Arizona bedded evaporites. Albuquerque (NM); Sandia National Laboratories. Report No. SAND96-1679C.

[PACES] PACES Project. 2016. Regional public gravity datasets. [Place unknown]; PACES Project. [Data set].

Pan B, Lei J, Zhang L, Guo Y. 2017. Research on the physical properties of supercritical CO_2 and the log evaluation of CO_2-bearing volcanic reservoirs. J Geophys Eng. 14:1052–1060. doi:10.1088/1742-2140/aa6f22

Peters, K.E., Curry, D.J., Kacewicz, M., 2012. An overview of basin and petroleum system modeling: definitions and concepts 1–16. doi:10.1306/13311426H4139

Raza A, Glatz G, Gholami R, Mahmoud M, Alafnan S. 2022. Carbon mineralization and geological storage of CO_2 in basalt: mechanisms and technical challenges. Earth-Sci Rev. 229:104036. doi:10.1016/j.earscirev.2022.104036

Reynolds SJ. 1997. Geologic data for the Phoenix South 30′ × 60′ quadrangle. Tucson (AZ); Arizona Geological Survey. DGI-05 v2.0.

Reynolds SJ, Grubensky MJ. 2007. Geologic data for the Phoenix North 30′ × 60′ quadrangle. Tucson (AZ); Arizona Geological Survey. DGI-04 v2.0.

Richard SM, Shipman TC, Greene L, Harris RC. 2007. Estimated depth to bedrock in Arizona. Tucson (AZ); Arizona Geological Survey. Digital Geologic Map DGM-52.

Richard SM, Spencer JE, Reynolds SJ, Pearthree PA, Demsey KA, Thompson LA, Snellen HL, Theim JP. 2022. Geologic map of the Salome 30′ × 60′ quadrangle, west-central Arizona. Tucson (AZ); Arizona Geological Survey. Digital Geologic Map DGM-157.

Sanguinito S, Hanson A, Haeri F, Myshakin E, Moore J, Crandall D. 2022. CO_2 storage prospective resource estimation Excel analysis (CO_2-SCREEN) user's manual: Python v4.1. Albany (OR); National Energy Technology Laboratory. Report No. DOE/NETL-2022/3729. doi:10.2172/1862020

Sarkodie-Kyeremeh J, Ampomah W, Tu J, Czarnota R. 2022. Advances in CO_2 geological storage: estimation of CO_2 storage efficiency factors for the San Juan Basin formations. In: Proceedings of the 16th Greenhouse Gas Control Technologies Conference (GHGT-16); 2022 Oct 23–27; Lyon (France). doi:10.2139/ssrn.4286058

Sass JH, Lachenbruch AH, Galanis SP Jr, Morgan P, Priest SS, Moses TH Jr, Munroe RJ. 1994. Thermal regime of the southern Basin and Range Province: 1. Heat flow data from Arizona and the Mojave Desert of California and Nevada. J Geophys Res Solid Earth. 99(B11):22093–22119. doi:10.1029/94JB01891

Selley RC, Sonnenberg SA. 2023. Methods of exploration. In: Selley RC, Sonnenberg SA, editors. Elements of petroleum geology. 4th ed. London (UK); Academic Press. p 43–166. doi:10.1016/B978-0-12-822316-1.00003-3

Spencer JE, Pearthree PA, Demsey KA, Thompson LA, Snellen HL, Korroch KM, Theim JP, Richard SM. 2022. Geologic map of the Little Horn Mountains 30′ × 60′ quadrangle, west-central Arizona. Tucson (AZ); Arizona Geological Survey. Digital Geologic Map DGM-153.

Spencer, J.E., Reynolds, S.J., 1989. Middle Tertiary tectonics of Arizona and adjacent areas. Geol. Evol. Ariz. Ariz. Geol. Soc. Dig. 17, 539–574.

Teixeira L, Lupinacci WM, Maul A. 2020. Quantitative seismic-stratigraphic interpretation of the evaporite sequence in the Santos Basin. Mar Pet Geol. 122:104690. doi:10.1016/j.marpetgeo.2020.104690

Towne D. 2014. Ambient groundwater quality of the Harquahala Basin: a 2009–2014 baseline study. Phoenix (AZ); Arizona Department of Environmental Quality. Open-File Report 14-04.

[U.S. EPA] U.S. Environmental Protection Agency. 2023. Greenhouse Gas Reporting Program (GHGRP): reporting year 2021 data, parts C and D (FLIGHT). Washington (DC); U.S. Environmental Protection Agency. [Internet]. https://www.epa.gov/ghgreporting/ghgrp-2021-reported-data

[USGS] U.S. Geological Survey. 2018. 2018 long-term national seismic hazard map. Reston (VA); U.S. Geological Survey. [Internet]. https://www.usgs.gov/programs/earthquake-hazards/science/2018-united-states-lower-48-seismic-hazard-long-term-model

Walton WC. 1970. Groundwater resource evaluation. New York (NY); McGraw-Hill.

Wilson TC, Thompson LA, Gootee BF. 2024. Phase I pre-feasibility study to evaluate carbon dioxide and hydrogen geologic storage potential in Harquahala Basin. Tucson (AZ); Arizona Geological Survey. Open-File Report 24-01. https://library.azgs.arizona.edu/item/AOFR-1712775909999-126

Witcher JC. 1995. Geothermal resource data base: Arizona. Idaho Falls (ID); U.S. Department of Energy. Report No. DOE/ID/13223-T9. doi:10.2172/204692

Derisking CO_2 Mineralization Storage in Basalt Reservoirs on page 183.

Part V – Working Groups

Economics Working Group

The goal of the CUSP Economics Working Group is to develop and maintain a consistent cost–benefit framework—defining cost and benefit categories, calibrating assumptions, and assembling capture-cost and emissions datasets—to underpin CUSP techno-economic and cost-benefit analyses. Its members include SNL, New Mexico Tech, Carbon Solutions LLC, University of Texas Permian Basin, Montana State University, Kansas Geological Survey, Stanford University, University of Utah, and University of Wyoming.

We hosted bimonthly meetings and facilitated discussions on economics of carbon capture, transport, utilization, and storage with this working group. We involved interested members from this working group in reports and peer-reviewed papers to recognize and attribute their contributions. The Economics Working Group collaboratively created materials pertaining to Economic Analysis of Geologic Carbon Sequestration establishing a clear, methodology for scoping projects. In parallel, the group built a shared CO_2 capture-cost and emissions database—harmonizing EPA GHGRP data with partner inventories and standardizing formats—to feed into the partnership's analysis. Sandia conducted a literature review and provided results on the capture costs to Carbon Solutions. The major deliverables led by SNL pertaining to this working group are the Blueprint for economic analysis of CCUS and the journal article (Mishra et al., 2025) in International Journal of GHG control mentioned above.

Targa Resources (Formerly Lucid Energy Delaware) Acid Gas Injection Project

Economic Risk–Related Objectives and Desired Outcomes

Economic assessment objectives included Developing a site-specific technoeconomic method for converting Targa's Red Hills AGI wells to UIC Class VI CO_2 storage, capturing all capital and operating cost components.

Economic Assessment

A detailed techno-economic model was constructed for the Red Hills AGI CCS project. We developed detailed CAPEX calculation method by disaggregating capital costs into site characterization, area-of-review and corrective action, injection-well construction, compressor/pipeline infrastructure, and monitoring/permitting categories, then aggregating these into the total capital cost (TCC). Operating expenses—including compressor electricity and water, well O&M, and postinjection monitoring—were computed and added to LTCC to yield the levelized cost of CO_2 storage per metric ton. The annualized CAPEX and OPEX per year were used to calculate the total annual cost which was then divided by annual injection amount to calculate CCS cost ($/metric ton). We worked closely with the industry partner and shared our

method, variables, literature-based data, equations used, and the assumptions made for the TEA. The TEA results were shared with the industry partner.

CCS Hub 2.0 Concept for ONEOK: Infrastructure Development for Handling of New Gaseous Products for Natural Gas Liquids Fractionation and Gas Processing Plants in Kansas and Oklahoma

Economic Risk–Related Objectives and Outcomes

Objectives for economic risk-related assessment includes:

- Quantify site-level economics (CAPEX, OPEX, levelized cost) and benefits (45Q revenues under Section 45Q of the U.S. Tax Code; Credit for Carbon…2021) for ONEOK's four injection wells under baseline, low-cost, and high-cost scenarios.
- Assess key economic risk categories—regulatory/policy, market/price, financing/interest-rate, and community/social-licensing—and identify mitigation strategies.
- Develop tailored guidance for Class VI permitting and 45Q compliance to streamline EPA and IRS applications.

Intended outcomes include delivering standardized cost-and-benefit metrics for each injection site, a ranked economic-risk matrix to guide mitigation strategies, and a clear permitting and financing roadmap to support ONEOK's CCS Hub development.

Risk Assessment

Economic risk assessment identifies and quantifies the key uncertainties that could undermine project viability. For the ONEOK sites, this project's analysis groups these into four categories—regulatory and policy risk, market and price risk, financing and interest-rate risk, and community and social-licensing risk—and applies scenario and sensitivity analyses to measure each category's potential impact on project NPV and benefit:cost ratios.

Economic Assessment

SNL conducted economic analysis to support the overarching goal of the project, which is to identify potential carbon dioxide (CO_2) reservoirs for long-term saline storage in the area surrounding ONEOK natural gas liquids fractionation plants near Bushton, KS, and Medford, OK, as well as several gas processing plants in Oklahoma that emit approximately 1 Mt of CO_2 per annum. SNL submitted a report on economic risk/feasibility assessment, which was included in the ONEOK report compiled and submitted by Brendan Bream, KGS.

We used a three-pronged approach for this task. First, we calculated the costs of CO_2 sequestration at the identified sites; second, we calculated the cost benefit ratio of sequestration projects; and finally, we evaluated the economic risks of the project. We followed the technoeconomic analysis and cost: benefit analysis methods discussed in Mishra et al. (2025) to calculate the cost of CO_2 storage at identified ONEOK sites and for the economic feasibility analysis of the CCS projects. We identified and discussed the factors of economic risk and discussed the potential impacts on the projects' economic viability.

The technoeconomic analysis conducted for the ONEOK site demonstrates that the total capital and operational costs associated with CO_2 injection are highly dependent on well depth, equipment selection, and site-specific geological conditions. The estimated levelized cost of CO_2 storage provides a useful benchmark for evaluating the economic feasibility of the proposed OneOK carbon sequestration projects. The levelized cost of CO2 storage calculated for the Bushton-LKC, Bushton-UArb, Buston-DArb, and Medford- WilBro sites are, respectively, $10.92 (9.08–12.76), $11.01 (9.17–12.85), $10.86 (9.02–12.69) and $11.13 (9.29–12.96) per metric ton CO_2. The cost–benefit and net present value analysis shows that all 4 of these wells are likely to be economically feasible, at least at the injection site level.

Economic risks associated with CCS projects are categorized as Regulatory and policy risks, market and price risks, financing and interest rate risks, and public licensing risk. The uncertainty in the continuation as well as the period (number of years), quantity (dollar value), and eligibility of CCS project for Section 45Q tax credits introduces economic risks for CCS projects. Under high-cost scenario combined with high pressure difference and depth, CCS projects are profitable only when Section 45Q Tax credits are fully realized. Finance risk is another major risk because CCS projects require large upfront capital. Our calculation shows that Bushton LKC requires $4.1 million to $16.4 million, Bushton UArb $4.2 million to $17 million, Bushton DArb $9 million to $35.6 million, and Medford $4.3 million to $17 million (for details, please refer ONEOK report). When financial returns are uncertain and the investment amounts are large investment, investors' confidence decreases. This adds to the financing risk. Similarly, interest rates fluctuations add risks by affecting the costs of borrowing. For large investment CCS projects, a small change in interest rate can impact the economic viability of the project, specifically if the debt-to-equity ratio is higher. Another major risk factor is market conditions. Inflation led increase in costs of equipment and inputs affect the capital expenses as well as the operational expenses thereby increasing the economic risks of CCS projects. The high-cost items such as the costs of compressors, costs of drilling, increased significantly from 2021 to 2025. Because CCS is energy heavy process, cost per kWh for instance can significantly affect the levelized cost of CO_2 storage. A higher cost of storage could convert a CCS project into an economically unviable project.

References

Credit for Carbon Oxide Sequestration, U.S.C.-2023 26 C.F.R. §1.45Q-1 (2021).

Mishra SK, Henderson MA, Heath JE, Tu DJ, Irwin A, Trentham R, Earnhart D, Fonquergne J, Gagarin H, Heath J. 2025. Can Section 45Q tax credit foster decarbonization? A case study of geologic carbon storage at acid gas injection wells in the Permian Basin. Int J Greenh Gas Control. 140:104284. doi:10.1016/j.ijggc.2024.104284

Data Working Group

Analytics Working Group

The Analytics Working Group served as the computational and decision-support engine of the Carbon Utilization and Storage Partnership (CUSP), providing the modeling consistency, data preparation, and methodological innovation that underpinned many of CUSP's technical deliverables. Unlike subtasks focused on a single basin, state, or technology, the Analytics Working Group worked across the entire CUSP region and spanned multiple subtasks, ensuring that the data, modeling assumptions, and scenario analyses used by partners were aligned and reproducible.

The group was led by Montana State University and strongly supported by Carbon Solutions, LANL, PNNL, and state partners from California, Kansas, Washington, Colorado, Utah, New Mexico, Arizona, and Nevada. This diverse membership allowed the group to combine algorithmic expertise with local data knowledge, producing analyses that were both technically rigorous and grounded in regional priorities.

Over the course of 5 years, the group's objectives evolved in a natural progression. In the early stages, the primary focus was supporting data collection: Defining what SimCCS requires as input, creating data templates and cost curve specifications, and working directly with state partners to identify, validate, and format emissions and storage data. This foundational work transitioned into scenario analysis for subregions of the CUSP footprint, beginning with Kansas and eventually including California, Nevada, Oklahoma, and the Four Corners. In these studies, the group developed optimized CCS network designs under a variety of capture targets, credit values, and routing constraints. In later years, the group focused on regional synthesis, producing readiness indices and geospatial mapping products that quantified each state's relative potential for CCS deployment.

Throughout the project, the Analytics Working Group contributed to or led several key subtasks, including:

- Subtask 3.1.1 – Identify data requirements for SimCCS modeling.
- Subtask 3.1.4 – Gather and catalog CO_2 emissions (point source) databases, assisting states with data curation.
- Subtask 4.5 – Focused scenario analysis, executing hundreds of SimCCS runs across CUSP-wide states and multistate regions.
- Subtask 5.1 – Development of regional readiness indices and mapping products.

These contributions were not limited to applied modeling. The group also developed new algorithms and formulations for multiphased buildout planning, robust design under storage uncertainty, repair-aware network design, and genetic algorithms for national-scale optimization. Many of these advances were peer-reviewed and published, ensuring they will continue to benefit the CCS community beyond the life of CUSP.

The outputs of the Analytics Working Group—cleaned datasets, reproducible scenarios, technical reports, open-source model improvements, and geospatial products—position the CUSP region for risk-aware, cost-effective CCS deployment. By addressing uncertainty, scaling challenges, and the need for phased infrastructure rollouts, this work supports DOE's long-term carbon management goals and helps de-risk early infrastructure investment decisions.

Report Organization

This report documents the Analytics Working Group's contributions in detail, presenting each phase of work in the chronological order in which it was undertaken over the life of the project. Phase 1 describes the early data and scenario guidance efforts that laid the foundation for consistent modeling across states. Phase 2 summarizes the regional scenario analyses, including Kansas, California, Nevada, Oklahoma, Utah, and the Four Corners region, with detailed results tables and figures. Phase 3 presents the group's model development contributions, including mathematical formulations, experimental setups, and case study findings. Phase 4 covers the readiness indices and mapping work that synthesized insights into region-wide metrics. The report concludes with cross-cutting lessons learned and overarching Analytics Working Group contributions and results.

Phase 1 – Foundational Data and Scenario Guidance

The initial phase of the Analytics Working Group's work focused on establishing a consistent foundation for CCS modeling across the CUSP region. Before full-scale scenario analyses could be undertaken, it was necessary to standardize data formats, ensure coverage of all major emissions sources and candidate storage locations, and align state partners on what SimCCS requires to generate meaningful optimization results.

Defining Data Requirements

A comprehensive specification of SimCCS data requirements was developed and distributed to all CUSP partners. This specification detailed the minimum data needed to construct a valid scenario, including

- Point-source data: Location coordinates, annual CO_2 emissions (Mt/year), fixed and variable capture costs, and maximum capture capacity.
- Storage site data: Location, estimated capacity, injectivity (where available), fixed development cost, and variable injection cost.
- Transport network data: Candidate pipeline corridors, cost–capacity curves for each diameter class, and right-of-way constraints.
- Economic and policy data: 45Q credit values (under Section 45Q of the U.S. Tax Code; Credit for Carbon…2021) and escalation schedules, LCFS credit values, and assumptions about EOR revenue.

Templates were provided in CSV and shapefile formats, along with guidance for quality control and unit consistency. These templates ensured that data collected by different states could be merged into larger regional studies without reformatting.

Partner Engagement and Education

The group conducted early webinars and presentations for state partners to explain how SimCCS uses input data to produce optimized infrastructure designs. These sessions demonstrated the three primary optimization modes available in SimCCS—CAP (minimum-cost capture of a specified quantity), PRICE (profit-maximizing under a credit value), and TIME (minimum cost subject to a fixed duration of injection)—and showed how pipeline routing cost surfaces are

generated. Special emphasis was placed on the importance of accurate cost curves and site characterizations, since these directly influence which sources and sinks are selected in an optimal solution.

Scenario Typology and Planning Guidance

To ensure comparability across states and regions, the Analytics Working Group developed a scenario typology that categorized potential analyses into a set of common archetypes. Example categories included

- Baseline CAP scenarios: capturing all emissions from selected industries at least cost.
- Profit-maximizing PRICE scenarios: determining which subset of emissions can be captured economically under current or projected credit levels.
- Sensitivity runs: varying storage capacities, cost multipliers, and credit levels to identify thresholds and breakpoints.
- Phased buildout scenarios: modeling infrastructure expansion over multiple decades to reflect realistic project sequencing.

The scenario planning guidance also addressed how to incorporate special considerations such as environmental justice (by adding spatial avoidance constraints), routing preferences (by weighting existing rights-of-way), and storage reliability (by including multiple candidate reservoirs to provide redundancy).

Phase 2 – Scenario Development and Evaluation

Throughout the CUSP project, the Analytics Working Group conducted focused scenario analysis of CUSP sub-regions encompassing local objectives and constraints. Data for the scenario analyses presented in this report were collected by CUSP partners, leveraging regional expertise in geology, energy infrastructure, and emissions data. These focused scenario analyses described in this section focus on evaluating the geological storage capacity, CO_2 capture potential, and transport infrastructure required to implement CCS projects at scale. Each region presents unique challenges and opportunities, shaped by local industrial emissions, geological formations, and existing infrastructure. By systematically analyzing these factors, the Analytics Working Group aimed to provide critical insights into how CCS can be deployed in a cost-effective and technically viable manner to help meet regional and national climate goals.

A critical tool in these analyses is SimCCS, an optimization software specifically designed to model the deployment of CCS infrastructure. SimCCS integrates geospatial, economic, and technical data to develop optimal strategies for CCS project design. It does so by solving a mixed-integer linear programming (MILP) problem that seeks to minimize overall project costs while adhering to constraints such as pipeline capacities, capture limits, and storage availability. SimCCS is flexible and can simulate multiple scenarios, allowing for variations in tax credits, capture rates, and infrastructure requirements. The tool's ability to model dynamic, multiphase projects makes it invaluable for identifying optimal CCS solutions across diverse geographic and industrial landscapes, as demonstrated in the scenario analyses for the CUSP region. Input data to parameterize SimCCS is provided by CO_2NCORD (CO_2 capture), CostMAP (CO_2 pipeline routing), and SCO_2T (CO_2 storage).

The data used for these scenario analyses encompass a wide array of factors, including regional CO_2 emissions, geological assessments of potential storage sites, and the availability of pipeline routes for transporting CO_2. The studies focus on key industrial emitters, such as power plants, refineries, and natural gas facilities, alongside potential storage sites in saline formations, hydrocarbon fields, and enhanced oil recovery (EOR) fields. For each site, the analyses explore different scenarios to capture both the technical feasibility and economic viability of CCS projects under varying conditions, such as differing 45Q tax credit values and project timeframes.

In the following subsections, the report presents the findings for each CUSP region, highlighting the specific results of the scenario analyses conducted. These findings provide actionable insights for developing large-scale CCS infrastructure across the Western USA, addressing both the economic challenges and environmental benefits of reducing CO_2 emissions through geological storage.

California: San Joaquin Basin CCS Opportunities

The Southern San Joaquin Basin in California offers significant promise for the deployment of CCS projects primarily due to its rich geological formations and proximity to large industrial CO_2 sources, as presented in **Figure 379** (Kim et al. 2023, Appendix A). The CCS potential of this region has been a major focus during the CUSP project, particularly in assessing the economic viability and logistical feasibility of capturing CO_2 from a variety of industrial sources and storing it in the subsurface. This analysis encompasses both saline formations and hydrocarbon fields, providing insights into the different types of storage sites and the challenges and opportunities that face CCS adoption in California.

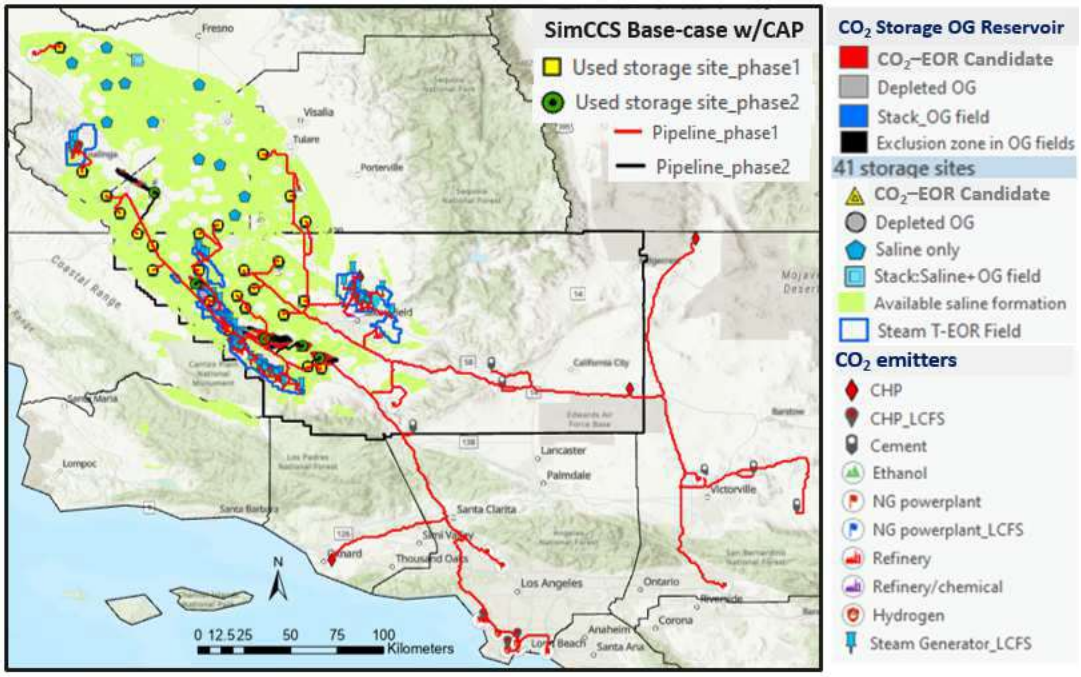


Figure 379 SimCCS solution for one scenario in the California study covering various emission industries and tax credits for an explicitly determined capture amount

Source Types and CO_2 Emitters

The industrial landscape of California presents a diverse array of CO_2 sources, making it a prime candidate for large-scale CCS deployment. In the Southern San Joaquin Basin, major CO_2 sources include combined heat and power (CHP) plants, refineries, cement production facilities, and natural gas-fired power plants. CHP systems are particularly relevant in this region due to their simultaneous production of electricity and steam, which makes them eligible for California's Low Carbon Fuel Standard (LCFS) credits.

The study identified capturable emissions from various sectors across Kern County and Southern California, focusing on linking these sources to storage sites. In particular, thermal EOR operations in Kern County are responsible for a large proportion of the region's industrial CO_2 emissions. The annual greenhouse gas emissions from oil and gas production operations in Kern County averaged 12.3 $MtCO_2$ between 2018 and 2019, making it a critical focus for CCS initiatives. The study also analyzed emissions from cogeneration plants, cement facilities, and hydrogen production plants, mapping these sources to storage locations based on the proximity and capture feasibility.

Case Studies and Technoeconomic Scenarios

Several case studies were performed to explore different scenarios for CO_2 capture and storage in the Southern San Joaquin Basin. SimCCS was used to evaluate the cost and infrastructure needs under various scenarios, focusing on both the 45Q tax credit and the LCFS credits as key financial incentives.

One key case study explored the impact of the 45Q tax credit, which was modeled to provide $85 per metric ton of CO_2 stored in saline formations and $60 per metric ton for CO_2 stored in EOR fields. This scenario showed that the Southern San Joaquin Basin is an economically viable CCS hub, with costs for capturing and transporting CO_2 remaining within feasible ranges due to the credit availability and high storage capacity of both saline formations and hydrocarbon fields. Another case study examined the volatility of LCFS credits, which have fluctuated between $65 and $150 per metric ton, and how this affects the financial viability of CCS deployment. These credits were found to be crucial for enhancing the economic returns from capturing emissions at CHP plants, oil and gas facilities, and refineries.

Seismic Fault Avoidance and Geologic Considerations

California's complex geology requires careful planning when designing CCS infrastructure, particularly in regions prone to seismic activity. One of the major technical challenges identified in the study was the need to avoid seismic faults when routing CO_2 pipelines and selecting storage sites. The Southern San Joaquin Basin contains several active fault systems, and the study employed detailed seismic risk assessments to ensure that CO_2 storage locations and transport routes are not compromised by seismic activity.

The study used seismic fault data in conjunction with SimCCS to map out optimal pipeline routes that minimize the risk of fault-induced damage. This involved creating buffer zones around known fault lines and avoiding areas with high seismic hazard potential when planning storage and pipeline infrastructure. By incorporating these factors into the SimCCS model, the

study ensured that both short-term operational safety and long-term storage integrity would be maintained.

Conclusions and Recommendations

The Southern San Joaquin Basin was identified as a key regional hub for CCS due to its large storage capacity, favorable proximity to CO_2 sources, and the financial incentives provided by both state and federal programs. The study concluded that with proper investment in CO_2 capture infrastructure, supported by the 45Q and LCFS credits, the region could feasibly store large quantities of CO_2 in both saline formations and hydrocarbon fields, making it a critical part of California's strategy to achieve net-zero emissions.

One of the key findings was the importance of phased deployment, allowing the infrastructure to grow over time as more CO_2 emitters are linked to the storage sites. This phased approach reduces initial capital expenditures and spreads out the costs of building pipelines and storage facilities. The study also highlighted the need for continued monitoring of seismic risks, as well as further investigation into the long-term storage capabilities of the region's saline formations.

Nevada: Resilience for CCS Networks in the Face of Uncertainty

The Nevada study investigated a critical aspect of CCS infrastructure: how to manage the risk of storage reservoir underperformance (or failure) in CCS networks. The challenge in CCS systems is not only to capture and transport CO_2 efficiently but also to ensure that storage reservoirs can reliably sequester CO_2 over the long term. This study modeled CCS infrastructure as a flow network, presented in **Figure 380**, where CO_2 sources, storage reservoirs (sinks), and pipelines are represented as edges in the graph. The research specifically explored scenarios in which storage reservoirs (represented as edges) fail, examining how such failures impact the overall cost and functionality of the CCS network. This analysis is particularly important in regions like Nevada, where CO_2 storage sites may be located far from industrial sources, and any failure in storage capacity could disrupt the entire system.

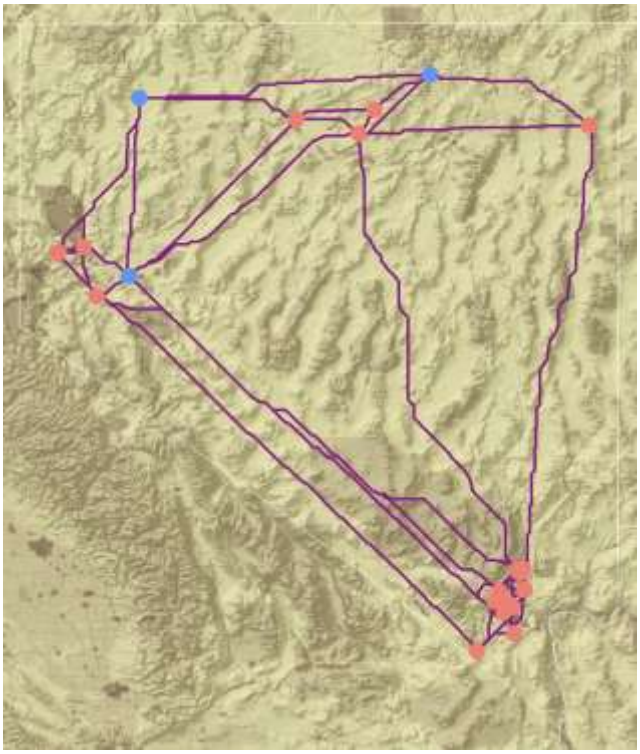


Figure 380 CCS data for the Nevada study consisting of sources (circles), sinks (squares), and possible pipeline routes (edges). The arrow indicates the sink that fails in the evaluated scenario.

CO_2 Sources and Storage Sites in Nevada

Nevada's industrial landscape presents several key CO_2 emission sources, primarily from power plants, natural gas facilities, and industrial manufacturing processes such as cement production. These emissions need to be captured and transported to distant storage sites. The vast distances between CO_2 emitters and potential storage reservoirs make Nevada an ideal case study for exploring how reservoir failures impact CCS networks.

The study identified several candidate storage reservoirs in Nevada and surrounding regions, each with different capacities and characteristics. These storage sites, often located in saline formations, serve as the "sinks" in the modeled flow network. The success of the CCS network depends on the reliability of these sinks to store CO_2 without operational issues such as capacity overruns, injectivity failures, or other disruptions that might prevent CO_2 injection.

Modeling Reservoir Failures in CCS Networks

A core focus of the Nevada study was modeling the potential failure of storage reservoirs within the CCS flow network. In this context, a reservoir failure is not a physical pipeline failure but rather an unexpected inability of the storage site to continue sequestering CO_2, either due to reaching capacity limits or operational difficulties with CO_2 injection. The study used a fixed-charge network flow (FCNF) model to represent the CCS infrastructure, where CO_2 sources, pipelines, and storage reservoirs are all modeled as edges. The failure scenarios specifically considered the edges representing storage reservoirs, allowing the study to simulate what happens when a storage reservoir can no longer accept CO_2.

The optimization model developed in the study aimed to find the most cost-effective flow of CO_2 through the network, ensuring that captured CO_2 is transported to available storage reservoirs. In failure scenarios, if a reservoir edge fails (i.e. the storage site is unable to sequester additional CO_2), the network must reroute the CO_2 to other available storage sites, increasing the transport distance and costs. This rerouting represents "repairing" the network, where additional costs are incurred due to the need to use alternative storage reservoirs that might be farther away or more expensive to access.

The study's multi-objective optimization framework provided a Pareto front of solutions, allowing decision-makers to evaluate the trade-offs between minimizing initial infrastructure costs and the costs of rerouting CO_2 in the event of reservoir failures. This approach is particularly important in regions like Nevada, where storage sites might be sparse and located far from emission sources, making rerouting CO_2 a potentially costly endeavor.

Key Findings: Balancing Infrastructure and Failure Costs

The results of the Nevada study highlighted the significant impact that reservoir failures can have on the overall cost and efficiency of CCS networks. The study found that while the initial infrastructure costs could be minimized by optimizing the CO_2 flow to the nearest and most cost-effective storage sites, this strategy left the network vulnerable to failures. In scenarios where a storage reservoir reached capacity or experienced operational issues, the costs of rerouting CO_2 to alternative storage sites were substantial.

The analysis showed that building more resilient networks, which incorporate additional storage reservoirs and redundancy, could reduce the long-term costs associated with reservoir failures. By investing in infrastructure that allows for multiple storage options, the network can more easily adapt to failures without significant cost increases. This is particularly relevant for Nevada, where the geographical distances between storage sites and CO_2 emitters make the rerouting of CO_2 a major cost driver in failure scenarios.

Moreover, the study identified critical reservoir edges—those storage locations whose failure would cause the most disruption to the network. By focusing additional investment on these critical edges, operators can mitigate the risk of costly rerouting and ensure more consistent CCS operations. This finding suggests that future CCS development in Nevada should prioritize storage reservoirs that offer both capacity and operational reliability, while also considering redundancy in storage options.

Conclusions and Infrastructure Recommendations

The Nevada study concluded that while optimizing initial CCS infrastructure is important, it is equally crucial to build networks that are resilient to storage reservoir failures. In regions like Nevada, where storage sites may be far from CO_2 emission sources, the cost of rerouting CO_2 in the event of a reservoir failure can be high, potentially undermining the economic viability of the CCS project. The study recommended investing in additional storage reservoirs and building redundancy into the network to reduce the risks associated with these failures.

Additionally, the study emphasized the importance of identifying critical storage reservoirs that play a pivotal role in the network's success. By reinforcing these critical edges and ensuring they are reliable, operators can mitigate the most significant risks to the network. This approach

would allow for more stable long-term CCS operations and reduce the likelihood of costly disruptions due to reservoir failures.

Kansas: Statewide CCS Deployment Potential.

Kansas presents a strong case for the large-scale deployment of CCS technologies, owing to its substantial industrial CO_2 emissions and abundant geological storage capacity. The Kansas Geological Survey collaborated with Montana State University to analyze the state's CCS potential, identifying 26 CO_2 sources across seven industries, with a combined capturable emissions rate of 33.76 $MtCO_2$ per year.

The study identified 46 storage sites with a combined storage potential of approximately 2.1 $GtCO_2$. These sites were ranked into three tiers based on their suitability for enhanced oil recovery (EOR) operations and geological storage. Tier 1 locations, with the highest suitability, were assigned an additional EOR sales value of $25 per metric ton of CO_2, in addition to the $35 per metric ton 45Q tax credit. Tier 2 and Tier 3 locations were assigned lower EOR values.

Scenarios run using SimCCS demonstrated that the deployment of CCS infrastructure in Kansas is economically feasible, particularly when the 45Q tax credits are applied. **Figure 381** presents the infrastructure calculated by SimCCS for one scenario. The study explored both CAP (capture all emissions) and PRICE (capture only profitable emissions) modes, concluding that Kansas could capture up to 33.76 $MtCO_2$ annually with the right infrastructure in place. However, under more constrained economic scenarios, capturing 16.78 $MtCO_2$ from the most profitable sources was deemed optimal.

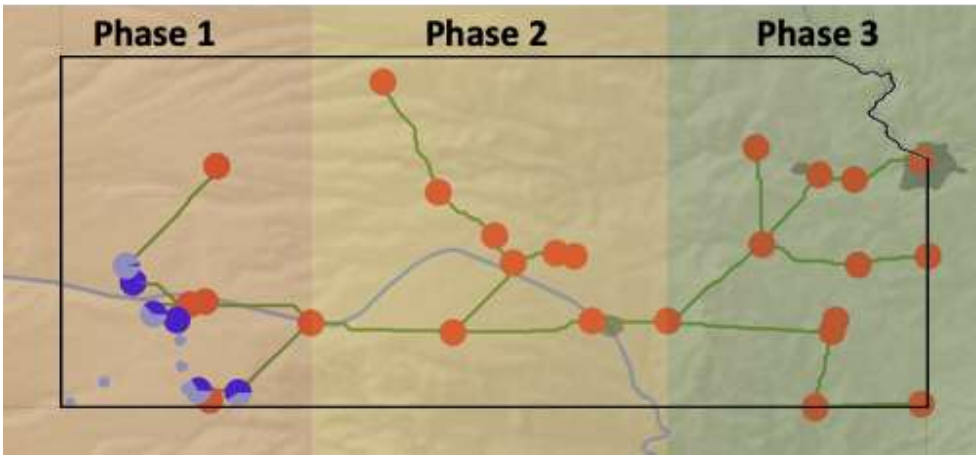


Figure 381 Infrastructure resulting from capturing all available emissions and restricting storage to the southwest corner of the state in a multiphase project

Four Corners Region: CO_2 Transport and Environmental Justice Concerns

The Four Corners region presents unique challenges and opportunities for CCS deployment, largely due to its complex land ownership and environmental justice (EJ) concerns. This study focused on the development of CO_2 transport infrastructure that accounts for the presence of tribal lands and disadvantaged communities.

Using SimCCS, the study evaluated pipeline routing scenarios with and without EJ considerations, as presented in **Figure 382**. It was found that incorporating EJ restrictions resulted in a 10.7% increase in total pipeline length, raising transport costs by approximately $0.80 per metric ton of CO_2. Despite this increase, the study emphasized the importance of adhering to EJ principles to ensure that pipeline infrastructure does not disproportionately impact vulnerable communities.

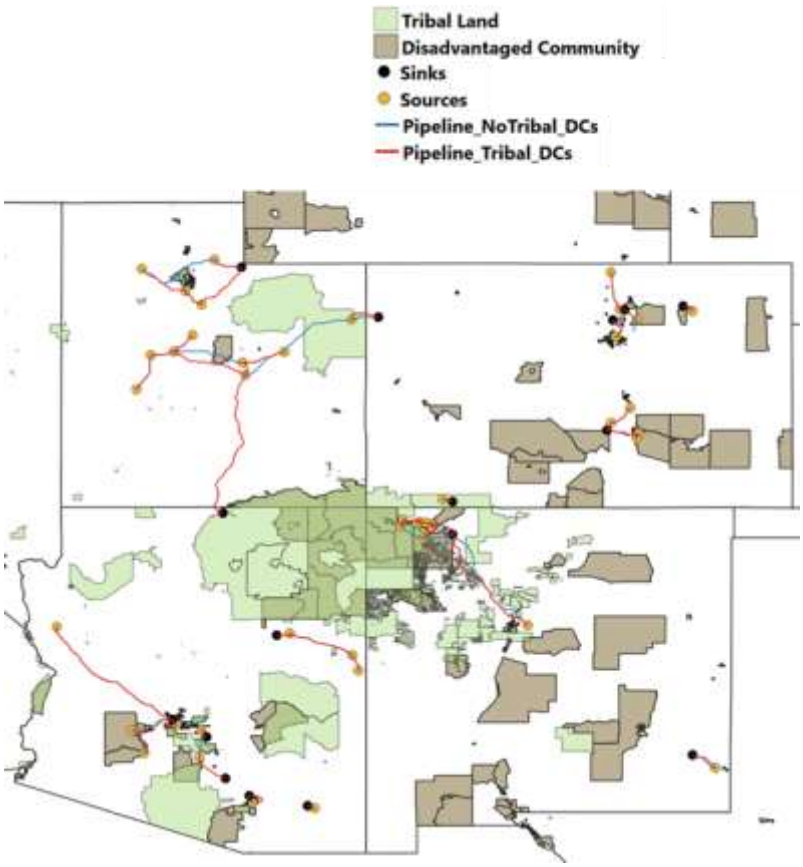


Figure 382 Optimized pipelines in the Four Corners Region study without considering environmental justice considerations

In addition to transport challenges, the study conducted a thorough risk assessment using reservoir simulation data to evaluate the potential for CO_2 leakage. The results showed that the region's geological formations are suitable for safe, long-term CO_2 storage, provided that appropriate monitoring and risk mitigation measures are in place.

Conclusion

The scenario analyses conducted for the CUSP region provide valuable insights into the opportunities and challenges of CCS deployment across diverse geological and industrial landscapes. Each region presents unique factors that influence the economic and technical feasibility of CCS, from the significant storage potential in California's Southern San Joaquin Basin to the phased approach pioneered by Kansas. By leveraging economic incentives such as the 45Q tax credit, combined with advanced optimization tools like SimCCS, these studies

highlight the critical role that targeted CCS infrastructure can play in achieving regional and national emissions reduction goals.

Phase 3 – Model Development

As the CUSP project progressed from data collection to full-scale scenario analysis, it became increasingly clear that new modeling capabilities were needed to address the challenges of realistic CCS deployment planning. Existing single-period MILP formulations were insufficient for representing phased infrastructure buildouts over decades. Computational bottlenecks limited the scale of problems that could be solved to optimality, preventing tractable national-level analyses or Monte Carlo ensembles. In addition, the ability to explore very large design spaces efficiently was essential for robust design under uncertainty.

To address these challenges, the Analytics Working Group led a sustained research effort to advance the state of CCS optimization modeling. This work resulted in multiple peer-reviewed publications and major enhancements to the SimCCS modeling framework. The contributions in this phase fall into three main categories:

- Multiphased mixed-integer linear programming (MILP) formulations that explicitly represent staged infrastructure deployment over time, enabling more realistic and cost-effective planning.
- Heuristic algorithms that generate near-optimal solutions orders of magnitude faster than exact MILP solvers, enabling national-scale studies and large scenario ensembles.
- A genetic algorithm (GA) specifically designed for the multi-capacity fixed-charge network flow problem (MC-FCNF), capable of efficiently exploring massive solution spaces and producing high-quality solutions under fixed runtime budgets.

Together, these contributions form the methodological backbone for risk-aware, large-scale CCS infrastructure planning. The following subsections present each contribution in detail, including mathematical formulations, algorithmic descriptions, experimental setups, and key results.

Phased Deployment

Planning the large-scale deployment of CCS is challenging because it requires concurrently selecting which CO_2 sources to capture from, which locations to store the CO_2, and where to route the transportation pipelines (Jones et al. 2022). Large scale CCS projects will inevitably experience variability in their economic conditions, source and reservoir availability, and project objectives over their lifetimes. Many current CCS infrastructure modeling approaches assume a static environment, where the infrastructure design is optimized based on a snapshot of available sources, reservoirs, and their associated economic and capacity parameters that are assumed to remain constant for the entire length of the project. While static models may rely on reasonable assumptions for many applications, there are some where this static assumption is limiting:

1. Sources or reservoirs may not be available throughout the entire project length, instead coming online after project initiation, or becoming inactive prior to project completion.
2. Government policies, such as increased (or decreased) tax credits (e.g. continuation or increase in 45Q credits in the United States) or modified carbon taxes, that change during the lifetime of a project could lead to increased CCS participation from sources or reservoirs.

3. Fluctuations in the price of oil could incentivize or disincentivize enhanced oil recovery (EOR) fields to purchase CO_2 from a CCS project over the life of the project thereby impacting CO_2 sales prices.
4. Financial constraints of the CCS project may require phased construction of the infrastructure over a significant period of time (e.g. 20 yr) instead of construction all at once.
5. An increase (or decrease) over time in the target CO_2 capture amount for a CCS project, due to meeting phased capture objectives.

None of these scenarios can be adequately addressed by a single-phase, static, infrastructure design model without significant degradation in solution quality. In this effort, we proposed a novel multiphased CCS infrastructure design model, formulated as a mixed integer linear program, that concurrently optimizes the design across multiple phases to construct a solution that is globally optimal for the full project instead of locally optimal for individual phases. We discuss the theoretical mechanism at play in the multiphased model's operation and show how it is able to solve more scenarios than the single-phase model is able to solve. We also present an evaluation using real CCS infrastructure data showing that the multiphased model is in fact able to determine cheaper infrastructure designs than the single-phase model when solving the same problem.

Model Formulation

In this section, we introduce the multiphased CCS infrastructure design model. We consider input consisting of a set of CO_2 emission sources, geologic storage reservoirs, candidate pipeline components, and project phases. Sources are parameterized with phase-specific unit capture costs and annual amounts of capturable CO_2 emissions. Reservoirs are parameterized with phase-specific unit injection costs and annual storage capacities, as well as total lifetime storage capacities.

Candidate pipeline components are the set of possible pipeline locations that the model is allowed to choose from when making deployment decisions. The candidate pipeline components are generated by the existing SimCCS process of calculating paths in a weighted cost surface. The weighted cost surface aggregates numerous properties from the underlying geography (e.g. population, land ownership, land cover, topography, rights of way) and produces a raster quantifying the relative costs of building pipelines between the neighboring cells. Paths between sources and reservoirs are then calculated and sparsified to produce the set of candidate pipeline components. The result of this effort is pipeline network routing at the resolution of the raster grid size. Pipelines component costs are represented as a set of linear functions (called *trends*) of pipeline capacity versus cost. The costs of the distinct pipeline trends were obtained from the NETL Transport Cost Model. Using pipeline trends instead of explicit pipeline capacities (i.e. diameters) reduces the number of integer variables in the model. It is assumed that the capacity of the largest pipeline trend is arbitrarily large. Pipeline construction costs are annualized by way of a capital recovery factor that accounts for project financing. The capital recovery factor includes the amount of time left in the modelled project. In this way, all pipelines are paid off in the project's time period, whether the pipeline opens in an early phase or a late one. The multiphased CCS infrastructure design problem is formulated as a Mixed Integer Linear Program (MILP) below:

Scenario Input Data:

S	Set of CO_2 sources
Q_{it}^{src}	Annual CO_2 production rate at source i in phase t ($MtCO_2$/yr)
V_{it}^{src}	Variable cost of capturing CO_2 from source i in phase t (\$/$MtCO_2$)
R	Set of storage sites
Q_{j}^{res}	Lifetime CO_2 capacity of storage site j ($MtCO_2$/yr)
Q_{jt}^{res}	Annual CO_2 capacity of storage site j in phase t ($MtCO_2$/yr)
V_{jt}^{res}	Variable cost of injecting CO_2 into storage site j in phase t (\$/$MtCO_2$)
P	Set of candidate pipelines
C	Set of possible capacities for each pipeline
Q_{kc}^{min}	Minimum capacity of pipeline k with capacity c ($MtCO_2$/yr)
Q_{kc}^{max}	Maximum capacity of pipeline k with capacity c ($MtCO_2$/yr)
F_{kc}^{pipe}	Fixed cost of opening pipeline k with capacity c (\$)
V_{kc}^{pipe}	Variable cost of transporting CO_2 via pipeline k with capacity c (\$/$MtCO_2$)
I	Set of all vertices (sources, sinks, candidate pipeline junctions)
N_t	Number of years in phase t
G_t	Annual target CO_2 capture amount during phase t (t/yr)

The decision variables of the infrastructure design MILP indicate which sources to open and how much CO_2 to capture from each, which storage locations to open and how much CO_2 to inject into each, and where to deploy pipelines and what capacity they need to be able to transport. Details on the decision variables are presented below.

Model Decision Variables:

$a_{it} \in \mathbb{R}^{\geq 0}$	Annual amount of CO_2 captured from source i in phase t ($MtCO_2$/yr)
$b_{jt} \in \mathbb{R}^{\geq 0}$	Annual amount of CO_2 injected into reservoir j in phase t ($MtCO_2$/yr)
$y_{kct} \in \{0,1\}$	Indicates if pipeline k with capacity c is opened in phase t
$x_{kct} \in \mathbb{R}^{\geq 0}$	Annual amount of CO_2 put in pipeline k with capacity c in phase t ($MtCO_2$/yr)
$p_{kct} \in \mathbb{R}^{\geq 0}$	Annual CO_2 capacity of pipeline k with capacity c in phase t ($MtCO_2$/yr)

The MILP is driven by the objective function representing the cost of the full project across all phases:

$$\min \overbrace{\sum_{i\in S}\sum_{t\in T}(V_{it}^{src}a_{it}N_t)}^{capture\ cost} + \overbrace{\sum_{k\in P}\sum_{c\in C}\sum_{t\in T}\left((F_{kc}^{pipe}y_{kct} + V_{kc}^{pipe}p_{kct})\sum_{r\geq t}N_r\right)}^{transport\ cost} + \overbrace{\sum_{j\in R}\sum_{t\in T}\left(V_{jt}^{res}b_{jt}N_t\right)}^{storage\ cost}$$

Constraints are used to enforce realistic operational restrictions including capacity restrictions and standard network construction requirements. The constraints are presented below.

Constraints:

$Q_{kc}^{\min}y_{kct} \leq p_{kct} \leq Q_{kc}^{\max}y_{kct}, \forall k \in P, \forall c \in C, \forall t \in T$	(A)
$x_{kct} \leq \sum_{r\leq t} p_{kcr}, \forall k \in P, \forall c \in C, \forall t \in T$	(B)
$\sum_{\substack{k\in P:\\ src(k)=n}}\sum_{c\in C} x_{kct} - \sum_{\substack{k\in P:\\ dest(k)=n}}\sum_{c\in C} x_{kct} = \begin{cases} a_{nt} & \text{if } n \in S \\ -b_{nt} & \text{if } n \in R, \forall n \in I, \forall t \in T \\ 0 & \text{if } n \in J \end{cases}$	(C)
$a_{it} \leq Q_{it}^{src}s_i, \forall i \in S, \forall t \in T$	(D)
$a_{i(t-1)} \leq a_{it}, \forall i \in S, \forall t \in T\ (t > 0)$	(E)
$\sum_{t\in T} N_t b_{jt} \leq Q_j^{res}r_j, \forall j \in R$	(F)
$b_{jt} \leq Q_{jt}^{res}, \forall j \in R, \forall t \in T$	(G)

$\sum_{i \in S} a_{it} \geq G_t, \forall t \in T$	(H)

Where constraint (A) restricts pipeline capacity by its minimum and maximum values. Constraint (B) ensures that new and existing pipeline capacity is sufficient for the amount of CO_2 to be transported. Constraint (C) enforces conservation of flow at each internal vertex. Constraint (D) ensures that the amount of CO_2 captured at each source is limited by the source's emission rate. Constraint (E) ensures that capture amounts do not decrease between consecutive phases. Constraint (F) limits lifetime storage for each reservoir by its maximum capacity. Constraint (G) limits the annual storage amount in each reservoir to the phase's annual capacity of the reservoir. Constraint (H) ensures each phase's total capture amount meets the phase's target. The version of the model with Constraint (H) is called the CAP version. Constraint (H) can be omitted to form a version of the model called the PRICE version that will only deploy cost negative (i.e. profitable) infrastructure. The PRICE version of the model is useful when considering scenarios with price incentives for CCS projects (e.g. tax credits such as 45Q).

Model Discussion

The multiphased model presented above will determine optimal values for the decision variables that minimize the objective function. The model needs to be parameterized with accurate, user-supplied, cost and capacity data. Determining accurate cost and capacity data for a specific CCS sources and reservoirs is a complicated effort and case study specific. With appropriate input data, the proposed multiphased model can be used to model all of the scenarios described earlier by manipulating instance input parameters:

1. Source or reservoir unavailability can be modelled by setting their capacities to zero in the phases they are unavailable in.
2. Modifications to tax credits and carbon taxes can be modelled by subtracting the credit amount from the capture or storage costs. If the credit is source dependent (e.g. California's Low Carbon Fuel Standard credit), then the credit should be subtracted from the capture costs of the sources that qualify for the credit.
3. If the credit is reservoir dependent (e.g. 45Q), then the credit should be subtracted from the storage costs of the reservoirs that qualify for the credit. The model is not equipped to manage a credit that is both source and reservoir dependent.
4. Proceeds from sales to EOR fields can be modelled by subtracting the unit (per metric ton) sales proceeds from the storage costs of each individual EOR field.
5. Phased capture objectives can be modelled by modifying the phase-specific annual CO_2 capture target.

The multiphased model presented above is a generalization of an existing single-phase CCS infrastructure design model. In the single-phase version of the model, the instance input parameters and MILP decision variables are constant throughout the entire project length while the objective of minimizing infrastructure cost remains the same. The infrastructure design for a multiphase CCS project can be naively approximated by sequential solutions of the single-phase model:

1. Find optimal infrastructure to support phase 1.

2. Mark opened infrastructure as purchased and find optimal additional infrastructure needed to support phase 2.
3. Repeat for remaining phases.

The limitation of this iterative approach is that infrastructure deployed in each phase is done without consideration given to future phases. This can lead to sub-optimal solutions for the full project. Instead of designing infrastructure one phase at a time, the multiphased model concurrently optimizes infrastructure for all phases. This results in infrastructure designs that are globally optimal for the full project instead of locally optimal for the individual phases. The multiphased model leverages three techniques for generating globally optimal solutions that improve upon iterative single-phase solutions:

- As-needed Infrastructure Deployment. In single-phase models, any infrastructure that is opened needs to be opened during the entire (single-phased) project. Alternatively, in the multiphased model, infrastructure can open (and close) over the course of the project. This flexibility can lead to cost savings when infrastructure is only opened when necessary. Figure 383 presents a scenario that illustrates this cost saving.

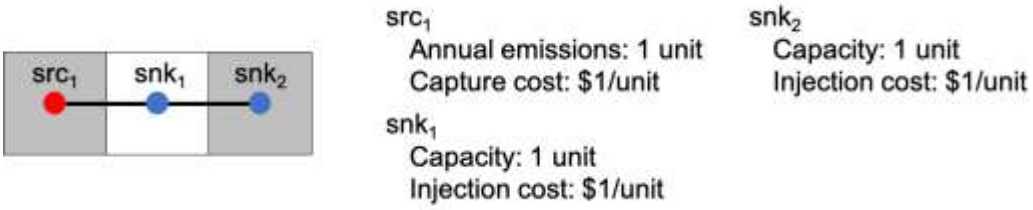


Figure 383 Consider the objective of capturing one unit per year for a two-year project. The single-phased and multiphased solutions will both capture all emissions from the source and fill all capacity in both sinks. However, the single-phased solution will deploy all sources and sinks at once, and build a one-capacity pipeline from src_1 to snk_1 and one half-capacity pipeline from snk_1 to snk_2. Alternatively, the multiphased solution will build a one-capacity pipeline from src_1 to snk_1 and fill snk_1 in the one-year phase one followed by an additional one-capacity pipeline from snk_1 to snk_2 to fill snk_2 in the one-year phase two. This will result in a cheaper solution since pipeline cost functions are subadditive (i.e. two one half-capacity pipelines are more expensive than a single one-capacity pipeline.)

- Infrastructure Overprovisioning. The aggregate of optimal single-phased solutions does not allow for overprovisioning early phases in anticipation of future phases. Since the multiphased model concurrently optimizes all phases, a pipeline can be deployed in one phase with a larger capacity (i.e. diameter) than is necessary if a larger capacity will be required in a future phase. This can provide beneficial economies of scale by constructing a single large pipeline in an early phase instead of multiple smaller pipelines across multiple phases. **Figure 384** presents a scenario that illustrates the power of overprovisioning in early phases.

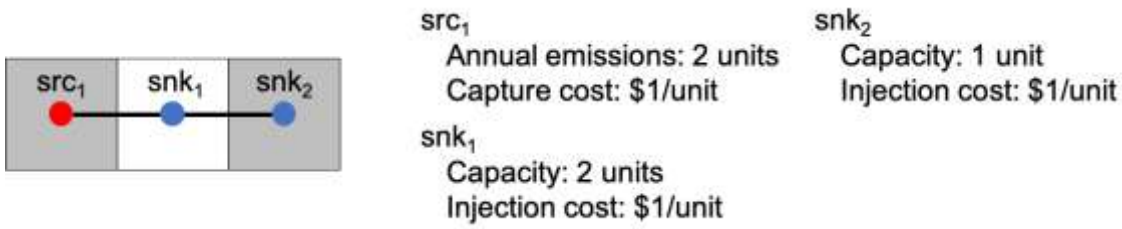


Figure 384 Suppose there are two available pipeline capacities: 1 unit per year and 2 units per year. Consider a two-phased scenario with an objective of capturing one unit in the first one-year phase and two units in the second one-year phase. Optimal single-phased solutions for each of the phases in isolation would result in a one-capacity pipeline connecting the source to snk_1 in phase 1 and a two-capacity pipeline connecting the source to snk_1 and one-capacity pipeline connecting snk_1 to snk_2 in phase 2. This would require building two pipelines over the life of the project between the source and snk_1. Alternatively, the optimal multiphased solution would build a single two-capacity pipeline between the source and snk_1 initially in phase 1. This pipeline would be overprovisioned for phase 1 but would not require new construction in phase 2.

- Targeted Routing. Optimal pipeline routing for a single phase without consideration given to future phases will not necessarily result in an optimal solution across all phases. Instead, it may be advantageous to select a routing that is sub-optimal for the current phase but leads to cheaper pipeline networks in subsequent phases. By concurrently optimizing all phases, the multiphase model will find globally optimal pipeline routes across all phases. **Figure 385** presents a scenario that illustrates this advantage of concurrently optimizing pipeline routes across multiple phases.

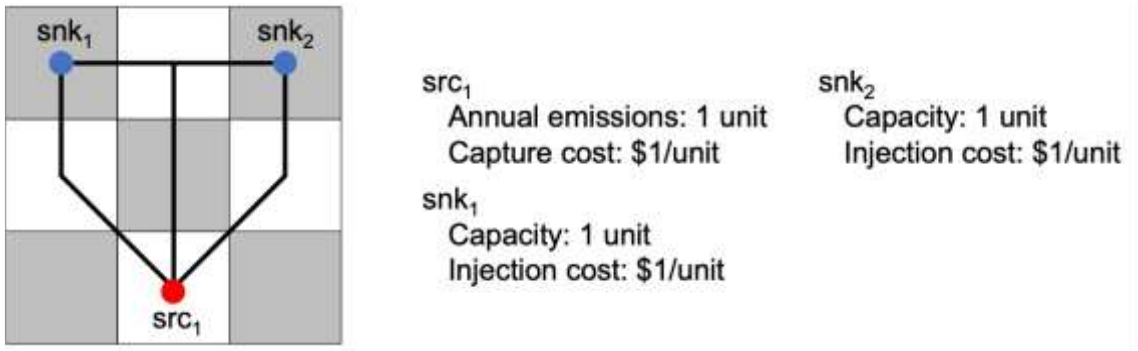


Figure 385 Suppose pipeline costs are proportional to length. Consider a two-phased scenario with an objective of capturing one unit in the first one-year phase and one unit in the second one-year phase. Optimal single-phased solutions for each of the phases in isolation would result in a direct pipeline between the source and snk_1 and the source and snk_2 for a total pipeline length of 4.83. Alternatively, a cheaper pipeline network can be selected by using the shared pipeline from src_1 to the cell between snk_1 and snk_2, and then pipelines from that cell to snk_1 and snk_2 for a total pipeline length of 4.

Heuristic Solvers

Deploying CCS infrastructure on a massive scale requires careful and comprehensive planning to ensure investments are made in a cost-effective manner (Whitman et al. 2022). At its core, designing CCS infrastructure is an optimization problem that aims to determine the most cost-effective locations and quantities of CO_2 to capture, route via pipeline, and inject for storage. Designing CCS infrastructure can naturally be formulated as a Mixed Integer Linear Program (MILP) that aims to minimize total cost, while capturing and injecting a target amount of CO_2.

The MILP is parameterized with a candidate pipeline network constructed from a weighted cost surface, and economic and capacity data about the possible source and sink locations. We show in this research that designing CCS infrastructure is a generalization of the well-studied NP-Hard fixed charge network flow (FCNF) problem. This means that optimal algorithms for designing CCS infrastructure do not efficiently scale as scenarios grow in size.

The intractability of designing CCS infrastructure impacts CCS infrastructure design studies in three ways. First, CCS infrastructure studies are moving from local scale projects with tens of sources and sinks to regional and national scale projects with thousands of sources and sinks. For instances of this size, MILP implementations have not been successful at executing in a reasonable time period (e.g. 40% gap after 72 hours). Second, many CCS infrastructure studies explore impacts of minute changes to input parameters that arise due to uncertainty (e.g. reservoir specific storage potential or injectivity). Studies of this type require ensemble runs, where thousands of differently parameterized instances are generated and solved, with results feeding the generation of more instances. Finally, studies are being proposed that consider continuous reservoir regions instead of discrete point locations. To solve these problems, the infrastructure design algorithm will need to be run many sequential times where, between runs, discrete reservoir locations are moved based on the previous iteration's solution. It is not possible to rely on MILP formulations to solve these types of problems. New optimization techniques need to be developed to address the problem of designing CCS infrastructure for massive deployments.

In this research, we introduce the CCS Infrastructure Design (CID) problem and develop custom optimization algorithms for it. We prove that CID is a generalization of the well-studied FCNF problem and characterize its computational complexity. We then introduce three fast algorithms for the CID problem. Finally, we evaluate the performance of the algorithms on realistic datasets and find that they reduce running time compared to an optimal MILP, with a minimal increase in solution costs. Reducing the time it takes to determine CCS infrastructure designs will support national-level scenarios, undertaking risk and sensitivity assessments, and understanding the impact of government policies (e.g. tax credits for CCS).

Problem Formulation

Given a set of CO_2 emitters (sources), geological reservoirs, and a candidate pipeline network, the goal of the CCS Infrastructure Design (CID) problem is to determine, in a cost-minimal fashion, which sources to capture from, which reservoirs to inject into, and which (and what diameter) pipelines to build to capture a pre-determined system-wide quantity of CO_2.

The sources and reservoirs are parameterized with an economic model consisting of fixed costs to open locations (millions of dollars), and variable costs to utilize the locations (dollars per metric ton of CO_2 captured/injected). These costs vary based on the ease of injection at that particular site. Candidate pipeline routes are constructed from a weighted cost surface. Pipelines have construction and per-metric-ton utilization costs dependent on their geographic location and the quantity of CO_2 they transport. Pipelines can intuitively be represented as a number of discrete pipeline sizes (i.e. diameters) and their associated costs and capacities. Pipeline costs include construction and operation costs (e.g. pumping stations, maintenance). In a mixed integer linear program (MILP) formulation, this representation requires an integer variable for each possible pipeline edge/size pair, which results in a large number of variables and quickly leads to

intractable formulations. To reduce the number of integer variables used in the MILP formulation, pipelines can be represented as a smaller set of linear functions (called *trends*) of pipeline capacity versus cost. The composition of these trends forms a pipeline capacity versus cost function that is increasing, piecewise linear, and subadditive. An example of two trends approximating the non-linear pipeline capacity versus cost function is presented in **Figure 386**. The pipeline costs that the trends approximate were determined using the National Energy Technology Laboratory's CO_2 Transport Cost Model. The increasing and subadditivity properties of the cost function enforces that a pipeline of a given capacity is cheaper than multiple pipelines of smaller capacities or a pipeline of a larger than necessary capacity. It is also assumed that the capacity of the largest pipeline trend is arbitrarily large. Using pipeline trends instead of explicit diameters} allows for simpler formulations compared to the discrete formulation while still ensuring that the cost model is realistic. All fixed construction costs are annualized by way of a capital recovery factor that accounts for project financing. The CID problem based on linearized pipelines is formulated as an MILP is a similar fashion as previously presented.

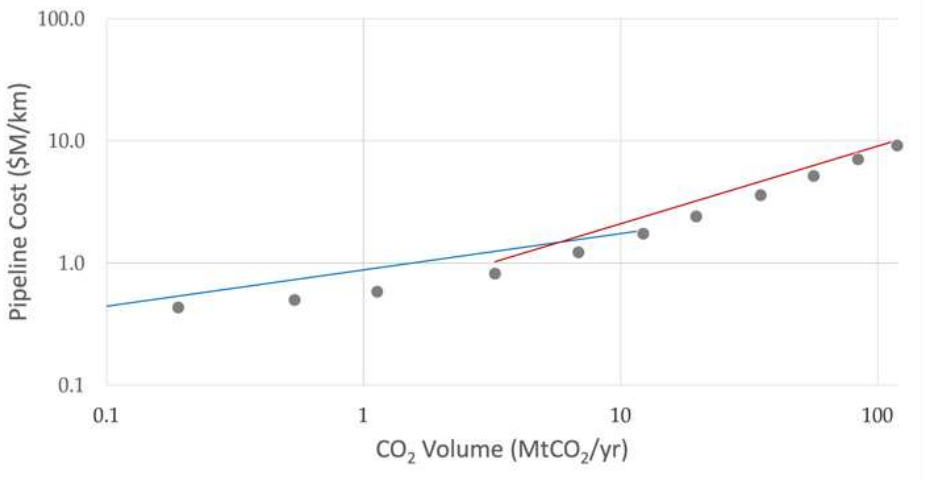


Figure 386 Two linear trends approximating the cost of a pipeline given the transportation volume

Computational Complexity

CID generalizes the Fixed Charge Network Flow (FCNF) problem: Consider a directed graph with edge capacities and fixed edge costs. Purchasing an edge incurs its fixed cost and allows it to host any amount of flow up to its capacity. A subset of the vertices is designated as sources and have an associated amount of flow they are able to supply. Likewise, a subset of the vertices is designated as sinks (analogous to reservoirs in the CID problem) and have an associated amount of flow they demand. The goal of the FCNF problem is to determine a least-cost set of edges that allows sufficient flow to be routed from the sources to the sinks to satisfy all of the sink demand.

Theorem: $\gamma \ln |V|$-approximation algorithm for the FCNF problem, where $0 < \gamma < 1$ is some constant, unless P=NP.

Proof: This complexity result is via an approximation-preserving reduction from the Dominating Set problem: Given a graph $G = (V, E)$, find a minimum sized $U \subseteq V$ such that for each vertex v in $V \setminus U$, there is some vertex u in U such that the edge (u, v) is in E.

Let $G = (V, E)$ be an instance of Dominating Set where $|V| = n$. G reduces to an FCNF instance $G' = (V', E')$ as follows: For each vertex v in V, make a new vertex v_{in}. Make a directed edge with cost zero and capacity one from the new vertex to the original one (the dotted red edges in **Figure 387**). For every edge $e = (u, v)$ in E, make the directed edges (u, v_{in}) and (v, u_{in}) with cost zero and capacity one (the solid black edges in **Figure 387**). Create a new vertex s and for each vertex v in V, make the directed edge (s, v) with cost one and infinite capacity (the dashed green edges in **Figure 387**). Let the original vertices V be the sinks and each have a demand of one. Let s be the single source and let its supply be $|V|$. **Figure 387** shows the reduction from Dominating Set to FCNF.

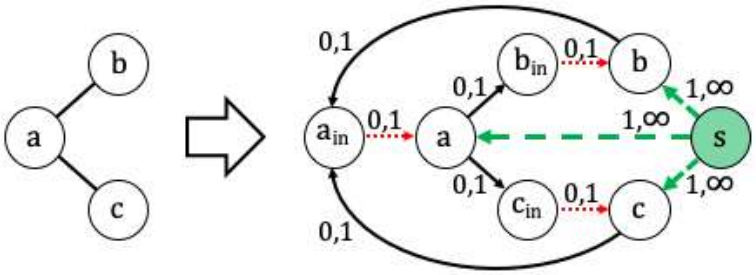


Figure 387 Dominating Set reduction to the FCNF problem where each edge is weighted as (cost, capacity)

Suppose that $U \subseteq V$ is a dominating set of G with $|U| = k$. For each vertex in $V \setminus U$, associate it with one neighbor that is in U. In this way, each vertex u in U is associated with a set of neighbors N_u that are in $V \setminus U$. U can now be translated into a source-sink flow of cost k in G'. For each vertex u in U, push $|N_u| + 1$ units of flow from the source s to u. One unit of that flow will be consumed by u and the additional $|N_u|$ units of flow will be distributed to the neighbors in N_u. Consider a vertex v in $V \setminus U$. This vertex has been associated with a single neighbor vertex u that is in U. Since v and u are neighbors in G, the directed edges (u, v_{in}) and (v_{in}, v) are in G' and form a path from u to v. The capacity of this path is one, so one unit of flow can be pushed to each vertex v in $V \setminus U$ from its associated neighbor vertex u in U. Therefore, this flow will satisfy all demand in G' and its cost will be k since the only costs incurred are the fixed unit costs for sending flow to the nodes directly connected to source s (i.e. the vertices in U).

Suppose there is a flow solution to G' of cost k. This means that every vertex in V receives one unit of flow from source s. Let U be the set of vertices receiving flow directly from source s. Since the only costs incurred in the flow network are on vertices receiving flow directly from source s, $|U| = k$. Consider a vertex v in $V \setminus U$. Suppose that v was able to forward flow to another vertex in V'. This would require v receiving more than one unit of flow, since v's demand for one unit needs to be satisfied. There are only two directed edges into v: (v_{in}, v) and (s, v). Since v is not in U, the directed edge (s, v) is not carrying any flow. Since the capacity of (v_{in}, v) is one, all of the flow carried on this edge must be used to satisfy v's demand. Therefore, there is no excess flow available for v to forward to another vertex in V'. This means that every vertex in $V \setminus U$ must be receiving flow from a neighbor that is in U, which means that U is a dominating set of V.

Since any dominating set in G of size k corresponds to a flow in G' of cost k and conversely, inapproximability results the Dominating Set problem hold for the FCNF problem. It has been shown that there exists a constant, $0 < \gamma < 1$, such that the Dominating Set problem cannot be

approximated within a factor of $\gamma \ln |V|$ unless P=NP, thus this result holds for the FCNF problem as well.

Corollary: The CID problem has the same inapproximability result as the FCNF problem.

Proof: CID generalizes the classic FCNF problem by allowing parallel edges representing different pipeline sizes. Other apparent differences between CID and FCNF are not actually generalizations of the FCNF model: Source and reservoir costs and capacities can be pushed to a new edge between the original source/reservoir and a new node. Also, allowing only a subset of the demand to be captured can be enforced with a new source node that feeds the original sources and a new reservoir node connected to the original reservoirs with the required demand (i.e. the target CO_2 capture amount).

As such, CID cannot be easier to approximate than FCNF.

Algorithms

Existing approaches to solving CCS infrastructure design type problems rely on exact techniques, specifically solving MILPs like the ones detailed throughout this report. The running time of MILP solvers does not scale linearly with linearly increasing input size. Large instances (e.g. thousands of vertices and pipeline components) cannot be solved by MILPs in a reasonable time, which motivates the search for sub-optimal techniques with better running time performance. In this section, we present three algorithms for CID.

Greedy Add

The first algorithm we introduce iteratively builds a solution by greedily selecting cheap (source, reservoir) pairs, as well as the cheapest appropriately sized pipelines connecting them. This algorithm is presented in Algorithm 1 and detailed below with references to the applicable lines of Algorithm 1.

First, for each (source, reservoir) pair, the maximum amount of CO_2 that is able to be transferred between the pair is determined. This value is calculated as the minimum of the source's uncaptured production, the reservoir's unused capacity, and the amount of the target capture remaining (line 4).

Second, the (source, reservoir) pair's capture and storage costs are calculated. Fixed costs are only included if the source or reservoir has not yet been opened (lines 6-11). Variable costs are included based on the amount of CO_2 that was determined to be transferred between the source and reservoir (line 5).

Third, the cheapest path between the source and reservoir for the amount of CO_2 that will be transferred is calculated. To calculate the cheapest path, the pipeline network first needs to be parameterized with costs that reflect the cost to transport that amount of CO_2 along each pipeline component. These costs need to take into account the following considerations:

1. Unused pipeline capacity that has already been purchased.
2. Upgrade costs associated with moving from one trend to a higher capacity trend.
3. Changes to the variable costs for CO_2 already being transported along that pipeline component associated with changing pipeline trends.

4. Cost savings associated with downsizing pipeline capacities due to redirecting CO_2 (i.e. pushing CO_2 in the opposite direction of CO_2 already being transported).

Parameterizing the pipeline network with costs is done in lines 13-27. Each pipeline component $e = (u, v)$ is sequentially considered as a directed edge. Depending on the pipeline trend already purchased and existing CO_2 flow on e or $e' = (v, u)$, there are three possibilities for the new pipeline's required volume and the existing pipeline's cost:

1. e is already hosting CO_2 (lines 14-16). In this case, the new volume of CO_2 on e will be the existing volume plus the new amount being transported. The old pipeline cost is the old cost of e.
2. e' is already hosting CO_2 (lines 17-19). Pipelines cannot transport CO_2 in both directions. If e' is already hosting CO_2, adding flow in the opposite direction on e represents redirecting CO_2 that was traveling from v to u. If e' is hosting less CO_2 than the amount being transported, the new volume of CO_2 on e will be the new amount minus the amount e' is currently hosting. If e' is hosting more CO_2 than the amount being transported, the new volume of CO_2 on e' would be the amount e' is currently hosting minus the new amount. In either case, the magnitude of the difference is the new volume of CO_2, so line 18 captures both with the absolute value. In both cases, the old pipeline cost is the old cost of e'.
3. Neither e nor e' is already hosting CO_2 (lines 20-22). In this case, the new volume of CO_2 on e will be the new amount being transported and there was no old pipeline cost.

The cost associated with using pipeline component e is then calculated by first determining the smallest trend that will fit the new volume of CO_2 (line 24). A pipeline of sufficient capacity is always available since the maximum capacity of the largest trend exceeds the target CO_2 capture amount. The new cost of the pipeline component is calculated as the fixed cost for the selected trend plus the utilization cost as a factor of the new volume of CO_2 (line 25). The cost of pipeline component e is set to be the new cost minus the old pipeline component cost (line 26). This is the cost to use pipeline component e, factoring in already purchased pipeline infrastructure. A consequence of this calculation is that the cost of e can be negative when e' is hosting CO_2. If redirecting CO_2 results in the new cost of the pipeline component being lower than the old cost of e', the cost to use e will be negative. Selecting e in this case represents redirecting some of the CO_2 that was traversing e', thereby enabling a smaller pipeline trend for the remaining CO_2, less utilization, and a cost savings. The cheapest path can then be calculated between the source and reservoir (line 28). Since there can be negative edge weights in the network, and possibly negative cycles, we implemented this step by setting the capacity of each edge to 1 and finding the minimum-cost flow of value 1.

After the costs for each (source, reservoir) pair are calculated, the pair that captures, transports, and injects CO_2 for the lowest cost per metric ton is added to the solution (lines 31-35). When the cheapest pair is selected, the infrastructure used to support the pair is updated for future iterations (lines 38-63)}. For the selected source and reservoir, they are added to the solution and their amounts captured and stored are updated (lines 39-40). The path between the source and reservoir is added one edge at a time (lines 42-63). In a similar fashion as was done to parameterize the costs for the pipeline network when finding cheapest paths, the new edge added to the solution depends on whether or not that edge (or its reverse) was already in the solution. If the edge was already in the solution, it will stay in the solution with a new volume of CO_2 being

the old volume plus the new amount being transported (lines 43-45). If the edge in the reverse direction is already in the solution, the edge added to the solution and its volume of CO_2 depends on if the reverse edge was hosting more or less than the new amount of CO_2 being transported (lines 46-53). If neither the edge nor the reverse direction edge is already in the solution, the edge is added with a volume of CO_2 being the new amount being transported (lines 54-56).

This process then repeats until the target quantity of CO_2 is captured. The running time for the algorithm is driven by lines 2-36. The running time for the algorithm is $O((|S||R|)^2(|K||C| + ShortestPath))$, where $|S|$ is the number of sources, $|R|$ is the number of reservoirs, $|K|$ is the number of pipeline components, $|C|$ is the number of trends, and $ShortestPath$ is the running time for the shortest path algorithm used. Line 2 repeats until the capture target is met by maximizing the transfer between some (source, reservoir) pair at each iteration of the algorithm. Since the transfer between each pair is maximized, it cannot be revisited in future iterations. This means that line 2 cannot repeat more than $|S||R|$ times. Line 3 repeats $|S||R|$ times. Line 13-27 runs in $|K||C|$ time and line 28 runs in whatever the running time is of the selected shortest path algorithm. When there are a reasonable number of trends, the shortest path algorithm at line 28 will dominate the running time.

Algorithm 1 Greedy Add

Input: Sources S, Reservoirs R, Candidate Pipelines K, Capture Target T
Output: $S' \subseteq S, R' \subseteq R, K' \subseteq K$

$S', R', K' = \emptyset$; $captured = 0$; minCost $= \infty$; minSet $= \emptyset$
while $captured < T$ **do**
  for $(src, res) \in S \times R$ **do**
    c = min(src.remainingProduction, res.remainingCapacity, $T - captured$)
    cost $= c \cdot$ (src.variableCost + res.variableCost)
    if src.captured $= 0$ **then**
      cost += src.fixedCost
    end if
    if res.stored $= 0$ **then**
      cost += res.fixedCost
    end if

    for directed edge $e = (u, v)$ in K **do**
      if $e = (u, v)$ in K' **then**
        vol = e.transported + c
        oldCost = e.costInK'
      else if $e' = (v, u)$ in K' **then**
        vol = |c - e'.transported|
        oldCost = e'.costInK'
      else
        vol = c
        oldCost = 0
      end if
      trend = smallestTrendWithCapacity(vol)
      newCost = trend.fixedCost + trend.variableCost $\cdot$ vol
      e.setCost(newCost - oldCost)
    end for
    $path$ = shortestPathInK(src, res)
    cost += $path$.cost

    cost /= c
    if cost < minCost **then**
      minCost = cost
      minSet = $\{src, res, path, c\}$
    end if
  end for

  Let $src, res, path$, and c be the references contained in minSet
  S'.add(src), R'.add(res)
  src.captured += c, res.stored += c, $captured$ += c

  for directed edge $e = (u, v)$ in $path$ **do**
    if $e = (u, v)$ in K' **then**
      newEdge = e
      vol = e.transported + c
    else if $e' = (v, u)$ in K' **then**
      if e'.transported < c **then**
        newEdge = e
        vol = c - e'.transported
      else
        newEdge = e'
        vol = e'.transported - c
      end if
    else
      newEdge = e
      vol = c
    end if
    K'.remove(e), K'.remove(e')
    trend = smallestTrendWithCapacity(vol)
    newEdge.transported = vol
    newEdge.costInK' = trend.fixedCost + trend.variableCost $\cdot$ vol
    K'.add(newEdge)
  end for
end while
return $\{S', R', K'\}$

Algorithm 1. Greedy Add

Iterative LP

The second algorithm we introduce iteratively solves linear programs that result from removing all integer variables from the mixed integer linear program formulation of the CID problem. Removing integer variables allows the resulting linear programs to be solved optimally in polynomial running time. However, the integer variables in the original mixed integer linear program formulation provided the mechanism to charge the fixed cost based on the binary decision of whether infrastructure was used or not. Each type of infrastructure entity (i.e. source, pipeline, or reservoir) in the CID problem has a fixed utilization cost F and variable utilization cost V. This means that the total cost for an entity is $Fw + Vx$, where w indicates if the entity is in use and x is the continuous amount of CO_2 processed by the entity. To approximate fixed costs with only continuous variables, entity costs are reformulated by removing the fixed utilization component and changing the variable utilization coefficient from V to $\frac{F}{\hat{x}} + V$, where $\hat{x}$ is an estimate of what the value of x will be when the linear program is solved. Therefore, the closer x is to $\hat{x}$, the closer the reformulated cost is to the true cost. This results in the following linear program, where $\hat{a}$, $\hat{p}$, and $\hat{b}$ are the estimated capture, transportation, and injection amounts:

$$\min \overbrace{\sum_{i \in S} \left(\frac{F_i^{src}}{\hat{a}_i} + V_i^{src} \right) a_i}^{capture\ cost} + \overbrace{\sum_{k \in P} \sum_{c \in C} \left(\alpha_{kc} + \frac{\beta_{kc}}{\hat{p}_{kc}} \right) p_{kc}}^{transport\ cost} + \overbrace{\sum_{j \in R} \left(\frac{F_j^{res}}{\hat{b}_j} + V_j^{res} \right) b_j}^{storage\ cost}$$

Subject to the standard CCS infrastructure design constraints and the following modified constraints:

$0 \leq p_{kc} \leq Q_{kc}^{\max}, \forall k \in P, \forall c \in C$	(I)
$a_i \leq Q_i^{src}, \forall i \in S$	(J)
$b_j L \leq Q_j^{res}, \forall j \in R$	(K)

These constraints are similar to the standard capacity limiting constraints. Constraint I limits the maximum capacity of a pipeline. Constraint J limits the amount captured at each source by its maximum production, and constraint K limits lifetime storage for each reservoir by its maximum capacity. An iterative scheme is used to generate estimated $\hat{a}$, $\hat{p}$, and $\hat{b}$ values: The estimated values are all initially set to one and the linear program is solved, resulting in solution values for a, p, and b. For each subsequent iteration, the estimated $\hat{a}$, $\hat{p}$, and $\hat{b}$ values are set to equal the previous iteration's a, p, and b values. In this way, if an infrastructure entity's utilization remains identical across iterations, its total cost will accurately reflect the correct fixed and variable costs, since $\left(\frac{F}{\hat{x}} + V\right) x = F + Vx$ when $x = \hat{x}$. However, there is no guarantee that the utilization values will stabilize between iterations, so we cannot depend on this process by itself to return high-quality solutions.

Two procedures are used to explicitly search for improved solutions, instead of just aiming to accurately reflect costs. Both of these procedures incentivize use of specific infrastructure based on usage in previous iterations of the algorithm. The *intensification* procedure prioritizes heavily-used infrastructure to improve existing solutions. The *diversification* procedure prioritizes seldom used infrastructure to encourage exploration of new solutions. Both of these procedures modify the $\hat{a}$, $\hat{p}$, and $\hat{b}$ values based on utilization statistics from previous iterations. The relevant utilization statistics are the same for each family of variables in the linear program (i.e. a, p, and b), so they can all be represented with a generic variable x:

$\text{avg}_n^{x_i}$	Average value of x_i in first n iterations
$\max_n^{x_i}$	Maximum value of x_i in first n iterations
$\text{rat}_n^{x_i}$	Equal to $\text{avg}_n^{x_i}/\max_n^{x_i}$
$\text{num}_n^{x_i}$	Number of times x_i was non-zero in first n iterations
μ_n^x	Average number of non-zero x's in first n iterations
σ_n^x	Standard deviation of number of non-zero x's in n iterations

This algorithm is presented in Algorithm 2 and detailed below. The algorithm alternates between intensification (lines 8-18) and diversification (lines 21-31)} phases until the maximum number of iterations is exceeded (line 2). In the intensification phases, entities that are already extensively deployed are defined as entities x_i where $\text{num}_n^{x_i} \geq \mu_n^x + \frac{1}{2}\sigma_n^x$ (line 10). For these entities, $\hat{x}_i$ is set to $\frac{1}{1-\text{rat}_n^{x_i}}$ (line 11) which makes the cost coefficient in the objective function for entity x_i equal to $F\left(1 - \text{rat}_n^{x_i}\right) + V$. On the other hand, uncommonly deployed entities are defined as entities x_i where $\text{num}_n^{x_i} < \mu_n^x$ (line 12). For these entities, $\hat{x}_i$ is set to $\frac{1}{2-\text{rat}_n^{x_i}}$ (line 13) which makes the cost coefficient in the objective function for entity x_i equal to $F\left(2 - \text{rat}_n^{x_i}\right) + V$. All other entities have $\hat{x}_i$ set to 1 (line 15), which makes the cost coefficient in the objective function for entity x_i equal to $F + V$. This results in incentivizing the use of extensively deployed entities (since $1 - \text{rat}_n^{x_i} \leq 1$), disincentivizing the use of uncommonly deployed entities (since $2 - \text{rat}_n^{x_i} \geq 1$).

In the diversification phases, extensively and uncommonly deployed entities are defined in the same way as in the intensification phases. For extensively deployed entities, $\hat{x}_i$ is set to $\frac{1}{1+\text{rat}_n^{x_i}}$ (line 24) which makes the cost coefficient in the objective function for entity x_i equal to $F\left(1 + \text{rat}_n^{x_i}\right) + V$. For uncommonly deployed entities, $\hat{x}_i$ is set to $\frac{1}{\text{rat}_n^{x_i}}$ (line 26) which makes the cost coefficient in the objective function for entity x_i equal to $F \cdot \text{rat}_n^{x_i} + V$. All other entities have $\hat{x}_i$ is set to 1 (line \$28\$), which makes the cost coefficient in the objective function for

entity x_i equal to $F + V$. This results in incentivizing the use of uncommonly deployed entities (since $\text{rat}_n^{x_i} \leq 1$), disincentivizing the use of extensively deployed entities (since $1 + \text{rat}_n^{x_i} \geq 1$).

This algorithm alternates between intensification and diversification phases until the maximum number of iterations is exceeded (line 2). At each iteration, $\hat{a}$, $\hat{p}$, and $\hat{b}$ are determined and the linear program described above is formulated and solved (lines 33-34). The resulting solution is used to update the utilization statistics and the next iteration begins (line 42). Changing from intensification phases to diversification phases and back is done whenever solution costs fail to improve within some threshold number of iterations (lines 3-5 and 35-41)}. Once the target number of iterations is completed, the set of sources, reservoirs, and pipeline components from the last iteration is returned. Finally, the real cost of this infrastructure must be calculated, since the cost used in the algorithm is not the actual cost, but the scaled cost defined in the objective of the linear program.

The running time for each iteration of the algorithm is driven by the formulation and solving of the linear program in lines 33-34. The linear program has $O(|S| + |K||C| + |R|)$ variables and $O(|K||C| + |I| + |S| + |R|)$ constraints, where $|S|$ is the number of sources, $|R|$ is the number of reservoirs, $|K|$ is the number of pipeline components, $|C|$ is the number of trends, and $|I|$ is the number of vertices in the pipeline network. The running time is then $O(numIterations \cdot |LP|)$, where $numIterations$ is the number of iterations enforced in line 2 and $|LP|$ is the running time associated with constructing and solving the linear program solver.

Algorithm 2 Iterative LP

1: $S', R', K' = \emptyset$; minCost $= \infty$; phase $= 1$; unimproved $= 0$
2: **for** $n < maxIterations$ **do**
3: **if** unimproved $\geq improvingThreshold$ **then**
4: phase $*= -1$
5: **end if**
6: **if** phase $== 1$ **then**
7: // Intensification
8: **for** each family of variables $x \in \{a, b, p\}$ **do**
9: **for** each i **do**
10: **if** $\text{num}_{n-1}^{x_i} \geq \mu_{n-1}^{x} + \frac{1}{2}\sigma_{n-1}^{x}$ **then**
11: $\hat{x}_i = \left(1 - \text{rat}_{n-1}^{x_i}\right)^{-1}$
12: **else if** $\text{num}_{n-1}^{x_i} < \mu_{n-1}^{x}$ **then**
13: $\hat{x}_i = \left(2 - \text{rat}_{n-1}^{x_i}\right)^{-1}$
14: **else**
15: $\hat{x}_i = 1$
16: **end if**
17: **end for**
18: **end for**
19: **else**
20: // Diversification
21: **for** each family of variables $x \in \{a, b, p\}$ **do**
22: **for** each i **do**
23: **if** $\text{num}_{n-1}^{x_i} \geq \mu_{n-1}^{x} + \frac{1}{2}\sigma_{n-1}^{x}$ **then**
24: $\hat{x}_i = \left(1 + \text{rat}_{n-1}^{x_i}\right)^{-1}$
25: **else if** $\text{num}_{n-1}^{x_i} < \mu_{n-1}^{x}$ **then**
26: $\hat{x}_i = \left(\text{rat}_{n-1}^{x_i}\right)^{-1}$
27: **else**
28: $\hat{x}_i = 1$
29: **end if**
30: **end for**
31: **end for**
32: **end if**
33: Formulate linear program from Section 4.2 as LP
34: $\{S_{LP}, R_{LP}, K_{LP}\} = LP.solve()$
35: **if** $cost(S_{LP}, R_{LP}, K_{LP}) <$ minCost **then**
36: minCost $= cost(S_{LP}, R_{LP}, K_{LP})$
37: $\{S', R', K'\} = \{S_{LP}, R_{LP}, K_{LP}\}$
38: unimproved $= 0$
39: **else**
40: unimproved $+= 1$
41: **end if**
42: Update utilization statistics: $\text{rat}_n^{x_i} = \frac{\text{avg}_n^{x_i}}{\max_n^{x_i}}, \text{num}_n^{x_i}, \mu_n^{x}, \sigma_n^{x}$
43: **end for**
44: **return** $\{S', R', K'\}$

Algorithm 2. Iterative LP

LP-Greedy Hybrid

The third algorithm we introduce is a hybrid of the first two algorithms. This algorithm is presented in Algorithm 3 and detailed below. First, an initial solution is generated by Algorithm 2 (line 1). The unit cost to transfer the maximum amount of CO_2 between each (source, reservoir) pair in the solution is then calculated (lines 4-29). Calculating this cost is done in a similar fashion to what was done in Algorithm 1 when finding the cheapest path for a (source, reservoir) pair: First, the maximum amount of CO_2 transferable between the (source, reservoir) pair in the solution is calculated as the minimum of the CO_2 captured at the source and injected at the reservoir (line 5). Second, the capture and storage costs associated with that amount of

CO_2 is calculated as the sum of the utilization costs (line 6) and applicable fixed costs (lines 7-12). Third, the shortest path in the solution between the (source, reservoir) pair is calculated by first parameterizing a network with the cost savings of removing this pair from the solution (lines 14-23). This is done by considering each directed edge in the solution that is hosting more CO_2 than the maximum transferable amount (lines 15-16). The cost of a new pipeline hosting the original amount of CO_2 minus the maximum transferable amount is calculated (lines 17-20). The cost of this edge in the cost network is set to be the difference between the cost of the pipeline in the solution and the new pipeline cost (line 21). The cheapest path for the (source, reservoir) pair is calculated by finding the shortest path in the cost network (line 24). These capture, transport, and storage costs and summed and the cost per metric ton of CO_2 calculated and recorded (line 27).

Once the pairwise costs of each (source, reservoir) pair is calculated, the cheapest (per metric ton of CO_2) reservoir for each source is identified (lines 31-35) and the most expensive pair is selected (line 36). The rationale for this step is that selecting the most expensive (source, reservoir) pair from the list of all pairs will likely select a pair with high transportation cost (i.e. physically distant from each other) that would not actually pair together to transfer CO_2 instead of a pair that would reasonably pair together. Instead, the list of cheapest pairs will reflect more likely pairings, of which we select the most expensive one for removal.

The most expensive of the cheapest, for each source, (source, reservoir) pairs is removed from the solution (lines 38-59). A pair is removed from the solution by removing the maximum transferable amount of CO_2 from the source and reservoir (lines 38-46). The cost and volume of CO_2 on each edge in the cheapest path between the (source, reservoir) pair is then calculated and updated (lines 48-59).

Finally, the cheapest replacement (source, reservoir) pairs are then added back to the solution using Algorithm 1 (line 62). Before Algorithm 1 is run, the solution variables in it (S', R', K') are set to be the S', R', and K' values from this algorithm (line 61). This process is repeated for a fixed number of iterations and improves the solution by replacing expensive (source, reservoir) pairs with cheaper ones.

The driver of the running time for each iteration of Algorithm 3 is not as clear as the preceding algorithms. Algorithm 2 is run only once, in line 1. Lines 4-29 takes $O(|S||R|(|K||C| + ShortestPath))$ time, where $|S|$ is the number of sources, $|R|$ is the number of reservoirs, $|K|$ is the number of pipeline components, $|C|$ is the number of trends, and $ShortestPath$ is the running time for the shortest path algorithm used. Line 62 calls Algorithm 1, which runs in $O((|S||R|)^2(|K||C| + ShortestPath))$ time, with possibly a different shortest path algorithm than Algorithm 3. In practice though, Algorithm 1 does not need to run many iterations, since the amount of captured CO_2 is still very close to the target. So, it is unlikely that Algorithm 1 will actually run for close to $|S||R|$ iterations in its line 2, whereas lines 4-29 in Algorithm 1 will run in $\Theta(|S||R|(|K||C| + ShortestPath))$ time each iteration. Nonetheless, the running time is $O(numIterations + |S||R|(|K||C| + ShortestPath) + (|S||R|)^2(|K||C| + ShortestPath))$, where $numIterations$ is the number of iterations enforced in line 2.

Algorithm 3 LP-Greedy Hybrid

Input: Sources S, Reservoirs R, Candidate Pipelines K, Capture Target T
Parameters: $maxIterationsHybrid, maxIterationsLP, improvingThreshold$
Output: $S' \subseteq S, R' \subseteq R, K' \subseteq K$

```
{S', R', K'} = IterativeLP(S, R, K, T, maxIterationsLP, improvingThreshold)
for n < maxIterationsHybrid do
    srcSnkPairCosts = ∅
    for (src, res) ∈ S' × R' do
        c = min(src.captured, res.stored)
        cost = c · (src.variableCost + res.variableCost)
        if c = src.captured then
            cost += src.fixedCost
        end if
        if c = res.stored then
            cost += res.fixedCost
        end if

        N = ∅
        for directed edge e = (u, v) in K' do
            if e.transported ≥ c then
                vol = e.transported - c
                oldCost = e.costInK'
                trend = smallestTrendWithCapacity(vol)
                newCost = trend.fixedCost + trend.variableCost · vol
                N.addEdgeWithCost(e, oldCost − newCost)
            end if
        end for
        path = shortestPathInN(src, res)
        cost += path.cost

        cost /= c
        srcSnkPairCosts.add((src, res, path, c, cost))
    end for

    cheapestSourcePairs = ∅
    for src ∈ S' do
        (src, res, path, c, cost) = srcSnkPairCosts.cheapestCostForSrc(src)
        cheapestSourcePairs.add((src, res, path, c, cost))
    end for
    Let (src, res, path, c, cost) be most expensive entry in cheapestSourcePairs

    src.captured -= c
    if src.captured = c then
        S'.remove(src)
    end if

    res.stored -= c
    if res.stored = c then
        R'.remove(res)
    end if

    for directed edge e = (u, v) in path do
        if e.transported > c then
            vol = e.transported - c
            trend = smallestTrendWithCapacity(vol)
            e.transported = vol
            e.costInK' = trend.fixedCost + trend.variableCost · vol
        else
            e.transported = 0
            e.costInK' = ∞
            K'.remove(e)
        end if
    end for

    Set GreedyAdd solution variables (S', R', K') to reference these S', R', K' values
    {S', R', K'} = GreedyAdd(S, R, K, T)
end for
return {S', R', K'}
```

Algorithm 3. LP-Greedy Hybrid

Genetic Algorithm

Solving CCS infrastructure design problems is fundamentally a computationally intractable problem (formally, it is an NP-Hard optimization problem; Eardley et al. 2025). CCS infrastructure design optimization is actually even NP-Hard to approximate within the natural logarithm of the number of vertices in the graph. As such, finding optimal solutions to large

instances is often computationally infeasible. The MILPs presented throughout this report are solvable with specialized software, but do not scale to national-level CCS case studies. In this Section, we introduce a novel genetic algorithm to solve CCS infrastructure design problems. The novel contribution of our genetic algorithm is the representation of a flow solution by an array of parameters that scale the fixed-costs for each edge in the network. This representation ensures that each array corresponds to a valid flow, thereby eliminating the need for computationally expensive repair functions that are required by other genetic algorithms for similar fixed-charge flow network problems. By avoiding costly repair functions, the proposed algorithm is able to efficiently find high-quality solutions to very large CCS infrastructure design problem instances. The proposed genetic algorithm is inspired by slope scaling techniques previously employed for the flow network problems. It is a *matheuristic*, as it employs mathematical programming to calculate a flow solution from a linear program parameterized with the fixed-cost scaling arrays.

Non-Integer Linear Program

In this section, we introduce a linear program (LP) that is a modification of the MILP presented in the Background Section. Since it is an LP, this new formulation can be solved optimally in polynomial time. This LP forms the foundation of the genetic algorithm discussed in later in this report. Two components of the ILP change to turn it into an appropriate LP:

1. The binary decision variables s_i, r_j, and p_{kc} are removed, thereby turning the model into an LP. Since the binary variables are removed, the fixed costs are then scaled and combined with the variable costs.
2. New scaling parameters s_i^s, r_j^s, and p_{kc}^s are introduced for component that will scale the fixed cost of each entity. These parameters form the representation of a flow solution in the genetic algorithm.

Let α_i, β_j, and δ_{kc} be the decision variable representing the amount of CO_2 processed by sources, sinks, and pipeline components respectively, analogous to the a_i, b_j, and d_{kc} continuous decision variable in the MILP.

Then, the objective function of the LP is:

$$\min \overbrace{\sum_{i \in S} \left(\frac{F_i^{src}}{s_i^s} + V_i^{src} \right) \alpha_i}^{capture\ cost} + \overbrace{\sum_{k \in P} \sum_{c \in C} \left(\frac{F_{kc}^{pipe}}{p_{kc}^s} + V_{kc}^{pipe} \right) \delta_{kc}}^{transport\ cost} + \overbrace{\sum_{j \in R} \left(\frac{F_j^{res}}{r_j^s} + V_j^{res} \right) \beta_j}^{storage\ cost}$$

The constraints in the LP mirror the constraints in the MILP:

$\delta_{kc} \leq Q_{kc}^{\max}, \forall k \in P, \forall c \in C$	(Q)
$\sum_{\substack{k \in P: \\ src(k)=n}} \sum_{c \in C} \delta_{kc} - \sum_{\substack{k \in P: \\ dest(k)=n}} \sum_{c \in C} \delta_{kc} = \begin{cases} \alpha_n & \text{if } n \in S \\ -\beta_n & \text{if } n \in R, \forall n \in S \cup R \cup J \\ 0 & \text{if } n \in J \end{cases}$	(R)
$\alpha_i \leq Q_i^{src}, \forall i \in S$	(S)

$\beta_j \leq Q_j^{res}, \forall j \in R$	(T)
$\sum_{i \in S} \alpha_i \geq T$	(U)

The output of this LP is a value for each α_i, β_j, and δ_{kc}. Of course, the optimal flow found by the LP is likely not an optimal solution for the MILP. The true cost of the LP's solution can be determined by calculating its value when input into the MILP's objective function. This is first done by defining resource-use indicator functions s_i^z, r_j^z, and p_{kc}^z and assigning them values as follows:

$$s_i^z = \begin{cases} 1, if\ \alpha_i > 0 \\ 0, if\ \alpha_i = 0 \end{cases} \quad r_j^z = \begin{cases} 1, if\ \beta_j > 0 \\ 0, if\ \beta_j = 0 \end{cases} \quad p_{kc}^z = \begin{cases} 1, if\ \delta_{kc} > 0 \\ 0, if\ \delta_{kc} = 0 \end{cases}$$

This makes the true cost of the LP's solution equal to:

$$\sum_{i \in S} (F_i^{src} s_i^z + V_i^{src} \alpha_i) + \sum_{k \in P} \sum_{c \in C} (F_{kc}^{pipe} p_{kc}^z + V_{kc}^{pipe} \delta_{kc}) + \sum_{j \in R} \left(F_j^{res} r_j^z + V_j^{res} \beta_j\right)$$

The genetic algorithm described below works by varying the s_i^s, r_j^s, and p_{kc}^s scaling parameters and scoring the resulting optimal α_i, β_j, and δ_{kc} values found by this true cost equation.

Genetic Algorithm

Genetic algorithms are a common evolutionary heuristic method used for searching and optimization. Genetic algorithms manage a population of *organisms* that each correspond to a solution to the problem. The population evolves over iterations of the algorithm using evolutionary processes observed in nature including selection, crossover, and mutation operations. Selection is the process of deciding which organisms of the population continue into the next iteration (i.e. next generation). This is the mechanism that allows the algorithm to prioritize organisms that correspond to better solutions to the problem and control the size of the population. Crossover is the generation of a new organism from two existing organisms, analogous to biological reproduction. Similarly, mutation is the slight modification of an organism into a new one corresponding to a different solution. Crossover and mutation operations are the mechanisms that allow the algorithm to search for new, and possibly better, solutions.

A number of genetic algorithms have been developed to solve various versions of the fixed-charge flow network problem. In these algorithms, organisms are broadly represented as either individual edges, or predefined routes through the network. Representing organisms as individual edges typically involves a binary variable for each edge indicating its availability for use. Alternatively, representing organisms as predefined routes involves a binary variable for each route in a set of predefined routes through the network. In the case of the individual edge representation, generating the initial population, crossover operations, and mutation operations often requires repairing the organism, as random sets of edges are unlikely to result in valid flows. Using predefined routes simplifies repairing operations but may still require repair in the event of capacity constraint violations and is likely to result in suboptimal solutions due to the

limited set of routing options. The genetic algorithms that use these representations address the issue by employing computationally expensive repair functions to make organisms correspond to valid flows. Instead of representing an organism in this fashion, we represent it as an array of the fixed-cost scaling parameters s_i^s, r_j^s, and p_{kc}^s. Then, the solution corresponding to this organism is the set of solution values α_i, β_j, and δ_{kc} found by the LP described earlier. The result of this representation is that we can guarantee the solution corresponding to any organism is a valid flow, since the LP enforces that. This avoids costly repair functions and is the key to the efficiency of our approach.

The motivation for using the fixed-cost scaling parameters as the organism representation is that it allows control over the amount of fixed-costs incurred, while also removing the integer variables from the optimal MILP. As the scaling parameter decreases to zero, the scaled fixed-cost increases to infinity, thereby dissuading selection of that edge by the LP. Conversely, as the scaling parameter increases to infinity, the scaled fixed-cost approaches zero, thereby encouraging selection of that edge by the LP. The genetic algorithm is tasked with searching for an organism of scaling parameters whose corresponding flow solution is as close to optimal for the MILP as possible. Given that the genetic algorithm is using the fixed-cost scaling parameters as a proxy for a solution instead of using a solution directly, an important question is whether or not there exists a set of scaling parameters that yields an optimal flow solution. A proof that such a set of scaling parameters is guaranteed to exist is presented later in this report. The key components and workflow of the genetic algorithm are described below:

Fitness Function

Genetic algorithms use fitness functions to rank and compare the population of organisms to aid the selection process. Our fitness function first determines the solution for a given organism by solving the LP to get the α_i, β_j, and δ_{kc} solution values. After the α_i, β_j, and δ_{kc} values are determined, the solution's true cost in the context of the optimal ILP is calculated using the LP's true cost solution equation. This value is used as the fitness of the organism, where lower values correspond to higher fitness.

Selection Function

To keep the size of the population computationally manageable, a selection function is employed to prune the population at each iteration. A selection function is also used to identify the organisms for crossover operations. Our genetic algorithm implements a binary tournament selection function in an effort to prioritize high fitness organisms, while not ignoring all low fitness organisms. In binary tournament selection, two random organisms are selected, and the one with the higher fitness is kept, while the other is discarded. This ensures that high-fitness organisms are likely to remain in the population while maintaining the possibility for low-fitness ones to survive as well. Binary tournament selection is repeated until the number of organisms in the population is at the desired size.

Crossover Function

A crossover function is used to generate a new child organism from two parent organisms already in the population. Our crossover function first randomly selects two parent organisms from the existing population. A child organism is constructed by taking a random interval of the

scaling parameter array from the first parent, combined with the remaining values from the second parent.

Mutation Function

In order to mimic evolution and introduce another element of randomness into the search, a mutation function is used to further alter child organisms. After a child organism is generated with the crossover function, it may be randomly selected for mutation. During a mutation operation, a number of scaling parameter values in the organism are selected and, with equal probability, either incremented up or down a random amount between zero and one. Mutated scaling parameter values are not allowed to go below a lower bound to avoid negative values and divide by zero issues.

Genetic Algorithm

Using the functions described above, our algorithm operates as follows: First, an initial population of organisms is randomly generated. Each organism in the initial population is initialized as a scaling parameter array filled with a random value between $\epsilon > 0$ and the average value of the fixed-costs in the input instance. After the initial population of organisms are created, the algorithm proceeds in an iterative fashion: At each iteration, the fitness of each organism is first calculated as described above. While the population size is less than some threshold, the crossover function is executed to generate child organisms. The child organisms are also subject to randomized mutations from the mutation function. Once the population has increased in size to the designated threshold, the selection function is run to reduce its size while statistically discarding the lower fitness organisms. The algorithm keeps executing iterations until the running time reaches a designated time limit.

CPLEX Polishing

Once the time limit has been reached, the most fit organism's α_i, β_j, and δ_{kc} solution values are used as a warm start for IBM's CPLEX optimization software. CPLEX polishing is run for one fifth of the total time limit resulting in the final flow values returned by the algorithm.

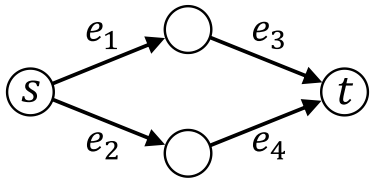
Optimal Search Viability

The purpose of this section is to show that the genetic algorithm is capable of finding the optimal solution of the ILP. This claim is not trivial, as the search space of the genetic algorithm is the set of possible scaling parameter arrays, which are merely a proxy for solution values, the property we are actually optimizing for. The original motivation for formulating the LP and representing the organisms in the genetic algorithm as scaling parameter arrays follows from the following false claim.

Claim: If each scaling parameter equals the optimal MILP solution value for that resource, then the optimal flow found by the resulting LP is also an optimal flow for the ILP.

The rationale for this claim is that if each scaling parameter and α_i, β_j, and δ_{kc} solution value both equal the optimal MILP flow values, then the cost of the LP's objective function will equal the optimal cost of the ILP's objective function. This claim is shown to be false with a simplified example in **Figure 388** with only pipeline costs and capacities as fixed costs (a_e), variable costs

(b_e), capacities (c_e), and a capture target of three. In this instance, the optimal ILP solution is to set the amount of flow on e_1 and e_3 to two and the amount of flow on e_2 and e_4 to one for a total cost of 20. Setting flow values for e_1 and e_3 to two and e_2 and e_4 to one yields the LP objective of minimizing $7\delta_{e_1} + 6\delta_{e_2}$. The optimal solution to this is to set the amount of flow on e_1 and e_3 to one and the amount of flow on e_2 and e_4 to two for a total cost of 21, thereby contradicting the claim.



	a_e	b_e	c_e
e_1	10	2	2
e_2	3	3	2
e_3	0	0	2
e_4	0	0	2

Figure 388 Counterexample to claim with only transportation costs and capacities having the displayed fixed costs (a_e), variable costs (b_e), capacities (c_e), and a capture target of three. In this instance, the optimal ILP solution is 20 with a flow of two units on e_1 and e_3 and one unit on e_2 and e_4. The corresponding optimal LP solution is 21 with a flow of one unit on e_1 and e_3 and two units on e_2 and e_4.

Since the motivation claim is false, along with the fact that the scaling parameter arrays are only proxies for the flow value solutions we seek, it remains to be shown that there actually exists a set of scaling parameter values that will result in the genetic algorithm finding optimal flow values for the ILP.

$s_i \in \{0, 1\}$	Indicates if source i is opened
$a_i \in \mathbb{R}^{\geq 0}$	Annual amount of CO_2 captured from source i ($MtCO_2$/yr)
$r_j \in \{0, 1\}$	Indicates if reservoir j is opened
$b_j \in \mathbb{R}^{\geq 0}$	Annual amount of CO_2 injected into reservoir j ($MtCO_2$/yr)
$p_{kc} \in \{0, 1\}$	Indicates if pipeline k with capacity c is opened
$d_{kc} \in \mathbb{R}^{\geq 0}$	Annual amount of CO_2 put in pipeline k with capacity c ($MtCO_2$/yr)

Theorem: For every problem instance, there exists a set of scaling parameter values such that the optimal flow found by the resulting LP is also an optimal flow for the ILP.

Proof: Without loss of generality, consider only a flow network with edge costs and capacities. This does not influence the conclusion in general since any CCS infrastructure modeling instance can be represented as a network with only edge costs and capacities. Let d_{kc}^{opt} be the optimal flow values found by the MILP and define the set of p_{kc}^{s} scaling parameter values as follows:

$$p_{kc}^{s} = \begin{cases} \epsilon > 0, if\ d_{kc}^{opt} = 0 \\ \infty, \quad if\ d_{kc}^{opt} > 0 \end{cases}$$

When p_{kc}^{s} is set to an ϵ -value near zero, the scaled fixed cost F_{kc}^{pipe}/p_{kc}^{s} makes those edges prohibitively expensive to include in LP solutions, so long as valid solutions exist that do not use those edges (such as the valid solution d_{kc}^{opt}). Likewise, if p_{kc}^{s} is set to a very large value, the scaled fixed cost is near zero. These p_{kc}^{s} values effectively restrict the LP to only selecting the edges and capacities with non-zero δ_{kc}^{opt} values.

Suppose that $H \subseteq P \times C$ is the set of edge-capacity pairs where p_{kc}^{opt} equals one. Then, given the p_{kc}^{s} values resulting from above, the objective for the LP becomes:

$$\sum_{k\in P}\sum_{c\in C}\left(\frac{F_{kc}^{pipe}}{p_{kc}^{s}} + V_{kc}^{pipe}\right)\delta_{kc} = \sum_{kc\in H} V_{kc}^{pipe}\delta_{kc}$$

Let δ_{kc}^{opt} be optimal flow values to the LP. We aim to show that δ_{kc}^{opt} is also an optimal flow for the MILP. First, δ_{kc}^{opt} is a valid solution to the MILP since δ_{kc}^{opt} is a valid flow of the MILP's target value on an identical graph with the same capacities. Showing that δ_{kc}^{opt} is optimal for the ILP can be accomplished by using δ_{kc}^{opt} to feed the definitions for p_{kc}^{z} and showing that:

$$\sum_{k\in P}\sum_{c\in C}\left(F_{kc}^{pipe}p_{kc}^{z-opt} + V_{kc}^{pipe}\delta_{kc}^{opt}\right) = \sum_{k\in P}\sum_{c\in C}\left(F_{kc}^{pipe}p_{kc}^{opt} + V_{kc}^{pipe}d_{kc}^{opt}\right)$$

p_{kc}^{z-opt} must equal one for all edges in H. If p_{kc}^{z-opt} equals zero for some edge in H, then the fixed costs incurred by δ_{kc}^{opt} are lower than the fixed costs incurred by d_{kc}^{opt}. Also, since δ_{kc}^{opt} is optimal for the LP,

$$\sum_{kc\in H} V_{kc}^{pipe}\delta_{kc}^{opt} \leq \sum_{kc\in H} V_{kc}^{pipe}d_{kc}^{opt}$$

Thus, if p_{kc}^{z-opt} equals zero for some edge in H, δ_{kc}^{opt} is a lower cost flow for the ILP than the optimal d_{kc}^{opt}, which is a contradiction. Therefore, d_{kc}^{opt} and δ_{kc}^{opt} must incur identical fixed costs and p_{kc}^{z-opt} must equal one for all edges in H.

Suppose that,

$$\sum_{kc\in H} V_{kc}^{pipe}\delta_{kc}^{opt} < \sum_{kc\in H} V_{kc}^{pipe}d_{kc}^{opt}$$

This implies that,

$$\sum_{kc\in H} F_{kc}^{pipe} + \sum_{kc\in H} V_{kc}^{pipe}\delta_{kc}^{opt} < \sum_{kc\in H} F_{kc}^{pipe} + \sum_{kc\in H} V_{kc}^{pipe}d_{kc}^{opt}$$

$$\Rightarrow \sum_{kc\in H}\left(F_{kc}^{pipe} + V_{kc}^{pipe}\delta_{kc}^{opt}\right) < \sum_{kc\in H}\left(F_{kc}^{pipe} + V_{kc}^{pipe}d_{kc}^{opt}\right)$$

$$\Rightarrow \sum_{k\in K}\sum_{c\in C}\left(F_{kc}^{pipe}p_{kc}^{z-opt}+V_{kc}^{pipe}\delta_{kc}^{opt}\right) < \sum_{k\in K}\sum_{c\in C}\left(F_{kc}^{pipe}p_{kc}^{opt}+V_{kc}^{pipe}d_{kc}^{opt}\right)$$

which is a contradiction, since d_{kc}^{opt} is an optimal flow value for the ILP, and thus cannot be more expensive than the valid flow δ_{kc}^{opt}. Thus,

$$\sum_{kc\in H}V_{kc}^{pipe}\delta_{kc}^{opt} = \sum_{kc\in H}V_{kc}^{pipe}d_{kc}^{opt}$$

which implies that,

$$\sum_{k\in K}\sum_{c\in C}\left(F_{kc}^{pipe}p_{kc}^{z-opt}+V_{kc}^{pipe}\delta_{kc}^{opt}\right) = \sum_{k\in K}\sum_{c\in C}\left(F_{kc}^{pipe}p_{kc}^{opt}+V_{kc}^{pipe}d_{kc}^{opt}\right)$$

Therefore, defining the p_{kc}^{s} values as above yields an LP whose optimal flow values correspond to optimal flow values of the ILP.

Case Study

To demonstrate the efficiency and effectiveness of the genetic algorithm, an evaluation was conducted using CCS data collected as part of the CUSP effort. The genetic algorithm was implemented and integrated into SimCCS. Initial performance simulations guided the parameterization of the genetic algorithm to have a population size of 10, and mutation and crossover probability of both 50%. A mutation probability of 50% means that each organism has a 50% chance of mutation, and a crossover probability of 50% means that 50% of the population (without organism repetition) is crossed over with a random other organism in each iteration of the genetic algorithm. All reported genetic algorithm values are the average of three runs. The optimal MILP from the Background Section was implemented in SimCCS using CPLEX as well. SimCCS was used as a standardized way to represent CCS data and for problem and solution visualization. Timing was coded directly into SimCCS to ensure only the algorithm of interest was being timed during simulation. Simulations were run on a machine with Ubuntu 20.04.5, an Intel Xeon W-2255 processor running at 3.7 GHz, and 64 GB of RAM. SimCCS on this machine used IBM's CPLEX optimization tool, version 22.1.1.0.

The genetic algorithm was tested on two CCS infrastructure design datasets. The first dataset covers the state of California and consists of 190 sources with a total annual emission rate of 88.3$ $MtCO_2$/yr, 102 sinks with a total lifetime storage capacity of 37.18 $GtCO_2$, and 1,188 possible pipeline components (i.e. edges in the graph) with a total length of 17,940.88 km and 11 possible capacities on each edge. A map of this dataset is presented in **Figure 389**.

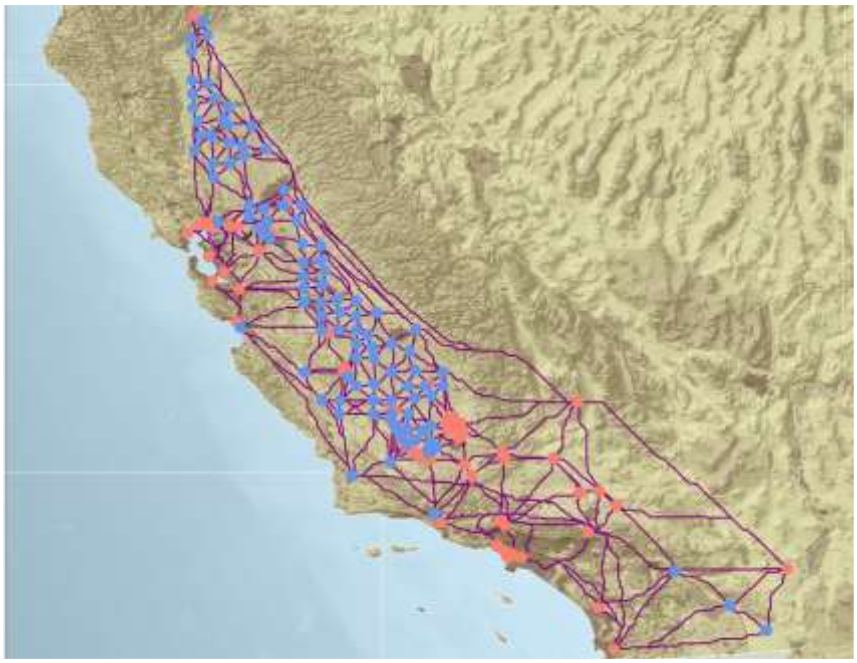


Figure 389 CCS dataset for the state of California consisting of sources (red), sinks (blue), and possible pipeline routes

The second dataset covers the contiguous United States and consists of 2,746 sources with a total annual emission rate of 532.61 $MtCO_2$/yr, 1,202 sinks with a total lifetime storage capacity of 2,691.86 $GtCO_2$, and 22,597 possible pipeline components with a total length of 424,674.41 km and 11 possible capacities on each edge. This data was collected by Carbon Solutions, LLC apart from the CUSP project as part of a study conducted by the Clean Air Task Force. Storage data was generated using the SCO_2T geologic sequestration tool. A map of this dataset is presented in **Figure 390**.

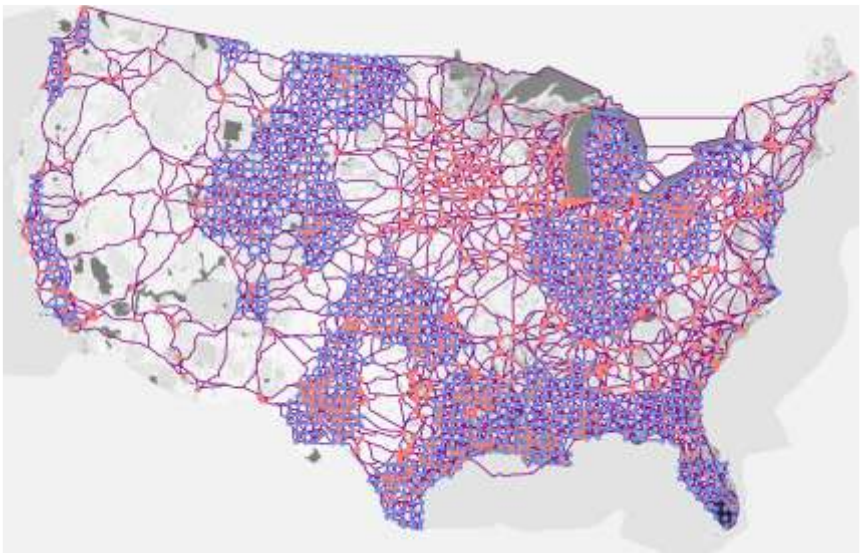


Figure 390 CCS dataset for the contiguous United States consisting of sources (red), sinks (blue), and possible pipeline routes

Candidate pipeline routes were generated in SimCCS using its candidate network generation algorithms. The National Energy Technology Laboratory's CO_2 Transport Cost Model was used by SimCCS to determine fixed construction and variable utilization costs for the 11 discrete pipeline capacity options.

To assess the efficiency of the genetic algorithm, its solution cost was compared to the solution cost found by CPLEX solving the optimal ILP, with both methods being allowed to run for set running time periods. For the California dataset, those running time periods were 0.5, 1, 2, 4, and 8 hours. The target flow amount (T) was set to 80 $MtCO_2$/yr for all of the California scenarios. For the contiguous United States dataset, the running time periods were 0.5, 1, 2, 4, 8 and 16 hours. The target flow amount was set to 500 $MtCO_2$/yr for the contiguous United States scenarios. **Figure 391**(a) presents each algorithm's solution cost over the running time periods for the California dataset, and **Figure 391**(b) presents the same results for the contiguous United States dataset. The cost of the best solution found by the genetic algorithm in the California dataset was within 0.5% of the ILP's solution across all running times. Conversely, the cost of the best solution found by the genetic algorithm in the contiguous United States dataset was 17% lower than the ILP's solution after one hour, 7% lower after four hours, and 2% lower after 16 hours. This suggests that the genetic algorithm may have utility for very large problem instances. The utility for small instances is likely limited, due to the speed of CPLEX.

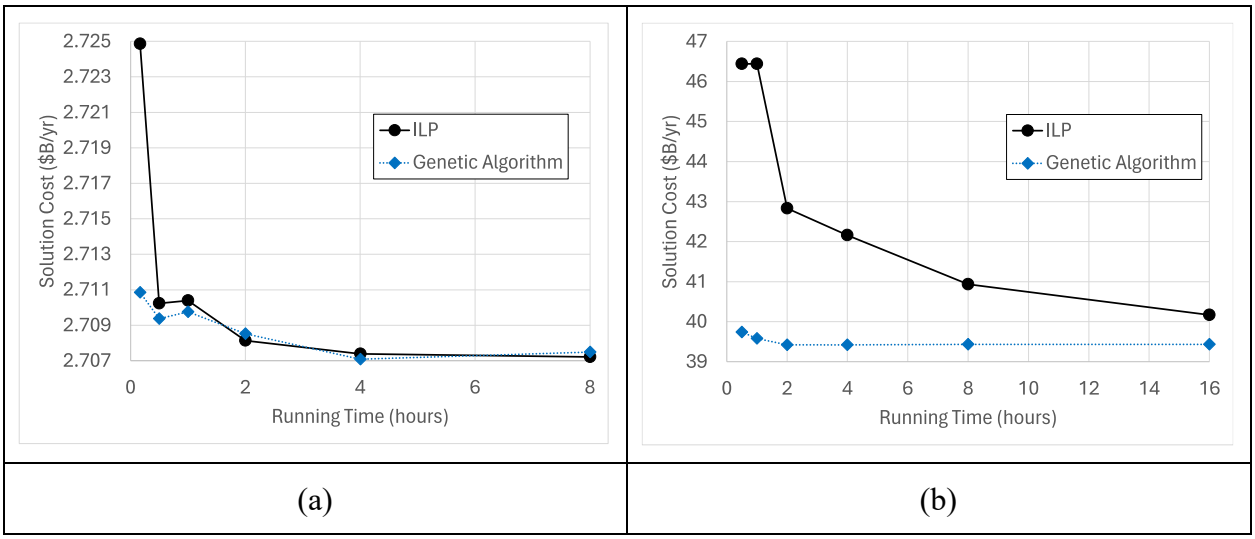


Figure 391 Solution cost versus running time for the genetic algorithm and optimal ILP on (a) the California dataset and (b) the contiguous United States dataset

Problem solvability is not only related to instance size, but also the amount of target flow being found. To identify the impact that target flow amount has on solution quality, scenarios were run on the contiguous United States dataset where the target flow amount was varied from 1 $MtCO_2$/yr to 532 $MtCO_2$/yr. The maximum annual capturable amount of CO_2 for this dataset is 532.61 $MtCO_2$/yr. Each algorithm was given two hours to solve each scenario. **Figure 392** presents each algorithm's solution cost for the various target flow amounts. Table 79 presents the specific solution cost values and the percent improvement of the genetic algorithm's solution over the ILP's solution. Other than in very low and high target flow amount scenarios, the genetic algorithm was fairly consistent in its improvement over the ILP. Interestingly, in the low target flow amount scenario, the genetic algorithm performed the best relative to the ILP. This

suggests that the genetic algorithm could have utility in a very large problem instance, even if the target flow amount is quite small. This is likely a very realistic scenario, where a relatively small target is sought amongst a very large space of options, and provides a compelling argument for the utility of the genetic algorithm.

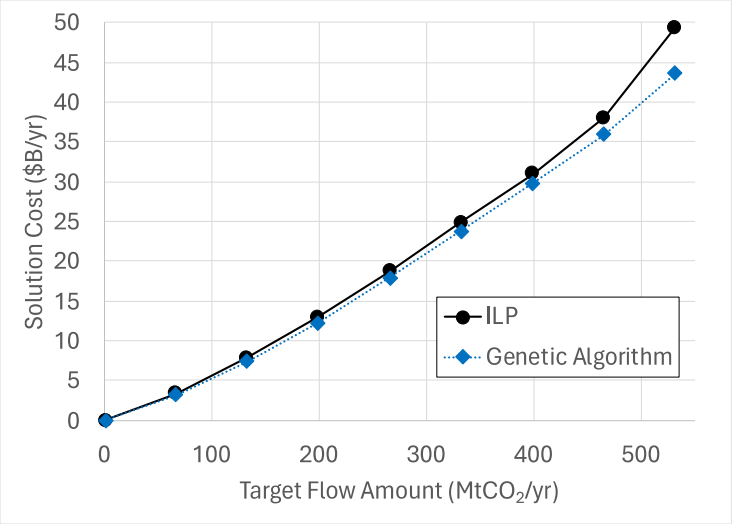


Figure 392 Solution cost versus target flow amount for the genetic algorithm and optimal ILP. Specific solution cost values are presented in Table 79

Table 79. Solution values with varying flow targets.

Target Flow Amount	MILP	Genetic Algorithm	% Improvement
1.00	0.04	0.03	25.00
66.50	3.35	3.22	3.88
133.00	7.84	7.41	5.48
199.50	13.00	12.25	5.77
266.00	18.78	17.94	4.47
332.50	24.84	23.77	4.31
399.00	31.06	29.86	3.86
465.50	38.05	35.98	5.44
532.00	49.44	43.58	11.65

Phase 4 – Readiness Indices and Mapping

A major effort of the Analytics Working Group was the development of a workflow for determining Regional Readiness Indices and applying that workflow to CUSP data to generate Regional Readiness Indices Maps. The outcome of this effort is described in detail in the Subtask 5.1 component of the final report.

Conclusions

Over the duration of the CUSP, the Analytics Working Group provided the computational, methodological, and integrative foundation that enabled consistent, data-driven CCS analyses across the western United States. The group's work evolved from early-stage data standardization and partner support to advanced model development and regional synthesis, culminating in the generation of the CUSP Readiness Indices (Maps) described in Subtask 5.1 – Development of Regional Readiness Indices.

By establishing a unified modeling framework, the Analytics Working Group ensured that each subtask's outputs were interoperable and grounded in reproducible computational methods. The adoption of standardized SimCCS data templates and cost specifications allowed state partners to produce compatible datasets and comparable regional scenarios. These foundational efforts supported extensive scenario analyses spanning California's San Joaquin Basin, Kansas, Nevada, the Four Corners region, and beyond—each revealing the diverse technical and economic realities of CCS deployment across varying geological, policy, and industrial contexts.

Methodologically, the group advanced the state of CCS infrastructure modeling by developing new formulations for multiphased build-out planning**,** risk-aware and repair-aware network design, and heuristic optimization algorithms capable of scaling to national problem sizes. These innovations improved the realism and tractability of CCS planning models, enabling assessment of phased deployment, uncertainty in storage performance, and trade-offs between cost and resilience. These advances were disseminated through peer-reviewed publications, expanding their utility to the wider CCS research and policy community.

The culmination of these efforts is reflected in the regional readiness framework produced under Subtask 5.1, which integrates geologic, economic, infrastructural, regulatory, and risk metrics into composite readiness indices. These indices quantify where CCS deployment is most feasible and identify barriers requiring further investment or policy action. Together, the readiness maps and supporting analyses form a decision-support tool that bridges scientific modeling and practical planning, providing a data-driven foundation for DOE, state agencies, and private stakeholders to prioritize CCS projects effectively.

In total, the Analytics Working Group's contributions position the CUSP region for informed, risk-aware, and cost-effective carbon management. By unifying data, methods, and modeling across jurisdictions, the group created a durable analytical framework that will continue to support regional decarbonization initiatives well beyond the life of the CUSP project.

References

Credit for Carbon Oxide Sequestration, U.S.C.-2023 26 C.F.R. §1.45Q-1 (2021).

Eardley C, Gomez D, Dupuis R, Papadopoulos M, Yaw S. 2025. A genetic algorithm for multi-capacity fixed-charge flow network design. In: Proceedings of the 25th Symposium on Algorithmic Approaches for Transportation Modeling, Optimization and Systems; 2025 Sep 18–19; Warsaw (Poland).

Jones E, Yaw S, Bennett J, Ogland-Hand J, Strahan C, Middleton R. 2022. Designing multi-phased CO_2 capture and storage infrastructure deployments. Renew Sustain Energy Transit. 2:100023. doi:10.1016/j.rset.2022.100023

Kim TW, Yaw S, Kovscek AR. 2023. Scoring, ranking, and technoeconomics of carbon capture and storage opportunities in the Central Valley of California. Int J Greenh Gas Control. 128:103968. doi:10.1016/j.ijggc.2023.103968

Whitman C, Yaw S, Hoover B, Middleton R. 2022. Scalable algorithms for designing CO_2 capture and storage infrastructure. Optim Eng. 23(2):1057–1083. doi:10.1007/s11081-021-09621-3

Outreach Working Group

Appendices

Bibliography